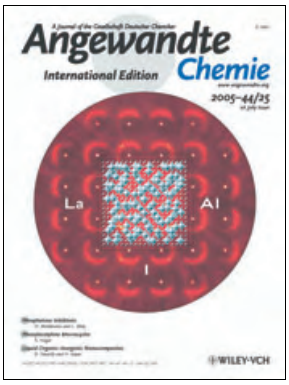
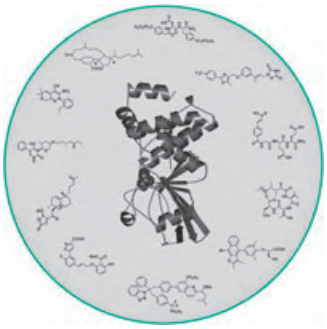
Cover Picture

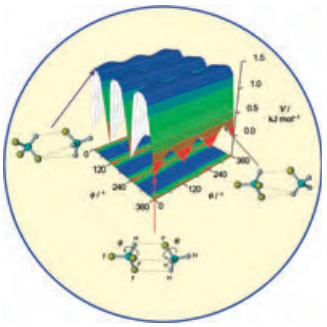


Oliver Oeckler, Thomas Weber, Lorenz Kienle, Hansjürgen Mattausch, and Arndt Simon*

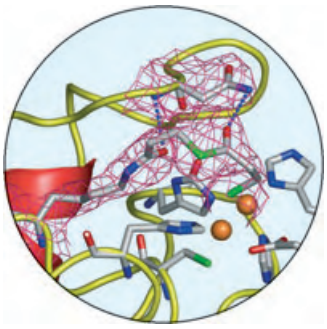
Diffuse diffraction data from disordered compounds can be interpreted with new numerical algorithms; however, there are few examples of quantitative structure refinement against all data and not only Bragg reflections. In the Communication on page 3917 ff., the authors demonstrate the application of evolutionary algorithms to solve the structure of an aluminum-stabilized lanthanum subiodide. The cover picture shows a diffraction pattern of the compound in the background and a section of the disordered structure model in the center.



Medicinal Chemistry
Protein tyrosine phosphatases have been analyzed as targets for therapeutic intervention for several years. H. Waldmann and L. Bialy discuss recent research activities in the development of small-molecule inhibitors of these enzymes in their Review on page 3814 ff.



Molecular Dynamics
Molecular clusters formed by hydrogen bridges can be highly dynamic systems, as described for a fluoromethane–trifluoromethane complex by W. Caminati et al. in their Communication on page 3840 ff.



Bioorganic Chemistry
Pathogenic bacteria that produce metallo-β-lactamases are recognized as a serious threat because of their resistance to antibiotics. In their Communication on page 3861 ff. H. Kurosaki et al. introduce an irreversible inhibitor for the metallo-β-lactamase IMP-1.

Contents

The following Communications have been judged by at least two referees to be "very important papers" and will be published online at www.angewandte.org soon:

*F. Studt, F. Tuczek**
Energetics and Mechanism of a Room Temperature Catalytic Synthesis of Ammonia (Schrock Cycle): Comparison with Biological Nitrogen Fixation

H. Zhu, J. Chai, H. Fan, H. W. Roesky, C. He, V. Jancik, H.-G. Schmidt, M. Noltemeyer, W. A. Merrill, P. P. Power*
A Stable Aluminacyclopropene LAl(η^2-C_2H_2) and Its End-On Azide Insertion to an Aluminaazacyclobutene

D. Loffreda, F. Delbecq, F. Vigné, P. Sautet*
Catalytic Hydrogenation of Unsaturated Aldehydes on Pt (111): Understanding the Selectivity from First-Principles Calculations

*C. Schaefer, G. C. Fu**
Catalytic Asymmetric Couplings of Ketenes with Aldehydes To Generate Enol Esters

M. Capdevila, J. Domènech, A. Pagani, L. Tío, L. Villarreal, S. Atrian*
Zn and Cd Metallothionein Recombinant Species from the Most Diverse Phyla May Contain Sulfide (S^{2-}) Ligands

*R. Shintani, W.-L. Duan, T. Nagano, A. Okada, T. Hayashi**
Chiral Phosphine–Olefin Bidentate Ligands in Asymmetric Catalysis: Rhodium-Catalyzed Asymmetric 1,4-Addition of Aryl Boronic Acids to Maleimides

Obituary

Hans Bethe (1906–2005) and Ligand Field Theory — *W. Kutzelnigg* — **3800**

Books

Modern Rhodium-Catalyzed Organic Reactions — P. Andrew Evans — *reviewed by B. Schmidt* — **3802**

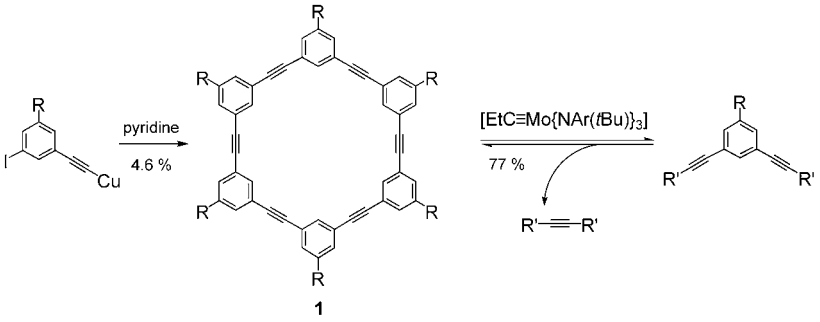
Acetylene Chemistry — François Diederich, Peter J. Stang, Rik R. Tykwinski — *reviewed by A. Hirsch* — **3803**

Highlights

Macrocycle Synthesis

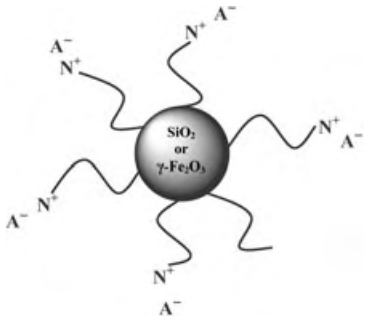
S. Höger* — **3806 – 3808**

Shape-Persistent Phenylene-Acetylene Macrocycles: Large Rings—Low Yield?



1

Reversibility makes the difference: 30 years after Staab reported the synthesis of the phenylene-acetylene macrocycle **1** in 4.6% yield starting from a simple precursor (see scheme), these structures are now available in nearly 80% yield, also from simple precursors.



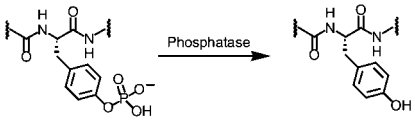
Go with the flow: Liquid inorganic salts formed by a combination of inorganic substances (for example, nanoparticles such as SiO_2 and Fe_2O_3 or polyoxometalates) with organic liquid salts (see picture: A^- is poly(ethylene glycol) sulfonate ion, ——N^+ is $C_3H_6N^+(CH_3)(C_{10}H_{21})_2$) combine the characteristics of both components in a homogenous material that can be used in batteries and solar cells.

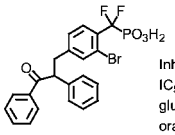
Ionic Liquids

B. Smarsly,* H. Kaper —— **3809 – 3811**

Liquid Inorganic–Organic Nanocomposites: Novel Electrolytes and Ferrofluids

Reviews





Inhibition of PTP1B:
IC_{50} = 0.12 μM, cellular activity (Sf9), glucose-lowering activity, orally bioavailable in rats

Tyrosine phosphatases and kinases govern the phosphorylation states of numerous proteins (see scheme) and modulate many cellular processes. Similar to the rise of tyrosine kinase inhibitors as established drug targets, inhibitors of tyrosine phosphatases also show promise in this regard, and only recently have moved into the spotlight.

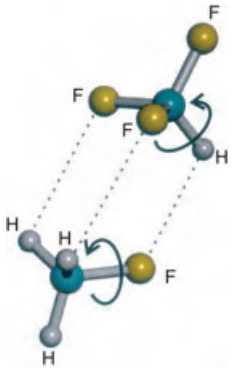
Medicinal Chemistry

L. Bialy, H. Waldmann* —— **3814 – 3839**

Inhibitors of Protein Tyrosine Phosphatases: Next-Generation Drugs?

Communications

A preferred conformation of the internally highly dynamic fluoromethane–trifluoromethane molecular complex results from the stabilization of the two subunits by three weak CH···F hydrogen bonds and electrostatic dipole–dipole interactions (see picture). The two subunits are not rigidly locked, but exhibit large amplitude motions by almost freely spinning around their symmetry axes as shown.



Molecular Complexes

W. Caminati,* J. C. López, J. L. Alonso, J.-U. Grabow —— **3840 – 3844**

Weak CH···F Bridges and Internal Dynamics in the $CH_3F{\cdot}CHF_3$ Molecular Complex

For the USA and Canada:
ANGEWANDTE CHEMIE International Edition (ISSN 1433-7851) is published weekly by Wiley-VCH PO Box 191161, D 69451 Weinheim, Germany. Air freight and mailing in the USA by Publications Expediting Inc. 200 Meacham Ave., Elmont, NY 11003. Periodicals postage paid at Jamaica NY 11431. US POSTMASTER: send address changes to *Angewandte Chemie*, Wiley-VCH, 111 River Street, Hoboken, NJ 07030. Annual subscription price for institutions: US$ 4948.00/4498.00 (valid for print and electronic / print or electronic delivery); for individuals who are personal members of a national chemical society, or whose institution already subscribes, or who are retired or self-employed consultants, print only: US$ 394.00. Postage and handling charges included. All Wiley-VCH prices are exclusive VAT.

 © 2005 Wiley-VCH Verlag GmbH & Co. KGaA, Weinheim

The best in chemistry –

for more than a hundred years



A Journal of the Gesellschaft Deutscher Chemiker

Angewandte
International Edition **Chemie**

www.angewandte.org

1888: ***The beginning of a success story***

Constant Innovations

1962: *First issue of the International Edition*
1976: *Graphical abstracts*
1979: *Cover pictures*
1988: *Centenary of Angewandte*
1989: *Routine use of color*
1991: *New section: Highlights*
1992: *Computerized editorial tracking system*
1995: *Internet service for readers*
1998: *Regular press service; full-text online*
2000: *New section: Essays; EarlyView: Communications available online ahead of the printed version*
2001: *New section: Minireviews*
2002: *Online submission of manuscripts*
2003: *Weekly publication; new section: News; new layout*
2004: *Backfiles (1962-1997); ManuscriptXpress: Online system for authors and referees*



Angewandte's advisors...

Rainer Metternich
Schering AG, Berlin

*»**Angewandte Chemie** keeps me up to date on the top new developments in chemistry. I am engaged in drug discovery, and this high-quality journal covering breakthrough discoveries in interdisciplinary research, particularly in bioorganic chemistry, is of the highest relevance to me. Each issue of Angewandte provides an outstanding source for innovations.«*

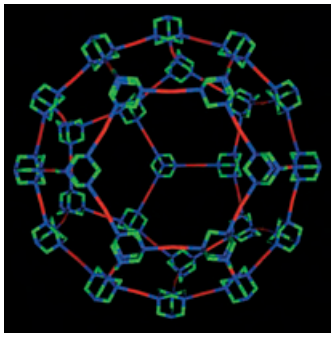
***Angewandte Chemie International Edition** is a journal of the German Chemical Society (GDCh)*

GDCh

WILEY InterScience® DISCOVER SOMETHING GREAT

WILEY-VCH

1804502_gu



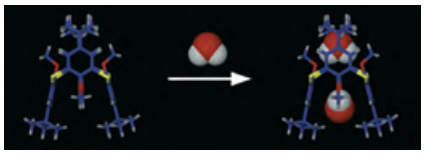
If you look for holes, you will find them in a novel 3D metal–organic framework complex with zeolite MTN topology. The framework of $[\{Cd(H_2O)_3\}_{34}(N_4C_6H_{12})_{17}]Cl_{68}\cdot 46\,H_2O\cdot 68$ DMF greatly expands the original structure of MTN and contains large cages with a volume of about 2522 Å^3 (see structure). MTN = zeolite socony mobil – thirty-nine, DMF = *N*,*N*-dimethylformamide.

Coordination Polymers

Q.-R. Fang, G.-S. Zhu,* M. Xue, J.-Y. Sun, Y. Wei, S.-L. Qiu,* R.-R. Xu **3845 – 3848**

A Metal–Organic Framework with the Zeolite MTN Topology Containing Large Cages of Volume 2.5 nm^3

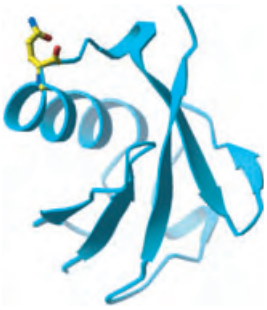
Burrowing water: The apohost phase of a substituted hydrophobic calixarene, grown by sublimation, forms lattice voids but not channels. Exposure of the crystals to liquid water results in a single-crystal-to-single-crystal phase transformation during which water molecules become embedded in the lattice voids (see picture); thus the classical view of diffusion might not be appropriate at the atomic scale.



Water Transport

P. K. Thallapally, G. O. Lloyd, J. L. Atwood,* L. J. Barbour* **3848 – 3851**

Diffusion of Water in a Nonporous Hydrophobic Crystal



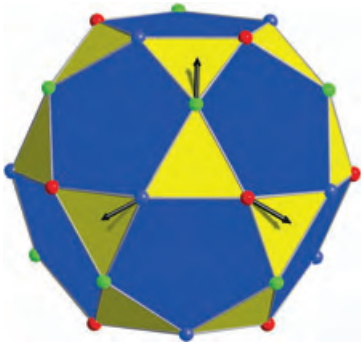
Striking similarity: An efficient synthetic route to native ubiquitin and its diastereomer [D-Gln 35]ubiquitin was realized by combining a one-pot native chemical ligation process with protein desulfurization. High-resolution X-ray crystallographic studies of the protein diastereomer (see picture) revealed a striking conservation of molecular structure.

Protein Structures

D. Bang, G. I. Makhatadze, V. Tereshko, A. A. Kossiakoff, S. B. Kent* **3852 – 3856**

Total Chemical Synthesis and X-ray Crystal Structure of a Protein Diastereomer: [D-Gln 35]Ubiquitin

Sphere we go: A spherical capsule is prepared simply by the interaction of linkers to pentagonal structural units. The metal centers (M) of the $\{(Mo^{VI})Mo^{VI}_5\}_{12}M_{30}$ type Keplerates formed (M = V^{IV}, Fe^{III}) describe an icosidodecahedron (see picture). For M = Fe^{III} the magnetic configuration of the 30 spin centers (colored spheres) can be pictured geometrically in terms of three sets, each of 10 spins, with different angular orientations (arrows). With M = V^{IV} the compound behaves according to the demands of quantum mechanics and a clear geometrical picture of the magnetism is not possible.



Polyoxometalates

A. Müller,* A. M. Todea, J. van Slageren, M. Dressel, H. Bögge, M. Schmidtmann, M. Luban, L. Engelhardt, M. Rusu **3857 – 3861**

Triangular Geometrical and Magnetic Motifs Uniquely Linked on a Spherical Capsule Surface

 © 2005 Wiley-VCH Verlag GmbH & Co. KGaA, Weinheim

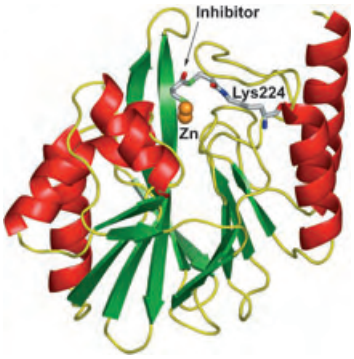
Contents

Bioorganic Chemistry

H. Kurosaki,* Y. Yamaguchi, T. Higashi, K. Soga, S. Matsueda, H. Yumoto, S. Misumi, Y. Yamagata, Y. Arakawa, M. Goto ——— **3861 – 3864**

Irreversible Inhibition of Metallo-β-lactamase (IMP-1) by 3-(3-Mercaptopropionylsulfanyl)propionic Acid Pentafluorophenyl Ester

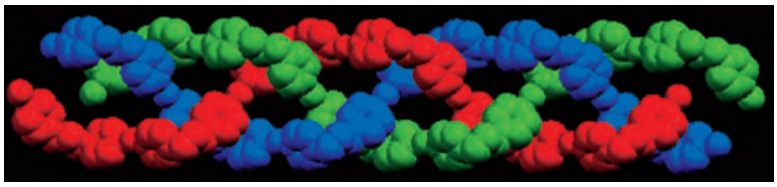
Resistance is futile: Pathogenic bacteria that produce metallo-β-lactamases are recognized as a serious threat because of their resistance to antibiotics. The title compound has now been shown to be an irreversible inhibitor for a metallo-β-lactamase (IMP-1). The X-ray crystallographic structure (see picture) has revealed that the inhibitor binds to IMP-1 with formation of a covalent amide bond with the amino group (N^{ζ}) of Lys 224.



Coordination Polymers

X.-J. Luan, Y.-Y. Wang,* D.-S. Li, P. Liu, H.-M. Hu, Q.-Z. Shi, S.-M. Peng ——— **3864 – 3867**

Self-Assembly of an Interlaced Triple-Stranded Molecular Braid with an Unprecedented Topology through Hydrogen-Bonding Interactions

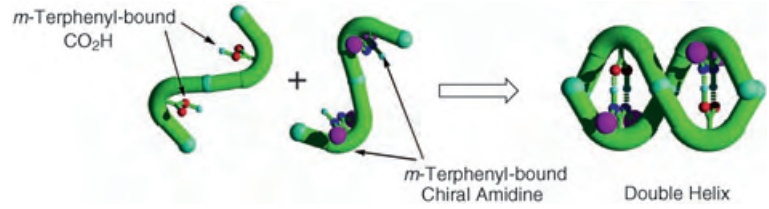


Molecular weaving: Mixing a Cu^{II} complex having a paddle-wheel structure with a highly flexible neutral 1,3-bis(4-pyridyl)-propane ligand (1:2 ratio) gives an interlaced braid which looks just like a hair plait (see X-ray crystallographic structure). The three strands are held together through hydrogen-bonding interactions.

Helical Structures

Y. Tanaka, H. Katagiri, Y. Furusho,* E. Yashima* ——— **3867 – 3870**

A Modular Strategy to Artificial Double Helices

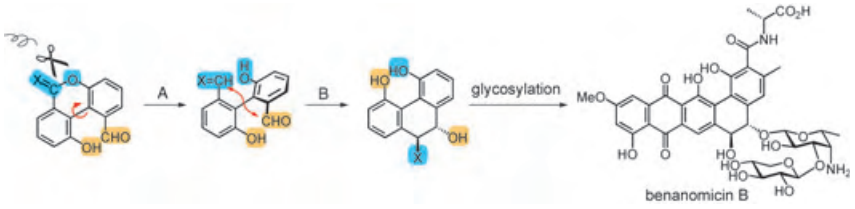


No metal required: Double-helical assemblies can be constructed through hydrogen bonds upon formation of amidinium–carboxylate salt bridges (see schematic representation). The double-helical structures formed including the helix sense are predictable by this approach.

Total Synthesis

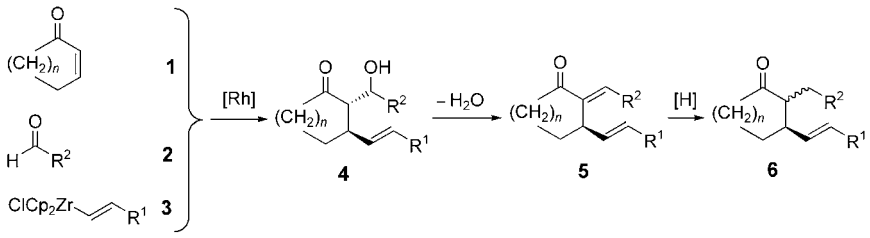
K. Ohmori, M. Tamiya, M. Kitamura, H. Kato, M. Oorui, K. Suzuki* ——— **3871 – 3874**

Regio- and Stereocontrolled Total Synthesis of Benanomicin B



Fully controlled total synthesis of benanomicin B was achieved by exploiting two key steps: a stereocontrolled ring-opening of a lactone (see scheme, step A), and a semipinacol cyclization of an acetal-aldehyde derivative discriminating the two hydroxy groups of the pseudo-C_2-symmetric 1,2-diol moiety (step B).

 © 2005 Wiley-VCH Verlag GmbH & Co. KGaA, Weinheim

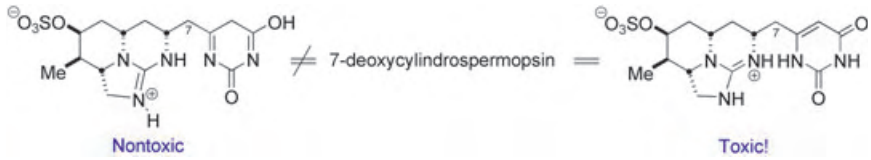


Three's not always a crowd: A three-component reaction involving α,β-unsaturated enones **1**, aldehydes **2**, and alkenyl zirconium species **3** in the presence of a Rh–binap catalyst leads, sequentially, to aldols **4**, enones **5**, and 2,3-disubstituted cycloalkanones **6** in good yields and with high *ee* values.

Multicomponent Reactions

K. C. Nicolaou,* W. Tang, P. Dagneau, R. Faraoni ——— **3874 – 3879**

A Catalytic Asymmetric Three-Component 1,4-Addition/Aldol Reaction: Enantioselective Synthesis of the Spirocyclic System of Vannusal A

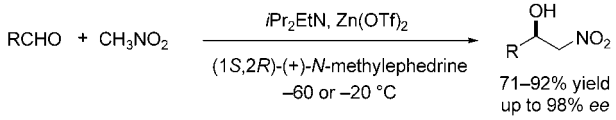


Naturally occurring! The cyanobacterial metabolite 7-deoxycylindrospermopsin has been synthesized and its natural occurrence confirmed by HPLC. Structural analysis and protein-inhibition studies show that the uracil unit does not appear to adopt the unconventional tautomeric structure (see scheme), as previously thought, and that oxygenation at C7 is not required for the inhibition of protein biosynthesis.

Natural Product Synthesis

R. E. Looper, M. T. C. Runnegar, R. M. Williams* ——— **3879 – 3881**

Synthesis of the Putative Structure of 7-Deoxycylindrospermopsin: C7 Oxygenation Is Not Required for the Inhibition of Protein Synthesis



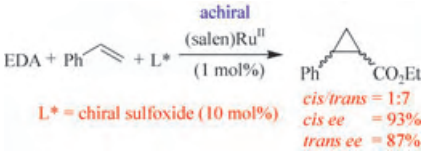
A simple assembly of commercially available materials, namely, zinc triflate ($Zn(OTf)_2$), a tertiary amine base (iPr_2EtN), and reusable (+)-*N*-methylephedrine, effectively activates the Henry reaction between aldehydes and nitromethane (see scheme). The catalytic system can be used in substoichiometric quantities and leads to good yields and enantioselectivities.

Henry Reaction

C. Palomo,* M. Oiarbide, A. Laso ——— **3881 – 3884**

Enantioselective Henry Reactions under Dual Lewis Acid/Amine Catalysis Using Chiral Amino Alcohol Ligands

An efficient and facile method is used to develop new (salen)ruthenium(II) catalysts for the asymmetric cyclopropanation of olefins, in which a chiral additive induces asymmetry in inexpensive and readily synthesized achiral (salen)ruthenium(II) catalysts (see scheme; EDA = ethyl diazoacetate). This approach is amenable to parallel-screening optimization and has great potential advantages over traditional catalyst development and synthetic methods.



Asymmetric Catalysis

J. A. Miller, B. A. Gross, M. A. Zhuravel, W. Jin, S. T. Nguyen* ——— **3885 – 3889**

Axial Ligand Effects: Utilization of Chiral Sulfoxide Additives for the Induction of Asymmetry in (Salen)ruthenium(II) Olefin Cyclopropanation Catalysts

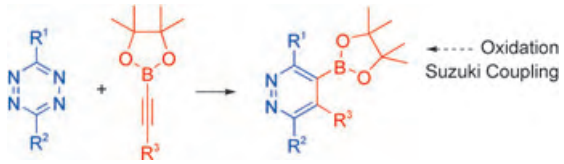
 © 2005 Wiley-VCH Verlag GmbH & Co. KGaA, Weinheim

Contents

Synthetic Methods

M. D. Helm, J. E. Moore, A. Plant, J. P. A. Harrity* ——— 3889 – 3892

Synthesis of Highly Substituted Pyridazines through Alkynyl Boronic Ester Cycloaddition Reactions



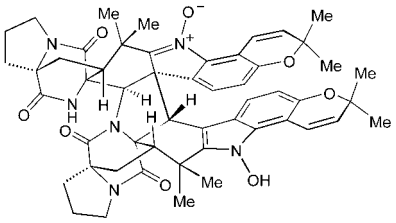
A highly regioselective transformation of tetrazines through a cycloaddition reaction with alkynyl boronic esters provides highly substituted pyridazine boronic esters as intermediates for C–O and C–C bond-forming reactions (see scheme). Functionalization reactions of the C–B bond, such as oxidation and the Suzuki cross-coupling, show the versatility of these species.

Natural Products Synthesis

P. S. Baran,* C. A. Guerrero, B. D. Hafensteiner, N. B. Ambhaikar ——— 3892 – 3895

Total Synthesis of Avrainvillamide (CJ-17,665) and Stephacidin B

Enantioselective total syntheses of the naturally occurring forms of the highly oxidized indole alkaloids avrainvillamide (CJ-17,665) and stephacidin B (see formula) are reported, facilitated by a remarkable oxidation of stephacidin A. A streamlined route to stephacidin A is also reported along with the absolute configuration determination of this family of natural products.

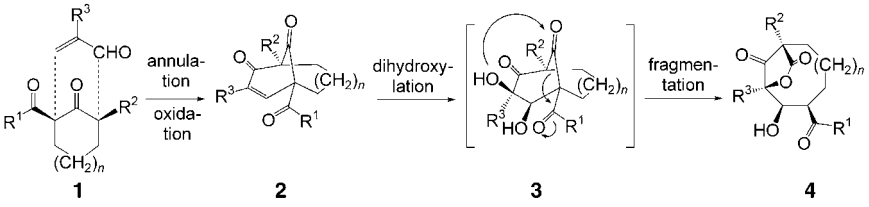


(–)-stephacidin B

Ring Systems

K. C. Nicolaou,* G. E. A. Carenzi, V. Jeso ——— 3895 – 3899

Construction of Highly Functionalized Medium-Sized Rings: Synthesis of Hyperforin and Perforatumone Model Systems

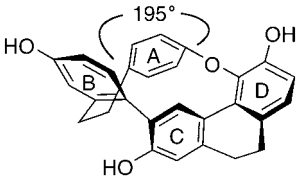


Bridging the gap: A sequence of reactions (**1**→**2**→**3**→**4**) leads to bridged, polyfunctional, medium-sized rings in synthetically useful yields. These rings are reminiscent of the molecular architectures of hyperforin and perforatumone.

Natural Product Synthesis

D. C. Harrowven,* T. Woodcock, P. D. Howes ——— 3899 – 3901

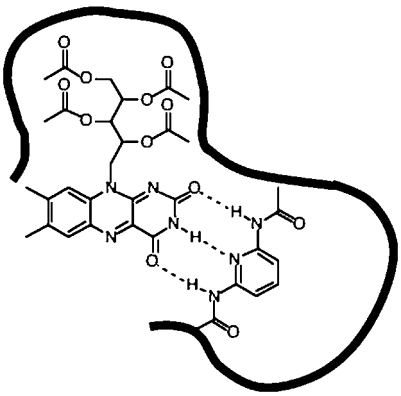
Total Synthesis of Cavicularin and Riccardin C: Addressing the Synthesis of an Arene That Adopts a Boat Configuration



cavicularin (**1**)

A transannular ring contraction induced by the addition of an aryl radical intermediate to a proximal arene facilitated the construction of the highly strained macrocyclic core of cavicularin (**1**). The precursor, an iodinated derivative of another natural product, riccardin C, was prepared from four commercially available arenes in a highly convergent sequence.

 © 2005 Wiley-VCH Verlag GmbH & Co. KGaA, Weinheim



Cheers! Specificity for riboflavin in water-rich media with an affinity on the order found for the corresponding biological receptor, riboflavin binding protein, is shown by a receptor containing a complementary hydrogen bonding array (see picture). Microcalorimetry performed at low receptor concentrations in a solution mimicking an alcoholic beverage indicated the presence of a small but uniform population of high-affinity sites ($K > 10^6\ M^{-1}$).

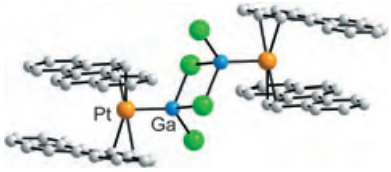
Bioorganic Chemistry

P. Manesiotis, A. J. Hall,* J. Courtois, K. Irgum, B. Sellergren* ____ 3902 – 3906

An Artificial Riboflavin Receptor Prepared by a Template Analogue Imprinting Strategy

---

Formal substitution of two terminal *trans* chlorine substituents in a Ga_2Cl_6 molecule by platinum groups leads to the platinum(0)–chrysene compound shown. The complex has been structurally characterized.

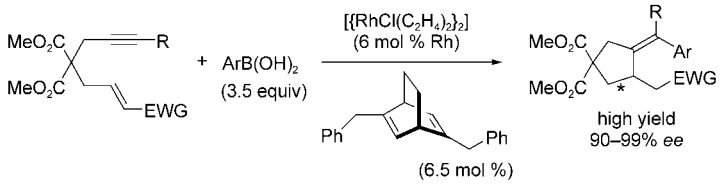


Platinum–Gallium Compounds

M. Gorlov, A. Fischer, L. Kloo* ____ 3906 – 3909

One-Step Synthesis of a Platinum(0)–Gallium(III) Chrysene Complex

---



A rhodium catalyst promotes the arylative cyclization of alkyne-tethered electron-deficient olefins in the presence of aryl boronic acids. High chemoselectivity was attained uniquely by the use of diene ligands, and high enantioselectivity was successfully realized by employing a C_2-symmetric chiral bicyclo[2.2.2]octadiene ligand (see scheme).

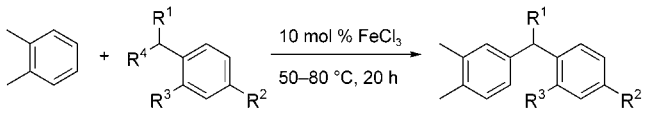
Asymmetric Catalysis

VIP

R. Shintani, A. Tsurusaki, K. Okamoto, T. Hayashi* ____ 3909 – 3912

Highly Chemo- and Enantioselective Arylative Cyclization of Alkyne-Tethered Electron-Deficient Olefins Catalyzed by Rhodium Complexes with Chiral Dienes

---



R^1 = H, Me, Ph, CH_2CO_2Et, CN
R^2 = H, OMe, Cl, F
R^3 = H, Cl, F
R^4 = OH, OAc, OCO_2Me, Cl

Green grow the diarylmethanes: Substituted arenes and heteroarenes can be easily benzylated in the presence of inexpensive and relatively nontoxic metal salts such as $FeCl_3$ (see scheme). This arylation method with benzyl alcohols is a state-of-the-art green route to diarylmethanes as water is the only by-product.

Arene Functionalization

I. Iovel, K. Mertins, J. Kischel, A. Zapf, M. Beller* ____ 3913 – 3917

An Efficient and General Iron-Catalyzed Arylation of Benzyl Alcohols and Benzyl Carboxylates

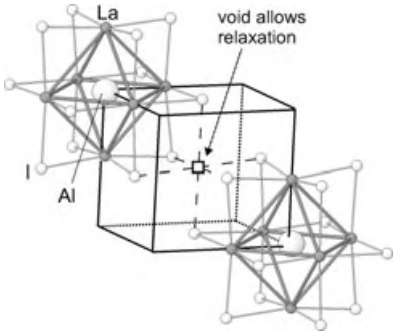
 © 2005 Wiley-VCH Verlag GmbH & Co. KGaA, Weinheim

Contents

Analysis of X-ray Data

O. Oeckler, T. Weber, L. Kienle, H. Mattausch, A. Simon* — **3917 – 3921**

Cluster Disorder and Ordering Principles in Al-Stabilized "LaI"

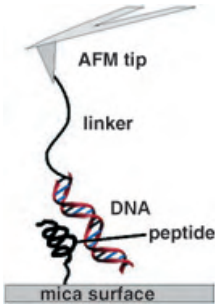


What appears to be "LaI" with a NaCl-type structure is in fact an Al-stabilized cluster compound consisting of disordered La_6AlI_{12} clusters that share I atoms (see picture). Quantitative analysis of diffuse diffraction data revealed both the constitution of this compound and the fact that this disorder is not statistical, but as uniform as possible for the composition $La_{\approx 0.7}I_{1-x}Al_x$ ($x \approx 0.14$) given the observed lattice.

DNA–Peptide Complexes

R. Eckel, S. D. Wilking, A. Becker, N. Sewald,* R. Ros, D. Anselmetti* — **3921 – 3924**

Single-Molecule Experiments in Synthetic Biology: An Approach to the Affinity Ranking of DNA-Binding Peptides



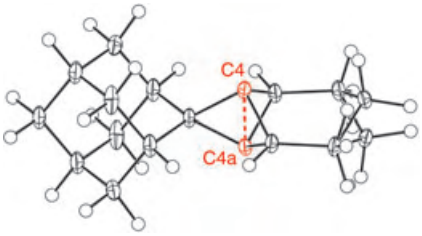
Peptide–DNA recognition: The specific binding of peptides to DNA representing a section of the binding sequence of a transcription activator has been demonstrated for the first time at the single-molecule level with AFM (experimental principle, see picture). The results underscore the importance of peptide length and cooperative effects as well as the contribution of single-point mutations on specific binding.

Propellanes

M. Messerschmidt, S. Scheins, L. Grubert, M. Pätzel, G. Szeimies, C. Paulmann, P. Luger* — **3925 – 3928**

Electron Density and Bonding at Inverted Carbon Atoms: An Experimental Study of a [1.1.1]Propellane Derivative

Synchrotron radiation was required for high-resolution diffraction experiments to determine the electron density and analyze the topology of a new [1.1.1]propellane derivative. A bond path with a bond critical point of significant electron density was found between the "inverted" bridgehead atoms C4···C4a (see picture), which is characteristic for a covalent bond; however, no charge accumulation at the bond critical point was seen.

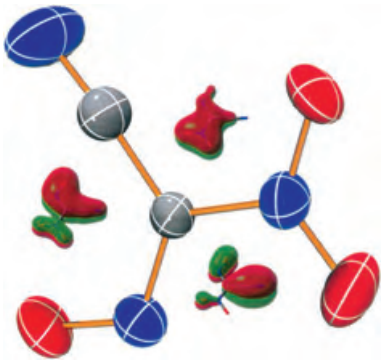


Stable Methanides

H. Brand, P. Mayer, A. Schulz,* J. J. Weigand — **3929 – 3932**

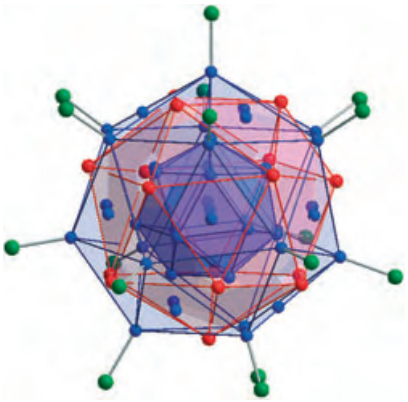
Nitro(nitroso)cyanomethanides

More bangs for the buck. Explosive nitro(nitroso)cyanomethanides $M'[C(NO_2)(NO)(CN)]$ ($M' =$ alkali metal, NMe_4) were prepared in a simple, two-step, high-yielding procedure, fully characterized, and shown to be stable at ambient temperature. The thermal properties were studied, and the structures of several nitro(nitroso)cyanomethanide salts were determined by X-ray diffraction. The structure and bonding in these compounds are discussed on the basis of calculations.



 © 2005 Wiley-VCH Verlag GmbH & Co. KGaA, Weinheim

Molecular alloys: The composition and properties of the title compounds suggests that they can be regarded as molecular alloys. The single-crystal structures of these phosphine-stabilized compounds are determined (see picture for structure of $[Cu_{45}Sb_{16}(PEt_2Me)_{16}]$; Sb red, Cu blue, P green) and confirmed by density functional theory (DFT) calculations.



Cluster Compounds

R. Ahlrichs, D. Fenske,* M. McPartlin, A. Rothenberger, C. Schrodt, S. Wieber ——— **3932 – 3936**

Phosphine-Stabilized Copper–Antimony Clusters: Syntheses, Structures, and Theoretical Investigations of $[Cu_{12}(SbSiMe_3)_6(PiPr_3)_6]$, $[Cu_{40}Sb_{12}(PMe_3)_{20}]$, and $[Cu_{45}Sb_{16}(PEt_2Me)_{16}]$

The issues for May 2005 appeared online on the following dates
Issue 21: May 17 · Issue 22: May 24 · Issue 23: May 30 · Issue 24: June 6

Sources

Product and Company Directory

You can start the entry for your company in "Sources" in any issue of *Angewandte Chemie*.

If you would like more information, please do not hesitate to contact us.

Wiley-VCH Verlag – Advertising Department
Tel.: 0 62 01 - 60 65 65
Fax: 0 62 01 - 60 65 50
E-Mail: MSchulz@wiley-vch.de

Service

Keywords ——— *3938*

Authors ——— *3939*

Angewandte's Sister Journals ——— *3940*

Preview ——— *3941*

Corrigendum

We failed to reference the interesting and relevant work of Gañán-Calvo and co-workers: A. M. Gañán-Calvo, *Phys. Rev. Lett.* **1998**, *80*, 285; A. M. Gañán-Calvo, J. M. Gordillo, *Phys. Rev. Lett.* **2001**, *87*, 274501; I. G. Loscertales, A. Barrero, I. Guerrero, R. Cortijo, M. Marquez, A. M. Gañán-Calvo, *Science* **2002**, *295*, 1695. We would also like to point the interested reader to other relevant reports, such as: I. Cohen, H. Li, J. L. Hougland, M. Mrksich, S. R. Nagel, *Science* **2001**, *292*, 265; S. Sugiura, M. Nakajima, H. Itou, M. Seki, *Macromol. Rapid. Commun.* **2001**, *22*, 773; T. Nisisako, T. Torii, T. Higuchi, *Chem. Eng. J.* **2004**, *101*, 23. Although the details of the fluid physics and the specific applications of our paper differ from those of the reports cited herein, the prior work of these authors illustrates the value of flow-focusing systems in making highly uniform droplets and the potential for using these droplets in materials science.
In addition, following the submission of our report, two other articles that document the use of microfluidic channels for the in situ preparation of anisotropic polymeric particles were published: W. Jeong, J. Kim, S. Kim, S. Lee, G. Mensing, D. J. Beebe, *Lab Chip* **2004**, *4*, 576; D. Dendukuri, K. Tsoi, T. A. Hatton, P. S. Doyle, *Langmuir* **2005**, *21*, 2113.

Generation of Monodisperse Particles by Using Microfluidics: Control over Size, Shape, and Composition

S. Xu, Z. Nie, M. Seo, P. Lewis, E. Kumacheva,* H. A. Stone, P. Garstecki, D. B. Weibel, I. Gitlin, G. M. Whitesides* ——— **724–728**

Angew. Chem. Int. Ed. **2005**, *44*

DOI 10.1002/anie.200462226

 © 2005 Wiley-VCH Verlag GmbH & Co. KGaA, Weinheim

Hans Bethe (1906–2005) and Ligand Field Theory

Hans Albrecht Bethe, probably the last of the pioneer generation of quantum mechanics and certainly one of the most important physicists of the 20th century, died on March 6, 2005, at almost 99 years of age. Rather than to extend another note of appreciation for Bethe's contributions to such fields as nuclear physics or astrophysics, it is more appropriate for this Journal to recall what chemistry owes him. Hans A. Bethe was born July 2, 1906 in Strassburg. He graduated from the University of Munich in 1928 after conducting research with Arnold Sommerfeld on electron scattering in crystals. He was active at various German universities and became assistant professor at the University of Munich in 1930. In 1929 his seminal paper on crystal field theory was published.[1] Between 1930 and 1935 Bethe worked in Rome (with Enrico Fermi) and at various English universities. After his departure from Nazi Germany he was offered a professorship at Cornell University (Ithaca, NY) in 1935 where, with the exception of some interruptions during World War II, he stayed until the end of his life.



Bethe's review on the theory of one- and two-electron atoms for the *Handbuch der Physik* of 1933 was the precursor of the famous *Bethe–Salpeter*.[2] For the serious study of atoms and molecules, this classic cannot be ignored. Of equal fundamental importance is a series of papers on nuclear physics[3] that soon became known as the Bethe bible. Most of Bethe's papers had no direct relation to chemistry. Nevertheless, his contributions to quantum electrodynamics (QED) are relevant even for theoretical chemistry. For example, his explanation of the Lamb shift, the QED correction to one-electron levels,[4] is gaining importance in the theory of heavy atoms and their molecules. Bethe's studies of the many-body problem in nuclear physics[5] have stimulated the treatment of the many-electron problem in quantum chemistry.

In 1967 Hans Bethe received the Nobel Prize in physics "*for his contributions to the theory of nuclear reactions, especially his discoveries concerning the energy production in stars*". His creation of crystal field theory may well have been deserving of the Nobel Prize in chemistry. Most of what can be learned about the formalism of the theory from modern textbooks of inorganic chemistry is found in Bethe's original papers.[1] Bethe investigated how the electronic states of open-shell ions, mainly those of transition metals, are influenced by the surrounding ions in a crystal. He proposed that the influence of the ligands can be described by an electrostatic 'crystal field'. This field lowers the symmetry with respect to the free atomic ions, which leads to a shift and splitting of the atomic states. The energy level scheme is determined by three parameters, the ligand field strength, the asymmetric portion of the electron interaction, and the spin–orbit interaction. Bethe distinguished three limiting cases of strong, intermediate, and weak fields. Currently, the term weak field is used for what Bethe described as the intermediate field (in which the electron interaction dominates over the ligand field strength), whereas the original weak field of Bethe is now known as the coupling case of the rare-earths (in which the spin–orbit interaction dominates). In the strong field, terms with low spin are preferred, as predicted by the aufbau principle. The present-day weak field favors terms with high spin in the spirit of Hund's rules. To appreciate Bethe's achievement fully, one must realize that around 1930, the theory of the representations of point groups had not yet been developed; he had to work them out himself. He also invented the double groups that are needed to describe relativistic states.

Bethe's theory had been applied to the magnetic properties of molecular complexes in the early 1930s.[6,7] However, more than 20 years would pass before ligand field theory, built upon crystal field theory, would become the standard model for understanding the spectra of transition metal complexes.[8–10] It is now known that the description of the effect of the ligands in terms of an electrostatic field is not very realistic, and that energy level splitting by the ligand environment is instead the result of chemical (overlap-dependent) forces.[11] One quality of Bethe's theory is that most of its results are the consequence of symmetry, and do not necessarily depend on the electrostatic model. For a considerable time, crystal field theory in Bethe's original meaning was distinguished from ligand field theory as a modification for molecular complexes, but this distinction is now of little more than historical interest. As even transition metal complexes are currently applicable to ab-initio calculations, crystal field theory is outdated as a scheme for approximate computations. However, it is still a valid model for a qualitative understanding of the spectra and other properties of transition metal complexes. It plays a similar fundamental role in inorganic chemistry as does the Debye–Hückel theory in organic chemistry.

Bethe was a participant in the Manhattan Project (the construction of the atomic bomb in the U.S.) as head of the theory group at Los Alamos. After the war, he became one of the most prominent advocates (even as an advisor to US presidents) for a change in energy policy and of nuclear disarmament and weapons test bans. Those who knew Hans Bethe well, describe him as a very modest and extremely friendly person.

Werner Kutzelnigg
Ruhr-Universität Bochum (Germany)

[1] H. A. Bethe, *Ann. Phys.* **1929**, *5*, 133; H. A. Bethe, *Z. Phys.* **1930**, *60*, 218.
[2] H. A. Bethe, E. E. Salpeter, *Quantum Mechanics of One- and Two-Electron Atoms*, Springer, Berlin, **1957**.
[3] a) H. A. Bethe, R. F. Bacher, *Rev. Mod. Phys.* **1936**, *8*, 82; b) H. A. Bethe, *Rev. Mod. Phys.* **1937**, *9*, 69; c) M. S. Livingston, H. A. Bethe, *Rev. Mod. Phys.* **1937**, *9*, 245.
[4] H. A. Bethe, *Phys. Rev.* **1947**, *72*, 339.
[5] H. A. Bethe, J. Goldstone, *Proc. Roy. Soc. A* **1957**, *238*, 551.
[6] a) W. G. Penney, R. Schlapp, *Phys. Rev.* **1932**, *41*, 194; b) R. Schlapp, W. G. Penney, *Phys. Rev.* **1932**, *42*, 666.
[7] a) J. H. van Vleck, *Phys. Rev.* **1932**, *41*, 208; b) J. H. van Vleck, *J. Chem. Phys.* **1935**, *3*, 807.

 © 2005 Wiley-VCH Verlag GmbH & Co. KGaA, Weinheim DOI: 10.1002/anie.200501634

[8] F. E. Ilse, H. Hartmann, *Z. Phys. Chem.* **1951**, *197*, 239.
[9] a) Y. Tanabe, S. Sugano, *J. Phys. Soc. Jap.* **1954**, *9*, 753; b) Y. Tanabe, S. Sugano, *J. Phys. Soc. Jap.* **1954**, *9*, 766.
[10] J. S. Griffith, *The Theory of Transition-Metal Ions*, University Press, Cambridge, **1971**.
[11] A critical analysis of ligand field theory is found in: W. Kutzelnigg, *Einführung in die Theoretische Chemie, Vol. 2*, VCH, Weinheim, **1978/1994**, pp. 407–468.

Unique – New - Fascinating



2004. XV, 295 pages, 173 figures, 66 tables. Hardcover.
ISBN 3-527-30828-8
€ 129.- /£ 90.- /US$ 185.-

MASAKATSU SHIBASAKI and YOSHINORI YAMAMOTO, (eds.)

Multimetallic Catalysts in Organic Synthesis

The reference comprehensively covers this hot topic presenting the information hitherto scattered throughout smaller reviews or single book chapters to provide an introduction to this rapidly expanding field.
In ten chapters, the international team of expert authors treats asymmetric syntheses, new transformations, and organometallic reactions using homo- and hetero-bimetallic catalysts. Written for advanced researchers, this very timely publication is of significant benefit to organic and organometallic chemists in both academia and industry.

15710411_kn

Register now for the free
WILEY-VCH Newsletter!
www.wiley-vch.de/home/pas

WILEY-VCH • P.O. Box 10 11 61 • D-69451 Weinheim, Germany
Fax: +49 (0) 62 01 - 60 61 84
e-mail: service@wiley-vch.de • http://www.wiley-vch.de

WILEY-VCH

 © 2005 Wiley-VCH Verlag GmbH & Co. KGaA, Weinheim

Macrocycle Synthesis

Shape-Persistent Phenylene-Acetylene Macrocycles: Large Rings—Low Yield?

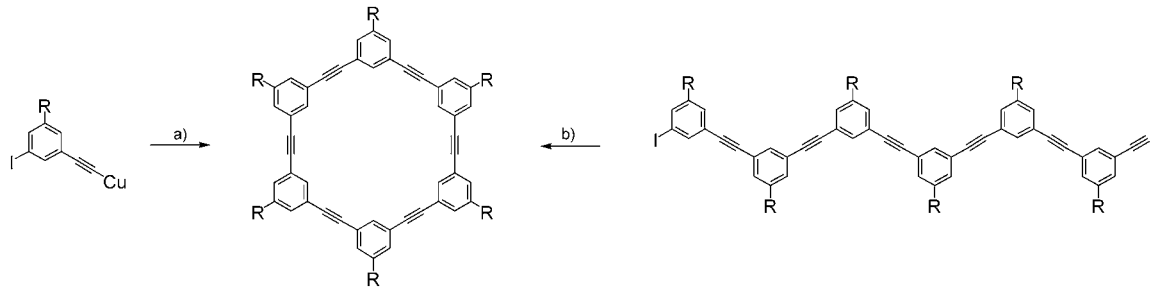
*Sigurd Höger**

Keywords:
alkynes · cyclophanes · macrocycles · metathesis · supramolecular chemistry

Shape-persistent macrocycles have gathered increasing interest over the past several years.[1] Rings that contain phenylethynyl, phenylbutadiynyl, or both moieties (phenylacetylene macrocycles, PAMs) are especially valuable candidates for investigations of the supramolecular chemistry of nanometer-scale rings. First, palladium-catalyzed aryl–alkyne bond formation is easily carried out (Sonogashira–Hagihara coupling); the coupling protocols have a great functional-group tolerance and acetylene protecting groups of various stabilities and polarities have been well-described. Second, the spacers between the aromatic rings avoid steric constrains between groups that are necessarily attached to the rigid backbone, to ensure the tractability of the macrocycles. The shape and size of the molecules depend on the substitution pattern of the arenes. Although pure *para*-substituted cyclic phenylacetylenes have been investigated,[2] most PAMs contain *meta*- or *ortho*-substituted arenes at their corners and *para*-substituted arenes for the expansion of interior space.

In 1974, Staab and Neunhoeffer reported the synthesis of the *m*-cyclophane **1a** by the intermolecular, sixfold Stephens–Castro coupling of the copper salt of *m*-iodophenylacetylene (Scheme 1).[3] The easily available starting material allowed the synthesis of 800 mg product, although the yield was only 4.6%. A much higher yield in the synthesis of this compound was reported by Moore and Zhang nearly 20 years later.[4] Instead of forming the ring precursor (and other oligomers) and the cyclization in a one-pot reaction, an α-iodo-ω-ethynyl precursor was prepared separately and then cyclized under high-dilution conditions in the final step to give **1b** in excellent (75%) yield. Apart from the high yield in the cyclization step (along with an easy purification of the product), this is the method of choice for the preparation of macrocycles with varying functional groups on the phenyl building blocks, as the precursor is built up stepwise. Cyclic pentamers, heptamers, and other defined oligomers that were not described until now are also available in high yield through this approach.

The repetitive precursor synthesis, however, is also responsible for the major disadvantage of this approach: it requires numerous deprotection/coupling steps. In addition to these two extreme strategies, numerous intermediate approaches can be found in the literature, for example, the dimerization of half-rings, trimerization of ring thirds, and so on. Similar approaches are also described for phenylenyl, phenylbutadienyl, and other shape-persistent rings.[5] Regardless of the specific C–C coupling reaction used, all protocols generally suffer from the same handicap: simple precursors are easily accessible, but give low yields of the desired shape-persistent ring, whereas high yields in the cyclization step require a time- and material-intensive multistep preparation of precursors.



Scheme 1. Synthesis of a hexameric phenylacetylene macrocycle; a) pyridine, reflux, 4.6% yield (Staab); b) $[Pd(dba)_2]$, PPh_3, CuI, 70°C, pseudo-high-dilution conditions, 75% yield (Moore); dba = dibenzylidene acetone.

[*] Prof. S. Höger
Universität Karlsruhe
Institute for Technical Chemistry and Polymer Chemistry
Engesserstrasse 18, 76131 Karlsruhe (Germany)
Fax: (+49) 721-608-3151
E-mail: hoeger@chemie.uni-karlsruhe.de

 © 2005 Wiley-VCH Verlag GmbH & Co. KGaA, Weinheim DOI: 10.1002/anie.200500681

Templates are an attractive way to overcome this problem and Sanders and co-workers were able to show that ethynylphenyl-substituted Zn porphyrins can be cyclodimerized or cyclotrimerized, depending on the specific pyridyl template present in the reaction media.[6] We showed that covalent templates also increase the yield of the desired cyclic products dramatically, thus allowing the preparation of symmetrically and even nonsymmetrically functionalized PAMs in high yields.[7] However, the supramolecular and covalent template approaches require the presence of appropriate functional groups that bind (or are bound) to the template.

Another approach involves preparation of the macrocycle under thermodynamic control. For cases in which the desired structure is the most stable under the given conditions and the cyclization reaction is reversible, it might be possible to obtain a single macrocyclic product in quantitative yield despite having begun the synthesis with small building blocks.[8,9]

Imine formation is a convenient way to generate macrocycles in high yields.[10,11] In recent years, the synthesis of arylacetylene macrocycles containing imine bonds was described, in which the cyclization step involves the formation of a Schiff base (Figure 1). For example, Moore and Zhao prepared the imine-containing macrocycle **2** in nearly quantitative yield by the condensation of the appropriate diamine and dialdehyde.[12] In this case, however, both starting materials (half rings) needed to be prepared separately through a multistep sequence.

Recently, shape-persistent imine-containing macrocycles have also been obtained from smaller building blocks. MacLachlan and Gallant prepared the soluble 30-membered ring **3** in 70% yield through the thermodynamically favored [3+3] cyclocondensation of the corresponding dialdehyde and diamine.[13] The product behaves like a crown ether, as it binds alkali metal ions. Based on titrations monitored by UV/Vis and NMR spectroscopy, it was suggested that upon complexation, the macrocycles aggregate toward tubular assemblies. Last year, the extension of this reaction sequence toward the preparation of larger macrocycles was presented. Condensation of the corresponding dialdehydes and diamines gave the macrocyclic products **4** and **5** in a one-pot, template-free synthesis in 68 and 40% yield, respectively.[14] Subsequent metallation of **4** has shown that this macrocycle can coordinate multiple transition metals in its salen-like pockets, and titration of **4** with Zn^{2+} strongly increases its fluorescence. Therefore, large rigid macrocycles with adjustable diameters and intraannular binding sites are available in good yield having started with rather simple building blocks.

Likewise, Moore and Zhang described a new approach toward arylacetylene macrocycles by using the reversibility of the alkyne metathesis reac-

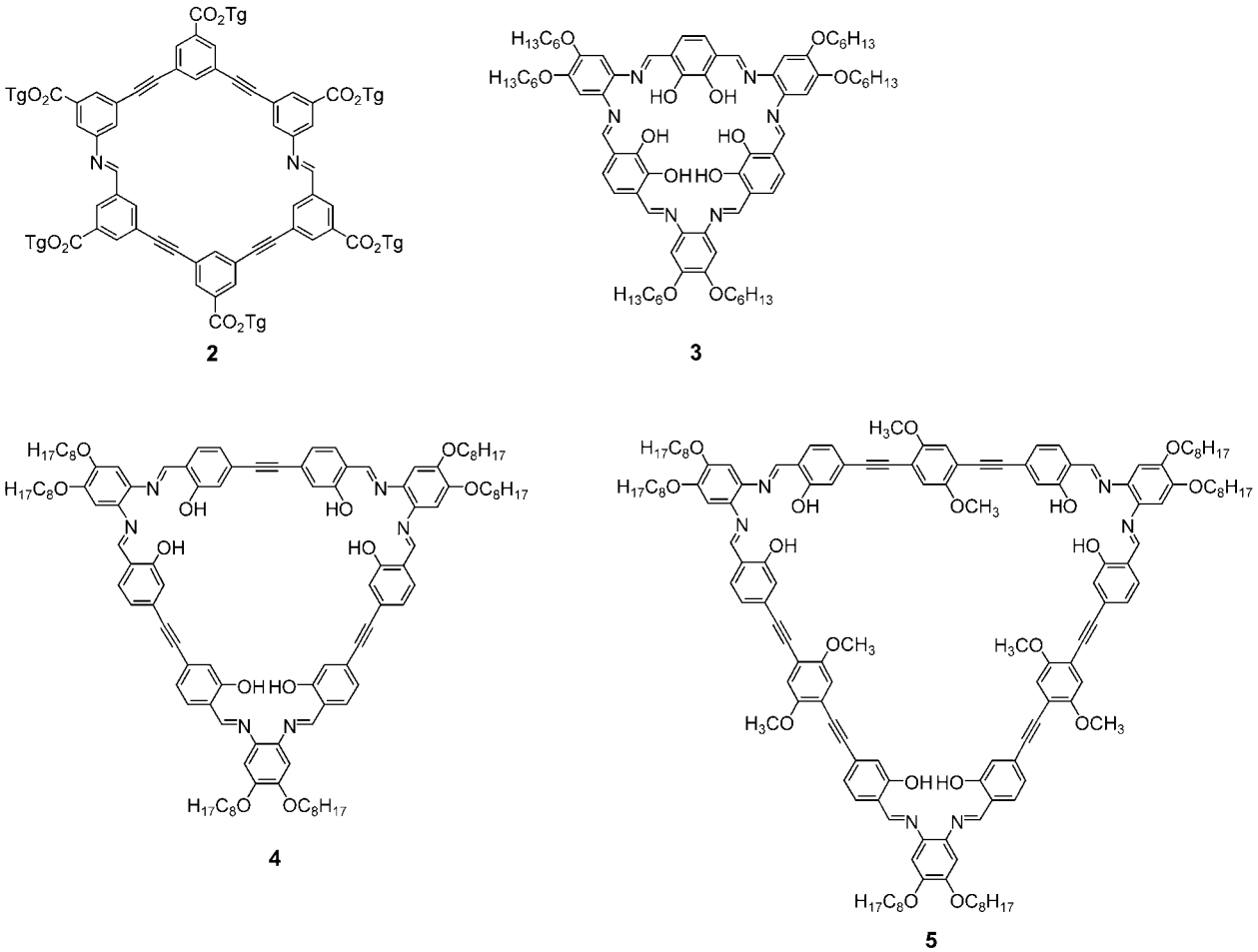


Figure 1. Shape-persistent macrocycles prepared by the formation of reversible imines; $Tg = (CH_2CH_2O)_3CH_3$.

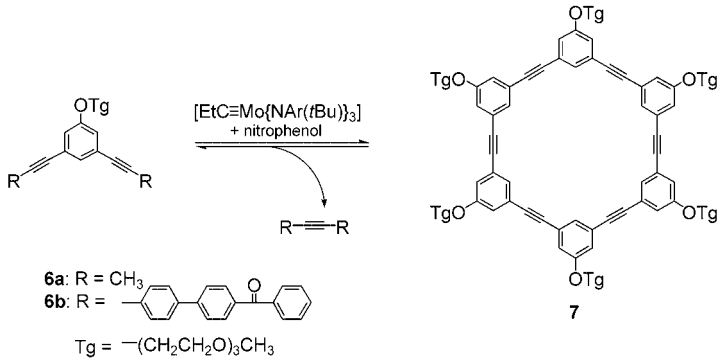
 © 2005 Wiley-VCH Verlag GmbH & Co. KGaA, Weinheim

tion.[15] Starting from the simple bisacetylene **6a** and a highly active Mo^{VI} alkylidyne catalyst, the macrocycle **7** was obtained in high yield (81%) when the reaction was carried out on the milligram scale under open driven conditions to remove the by-product, 2-butyne (Scheme 2).[16]

Several *m*-cyclophanes of this type were synthesized with similar yields, demonstrating the general applicability of this concept. However, attempts to increase the scale of the reaction were not successful; mainly oligomeric products were produced. It was suggested that either the 2-butyne by-product could not be removed quickly enough from the reaction mixture if the metathesis is performed on the gram scale, or that air could have led to decomposition of the catalysts. Accordingly, an alternative approach for shifting the metathesis equilibrium was explored.[17] Instead of removing a volatile by-product under vacuum, an insoluble by-product may separate from the reaction mixture in a closed system. Indeed, under optimized reaction conditions, it was possible to prepare more than 5 g (77%) of **7** in one batch when the benzoylbiphenyl-substituted arylacetylene **6b** was cyclized in CCl_4.

30 years after the report of Staab and Neunhoeffer on *m*-cyclophane **1**, arylacetylene macrocycles have now become available in high yields even with the use of small molecules as precursors. Although the structural variability that can be obtained through repetitive precursor synthesis is not yet known, the syntheses described herein will clearly open new possibilities for future investigations of the structure–property relationships in this interesting class of compounds.

Published online: May 13, 2005



Scheme 2. Alkyne metathesis for the preparation of hexameric phenylacetylene macrocycles in high yields.

[1] Recent reviews: a) J. S. Moore, *Acc. Chem. Res.* **1997**, *30*, 402–413; b) S. Höger, *J. Polym. Sci. Part A* **1999**, *37*, 2685–2698; c) M. M. Haley, J. J. Pak, S. C. Brand, *Top. Curr. Chem.* **1999**, *201*, 81–130; d) C. Grave, A. D. Schlüter, *Eur. J. Org. Chem.* **2002**, 3075–3098; e) D. Zhao, J. S. Moore, *Chem. Commun.* **2003**, 807–818; f) S. Höger, *Chem. Eur. J.* **2004**, *10*, 1320–1329; g) *Acetylene Chemistry* (Eds.: F. Diederich, P. J. Stang, R. R. Tykwinsky), Wiley-VCH, Weinheim, **2005**.

[2] a) T. Kawase, H. R. Darabi, M. Oda, *Angew. Chem.* **1996**, *108*, 2803–2805; *Angew. Chem. Int. Ed. Engl.* **1996**, *35*, 2664–2666; b) T. Kawase, K. Tanaka, N. Shiono, Y. Seirai, N. Shiono, M. Oda, *Angew. Chem.* **2004**, *116*, 1754–1756; *Angew. Chem. Int. Ed.* **2004**, *43*, 1722–1724.

[3] H. A. Staab, K. Neunhoeffer, *Synthesis* **1974**, 424.

[4] a) J. S. Moore, J. Zhang, *Angew. Chem.* **1992**, *104*, 873–874; *Angew. Chem. Int. Ed. Engl.* **1992**, *31*, 922–924; b) J. Zhang, D. J. Pesak, J. L. Ludwick, J. S. Moore, *J. Am. Chem. Soc.* **1994**, *116*, 4227–4239.

[5] For examples, see: a) H. Staab, F. Binning, *Chem. Ber.* **1967**, *100*, 293–305; b) V. Hensel, K. Lützow, J. Jakob, K. Gessler, W. Saenger, A. D. Schlüter, *Angew. Chem.* **1997**, *109*, 2768–2770; *Angew. Chem. Int. Ed. Engl.* **1997**, *36*, 2654–2656; c) Y. Tobe, N. Utsumi, A. Nagano, K. Naemura, *Angew. Chem.* **1998**, *110*, 1347–1349; *Angew. Chem. Int. Ed.* **1998**, *37*, 1285–1287.

[6] a) H. L. Anderson, J. K. M. Sanders, *Angew. Chem.* **1990**, *102*, 1478–1480; *Angew. Chem. Int. Ed. Engl.* **1990**, *29*, 1400–1403; b) D. W. J. McCallien, J. K. M. Sanders, *J. Am. Chem. Soc.* **1995**, *117*, 6611–6612.

[7] a) S. Höger, A.-D. Meckenstock, H. Pellen, *J. Org. Chem.* **1997**, *62*, 4556–4557; b) S. Höger, A.-D. Mechenstock, *Tetrahedron Lett.* **1999**, *40*, 1735–1736; c) S. Höger, A.-D. Meckenstock, *Chem. Eur. J.* **1999**, *5*, 1686–1691; d) S. Höger, *Macromol. Symp.* **1999**, *142*, 185–191; e) M. Fischer, S. Höger, *Eur. J. Org. Chem.* **2003**, 441–446.

[8] For an example summary, see: S. J. Rowan, S. J. Cantrill, G. R. L. Cousins, J. K. M. Sanders, J. F. Stodart, *Angew. Chem.* **2002**, *114*, 938–993; *Angew. Chem. Int. Ed.* **2002**, *41*, 898–952.

[9] Topical examples of this strategy through self-assembled metalloorganic frameworks: a) M. Fujita, K. Umemoto, M. Yoshizawa, N. Fujita, T. Kusokawa, K. Biradha, *Chem. Commun.* **2001**, 509–518; b) S. R. Seidel, P. J. Stang, *Acc. Chem. Res.* **2002**, *35*, 972–983.

[10] a) S. Akine, T. Taniguchi, T. Nabeshima, *Tetrahedron Lett.* **2001**, *42*, 8861–8864; b) J. Gawroński, H. Kolbon, M. Kwit, A. Katrusiak, *J. Org. Chem.* **2000**, *65*, 5768–5773.

[11] One of the most impressive recent examples are the Borromean rings of Stoddart: K. S. Chichak, S. J. Cantrill, A. R. Pease, S.-H. Chiu, G. W. V. Cave, J. L. Atwood, J. F. Stoddart, *Science* **2004**, *304*, 1308–1312.

[12] D. Zhao, J. S. Moore, *J. Org. Chem.* **2002**, *67*, 3548–3554. Imine metathesis reactions in various solvents suggest that the formation of stacked-ring assemblies is the thermodynamic driving force for the exclusive formation of cyclodimers: D. Zhao, J. S. Moore, *Macromolecules* **2003**, *36*, 2712–2720.

[13] A. J. Gallant, M. J. MacLachlan, *Angew. Chem.* **2003**, *115*, 5465–5468; *Angew. Chem. Int. Ed.* **2003**, *42*, 5307–5310.

[14] C. Ma, A. Lo, A. Abdolmaleki, M. J. MacLachlan, *Org. Lett.* **2004**, *6*, 3841–3844.

[15] W. Zhang, J. S. Moore, *J. Am. Chem. Soc.* **2004**, *126*, 12796.

[16] With the "instant catalysts" described by Bunz, the cyclohexamer was obtained in only 6% yield, similar to synthesis of Staab: a) P.-H. Ge, W. Fu, W. A. Herrmann, E. Herdtweck, C. Campana, R. D. Adams, U. H. F. Bunz, *Angew. Chem.* **2000**, *112*, 3753–3756; *Angew. Chem. Int. Ed.* **2000**, *39*, 3607–3610; b) U. H. F. Bunz, *Acc. Chem. Res.* **2001**, *34*, 998–1010.

[17] Previous experiments by Moore and coworkers have shown that high conversions in the metathesis reaction could be obtained in a closed system if the reaction product is insoluble in the reaction mixture: W. Zhang, S. Kraft, J. S. Moore, *J. Am. Chem. Soc.* **2004**, *126*, 329–335.

 © 2005 Wiley-VCH Verlag GmbH & Co. KGaA, Weinheim

Ionic Liquids

Liquid Inorganic–Organic Nanocomposites: Novel Electrolytes and Ferrofluids

Bernd Smarsly and Helena Kaper*

Keywords:
conducting materials · ferrofluids · ionic liquids · organic–inorganic hybrid materials · polyoxometalates

Inorganic–organic nanocomposite materials have been frequently proposed in the past years as the key to various challenges in the field of future technology such as energy supply, storage and production (fuel cells, batteries, solar cells) and information technology. Ideally, the partitioning of the inorganic and organic species on the nanometer scale is expected to create a homogenous composite showing the advantageous physico-chemical properties of both moieties.[1] To date, for the organic moiety, the main focus of research has been on polymers (e.g. in proton-exchange membranes in fuel cells).[2] Attractive candidates for the inorganic parts are semiconductors, (such as TiO_2, CdS) and magnetic oxides. One of the most prominent recent examples of such nanocomposites are novel solid-state solar cells. They are based on films containing semiconductive, nanocrystalline TiO_2, an electrolyte, and a sensitizing dye.[3] Further important examples of inorganic components are magnetic nanoparticles, such as Fe_2O_3, which could be used for any kind of fluidic magnetic material.[4] Considering these potential applications, composites should fulfill the following requirements (among others): high conductivity of the electrolyte, low vapor pressure and reasonable thermal stability of the organic part (with respect to the conductivity, etc.), optimized viscosity, homogenous distribution of the inorganic and organic phases on the nanometer scale (no macroscopic phase separation), solvent-free processing, a reasonable chemical stability (electrochemical, redox, and hydrolytic stability) and improved processing properties with regard to fluidity requirements (films). The properties of the inorganic and organic species should be maintained in the composite, but eventually also new desired properties could be obtained. However, many of these basic demands are not matched yet by currently available materials. For instance, some of the delicate problems of water-based ion conductive nanocomposite membranes used in fuel cells are related to the nature of water in the membrane, differences in mechanical strength and the ductility as a function of the water content.[2,5] Also, water-based electrolytes are only operable at relative low temperatures, which represents a significant hurdle for fuel cell applications. The interest in non-aqueous electrolytes with low viscosity is therefore driven by the development of rechargeable batteries and fuel cells.[6] Ionic liquids (ILs; organic salts with melting points below 80 °C) have been identified as ideal materials to solve some of these shortcomings of water-based electrolytes because they combine high conductivity (both protic and aprotic ILs are known) with low viscosity and an extremely low vapor pressure.[7] It was recently reported that certain ILs even reach the conductivity and ionicity of water, and also have a sufficiently high ductility.[6,8] These properties make them promising candidates as electrolyte medium in fuel cell and solar cell devices.[9] While most of the developments in the field of ILs focused on optimizing the conductivity and vapor pressure, the generation of nanocomposites of ILs with inorganic species has been neglected up to now. As shown recently, certain ILs also act as a template to create highly ordered mesostructured oxidic materials.[10,11] Hence, these materials fulfill several of the aforementioned requirements for useful nanocomposites.

In the light of these recent developments, Giannelis and co-workers have reported a further important attempt to prepare the so far unavailable organic–inorganic nanocomposites with "liquid-like" behavior. They described a composite based on polyoxometalates (POMs).[12] POMs are composed of transition-metal-ion clusters in which the metal centers coordinate to oxygen atoms and have an octahedral coordination environment. POMs can form various shapes such as balls and wheels.[13] Solid POM protonic conductors are potentially interesting as electrolytes in fuel cells, however, this potential is limited by the sensitivity of their protonic conductivity, in particular towards humidity and higher temperatures. An elegant strategy to reduce the sensitivity substantially is shielding the surface of the POMs with suitable ionic organic molecules. Kurth et al. and Polarz et al. had already reported the formation of ordered, mesostructured aggregates of molybdenum-based POMs with ionic surfactants, which could even be imbedded in organic species.[14,15]

[*] B. Smarsly, H. Kaper
Max-Planck Institute of Colloids and Interfaces
Research Campus Golm
Am Mühlenberg, 14476 Potsdam-Golm (Germany)
Fax: (+49) 331-567-9508
E-mail: smarsly@mpikg.mpg.de

 DOI: 10.1002/anie.200500690 © 2005 Wiley-VCH Verlag GmbH & Co. KGaA, Weinheim

Giannelis and co-workers went a step further and obtained a solvent-free POM-containing liquid salt with zero vapor pressure, good thermal stability, high proton conductivity, and superionic behavior.[12] Selected poly(ethylene glycol) (PEG) containing quaternary ammonium cations were attached to POMs: in a simple procedure, a commercially available heteropolyacid POM such as $H_3PW_{12}O_{40}$ was treated with species such as $(CH_3)(C_{18}H_{37})N^+$-$[(CH_2CH_2O)_nH][(CH_2CH_2O)_mH]Cl^-$ ("S^+Cl^-"), leading to a partial exchange of surface protons of the POM (yield about 40%) to give $H_{3-x}S_xPW_{12}O_{40}$ ($x \approx 2$). This method takes advantage of the low viscosity and melting points of organic species such as S^+ (the coupling with PEG oligomers is an established technique to reduce the melting point and viscosity of organic salts[7]). This modified POM has a viscosity of 75 Pa s at room temperature, which drops to 0.5 Pa s at 120 °C. For comparison, water has a viscosity of approximately 10^{-3} Pa s and honey of 0.104 Pa s at room temperature, and the viscosity of ILs is usually significantly smaller than that of the "liquid" POMs (in general below 0.1 Pa s).[7a,8]

While still showing a high viscosity, this POM-based "inorganic liquid" show a reasonable conductivity over a broad temperature range, for example, 6×10^{-4} S cm^{-1} at 140 °C. Furthermore, in comparison to a corresponding solid potassium-substituted POM, the ionic conductivity of the liquid POM salt is extremely high, it exceeds that of the potassium-exchanged analogue by three orders of magnitude. This high conductivity has been attributed to superionic behavior.[12] Hence, the proton conductivity and the liquid-like character of this POM suggests applications in fuel cells or catalysis. Moreover, through the IL, the magnetic, electrochemical, and optical characteristics of POMs might be exploited in the field of organic chemistry.

Giannelis and co-workers also offer an approach towards the generation of inorganic liquid-like oxidic nanoparticles through surface functionalization by organosilanes (Figure 1).[16] In the first step, the surface of the silica nanoparticles is modified through condensation of surface silanol groups with a charged organosilane $(CH_3O)_3Si(CH_2)_3N^+$-$(CH_3)(C_{10}H_{21})_2Cl^-$. A solution of the organosilane in methanol was added to a suspension of silica particles in water, and the precipitate, which forms immediately, was aged at room temperature for 24 h. The nature of the counterion determines whether a salt is obtained that is liquid at room-temperature. While a simple chloride ion gives a typical solid salt, a subsequent ion exchange with a more complex PEG-containing sulfonate ion leads to the desired liquid salt. For this step, the chloride analogue was treated with a solution of $R(OCH_2CH_2)_7O$-$(CH_2)_3SO_3^-K^+$ ($R = C_{13-15}$ alkyl chain) in water at 70 °C for 24 h. A high organic content of around 75 wt.% was achieved and the material had a liquid-like ionic-conductivity temperature dependence and rheological performance ($G'' > G'$). In contrast, isostearate (50 wt.% organic content) and oleate (40 wt.% organic content) as counterions resulted in quite viscous gel-like materials at room temperature that only reached a low viscosity at temperatures above 120 °C. These results show the substantial dependence of the macroscopic properties on the chemical composition.

The liquid salt obtained from the silica nanoparticles was used to dissolve and polymerize pyrrole (Figure 2), thus demonstrating that such inorganic liquid salts can serve as a reaction medium in which interesting inorganic–organic composites with extra functionality can be generated.



Figure 1. Schematic representation of silica or γ-Fe_2O_3 nanoparticles linked to liquid organic salts; A^- poly(ethylene glycol) sulfonate ion.

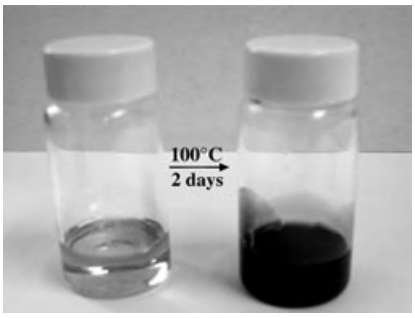


Figure 2. Liquid salt, based on silica nanoparticles, containing pyrrole before (left) and after (right) polymerization.

The preparation of liquid salts of maghemite (γ-Fe_2O_3) is a significant extension of the reported strategies for surface-functionalized iron oxide nanoparticles.[17] The synthesis is quite similar to the one used for the silica particles. The silane solution was added to a suspension of Fe_2O_3 in alkaline water (pH 10), giving the maghemite chloride salt. Then the desired sulfonate derivative was obtained through ion exchange with the PEG-containing sulfonate ion. Since the superparamagnetism of the nanoparticles remained unaffected through this procedure, a solvent-free, ionically conductive ferrofluid (a "magnetic liquid electrolyte") was obtained. Unlike the "SiO_2 liquids", the maghemite system showed a liquid-like behavior with only moderate viscosity at room temperature and flowed easily at 40 °C. For both types of inorganic nanoparticles, rheological properties can be expected to be improved by the suitable choice of the organic counterion. Further work has to focus on the improvement of the still low ion conductivity and high viscosity of the "inorganic liquids", which limit their application as electrolytes or reaction mediums.

Besides surface functionalization of nanoparticles through counterion exchange, other successful "nanochemical" approaches towards ferrofluids were described recently: Landfester et al. introduced straightforward and reliable strategies to obtain stable emulsions of magnetic iron oxide particles both in aqueous and non-aqueous media, with loadings up to 40%.[18] One advantage is that such emulsions have a much lower viscosity than the liquid salts, eventually improving their processing properties. However, the materi-

 © 2005 Wiley-VCH Verlag GmbH & Co. KGaA, Weinheim

als introduced by Giannelis and co-workers for the first time show ionic conductivity in addition to the liquid and magnetic properties, which is difficult to achieve by emulsion strategies.

The "inorganic liquid salts" can be regarded as important examples of the potential of nanochemistry to create materials with completely new properties: the combination of the physical properties of inorganic species such as binary oxide nanoparticles or POMs with those of organic liquid salts generated a "chimera", showing properties, which before had not been considered to be compatible in one homogeneous material. Once again, organic liquid salts ("ionic liquids") have demonstrated their potential to significantly contribute to solutions for future technologies.[7,10] But perhaps it is not even necessary to establish a covalent linkage between the organic liquid salt and the nanoparticles: Recently, Antonietti and co-workers reported on a low-temperature synthesis of crystalline TiO_2 nanoparticles within ionic liquids of low viscosity.[11] Also in this case the inorganic species were well dispersed in the liquid organic salt, but without a covalent bond between the organic part and the inorganic particles. This concept and the approach of Giannelis and co-workers could be suitable general strategies in quite different areas such as batteries and solar cells: noteworthy was that the addition of certain liquid salt electrolytes significantly improved the stability of titania-based solar cells of the Grätzel-type.[9] A "vision" in this field is the use of dye-sensitized "TiO_2 liquids" to improve their processing properties and conversion rate of such solar cells.

The fabrication of "inorganic liquids" now presents a new conceptual methodology in materials chemistry: combining suitable nanoparticles and well-chosen ionic liquids opens new vistas towards a facile, rational strategy to create inorganic liquids with optimized conductive and rheological properties.

Published online: May 11, 2005

[1] *Functional Hybrid Materials* (Eds.: P. Gómez-Romero, C. Sanchez), Wiley-VCH, Weinheim, **2003**.

[2] M. A. Hickner, H. Ghassemi, Y. S. Kim, B. R. Einsla, J. E. McGrath, *Chem. Rev.* **2004**, *104*, 4587 – 4612.

[3] M. Grätzel, *Nature* **2001**, *414*, 338 – 344.

[4] R. Kaiser, G. Miskolcz, *IEEE Transactions on Magnetics MA G6* **1970**, *3*, 694.

[5] Y. S. Kim, M. A. Hickner, L. Dong, B. S. Pivovar, J. E. McGrath, *J. Membr. Sci.* **2004**, *243*, 317 – 326.

[6] W. Xu, C. A. Angell, *Science* **2003**, *302*, 422 – 425.

[7] a) *Ionic Liquids in Synthesis* (Eds.: P. Wasserscheid, T. Welton), Wiley-VCH, Weinheim, **2002**; b) P. Wasserscheid, W. Keim, *Angew. Chem.* **2000**, *112*, 3926 – 3945; *Angew. Chem. Int. Ed.* **2000**, *39*, 3772 – 3789.

[8] P. Bonhôte, A. P. Dias, N. Papageorgiou, K. Kalyanasundaram, M. Grätzel, *Inorg. Chem.* **1996**, *35*, 1168 – 1178.

[9] P. Wang, C. Klein, J. E. Moser, R. Humphry-Baker, N. L. Cevey-Ha, R. Charvet, P. Comte, S. M. Zakeeruddin, M. Grätzel, *J. Phys. Chem. B* **2004**, *108*, 17553 – 17559.

[10] a) M. Antonietti, D. B. Kuang, B. Smarsly, Z. Yong, *Angew. Chem.* **2004**, *116*, 5096 – 5100; *Angew. Chem. Int. Ed.* **2004**, *43*, 4988 – 4992; b) Y. Zhou, M. Antonietti, *J. Am. Chem. Soc.* **2003**, *125*, 14960 – 14961.

[11] a) Y. Zhou, M. Antonietti, *Chem. Mater.* **2004**, *16*, 544 – 550; b) Y. Zhou, M. Antonietti, *Adv. Mater.* **2003**, *15*, 1452 – 1455; c) B. Smarsly, D. Kuang, M. Antonietti, *Colloid Polym. Sci.* **2004**, *282*, 892 – 900; d) D. Kuang, T. Brezesinski, B. Smarsly, *J. Am. Chem. Soc.* **2004**, *126*, 10543 – 10544.

[12] A. B. Bourlinos, K. Raman, R. Herrera, Q. Zhang, L. A. Archer, E. P. Giannelis, *J. Am. Chem. Soc.* **2004**, *126*, 15359 – 15360.

[13] a) D. E. Katsoulis, *Chem. Rev.* **1998**, *98*, 359 – 387; b) *Polyoxometalates: From Platonic Solids to Anti-Retroviral Activity* (Eds A. Müller, M. T. Pope), Kluwer Academic, Dordrecht, **1994**; c) A. Müller, E. Krickemeyer, J. Meyer, H. Bögge, F. Peters, W. Plass, E. Diemann, S. Dillinger, F. Nonnenbruch, M. Randerath, C. Menke, *Angew. Chem.* **1995**, *107*, 2293 – 2295; *Angew. Chem. Int. Ed. Engl.* **1995**, *34*, 2122 – 2124.

[14] D. G. Kurth, P. Lehmann, D. Volkmer, H. Cölfen, M. J. Koop, A. Müller, A. D. Chesne, *Chem. Eur. J.* **2000**, *6*, 385 – 393.

[15] S. Polarz, B. Smarsly, M. Antonietti, *ChemPhysChem* **2001**, *2*, 457 – 461.

[16] A. B. Bourlinos, R. Herrera, N. Chalkias, D. D. Jiang, Q. Zhang, L. A. Archer, E. P. Giannelis, *Adv. Mater.* **2005**, *17*, 234 – 237.

[17] a) A. B. Bourlinos, A. Bakandritsos, V. Georgakilas, D. Petridis, *Chem. Mater.* **2002**, *14*, 3226 – 3228; b) A. K. Boal, B. L. Frankamp, O. Uzun, M. T. Tuominen, V. C. Rotello, *Chem. Mater.* **2004**, *16*, 3252 – 3256.

[18] L. P. Ramírez, K. Landfester, *Macromol. Chem. Phys.* **2003**, *204*, 22 – 31.

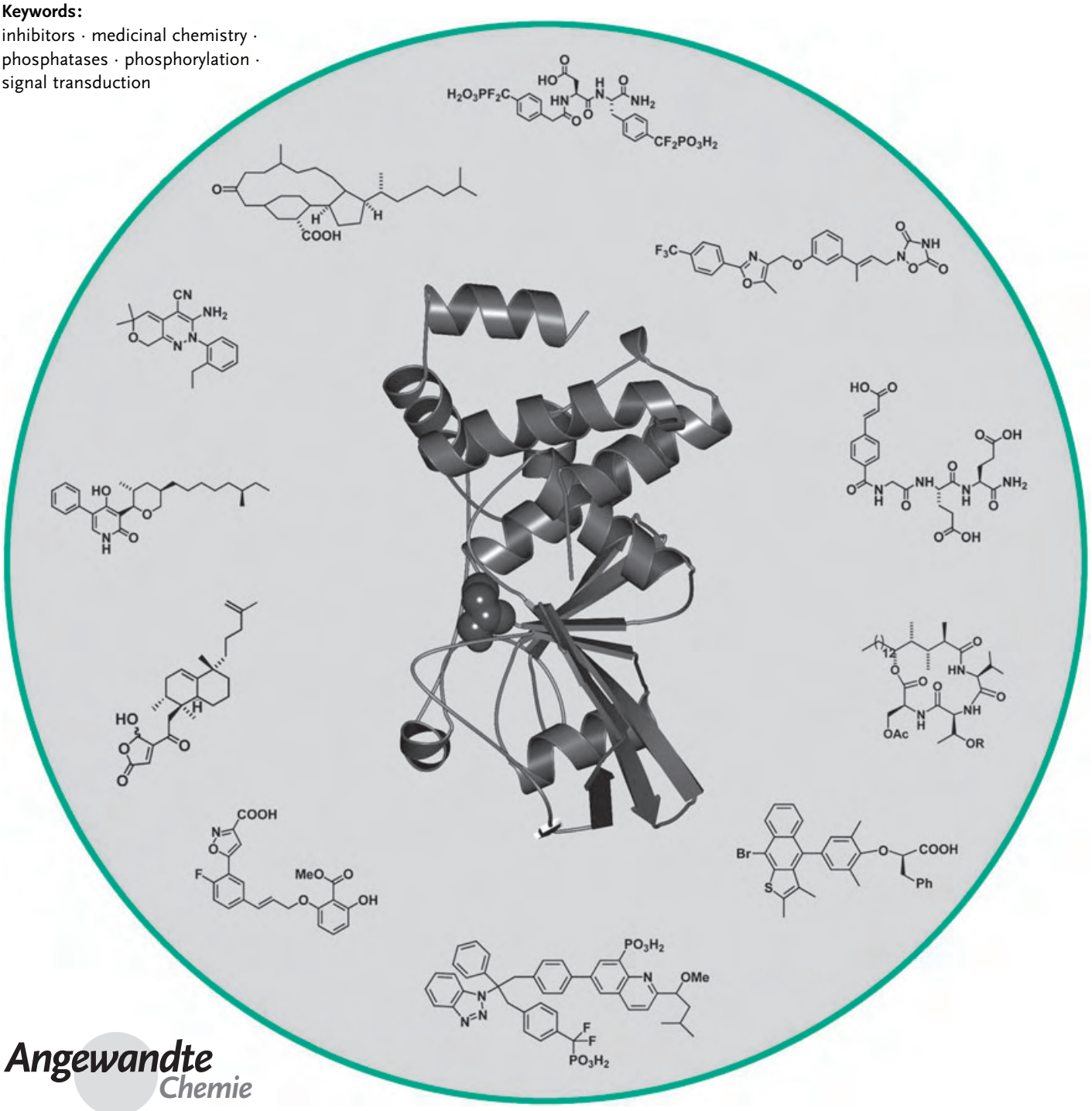
 © 2005 Wiley-VCH Verlag GmbH & Co. KGaA, Weinheim

Medicinal Chemistry

Inhibitors of Protein Tyrosine Phosphatases: Next-Generation Drugs?

*Laurent Bialy and Herbert Waldmann**

Keywords:
inhibitors · medicinal chemistry · phosphatases · phosphorylation · signal transduction



© 2005 Wiley-VCH Verlag GmbH & Co. KGaA, Weinheim
DOI: 10.1002/anie.200461517

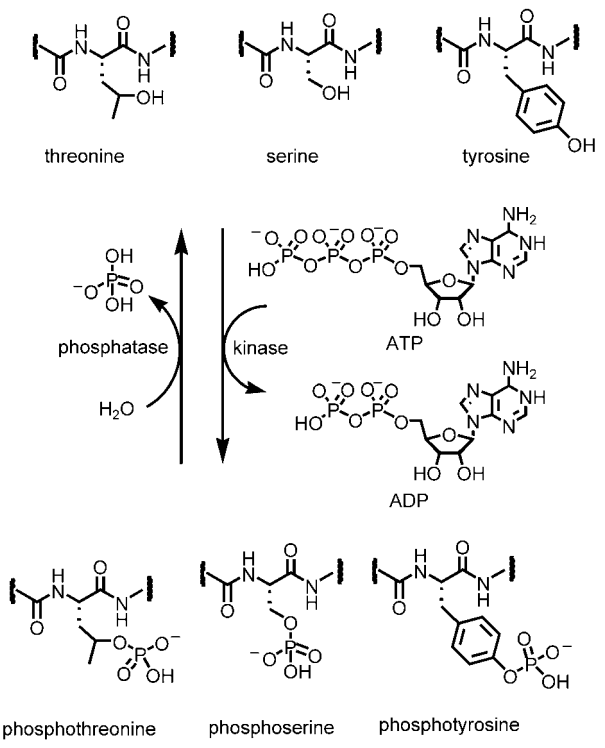
The protein tyrosine phosphatases (PTPs) constitute a family of closely related key regulatory enzymes that dephosphorylate phosphotyrosine residues in their protein substrates. Malfunctions in PTP activity are linked to various diseases, ranging from cancer to neurological disorders and diabetes. Consequently, PTPs have emerged as promising targets for therapeutic intervention in recent years. In this review, general aspects of PTPs and the development of small-molecule inhibitors of PTPs by both academic research groups and pharmaceutical companies are discussed. Different strategies have been successfully applied to identify potent and selective inhibitors. These studies constitute the basis for the future development of PTP inhibitors as drugs.

From the Contents

1. Introduction	3815
2. PTPs and Diseases	3816
3. PTPs and Dual-Specificity Phosphatases: General Classification	3816
4. Structure of the Catalytic PTP Domain and Mechanism of Enzymatic Catalysis	3817
5. Intracellular PTPs	3819
6. Receptor Protein Tyrosine Phosphatases (RPTPs)	3821
7. PTP Inhibitors	3822
8. Conclusions and Future Prospects	3835

1. Introduction

Protein phosphorylation and dephosphorylation reactions are employed by living organisms for the regulation of innumerable cellular processes; aberrancies in protein phosphorylation contribute to the development of many human diseases such as cancer and diabetes.[1] Phosphorylation states are governed by protein kinases (PKs), which catalyze protein phosphorylation, and protein phosphatases (PPs), which are responsible for dephosphorylation (Scheme 1). Given this complementary relationship and the fact that PKs are established targets for drug discovery,[2] it is surprising that the development of small-molecule inhibitors of PPs has emerged only recently as a rapidly growing area of investigation in clinical biology and medicinal chemistry. Protein phosphatases have been classified by structure and substrate specificity into protein serine/threonine phosphatases (PSTPs) and protein tyrosine phosphatases (PTPs). Among the PPs, the development of small-molecule inhibitors of PTPs[3] has attracted considerable attention in both basic research and pharmaceutical investigations.[4] This development was undoubtedly triggered by the discovery that disruption of the *ptp1b* gene in mice confers resistance to obesity and increases insulin sensitivity without negative side effects (Section 5.2).[5] Moreover, the use of antibodies to modulate the activity of CD45, the first transmembrane phosphatase discovered, has been shown to prevent rejection of organ transplants and the formation of Alzheimer plaques in animal models.[6] In this review, we discuss the recent advances in the field of PTP inhibitor discovery with a focus on phosphatases that could be among the targets of the next drug generation. The inhibition of PSTPs has been investigated intensively, mainly through research in basic chemical biology. This topic has been discussed elsewhere[7] and is therefore not a subject in this review.



Scheme 1. Phosphorylation and dephosphorylation reactions catalyzed by kinases and phosphatases.

[*] Dr. L. Bialy, Prof. Dr. H. Waldmann
Max-Planck-Institut für molekulare Physiologie
Abteilung Chemische Biologie
Otto-Hahn-Strasse 11, 44227 Dortmund (Germany)
and
Universität Dortmund
Fachbereich 3, Organische Chemie
Fax.: (+49) 231-133-2499
E-mail: herbert.waldmann@mpi-dortmund.mpg.de

 DOI: 10.1002/anie.200461517 © 2005 Wiley-VCH Verlag GmbH & Co. KGaA, Weinheim

2. PTPs and Diseases

PTPs exert key regulatory functions, and thus it does not come as a surprise that the perturbation of PTP activity has been linked to various diseases (Table 1). On the one hand, mutations which inactivate PTPs have been correlated with genetic disorders like the lafora disease[8] and the autoimmune disease, systemic lupus erythematosus (SLE).[9] On the other hand, many PTPs act as tumor suppressors[10] and are mutated or underexpressed in diverse cancers.

More interestingly, some PTPs enhance disease which indicates that their inhibition could be of immense therapeutic interest. For example, the bisphosphonate alendronate (**1**, Section 7.2, Figure 5) is a drug used to treat osteoporosis. It inhibits PTP-ε, a phosphatase that plays a significant role in the development of osteoclasts, which are responsible for bone resorption.[11] It has been proposed that the main action of alendronate comes at least partially from its inhibitory activity toward PTP (alendronate is also thought to exert its action through the inhibition of enzymes of the mevalonate pathway). Many immune diseases and allergic reactions involve the receptor phosphatase CD45.[12] In cancer, the Cdc25 phosphatases enhance cell growth by stimulation of the cell cycle. The inhibition of Cdc25 could therefore be useful as a course of anticancer therapy.[13] Another interesting target that is currently under investigation by Incyte is the dual-specificity phosphatase MKP-1, which inactivates the JNK kinase and is overexpressed in various cancers.[14] Many PTPs are major players in the field of neurological disorders. The inhibition of CD45 is especially likely to be a successful approach toward therapeutic treatments for Alzheimer's disease.[15] Many bacteria like *Salmonella typhimurium* (the typhus pathogen) and *Yersinia pestis* (the plague pathogen) use their own phosphatases (such as YopH of *Yersinia*,[16] which blocks phagocytosis by macrophages), or the host-derived phosphatases (such as RPTP-β of *Helicobacter*)[17] to infect their hosts or escape from an immune response. PTP inhibition would thus constitute a valuable strategy against infectious diseases and bioterrorism. Another area which could benefit from PTP inhibitors is in the treatment of type 2 diabetes and obesity. In this respect, the phosphatase PTP1B is a particularly promising target[5] (Section 5.2).

Table 1 shows some PTPs which play a major role in the development of disease. Some of these phosphatases constitute potential therapeutic targets. This review summarizes the efforts which have been made in the development of small-molecule phosphatase inhibitors for new therapeutic strategies. Other strategies, such as antisense (ISIS is currently developing an antisense drug against PTP1B (ISIS 113715), which has entered phase II clinical trials for the treatment of type 2 diabetes) and antibody treatments, are not discussed herein.

3. PTPs and Dual-Specificity Phosphatases: General Classification

The PTP superfamily (107 human PTP genes have been identified) is divided into four categories according to the amino acid sequence of PTP catalytic domains (Figure 1).[46] The first category is made up of the type I cysteine-based PTPs, which share a characteristic motif of ≈250 residues. This highly conserved "PTP-domain" catalyzes the enzymatic reaction in which an active-site cysteine group plays a central role (Section 4). The classical PTPs (nonreceptor and receptor PTPs) that are specific for phosphotyrosine substrates are members of this class. Some receptor PTPs contain two PTP domains, although usually only one is active. The dual-specificity phosphatases (DSP) also belong to this first group of PTPs, but in contrast to the classical PTPs they catalyze the dephosphorylation of both tyrosine and serine/threonine residues of their protein substrates. The DSP family contains special types of tyrosine phosphatases, which are mentioned only briefly in this review; these include members of the myotubularin (MTM) family,[47b] the C-terminally prenylated PRL-type phosphatases,[47c] RNA triphosphatases,[47d] and PTEN-type phosphatases,[47e] which accept inositol phosphates as substrates.

The second PTP group is the class II cysteine-based PTPs. This type of phosphatase is especially common in bacteria, whereas only one gene (*lmptp*) has been found in humans. Class II PTPs are not discussed in this review.[47a]

Although they are also able to catalyze the dephosphorylation of both tyrosine and serine/threonine substrates, the



Herbert Waldmann, born in 1957, received his PhD in 1985 with Horst Kunz at the University of Mainz. After postdoctoral studies at Harvard University with George Whitesides and a lectureship at the University of Mainz, he accepted a professorship at the University of Bonn in 1991. In 1993 he moved to the University of Karlsruhe as full professor of organic chemistry. In 1999 he was appointed as Director at the Max Planck Institute of Molecular Physiology in Dortmund (Department of Chemical Biology) and as full professor of biochemistry at the University of Dortmund. His honors include the Friedrich Weygand Award, the Carl Duisberg Award, the Otto Bayer Award, the Steinhofer Award, and the Max Bergmann Medal.



Laurent Bialy, born in 1974 in Karlsruhe, studied chemistry between 1992 and 1998 in Karlsruhe. He finished his PhD in 2002 at the Max Planck Institute for Molecular Physiology and the University of Dortmund on the synthesis and biological evaluation of the phosphatase inhibitor cytostatin and its analogues. As a postdoc with Mark Bradley at the University of Southampton, he investigated applications of PNA–peptide conjugates and microarray technology to the field of combinatorial chemistry. He is the laureate of the International DSM Award, the Prize of the Chemical Society of Karlsruhe, and the Klaus Grohe Award for medicinal chemistry.

 © 2005 Wiley-VCH Verlag GmbH & Co. KGaA, Weinheim

Table 1: Protein tyrosine phosphatases linked to various diseases.

Disease Class	PTPs Involved	Physiological Effect(s)
immune diseases, organ transplantation, inflammation	SHP-1	mutation causes moth-eaten phenotype;[18][a] negative regulator of allergic responses[19]
	CD45	inhibitors as potential drugs against xenograft rejection[6]
	PTP-ε	immune response[20]
cancer	PTEN[a]	tumor-suppressor gene[21]
	PTP-α	activates kinases Src/Fyn[22]
	Cdc25A, Cdc25B	stimulate cell cycle progression; oncogenic roles[13]
	FAP-1[a]	apoptosis induction[23]
	HePTP[a]	regulates ERK; changes in expression linked to hematopoietic malignancies[24]
	PRL-3	tumor metastasis[25]
	PTP1B	dephosphorylates and activates c-Src in human breast cancer cell lines[26]
	JSP-1	activates the MAPK JNK[27]
	SAP-1[a]	negatively regulates integrin signaling; downregulated in hepatocellular carcinoma[28]
	RPTP-β/PTP-ζ[a]	highly expressed in a glioblastoma cell line[29]
	SHP-2[a]	mutation causes juvenile myelomonocytic leukemia[30]
	SHP-1[a]	tumor suppressor by degradation of JAK kinases[31]
	PTP-χ[a]	frequently deleted in renal and lung cancers[32]
	CD45	correlates with proliferation rate of myeloma cells[33]
	PacP (prostatic acid phosphatase)[a]	decreased activity in prostate cancer cell lines[34]
	MKP-1	overexpressed in cancers[14]
neurological diseases and neuroprotection	Laforin[a]	mutation causes lafora progressive myoclonus epilepsy[8]
	LAR	downregulation prevents apoptosis, inhibition could be useful for nerve regeneration[35]
	PTP-σ	nerve regeneration is faster in PTP-σ knock-out mice[36]
	CD45	Alzheimer's disease[15]
	SHP-1	neuroprotection[37,38]
	SHP-2[a]	neuroprotection[39]
infectious diseases	*Yersinia* YopH	essential for virulence[16]
	Salmonella SptP	essential for virulence[16]
	SHP-1	leishmaniasis[40]
	SHP-2	activated by *Helicobacter pylori*[41]
	MPtpA, MPtpB	*Mycobacterium tuberculosis*[42]
	RPTP-α, RPTP-β/PTP-ζ	target of VacA from *Helicobacter pylori*[17]
diabetes	PTP1B	PTP1B knockout mice are resistant to diabetes[5]
	LAR	overexpression causes insulin resistance[43]
osteoporosis	PTP-ε	alendronate = inhibitor[11]
	GLEPP-1	renal receptor-like PTP, inactivation results in altered podocyte structure[44]
obesity	PTP1B	PTP1B knockout mice are resistant to obesity[5]
	SHP-2	negatively regulates leptin signaling which is important in obesity[45]

[a] Disease caused by inactive phosphatase; inhibition would therefore be counterproductive in these cases.

Cdc25 phosphatases form the third category of cysteine-based PTPs as class III enzymes. They are involved primarily in cell-cycle progression. Phosphatases based on aspartate instead of cysteine as a key catalytic residue form class IV of the PTPs; members of the haloacid dehalogenase (HAD) superfamily[47f] belong to this group, and are treated only briefly in this review.

PTPs are crucial for the regulation of cellular processes and therefore it is not surprising that PTPs themselves are highly regulated enzymes. Regulation mechanisms include gene expression, subcellular localization, alternative splicing, phosphorylation, and even reversible oxidation of the catalytic cysteine residue.[48]

4. Structure of the Catalytic PTP Domain and Mechanism of Enzymatic Catalysis[46]

The crystallographic structures of more than 20 PTPs have been solved and, together with mutagenesis experiments, have strongly contributed to our understanding of catalysis and substrate recognition.[49] PTPs are α/β proteins composed of β barrels flanked by α helices. The catalytic site is located in a groove at the protein surface which is deeper for classical PTPs (9 Å) than for DSPs (6 Å), a difference which explains the higher substrate selectivity of the classical PTPs. The characteristic motif $(H/V)C(X)_5R(S/T)$ and a

 © 2005 Wiley-VCH Verlag GmbH & Co. KGaA, Weinheim

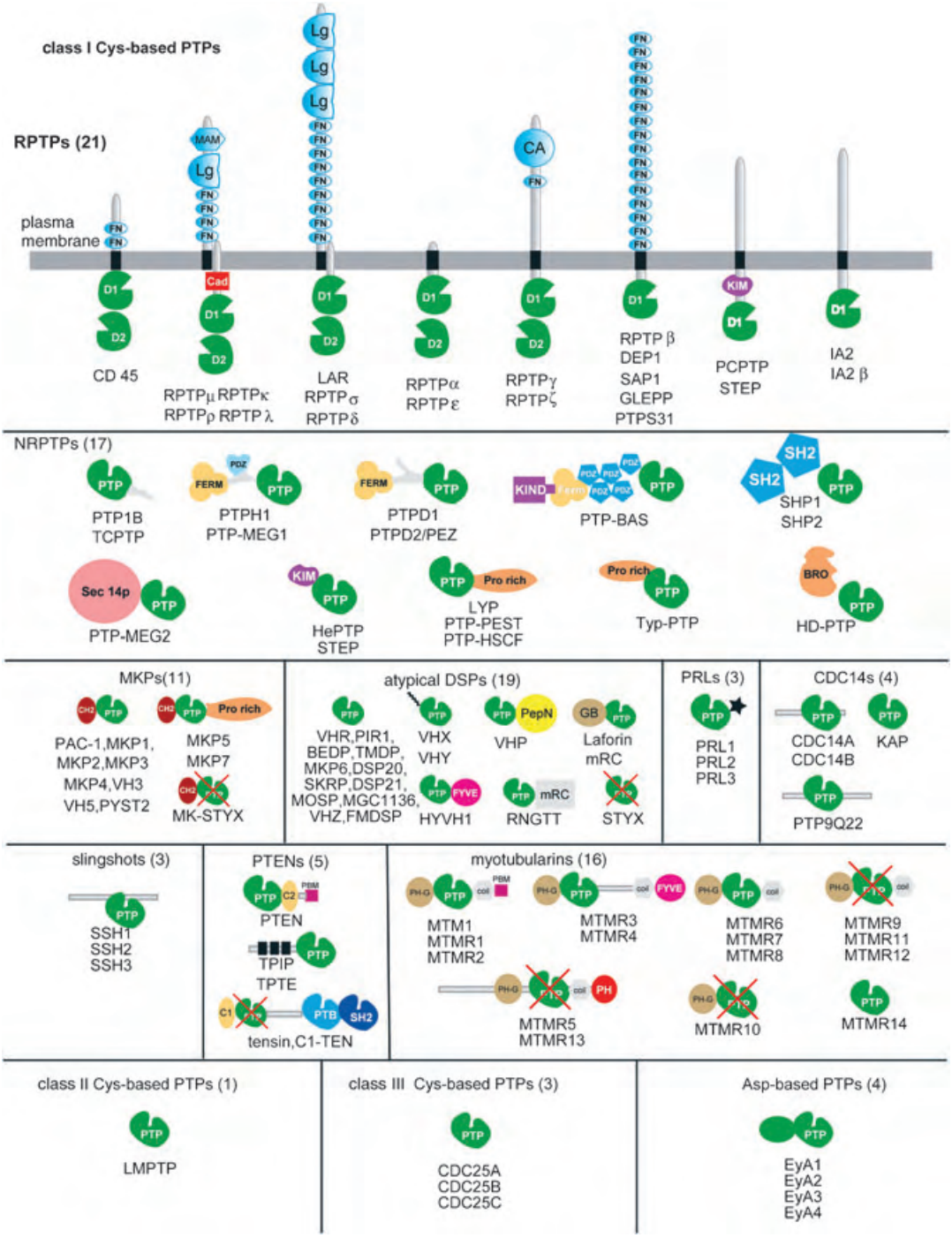


Figure 1. The PTPs are classified according to their overall composition and cellular localization (from Ref. [46b] with permission).

surface loop rich in acidic residues are further elements common to the PTP domain (Figure 2).[50]

The general mechanism is explained herein for PTP1B,[51] a phosphatase important in the insulin cascade (Section 5.2), whose mechanism is likely reflective of that for most PTPs.[46] The negatively charged phosphate substrate is stabilized by hydrogen bonds to residues of the phosphate-binding loop (P loop) and a highly conserved arginine group (Arg 221 of PTP1B; Figure 2). Furthermore, a nearby α-helix dipole stabilizes the phosphate. Upon substrate binding, the enzyme undergoes a conformational change that brings the WPD loop over the substrate-binding pocket and generates further stabilizing interactions, which are essential for substrate selectivity and catalytic activity. In the closed state, Asp 181 is positioned near the substrate and forms a hydrogen bond with the phenolic oxygen atom of phosphotyrosine. Furthermore, the phenyl ring of phosphotyrosine is sandwiched by and forms hydrophobic interactions with Tyr 46 and Phe 182.

 © 2005 Wiley-VCH Verlag GmbH & Co. KGaA, Weinheim

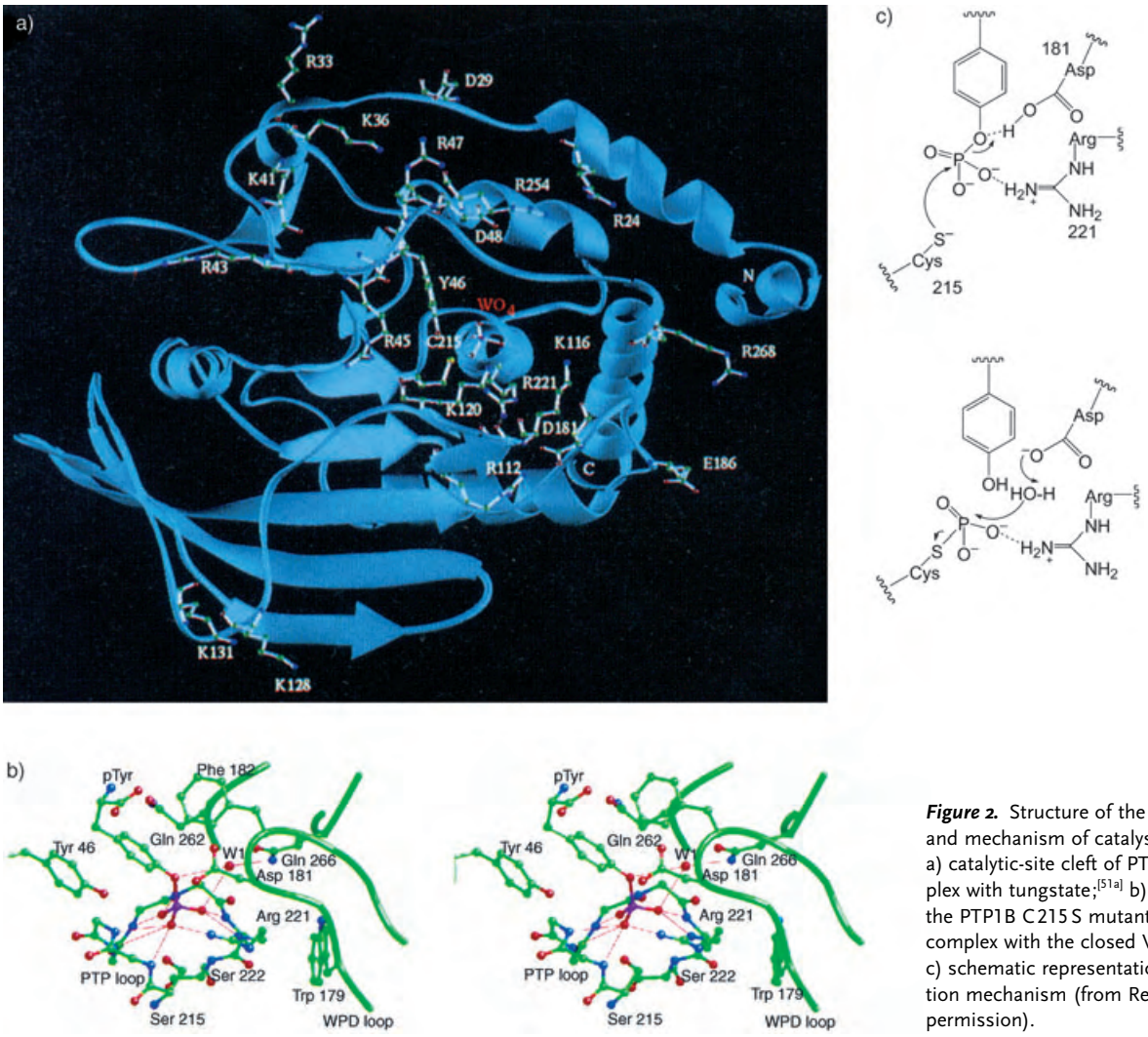


Figure 2. Structure of the catalytic site and mechanism of catalysis by PTP1B: a) catalytic-site cleft of PTP1B in complex with tungstate;[51a] b) stereo view of the PTP1B C215S mutant Tyr(P) in complex with the closed WPD loop;[51b] c) schematic representation of the reaction mechanism (from Ref. [51] with permission).

The central step of catalysis is a nucleophilic attack by a deprotonated cysteine residue (Cys215), which results in the formation of a covalent thiophosphoryl intermediate.[52] Mutational analysis has shown that substitution of the active-site cysteine totally abolishes enzymatic activity.[53] The active-site cysteine is particularly acidic in PTPs, as the thiolate anion is stabilized by several hydrogen bonds, one of which is formed with the proximal OH group of a conserved Ser/Thr moiety.[54] The geometry of the pentacoordinate intermediate is stabilized by ionic interactions with the positively charged Arg221.[55] The acidic Asp181 stabilizes the formation of a negative charge by protonation.[56] In a second step, the intermediate is attacked by a water molecule that is deprotonated by Asp181 (at this point in its basic form), thereby releasing the cysteine and regenerating the enzyme after dissociation of the product.[57] The conserved Ser/Thr group found proximal to the conserved Arg residue (Arg221) in the catalytic loop facilitates the hydrolysis of the enzyme-phosphoryl adduct, possibly through hydrogen-bond stabilization of a negative charge on the sulfur atom in the hydrolysis step of the phosphoryl-enzyme intermediate.[58]

5. Intracellular PTPs

5.1. SHP1 and SHP2

In addition to the PTP domain, the SHP phosphatases have a phosphotyrosine binding SH2 (SH2 = Src homology 2) domain of ≈100 amino acid residues, which is also present in many other signaling proteins.[59] SHP1 is mainly expressed in hematopoietic cells and exerts negative regulatory functions in signaling pathways of cytokine receptors, antigen receptors, and receptor tyrosine kinases.[60] SHP1 interacts with numerous growth factor receptors that have tyrosine kinase activity (such as the EGF receptor)[61] and cytokine receptors (like IL-R[62] and Epo-R[63]).[60] Dysfunction of SHP1 in lymphocytes has been correlated with cancers like lymphoma and leukemia;[64] SHP1 acts as tumor suppressor.[31] In contrast, SHP2 is ubiquitously expressed and exerts positive functions in receptor tyrosine kinase signaling.[65] It interacts with many signaling proteins through its SH2 domain, like the PDGF receptor,[66] the EGF receptor,[67] and IRS-1[68]. Both proteins contain two SH2 domains, of which the N-terminal domain

 © 2005 Wiley-VCH Verlag GmbH & Co. KGaA, Weinheim

binds to the catalytic PTP domain, thereby acting in an autoinhibitory manner.[69] For example, binding of Epo-R to the N-terminal SH2 domain of SHP1 releases the catalytic PTP domain, thereby activating SHP1.[70] SHP1 and SHP2 could be valuable targets for the treatment of infectious diseases, as sodium stibogluconate, a known agent against leishmaniasis, has been found to inhibit SHP1 and SHP2.[40] SHP2 is involved in many biological pathways and has been correlated with clinical diseases such as the Noonan syndrome,[71] neutropenia,[72] diabetes,[73] and juvenile myelomonocytic leukemia.[30]

5.2. PTP1B

PTP1B was the first mammalian PTP to be purified and characterized.[74] In addition to the PTP catalytic domain, it contains a proline-rich sequence and an anchor domain which localizes the enzyme to the endoplasmic reticulum (ER). Following enzymatic cleavage from the anchor domain, the phosphatase can diffuse to its cytosolic substrates. PTP1B plays a key role in the insulin-dependent signaling cascade (Figure 3) and has attracted considerable attention as a possible target for the treatment of type 2 diabetes.

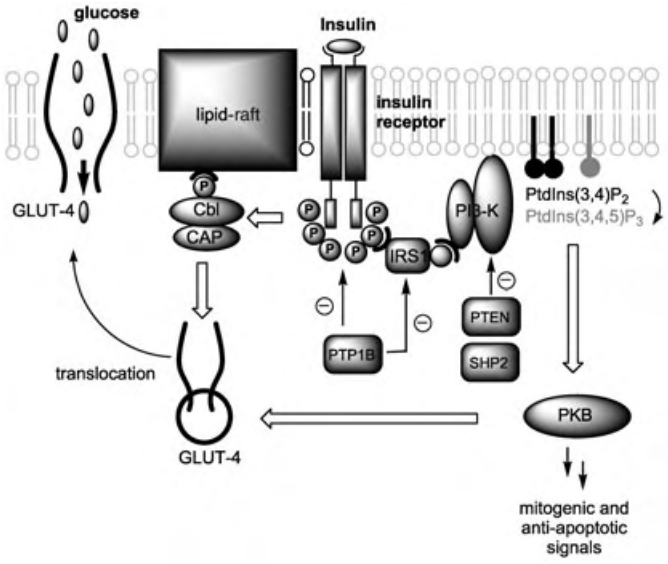


Figure 3. Schematic illustration of insulin-dependent signaling and relevant interactions with PTP1B; other phosphatases such as PTEN and SHP-2 have also been reported to exert functions in this pathway (adapted from Ref. [4] with permission).

Insulin is an anabolic peptide hormone which is secreted by the pancreatic β cells. It binds to the extracellular (α) domains of the dimeric insulin receptor (IR), which belongs to the family of receptor tyrosine kinases. Upon binding insulin, the IR undergoes autophosphorylation at tyrosine residues in the cytosolic (β) domains in a manner similar to other receptor tyrosine kinases.[75] In its phosphorylated state, the IR recruits and phosphorylates additional cytosolic molecules like the insulin receptor substrate 1, IRS-1. Phosphorylated IRS-1 is recognized by other SH2 domain-containing proteins, particularly the phosphatidylinositol 3 kinase (PI-3-K), which itself phosphorylates further substrates. By means of this cascade, insulin triggers numerous biological processes such as glycogen synthesis, fatty acid synthesis, protein synthesis and mitotic processes.[76] Of central importance is the translocation of the glucose transporter GLUT-4 from intracellular vesicles to the cell membrane which enables the cellular uptake of glucose from plasma.[77]

Type 2 diabetes, which accounts for 95% of all diabetes cases, is characterized by a deficient insulin cascade and is therefore also termed insulin resistance. PTP1B works as an insulin antagonist through the dephosphorylation and inactivation of the IR at Tyr 1150 and Tyr 1151. This has been shown by substrate trapping with an inactive C215S mutant[78] and kinetic as well as crystallographic data.[79] There are presumably additional substrates of PTP1B, with IRS-1 as a possible example.[80] The insulin antagonizing activity of PTP1B has been confirmed by many experiments. The most spectacular results were obtained from PTP1B knockout mice, in which the *ptp1b* gene has been deactivated.[5] PTP1B is not needed for embryonic development, so the mutation is not lethal. The animals showed hypersensitivity to insulin and resistance to obesity. No negative side effects of the mutation could be detected. These results have triggered intense efforts in pharmaceutical companies to identify PTP1B inhibitors as potential drugs against diabetes or obesity.[4]

In addition to its central role in the insulin cascade, PTP1B is involved in other important pathways. Of particular significance is its overexpression in human breast and ovarian cancers.[81] PTP1B dephosphorylates and thereby activates the kinase c-Src in human cancer cell lines.[26] Besides these activation functions, PTP1B also has negative-regulatory functions, for example in EGF receptor signaling[82] and integrin-mediated cell adhesion.[83] In light of these multiple functions, it comes as a surprise that PTP1B knockout mice do not show serious side effects.

5.3. Dual-Specificity Phosphatases[48]

DSPs contain the conserved active-site motif of the PTPs, $(H/V)C(X)_5R(S/T)$, but otherwise share little primary sequence identity. They accept a broader range of substrates and display catalytic activity against phosphotyrosine, phosphoserine, phosphothreonine, and even nonprotein substrates like phospholipids and RNA in vitro. The prototype of this family is VH-1, an enzyme identified in the *Vaccinia* virus.[84]

5.3.1. VHR

VHR is a human dual-specificity phosphatase.[85] It dephosphorylates and inactivates the extracellular regulated kinases (ERKs; members of the MAP kinase family).[86] The crystallographic structure of VHR has been disclosed and shows that the substrate-binding pocket is shallower than that

 © 2005 Wiley-VCH Verlag GmbH & Co. KGaA, Weinheim

of PTP1B.[87] This difference could explain why DSPs can accommodate not only phosphotyrosine but also phosphoserine and phosphothreonine. Other members of the DSP family have been identified and show additional binding domains, like the Cdc25 homology (CH) domains which play an essential role in substrate binding and recognition. DSPs are found in the cytosol and in the nucleus and their expression is tissue-dependent.

The main role of VHR seems to be the dephosphorylation and inactivation of the MAP kinases in the activation loop TXY (in which both T and Y must be phosphorylated for enzymatic activity), which plays an essential role in signal transduction cascades.[48] Interestingly, different DSPs show a surprisingly high selectivity in the recognition of their substrates and contribute to the correct spatial and temporal regulation of MAP kinases.[48]

5.3.2. Cdc25 Phosphatases

This enzyme family is classified separately from the DSP family because they are different from other DSPs on the primary and tertiary structure levels. The Cdc25 phosphatases are present as three homologs in humans: A, B, and C.[88] They have attracted particular attention as regulators of the cell cycle, as they dephosphorylate the cyclin-dependent kinases.[89] Cdc25B has attracted considerable interest, as its overexpression has been correlated to the malignancy of tumors.[13] Thus, selective inhibitors of Cdc25B could be interesting candidates for anticancer drug development. Cdc25B activates the Cdc2–cyclin B complex in the cytoplasm (prior to its translocation to the nucleus) by dephosphorylating Cdc2 at Tyr 15, which is placed in close proximity to the ATP binding site of the enzyme.[90] The Cdc2–cyclin B complex phosphorylates and activates Cdc25C, which in turn dephosphorylates and activates nuclear Cdc2–cyclin B. The ensuing positive feedback mechanism triggers the transition from G2- to M-phase.[91]

The Cdc25A phosphatase is expressed in early G_1-phase and is responsible for the $G_1 \rightarrow S$ transition.[92] It is necessary for the activation of the cyclin E–Cdk2 complex, and is itself phosphorylated by this complex in a positive feedback loop similar to that described above for Cdc25C (for a more detailed discussion, see Ref. [93]). The inappropriate activation and/or amplification of Cdc25A and Cdc25B have been suggested to play an important role in various human cancers.[13] Several crystal structures have been published for the catalytic domains of Cdc25A and Cdc25B.[94]

5.4. Other Phosphatases

Other phosphatases have been described which exert quite diverse functions. Some of them accept phospholipids as substrates, like the phosphatase PTEN (a tumor suppressor) and myotubularin (MTM), which dephosphorylate specific inositol phosphates.[95] Members of the MTM family have been associated with human muscular and neurodegenerative diseases.[96] Another class of DSPs is formed by the enzymes Mce1 and BVP, which dephosphorylate RNA triphosphates.[97] Members of the haloacid dehalogenase (HAD) superfamily define a further protein tyrosine phosphatase class that is unrelated to the family of "classical" PTPs. It was shown recently that the nuclear transcription factor "Eyes absent", a HAD superfamily member, is a tyrosine phosphatase that hydrolyzes its substrates with a nucleophilic aspartic acid residue instead of a cysteine group, used by classical PTPs.[98] Another phosphatase type is exemplified by the prenylated enzyme PRL-3, which is overexpressed in metastatic tumors and might be an interesting therapeutic target for anticancer therapy.[25]

6. Receptor Protein Tyrosine Phosphatases (RPTPs)

Receptor PTPs contain an extracellular domain that consists of several structural motifs (immunoglobulin-like, fibronectin type, etc.), which are also found in other cell-adhesion molecules. This suggests a role for these PTPs in mediating cell–cell and cell–matrix interactions. Besides a single transmembrane domain, they contain intracellular domains, which are formed by one or two PTP domains (usually only one is catalytically active) and other noncatalytic domains involved in the regulation or subcellular localization of the enzymes. By structural and evolutionary analysis the RPTPs have been classified into eight distinct subfamilies, whereas the NRPTPs (nonreceptor PTPs) have been classified into nine subtypes[99] (Figure 1). Interestingly, there is a strong relationship between PTP domain sequence similarity and overall structural composition of the full-length proteins.[100]

The exact roles of the RPTPs have yet to be elucidated, and herein we discuss only some general features of this type of PTP, with particular emphasis on CD45, the first and best-characterized transmembrane phosphatase. It is present in hematopoietic cells and is essential for antigen receptor signaling in T cells and B cells.[12] CD45 is expressed in various isoforms that differ in their extracellular domains as a result of alternative exon splicing in the N-terminal region.[12] The variable, N-terminal extracellular domain consists of ≈ 200 amino acid residues and is heavily glycosylated. Therefore significant differences are present in the glycosylation patterns between different isoforms. The N-terminal region is followed by a cysteine-rich region, three fibronectin type 3 repeats, and a single transmembrane region (Figure 4). On the cytoplasmic side, the phosphatase is composed of two phosphatase subunits (D1 and D2). However, only the membrane-proximal domain D1 is responsible for phosphatase activity, whereas D2 is involved in protein–protein interactions and proper phosphatase folding. Expression of the different CD45 isoforms is cell-type specific and is also dependent on the state of differentiation of hematopoietic cells.[12]

Some extracellular ligands of RPTPs have been identified, such as the secreted protein galectin-1 (for CD45), which may have an inhibitory effect toward the phosphatase activity of CD45,[101] an extracellular matrix complex between laminin and nidogen (for LAR),[102] and the growth factor pleiotrophin, which appears to bind and inhibit PTP-ζ.[29]

 © 2005 Wiley-VCH Verlag GmbH & Co. KGaA, Weinheim

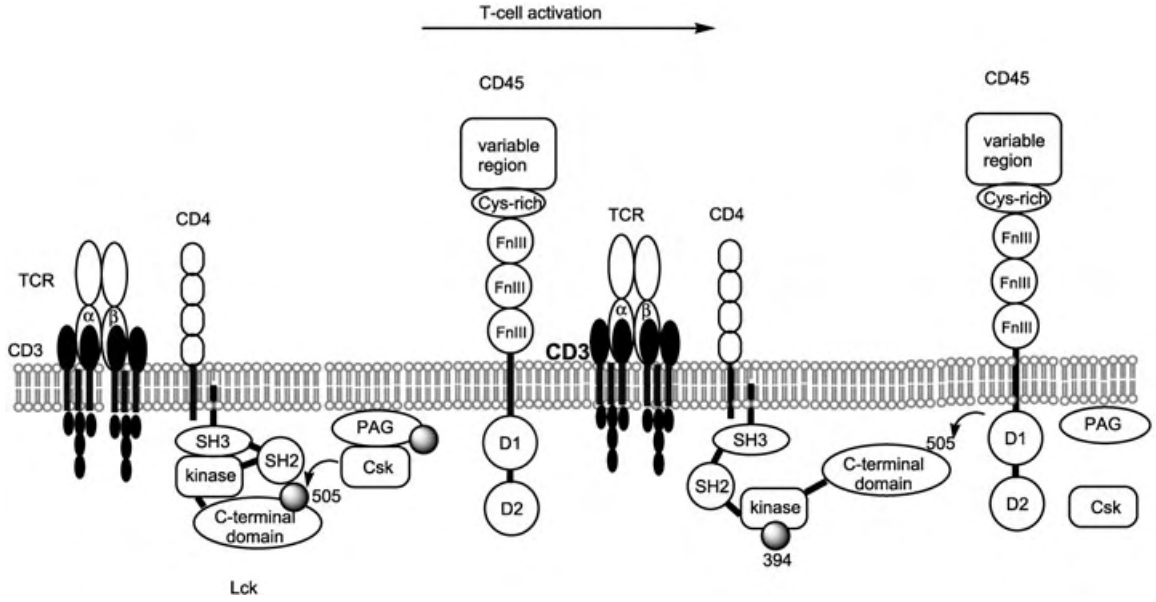


Figure 4. The role of CD45 in T-cell signaling.

RPTPs also seem to form homodimeric and heterodimeric complexes.[103] Importantly, the dimerization of RPTPs regulates their catalytic activity, which is reminiscent of the activation of receptor protein tyrosine kinases (RPTKs) by dimerization.[104] For example, it has been shown that for CD45, dimerization results in the inhibition of catalytic activity. The inhibitory wedge structure of one D1 domain (the membrane-proximal, catalytically active PTP domain) binds and inhibits the D1 domain of the second phosphatase.[105] Heterodimerization of RPTPs could play an important role in the cross-talk between different RPTP-mediated pathways.

In recent years, an increasing number of intracellular RPTP substrates have been identified, thus elucidating their physiological function. The first substrate type consists of the PTKs. For example, CD45 is critically involved in the activation of T cells. CD4 facilitates T-cell receptor (TCR) association with the kinase Lck (a Src-type kinase). By activating Lck through the dephosphorylation of an inhibitory residue (Tyr 505), CD45 plays a determining role in T-cell signaling (Figure 4). In the inactive form, Tyr 505 is kept in a phosphorylated state by the kinase Csk, which is associated through its SH2 domain with the transmembrane phosphoprotein, PAG (phosphoprotein associated with glycosphingolipid-enriched microdomains).[106] Upon cell activation, PAG is dephosphorylated and Csk is released into the cytosol, where it can no longer maintain the phosphorylated state of Lck Tyr 505. CD45 can associate with the SH2 domain and the N-terminal region of Lck. Upon dephosphorylation by CD45, Tyr 505 no longer binds to an intramolecular SH2 domain, causing a major conformational change in Lck. The accessible SH2 domain is free to bind substrate phosphoproteins. Moreover, the conformational change allows auto- and transphosphorylation of Lck Tyr 394, which displaces the activation loop and creates a more accessible catalytic cleft.[12] Interestingly, CD45 also has a negative function and dephosphorylates the same Tyr 394 residue, thus terminating Lck activity.[12]

CD45 has similar stimulatory activity toward other Src kinases, such as Lyn in B cells.[107] Besides these stimulatory activities, RPTPs can inhibit kinases such as Janus kinases,[12,108] and LAR through insulin receptor signaling.[109] RPTPs appear to be involved in various processes such as cell adhesion,[103] neuronal development,[110] and ion channel-mediated processes.[111] CD45 has gathered particular attention as its inhibition by antibodies blocks T-cell activation in vitro[112] and graft rejection in mice.[113] Thus, selective inhibitors of CD45 could find applications in the treatment of autoimmune disease and the treatment of transplant rejection. Decreased CD45 expression and/or activity has been discovered in SLE patients.[9] A point mutation in the CD45 gene (*ptprc*) has been associated with autoimmune diseases like multiple sclerosis[113] and autoimmune hepatitis.[114] Moreover, the modulation of CD45 activity by antibodies inhibits the formation of Alzheimer plaques.[15] The negative regulation of cytokine receptor signaling by CD45 could explain the loss of CD45 activity that has been observed in several cancers, such as leukemia.[115] CD45 has been correlated with the proliferation of myeloma cells and could therefore be a potential therapeutic target for the treatment of multiple myelomas.[33]

7. PTP Inhibitors

Below, we discuss the development of PTP inhibitors, which are classified according to type. Only those inhibitors were chosen that exhibit cellular activity which is not necessarily linked to phosphatase inhibition in vitro.

 © 2005 Wiley-VCH Verlag GmbH & Co. KGaA, Weinheim

7.1. Unspecific and Inorganic PTP Inhibitors

Vanadate-based compounds have been used as unspecific phosphatase inhibitors. They work by mimicking the phosphate group of the natural enzyme substrate. They have been shown to work as insulin mimetics and also exhibit antimetastatic activity.[116] Other mainly inorganic compounds, like nitric oxide and phenyl arsine oxide, are thought to exert their pharmacological effects by phosphatase inhibition,[117] although other enzymes are likely to be targets for these compounds as well; this severely limits their therapeutic usefulness.

7.2. Natural Products and Derivatives as PTP Inhibitors

Natural products have been a rich source of PTP inhibitors and a good starting point for the development of synthetic analogues. 4-Isoavenaciolide (**2**, Figure 5) was isolated from a fungal strain and identified as an irreversible inhibitor of VHR with an IC_{50} of 1.2 μM.[118] Some other phosphatases like Cdc25B, Laforin, and PTP1B were inhibited with similar potency, whereas CD45 and serine/threonine phosphatases like PP2A and PP1 were not inhibited. An investigation into the mechanism of inhibition showed that two inhibitor molecules covalently bind to two of the four cysteine residues of VHR, namely Cys124 in the active-site and Cys171 on the protein surface. The results were rationalized by the proposal of a hydrophobic cleft near the cysteine residue that is required for efficient binding.

The alkaloid nornuciferine (**3**) inhibits CD45 with an IC_{50} value of 5.3 μM. T-cell receptor-dependent production of IL-2 was inhibited, whereas other phosphatases like calcineurin (PP2B), alkaline phosphatase, and acid phosphatase were not inhibited.[119] Nornuciferine was also shown to be active against leishmaniasis.[120] and is thought to be the antidepressive component in the fruit of *Annona muricata*.[121] The total syntheses of nornuciferine and other natural products of this class have been described.[122]

The stevastelins (e.g. **4a–c**), an interesting class of depsipeptides, have been isolated as immunosuppressive agents from *Penicillium* spp. and inhibit T-cell proliferation.[123] It has been shown that these natural products act through inhibition of the dual-specificity phosphatase VHR and thus cell-cycle progression. A structure–activity relationship of this natural product class was established through the evaluation of a small subset of analogues. It was shown that the long alkyl side chain and the free hydroxy group of the threonine residue (type A stevastelins; **4c**) are required for activity against Jurkat cells. Derivatization of the hydroxy group either by sulfatation (**4a**) or phosphorylation (**4b**) abolished the in-vivo inhibitory activity of the compounds against Il-2 and Il-6-dependent gene expression in Jurkat cells. In contrast, the sulfated compounds (type A) showed good in-vitro inhibitory activity against VHR in the micromolar range, but not against the PTP CD45 and the PSTPs PP2A and PP2B. The desulfated compounds showed a decrease in PTP inhibition by one order of magnitude. These findings were rationalized by suggesting that the compounds may be threonine-phosphorylated or sulfated by cellular enzymes after cellular uptake of the uncharged (type B) compounds. The stevastelins constitute a novel, calcineurin-independent class of immunosuppressive agents and have therefore been the targets of several total syntheses.[124]

The tetronic acid derivative RK-682 (**5a**) was isolated from a *Streptomyces* strain and identified as a competitive inhibitor of the DSP VHR and CD45. It arrests the cell-cycle progression of mammalian cells in the G_1 phase.[125] The synthesis of derivatives and a subsequently derived structure–activity relationship revealed that the highly acidic 3-acyltetronic acid moiety functions as a phosphate mimic. [126] The hydrophobic side chain at C3 and the enolic hydroxy group at C4 were found to be important for VHR inhibition, whereas removal of the hydroxy group from the C5 arm did not interfere with inhibition. None of the compounds showed any activity against the PSTPs PP1, PP2A, or PP2C. Some derivatives showed inhibition of Cdc25B at the submicromo-

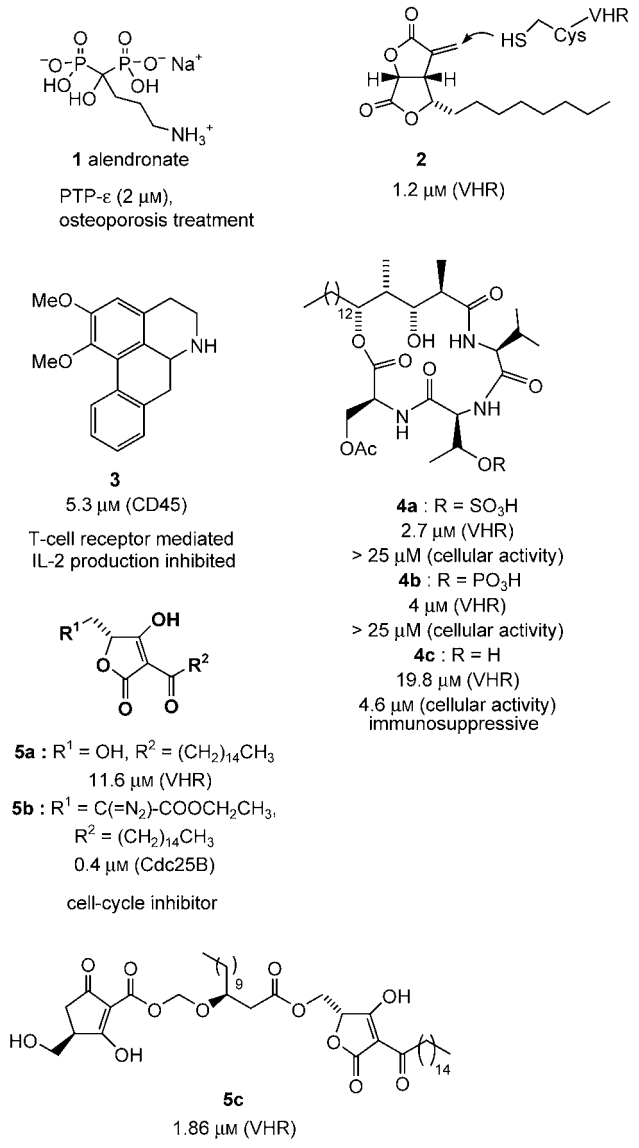


Figure 5. Natural-product-derived PTP inhibitors; the IC_{50} values are shown for all compounds unless mentioned otherwise.

 © 2005 Wiley-VCH Verlag GmbH & Co. KGaA, Weinheim

lar level and inhibition of VHR in the micromolar range. Interestingly, **5b** exhibited some selectivity toward Cdc25B ($IC_{50} = 0.4\ \mu M$) over VHR ($IC_{50} = 12.4\ \mu M$) and PTP-S2 ($IC_{50} > 100\ \mu M$), whereas the natural product **5a** showed the opposite trend in selectivity ($IC_{50} = 11.6\ \mu M$ (VHR) and $> 100\ \mu M$ (Cdc25B)).[127] This example clearly demonstrates how selectivity toward related enzymes can be tuned within a natural product library. Molecular modeling, the crystallographic structure of VHR, and a detailed kinetic analysis were used to propose a model in which the acyltetronic acid anion is a phosphate mimic with multiple hydrogen bonds to the active-site loop (Cys124–R130). A second molecule of tetronic acid is involved in the inhibition and interacts with Arg158.[128] Both C_3 alkyl side chains interact with the hydrophobic groove of the enzyme (Figure 6). Based on this

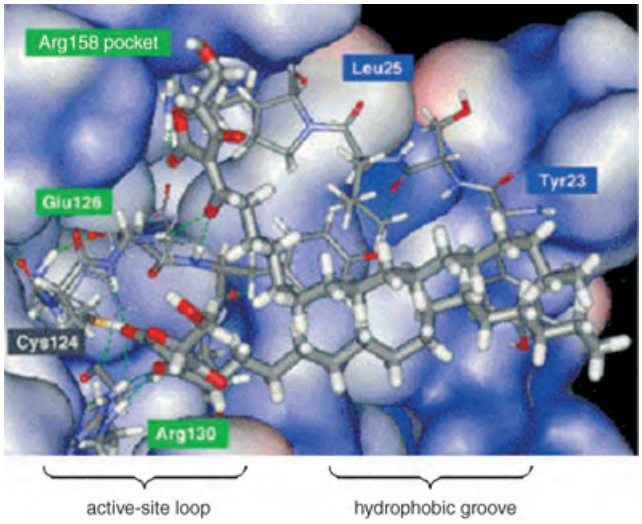


Figure 6. Binding of two molecules of **5a** to VHR (from Ref. [128] with permission).

model, a dimeric inhibitor **5c** was designed. This compound showed increased potency against VHR in comparison with the natural product ($IC_{50} = 1.83\ \mu M$). Interestingly, the arginine group (Arg158) involved in binding the second tetronic acid moiety is in a sequence region that is less conserved among various phosphatases. Therefore, this new type of dimeric inhibitor might constitute an excellent starting point for the generation of new, highly selective protein phosphatase inhibitors.

Another highly interesting natural product, dysidiolide (see the 6-epimer **6**), was isolated 1996 from the marine sponge *Dysidea etheria* (Figure 7).[129] Dysidiolide is a sesterterpene with a γ-hydroxybutenolide group and was identified as an inhibitor of Cdc25A ($IC_{50} = 9.4\ \mu M$). Other phosphatases like calcineurin, CD45, and LAR were not inhibited at this concentration. Moreover, dysidiolide inhibited growth of A-459 lung carcinoma cells and P388 murine leukemia cells at micromolar concentrations. However, whether dysidiolide works as a phosphatase inhibitor subsequently came into question. It was concluded that the inhibitory activity of isolated samples of the natural product could stem from an

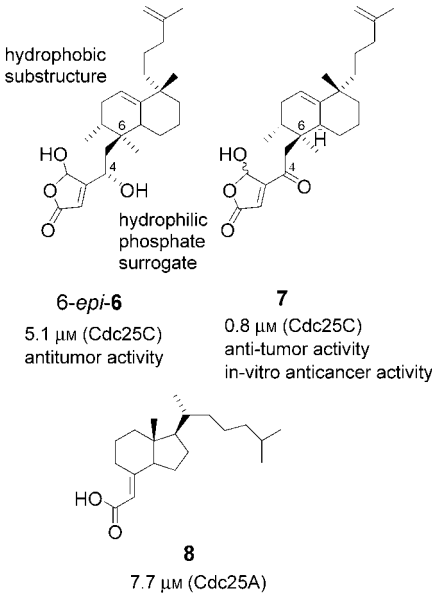


Figure 7. Inhibitors derived from dysidiolide; IC_{50} values are given.

unidentified impurity.[130] Several total syntheses[131] and the synthesis of simple analogues[132] of dysidiolide have been reported. Similar natural products with antitumor activity have been described.[133] Based on their total synthesis of dysidiolide, Shirai and co-workers synthesized a series of analogues of the natural product in solution.[134] This study showed that the bicyclic structure could not be replaced with a cyclohexane ring without destroying the activity. Variation of the stereochemistry at C4 and C6 did not interfere with activity. Clearly, the orientation of the hydroxybutenolide unit relative to the hydrophobic portion is not important. Indeed, some of the diastereomers showed even stronger inhibition of Cdc25A and B than the natural product itself.

In the context of a program in which natural products are used as biologically validated starting points for the development of compound libraries, the solid-phase synthesis of a small collection of dysidiolide analogues was reported. The library was screened against Cdc25C and various cancer cell lines, including the colon cancer cell line HCT116, the prostate cancer cell line PC3, and the breast cancer cell line MDA-MB231.[135] The key steps of the synthesis included an asymmetric Diels–Alder reaction for the construction of a bicyclic hydrophobic substructure and the singlet-oxygen-mediated oxidation of a furan ring to the γ-hydroxybutenolide group. A traceless linker that is cleaved by ring-closing metathesis was used for solid-phase attachment. By this strategy, inhibitors of Cdc25C that are more potent than 6-*epi*-dysidiolide ($IC_{50} = 5.1\ \mu M$), for example, the ketone **7** ($IC_{50} = 0.8\ \mu M$), were obtained (Figure 7). Anticancer activity was also observed at micromolar levels in vitro for these analogues, although the activity did not strictly parallel that of phosphatase inhibition.

In the initial report of the isolation and structure elucidation of dysidiolide, the hydroxybutenolide moiety was already proposed to be a nonionic phosphate surrogate, whereas the decalin scaffold bearing the alkyl side chain was

 © 2005 Wiley-VCH Verlag GmbH & Co. KGaA, Weinheim

proposed to exert hydrophobic interactions with the enzyme. Based on this hypothesis, Shirai and co-workers described simplified analogues of the natural product which were synthesized from vitamin D_3 and which contained a carboxylic acid group instead of the hydroxybutenolide moiety. Among these compounds, **8** showed both Cdc25A inhibition and antitumor activity in the micromolar range, comparable to the natural product (Figure 7).[132a]

An interesting approach to the synthesis of micromolar inhibitors of similar structure has been described by Zalkow and co-workers (Figure 8). By silica-mediated pyrolysis of

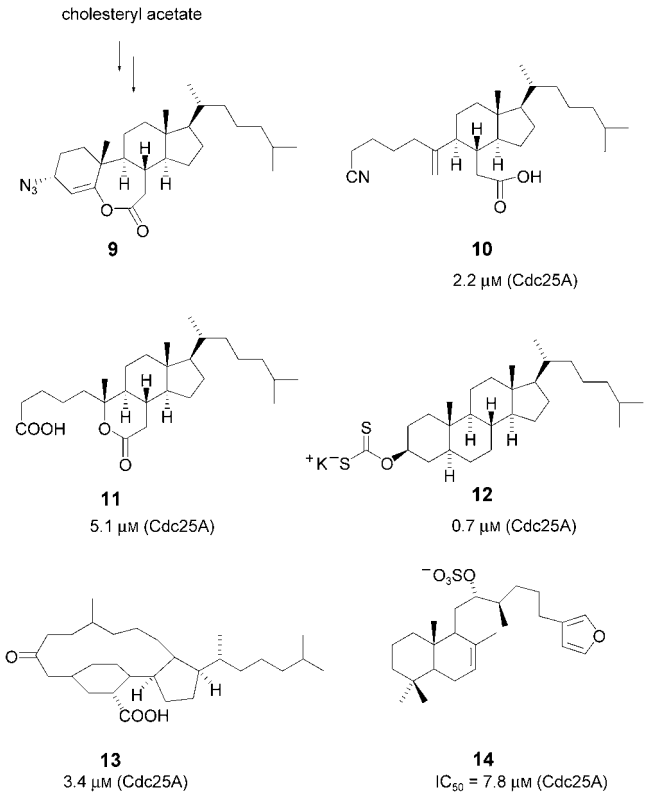


Figure 8. Cholesterol-derived PTP inhibitors **9**–**13** and the natural product, sulfircin (**14**); IC_{50} values are given.

azide **9**, itself readily synthesized from cholesteryl acetate, ten compounds were isolated and subjected to further chemical transformations, leading to a panel of analogues. Among them, nitrile **10** was identified as a reversible, noncompetitive inhibitor of Cdc25A, B and C ($IC_{50} = 2.2$, 8.3, 12.2 μM). The authors proposed that the cyano group may bind to an arginine residue located in a region distinct from the substrate binding site. Whereas CD45 was also inhibited by this compound, acid **11** and *O*-cholestanyl xanthate **12** were highly selective for Cdc25A (**11**: $IC_{50} = 5.1$ μM; **12**: 0.7 μM) relative to CD45 ($IC_{50} > 100$ μM).[132b] Interestingly, although most of the compounds showed inhibition of cancer cell lines in vitro, this did not necessarily correlate with the inhibition of phosphatase activity. Thus, simple steroidal derivatives like **12** functionalized with a phosphate surrogate chain, although excellent phosphatase inhibitors, were weaker inhibitors of tumor cell growth than more complex structures like **11**. The authors suggested that poor cellular uptake and metabolic degradation may be important factors in modulating the anticancer activity of these phosphatase inhibitors.

Researchers at Schering synthesized a series of micromolar inhibitors of Cdc25B, based on a rigid steroid-derived macrocyclic scaffold.[136] Among these, compound **13** is the most potent ($IC_{50} = 5.6$ μM). It is believed that the keto functionality serves as a phosphate mimic, and the carboxyl group binds to the side chains of either Arg544 or Arg482, which flank the binding site (Figure 8).

Another natural product, sulfircin (**14**, Figure 8), was isolated from a marine sponge[137] and exhibited an IC_{50} value of 7.8 μM against Cdc25A, although selectivity over other PTPs was poor. Analogues of this natural product have been synthesized, and the sulfate group can be replaced by a malonate group.[138]

Dnacin A1 and B1 (**15a** and **15b**, Figure 9), two naphthyridinomycin-type antibiotics with antitumor activity have

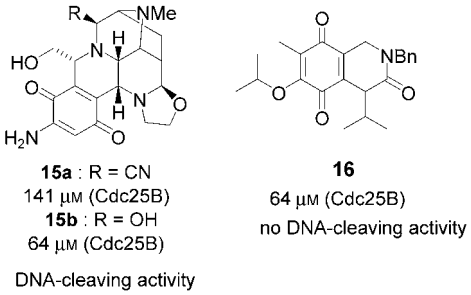


Figure 9. Dnacins A1 and B1 as well as a simplified analogue; IC_{50} values are given.

been isolated from *Actinomycetes* strains.[139] They are weak, noncompetitive inhibitors of Cdc25B ($IC_{50} = 141$ μM and 64 μM).[139] However, these natural products also showed the ability to cleave DNA through the generation of superoxide radicals. Recently, Wipf and co-workers synthesized analogues of the natural product (for example, **16**) which still showed PTP inhibition in the micromolar range, but no DNA-cleaving activity. They were thus able to "separate" the two biological mechanisms of this interesting class of compounds.[140] It was also shown that PTP1B and VHR were inhibited as well as Cdc25A and B. For two compounds, selectivity for Cdc25 and PTP1B over VHR was observed. The authors concluded that truncated analogues that lack the bridged piperidine moieties were good leads for the design of novel Cdc25 inhibitors without DNA-cleaving activity.

A new lead compound for the development of PTP inhibitors was derived from the antitumor 2-pyridone TMC-69.[141a–c] The synthesis of the hydrogenated enantiomers (17*S*)-**17** and (17*R*)-**17** (Figure 10) and their biological evaluation against a panel of phosphatases showed, in contrast to previous reports, that the structures are moderate (micromolar) inhibitors of PTP1B, VHR, and PP1 (a serine/threonine phosphatase), whereas Cdc25A is only weakly inhibited.[141d]

The natural product dephostatin **18a** was found to be a micromolar, competitive PTP inhibitor in *Streptomyces* sp-

 © 2005 Wiley-VCH Verlag GmbH & Co. KGaA, Weinheim

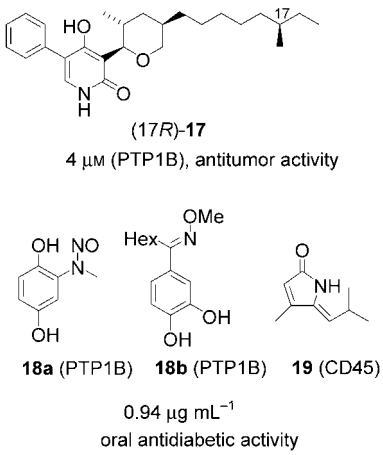


Figure 10. Analogues of the antitumor 2-pyridone TMC-69 are PTP inhibitors; IC_{50} values are given.

p.[142a,b] More selective and stable analogues without the potentially carcinogenic nitrosamino unit were later designed by molecular modeling. C–H π interactions of the alkyl side chain are thought to play an important role in the binding of these inhibitors, which essentially function as tyrosine mimics. The most potent inhibitor, compound **18b**, is a micromolar inhibitor of PTP1B ($IC_{50} = 0.94\ \mu g\,mL^{-1}$). These compounds also show moderate selectivity towards PTP1B and SHPTP-1 (30-fold over CD45 and >100-fold over LAR). More importantly, they show oral antidiabetic activity in mice by decreasing high blood glucose levels. No serious toxicity was observed.[142c]

In 1997, Alvi et al. isolated a natural product from the marine fungus *Corollospora pulchella* with inhibitory activity toward CD45: pulchellalactam (**19**).[143] This natural product contains 3-pyrrol-2-one as a core structure, and could constitute an interesting pharmacophore for the development of phosphatase inhibitors.

In a recent study, a range of glycolipids, among them glucolipsin A, cycloviracin B_1, caloporoside, woodrosin I, sophorolipid, tricolorin G, and analogues thereof were screened against phosphatases PTP1B and Cdc25A.[144] Most of the structures (some of which are shown in Figure 11; **20**–**22**) were identified as micromolar inhibitors of Cdc25A, whereas PTP1B was not inhibited. These results are surprising, as glycolipids had not been identified previously as phosphatase inhibitors. Analogues and synthetic precursors of the natural products roseophilin and the prodigiosins[145] were identified as inhibitors of Cdc25A, PTP1B, and VHR (**23a–c**; Figure 11). Whereas none of the compounds inhibited PP1, some micromolar inhibitors of phosphatases were identified, thus illustrating once more the utility of natural compounds as starting points for the identification of phosphatase inhibitors.[146]

7.3. Mechanism-Based Small-Molecule Inhibitors

Apart from inspiration from a rich pool of natural products, more rational approaches have been successful in

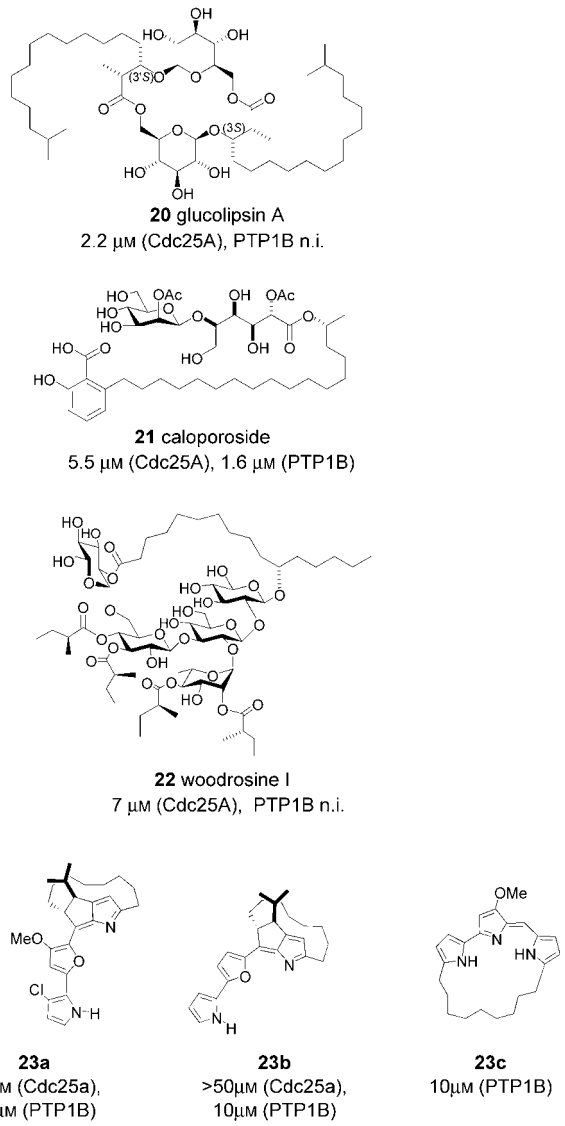


Figure 11. Structures of glycolipids and alkaloids identified as phosphatase inhibitors; IC_{50} values are given; (n.i. = no inhibition).

the development of PTP inhibitors, such as molecular modeling based on X-ray crystallographic structures of PTPs. Most of this work has focused on the development of competitive inhibitors that bear a nonhydrolyzable phosphotyrosine mimetic group.

7.3.1. Nonhydrolyzable Tyrosine Phosphate Mimetics

A rational concept for the design of competitive PTP inhibitors has been realized through the replacement of the phosphate portion of peptidic substrates with nonhydrolyzable phosphate mimetics. A range of simple anionic mimetic structures has been developed and successfully converted into PTP inhibitors. Thus, the phosphotyrosyl group has been replaced by sulfotyrosyl,[147a] thiophosphoryltyrosyl,[147b] *O*-dithiophosphoryltyrosyl,[147c] *O*-boranophosphoryltyrosyl,[147c] phosphonomethylphenylalanine (Pmp),[147d] *O*-malonyltyrosyl,[147e] fluoro *O*-malonyltyrosyl,[147f] and most successfully,

 © 2005 Wiley-VCH Verlag GmbH & Co. KGaA, Weinheim

difluorophosphonomethylphenylalanine (F_2Pmp) groups.[147g] In the latter compound, the fluorine atoms form hydrogen bonds with N–H groups of PTP, which increases the binding affinity by several orders of magnitude.[147h]

Early inhibitor designs relied on peptidic structures as templates for the phosphotyrosine mimetic. For example, the hexapeptide Asp-Ala-Asp-Glu-F_2Pmp-Leu-NH_2 was developed by Burke et al., and has an IC_{50} of 0.2 μM for PTP1B.[147g] However, peptides are generally poor candidates for drug development, as they are susceptible to protease degradation and have poor permeability through the cell membrane. Interestingly, simple aromatic difluoromethylphosphonates have already shown weak PTP inhibition and even exert biological activity like promotion of neovascularization.[148] Biphenyl- and naphthyl-substituted compounds showed higher potency than phenyl derivatives, as hydrophobic interactions play a dominant role in the stabilization of inhibitor–enzyme interactions.[149]

The main drawback of double-negatively charged phosphotyrosine mimetics is their inherent lack of cell-membrane permeability.[150] Indeed, most of the compounds, despite their strong inhibition of phosphatases in vitro, are not biologically active in cell-based assays. Therefore, considerable efforts have been undertaken by academic groups and pharmaceutical companies to develop nonpeptidic, small-molecule PTP inhibitors (especially PTP1B inhibitors) with more "druglike" character and less negatively charged phosphotyrosine mimetic groups.[4] In the following section we discuss some of the inhibitors generated under this principle, with a focus on new developments.

Researchers at Merck Frosst developed a series of difluoromethylphosphonates substituted with a deoxybenzoin side chain which showed strong (nanomolar) PTP1B inhibition and, perhaps surprisingly, cellular activity. Moreover, compound **24** (Figure 12), with an *ortho*-bromo substituent on the phenyl ring, proved to be orally bioavailable and displayed glucose-lowering activity in rat models.[151] Unfortunately, only poor selectivity over the closely related phosphatase TCPTP was observed. The lack of information about the binding mode of these inhibitors impaired a further improvement in selectivity.

Moran et al. demonstrated that cinnamic acids (for example, **25a**; Figure 12) are potent inhibitors ($K_i = 79$ nM) of PTP1B.[152] Unfortunately, these structures are likely to covalently modify the enzymes, a feature which may be undesirable in drug development. Similar cinnamic aldehydes (such as **25b**) with a tripeptide moiety were later reported by Pei and co-workers that lead to micromolar inhibitors of PTP1B and the catalytic domain of SHP-1, whereas the dual-specificity phosphatase VHR showed only weak inhibition.[153] Surprisingly, **25b** acts as an activator of SHP-1 by binding to the inhibitory N-terminal SH2-domain of the enzyme.[154] NMR spectroscopic analysis of the mode of inhibition suggests that an enamine is formed reversibly between the aldehyde moiety and Arg221 of PTP1B.

Taylor and co-workers described the difluoromethylenesulfonic acid (F_2Smp) as a monoanionic phosphate surrogate and incorporated this moiety into peptides and compared it to other phosphate mimetics in the same peptidic template.[155]

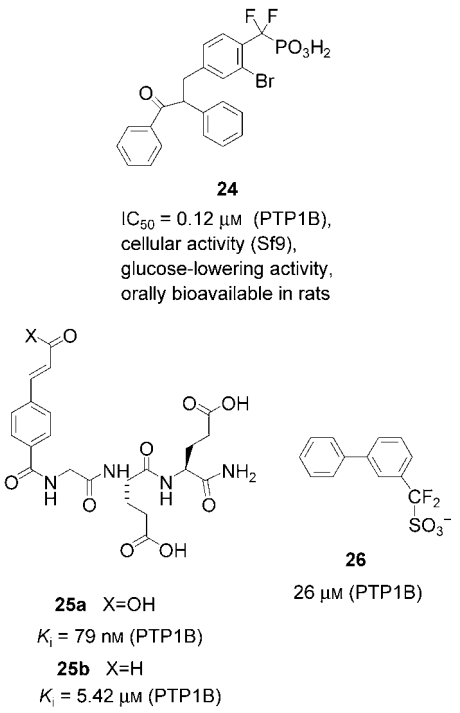


Figure 12. Cinnamic aldehydes, acids and difluoromethylenesulfonic acids as phosphotyrosyl mimetics.

This work showed that whereas F_2Smp is less potent than the bisanionic F_2Pmp, it performs similarly to other monoanionic surrogates. The same research group also synthesized a range of simple nonpeptidic aromatic derivatives with IC_{50} values toward PTP1B that range between 26 and 197 μM (for example, **26;** Figure 12).

Researchers at Pharmacia replaced the *O*-malonyltyrosine moiety (**27a**) by a more potent 2-carboxymethoxybenzoic acid group (**27b**; Figure 13). To overcome problems caused by poor cell-membrane permeability, one carboxylic acid moiety was replaced by a tetrazole unit as a carboxyl group bioisostere (**28**).[156] The resulting compound **29** showed PTP1B inhibition ($K_i = 2$ μM) and modest cellular activity (insulin-stimulated 2-deoxyglucose uptake by L6 myocytes). Another successful approach was in the use of the corresponding diester moiety **27c** as a prodrug. This compound is more cell-membrane permeable than the diacid, and can be cleaved in the cell by enzymes to release the active PTP inhibitor.[157] Replacement of the Boc group in **29** by arylalkanoyl groups yielded inhibitors (for example, **30**) with submicromolar K_i values against PTP1B and improved insulin-stimulated glucose transport by L6 myocytes at 100 μM. Moreover, the compounds showed selectivity over LAR and SHP-2.[158]

The binding modes of these inhibitors have been investigated by X-ray crystallographic analysis (Figure 14).[157] The peptide backbone adopts a β-strand conformation and forms hydrogen bonds with Asp48 and Arg 47 (PTP1B numbering). The two phenyl rings form hydrophobic interactions with the side chains of Tyr46, Val49, Ala217, Ile 219, Gln 262, and Phe 182. Interestingly, binding of the inhibitors by the enzyme results in closure of the WPD loop in a manner similar to

 © 2005 Wiley-VCH Verlag GmbH & Co. KGaA, Weinheim

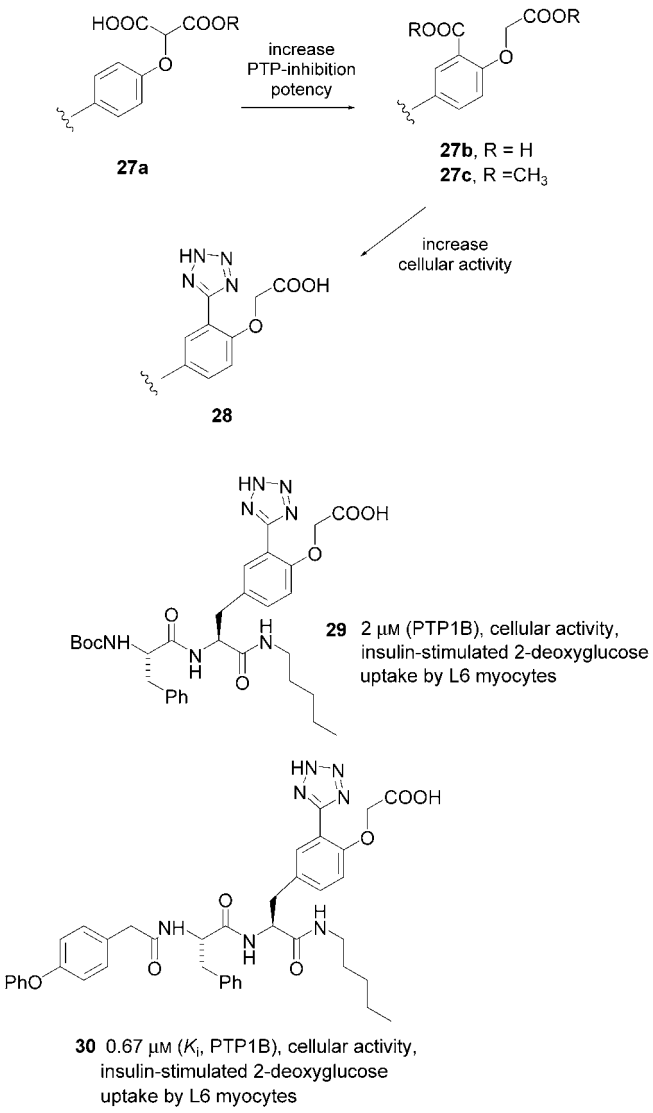


Figure 13. Improvement of PTP inhibition and cellular activity starting from *O*-malonyltyrosyl derivatives; the tetrazole group is a well-established carboxylic acid bioisostere; K_i values are given.

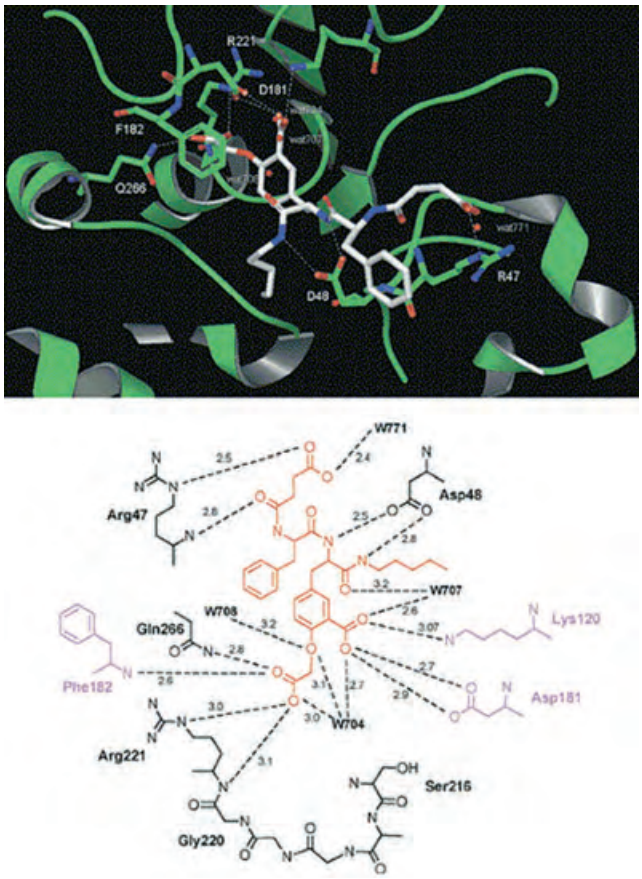


Figure 14. Binding mode of an inhibitor of type **27b** (white) to the active site of PTP1B (green); (W = water molecule; from Ref. [157] with permission).

substrate binding, as described earlier. Relative to the phosphate groups of substrates, the carboxylic groups are closer to the WPD loop and form hydrogen bonds with water molecules inside the active site as well as with amide groups.

Researchers at Novo Nordisk identified a similar structure, 2-(oxalylamino)benzoic acid (**31**) as a phosphotyrosine mimetic (Figure 15). Based on this structural element, analogues such as thiophene **32** were developed with submicromolar IC_{50} values for PTP1B and good oral bioavailability in rats.[159] The X-ray crystallographic structure of **32** in complex with PTP1B revealed that the oxalylamino carboxyl group forms hydrogen bonds with the main chain amide nitrogen atom of Gly220 and Arg221 and a salt bridge with the guanidinium side chain of Arg221. The other carboxyl group forms a salt bridge with Lys120. Upon binding of the inhibitor, the WPD loop is closed similarly to the binding mode of phosphotyrosine. In this conformation, Phe182 forms favorable aromatic–aromatic interactions with the thiophene ring of **32** while the tetrahydropyridine ring interacts with Ile219, Val49 and Tyr46. Another remarkable interaction is present between the nitrogen atom of the tetrahydropyridine ring and Asp48. The corresponding position in many other phosphatases such as SHP-1, PTP-α, and LAR is occupied by an Asn residue, which would exert a repulsive interaction with the same nitrogen atom, thereby contributing to the PTP selectivity of this class of inhibitors. To overcome the poor cellular uptake of such highly charged compounds, a prodrug approach (ethyl ester) was used, and these compounds showed cellular activity (enhancement of 2-deoxyglucose accumulation in C2C12 cells) in the high micromolar range (100 μM).

The same phosphotyrosine mimetic was used by researchers at Abbott for the development of nanomolar PTP1B inhibitors (Section 7.3.2).

Researchers at Molecumetics designed a phenylalanine derivative[160] based on earlier work by Ham et al.[161] When incorporated into a library containing triazolopyridazine β-strand templates, micromolar irreversible inhibitors of PTP1B were obtained (for example, **33**; Figure 15).

Researchers at Wyeth–Ayerst developed and optimized PTP-inhibitors with benzofuran or benzothiophene rings. The most potent inhibitors obtained showed IC_{50} values against PTP1B in the range of 20–50 nM, and some compounds

 © 2005 Wiley-VCH Verlag GmbH & Co. KGaA, Weinheim

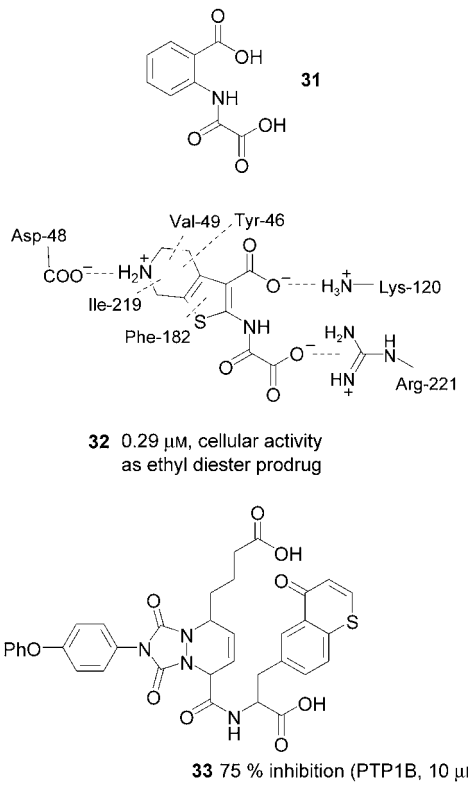


Figure 15. Phosphotyrosine mimetics: inhibitors developed at Novo Nordisk and Molecumetics; IC_{50} values are given.

normalized plasma glucose levels at intraperitoneal doses of 1 mg kg^{-1}, with **34** as the best compound in vivo (Figure 16).[162] Furthermore the compound showed 10- to 100-fold selectivity for PTP1B over other PTPs. A model for the binding of this class of compounds has been developed based on X-ray crystallographic data. The carboxylic acid group binds to two water molecules that bridge the guanidine group of Arg221 (PTP1B), which normally binds the phosphate group of the substrate. Thus, this moiety acts as a phosphate mimetic in a broader sense. The biphenyl ring proximal to the carboxylic acid group is sandwiched between Tyr46 and Phe182, which resembles the binding of the phenyl ring of phosphotyrosine substrates. Other interactions that contribute to the high affinity of the inhibitor are mainly hydrophobic in nature. The second biphenyl ring binds the positively charged ammonium group of the Lys120 side chain, while the 2-benzyl-benzofuran/benzothiophene moiety interacts with the Lys116 side chain and the aromatic ring of Phe182.

In the same report, a similar compound with a salicylic acid moiety as the polar group was described (**35;** Figure 16). Interestingly, the mode of binding is quite different in this case, as determined by X-ray crystallographic analysis of this compound in complex with PTP1B. A molecule of **35** forms amide hydrogen bonds with Lys120 and Tyr46 and interacts with one H_2O molecule bridging Arg221, while the hydrophobic moieties point toward the opposite side relative to the case of inhibitor **34** (Figure 17). A similar compound, Ertiprotafib (PTP-112, **36**; Figure 16) was developed by

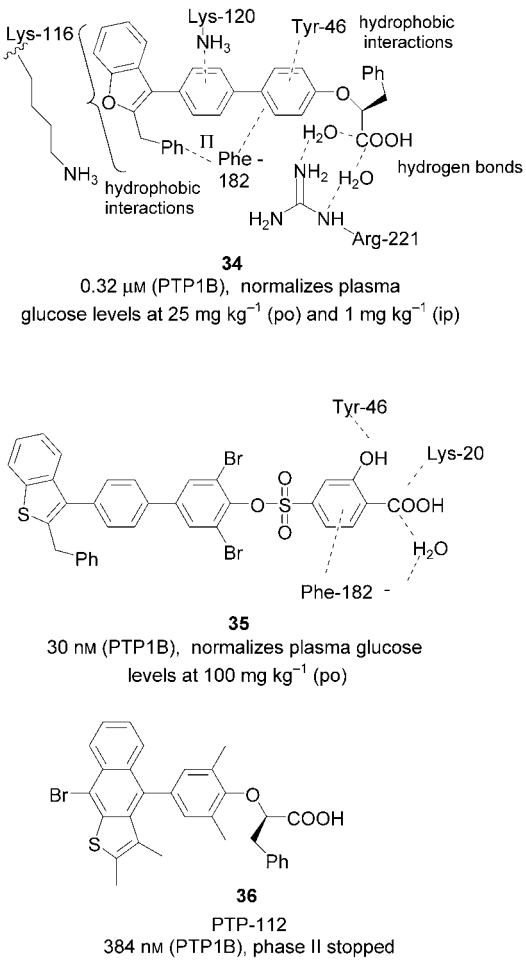


Figure 16. Benzofuran-derived carboxylic acids and their interactions with key residues of PTP1B; (po = peroral; ip = intraperitoneal).

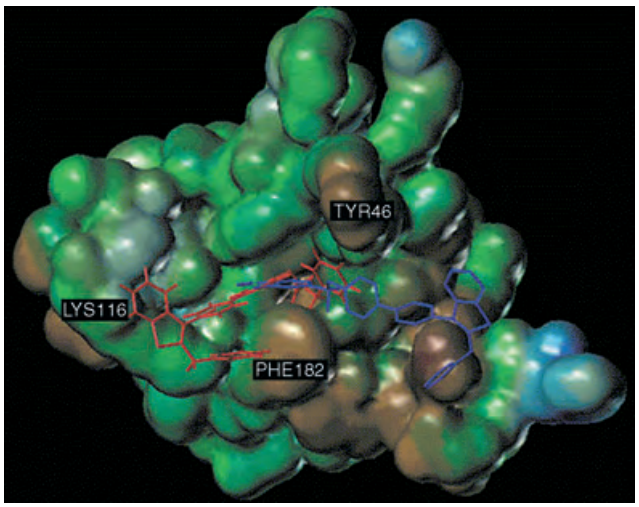


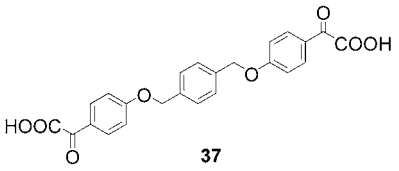
Figure 17. Different binding modes of compounds of type **34** (red) and **35** (blue); the protein surface is colored: lipophilic regions are brown and hydrophilic regions are blue/green (from Ref. [162] with permission).

Wyeth as a drug for the treatment of diabetes type 2. However, development was stopped in 2002 at phase II clinical trials because of unsatisfactory clinical efficacy and

 © 2005 Wiley-VCH Verlag GmbH & Co. KGaA, Weinheim

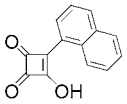
the occurrence of dose-limiting side effects.[4,63] Ertiprotafib has also been shown to be a PPAR modulator, and some of its biological effects may be linked to this activity.[63b]

A further phosphate mimetic, α-ketocarboxylic acid, was developed by Seto and co-workers.[164] When this mimetic was incorporated into peptides, weak inhibitors were obtained ($IC_{50} = 150$ μM toward *Yersinia* PTP). However, much higher affinities were obtained with dimeric structures like **37** (Figure 18).[165] (The use of dimeric phosphotyrosine mimetics



37

0.7 μM (*Yersinia* PTP),
2.7 μM (PTP1B),
250 μM (LAR)



38

47 μM (*Yersinia* PTP),
400 μM (PTP1B)

Figure 18. Phosphotyrosine mimetics: α-ketocarboxylic acids and squaric acids; IC_{50} values are given.

is discussed in greater detail in the following Section 7.3.2.) The same research group also showed that aryl-substituted squaric acids can serve as phosphotyrosine mimetics.[166] Among the compounds tested, the naphthyl-substituted squaric acid **38** showed the highest inhibition ($IC_{50} = 47$ μM against *Yersinia* PTP; Figure 18). Furthermore, a kinetic analysis revealed that the compounds act as reversible competitive inhibitors, thus confirming that they are phosphotyrosine mimetics.

7.3.2. ***Two-Site-Binders as Selective Inhibitors of PTP1B***

A major problem in finding selective inhibitors for PTPs is the high sequence homology of the catalytic site shared by the enzymes (up to 80% homology between TCPTP and PTP1B). In this respect the discovery by Zhang and co-workers[167] of a second, noncatalytic binding site on PTP1B in the vicinity of the active site which shows less homology among the phosphatases is of particular importance for the development of a new class of more selective inhibitors of PTP1B. By resolving the crystallographic structure of a catalytically inactive mutant (C215S) of PTP1B in complex with the small-molecule substrates bis(*para*-phosphophenyl)methane or phosphotyrosine, it was found that the substrates could bind the enzyme at two sites (Figure 19). In the catalytic site, the phosphotyrosine forms ionic interactions with Arg221, hydrogen bonds with the main-chain nitrogen atoms of Ser216–Arg221, and aromatic–aromatic contacts with Tyr46

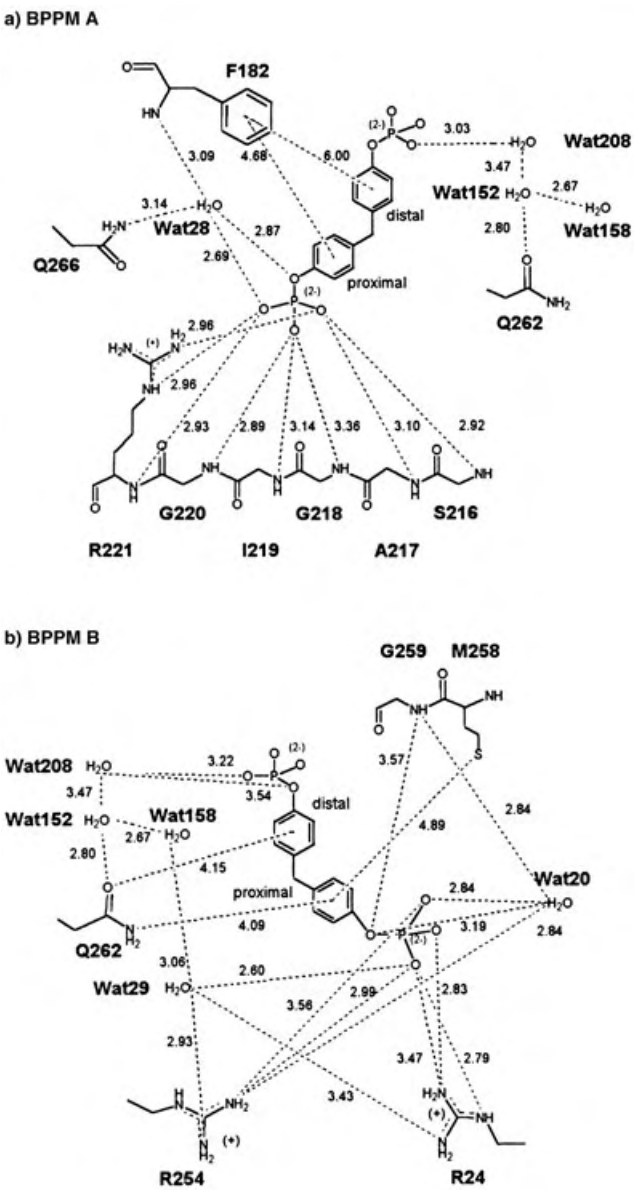


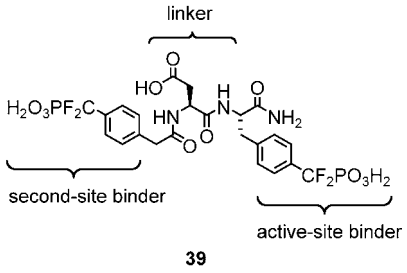
Figure 19. The PTP1B inhibitor BPPM can bind to the enzyme in two different modes, suggesting the presence of two aryl phosphate binding sites in PTP1B: the first mode (a) is similar to the binding of phosphotyrosine substrates, whereas the second mode (b) involves amino acids that are less conserved among phosphatases (from Ref. [167a] with permission).

and Phe182. Unexpectedly, a second binding site in the vicinity of the catalytic site was found. In this site, phosphotyrosine forms ionic interactions with Arg24 and Arg254, polar interactions with Met258 and Gln262, and van der-Waals contacts with Ile219, Asp48 and Arg254.

This observation constitutes a new paradigm for ligand design, as the second aryl phosphate binding site is less conserved among phosphatases (apart from Arg254 and Gln262, which are present in all PTPs). Thus, a bidentate ligand that binds the two sites has a better chance to be more selective than a classical active-site binding compound. The authors later successfully applied this paradigm to the

 © 2005 Wiley-VCH Verlag GmbH & Co. KGaA, Weinheim

development of potent and remarkably selective PTP1B inhibitors.[167b] They first synthesized a 184-membered library of compounds with three distinct moieties: an invariable, active-site binding aryl phosphate group, an amino acid as linker (23 members) and a second-site binding fragment (8 compounds). The compounds were screened for binding to the inactive C215S mutant form of PTP1B. A further advantage to the use of this enzyme is that inhibitors emerging from these studies are less likely to act through irreversible alkylation or oxidation of the catalytically active cysteine group, a characteristic undesirable in drug development.[168] The most powerful binder was then converted into a nonhydrolyzable phosphate mimetic, the corresponding difluoromethylphosphonate, to give compound **39,** which gave a K_i value of 2.4 nM (Figure 20). Besides this remarkable



39

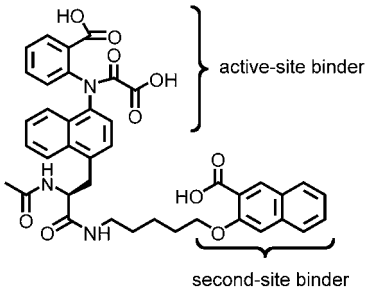
2.4 nM (K_i, PTP1B)

Figure 20. Two-site-binders: an alternative approach to the design of selective and potent PTP inhibitors.

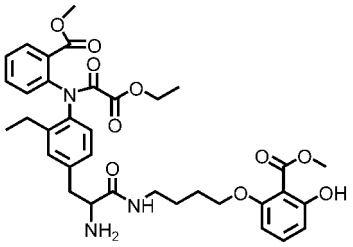
potency, the compound showed excellent selectivity (in most cases by three orders of magnitude) over other intracellular PTPs, receptor-like PTPs, and DSPs. The selectivity against the most closely related TCPTP was tenfold. TCPTP is implicated in regulation of T-cell activation[169] and a mutation has been shown to be lethal for embryonic development in mice.[170] Therefore, from a therapeutic point of view, selectivity of PTP1B over TCPTP is highly desirable.

The exceptional potency and selectivity of compound **39** was later rationalized by the crystallographic structure of a similar compound in complex with PTP1B.[171] Whereas the active-site-targeting phenyldifluoromethylphosphonyl group bound the active site in the expected fashion, the authors found that the aspartic acid linker and the distal difluoromethylphosphonyl group developed interactions mainly with Lys41, Arg47 and Asp48. Other groups previously identified similar interactions by crystallization of a bisphosphonate inhibitor with PTP1B.[172] Thus the second phosphonate group binds near Arg47 rather than the previously identified secondary binding site.

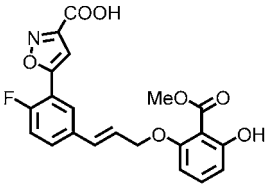
Researchers at Abbott applied this concept to the development of nanomolar PTP1B inhibitors with good to excellent selectivities over other phosphatases.[173a] Their "linked-fragment approach" was based on a NMR spectroscopic screen for compounds that bind weakly to the active site as well as the second site. The investigation started with a 10000-membered library of compounds with ^{13}C-enriched PTP1B ("SAR by NMR"). Guided by X-ray crystallographic data from protein–ligand complexes and linkage of the identified fragments, compound **40** was designed (Figure 21), a 22 nM inhibitor of PTP1B. The diaryloxamic acid moiety binds to the active site, and the naphthoic acid



40 22 nM (K_i, PTP1B), poor cell-membrane permeability



41 prodrug, increased insulin-induced PKB phosphorylation of FAO cells



42 6.9 μM (PTP1B), 30-fold selectivity over TC-PTP, cellular activity in COS cells

Figure 21. Two-site-binders developed as selective PTP1B inhibitors (30-fold selectivity over TCPTP for **42**).

group binds the second site. Other phosphatases like LAR, SHP-2, and CD45 were inhibited at much higher concentrations (1–54 μM), whereas the compound was twofold less effective toward the most closely related phosphatase, TCPTP. By analysis of X-ray crystallographic data of the protein–inhibitor complex, the authors developed a model of inhibition for compound **40** (Figure 22). The oxamic acid moiety works as a phosphate mimetic and binds to the open form of the enzyme, where the Trp179–Ser187 loop retains a conformation similar to that of the unoccupied enzyme. The benzoic ring of the oxamic acid moiety makes hydrophobic contacts with Gln262, while the carboxylate interacts with Arg221. The naphthalene moiety makes hydrophobic interactions with Tyr46, while the adjacent C_4-diamido chain extends out of the active site to form hydrogen bonds with Asp48. The naphthoic acid group is placed in the second binding site, forming ionic interactions with Arg254 and Arg24; the naphthalene ring forms weak hydrophobic

 © 2005 Wiley-VCH Verlag GmbH & Co. KGaA, Weinheim

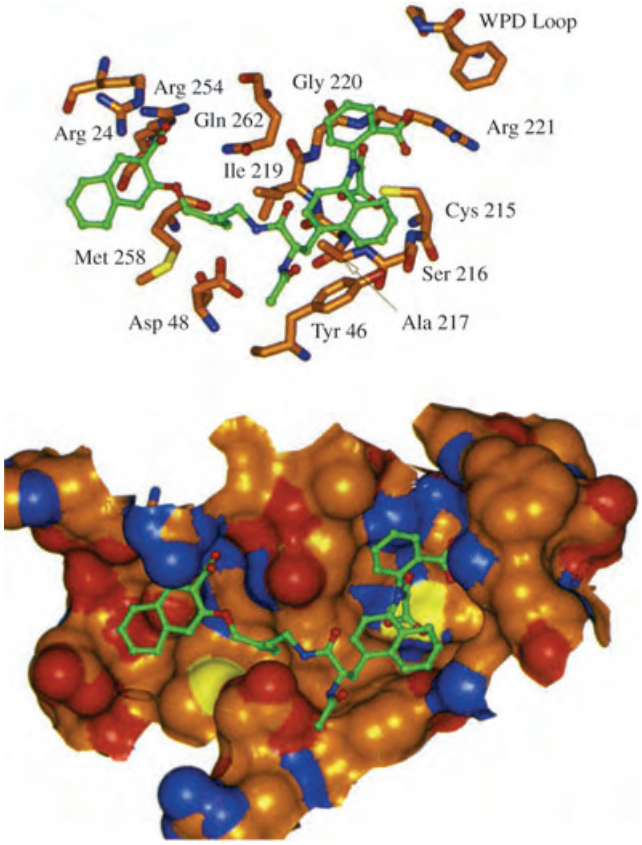
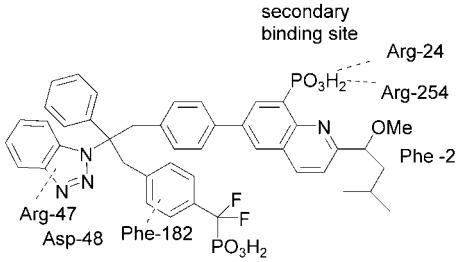


Figure 22. Inhibitor **40** bound to PTP1B (from Ref. [173a] with permission).

interactions with Met258. Although a good phosphatase inhibitor in vitro, compound **40** showed poor cellular membrane permeability as a result of its high polarity. To circumvent this problem, a prodrug approach was applied, leading to diester **41**, which showed increased insulin-induced PKB phosphorylation of FAO cells.[173b] In another approach, the same research group used NMR spectroscopic screening, but started from less polar compounds.[173c] From this study, compound **42** was produced in which the oxamic acid unit was replaced by isoxazole carboxylic acid. Compound **42** shows a K_i (PTP1B) value of 6.9 μM, a 30-fold selectivity preference over TCPTP, and no inhibition of other phosphatases (LAR, CD45, Cdc25, and SHP-2) up to 300 μM. It is therefore one of the most selective PTP1B inhibitors described to date. Moreover, **42** showed activity in the leptin pathway in COS-7 cells (for similar studies by Abbott see Ref. [173]).

Although it is a remarkable advance in the development of more potent inhibitors of PTPs, there has been some reservation concerning the utility of this concept to the development of truly selective PTP inhibitors, as some of the residues involved in the binding of the second aryl moiety (especially Arg47) are also present in phosphatases other than PTP1B, with particular regard to TCPTP.[172a]

Other amino acid residues like Phe52 and Ala27 (PTP1B) have also been targets of research at Merck Frosst, as the corresponding positions in TCPTP have different residues (Tyr and Ser, respectively). Based on X-ray crystallographic structural data, inhibitor **43** was developed (Figure 23) which employs a phenyldifluoromethylphosphonate group as a primary active-site binding motif, a benzotriazole group that interacts with Arg47 and Asp48, and a substituted quinoline moiety directed toward Phe52 and Ala27, tethered by a rigid



43
5 nM (PTP1B), cellular activity,
7-fold selectivity over TCPTP

Figure 23. Structure of PTP inhibitor **43** and interactions with PTP1B.

biphenyl linker to the rest of the molecule. The phosphonate moiety of the quinoline interacts with Arg24 and Arg254, the residues of the original secondary binding site as defined by Zhang,[167] whereas the methoxy and the isobutyl groups interact with Phe52 (Figure 24). Although a very potent

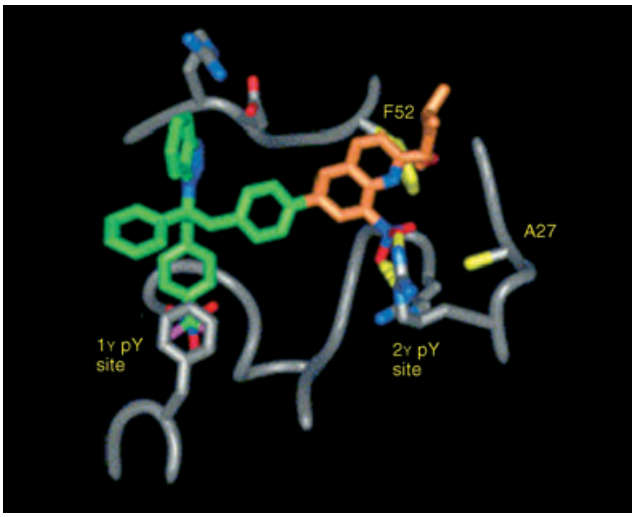


Figure 24. X-ray crystallographic structure of **43** in complex with PTP1B: the key interaction with Phe52 (which corresponds to a tyrosine residue in TCPTP) causes a sevenfold selectivity over TCPTP (from Ref. [174] with permission).

PTP1B inhibitor ($IC_{50} = 5$ nM) with cellular activity ($IC_{50} =$ 58 nM, compare with **24**; Figure 12), compound **43** was only moderately selective over TCPTP (sevenfold), again illustrating the difficulty in finding truly selective PTP1B inhibitors.[174]

 © 2005 Wiley-VCH Verlag GmbH & Co. KGaA, Weinheim

7.3.3. *Quinones*

Many PTP inhibitors contain a quinone functionality, in which case one would intuitively expect the active-site cysteine residue to be oxidized, or to form covalent adducts with such compounds. However, the modes of inhibition of quinone-derived inhibitors sometimes differ from the expected scenarios.

In an interesting approach, Wipf and co-workers screened 10070 compounds of the National Cancer Institute (NCI) for inhibitors of Cdc25.[175] They identified 21 compounds with IC_{50} values less than 1 μM. Furthermore, they found that 75% of the hits were quinones; more than 40% were *para*-naphthoquinones, among them compound **44** (NSC95397, IC_{50}(Cdc25B) = 0.125 μM; Figure 25). This compound is

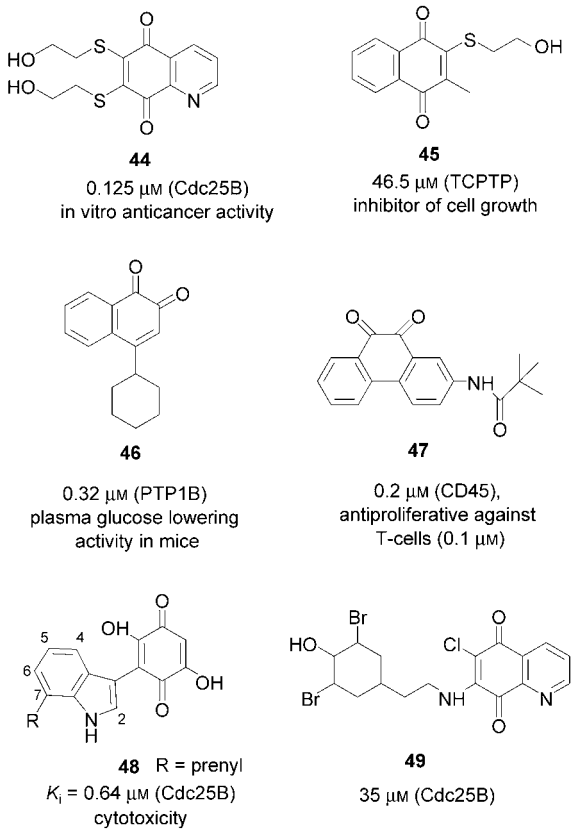


Figure 25. Quinone-derived PTP inhibitors; IC_{50} values are given.

closely related to naphthoquinone **45**, a vitamin K analogue which had been described before as an inhibitor.[176] The compounds show only moderate selectivity against other phosphatases like PTP1B and VHR. They inhibit irreversibly, have anticancer activity in vitro against one prostate and two breast cancer cell lines and induce cell-cycle arrest of tsFT210 cells at micromolar concentrations. With the known structure of Cdc25B, Wipf and co-workers proposed a binding mode of the naphthoquinone moiety at the surface of the enzyme in a secondary, sulfate-binding site located adjacent to the active site.[175,94b] In this model, the carbonyl oxygen atoms of the quinone form hydrogen bonds to two arginine residues: Arg482 and Arg544. The aromatic ring is bound by hydrophobic interactions with other amino acids (Arg479, Thr547, Tyr428, Phe543) in the interior of the pocket. To confirm their model, a set of analogues was synthesized. It was shown that the aromatic moiety and the *para*-quinone were needed for inhibition. Further substitution of the thiol side chains did not improve activity. This model also explains why so many *para*-quinone compounds of the NCI library do not inhibit Cdc25; the binding site is close enough to the catalytic cysteine group (Cys473) to allow covalent modification by the electrophilic quinone moiety.[177]

In a similar approach, Choi and co-workers identified the 1,2-naphthoquionone moiety as the pharmacophore for PTP1B.[178] They found that some substituted compounds like **46** showed remarkable activity against PTP1B (IC_{50} = 0.32 μM). Furthermore, a 10- to 60-fold selectivity over other phosphatases (like CD45, LAR, Yop, PP1, and Cdc25B) was demonstrated. The compounds lowered plasma glucose levels in mice.

A similar series of compounds, namely phenanthrenediones (for example, **47**; Figure 25) which showed cellular activity, was investigated by researchers at AstraZeneca.[179] The most effective compounds obtained inhibited CD45 in the single-digit micromolar range, whereas PTP1B was not inhibited at 30 μM. The compounds acted as reversible competitive inhibitors. Furthermore, some compounds inhibited the proteases cathepsin L and S, but not cathepsin B.

A difficult aspect in the search for inhibitors of dual-specifity phosphatases like Cdc25 is the open and shallow shape of the active site, which is directly linked to the low specificity of these enzymes towards their substrates. In this respect, the indolyldihydroxyquinone moiety has been described by Rudolph and co-workers as a promising lead for the development of reversible, competitive inhibitors of Cdc25 with submicromolar inhibition constants (**48**; Figure 25).[180] The substitution pattern of the indole moiety was varied systematically, showing that variation at positions 2 and 4 led to a significant decrease of potency, substitution at positions 1 and 5 had little effect, whereas modification at positions 6 and 7 led to stronger Cdc25 inhibition. All isoforms of Cdc25 (A, B, and C) were inhibited, while the activity of PTP1B was unaffected up to 50 μM. Although similar to previously described quinone-based phosphatase inhibitors (for example, NSC668394 (**49**); Figure 25), the authors demonstrated that the mode of inhibition was different (reversible and competitive). The finding that the quinone moiety does not covalently modify the enzyme was rationalized with the rather electron-rich nature of the quinone (two hydroxy groups, one indolyl group). To understand the mechanism of inhibition, several site-directed mutants and a C-terminally truncated variant of Cdc25B were tested. The authors showed that three amino acids, Glu474, Phe475 (which are part of the characteristic HCX_5R loop), and Arg482 as well as the C-terminal tail were important for the inhibition mode. Arg482 has been proposed before to bind other quinone-based Cdc25 inhibitors.[175] The C-terminal portion has been shown to play an essential role in the interaction with the natural substrate of Cdc25, the Cdk2–cyclin A complex.[181] It is interesting to note that the IC_{50}

 © 2005 Wiley-VCH Verlag GmbH & Co. KGaA, Weinheim

values of the inhibitors determined with the natural substrate proved to be higher (albeit still in the micromolar range) than those determined with the commonly used artificial substrate 3-*O*-methylfluorescein phosphate. Cell toxicity of the inhibitors in vitro, possibly through apoptotic mechanisms, was demonstrated. Remarkably, no increase in phosphorylation of the Cdks was detected. The observed nonspecific binding of the inhibitors to serum albumin could be a problem for their future development as drug candidates.

7.3.4. Other Approaches

Starting from a pharmacophore model derived from natural product inhibitors of the serine/threonine phosphatase PP1,[182] a combinatorial approach was used to generate new inhibitors (for example, **50**; Figure 26) which are active toward PTPs and DSPs.[183] This is remarkable, as serine/threonine phosphatases are quite different from their PTP counterparts. The mechanism of inhibition remains unclear; a kinetic analysis has shown that they act as partially competitive, reversible inhibitors of Cdc25B, whereas they exhibit noncompetitive inhibition toward other phosphatases. The compounds inhibit tumor cell growth in culture. Hydrophobic interactions with the enzyme play an important role in inhibition, while both the carboxylic acid and the oxazole moieties form hydrogen-bond interactions. The cyclohexyldiamine linker confers conformational rigidity and thereby enhances the potency of the compounds.

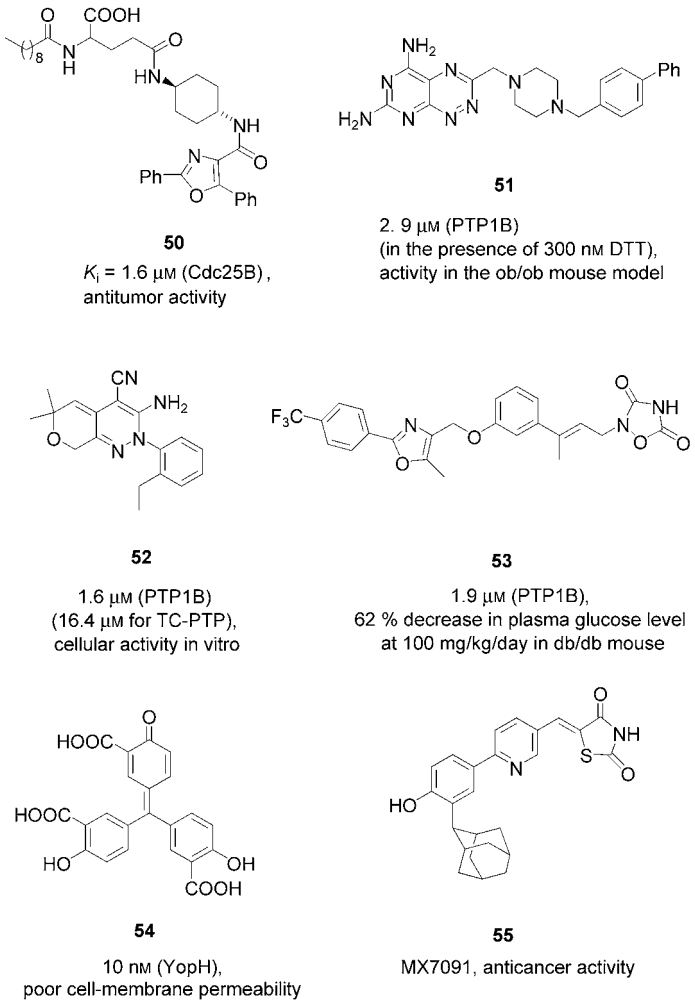


Figure 26. Further PTP inhibitors obtained from diverse approaches; IC_{50} values are given except for **50** and **55**.

PTPs contain a cysteine residue which is essential for catalytic activity. Oxidation of this cysteine inactivates the enzyme, a mechanism also relevant for the in-vivo regulation of enzymes, for example, in the early phases of the insulin signal-transduction cascade, in which a burst of intracellular hydrogen peroxide inhibits PTP1B upon insulin stimulation. As a result, the cascade is enhanced.[135] This process is reversible, as the resulting oxidation product is reduced by glutathione. A similar mechanism is probably responsible for the in-vitro inhibition of PTP1B by pyrimidotriazinediamine-based compounds (for example, **51**; Figure 26) developed at Roche, which show a reversible inhibition of the enzyme in the presence of DTT.[184] Although the compounds are active in vivo in the ob/ob mouse model at 30 mg kg^{-1}, they show little selectivity over other phosphatases such as LAR, PTP-α, and SHP-2.

Researchers at Biovitrum described another inhibitor type, the pyridazine analogues (for example, **52**; Figure 26).[185] They act as noncompetitive reversible inhibitors, with IC_{50} values in the low micromolar range. Therefore, they bind to a site different from the active site. Additional positive aspects include their high selectivity over TCPTP (20-fold in the case of some analogues) and their cell-membrane permeability. They exhibited oral bioavailability and increased insulin-stimulated phosphorylation of the insulin receptor.

Further small-molecule inhibitors of PTP were discovered more or less by chance. For example, researchers at Wyeth–Ayerst described azolidinone derivatives that have submicromolar IC_{50} values against PTP1B; some of these derivatives, like **53**, (Figure 26) normalized plasma glucose and insulin levels in diabetic mouse models.[186] However, the authors pointed out that the compounds may also act as agonists toward the peroxisome proliferator-activated receptor γ (PPAR-γ).

In an effort to identify agents that work against the plague, Zhang and co-workers identified a highly potent and selective inhibitor against the *Yersinia* phosphatase YopH (which is essential for virulence) by screening 720 commercially available carboxylic acids.[187] Aurintricarboxylic acid (**54**) inhibited YopH with an IC_{50} of 10 nM and 6–120-fold selectivity over other phosphatases, such as PTP1B (61 nM) and CD45 (250 nM). The compound also restored T-cell activity in YopH-transfected Jurkat cells, although electroporation was necessary to enable cellular uptake of the highly charged compound.

Incyte is currently developing inhibitors against the dual-specificity phosphatase MKP-1. MKP-1 inhibits apoptosis through the inactivation of the kinase JNK. One MKP-1 inhibitor, MX7091 (**55**; Figure 26) proved to be more effica-

 © 2005 Wiley-VCH Verlag GmbH & Co. KGaA, Weinheim

cious against solid tumors than paclitaxel in mice and exhibited synergistic effects when combined with cisplatin.[14]

8. Conclusions and Future Prospects

We have given an overview of the structure, functions and possible therapeutic relevance of selected PTPs. Today, the structures and catalytic mechanisms of several phosphatases are reasonably well-understood. Although major progress has been made toward an understanding of the involvement of PTPs in signal-transduction pathways, and in the development of diseases and infections, there is still a lot of work to be done in this field, as well as for the search for other PTPs and their biological relevance.

Ever since the discovery that the PTP1B knockout is not a lethal mutation in mice, but instead confers protection from obesity and improved insulin sensitivity, scientists in both academia and pharmaceutical industry have realized that the inhibition of PTPs may be a valuable tool for molecular biology research, as is the well-established case for the serine/threonine phosphatases. PTP inhibition could also be a possible source of valuable drugs against major diseases like diabetes and obesity. Moreover, the treatment of other diseases (infectious, autoimmune or neurological disorders, and cancer) is expected to profit from PTP inhibitor research. Although a few natural products have been identified as PTP inhibitors, the major strategy adopted today has been the design of small molecules based on nonhydrolyzable phosphotyrosine mimetics. Whereas very potent in-vitro PTP inhibitors have been identified, two major challenges characterize this field: increasing cell-membrane permeability through the design of noncharged (or less-charged) compounds, which is a prerequisite for activity in vivo, and the identification of truly selective inhibitors—a task quite difficult, regarding the highly conserved nature of the PTP active site. The finding of a second aryl phosphate binding site on PTP1B has been a major step in getting closer to achieving this goal. However, a further increase of selectivity over other phosphatases, which exert vital cellular functions (like the T-cell PTP) is required to decrease the risk of undesirable side-effects.

The aforementioned tasks appear to be within reach, given the progress already made in the development of PTP1B inhibitors and the power of modern medicinal chemistry research. In line with this notion, the phosphatases have already been considered by pharmaceutical researchers to make up a considerable part (4%) of the "druggable genome",[188] and an in-depth analysis of the genome revealed that there are 107 protein tyrosine phosphatases[189] which will most likely be the prime candidates for drug development. For several years, various phosphatases have been forming an integral part of the screening units of pharmaceutical companies, and an initial candidate has already been subjected to clinical trials (Section 7.3.1). Notably, in comparison with other target classes that belong to the "druggable genome", phosphatases are only beginning to move into the focus of pharmaceutical research, and today the field is clearly still in its infancy. However, given the crucial roles these enzymes play in innumerable biological processes, it appears almost certain that phosphatase inhibitors will be an integral part of the drugs of the next generation.

This work was supported by the Max Planck Gesellschaft, the Deutsche Forschungsgemeinschaft and the Fonds der Chemischen Industrie.

Received: August 3, 2004
Published online: May 18, 2005

[1] T. Hunter, *Cell* **2000**, *100*, 113–127.
[2] Reviews: a) A. J. Bridges, *Chem. Rev.* **2001**, *101*, 2541–2572; b) M. E. M. Noble, J. A. Endicott, L. N. Johnson, *Science* **2004**, *303*, 1800–1805; c) K. Grosios, P. Traxler, *Drugs Future* **2003**, *28*, 679–697; d) L. K. Shawver, D. Slamon, A. Ullrich, *Cancer Cell* **2002**, *1*, 117–123.
[3] Review: Z. Y. Zhang, *Annu. Rev. Pharmacol. Toxicol.* **2002**, *42*, 209–234.
[4] Reviews: a) R. H. van Huijsduijnen, A. Bombrun, D. Swinnen, *Drug Discovery Today* **2002**, *7*, 1013–1019; b) G. Liu, *Curr. Med. Chem.* **2003**, *10*, 1407–1421; c) M. A. Lyon, A. P. Ducruet, P. Wipf, J. S. Lazo, *Nat. Rev. Drug Discovery* **2002**, *1*, 961–976.
[5] a) M. Elchebly, P. Payette, E. Michaliszyn, W. Cromlish, S. Collins, A. L. Loy, D. Normandin, A. Cheng, J. Himms-Hagen, C. C. Chang, C. Ramachandran, M. J. Gresser, M. L. Tremblay, *Science* **1999**, *283*, 1544–1548; b) L. D. Klaman, O. Boss, O. D. Peroni, J. K. Kim, J. L. Martino, J. M. Zabolotny, N. Moghal, M. Lubkin, Y. B. Kim, A. H. Sharpe, A. Stricker-Krongrad, G. I. Shulman, B. G. Neel, B. B. Kahn, *Mol. Cell. Biol.* **2000**, *20*, 5479–5489.
[6] A. I. Lazarovits, S. Poppema, Z. Zhang, M. Khandaker, C. E. LeFeuvre, S. K. Singhal, B. M. Garcia, N. Ogasa, A. M. Jevnikar, M. J. White, G. Singh, C. R. Stiller, R. Z. Zhong, *Nature* **1996**, *380*, 717–720.
[7] Reviews: a) R. E. Honkanen, T. Golden, *Curr. Med. Chem.* **2002**, *9*, 2055–2075; b) K. Hinterding, D. Alonso-Diáz, H. Waldmann, *Angew. Chem.* **1998**, *110*, 716–780; *Angew. Chem. Int. Ed.* **1998**, *37*, 688–749.
[8] a) B. A. Minassian, L. Ianzano, M. Meloche, E. Andermann, G. A. Rouleau, A. V. Delgado-Escueta, S. W. Scherer, *Neurology* **2000**, *55*, 341–346; b) S. Ganesh, K. L. Agarwala, K. Ueda, T. Akagi, K. Shoda, T. Usui, T. Hashikawa, H. Osada, A. V. Delgado-Escueta, K. Yamakawa, *Hum. Mol. Genet.* **2000**, *9*, 2251–2261.
[9] T. Takeuchi, M. Pang, K. Amano, J. Koide, T. Abe, *Clin. Exp. Immunol.* **1997**, *109*, 20–26.
[10] T. Hunter, *Cell* **1989**, *58*, 1013–1016.
[11] A. Schmidt, S. J. Rutledge, N. Endo, E. E. Opas, H. Tanaka, G. Wesolowski, C. T. Leu, Z. Huang, C. Ramachandaran, S. B. Rodan, G. A. Rodan, *Proc. Natl. Acad. Sci. USA* **1996**, *93*, 3068–3073.
[12] CD45 reviews: a) M. L. Hermiston, Z. Xu, A. Weiss, *Annu. Rev. Immunol.* **2003**, *21*, 107–137; b) J. Irie-Sasaki, T. Sasaki, J. M. Penninger, *Curr. Top. Med. Chem.* **2003**, *3*, 783–796.
[13] For example, see: a) K. Galaktionov, A. K. Lee, J. Eckstein, G. Draetta, J. Meckler, M. Loda, D. Beach, *Science* **1995**, *269*, 1575–1577; b) D. Dixon, T. Moyana, M. J. King, *Exp. Cell Res.* **1998**, *240*, 236–243; c) Y. Kudo, W. Yasui, T. Ue, S. Yamamoto, H. Yokosaki, H. Nikai, E. Tahara, *Jpn. J. Cancer Res.* **1997**, *88*, 9947–9952.
[14] a) H. Wang, Z. Cheng, C. C. Malbon, *Cancer Lett.* **2002**, 229–237; b) http://www.albmolecular.com/features/tekreps/vol08/no17.

 © 2005 Wiley-VCH Verlag GmbH & Co. KGaA, Weinheim

[15] J. Tan, T. Town, T. Mori, Y. J. Wu, M. Saxe, F. Crawford, M. Mullan, *J. Neurosci.* **2000**, *20*, 7587 – 7594.
[16] Review: R. DeVinney, O. Steele-Mortimer, B. B. Finlay, *Trends Microbiol.* **2000**, *8*, 29 – 32.
[17] a) K. Yahiro, T. Niidome, M. Kimura, T. Hatakeyama, H. Aoyagi, H. Kurazono, K. Imagawa, A. Wada, J. Moss, T. Hirayama, *J. Biol. Chem.* **1999**, *274*, 36693 – 36699; b) K. Yahiro, A. Wada, N. Nakayama, T. Kimura, K. Ogushi, T. Niidome, H. Aoyagi, K. Yoshino, K. Yonezawa, J. Moss, T. Hirayama, *J. Biol. Chem.* **2003**, *278*, 19183 – 19189.
[18] L. D. Schultz, P. A. Schweitzer, T. V. Rajan, T. Yi, J. N. Ihle, R. J. Matthews, M. L. Thomas, D. R. Beier, *Cell* **1993**, *73*, 1445 – 1454.
[19] T. Kamata, M. Yamashita, M. Kimura, K. Murata, M. Inami, C. Shimizu, K. Sugaya, C.-R. Wang, M. Taniguchi, T. Nakayama, *J. Clin. Invest.* **2003**, *111*, 109 – 119.
[20] J. L. Thompson, J. H. Jiang, N. Madamanchi, M. S. Runge, C. Patterson, *Am. J. Physiol.* **2001**, *281*, H396 – 403.
[21] A. Di Cristofano, P. P. Pandolfi, *Cell* **2000**, *100*, 387 – 390.
[22] S. Ponniah, D. Z. Wang, K. L. Lim, C. J. Pallen, *Curr. Biol.* **1999**, *9*, 535 – 538.
[23] G. Bompard, C. Puech, C. Prebois, F. Vignon, G. Freiss, *J. Biol. Chem.* **2002**, *277*, 47861 – 47869.
[24] S. M. Pettiford, R. Herbst, *Leukemia* **2003**, *17*, 366 – 378.
[25] S. Saha, A. Bardelli, P. Buckhaults, V. E. Velculescu, C. Rago, B. St Croix, K. E. Romans, M. A. Choti, C. Lengauer, K. W. Kizler, B. Vogelstein, *Science* **2001**, *294*, 1343 – 1346.
[26] J. D. Bjorge, A. Pang, D. J. Fujita, *J. Biol. Chem.* **2000**, *275*, 41439 – 41446.
[27] Y. Shen, R. Luche, B. Wei, M. L. Gordon, C. D. Diltz, N. K. Tonks, *Proc. Natl. Acad. Sci. USA* **2001**, *98*, 13613 – 13618.
[28] a) Y. Seo, T. Matozaki, M. Tsuda, Y. Hayashi, H. Itoh, M. Kasuga, *Biochem. Biophys. Res. Commun.* **1997**, *231*, 705 – 711; b) H. Nagano, T. Noguchi, K. Inagaki, S. Yoon, T. Matozaki, H. Itoh, M. Kasuga, Y. Hayashi, *Oncogene* **2003**, *22*, 4656 – 4663.
[29] K. Meng, A. Rodriguez-Pena, T. Dimitrov, W. Chen, M. Yamin, M. Noda, T. F. Deuel, *Proc. Natl. Acad. Sci. USA* **2000**, *97*, 2603 – 2608.
[30] M. L. Loh, S. Vattikuti, S. Schubert, M. G. Reynolds, E. Carlson, K. H. Lieuw, J. W. Cheng, C. M. Lee, D. Stokoe, J. M. Bonifas, N. P. Curtiss, J. Gotlib, S. Meschinchi, M. M. Le Beau, P. D. Emanuel, K. M. Shannon, *Blood* **2004**, *103*, 2325 – 2331.
[31] C. Y. Wu, Q. Guan, Y. J. Wang, Z. J. Zhao, G. W. Zhou, *J. Cell. Biochem.* **2003**, *90*, 1026 – 1037.
[32] T. Tsukamoto, T. Takahashi, R. Ueda, K. Hibi, H. Saito, *Cancer Res.* **1992**, *52*, 3506 – 3509.
[33] R. Bataille, N. Robillard, C. Pellat-Deceunynck, M. Amiot, *Immunol. Rev.* **2003**, *194*, 105 – 111.
[34] T. Igawa, F.-F. Lin, P. Rao, M.-F. Lin, *Prostate* **2003**, *55*, 247 – 258.
[35] M. A. Tisi, Y. Xie, T. T. Yeo, F. M. Longo, *J. Neurobiol.* **2000**, *42*, 477 – 486.
[36] J. McLean, J. Batt, L. C. Doering, D. Rotin, J. R. Bain, *J. Neurosci.* **2002**, *22*, 5481 – 5491.
[37] A. Horvat, F. W. Schwaiger, G. Hager, F. Brocker, R. Streif, P. G. Knyazev, A. Ullrich, G. W. Kreutzberg, *J. Neurosci.* **2001**, *21*, 865 – 874.
[38] M. B. Marrero, R. L. Papke, B. S. Bhatti, S. Shaw, M. Bencherif, *J. Pharmacol. Exp. Ther.* **2003**, *309*, 16 – 27.
[39] Z. Z. Chong, S. H. Lin, J. Q. Kang, K. Maiese, *Cell. Mol. Neurobiol.* **2003**, *23*, 561 – 578.
[40] M. K. Pathak, T. Yi, *J. Immunol.* **2001**, *167*, 3391 – 3397.
[41] H. Higashi, R. Tsutsumi, S. Muto, T. Sugiyama, T. Azuma, M. Asaka, M. Hatakeyama, *Science* **2002**, *295*, 683 – 686.
[42] A. Koul, A. Choidas, M. Treder, A. K. Tyagi, K. Drlica, Y. Singh, A. Ullrich, *J. Bacteriol.* **2000**, *182*, 5425 – 5432.
[43] J. M. Zablotny, Y. B. Kim, O. D. Peroni, J. K. Kim, M. A. Pani, O. Boss, L. D. Klaman, S. Kamatkar, G. I. Shulman, B. B. Kahn, B. G. Neel, *Proc. Natl. Acad. Sci. USA* **2001**, *98*, 5187 – 5192.
[44] S. M. Suhr, S. Pamula, D. J. Baylink, K. H. W. Lau, *J. Bone Miner. Res.* **2001**, *16*, 1795 – 1803.
[45] A. Kita, S. Uotani, H. Kuwahara, R. Takahashi, K. Oshima, H. Mizuguchi, T. Hayakawa, Y. Nagayama, Y. Yamaguchi, K. Eguchi, *Biochem. Biophys. Res. Commun.* **2003**, *302*, 805 – 809.
[46] a) Z.-Y- Zhang, *Acc. Chem. Res.* **2003**, *36*, 385 – 392; b) A. Alonso, J. Sasin, N. Bottini, I. Friedberg, I. Friedberg, A. Osterman, A. Godzik, T. Hunter, J. Dixon, T. Mustelin, *Cell* **2004**, *117*, 699 – 711.
[47] a) G. Raugei, G. Ramponi, P. Chiarugi, *Cell. Mol. Life Sci.* **2002**, *59*, 941 – 949; b) M. J. Wishart, G. S. Taylor, J. T. Slama, J. E. Dixon, *Curr. Opin. Cell Biol.* **2001**, *13*, 172 – 181; c) Q. Zeng, X. Si, H. Horstmann, Y. Xu, W. Hong, C. J. Pallen, *J. Biol. Chem.* **2000**, *275*, 21444 – 21452; d) T. Takagi, C. R. Moore, F. Diehn, S. Buratowski, *Cell* **1997**, *89*, 867 – 873; e) M. L. Sulis, R. Parsons, *Trends Cell Biol.* **2003**, *13*, 478 – 483; f) S.-A. Kim, P. O. Vacratsis, R. Firestein, M. L. Cleary, J. E. Dixon, *Proc. Natl. Acad. Sci. USA* **2003**, *100*, 4492 – 4497.
[48] X.-L. Zhan, M. J. Wishart, K.-L. Guan, *Chem. Rev.* **2001**, *101*, 2477 – 2496.
[49] http://ptp.cshl.edu/.
[50] D. Barford, *Biochem. Soc. Trans.* **1999**, *27*, 751 – 766.
[51] a) D. Barford, A. J. Flint, N. K. Tonks, *Science* **1994**, *263*, 1397 – 1404; b) A. D. B. Pannifer, A. J. Flint, N. K. Tonks, D. Barford, *J. Biol. Chem.* **1998**, *273*, 10454 – 10462.
[52] K. L. Guan, J. E. Dixon, *J. Biol. Chem.* **1991**, *266*, 17026 – 17030.
[53] M. Streuli, N. X. Krueger, T. Thai, M. Tang, H. Saito, *EMBO J.* **1990**, *9*, 2399 – 2407.
[54] J. A. Stuckey, E. B. Fauman, H. L. Schubert, Z.-Y. Zhang, J. E. Dixon, M. A. Saper, *Nature* **1994**, *370*, 575 – 578.
[55] Y. L. Zhang, F. Hollfelder, S. J. Gordon, L. Chen, Y. F. Keng, *Biochemistry* **1999**, *38*, 12111 – 12123.
[56] Z.-Y. Zhang, Y. Wang, E. J. Dixon, *Proc. Natl. Acad. Sci. USA* **1994**, *91*, 1624 – 1627.
[57] J. M. Denu, D. L. Lohse, J. Vijayalakshmi, M. A. Saper, J. E. Dixon, *Proc. Natl. Acad. Sci. USA* **1996**, *93*, 2493 – 2498.
[58] Z.-Y. Zhang, B. A. Palfey, L. Wu, Y. Zhao, *Biochemistry* **1995**, *34*, 16389 – 16396.
[59] T. Pawson, G. Gish, *Cell* **1992**, *71*, 359 – 362.
[60] C. Wu, M. Sun, L. Liu, G. W. Zhou, *Gene* **2003**, *306*, 1 – 12.
[61] S. Tomic, U. Greiser, R. Lammers, A. Kharitonenkov, E. Imyanitov, A. Ullrich, F. D. Bohmer, *J. Biol. Chem.* **1997**, *272*, 5966 – 5973.
[62] T. Yi, A. L. F. Mui, G. Krystal, J. N. Ihle, *Mol. Cell. Biol.* **1993**, *13*, 7577 – 7586.
[63] a) U. Klingmueller, U. Lorenz, L. C. Cantley, B. G. Neel, H. F. Lodish, *Cell* **1995**, *80*, 729 – 738; b) B. F. Burkey, M. Dong, L. Wennogle, R. Babb, M. Dressman, A. Islam, R. Deacon, C. Dragland, E. Kaplan, J. Tomesch, J. P. Gao, *Diabetes* **2002**, *51*, A34-A34, 138 Suppl.
[64] M. Tabrizi, W. Yang, H. Jiao, E. M. de Vries, L. C. Platanias, M. Arico, T. Yi, *Leukemia* **1998**, *12*, 200 – 206.
[65] C.-K. Qu, *Biochim. Biophys. Acta* **2002**, *1592*, 297 – 301.
[66] G.-S. Feng, C. C. Hui, T. Pawson, *Science* **1993**, *259*, 1607 – 1611.
[67] W. Vogel, R. Lammers, J. Huang, A. Ullrich, *Science* **1993**, *259*, 1611 – 1614.
[68] M. R. Kuhne, T. Pawson, G. E. Lienhard, G.-S. Feng, *J. Biol. Chem.* **1993**, *268*, 11479 – 11481.
[69] D. Pei, U. Lorenz, U. Klingmueller, B. G. Neel, C. T. Walsh, *Biochemistry* **1994**, *33*, 15483 – 15493.
[70] D. Pei, J. Wang, C. T. Walsh, *Proc. Natl. Acad. Sci. USA* **1996**, *93*, 1141 – 1145.

 © 2005 Wiley-VCH Verlag GmbH & Co. KGaA, Weinheim

[71] M. Tartaglia, E. L. Mehler, R. Goldberg, G. Zampino, H. G. Brunner, H. Kremer, I. van der Burgt, A. H. Crosby, A. Ion, S. Jeffery, K. Kalidas, M. A. Patton, R. S. Kucherlapati, B. D. Gelb, *Nat. Genet.* **2001**, *29*, 465 – 468.
[72] N. Tidow, B. Kasper, K. Welte, *Exp. Hematol.* **1999**, *27*, 1038 – 1045.
[73] J. A. Bonini, J. Colca, C. Hofmann, *Biochem. Biophys. Res. Commun.* **1995**, *212*, 933 – 938.
[74] N. K. Tonks, C. D. Diltz, E. H. Fischer, *J. Biol. Chem.* **1988**, *263*, 6731 – 6737.
[75] M. F. White, C. R. Kahn, *J. Biol. Chem.* **1994**, *269*, 1 – 4.
[76] A. Cheng, N. Dubé, F. Gu, M. L. Tremblay, *Eur. J. Biochem.* **2002**, *269*, 1050 – 1059.
[77] J. E. Pessin, D. C. Thurmond, J. S. Elmendorf, K. J. Coker, S. Okada, *J. Biol. Chem.* **1999**, *274*, 2593 – 2596.
[78] a) B. L. Seely, P. A. Staubs, D. R. Reichhart, P. Berhanu, K. L. Milarski, A. R. Saltiel, J. Kusari, *Diabetes* **1996**, *45*, 1379 – 1385; b) D. Bandyopadhyay, A. Kusari, K. A. Kenner, F. Liu, J. Chernoff, T. A. Gustafson, J. Kusari, *J. Biol. Chem.* **1997**, *272*, 1639 – 1645.
[79] A. Salmeen, J. N. Andersen, M. P. Myers, N. K. Tonks, D. Barford, *Mol. Cell* **2000**, *6*, 1401 – 1412.
[80] B. J. Goldstein, A. Bittner-Kowalsczyk, M. F. White, M. Tarbeck, *J. Biol. Chem.* **2000**, *275*, 4283 – 4289.
[81] J. R. Wiener, B. J. M. Kerns, E. L. Harvey, M. R. Conaway, J. D. Igleheart, A. Berchuck, R. C. Bast, Jr., *J. Natl. Cancer Inst.* **1994**, *86*, 372 – 378.
[82] a) F. Liu, J. Chernoff, *Biochem. J.* **1997**, *327*, 139 – 145; b) A. J. Flint, T. Tiganis, D. Barford, N. K. Tonks, *Proc. Natl. Acad. Sci. USA* **1997**, *94*, 1680 – 1685.
[83] J. Balsamo, C. Arregui, T. Leung, J. Lilien, *J. Cell Biol.* **1998**, *143*, 523 – 532.
[84] K. L. Guan, S. S. Broyles, J. E. Dixon, *Nature* **1991**, *350*, 359 – 362.
[85] T. Ishibashi, D. P. Bottaro, A. Chan, T. Miki, S. A. Aaronson, *Proc. Natl. Acad. Sci. USA* **1992**, *89*, 12170 – 12174.
[86] J. L. Todd, K. G. Tanner, J. M. Denu, *J. Biol. Chem.* **1999**, *274*, 13271 – 13280.
[87] J. Yuvaniyama, J. M. Denu, J. E. Dixon, M. A. Saper, *Science* **1996**, *272*, 1328 – 1331.
[88] a) K. S. Sadhu, I. Reed, H. Rihardson, P. Russell, *Proc. Natl. Acad. Sci. USA* **1990**, *87*, 5139 – 5143; b) J. B. Millar, J. Blevitt, L. Gerace, K. Sadhu, C. Featherstone, P. Russell, *Proc. Natl. Acad. Sci. USA* **1991**, *88*, 10500 – 10504; c) A. Nagata, M. Igarashi, S. Jinno, K. Suto, H. Okayama, *New Biol.* **1991**, *3*, 959 – 968.
[89] A. J. Obaya, J. M. Sedivy, *Cell. Mol. Life Sci.* **2002**, 126 – 142.
[90] a) C. Norbury, J. Blow, P. Nurse, *EMBO J.* **1991**, *10*, 3321 – 3329; b) C. Lammer, S. Wagerer, R. Saffrich, D. Mertens, W. Ansorge, I. Hoffmann, *J. Cell Sci.* **1998**, *111*, 2445 – 2453.
[91] a) I. Hoffmann, P. R. Clarke, M. J. Marcote, E. Karsenti, G. Draetta, *EMBO J.* **1993**, *12*, 53 – 63; b) U. Strausfeld, A. Fernández, J.-P. Capony, F. Girard, N. Lautredou, J. Derancourt, J. C. Labbe, N. J. Lamb, *J. Biol. Chem.* **1994**, *269*, 5989 – 6000.
[92] I. Hoffmann, G. Draetta, E. Karsenti, *EMBO J.* **1994**, *13*, 4302 – 4310.
[93] I. Hoffmann, *Protoplasma* **2000**, *211*, 8 – 11.
[94] a) E. B. Faumann, J. P. Cogswell, B. Lovejoy, W. J. Rocque, W. Holmes, V. G. Montana, H. Piwnica-Worms, M. J. Rink, M. A. Saper, *Cell* **1998**, *93*, 617 – 625; b) R. A. Reynolds, A. W. Yem, C. L. Wolfe, J. Deibel, C. G. Chidester, K. D. Watenpaugh, *J. Mol. Biol.* **1999**, *293*, 559 – 568.
[95] M. L. Sulis, R. Parsons, *Trends Cell Biol.* **2003**, *13*, 478 – 483.
[96] S.-A. Kim, P. O. Vacratsis, R. Firestein, M. L. Cleary, J. E. Dixon, *Proc. Natl. Acad. Sci. USA* **2003**, *100*, 4492 – 4497.
[97] A. Martins, S. Shuman, *Biochemistry* **2002**, *41*, 13403 – 13409.
[98] P. J. Rayapureddi, C. Kattamuri, B. D. Steinmetz, B. J. Frankfort, E. J. Ostrin, G. Mardon, R. S. Hedge, *Nature* **2003**, *426*, 295 – 298.
[99] S. M. Braday-Kalnay, N. K. Tonks, *Curr. Opin. Cell Biol.* **1995**, *7*, 650 – 657.
[100] J. N. Andersen, O. H. Mortensen, G. H. Peters P. G. Drake, L. F. Iversen, O. H. Olsen P. G. Jansen, H. S. Andersen, N. K. Tonks, N. P. H. Møller, *Mol. Cell. Biol.* **2001**, *21*, 7117 – 7136.
[101] H. Walzel, U. Schulz, P. Neels, J. Brock, *Immunol. Lett.* **1999**, *67*, 193 – 202.
[102] P. O'Grady, T. C. Thai, H. Saito, *J. Cell Biol.* **1998**, *141*, 1675 – 1684.
[103] Review: P. J. Beltran, J. L. Bixby, *Front. Biosci.* **2003**, *8*, D87-D99.
[104] Review: S. Brunelleschi, L. Penego, M. M. Santoro, G. Gaudino, *Curr. Pharm. Des.* **2002**, *8*, 1959 – 1972.
[105] A. Petrone, J. Sap, *J. Cell Sci.* **2000**, *113*, 2345 – 2354.
[106] a) M. Bergmann, T. Mustelin, C. Oetken, J. Partanen, N. A. Flint, K. E. Amrein, M. Autero, P. Burn, K. Alitalo, *EMBO J.* **1992**, *11*, 2919 – 2924; b) L. M. L. Chow, M. Fournel, D. Davidson, A. Veillette, *Nature* **1993**, *365*, 156 – 160.
[107] a) T. Katagiri, M. Ogimoto, K. Hasegawa, K. Mizuno, H. Yakura, *J. Biol. Chem.* **1995**, *270*, 27987 – 27990; b) S. Yanagi, H. Sugawara, M. Kurosaki, H. Sabe, H. Yamamura, T. Kurosaki, *J. Biol. Chem.* **1996**, *271*, 30487 – 30492.
[108] J. Irie-Sasaki, T. Sasaki, W. Matsumoto, A. Opavsky, M. Cheng, G. Welstead, E. Griffiths, C. Krawczyk, C. D. Richardson, K. Aitken, N. Iscove, G. Koretzky, P. Johnson, P. Liu, D. M. Rothstein, J. M. Penninger, *Nature* **2001**, *409*, 349 – 354.
[109] B. J. Goldstein, F. Ahmad, W. Ding, P. M. Li, W. R. Zhang, *Mol. Cell. Biochem.* **1998**, *182*, 91 – 99.
[110] For example, see: a) A. Petrone, F. Battalia, C. Wang, A. Dusa, J. Su, D. Zagzag, R. Bianchi, P. Casaccia-Bonnefil, O. Arancio, J. Sap, *EMBO J.* **2003**, *22*, 4121 – 4131; b) N. Sakaguchi, H. Muramatsu, K. Ichihara-Tanaka, N. Madea, M. Noda, T. Yamamoto, M. Michikawa, S. Ikematsu, S. Sakuma, T. Muramatsu, *Neurosci. Res.* **2003**, *45*, 219 – 224; c) M. J. Wallace, J. Batt, C. A. Fladd, J. T. Henderson, W. Skarnes, D. Rotin, *Nature Genet.* **1999**, *21*, 334 – 338.
[111] W. Tsai, A. D. Morielli, T. G. Cachero, E. G. Peralta, *EMBO J.* **1999**, *18*, 109 – 118.
[112] T. C. R. Prickett, D. N. J. Hart, *Immunology* **1990**, *69*, 250 – 256.
[113] M. Jacobsen, D. Schweer, A. Ziegler, *Nat. Genet.* **2000**, *26*, 495 – 499.
[114] A. Vogel, C. P. Strassburg, M. P. Manns, *Genes Immun.* **2003**, *4*, 79 – 81.
[115] For example, see: R. Ratei, C. Sperling, L. Karawajew, G. Schott, M. Schrappe, J. Harbott, H. Riehm, W. D. Ludwig, *Ann. Hematol.* **1998**, *77*, 107 – 114.
[116] Y. Shechter, J. Meyerovitch, Z. Farfel, J. Sach, R. Bruck, S. Bar-Meir, S. Amir, H. Degani, S. J. D. Karlish in *Vanadium in Biological Systems: Physiology and Biochemistry* (Ed.: N. D. Chasteen), Kluwer, Dordrecht, pp. 129 – 142.
[117] A. Caselli, P. Chiarugi, G. Camici, G. Manao, G. Ramponi, *FEBS Lett.* **1995**, *374*, 249 – 252.
[118] K. Ueda, T. Usui, H. Nakayama, M. Ueki, K. Takio, M. Ubukata, H. Osada, *FEBS Lett.* **2002**, *525*, 48 – 52.
[119] M. Miski, X. Shen, R. Cooper, A. M. Gillum, D. K. Fisher, R. W. Miller, T. J. Higgins, *Bioorg. Med. Chem. Lett.* **1995**, *5*, 1519 – 1522.
[120] H. Montenegro, M. Guterrez, L. I. Romero, E. Ortega-Barria, T. L. Capson, L. C. Rios, *Planta Med.* **2003**, *69*, 677 – 679.
[121] J. A. Hasrat, T. DeBruyne, J. P. DeBacker, G. Vauquelin, A. J. Vlietinck, *J. Pharm. Pharmacol.* **1997**, *49*, 1145 – 1149.
[122] M. M. V. Ramana, P. V. Potnis, *Tetrahedron Lett.* **1996**, *37*, 1671 – 1674.

 © 2005 Wiley-VCH Verlag GmbH & Co. KGaA, Weinheim

[123] a) T. Morino, A. Masuda, M. Yamada, M. Nishimoto, T. Nishikiori, S. Saito, *J. Antibiot.* **1994**, *47*, 1341 – 1343; b) T. Morino, K. Shimada, A. Masuda, M. Nishimoto, S. Saito, *J. Antibiot.* **1994**, *47*, 1049 – 1051.

[124] a) F. Sarabia, S. Chammaa, F. Jorge Lopez-Herrera, *Tetrahedron Lett.* **2002**, *43*, 2961 – 2965; b) K. Kurosawa, T. Nagase, N. Chida, *Chem. Commun.* **2002**, 1280 – 1281.

[125] T. Hamaguchi, T. Sudo, H. Osada, *FEBS Lett.* **1995**, *372*, 54 – 58.

[126] M. Sodeoka, R. Sampe, S. Kojima, Y. Baba, T. Usui, K. Ueda, H. Osada, *J. Med. Chem.* **2001**, *44*, 3216 – 3222.

[127] M. Sodeoka, R. Sampe, T. Kagamizono, H. Osada, *Tetrahedron Lett.* **1996**, *37*, 8775 – 8778.

[128] T. Usui, S. Kojima, S. Kidokoro, K. Ueda, H. Osada, M. Sodeoka, *Chem. Biol.* **2001**, *8*, 1209 – 1220.

[129] S. P. Gunasekera, P. J. McCarthy, M. Kelly-Borges, *J. Am. Chem. Soc.* **1996**, *118*, 8759 – 8760.

[130] J. L. Blanchard, D. M. Epstein, M. D. Boisclair, J. Rudolph, K. Pal, *Bioorg. Med. Chem. Lett.* **1999**, *9*, 2537 – 2538.

[131] a) E. J. Corey, B. E. Roberts, *J. Am. Chem. Soc.* **1997**, *119*, 12425 – 12431; b) J. Boukouvalas, Y. Cheng, J. Robichaud, *J. Org. Chem.* **1998**, *63*, 228 – 229; c) S. T. Magnuson, L. Sepp-Lorenzino, N. Rosen, S. Danishefsky, *J. Am. Chem. Soc.* **1998**, *120*, 1615 – 1616; d) M. Takahashi, K. Dodo, Y. Yashimoto, R. Shirai, *Tetrahedron Lett.* **2000**, *41*, 2111 – 2114; e) M. Jung, N. Nishimura, *Org. Lett.* **2001**, *3*, 2113 – 2115.

[132] a) K. Dodo, M. Takahashi, Y. Yamada, Y. Sugimoto, Y. Hashimoto, R. Shirai, *Bioorg. Med. Chem. Lett.* **2000**, *10*, 615 – 617; b) H. Peng, W. Xie, D. M. Otterness, J. P. Cogswell, R. T. McConnll, H. L. Carter, G. Powis, R. T. Abraham, L. H. Zalkow, *J. Med. Chem.* **2001**, *44*, 834 – 848.

[133] For example, see: H. Miyaoka, M. Yamanishi, Y. Kajiwara, Y. Yamada, *J. Org. Chem.* **2003**, *68*, 3476.

[134] a) M. Takahashi, K. Dodo, Y. Sugimoto, Y. Sugimoto, Y. Aoyagi, Y. Yamada, Y. Hashimoto, R. Shirai, *Bioorg. Med. Chem. Lett.* **2000**, *10*, 2571 – 2574; b) R. Shimazawa, T. Suzuki, K. Dodo, R. Shirai, *Bioorg. Med. Chem. Lett.* **2004**, *14*, 3291 – 3294.

[135] a) D. Brohm, S. Metzger, A. Bhargava, O. Müller, F. Lieb, H. Waldmann, *Angew. Chem.* **2002**, *114*, 319 – 323; *Angew. Chem. Int. Ed.* **2002**, *41*, 307 – 311; b) D. Brohm, N. Philippe, S. Metzger, A. Bhargava, O. Müller, F. Lieb, H. Waldmann, *J. Am. Chem. Soc.* **2002**, *124*, 13171 – 13178.

[136] S. Bäuerle, T. Blume, J. Günther, D. Henschel, R. Hillig, M. Husemann, A. Mengel, C. Parchmann, E. Schmid, W. Skuballa, *Bioorg. Med. Chem. Lett.* **2004**, *14*, 1673 – 1677.

[137] A. E. Wright, P. J. McCarthy, G. K. Schulte, *J. Org. Chem.* **1989**, *54*, 3472.

[138] R. E. Cebula, J. L. Blanchard, M. D. Boisclair, K. Pal, N. J. Bockovich, *Bioorg. Med. Chem. Lett.* **1997**, *7*, 2015 – 2020, and references therein.

[139] T. Horiguchi, K. Nishi, S. Hakoda, S. Tanida, A. Nagata, H. Okoyama, *Biochem. Pharmacol.* **1994**, *48*, 2139.

[140] P. Wipf, C. R. Hopkins, E. O. Phillips, J. S. Lazo, *Tetrahedron* **2002**, *58*, 6367 – 6372.

[141] a) N. Hirano, J. Kohno, S. Tsunoda, M. Nishio, N. Kishi T. Okuda, K. Kawano, S. Komatsubara, *Tetrahedron* **2001**, *57*, 421 – 427; b) J. Kohno, N. Hirano, K. Sugawara, M. Nishio, T. Hashiyama, N. Nakanishi, S. Komatsubara, *Tetrahedron* **2001**, *57*, 1731 – 1735; c) K. Sugawara, J. Kohno, N. Nakanishi, T. Hashiyama, *Tennen YuKi Kagobutsu Toronkai Koen Yoshishu* **2000**, *42*, 661 – 666; d) A. Fürstner, F. Feyen, H. Prinz, H. Waldmann, *Angew. Chem.* **2003**, *115*, 5519 – 5522; *Angew. Chem. Int. Ed.* **2003**, *42*, 5361 – 5364.

[142] a) M. Imoto, H. Kakeya, T. Sawa, C. Hayashi, M. Hamada, T. Takeuchi, K. Umezawa, *J. Antibiot.* **1993**, *46*, 1342 – 1346; b) H. Kakeya, M. Imoto, Y. Takahashi, H. Naganawa, T. Takeuchi, K. Umezawa, *J. Antibiot.* **1993**, *46*, 1716 – 1719; c) K. Umezawa, M. Kawakami, T. Watanabe, *Pharmacol. Ther.* **2003**, *99*, 15 – 24.

[143] K. A. Alvi, A. Casey, B. G. Nair, *J. Antibiot.* **1997**, *51*, 515 – 517.

[144] A. Fürstner, J. Ruiz-Caro, H. Prinz, H. Waldmann, *J. Org. Chem.* **2004**, *69*, 459 – 467.

[145] For a review see: A. Fürstner, *Angew. Chem.* **2003**, *115*, 3706 – 3728; *Angew. Chem. Int. Ed.* **2003**, *42*, 3582 – 3603.

[146] A. Fürstner, K. Reinecke, H. Prinz, H. Waldmann, *ChemBioChem* **2004**, *5*, 1575 – 1579.

[147] a) A. S. Liotta, H. K. Kole, H. M. Fales, J. Roth, M. Bernier, *J. Biol. Chem.* **1994**, *269*, 22996 – 23001; b) K. T. Hiriyanna, W. R. Buck, S. S. Shen, T. S. Ingebritsen, *Exp. Cell Res.* **1995**, *216*, 21 – 29; c) K. E. Jenkins, A. P. Higson, P. H. Seeberger, M. H. Caruthers, *J. Am. Chem. Soc.* **2002**, *124*, 6584 – 6593; d) I. Marseigne, B. P. Roques, *J. Org. Chem.* **1988**, *53*, 3621 – 3624; e) H. K. Kole, M. Akamatsu, B. Ye, X. Yan, D. Barford, P. P. Roller, T. R. Burke, *Biochem. Biophys. Res. Commun.* **1995**, *209*, 817 – 822; f) T. R. Burke, B. Ye, M. Akamatsu, H. Ford, X. Yan, H. K. Kole, G. Wolf, S. E. Shoeson, P. P. Roller, *J. Med. Chem.* **1996**, *39*, 1021 – 1027; g) T. R. Burke, H. K. Kole, P. P. Roller, *Biochem. Biophys. Res. Commun.* **1994**, *204*, 129; h) L. Chen, L. Wu, A. Otaka, M. S. Smyth, P. P. Roller, T. R. Burke, J. Denhertog, Z. Y. Zhang, *Biochem. Biophys. Res. Commun.* **1995**, *216*, 976 – 984.

[148] S. Soeda, T. Shimada, S. Koyanagi, T. Yokomatsu, T. Murano, S. Shibuya, H. Shimeno, *FEBS Lett.* **2002**, *524*, 54 – 58.

[149] V. S. Murthy, V. M. Kulkarni, *Bioorg. Med. Chem.* **2002**, *10*, 897 – 906.

[150] T. R. Burke, Jr., B. Ye, X. Yan, S. Wang, Z. Jia, L. Chen, Z.-Y. Zhang, D. Barford, *Biochemistry* **1996**, *35*, 15989 – 15989.

[151] C. Dufresne, P. Roy, Z. Wang, E. Asante-Appiah, W. Cromlish, Y. Boie, F. Forghani, S. Desmarais, Q. Wang, K. Skorey, D. Waddleton, C. Ramachandran, B. P. Kennedy, L. Xu, R. Gordon, C. C. Chan, Y. Leblanc, *Bioorg. Med. Chem. Lett.* **2004**, *14*, 1039 – 1042.

[152] E. J. Moran, S. Sarshr, J. E. Cargill, M. M. Shahbaz, A. Lio, A. M. M. Mjalli, R. W. Armstrong, *J. Am. Chem. Soc.* **1995**, *117*, 10787 – 10788.

[153] H. Fu, J. Park, D. Pei, *Biochemistry* **2002**, *41*, 10700 – 10709.

[154] J. Park, H. Fu, D. Pei, *Biochemistry* **2003**, *42*, 5159 – 5167.

[155] C. Leung, J. Grzyb, J. Lee, N. Meyer, G. Hum, C. Jia, S. Liu, S. D. Taylor, *Bioorg. Med. Chem. Lett.* **2002**, *12*, 2309 – 2323.

[156] C. Liljebris, S. D. Larsen, D. Ogg, B. J. Palazuk, J. E. Bleasdale, *J. Med. Chem.* **2002**, *45*, 1785 – 1798.

[157] J. E. Bleasdale, D. Ogg, B. J. Palazuk, C. S. Jacob, M. L. Swanson, W.-Y. Wang, D. P. Thompson, R. A. Conradi, W. R. Mathews, A. L. Laborde, C. W. Stuchly, A. Heijbel, K. Bergdahl, C. A. Bannow, C. W. Smith, C. Liljebris, H. J. Schostarez, P. D. May, F. C. Stevens, S. D. Larsen, *Biochemistry* **2001**, *40*, 5642.

[158] S. D. Larsen, F. C. Stevens, T. J. Lindberg, P. M. Bodnar, T. J. O'Sullivan, H. J. Schostarez, B. J. Palazuk, J. E. Bleasdale, *Bioorg. Med. Chem. Lett.* **2003**, *13*, 971 – 975.

[159] a) L. F. Iversen, H. S. Andersen, S. Branner, S. B. Mortensen, G. H. Peters, K. Norris, O. H. Olsen, C. B. Jeppesen, B. F. Lundt, W. Ripka, K. B. Møller, N. P. H. Møller, *J. Biol. Chem.* **2000**, *275*, 10300 – 10307; b) H. S. Andersen, O. H. Olsen, L. F. Iversen, A. L. P. Sørensen, S. B. Mortensen, M. S. Christensen, S. Branner, T. K. Hansen, J. F. Lau, L. Jeppesen, E. J. Moran, J. Su, F. Bakir, L. Judge, M. Shahbaz, T. Collins, T. Vo, M. J. Newman, W. C. Ripka, N. P. H. Møller, *J. Med. Chem.* **2002**, *45*, 4443 – 4459.

[160] Z. Yan, M. Kahn, M. Qabar, J. Urban, H.-O. Kim, M. A. Blaskovich, *Bioorg. Med. Chem. Lett.* **2003**, *13*, 2083 – 2085.

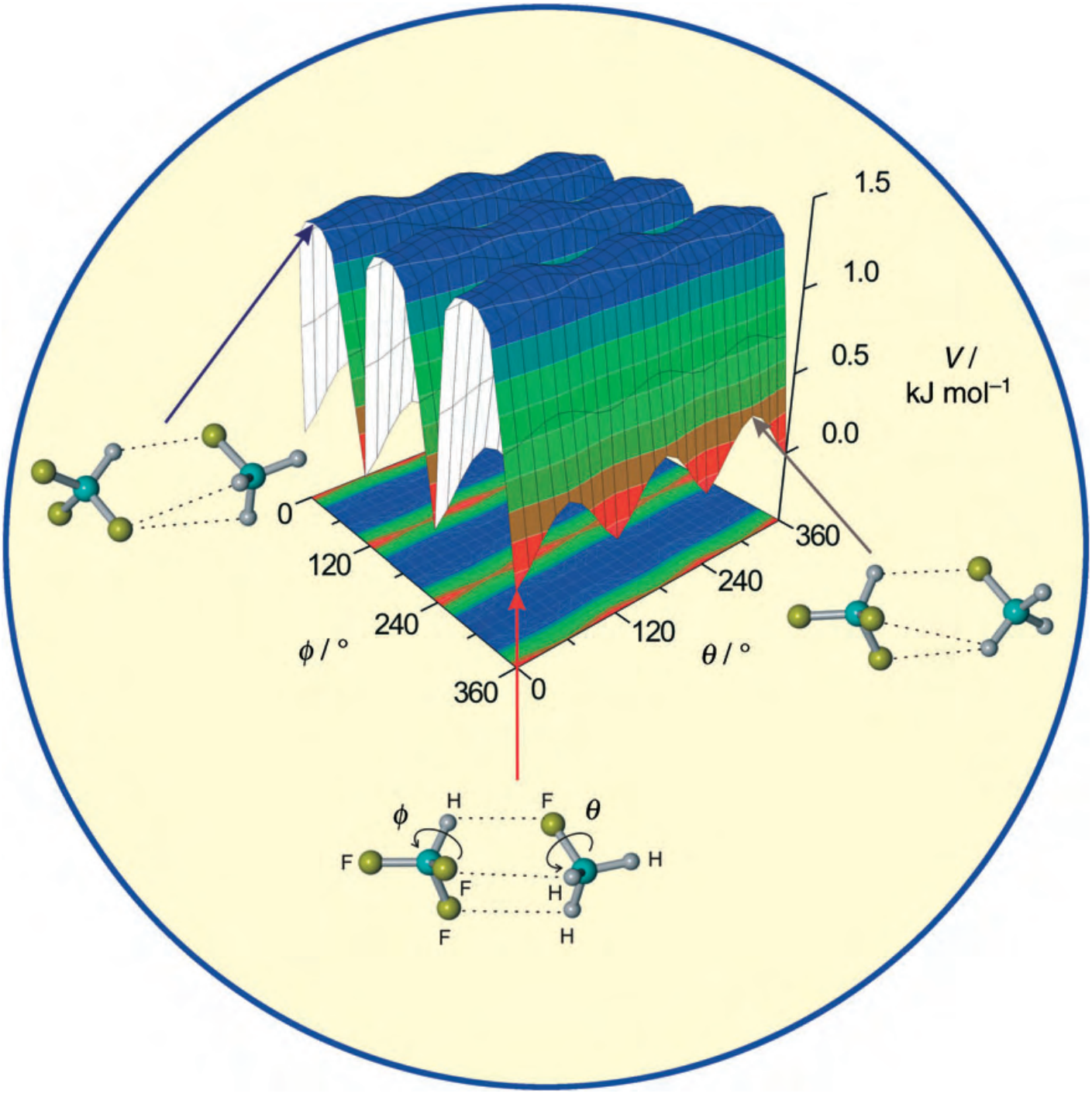
[161] S. W. Ham, J. Park, S.-J. Lee, J. S. Yoo, *Bioorg. Med. Chem. Lett.* **1999**, *9*, 185.

 © 2005 Wiley-VCH Verlag GmbH & Co. KGaA, Weinheim

[162] M. S. Malamas, J. Sredy, C. Moxham, A. Katz, W. Xu, R. McDevitt, F. O. Adebayo, D. R. Sawicki, L. Seestaller, D. Sullivan, J. R. Taylor, *J. Med. Chem.* **2000**, *43*, 1293 – 1310.
[163] http://www.wyeth.com.
[164] Y. T. Chen, J. Xie, C. T. Seto, *J. Org. Chem.* **2003**, *68*, 4123 – 4125.
[165] Y. T. Chen, C. T. Seto, *J. Med. Chem.* **2002**, *45*, 3946 – 3952.
[166] J. Xie, A. B. Comeau, C. T. Seto, *Org. Lett.* **2004**, *6*, 83 – 86.
[167] a) Y. A. Puius, Y. Zhao, M. Sullivan, D. S. Lawrence, S. C. Almo, Z.-Y. Zhang, *Proc. Natl. Acad. Sci. USA* **1997**, *94*, 13420 – 13425; b) K. Shen; Y.-F. Keng, L. Wu, X.-L. Guo, D. S. Lawrence, Z.-Y. Zhang, *J. Biol. Chem.* **2001**, *276*, 47311.
[168] K. I. Skorey, B. P. Kennedy, R. W. Friesen, C. Ramachandran, *Anal. Biochem.* **2001**, *291*, 269 – 278.
[169] K. E. You-Ten, E. S. Muise, A. Itié, E. Michaliszyn, J. Wagner, S. Jothy, W. S. Lapp, M. L. Tremblay, *J. Exp. Med.* **1997**, *186*, 683.
[170] K. E. YouTen, E. S. Muise, A. Itie, E. Michaliszyn, J. Wagner, S. Jothy, W. S. Lapp, M. L. Tremblay, *J. Exp. Med.* **1997**, *186*, 683 – 693.
[171] J. P. Sun, A. A. Fedorov, S. Y. Lee, X. L. Guo, K. Shen, D. S. Lawrence, S. C. Almo, Z. Y. Zhang, *J. Biol. Chem.* **2003**, *278*, 12406 – 12414.
[172] a) Z. Jia, Q. Ye, A. N. Dinaut, Q. Wang, D. Waddleton, P. Payette, C. Ramachandran, B. Kennedy, G. Hum, S. D. Taylor, *J. Med. Chem.* **2001**, *44*, 4584 – 4594; b) E. Asante-Appiah, S. Patel, C. Dufresne, P. Roy, Q. Wang, V. Patel, R. W. Friesen, C. Ramachandran, J. W. Becker, Y. Leblanc, B. P. Kennedy, G. Scapin, *Biochemistry* **2002**, *41*, 9043 – 9051.
[173] a) B. C. Szczepankiewicz, G. Liu, P. J. Hajduk, C. Abad-Zapatero, Z. Pei, Z. Xin, T. H. Lubben, J. M. Trevillyan, M. A. Stashko, S. J. Ballaron, H. Liang, F. Huang, C. W. Hutchins, S. W. Fesik, M. R. Jirousek, *J. Am. Chem. Soc.* **2003**, *125*, 4087 – 4096; b) G. Liu, Z. Xin, H. Liang, C. Abad-Zapatero, P. J. Hajduk, D. A. Janowick, B. G. Szczepankiewicz, Z. Pei, C. W. Hutchins, S. J. Ballaron, M. A. Stashko, T. H. Lubben, C. E. Berg, C. M. Rondinone, J. M. Trevillyan, M. R. Jirousek, *J. Med. Chem.* **2003**, *46*, 3437 – 3440; c) G. Liu, Z. Xin, Z. Pei, P. J. Hajduk, C. Abad-Zapatero, C. W. Hutchins, H. Zhao, T. M. Lubben, S. J. Ballaron, D. L. Haasch, W. Kaszubska, C. M. Rondinone, J. M. Trevillyan, M. R. Jirousek, *J. Med. Chem.* **2003**, *46*, 4232 – 4235; d) Z. Xin G. Liu, C. Abad-Zapatero, Z. Pei, B. G. Szczepankiewicz, X. Li, T. Zhang, C. W. Hutchins, P. J. Hajduk, S. J. Ballaron, M. A. Stashko, T. H. Lubben, J. M. Trevillyan, M. R. Jirousek, *Bioorg. Med. Chem. Lett.* **2003**, *13*, 3947 – 3950; e) Z. Pei, X. Li, G. Liu, C. Abad-Zapatero, T. Lubben, T. Zhang, S. J. Ballaron, C. W. Hutchins, J. M. Trevillyan, M. R. Jirousek, *Bioorg. Med. Chem. Lett.* **2003**, *13*, 3129 – 3132.
[174] C. K. Lau, C. I. Bayly, J. Y. Gauthier, C. S. Li, M. Therien, E. Asante-Appiah, W. Cromlish, Y. Boie, F. Forghani, S. Desmarais, Q. Wang, K. Skorey, D. Waddleton, P. Payette, C. Ramachandran, B. P. Kennedy, G. Scapin, *Bioorg. Med. Chem. Lett.* **2004**, *14*, 1043 – 1048.
[175] J. S. Lazo, K. Nemoto, K. E. Pestell, K. Cooley, E. C. Southwick, D A. Mitchell, W. Furey, R. Gussio, D. W. Zaharevitz, B. Joo, P. Wipf, *Mol. Pharmacol.* **2002**, *61*, 720 – 728.
[176] Y Nishikawa, M. Wang, J. Kerns, C. S. Wilcox, B. I. Carr, *J. Biol. Chem.* **1999**, *274*, 34803 – 34810.
[177] K. Tamura, E. C. Southwick, J. Kerns, K. Rosi, B. I. Carr, C. Wilcox, J. S. Lazo, *Cancer Res.* **2000**, *60*, 1317 – 1325.
[178] J. H. Ahn, S. Y. Cho, J. D. Ha, S. Y. Chu, S. H. Jung, Y. S. Jung, J. Y. Baek, I. K. Choi, E. Y. Shin, S. K. Kang, S. S. Kim, H. G. Cheon, S.-D. Yang, J.-K. Choi, *Bioorg. Med. Chem. Lett.* **2002**, *12*, 1941 – 1946.
[179] R. A. Urbanek, S. J. Suchard, G. B. Steelman, K. S. Knappenberger, L. A. Sygowski, C. A. Veale, M. J. Chapdelaine, *J. Med. Chem.* **2001**, *44*, 1777 – 1793.
[180] J. Sohn, B. Kiburz, Z. Li, L. Deng, A. Safi, M. C. Pirrung, J. Rudolph, *J. Med. Chem.* **2003**, *46*, 2580 – 2588.
[181] M. Wilborn, S. Free, A. Ban, J. Rudolph, *Biochemistry* **2001**, *40*, 14200 – 14206.
[182] P. Wipf, A. Cunningham, R. L. Rice, J. S. Lazo, *Bioorg. Med. Chem.* **1997**, *5*, 165 – 177.
[183] A. P. Ducruet, R. L. Rice, K. Tamura, F. Yokokawa, S. Yokokawa, P. Wipf, J. S. Lazo, *Bioorg. Med. Chem.* **2000**, *8*, 1451 – 1466.
[184] K. R. Guertin, L. Setti, L. Qi, R. M. Dunsdon, B. W. Dymock, P. S. Jones, H. Overton, M. Taylor, G. Williams, J. A. Sergi, K. Wang, Y. Peng, M. Renzetti, R. Boyce, F. Falcioni, R. Garippa, A. Olivier, *Bioorg. Med. Chem. Lett.* **2003**, *13*, 2895 – 2898.
[185] C. Liljebris, J. Martinsson, L. Tedenborg, M. Williams, E. Barker, J. E. S. Duffy, A. Nygren, S. James, *Bioorg. Med. Chem.* **2002**, *10*, 3197 – 3212.
[186] M. S. Malamas, J. Sredy, I. Gunawan, B. Milan, D. R. Sawicki, L. Seestaller, D. Sullivan, B. R. Flam, *J. Med. Chem.* **2000**, *43*, 995 – 1010.
[187] F. Liang, Z. Huang, S.-Y. Lee, J. Liang, M. I. Ivanov, A. Alonso, J. B. Bliska, D. S. Lawrence, T. Mustelin, Z.-Y. Zhang, *J. Biol. Chem.* **2003**, *278*, 41734 – 41741.
[188] A. L. Hopkins, E. R. Groom, *Nat. Rev. Drug Discovery* **2002**, *1*, 727 – 730.
[189] A. Alonso, J. Sasin, N. Bottini, I. Friedberg, I. Friedberg, A. Osterman, A. Godzik, T. Hunter, J. Dixon, T. Mustelin, *Cell* **2004**, *117*, 699 – 711.

 © 2005 Wiley-VCH Verlag GmbH & Co. KGaA, Weinheim

Communications



Molecular clusters formed by hydrogen bridges can be highly dynamic systems, as shown here for a fluoromethane–trifluoromethane molecular complex: The two subunits are not rigidly locked, but almost freely spin around their symmetry axes. For more information, see the Communication by W. Caminati et al. on the following pages.

 © 2005 Wiley-VCH Verlag GmbH & Co. KGaA, Weinheim DOI: 10.1002/anie.200500775

Molecular Complexes

Weak CH···F Bridges and Internal Dynamics in the $CH_3F{\cdot}CHF_3$ Molecular Complex**

Walther Caminati, Juan C. López, José L. Alonso, and Jens-Uwe Grabow*

Herein, we report the effects of weak CH···F hydrogen bonds and dipole–dipole interaction energies on the conformation of the molecular complex fluoromethane–trifluoromethane and the internal dynamics of the two symmetric top subunits, which rotate almost freely with respect to each other.

The non-covalent interactions CH···F and CH···O, which play important roles in biological, atmospheric, and supramolecular chemistry, have been classified as weak hydrogen bonds (WHBs).[1] Studies on WHBs have been mainly performed by X-ray diffraction[2] and, to a lesser extent, by IR spectroscopy on solutions of rare gases.[3] The experimental data on WHB obtained from investigations in the solid or solution states are contaminated by other intermolecular interactions that take place in condensed phases and do not give information on the internal dynamics of the subunits held together by these interactions.

The few rotationally resolved investigations of molecular adducts in which the monomers are held together by CH···F and CH···O WHBs have shown the specificity and directionality of these interactions.[4–9] For example, the dimer of difluoromethane is stabilized only by CH···F bridges[4] and several theoretical investigations have been reported on this type of interaction.[10–12]

The heterodimer fluoromethane–trifluoromethane ($CH_3F{\cdot}CHF_3$) is also expected to contain only CH···F linkages, and an investigation of this dimer is of particular interest to assess the relative weights of the WHBs and dipole–dipole interaction energies. In Figure 1 two plausible conformations of $CH_3F{\cdot}CHF_3$ (A and B) are shown in which three WHBs stabilize the two subunits. In A the three hydrogen s orbitals in CH_3F can probably better overlap with the three fluorine p orbitals of the opposing molecule, but B has a more favorable electrostatic potential energy from the dipole–dipole interaction, with the two dipole moments almost antiparallel to each other. To elucidate the balance between these two stabilization mechanisms, we studied the rotational spectrum of $CH_3F{\cdot}CHF_3$ isolated in the interaction-free matrix of a supersonic jet by employing Fourier-transform microwave spectroscopy (see Experimental Section for details). We could assign only the spectrum of species B: 32, 12, and 11 rotational transitions (see Supporting Information) have been measured for the normal, $CH_3F{\cdot}^{13}CHF_3$, and $^{13}CH_3F{\cdot}CHF_3$ isotopomers, respectively. At an overall point group symmetry of C_s, the molecular complex has two inequivalent internal rotors of C_{3v} symmetry. By taking the feasible large amplitude motions into account within the permutation-inversion (PI) group theory formalism,[13] the appropriate molecular symmetry (MS) group will be G_{18} and the torsional wavefunctions can accordingly be symmetry-classified as A_1, E_1, E_2, E_3, and E_4.[14] All measured transitions were split into a non- and a doubly degenerate (designated A_1 and E_1, respectively) component line as a result of the internal rotation of the CHF_3 group around its symmetry axis. The three other components, E_2, E_3, and E_4, which arise from the internal rotation of the CH_3F group and the interaction between both groups, were not observed. For a very low tunneling barrier, the corresponding splittings are predicted to be very large and thus difficult to locate. The combined analysis of the rotational transition frequencies for the A_1 and E_1 states of the internal rotations of the CHF_3 group[15] yielded the spectroscopic constants shown in Table 1. The internal rotation parameters[16] included therein are: 1) I_α, the moment of inertia of the CHF_3 top, 2) $\measuredangle(a,i)$, the angle between the internal rotation axis of the CHF_3 top and the principal axis of inertia a of the complex, and 3) V_3, the barrier to internal rotation of the CHF_3 top. For the two less abundant isotopomers the results were similar; the larger standard errors are a result of the smaller experimental data set. The effective moment of inertia determined from the A_1–E_1 splitting pattern for an internal rotor (see Table 2) in

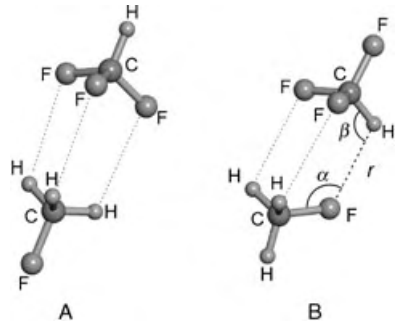


Figure 1. Plausible conformations (A and B) of $CH_3F{\cdot}CHF_3$ highlighting the structural parameters (r, α, and β).

[*] Prof. Dr. W. Caminati
Dipartimento di Chimica "G. Ciamician" dell'Università
Via Selmi 2, 40126 Bologna (Italy)
Fax: (+39) 051-209-9456
E-mail: walther.caminati@unibo.it
Prof. Dr. J. C. López, Prof. Dr. J. L. Alonso
Departamento de Química-Física y Química-Inorgánica
Facultad de Ciencias
Universidad de Valladolid
47005 Valladolid (Spain)
Priv.-Doz. Dr. J.-U. Grabow
Institut für Physikalische Chemie und Elektrochemie
Lehrgebiet A
Callinstrasse 3–3a, 30167 Hannover (Germany)

[**] We would like to thank the Ministers of Education of Italy and Spain, and the Deutscher Akademischer Austauschdienst (DAAD) of Germany for the support given through three bilateral programs: 1) Italy–Spain (Azione Integrata It294-2001, Acción Integrada HI-2000-0092); 2) Germany–Italy (PPP D/0231300 and Progetto VIGONI 2003 21-2002); 3) Spain–Germany (Acciones Integradas HA-2002-0014 and PPP D/0246239). W.C. thanks the University of Bologna, and J.C.L. and J.L.A. thank the Dirección General de Investigación—Ministerio de Ciencia y Tecnología the Junta de Castilla y León—for financial support.

 © 2005 Wiley-VCH Verlag GmbH & Co. KGaA, Weinheim

Table 1: Spectroscopic constants for adduct $CH_3F{\cdot}CHF_3$.[a]

Parameter	$CH_3F{\cdot}CHF_3$	$CH_3F{\cdot}^{13}CHF_3$	$^{13}CH_3F{\cdot}CHF_3$
A [MHz]	6451.696(2)	6456(5)	6440(2)
B [MHz]	1459.976(6)	1456.23(2)	1430.48(1)
C [MHz]	1413.440(6)	1410.10(2)	1386.47(1)
D_J [kHz]	2.740(3)	2.720(7)	2.668(3)
D_{JK} [kHz]	53.44(2)	52.2(5)	51.2(2)
D_K [kHz]	16.3(3)	16.3[b]	16.3[b]
d_J [kHz]	0.222(2)	0.219(5)	0.204(2)
d_K [kHz]	1.4(9)	1.4[b]	1.4[b]
I_α [u Å^2]	86.0(3)	89(3)	86(2)
$\measuredangle(a,i)$ [°][c]	51.4(1)	53(2)	50.6(8)
V_3 [kJ mol^{-1}]	0.840(5)	0.80(3)	0.88(2)
N[d]	64	24	22
σ [kHz][e]	3.2	4.1	1.5
P_{bb} [u Å^2]	44.865(1)[f]	44.82(4)	44.85(2)

[a] A_1 and E_1 states of the internal rotation; I^r representation of Watson's S-reduced Hamiltonian.[15]. Standard errors in parentheses are given in units of the last digit.[b] Parameters were fixed to those of the normal species. [c] $\measuredangle(a,i)$ is the angle between the inertial axes a and the internal rotation axis I; $\measuredangle(b,i)$ is the complement of $\measuredangle(a,i)$ at 90°, while $\measuredangle(c,i)$ is 90° from the symmetry axis. [d] Number of transition frequencies in the fit. [e] Root-mean-square deviation of the fit. [f] Smaller than the sum (46.17 u Å^2) of the P_{bb} values of isolated CHF_3 and CH_3F (44.62 and 1.55 u Å^2, respectively).

Table 2: Comparison of the internal rotation parameters for the CF_3 and CH_3 internal rotors of $CH_3F{\cdot}CHF_3$.

Internal rotor	CF_3	CH_3
I_α [u Å^2]	85.0	3.20
V_3 [kJ mol^{-1}]	0.840	0.36
s	67.92	2.5
Δ_{AE} [MHz][a]	2.6×10^{-1}	1.2×10^{5}
N_{levels}[b]	12	2

[a] Energy spacing between the A_1 and E_1 or E_2 sublevels, that is, $W(E_1)-W(A_1)$ and $W(E_2)-W(A_1)$, respectively, of the vibrational ground state. [b] Number of bound levels below the corresponding V_3 barrier.

$CH_3F{\cdot}CHF_3$ is only slightly smaller than the value of 89.23(2) u Å^2 for isolated CHF_3.[17] This result indicates that the motion responsible for the A_1–E_1 spectral separations is essentially the rotation of the CHF_3 group around an axis close to its C_3 symmetry axis.

The A_1–E_2 torsional splitting was deduced also for the internal rotation of the lighter CH_3F group. This splitting is related to the unexpectedly low value of the planar moment of inertia, P_{bb}, of the complex. The planar moments of inertia, defined as $P_{aa}=1/2\,(-I_{aa}+I_{bb}+I_{cc})$, and cyclic permutations give the extensions of the molecular system in the directions of the considered principal axis. For the $CH_3F{\cdot}CHF_3$ complex the value of P_{bb} should correspond to the sum of the values of P_{bb} for the two isolated symmetric tops (1.55 and 44.62 u Å^2),[17,18] that is, 46.17 u Å^2. This is the case, for example, for oxirane·CHF_3,[6] for which P_{bb} (63.86 u Å^2) is almost exactly the sum of the P_{aa} value of oxirane and the P_{bb} value of CHF_3 (19.43 and 44.62 u Å^2, respectively). In $CH_3F{\cdot}CHF_3$, P_{bb} is 44.69 u Å^2, which is lower by 1.48 u Å^2 than the sum value (46.17 u Å^2). Such an unusually low value of P_{bb} is indicative of an exceptionally low V_3 barrier to the internal rotation of the methyl group. In fact, rotational constants are effective quantities that include the "pseudo" contributions due to the internal rotation of the methyl group, according to Equation (1),[19] in which A_r, B_r, and C_r are the "rigid" rotational constants in the limit of the very high barrier; $W_{00}^{(n)}$ are Hersbach's barrier-dependent perturbation sums relative to the A sublevels of the ground state;[20] F is the reduced constant of the motion; $\rho_g=\lambda_g I_\alpha/I_g$.

$$\begin{aligned} A_{00} &= A_r + W_{00}^{(2)}\,F\,\rho_a^2 \\ B_{00} &= B_r \\ C_{00} &= C_r + W_{00}^{(2)}\,F\rho_c^2 \end{aligned} \qquad (1)$$

The experimentally determined value of P_{bb} is obtained at $V_3=30\ \mathrm{cm}^{-1}$. As the curve V_3 versus P_{bb} is very steep at that point, we can set an estimated error of $10\ \mathrm{cm}^{-1}$. The parameters relevant to the internal rotations of CH_3F and CHF_3 are compared in Table 2. Although the two V_3 barriers are relatively similar, the reduced barriers s, which contain both potential- and kinetic-energy factors, are very different from each other. Correspondingly, the A_1–E_1 and A_1–E_2 splittings, that is, the Δ_{AE} energy spacings between the A_1 and E_1 or E_2 sublevels, respectively, of the vibrational ground state, differ by six orders of magnitude.

For several molecular complexes, it has been possible to estimate the force constant (k_s) of the stretching motions between the two moieties that lead to dissociation, by using approximated Equation (2),[21] in which μ, R_{CM}, B, C, and D_J are the reduced mass, the distance between the monomer centers of mass, the rotational constants, and the first-order centrifugal distortion constant, respectively, of the adduct, and h is Planck's constant. However, in the case of $CH_3F{\cdot}CHF_3$, the effective parameter D_J contains contributions from one of the large amplitude motions, that is, the internal rotation of the CH_3F group. These contributions can be calculated with Equation (3).[22]

$$k_s = 16\,\pi^4\,(\mu\,R_{CM})^2\,[4\,B^4+4\,C^4-(B-C)^2(B+C)^2]/(h\,D_J) \qquad (2)$$

$$D_J = -1/2\,(\rho_b^4+\rho_c^4)\,W_{00}^{(4)}\,F \qquad (3)$$

The estimated correction (0.029 kHz) to the effective value in Table 1 is very small. Thus, by using the value of 2.711 kHz in Equation (2), a value $k_s=5.2\ \mathrm{N\,m^{-1}}$, which corresponds to a harmonic stretching frequency of $62\ \mathrm{cm}^{-1}$, was obtained. The dissociation energy (E_D) has been evaluated to be $5.3\ \mathrm{kJ\,mol^{-1}}$ by assuming a Lennard–Jones potential function and using the approximated equation[23] $E_D=1/72\,k_s R_{CM}^2$. Such a dissociation energy corresponds to a binding energy of $1.8\ \mathrm{kJ\,mol^{-1}}$ for each C–H···F linkage. This value is very similar to that found for the dimer of difluoromethane, which also displays three C–F···H–C interactions.[4]

If we assume the geometries of isolated CHF_3[17] and CH_3F[18] to remain unaltered in the adduct, we have sufficient experimental data to obtain a plausible r_0 structure, that is, to determine the three parameters r, α, and β shown in Figure 1. First, we calculated the rigid values of the rotational constants by applying the CH_3 corrections indicated in Equation (1) to the effectively determined rotational constants. Then we

 © 2005 Wiley-VCH Verlag GmbH & Co. KGaA, Weinheim

fitted the nine available rotational constants to obtain the three parameters. In the fit, we allowed these parameters to change, with respect to the ab initio values, at "confidence intervals" of 0.01 Å for the bond distance and at 2° for the two angles, respectively, according to the diagnostic least-squares procedure described by Curl.[24] The three parameters, r, α, and β, are reported in Table 3, together with the derived distance of the other hydrogen bonds. The substitution coordinates[25] of the carbon atoms of the CH_3F and CHF_3 subunits (see Table 3 footnotes) allow the C–C distances, which are also listed in Table 3, to be determined.

Table 3: Relevant structural parameters of $CH_3F{\cdot}CHF_3$ (see Figure 1).

r_0 parameters	r_0[a]	r_s[b]	ab initio[c]
$r(F_{CH_3F}\cdots H_{CHF_3})$ [Å][a]	2.427(10)	–	2.405
α [°][a]	124.1(3)	–	122.3
β [°][a]	115.5(3)	–	109.9
$r(F_{CHF_3}\cdots H_{CH_3F})$ [Å][d]	3.052(15)	–	2.842
$r(C_{CH_3F}\cdots C_{CHF_3})$ [Å][d]	3.645	3.60(2)[e]	3.522

[a] $r(F_{CH_3F}\cdots H_{CHF_3})$, which coincides with r of Figure 1, α, and β are the fitted parameters. The remaining parameters have been derived from the obtained partial r_0 geometry. [b] From the substitution coordinates of CH_3F and CHF_3 carbon atoms. [c] Computed values at MP2/6-311++G(2df,2p) level. [d] Derived parameter. [e] C···C distance between the carbon atoms of CH_3F and CHF_3. From r_s coordinates of C_{CHF_3} [$|a|$ = 0.84(6); $|c|$ = 0.43(4) Å] and of C_{CH_3F} [$|a|$ = 2.619(7); $|c|$ = 0.57(3) Å]. $|b|$ is fixed to 0 because imaginary.

Ab initio computations at the MP2/6-311++G(2df,2p) level[26] at different points of the $CH_3F{\cdot}CHF_3$ potential-energy surface have been performed to investigate the conformational behavior of the dimer. Conformer B is predicted to be the global minimum. Some of the calculated structural parameters for this conformer are compared to the experimental values in Table 3. The counterpoise (CP)-corrected dissociation energy for this conformer is calculated to be 10.0 kJ mol^{-1}, which is higher than that determined from the centrifugal distortion. Conformer A is predicted to be also a stable minimum, some 714 cm^{-1} (619 cm^{-1} after CP corrections) higher in energy than species B.

Other plausible conformers shown in Figure 2 were also considered. However, at this level of theory these conformers are predicted to be transition configurations with one negative frequency. Figure 3 shows the calculated potential-energy curves that describe the internal rotation of CHF_3 and CH_3F around their local C_3 axes. As indicated, the measured V_3 values thus give the experimental energies of configurations C and D with respect to B. They are in good agreement with the ab initio values, although the results of ab initio calculations lead us to anticipate that the shape of the potential-energy surface is more complicated.

In summary, we have shown how rotational spectroscopy can supply detailed information on the chemical features of weak hydrogen bonds and provide insight on the internal dynamics of the unit constituents of molecular complexes with unrivaled precision. In the case of $CH_3F{\cdot}CHF_3$ studied here, the CH_3F moiety "sees" CHF_3 in a well-defined position, while the CHF_3 unit "sees" CH_3F as a "cone".

Experimental Section

Commercial samples of CH_3F (Aldrich) and CHF_3 (Linde gas) were used without further purification. The spectra of the isotopic ^{13}C-containing species were measured in natural abundance.

The rotational spectrum in the 6–18.5 GHz frequency region was measured using a coaxially oriented beam-resonator arrangement-(COBRA)-type[27] pulsed supersonic jet Fourier-transform microwave (FT-MW) spectrometer,[28] as described elsewhere[29] and recently updated with the FTMW++ set of programs.[30]

A gaseous mixture of CH_3F (1%) and CHF_3 (1%) in He at a total pressure of 2.0 bar was expanded through the solenoid valve (General Valve, Series 9, nozzle diameter 0.5 mm) into the Fabry–Pérot cavity. The spectral line positions were determined after Fourier transformation of the 8000-data-point time-domain signal, recorded at intervals of 100 ns. Each rotational transition is split by the Doppler effect as a result of the coaxial arrangement of the supersonic jet and resonator axes in the COBRA-FTMW spectrometer. The rest frequency is calculated as the arithmetic mean of the frequencies of the Doppler components. The estimated accuracy of frequency measurements is greater than 3 kHz. Lines separated by more than 7 kHz are resolvable.

Received: March 2, 2005
Published online: May 2, 2005

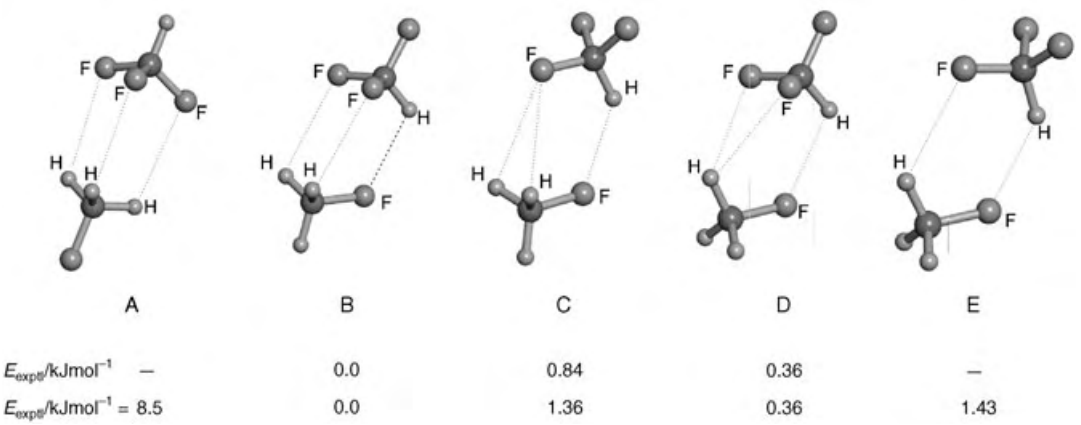


Figure 2. Relative energies of configurations A and C–E with respect to the observed conformer B. Configurations C–E are transition states (saddle points), not stable minima. In particular, the energies of C and D correspond to the two V_3 barriers.

 © 2005 Wiley-VCH Verlag GmbH & Co. KGaA, Weinheim

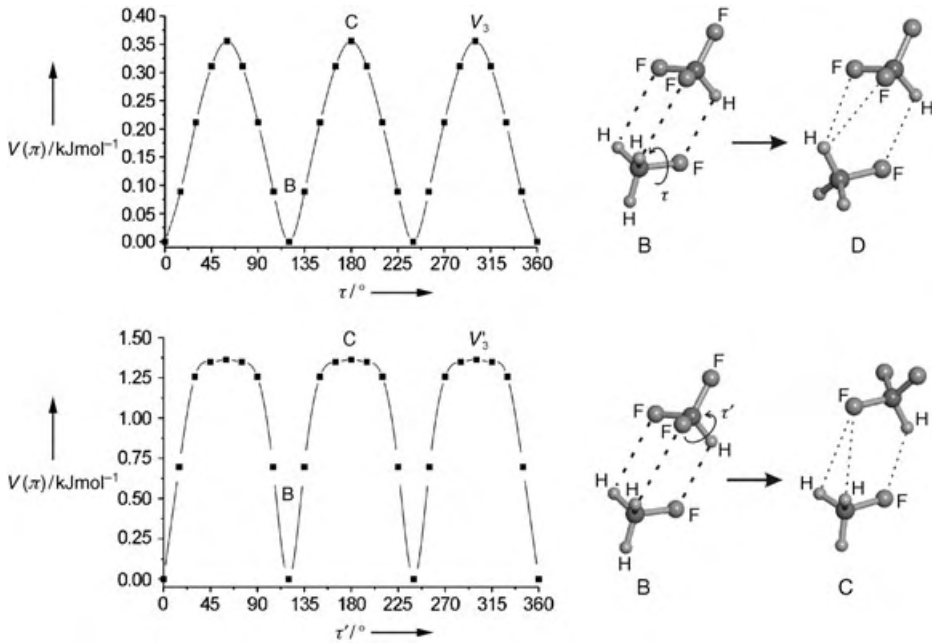


Figure 3. Local potential-energy curves for the two large amplitude tunneling motions in $CH_3F{\cdot}CHF_3$.

Keywords: halomethanes · hydrogen bonds · molecular complexes · molecular dynamics · rotational spectroscopy

[1] "The Weak Hydrogen Bond in Structural Chemistry and Biology": *IUCr Monographs on Crystallography, Vol. IX* (Eds.: G. R. Desiraju, T. Steiner), Oxford University Press, Oxford, **2001**.

[2] T. Steiner, *Angew. Chem.* **2002**, *114*, 50; *Angew. Chem. Int. Ed.* **2002**, *41*, 48.

[3] S. N. Delanoye, W. A. Herrebout, B. J. van der Veken, *J. Am. Chem. Soc.* **2002**, *124*, 11854.

[4] a) W. Caminati, S. Melandri, P. Moreschini, P. G. Favero, *Angew. Chem.* **1999**, *111*, 3105; *Angew. Chem. Int. Ed.* **1999**, *38*, 2924; b) S. Blanco, J. C. López, A. Lesarri, J. L. Alonso, *J. Mol. Struct.* **2002**, *612*, 255.

[5] Y. Tatamitani, B. Liu, J. Shimada, T. Ogata, P. Ottaviani, A. Maris, W. Caminati, J. L. Alonso, *J. Am. Chem. Soc.* **2002**, *124*, 2739.

[6] J. L. Alonso, S. Antolínez, S. Blanco, A. Lesarri, J. C. López, W. Caminati, *J. Am. Chem. Soc.* **2004**, *126*, 3244.

[7] Y. Tatamitami, T. Ogata, *J. Mol. Spectrosc.* **2003**, *222*, 102.

[8] S. Blanco, J. C. López, A. Lesarri, W. Caminati, J. L. Alonso, *ChemPhysChem* **2004**, *5*, 1779.

[9] G. C. Cole, A. C. Legon, *Chem. Phys. Lett.* **2003**, *369*, 31.

[10] E. Espinosa, I. Alkorta, J. Elguero, E. Molins, *J. Chem. Phys.* **2002**, *117*, 5529.

[11] E. Kryachko, S. Scheiner, *J. Phys. Chem. A* **2004**, *108*, 2527.

[12] E. Ebrahimi, H. Roohi, S. M. Habibi, *J. Mol. Struct. (Theochem)* **2004**, *684*, 87.

[13] H. C. Longuet Higgins, *Mol. Phys.* **1963**, *6*, 445.

[14] H. Dreizler, *Z. Naturforsch.* **1961**, *16*, 1354. For a typical example, see: J. Sheridan, W. Bossert, A. Bauder, *J. Mol. Spectrosc.* **1980**, *80*, 1.

[15] H. Hartwig, H. Dreizler, *Z. Naturforsch. A* **1996**, *51*, 923, according to the I^r representation of Watson's *S*-reduced Hamiltonian: J. K. G. Watson in *Vibrational Spectra and Structure, Vol. 6* (Ed.: J. R. Durig), Elsevier, New York, **1977**, pp. 1–89.

[16] R. C. Woods, *J. Mol. Spectrosc.* **1966**, *21*, 4.

[17] Y. Kawashima, A. P. Cox, *J. Mol. Spectrosc.* **1978**, *72*, 423.

[18] R. Bocquet, W. D. Chen, D. Papousek, G. Wlodarczak, J. Demaison, *J. Mol. Spectrosc.* **1994**, *164*, 456.

[19] D. R. Herschbach, J. D. Swalen, *J. Chem. Phys.* **1958**, *29*, 761.

[20] D. R. Herschbach, *J. Chem. Phys.* **1959**, *31*, 91.

[21] a) D. J. Millen, *Can. J. Chem.* **1985**, *63*, 1477; b) W. G. Read, E. J. Campbell, G. Henderson, *J. Chem. Phys.* **1983**, *78*, 3501.

[22] W. Caminati, *J. Mol. Spectrosc.* **1982**, *90*, 315.

[23] R. P. A. Bettens, R. M. Spycher, A. Bauder, *Mol. Phys.* **1995**, *86*, 487.

[24] R. F. Curl, *J. Comput. Phys.* **1957**, *27*, 343.

[25] J. Kraitchman, *Am. J. Phys.* **1953**, *21*, 17.

[26] Gaussian 03 (Revision B.04), M. J. Frisch, G. W. Trucks, H. B. Schlegel, G. E. Scuseria, M. A. Robb, J. R. Cheeseman, J. A. Montgomery, Jr., T. Vreven, K. N. Kudin, J. C. Burant, J. M. Millam, S. S. Iyengar, J. Tomasi, V. Barone, B. Mennucci, M. Cossi, G. Scalmani, N. Rega, G. A. Petersson, H. Nakatsuji, M. Hada, M. Ehara, K. Toyota, R. Fukuda, J. Hasegawa, M. Ishida, T. Nakajima, Y. Honda, O. Kitao, H. Nakai, M. Klene, X. Li, J. E. Knox, H. P. Hratchian, J. B. Cross, C. Adamo, J. Jaramillo, R. Gomperts, R. E. Stratmann, O. Yazyev, A. J. Austin, R. Cammi, C. Pomelli, J. W. Ochterski, P. Y. Ayala, K. Morokuma, G. A. Voth, P. Salvador, J. J. Dannenberg, V. G. Zakrzewski, S. Dapprich, A. D. Daniels, M. C. Strain, O. Farkas, D. K. Malick, A. D. Rabuck, K. Raghavachari, J. B. Foresman, J. V. Ortiz, Q. Cui, A. G. Baboul, S. Clifford, J. Cioslowski, B. B. Stefanov, G. Liu, A. Liashenko, P. Piskorz, I. Komaromi, R. L. Martin, D. J. Fox, T. Keith, M. A. Al-Laham, C. Y. Peng, A. Nanayakkara, M. Challacombe, P. M. W. Gill, B. Johnson, W. Chen, M. W. Wong, C. Gonzalez, J. A. Pople, Gaussian, Inc., Pittsburgh, PA, **2003**.

[27] J.-U. Grabow, W. Stahl, *Z. Naturforsch. A* **1990**, *45*, 1043; J.-U. Grabow, doctoral thesis, Christian-Albrechts-Universität zu Kiel, Kiel, **1992**; J.-U. Grabow, W. Stahl, H. Dreizler, *Rev. Sci. Instrum.* **1996**, *67*, 4072.

[28] T. J. Balle, W. H. Flygare, *Rev. Sci. Instrum.* **1981**, *52*, 33.

[29] W. Caminati, A. Millemaggi, J. L. Alonso, A. Lesarri, J. C. Lopez, S. Mata, *Chem. Phys. Lett.* **2004**, *392*, 1.

[30] J.-U. Grabow, *56th Ohio State University International Conference on Molecular Spectroscopy*, MG01, Columbus **2001**; J.-U. Grabow, Habilitationsschrift, Universität Hannover, Hannover **2004**; http://www.pci.uni-hannover.de/~lgpca/spectroscopy/ftmw.

 © 2005 Wiley-VCH Verlag GmbH & Co. KGaA, Weinheim

Coordination Polymers

A Metal–Organic Framework with the Zeolite MTN Topology Containing Large Cages of Volume 2.5 nm^3 **

Qianrong Fang, Guangshan Zhu, Ming Xue, Jinyu Sun, Yen Wei, Shilun Qiu,* and Ruren Xu*

Metal–organic framework (MOF) coordination polymers have attracted tremendous attention because of their intriguing molecular topologies and their potentially useful ion-exchange, adsorption, catalytic, fluorescence, and magnetic properties.[1–7] By taking advantage of the well-defined coordination geometries of metal centers as nodes, the structures of various minerals, such as quartz diamond,[8,9] perovskite,[10] rutile,[11] PtS,[12,13] and feldspar,[14] with specific functionalities, have been artificially reproduced by replacing monoatomic anions (O^{2-}, S^{2-}) with polyatomic organic bridging ligands as linkers. To meet the increasing demand for large-pore frameworks that are suitable for catalyzing reactions of large molecules, successful synthetic strategies for the preparation of large-pore metal–organic polymers with a genuine zeolite topology are still a huge challenge.

The expansion and decoration of the topological networks of inorganic materials, which is an effective and powerful synthetic strategy, has been shown to produce a new generation of highly porous metal–organic polymers.[15,16] During the course of our work, Férey et al. described a novel metal–organic hybrid compound, $[Cr_3F(H_2O)_3O\{C_6H_3(CO_2)_3\}_2]\cdot n\,H_2O$ (MIL-100, $n \approx 28$),[17] with the zeolite MTN topology from Cr^{3+} ions and benzene-1,3,5-tricarboxylate, whose structure was determined by powder X-ray diffraction simulation. Our strategy for preparing such a metal–organic framework with large pores is based on expanding the zeolite topologies[18,19] by constructing metal–organic tetrahedral building blocks with four connections. In this work, we consider the hexamethylenetetramine (hmt) ligand to be the best candidate because it contains four coordinating N atoms, similar to the mode of the SiO_4 building block in zeolites. The cadmium ion was chosen as the bridge on account of the equatorial-plane locations of its trigonal-bipyramidal coordination geometry; these locations are easily coordinated by water molecules. Thus, a metal–organic tetrahedral building block TM_4 (T = tetrahedrally coordinated molecule; M = transition-metal ion), in which the M-T-M angles range from 108 to 120°, was constructed from an hmt molecule and four cadmium ions. We present herein a new metal–organic framework with zeolite topology constructed from this tetrahedral building block. The novel open-framework metal–organic polymer $[\{Cd(H_2O)_3\}_{34}(N_4C_6H_{12})_{17}]Cl_{68}\cdot 46\,H_2O\cdot 68\,DMF$ (**1**; DMF = *N*,*N*-dimethylformamide) possesses the zeolite MTN topology (MTN = zeolite socony mobil – thirty-nine) with two types of 5^{12} and 6^45^{12} cages. The 6^45^{12} cage has a volume of about 2522 Å^3 (a van der Waals sphere with a diameter of 16.8 Å would just fit inside the void). To the best of our knowledge, architectures with large cages have rarely been reported so far for metal–organic polymers (such as MOF-101[20] and MIL-100[17]).

Polymer **1** was synthesized under mild conditions. In a typical procedure, a mixture of $CdCl_2\cdot 2.5\,H_2O$ and hmt (10:1) was prepared in DMF/ethanol/H_2O (5:3:3) containing HCl, and then a solution of triethylamine in DMF was allowed to diffuse into the above mixture at room temperature to adjust the pH value of the solution. After standing for a month, colorless octahedron-shaped crystals of **1** were collected with a 67% yield based on cadmium. This complex is stable in air, soluble in water, methanol, and ethanol, slightly soluble in DMF, but insoluble in acetonitrile and nitromethane.

X-ray crystallographic analysis revealed that polymer **1**[21] consists of a 3D open framework with the zeolite MTN topology. Each cadmium ion is coordinated by two nitrogen atoms from two different hmt ligands and three coordinated water molecules (Figure 1). The hmt ligands adopt a tetrahe-

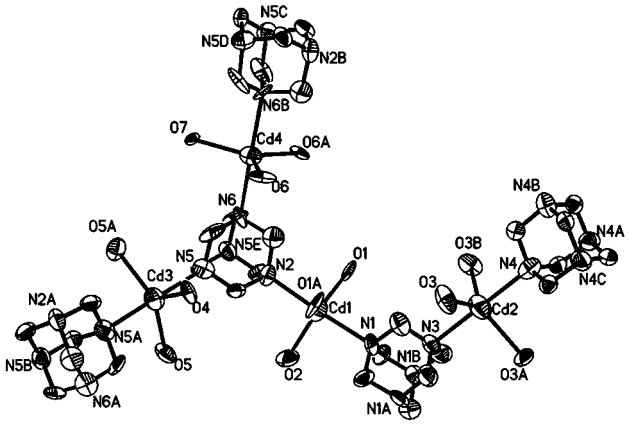


Figure 1. The coordination geometry of the cadmium ions in the asymmetric unit of polymer **1**. Thermal ellipsoids are shown at the 50% probability level. Selected bond lengths [Å] and angles [°]: Cd1–N1 2.455(8), Cd1–N2 2.385(7), Cd1–O1 2.445(4), Cd1–O2 2.466(7), Cd2–N3 2.468(13), Cd2–N4 2.421(16), Cd2–O3 2.459(6), Cd3–N5 2.440(6), Cd3–O4 2.485(5), Cd3–O5 2.419(5), Cd4–N6 2.513(8), Cd4–O6 2.453(4), Cd4–O7 2.448(7); N2-Cd1-N1 177.1(3), N2-Cd1-O1 90.12(13), O1-Cd1-N1 88.51(12), N2-Cd1-O2 90.2(3), N1-Cd1-O2 92.6(3), O1-Cd1-O2 118.36(13), N4-Cd2-N3 180.0(6), N4-Cd2-O3 89.64(17), N3-Cd2-O3 90.36(17), O5-Cd3-N5 92.50(17), N5-Cd3-O4 87.53(13), O5-Cd3-O4 114.69(15), O7-Cd4-N6 90.51(16), O6-Cd4-N6 89.74(8), O7-Cd4-O6 121.13(17).

[*] Q.-R. Fang, Prof. G.-S. Zhu, M. Xue, J.-Y. Sun, Prof. S.-L. Qiu, Prof. R.-R. Xu
State Key Laboratory of Inorganic Synthesis and Preparative Chemistry Jilin University
Changchun 130012 (P.R. China)
Fax: (+86) 431-516-8331
E-mail: zhugs@mail.jlu.edu.cn
sqiu@mail.jlu.edu.cn
Prof. Y. Wei
Department of Chemistry, Drexel University
Philadelphia, PA 19104 (USA)

[**] This work was funded by the State Basic Research Project (no. G2000077507) and the National Nature Science Foundation of China (grant nos. 29873017, 20273026, and 20101004). MTN = zeolite socony mobil – thirty-nine. We are very grateful for the help provided by one of the referees.

Supporting information for this article is available on the WWW under http://www.angewandte.org or from the author.

 DOI: 10.1002/anie.200462260 © 2005 Wiley-VCH Verlag GmbH & Co. KGaA, Weinheim

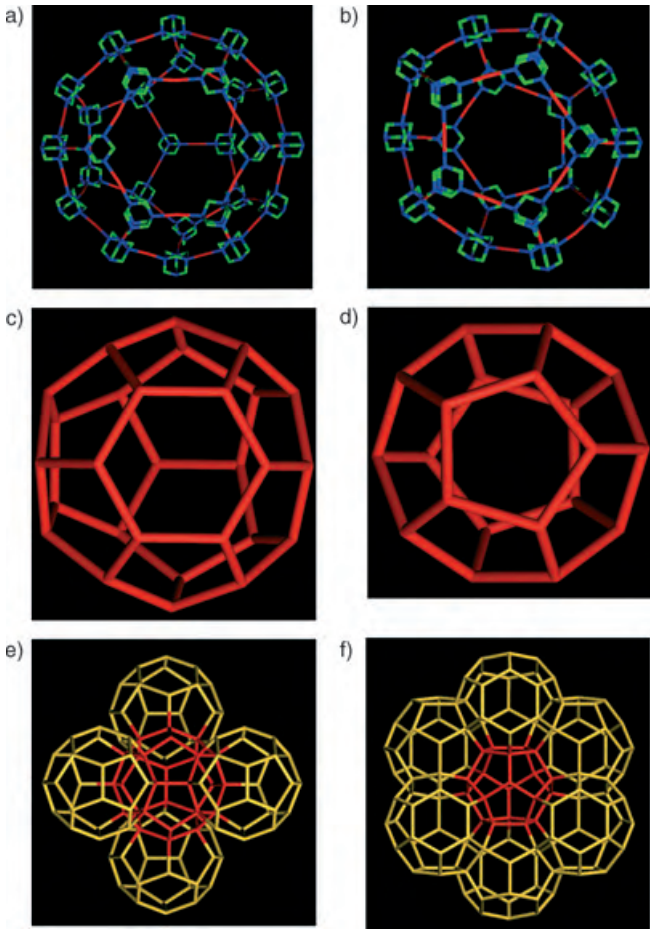


Figure 2. a) A large cage constructed from four six-membered rings (six {Cd_4(hmt)} tetrahedra) and twelve five-membered rings (five {Cd_4(hmt)} tetrahedra) and b) a small cage constructed from twelve five-membered rings (five {Cd_4(hmt)} tetrahedra) in the structure of polymer **1**. Cd red, N blue, C green; for clarity, the oxygen and hydrogen atoms are not shown. The topologies of the 6^45^{12} and 5^{12} cages are shown in (c) and (d), respectively. e) The 6^45^{12} cage in (c; red) sharing its four six-membered rings with four others (yellow). f) The 5^{12} cage in (d; red) sharing its six six-membered rings with six 6^45^{12} cages (c; yellow).

dral coordination geometry, with four different cadmium ions occupying the four coordination sites. The Cd–O lengths (2.419(5)–2.485(5) Å) are within the normal range,[22] and the Cd–N lengths (2.385(7)–2.513(8) Å) are close to those reported for other cadmium–nitrogen donor compounds.[23]

The framework of polymer **1** contains two kinds of cages composed of tetrahedral {Cd_4(hmt)} building blocks. The large 6^45^{12} cage (Figure 2a,c) consists of four six-membered rings (made of six tetrahedrally coordinated hmt molecules) of about 12.3×13.1 Å^2 (as measured between the centers of opposite atoms) and twelve five-membered rings of about 10.4×10.4 Å^2 in diameter. The small 5^{12} cage (Figure 2b,d) consists of twelve five-membered rings. Each 6^45^{12} cage in polymer **1** shares its six-membered rings with four neighboring 6^45^{12} cages (Figure 2e) and five-membered rings with twelve neighboring 5^{12} cages, while each 5^{12} cage in **1** shares its five-membered rings with six neighboring 6^45^{12} cages (Figure 2f) and six neighboring 5^{12} cages. In this way, all of these cages give rise to the 3D framework of polymer **1** with the MTN topology.[24] Figure 3 shows two kinds of windows for the five- and six-membered rings along the [110] direction. The same structure exists along five other directions (such as [101], [011], [$\bar{1}$10], 10$\bar{1}$], and [01$\bar{1}$]).

Unlike most zeolites, polymer **1** has a positively charged framework. The charge-balancing chlorine anions in the cages could not be directly located in the crystal structure analysis. However, inductively coupled plasma analysis[25] and mass-spectrometric analysis[26] indicated that the molar ratio of cadmium to chlorine is 1:2. In addition, elemental analysis[27] and thermal gravimetric analysis (TGA)[28] showed that each formula unit of polymer **1** includes about 46 guest H_2O and 68 DMF molecules. Anion exchange was carried out for the cationic framework[29–31] by substituting SCN^- for Cl^- in the cages. Typically, a 200-mg sample of the coordination polymer was treated at room temperature with 5 mL of DMF containing 3 M KSCN. After stirring for 20 min the product was filtered, washed with pure DMF, and then dried in air. The IR spectra of the exchanged product show new SCN^- bands (2075 cm^{-1}); the other signals of the IR spectrum and the powder XRD pattern remain virtually unchanged, which

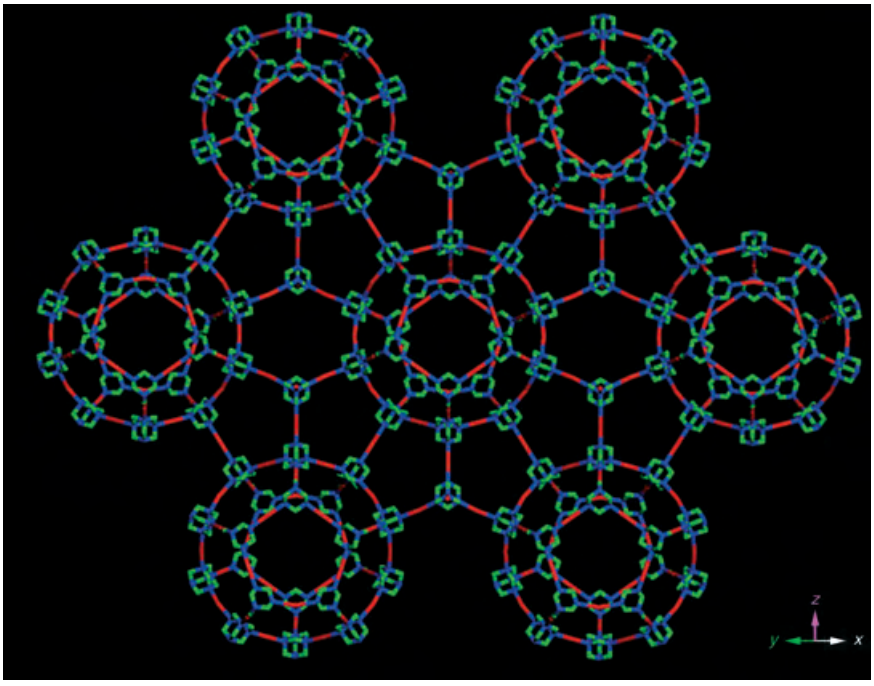


Figure 3. Infinite 3D coordination framework of polymer **1** viewed along the [110] direction. The windows of the six-membered rings (six {Cd_4(hmt)} tetrahedra) are about 12.3×13.1 Å^2 (measured between atom centers), and the windows of the five-membered rings (five {Cd_4(hmt)} tetrahedra) are about 10.4×10.4 Å^2 in this structure. Cd red, N blue, C green; for clarity, the oxygen and hydrogen atoms are not shown.

 © 2005 Wiley-VCH Verlag GmbH & Co. KGaA, Weinheim

suggests that the skeleton is retained after anion exchange (see Supporting Information).

In conclusion, the novel 3D metal–organic framework polymer **1** with the zeolite MTN topology has been synthesized from the metal–organic tetrahedral building block TM_4. The framework of **1** greatly expands the original structure of MTN and possesses large cages with a volume of about 2522 Å^3. Other structures with zeolite or zeolite-like topologies and large cages should be obtainable by following a similar synthetic strategy. We believe that such metal–organic framework coordination polymers will come to be seen as a genuine third generation of zeolites that contain the same structures as traditional zeolites but offer several fundamental advantages, including ion-exchange, adsorption, and catalytic properties.

Experimental Section

1: $CdCl_2 \cdot 2.5\,H_2O$ (0.228 g, 0.1 mmol), HCl (0.1 mL, 2 M solution), hmt (0.014 g, 0.01 mmol), DMF (5 mL), ethanol (3 mL), and H_2O (3 mL) were placed in a 25-mL vial and stirred. After stirring in air for 1 h, the vial was placed in a 100-mL beaker containing a solution of triethylamine (0.1 mL) in DMF (8 mL), and then sealed and left for 30 days at room temperature. The resulting colorless octahedron-shaped crystals of **1** were collected (67% yield based on cadmium). The complex is stable in air, soluble in water, methanol, and ethanol, slightly soluble in DMF, but insoluble in acetonitrile and nitromethane. FTIR (KBr): $\tilde{\nu} = 3448$ (s), 2939 (w), 2360 (w), 1651 (s), 1466 (w), 1388 (w), 1242 (m), 1111 (w), 1011 (s), 818 (m), 694 (m), 579 (w) cm^{-1}.

Received: October 10, 2004
Revised: February 26, 2005
Published online: April 29, 2005

Keywords: cadmium · coordination polymers · organic–inorganic hybrid composites · zeolite analogues

[1] M. Eddaoudi, D. B. Moler, H. Li, B. Chen, T. M. Reineke, M. O'Keeffe, O. M. Yaghi, *Acc. Chem. Res.* **2001**, *34*, 319–330.
[2] B. Moulton, M. J. Zaworotko, *Chem. Rev.* **2001**, *101*, 1629–1658.
[3] S. L. James, *Chem. Soc. Rev.* **2003**, *32*, 276–288.
[4] H. Li, M. Eddaoudi, M. O'Keeffe, O. M. Yaghi, *Nature* **1999**, *402*, 276–279.
[5] J. S. Seo, D. Whang, H. Lee, S. I. Jun, J. Oh, Y. J. Jeon, K. Kim, *Nature* **2000**, *404*, 982–986.
[6] J. Pang, E. J. P. Marcotte, C. Seward, R. S. Brown, S. N. Wang, *Angew. Chem.* **2001**, *113*, 4166–4169; *Angew. Chem. Int. Ed.* **2001**, *40*, 4042–4045.
[7] K. Barthelet, J. Marrot, D. Riou, G. Férey, *Angew. Chem.* **2002**, *114*, 291–294; *Angew. Chem. Int. Ed.* **2002**, *41*, 281–284.
[8] J. Y. Sun, L. H. Weng, Y. M. Zhou, J. X. Chen, Z. X. Chen, Z. C. Liu, D. Y. Zhao, *Angew. Chem.* **2002**, *114*, 4651–4653; *Angew. Chem. Int. Ed.* **2002**, *41*, 4471–4473.
[9] B. F. Hoskins, R. Robson, *J. Am. Chem. Soc.* **1990**, *112*, 1546–1554.
[10] L. Carlucci, G. Ciani, D. M. Proserpio, A. Sirni, *Angew. Chem.* **1995**, *107*, 2037–2040; *Angew. Chem. Int. Ed. Engl.* **1995**, *34*, 1895–1898.
[11] S. R. Batten, B. F. Houskins, R. Robson, *J. Chem. Soc. Chem. Commun.* **1991**, 445–447.
[12] R. W. Gable, B. F. Houskins, R. Robson, *J. Chem. Soc. Chem. Commun.* **1990**, 762–763.
[13] B. Chen, M. Eddaoudi, T. M. Reineke, J. W. Kampf, M. O'Keeffe, O. M. Yaghi, *J. Am. Chem. Soc.* **2000**, *122*, 11559–11560.
[14] S. W. Keller, *Angew. Chem.* **1997**, *109*, 295–297; *Angew. Chem. Int. Ed. Engl.* **1997**, *36*, 247–248.
[15] B. Chen, M. Eddaoudi, S. T. Hyde, M. O'Keeffe, O. M. Yaghi, *Science* **2001**, *291*, 1021–1023.
[16] M. O'Keeffe, M. Eddaoudi, H. Li, T. M. Reineke, O. M. Yaghi, *J. Solid State Chem.* **2000**, *152*, 3–20.
[17] G. Férey, C. Serre, C. Mellot-Draznieks, F. Millange, S. Surblé, J. Dutour, I. Margiolaki, *Angew. Chem.* **2004**, *116*, 6456–6461; *Angew. Chem. Int. Ed.* **2004**, *43*, 6296–6301.
[18] Y. Q. Tian, C. X. Cai, Y. Ji, X. Z. You, S. M. Peng, G. H. Lee, *Angew. Chem.* **2002**, *114*, 1442–1444; *Angew. Chem. Int. Ed.* **2002**, *41*, 1384–1386.
[19] B. F. Abrahams, A. Hawley, M. G. Haywood, T. A. Hudson, R. Robson, D. A. Slizys, *J. Am. Chem. Soc.* **2004**, *126*, 2894–2904.
[20] M. Eddaoudi, J. Kim, M. O'Keeffe, O. M. Yaghi, *J. Am. Chem. Soc.* **2002**, *124*, 376–377.
[21] A colorless crystal of **1** ($0.30 \times 0.30 \times 0.28$ mm^3) was selected for X-ray structural analysis on a Bruker SMART CCD diffractometer at 298 K. The compound crystallized in the space group $Fd\bar{3}m$, cubic, $a = 48.9411(12)$ Å, $V = 117225(5)$ Å^3, $Z = 8$, $\lambda = 0.71073$ Å, $\rho_{calcd} = 1.185$ Mg m^{-3}, $\mu(Mo_{K\alpha}) = 1.558$ mm^{-1}, $F(000) = 40800$. A total of 108996 reflections were collected in the range $3.72 < \theta < 28.27$, of which 6526 were unique. The structure was solved and refined by full-matrix least-squares on F^2 (SHELXL-97; G. M. Sheldrick, SHELXL-97, program for X-ray crystal structure refinement, University of Göttingen, Göttingen, Germany). Non-hydrogen atoms were refined anisotropically. Hydrogen atoms were fixed at calculated positions and refined in a riding mode. Final $R1$ value 0.1891 (0.0799 after SQUEEZE) for 3121 independent reflections ($I > 2\sigma(I)$). The solvent-accessible volume was assessed using the PLATON software (A. L. Spek, *Acta Crystallogr., Sect. A* **1990**, *46*, C34) and the contribution of the chlorine anions and the disordered solvent to the diffraction pattern was subtracted from the observed data by the "SQUEEZE" method as implemented in PLATON (P. van der Sluis, A. L. Spek, *Acta Crystallogr., Sect. A* **1990**, *46*, 194). The SQUEEZE-bypass method referred to therein is widely used in crystallographic analysis of compounds containing substantial amounts of disordered solvent that cannot be located precisely from diffraction data. CCDC-253194 contains the supplementary crystallographic data for this paper. These data can be obtained free of charge from the Cambridge Crystallographic Data Centre via www.ccdc.cam.ac.uk/data_request/cif.
[22] H. K. Fun, S. S. S. Raj, R. G. Xiong, J. L. Zuo, Z. Yu, X. Z. You, *J. Chem. Soc. Dalton Trans.* **1999**, 1915–1916.
[23] M. L. Tong, B. H. Ye, J. W. Cai, X. M. Chen, S. W. Ng, *Inorg. Chem.* **1998**, *37*, 2645–2650.
[24] J. L. Schlenker, F. G. Dwyer, E. E. Jenkins, W. J. Rohrbaugh, G. T. Kokotailo, W. M. Meier, *Nature* **1981**, *294*, 340–342.
[25] Inductively coupled plasma (ICP) analysis (Perkin-Elmer Optima 3300 DV ICP instrument) indicated that each gram of the complex contains 1.569×10^{-4} mol of cadmium.
[26] Polymer **1** (0.05148 g) and H_2O (15.0 mL) were placed in a 25-mL vial and stirred. A solution of $AgNO_3$ (0.5 g) in H_2O (3.0 mL) was then slowly added. After stirring in air for 1 h, the precipitate of AgCl was filtered off, washed with H_2O (3×4 mL), and calcined in a crucible at a constant rate (10 °C min^{-1}) to 800 °C for 30 min. The final quantity of AgCl was 0.04493 g, which gives 3.135×10^{-4} mol of chlorine per gram of complex.
[27] Elemental analysis (%; Perkin-Elmer 2400 elemental analyzer) calcd for $C_{306}H_{976}O_{216}N_{136}Cd_{34}Cl_{68}$: C 22.61, H 6.05, N 11.72; found: C 22.53, H 6.11, N 11.65.

 © 2005 Wiley-VCH Verlag GmbH & Co. KGaA, Weinheim

[28] TGA shows a weight loss of 5.24% during the first step (35–75°C), which corresponds to the loss of 46 guest water molecules (calcd: 5.10%). The weight loss of 11.18% during the second step (75–130°C) is attributed to the removal of 25 guest DMF molecules (calcd: 11.24%). The weight loss of 30.41% during the third step (140–245°C) is in accordance with the removal of 43 guest DMF molecules and 102 coordinated water molecules (calcd: 30.64%). (The IR spectrum of **1** displays bands at $\tilde{\nu}=$ 1651 and 2939 cm^{-1} because of $\nu_{C=O}$ and the asymmetric stretching vibration of the methyl group of the guest DMF molecules, respectively.) Decomposition of **1** began above 300°C.
[29] O. S. Jung, Y. J. Kim, K. M. Kim, Y. A. Lee, *J. Am. Chem. Soc.* **2002**, *124*, 7906–7907.
[30] O. M. Yaghi, H. Li, *J. Am. Chem. Soc.* **1996**, *118*, 295–296.
[31] O. M. Yaghi, H. Li, C. Davies, D. Richardson, T. L. Groy, *Acc. Chem. Res.* **1998**, *31*, 474–484.

 © 2005 Wiley-VCH Verlag GmbH & Co. KGaA, Weinheim

Water Transport

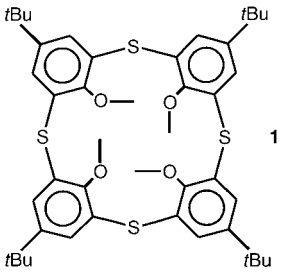
Diffusion of Water in a Nonporous Hydrophobic Crystal**

Praveen K. Thallapally, Gareth O. Lloyd, Jerry L. Atwood, and Leonard J. Barbour**

The transport of water molecules across cell membranes in biological systems is significantly enhanced by the presence of aquaporins,[1] proteins that associate as tetramers to form cylindrical transmembrane pores 2 to 3 nm long and about 0.3 nm wide at their narrowest point. Water travels through these channels at bulk diffusion rates,[2] presumably as single-file, hydrogen-bonded chains consisting, at any instant, of about seven to nine water molecules.[3] While interest in the transport properties of aquaporins has mainly focused on their selectivity for water over protons,[4] the influence of the channel size on water permeation has also received significant attention.[4f,5]

The shape, dimensions, and electrostatic profile of biological pores are considered to be the major determinants of their function. Intuitively, the simple notion of molecular transport through any matrix implies the presence of suitably sized channels defined and bounded by van der Waals surfaces. For example, molecular-scale hydrodynamics is only expected to occur if the narrowest site of the channel is at least wide enough to admit a single water molecule. Our own recent work with crystals composed of relatively small organic molecules has raised questions about the transport of small, mobile molecular species in solid media and we have shown that the conventional conception of crystal porosity may be flawed.[6] We have now extended our investigations of transport phenomena within seemingly nonporous crystals to include studies of water diffusion processes.

Crystals of pure 5,11,17,23-tetra-*tert*-butyl-25,26,27,28-tetramethoxy-2,8,14,20-tetrathiacalix[4]arene (**1**) were prepared



by sublimation at 240 °C under reduced pressure. Visual examination of the crystals revealed two different morphologies: primarily parallelepipeds (**1a**), interspersed with a relatively small number of square plates (**1b**). The structures of both crystal forms were elucidated by single-crystal X-ray diffraction analysis and found to be polymorphic variants of one another. In both cases the calixarene assumes the 1,3-alternate conformation, and the molecule is approximately box-shaped, with estimated dimensions of $10 \times 10 \times 14$ Å^3. The space group of polymorph **1a** is $C2/c$ and the molecules are arranged in two distinct orientations, each with the principal molecular axis canted at an angle of 83° with respect to the other. However, in the context of the present study, the structure of **1a** is of limited interest. The space group of polymorph **1b** is $P\bar{4}2_1m$ and the structure possesses two crystallographically unique molecules of **1** (Figure 1). One of the molecules ($\mathbf{1b_1}$) is situated on the intersection of the two mirror planes at (110) and (−110) while the other ($\mathbf{1b_2}$) straddles a position of $\bar{4}$ site symmetry at 0,0,0. All of the calixarene molecules in the crystal are aligned with their principal molecular axes parallel to [001] and the extended structure consists of columns of $\mathbf{1b_1}$ and $\mathbf{1b_2}$ stacked end-to-end along this direction. Although $\mathbf{1b_1}$ and $\mathbf{1b_2}$ have the same overall conformation, remarkably subtle yet ultimately critical metric differences exist between them.

It is useful to briefly discuss the shape of the 1,3-alternate conformation of **1** in relation to its potential as a host molecule. In the context of host–guest chemistry, calix[4]-arenes are usually of more interest when they incorporate phenolic rather than methoxy groups at the lower rim. A cyclic hydrogen-bonded arrangement of hydroxy groups enforces a truncated cone conformation, thus giving rise to

[*] Dr. P. K. Thallapally, Prof. J. L. Atwood
Department of Chemistry
University of Missouri-Columbia
Columbia, MO 65211 (USA)
Fax: (+1) 573-884-9606
E-mail: atwoodj@missouri.edu
G. O. Lloyd, Prof. L. J. Barbour
Department of Chemistry
University of Stellenbosch
7602 Matieland (South Africa)
Fax: (+27) 21-808-3849
E-mail: ljb@sun.ac.za

[**] We acknowledge the National Science Foundation (USA) and the National Research Council (South Africa) for support of this work.

Supporting information for this article is available on the WWW under http://www.angewandte.org or from the author.

 © 2005 Wiley-VCH Verlag GmbH & Co. KGaA, Weinheim DOI: 10.1002/anie.200500749

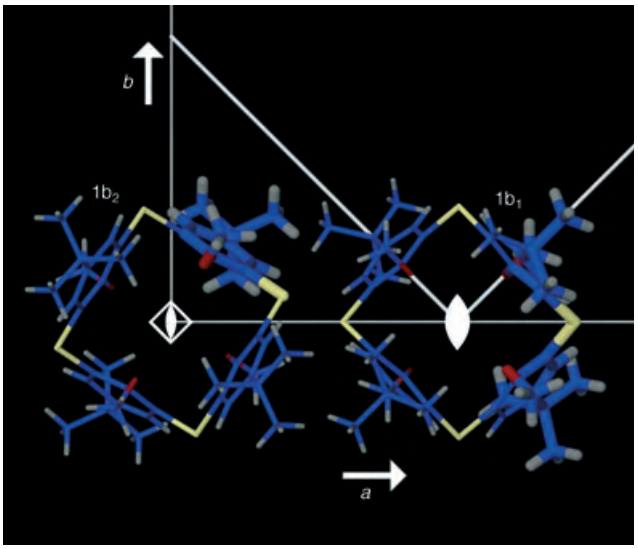


Figure 1. Perspective view of **1b** projected along [001]. The space group is $P\bar{4}2_1m$ (no. 113) with $a=b=19.494(2)$, $c=12.102(1)$ Å. Two crystallographically unique molecules are shown in capped-stick representation and the asymmetric unit in each case is indicated by thick bonds. As indicated, molecule $\mathbf{1b_1}$ resides on a 2*mm* axis while $\mathbf{1b_2}$ occupies a position of $\bar{4}$ site symmetry.

a molecular cleft large enough to accommodate small molecular moieties. Substitution of the phenolic protons usually causes distortion of the molecule to form the pinched cone, the 1,2-alternate, or the 1,3-alternate conformation. None of these substituted conformations result in the formation of a sizeable cleft, and the molecular host properties specifically associated with the cone conformation are generally forfeited.

Each pair of distal aromatic rings in the 1,3-alternate conformation of **1** forms a pincerlike arrangement. At each extremity of the molecule along its principal axis the "pincer" enfolds a small cleft with a narrow entrance guarded by two *para-tert*-butyl moieties. It is interesting to note that **1b** contains two crystallographically distinct molecules of **1**, with three of the four clefts unique. As a consequence of its $\bar{4}$ site symmetry, both clefts of $\mathbf{1b_2}$ are identical, and the dihedral angle between the distal rings is 26.0°. Two unique clefts are present in $\mathbf{1b_1}$ and the dihedral angles between their distal rings are 20.7° and 35.6°. This observation implies that one cleft is significantly larger than the other. The radius of the largest sphere capable of passing through the center of $\mathbf{1b_2}$ along its principal axis is 0.97 Å and the corresponding value for $\mathbf{1b_1}$ is 0.89 Å (note that the van der Waals radius of a hydrogen atom is often taken to be about 1.2 Å).

After collection of X-ray diffraction data, the crystal of **1b** was immersed in water for 8 h. Data were then recollected, and yielded structure **1c**. The space group of **1c** is also $P\bar{4}2_1m$ ($a=b=19.516(2)$, $c=12.096(1)$ Å) and structure solution reveals the same arrangement and relative conformations of the calixarene moietiess (correspondingly designated $\mathbf{1c_1}$ and $\mathbf{1c_2}$) as observed in **1b** (distal ring dihedral angles are 26.4° for $\mathbf{1c_2}$, and 20.2° and 35.0° for $\mathbf{1c_1}$). FT-IR analysis of carefully dried crystals, after similar treatment with water, indicated the presence of water molecules in **1c** and an overall calixarene:water ratio of 1:1 was determined by thermogravimetric analysis. In accordance with these results, least-squares refinement of **1c** yielded difference electron density peaks consistent with the presence of water oxygen atoms in the structure. Each of the two clefts of $\mathbf{1c_2}$ contains a water molecule at 50% site occupancy. The larger of the two clefts of $\mathbf{1c_1}$ contains one water molecule, while the smaller cleft remains unoccupied. A lower-symmetry structure of an inclusion complex of **1** with both water and dichloromethane has been previously published.[7]

The structure of **1b** is most likely dictated by complex packing considerations that do not favor a more symmetrical arrangement containing a single, unique conformation of **1**. Our experimental results show unequivocally that exposure of single crystals of **1b** to liquid water results in water molecules becoming lodged within some of the pincerlike clefts of the calixarenes. The water uptake is stoichiometric and the lattice structure remains otherwise unchanged. It appears that the three crystallographically different but similar molecular clefts exhibit remarkably subtle degrees of selectivity towards the guest water molecules. Figure 2 shows the two unique clefts of $\mathbf{1c_1}$ represented as Connolly[8] surfaces. The *tert*-butyl groups guarding the mouth of the smaller of the two clefts (Figure 2a) are rotated such that the cleft volume is maximized. Although the void is large enough to accommodate a water molecule, it remains unoccupied in **1c** (Figure 2c). The cleft at the other end of the calixarene

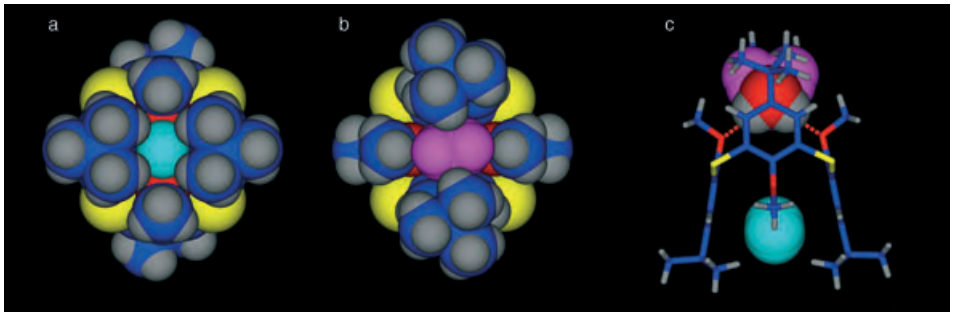


Figure 2. Molecule $\mathbf{1c_1}$ with its two clefts shown as Connolly surfaces. A probe radius of 1.4 Å was used to calculate the surfaces representing the voids. a) At one extremity of the host molecule, the unoccupied void (16.1 Å^3) is shown as a light blue surface. b) The fully occupied void (35.8 Å^3) at the other end of the molecule is shown as a purple surface. c) A side-view of **1** showing a section through the two cavity surfaces. The water molecule within the larger cavity is shown in van der Waals representation. Hydrogen bonds are indicated as dashed red lines.

 © 2005 Wiley-VCH Verlag GmbH & Co. KGaA, Weinheim

(Figure 2b) is larger, as a result of the greater angle between its distal aromatic rings. The two *tert*-butyl groups at this end are each disordered over two distinct positions. Four combinations of positions of these groups relative to one another are possible, but only two are geometrically unique (the combination defining the maximal void space is shown in Figure 2). This cleft accommodates one water molecule which donates two hydrogen bonds (O···O = 2.998 Å) to the methoxy oxygen atoms at the base of the cleft (Figure 2c).

The two molecular clefts in $\mathbf{1c_2}$ (shown as Connolly surfaces in Figure 3) are equivalent in size and shape, and

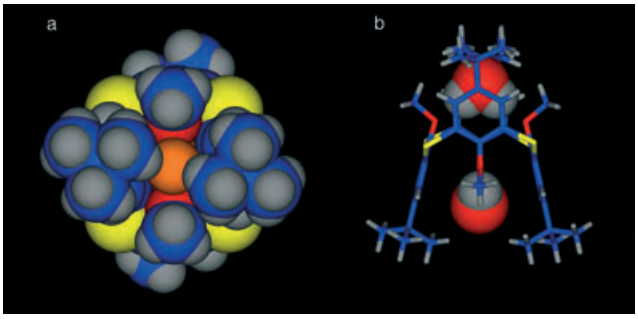


Figure 3. Connolly surfaces (orange) representing the two symmetry-related clefts (13.5 Å^3 each) in $\mathbf{1c_2}$. a) A view along the principal axis of the host molecule shows that the mouth of the cleft is guarded by two *tert*-butyl groups. b) A side-view of **1** showing two water molecules, each at 50% site occupancy, in space-filling representation.

each is barely large enough to accommodate a single molecule of water (ca. 19.7 Å^3) in a hydrogen-bonded environment (assuming that hydrogen bonding involves a small amount of van der Waals overlap of molecules). The *tert*-butyl groups do not appear to be disordered, and are positioned relative to one another so as to minimize the total void volume as well as the opening to the cleft. In the final crystallographic model, $\mathbf{1c_2}$ acts as host to only one water molecule that is disordered equally over the two possible sites. The water molecule donates two hydrogen bonds (O···O = 2.995 Å) to the calixarene methoxy oxygen atoms.

From our thermogravimetric and X-ray structural analyses we infer that any molecule of **1** only accommodates a maximum of one water molecule, even though there is enough space for two. Indeed, repeated soaking experiments lasting from eight hours to several days yielded consistent host:guest ratios of 1:1. The two distal *tert*-butyl groups at the mouth of each cleft are too close to one another to allow a water molecule to enter without conformational distortion of the calixarene. We believe that water uptake occurs through a complex mechanism involving rotation of the *tert*-butyl groups, with concomitant flexing of the host molecule whereby the distal aromatic rings lining the target cleft move apart. Such flexing most likely occurs as rotation about the C–S bonds of the thioether linkages. Thus the aromatic rings of the remaining cleft would be required to pinch closer together to compensate energetically for bond strain. Once a water molecule is admitted into the cleft, the host molecule can return to its original conformation. The water molecule now finds itself in a favorable environment where it is stabilized by two hydrogen bonds to symmetrically placed methoxy oxygen atoms. According to our assumption, the incorporation of a water molecule into one of the calixarene clefts inhibits uptake of water by the remaining cleft. The water molecule serves as a steric brace to the pinching motion that is required to open the opposite cleft of the host in order to capture a second water molecule. One of the voids of $\mathbf{1c_1}$ is significantly larger than the other and is also guarded by rotationally compliant *tert*-butyl groups. Hence, it is plausible that water uptake by this void is kinetically favored over that of the other, and the crystallographic model with a single water molecule at only one end of $\mathbf{1c_1}$ seems reasonable. Since both of the host cavities of $\mathbf{1c_2}$ are equivalent, we propose that a water site occupancy of 50% in each cavity implies that each molecule of **1** only captures one water molecule, but that the two cavities are equally favored.

Although we have discussed the possible mechanism by which water molecules enter the voids of isolated host molecules, careful scrutiny of the packing mode of the calixarene molecules reveals that the host framework is nonporous. This observation raises the intriguing question of how the water molecules diffuse through the lattice before becoming lodged within the calixarene cavities. Since structures **1b** and **1c** were determined using the same crystal, we can disregard the possibility of a water-inclusion process involving crystal dissolution and regrowth. Indeed, compound **1** is highly hydrophobic with no discernable water solubility, even in boiling water.

The calixarene molecules are stacked in columns parallel to [001]. Connolly surface plots (Figure 4a) reveal lattice voids (shown in green) embedded within bundles composed of four nearest-neighbor calixarene columns. These voids are isolated from one another by *tert*-butyl and methoxy methyl groups and do not merge to form channels. Assuming that the

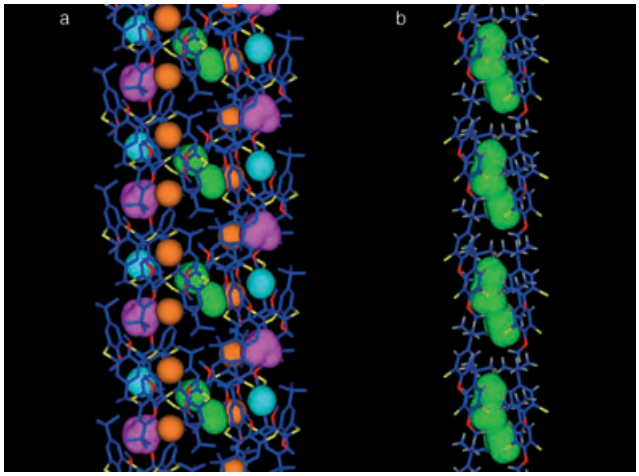


Figure 4. Four adjacent columns of **1** in **1c**, viewed perpendicular to [001]. a) The Connolly surfaces of the molecular clefts in **1** are shown in blue, purple, and orange (see Figures 2 and 3). The lattice voids between the calixarene atoms are shown in green (45.6 Å^3). Hydrogen atoms are omitted for clarity. b) The *tert*-butyl groups of **1** have been rotated to allow maximum extension of the lattice voids (91.4 Å^3) along [001]. Only the calixarene aromatic rings defining the lattice voids are shown.

 © 2005 Wiley-VCH Verlag GmbH & Co. KGaA, Weinheim

tert-butyl groups can rotate in a concerted fashion during water uptake, it is possible to construct a model in which the lattice voids can be extended maximally towards one another along [001] (Figure 4b). However, there appears to be no set of orientations for the *tert*-butyl groups that allows the lattice voids to transform into channels. Therefore, no rational pathway can be traced whereby water molecules might be transported through the crystal lattice. Moreover, with the exception only of the location between the two methoxy oxygen atoms embedded within each calixarene cleft, the entire host framework presents a highly hydrophobic environment. In summary of the above, the molecular clefts of the host molecules constitute the only hydrophilic regions of the crystal structure, and there are no channels leading to these clefts.

The uptake of an individual water molecule can be simplified as a two-step process involving diffusion through the lattice, followed by complexation by the host molecule. While water molecules travel through the nonporous hydrophobic lattice with seemingly little concern for van der Waals surface constraints, they appear to be quite selective with regard to the size, shape, and electrostatic profile of their final resting places. Carbon nanotubes have been studied extensively as model systems for small hydrophobic channels by using molecular dynamics simulations.[4f–h,9] These studies indicate that water can be transported quite rapidly through such channels in single file. However, for diffusion to occur, it is generally understood that the channels must be of a suitable diameter (as defined by the van der Waals surfaces of the constituent atoms) to allow free passage of the water molecules. Indeed, this is taken to be a universal requirement for the diffusion of any substance through any matrix.[10]

The double-ended host molecule features two pincerlike clefts, each defining a void approximately the size of a single water molecule. Encapsulation of water at one extremity of the molecular receptor appears to inhibit guest inclusion at the other end. This observation is easily rationalized in terms of conformational flexibility of the host molecule during guest complexation, as well as by our comprehension of van der Waals interactions. However, conventional wisdom does not explain why water molecules display seemingly little regard for van der Waals constraints during the dynamic diffusion process: it is only when they finally come to rest that the water molecules appear to obey spatial restrictions imposed by van der Waals surface contacts. These findings have potentially important implications for both theoretical and experimental studies of water-transport phenomena, particularly across biological membranes.

Our results imply that the classical view of diffusion might be inappropriate when applied at the atomic scale. We have shown that water molecules have the ability to burrow through a rigid medium such as a crystal without the clear presence of suitable channels. It is our belief that the lattice and molecular voids in the structure of **1b** are essential to the diffusion process. Although these voids do not merge to form channels, they are situated relatively close to one another at the atomic scale. In such cases, it is perhaps possible for water molecules to exploit the voids as "stepping stones" to travel through the lattice. The water-transport mechanism would thus involve water molecules hopping between voids until a thermodynamically favorable location can be found. The implications of these findings are that, either crystals are not as rigid as generally presumed, or that van der Waals surfaces do not behave as classical barriers to small molecules in motion.

Received: February 28, 2005
Published online: May 13, 2005

Keywords: calixarenes · diffusion · host–guest systems · supramolecular chemistry · water transport

[1] a) G. M. Preston, T. P. Carroll, W. B. Guggino, P. Agre, *Science* **1992**, *256*, 385–387; b) P. Agre, M. Bonhivers, M. J. Borgnia, *J. Biol. Chem.* **1998**, *273*, 14659–14662; c) M. J. Borgnia, S. Nielsen, A. Engel, P. Agre, *Annu. Rev. Biochem.* **1999**, *68*, 425–458; d) M. Yasui, T. H. Kwon, M. A. Knepper, S. Nielsen, P. Agre, *Proc. Natl. Acad. Sci. USA* **1999**, *96*, 5808–5813.

[2] M. L. Zeidel, S. V. Ambudkar, B. L. Smith, P. Agre, *Biochemistry* **1992**, *31*, 7436–7440.

[3] a) M. Ø. Jensen, E. Tajkhorshid, K. Schulten, *Biophys. J.* **2003**, *85*, 2884–2899; b) A. Yarnell, *Chem. Eng. News* **2004**, *82*, 42.

[4] a) C. J. T. Grotthuss, *Ann. Chim.* **1806**, *LVIII*, 54–74; b) B. L de Groot, H. Grubmüller, *Science* **2001**, *294*, 2353–2357; c) E. Tajkhorshid, P. Nollert, M. Ø. Jensen, L. J. W. Miercke, J. O'Connell, R. M. Stroud, K. Schulten, *Science* **2002**, *296*, 525–530; d) B. L. de Groot, T. Frigato, V. Helms, H. Grubmüller, *J. Mol. Biol.* **2003**, *333*, 279–293; e) A. Burykin, A. Warshel, *Biophys. J.* **2003**, *85*, 3696–3706; f) G. Hummer, J. C. Rasaiah, J. P. Noworyta, *Nature* **2001**, *414*, 188–190; g) F. Zhu, K. Schultern, *Biophys. J.* **2003**, *85*, 236–244; h) A. Berezhkovskii, G. Hummer, *Phys. Rev. Lett.* **2002**, *89*, 64503/1–64503/4.

[5] a) J. Wang, Y. Zhu, J. Zhou, X.-H. Lu, *Phys. Chem. Chem. Phys.* **2004**, *6*, 829–835; b) M. S. P. Sansom, P. C. Biggin, *Nature* **2001**, *414*, 156–157; c) O. Beckstein, M. S. P. Sansom, *Proc. Natl. Acad. Sci. USA* **2003**, *100*, 7063–7068; d) H. Grubmüller, *Proc. Natl. Acad. Sci. USA* **2003**, *100*, 7421–7422.

[6] J. L. Atwood, L. J. Barbour, A. Jerga, B. L. Schottel, *Science* **2002**, *298*, 1000–1002.

[7] P. Lhoták, M. Himl, I. Stibor, J. Sýkora, H. Dvořáková, J. Lang, H. Petříčková, *Tetrahedron* **2003**, *59*, 7581–7585.

[8] a) M. L. Connolly, *Science* **1983**, *221*, 709–713; b) M. L. Connolly, *J. Am. Chem. Soc.* **1985**, *107*, 1118–1124.

[9] a) A. Kalra, S. Garde, G. Hummer, *Proc. Natl. Acad. Sci. USA* **2003**, *100*, 10175–10180; b) S. Joseph, R. J. Mashi, E. Jakobsson, N. R. Aluru, *Nano Lett.* **2003**, *3*, 1399–1403.

[10] T. K. Maji, K. Uemura, H.-C. Chang, R. Matsuda, S. Kitagawa, *Angew. Chem.* **2004**, *116*, 3331–3334; *Angew. Chem. Int. Ed.* **2004**, *43*, 3269–3272.

 © 2005 Wiley-VCH Verlag GmbH & Co. KGaA, Weinheim

Protein Structures

Total Chemical Synthesis and X-ray Crystal Structure of a Protein Diastereomer: [D-Gln35]Ubiquitin**

*Duhee Bang, George I. Makhatadze, Valentina Tereshko, Anthony A. Kossiakoff, and Stephen B. Kent**

Proteins found in nature contain polypeptide chains made up of L-amino acids and glycine. The sequence of amino acids in the polypeptide chain defines the folded tertiary structure of the protein molecule, and the protein owes its biological activity to that folded structure. Non-natural amino acids have been used to construct proteins that are not found in nature to investigate the role of amino acid chemical structure in the formation and stability of the folded protein molecule.[1] In particular, substitution of D-amino acid residues into the protein molecule has been explored for its effects on the binding of insulin to insulin receptors.[2] More recently, D-amino acid substitution has been proposed for enhancing protein stability,[3a] and the structure–function relationships in the K^+ ion channel selectivity filter have been explored by incorporation of a D-Ala residue in place of a Gly residue.[3b] However, despite their potential importance for investigating protein structure–function relationships, there is little detailed knowledge of how the incorporation of a D-amino acid residue affects the local and global conformations that define the folding, stability, and function of the protein molecule.

We set out to understand how a native protein would incorporate a D-amino acid residue into its overall architecture. To definitively explore the perturbation of the local and global conformation in a protein molecule that results from incorporation of D-amino acids, we synthesized and determined the X-ray crystal structure of the chemically engineered globular protein ubiquitin (76 amino acids) with a D-amino acid residue in place of the Gly35 residue in the C-cap region of an α helix. This residue was targeted because the conformation of the Gly35 residue ($\phi = 81°$, $\varphi = 5°$) in native ubiquitin[4] is only allowed for an L-amino acid in a left-handed α helix or for a D-amino acid residue. Herein, we report: 1) an efficient strategy for the total chemical synthesis of ubiquitin; 2) the direct observation of the conservation of amino acid configuration after protein desulfurization by Raney-nickel reduction (that is, L-Cys→L-Ala); 3) high-resolution crystal structures for native ubiquitin and for the ubiquitin protein diastereomer [D-Gln35]ubiquitin; and 4) a striking similarity between the molecular structures of native ubiquitin and the ubiquitin protein diastereomer. The significance of these results is also discussed.

Our research focuses on the investigation of protein folding and stability by using chemical techniques, so we set out to establish an efficient total chemical synthesis of the model protein ubiquitin and its various analogues.[5] We sought to use the recently developed one-pot ligation method[9] to covalently assemble three unprotected peptide segments. However, the ubiquitin molecule does not have the cysteine residues that are needed for native chemical ligation[10] (the amino acid sequence of ubiquitin is shown in Scheme 1a). We noted that human erythrocytic ubiquitin has two alanine residues, which are in positions 28 and 46 and so are suitably located for use as ligation sites (Swiss-Prot accession number P62988).[4] Thus, we adopted a protein-desulfurization strategy[11] that enables the use of native chemical ligation at Cys28 and cys46, after which the cysteine residues are converted into the native Ala28 and Ala46 residues. Our synthetic strategy is shown in Scheme 1b.

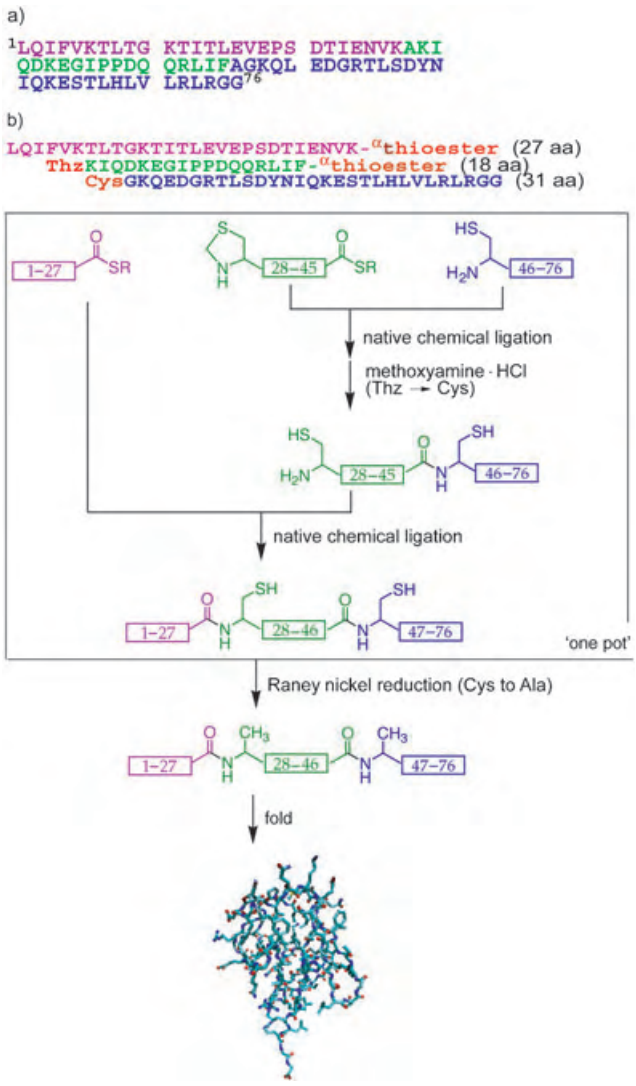
Data for the synthesis of native ubiquitin are shown in Figure 1. The C-terminal peptide and the peptide-$^{\alpha}$thioesters were prepared by solid-phase peptide synthesis by using manual stepwise Boc-chemistry (Boc = butoxycarbonyl) "in situ neutralization" protocols.[12] Several hundred milligrams of high-purity peptide were obtained by preparative reverse-phase HPLC from each 0.4-mmol-scale synthesis. The recovered peptide yields were approximately 30% for the (1–27)-$^{\alpha}$thioester and (Cys^{46}–76) peptides and approximately 45% for the (Thz^{28}–45)-$^{\alpha}$thioester (Thz = 1,3-thiazolidine-4-carboxo group) sequences, based on the starting aminoacyl resin. These three peptides were used as the substrates for the one-pot three-segment ligation on a tens-of-milligrams scale:

[*] D. Bang, V. Tereshko, Prof. A. A. Kossiakoff, Prof. S. B. Kent
Institute for Biophysical Dynamics
The University of Chicago
Chicago, IL 60637 (USA)
Fax: (+1) 773-702-0439
E-mail: skent@uchicago.edu
V. Tereshko, Prof. A. A. Kossiakoff, Prof. S. B. Kent
Department of Biochemistry and Molecular Biology
The University of Chicago
Chicago, IL 60637 (USA)
D. Bang, Prof. S. B. Kent
Department of Chemistry
The University of Chicago
Chicago, IL 60637 (USA)
Prof. G. I. Makhatadze
Department of Biochemistry and Molecular Biology
Pennsylvania State University
Hershey, PA 17033 (USA)

[**] D.B. was supported by funding from the NSF MRSEC program at the University of Chicago (grant DMR 0213745). We acknowledge funding from DOE GTL program grant no. DE-FG02–04ER63786 (to S.B.K) and NIH grant no. GM54537 (to G.I.M). Portions of this work were performed at the DND-CAT (sector 5-ID) and IMCA-CAT (sector 17-ID) of the Advanced Photon Source. Use of the Advanced Photon Source was supported by the US Department of Energy, Office of Science, Office of Basic Energy Sciences, under contract no. W-31–109-Eng-38. Use of the DND-CAT beamline is supported by the E.I. DuPont de Nemours, The Dow Chemical Company, the US National Science Foundation through grant no. DMR-9304725, and the State of Illinois through the Department of Commerce and the Board of Higher Education Grant IBHE HECA NWU 96. Use of the IMCA-CAT beamline at the Advanced Photon Source was supported by the companies of the Industrial Macromolecular Crystallography Association through a contract with the Illinois Institute of Technology.

Supporting information for this article is available on the WWW under http://www.angewandte.org or from the author.

 © 2005 Wiley-VCH Verlag GmbH & Co. KGaA, Weinheim DOI: 10.1002/anie.200463040



Scheme 1. a) Target amino acid sequence for human erythrocytic [Met 1 Leu]ubiquitin. b) Peptide segments and strategy used for the total chemical synthesis of ubiquitin.

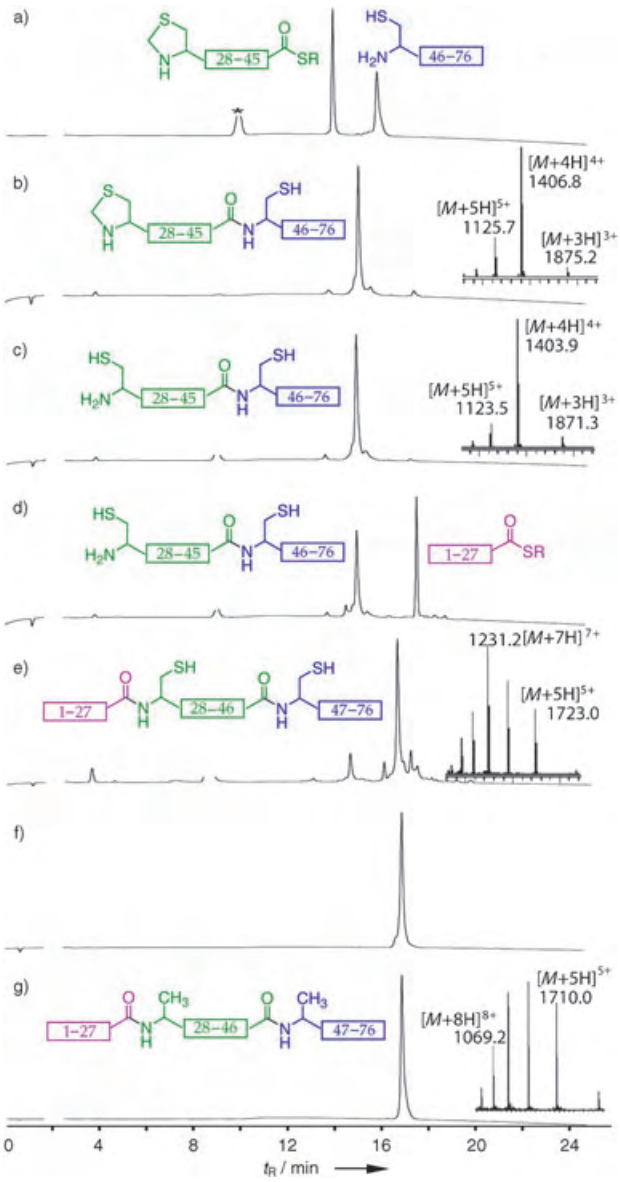


Figure 1. Data for the synthesis of native ubiquitin. Reactions were monitored by LC–MS. The UV profile at 214 nm is shown, together with ESIMS data (inset) corresponding to each major product. The chromatographic separations were performed using a linear gradient (10–50%) of buffer B in buffer A over 20 min (buffer A = 0.1% trifluoroacetic acid (TFA) in water; buffer B = 0.08% TFA in acetonitrile). a) $t = 0$ h, b) $t = 12$ h, c) $t = 16$ h, d) $t = 17$ h, e) $t = 40$ h, f) purified, and g) desulfurized and purified. Observed and calculated masses of the synthetic intermediates and final products were: b) observed mass (obs) 5623.1 ± 0.5 Da, calculated mass using average isotopes (calcd) 5623.4 Da; c) obs = 5611.6 ± 0.7 Da, calcd = 5611.4 Da; e) obs = 8610.2 ± 1.0 Da, calcd = 8610.9 Da; g) obs = 8546.0 ± 1.1 Da, calcd = 8546.8 Da.

the first ligation of the (Thz^{28}–45)-$^{\alpha}$thioester and (Cys^{46}–76) peptides was performed in phosphate buffer (100 mM, pH 6.8) containing guanidinium hydrochloride (6 M) and thiophenol (1% (v/v)) at a concentration of 3 mg mL^{-1} for each peptide (Figure 1a,b). Methoxyamine·hydrochloride (0.2 M) was added to convert the Thz peptide into the Cys peptide ligation product at pH 4.0 (Figure 1c). Readjustment of the solution to pH 6.8 was followed by addition of the third peptide segment, (1–27)-$^{\alpha}$thioester, to effect the second ligation (Figure 1d,e). The ligated full-length 76 residue polypeptide was purified by reverse-phase HPLC (Figure 1f) and lyophilized for the subsequent Raney-nickel desulfurization reaction.

Desulfurization with Raney nickel has been applied to proteins to convert cysteine residues into alanine residues.[13] No change in the absolute configuration at the α carbon atoms of the cysteine/alanine residues was observed in model studies on acylated cysteine.[14,15] Yan and Dawson used Raney-nickel reduction subsequent to native chemical ligation at Cys to extend the use of chemical ligation to the synthesis of proteins that do not contain Cys.[11] One disdavantage of the Raney-nickel reduction is that desulfurization not only affects the cysteine residues but also results in the demethylthiolation of the methionine side chain (although at a slower rate).[11] The first residue of ubiquitin

 © 2005 Wiley-VCH Verlag GmbH & Co. KGaA, Weinheim

is a methionine, so for synthetic convenience, we replaced Met 1 in ubiquitin with Leu 1 (Scheme 1 a).[16]

We prepared the Raney nickel as described:[11] Nickel acetate (600 mg) was dissolved in distilled water (15 mL) and then sodium borohydride (100 mg) was added slowly. The black nickel precipitate was collected by filtration and then washed extensively with distilled water. We carried out the conversion of Cys 28 and Cys 46 into Ala 28 and Ala 46 in the synthetic polypeptide by adding the freshly prepared nickel precipitate to the peptide solution (ca. 20 mg of purified 76 amino acid polypeptide at a concentration of 3 mg of lyophilized peptide per 1 mL of 0.1 M phosphate buffer containing 6 M guanidinium hydrochloride). We observed that oxidized cysteine residues retarded the rate of the reaction (the same observation has been made previously[13]). We added TCEP (tris(2-carboxyethyl)phosphane hydrochloride; 10 mM) to our reaction mixture to insure that the two cysteine residues were fully reduced. The final pH value of the reaction mixture was 6.0. The Raney-nickel reduction was complete in 12 hours and a mass decrease of 64 Da was observed, as expected for the loss of two sulfur atoms (Figure 1 g).

Essentially identical results were obtained for the total chemical synthesis of the [D-Gln 35]ubiquitin protein molecule (Figure 2). The folded structure of chemically synthesized ubiquitin was confirmed by dissolution of the lyophilized polypeptide under native conditions and the procurement of circular dichroism spectra, which were consistent with the native protein structure (data not shown). The folded protein was obtained at the high concentrations necessary for crystallization by dissolution of the the synthetic polypeptide (20 mg mL^{-1}) in phosphate buffer containing guanidinium hydrochloride (6 M) and was then dialyzed against distilled water.

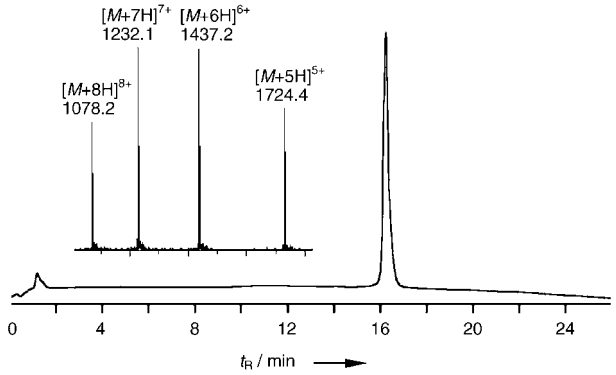


Figure 2. HPLC profile of purified [D-Gln 35]ubiquitin at 214 nm and ESIMS data (inset) corresponding to the product peak (observed mass = 8617.4 ± 0.5 Da; calculated mass = 8617.9 Da (average isotopes)).

We performed several syntheses of both the native ubiquitin and the [D-Gln 35]ubiquitin diastereomer to produce enough protein material for the screening of crystallization conditions and for the optimization of the growth of high-quality crystals. An average yield of recovered product of 36 % from the overall preparation of the full-length polypeptide containing Cys 28 and Cys 46 was obtained using the protocols described above (Figure 1 a–f). The yields of recovered product from the desulfurization reaction were 75 % on average (Figure 1 f–g). Ten- to twenty-milligram quantities of wild-type ubiquitin and its diastereomer were produced in each synthesis. The average synthetic yields were 27 % based on the peptides used. Therefore, excellent yields of high-quality protein constructs were obtained from the synthetic strategy reported herein, and furthermore we could apply this multisegment strategy to the ready synthesis of analogues. Thus, we could reuse the peptides (1–27)-$^{\alpha}$thioester and (Cys^{46}–76) and it was only necessary to remake the short [Gly 35D-Gln](Thz^{28}–45)-$^{\alpha}$thioester for the synthesis of the diastereomer analogue protein.

At first, we considered a protein NMR experiment to investigate the local and global structure of the ubiquitin diastereomer. However, we concluded that high-resolution crystallography would be better suited to explore even small configuration changes caused by the incorporation of D-Gln 35 into the protein molecule and to definitively show the local and global structural changes of a protein diastereomer compared to the wild-type protein molecule. Ubiquitin is reported to be difficult to crystallize.[4,17–19] Attempts to form ubiquitin crystals under the conditions used in the first successful crystallization[17] have since failed.[4,17–19] Instead, most of the crystals of sufficient quality for X-ray crystallographic studies have been produced by seeding with samples of the original crystal.

We carried out extensive screening of crystallization conditions for ubiquitin, but without seeding we were unable to obtain crystals. However, we were aware that solid-state NMR spectroscopy researchers were using ubiquitin nanocrystals to study protein structures.[20] The conditions reported for the production of ubiquitin nanocrystals used cadmium salts not usually included in commercially available crystal screening kits. By using cadmium salts in combination with the crystal screening kits, we were able to grow two different forms of ubiquitin crystals under different conditions. Subsequent rounds of optimization led to crystals of both the wild-type ubiquitin and its diastereomer that were of sufficient quality for X-ray crystallographic studies. Crystal formation could be reproducibly obtained by mixing ubiquitin solution (2 μL, 20 mg mL^{-1}) and $CdCl_2$ solution (2 μL, 50 mM), and poly(ethylene glycol) 2000 monomethyl ether (PEG MME; 20 %, *w*/*v*) in bis–tris buffer (bis(2-hydroxyethyl)iminotris(hydroxymethyl)methane; 0.1 M, pH 6.5).

X-ray diffraction data were collected using synchrotron radiation at the Advanced Photon Source at the Argonne National Laboratory. Cubic ($P4_332$) and orthorhombic ($P2_12_12_1$) space groups were identified for both the wild-type and diastereomer crystals. In particular, the orthorhombic crystals were highly ordered and diffracted well to 1.3 Å (a complete data set was obtained to only 1.5 Å because of the geometric limitations of the CCD detector). The structures of the native ubiquitin and the diastereomer protein were solved by the molecular replacement method, in which the ubiquitin structure PDB accession number 1UBQ was used as the test model.[21] Subsequent refinement procedures were carried out

 © 2005 Wiley-VCH Verlag GmbH & Co. KGaA, Weinheim

using the CNS and refmac refinement packages (see the Supporting Information for data collection and refinement statistics for both native ubiquitin and [D-Gln35]ubiquitin).

The synthetic native ubiquitin protein had the same molecular structure as that previously reported.[4] The stereochemical configuration of the D-Gln35 residue was directly confirmed by the high-resolution electron-density map of the ubiquitin diastereomer, in which the side chain of D-Gln35 could be seen pointing in the opposite direction to that expected for the side chain of an L-Gln residue (Figure 3). Thus, the ubiquitin diastereomer can incorporate D-Gln35 into its overall fold without perturbing the global architecture of the protein molecule (Figure 4). Both Gly35 and D-Gln35 were in a left-handed conformation ($\phi = 80°$ for Gly35 and $\phi = 77°$ for Gln35; see the Supporting Information).

Comparison of the wild-type and diastereomer structures showed a striking similarity in both the local and global conformations (Figure 4). The root-mean-square difference (rmsd) value for the comparison of the Cα atoms at corresponding positions in the two protein structures was 0.39 Å, and the rmsd value for all corresponding main-chain atoms in the local region (from residue 31 to 37) near the D-Gln35 substitution was 0.24 Å (see the Supporting Information). These values are within the experimental variation expected for two proteins of identical structure at the resolution of the analysis. This striking similarity 1) validates the replacement of natural amino acid residues occupying left-handed conformations in native protein molecules by D-amino acids and 2) provides experimental support for the assumption that replacement of a Gly residue occupying a left-handed conformation by a D-amino acid does not alter the local and global conformations of the protein molecule.

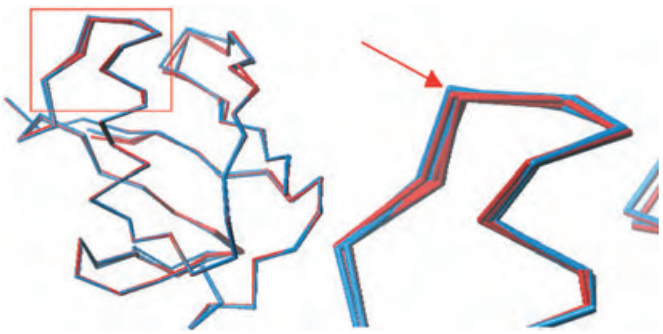


Figure 4. Superposition of the molecular structures of the three native and three [D-Gln35]ubiquitin protein molecules found in the unit cell for the two different proteins. Left: the backbone of Cα-atom traces of the two proteins are shown superimposed; [D-Gln35]ubiquitin (blue); native ubiquitin (red). Right: close up of nine residues near D-Gln35/Gly35 (arrow).

The conservation of the L configuration of Ala28 and Ala46 after the desulfurization reaction could be directly observed in the electron-density map of the synthetic proteins (Figure 5). The conservation of the L configuration during the Raney-nickel reduction further validates the synthetic strategy that Yan and Dawson devised to prepare cysteine-free proteins by using native chemical ligation followed by a desulfurization reaction.[11]

In summary, we have developed an efficient route to cysteine-free ubiquitin molecules by combining one-pot three-peptide-segment native chemical ligation[9] and protein desulfurization[11] for chemical protein synthesis to produce large quantities of high-quality protein materials for X-ray crystallographic studies. We have also verified a striking

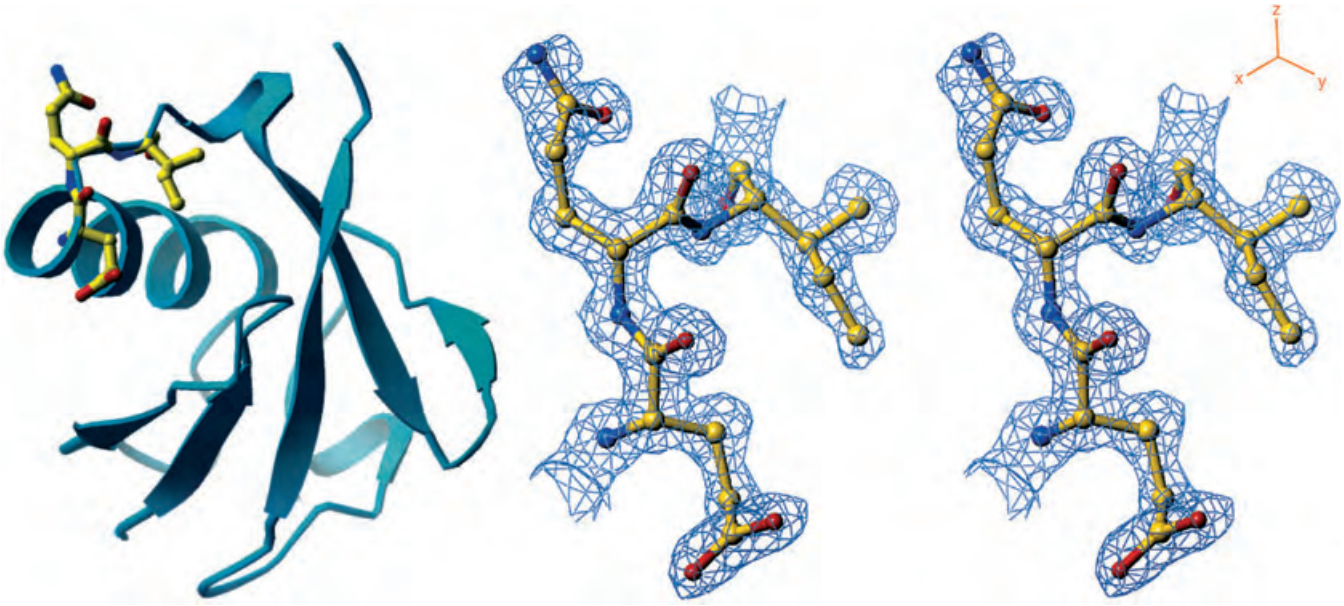


Figure 3. Left: structure of the [D-Gln35]ubiquitin diastereomer; the sequence Glu34–D-Gln35–Ile36 is highlighted in yellow. Right: stereoview of the local conformation near the D-Gln35 residue; the residues Glu34–D-Gln35–Ile36 are shown fitted to the $2F_o - F_c$ electron-density map contoured at 1σ. (It was not possible to unambiguously differentiate the oxygen and nitrogen atoms in the carboxamide side chain at a resolution of 1.5 Å; therefore, the assignment shown is arbitrary.)

 © 2005 Wiley-VCH Verlag GmbH & Co. KGaA, Weinheim

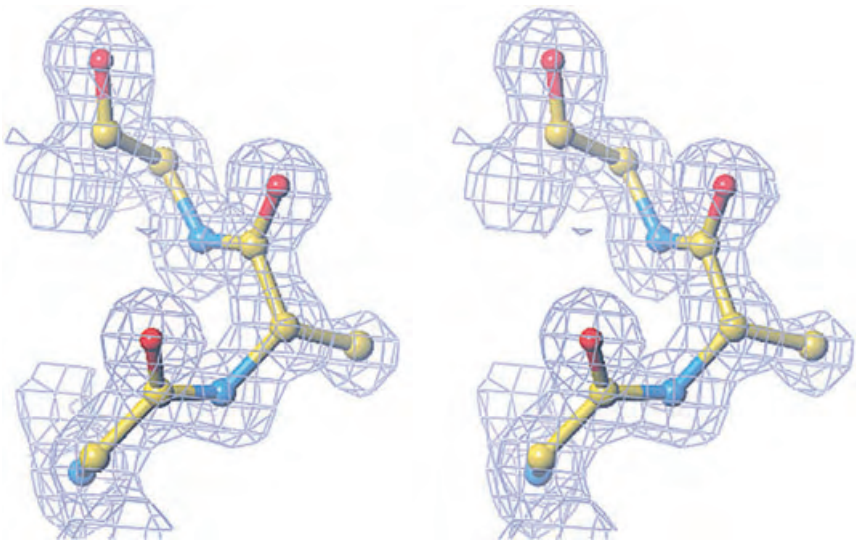


Figure 5. Stereoview showing Ala 46 fitted to the $2F_o-F_c$ electron-density map contoured at 1σ. The conservation of configuration in the desulfurization reaction (L-Cys→L-Ala) is apparent. Occupancy and thermal factor refinement indicated that the Cβ atoms showed full occupancy for the L conformation of the alanine side chain, within experimental uncertainty (<10%), with an accompanying low thermal factor ($B=3$ Å^2).

conservation of molecular structure between the folded conformations of a protein diastereomer and the corresponding wild-type protein by using high-resolution X-ray crystallography. This study provides experimental support that replacement of a native Gly residue that occupies a left-handed conformation by a D-amino acid does not significantly perturb the local or global conformations of a protein molecule. We are currently using the ubiquitin synthesis and crystallographic methods reported herein, in combination with other modern biophysical techniques, to systematically dissect the molecular basis of stability in this model protein.

Received: December 23, 2004
Published online: April 18, 2005

Keywords: chemical ligation · diastereomers · protein structures · protein synthesis · X-ray diffraction

[1] a) A. Wlodawer, M. Miller, M. Jaskolski, B. K. Sathyanarayana, E. Baldwin, I. T. Weber, L. M. Selk, L. Clawson, J. Schneider, S. B. H. Kent, *Science* **1989**, *245*, 616–621; b) M. Baca. S. B. H. Kent, *Proc. Natl. Acad. Sci. USA* **1993**, *90*, 11638–11642; c) M. Baca, S. B. H. Kent, *Tetrahedron* **2000**, *56*, 9503–9513; d) G. Simmons, P. R. Clapham, L. Picard, R. E. Offord, M. M. Rosenkilde, T. W. Schwartz, R. Buser, T. N. Wells, A. E. Proudfoot, *Science* **1997**, *276*, 276–279; e) Z. Zhang, J. Gildersleeve, Y. Y. Yang, R. Xu, J. A. Loo, X. Uryu, C. H. Wong, P. G. Schultz, *Science* **2004**, *303*, 371–373.

[2] M. Kobayashi, S. Ohgaku, M. Iwasaki, H. Maegawa, Y. Shigeta, K. Inouye, *Biochem. Biophys. Res. Commun.* **1982**, *107*, 329–336.

[3] a) B. Anil, B. Song, Y. Tang, R. D. P. Raleigh, *J. Am. Chem. Soc.* **2004**, *126*, 13194–13195; b) F. I. Valiyaveetil, M. Sekedat, R. MacKinnon, T. W. Muir, *Proc. Natl. Acad. Sci. USA* **2004**, *101*, 17045–17049.

[4] S. Vijay-Kumar, C. E. Bugg, W. J. Cook, *J. Mol. Biol.* **1987**, *194*, 531–544.

[5] The synthesis of crystalline ubiquitin by stepwise solid-phase methods has been previously reported; see Refs. [6]–[8].

[6] R. Ramage, O. Ogunjobi, J. Green, *Tetrahedron Lett.* **1989**, *30*, 2149–2152.

[7] O. Ogunjobi, R. Ramage, *Biochem. Soc. Trans.* **1990**, *18*, 1322–1323.

[8] R. Ramage, J. Green, T. W. Muir, O. M. Ogunjobi, S. Love, K. Shaw, *Biochem. J.* **1994**, *299*, 151–158.

[9] D. Bang, S. B. Kent, *Angew. Chem.* **2004**, *116*, 2588–2592; *Angew. Chem. Int. Ed.* **2004**, *43*, 2534–2538.

[10] P. E. Dawson, T. W. Muir, I. Clark-Lewis, S. B. Kent, *Science* **1994**, *266*, 776–779.

[11] L. Z. Yan, P. E. Dawson, *J. Am. Chem. Soc.* **2001**, *123*, 526–533.

[12] M. Schnolzer, P. Alewood, A. Jones, D. Alewood, S. B. Kent, *Int. J. Pept. Protein Res.* **1992**, *40*, 180–193.

[13] M. T. Perlstein, M. Z. Atassi, S. H. Cheng, *Biochim. Biophys. Acta* **1971**, *236*, 174–182.

[14] G. S. Fonken, R. Mozingo, *J. Am. Chem. Soc.* **1947**, *69*, 1212–1213.

[15] R. Mozingo, D. E. Wolf, S. A. Harris, K. Fokers, *J. Am. Chem. Soc.* **1943**, *65*, 1013–1016.

[16] Leu 1 ubiquitin has full biological activity: C. G. Benitez-Cardoza, K. Stott, M. Hirshberg, H. M. Went, D. N. Woolfson, S. E. Jackson, *Biochemistry* **2004**, *43*, 5195–5203.

[17] S. Vijay-Kumar, C. E. Bugg, K. D. Wilkinson, W. J. Cook, *Proc. Natl. Acad. Sci. USA* **1985**, *82*, 3582–3585.

[18] S. Vijay-Kumar, C. E. Bugg, K. D. Wilkinson, R. D. Vierstra, P. M. Hatfield, W. J. Cook, *J. Biol. Chem.* **1987**, *262*, 6396–6399.

[19] D. Alexeev, S. M. Bury, M. A. Turner, O. M. Ogunjobi, T. W. Muir, R. Ramage, L. Sawyer, *Biochem. J.* **1994**, *299*, 159–163.

[20] R. W. Martin, K. W. Zilm, *J. Magn. Reson.* **2003**, *165*, 162–174.

[21] The PDB accession numbers for the crystal structures are: 1YIW for wild type ubiquitin and 1J1 for [D-Gln 35]ubiquitin.

 © 2005 Wiley-VCH Verlag GmbH & Co. KGaA, Weinheim

Polyoxometalates

Triangular Geometrical and Magnetic Motifs Uniquely Linked on a Spherical Capsule Surface**

Achim Müller, Ana Maria Todea, Joris van Slageren, Martin Dressel, Hartmut Bögge, Marc Schmidtmann, Marshall Luban, Larry Engelhardt, and Mariana Rusu*

Dedicated to Professor Francis Sécheresse on the occasion of his 60th birthday

Polygons can be placed on spherical surfaces such that periodical structures of a cyclic nature result, while these can be considered as discrete models for two-dimensional (extended) structures. If we wish to construct a chemical structure on a spherical capsule surface in the same way, we have to remember that 1) pentagons are the basic units for sphere constructions, as is well known, for example, from virus structures, 2) they exist, for example, in the form of $\{(Mo^{VI})Mo^{VI}_5\}$ type units, and that 3) they occur in Keplerates of the type $\{(Mo^{VI})Mo^{VI}_5\}_{12}\{Linker\}_{30}$[1–5] (linker can be of the mononuclear M (M = metal center) or dinuclear type M_2; for the definition of Keplerates, see ref. [5b]). However, until now it was not possible to synthesize a spherical capsule surface directly by the addition of linkers to the pentagonal units that are available in a dynamic library.[1–5] It is significant that in the Keplerates the linkers describe generic Archimedean solids: in the case of dinuclear linkers M_2 a distorted truncated icosahedron, $\{M_2\}_{30}$, and in the case of mononuclear linkers the unique icosidodecahedron (Figure 1)[6] $\{M_{30}\}$, which has—geometrically speaking—linked M_3 triangles. Surprisingly the related consequences for chemistry have not been discussed until now. In the $\{M_{30}\}$ situation, there is a network of corner-shared triangles on the sphere surface, this can result unique magnetic properties as in the case of the "classical" Keplerate $\{(Mo^{VI})Mo^{VI}_5\}_{12}Fe^{III}_{30}$.[7,8] This is the first laboratory example of a "zero-dimensional" system that at low temperatures embodies characteristics of geometrical frustration/magnetic ordering[8b] which otherwise have only been observed in selected one-, two-, and three-dimensional lattice spin systems.[9] Herein we report on the spherical cluster **1a** where the twelve $\{(Mo^{VI})Mo^{VI}_5\}$ type units fix 30 d^1 V^{IV} linkers/centers with spin $S = 1/2$ in the form of an icosidodecahedron, and thus 1) demonstrating for the first time that the spherical capsule/Keplerate can be directly constructed from the mononuclear linkers and the appropriate molybdate library,[5c] 2) providing the chance to obtain new information regarding the unique molecular magnetism of the $\{M_{30}\}$ type network of linkers/triangles, and 3) clarifying the quantum effects of the spin $S = 1/2$ vanadyl linkers especially in connection with the two-dimensional $S = 1/2$ Kagomé lattice which contains linked triangles and exhibits unique magnetic properties.[9a]

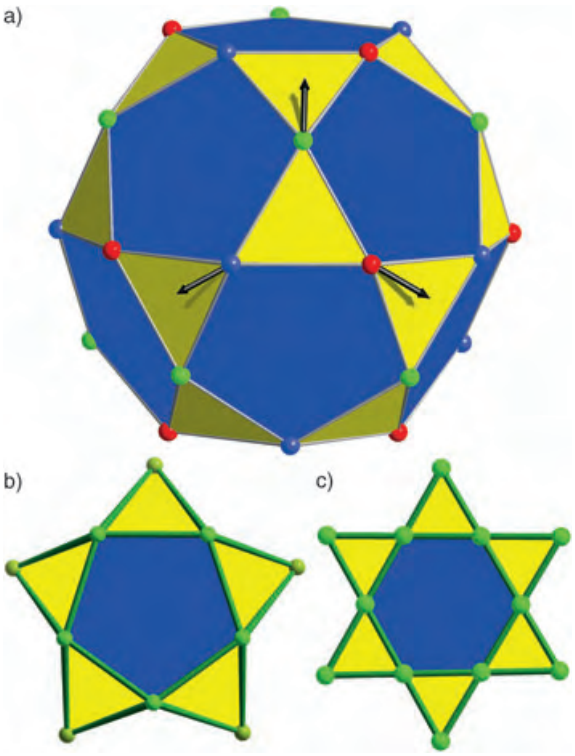


Figure 1. a) The M centers (small colored spheres) of the $\{(Mo^{VI})Mo^{VI}_5\}_{12}M_{30}$ type Keplerates (e.g., M = V^{IV}, Fe^{III}) describe the icosidodecahedron shown, which is unique among the icosahedral Archimedean solids as all edges are equivalent and all dihedral angles equal. Referring to the special situation of M = Fe^{III}, there are three groups ("sublattices") of 10 spins (colors: red, blue, green), with all spins of a sublattice pointing in the same direction, while nearest-neighbor spin vectors (three are highlighted) differ in angular orientation by 120°. Also shown: b) A fragment highlighting five linked triangles around a pentagon. c) A fragment of a planar Kagomé lattice with six linked triangles around a hexagon.

After adding vanadyl sulfate to an acidified molybdate solution, in the presence of K^+ ions, compound **1** precipitates after some time in high yield. (A simpler expression for the

[*] Prof. Dr. A. Müller, A. M. Todea, Dr. H. Bögge, M. Schmidtmann
Lehrstuhl für Anorganische Chemie I
Fakultät für Chemie der Universität
Postfach 100131, 33501 Bielefeld (Germany)
Fax: (+49) 521-106-6003
E-mail: a.mueller@uni-bielefeld.de
Dr. J. van Slageren, Prof. Dr. M. Dressel
1. Physikalisches Institut
Universität Stuttgart
Pfaffenwaldring 57, 70550 Stuttgart (Germany)
Prof. Dr. M. Luban, L. Engelhardt
Ames Laboratory and Department of Physics and Astronomy
Iowa State University, Ames, Iowa 50011 (USA)
Prof. Dr. M. Rusu
Faculty of Chemistry, Babes-Bolyai University
3400 Cluj-Napoca (Romania)

[**] A.M., M.D., and J.v.S. gratefully acknowledge the financial support of the Deutsche Forschungsgemeinschaft, A.M. additionally the Fonds der Chemischen Industrie, the German-Israeli Foundation for Scientific Research & Development, the Volkswagenstiftung, and the European Union. M.L. thanks Dr. P. Kögerler and Prof. Dr. C. Schröder for valuable discussions. Ames Laboratory is operated for the U.S. Department of Energy by Iowa State University under Contract No. W-7405-Eng-82.

 DOI: 10.1002/anie.200500697 © 2005 Wiley-VCH Verlag GmbH & Co. KGaA, Weinheim

cluster anion **1a** without referring to structural differences is given as well.)

$$Na_8K_{14}(VO)_2[\{(Mo^{VI})Mo^{VI}_5O_{21}(H_2O)_3\}_{10}\{(Mo^{VI})Mo^{VI}_5O_{21}(H_2O)_3(SO_4)\}_2\{V^{IV}O(H_2O)\}_{20}\{V^{IV}O\}_{10}(\{KSO_4\}_5)_2]\cdot \approx 150\,H_2O \quad \mathbf{1}$$

$$[K_{10} \subset \{(Mo^{VI})Mo^{VI}_5O_{21}(H_2O)_3(SO_4)\}_{12}\{(V^{IV}O)_{30}(H_2O)_{20}\}]^{26-} \quad \mathbf{1a}$$

Compound **1**, which crystallizes in the monoclinic space group *C*2/*c*, was characterized by elemental analysis, thermogravimetry (to determine the crystal water content), redox titrations (to determine the number of V^{IV} centers), spectroscopic methods (IR, Raman, UV/Vis), single-crystal X-ray structure analysis (including bond valence sum (BVS) calculations),[10] and susceptibility measurements (including related quantum Monte Carlo calculations).

The cluster anion **1a** of **1** is of the expected $(Pentagon)_{12}(Linker)_{30}$ type and is a slightly compressed sphere, while the heptacoordinate Mo^{VI} centers of the 12 pentagonal units correspondingly describe a slightly distorted icosahedron and the 30 V^{IV} centers—acting as linkers for the pentagonal $\{(Mo^{VI})Mo^{VI}_5\}$ type units—describe a (slightly distorted) icosidodecahedron (Figure 2; the V^{IV}–V^{IV} distances in the distorted Archimedean solid vary from 6.3 to 6.6 Å). The distortion is in agreement with the fact that 20 V^{IV} centers in the equatorial region have octahedral coordination and the two sets of five V^{IV} centers in the polar area have square-pyramidal coordination; the distances from the 10 equatorial V^{IV} units to the center of the cluster are a little shorter (10.3 Å) than the related distances of the other 20 V^{IV} units (10.6 Å). Ten of the twelve $[SO_4]^{2-}$ ligands are coordinated by three oxygen atoms to three adjacent Mo^{VI} centers of the $\{(Mo^{VI})Mo^{VI}_5\}$ groups such that two $\{KSO_4\}_5$ rings parallel to the equator result, with the K^+ ions (formally) bridging the $[SO_4]^{2-}$ ions (Figure 3). The other two sulfate groups are disordered and act as ligands to the two polar $\{(Mo^{VI})Mo^{VI}_5\}$ groups. The structure of **1a** comprising the twenty triangular and twelve pentagonal faces of the icosidodecahedron built up by 30 V^{IV} centers shows an interesting relation to the much less symmetrical cluster anion **2a** which has a non-complete spherical $\{V_3\}$ type net. In **2a**, a strongly distorted icosidodecahedron is described by 10 Mo^{VI} and 20 V^{IV} centers, while the equatorial $\{V_{20}\}$ belt—formed by 10 linked $\{V_3\}$ triangles—is identical to the related equatorial segment of **1a**.

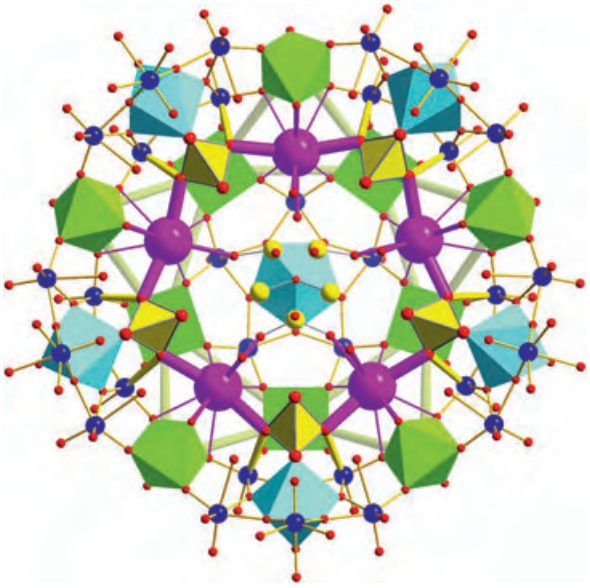


Figure 3. Combined polyhedral and ball-and-stick representation of a fragment of **1a** (view in direction of the C_5 axis) showing one of the two $\{KSO_4\}_5$ rings and the coordination of $\{SO_4\}$ groups to Mo centers as well as the disorder of one of the two sulfate groups (color code as in Figure 2, additional light blue pentagonal bipyramids: $\{MoO_7\}$).

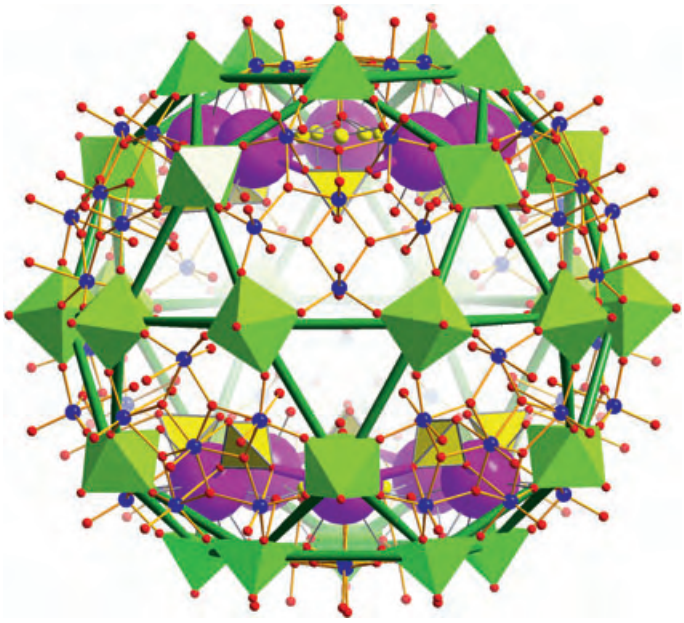


Figure 2. Combined polyhedral and ball-and-stick representation of the structure of **1a** showing the triangles and pentagons of the icosidodecahedron (green sticks), and additionally the basic $\{VO_5\}$ and $\{VO_6\}$ units as green polyhedra; as the interaction between the "lattice K^+" ions and the 20 pores is not homogeneous, this interaction was not considered here (blue Mo, red O, purple K, yellow tetrahedra: $\{SO_4\}$ groups; yellow spheres: disordered S atoms).

$$[\{Mo^{VI}O_3(H_2O)\}_{10}\{(Mo^{VI})Mo^{VI}_5O_{21}(H_2O)_3\}_{10}\{V^{IV}O(H_2O)\}_{20}(\{Mo^{VI}O_2(H_2O)_2\}_{5/2})_2(\{NaSO_4\}_5)_2]^{20-} \quad \mathbf{2a}$$[7d]

The presence of K^+ and $[SO_4]^{2-}$ ions in the reaction medium seems to be of fundamental importance for the structure formation, as the potassium cations of the two $\{KSO_4\}_5$ rings of **1a** attract the two negatively charged polar $\{(Mo^{VI})Mo^{VI}_5\}$ units thus causing the slight compression of the sphere. This distortion leads to an inclination of the adjacent $\{VO_5\}$ polyhedra and thus prevents an octahedral coordination of the 10 polar V^{IV} centers. The sixth (H_2O) ligand required for octahedral coordination would be too close to the $[SO_4]^{2-}$ ligands of the $\{KSO_4\}_5$ rings.

The investigations nicely show that $\{(Mo^{VI})Mo^{VI}_5\}$ type units are potentially available in a dynamic polymolybdate library; remarkably, they can be "used" in the present case as

 © 2005 Wiley-VCH Verlag GmbH & Co. KGaA, Weinheim

virtual units in the presence of potential linkers. In aqueous solution at low pH values, the pentagonal structural unit occurs in the $[Mo^{VI}_{36}O_{112}(H_2O)_{16}]^{8-}$ ion,[11] which is the only(!) abundant species under those conditions. Correspondingly, **1a** is formed from that solution in the presence of VO^{2+} linkers by a "split-and-link" process with the $\{(Mo^{VI})Mo^{VI}_5\}$ unit being formed from the $\{Mo_{36}\}$ species after the addition of the linkers. The option to extend this to mixed-metal species such as $\{Mo^{V}_8V^{IV}_{22}\}$,[12] $\{Mo^{V}_4V^{IV}_{26}\}$, or $\{Fe^{III}_{22}V^{IV}_8\}$[13] will be reported elsewhere.

Turning to the magnetic properties, two circumstances are of pivotal importance for the possible occurrence of geometrical frustration in the type of system considered herein: First, the 30 mononuclear magnetic Keplerate linkers occupy the vertices of an icosidodecahedron, which may be pictured as 20 linked (corner sharing) triangles arranged around 12 pentagons and corresponds to an equidistant distribution of the spins on the surface of a spherical cluster; second, each magnetic center ("spin vector") interacts with its four nearest-neighbors by isotropic antiferromagnetic exchange as a consequence of the special geometry of the unique $\{M_{30}\}$ type quasi-regular solid (Figure 1). Analogous to what occurs for the Kagomé spin system (planar lattice of triangles framed around hexagons; Figure 1c),[9] the geometric frustration of the individual Keplerate can be achieved by the cooperative interactions among the full set of spin vectors. In the special case of the above mentioned $\{(Mo^{VI})Mo^{VI}_5\}_{12}Fe^{III}_{30}$, we may refer to it as a "classical" Keplerate (because of the relatively high spin, $S = 5/2$, of individual Fe^{III} centers) and the spin frustration/magnetic ordering may therefore be visualized in geometrical terms[8c] (Figure 1). The 30 spin vectors are composed of three groups ("sublattices") of 10 spins each; all spins of a given sublattice point in the same direction, and any pair of nearest-neighbor spin vectors differ in angular orientation by 120° (Figure 1).[8c] In **1a** we have replaced the Fe^{III} centers by VO^{2+} ions which have the much smaller spin of $S = 1/2$, that is, "quantum spins". In addition, in **1a** the 3d electrons are not "localized" at the vertices of the icosidodecahedron as is approximately the case in the $\{Fe^{III}_{30}\}$ Keplerate.[14] However, the spin frustration of these quantum spins can not be visualized in geometric terms. More generally the magnetism of the "quantum" Keplerate **1a** is expected to be significantly different from that of its classical counterpart $\{Fe_{30}\}$, and more properties are expected to emerge.

Our experimental susceptibility data versus T, recorded for an applied field of $H = 0.1$ T, and corrected for the d^1 centers of two VO^{2+} ions which are magnetically/structurally independent from the cluster skeleton **1a**, are shown in Figure 4.[15] These results show the strong antiferromagnetic coupling in **1a**, in contrast to the $\{(Mo^{VI})Mo^{VI}_5\}_{12}Fe^{III}_{30}$ case.[16] The behavior of $T\chi$ at low T is qualitatively what could be expected for a spin system having a ground state with $S = 0$ and with very strong exchange coupling. This situation can be explained by a strong delocalization of the 3d electrons which arises because the 3d V levels are comparable in energy with the LUMOs of the molybdate fragment system.[16] This is a completely different situation than the classical $\{Fe_{30}\}$ type Keplerate where the exchange interaction is very weak, and

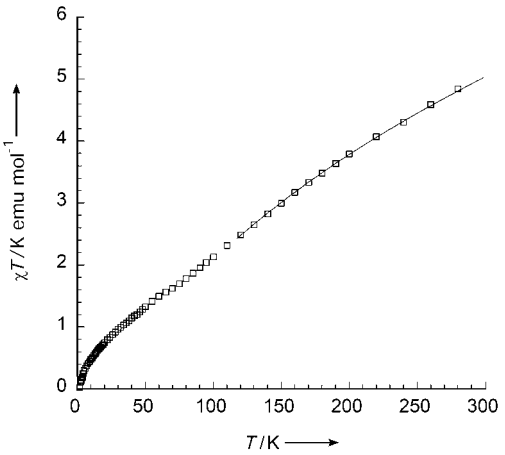


Figure 4. Magnetic susceptibility of $\{V_{30}\}$ versus temperature: Experimental data corrected for the two d^1/VO^{2+} centers (□);[15] quantum Monte Carlo results (solid curve).

therefore the room temperature value of $T\chi$ corresponds to 30 uncoupled $S = 5/2$ ions. The quantum Monte Carlo (QMC) method provides accurate values of susceptibility for the Heisenberg model of the $\{V_{30}\}$ system for $T > 0.5J/k_B$, and as seen in Figure 4, a very good fit to $T\chi$ is achieved for $T >$ 120 K for the choices $J/k_B = 245$ K and $g = 1.95$. Unfortunately, reliable results cannot be obtained for lower temperatures using the QMC method owing to the "sign problem" that occurs for spin systems with antiferromagnetic exchange based on lattice geometries where the classical counterpart exhibits spin frustration.

To summarize: We have demonstrated that it is possible to "use" pentagonal units as "building units" which play, geometrically speaking, the same role as the pentagonal units in other sphere-based constructions, such as spherical viruses, fullerenes, and geodesic domes; in our context they are used as a glue for trapping magnetic centers, such that triangles are linked to form an icosidodecahedron, that is, a part of a Keplerate. As the "quantum" Keplerate **1a** obtained is a new example of a frustrated magnetic system which shares a topological feature with the classical Keplerate $\{(Mo^{VI})Mo^{VI}_5\}_{12}Fe^{III}_{30}$ and the Kagomé-lattice antiferromagnet, its exploration is expected to provide a deeper understanding of basic aspects of magnetic frustration and the role played by the size of the intrinsic spin of the interacting magnetic ions. This study should also shed light on the parallel problem, and the focus of an intense effort, to characterize and understand the $S = 1/2$ Kagomé lattice, which is considered to have unique magnetic/electronic properties originating in the small value of S.[9] The behavior of the magnetization of the quantum Keplerate **1a** in high magnetic fields will be of key importance in studies aimed at elucidating the characteristics of its magnetic frustration.[17]

Experimental Section

A solution of $VOSO_4 \cdot 5H_2O$ (2.53 g, 10 mmol) in H_2O (35 mL) was added to a stirred solution of $Na_2MoO_4 \cdot 2H_2O$ (2.42 g, 10 mmol) in H_2SO_4 (0.5 M; 8 mL) in an conical flask. The resulting dark purple

 © 2005 Wiley-VCH Verlag GmbH & Co. KGaA, Weinheim

mixture was stirred at room temperature for 30 min (flask closed with a rubber stopper) and then treated with KCl (0.65 g, 8.72 mmol). After additional stirring for 30 min the solution was stored in the flask which was closed with a rubber stopper. After 5 days, the purple-black rhombic crystals of **1** were collected by filtration, washed with cold water, and finally dried in air. Yield: 1 g; elemental analysis: calcd (%) for $Na_8K_{24}Mo_{72}V_{32}S_{12}O_{538}H_{412}$: Na 0.96, K 4.92, V 8.55, S 2.02; found: Na 1.0, K 5.1, V 8.5, S 2.1. IR (KBr pellet): $\tilde{\nu}=1622$ (m), ($\delta(H_2O)$) 1198 (w), 1130 (w), 1055 (w) ($\nu_{as}(SO_4)$ triplet), 964 (s) (ν(V=O)/ν(Mo=O)), 791 (vs), 631 (w), 575 (s), 449 (w) cm^{-1}; FT-Raman (solid; $\lambda_e=1064$ nm): $\tilde{\nu}=941$ (w, ν(V=O)/ν(Mo=O)), 872 (s, $A_{1g}O_{br}$ breathing) cm^{-1}; UV/Vis (in H_2O): $\lambda=510$ (vs), 689 (w), 845 (w) nm.

Received: February 24, 2005
Published online: May 25, 2005

Keywords: magnetochemistry · mixed-valence compounds · molybdenum · polyoxometalates · vanadium

[1] A. Müller, E. Beckmann, H. Bögge, M. Schmidtmann, A. Dress, *Angew. Chem.* **2002**, *114*, 1210–1215; *Angew. Chem. Int. Ed.* **2002**, *41*, 1162–1167.

[2] a) In this context we should refer first to the fact that molybdenum oxide building units—abundant as virtual ingredients in a dynamic library in aqueous solution—display a unique type of flexibility and that the units can adjust their size and shape by a type of "split-and-link process" depending on the relevant boundary conditions.[1] (Pentagonal $\{(Mo^{VI})Mo^{VI}_5\}$ building blocks, for instance, occur in spherical capsules/Keplerates of the $\{Pentagon\}_{12}\{Linker\}_{30}$ type.[1–5]) The flexibility is nicely shown by the reaction of $[PMo_{12}O_{40}]^{3-}$ with Fe^{III} leading to a fragmentation of the Keggin ion while the fragments and the Fe^{III} ions form the (present type of) spherical system $\{(Mo^{VI})Mo^{VI}_5\}_{12}Fe^{III}_{30}$ which has the pentagonal units and encapsulated non-decomposed Keggin ions; see b) A. Müller, S. K. Das, H. Bögge, M. Schmidtmann, A. Botar, A. Patrut, *Chem. Commun.* **2001**, 657–658.

[3] A. Müller, S. Roy, *Coord. Chem. Rev.* **2003**, *245*, 153–166.

[4] A. Müller, S. Roy in *The Chemistry of Nanomaterials: Synthesis, Properties and Applications* (Eds.: C. N. R. Rao, A. Müller, A. K. Cheetham), Wiley-VCH, Weinheim, **2004**, pp. 452–475.

[5] a) A. Müller, P. Kögerler, C. Kuhlmann, *Chem. Commun.* **1999**, 1347–1358; b) A. Müller, P. Kögerler, A. W. M. Dress, *Coord. Chem. Rev.* **2001**, *222*, 193–218; c) The related direct synthetic conditions, simply based on addition of the finally appearing linker to the relative medium, are reported herein for the first time. Earlier Keplerate syntheses were more complex.

[6] The (quasi-regular) icosidodecahedron is a hybrid of the icosahedron and the dodecahedron and thus contains 20 trigonal and 12 pentagonal faces which intersect at each corner. Unlike the other related Archimedean solids, such as the $\{M_{60}\}$-type truncated icosahedron, it comprises not only equivalent vertices but also equivalent edges and equal dihedral angles (Figure 1); see a) M. O'Keeffe, B. G. Hyde, *Crystal Structures, I. Patterns and Symmetry*, Mineralogical Society of America, Washington, DC, **1996**; b) H. S. M. Coxeter, *Introduction to Geometry*, Wiley, New York, **1989**; c) H. S. M. Coxeter, *Regular Polytopes*, 3rd ed., Dover, New York, **1973**, in which we read (p. 18): "*A quasi-regular polyhedron (like the icosidodecahedron) is defined as having regular faces, while its vertex figures, though not regular, are cyclic and equiangular (i.e., inscriptible in circles and alternate-sided). It follows from this definition that the edges are all equal, say of length 2L, that the dihedral angles are all equal, and that the faces are of two kinds, each face of one kind being entirely surrounded by faces of the other kind.*"); d) A. Holden, *Shapes, Space and Symmetry*, Dover, New York, **1991**.

[7] a) A. Müller, S. Sarkar, S. Q. N. Shah, H. Bögge, M. Schmidtmann, Sh. Sarkar, P. Kögerler, B. Hauptfleisch, A. X. Trautwein, V. Schünemann, *Angew. Chem.* **1999**, *111*, 3435–3439; *Angew. Chem. Int. Ed.* **1999**, *38*, 3238–3241; b) D. Gatteschi, R. Sessoli, A. Müller, P. Kögerler in *Polyoxometalate Chemistry: From Topology via Self-Assembly to Applications* (Eds.: M. T. Pope, A. Müller), Kluwer, Dordrecht, **2001**, pp. 319–328; c) D. Gatteschi, *Europhys. News* **2003**, *34*(6), 214–216 (Magnetism Special Issue); D. Gatteschi in *Organic conductors, superconductors and magnets: from synthesis to molecular electronics* (Eds.: L. Ouahab, E. Yagubskii), Kluwer, Dordrecht, **2004**, pp. 179–196; d) see also A. Müller, M. Koop, H. Bögge, M. Schmidtmann, F. Peters, P. Kögerler, *Chem. Commun.* **1999**, 1885–1886. In the related compound discrete hydrated VO^{2+} groups are also present (evidenced by ESR); these can, as usual, be easily integrated into the crystal-water lattice, which leads to a corresponding lower alkali cation concentration.

[8] a) M. Axenovich, M. Luban, *Phys. Rev. B* **2001**, *63*, 100407; b) C. Schröder, H. Nojiri, J. Schnack, P. Hage, M. Luban, P. Kögerler, *Phys. Rev. Lett.* **2005**, *94*, 017205; c) A. Müller, M. Luban, C. Schröder, R. Modler, P. Kögerler, M. Axenovich, J. Schnack, P. Canfield, S. Bud'ko, N. Harrison, *ChemPhysChem* **2001**, *2*, 517–521.

[9] When frustration originates purely from the geometry or topology of the lattice it is termed geometric frustration. The corresponding compounds are called geometrically frustrated antiferromagnetic materials (GFAF) and can have exotic magnetic ground states; see: a) J. Greedan, *J. Mater. Chem.* **2001**, *11*, 37–53; b) *Magnetic Systems with Competing Interactions* (Ed.: H. Diep), World Scientific, Singapore, **1994**; c) *Quantum Magnetism* (Eds.: U. Schollwöck, J. Richter, D. J. J. Farnell, R. F. Bishop), Springer, Berlin, **2004**; d) Y. Narumi, K. Katsumata, Z. Honda, J.-C. Domenge, P. Sindzingre, C. Lhuillier, Y. Shimaoka, T. C. Kobayashi, K. Kindo, *Europhys. Lett.* **2004**, *65*, 705–711.

[10] Crystal data for **1**: $H_{412}K_{24}Mo_{72}Na_8O_{538}S_{12}V_{32}$, $M_r=19068.10\ g\,mol^{-1}$, monoclinic, space group $C2/c$, $a=47.155(2)$, $b=42.5364(18)$, $c=26.5344(12)$ Å, $\beta=90.2510(10)°$, $V=53222(4)$ Å^3, $Z=4$, $\rho=2.380\ g\,cm^{-3}$, $\mu=2.530\ mm^{-1}$, $F(000)=36848$, crystal size $=0.30\times0.20\times0.02\ mm^3$. Crystals of **1** were removed from the mother liquor and immediately cooled to 183(2) K on a Bruker AXS SMART diffractometer (three circle goniometer with 1 K CCD detector, $Mo_{K\alpha}$ radiation, graphite monochromator; hemisphere data collection in ω at 0.3° scan width in three runs with 606, 435, and 230 frames ($\phi=0$, 88, and 180°) at a detector distance of 5 cm). A total of 158364 reflections ($1.50<\Theta<26.99°$) were collected of which 57718 reflections were unique ($R(\mathrm{int})=0.0612$). An empirical absorption correction using equivalent reflections was performed with the program SADABS. The structure was solved with the program SHELXS-97 and refined using SHELXL-97 to $R=0.0567$ for 40563 reflections with $I>2\sigma(I)$, $R=0.0916$ for all reflections; max/min residual electron density 3.456 and $-2.026\ e\,Å^{-3}$. (SHELXS/L, SADABS from G. M. Sheldrick, University of Göttingen **1997**; structure graphics with DIAMOND 2.1 from K. Brandenburg, *Crystal Impact GbR*, **2001**.) As usual the cations not bound to the capsule as well as the crystal water molecules could not be found completely due to disorder. As this is also the case for the $[VO(H_2O)_5]^{2+}$ centers, the H_2O ligand sphere was not considered in the formula. Further details on the crystal structure investigations may be obtained from the Fachinformationszentrum Karlsruhe, 76344 Eggenstein-Leopoldshafen, Germany (fax: (+49) 7247-808-666; e-mail: crysdata@fiz-karlsruhe.de), on quoting the depository number CSD-415055.

[11] See for example, a) P. Kögerler, A. Müller in *Polyoxometalate Molecular Science* (Eds.: J. J. Borrás-Almenar, E. Coronado, A.

 © 2005 Wiley-VCH Verlag GmbH & Co. KGaA, Weinheim

Müller, M. T. Pope), Kluwer, Dordrecht, **2003**, pp. 297–323; b) A. Müller, F. Peters, M. T. Pope, D. Gatteschi, *Chem. Rev.* **1998**, *98*, 239–271.

[12] A. Müller, B. Botar, H. Bögge, P. Kögerler, A. Berkle, *Chem. Commun.* **2002**, 2944–2945.

[13] A. Müller, S. K. Das, H. Bögge, M. Schmidtmann, M. Dressel, J. van Slageren, unpublished results.

[14] In spite of these expected differences, there are some important features common to the two Keplerates, such as similar characteristics of the ground state and the low-lying excitation states, which arise because of their otherwise common geometrical structure and the existence of antiferromagnetic exchange between nearest-neighbor spins. As one example, the total spin quantum number of the ground state eigenvector for the "quantum" Keplerate **1** is expected to be $S=0$, as it is for the "classical" Keplerate $\{Fe_{30}\}$, and its direct manifestation would be in the vanishing of T_χ (proportional to $\langle S^2\rangle$), in the low-temperature regime; χ is the zero-field susceptibility.

[15] The raw M/H ($\equiv\chi$) data display a rapid rise on decreasing the temperature below 50 K that is very accurately simulated by a term proportional to $1/T$ (Curie behavior). This observation suggests the presence of additional non-interacting paramagnetic centers in the sample. In fact, fitting the low temperature data leads to a value of approximately 2 $S=1/2$ centers. These centers are considered to be the non-interacting VO^{2+} (d^1) ions. In large cluster systems like **1**, they can take the same place as the other diamagnetic cations, which are usually disordered in the large voids between the clusters and can therefore not be discovered by single-crystal structure analysis (see ref. [10]). On subtracting the contribution of these discrete paramagnetic centers, we obtain a corrected magnetization M' as well as the corrected susceptibility data, $T\chi \equiv T'/H$, shown in Figure 4. The Curie behavior of the paramagnetic centers shows that they do not interact with each other and with the $\{V_{30}\}$ cluster. The possibility that the finite $T\chi$ value at low temperatures is due to a non-zero spin ground state can be precluded. Regarding the presented $T\chi$ curve: As always there is uncertainty as to the appropriate choices for diamagnetic and temperature-independent paramagnetism (TIP) corrections. Additionally, because of the large voids between the clusters the VO^{2+} groups need not be present stoichiometrically in the compound; correspondingly, there is a very small error limit in the given/used number of two VO^{2+} groups which influences the correction of the raw magnetic data ($(VO)_{1.8}$ could, for example, correspond to $K_{14.4}$).

[16] The exchange coupling difference between the classical and quantum Keplerates discussed herein is analogous to that of the cluster pair with 6 V^{IV} and 6 Fe^{III} centers embedded in the $\{Mo_{57}\}$ type skeleton; see D. Gatteschi, R. Sessoli, W. Plass, A. Müller, E. Krickemeyer, J. Meyer, D. Sölter, P. Adler, *Inorg. Chem.* **1996**, *35*, 1926–1934.

[17] Note added in proof, April 27, 2005: Very recent measurements by H. Nojiri (Tohoku University) of M versus H at 0.5 K up to 27 Tesla, as well as ESR measurements at 190 GHz for several temperatures, show features which are fully consistent with our physical interpretation of a strong intracluster exchange constant and approximately two VO^{2+} ions per formula unit that are magnetically independent of the $\{V_{30}\}$ cluster. Full details will be published elsewhere.

 © 2005 Wiley-VCH Verlag GmbH & Co. KGaA, Weinheim

Bioorganic Chemistry

Irreversible Inhibition of Metallo-β-lactamase (IMP-1) by 3-(3-Mercaptopropionylsulfanyl)-propionic Acid Pentafluorophenyl Ester**

Hiromasa Kurosaki, Yoshihiro Yamaguchi, Toshihiro Higashi, Kimitaka Soga, Satoshi Matsueda, Haruka Yumoto, Shogo Misumi, Yuriko Yamagata, Yoshichika Arakawa, and Masafumi Goto*

Pathogenic bacteria that produce metallo-β-lactamases (MBLs) are emerging as a new challenge to the medical community. These enzymes catalyze the hydrolysis of a wide spectrum of β-lactams, including carbapenems such as imipenem, some of which are coded in transferable plasmids.[1,2] Among the currently known MBLs, IMP-1, a member of subclass B1, which is encoded by the bla_{IMP} gene included in the integron structure,[2,3] rapidly spreads by facile horizontal gene transfer to other bacteria.[4] Moreover, many of the currently used serine β-lactamase inhibitors such as clavulanic acid, sulbactam, and tazobactam are ineffective against MBLs. Thus, the development of inhibitors of MBLs is important for the continuing application of such widely prescribed β-lactam antibiotics. Several such inhibitors have been reported to date;[5–11] for example, Payne et al. demonstrated[6] that mercaptoacetic acid, a hydrolysis product of mercaptoacetic acid thiol esters that are hydrolyzed by MBLs (β-lactamase II, CfiA, and CphA), binds irreversibly to the enzyme through formation of a disulfide bond with the active site cysteine residue under aerobic conditions, as evidenced

[*] Prof. Dr. H. Kurosaki, Y. Yamaguchi, T. Higashi, K. Soga, S. Matsueda, H. Yumoto, Prof. Dr. M. Goto
Department of Structure-Function Physical Chemistry
Graduate School of Pharmaceutical Sciences
Kumamoto University
Oe-honmachi 5-1, Kumamoto 862-0973 (Japan)
Fax: (+81) 96-371-4314
E-mail: ayasaya@gpo.kumamoto-u.ac.jp
Prof. Dr. S. Misumi
Department of Pharmaceutical Biochemistry
Graduate School of Pharmaceutical Sciences
Kumamoto University
Oe-honmachi 5-1, Kumamoto 862-0973 (Japan)
Prof. Dr. Y. Yamagata
Department of Structural Biology
Graduate School of Pharmaceutical Sciences
Kumamoto University
Oe-honmachi 5-1, Kumamoto 862-0973 (Japan)
Prof. Dr. MD. Y. Arakawa
Department of Bacterial Pathogenesis and Infection Control
National Institute of Infectious Diseases
4-7-1 Gakuen, Musashi-Murayama, Tokyo 208-0011 (Japan)

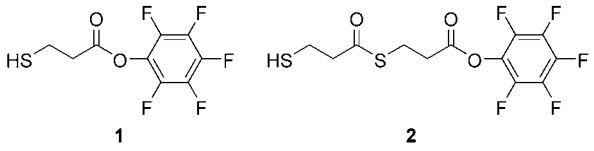
[**] This work was supported by H15-Shinkou-9 from the Ministry of Health Labor and Welfare of Japan and by a Grant-in-Aid for Scientific Research (B) (No. 16390017) from the Japan Society for the Promotion of Science.

Supporting information for this article is available on the WWW under http://www.angewandte.org or from the author.

 DOI: 10.1002/anie.200500835 © 2005 Wiley-VCH Verlag GmbH & Co. KGaA, Weinheim

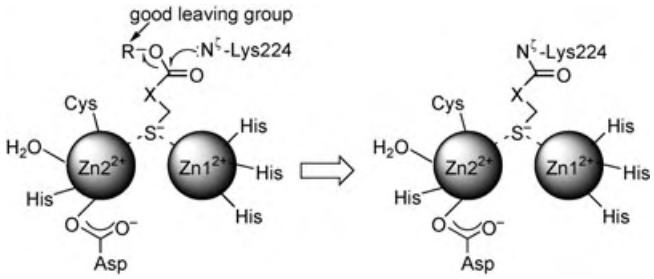
by both tryptic digestion and electrospray mass spectrometry studies.

Our ultimate goal was to develop an irreversible inhibitor of IMP-1. We report here on the design and inhibition properties of three-dimensional structure-based irreversible inhibitors of IMP-1, **1** and **2**, and the crystal structure of a covalently bound complex formed between the hydrolysis product of **2** and IMP-1.



1 **2**

The strategy for the irreversible inhibition of IMP-1 is shown in Scheme 1: The thiol group in **2** coordinates to one or



Scheme 1. Strategy for the irreversible inhibition of thiol compounds with a good leaving group.

two Zn^{II} ion(s) in the active site as an anchor. Lys224 (following BBL numbering[12]) is conserved in almost all MBLs of subclass B1. In the first IMP-1 structure reported (PDB code 1DD6),[7] Lys224 is located at a distance of about 6 Å from the two Zn^{II} ions. Lys224 is thought to be important for substrate binding[6,13] and may attack an activated ester, thus forming a covalently bound inhibitor–enzyme adduct that irreversibly inhibits the enzyme. At this point, water molecules, from the solvation shell surrounding Lys224, may act as acceptors of H^+ ions from the positively charged N^{ζ} group of Lys224.

The coupling reaction of one equivalent of 3-mercaptopropionic acid (MPA) and 1-hydroxy-1*H*-benzotriazole (HOBt) with pentafluorophenol in the presence of one equivalent of *N*,*N*′-dicyclohexylcarbodiimide (DCC) in ethyl acetate at 0 °C afforded **1**, a synthetic intermediate of **2**, in 15 % yield (see Supporting Information). The desired inhibitor **2** was prepared in 45 % yield by treating **1** with MPA in the presence of DCC in ethyl acetate at 0 °C (see Supporting Information).

The time-dependent inactivation of IMP-1 by **1** and **2** was determined by incubating various amounts of inhibitor with 10 nM IMP-1 in 50 mM tris-HCl/0.5 M NaCl buffer (pH 7.4, tris = tris(hydroxymethyl)aminomethane) at 15 °C (see Supporting Information). The inactivation of IMP-1 by **1** and **2** was both time and concentration dependent. Plots of the natural logarithm of the residual activity against incubation time were linear, thus suggesting that the observed rate of inactivation follows pseudo-first-order kinetics (Figure 1 a and b). The double reciprocal plots of these slopes (k_{obs}) versus concentration of **1** and **2** gave straight lines (Figure 1 c

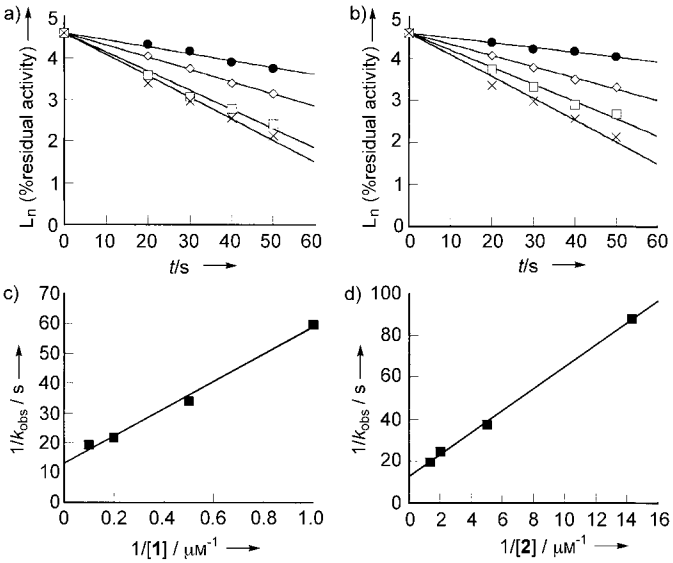


Figure 1. Time- and concentration-dependent inactivation of IMP-1 by **1** (a) and **2** (b) in 50 mM tris-HCl/0.5 M NaCl buffer (pH 7.4) at 15 °C. Inhibition concentrations: ●: 1 μM; ◇: 2 μM; □: 5 μM; and ×: 10 μM for **1**, and ●: 0.07 μM; ◇: 0.2 μM; □: 0.5 μM; and ×: 0.75 μM for **2**. Each point shown represents the mean of three experiments. Double reciprocal plots of k_{obs} versus concentration of **1** (c) and **2** (d).

and d). The regression line did not pass through the origin, but intercepted the positive *y*-axis, thus indicating the initial formation of a dissociable complex between IMP-1 and inhibitor before inactivation.[14] The k_{inact} and K_i values were calculated from these plots to be $0.076 \pm 0.002\ s^{-1}$ and 3.452 ± 0.030 μM for **1** and $0.080 \pm 0.002\ s^{-1}$ and 0.423 ± 0.013 μM for **2**. These results show that the second-order rate constant for inactivation (k_{inact}/K_i) with **2** increases by about ninefold over that with **1**.

To determine whether **1** or **2** inhibits IMP-1 irreversibly, 10 μM IMP-1 was incubated with 1 mM **1** or **2** at 0 °C for various periods of time (0–2 h) and the mixtures were then filtered through gel (Sephadex G-25) to separate the protein from the excess inhibitor (see Supporting Information). The activity of the resulting protein was measured using nitrocefin as the substrate. The control, without inhibitor, shows no loss of activity of IMP-1 after filtration through the gel. On the other hand, the inactivation of IMP-1 by **1** and **2** resulted in a nearly 100 % inhibition, clearly showing that both inhibitors inhibited IMP-1 very rapidly and irreversibly. Furthermore, the irreversibility of the binding of **1** and **2** was also confirmed by dialysis at 4 °C for 16 h (see Supporting Information): in neither of these cases was any activity recovered, thus verifying that **1** and **2** are irreversible inhibitors.

After the incubation of 100 μM **2** with 10 μM IMP-1 for 30 minutes and gel filtration, the sample was analyzed by MALDI-TOF mass spectrometry (see Supporting Information). The MALDI-TOF mass spectrum of the intact IMP-1

 © 2005 Wiley-VCH Verlag GmbH & Co. KGaA, Weinheim

showed the parent signal at *m*/*z* 25113.2 while that treated with **2** showed a peak at *m*/*z* 25290.1 (see Supporting Information). The increase in mass of *m*/*z* 176.9 corresponds to the mass of $SCH_2CH_2COSCH_2CH_2CO$ (this unit is denoted **2**-P), which indicates that this moiety of **2** is covalently attached to IMP-1 in a ratio of 1:1.

To identify the site of amino acid attachment and to determine the three-dimensional structure, crystals of IMP-1 treated with **2** were prepared by the hanging-drop method and the molecular structure was determined (see Supporting Information). The structure of the inhibitor bound IMP-1 (**2**-P/IMP-1) at a resolution of 2.63 Å was refined to an *R*-factor value of 22.8 % and an R_{free} value of 24.3 % using 2.63- to 44.7-Å data.[15] There are two **2**-P/IMP-1 molecules, A and B, in the asymmetric unit. The two molecules are almost identical with a root-mean-square deviation of 0.31 Å when all C^{α} atoms between A and B are superimposed. The overall structure of each molecule adopts a αβ/βα sandwich structure as found in the native enzyme, the three-dimensional structure of which was not greatly perturbed by the inhibitor. The overall structure of molecule A is shown in Figure 2a.

The thiolate group in **2**-P bridges between the two Zn^{II} ions in the active site (distances Zn1···inhibitor(S), 2.2/2.2; Zn2···inhibitor(S), 2.3/2.5 Å in molecules A/B; Figure 2b). The geometry around Zn2 is changed from a trigonal bypyramid in the native structure to a distorted tetrahedral structure, as previously reported by Concha et al.[7] (angles (Asp120)$O^{\delta 2}$-Zn2-Cys221(S^{γ}), 101/101°; (Asp120)$O^{\delta 2}$-Zn2-His263($N^{\varepsilon 2}$), 99/104°; Asp120 $O^{\delta 2}$-Zn2-inhibitor(S), 122/112°; (Cys221)S^{γ}-Zn2-His263($N^{\varepsilon 2}$), 109/116°; (Cys221)S^{γ}-Zn2-inhibitor(S), 107/113°; (His263)$N^{\varepsilon 2}$-Zn2-inhibitor(S), 117/111° in molecules A/B.

The $2|F_o|-|F_c|$ electron density map clearly indicates the formation of a covalent amide bond between the ester and side chain N^{ζ} atom of Lys224 with the concomitant displacement of the pentafluorophenolate group, which is not seen in the electron density.

The carbonyl oxygen atom of the amide group formed between the inhibitor and IMP-1 forms a hydrogen bond with the main-chain nitrogen atom of Asn233 (ca. 3.1/3.3 Å in molecules A/B) while the carbonyl oxygen atom of the thioester group of the inhibitor is hydrogen bonded to the side chain nitrogen atom of Asn233 (ca. 3.0/3.5 Å in molecules A/B).

In summary, the synthesis of a covalent, irreversible inhibitor **2** of IMP-1 is described. An X-ray crystal structure of the inhibitor covalently bound to IMP-1 confirmed this strategy. These findings shed further light on the design of inhibitors based on the three-dimensional structure of MBLs related to IMP-1.

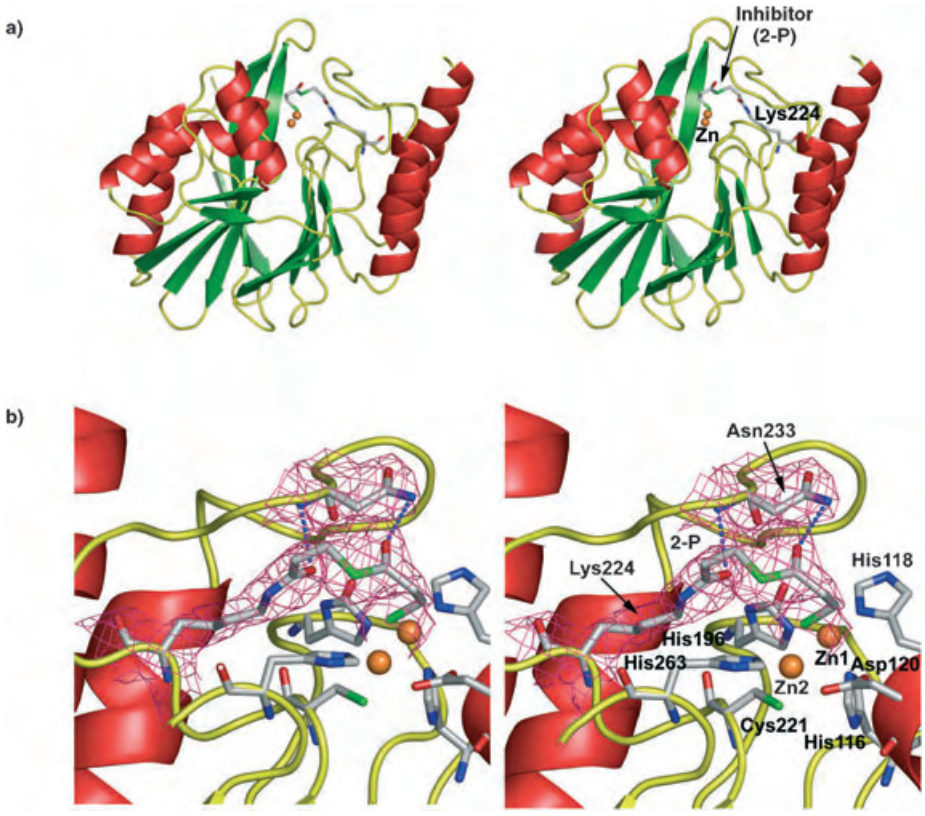


Figure 2. a) The overall structure of IMP-1 complexed with 2-P. α-Helices, β-strands, and loops are shown in red, green, and yellow, respectively. Zn^{2+} ions are represented as orange spheres. The inhibitor and Lys224 are displayed as sticks (C, N, O, and S atoms colored gray, blue, red, and green, respectively). b) The crystal structure of IMP-1 modified by **2**-P. The electron density of Asn233 as well as Lys224 and its covalently attached inhibitor molecule is shown countoured at 1.0σ in a $2|F_o|-|F_c|$ map. Hydrogen bonds are indicated by blue dashed lines.

Received: March 7, 2005
Published online: May 13, 2005

Keywords: bioorganic chemistry · inhibitors · lactams · metalloenzymes · structure elucidation

[1] Y. Arakawa, M. Murakami, K. Suzuki, H. Ito, R. Wacharotayankun, S. Ohsuka, N. Kato, M. Ohta, *Antimicrob. Agents Chemother.* **1995**, *39*, 1612–1615.
[2] M. L. Riccio, N. Franceschini, L. Boschi, B. Caravelli, G. Cornaglia, R. Fontana, G. Amicosante, G. M. Rossolini, *Antimicrob. Agents Chemother.* **2000**, *44*, 1229–1235.
[3] N. Laraki, M. Galleni, I. Thamm, M. L. Riccio, G. Amicosante, J. M. Frère, G. M. Rossolini, *Antimicrob. Agents Chemother.* **1999**, *43*, 890–901.
[4] D. M. Livermore, N. Woodford, *Curr. Opin. Microbiol.* **2000**, *3*, 489–495.
[5] M. Goto, T. Takahashi, F. Yamashita, A. Koreeda, H. Mori, M. Ohta, Y. Arakawa, *Biol. Pharm. Bull.* **1997**, *20*, 1136–1140.
[6] D. J. Payne, J. H. Bateson, B. C. Gasson, D. Proctor, T. Khushi, T. H. Farmer, D. A. Tolson, D. Bell, P. W. Skett, A. C. Marshall, R. Reid, L. Ghosez, Y. Combret,

 © 2005 Wiley-VCH Verlag GmbH & Co. KGaA, Weinheim

J. Marchand-Brynaert, *Antimicrob. Agents Chemother.* **1997**, *41*, 135 – 140.
[7] N. O. Concha, C. A. Janson, P. Rowling, S. Pearson, C. A. Cheever, B. P. Clarke, C. Lewis, M. Galleni, J. M. Frère, D. J. Payne, J. H. Bateson, S. S. Abdel-Meguid, *Biochemistry* **2000**, *39*, 4288 – 4298.
[8] J. H. Toney, G. G. Hammond, P. M. Fitzgerald, N. Sharma, J. M. Balkovec, G. P. Rouen, S. H. Olson, M. L. Hammond, M. L. Greenlee, Y. D. Gao, *J. Biol. Chem.* **2001**, *276*, 31913 – 31918.
[9] S. Bounaga, M. Galleni, A. P. Laws, M. I. Page, *Bioorg. Med. Chem.* **2001**, *9*, 503 – 510.
[10] S. Siemann, D. P. Evanoff, L. Marrone, A. J. Clarke, T. Viswanatha, G. I. Dmitrienko, *Antimicrob. Agents Chemother.* **2002**, *46*, 2450 – 2457.
[11] I. García-Sáez, J. Hopkins, C. Papamicael, N. Franceschini, G. Amicosante, G. M. Rossolini, M. Galleni, J. M. Frère, O. Dideberg, *J. Biol. Chem.* **2003**, *278*, 23868 – 23873.
[12] M. Galleni, J. Lamotte-Brasseur, G. M. Rossolini, J. Spencer, O. Dideberg, J. M. Frère, *Antimicrob. Agents Chemother.* **2001**, *45*, 660 – 663.
[13] S. Haruta, E. T. Yamamoto, Y. Eriguchi, T. Sawai, *FEMS Microbiol. Lett.* **2001**, *197*, 85 – 89.
[14] R. Kitz, I. B. Wilson, *J. Biol. Chem.* **1962**, *237*, 3245 – 3249.
[15] The X-ray coordinates for the **2**-P/IMP-1 complex have been deposited in the Protein Data Bank under the code number: 1VGN.

 © 2005 Wiley-VCH Verlag GmbH & Co. KGaA, Weinheim

Coordination Polymers

Self-Assembly of an Interlaced Triple-Stranded Molecular Braid with an Unprecedented Topology through Hydrogen-Bonding Interactions**

Xin-Jun Luan, Yao-Yu Wang, Dong-Sheng Li, Ping Liu, Huai-Ming Hu, Qi-Zhen Shi, and Shie-Ming Peng*

The current interest in the crystal engineering of coordination polymers[1] stems from their potential applications as materials[2] for molecular selection, ion exchange, and catalysis, as well as because of their intriguing variety of architectures and topologies. Many recent examples have illustrated that topological types unprecedented in inorganic compounds and in minerals can be observed within coordination polymer frameworks.[3] Particularly attractive is the finding of species with novel modes of supramolecular intertwining, such as helices, rotaxanes, catenanes, and knots,[4] which contribute more and more to our increasing knowledge of the self-assembly processes and the supramolecular self-organization of coordination polymers. The amount of predefined information can be reduced by incorporating a higher degree of flexibility into the building blocks, and more unpredictable structures can arise from identical metal–ligand combinations. For example, rigid polyfunctional ligands are well known to form grids,[5] brick-wall structures,[6] honeycombs,[7] diamondoid nets,[8] and other noteworthy species,[9] while long flexible polyfunctional ligands have shown the ability to produce unique interwoven extended structural motifs, such as polycatenanes,[10] polyrotaxanes,[11] double helices,[12] triple helices,[13] and other uncommon species.[14] Some of the interwoven structures may be predictable; however, structural control of metal–organic reactions (especially those involving flexible ligands) remains a great challenge, and unexpected structures with unprecedented topologies often result. Herein we report a fascinating interlaced triple-stranded braid based on a Cu^{II} complex with the highly flexible 1,3-bis(4-pyridyl)propane (bpp) ligand. To the best of our knowledge, this species presents a remarkable and unprecedented topology of a triple-stranded molecular braid which looks just like a hair plait. Moreover, it shows an interesting behavior in which the interlaced chains are self-recognized by hydrogen bonds between them.

Slow evaporation of the methanol/acetonitrile solvent from a solution of bpp and $[Cu_2(maa)_4{\cdot}2H_2O]$ (Hmaa = 2-methylacrylic acid) in a 2:1 stoichiometry led to crystals of $[Cu_4(bpp)_4(maa)_8(H_2O)_2]{\cdot}2H_2O$ (**1**).

The structure of **1** was determined unambiguously by X-ray crystallographic analysis.[15] This system crystallized in the centrosymmetric space group $P\bar{1}$, with three independent copper centers per asymmetric unit (Figure 1). Each Cu^{II} center has a different coordination environment: distorted square pyramid, ideal square-planar, and distorted octahedral geometries. Although it is well known that Cu^{II} ions can give rise to tetracoordinate, pentacoordinate, and hexacoordinate geometries, complexes in which the three coordination styles all exist hasn't been reported to date. The complex reported herein contains the three modes of coordination for Cu^{II} ions in the arrangement $(\text{-}Cu^5\text{-}Cu^6\text{-}Cu^5\text{-}Cu^4\text{-})_n$ (Cu^x, x = coordination number). In addition, the terminally coordinated maa anions exhibit a versatile coordination behavior and display different bonding modes with the copper cations: monodentate for Cu1 and Cu2 and chelating for Cu3. In the complex, bpp is employed as a bridging ligand for the construction of a one-dimensional chain along the *c* axis which has alternating helical sections (alternating right and left turns of the strand when looking down the "growth axis"). However, the single strand chain is not a helical structure, because the strand contains centers of inversion and does not have defined chirality. Interestingly, bpp can adopt different conformations with respect to the relative orientations of the CH_2 groups: the bpp ligand between Cu1 and Cu2 adopts a *trans– gauche* (TG) conformation, in which N···N is 8.684(2) Å, whereas the

[*] X.-J. Luan, Prof. Dr. Y.-Y. Wang, Dr. D.-S. Li, Dr. P. Liu, Prof. Dr. H.-M. Hu, Prof. Dr. Q.-Z. Shi
Department of Chemistry
Shaanxi Key Laboratory of Physico-Inorganic Chemistry
Northwest University
Xi'an, Shaanxi, 710069 (P.R. China)
Fax: (+86) 29-8837-3398
E-mail: wyaoyu@nwu.edu.cn
Prof. Dr. S.-M. Peng
Department of Chemistry
National Taiwan University (Taiwan)

[**] This work was supported by the National Natural Science Foundation of China (No. 20471048) and TRAPOYT.

 © 2005 Wiley-VCH Verlag GmbH & Co. KGaA, Weinheim DOI: 10.1002/anie.200500744

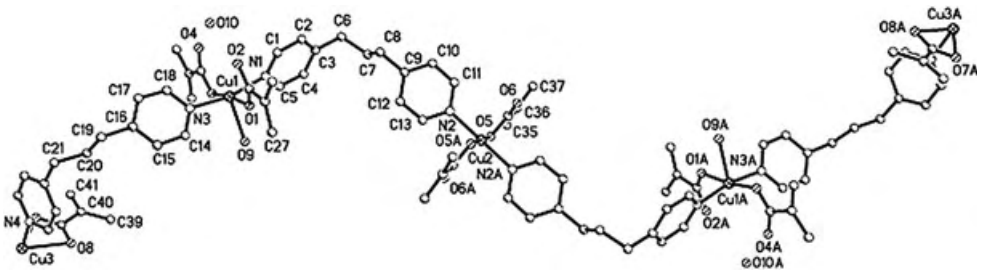


Figure 1. A view of the coordination environments at the three Cu^{II} centers in **1**. Selected bond lengths [Å]: Cu1-O1 1.918(2), Cu1-O3 1.920(2), Cu1-O9 2.329(2), Cu1-N1 2.027(2), Cu1-N3 2.026(3), Cu2-O5 1.991(2), Cu2-N2 1.995(3), Cu3-O7 2.111(3), Cu3-O8 2.361(3), Cu3-N4 1.985(2).

bpp ligand between Cu1 and Cu3 adopts a TT conformation, in which N···N is longer (9.375(2) Å). The chain in **1**, therefore, results from metal–ligand interactions coupled with various other factors and can be described as $(\text{-bpp}^{TT}\text{-Cu}^{5}\text{-bpp}^{TG}\text{-Cu}^{6}\text{-bpp}^{TG}\text{-Cu}^{5}\text{-bpp}^{TT}\text{-Cu}^{4}\text{-})_n$. The periodicity of the chain is 44.280(2) Å and contains four Cu^{II} centers per repeat unit.

The crystal structure of **1** shows the presence of a neutral interlaced triple-stranded braid, which is formed by the interweaving of three single-stranded chains with alternating helical parts that extend along the *c* axis (Figure 2). The repeat distance of the braid (14.760 Å) is 1/3 of the repeat distance of the single chain. Cu^{II} atoms are arranged in a line in the middle of the braid, and the distance between the adjacent Cu^{II} centers is 7.380 Å, which is half of the repeat distance of the braid. Discrete triple-stranded intertwining chains generally show a triple-helix topology in supramolecular chemistry.[13] In contrast, the structure of **1** can be described as a molecular braid with an unprecedented topology. To the best of our knowledge, this is the first example of a molecular braid which mimics perfectly a hair plait. Careful examination of the structure indicates that strong intermolecular hydrogen bonds of O9–H9A···O8 (2.764(1) Å) and O9–H9···O6 (2.800(2) Å) exist between the three independent chains in the braid (Figure 3). It is clear that two hydrogen atoms of one coordinated water molecule serve as the acceptors, while the two oxygen atoms of different coordinated maa anions serve as the donors in each self-recognition site. Self-recognition often operates between groups during the assembly of amino acid molecules in crystals, in the majority of cases, through the formation of hydrogen bonds. In the current complex, the molecular braid structure can be considered to be dependent on self-recognition between the three chains. That is, the hydrogen bonds,

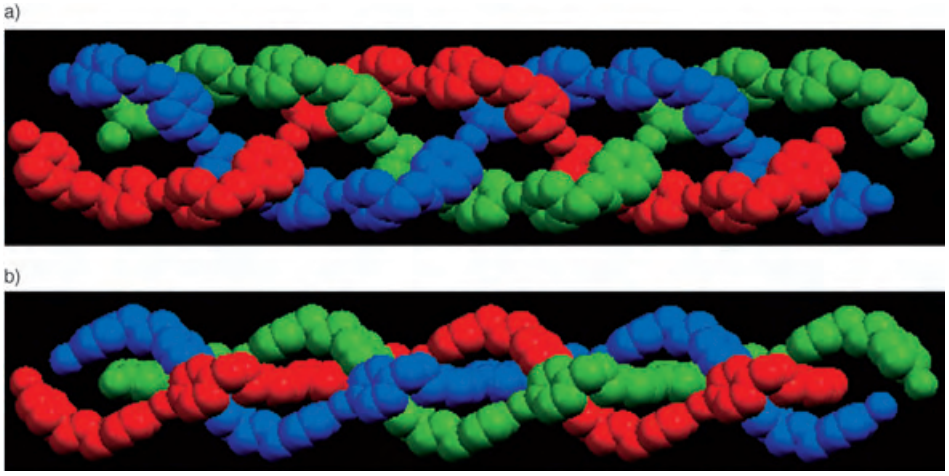


Figure 2. a) Top view of the interlaced triple-stranded braid of **1** and b) side view of **1**. The maa anions are omitted for clarity, and the triple-stranded chains are colored red, blue, and green.

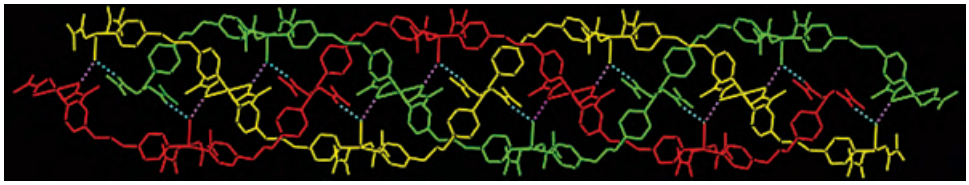


Figure 3. Self-assembly of the triple-stranded braid through formation of hydrogen bonds (O9–H9···O8, 2.764(1) (violet), O9–H9···O6, 2.800(2) Å (light blue)).

 © 2005 Wiley-VCH Verlag GmbH & Co. KGaA, Weinheim

through which the molecular braid is aligned exactly, operate between the three interwoven chains. Thus, the formation of the molecular braid in this case is expected to occur in two steps: initial construction of an infinite interwoven chain of ligated Cu^{II} ions, followed by hydrogen-bonding between the infinite chains. Thermogravimetric analysis (TGA) of the crystalline complexes **1** showed that after the loss of uncoordinated water molecules (2.0%) below 65°C, no weight loss occurred until approximately 235°C, which indicates the molecular braid is thermally stabile. Detailed analysis of the crystal structure also indicates that the main factor governing this phenomenon is not only the hydrogen bonds between the chains, as expected, but also by the braid framework, that is, by the interweaving of the single polymeric strands (which have alternating right and left turns looking down the "growth axis"). The rigidity of the braid framework means that the braids cannot approach one another sufficiently closely in the crystal; thus, the framework promotes the formation of an interlaced triple-stranded braid.

Another interesting structural feature of **1** is that there are many uncoordinated oxygen atoms that become arranged along the two sides on formation of the braid. In the process of self-assembly, uncoordinated oxygen atoms can act as hydrophilic sites and easily form hydrogen bonds with water molecules that approach the host (O10–H10A···O2 2.884(2) Å, O10–H10B···O4 2.798(1) Å; Figure 4). As a result, guest water molecules seem to cling to the surface of the braid.

In conclusion, the results demonstrate that an unusual complex comprising an interlaced triple-stranded braid is synthesized from the reaction of a Cu^{II} complex having a paddle-wheel structure with a flexible neutral organic ligand in the ratio of 1:2, which is different to the typical reaction route.[16] To the best of our knowledge, this complex–ligand combination represents a unique case in which the supramolecular assembly results in a molecular braid with an unprecedented topology. This example thus brings a new member to the family of suprastructures composed of identical units.

Experimental Section

$[Cu_2(maa)_4]\cdot 2H_2O$: Reaction of $[Cu_2(OH)_2CO_3]$ (2.211 g, 10 mmol) with 2-methylacrylic acid (3.442 g, 40 mmol) in methanol under reflux for 2 h afforded blue-green crystals of $[Cu_2(maa)_4\cdot 2H_2O$ in approximately 87% yield. Elemental analysis calcd (%) for $C_{16}H_{24}Cu_2O_{10}$: C 38.17, H 4.80; found: C 38.28, H 4.83. IR (KBr): $\tilde{\nu}$ = 2968, 2932, 1681, 1645, 1594, 1497, 1414, 1299, 1225, 1008, 951, 856, 826, 638, 445 cm^{-1}.

1: A solution of bpp (0.040 g, 0.200 mmol) in acetonitrile (10 mL) was added to a solution of $Cu_2(maa)_4\cdot 2H_2O$ (0.050 g, 0.100 mmol) in methanol (10 mL). The clear mixture was stirred for a few minutes and then allowed to evaporate at room temperature. Well-shaped blue needles of **1** appeared after several days. The crystalline product was filtered, washed with ethanol, and dried in air. Yield, 65%. Elemental analysis calcd for $C_{84}H_{104}Cu_4N_8O_{20}$: C 56.05, H 5.82, N 6.22; found: C 56.12, H 5.85, N 6.28. IR (KBr): $\tilde{\nu}$ = 3421, 2953, 1650, 1618, 1591, 1453, 1427, 1379, 1232, 939, 835, 810, 627, 523 cm^{-1}.

Received: February 28, 2005
Published online: May 13, 2005

Keywords: coordination polymers · copper · self-assembly · supramolecular chemistry · topology

[1] a) B. F. Hoskins, R. Robson, *J. Am. Chem. Soc.* **1990**, *112*, 1546; b) O. M. Yaghi, H. Li, C. Davis, D. Richardson, T. L. Groy, *Acc. Chem. Res.* **1998**, *31*, 474; c) S. R. Batten, R. Robson, *Angew. Chem.* **1998**, *110*, 1558; *Angew. Chem. Int. Ed.* **1998**, *37*, 1460; d) F. M. Tabellion, S. R. Seidel, A. M. Arif, P. J. Stang, *Angew. Chem.* **2001**, *113*, 1577; *Angew. Chem. Int. Ed.* **2001**, *40*, 1529; e) O. M. Yaghi, M. O'Keeffe, N. W. Ockwig, H. K. Chae, M. Eddaoudi, J. Kim, *Nature* **2003**, *423*, 705.

[2] a) C. Janiak, *Angew. Chem.* **1997**, *109*, 1499; *Angew. Chem. Int. Ed. Engl.* **1997**, *36*, 1431; b) D. M. L. Goodgame, D. A. Grachvogel, D. J. Williams, *Angew. Chem.* **1999**, *111*, 217; *Angew. Chem. Int. Ed.* **1999**, *38*, 153; c) M. Eddaoudi, J. Kim, N. Rosi, D. Vodak, J. Wachter, M. O'Keeffe, O. M. Yaghi, *Science* **2001**, *295*, 469; d) R. Matsuda, R. Kitaura, S. Kitagawa, Y. Kubota, T. C. Kobayashi, S. Horike, M. Takata, *J. Am. Chem. Soc.* **2004**, *126*, 14063.

[3] a) L. Carlucci, G. Ciani, P. Macchi, D. M. Proserpio, *Chem. Commun.* **1998**, 1837; b) M. J. Zaworotko, *Chem. Commun.* **2001**, 1; c) M. L. Tong, X. M. Chen, S. R. Batten, *J. Am. Chem. Soc.* **2003**, *125*, 16170; d) X. H. Bu, M. L. Tong, H. C. Chang, S. Kitagawa, S. R. Batten, *Angew. Chem.* **2004**, *116*, 194; *Angew. Chem. Int. Ed.* **2004**, *43*, 192.

[4] J.-M. Lehn, *Supramolecular Chemistry*, VCH, Weinheim, **1995**.

[5] a) M. Fujita, Y. J. Kwon, S. Washizu, K. Ogura, *J. Am. Chem. Soc.* **1994**, *116*, 1151; b) L. R. MacGillivray, R. H. Groeneman, J. L. Atwood, *J. Am. Chem. Soc.* **1998**, *120*, 2676.

[6] M. Fujita, Y. J. Kwon, O. Sasaki, K. Yamaguti, K. Ogura, *J. Am. Chem. Soc.* **1995**, *117*, 7287.

[7] a) G. B. Gardner, D. Venkataraman, J. S. Moore, S. Lee, *Nature* **1995**, *374*, 792; b) S. R. Batten, B. F. Hoskins, B. Moubaraki, K. S. Murray, R. Robson, *Chem. Commun.* **2000**, 1095.

[8] a) L. R. MacGillivray, S. Subramanion, M. J. Zaworotko, *J. Chem. Soc. Chem. Commun.* **1994**, 1325; b) O. M. Yaghi, H. Li, *J. Am. Chem. Soc.* **1995**, *117*, 10401; c) O. R. Evans, R. G. Xiong, Z. Y. Wang, G. K. Wong, W. B. Lin, *Angew. Chem.* **1999**, *111*, 557; *Angew. Chem. Int. Ed.* **1999**, *38*, 536.

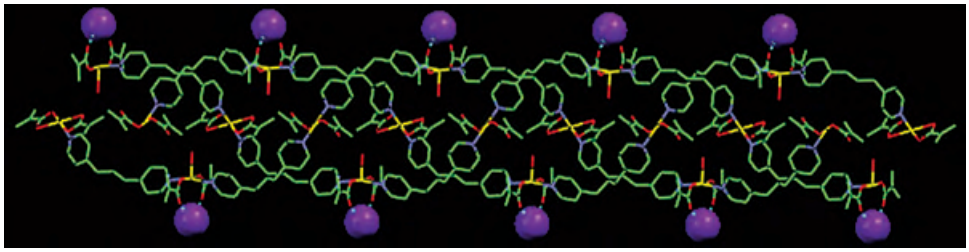


Figure 4. The triple-stranded-braid polymer of **1** with water guest molecules shown as space-filling models.

 © 2005 Wiley-VCH Verlag GmbH & Co. KGaA, Weinheim

[9] a) M. Eddaoudi, J. Kim, M. O'Keeffe, O. M. Yaghi, *J. Am. Chem. Soc.* **2002**, *124*, 376; b) B. Moulton, H. Abourahma, M. W. Bradner, J. J. Lu, G. J. McManus, M. J. Zaworotko, *Chem. Commun.* **2003**, 1342; c) X. L. Wang, C. Qin, E. B. Wang, Y. G. Li, C. W. Hu, L. Xu, *Chem. Commun.* **2004**, 378.

[10] a) D. M. L. Goodgame, S. Menzer, A. M. Smith, D. J. Williams, *Angew. Chem.* **1995**, *107*, 605; *Angew. Chem. Int. Ed. Engl. Angew. Chem. Int. Ed.* **1995**, *34*, 574; b) A. J. Blake, N. R. Champness, A. Khlobystov, D. A. Lemenovkii, W. S. Li, M. Schröder, *Chem. Commun.* **1997**, 2027; c) L. Carlucci, G. Ciani, M. Moret, D. M. Proserpio, S. Rizzato, *Angew. Chem.* **2000**, *112*, 1566; *Angew. Chem. Int. Ed.* **2000**, *39*, 1506; d) L. Carlucci, G. Ciani, D. M. Proserpio, *CrystEngComm* **2003**, *5*, 269.

[11] a) D. Whang, K. Kim, *J. Am. Chem. Soc.* **1997**, *119*, 451; b) B. F. Hoskins, R. Robson, D. A. Slizys, *J. Am. Chem. Soc.* **1997**, *119*, 2952; c) M. L. Tong, Y. M. Wu, J. Ru, X. M. Chen, H. C. Chang, S. Kitagawa, *Inorg. Chem.* **2002**, *41*, 4846; d) I. Poleschak, J. M. Kern, J.-P. Sauvage, *Chem. Commun.* **2004**, 474; e) Q. C. Wang, D. H. Qu, J. Ren, K. C. Chen, H. Tian, *Angew. Chem.* **2004**, *116*, 2715; *Angew. Chem. Int. Ed.* **2004**, *43*, 2661.

[12] a) L. Carlucci, G. Ciani, D. W. Gudenberg, D. M. Proserpio, *Inorg. Chem.* **1997**, *36*, 3812; b) O. Mamula, A. von Zelewsky, T. Bark, G. Bernardinelli, *Angew. Chem.* **1999**, *111*, 3129; *Angew. Chem. Int. Ed.* **1999**, *38*, 2945; c) X. M. Chen, G. F. Liu, *Chem. Eur. J.* **2002**, *8*, 4811.

[13] a) D. M. Ciurtin, N. G. Pschirer, M. D. Smith, U. H. F. Bunz, H. C. zur Loye, *Chem. Mater.* **2001**, *13*, 2743; b) P. Grosshans, A. Jouaiti, V. Bulach, J. M. Planeix, M. W. Hosseini, J. F. Nicoud, *Chem. Commun.* **2003**, 1336; c) Y. Cui, H. L. Ngo, W. B. Lin, *Chem. Commun.* **2003**, 1388.

[14] a) D. M. L. Goodgame, S. Menzer, A. M. Smith, D. J. Williams, *Chem. Commun.* **1997**, 339; b) T. Y. Niu, X. Q. Wang, A. J. Jacobson, *Angew. Chem.* **1999**, *111*, 2059; *Angew. Chem. Int. Ed.* **1999**, *38*, 1934; c) L. Carlucci, G. Ciani, D. M. Proserpio, L. Spadacini, *CrystEngComm* **2004**, *6*, 96; d) L. Carlucci, G. Ciani, D. M. Proserpio, *Chem. Commun.* **2004**, 380.

[15] Crystal data for **1**: $C_{84}H_{104}Cu_4N_8O_{20}$, triclinic, space group $P\bar{1}$, $a = 12.0997(14)$, $b = 12.8855(16)$, $c = 14.7601(17)$ Å, $\alpha = 89.462(2)$, $\beta = 86.349(2)$, $\gamma = 76.122(2)°$, $V = 2229.5(5)$ Å^3, $Z = 4$, $\rho_{calcd} = 1.341\ g\,cm^{-3}$. In the final least-squares refinement cycles on $|F|^2$, the model converged at $R_1 = 0.0397$, $wR_2 = 0.1041$, and GOF = 1.038 for 7233 independent reflections ($I > 2\sigma(I)$). The data collections were performed at 293(2) K on a Bruker SMART CCD area-detector diffractometer, using $Mo_{K\alpha}$ radiation ($\lambda = 0.71073$ Å) and the ω-scan method within the limits $1.74 < \theta < 24.41$. Absorption corrections were made with the program SADABS,[17] and the crystallographic package SHELXTL[18] was used for all calculations. All diagrams were generated using the SHELX-97 and MERCURY programs. CCDC-257085 contains the supplementary crystallographic data for this paper. These data can be obtained free of charge from the Cambridge Crystallographic Data Centre via www.ccdc.cam.ac.uk/data_request/cif.

[16] W. J. Belcher, C. A. Longstaff, M. R. Neckenig, J. W. Steed, *Chem. Commun.* **2002**, 1602.

[17] G. M. Sheldrick, SADABS. Software for empirical absorption corrections, University of Göttingen, Gemany, **2000**.

[18] SHELXTL Reference Manual, Version 5.1, Bruker AXS, Analytical X-Ray Systems, Inc., Madison, WI, USA, **1997**.

 © 2005 Wiley-VCH Verlag GmbH & Co. KGaA, Weinheim

Helical Structures

A Modular Strategy to Artificial Double Helices**

Yoshie Tanaka, Hiroshi Katagiri, Yoshio Furusho, and Eiji Yashima**

The fascination of the structure, dynamics, and recognition properties of naturally occurring helical polymers, such as the α-helix of peptides and the double helix of DNA structures have prompted chemists to design and synthesize artificial helical polymers and oligomers.[1] Although a number of synthetic polymers and oligomers that fold into single-helical conformations have been reported, only a few structural motifs are available for constructing double-helical structures. The most widely used approach is the utilization of metal-directed self-assembly, in which ligand-containing strands form double-, triple-, or quadruple-helical complexes, that is, helicates;[2] the three-dimensional structures of helicates are determined by the geometry of the template metal ions. Hydrogen-bonding-driven self-assembly is another common approach to constructing supramolecular duplexes.[3] In most cases, however, their three-dimensional structures have been characterized as ladder- or zipperlike linear conformations. It was recently disclosed that some oligoamides give rise to double-helical assemblies by making use of interstrand hydrogen-bonding and aromatic–aromatic interactions.[4] Although the hydrogen-bonding interaction is a readily available and versatile tool for constructing supramolecular assemblies,[5] it is still difficult and challenging to design double helices with predictable structures.[4c] Herein, we describe the design and synthesis of hydrogen-bonding-driven double helices by a modular strategy in which intertwined supramolecular binary complexes are employed.

Our strategy is based on the crescent-shaped *m*-terphenyl derivatives (Figure 1). Crescent-shaped molecules, such as bipyridine and phenanthroline derivatives, have often been used to construct intertwined supramolecular complexes and

[*] Dr. Y. Tanaka, Dr. H. Katagiri, Dr. Y. Furusho, Prof. E. Yashima
Yashima Super-structured Helix Project
Exploratory Research for Advanced Technology (ERATO)
Japan Science and Technology Agency (JST)
Creation Core Nagoya 101
2266-22 Anagahora, Shimoshidami
Moriyama-ku, Nagoya 463-0003 (Japan)
Fax: (+81) 52-739-2081
E-mail: furusho@yp-jst.jp
yashima@apchem.nagoya-u.ac.jp
Prof. E. Yashima
Institute for Advanced Research
Nagoya University
Chikusa-ku, Nagoya 464-8601 (Japan)
Fax: (+81) 52-789-3185

[**] We thank Dr. Mikio Yamasaki of Rigaku Cooperation for the X-ray crystal-structure analysis.

Supporting information for this article is available on the WWW under http://www.angewandte.org or from the author.

 DOI: 10.1002/anie.200501028 © 2005 Wiley-VCH Verlag GmbH & Co. KGaA, Weinheim

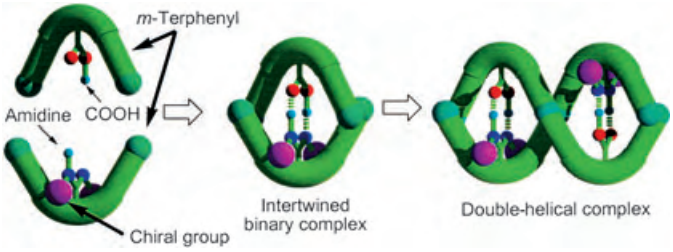
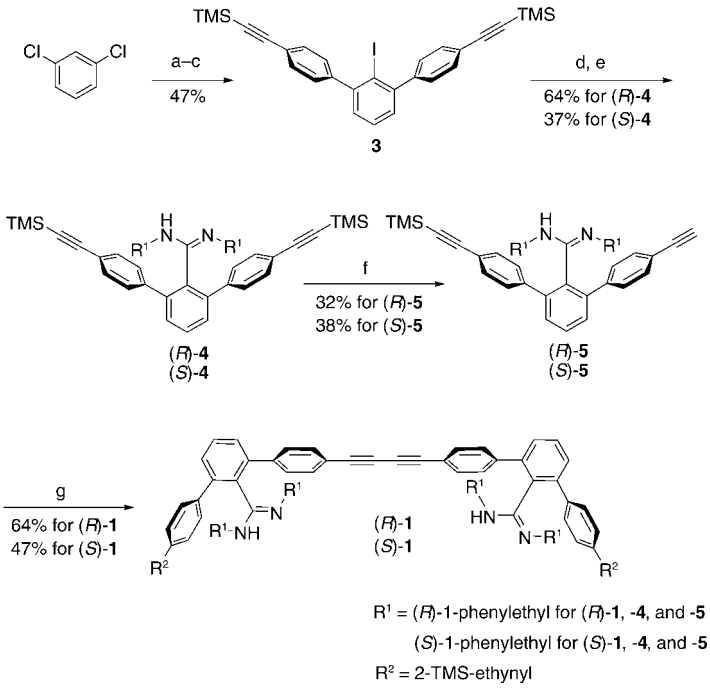


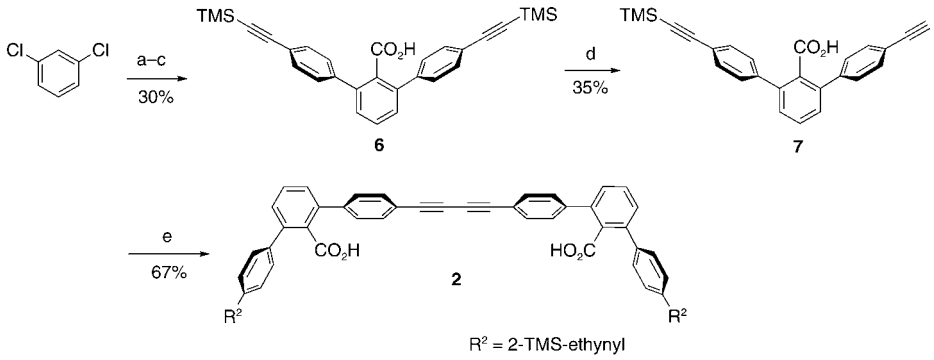
Figure 1. Schematic illustration of the modular strategy for the construction of artificial double-helical assemblies.

interlocked molecules.[6] We chose amidinium–carboxylate salt bridges as the supramolecular junction for the *m*-terphenyl derivatives because the charge-assisted hydrogen bonding between amidines and carboxylic acids is quite strong even in polar solvents and has a well-defined geometry.[7] Chiral groups were introduced onto the nitrogen atoms of the amidine moieties to control the chirality of the double helices. The formation of the salt bridge leads to a supramolecular binary complex, in which the two *m*-terphenyl derivatives are intertwined around the salt bridge (Figure 1). Connecting the intertwined complexes together should result in the formation of the double-helical structure.

The chiral diamidine (*R*)-**1** and its antipode (*S*)-**1** were prepared according to Scheme 1.[8] The iodide **3** was obtained by the Hart coupling of *m*-dichlorobenzene with 4-trimethylsilylethynylphenylmagnesium bromide followed by quenching with iodine.[9] Iodide **3** was lithiated and then treated with *N*,*N*′-bis[(*R*)-1-phenylethyl]carbodiimide[10a] to yield the amidine (*R*)-**4**.[11] (*R*)-**4** was treated with tetra-*n*-butylammonium fluoride (TBAF) to give the monosilane (*R*)-**5**, which was dimerized by oxidative coupling using the Sonogashira reagents to afford the diamidine (*R*)-**1**. The antipode (*S*)-**1** was synthesized in a similar manner except that *N*,*N*′-bis[(*S*)-1-phenylethyl]carbodiimide was used.[10b] Similarly, the dicarboxylic acid **2** was prepared according to Scheme 2. Carboxylic acid **6** was obtained by Hart coupling using CO_2 as the quencher. The monodesilylation of **6** was achieved by treatment with TBAF to yield the monosilane **7**, which was subsequently dimerized by oxidative coupling to afford **2**.



Scheme 1. Synthesis of diamidines **1**: a) *n*BuLi/THF, −78 °C; b) 4-trimethylsilylethynylphenylmagnesium bromide, −78 °C to RT; c) I_2, RT; d) *n*BuLi, TMEDA/Et_2O, 0 °C; e) *N*,*N*′-bis[(*R*)-1-phenylethyl]carbodiimide for (*R*)-**4**, *N*,*N*′-bis[(*S*)-1-phenylethyl]carbodiimide for (*S*)-**4**/THF, RT; f) nBu_4NF/THF, 0 °C; g) $[PdCl_2(PPh_3)_2]$, CuI, Et_3N/THF, RT. TMEDA = *N*,*N*,*N*′*N*′-tetramethyl-1,2-ethanediamine.



Scheme 2. Synthesis of dicarboxylic acid **2**: a) *n*BuLi/THF, −78 °C; b) 4-trimethylsilylethynylphenylmagnesium bromide, −78 °C to RT; c) CO_2, RT; d) nBu_4NF/THF, 0 °C; e) $[PdCl_2(PPh_3)_2]$, CuI, Et_3N/THF, RT.

Complexation of the diamidine (*R*)-**1** with the dicarboxylic acid **2** was first investigated by ^1H NMR spectroscopy (Figure 2). The ^1H NMR spectrum of **1** in $CDCl_3$ was complicated at 25 °C, because of the presence of several conformers originating from the *E*–*Z* isomerism of the C=N double bonds and the restricted rotation about the C–C bond between the amidine and the *m*-terphenyl groups.[11] In contrast, the ^1H NMR spectrum of the complex (*R*)-**1**·**2** showed a simple spectrum, thus indicating the presence of only one isomer. This result is consistent with the formation of a salt bridge between (*R*)-**1** and **2**, through which the geometry around the amidine residues is fixed in the *E* configuration. The resonances of the NH protons (c′ and c″) were observed as two doublets at a low magnetic field of approximately $\delta = 13.5$ ppm, which is indicative of the formation of a salt bridge. The CH_3 protons of the amidine groups (d′ and e′) were also evident. The non-equivalency of these signals is attributed to the formation of a duplex between (*R*)-**1** and **2**, which was also supported by 2D NMR spectroscopic and electrospray ionization mass spectrometry (ESI-MS) studies.[8] The association constant of **1** and **2** at

 © 2005 Wiley-VCH Verlag GmbH & Co. KGaA, Weinheim

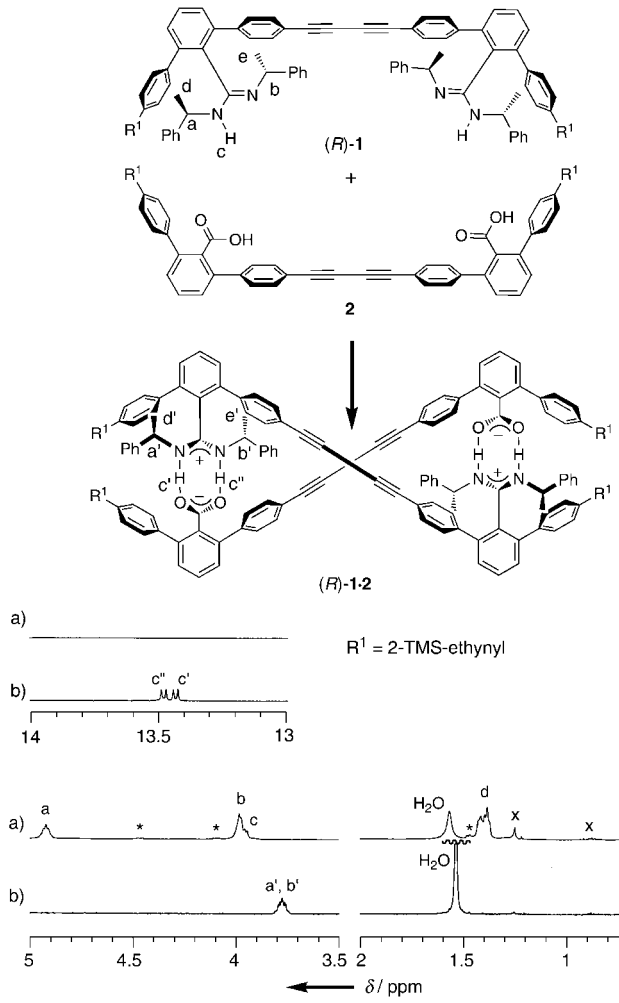


Figure 2. Partial ^{1}H NMR (500 MHz, $CDCl_3$, 25 °C) spectra of a) diamidine (*R*)-**1** (7.1 mM) and b) complex (*R*)-**1·2** (0.4 mM). The asterisks denote the signals for the corresponding *Z* isomer of (*R*)-**1**. "x" indicates impurities.

25 °C in $CDCl_3$ was estimated to be $>10^6\,M^{-1}$ by ^{1}H NMR spectroscopy.[8]

The X-ray structural analysis unambiguously revealed that the complex (*R*)-**1·2** adopted a right-handed double-helical structure in the solid state (Figure 3).[8,12] The amidine and carboxy groups formed two identical salt bridges with two hydrogen bonds for each and average N···O distances of 2.73 Å. The two amidinium–carboxylate salt bridges enabled the two strands to be held together. All the benzene rings of the *m*-terphenyl groups were chirally twisted clockwise by about 48–61°, and the two strands were wound up to form the right-handed double-helical structure.

Circular dichroism (CD) measurements were then performed to examine if the complexes (*R*)- and (*S*)-**1·2** maintained their single-handed double-helical structures in solution (Figure 4). Both enantiomers of **1·2** showed intense mirror-image CD signals between approximately 260 and

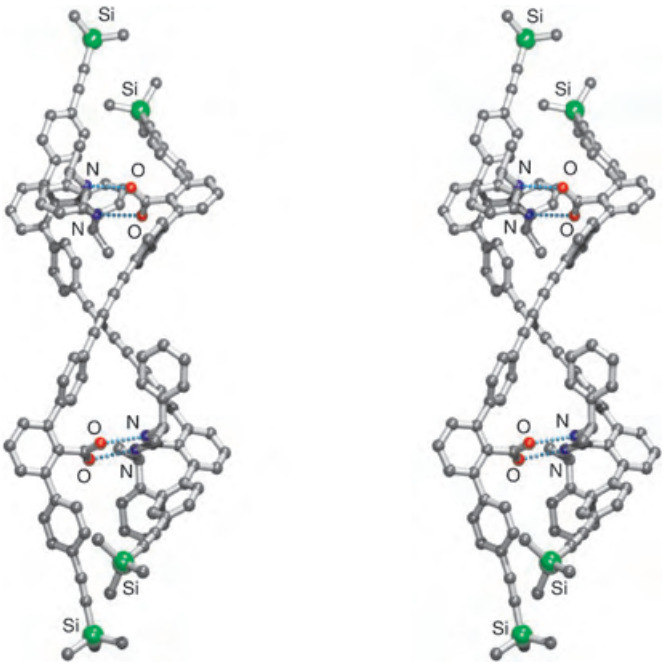


Figure 3. Stereoview of the crystal structure of (*R*)-**1·2**. The hydrogen atoms and included solvents are omitted for clarity. The intermolecular hydrogen bonds between N and O are shown by dashed lines.

370 nm in $CHCl_3$, whereas (*R*)- and (*S*)-**1** exhibited very weak Cotton effects in this region. The significant enhancement of the Cotton effects for the complexes **1·2**, especially in the absorption region of the diacetylene linkages (ca. 300–370 nm), indicates that the single-handed double-helical structures of (*R*)- and (*S*)-**1·2** are likely retained in $CHCl_3$. This presumption was supported by the variable-temperature ^{1}H NMR spectroscopic measurements of (*R*)-**1·2** in $CDCl_3$; no signals corresponding to the opposite diastereomeric left-handed double helix were observed, even at temperatures as low as −60 °C. Thus, (*R*)-**1·2** seems to adopt a predominantly right-handed double-helical structure, although the possibility that the inversion of the double helices is still fast on the NMR time scale even at −60 °C can not be ruled out.

It should be noted that (*R*)-**1·2** even exhibited intense Cotton effects in DMSO, although the intensities were reduced to 67 % of those in $CHCl_3$ (Figure 4). The ^{1}H NMR

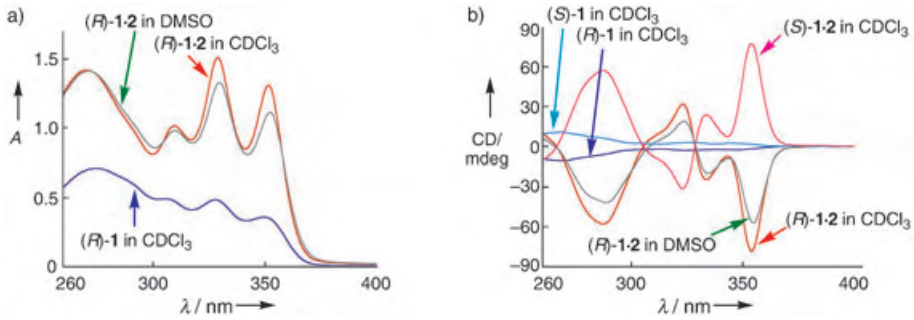


Figure 4. a) UV/Vis spectra (0.1 mM, 20 °C) of amidine (*R*)-**1** in $CDCl_3$ (blue), and complex (*R*)-**1·2** in $CDCl_3$ (red) and in DMSO (green). b) CD spectra (0.1 mM, 20 °C) of (*R*)-**1** (blue), (*S*)-**1** (light blue), (*R*)-**1·2** (red), and (*S*)-**1·2** (pink) in $CDCl_3$, and (*R*)-**1·2** in DMSO (green).

 © 2005 Wiley-VCH Verlag GmbH & Co. KGaA, Weinheim

spectrum of **1·2** showed that 60% of the complex **1·2** retained its duplex structure, whereas the rest of **1·2** underwent dissociation into **1** and **2** in [D_6]DMSO (0.1 mM, 25 °C).[8] In sharp contrast, (*R*)-**4·6**, a simple model for (*R*)-**1·2**, showed a weak CD spectrum similar to that of (*R*)-**4** in DMSO.[8] In fact, it was shown by ^{1}H NMR spectroscopic analysis that **4·6** dissociated into **4** and **6** in [D_6]DMSO.[8] Consequently, the complexation of **1·2** was more stable than that of the simpler **4·6**.

In summary, we have successfully prepared the first artificial single-handed double helices through formation of salt bridges between chiral diamidines ((*R*)- and (*S*)-**1**) and the achiral dicarboxylic acid **2.** Both single-handed double helices are stable in the solid state as well as in solution. The modular strategy, we believe, can act as a new design rationale for the formation of hydrogen-bond-driven double helices in which the three-dimensional structures including the helix sense are predictable.

Received: March 22, 2005
Published online: May 18, 2005

Keywords: chirality · helical structures · hydrogen bonds · salt bridges · supramolecular chemistry

[1] For reviews on artificial helical polymers and oligomers, see a) M. M. Green, J.-W. Park, T. Sato, A. Teramoto, S. Lifson, R. L. B. Selinger, J. V. Selinger, *Angew. Chem.* **1999**, *111*, 3329–3345; *Angew. Chem. Int. Ed.* **1999**, *38*, 3138–3154; b) D. J. Hill, M. J. Mio, R. B. Prince, T. S. Hughes, J. S. Moore, *Chem. Rev.* **2001**, *101*, 3893–4011; c) T. Nakano, Y. Okamoto, *Chem. Rev.* **2001**, *101*, 4013–4038; d) J. J. L. M. Cornelissen, A. E. Rowan, R. J. M. Nolte, N. A. J. M. Sommerdijk, *Chem. Rev.* **2001**, *101*, 4039–4070; e) L. Brunsveld, B. J. B. Folmer, E. W. Meijer, R. P. Sijbesma, *Chem. Rev.* **2001**, *101*, 4071–4097; f) M. Fujiki, *Macromol. Rapid Commun.* **2001**, *22*, 539–563; g) E. Yashima, K. Maeda, T. Nishimura, *Chem. Eur. J.* **2004**, *10*, 42–51.

[2] For reviews on helicates, see a) J.-M. Lehn, *Supramolecular Chemistry*, VCH, Weinheim, **1995**; b) C. Piguet, G. Bernardinelli, G. Hopfgartner, *Chem. Rev.* **1997**, *97*, 2005–2062; c) M. Albrecht, *Chem. Rev.* **2001**, *101*, 3457–3497.

[3] a) J. Sánchez-Quesada, C. Steel, P. Prados, J. de Mendoza, *J. Am. Chem. Soc.* **1996**, *118*, 277–278; b) A. P. Bisson, C. A. Hunter, *Chem. Commun.* **1996**, 1723–1724; c) J. L. Sessler, R. Wang, *J. Am. Chem. Soc.* **1996**, *118*, 9808–9809; d) B. Gong, Y. Yan, H. Zeng, E. Skrzypczak-Jankunn, Y. W. Kim, J. Zhu, H. Ickes, *J. Am. Chem. Soc.* **1999**, *121*, 5607–5608; e) B. J. B. Folmer, R. P. Sijbesma, H. Koojiman, A. L. Spek, E. W. Meijer, *J. Am. Chem. Soc.* **1999**, *121*, 9001–9007; f) P. S. Corbin, S. C. Zimmerman, *J. Am. Chem. Soc.* **2000**, *122*, 3779–3780; g) E. A. Archer, N. T. Goldberg, V. Lynch, M. J. Krische, *J. Am. Chem. Soc.* **2000**, *122*, 5006–5007; h) J. S. Nowick, D. M. Chung, K. Maitra, S. Maitra, K. D. Stigers, Y. Sun, *J. Am. Chem. Soc.* **2000**, *122*, 7654–7661; i) G. Schmuck, W. Wienand, *J. Am. Chem. Soc.* **2003**, *125*, 452–459; j) T. Moriuchi, T. Tamura, T. Hirao, *J. Am. Chem. Soc.* **2004**, *126*, 9356–9357.

[4] a) V. Berl, I. Huc, R. G. Khoury, M. J. Krische, J.-M. Lehn, *Nature* **2000**, *407*, 720–723; b) V. Berl, I. Huc, R. G. Khoury, J.-M. Lehn, *Chem. Eur. J.* **2001**, *7*, 2810–2820; c) I. Huc, *Eur. J. Org. Chem.* **2004**, 17–29; the two strands of poly(methyl methacrylate) were reported to form a double helix in the solid state through van der Waals interactions; d) H. Kusanagi, *Polym. J.* **1996**, *28*, 708–711.

[5] L. J. Prins, D. N. Reinhoudt, P. Timmerman, *Angew. Chem.* **2001**, *113*, 2446–2492; *Angew. Chem. Int. Ed.* **2001**, *40*, 2382–2492.

[6] *Molecular Catenanes, Rotaxanes and Knots* (Eds.: J.-P. Sauvage, C. Dietrich-Buchecker), Wiley-VCH, Weinheim, **1999**.

[7] For recent examples of amidinium–carboxylate salt bridges, see a) J. Otsuki, K. Iwasaki, Y. Nakano, M. Itou, Y. Araki, O. Ito, *Chem. Eur. J.* **2004**, *10*, 3461–3466; b) G. Cooke, F. M. A. Duclairoir, A. Kraft, C. Rosair, V. M. Rotello, *Tetrahedron Lett.* **2004**, *45*, 557–560; c) N. H. Damrauer, J. M. Hodgkiss, J. Rosenthal, D. G. Nocera, *J. Phys. Chem. B* **2004**, *108*, 6315–6321; d) F. Corbellini, L. Di Constanzo, M. Cregs-Calama, S. Geremia, D. N. Reinhoudt, *J. Am. Chem. Soc.* **2003**, *125*, 9946–9947; e) A. Kraft, L. Peters, H. R. Powell, *Tetrahedron* **2002**, *58*, 3499–3505; f) G. Wulff, R. Schönfeld, *Adv. Mater.* **1998**, *10*, 957–959.

[8] See the Supporting Information for details of the synthesis, structures, and characterization of compounds **1**–**7**.

[9] A. Saednya, H. Hart, *Synthesis* **1996**, 1455–1458.

[10] a) R. R. Hiatt, M.-J. Shaio, F. Georges, *J. Org. Chem.* **1979**, *44*, 3265–3266; b) R. Chinchilla, C. Nájera, P. Sánchez-Agulló, *Tetrahedron: Asymmetry* **1994**, *5*, 1393–1402.

[11] a) R. T. Boeré, V. Klassen, G. Wolmershäuser, *J. Chem. Soc. Dalton Trans.* **1998**, 4147–4154; b) J. A. R. Schmidt, J. Arnold, *Chem. Commun.* **1999**, 2149–2150; c) J. A. R. Schmidt, J. Arnold, *J. Chem. Soc. Dalton Trans.* **2002**, 2890–2899.

[12] Crystal data for (*R*)-**1·2** ($C_{141}H_{140}N_4O_9Si_4$): $M_r = 2147.03$, crystal dimensions $0.30 \times 0.24 \times 0.14$ mm^3, orthorhombic, space group $P2_12_12_1$, $Z = 4$, $\rho_{calcd} = 1.132$ g cm^{-3}, $\mu(Cu_{K\alpha}) = 8.92$ cm^{-1}, $F(000) = 4568$, $2\theta_{max} = 136.4°$ were $a = 13.6965(5)$, $b = 22.7967(11)$, $c = 40.3486(17)$ Å, and $V = 12598.2(9)$ Å^3. A total of 124842 reflections were collected, of which 22862 reflections were independent ($R_{int} = 0.044$). The structure was refined to final $R_1 = 0.072$ for 15968 data [$I > 2\sigma(I)$] with 1430 parameters and $wR_2 = 0.2360$ for all data, GOF = 1.039, and residual electron density max./min. = 0.49/−0.32 e Å^{-3}. CCDC-266647 contains the supplementary crystallographic data for this paper. These data can be obtained free of charge from the Cambridge Crystallographic Data Centre via www.ccdc.cam.ac.uk/data_request/cif.

 © 2005 Wiley-VCH Verlag GmbH & Co. KGaA, Weinheim

Total Synthesis

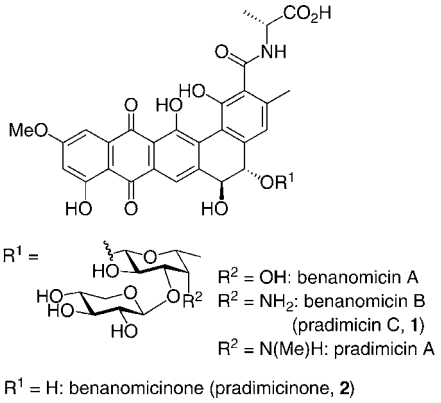
Regio- and Stereocontrolled Total Synthesis of Benanomicin B**

*Ken Ohmori, Minoru Tamiya, Mitsuru Kitamura, Hirohisa Kato, Mami Oorui, and Keisuke Suzuki**

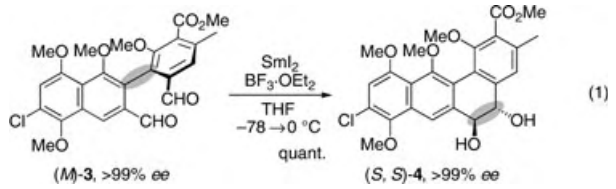
In memory of Tsuguo Mizuochi

Benanomicin/pradimicin antibiotics (BPAs) constitute a class of natural products with a unique structure consisting of a benzo[*a*]naphthacene core, an amino acid, and a disaccharide.[1] Their potent antifungal and anti-HIV activity is attributed to the specific, Ca^{2+}-mediated binding of BPAs to the mannose-rich oligosaccharides presented on the fungi or virus surfaces.[2] Stimulated by these intriguing biological properties and structural novelty, we initiated a synthesis study of BPAs.

In a previous synthesis study we reported the stereoselective synthesis of the common aglycon benanomicinone (pradimicinone, **2**)[3] by exploiting the complete transfer of



the axial chirality into the central chiralities in the pinacol cyclization of biaryl dicarbaldehyde (*M*)-**3** into the *trans*-1,2-diol (*S*,*S*)-**4** [Eq. (1)].



[*] Dr. K. Ohmori, M. Tamiya, Dr. M. Kitamura, Dr. H. Kato, M. Oorui, Prof. Dr. K. Suzuki
Department of Chemistry
Tokyo Institute of Technology
SORST-JST Agency
2-12-1 O-okayama, Meguro-ku, Tokyo 152-8551 (Japan)
Fax: (+81) 3-5734-2788
E-mail: ksuzuki@chem.titech.ac.jp

[**] We thank Meiji Seika Kaisha Ltd. for providing an authentic sample of benanomicins A and B. This work was partially supported by the 21st Century COE program (Tokyo Institute of Technology).

Two additional issues must be addressed en route to the fully controlled total synthesis (Figure 1): a) introduction of the sugar moiety into the aglycon in a regioselective manner, and b) stereoselective access to the chiral, nonracemic biaryl

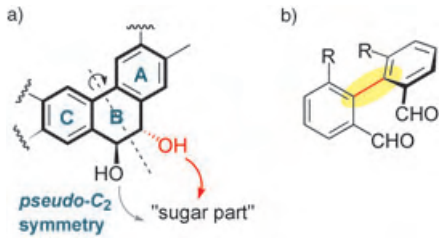
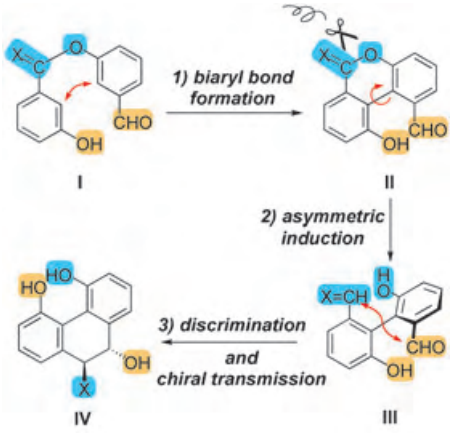


Figure 1. Tactical issues for the total synthesis of BPAs. a) regioselective introduction of the sugar moiety and b) stereocontrol of the axial chirality.

dicarbaldehyde (*M*)-**3**, as the key cyclization precursor. Conjugation of the disaccharide was an intriguing challenge, because of the local pseudo-C_2 symmetry of the 1,2-diol on the B ring. Although a subsidiary issue, the enantioselective synthesis of (*M*)-**3** was a serious bottleneck in the sequence of our synthesis. Herein, we describe clean solutions to these problems, which have culminated in the first total synthesis of benanomicin B (**1**).

Scheme 1 features three key points in our strategy; 1) construction of sterically encumbered biaryl structure **II**

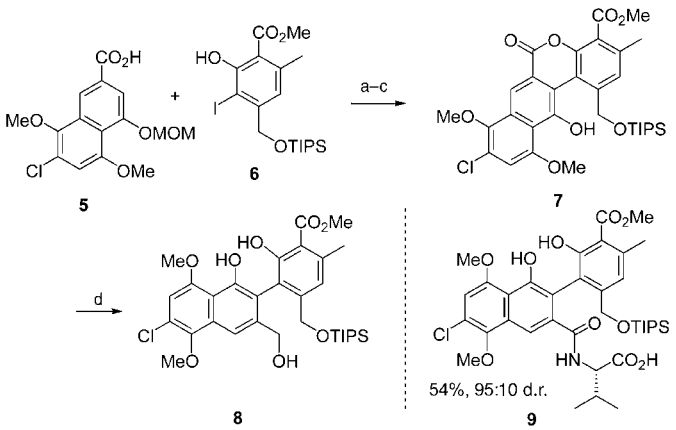


Scheme 1. Overview of our synthesis strategy.

by formation of an internal C–C bond in the tethered derivative **I**; 2) The asymmetric cleavage of the C–O tether in **II** by employing a chiral agent to give the axially chiral biaryl **III**; and 3) Reconnection at two carbonyl groups to give the tricyclic product **IV**. A special requirement for the third stage was the capability of an axial-to-central chirality transfer with concomitant discrimination of the two oxy functions.

The first task was to prepare optically pure **8** as a key precursor for the pinacol cyclization (Scheme 2). We applied an asymmetric ring opening of biaryl lactones pioneered by Bringmann et al. for introducing the biaryl chirality.[4] The substrate for this purpose, the biaryl lactone **7**, was prepared

 DOI: 10.1002/anie.200501210 © 2005 Wiley-VCH Verlag GmbH & Co. KGaA, Weinheim

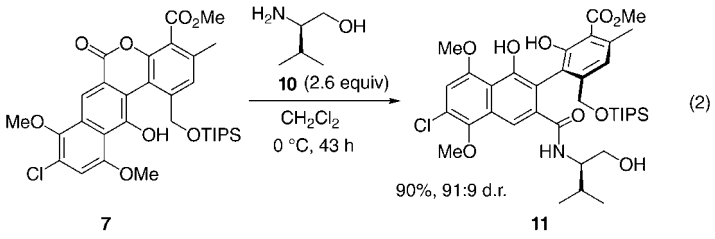


Scheme 2. Preparation and the ring-opening reaction of **7**. a) 2,4,6-trichlorobenzoyl chloride, Et_3N, DMAP, toluene, 25 °C, 20 min (99 %). b) CF_3CO_2H, CH_2Cl_2, 25 °C, 4 h (96 %). c) $Pd(OAc)_2$ (30 mol %), PPh_3 (60 mol %), $tBuCO_2Na$ (3 equiv), DMA, 110 °C, 20 min (60 %). d) L-valine (3.3 equiv), $NaBH_4$ (3.0 equiv), THF, (8 %, 2 % *ee*). DMAP = 4-*N*,*N*-dimethylaminopyridine, DMA = *N*,*N*-dimethylacetamide.

in high yield by the Yamaguchi esterification[5] of carboxylic acid **5**[3b] with phenol **6**[6] followed by the Pd-mediated cyclization.[3b,7]

Initial attempts were centered at the enantioselective reduction of **7** with $NaBH_4$ by using stoichiometric amounts of various chiral modifiers,[8–10] all of which resulted in disappointing enantioselectivities. Unexpectedly, however, we obtained an important hint when L-valine was employed: thus, although the reaction itself was not very effective (8 % yield and 2 % *ee*), a sizable amount of a highly polar by-product was noted, which was proved to be the amide **9**—the direct adduct of the amino acid. An important observation was that amide **9** was highly enriched in one of the diastereomers (90:10 d.r.).

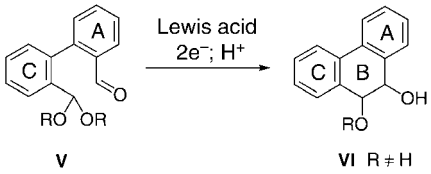
Encouraged by this finding, we decided to pursue a diastereoselective ring-opening reaction, and optimization experiments showed that D-valinol (**10**) was an excellent chiral nucleophile, which afforded amide alcohol **11** in 90 % yield with 91:9 diastereoselectivity [Eq. (2)].[11] Purification of



(2)

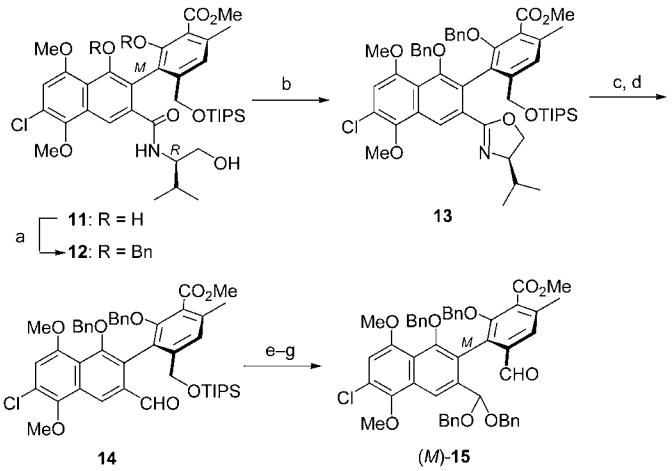
the major diastereomeric product by column chromatography (silica gel, hexane/EtOAc = 1/2) gave single crystals that were suitable for X-ray crystallographic analysis.[12] This analysis proved the compound had the requisite *M* configuration around the biaryl axis.

Now the stage was set for the pivotal stage: construction of the B-ring diol with discrimination of the two oxy functions, for which we planned the semipinacol cyclization of acetal-aldehyde **V** [Eq. (3)]. Activation of the acetal with Lewis acid followed by a net two-electron reduction would hopefully give the mono-masked diol **VI**.[13]



(3)

With this strategy in mind, we envisioned the acetal-aldehyde (*M*)-**15** as the key substrate, which was readily available from the lactone ring-opening product **11** (Scheme 3). After selective benzylation of two of the phenol



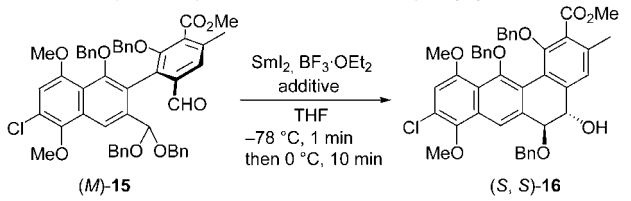
Scheme 3. a) BnBr, Cs_2CO_3, DMF, 0 °C → RT, 70 min (97 %). b) I_2, PPh_3, imidazole, CH_2Cl_2, 0 °C, 20 min (quant.). c) MeOTf, 2,6-di-*tert*-butylpyridine, CH_2Cl_2, RT, 1 h. d) L-Selectride, 0 °C, 20 min; SiO_2, RT, 17 h (96 % from **13**). e) BnOTMS, TMSOTf, toluene, −15 °C, 6 h. f) nBu_4NF, THF, 0 °C, 1 h. g) MnO_2, CH_2Cl_2, RT, 16 h (94 % from **14**). TIPS = triisopropylsilyl; Bn = benzyl, Tf = trifluoromethanesulfonyl, L-selectride = lithium tri-*sec*-butylborohydride, TMS = trimethylsilyl.

groups in **11**, the hydroxyamide moiety in the product **12** was converted into an oxazoline functionality by treatment with PPh_3 and I_2 to give **13** in high yield. After N-methylation of **13**, reduction and exposure to silica gel gave the corresponding aldehyde **14** cleanly in 96 % yield.[14] Conversion of **14** into the corresponding dibenzyl acetal[15] followed by detachment of the silyl group and oxidation afforded the enantiopure acetal-aldehyde (*M*)-**15** for the key cyclization.

The initial attempts at the semipinacol cyclization of (*M*)-**15** by using SmI_2 and $BF_3{\cdot}OEt_2$ suffered from not only modest yields, but also the lack of reproducibility (Table 1).[16] The yields widely fluctuated in the range 10–50 %, even by a slight change in reaction parameters (temperature, reaction time, amounts of reducing agent, and Lewis acid). After extensive effort, we finally found that the presence of a suitable proton source was the key to secure the reproducibility. A clean reaction occurred in the presence of H_2O to give semipinacol

 © 2005 Wiley-VCH Verlag GmbH & Co. KGaA, Weinheim

Table 1: Semipinacol cyclization of acetal-aldehyde (*M*)-**15**.[a]



Entry	Additive[b]	Yield [%]	*trans*/*cis*	*ee* [%]
1	none	0–50	>99/<1	>99
2	H_2O	82	>99/<1	>99
3	MeOH	95	>99/<1	>99

[a] 2.5 equiv of SmI_2, 3.0 equiv of $BF_3{\cdot}OEt_2$. [b] 1.0 equiv.

16 in 82% yield; furthermore, methanol proved to be even more effective (95% yield). The reaction proceeded with stereochemical integrity, namely it was *trans*-selective and with complete chiral transmission, and (*M*)-**15** (>99% *ee*) was cleanly converted into (*S*,*S*)-**16** (>99% *ee*).[17]

Having finally overcome two major synthetic hurdles, the stage was set for the introduction of the amino acid and the sugar moieties (Scheme 4). Thus, tetracycle **16** was saponified, and condensed with D-alanine methyl ester by using the benzotriazole derivative BOP to give the corresponding amide **17** in excellent yield. The metallocene-based activator $[Cp_2HfCl_2]/2\,AgOTf$,[18] allowed the coupling of glycosyl fluoride **18**[19] with the acceptor **17** to give the β-glycoside **19** in 72% yield along with its α-anomer in 9% yield.

After oxidation of **19** by $Ce(NH_4)_2(NO_3)_6$ (CAN), the resulting chloroquinone **20** was subjected to a Diels–Alder reaction with siloxydiene **21**,[3b,20] from which pentacycle **22** was obtained in a fully regiocontrolled manner, thus completing the full carbon framework. Removal of the four acyl groups and hydrolysis of the methyl ester moiety in **22** was achieved by treatment with 1M NaOH to give **23**. Final hydrogenolysis of **23** in the presence of aqueous HCl gave benanomicin B hydrochloride (**1**·HCl), which was fully identical with an authentic sample.[21]

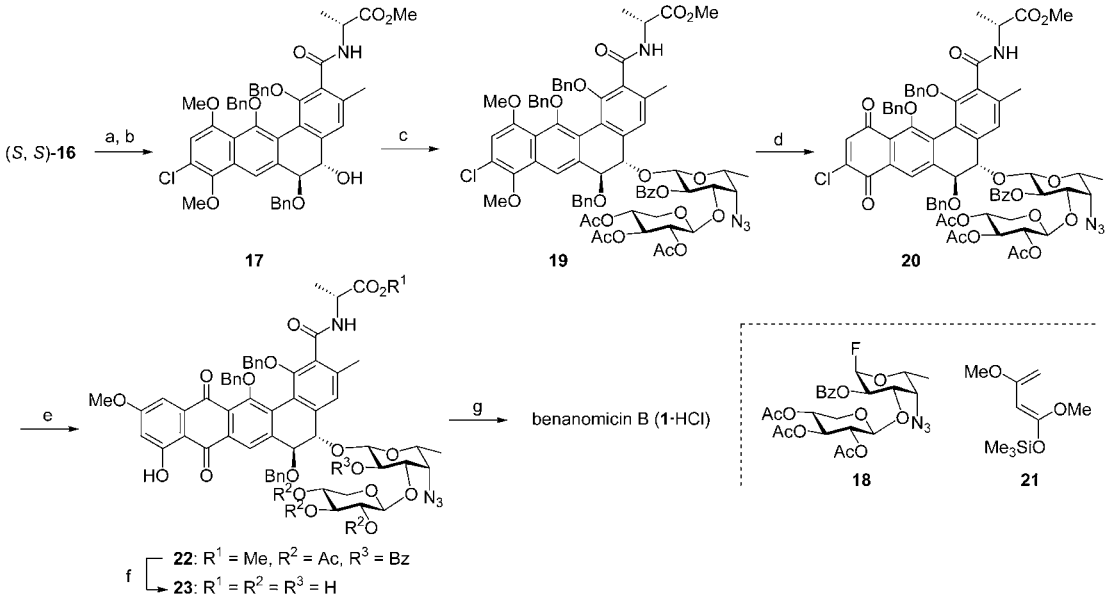
In conclusion, the first total synthesis of benanomicin B (**1**) was achieved based on a chiral transmission strategy. Stereoselective incorporation of valinol into lactone **7** effectively gave the axially chiral product **11**. The semipinacol cyclization of acetal-aldehyde (*M*)-**15** successfully provided the semiprotected *trans*-diol (*S*,*S*)-**16**, which allowed the selective introduction of the sugar moiety, thus enabling access to **1**.

Received: April 6, 2005
Published online: May 18, 2005

Keywords: antibiotics · atropisomerism · biaryls · samarium · total synthesis

[1] a) T. Oki, M. Konishi, K. Tomatsu, K. Tomita, K. Saitoh, M. Tsunakawa, M. Nishio, T. Miyaki, H. Kawaguchi, *J. Antibiot.* **1988**, *41*, 1701–1704; b) T. Takeuchi, T. Hara, H. Naganawa, M. Hamada, H. Umezawa, S. Gomi, M. Sezaki, S. Kondo, *J. Antibiot.* **1988**, *41*, 807–811.

[2] a) M. Watanabe, S. Gomi, H. Tohyama, K. Ohtsuka, S. Shibahara, S. Inouye, H. Kobayashi, S. Suzuki, S. Kondo, T. Takeuchi, H. Yamaguchi, *J. Antibiot.* **1996**, *49*, 366–373; b) T. Ueki, K. Numata, Y. Sawada, T. Nakajima, Y. Fukagawa, T. Oki, *J. Antibiot.* **1993**, *46*, 149–161; c) T. Mizuochi, M. Nakata, *Jpn. J. Clin. Med.* **1995**, *53*, 2340–2349.



Scheme 4. The final stage toward **1**. a) 5M NaOH, EtOH, in sealed tube, 100°C, 2 h. b) D-Ala-OMe·HCl, BOP, Et_3N, DMF, RT, 1 h (84% from **16**). c) **18**, $[Cp_2HfCl_2]/2\,AgOTf$, 4-Å MS, CH_2Cl_2, −78°C, 20 min then −35°C, 11 h (72% for the β anomer **19**, 9% for the α anomer). d) $Ce(NH_4)_2(NO_3)_6$, CH_3CN, H_2O, 0°C, 5 min. e) **21**, THF, RT, 2 h; SiO_2, RT, 12 h; K_2CO_3, CH_2Cl_2, THF, 3 h (74% from **19**). f) 5M NaOH, MeOH, 25°C, 9 h. g) H_2, Pd/C, MeOH, 1M HCl, DMF, 2 h (53% from **22**). D-Ala-OMe = D-alanine methyl ester, DMAP = 4-*N*,*N*-dimethylaminopyridine, DMA = *N*,*N*-dimethylacetamide, BOP = benzotriazol-1-yloxytris(dimethylamino)phosphonium hexafluorophosphate, Tf = trifluoromethanesulfonyl, MS = molecular sieves, Bz = benzoyl.

 © 2005 Wiley-VCH Verlag GmbH & Co. KGaA, Weinheim

[3] a) K. Ohmori, M. Kitamura, K. Suzuki, *Angew. Chem.* **1999**, *111*, 1304 – 1307; *Angew. Chem. Int. Ed.* **1999**, *38*, 1226 – 1229; b) M. Kitamura, K. Ohmori, T. Kawase, K. Suzuki, *Angew. Chem.* **1999**, *111*, 1308 – 1311; *Angew. Chem. Int. Ed.* **1999**, *38*, 1229 – 1232.

[4] For enantioselective reactions, see a) G. Bringmann, T. Hartung, *Angew. Chem.* **1992**, *104*, 782 – 783; *Angew. Chem. Int. Ed. Engl.* **1992**, *31*, 761 – 762; b) G. Bringmann, R. Walter, R. Weirich, *Tetrahedron* **1993**, *49*, 7891 – 7902; c) G. Bringmann, M. Breuning, *Synlett* **1998**, 634 – 636; for diastereoselective reactions, see d) *Angew. Chem.* **1989**, *101*, 1725 – 1726; *Angew. Chem. Int. Ed. Engl.* **1989**, *28*, 1672 – 1673; e) G. Bringmann, M. Breuning, R. Walter, A. Wuzik, K. Peters, E.-M. Peters, *Eur. J. Org. Chem.* **1999**, 3047 – 3055; f) G. Bringmann, M. Breuning, S. Tasler, H. Endress, C. L. J. Ewers, L. Göbel, K. Peters, E.-M. Peters, *Chem. Eur. J.* **1999**, *5*, 3029 – 3038; for a review, see g) G. Bringmann, M. Breuning, S. Tasler, *Synthesis* **1990**, *102*, 1006 – 1019; *Angew. Chem. Int. Ed. Engl.* **1990**, *29*, 977 – 991, and references therein.

[5] J. Inanaga, K. Hirata, H. Saeki, T. Katsuki, M. Yamaguchi, *Bull. Chem. Soc. Jpn.* **1979**, *52*, 1989 – 1993.

[6] Prepared from the known orsellinic acid derivative, namely, methyl 4-hydroxymethyl-2-methoxymethoxy-6-methylbenzoate,[3b] by a three-step sequence [1) iPr$_3$SiCl, imidazole, DMF; 2) TFA, CH_2Cl_2; 3) $BnMe_3NCl{\cdot}ICl$, $NaHCO_3$, MeOH, CH_2Cl_2 (83 % over 3 steps)].

[7] a) P. P. Deshpande, O. R. Martin, *Tetrahedron Lett.* **1990**, *31*, 6313 – 6316; b) T. Hosoya, E. Takashiro, T. Matsumoto, K. Suzuki, *J. Am. Chem. Soc.* **1994**, *116*, 1004 – 1015.

[8] Initial attempts at the enantioselective ring opening of **7** were centered on the borane activated by chiral oxazaborolidines,[9] which uniformly led to poor enantioselectivity. Attempts were also made to use $NaBH_4$ with stoichiometric amounts of various chiral compounds, such as L-(+)-tartaric acid diethyl ester,[10a] *N*,*N*-dibenzoylcycteine,[10b] and (*S*)-(−)-1,1′-binaphthol.[10c]

[9] a) E. J. Corey, C. J. Helal, *Angew. Chem.* **1998**, *110*, 2092 – 2118; *Angew. Chem. Int. Ed.* **1998**, *37*, 1986 – 2012, and references therein.

[10] a) M. Yatagai, T. Ohnuki, *J. Chem. Soc. Perkin Trans. 1* **1990**, 1826 – 1828; b) K. Soai, T. Yamanoi, H. Oyamada, *Chem. Lett.* **1984**, 251 – 254; c) R. Noyori, I. Tomino, Y. Tanimoto, M. Nishizawa, *J. Am. Chem. Soc.* **1984**, *106*, 6709 – 6716.

[11] The diastereomer ratio was assessed by ^{1}H NMR spectroscopic analysis ($CDCl_3$, 400 MHz).

[12] The major diastereomer of **11** gave a single crystal (EtOAc/hexane) suitable for X-ray analysis, which confirmed the stereostructure of **11**. CCDC-262629 contains the supplementary crystallographic data for this paper. These data can be obtained free of charge via www.ccdc.cam.ac.uk/conts/retrieving.html (or from the Cambridge Crystallographic Data Centre, 12 Union Road, Cambridge CB21EZ, UK; fax: (+44) 1223-336-033; or deposit@ccdc.cam.ac.uk).

[13] K. Ohmori, M. Kitamura, Y. Ishikawa, H. Kato, M. Oorui, K. Suzuki, *Tetrahedron Lett.* **2002**, *43*, 7023 – 7026.

[14] a) A. I. Meyers, M. Shipman, *J. Org. Chem.* **1991**, *56*, 7098 – 7102; b) S. Boisnard, L. Neuville, M. Bois-Choussy, J. Zhu, *Org. Lett.* **2000**, *2*, 2459 – 2462.

[15] T. Tsunoda, M. Suzuki, R. Noyori, *Tetrahedron Lett.* **1980**, *21*, 1357 – 1358.

[16] For preparation of SmI_2/THF, see P. Girard, J. L. Namy, H. B. Kagan, *J. Am. Chem. Soc.* **1980**, *102*, 2693 – 2698.

[17] The enantiomeric purity of **15** was assessed by HPLC analysis (Daicel Chemical Industries, Ltd, CHIRALPAK AD-H (25 cm, 0.46 cm diameter), hexane/iPrOH 9/1, flow rate 0.5 mL min^{-1}, $t_R = 11.4$ min for the *M* isomer, 15.2 min for the *S* isomer). Also, **16** was analyzed (Daicel Chemical Industries Ltd, CHIRALPAK AD-H (25 cm, 0.46 cm diameter), hexane/iPrOH 8/2, flow rate 0.5 mL min^{-1}, $t_R = 14.2$ min for the *S*,*S* isomer, 23.1 min for the *R*,*R* isomer).

[18] a) K. Suzuki, H. Maeta, T. Matsumoto, G. Tsuchihashi, *Tetrahedron Lett.* **1988**, *29*, 3571 – 3574; b) K. Suzuki, H. Maeta, T. Matsumoto, *Tetrahedron Lett.* **1989**, *30*, 4853 – 4856.

[19] H. Kato, K. Ohmori, K. Suzuki, *Tetrahedron Lett.* **2000**, *41*, 6827 – 6832.

[20] J. Savard, P. Brassard, *Tetrahedron* **1984**, *40*, 3455 – 3464.

[21] Although the ^{1}H NMR spectra of free benanomicin B (**1**) are highly dependent on the pH value and temperature, the mixed sample of synthetic/authentic benanomicin B hydrochloride showed fully coincided ^{1}H NMR spectra. Furthermore, all physical data (^{1}H and ^{13}C NMR, IR, HRMS (FAB), $[\alpha]_D$, and m.p.) of the synthetic material were fully identical with those of **1**·HCl.[1b]

 © 2005 Wiley-VCH Verlag GmbH & Co. KGaA, Weinheim

Multicomponent Reactions

A Catalytic Asymmetric Three-Component 1,4-Addition/Aldol Reaction: Enantioselective Synthesis of the Spirocyclic System of Vannusal A**

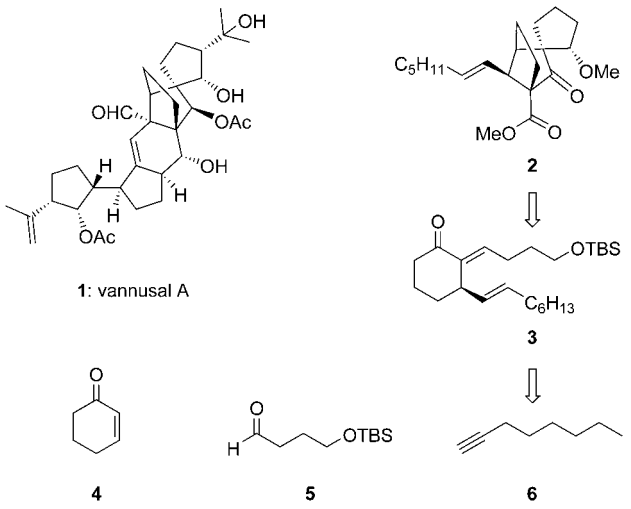
K. C. Nicolaou, Wenjun Tang, Philippe Dagneau, and Raffaella Faraoni*

The advantages of multicomponent reactions over the more common two-component processes have been widely demonstrated and reviewed.[1] Efficient asymmetric versions of such reactions offer even greater benefits to the art of chemical synthesis, as these can provide expedient access to polyfunctionalized molecules in enantioenriched form, starting from simple prochiral building blocks.[2,3] During a program directed towards the total synthesis of vannusal A (**1**, Scheme 1), an architecturally complex marine natural product isolated from the ciliate *Euplotes vannus*,[4] the key optically enriched spirocyclic intermediate **2** was required. This demand led us to the development of an asymmetric multicomponent reaction that combined α,β-unsaturated

[*] Prof. Dr. K. C. Nicolaou, Dr. W. Tang, P. Dagneau, Dr. R. Faraoni
Department of Chemistry and
The Skaggs Institute for Chemical Biology
The Scripps Research Institute
10550 North Torrey Pines Road, La Jolla, CA 92037 (USA)
Fax: (+1) 858–784–2469
E-mail: kcn@scripps.edu
and
Department of Chemistry and Biochemistry
University of California, San Diego
9500 Gilman Drive, La Jolla, CA 92093 (USA)

[**] We thank Dr. D. H. Huang and Dr. G. Siuzdak for NMR spectroscopic and mass spectrometric assistance, respectively. Financial support for this work was provided by grants from the National Institutes of Health (USA) and the Skaggs Institute for Chemical Biology, and a fellowship from the Swiss National Science Foundation (to R.F.).

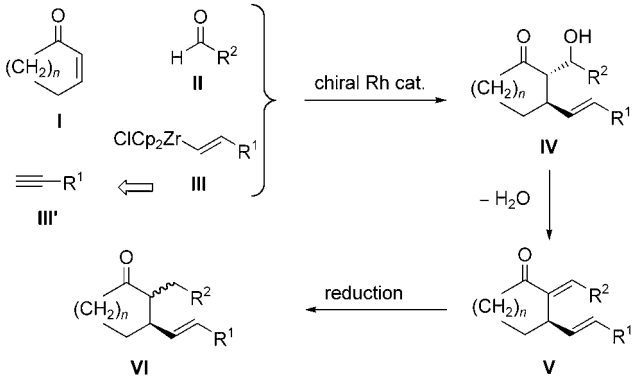
 © 2005 Wiley-VCH Verlag GmbH & Co. KGaA, Weinheim DOI: 10.1002/anie.200500789



Scheme 1. Stucture of vannusal A (**1**) and retrosynthetic analysis of spirocyclic building block **2**.

enones, aldehydes, and alkenyl zirconium species in the presence of a chiral rhodium catalyst to give enantioselective access to 2,3-disubstituted cycloalkanones. Herein we report this new synthetic technology and describe its application to the construction of enantioenriched building block **2**, which represents the spiro domain of vannusal A (**1**).

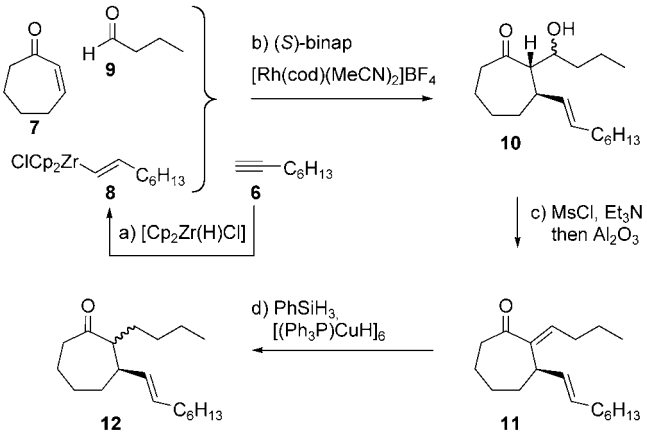
Scheme 2 shows the general strategy for the intended three-component (**I**, **II**, and **III**) catalytic asymmetric con-



Scheme 2. General scheme for the catalytic asymmetric three-component reaction (**I** + **II** + **III**→**IV**→**V**→**VI**).

struction of aldol-type compounds **IV**, α,β-unsaturated enones of type **V**, and 2,3-disubstituted cyclic ketones of type **VI**. This proposed multicomponent reaction was partially based on the pioneering work of Oi, Sato, and Inoue,[5] who demonstrated the efficient rhodium-catalyzed addition of alkenyl zirconium species to enones (under non-aqueous conditions) to afford 1,4-adducts. Furthermore, the elegant studies of the Hayashi group[6] on the catalytic cycle of the rhodium-catalyzed conjugate addition of *B*-aryl-9-BBN to a reactive vinyl ketone, which showed that a transient rhodium enolate can react with electrophiles, were key to this proposal. Both studies, however, stopped short of a three-component process capable of delivering enantiomerically enriched products as reported herein. According to our plan, a chiral rhodium complex was to act as a catalyst to induce the asymmetric 1,4-addition of zirconium species **III** to α,β-unsaturated ketone **I**. This should, in turn, furnish a rhodium enolate intermediate, whose trapping with aldehyde **II** was expected to lead first to aldol **IV** and thence to enone **V** and disubstituted cyclic ketones **VI** (by sequential elimination of water and reduction, respectively). It was, therefore, hoped that the products from this multicomponent reaction would include any one or more desired compounds **IV** to **VI** (Scheme 2).

This work was initiated with some considerable success, as demonstrated in Scheme 3 in the case of α,β-unsaturated

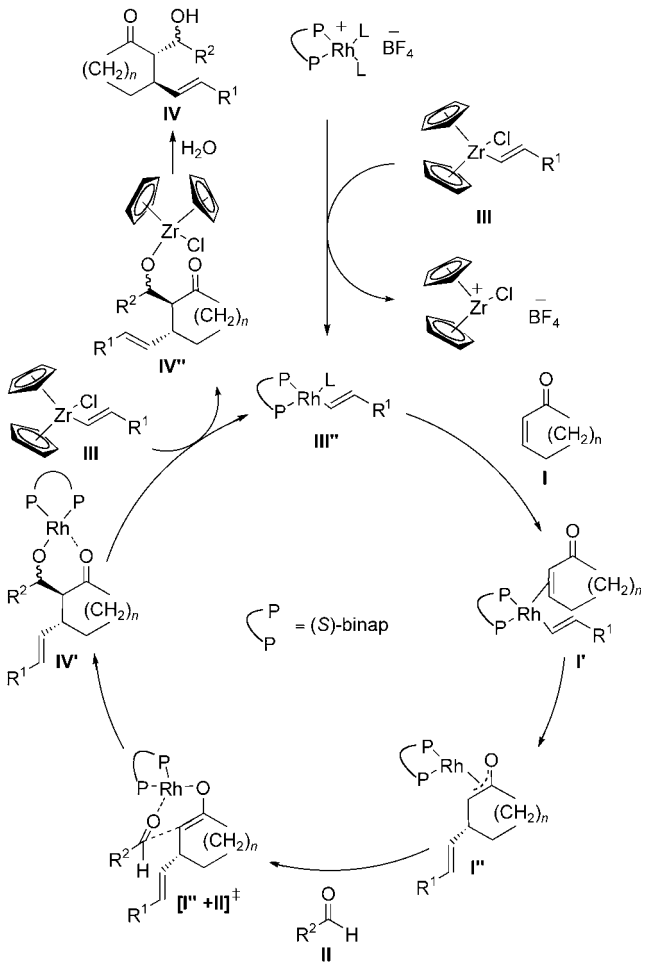


Scheme 3. Proof of principle of the catalytic asymmetric three-component reaction. Reagents and conditions: a) $[Cp_2Zr(H)Cl]$, THF, 30 min; b) **7** (1.2 equiv), **8** (1.2 equiv), **9** (1.0 equiv), $[Rh(cod)(MeCN)_2]BF_4$ (0.05 equiv), (*S*)-binap (0.06 equiv), THF, 25 °C, 12 h, 50% (**10**; ≈4:1 isomeric ratio); c) MsCl (3.0 equiv), Et_3N (6.0 equiv), 0→25 °C, 30 min; then Al_2O_3 (excess), 12 h, 95% (**11**, *E*:*Z*≈20:1, 98% *ee*); d) $PhSiH_3$ (1.5 equiv), $[(Ph_3P)CuH]_6$ (1 mol%), toluene, 25 °C, 6 h, 85% (*trans*/*cis*≈1:3). cod = cyclooctadiene, (*S*)-binap = (*S*)-(−)-2,2′-bis(diphenylphosphino)-1,1′-binaphthyl, Ms = methanesulfonyl.

cycloheptenone (**7**). Thus, mixing of **7** with the zirconium species **8** (derived from 1-octyne and $[Cp_2Zr(H)Cl]$)[7] and aldehyde **9** in the presence of $[Rh(cod)(MeCN)_2]BF_4$[5] and (*S*)-binap as the catalyst system in THF at 25 °C for 12 h led to the formation of **10** as a mixture of two diastereoisomers (≈4:1, 50% combined yield). This mixture was subjected to a standard mesylation/elimination sequence to produce enone **11** (*E*/*Z*≈20:1; Table 2) in 95% overall yield. Furthermore, and gratifyingly, the enantiopurity of this enone ($[\alpha]_D^{33}$ = +118.5 ($CHCl_3$, c = 1.0)) was found to be 98% *ee* by chiral HPLC (Chiralcel, OD-H). Finally, this enone **11** was reduced with $PhSiH_3$ in the presence of a catalytic amount of $[(Ph_3P)CuH]_6$[8] (1 mol%) to afford 2,3-disubstituted cycloheptanones **12** (*trans*/*cis*≈1:3; 85% combined yield).

With regards to a mechanism for this process, we envisage a similar catalytic cycle (see Scheme 4) to those previously proposed by the Oi and Inoue group[5] and the Hayashi group[6] to explain their enantioselective 1,4-addition of zirconium species, aryl boronic acids, or *B*-aryl-9-BBN

 © 2005 Wiley-VCH Verlag GmbH & Co. KGaA, Weinheim

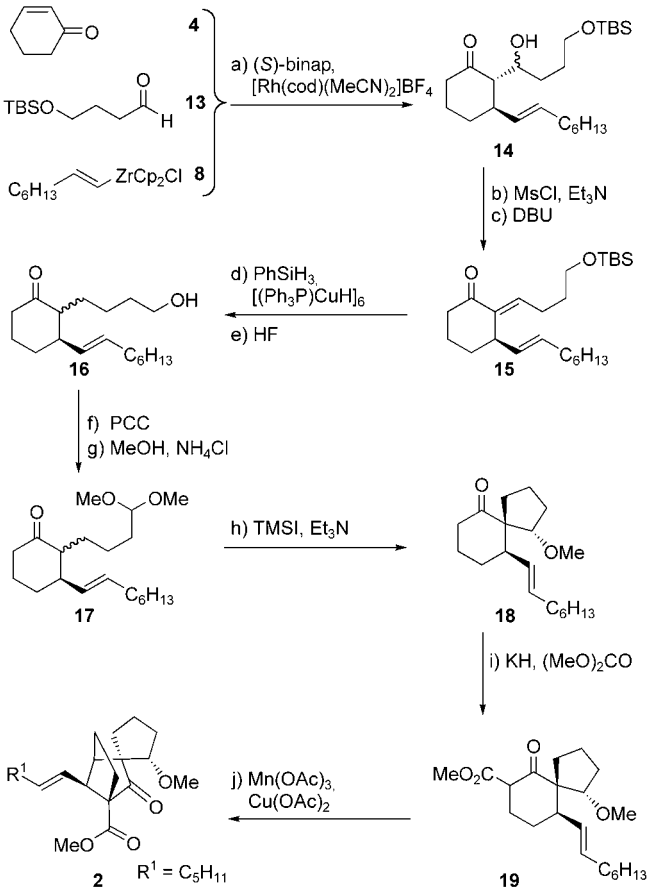


Scheme 4. Proposed mechanism for the asymmetric three-component, rhodium-catalyzed 1,4-addition/aldol reaction (**I** + **II** + **III**→**IV**). L = CH_3CN, cod (cycloocta-1,5-diene), or thf.

reagents to α,β-unsaturated enones. Thus, transmetalation of the alkenyl zirconium species **III** may lead to the rhodium alkenyl complex **III″**, which could react with cyclic enone **I** to form the π-coordination complex **I′**. Rearrangement of **I′**, upon transfer of the alkenyl group onto the 4-position of the enone, should lead to the rhodium enolate **I″**. This chiral enolate may then engage the aldehyde **II** in an aldol reaction, generating rhodium complex **IV′** through a six-membered-ring transition state [**I″** + **II**]‡. Transmetalation of **IV′** with another alkenyl zirconium species **III** could then lead to zirconium alkoxide **IV″** and regeneration of rhodium alkenyl complex **III″**. Hydrolysis of **IV″** provides aldol product **IV**. Both the chemoselectivity of the rhodium alkenyl species **III″** in differentiating between the conjugated ketone **I** and an aldehyde **II**, as well as the ability of the postulated transient rhodium enolate to engage the aldehyde component in an aldol reaction,[9,10] are crucial for the success of this process.

Next, we examined the generality and scope of the present enantioselective reaction. As demonstrated in Table 1, this process proceeded well with five- (Table 1, entries 7 and 8), six- (Table 1, entries 1–6), and seven-membered cyclic enones (Table 1, entries 9–11), as well as an acyclic ketone (Table 1, entry 12). Thus, a series of aldol products **IV** were obtained in good yields (30–62%) through the three-component 1,4-addition/aldol reaction. Good to excellent enantioselectivities (78–98% *ee*) were observed for the corresponding enones **V**. Various aliphatic aldehydes that carry linear or branched chains or ring systems at their α sites were employed successfully. It is noteworthy that benzaldehyde and trimethyl acetaldehyde did not prove to be suitable substrates for these reactions. The alkenyl zirconium species employed in these asymmetric processes were derived from terminal alkynes with different aliphatic or functionalized carbon chains.

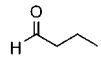
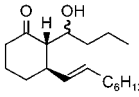
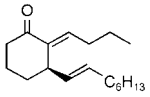
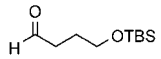
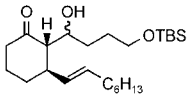
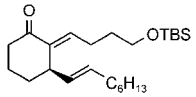
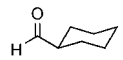
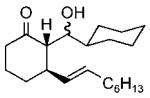
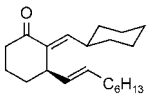
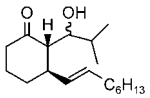
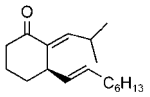
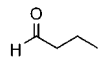
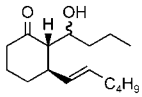
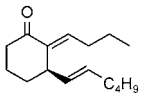
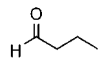
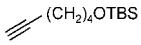
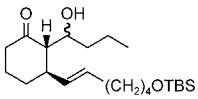
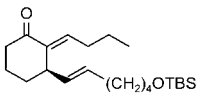
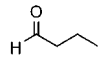
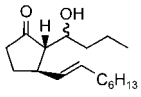
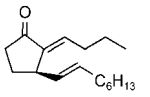
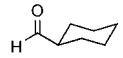
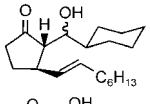
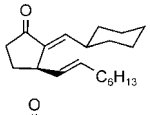
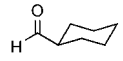
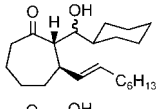
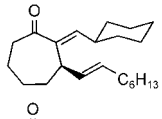
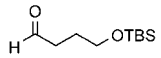
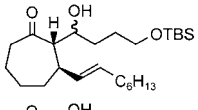
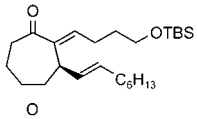
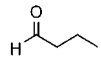
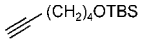
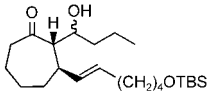
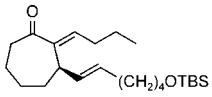
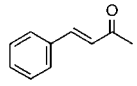
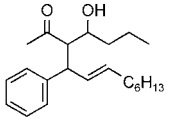
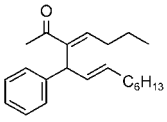
The developed technology was successfully applied to the synthesis of the spiro system **2** of vannusal A (**1**), as depicted in Scheme 5. Thus, enone **4**, alkenyl zirconium species **8** (generated in situ from 1-octyne and $[Cp_2Zr(H)Cl]$)[7] and aldehyde **13** were combined in the presence of $[Rh(cod)(MeCN)_2]BF_4$ (5 mol%) and (*S*)-binap (6 mol%) in THF at



Scheme 5. Construction of spirocyclic building block **2** of vannusal A. Reagents and conditions: a) $[Rh(cod)(MeCN)_2]BF_4$ (5 mol%), (*S*)-binap (6 mol%), THF, 25 °C, 12 h, 52%; b) MsCl (2.0 equiv), Et_3N (3.0 equiv), CH_2Cl_2, 25 °C, 30 min; c) DBU (2.0 equiv), THF, 25 °C, 2 h, (**15**, *E*:*Z* ≈ 13:1), 85% (over two steps); d) $PhSiH_3$ (1.5 equiv), $[(Ph_3P)CuH]_6$ (1 mol%), toluene, 25 °C, 6 h, (*trans*/*cis* ≈ 2:1); e) aqueous HF (48%;10 equiv), THF, 25 °C, 2 h, 79% (over two steps); f) PCC (1.5 equiv), CH_2Cl_2, 25 °C, 2 h, 91%; g) MeOH, NH_4Cl (0.01 equiv), reflux, 2 h, 98%; h) TMSI (1.5 equiv), Et_3N (1.2 equiv), CH_2Cl_2, 0 to 25 °C, 2 h, 50%; i) KH (5.0 equiv), $(MeO)_2CO$ (10 equiv), THF, reflux, 2 h; j) $Mn(OAc)_3$ (2.5 equiv), $Cu(OAc)_2$ (1.2 equiv), EtOH, reflux, 2 h, 68% (over two steps), (**2**, 96% *ee*). DBU = 1,8-diazabicyclo-[5.4.0]undec-7-ene, PCC = pyridinium chlorochromate, TMS = trimethylsilyl.

 © 2005 Wiley-VCH Verlag GmbH & Co. KGaA, Weinheim

Table 1: Catalytic asymmetric three-component 1,4-addition/aldol reaction of enones **I**, aldehydes **II**, and alkenyl zirconium species **III**: preparation of enantiomerically enriched 2,3-disubstituted aldols **IV** and enones **V**.[a]

Entry	I	II	III′	IV	Yield [%][b]	Ratio[c]	V[d]	Yield [%][e]	*ee* [%][f]	$[\alpha]_D$
1					53	2:1		85	96	+
2					52	1.4:1		85	96	+
3					51	4:1		89[g]	96	+
4					41	5.9:1		83[h]	95	+
5					30	1.1:1		88	94	+
6					58	1:1		80	96	+
7					55	1:1		91	78	+
8					62	5.3:1		94	79	+
9					50	1.3:1		80	98	+
10					34	3.1:1		90	93	+
11					61	3.7:1		82	94	+
12					48	mixture[i]		85	85	+

[a] Reactions were carried out at ambient temperature on a 1.0-mmol scale (aldehyde) in THF in the presence of catalytic amounts of $[Rh(cod)(MeCN)_2]BF_4$ and (*S*)-binap (see Experimental Section for more details). [b] Yields of isolated products. [c] Ratios were determined by ^{1}H NMR spectroscopy. The relative configurations were not determined. [d] The *E* enones were predominantly formed along with small amounts of the *Z* enones ($E/Z > 9:1$), unless otherwise specified. The absolute configurations of products in entries 1–11 were tentatively assigned by analogy with their corresponding 1,4-addition products.[5]. [e] Overall yield of mesylation–elimination (**IV**→**V**). [f] The *ee* values of the *E* enones were determined by chiral HPLC (chiralpak AD or chiralcel OD-H columns). [g] $E/Z \approx 3:1$. [h] $E/Z \approx 5:1$. [i] Four isomers by ^{1}H NMR spectroscopy.

25 °C. After 12 h of stirring, aldol product **14** was obtained (52% yield, ≈1.4:1 ratio of diastereomers). Mesylation of this mixture, followed by exposure of the resulting products to DBU, furnished enone **15** ($E/Z \approx 13:1$; Table 2) in 85% overall yield. The conjugated double bond within **15** was selectively reduced with $PhSiH_3$ in the presence of a catalytic amount of $[(Ph_3P)CuH]_6$[8] (1 mol%) which led, after desilylation, to disubstituted cyclohexanones **16** (*trans*/*cis* ≈ 2:1, 79% combined yield). From this point, the synthesis followed the sequence established previously on a similar, racemic, substrate.[11] Thus, oxidation of hydroxyketone **16** with PCC, followed by acetalization of the resulting aldehyde, led to **17** (90% yield). Treatment of this acetal **17** with TMSI in the presence of Et_3N gave methoxy spiroketone **18** (48% yield of the desired diastereoisomer; Table 2). Finally, carboxymethylation of the latter compound **18**, followed by exposure to the radical oxidation conditions of $Mn(OAc)_3$–$Cu(OAc)_2$, afforded the desired vannusal A key building block **2** (68%;

 © 2005 Wiley-VCH Verlag GmbH & Co. KGaA, Weinheim

Table 2). Intermediate **2** ($[\alpha]_D^{33} = -1.0$ ($CHCl_3$, $c = 1.0$)) was thus obtained with 96% *ee*, as determined by chiral HPLC (Chiralcel OD-H).

The methodology presented herein represents a convenient entry into multifunctionalized and relatively complex building blocks, starting from comparatively simple and readily available starting materials. Its scope incorporates substituted acyclic as well as cyclic ketones. Good to excellent enantiomeric excess was attained in all cases studied. Application of this catalytic asymmetric three-component reaction to the construction of the spirocyclic domain of vannusal A powerfully demonstrates the applicability and versatility of this process. The total synthesis of this challenging triterpene **1** is well underway in our laboratories.

Experimental Section

General procedure: The alkyne (1.25 mmol, 1.25 equiv) was added to $[Cp_2Zr(H)Cl]$[12] (1.2 mmol; 1.2 equiv) in anhydrous THF (4 mL) under argon. The mixture was stirred at 25 °C for 30 min until it became homogeneous. In a separate flask, $[Rh(cod)(MeCN)_2]BF_4$ (0.05 mmol, 0.05 equiv) and (*S*)-binap (0.06 mmol, 0.06 equiv) were dissolved in anhydrous THF (4 mL) under argon and stirred at 25 °C for 30 min. The enone (1.2 mmol, 1.2 equiv) was then added to the resulting red catalyst solution, followed by the aldehyde (1.0 mmol; 1.0 equiv). The zirconium reagent was transferred to this solution through a cannula, and the resulting mixture was stirred at 25 °C for 12 h. The mixture was concentrated under reduced pressure, and the residue taken up in diethyl ether and directly filtered through a small pad of celite and then concentrated. The resultant crude mixture was purified by flash column chromatography (silica gel), with Et_2O/hexanes mixtures as eluant, to provide aldol products **IV** as colorless oils. Triethylamine (1.8 mmol, 6.0 equiv) and methanesulfonyl chloride (0.9 mmol, 3.0 equiv) were added to a stirred solution of the aldol product **IV** (0.3 mmol) in CH_2Cl_2 (4 mL) at 0 °C. The resulting mixture was allowed to warm to 25 °C within 30 min, and then basic alumina (2 g) was added (alternatively, DBU/THF could be employed for the elimination step). The mixture was then stirred vigorously at 25 °C for 12 h, filtered, and concentrated. The residue was purified by flash column chromatography (silica gel) with EtOAc/hexanes mixtures as eluant to provide enone product **V**.

Table 2: Selected physical properties for compounds **2**, **11**, **15**, and **18**.

2: $R_f = 0.43$ (silica gel, EtOAc/hexanes 1:5); $[\alpha]_D^{33} = -1.0$ ($c = 1.0$, $CHCl_3$); IR (film): $\tilde{\nu}_{max} = 1731\ cm^{-1}$; ^1H NMR (600 MHz, $CDCl_3$): $\delta = 5.61$ (dt, $J = 15.0$, 7.2 Hz, 1H), 5.36 (dd, $J = 15.0$, 7.2 Hz, 1H), 3.68 (s, 3H), 3.54 (dd, $J = 6.6$, 3.0 Hz, 1H), 3.26 (s, 3H), 2.85 (d, $J = 7.2$ Hz, 1H), 2.13–1.80 (m, 9H), 1.73 (m, 1H), 1.57 (m, 1H), 1.45 (m, 1H), 1.33–1.17 (m, 7H), 0.86 ppm (t, $J = 7.2$ Hz, 3H); ^{13}C NMR (150 MHz, $CDCl_3$): $\delta = 212.1$, 171.4, 136.0, 124.5, 87.6, 69.4, 62.6, 58.3, 53.3, 52.7, 52.1, 36.8, 33.6, 32.1, 32.0, 29.8, 24.4, 23.3, 22.7, 22.4, 14.9 ppm; HRMS (ESI-TOF) (*m*/*z*): calcd for $C_{21}H_{33}O_4^+$ $[M+H]^+$: 349.2373; found: 349.2357

11: $R_f = 0.46$ (silica gel, EtOAc/hexanes 1:5); $[\alpha]_D^{33} = +118.5$ ($c = 1.0$, $CHCl_3$); IR (film) $\tilde{\nu}_{max} = 2957$, 2929, 2855, 1684, 1611, 1458, 1326, 1286, 1208, 1122, 974, 938 cm^{-1}; ^1H NMR (400 MHz, $CDCl_3$): $\delta = 6.52$ (t, $J = 7.6$ Hz, 1H), 5.51 (dd, $J = 15.7$, 4.0 Hz, 1H), 5.30 (m, 1H), 3.60 (m, 1H), 2.59 (dt, $J = 13.5$, 2.0 Hz, 1H), 2.46 (m, 1H), 2.11–1.97 (m, 5H), 1.88–1.79 (m, 1H), 1.78–1.70 (m, 2H), 1.59–1.50 (m, 1H), 1.49–1.20 (m, 11H), 0.92 (t, $J = 7.4$ Hz, 3H), 0.87 ppm (t, $J = 6.8$ Hz, 3H); ^{13}C NMR (100 MHz, $CDCl_3$): $\delta = 216.2$, 143.0, 140.0, 131.6, 130.7, 43.4, 37.8, 34.2, 32.7, 31.7, 30.0, 29.4, 28.8, 25.8, 25.1, 22.6, 22.1, 14.1, 14.0 ppm; HRMS (ESI TOF) (*m*/*z*): calcd for $C_{19}H_{33}O^+$ $[M+H]^+$: 277.2526; found: 277.2531

15: $R_f = 0.41$ (silica gel, EtOAc/hexanes 1:5); $[\alpha]_D^{33} = +73.5$ ($c = 1.0$, $CHCl_3$); IR (film) $\tilde{\nu}_{max} = 2928$, 2856, 1688, 1616, 1471, 1463, 1256, 1102, 970, 837, 776 cm^{-1}; ^1H NMR (500 MHz, $CDCl_3$): $\delta = 6.64$ (t, $J = 7.5$ Hz, 1H), 5.34 (dd, $J = 15.4$, 4.8 Hz, 1H), 5.23 (m, 1H), 3.60 (m, 3H), 2.48 (d, $J = 17.6$ Hz, 1H), 2.23 (m, 2H), 2.08 (m, 1H), 1.96 (m, 2H), 1.91–1.78 (m, 3H), 1.78–1.71 (m, 1H), 1.68–1.56 (m, 2H), 1.32–1.20 (m, 8H), 0.88 (m, 12H), 0.03 ppm (s, 6H); ^{13}C NMR (125 MHz, $CDCl_3$): $\delta = 201.8$, 140.2, 138.5, 131.9, 131.3, 62.4, 40.2, 38.6, 32.5, 31.7, 31.6, 29.8, 29.4, 28.8, 25.9, 24.1, 22.6, 19.0, 14.0, −5.3 ppm; HRMS (ESI-TOF) (*m*/*z*): calcd for $C_{24}H_{45}O_2Si^+$ $[M+H]^+$: 393.3183; found: 393.3184

18: $R_f = 0.38$ (silica gel, EtOAc/hexanes 1:10); $[\alpha]_D^{33} = +44.6$ ($c = 1.0$, $CHCl_3$); IR (film): $\tilde{\nu} = 1710\ cm^{-1}$; ^1H NMR (400 MHz, $CDCl_3$): $\delta = 5.37$ (dt, $J = 14.8$, 6.8 Hz, 1H), 5.21 (ddt, $J = 14.8$, 9.6, 1.2 Hz, 1H), 3.92 (dd, $J = 4.8$, 2.4 Hz, 1H), 3.21 (s, 3H), 2.49 (m, 1H), 2.38–2.30 (m, 2H), 2.25–2.10 (m, 2H), 1.96–1.56 (m, 8H), 1.45 (m, 1H), 1.37–1.18 (m, 9H), 0.85 ppm (t, $J = 6.8$ Hz, 3H); ^{13}C NMR (150 MHz, $CDCl_3$): $\delta = 212.8$, 133.9, 129.7, 88.3, 65.3, 57.4, 48.7, 42.1, 33.3, 32.5, 30.2, 30.0, 29.9, 29.6, 29.6, 23.6, 23.5, 21.6, 14.9 ppm; HRMS (ESI-TOF) (*m*/*z*): calcd for $C_{19}H_{33}O_2^+$ $[M+H]^+$: 293.2471; found: 293.2475

Received: March 3, 2005
Published online: May 18, 2005

Keywords: aldol reaction · asymmetric catalysis · multicomponent reactions · natural products · nucleophilic addition

[1] For selected reviews on multicomponent reactions, see: a) L. Weber, K. Illgen, M. Almstetter, *Synlett* **1999**, 366–374; b) H. Bienaymé, C. Hulme, G. Oddon, P. Schmitt, *Chem. Eur. J.* **2000**, *6*, 3321–3329; c) L. Weber, *Curr. Opin. Chem. Biol.* **2000**, *4*, 295–302; d) L. Weber, *Drug Discovery Today* **2002**, *7*, 143–147; e) A. Tuch, S. Wallé, *Handbook of Combinatorial Chemistry, Vol. 2* (Eds.: K. C. Nicolaou, R. Hanko, W. Hartwig), Wiley-VCH, Weinheim, **2002**, pp. 685–705; f) R. V. A. Orru, M. de Greef, *Synthesis* **2003**, 1471–1499.

[2] For an excellent review on asymmetric multicomponent reactions, see: M. Yus, D. J. Ramón, *Angew. Chem.* **2005**, *117*, 1602–1634; *Angew. Chem. Int. Ed.* **2005**, *44*, 1628–1661.

[3] For examples of catalytic asymmetric 1,4-addition/aldol reactions involving cyclic enones, see: a) K.-I. Yamada, T. Arai, M. Shibasaki, *J. Org. Chem.* **1998**, *63*, 3666–3672; b) L. A. Arnold, R. Naasz, A. J. Minnaard, B. L. Feringa, *J. Am. Chem. Soc.* **2001**, *123*, 5841–5842; c) L. A. Arnold, R. Naasz, A. J. Minnaard, B. L. Feringa, *J. Org. Chem.* **2002**, *67*, 7244–7254.

[4] G. Guella, F. Nini, F. Pietra, *Angew. Chem.* **1999**, *111*, 1217–1220; *Angew. Chem. Int. Ed.* **1999**, *38*, 1134–1136.

[5] S. Oi, T. Sato, Y. Inoue, *Tetrahedron Lett.* **2004**, *45*, 5051–5055.

[6] a) K. Yoshida, M. Ogasawara, T. Hayashi, *J. Am. Chem. Soc.* **2002**, *124*, 10984–10985; b) T. Hayashi, K. Yamasaki, *Chem. Rev.* **2003**, *103*, 2829–2844.

[7] J. Schwartz, J. A. Labinger, *Angew. Chem.* **1976**, *88*, 402–409; *Angew. Chem. Int. Ed. Engl.* **1976**, *15*, 333–340.

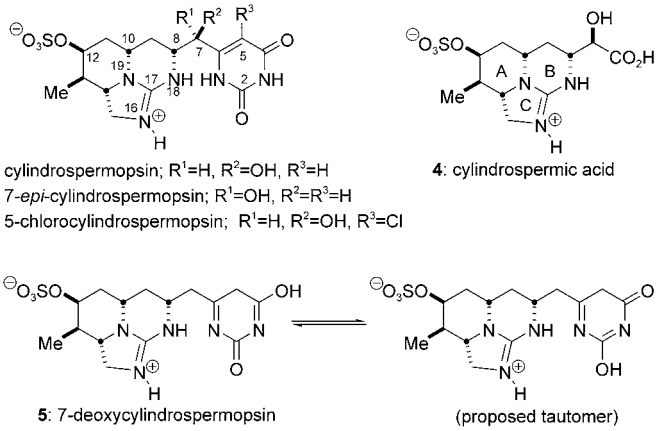
[8] B. H. Lipshutz, J. Keith, P. Papa, R. Vivian, *Tetrahedron Lett.* **1998**, *39*, 4627–4630.

[9] For previous examples of aldol reactions mediated by rhodium enolates, see: a) G. A. Slough, R. G. Bergman, C. H. Heathcock, *J. Am. Chem. Soc.* **1989**, *111*, 938–949; b) S. J. Taylor, M. O. Duffey, J. P. Morken, *J. Am. Chem. Soc.* **2000**, *122*, 4528–4529; c) H.-Y. Jang, R. R. Huddleston, M. J. Krische, *J. Am. Chem. Soc.* **2002**, *124*, 15156–15157; d) H.-Y. Jang, M. J. Krische, *Acc. Chem. Res.* **2004**, *37*, 653–661; e) H.-Y. Jang, M. J. Krische, *Eur. J. Org. Chem.* **2004**, 3953–3958; f) A. E. Russell, N. O. Fuller,

 © 2005 Wiley-VCH Verlag GmbH & Co. KGaA, Weinheim

S. J. Taylor, P. Aurriset, J. P. Morken, *Org. Lett.* **2004**, *6*, 2309–2312.
[10] Another aldol reaction pathway, involving transmetalation of the rhodium enolate **I**′ with the alkenyl zirconium species **III** to generate the zirconium enolate, followed by the engagement of an aldehyde **II** for the subsequent aldol reaction, cannot be excluded at this time in this three-component reaction.
[11] K. C. Nicolaou, M. P. Jennings, P. Dagneau, *Chem. Commun.* **2002**, 2480–2481.
[12] [$Cp_2Zr(H)Cl$] was purchased from Strem Chemicals, Inc.

 © 2005 Wiley-VCH Verlag GmbH & Co. KGaA, Weinheim



Scheme 1. Structures of the cylindrospermopsins and chlorination products.

Natural Product Synthesis

Synthesis of the Putative Structure of 7-Deoxycylindrospermopsin: C7 Oxygenation Is Not Required for the Inhibition of Protein Synthesis**

*Ryan E. Looper, Maria T. C. Runnegar, and Robert M. Williams**

Cylindrospermopsin (**1**) and its naturally occurring epimer, 7-*epi*-cylindrospermopsin (**2**; Scheme 1), are attracting increasing attention as threats to public health.[1] These alkaloids are hepatotoxic metabolites of the cyanobacterium *Cylindrospermopsis raciborskii* and of three other types of cyanobacteria, and they pose a serious public-health problem when they occur in water supplies. Both **1** and **2** are potent inhibitors of protein synthesis both in vitro ($IC_{50} = 200$ and 480 nM, respectively) and in vivo ($IC_{50} = 1.28$ and 2.66 μM, respectively).[2] A number of researchers have shown that these compounds inhibit the translation of mRNA into protein.[2,3] Despite two decades of research, the exact mechanism of this inhibition remains unknown. Investigations into the removal of these toxins from water supplies have led to the isolation of both 5-chlorocylindrospermopsin (**3**) and cylindrospermic acid (**4**).[4] Both of these by-products were shown to be nontoxic by mouse bioassay. Furthermore, a related metabolite (**5**), described as 7-deoxycylindrospermopsin, has been isolated and shown to be nontoxic.[5] Interestingly, **5** is thought to exist as a mixture of tautomers (which are illustrated in Scheme 1), as its ^{1}H NMR spectrum lacked a signal for the vinylic proton on the uracil unit and the resonances were generally broad. These structure–activity relationships have led to conjecture about the steric and electronic requirements of the uracil unit and its role in the toxicity of these compounds.[1,4]

Our continuing interest in the synthesis of these intriguing natural products and elucidation of their mode of action led us to pursue the synthesis of 7-deoxycylindrospermopsin for several reasons:[6] First, the absorption maximum (λ_{max}) for **5** at 263 nm, which is consistent with the presence of a uracil unit and not the tautomers shown in Scheme 1.[7] Second, the configuration of C7 arises biosynthetically from the methyl group of an acetate unit;[8] thus, the synthesis of 7-deoxycylindrospermopsin would allow us to explore its intermediacy in the biogenesis of **1** and **2**. Last, the involvement of cytP450 oxidases in the toxicity of **1** suggests a possible oxidation event at C7,[9] thus potentially explaining the redundancy of the configuration of C7 and also implicating 7-deoxycylindrospermopsin as a potential toxin if it intercepted a common metabolic pathway.

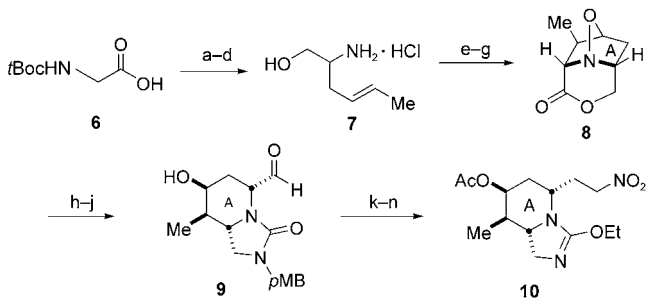
Noting that the optical rotation of **5** has not been reported, we began by synthesizing it in a racemic fashion (Scheme 2). Diimide-mediated coupling of 3-buten-2-ol with *N*-Boc-glycine (**6**) afforded an allylic ester that underwent a smooth enolate Claisen rearrangement on treatment with 2.2 equivalents of NaHMDS.[10] Reduction of the acid and acidic removal of the Boc group gave crotyl glycinol salt **7** in good yield. Isourea **10** was obtained in nine further steps.[6b] A highlight of this sequence is the intramolecular dipolar cycloaddition to afford **8**, in which three contiguous stereogenic centers were constructed[6a] in ring A in a selectivity of approximately 10:1. An acid-mediated oxidation employing tetramethylpiperidine-1-oxyl allowed a selective oxidation of

[*] R. E. Looper, Prof. Dr. R. M. Williams
Department of Chemistry
Colorado State University
Fort Collins, CO 80523 (USA)
Fax: (+1) 970-49-1-3944
E-mail: rmw@chem.colostate.edu
Dr. M. T. C. Runnegar
Research Center for Liver Diseases
University of Southern California Medical Center
Los Angeles, CA 90033 (USA)

[**] This work was supported by the National Institutes of Health (NIH) Grants GM068011 and DK51788 (to R.M.W. and M.T.C.R, respectively) and the National Science Foundation Grant CHE0202827 (to R.M.W). The Cell Culture Core of the USC Center for Liver Disease (P30 DK 48522) provided the rat hepatocytes used in these studies. We are grateful to Array Biopharma for fellowship support to R.E.L. We thank Dr. A. Humpage of the Australian Water Quality Center, South Australia for providing a sample of natural 7-deoxycylidrospermopsin; Dr. G. Shaw for providing a spectra of **5**; and Dr. C. Rithner for helpful discussions concerning the NMR analysis.

Supporting information for this article is available on the WWW under http://www.angewandte.org or from the author.

 DOI: 10.1002/anie.200500520 © 2005 Wiley-VCH Verlag GmbH & Co. KGaA, Weinheim



Scheme 2. a) 3-Buten-2-ol, DIC, DMAP, CH_2Cl_2 (96%); b) 2.2 equiv NaHMDS, THF, 0°C→RT (99%); c) EtOCOCl, Et_3N, THF, $NaBH_4$, H_2O; d) AcCl, MeOH (60%, 2 steps); e) $BrCH_2CO_2Ph$, iPr_2NEt, MeCN (63–80%); f) *m*CPBA, Na_2HPO_4, CH_2Cl_2, −78°C (84%); g) PhMe, 200°C, sealed tube, (78%); h) DIBAL-H, CH_2Cl_2, −78°C (87%); i) *p*MBNH$_2$, H_2/Pd/C, EtOAc then (*p*-O_2NPhO)$_2$CO, MeCN (81%); j) TEMPO, PhI(OAc)$_2$, 1 mol% MsOH, $CDCl_3$ (75%); k) $MeNO_2$, *n*BuLi, THF, RT (84%); l) Ac_2O, DMAP, CH_2Cl_2 then $NaBH_4$, EtOH (67%); m) TFA (neat), reflux (80%); n) Et_3OBF_4, Cs_2CO_3, CH_2Cl_2 (78%). DIC = diisopropylcarbodiimide, DMAP = 4-dimethylaminopyridine, HMDS = hexamethyldisilazide, Ac = acetyl, *m*CPBA = 3-chloroperoxybenzoic acid, DIBAL-H = diisobutylaluminum hydride, *p*MB = *para*-methoxybenzyl, TEMPO = tetramethylpiperidine-1-oxyl, MsOH = methanesulfonic acid, TFA = trifluoroacetic acid. Boc = *tert*-butoxycarbonyl.

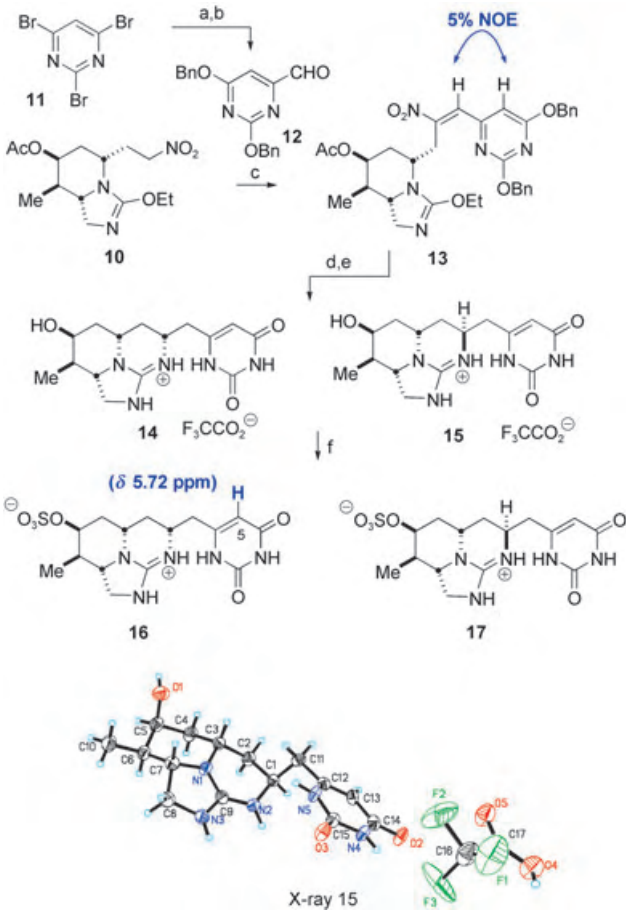
the hydroxymethyl group, thus affording good yields of the sensitive ureido aldehyde **9**.[11]

Intrigued by the possibility of conducting a reductive guanidinylation sequence and simultaneously unmasking the uracil unit, we first synthesized the dibenzyloxypyrimidine aldehyde **12** (Scheme 3): A slightly modified procedure permitted the substitution of 2,4,6-tribromopyrimidine (**11**) with benzyl ether groups,[12] and formylation of the lithiated pyrimidine with dimethylformamide (DMF) afforded **12** in good yield. Treatment of **10** with **12** in the presence of acetic anhydride and excess cesium fluoride couples these two units directly and allows dehydration to occur in a single operation, thus affording **13** in 67% yield. This nitroalkene was produced as a single geometric isomer, which is presumed to be the *E* isomer from studies of the NOE interactions of the pyrimidine proton. Attempts to reduce the nitroalkene directly to the corresponding saturated amine led predominantly to hydrolysis of the presumed enamine intermediate.

To obviate this reactivity, sodium borohydride was employed to reduce **13** to the nitroalkane. Hydrogenolysis of this mixture reduced the nitroalkene, thus effecting reductive guanidinylation, and cleanly cleaved the benzyl ether groups to afford the uracil/guanidine compounds in an approximate 1:1 mixture of isomers. Brief exposure of this mixture to HCl facilitated the removal of the acetate group at C12 to give **14** and **15**. The configuration of **15** was ultimately determined by X-ray crystallographic analysis.[13] It should be noted that the guanidine moieties were obtained as trifluoroacetate salts after purification by HPLC. This method of purification has been used in all of the previous syntheses of **2**.[6b,14] The small amount of synthetic material produced did not allow this counterion to be detected by ^{13}C NMR spectroscopy, but it is presumed to accompany the non-zwitterionic guanidines purified by HPLC with trifluoroacetic acid (TFA) in the eluent.

The reductive guanidinylation sequence is sufficiently clean to effect the direct sulfonation of **14** and **15** at O12 to give sulfates **16** and **17** in a combined yield of 66% from **13** after a single purification by HPLC. In the ^1H NMR spectrum of **16**, the uracil proton at C5 is clearly evident at $\delta =$ 5.72 ppm, and the resonances are well defined and closely match those of **1**, except for the methylene protons at C7. In an attempt to reconcile these differences, this spectrum was compared with the spectrum that had led to the elucidation of the structure of **5**. However, it is clear that the natural material is a mixture of compounds, and it was not possible to conclude whether **16** was a minor component of that mixture.

Most significantly, our synthetic 7-deoxycylindrospermopsin (**16**) proved to be a potent inhibitor of protein synthesis in vitro, as measured in the rabbit reticulocyte lysate system.[9b] Protein synthesis was completely inhibited at 12 μM and partially inhibited at 500 nM. This effect on protein synthesis was also evaluated in whole cells (Table 1).[2] As seen, **16** completely inhibits protein synthesis at 10 μM, thus displaying a potency that is within an order of magnitude of natural **1**. Synthetic **16** also inhibits the synthesis of glutathione (GSH), in a similar fashion to **1**.[3,9a]



Scheme 3. a) BnOH, *n*BuLi, THF/DMF (80%); b) *n*BuLi, Et_2O, DMF, then 10% HCl (73%); c) **12**, CsF, Ac_2O, MeCN (67%); d) $NaBH_4$, EtOH then Pd(OH)$_2$, H_2, 5% AcOH/MeOH; e) HCl (conc.), reflux for 0.5 h (**14** = 33%, **15** = 30%; 2 steps); f) SO_3·py, DMF, 3-Å MS (**16** = 33% from **13**, **17** = 33% from **13**). Bn = benzyl, py = pyridine, MS = molecular sieves.

 © 2005 Wiley-VCH Verlag GmbH & Co. KGaA, Weinheim

Table 1: Inhibition of protein synthesis in rat hepatocytes.

Compound	Conc. [μM][a]	Protein [%][b]	GSH [%][c]
1	0.20	58	100
	1.03	15	80
	1.55	7	60
16	2	64	100
	5	28	95
	10	8	45
17	40	73	100
	80	56	100

[a] Calculated from $\varepsilon = 4600\ mol^{-1}\ dm^3\ cm^{-1}$ at 263 nm. [b] Measured by the incorporation of [^{35}S]methionine into protein (given as % of control values). [c] Measured as nmol of GSH per mg of protein (given as % of control values).

Contrary to previously reported findings,[5] we found that a sample of natural 7-deoxycylindrospermopsin also inhibits protein synthesis with potency similar to the synthetic 7-deoxycylindrospermopsin (**16**). These two materials were shown by HPLC analysis to be identical, thus corroborating the natural occurrence of **16**.[15,16]

The synthesis detailed herein should cast doubt on the notion of uracil tautomers in the purported structure of 7-deoxycylindrospermopsin. It appears unlikely that an oxygenation event at C7 or C8 occurs in the metabolism of **1**, **2**, or **16** (to generate an enol ketone), as the C8 diastereomer **17** is two orders of magnitude less toxic. Compounds **14** and **16** have been labeled with $^{13}CH_3NO_2$ to investigate their intermediacy in the biosynthesis of **1** and **2**. These studies will be reported in due course.

Received: February 11, 2005
Published online: May 18, 2005

Keywords: alkaloids · cyanobacteria · cycloaddition · guanidine · toxicology

[1] For an excellent review of the cylindrospermopsins, see: D. J. Griffiths, M. L. Saker, *Environ. Toxicol.* **2003**, *18*, 78; for NIH and EPA involvement, see: http://www.epa.gov/safewater/standard/ucmr/ and http://ntp-server.niehs.nih.gov/htdocs/Results_status/ResstatC/M000072.html.
[2] M. T. Runnegar, C. Y. Xie, B. B. Snider, G. A. Wallace, S. M. Weinreb, J. Kuhlenkamp, *Toxicol. Sci.* **2002**, *67*, 81.
[3] M. T. Runnegar, S. M. Kong, Y. Z. Zhong, J. L. Ge, S. C. Lu, *Biochem. Biophys. Res. Commun.* **1994**, *201*, 235; M. Runnegar, S. Lu, *FASEB J.* **1994**, *8*, A419.
[4] R. Banker, S. Carmeli, M. Werman, B. Teltsch, R. Porat, A. Sukenik, *J. Toxicol. Env. Heal. A* **2001**, *62*, 281.
[5] R. L. Norris, G. K. Eaglesham, G. Pierens, G. R. Shaw, M. J. Smith, R. K. Chiswell, A. A. Seawright, M. R. Moore, *Environ. Toxicol.* **1999**, *14*, 163.
[6] a) R. E. Looper, R. M. Williams, *Tetrahedron Lett.* **2001**, *42*, 769; b) R. E. Looper, R. M. Williams, *Angew. Chem.* **2004**, *116*, 2990; *Angew. Chem. Int. Ed.* **2004**, *43*, 2930.
[7] R. H. Li, W. W. Carmichael, S. Brittain, G. K. Eaglesham, G. R. Shaw, Y. D. Liu, M. M. Watanabe, *J. Phycol.* **2001**, *37*, 1121.
[8] D. L. Burgoyne, T. K. Hemscheidt, R. E. Moore, M. T. Runnegar, *J. Org. Chem.* **2000**, *65*, 152.
[9] a) M. T. Runnegar, S. M. Kong, Y. Z. Zhong, S. C. Lu, *Biochem. Pharmacol.* **1995**, *49*, 219; b) K. Terao, S. Ohmori, K. Igarashi, I. Ohtani, M. F. Watanabe, K. I. Harada, E. Ito, M. Watanabe, *Toxicon* **1994**, *32*, 833.
[10] U. Kazmaier, *Angew. Chem.* **1994**, *106*, 1046; *Angew. Chem. Int. Ed. Engl.* **1994**, *33*, 998.
[11] A. De Mico, R. Margarita, L. Parlanti, A. Vescovi, G. Piancatelli, *J. Org. Chem.* **1997**, *62*, 6974.
[12] R. F. Schinazi, W. H. Prusoff, *J. Org. Chem.* **1985**, *50*, 841.
[13] CCDC-258351 contains the supplementary crystallographic data for this paper. These data can be obtained free of charge from the Cambridge Crystallographic Data Centre via www.ccdc.cam.ac.uk/data_request/cif.
[14] a) G. R. Heintzelman, W. K. Fang, S. P. Keen, G. A. Wallace, S. M. Weinreb, *J. Am. Chem. Soc.* **2001**, *123*, 8851; b) G. R. Heintzelman, W. K. Fang, S. P. Keen, G. A. Wallace, S. M. Weinreb, *J. Am. Chem. Soc.* **2002**, *124*, 3939; c) J. D. White, J. D. Hansen, *J. Am. Chem. Soc.* **2002**, *124*, 4950.
[15] Co-HPLC-injection of **16** and natural 7-deoxycylindrospermopsin (Agilent zorbax C18 column (4.6 × 150 mm) with MeOH/TFA/H_2O (0.04:0.001:1) as the elutant at 2.0 mL min^{-1} with monitoring at 262 nm) gave a single peak at 5.48 min.
[16] For an excellent review of structural reassignments by total synthesis, see: K. C. Nicolaou, S. A. Snyder, *Angew. Chem.* **2005**, *117*, 1036; *Angew. Chem. Int. Ed.* **2005**, *44*, 1012.

 © 2005 Wiley-VCH Verlag GmbH & Co. KGaA, Weinheim

Henry Reaction

Enantioselective Henry Reactions under Dual Lewis Acid/Amine Catalysis Using Chiral Amino Alcohol Ligands**

Claudio Palomo, Mikel Oiarbide, and Antonio Laso*

There is increasing interest in developing catalytic asymmetric C–C bond-forming processes.[1] In this endeavor the Henry reaction[2] is prominent because of the versatile chemistry of the nitro group.[3] Remarkably, however, while this reaction is closely related to the aldol addition reaction, it has been much less developed than the latter and only a few examples of efficient catalytic enantioselective Henry reactions are known to date.[4] The most outstanding examples include the use of metal-based bifunctional chiral catalysts, as reported by the groups of Shibasaki,[5] Trost,[6] and Evans,[7] which rely on concurrent activation of the aldehyde and the nitroalkane.[8,9] This concurrent activation in Henry reactions has also been

[*] Prof. Dr. C. Palomo, Prof. Dr. M. Oiarbide, A. Laso
Departamento de Química Orgánica I
Facultad de Química
Universidad del País Vasco
Apdo. 1072, 20080 San Sebastián (Spain)
Fax: (+34) 943-015-270
E-mail: qoppanic@sc.ehu.es

[**] This work was financially supported by the University of the Basque Country and the Ministerio de Educación y Ciencia (MEC, Spain). A predoctoral grant to A.L. from the MEC is acknowledged.

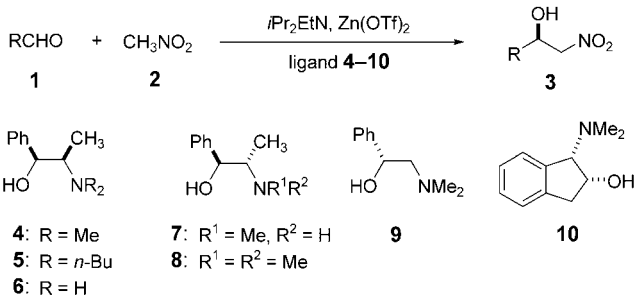
Supporting information for this article is available on the WWW under http://www.angewandte.org or from the author.

 DOI: 10.1002/anie.200463075 © 2005 Wiley-VCH Verlag GmbH & Co. KGaA, Weinheim

realized by the combined use of discrete Lewis acids and Brønsted bases as structurally independent entities.[10] While this approach allows the straightforward scrutiny of a wide range of Lewis acids and Brønsted bases during the optimization of the catalyst system, it is apparently troublesome because of the chemical incompatibility of Lewis acids and Brønsted bases[11] and the occurrence of a nonselective, base-initiated Henry side reaction.[12] Herein, we report that highly enantioselective direct Henry reactions can be triggered by a combination of a simple Zn^{II} salt, an amine base, and a chiral amino alcohol ligand.

On the basis of precedents in the literature, the combination of a metal triflate salt, a tertiary amine base, and a chiral amino alcohol ligand was initially selected.[13,14] Accordingly, the Henry reaction of nitromethane **2** with hydrocinnamaldehyde **1a** and benzaldehyde **1i** (see Table 3), as representative aliphatic and aromatic aldehydes, respectively, was examined in the presence of stoichiometric quantities of $Zn(OTf)_2$, diisopropylethylamine, and a series of commercially available chiral amino alcohol ligands[15,16] (**4**–**10**; Scheme 1). As the data collected in Table 1 show, (+)-*N*-methylephedrine ((+)-NME; **4**) was prominent in providing both nitroaldol products **3a** and **3i** in good yields and, most importantly, with 90% and 70% *ee*, respectively. When **5**, **8**, or **10** were employed as the ligand, the efficiency of the reaction was maintained although a decrease in enantioselectivity was observed, whereas the reactions of the two aldehydes in the presence of the related amino alcohol ligands **6**, **7**, and **9** were sluggish.

In subsequent experiments, it was found that substoichiometric quantities of the promoter system sufficed for the reaction between nitromethane (**2**) and **1a** (Table 2).[17] The



Scheme 1. Henry reaction of nitromethane (**2**) and an aldehyde **1** promoted by zinc triflate, iPr_2EtN, and a chiral amino alcohol ligand (**4**–**10**).

Table 1: Effect of the structure of the amino alcohol ligand on the efficiency of the Henry reaction between nitromethane (**2**) and either hydrocinnamaldehyde (**1a**) or benzaldehyde (**1i**) under stoichiometric conditions.[a]

	Product **3a** (R = $PhCH_2CH_2$)		Product **3i** (R = Ph)	
Ligand	Conv. [%][b]	*ee* [%][c]	Conv. [%][b]	*ee* [%][c]
4	>99	90	>99	70
5	>99	40	>99	20
6	0	–	20	8
7	37	24	60	40
8	>99	0	85	0
9	35	0	0	–
10	>99	8	90	20

[a] Reactions conducted on a 1-mmol scale (**1**) using nitromethane as solvent (1 mL). 1:1:1:1.5 molar ratio of aldehyde/$Zn(OTf)_2$/iPr_2EtN/(+)-NME. [b] Determined by ^1H NMR spectroscopy (500 MHz) after 15–16 h reaction at −20°C. [c] Determined by HPLC. See Supporting Information for further details.

Table 2: Effect of the quantities of metal triflate, amine base, and amino alcohol ligand on the reaction between hydrocinnamaldehyde (**1a**, R = $PhCH_2CH_2$) and nitromethane (**2**).[a]

Entry	$Zn(OTf)_2$ [%][b]	iPr_2EtN [%][b]	(+)-NME [%][b]	Conv. [%][c]	*ee* [%][d]
1	30	30	30	>99	80
2	30	30	45	90	90
3	30	20	45	48	50
4	30	0	45	≤14	≤12
5	30	0	75	88	64
6	20	20	45	>99	84
7	10	10	45	>99	70
8	0	0	135	70	0

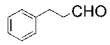
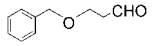
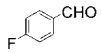
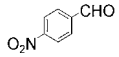
[a] Reactions conducted on a 1-mmol scale (**1**) in nitromethane (1 mL) for 15–16 h at −20°C. [b] Percentage values refer to the mole percentage (% mol) of the catalyst constituents with respect to the aldehyde. [c] Percentage conversion of the reaction. [d] Determined by HPLC.

threshold loading for satisfactory results was set at 30 mol% of metal salt, relative to the aldehyde, with lower loadings usually accompanied by a diminished selectivity (entries 6 and 7).[18] The optimum result (90% yield, 90% *ee*) was obtained by using $Zn(OTf)_2$, iPr_2EtN, and (+)-NME (**4**) in a percentage mole ratio of 30:30:45 (entry 2). Lowering the loading of (+)-NME to 30 mol% slightly diminished the selectivity (entry 1), whereas increasing the ligand loading above 45 mol% did not improve the result. The quantity of iPr_2EtN was crucial too. Lower loading or absence of iPr_2EtN (entries 3 and 4) led to diminished yields and *ee* values. Interestingly, the absence of iPr_2EtN could be partially compensated by increasing the quantity of the ligand (Table 2, entry 5) which is consistent with the amino alcohol ligand playing the double role of chiral inductor and base. Also, while a stoichiometric quantity of (+)-NME (**4**) alone promoted the reaction (entry 8), the product was obtained as a racemic mixture. Amongst the solvents examined, namely methylene chloride, toluene, diethyl ether, and tetrahydrofuran, all worked similarly well and lead to high enantioselectivities except for THF.

A representative selection of aldehydes **1** were evaluated under the optimized conditions and the results obtained are summarized in Table 3. The enantioselectivities obtained were above 90% for essentially all the aliphatic aldehydes explored and even for the branched or sterically hindered aldehydes, which gave values of up to 98% *ee*. Aromatic aldehydes were also tolerated with equal chemical efficiency although the enantioselectivities were comparatively moderate. Typically, the reactions were carried out at −20°C, but lower temperatures (−40°C, or even −60°C under stoichio-

 © 2005 Wiley-VCH Verlag GmbH & Co. KGaA, Weinheim

Table 3: Scope of the aldehyde **1** for the Henry reaction with nitromethane under substoichiometric conditions of $Zn(OTf)_2$/iPr_2EtN/(+)-NME.[a]

	Aldehyde	*T* [°C]	*t* [h]	Yield [%][b]	*ee* [%][c]
1a		−20	16	90	90
1b		−20	16	83	92
		−40[d]	20	81	94
1c		−20	16	92	92
1d		−20	16	75	90
		−30	16	75	92
1e		−20	15	68	97
		−40[d]	17	78	98
1f		−20	16	72	90
		−40[d]	20	74	94
1g		−20	16	71	96
1h		−20	16	87	74
		−60[d]	16	82	87
1i		−60[d]	45	82 (91)	92
1j		−60[d]	45	68 (80)	89
1k		−60[d]	60	77	84

[a] Reactions conducted on the 1-mmol scale (**1**) in dry nitromethane (1 mL) using $Zn(OTf)_2$ (30 mol%), iPr_2EtN (30 mol%), and (+)-NME (45 mol%), otherwise stated. [b] Isolated yields after chromatography. The numbers in parentheses refer to the percentage conversion. If not specified, conversions are >99%. [c] Determined by HPLC. [d] Using a 1:1 (v/v) mixture of nitromethane and CH_2Cl_2 as solvent, and a ratio of 1:1:1:1.5 of aldehyde/$Zn(OTf)_2$/iPr_2EtN/ligand.

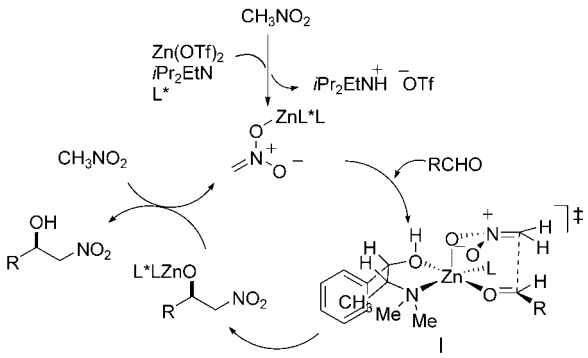


Figure 1. Proposed reaction pathway and transition state (I) for the catalytic Henry reaction. L* = (+)-NME (**4**).

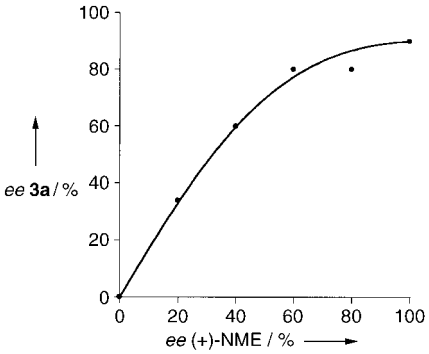


Figure 2. Positive nonlinear effect for the Henry reaction of nitromethane and hydrocinnamaldehyde under substoichiometric conditions.

metric conditions) could also be used effectively to enhance the enantioselectivity. Enals, however, constitute a limitation of the present Henry reaction as they were either recovered unconverted or led to a complex mixture of unidentifiable products. Of practical relevance, the source of chirality, (+)-NME (**4**), could be easily recovered in near-quantitative yield after the reaction by simple aqueous acid/base workup and reused (see Experimental Section).

While the present Henry reaction[19] is simple in execution and uses readily available reagents, the elucidation of its mechanism is appealing. The sense of the asymmetric induction imparted may be correctly predicted by transition model I (Figure 1), which is in accord with previously reported steric and electronic considerations.[7] However, the nonlinear effect observed for the substoichiometric reaction suggests a higher order molecularity of the catalytically active species. In this respect, the data collected in Figure 2 for the Henry reaction of nitromethane (**2**) with hydrocinnamaldehyde (**1a**) seem to fit well with Kagan's two-ligand model.[20] However, control experiments indicate that there is not an appreciable variation of the nonlinear magnitude measured at different values of catalyst loading, while the enantiomeric composition of the product remains essentially constant regardless of the level of conversion of the reaction.[21] Accordingly, it also appears that both the reservoir effect and the possible interaction of the catalytic species with the forming nitroaldol may be discarded as factors of the observed nonlinearity. Studies directed to clarify these mechanistic aspects as well as the extension of this Lewis acid–Brønsted base dual-activation strategy to other reactions is currently underway.

Experimental Section

In a typical procedure, diisopropylethylamine (1.04 mL, 6 mmol) was added to a suspension of $Zn(OTf)_2$ (2.18 g, 6 mmol) in CH_3NO_2 (**2**; 15 mL), and the slurry was stirred for 1 h at 25 °C. (1*S*,2*R*)-(+)-*N*-Methylephedrine (**4**; 1.61 g, 9 mmol) was then added, and the resulting yellow mixture was stirred for an additional 2 h at room temperature. After cooling the mixture to −20 °C a solution of trimethylacetaldehyde (**1g**; 2.17 mL, 20 mmol) in **2** (5 mL) was added by syringe, and the mixture was stirred at the same temperature for 17 h. The reaction was quenched with a saturated aqueous solution of NH_4Cl (20 mL), the mixture was extracted with Et_2O (3 × 20 mL), and the combined organic layer was washed with HCl (12 N; 2 × 10 mL) and saturated NH_4Cl (1 × 10 mL). The organic layer was dried with $MgSO_4$ and filtered, and the solvent was removed by evaporation. The crude product was purified by column chromatography to give (*R*)-3,3-dimethyl-1-nitrobutan-2-ol (**3g**) as the major product (2.3 g, 83% yield, 96% *ee*; Chiralcel OD, 98:2 hexane/*i*PrOH, 0.8 mL min^{-1}). *R* major t_r = 16.5 min, *S* minor t_r = 19 min; $[\alpha]_D^{25} = -37.2$ ($c = 1$, CH_2Cl_2).[22] To recover the chiral ligand from the aqueous phase, a solution of NaOH (20% w/v) was added dropwise to the aqueous phase, cooled in an ice bath, until pH 10. The mixture was extracted with CH_2Cl_2 (3 × 10 mL), and the organic layer was dried

 © 2005 Wiley-VCH Verlag GmbH & Co. KGaA, Weinheim

over $MgSO_4$ and filtered, and the solvent was evaporated to afford chemically and optically pure (1*S*,2*R*)-*N*-methylephedrine (2.8 g, 97% recovered).

Received: December 27, 2004
Revised: February 2, 2005
Published online: May 13, 2005

Keywords: amines · amino alcohols · asymmetric catalysis · Henry reaction · Lewis acids

[1] *Comprehensive Asymmetric Catalysis*, *Vol. III* (Eds.: E. N. Jacobsen, A. Pfaltz, H. Yamamoto), Springer, Berlin, **1999**.
[2] a) G. Rosini in *Comprehensive Organic Synthesis*, *Vol. 2* (Eds.: B. M. Trost, I. Fleming, C. H. Heathcock), Pergamon, New York, **1991**, pp. 321 – 340; b) F. A. Luzio, *Tetrahedron* **2001**, *57*, 915 – 945.
[3] N. Ono, *The Nitro Group in Organic Synthesis*, Wiley-VCH, New York, **2001**.
[4] C. Palomo, M. Oiarbide, A. Mielgo, *Angew. Chem.* **2004**, *116*, 5558 – 5560; *Angew. Chem. Int. Ed.* **2004**, *43*, 5442 – 5444.
[5] a) H. Sasai, T. Suzuki, S. Arai, T. Arai, M. Shibasaki, *J. Am. Chem. Soc.* **1992**, *114*, 4418 – 4420; b) T. Arai, Y. M. A. Yamada, N. Yamamoto, H. Sasai, M. Shibasaki, *Chem. Eur. J.* **1996**, *2*, 1368 – 1372; c) H. Sasai, S. Watanabe, T. Suzuki, M. Shibasaki, *Org. Synth.* **2001**, *74*, 571 – 577 (*Coll. Vol. 10*).
[6] a) B. M. Trost, V. S. C. Yeh, *Angew. Chem.* **2002**, *114*, 889 – 891; *Angew. Chem. Int. Ed.* **2002**, *41*, 861 – 863; b) B. M. Trost, V. S. C. Yeh, H. Ito, N. Bremeyer, *Org. Lett.* **2002**, *4*, 2621 – 2623.
[7] D. A. Evans, D. Seidel, M. Rueping, H. W. Lam, J. T. Shaw, C. W. Downey, *J. Am. Chem. Soc.* **2003**, *125*, 12692 – 12693.
[8] For enantioselective fluoride-mediated Henry reactions that used silyl nitronates as preactivated forms of nitroalkanes, see: a) T. Risgaard, K. V. Gothelf, K. A. Jørgensen, *Org. Biomol. Chem.* **2003**, *1*, 153 – 156; b) T. Ooi, K. Doda, K. Maruoka, *J. Am. Chem. Soc.* **2003**, *125*, 2054 – 2055.
[9] For reviews on the concept of dual acid/base catalysis, see: a) M. Shibasaki, N. Yoshikawa, *Chem. Rev.* **2002**, *102*, 2187 – 2209; b) M. Shibasaki, M. Kanai, K. Funabashi *Chem. Commun.* **2002**, 1989 – 1999; c) G. J. Rowlands, *Tetrahedron* **2001**, *57*, 1865 – 1882; d) J.-A. Ma, D. Cahard, *Angew. Chem.* **2004**, *116*, 4666 – 4683; *Angew. Chem. Int. Ed.* **2004**, *43*, 4566 – 4583.
[10] For reactions employing bis(oxazoline)-based Cu^{II} complexes and triethylamine, see: a) C. Christensen, K. Juhl, K. A. Jørgensen, *Chem. Commun.* **2001**, 2222 – 2223; b) C. Christensen, K. Juhl, R. G. Hazell, K. A. Jørgensen, *J. Org. Chem.* **2002**, *67*, 4875 – 4881; c) S.-F. Lu, D.-M. Du, S.-W. Zhang, J. Xu, *Tetrahedron: Asymmetry* **2004**, *15*, 3433 – 3441; For reactions employing chiral imine based Co^{II} complexes and diisopropylethylamine, see: d) Y. Kogami, T. Nakajima, T. Ashizawa, S. Kezuka, T. Ikeno, T. Yamada, *Chem. Lett.* **2004**, 614 – 615; e) Y. Kogami, T. Nakajima, T. Ikeno, T. Yamada, *Synthesis* **2004**, 1947 – 1950.
[11] For a solution to this problem within the context of the double catalytic activation strategy, see: S. Kanemasa, K. Itoh, *Eur. J. Org. Chem.* **2004**, 4741 – 4753.
[12] Base-catalyzed, nonselective Henry reactions are long known. For the incidence of such a process in the efficiency of asymmetric catalysis, see Ref. [10b].
[13] For the enolization of carbonyl compounds using metal triflates in combination with tertiary amines, see: a) D. A. Evans, J. S. Tedrow, J. T. Shaw, C. W. Downey, *J. Am. Chem. Soc.* **2002**, *124*, 392 – 393; b) D. A. Evans, C. W. Downey, J. L. Hubbs, *J. Am. Chem. Soc.* **2003**, *125*, 8706 – 8707; c) C. J. Cowden, I. Paterson, *Org. React.* **1997**, *51*, 1 – 200; d) *Modern Aldol Reactions* (Ed.: R. Mahrwald), Wiley-VCH, Weinheim, **2004**.
[14] For amino-alcohol–Zn^{II} complexes in enantioselective carbonyl alkylations, see: a) K. Soai, S. Niwa, S. *Chem. Rev.* **1992**, *92*, 833 – 856; b) L. Pu, H.-B. Yu, *Chem. Rev.* **2001**, *101*, 757 – 824; and in carbonyl alkynylations, see: c) E. M. Carreira, *Acc. Chem. Res.* **2000**, *33*, 373 – 381; d) L. Pu, *Tetrahedron* **2003**, *59*, 9873 – 9886; e) P. G. Cozzi, R. Hilgraf, N. Zimmermann, *Eur. J. Org. Chem.* **2004**, 4095 – 4105.
[15] Other reports of Henry reactions using Zn^{II}–amino-alcohol complexes have met with essentially complete failure. See: a) G. Klein, S. Pandiaraju, O. Reiser, O. *Tetrahedron Lett.* **2002**, *43*, 7503 – 7506; b) Y.-W. Zhong, P. Tian, G.-Q. Lin, *Tetrahedron: Asymmetry* **2004**, *15*, 771 – 776; and with Zn^{II} complexes with chiral thioaza ligands, see: c) J. Gao, A. E. Martell, *Org. Biomol. Chem.* **2003**, *1*, 2801 – 2806. Also, see Ref. [10c].
[16] Ligand **10** was prepared by the reductive methylation of indanol. See: S. Yao, J.-C. Meng, G. Siuzdak, M. G. Finn, *J. Org. Chem.* **2003**, *68*, 2540 – 2546. The remaining ligands were purchased from Aldrich.
[17] Other combinations of metal salts and Brønsted bases were also examined, with either inferior results or complete failure of the reaction observed. See Supporting Information for more details.
[18] Remarkably, the reaction between nitromethane (**2**) and pivalaldehyde (**1d**) under a low catalyst loading of $Zn(OTf)_2$/$i$$Pr_2$EtN/(+)-NME (10:10:15 mol% each) led to product **3d** in 75% yield and in 90% *ee*.
[19] Under the optimized conditions for nitromethane, the reaction between nitroethane and benzaldehyde gave a mixture of *anti*- and *syn*-nitroaldols in a 65:35 ratio.
[20] a) C. Girard, H. B. Kagan, *Angew. Chem.* **1998**, *110*, 3088 – 3127; *Angew. Chem. Int. Ed.* **1998**, *37*, 2922 – 2959; b) H. B. Kagan, *Adv. Synth. Catal.* **2001**, *343*, 227 – 233.
[21] Similar results have also been observed in reactions with butyraldehyde and heptanal. See Supporting Information for details.
[22] By using (1*R*,2*S*)-(−)-*N*-methylephedrine as the ligand under otherwise identical reaction conditions, the corresponding (*S*)-nitroaldol was obtained (80% yield, 96% *ee*). $[\alpha]_D^{25} = +36.8$ ($c = 1$, CH_2Cl_2) ($[\alpha]_D^{25} = +29.39$ ($c = 3.39$, CH_2Cl_2), 93% *ee*).[7]

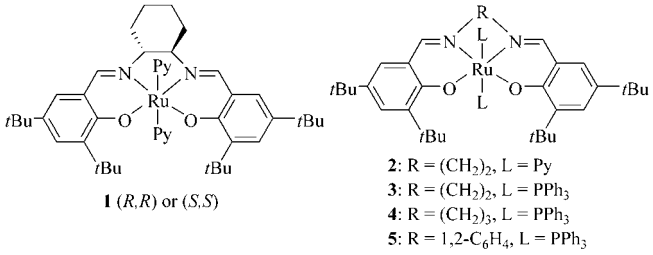
Asymmetric Catalysis

Axial Ligand Effects: Utilization of Chiral Sulfoxide Additives for the Induction of Asymmetry in (Salen)ruthenium(II) Olefin Cyclopropanation Catalysts**

*Jason A. Miller, Bradley A. Gross, Michael A. Zhuravel, Wiechang Jin, and SonBinh T. Nguyen**

The enantioselective synthesis of compounds containing the cyclopropyl fragment has recently received considerable attention, largely because of the frequent occurrence of cyclopropanes in natural products and their importance as valuable synthetic intermediates.[1–3] Although many methods have been developed, transition-metal-catalyzed asymmetric cyclopropanation has emerged as one of the most efficient routes for the formation of optically pure cyclopropanes.[1,4] However, the syntheses of the necessary chiral catalysts for this important transformation are often rather laborious. A general and facile method for the asymmetric synthesis of a cyclopropanation catalyst has yet to be developed.

Recently, we have focused on cultivating efficient methods for the development of asymmetric catalysts. We began by improving on our previously reported (salen)ruthenium(II) asymmetric cyclopropanation system. This catalyst system has been shown to be highly effective for the cyclopropanation of olefins with the carbene precursor ethyl diazoacetate (EDA).[5] However, although the use of chiral catalyst **1** (Scheme 1) has led to exceptional selectivity and high yields for the cyclopropanation of olefins with EDA, these results



Scheme 1. Asymmetric **1** and achiral (salen)ruthenium(II) cyclopropanation catalysts **2**–**5**. Py = pyridine.

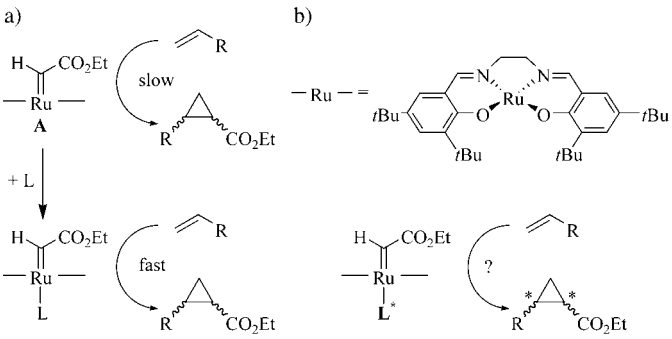
[*] Dr. J. A. Miller, B. A. Gross, Dr. M. A. Zhuravel, Dr. W. Jin, Prof. S. T. Nguyen
Department of Chemistry
Northwestern University
2145 Sheridan Road, Evanston, IL 60208-3113 (USA)
Fax: (+1) 847-491-7713
E-mail: stn@northwestern.edu

[**] This work was supported by the National Institute of Health and the DuPont Company. J.A.M. is an ACS Division of Organic Chemistry Nelson J. Leonard Fellow sponsored by Organic Synthesis, Inc., and S.T.N. is an Alfred P. Sloan Research Fellow. We also thank the Packard Foundation for partial financial support and Prof. M. J. Hynes for his help with the WinEQNMR program. Salen = N,N′-bis(salicylidene)ethylenediamine.

Supporting information for this article is available on the WWW under http://www.angewandte.org or from the author.

can not necessarily be extended to all olefin substrates. For some olefins, multiple catalysts containing different chiral diamine backbones must be examined before optimal results can be achieved. The synthesis of a series of chiral salen-based catalysts with differing backbones is both expensive and time consuming so an alternative approach is needed to expedite the screening of new olefins and diazo compounds for the cyclopropanation reaction.

Previous work in our group has demonstrated a significant ligand-accelerated catalysis effect for certain substrates through what is presumed to be axial ligand binding and further activation of the ruthenium carbene cyclopropanation intermediate (Scheme 2a).[6] We hypothesized that this could be used to our advantage and an optically pure Lewis base

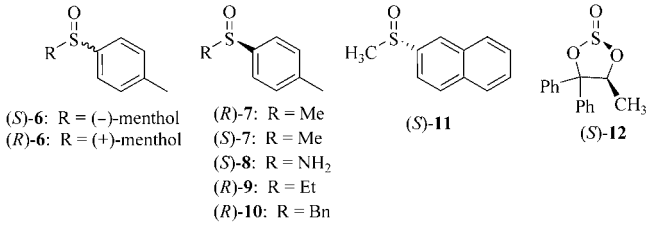


Scheme 2. a) Ligand-accelerated catalysis in olefin cyclopropanation catalyzed by a (salen)ruthenium(II) complex. b) A chiral Lewis base **L*** ligated axially to an achiral (salen)ruthenium–carbene cyclopropanation intermediate could induce asymmetry.

could be used to bind axially to an achiral catalyst as an alternative to using the preformed chiral (salen)ruthenium(II) catalyst **1**. The Lewis base, if paired correctly with the catalyst (both electronically and sterically), should force an achiral salen ligand into an asymmetric conformation, thus transferring enantioselectivity to the cyclopropanation reaction occurring on the opposite axial face of the catalyst. This approach would allow the use of the inexpensive and readily synthesized achiral catalysts **2**–**5** and the facile screening of a nearly endless library of chiral Lewis bases **L*** that can function as ligands to the metal carbene intermediate (Scheme 2b). Related strategies were previously employed by Katsuki and co-workers with varying degrees of success for the (salen)manganese(III)-catalyzed asymmetric epoxidation of olefins through the application of chiral amines[7,8] and chiral pyridine *N*-oxides.[9] Walsh and co-workers also reported considerable enhancement in selectivity when chiral additives were used to convey asymmetry into an achiral titanium precatalyst for the addition of an ethyl nucleophile to aldehydes.[10–12] A recent review by Walsh et al. touched on the potential application of this novel and exciting approach to catalyst screening.[13]

Herein, we describe the first example of an asymmetric cyclopropanation mediated by a combination of achiral (salen)ruthenium(II) catalysts **2**–**5** and a catalytic amount of chiral sulfoxide additives (**6**–**12**; Scheme 3). Sulfoxides were chosen as a test class of chiral Lewis bases because they have

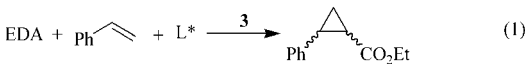
 DOI: 10.1002/anie.200460887 © 2005 Wiley-VCH Verlag GmbH & Co. KGaA, Weinheim



Scheme 3. Sulfoxide Lewis bases used as chiral additives for the cyclopropanation of olefins with achiral (salen)ruthenium(II) complexes.

been recently used as ligands in asymmetric catalysis.[14,15] Sulfoxide ruthenium(II) complexes are well known[12,16] and chiral sulfoxides have centers of asymmetry that are very close to the ruthenium center during coordination and should have a high probability of transmitting chirality to a flexible salen ligand.

We screened several chiral sulfoxides (**6**–**12**) individually as catalytic additives for the cyclopropanation of styrene with EDA catalyzed by the achiral catalyst **3** [Eq. (1); Table 1]. In



(1)

Table 1: The cyclopropanation of styrene and EDA with **3** and chiral sulfoxides **6**–**9**.[a]

L*	Yield [%][b]	*cis*/*trans*	*cis ee* [%][c]	*trans ee* [%][c]
none	92	1:7.5	–	–
(*S*)-**6**	86	1:7.3	23 (*S*,*R*)	5 (*S*,*S*)
(*R*)-**6**	87	1:7.2	23 (*R*,*S*)	5 (*R*,*R*)
(*S*)-**7**	84	1:7.5	50 (*S*,*R*)	42 (*S*,*S*)
(*R*)-**7**	86	1:7.6	57 (*R*,*S*)	46 (*R*,*R*)
(*S*)-**8**	85	1:7.2	40 (*R*,*S*)	10 (*R*,*R*)
(*R*)-**9**	96	1:7.4	51 (*R*,*S*)	29 (*R*,*R*)
(*R*)-**10**	90	1:7.3	56 (*R*,*S*)	45 (*R*,*R*)
(*S*)-**11**	90	1:7.3	41 (*S*,*R*)	45 (*S*,*S*)
(*S*)-**12**	87	1:7.4	33 (*R*,*S*)	16 (*R*,*R*)

[a] Reaction conditions: EDA (0.5 mmol), styrene (2.5 mmol), **3** (1 mol%), **L*** (10 mol%), CH_2Cl_2 (5 mL), RT, 12 h. [b] Yield determined by GC analysis based on EDA with undecane as an internal standard. [c] Absolute configuration determined from chiral GC analysis versus known standards.

general, the addition of these chiral additives does not affect either the yield or diastereoselectivity of the reaction. Furthermore, reversing the chirality of the sulfoxide (that is, (*S*)-**6** versus (*R*)-**6** and (*S*)-**7** versus (*R*)-**7**) leads to opposite enantioselectivities, thus lending support to the supposition that the chirality of the product is a direct result of the Lewis base additive.

These preliminary results were quite promising. Even with a very low concentration of additive in solution (10 mol% relative to EDA), *ee* values of up to 57% were noted. These results suggested to us that (*R*)-(+)-methyl *p*-tolyl sulfoxide (*R*)-**7** was the best chiral additive for the cyclopropanation of styrene. This was somewhat surprising in light of the small size of the methyl substituent on (*R*)-**7** relative to the larger menthol substituents on additive **6**. The use of additives with amino ((*S*)-**8**), ethyl ((*R*)-**9**), and benzyl ((*R*)-**10**) substituents on the *p*-tolyl sulfoxide was also investigated to probe for the optimal steric environment; however, none of these compounds proved as successful as (*R*)-**7**. (*S*)-Methyl 2-naphthyl sulfoxide ((*S*)-**11**) was used to determine the effect of adding steric bulk to the other side of the sulfoxide. Surprisingly, this also yielded lower enantioselectivities than (*R*)-**7**. Additive (*R*)-**7** was, however, expected to produce higher enantioselectivities than the cyclic compound (*S*)-**12**, in which the cone angle of the chiral center is considerably smaller.

As we previously reported, the olefin cyclopropanation product can be readily separated from a reaction mixture containing solvent, catalyst, and excess olefin.[17] This same isolation strategy can also be applied in the current case when a chiral Lewis base is also present in solution. As a representative example, the optically enriched styrene cyclopropanation product produced in the presence of additive (*R*)-**7** could be isolated in excellent yield (94%). Further details on the isolation procedure can be found in the Experimental Section.

Additive (*R*)-**7** was then subjected to a range of reaction conditions and catalysts to optimize the enantioselectivity for the cyclopropanation of styrene (Table 2). The enantioselectivity of the reaction increased to nearly 70% with respect to the *cis* isomer when 50 mol% of (*R*)-**7** was used with **3** (Table 2, entry 5). The same increase was noted when the solvent amount was decreased and the amount of sulfoxide added was maintained at 10 mol% (Table 2, entries 6 and 7). Decreasing the temperature of the reaction also positively affected the *ee* value of the products; when the reaction temperature was lowered to −78 °C and the additive concentration increased, the *cis* and *trans* products were obtained in 93 and 87% *ee*, respectively (Table 2, entry 9). These promising results are amongst the highest *ee* values reported for asymmetric induction resulting from the action of a chiral additive on an achiral catalyst.

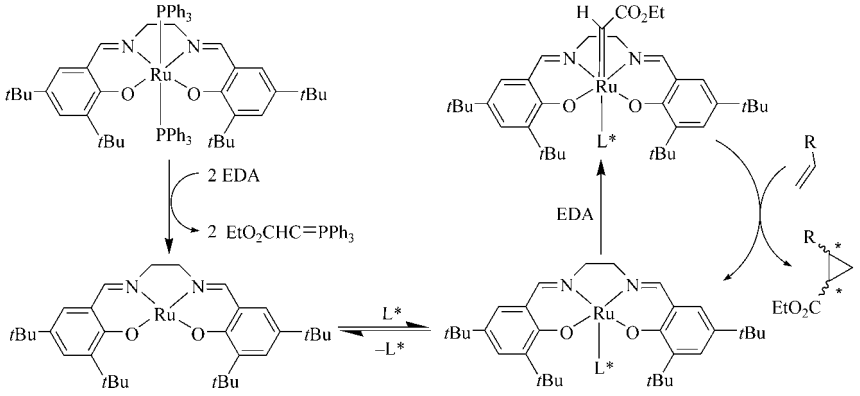
Table 2: Optimization of reaction conditions for the cyclopropanation of styrene and EDA with sulfoxide (*R*)-**7**.[a]

Entry	Cat.	(*R*)-**7** [mol%]	CH_2Cl_2 [mL]	*T* [°C]	Yield [%][b]	*cis*/*trans*	*cis ee* [%][c]	*trans ee* [%][d]
1	**2**	10	5.0	25	87	1:7.6	41	19
2	**3**	10	5.0	25	86	1:7.6	57	46
3	**4**	10	5.0	25	90	1:5.7	27	13
4	**5**	10	5.0	25	89	1:7.8	0	0
5	**3**	50	5.0	25	88	1:7.3	67	57
6	**3**	10	3.5	25	88	1:7.0	65	57
7	**3**	10	2.5	25	85	1:6.9	72	64
8	**3**	10	2.5	0	90	1:7.4	85	81
9	**3**	10	0.0[e]	−78[f]	92	1:6.7	93	87

[a] Reaction conditions: EDA (0.5 mmol), styrene (2.5 mmol), cat. (1 mol%), 12 h. [b] Yield determined by GC analysis based on EDA with undecane as an internal standard. [c] *R*,*S* configuration in all cases. [d] *R*,*R* configuration in all cases. [e] Reaction was carried out in neat styrene. [f] Original temperature followed by slow warming to RT over 6 h.

 © 2005 Wiley-VCH Verlag GmbH & Co. KGaA, Weinheim

We propose that the mechanism of asymmetric induction for Equation (1) involves the axial coordination of the chiral sulfoxide to the ruthenium center as a key induction step in the reaction stereoselectivity (Scheme 4). Initial reaction of



Scheme 4. Proposed mechanism of asymmetric induction through a chiral additive.

EDA with the axial triphenylphosphane ligands of **3**–**5** causes the rapid formation of phosphorus ylides, which do not bind significantly to the metal center.[18] This leaves the axial positions of the catalyst open to coordination by the chiral sulfoxide. The chiral additive can then bind preferentially to one of the two chiral conformers of the achiral (salen)ruthenium complex,[7–9] thus effectively forcing the larger achiral salen ligand to adopt a preferred chiral conformation. Therefore, the asymmetry of the additive is transmitted/amplified to the opposite axial position where a ruthenium carbene can interact stereoselectively with an olefin to complete the cyclopropanation cycle. Balsells and Walsh termed this phenomenon *chiral environment amplification*.[12] The catalytic formation of cyclopropanes through this induced chiral environment, especially when coupled with ligand-accelerated catalysis (Scheme 2a), would afford an excess of one enantiomer, as expected from our work with preformed chiral (salen)ruthenium(II) complexes.[5] Catalyst **5**, with the rigid phenylene diamine backbone, yielded no enantioselectivity when chiral sulfoxide (*R*)-**7** was used as an additive (entry 4), which is consistent with our proposed mechanism.

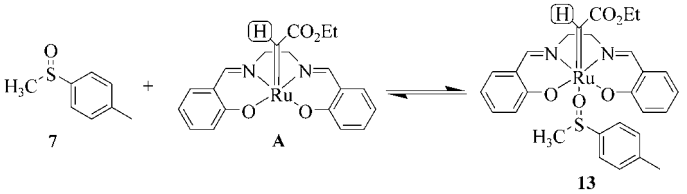
Catalyst **4**, which contains the propylenediamine backbone, yields the same sense of chiral induction as the ethylenediamine analogue **3** in the presence of (*R*)-**7** (Table 2, entries 3 and 2), as could be predicted from the proposed mechanism in Scheme 4. It is also reassuring that the *cis*/*trans* ratio is very close to that when the reaction is carried out in the absence of a chiral additive (1:6.2).

The addition of either (*R*)-**7** or (*S*)-**7** to the cyclopropanation reaction of styrene with EDA using the chiral preformed catalyst **1** (*R*,*R* or *S*,*S*) results in no increase or decrease in the enantiomeric excess of the cyclopropane product compared to use of the chiral catalyst alone. These match/mismatch experiments suggest that the backbone of a chiral catalyst overrides the chirality of an additive and, therefore, plays a larger role in asymmetric induction.

The use of (*R*)-**7** and catalyst **2**, which contains pyridine axial ligands, together with led to lower optical enrichment of the product cyclopropanes compared to when **3**, which loses both PPh_3 moieties at the beginning of the catalytic cycle, was employed (see entries 1 and 2). This effect is most likely because of competition between the pyridine and the additive for the axial position of the catalyst. Pyridine binds strongly to the ruthenium(II) center,[5] so coordination of the chiral additive is hindered. Titration data suggest that this is indeed the case, as addition of increasing amounts of pyridine to a mixture of (*R*)-**7** and **3** leads to linearly decreasing enantiomeric excess.

Control experiments with either a chiral sulfoxide/EDA system or preformed sulfoxide ylides,[19] both with and without the (salen)ruthenium(II) catalyst **3**, confirm that the metal center is necessary for catalytic activity and that the reaction does not occur through a pathway that requires the formation of a sulfoxide ylide. These results are consistent with our proposed mechanism and fully support the idea of chiral induction by an axial ligand.

Further support for our proposed mechanism was obtained by examining the binding mode of the sulfoxide to **A** by NMR spectroscopy.[20] The changes in the chemical shift of the resonances for the α-methyl protons in **7** when it was alone in solution and when it was in solution with the carbene complex **A** were compared ($\delta = 2.07$ versus $\delta = 2.14$ ppm, respectively), thus indicating that **7** binds through the sulfoxide oxygen atom. This small change in chemical shift (< 0.1 ppm) is diagnostic of the oxygen-atom binding mode; binding through the sulfur atom produces a much larger change (> 1 ppm).[15] Furthermore, analysis of the carbene proton of the (salen)ruthenium carbene cyclopropanation intermediate allowed us to calculate the binding constant for the formation of the bound complex **13** [Eq. (2); salen *t*Bu



(2)

groups omitted for clarity]. Figure 1 shows that increasing concentrations of sulfoxide in solution leads to a downfield shift of the carbene proton. These data were used to calculate a binding constant of $K_{eq} = 129 \pm 6\ M^{-1}$ using WinEQNMR software.[21]

Although binding at the ruthenium center to the oxygen atom of the sulfoxide group is inferred by our spectroscopic observations (see above), it is possible that a Curtin–Hammett situation may occur in which the oxygen-bound complex is not necessarily the active species responsible for the excellent cyclopropanation enantioselectivities. That is,

 © 2005 Wiley-VCH Verlag GmbH & Co. KGaA, Weinheim

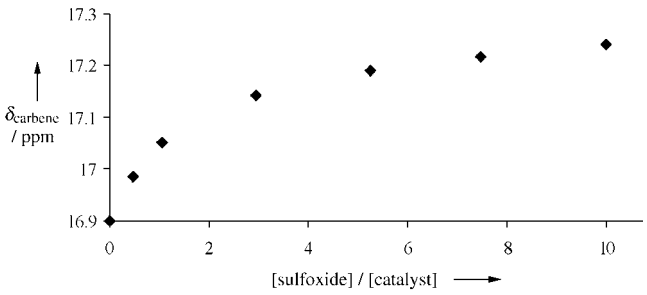


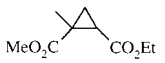
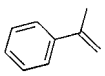
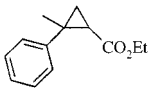
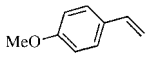
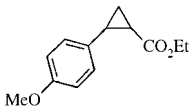
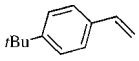
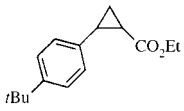
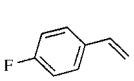
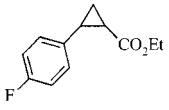
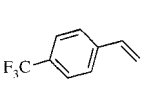
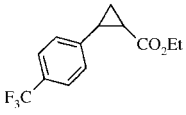
Figure 1. Changes in the chemical shift of the ruthenium carbene proton on addition of sulfoxide **7**.

the sulfur-bound carbene complex could be present in a minute quantity that cannot be observed by NMR spectroscopy but is primarily responsible for the asymmetric induction. Further mechanistic experiments are in progress to help elucidate this possibility and the results will be published at a later date.

We have also extended this sulfoxide-induced chiral amplification strategy to the cyclopropanation of other olefins (Table 3). Quite promising enantioselectivities were observed for these substrates despite having a limited library of chiral sulfoxides, such as **6**–**12**. As observed with styrene, diastereoselectivities remained similar both with and without the chiral additives. These exciting results prove that styrene is not a unique case and that this method is, in fact, applicable to other olefins. Interestingly, although additive (*R*)-**7** induces the greatest enantioselectivities for styrene and its *para*-substituted derivatives, it is not the best chiral Lewis base for all other substrates: methyl methacrylate gave the best results when (*R*)-benzyl *p*-tolyl sulfoxide (*R*)-**10** was utilized, whereas (α-methyl)styrene required the use of (*R*)-**6**. Table 3 shows representative results for these two substrates with some of the optimally performing sulfoxides. These results show that a combinatorial approach can be used to simultaneously screen the substrate and chiral additives for optimum selectivity and reaction conditions. As with styrene, the cyclopropanation products of the substrates listed in Table 3 can be readily isolated in yields closely matching those calculated by GC-calibration techniques.

In conclusion, we have found an efficient and facile method for the development of new (salen)ruthenium(II) catalysts for the asymmetric cyclopropanation of olefins. This exciting modular approach is amenable to parallel-screening optimization and has great potential advantages over traditional catalyst development and synthetic methods. We feel that this approach may also be extended to other types of catalysis where one metal coordination site is free during a reaction. The initial selectivities with this achiral catalyst/chiral Lewis base system are very promising and provide a solid proof-of-concept that chirality can be introduced into a complex cyclopropanation system through the addition of a simple optically active additive. Screening experiments with other classes of chiral additives is underway and optimization data will be reported in due course.

Table 3: Optimized results for the cyclopropanation of various olefins with EDA by using chiral sulfoxides to induce asymmetry into achiral catalyst **3**.[a]

Substrate	Product	Additive	Yield [%][b]	*cis*/*trans*	*cis ee*	*trans ee*
		(*R*)-**6**	86	1:45.7	–	47
		(*R*)-**7**	98	1:40.2	–	68
		(*R*)-**10**	98 (84[c])	1:45.8	–	80
		(*R*)-**6**	97 (89[c])	1:1.1	43	53
		(*R*)-**7**	97	1:1.4	10	3
		(*R*)-**10**	97	1:1.3	0	0
		(*R*)-**7**	97 (97[c])	1:5.9	89	87
		(*R*)-**7**	95 (88[c])	1:4.8	93	87
		(*R*)-**7**	86 (92[c])	1:5.8	80	83
		(*R*)-**7**	98 (98[c])	1:7.8	79	86

[a] Reaction conditions: EDA (0.5 mmol), olefin (2.5 mmol), **3** (1 mol%), additive (10 mol%), 12 h. [b] Yield determined by GC analsis relative to styrene cyclopropane based on EDA with undecane as an internal standard. [c] Yield of isolated cyclopropane (see the Supporting Information for details).

Experimental Section

General procedure for the asymmetric cyclopropanation of olefins with EDA using (salen)ruthenium(II) complexes **1**–**5** and chiral sulfoxide additives **6**–**12**:[22] A mixture of achiral ruthenium catalyst (0.005 mmol), olefin (2.5 mmol), and sulfoxide (0.05 mmol for 10 mol% and 0.25 mmol for 50 mol%) in CH_2Cl_2 (2.5 mL) was placed in a 25-mL round-bottom flask under N_2 in a drybox. A three-times degassed CH_2Cl_2 (2.5 mL) solution of EDA (0.50 mmol) and undecane internal standard (0.50 mmol) was slowly added by a gas-tight syringe over a period of 20 min under N_2. After the addition was complete, the reaction mixture was allowed to stir for 12 h at room temperature. A sample of the solution was then passed through a short plug of silica gel (0.3 × 3 cm) to remove the catalyst and the plug was washed with CH_2Cl_2 (15 mL). The combined organic solutions were analyzed by using standard-phase GC for diasteroselectivity and either chiral-phase GC or HPLC for enantioselectivity.

Received: June 7, 2004
Revised: February 9, 2005
Published online: May 18, 2005

 © 2005 Wiley-VCH Verlag GmbH & Co. KGaA, Weinheim

Keywords: cyclopropanation · ligand-accelerated catalysis · ruthenium · salen · sulfoxides

[1] M. P. Doyle, D. C. Forbes, *Chem. Rev.* **1998**, *98*, 911 – 935.
[2] M. P. Doyle, M. A. McKervey, T. Ye, *Modern Catalytic Methods for Organic Synthesis with Diazo Compounds*, Wiley, New York, **1998**.
[3] J. Salaün, *Chem. Rev.* **1989**, *89*, 1247 – 1270.
[4] H. Lebel, J.-F. Marcoux, C. Molinaro, A. B. Charette, *Chem. Rev.* **2003**, *103*, 977 – 1050.
[5] J. A. Miller, W. Jin, S. T. Nguyen, *Angew. Chem.* **2002**, *114*, 3077 – 3080; *Angew. Chem. Int. Ed.* **2002**, *41*, 2953 – 2956.
[6] R. A. Eveland, J. A. Miller, S. T. Nguyen, unpublished data.
[7] T. Hashihayata, Y. Ito, T. Katsuki, *Synlett* **1996**, *11*, 1079 – 1081.
[8] T. Hashihayata, Y. Ito, K. Tsutomu, *Tetrahedron* **1997**, *53*, 9541 – 9552.
[9] K. Miura, T. Katsuki, *Synlett* **1999**, *6*, 783 – 785.
[10] T. J. Davis, J. Balsells, P. J. Carroll, P. J. Walsh, *Org. Lett.* **2001**, *3*, 2161 – 2164.
[11] A. M. Costa, C. Jimeno, J. Gavenonis, P. J. Carroll, P. J. Walsh, *J. Am. Chem. Soc.* **2002**, *124*, 6929 – 6941.
[12] J. Balsells, P. J. Walsh, *J. Am. Chem. Soc.* **2000**, *122*, 1802 – 1803.
[13] P. J. Walsh, A. E. Lurain, J. Balsells, *Chem. Rev.* **2003**, *103*, 3297 – 3344.
[14] J. Priego, O. G. Mancheno, S. Cabrera, J. C. Carretero, *J. Org. Chem.* **2002**, *67*, 1346 – 1353.
[15] I. Fernandez, N. Khiar, *Chem. Rev.* **2003**, *103*, 3651 – 3705.
[16] M. Calligaris, O. Carugo, *Coord. Chem. Rev.* **1996**, *153*, 83 – 154.
[17] J. A. Miller, E. J. Hennessy, W. J. Marshall, M. A. Scialdone, S. T. Nguyen, *J. Org. Chem.* **2003**, *68*, 7884 – 7886.
[18] R. A. Eveland, PhD Thesis, Northwestern University, Evanston, **2000**, p. 190.
[19] F. Dost, J. Gosselck, *Tetrahedron Lett.* **1970**, 5091 – 5093.
[20] The sulfoxide can bind to the ruthenium center through either the S atom, O atom, or the S=O bond; see references [15, 16].
[21] M. J. Hynes, *J. Chem. Soc. Dalton Trans.* **1993**, 311 – 312.
[22] Detailed procedures for the catalytic screening, product isolation, pyridine addition, and control experiments as well as details of the sulfoxide binding studies, the syntheses of catalysts **1**–**5**, synthesis of sulfoxides **9**–**11**, and GC and HPLC analytical methods are available in the Supporting Information.

 © 2005 Wiley-VCH Verlag GmbH & Co. KGaA, Weinheim

Synthetic Methods

Synthesis of Highly Substituted Pyridazines through Alkynyl Boronic Ester Cycloaddition Reactions**

*Matthew D. Helm, Jane E. Moore, Andrew Plant, and Joseph P. A. Harrity**

Aryl boronic acids and esters represent one of the most heavily used classes of synthetic intermediates in recent times.[1] The versatility of the C–B bond allows the organoboron species to be transformed into numerous new synthetic compounds through various functional group interconversions and C–C bond-forming reactions. In an effort to develop new strategies toward the synthesis of highly substituted and functionalized aromatic boronic esters, we have embarked on a program that endeavors to access these compounds through a series of benzannulation protocols. Specifically, we have prepared benzenoid-derived boronic esters through a chromium-mediated benzannulation reaction[2] and isoxazole boronic esters through a [3+2] cycloaddition.[3] More recently, we investigated the use of [4+2] cycloaddition reactions to broaden the scope of our approach. Previous studies in this area have demonstrated that alkynyl boronic esters, alkynyl dihaloboranes, and alkynyl dialkyl boranes can all function as dienophiles.[4] We report herein our efforts to exploit this strategy for the synthesis of pyridazine boronic esters.

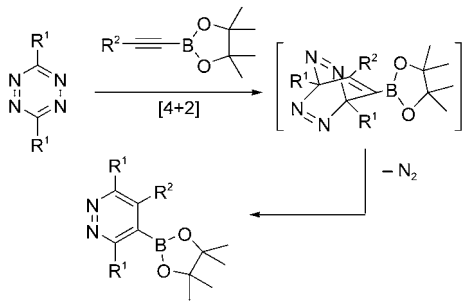
The inverse-electron-demand Diels–Alder reaction of 3,6-disubstituted 1,2,4,5-tetrazines (developed by Carboni and Lindsey) is an effective method for the synthesis of highly substituted pyridazines and other aromatic systems.[5,6] We envisaged that employing alkynyl boronic esters in this reaction would allow the rapid assembly of highly substituted pyridazine boronic esters with potential control of the regiochemistry around the heteroaromatic ring (Scheme 1). Indeed, Seitz and Haenel gave three examples of cycloaddition reactions of ethynyl boronic esters with symmetrical tetrazines that provided the corresponding pyridazines in good yield.[7] The authors did not explore the use of more heavily substituted alkynyl boronic esters or investigate the regiochemistry of this reaction. Nonetheless, it is notable that, to the best of our knowledge, this report is the only

[*] M. D. Helm, J. E. Moore, Dr. J. P. A. Harrity
Department of Chemistry
University of Sheffield
Sheffield, S3 7HF (UK)
Fax: (+44) 114-222-9346
E-mail: j.harrity@sheffield.ac.uk
Dr. A. Plant
Research Chemistry, Syngenta
Jealott's Hill International Research Centre
Bracknell, Berkshire, RG42 6EY (UK)

[**] The authors are grateful to the EPSRC and Syngenta for a studentship (M.D.H.) and to H. Adams for help obtaining the X-ray diffraction data.

Supporting information for this article is available on the WWW under http://www.angewandte.org or from the author.

 DOI: 10.1002/anie.200500288 © 2005 Wiley-VCH Verlag GmbH & Co. KGaA, Weinheim

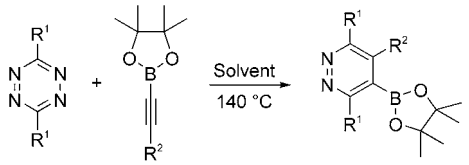


Scheme 1. Synthesis of pyridazine boronic esters through cycloaddition reactions of tetrazines.

documented method for the preparation of pyridazine boronic esters.

We began our studies by investigating the cycloaddition reactions of some substituted alkynyl boronic esters with the readily prepared symmetrical tetrazines **1** and **2**[8] (the results are summarized in Table 1). The preliminary results were encouraging, and we were pleased to find that the ester-substituted tetrazine **1** participated smoothly in the cycloaddition process at 140 °C to form the corresponding pyridazine boronic esters **9**–**12** in moderate to high yield. An interesting solvent effect was also observed, whereby the reactions proceeded more quickly and cleanly when conducted in nitrobenzene (Table 1, compare entries 1, 3, 5, and 7 with entries 2, 4, 6, and 8). Furthermore, the bis(3,5-dimethylpyrazol-1-yl) (DMPY) substituted tetrazine **2** furnished the corresponding heteroaromatic boronic esters **13**–**15** in high yield; moreover, these substrates were stable to chromatography on silica gel, whereas the purification of the ester-substituted boronic esters was more successful when florisil was used. Finally, the parent tetrazine **3** also participated in cycloaddition reactions with alkynes **5** and **7** to provide the simpler pyridazines **16** and **17** in good yield.

Table 1: Cycloaddition reactions of alkynyl boronic esters with symmetrical tetrazines.



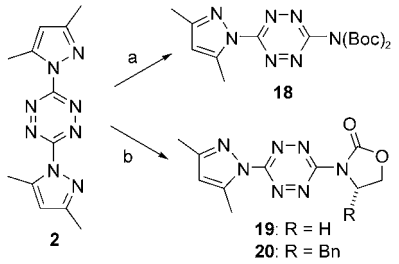
1–3 **4–8** **9–17**

Entry	R^1	$R^{2[a]}$	Solvent	*t* [h]	Product	Yield [%]
1	CO_2Me (**1**)	Me (**4**)	xylene	16	**9**	39
2	CO_2Me (**1**)	Me (**4**)	nitrobenzene	3	**9**	44
3	CO_2Me (**1**)	*n*Bu (**5**)	xylene	16	**10**	62
4	CO_2Me (**1**)	*n*Bu (**5**)	nitrobenzene	6	**10**	75
5	CO_2Me (**1**)	Ph (**6**)	xylene	16	**11**	68
6	CO_2Me (**1**)	Ph (**6**)	nitrobenzene	4	**11**	75
7	CO_2Me (**1**)	TMS (**7**)	xylene	16	**12**	62
8	CO_2Me (**1**)	TMS (**7**)	nitrobenzene	4	**12**	89
9	DMPY (**2**)	Me (**4**)	xylene	16	**13**	82
10	DMPY (**2**)	Me (**4**)	nitrobenzene	7	**13**	81
11	DMPY (**2**)	Ph (**6**)	xylene	16	**14**	80
12	DMPY (**2**)	Ph (**6**)	nitrobenzene	6	**14**	84
13	DMPY (**2**)	TMS (**7**)	xylene	16	**15**	70
14	DMPY (**2**)	TMS (**7**)	nitrobenzene	8	**15**	69
15	H (**3**)	Ph (**6**)	nitrobenzene	6	**16**	60
16	H (**3**)	H (**8**)	nitrobenzene	6	**17**	64

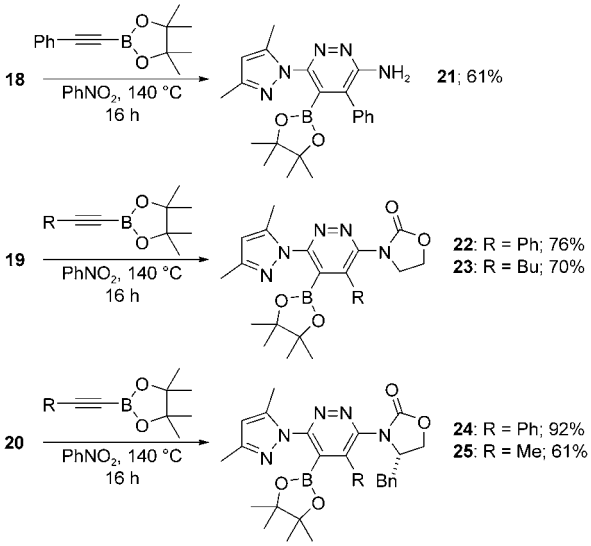
[a] TMS = trimethylsilane.

We next turned our attention to investigating the cycloaddition reactions of unsymmetrical tetrazines with a view to developing a regioselective method for preparing the corresponding pyridazine boronic esters. It has been reported that the DMPY group can be readily displaced with a variety of O- and N-containing nucleophiles,[9] and therefore **2** was employed as a common intermediate for the preparation of unsymmetrical tetrazines (Scheme 2). The treatment of **2** with ammonia followed by Boc_2O furnished a Boc-protected tetrazine **18**. Furthermore, oxazolidinone-substituted tetrazines **19** and **20** were readily prepared by addition of the appropriate amino alcohol followed by acylation with triphosgene.

Cycloaddition reactions with model alkynes were carried out under the conditions optimized in the earlier studies (Scheme 3). Accordingly, heating a solution of **18** and a phenyl-substituted alkynyl boronic ester in nitrobenzene resulted in smooth conversion into pyridazine **21**, which was isolated as the free amine[10] and, notably, as a single regioisomer. NOE interaction studies were used to determine the regiochemistry of this cycloaddition reaction, and it was



Scheme 2. a) 1. NH_3 (excess), toluene, 98%; 2. Boc_2O (2.2 equiv), DMAP (10 mol%), THF (**18**: 70%); b) 1. $H_2N(CH_2)_2OH$ (1.2 equiv), MeOH; 2. triphosgene (1.2 equiv), Et_3N (2.1 equiv), CH_2Cl_2 (**19**: 73% over 2 steps); or 1. (*S*)-$H_2NCH(Bn)CH_2OH$ (1.2 equiv), MeOH; 2. triphosgene (1.2 equiv), Et_3N (2.0 equiv), CH_2Cl_2 (**20**: 63% over 2 steps). Boc = *tert*-butoxycarbonyl, DMAP = 4-dimethylaminopyridine, Bn = benzyl.



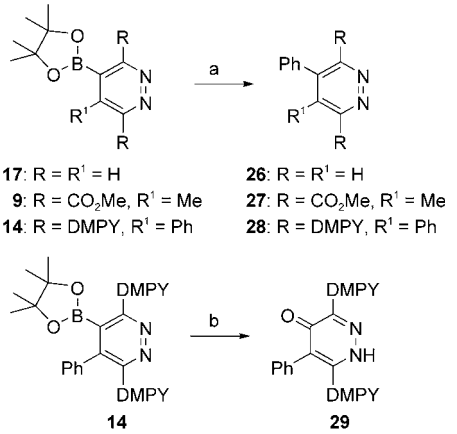
Scheme 3. Preparation of unsymmetrical tetrazines.

 © 2005 Wiley-VCH Verlag GmbH & Co. KGaA, Weinheim

shown that the boronic ester is adjacent to the pyrazolyl ring. We extended this promising reaction to the oxazolidinone-substituted tetrazine **19** to afford **22** and **23** and were pleased that, once again, single regioisomers were isolated. Crystals of **22** suitable for X-ray crystallographic analysis were obtained, and it was confirmed that the boronic ester moiety was again incorporated adjacent to the pyrazole ring.[11] Finally, we extended the cycloaddition chemistry to the chiral oxazolidinone-substituted tetrazine **20** and synthesized chiral pyridazine boronic esters **24** and **25** with equally satisfying results.[12]

With a series of pyridazine boronic esters in hand, our final goal was to investigate functionalization reactions of the C–B bond. The primary objective was to establish the viability of these substrates for Suzuki cross-coupling reactions. It was anticipated that these reactions would require significant optimization as electron-deficient boronic acid derivatives are known to be prone to protodeboronation.[13] Also, the significant steric crowding around the boronate moiety in these compounds further suggested that they would be very challenging substrates. Accordingly, we initiated our studies by examining the cross-coupling of the parent pyridazine boronic ester **17** (Scheme 4). After significant optimization, we were pleased to find that **26** was successfully generated in high yield by employing the protocol of Netherton and Fu[14] for the Suzuki reaction. Pleasingly, these conditions could also be applied to the cross-coupling reaction of the hindered diester **9** to provide the coupled product **27** in 57% yield. Finally, the cross-coupling reaction of **14** with iodobenzene proved to be extremely difficult and resulted in the formation of a substantial quantity of protodeboronated material with a small amount of desired product. Nonetheless, the use of microwave irradiation allowed the desired product **28** to be isolated in 51% yield within a short reaction time.[15] Finally, we explored a simple oxidation of **14** to the 1*H*-pyridazin-4-one **29** and were pleased to find that this transformation proceeded smoothly and in high yield (Scheme 4).

In conclusion, we have reported that the cycloaddition of tetrazines with alkynyl boronic esters provides a direct and regioselective method for the synthesis of highly functionalized pyridazine boronic esters. We have also shown that these intermediates can undergo C–O and C–C bond-forming reactions; the latter transformation requires bulky and electron-rich phosphine ligands to promote catalytic cross-coupling over protodeboronation.



17: R = R¹ = H
9: R = CO_2Me, R¹ = Me
14: R = DMPY, R¹ = Ph

26: R = R¹ = H
27: R = CO_2Me, R¹ = Me
28: R = DMPY, R¹ = Ph

14 **29**

Scheme 4. a) **26**: $[Pd_2(dba)_3]$ (5 mol%), $[(tBu)_3PH]BF_4$ (12 mol%), PhI, K_3PO_4, MeCN, 85°C, 90 min (72%); **27:** $[Pd_2(dba)_3]$ (5 mol%), $[(tBu)_3PH]BF_4$ (12 mol%), PhI, K_3PO_4, MeCN, 50°C, 90 min (57%); **28:** $[Pd_2(dba)_3]$ (5 mol%), $[(tBu)_3PH]BF_4$ (12 mol%), PhI, K_3PO_4, MeCN, 170°C, microwave irradiation, 15 min (51%); b) *i*PrOH, H_2O_2, Na_2CO_3, 85°C (**29**: 96%).

Experimental Section

Typical cycloaddition procedure, as exemplified by the formation of **16**: 4,4,5,5-Tetramethyl-2-phenylethynyl[1,3,2]dioxaborolane (**6**; 306 mg, 1.34 mmol) and 1,2,4,5-tetrazine (**3**; 100 mg, 1.22 mmol) were dissolved in nitrobenzene (2 mL) and heated at 140°C for 6 h. The nitrobenzene was removed in vacuo, and the product recrystallized from ethyl acetate to give **16** (206 mg, 60%) as a light-yellow solid. M.p. 130.5–132.7°C; ^{1}H NMR (250 MHz, $CDCl_3$): $\delta = 1.25$ (s, 12H), 7.40–7.50 (m, 5H), 9.22 (d, $J = 1.0$ Hz, 1H), 9.31 ppm (d, $J = 1.0$ Hz, 1H); ^{13}C NMR (62.9 MHz, [D$_6$]DMSO): $\delta = 24.4$, 84.8, 128.7, 129.0, 129.4, 136.0, 143.3, 150.8, 153.6 ppm; FTIR: 3063 (w), 2978 (m), 1573 (w), 1288 (w), 1148 (s), 1076 cm^{-1} (m). HRMS calcd for $C_{16}H_{19}N_2O_2B$: *m/z* 282.1540, found: 282.1550.

Received: January 25, 2005
Published online: May 19, 2005

Keywords: boronic esters · cross-coupling · cycloaddition · heterocycles · regioselectivity

[1] a) M. Masahiro, *Angew. Chem.* **2004**, *116*, 2251; *Angew. Chem. Int. Ed.* **2004**, *43*, 2201; b) S. Kotha, K. Lahiri, D. Kashinath, *Tetrahedron* **2002**, *58*, 9633; c) J. Hassan, M. Sevignon, C. Gozzi, E. Schulz, M. Lemaire, *Chem. Rev.* **2002**, *102*, 1359; d) A. Suzuki, *Pure Appl. Chem.* **1994**, *66*, 213.

[2] a) M. W. Davies, C. N. Johnson, J. P. A. Harrity, *Chem. Commun.* **1999**, 2107; b) M. W. Davies, C. N. Johnson, J. P. A. Harrity, *J. Org. Chem.* **2001**, *66*, 3525.

[3] a) M. W. Davies, R. A. J. Wybrow, C. N. Johnson, J. P. A. Harrity, *Chem. Commun.* **2001**, 1558; b) J. E. Moore, K. M. Goodenough, D. Spinks, J. P. A. Harrity, *Synlett* **2002**, 2071.

[4] For [4+2] cycloaddition reactions of alkynyl boronic esters and related compounds, see: a) G. Hilt, S. Lüers, K. I. Smolko, *Org. Lett.* **2005**, *7*, 251; b) G. Hilt, K. I. Smolko, *Angew. Chem.* **2003**, *115*, 2901; *Angew. Chem. Int. Ed.* **2003**, *42*, 2795; c) D. S. Matteson, J. O. Waldbillig, *J. Org. Chem.* **1963**, *28*, 366; d) W. G. Woods, P. L. Strong, *J. Organomet. Chem.* **1967**, *7*, 371; e) D. A. Singleton, S.-W. Leung, *J. Org. Chem.* **1992**, *57*, 4796; f) S.-W. Leung, D. A. Singleton, *J. Org. Chem.* **1997**, *62*, 1955; g) M. A. Silva, S. C. Pellegrinet, J. M. Goodman, *J. Org. Chem.* **2002**, *67*, 8203.

[5] a) R. A. Carboni, R. V. Lindsey, *J. Am. Chem. Soc.* **1959**, *81*, 4342; b) D. L. Boger, S. M. Sakya, *J. Org. Chem.* **1988**, *53*, 1415; c) G. L. Rusinov, R. I. Ishmetova, N. I. Latosh, I. N. Ganebnych, O. N. Chupakhin, V. A. Potemkin, *Russ. Chem. Bull.* **2000**, *49*, 355; d) D. L. Boger, *Chem. Rev.* **1986**, *86*, 781.

[6] For cycloaddition reactions that involve heteroatom-substituted alkynes, including Si, Sn, and Ge, see: a) J. Sauer, D. K. Heldmann, J. Hetzenegger, J. Krauthan, H. Sichert, J. Schuster, *Eur. J. Org. Chem.* **1998**, 2885; b) T. J. Sparey, J. Harrison, *Tetrahedron Lett.* **1998**, *39*, 5873; c) J. Sauer, D. K. Heldmann, *Tetrahedron* **1998**, *54*, 4297.

[7] G. Seitz, F. Haenel, *Arch. Pharm.* **1994**, *327*, 673.

[8] a) D. L. Boger, R. S. Coleman, J. S. Panek, J. Sauer, F. X. Huber, *J. Org. Chem.* **1985**, *50*, 5377; b) M. D. Coburn, G. A. Buntain, B. W. Harris, M. A. Hiskey, K.-Y. Lee, D. G. Ott, *J. Heterocycl. Chem.* **1991**, *28*, 2049.

[9] a) N. I. Latosh, G. L. Rusinov, I. N. Ganebnykh, O. N. Chupakhin, *Russ. J. Org. Chem.* **1999**, *35*, 1363; b) Z. Novák, B. Bostai, C. Márton, K. Lörincz, A. Kotschy, *Heterocycles* **2003**, *60*, 2653.

 © 2005 Wiley-VCH Verlag GmbH & Co. KGaA, Weinheim

[10] For a related deprotection of a Boc-protected amine during tetrazine cycloaddition reactions, see: D. L. Boger, R. P. Schaum, R. M. Garbaccio, *J. Org. Chem.* **1998**, *63*, 6329.
[11] CCDC-260811 contains the supplementary crystallographic data for this paper. These data can be obtained free of charge from the Cambridge Crystallographic Data Centre via www.ccdc.cam.ac.uk/data_request/cif.
[12] The regiochemistry of compounds **21**, **23**, and **24** was determined by NOE interaction studies and NOESY spectroscopic analysis (see the Supporting Information); the regiochemistry of **25** was determined by inference.
[13] a) S. Gronowitz, V. Bobosik, K. Lawitz, *Chem. Scr.* **1984**, *23*, 120; b) C. Coudret, V. Mazenc, *Tetrahedron Lett.* **1997**, *38*, 5293.
[14] M. R. Netherton, G. C. Fu, *Org. Lett.* **2001**, *3*, 4295.
[15] It is likely that the DMPY groups are responsible for retarding the rate of metal-catalyzed arylation; indeed, the DMPY-substituted tetrazine **2** can act as a good ligand for transition-metal salts, see: J. Faragó, Z. Novák, G. Schlosser, A. Csámpai, A. Kotschy, *Tetrahedron* **2004**, *60*, 1991.

 © 2005 Wiley-VCH Verlag GmbH & Co. KGaA, Weinheim

Natural Product Synthesis

Total Synthesis of Avrainvillamide (CJ-17,665) and Stephacidin B**

Phil S. Baran, Carlos A. Guerrero, Benjamin D. Hafensteiner, and Narendra B. Ambhaikar*

The stephacidins and related alkaloids are a distinctive class of bioactive prenylated indole alkaloids[1] isolated from various terrestrial and marine fungal sources.[2–4] Recently, we reported an enantioselective route to stephacidin A (**1**, Figure 1).[5] Although our synthesis permitted the assignment of relative configuration, the lack of an authentic sample and an optical rotation measurement left the absolute configuration of **1** a mystery.[7] The highest oxidized member in this family of natural products, avrainvillamide (**3**, first isolated by Fenical et al.),[2c,6] also posed some unanswered questions. Specifically, the unique oxidation pattern (3-alkylidene-3*H*-indole-1-oxide) present in **3** is the first of its sort in a natural product[2] and required new methodology for its installation. Although it appeared logical to target **3** through a natural progression of oxidative transformations from the parent stephacidin A (**1**), the execution of this plan was uncertain. For instance, the benzopyran subunit of **1** is susceptible to oxidation under many of the conditions used for the oxidation of amines to nitrones.[8] Herein, we present the following results: 1) a streamlined enantioselective synthesis of both antipodes of **1**, 2) the absolute configuration of this family of alkaloids, 3) the verification of the structure of avrainvillamide (CJ-17,665; (+)-**3**) through reisolation and total synthesis, 4) an approach to the chemoselective conversion of (+)-**1** into (+)-**3**, and 5) the spontaneous dimerization of (+)-**3** to stephacidin B ((−)-**2**).

Our first synthesis[5] of (−)-**1** could be shortened and rendered more amenable to scale-up by making the modifications as illustrated in Scheme 1. The superfluous protection and oxidation of the ester side chain was avoided by using proline derivative **6**,[9] which was able to undergo peptide coupling with **5**[5] without intramolecular cyclization to form a γ-lactam. This undesired cyclization could be avoided when amine **6** was immediately subjected to peptide coupling to furnish **7**. The yield of the key enolate coupling (**8** to **9**) was improved (61% yield along with 8% recovered starting materials), and the reproducibility of the thermal annulation (**10** to **1**) was enhanced by using sulfolane as solvent at a higher temperature (240 °C). By this route, (+)-**1** or (−)-**1** could be prepared in seven steps (12% overall yield) from readily available **5** and (*R*)- or (*S*)-**6**, respectively. Although one could make an educated guess regarding the absolute configuration of these natural products by comparison to the paraherquamides, brevianamides, and other bicyclo-[2.2.2]diazaoctane alkaloids,[1] we elected to use natural (*S*)-proline until this uncertainty was resolved.

On the basis of the assumption that **3** is produced in nature by oxidation of **1**, we collaborated with Professor Fenical et al. (Scripps Institution of Oceanography) to obtain a sample of natural **3** as the original isolated compound was no longer available. Our hope was that **3** could be reduced to **1** to ascertain its absolute configuration. Careful analysis of the crude extracts indicated the presence of not only avrainvillamide (**3**) but also stephacidin A (**1**). Stephacidin B (**2**) was not detected by LC-MS. With a natural sample of (+)-**1** in hand the issue of absolute configuration could be addressed.[10] As shown in Figure 2, comparison of the CD spectra of synthetic (−)-**1** and natural (+)-**1** revealed that the enantiomer had been synthesized previously in these laboratories. The use of (*R*)-proline to secure the enantiomer of amine **6** eventually led to the preparation of (+)-**1** with the correct absolute configuration (synthetic (+)-**1**: $[\alpha]_D = +68.5$ ($c = 0.35$, 1:1 CH_2Cl_2/MeOH); natural (+)-**1**: $[\alpha]_D = +61.5$ ($c = 0.26$, 1:1 CH_2Cl_2/MeOH).

[*] Prof. Dr. P. S. Baran, C. A. Guerrero, B. D. Hafensteiner, Dr. N. B. Ambhaikar
Department of Chemistry
The Scripps Research Institute
10650 North Torrey Pines Road, La Jolla, CA 92037 (USA)
Fax: (+1) 858-784-7375
E-mail: pbaran@scripps.edu

[**] We are deeply grateful to Professor William Fenical (Scripps Institution of Oceanography) for his invaluable advice and support, and for generously providing samples of the crude extracts of *Aspergillus sp.* (CNC358). We are indebted to Professor Axel Zeeck, Dr. Jennifer Qian-Cutrone of BMS, and Pfizer for authentic samples of avrainvillamide, stephacidin B, and CJ-17,665, respectively. Ms. Sarah Siegel of the Kelly group is acknowledged for expertise in obtaining CD spectra. We thank Dr. D.-H. Huang and Dr. L. Pasternak for assistance with NMR spectroscopic studies, and Dr. G. Suizdak for assistance with mass spectrometry measurements. We thank Biotage for a generous donation of process vials that were used extensively during these studies. Financial support for this work was provided by The Scripps Research Institute, Eli Lilly & Co, GlaxoSmithKline, the Searle Scholarship fund, and the NIH (predoctoral fellowship to C.A.G.). CJ-17,665 is the name given to avrainvillamide isolated independently from a soil sample collected in Venezuela.

Supporting information for this article is available on the WWW under http://www.angewandte.org or from the author.

 © 2005 Wiley-VCH Verlag GmbH & Co. KGaA, Weinheim DOI: 10.1002/anie.200500655

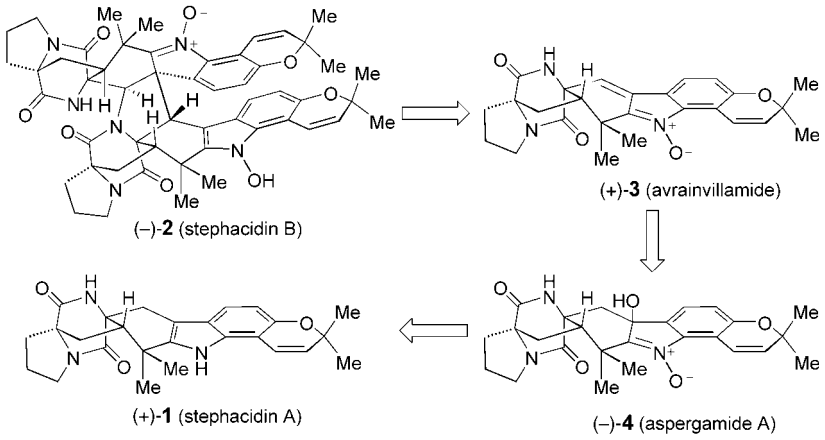
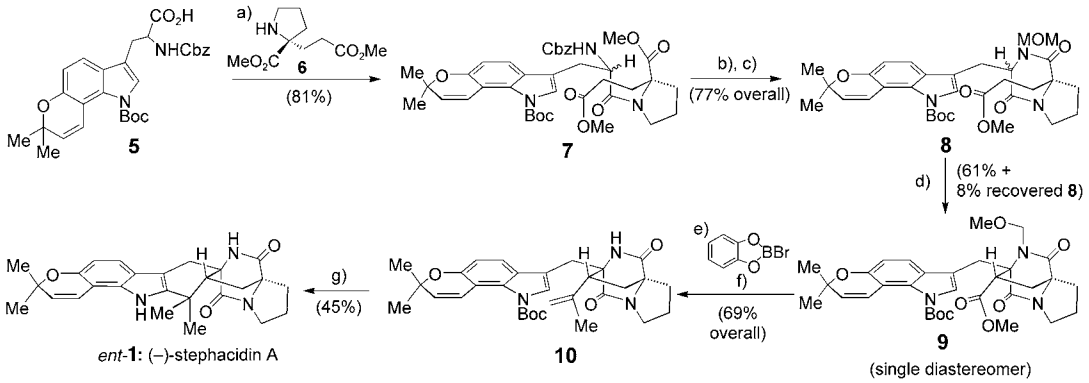


Figure 1. Structures of the stephacidins and related alkaloids along with their proposed[2,3] biogenetic relationships and absolute configuration.

With a shorter synthetic route and the absolute configuration of **1** determined, attention was turned to exploring its conversion into **3**. In the meantime, we had received a sample of aspergamide A (**4**) from Professor Axel Zeeck.[10] Surprisingly, analysis of the material indicated that it had transformed to (+)-**3** by dehydration (Scheme 2). We therefore targeted **4** as a logical precursor to **3**. In principle, the conversion of **1** into **3** could be carried out by chemoselective oxidation of the indole at C3 followed by conversion of the resulting C3-hydroxyindolenine into the corresponding nitrone. In the event, photooxidation with $^1O_2$[11] gave hydroxyindolenine **11** in good yield (Scheme 2). However, all attempts to carry out further oxidation to aspergamide A (**4**) met with failure. A variety of oxidants



Scheme 1. Second-generation enantioselective total synthesis of stephacidin A (**1**). Reagents and conditions: a) **6** (1.0 equiv), HATU (1.1 equiv), iPr$_2$EtN (3.0 equiv), DMF, 25 °C, 12 h, 81%; b) [Pd$_2$(dba)$_3$·CHCl$_3$] (0.2 equiv), Et$_3$SiH (40 equiv), Et$_3$N (2.0 equiv), CH$_2$Cl$_2$, 25 °C, 3.5 h; then DMF/MeOH (3:1), 4 h; 80% overall; c) NaHMDS (1.1 equiv), THF, −78 °C, 30 min then MOMCl (1.4 equiv), THF, −78→25 °C, 1.5 h, 95%; d) LDA (2.2 equiv), THF, −78 °C, 5 min then Fe(acac)$_3$ (2.2 equiv), THF, −78→25 °C, 1 h, 61% **9** with 8% recovered **8**; e) *B*-bromocatecholborane (1.5 equiv), CH$_2$Cl$_2$, 0 °C, 40 min, 78%; f) MeMgBr (5.0 equiv), toluene, 25 °C, 1 h, then Burgess reagent (2.0 equiv), benzene, 50 °C, 30 min, 88% overall; g) sulfolane, 240 °C, 1 h, 45%. Cbz = carbobenzyloxy; Boc = *tert*-butoxycarbonyl; HATU = *O*-(7-azabenzotriazol-1-yl)-*N*,*N*,*N*′,*N*′-tetramethyluronium hexafluorophosphate; DMF = *N*,*N*-dimethylformamide; dba = *trans*, *trans*-dibenzylideneacetone; NaHMDS = sodium bis(trimethylsilyl) amide; MOM = methoxymethyl; LDA = lithium diisopropylamide; acac = acetylacetonate; Burgess reagent = MeO$_2$CN$^-$SO$_2$N$^+$Et$_3$.

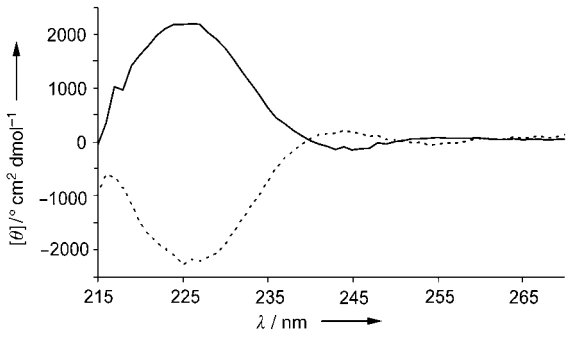
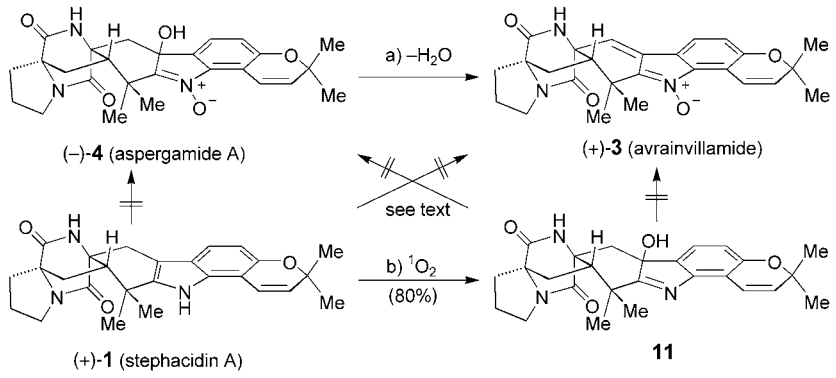


Figure 2. Circular dichroism (CD) spectra (CH$_2$Cl$_2$, 25 °C) of synthetic (−)-**1** (----) and natural (+)-**1** (——). [θ] = molar ellipticity.

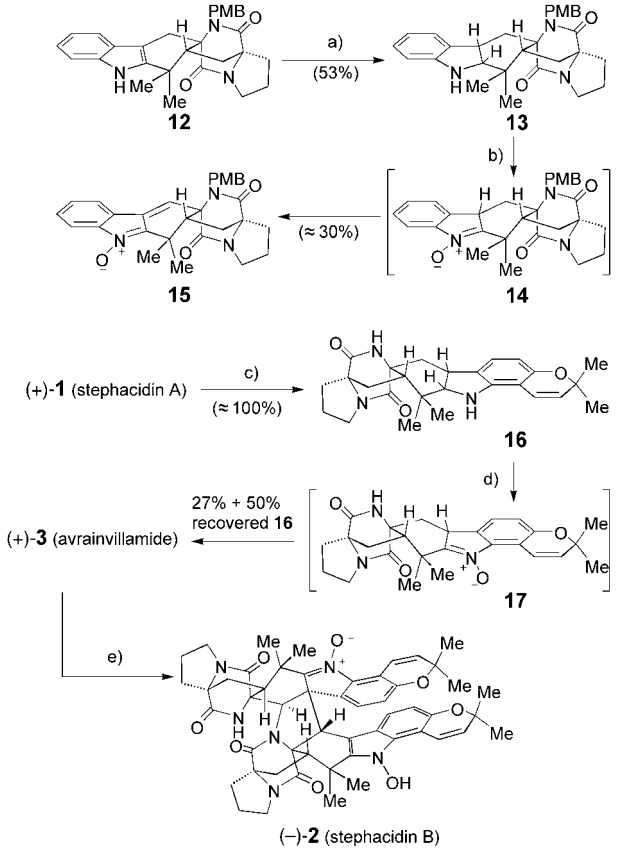


Scheme 2. Attempted conversion of **1** into **3** or **4**. Reagents and conditions: a) likely occurred gradually during storage/shipping, 100%; b) sunlamp, cat. methylene blue, $^3O_2$, MeOH, −28 °C, 30 min; then DMS (100 equiv), −28→25 °C, 10 min, 80%. DMS = dimethyl sulfide.

 © 2005 Wiley-VCH Verlag GmbH & Co. KGaA, Weinheim

that were screened to convert either **1** or **11** into either **3** or **4** were similarly unsuccessful. These shortcomings forced a reevaluation of our planned pathway to avrainvillamide.

In 1971, Somei put forth a provocative hypothesis for the role of 1-hydroxyindoles (tautomers of saturated indolic nitrones) in the biosynthesis and functionalization of indole alkaloids in nature.[12] These highly reactive species are susceptible to nucleophilic attack and dimerization, and undergo a variety of interesting rearrangements. These pioneering studies led us to hypothesize that perhaps such a species would be a viable precursor to **3**. As a proof of principle, model compound **12** was synthesized by a route that paralleled our synthesis of **1**.[13] As shown in Scheme 3, chemoselective reduction of the indole C2–C3 π bond with sodium cyanoborohydride in acetic acid (Gribble reduction)[14] gave indoline **13** (53% yield), poised for Somei oxidation.[12] Treatment of **13** with catalytic $Na_2WO_4{\cdot}2H_2O$ and excess H_2O_2 did not lead to appreciable amounts of the expected 1-hydroxyindole **14**. Instead, we were pleased to find that the major constituent in the crude reaction mixture was the bright yellow α,β-unsaturated nitrone **15** isolated in approximately 30% yield (unoptimized).



Scheme 3. Synthesis of simple avrainvillamide model **15** and the successful conversion of (+)-**1** into (+)-**3** and (−)-**2**. Reagents and conditions: a) $NaBH_3CN$ (10 equiv), AcOH, 25 °C, 12 h, 53%; b) $Na_2WO_4{\cdot}2H_2O$ (0.2 equiv), aq. 35% H_2O_2 (50 equiv), MeOH, H_2O, 25 °C, 6 h, ca. 30%; c) $NaBH_3CN$ (50 equiv), AcOH, 25 °C, 24 h, 93%; d) SeO_2 (0.25 equiv), 35% H_2O_2 (50 equiv), dioxane, 25 °C, 40 h, 27% **3** with 50% recovered **16**; e) Procedure A: Preparative TLC (SiO_2, EtOAc); Procedure B:[6] Et_3N (excess), CH_3CN, 25 °C, 1 h; Procedure C: DMSO, then solvent removal, approx. 2:1 mixture of **3** to **2**, purified by preparative TLC. PMB = *p*-methoxybenzyl; DMSO = dimethyl sulfoxide.

With a method in hand for the desired oxidative conversion, we turned our attention to stephacidin A (**1**) once again. Gribble reduction of synthetic (+)-**1** furnished indoline **16** (Scheme 3) in essentially quantitative yield as a separable but inconsequential mixture of diastereomers. This mixture was subjected to Somei oxidation, which unfortunately provided about 20% yield of (+)-**3** mixed with some inseparable impurities. Alternatively, indoline **16** could be treated with catalytic SeO_2[15] and excess H_2O_2 to provide pure (+)-**3** in 27% isolated yield along with 50% recovered **16** (spectroscopically identical to the samples obtained from Prof. Zeeck and Prof. Fenical and that reported by Myers;[6] synthetic (+)-**3**: $[\alpha]_D = +11$ ($c = 0.1$, $CHCl_3$); natural (+)-**3**: $[\alpha]_D = +10.6$ ($c = 0.17$, $CHCl_3$). We speculate that this cascade oxidation proceeds via the putative intermediate 1-hydroxyindole **17**, which is further oxidized directly to **3** or perhaps first to **4** (Figure 1) followed by loss of water to form (+)-**3**.

In accord with Herzon and Myers' observations in the unnatural series,[6] synthetic (+)-**3** underwent spontaneous dimerization to (−)-**2** under a variety of conditions, including exposure to silica gel (during preparative TLC), base (Et_3N),[6] or even simple evaporation from DMSO (synthetic (−)-**2** was spectroscopically identical to a sample obtained from BMS[2a] and to that reported by Myers;[6] optical rotation of synthetic (−)-**2**: $[\alpha]_D = -33$ ($c = 0.1$, $CDCl_3$); natural (−)-**2** (as received from BMS): $[\alpha]_D = -21.1$ ($c = 0.19$, $CDCl_3$); (+)-**2**:[6] $[\alpha]_D = +91$ ($c = 0.25$, CH_3CN)). The ease with which the dimerization took place actually hampered purification of **3**. Likewise, **2** underwent facile retrodimerization back to a mixture of **3** and **2** during chromatography. A final issue that needed to be addressed was the true identity of CJ-17,665[2d] as slight differences between synthetic **3** and the reported ^{1}H NMR spectra of CJ-17,665 were observed by both us and Herzon and Myers.[6] Comparison (LC-MS, TLC, NMR spectroscopy) with an authentic sample from Pfizer confirms that it is indeed **3**, and, perhaps not surprisingly, the sample contained approximately 20% of stephacidin B (**2**) as judged by ^{1}H NMR spectral analysis and LC-MS.[16] Interestingly, the sample from Pfizer was provided as a (yellow) solution in DMSO, whereas the sample from Professor Zeeck (see above) was a yellow–green powder and contained no stephacidin B (as judged by ^{1}H NMR spectroscopy), which implies that dimerization does not occur over time in the solid state.

The spontaneous (and reversible) dimerization of **3** to **2** is consistent with the known tendency of saturated indolic nitrones (a tautomeric form of a 1-hydroxyindole) to dimerize.[12] Taken together, these findings add further support for Somei's hypothesis regarding the potentially widespread significance of fleeting 1-hydroxyindoles in nature. The new selenium- and tungsten-based protocols reported herein to chemoselectively generate an unsaturated nitrone group from an easily accessible indoline should facilitate the synthesis of avrainvillamide and stephacidin mimics for biological explorations.[16]

Received: February 22, 2005
Revised: March 30, 2005
Published online: May 18, 2005

 © 2005 Wiley-VCH Verlag GmbH & Co. KGaA, Weinheim

Keywords: alkaloids · natural products · stephacidin · total synthesis

[1] a) R. M. Williams, E. M. Stocking, J. F. Sanz-Cervera, *Top. Curr. Chem.* **2000**, *209*, 97 – 173; b) M. Somei, F. Yumada, *Nat. Prod. Rep.* **2005**, *22*, 73 – 103.

[2] a) J. Qian-Cutrone, S. Huang, Y.-Z. Shu, D. Vyas, C. Fairchild, A. Menendez, K. Krampitz, R. Dalterio, S. E. Klohr, Q. Gao, *J. Am. Chem. Soc.* **2002**, *124*, 14556 – 14557; b) J. Qian-Cutrone, K. D. Krampitz, Y.-Z. Shu, L.-P. Chang, S. E. Lowe, U.S. Patent 6,291,461, **2001** [*Chem. Abstr.* **2001**, *135*, 236411]; c) Isolation of avrainvillamide from a marine fungus off the coast of the Bahamas: W. Fenical, P. R. Jensen, X. C. Cheng, U.S. Patent 6,066,635, **2000** [*Chem. Abstr.* **2000**, *132*, 346709]; d) Avrainvillamide was isolated independently from a soil sample collected in Venezuela and named CJ-17,665: Y. Sugie, H. Hirai, T. Inagaki, M. Ishiguro, Y. Kim, Y. Kojima, T. Sakakibara, A. Sakemi, Y. Suzuki, L. Brennan, J. Duignan, L. H. Huang, J. Sutcliffe, N. Kojima, *J. Antibiot.* **2001**, *54*, 911 – 916.

[3] F. von Nussbaum, *Angew. Chem.* **2003**, *115*, 3176 – 3179; *Angew. Chem. Int. Ed.* **2003**, *42*, 3068 – 3071.

[4] For studies towards the total synthesis of the stephacidins or avrainvillamide, see: A. G. Myers, S. B. Herzon, *J. Am. Chem. Soc.* **2003**, *125*, 12080 – 12081; L. A. Adams, C. R. Gray, R. M. Williams, *Tetrahedron Lett.* **2004**, *45*, 4489 – 4493.

[5] P. S. Baran, C. A. Guerrero, N. B. Ambhaikar, B. D. Hafensteiner, *Angew. Chem.* **2005**, *117*, 612 – 615; *Angew. Chem. Int. Ed.* **2005**, *44*, 606 – 609.

[6] While this manuscript was under review, beautiful total syntheses of (−)-avrainvillamide and (+)-stephacidin B were reported: S. B. Herzon, A. G. Myers, *J. Am. Chem. Soc.* **2005**, *127*, 5342 – 5344.

[7] J. Qian-Cutrone, Bristol-Meyers-Squibb, personal communication.

[8] For example, see: V. B. Sharma, S. L. Jain, B. Sain, *Tetrahedron Lett.* **2003**, *44*, 3235 – 3237.

[9] Proline **6** was synthesized by hydroboration, oxidation, esterification, and deprotection of the corresponding Cbz-protected enantiopure allylated proline, see: D. Seebach, M. Boes, R. Naef, W. B. Schweizer, *J. Am. Chem. Soc.* **1983**, *105*, 5390 – 5398; M. G. Hinds, J. H. Welsh, D. M. Brennand, J. Fischer, M. J. Glennie, N. G. J. Richards, D. L. Turner, J. A. Robinson, *J. Med. Chem.* **1991**, *34*, 1777 – 1789.

[10] J. Fuchser, PhD Thesis, University of Göttingen, **1995**.

[11] M. Nakagawa, H. Watanabe, S. Kodato, H. Okajima, T. Hino, J. L. Flippen, B. Witkop, *Proc. Natl. Acad. Sci. USA* **1977**, *74*, 4730 – 4733.

[12] For extensive reviews, see: M. Somei, *Heterocycles* **1999**, *50*, 1157 – 1211; M. Somei, *Adv. Het. Chem.* **2002**, *82*, 101 – 155.

[13] Model **12** had identical spectral properties to those reported, see: R. M. Williams, T. Glinka, E. Kwast, H. Coffman, J. K. Stille, *J. Am. Chem. Soc.* **1990**, *112*, 808 – 821.

[14] G. W. Gribble, P. D. Lord, J. Skotnicki, S. E. Dietz, J. T. Eaton, J. L. Johnson, *J. Am. Chem. Soc.* **1974**, *96*, 7812 – 7814.

[15] S.-I. Murahashi, T. Shiota, *Tetrahedron Lett.* **1987**, *28*, 2383 – 2386.

[16] Detailed experimental procedures and copies of all spectral data for **15**, (+)-**1**, (+)-**3**, and (−)-**2** are available in the Supporting Information.

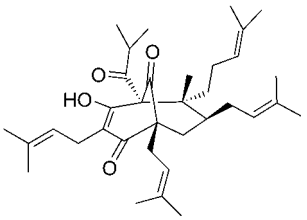
 © 2005 Wiley-VCH Verlag GmbH & Co. KGaA, Weinheim

Ring Systems

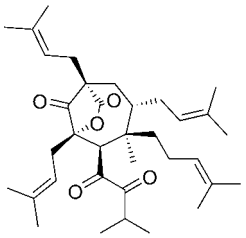
Construction of Highly Functionalized Medium-Sized Rings: Synthesis of Hyperforin and Perforatumone Model Systems**

K. C. Nicolaou, Giacomo E. A. Carenzi, and Valer Jeso*

Hyperforin[1] (**1**) and perforatumone[2] (**2**) are two secondary metabolites with unique molecular architectures and were



1: hyperforin



2: perforatumone

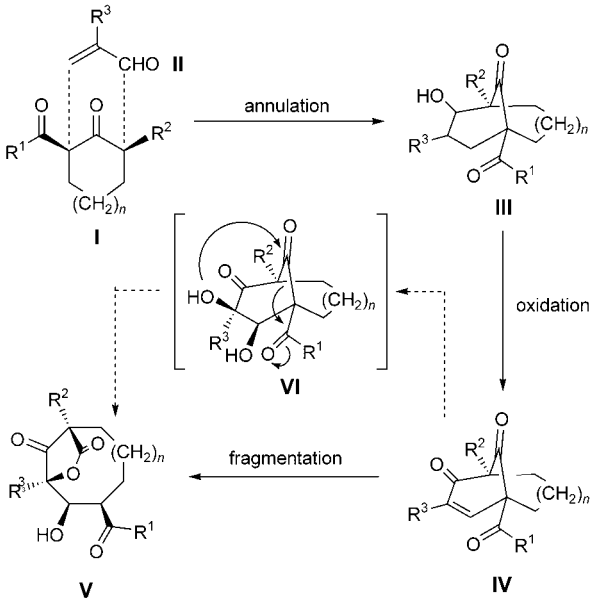
isolated from *Hypericum perforatum* (St. John's wort),[3] famous for its antidepressant properties. Despite their relatively small size, these structures constitute thorny synthetic challenges and remain to this day defiant to chemical synthesis.[4] As part of our efforts to develop synthetic routes to these and other natural and designed polyprenylated phloroglucinol derivatives, we sought a general method of entry into bridged medium-sized rings reminiscent of this class of compounds. Herein we report a novel synthetic sequence to such polyfunctional systems from simple cyclic ketones that involves a series of cascade reactions and delivers model systems of both hyperforin and perforatumone in a stereoselective manner.

Scheme 1 depicts the hypothetical strategy devised for reaching bridged medium (and potentially large)-sized rings of type **III**, **IV**, and **V** from simple building blocks such as disubstituted cyclic ketones **I** and α,β-unsaturated aldehydes **II**. Implementation of this strategy would require annulation of cyclic ketone **I** with the α,β-unsaturated aldehyde **II** to

[*] Prof. Dr. K. C. Nicolaou, Dr. G. E. A. Carenzi, V. Jeso
Department of Chemistry and
The Skaggs Institute for Chemical Biology
The Scripps Research Institute
10550 North Torrey Pines Road, La Jolla, California 92037 (USA)
Fax: (+1) 858-784-2469
E-mail: kcn@scripps.edu
and
Department of Chemistry and Biochemistry
University of California, San Diego
9500 Gilman Drive, La Jolla, California 92093 (USA)

[**] We thank Dr. D. H. Huang, Dr. G. Siuzdak, and Dr. R. Chadha for NMR spectroscopic, mass spectrometric, and X-ray crystallographic assistance, respectively. Financial support for this work was provided by grants from the National Institutes of Health (USA) and the Skaggs Institute for Chemical Biology, and a postdoctoral fellowship from Indena S.p.A (to G.E.A.C.).

 DOI: 10.1002/anie.200500776 © 2005 Wiley-VCH Verlag GmbH & Co. KGaA, Weinheim

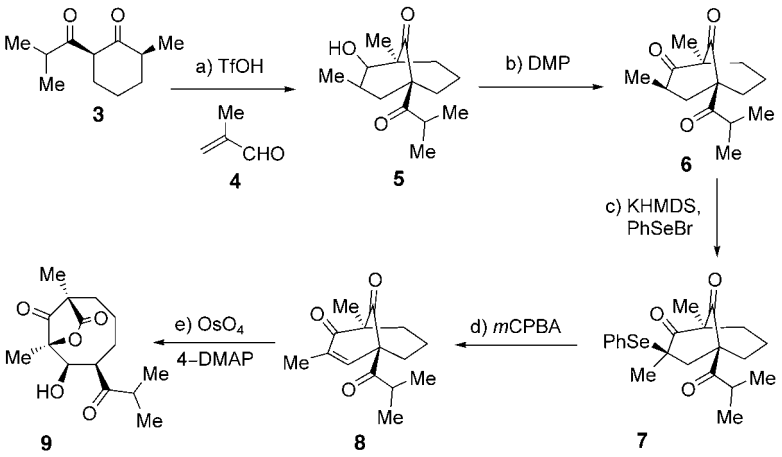


Scheme 1. General strategy for the construction of polyfunctional, bridged medium-sized rings **III**, **IV**, and **V**.

afford the bridged bicyclic system **III**, followed by oxidation of the latter compound to the α,β-unsaturated enone **IV**. Dihydroxylation and subsequent fragmentation of **IV** was expected to afford the ring-expanded product **V** via intermediate **VI**. Notably, besides the two-carbon expansion involved in the fragmentation reaction (**VI**→**V**), this process would concurrently form a new bridge, which being a lactone, can be conveniently disassembled to afford further multifunctional products. Noteworthy is also the choice of annulation partners **I** and **II** in which the fine-tuning of the reactivity of each compound at its two reactive ends was deemed crucial to the success of the anticipated cascade reaction to afford **III**. Favoring the proposed fragmentation was the proximity of the attending hydroxy group to the attached bridging carbonyl moiety, the closeness of its trajectory to the Bürgi–Dunitz angle,[5] and the strain released upon the event.

Delightfully, implementation of this plan with cyclohexanone derivative **3** and 2-methylacrolein (**4**) as starting materials proved successful (Scheme 2). Thus, mixing of diketone **3**[6] with acrolein **4** in CH_2Cl_2, followed by addition of TfOH[7] at −78 °C and slowly allowing the reaction mixture to reach ambient temperature, led to the formation of bicyclic hydroxy diketone **5** in 63% yield, presumably through: 1) initial activation (enolization) of the carbon atom between the two carbonyl groups of the cyclic diketone **3**, followed by 2) intermolecular 1,4-addition to the α,β-unsaturated aldehyde **4**, 3) protonation, and 4) intramolecular aldol reaction.[8] This annulation process is remarkable, not only for its efficiency, but also for its stereoselectivity: only two diastereomers of **5** (≈2:1) were obtained. Four diastereomers could plausibly be formed in this reaction, but the stereochemistry of the observed two was neither determined nor of consequence as both stereocenters were destroyed in the subsequent steps (see below). Continuing with the sequence (Scheme 1), the hydroxy group within the bicyclic product **5** (mixture of two compounds) was oxidized with DMP (81%) to afford tricarbonyl compound **6** (single compound), whose regioselective unsaturation (to afford enone **8** (Scheme 2)) proceeded smoothly through phenylselenide **7** (produced by sequential exposure to KHMDS and PhSeBr, 71%) by oxidation to the corresponding selenoxide with *m*CPBA (98%). Finally, stereoselective dihydroxylation of enone **8** from the *exo* face (OsO_4/4-DMAP) led conveniently to the targeted product **9** (Scheme 2; Table 3) in 68% yield, presumably through fragmentation[9] of the dihydroxy tricarbonyl compound corresponding to **VI** (Scheme 1) whose existence is apparently transient (not detected by TLC). While the resemblance of structures **5**–**8** to that of hyperforin (**1**) is obvious, the architecture of fragmentation product **9** contains one extra carbon in its medium-sized ring compared with that of perforatumone (**2**). Nevertheless, this sequence proved quite useful in synthesizing several other polyfunctional ring systems, including a bridged seven-membered ring corresponding to **2** (i.e. compound **25**, Table 2, Figure 1[10]).

The success of this process encouraged us to explore its optimization, generality, and scope. Table 1 lists the results of a number of experiments carried out to optimize the initial annulation procedure. Besides TfOH, a number of Lewis acids such as $Bi(OTf)_3$,[11] TMSOTf, $Sn(OTf)_2$, $Y(OTf)_3$, and AgOTf performed well, although it is not clear whether they act through the generation of TfOH. Optimizations for this step were also carried out for the five-membered (compound **10**, Table 2) and seven-membered rings (compound **11**, Table 2), as shown in Table 1. From these results we conclude



Scheme 2. Synthesis of polyfunctional ring systems. Reagents and conditions: a) TfOH (0.3 equiv), CH_2Cl_2, −78→25 °C, 1.5 h, 63%; b) DMP (1.5 equiv), py, CH_2Cl_2, 25 °C, 81%; c) KHMDS (1.15 equiv), THF, −41 °C, 2 h; then PhSeBr (1.4 equiv), −41 °C, 15 min, 71%; d) *m*CPBA (2.0 equiv), CH_2Cl_2, −10→0 °C, 30 min, 98%; e) OsO_4 (1.1 equiv), 4-DMAP (1.1 equiv), *t*BuOH/H_2O (1:1), 25 °C, 1 h, 68%. Tf = trifluoromethanesulfonyl; DMP = Dess–Martin periodinane; py = pyridine; KHMDS = potassium bis(trimethylsilyl)amide; *m*CPBA = *m*-chloroperbenzoic acid, 4-DMAP = 4-dimethylaminopyridine.

 © 2005 Wiley-VCH Verlag GmbH & Co. KGaA, Weinheim

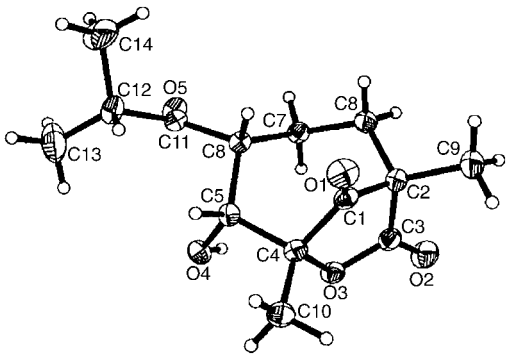


Figure 1. ORTEP drawing of **25** drawn at the 30% probability level.

that the best catalysts for this reaction can be found from the collection of TfOH, TMSOTf, and the triflate salts of Bi, Sn, Y, and Ag.

As shown in Table 2, the five- to ten-membered ring disubstituted ketones (**10**, **3**, **11**–**14**) entered and completed the sequence to the final lactone-bridged fragmentation products (**25**, **9**, **26**–**29**, respectively) via the corresponding intermediate compounds (**15**, **5**, **16**–**19**, and **20**, **8**, **21**–**24**) in varying yields. Thus, while the five- to eight-membered ring ketones performed well and yielded the seven- to ten-membered ring systems (Table 2, entries 1–4), the larger-ring ketones behaved erratically both in the initial (annulation) and in the final (fragmentation) steps to afford the expected products in low yields (Table 2, entries 5 and 6). The higher flexibility of the larger-ring substrates may be responsible for the poor performance of these ring-forming and -rupturing reactions, a hypothesis that was supported by the refusal of an open-chain disubstituted ketone (i.e. 2,4,6-trimethylheptan-3,5-dione) to enter the initial productive step (i.e. the annulation step).

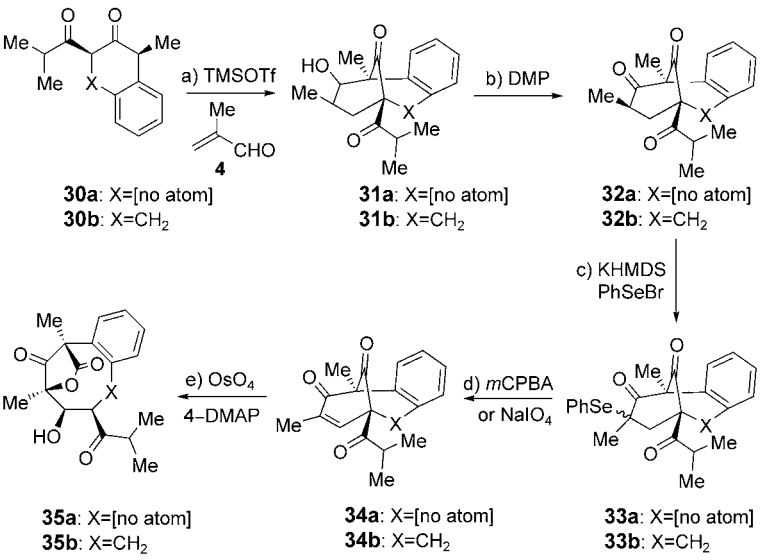
As a further demonstration of the generality of the developed synthesis of polyfunctional medium-sized rings, we attempted the construction of the fully substituted seven- and eight-membered bridged ring systems **31a,b**–**35a,b** (Scheme 3). Each carbon atom of these benzenoid fused ring systems is uniquely substituted, making them both synthetically challenging and potentially useful as biological probes. Thus, the substituted diketones **30a** and **30b** upon reaction with methyl acrolein (**4**) under the influence of TMSOTf, formed the annulated products **31a** (41%) and **31b** (31%), respectively. The latter compounds were then oxidized with DMP to the corresponding triketones **32a** (60%) and **32b** (61%), which were subjected to the phenylselenenylation/oxidation procedure to afford enones **34a** (74%) and **34b** (56%) via **33a** and **33b**. Finally, exposure of **34** to the OsO_4/4-DMAP conditions led directly to the targeted products **35a** (38%; Table 3) and **35b** (31%) through the postulated dihydroxylation/fragmentation cascade (yields unoptimized).

The described synthetic technology offers rapid and convenient build-up of molecular complexity from simple and readily available starting materials. Its application to the synthesis of natural and designed molecules containing medium-sized rings (seven- to ten-membered) appears particularly attractive and should be forthcoming.

Table 1: Optimization of annulation conditions (**I** + **II**→**III**)[a]

Entry	Substrate	Solvent	Equiv	*t* [h]	Product	Yield [%][b]
1	**3**	TfOH	0.3	1.5	**5**	63
2	**3**	$Bi(OTf)_3$	0.3	6	**5**	58
3	**3**	TMSOTf	0.5	1.5	**5**	65
4	**3**	$Sn(OTf)_2$	0.3	24	**5**	68
5	**3**	$Y(OTf)_3$	0.3	40	**5**	43
6	**3**	AgOTf	0.3	40	**5**	53
7	**3**	$CeCl_3$	0.3	24	**5**	0
8	**3**	Nafion	0.3	24	**5**	0
9	**10**	TfOH	0.3	3.5	**15**	33
10	**10**	$Bi(OTf)_3$	0.3	24	**15**	29
11	**10**	TMSOTf	0.5	3	**15**	46
12	**10**	$Sn(OTf)_2$	0.3	24	**15**	33
13	**10**	$Y(OTf)_3$	0.3	30	**15**	37
14	**10**	Nafion	1	24	**15**	0
15	**10**	Dowex	1	24	**15**	0
16	**10**	$Nd(OTf)_3$	0.3	24	**15**	trace
17	**10**	$Eu(OTf)_3$	0.3	24	**15**	trace
18	**10**	TfOH	0.3	24	**16**	56
19	**11**	$Bi(OTf)_3$	0.3	18	**16**	58
20	**11**	TMSOTf	0.5	3	**16**	47
21	**11**	$Sn(OTf)_2$	0.3	24	**16**	51
22	**11**	AgOTf	0.3	30	**16**	trace

[a] See Scheme 1 and Table 2. Reactions were carried out in CH_2Cl_2 at −78→25 °C on a 0.5-mmol scale. [b] Yields of chromatographically and spectroscopically homogeneous materials.

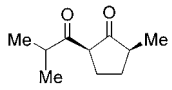
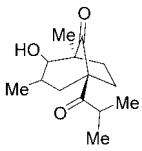
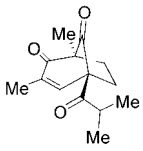
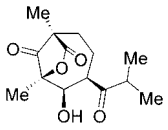
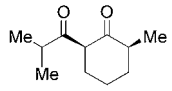
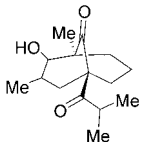
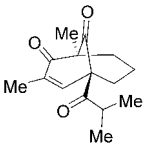
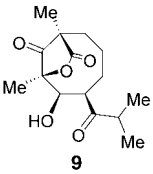
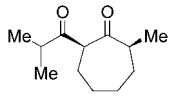
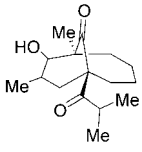
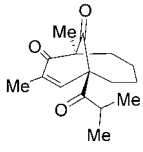
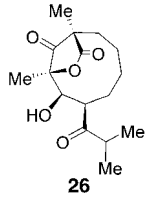
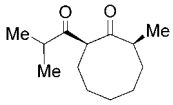
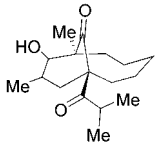
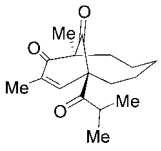
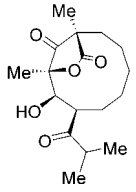
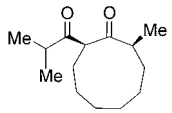
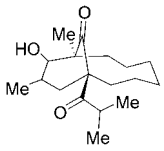
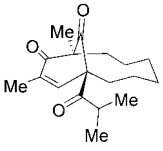
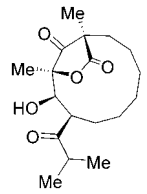
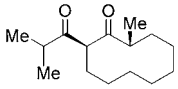
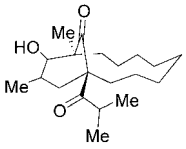
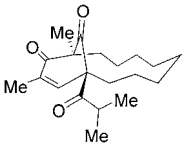
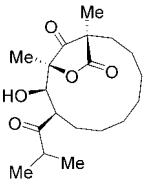


Scheme 3. Synthesis of fused benzenoid medium-sized ring systems **35a** and **35b**. Reagents and conditions: a) TMSOTf (0.5 equiv), CH_2Cl_2, −78→25 °C, 1.5 h, 41% (**31a**), 31% (**31b**); b) DMP (1.5 equiv), py (10 equiv), CH_2Cl_2, 25 °C, 3 h, 60% (**32a**), 61% (**32b**); c) KHMDS (1.15 equiv), THF, −41 °C, 2 h; then PhSeBr (1.4 equiv), −41 °C, 52% (**33a**), KHMDS (1.15 equiv), THF, −41 °C, 2 h; then PhSeBr (1.4 equiv), −78 °C, 50% (**33b**); d) *m*CPBA (2.0 equiv), CH_2Cl_2, −10→0 °C, 30 min, 74% (**34a**), $NaIO_4$ (10.0 equiv), $NaHCO_3$ (5.0 equiv), MeOH/H_2O (4:1), 0→25 °C, 56% (**34b**); e) OsO_4 (1.1 equiv), 4-DMAP (1.1 equiv), *t*BuOH/H_2O (1:1), 25 °C, 38% (**35a**) 31% (**35b**). TMS = trimethylsilyl.

Received: March 2, 2005
Published online: May 13, 2005

 © 2005 Wiley-VCH Verlag GmbH & Co. KGaA, Weinheim

Table 2: Synthesis of highly functionalized medium ring systems by annulation-oxidation-fragmentation cascade[a]

Entry	Substrate	Annulation Product	Yield [%][b]	Oxidation Product	Yield [%][b,c]	Fragmentation Product	Yield [%][b]
1[d]	 **10**	 **15**	46	 **20**	37	 **25**	39
2[e]	 **3**	 **5**	68	 **8**	57	 **9**	68
3[f]	 **11**	 **16**	58	 **21**	38	 **26**	53
4[g]	 **12**	 **17**	30	 **22**	35	 **27**	56
5[d]	 **13**	 **18**	4[h]	 **23**	58	 **28**	21
6[d]	 **14**	 **19**	4[h]	 **24**	60	 **29**	27

[a] Reactions were carried out on a 0.1–5.0-mmol scale under the conditions specified in Scheme 2. [b] Yields of chromatographically and spectroscopically homogeneous materials. [c] Overall yield for the three steps from annulation product. [d] TMSOTf was used as a catalyst for the annulation step. [e] $Sn(OTf)_2$ was used as a catalyst for the annulation step. [f] $Bi(OTf)_3$ was used as a catalyst for the annulation step. [g] TfOH was used as a catalyst for the annulation step. [h] Yield estimated from the pure ketone obtained after oxidation with DMP (the annulation product was contaminated by inseparable oligomeric material).

Keywords: annulation · fragmentation · medium-sized rings · natural products · synthetic methods

[1] a) A. I. Gurevich, V. N. Dobrynin, M. N. Kolosov, S. A. Popravko, I. D. Ryabova, B. K. Chennov, N. A. Derbentseva, B. E. Aizenman, A. D. Garagulya, *Antibiotiki* **1971**, *6*, 510–513; b) N. S. Bystrov, B. K. Chernov, V. N. Dobrynin, M. N. Kolosov, *Tetrahedron Lett.* **1975**, 2791–2794.

[2] J. Wu, X.-F. Cheng, L. J. Harrison, S.-H. Goh, K.-Y. Sim, *Tetrahedron Lett.* **2004**, *45*, 9657–9659.

[3] For a review on the chemistry, pharmacology, and clinical properties of St. John's wort (*Hypericum perforatum L.*) see: J. Barnes, L. A. Anderson, J. D. Phillipson, *J. Pharm. Pharmacol.* **2001**, *53*, 583–600.

 © 2005 Wiley-VCH Verlag GmbH & Co. KGaA, Weinheim

Table 3: Selected physical properties for compounds **8**, **9**, and **35a**.

8: $R_f = 0.48$ (silica gel, hexanes/EtOAc 7:3); IR (film): $\tilde{\nu}_{max} = 2978$, 2931, 1725, 1707, 1666, 1448, 1378, 1278, 1102 cm^{-1}; ^1H NMR (300 MHz, $CDCl_3$): $\delta = 6.91$ (s, 1H), 2.89 (sept, $J = 6.6$ Hz, 1H), 2.35 (td, $J = 7.2$ Hz, 1H), 2.01–1.99 (m, 1H), 1.96 (s, 3H), 1.88–1.83 (m, 1H), 1.68–1.46 (m, 3H), 1.21 (s, 3H), 1.14 (d, $J = 6.6$ Hz, 3H), 1.11 ppm (d, $J = 6.6$ Hz, 3H); ^{13}C NMR (75 MHz, $CDCl_3$): $\delta = 212.4$, 207.9, 199.7, 140.3, 140.2, 66.4, 62.5, 41.7, 38.8, 32.5, 20.1, 19.9, 18.4, 16.2, 16.0 ppm; HRMS (FAB) (%): calcd for $C_{15}H_{20}O_3Na$ [M+Na^+]: 271.1305; found: 271.1304

9: $R_f = 0.18$ (silica gel, hexanes/EtOAc 7:3); IR (film): $\tilde{\nu}_{max} = 3459$, 2978, 2931, 1742, 1707, 1454, 1378 cm^{-1}; ^1H NMR (300 MHz, $CDCl_3$): $\delta = 4.20$ (br s, 1H), 3.17–3.13 (m, 1H), 2.70 (sept, $J = 6.8$ Hz, 1H), 2.39–2.30 (m, 1H), 1.97–1.93 (m, 1H), 1.86–1.80 (m, 2H), 1.55 (s, 3H), 1.42–1.32 (m, 1H), 1.26 (s, 3H), 1.06 (d, $J = 6.8$ Hz, 3H), 1.02 ppm (d, $J = 6.8$ Hz, 3H); ^{13}C NMR (75 MHz, $CDCl_3$): $\delta = 217.2$, 216.8, 175.8, 91.9, 76.7, 51.1, 48.7, 39.7, 38.7, 23.1, 22.6, 22.4, 20.2, 19.7, 17.6 ppm; HRMS (FAB) (m/z): calcd for $C_{15}H_{23}O_5$ [M+H^+]: 283.1540; found: 283.1548

35a: $R_f = 0.11$ (silica gel, hexanes/EtOAc 7:3); IR (film): $\tilde{\nu}_{max} = 3434$, 2967, 2919, 1758, 1725, 1453, 1372, 1243, 1095, 1057 cm^{-1}; ^1H NMR (300 MHz, $CDCl_3$): $\delta = 7.47$–7.32 (m, 3H), 7.07–7.00 (m, 1H), 5.06 (d, $J = 3.3$ Hz, 1H), 4.35 (d, $J = 3.3$ Hz, 1H), 2.72 (sept, $J = 6.8$ Hz, 1H), 1.89 (s, 3H), 1.40 (s, 3H), 1.19 (d, $J = 6.8$ Hz, 1H), 1.05 ppm (d, $J = 6.8$ Hz, 1H); ^{13}C NMR (75 MHz, $CDCl_3$): $\delta = 211.7$, 201.4, 168.9, 136.1, 132.0, 130.9, 130.0, 129.3, 126.3, 80.2, 73.0, 60.4, 58.3, 38.7, 22.7, 19.7, 19.6, 16.0 ppm; HRMS (FAB) (m/z): calcd for $C_{18}H_{21}O_5$ [M+H^+]: 317.1383; found: 317.1390

[4] For synthetic studies toward members of this class of natural products, see: a) K. C. Nicolaou, J. A. Pfefferkorn, S. Kim, H. X. Wei, *J. Am. Chem. Soc.* **1999**, *121*, 4724–4725; b) K. C. Nicolaou, J. Pfefferkorn, G.-Q. Cao, S. Kim, J. Kessabi, *Org. Lett.* **1999**, *1*, 807–810; c) H. Usuda, M. Kanai, M. Shibasaki, *Org. Lett.* **2002**, *4*, 859–862; d) H. Usuda, M. Kanai, M. Shibasaki, *Tetrahedron Lett.* **2002**, *43*, 3621–3624; e) S. J. Spessard, B. M. Stoltz, *Org. Lett.* **2002**, *4*, 1943–1946; f) G. A. Kraus, T. H. Nguyen, I. Jeon, *Tetrahedron Lett.* **2003**, *44*, 659–661; g) R. Ciochina, R. B. Grossman, *Org. Lett.* **2003**, *5*, 4619–4621.

[5] a) H.-B. Bürgi, J. D. Dunitz, E. Shefter, *Acta Crystallogr. Sect. B.* **1974**, *30*, 1517–1527; b) H.-B. Bürgi, *Angew. Chem.* **1975**, *87*, 461–475; *Angew. Chem. Int. Ed. Engl.* **1975**, *14*, 460–473.

[6] The starting 1,3-diketones were synthesized from the corresponding 2-methyl cyclic ketones: A. R. Katritzky, A. Pastor, *J. Org. Chem.* **2000**, *65*, 3679–3682.

[7] For the use of TfOH and related catalysts to induce Michael additions of β-ketoesters to α,β-unsaturated carbonyl compounds, see: a) H. Kotsuki, K. Arimura, T. Ohishi, R. Maruzasa, *J. Org. Chem.* **1999**, *64*, 3770–3773; for the use of a palladium triflate catalyst to facilitate Michael addition of 1,3-dicarbonyl compounds to enones, see: b) Y. Hamashima, D. Hotta, M. Sodeoka, *J. Am. Chem. Soc.* **2002**, *124*, 11240–11241.

[8] For related annulations, see: a) D. Gravel, M. Labelle, *Can. J. Chem.* **1985**, *63*, 1874–1883; b) T. Kawabata, M. Kato, T. Mizugaki, K. Ebitani, K. Kaneda, *Chem. Eur. J.* **2005**, *11*, 288–297.

[9] For related fragmentations, see: a) L. Verotta, E. Lovaglio, O. Sterner, G. Appendino, E. Bombardelli, *Eur. J. Org. Chem.* **2004**, 1193–1197; b) L. Verotta, E. Lovaglio, O. Sterner, G. Appendino, E. Bombardelli, *J. Org. Chem.* **2004**, *69*, 7869–7874.

[10] CCDC-265275 (**25**) contains the supplementary crystallographic data for this paper. These data can be obtained free of charge from the Cambridge Crystallographic Data Centre via www.ccdc.cam.ac.uk/data_request/cif.

[11] H. Gaspard-Iloughmane, C. Le Roux, *Eur. J. Org. Chem.* **2004**, 2517 2532.

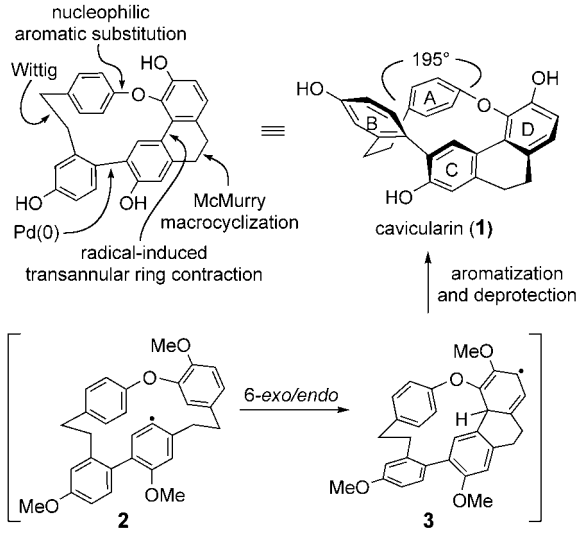
 © 2005 Wiley-VCH Verlag GmbH & Co. KGaA, Weinheim

Natural Product Synthesis

Total Synthesis of Cavicularin and Riccardin C: Addressing the Synthesis of an Arene That Adopts a Boat Configuration**

David C. Harrowven, Timothy Woodcock, and Peter D. Howes*

From a structural perspective cavicularin (**1**), from the liverwort *Cavicularia densa*,[1] is one of the most unusual natural products to have been isolated in the last decade. It comprises a macrocyclic core that contains dibenzyl and dihydrophenanthrene units conjoined by a biaryl bond and an ether linkage. This core imparts such strain on the system that one of the arenes, ring A, adopts a boatlike configuration and is twisted out of the plane by some 15° in the solid state. Herein, we describe the first total synthesis of cavicularin (**1**), in which a radical-induced transannular ring contraction features as a key step (Scheme 1).



Scheme 1. Synthetic strategy to cavicularin (**1**).

In planning the synthesis of cavicularin, we identified two problems that required special consideration: one was the obvious kinetic barrier to closure of the strained macrocycle;

[*] Dr. D. C. Harrowven, T. Woodcock
School of Chemistry, University of Southampton
Highfield, Southampton, SO171BJ (UK)
Fax: (+44) 2380-596805
E-mail: dch2@soton.ac.uk
Dr. P. D. Howes
GlaxoSmithKline Medicines Research Centre
Gunnels Wood Road, Stevenage, SG12NY (UK)

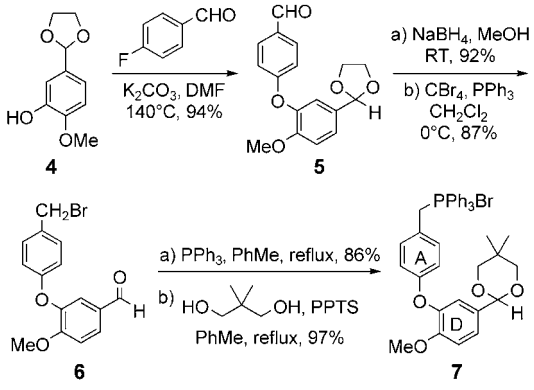
[**] Financial support from GlaxoSmithKline, Pfizer, and the EPSRC is gratefully acknowledged. Dr. Mark Bunnage (Pfizer) is thanked for helpful discussions.

Supporting information for this article is available on the WWW under http://www.angewandte.org or from the author.

 DOI: 10.1002/anie.200500466 © 2005 Wiley-VCH Verlag GmbH & Co. KGaA, Weinheim

the other was a thermodynamic constraint imposed by the need to distort arene A. We felt that both of these problems could be resolved by employing a radical-induced, transannular ring-contraction strategy, such as **2**→**3** (Scheme 1).[2] In particular, by employing a larger and less-strained macrocycle as a precursor the kinetic burden would be transferred to the ring-contraction step, in which the close proximity of the aryl radical intermediate to arene D offered good prospects for a favorable outcome. It also seemed likely that cyclization could proceed without significant distortion of arene A. Indeed, that would occur in the second phase of the reaction with the collapse of **3** to cavicularin trimethyl ether, with the thermodynamic cost of bending the arene compensated by the rearomatization of arene D.[3,4]

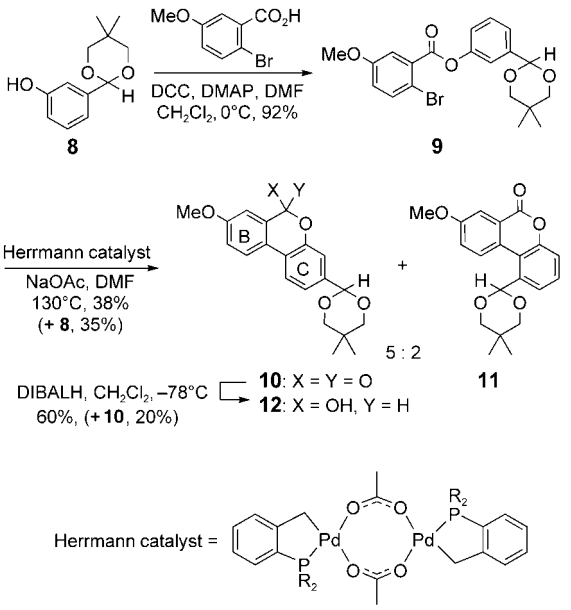
Our synthesis began with the protection of isovanillin as its dioxolane acetal **4**. Union of **4** with 4-fluorobenzaldehyde then gave diaryl ether **5**,[6] which was reduced with sodium borohydride to the corresponding alcohol. Bromination with CBr_4/PPh_3 additionally unmasked the latent aldehyde function to give **6**, which, on sequential treatment with PPh_3 and neopentyl glycol, led to the suitably functionalized AD ring system **7** (Scheme 2).



Scheme 2. Synthesis of the AD ring biaryl ether **7**. DMF = *N*,*N*-dimethylformamide, PPTS = pyridinium *p*-toluenesulfonate.

Construction of the BC ring system began with the protection of 3-hydroxybenzaldehyde as its neopentyl glycol acetal **8**. Coupling of **8** and 2-bromo-5-methoxybenzoic acid in the presence of DCC then gave ester **9**, which, on heating in the presence of the Herrmann catalyst, underwent cyclization to benzo[*c*]chromen-6-ones **10** and **11** (Scheme 3).[6] Though low-yielding, the rapidity with which this sequence led to the BC ring system of cavicularin (**1**) offered practical advantages over the alternative routes investigated. Most notably, reduction of **10** with DIBALH provided lactol **12**, which was appropriately functionalized for union with **7** and primed to facilitate regioselective iodination of arene C at a later stage.

The coupling of phosphonium salt **7** and lactol **12** by using standard Wittig protocols proved troublesome at first. However, through the simple expedient of adding 18-crown-6 to the reaction mixture, stilbene **13** was formed in 66% yield as a mixture of *E* and *Z* isomers in 2:1 ratio.[7] Next, reduction of the alkene gave phenol **14**, which was selectively iodinated under basic conditions to give tetraarene **15**.[8] Protection of



Scheme 3. Synthesis of the BC ring system. DCC = dicyclohexylcarbodiimide, DMAP = 4-dimethylaminopyridine, DIBALH = diisobutylaluminum hydride, R = *o*-tolyl.

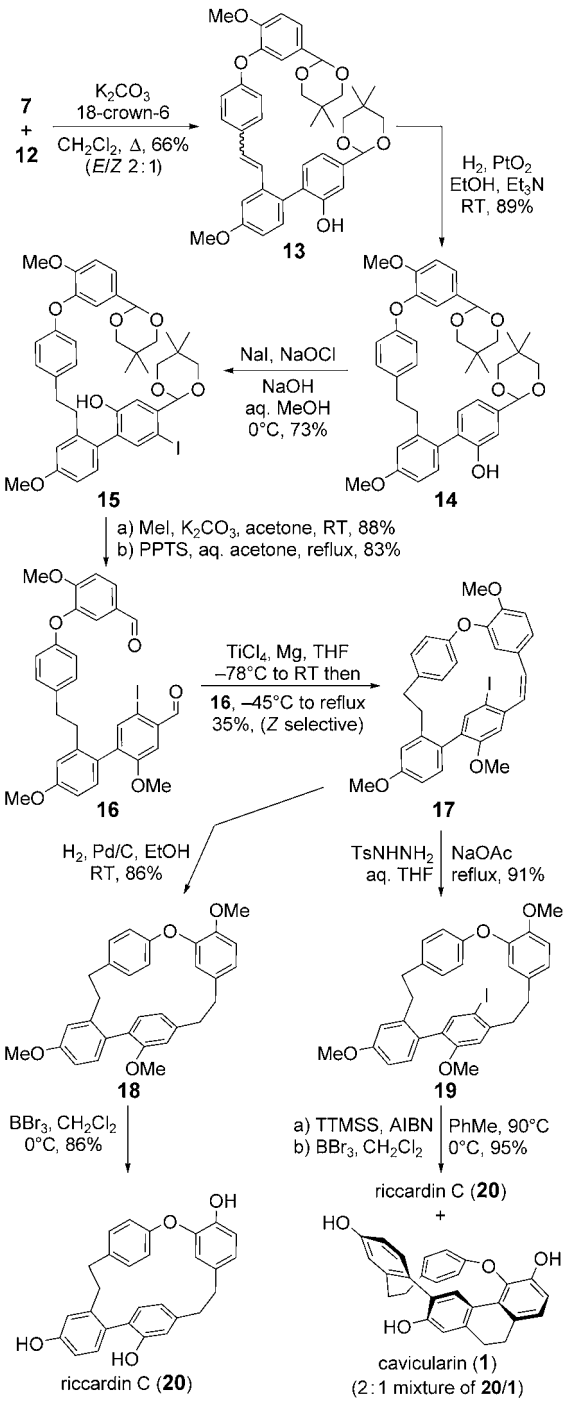
the phenol group as its methyl ether and removal of the acetal functions then provided dialdehyde **16**, which underwent macrocyclization on treatment with low-valent titanium to yield (*Z*)-**17** (Scheme 4).[9]

We were now in a position to address the synthesis of riccardin C (**20**) and cavicularin (**1**). Catalytic hydrogenation of **17** using palladium on carbon simultaneously effected hydrogenolysis of the aryl iodide to give riccardin C trimethyl ether (**18**). Deprotection of the phenolic groups with boron tribromide then gave riccardin C (**20**) in 86% yield.[10,11] Reduction of the alkene in **17** also proceeded smoothly to give **19** without concomitant reduction of the aryl iodide.[12] A solution of macrocycle **19** in toluene was then heated at 90 °C with TTMSS and AIBN to induce homolysis of the carbon–iodine bond.[13] This procedure gave an inseparable mixture of riccardin C trimethyl ether (**18**) and cavicularin trimethyl ether in 2:1 ratio. Exposure of the mixture to boron tribromide provided riccardin C (**20**) and cavicularin (**1**), which were readily separated by column chromatography. Pleasingly, data recorded on our synthetic samples matched those reported for the natural products.[1,10,11]

In summary, we have completed the first total synthesis of cavicularin (**1**), a cyclic dibenzyldihydrophenanthrene ether from *Cavicularia densa*, in which one of the arenes is under such strain that it is forced to adopt a boat configuration. The key step involved the addition of an aryl radical intermediate to a proximal arene to facilitate a transannular ring contraction with concomitant bending of aromatic ring A (Scheme 1). The macrocyclic precursor **19** was also transformed into riccardin C (**20**) to complete the shortest synthesis of this natural product described to date.[11]

Received: February 7, 2005
Published online: May 18, 2005

 © 2005 Wiley-VCH Verlag GmbH & Co. KGaA, Weinheim



Scheme 4. Total synthesis of cavicularin (**1**) and riccardin C (**20**). Ts = *p*-toluenesulfonyl, TTMSS = tris(trimethylsilyl)silane, AIBN = azobis(isobutyronitrile).

Keywords: arenes · macrocycles · radical reactions · ring contraction · total synthesis

[1] M. Toyota, T. Yoshida, Y. Kan, S. Takaoka, Y. Asakawa, *Tetrahedron Lett.* **1996**, *37*, 4745 – 4748.

[2] D. C. Harrowven, M. I. T. Nunn, D. R. Fenwick, *Tetrahedron Lett.* **2002**, *43*, 3185 – 3187.

[3] A related reaction has been used in the synthesis of [5]helicenes that provides precedent for this hypothesis; see: a) D. C. Harrowven, M. I. T. Nunn, D. R. Fenwick, *Tetrahedron Lett.* **2002**, *43*, 3189 – 3191; b) D. C. Harrowven, M. I. T. Nunn, D. R. Fenwick, *Tetrahedron Lett.* **2002**, *43*, 7345 – 7347.

[4] The mechanism of rearomatization has been the subject of much discussion; for some leading references, see: a) D. C. Harrowven, B. J. Sutton, S. Coulton, *Tetrahedron* **2002**, *58*, 3387 – 3400; b) A. L. J. Beckwith, V. W. Bowry, W. R. Bowman, E. Mann, J. Parr, J. M. D. Storey, *Angew. Chem.* **2004**, *116*, 97 – 100; *Angew. Chem. Int. Ed.* **2004**, *43*, 95 – 98.

[5] a) G. W. Yeager, D. N. Schissel, *Synthesis* **1991**, 63 – 68; b) O. Dann, J. Ruff, H.-P. Wolff, H. Griessmeier, *Liebigs Ann. Chem.* **1984**, 409 – 425; c) G. M. Keserüe, Z. Dienes, M. Nogradi, M. Kajtar-Peredy, *J. Org. Chem.* **1993**, *58*, 6725 – 6728.

[6] a) D. E. Ames, A. Opalko, *Tetrahedron* **1984**, *40*, 1919 – 1926; b) T. Harayama, H. Yasuda, *Heterocycles* **1997**, 61 – 64; c) A. V. R. Rao, T. K. Chakraborty, S. P. Joshi, *Tetrahedron Lett.* **1992**, *33*, 4045 – 4048; d) G. Bringmann, D. Menche, J. Muehlbacher, M. Reichert, N. Saito, S. S. Pfeiffer, B. H. Lipshutz, *Org. Lett.* **2002**, *4*, 2833 – 2836.

[7] T. Eicher, S. Fey, W. Puhl, E. Büchel, A. Speicher, *Eur. J. Org. Chem.* **1998**, 877 – 888.

[8] K. J. Edgar, S. N. Falling, *J. Org. Chem.* **1990**, *55*, 5287 – 5291.

[9] For a related macrocyclization reaction leading to bazzanin A tetramethyl ether, see: A. Speicher, J. Kolz, R. P. Sambanje, *Synthesis* **2002**, 2503 – 2512.

[10] Riccardin C was first isolated from the liverwort *Reboulia hemisphaerica*, see: a) Y. Asakawa, R. Matsuda, *Phytochemistry* **1982**, *21*, 2143 – 2144; b) Y. Asakawa, M. Toyota, Z. Taira, T. Takemoto, M. Kido, *J. Org. Chem.* **1983**, *48*, 2164 – 2167; it displays in vitro cytotoxicity against nasal epidermoid carcinoma cells and weak inhibitory activity against HIV-1 reverse transcriptase, see: c) T. Yoshida, T. Hashimoto, S. Takaoka, Y. Kan, M. Tori, Y. Asakawa, J. M. Pezzuto, T. Pengsuparp, G. A. Cordell, *Tetrahedron* **1996**, *52*, 14487 – 14500.

[11] For previous total syntheses of riccardin C, see: a) A. Gottsegen, M. Nogradi, B. Vermes, M. Kajtar-Peredy, E. Bihatsi-Karsai, *J. Chem. Soc. Perkin Trans. 1* **1990**, 315 – 320; b) A. Gottsegen, M. Nogradi, B. Vermes, M. Kajtar-Peredy, E. Bihatsi-Karsai, *Tetrahedron Lett.* **1988**, *29*, 5039 – 5040, and reference [6].

[12] D. C. Harrowven, B. J. Sutton, S. Coulton, *Org. Biomol. Chem.* **2003**, *1*, 4047 – 4057.

[13] C. Chatgilialoglu, *Organosilanes in Radical Chemistry*, Wiley, Chichester, UK, **2003**.

 © 2005 Wiley-VCH Verlag GmbH & Co. KGaA, Weinheim

Bioorganic Chemistry

An Artificial Riboflavin Receptor Prepared by a Template Analogue Imprinting Strategy**

Panagiotis Manesiotis, Andrew J. Hall, Julien Courtois, Knut Irgum, and Börje Sellergren**

Molecular imprinting has resulted in a range of robust polymer-based receptors that are being considered for use in a variety of applications based on molecular recognition.[1] The technique entails polymerization of mono- and polyfunctional monomers in the presence of a template, whose subsequent removal leaves sites that can be reoccupied by the template or a closely related compound. These synthetic receptors are distinguished by their robustness and ease of synthesis, but they also have drawbacks, notably their poor water compatibility and, with notable exceptions,[2–5] the lack of strategies for imprinting water-soluble target molecules. One approach towards overcoming the latter is to use a non-aqueous imprinting protocol, in which lipophilic templates representing a close structural analogue or substructure of the target are employed.[6,7] Here, a solvent/porogen is chosen such that the intrinsically weak monomer–template interactions based, for example, on hydrogen bonding, electrostatics, or charge transfer, are stabilized. Thus, the use of solvents with low polarity and hydrogen bonding strength is generally favored. Although polymers prepared by this route have displayed selective binding of their targets under aqueous conditions, the effects were typically too weak to be of practical value. Following this approach, we report here on molecularly imprinted polymers (MIPs) that recognize their targets (riboflavin) effectively under such conditions (Figure 1). Careful fine-tuning of the synthesis conditions with respect to the choice of template and cross-linking monomer proved critical and resulted in a polymer which strongly and selectively bound riboflavin in water-rich media similar to those found in common alcoholic beverages.[8]

[*] Dipl.-Chem. P. Manesiotis, Dr. A. J. Hall, Priv.-Doz. Dr. B. Sellergren
Institut für Umweltforschung
Universität Dortmund
Otto Hahn Strasse 6, 44221 Dortmund
Fax: (+49) 231-755-4084
E-mail: andy@infu.uni-dortmund.de
borje@infu.uni-dortmund.de
Dipl.-Chem. J. Courtois, Prof. Dr. K. Irgum
Department of Chemistry
Umeå Universitet
90187 Umeå (Sweden)

[**] This work was supported in part by the European Community's programme for Training and Mobility of Researchers (TMR) under contract: FMRX-CT-98-0173 (MICA) and the European Community's Improving Human Potential Programme under contract HRPN-CT-2002–00189 (AquaMIP). Further financial support from Heineken Technical Services (Zoeterwoude, NL) is gratefully acknowledged.

Supporting information for this article is available on the WWW under http://www.angewandte.org or from the author.

For the design of the polymers, we first turned our attention to the functional monomer. The flavin ring system contains an imide functionality which contains an acceptor-donor-acceptor (ADA) array of hydrogen-bonding sites capable of interacting with receptors containing a complimentary DAD array. Representative of such molecules are 2,6-bisamidopyridines, whose ability to bind to imide functionalities has been widely studied.[9] Accordingly, we chose 2,6-bis(acrylamido)pyridine (BAAPy) as our functional monomer (Scheme 1).[10,11]

With regards the choice of template, we focused on flavin and riboflavin derivatives having high solubility in typical imprinting solvents, in this case chloroform (Scheme 1), initially attempting to use N(10)-alkylflavins.[12] However, the solubility of these compounds in chloroform was found to be too low (ca. 16 mM for **1** and only ca. 6 mM for **2**) for a conventional template/monomer molar ratio to be used. As expected, polymers prepared using these analogues as templates exhibited low imprinting factors and capacities (see below). Riboflavin tetraesters performed better in this regard, their solubility in chloroform being far greater than that of the N(10)-alkylflavins described above (RfAc: 0.2 M, RfPr: 0.6 M, RfBu: 0.8 M). Furthermore, the use of these tetraesters of various sizes allowed the investigation of other effects of the templating process, for example, size-exclusion phenomena. A ^{1}H NMR titration was performed in $CDCl_3$ using **1** as the guest and BAAPy as the host to check the likely effects of these pairings of template(s) and functional monomer. The raw data were fitted by nonlinear regression to a 1:1 binding isotherm and an association constant of $K_a = 570 \pm 35\ M^{-1}$ was extracted.[13] This value is in accordance with association constants obtained previously with similar systems,[14] and implies that the major part of the template is complexed prior to polymerization. The magnitude of the K_a value, along with the observed complexation-induced shifts of protons in the NMR spectra of both the host and guest, support the presence of a three-point hydrogen-bonded complex as depicted in Figure 1.

The use of the riboflavin esters as templates leads to MIPs[15] that exhibit extremely strong retention of their respective templates (Figure 2). Indeed, modification of the mobile phase with acetic acid was necessary to reduce the retentions to a workable time frame. Anticipating that the primary electrostatic driving force causing this retention was the three-point hydrogen-bond array, we also challenged the RfAc-imprinted and control polymers with the *N*-methylated template analogue **6**. We observed total suppression of the retention on both the imprinted and control polymers, thus providing proof that the complexation mode observed in solution is also preserved in the polymer. Furthermore, evidence of size-exclusion effects is seen in the different polymers. Thus, P(RfAc) retains its template to a greater extent than the other analytes, while the retentions of RfAc and RfPr on P(RfPr) are very similar. This result suggests that the polymeric binding site formed around RfAc is able to exclude the larger analytes, while the polymeric binding sites formed around RfPr appear to still offer a "good fit" for the smaller analyte. The larger analyte RfBu is less strongly retained on both these polymers. However, the retention of

 © 2005 Wiley-VCH Verlag GmbH & Co. KGaA, Weinheim DOI: 10.1002/anie.200500342

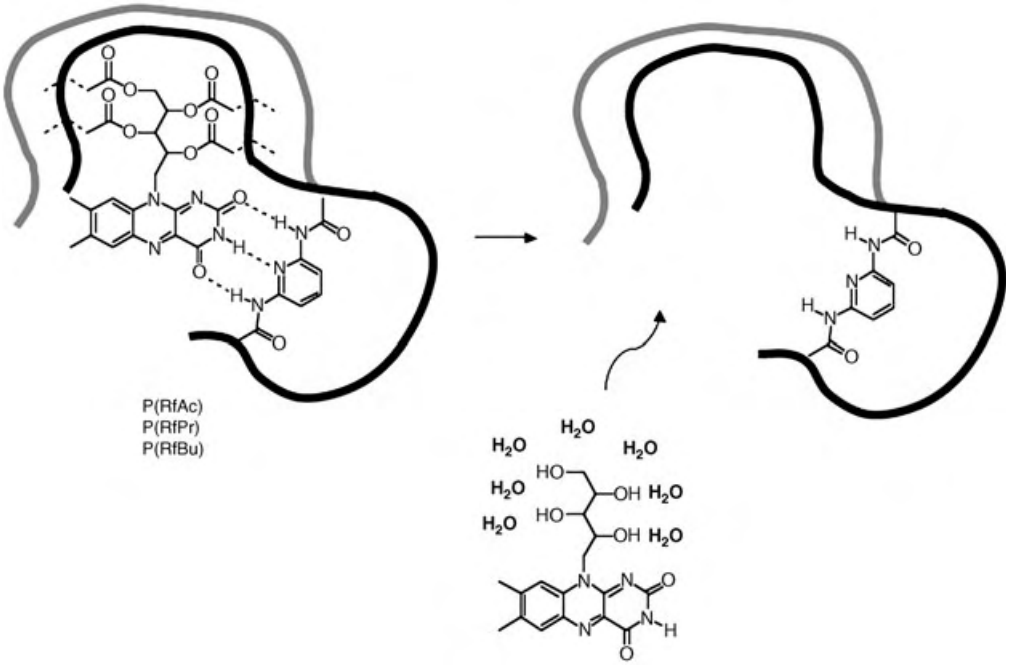
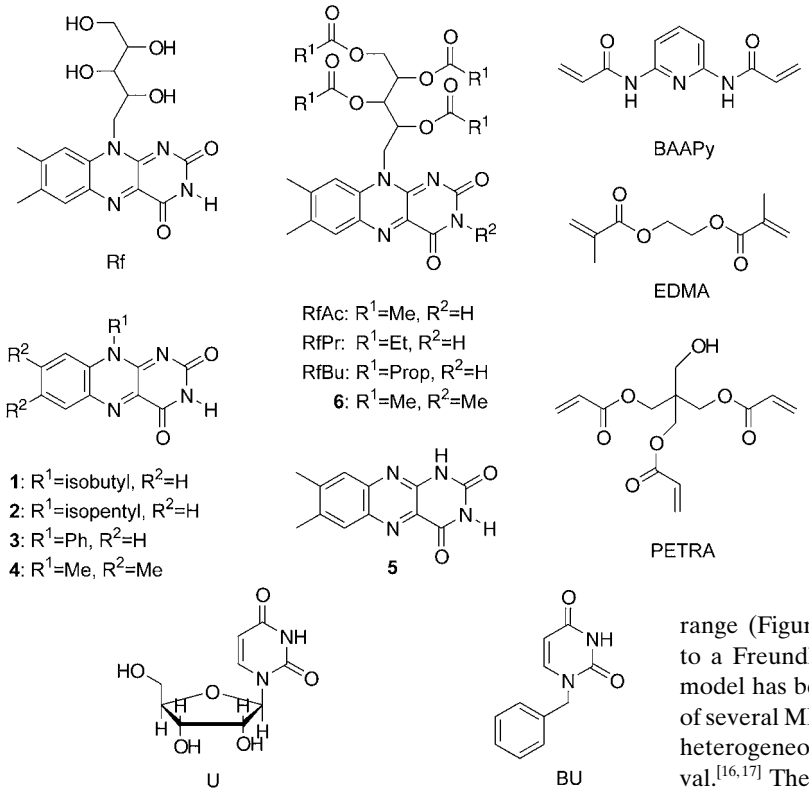


Figure 1. Fine-tuning of the size of a binding cavity complementary to the ribose chain of riboflavin (Rf) using riboflavin tetraesters as templates.



Scheme 1. The monomersand templates investigated in the study.

RfBu is strongest on P(RfBu), perhaps indicating that, while the binding sites formed in these polymers are large enough to accommodate RfAc and RfPr, there is a lessening of secondary interactions provided by the polymeric matrix, as the templated cavity is now too large for these smaller analytes. This view is further supported by the much lower retentions of the other smaller analytes (BU and **3**–**5**) on all polymers. The large imprinting factors arise from two effects, namely the pronounced retention of the riboflavin analytes on the MIPs coupled with low retention on the control, non-imprinted polymer P(N). This observation suggests that the binding sites provided by the functional monomer units in P(N) are located in areas of the polymeric matrix that cannot be accessed by the larger tetraester analytes. This assumption is again supported by the comparatively stronger retentions of the smaller analogue analytes on P(N).

Insights into the affinities and abundance of these sites were obtained by frontal analysis (low concentration range, 0–1 mM) and batch partitioning experiments (higher concentration range, 0–20 mM). In the low concentration range (Figure 3 a) the isotherms could be excellently fitted to a Freundlich multiple site model (Figure 3 a inset). This model has been shown to describe well the binding behavior of several MIPs in the low concentration range and indicates a heterogeneous distribution of binding sites within this interval.[16,17] The isotherms obtained in the higher concentration interval (Figure 3 b) display a sigmoidal-type saturation behavior, the origin of which is currently unclear.

As suggested from the earlier chromatographic results, binding to the non-imprinted polymer is confirmed to be weak. The isotherms of the imprinted polymers also agree with the relative retentions observed in the chromatographic investigation. Thus, P(RfAc) shows the highest binding capacity, exceeding that of P(N) by more than 30 $\mu mol\,g^{-1}$

 © 2005 Wiley-VCH Verlag GmbH & Co. KGaA, Weinheim

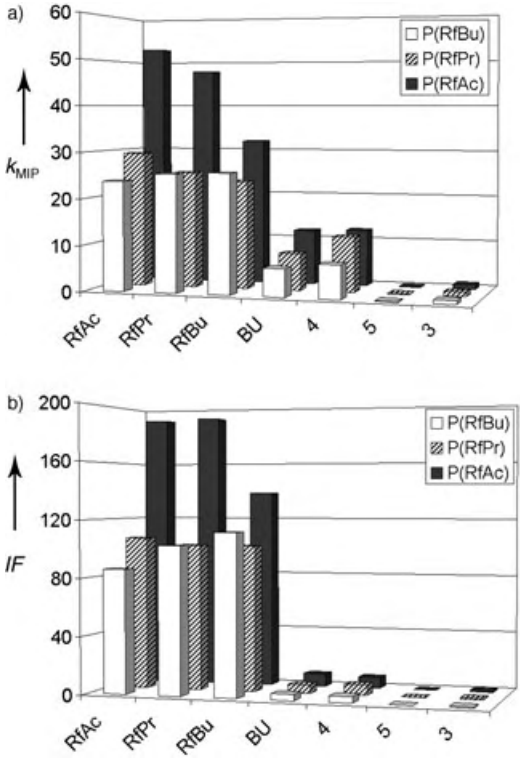


Figure 2. a) Retention factors (k) and b) imprinting factors (IF) obtained in the chromatographic evaluation of the riboflavin tetraester imprinted polymers (P(RfAc), P(RfPr), P(RfBu)) and a control, non-imprinted, polymer (P(N)) using acetonitrile/acetic acid (99/1 v/v) as the mobile phase. k and IF are defined as follows: $k=(t-t_0)/t_0$; $IF=k_{MIP}/k_{NIP}$; where t = retention time of the solute; t_0 = retention time of a nonretained void marker; $k_{MIP}(k_{NIP})$ = retention factors for a given solute using the imprinted (or non-imprinted) polymer as stationary phase.

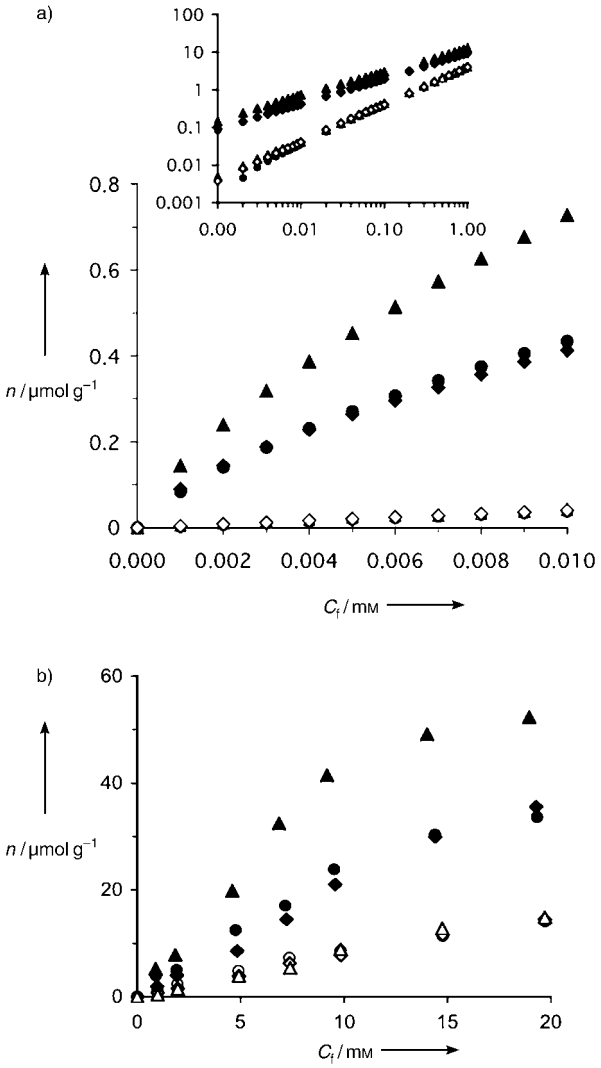


Figure 3. Binding isotherms of riboflavin tetraesters (RfAc: triangles, RfPr: circles, RfBu: diamonds) on their respective complementary polymers (P(RfAc), P(RfPr), P(RfBu): filled symbols) and on a control non-imprinted polymer (P(N); open symbols) as determined a) by frontal analysis using the staircase method or b) by a batch partitioning experiment in acetonitrile/acetic acid (99/1 v/v). In (b) the polymers (10 mg) were equilibrated for 24 h with solutions (0.5 mL) containing different concentrations of the riboflavin tetraesters.

at saturation. The binding curves of P(RfPr) and P(RfBu) exhibit similar shapes, but with lower binding of the templates. Thus, the reason for the stronger retention of RfAc on its complementary polymer appears to be a consequence of a larger number of sites rather than the presence of sites of higher affinity. Nevertheless, high-energy binding sites are clearly present. Thus, at a free concentration (C_f) of 1 μM, P(RfAc) adsorbed 0.15 μmol RfAc g^{-1} polymer with negligible nonspecific adsorption, thus indicating the presence of sites with $K_a > 10^6\,M^{-1}$.

The primary goal of our study was the recognition of riboflavin in aqueous-based media. To this end, the above polymers were tested, again in the chromatographic mode, for their ability to retain Rf under such conditions (Figure 4).

Retention of Rf by **P1** is weak and only minimally different from the retention of Rf by the control P(N). Thus, although **P1** is able to recognize its template over analogous molecules in organic media, **1** is a poor template for the preparation of MIPs that exhibit Rf recognition in aqueous media. For the MIPs prepared using the riboflavin esters as templates, much stronger retentions of Rf are observed, with P(RfAc), P(RfPr), and P(RfBu) all capable of retaining Rf to a much greater extent than either P(N) or **P1**. The relative retention of Rf on these polymers agrees with their relative binding capacities for their own templates (Figure 3). Thus, P(RfAc) emerges as the MIP best able to retain Rf under the conditions tested, which implies that the binding sites formed around this tetraester offer a good fit for the ribose chain of Rf as well.

These encouraging results were somewhat offset by the performance of the polymers in pure water or water containing small amounts of additives. In this case, nonspecific, hydrophobically driven binding dominated the retention, thus leading to much lower imprinting factors. To suppress this contribution, the polar cross-linking monomer pentaerythritol triacrylate (PETRA) was used in place of EDMA. The corresponding polymer (P(RfAc)′) retained Rf strongly, with a retention almost two times higher than P(RfAc). Furthermore, the retention displayed by the control polymer (P(N)′) was lower than that of the corresponding EDMA-based

 © 2005 Wiley-VCH Verlag GmbH & Co. KGaA, Weinheim

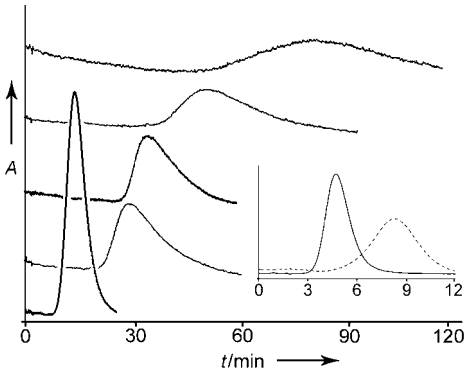


Figure 4. Elution profiles of riboflavin (10 µl of a 1 mM solution) injected on columns packed with from bottom to top (main figure): P**1**, P(RfBu), P(RfPr), P(RfAc), and P(RfAc)′. The inset shows the elution profiles of riboflavin on columns packed with P(N) (dashed line) and P(N)′ (solid line). Mobile phase = water/acetonitrile/ethanol (85.5/10/4.5 v/v/v).

control P(N) (see inset in Figure 4). Thus, it appears that the hydroxy groups of the cross-linking monomer create both a more hydrophilic backbone with lower affinity for nonpolar compounds and provide additional stabilizing interactions in the imprinted sites, presumably through hydrogen bonds to the ester function of RfAc. Frontal analysis on this polymer confirmed these findings. Thus P(RfAc)′ bound roughly two times more template at a given solution concentration than P(RfAc) and displayed more uniform high-affinity sites.

P(RfAc)′ was then subjected to a thermodynamic investigation using isothermal titration microcalorimetry (ITC). This technique has proven extremely versatile for the thermodynamic characterization of receptor–ligand interactions,[18] including an imprinted system,[19] and is based on the measurement of the heat changes occurring upon titration of a receptor (or a ligand) with its binding partner. The addition of a dilute solution of Rf to a suspension of the polymer particles ($0.9\,mg\,mL^{-1}$) in a beverage-mimicking solution (water/formic acid/ethanol: 90.6/4.7/4.7 (v/v/v)) led to exothermic heat pulses, thus indicating noncovalent interactions between the titrant and the suspended polymer particles. The heat generated per addition was calculated by integrating the heat pulses and thereafter plotted against the total concentration of Rf in the cell (Figure 5 a). Within this small concentration interval, limited by the analyte solubility, the heat generated per addition was constant, with no evidence of saturation. Nevertheless, clear differences between the polymers were observed. Interaction of Rf with the imprinted polymer was exothermic, exceeding that with the nonimprinted polymer by more than $1.3\,kcal\,mol^{-1}$, with the latter signal coinciding with the background signal obtained by addition of riboflavin in the absence of polymer.

The presence of highly discriminating imprinted sites was further supported by the absence of any such effect when the control analyte uridine was added. Uridine, which contains both the imide and ribose substructures, could be expected to cross-react with sites designed to bind riboflavin. However, the signal observed when this analyte was added to the different polymers did not differ from the blank runs.

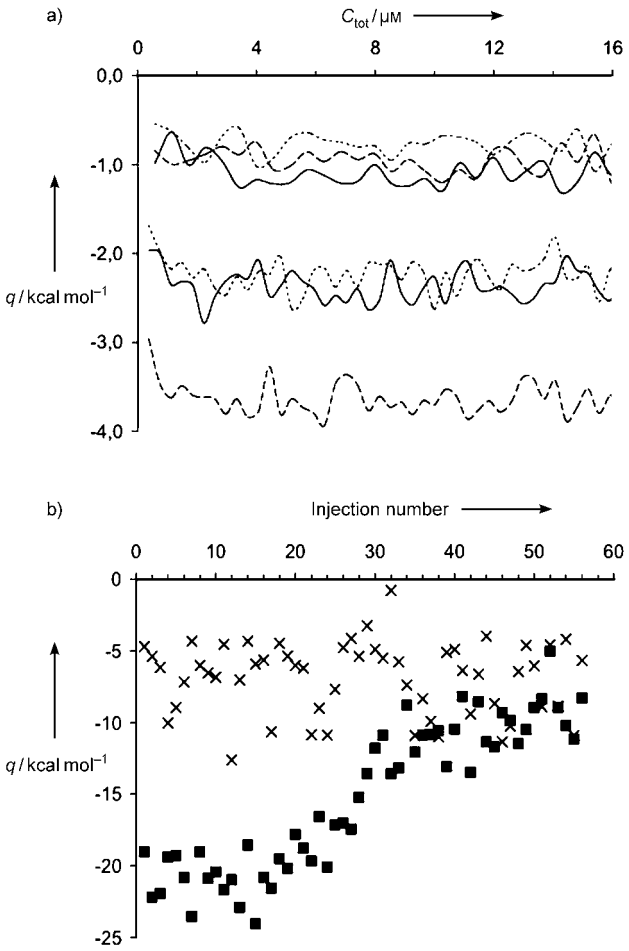


Figure 5. ITC titration profiles showing in a) the energy released (q) versus the total concentration of the titrant in the cell (C_{tot}) for the titration of P(RfAc)′ (dashed lines), P(N)′ (solid lines), or blank (dotted lines) with Rf (lower three profiles) or U (upper three profiles) in water/ethanol/formic acid: 90.6/4.7/4.7 (v/v/v), and b) the energy released versus the injection number for the titration of solutions of Rf (■) or U (X) (1 µM in 50 mM aqueous sodium phosphate buffer pH 7) by RfBP.

Unfortunately, the limited solubility of riboflavin meant that only a fraction of the binding sites could be investigated in these experiments. Thus, none of the thermodynamic quantities typically furnished by this type of experiment could be estimated. However, the presence of a specific exotherm at a low total concentration of analyte (<400 nM) implies that binding sites with affinities $>10^6\,M^{-1}$ are present. The absence of saturation effects further indicates that the sites within this population are relatively uniform.

Finally, we compared the imprinted receptor with its biological counterpart—riboflavin binding protein (RfBP). This protein was titrated by the classical technique in two different solvent systems. Pronounced exothermic heat pulses were observed under neutral conditions, with saturation clearly occurring close to a receptor:ligand stoichiometry of 1:1. Analysis of the saturation curve provided a binding constant of $9.0(\pm0.5)\times10^5\,M^{-1}$ (four independent measurements), with an associated enthalpy of $9.4(\pm0.1)\,kcal\,mol^{-1}$. Similar to the situation with the imprinted receptor, no signal

 © 2005 Wiley-VCH Verlag GmbH & Co. KGaA, Weinheim

was observed when the control analyte uridine was used as the titrant. A different picture emerged when the protein was assessed in the beverage-mimicking solution used to evaluate the imprinted polymer. A pronounced exotherm was observed under these conditions upon each addition, with no apparent binding-related signals, which implies that the protein denatures under conditions where the imprinted polymer retains its ability to bind the target. Notably, this occurs in a solvent system which resembles that found in common alcoholic beverages.[8]

We are currenttly investigating means to further enhance the affinity of the polymers for riboflavin and to suppress the nonspecific binding occurring in pure water.

Received: January 28, 2005
Published online: May 13, 2005

Keywords: hydrogen bonds · imprinting · molecular recognition · receptors · riboflavin

[1] "Molecularly imprinted polymers. Man-made mimics of antibodies and their applications in analytical chemistry" in *Techniques and instrumentation in analytical chemistry, Vol. 23* (Ed.: B. Sellergren), Elsevier Science, Amsterdam, **2001**.
[2] G. Wulff, T. Gross, R. Schönfeld, *Angew. Chem.* **1997**, *109*, 2050; *Angew. Chem. Int. Ed. Engl.* **1997**, *36*, 1962.
[3] C. Lübke, M. Lübke, M. J. Whitcombe, E. N. Vulfson, *Macromolecules* **2000**, *33*, 5098.
[4] M. Subat, A. S. Borovik, B. König, *J. Am. Chem. Soc.* **2004**, *126*, 3185.
[5] P. Manesiotis, A. J. Hall, M. Emgenbroich, M. Quaglia, E. de Lorenzi, B. Sellergren, *Chem. Commun.* **2004**, 2278.
[6] A. Rachkov, N. Minoura, *Biochim. Biophys. Acta* **2001**, *1544*, 255.
[7] M. Quaglia, K. Chenon, A. J. Hall, E. De Lorenzi, B. Sellergren, *J. Am. Chem. Soc.* **2001**, *123*, 2146.
[8] C. Laane, G. de Roo, E. van den Ban, M.-W. Sjauw-En-Wa, M. G. Duyvis, W. A. Hagen, W. J. H. van Berkel, R. Hilhorst, D. J. M. Schmedding, D. J. Evans, *J. Inst. Brew.* **1999**, *105*, 392.
[9] S. K. Chang, D. Van Engen, E. Fan, A. D. Hamilton, *J. Am. Chem. Soc.* **1991**, *113*, 7640.
[10] P. Manesiotis, A. J. Hall, B. Sellergren, *J. Org. Chem.* **2005**, *70*, 2729
[11] K. Tanabe, T. Takeuchi, J. Matsui, K. Ikebukuro, K. Yano, I. Karube, *J. Chem. Soc. Chem. Commun.* **1995**, *22*, 2303.
[12] a) R. Deans, V. M. Rotello, *J. Org. Chem.* **1997**, *62*, 4528–4529; b) M. D. Greaves, V. M. Rotello, *J. Am. Chem. Soc.* **1997**, *119*, 10569.
[13] K. A. Connors, *Binding constants. The measurement of molecular complex stability*, Wiley, New York, **1987**.
[14] L. Yu, H.-J. Schneider, *Eur. J. Org. Chem.* **1999**, 1619.
[15] The polymers were prepared by radical polymerization (azobisisobutyronitrile (AIBN), 60 °C) of BAAPy (1 mmol), crosslinking monomer (EDMA (20 mmol) or PETRA (12 mmol)) in chloroform in the presence (MIPs) or absence (P(N) or P(N)′) of template (1 mmol).
[16] Y. Chen, M. Kele, P. Sajonz, B. Sellergren, G. Guiochon, *Anal. Chem.* **1999**, *71*, 928.
[17] R. J. Umpleby II, S. C. Baxter, Y. Chen, R. N. Shah, K. D. Shimizu, *Anal. Chem.* **2001**, *73*, 4584.
[18] I. Jelesarov, H. R. Bosshard, *J. Mol. Recognit.* **1999**, *12*, 3.
[19] A. Weber, M. Dettling, H. Brunner, G. E. M. Tovar, *Macromol. Rapid Commun.* **2002**, *23*, 824.

 © 2005 Wiley-VCH Verlag GmbH & Co. KGaA, Weinheim

Platinum–Gallium Compounds

One-Step Synthesis of a Platinum(0)–Gallium(III) Chrysene Complex**

*Mikhail Gorlov, Andreas Fischer, and Lars Kloo**

Recent investigations of gallium(III) halide–aromatic solvent systems with respect to platinum-group metal halides have shown them to be very efficient reducing media.[1,2] Another attractive feature of gallium(III) halides is their aptitude to abstract halide ions from other metal halides, which facilitates metal–metal bond formation. Taking advantage of these properties, we have prepared and crystallographically characterized a series of dipalladium(I) and diplatinum(I) complexes $[M_2(\eta^6\text{-arene})_2(GaX_4)_2]$ (arene = benzene, its alkylated derivatives, or naphthalene; $X = Cl^-$ or Br^-).[1,2]

The reactions of $GaCl_3$ with $PtCl_2$ and polycyclic aromatic hydrocarbons (PAH), such as anthracene, tetracene, or pentacene, turned out to be complicated, probably because of the interaction between the strong Lewis acid $GaCl_3$ and the PAHs; only dark oily products have so far been obtained from these systems. In spite of this, the reaction of platinum(II) and gallium(III) chlorides in the presence of chrysene in 1,2,4-trichlorobenzene leads to the formation of a dark violet solution, from which red crystals can be isolated within a few weeks. An X-ray single-crystal structure determination revealed that the crystalline product is the Pt–Ga compound **1**.[3] The formation of this complex can be described schematically with Equation (1).

$$2\,PtCl_2 + 12\,GaCl_3 + 4\,\text{chrysene} \xrightarrow{+4e^-} [Pt_2Ga_2Cl_2(\mu\text{-}Cl)_2(\text{chrysene})_4](Ga_3Cl_{10})_2 + 4GaCl_4^- \quad (1)$$

The main structural feature of compound **1** is a centrosymmetric $(PtGaCl_2)_2$ unit, where each Pt center is coordinated by two chrysene molecules (Figure 1). This structural unit can be derived from the structure of Ga_2Cl_6 by replacing one terminal Cl substituent on each Ga atom by the Pt-containing group. The geometry is thus that of two edge-sharing tetrahedra. The Ga–Cl bond lengths are 213.6 pm for the terminal Cl substituents and 230.0 and 240.5 pm for the two bridging Cl substituents. They are thus of the same order of magnitude as in Ga_2Cl_6, and are much shorter than would be expected for gallium(I), thus suggesting a +3 oxidation state for Ga. The Ga–Pt distance (233.6 pm) is similar to Ga–Pt bond lengths in related compounds.[4–8] The overall charge

[*] Dr. M. Gorlov, Dr. A. Fischer, Prof. Dr. L. Kloo
Division of Inorganic Chemistry
Royal Institute of Technology
10044 Stockholm (Sweden)
Fax: (+46) 879-09-349
E-mail: Larsa@kth.se

[**] This work was supported by the Swedish Research Council and the Göran Gustafsson Foundation.

Supporting information for this article is available on the WWW under http://www.angewandte.org or from the author.

 © 2005 Wiley-VCH Verlag GmbH & Co. KGaA, Weinheim DOI: 10.1002/anie.200462373

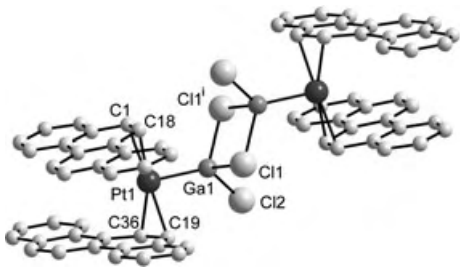


Figure 1. Structure of the cation $[Pt_2Ga_2Cl_2(\mu\text{-}Cl)_2(chrysene)_4]^{2+}$. Selected bond lengths [pm]: Pt1–Ga1 233.6(2), Pt1–C1 222(2), Pt1–C18 221(2), Pt1–C19 223(2), Pt1–C36 219.4(14), Ga1–Cl2 213.6(4), Ga1–Cl1 240.5(4), Ga1–Cl1^{i} 230.0(4). Symmetry operation: I: $2-x$, $1-y$, $1-z$.

of +2 of this unit is unequivocally determined by the fact that there are two $[Ga_3Cl_{10}]^-$ anions present in the structure. The formal oxidation state of Pt in this structure is thus zero.

Each platinum atom is connected to two planar chrysene molecules. The Pt–C bond lengths in **1** (219.4–223.2 pm) are comparable to those in a diplatinum(I) naphthalene complex (219.9–225.8 pm),[1] but they are shorter than those in some other platinum(II) complexes containing arene ligands (for example, 233–234 pm in the 9,10-dihydro-9,10-ethenoanthracene complex).[9]

It should be emphasized that the isolation of compound **1** demonstrates the diversity of reaction routes based on platinum or palladium halides in combination with aluminum or gallium halides in arene-based media. Indeed, only compounds with a dimetallic M_2^{2+} (M = Pd, Pt) core have so far been isolated from these systems.[1,2,10] In the only platinum complex isolated from related systems the platinum center is coordinated by naphthalene. In spite of that, the chrysene complex **1** has a unique structure. The shortest distance between the benzene rings of adjacent chrysene ligands is 358.8 pm, which may indicate a π–π interaction between the chrysene ligands, possibly providing additional stability to **1**.

The crystal packing of **1** is shown in Figure 2. Organic layers of coordinated chrysene molecules are separated by inorganic layers composed of gallium and chlorine atoms, which belong to the central part of the cation and the $[Ga_3Cl_{10}]^-$ anions. The shortest distance between chrysene ligands of adjacent molecules is 360 pm.

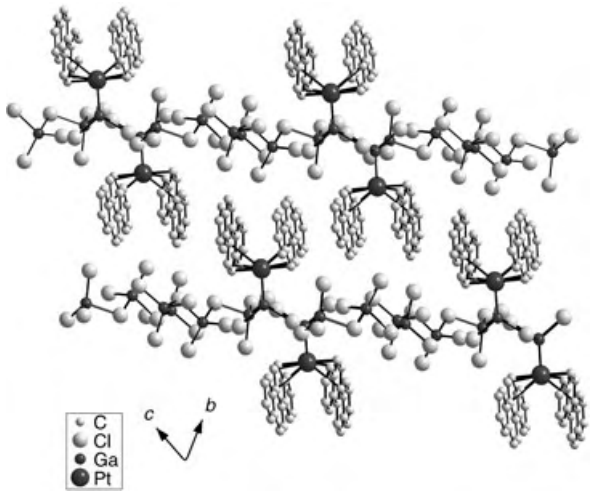


Figure 2. View of the crystal packing of **1**.

Compound **1** is the first platinum–chrysene compound whose structure has been confirmed by X-ray diffraction.[3] It should be noted that among platinum-group metals only ruthenium–chrysene compounds have been described previously.[11–13] In contrast to these compounds, which have an η^6-type coordination, the chrysene in **1** is coordinated in an η^2-mode. Moreover, in the case of the ruthenium complexes exterior ring(s) of chrysene are bound to the metal atom(s), while in **1** the inner ring is coordinated to platinum.

Another remarkable feature of **1** is the presence of a direct platinum–gallium bond whose length is 233.6(2) pm. The platinum–gallium distance is comparable to those in platinum(0)–gallium(I) complexes described in the literature.[4–8] This is remarkable, since electron bookkeeping based on the structure of **1** (vide supra) suggests a platinum(0)–gallium(III) interaction, which means two electrons less on the metal centers available for covalent interaction. In spite of this essentially the same Pt–Ga separation is observed.

To get some further insight into the oxidation states of the atoms involved, X-ray photoelectron spectroscopy (XPS) data were collected for **1**. The binding energies (BE) for **1** are presented in Table 1. Charge-transfer to the ligands has an important impact, and the binding energy of the Pt4f(7/2) electrons in **1** more resembles that of a formal oxidation state of +2 [for example, the BEs of Pt4f(7/2) in $K_2[Pt^{II}Cl_4]$ and $[Pt^0(PPh_3)_4]$ are 73.4 and 71.6 eV, respectively].[14] Thus, the XPS results do not provide the clear-cut information about formal oxidation states hoped for.

Table 1: The XPS data of **1**.

	Line C1s	Pt4f(7/2)	Cl2p(3/2)	Ga2p(3/2)	Ga3d
BE [eV]	284.7 285.6	72.9	199.7 200.4	1120.0	22.2

To shed some further light on the formal oxidation states of the metal centers in **1**, quantum chemical calculations were performed for a series of model compounds. $[(C_6H_6)_2Pt–Ga_2Cl_5]^+$ was chosen as a simplified model of **1** as it essentially represents the cation in **1** terminated by an extra chloride ion, instead of a second $(C_6H_6)_2Pt$ entity, and chrysene molecules replaced by more simple η^2-coordinated benzene molecules. The Natural Bond Order (NBO) charge of platinum in the geometrically optimized model was calculated to be +0.27 at the B3LYP level. This is larger than that found in the isolated, neutral $(C_6H_6)_2Pt$ entity (+0.14) but significantly smaller than that in a formal platinum(II) compound such as $[PtCl_4]^{2-}$ (+0.48). The corresponding $[(C_6H_6)_2Pt]^{2+}$ unit, which thus contains two electrons less, displays a Pt charge of +0.73. The corresponding NBO charge of the gallium atom directly connected to platinum is +1.04 and of the one furthest away

 © 2005 Wiley-VCH Verlag GmbH & Co. KGaA, Weinheim

+1.17. Both values are close to those found in compounds with formal gallium(III) (viz. +1.12 in $[GaCl_4]^-$). These results confirm the assignment of both gallium atoms in **1** as gallium(III). The optimized Pt–Ga distance obtained is 241.8 pm, which is slightly longer than the experimentally obtained. The closest Pt–C distances range from 228 to 232 pm.

Susceptibility measurements of **1** show the compound to be diamagnetic, thus ruling out a qualitative electron transfer from platinum to the chrysene ligands to give a formal platinum(II) center and anionic arene ligands. Logically, therefore, the platinum centers must be formally assigned as platinum(0).

The bonding situation in known compounds with a platinum(0)–gallium(I) interaction closely resembles that in $[Ni(CO)_4]$. The platinum(0) center is surrounded by neutral phosphine and/or cyclopentadienylgallium(I) entities in a quasi-tetrahedral fashion,[4–8] and the bonding can be described in terms of a perturbed T_d symmetry involving both σ- and π-bonding.[15–17] In a series of such compounds, quantum chemical calculations have been used to assign the NBO charge on Pt to about −0.6. Gallium typically displays an NBO charge from +0.5 to +0.7, substantially lower than in the model of **1**.

The bonding situation in **1** is clearly different, and the platinum(0)–gallium(III) interaction is best described as dative, similar to that between Cl^- and gallium(III), and the similar Pt–Ga separation observed must be simply a coincidence.

The presence of hydride ligands bound to platinum and/or gallium atoms can also formally be proposed. However, neither chemical, structural, or spectroscopic, nor theoretical results give any support to the presence of hydride ligands in **1**.[18] As a bonus, it should be noted that the title compound contains the first example of a structurally characterized decachlorotrigallate anion, whose existence has only been shown by spectroscopic techniques until now.[19]

The nature of the reducing agent in this system is not clear, although two possibilities can be proposed. First of all, chrysene can be oxidized by gallium(III) chloride (presumable products are chlorinated chrysenes and/or products of chrysene polymerization) and thereby chrysene may act as the reductant. However, the Pt:Ga:chrysene molar ratio is 1:2:1, which means that no excess of chrysene was used. The solvent, 1,2,4-trichlorobenzene, can also be chlorinated, but, as noted earlier,[1] chlorinated benzene–$GaCl_3$ systems are inert with respect to the reduction of platinum-group metal chlorides.

The reactions between $PtBr_2$ and $GaBr_3$, $PtCl_2$ and $AlCl_3$, and $PtBr_2$ and $AlBr_3$ in the presence of chrysene in 1,2-dichlorobenzene were also studied. In spite of the formation of deeply colored solutions, no crystals could be isolated. Attempts to obtain the analogous palladium compounds were unsuccessful, both in the gallium and aluminum halide systems.

In conclusion, this work describes the one-step synthesis of a platinum(0)–gallium(III) compound from readily available $PtCl_2$. The complex, with two Pt–Ga bonds, contains platinum chrysene units and Ga_3Cl_{10} groups, the latter of which have been crystallographically confirmed for the first time.

Experimental Section

General: $GaCl_3$ (Aldrich, 99.99%), $GaBr_3$ (Alfa Aesar, 99.999%), $PtCl_2$ (Aldrich, 99.9+%), $PtBr_2$ (Alfa Aesar, 99.9%) $AlCl_3$ (Alfa Aesar, 99.985%), $AlBr_3$ (Alfa Aesar, 99.998%), $PdCl_2$ (Alfa Aesar, 99.999%), $PdBr_2$ (Aldrich, 99%), and chrysene (Aldrich, 98%) were used as received. 1,2,4-Trichlorobenzene (Aldrich, 99%) and 1,2-dichlorobenzene (Fluka Chemika, ≥99%) were dried over molecular sieves. All experiments were performed in a glove box under an inert atmosphere of deoxygenated and dried nitrogen (< 1 ppm H_2O and O_2).

XPS spectra were recorded with a Kratos Axis Ultra electron spectrometer fitted with a monochromatic $Al_{K\alpha}$ source operating at 180 W. The BE scale was referenced to the C 1s line of *p*-quaterphenyl (284.7 eV). The uncertainty in the BE values is ±0.1 eV, and ±10% in atomic ratios. Processing of the spectra was accomplished with Kratos software. Special care (glove bag) was taken during transfer of the air-sensitive samples for analysis by ensuring a dry nitrogen atmosphere. The samples were pre-cooled and XPS analyses were carried out at liquid-nitrogen temperature.

NMR spectra were obtained on a Bruker AMX 500 MHz spectrometer. The spectra were recorded at 300 K in 1,2,4-trichlorobenzene solution under an inert atmosphere.

1: 1,2,4-Trichlorobenzene was added to a solid mixture of $PtCl_2$ (30 mg, 0.113 mmol), $GaCl_3$ (40 mg, 0.226 mmol), and chrysene (26 mg, 0.113 mmol). The mixture was stirred for 15 min. A red crystalline product was obtained after 4–5 weeks. Crystals of **1** are unstable: 2–3 weeks after their formation most of the crystals had decomposed, even in the dark and when in contact with the mother liquor.

Quantum chemical calculations were performed at the Hartree–Fock and hybrid density functional level (B3LYP) using the Gaussian 98 program package.[20] Basis sets for H, C, and Cl were of 6-31G quality supplemented with additional diffuse and polarization functions. Valence basis sets for Ga and Pt were fully noncontracted of (7s6p6d) and (8s7p6d1f) quality, respectively. Quasi-relativistic effective core potentials replaced 18 and 60 electrons for Ga and Pt, respectively.[21] Natural Bond Order populations were evaluated using the integrated Gaussian NBO version 3.1.

Received: October 10, 2004
Revised: March 23, 2005
Published online: May 13, 2005

Keywords: ab initio calculations · cluster compounds · gallium · platinum

[1] M. Gorlov, A. Fischer, L. Kloo, *Inorg. Chim. Acta* **2003**, *350*, 449.
[2] M. Gorlov, A. Fischer, L. Kloo, *J. Organomet. Chem.* **2004**, *689*, 489.
[3] Crystal structure determination of **1**: triclinic, space group $P\bar{1}$, $a = 1237.9(2)$, $b = 1216.62(11)$, $c = 1618.5(2)$ pm, $\alpha = 62.750(4)$, $\beta = 83.700(6)$, $\gamma = 89.62(2)°$, $V = 2151.3(6) \times 10^6$ pm^3, $\rho_{calcd} = 2.09$ g cm^{-3}, $2\theta_{max} = 35.5°$, $Ag_{K\alpha}$ radiation, $\lambda = 56.090$ pm, $T = 299$ K. The diffraction data were collected on a Bruker-Nonius KappaCCD diffractometer. All non-H atoms were refined with anisotropic temperature parameters. Numerical absorption corrections were applied. The structure was solved with SHELXS-97 and refined on F^2 with SHELXL-97. Final R values: $R_1 = 0.0687$, $wR_2 = 0.153$; GOF = 1.180 for 5381 unique reflections and 478 parameters. Max./min. residual electron density 1.47/−1.48. CCDC-252705 contains the supplementary crystallographic data for this paper. These data can be obtained free of charge from the Cambridge Crystallographic Data Centre via www.ccdc.cam.ac.uk/data_request/cif.

 © 2005 Wiley-VCH Verlag GmbH & Co. KGaA, Weinheim

[4] C. Gemel, T. Steinke, D. Weiss, M. Cokoja, M. Winter, R. A. Fischer, *Organometallics* **2003**, *22*, 2705.
[5] D. Weiss, M. Winter, K. Merz, A. Knufer, R. A. Fischer, N. Fröhlich, G. Frenking, *Polyhedron* **2002**, *21*, 535.
[6] D. Weiss, T. Steinke, M. Winter, R. A. Fischer, N. Fröhlich, J. Uddin, G. Frenking, *Organometallics* **2000**, *19*, 4583.
[7] D. Weiss, M. Winter, R. A. Fischer, C. Yu, K. Wichmann, G. Frenking, *Chem. Commun.* **2000**, 2495.
[8] R. A. Fischer, H. D. Kaesz, S. I. Khan, H. J. Muller, *Inorg. Chem.* **1990**, *29*, 1601.
[9] L. L. Wright, S. J. Moore, J. A. McIntyre, S. M. Dowling, J. D. Overcast, G. R. Grisel IV, K. N. Nelson, P. R. Rupert, W. T. Pennington, *Organometallics* **1999**, *18*, 4558.
[10] a) G. Allegra, A. Immirzi, L. Porri, *J. Am. Chem. Soc.* **1965**, *87*, 1394; b) G. Allegra, G. T. Casagrande, A. Immirzi, L. Porri, G. Vitulli, *J. Am. Chem. Soc.* **1970**, *92*, 289.
[11] L. C. Porter, J. R. Polam, S. Bodige, *Inorg. Chem.* **1995**, *34*, 998.
[12] I. Chavez, M. Otero, E. Román, U. Mueller, *J. Organomet. Chem.* **1992**, *427*, 369.
[13] I. Chavez, A. Cisternas, M. Otero, E. Román, U. Mueller, *Z. Naturforsch. B* **1990**, *45*, 658.
[14] T. W. Hanks, R. A. Ekeland, K. Emerson, R. D. Larsen, P. W. Jennings, *Organometallics* **1987**, *6*, 28.
[15] V. Jonas, W. Thiel, *J. Chem. Phys.* **1995**, *102*, 8474.
[16] A. W. Ehlers, S. Dapprich, S. F. Vyboishchikov, G. Frenking, *Organometallics* **1996**, *15*, 105.
[17] M. Doerr, G. Frenking, *Z. Anorg. Allg. Chem.* **2002**, *628*, 843.
[18] From a chemistry point of view, the co-existence of gallium(III) and a hydride in the cation of **1** is highly unlikely. Both the Lewis acidity and reduction propensity of gallium(III) would most likely lead to direct reaction. The X-ray structure analysis supplied no indications of the presence of hydride ligands in **1**. A solution of **1** in 1,2,4-trichlorobenzene shows no hydrides in the negative chemical-shift region in the ^{1}H NMR spectrum. In addition, the introduction of hydrides into the theoretical model to give $[(C_6H_6)_2Pt(H_2)Ga_2Cl_5]^+$, with a formal platinum(II)and hydrides initially placed as bridging atoms along the Pt–Ga bond (which is the structurally most elusive position), gave rise to an extraction of one hydride by the $[Ga_2Cl_5]^+$ entity to give a neutral Ga_2Cl_5H molecule that is well separated from platinum, thus highlighting the expected Lewis acidity of gallium(III).
[19] S. Ulvenlund, A. Wheatley, L. A. Bengtsson, *J. Chem. Soc. Dalton Trans.* **1995**, 245.
[20] Gaussian 98 (Revision A.7): M. J. Frisch et al., see Supporting Information.
[21] a) D. Andrae, U. Häußermann, M. Dolg, H. Stoll, H. Preuss, *Theor. Chim. Acta* **1990**, *77*, 123; b) T. Leininger, A. Berning, A. Nicklass, H. Stoll, H.-J. Werner, H. J. Flad, *Chem. Phys.* **1997**, *217*, 19.

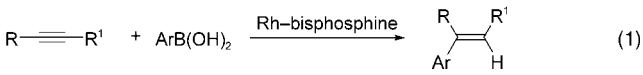
 © 2005 Wiley-VCH Verlag GmbH & Co. KGaA, Weinheim

Asymmetric Catalysis

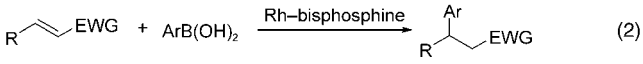
Highly Chemo- and Enantioselective Arylative Cyclization of Alkyne-Tethered Electron-Deficient Olefins Catalyzed by Rhodium Complexes with Chiral Dienes**

*Ryo Shintani, Akihiro Tsurusaki, Kazuhiro Okamoto, and Tamio Hayashi**

Multiple carbon–carbon bond-forming reactions catalyzed by transition metals are a powerful method for the construction of structurally complex molecules in a convergent manner from relatively simple precursors.[1] Compounds that bear two or more electrophilic sites at appropriate positions are potentially useful for the preparation of complex cyclic materials by sequential addition and cyclization of nucleophiles in a cascade manner.[2,3] However, if these electrophilic sites are all reactive toward the incoming nucleophile, chemoselectivity of the initial nucleophilic attack becomes an important issue. In this context, alkyne-tethered electron-deficient olefins should be an interesting class of substrates, as both internal alkynes[4] and electron-deficient olefins[5] are good electrophiles in a rhodium–bisphosphine-catalyzed addition of aryl boronic acids [Eq. (1) and Eq. (2); EWG = electron-withdrawing group]. Herein, we describe how a rhodium–diene catalyst, rather than a rhodium–bisphosphine catalyst, can effectively catalyze an arylative cyclization of alkyne-tethered electron-deficient olefins with high chemoselectivity, and that high enantioselectivity can also be attained by the use of chiral diene ligands in this process (Scheme 1).



(1)



(2)

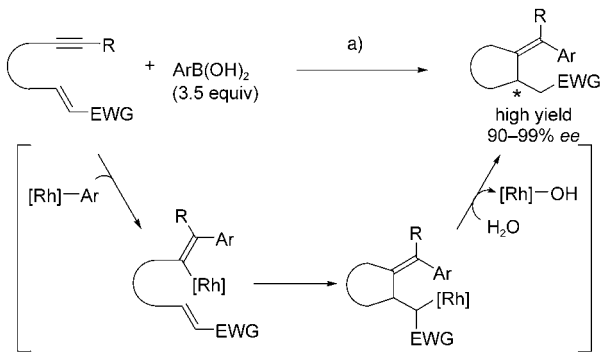
In an initial investigation, we employed alkyne-tethered enoate **1a** as a model substrate in combination with $PhB(OH)_2$ to examine the effect of the ligand in the presence of 6 mol% rhodium (Table 1). Although the reaction proceeds smoothly when (*S*)-binap is used as a ligand, a mixture

[*] Dr. R. Shintani, A. Tsurusaki, K. Okamoto, Prof. Dr. T. Hayashi
Department of Chemistry
Graduate School of Science
Kyoto University
Sakyo, Kyoto 606-8502 (Japan)
Fax: (+81) 75-753-3988
E-mail: thayashi@kuchem.kyoto-u.ac.jp

[**] Support was provided in part by a grant-in-aid for scientific research by the Ministry of Education, Culture, Sports, Science, and Technology, Japan (21 COE on Kyoto University Alliance for Chemistry).

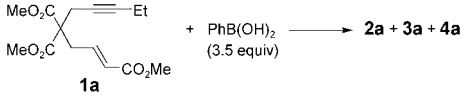
Supporting information for this article is available on the WWW under http://www.angewandte.org or from the author.

 DOI: 10.1002/anie.200500843 © 2005 Wiley-VCH Verlag GmbH & Co. KGaA, Weinheim



Scheme 1. a) [{RhCl(C_2H_4)$_2$}$_2$] (6 mol% Rh), (*S*,*S*)-Bn-bod* (6.5 mol%), KOH (0.3 equiv), dioxane/H_2O (10:1), 60°C, 4 h.

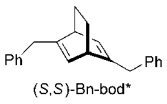
Table 1: Rhodium-catalyzed asymmetric arylative cyclization of model substrate **1a**: effect of the ligand.[a]



1a

	Yield [%]		
	2a	**3a**	**4a**
(*S*)-binap	23 (95% *ee*)	22	45
dppf	3	9	32
(*S*,*S*)-Bn-bod*	83 (99% *ee*)	5	5
cod	72	3	8

[a] Conditions: [{RhCl(C_2H_4)$_2$}$_2$] (6 mol% Rh), ligand (6.5 mol%), KOH (0.3 equiv), dioxane/H_2O (10:1), 60°C, 4 h. (*S*)-binap = 2,2′-bis(diphenylphosphino)-1,1′-binaphthyl, dppf = 1,1′-bis(diphenylphosphino)ferrocene, cod = cycloocta-1,5-diene.

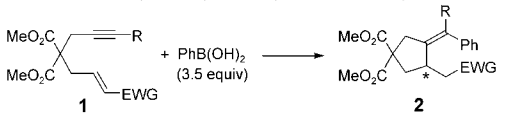


(*S*,*S*)-Bn-bod*

of three different phenylated products (**2a**, **3a**,[6] and **4a**) are obtained rather nonselectively (23, 22, and 45% yields, respectively). The use of other bisphosphine ligands such as dppf leads to somewhat lower reactivity (51% conversion), which tends to give 1,4-adduct **4a** as the major product. In contrast, the use of chiral diene ligand (*S*,*S*)-Bn-bod*[2f,7] dramatically changes the course of the reaction and preferentially leads to product **2a**, which is obtained in 83% yield and with 99% *ee* (compare with 95% *ee* when (*S*)-binap is used), with a small amount of **3a** and **4a** (5% yield for each) also formed. The employment of other diene ligands such as cod also provides compound **2a** as the major product.

Under these conditions with Rh(*S*,*S*)-Bn-bod* as a catalyst, several alkyne-tethered electron-deficient olefins can be successfully used as shown in Table 2. Thus, not only methyl or ethyl esters (entries 1–3) but also phenyl ketone (entry 4) can be employed as an electron-withdrawing group

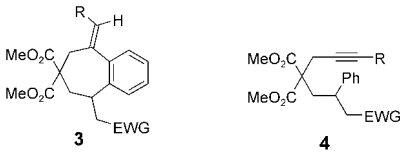
Table 2: Rhodium-catalyzed arylative cyclization: scope of substrate **1**.[a]



1 **2**

Entry	Substrate	R; EWG	Yield [%][b]	*ee* [%][c]	$[\alpha]_D^{20}$ (in $CHCl_3$)
1	**1a**	Et; CO_2Me	93	99	−65.8 (*c* = 0.97)
2	**1b**	Me; CO_2Me	86	99	−67.0 (*c* = 0.97)
3	**1c**	Et; CO_2Et	89	99	−73.5 (*c* = 1.02)
4	**1d**	Et; COPh	87	90	−90.2 (*c* = 1.45)

[a] Conditions: [{RhCl(C_2H_4)$_2$}$_2$] (6 mol% Rh), (*S*,*S*)-Bn-bod* (6.5 mol%), KOH (0.3 equiv), dioxane/H_2O (10:1), 60°C, 4 h. [b] Contaminated with up to 10% of **3** and **4** (≈1:1) in all cases. [c] *ee* values were determined by HPLC on a chiralpak AD-H column.

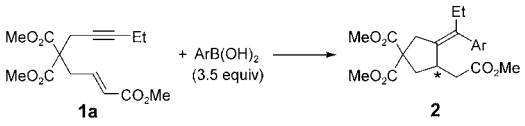


3 **4**

on the olefin to furnish five-membered carbocycles with high chemo- and enantioselectivities (90–99% *ee*).

With respect to the scope of the nucleophilic component, sterically and electronically diverse arrays of aryl boronic acids can be used under the same conditions to afford the five-membered products uniformly with high chemoselectivity and with excellent enantioselectivity (Table 3; 97–99% *ee*).

Table 3: Rhodium-catalyzed asymmetric arylative cyclization: scope of the aryl boronic acid.[a]



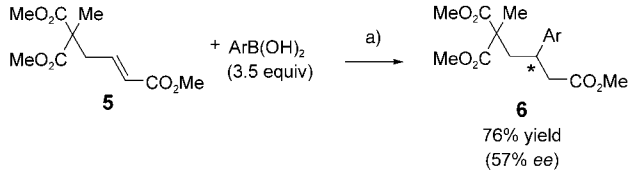
1a **2**

Entry	Ar	Yield [%][b]	*ee* [%][c]	$[\alpha]_D^{20}$ (in $CHCl_3$)
1	Ph	93	99	−65.8 (*c* = 0.97)
2	4-MeC_6H_4	87	99	−87.7 (*c* = 1.11)
3	4-$MeOC_6H_4$	86	99	−90.9 (*c* = 1.14)
4	4-FC_6H_4	88	97	−72.5 (*c* = 1.28)
5	3-ClC_6H_4	84	99	−77.4 (*c* = 1.29)
6	3,5-$Me_2C_6H_3$	83	99	−63.5 (*c* = 1.07)
7	2-naphthyl	80	98	−82.8 (*c* = 0.94)

[a] Conditions: [{RhCl(C_2H_4)$_2$}$_2$] (6 mol% Rh), (*S*,*S*)-Bn-bod* (6.5 mol%), KOH (0.3 equiv), dioxane/H_2O (10:1), 60°C, 4 h. [b] Contaminated with 7–11% of **3**/**4** (≈1:1) in all cases. [c] *ee* values were determined by HPLC on a Chiralpak AD-H column.

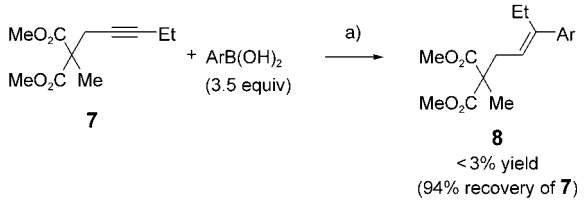
To gain insight into the origin of the difference in chemoselectivity between rhodium–bisphosphine and rhodium–diene catalysts in these arylative cyclization reactions, we conducted the following experiments. Reaction of α,β-enoate **5** with an aryl boronic acid (Ar = 3,5-$Me_2C_6H_3$) in the presence of 6 mol% Rh–(*S*)-binap produced the corresponding 1,4-adduct **6** in 76% yield (Scheme 2). In contrast, the use of alkyne **7** as a substrate under Rh–(*S*)-binap catalysis resulted in 94% recovery of **7** with almost no formation of

 © 2005 Wiley-VCH Verlag GmbH & Co. KGaA, Weinheim



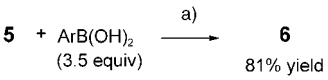
Scheme 2. a) [{RhCl(C_2H_4)$_2$}$_2$] (6 mol% Rh), (*S*)-binap (6.5 mol%), KOH (0.3 equiv), dioxane/H_2O (10:1), 60°C, 4 h.

arylated product **8** (Scheme 3). Compared to these results, both α,β-enoate **5** and alkyne **7** reacted with the aryl boronic acid (Ar = 3,5-$Me_2C_6H_3$) in the presence of 6 mol% Rh–cod

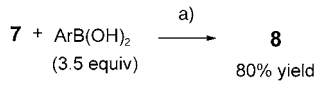


Scheme 3. a) [{RhCl(C_2H_4)$_2$}$_2$] (6 mol% Rh), (*S*)-binap (6.5 mol%), KOH (0.3 equiv), dioxane/H_2O (10:1), 60°C, 4 h.

catalyst to furnish the corresponding arylated products **6** and **8** in over 80% yield (Scheme 4 and Scheme 5). To distinguish the reactivity between the two, we conducted a competition

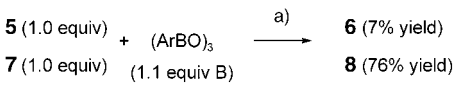


Scheme 4. a) [{RhCl(cod)}$_2$] (6 mol% Rh), KOH (0.3 equiv), dioxane/H_2O (10:1), 60°C, 4 h.



Scheme 5. a) [{RhCl(cod)}$_2$] (6 mol% Rh), KOH (0.3 equiv), dioxane/H_2O (10:1), 60°C, 4 h.

experiment using a 1:1 mixture of **5** and **7** with 1.1 equivalents of aryl boron species (Ar = 3,5-$Me_2C_6H_3$) in the presence of 6 mol% Rh–cod (Scheme 6). Under these conditions, α,β-enoate **5** was recovered in 90% yield and alkyne **7** was completely comsumed to give product **8** in 76% yield. These results indicate that a Rh–bisphosphine catalyzes the 1,4-addition of α,β-enoates more effectively than the arylation of alkynes, and that a Rh–diene catalyst displays higher activity



Scheme 6. a) [{RhCl(cod)}$_2$] (6 mol% Rh), KOH (0.3 equiv), dioxane/H_2O (10:1), 60°C, 4 h.

in the arylation of alkynes than in the 1,4-addition of α,β-enoates. This conclusion should partially explain the observed high chemoselectivity in the arylative cyclization of **1** with a rhodium–diene catalyst.[8]

In summary, we have developed a rhodium-catalyzed arylative cyclization of alkyne-tethered electron-deficient olefins with aryl boronic acids, and high chemo- and enantioselectivities have been observed by the use of a chiral diene ligand. We hope to further develop chiral diene ligands and their application to various transition-metal-catalyzed asymmetric processes.

Experimental Section

Procedure for Table 1: An aqueous solution of KOH (0.3 M in H_2O; 0.2 mL, 60 μmol) was added to a solution of [{RhCl(C_2H_4)$_2$}$_2$] (2.3 mg, 12 μmol Rh) and ligand (13 μmol) in 1,4-dioxane (1.0 mL), and the mixture was stirred for 5 min at room temperature. $PhB(OH)_2$ (85.4 mg, 0.70 mmol) and **1a** (59.3 mg, 0.20 mmol) were then added along with additional 1,4-dioxane (1.0 mL), and the resulting solution was stirred for 4 h at 60°C. The reaction mixture was directly passed through a pad of silica gel with Et_2O, and the solvent was removed under vacuum. The residue was purified by preparative TLC (silica gel) with a mixture of Et_2O/hexane (1:1) as eluent.

With (*S*)-binap as ligand, a mixture of **2a**, **3a**, and **4a** (26:24:50, as determined by ^{1}H NMR spectroscopy) was obtained as a pale yellow oil (67.7 mg, 90% combined yield). The *ee* value for **2a** was determined on a Daicel Chiralpak AD-H column with hexane/2-propanol (90:10) and a flow rate of 0.3 mL min^{-1}. Retention times: 29.8 min ((+)-enantiomer) and 33.5 min ((−)-enantiomer, 95% *ee*).

With (*S*,*S*)-Bn-bod* as ligand, a mixture of **2a**, **3a**, and **4a** (90:5:5, as determined by ^{1}H NMR spectroscopy) was obtained as a yellow oil (69.5 mg, 93% combined yield). **2a**: 99% *ee*; $[\alpha]_D^{20} = -65.8$ ($c = 0.97$, $CHCl_3$).

Received: March 7, 2005
Published online: May 18, 2005

Keywords: asymmetric catalysis · chemoselectivity · cyclization · diene ligands · rhodium

[1] For reviews, see: a) J. Montgomery, *Angew. Chem.* **2004**, *116*, 3980; *Angew. Chem. Int. Ed.* **2004**, *43*, 3890; b) E. Negishi, C. Copéret, S. Ma, S. Y. Liou, F. Liu, *Chem. Rev.* **1996**, *96*, 365; c) L. F. Tietze, *Chem. Rev.* **1996**, *96*, 115; for recent examples, see: d) K. Agapiou, D. F. Cauble, M. J. Krische, *J. Am. Chem. Soc.* **2004**, *126*, 4528; e) K. Subburaj, J. Montgomery, *J. Am. Chem. Soc.* **2003**, *125*, 11210.

[2] For examples of rhodium-catalyzed processes, see: a) D. F. Cauble, J. D. Gipson, M. J. Krische, *J. Am. Chem. Soc.* **2003**, *125*, 1110; b) B. M. Bocknack, L.-C. Wang, M. J. Krische, *Proc. Natl. Acad. Sci. USA* **2004**, *101*, 5421; c) M. Lautens, J. Mancuso, *Org. Lett.* **2002**, *4*, 2105; d) M. Lautens, J. Mancuso, *J. Org. Chem.* **2004**, *69*, 3478; e) M. Lautens, T. Marquardt, *J. Org. Chem.* **2004**, *69*, 4607; f) R. Shintani, K. Okamoto, Y. Otomaru, K. Ueyama, T. Hayashi, *J. Am. Chem. Soc.* **2005**, *127*, 54; g) T. Miura, M. Shimada, M. Murakami, *J. Am. Chem. Soc.* **2005**, *127*, 1094; h) T. Miura, T. Sasaki, H. Nakazawa, M. Murakami, *J. Am. Chem. Soc.* **2005**, *127*, 1390; for an example of cobalt-catalyzed reductive cyclizations, see: i) T.-G. Baik, A. L. Luis, L.-C. Wang, M. J. Krische, *J. Am. Chem. Soc.* **2001**, *123*, 5112.

 © 2005 Wiley-VCH Verlag GmbH & Co. KGaA, Weinheim

[3] For an overview, see: a) J. Montgomery, *Acc. Chem. Res.* **2000**, *33*, 467; b) R. A. Widenhoefer, *Acc. Chem. Res.* **2002**, *35*, 905; c) H.-Y. Jang, M. J. Krische, *Acc. Chem. Res.* **2004**, *37*, 653.
[4] T. Hayashi, K. Inoue, N. Taniguchi, M. Ogasawara, *J. Am. Chem. Soc.* **2001**, *123*, 9918.
[5] a) M. Sakai, H. Hayashi, N. Miyaura, *Organometallics* **1997**, *16*, 4229; b) Y. Takaya, M. Ogasawara, T. Hayashi, M. Sakai, N. Miyaura, *J. Am. Chem. Soc.* **1998**, *120*, 5579; for reviews, see: c) T. Hayashi, K. Yamasaki, *Chem. Rev.* **2003**, *103*, 2829; d) K. Fagnou, M. Lautens, *Chem. Rev.* **2003**, *103*, 169.
[6] Compound **3a** is presumably formed through a pathway similar to that reported in ref. [2h].
[7] a) N. Tokunaga, Y. Otomaru, K. Okamoto, K. Ueyama, R. Shintani, T. Hayashi, *J. Am. Chem. Soc.* **2004**, *126*, 13584; b) Y. Otomaru, K. Okamoto, R. Shintani, T. Hayashi, *J. Org. Chem.* **2005**, *70*, 2503.
[8] This conclusion does not necessarily fully explain the low chemoselectivity in the reaction of **1a** with phenylboronic acid in the presence of a Rh–bisphosphine catalyst (Table 1).

 © 2005 Wiley-VCH Verlag GmbH & Co. KGaA, Weinheim

Arene Functionalization

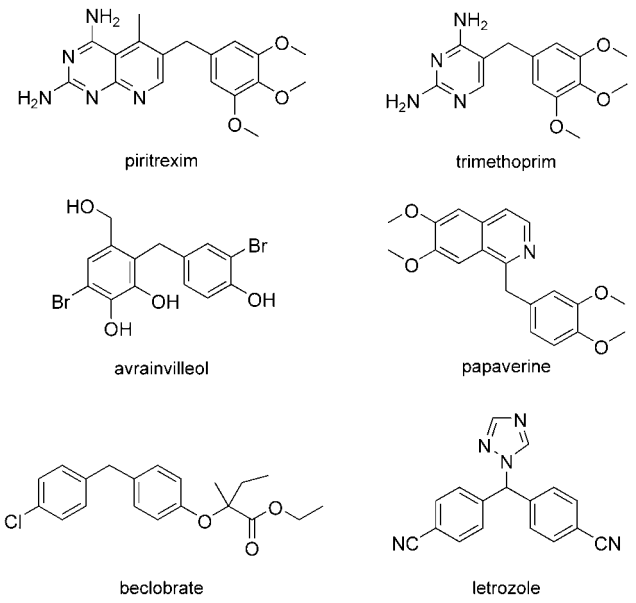
An Efficient and General Iron-Catalyzed Arylation of Benzyl Alcohols and Benzyl Carboxylates**

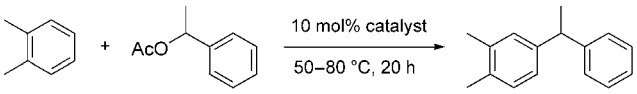
*Irina Iovel, Kristin Mertins, Jette Kischel, Alexander Zapf, and Matthias Beller**

Dedicated to Professor Dirk Walther on the occasion of his 65th birthday

Functionalized arenes and heteroarenes are of outstanding importance as pharmaceuticals, agrochemicals, fine and bulk chemicals. Hence, the development of environmentally benign C–C coupling reactions of arenes is an important topic of organometallic chemistry and catalysis. Elegant examples of direct C–H transformations of arenes[1] include the addition of olefins to acetophenones (Murai reaction)[2] and aromatic imines,[3] novel additions of olefins to electron-rich arenes[4] and heterocycles,[5] the addition of aromatics to alkynes,[6] the carbonylation of heterocycles,[7] and the cyclization of arene–alkyne substrates[8] as well as the C-arylation of heteroarenes.[9] In addition, recently significant progress has been seen in Friedel–Crafts-like alkylations[10] in which the use of lanthanide and actinide triflates[11] as well as heterogeneous catalysts[12] is especially noteworthy. Very recently we demonstrated that also various late-transition-metal salts, such as $IrCl_3$, $RhCl_3$, or H_2PtCl_6, are capable of catalyzing the addition of benzyl acetates to arenes and heteroarenes with high yield and selectivity under ambient conditions.[13,14] The resulting diarylmethane motif is an integral part of a number of biologically active compounds and pharmaceuticals such as piritrexim, trimethoprim, avrainvilleol, papaverine, beclobrate, or letrozole. In addition, diarylmethanes are utilized for the preparation of fluorenyl-based electroactive and photoactive oligomers and polymers.[15]

Although the selectivity of our recently developed procedure is often good to very good, to date a significant amount (5–10 mol%) of an expensive late-transition-metal catalyst has to be applied. Thus, we are interested in alternative, more practical catalyst systems, which can be used in the synthesis of all types of diarylmethanes. In looking for new and improved catalysts the reaction of *o*-xylene and 1-phenylethyl acetate was studied as a model reaction. The performance of different Brønsted acids and transition-metal salts was compared without additional solvent at 50–80 °C (Scheme 1). With regard to the catalyst, our attention focused in this study mainly on inexpensive and relatively nontoxic metal salts based on Fe, Cu, Co, Zn, and Mn. Table 1 shows a summary of the results.





Scheme 1. Reaction of *o*-xylene with 1-phenylethyl acetate.

Table 1: Reaction of *o*-xylene with 1-phenylethyl acetate (Scheme 1).[a]

Entry	Catalyst	Conversion [%]	Yield of **1** [%] (Regioselectivity[b])
1	HCl	5	0
2	*p*-TSA[c]	52	2
3	HOAc	8	0
4	$CoCl_2$	13	0
5	CuBr	0	0
6	CuCl	14	0
7	$CuBr_2$	22	0
8	$CuCl_2$	17	0
9	$CuCl_2 \cdot 2H_2O$	26	11
10	$FeCl_2$	16	0
11	$Fe(OAc)_2$	13	0
12	$[Fe(acac)_3]$[d]	5	0
13[e]	$FeCl_3$	100	99 (>99:1)
14[e]	$FeCl_3 \cdot 6H_2O$	100	99 (>99:1)
15	$Fe(ClO_4)_3 \cdot H_2O$	100	99 (92:8)
16	$Fe(BF_4)_2$[f]	98	63 (94:6)
17	MnO_2	14	0
18	$MnCl_2$	4	0
19	$MnSO_4 \cdot H_2O$	15	0
20	$ZnCl_2$	50	21
21	$Zn(OAc)_2 \cdot 2H_2O$	13	0

[a] Reaction conditions: 1-phenylethyl acetate (0.5 mmol), *o*-xylene (5 mL), catalyst (10 mol%), 80 °C, 20 h. [b] 1-(3,4-Dimethylphenyl)-1-phenylethane: 1-(2,3-dimethylphenyl)-1-phenylethane. [c] TSA = *p*-toluene sulfonic acid. [d] acac = acetylacetone. [e] 50 °C. [f] The catalyst was employed as 43.5% aqueous solution.

[*] Dr. I. Iovel, Dipl.-Chem. K. Mertins, Dipl.-Chem. J. Kischel, Dr. A. Zapf, Prof. Dr. M. Beller
Leibniz-Institut für Organische Katalyse an der Universität Rostock e.V. (IfOK)
Buchbinderstrasse 5–6, 18055 Rostock (Germany)
Fax: (+49) 381-466-9324
E-mail: matthias.beller@ifok.uni-rostock.de

[**] This work has been financed by the state of Mecklenburg-Vorpommern and the Bundesministerium für Bildung und Forschung ("Nachhaltige Aromatenchemie"). We thank Prof. Dr. M. Michalik, Dr. W. Baumann, Dr. C. Fischer, Mrs. H. Baudisch, Mrs. A. Lehmann, Mrs. C. Mewes, and Ms. K. Reincke (all IfOK) for excellent analytic support.

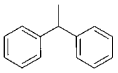
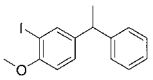
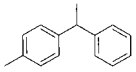
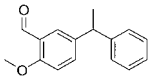
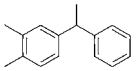
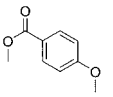
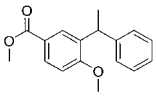
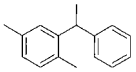
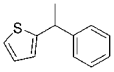
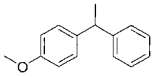
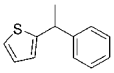
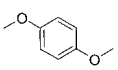
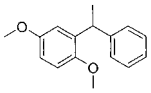
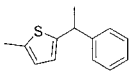
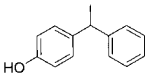
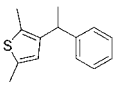
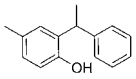
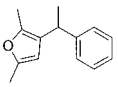
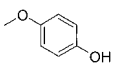
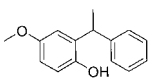
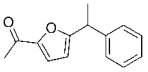
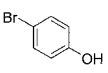
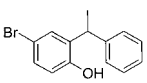
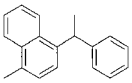
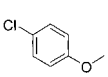
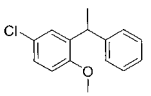
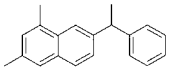
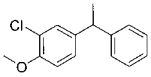
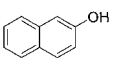
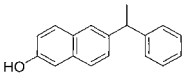
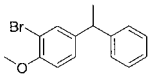
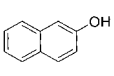
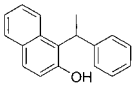
 DOI: 10.1002/anie.200462522 © 2005 Wiley-VCH Verlag GmbH & Co. KGaA, Weinheim

While in the presence of catalytic amounts (10 mol%) of various Brønsted acids (HCl, HOAc, *p*-toluenesulfonic acid) no or only low yields (<2%) of the product 1-(3,4-dimethylphenyl)-1-phenylethane (**1**) are obtained (Table 1, entries 1–3), iron(III) salts proved to be excellent catalysts for the test reaction (Table 1, entries 13–15).[16] The best results (>99% of **1**) are obtained in the presence of $FeCl_3$ (Table 1, entries 13, 14). Advantageously, even hydrated $FeCl_3$ can be used under mild conditions (50°C) and the reaction is not sensitive towards air or moisture. Although screening reactions have been run for convenience for 20 h, it is noteworthy that the reaction with $FeCl_3$ is finished within 1 h at 80°C. With other metal salts a significant difference between the conversion and the yield of **1** is observed in some cases. In these reactions, side-reactions of 1-phenylethyl acetate, such as elimination of acetic acid to give styrene that then undergoes oligomerization and polymerization, took place.

We were interested in the reactivity of different arenes and heteroarenes (Table 2). However, only the most active and selective catalyst ($FeCl_3$) was tested. As expected a variety of electron-rich aromatics, such as toluene, anisole, 1,4-dimethoxybenzene, 1-methylnaphthalene, 1,3-dimethylnaphthalene, 2-naphthol (all >99% yield), and 1,4-xylene (97%), gave the corresponding products in excellent yields. In addition, heteroarenes, such as 2-methylthiophene, 2,5-dimethylthiophene (>99%), 2,5-dimethylfuran (87%), and 2-acetylfuran (92%), react very well.

Even non-activated substrates, for example, benzene (50%) and functionalized starting materials, such as 4-bromophenol (86%), 2- and 4-chloroanisole (>99%), 2-

Table 2: Benzylation of different arenes with 1-phenylethyl acetate.[a]

Entry	Arene	Main Product	Solvent (*T* [°C])	Yield [%] (Regioselectivity)	Entry	Arene	Main Product	Solvent (*T* [°C])	Yield [%] (Regioselectivity)
1			–[b] (140)	50 (–)	14			CH_2Cl_2 (50)	88 (>99:1)
2			–[b] (50)	>99 (84:13:3)	15			$MeNO_2$ (120)[c]	93 (>99:1)
3			–[b] (50)	>99 (>99:1)	16			$MeNO_2$ (50)	>99 (>99:1)
4			–[b] (80)	97 (–)	17			CH_2Cl_2 (50)	62 (83:17)
5			–[b] (50)	>99 (84:16)	18			$MeNO_2$ (50)	66 (77:23)
6			CH_2Cl_2 (50)	>99 (–)	19			$MeNO_2$ (50)	>99 (85:15)
7			$MeNO_2$ (50)	>99 (80:20)	20			CH_2Cl_2 (50)	>99 (–)
8			CH_2Cl_2 (50)	>99 (>99:1)	21			CH_2Cl_2 (50)	87 (–)
9			CH_2Cl_2 (50)	>99 (78:22)	22			$MeNO_2$ (50)	92 (>99:1)
10			CH_2Cl_2 (50)	86 (>99:1)	23			$MeNO_2$ (50)	>99 (93:7)
11			CH_2Cl_2 (50)	>99 (>99:1)	24			CH_2Cl_2 (50)	>99 (75:14:11)
12			CH_2Cl_2 (50)	>99 (>99:1)	25			CH_2Cl_2 (50)	87 (69:15:10:6)
13			CH_2Cl_2 (50)	97 (>99:1)	26			$MeNO_2$ (50)	>99 (88:8:4)

[a] Reaction conditions: arene (2.0 mmol), 1-phenylethyl acetate (0.5 mmol), solvent (5 mL), $FeCl_3$ (10 mol%), 20 h. Yield determined by GC with decane as internal standard. [b] 5 mL arene, no solvent. [c] 2 h reaction time.

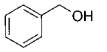
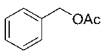
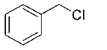
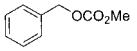
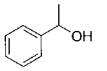
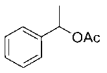
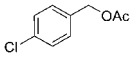
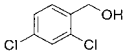
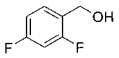
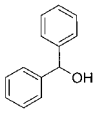
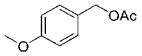
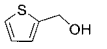
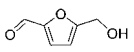
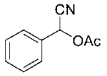
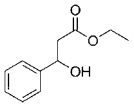
 © 2005 Wiley-VCH Verlag GmbH & Co. KGaA, Weinheim

bromoanisole (97%), 2-iodoanisole (88%), and also 2-methoxybenzaldehyde (93%) and methyl 4-methoxybenzoate (>99%), gave the corresponding products highly selectively. Note that this reaction catalyzed by $FeCl_3$ is one of the few successful Friedel–Crafts alkylations which work well also with non-activated arenes, and entry 15 (Table 2) constitutes one of the rare cases of a selective Friedel–Crafts reaction in the presence of an aldehyde group.

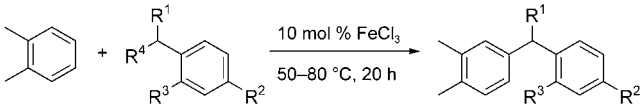
The scope and limitation of the benzylation reagent are shown in Table 3 in more detail: as well as 1-phenylethyl acetate, also benzyl alcohol, benzyl acetate, benzyl chloride, benzyl methyl carbonate, 1-phenylethanol, 1,1-diphenylmethanol, 4-chlorobenzyl acetate, 2,4-dichloro- and 2,4-difluorobenzyl alcohol react with *o*-xylene in the presence of $FeCl_3$ at 80°C (Table 3, entries 1–10). In all cases the corresponding products are obtained in good to excellent yields (96 to >99%). To our surprise there is basically no difference between the reaction of benzyl acetate and benzyl alcohol, although in the latter case stoichiometric amounts of water are produced which are expected to deactivate the catalyst.

Applying 4-methoxybenzyl acetate, 2-(hydroxymethyl)-thiophene, or 5-(hydroxymethyl)-2-furfural the desired products are observed in somewhat lower yields (66, 61, and 37%, respectively) owing to "self-arylation" of the benzylating reagent (Table 3, entries 11–13). In general, the regioselectivity of the reaction is good to excellent (89 to >99%). However, in a few cases applying halogen derivatives and heterocyclic reagents the regioselectivity is somewhat lower (62–75%). From a standpoint of general applicability it is interesting to note that the method allows for the use of benzyl alcohols or acetates which are functionalized in the benzylic position (Scheme 2). Hence, easily available aromatic cyanohydrins can be arylated despite the decreased stability of the intermediate carbocation (Table 3, entry 14). To our knowledge this is the first example of such an arylation reaction. Another example for a functionalized substrate is ethyl 3-phenyl-3-hydroxypropanoate, which yields the corresponding 3,3-diarylpropanoate in 98% yield (Table 3, entry 15).

Table 3: Variation of the benzylating agent in the reaction with o-xylene (Scheme 2).[a]

Entry	Benzylating agent	Yield [%]	Regioselectivity[b]
1		99	99:1
2		99	99:1
3		>99	67:33
4		96	99:1
5		>99	89:11
6[c]		99	>99:1
7		>99	64:36
8		>99	69:31
9		99	69:31
10		>99	93:7
11		66	99:1
12		61	75:25
13[d]		37	62:38
14		31	>99:1
15		98	99:1

[a] Reaction conditions: benzylating agent (0.5 mmol), *o*-xylene (5 mL), $FeCl_3$ (10 mol%), 80°C, 24 h. Yield determined by GC with decane as internal standard. [b] 4-alkylated *o*-xylene : 3-alkylated *o*-xylene. [c] 50°C. [d] Stepwise addition of the reagent.



R^1 = H, Me, Ph, CH_2CO_2Et, CN
R^2 = H, OMe, Cl, F
R^3 = H, Cl, F
R^4 = OH, OAc, OCO_2Me, Cl

Scheme 2. Reaction of *o*-xylene with different benzylating reagents.

In summary, we have developed a general method for the arylation of benzyl carboxylates and benzyl alcohols. Using iron catalysts[17] an easy and practical synthesis of many kinds of diarylmethanes and arylheteroarylmethanes is possible. Typically reactions proceed under mild conditions (50–80°C, without strong acid or base) and it is not necessary to exclude air or moisture. Of special importance is the tolerance of a wide variety of functional groups, such as CHO, CO_2R, I, Br, Cl, F, OH, OMe, as well as the thiophene and furan derivatives, which is a rare feature of Friedel–Crafts-type chemistry. Using benzyl alcohols this arylation method is a state-of-the-art green route to diarylmethanes, because water is the only side-product in this transformation.

Experimental Section

General: All reactions were carried out without any special precautions against air. ^1H and ^{13}C NMR spectra were recorded on a Bruker ARX 400 spectrometer. Chemical shifts (δ) are given in ppm and refer to the residual solvent as the internal standard. Gas chromatography was performed on a Hewlett Packard HP 6890 chromatograph with a HP5 column. Mass spectra were recorded on an AMD 402/3

 © 2005 Wiley-VCH Verlag GmbH & Co. KGaA, Weinheim

mass spectrometer. Chemicals and solvents were purchased from Fluka or Aldrich and used as received.

Benzylation of *o*-xylene: In a pressure tube, 1-phenylethyl acetate (0.5 mmol) and catalyst (10 mol%, 0.05 mmol) were dissolved in *o*-xylene (5 mL). Then hexadecane or decane (50 μL) was added as internal GC standard. After stirring for 20 h at 80 °C aliquots were taken from the reaction mixture and subjected to GC analysis for determination of yield and conversion. For isolation of the products the reaction was quenched with water. The water phase was extracted with dichloromethane. The combined organic layers were dried over $MgSO_4$ and the solvents were distilled off. The product was purified by silica gel column chromatography (70–230 mesh, *n*-heptane/ethyl acetate (50:1)).

^{1}H NMR (400 MHz, $CDCl_3$, 25 °C): $\delta = 1.5$ (d, ^3J(H,H) = 7.2 Hz, 3H; $CHCH_3$), 2.1 (s, 6H; $2ArCH_3$), 4.0 (q, ^3J(H,H) = 7.2 Hz, 1H; CH), 6.9–7.2 ppm (m, 8H; CH aromat.); ^{13}C NMR (101 MHz, $CDCl_3$, 25 °C): $\delta = 18.3$, 18.8, 20.9, 43.2, 123.8, 124.8, 126.5, 127.3, 127.9, 128.6, 133.1, 135.4, 142.8, 145.6 ppm; MS (70 eV): *m*/*z* (%): 210 (40) [M^+], 195 (100) [$C_{15}H_{15}^+$], 91 (10) [$C_7H_7^+$].

Received: November 5, 2004
Published online: May 18, 2005

Keywords: arylation · benzylation · Friedel–Crafts reaction · homogeneous catalysis · iron

[1] G. Dyker, *Angew. Chem.* **1999**, *111*, 1808 – 1822; *Angew. Chem. Int. Ed.* **1999**, *38*, 1698 – 1712.

[2] a) S. Murai, F. Kakiuchi, S. Sekine, Y. Tanaka, A. Kamatami, M. Sonoda, N. Chatani, *Nature* **1993**, *366*, 529 – 531; b) F. Kakiuchi, S. Sekine, Y. Tanaka, A. Kamatami, M. Sonoda, N. Chatani, S. Murai, *Bull. Chem. Soc. Jpn.* **1995**, *68*, 62 – 83; c) F. Kakiuchi, S. Murai, *Acc. Chem. Res.* **2002**, *35*, 826 – 834; d) F. Kakiuchi, T. Uetsuhara, Y. Tanaka, N. Chatani, S. Murai, *J. Mol. Catal. A* **2002**, *182*, 511 – 514; e) Y. Guari, A. Castellanos, S. Sabo-Etienne, B. Chaudret, *J. Mol. Catal. A* **2004**, *212*, 77 – 82.

[3] a) F. Kakiuchi, M. Yamauchi, N. Chatani, S. Murai, *Chem. Lett.* **1996**, 111 – 112; b) C.-H. Jun, J.-B. Hong, Y.-H. Kim, K.-Y. Chung, *Angew. Chem.* **2000**, *112*, 3582 – 3584; *Angew. Chem. Int. Ed.* **2000**, *39*, 3440 – 3442; c) C.-H. Jun, C. W. Moon, J.-B. Hong, S.-G. Lim, K.-Y. Chung, Y.-H. Kim, *Chem. Eur. J.* **2002**, *8*, 485 – 492; d) Y.-G. Lim, J.-S. Han, B. T. Koo, J.-B. Kang, *J. Mol. Catal. A* **2004**, *209*, 41 – 49.

[4] a) G. Dyker, E. Muth, A. S. K. Hashmi, L. Ding, *Adv. Synth. Catal.* **2003**, *345*, 1247 – 1252; for a recent review on stereoselective Friedel–Crafts type reactions with unsaturated compounds see: b) M. Bandini, A. Melloni, A. Umani-Ronchi, *Angew. Chem.* **2004**, *116*, 560 – 566; *Angew. Chem. Int. Ed.* **2004**, *43*, 550 – 556.

[5] a) R. K. Thalji, K. A. Ahrendt, R. G. Bergman, J. A. Ellman, *J. Am. Chem. Soc.* **2001**, *123*, 9692 – 9693; b) K. A. Ahrendt, R. G. Bergman, J. A. Ellman, *Org. Lett.* **2003**, *5*, 1301 – 1303.

[6] a) F. Kakiuchi, Y. Yamamoto, N. Chatani, S, Murai, *Chem. Lett.* **1995**, 681 – 682; b) C. G. Jia, W. T. Lu, J. Oyamada, T. Kitamura, K. Matsuda, M. Irie, Y. Fujiwara, *J. Am. Chem. Soc.* **2000**, *122*, 7252 – 7263; c) T. Kitamura, K. Yamamoto, M. Kotani, J. Oyamada, C. Jia, Y. Fujiwara, *Bull. Chem. Soc. Jpn.* **2003**, *76*, 1889 – 1895; d) M. T. Reetz, K. Sommer, *Eur. J. Org. Chem.* **2003**, 3485 – 3496.

[7] a) E. J. Moore, W. R. Pretzer, T. J. O'Connell, J. Harris, L. Labounty, L. Chou, S. S. Grimmer, *J. Am. Chem. Soc.* **1992**, *114*, 5888 – 5890; b) N. Chatani, T. Fukuyama, F. Kakiuchi, S. Murai, *J. Am. Chem. Soc.* **1996**, *118*, 493 – 494.

[8] a) S. J. Pastine, S. W. Youn, D. Sames, *Tetrahedron* **2003**, *59*, 8859 – 8868; b) S. J. Pastine, D. Sames, *Org. Lett.* **2003**, *5*, 4053 – 4055; c) S. J. Pastine, S. W. Youn, D. Sames, *Org. Lett.* **2003**, *5*, 1055 – 1058; d) V. Mamane, P. Hannen, A. Fürstner, *Chem. Eur. J.* **2004**, *10*, 4556 – 4575.

[9] a) B. Sezen, D. Sames, *Org. Lett.* **2003**, *5*, 3607 – 3610; b) B. Sezen, D. Sames, *J. Am. Chem. Soc.* **2003**, *125*, 5274 – 5275; c) B. Sezen, D. Sames, *J. Am. Chem. Soc.* **2003**, *125*, 10580 – 10585.

[10] a) G. A. Olah, R. Krishnamurti, G. K. S. Prakash in *Comprehensive Organic Synthesis, Vol. 3* (Eds.: B. M. Trost, I. Fleming), Pergamon, Oxford, **1991**, pp. 293 – 339; b) T. Tsuchimoto, Y. Ozawa, R. Negoro, E. Shirakawa, Y. Kawakami, *Angew. Chem.* **2004**, *116*, 4327 – 4329; *Angew. Chem. Int. Ed.* **2004**, *43*, 4231 – 4233, and references therein.

[11] a) M. T. E. Gihani, H. Heaney, K. F. Shuhaibar, *Synlett* **1996**, 871 – 872; b) S.-I. Fukuzawa, T. Tsuchimoto, T. Hiyama, *J. Org. Chem.* **1997**, *62*, 151 – 156; c) T. Tsuchimoto, K. Tobita, T. Hiyama, S.-I. Fukuzawa, *J. Org. Chem.* **1997**, *62*, 6997 – 7005; d) G. V. M. Sharma, A. K. Mahalingam, *J. Org. Chem.* **1999**, *64*, 8943 – 8944; e) I. Shiina, M. Suzuki, *Tetrahedron Lett.* **2002**, *43*, 6391 – 6394; f) M. Noji, T. Ohno, K. Fuji, N. Futabe, H. Tajima, K. Ishii, *J. Org. Chem.* **2003**, *68*, 9340 – 9347; g) T. Mukaiyama, H. Kamiyama, H. Yamanaka, *Chem. Lett.* **2003**, *32*, 814 – 815.

[12] Selected recent examples: a) X. Hu, G. K. Chuah, S. Jaenicke, *Appl. Catal.* **2001**, *217*, 1 – 2; b) V. R. Choudhary, S. K. Jana, *J. Catal.* **2001**, *201*, 225 – 235; c) A. B. Deshpande, A. R. Bajpai, S. D. Samant, *Appl. Catal.* **2001**, *209*, 229 – 235; d) V. R. Choudhary, S. K. Jana, V. S. Narkhede, *Appl. Catal.* **2002**, *235*, 207 – 215; e) N. B. Shrigadi, A. B. Shinde, S. D. Samant, *Appl. Catal.* **2003**, *252*, 23 – 35; f) K. Bachari, J. M. M. Millet, B. Benaichouba, O. Cherifi, F. Figueras, *J. Catal.* **2004**, *121*, 55 – 61; g) M. Salavati-Niasari, J. Hasanalian, H. Najafian, *J. Mol. Catal. A* **2004**, *209*, 209 – 214; for the reaction of benzene with benzyl chloride catalyzed by Envirocat EPZ10 see: h) K. Martin in *Handbook of Green Chemistry and Technology* (Eds.: J. Clark, D. Macquarrie), Blackwell Science, Oxford, **2002**, pp. 321 – 337; the catalyst can be reused with little or no decrease in activity and the yield of diphenylmethane remained at 70–75%.

[13] K. Mertins, I. Jovel, J. Kischel, A. Zapf, M. Beller, *Angew. Chem.* **2005**, *117*, 242 – 246; *Angew. Chem. Int. Ed.* **2005**, *44*, 238 – 242.

[14] For other examples using transition-metal complexes see: a) G. Dyker, D. Hildebrandt, J. Liu, K. Merz, *Angew. Chem.* **2003**, *115*, 4536 – 4538; *Angew. Chem. Int. Ed.* **2003**, *42*, 4399 – 4402; b) Y. Nishibayashi, M. Yoshikawa, Y. Inada, M. D. Milton, M. Hidai, S. Uemura, *Angew. Chem.* **2003**, *115*, 2663 – 2666; *Angew. Chem. Int. Ed.* **2003**, *42*, 2681 – 2684; c) Y. Nishibayashi, Y. Inada, M. Yoshikawa, M. Hidai, S. Uemura, *Angew. Chem.* **2003**, *115*, 1533 – 1536; *Angew. Chem. Int. Ed.* **2003**, *42*, 1495 – 1498.

[15] a) P. J. Skabara, I. M. Serebryako, I. F. Perepichka, *Synth. Met.* **1999**, *102*, 1336 – 1337; b) M. S. Khan, M. R. A. Al-Mandhary, M. K. Al-Suti, B. Ahrens, M. F. Mahon, L. Male, P. R. Raithby, C. E. Boothby, A. Kohler, *Dalton Trans.* **2003**, 74 – 84; c) J. Jacob, L. Oldridge, J. Y. Zhang, M. Gaal, E. J. W. List, A. C. Grimsdale, K. Müllen, *Curr. Appl. Phys.* **2004**, *4*, 339 – 342.

[16] Fe-catalysts have been used for reactions of benzyl chloride with non-functionalized arenes. Stoichiometric amounts of unwanted HCl are formed and corrosion problems occur. For examples see: a) Y. V. Pozdnyakovich, R. P. Savyak, S. M. Shein, *J. Org. Chem. USSR (Engl. Transl.)* **1983**, *19*, 1484 – 1490; Y. V. Pozdnyakovich, R. P. Savyak, S. M. Shein, *Zh. Org. Khim.* **1983**, *19*, 1674 – 1681; b) Y. V. Pozdnyakovich, R. P. Savyak, S. M. Shein, *Zh. Org. Khim.* **1986**, *22*, 584 – 589; c) S. G. Pai, A. R. Bajpai, A. B. Deshpande, S. D. Samant, *Synth. Commun.* **1997**, *27*, 2267 – 2273; d) V. R. Choudhary, S. K. Jana, B. P. Kiran, *Catal. Lett.* **1999**, *59*, 217 – 219; e) S. G. Pai, A. R. Bajpai, A. B. Deshpande, S. D. Samant, *J. Mol. Catal. A* **2000**, *156*, 233 – 243; f) V. R.

 © 2005 Wiley-VCH Verlag GmbH & Co. KGaA, Weinheim

Choudhary, S. K. Jana, A. S. Mamman, *Microporous Mesoporous Mater.* **2002**, *56*, 65–71; g) V. R. Choudhary, S. K. Jana, *Appl. Catal.* **2002**, *224*, 51–62; h) V. R. Choudhary, S. K. Jana, *J. Mol. Catal. A* **2002**, *180*, 267–276.

[17] For an actual review on the use of Fe-catalysts in organic synthesis see: C. Bolm, J. Legros, J. Le Paih, L. Zani, *Chem. Rev.* **2004**, *104*, 6217–6254.

 © 2005 Wiley-VCH Verlag GmbH & Co. KGaA, Weinheim

Analysis of X-ray Data

Cluster Disorder and Ordering Principles in Al-Stabilized "LaI"**

*Oliver Oeckler, Thomas Weber, Lorenz Kienle, Hansjürgen Mattausch, and Arndt Simon**

Diffuse X-ray scattering is frequently dismissed in conventional structure analyses. However, it contains valuable information in many respects, particularly concerning the chemical constitution of a crystal. Most investigations on diffuse scattering so far have been restricted to qualitative discussions, trial-and-error simulations, and analytical Fourier calculations.[1] The quantitative measurement of the continuous intensity distribution in reciprocal space has become routinely feasible with the advent of area detectors. As computing power is still a bottleneck for complex numerical methods, quantitative structure refinement against diffuse data has been performed in only a few investigations.[2] Such refinements will become more and more accessible in the future. Here we present a case where only the refinement against diffuse scattering data led to detailed insight into the chemical nature of a compound.

Some time ago the preparation and structure of LaI was described in this journal.[3] It crystallizes in the hexagonal NiAs structure type. Now we have found a phase with the approximate composition $(La_{1-x}Al_x)I$ ($x < 0.15$) for which on the basis of sharp Bragg reflections a NaCl-type structure ($a =$ 6.323 Å) can be refined down to $R \approx 5\,\%$.[4] In spite of the convincing value, this structural characterization is incomplete and even misleading. A correct structural model can be derived only by taking into account the pronounced diffuse scattering that shows up as sections of hollow spheres in Figure 1.

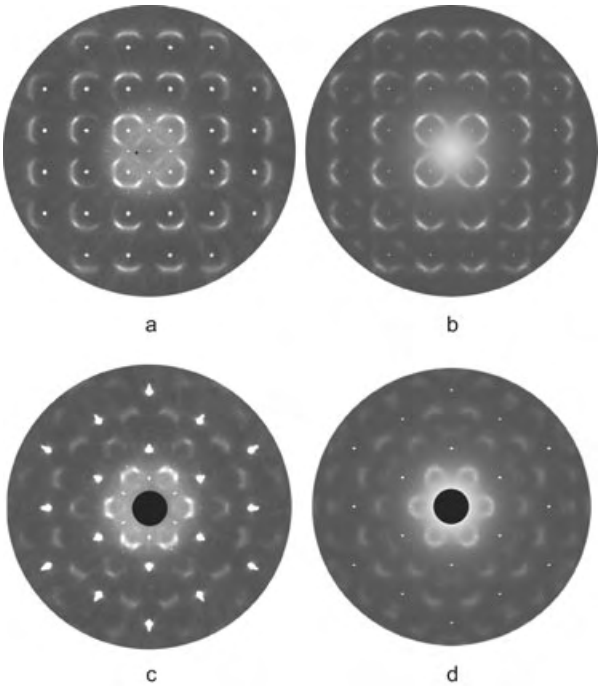


Figure 1. Experimental (a, c) and calculated (b, d) X-ray diffraction patterns for $La_{\approx 0.7}I_{1-x}Al_x$ ($x \approx 0.14$); first layer perpendicular [100] (a, b) and zero layer perpendicular [111] (c, d). The calculated images are based on the best refinement result.

A hint to the correct interpretation of the diffraction data comes from the extended cluster chemistry of the rare-earth metals.[5] Their metal-rich halides are composed of discrete or condensed clusters, and the M_6X_{12}-type cluster stabilized by an endohedral atom Z is frequently observed. The $M_6X_{12}Z$ entity can be viewed as a section of the rock-salt structure.[6] Hence, one way of addressing the disorder problem is to start from a hypothetical NaCl-type LaI, in which some iodine atoms are replaced by endohedral atoms Z = Al, and the La atoms that are not part of the La_6Al units are removed. If we assume the presence of such $La_6I_{12}Al$ clusters[7] in the title compound, the occurrence of structured and narrow diffuse scattering indicates their nonrandom distribution, which is quite common with metal-rich cluster compounds of lanthanoids and other elements.[8]

Some conclusions can be drawn from the qualitative analysis of the diffuse intensity. Generally speaking, the presence of spheres and their location only around odd Bragg reflections can be interpreted as due to some spherical modulation[9] characterized by the complementary behavior of cation and anion sites, and the higher intensity on the large-

[*] Dr. L. Kienle, Dr. H. Mattausch, Prof. Dr. A. Simon
Max-Planck-Institut für Festkörperforschung
Heisenbergstrasse 1, 70569 Stuttgart (Germany)
Fax: (+49) 711-689-1642
E-mail: a.simon@fkf.mpg.de
Dr. O. Oeckler
Department Chemie und Biochemie
Lehrstuhl für Anorganische Festkörperchemie
Ludwig-Maximilians-Universität
Butenandtstrasse 5–13(D), 81377 Munich (Germany)
Dr. T. Weber
Laboratorium für Kristallographie
ETH-Hönggerberg
Wolfgang-Pauli-Strasse 10, 8093 Zurich (Switzerland)

[**] O. Oeckler thanks the Max Planck Society for supporting his stay in Zurich. The authors are indebted to R. Eger for preparative work and V. Duppel for recording SAED patterns and HRETM images.

 DOI: 10.1002/anie.200500594 © 2005 Wiley-VCH Verlag GmbH & Co. KGaA, Weinheim

angle side indicates lattice distortions due to a "size effect",[10] where a smaller structural motif (e.g. a cluster) is a stronger scatterer than a larger structural motif. However, from these and other possible qualitative considerations no reliable statements can be made concerning the kind of chemical entities, their interconnection, and their nonrandom arrangement. Here we demonstrate a quantitative structure solution by a new, very efficient evolutionary algorithm.[2a,11]

The first important step is the modeling of the disorder with a realistic atom arrangement using as few parameters as possible, because diffuse data contain limited information and precision in comparison to Bragg data. A (defect-)NaCl-type structure can be derived starting from a *fcc* lattice of I atoms by statistically substituting a variable number of atoms (11–15%) by La_6Al units to create a set of 80 different structures, each defined by a specific set of parameters. In Monte Carlo (MC) calculations we used a set of 13 parameters, including "interaction energies" for edge- and corner-sharing octahedrons and all possible relative cluster positions up to a distance of 13.4 Å. Furthermore, the cluster concentration and local relaxation around vacancies and interstitial atoms are parameters of the disorder model obtained by "energy minimization" with respect to the specific parameter set.

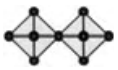
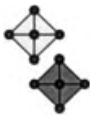
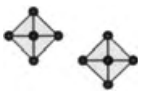
The pixelwise comparison of the scattering intensities calculated for these model structures with observed intensities is quantified by an *R*-factor for each structure ("individual"). Then the next generation of structures strictly related to the specific parents, and hence comprising the same number of individuals as the starting set, is created by admixing a certain percentage of another parent's parameter set, and those members of the new generation are dismissed whose structures lead to an inferior fit with the experimental data. In a later generation the calculation converges to a set of statistically identical structures which optimally represents the experimental scattering pattern. This final structure model is analyzed in terms of the structural features actually present.[12]

Figure 2 illustrates that the final structure model exhibits a uniform cluster distribution in contrast to the random arrangement for the refined cluster concentration x. This refinement yields $x = 0.136$ and the chemical formula $La_{0.69}I_{0.86}Al_{0.14}$, which is confirmed by chemical analyses. The deviation of La and I atoms from the ideal NaCl-type positions as refined from diffuse data is in good agreement with the corresponding numbers derived from Bragg data;[13] however, now the displacements can be interpreted directly in terms of a contraction of the clusters. The cluster geometry is in very good agreement with that of $La_6I_{12}Al$ or related clusters in other compounds.[7]

Based on this result, a reasonable interpretation of Bragg data can be obtained, too, in a constrained refinement[14] assuming one anion site with x Al and $(1-x)$ I and implying La_6Al octahedrons by placing $6x$ La on the cation site. In accordance with the result from diffuse data, x amounts to 0.110(1). However, information on the interconnection of clusters can *only* be derived from the final structure model.

From Table 1 we conclude that edge- or corner-sharing octahedrons are very unfavorable in this compound as their frequency amounts to 49% and 31%, respectively, of the random arrangement. Double octahedrons have been frequently observed in other systems;[5a,d] however, the present disordered NaCl-type matrix obviously cannot adjust to the high degree of strain induced by the contraction due to metal–metal bonding in such an entity. Configurations that do not allow complete relaxation are observed less frequently, and the tendency to avoid local strain is evident from the most favorable relative cluster position in which the centers are on opposite corners in the [111] direction of the NaCl cell as shown in Figure 3. Short La–I contacts are avoided (3.16 Å in the average NaCl structure instead of 3.28–3.40 Å in comparable compounds) both by contraction of the La_6 unit as well as by displacement of the I atoms towards the void.

Table 1: Comparison of relative cluster positions (characterized by lattice vectors corresponding to a NaCl unit cell) for a) random cluster distribution with $x = 0.136$ before MC calculation and b) the final model crystal. The frequencies of intercluster arrangements are denoted n_i for (a) and n_f for (b).

Relative cluster positions		n_i	n_f	n_f/n_i
	[0.5,0.5,0]	55856	27108	0.49
	[100]	27875	8687	0.31
	[0.5,0.5,1]	111602	95275	0.85
	[110][a]	55976	59479	1.06
	[1.5,0.5,0]	111759	148168	1.33
	[111][b]	37203	59708	1.60

[a] Face centered (fc) in a 2***a***2***b***2***c*** supercell. [b] Bod centered (bc) in a 2***a***2***b***2***c*** supercell.

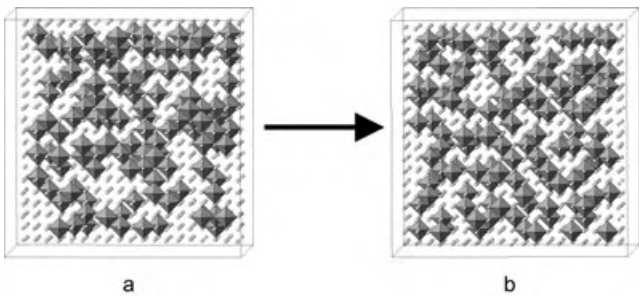


Figure 2. Representative parts of the model crystal ($x = 0.136$; shaded: La_6Al octahedrons, spheres: I atoms) before MC calculation and the final model crystal (after MC simulation with the refined parameters).

 © 2005 Wiley-VCH Verlag GmbH & Co. KGaA, Weinheim

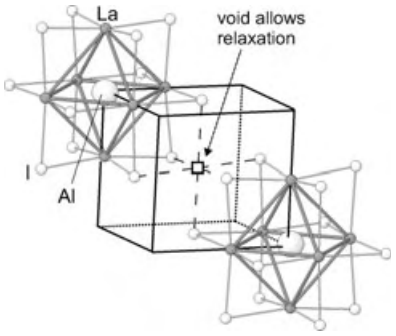


Figure 3. Pair of clusters in the relative position [111] of the average NaCl cell (cell dimensions are outlined). Short La–I distances can be avoided by both cluster contraction and displacement of I atoms towards the void.

Additional evidence for the preference of this relative cluster orientation has also been obtained from high-resolution electron microscopy (HRTEM) studies.[15] Images taken along the zone axis [111] (Figure 4) show the disordered

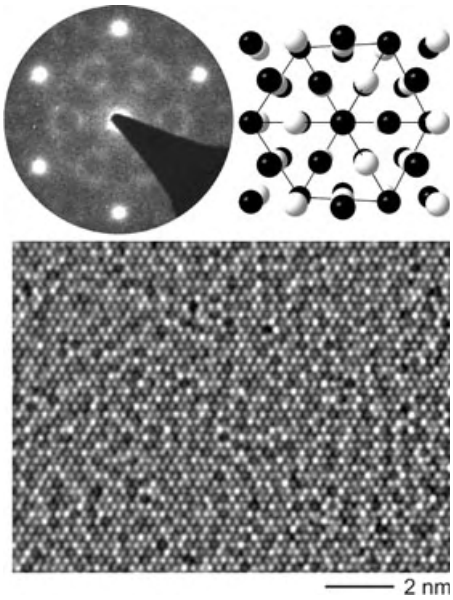


Figure 4. Electron diffraction pattern (top, left) and HRTEM image (bottom) of disordered crystal along the zone axis [111]. The hexagonal arrangement of dots results from the average symmetry of the structure along [111]. The bright and dark contrasts of the experimental image can be correlated with the projection of the real structure (top, right). Simulated images ($\Delta f = -65$) indicate that bright dots correspond to rows of the heavy atoms La and I, while dark dots indicate a sequence of these atoms replaced by Al and voids.

structure as light spots for rows of La and I, and dark spots for rows in which Al and voids alternate statistically. Prolonged exposure to the electron beam as well as long annealing times does not remove the disorder. Based on our investigations we explain this behavior as a consequence of the impossibility of the title compound to order in small unit cells with high symmetry.

However, allowing for slight compositional variations, ordered variants of this structure are sometimes observed in electron diffraction patterns (cf. Figure 5) which show the diffuse scattering to develop into superstructure reflections.

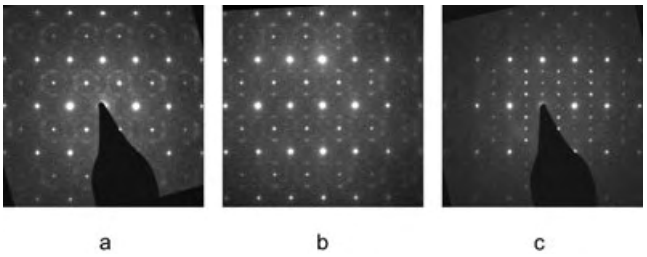


Figure 5. Electron diffraction patterns (zone axis [110]) of several crystals in one sample of the approximate composition $La_{\approx 0.7}I_{1-x}Al_x$ ($x \approx 0.14$). a) The most frequently observed pattern, corresponding to X-ray single-crystal diffraction, b) a crystallite with partial ordering, c) an ordered crystallite with a distinct superstructure.

All reasonable refinements from X-ray Bragg data[16] lead to structure models in which a certain degree of disorder remains; however, a body centering of ordered clusters in a $2\boldsymbol{a}2\boldsymbol{b}2\boldsymbol{c}$ NaCl-type cell is a feature common to all models. This partial ordering corresponds exactly to the preferred cluster arrangement in the disordered structure of the title compound.

Summing up, the title compound and its disorder can be well understood. The cluster distribution is far from a statistically random function. The *uniform* (not *random*) distribution avoids short intercluster distances which leads to an approximately harmonic radial distribution function of intercluster vectors that is reflected in the diffuse spheres. The preferred relative cluster arrangement (Figure 2) allows a unique possibility to avoid short distances in a dense packing by contraction of both Ln_6 units around endohedral Al atoms and of I_6 octahedrons around voids.

Finally, we point out that our investigation, though addressing a special system, is quite relevant to the extended structural chemistry of NaCl-type transition-metal oxides, nitrides, and carbides. They form ordered cluster structures in a few instances, for example, NbO[17] and TiO,[6a,18] and frequently show diffuse scattering effects due to local order and long-range disorder.[19]

Experimental Section

Single crystals of $La_{\approx 0.7}I_{1-x}Al_x$ ($x \approx 0.14$) were first obtained from La, LaI_3, and Al in different reactions (e.g. the nominal composition $La_3Al_2I_2$) during a systematic investigation of the La/I/Al system. EDX analyses (Tescan scanning electron microscope, Oxford EDX detector) of several crystals confirmed the given composition. The best method for obtaining pure samples was by heating a stoichiometric mixture of La, LaI_3, and AlI_3 in a tantalum ampule at 875 °C for 7 days. These samples are single phase according to X-ray powder diagrams (Stoe STADI P diffractometer, $Mo_{K\alpha}$ radiation). Since the starting materials as well as the product are very moisture sensitive, all manipulations must be carried out in a glove box or by Schlenk techniques under purified argon atmosphere. Elemental analysis (double determinations) by the Mikroanalytisches Labor Pascher,

 © 2005 Wiley-VCH Verlag GmbH & Co. KGaA, Weinheim

Remagen, $La_{0.7}I_{0.86}Al_{0.14}$ (212.1 amu) calcd (in wt%): La 46.2, I 51.9, Al 1.8; found: La 43.7, I 54.4, Al 1.8.

Received: February 17, 2005
Published online: May 13, 2005

Keywords: cluster compounds · diffuse scattering · disorder · lanthanum · subiodides

[1] A good overview including many references has been given by H. Jagodzinski, F. Frey in *International Tables for Crystallography*, *Vol. B* (Ed.: H. Shmueli), Kluwer, Dordrecht, **2001**, pp. 407–442. Simulation methods are discussed in R. T. Welberry, *Diffuse X-ray Scattering and Models of Disorder*, Oxford University Press, Oxford, **2004**.

[2] Methods that have been used for a quantitative fit of diffuse data include reverse Monte Carlo, least-squares, and evolutionary (genetic) algorithms: a) T. Weber, H.-B. Bürgi, *Acta Crystallogr. Sect. A* **2002**, *58*, 526; b) T. Proffen, T. R. Welberry, *Acta Crystallogr. Sect. A* **1997**, *53*, 202; c) T. R. Welberry, T. Proffen, M. Bown, *Acta Crystallogr. Sect. A* **1998**, *54*, 661.

[3] J. D. Martin, J. D. Corbett, *Angew. Chem.* **1995**, *107*, 234; *Angew. Chem. Int. Ed. Engl.* **1995**, *34*,233.

[4] Split positions and variation of site occupancies further reduce R_1 to about 3%; however, the mixed La/Al occupation of the cation site assumed here is not consistent with the correct average structure.[14]

[5] a) A. Simon, H. Mattausch, G. J. Miller, W. Bauhofer, R. K. Kremer in *Handbook on the Physics and Chemistry of Rare Earths*, *Vol. 15* (Eds.: K. A. Gschneidner, L. Eyring), Elsevier, Amsterdam, **1991**, p. 191; b) J. D. Corbett, *J. Chem. Soc. Dalton Trans.* **1996**, 575; c) G. Meyer, *Chem. Rev.* **1998**, *98*, 3295; d) H. Mattausch, E. Warkentin, O. Oeckler, A. Simon, *Z. Anorg. Allg. Chem.* **2000**, *626*, 2117; e) H. Mattausch, G. V. Vajenine, O. Oeckler, R. K. Kremer, A. Simon, *Z. Anorg. Allg. Chem.* **2001**, *627*, 2542.

[6] a) A. Simon, *Angew. Chem.* **1981**, *93*, 23; *Angew. Chem. Int. Ed. Engl.* **1981**, *20*, 1; b) A. Simon, *Angew. Chem.* **1988**, *100*, 164; *Angew. Chem. Int. Ed. Engl.* **1988**, *27*, 160; c) H. G. von Schnering, *Angew. Chem.* **1981**, *93*, 44; *Angew. Chem. Int. Ed. Engl.* **1981**, *20*, 33.

[7] Compounds are well characterized with Al-centering trigonal Ln_6 prisms (H. Mattausch, O. Oeckler, C. Zheng, A. Simon, *Z. Anorg. Allg. Chem.* **2001**, *627*, 1523). Octahedral clusters have been observed in comparable compounds, e.g. boride halides,[5a,c] and a few Al-containing octahedral clusters are known as well.

[8] Other disordered cluster compounds have been discussed, cf. for example: J. Köhler, G. Svensson, A. Simon, *Angew. Chem.* **1992**, *104*, 1463; *Angew. Chem. Int. Ed. Engl.* **1992**, *31*, 1437; O. Oeckler, L. Kienle, H. Mattausch, A. Simon, *Angew. Chem.* **2002**, *114*, 4431; *Angew. Chem. Int. Ed.* **2002**, *41*, 4257. In the latter case, a reasonable structural model was not evident from the averaged structure, but a "semiquantitative" analysis of diffuse diffraction data was successful.

[9] T. R. Welberry, *Acta Crystallogr. Sect. A* **2001**, *57*, 244.

[10] T. R. Welberry, *J. Appl. Crystallogr.* **1986**, *19*, 382.

[11] This algorithm mimics the principles of Darwinism (for a detailed overview, cf. Z. Michalewicz, *Genetic Algorithms + Data Structures = Evolution Programs*, Springer, Berlin, **1996**). It starts from a "population" of diverse structure models, each one characterized by its "genes", that is, a set of parameters defining a model crystal as the "phenotype". Its "fitness" corresponds to the crystallographic *R* factor based on all individual pixels of the diffraction image and not only on a set of Bragg intensities. A new generation is created from the parent population by recombination and variation ("mutation") of the parameters ("genes"). Here, we used so-called differential evolution (K. Price, R. Storn, *Dr Dobb's J.* **1997**, April issue, 18; R. Storn, K. Prince, *J. Global Optimization* **1997**, *11*, 341; and ref. [2a]) replacing parents by "fitter" children (models with better *R* factors) and discarding "unfit" members of each new generation.

[12] Refinement of the disordered structure based on diffuse data: Measurement of diffuse data: Huber four-circle goniometer, MAR345 image-plate detector, $Ag_{K\alpha}$ ($\lambda = 0.56086$ Å), graphite monochromator, $2\vartheta_{max} = 45°$, beam normal to oscillation axis and normal to detector, 492 frames, $\Delta\phi = 0.5°$/frame, reconstruction of undistorted reciprocal layers with XCAVATE (M. A. Estermann, W. Steurer, *Phase Transitions* **1998**, *67*, 165). Monte Carlo model: An initial model structure containing a random distribution of clusters was modified by swapping cluster and noncluster positions. The energy difference between the old and the new configuration was calculated based on the model parameters, and the new configuration was accepted with a probability following a Boltzmann distribution. Finally, local relaxations around vacancies and interstitial atoms were applied. Neither the cluster interaction nor the total energy can be interpreted as actual energy values, and the parameters of the structure model cannot be directly analyzed. All "interactions" are simply abstract parameters, but the result of the corresponding MC simulation bears physical significance. The model parameters were refined in analogy to T. Weber, H.-B. Bürgi, *Acta Crystallogr. Sect. A* **2002**, *58*, 526 with $f_m = f_r = 0.6$. The number of lots was subsequently increased after no improvement was found during one generation. The final results are based on 125 lots, $R(\text{final}) = 0.09$ (based on F^2).

[13] Atom shifts from Bragg data are just a mean displacement ("octahedral" split position) from the atom positions of the NaCl type: 0.25(1) Å for La and 0.22(1) Å for I. They can be compared only approximately with the results from diffuse data, which model the actual situation more clearly: an "attractive force" between Al and La yields a refined La–Al distance of 2.8 Å. A "repulsive force" between La and I (avoiding short contacts) leads to an average distance of 3.3 Å for the inner and 3.5 Å for the outer ligands. The root-mean-square displacements as obtained from the Monte Carlo modeling were 0.40 Å for La and 0.19 Å for *I* (based on diffuse data only).

[14] Refinement of the average structure of $La_{\approx 0.7}I_{1-x}Al_x$ ($x \approx 0.14$): Enraf Nonius CAD4 four-circle diffractometer, $Mo_{K\alpha}$ ($\lambda = 0.70173$ Å), $2\vartheta_{max} = 70°$, crystal dimensions $0.11 \times 0.09 \times 0.08$ mm^3, cubic, space group $Fm\bar{3}m$ (No. 225), $a = 6.323(1)$ Å, $V = 252.80(7)$ Å^3, $Z = 4$, calcd density $\rho = 5.44$ g cm^{-3}, $\mu(Mo_{K\alpha}) = 21.7$ mm^{-1}, 590 measured reflections, 48 independent ($R_{int} = 0.055$), least-squares refinement based on F^2 (G. M. Sheldrick, SHELXL-97, Program for the Refinement of Crystal Structures, Universität Göttingen, Göttingen (Germany), **1997**); *R* values [all data/data with $I > 2\sigma(I)$]: $R_1 = 0.033/0.029$, $wR_2 = 0.068/0.066$, GooF = 1.14 for 41 observed reflections [$I > 2\sigma(I)$] and 6 parameters. Further details on the crystal structure investigations may be obtained from the Fachinformationszentrum Karlsruhe, 76344 Eggenstein-Leopoldshafen, Germany (fax: (+49) 7247-808-666; e-mail: crysdata@fiz-karlsruhe.de), on quoting the depository number CSD-391280.

[15] HRTEM along several zone axes was performed with a Philips CM30 ST electron microscope (300 kV, LaB_6 cathode, Gatan multiscan CCD camera). The multislice formalism (P. A. Stadelmann, *Ultramicroscopy* **1987**, *21*, 131–146) was used for image simulations.

[16] A quantitative analysis of the diffuse data from crystals with partial long-range ordering could not be performed due to moderate crystal quality and very weak diffuse intensity as well as limited computational resources. As it is common for many partially ordered cubic structures, the space group assignment (including possible twinning) remains ambiguous in this case.

 © 2005 Wiley-VCH Verlag GmbH & Co. KGaA, Weinheim

[17] H. Schäfer, H. G. Schnering, *Angew. Chem.* **1964**, *76*, 833.
[18] D. Watanabe, J. R. Castles, A. Jostsons, A. S. Malin, *Acta Crystallogr.* **1967**, *23*, 307.
[19] a) J. Billingham, P. S. Bell, M. H. Lewis, *Acta Crystallogr. Sect. A* **1972**, *28*, 602; b) M. Sauvage, E. Parthé, *Acta Crystallogr. Sect. A* **1972**, *28*, 607; c) R. DeRidder, G. van Tendeloo, S. Amelinckx, *Acta Crystallogr. Sect. A* **1976**, *32*, 216; d) K. Oshima, J. Harada, M. Morinaga, P. Georgopoulus, J. B. Cohen, *Acta Crystallogr. Sect. A* **1988**, *44*, 167; e) S. Matsumura, T. Hino, S. Hata, K. Oki, *Mater. Trans.* **1996**, *37*, 1748; f) P. Li, J. M. Howe, *Acta Mater.* **2003**, *51*, 1261.

 © 2005 Wiley-VCH Verlag GmbH & Co. KGaA, Weinheim

DNA–Peptide Complexes

Single-Molecule Experiments in Synthetic Biology: An Approach to the Affinity Ranking of DNA-Binding Peptides**

Rainer Eckel, Sven David Wilking, Anke Becker, Norbert Sewald, Robert Ros, and Dario Anselmetti**

Gene expression in eukaryotes is controlled at the transcriptional level by the specific binding of transcription factors to defined DNA sequences. In this way, cell growth, differentiation, and development are regulated. The possibility to influence and control cell metabolism through modified synthetic transcription factors[1–4] offers fascinating prospects for molecular cell biology in the framework of biomimetics and synthetic biology.[5,6] The design and synthesis of biologically active artificial enzymes and new protein-based materials can be investigated by the combination of bioorganic bottom-up synthesis and single-molecule affinity nanotechnology. With this approach important questions can be addressed, such as the extent to which a single recognition helix contributes to the specific binding of a complete protein to DNA, the effect that a single amino acid point mutation has upon biological specificity and affinity, and the minimal peptide sequence length to ensure binding specificity. This approach would also aid in the design of artificial proteins that contain a purely synthetic helix-turn-helix (HTH) binding motif.

In this context, it is of considerable interest to elucidate the DNA-binding specificity of synthetic peptides with a primary sequence akin to the binding domain of a transcription factor. We studied a 20-residue peptide that represents the native sequence of a binding epitope of the transcription activator PhoB (*E. coli*) and three single point mutants of this peptide.

PhoB is a transcription activator which, after phosphorylation by PhoR, binds to the phosphate box in the promoter region of the phosphate regulon *pho* and activates the expression of genes involved in phosphate metabolism.[7–9] The protein[9] consists of a regulatory phosphorylation domain in the N-terminal region (PhoB 1–127) and a DNA-binding domain in the C-terminal region (PhoB 128–229). Deletion experiments showed that PhoB 139–229 binds to double-stranded DNA and recognizes the sequence TGTCA. The NMR solution structure of the regulatory domain and the DNA-binding domain (PhoB126–229),[10] as well as the X-ray crystal structure of the complex with DNA have been reported (Figure 1a).[11] Structurally, the DNA-binding domain of PhoB belongs to the family of *winged* helix-turn-helix proteins with the topology β^1-β^2-β^3-β^4-α^1-β^5-α^2-α^3-β^6-β^7, in which the rigid turn is replaced by a loop. This family is characterized by an N-terminal four-stranded β sheet (β^1-β^2-β^3-β^4), one α helix (α^1) connected through a short β sheet (β^5) to another α helix (α^2), followed by a third α helix (α^3) and a β hairpin (β^6-β^7). The DNA-recognizing helix α^3, is amphiphilic and is connected to α^2 by a loop.[12] The β hairpin (β^6-turn-β^7) is often called the *recognition wing*.[13]

The single amino acid residues of DNA-binding peptides and proteins contribute differently to affinity and specificity. Whereas cationic side chains (Lys, Arg) often form sequence-independent ionic interactions with the phosphate backbone, the sequence information of the DNA is read through hydrogen bonds and van der Waals interactions with the peptide. Binding of the recognition helix α^3 of PhoB takes place in the DNA major groove.[11] Arg201 interacts through a hydrogen bond with the carbonyl oxygen atom of a guanine base while Arg193, His198, Arg200, and Arg203 form salt bridges with phosphate groups. Furthermore, van der Waals contacts with Thr194 and Val197 are involved in specific recognition. Arg219 in the *recognition wing* is bound to deoxyribose moieties through hydrogen bonds.

In the work reported herein, the contribution that single amino acid residues in the DNA-binding helix α^3 contribute to intermolecular affinity was investigated on the single-molecule level. We synthesized peptides in which the amino acid residues that interact with the DNA phosphate backbone in the X-ray crystal structure through salt bridges were individually exchanged by alanine (Table 1). The synthesized peptides comprised the native sequence PhoB(190–209) as well as the point-mutated peptides PhoB(190–209) R193A, PhoB(190–209) H198A and PhoB(190–209) R203A. Accord-

[*] Dipl.-Chem. R. Eckel, Priv.-Doz. Dr. R. Ros, Prof. Dr. D. Anselmetti
Experimental Biophysics and Applied Nanoscience
Bielefeld University
Universitätsstraße 25, 33615 Bielefeld (Germany)
Fax: (+49) 521-106-2959
E-mail: dario.anselmetti@physik.uni-bielefeld.de
Dipl.-Chem. S. D. Wilking, Prof. Dr. N. Sewald
Organic and Bioorganic Chemistry
Bielefeld University
Universitätsstraße 25, 33615 Bielefeld (Germany)
Fax: (+49) 521-106-8094
E-mail: norbert.sewald@uni-bielefeld.de
Priv.-Doz. Dr. A. Becker
Genetics
Bielefeld University (Germany)

[**] The authors thank the Deutsche Forschungsgemeinschaft (SFB 613) for financial support, Tanja Beschnitt for help with DNA preparation, and Kay Lofthouse for a careful reading of the manuscript.

Supporting information for this article is available on the WWW under http://www.angewandte.org or from the author.

 DOI: 10.1002/anie.200500152 © 2005 Wiley-VCH Verlag GmbH & Co. KGaA, Weinheim

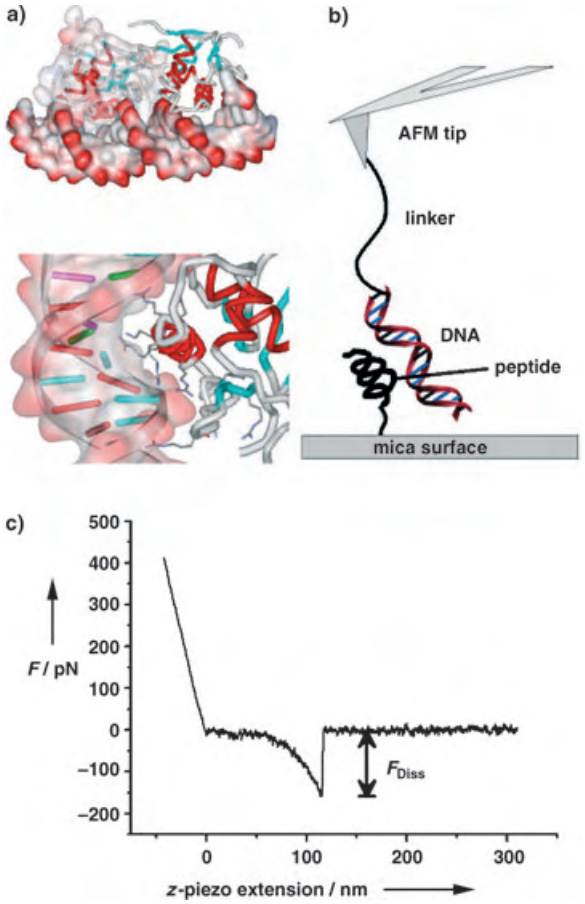


Figure 1. a) Upper image: X-ray crystal structure of the 2:1 complex of PhoB(124–229) with DNA,[10] lower image: Section from the X-ray crystal structure showing the recognition helix α^3; b) force spectroscopy setup (schematic representation); c) typical force–distance curve (only retractive part shown).

Table 1: Synthesized peptides from the epitope PhoB(190–209).

Mutation	Peptide Sequence	k_{off} [s^{-1}][a]	x_β [Å][a]
–	Ac-VEDRTVDVHIRRLRKALEPG-Linker	3.1 ± 2.1	6.8 ± 1.2
R193A	Ac-VED**A**TVDVHIRRLRKALEPG-Linker	0.071 ± 0.053	9.3 ± 2.6
H198A	Ac-VEDRTVDV**A**IRRLRKALEPG-Linker	49.5 ± 21.2	7.2 ± 3.5
R203A	Ac-VEDRTVDVHIRRL**A**KALEPG-Linker	no binding	no binding

[a] k_{off}: dissociation rate constant for the peptide–DNA complex; x_β: molecular reaction length.

ing to CD spectroscopy measurements, all peptides exhibit an α-helical structure. N-terminal functionalized fragments of the PhoB helix α^3 were synthesized on the solid phase with 2-chlorotritylresin preloaded with a suitable linker according to the Fmoc/*t*Bu protection scheme.[14] The peptides were purified by HPLC with acetonitrile/water/TFA gradients. The interaction of the synthesized peptides with the corresponding DNA was investigated with AFM force spectroscopy.

A broad affinity range for specific molecular recognition between single binding partners from 10^{-5} M[15] to 10^{-15} M[16,17] can be investigated with single-molecule force spectroscopy. The deflection of a micro-fabricated force sensor (cantilever) is used to detect forces in the pico-Newton range. The AFM principle permits investigation of molecular binding forces under physiological conditions, and AFM force spectroscopy has found applications in the study of a variety of specific biological receptor–ligand interactions[16–22] as well as in supramolecular host–guest systems.[15] The direct investigation of specific, native protein–DNA interactions has been reported recently.[23–25]

In our studies reported herein, we applied AFM single-molecule force spectroscopy to study the specific binding between the peptides listed in Table 1 and the DNA target sequence. Each peptide was covalently immobilized to an amino-functionalized mica surface in a directed manner with the short C-terminal linker 1,8-diamino-3,6-dioxaoctane and the cross-linker BS^3 (bis(sulfosuccinimidyl)suberate; Figure 1b). This immobilization prevents unfolding of the peptide caused by physisorption on the surface. PCR-amplified genomic DNA containing the 600-bp PhoB binding motif from *E. coli* was chosen as the binding partner, and was bound to an AFM tip with a bifunctional polyethylene glycol (PEG) linker (molar mass: 3400 g mol^{-1}, corresponding to an average length of 30 nm).[26] The application of the PEG linker serves various purposes. First, it adds steric flexibility to the system and ensures that dissociation occurs far from the surface. Second, the linker facilitates the distinction between single and multiple dissociation events, and decreases non-specific adhesion. Third, the elastic stretching of the linker ensures a gradual increase in force until the point of bond rupture, and allows precise measurement of the molecular elasticity of the complex (Figure 1c). As the elasticity is determined for each rupture event individually, variations in the entropic portion of the rupture peaks are included and do not affect the statistical interpretation.

Compilation of the rupture forces to histograms and statistical analysis of the resulting force distribution yields the most probable dissociation forces at a given retract velocity. Each histogram represents the analysis of 2000 force curves; the binding probabilities given in the figures (Figure 2 and Supporting Information) refer to the ratio of rupture events divided by the total number of force curves recorded (for example, 300 binding events out of 2000 force curves results in a binding probability of 15%). The maximum of the force distribution was taken as the most probable dissociation force.

Competition experiments were performed to determine if binding between the peptides and the DNA target sequence occurs specifically. For each mutant, a series of force spectroscopy experiments in standard buffer solution (100 mM Na_2HPO_4, 50 mM NaCl, pH 7.4) was followed by a series of experiments with an excess of free binding partner (peptide or DNA) as competitor in solution. This was followed by washing the sample with standard buffer and then performing another series of experiments in standard buffer. Figure 2 shows the results of the competition for the native peptide: part (a) shows the force distribution in standard buffer solution, with a total binding probability of ≈33%; part (b) shows the competition with free peptide in

 © 2005 Wiley-VCH Verlag GmbH & Co. KGaA, Weinheim

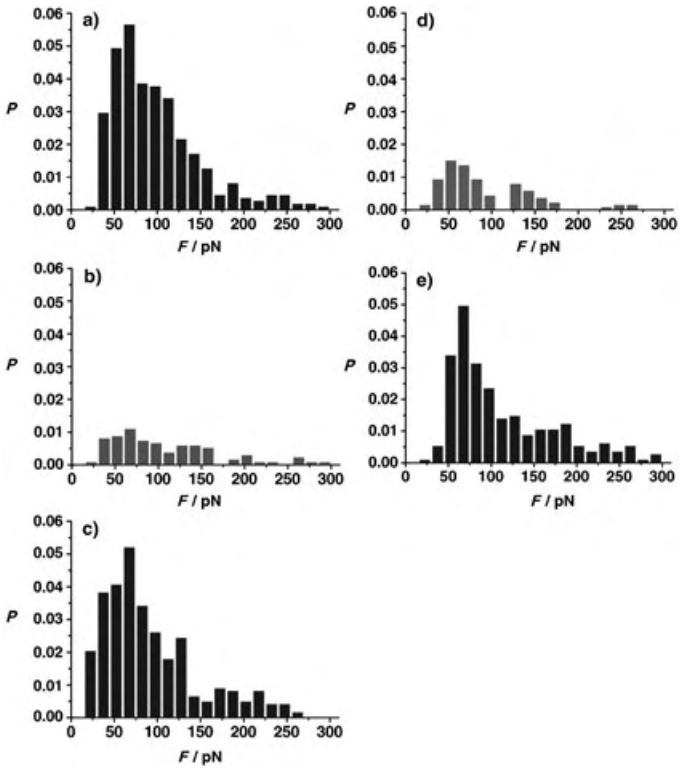


Figure 2. Competition experiments with the native peptide sequence: a) force spectroscopy experiment in standard buffer solution (100 mM NaH_2PO_4, 50 mM NaCl, pH 7.4) without competitor; b) experiment in buffer solution with an excess of free peptide as competitor; c) experiment after washing with standard buffer solution; d) experiment in buffer solution with excess of free DNA as competitor; e) as in c).

buffer solution, in which a significant decrease in total binding probability is apparent; part (c) illustrates how the original binding probability and activity of the interaction is restored after washing the sample in standard buffer; part (d) shows the analogous competition experiment with excess free DNA in buffer solution, and part (e) illustrates the reactivation of the interaction. In additional control experiments with EBNA DNA fragments, which lack the PhoB binding sequence, no binding was observed at all (data not shown; EBNA = Epstein–Barr virus nuclear antigen). These results clearly prove that the binding of the peptide with the native sequence takes place specifically at the binding sequence on the DNA.

The same conclusion applies to the results of the competition experiments performed with the peptide mutants R193A and H198A. Again, competition was successful both with free peptide and with free DNA as competitor (Supporting Information). For H198A, however, the total binding probability was distinctly lower than those of the native peptide and the mutant R193A. In contrast, binding experiments with the mutant R203A yielded very few binding events, rendering statistical analysis impossible. In summary, there is evidence that the native sequence and the mutants R193A and H198A specifically recognize the PhoB target sequence. As it was doubted recently that short peptide sequences with only one α helix are capable of specific DNA binding,[1] our results are quite remarkable given that the 20-residue peptides represent a rather small epitope from the binding domain of the protein.

Dynamic force spectroscopy experiments were performed with the native sequence and the mutants R193A and H198A to obtain information on the dissociation kinetics and energy landscapes. In force-induced thermally driven dissociation of a metastable molecular complex,[27–29] the measured dissociation forces depend on the temporal force evolution on the complex, commonly referred to as the loading rate. It is given as the product of the molecular elasticity and the retract velocity of the cantilever. In our experiments, the molecular elasticity was determined by fitting the last 20 data points prior to bond rupture in the force–distance curve. The retract velocity was varied in the range of 10–6000 nm s^{-1}.

The results of the dynamic experiments are shown in Figure 3. The dissociation forces (derived from analysis of the

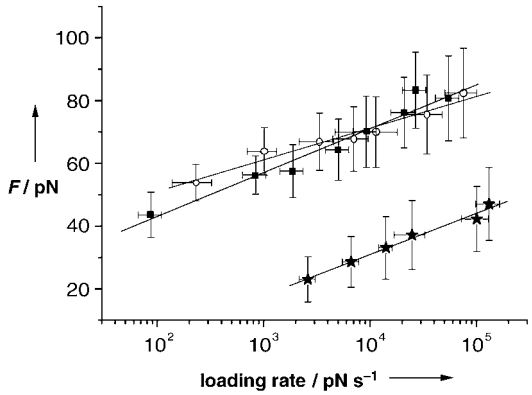


Figure 3. Dynamic force spectroscopy: ■ = native sequence; ○ = R193A; ⋆ = H198A.

respective force histograms) are plotted logarithmically against the loading rate. The linear fit of the data provides two important parameters. First, extrapolation to zero external force $F = 0$ gives the thermal off-rate k_{off}. For the native sequence, the thermal off-rate amounts to $k_{off} = (3.1 \pm 2.1)\ s^{-1}$ (Table 1), which corresponds to a time constant (lifetime) for complex dissociation of $\tau = (320 \pm 220)$ ms. The complex between DNA and the mutant R193A, interestingly, dissociates more slowly, with $k_{off} = (0.071 \pm 0.053)\ s^{-1}$, indicating a longer complex lifetime of $\tau = (14.1 \pm 10.5)$ s. In contrast, the mutant H198A exhibits a considerably higher off-rate: $k_{off} = (49.5 \pm 21.2)\ s^{-1}$, corresponding to a shorter lifetime of $\tau = (20 \pm 8)$ ms. This is not surprising, as in mutant H198A the basic residue His 198 from the native sequence was replaced by alanine. Hence, the charge-controlled contribution to the binding of the peptide with DNA should be decreased. Surprisingly, the mutant R193A, in which Arg 193 was replaced by an alanine, exhibits a lower off-rate and consequently, a longer complex lifetime than the native peptide sequence. This result can presumably be attributed to an enhanced α-helical conformation of the peptide in solution, a finding which will be examined more closely in future experiments. In comparison with recent single-molecule experiments with complete transcription-activating proteins bearing a HTH DNA-binding motif,

 © 2005 Wiley-VCH Verlag GmbH & Co. KGaA, Weinheim

which exhibit lower dissociation rates (2×10^{-4} to $1.3\times10^{-2}\,s^{-1}$)[23] and lifetimes (100–1000 s), this interesting fact indicates the presence and importance of cooperative binding effects—an issue which must be addressed in the future as well.

The affinity of a ligand to its receptor, represented in the case of a 1:1 kinetics by the dissociation equilibrium constant $K_D = k_{off}/k_{on}$, is governed by the dissociation rate k_{off}.[22] Assuming diffusion-controlled association with a typical on-rate constant of $k_{on} = 10^5\,M^{-1}s^{-1}$ [24,30–32] for the binding of a peptide to the target DNA, equilibrium constants of $K_D = 3\times10^{-6}\,M$ (native sequence), $K_D = 7\times10^{-8}\,M$ (mutant R193A), and $K_D = 5\times10^{-5}\,M$ (mutant H198A) can be estimated. According to $\Delta G° = RT\ln K_D$, the corresponding Gibbs′ free energy differences of complex formation can be estimated to $\Delta G° = -31\,kJ\,mol^{-1}$ (native sequence), $\Delta G° = -41\,kJ\,mol^{-1}$ (mutant R193A), and $\Delta G° = -25\,kJ\,mol^{-1}$ (mutant H198A).

From the inverse slope of the linear fit to the data (Figure 3), a molecular reaction length x_β can be obtained as a second parameter, which amounts to values of 6.8 ± 1.2 Å for the native peptide and 7.2 ± 3.5 Å for the mutant H198A (Table 1). However, for peptide R193A, which exhibits the longest complex lifetime, a larger value of $x_\beta = 9.3\pm2.6$ Å is found. This is consistent with the previous results, as it indicates that the final activation barrier is located late along the reaction coordinate. This suggests the possibility for the complex to re-associate (assuming microscopic reversibility) over a larger distance along the reaction coordinate, which corresponds to a longer lifetime of the complex.

In summary, the specific interaction of synthetic peptides that comprise only the recognition helix of a transcription activator with DNA could be investigated for the first time at the single-molecule level. The molecular binding forces observed for single peptide–DNA complexes upon induced dissociation were analyzed quantitatively with AFM force spectroscopy. Competition experiments have proven the specific binding of two peptide mutants to DNA. The results of dynamic force spectroscopy experiments indicate a dependence of the binding forces on external load, which is consistent with thermally driven dissociation. These experiments yield values for the dissociation rates of the corresponding complexes, which allow a direct affinity ranking of synthetic peptides with single point mutations. Furthermore, our results indicate the importance of peptide length, cooperative binding effects, and the contribution of single point mutations to the specific binding of (synthetic) peptides to DNA. These results prove the potential of combining chemical synthesis strategies for biomimetics (synthetic biology) with the high sensitivity of AFM single-molecule force spectroscopy to investigate, quantify, and control the mechanisms and properties of molecular recognition processes (molecular nanotechnology).

Received: January 14, 2005
Revised: March 3, 2005
Published online: May 20, 2005

Keywords: molecular recognition · peptides · point mutations · scanning probe microscopy · single-molecule studies

[1] M. E. Vázquez, A. M. Caamaño, J. L. Mascarenas, *Chem. Soc. Rev.* **2003**, *32*, 338 – 349.
[2] M. E. Vázquez, A. M. Caamaño, J. Martínez-Costas, L. Castedo, J. L. Mascarenas, *Angew. Chem.* **2001**, *113*, 4859 – 4861; *Angew. Chem. Int. Ed.* **2001**, *40*, 4723 – 4725.
[3] A. M. Caamaño, M. E. Vázquez, J. Martínez-Costas, L. Castedo, J. L. Mascarenas, *Angew. Chem.* **2000**, *112*, 3234 – 3237; *Angew. Chem. Int. Ed.* **2000**, *39*, 3104 – 3107.
[4] C. Melander, R. Burnett, J. M. Gottesfeld, *J. Biotechnol.* **2004**, *112*, 195 – 220.
[5] P. Ball, *Nanotechnology* **2005**, *16*, R1-R8.
[6] S. A. Benner, *Nature* **2003**, *421*, 118 – 118.
[7] S.-K. Kim, S. Kimura, H. Shinagawa, A. Nakata, K.-S. Lee, B. L. Wanner, K. Makino, *J. Bacteriol.* **2000**, *182*, 5596 – 5599.
[8] K. Makino, H. Shinagawa, M. Amemura, A. Nakata, *J. Mol. Biol.* **1986**, *190*, 37 – 44.
[9] K. Makino, M. Amemura, T. Kawamoto, K. Kimura, H. Shinagawa, A. Nakata, M. Suzuki, *J. Mol. Biol.* **1996**, *259*, 15 – 26.
[10] Brookhaven Data Base: 1QQI. 2004.
[11] A. G. Blanco, M. Sola, F. X. Gomis-Rüth, M. Coll, *Structure* **2002**, *10*, 701 – 713.
[12] H. Okamura, S. Hanaoka, A. Nagadoi, K. Makino, Y. Nishimura, *J. Mol. Biol.* **2000**, *295*, 1225 – 1236.
[13] E. Martínez-Hackert, A. M. Stock, *J. Mol. Biol.* **1997**, *269*, 301 – 312.
[14] S. D. Wilking, N. Sewald, *J. Biotechnol.* **2004**, *112*, 109 – 114.
[15] R. Eckel, R. Ros, B. Decker, J. Mattay, D. Anselmetti, *Angew. Chem.* **2005**, *117*, 489 – 492; *Angew. Chem. Int. Ed.* **2005**, *44*, 484 – 488.
[16] E.-L. Florin, V. T. Moy, H. E. Gaub, *Science* **1994**, *264*, 415 – 417.
[17] G. U. Lee, D. A. Kidwell, R. J. Colton, *Langmuir* **1994**, *10*, 354 – 357.
[18] U. Dammer, O. Popescu, P. Wagner, D. Anselmetti, H.-J. Güntherodt, G. N. Misevic, *Science* **1995**, *267*, 1173 – 1175.
[19] T. Strunz, K. Oroszlan, R. Schäfer, H.-J. Güntherodt, *Proc. Natl. Acad. Sci. USA* **1999**, *96*, 11277 – 11282.
[20] R. Ros, F. Schwesinger, D. Anselmetti, M. Kubon, R. Schäfer, A. Plückthun, L. Tiefenauer, *Proc. Natl. Acad. Sci. USA* **1998**, *95*, 7402 – 7405.
[21] U. Dammer, M. Hegner, D. Anselmetti, P. Wagner, M. Dreier, W. Huber, H.-J. Güntherodt, *Biophys. J.* **1996**, *70*, 2437 – 2441.
[22] F. Schwesinger, R. Ros, T. Strunz, D. Anselmetti, H.-J. Güntherodt, A. Honegger, L. Jermutus, L. Tiefenauer, A. Plückthun, *Proc. Natl. Acad. Sci. USA* **2000**, *97*, 9972 – 9977.
[23] F. W. Bartels, B. Baumgarth, D. Anselmetti, R. Ros, A. Becker, *J. Struct. Biol.* **2003**, *143*, 145 – 152.
[24] B. Baumgarth, F. W. Bartels, D. Anselmetti, A. Becker, R. Ros, *Microbiology* **2005**, *151*, 259 – 268.
[25] F. Kühner, L. T. Costa, P. M. Bisch, S. Thalhammer, W. M. Heckl, H. E. Gaub, *Biophys. J.* **2004**, *87*, 2683 – 2690.
[26] P. Hinterdorfer, W. Baumgartner, H. Gruber, K. Schilcher, H. Schindler, *Proc. Natl. Acad. Sci. USA* **1996**, *93*, 3477 – 3481.
[27] G. I. Bell, *Science* **1978**, *200*, 618 – 627.
[28] E. Evans, K. Ritchie, *Biophys. J.* **1997**, *72*, 1541 – 1555.
[29] R. Merkel, P. Nassoy, A. Leung, K. Ritchie, E. Evans, *Nature* **1999**, *397*, 50 – 53.
[30] M. Schlosshauer, D. Baker, *Protein Sci.* **2004**, *13*, 1660 – 1669.
[31] M. Vijayakumar, K.-W. Wong, G. Schreiber, A. R. Fersht, A. Szabo, H.-X. Zhou, *J. Mol. Biol.* **1998**, *278*, 1015 – 1024.
[32] O. G. Berg, R. B. Winter, P. H. von Hippel, *Biochemistry* **1981**, *20*, 6929 – 6948.

 © 2005 Wiley-VCH Verlag GmbH & Co. KGaA, Weinheim

Propellanes

Electron Density and Bonding at Inverted Carbon Atoms: An Experimental Study of a [1.1.1]Propellane Derivative**

*Marc Messerschmidt, Stephan Scheins, Lutz Grubert, Michael Pätzel, Günter Szeimies, Carsten Paulmann, and Peter Luger**

The most exciting problem in the chemistry of small-ring propellanes is the nature of the central bond that connects the two "inverted" bridgehead carbon atoms common to the three "wings" of the cage structure (see Figure 1). For several

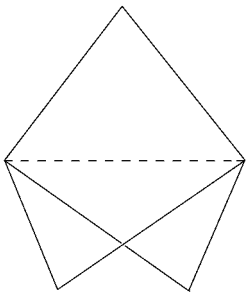
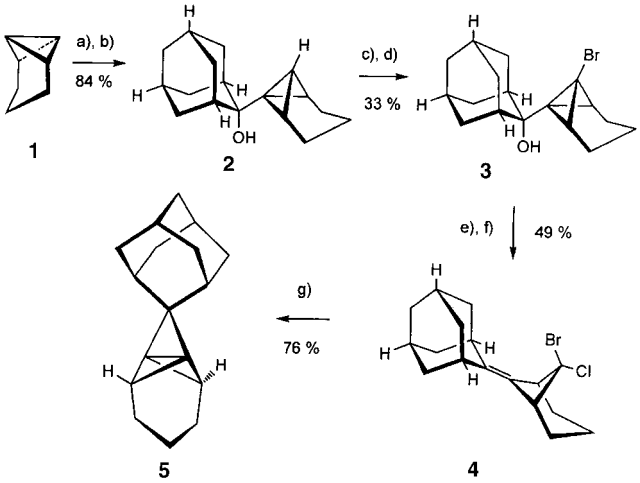


Figure 1. Structure of [1.1.1]propellane. The dashed line connects the inverted carbon atoms.

[1.1.1]propellanes, the X-ray structures showed distances of 1.59 (±0.01) Å[1] between these atoms—only slightly longer than the standard C–C bond length in saturated hydrocarbons.

The results of intensive theoretical work devoted to the question of covalent bonding seem to converge to the conclusion that the inverted carbon atoms are covalently bonded; this is supported by the existence of a bond critical point.[2] On the other hand, the electron deformation density is not accumulated in this region,[3] which was, however, regarded by Wiberg et al. *"as an artefact of the promolecule density distribution and not as a reflection of the relative properties of the two charge distributions of interest"* (quotation from ref. [2]). An experimental investigation of the electron density of two [1.1.1]propellane derivatives agreed qualitatively with the theoretical results.[4] Since no quantitative topological analysis was applied, a conclusion on the existence of a bond critical point could not been drawn from the experiments. Therefore, it was necessary to readdress the issue of electron density in [1.1.1]propellanes, and we present here quantitative results of a synchrotron experiment carried out with propellane **5** (Scheme 1).

Propellane **5** was prepared in four steps from tricycloheptane **1**[6] (Scheme 1). After metalation of **1** with butyllithium, the resulting lithium species was treated with adamantan-2-one to afford the tertiary alcohol **2**. The substitution of the second bridgehead hydrogen atom by bromine was achieved by twofold lithiation of **2** followed by reaction with tosyl bromide. Reaction of **3** with the dimethyl sulfide/*N*-chlorosuccinimide reagent furnished the olefin **4** bearing a geminal halogen moiety. The key step of the synthesis is the intramolecular addition of the carbene, [5] generated by treatment of **4** with methyllithium, to the C–C double bond, to afford the target propellane **5** in 10% overall yield.



Scheme 1. a) BuLi (0.8 equiv Et_2O), 0 °C→RT, 72 h, b) adamantan-2-one (0.9 equiv in Et_2O), 0 °C→RT; c) BuLi (2.25 equiv in Et_2O), 0 °C→RT, 72 h, d) *para*-toluenesulfonyl bromide (0.55 equiv), RT; e) Me_2S (1.0 equiv in CH_2Cl_2), NCS (1.0 equiv in CH_2Cl_2), −25 °C→RT; f) chromatography, silica gel, hexane; g) MeLi (1.25 equiv in Et_2O), −25 °C→RT.

Single crystals of **5** were obtained from a cold pentane solution at 258 K. The rather small crystals, which did not diffract sufficiently in the outer regions of reciprocal space with our laboratory setup, made it necessary to collect high-resolution data at a synchrotron beam line.[7] Propellane **5** crystallizes in the space group *Pmmn* and is situated at an *mm2* site of symmetry in the crystal; this results in nine independent carbon atoms (Figure 2). This symmetry is possible only with a 1:1 disorder for one methylene group (C1/C1a, see Figure 2).[8]

For comparison of the experimentally obtained electron density with the theoretical, ab initio calculations, which

[*] Dr. M. Messerschmidt, Dipl.-Chem. S. Scheins, Prof. Dr. P. Luger
Institut für Chemie/Kristallographie
Freie Universität Berlin
Takustrasse 6, 14195 Berlin (Germany)
Fax: (+49) 30-838-53464
E-mail: luger@chemie.fu-berlin.de
Dr. L. Grubert, Dr. M. Pätzel, Prof. Dr. G. Szeimies
Institut für Chemie
Humboldt-Universität zu Berlin
Brook-Taylor-Strasse 2, 12489 Berlin (Germany)
Dr. C. Paulmann
Mineralogisch-Petrographisches Institut
Universität Hamburg
Grindelallee 48, 20146 Hamburg (Germany)

[**] This research was supported by the Deutsche Forschungsgemeinschaft (grant Lu 222/24-1 and Lu 222/24-3).

 DOI: 10.1002/anie.200500169 © 2005 Wiley-VCH Verlag GmbH & Co. KGaA, Weinheim

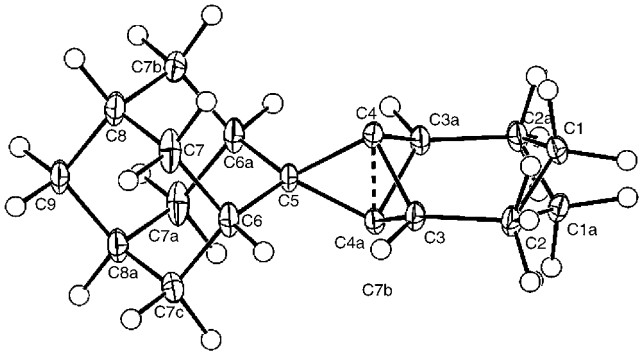


Figure 2. ORTEP representation[19] of the molecular structure of **5** in the crystal with atom numbering (not identical to the numbering in keeping with IUPAC nomenclature). The C1/C1a methylene groups exhibit the 1:1 disorder. Displacement ellipsoids (at 100 K) are shown at a 50% probability.

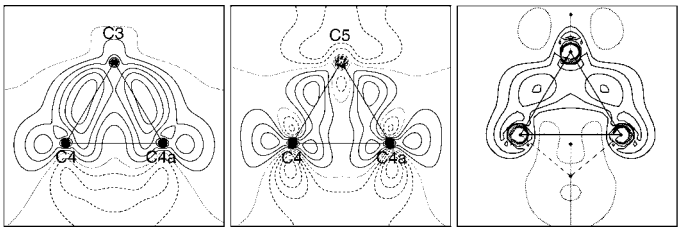


Figure 3. Static deformation densities in the [1.1.1]propellane cage. Left/middle: Experimental distribution in the wing containing C3/C5. Right: Distribution from the B3LYP/6-311G** calculation. Contour interval 0.1 e Å^{-3}, solid/dotted/dashed lines: positive/zero/negative values.



Figure 4. Laplace distributions in the same sections as defined in Figure 3. Contour interval 5 e Å^{-5}, blue/red: positive/negative values.

initially were performed by Wiberg et al.[2] with HF methods, were now completed at the density functional B3LYP level of theory.[9]

The deformation densities visualize the difference between the multipol model and a promolecule that consists of neutral spherical atoms. Therefore, it is open whether they reproduce properly the charge accumulation in strained systems, as was already pointed out in Wiberg's statement cited above.[2] For the two experimentally independent wings of the propellane cage of **5** the static deformation densities are shown in Figure 3 along with the corresponding densities derived from theory. The features of the two experimental maps show some differences, which can be caused by the different crystal environments or by the fact that the C3-containing map displays a region close to the disordered part of the molecule. Nevertheless, the major features are comparable. The bonding densities on the wings have maxima clearly outside the direct internuclear vectors, showing the so-called banana bonds that are typically found in very strained ring systems.[10,11] The second common feature is the absence of density accumulation in the region between the inverted carbon atoms, as is also shown in the theoretical distribution (Figure 3, right).

Regardless of whether the deformation density is an artefact of the promolecule distribution, the Laplacian $\nabla^2\rho(\boldsymbol{r})$, which is directly obtained from the total electron density, should provide more reliable and detailed information on the bonding situation. As shown in Figure 4, the bonds on the wings have saddle-shaped regions with a clear charge accumulation over the whole bond, as is characteristic for covalent bonds. In contrast, the central bond through the cage shows, in good agreement with theory, no charge accumulation at the center.

Quantitative results were obtained from the bond critical points (bcps), all of which were found in the experimental density of **5** and characterized using Bader's theory of "Atoms in Molecules".[12] They are summarized in Table 1, where also, for comparison, corresponding topological data are given for the cage of a [1.1.1]bicyclopentane derivative, of which the experimental electron density was described earlier.[11] There is a relationship between the two types of cages, in that formally the addition of two substituents to the propellane bridgehead atoms breaks the bond in question and yields the corresponding bicyclopentane molecule, where the intracage distance increases to 1.8–1.9 Å.[1]

As shown in Table 1 the bonds in the wings are described by experiment and theory as covalent. The experimental

Table 1: Summary of selected topological parameters of **5** and a [1.1.1]bicyclopentane derivative.

Atoms	Distance [Å]	ρ [e Å^{-3}]	$\nabla^2\rho$ [e Å^{-5}]	Type	Method
1) Compound **5**					
C3-C4	1.526	1.79(2)	−11.6(1)	bcp	exptl
C4-C5	1.532	1.55(2)	−13.0(1)	bcp	exptl
	1.518	1.61	−10.3	bcp	B3LYP
C4-C4a	1.579	1.31(3)	10.3(1)	bcp	exptl
	1.578	1.27	2.0	bcp	B3LYP
C4-C4a-C3		1.29(2)	8.71(5)	rcp	exptl
C4-C4a-C5		1.21(2)	4.34(5)	rcp	exptl
		1.25	2.88	rcp	B3LYP
2) [1.1.1]Bicyclopentane derivative[11]					
wing bonds:					
range	1.549–1.561	1.53(3)–1.67(3)	−9.7(1)– −13.1(1)	bcp	exptl
average	1.556(4)	1.61(5)	−11.8(13)	bcp	exptl
		1.55(2)	−10.9(4)	bcp	B3LYP
bridgehead atoms	1.868(1)	0.68(2)	11.09(6)	ccp	exptl
		0.67	11.3	ccp	B3LYP

 © 2005 Wiley-VCH Verlag GmbH & Co. KGaA, Weinheim

densities on the bond critical points fall roughly in the range also found for the six wing bonds in the [1.1.1]bicyclopentane derivative, although these bonds are slightly shorter in **5**. In total, the agreement for the wing bonds is reasonable for the two compounds; both ρ_{bcp} and $\nabla^2\rho_{bcp}$, and experimental and theoretical descriptions are all in good agreement as well.

Of major interest is the central bond through the cage. While for the bicyclopentane only a cage critical point (ccp) could be located inside the cage, a bond critical point is found unambiguously also in the experimental electron density of the propellane **5**. For the much shorter contact between the bridgehead atoms, the bcp has nearly twice the density of the bicyclopentane ccp, which is in good agreement with theoretical calculations. The Laplacian at this bond critical point is positive, as is seen normally for noncovalent interactions. Its higher value in the experiment indicates that the experimental bond path has a stronger curvature than the theoretical.

By using an exponential relation introduced by Bader et al.,[13] a bond order n can be derived from the electron density at the bond critical point. For C4–C4a and the experimental value $\rho_{bcp} = 1.31(3)\ e\,Å^{-3}$ we obtained a bond order of $n = 0.71$, which is in line with $n = 0.73$ determined by Wiberg et al.[2] in earlier theoretical studies and comparable to $n = 0.69(1)$ recently reported for the lengthened bond in the cyclopropane ring of a barbaralane derivative.[14] It should, however, be noted that the determination of bond orders smaller than one is uncertain because the extrapolation to zero bond order is not well defined. The existence of a bond path is further supported by the location of ring critical points (rcps) in the two crystallographically independent wings of **5** with densities found very close to theoretical values (see Table 1). Such ring critical points were not located in the bicyclopentane cage.

This study shows that a high-resolution data set could be obtained even from otherwise weakly diffracting crystals thanks to the use of very intense synchrotron primary radiation. This data set served as the experimental basis for the determination of the electron density of the [1.1.1]propellane **5** and its topological analysis. Although a small part of the molecule was affected by disorder, all expected topological descriptors in terms of critical points could be located and a general good agreement was seen between experiment and theory. In contrast to a related [1.1.1]bicyclopentane derivative,[11] a bond critical point was found between the bridgehead atoms in **5**. This bond is unusual according to topological analysis: it has a bond path with a bond critical point of significant density, as is characteristic for a covalent bond, but no charge accumulation is evident at the bond critical point where the Laplacian is positive. These findings, confirming small-ring propellanes as a unique class of hydrocarbons, have been obtained for the first time by quantitative topological results derived from experimental electron density distribution.

Experimental Section

2: The solvent was removed from a solution of butyllithium (50 mL, 1.6 M in hexane, 80 mmol) under reduced pressure and under nitrogen. The residue was dissolved in about the same volume of Et_2O. To this first solution was added a solution of **1** (9.4 g, 100 mmol) in Et_2O (100 mL) at 0 °C within 30 min. The reaction solution was allowed to warm to room temperature and was stirred for further 72 h. Then the reaction mixture was cooled to 0 °C, and adamantan-2-one (11.25 g, 75 mmol) dissolved in Et_2O (100 mL) was added dropwise. After stirring for 5 h the mixture was hydrolyzed with 1 M NaOH. The ether phase was washed twice with 1 M NaOH, the organic layer was dried ($MgSO_4$), and the solvent was removed under reduced pressure. The solid residue was dissolved in diisopropyl ether. Recrystallization at −10 °C afforded **2** (16.5 g, 84 %) as colorless crystals. M.p. 122–124 °C (diisopropyl ether). ^{1}H NMR (600 MHz, $CDCl_3$, TMS): $\delta = 2.45$ (m, 2H, H-6′ and H-2′), 2.19 (m, 2H, H-4a and H-9a), 2.11 (m, 2H, H-8a and H-10a), 1.88 (m, 1H, H-5), 1.81 (m, 1H, H-7), 1.74 (m, 7H, H-1, 3, 6, 8b, 10b and H-7′), 1.58 (m, 2H, H-4b and H-9b), 1.42 (m, 1H, H-3a′), 1.38 (m, 4H, H-3b′, 4′, 5b′), 1.31 (m, 1H, H-5a′), 1.03 ppm (s, 1H, OH); ^{13}C NMR (75 MHz, $CDCl_3$, TMS): $\delta = 73.9$ (C-2), 39.5 (2C, C-2′ and C-6′), 38.1 (C-6), 38.0 (2C, C-1 and C-3), 34.9 (2C, C-8 and C-10), 33.0 (2C, C-4 and C-9), 27.5 (C-5), 27.1 C-7), 26.7 (C-1′), 20.8 (C-4′), 19.9 (2C, C-3′ and C-5′) 13.5 ppm (C-7′).

3: Carbinol **2** (5.76 g, 40 mmol) in Et_2O (100 mL) was added dropwise with stirring at 0 °C to butyllithium (56 mL, 1.6 M in Et_2O, 90 mmol). Stirring was continued for 72 h at room temperature. The reaction mixture was again cooled in an ice bath, charged with 4-toluenesulfonyl bromide (11.75 g, 50 mmol) in small portions, stirred for 5 h at room temperature, and then hydrolyzed with 1 N NaOH in an ice bath. The layers were separated, the aqueous part extracted three times with Et_2O, and the combined ether layers dried with $MgSO_4$. After filtration and removal of the solvents and volatile products under reduced pressure (5×10^{-5} Torr) and elevated bath temperature (up to 80 °C), the solid residue was dissolved in Et_2O. Recrystallization at −10 °C afforded **3** (2.5 g, 33 %) as colorless crystals. M.p. 77–78 °C (Et_2O). MS (CI) m/z (%): 322//324 (0.5) [$M^{+\bullet}$], 243 (23) [$M-Br^{+\bullet}$], 171//173 (6) [$M-Ad\text{-}OH^{+}$], 162 (58), 151 (42), 91 (100), 79 (64), 77 (45), 67 (35), 55 (40), 41 (55), 39 (33); ^{1}H NMR (300 MHz, $CDCl_3$, TMS): $\delta = 2.85$ (m, 2H, H-6′ and H-2′), 2.28 (m, 2H, H-4a and H-9a), 1.99 (m, 2H, H-8a and H-10a), 1.88 (s 1H, OH), 1.82 (m, 4H, H-1, 3, 5, 7), 1.72 (m, 4H, H-6, 8b, 10b), 1.57 (m, 2H, H-4b and H-9b), 1.54 (m, 2H, H-3a′ and H-5a′), 1.38 ppm (m, 4H, H-3b′, 4′, 5b′); ^{13}C NMR (75 MHz, $CDCl_3$, TMS): $\delta = 75.8$ (C-2), 46.6 (2C, C-2′ and C-6′), 38.4 (2C, C-1 and C-3), 38.0 (C-6), 34.6 (2C, C-8 and C-10), 33.0 (C-7′), 32.6 (2C, C-4 and C-9), 27.9 (C-1′), 27.3 (C-5), 27.0 (C-7), 19.9 (C-4′), 19.0 ppm (2C, C-3′ and C-5′).

4: *N*-Chlorosuccinimide (2.4 g, 0.018 mol) and dimethyl sulfide (1.32 mL, 0.018 mol) were mixed at 0 °C in dichloromethane (75 mL). The milky suspension was cooled to −25 °C, and a solution of **3** (4.83 g, 0.015 mol) in 25 mL dichloromethane was added dropwise with stirring. The bath temperature was increased to 25 °C, and stirring was continued for 4 h. The dichloromethane solution was extracted three times with 1 M NaOH and twice with brine, dried with $MgSO_4$, and filtered, and the solvent was removed under reduced pressure. The volatile products were removed in vacuo (10^{-5} Torr, 40 °C). The residue was purified by chromatography (silica gel, *n*-hexane) The solvent was removed and the target compound **4** (2.5 g, 49 %) was obtained as colorless crystals. M.p. 55 °C (*n*-hexane). MS (CI) m/z (%): 340/342/344 (3/4/1) [$M^{+\bullet}$], 213 (100), 131 (16), 91 (36), ^{1}H NMR (600 MHz, $CDCl_3$, TMS): $\delta = 3.39$ (d, 2H, H-1′ and H-5′), 2.53 (s, br, 2H, H-1 and H-3), 2.30 (m 2H, H-2′ and H-4′) 1.93 (m, 2H, H-5 and H-7) 2.85 (m 10H, H-2′, 4′, 4, 6, 8, 9, 10), 1.71 (d, br., 2H, H-4 and H-9) 1.63 (m, 1H, H-3′), 1.45 ppm (m, 1H, H-3′); ^{13}C NMR (75 MHz, $CDCl_3$, TMS): $\delta = 140.2$ (C-6′), 121,4 (C-2), 70.9 (C-7′), 59.1 (2C, C-1′ and C-5′) 39.2 (2C, C-4 and C-9), 38.3 (2C, C-8 and C-10), 37.1 (C-6), 33.9 (2C, C-1 and C-3), 29.6 (2C, C-2′ and C-4′) 28.3 (2C, C-5 and C-7), 14.7 ppm (C-3′).

5: Methyllithium in Et_2O (6.1 mL, 1.5 M, 9.1 mmol MeLi) was diluted at 0 °C with Et_2O (10 mL) and cooled down to −25 °C. This solution was stirred and a solution of dihalide **4** (2.5 g, 7.25 mmol) in Et_2O (40 mL) was added dropwise. The mixture was allowed to warm

 © 2005 Wiley-VCH Verlag GmbH & Co. KGaA, Weinheim

to room temperature and kept at this temperature for 5 h. The reaction mixture was cooled in an ice bath, then 2 N NaOH (5 mL) was added with stirring. After separation of the phases, the organic layer was extracted twice with water and dried with $MgSO_4$. Removal of the solvent afforded a crystalline residue. Recrystallization yielded **5** (1.25 g, 76 %) as colorless needles. M.p. 81–83 °C (*n*-pentane at −10 °C). ^{1}H NMR (600 MHz, $CDCl_3$, TMS): $\delta = 3.25$ (s, 2H, H-2′ and H-6′), 1.70 (br s, 2H, H-1 and H-3), 1.57 (br s, 2H, H-5 and H-7), 1.55 (br s, 4H, H-4, 8, 9, 10), 1.45 (m, 6H, H-4, 8, 9, 10 and H-6), 1.34 (m, 4H, H-3′ and H-5′), 0.96 ppm (m, 2H, H-4′); ^{13}C NMR (75 MHz, $CDCl_3$, TMS): $\delta = 102.2$ (C-8′=C-2), 80.8 (2C, C-2′ and C-6′), 40.0 (4C, C-4, 8, 9, 10), 39.1 (C-6), 29.2 (2C, C-5 and C-7), 28.7 (2C, C-1 and C-3), 22.3 (2C, C-3′ and C-5′), 20.8 (C-4′), 20.2 ppm (2C, C-1′ and C-7′).

Received: January 17, 2005
Published online: May 13, 2005

Keywords: density functional calculations · electron density · propellanes · solid-state structures · strained molecules

[1] M. D. Levin, P. Kaszynski, J. Michl, *Chem. Rev.* **2000**, *100*, 169–234; see Table 2 on p. 176.
[2] K. B. Wiberg, R. F. W. Bader, C. D. H. Lau, *J. Am. Chem. Soc.* **1987**, *109*, 985–1001, and references therein.
[3] See ref. [1] and references therein.
[4] P. Seiler, J. Belzner, U. Bunz, G. Szeimies, *Helv. Chim. Acta* **1988**, *71*, 2100.
[5] M. Kenndorf, A. Singer, G. Szeimies, *J. Prakt. Chem.* **1997**, *339*, 217–232.
[6] W. R. Moore, H. R. Ward, R. F. Merritt, *J. Am. Chem. Soc.* **1961**, *83*, 2019; A. P. Molchanov, S. A. Kalyamin, R. R. Kostikov, *J. Org. Chem. USSR (Engl. Transl.)* **1992**, *28*, 102–107; *Zh. Org. Khim.* **1992**, *28*, 122–128.
[7] Crystal structure analysis of **5**, $C_{17}H_{22}$, at 100 K: Crystal size $0.4 \times 0.2 \times 0.1$ mm^3, orthorhombic, *Pmmn*, $a = 6.706(1)$, $b = 7.332(1)$, $c = 12.521(2)$ Å, $V = 608.99(14)$ Å^3, $\rho_{calcd} = 1.240$ g cm^{-3}, $\sin\theta/\lambda_{max} = 1.18$ Å^{-1}. The structure was solved by direct methods and at first spherically refined using full matrix least squares methods (SHELXTL).[20] The synchrotron experiments were carried out at beamline F1 (κ-axis geometry) at Desy/Hasylab. A Bruker CCD area detector and Oxford Cryosystem N_2 gas stream device were used. The measurement strategy was determined with ASTRO,[15] the measurement was controlled with SMART,[15] and the integration and correction of the data was done with SAINT[15] and SORTAV.[16] Si double-crystal monochromator, $\lambda = 0.5600$ Å, $T = 100$ K, 26569 reflections measured, 4087 unique ($R_{int} = 4.4$ %), 2371 reflections with ($I > 3\sigma(I)$) were included in multipole refinements which were carried out then based on the formalism of Hansen and Coppens[17] with the program system XD.[18] Hexadecapoles were used for the heavy atoms and dipoles for the H atoms. Atomic site symmetry was applied according to corresponding special positions in the crystal structure. The disorder was considered by a 1:1 population. After convergence $R(F) = 3.56$ % for 217 parameters, $Rw(F) = 3.47$ %, min./max. residual density: −0.23/0.28 e Å^{-3}. The topological analysis, derivation of electronic properties, and graphical visualization (Figures 3 and 4) were also done with XD. CCDC 257891 contains the supplementary crystallographic data for this paper. These data can be obtained free of charge from the Cambridge Crystallographic Data Centre via www.ccdc.cam.ac.uk/data_request/cif.
[8] Attempts to solve and refine the structure in the corresponding acentric space group $Pmn2_1$ confirmed the disorder, although it is not forced by the symmetry of this space group.
[9] To predict the influence of the substituents on the propellane cage, several calculations at HF and B3LYP level of theory were performed with the basis set 6-311G**.[21] All calculations resulted in an almost D_{3h}-symmetric propellane cage and showed no significant influence of the substituents on the interesting bond features of the propellane cage. Therefore results of the unsubstituted propellane were used for all further comparisons. These are in line with earlier calculations,[2] except for minor quantitative differences in the bond topological descriptors. The partitioning procedure which uses the zero-flux surfaces of $\nabla\rho(\boldsymbol{r})$ to obtain atomic properties was applied to the theoretical density of propellane[22] derived from the above-mentioned calculation. It yielded practically zero charges for all atoms and volumes of 13.5 Å^3 and 10.1 Å^3 for the bridgehead and the wing carbon atoms, respectively.
[10] T. Koritsánszky, J. Buschmann, P. Luger, *J. Phys. Chem.* **1996**, *100*, 10541–10553.
[11] P. Luger, M. Weber, G. Szeimies, M. Pätzel, *J. Chem. Soc. Perkin Trans. 2* **2001**, 1956–1960.
[12] R. F. W. Bader, *Atoms in Molecules, A Quantum Theory*, Clarendon, Oxford, **1990**; R. F. W. Bader, P. Lode, A. Popelier. T. A. Keith, *Angew. Chem.* **1994**, *106*, 647; *Angew. Chem. Int. Ed. Engl.* **1994**, *33*, 620.
[13] R. F. W. Bader, T. S. Slee, D. Cremer, E. Kraka, *J. Am. Chem. Soc.* **1983**, *105*, 5061–5068.
[14] P. Luger, M. Messerschmidt, S. Scheins, A. Wagner, *Acta Crystallogr. Sect. A* **2004**, *60*, 390–396.
[15] Programs of ASTRO 1995–1996, SMART 1996, SAINT 1994–1996, Bruker-ASS Inc. Madison, WI (USA).
[16] R. H. Blessing, *Acta Crystallogr. Sect. A* **1995**, *51*, 33.
[17] N. K. Hansen, P. Coppens, *Acta Crystallogr. Sect. A* **1978**, *34*, 909.
[18] T. Koritsánszky, T. Richter, P. Macchi, A. Volkov, C. Gatti, S. Howard, P. R. Mallinson, L. Farrugia, Z. W. Su, N. K. Hansen, XD—A Computer Program Package for Multipole Refinement and Analysis of Electron Densities from Diffraction Data. User Manual. Tech. rep., Freie Universität Berlin, **2003**.
[19] M. N. Burnett, C. K. Johnson, ORTEP-III, Oak Ridge Thermal Ellipsoid Plot Program for Crystal Structure Illustrations. Tech. rep., Oak Ridge National Laboratory Report ORNL-6895, Oak Ridge, TN, **1996**.
[20] G. M. Sheldrick, *Acta Crystallogr. Sect. A* **1990**, *46*, 467; G. M. Sheldrick, SHELX-TL 5.03, Software Package for the Crystal Structure Determination, Siemens Analytical X-ray Instrument Division, Madison, WI, USA, **1994**.
[21] Gaussian 98 (Revision A.7), M. J. Frisch, G. W. Trucks, H. B. Schlegel, G. E. Scuseria, M. A. Robb, J. R. Cheeseman, V. G. Zakrzewski, J. A. M. Jr., R. E. Stratmann, J. C. Burant, S. Dapprich, J. M. Millam, A. D. Daniels, K. N. Kudin, M. C. Strain, O. Farkas, J. Tomasi, V. Barone, M. Cossi, R. Cammi, B. Mennucci, C. Pomelli, C. Adamo, S. Clifford, J. Ochterski, G. A. Petersson, P. Y. Ayala, Q. Cui, K. Morokuma, D. K. Malick, A. D. Rabuck, K. Raghavachari, J. B. Foresman, J. Cioslowski, J. V. Ortiz, A. G. Baboul, B. B. Stefanov, G. Liu, A. Liashenko, P. Piskorz, I. Komaromi, R. Gomperts, R. L. Martin, D. J. Fox, T. Keith, M. A. Al-Laham, C. Y. Peng, A. Nanayakkara, C. Gonzalez, M. Challacombe, P. M. W. Gill, B. Johnson, W. Chen, M. W. Wong, J. L. Andres, C. Gonzalez, M. Head-Gordon, E. S. Replogle, J. A. Pople, Gaussian, Inc., Pittsburgh, PA, **1998**.
[22] P. Popelier, R. Bone, MORPHY, a program written by P. L. A. Popelier with a contribution from R. G. A. Bone, Tech. rep. UMIST, Manchester, England, EU, **1998**.

 © 2005 Wiley-VCH Verlag GmbH & Co. KGaA, Weinheim

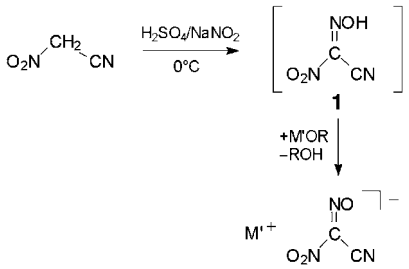
Stable Methanides

Nitro(nitroso)cyanomethanides**

Harald Brand, Peter Mayer, Axel Schulz, and Jan J. Weigand*

Methanide anions of the type $[HCR^1R^2]^-$ and $[CR^1R^2R^3]^-$ ($R^{1,2,3}$ = CN, NO, NO_2 and all possible permutations of $R^{1,2,3}$) can be considered to be resonance-stabilized, nonlinear pseudohalides.[1] The term pseudohalogen/pseudohalide was first introduced by Birckenbach in 1925 and applied to linear species such as CN/CN^-, CNO/CNO^-, N_3/N_3^-, OCN/OCN^-, and SCN/SCN^-.[2] In the same year Grimm developed the hydride displacement law,[3] according to which the pseudo-elements CH_3, NH_2, and OH have properties similar to those of fluorine; for example, they form singly charged anions. Successive substitution of the hydrogen atoms in CH_3 (CH_3^-) and NH_2 (NH_2^-) by electron-withdrawing groups in resonance with π bonds, such as CN, NO, and NO_2, leads to the class of resonance-stabilized, nonlinear pseudohalogens (pseudohalides).[4] Prominent examples of methanides are di- and tricyanomethanides,[5,6] di- and trinitromethanides,[7,8] dinitrosomethanide,[9] and the mixed substituted species such as nitrosodicyanomethanide $[(ON)C(CN)_2]^-$ and nitrodicyanomethanide $[(O_2N)C(CN)_2]^-$.[10] Nitro(nitroso)cyanomethanide, a methanide with three different characteristic groups, is not known yet. Here we wish to report the synthesis and full characterization of the alkali-metal and tetramethylammonium salts of nitro(nitroso)cyanomethanide, a simple new class of salts with surprising thermal stability.

Nitro(nitroso)cyanomethanides (NNCM) were synthesized readily in a two-step reaction (Scheme 1). First, nitroacetonitrile was nitrosated with sodium nitrite in water to give the metastable cyanomethylnitrolic acid (**1**), which was extracted with diethyl ether. Then an anhydrous ether solution of **1** was treated with a solution of M′OR (M′ = alkali metal, NR_4; R = H, alkyl) in 2-propanol, resulting in a red precipitate of M′NNCM. The beautiful red alkali-metal NNCM salts were purified easily by recrystallization from methanol (yield 50–60%).

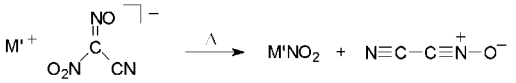


Scheme 1. Synthesis of nitro(nitroso)cyanomethanide salts (M′ = alkali metal, NR_4; R = H, alkyl).

Metastable cyanomethylnitrolic acid and its red color in basic water solution have already been observed by Steinkopf.[11] Moreover, he postulated the existence of the silver salt of **1**. The intermediate formation of the silver salt was also postulated by Pillai and Boyer in the reaction of ICH_2CN with $AgNO_2$, which finally gave $NC{-}CH_2{-}O{-}N{=}C(NO_2)CN$ as the only isolable product.[12]

Crystals of LiNNCM and NaNNCM are very hygroscopic (they deliquesce within seconds), while crystals of KNNCM and CsNNCM can be handled without inert gas for some minutes. Interestingly, the red color of the NNCM salts darkens the heavier the alkali-metal counterion is: LiNNCM exhibits a bright orange-red color while CsNNCM displays a purple color.

Similar to the alkali-metal dinitrosomethanide salts,[9] pure dry alkali-metal NNCM salts are stable at ambient temperature, are heat and shock sensitive, and decompose slowly in polar solvents releasing N_2O gas (detected by ^{14}N NMR experiments). To determine the gases formed when M′NNCM explodes, combined IR and HRMS pyrolysis experiments were carried out. The only gaseous products observed were NC–CNO, N_2O, CO_2, NO, and CO. An intriguing feature of NNCM salts is the liberation of cyanogen *N*-oxide (NC–CNO)[13] upon gentle heating (e.g. KNNCM: $80\,^\circ C < T < T_{onset}$) and the formation of $M'NO_2$ in the solid state as well as in solution (Scheme 2).[14] Differential scanning calorimetry (DSC) experiments revealed that M′NNCM salts (M′ = K, Cs, NMe_4) undergo exothermic decomposition. For example, for the explosion of KNNCM: $\Delta H = -37.25\ kcal\,mol^{-1}$; onset of decomposition: 101.7 °C ($\beta = 5\,^\circ C\,min^{-1}$) in a temperature range of 90–117 °C; estimated activation energy of ca. 31.9(±0.5) $kcal\,mol^{-1}$.[15] We assume that the presence of a π system delocalized over the entire anion accounts for the remarkable kinetic stability of NNCM salts (see below). Nitro-, nitrosodicyanomethanide, and dinitrosomethanide salts possess a higher thermal stability than M′NNCM salts.[9,10] It is interesting to note that we were able to detect the NNCM anion in a FAB^- mass spectrometry experiment that was carried out with crystals of KNNCM.



Scheme 2. Decomposition of M′NNCM (M′ = alkali metal) upon gentle heating.

^{14}N NMR spectra of the NNCM anion in DMSO solution display three resonances in the ranges typical for C–NO (265 ppm, cf. 332 ppm $[HC(NO)_2]^-$),[9] $C{-}NO_2$ (−15 ppm, cf. −25 ppm $H_2C(NO_2)_2$),[16] and C–CN species (−107 ppm, cf. −105 ppm $[C(NO)(CN)_2]^-$).[16] The ^{13}C NMR spectrum shows

[*] H. Brand, Dr. P. Mayer, Dr. A. Schulz, J. J. Weigand
Department Chemie und Pharmazie
Ludwig-Maximilians-Universität München
Butenandtstrasse 5–13 (Haus D), 81377 München (Germany)
Fax: (+49) 89-2180-77492
E-mail: axel.schulz@cup.uni-muenchen.de

[**] A.S. thanks Professor Dr. T. M. Klapötke (LMU München) for his generous support and Professor Dr. W. Beck for his interest and advice.

Supporting information for this article is available on the WWW under http://www.angewandte.org or from the author.

 DOI: 10.1002/anie.200500495 © 2005 Wiley-VCH Verlag GmbH & Co. KGaA, Weinheim

singlet resonances at 149.6 ppm (*C*-CN, cf. 150.3 ppm $[C(NO_2)_3]^-$)[17] and 119.5 ppm (C-*C*N, cf. 117.2 ppm $[C(NO_2)(CN)_2]^-$).[10] The characteristic frequencies of the NO (1380–1400 cm^{-1}), NO_2 (1490–1510 cm^{-1}), and CN (2210–2230 cm^{-1}) groups can be detected in the Raman and IR spectra of all M′NNCM salts (M′ = alkali metal, Me_4N).[18a]

KNNCM crystallizes in beautiful red rods in the monoclinic space group $P2_1/c$ with four units per cell.[19] The structure consists of an infinite three-dimensional network of repeating $K[C(NO_2)(NO)(CN)]$ units. Each anion is bonded to six potassium cations and vice versa (Figure 1). Specifically,

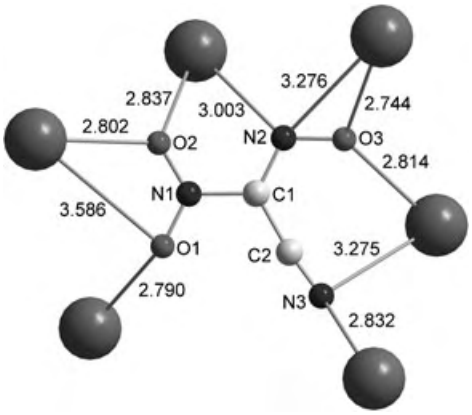


Figure 1. Coordination environment of NNCM in KNNCM; bond lengths [Å]: C1–N1 1.418(3), C1–N2 1.323(3), C1–C2 1.422(4), C2–N3 1.138(3), N1–O1 1.233(3), N1–O2 1.236(3), N2–O3 1.273(3); angles [°]: C1-C2-N3 173.2(3), C1-N1-O1 117.5(2), C1-N1-O2 119.7(2), C1-N2-O3 115.6(2), N1-C1-N2 117.4(2), N1-C1-C2 117.7(2), N2-C1-C2 124.9(2).

the oxygen atoms of the nitro group are bonded to three potassium centers with K–O distances of 2.790(2) to 3.586(2) Å, while the oxygen atom of the NO group is attached to two potassium centers (d(K–O) = 2.814(2) and 2.744(2) Å). Additionally, two K–N interactions are found for the N atom of the NO group (3.003(2) and 3.276(2) Å). The nitrogen atom of the CN group coordinates to two neighboring potassium centers with K–N distances of 2.832(2) and 3.275(3) Å. Hence, as shown in Figure 1, each potassium center is surrounded by four nitrogen and five oxygen atoms. The potassium coordination sphere consists of six NNCM ligands which leads to the interesting three-dimensional network arrangement of the ions (Figure 2). A view along the *a* axis reveals stacked chains of K^+ and $NNCM^-$ ions.[18b,c]

As depicted in Figure 1, the NNCM anion is nearly planar[20] (sum of angles at C1 = 359.9°) like most of the known NO-, NO_2-, and CN-substituted methanide anions (except trinitromethanide, in which the balance between resonance stabilization and steric repulsion results in the torsion of one NO_2 group out of the plane).[8a,21] Inspection of the conformational space at the B3LYP/aug-cc-pvTZ level yielded two different planar structures of the NNCM ion: a *cis* isomer (as shown in Figure 1, O3 in *cis* position to C2) and a *trans* arrangement. In agreement with the experiment our calculations indicated that the *cis* form is the most stable isomer (ΔE^{tot}(*cis*–*trans*) = +4.6 kcal mol^{-1}). As expected, all

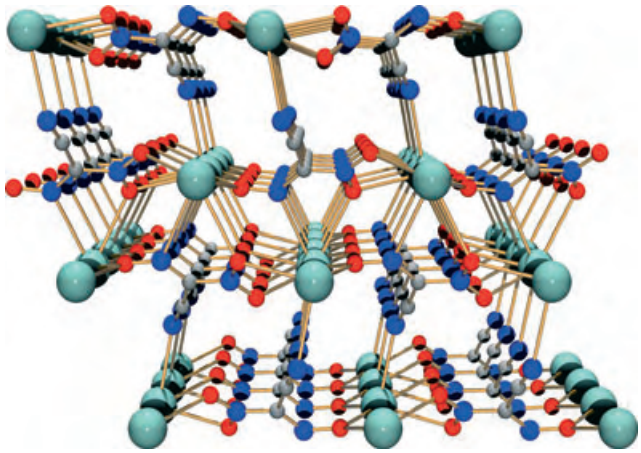
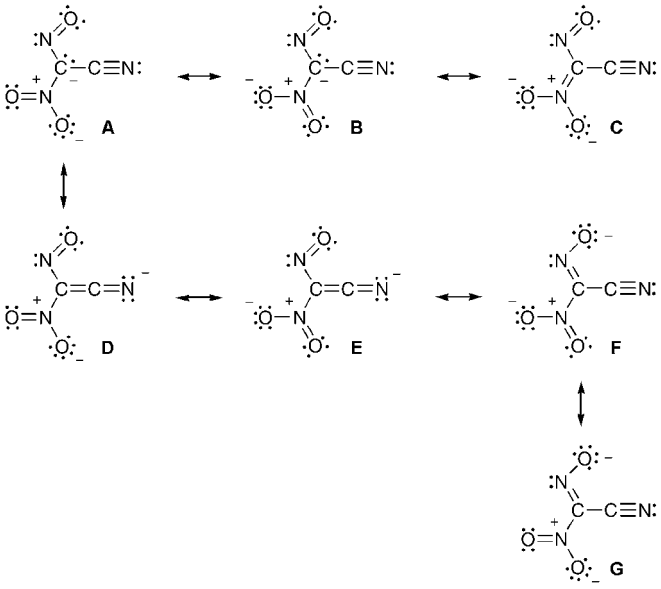


Figure 2. Packing diagram of KNNCM (view along 100).

N–O bonds (KNNCM: 1.233(3), 1.236(3), and 1.273(3) Å) are significantly shorter than the C1–N1, C1–N2, and C1–C2 bonds (KNNCM: 1.418(3), 1.323(3), and 1.422(4) Å).[18c] This is comparable to the situation found in the structure of dinitrosomethanide[9] and the nitroso- and nitrodicyanomethanides.[10] The $C–N_{nitroso}$ bond is significantly shorter than the $C–N_{nitro}$ bond, indicating a stronger π interaction along the $C–N_{nitroso}–O$ moiety. These short C–N bonds together with the planarity indicate that the π bonds are delocalized over the whole anionic species.

MO[18d] and natural bond orbital (NBO)[22] calculations of the NNCM ion support the existence of a 10π-electron, eight-center bond (Scheme 3 and Figure 3).[23] According to NBO analysis **A** and **B** in Scheme 3, are the energetically preferred Lewis representations. Investigation of the intramolecular donor–acceptor interactions utilizing the NBO partitioning scheme clearly indicates a highly delocalized 10π-system



Scheme 3. Lewis structures of NNCM corresponding to the results of NBO analysis.

 © 2005 Wiley-VCH Verlag GmbH & Co. KGaA, Weinheim

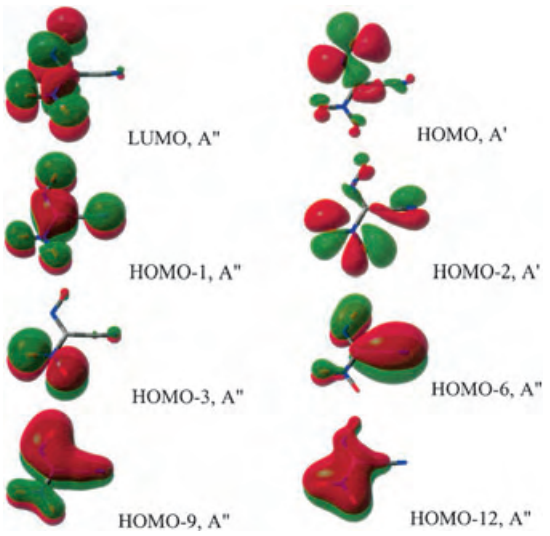


Figure 3. Selected molecular orbitals (B3LYP/aug-cc-pvTZ) of *cis* NNCM (the five occupied π MOs are those with A″ symmetry).

corresponding to the resonance structures **A**–**G**. The calculated natural atomic orbital population (NAO) net charges are $q(O) = -0.459$ (O1), -0.430 (O2), -0.464 (O3); $q(N) =$ 0.475 (N1), 0.022 (N2), -0.382 (N3); $q(C) = -0.025$ (C1), 0.263 *e* (C2). This indicates that the negative charge is found mainly on the three O atoms and the N atom of the CN group.

The UV/Vis spectra of the red solutions of NNCM alkali-metal salts in methanol exhibit one very strong characteristic $\pi \rightarrow \pi^*$ and one weak $n \rightarrow \pi^*$ electronic transition at roughly 328 and 489 nm, respectively, which could be assigned on the basis of TD-B3LYP calculations (Figure 3).[18d] The red color arises from the weak $n \rightarrow \pi^*$ HOMO–LUMO electronic transition in the anion. The HOMO describes a lone pair that lies in the anion plane. A closer inspection of the orbital coefficients of the HOMO shows rather large coefficients for the nitroso group; hence, it can be concluded that the nitroso group is mainly responsible for the red color.

In conclusion, we present here an easy, high-yielding synthetic procedure and first full characterization of alkali-metal and tetramethylammonium salts of nitro-(nitroso)cyanomethanides. The presence of a π system delocalized over the entire anion accounts for the remarkable thermal stability of alkali-metal NNCM salts, and the NNCM anion can be regarded as a nonlinear, resonance-stabilized pseudohalide. Because of the three different functional groups, NNCM salts may have great synthetic potential, for example, as a source for NC–CNO release in situ.[14b]

Experimental Section

Caution: Although ammonium and alkali-metal NNCM salts are kinetically stable compounds, they are nonetheless high-energy materials and appropriate safety precautions should be taken, especially when these compounds are prepared on a larger scale (see the Supporting Information).

Synthesis of KNNCM:[24] A solution of H_2SO_4 (100%; 1.10 g, 11.2 mmol) in water (3 mL) was added dropwise to a stirred solution of nitroacetonitrile (1.80 g, 20.9 mmol)[25] and sodium nitrite (1.50 g, 21.7 mmol) in water (30 mL) at 0 °C. The reaction mixture was stirred at 0 °C for 30 min, and then **1** was extracted with diethyl ether (4 × 25 mL). The combined extracts were dried over anhydrous calcium chloride, filtered, and cooled to 0 °C with stirring. A solution of KO*t*Bu (1.40 g, 12.5 mmol) in 2-propanol (10 mL) was added dropwise, resulting in a red precipitate, which was recrystallized from methanol to give red crystals (rods) of KNNCM (1.82 g, 11.9 mmol, 57%). M.p. 105 °C (decomp.), Raman (200 mW, 25 °C, 100 scans):[18a] $\tilde{\nu}(I_{rel}) = 2225$ (4), 1501 (3), 1400 (7), 1344 (10), 1258 (2), 1214 (9), 848 (2), 834 (2), 806 (1), 777 (1), 570 (0.5), 537 (1), 489 (0.3), 258 (1), 180 (2), 154 cm^{-1} (1); UV/Vis (methanol):[18d] $\lambda_{max}(\varepsilon) = 489$ (60), 328 (11055), 245 nm (5493 $cm^{-2}mmol^{-1}$); ^{13}C NMR ([D$_6$]DMSO, 101 MHz, 25 °C): $\delta = 119.5$ (s, C-*C*N), 149.6 ppm (s, *C*-CN); ^{14}N NMR ([D$_6$]DMSO, 28.9 MHz, 25 °C): $\delta = -107$ (s, $\Delta\nu^{1/2} = 240$ Hz, C-C*N*), -15 (s, $\Delta\nu^{1/2} = 80$ Hz, C-*N*O$_2$), 265 ppm (s, $\Delta\nu^{1/2} = 320$ Hz, C-*N*O); MS (FAB$^-$, xenon, 6 keV, *m*NBA matrix): 267 [NNCM + NBA]$^-$, 114 [NNCM]$^-$; MS (EI, 70 eV, >5%, explosion gases); *m*/*z* (%): 68 (6) [NCCNO]$^+$, 52 (28) [(CN)$_2$]$^+$, 44 (100) [CO$_2$]$^+$ and [N$_2$O]$^+$, 32 (8) [O$_2$]$^+$, 30 (41) [NO]$^+$, 28 (30) [CO]$^+$, 27 (6) [HCN]$^+$; Elemental analysis for $KC_2N_3O_3$ (153.139) calcd C 15.69, N 27.44; found C 16.16, N 26.24.

Received: February 9, 2005
Published online: May 17, 2005

Keywords: bonding analysis · methanides · pseudohalogens · structure elucidation

[1] A. M. Golub, H. Köhler, *Chemie der Pseudohalogenide*, VEB Deutscher Verlag der Wissenschaften, Berlin, **1979**.
[2] a) L. Birckenbach, K. Kellermann, *Ber. Dtsch. Chem. Ges.* **1925**, *58*, 786–794; b) L. Birckenbach, K. Kellermann, *Ber. Dtsch. Chem. Ges.* **1925**, *58*, 2377; c) L. Birckenbach, K. Huttner, W. Stein, *Ber. Dtsch. Chem. Ges. A* **1929**, *62*, 2065–2075; L. Birckenbach, K. Huttner, W. Stein, *Ber. Dtsch. Chem. Ges. A* **1929**, *62*, 2261–2277; d) L. Birckenbach, M. Linhard, *Ber. Dtsch. Chem. Ges. A* **1930**, *63*, 2528–2544; L. Birckenbach, M. Linhard, *Ber. Dtsch. Chem. Ges. A* **1930**, *63*, 2544–2558; L. Birckenbach, M. Linhard, *Ber. Dtsch. Chem. Ges. A* **1930**, *63*, 2588.
[3] a) H. G. Grimm, *Z. Elektrochem. Angew. Phys. Chem.* **1925**, *31*, 474–480; b) Atoms in the periodic system anywhere up to four places before an inert gas change their properties by uniting with 1, 2, 3, or 4, H atoms, so that the resulting complexes behave like pseudoatoms similar to elements of the groups before them in the periodic table.
[4] Substitution of H in OH$^-$ by CN and NO results in the formation of the well-known pseudohalides OCN$^-$ and NO$_2^-$, respectively.[1]
[5] a) W. Hiller, S. Frey, J. Straehle, G. Boche, W. Zarges, K. Harms, M. Marsch, R. Wollert, K. Dehnicke, *Chem. Ber.* **1992**, *125*, 87–92; b) M. Armand, Y. Choquette, M. Gauthier, Ch. Michot, EP 850921 A1, **1998**.
[6] a) J. R. Witt, D. Britton, *Acta Crystallogr. B* **1971**, *27*, 1835–1836; b) L. Jäger, M. Kretschmann, H. Köhler, *Z. Anorg. Allg. Chem.* **1992**, *611*, 68–72; c) H. Köhler, M. Jeschke, V. I. Nefedov, *Z. Anorg. Allg. Chem.* **1987**, *552*, 210–214; d) P. Andersen, B. Klewe, E. Thom, *Acta Chem. Scand.* **1967**, *21*, 1530–1542.
[7] a) Z. S. Kosturkevich, Yu. T. Struchkov, *Z. Strukt. Khim.* **1964**, *5*, 320–31; Z. S. Kosturkevich, Yu. T. Struchkov, *Z. Strukt. Khim.* **1964**, *5*, 322–323; b) V. Grakauskas, US 4 233 249, **1980**; c) V. Grakauskas, A. M. Guest, *J. Org. Chem.* **1978**, *43*, 3485–3488.
[8] a) C. B. Jeffrey, M. N. Burnett, A. A. Gakh, *Acta Crystallogr. A* **1998**, *54*, 1229–1233; b) L. Liang, *Org. Synth.* **1941**, *21*, 105–107; c) K. D. Scherfise, F. Weller, K. Dehnicke, *Z. Naturforsch. B* **1985**, *40*, 906–912; d) H. L. Ammon, C. S. Choi, R. S. Damvarapu, S. Iyer, J. Alster, *Acta Crystallogr. A* **1990**, *46*, 295–298;

 © 2005 Wiley-VCH Verlag GmbH & Co. KGaA, Weinheim

e) Z. Berkovitch-Yellin, L. Leiserowitz, *Acta Crystallogr. A* **1984**, *40*, 159 – 165.
[9] H. Brand, P. Mayer, K. Polborn, A. Schulz, J. J. Weigand, *J. Am. Chem. Soc.* **2005**, *127*, 1360 – 1361.
[10] N. Arulsamy, D. S. Bohle, B. G. Doletski, *Inorg. Chem.* **1999**, *38*, 2709 – 2715.
[11] W. Steinkopf, *Ber. Dtsch. Chem. Ges.* **1909**, *42*, 617 – 621.
[12] P. Pillai, J. H. Boyer, *Org. Prep. Proced. Int.* **1982**, *14*, 365 – 369.
[13] a) For detailed temperature-dependent data for gas-phase IR spectra and HRMS, see the Supporting Information; b) C. Grundmann, H. D. Frommeld, *J. Org. Chem.* **1966**, *31*, 4235 – 4237; c) B. Guo, T. Pasinszki, N. P. C. Westwood, K. Zhang, P. F. Bernath, *J. Chem. Phys.* **1996**, *105*, 4457 – 4460; d) T. Pasinszki, N. P. C. Westwood, *J. Phys. Chem.* **1996**, *100*, 16856 – 16863; e) T. Pasinszki, N. P. C. Westwood, *J. Chem. Soc. Chem. Commun.* **1995**, *18*, 1901 – 1902; f) G. Maier, J. H. Teles, *Angew. Chem.* **1987**, *99*, 152 – 153; *Angew. Chem. Int. Ed. Engl.* **1987**, *26*, 155 – 156.
[14] a) The release of nitrile oxides has also been described in the decomposition of nitrolic acids ($RC(=NOH)NO_2$) yielding HNO_2 and RCNO; b) C. Grundmann, P. Günanger, *The Nitrile Oxides*, Springer, New York, **1971**.
[15] a) T. Ozawa, *Bull. Chem. Soc. Jpn.* **1965**, *38*, 1881 – 1886; b) H. E. Kissinger, *Anal. Chem.* **1957**, *29*, 1702 – 1706; c) Standard Test Method for Arrhenius Kinetic Constants for Thermally Unstable Materials, ASTM Designation E698–99, **1999**.
[16] M. Witanowski, L. Stefaniak, G. A. Webb, *Annu. Rep. NMR Spectrosc.* **1993**, *31*, 1 – 480.
[17] A. A. Gakh, J. C. Bryan, M. N. Burnett, P. V. Bonnesen, *J. Mol. Struct.* **2000**, *520*, 221 – 228.
[18] a) For the approximate assignment of all normal modes on the basis of DFT calculations and trends see Table S8 in the Supporting Information. b) When the coordination environment on the anion was changed by introducing the bulky cation Me_4N^+, noncoordinated cations and anions were observed in solid state instead of the three-dimensional network, and the anions do not adopt the parallel eclipsed stacking found in KNNCM (Figure S4). c) For comparison, see X-ray data of (NMe_4)NNCM (Tables S4 and S5). d) See Figure S7 and Table S10.
[19] Crystal data for KNNCM: $M_r(C_2N_3O_3K) = 153.14$, crystal dimensions ca. $0.32 \times 0.10 \times 0.03$ mm, monoclinic, space group $P2_1/c$, $a = 4.8112(3)$, $b = 7.5510(5)$, $c = 14.9095(10)$ Å, $\alpha = \gamma = 90.0$, $\beta = 93.086(4)°$, $V = 540.87(6)$ Å^3, $Z = 4$, $\rho_{calcd} = 1.881$ g cm^{-3}, $F(000) = 304$, Nonius Kappa CCD, $\lambda(Mo_{K\alpha}) = 0.71073$ Å, $T = 200$ K, $\mu = 0.909$ mm^{-1}, $3.84 \leq \theta \geq 25.98$, of 4842 reflections collected, 1041 were independent, 804 were observed, ($R_{int} = 0.053$), The R values are $R_1 = 0.0359$ ($I > 2\sigma(I)$) and $wR_2 = 0.0787$ (all data); max./min. residual electron density: 0.258/ −0.378 e Å^3. All structures were solved by direct methods (structure solution program: SIR97)[26] and refined by full-matrix least squares methods with SHELXL-97[27] and anisotropical thermal parameters for all atoms. Crystal data for (NMe_4)NNCM are given in the Supporting Information. CCDC 261891 and CCDC 261892 contain the supplementary crystallographic data for this paper. These data can be obtained free of charge via www.ccdc.cam.ac.uk/conts/retrieving.html (or from the Cambridge Crystallographic Data Centre, 12 Union Road, Cambridge CB21EZ, UK; fax: (+44) 1223-336-033; or deposit@ccdc.cam.ac.uk).
[20] Largest deviations from the ideal least-square plane (all atoms included) are 0.040(2) Å (O1, NMe_4NNCM) and 0.090(2) Å (O2, KNNCM).
[21] a) Calculations predict a propeller-type D_3-symmetric anion: J. Cioslowski, S. T. Mixon, E. D. Fleischmann, *J. Am. Chem. Soc.* **1991**, *113*, 4751 – 4755; b) Additionally, our B3LYP/aug-cc-pvTZ calculations revealed a nonplanar C_{2v} structure as the global minimum (0.5 kcal mol^{-1} lower in energy than the D_3-symmetric isomer).
[22] a) E. D. Glendening, A. E. Reed, J. E. Carpenter, F. Weinhold, *NBO Version 3.1*; b) A. E. Reed, L. A. Curtiss, F. Weinhold, *Chem. Rev.* **1988**, *88*, 899 – 926.
[23] All MOs are shown in Figure S7 of the Supporting Information.
[24] The other ammonium and alkali-metal NNCM salts can be obtained either by ion-exchange reactions or by the described synthetic procedure (see the Supporting Information).
[25] G. H. Reidlinger, H. Junek, *Synthesis* **1991**, *10*, 835 – 838.
[26] A. Altomare, M. C. Burla, M. Camalli, G. L. Cascarano, C. Giacorazzo, *J. Appl. Crystallogr.* **1999**, *32*, 115 – 119.
[27] G. M. Sheldrick, *SHELXL-97*, *Program for Solution of Crystal Structures*; University of Göttingen: Göttingen, Germany, **1997**.

 © 2005 Wiley-VCH Verlag GmbH & Co. KGaA, Weinheim

Cluster Compounds

Phosphine-Stabilized Copper–Antimony Clusters: Syntheses, Structures, and Theoretical Investigations of $[Cu_{12}(SbSiMe_3)_6(PiPr_3)_6]$, $[Cu_{40}Sb_{12}(PMe_3)_{20}]$, and $[Cu_{45}Sb_{16}(PEt_2Me)_{16}]$**

Reinhart Ahlrichs, Dieter Fenske, Mary McPartlin, Alexander Rothenberger, Claudia Schrodt, and Stephan Wieber*

Dedicated to *Professor Herbert W. Roesky on the occasion of his 70th Birthday*

Recently we have started to study the synthesis and structural analysis of copper complexes containing heavier elements of Group 15.[1] Despite the extensive amount of work that has been carried out in the area of transition-metal complexes of heavier Group 15 elements, there are only a few accounts of antimony- or bismuth-containing copper complexes.[2] Most

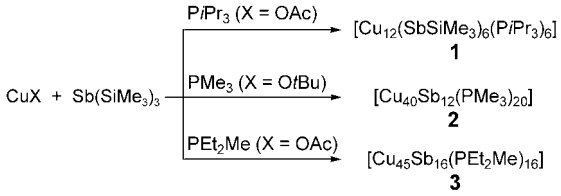
[*] Prof. D. Fenske, Dr. A. Rothenberger, Dipl.-Chem. S. Wieber
Institut für Anorganische Chemie
Universität Karlsruhe
Engesserstrasse 15, 76131 Karlsruhe (Germany)
Fax: (+49) 721-608-8440
E-mail: dieter.fenske@chemie.uni-karlsruhe.de
Prof. R. Ahlrichs
Institut für Physikalische Chemie
Universität Karlsruhe
Fritz-Haber-Weg 4, 76131 Karlsruhe (Germany)
Prof. M. McPartlin
School of Applied Chemistry
University of North London
Holloway Road, London N7 8DB (UK)
Dipl.-Chem. C. Schrodt
Institut für Nanotechnologie
Forschungszentrum Karlsruhe GmbH
Postfach 3640, 76021 Karlsruhe (Germany)

[**] We gratefully acknowledge the DFG (Zentrum für funktionelle Nanostrukturen), the INT at the Forschungszentrum Karlsruhe (A.R., S.W.) and the Fonds der Chemischen Industrie for financial support.

 © 2005 Wiley-VCH Verlag GmbH & Co. KGaA, Weinheim DOI: 10.1002/anie.200500593

of these complexes are adducts of copper(I) salts with tertiary stibanes or bismuthines ER_3 (E = Sb, Bi; R = aryl or alkyl) as terminal ligands.[3] The first copper(I) antimonide complex $[\{Mes_2SbCu(PMe_3)_2\}_2]$ (Mes = 2,4,6-trimethylphenyl) was prepared by the metathesis reaction of Mes_2SbLi with CuCl.[4] Our approach to the syntheses of copper(I) antimonides reported herein involves the reaction of $Sb(SiMe_3)_3$ with copper(I) salts in the presence of tertiary phosphines (see Scheme 1).[1] By this approach we have already synthesized the copper–antimony clusters $[Cu_{10}(Sb_3)_2(SbSiMe_3)_2(dppm)_6]$, $[Cu_{17}Sb_8(dppm)_7]$, and $[Cu_{20}Sb_{10}(PCy_3)_8]$ (dppm = 1,2-bis-(diphenylphosphino)methane, Cy = cyclohexyl).[1a,c] The different ratio of Cu:Sb present in complexes **2** and **3** suggests copper atoms in the oxidation states 0, +I, or +II. UV/Vis studies and magnetic measurements on these type of compounds, however, did not confirm the presence of metal centers in various oxidation states and instead showed that these compounds are best described as phosphine-stabilized molecular copper–antimony alloys. On our way towards the selective synthesis of molecular alloys and the correlation of their properties with those of CuSb phases which have similar Cu:Sb ratios, we report herein the structure of an intermediate copper–antimony cluster and the two largest molecular CuSb alloys belonging to this class of compounds.[5] The structures of the complexes were established by X-ray crystallography and the results assessed with structures obtained from DFT studies.

The reaction of CuOAc with $Sb(SiMe_3)_3$ in the presence of P*i*Pr$_3$ produced $[Cu_{12}(SbSiMe_3)_6(PiPr_3)_6]$ (**1**, Scheme 1).[19] In the solid state **1** consists of a distorted centrosymmetric octahedral arrangement of six $\{SbSiMe_3\}$ units. The copper atoms Cu(2,3,6) and their symmetry equivalents are each coordinated by one phosphorus atom of a P*i*Pr$_3$ ligand and two antimony atoms from an edge of the distorted Sb_6 octahedron (Figure 1 a; Cu–P 2.227(2)–2.253(3), nonbonding Sb···Sb distances are ca. 4.0–4.8 Å). The remaining copper



Scheme 1. Synthesis of Cu–Sb clusters **1**–**3** (X = O*t*Bu, OAc).

atoms Cu(1,4,5) and their symmetry equivalents are located on the faces of the Sb_6 octahedron and are coordinated by three Sb atoms. All the copper atoms have distorted trigonal-planar coordination environments. A remarkable feature of **1** is that trimethylsilyl groups are still present despite the stoichiometric supply of starting materials (CuOAc:Sb-$(SiMe_3)_3$ = 3:1). An explanation for this observation could be the presence of bulky *i*Pr$_3$P ligands which prevent **1** from further reactions with CuOAc. Compound **1** can be described as a "classical" Cu–Sb complex where charges can formally be assigned to give twelve Cu^+ centers and six $[SbSiMe_3]^{2-}$ ligands. Similar short Cu···Cu distances such as those in **1** (ca. 2.4 Å) were also observed in a range of other copper(I) complexes.[6] Sb–Cu bond lengths of approximately 2.5 Å are characteristic and are similar to distances observed in other Cu–Sb complexes.[1] Inspired by the structural diversity of copper clusters bridged by Group 16 elements, the reaction conditions(R groups of tertiary phosphines, anions of the Cu^I salts, and solvents), were modified. Particular synthetic targets were larger CuSb clusters which could be regarded as molecular representatives of the various crystallographically characterized CuSb intermetallic phases.[5] The reactions of PMe_3 with one equivalent of CuO*t*Bu and then with $Sb(SiMe_3)_3$ produced black crystals of the copper–antimony clusters $[Cu_{40}Sb_{12}(PMe_3)_{20}]$ (**2**) (Figure 1 b) and a complex which has the approximate composition $[Cu_{40}Sb_{21}(PMe_3)_{16}]$

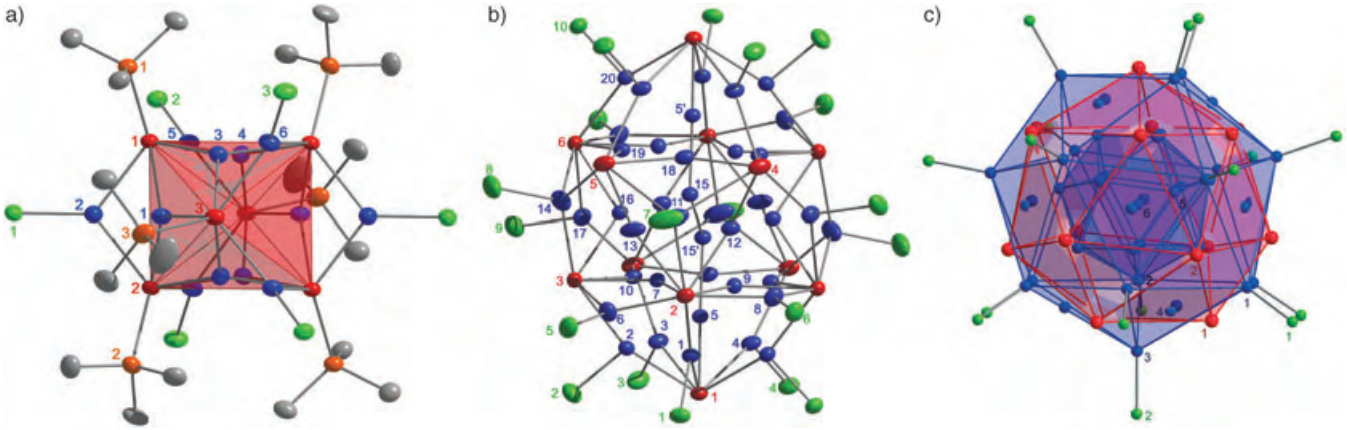


Figure 1. a) Molecular structure of **1** (Sb red, Cu blue, P green, Si orange). *i*Pr groups have been omitted for clarity; thermal ellipsoids set at 50% probability. Selected ranges of bond lengths [Å]: Cu–Sb: 2.600(1) for Sb1-Cu2 to 2.778(1) for Sb3-Cu1, Sb–Si: 2.537(2) for Sb3-Si3 to 2.547(2) for Sb2-Si2, shortest Cu-Cu distances 2.381(2) for Cu1-Cu4a to 2.541(2) for Cu1-Cu2, Cu-P: 2.228(2) for Cu5-P2 to 2.253(2) for Cu6-P3. B) Molecular structure of **2** (Sb red, Cu blue, P green). Methyl groups have been omitted for clarity; thermal ellipsoids set at 50% probability. Selected ranges of bond lengths [Å]: Cu–Sb: 2.454(1) for Sb1-Cu5 to 3.162(2) for Sb4-Cu11, shortest Cu–Cu distances 2.316(2) for Cu15–Cu15′ to 2.923(2) for Cu3-Cu4, Cu–P: 2.220(2) for Cu11-P7 to 2.265(2) for Cu3-P3. c) Polyhedral representation of **3** (Sb red, Cu blue, P green; C and H atoms have been omitted for clarity). Selected ranges of bond lengths [Å]: Cu–Sb: 2.5798(8) for Sb1-Cu4′ to 2.922(1) for Sb1-Cu2, Cu···Cu distances 2.442(2)–2.923(2), Cu–P: 2.186(4) for Cu1-P1 and 2.188(8) for Cu3-P2.

 © 2005 Wiley-VCH Verlag GmbH & Co. KGaA, Weinheim

(**2a**). Crystals of **2** and **2a** can be separated manually under perfluoroether oil but decompose once placed under vacuum as a result of the loss of lattice-bound solvent. For these reasons a characterization of **2** was only possible by X-ray crystallography.[19]

The solid-state structure of **2** consists of a distorted Sb_{12} icosahedron (nonbonding Sb···Sb distances ca. 5 Å). The twenty copper atoms located on the cluster surface are all coordinated to phosphorus atoms of PMe_3 ligands and bridge the edges or cap Sb_3 faces of the icosahedral Sb_{12} unit. The copper atoms not coordinated by PMe_3 ligands are located inside the cluster. They bridge edges of the icosahedron and the atoms Cu(5), Cu(15), and their symmetry equivalents form a Cu_4 chain inside the cluster. The Cu···Cu distance of 2.316(2) Å between Cu(15) and Cu(15′) is to our knowledge the shortest Cu–Cu distance observed to date in a molecular complex and is close to the distance observed in Cu_2(g) 2.2 Å.[7] The Sb–Cu bond lengths in **2** (2.453(1)–3.162(2) Å) are characteristic for Cu–Sb complexes and are in the range of distances observed in Cu_2Sb alloy.[8] Further experiments to elucidate the electronic structure and in particular the oxidation-state of the copper atoms involved were hindered by the unselective formation of **2** which makes it impossible to prepare larger amounts of pure **2** as it can not be separated from the byproducts. Since the composition of **2** is non-stoichiometric with four excess electrons, density functional theory (DFT) calculations[9,10] were carried out to investigate its electronic structure. The results show typical semiconductor features: the occupied valence band and the empty conduction band are separated by a band gap of about 1.5 eV,[11] whereas orbital energies within these bands differ by typically 0.1 eV. A similar situation was observed in clusters of the composition $[Cu_{26}Te_{12}(PEt_2Ph)_{12}]$, $[Cu_{32}As_{10}(dppm)_8]$.[12] In agreement with the small difference in electronegativities of Cu and Sb (Pauling scale: Cu 1.6, Sb 1.9), a valence band composed of 5p(Sb) and (4s)Cu orbitals is formed, which accommodates the four excess electrons. An "ionic" model of **2** which could consist of Cu^+ and Sb^{3-} ions and Cu^0 is inappropriate. A structural model of **2a** was also investigated using DFT methods and the results showed that the solution we obtained in the space group $F23$ was wrong. The DFT analysis was necessary because highly symmetric structures of large Cu–Sb clusters can sometimes not be determined reliably by X-ray crystallographic methods alone. This is due to the intrinsic problem that a crystal structure represents the arrangement of atoms averaged over a lot of molecules. For large clusters containing more than 60 metal atoms this means that metal atom positions in different cluster molecules can sometimes be occupied by Cu or Sb atoms. To gain further insight into this problem we have performed similar reactions of CuOAc and $Sb(SiMe_3)_3$ in the presence of phosphines and the reaction with PEt_2Me gave rise to another cluster containing the same number of metal atoms as **2a**. Black crystals were obtained from this reaction in addition to an amorphous black precipitate. The X-ray analyses has shown that the structure can be solved in the cubic space group $F\bar{4}3m$.[19] The cluster has the composition $[Cu_{45}Sb_{16}(PEt_2Me)_{16}]$ (**3**) and consists of two metal shells (see Figure 1c).

The atom Cu(6) is in the center of **3** and is surrounded by a regular arrangement of 16 Cu atoms forming a slightly distorted Frank–Kasper polyhedron (Cu(6)···Cu 2.629(2) and 2.771(1) Å). Sixteen Cu atoms of the outer shell have a tetrahedral coordination environment and each one is bonded to a P atom of a PEt_2Me ligand and three Sb atoms. These Cu atoms and the outer Sb atoms are located on the corners of another Frank–Kasper polyhedron (with nonbonding Cu···Cu distances of ca. 4.1–4.9 Å; Sb···Sb ca. 3.5 and 4.5 Å). Each of the remaining twelve surface Cu atoms is coordinated trigonally planar by three Sb atoms and is located in the center of the Sb_3 faces of the Sb_{16} shell. These outer three-coordinate Cu atoms are also located in the center of a trigonal face of the polyhedron formed by the sixteen $\{Cu(PEt_2Me)\}$ units. The organic groups of the phosphine ligands prevent the coordination of additional phosphine ligands to the three-coordinate Cu atoms.[13] Having solved the structure of **3** we were unable to unequivocally identify the atom type in the center of the cluster (herein refined as Cu(6)) by crystallographic methods alone. Other analytical tools, such as elemental analysis and mass spectrometric methods, also failed to give us clear evidence. Again the accuracy of the X-ray structure determination was assessed by DFT methods. Calculations for the isomorphous cluster cores $[Cu_{40}Sb_{21}]$ (**2a**), $[Cu_{41}Sb_{20}]$, $[Cu_{44}Sb_{17}]$, and $[Cu_{45}Sb_{16}]$ with PMe_3 ligands in molecular symmetry T were performed.[14] Figure 2 shows the deviation between measured and calculated bond lengths in **3**.

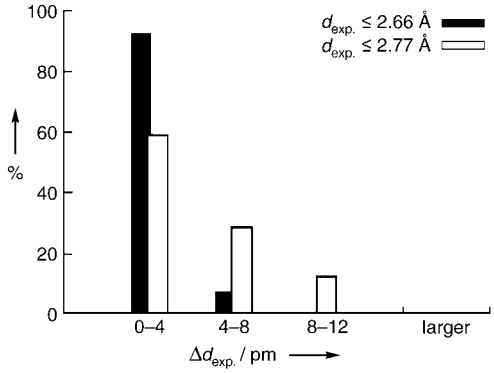


Figure 2. Deviations of selected calculated from experimentally determined metal···metal distances (d_{exp}) in **3**.

This deviation is most meaningful for short and strong bonds which are those described best by theory. $[Cu_{45}Sb_{16}L_{16}]$ ($L = PMe_3$) gives a perfect match: short bonds (≤ 2.66 Å) deviate by only up to 0.08 Å, and the deviation is less than 0.04 Å in over 90% of cases. Even for a larger cutoff, bonds ≤ 2.77 Å, which includes relatively weak bonds there are no discrepancies larger than 0.12 Å. All the calculated cluster cores contain 61 metal atoms stabilized by phosphine ligands, but for Cu:Sb $\neq$ 45:16 they show unacceptably large deviations from X-ray results and can be reliably excluded.[15] The electronic structure of **3** shows remarkable features. The odd numbers of electrons leads to an open-shell structure with a singly occupied tHOMO in molecular symmetry T resulting

 © 2005 Wiley-VCH Verlag GmbH & Co. KGaA, Weinheim

in a ^{2}T state that will undergo a (slight) Jahn–Teller distortion. The high-lying HOMO, $\varepsilon_{HOMO} = -1.902$ eV, and a band gap of 0.85 eV between HOMO and HOMO-1 indicate that **3** is a strong reducing agent.[16]

In addition to the synthesis of the molecular CuSb alloys **2** and **3**, which are nonclassical compounds in a sense that they cannot be described by localized charges, calculations of the largest CuSb clusters have shown that DFT calculations can assist in the correct assignment of atom types in highly symmetric crystal structures. It can be assumed that the synthesis of even larger CuSb alloy complexes does not simply proceed via elimination of volatile trimethylsilyl-containing leaving groups but instead via aggregates similar to **3** which could act as reducing agents in reactions with other metal cations present in solution.

Experimental Section

All operations were carried out in an atmosphere of purified Argon. THF was heated under reflux over potassium and freshly distilled. Hexane and diethyl ether were dried over $LiAlH_4$. PMe_3, $Sb(SiMe_3)_3$, CuO*t*Bu, and CuOAc were prepared according to published procedures.[17]

1: CuOAc (0.27 g, 2.20 mmol) was dissolved in Et_2O (9 mL) and P*i*Pr$_3$ (0.83 mL, 4.04 mmol) was added. The dark yellow solution was cooled to −78 °C and $Sb(SiMe_3)_3$ (2.4 mL, 0.73 mmol; 0.31 M in hexane) was added and solution then stored at −78 °C for 12 h. The reaction was then allowed to warm to −40 °C and stored for one week. Dark brown crystals of **1** were isolated (0.15 g, 31 %), which decomposed at room temperature.

2: PMe_3 (0.36 mL, 4.00 mmol) was added to CuO*t*Bu (0.27 g, 2.00 mmol) in THF (5 mL). The yellow solution was briefly heated to reflux and then allowed to cool to room temperature. At −78 °C $Sb(SiMe_3)_3$ (3.9 mL; 0.66 mmol; 0.17 M in hexane) was then added. After storage at −40 °C for two weeks the mixture was then stored at room temperature for another two weeks producing black crystals of **2** (eight molecules of THF as lattice-bound solvent) (ca. 0.10 g, 33 %), which decomposed at room temperature.

3: A solution of CuOAc (0.25 g, 2.00 mmol) in THF (8 mL) and $PMeEt_2$ (0.52 mL, 4.00 mmol) was cooled to −78 °C and $Sb(SiMe_3)_3$ (2.0 mL, 2.00 mmol; 1 M in hexane) was added. The reaction was stored at −78 °C for 12 h, allowed to warm to −40 °C, and stored for two weeks. Black crystals of **3** were isolated (ca. 0.08 g, 28 %), which decomposed at room temperature.

X-ray Crystallographic Study: Data were collected on a Stoe IPDS II diffractometer using graphite-monochromated $Mo_{K\alpha}$ radiation ($\lambda = 0.71073$ Å). The structures were solved by direct methods and refined by full-matrix least-squares on F^2 (all data) using the SHELXTL program package.[18,19] Hydrogen atoms were placed in calculated positions, non-hydrogen atoms were assigned anisotropic thermal parameters, atoms of lattice-bound solvent molecules were refined with isotropic thermal parameters. To identify further possible by-products, unit cell dimensions of crystals from different samples were repeatedly determined and in each case **1**–**3** were the only products we were able to characterize. CCDC 263819–263821 contain the supplementary crystallographic data for this paper. These data can be obtained free of charge from the Cambridge Crystallographic Data Centre via www.ccdc.cam.ac.uk/data_request/cif.

Received: February 17, 2005
Published online: May 18, 2005

Keywords: antimony · cluster compounds · copper · density functional calculations · molecular alloys

[1] a) J. Besinger, J. Treptow, D. Fenske, *Z. Anorg. Allg. Chem.* **2002**, *628*, 512–515; b) D. Fenske, A. Rothenberger, S. Wieber, *Z. Anorg. Allg. Chem.* **2003**, *629*, 929–930; c) R. Ahlrichs, C. E. Anson, R. Clerac, D. Fenske, A. Rothenberger, M. Sierka, S. Wieber, *Eur. J. Inorg. Chem.* **2004**, 2933–2936.

[2] a) J. L. Stark, B. Harms, I. Guzmann-Jimenez, K. H. Whitmire, R. Gautier, J.-F. Halet, J.-Y. Saillard, *J. Am. Chem. Soc.* **1999**, *121*, 4409–4418; b) A. H. Cowley, N. C. Norman, M. Pakulski, *J. Am. Chem. Soc.* **1984**, *106*, 6844–6845; c) H. G. Ang, C. M. Hay, B. F. G. Johnson, J. Lewis, P. R. Raithby, A. J. Whitton, *J. Organomet. Chem.* **1987**, *330*, C5–C11; d) L. Balazs, H. J. Breunig, E. Lork, C. Silvestru, *Eur. J. Inorg. Chem.* **2003**, 1361–1365.

[3] a) W. Levason, M. L. Matthews, G. Reid, M. Webster, *Dalton Trans.* **2004**, 554–561; b) G. A. Bowmaker, R. D. Hart, A. H. White, *Aust. J. Chem.* **1997**, *50*, 621–626.

[4] A. H. Cowley, R. A. Jones, C. M. Nunn, D. L. Westmoreland, *Angew. Chem.* **1989**, *101*, 1089–1090; *Angew. Chem. Int. Ed. Engl.* **1989**, *28*, 1018–1019.

[5] ASM Speciality Handbook, *Copper and Copper Alloys* (Eds.: J. R. Davis), Davis & Associates, ASM International, **2001**.

[6] A CSD search of Cu···Cu distances ≤ 2.4 Å produced 24 hits, selected examples: a) J. Beck, J. Strähle, *Angew. Chem.* **1985**, *97*, 419–420; *Angew. Chem. Int. Ed. Engl.* **1985**, *24*, 409–410; b) A. Heine, R. Herbst-Irmer, D. Stalke, *J. Chem. Soc. Chem. Commun.* **1993**, 1729–1731.

[7] K. P. Huber, G. Herzberg, *Molecular Spectra and Molecular Structure IV. Constants of Diatomic Molecules*, Van Nostrand Reinhold, New York, **1979**.

[8] Cu–Sb distances in Cu_2Sb alloy are 2.701(1)–2.834(1) Å, Cu···Cu 2.602(1), a) W. B. Pearson, *A Hanbook of Lattice Spacings and Structures of Metals and Alloys*, *Vol. 2*, Pergamon, New York, **1967**; b) J. Nuss, M. Jansen, *Z. Anorg. Allg. Chem.* **2002**, *628*, 1152–1157, and references therein.

[9] All calculations were performed with the TURBOMOLE program. a) R. Ahlrichs, M. Bär, M. Häser, H. Horn, C. Kölmel, *Chem. Phys. Lett.* **1989**, *162*, 165–169; b) O. Treutler, R. Ahlrichs, *J. Chem. Phys.* **1995**, *102*, 346–354. We employed the Becke–Perdew (BP-86) exchange-correlation functional and the very efficient MARIJ technique; c) A. D. Becke, *Phys. Rev. A* **1988**, *38*, 3098–3100; d) S. J. Vosko, L. Wilk, M. Nusair, *Can. J. Phys.* **1980**, *58*, 1200–1211; e) J. P. Perdew, *Phys. Rev. B* **1986**, *33*, 8822–8824; Erratum: J. P. Perdew, *Phys. Rev. B* **1986**, *34*, 7406; f) K. Eichkorn, O. Treutler, H. Öhm, M. Häser, R. Ahlrichs, *Chem. Phys. Lett.* **1995**, *242*, 652–660; g) M. Sierka, A. Hogekamp, R. Ahlrichs, *J. Chem. Phys.* **2003**, *118*, 9136–9148. We used also the Becke-Lee-Yang-Parr (B3LYP) exchange-correlation functional; h) C. Lee, W. Yang, R. G. Parr, *Phys. Rev. B* **1988**, *37*, 785–789; i) A. D. Becke, *J. Chem. Phys.* **1993**, *98*, 5648–5652. We used RECP (relativistic effective core potential) for Sb; j) D. Andrae, U. Häussermann, M. Dolg, H. Stoll, H. Preuss, *Theor. Chim. Acta* **1990**, *77*, 123–141.

[10] The basis and the auxiliary basis sets were of TZVP quality (triple zeta valence with a set of polarization functions)–for Hydrogen we used a smaller but sufficient SV(P) basis–taken from the standard TURBOMOLE basis set file. a) A. Schäfer, H. Horn, R. Ahlrichs, *J. Chem. Phys.* **1992**, *97*, 2571–2577; b) A. Schäfer, C. Huber, R. Ahlrichs, *J. Chem. Phys.* **1994**, *100*, 5829–5835; c) K. Eichkorn, F. Weigend, O. Treutler, R. Ahlrichs, *Theor. Chem. Acc.* **1997**, *97*,119–124; d) ftp://ftp.chemie.uni-karlsruhe.de/pub/.

[11] Band gaps of 0.6 eV were calculated using the BP86 functional, which usually underestimates the gap; 1.6 eV were obtained using the B3LYP functional.

 © 2005 Wiley-VCH Verlag GmbH & Co. KGaA, Weinheim

[12] R. Ahlrichs, J. Besinger, A. Eichhöfer, D. Fenske, A. Gbureck, *Angew. Chem.* **2000**, *112*, 4089 – 4093; *Angew. Chem. Int. Ed.* **2000**, *39*, 3929 – 3933.

[13] A. Eichhöfer, J. F. Corrigan, D. Fenske, E. Tröster, *Z. Anorg. Allg. Chem.* **2000**, *626*, 338 – 348.

[14] In addition to basis sets and RECPs specified in reference [9] and [10], we employed also a smaller core RECP-28; B. Metz, M. Schweizer, H. Stoll, M. Dolg, W. Liu, *J. Chem. Phys.* **2000**, *113*, 2563 – 2569. The corresponding TZVP basis set has very recently been optimized and added to the TURBOMOLE basis set library.

[15] The cutoffs have been chosen at gaps in the X-ray diffraction distance statistics. The results were checked and confirmed with slightly modified conditions (basis sets and ligands employed, e.g., PH_3 or PMe_3).

[16] The LUMO also has t symmetry and is just 0.05 eV above the HOMO indicating a series of low-lying electronic states (within 0.1 eV).

[17] a) M. L. Luetkens, A. P. Sattelberger, H. H. Murray, J. D. Basil, J. P. Fackler, *Inorg. Synth.* **1989**, *26*, 7 – 12; b) G. Becker, A. Münch, C. Witthauer, *Z. Anorg. Allg. Chem.* **1982**, *492*, 15 – 27; c) T. Greiser, E. Weiss, *Chem. Ber.* **1976**, *109*, 3142; d) D. A. Edwards, R. J. Richards, *J. Chem. Soc. Dalton Trans.* **1973**, 2463 – 2468.

[18] SHELXTL-97, G. M. Sheldrick, University of Göttingen, **1997**.

[19] Crystal data for **1**: $C_{72}H_{180}Cu_{12}P_6Sb_6Si_6$; $M_r = 2893.50$; monoclinic, space group $P2_1/n$, $Z = 2$; $a = 15.5505(8)$, $b = 18.2888(17)$, $c = 19.385(4)$ Å, $\beta = 90.524(6)°$, $V = 5512.8(13)$ Å^3, $T = 130(2)$ K, $F(000) = 2880$; $\rho_{calcd} = 1.743$ g cm^{-3}. 23193 reflections measured, of which 10011 were unique ($R_{int} = 0.0612$). 460 parameters; final $wR_2 = 0.0896$ (all data); $R_1 = 0.0419$ $\{I > 2\sigma(I)\}$; largest difference peak and hole 0.998 and -1.301 e Å^{-3}; disordered components were refined with isotropic thermal parameters. Crystal data for **2**·8THF: $C_{92}H_{244}Cu_{40}O_8P_{20}Sb_{12}$; $M_r = 6100.87$; monoclinic, space group $P2_1/n$, $Z = 2$; $a = 18.283(4)$, $b = 22.227(4)$, $c = 21.510(4)$ Å, $\beta = 91.75(3)°$; $V = 8737(3)$ Å^3, $T = 100(2)$ K, $F(000) = 5864$, $\rho_{calcd} = 2.319$ g cm^{-3}. 64873 reflections measured, of which 21361 were unique ($R_{int} = 0.0821$). 767 parameters; final $wR_2 = 0.1504$ (all data); $R_1 = 0.0515$ $\{I > 2\sigma(I)\}$; largest difference peak and hole 3.200 and -1.834 e Å^{-3}; disordered components were refined with isotropic thermal parameters. Crystal data for **3**: $C_{80}H_{208}Cu_{45}P_{16}Sb_{16}$; $M_r = 6473.28$; cubic, space group $F\bar{4}3m$, $Z = 4$; $a = 27.200(3)$; $V = 20124(4)$ Å^3, $T = 100(2)$ K, $F(000) = 12196$, $\rho_{calcd} = 2.137$ g cm^{-3}. 30390 reflections measured, of which 2408 were unique ($R_{int} = 0.0502$). 62 parameters; final $wR_2 = 0.1419$ (all data); $R_1 = 0.0455$ $\{I > 2\sigma(I)\}$; largest difference peak and hole 1.022 and -0.969 e Å^{-3}; the α-C atoms in Et_2MeP ligands were placed in idealized positions and refined with isotropic thermal parameters. Methyl groups in ethyl substituents of Et_2MeP were not located. Further details are given in the Experimental Section.

 © 2005 Wiley-VCH Verlag GmbH & Co. KGaA, Weinheim

Cover Picture

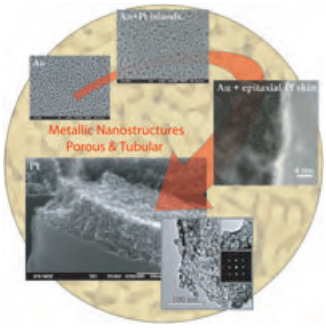


Sébastien Bonhommeau, Gábor Molnár, Ana Galet, Antoine Zwick, José-Antonio Real, John J. McGarvey, and Azzedine Bousseksou*

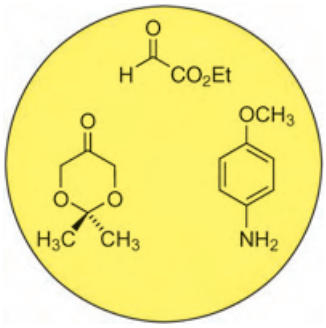
A reversible spin transition occurs when a single laser pulse (8 ns) is applied in the hysteresis loop (black curve) of the spin-crossover complex [Fe(pyrazine){Pt(CN)$_4$}] (structure shown). This bi-directional, photoinduced spin switching occurs at room temperature over a wide region of bistability and involves magnetization as well as color changes (low spin: red; high spin: yellow). More details on this phenomenon are given in the Communication by A. Bousseksou and co-workers on page 4069 ff.



Kinetic Resolution
The development of kinetic resolution from its initial discovery and its fascinating course through historical milestones to current techniques is retraced by E. Vedejs and M. Jure in their Review on page 3974 ff.



Materials Science
The design and synthesis of nanotubular mesoporous platinum by an epitaxial casting method using nanoporous gold membrane molds is described by J. Erlebacher and co-workers in their Communication on page 4002 ff.



Stereoselective Mannich Reactions
In two independent studies, B. Westermann and C. Neuhaus as well as D. Enders et al. describe on page 4077 ff. and page 4079 ff. an (*S*)-proline-catalyzed three-component Mannich reaction to form protected amino sugars.

Contents

VIP *The following Communications have been judged by at least two referees to be "very important papers" and will be published online at www.angewandte.org soon:*

*F. Studt, F. Tuczek**
Energetics and Mechanism of a Room Temperature Catalytic Synthesis of Ammonia (Schrock Cycle): Comparison with Biological Nitrogen Fixation

H. Zhu, J. Chai, H. Fan, H. W. Roesky, C. He, V. Jancik, H.-G. Schmidt, M. Noltemeyer, W. A. Merrill, P. P. Power*
A Stable Aluminacyclopropene LAl(η^2-C_2H_2) and Its End-On Azide Insertion to an Aluminaazacyclobutene

D. Loffreda, F. Delbecq, F. Vigné, P. Sautet*
Catalytic Hydrogenation of Unsaturated Aldehydes on Pt (111): Understanding the Selectivity from First-Principles Calculations

*C. Schaefer, G. C. Fu**
Catalytic Asymmetric Couplings of Ketenes with Aldehydes to Generate Enol Esters

M. Capdevila, J. Domènech, A. Pagani, L. Tío, L. Villarreal, S. Atrian*
Zn and Cd Metallothionein Recombinant Species from the Most Diverse Phyla May Contain Sulfide (S^{2-}) Ligands

*R. Shintani, W.-L. Duan, T. Nagano, A. Okada, T. Hayashi**
Chiral Phosphine–Olefin Bidentate Ligands in Asymmetric Catalysis: Rhodium-Catalyzed Asymmetric 1,4-Addition of Aryl Boronic Acids to Maleimides

News

K. Nakanishi Awarded Gold Nagoya Medal 2005 ——— **3956**

M. Suginome Receives Silver Nagoya Medal 2005 ——— **3956**

M. Shibasaki Receives Japan Academy Prize ——— **3956**

Books

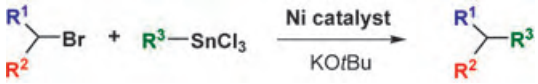
Fritz Haber: Chemist, Nobel Laureate, German, Jew — Dietrich Stoltzenberg — *reviewed by B. Friedrich* ——— **3957**

Highlights

Cross-Coupling Reactions

A. M. Echavarren* ——— **3962 – 3965**

Couplings with Monoorganotin Compounds: A "Radical" Twist from the Original Stille Reaction

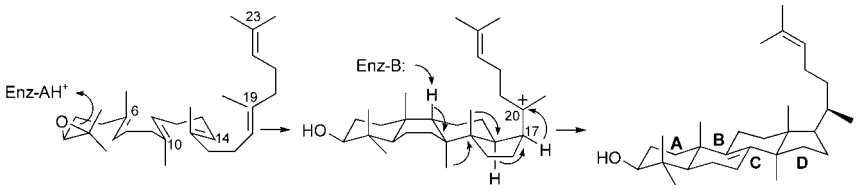


Revamped for the 21st century: The original Stille protocols for cross-couplings are difficult to recognize in the newer nickel-catalyzed reactions of monoorganotin compounds with secondary alkyl halides (see scheme). This new coupling scheme avoids the formation of toxic byproducts.

Cyclizations

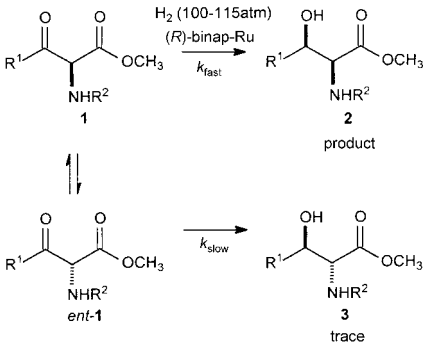
K. U. Wendt* ——— **3966 – 3971**

Enzyme Mechanisms for Triterpene Cyclization: New Pieces of the Puzzle



Cationic polycyclization cascades: The stereoselective transformations of linear polyolefins to give cyclic triterpenes (see scheme) have fueled half a century of intense research. Structures of triterpene cyclases complexed with the substrate analogue 2-azasqualene and the reaction product lanosterol provide new insights into the elegant mechanisms of these enyzmes.

Reviews



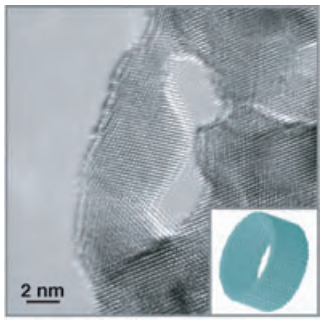
Among the numerous synthetic methods for the preparation of chiral products with high enantiomeric excess, kinetic resolution is the oldest. It is unique, as it has been applied to practically every type of chiral substrate, and can be combined with any method of enantioselective synthesis. The scheme shows an example of dynamic kinetic resolution through the enantioselective catalytic hydration of an equilibrated racemic β-ketoester.

Chiral Resolution

E. Vedejs,* M. Jure* ——— **3974 – 4001**

Efficiency in Nonenzymatic Kinetic Resolution

Communications



A network of platinum nanotubes with diameters of about 15 nm and walls 1 nm thick that interconnect to form an open, doubly bicontinuous structure (see high-resolution electron micrograph) is formed by coating platinum on a nanoporous gold template then dissolving away the mold. The structure is stable at 125 °C for at least 24 hours, but starts to deform at 150 °C and eventually forms nanoparticles.

Materials Science

Y. Ding, A. Mathur, M. Chen, J. Erlebacher* ——— **4002 – 4006**

Epitaxial Casting of Nanotubular Mesoporous Platinum

Z for zinc and Z-DNA: As a result of different binding modes, a cationic zinc porphyrin discriminates between B and Z conformations of DNA and holds promise as a probe for Z-DNA. A very intense induced circular dichroism (ICD) effect with a bisignate spectrum is observed upon interaction of the porphyrin with Z-DNA (see graphic; porphyrin red, Z-DNA green), whereas only a weak ICD spectrum results upon its interaction with B-DNA.



Chiroptical Probes

M. Balaz, M. De Napoli, A. E. Holmes, A. Mammana, K. Nakanishi, N. Berova,* R. Purrello* ——— **4006 – 4009**

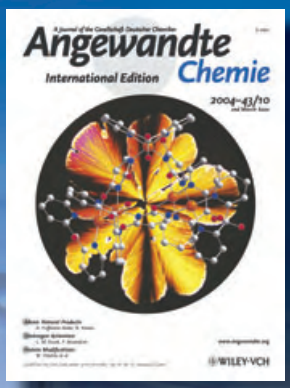
A Cationic Zinc Porphyrin as a Chiroptical Probe for Z-DNA

For the USA and Canada:
ANGEWANDTE CHEMIE International Edition (ISSN 1433-7851) is published weekly by Wiley-VCH PO Box 191161, D 69451 Weinheim, Germany. Air freight and mailing in the USA by Publications Expediting Inc. 200 Meacham Ave., Elmont, NY 11003. Periodicals postage paid at Jamaica NY 11431. US POSTMASTER: send address changes to *Angewandte Chemie*, Wiley-VCH, 111 River Street, Hoboken, NJ 07030. Annual subscription price for institutions: US$ 4948.00/4498.00 (valid for print and electronic / print or electronic delivery); for individuals who are personal members of a national chemical society, or whose institution already subscribes, or who are retired or self-employed consultants, print only: US$ 394.00. Postage and handling charges included. All Wiley-VCH prices are exclusive VAT.

 © 2005 Wiley-VCH Verlag GmbH & Co. KGaA, Weinheim

The best in chemistry –

for more than a hundred years



A Journal of the Gesellschaft Deutscher Chemiker

Angewandte International Edition **Chemie**

www.angewandte.org

1888: ***The beginning of a success story***

Constant Innovations

1962: *First issue of the International Edition*
1976: *Graphical abstracts*
1979: *Cover pictures*
1988: *Centenary of Angewandte*
1989: *Routine use of color*
1991: *New section: Highlights*
1992: *Computerized editorial tracking system*
1995: *Internet service for readers*
1998: *Regular press service; full-text online*
2000: *New section: Essays; EarlyView: Communications available online ahead of the printed version*
2001: *New section: Minireviews*
2002: *Online submission of manuscripts*
2003: *Weekly publication; new section: News; new layout*
2004: *Backfiles (1962-1997); ManuscriptXpress: Online system for authors and referees*



Angewandte's advisors...

Colin L. Raston
University of Western Australia

» Why would you not want to publish in ***Angewandte Chemie*** *and be part of the 'action'? The cutting edge papers hitting the community on a weekly basis keep you up to date on the major development across the chemical sciences and beyond. «*

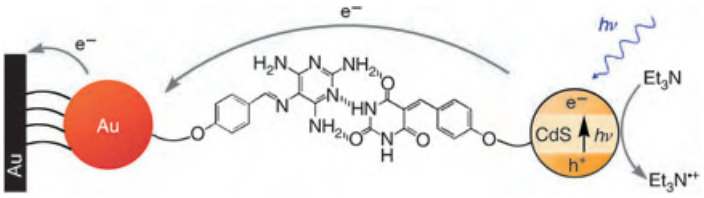
Angewandte Chemie International Edition *is a journal of the German Chemical Society (GDCh)*

GDCh

WILEY InterScience® DISCOVER SOMETHING GREAT

WILEY-VCH

1686501_gu

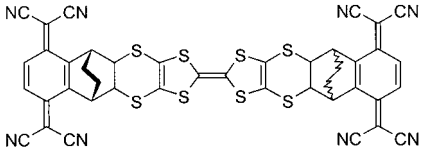


Trapping the light fantastic-ally! Enhanced photocurrents are observed for hydrogen-bonded gold nanoparticle/CdS nanoparticle arrays associated with a gold electrode surface (see scheme) as a result of charge separation and controlled electron transfer at the electrode interface.

Nanotechnology

R. Baron, C.-H. Huang, D. M. Bassani,* A. Onopriyenko, M. Zayats, I. Willner* _____ **4010 – 4015**

Hydrogen-Bonded CdS Nanoparticle Assemblies on Electrodes for Photoelectrochemical Applications



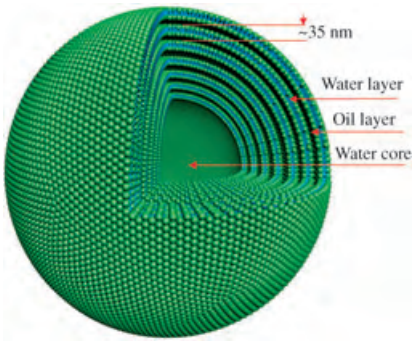
A one-component acceptor-donor-acceptor compound based on a rigid TCNQ-σ-TTF-σ-TCNQ system (see picture) exhibits a unique case of both intramolecular charge and electron transfer through space that is strongly dependent on the polarity of the medium. The strong dependence of the ground-state electronic structure on the solvent polarity provides an unprecedented case of solvatochromism.

Donor–Acceptor Systems

E. Tsiperman, J. Y. Becker,* V. Khodorkovsky,* A. Shames, L. Shapiro _____ **4015 – 4018**

A Rigid Neutral Molecule Involving TTF and TCNQ Moieties with Intrinsic Charge- and Electron-Transfer Properties that Depend on the Polarity of the Solvent

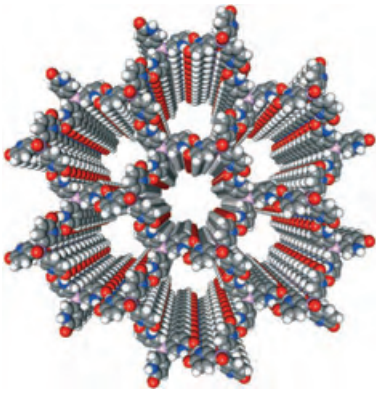
No added salt: Transmission electron microscopy and small-angle X-ray scattering studies have shown that uni- and multilamellar vesicles with radii of 25.5 and 366 nm (see schematic diagram; the hydrophilic cation/anion groups are shown as green spheres and the hydrocarbon chains in blue), respectively, are formed from trimethyltetradecylammonium hydroxide and oleic acid in water. The multilamellar phase consists of seven bilayers.



Phase Transitions

A. Song, S. Dong, X. Jia, J. Hao,* W. Liu,* T. Liu _____ **4018 – 4021**

An Onion Phase in Salt-Free Zero-Charged Catanionic Surfactant Solutions



Carefully selected combinations of directional forces can be used to rationally engineer crystals with particular anisotropic features. This approach has led to the generation of cleavable molecular crystals with parallel 15-Å channels by dipole-directed stacking of hydrogen-bonded sheets (see crystal structure). The network remains undeformed when guests included in the channels are exchanged.

Dipoles in Crystal Engineering

N. Malek, T. Maris, M.-È. Perron, J. D. Wuest* _____ **4021 – 4025**

Molecular Tectonics: Porous Cleavable Networks Constructed by Dipole-Directed Stacking of Hydrogen-Bonded Sheets

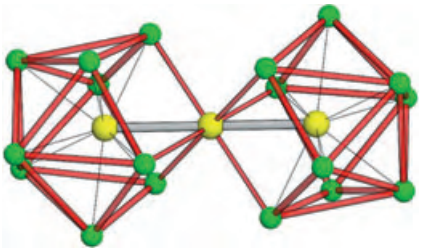
 © 2005 Wiley-VCH Verlag GmbH & Co. KGaA, Weinheim

Contents

Zintl Anions

J. M. Goicoechea, S. C. Sevov* ——— 4026 – 4028

$[(Ni\text{-}Ni\text{-}Ni)@(Ge_9)_2]^{4-}$: A Linear Triatomic Nickel Filament Enclosed in a Dimer of Nine-Atom Germanium Clusters

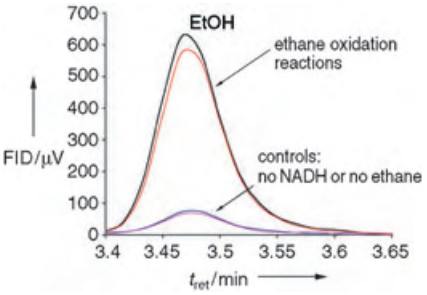


Under wraps: A linear nickel filament is "wrapped" inside an eighteen-atom germanium enclosure made of two nine-atom deltahedral clusters (see structure; green Ge, yellow Ni).

Enzyme Engineering

F. Xu, S. G. Bell, J. Lednik, A. Insley, Z. Rao,* L.-L. Wong* ——— 4029 – 4032

The Heme Monooxygenase Cytochrome $P450_{cam}$ Can Be Engineered to Oxidize Ethane to Ethanol

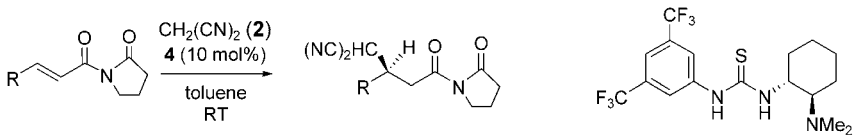


A NADH turnover rate of 741 min^{-1} in the oxidition of ethane to ethanol is observed with an engineered form of the heme monooxygenase cytochrome $P450_{cam}$—the first example of such activity for a P450 enzyme (GC analysis shown). Ethanol is formed at 78 min^{-1} (10.5% coupling). The mutant is ≈45% high-spin in the absence of substrate, making it a useful platform for P450 structure–function studies.

Organocatalysis

Y. Hoashi, T. Okino, Y. Takemoto* ——— 4032 – 4035

Enantioselective Michael Addition to α,β-Unsaturated Imides Catalyzed by a Bifunctional Organocatalyst



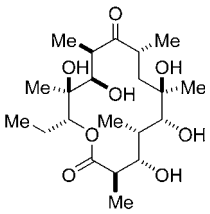
1 3 4

High enantioselectivities (up to 94% *ee*) were attained in the Michael addition of a variety of α,β-unsaturated imides **1** and malononitrile (**2**) catalyzed by bifunctional thiourea **4**. The pyrrolidinone moiety of **1** plays a key role in the reaction. The reaction provides access to a variety of Michael adducts **3** (see scheme; R = aryl and alkyl groups).

Natural Product Synthesis

D. Muri, N. Lohse-Fraefel, E. M. Carreira* ——— 4036 – 4038

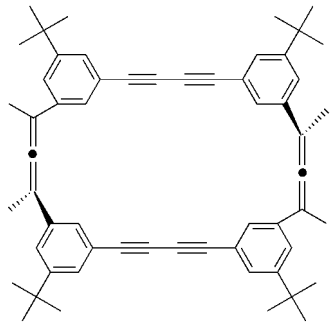
Total Synthesis of Erythronolide A by Mg^{II}-Mediated Cycloadditions of Nitrile Oxides



erythronolide A

A cycloaddition comes of age: The focal points of a stereoselective total synthesis of erythronolide A (see structure) are two Mg^{II}-mediated cycloadditions of nitrile oxides. Of broader significance, the strategy not only facilitates the synthesis of specific polyketide targets (i.e. natural products) but also opens up new possibilities for the preparation of non-natural analogues.

 © 2005 Wiley-VCH Verlag GmbH & Co. KGaA, Weinheim

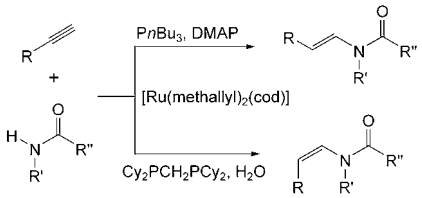


A cyclophane with allene and acetylene bridges has been prepared as a single enantiomer. This acetylenic allenophane (see structure) was synthesized by a series of palladium- and copper-mediated coupling reactions. The allene bridge was derived from the ring opening of a chiral epoxy alkyne, which was prepared by a Sharpless asymmetric epoxidation of an allylic alcohol.

Asymmetric Synthesis

M. D. Clay, A. G. Fallis* ____ **4039 – 4042**

Acetylenic Allenophanes: An Asymmetric Synthesis of a Bis(alleno)-bis(butadiynyl)-*meta*-cyclophane

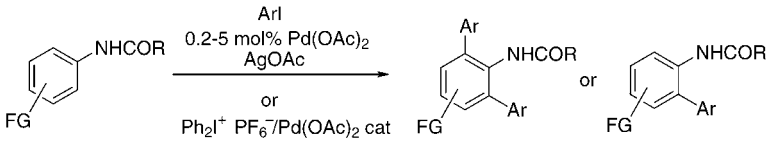


The base-free anti-Markovnikov addition of secondary amides, anilides, lactams, ureas, bislactams, and carbamates to terminal alkynes is accomplished, for the first time, by a ruthenium-catalyzed reaction. Two complementary protocols provide stereoselective synthetic entries to either the *E* or the *Z* isomers (see scheme; cod = cycloocta-1,5-diene; DMAP = 4-(*N*,*N*-dimethylamino)pyridine).

Homogeneous Catalysis

L. J. Gooßen,* J. E. Rauhaus, G. Deng ____ **4042 – 4045**

Ru-Catalyzed Anti-Markovnikov Addition of Amides to Alkynes: A Regio- and Stereoselective Synthesis of Enamides

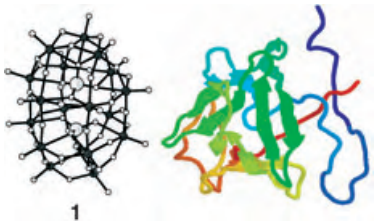


A thousand turnovers in bi- and triaryl formation: Substituted anilides have been *ortho*-arylated by aryl iodides under palladium catalysis (see scheme). This method is highly tolerant of the presence of additional functional groups (FGs). Even an iodo functionality on the anilide moiety and a bromo functionality on the aryl iodide are compatible with this methodology.

C–H Activation

O. Daugulis,* V. G. Zaitsev ____ **4046 – 4048**

Anilide *ortho*-Arylation by Using C–H Activation Methodology



Protein binders: Three representative polyoxometalate (POM) compounds, for example **1**, which is of the Wells–Dawson class, were found to interact with the basic fibroblast growth factor (bFGF, right). The binding induces dramatic conformational changes in the growth factor. POMs are promising leads for compounds that may represent a new avenue for the development of therapeutic agents against bFGF-induced angiogenesis.

Polyoxometalates

Q. Wu, J. Wang, L. Zhang, A. Hong, J. Ren* ____ **4048 – 4052**

Molecular Recognition of Basic Fibroblast Growth Factor by Polyoxometalates

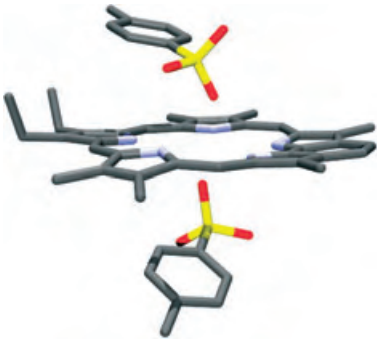
 © 2005 Wiley-VCH Verlag GmbH & Co. KGaA, Weinheim

Contents

Sapphyrins

P. K. Panda, Y.-J. Kang, C.-H. Lee* _____ **4053 – 4055**

A Benzodipyrrole-Derived Sapphyrin



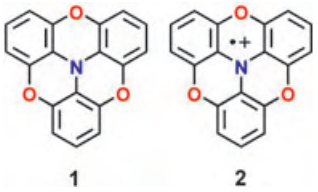
Within the framework: The fused benzodipyrrole unit within the sapphyrin **1** has a significant influence on its structure as compared to those of usual sapphyrins. The fused benzene ring partly inhibits distortion of the macrocycle about the dipyrrole unit (see structure of **1**·2 H^+2 (p-$CH_3C_6H_4SO_3^-$); C gray, N blue, O red, S yellow) and contributes to the significant red-shift of Q-bands.

Heterocyclic Chemistry

M. Kuratsu, M. Kozaki, K. Okada* _____ **4056 – 4058**

2,2′:6′,2″:6″,6-Trioxytriphenylamine: Synthesis and Properties of the Radical Cation and Neutral Species

A flat radical: Oxygen-bridged triphenylamine **1** and its radical cation **2** were prepared. The neutral compound has a shallow bowl structure, whereas the radical cation is planar. The properties of the highly stable radical cation were clarified; such compounds have potential applicability in electronic and magnetic materials.



Tumor Imaging Agents

O. Raguin, M.-C. Fournié-Zaluski, A. Romieu, A. Pèlegrin, F. Chatelet, D. Pélaprat, J. Barbet, B. P. Roques,* A. Gruaz-Guyon* _____ **4058 – 4061**

A Labeled Neutral Endopeptidase Inhibitor as a Potential Tool for Tumor Diagnosis and Prognosis

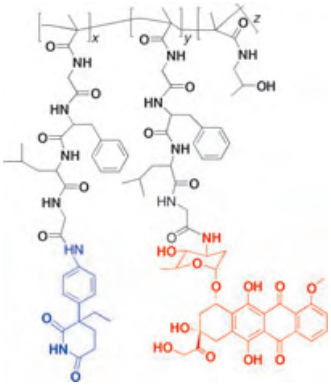


Specific targeting of tumors with radioactive isotopes is the key for high-sensitivity scintigraphy detection. A labeled neutral endopeptidase (NEP) inhibitor is described that accumulates in vivo in tumor cells expressing this enzyme, which makes it a potential tool for noninvasive evaluation of NEP expression. Its structure (black with the label depicted in red, DTPA = diethylenetriaminepentaacetic acid) is shown in a model of the NEP active site (blue).

Drug Design

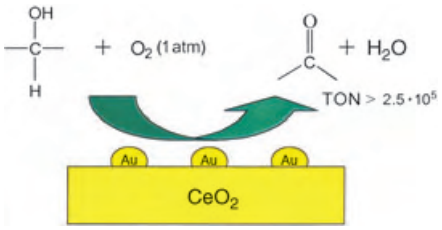
M. J. Vicent,* F. Greco, R. I. Nicholson, A. Paul, P. C. Griffiths, R. Duncan* _____ **4061 – 4066**

Polymer Therapeutics Designed for a Combination Therapy of Hormone-Dependent Cancer



Designer drug: A polymer therapeutic was designed for a combination therapy of breast cancer. *N*-(2-Hydroxypropyl)methacrylamide was used as the model polymer platform to prepare a unimolecular polymer conjugate (see picture, radius of gyration: 12.8 nm) that combines an endocrine (the aromatase inhibitor aminoglutethimide, blue) and a chemotherapeutic agent (the anthracycline antibiotic doxorubicin, red).

© 2005 Wiley-VCH Verlag GmbH & Co. KGaA, Weinheim



Ceria nanoparticles as a support stabilize positive gold species and provide oxygen vacancies. The resulting solid exhibits an exceedingly high efficiency for the solventless aerobic oxidation of primary and secondary alcohols to carbonyl compounds (see picture).

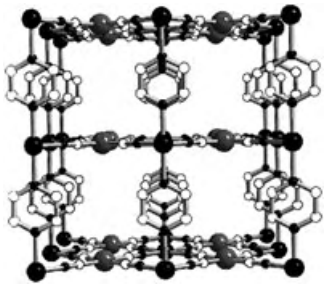
Supported Catalysts

A. Abad, P. Concepción, A. Corma,*
H. García ——— **4066 – 4069**

A Collaborative Effect between Gold and a Support Induces the Selective Oxidation of Alcohols

---

In the loop: A reversible spin transition was observed by Raman spectroscopy on application of a single laser pulse (8 ns) in the hysteresis loop of the spin-crossover complex [Fe(pyrazine){$Pt(CN)_4$}]. This bidirectional, photoinduced spin switching occurs at room temperature over a wide region of bistability and involves magnetization as well as color changes (see picture).



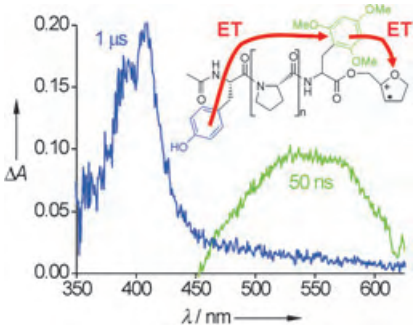
Spin Crossover

S. Bonhommeau, G. Molnár, A. Galet, A. Zwick, J.-A. Real, J. J. McGarvey, A. Bousseksou* ——— **4069 – 4073**

One Shot Laser Pulse Induced Reversible Spin Transition in the Spin-Crossover Complex [$Fe(C_4H_4N_2)${$Pt(CN)_4$}] at Room Temperature

---

Hopping holes: Oligopeptides with a photosensitive charge-injection system were synthesized and irradiated by a nanosecond laser. A multistep electron-transport process occurred which uses aromatic side chains as hole carriers (see scheme). The rates of this process indicate through-space electron transfer (a hopping mechanism).



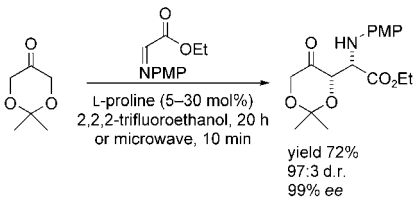
Electron Transfer in Peptides

B. Giese,* M. Napp, O. Jacques, H. Boudebous, A. M. Taylor, J. Wirz ——— **4073 – 4075**

Multistep Electron Transfer in Oligopeptides: Direct Observation of Radical Cation Intermediates

---

The C_3 equivalent dihydroxyacetone was used in its protected form in proline-catalyzed Mannich reactions (see scheme). As little as 5 mol% catalyst is required when using 2,2,2-trifluoroethanol as solvent. The reaction is improved further (reaction time 10 min) under microwave conditions. PMP = *p*-methoxyphenyl.



Organocatalysis

B. Westermann,*
C. Neuhaus ——— **4077 – 4079**

Dihydroxyacetone in Amino Acid Catalyzed Mannich-Type Reactions

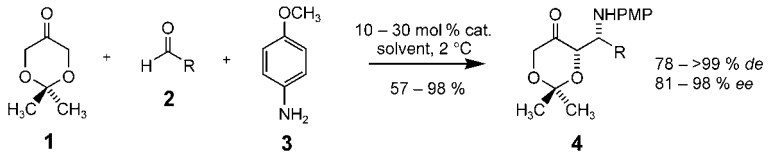
© 2005 Wiley-VCH Verlag GmbH & Co. KGaA, Weinheim

Contents

Amino Sugars

D. Enders,* C. Grondal, M. Vrettou, G. Raabe _____ 4079 – 4083

Asymmetric Synthesis of Selectively Protected Amino Sugars and Derivatives by a Direct Organocatalytic Mannich Reaction

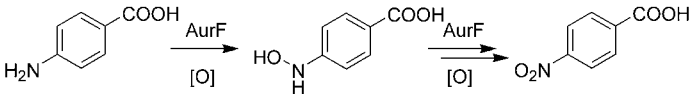


Short and sweet: Starting from the commercially available precursors **1**–**3**, selectively protected amino sugars and derivatives are obtained in one step and with high diastereo- and enantiomeric purity by means of a proline-catalyzed three-component Mannich reaction (see scheme, PMP = *para*-methoxyphenyl). This efficient organocatalytic procedure can be carried out smoothly on a multigram scale.

Enzyme Catalysis

R. Winkler, C. Hertweck* ___ 4083 – 4087

Sequential Enzymatic Oxidation of Aminoarenes to Nitroarenes via Hydroxylamines



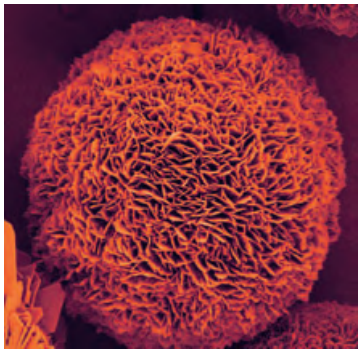
The at-line detection of an amino group oxidation catalyzed by the N-oxygenase AurF provides the first direct evidence for a stepwise enzymatic oxidation of aromatic amines to nitro groups via a hydroxylamine intermediate (see scheme). The sequential nature of this reaction is further supported by biotransformation of the intermediate and the identification of a *p*-aminobenzoate-derived azoxy side product.

Crystal Engineering

S. Wohlrab, H. Cölfen,* M. Antonietti _____ 4087 – 4092

Crystalline, Porous Microspheres Made from Amino Acids by Using Polymer-Induced Liquid Precursor Phases

Precipitation of charged amino acids in the presence of oppositely charged polyelectrolytes leads to liquid droplets of the corresponding polymer/amino acid complexes in water. The resulting emulsions are stable against crystallization and Ostwald ripening for several months but can also be used as a starting situation for crystallization of spherical, porous crystal superstructures (see SEM image of L-lysine).

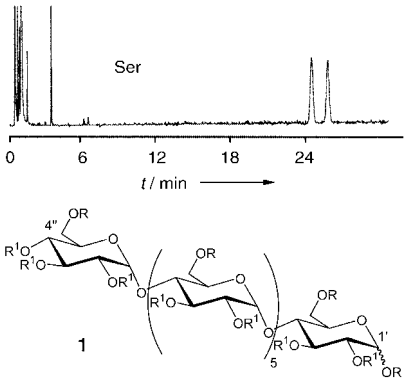


Enantiomer Separation

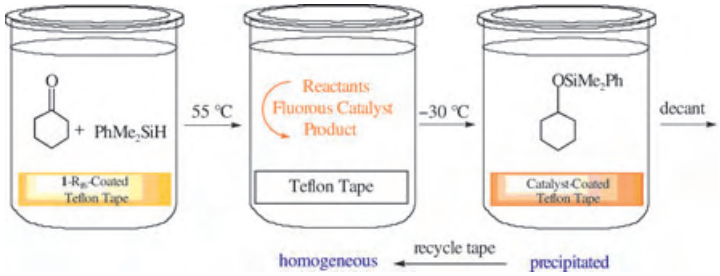
G. Sicoli, Z. Jiang, L. Jicsinsky, V. Schurig* _____ 4092 – 4095

Modified Linear Dextrins ("Acyclodextrins") as New Chiral Selectors for the Gas-Chromatographic Separation of Enantiomers

Cyclic or acyclic: Not only modified cyclodextrins but also modified linear dextrins like the silylated (R)and acetylated (R^1) maltoheptaose derivatives **1** are suitable selectors for separating racemic *N*-trifluoroacetyl-*O*-alkyl esters of α-amino acids by gas chromatography. In the example shown, racemic *N*-trifluoroacetylserine *O*-ethyl ester is resolved.



 © 2005 Wiley-VCH Verlag GmbH & Co. KGaA, Weinheim



Nothing sticks to Teflon? Going one better than "soap on a rope", a recyclable fluorous rhodium hydrosilylation catalyst is described that is released from Teflon tape into dibutyl ether upon warming, and readsorbed upon cooling (see scheme).

Catalyst Recycling

L. V. Dinh, J. A. Gladysz* — **4095 – 4097**

"Catalyst-on-a-Tape"—Teflon: A New Delivery and Recovery Method for Homogeneous Fluorous Catalysts

Sources

Product and Company Directory

You can start the entry for your company in "Sources" in any issue of *Angewandte Chemie*.

If you would like more information, please do not hesitate to contact us.

Wiley-VCH Verlag – Advertising Department
Tel.: 0 62 01 - 60 65 65
Fax: 0 62 01 - 60 65 50
E-Mail: MSchulz@wiley-vch.de

Service

Keywords — *4098*

Authors — *4099*

Preview — *4101*

Corrigendum

The compounds in Equation (1) of this Communication were renumbered before printing, yet the requisite change to the text was not made. The sentence that begins on the last line preceding Equation (1) should therefore read: "Compound **1** exhibits strong fluorescence not only in concentrated solution but also in the solid state."

A Novel Fluorescent Dye with Strong, Anisotropic Solid-State Fluorescence, Small Stokes Shift, and High Photostability

H. Langhals,* O. Krotz, K. Polborn, P. Mayer — **2427–2428**

Angew. Chem. Int. Ed. **2005**, *44*

DOI 10.1002/anie.200461610

 © 2005 Wiley-VCH Verlag GmbH & Co. KGaA, Weinheim



Awarded...

K. Nakanishi Awarded Gold Nagoya Medal 2005

Koji Nakanishi, Centennial Professor of Chemistry at Columbia University, will receive the Gold Nagoya Medal 2005 in November. Since 1995, this annual award has been given to organic chemists who have made original and significant contributions to their field. During the award ceremony at the University of Nagoya, he will discuss ginkgolides and bilobalide, about which he and K. Strømgaard co-authored a Review in *Angewandte Chemie* last year.[1]



K. Nakanishi

Nakanishi has 60 years of chemistry research behind him! He received his BSc in Chemistry in 1947 at the University of Nagoya. He spent the following two years working with Professor L. Fieser at Harvard University. Afterward, he returned to the University of Nagoya, where he completed his PhD in 1954 with Professor Y. Hirata. He spent the following years there as an assistant professor until 1958, when he accepted a full professorship in chemistry at Tokyo Kyoiku University. His next position was held between 1963 and 1969 at Tohoku University in Sendai. He has been a faculty member at Columbia University in New York since 1969. His research involves the isolation as well as structural and bioorganic studies of bioactive compounds, retinal proteins, ligand–neuroreceptor interactions, and the development of spectroscopic methods. Nakanishi is an editorial board member for several journals and is editor-in-chief of *The Chemical Record*, issued by a series of Japanese chemical societies.

M. Suginome Receives Silver Nagoya Medal 2005

Michinori Suginome, professor of chemistry at Kyoto University, will be awarded with the Silver Nagoya Medal 2005 in November. The silver medal has been presented each year since 1999 to young Japanese scientists whose research has had a major influence on the field of synthetic organic chemistry. Professor Suginome is being recognized for his contributions to synthetic organic chemistry through work with boron and silicon compounds in combination with catalysts to develop new synthetic methods toward biologically relevant molecules.



M. Suginome

Suginome studied chemistry at the University of Kyoto, where he received his PhD in 1993 under the direction of Professor Y. Ito. In the same year, he accepted an assistant professorship at the University of Kyoto. He visited the Massachusetts Institute of Technology between 1998 and 1999 to conduct research with Professor G. Fu. He was promoted to associate professor in 2002 and to full professor in 2004 at the University of Kyoto. His research interests include organometallic chemistry as well as organic synthesis and polymer synthesis. His work in the synthesis of α,β-unsaturated β-boryl nitriles by palladium-catalyzed cyanoboranation of alkynes appears in this year's volume of *Angewandte Chemie*.[2]

M. Shibasaki Receives Japan Academy Prize

Masakatsu Shibasaki, professor of chemistry at the University of Tokyo, will be awarded with the Japan Academy Prize in a ceremony in the presence of the Emperor and Empress of Japan on June 13th. The prize is accompanied by an endowment of one million yen. He is being recognized for his lifetime achievement in the creation of new asymmetric catalysts and their application toward the efficient synthesis of medicinal compounds.

Professor Shibasaki received his PhD from the University of Tokyo in 1974 under the direction of Professor Shun-ichi Yamada before conducting postdoctoral research with Professor E. J. Corey at Harvard University. In 1997 he returned to Japan and joined Teikyo University as an associate professor. In 1983 he moved to Sagami Chemical Research Center as a group leader, and in 1986 accepted a professorship at Hokkaido University until 1991. He then returned to the University of Tokyo, where he holds his current position. Shibasaki's research interests include asymmetric catalysis and the asymmetric synthesis and medicinal chemistry of biologically active compounds. His report in *Angewandte Chemie* describes the design and application of chirally economical, non-C_2-symmetric linked-binol derivatives with readily tunable properties.[3] Shibasaki is a member of the editorial board of *Chemistry—A European Journal*.



M. Shibasaki

[1] K. Strømgaard, K, Nakanishi, *Angew. Chem.*, **2004**, *116*, 1670–1689; *Angew. Chem. Int. Ed.* **2004**, *43*, 1640–1658.

[2] M. Suginome, A. Yamamoto, M. Murakami, *Angew. Chem.* **2005**, *117*, 2432–2434; *Angew. Chem. Int. Ed.* **2005**, *44*, 2380–2382.

[3] T. Yoshida, H. Morimoto, N. Kumagai, S. Matsunaga, M. Shibasaki, *Angew. Chem.* **2005**, *117*, 3536–3540; *Angew. Chem. Int. Ed.* **2005**, *44*, 3470–3474.

 © 2005 Wiley-VCH Verlag GmbH & Co. KGaA, Weinheim DOI: 10.1002/anie.200501894

Cross-Coupling Reactions

Couplings with Monoorganotin Compounds: A "Radical" Twist from the Original Stille Reaction

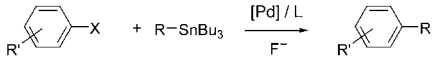
*Antonio M. Echavarren**

Keywords:
cross-coupling · nickel · palladium · reaction mechanisms · stannanes

The Stille cross-coupling reaction of tetraorganostannanes R_4Sn' with organic electrophiles is one of the most reliable methods for the selective formation of carbon–carbon bonds,[1] in particular C_{sp^2}–C_{sp^2} bonds.[2–4] However, this method suffers the disadvantage that only one of the four groups at tin is transferred to the organic electrophile. Also, the triorganotin halide R_3SnX that forms stoichiometrically as a byproduct is toxic and, on occasions, its separation from the desired product can be rather difficult.

Recent developments in cross-coupling methodology allow Stille reactions to be performed under milder conditions.[2,3] This is more clearly seen by comparing the best current methods for the coupling of aryl bromides with Stille's original procedure published in 1987 (Table 1).[5] Fu and co-workers discovered that palladium complexes $[Pd_2(dba)_3]/PtBu_3$ or $[Pd(PtBu_3)_2]$, that bear bulky phosphane groups, are excellent catalysts for the coupling of aryl bromides at room temperature.[6] Verkade and co-workers developed related conditions for the Stille coupling reaction by using proazaphosphatranes as P ligands.[7] Concurrently, Baldwin and co-workers found a synergetic effect of fluoride anion and Cu^I ions that allowed the coupling of aryl bromides to be carried out under mild conditions.[8] For the coupling of aryl chlorides, the least reactive of the common aryl electrophiles,[9] relatively harsh conditions are still required.

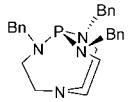
Table 1: Comparison of some of the best methods for Stille couplings with aryl bromides and chlorides.[a]



X = Cl, Br

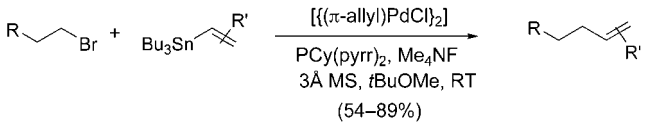
Method	Ar–Br	Ar–Cl
Stille[5]	$[Pd(PPh_3)_4]$ (2%), toluene, 110°C	–
Fu[6]	$[Pd_2(dba)_3]$ (0.5–1.5%), $PtBu_3$ (1.1–3.3%),[b] toluene or NMP, RT, (CsF, 2.2 equiv for R = Ar)	as for Ar–Br, but in dioxane at 100°C with CsF (2.2 equiv)
Verkade[7]	$[Pd_2(dba)_3]$ (1.5%), L[c] (3%), CsF (2.2 equiv), THF, RT	as for Ar–Br, but in dioxane at 110°C
Baldwin[8]	$PdCl_2$ (2%), $PtBu_3$ (4%), CuI (4%), CsF (2 equiv), DMF, 45°C	as for Ar–Br, but at 100°C

[a] Bn = benzyl, dba = dibenzylideneacetone, NMP = *N*-methylpyrrolidone, DMF = *N*,*N*-dimethylformamide.
[b] $[Pd(PtBu_3)_2]$ could also be used as catalyst.

[c] L = 

Part of the success of these new methods for the coupling of ordinary aryl chlorides relies on the use of fluoride anion to enhance the reactivity of the stannane. Fu and co-workers found that activation by fluoride anion is also crucial in the coupling of stannanes with primary alkyl bromides that bear β-hydrogen atoms (Scheme 1).[10] This result represented a significant development in this area.[11,12] Fluoride ion probably gives rise to pentacoordinated species with enhanced reactivity in the transmetalation step, as demonstrated by García Martínez et al. using hypervalent difluorostannate reagents **1**, which are easily prepared by reaction of triorganostannyl fluorides (Scheme 2).[13]

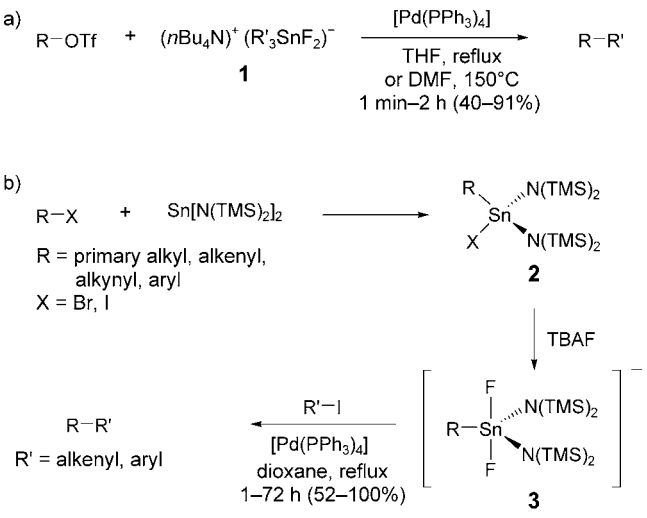
Fouquet et al. reported that monoalkylstannanes **2**, prepared in situ from RX and Lappert's stannylene $Sn[(Me_3Si)_2N]_2$, are activated by tetrabutylammonium fluoride (TBAF) to form reagents **3**, which react with alkenyl or aryl iodides (Scheme 2).[14] The accelerating effect of fluoride ion in the Stille coupling reaction had been discovered earlier using TBAF by Fugami et al.[15] Significantly, selective aryl transfer was attained in the palladium-



Scheme 1. Cy = cyclohexyl, pyrr = pyrrolidinyl, MS = molecular sieves.

[*] Prof. Dr. A. M. Echavarren
Institute of Chemical Research of Catalonia (ICIQ)
43007 Tarragona (Spain)
and
Departamento de Química Orgánica
Universidad Autónoma de Madrid (Spain)
Fax: (+34) 977-920-225
E-mail: aechavarren@iciq.es

 © 2005 Wiley-VCH Verlag GmbH & Co. KGaA, Weinheim DOI: 10.1002/anie.200500918



Scheme 2. a) See ref. [13]; Tf = trifluoromethanesulfonyl. b) See ref. [14]; TMS = trimethylsilyl.

catalyzed reaction between di-*n*-butyl-*p*-tolylstannyl chloride and *p*-iodoanisole to give 4-methoxy-4′-methylbiphenyl. Recently, Thiele and Mitchell reported palladium-catalyzed alkenyl transfers from an alkenyldi-*n*-butylstannyl chloride or bromide in the presence of excess TBAF, although the yields of product were only low to moderate.[16]

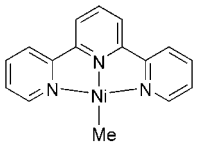
Bumagin and co-workers[17] and Collum and co-workers[18] succeeded in performing Stille reactions with monoorganotin compounds $RSnX_3$ (Scheme 3). These couplings were performed under basic conditions in aqueous solutions at 90–100 °C with $PdCl_2$ or, preferentially, with palladium complexes of water-soluble phosphanes.[19]

As part of a study on the cross-coupling of alkyl halides, the groups of Knochel[20] and Fu[21] found that nickel catalysts were particularly effective in this context.[22] This led Fu et al. recently to develop a coupling of secondary alkyl bromides with monoorganostannanes $RSnCl_3$ that drastically departs from conventional Stille reactions (Scheme 4).[23] In this case, activation of the stannane is carried out with KO*t*Bu. The byproducts of the reaction are nontoxic inorganic tin species that can be easily removed. This and related methods are significant steps forward in synthetic methodology.

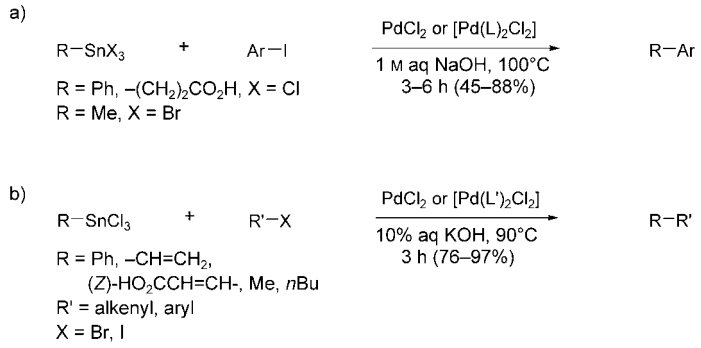
Nickel-catalyzed couplings with different Ar–M reagents are compared in Table 2.[22] Although the Suzuki-type coupling (entry 1) proceeds with only 4 mol% catalyst,[21b] reaction with the stannane (entry 3) uses a catalyst formed from bipyridine and $NiCl_2$,[23] a less sensitive and much cheaper source of nickel than $[Ni(cod)_2]$.

Another distinct advantage of this coupling is the ready availability of monoorganostannanes $RSnCl_3$ by redistribution of commercially available tetraorganostannanes such as **4** and **5** with $SnCl_4$ (Scheme 5).[23]

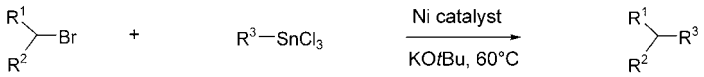
As shown in the coupling of cholesteryl iodide **6**, retention of configuration was observed to give **7** (Scheme 5). It remains to be seen if the C-3 epimer of **6**, with an axial leaving group, would also react with retention of configuration. Importantly, note that the Suzuki and Hiyama couplings of *exo*- (**8**) and *endo*-2-bromonorbornene (**9**) give selectively the *exo*-coupled product **10** (Scheme 6).[21b,c] These and other results[23] point to a radical mechanism for the oxidative addition step involving Ni^I species, which is supported by the recent finding that Ni^I complex **11** is the



11

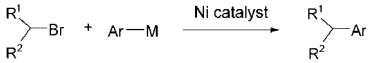


Scheme 3. a) See ref. [17]; L = $Ph_2P(m\text{-}C_6H_4SO_3Na)$. b) See ref. [18]; L′ = $PhP(m\text{-}C_6H_4SO_3Na)_2$.



Scheme 4.

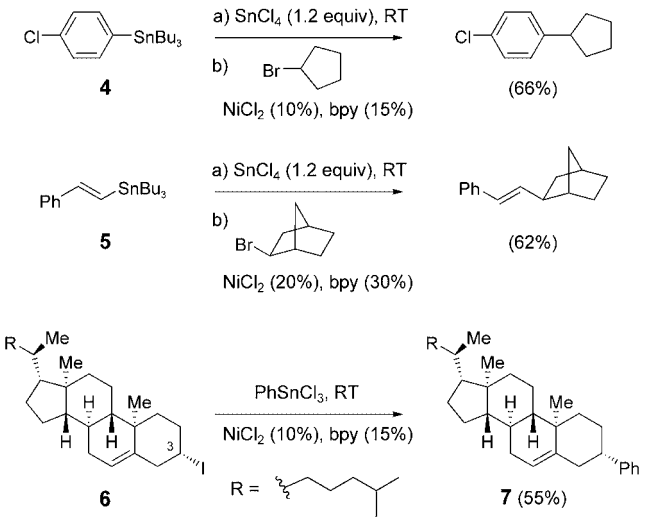
Table 2: Nickel-catalyzed cross-couplings of secondary alkyl bromides with Ar–M reagents.[a]



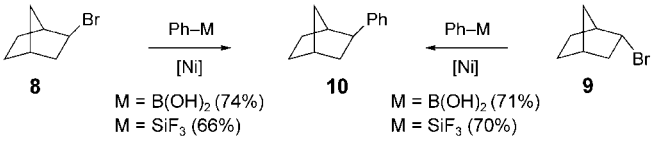
Entry	M	Ni catalyst	Additives	Solvent
1[20b]	$B(OH)_2$	$[Ni(cod)_2]$ (4%), bphen (8%)	KO*t*Bu (1.6 equiv)	*s*BuOH
2[20c]	SiF_3	$NiBr_2$·diglyme (6.5%), bphen (7.5%)	CsF (3.8 equiv)	DMSO
3[22]	$SnCl_3$	$NiCl_2$ (10%), bpy (15%)	KO*t*Bu (7 equiv)	*t*BuOH/*i*BuOH (1:1)

[a] cod = 1,5-cyclooctadiene, bphen = 4,7-diphenylphenanthroline (bathophenanthroline), diglyme = diethylene glycol dimethyl ether, DMSO = dimethyl sulfoxide, bpy = 2,2′-bipyridine.

 © 2005 Wiley-VCH Verlag GmbH & Co. KGaA, Weinheim



Scheme 5.

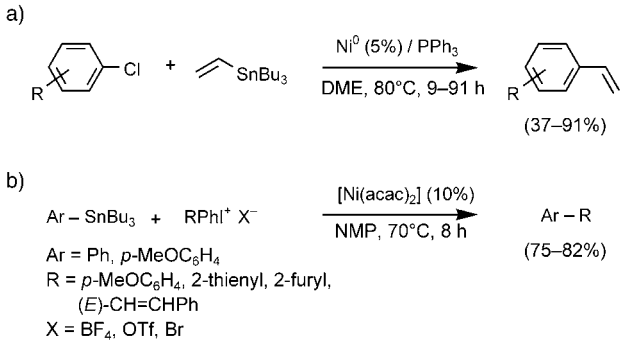


Scheme 6. [Ni] = Ni catalyst.

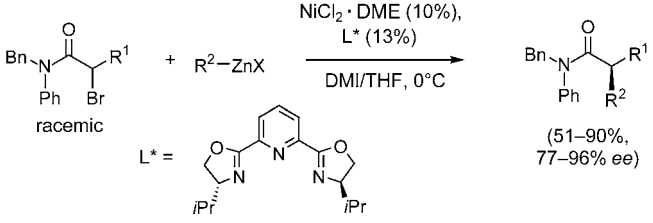
active catalyst in the coupling of *n*-pentylzinc bromide with alkyl bromides and iodides.[24]

Nickel catalysts in Stille-type couplings had already been used by Shirakawa et al. for the synthesis of styrenes from aryl chlorides (Scheme 7 a).[25,26] The reactive Ni^0 catalyst, presumably $[Ni(PPh_3)_4]$, was prepared from $[Ni(acac)_2]$ (acac = acetylacetonate) and PPh_3 in the presence of iBu_2AlH as reductant. Aryl bromides also react with alkenyl-, allyl-, and alkynylstannanes in the presence of this catalyst. Stannanes are also able to reduce Ni^{II} in situ as shown in the coupling of hypervalent iodonium salts with aryltri-*n*-butyltin (Scheme 7 b).[27] Aryl–aryl couplings have also been reported for arylboronic acids in the presence of nickel catalysts.[28]

The original Stille protocols can hardly be recognized in the Ni-catalyzed reaction of monoorganotin compounds.[23] This coupling raises intriguing mechanistic questions and paves the way to the development of asymmetric couplings of secondary alkyl halides by using chiral ligands. Indeed, recently Fisher and Fu have successfully reported asymmetric Ni-catalyzed Negishi couplings of α-bromoamides (Scheme 8).[29] New procedures for the formation of C_{sp^2}–C_{sp^2} and C_{sp^2}–C_{sp^3} bonds can also be foreseen by using nickel catalysts and monoorganotins $RSnX_3$ or related reagents.



Scheme 7. a) See ref. [25]; DME = 1,2-dimethoxyethane. b) See ref. [27].



Scheme 8. See ref. [29]. DMI = dimethylimidazolidin-2-one.

Published online: June 1, 2005

[1] J. K. Stille, *Angew. Chem.* **1986**, *98*, 504–519; *Angew. Chem. Int. Ed. Engl.* **1986**, *25*, 508–524.

[2] V. Farina, V. Krishnamurthy, W. K. Scott, *Organic Reactions*, *Vol. 50*, Wiley, New York, **1997**.

[3] T. N. Mitchell in *Metal-Catalyzed Cross-Coupling Reactions* (Eds.: A. de Meijere, F. Diederich), Wiley-VCH, Weinheim, **2004**, chapt. 3.

[4] P. Espinet, A. M. Echavarren, *Angew. Chem.* **2004**, *116*, 4808–4839; *Angew. Chem. Int. Ed.* **2004**, *43*, 4704–4734.

[5] D. R. McKean, G. Parrinello, A. F. Renaldo, J. K. Stille, *J. Org. Chem.* **1987**, *52*, 422–424.

[6] a) A. F. Littke, G. C. Fu, *Angew. Chem.* **1999**, *111*, 2568–2570; Angew . *Chem. Int. Ed.* **1999**, *38*, 2411–2413; b) A. F. Littke, L. Schwarz, G. C. Fu, *J. Am. Chem. Soc.* **2002**, *124*, 6343–6348.

[7] a) W. Su, S. Urgaonkar, J. G. Verkade, *Org. Lett.* **2004**, *6*, 1421–1424; b) W. Su, S. Urgaonkar, P. A. McLaughlin, J. G. Verkade, *J. Am. Chem. Soc.* **2004**, *126*, 16433–16439.

[8] S. P. H. Mee, V. Lee, J. E. Baldwin, *Angew. Chem.* **2004**, *116*, 1152–1156; *Angew. Chem. Int. Ed.* **2004**, *43*, 1132–1136.

 © 2005 Wiley-VCH Verlag GmbH & Co. KGaA, Weinheim

[9] A. F. Littke, G. C. Fu, *Angew. Chem.* **2002**, *114*, 4350 – 4386; *Angew. Chem. Int. Ed.* **2002**, *41*, 4176 – 4211.
[10] a) K. Menzel, G. C. Fu, *J. Am. Chem. Soc.* **2003**, *125*, 3718 – 3719; b) H. Tang, K. Menzel, G. C. Fu, *Angew. Chem.* **2003**, *115*, 5233 – 5236; *Angew. Chem. Int. Ed.* **2003**, *42*, 5079 – 5082.
[11] A. C. Frisch, M. Beller, *Angew. Chem.* **2005**, *117*, 680 – 695; *Angew. Chem. Int. Ed.* **2005**, *44*, 674 – 688.
[12] For pioneering work on the coupling of stannanes with secondary alkyl bromides that comprise β hydrogens, see: R. Sustmann, J. Lau, M. Zipp, *Tetrahedron Lett.* **1986**, *27*, 5207 – 5210.
[13] a) A. García Martínez, J. Osío Barcina, A. de Fresno Cerezo, L. R. Subramanian, *Synlett* **1994**, 1047 – 1048; b) A. García Martínez, J. Osío Barcina, M. R. Colorado Heras, Á. de Fresno Cerezo, *Org. Lett.* **2000**, *2*, 1377 – 1378; c) A. García Martínez, J. Osío Barcina, M. R. Colorado Heras, Á. de Fresno Cerezo, *Organometallics* **2001**, *20*, 1020 – 1023.
[14] a) E. Fouquet, M. Pereyre, A. L. Rodriguez, *J. Org. Chem.* **1997**, *62*, 5242 – 5243; b) E. Fouquet, A. L. Rodriguez, *Synlett* **1998**, 1323 – 1324; c) A. Herve, A. L. Rodriguez, E. Fouquet, *J. Org. Chem.* **2005**, *70*, 1953 – 1956.
[15] K. Fugami, S. Ohnuma, M. Kameyama, T. Saotome, M. Kosugi, *Synlett* **1999**, 63 – 64.
[16] C. M. Thiele, T. N. Mitchell, *Appl. Organomet. Chem.* **2004**, *18*, 83 – 85.
[17] A. I. Roshchin, N. A. Bumagin, I. P. Beletskaya, *Tetrahedron Lett.* **1995**, *36*, 125 – 128.
[18] R. Rai, K. B. Aubrecht, D. B. Collum, *Tetrahedron Lett.* **1995**, *36*, 3111 – 3114.
[19] For palladium-catalyzed couplings of $ArGeCl_3$ with ArX under aqueous basic conditions, see: T. Enokido, K. Fugami, M. Endo, M. Kameyama, M. Kosugi, *Adv. Synth. Catal.* **2004**, *346*, 1685 – 1688.
[20] a) A. Devasagayaraj, T. Stüdemann, P. Knochel, *Angew. Chem.* **1995**, *107*, 2952 – 2954; *Angew. Chem. Int. Ed. Engl.* **1995**, *34*, 2723 – 2725; b) R. Giovannini, P. Knochel, *J. Am. Chem. Soc.* **1998**, *120*, 11186 – 11187; c) M. Piber, A. E. Jensen, M. Rottländer, P. Knochel, *Org. Lett.* **1999**, *1*, 1323 – 1326; d) R. Giovannini, T. Stüdemann, A. Devasagayaraj, G. Dussin, P. Knochel, *J. Org. Chem.* **1999**, *64*, 3544 – 3553; e) A. E. Jensen, P. Knochel, *J. Org. Chem.* **2002**, *67*, 79 – 85.
[21] a) J. Zhou, G. C. Fu, *J. Am. Chem. Soc.* **2003**, *125*, 14726 – 14727; b) J. Zhou, G. C. Fu, *J. Am. Chem. Soc.* **2004**, *126*, 1340 – 1341; c) D. A. Powell, G. C. Fu, *J. Am. Chem. Soc.* **2004**, *126*, 7788 – 7789.
[22] M. R. Netherton, G. C. Fu, *Adv. Synth. Catal.* **2004**, *346*, 1525 – 1532.
[23] D. A. Powell, T. Maki, G. C. Fu, *J. Am. Chem. Soc.* **2005**, *127*, 510 – 511.
[24] T. J. Anderson, G. D. Jones, D. A. Vicic, *J. Am. Chem. Soc.* **2004**, *126*, 8100 – 8101.
[25] a) E. Shirakawa, K. Yamasaki, T. Hiyama, *J. Chem. Soc. Perkin Trans. 1* **1997**, 2449 – 2450; b) E. Shirakawa, K. Yamasaki, T. Hiyama, *Synthesis* **1998**, 1544 – 1549.
[26] For coupling of (η^3-allyl)nickel intermediates with alkynyltins, see: D.-M. Cui, N. Hashimoto, S. Ikeda, Y. Sato, *J. Org. Chem.* **1995**, *60*, 5752 – 5756.
[27] S.-K. Kang, H.-C. Ryu, S.-W. Lee, *J. Chem. Soc. Perkin Trans. 1* **1999**, 2661 – 2663.
[28] Z.-Y. Tang, Q.-S. Hu, *J. Am. Chem. Soc.* **2004**, *126*, 3058 – 3059.
[29] C. Fisher, G. C. Fu, *J. Am. Chem. Soc.* **2005**, *127*, 4594 – 4595.

 © 2005 Wiley-VCH Verlag GmbH & Co. KGaA, Weinheim

Cyclizations

Enzyme Mechanisms for Triterpene Cyclization: New Pieces of the Puzzle**

*K. Ulrich Wendt**

Keywords:
bioorganic chemistry · enzyme catalysis · steroids · structural biology · terpenes

The remarkable stereoselective cyclizations of 2,3-oxidosqualene (**1**) and squalene (**2**) to give polycyclic triterpenes have fascinated bioorganic chemists for over half a century.[1–3] These reactions are catalyzed by related enyzmes, the squalene cyclases and 2,3-oxidosqualene cyclases, which occur in a wide variety of microorganisms and in higher eukaryotes. Different active-site geometries of these enzymes give rise to structurally diverse polycyclic triterpenes that serve as precursors of hopanoids and steroids.[2] Consequently, the 2,3-oxidosqualene cyclases have been investigated as potential targets for anticholestermic and antifungal therapies.[4]

Detailed studies with nonnatural substrates have established the overall pathways of the enzymatic reactions (Scheme 1) involving: 1) binding of the polyolefinic substrate in a folded conformation, 2) initiation of the reaction by protonation of a double bond (squalene) or an epoxide (2,3-oxidosqualene), 3) ring formation, 4) in some cases skeletal rearrangement by 1,2-methyl and -hydride shifts (e.g. 2,3-oxidosqualene–lanosterol cyclase; OSC), and 5) termination by deprotonation or addition of water.[1–3]

Crystal structures of the monotopic membrane protein squalene–hopene cyclase (SHC) have provided a three-dimensional framework, which together with a wealth of bioorganic and mutational data, yielded the first biomolecular mechanism for enzymatic triterpene cyclization.[3,5] In brief, the structures show how the hydrophobic substrates are channeled from the membrane interior into a buried active-site cavity, where the reaction is initiated through protonation by an acidified aspartic acid residue ($Asp376^{SHC}$/$Asp455^{OSC}$).[5,6] During subsequent ring formation, the cation proceeds away from the catalytic acid, and the intermediates are shielded by the aromatic residues that line the active-site cavity with their π-electron-rich faces.[7] Deprotonation of the terminal cation has been shown to occur through polarized water (SHC) or a basic residue such as $His232^{OSC}$.[3]

Key questions around these complex reactions have remained unanswered: How is the energetically unfavorable chair–boat–chair conformation of the substrate induced in OSC? To what extend is ring formation concerted with the initial protonation step? Do C-ring formation (OSC and SHC) and D-ring formation (SHC) proceed through Markovnikov additions to intermediates **5**, **11**, and **13**, or does the reaction proceed along other pathways? What is the catalytic base in OSC?

Recent findings provide two important additional snapshots of the triterpene polycyclization cascades. Reinert et al. have determined the structure of SHC in complex with the substrate mimic 2-azasqualene, providing a view on the meandering conformation of the substrate prior to the initial protonation step (Figure 1).[8] Thoma et al. have succeeded in determining the long-awaited structure of human OSC in complex with the reaction product lanosterol (Figure 1).[9] In this article the contributions of these studies are highlighted along the principal steps of the enzymatic reaction.

Initiation

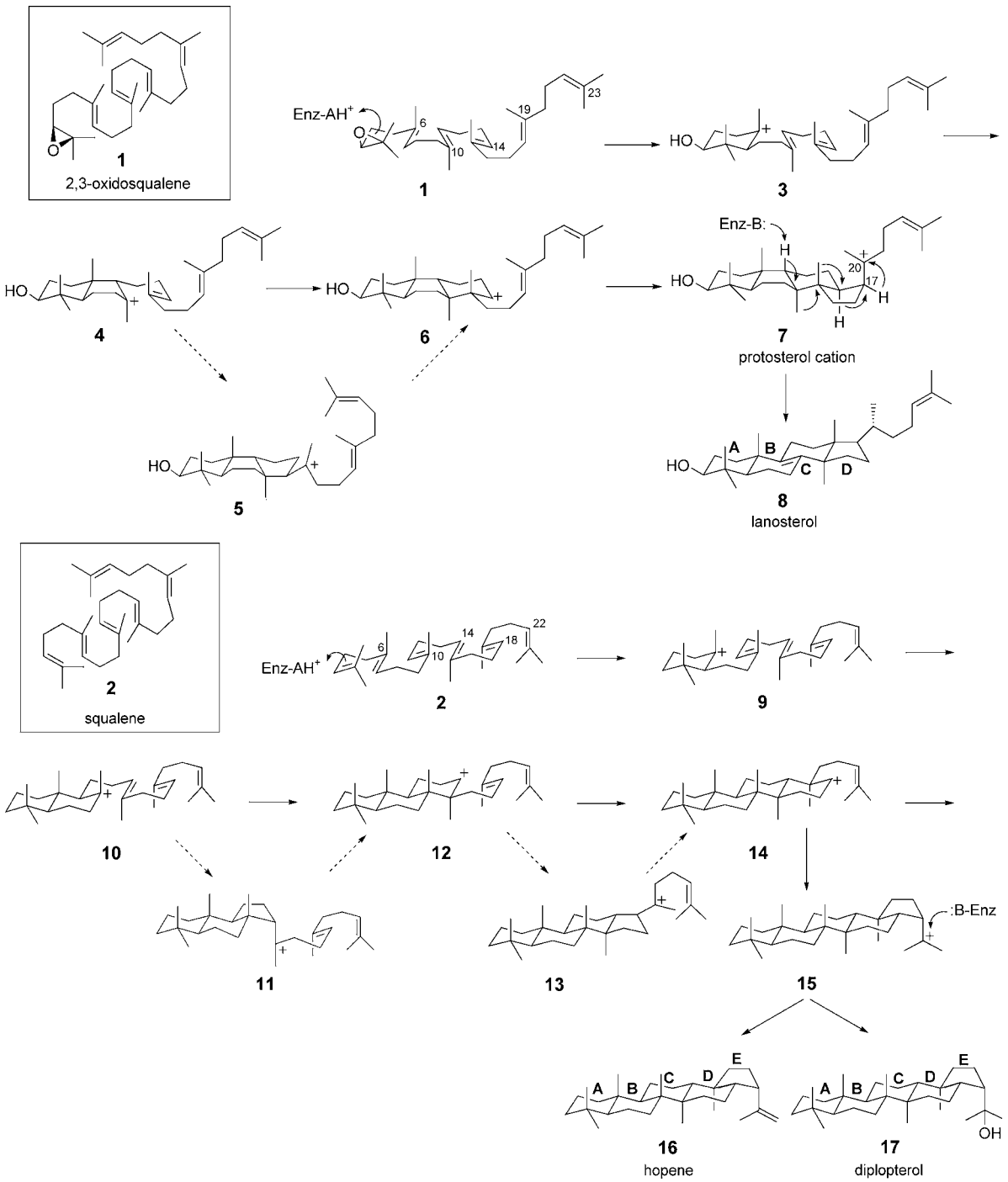
Since epoxides are more readily protonated than alkenes, one would expect that the catalytic acid of OSC need not be as acidic as that of SHC. In SHC, the catalytic acid $Asp376^{SHC}$ faces the substrate with its more acidic *anti* proton.[3,10] $Asp376^{SHC}$ is hydrogen-bonded to $His451^{SHC}$, a residue that is likely to carry a positive charge prior to the proton transfer and thus acidifies $Asp376^{SHC}$ (Figure 1). A negative countercharge on the hydrogen-bonded pair $Asp374^{SHC}$:$Asp377^{SHC}$ (2.6 Å distance) resides in an appropriate position to stabilize the C2 and C6 cations (squalene numbering). Three hydrogen bonds connect $Asp376^{SHC}$ with the bulk solvent such that reprotonation can occur while the cyclizing cation migrates away from the catalytic acid.[5]

The structure determined by Thoma et al. confirms $Asp455^{OSC}$ as the catalytic acid of OSC (Figure 1).[9,11] As predicted for this structure, $Asp455^{OSC}$ is not polarized by a positively charged histidine, and consequently the countercharged $Asp377^{SHC}$:$Asp374^{SHC}$ pair is missing as well.[3,5,9] Surprisingly, $Asp455^{OSC}$ is hydrogen-bonded to two cysteine residues, and it directs its less acidic *syn* proton toward the active-site cavity.[9,10] As in SHC, reprotonation can

[*] Dr. K. U. Wendt
Aventis Pharma Deutschland GmbH
Industrial Park Hoechst
65926 Frankfurt (Germany)
Fax: (+49) 69-30580169
E-mail: ulrich.wendt@sanofi-aventis.com

[**] I thank Alexander Schiffer, Christian von der Heyden, and Matthias Urmann for critical comments on the manuscript.

 © 2005 Wiley-VCH Verlag GmbH & Co. KGaA, Weinheim DOI: 10.1002/anie.200500804



Scheme 1. Overall mechanisms for reactions catalyzed by 2,3-oxidosqualene–lanosterol cyclase (OSC, top) and squalene–hopene cyclase (SHC, bottom).

occur through a chain of rigidly held water molecules that connect $Asp455^{OSC}$ with the bulk solvent. Overall, the Brønsted acidity of the OSC catalytic acid appears to be lower than that of SHC, potentially in order to enable the enzyme to discriminate between the olefin and epoxide sides of its natural substrate.

Ring Formation

The complex structure of OSC with lanosterol suggests how the energetically unfavorable boat conformation of the B-ring is induced. Thoma et al. suggest that in the otherwise highly conserved "upper" part of the active site, $Tyr98^{OSC}$ (Leu36 in SHC) is well positioned to induce this conformation by pushing the methyl group at C10 of 2,3-oxidosqualene below the molecular plane (Figure 2).[9]

For OSC, temporal overlap between the initial protonation step and A- and potentially B-ring cyclization has been inferred from nonenzymatic data and substrate-analogue studies and is sup-

 © 2005 Wiley-VCH Verlag GmbH & Co. KGaA, Weinheim

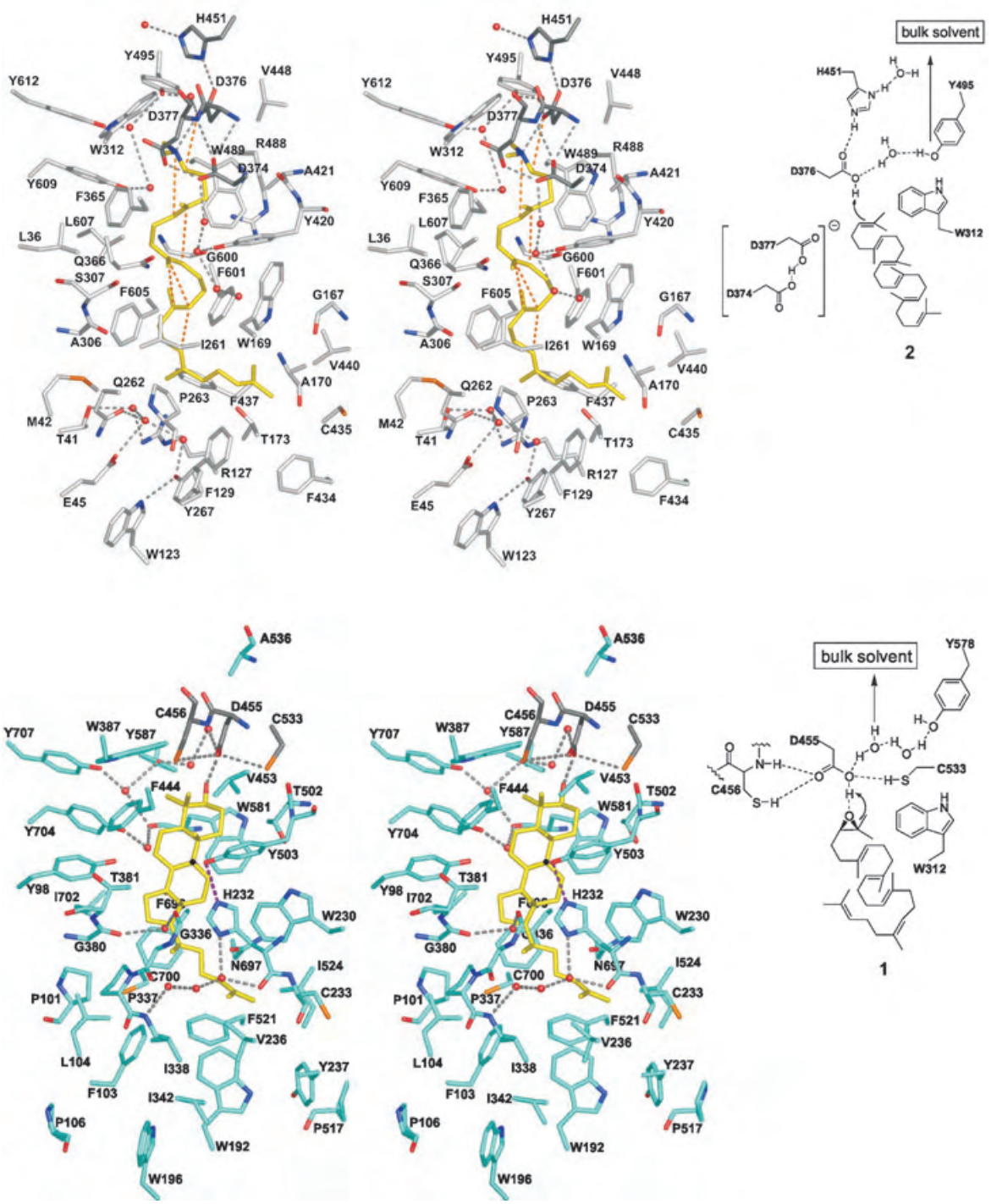


Figure 1. Active sites (stereoview in left and middle panels), and schemes of the initiation sites (right panels). Upper stereoview: *A. acidocaldarius* SHC (gray) with 2-azasqualene (yellow; PDB entry 1ump).[8] Highlighted are polar residues around the catalytic acid $Asp376^{SHC}$ (dark gray), structural water molecules (red spheres), and polar interactions (gray dashes). Trajectories for the first four ring-formation steps are indicated according to Reinert et al. (orange dashes).[8] Lower stereoview: *H. sapiens* OSC (turquoise) with lanosterol (yellow; PDB entry 1w6k).[9] Polar residues around catalytic acid $Asp455^{OSC}$, polar interactions, and structural water are shown as above. The $His232^{OSC}$:$Tyr503^{OSC}$ catalytic base dyad (purple dash) is proposed to accept a proton from C9 of the lanosterol cation (black dot).[9]

ported by computational results.[12–14] Computational studies have suggested an analogous mechanism for SHC.[15] The SHC complex with the substrate mimic 2-azasqualene shows a conformation in which the first four isoprene units orient themselves in a way such that only small displacements are required for the formation of a 6-6-6- or 6-6-5-tricycle (Figure 1).[8] For D-ring formation, a productive approach of the C18–C19 double bond towards C14 requires rotation around the C17–C18 bond and is therefore unlikely to occur in concert with the initial protonation step. The

 © 2005 Wiley-VCH Verlag GmbH & Co. KGaA, Weinheim

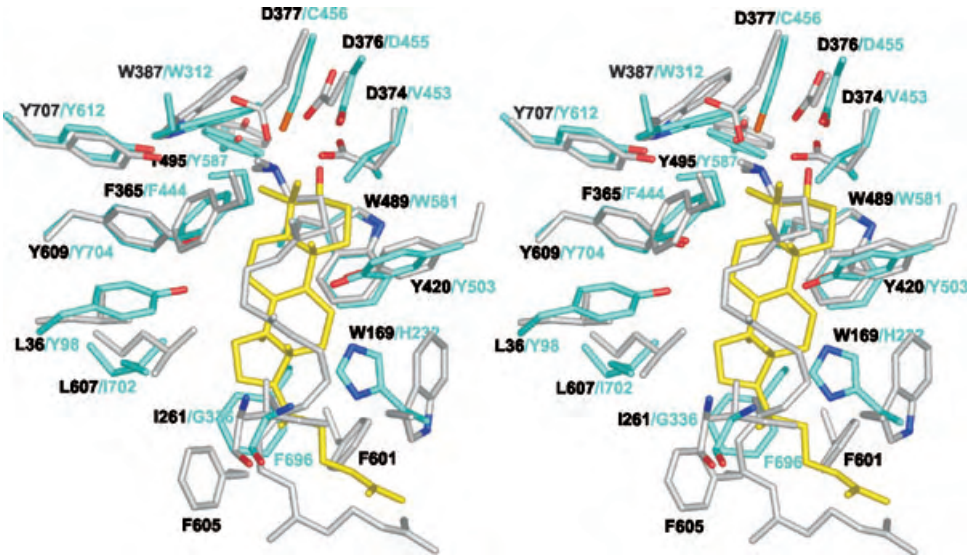
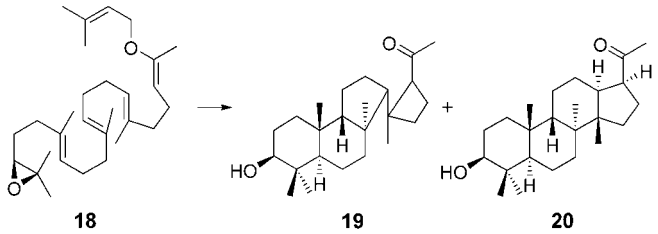


Figure 2. Stereoview of the superposition of selected residues of *H. sapiens* OSC (turquoise, turquoise labels) with lanosterol (yellow) and *A. acidocaldarius* SHC with 2-azasqualene (gray, black labels).[8,9]

observed conformation of 2-azasqualene appears to favor Markovnikov-type closure to a 6-6-6-5-tetracycle.[8] Furthermore, Reinert et al. show that the E ring is not prefolded in 2-azasqualene. They argue convincingly that the approach of the C22–C23 double bond to C18 involves a significant reorientation of the substrate, which has a considerable activation barrier, and they conclude that the cascade pauses at the 6-6-6-5-cation **13**.[8] This pause would provide time for side reactions to occur and thereby corresponds well to the observation of various 6-6-6-5 side products in the reaction of SHC with the natural substrate squalene.[8,16]

The concept of a Markovnikov-type C-ring closure with subsequent ring expansion was initially suggested by Corey et al. and was based on the finding that cyclization of 20-oxaoxidosqualene (**18**) with *S. cerevisiae* OSC yields the 6-6-5 fused-ring product **19** in addition to the expected 6-6-6-5 product **20** (Scheme 2).[17] Observations of numerous partially cyclized 6-6-5 and 6-6-6-5 side products arising from site-directed mutagenesis and substrate-analogue studies have been considered to support the relevance of cations **5**, **11**, and **13** for the mechanisms of SHC and OSC.[3] In contrast, the corresponding 6-6-6 products arising from cations **6** (OSC) and **12** (SHC) have not been trapped,[3] and 6-6-6-6 side products arising from cation **14** have been isolated in only trace amounts.[18] Based on these observations one could assume that **6**, **12**, and **14** may not be stable species in the reaction pathway. However, the isolation of side products arising from aborted cyclizations provides no conclusive evidence for the true reaction pathway of the enzyme.



Scheme 2. Products arising from the cyclization of 20-oxaoxidosqualene (**18**) catalyzed by *S. cerevisiae* OSC.[17]

Based on molecular dynamics simulations, Gao et al. recently suggested the 6-6 cation **10** as the only reaction intermediate of SHC with a significant lifetime. Intermediate **10** would react to **15** via a single transition state.[15] This proposal appears to be in contrast with that of Reinert et al., who suggest rapid formation of the 6-6-6-5 intermediate **13**, followed by first a slow conformational rearrangement of the remaining noncyclized substrate and subsequent concerted D-ring expansion and E-ring formation.[8] Resolving this dilemma will likely require knowledge of the conformation of the noncyclized isoprene chain in structures of SHC with analogues of intermediates **10**–**13**.

For OSC, Thoma et al. show that $His\,232^{OSC}$ and $Phe\,696^{OSC}$ are well positioned for π–cation interactions with the C20-protosteryl cation **7** as well as with a charge on C14 (2,3-oxidosqualene numbering), which would arise in a potential intermediate **6** (Figure 1).[9] As shown for SHC, the detailed understanding of C-ring formation in OSC would benefit from complex structures with 2-azasqualene and with analogues of intermediates **4**–**6**. As expected, $Phe\,605^{SHC}$, which has been shown to be critical for E-ring formation by SHC, is nonconserved in OSC, where only four rings are formed (Figure 2).[3]

In contrast to squalene cyclases, OSCs exhibit a conserved deletion of $Gly\,600^{SHC}$.[19] It has been shown that the corresponding $\Delta Gly\,601^{SHC}$ mutant of *A. acidocaldarius* SHC transforms (3*S*)-2,3-oxidosqualene into a mixture of

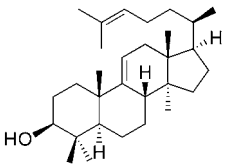
 © 2005 Wiley-VCH Verlag GmbH & Co. KGaA, Weinheim

mono- and tricyclic fused-ring products but is inactive towards (3*R*)-2,3-oxidosqualene and the natural product squalene.[20] In view of the available crystal structures, this result cannot be explained and requires further investigation.

Rearrangement, Elimination, and Product Release

In SHC, the reaction is terminated by a polarized water molecule X[5] that deprotonates the hopenyl cation **15** to give hopene (**16**) or adds to diplopterol (**17**). The water molecule X has not been observed in any SHC structures.[8] Based on molecular dynamics simulations Reinert et al. suggest that the cyclizing squalene contracts from both sides towards its center. The resulting position of the hopenyl cation **15** allowed the definition of a putative position for water X in proximity to a defined water network around Glu45^{SHC}.[5,8]

In the active site of OSC the C20-lanosterol cation **7** is rearranged and then deprotonated at C9 (lanosterol numbering; Scheme 1 and Figure 1). Thoma et al. propose that a gradient in the π-electron density of different active-site regions is the driving force for the rearrangement from **7** to **8**. However, the nonenzymatic reaction of **21** generates 24,25-dihydroparkeol benzoate (**22**, Scheme 3).[21] This observation suggests that rearrangement from **7** to **8** requires only minimal assistance from the enzyme. Therefore, the appropriate positioning of the catalytic base may be a more relevant determinant for the rearrangement than the π-electron gradient of the active site. Thoma et al. confirm that His232^{OSC} is the only basic residue in proximity to the termination site,[3,11] and they demonstrate that His232^{OSC} forms a hydrogen bond with the Tyr503^{OSC} hydroxy group, which is in a better position to accept the proton from C9 of the lanosterol cation than His232^{OCS} itself (Figure 1).[9] The assignment of His232^{OSC}:Tyr503^{OSC} as the catalytic base dyad of OSC is supported by additional data: 1) The essential character of the corresponding His234 of the *S. cerevisiae* OSC[11] and 2) the finding that the Tyr510Ala mutant of *S. cerevisiae* forms parkeol (**23**), [22] a product that corresponds to that of the nonenzymatic rearrangement of **21** to **22**.[22]

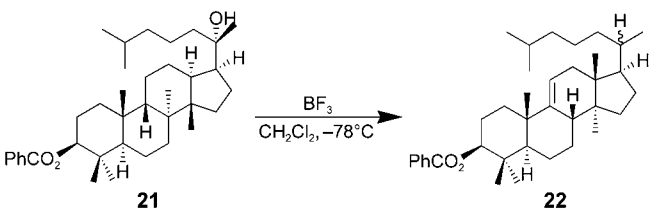


23

The release of the bulky reaction products from the hydrophobic active site back to the membrane is an intriguing feature of the triterpene cyclases. For SHC it has been suggested that a loop region that lines the channel connecting the active site with the membrane interior is likely to be mobile enough to open for product passage.[5,8] Inspection of the OSC structure shows that the related regions are mobile as well, so that a similar mechanism can be expected for both enzymes.

Outlook

Key features of the mechanisms of enzymatic triterpene cyclization have been clarified by a combination of bioorganic chemistry, structural biology, and mutational analyses. A more detailed experimental analysis of these complex mechanisms is currently hampered by the fact that even small steric changes of the enzyme or substrate can alter the conformation and positioning of the cyclizing polyolefin chain in such manner that the reaction pathway is influenced distant from the site of mutation.[3,19] Clarification of the exact reaction trajectories and delineation of the steric and electronic contributions of individual active-site residues therefore requires structures of native and mutated cyclases in complex with substrate and transition-state analogues.



21 **22**

Scheme 3. Nonenzymatic rearrangement of **21**.[21]

Published online: June 1, 2005

[1] a) R. B. Woodward, K. Bloch, *J. Am. Chem. Soc.* **1953**, *75*, 2023–2024; b) G. Stork, A. W. Burgstahler, *J. Am. Chem. Soc.* **1955**, *77*, 5068–5077; c) A. Eschenmoser, L. Ruzika, O. Jeger, D. Arigoni, *Helv. Chim. Acta* **1955**, *38*, 1890–1904; d) R. K. Maugdal, T. T. Tchen, K. Bloch, *J. Am. Chem. Soc.* **1958**, *80*, 2589–2590; e) J. W. Cornforth, R. H. Cornforth, C. Donninger, G. Popjak, Y. Shimizu, S. Ichii, E. Forchielli, E. Caspi, *J. Am. Chem. Soc.* **1965**, *87*, 3224–3228; f) E. J. Corey, W. E. Russey, P. R. Oritz de Montellano, *J. Am. Chem. Soc.* **1966**, *88*, 4750–4751; g) E. J. Corey, W. E. Russey, *J. Am. Chem. Soc.* **1966**, *88*, 4751–4752; h) E. E. van Tamelen, J. D. Willet, R. B. Clayton, K. E. Lord, *J. Am. Chem. Soc.* **1966**, *88*, 4752–4754.

[2] I. Abe, M. Rohmer, G. D. Prestwich, *Chem. Rev.* **1993**, *93*, 2189–2206.

[3] a) K. U. Wendt, G. E. Schulz, E. J. Corey, D. R. Liu, *Angew. Chem.* **2000**, *39*, 2930–2952; *Angew. Chem. Int. Ed.* **2000**, *39*, 2812–2833; b) T. Hoshino, T. Sato, *Chem. Commun.* **2002**, 291–301.

[4] a) O. H. Morand, J. D. Aebi, H. Dehmlow, Y.-H. Ji, N. Gains, H. Lengsfeld, J. Himber, *J. Lipid Res.* **1997**, *38*, 373–390; b) S. Jolidon, A. Polak-Wyss, P. G. Hartmann, P. Guerry, *Recent Advances in the Chemistry of Antiinfective Agents* (Ed.: P. H. Bentley), Royal Society of Chemistry, Cambridge, **1993**, pp. 223–233; c) A. Lenhart, D. J. Reinert, J. D. Aebi, H. Dehmlow, O. H. Morand, G. E. Schulz, *J. Med. Chem.* **2003**, *46*, 2083–2092.

[5] a) K. U. Wendt, K. Poralla, G. E. Schulz, *Science* **1997**, *277*, 1811–1815; b) K. U. Wendt, A. Lenhart, G. E. Schulz, *J. Mol. Biol.* **1999**, *286*, 175–187.

[6] Sequence numbering corresponds to *A. acidocaldarius* squalene–hopene cyclase (SHC) and *H. sapiens* 2,3-oxidosqualene–lanosterol cyclase (OSC).

[7] For SHC/OSC the conserved residues Trp312^{SHC}/Trp387^{OSC}, Trp489^{SHC}/Trp581^{OSC}, Phe365^{SHC}/Phe444^{OSC} orient their π faces towards the active-site cavity and were suggested to interact

 © 2005 Wiley-VCH Verlag GmbH & Co. KGaA, Weinheim

with the carbocations forming at C2, C6, C10 (squalene numbering). Trp 169^{SHC}/His 232^{OSC} and Phe 601^{SHC}/Phe 696^{OSC} reside in proximity to the site of C- and D-ring formation and interact with the respective intermediates. Phe 605^{SHC} is conserved in squalene cyclases only and has been shown to be involved in E-ring formation. Numerous analyses have been performed in order to delineate the steric and electronic contributions of these and other residues and have been reviewed recently.[3]

[8] D. J. Reinert, G. Balliano, G. E. Schulz, *Chem. Biol.* **2004**, *11*, 121 – 126.

[9] R. Thoma, T. Schulz-Gasch, B. D'Arcy, J. Benz, J. Aebi, H. Dehmlow, M. Hennig, M. Stihle, A. Ruf, *Nature* **2004**, *432*, 118 – 122.

[10] a) R. D. Gandour, *Bioorg. Chem.* **1981**, *10*, 169 – 176; b) J. Gao, J. J. Pavelites, *J. Am. Chem. Soc.* **1992**, *114*, 1912 – 1914.

[11] a) E. J. Corey, H. Cheng, C. H. Baker, S. P. T. Matsuda, D. Li, X. Song, *J. Am. Chem. Soc.* **1997**, *119*, 1277 – 1288; b) E. J. Corey, H. Cheng, C. H. Baker, S. P. T. Matsuda, D. Li, X. Song, *J. Am. Chem. Soc.* **1997**, *119*, 1289 – 1296.

[12] E. J. Corey, D. D. Staas, *J. Am. Chem. Soc.* **1998**, *120*, 3526 – 3527.

[13] a) C. Jenson, W. L. Joergensen, *J. Am. Chem. Soc.* **1997**, *119*, 10846 – 10854; b) B. A. Hess, *Org. Lett.* **2003**, *5*, 165 – 167; c) B. A. Hess, *J. Am. Chem. Soc.* **2002**, *124*, 10286 – 10287.

[14] D. Gao, Y.-K. Pan, K. Byun, J. Gao, *J. Am. Chem. Soc.* **1998**, *120*, 4045 – 4046.

[15] R. Rajamani, J. Gao, *J. Am. Chem. Soc.* **2003**, *125*, 12768 – 12781.

[16] C. Pale-Grosdemange, C. Feil, M. Rohmer, K. Poralla, *Angew. Chem.* **1998**, *110*, 2355 – 2358; *Angew. Chem. Int. Ed.* **1998**, *37*, 2237 – 2240.

[17] E. J. Corey, S. C. Virgil, H. Cheng, C. H. Baker, S. P. T. Matsuda, V. Sigh, S. Sarshar, *J. Am. Chem. Soc.* **1995**, *117*, 11819 – 11820.

[18] T. Hoshino, T. Abe, M. Kouda, *Chem. Commun.* **2000**, 441 – 442.

[19] T. Schulz-Gasch, M. Stahl, *J. Comput. Chem.* **2003**, *24*, 741 – 7523.

[20] T. Hoshino, K. Shimizu, T. Sato. *Angew. Chem.* **2004**, *116*, 6868 – 6871; *Angew. Chem. Int. Ed.* **2004**, *43*, 6700 – 6703.

[21] E. J. Corey, S. C. Virgil, *J. Am. Chem. Soc.* **1990**, *112*, 6429 – 6431.

[22] T.-K. Wu, C.-H. Chang, *ChemBioChem* **2004**, *5*, 1712 – 1715.

Deadline for recruitment adverts

29/05	July 18	Publication date: July 1
30/05	July 25	Publication date: July 8

Angewandte Chemie International Edition
Advertising Sales Department:
Marion Schulz
Phone: 0 62 01 – 60 65 65
Fax: 0 62 01 – 60 65 50
E-Mail: MSchulz@wiley-vch.de

Place an advert in the printed version and have it made available online for 1 month, free of charge!

HUMBOLDT-UNIVERSITÄT ZU BERLIN

The Faculty of Mathematics and Natural Sciences I, Institute of Chemistry at Humboldt-Universität zu Berlin announces the position of a

Full Professor (W3)
"Organic Chemistry and Functional Materials".
to commence on or after October 1st, 2006.

Applicants should have an outstanding record of achievement in important areas of synthetic organic chemistry as applied to functional materials. A research focus on organic chemistry of polymers, conjugated systems, catalytic, sensory or biosensory materials is desired. The research activities of the candidate should complement research areas in the institute of chemistry. The ideal candidate has a record of close collaborations. She/he will be expected to further the scientific exchange with research institutes within and outside Humboldt-Universität and with high tech companies at the science park Berlin-Adlershof and in the greater Berlin area. The candidate will be involved in the teaching of students covering the entire field of organic chemistry.
Applicants must meet the requirements for a university professor as stipulated in § 100 BerlHG.

Humboldt-Universität is an equal opportunity employer, committed to the advancement of individuals without regard to ethnicity, religion, sex, age, disability or any other protected status.

Applications with necessary documents should be sent to Dekan der Mathematisch-Naturwissenschaftlichen Fakultät I, Humboldt-Universität zu Berlin, **code number PR/013/05**, 12489 Berlin, Newtonstr. 14, not later than 30.09. 2005.



Life's Simple Pleasures!

No need to waste precious time looking for the right information – Register now for the free **Wiley-VCH Alerting Service.**

To receive regular news per e-mail tailored precisely to your needs and interests, just fill in the registration form at
www.wiley-vch.de/home/pas/

It's simple – and it's fast.

WILEY-VCH

13283407_gu

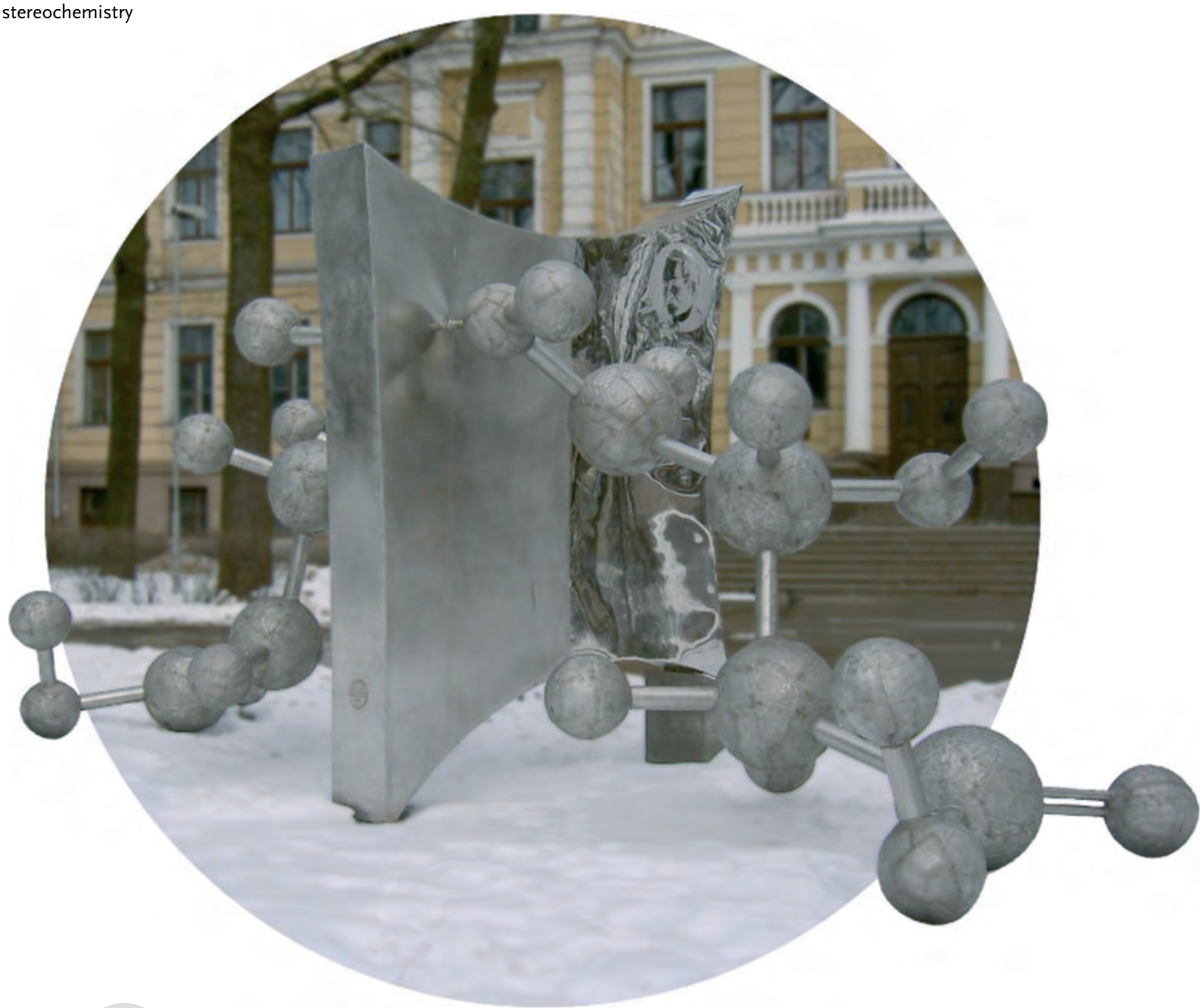
 © 2005 Wiley-VCH Verlag GmbH & Co. KGaA, Weinheim

Chiral Resolution

Efficiency in Nonenzymatic Kinetic Resolution

Edwin Vedejs and Mara Jure**

Keywords:
diastereoselectivity · enantiomer resolution · enantioselectivity · kinetic resolution · stereochemistry



Angewandte Chemie

 © 2005 Wiley-VCH Verlag GmbH & Co. KGaA, Weinheim DOI: 10.1002/anie.200460842

The Walden memorial at the Technical University in Riga is pictured in the frontispiece to mark the recent centennial of the Walden inversion. This is a rare public monument to key events from the first era of exploration in stereocontrolled synthesis, and may be the only such monument to use the language of organic chemistry expressed at the molecular level. The reaction of racemic substrates with chiral nucleophiles is one of many methods currently known to achieve kinetic resolution, a phenomenon that ranks as the oldest and most general approach for the synthesis of highly enantioenriched substances. The first nonenzymatic kinetic resolutions as well as the original forms of the Walden inversion were studied in the 1890s. All of these investigations were conducted within the first generation following the demonstration that carbon is tetrahedral, and provided abundant evidence that the principles and importance of enantiocontrolled syntheses were understood. However, a reliable, rapid technique to quantify results and guide the optimization process was still lacking. Many decades passed before this problem was solved by the advent of HPLC and GLPC assays on chiral supports, which stimulated explosive growth in the synthesis of nonracemic substances by kinetic resolution. The Walden monument is accessible to passers-by for hands-on inspection as well as for contemplation and learning. In a similar way, kinetic resolution is experimentally accessible and can be thought-provoking at several levels. We follow the story of kinetic resolution from the early discoveries through fascinating historical milestones and conceptual developments, and close with a focus on modern techniques that maximize efficiency.

From the Contents

1. Introduction 3975
2. History of Kinetic Resolution 3976
3. Kinetic Resolution and Highly Enriched Chiral Substances 3977
4. Improved Efficiency in Kinetic Resolutions 3978
5. Kinetic Resolution of Important Functional Group Categories 3989
6. Data Treatment and Assay Methods 3994
7. Current State and Perspectives of Nonenzymatic KR 3995

1. Introduction

Among the numerous synthetic methods that are capable of producing chiral substances with high enantiomeric excess (*ee*) values, kinetic resolution (KR) has the distinction of being the oldest (for its historical development, see Section 2). KR is also unique among the available methodologies because it allows the preparation of samples that are enantiomerically pure, well beyond the assay limits of modern analytical techniques. This feature has stimulated academic interest as well as speculation about possible connections with the origin of enantiomerically pure natural substances (Section 3). A third distinction is that KR can be applied to virtually every class of chiral substrates and can be used in combination with all methods of enantioselective synthesis.

With so many possibilities, the topic of KR must be reviewed selectively. Herein, we expand on some aspects of the comprehensive review from 1987 by Kagan and Fiaud[1] to emphasize developments that have improved the efficiency of KR, to comment briefly on interesting new examples, and to make connections with historical origins for key techniques and concepts. Because more than 50 specialized reviews have appeared since 1987,[2,3] we mention some topics very briefly and bypass enzymatic KR techniques almost entirely. The latter field has been the subject of many recent reviews,[3] and is mentioned only where needed for the purpose of comparison. Even with these limitations in scope, the subject remains large (>400 papers on nonenzymatic KR since 1987). The reader is referred to specialized reviews to appreciate the breadth of some important topics mentioned in specific context below.

The definition of KR according to the 1996 IUPAC recommendation follows: "The achievement of partial or complete resolution by virtue of unequal rates of reaction of the enantiomers in a racemate with a chiral agent (reagent, catalyst, solvent, etc.)".[4] We prefer this wording over older definitions[1,5] because it does not focus on the recovery of unreacted substrate and therefore fits better with recent variations that feature total conversion into products, such as dynamic kinetic resolution (DKR; Section 4).

[*] Prof. E. Vedejs
Department of Chemistry
University of Michigan
Ann Arbor MI 48109 (USA)
Fax: (+1) 734-615-1628
E-mail: edved@umich.edu
Prof. M. Jure
Faculty of Chemical Technology
Riga Technical University
14/24 Azenes
Riga LV-1048 (Latvia)
Fax: (+370) 371-761-5765
E-mail: mara@mail.ktf.rtu.lv

 DOI: 10.1002/anie.200460842 © 2005 Wiley-VCH Verlag GmbH & Co. KGaA, Weinheim

In the simplest cases of KR, the substrate enantiomers interact with a chiral reagent or catalyst to generate two diastereomeric transition states. The free energies of these competing transition states define the rate constants for conversion of the fast-reacting and slow-reacting enantiomers, and the ratio k_{fast}/k_{slow} (equal to k_{rel} or the enantioselectivity s) controls the product distribution. As discussed later, additional factors are important for cases in which the preparative focus is on the isolation of products (DKR, PKR).

It is convenient to relate the variables in simple KR experiments with Equation (1) (based on *ee* of the recovered substrate) or, for cases in which the product is also chiral, with Equation (2) (based on *ee*′ of the product).

$$s = \frac{\ln[(1-C)(1-ee)]}{\ln[(1-C)(1+ee)]} \quad (1)$$

$$s = \frac{\ln[1-C(1+ee\prime)]}{\ln[1-C(1-ee')]} \quad (2)$$

Equation (2), when applicable, can be used to check for self-consistency and to calculate an accurate value for conversion (C), as values of *ee* and *ee*′ can usually be measured easily and with high precision, whereas the precise determination of C is relatively difficult. The derivation and history of this treatment can be found in reviews by Kagan and Fiaud[1] and (in the case of enzymatic KR) by Sih and Wu,[3a] together with graphical representations of enantiomeric purity as a function of s and C. For the present purposes, the numerical summary of *ee* or *ee*′ as a function of selected values of conversion and enantioselectivity is sufficient (Tables 1 and 2).

Although Equation (1) is widely used, caution is appropriate because the equation assumes simple first-order kinetics for the substrate, and the absence of nonlinear effects involving the catalyst. Jacobsen and co-workers have noted cases of KR with organometallic catalysts in which this expression is not obeyed.[2q] We recommend measuring s at two or more conversion values to test the kinetic assumptions. If s is found to vary with conversion, then Equation (1) does not apply, and the data must be expressed in terms of material recovery and *ee*. If this is necessary, then care should be taken to measure and report the ratio of products and starting materials so that comparisons and evaluation of results are easier.

Table 1: Conversion C and theoretical yield limits for *ee* values of 90, 95, and 99% in the unconverted substrates in kinetic resolution as a function of enantioselectivity s [Eq. (1) and Eq. (2)].

s	C [%]	$Yield_{90}$ [%][a]	C [%]	$Yield_{95}$ [%][b]	C [%]	$Yield_{99}$ [%][c]
2	97.2	2.8	98.6	1.4	99.7	0.3
5	74.7	25.3	79.4	20.6	86.6	13.4
10	62.0	38.0	65.8	34.2	72.0	28.0
15	57.3	42.7	60.5	39.5	65.5	34.5
20	54.9	45.1	57.7	42.3	61.9	38.1
25	53.4	46.6	55.9	44.1	59.6	40.4
30	52.4	47.6	54.8	45.2	58.1	41.9
35	51.7	48.3	53.9	46.1	56.9	43.1
40	51.1	48.9	53.3	46.7	56.1	43.9
45	50.7	49.3	52.8	47.2	55.4	44.6
50	50.4	49.6	52.4	47.6	54.8	45.2
55	50.1	49.9	52.0	48	54.4	45.6
60	49.9	50.1	51.8	48.2	54.0	46.0

[a] Theoretical yield limit for the recovery of substrate with 90% *ee*. [b] As in [a] with 95% *ee*. [c] As in [a] with 99% *ee*.

Table 2: Product *ee*′ values (in %) in kinetic resolution as a function of conversion C and enantioselectivity s.

s	$C=1\%$	$C=10\%$	$C=20\%$	$C=30\%$	$C=40\%$	$C=50\%$
2	33.2	31.8	30.1	28.2	26.1	23.6
10	81.7	80.3	78.5	75.9	72.4	67.1
20	90.4	89.6	88.3	86.6	83.9	78.7
30	93.4	92.9	92.0	90.7	88.6	83.8
50	96.0	95.5	95.1	94.2	92.7	88.7
100	98.0	97.8	97.5	97.0	96.2	93.3
200	99.0	98.9	98.7	98.5	98.1	96.1
500	99.6	99.6	99.5	99.4	99.2	98.1

2. History of Kinetic Resolution

This story has been told many times, but it is worth repeating. In 1858, Pasteur observed that fermentation of racemic ammonium tartrate with *Penicillium glaucum* selectively destroys the dextrorotatory isomer.[6] The structural basis for this phenomenon was not yet known, but Pasteur understood that the reactive and unreactive isomers were related as mirror image forms of each other. By 1890, Fischer had observed several other enzymatic resolutions in the carbohydrate series, and had correctly deduced that the



Edwin Vedejs earned his BS degree in chemistry from the University of Michigan in 1962, and his PhD from the University of Wisconsin in 1966, under the direction of H. Muxfeldt. After a year of postdoctoral research with E. J. Corey, he returned to Wisconsin in 1967 to accept a faculty position. In 1999, he moved to the University of Michigan where he is currently the Moses Gomberg Professor of Chemistry. His research interests are in main group element chemistry and the mechanistic and conceptual aspects of organic synthesis and stereochemistry.



Mara Jure received her engineering diploma in 1986 and her PhD in 1990 from the Riga Polytechnical Institute (Latvia), where she began her academic career. She later worked as research associate in the group of Edwin Vedejs at the University of Wisconsin, Madison. Since 2001, she has been a professor of chemical technology of biologically active compounds at the Riga Technical University. Her current research interests concern heterocyclic chemistry.

 © 2005 Wiley-VCH Verlag GmbH & Co. KGaA, Weinheim

natural *d*-hexoses are consumed upon fermentation with brewer's yeast, whereas the *l* enantiomers remain unchanged.[7][*] This work was part of Fischer's monumental studies that defined relative and absolute configuration of monosaccharides, and the stereochemical issues were already described in perfect detail.

Fischer's fermentation experiments probably included the first examples in which a racemic, synthetic substance was converted into a single enantiomer with $>99\,\%$ *ee* by using KR. This supposition assumes total conversion of the more reactive *d* sugar into fermentation products as well as total enantioselectivity, as seems likely in the hexose experiments. Fischer understood the implications, but he may not have shared the current fascination with $>90\,\%$ *ee*, and did not quantify the optical purity of residual *l* sugars in typical experiments beyond showing that the optical rotation is opposite in sign relative to that of the *d* sugar.

The first example of the KR phenomenon with nonenzymatic reagents was reported a few years later. Marckwald and McKenzie observed enantioselective esterification of racemic mandelic acid by (−)-menthol upon heating the reactants,[8] and were able to recover a small amount of the less-reactive *l*-mandelic acid in pure form after multiple crystallizations. They also explained the relative reactivity issues responsible for the observed optical enrichment. Shortly thereafter, Dakin published the first examples of KR by using a lipase catalyst (in the hydrolysis of racemic ethyl mandelate with crude pig liver lipase).[9] This work is noteworthy because, as clearly demonstrated with polarimetry, the product *ee* depends on conversion (25 % *ee* at 5 % conversion; 5 % *ee* at 94 % conversion). Whereas the earlier reports by Pasteur and Fischer could have been taken to imply that natural catalysts accept only a single enantiomer, the results by Dakin showed that enzymes are not perfectly enantioselective, and that relative reactivity issues and percent conversion must be taken into account.

Subsequent reports by Fajans and Bredig revealed that the relationship between reaction rates, enantioselectivity ($s = k_{fast}/k_{slow}$), enantiomeric purity of reactants and products, and conversion in KR experiments was understood by 1910.[10] Fajans also reported the first examples of *catalytic* nonenzymatic KR (in the decarboxylation of camphor-3-carboxylic acid in the presence of chiral alkaloids; $s = 1.1$–1.5). His kinetic treatment would have shown that the *ee* value of unconverted substrate continuously increases as the conversion approaches 100 %, but only the product of decarboxylation (camphor) was assayed (with polarimetry).

3. Kinetic Resolution and Highly Enriched Chiral Substances

The possibility that nonenzymatic KR might allow the preparation of enantiomerically pure chiral substances may have been fully understood after the first enzymatic experiments, but it was not discussed explicitly until a report by Kuhn and Knopf appeared in 1930.[11] This paper was not at all concerned with synthesis applications. Instead, it focused on the origin of enantiomerically pure natural products. Kuhn and Knopf showed that the photodecomposition of 2-azido-*N*,*N*-dimethylpropionamide by circularly polarized light (CPL) results in optically active recovered starting material ($\approx 0.5\,\%$ *ee*). This form of KR occurs because the enantiomers differ in their absorption coefficients for CPL, which results in differing rates of photodecomposition. A single data point corresponding to 30–40 % conversion was measured, but the discussion included a derivation of kinetic expressions and relevant commentary to show that the optical activity of recovered starting material would continuously increase with an increase in conversion.

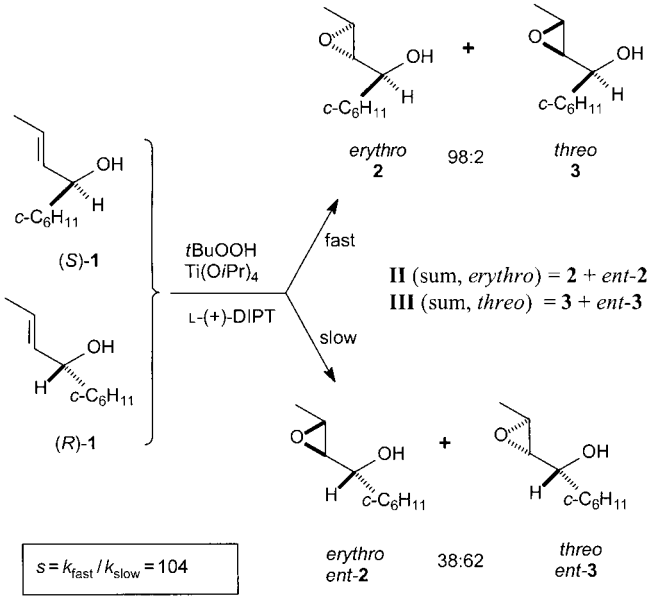
In one hypothetical scenario, the authors used kinetic equations to argue that even a small difference in absorption coefficients resulting in 1 % *ee* for the unreacted substrate at $\approx 60\,\%$ recovery would produce 10 % *ee* at 0.67 % recovery, or 76 % *ee* at $5 \times 10^{-20}\,\%$ recovery! The same principle is evident in Table 1, although the limits for enantioselectivity are set higher, and the percent conversions are lower. If yield is not a concern, then $>99\,\%$ *ee* can be easily achieved with KR. It is this feature that intrigued Kuhn and Knopf because they recognized that CPL is a natural phenomenon, and that it might induce formation of an enantiomerically pure substance under conditions of exceptionally high conversion. Subsequent studies by Kagan and co-workers demonstrated KR in the photodecomposition of racemic camphor by CPL, and reported a more substantial 20 % *ee* at 1 % recovery of the substrate.[12] The previous findings with 2-azido-*N*,*N*-dimethylpropionamide were confirmed, and the increase in *ee* with conversion was shown to correspond to the original mathematical model.

A milestone in the use of KR for the preparation of highly enantioenriched substances came in 1981 when Sharpless and co-workers reported KR experiments with racemic allylic alcohol substrates and the diisopropyl tartrate/*tert*-butylhydroperoxide (TBHP)/Ti(O*i*Pr)$_4$ reagent.[13] One of the best examples is shown in the conversion of (*R*,*S*)-**1** into the *erythro* and *threo* products **II** (**2** + *ent*-**2**) and **III** (**3** + *ent*-**3**), respectively (Scheme 1). Because the enantioselectivity was quite high ($s = 104$) the problem was no longer in the recovery of trace residual substrate for assay. Instead, the problem was to find an assay method sufficient to measure *ee* values in excess of 96 % for recovered (*S*)-**1**, not to mention the 99.99999999999 % *ee* calculated for a related example (2-methylhept-1-en-3-ol at 60 % conversion, $s = 138$) according to the relationship established by Equation (1). The problem of assay precision in the range of 96–99.9 % *ee* would soon be solved with the development and broad availability of chiral supports (not "chiral chromatography"!) for HPLC and GPLC assays. The problem of confirming 13 significant figures in the larger number can be entrusted to the mathematical approach in view of the proven predictive value of Equation (1).

The principles were understood long before the Sharpless study, and Horeau had described the mathematical basis as

[*] The stereochemical descriptors *d* and *l* for right- and left-handed compounds, respectively, are considered antiquated and are used herein for historical reasons. Recommended descriptors for the respective directions of optical rotation are (+) and (−).

 © 2005 Wiley-VCH Verlag GmbH & Co. KGaA, Weinheim



Scheme 1. Kinetic resolution of the allyl alcohol (*R*,*S*)-**1** as reported by Sharpless and co-workers.[13]

well as an example of KR to prepare samples with $>99.9\%$ *ee* by 1975.[14] However, the Sharpless paper certainly awakened the synthetic chemistry community to the preparative potential of nonenzymatic KR. Within several years, explosive growth in the field was evident, as summarized in several reviews.[1,2a–d] More recent studies have greatly expanded the scope of nonenzymatic KR and have added conceptual developments as well as technology for rapid-throughput screening. All of this would probably have impressed the pioneering researchers in the field, yet they would have understood the concepts, because most of the fundamentals of KR were known by 1910. It has taken time to develop these concepts to the current level of utility, and progress in the field has been closely tied to the advent of sensitive assay methodology for enantiomeric excess.

4. Improved Efficiency in Kinetic Resolutions

If the racemic substrate is simple or inexpensive, and the theoretical limit of 50% yield for KR is not a serious problem, good results can be obtained even with relatively modest values of *s*. Table 1 shows that $>40\%$ recovery of substrate with 95% *ee* is possible with $s=20$ or higher. If substrate recovery is the objective, then there is little to be gained by optimizing catalysts for higher *s* values, as may be observed by comparing the entries for $s=20$ (42% yield limit) with those for which $s=60$ (48% yield limit).

The situation is quite different for cases in which the recovery of enantioenriched product is also important, and the objective is to recover both enriched enantiomers with high efficiency (combined yield of 90% or more). Table 2 shows that product enrichment to the level of 95% *ee*′ requires that $s=50$ or above. However, $s=50$ is not good enough for efficient recovery because the *ee*′ value drops rapidly as conversion approaches or exceeds 50%.

For typical KR experiments in which the kinetic assumptions for Equations (1) and (2) are satisfied, the values of *ee* (substrate) and *ee*′ (product) become equal at 50% conversion. The column for $C=50\%$ in Table 2 can therefore be used to evaluate the enantioselectivity *s* needed if highly efficient recovery of both enantiomers is desired. If the goal of a simple KR experiment is to obtain both enantiomers in 95% *ee* or more, then it would be necessary to have $s=200$ or higher. Although such levels of enantioselectivity are known for some of the best nonenzymatic methods, they are not yet routine. Fortunately, there are alternative approaches that allow efficient recovery of material, as discussed in Sections 4.1–4.3.

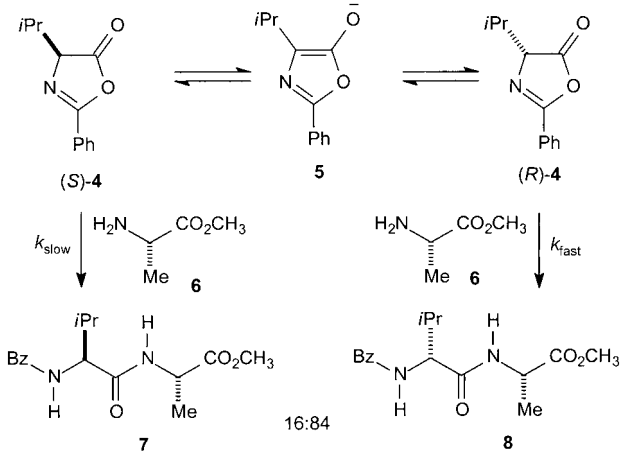
4.1. Dynamic Kinetic Resolution (DKR)

The theoretical limit of 50% yield for the simplest versions of KR has stimulated the search for more efficient procedures. Dynamic kinetic resolution (DKR) is the most important of these techniques. In DKR,[2e–m] the enantiomers of a racemic substrate are induced to equilibrate at a rate that is faster than that of the slow-reacting enantiomer in reaction with the chiral reagent (Curtin–Hammet kinetics). If the enantioselectivity *s* (k_{fast}/k_{slow}) is sufficient, then isolation of a highly enriched nonracemic product is possible with a theoretical yield of 100% based on the racemic substrate. This is an advantage over simple KR in which the realistic expectation for recovery is often 40% or less, owing to losses incurred during the separation of products from starting materials.[13] A second advantage of considerable importance is that the levels of enantioselectivity required for DKR are lower than those needed for KR for similar efficiency in material recovery. The key difference with DKR is that there is no decay in product *ee* as percent conversion increases, in contrast to KR. This means that even a modest *s* value of 20 allows the preparation of product with $>90\%$ *ee* and $>90\%$ recovery. On the other hand, DKR does not permit the same degree of enrichment as does KR because there is no conversion-dependent increase in substrate *ee*.

4.1.1. DKR by Enolization

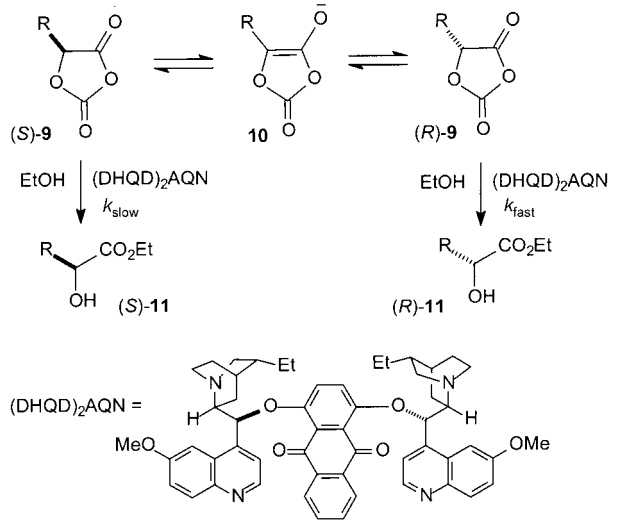
Possibly the first clear example of DKR appears in a 1966 study by Weygand et al.,[14] involving the reaction of racemic azlactones with chiral amino esters to form dipeptides (Scheme 2). The best example is shown, in which (*R*,*S*)-**4** and methyl alaninate (**6**) afford dipeptide **8** as the major product. Similar transformations were probably encountered much earlier in attempts to prepare peptides from activated *N*-acylamino acids, but Weygand's report is distinct because it demonstrates the mechanistic and preparative aspects of what is now recognized as DKR. A typical Curtin–Hammett kinetics scheme was shown, illustrating the interconversion of enantiomeric azlactones via enolate **5**. The diastereomeric ratios for the peptide products **7** and **8** (d.r. $\approx$ 1:5) require at least partial racemization, and demonstrate that DKR had occurred.

 © 2005 Wiley-VCH Verlag GmbH & Co. KGaA, Weinheim



Scheme 2. One of the first examples of DKR by Weygand et al. [14] Treatment of the azlactone (*R*,*S*)-**4** with alanine methyl ester (**6**) gives dipeptide **8** as the major product.

Several recent studies have exploited the same facile interconversion of azlactone enantiomers in DKR by using nonenzymatic chiral reagents or catalysts.[15] Furthermore, highly effective enzymatic adaptations that involve azlactone cleavage have been reported.[16] As discussed in the review literature,[3l] the concept has also been applied by using one or more enzymatic catalysts to obtain highly enantioselective ring cleavage of racemic hydantoins under conditions in which enolization is facile. In a related nonenzymatic application, Tang and Deng found that the commercially available cinchona derivative $(DHQD)_2AQN$ (which is also used in enantioselective Sharpless osmylation) is an effective catalyst for the enolization and ethanolysis of 5-substituted 1,3-dioxolan-2,4-diones (*R*,*S*)-**9** (Scheme 3).[17] The reaction works well for several cases in which the substituent R is aryl (Table 3, entries 1–3), but the 2-chloro derivative (Table 3, entry 4) gives lower enantioselectivity for (*R*)-**11** if the reaction is allowed to go to completion. For this example, the enantioselectivity is higher in the early stages of the reaction, which indicates that the interconversion of enantiomers (*S*)-**9** and (*R*)-**9** via enolate **10** is not rapid enough to satisfy the conditions for efficient DKR. For cases in which R = benzyl or *n*-butyl (Table 3, entries 5 and 6) enolization becomes so slow that the reactions proceed as simple kinetic resolutions. Fortunately, the enantioselectivities are quite high, allowing the recovery of unreacted (*S*)-**9** as well as the product (*R*-**11**) with $>90\,\%$ *ee*. The transition from KR to DKR occurs as the substituent R is changed from alkyl to aryl and reflects the relative ease of enolization.



Scheme 3. Nonenzymatic DKR with the use of the cinchona derivative $(DHQD)_2AQN$ reported by Tang and Deng (see Table 3).[17]

Table 3: DKR of 5-aryl-1,3-dioxolane-2,4-diones (see Scheme 3).

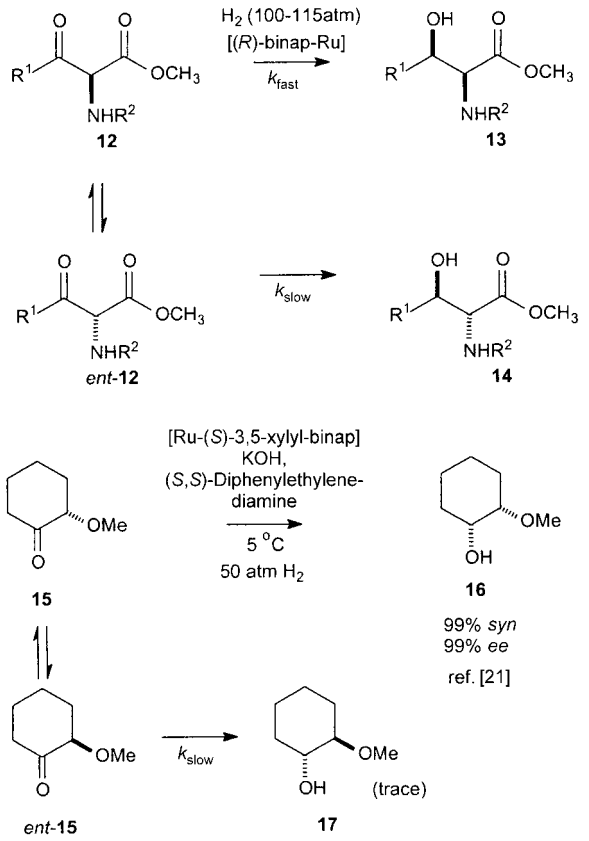
Entry	R	*t* [h]	*T* [°C]	Yield **11** [%]	*ee* [%]
1	C_6H_5	24	−78	71	95
2	4-ClC_6H_4	24	−78	70	96
3	1-naphthyl	14	−40	74	91
4	2-ClC_6H_4	10	−60	66	62
5	$C_6H_5CH_2$	12	−78	47[a]	96
6	*n*-C_4H_9	36	−78	46[b]	92

[a] KR conditions, unconverted **9** ≈39%, 95% *ee*, $s=133$. [b] KR conditions, unconverted **9** 36%, 95% *ee*, $s=57$.

To our knowledge, the first use of the term "dynamic kinetic resolution" appears in the title of the classic 1989 work by Noyori et al.[18] This paper describes the catalytic enantioselective hydrogenation of equilibrating racemic β-keto esters **12** and *ent*-**12** to afford the *syn* alcohol **13** in very high *ee*, together with a trace of the *anti* diastereomer **14** (Scheme 4, Table 4). This work has been reviewed[2e,f,l] and modified for applications by other groups.[19–21] Scheme 4 illustrates an impressive recent example of the efficiency of this method which allows the simultaneous control of absolute configuration as well as *syn* stereochemistry of two adjacent stereocenters with yields of 95% or more. The method also works with cyclic keto esters and lactones,[2f,18] and even with enolizable 2-substituted cyclohexanones.[21] The optimized example of the conversion of *rac*-**15** into **16** is shown in Scheme 4,[21a] but the previously reported hydrogenation of 2-isopropylcyclohexanone is also highly enantioselective.[21b]

In another example of DKR involving enolization to interconvert ketone enantiomers, Jurkauskas and Buchwald were able to hydrogenate 3,5-disubstituted racemic cyclopent-2-enones *rac*-**18** to highly enriched (89–95% *ee*) cyclopentanones **19** by using poly(methylhydrosiloxane) (PMHS) and a chiral catalyst consisting of *p*-tol-binap/CuCl in the presence of sodium *tert*-butoxide (Scheme 5).[22] The reaction proceeds with yields of 90% or more, and with $>90\,\%$ selectivity for the *syn*-disubstituted products (Table 5). If the *tert*-butanol additive is omitted, interconversion via the enolate is no longer fast enough to allow DKR, and the reaction proceeds as a simple KR process with $s=25$–52. Selectivities of this magnitude are sufficient for the recovery of unreacted **18** with $>90\,\%$ *ee* at ≈45% recovery (Table 1). By comparison, the conditions that promote DKR allow $>90\,\%$ recovery and comparable enantioselectivity.[23]

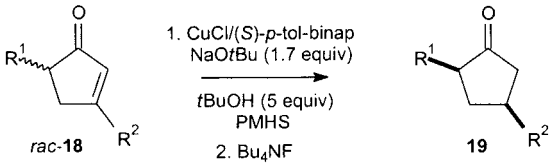
 © 2005 Wiley-VCH Verlag GmbH & Co. KGaA, Weinheim



Scheme 4. DKR of equilibrating racemic ketones by catalytic enantioselective hydration (see Table 4).

Table 4: DKR of **12**/*ent*-**12** under hydrogenation conditions (see Scheme 4).[a]

Catalyst	R^1	R^2	*T* [°C]	*ee* [%]	Ref.
$[RuBr_2\{(R)\text{-binap}\}]$	CH_3	Ac	15	98	[18]
[(*R*)-MeO-biphep]/HBr/ $[(cod)Ru(2\text{-methallyl})_2]$	$PhthN(CH_2)_3$	Ac	50	"opt. pure"	[19]
$[RuCl_2\{(S)\text{-binap}\}](dmf)_n$	*i*Pr	Bz	50	98	[20]



Scheme 5. DKR by hydration of 3,5-disubstituted racemic cyclopent-2-enones to cyclopentanones **19** in the presence of poly(methylhydrosiloxane), a *p*-tol-binap/CuCl-based chiral catalyst, and sodium *tert*-butoxide as reported by Jurkauskas and Buchwald (see Table 5).[22]

Table 5: DKR in the 1,4-reduction of *rac*-**18** (see Scheme 5).

Entry	R^1	R^2	*T* [°C]	Yield [%]	*syn*/*anti*	*ee* [%]
1	Me	CH_2CH_2Ph	−50	89	91:9	91
2	*t*Bu	CH_2CH_2Ph	0	94	93.5:6.5	94
3	$tBuO_2CCH_2$	CH_2CH_2Ph	−50	93	90:10	93
4	$PhCH_2$	*i*Pr	−50	95	91.5:8.5	93
5	Me	Ph	−50	90	96.5:3.5	91

4.1.2. ***DKR Involving Carbon–Metal Bond Equilibration***

A large and diverse category of DKR applications is the reversible thermal inversion of configuration at a stereogenic, metal-substituted carbon atom as a way to interconvert enantiomers. The 1989 report by Noyori et al. cited possible examples of this phenomenon that involve equilibration at a secondary carbon–metal (C–M) bond.

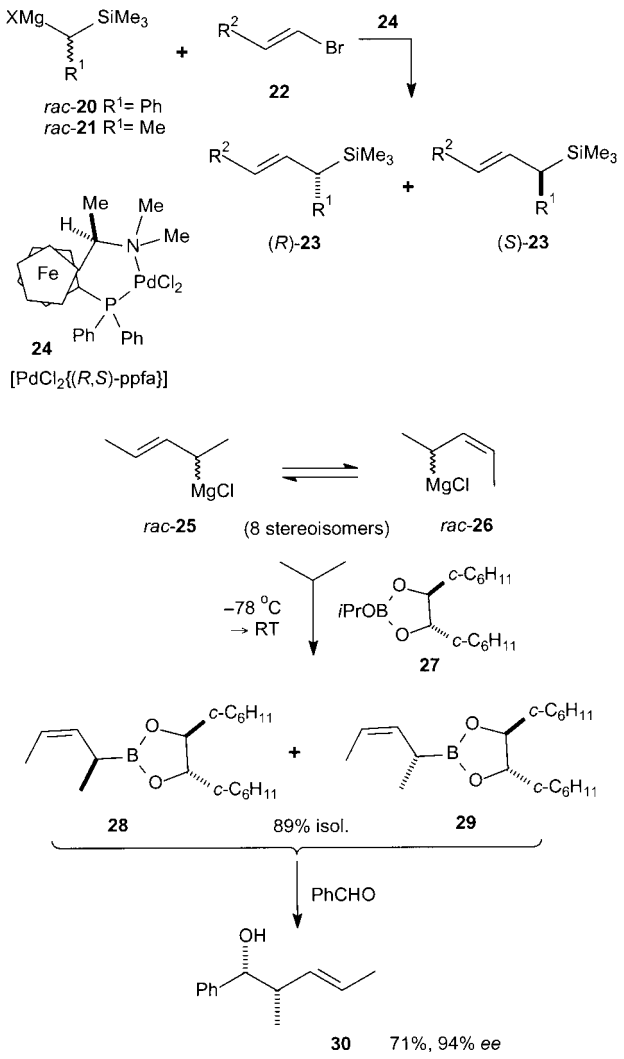
Many examples of simple KR have been reported with C–M substrates.[24–30] One of the first reports described the nickel-catalyzed coupling of 2-butylmagnesium bromide with chlorobenzene in the presence of a chiral phosphine ligand to give 2-phenylbutane in 52% yield and 17.5% *ee*.[24a] If the secondary Grignard reagent is capable of inversion of configuration at the C–Mg bond, then the conditions for DKR might be satisfied. However, the relatively low yield and *ee* might also be the result of simple KR if the reaction was not taken to completion. Subsequent studies by other researchers increased the yield and enantioselectivity in related palladium-catalyzed coupling reactions of the more easily inverted benzylic Grignard reagents by using the optimized catalyst **24**.[25] The principle is illustrated in Scheme 6 and Table 6 with silylated Grignard reagents *rac*-**20** and *rac*-**21**.[25c]

For cases in which the C–Mg bond is benzylic (Table 6, entries 1 and 2), interconversion of the enantiomers is easy and DKR conditions are largely maintained. This is shown by the relatively small decrease in *ee* as the excess of *rac*-**20** over the halide **22** is decreased (compare entries 1 and 2 in Table 6). The trimethylsilylethyl Grignard reagent *rac*-**21** (Table 6, entry 3) works especially well and affords **23** with excellent *ee* if employed in excess. As shown in entry 4, DKR conditions are no longer satisfied by using a deficiency of *rac*-**21**. This observation is consistent with the greater configurational stability of **21** (methyl-substituted) over the phenyl-substituted Grignard reagent **20**, and suggests that with a deficiency of *rac*-**21** a simple KR pathway is taken.

Scheme 6 also shows an interesting example of an allylic Grignard reagent in which equilibrating *Z* and *E* isomers as well as enantiomers (**25** and **26**) are intercepted by a stoichiometric amount of a chiral borate **27**. In keeping with earlier precedents of double-bond geometry, the reaction affords isolable (*Z*)-(1-methyl-2-butenyl)boronic esters **28** and **29** with a remarkable diastereoselectivity of 97:3. The product ratio was inferred from an analysis of enantiomeric excess of the product of benzaldehyde trapping **30** (94% *ee*).[24e] On the basis of the product ratio, the facile interconversion between all possible stereoisomers must be facile to maintain DKR conditions.

A variety of organolithium reagents undergo inversion of configuration at or below room temperature,[26] and are therefore potentially useful in DKR applications. As might be expected with the relatively reactive benzyllithium **31**, reaction with the chiral electrophile (*S*)-**32** occurs with modest selectivity to give an unassigned ratio of 63:37 for the formation **33** and **34** (Scheme 7).[27a,b] If the enantiomers of **31** were stable to interconversion under the reaction conditions, then the product ratio would have to be 1:1, the same as the enantiomeric ratio (this is one variation of the

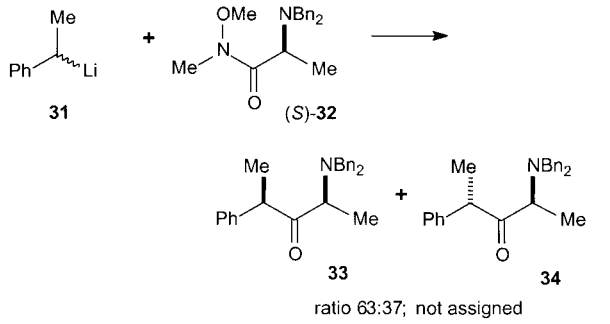
 © 2005 Wiley-VCH Verlag GmbH & Co. KGaA, Weinheim



Scheme 6. DKR in alkyl coupling reactions with Grignard-reagents (see Table 6).

Table 6: DKR in the alkenylation of *rac*-**20** and *rac*-**21** (see Scheme 6).

Entry	R^1	R^2	Equiv Grignard/halide	*T* [°C]	Yield [%]	*ee* [%]
1	Ph	H	2–3	19	63	85
2	Ph	H	1.5	19	52	77
3	Me	Ph	2	−10	88	93
4	Me	Ph	<1	−10	93	14

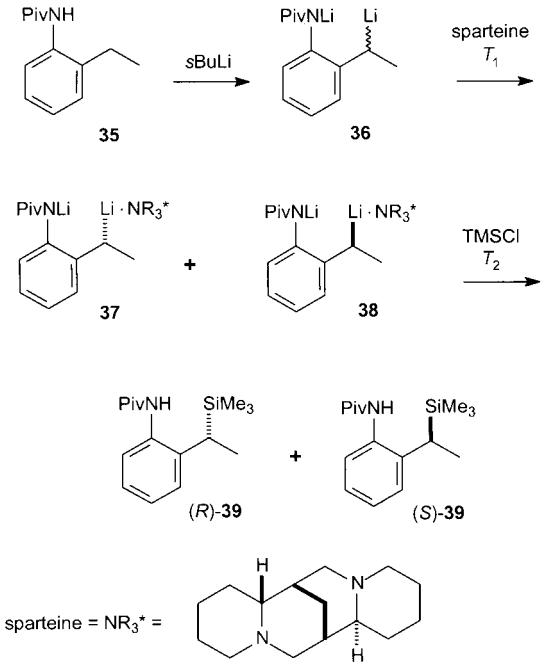


Scheme 7. Example of the DKR of an organolithium reagent with the chiral electrophile (*S*)-**32**; Bn = benzyl.

Hoffmann test for configurational stability).[27c] As the ratio of **33** to **34** is not 1:1, at least some degree of benzyllithium interconversion must occur, and electrophilic trapping takes place with at least partial DKR. However, DKR is by no means assured in other organolithium trapping experiments, and there are a number of mechanistic possibilities to consider.

4.1.3. *DKR versus Dynamic Thermodynamic Resolution (DTR) of Carbon–Metal Bonds*

Numerous reactions of heteroatom-stabilized organolithium species involve potentially interconverting carbon–lithium bonds, and some of the most useful examples are encountered in reactions conducted in the presence of sparteine or other chiral complexing agents.[28,29] A recent review by Beak et al. evaluates the mechanistic alternatives.[29] In a representative case, sparteine forms a coordination complex with the racemic organolithium species **36** under equilibrium conditions (−25 °C) to generate diastereomers **37** and **38** in solution (Scheme 8). If the solution is cooled to



Scheme 8. Silylation of **37** + **38** in the presence of sparteine (see Table 7); TMS = trimethylsilyl, Piv = pivaloyl.

−78 °C and treated with 0.1 equiv of TMSCl, then products (*R*)-**39** and (*S*)-**39** are formed in a ratio of 91:9 (Table 7, entry 1). If this ratio were the result of ideal DKR conditions, then the precursors **37** and **38** would have to be in rapid equilibrium, and the product ratio would be unaffected by the stoichiometry of TMSCl. However, the corresponding experiment with excess TMSCl afforded a much lower ratio of products (Table 7, entry 2). Furthermore, addition of sparteine at −25 °C prior to silylation at −78 °C with 0.1 equiv of TMSCl gives an exceptionally high *R*/*S* product ratio of 99:1 (Table 7, entry 3). These results indicate that **37** does not

 © 2005 Wiley-VCH Verlag GmbH & Co. KGaA, Weinheim

Table 7: Silylation of **37**+**38** in the presence of sparteine (see Scheme 8).

Entry	Equiv TMSCl	T_1 [°C]	T_2 [°C]	(*R*)-**39**/(*S*)-**39**	*ee* [%]
1	0.1	−78	−78	91:9	82
2	2.3	−78	−78	56:44	12
3	0.1	−25	−78	99:1	98
4	2.1	−25	−78	92:8	84

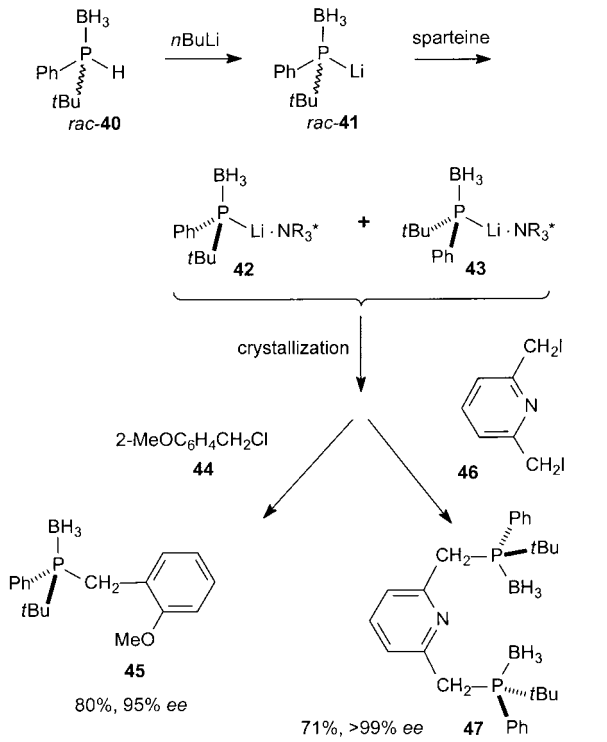
interconvert with **38** at −78 °C, and that the major diastereomer **37** is also the more reactive isomer. Entry 4 of Table 7 describes an experiment in which equilibration with sparteine at −25 °C is followed by the addition of excess TMSCl at −78 °C. In this case, both **37** and **38** must be completely consumed. As **37** and **38** do not interconvert at −78 °C, the ratio of (*R*)-**39**/(*S*)-**39** reflects the thermodynamic ratio of **37** and **38** established by the preceding equilibration at −25 °C. Thus, none of the four experiments involves dominant DKR.

Beak et al. classified the scenario of entry 4 in Table 7 as a dynamic thermodynamic resolution (DTR).[29] This is defined as a two stage process: 1) a thermodynamic ratio of reactive intermediates is established by equilibration of diastereomers; 2) a subsequent reaction is conducted at a lower temperature where the equilibrium is frozen out, resulting in chiral products.

In principle, the DTR phenomenon is possible in a variety of organometallic environments in which an equilibrating pair of enantiomers is modified for further reaction by complexation with an enantiomerically pure ligand. This concept has considerable potential for the control of configuration at labile carbon–metal bonds, as underscored in a recent study of 2-lithiopyrrolidines by Coldham et al.[28f] However, DTR is distinct from DKR, so the reader is referred to the review by Beak et al. for further examples.[29]

In the first stage of DTR, diastereomeric species interconvert through inversion of configuration at one of the asymmetric atoms. If the process occurs in solution, then the first stage is referred to as an "asymmetric transformation of the first kind".[30] The more interesting variation occurs if one of the isomers crystallizes from solution. In this situation, events are controlled by the thermodynamics of phase equilibrium. The more stable crystal lattice can be formed exclusively because two equilibrating solid phases with different stabilities cannot be present simultaneously unless the temperature happens to match the critical temperature for a phase transition.[31,32] Eliel et al. define this striking phenomenon as a crystallization-induced asymmetric transformation, also known previously as an "asymmetric transformation of the second kind".[30]

A more recent case in which DKR and DTR are possible in principle was reported by Wolfe and Livinghouse.[33] The conversion of the phosphine–borane complex *rac*-**40** into the chiral phosphine **45** (95 % *ee*) was carried out by deprotonation, treatment of *rac*-**41** with sparteine,[33] equilibration of the resulting mixture of diastereomers **42** and **43**, and alkylation with the benzylic halide **44** (Scheme 9). High *ee* values were only observed upon warming the mixture of **42** and **43** to 25 °C, and stirring the resulting suspension for one hour,



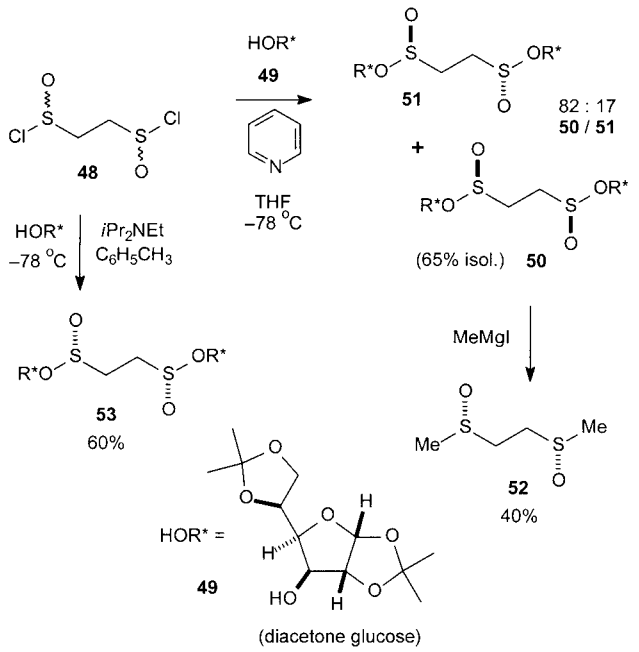
Scheme 9. Example of DKR as a likely consequence of DTR as reported by Wolfe and Livinghouse.[33]

followed by cooling to −78 °C prior to alkylation. If the sample was not warmed above 0 °C, the *ee* value of **45** was not more than 35 %. Therefore, the product ratio cannot be controlled solely by the differences in relative reactivity between rapidly interconverting **42** and **43** (commensurate with DKR). The result is consistent with a DTR interpretation, and may involve crystallization-induced asymmetric transformation in the first stage if the formation of a suspension ("voluminous precipitate") results from the crystallization of **42**. A similar sequence with the difunctional halide **46** in the alkylation step gave the interesting diphosphine **47** in >99 % *ee* (Scheme 9). The higher *ee* reflects an upgrade resulting from the formation of separable diastereomers as minor by-products in the alkylation step.

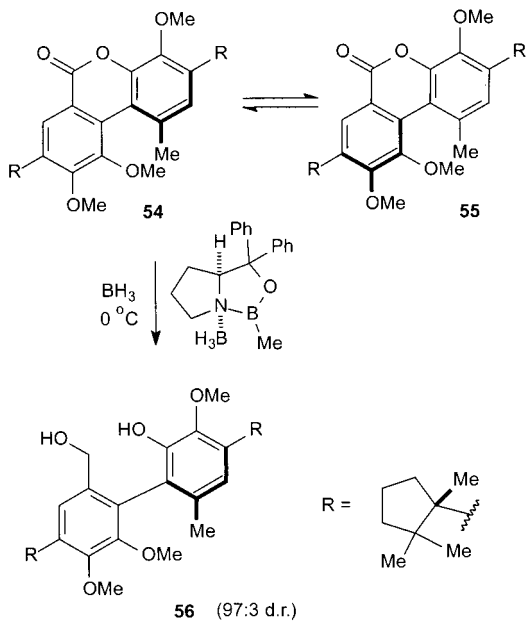
4.1.4. DKR with S(O)Cl and P(O)Cl Derivatives

Equilibration of configuration at sulfinyl sulfur or phosphinyl phosphorus atoms can also be used in DKR experiments.[34a,b] The most impressive example is shown in Scheme 10: the difunctional bis(sulfinyl chloride) **48** in reaction with the chiral alcohol diacetone glucose (**49**) (HOR*).[34a] Thus, a mixture of enantiomers and diastereomers of **48** is treated with **49** in the presence of pyridine to afford a mixture of diastereomeric bis(sulfinates) **50** and **51** in a ratio of 82:17, with the remaining 1 % as a third isomer **53**. Crystallization affords pure **50**, and Grignard displacement occurs with inversion to produce the interesting C_2-symmetric bis(sulfoxide) **52** in moderate yield. Evidently, the isomers of **48** are in equilibrium at −78 °C, and formation of **50** is favored kinetically. If the first step in the sequence is modified by the

 © 2005 Wiley-VCH Verlag GmbH & Co. KGaA, Weinheim



Scheme 10. DKR of a mixture of enantiomers and diastereomers of bis(sulfinyl chloride) **48** with the chiral alcohol diacetone glucose (**49**).



Scheme 11. DKR of enantiomeric atropisomers as reported by Bringmann, et al.[35a]

replacement of pyridine with the Hünig base, and the solvent is changed to toluene, then the kinetic selectivity is inverted; **53** becomes the dominant product. In this manner, either enantiomeric series of C_2-symmetric bis(sulfoxides) is accessible.

The same methodology also works with simple sulfinyl chlorides, and provides a route to unsymmetrical chiral sulfoxides.[34a] A conceptually similar DKR approach has been used to prepare chiral phosphites, aminophosphines, and phosphines.[34b–e] These methods are attractive alternatives to simple KR of sulfur- or phosphorus-containing substrates.[34f,g]

4.1.5. DKR with Atropisomers

In principle, DKR is possible if interconverting, enantiomeric atropisomers are treated with enantioselective reagents.[35] The concept is illustrated in Scheme 11,[35a] although it is not technically a case of DKR because the process involves equilibrating diastereomers **54** and **55** (note that chirality is present in the remote substituent R). The recognition process occurs far from the chiral substituent, and involves the selective reduction of the lactone carbonyl group of isomer **54** by diborane with a chiral oxazaborolidinone catalyst. After the constraint imposed by the lactone ring is removed, the atropisomers interconvert much more slowly, and **56** is isolated with excellent diastereomeric purity (97:3 d.r.). Structure **56** is an intermediate in the synthesis of mastigophorene A by Bringmann et al.[35a]

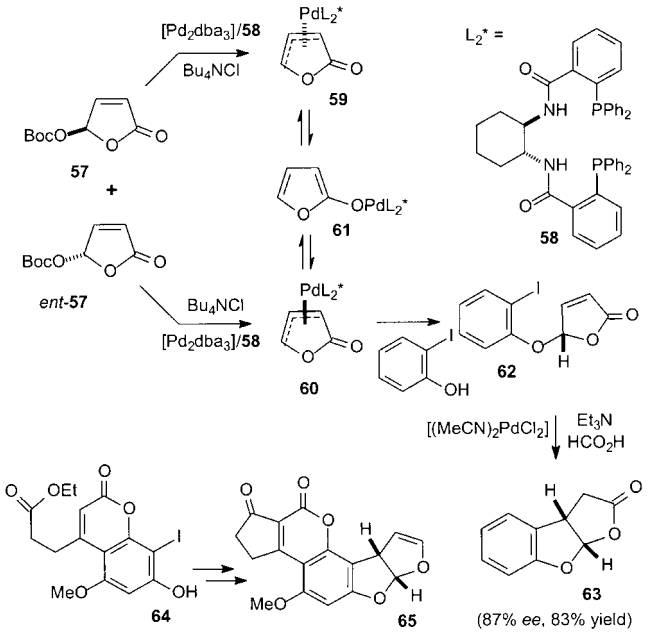
4.1.6. DKR with Transition-Metal Intermediates

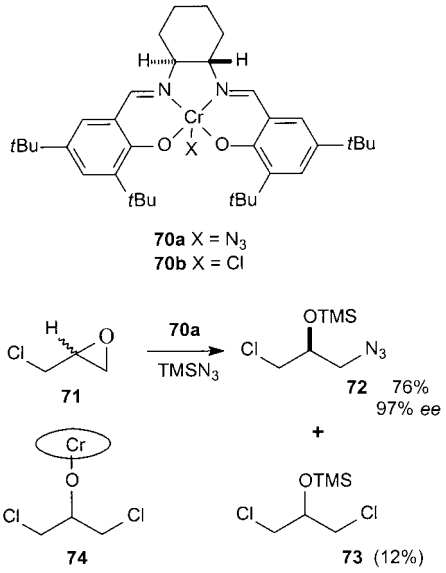
Catalytic cycles that are capable of converting both enantiomers of a racemic substrate into a common intermediate have been recognized which provide additional opportunities for DKR. Simple KR via π-allyl intermediates is well-known,[36] but recent investigations have encountered cases in which DKR is also possible if allylpalladium intermediates are generated catalytically from allylic carbonates (Scheme 12).[37,38] Thus, treatment of the racemic butenolide **57** with $[Pd_2dba_3]$ in the presence of the chiral ligand **58** under carefully optimized conditions results in the reversible formation of diastereomeric π-allylpalladium intermediates **59** and **60**.[37a,b] If a Cl^- ion source is included in the system, then **59** and **60** interconvert via the "enolate complex" **61**, and DKR becomes possible. If the experiment is conducted in the presence of *o*-iodophenol, the intermediate **60** is intercepted selectively, and **62** is formed in 83% yield (87% *ee*). Subsequent reductive Heck cyclization to **63** was also demonstrated, and the analogous sequence from **64** was used by Trost and Toste in an elegant synthesis of aflatoxin B (**65**).[37a,b]

One further example of palladium-mediated DKR illustrates an unusual pathway for the conversion of both enantiomers of a complex racemic substrate into a common intermediate.[38a] The treatment of racemic tetracarboxylate **66** (an ester of *rac*-conduritol B) with a palladium source, a soluble benzoate salt, and the chiral ligand **58** results in a remarkable conversion into the bis(benzoate) **69** (85% yield, >99% *ee*; Scheme 12). Selective oxidative insertion of palladium into bond **a** in preference to bond **b** initiates the events leading from **66** to **67**. However, the same intermediate can also be formed from *ent*-**66** by selective insertion into bond **d** in preference to bond **c**. This provides an efficient pathway to **68** and ultimately to **69** from either enantiomer of the starting compound **66**.

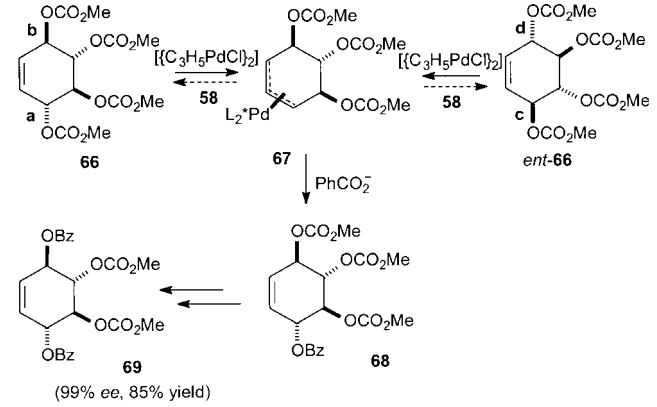
Another approach to the generation of a common intermediate from a racemic mixture through organometallic catalysis is described by Schaus and Jacobsen (Scheme 13).[39]

 © 2005 Wiley-VCH Verlag GmbH & Co. KGaA, Weinheim





Scheme 13. DKR through the production of a common intermediate from a racemic mixture by organometallic catalysis. [39]



Scheme 12. Palladium-mediated DKR through catalytic production of allylpalladium intermediates; Boc = *tert*-butoxycarbonyl, dba = dibenzylideneacetone, Bz = benzoyl.

The intent was to evaluate catalyst **70a** for the conversion of epichlorohydrin **71** into **72** with trimethylsilyl azide under conditions expected to allow simple KR. However, the recovered epichlorohydrin did not show the expected enrichment of *ee*, apparently the result of competing racemization under the reaction conditions. This observation suggested a DKR application, and an optimized experiment was developed with controlled addition of the azide to provide **72** in 76% yield (97% *ee*). The formation of a common intermediate **74** was proposed to explain racemization of **71** during the DKR process, as well as formation of the by-product **73** through interaction of a modified catalyst **70b** with the starting epichlorohydrin.

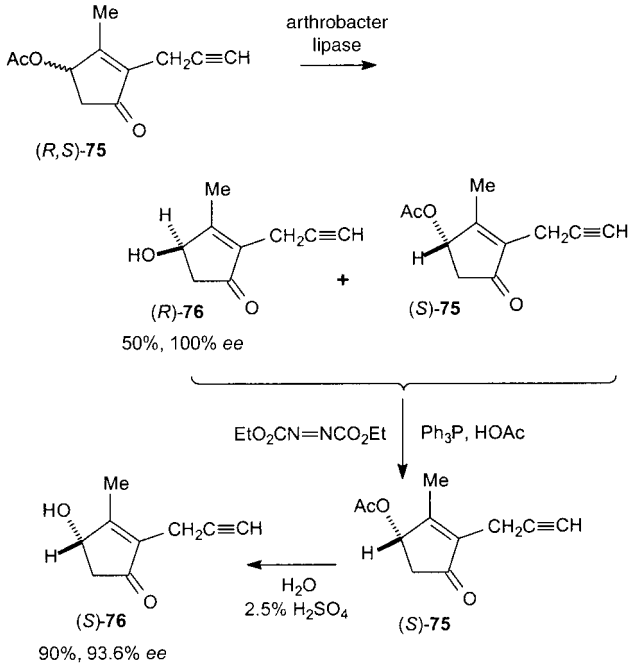
A variety of other methods for the interconversion of enantiomers of labile substrates have been exploited for DKR,[2g,i,40] and some have been used in combination with enzymatic catalysis. Some of the best examples feature equilibrating racemic cyanohydrins and racemic heterobenzylic alcohols as substrates for DKR in the presence of lipase acyl-transfer catalysts, a topic that has been described extensively in the review literature.[3a–j] Some of the most recent work in this area emphasizes the simultaneous use of enzymatic catalysts and transition-metal racemization catalysts; specialized reviews on this topic are also available.[2j,m]

4.2. Kinetic Resolution with Subsequent Enantioconvergent Processing of Intermediates or Products

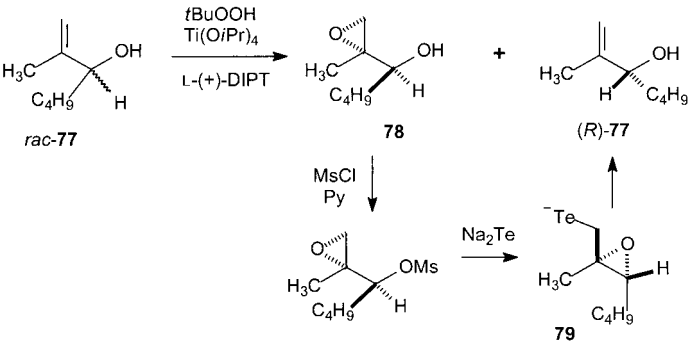
A racemic substrate can be efficiently converted into a single enantiomer if simple KR is combined with the stereospecific conversion of one enantiomer into a product derived from the other. Early experiments to demonstrate enantioconvergent processing relied on lipase-mediated KR to afford a mixture of a secondary alcohol and the enantiomeric secondary ester.[3p,41] Simple Mitsunobu esterification was then used as the enantioconvergent step to transform the alcohol into the ester by inversion of configuration. One of the best examples is shown in Scheme 14.[41a] Through the lipase-catalyzed hydrolysis of racemic ester (*R*,*S*)-**75**, a mixture of alcohol (*R*)-**76** and acetate ester (*S*)-**75** was obtained with perfect selectivity. After the mixture was subjected to Mitsunobu conditions, a single product consisting of (*S*)-**75** was isolated. Ester hydrolysis with dilute acid then produced the alcohol (*S*)-**76** in 90% overall yield and 93.6% *ee*. Evidently, the Mitsunobu inversion from (*R*)-**76** to (*S*)-**75** occurs with ≈97% stereospecificity. In principle, the same enantioconvergent approach can be used with a variety of secondary alcohols, and several simpler examples have been demonstrated.[41b]

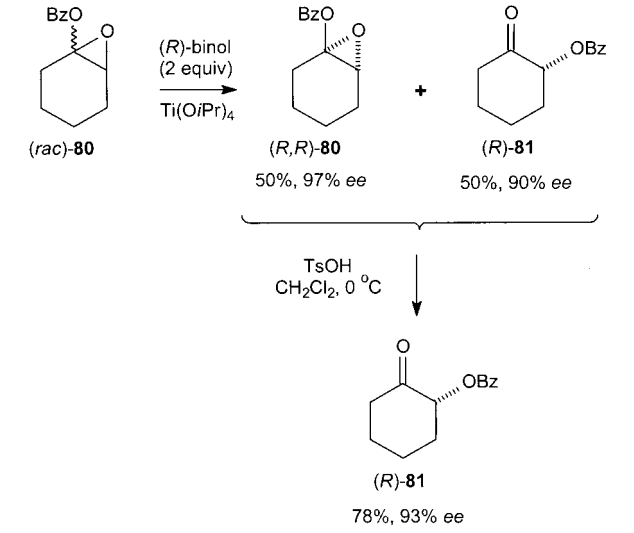
Among the few cases in which nonenzymatic catalysts were used for enantioconvergence is a study by Discordia and Dittmer (Scheme 15).[42] Standard Sharpless epoxidation KR was performed to convert *rac*-**77** into a mixture of epoxide **78**

 © 2005 Wiley-VCH Verlag GmbH & Co. KGaA, Weinheim



Scheme 14. KR by lipase-catalyzed hydrolysis of a racemic ester and subsequent enantioconvergent transformation. [41a]



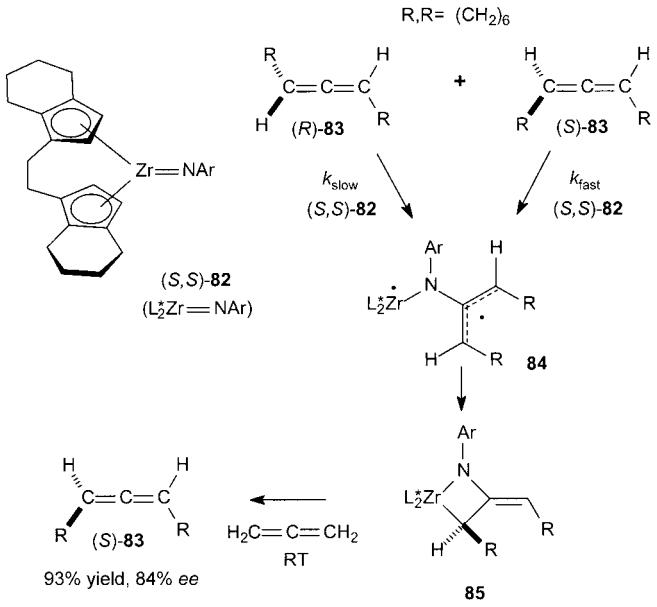


Scheme 15. Enantioconvergent transformations with nonenzymatic catalysts as reported by Discordia and Dittmer (top)[42] and Shi and co-workers (bottom);[43] Py = pyridine, Ms = methanesulfonyl, Ts = *p*-toluenesulfonyl.

and the slow-reacting alcohol (*R*)-**77**. After isolation of **78**, treatment with methanesulfonyl chloride followed by reaction with a telluride ion source resulted in a sequence of intermolecular and intramolecular displacement steps to afford the transient epoxide **79** with inversion of configuration. Subsequent 1,2-elimination by an unknown mechanism then converted **79** into (*R*)-**77**, identical to the slow-reacting enantiomer from the initial Sharpless KR (88% combined yield, 94% *ee*).

An intriguing report by Shi et al. illustrates another epoxidation approach (Scheme 15) that results in enantioconvergence.[43] A racemic mixture of epoxides **80** was prepared by the epoxidation of cyclohexenyl benzoate. Upon treatment of the racemic epoxide with a chiral Lewis acid generated from (*R*)-binol and titanium tetra(isopropoxide), the (*S*,*S*)-epoxide was selectively converted into α-benzoyloxycyclohexanone (*R*)-**81**. The reaction proceeds by simple KR that occurs with inversion of configuration and with excellent enantioselectivity ($s > 100$). The product mixture was then treated with toluenesulfonic acid to convert the slow-reacting epoxide (*R*,*R*)-**80** into (*R*)-**81** with retention of configuration (78% overall yield, 93% *ee*). Thus, enantioconvergence was achieved in the first stage (rearrangement of (*S*,*S*)-**80** to (*R*)-**81**), whereas structural convergence was effected in the second stage. Several other examples of this two-stage process were reported by Shi and co-workers.[43]

Another case in which enantioconvergence occurs at the stage of a reactive intermediate was reported by Bergman and co-workers. Kinetic resolution of chiral allenes can be effected with the chiral zirconium imido complex **82** (Scheme 16).[44] However, for 1,2-cyclononadiene **83**, both the fast-reacting and slow-reacting enantiomers eventually afford the same major product **85**, apparently via the diradical intermediate **84**. Upon treatment of **85** with excess allene at room temperature,



Scheme 16. Enantioconvergence at the stage of a reactive intermediate in the kinetic resolution of a chiral allene. [44]

 © 2005 Wiley-VCH Verlag GmbH & Co. KGaA, Weinheim

the 1,2-cyclononadiene is displaced and is recovered in 93% overall yield and with 84% *ee*.

The above case is conceptually related to some of the DKR experiments mentioned in Section 4.1.6.[37,38] For example, the formation of a single allylpalladium complex **67** from either enantiomer **66** or *ent*-**66** was described in Scheme 12. If conversion into **67** is reversible, as suggested in a generalized reaction Scheme by the authors,[38a] then the experiment involves DKR by the conventional definition. However, if conditions were found under which **67** is formed irreversibly from both **66** and *ent*-**66**, it would still be possible to obtain a single product in high yield and high *ee*. In this case, the experiment would be an example of enantioconvergence, and not DKR.

By similar logic, the example illustrated in Scheme 16 might involve DKR if **84** were formed reversibly from (*R*)-**83** and (*S*)-**83**. However, this possibility is ruled out because unreacted 1,2-cyclononadiene did not racemize under the reaction conditions. Therefore, the process appears to be enantioconvergent, and does not involve DKR. In view of the potential for efficient processing of both enantiomers of a substrate, the prospect of future reports of further examples of this phenomenon is exciting.

4.3. Divergent Reactions on a Racemic Mixture and Parallel Kinetic Resolution

Efficient recovery of highly enantioenriched products starting from a racemic mixture is possible if each substrate enantiomer can be selectively converted into a distinct, easily separated product. Generally accepted terminology for such reactions has not yet reached the consensus stage,[2ee,45–47] although relevant examples that involve a single chiral reagent had been recognized many years ago.[45] Herein, we use Kagan's recent classification of this potentially diverse family of transformations as "divergent reactions on a racemic mixture" (divergent RRM).[46b] This terminology applies broadly to a number of possible scenarios, some of which involve a component of kinetic resolution, whereas others do not.

By 1967, Guetté and Horeau had already demonstrated that reaction of racemic ketones with a chiral hydride donor affords alcohol diastereomers with significant *ee* values.[45] The results were correlated by using material balance relationships for the case in which the chiral substrate is completely converted into two products. Subsequent papers by Kagan extended the mathematical treatment to a broader range of divergent RRM scenarios (partial conversion, more than two products).[46] Furthermore, Kagan recognized that the Sharpless epoxidation of **1**, already mentioned in a different historical context (Scheme 1), is an example of divergent RRM because the reaction affords diastereomeric *erythro* and *threo* epoxides.

Sharpless and co-workers had shown that the minor *threo* diastereomer **III** (**3** + *ent*-**3**) is formed in an enantiomeric ratio of 24:1 (92% *ee* favoring *ent*-**3**) if the reaction of racemic alcohol **1** (= **I**) is allowed to proceed to completion.[13] The *ee* value of products **II** from racemic **1** was not reported, but may be inferred as 44% *ee* if the product enantiomeric ratios of Scheme 1, deduced from the reactions of pure enantiomers (*R*)-**1** and (*S*)-**1**, also apply to the reaction of racemic **1**. Further insight can be obtained by applying the mathematical model of Horeau to the reaction of the racemic alcohol **1** [Eq. (3)].

given : $\mathbf{II} = \mathbf{2} + \textit{ent}\text{-}\mathbf{2} = \textit{erythro}$ diastereomer;
$\mathbf{III} = \mathbf{3} + \textit{ent}\text{-}\mathbf{3} = \textit{threo}$ diastereomer

from Scheme 1 : $(R,S)\text{-}\mathbf{1} \rightarrow \mathbf{II} + \mathbf{III}$

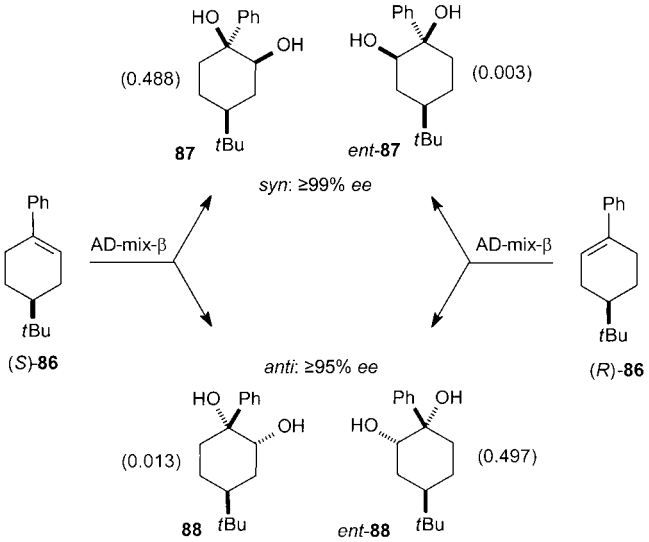
Horeau equation : $x_{\mathbf{II}}(ee_{\mathbf{II}}) + x_{\mathbf{III}}(ee_{\mathbf{III}}) = 0$ (3)

The terms $x_{\mathbf{II}}$ and $x_{\mathbf{III}}$ refer to the mole fractions of diastereomers **II** and **III**, and $ee_{\mathbf{II}}$ and $ee_{\mathbf{III}}$ represent their respective enantiomeric purities (Horeau's derivation uses *ee* values as decimals with opposite signs for cases in which the major enantiomers have opposite absolute configurations). From the measured value of $ee_{\mathbf{III}}$ for **III** (92%), it is possible to calculate the value of $ee_{\mathbf{II}}$ if the mole fractions of **II** and **III** are known (that is, from the diastereomeric ratio). This data was not reported for the reaction of racemic **1**, but may be inferred from Scheme 1 as $x_{\mathbf{II}} = 68\%$ and $x_{\mathbf{III}} = 32\%$. The predicted value of $ee_{\mathbf{II}}$ from Equation 3 is 44%, the same as inferred above from the product ratios shown in Scheme 1. Thus, Equation (3) may be used to check for self-consistency in diastereomeric and enantiomeric ratio data.

Equation (3) requires the major product, **II**, in a divergent RRM process to have the lower *ee* value. This is a consequence of the material balance relationship, and a lower degree of reagent control (for example, 38:62 in the path from enantiomer (*R*)-**1** to the products *ent*-**2** and *ent*-**3**, Scheme 1). On the other hand, Equation (3) predicts that both products can be formed with high *ee* and high yield if both enantiomers react with high reagent control (high diastereoselectivity), as discussed in the following examples. We classify these reactions as stereodivergent RRM to indicate that individual enantiomers may react with different levels of diastereoselectivity.

Examples of efficient stereodivergent RRM are known under Sharpless osmylation conditions,[48] one of which is summarized in Scheme 17. The racemic cyclohexene **86** was treated with the commercially available Sharpless osmylation reagent (AD mix β) to give separable diastereomers **87** ($\geq$99% *ee*) and **88** ($\geq$95% *ee*) in 82% combined yield.[48g] The Horeau relationship [Eq. (3)] allows calculation of the detailed product ratios from the conservative *ee* limits (taken as 99% *ee* and 95% *ee*, respectively) and the mole-fraction relationship (sum of **87** + *ent*-**87** + **88** + *ent*-**88** = 1). The predicted mole fractions (Scheme 17, in parentheses) show that the osmylation occurs with excellent reagent control. The major product from each enantiomeric alkene corresponds to osmylation of the pro-*R* face of the phenyl-substituted carbon. The directing influence of the *tert*-butyl substituent is relatively small, as shown by the calculated diastereomeric ratio of (*R*)-**86** (37.5:1 *syn*/*anti*) in comparison with that of (*S*)-**86** (1:166 *syn*/*anti*). Assuming that conventional purification would separate the diastereomers efficiently, the result would

 © 2005 Wiley-VCH Verlag GmbH & Co. KGaA, Weinheim



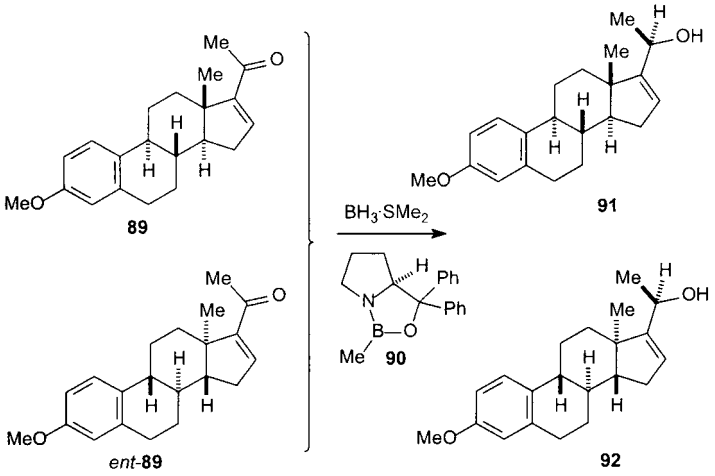
Scheme 17. Stereodivergent RRM in the osmylation of racemic cyclohexene **86** with AD mix β.

be to enrich the enantiomers to a level of $\geq 95\%$ *ee* with a theoretical recovery limit equal to the overall yield (82%).

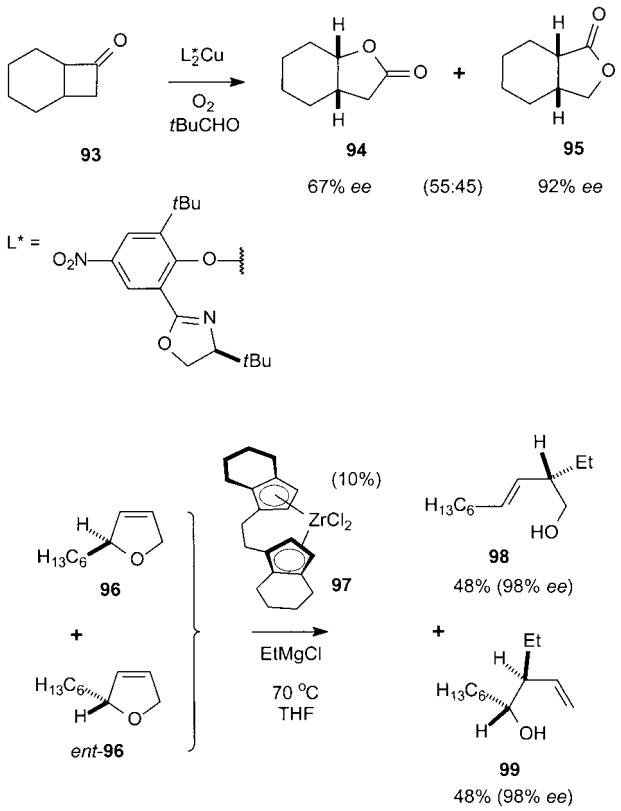
The ideal situation for stereodivergent RRM is to have total reagent control. In this case, the asymmetric carbons in the racemic substrate would have no influence on the diastereomeric ratio and would serve only to enable the separation of product diastereomers. Scheme 18 illustrates an example of enantiofacially controlled ketone reduction in which the efficiency may have reached the ideal limit.[49] The reduction of racemic **89** with dimethylsulfide borane and the oxazaborolidine catalyst **90** affords a 1:1 mixture of diastereomers **91** (>99% *ee*) and **92** (>99% *ee*) in 95% combined yield after chromatographic separation. The same phenomenon had been encountered earlier with racemic ketones under enzymatic reduction conditions,[50a–j] or by the use of nonenzymatic hydride donors in the presence of chiral additives, although the level of enantiofacial control in the latter examples was usually lower.[45,50k–o] For the example in Scheme 18, the highly selective reduction allows the preparation of both enantiomeric steroids by using a simple technique to separate the product diastereomers and thus the enantiomers as well.

In principle, stereodivergent RRM is possible in a variety of addition reactions in which an sp^2-hybridized carbon atom is converted into an asymmetric carbon atom. A relevant study has appeared involving the hetero-Diels–Alder reaction of racemic enals and achiral enol ethers. Highly selective stereodivergent RRM was observed, resulting in the synthesis of diastereomeric dihydropyrans with good *ee* by using a chiral chromium Lewis acid catalyst (Chavez and Jacobsen).[51]

The Horeau relationship [Eq. (3)] also applies to a reaction category that we classify as regiodivergent RRM. The only new feature is that product separation depends on the formation of a distinct regioisomer from each substrate enantiomer. Early reports of this phenomenon involved a variety of enzymatic oxidations,[52] including a number of highly efficient Baeyer–Villiger reactions.[52j–n] Synthetic catalysts for analogous Baeyer–Villiger oxidations are now available,[53] as illustrated for the conversion of racemic **93** into a separable mixture of the regioisomers **94** and **95** (Scheme 19).[53a]



Scheme 18. Separation of both enantiomers of a steroid **89** and *ent*-**89** by stereodivergent RRM (highly selective reduction).



Scheme 19. Top: regiodivergent RRM under Baeyer–Villiger oxidation conditions with a synthetic catalyst.[53a] Bottom: ring opening of a racemic dihydrofuran with nearly perfect reagent control.

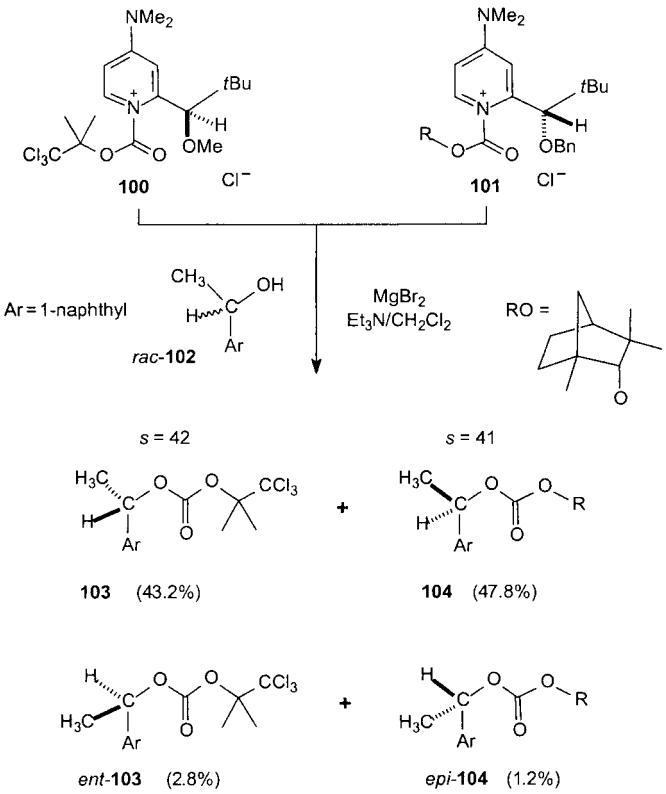
 © 2005 Wiley-VCH Verlag GmbH & Co. KGaA, Weinheim

Other interesting examples of regiodivergent RRM have been reported recently,[54–58] including regioselective C–O bond cleavage,[54] Sharpless epoxidations,[55] transition-metal-catalyzed diazo insertions and cyclopropanations,[56] and a rhodium-catalyzed ynal cyclization in which one enantiomer affords a cyclopentenone product while the other produces the isomeric alkylidenecyclobutanone.[57] In one of the most impressive examples, the ring opening of racemic dihydrofuran **96** by a Grignard reagent in the presence of the chiral zirconocene catalyst **97** was carried out with near-perfect control, as shown in Scheme 19.[58] Excellent recovery and selectivity (96% yield of separated isomers **98** and **99**, each with 98% *ee*) were observed, resulting from dominant reagent control.

The examples of stereodivergent and regiodivergent RRM discussed above feature a single reagent that reacts in a different way with each enantiomer. This difference is the basis for enantiodivergence. If reagent control is sufficiently high and the products can be separated, then the process allows efficient separation of enantiomers. Although the experimental setup resembles that of simple KR (a chiral reagent is used to modify a racemic mixture), there is a crucial difference: in divergent RRM, the reaction is taken to completion. If this were done in a simple KR situation in which the divergence of enantiomers to give distinct products is not possible, the product would be racemic. Simple KR may or may not take place as divergent RRM experiments are performed, but KR has nothing to do with the desired outcome in RRM using a single chiral reagent because the relative reactivities of the enantiomers are unimportant.

Parallel kinetic resolution (PKR) is a variation of divergent RRM in which two complementary chiral reagents are employed for selective modification of a racemic substrate to afford distinct products.[47] The experiment consists of two simple KR reactions conducted "in parallel", in contrast to divergent RRM with a single reagent. In PKR, the relative reactivities of enantiomers are very important, and the two chiral reagents are chosen so that each substrate enantiomer reacts at a similar rate. Under these conditions, the enantiomeric ratio of the unreacted substrate remains close to 1:1 regardless of conversion, and product *ee* reflects the inherent enantioselectivities of each reagent. In these respects, PKR resembles DKR.

The first example of a preparative PKR experiment is shown in Scheme 20 with quasienantiomeric pyridinium carboxylates **100** and **101** as the chiral reagents.[47] The reagents were selected for their similar reactivities and complementary enantioselectivities in simple KR experiments (**100**, $s = 42$, selective for (*S*)-**102**; **101**, $s = 41$, selective for (*R*)-**102**). The chiral R group (fenchyl) in reagent **101** plays no role other than to provide steric bulk as needed to match the reactivity of **100**. For the PKR experiment, **100** and **101** were mixed and allowed to react with *rac*-**102**. The quasienantiomeric esters **103** (e.r. 94.5:5.5 *S*/*R*) and **104** (d.r. 97.5:2.5 **104**/*epi*-**104**) were obtained as the major products in >95% combined yield. Reductive cleavage of the trichlorobutyl protecting group from **103** allowed easy product and enantiomer separation to a level of 89% *ee* or more, and with a substantial improvement in recovery of enantioenriched products (>95%) over simple KR.

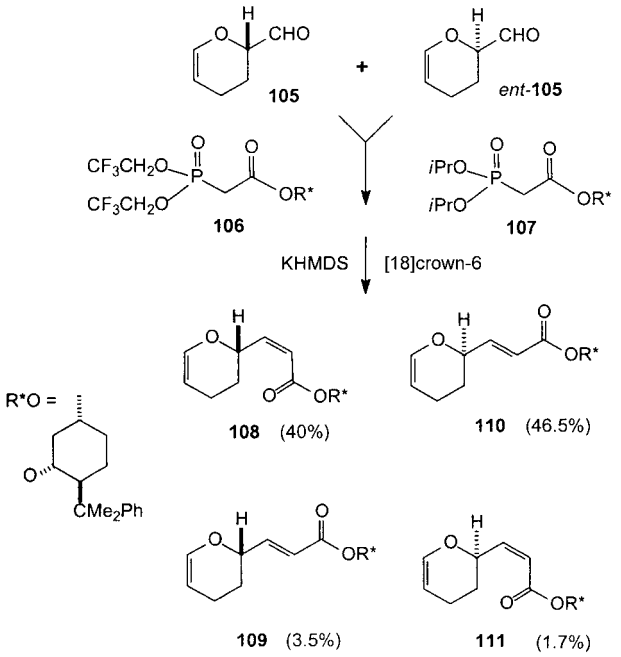


Scheme 20. Preparative PKR using chiral reagents with complementary enantioselectivities.[47]

Brooks et al. may have encountered an earlier example of the two-reagent process in the reduction of a racemic ketone with bakers' yeast. In this case, two different enzymes were involved in enantiomer discrimination, although one of the products in their experiment was achiral.[59a] The optimum conditions required for conducting two parallel, complementary enantioselective reactions were not discussed in this report. However, another early study by Preston not only discussed the principles, but also conducted relevant experiments with two complementary chiral reagents.[59b] These were probably the first attempts designed specifically to achieve PKR (termed "simultaneous kinetic resolution" by Preston), but evidence for PKR was largely based on NMR spectroscopic analysis because the product mixtures could not be separated.

An intriguing study of reagent selectivity has been reported in connection with another example of PKR (Scheme 21).[60] In this case, differing phosphonate alkoxy groups in the phenmenthyl-derived reagents **106** and **107** allowed complementary selectivity for individual enantiomers of the substrate **105**. Evidently, the phosphorous-bound alkoxy groups invert reagent enantioselectivity and *E*/*Z* selectivity, which results in divergent processing of the substrate enantiomers (enantiodivergence) to afford diastereomers **108–111**. Even if the chiral auxiliary OR* were removed, separation of *E* and *Z* isomers would still provide a

 © 2005 Wiley-VCH Verlag GmbH & Co. KGaA, Weinheim



Scheme 21. An example of complementary selectivity with reagents **106** and **107** for the individual enantiomers of a substrate.[60]

basis for the separation of enantiomers because of the high diastereomeric ratios of *Z* isomers (**108** > **111**) and *E* isomers (**110** > **109**). The authors also report other highly selective variations of PKR with different chiral auxiliaries on each substrate enantiomer[60a] and enantioconvergent processing via allylpalladium intermediates to give one dominant product with enhanced efficiency.

All of the two-reagent divergent RRM (PKR) applications require the compatibility of both reagents as well as similar reaction rates and enantioselectivities for optimum results. These requirements are easier to satisfy by using two stoichiometric chiral reagents,[47,59–63] although a doubly catalytic example of PKR has also been reported.[63] In contrast, the single reagent version (divergent RRM) is easier to perform in the catalytic mode if the necessary level of reagent control is achieved, and if a structural basis for enantiodivergence is present.

As shown above, PKR experiments can be stereodivergent, regiodivergent, or structurally divergent in other ways, provided that a distinct modification is made to each enantiomer that allows conventional separation.[47,59a,60–63] The Horeau relationship [Eq. (3)] still applies because it is based on material balance, yet PKR experiments involve a kinetically distinct situation[64] from the single-reagent version (divergent RRM). In the literature, PKR terminology has often been used to describe divergent RRM, but we recommend that PKR be reserved for the two-reagent experiment as a special case of divergent RRM.[45] As already noted, single reagent divergent RRM does not depend on the existence of any KR component, whereas the two-reagent version (PKR) requires two simultaneous enantiocomplementary KR reactions.

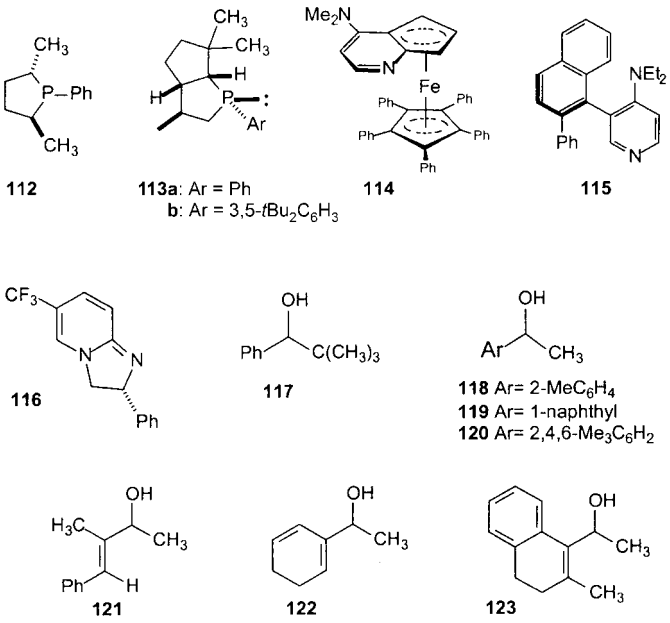
5. Kinetic Resolution of Important Functional Group Categories

5.1. Alcohols

As the most versatile class of substrates for synthesis applications, alcohols have received the most attention in the context of KR. A number of examples have already been encountered in connection with the techniques for improving efficiency, especially in the context of DKR with the Noyori hydrogenation methodology. Furthermore, KR with enantioconvergent processing of products is easily applied to secondary alcohol-containing structures because there are good methods available to invert alcohol group configuration, such as the Mitsunobu reaction as mentioned earlier. Recent developments in the preparation of alcohol derivatives with nonenzymatic KR is therefore discussed in detail herein, with an emphasis on catalytic methods.[2u–y]

5.1.1. KR of Alcohols with Chiral Nucleophiles as Catalysts

Major advances have been made in the development of chiral synthetic catalysts for acyl transfer through the activation of anhydrides. Studies in this area can be traced to the experiments of Wegler in the 1930s in which alkaloids were used to mediate enantioselective acylations with acetyl chloride and acetic anhydride, and to subsequent work with stoichiometric acyl-transfer agents.[65] The first example of KR of alcohols with $s > 10$ under nonenzymatic catalytic conditions was reported in 1996 in which the chiral phosphine **112** (Scheme 22) was used to activate *m*-chlorobenzoic anhydride.[66] Since that time, rapid progress has been made with other chiral nucleophiles, including structures **113**–**116**.[67–72] Hindered secondary benzylic and allylic alcohols



Scheme 22. Catalysts **112**–**116** for the kinetic resolution of alcohols **117**–**123** under nonenzymatic conditions (see Table 8).

 © 2005 Wiley-VCH Verlag GmbH & Co. KGaA, Weinheim

are excellent substrates, provided that the hydroxy group and double bond are not constrained within a ring (Table 8).

Nucleophilic catalysts **124**–**127** (Scheme 23) have been shown to activate anhydrides for the kinetic resolution of several 2-substituted cycloalkanols, 1,2-diol monoesters, and 2-amido alcohols with impressive enantioselectivity (Table 9; tertiary amine additives are required for good catalyst turnover, but are not specified in the table).[73–78] Lower selectivity was observed with a primary alcohol **133** (s = 6.8),[73b] but promising results have been obtained with analogous tertiary alcohols.[75f] These examples suggest that nonenzymatic catalysts may soon be capable of competing with lipases in terms of substrate generality. The peptide-based catalysts reported by Miller and co-workers are especially promising in this regard.[75] The first-generation tetrapeptide catalyst **126a** was initially optimized for functional-group recognition in the acetamido alcohol *rac*-**131** (s = 28),[75a] but the more recent octapeptide **126b** is highly selective in the KR of other substrates, including benzylic alcohols **117** (s = 30), **119** (s > 50), and the 2-phenylcyclohexanol *rac*-**129** (s > 50),[75c] whereas related octapeptides distinguish between the enantiomers of *rac*-**131** with s = 50–51.[75b] Several other chiral DMAP derivatives are known that have been used to catalyze O-acylation, but the selectivities are lower.[77,78]

An enantioselective acylation and KR of alcohols has been demonstrated with a polymer-supported amine catalyst in combination with the soluble reagents benzoyl chloride/triethylamine.[79] Furthermore, polymeric reagents have been employed to help separate unreacted substrate from the product of lipase-catalyzed KR.[80] Phase isolation is also important in the doubly catalytic PKR experiment discussed earlier.[63] Catalytic PKR relies on an insoluble, polymer-supported mixed anhydride that is selectively activated as an acyl donor with the soluble phosphine catalyst *ent*-**113b** while an insoluble lipase catalyst activates the soluble vinyl pivalate as the lipase-activated acyl donor.[63] Phase isolation of the mixed anhydride and the lipase allows two enantiocomplementary esterifications to be conducted simultaneously without harm to either catalyst.

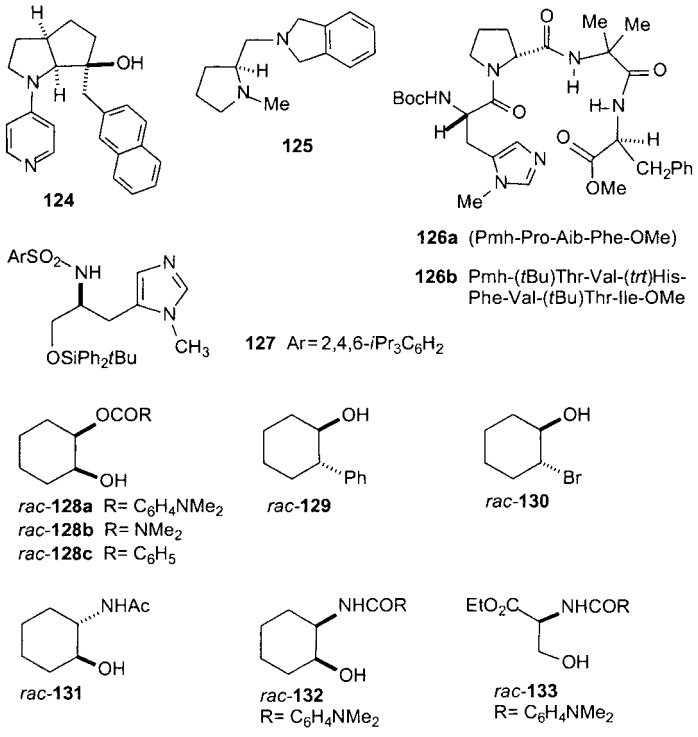
A different approach to solubility-based product separation uses lipase-catalyzed acylation with fluorinated acyl donors, followed by extraction with fluorine-containing solvents.[81] Alternatively, lipase-catalyzed saponification of a racemic fluorinated ester can be conducted under triphasic conditions in a U-tube such that the product alcohol collects in one methanolic phase.[82] The unreacted ester remains in the fluorinated solvent phase during lipase hydrolysis, and is then saponified by contact with aqueous hydroxide in a second methanol layer. This technique allows separation and recovery of each enantiomeric alcohol (89% *ee* or more) without chromatography or solvent extraction. Similar experiments with nonenzymatic acylation catalysts should

Table 8: KR of unsaturated alcohols (see Scheme 22).

Alcohol	Catalyst	$(RCO)_2O$	Solvent	T [°C]	s	Ref.
117	**112**	$(m\text{-ClBz})_2O$	CH_2Cl_2	RT	13	[66]
117	**114**	Ac_2O	*t*-amyl alcohol	0	95	[67]
117	**113a**	Bz_2O	toluene	−40	67	[68]
117	**116**	$(EtCO)_2O$	$CHCl_3$	0	85	[72]
118	**114**	Ac_2O	*t*-amyl alcohol	0	66	[67]
118	**113b**	$(i\text{PrCO})_2O$	heptane	−40	188	[68]
118	**116**	$(EtCO)_2O$	$CHCl_3$	0	26	[72]
119	**114**	Ac_2O	*t*-amyl alcohol	0	65	[67]
119	**113b**	$(i\text{PrCO})_2O$	toluene	−40	99	[68]
119	**115**	$(i\text{PrCO})_2O$	toluene	−78	29	[69a]
119	**116**	$(EtCO)_2O$	$CHCl_3$	0	56	[72]
120	**113b**	$(i\text{PrCO})_2O$	toluene	−40	370	[68]
121	**114**	Ac_2O	*t*-amyl alcohol	0	80	[70]
121	**113b**	$(i\text{PrCO})_2O$	toluene	−40	21	[71]
122	**113b**	$(i\text{PrCO})_2O$	toluene	−40	34	[68]
123	**113b**	$(i\text{PrCO})_2O$	toluene	−40	82	[71]

Table 9: KR of miscellaneous alcohols (see Scheme 23).

Alcohol	Catalyst	$(RCO)_2O$	Solvent	T [°C]	s	Ref.
128a	**124**	$(i\text{PrCO})_2O$	toluene	RT	12.3	[73a]
128a	**127**	$(i\text{PrCO})_2O$	CCl_4	RT	27	[76]
128b	**127**	$(i\text{PrCO})_2O$	CCl_4	0	64	[76]
128c	**115**	$(i\text{PrCO})_2O$	toluene	−78	20	[69b]
129	**125**	BzCl	CH_2Cl_2	−78	160	[74a]
130	**125**	BzCl	CH_2Cl_2	−78	130	[74a]
131	**126a**	Ac_2O	toluene	0	28	[75a]
132	**124**	$(i\text{PrCO})_2O$	toluene	−40	54	[73b]
133	**124**	$(i\text{PrCO})_2O$	toluene	20	6.8	[73b]
117	**126b**	Ac_2O	toluene	−65	30	[75c]
129	**126b**	Ac_2O	toluene	−65	>50	[75c]

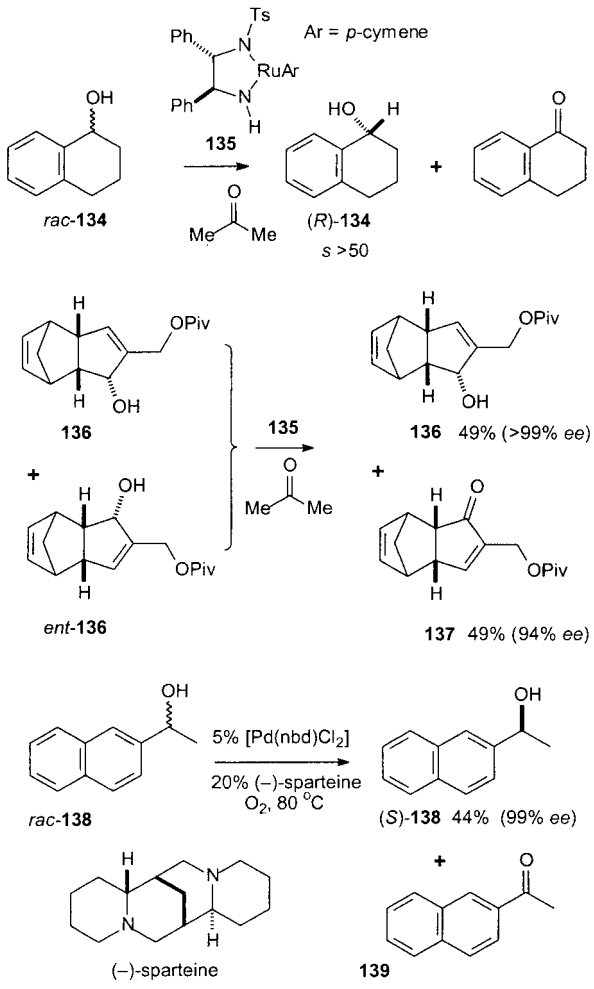


Scheme 23. Catalysts **124**–**127** for the kinetic resolution of alcohols **128**–**133** (see Table 9).

be possible, and deserve evaluation for preparative applications. Enantioselective acylation with chiral Lewis acid catalysts is another topic for which further exploration may be worthwhile.[83]

5.1.2. Oxidative KR of Alcohols

There has been considerable interest in kinetic resolutions that are based on the oxidation of a chiral secondary alcohol to a prochiral ketone, as the (achiral) product of the reaction can usually be recycled to the racemic starting material by simple hydride reduction. In principle, product recycling allows improved material recovery and greater efficiency. The first broadly applicable method for this purpose was developed by Noyori and co-workers under catalytic hydride transfer conditions similar to those used for the asymmetric hydrogenation of ketones. The methodology works well with benzylic alcohols, as is the case in the conversion of *rac*-**134** into (*R*)-**134** with the chiral ruthenium catalyst **135** to abstract hydride in the presence of acetone as the ultimate stoichiometric hydride acceptor (Scheme 24).[84] This reaction is essentially the reverse of the Noyori hydrogenation of ketones, a transformation that employs the same catalyst in the presence of isopropanol as the stoichiometric hydride donor.



Scheme 24. Examples of kinetic resolution in the oxidation of chiral secondary alcohols to prochiral ketones; nbd = norbornadiene.

The same conditions are effective with allylic alcohols, and allow the kinetic resolution of *rac*-**136**. The reaction proceeds with exceptional selectivity to give highly enriched alcohol **136** (> 99% *ee*, 49% yield) as well as ketone **137** (94% *ee*, 49% yield).[85] As ketone **137** is chiral, simple hydride reduction would not be applicable for the purposes of improving efficiency through product recycling, in contrast to the tetralone case discussed above. On the other hand, one can imagine methodology that might allow the enantioconvergent transformation of **137** into **136**. Even higher selectivities ($s > 360$) have been reported for the oxidative KR of substituted 1-phenylethanols with modified ruthenium catalysts,[86] but the corresponding acetophenone hydrogenations are also highly enantioselective and would be preferred for efficient preparation of the alcohols.

Conceptually related oxidative KR methods have been developed with palladium catalysis in the presence of sparteine as a chiral ligand.[87] Selectivities are generally lower than with the ruthenium catalysts ($s = 47$ in the best case from *rac*-**138**; $s = 24$ or less in most other reported examples with Pd or other metals and ligands).[88] The use of oxygen as the oxidant with hydrocarbon solvents raises some safety issues that would need attention as the technology is developed.

Another reaction type involving oxidative KR has been encountered in the metal-catalyzed decomposition of racemic hydroperoxides.[89] Catalyzed Baeyer–Villiger reactions of cyclic ketones might also be placed in this category, although oxidation occurs at the carbonyl carbon atom to produce a lactone product.[53]

5.1.3. KR by Mitsunobu Reaction of Alcohols

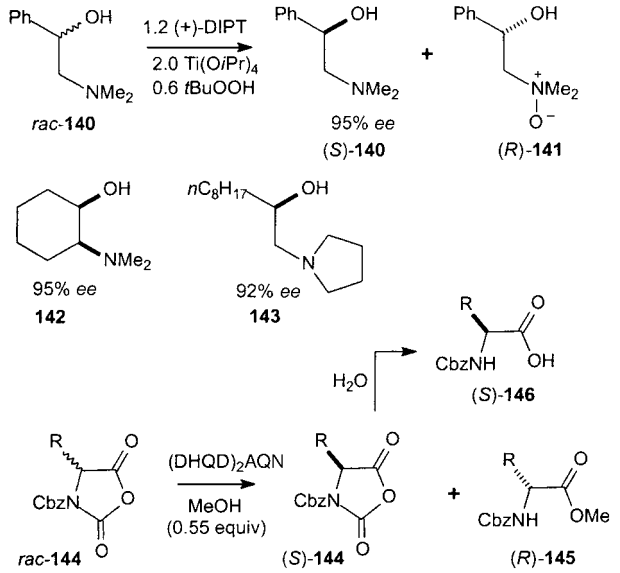
Several recent studies have described the KR of alcohols through nucleophilic substitution that results from azodicarboxylate activation with chiral phosphines,[90] or use of an achiral phosphine in combination with ketopinic acid as a chiral nucleophile.[91] The latter approach requires a stoichiometric quantity of ketopinic acid, whereas the former involves conversion of one equivalent of the chiral phosphine into the phosphine oxide. The ketopinic acid method can be used under DKR conditions with several benzylic alcohol substrates, resulting in the formation of a single ester product with > 95% *de*. Apparently, racemization occurs by ionization of the alkoxyphosphonium salt intermediate in the Mitsunobu sequence.[91] In principle, this might allow increased efficiency, but both of the reported Mitsunobu KR variants have the disadvantage of using stoichiometric chiral reagents.

5.2. Amines

Nonenzymatic methodology for the KR of amines and their derivatives is much less developed than that of the KR of alcohols. Indeed, the earliest catalytic example, the oxidative KR of β-hydroxy-*N*,*N*-dialkylamines described by Sharpless

 © 2005 Wiley-VCH Verlag GmbH & Co. KGaA, Weinheim

and co-workers, is still among the best applications.[92,93] Several specific examples, **140**–**143**, are shown in Scheme 25. A few other cases have already been mentioned in which nitrogen-containing molecules have been used in some of the



Scheme 25. Examples of nonenzymatic methods for the KR of amine derivatives (see Table 10); cbz = benzyloxycarbonyl.

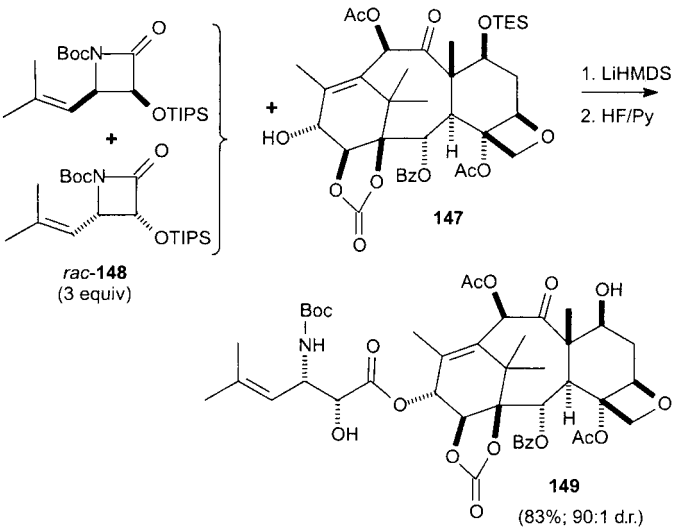
techniques for efficient KR, but in these cases the nitrogen substituent serves as a spectator group (see Schemes 2 and 4). A related example of this type is the catalytic methanolysis of oxazolidinediones described by Deng and co-workers (illustrated in the reaction of *rac*-**144** to (*S*)-**144**; Table 10).[94] With

Table 10: KR of oxazolidinediones **144**

Entry	R	*t* [h]	*T* [°C]	*s*
1	C_6H_5	16	−78	170
2	$CH_3(CH_2)_5$	37	−60	78
3	$C_6H_5CH_2$	17	−60	114
4	$BnOCH_2$	72	−78	69

some substrates, this method is selective enough to produce both the product (*R*)-**145** and the unreacted (*S*)-**144** in high *ee*. Because (*S*)-**144** is easily hydrolyzed to (*S*)-**146**, both enantiomers of the amino acid can be obtained with >90% *ee*. In the case of the aryl derivatives (for example, **144** with R = phenyl), a similar experiment can be performed under DKR conditions at room temperature to afford the ester in 91% yield and 90% *ee*).[94b] Several other interesting methods for the KR of nitrogen-containing compounds are known under catalytic[95,96] or stoichiometric[97] conditions in which issues of scope and efficiency remain to be explored.

One of the most remarkable stoichiometric KR examples of a nitrogen-containing substrate was described by Ojima and co-workers (Scheme 26). Enantiopure baccatin analogues such as **147** act as the resolving agents for a racemic chiral β-lactam **148** (threefold excess) to afford **149** (taxoid



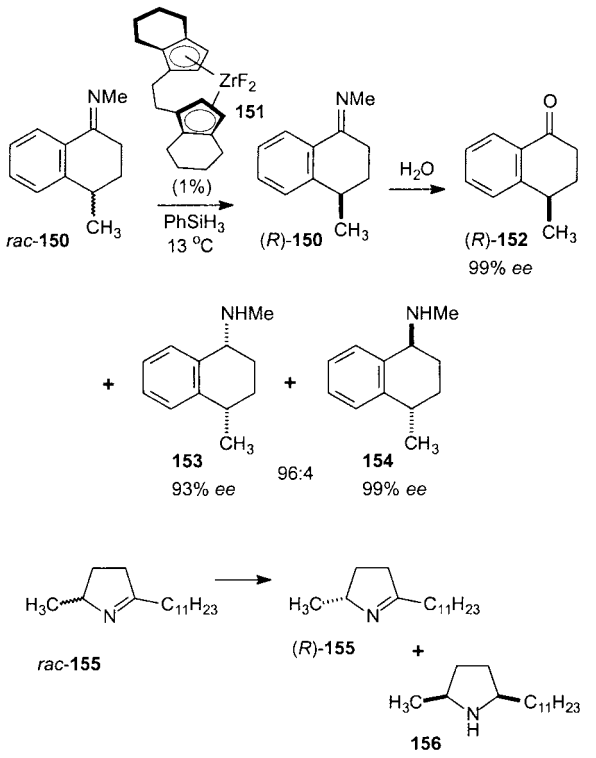
Scheme 26. Stoichiometric KR of an azetidine derivative as reported by Ojima and co-workers;[98] TIPS = triisopropylsilyl, TES = triethylsilyl.

series) with a diastereomeric ratio of 90:1 in favor of the isomer shown.[98] The efficiency of KR in this example is so high that the racemic β-lactam **148** can be used for preparative amide-bond formation without significant loss of the more complex reactant **147**.

Potentially valuable catalytic KR methodology that relies directly on the nitrogen substituent is highlighted by examples of aziridine carbonylation[95] and N-acylation,[96] as well as KR methods that use racemic imines as substrates.[99–101] Some useful examples involving imine hydrogenation are shown in Scheme 27. Yun and Buchwald demonstrated the reduction of imine *rac*-**150** with the chiral precatalyst [Zr(ebthi)] **151** and phenylsilane as the stoichiometric reducing agent. Aqueous workup gave the ketone **152** (>99% *ee*) and two isomeric amines **153** and **154**, both with high *ee*.[100] The two saturated amine products are the result of a stereoselective reduction involving the more reactive enantiomer, whereas **152** is formed by hydrolysis of the less reactive enantiomer (*R*)-**150** resulting from simple KR with $s = 61$. The Buchwald group has also shown that reductive KR is possible with cyclic imines, as in the reaction of *rac*-**155** to afford (*R*)-**155** (>95% *ee*, 41% yield) and **156** (>95% *ee*, 41% yield) with a similar catalytic system.[101]

5.3. Alkenes

Alkenes continue to play a central role as substrates for KR. This subject is discussed briefly because nearly all of the most important applications have been extensively reviewed.[2a–d,o–q] A number of examples have already been mentioned in the context of stereodivergent or regiodivergent RRM, for example, the Sharpless KR of allylic alcohols and osmylations. More recently, epoxidation methodology for the KR of simple alkenes has become available with chiral dioxiranes[102a] and the Jacobsen epoxidation catalyst.[102b]

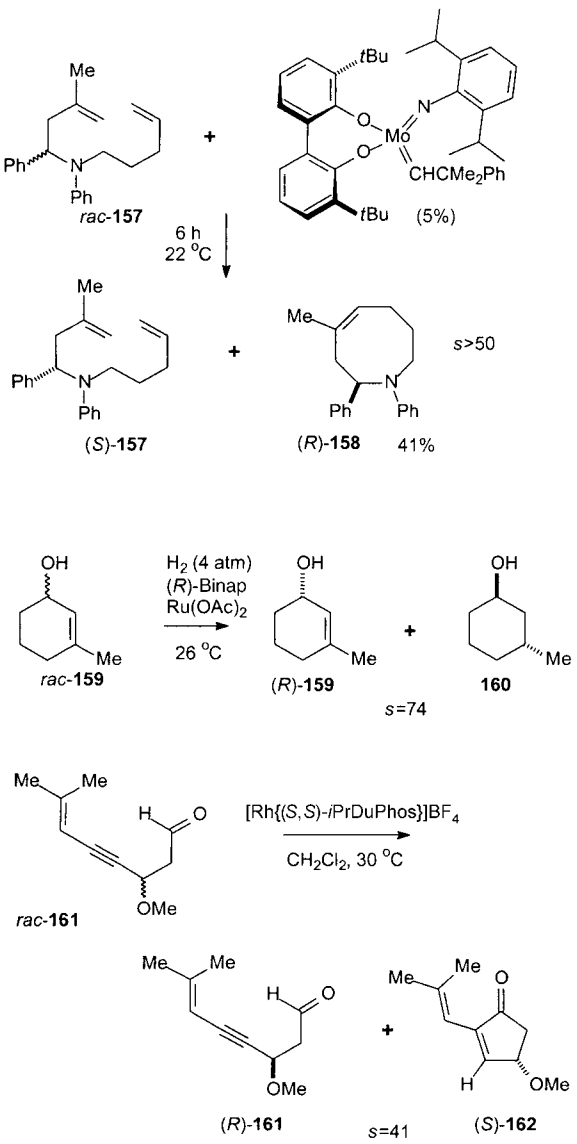


Scheme 27. Reductive KR of imines as reported by Buchwald and coworkers.[100,101]

Epoxidation methodology for the KR of allenes has also appeared.[102c]

Transition-metal-catalyzed alkene KR methodology continues to attract the most attention, and excellent reviews are available.[2o,q,z] The zirconium-catalyzed carbomagnesation of allylic ethers has already been mentioned in the context of DKR (Scheme 19), and simple KR examples are also known.[103] Other interesting examples of metal-catalyzed KR applications include the ring-closing metathesis of dienes (**157** to **158**; Scheme 28),[104] the catalytic hydrogenation of chiral allylic alcohols[105a,b] and unsaturated esters,[105c,d] and the zirconium-catalyzed polymerization of chiral alkenes.[106] Among the examples of hydrogenation, the best allylic alcohol case is shown in Scheme 28 (**159** to **160**).[105b] The substrate *rac*-**159** is a constrained, cyclic allylic alcohol with which the Sharpless epoxidation KR method is not effective, but with which the ruthenium-catalyzed hydrogenation occurs with excellent enantioselectivity ($s = 74$) and, in principle, allows recovery of highly enriched (*R*)-**159** near the 50%-yield limit.

KR based on the catalytic internal cyclization of functionalized alkynes has been reported most recently,[107] for example, the hydroacylation of unsaturated aldehydes (**161**→**162**; Scheme 28).[107b] In an intriguing variation of this process with a related substrate, Tanaka and Fu observed that a similar rhodium catalyst containing the tol-binap ligand allows conversion of one enantiomeric ynal into an alkylidene cyclobutanone while the other enantiomer affords the cyclopentenone as usual.[57] As mentioned in Section 4.3, this example can be classified as an unusual case of regiodivergent RRM. A related KR process that involves internal cyclo-

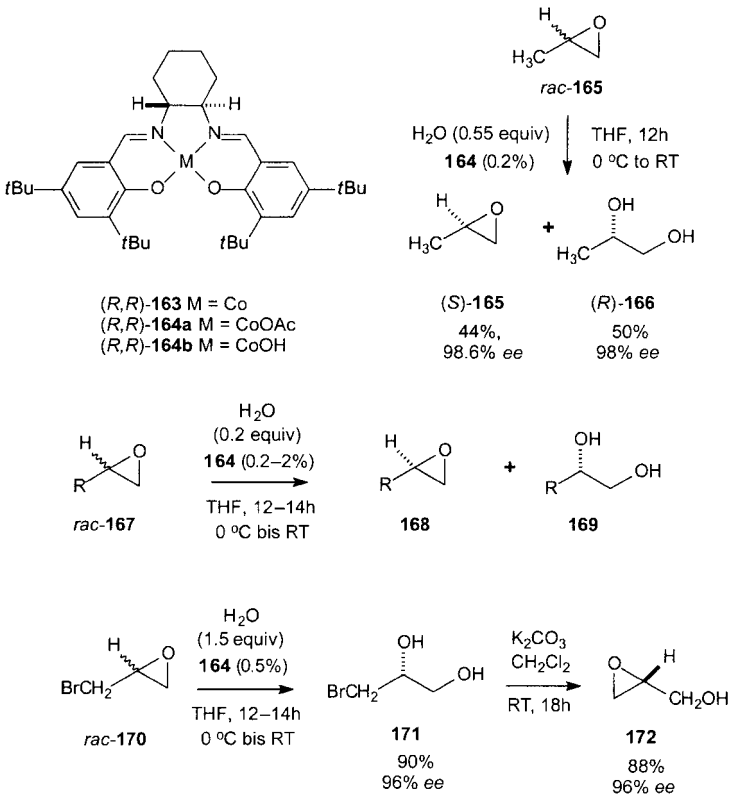


Scheme 28. Examples of kinetic resolution of olefins.

isomerization of oxygen-tethered enynes has also been reported. A chiral rhodium catalyst was used to convert allyl propargyl ethers into highly enantioenriched 4-alkylidene-3-alkenyltetrahydrofurans.[107c] More familiar reactions of chiral alkenes have also been used in KR processes, including thermal cycloadditions[108] and photoinitiated reactions in the presence of chiral additives.[109]

5.4. Epoxides

The Jacobsen methodology for enantioselective epoxide ring opening by nucleophiles is the most important recent development in nonenzymatic KR,[2q,r,t,110,111] especially the hydrolytic ring opening of epoxides (HKR; Scheme 29).[2q,r,110j] An example of the HKR process is illustrated by the conversion of propylene oxide (*rac*-**165**) into a mixture of (*S*)-**165** (44% yield, 98.6% *ee*) and propylene glycol (*R*)-**166**



Scheme 29. Examples of enantioselective epoxide ring-opening reactions with applications in hydrolytic KR (see Table 11).

(50% yield, 98% *ee*) with 0.55 equiv water and the cobalt(III) catalyst **164a** (0.2%).[110j] Both enantiomers of the precatalyst **163** are commercially available, and the conversion into **164a** is easily performed by air oxidation in the presence of acetic acid. Among the advantages of the HKR process are its broad applicability over a range of simple as well as functionalized terminal epoxides, high enantioselectivity, and low catalyst loading. A number of applications of this methodology have already appeared from other research groups.[111]

High enantiomeric purity for the product (*R*)-**166** as well as for the recovered epoxide (*S*)-**165** reflects a remarkably high enantioselectivity $s = 500$.[110j] Most of the other terminal epoxide examples summarized under the generalized structure **167** react with somewhat lower selectivity (Table 11). However, the *s* values are still high enough to permit preparation of diol products **169** with >95% *ee* if epoxide conversion is in the range of 15–20%. The extent of hydrolytic ring opening is controlled by limiting the amount of added water to 0.2 equiv. Recent studies have shown that the consistently high enantioselectivity of the Jacobsen HKR process is the result of an unusual mechanism in which **164a** or **164b** serves as a Lewis acid to activate the epoxide while **164b** is responsible for the nucleophilic cleavage step.[110m] Thus, **164b** functions as a precatalyst as well as a cocatalyst.

Table 11: Hydrolytic epoxide ring opening of *rac*-**167** (see Scheme 29).

R	*s*	R	*s*	R	*s*
CH_3	500	CH_2Cl	190	CO_2CH_3	120
*n*Bu	310	CF_3	620	$COCH_3$	81
CH_2Ph	96	CH_2OTBS	250	C_6H_5	130
c-C_6H_{11}	630	$(CH_2)_2OBn$	82	$CH{=}CH_2$	120
*t*Bu	76	CH_2CO_2Et	130	$CCSiMe_2tBu$	420

An interesting HKR result is observed with *rac*-**170** (Scheme 29), a case in which enantioselectivity is not especially high ($s = 49$).[110j] However, the epoxide substrate undergoes racemization under the reaction conditions to make DKR possible. Thus, treatment of *rac*-**170** with 1.5 equiv water in the presence of catalyst **164** (0.5%) affords the diol **171** in 90% yield (96% *ee*). Further reaction with potassium carbonate affords glycidol **172** in excellent yield and enantiomeric purity. Other interesting KR applications of the Jacobsen catalyst include the catalyzed cleavage of epoxides by other nucleophiles such as azide and phenoxide.[2t]

Several other methods for the KR of epoxides are known. They are not competitive with the Jacobsen procedure for terminal epoxides, but the methodology can be used for 1,2-disubstituted epoxides with which the Jacobsen catalyst is less reactive. Reports of this include epoxide ring opening induced by chiral organometallic agents,[112a–c] and conversion of epoxides into allylic alcohols by elimination in the presence of chiral metal amides.[112d–g] The kinetic resolution of epoxides with a Jacobsen-type salen chromium catalyst and indole as nucleophile has also been reported.[111i]

5.5. Miscellaneous Functional Group Categories

This Section contains a brief overview of the relevant literature citations for the various KR methodologies organized by functional group class: aldehydes (Horner–Emmons olefination,[60] hydroacylation[107]); allylic alcohols (Sharpless epoxidation);[13,55] allylic carboxylates (palladium-catalyzed substitution);[36–38] allylic ethers (carbometallation);[58] alkenes (osmylations);[48,49] atropisomers;[35] azlactone cleavage;[14–16] 1,3-dioxolan-2,4-dione cleavage;[17] enones (hydrogenation,[22] cuprate addition[23e]); Grignard reagents;[24a–f,25] halides (palladium-catalyzed amine coupling);[113] ketones (aldol reaction,[23a] Baeyer–Villiger oxidation,[53] Horner–Emmons olefination,[23b] enolization,[23c] organozinc addition,[23d] reduction,[23f,50,51] Noyori hydrogenation[18–21]); lactones;[28e] organolithium reagents;[28,29] phosphorus compounds;[33,34b–e] and sulfur compounds.[34a,c]

6. Data Treatment and Assay Methods

Recent advances in this area are beyond the scope of this review, and are mentioned only in brief outline to provide some leading references. Mathematical treatments have appeared that focus on DKR,[114] sequential KR (two stages of KR conducted in sequence to improve enantiomeric purity),[115] catalytic KR with enantiomerically impure catalyst,[116] nonlinear effects in KR,[116b–d] and KR involving *meso*/*d,l* isomer mixtures.[117] Access to programs that perform the simple KR calculations of Equation (1) and Equation (2) is now possible through the Internet,[118] and a program for

 © 2005 Wiley-VCH Verlag GmbH & Co. KGaA, Weinheim

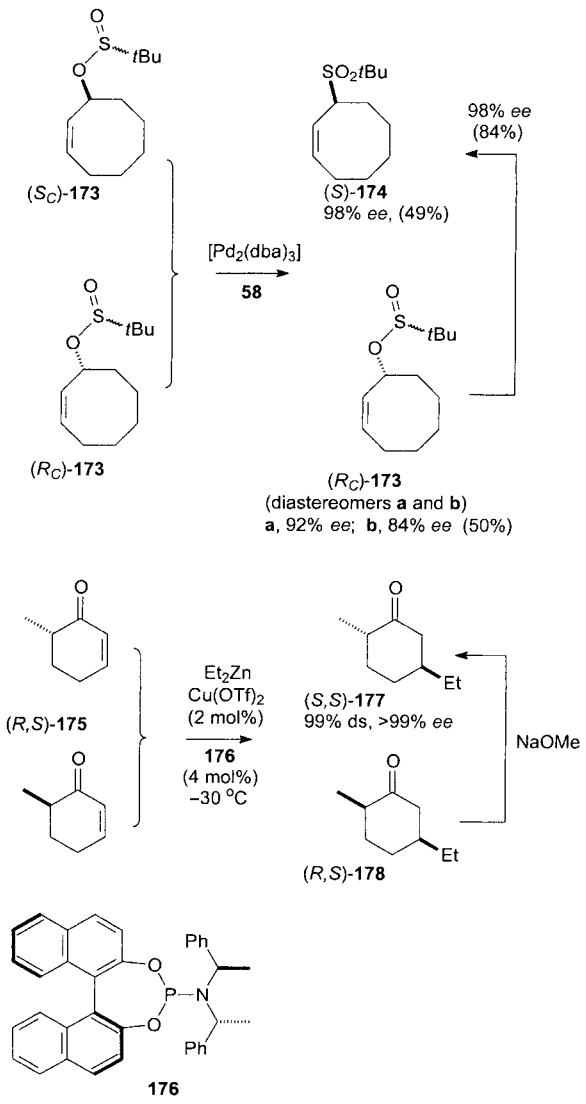
calculating enantioselectivities *s* and plotting *ee* as a function of conversion is available in a free downloadable version.[119]

A variety of assay techniques designed for high-throughput screening have been applied to KR experiments, including methods based on mass spectroscopy[120] and fluorimetry.[121] Techniques have also been reported that speed up the measurement of enantiomeric excess for large numbers of samples.[122] A method for the evaluation of the KR potential of racemic catalysts has also been described.[123]

7. Current State and Perspectives of Nonenzymatic KR

Several KR and DKR techniques have become important for the synthesis of enantiomerically enriched substances on the preparative scale, including the Sharpless epoxidation of allylic alcohols,[13] the Noyori hydrogenation of enolizable ketones,[18] and the Jacobsen hydrolytic cleavage of terminal epoxides.[2q,r,t] Numerous other KR techniques of fundamental interest have served as a proving ground for conceptual advances in enantioselective synthesis. Much of the work to improve KR efficiency can be viewed in this context, and this has been the focus of the current review.

Some of the preparative applications of simple KR will eventually be replaced by advances in enantioselective synthesis methodology with chiral catalysts and achiral substrates, procedures that are not subject to the 50%-yield limit. This limit does not apply to DKR, but neither does the possibility of improving substrate *ee* with conversion. This is the unique advantage of KR, even for modest levels of enantioselectivity *s*. At the current stage of development, almost any chiral substance can be prepared with exceptional levels of enrichment (>99% *ee*) with KR, if yields in the range of 30–40% are acceptable. As the nonenzymatic KR methodologies become more selective and more versatile, new ways will be found to improve efficiency.



Scheme 30. Examples in which kinetic resolution is combined with an equilibration step for the conversion of both enantiomers into a single product.

Addendum (December 8, 2004)

A number of interesting developments in kinetic resolution have been reported since the bulk of this manuscript was written. Many of these have been covered by the insertion of relevant references according to conceptual or functional group categories, but two selected examples of unusual interest are described in Scheme 30. In both cases, kinetic resolution is combined with an equilibration step for the conversion of both enantiomers into a single product. In the first example from racemic **173** (a mixture of two sulfinate diastereomers and enantiomers), Gais and co-workers demonstrated the rearrangement of an allylic sulfinate into the sulfone (*S*)-**174** with the remarkably high 98% *ee* for the apparent product of simple KR.[124] The unusual sequence is initiated with a palladium catalyst in the presence of the Trost chiral diphosphine **58**, and affords the slow-reacting enantiomer (R_C)-**173** together with the original sulfur diastereomers (S_S and R_S, labeled **a** and **b**, respectively), but both with significant enantiomeric enrichment (92% *ee* and 84% *ee*). With a higher loading of both the palladium source and chiral ligand **58**, however, complete conversion was observed and gave only the sulfone (*S*)-**174**, again with 98% *ee*. This result requires some form of deracemization and equilibration at the sulfur and carbon atoms on the way to products, and was attributed to the formation of ion pair intermediates.

In the second example of Scheme 30, Alexakis and co-workers reported an intriguing 1,4-addition process from racemic enone **175** in which stereodivergent RRM occurs in the first stage to afford the diastereomers (*S*,*S*)-**177** and (*R*,*S*)-**178**.[125] The diastereomer mixture was then treated with NaOMe to equilibrate the enolizable α-carbon, resulting in the conversion of the *cis* diastereomer **178** into the *trans* diastereomer **177**. Because this process does not alter configuration at the β′ carbon atom, the net result is an enantioconvergent process in which (*R*,*S*)-**175** is converted into (*S*,*S*)-**177** with excellent *ee*.

 © 2005 Wiley-VCH Verlag GmbH & Co. KGaA, Weinheim

Both of the examples in Scheme 30 were selected to underscore the principal message of this account. Many of the recent extensions and modifications of simple KR are academically fascinating, but not always practical. On the other hand, the investigation of simple KR phenomena has resulted in permutations such as DKR or stereodivergent RRM. As shown by the examples of Scheme 30, these adaptations can be exceptionally efficient.

Received: June 1, 2004
Published online: June 8, 2005

[1] H. B. Kagan, J. C. Fiaud, *Top. Stereochem.* **1988**, *18*, 249 – 330.
[2] Reviews of Sharpless epoxidation: a) M. G. Finn, K. B. Sharpless in *Asymmetric Synthesis Vol. 5* (Ed.: J. D. Morrison), Academic Press, New York, **1985**, pp. 247 – 308; b) K. B. Sharpless, T. R. Verhoeven, *Aldrichimica Acta* **1979**, *12*, 63 – 74; c) A. Pfenninger, *Synthesis* **1986**, 89 – 116; d) "Sharpless KR": D. B. Smith, S. L. Schreiber, *Chemtracts: Org. Chem.* **1988**, *1*, 26 – 28; DKR reviews: e) B. Ganem, *Chemtracts: Org. Chem.* **1990**, *3*, 165 – 167; f) R. Noyori, M. Tokunaga, M. Kitamura, *Bull. Chem. Soc. Jpn.* **1995**, *68*, 36 – 56; g) R. S. Ward, *Tetrahedron: Asymmetry* **1995**, *6*, 1475 – 1490; h) S. Caddick, K. Jenkins, *Chem. Soc. Rev.* **1996**, *25*, 447 – 456; i) R. Sturmer, *Angew. Chem.* **1997**, *109*, 1221 – 1222; *Angew. Chem. Int. Ed. Engl.* **1997**, *36*, 1173 – 1174; j) M. T. El Gihani, J. M. J. Williams, *Curr. Opin. Chem. Biol.* **1999**, *3*, 11 – 15; k) V. Ratovelomanana-Vidal, J.-P. Genet, *Can. J. Chem.* **2000**, *78*, 846 – 851; l) F. F. Huerta, A. B. E. Minidis, J.-E. Baeckvall, *Chem. Soc. Rev.* **2001**, *30*, 321 – 331; m) H. Pellissier, *Tetrahedron* **2003**, *59*, 8291 – 8327; Parallel kinetic resolution: n) J. Eames, *Angew. Chem.* **2000**, *112*, 913 – 916; *Angew. Chem. Int. Ed.* **2000**, *39*, 885 – 888; general reviews of preparative KR: o) A. H. Hoveyda, M. T. Didiuk, *Curr. Org. Chem.* **1998**, *2*, 489 – 526; p) G. R. Cook, *Curr. Org. Chem.* **2000**, *4*, 869 – 885; q) J. M. Keith, J. F. Larrow, E. N. Jacobsen, *Adv. Synth. Catal.* **2001**, *343*, 5 – 26; reviews of epoxide cleavage: r) "Jacobsen KR": M. Tokunaga, J. F. Larrow, F. Kakiuchi, E. N. Jacobsen, *Science* **1997**, *277*, 936 – 938; s) A. C. Rondon, J. S. Panek, *Chemtracts* **1997**, *10*, 1058 – 1061; t) E. N. Jacobsen, *Acc. Chem. Res.* **2000**, *33*, 421 – 431; Reviews of alcohol KR: u) P. Somfai, *Angew. Chem.* **1997**, *109*, 2849 – 2851; *Angew. Chem. Int. Ed. Engl.* **1997**, *36*, 2731 – 2733; v) Y. O. Long, L. A. Paquette, *Chemtracts* **2000**, *13*, 1 – 8; w) G. C. Fu, *Acc. Chem. Res.* **2000**, *33*, 412 – 420; x) K. M. Nicholas, E. M. Ferreira, B. M. Stoltz, D. R. Jensen, J. S. Pugsley, M. S. Sigman, *Chemtracts* **2001**, *14*, 654 – 658; y) E. R. Jarvo, S. J. Miller, *Tetrahedron* **2002**, *58*, 2481 – 2495; *Comprehensive Asymmetric Catalysis*, *Suppl. 1*, (Eds.: E. N. Jacobsen, A. Pfaltz, H. Yamamoto), Springer, Heidelberg, **2004**, chap. 43; Miscellaneous reviews: catalysis: z) J. M. Brown, *Chem. Ind.* **1988**, 612 – 617; P. I. Dalko, L. Moisan, *Angew. Chem.* **2001**, *113*, 3840 – 3864; *Angew. Chem. Int. Ed.* **2001**, *40*, 3726 – 3748; axial chirality: aa) G. Bringmann, D. Menche, *Acc. Chem. Res.* **2001**, *34*, 615 – 624; Horner–Wadsworth–Emmons reaction: bb) M. Yamaguchi, M. Hirama, *Chemtracts: Org. Chem.* **1994**, *7*, 401 – 405; Organolithium compounds: cc) H. Kunz, H. Waldmann, *Chemtracts: Org. Chem.* **1990**, *3*, 421 – 424; Ferrocenes: dd) H. B. Kagan, O. Riant, *Adv. Asymmetric Synth.* **1997**, *2* 189 – 235; Terminology and stereochemical classification: ee) K. Faber, *Chem. Eur. J.* **2001**, *7*, 5004 – 5010.
[3] Reviews of enzymatic KR: Lipases: a) C. J. Sih, S.-H. Wu, *Top. Stereochem.* **1989**, *19*, 63; b) C.-S. Chen, C. J. Sih, *Angew. Chem.* **1989**, *101*, 711 – 724; *Angew. Chem. Int. Ed. Engl.* **1989**, *28*, 695 – 707; c) A. M. Klibanov, *Acc. Chem. Res.* **1990**, *23*, 114 – 120; d) P. Andersch, M. Berger, J. Hermann, K. Laumen, M. Lobell, R. Seemayer, C. Waldinger, M. P. Schneider, *Methods Enzymol.* **1997**, *286*, 406 – 433; e) J. J. Lalonde, M. N. Navia, A. L. Margolin, *Methods Enzymol.* **1997**, *286*, 443 – 464; f) R. D. Schmid, R. Verger, *Angew. Chem.* **1998**, *110*, 1694 – 1720; *Angew. Chem. Int. Ed.* **1998**, *37*, 1609 – 1633; g) M. T. Reetz, K. E. Jaeger, *Chem. Phys. Lipids* **1998**, *93*, 3 – 14; h) S. M. Roberts, *J. Chem. Soc. Perkin Trans. 1* **1999**, 1 – 21; i) V. E. U. Costa, H. L. N. de Amorim, *Quimica* **1999**, *22*, 863 – 873; j) M. T. Reetz, M. Hermes, M. H. Becker, *Appl. Microbiol. Biotechnol.* **2001**, *55*, 531 – 536; Miscellaneous reviews of enzymatic KR: k) S. M. Roberts, N. J. Turner, A. J. Willetts, *Chimia* **1993**, *47*, 85 – 92; l) H. Stecher, K. Faber, *Synthesis* **1997**, 1 – 16; m) R. V. Orru, K. Faber, *Curr. Opin. Chem. Biol.* **1999**, *3*, 16 – 21; n) M. T. Reetz, K. E. Jaeger, *Chem. Eur. J.* **2000**, *6*, 407 – 412; o) A. Archelas, R. Furstoss, *Curr. Opin. Chem. Biol.* **2001**, *5*, 112 – 119; p) A. Steinreiber, K. Faber, *Curr. Opin. Chem. Biol.* **2001**, *5*, 12, 552 – 558.
[4] G. P. Moss, *Pure Appl. Chem.* **1996**, *68*, 2193 – 2222.
[5] E. L. Eliel, S. H. Wilen, L. N. Mander, *Stereochemistry of Organic Compounds*, Wiley, New York, **1994**.
[6] M. L. Pasteur, *C. R. Hebd. Seances Acad. Sci.* **1858**, *46*, 615 – 618.
[7] E. Fischer, *Ber. Dtsch. Chem. Ges.* **1890**, *23*, 370 – 394.
[8] a) W. Marckwald, A. McKenzie, *Ber. Dtsch. Chem. Ges.* **1899**, *32*, 2130 – 2136; b) W. Marckwald, A. McKenzie, *Ber. Dtsch. Chem. Ges.* **1901**, *34*, 469 – 478; For quantitation of the results, see: E. P. Schultz, P. A. F. Lehmann, *Rev. Soc. Quim. Mex.* **1969**, *13*, 167A – 170A [*Chem. Abstr.* **1970**, 32039].
[9] H. D. Dakin, *J. Physiol.* **1904**, *30*, 253 – 263.
[10] G. Bredig, K. Fajans, *Ber. Dtsch. Chem. Ges.* **1908**, *41*, 752 – 763. K. Fajans, *Z. Phys. Chem.* **1910**, *73*, 25 – 96.
[11] W. Kuhn, E. Knopf, *Z. Phys. Chem. Abt. A* **1930**, 7, 292 – 310.
[12] C. Balavoine, A. Moradpour, H. B. Kagan, *J. Am. Chem. Soc.* **1974**, *96*, 5152 – 5157.
[13] V. S. Martin, S. S. Woodard, T. Katsuki, Y. Yamada, M. Ikeda, K. B. Sharpless, *J. Am. Chem. Soc.* **1981**, *103*, 6237 – 6240.
[14] F. Weygand, W. Steglich, X. Barocio de la Lama, *Tetrahedron Suppl.* **1966**, *8*, 9 – 13.
[15] J. Liang, J. C. Ruble, G. C. Fu, *J. Org. Chem.* **1998**, *63*, 3154 – 3155. K. Gottwald, D. Seebach, *Tetrahedron* **1999**, *55*, 723 – 738.
[16] J. Z. Crich, R. Brieva, P. Marquart, R.-L. Gu, S. Flemming, C. J. Sih, *J. Org. Chem.* **1993**, *58*, 3252 – 3258, and references therein.
[17] L. Tang, L. Deng, *J. Am. Chem. Soc.* **2002**, *124*, 2870 – 2871.
[18] R. Noyori, T. Ikeda, T. Ohkuma, M. Widhalm, M. Kitamura, H. Takaya, S. Akutagawa, N. Sayo, T. Saito, *J. Am. Chem. Soc.* **1989**, *111*, 9134 – 9135.
[19] E. Coulon, M. C. Cano de Andrade, V. Ratovelomanana-Vidal, J.-P. Genet, *Tetrahedron Lett.* **1998**, *39*, 6467 – 6470.
[20] K. Makino, N. Okamoto, O. Hara, Y. Hamada, *Tetrahedron: Asymmetry* **2001**, *12*, 1757 – 1762; K. Makino, T. Goto, Y. Hiroki, Y. Hamada, *Angew. Chem.* **2004**, *116*, 900 – 902; *Angew. Chem. Int. Ed.* **2004**, *43*, 882 – 884.
[21] a) T. Matsumoto, T. Murayama, S. Mitsuhashi, T. Miura, *Tetrahedron Lett.* **1999**, *40*, 5043 – 5046; b) T. Ohkuma, H. Ooka, M. Yamakawa, T. Ikariya, R. Noyori, *J. Org. Chem.* **1996**, *61*, 4872 – 4873; c) N. J. Alcock, I. Mann, P. Peach, M. Wills, *Tetrahedron: Asymmetry* **2002**, *13*, 2485 – 2488.
[22] V. Jurkauskas, S. L. Buchwald, *J. Am. Chem. Soc.* **2002**, *124*, 2892 – 2893.
[23] KR of ketones: aldol reaction: a) K. Chibale, S. Warren, *Tetrahedron Lett.* **1992**, *33*, 4369 – 4372; C. Agami, N. Platzer, C. Puchot, H. Sevestre, *Tetrahedron* **1987**, *43*, 1091 – 1098; Horner–Emmons reaction: b) K. Narasaka, E. Hidai, Y. Hayashi, J. L. Gras, *J. Chem. Soc. Chem. Commun.* **1993**, 102 – 104; T. Rein, J. Anvelt, A. Soone, R. Kreuder, C. Wulff, O. Reiser, *Tetrahedron Lett.* **1995**, *36*, 2303 – 2306; M. Yamaguchi, M.

 © 2005 Wiley-VCH Verlag GmbH & Co. KGaA, Weinheim

Hirama, *Chemtracts: Org. Chem.* **1994**, 7, 401 – 405; K. Tanaka, T. Watanabe, K. Shimamoto, P. Sahakitpichan, K. Fuji, *Tetrahedron Lett.* **1999**, *40*, 6599 – 6602; Enantioselective deprotonation: c) H. D. Kim, H. Kawasaki, M. Nakajima, K. Koga, *Tetrahedron Lett.* **1989**, *30*, 6537 – 6540; K. Bambridge, N. S. Simpkins, B. P. Clark, *Tetrahedron* Lett. **1992**, *33*, 8141 – 8144; P. Coggins, N. S. Simpkins, *Synlett* **1992**, 313 – 314; K. Bambridge, B. P. Clark, N. S. Simpkins, *J. Chem. Soc. Perkin Trans. 1* **1995**, 2535 – 2541; H-D. Kim, *Arch. Pharmacal Res.* **1995**, *18*, 369 – 370; D. E. Ward, W.-L. Lu, *J. Am. Chem. Soc.* **1998**, *120*, 1098 – 1099; D. A. Greenhalgh, N. S. Simpkins, *Synlett* **2002**, 2074 – 2076; Alkylzinc addition: d) M. Hayashi, H. Miwata, N. Oguni, *J. Chem. Soc. Perkin Trans. 1* **1991**, 1167 – 1171; Cuprate addition: e) K. H. Ahn, R. B. Klassen, S. J. Lippard, *Organometallics* **1990**, *9*, 3178 – 3181; R. Naasz, L. A. Arnold, A. J. Minnaard, B. L. Feringa, *Angew. Chem.* **2001**, *113*, 953 – 965; *Angew. Chem. Int. Ed.* **2001**, *40*, 927 – 930; L. M. Mediavilla, A. Alexakis, N. Krause, *Tetrahedron Lett.* **2002**, *43*, 7887 – 7890; Reduction with $ClB(ipc)_2$ (ipc = isopinocampheyl): f) P. V. Ramachandran, G.-M. Chen, H. C. Brown, *J. Org. Chem.* **1996**, *61*, 88 – 94.

[24] KR of organometallic reagents; C–Mg bonds: a) J. D. Morrison, A. Tomash, R. W. Ridgeway, *Tetrahedron Lett.* **1969**, *10*, 565 – 567; b) G. Consiglio, C. Botteghi, *Helv. Chim. Acta* **1973**, *56*, 460 – 463; c) N. Nomura, T. V. RajanBabu, *Tetrahedron Lett.* **1997**, *38*, 1713 – 1716; d) G. C. Lloyd-Jones, C. P. Butts, *Tetrahedron* **1998**, *54*, 901 – 914; e) R. Stürmer, *Angew. Chem.* **1990**, *102*, 62; *Angew. Chem. Int. Ed. Engl.* **1990**, *29*, 59 – 60; C–B bonds: f) N. N. Joshi, C. Pyun, V. K. Mahindroo, B. Singaram, H. C. Brown, *J. Org. Chem.* **1992**, *57*, 504 – 511; C-Zn bonds: g) J.-F. Poisson, J. F. Normant, *J. Am. Chem. Soc.* **2001**, *123*, 4639 – 4640.

[25] a) T. Hayashi, M. Konishi, M. Fukushima, T. Mise, M. Kagotani, M. Tajika, M. Kumada, *J. Am. Chem. Soc.* **1982**, *104*, 180 – 186; b) T. Hayashi, M. Konishi, M. Fukushima, K. Kanehira, T. Hioki, M. Kumada, *J. Org. Chem.* **1983**, *48*, 2195 – 2202; c) T. Hayashi, M. Konishi, Y. Okamoto, K. Kabeta, M. Kumada, *J. Org. Chem.* **1986**, *51*, 3772 – 3781.

[26] A. Basu, S. Thayumanavan, *Angew. Chem.* **2002**, *114*, 740 – 763; *Angew. Chem. Int. Ed.* **2002**, *41*, 716 – 738.

[27] a) R. W. Hoffmann, T. Ruehl, J. Harbach, *Liebigs Ann. Chem.* **1992**, 719 – 724; b) R. W. Hoffmann, T. Ruehl, F. Chemla, T. Zahneisen, *Liebigs Ann. Chem.* **1992**, 725 – 730; c) R. Hirsch, R. W. Hoffmann, *Chem. Ber.* **1992**, *125*, 975 – 982.

[28] a) D. Hoppe, T. Hense, *Angew. Chem.* **1997**, *109*, 2376 – 2410; *Angew. Chem. Int. Ed. Engl.* **1997**, *36*, 2282 – 2316; b) P. Beak, A. Basu, D. J. Gallagher, Y. S. Park, S. Thayumanavan, *Acc. Chem. Res.* **1996**, *29*, 552 – 560; c) M. J. Woltering, R. Froehlich, B. Wibbeling, D. Hoppe, *Synlett* **1998**, 797 – 800; J. Van Bebber, H. Ahrens, R. Frohlich, D. Hoppe, *Chem. Eur. J.* **1999**, *5*, 1905 – 1916; B. Weber, J. Schwerdtfeger, R. Froehlich, A. Gohrt, D. Hoppe, *Synthesis* **1999**, 1915 – 1924; H. Laqua, R. Froehlich, B. Wibbeling, D. Hoppe, *J. Organomet. Chem.* **2001**, *624*, 96 – 104; d) D. J. Pippel, M. D. Curtis, H. Du, P. Beak, *J. Org. Chem.* **1998**, *63*, 2 – 3; e) S. H. Lim, P. Beak, *Org. Lett.* **2002**, *4*, 2657 – 2660; f) I. Coldham, S. Dufour, T. F. N. Haxell, S. Howard, G. P. Vennall, *Angew. Chem.* **2002**, *114*, 4043 – 4045; *Angew. Chem. Int. Ed.* **2002**, *41*, 3887 – 3889.

[29] P. Beak, D. R. Anderson, M. D. Curtis, J. M. Laumer, D. J. Pippel, G. A. Weisenburger, *Acc. Chem. Res.* **2000**, *33*, 715 – 727.

[30] a) See Ref. [5], pp. 1192–1193 for the definitions; b) The terminology of DTR does not distinguish between the process in solution (asymmetric transformation of the first kind) and the very different heterogeneous experiment in which crystallization of the labile intermediate is responsible for the high selectivity. Important information may be difficult to find in the literature unless authors continue to use the older asymmetric transformation terminology as appropriate for the first stages of DTR.

[31] J. Jacques, A. Collet, S. H. Wilen, *Enantiomers, Racemates, and Resolutions*, Krieger, Malabar, **1994**, chap. 6.

[32] E. Vedejs, R. W. Chapman, S. Lin, M. Muller, D. R. Powell, *J. Am. Chem. Soc.* **2000**, *122*, 3047 – 3052; E. Vedejs, Y. Donde, *J. Org. Chem.* **2000**, *65*, 2337 – 2343, and references therein.

[33] B. Wolfe, T. Livinghouse, *J. Am. Chem. Soc.* **1998**, *120*, 5116 – 5117.

[34] a) N. Khiar, F. Alcudia, J.-L. Espartero, L. Rodriguez, I. Fernandez, *J. Am. Chem. Soc.* **2000**, *122*, 7598 – 7599; N. Khiar, C. S. Araujo, F. Alcudia, I. Fernandez, *J. Org. Chem.* **2002**, *67*, 345 – 356; b) O. I. Kolodiazhnyi, E. V. Gryshkun, *Tetrahedron: Asymmetry* **1996**, *7*, 967 – 970; c) O. I. Kolodiazhnyi, E. V. Gryshkun, N. V. Andrushko, M. Freytag, P. G. Jones, R. Schmutzler, *Tetrahedron: Asymmetry* **2003**, *14*, 181 – 183; d) Y. Hayakawa, M. Hyodo, K. Kimura, *Chem. Commun.* **2003**, 1704 – 1705; e) J. R. Moncarz, T. J. Brunker, D. S. Glueck, R. D. Sommer, A. L. Rheingold, *J. Am. Chem. Soc.* **2003**, *125*, 1180 – 1181; f) F. A. Davis, J. M. Billmers, *J. Org. Chem.* **1983**, *48*, 2672 – 2675; M. L. Phillips, D. M. Berry, J. A. Panetta, *J. Org. Chem.* **1992**, *57*, 4047 – 4049; N. Komatsu, M. Hashizume, T. Sugita, S. Uemura, *J. Org. Chem.* **1993**, *58*, 4529 – 4533; A. Scettri, F. Bonadies, A. Lattanzi, A. Senatore, A. Soriente, *Tetrahedron: Asymmetry* **1996**, *7*, 657 – 658; A. Lattanzi, F. Bonadies, A. Senatore, A. Soriente, A. Scettri, *Tetrahedron: Asymmetry* **1997**, *8*, 2473 – 2478; M. L. Phillips, J. A. Panetta, *Tetrahedron: Asymmetry* **1997**, *8*, 2109 – 2114; W. Adam, M. N. Korb, K. J. Roschman, C. R. Saha-Moeller, R. Chantu, *J. Org. Chem.* **1998**, *63*, 3423 – 3428; g) H. J. Bestmann, I. Tomoskozi, *Tetrahedron* **1968**, *24*, 3299 – 3319; J. M. Brown, P. J. Maddox, *Chirality* **1991**, *3*, 345 – 354; A. Goti, S. Cicchi, A. Brandi, K. M. Pietrusiewicz, *Tetrahedron: Asymmetry* **1991**, *2*, 1371 – 1378; J. Clayden, E. W. Collington, S. Warren, *Tetrahedron Lett.* **1992**, *33*, 7043 – 7046; J. Clayden, E. W. Collington, S. Warren, *Tetrahedron Lett.* **1993**, *34*, 1327 – 1330; A. Brandi, S. Cicchi, A. Goti, M. Koprowski, K. M. Pietrusiewicz, *J. Org. Chem.* **1994**, *59*, 1315 – 1318; J. Clayden, S. Warren, *J. Chem. Soc. Perkin Trans. 1* **1994**, 2811 – 2823; P. Kelbasinski, P. Goralczyk, M. Mikolajczyk, M. W. Wieczorek, W. R. Majzner, *Tetrahedron: Asymmetry* **1998**, *9*, 2641 – 2650; P. B. Wyatt, P. Blakskjaer, *Tetrahedron Lett.* **1999**, *40*, 6481 – 6483; K. M. Pietrusiewitz, W. Holody, M. Koprowski, S. Cicchi, A. Goti, A. Brandi, *Phosphorus Sulfur Silicon Relat. Elem.* **1999**, *144–146*, 389 – 392; W. Perlikowska, M. Gouygou, J.-C. Daran, G. Balavoine, M. Mikolajczyk, *Tetrahedron Lett.* **2001**, *42*, 7841 – 7845.

[35] a) G. Bringmann, T. Pabst, P. Henschel, J. Kraus, K. Peters, E.-M. Peters, D. S. Rycroft, J. D. Connolly, *J. Am. Chem. Soc.* **2000**, *122*, 9127 – 9133; b) V. Chan, J. G. Kim, C. Jimeno, P. J. Carroll, P. J. Walsh, *Org. Lett.* **2004**, *6*, 2051 – 2053; c) Simple KR of axially chiral substrates: T. Itoh, J.-I. Chika, *J. Org. Chem.* **1995**, *60*, 4968 – 4969; G. Bringmann, J. Hinrichs, *Tetrahedron: Asymmetry* **1997**, *8*, 4121 – 4126; J. Blum, D. Gelman, Z. Aizenshtat, S. Wernik, H. Schumann, *Tetrahedron Lett.* **1998**, *39*, 5611 – 5614.

[36] KR of B-allyl complexes with oxygen nucleophiles: a) B. M. Trost, E. J. Hembre, *Tetrahedron Lett.* **1999**, *40*, 219 – 222; B. J. Lüssem, H.-J. Gais, *J. Am. Chem. Soc.* **2003**, *125*, 6066 – 6067; C. Fischer, C. Defieber, T. Suzuki, E. M. Carreira, *J. Am. Chem. Soc.* **2004**, *126*, 1628 – 1629; Sulfur nucleophiles: b) H.-J. Gais, H. Eichelmann, N. Spalthoff, F. Gerhards, M. Frank, G. Raabe, *Tetrahedron: Asymmetry* **1998**, *9*, 235 – 248; H.-J. Gais, N. Spalthoff, T. Jagusch, M. Frank, G. Raabe, *Tetrahedron Lett.* **2000**, *41*, 3809 – 3812; H.-J. Gais, T. Jagusch, N. Spalthoff, F. Gerhards, M. Frank, G. Raabe, *Chem. Eur. J.* **2003**, *9*, 4202 – 4221; H.-J. Gais, T. Jagusch, O. Bondarev, *J. Org. Chem.* **2004**,

 © 2005 Wiley-VCH Verlag GmbH & Co. KGaA, Weinheim

69, 2731 – 2736; Regiodivergent RRM: c) F. Ozawa, A. Kubo, Y. Matsumoto, T. Hayashi, E. Nishioka, K. Yanagi, K. Moriguchi, *Organometallics* **1993**, *12*, 4188 – 4196; Carbon nucleophiles: d) S. R. Gilbertson, P. Lan, *Org. Lett.* **2001**, *3*, 2237 – 2240; J. W. Faller, J. C. Wilt, J. Parr, *Org. Lett.* **2004**, *6*, 1301 – 1304; KR and DKR: e) D. L. Hughes, M. Palucki, N. Yasuda, R. A. Reamer, P. J. Reider, *J. Org. Chem.* **2002**, *67*, 2762 – 2768.

[37] a) B. M. Trost, F. D. Toste, *J. Am. Chem. Soc.* **1999**, *121*, 3543 – 3544; b) B. M. Trost, F. D. Toste, *J. Am. Chem. Soc.* **2003**, *125*, 3090 – 3100; c) B. M. Trost, O. R. Thiel, H.-C. Tsui, *J. Am. Chem. Soc.* **2002**, *124*, 11616 – 11617; d) B. M. Trost, R. C. Bunt, R. C. Lemoine, T. L. Calkins, *J. Am. Chem. Soc.* **2000**, *122*, 5968 – 5976; e) T. Nishimata, K. Yamaguchi, M. Mori, *Tetrahedron Lett.* **1999**, *40*, 5713 – 5716; f) J. M. Longmire, B. Wang, X. Zhang, *Tetrahedron Lett.* **2000**, *41*, 5435 – 5439.

[38] a) B. M. Trost, D. E. Patterson, E. J. Hembre, *J. Am. Chem. Soc.* **1999**, *121*, 10834 – 10835; For related conduritol examples, see B. M. Trost, D. E. Patterson, E. J. Hembre, *Chem. Eur. J.* **2001**, *7*, 3768 – 3775; b) The key events of Scheme 12 were described with modified terminology, and were referred to as dynamic kinetic asymmetric transformations, or DYKAT. A personal communication from Prof. Trost provides the following definition: "*Dynamic kinetic asymmetric transformation is the preferential formation of one enantiomer of a product in a chemical transformation arising from both enantiomers of a racemic starting material that is structurally different from the starting material.*" This definition of DYKAT has the same meaning as generally accepted for DKR, but is more accurate in the sense that "resolution" is usually defined to imply the recovery of resolved, unreacted substrate.

[39] S. E. Schaus, E. N. Jacobsen, *Tetrahedron Lett.* **1996**, *37*, 7937 – 7940.

[40] DKR: a) Acylation of axially chiral amides: S. Yamada, E. Noguchi, *Tetrahedron Lett.* **2001**, *42*, 3621 – 3624; b) Wittig olefination of axially chiral aldehyde: W.-M. Dai, C. W. Lau, *Tetrahedron Lett.* **2001**, *42*, 2541 – 2544; c) Zirconaaziridine carboxylation: J. A. Tunge, D. A. Gately, J. R. Norton, *J. Am. Chem. Soc.* **1999**, *121*, 4520 – 4521; J.-X. Chen, J. A. Tunge, J. R. Norton, *J. Org. Chem.* **2002**, *67*, 4366 – 4369; d) Metallocene–binap–Rh complex: T. K. Hollis, L.-S. Wang, F. Tham, *J. Am. Chem. Soc.* **2000**, *122*, 11737 – 11738; e) α-Bromo esters with pseudoephedrine: S.-K. Lee, J. Nam, Y. S. Park, *Synlett* **2002**, 790 – 792; f) The terminology of DKR has also been applied to reactions of equilibrating substrates derivatized with chiral auxiliaries.[2g,h] We do not classify these examples under DKR because the equilibria involve interconversion of enantiomerically pure diastereomers, not enantiomers in a racemate. These are examples of asymmetric transformation as currently defined by Eliel, not resolutions (see Ref. [5], pp. 1192–1193). For representative examples, see: J. A. O'Meara, M. Jung, T. Durst, *Tetrahedron Lett.* **1995**, *36*, 5096 – 5099; H. Kubota, A. Kubo, M. Takahashi, R. Shimizu, T. Date, K. Okamura, K.-I. Nunami, *J. Org. Chem.* **1995**, *60*, 6776 – 6784; A. Kubo, H. Kubota, M. Takahashi, K.-I. Nunami, *Tetrahedron Lett.* **1996**, *37*, 4957 – 4960; S. Caddick, K. Jenkins, *Tetrahedron Lett.* **1996**, *37*, 1301 – 1304; G. R. Cook, P. S. Shanker, K. Pararajasingham, *Angew. Chem.* **1999**, *111*, 226 – 228; *Angew. Chem. Int. Ed.* **1999**, *38*, 110 – 113; g) DKR of Morita–Baylis–Hillman adducts by chiral phosphine catalyzed allylic amination: C.-W. Cho, J.-R. Kong, M. J. Krische, *Org. Lett.* **2004**, *6*, 1337 – 1339; h) DKR in the allylation of benzylic trimethylsilyl ethers and of aminals and acetal derivatives with allyltrimethylsilane in the presence of a catalytic chiral titanium complex as a Lewis acid: M. Braun, W. Kotter, *Angew. Chem.* **2004**, *116*, 520 – 523; *Angew. Chem. Int. Ed.* **2004**, *43*, 515 – 517.

[41] a) H. Danda, T. Nagatomi, A. Maehara, T. Umemura, *Tetrahedron* **1991**, *47*, 8701 – 8716; H. Danda, Y. Furukawa, T. Umemura, *Synlett* **1991**, 441 – 442; b) S. Takano, M. Suzuki, K. Ogasawara, *Tetrahedron: Asymmetry* **1993**, *4*, 1043 – 1046; c) M.-J. Kim, I. Lee, *Synlett* **1993**, 767 – 768; d) E. Vänttinen, L. Kanerva, *Tetrahedron: Asymmetry* **1995**, *6*, 1779 – 1786.

[42] R. P. Discordia, D. C. Dittmer, *J. Org. Chem.* **1990**, *55*, 1414 – 1415.

[43] X. Feng, L. Shu, Y. Shi, *J. Org. Chem.* **2002**, *67*, 2831 – 2836.

[44] Z. K. Sweeney, J. L. Salsman, R. A. Andersen, R. G. Bergman, *Angew. Chem.* **2000**, *112*, 2429 – 2433; *Angew. Chem. Int. Ed.* **2000**, *39*, 2339 – 2343.

[45] J. P. Guetté, A. Horeau, *Bull. Soc. Chim. Fr.* **1967**, 1747 – 1752.

[46] a) H. B. Kagan, *Croat. Chem. Acta* **1996**, *68*, 669 – 680; b) H. B. Kagan, *Tetrahedron* **2001**, *57*, 2449 – 2468.

[47] E. Vedejs, X. Chen, *J. Am. Chem. Soc.* **1997**, *119*, 2584 – 2585.

[48] a) M. S. VanNieuwenhze, K. B. Sharpless, *J. Am. Chem. Soc.* **1993**, *115*, 7864 – 7865; b) E. J. Corey, M. C. Noe, A. Guzman-Perez, *J. Am. Chem. Soc.* **1995**, *117*, 10817 – 10824; c) J. M. Gardiner, M. Noerret, I. H. Sadler, *Chem. Commun.* **1996**, 2709 – 2710; d) J. M. Gardiner, M. Norret, I. H. Sadler, *Tetrahedron Lett.* **1996**, *37*, 8447 – 8450; e) E. J. Corey, A. Guzman-Perez, *Tetrahedron Lett.* **1997**, *38*, 5941 – 5944; f) B. B. Lohray, E. Nandanan, V. Bhushan, *Indian J. Chem.* **1997**, *35*, 226 – 231; g) D. P. G. Hamon, K. L. Tuck, H. S. Christie, *Tetrahedron* **2001**, *57*, 9499 – 9508; h) R. Rios, C. Jimeno, P. J. Carroll, P. J. Walsh, *J. Am. Chem. Soc.* **2002**, *124*, 10272 – 10273; i) For simple KR of fullerene C_{76} by osmylation, see: J. M. Hawkins, A. Meyer, *Science* **1993**, *260*, 1918 – 1920.

[49] M. Kurosu, Y. Kishi, *J. Org. Chem.* **1998**, *63*, 6100 – 6101.

[50] Stereodivergent RRM in the enzymatic reduction of racemic ketones: a) M. Nakazaki, H. Chikamatsu, K. Naemura, Y. Hirose, T. Shimizu, M. Asao, *J. Chem. Soc. Chem. Commun.* **1978**, 668 – 670; b) M. Nakazaki, H. Chikamatsu, Y. Hirose, T. Shimizu, *J. Org. Chem.* **1979**, *44*, 1043 – 1048; c) M. Nakazaki, H. Chikamatsu, K. Naemura, M. Nishino, H. Murakami, M. Asao, *J. Org. Chem.* **1979**, *44*, 4588 – 4593; d) J. Davies, J. B. Jones, *J. Am. Chem. Soc.* **1979**, *101*, 5405 – 5410; e) M. Nakazaki, H. Chikamatsu, K. Naemura, M. Asao, *J. Org. Chem.* **1980**, *45*, 4432 – 4440; f) M. Nakazaki, H. Chikamatsu, M. Asao, *J. Org. Chem.* **1981**, *46*, 1147 – 1151; g) M. Nakazaki, H. Chikamatsu, T. Fujii, T. Nakatsuji, *J. Org. Chem.* **1981**, *46*, 585 – 589; h) O. Abril, G. M. Whitesides, *J. Am. Chem. Soc.* **1982**, *104*, 1552 – 1554; i) M. Nakazaki, H. Chikamatsu, Y. Sasaki, *J. Org. Chem.* **1983**, *48*, 2506 – 2511; j) J. R. Dehli, V. Gotor, *J. Org. Chem.* **2002**, *67*, 1716 – 1718; Nonenzymatic reduction of racemic ketones with chiral hydride donors: k) K. Yamamoto, K. Tsuruoka, J. Tsuji, *Chem. Lett.* **1977**, 1115 – 1116; l) S. El Baba, J.-C. Poulin, H. B. Kagan, *Tetrahedron* **1984**, *40*, 4275 – 4284; m) H.-G. Scmaltz, H. Jope, *Tetrahedron* **1998**, *54*, 3457 – 3464; n) P. Dorizon, C. Martin, J.-C. Daran, J.-C. Fiaud, H. B. Kagan, *Tetrahedron: Asymmetry* **2001**, *12*, 2625 – 2630; o) C. Fehr, J. Galindo, O. Etter, *Eur. J. Org. Chem.* **2004**, 1953 – 1957 (This example includes convergent processing of enantiomers as well as stereodivergent RRM).

[51] D. E. Chavez, E. N. Jacobsen, *Org. Lett.* **2003**, *5*, 2563 – 2565.

[52] a) L. L. Smith, G. Greenspan, R. Rees, T. Foell, *J. Am. Chem. Soc.* **1966**, *88*, 3120 – 3128; b) R. A. Johnson, H. C. Murray, L. M. Reineke, G. S. Fonken, *J. Org. Chem.* **1968**, *33*, 3207 – 3217; c) R. A. Johnson, H. C. Murray, L. M. Reinke, G. S. Fonken, *J. Org. Chem.* **1969**, *34*, 2279 – 2284; d) R. A. Johnson, H. C. Murray, L. M. Reineke, *J. Am. Chem. Soc.* **1970**, *92*, 4872 – 4879; e) D. R. Thakker, H. Yagi, H. Akagi, M. Koreeda, A. Y. H. Lu, W. Levin, A. W. Wood, A. H. Conney, D. M. Jerina, *Chem.-Biol. Interact.* **1977**, *16*, 281 – 300; f) W. Levin, M. K. Buening, A. W. Wood, R. L. Chang, B. Kedzierski, D. R. Thakker, D. R. Boyd, G. S. Gadaginamath, R. N. Armstrong,

H. Yagi, J. M. Karle, T. J. Slaga, D. M. Jerina, A. H. Conney, *J. Biol. Chem.* **1980**, *255*, 9067 – 9074; g) M. W. Chou, P.-L. Chiu, P. P. Fu, S. K. Yang, *Carcinogenesis* **1983**, *4*, 629 – 638; h) J.-D. Fourneron, A. Archelas, B. Vigne, R. Furstoss, *Tetrahedron* **1987**, *43*, 2273 – 2284; i) M. Shou, S. K. Yang, *Chirality* **1990**, *2*, 141 – 149; j) K. Konigsberger, V. Alphand, R. Furstoss, H. Griengl, *Tetrahedron Lett.* **1991**, *32*, 499 – 502; k) V. Alphand, R. Furstoss, *J. Org. Chem.* **1992**, *57*, 1306 – 1309; l) F. Petit, R. Furstoss, *Tetrahedron: Asymmetry* **1993**, *4*, 1341 – 1352; m) M. Mischitz, K. Faber, *Tetrahedron Lett.* **1994**, *35*, 81 – 84; n) B. Adger, M. T. Bes, G. Grogan, R. McCaque, S. Pedragossa-Moreau, S. M. Roberts, R. Villa, P. W. H. Wan, A. J. Willetts, *J. Chem. Soc. Chem. Commun.* **1995**, 1563 – 1564; o) S. Pietz, R. Frohlich, G. Haufe, *Tetrahedron* **1997**, *53*, 17055 – 17066; p) M. Wüst, R. B. Croteau, *Biochemistry* **2002**, *41*, 1820 – 1827.

[53] a) C. Bolm, G. Schlinghoff, *J. Chem. Soc. Chem. Commun.* **1995**, 1247 – 1248; C. Bolm, O. Beckmann, C. Palazzi, *Can. J. Chem.* **2001**, *79*, 1593 – 1597; b) see also: H. D. Kim, H. Kawasaki, M. Nakajima, K. Koga, *Tetrahedron: Asymmetry* **1990**, *1*, 295 – 298; A. Gusso, C. Baccin, F. Pinna, G. Strukul, *Organometallics* **1994**, *13*, 3442 – 3451; M. Lopp, A. Paju, T. Kanger, T. Pehk, *Tetrahedron Lett.* **1996**, *37*, 7583 – 7586; M. Aoki, D. Seebach, *Helv. Chim. Acta* **2001**, *84*, 187 – 207.

[54] Enantiodivergent C–O bond cleavage in cyclic anhydrides: a) D. Seebach, Y. Jaeschke, K. Gottwald, K. Matsuda, R. Formisano, D. A. Chaplin, M. Breuning, G. Bringmann, *Tetrahedron* **1997**, *53*, 7539 – 7556; Y. Chen, L. Deng, *J. Am. Chem. Soc.* **2001**, *123*, 11302 – 11303; Enantiodivergent cleavage involving allylic C–O bonds: b) G. R. Cook, S. Sankaranarayanan, *Org. Lett.* **2001**, *3*, 3531 – 353 (allylpalladium displacement); F. Bertozzi, P. Crotti, F. Macchia, M. Pineschi, B. L. Feringa, *Angew. Chem.* **2001**, *113*, 956 – 958; *Angew. Chem. Int. Ed.* **2001**, *40*, 930 – 932; M. Pineschi, F. Del Moro, P. Crotti, V. Di Bussolo, F. Macchia, *J. Org. Chem.* **2003**, *68*, 2099 – 105 (vinyl oxirane displacement by alkylzinc reagents).

[55] Z.-C. Yang, X.-B. Jiang, Z.-M. Wang, W.-S. Zhou, *J. Chem. Soc. Chem. Commun.* **1995**, 2389 – 2390; Z.-C. Yang, W.-S. Zhou, *Tetrahedron Lett.* **1995**, *36*, 5617 – 5618; T. Honda, N. Sano, K. Kanai, *Heterocycles* **1995**, *41*, 425 – 430; T. Honda, H. Mizutani, K. Kanai, *J. Chem. Soc. Perkin Trans. 1* **1996**, 1729 – 1739; For related epoxidations, see S. L. Schreiber, T. S. Schreiber, D. B. Smith, *J. Am. Chem. Soc.* **1987**, *109*, 1525 – 1529.

[56] S. F. Martin, M. R. Spaller, S. Liras, B. Hartmann, *J. Am. Chem. Soc.* **1994**, *116*, 4493 – 4494; M. P. Doyle, A. B. Dyatkin, A. V. Kalinin, D. A. Ruppar, S. F. Martin, M. R. Spaller, S. Liras, *J. Am. Chem. Soc.* **1995**, *117*, 11021 – 11022; H. M. L. Davies, C. Venkataramani, *Org. Lett.* **2001**, *3*, 1773 – 1775.

[57] K. Tanaka, G. C. Fu, *J. Am. Chem. Soc.* **2003**, *125*, 8078 – 8079.

[58] M. S. Visser, A. H. Hoveyda, *Tetrahedron* **1995**, *51*, 4383 – 4394.

[59] a) D. W. Brooks, M. Wilson, M. Webb, *J. Org. Chem.* **1987**, *52*, 2244 – 2248; This paper reports an enzymatic version of the product-divergent PKR experiment, although one of the products is achiral; b) S. C. Preston, *Asymmetric Synthesis via Iron Acyl Complexes*, PhD Dissertation, Oxford University, **1989**; Preston lists the following points among the criteria for "simultaneous resolution": 1) [reagents] X and Y must display high degrees of chirality discrimination of opposite sense in their reactions with the substrate enantiomers *R* and *S*. 2) The two reactions must have similar rate coefficients (i.e., $k_R = k_S$). 3) The reactions must proceed in the same vessel without detrimental mutual effects. 4) [products] A and B must be readily separable.

[60] a) T. M. Pedersen, J. F. Jensen, R. E. Humble, T. Rein, D. Tanner, K. Bodmann, O. Reiser, *Org. Lett.* **2000**, *2*, 535 – 538; b) T. M. Pedersen, E. L. Hansen, J. Kane, T. Rein, P. Helquist, P.-O. Norrby, D. Tanner, *J. Am. Chem. Soc.* **2001**, *123*, 9738 – 9742.

[61] The equivalent of a two-reagent PKR process has been achieved by using a single, unsymmetrical imide that selectively transfers one of two different acyl groups to enantiomeric amines: A. G. Al-Sehemi, R. S. Atkinson, C. K. Meades, *Chem. Commun.* **2001**, 2684 – 2685; A. G. Al-Sehemi, R. S. Atkinson, J. Fawcett, *J. Chem. Soc. Perkin Trans. 1* **2002**, 257 – 274.

[62] PKR with quasienantiomeric nitrones for the [2+3] cycloaddition to a racemic enol ether: a) K. M. Pietrusiewitz, W. Holody, M. Koprowski, S. Cicchi, A. Goti, A. Brandi, *Phosphorus Sulfur Silicon Relat. Elem.* **1999**, *144–146*, 389 – 392; F. Cardona, S. Valenza, A. Goti, A. Brandi, *Eur. J. Org. Chem.* **1999**, 1319 – 1332; PKR using quasienantiomeric *N*-lithioamides for Michael addition to a racemic enoate: b) S. G. Davies, D. Diez, M. M. El Hammouni, A. C. Garner, N. M. Garrido, M. J. C. Long, R. M. Morrison, A. D. Smith, M. J. Sweet, J. M. Withey, *Chem. Commun.* **2003**, 2410 – 2411; PKR in the reaction of a racemic cyclopropene carboxylate with quasienantiomeric *N*-lithiooxazolidinones: c) L.-a. Liao, F. Zhang, O. Dmitrenko, R. D. Bach, J. M. Fox, *J. Am. Chem. Soc.* **2004**, *126*, 4490 – 4491.

[63] E. Vedejs, E. Rozners, *J. Am. Chem. Soc.* **2001**, *123*, 2428 – 2429.

[64] J. Brandt, C. Jochum, I. Ugi, P. Jochum, *Tetrahedron* **1977**, *33*, 1353 – 1363.

[65] a) R. Wegler, *Justus Liebigs Ann. Chem.* **1932**, *498*, 62 – 76; b) D. A. Evans, J. C. Anderson, M. K. Taylor, *Tetrahedron Lett.* **1993**, *34*, 5563 – 5566; S. Yamada, T. Ohe, *Tetrahedron Lett.* **1996**, *37*, 6777 – 6780; S. Yamada, H. Katsumata, *J. Org. Chem.* **1999**, *64*, 9365 – 9373; c) E. Vedejs, X. Chen, *J. Am. Chem. Soc.* **1996**, *118*, 1809 – 1810, and references therein.

[66] E. Vedejs, O. Daugulis, S. T. Diver, *J. Org. Chem.* **1996**, *61*, 430 – 431.

[67] J. C. Ruble, J. Tweddell, G. C. Fu, *J. Org. Chem.* **1998**, *63*, 2794 – 2795.

[68] E. Vedejs, O. Daugulis, *J. Am. Chem. Soc.* **1999**, *121*, 5813 – 5814; E. Vedejs, O. Daugulis, *J. Am. Chem. Soc.* **2003**, *125*, 4166; E. Vedejs, O. Daugulis, L. A. Harper, J. A. MacKay, D. R. Powell, *J. Org. Chem.* **2003**, *68*, 5020.

[69] a) A. C. Spivey, T. Fekner, S. E. Spey, *J. Org. Chem.* **2000**, *65*, 3154 – 3159; b) A. C. Spivey, F. Zhu, M. B. Mitchell, S. G. Davey, R. L. Jarvest, *J. Org. Chem.* **2003**, *68*, 7379 – 7385.

[70] S. Bellemin-Laponnaz, J. Tweddell, J. C. Ruble, F. M. Breitling, G. C. Fu, *Chem. Commun.* **2000**, 1009 – 1010.

[71] E. Vedejs, J. A. MacKay, *Org. Lett.* **2001**, *3*, 535 – 536.

[72] V. B. Birman, E. W. Uffman, H. Jiang, X. Li, C. J. Kilbane, *J. Am. Chem. Soc.* **2004**, *126*, 12226 – 12227.

[73] a) T. Kawabata, M. Nagato, K. Takasu, K. Fuji, *J. Am. Chem. Soc.* **1997**, *119*, 3169 – 3170; b) T. Kawabata, K. Yamamoto, Y. Momose, H. Yoshida, Y. Nagaoka, K. Fuji, *Chem. Commun.* **2001**, 2700 – 2701; c) T. Kawabata, R. Stragies, T. Fukaya, K. Fuji, *Chirality* **2003**, *15*, 71 – 76; d) T. Kawabata, R. Stragies, T. Fukaya, Y. Nagaoka, H. Schedel, K. Fuji, *Tetrahedron Lett.* **2003**, *44*, 1545 – 1548.

[74] a) T. Sano, K. Imai, O. Kousaburo, T. Oriyama, *Chem. Lett.* **1999**, 265 – 266; for related acylations, see: b) T. Sano, H. Miyata, T. Oriyama, *Enantiomer* **2000**, *5*, 119 – 123; c) T. Oriyama, Y. Mori, K. Imai, R. Sasaki, *Tetrahedron Lett.* **1996**, *37*, 8543 – 8546.

[75] a) G. T. Copeland, E. R. Jarvo, S. J. Miller, *J. Org. Chem.* **1998**, *63*, 6784 – 6785; b) M. M. Vasbinder, E. R. Jarvo, S. J. Miller, *Angew. Chem.* **2001**, *113*, 2906 – 2909; *Angew. Chem. Int. Ed.* **2001**, *40*, 2824 – 2827; c) G. T. Copeland, S. J. Miller, *J. Am. Chem. Soc.* **2001**, *123*, 6496 – 6502; d) E. R. Jarvo, C. A. Evans, G. T. Copeland, S. J. Miller, *J. Org. Chem.* **2001**, *66*, 5522 – 5527; e) N. Papaioannou, J. T. Blank, S. J. Miller, *J. Org. Chem.* **2003**, *68*, 2728 – 2734; M. B. Fierman, D. J. O'Leary, W. E. Steinmetz, S. J. Miller, *J. Am. Chem. Soc.* **2004**, *126*, 6967 – 6971.

 © 2005 Wiley-VCH Verlag GmbH & Co. KGaA, Weinheim

[76] K. Ishihara, Y. Kosugi, M. Akakura, *J. Am. Chem. Soc.* **2004**, *126*, 12212 – 12213.

[77] a) G. Naraku, N. Shimomoto, T. Hanamoto, J. Inanaga, *Enantiomer* **2000**, *5*, 135 – 138; b) B. Pelotier, G. Priem, I. B. Campbell, S. J. F. Macdonald, M. S. Anson, *Synlett* **2003**, 679 – 683; G. Priem, B. Pelotier, S. J. F. Macdonald, M. S. Anson, I. B. Campbell, *J. Org. Chem.* **2003**, *68*, 3844 – 3848.

[78] S. A. Shaw, P. Aleman, E. Vedejs, *J. Am. Chem. Soc.* **2003**, *125*, 13368.

[79] B. Clapham, C.-W. Cho, K. D. Janda, *J. Org. Chem.* **2001**, *66*, 868 – 873.

[80] A. Cordova, M. R. Tremblay, B. Clapham, K. D. Janda, *J. Org. Chem.* **2001**, *66*, 5645 – 5648.

[81] B. Hungerhoff, H. Sonnenschein, F. Theil, *J. Org. Chem.* **2002**, *67*, 1781 – 1785.

[82] Z. Luo, S. M. Swaleh, F. Theil, D. P. Curran, *Org. Lett.* **2002**, *4*, 2585 – 2587.

[83] M.-H. Lin, T. V. RajanBabu, *Org. Lett.* **2002**, *4*, 1607 – 1610.

[84] S. Hashiguchi, A. Fujii, K.-J. Haack, K. Matsumura, T. Ikariya, R. Noyori, *Angew. Chem.* **1997**, *109*, 300 – 303; *Angew. Chem. Int. Ed. Engl.* **1997**, *36*, 288 – 290.

[85] Y. Iura, S. Tsutomu, K. Ogasawara, *Tetrahedron Lett.* **1999**, *40*, 5735 – 5738.

[86] N. Yoshiaki, I. Takei, S. Uemure, M. Hidai, *Organometallics* **1999**, *18*, 2291 – 2293.

[87] a) E. M. Ferreira, B. M. Stoltz, *J. Am. Chem. Soc.* **2001**, *123*, 7725 – 7726; R. M. Trend, B. M. Stolz, *J. Am. Chem. Soc.* **2004**, *126*, 4482 – 4483; b) D. R. Jensen, J. S. Pugsley, M. S. Sigman, *J. Am. Chem. Soc.* **2001**, *123*, 7475 – 7476; J. A. Mueller, M. S. Sigman, *J. Am. Chem. Soc.* **2003**, *125*, 7005 – 7013; D. R. Jensen, M. S. Sigman, *Org. Lett.* **2003**, *5*, 63 – 65.

[88] W. Leitner, J. M. Brown, *J. Am. Chem. Soc.* **1993**, *115*, 152 – 159; M. Kuroboshi, H. Yoshihisa, M. N. Cortona, Y. Kawakami, Z. Gao, H. Tanaka, *Tetrahedron Lett.* **2000**, *41*, 8131 – 8135; K. Masutani, T. Uchida, R. Irie, T. Katsuki, *Tetrahedron Lett.* **2000**, *41*, 5119 – 5123; J. A. Mueller, D. R. Jensen, M. S. Sigman, *J. Am. Chem. Soc.* **2002**, *124*, 8202 – 8203; W. Sun, H. Wang, C. Xia, J. Li, P. Zhao, *Angew. Chem.* **2003**, *115*, 1072 – 1074; *Angew. Chem. Int. Ed.* **2003**, *42*, 1042 – 1044.

[89] H.-J. Hamann, E. Hoeft, *Tetrahedron: Asymmetry* **1996**, *7*, 2217 – 2218; A. Lattanzi, F. Bonadies, A. Scettri, *Tetrahedron: Asymmetry* **1997**, *8*, 2141 – 2151; T. Hamada, R. Irie, J. Mihara, K. Hamachi, T. Katsuki, *Tetrahedron* **1998**, *54*, 10017 – 10028.

[90] R. Hulst, A. van Basten, K. Fitzpatrick, R. M. Kellogg, *J. Chem. Soc. Perkin Trans. 1* **1995**, 2961 – 2963; G. Sekar, H. Nishiyama, *Chem. Commun.* **2001**, 1314 – 1315; G. Sekar, H. Nishiyama, *J. Am. Chem. Soc.* **2001**, *123*, 3603 – 3604.

[91] S. Chandrasekhar, G. Kulkarni, *Tetrahedron Lett.* **2002**, *43*, 615 – 619.

[92] L. S. Miyano, L. D. L. Lu, S. M. Viti, K. B. Sharpless, *J. Org. Chem.* **1983**, *48*, 3611 – 3613; S. Miyano, L. D. L. Lu, S. M. Viti, K. B. Sharpless, *J. Org. Chem.* **1985**, *50*, 4350 – 4360.

[93] M. Hayashi, F. Okamura, T. Toba, N. Oguni, K. B. Sharpless, *Chem. Lett.* **1990**, 547 – 548.

[94] a) J. Hang, S.-K. Tian, L. Tang, L. Deng, *J. Am. Chem. Soc.* **2001**, *123*, 12696 – 12697; b) J. Hang, H. Li, L. Deng, *Org. Lett.* **2002**, *4*, 3321 – 3324.

[95] Carbonylation of aziridines: S. Calet, F. Urso, H. Alper, *J. Am. Chem. Soc.* **1989**, *111*, 931 – 934.

[96] Acylation of arylethylamines with catalyst **114**: S. Arai, S. Bellemin-Laponnaz, G. C. Fu, *Angew. Chem.* **2001**, *113*, 240 – 242; *Angew. Chem. Int. Ed.* **2001**, *40*, 234 – 236.

[97] Stoichiometric chiral reagents: a) M. D. Weingarten, K. Sekanina, W. C. Still, *J. Am. Chem. Soc.* **1998**, *120*, 9112 – 9113; b) M. Calmes, C. Glot, T. Michel, M. Rolland, J. Martinez, *Tetrahedron: Asymmetry* **2000**, *11*, 737 – 741; *N*-Acylation: c) Y. Ie, G. C. Fu, *Chem. Commun.* **2000**, 119 – 120; A. G. Al-Sehemi, R. S. Atkinson, J. Fawcett, D. R. Russell, *Tetrahedron Lett.* **2000**, *41*, 2239 – 2242; d) Selective cleavage of epimeric aziridinyl esters by an achiral alkoxide has been described with KR terminology, but the substrate is not racemic: V. Alezra, C. Bouchet, L. Micouin, M. Bonin, H.-P. Husson, *Tetrahedron Lett.* **2000**, *41*, 655 – 658.

[98] I. Ojima, J. C. Slater, *Chirality* **1997**, *9*, 487 – 494; S. Lin, X. Geng, C. Qu, R. Tynebor, D. J. Gallagher, E. Pollina, J. Rutter, I. Ojima, *Chirality* **2000**, *12*, 431 – 441.

[99] C. Lensink, J. G. de Vries, *Tetrahedron: Asymmetry* **1993**, *4*, 215 – 222.

[100] J. Yun, S. L. Buchwald, *J. Org. Chem.* **2000**, *65*, 767 – 774.

[101] A. Viso, N. E. Lee, S. L. Buchwald, *J. Am. Chem. Soc.* **1994**, *116*, 9373 – 9374.

[102] Alkene KR by epoxidation: dioxirane examples: a) M. Frohn, X. Zhou, J.-R. Zhang, Y. Tang, Y. Shi, *J. Am. Chem. Soc.* **1999**, *121*, 7718 – 7719; D. Yang, G.-S. Jiao, Y.-C. Yip, T.-H. Lai, M.-K. Wong, *J. Org. Chem.* **2001**, *66*, 4619 – 4624; metal-catalyzed alkene epoxidation: b) S. L. Van der Velde, E. N. Jacobsen, *J. Org. Chem.* **1995**, *60*, 5380 – 5381; allene KR: c) Y. Noguchi, H. Takiyama, T. Katsuki, *Synlett* **1998**, 543 – 545.

[103] J. P. Morken, M. T. Didiuk, M. S. Visser, A. H. Hoveyda, *J. Am. Chem. Soc.* **1994**, *116*, 3123 – 3124; Visser, J. P. A. Harrity, A. H. Hoveyda, *J. Am. Chem. Soc.* **1996**, *118*, 3779 – 3780; C. W. Johannes, M. S. Visser, G. S. Weatherhead, A. H. Hoveyda, *J. Am. Chem. Soc.* **1998**, *120*, 8340 – 8347.

[104] KR by olefin metathesis: O. Fujimura, R. H. Grubbs, *J. Am. Chem. Soc.* **1996**, *118*, 2499 – 2500; J. B. Alexander, D. S. La, D. R. Cefalo, A. H. Hoveyda, R. R. Schrock, *J. Am. Chem. Soc.* **1998**, *120*, 4041 – 4042; D. S. La, J. B. Alexander, D. R. Cefalo, D. D. Graf, A. H. Hoveyda, R. R. Schrock, *J. Am. Chem. Soc.* **1998**, *120*, 9720 – 9721; O. Fujimura, R. H. Grubbs, *J. Org. Chem.* **1998**, *63*, 824 – 832; S. J. Dolman, E. S. Satteley, A. H. Hoveyda, R. R. Schrock, *J. Am. Chem. Soc.* **2002**, *124*, 6991 – 6997.

[105] KR by alkene hydrogenation: Hydroxyalkylacrylates: a) J. M. Brown, I. Cutting, *J. Chem. Soc. Chem. Commun.* **1985**, 578 – 579; Allylic alcohols: b) M. Kitamura, I. Kasahara, K. Manabe, R. Noyori, H. Takaya, *J. Org. Chem.* **1988**, *53*, 708 – 710; J. W. Faller, M. Tokunaga, *Tetrahedron Lett.* **1993**, *34*, 7359 – 7362; Aminoalkylacrylates: c) M. Takagi, K. Yamamoto, *Tetrahedron* **1991**, *47*, 8869 – 8882; α,β-Unsaturated acids: d) W. Leitner, J. M. Brown, H. Brunner, *J. Am. Chem. Soc.* **1993**, *115*, 152 – 159.

[106] C. R. Baar, C. J. Levy, E. Y.-J. Min, L. M. Henling, M. W. Day, J. E. Bercaw, *J. Am. Chem. Soc.* **2004**, *126*, 8216 – 8231.

[107] Ynal cyclization: a) M. Imai, M. Tanaka, H. Suemune, *Tetrahedron* **2001**, *57*, 1205 – 1211; b) K. Tanaka, G. C. Fu, *J. Am. Chem. Soc.* **2002**, *124*, 10296 – 10297; Enyne cyclization: c) A. Lei, M. He, X. Zhang, *J. Am. Chem. Soc.* **2003**, *125*, 11472 – 11473.

[108] Racemic dienophiles: a) B. Wegener, M. Hansen, E. Winterfeldt, *Tetrahedron: Asymmetry* **1993**, *4*, 345 – 350; M. Goeres, E. Winterfeldt, *J. Chem. Soc. Perkin Trans. 1* **1994**, 3525 – 3531; Racemic dienes: b) M. C. Carreno, A. Urbano, C. D. Vitta, *J. Org. Chem.* **1998**, *63*, 8320 – 8330; M. C. Carreno, S. Garcie-Cerrada, A. Urbano, C. D. Vitta, *Tetrahedron: Asymmetry* **1998**, *9*, 2965 – 2969.

[109] Chiral amines and 1-acetyl-*trans*-cyclooctene: a) F. Henin, J. Muzart, J. P. Pete, H. Rau, *Tetrahedron Lett.* **1990**, *31*, 1015 – 1016; F. Henin, J. Muzart, J. P. Pete, H. Rau, *New J. Chem.* **1992**, *16*, 979 – 985; *ortho*-photocycloaddition of double bonds to benzene rings: b) P. J. Wagner, K. McMahon, *J. Am. Chem. Soc.* **1994**, *116*, 10827 – 10828; 1,3-dipolar cycloadditions: c) F. Cardona, A. Gotti, A. Brandi, *Eur. J. Org. Chem.* **2001**, 2999 – 3011.

 © 2005 Wiley-VCH Verlag GmbH & Co. KGaA, Weinheim

[110] a) J. F. Larrow, E. N. Jacobsen, *J. Am. Chem. Soc.* **1994**, *116*, 12129 – 12130; b) J. F. Larrow, S. E. Schaus, E. N. Jacobsen, *J. Am. Chem. Soc.* **1996**, *118*, 7420 – 7421; c) B. D. Brandes, E. N. Jacobsen, *Tetrahedron: Asymmetry* **1997**, *8*, 3927 – 3933; d) M. E. Furrow, S. E. Schaus, E. N. Jacobsen, *J. Org. Chem.* **1998**, *63*, 6776 – 6777; e) J. M. Ready, E. N. Jacobsen, *J. Am. Chem. Soc.* **1999**, *121*, 6086 – 6087; f) M. H. Wu, K. B. Hansen, E. N. Jacobsen, *Angew. Chem.* **1999**, *111*, 2167 – 2170; *Angew. Chem. Int. Ed.* **1999**, *38*, 2012 – 2014; Polymer-supported salen catalysts: g) S. Peukert, E. N. Jacobsen, *Org. Lett.* **1999**, *1*, 1245 – 1248; Dendrimeric salen catalysts: h) R. Breinbauer, E. N. Jacobsen, *Angew. Chem.* **2000**, *112*, 3750 – 3753; *Angew. Chem. Int. Ed.* **2000**, *39*, 3604 – 3607; Oligomeric catalysts: i) J. M. Ready, E. N. Jacobsen, *J. Am. Chem. Soc.* **2001**, *123*, 2687 – 2688; j) S. E. Schaus, B. D. Brandes, J. F. Larrow, M. Tokunaga, K. B. Hansen, A. E. Gould, M. E. Furrow, E. N. Jacobsen, *J. Am. Chem. Soc.* **2002**, *124*, 1307 – 1315; k) D. E. White, E. N. Jacobsen, *Tetrahedron: Asymmetry* **2003**, *14*, 3633 – 3638; l) S. K. Kim, E. N. Jacobsen, *Angew. Chem.* **2004**, *116*, 4042 – 4044; *Angew. Chem. Int. Ed.* **2004**, *43*, 3952 – 3954; m) L. P. C. Nielsen, C. P. Stevenson, D. G. Blackmond, E. N. Jacobsen, *J. Am. Chem. Soc.* **2004**, *126*, 1360 – 1362.

[111] a) P. S. Savle, M. J. Lamoreaux, J. F. Berry, R. D. Gandour, *Tetrahedron: Asymmetry* **1998**, *9*, 1843 – 1846; b) C. Jin, R. D. Ramirez, A. S. Gopalan, *Tetrahedron Lett.* **2001**, *42*, 4747 – 4750; c) J. S. Yadav, A. Bandyopadhyay, A. C. Kunwar, *Tetrahedron Lett.* **2001**, *42*, 4907 – 4911; d) K. Kulig, U. Holzgrabe, B. Malawska, *Tetrahedron: Asymmetry* **2001**, *12*, 2533 – 2536; e) G. C. Paddon-Jones, C. S. P. McErlean, P. Hayes, C. J. Moore, W. A. Koenig, W. Kitching, *J. Org. Chem.* **2001**, *66*, 7487 – 7495; f) S. Chow, W. Kitching, *Tetrahedron: Asymmetry* **2002**, *13*, 779 – 793; g) S. Lochynski, B. Frackowiak, T. Librowski, R. Czarnecki, J. Grochowski, P. Serda, M. Pasenkiewicz-Gierula, *Tetrahedron: Asymmetry* **2002**, *13*, 873 – 878; h) N. Maezaki, N. Kojima, M. Asai, H. Tominaga, T. Tanaka, *Org. Lett.* **2002**, *4*, 2977 – 2980; i) M. Bandini, P. G. Cozzi, P. Melchiorre, A. Umani-Ronchi, *Angew. Chem.* **2004**, *116*, 86 – 89; *Angew. Chem. Int. Ed.* **2004**, *43*, 84 – 87.

[112] KR of epoxides: a) Organoaluminum reagents: Y. Naruse, T. Esaki, H. Yamamoto, *Tetrahedron Lett.* **1988**, *29*, 1417 – 1420; Chiral titanium complex: b) A. Ishikawa, T. Katsuki, *Tetrahedron Lett.* **1991**, *32*, 3547 – 3550; Molybdenum(VI) complexes: c) F. Betschinger, K. Hintzer, U. Leyrer, V. Schurig, *Stud. Surf. Sci. Catal.* **1991**, *66*, 513 – 520; V. Schurig, F. Betschinger, *Bull. Soc. Chim. Fr.* **1994**, *131*, 555 – 560; Chiral lithium amide base: d) M. Asami, N. Kanemaki, *Tetrahedron Lett.* **1989**, *30*, 2125 – 2128; e) A. Bigi, A. Mordini, A. Thurner, F. Faigl, G. Poli, L. Toke, *Tetrahedron: Asymmetry* **1998**, *9*, 2293 – 2299; f) M. Asami, S. Sato, K. Honda, S. Inoue, *Heterocycles* **2000**, *52*, 1029 – 1032; g) M. J. Soedergren, S. K. Bertilsson, P. G. Andersson, *J. Am. Chem. Soc.* **2000**, *122*, 6610 – 6618; h) A. Gayet, S. Bertilsson, P. G. Andersson, *Org. Lett.* **2002**, *4*, 3777 – 3779.

[113] K. Rossen, P. J. Pye, A. Maliakal, R. P. Volante, *J. Org. Chem.* **1997**, *62*, 6462 – 6463.

[114] M. Kitamura, M. Tokunaga, R. Noyori, *Tetrahedron* **1993**, *49*, 1853 – 1860.

[115] A. J. J. Straathof, J. L. L. Rakels, J. J. Heijnen, *Biotechnol. Bioeng.* **1995**, *45*, 536 – 538; W. Kroutil, A. Kleewein, K. Faber, *Tetrahedron: Asymmetry* **1997**, *8*, 3251 – 3261; W. Kroutil, A. Kleewein, K. Faber, *Tetrahedron: Asymmetry* **1997**, *8*, 3263 – 3274.

[116] a) R. F. Ismagilov, *J. Org. Chem.* **1998**, *63*, 3772 – 3774; b) T. O. Lukas, C. Girard, D. R. Fenwick, H. B. Kagan, *J. Am. Chem. Soc.* **1999**, *121*, 9299 – 9306; c) D. W. Johnson, Jr., D. A. Singleton, *J. Am. Chem. Soc.* **1999**, *121*, 9307 – 9312; d) D. G. Blackmond, *J. Am. Chem. Soc.* **2001**, *123*, 545 – 553.

[117] D. E. Ward, Y. Liu, D. How, *J. Am. Chem. Soc.* **1996**, *118*, 3025 – 3026; D. E. Ward, D. How, Y. Liu, *J. Am. Chem. Soc.* **1997**, *119*, 1884 – 1894.

[118] a) Chemical calculations program "Magnus": http://www.ch.cam.ac.uk./magnus (J. M. Goodman et al.); b) J. M. Goodman, A.-K. Köhler, S. C. M. Alderton, *Tetrahedron Lett.* **1999**, *40*, 8715 – 8718.

[119] Program "Selectivity": http://www.cis.TUGraz.at/orgc (K. Faber, H. Hönig: Windows version; K. Faber, A. Kleewein: Mac version).

[120] a) M. G. Finn, *Chirality* **2002**, *14*, 534 – 540; b) A. Horeau, A. Nouaille, *Tetrahedron Lett.* **1990**, *31*, 2707 – 2710; J. Guo, J. Wu, G. Siuzdak, M. G. Finn, *Angew. Chem.* **1999**, *111*, 1868 – 1871; *Angew. Chem. Int. Ed.* **1999**, *38*, 1755 – 1758; M. T. Reetz, M. H. Becker, H.-W. Klein, D. Stockigt, *Angew. Chem.* **1999**, *111*, 1872 – 1875; *Angew. Chem. Int. Ed.* **1999**, *38*, 1758 – 1761; D. D. Diaz, S. Yao, M. G. Finn, *Tetrahedron Lett.* **2001**, *42*, 2617 – 2619.

[121] G. T. Copeland, S. J. Miller, *J. Am. Chem. Soc.* **2001**, *123*, 6496 – 6502.

[122] M. T. Reetz, K. M. Kuhling, S. Wilensek, H. Husmann, U. W. Hausig, M. Hermes, *Catal. Today* **2001**, *67*, 389 – 396; G. A. Korbel, L. Gojko, M. D. Shair, *J. Am. Chem. Soc.*, **2001**, *123*, 361 – 362.

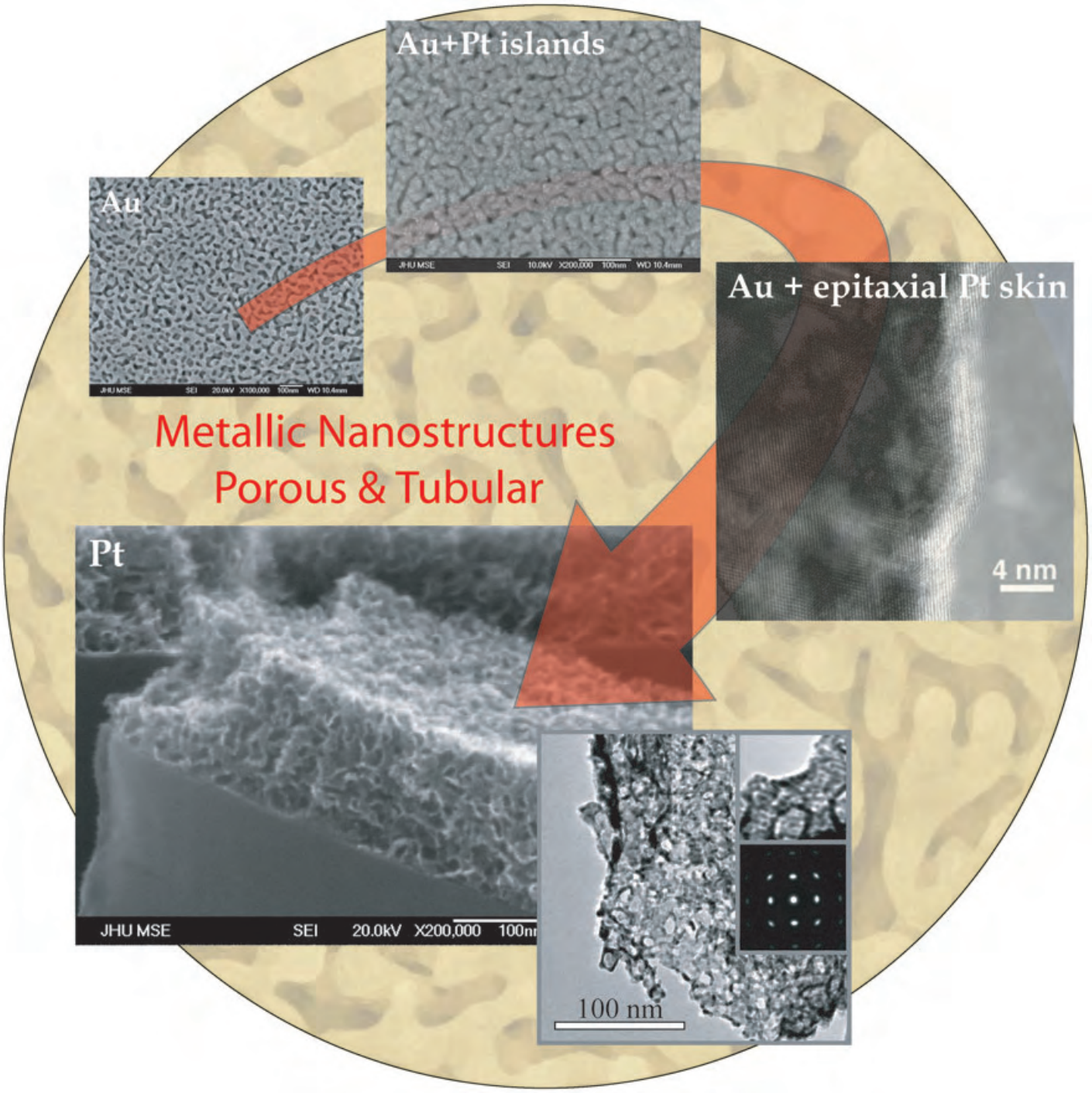
[123] B. Dominguez, N. S. Hodnett, G. C. Lloyd-Jones, *Angew. Chem.* **1999**, *111*, 4419 – 4421; *Angew. Chem. Int. Ed.* **2001**, *40*, 4289 – 4291.

[124] H.-J. Gais, T. Jagusch, O. Bondarev, *J. Org. Chem.* **2004**, *69*, 2731 – 2736.

[125] L. M. Mediavilla, A. Alexakis, N. Krause, *Tetrahedron Lett.* **2002**, *43*, 7887 – 7890.

 © 2005 Wiley-VCH Verlag GmbH & Co. KGaA, Weinheim

Communications



Epitaxial casting of platinum on nanoporous gold membrane molds leads to the formation of nanotubular mesoporous platinum, a new material with high mechanical stability and interesting capillary behavior. For more information on the synthesis and properties of this network of platinum nanotubes see the Communication by J. Erlebacher and co-workers on the following pages.

 © 2005 Wiley-VCH Verlag GmbH & Co. KGaA, Weinheim DOI: 10.1002/anie.200463106

Materials Science

Epitaxial Casting of Nanotubular Mesoporous Platinum**

*Yi Ding, Anant Mathur, Mingwei Chen, and Jonah Erlebacher**

Mesoporous precious metals (pore size 2–50 nm), especially platinum, are particularly sought after because of their immense technological importance in, for example, catalysis,[1] sensing,[2] and actuation.[3] A common approach to the fabrication of these materials is the replication of porous alumina[4] or liquid-crystal templates.[5,6] Templating generally offers a high degree of control over the pore size as well as microstructure periodicity, but most techniques in this class result in materials with one-dimensional porosity, such as an array of tubes. This characteristic is desirable for some optoelectronic applications, but for applications such as sensing or catalysis, materials with open porosity extending in all dimensions are favored to allow unlimited transport of the molecules of the medium;[1] in fact, the most useful materials often exhibit bicontinuous microstructures in which both the void space and the scaffold are completely interconnected, with the scaffold imparting mechanical stability and electrical pathways to catalytically active sites. Two important classes of bicontinuous mesoporous materials are aerogels[1] and nanoporous metals made by dealloying.[7]

Here we report the design and fabrication of nanotubular mesoporous platinum (NMP), a new material that can be described as a network of platinum nanotubes with diameters of about 15 nm and walls 1 nm thick that interconnect to form an open, doubly bicontinuous structure that may possess the highest surface area to volume ratio known (or possible) for a macroscopic sample of metal. NMP possesses a higher order of geometric complexity than most known porous materials in that the walls separate two distinct void spaces, one with predominantly negative curvature, the other with predominantly positive curvature. As such, the material exhibits interesting capillary behavior, and we envision application in nanofluidic systems as well as in ultrahigh surface area catalysis. Intriguingly, NMP exhibits structural characteristics of a macroscopic metal, in the sense that grains of micrometer size or larger are typical and that the nanotubular network within each grain exists as a single crystal with characteristic dimensions several orders of magnitude smaller.

The nanotubular mesoporous platinum is formed by epitaxial casting[8] using nanoporous gold (NPG) membrane molds. Our typical starting material is comprised of free-standing NPG membranes 100 nm thick for which the in-plane grain size is on the order of micrometers, but in principle this fabrication method is not limited to any particular size and shape of sample. NPG is a three-dimensional bicontinuous mesoporous metal with a tunable ligament size on the order 10–100 nm.[7] The crystallographic coherence of NPG extends to the scale of the grains of the Au/Ag alloy. In this sense, NPG is markedly different from most other nanoporous materials that are essentially controlled aggregates of nanoparticles.[9] Epitaxial casting is a new casting method in which an epitaxial skin of a second material coats a mold that is subsequently dissolved away. In previous work, we discovered that platinum could be grown epitaxially onto NPG by an electroless plating process,[10] which resulted in a composite core–shell nanoporous structure. More specifically, we found that a coating of Pt with an average thickness of about 1 nm took the form of a conformal coating of uniformly sized epitaxial islands on the NPG substrate. Past studies of Pt films on planar gold[11] exhibited a heteroepitaxial growth mode where initial layer-by-layer growth was followed by accommodation of misfit strain (4% in Pt/Au system) through injection of misfit dislocations (MD) at the interface. The critical thickness for injection of MDs was typically 1 nm. The presence of coherent islands with no MDs in the present case suggested that the approximately 5-nm radius of curvature allowed out-of-plane relaxation to occur by islanding, a characteristic feature of the Stranski–Krastanov growth mode. The presence of large epitaxial strains was confirmed during the course of this study by the behavior of the material after annealing at a moderate temperature (300 °C for 30 minutes), during which it was observed that the islands smoothed out to form a uniform coating with injection of misfit dislocations at the Pt/Au interface. At this point of processing, surprisingly, we found that we could completely dissolve the gold away in aqueous gold etchant (KI: 10 wt%, I_2: 5 wt%) to leave the 1-nm-thick Pt shell, still single crystalline within individual grains and retaining the bicontinuous void space of the original NPG but adding a second, tubular void region where the gold had been prior to etching.

Figure 1b shows a representative scanning electron microscopy (SEM) image of NMP. The average diameter of the tubular ligaments is about 15 nm, which is consistent with the ligament size of the NPG template (Figure 1a). Tube openings (see inset to Figure 1c) are frequently seen at the sample edges, and the shell thickness of the tubes is estimated to be around 1–2 nm. This thickness may be adjusted by varying the amount of platinum plated onto the NPG mold. A 1-nm-thick shell is only 4–6 atoms thick, which is smaller than the diameter of typical Pt nanoparticles by more than a factor

[*] Y. Ding, A. Mathur, Prof. Dr. J. Erlebacher
Department of Materials Science and Engineering
Johns Hopkins University
Baltimore, MD 21218 (USA)
Fax: (+1) 410-516-5293
E-mail: jonah.erlebacher@jhu.edu
Prof. Dr. M. Chen[+]
Department of Mechanical Engineering
Johns Hopkins University
Baltimore, MD 21218 (USA)
[+] Current address:
Institute for Materials Research
Tohoku University
Sendai 980-8577 (Japan)

[**] This work was supported by the National Science Foundation under grant DMR-0092756, and the Lawrence Livermore National Laboratory under contract W-7405-ENG-48.

Supporting information for this article is available on the WWW under http://www.angewandte.org or from the author.

 © 2005 Wiley-VCH Verlag GmbH & Co. KGaA, Weinheim

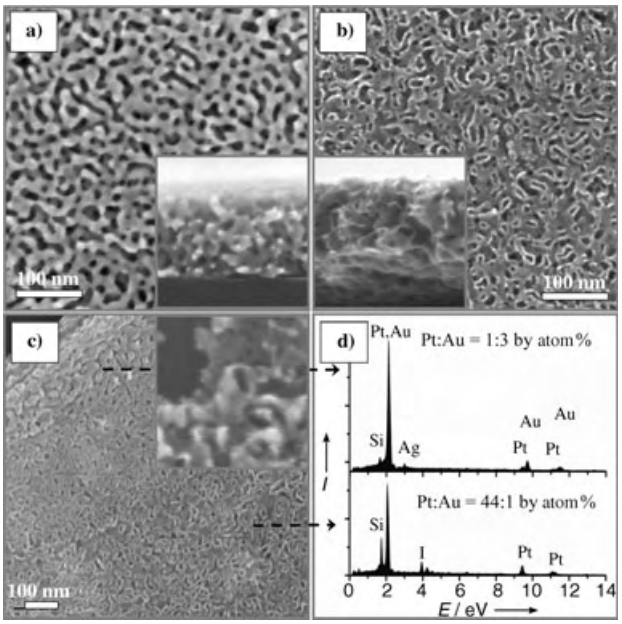


Figure 1. a) Plan-view and cross-section (inset) SEM images of NPG. b) Plan-view and cross-section (inset) SEM images of NMP. c) SEM image of a Pt-coated NPG sample within which gold has been only partially removed; the inset shows a tube opening of NMP. d) EDS analysis indicates a gradual structure transition from Pt/NPG to NMP. The NPG mode was made by dealloying white gold leaf in nitric acid for 10 minutes. The NPG surface was coated with platinum by electroless plating. Typical plating time is on the order of minutes, and thicker platinum layers may be formed with longer plating times. Experimental details have been reported in Ref. [10]. SEM images were acquired on a JEOL JSM-6700F SEM, equipped with a EDAX Genesis 4000 microanalysis system, under an accelerating voltage of 20 kV.

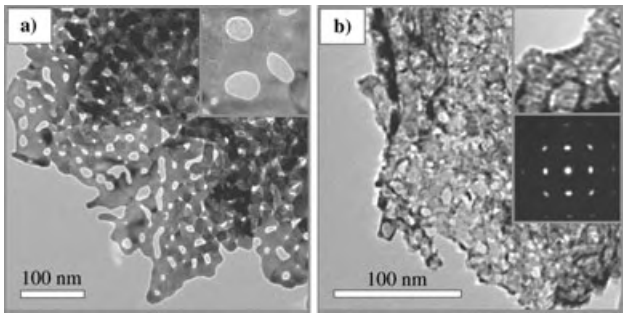


Figure 2. Bright-field TEM images of: a) NPG and b) NMP. The insets in (a) and (b) show three-way junctions of solid and tubular ligaments, and the electron-diffraction pattern shown as a lower inset in (b) indicates that NMP is a single crystal over a scale that is orders of magnitude greater than the pore size.

of two.[12,13] Note that all the tube edges of the structure show brighter contrast, a characteristic feature of tubular morphologies when observed by SEM. Figure 1c shows a Pt-coated NPG sample within which gold has been only partially removed. In this image, a gradual structure change from Pt/NPG to NMP can be clearly seen. Energy dispersive spectroscopy analysis (EDS) confirms this change. A Pt/Au ratio of 1:3 is found in the Pt/NPG region (Figure 1d), while the gold concentration is on the order of the detection limit of the instrument (ca. 1 atom%) in the NMP area and indicative of the nearly complete removal of the gold backbone.[14] If it is assumed that Pt/NPG has the idealized structure of coaxial cylinders with a diameter of 15 nm, one can calculate the shell thickness of the platinum layer to be about 1.1 nm (4 atomic layers), which is consistent with the SEM observation. We have also performed a virtual experiment (computer simulation) of coating a simulated NPG structure made by using literature methods[7], and then removing the porous gold substrate. The simulated morphology shows the original porous channels and hollow ligaments, and is remarkably similar to the experimental morphology (see the Supporting Information).

Complementary structural information is given by transmission electron microscopy (TEM) images and selected-area electron diffraction patterns (Figure 2). NPG and NMP appear as very complicated morphologies under TEM because of a 3D to 2D projection of highly interconnected wires (for NPG) and tubes (for NMP). The insets of Figure 2 show areas of three-way junctions of solid and tubular ligaments. NMP shows darker edges along the edges of its tubular ligaments than nanoporous gold. These darker edges correspond to electron attenuation by wall features parallel to the electron beam. As mentioned above, the epitaxial relationship between Pt and the NPG substrate mold suggests that large (approximately micrometer) grains of NMP are retained upon etching away the gold. The selected-area electron diffraction pattern shows this is indeed the case, as illustrated in the inset of Figure 2b, which shows a single-crystal square lattice recorded from a $\langle 001 \rangle$ zone axis of face-centered cubic (fcc) Pt. The stretched diffraction spots indicate minor lattice distortion possibly resulting from surface stresses or simply sample preparation.[3,15] Further characterization of epitaxial casting leading to NMP formation is given by high-resolution electron microscopy (HREM) images. The micrograph in Figure 3a clearly shows the epitaxial relationship between the annealed Pt overlayer and the NPG substrate. EDS analysis using an electron beam of about 1 nm shows that the bright area with a thickness of 5–8 atomic layers is a platinum skin. After removing the Au backbone, the Pt nanotubules with thin shells and nanosized holes can be clearly seen in HREM images. Figure 3b shows an example of this tubular structure, where a tubule appears to slightly tilt out of the plane as shown schematically in the insert in Figure 3b. The internal diameter of the tubule is around 10 nm, close to the ligament size of NPG. One side of the tubule was imaged along a $\langle 111 \rangle$ orientation of fcc Pt. The thickness of the sheet was estimated by simulating the atomic image, and the best match between the HREM and simulated images was obtained at a sample thickness of about 2 nm, which is consistent with the thickness of tubular shells observed in the cross-sectional image (Figure 3a). The HREM images also clarify the geometry of the tubular ligaments which are seen not to be single-valued in surface curvature; instead, they are more like hyperboloids of revolution for which each point is a saddle, thus possessing both positive and negative principal curvatures.

 © 2005 Wiley-VCH Verlag GmbH & Co. KGaA, Weinheim

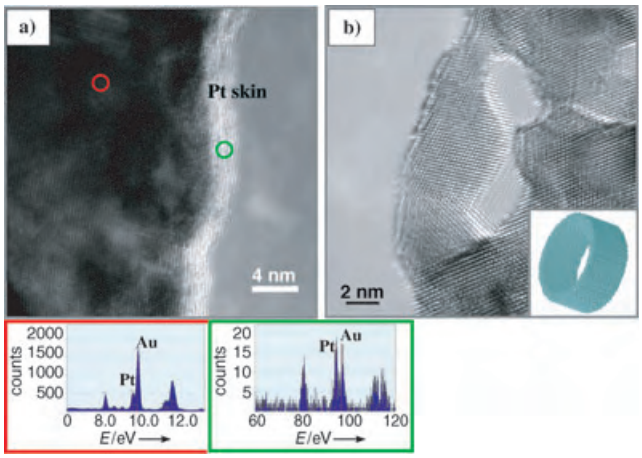


Figure 3. HREM images of Pt/NPG and NMP. a) A uniform skin of heteroepitaxial Pt on nanoporous gold was made by platinum deposition followed by thermal annealing at 300 °C for 30 minutes. The bright area with a thickness of 5–8 atomic layers is the platinum skin, as demonstrated by EDS analysis. The observation of gold in the shell region arises from sample drifting during imaging. b) Side-view of a tube opening of NMP. Lattice distortion and dislocations are observed. The inset is an atomistic model consistent with the projection of the tube opening shown in (b). TEM analysis was performed on a 300 kV, field-emission Philips CM300FEG in the Electron Microscopy Center at Johns Hopkins University.

Since NMP has atomically thin tube walls it has a very high surface area and total surface free energy. This situation imparts an intrinsic metastability to the material which could potentially lead to morphological coarsening, a problem akin to the sintering problems plaguing nanoparticle-based catalysts. The likely mechanism for such coarsening in NMP at moderate temperatures is surface diffusion, for which the characteristic coarsening time t depends on the characteristic length scale l of the structure material according to the relationship $t \approx l^4$; [16] thus, NMP with $l \approx 1$ nm should coarsen 10^{12} times faster than 1-μm-sized solid platinum grains should sinter. We do know, however, that platinum surface self-diffusivities are three to four orders of magnitude slower than gold,[17] and NPG does coarsen at room temperature, particularly in certain electrolytic environments.[18] To examine this stability problem for nanotubular mesoporous platinum we studied the morphological stability of NMP by annealing it at elevated temperatures (see the Supporting Information). It was found that NMP is stable at 125 °C for at least 24 h. At 150 °C, the tube walls start to deform, and eventually evolve into Pt nanoparticles (Pt-NPG, in contrast, is stable at these temperatures). This behavior indicates that NMP may be useful for catalytic reactions at moderate temperatures, such as in a H_2/O_2 fuel cell.

The thermal stability of NMP is also interesting from the standpoint of fundamental thermodynamics. It has been predicted that the melting point of small particles is suppressed relative to that of bulk particles.[19] We estimate for Pt that a suppression of the melting point below 300 °C requires a radius of curvature less than approximately 1 nm. The principal curvatures of the network are greater than this (ca. 7–10 nm), so we expect NMP to be stable with regards to this instability. However, small pinholes in the tubular network may occasionally open up which may locally melt and then resolidify when the mass of the melted regions increases to the point that the solid is again thermodynamically stable. In this context, it is interesting to note the similarity of the NMP sample annealed at 300 °C to a network of solidified droplets.

The whole network and each individual tubular segment in NMP are essentially one crystallographic lattice. This characteristic feaure enhances the mechanical rigidity of the material, and one may be able to use this interconnected 3D channel structure as a model system with which to study nano-/microfluidic transport phenomena or confined reactions on the nanoscale.[20] To further develop this concept, we have made a platinum–palladium bicontinuous mesoporous composite structure by refilling the tubes of NMP[21] with palladium chloride. Samples were made by touching the edge of a sample of NMP with a drop of concentrated $PdCl_2$ solution. Strong capillary forces drove the liquid into the tube channels, an effect that caused a change in the appearance that was visible to the naked eye, and then the samples were subsequently dried and imaged by SEM. Figure 4 shows the structure of such a sample at the filled/

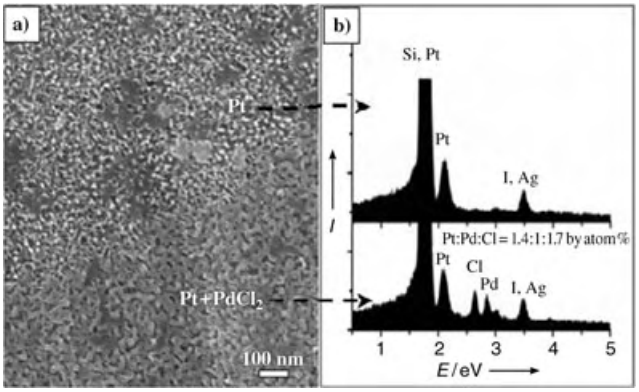


Figure 4. a) SEM image of NMP that has been partially filled with $PdCl_2$. b) EDS analysis showing the difference in pore composition between unfilled and refilled regions.

unfilled boundary. The area with $PdCl_2$ looks very similar to the morphology of unetched Pt/NPG, that is, the edge contrast arising from the tubular morphology disappears and the region in the upper section of the micrograph is clearly unfilled. Compositional analysis from both areas (Figure 4b) supports this view. It is interesting to find that liquid transport occurs preferentially through tubes rather than pores, possibly because of the much stronger capillary forces of tubes, which have very high negative curvature.

The surprising mechanical stability imparted by the nanostructure of NMP enables it to be produced in macroscopic quantities (membrane samples on the order of one square centimeter are routinely made). This feature should enable its easy integration into technologies for catalysis, nano-/microfluidic transport, as well as supplying a new

 © 2005 Wiley-VCH Verlag GmbH & Co. KGaA, Weinheim

material to probe the nanoscale limits of materials research focusing on structural, physical, and mechanical properties.

Received: December 30, 2004
Revised: April 11, 2005
Published online: May 18, 2005

Keywords: materials science · mesoporous materials · nanostructures · nanotubes · platinum

[1] D. R. Rolison, *Science* **2003**, *299*, 1698 – 1701.
[2] C. R. Martin, P. Kohli, *Nat. Rev. Drug Discovery* **2003**, *2*, 29 – 37.
[3] J. Weissmüller, R. N. Viswanath, D. Kramer, P. Zimmer, R. Würschum, H. Gleiter, *Science* **2003**, *300*, 312 – 315.
[4] H. Masuda, K. Fukuda, *Science* **1995**, *268*, 1466 – 1468.
[5] G. S. Attard, P. N. Bartlett, N. R. B. Coleman, J. M. Elliott, J. R. Owen, J. H. Wang, *Science* **1997**, *278*, 838 – 840.
[6] T. Kijima, T. Yoshimura, M. Uota, T. Ikeda, D. Fujikawa, S. Mouri, S. Uoyama, *Angew. Chem.* **2004**, *116*, 230 – 234; *Angew. Chem. Int. Ed.* **2004**, *43*, 228 – 232.
[7] J. Erlebacher, M. J. Aziz, A. Karma, N. Dimitrov, K. Sieradzki, *Nature* **2001**, *410*, 450 – 453.
[8] J. Goldberger, R. R. He, Y. F. Zhang, S. Lee, H. Q. Yan, H. J. Choi, P. D. Yang, *Nature* **2003**, *422*, 599 – 602.
[9] O. D. Velev, P. M. Tessier, A. M. Lenhoff, E. W. Kaler, *Nature* **1999**, *401*, 548.
[10] Y. Ding, M. W. Chen, J. Erlebacher, *J. Am. Chem. Soc.* **2004**, *126*, 6876 – 6877.
[11] J. W. Matthews, W. A. Jesser, *Acta Metall.* **1967**, *15*, 595 – 600.
[12] Y. Sun, B. Mayers, Y. Xia, *Adv. Mater.* **2003**, *15*, 641 – 646.
[13] Y. Luo, S. K. Lee, H. Hofmeister, M. Steinhart, U. Gosele, *Nano Lett.* **2004**, *4*, 143 – 147.
[14] Our current data can not exclude the possibility of a surface alloy (1–2 atomic layers) forming between Au and Pt; see, for example, F. Besenbacher, I. horkendorff, B. S. Clausen, B. Hammer, A. M. Molenbroek, J. K. Nørskov, I. Stensgaard, *Science* **1998**, *279*, 1913 – 1915.
[15] X. Y. Kong, Y. Ding, R. Yang, Z. L. Wang, *Science* **2004**, *303*, 1348 – 1351.
[16] C. Herring, *J. Appl. Phys.* **1950**, *21*, 301 – 303.
[17] E. G. Seebauer, C. E. Allen, *Prog. Surf. Sci.* **1995**, 49, 265 – 330.
[18] Y. Ding, Y.-J. Kim, J. Erlebacher, *Adv. Mater.* **2004**, *16*, 1897 – 1900.
[19] J. W. Cahn, *Acta Metall.* **1980**, *28*, 1333 – 1338.
[20] A. Karlsson, R. Karlsson, M. Karlsson, A.-S. Cans, A. Strömberg, F. Ryttsén, O. Orwar, *Nature* **2001**, *409*, 150 – 151.
[21] In this work, we made the distinction between tubular/tubes and porous/pores by referring to pores as the original porous empty space between ligaments (also seen in NPG), and tubes as hollow channels originally occupied by gold (only seen in NMP).

 © 2005 Wiley-VCH Verlag GmbH & Co. KGaA, Weinheim

Chiroptical Probes

A Cationic Zinc Porphyrin as a Chiroptical Probe for Z-DNA**

Milan Balaz, Massimo De Napoli, Andrea E. Holmes, Angela Mammana, Koji Nakanishi, Nina Berova, and Roberto Purrello**

DNA is a polymorphic polymer that can adopt a variety of secondary structures ranging from the canonical right-handed B form to the left-handed Z conformation.[1] The latter conformation is less common than the right-handed B-DNA because under physiological conditions Z-DNA has a higher energy.[2–4] Although the biological role of Z-DNA still remains to be clarified, it has recently been inferred that certain classes of proteins bind to it both tightly and specifically.[5–8]

The different handedness of the two DNA forms is reported in the spectral region below 300 nm of circular dichroism (CD) spectra. B-DNA is characterized by a complex positive band centered at 274 nm and a negative Cotton effect at 253 nm, while Z-DNA exhibits a negative Cotton effect at 293 nm and a positive Cotton effect at 263 nm. Determination and sensing of Z-DNA based on these spectral differences, however, can be hampered by the concomitant presence of the two forms of DNA and/or other biomolecules such as proteins that make the region below 300 nm in the CD spectra difficult to analyze. To solve this problem, it is desirable to design chiroptical probes that discriminate between the B and Z structures and absorb above 300 nm, a region that is free from interferences, to provide characteristic induced circular dichroism (ICD) signals.

Recognition of B- and Z-DNA has been achieved by using the Δ or Λ enantiomers, respectively, of chiral complexes of transition metals (Fe, Ru, and Rh).[9,10] Recently, it has been reported that the enantiomeric pairs of daunorubicin or helicene display structural selectivity in binding to B- or Z-DNA.[11] However, none of these systems can be used as chiroptical probes because recognition of the Z or B forms is not reflected in unique spectroscopic features, such as new CD bands, which unequivocally show the detection event.

[*] Dr. M. Balaz, Dr. A. E. Holmes, Prof. K. Nakanishi, Prof. N. Berova
Department of Chemistry
Columbia University
3000 Broadway, NY, 10027 (USA)
Fax: (+1) 212-932-1289
E-mail: ndb1@columbia.edu

M. De Napoli, A. Mammana, Prof. R. Purrello
Dipartimento di Scienze Chimiche
Università di Catania
Viale Andrea Doria 6, 95125 Catania (Italy)
Fax: (+39) 095-580-138
E-mail: rpurrello@dipchi.unict.it

[**] R.P. thanks the MIUR (PRIN, FIRB) for financial support.

Supporting information for this article is available on the WWW under http://www.angewandte.org or from the author.

 © 2005 Wiley-VCH Verlag GmbH & Co. KGaA, Weinheim DOI: 10.1002/anie.200501149

Porphyrins and their metallo-derivatives are very attractive molecules because of their unique spectroscopic and geometric properties. They have been covalently linked to specific chiral sequences, and their CD spectral properties have been used to resolve complicated stereochemical issues[12–15] as well as monitor polynucleotide dynamics.[16] Also, the noncovalent interactions of cationic or anionic water-soluble achiral porphyrins with chiral templates have been exploited to build supramolecular species to detect and/or amplify the handedness of the matrix.[17,18] Achiral cationic porphyrins are indeed good candidates as noncovalent probes for right- and left-handed DNA.[19] Up to now, cationic porphyrins and metalloporphyrins have been used as reporters of different sequences of DNA bases,[20–22] but have never been employed for recognizing the handedness of a DNA helix.

Circular dichroism spectroscopy has been very useful for distinguishing the three main DNA-binding modes of porphyrins: intercalation (negative CD), outside groove binding (positive CD), and outside stacking (bisignate CD).[20,21] However, few studies have been performed on the interactions of cationic porphyrins with Z-DNA because the intercalation of porphyrins reverts the helix back to the B form.[23] The latter data suggest that pentacoordinated cationic metalloporphyrins, such as the zinc(II) derivative of *meso*-tetrakis(4-*N*-methylpyridyl)porphyrin (ZnT4, **1**; Figure 1), should be an ideal chiroptical probe for Z-DNA because the axially coordinated water molecule hinders intercalation[24–28] and prevents the Z-to-B transition.

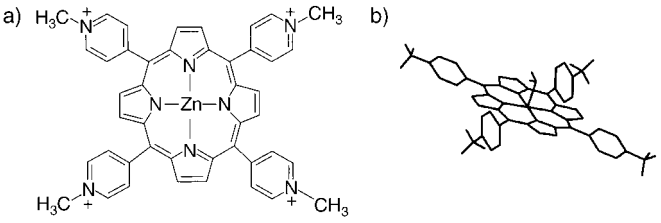


Figure 1. a) Chemical structure of zinc(II) porphyrin **1** and b) its 3D structure which shows the axially coordinated water molecule.

In our study we used poly(dG-dC)$_2$ (poly(deoxyguanylic-deoxycytidylic) acid; average base length 960), as this alternating purine–pyrimidine sequence favors the Z conformation. The B-to-Z transition can be induced in vitro by molar concentrations of NaCl, millimolar concentrations of multivalent cations such as $Co(NH_3)_6^{3+}$, or micromolar concentrations of protonated spermine.[29,30] Among these, spermine seems to be the most appropriate choice as this tetraamine, which is fully protonated at pH 7, is ubiquitous in cells and other biological systems.[31]

With B-DNA (Figure 2, blue line) only a small ICD signal is detectable in the visible region, while with Z-DNA (Figure 2, red line) a very intense bisignate curve, with $\Delta\varepsilon = -154\,M^{-1}cm^{-1}$ at $\lambda = 449$ nm and $\Delta\varepsilon = +87\,M^{-1}cm^{-1}$ at $\lambda = 433$ nm, is observed even at concentrations as low as 1 μM of **1**. The ICD spectra remain remarkably different at concentrations of **1** ranging from 1 to 8 μM (see Supporting Information) which thus shows that ZnT4 (**1**) can be highly diagnostic of the different DNA structures. The region below 300 nm in the CD spectra suggests changes in the Z-DNA helix upon interactions with **1** which become more apparent with increasing concentrations of porphyrin.

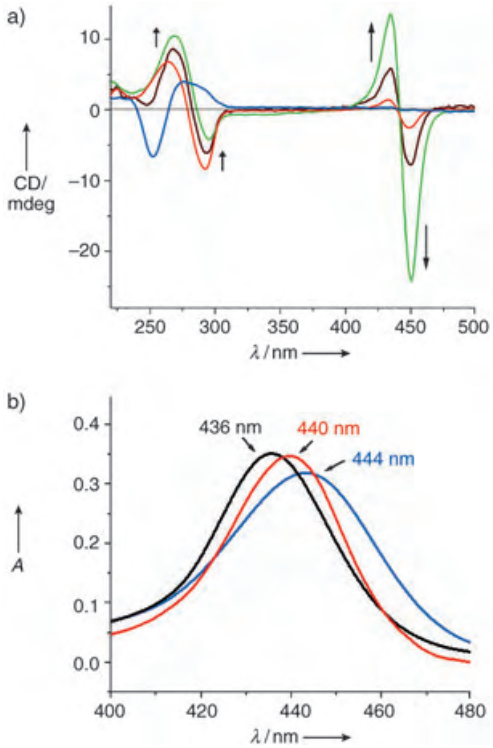


Figure 2. a) Circular dichroism (CD) spectra of Z-DNA (50 μM) in the presence of **1** (1 μM (red), 4 μM (brown), and 8 μM (green)), and B-DNA (50 μM) in the presence of **1** (1 μM; blue). b) Variation of the Soret band in the UV/Vis spectra of unbound **1** (black), **1**+Z-DNA (red), and **1**+B-DNA (blue).

So far,[21,32] observation of a ICD bisignate signal has been related to the aggregation of porphyrins. However, absorption data of ZnT4 (**1**) in the presence of Z-DNA (Figure 2b) does not support porphyrin aggregation, which should lead to quite extensive hypochromicity and broadening of the Soret band. None of these changes are observed upon binding of **1** to Z-DNA. To understand the origin of the bisignate signal we also performed fluorescence measurements, as porphyrin aggregation usually leads to severe quenching of the fluorescent emission. While the fluorescence of ZnT4 (**1**) is quenched upon complexation with B-DNA, it is only marginally affected in the presence of the Z form (Figure 3). In particular, the emission of **1** at $\lambda = 633$ nm is blue-shifted to 622 nm and quenched slightly upon binding to Z-DNA, while the intensity of the band at 670 nm increases by about 10%. This behavior clearly indicates the absence of close π–π interactions. The increase in fluorescence of **1** upon binding to Z-DNA suggests that the porphyrins lose some vibrational freedom as a result of a tighter interaction with Z-DNA than that found with B-DNA.

While the presence of the bisignate signal implies electronic communication between the porphyrin chromo-

 © 2005 Wiley-VCH Verlag GmbH & Co. KGaA, Weinheim

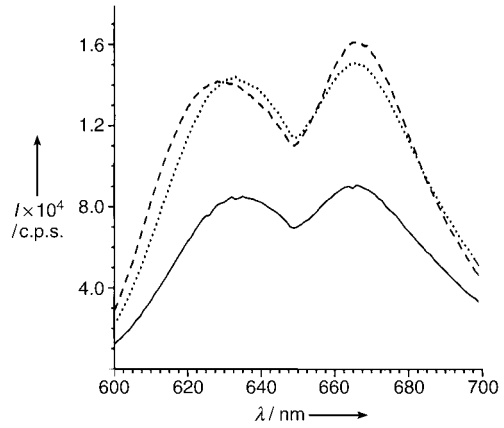


Figure 3. Fluorescence spectra (*I*/counts per second) of **1** unbound (••••), in the presence of Z-DNA (50 μM; -----), and in the presence of B-DNA (50 μM; ——).

phores (Figure 2), this is not inferred from either the absorption or fluorescence spectra (Figure 2b and Figure 3, respectively).

To better understand the binding modes, resonance light scattering (RLS) measurements were performed.[33] One advantage of RLS compared with other scattering techniques is that it provides information on the coupling between the transition dipole moments of interacting chromophores. RLS data provided a clear difference in the interactions of **1** with B- and Z-DNA (Figure 4). The RLS spectrum for the system

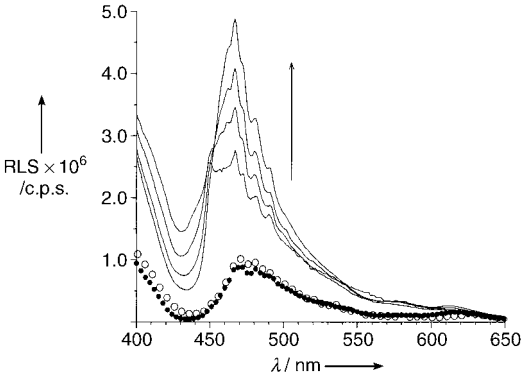


Figure 4. Resonance light scattering (RLS/counts per second) spectra of unbound **1** (2 μM; ○), **1** (2–8 μM) in the presence of B-DNA (50 μM; ●), and **1** (2, 4, 6, and 8 μM) in the presence of Z-DNA (50 μM; ——).

1·B-DNA is superimposable on that of free ZnT4 (**1**) at the same concentration, and its intensity did not change upon changing the concentration of **1**. In contrast, the intensity of the RLS spectrum of **1** in the presence of Z-DNA (**1**·Z-DNA) was higher than that of unbound **1** at the same concentration and increases with increasing concentrations of **1** (Figure 4). Therefore, in agreement with ICD data, RLS indicates that the porphyrins ZnT4 (**1**) are electronically coupled on Z-DNA but not on B-DNA.

Thus the CD, absorption, fluorescence, and RLS spectra show a profound difference in the binding modes of **1** with the two forms of DNA, B and Z . ICD and RLS data reveal that the porphyrin probes are dispersed disorderly on B-DNA and, therefore, not involved in interporphyrin coupling. In contrast, the structure of Z-DNA induces an ordered distribution of **1** which allows electronic coupling between porphyrin molecules that are not in close π–π contact (according to fluorescence measurements).

The different modes of interporphyrin coupling observed with B- or Z-DNA suggests that interaction of ZnT4 (**1**) with Z-DNA involves an additional binding site. Moreover, it is quite unlikely that only the different geometry of the phosphate backbone of the two DNA forms might cause such a different distribution of the porphyrin molecules. Inspection of the structure of Z-DNA reveals that the alternate *anti* and *syn* conformation of nucleobases leads to exposure of guanine atoms N7 and C8, which are both shielded in the B form.[1,3] In Z-DNA, nitrogen atom N7 is available for coordination with transition-metal ions, as shown previously by IR,[34,35] and therefore can provide a site for axial coordination with the central zinc atom of **1**. This hypothesis is corroborated by recent fluorescence studies which reported that the interactions of a cationic zinc(II) porphyrin with polynucleotides caused a blue shift in the emission of the porphyrin despite the red shift in the absorption Soret band,[28,36] similar to what is observed here in the emission of **1**·Z-DNA. The "anomalous" shift of the emission maximum of the porphyrin was interpreted in that case as arising from a change in the binding with respect to the fifth ligand, that is, upon changing from a molecule of water to DNA. The change in the fifth ligand around the Zn(II) ion may also be the case here for **1**·Z-DNA, with substitution of the axial water molecule in ZnT4 (**1**) by guanine N7 of Z-DNA.

Compelling evidence for the occurrence of this binding event came from a competition experiment. Figure 5 shows the decrease in ICD in the Soret region of **1**·Z-DNA and the partial restoration of the original CD features of unbound Z-DNA upon addition of micromolar concentrations of Ni^{II} ions to a solution of the DNA–porphyrin complex. This behavior can be explained by the complexation of Ni^{II} ions to site N7 in Z-DNA and the simultaneous release of porphyrins **1**, together with the strains related to their binding as shown

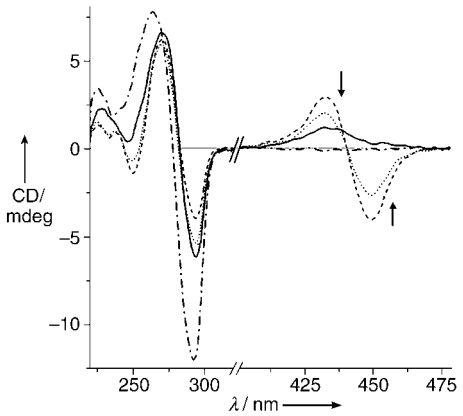


Figure 5. CD spectra of Z-DNA (–•–•), complex **1**·Z-DNA (-----), and **1**·Z-DNA after the addition of $NiCl_2$ (5 μM (••••) and 46 μM (——)).

 © 2005 Wiley-VCH Verlag GmbH & Co. KGaA, Weinheim

by the decrease of the ICD of **1** and the partial restoration of the CD spectrum of Z-DNA in Figure 5. A possible model of the **1**·Z-DNA complex is shown schematically in Figure 6b.

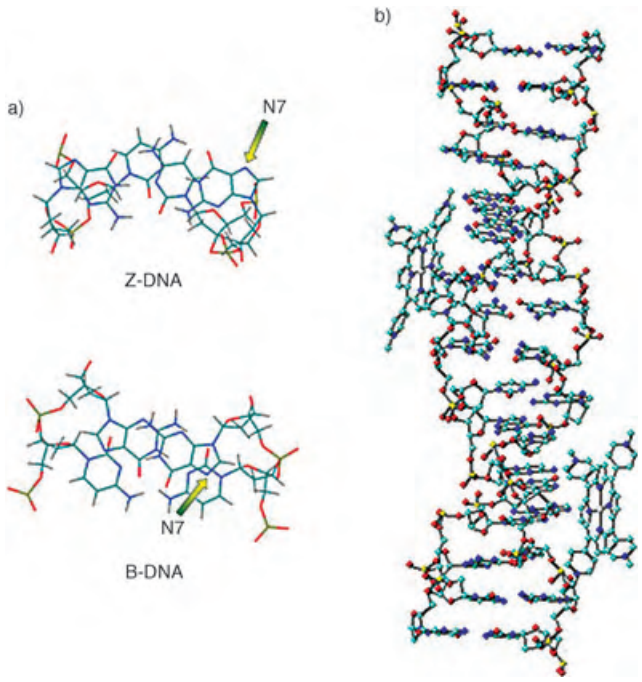


Figure 6. a) Stacking diagram demonstrating the overlap of successive bases (CpG = cytidine-phosphate–guanosine) along the helices of Z- and B-DNA (the arrows point to guanine N7 to highlight their different environments in the two forms), and b) schematic of the proposed structure of the complex **1**·Z-DNA.

In conclusion we have shown that cationic zinc porphyrin **1** is a promising chiroptical probe, which operates at micromolar concentrations, for the structure of left-handed Z-DNA. By application of different spectroscopic techniques, we have proposed the possible origin for a clear-cut discrimination between B- and Z-DNA in the presence of zinc porphyrin **1**. We have clarified the interaction of **1** with left-handed Z-DNA which in turn has led us to propose a structure for the complex **1**·Z-DNA. Studies aimed to better understand the interaction between Z-DNA and porphyrin molecules as well as the design of new porphyrin derivatives with improved discrimination abilities are underway.

Received: March 31, 2005
Published online: May 25, 2005

Keywords: chirality · circular dichroism · DNA · porphyrinoids · sensors

[1] P. Belmont, J. F. Constant, M. Demeunyck, *Chem. Soc. Rev.* **2001**, *30*, 70.
[2] T. M. Jovin, D. M. Soumpasis, L. P. McIntosh, *Annu. Rev. Phys. Chem.* **1987**, *38*, 521.
[3] A. Rich, A. Nordheim, A. H.-J. Wang, *Annu. Rev. Biochem.* **1984**, *53*, 791.
[4] A. Rich, S. Zhang, *Nat. Rev. Genet.* **2003**, *4*, 566.
[5] A. Herbert, J. Alfken, Y.-G. Kim, I. S. Mian, K. Nishikura, A. Rich, *Proc. Natl. Acad. Sci. USA* **1997**, *94*, 8421.
[6] Y.-G. Kim, K. Lowenhaupt, S. Maas, A. Herbert, T. Schwartz, A. Rich, *J. Biol. Chem.* **2000**, *275*, 26828.
[7] Y.-G. Kim, K. Lowenhaupt, D.-B. Oh, K. K. Kim, A. Rich, *Proc. Natl. Acad. Sci. USA* **2004**, *101*, 1514.
[8] T. Schwartz, M. A. Rould, K. Lowenhaupt, A. Herbert, A. Rich, *Science* **1999**, *284*, 1841.
[9] B. Norden, F. Tjerneld, *FEBS Lett.* **1976**, *67*, 368.
[10] C. S. Chow, J. K. Barton, *Methods Enzymol.* **1992**, *212*, 219.
[11] Y. Xu, Y. X. Zhang, H. Sugiyama, T. Umano, H. Osuga, K. Tanaka, *J. Am. Chem. Soc.* **2004**, *126*, 6566.
[12] X. F. Huang, N. Fujioka, G. Pescitelli, F. E. Koehn, R. T. Williamson, K. Nakanishi, N. Berova, *J. Am. Chem. Soc.* **2002**, *124*, 10320.
[13] G. Pescitelli, S. Gabriel, Y. K. Wang, J. Fleischhauer, R. W. Woody, N. Berova, *J. Am. Chem. Soc.* **2003**, *125*, 7613.
[14] S. Matile, N. Berova, K. Nakanishi, J. Fleischhauer, R. W. Woody, *J. Am. Chem. Soc.* **1996**, *118*, 5198.
[15] S. Matile, N. Berova, K. Nakanishi, *Chem. Biol.* **1996**, *3*, 379.
[16] M. Balaz, A. E. Holmes, M. Benedetti, P. C. Rodriguez, N. Berova, K. Nakanishi, G. Proni, *J. Am. Chem. Soc.* **2005**, *127*, 4172.
[17] E. Bellacchio, R. Lauceri, S. Gurrieri, L. M. Scolaro, A. Romeo, R. Purrello, *J. Am. Chem. Soc.* **1998**, *120*, 12353.
[18] R. Lauceri, A. Raudino, L. M. Scolaro, N. Micali, R. Purrello, *J. Am. Chem. Soc.* **2002**, *124*, 894.
[19] R. F. Pasternack, A. Giannetto, P. Pagano, E. J. Gibbs, *J. Am. Chem. Soc.* **1991**, *113*, 7799.
[20] R. J. Fiel, J. C. Howard, E. H. Mark, N. DattaGupta, *Nucleic Acids Res.* **1979**, *6*, 3093.
[21] R. F. Pasternack, *Chirality* **2003**, *15*, 329.
[22] S. Lee, S. H. Jeon, B.-J. Kim, S. W. Han, H. G. Jang, S. K. Kim, *Biophys. Chem.* **2001**, *92*, 35.
[23] R. F. Pasternack, D. Sidney, P. A. Hunt, E. A. Snowden, E. J. Gibbs, *Nucleic Acids Res.* **1986**, *14*, 3927.
[24] R. F. Pasternack, E. J. Gibbs, J. J. Villafranca, *Biochemistry* **1983**, *22*, 2406.
[25] J. A. Strickland, L. G. Marzilli, K. M. Gay, W. D. Wilson, *Biochemistry* **1988**, *27*, 8870.
[26] N. E. Geacintov, V. Ibanez, M. Rougee, R. V. Bensasson, *Biochemistry* **1987**, *26*, 3087.
[27] V. S. Chirvony, V. A. Galievsky, S. N. Terekhov, B. M. Dzhagarov, V. V. Ermolenkov, P.-Y. Turpin, *Biospectroscopy* **1999**, *5*, 302.
[28] J. M. Kelly, M. J. Murphy, D. J. McConnell, C. Ohuigin, *Nucleic Acids Res.* **1985**, *13*, 167.
[29] M. Behe, G. Felsenfeld, *Proc. Natl. Acad. Sci. USA* **1981**, *79*, 1619.
[30] A. Parkinson, M. Hawken, M. Hall, K. J. Sanders, A. Rodger, *Phys. Chem. Chem. Phys.* **2000**, *2*, 5469.
[31] A. C. Childs, D. J. Mehta, E. W. Gerner, *Cell. Mol. Life Sci.* **2003**, *60*, 1394.
[32] R. F. Pasternack, E. J. Gibbs, *ACS Symp. Ser.* **1989**, *402*, 59.
[33] R. F. Pasternack, P. J. Collings, *Science* **1995**, *269*, 935.
[34] J. A. Taboury, P. Bourtayre, J. Liquier, E. Taillandier, *Nucleic Acids Res.* **1984**, *12*, 4247.
[35] D. M. Loprete, K. A. Hartman, *Biochemistry* **1993**, *32*, 4077.
[36] S. A. Bejune, A. H. Shelton, D. R. McMillin, *Inorg. Chem.* **2003**, *42*, 8465.

 © 2005 Wiley-VCH Verlag GmbH & Co. KGaA, Weinheim

Nanotechnology

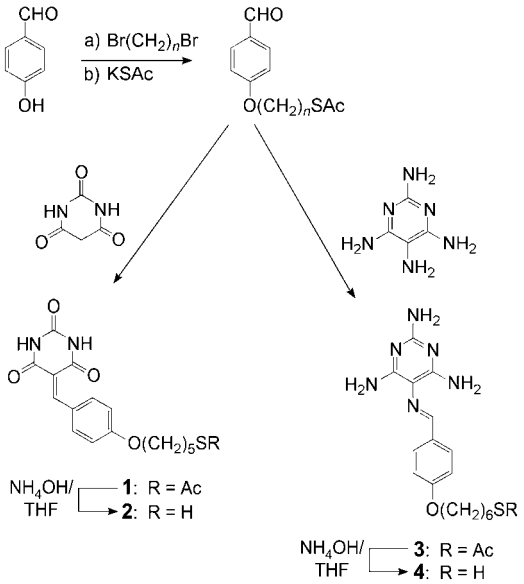
Hydrogen-Bonded CdS Nanoparticle Assemblies on Electrodes for Photoelectrochemical Applications**

Ronan Baron, Chih-Hao Huang, Dario M. Bassani, Avital Onopriyenko, Maya Zayats, and Itamar Willner**

The organization of functional semiconductor nanoparticles on surfaces has been extensively examined in recent years,[1] and the use of organized semiconductor nanoparticle systems for photoelectrochemical applications has attracted specific research efforts.[2] For example, core–shell nanoparticle systems were reported to behave as organized matrices that assist charge separation and enhance photocurrent generation when deposited on electrodes.[3] Similarly, the electropolymerization of CdS semiconductor nanoparticles in conductive bis-aniline films proved to result in an organized system that facilitated the charge separation of electron–hole pairs, generated upon photoexcitation of the semiconductor nanoparticles, and the transport of conduction-band electrons to the electrode and led to improved photocurrents.[4] The deposition of layered semiconductor nanoparticles on surfaces by using electrostatic interactions[5] or covalent bonds[6] has been described. Likewise, the assembly of semiconductor nanoparticles on electrode supports by using molecular[7] or supramolecular[8] cross-linkers and hybrid layered metal nanoparticle/semiconductor nanoparticle assemblies[9a] or carbon nanotube/semiconductor nanoparticle systems[9b] were studied. The relationship between structure and photoelectrochemical function in these nanostructures was characterized, and the assembly of these hybrid systems proved to be an effective means to improve the generation of photocurrents by assisting charge separation.

In other organized systems, hydrogen-bonded interactions are an important motif in the generation of supramolecular structures.[10] However, the use of hydrogen bonds to assemble nanoparticle structures has been less explored. The aggregation of silver nanoparticles[11] or gold nanoparticles[12] by interparticle hydrogen bonds of the capping monolayers was reported. Also, modified gold nanoparticles that form hydrogen-bonded host–guest complexes have been synthesized[13] and applied to the development of an electrochemical sensor for phosphate.[13b] To date, the use of hydrogen bonds to fabricate layered nanoparticle structures on surfaces is little explored, but the formation of a multilayer of gold nanoparticles, modified by carboxylic acids, using polyvinylpyridine as the cross-linker in a layer-by-layer deposition process was examined.[14] However, the assembly of functional hydrogen-bonded layered nanoparticle structures on surfaces is unknown. Herein, we report the assembly of cadmium sulfide nanoparticles and gold nanoparticle/cadmium sulfide nanoparticle hybrids on gold surfaces through complementary barbiturate–triaminodiazine hydrogen-bonded interactions and the application of the systems for the generation of photocurrents.

The thioacetyl-protected barbiturate **1** and its complementary hydrogen-bonding aminopyrimidine partner **3** (Scheme 1) were used to modify the CdS or Au nanoparticles.



Scheme 1. Synthesis and structures of barbiturate compounds **1** and **2** as well as their triaminodiazine complements **3** and **4**. $n = 5$ for **1** and **2**; $n = 6$ for **3** and **4**.

The capped nanoparticles were then organized on surfaces by using complementary hydrogen bonds as the driving force. The CdS nanoparticles (4–5 nm diameter) were prepared according to reported methods,[15] and the resulting nanoparticles were treated in a solution of heptane/THF with the thiol derivatives **2** or **4**. The average loading of the CdS nanoparticles with **2** or **4** was determined spectroscopically by monitoring the absorption spectra of the CdS nanoparticles in solution before and after thiol modification. The subtraction of the respective absorbance spectra led to the net absorbance of the capping reagents associated with the CdS nanoparticles.

[*] C.-H. Huang, Dr. D. M. Bassani
Centre de Recherche en Chimie Moléculaire
LCOO CNRS UMR 5802
Université Bordeaux 1
351, Cours de la Libération, 33405 Talence cedex (France)
Fax: (+33) 5-4000-6158
E-mail: d.bassani@lcoo.u-bordeaux1.fr
Dr. R. Baron, A. Onopriyenko, M. Zayats, Prof. I. Willner
Institute of Chemistry and
the Farkas Center for Light-Induced Processes
The Hebrew University of Jerusalem
Jerusalem 91904 (Israel)
Fax: (+972)-2-652-7715
E-mail: willnea@vms.huji.ac.il

[**] This work was supported by the German–Israeli Program (DIP) as well as the French MRT and CNRS (AC Nanosciences–Nanotechnologies). M.Z. acknowledges the Israeli Ministry of Science for a Levi Eshkol fellowship. The authors are grateful to Prof. D. Mandler and A. Becker (The Hebrew University of Jerusalem) for assistance with the FTIR measurements.

Supporting information for this article is available on the WWW under http://www.angewandte.org or from the author.

 © 2005 Wiley-VCH Verlag GmbH & Co. KGaA, Weinheim DOI: 10.1002/anie.200463055

From the absorbance value at $\lambda = 270$ nm of a solution of known concentration of the CdS nanoparticles (the extinction coefficient (ε) of 4–5-nm CdS nanoparticles is $7 \times 10^5\,\text{M}^{-1}\,\text{cm}^{-1}$),[16] we estimate the average loading of **2** and **4** to be 172 and 190 units per particle, respectively.

Figure 1 depicts the methods to assemble the hydrogen-bonded CdS nanoparticles on gold electrodes. The systems were assembled on Au/quartz piezoelectric crystals to enable

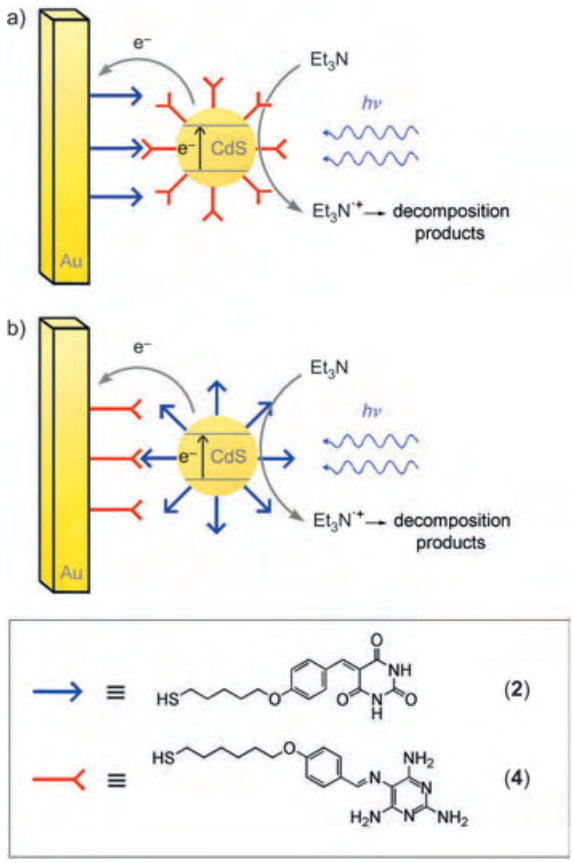


Figure 1. Schematic presentation of hydrogen-bonded CdS nanoparticle assemblies in which a) **2** is bound to the gold electrode and **4** is bound to the CdS nanoparticles, and b) **4** is bound to the electrode and **2** is associated with the CdS nanoparticles.

the characterization of the loading of the different components on the surfaces by microgravimetric quartz-crystal-microbalance (QCM) analyses. In one configuration, Figure 1 a, the thiolated barbiturate **2** was linked to the Au/quartz surface. From the frequency change (Δf), its surface coverage was calculated to be 6.6×10^{-10} mole cm^{-2}. The monolayer-modified surface was then treated with the **4**-functionalized CdS nanoparticles in dry THF. From the frequency change ($\Delta f = -420$ Hz in air), we estimate the surface coverage of the CdS nanoparticles to be 3.1×10^{12} particles cm^{-2} (note, the calculation took into account the loading of the CdS nanoparticles with **4**). Thus, presumably, about 32 monolayer units participate in the hydrogen-bonded association of a CdS nanoparticle to the surface. Further support that the CdS nanoparticles are linked to the electrode by hydrogen bonds was obtained by FT-IR experiments. For the monolayer of thiolated barbiturate **2** on the gold-coated glass, a broad band at $\tilde{\nu} = 3250$ cm^{-1} for the N-H group and three sharp bands at $\tilde{\nu} = 1747$, 1716, and 1687 cm^{-1} for the three different carbonyl functionalities were observed. These bands are consistent with the reported values of IR peaks for barbiturate derivatives.[17] A drop of a solution that contained the CdS nanoparticles capped with the thiolated triaminodiazine **4** was dried on the gold surface, and the residue revealed a broad band at $\tilde{\nu} = 3255$ cm^{-1} (N-H) and an intense band at 1574 cm^{-1} (C=N). For the hydrogen-bonded assembly in which the **4**-capped CdS nanoparticles are linked to the **2**-functionalized gold surface, two bands at $\tilde{\nu} = 3262$ and 3031 cm^{-1} were observed. The appearance of a wide band at $\tilde{\nu} = 3031$ cm^{-1} was previously attributed to the hydrogen-bonded N–H bond between the aminoazine and barbiturate carbonyl functionalities.[18] Similarly, the three sharp bands of the carbonyl group of the barbiturate monolayer are reduced to two bands and shifted to $\tilde{\nu} = 1702$ and 1698 cm^{-1} upon formation of the hydrogen-bonded assembly with the **4**-capped CdS nanoparticles. These shifts are in good agreement with the reported IR bands of hydrogen-bonded assemblies between barbiturate and triaminodiazine derivatives.[17]

In the second configuration of the hydrogen-bonded CdS nanoparticles, as depicted in Figure 1 b, **4** was assembled on the Au/quartz crystal with a surface coverage of 6.4×10^{-10} mole cm^{-2}. The **2**-functionalized CdS nanoparticles were then bound through hydrogen bonds to the surface with a surface coverage of 3.3×10^{12} particles cm^{-2}. The formation of this hydrogen-bonded CdS nanoparticle assembly was also supported by FTIR measurements. Similar to the spectral changes discussed in detail above for system a, analogous shifts for system b were observed. New stretching frequencies for the hydrogen-bonded carbonyl group at $\tilde{\nu} =$ 1700 and 1705 cm^{-1} as well as the non-bonded carbonyl functionalities associated with the particles at $\tilde{\nu} = 1730$, 1716, and 1683 cm^{-1} are the most indicative bands for the formation of the hydrogen-bonded system. A new, less intense band at $\tilde{\nu} = 3035$ cm^{-1}, which corresponds to the hydrogen-bonded N–H bond to the barbiturate carbonyl functions that cap the CdS nanoparticles, was also observed.

The resulting surfaces were also characterized by absorption spectroscopy. Figure 2 a shows the absorption spectrum of the gold surface functionalized with CdS nanoparticles, generated by the association of the **4**-modified CdS nanoparticles with the **2**-functionalized surface. Figure 2 b shows the photocurrent action spectrum of the electrodes modified with CdS nanoparticles, prepared according to system a (Figure 1 a). The photocurrents were recorded in anhydrous THF in the presence of triethylamine (Et_3N) as the electron donor and tetra-*n*-butylammonium hexafluorophosphate as the electrolyte. The photocurrent action spectrum follows the absorbance pattern of the CdS nanoparticles. Furthermore, control experiments indicated that in the absence of either the electron donor or the CdS nanoparticles, no photocurrent was generated in the system. Figure 2 c shows the effect of the applied potential on the magnitude of the resulting photocurrent. As the applied potential is negatively shifted, the photocurrent decreases and is completely blocked at about −0.5 V (vs SCE). These results allow us to define the

 © 2005 Wiley-VCH Verlag GmbH & Co. KGaA, Weinheim

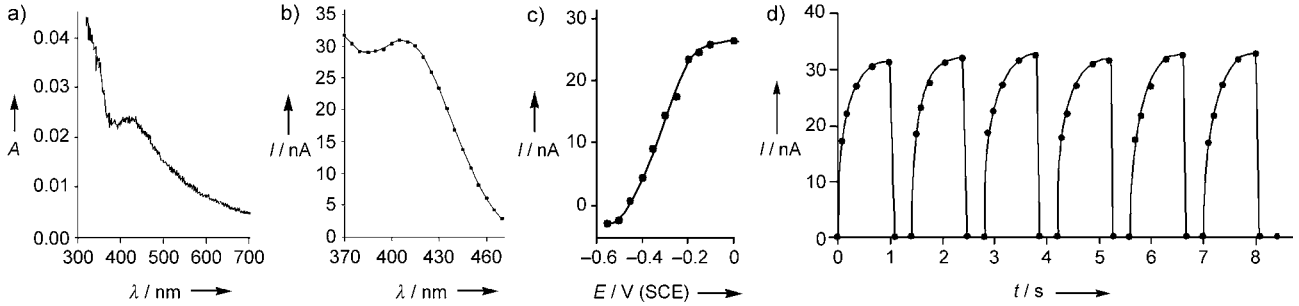


Figure 2. a) Absorbance spectrum of the CdS nanoparticle layer on a gold-coated glass support prepared according to Figure 1 a; b) photocurrent action spectrum corresponding to the CdS nanoparticle assembly shown in Figure 1 a; c) photocurrent recorded as a function of the applied potential at $\lambda = 410$ nm (SCE = standard calomel electrode); d) light-induced "ON" and "OFF" states of switchable photocurrents generated upon irradiation of the functionalized electrode at $\lambda = 410$ nm. All data were recorded in THF solutions containing triethylamine (2×10^{-2} M) and tetra-*n*-butylammonium hexafluorophosphate (0.1 M).

mechanism for the generation of photocurrents in the system. Upon photoexcitation of the CdS nanoparticles, an electron–hole pair is generated in the nanoparticles. The transfer of conduction-band electrons to the electrode followed by the oxidation of the electron donor by valence-band holes leads to the formation of the steady-state photocurrent. Biasing the electrode potential at −0.5 V (vs SCE) blocks the transfer of conduction-band electrons to the electrode which prohibits the generation of photocurrents. By knowing the absorbance features of the CdS nanoparticle interface, the efficiency of light to electrical-energy conversion was calculated to be 0.5%. The functionalized electrode revealed reasonable stability. Figure 2 d shows the cyclic "ON" and "OFF" formation of light-induced photocurrents in the system. The electrode was stable for at least 3 days upon storage in the dark under dry conditions, whilst less than 10% decrease in the photocurrents were observed after immersion for 5 hours in the THF/electrolyte solution.

Further support that the CdS nanoparticle interface is stabilized by hydrogen-bonding interactions was obtained by examining the effect on the resulting photocurrent of the addition of 10% water to the THF/electrolyte solution (Figure 3). As the time interval after the addition of H_2O becomes longer, the resulting photocurrent decreases. Simultaneous QCM analyses indicated that the addition of H_2O to the CdS nanoparticle modified Au/quartz surface resulted in the dissociation of CdS nanoparticles from the electrode support. Interestingly, however, we did not notice desorbtion of the photoactive interface within 10 minutes after the addition of 2% H_2O to the THF/electrolyte solution. Increasing the concentration of H_2O enhanced the dissociation rate of the CdS nanoparticles. The relative stability of the CdS nanoparticle interface is therefore attributed to the multipoint hydrogen-bonded association of the nanoparticles to the monolayer which results in the synergetic binding of the nanoparticles to the surface.

The photocurrent action spectrum observed for the system described in Figure 1 b is depicted in the Supporting Information. The efficiency of conversion of light to electrical energy in this system was estimated to be about 0.4%. This electrode reveals similar properties and functions to the electrode configuration outlined in Figure 1 a. The addition of

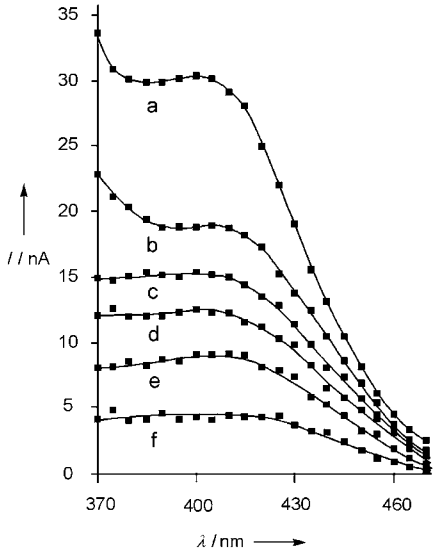


Figure 3. Effect of added water on the photocurrent spectra generated by the CdS nanoparticle assembly shown in Figure 1 a. Data recorded in THF solutions containing triethylamine (2×10^{-2} M) and tetra-*n*-butylammonium hexafluorophosphate (0.1 M). Photocurrent spectra were recorded a) before and (b–f) after the addition of 10% water to the solution in THF: b) 4 min, c) 8 min, d) 12 min, e) 16 min, and f) 20 min.

10% of H_2O to this system similarly resulted in the time-dependent degradation of the hydrogen-bonded interface and decrease of the photocurrent.

In light of previous observations that employed layered gold nanoparticle/CdS nanoparticle hybrid systems for the enhanced generation of photocurrents,[9a] we decided to use hydrogen bonds as a means to construct gold nanoparticle/CdS nanoparticle composites (Figure 4). Citrate-stabilized gold nanoparticles[19] (12 ± 1 nm) were linked by a thiolated monolayer to a Au/quartz surface and a semitransparent (Au film thickness ≈ 50 nm) gold-coated glass slide. Then a monolayer of **4** was assembled on the gold nanoparticles, with an average loading of 5.8×10^3 molecules of **4** per particle determined by QCM measurements. CdS nanoparticles functionalized with **2** were then linked through hydrogen bonds to the gold nanoparticles. QCM measurements of the

 © 2005 Wiley-VCH Verlag GmbH & Co. KGaA, Weinheim

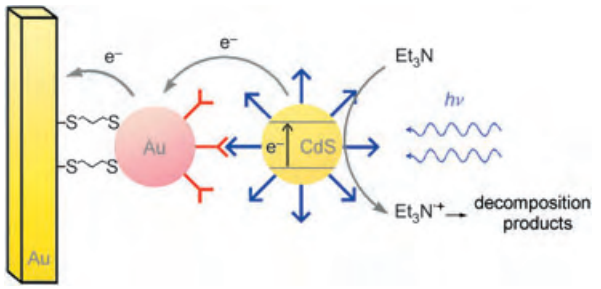


Figure 4. Schematic representation of the layered hydrogen-bonded gold nanoparticle/CdS nanoparticle assembly associated with a gold electrode in which the gold nanoparticles are functionalized with **4** and the CdS nanoparticles are modified with complementary **2**.

parallel assembly of the layered nanoparticle system on a Au/quartz piezoelectric crystal indicated that the surface coverage of the base dithiol monolayer was 8×10^{-10} mole cm^{-2} and the surface coverage of the gold nanoparticles and the CdS nanoparticles corresponded to 7.0×10^{10} and 2.6×10^{12} particles cm^{-2}, respectively.

Figure 5a, curve 1, shows the absorption spectrum of the primary layer of gold nanoparticles on the gold surface. The characteristic plasmon absorbance is clearly visible at $\lambda=$ 520 nm. From the values of the absorbance and the extinction

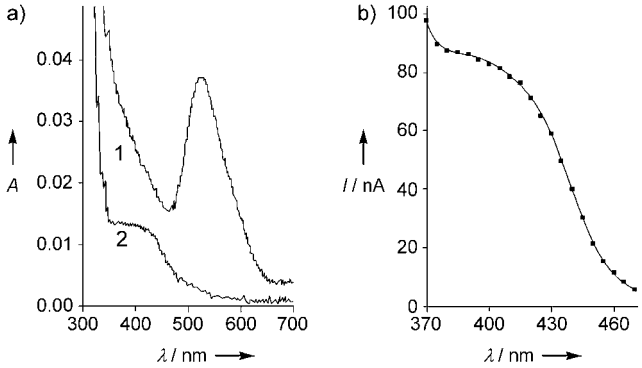


Figure 5. a) Absorbance spectra on a gold-coated glass support of 1) the gold nanoparticle layer and 2) the gold nanoparticle/CdS nanoparticle assembly shown in Figure 4. b) Photocurrent action spectrum corresponding to the gold nanoparticle/CdS nanoparticle assembly. Data recorded in THF solutions containing triethylamine (2×10^{-2} M) and tetra-*n*-butylammonium hexafluorophosphate (0.1 M).

coefficient of 12-nm gold nanoparticles ($\varepsilon=3\times10^{8}$ M^{-1} cm^{-1}),[20] the surface coverage of the gold nanoparticles was estimated to be 6.9×10^{10} particles cm^{-2}, in excellent agreement with the QCM measurements. Figure 5a, curve 2, shows the corrected absorption spectrum of the system after linking the **2**-functionalized CdS nanoparticles to the surface, with the background absorbance of the primary gold nanoparticles subtracted from the spectrum of the composite. The absorbance spectrum of the CdS nanoparticles is clearly identified and exhibits a characteristic shoulder at $\lambda=420$ nm.

Photocurrents from the electrode functionalized with the gold nanoparticle/CdS nanoparticle array were then measured. Figure 5b shows the photocurrent action spectrum of the system. The results are compared to the related hydrogen-bonded CdS nanoparticle assembly that lacks the gold nanoparticles (Figure 1b). The depicted photocurrent action spectra were normalized to exhibit identical surface coverage of the CdS nanoparticles. The photocurrent observed in the gold nanoparticle/CdS nanoparticle composite system is approximately 2.6-fold enhanced relative to the system that lacks the gold nanoparticles. The enhanced photocurrent in the gold nanoparticle/CdS nanoparticle composite system is attributed to the charge separation of the electron–hole pair that is generated upon the photochemical excitation of the CdS nanoparticles; that is, the transfer of the conduction-band electrons to the gold nanoparticles spatially separates the electron–hole pair, thus leading to the retardation of the electron–hole recombination. This delay facilitates the effective scavenging of the valence-band holes by the electron donor as well as the transfer of the electrons trapped by the gold nanoparticles to the electrode, processes that lead to the enhanced generation of photocurrents. There is a substantial difference between the hydrogen-bonded bulk gold surface/CdS nanoparticle configurations (Figure 1a and b) and the hydrogen-bonded gold nanoparticle/CdS nanoparticle array (Figure 4) in facilitating charge separation. A comparison of the surface coverage of molecular components on the functionalized gold nanoparticles or the CdS nanoparticles with the surface coverage by **2**, **4**, or propanedithiol on the bulk gold surfaces indicates that the surface coverage of the bulk gold support is 50- to 100-fold higher than the loadings of the particles. This result implies that the CdS nanoparticles which are linked to the electrode exist in a rigid configuration, whereas structural flexibility exists within the gold nanoparticle/CdS nanoparticle array. This flexibility facilitates the quenching of the conduction-band electrons and enhances charge separation. Furthermore, note that the schematic configuration depicted in Figure 4 is a simplified configuration. The CdS nanoparticles as well as the gold nanoparticles exhibit irregular surface roughness. As a result, the nanoparticles may exist at a substantially closer distance than that dictated by the hydrogen-bonded complex which would facilitate the interparticle charge transport. The special separation of the electron and hole in two different particles then retards the recombination reactions and enhances the photocurrent.

The addition of water to the composite gold nanoparticle/CdS nanoparticle system resulted in the dissociation of the CdS nanoparticles, as observed from microgravimetric QCM measurements, absorption spectra, and photocurrent measurements (see Figure 6). These results imply that the CdS nanoparticles are linked to the gold nanoparticles by complementary hydrogen bonds that are dissociated by water, whereas the gold nanoparticles themselves are tightly bound to the gold support by the dithiol bridging monolayer.

In conclusion, the present study has employed complementary hydrogen bonds to fabricate metal and semiconductor nanoparticle arrays on surfaces and has demonstrated the functional use of the resulting nanostructures for the generation of photocurrents. Although the results may have a limited impact for energy conversion owing to the low photocurrent values, the study highlights fundamental effects

 © 2005 Wiley-VCH Verlag GmbH & Co. KGaA, Weinheim

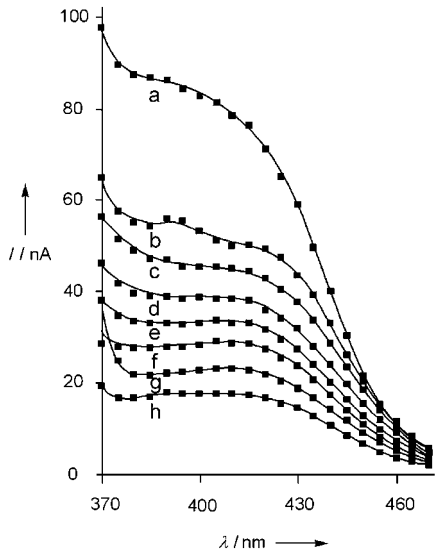


Figure 6. Effect of added water on the photocurrent spectra generated by the gold nanoparticle/CdS nanoparticle assembly shown in Figure 4. Data were recorded in THF solutions containing triethylamine (2×10^{-2} M) and tetra-*n*-butylammonium hexafluorophosphate (0.1 M). Photocurrent spectra were recorded a) before and (b–f) after the addition of 10% water to the solution in THF: b) 4 min, c) 8 min, d) 12 min, e) 16 min, f) 20 min, g) 24 min, and h) 28 min.

of hydrogen-bonded complexes on charge transport at semiconductor nanoparticle/electrode interfaces. The fact that the presented systems are in a monolayer/bilayer nanoparticle configuration suggests, however, that by tailoring hydrogen-bonded composites of higher complexity the resulting photocurrents could be further enhanced.

Experimental Section

Photocurrent experiments were performed using a homebuilt instrument described previously.[7] All spectra were recorded under argon on solutions in THF (0.1M) that contained triethylamine (Et_3N; 2×10^{-2} M) as a sacrificial electron donor and tetra-*n*-butylammonium hexafluorophosphate (0.1M) as electrolyte. The electrodes used were piezoelectric Au/quartz crystals, which allowed us to determine the surface coverage as well as record the photocurrent. The photocurrent spectra were normalized by using the surface coverage of CdS nanoparticles on the piezoelectric crystals.

Absorbance spectra and quantum efficiencies were measured using glass slides coated with a 3-nm layer of chromium and a 50-nm layer of gold (Analytical-μ Systems, Germany). The absorbance spectra were obtained after subtraction of the background absorbance of the gold coating. The quantum efficiency was calculated by determining the light intensity absorbed by the CdS nanoparticle systems and the photocurrent intensities generated by the respective electrodes. The intensity of the light absorbed by the CdS nanoparticle layered system was determined by monitoring the intensity of the light transmitted through the gold-coated glass and the light reflected from the coated surface, and then subtracting the respective values for the transmitted/reflected light for the gold surface modified with CdS nanoparticles. To determine the intensity of absorbed light in the gold nanoparticle/CdS nanoparticle system, the intensity of the transmitted/reflected light in the gold nanoparticle/CdS nanoparticle system was substracted from the intensities of the transmitted/reflected light from the gold surface modified with gold nanoparticles.

Preparation of the CdS nanoparticle assemblies: (The characterization of compounds **1** and **3** is detailed in the Supporting Information.) The acetyl protecting groups in compounds **1** and **3** were removed by hydrolysis under basic conditions in THF by the addition of approximately 10 mg of NH_4OH. CdS nanoparticles, which were prepared according to the reported methods,[15] were capped by mixing solutions of CdS nanoparticles (4 mL) with a solution of **1** or **3** (5×10^{-3} M) in THF (2 mL). The mixture was stirred overnight, then pyridine (0.5 mL) was added, and the resulting particles were collected by centrifugation, washed with THF (×3), and dissolved in THF (2 mL). This solution of nanoparticles was then used to assemble the functionalized electrodes.

The electrode configurations shown in Figure 1a and b were prepared by the following procedure: Au/quartz-crystal electrodes and gold-plated glass electrodes were cleaned in boiling ethanol prior to modification. The electrodes were then modified with either **2** or **4** (5×10^{-3} M overnight in THF) and then immersed for 30 min in the solution of the CdS nanoparticles in THF that were capped with the complementary compound. After each modification step, the electrodes were washed with THF (×3).

For the configuration presented in Figure 4, the electrodes were modified with a propanedithiol monolayer (10^{-2} M, overnight in methanol) and then immersed overnight in an aqueous solution of citrate-stabilized gold nanoparticles. The electrodes were then modified by the procedure described above for the configuration of Figure 1b.

FT-IR spectra were obtained using a Bruker Equinox 55 instrument. The measurements were made directly on gold-coated glass slides in the dry phase under argon, and 1000 scans were averaged for each curve.

The estimation of the number of hydrogen bonds between the CdS nanoparticles and the complementary base monolayer associated with the gold support was based on some rough geometrical approximations. By knowing the average particle diameter, the footprint area of the particles with the monolayer was calculated. By knowing the total loading of the CdS nanoparticles with **2** or **4** (the surface coverage of the gold surface is substantially higher than the coverage of the particles), we were able to estimate the number of hydrogen bonds between the nanoparticles and the surface by also assuming that all the units associated with the footprint area form the hydrogen bonds with the surface.

Received: December 24, 2004
Revised: March 6, 2005
Published online: May 24, 2005

Keywords: gold · hydrogen bonds · nanostructures · photoelectrochemistry · semiconductors

[1] a) A. N. Shipway, E. Katz, I. Willner, *ChemPhysChem* **2000**, *1*, 18–52; b) A. N. Shipway, I. Willner, *Chem. Commun.* **2001**, 2035–2045; c) E. Katz, I. Willner, *Angew. Chem.* **2004**, *116*, 6166–6235; *Angew. Chem. Int. Ed.* **2004**, *43*, 6042–6108.

[2] a) C. Nasr, S. Hotchandani, W. Y. Kim, R. S. Schmehl, P. V. Kamat, *J. Phys. Chem. B* **1997**, *101*, 7480–7487; b) V. Pardo-Yissar, E. Katz, J. Wasserman, I. Willner, *J. Am. Chem. Soc.* **2003**, *125*, 622–623; c) D. Dong, D. Zheng, F.-Q. Wang, X.-Q. Yang, N. Wang, Y.-G. Li, L.-H. Guo, J. Cheng, *Anal. Chem.* **2004**, *76*, 499–501.

[3] a) N.-G. Park, M. G. Kang, K. M. Kim, K. S. Ryu, S. H. Chang, D.-K. Kim, J. van de Lagemaat, K. D. Benkstein, A. J. Frank, *Langmuir* **2004**, *20*, 4246–4253; b) A. Zaban, S. G. Chen, S. Chappel, B. A. Gregg, *Chem. Commun.* **2000**, 2231–2232.

[4] E. Granot, F. Patolsky, I. Willner, *J. Phys. Chem. B* **2004**, *108*, 5875–5881.

 © 2005 Wiley-VCH Verlag GmbH & Co. KGaA, Weinheim

[5] a) N. A. Kotov, I. Dekany, J. H. Fendler, *J. Phys. Chem.* **1995**, *99*, 13065 – 13069; b) K. Ariga, Y. Lvov, M. Onda, I. Ichinose, T. Kunitake, *Chem. Lett.* **1997**, 125 – 126; c) Z. Tang, Y. Wang, N. A. Kotov, *Langmuir* **2002**, *18*, 7035 – 7040.
[6] a) V. L. Colvin, A. N. Goldstein, A. P. Alivisatos, *J. Am. Chem. Soc.* **1992**, *114*, 5221 – 5230; b) S. Westenhoff, N. A. Kotov, *J. Am. Chem. Soc.* **2002**, *124*, 2448 – 2449.
[7] L. Sheeney-Haj-Ichia, J. Wasserman, I. Willner, *Adv. Mater.* **2002**, *14*, 1323 – 1326.
[8] L. Sheeney-Haj-Ichia, I. Willner, *J. Phys. Chem. B* **2002**, *106*, 13094 – 13097.
[9] a) L. Sheeney-Haj-Ichia, S. Pogorelova, Y. Gofer, I. Willner, *Adv. Funct. Mater.* **2004**, *14*, 416 – 424; b) L. Sheeney-Haj-Ichia, B. Basnar, I. Willner, *Angew. Chem.* **2005**, *117*, 80 – 85; *Angew. Chem. Int.* Ed. **2005**, *44*, 78 – 83.
[10] a) D. Coman, I. M. Russu, *J. Am. Chem. Soc.* **2003**, *125*, 6626 – 6627; b) M. Peters, I. Rozas, I. Alkorta, J. Elguero, *J. Phys. Chem. B* **2003**, *107*, 323 – 330; c) H.-C. Lin, H.-Y. Sheu, C.-L. Chang, C. Tsai, *J. Mater. Chem.* **2001**, *11*, 2958 – 2965.
[11] S. Mandal, A. Gale, N. Lala, R. Gonnade, V. Gavnir, M. Sastry, *Langmuir* **2001**, *17*, 6262 – 6268.
[12] a) L. Han, J. Luo, N. N. Kariuki, M. M. Maye, V. W. Jones, C. J. Zhong, *Chem. Mater.* **2003**, *15*, 29 – 37; b) A. K. Boal, V. M. Rotello, *Langmuir* **2000**, *16*, 9527 – 9532.
[13] a) A. K. Boal, V. M. Rotello, *J. Am. Chem. Soc.* **2002**, *124*, 5019 – 5024; b) A. Labande, J. Ruiz, D. Astruc, *J. Am. Chem. Soc.* **2002**, *124*, 1782 – 1789; c) U. Drechsler, B. Erdogan, V. Rotello, *Chem. Eur. J.* **2004**, *10*, 5570 – 5579.
[14] E. Hao, T. Lian, *Chem. Mater.* **2000**, *12*, 3392 – 3396.
[15] M. Miyake, H. Matsumoto, M. Nishizawa, T. Sakata, H. Mori, S. Kuwabata, H. Yoneyama, *Langmuir* **1997**, *13*, 742 – 746.
[16] W. W. Yu, L. Qu, W. Guo, X. Peng, *Chem. Mater.* **2003**, *15*, 2854 – 2860.
[17] W.-S. Yang, S.-G. Chen, X.-D. Chai, Y.-W Cao, R. Lu, W.-P. Chai, Y.-J. Jiang, T.-J. Li, J.-M. Lehn, *Synth. Met.* **1995**, 71, 2107 – 2108.
[18] Z. Sideratou, D. Tsiourvas, C. M. Paleos, E. Peppas, J. Anastassopoulou, T. Theophanides, *J. Mol. Struct.* **1999**, *484*, 91 – 101.
[19] K. C. Grabar, R. G. Freeman, M. B. Hommer, M. J. Natan, *Anal. Chem.* **1995**, *67*, 735 – 743.
[20] S. Link, M. El-Sayed, *J. Phys. Chem. B* **1999**, *103*, 8410 – 8426.

 © 2005 Wiley-VCH Verlag GmbH & Co. KGaA, Weinheim

Donor–Acceptor Systems

A Rigid Neutral Molecule Involving TTF and TCNQ Moieties with Intrinsic Charge- and Electron-Transfer Properties that Depend on the Polarity of the Solvent**

Evgeny Tsiperman, James Y. Becker, Vladimir Khodorkovsky,* Alex Shames, and Lev Shapiro*

Since the discovery[1] of the first organic metal in 1973, much attention has been devoted to the investigation of TTF, its derivatives, and analogues as electron-donor components for many charge-transfer (CT) complexes and ion-radical salts.[2] A proposed model of a unimolecular rectifier[3] involving TTF and TCNQ moieties linked covalently through a rigid saturated spacer has stimulated intensive studies in this direction. A concept involving a number of donor and acceptor units incorporated in a single molecule was later developed[4] that would enable the properties related to molecular organic conductors to be controlled. So far, the realization of this notion has been limited to linking moderate acceptors to TTF derivatives and weak donors to TCNQ fragments,[5] while the incorporation of TTF and TCNQ moieties in a single molecule has proved to be an elusive goal.[6]

In 2003, Bryce and co-workers published[7] a synthesis of a TTF-σ-TCNQ molecule containing a nonconjugated flexible spacer. This compound is expected to exhibit a high degree of intramolecular CT in both solution and the solid state. However, while its IR data are consistent with a degree of charge transfer of about 0.85 in the solid state, only less than 1% biradicals were observed by EPR and UV/Vis/NIR spectroscopy. Also, the redox potentials shifted by only 20 mV with respect to those of the individual donor and acceptor components, thus indicating only a small degree of donor–acceptor interaction. Furthermore the authors' claim of a thermally induced electron transfer in their system, which was based on temperature-dependent EPR measurements, is somewhat misleading. Their calculated HOMO/LUMO gap (0.17–0.75 eV) and measured energy of the CT transition (0.75 eV, red edge 0.45 eV) are much higher than the energy

[*] E. Tsiperman, Prof. J. Y. Becker, Prof. V. Khodorkovsky, Dr. L. Shapiro
Department of Chemistry
Ben-Gurion University of the Negev
P.O.B. 653, Beer-Sheva 84105 (Israel)
Fax: (+972) 8-647-2943
E-mail: becker@bgu.ac.il
hodor@bgu.ac.il

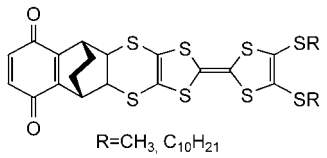
Dr. A. Shames
Department of Physics
Ben-Gurion University of the Negev
P.O.B. 653, Beer-Sheva 84105 (Israel)

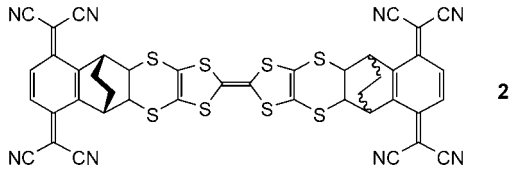
[**] V.K. was on leave at the Université de la Mediterranée, UMR CNRS 6114, 13288 Marseille 09 (France) during the preparation of this manuscript. TTF = tetrathiafulvalene; TCNQ = tetracyanoquinodimethane.

 DOI: 10.1002/anie.200500812 © 2005 Wiley-VCH Verlag GmbH & Co. KGaA, Weinheim

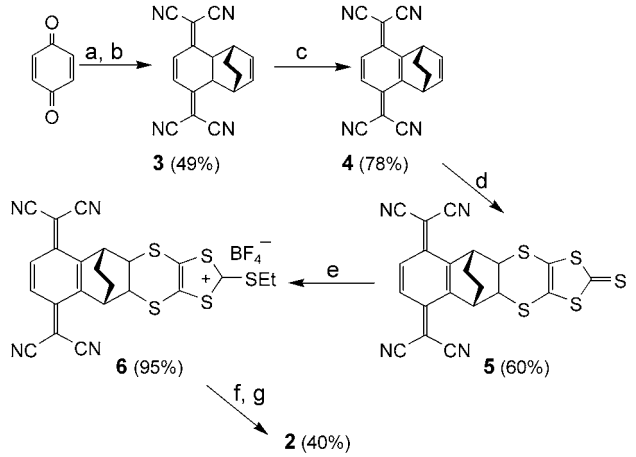
at room temperature (0.025 eV), and therefore, thermal ion-radical generation should be totally excluded. In our view, the discrepancies could stem from the flexible nature of the spacer used allowing several conformations, thus leading to difficulties in the interpretation of the observed results. Consequently, it would be more adequate to study TCNQ–TTF systems involving rigid spacers.

Recently[8] we reported the synthesis of compound **1** containing a TTF moiety covalently linked to *p*-benzoquinone through a rigid saturated spacer with a bent structure





that allows an intrinsic through-space charge transfer. Herein, we describe the synthesis, electrochemistry, and spectroscopic results of the rigid TCNQ-σ-TTF-σ-TCNQ derivative **2**. The synthesis was based on the known TCNQ derivative **4** (Scheme 1),[9] which was prepared by a novel procedure, since the reported oxidation was not reproducible in our hands. Intermediate **5** exhibited CT properties as a result of intramolecular through-space interactions between the TCNQ and trithiocarbonate moieties. The combination of zinc dust and bromine in dry acetonitrile[10] was utilized for the self-coupling of 2-ethylthio-1,3-dithiolium salt **6** to obtain



Scheme 1. Synthesis of TCNQ-σ-TTF-σ-TCNQ system **2**: a) PBQ (19 mmol), cyclohexadiene (60 mmol), EtOH (10 mL), b) $TiCl_4$/pyridine (80 mmol/100 mmol), malononitrile (55 mmol), CH_2Cl_2 (450 mL); c) **3** (1.8 mmol), MnO_2 (10–20 mmol), toluene (40 mL); d) **4** (1,4 mmol), 1,3-dithiole-2,4,5-trithione (1.4 mmol), thiophene (20 mL); e) **5** (0.8 mmol), $(EtO)_3CH/BF_3{\cdot}Et_2O$ (5 mmol/3 mmol), CH_2Cl_2 (40 mL); f) **6** (0.8 mmol), Zn/Br_2 (8 mmol/6 mmol), dry CH_3CN (20 mL); g) DDQ (3.5 mmol), dry CH_3CN (20 mL). PBQ = *para*-benzoquinone, DDQ = 2,3-dichloro-5,6-dicyano-1,4-benzoquinone.

a reduced form of **2**. Oxidation of the TCNQ moieties with DDQ in boiling acetonitrile afforded the final product **2**, as a greenish brown powder.

The UV/Vis/NIR spectrum of **2** in CH_2Cl_2 (Figure 1) shows a broad absorption band centered at about 1330 nm ($\varepsilon \approx 750 \pm 40\ cm^{-1}M^{-1}$). The extinction coefficient is concentration and temperature independent and the spectrum

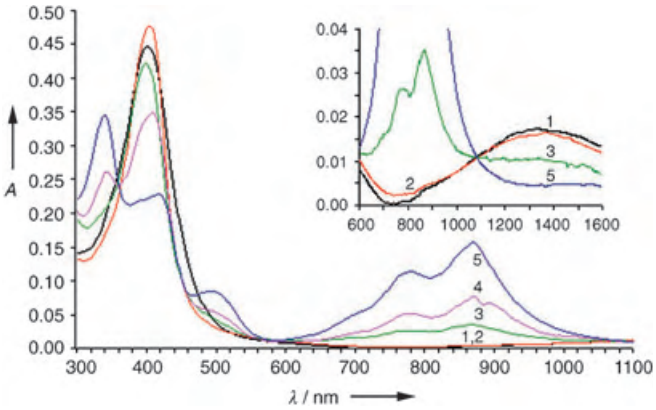


Figure 1. Absorption spectra of **2** in toluene (black, line 1), CH_2Cl_2 (red, line 2), CH_3CN (green, line 3), CH_2Cl_2 + DMF (magenta, line 4), and DMF (blue, line 5).

remains unchanged upon irradiation. The spectrum in toluene is essentially the same, with a similar minimum at about 750 nm. No radicals have been detected by EPR spectroscopy in either solvent. Therefore, the band at approximately 1330 nm can be attributed to an intramolecular CT transition from the TTF to the TCNQ moieties. In comparison, the cation radical and the dianion diradical of **2**[11] exhibit the expected absorption bands between 650 and 1050 nm, centered at about 850 nm, that are characteristic of these species.[12]

The cyclic voltammogram of **2** (Figure 2) in dichloromethane exhibits two $2e^-$ reversible reduction waves at $E^{1/2}_{red1} = 0.14$ V and $E^{1/2}_{red2} = -0.39$ V, which represent the consecutive reduction steps of the two identical TCNQ moieties

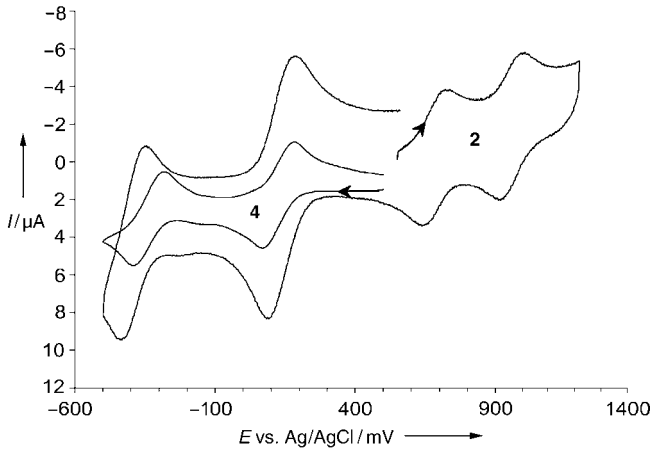


Figure 2. Cyclic voltammograms of **2** and **4** in CH_2Cl_2; 0.1 M $TBA^+PF_6^-$, on glassy carbon electrode versus Ag/AgCl; scan rate 100 $mV s^{-1}$. TBA = tetrabutylammonium.

 © 2005 Wiley-VCH Verlag GmbH & Co. KGaA, Weinheim

(**4** shows (Figure 2) $E^{1/2}_{red1} = 0.10$ V, $E^{1/2}_{red2} = -0.34$ V), and two reversible $1e^-$ oxidation waves at $E^{1/2}_{ox1} = 0.69$ V and $E^{1/2}_{ox2} = 0.96$ V, for the oxidation of the TTF fragment. As can be seen by comparing the oxidation of **2** with that of BEDT-TTF (bis(ethylenedithio)tetrathiafulvalene; $E^{1/2}_{ox1} = 0.48$ V, $E^{1/2}_{ox2} = 0.90$ V), the two waves are shifted by about 200 and 60 mV, respectively. These shifts indicate a relatively high degree of CT between the TTF and one (or both) of the TCNQ fragments, thus causing the TTF moiety to be partially charged, and therefore, more difficult to oxidize. The positive shift of the first reduction potential of **2** with respect to that of **4**, which was observed under various experimental conditions, is not fully understood yet.

A significant degree of CT in solid **2** was also observed by IR spectroscopic analysis, with the band corresponding to the cyano groups shifted to a smaller wave number with respect to the similar band in **4** and **5**. On the basis of the well-studied and widely used correlation between the degree of CT and the stretching frequency of the CN groups in TCNQ,[13] we estimated the degree of CT in solid **2** to be of about 0.2. This estimation is based on the absorption bands of the CN groups in the IR spectra of **2** (2206 cm^{-1}), **5** (2213 cm^{-1}), and their corresponding lithium salts (2175 cm^{-1} for both). It is noteworthy that our result is consistent with the absence of signals in the EPR spectrum of solid **2**.

Thus, both in the solid state and relatively nonpolar solvents, derivative **2** exists as an intramolecular CT complex with a degree of CT about 0.2. However, **2** undergo gradual changes in its properties when the polarity of the is solvent increased. For example, the shape of the UV/Vis/NIR spectrum changes completely in DMF solution (Figure 1): the broad NIR absorption band disappears and a strong band centered at 850 nm appears. The spectrum becomes similar to the superimposed spectra of the cation radical and dianion biradical of **2**. The solution also shows a strong EPR signal with $g = 2.0055$, which is an average of the g-factors of the corresponding cation and anion radicals. According to a simulation we performed, the signal is split by four equivalent hydrogen atoms (Figure 3). Both ion radicals and CT complexes can be observed in less-polar solvents or mixtures of solvents (Figure 1).

In summary, a strategy has been developed for preparing a novel system involving TTF and TCNQ moieties covalently linked through rigid saturated spacers. We have shown the first example of a rigid unimolecular system of type TCNQ-σ-TTF-σ-TCNQ that is capable of both through-space intramolecular charge and electron transfer, depending on the polarity of the surroundings. The strong dependence of the ground-state electronic structure on the polarity of solvents, which is a unique and unprecedented case of solvatochromism, can be useful for imaging since the more polar zones will contain larger amounts of ion radicals. The observed polarizing effect in the solid state was not sufficiently strong to give rise to ion radicals, but subtle changes in molecular structure could bring about drastic changes in molecular packing that may lead to different degrees of charge transfer.

Received: March 4, 2005
Published online: May 25, 2005

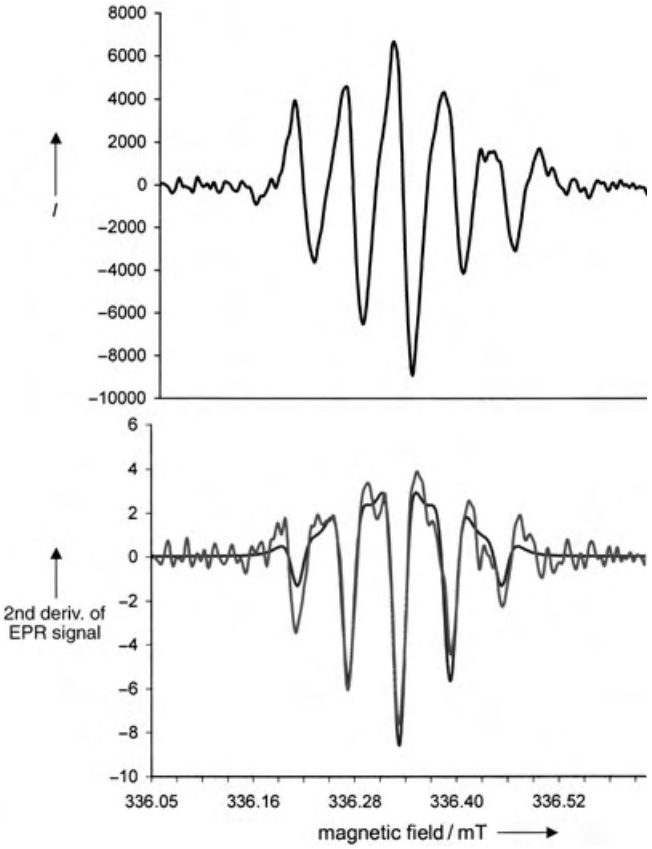


Figure 3. EPR signal of **2** in DMF (black: experimental; gray: simulated).

Keywords: charge transfer · donor–acceptor systems · electron transfer · solvent effects · tetrathiafulvalenes

[1] J. P. Ferraris, D. O. Cowan, V. Walatka, J. H. Perlstein, *J. Am. Chem. Soc.* **1973**, *95*, 948; L. B. Coleman, M. J. Cohen, D. J. Sandman, F. G. Yamagishi, A. F. Garito, A. Heeger, *Solid State Commun.* **1973**, *12*, 1125.

[2] V. Yu. Khodorkovsky, J. Y. Becker in *Organic Conductors: Fundamentals and Applications* (Ed.: J. P. Farges), Marcel Dekker, New-York, **1994**, chap. 3, p. 75; J. M. Williams, A. J. Schultz, U. Geiser, K. D. Carlson, A. M. Kini, H. H. Wang, W.-K. Kwok, M.-H. Whangbo, J. E. Shirber, *Science* **1991**, *252*, 1501; A. E. Underhill, *J. Mater. Chem.* **1992**, *2*, 1; *J. Mater. Chem.* **1995**, *5*, 1469 (special issue on molecular conductors).

[3] A. Aviram, M. A. Ratner, *Chem. Phys. Lett.* **1974**, *29*, 277.

[4] S. S. Shaik, *J. Am. Chem. Soc.* **1982**, *104*, 5328; J. Y. Becker, J. Bernstein, S. Bittner, N. Levi, S. S. Shaik, *J. Am. Chem. Soc.* **1983**, *105*, 4468.

[5] M. R. Bryce, *Adv. Mater.* **1999**, *11*, 11; J. L. Segura, N. Martín, *Angew. Chem.* **2001**, *113*, 1416; *Angew. Chem. Int. Ed.* **2001**, *40*, 1372; J. Y. Becker, J. Bernstein, S. Bittner, N. Levi, S. S. Shaik, N. Zer-Zion, *J. Org. Chem.* **1988**, *53*, 1689.

[6] C. A. Panetta, J. Baghdadchi, R. M. Metzger, *Mol. Cryst. Liq. Cryst.* **1984**, *107*, 103.

[7] D. F. Perepichka, M. R. Bryce, C. Pearson, M. C. Petty, E. J. L. McInnes, J. P. Zhao, *Angew. Chem.* **2003**, *115*, 4784; *Angew. Chem. Int. Ed.* **2003**, *42*, 4636.

[8] E. Tsiperman, T. Regev, J. Y. Becker, J. Bernstein, A. Ellern, V. Khodorkovsky, A. Shames, L. Shapiro, *Chem. Commun.* **1999**, 1125.

 © 2005 Wiley-VCH Verlag GmbH & Co. KGaA, Weinheim

[9] K. Nakasuju, M. Nakatsuka H. Yamochi, I. Murata, S. Harada, N. Kasai, K. Yamamura, J. Tanaka, G. Saito, T. Enoki, H. Inokuchi, *Bull. Chem. Soc. Jpn.* **1986**, *59*, 207.
[10] Based on E. Fanghänel, L. van Hinh, G. Schukat, *Z. Chem.* **1976**, *16*, 317.
[11] $\mathbf{2}^{+\cdot}$ was obtained by means of electrochemical oxidation at 0.6 V; $\mathbf{2}^{-\cdot,-\cdot}$ was prepared by treating **2** with LiI in dry acetonitrile.
[12] V. Khodorkovsky, L. Shapiro, P. Krief, A. Shames, M. Giffard, A. Gorgues, G. Mabon, *Chem. Commun.* **2001**, 2736; L. R. Melby, R. J. Harder, W. R. Hertler, W. Mahler, R. E. Benson, W. E. Mochel, *J. Am. Chem. Soc.* **1962**, *84*, 3374.
[13] J. S. Chappel, A. N. Bloch, W. A. Bryden, M. Maxfield, T. O. Poehler, D. O. Cowan, *J. Am. Chem. Soc.* **1981**, *103*, 2442.

 © 2005 Wiley-VCH Verlag GmbH & Co. KGaA, Weinheim

Phase Transitions

An Onion Phase in Salt-Free Zero-Charged Catanionic Surfactant Solutions**

Aixin Song, Shuli Dong, Xiangfeng Jia, Jingcheng Hao, Weimin Liu,* and Tianbo Liu*

Mixtures of cationic and anionic (catanionic) single-chain surfactants can readily form bilayers in aqueous solutions,[1] in which uni- and multilamellar onion phases (the so-called vesicle phase) are often observed to be in equilibrium.[2] Since vesicles represent simple model systems for biological membranes and have practical applications (for example, for controlled drug or DNA release),[3] investigations of vesicle phases are of considerable interest in different areas, including surfactants, materials, and life sciences. Recently, two new self-assembled structures of controlled size (nanodisks and regular hollow icosahedra) were observed in dilute catanionic surfactants with H^+ and OH^- counterions by Zemb and coworkers.[4–6] Such so-called "true" catanionic systems, with a nonswelling but finite uptake of water, and with a spacing of the same order as described in the current study were studied and documented by Jokela et al.[7] It was also later established by Rand, Parsegian, and Leiken[8] that the lamellar phase at maximum swelling of salt-free catanionic systems with a zero osmotic pressure, that is, the repulsive hydration interaction is compensated by van der Waals force at that point. The molar ratio r of the anionic to cationic components controls the structural surface charge and, hence, controls the long-range repulsive interaction independently of the weight volume fraction (ϕ), which in turn controls the average colloid–colloid distance. The salt-free catanionic systems can be represented in a ternary phase diagram whose two independent variables are ϕ and r.[6]

Herein we report, for the first time to our knowledge, the discovery of a "true", salt-free concentrated catanionic uni- and multilamellar onion phase that differs from the catanionic surfactant systems with excess salt that are formed by the combination of the counterions, as evident from our freeze-fracture transmission electron microscopy (FF-TEM) observations and small-angle X-ray scattering (SAXS) measurements. This molecular catanionic couple comprises the longest hydrocarbon chains described to date, so it was essential to determine if the carbon chains were in a frozen (gel) or liquid state. The size of the unilamellar vesicles ranges from about 20 to 700 nm and that of the large onions are several micrometers. The interlamellar spacing between the bilayers of onions is about 35 nm, thus suggesting rather compact packing of the bilayers. The high osmotic pressure sustains the highly stable colloidal suspension of the catanionic onion phase. The observations of the onion phase may prove valuable and stimulating to fellow specialists, not least as "true" catanionic surfactant systems do not seem to be exhaustively investigated yet.

The "true" salt-free catanionic vesicle phase was obtained by mixing aqueous solutions of trimethyltetradecylammonium hydroxide (TTAOH) and oleic acid (OA; see Figure 3). The stock solution of TTAOH (pH 12–13) was prepared from the commercial bromide form (TTABr) by anion exchange with a strong base at 40 °C until no bromide ions could be detected by precipitation with $AgNO_3$ in excess HNO_3. The resulting ion exchange with hydroxide ions was $>99\,\%$ (as determined from the detection limit of Br^- ions (Br^- sensitivity)).[9] The critical micelle concentration (cmc) of TTAOH was determined by surface tension measurements to be 1.8 mmol L^{-1}. The phase behavior on mixing 100 mM TTAOH with increasing concentrations of OA (up to 200 mM) was studied (not shown here). OA can dissolve in the aqueous solution containing TTAOH micelles. A single transparent, low viscous solution, which is the L_1 phase (spherical micelle phase), is evident at $c_{OA} = 0$–49.5 mM. The single transparent but viscous L_1 phase (rodlike micelles) is obtained between $c_{OA} = 49.5$ and about 62.5 mM; the viscosity of the samples in this region is much higher, which is evident since the surface of the L_1 phase could not be inclined on tilting the sample tube. A macroscopic phase separation into a birefringent Lα phase on top of the viscous L_1 phase at the bottom of the

[*] S. Dong, X. Jia, Prof. Dr. J. Hao
Key Laboratory for Colloid and Interface Chemistry
Shandong University
Ministry of Education
Jinan 250100 (P.R. China)
Fax: (+86) 531-856-4464
E-mail: jhao@sdu.edu.cn
A. Song, Prof. Dr. J. Hao, Prof. Dr. W. Liu
State Key Laboratory of Solid Lubrication
Lanzhou Institute of Chemical Physics
Chinese Academy of Sciences
Lanzhou 730000 (P.R. China)
Fax: (+86) 931-827-7088
E-mail: wmliu@l2b.ac.cn
Dr. T. Liu
Department of Chemistry
Lehigh University
Bethlehem, PA 18015 (USA)

[**] This work was supported by the NFSC (20473049, 20428101), the Alexander von Humboldt Foundation, the Program of Hundreds Talent of the Chinese Academy of Sciences, Scientists' Awards of Young-Middle Age (03BS083), the NSF-Shandong Province (Z2004B04; J.H.), and the NSFC (50421502; W.L.).

 © 2005 Wiley-VCH Verlag GmbH & Co. KGaA, Weinheim DOI: 10.1002/anie.200500353

tube occurs between 62.5 and approximately 90 mM. From $c_{OA} = 90$ to about 180 mM, a very stable, slightly turbid, bluish, and viscoelastic solution is seen. When $c_{OA} > 180$ mM, this birefringent Lα phase again separates into a two-phase emulsion/viscous layer. The upper phase is an emulsion phase and the lower phase contains the oleic acid component.

The birefringent Lα phase consists of both uni- and multilamellar vesicles, as shown in Figure 1 for two typical samples of TTAOH/OA by means of FF-TEM. The features of the vesicular structures in the two samples are apparent; uni- and multilamellar vesicles can both be seen throughout the samples. The diameters of the unilamellar vesicles, which range from about 20 to over 700 nm, are similar to those formed by single-tailed catanionic surfactants[10] and natural lipids such as lecithine.[11] The vesicles are completely dispersed in solutions and do not tend to associate with each other. Very large multilamellar vesicles with diameters of more than 3 μm can also be seen. The interlamellar spacing between the bilayers is rather small, in the range of about (36 ± 2) nm (Figure 1c), thus suggesting quite compact packing of the bilayers. An important feature is evident in Figure 1a and b: the multilamellar onion phase in the system containing excess cationic component (namely with positive charges; $r_{TTAOH}/r_{OA} = 100{:}94$) has less bilayers than those of ones with zero charges (at $r_{TTAOH}/r_{OA} = 100{:}100$), thus suggesting that the imbalance in the molar ratio of cationic and anionic surfactants does not favor the formation of multilamellar "onions" with quite a compact packing of bilayers.

Small-angle X-ray scattering (SAXS) measurements were carried out on one sample with the birefringent, viscoelastic Lα phase (containing 100 mmol L^{-1} TTAOH and 100 mmol L^{-1} OA), and clearly revealed the formation of lamellar aggregate structures (Figure 2). Three scattering peaks at $q = 0.18$, 0.36, and 0.54 nm^{-1} were observed. The relative peak positions $q_1{:}q_2{:}q_3$ are 1:2:3, which is typical for a Bragg scattering pattern from a one-dimensional lamellar structure (corresponding to the 001, 002, and 003 planes). The interlayer distance d $(= 2\pi/q_{max})$ was determined to be around 35 nm (Figure 3), which is completely consistent with the value obtained from the FF-TEM images. Such a lamellar structure has been commonly observed in mixtures of polyelectrolyte/surfactant complexes[12] and cationic/anionic

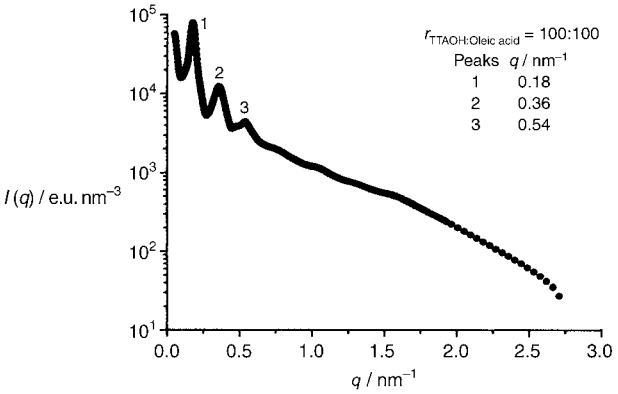


Figure 2. A SAXS profile of one Lα phase in the sample prepared from 100 mmol L^{-1} TTAOH/100 mmol L^{-1} OA. The scattering peaks for the TTAOH/OA mixture can be indexed to a lamellar structure.

surfactant systems[13] with excess salts; very few observations have been reported of such an onion-phase structure in salt-free catanionic systems. The observation of an onion phase in the salt-free catanionic surfactant system should open up new studies on such catanionic systems, and shed new light on the "true", salt-free catanionic onion phase. Meanwhile, the viscoelastic onion phase which contains no dispersed materials will find many applications where such salt-free viscoelastic phases are required with the morphology (spherical core-shell structure) obtained with our catanionic mixtures, for example, in producing mesoporous materials, to orient solubilized molecules, as well as in pharmaceuticals. The SAXS measurements clearly show that the bilayers of vesicles with zero charge have large spacing. This situation arises since electrostatic effects add to the hydration force to compensate for the attractive force and produce low osmotic pressure, probably about 1000 Pa—as reported by Meister et al.[14]

Electrostatic and hydrophobic interactions are responsible for the formation of aggregates in all catanionic surfactant systems investigated in the literature. These catanionic surfactant systems contain dissociated small electrolytes from the counterions of both the anionic and cationic surfactants, which lead to some exclusive properties. For example, the mixed solutions have high ionic strength between the aggregates, electrostatic repulsions are screened,

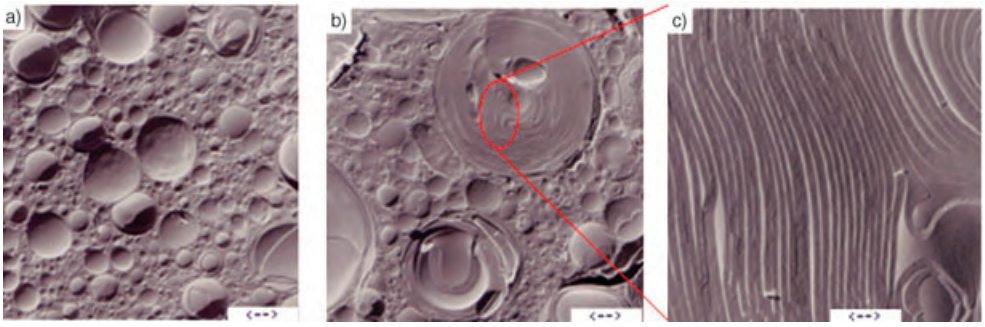


Figure 1. FF-TEM images of two samples: a) 94 mmol L^{-1} OA in 100 mmol L^{-1} TTAOH micellar solution, the scale bar corresponds to 0.350 μm, and b) 100 mmol L^{-1} OA in 100 mmol L^{-1} TTAOH micellar solution, the scale bar corresponds to 0.583 μm. c) Magnification of the multilamellar vesicles to determine the interlamellar spacing between two adjacent bilayers; the scale bar corresponds to 0.14 μm. The sample was frozen from room temperature in liquid propane cooled by liquid N_2: for further details see reference [2].

 © 2005 Wiley-VCH Verlag GmbH & Co. KGaA, Weinheim

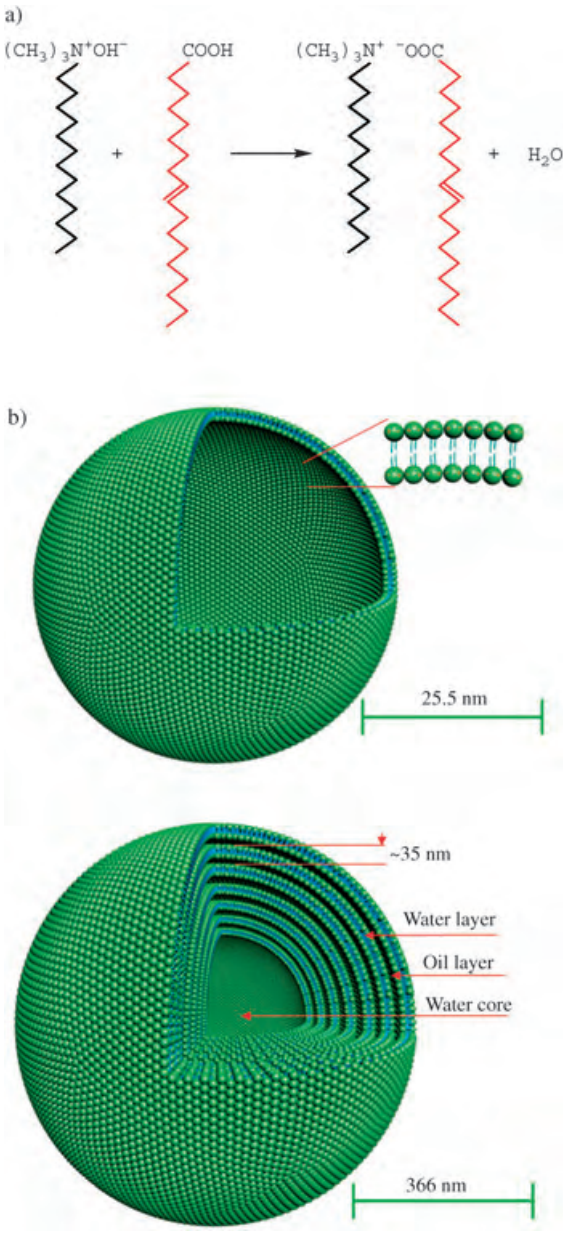


Figure 3. a) Formation of the salt-free catanionic surfactants. b) Models of unilamellar vesicle (top) with 25.5-nm radius and multilamellar vesicles (below) with 366-nm radius. The analysis of experimental data is shown for the multilamellar vesicles. The hydrophobic double-chain hydrocarbons are shown as blue rods and the hydrophilic-charged cationic-anionic groups as green spheres. A sector in each model has been cut out to enhance the visibility. Seven bilayers comprise the multilamellar onion phase.

and osmotic pressure of aggregates is <100 Pa. Moreover, when mixing cationic and anionic surfactants in solutions, the strong reduction in area per head group resulting from ion pairing induces lamellar structures. Thus vesicles, flexible cylinders, as well as flat lamellae can be prepared and observed.[10,13]

In the current study, a low osmotic pressure is produced by unscreened electrostatic repulsion, which sustains the highly stable colloidal suspension, the "onion phase". However, it is quite different from the excess-salt catanionic surfactants, because solid surfactant precipitates do not form in the salt-free systems at relatively high surfactant concentrations (100 mmol L^{-1}, or 3–5 wt% surfactants) and a 1:1 cationic/anionic surfactant ratio (zero charge). Thus, the observation of an onion phase in the current study constitutes a salt-free concentrated catanionic surfactant system with the longest hydrocarbon chains having an unsaturated bond to date. Such a well-defined salt-free onion-phase system should be much more useful than the excess-salt catanionic surfactant systems, because of the interactions and effects controlling the assembly of the surfactants and/or the formation of different new surfactant phases, the more theoretically predictable behavior, and the fact that solid surfactant precipitates do not form at a 1:1 cationic and anionic surfactant ratio.

Experimental Section

Materials**:** Trimethyltetradecylammonium bromide (TTABr) was purchased from Acros Organics, New Jersey, USA and recrystallized three times from the mixed solvent of diethyl ether/ethanol. The TTAOH stock solution was prepared from the TTABr solution (120 mM) by anion exchange with a strong base (Ion exchanger III, Merck) at 40 °C. Bromide ions could not be detected by $AgNO_3$ in the TTAOH stock solution ($Ag^+ + Br^- \rightarrow AgBr\downarrow$), so the ion exchange with hydroxide is $>99\%$.[9] The critical micelle concentration (cmc) of TTAOH (0.0018 mol L^{-1}) was determined by using surface tension measurements. Oleic acid (OA) was obtained from Shanghai Chemical Co. with ionic impurities of sodium (0.1% molar fraction) and calcium (0.05% molar fraction). The fatty acids are quasi-insoluble in water, however, they can be mixed with TTAOH solution to provide clear solutions by heating to 40 °C.

Methods: The phase diagram of 100 mM TTAOH with the variable oleic acid concentrations was established by observing the solutions in test tubes at 25.0 ± 0.1 °C. The samples were homogenized by mixing and heating to about 40 °C for a few minutes, and then the hot solutions were cooled to room temperature with permanent shaking during cooling. The solutions were allowed to equilibrate for at least four weeks at 25.0 ± 0.1 °C and did not contain any trace of insoluble materials. All the experiments described were done at 25 ± 0.1 °C unless specified otherwise.

The microstructure of the samples with birefringence between the polarizers was examined by freeze-fracture transmission electron microscopy (FF-TEM). A small amount of sample (ca. 4 μL) was placed on a 0.1-mm thick copper disk covered with a second copper disk. The copper sandwich with the sample was frozen by plunging it into liquid propane which had been cooled by liquid nitrogen. A freeze-fracture apparatus (Balzer BAF 400, Germany) was used at a temperature of −140 °C for fracturing and replication. Pt/C was deposited at an angle of 45°. The replicas were examined with a Zeiss CEM 902 transmission electron microscope operated at 80 kV.

SAXS measurements were carried out at room temperature on a modified Kratky compact camera. The evacuated camera was mounted on a sealed X-ray tube equipped with a copper target. The scattering intensities were measured with a linear position-sensitive, gas-filled detector (Mbraun, Germany) by monitoring the scattering curves in the q range ($q = 4\pi/\lambda \sin\theta/2$, where θ is the scattering angle and λ is the wavelength of radiation). The sample solutions were injected into a 1 mm diameter quartz capillary mounted in a steel cuvette. The data collection time for each scattering curve amounted to about 15 h.

Received: January 30, 2005
Published online: June 10, 2005

 © 2005 Wiley-VCH Verlag GmbH & Co. KGaA, Weinheim

Keywords: electron microscopy · phase transitions · surfactants · X-ray spectroscopy

[1] a) E. Sackman, R. Lipowsky, *Handbook of biological physics, Vol. 1B* (Ed.: A. J. Hoff), North-Holland, Amsterdam, **1995**; b) H. T. Jung, S. Y. Lee, E. W. Kaler, B. Coldren, J. A. Zasadziski, *Proc. Natl. Acad. Sci. USA* **2002**, *99*, 15318; c) H. T. Jung, B. Coldren, J. A. Zasadzinski, D. J. Iampietro, E. W. Kaler, *Proc. Natl. Acad. Sci. USA* **2001**, *98*, 1353.
[2] J. Hao, H. Hoffmann, K. Horbaschek, *J. Phys. Chem. B* **2000**, *104*, 10144.
[3] *Vesicles*, *Vol. 62* (Ed.: E. Rosoff), Marcel Dekker, New York, **1996** (Surfactant Science Series).
[4] Th. Zemb, M. Dubois, B. Demé, Th. Gulik-Krzwicki, *Science* **1999**, *283*, 816.
[5] M. Dubois, B. Demé, Th. Gulik-Krzwicki, J. C. Dedieu, C. Vautrin, S. Désert, E. Perez, Th. Zemb, *Nature* **2001**, *411*, 672.
[6] M. Dubois, V. Lizunov, A. Meister, Th. Gulik-Krzywicki, J. M. Verbavatz, E. Perez, J. Zimmerberg, Th. Zemb, *Proc. Natl. Acad. Sci. USA* **2004**, *101*, 15082.
[7] a) P. Jokela, B. Jonsson, A. Khan, *J. Phys. Chem.* **1987**, *91*, 3291; b) P. Jokela, B. Jonsson, H. Wennerstrom, *Prog. Colloid Polym. Sci.* **1985**, *70*, 17; c) P. Jokela, B. Jonsson, B. Eichmuller, K. Fontell, *Langmuir*, **1988**, *4*, 187.
[8] a) R. P. Rand, V. A. Parsegian, *Biochim. Biophys. Acta* **1989**, *988*, 351; b) S. Leikin, V. A. Parsegian, *Annu. Rev. Phys. Chem.* **1993**, *44*, 369, and references therein.
[9] Q. Cai, Z. Guo, C. Yu, W. Zhang, Z. Yang, *Anal. Bioanal. Chem.* **2003**, *377*, 740.
[10] E. W. Kaler, A. K. Murthy, B. E. Rodriguez, J. N. Zasadzinski, *Science* **1989**, *245*, 1371.
[11] J. M. Gebicki, M. Hicks, *Nature* **1973**, *243*, 232.
[12] a) C. K. Ober, G. Wegner, *Adv. Mater.* **1997**, *9*, 17; b) D. G. Kurth, P. Lehmann, M. Schütte, *Proc. Natl. Acad. Sci. USA* **2000**, *99*, 5704.
[13] J. Hao, H. Hoffmann, *Curr. Opin. Colloid Interface Sci.* **2004**, *9*, 273, and references therein.
[14] A. Meister, M. Dubois, L. Belloni, T. Zemb, *Langmuir* **2003**, *19*, 7259.

 © 2005 Wiley-VCH Verlag GmbH & Co. KGaA, Weinheim

Dipoles in Crystal Engineering

Molecular Tectonics: Porous Cleavable Networks Constructed by Dipole-Directed Stacking of Hydrogen-Bonded Sheets**

*Nadia Malek, Thierry Maris, Marie-Ève Perron, and James D. Wuest**

An exciting challenge in contemporary science is learning how to make ordered molecular materials with predetermined structures and properties. The effort to reach this goal continues to yield new knowledge of both fundamental and practical value. Of particular interest are ordered molecular materials produced spontaneously by methods of self-assembly, such as crystallization. Although detailed predictions of the structure of molecular crystals remain unreliable,[1] crystal engineering provides increasingly effective strategies for identifying compounds predisposed to crystallize in particular ways.[2] One such strategy, which has been called molecular tectonics,[3,4] relies on special compounds that participate in multiple directional interactions. Such compounds, called tectons from the Greek word for builder, are programmed to associate and to form networks in which each molecule is placed in a predictable position with respect to its neighbors. Herein, we show how two different directional forces, hydrogen bonding and dipole-dipole interactions,[5] can be used in potent combination to engineer molecular networks with predictable cleavage and high porosity.[6]

Tetrahedral tectons **1** with peripheral sites of association (●) are predisposed to form three-dimensional four-connected networks, whereas trigonal analogues **2** favor sheets (Figure 1). In the first case, the entire three-dimensional structure is programmed by the tectons and maintained by strong interactions in all directions; in the second case, however, the ultimate structure must result from the stacking or interpenetration of sheets,[7] governed by forces that are not normally subject to rational control. Examples of structural polytypism resulting from subtle variations in the stacking of sheets are numerous in chemistry and include the diverse phases of graphite,[8] sheet silicates in which the layers have different offsets,[9] and various hydrogen-bonded molecular sheets.[10] For many applications, polytypism is undesirable because it makes full structural predictions unreliable, even when the positions of all the atoms in individual sheets are well established.

[*] Dr. N. Malek, Dr. T. Maris, M.-È. Perron, Prof. Dr. J. D. Wuest
Département de Chimie
Université de Montréal
Montréal, Québec H3C 3J7 (Canada)
Fax: (+1) 514-340-3721
E-mail: james.d.wuest@umontreal.ca

[**] We are grateful to the Natural Sciences and Engineering Research Council of Canada, the Ministère de l'Éducation du Québec, the Canada Research Chairs Program, and the Canada Foundation for Innovation for financial support.

Supporting information for this article is available on the WWW under http://www.angewandte.org or from the author.

 DOI: 10.1002/anie.200500198 © 2005 Wiley-VCH Verlag GmbH & Co. KGaA, Weinheim

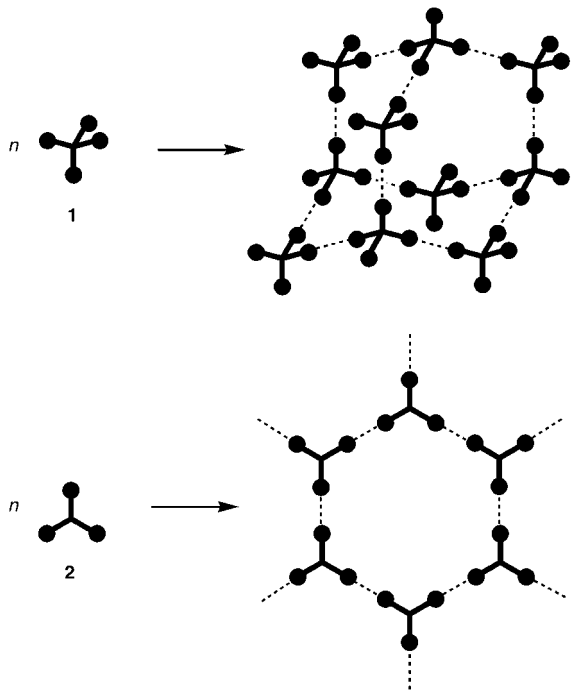


Figure 1. Representations of the hypothetical three-dimensional network built from tetrahedral tecton **1** and the two-dimensional network formed by trigonal tecton **2**.

A potentially effective element of control can be introduced by incorporating a dipole at each trigonal center to create tecton **3** (Figure 2). Assembly directed cooperatively

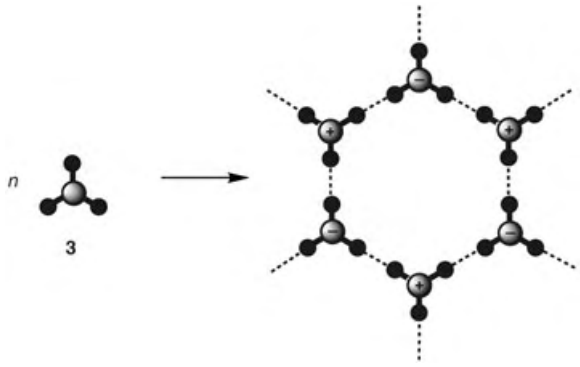
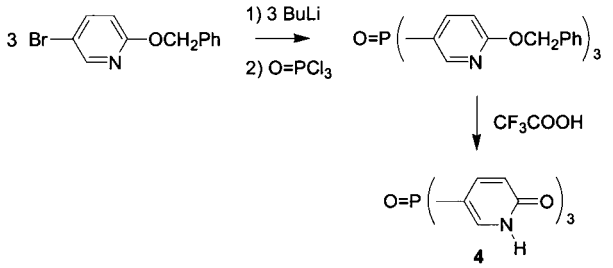


Figure 2. Hypothetical sheet resulting from trigonal tecton **3** with a dipolar core (white circle) showing the expected antiparallel alignment of adjacent dipoles (represented by inscribing + and − in the cores).

by the normal association of the sticky sites (●) and by antiparallel orientation of neighboring dipoles should produce the sheet shown in Figure 2. Such sheets are then predisposed to create a hexagonal three-dimensional array by stacking in registry, directed by the formation of head-to-tail columns of dipoles that lie perpendicular to the sheets. An encouraging precedent for the dipole-directed assembly of sheets is provided by the structure of the most stable polymorph of phosphorus pentoxide.[11] In this structure, PO_4 tetrahedra share three corners to form covalently bonded sheets composed of 12-membered rings. Adjacent P=O bonds are oriented perpendicularly toward opposite faces of each sheet, and their alignment suggests that dipolar interactions control the stacking of the sheets.

The feasibility of using dipoles to direct the stacking of hydrogen-bonded molecular sheets was tested by studying phosphine oxide **4** (Scheme 1). Three pyridinone groups are



Scheme 1. Synthesis of phosphine oxide **4**.

incorporated in compound **4** to ensure strong intermolecular hydrogen bonding through a reliable supramolecular synthon,[12–14] and the P=O bond introduces a large and unambiguous dipole, which is approximately 4.5 D in triphenylphosphine oxide.[15] Compound **4** was prepared in 89% overall yield from 5-bromo-2-(phenylmethoxy)pyridine[16] by the route summarized in Scheme 1. Crystallization was achieved by allowing hexane to diffuse into solutions of compound **4** in either CH_3COOH or CH_3CH_2COOH. Both crystallizations produced hexagonal prisms of composition **4**·3 RCOOH, as determined by X-ray crystallography, thermogravimetry, and ^{1}H NMR spectroscopy of dissolved samples. X-ray diffraction established that crystals grown under both conditions belong to the trigonal space group $P\bar{3}$ and are isomorphous, so only views of the structure containing CH_3COOH are shown (Figures 3 and 4).

The structure produced by crystallizing tecton **4** can be interpreted as a direct consequence of the combined effects of hydrogen bonding and dipolar interactions. Characteristic intermolecular hydrogen bonding of the three pyridinone groups defines a porous sheet composed of cyclic hexamers (Figure 3). It is noteworthy that hydrogen bonding of carboxylic acid solvents with compound **4** does not prevent normal association of its pyridinone groups. Since the P atom is approximately tetrahedral (∢O-P-C 112.08(11)° in crystals grown from CH_3COOH/hexane), the pyridinone groups do not diverge from the core in a single plane, and the resulting sheet is corrugated (Figure 4). Each cyclic hexamer has a chair conformation with the P=O dipoles oriented axially, and adjacent dipoles are antiparallel and directed toward opposite faces of the sheet. Like other triarylphosphine oxides,[17–19] compound **4** adopts a chiral conformation in the crystalline state, and molecules with dipoles oriented in one direction are enantiomers of those with dipoles aligned in the opposite direction. The intertectonic distance between the P atoms of neighboring hydrogen-bonded molecules is 11.82 Å, and the pores in individual sheets are approximately 15.1 Å in diameter.[20]

 © 2005 Wiley-VCH Verlag GmbH & Co. KGaA, Weinheim

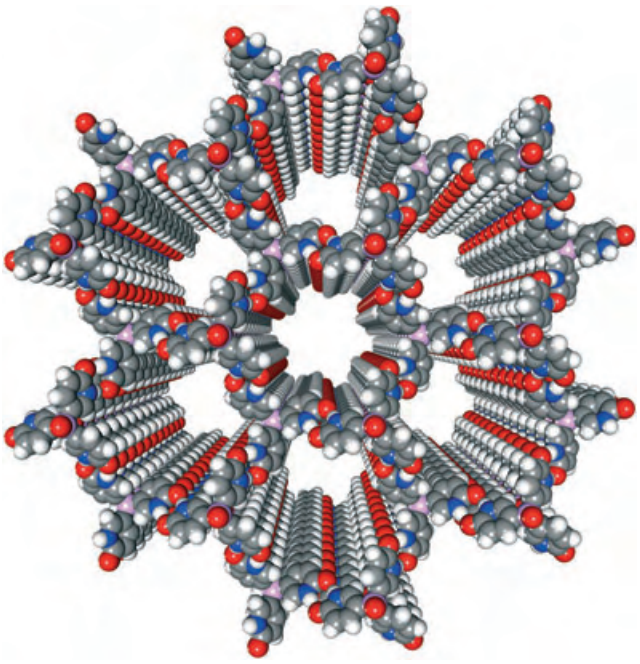


Figure 3. Perspective view along the *c* axis of the network constructed by crystallizing phosphine oxide **4** from CH_3COOH/hexane. Guests are omitted, and atoms are shown as spheres of van der Waals radii to reveal the cross-sections of the channels. Atoms of hydrogen are shown in white, carbon in gray, nitrogen in blue, oxygen in red, and phosphorus in pink.

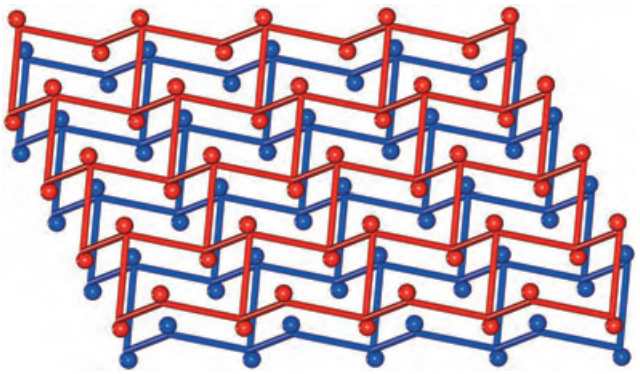


Figure 4. Representation of the dipole-directed stacking of corrugated sheets observed in crystals of phosphine oxide **4** grown from CH_3COOH/hexane, as viewed with the *c* axis approximately vertical. Two adjacent sheets are shown, one in red and the other in blue, and P=O dipoles are represented by lobes of the same color. The sheets are defined by lines joining the central phosphorus atom of each tecton to the centers of the three hydrogen-bonded neighbors.

As planned, the sheets then stack in registry in a way that appears to be directed by head-to-tail alignment of P=O dipoles in adjacent layers (Figure 4). In the resulting structure, the average intertectonic distance between the closest P atoms of neighboring sheets is 5.39 Å. As a result of the registry the pores in each sheet are aligned with those in adjacent sheets, thereby creating impressive parallel channels that run perpendicular to the sheets and contain partially ordered molecules of CH_3COOH and CH_3CH_2COOH. Approximately 50% of the volume of the crystals of compound **4** is available for including guests.[21,22] This degree of porosity is impressive but somewhat smaller than that of the very best three-dimensional molecular networks,[23] perhaps because tecton **4** favors association in two dimensions to form sheets that can then pack closely. However, the channels are among the largest ever observed in molecular crystals. It is instructive to compare the network constructed from compound **4** with those of crystalline inorganic analogues that have similar parallel channels and have been cited repeatedly as benchmarks in the field of microporous materials. In particular, gross structural features of the network built from tecton **4** (porosity 50%, 15-Å channels) resemble those of the synthetic aluminophosphate VPI-5 (porosity 43%, 13-Å channels)[24] and the natural Fe^{III} phosphate cacoxenite (porosity 49%, 17-Å channels).[25,26] These analogies underscore the potential of engineering porous networks from purely molecular precursors. Moreover, the network derived from compound **4** was built by design and can be assembled at 25 °C as large single crystals with a structure that can be solved by straightforward X-ray diffraction, unlike VPI-5, cacoxenite, and many related inorganic and metal–organic materials.[26]

The behavior of compound **4** differs significantly from that of structurally similar molecules lacking the same capacity to take part in directional interactions. For example, compound **4** yields isomorphous structures when crystallized from either CH_3COOH/hexane or CH_3CH_2COOH/hexane, whereas triphenylphosphine oxide crystallizes under different conditions as multiple polymorphs.[17,18] Some of these polymorphs do not incorporate the head-to-tail alignment of P=O dipoles observed in crystals of compound **4**, which suggests that the contribution of dipolar interactions to the overall lattice energy is important but not dominant. In addition, compound **4** forms a highly porous network, whereas all known polymorphs of triphenylphosphine oxide are close-packed, and enclathration of guests is not observed.[17,18,27] Together, these comparisons show how the behavior of tectons differs markedly from that of models lacking oriented arrays of sticky sites, and they confirm that tectonic association normally reduces opportunities for polymorphism and favors the formation of networks that are not close-packed.

In the open network constructed from phosphine oxide **4**, each tecton forms a total of six hydrogen bonds with its three neighbors in the same sheet, and it participates in attractive dipole–dipole interactions with the two closest neighbors in adjacent sheets. In contrast, included guests are weakly bound to the network and are located in large channels that in principle offer easy escape from the network. As observed in other porous molecular networks held together by multiple hydrogen bonds, crystals of compound **4** are permeable, and guests can be exchanged in single crystals without loss of crystallinity. For example, crystals of composition $\mathbf{4}\cdot 3\,CH_3COOH$ and approximate dimensions $0.5\times0.5\times2.0\ mm^3$ were suspended in CH_2=CHCOOH/hexane at 25 °C for 3 days.[28] The recovered sample remained transparent and morphologically unchanged. Furthermore, it continued to diffract and to show uniform extinction between crossed polarizers. Analysis of dissolved samples by ^1H NMR spec-

 © 2005 Wiley-VCH Verlag GmbH & Co. KGaA, Weinheim

troscopy confirmed that CH_3COOH had been replaced completely to give new crystals of composition **4**·3 CH_2=CHCOOH. The quality of the exchanged crystals was high enough to allow their structure to be solved by single-crystal X-ray diffraction. The exchanged crystals proved to be isomorphous, with unit cell parameters essentially identical to those of the initial crystals (±4%). The close similarity of the structures of crystals containing CH_3COOH, CH_3CH_2COOH, or CH_2=CHCOOH suggests that the network built from tecton **4** is resistant to deformation.[12]

The three-dimensional architecture generated by crystallizing compound **4** consists of sheets held together by a high density of strong hydrogen bonds, stacked in the perpendicular direction by a lower density of weaker dipolar interactions. As a result, we reasoned that the mechanical properties of the crystals would be highly anisotropic. In particular, we expected cleavage of the crystals to show marked directional preferences, perhaps similar to those observed in micas and other lamellar inorganic materials, and we hoped to be able to make thin sections by cleaving crystals perpendicular to the axes of the channels. Unlike sections cleaved from lamellar inorganic materials, which are typically dense and nonporous,[29] those split from crystals of compound **4** are expected to be selectively permeable and to have well-defined pores of nanometric dimensions.

Indexation of hexagonal prisms of compound **4** grown from CH_3COOH established that the long axis of the crystals corresponds to the crystallographic *c* axis, so the channels run from one end of the prisms to the other. Stress was induced in the crystals by removing them from their mother liquors and exposing them to air, thereby initiating slow loss of included guests. Close examination of a typical stressed crystal (Figure 5) reveals multiple planes of fracture, all lying perpendicular to the *c* axis. This fractographic analysis[30] confirmed that the crystals are mechanically fragile and susceptible to preferential basal cleavage between adjacent hydrogen-bonded sheets, as expected. Moreover, pressing gently on crystals with a microscalpel held perpendicular to the length of the prism readily cleaved sections as thin as 30 μm, such as the one shown in Figure 5. The prism faces in ideal prisms free of defects should not show significant permeability; instead, guests should enter or exit only at the terminations, then reach the core by diffusion.[31] In real crystals, however, fractures may provide additional surfaces for the exchange of guests. In a prism with *N* complete basal fractures of the type observed, the surface available for exchange will in principle be multiplied by a factor of $2N+2$, and the rate of exchange will increase accordingly. Similar phenomena may account in part for the high rate of exchange observed in other permeable molecular crystals.

Together, these observations underscore the potential of molecular tectonics as a strategy for the purposeful construction of ordered materials with new properties, and they show how carefully selected combinations of directional forces can be used to engineer crystals with particular anisotropic features.

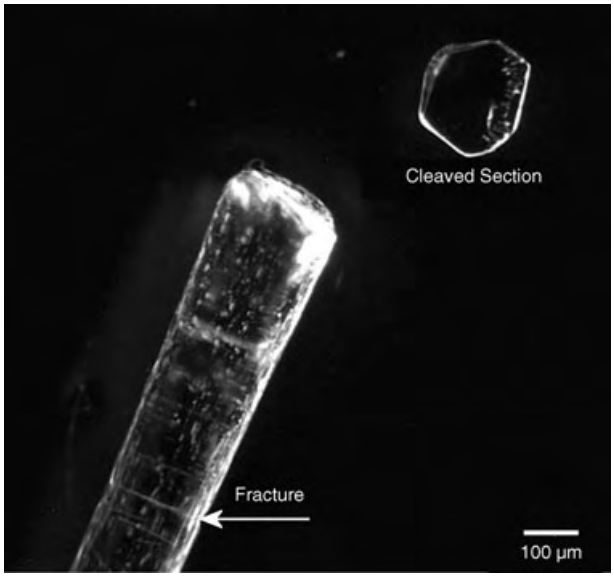


Figure 5. Optical micrograph showing 1) an intact single crystal of phosphine oxide **4** (lower left) grown from CH_3COOH/hexane, then stressed by partial evaporation of guests to induce the formation of basal fractures and 2) a thin section (upper right) cleaved from the same single crystal.

Experimental Section

For experimental details, see reference [32]. X-ray crystal structural analyses:[33] Data were collected at 223 K using a Bruker SMART 2000 CCD diffractometer with $Cu_{K\alpha}$ radiation ($\lambda = 1.54178$ Å). Intensities were integrated using SAINT[34] and corrected for absorption and other effects using SADABS.[35] Structures were solved and refined using the SHELX suite of programs.[36]

Crystal data for tecton **4**·3 CH_3COOH: crystal size $0.40 \times 0.15 \times 0.15\ mm^3$, trigonal, space group $P\bar{3}$, $a = b = 16.9535(8)$, $c = 5.2396(3)$ Å, $V = 1304.21(11)$ Å^3, $Z = 2$. Least-squares refinement of 137 parameters using 73 restraints for 1404 reflections with $I > 2\sigma(I)$ out of 1659 reflections gave residual factors $R_1 = 0.0772$, w$R_2 = 0.2660$, and GOF = 1.086.

Crystal data for tecton **4**·3 CH_3CH_2COOH: crystal size $0.40 \times 0.40 \times 0.20\ mm^3$, trigonal, space group $P\bar{3}$, $a = b = 17.1474(4)$, $c = 5.3885(2)$ Å, $V = 1372.13(7)$ Å^3, $Z = 2$. Least-squares refinement of 117 parameters using 2 restraints for 1403 reflections with $I > 2\sigma(I)$ out of 1691 reflections led to residual factors $R_1 = 0.0682$, w$R_2 = 0.1984$, and GOF = 1.071.

Crystal data for tecton **4**·3 CH_2=CHCOOH: crystal size $0.60 \times 0.25 \times 0.25\ mm^3$, trigonal, space group $P\bar{3}$, $a = b = 17.4823(8)$, $c = 5.0683(8)$ Å, $V = 1341.5(2)$ Å^3, $Z = 2$. Least-squares refinement of 115 parameters using 30 restraints for 699 reflections with $I > 2\sigma(I)$ out of 1211 reflections gave residual factors $R_1 = 0.0956$, w$R_2 = 0.2542$, and GOF = 1.031.

Received: January 18, 2005
Published online: May 27, 2005

Keywords: crystal engineering · dipoles · hydrogen bonding · layered compounds · porous networks

[1] a) J. D. Dunitz, *Chem. Commun.* **2003**, 545; b) G. R. Desiraju, *Nat. Mater.* **2002**, *1*, 77; c) A. Gavezzotti, *Acc. Chem. Res.* **1994**, *27*, 309; d) J. Maddox, *Nature* **1988**, *335*, 201.

[2] a) D. Braga, *Chem. Commun.* **2003**, 2751; b) K. Biradha, *CrystEngComm* **2003**, *5*, 374; c) M. D. Hollingsworth, *Science* **2002**, *295*, 2410; d) *Crystal Engineering: From Molecules and*

 © 2005 Wiley-VCH Verlag GmbH & Co. KGaA, Weinheim

Crystals to Materials (Eds.: D. Braga, F. Grepioni, A. G. Orpen), Kluwer, Dordrecht, Netherlands, **1999**; e) G. R. Desiraju, *Crystal Engineering: The Design of Organic Solids*, Elsevier, Amsterdam, **1989**.

[3] a) S. Mann, *Nature* **1993**, *365*, 499; b) M. Simard, D. Su, J. D. Wuest, *J. Am. Chem. Soc.* **1991**, *113*, 4696.

[4] M. W. Hosseini, *CrystEngComm* **2004**, *6*, 318.

[5] For references to the use of dipoles in crystal engineering, see a) R. Paulini, K. Müller, F. Diederich, *Angew. Chem.* **2005**, *117*, 1820; *Angew. Chem. Int. Ed.* **2005**, *44*, 1788; b) S. Lee, A. B. Mallik, D. C. Fredrickson, *Cryst. Growth Des.* **2004**, *4*, 279; c) B. Jagadish, M. D. Carducci, C. Bosshard, P. Günter, J. I. Margolis, L. J. Williams, E. A. Mash, *Cryst. Growth Des.* **2003**, *3*, 811; d) S. George, A. Nangia, M. Bagieu-Beucher, R. Masse, J.-F. Nicoud, *New J. Chem.* **2003**, *27*, 568; e) J. Zyss, S. Brasselet, V. R. Thalladi, G. R. Desiraju, *J. Chem. Phys.* **1998**, *109*, 658; f) F. H. Allen, C. A. Baalham, J. P. M. Lommerse, P. R. Raithby, *Acta Crystallogr. Sect. B* **1998**, *54*, 320; g) A. Gavezzotti, *J. Phys. Chem.* **1990**, *94*, 4319.

[6] For reviews of porous molecular networks, see a) A. Nangia, *Curr. Opin. Solid State Mater. Sci.* **2001**, *6*, 115; b) P. J. Langley, J. Hulliger, *Chem. Soc. Rev.* **1999**, *28*, 279.

[7] For discussions of interpenetration in networks, see a) S. R. Batten, *CrystEngComm* **2001**, *18*, 1; b) S. R. Batten, R. Robson, *Angew. Chem.* **1998**, *110*, 1558; *Angew. Chem. Int. Ed.* **1998**, *37*, 1460.

[8] F. P. Bundy, W. A. Bassett, M. S. Weathers, R. J. Hemley, H. K. Mao, A. F. Goncharov, *Carbon* **1996**, *34*, 141.

[9] F. Liebau, *Structural Chemistry of Silicates*, Springer, Berlin, **1985**.

[10] For recent references, see a) M. D. Ward, M. J. Horner, *CrystEngComm* **2004**, *6*, 401; b) K. Sada, K. Inoue, T. Tanaka, A. Tanaka, A. Epergyes, S. Nagahama, A. Matsumoto, M. Miyata, *J. Am. Chem. Soc.* **2004**, *126*, 1764; c) D. Maspoch, N. Domingo, D. Ruiz-Molina, K. Wurst, J. Tejada, C. Rovira, J. Veciana, *J. Am. Chem. Soc.* **2004**, *126*, 730; d) Y. Du, C. J. Creighton, B. A. Tounge, A. B. Reitz, *Org. Lett.* **2004**, *6*, 309; e) D. K. Kumar, D. A. Jose, P. Dastidar, A. Das, *Chem. Mater.* **2004**, *16*, 2332; f) C. Ruiz-Pérez, P. A. Lorenzo-Luis, M. Hernández-Molina, M. M. Laz, P. Gili, M. Julve, *Cryst. Growth Des.* **2004**, *4*, 57; g) C. Glidewell, J. N. Low, J. M. S. Skakle, J. L. Wardell, *Acta Crystallogr. Sect. C* **2004**, *60*, o120; h) S. H. Dale, M. J. R. Elsegood, A. E. L. Coombs, *CrystEngComm* **2004**, *6*, 328; i) K. K. Arora, V. R. Pedireddi, *J. Org. Chem.* **2003**, *68*, 9177; j) N. Shan, A. D. Bond, W. Jones, *New J. Chem.* **2003**, *27*, 365; k) K. Moon, W.-Z. Chen, T. Ren, A. E. Kaifer, *CrystEngComm* **2003**, *5*, 451; l) F. A. A. Paz, J. Klinowski, *CrystEngComm* **2003**, *5*, 238; m) B.-Q. Ma, P. Coppens, *Chem. Commun.* **2003**, 2290; n) B. R. Bhogala, A. Nangia, *Cryst. Growth Des.* **2003**, *3*, 547.

[11] a) E. H. Arbib, B. Elouadi, J. P. Chaminade, J. Darriet, *J. Solid State Chem.* **1996**, *127*, 350; b) D. Stachel, I. Svoboda, H. Fuess, *Acta Crystallogr. Sect. C* **1995**, *51*, 1049.

[12] a) O. Saied, T. Maris, J. D. Wuest, *J. Am. Chem. Soc.* **2003**, *125*, 14956; b) X. Wang, M. Simard, J. D. Wuest, *J. Am. Chem. Soc.* **1994**, *116*, 12119.

[13] For related studies of phosphines and phosphine oxides bearing a single pyridinone ring, see M. Akazome, S. Suzuki, Y. Shimuzu, K. Henmi, K. Ogura, *J. Org. Chem.* **2000**, *65*, 6917.

[14] a) A. Nangia, G. R. Desiraju, *Top. Curr. Chem.* **1998**, *198*, 57; b) G. R. Desiraju, *Angew. Chem.* **1995**, *107*, 2541; *Angew. Chem. Int. Ed. Engl.* **1995**, *34*, 2311.

[15] R. R. Carlson, D. W. Meek, *Inorg. Chem.* **1974**, *13*, 1741.

[16] a) É. Boucher, M. Simard, J. D. Wuest, *J. Org. Chem.* **1995**, *60*, 1408; b) W. A. Lott, E. Shaw, *J. Am. Chem. Soc.* **1949**, *71*, 70.

[17] A. L. Spek, *Acta Crystallogr. Sect. C* **1987**, *43*, 1233.

[18] a) J. A. Thomas, T. A. Hamor, *Acta Crystallogr. Sect. C* **1993**, *49*, 355; b) C. P. Brock, W. B. Schweizer, J. D. Dunitz, *J. Am. Chem. Soc.* **1985**, *107*, 6964.

[19] a) R. F. See, A. D. Dutoi, J. C. Fettinger, P. J. Nicastro, J. W. Ziller, *J. Chem. Crystallogr.* **1998**, *28*, 893; b) C. M. Whitaker, K. L. Kott, R. J. McMahon, *J. Org. Chem.* **1995**, *60*, 3499.

[20] The dimensions of a channel in a particular direction correspond to those of an imaginary cylinder that could be passed through the hypothetical open network in the given direction in contact with the van der Waals surface. Such values are inherently conservative because 1) they measure the cross-section at the most narrow constriction, and 2) they systematically underestimate the sizes of channels that are not uniform and linear.

[21] The percentage of volume accessible to guests was estimated by the PLATON program.[22] PLATON calculates the accessible volume by allowing a spherical probe of variable radius to roll over the internal van der Waals surface of the crystal structure. PLATON uses a default value of 1.20 Å for the radius of the probe, which is an appropriate model for small guests such as water. The van der Waals radii used to define surfaces for these calculations are as follows: C: 1.70 Å, H: 1.20 Å, N: 1.55 Å, O: 1.52 Å, and P: 1.80 Å. If V is the volume of the unit cell and V_g is the guest-accessible volume as calculated by PLATON, then the porosity P in % is given by 100 V_g/V.

[22] a) A. L. Spek, *PLATON, A Multipurpose Crystallographic Tool*, Utrecht University, Utrecht, The Netherlands, **2001**; b) P. van der Sluis, A. L. Spek, *Acta Crystallogr. Sect. A* **1990**, *46*, 194.

[23] J.-H. Fournier, T. Maris, J. D. Wuest, *J. Org. Chem.* **2004**, *69*, 1762.

[24] a) L. B. McCusker, Ch. Baerlocher, E. Jahn, M. Bülow, *Zeolites* **1991**, *11*, 308; b) M. E. Davis, C. Saldarriaga, C. Montes, J. Garces, C. Crowder, *Nature* **1988**, *331*, 698.

[25] P. B. Moore, J. Shen, *Nature* **1983**, *306*, 356.

[26] For reviews of related work, see a) J. L. C. Rowsell, O. M. Yaghi, *Microporous Mesoporous Mater.* **2004**, *73*, 3; b) M. E. Davis, *Nature* **2002**, *417*, 813; c) A. K. Cheetham, G. Férey, T. Loiseau, *Angew. Chem.* **1999**, *111*, 3466; *Angew. Chem. Int. Ed.* **1999**, *38*, 3268.

[27] Triphenylphosphine oxide is known to cocrystallize with many compounds that can serve as donors of hydrogen bonds; M. C. Etter, P. W. Baures, *J. Am. Chem. Soc.* **1988**, *110*, 630.

[28] Under these conditions, exchange is driven to completion by a large excess of the new guest.

[29] For rare exceptions, see H.-K. Jeong, S. Nair, T. Vogt, L. C. Dickinson, M. Tsapatsis, *Nat. Mater.* **2003**, *2*, 53.

[30] C. A. Zapffe, C. O. Worden, *Acta Crystallogr.* **1949**, *2*, 377.

[31] For a related study of diffusion in molecular crystals, see T. Hertzsch, F. Budde, E. Weber, J. Hulliger, *Angew. Chem.* **2002**, *114*, 2385; *Angew. Chem. Int. Ed.* **2002**, *41*, 2281.

[32] See the Supporting Information for a detailed description of the synthesis and spectroscopic characterization of tecton **4**, its crystallization and structure, and exchanges of guests in single crystals.

[33] CCDC-260634–260636 contain the supplementary crystallographic data for this paper. These data can be obtained free of charge from the Cambridge Crystallographic Data Centre via www.ccdc.cam.ac.uk/data_request/cif.

[34] SAINT (Release 6.06), Integration Software for Single Crystal Data, Bruker AXS Inc., Madison, Wisconsin (USA), **1999**.

[35] G. M. Sheldrick, SADABS, Bruker Area Detector Absorption Corrections, Bruker AXS Inc., Madison, Wisconsin (USA), **1996**.

[36] G. M. Sheldrick, SHELXS-97, Program for the Solution of Crystal Structures and SHELXL-97, Program for the Refinement of Crystal Structures, University of Göttingen (Germany), **1997**.

 © 2005 Wiley-VCH Verlag GmbH & Co. KGaA, Weinheim

Zintl Anions

[(Ni-Ni-Ni)@(Ge$_9$)$_2$]$^{4-}$: A Linear Triatomic Nickel Filament Enclosed in a Dimer of Nine-Atom Germanium Clusters**

*Jose M. Goicoechea and Slavi C. Sevov**

The chemistry of nine-atom deltahedral Zintl anions of Group 14 has advanced greatly in recent years. Redox reactions of these clusters have led to dimers, trimers, tetramers, and infinite chains of germanium clusters such as [Ge$_9$-Ge$_9$]$^{6-}$,[1] [Ge$_9$=Ge$_9$=Ge$_9$]$^{6-}$,[2] [Ge$_9$=Ge$_9$=Ge$_9$=Ge$_9$]$^{8-}$,[3,4] $_\infty$[-(Ge$_9$)$^{2-}$-],[5,6] and $_\infty$[-(HgGe$_9$)$^{2-}$-].[7] Similar redox reactions combined with nucleophilic addition of various anions have produced, for the first time, substituted clusters such as [Ge$_9$-SnPh$_3$]$^{3-}$, [Ph$_3$Sn-Ge$_9$-SnPh$_3$]$^{2-}$, [Ph$_2$Sb-Ge$_9$-SbPh$_2$]$^{2-}$, and [Ph$_3$Sn-Ge$_9$-Ge$_9$-SnPh$_3$]$^{3-}$.[8–10] Also, it has been known for quite some time that ligand-exchange reactions with organometallic compounds can add a transition-metal vertex to the cluster and form species such as [Sn$_9$M(CO)$_3$]$^{4-}$ for M = Cr, Mo, W.[11–13] More recent experiments with [Pt(PPh$_3$)$_4$], [Ni(CO)$_2$(PPh$_3$)$_2$], and [Ni(cod)$_2$] (cod = 1,5-cyclooctadiene) have shown that the nine-atom cluster can accommodate a central transition-metal atom to form [Ni@(Ge$_9$Ni-PPh$_3$)]$^{2-}$,[14] [Ni@(Sn$_9$Ni-CO)]$^{2-}$, and [Pt@(Sn$_9$Pt-PPh$_3$)]$^{2-}$.[15] Note that these species also contain a ligated transition-metal atom in the form of {Ni-PPh$_3$}, {Ni-CO}, or {Pt-PPh$_3$} fragments as a vertex of the cluster and are thus ten-atom clusters. Similar reactions involving Pb$_9$ clusters resulted in cluster enlargement and formation of the first ligand-free, transition-metal centered deltahedral clusters [Ni@Pb$_{10}$]$^{2-}$ and [Pt@Pb$_{12}$]$^{2-}$ with the shapes of a bicapped square antiprism and an icosahedron, respectively.[16,17] Also, a reaction of the As$_7^{3-}$ ions with [Ni(cod)$_2$] leads to a large cluster of 20 arsenic atoms around an arsenic-centered {Ni$_{12}$} core.[18]

Herein we report the synthesis and characterization of a ligand-free anion that contains a linear trimer of nickel enclosed inside two nine-atom germanium clusters, [(Ni-Ni-Ni)@(Ge$_9$)$_2$]$^{4-}$ (**1**; Figure 1). This compound is the first ligand-free deltahedral formation of Group 14 with more than one transition-metal atom inside. The anion was structurally characterized in the species [K(2,2,2-crypt)]$_4$[Ni$_3$@(Ge$_9$)$_2$]·2tol (2,2,2-crypt = 4,7,13,16,21,24-hexaoxa-1,10-diazabicyclo-[8.8.8]hexacosane, tol = toluene) made in a high yield by a reaction of an ethylenediamine(en) solution of K$_4$Ge$_9$ with a threefold excess of [Ni(cod)$_2$].

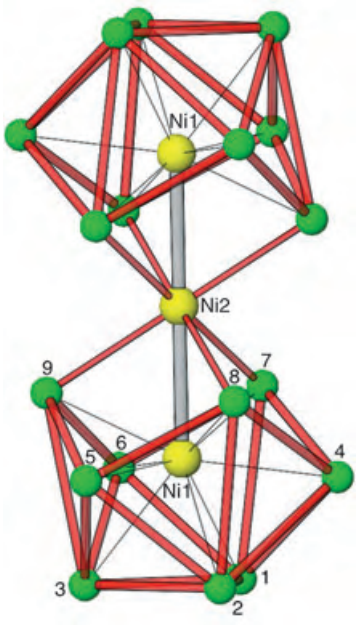


Figure 1. The anion **1**. Ge: green. The Ni–Ni bond length is 2.395(1) Å. Ni2 is at an inversion center and is octahedrally coordinated by germanium with distances [Å] from Ni2 to: Ge7 2.529(1), Ge8 2.540(1), Ge9 2.505(1) Å, and angles in the range 86.09(4)–93.91(4)°. Each Ge$_9$ cluster is a tricapped (atoms 4, 5, 6) trigonal prism (triangular bases of atoms 1-2-3 and 7-8-9) in which one of the triangular bases (7-8-9) has been opened by insertion of the nickel trimer. Distances [Å] from Ni1 to: Ge1 2.475, Ge2 2.487, Ge3 2.510, Ge4 2.446, Ge5 2.456, Ge6 2.453, Ge7 2.338, Ge8 2.340, Ge9 2.362. Other distances [Å]: Ge1-Ge7 3.016, Ge2-Ge8 3.052, Ge3-Ge9 3.061, Ge1-Ge2 2.654, Ge1-Ge3 2.634, Ge1-Ge4 2.726, Ge1-Ge6 2.749, Ge2-Ge3 2.640, Ge2-Ge4 2.712, Ge2-Ge5 2.713, Ge3-Ge5 2.724, Ge3-Ge6 2.738, Ge4-Ge7 2.662, Ge4-Ge8 2.621, Ge5-Ge8 2.653, Ge5-Ge9 2.604, Ge6-Ge7 2.621, Ge6-Ge9 2.612. (The standard deviations for all distances are 1 or 2×10^{-3} Å.).

The two end atoms of the nickel trimer center the two nine-atom germanium clusters while the central nickel atom is positioned at an inversion center and plays the role of a tenth (shared) vertex for each cluster. A closer look at the nine-atom germanium clusters reveals that, similar to many empty clusters, they can be described as distorted tricapped trigonal prisms (Figure 1). Typically, the distortion in empty clusters is expressed in elongation of one, two, or all three of the vertical prismatic edges 1-7, 2-8, and 3-9. The nickel-centered clusters in **1** show the same distortion, all three edges being significantly longer, 3.061(2), 3.052(2), and 3.016(2) Å, than the remaining Ge–Ge distances, 2.604(1)–2.749(2) Å. However, the clusters in **1** are additionally distorted by the opening of one of the triangular bases of the prisms, the base made of atoms 7-8-9. This distortion is clearly caused by the insertion of the additional nickel atom, Ni2, as a vertex of the two nine-atom germanium clusters (Figure 1) and results in two nickel-centered ten-atom clusters made of one nickel and nine germanium atoms, {Ni@Ge$_9$Ni}. The two clusters form a dimer by sharing the nickel vertex, and the formula of **1** can be

[*] J. M. Goicoechea, Prof. S. C. Sevov
Department of Chemistry and Biochemistry
University of Notre Dame
Notre Dame, IN 46556 (USA)
Fax: (+1) 574-631-6652
E-mail: ssevov@nd.edu

[**] This work was supported by the National Science Foundation (CHE-0446131). We thank Bill Boggess for helping with the mass spectrometry.

Supporting information for this article is available on the WWW under http://www.angewandte.org or from the author.

 © 2005 Wiley-VCH Verlag GmbH & Co. KGaA, Weinheim DOI: 10.1002/anie.200500600

written as $[(Ni@Ge_9)Ni(Ni@Ge_9)]^{4-}$. Interestingly, the corresponding monomer, $[Ni@(Ge_9Ni\text{-}PPh_3)]^{2-}$ (**2**),[14] also exists, as mentioned above, and has exactly the same shape (as does $[Pt@(Sn_9Pt\text{-}PPh_3)]^{2-}$) as the {Ni@$Ge_9$Ni} unit of **1**.[15] The only difference is that the outer nickel atom in **2** is ligated (Figure 2b). The monomer, in turn, can be viewed as being

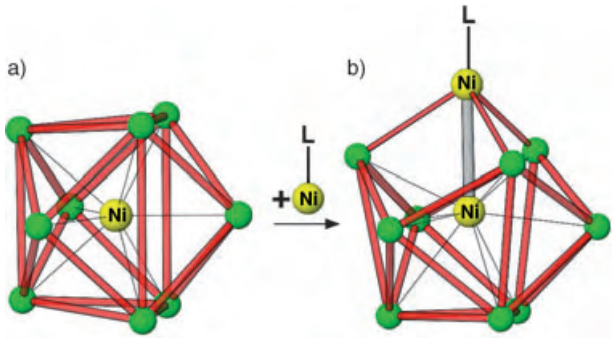


Figure 2. a) The centered nine-atom germanium cluster $[Ni@Ge_9]^{3-}$ (**3**) with the shape of elongated tricapped trigonal prism characterized in $[K(2,2,2\text{-crypt})]_6[Ni@Ge_9]_2\cdot 3en$. b) The $[Ni@Ge_9Ni\text{-}PPh_3]^{2-}$ (**2**) ion can be viewed as being made from $[Ni@Ge_9]^{3-}$ by insertion of an Ni–L fragment and opening of one of the bases of the trigonal prism.

made by insertion of a Ni–L (L = ligand) fragment along the pseudo threefold axis of a hypothetical nickel-centered $[Ni@Ge_9]$ tricapped trigonal prism and opening of the corresponding triangular base (Figure 2). We searched for these hypothetical species by carrying out reactions of Ge_9 clusters (K_4Ge_9 dissolved in ethylenediamine) with smaller excesses of $[Ni(cod)_2]$. These reactions were successful and produced a crystalline compound, $[K(2,2,2\text{-crypt})]_6[Ni@Ge_9]_2\cdot 3en$, that contained the anticipated nickel-centered clusters $[Ni@Ge_9]^{3-}$ (**3**; Figure 2a). The structure determination of this compound was somewhat problematic owing to its extremely large unit cell, the presence of two crystallographically different $[Ni@Ge_9]^{3-}$ clusters per cell, and the observed disorder in some of the germanium atoms of the clusters. Nevertheless, it is clear that the clusters are nickel-centered tricapped trigonal prisms elongated along the three vertical prismatic edges (edge distances within 3.089–3.560 Å). Thus, the existence of these clusters completes the series of species in the formation of **1**, that is, $[Ge_9]\rightarrow[Ni@Ge_9]\rightarrow[Ni@Ge_9NiL]\rightarrow[(Ni@Ge_9)Ni(Ni@Ge_9)]$.

The three nickel atoms of **1** form a linear trimer, a filament that is "protected" by the two germanium clusters. The Ni–Ni distance of 2.395(1) Å compares very well with bonding distances in nickel dimers, trimers, and larger clusters. For example, the distances in the triangular $[(\mu^3\text{-}NtBu)(NiCp)_3]$ (Cp = C_5H_5),[19] $(\mu^3\text{-}CO)_2(NiCp^*)_3$ (Cp* = C_5Me_5),[20] and $(\mu^3\text{-}CS)_2(NiCpMe)_3$ (CpMe = C_5H_4Me)[21] are in the range 2.335–2.442 Å. These distances are 2.419 and 2.428 Å in the octahedral $[(NiCp)_6]^+$ ion,[22] and the distance in the dimeric $[(NiCpMe)_2(\mu\text{-}CO)_2]$ is 2.390 Å.[23] The Ni–Ni distance in the monomeric cluster $[Ni@(Ge_9Ni\text{-}PPh_3)]^{2-}$ is also very similar, 2.361 Å.[14] The only other linear trimer of metal atoms that are part of fused clusters happens to be a ruthenium trimer in $[(Cp^*RuB_4H_{10})Ru(Cp^*RuB_4H_{10})]$.[24] Each cluster in this case is a pentagonal pyramid with a {Cp*Ru} moiety at its apex and a shared ruthenium atom in the base (the clusters are shared in a transoid fashion giving linear Ru-Ru-Ru). Furthermore, as with **2**, the corresponding monomeric cluster $[Cp^*RuB_4H_{10}Ru\text{-}Cp^*]$ is also known.[25]

The charge of 4− of **1** can be understood as the sum of the charges of $[Ni@(Ge_9Ni\text{-}L)]^{2-}$ and $[Ni@Ge_9]^{2-}$. The latter formally replaces the ligand L in the former, that is, $[Ni@(Ge_9Ni\text{-}L)]^{2-} + [Ni@Ge_9]^{2-}\rightarrow[(Ni@Ge_9)Ni(Ni@Ge_9)]^{4-} + L$. Note that the Ni–L fragment does not provide cluster-bonding electrons and, therefore, $[Ni@Ge_9Ni\text{-}L]^{2-}$ and $[Ni@Ge_9]^{2-}$ have the same numbers of such electrons, 20, despite the different numbers of vertices. This situation makes $[Ni@Ge_9Ni\text{-}L]^{2-}$, as well as each half of **1**, *hypo*-electronic because a deltahedron with 10 vertices should have $2n+2 = 22$ ($n = 10$) cluster-bonding electrons according to Wade's rules.[26] The reason for the deviation is clearly the shape of the cluster which differs greatly from the shape expected for a 10-atom deltahedron (a bicapped square antiprism). The same unusual shape and electron count was also observed for 10-atom indium clusters centered by Ni, Pd, or Pt, $[M@In_{10}]^{10-}$.[27] The relation between the shape and the electron count was explained in molecular orbital terms for these clusters. In short, the central d^{10} atom does not bring additional cluster-bonding electrons but provides central orbitals for overlap with the cluster orbitals and, therefore, improves the bonding within the cluster. A nine-atom deltahedron with the shape of a tricapped trigonal prism (20 cluster-bonding electrons) has a LUMO that is bonding within the triangular bases of the prism but is antibonding between them. Therefore, elongation of the prismatic edges (those between the triangular bases) reduces the antibonding character of the orbital while opening of a triangular base reduces its bonding character. Thus, the position of this orbital, and therefore its occupancy, depends very strongly on which of these distortions prevails in each particular case. Note that the addition of a tenth vertex along the threefold axis of the prism to cap one of the bases does not change the electronic requirements. The orbital in question is empty for $[M@In_{10}]^{10-}$, $[Ni@Ge_9Ni\text{-}L]^{2-}$, and the two halves of **1**, while it is occupied by a single electron in $[Ni@Ge_9]^{3-}$ (and many examples of $[Ge_9]^{3-}$).[28] Furthermore, as for empty nine-atom germanium clusters,[9,10] centered clusters with different charges may be in equilibria between themselves and solvated electrons. This situation would provide $[Ni@Ge_9]^{2-}$ ions in the solution in addition to $[Ni@Ge_9]^{3-}$.

The new ions $[(Ni@Ge_9)Ni(Ni@Ge_9)]^{4-}$ are intact in solution, that is, they do not form simply upon crystallization. This was demonstrated by electrospray mass spectroscopy of a dimethylformamide (DMF) solution of $[K(2,2,2\text{-crypt})]_4[Ni_3@(Ge_9)_2]\cdot 2tol$. The spectrum, acquired in negative-ion mode, shows clearly the signal for the dianion $[Ni_3@(Ge_9)_2]^{2-}$ with an isotope distribution matching perfectly the calculated one (Figure 3). The new compound is EPR silent (crystalline sample at room temperature), which indicates that the nickel centers have a Ni^0, d^{10} configuration.

 © 2005 Wiley-VCH Verlag GmbH & Co. KGaA, Weinheim

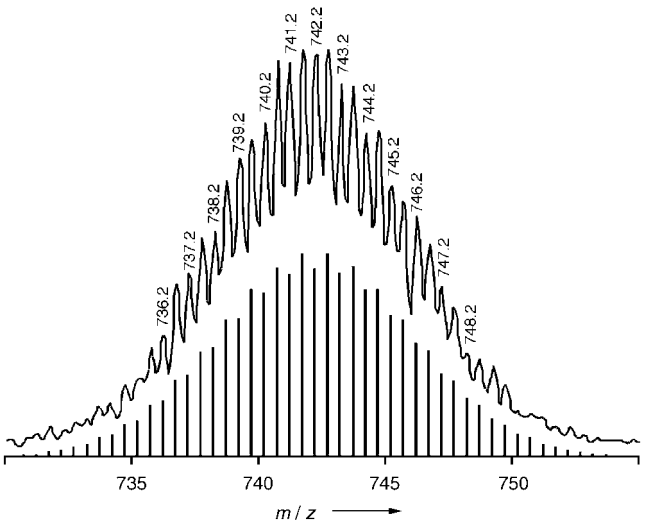


Figure 3. The electrospray mass spectrum (negative-ion mode) of a solution of $[K(2,2,2\text{-crypt})]_4[Ni_3@(Ge_9)_2]\cdot 2\,tol$ in DMF. The spectrum shows the dianion $[Ni_3@(Ge_9)_2]^{2-}$ (top) and its theoretical isotope distribution (bottom).

Experimental Section

All manipulations were carried out under an inert atmosphere using standard Schlenk-line and/or glovebox techniques. Ethylenediamine (Acros, 99%) was distilled over sodium metal, collected and redistilled over K_4Sn_9 and/or K_4Pb_9 intermetallics. The K_4Ge_9 precursor was synthesized from a stoichiometric mixture of the elements (K: 99+%, Strem; Ge: 99.999%, Alfa-Aesar) heated at 900°C for 2 days in sealed niobium containers jacketed in evacuated fused-silica ampoules. 2,2,2-crypt (Acros, 98%) and $[Ni(cod)_2]$ (Strem, 98+%) were used as received after they had been carefully dried under vacuum. Electrospray mass-spectra were recorded from DMF solutions (10–20 μM) of $[K(2,2,2\text{-crypt})]_4\mathbf{1}\cdot 2\,tol$ on a Micromass Quattro-LC triple quadrupole mass spectrometer (125°C source temperature, 150°C desolvation temperature, 3 kV capillary voltage, and 25 V cone voltage).

$[K(2,2,2\text{-crypt})]_4[Ni_3@(Ge_9)_2]\cdot 2\,tol$: K_4Ge_9 (78 mg, 0.096 mmol) and 2,2,2-crypt (145 mg, 0.384 mmol) were dissolved in ethylenediamine (2 mL) in a test tube inside a glovebox yielding an intensely red solution. $[Ni(cod)_2]$ (82 mg, 0.298 mmol) was added to this solution, and the mixture was allowed to stir for 3 h yielding a dark reddish brown suspension. The suspension was filtered, and the resulting dark brown filtrate was layered with toluene and left undisturbed. It yielded dark greenish brown plates of $[K(2,2,2\text{-crypt})]_4[Ni_3@(Ge_9)_2]\cdot 2\,tol$ after 2–3 days (ca. 65%).

$[K(2,2,2\text{-crypt})]_6[Ni@Ge_9]_2\cdot 3\,en$: K_4Ge_9 (84 mg, 0.104 mmol) and 2,2,2-crypt (117 mg, 0.310 mmol) were dissolved in ethylenediamine (2 mL) yielding a bright red solution. $[Ni(cod)_2]$ (64 mg, 0.232 mmol) was added to this solution, and the mixture was allowed to stir for 2 h. The resulting dark red–brown solution was filtered. The filtrate was collected and layered with toluene, and left undisturbed to allow for crystallization. The solution afforded large bright red blocks of $[K(2,2,2\text{-crypt})]_6[Ni@Ge_9]_2\cdot 3\,en$ after 2–3 days.

Data sets were collected on a Bruker APEX diffractometer with a CCD area detector at 100 K with $Mo_{K\alpha}$ radiation. The crystals were selected under Paratone-N oil, mounted on fibers, and positioned in the cold stream of the diffractometer. The structures were solved and refined (on F^2) with the aid of the SHELXTL V5.1 package.[29] Crystal data for $[K(2,2,2\text{-crypt})]_4[Ni_3@(Ge_9)_2]\cdot 2\,tol$: monoclinic, $P2_1/n$, $a=14.439(2)$, $b=28.830(4)$, and $c=16.563(2)$ Å, $\beta=115.716(3)°$, $V=6211.9(1)$ Å^3, $R1=0.0735$ for the observed data. Crystal data for $[K(2,2,2\text{-crypt})]_6[Ni@Ge_9]_2\cdot 3\,en$: monoclinic, $P2_1/n$, $a=14.744(1)$, $b=21.437(1)$, and $c=53.575(4)$ Å, $\beta=93.459(2)°$, $V=16\,903(2)$ Å^3, $R1=0.0932$ for the observed data. CCDC-263116 for $[K(2,2,2\text{-crypt})]_4[Ni_3@(Ge_9)_2]\cdot 2\,tol$ and CCDC-263117 for $[K(2,2,2\text{-crypt})]_6[Ni@Ge_9]_2\cdot 3\,en$ contain the supplementary crystallographic data for this paper. These data can be obtained free of charge from the Cambridge Crystallographic Data Centre via www.ccdc.cam.ac.uk/data_request/cif.

Received: February 17, 2005
Revised: April 7, 2005
Published online: June 1, 2005

Keywords: cluster compounds · germanium · nickel · zintl anions

[1] L. Xu, S. C. Sevov, *J. Am. Chem. Soc.* **1999**, *121*, 9245.
[2] A. Ugrinov, S. C. Sevov, *J. Am. Chem. Soc.* **2002**, *124*, 10990.
[3] A. Ugrinov, S. C. Sevov, *Inorg. Chem.* **2003**, *42*, 5789.
[4] L. Yong, S. D. Hoffman, T. F. Fässler, *Z. Anorg. Allg. Chem.* **2004**, *630*, 1977.
[5] C. Downie, Z. Tang, A. M. Guloy, *Angew. Chem.* **2000**, *112*, 345; *Angew. Chem. Int. Ed.* **2000**, *39*, 337; .
[6] C. Downie, J. G. Mao, A. M. Guloy, *Inorg. Chem.* **2001**, *40*, 4721.
[7] A. Nienhaus, R. Hauptmann, T. F. Fässler, *Angew. Chem.* **2002**, *114*, 3352; *Angew. Chem. Int. Ed.* **2002**, *41*, 3213; .
[8] A. Ugrinov, S. C. Sevov, *J. Am. Chem. Soc.* **2002**, *124*, 2442.
[9] A. Ugrinov, S. C. Sevov, *J. Am. Chem. Soc.* **2003**, *125*, 14059.
[10] A. Ugrinov, S. C. Sevov, *Chem. Eur. J.* **2004**, *10*, 3727.
[11] B. W. Eichhorn, R. C. Haushalter, W. T. Pennington, *J. Am. Chem. Soc.* **1988**, *110*, 8704.
[12] B. Kesanli, J. C. Fettinger, D. R. Gardner, B. W. Eichhorn, *Chem. Eur. J.* **2001**, *7*, 5277.
[13] J. Campbell, H. P. A. Mercier, F. Holger, D. Santry, D. A. Dixon, G. J. Schrobilgen, *Inorg. Chem.* **2002**, *41*, 86.
[14] D. R. Gardner, J. C. Fettinger, B. W. Eichhorn, *Angew. Chem.* **1996**, *108*, 3032; *Angew. Chem. Int. Ed. Engl.* **1996**, *35*, 2852.
[15] B. Kesanli, J. Fettinger, D. R. Gardner, B. Eichhorn, *J. Am. Chem. Soc.* **2002**, *124*, 4779.
[16] E. N. Esenturk, J. Fettinger, B. Eichhorn, *Chem. Commun.* **2005**, 247.
[17] E. N. Esenturk, J. Fettinger, Y. F. Lam, B. Eichhorn, *Angew. Chem.* **2004**, *116*, 2184; *Angew. Chem. Int. Ed.* **2004**, *43*, 2132.
[18] M. J. Moses, J. C. Fettinger, B. W. Eichhorn, *Science* **2003**, *300*, 5620.
[19] N. Kamijo, T. Wantabe, *Bull. Chem. Soc. Jpn.* **1974**, *47*, 373.
[20] J. J. Maj, A. D. Rae, L. F. Dahl, *J. Am. Chem. Soc.* **1982**, *104*, 3054.
[21] T. E. North, J. B. Thoden, B. Spencer, A. Bjarnason, L. F. Dahl, *Organometallics* **1992**, *11*, 4326.
[22] M. S. Pasquette, L. F. Dahl, *J. Am. Chem. Soc.* **1980**, *102*, 6621.
[23] L. R. Byers, L. F. Dahl, *Inorg. Chem.* **1980**, *19*, 680.
[24] X. Lei, M. Shang, T. P. Fehlner, *Angew. Chem.* **1999**, *111*, 2186; *Angew. Chem. Int. Ed.* **1999**, *38*, 1986.
[25] X. Lei, M. Shang, T. P. Fehlner, *J. Am. Chem. Soc.* **1999**, *121*, 1275.
[26] K. J. Wade, *Adv. Inorg. Chem. Radiochem.* **1976**, *18*, 1.
[27] S. C. Sevov, J. D. Corbett, *J. Am. Chem. Soc.* **1993**, *115*, 9089.
[28] Reviews: a) T. F. Fässler, *Coord. Chem. Rev.* **2001**, *215*, 377; b) J. D. Corbett, *Struct. Bonding (Berlin)* **1997**, *87*, 157.
[29] a) G. M. Sheldrick, *Acta Crystallogr. Sect. A* **1990**, *46*, 467; b) G. M. Sheldrick, SHELXTL V5.1, Bruker-AXS, Madison, WI, USA.

 © 2005 Wiley-VCH Verlag GmbH & Co. KGaA, Weinheim

Enzyme Engineering

The Heme Monooxygenase Cytochrome $P450_{cam}$ Can Be Engineered to Oxidize Ethane to Ethanol**

Feng Xu, Stephen G. Bell, Jaka Lednik, Andrew Insley, Zihe Rao, and Luet-Lok Wong**

The selective catalytic oxidation of alkanes to alcohols under ambient conditions is a great scientific challenge and is of potential industrial and economic importance. Heterogeneous catalysts require elevated temperatures and pressures, and further oxidation to aldehydes and carbon dioxide is prevalent. Although biological catalysts are attractive because they operate under mild conditions, the only enzymes capable of oxidizing ethane and methane are the copper and non-heme iron methane monooxygenases.[1–5] Of the other classes of monooxygenases, the heme-dependent cytochrome P450 enzymes, which use two electrons from NAD(P)H to activate oxygen and generate a ferryl intermediate $[(Por)^{+}Fe^{IV}=O]$ to attack C–H bonds, are known to oxidize a wide range of organic molecules, but not ethane and methane (Por = porphyrin).[6,7] We have explored the engineering of $P450_{cam}$ from *Pseudomonas putida* [8] for alkane oxidation.[9,10] The approach of varying the $P450_{cam}$ active-site volume to fit a non-natural substrate was first used by Loida and Sligar for ethylbenzene oxidation.[11,12] We have used bulky amino acid substitutions in the $P450_{cam}$ active site to promote the binding and oxidation of gaseous alkanes. The mutants showed fast and efficient *n*-butane oxidation, but propane oxidation activity was modest, and no ethane oxidation was observed.[10] This approach of decreasing the active-site volume has been combined with directed evolution to engineer $P450_{BM\text{-}3}$ from *Bacillus megaterium* to oxidize propane with a turnover rate of 54 min^{-1}.[13] Herein, we report the engineering of $P450_{cam}$ to provide the first example of ethane oxidation by a P450 enzyme.

[*] F. Xu,[+] Prof. Z. Rao
Laboratory of Structural Biology
School of Life Sciences and Engineering
Tsinghua University, Beijing 100084 (China)
Fax: (+86) 10-6277-3145
E-mail: raozh@xtal.tsinghua.edu.cn
Prof. Z. Rao
Institute of Biophysics
15 Datun Road, Chaoyang District, Beijing 100101 (China)
Fax: (+86) 10-6486-7566
Dr. S. G. Bell,[+] J. Lednik, A. Insley, Dr. L.-L. Wong
Department of Chemistry, University of Oxford
Inorganic Chemistry Laboratory
South Parks Road, Oxford, OX1 3QR (UK)
Fax: (+44) 1865-272690
E-mail: luet.wong@chem.ox.ac.uk
[+] These authors contributed equally to this work.

[**] L.-L.W. acknowledges support from the Biotechnology and Biological Sciences Research Council (UK) (B10666) and the Higher Education Funding Council for England.

The most active $P450_{cam}$ mutant for propane oxidation reported previously was the F87W/Y96F/T101L/L1244M/V247L mutant (the EB mutant).[10] We determined the crystal structure of the substrate-free form of the precursor mutant F87W/Y96F/V247L to a resolution of 2.1 Å to provide insight into the effects of the mutations.[14] The active-site structure is shown in Figure 1. The most interesting feature is that there

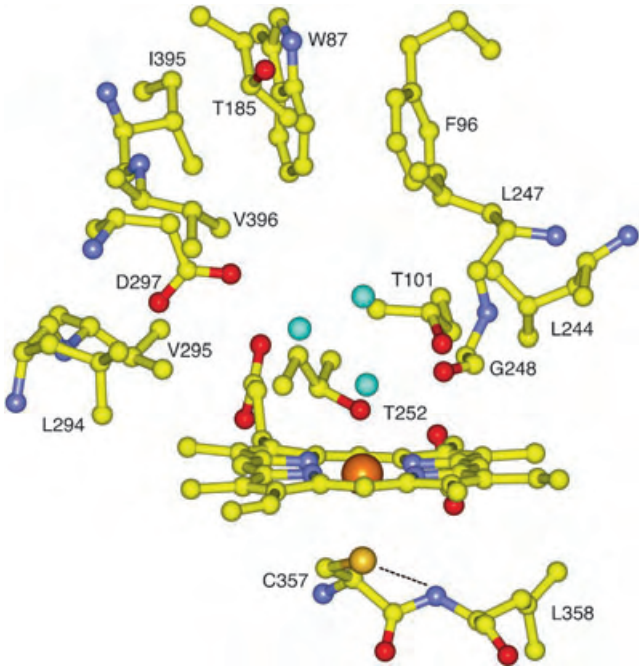


Figure 1. The active-site structure of the substrate-free form of the F87W/Y96F/V247L mutant of $P450_{cam}$ highlighting the cluster of three water molecules (light blue) in the substrate pocket and the hydrogen bond between the thiolato side chain of C357 and the main-chain amide of L358.

are only three water molecules in the active site, compared with six in the wild-type enzyme structure.[15] This probably results from the decreased active site volume, and is consistent with the increased activity of the mutant for the oxidation of small molecules such as propane. In the work discussed herein, we introduced additional mutations to the EB mutant to further decrease the size of the substrate-binding pocket. We examined the structure (Figure 1) for cavities within the active site that could bind a small molecule such as ethane away from the heme iron center. Mutations were then introduced to close such cavities. The $P450_{cam}$ active site is highly irregular in shape, and cavities were found between L294 and T252, L247 and G248, and in the A296–D297 region. The cavity between the W87, L247, and V396 side chains at the top of the active site is covered by T185. Therefore, the mutations L294M, G248A, and T185M were introduced to force ethane to bind closer to the heme iron center.

Morishima and co-workers recently reported the interesting effects of the L358P mutation.[16,17] The main-chain amide of L358 forms a hydrogen bond to the thiolato side chain of C357, thus modulating the donor strength of this heme-

 DOI: 10.1002/anie.200462630 © 2005 Wiley-VCH Verlag GmbH & Co. KGaA, Weinheim

proximal ligand.[18] The L358P mutation removes this hydrogen bond and alters the reduction potential of the heme, but it also promotes the oxidation of non-natural substrates.[16] We therefore investigated the effect of this mutation on alkane oxidation. While this work was in progress, the crystal structure of the L358P mutant was reported.[17] Among the interesting structural changes, it was found that the heme was pushed into the substrate pocket towards the substrate; a general tightening of the pocket was also observed. These changes may promote the binding of non-natural substrates that do not fit as well into the pocket as does camphor.

As none of the previous $P450_{cam}$ mutants oxidized ethane, we first examined the propane oxidation activity of the new mutants;[19] those with the highest activity were then tested for ethane oxidation. The results are given in Table 1. All the mutants showed $>90\%$ high-spin heme content upon propane binding (data not shown). The L294M mutation increased the NADH oxidation rate for propane by 50% relative to the EB mutant, but decreased the coupling efficiency (product yield based on NADH consumed). Overall, the propane oxidation rate was slightly increased. Interestingly, the EB/L294M mutant gave readily detectable amounts of propan-1-ol, whereas all previous $P450_{cam}$ mutants gave propan-2-ol exclusively. Hence the L294M mutation decreased the mobility of propane within the active site such that the higher intrinsic reactivity of secondary C–H bonds in the radical mechanism no longer dominated over that of the larger number of the less reactive, primary C–H bonds. The T185M mutation significantly increased the coupling, resulting in another increase in the propane oxidation activity. The L358P mutation increased both the activity and coupling, in agreement with previous reports on the effects of this mutation on the oxidation of non-natural substrates. Adding the G248A mutation increased both the activity and coupling further. The fast propane oxidation rate ($500\ min^{-1}$) and excellent coupling (86%) of the EB/L294M/T185M/L1358P/G248A mutant indicated good fit between the engineered $P450_{cam}$ active site and propane.

The EB/L294M/T185M/L1358P/G248A mutant was examined for ethane oxidation. The heme shifted to $>85\%$ high spin in the presence of ethane (Figure 2). We were surprised that the NADH oxidation activity ($741\ min^{-1}$)[20] was higher than that for propane. GC analysis showed that ethane was oxidized to ethanol (no ethanal was formed) at a rate of $78.2\ min^{-1}$, which corresponds to 10.5% coupling (Figure 3).[21] There was more peroxide uncoupling (40%) than observed with propane (15%). Therefore, the oxidase uncoupling pathway accounted for $\approx 50\%$ of the NADH consumed in ethane oxidation. This pathway becomes significant if the ethane substrate is bound too far away from the ferryl oxygen atom for rapid substrate oxidation,[12] such that two-electron reduction of the ferryl to the ferric state competes with substrate oxidation. The drop in coupling from propane (86%) to ethane (10%) is surprisingly large, indicating the stringent requirement of the active site architecture to localize ethane close to the heme iron center. It also explains why the other mutants did not show readily detectable ethane oxidation activity.

The EB/L294M/T185M/L1358P/G248A mutant also had the interesting property of being $\approx 45\%$ high spin even in the absence of substrate (Figure 2), whereas all other mutants

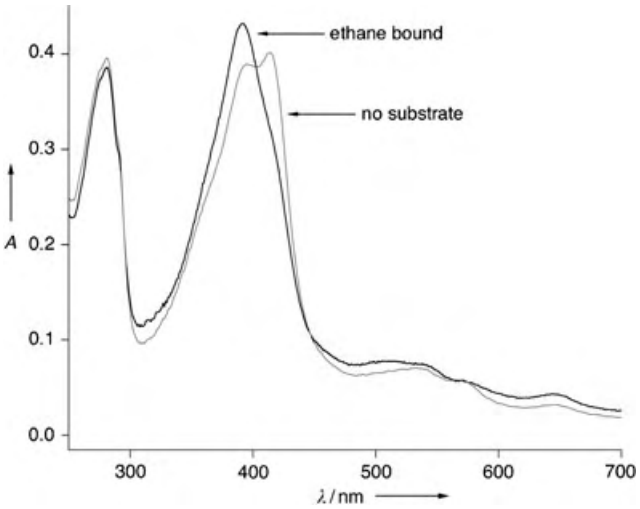


Figure 2. The Soret region of the electronic spectrum of the EB/L294M/T185M/L1358P/G248A mutant of $P450_{cam}$ showing the partial high-spin heme nature of the mutant in the absence of substrate and the $>85\%$ high-spin heme content upon binding of ethane.

Table 1: Propane and ethane oxidation activity of $P450_{cam}$ mutants.[a]

$P450_{cam}$ enzyme	Propane				Ethane			
	NADH rate	product rate[b]	coupling [%][c]	H_2O_2 [%]	NADH rate	product rate[b]	coupling [%][c]	H_2O_2 [%]
F87W/Y96F/T101L/V247L/L1244M[d] (EB mutant)	266	176 (<2%)	66.2	25.0	<20	–	–	–
EB/L294M	414	193 (5.8%)	46.8	38.0	<20	–	–	–
EB/L294M/T185M	302	228 (3.4%)	75.6	23.4	45	–	–	–
EB/L294M/T185M/L1358P	462	379 (3.6%)	81.9	12.4	269	<10	<4	30.0
EB/L294M/T185M/L1358P/G248A	590	505 (4.2%)	85.6	15.0	741	78.2	10.5	39.6

[a] The rates of NADH turnover and product formation are given in nmol (nmol P450)$^{-1}$ min^{-1}. The data represent the averages of at least four experiments, with all data for each parameter within 15% of the mean. [b] The dominant product of propane oxidation was propan-2-ol; the percentage of propan-1-ol is shown in brackets. Ethane was oxidized to ethanol with no evidence for ethanal formation (by GC). [c] The percentage of NADH consumed that was channeled to product formation. [d] Data from Ref. [10]. (–: The ethanol product concentration was not sufficiently high above the background to be reliably determined.)

 © 2005 Wiley-VCH Verlag GmbH & Co. KGaA, Weinheim

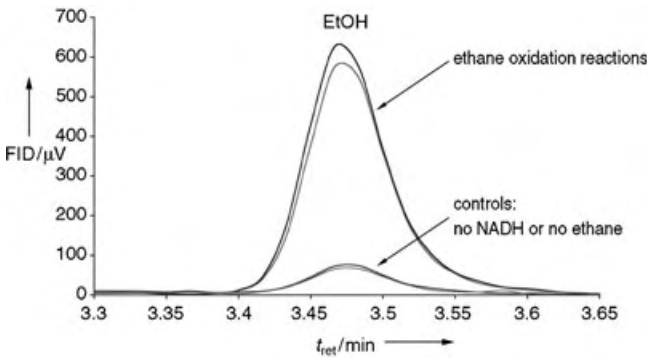


Figure 3. GC analysis of ethane oxidation assays with the EB/L294M/T185M/L1358P/G248A mutant. The controls with no ethane or no NADH added show the residual background peak from ethanol (< 1 μM) present in the water used to prepare the buffers. The apparent difference in the ethanol product peak areas for two separate incubations was corrected by the ratio to the pentan-1-ol internal standard peak. t_{ret} = retention time.

were low spin. The six-water cluster in substrate-free $P450_{cam}$ has strong hydrogen bonding, and the heme-bound water ligand is likely to have significant hydroxide ion character. Raag and Poulos noted the importance of hydrogen bonding to the heme ligand water: wild-type $P450_{cam}$ with non-natural substrates bound could have a six-coordinate heme, yet the iron center was high spin. Therefore, the presence of this sixth ligand on its own was not sufficient to bring the heme to a low-spin state.[22] Model compound studies have also shown that the P450 heme group is low spin if the axial water ligand is hydrogen bonded to other groups, but is high spin if there is no such hydrogen bonding.[23] The axial water ligand in the F87W/Y96F/V247L mutant is hydrogen bonded to two other waters, and the heme is low spin. As the EB/L294M/T185M/L1358P/G248A mutant contains five additional bulky substitutions within the active site, it is very likely that the three-water cluster observed in the F87W/Y96F/V247L mutant would be perturbed significantly, leaving only two or even one water molecule in the active site. Fewer active site water molecules and weakened hydrogen bonding allows ethane to bind more readily, and in this case, to induce a heme-group shift to > 90% high spin and a fast NADH turnover rate. Hence the EB/L294M/T185M/L1358P/G248A mutant has not only the interesting property of ethane oxidation, but its active site water structure could provide new insight into the origin of the heme spin state equilibrium in P450 enzymes.

In summary, we have engineered a cytochrome P450 enzyme to oxidize ethane to ethanol by decreasing the active site volume with bulky substitutions, and by altering the hydrogen bonding to the proximal ligand by the L358P mutation first reported by Morishima.[16,17] The high spin heme content of the EB/L294M/T185M/L1358P/G248A mutant in the absence of substrate suggests that it may also be a useful platform for structure–function studies of P450 enzymes. Finally, the high NADH oxidation rate of this mutant with ethane suggests that, as we had shown for *n*-butane and propane, fast ethane oxidation will be possible once the uncoupling pathways are suppressed by localizing ethane close to the ferryl oxygen atom.

Received: November 16, 2004
Revised: March 17, 2005
Published online: May 24, 2005

Keywords: alkane oxidation · heme proteins · iron · metalloenzymes · protein engineering

[1] J. D. Lipscomb, *Annu. Rev. Microbiol.* **1994**, *48*, 371.
[2] J. C. Murrell, B. Gilbert, I. R. McDonald, *Arch. Microbiol.* **2000**, *173*, 325.
[3] D. A. Kopp, S. J. Lippard, *Curr. Opin. Chem. Biol.* **2002**, *6*, 568.
[4] J. G. Leahy, P. J. Batchelor, S. M. Morcomb, *FEMS Microbiol. Rev.* **2003**, *27*, 449.
[5] S. I. Chan, K. H. Chen, S. S. Yu, C. L. Chen, S. S. Kuo, *Biochemistry* **2004**, *43*, 4421.
[6] *Cytochrome P450: Structure, Mechanism, and Biochemistry*, 2nd ed. (Ed.: P. R. Ortiz de Montellano), Plenum, New York, **1995**.
[7] M. J. Cryle, J. E. Stok, J. J. De Voss, *Aust. J. Chem.* **2003**, *56*, 749.
[8] I. C. Gunsalus, G. C. Wagner, *Methods Enzymol.* **1978**, *52*, 166.
[9] S. G. Bell, J.-A. Stevenson, H. D. Boyd, S. Campbell, A. D. Riddle, E. L. Orton, L.-L. Wong, *Chem. Commun.* **2002**, 490.
[10] S. G. Bell, E. Orton, H. Boyd, J.-A. Stevenson, A. Riddle, S. Campbell, L.-L. Wong, *Dalton Trans.* **2003**, 2133.
[11] P. J. Loida, S. G. Sligar, *Protein Eng.* **1993**, *6*, 207.
[12] P. J. Loida, S. G. Sligar, *Biochemistry* **1993**, *32*, 11530.
[13] M. W. Peters, P. Meinhold, A. Glieder, F. H. Arnold, *J. Am. Chem. Soc.* **2003**, *125*, 13442.
[14] We had reported earlier that one molecule in the *P*1 asymmetric unit in the X-ray crystal structure of the F87W/Y96F/V247L mutant complexed with 1,3,5-trichlorobenzene had low substrate occupancy, and that the density above the heme could be modeled with three water molecules, but their locations could not be refined (X. Chen, A. Christopher, J. P. Jones, S. G. Bell, Q. Guo, F. Xu, Z. Rao, L. L. Wong, *J. Biol. Chem.* **2002**, *277*, 37519). The structure of the substrate-free form of the mutant was therefore determined. Procedures for crystallization of the mutant at 291 K by the hanging drop vapor diffusion method and data collection and refinement were as reported previously. Crystals of the F87W/Y96F/V247L mutant belonged to the space group $P2_1$, with unit-cell dimensions: $a = 66.8$ Å, $b = 62.1$ Å, $c = 94.9$ Å, $\alpha = 90°$, $\beta = 90.5°$, $\gamma = 90°$. A total of 236028 reflections were measured, with R_{merge} of 7.6% for 45978 unique reflections and 99.9% completeness (50–2.1 Å). Data were collected to 100% completeness in the highest resolution shell. The structure was solved by molecular replacement based on the crystal structure of wild-type $P450_{cam}$ (PDB code: 2CPP), but with the camphor removed. After initial refinement, the difference Fourier map for both molecules in the unit cell showed well-defined triangle-shaped electron density above the heme group that was modeled by three water molecules. The final refinement parameters were $R_{work} = 19.1\%$ and $R_{free} = 24.3\%$. Full details will be published elsewhere.
[15] T. L. Poulos, B. C. Finzel, A. J. Howard, *Biochemistry* **1986**, *25*, 5314.
[16] S. Yoshioka, S. Takahashi, K. Ishimori, I. Morishima, *J. Inorg. Biochem.* **2000**, *81*, 141.
[17] S. Nagano, T. Tosha, K. Ishimori, I. Morishima, T. L. Poulos, *J. Biol. Chem.* **2004**, *279*, 42844.
[18] T. L. Poulos, B. C. Finzel, A. J. Howard, *J. Mol. Biol.* **1987**, *195*, 687.

 © 2005 Wiley-VCH Verlag GmbH & Co. KGaA, Weinheim

[19] General methods for mutagenesis, enzyme expression and purification, activity and GC analysis for propane were carried out as described previously.[10]
[20] The ethane oxidation assays required extra precautions. Ethanol was present in varying concentrations in most components of an activity assay, even in the ultra pure water obtained from water purification systems. Only water containing <500 nM ethanol (GC) were used for buffer preparation. Buffer solutions were then analyzed by GC to ensure that there was no ethanol in the chemicals used. Commercial NADH contains ethanol as a stabilizer. This ethanol was removed by washing with diisopropyl ether: 0.5-mL aliquots of a NADH solution (20 mg mL^{-1}) were mixed with 2 mL diisopropyl ether, vortexed and then centrifuged at 3000 rpm for 5 min. The organic layer was removed, and the wash repeated a further four times. The resulting solution of NADH was analyzed by GC to determine the ethanol concentration, and then lyophilized. This procedure gave <1 μM ethanol background in the reaction mixtures. NADH turnover incubations were carried out at 30 °C in 4-mL capacity cuvettes equipped with screw caps and Teflon septum seals. Incubation mixtures contained Tris (50 mM, pH 7.4), KCl (200 mM), $P450_{cam}$ (1 μM), putidaredoxin (16 μM), and putidaredoxin reductase (1 μM). In a typical reaction, the volume of buffer required to take the final volume to 2.5 mL was $\approx$1.6 mL. Half of this required volume of buffer was saturated with ethane, and the other half was a buffer solution saturated with oxygen. A sample was taken (the no-NADH control), and the cuvette sealed with a Teflon-backed screw cap. The mixtures were equilibrated at 30 °C for 2 min, and the reaction was initiated by the addition of NADH through a hypodermic syringe needle pushed through the Teflon septum. NADH was added as a stock solution (20 mg mL^{-1}) in Tris (50 mM, pH 7.4) to $\approx$200 μM (final A_{340} $\approx$1.2), and the absorbance at $\lambda = 340$ nm was monitored. The rate of NADH consumption was calculated from the slope of the time-course plot by using $\varepsilon_{340} = 6.22$ mM^{-1} cm^{-1}. A total of five experiments were carried out for each mutant tested. For each mutant, a control incubation with no substrate was also carried out to ensure that the ethane contained no ethanol.
[21] A 90-μL aliquot of a reaction mixture or control was added to a 10-μL aliquot of an aqueous solution of pentan-1-ol (200 μM) as internal standard. A 2-μL aliquot of each mixture was injected directly onto the SPB-1 GC column (0.5 mm × 60 m). The column temperature was held at 40 °C for 4 min and then increased at 5 °C min^{-1} to 100 °C. The retention times were: ethanol, 3.50 min; propan-2-ol, 4.80 min; propan-1-ol, 6.50 min; pentan-1-ol, 16.0 min. The concentration of product in a reaction mixture was determined by calibrating the FID response to the product.[10] Peroxide uncoupling was determined by a standard horseradish peroxidase/phenol/4-aminoantipyrine assay.
[22] R. Raag, T. L. Poulos, *Biochemistry* **1989**, *28*, 917.
[23] M. Lochner, M. Meuwly, W. D. Woggon, *Chem. Commun.* **2003**, 1330.

 © 2005 Wiley-VCH Verlag GmbH & Co. KGaA, Weinheim

Organocatalysis

Enantioselective Michael Addition to α,β-Unsaturated Imides Catalyzed by a Bifunctional Organocatalyst**

*Yasutaka Hoashi, Tomotaka Okino, and Yoshiji Takemoto**

The catalytic asymmetric formation of a carbon–carbon bond represents one of the most challenging fields in organic chemistry. A number of asymmetric Michael additions to α,β-unsaturated carbonyl acceptors catalyzed by chiral catalysts have been reported.[1] However, the acceptors employed in the asymmetric Michael additions of 1,3-dicarbonyl compounds generally have been restricted to enones[2–4] and nitroalkenes.[5] Similarly, although organocatalysts that bear chiral secondary amine groups have been shown to be efficient catalysts for the Michael reaction with such acceptors,[6] their applications to α,β-unsaturated acid derivatives seems to be difficult. Therefore, the development of general and highly enantioselective versions of the reactions of α,β-unsaturated acid derivatives still remains a challenging goal. Quite recently, two groups achieved the initial breakthroughs on these problems. The Jacobsen and Kanemasa groups independently reported the highly enantioselective metal-catalyzed Michael additions of malononitrile, which is equivalent to a 1,3-dicarbonyl compound, to α,β-unsaturated imides.[7,8] However, there have been no reports of such asymmetric Michael addition without any metal catalysts. Herein, we report the first enantioselective Michael reactions of malononitrile to acyclic α,β-unsaturated imides in the presence of a chiral organocatalyst.

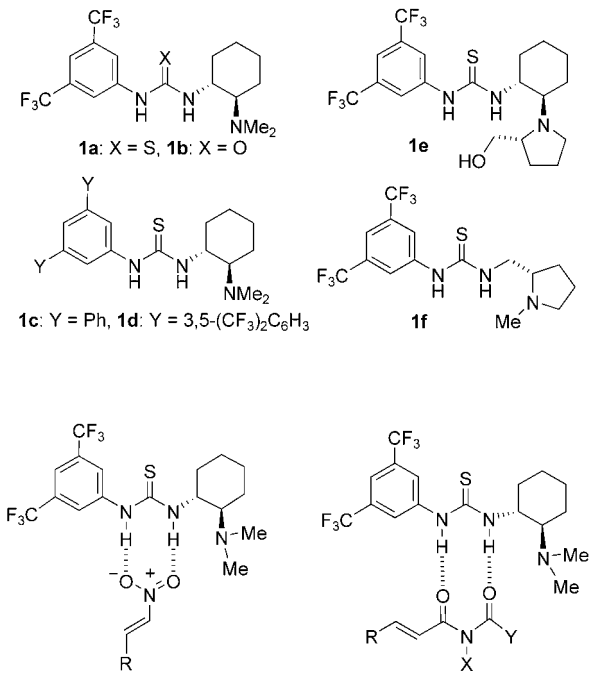
Although we recently reported that the bifunctional-thiourea-catalyzed Michael reaction of 1,3-dicarbonyl compounds to nitroalkenes proceeded with high enantioselectivity (up to 93% *ee*),[9] the same reaction of other nucleophiles such as malononitrile to nitroalkenes gave the corresponding product with low enantioselectivity. To extend the synthetic utility of the bifunctional thiourea **1a** in the asymmetric reaction, we undertook the screening of proper Michael acceptors other than nitroalkenes to react with malononitrile. For the purpose, α,β-unsaturated imides seem to have an ideal structure to form hydrogen bonds with the thiourea catalyst **1a** as shown in Scheme 1.[10,11]

[*] Y. Hoashi, T. Okino, Prof. Dr. Y. Takemoto
Graduate School of Pharmaceutical Sciences
Kyoto University
Yoshida, Sakyo-ku, Kyoto 606-8501 (Japan)
Fax: (+81) 75-753-4569
E-mail: takemoto@pharm.kyoto-u.ac.jp

[**] This work was supported by grants from the 21st Century COE Program "Knowledge Information Infrastructure for Genome Science" and KAKENHI (16390006).

Supporting information for this article is available on the WWW under http://www.angewandte.org or from the author.

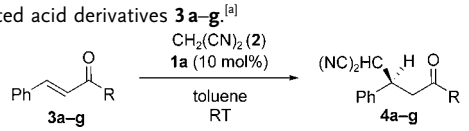
 © 2005 Wiley-VCH Verlag GmbH & Co. KGaA, Weinheim DOI: 10.1002/anie.200500459



Scheme 1. Hydrogen-bond interaction with thiourea **1a**.

We first investigated the Michael addition of malononitrile (**2**) to several types of α,β-unsaturated acid derivatives **3a**–**g** (Table 1). The reaction of **2** (2 equiv) with a solution of imides **3** in toluene (0.5 M) was carried out at room temperature in the presence of **1a** (10 mol%). Although the conjugate addition of **2** with amide **3a** gave no desired product, the same reaction with *N*-acyl-1,3-oxazolidinone **3b**[10e] was completed after 96 h to give the Michael adduct **4b** in 89% yield (Table 1, entries 1 and 2). The enantiopurity of **4b** was revealed to be 83% ee by means of HPLC analysis. In the hope of enhancing the hydrogen-bonding interaction with thiourea **1a**, we employed *N*-acyl-1,3-imidazolidinone **3c**, which bears a cyclic urea moiety, as a Michael acceptor, but both the yield of **4c** and enantioselectivity were poorer (59%, 81% *ee*; Table 1, entry 3). In contrast with **3c**, *N*-acylpyrrolidinone **3d** was revealed to be a good acceptor of **2**, providing the corresponding product **4d** in 93% yield with the best enantioselectivity (87% *ee*) (Table 1, entry 4). Use of *N*-acylpiperidinone **3e** and acyclic imide **3f** for the Michael addition reaction resulted in a significant decrease in both chemical yield and enantioselectivity (Table 1, entries 5 and 6). On the other hand, the conjugate addition of **2** with imide **3g** proceeded smoothly, but the enantioselectivity (84% *ee*) was somewhat lower than that with **3d** (Table 1, entry 7). Notably, the same reaction with **3d** under dilute conditions (0.1 M solution in toluene) improved the stereoselectivity up to 93% *ee*.

Table 1: Enantioselective Michael addition of malononitrile **2** with α,β-unsaturated acid derivatives **3a**–**g**.[a]



Entry	Substrate (R)	Product	*t* [h]	Yield [%][b]	*ee* [%][c]
1	**3a**	**4a**	48	0	–
2	**3b**	**4b**	96	89	83
3	**3c**	**4c**	120	59	81
4	**3d**	**4d**	60	93	87
5	**3e**	**4e**	140	42	59
6	**3f**	**4f**	216	27	56
7	**3g**	**4g**	8	94	84

[a] The reaction was conducted with **1a** (10 mol%), **2** (2 equiv), and **3a**–**g** in toluene (0.5 M). [b] Yield of isolated product. [c] The *ee* values were determined by HPLC analysis of **4a**–**g** with a chiral column.

Encouraged by the excellent results obtained with *N*-acylpyrrolidinone **3d** and thiourea **1a**, we explored the effectiveness of a bifunctional urea **1b** and other bifunctional thioureas **1c**–**f** for the Michael addition (Table 2). The reaction of **2** with **3d** in the presence of urea **1b** gave a similar result, affording the desired product **4d** in somewhat lower yield (78%, 87% *ee*; Table 2, entry 1). However, the introduction of phenyl and 3,5-bis(trifluoromethyl)phenyl groups on the aromatic ring of **1a** as well as modification of its dimethylamino group led to significant decrease in reaction rate and enantioselectivity (Table 2, entries 2–4). Furthermore, the (*N*-methylpyrrolidin-2-yl)methyl derivative **1f** was not catalytically active in the Michael reaction and resulted in a low yield of **4d**. These results demonstrated that the original thiourea **1a** was the best choice as a chiral organocatalyst.

Table 2: Enantioselective Michael addition of **2** and imide **3d** in the presence of several bifunctional thioureas **1a**–**f**.

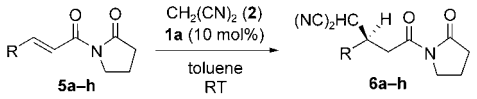
Entry	**1**	*t* [h]	Yield [%][a]	*ee* [%][b]
1	**b**	48	78	87 (*R*)
2	**c**	120	66	60 (*R*)
3	**d**	120	78	69 (*R*)
4	**e**	120	61	48 (*R*)
5	**f**	120	13	3 (*S*)

[a] Yield of isolated product. [b] Determined by HPLC analysis of **4d** with a chiral column.

Having established the optimal reaction conditions for the enantioselective Michael reaction of malononitrile (**2**), we next screened a series of analogues **5a**–**h**, which bear various β substituents. As illustrated in Table 3, imides **5a**–**h** underwent conjugate addition of **2** in the presence of catalyst **1a** in high yields and enantioselecivities, which were almost independent of the β substituents in terms of steric hindrance and electronic properties. The reaction with aryl-substituted

 © 2005 Wiley-VCH Verlag GmbH & Co. KGaA, Weinheim

Table 3: Asymmetric Michael addition of **2** and various α,β-unsaturated imides **5a–h** with **1a**.

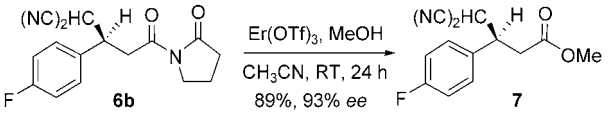


Entry	**5** (R)	*t* [h][a]	**6**	Yield [%][a, b]	*ee* [%][a, c]
1	**a** (*p*-ClC_6H_4)	72 (192)	**a**	85 (88)	89 (93)
2	**b** (*p*-FC_6H_4)	48 (168)	**b**	99 (84)	88 (93)
3	**c** (*p*-$MeOC_6H_4$)	216	**c**	77	85
4	**d** (1-naphthyl)	48 (168)	**d**	93 (87)	88 (93)
5	**e** (2-furyl)	192	**e**	79	85
6	**f** ($PhCH_2CH_2$)	24 (144)	**f**	96 (98)	88 (94)
7	**g** (Me)	24 (120)	**g**	82 (86)	84 (93)
8	**h** (*t*Bu)	168	**h**	78	92

[a] The values in parentheses were obtained from reactions carried out in a 0.1 M solution. [b] Yield of isolated products, after chromatography, of reactions carried out in a 0.5 M solution. [c] Determined by chiral HPLC analysis.

imides **5a–c** proceeded with high enantioselectivity to furnish the addition adducts **6a–c**, while the rate of the reaction was somewhat lower for **5c** (R = *p*-methoxyphenyl) owing to the electron-rich substrate (Table 2, entries 1–3). Similarly, imides **5d–e** bearing 1-naphthyl and furyl groups as the β substituent underwent clean reaction as well, and gave the corresponding adducts **6d–e** with 85–88% *ee* (Table 2, entries 4–5). In contrast to the previously reported Michael addition with nitroalkenes,[9] the present reaction of **2** with imides **5f–h**, which bear alkyl groups as the β substituent, occurred smoothly to afford the desired products **6f–h** in good yields with high enantioselectivities similar to those of **5a–e**. The highest enantioselectivity (92% *ee*) was obtained under the standard conditions in the case of *tert*-butyl derivative **5h**. Furthermore, it is noteworthy that when the reactions were carried out in a 0.1M solution, the all the corresponding products were obtained with higher enantioselectivities (> 93% *ee*).

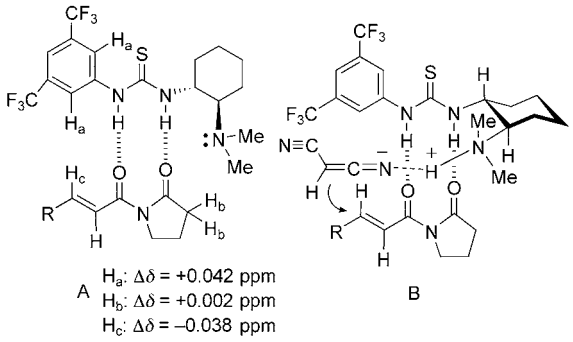
The absolute configuration of the Michael adduct **6b** was determined by the transformation of **6b** into a known compound **7**[7b] (Scheme 2). Treatment of **6b** with a catalytic



Scheme 2. Transformation of Michael adduct **6b** to methyl ester **7**.

amount of $Er(OTf)_3$ in methanol provided methyl ester **7** ($[\alpha]_D^{24} = +22$; $c = 0.70$, CH_3CN) in 89% yield. By comparing $[\alpha]_D$ value with that of an authentic sample ($[\alpha]_D^{24} = +19$; $c = 1.0$, CH_3CN),[7b] the absolute configuration of **6b** was determined to be *R*, and those of the other adducts **6a** and **6c–h** were also assumed to be *R* based on this result.

The formation of a substrate–catalyst complex **1a**·**3d** (**A**; R = Ph) was supported by ^1H NMR spectroscopic experiments (1:1 mixture of **1a** and **3d** in [D_8]toluene), as shown in Scheme 3. From these results, we propose a ternary complex



Scheme 3. ^1H NMR spectroscopic experiments of a substrate–catalyst complex **A** and proposed transition state **B** for the Michael reaction with **1a**.

B of catalyst **1a**, malononitrile (**2**), and imide **5** as a plausible transition state in which **5** and the anion of **2** coordinate to the thiourea moiety and the tertiary amine group of **1a**, respectively, through hydrogen-bonding interactions. The predominant production of *R* adducts is reasonably explained by this transition-state model.

In summary, we have developed the first highly enantioselective organocatalytic Michael reaction of malononitrile (**2**) with α,β-unsaturated imides **5a–h** in the presence of a bifunctional thiourea **1a**. The pyrrolidinone moiety of α,β-unsaturated imides is demonstrated to play a key role in the thiourea-catalyzed Michael reaction. The reaction is applicable to a variety of α,β-unsaturated imides that bear aryl and alkyl groups as a β substituent, and high enantioselectivities are attained. Unfortunately, the Michael addition of other carbon nucleophiles such as malonates and β-ketoesters with **4d** gave no desired products owing to their low reactivities. Further investigations into the mechanism and synthetic application are underway and will be reported in due course.

Received: February 7, 2005
Published online: May 20, 2005

Keywords: imides · Michael addition · nitriles · organocatalysis · thiourea

[1] For a review, see: a) K. Fagnou, M. Lautens, *Chem. Rev.* **2003**, *103*, 169–196; b) E. R. Jarvo, S. J. Miller, *Tetrahedron* **2002**, *58*, 2481–2495; c) J. Christoffers, A. Mann, *Angew. Chem.* **2001**, *113*, 4725–4732; *Angew. Chem. Int. Ed.* **2001**, *40*, 4591–4597; d) N. Krause, A. Hoffmann-Röder, *Synthesis* **2001**, 171–196; e) M. P. Sibi, S. Manyem, *Tetrahedron* **2000**, *56*, 8033–8061; f) *Comprehensive Asymmetric Catalysis* (Eds.: E. N. Jacobsen, A. Pfaltz, H. Yamamoto), Springer, Berlin, **1999**; g) J. Leonard, E. Díez-Barra, S. Merino, *Eur. J. Org. Chem.* **1998**, 2051–2061.

[2] For the conjugate addition of malonates, see: a) M. Watanabe, K. Murata, T. Ikariya, *J. Am. Chem. Soc.* **2003**, *125*, 7508–7509; b) R. T. Dere, R. R. Pal, P. S. Patil, M. M. Salunkhe, *Tetrahedron Lett.* **2003**, *44*, 5351–5353; c) S. Velmathi, S. Swarnalakshmi, S. Narasimhan, *Tetrahedron: Asymmetry* **2003**, *14*, 113–117; d) R. Takita, T. Ohshima, M. Shibasaki, *Tetrahedron Lett.* **2002**, *43*, 4661–4665; e) E. F. DiMauro, M. C. Kozlowski, *Organometallics* **2002**, *21*, 1454–1461; f) N. Prabagaran, G. Sundararajan, *Tetrahedron: Asymmetry* **2002**, *13*, 1053–1058; g) G. Kumar-

 © 2005 Wiley-VCH Verlag GmbH & Co. KGaA, Weinheim

aswamy, M. N. V. Sastry, N. Jena, *Tetrahedron Lett.* **2001**, *42*, 8515 – 8517; h) D. Y. Kim, S. C. Huh, S. M. Kim, *Tetrahedron Lett.* **2001**, *42*, 6299 – 6301; i) S. C. Jha, N. N. Joshi, *Tetrahedron: Asymmetry* **2001**, *12*, 2463 – 2466; j) Y. S. Kim, S. Matsunaga, J. Das, A. Sekine, T. Ohshima, M. Shibasaki, *J. Am. Chem. Soc.* **2000**, *122*, 6506 – 6507; k) M. Ostendorf, S. van der Neut, F. P. J. T. Rutjes, H. Hiemstra, *Eur. J. Org. Chem.* **2000**, 105 – 113; l) H. Sasai, T. Arai, M. Shibasaki, *J. Am. Chem. Soc.* **1994**, *116*, 1571 – 1572; m) N. End, L. Macko, M. Zehnder, A. Pfaltz, *Chem. Eur. J.* **1998**, *4*, 818 – 824; n) M. Yamaguchi, T. Shiraishi, M. Hirama, *J. Org. Chem.* **1996**, *61*, 3520 – 3530; o) H. Sasai, T. Arai, M. Shibasaki, *J. Am. Chem. Soc.* **1994**, *116*, 1571 – 1572; p) A. Kawara, T. Taguchi, *Tetrahedron Lett.* **1994**, *35*, 8805 – 8808.

[3] For the conjugate addition of 1,3-dicarbonyl compounds, see: a) K. Majima, R. Takita, A. Okada, T. Ohshima, M. Shibasaki, *J. Am. Chem. Soc.* **2003**, *125*, 15837 – 15845; b) Y. Hamashima, H. Takano, D. Hotta, M. Sodeoka, *Org. Lett.* **2003**, *5*, 3225 – 3228; c) M. Nakajima, S. Yamamoto, Y. Yamaguchi, E. Nakamura, S. Hashimoto, *Tetrahedron* **2003**, *59*, 7307 – 7313; d) Y. Hamashima, D. Hotta, M. Sodeoka, *J. Am. Chem. Soc.* **2002**, *124*, 11240 – 11241; e) M. Nakajima, Y. Yamaguchi, S. Hashimoto, *Chem. Commun.* **2001**, 1596 – 1597; f) J. Christoffers, U. Rößler, T. Werner, *Eur. J. Org. Chem.* **2000**, 701 – 705; g) M. Shibasaki, H. Sasai, T. Arai, *Angew. Chem.* **1997**, *109*, 1290 – 1311; *Angew. Chem. Int. Ed. Engl.* **1997**, *36*, 1236 – 1256; h) G. Desimoni, G. Dusi, G. Faita, P. Quadrelli, P. Righetti, *Tetrahedron* **1995**, *51*, 4131 – 4144; for the conjugate addition of other nucleophiles, see: i) M. S. Taylor, D. N. Zalatan, A. M. Lerchner, E. N. Jacobsen, *J. Am. Chem. Soc.* **2005**, *127*, 1313 – 1317; j) M. Sawamura, H. Hamashima, Y. Ito, *Bull. Chem. Soc. Jpn.* **2000**, *73*, 2559 – 2562; k) A. J. Blacker, M. L. Clarke, M. S. Loft, M. F. Mahon, J. M. J. Williams, *Organometallics* **1999**, *18*, 2867 – 2873; l) K. Funabashi, Y. Saida, M. Kanai, H. Sasai, M. Shibasaki, *Tetrahedron Lett.* **1998**, *39*, 7557 – 7558; m) M. Sawamura, H. Hamashima, Y. Ito, *J. Am. Chem. Soc.* **1992**, *114*, 8295 – 8296.

[4] For the conjugate addition of nitroalkanes, see: a) M. T. Allingham, A. Howard-Jones, P. J. Murphy, D. A. Thomas, P. W. R. Caulkett, *Tetrahedron Lett.* **2003**, *44*, 8677 – 8680; b) G. Sundararajan, N. Prabagaran, *Org. Lett.* **2001**, *3*, 389 – 392; c) E. J. Corey, F.-Y. Zhang, *Org. Lett.* **2000**, *2*, 4257 – 4259; d) K. Funabashi, Y. Saida, M. Kanai, T. Arai, H. Sasai, M. Shibasaki, *Tetrahedron Lett.* **1998**, *39*, 7557 – 7558; e) P. Bakó, A. Szöllósy, P. Bombicz, L. Tóke, *Synlett* **1997**, 291 – 292; f) E. Keller, N. Veldman, A. L. Spek, B. L. Feringa, *Tetrahedron: Asymmetry* **1997**, *8*, 3403 – 3413; g) M. Yamaguchi, Y. Igarashi, R. S. Reddy, T. Shiraishi, M. Hirama, *Tetrahedron* **1997**, *53*, 11223 – 11236.

[5] a) H. Li, Y. Wang, L. Tang, F. Wu, X. Liu, C. Guo, B. M. Foxman, L. Deng, *Angew. Chem.* **2005**, *117*, 107 – 110; *Angew. Chem. Int. Ed.* **2005**, *44*, 105 – 108; b) M. Watanabe, A. Ikagawa, H. Wang, K. Murata, T. Ikariya, *J. Am. Chem. Soc.* **2004**, *126*, 11148 – 11149; c) H. Li, Y. Wang, L. Tang, L. Deng, *J. Am. Chem. Soc.* **2004**, *126*, 9906 – 9907; d) D. M. Barnes, J. Ji, M. G. Fickes, M. A. Fitzgerald, S. A. King, H. E. Morton, F. A. Plagge, M. Preskill, S. H. Wagaw, S. J. Wittenberger, J. Zhang, *J. Am. Chem. Soc.* **2002**, *124*, 13097 – 13105; e) O. M. Berner, L. Tedeschi, D. Enders, *Eur. J. Org. Chem.* **2002**, 1877 – 1894; f) J. Ji, D. M. Barnes, J. Zhang, S. A. King, S. J. Wittenberger, H. E. Morton, *J. Am. Chem. Soc.* **1999**, *121*, 10215 – 10216; g) H. Brunner, B. Kimel, *Monatsh. Chem.* **1996**, *127*, 1063 – 1072.

[6] a) N. Halland, T. Hansen, K. A. Jørgensen, *Angew. Chem.* **2003**, *115*, 5105 – 5107; *Angew. Chem. Int. Ed.* **2003**, *42*, 4955 – 4957; b) N. Halland, P. S. Aburel, K. A. Jørgensen, *Angew. Chem.* **2003**, *115*, 685 – 689; *Angew. Chem. Int. Ed.* **2003**, *42*, 661 – 665; c) P. Melchiorre, K. A. Jørgensen, *J. Org. Chem.* **2003**, *68*, 4151 – 4157; d) O. Andrey, A. Alexakis, G. Bernardinelli, *Org. Lett.* **2003**, *5*, 2559 – 2561; e) A. Alexakis, O. Andrey, *Org. Lett.* **2002**, *4*, 3611 – 3614; f) D. Enders, A. Seki, *Synlett* **2002**, 26 – 28; g) N. Halland, R. G. Hazell, K. A. Jørgensen, *J. Org. Chem.* **2002**, *67*, 8331 – 8338; h) J. M. Betancort, C. F. Barbas III, *Org. Lett.* **2001**, *3*, 3737 – 3740; i) J. M. Betancort, K. Sakthivel, R. Thayumanavan, C. F. Barbas III, *Tetrahedron Lett.* **2001**, *42*, 4441 – 4444; j) S. Hanessian, V. Pham, *Org. Lett.* **2000**, *2*, 2975 – 2978.

[7] a) I. T. Raheem, S. N. Goodman, E. N. Jacobsen, *J. Am. Chem. Soc.* **2004**, *126*, 706 – 707; b) M. S. Taylor, E. N. Jacobsen, *J. Am. Chem. Soc.* **2003**, *125*, 11204 – 11205.

[8] a) S. Kanemasa, K. Ito, *Eur. J. Org. Chem.* **2004**, 4741 – 4753; b) K. Itoh, Y. Oderaotoshi, S. Kanemasa, *Tetrahedron: Asymmetry* **2003**, *14*, 635 – 639; c) K. Itoh, S. Kanemasa, *J. Am. Chem. Soc.* **2002**, *124*, 13394 – 13395.

[9] a) T. Okino, Y. Hoashi, T. Furukawa, X. Xu, Y. Takemoto, *J. Am. Chem. Soc.* **2005**, *127*, 119 – 125; b) T. Okino, S. Nakamura, T. Furukawa, Y. Takemoto, *Org. Lett.* **2004**, *6*, 625 – 627; c) T. Okino, Y. Hoashi, Y. Takemoto, *J. Am. Chem. Soc.* **2003**, *125*, 12672 – 12673.

[10] a) D. J. Maher, S. J. Connon, *Tetrahedron Lett.* **2004**, *45*, 1301 – 1305; b) T. Okino, Y. Hoashi, Y. Takemoto, *Tetrahedron Lett.* **2003**, *44*, 2817 – 2821; c) P. R. Schreiner, *Chem. Soc. Rev.* **2003**, *32*, 289 – 296; d) A. Wittkopp, P. R. Schreiner, *Chem. Eur. J.* **2003**, *9*, 407 – 414; e) P. R. Schreiner, A. Wittkopp, *Org. Lett.* **2002**, *4*, 217 – 220; f) D. P. Curran, L. H. Kuo, *Tetrahedron Lett.* **1995**, *36*, 6647 – 6650; g) D. P. Curran, L. H. Kuo, *J. Org. Chem.* **1994**, *59*, 3259 – 3261.

[11] For catalytic asymmetric reactions in the presence of chiral urea and thiourea catalysts, see: a) A. Berkessel, F. Cleemann, S. Mukherjee, T. N. Müller, J. Lex, *Angew. Chem.* **2005**, *117*, 817 – 821; *Angew. Chem. Int. Ed.* **2005**, *44*, 807 – 811; b) T. P. Yoon, E. N. Jacobsen, *Angew. Chem.* **2005**, *117*, 470 – 472; *Angew. Chem. Int. Ed.* **2005**, *44*, 466 – 468; c) M. S. Taylor, E. N. Jacobsen, *J. Am. Chem. Soc.* **2004**, *126*, 10558 – 10559; d) G. D. Joly, E. N. Jacobsen, *J. Am. Chem. Soc.* **2004**, *126*, 4102 – 4103; e) Y. Sohtome, A. Tanatani, Y. Hashimoto, K. Nagasawa, *Chem. Pharm. Bull.* **2004**, *52*, 477 – 480; f) Y. Sohtome, A. Tanatani, Y. Hashimoto, K. Nagasawa, *Tetrahedron Lett.* **2004**, *45*, 5589 – 5592; g) A. G. Wenzel, M. P. Lalonde, E. N. Jacobsen, *Synlett* **2003**, 1919 – 1922; h) A. G. Wenzel, E N. Jacobsen, *J. Am. Chem. Soc.* **2002**, *124*, 12964 – 12965; i) P. Vachal, E. N. Jacobsen, *J. Am. Chem. Soc.* **2002**, *124*, 10012 – 10014; j) J. T. Su, P. Vachal, E. N. Jacobsen, *Adv. Synth. Catal.* **2001**, *343*, 197 – 200; k) M. S. Sigman, P. Vachal, E. N. Jacobsen, *Angew. Chem.* **2000**, *112*, 1336 – 1338; *Angew. Chem. Int. Ed.* **2000**, *39*, 1279 – 1281; l) P. Vachal, E. N. Jacobsen, *Org. Lett.* **2000**, *2*, 867 – 870; m) M. S. Sigman, E. N. Jacobsen, *J. Am. Chem. Soc.* **1998**, *120*, 4901 – 4902.

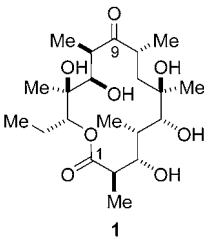
 © 2005 Wiley-VCH Verlag GmbH & Co. KGaA, Weinheim

Natural Product Synthesis

Total Synthesis of Erythronolide A by Mg^{II}-Mediated Cycloadditions of Nitrile Oxides**

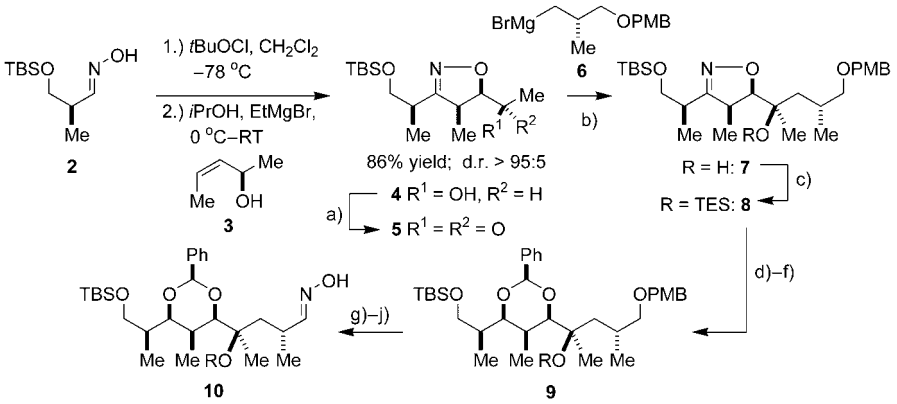
*Dieter Muri, Nina Lohse-Fraefel, and Erick M. Carreira**

Since its discovery in 1952,[1] erythromycin A has captured the imagination of research groups all over the world. The total syntheses of erythromycin A and its related derivatives (erythronolide A, erythromycin B, erythronolide B, (9*S*)-dihydroerythronolide A, 6-deoxyerythronolide B, 9,12-anhydroerythronolide A) have become benchmarks for the study of new methodologies in polyketide synthesis.[2–4] We have recently reported a general approach for the synthesis of polyketide building blocks by means of Kanemasa's Mg^{II}-mediated cycloadditions of nitrile oxides to allylic alcohols.[5] The nature of this approach allows the modular preparation of the entire spectrum of functionality and stereochemical permutations found in polyketide-derived structures. In this communication, we demonstrate the power and generality of this cycloaddition in the context of the total synthesis of erythronolide A (**1**). Erythronolide A was completed in 21 linear steps from the readily available oxime **2**.[5a] Of additional importance, we demonstrate the potential of the strategy to provide access to nonnatural analogues (ketolides) of this important agent.



1

The synthesis commences with the cycloaddition of oxime **2** to allylic alcohol **3**; the former is available in three steps from (*S*)-methyl-3-hydroxyisobutyrate (Roche ester)[6] and the latter in two steps by Noyori reduction of propargylic ketone and semihydrogenation over the Lindlar catalyst.[7] Oxime **2** was treated with *t*BuOCl (−78 °C), which, after addition to a solution of *i*PrOH, EtMgBr, and **3**, provided isoxazoline **4** in 86 % yield on a 35-mmol scale and with a diastereomeric ratio of >95:5 as determined by ^{1}H NMR spectroscopy (Scheme 1). Oxidation of the secondary hydroxy group in **4** under conditions described by Ley et al. [8] and treatment with Grignard reagent **6**[9] afforded tertiary alcohol **7** in 64 % yield



Scheme 1. Conditions: a) TPAP, NMO, CH_2Cl_2, RT, 1.5 h, 82 %; b) **6**, THF, −78 °C, 1 h, 64 %, (d.r. > 98:2); c) TESOTf, 2,6-lutidine, CH_2Cl_2, 0 °C, 1 h, 93 %; d) Raney Ni (W2), $B(OH)_3$, H_2, $MeOH/H_2O$, RT, 2 h, 89 %; e) $Zn(BH_4)_2$, CH_2Cl_2, −30 °C, 2.5 h, 60 % (d.r. > 95:5); f) $PhCH(OMe)_2$, CSA (10 mol %), toluene, 50 mbar, RT, 1.5 h, 87 %; g) DDQ, pH 7 buffer, CH_2Cl_2, 0 °C, 2 h, 85 %; h) TEMPO (15 mol %), NaOCl, KBr (10 mol %), pH 8.6 buffer, CH_2Cl_2, 0 °C, 10 min; j) $H_2NOH{\cdot}HCl$, pyridine, EtOH, RT, 20 min, 85 % (over 2 steps). CSA = camphorsulfonic acid, DDQ = 2,3-dichloro-5,6-dicyanobenzoquinone, NMO = *N*-methylmorpholine *N*-oxide, PMB = *para*-methoxybenzyl, TBS = *tert*-butyldimethylsilyl, TEMPO = 2,2,6,6-tetramethyl-1-piperidinyloxyl, TESOTf = triethylsilyl trifluoromethanesulfonate, TPAP = tetrapropylammonium perruthenate.

(98:2 d.r., ^{1}H NMR). The tertiary hydroxy group was protected as triethylsilyl ether (93 % yield). Reductive cleavage of the N–O bond (Raney Ni, $B(OH)_3$, 93 % yield),[10] *syn* reduction of the ensuing hydroxy ketone ($Zn(BH_4)_2$, 60 % yield),[11] and protection of the isolated 1,3-diol provided **9** (87 % yield) as a single diastereomer (^{1}H NMR). Adduct **9** was converted to oxime **10** by a short three-step sequence of reactions in 72 % overall yield.

With oxime **10** in hand, we were ready for the second cycloaddition of a nitrile oxide. We were pleased to observe that this highly functionalized nitrile oxide smoothly underwent Mg^{II}-mediated 1,3-dipolar cycloaddition with allylic alcohol **3** under our standard reaction conditions (Scheme 2).[6] Isoxazoline **11** was obtained in excellent yield (86 %) as a single diastereomer as determined by ^{1}H NMR spectroscopy. The nitrile oxide derived from **10** represents one of the most complex substrates used in dipolar cycloaddition reactions and attests to the versatility of the cycloaddition strategy for the synthesis of polyketides.

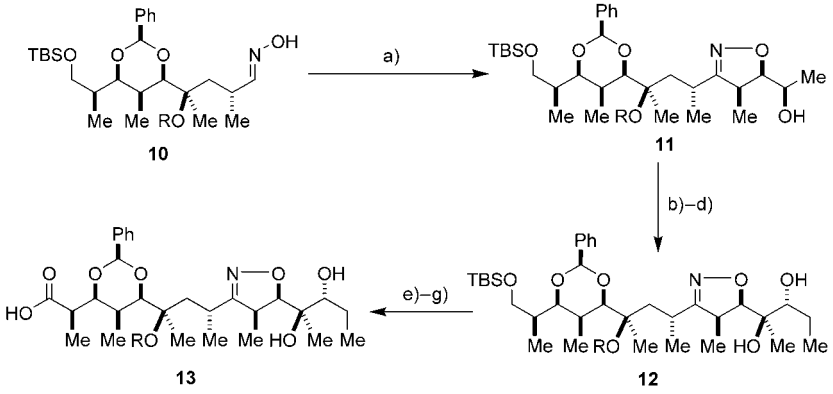
Oxidation of the secondary hydroxy group in **11** with TEMPO/NaOCl provided the corresponding ketone in 93 % yield, which was subjected to Wittig olefination[12] ($PrPPh_3Br$ and *t*BuLi) to give a trisubstituted olefin in 78 % yield and 33:1 *Z*/*E* ratio. Dihydroxylation of this olefin with $(DHQD)_2PHAL/K_2OsO_4{\cdot}2H_2O$ (4 mol %) furnished the 1,2-diol **12** in 81 % yield and 96:4 d.r.[13,14] Selective deprotection of the primary *tert*-butyldimethylsilyl ether over the tertiary triethylsilyl ether could be accomplished with HF·pyridine/pyridine (1:3).[15] Chemoselective two-step oxi-

[*] D. Muri, N. Lohse-Fraefel, Prof. Dr. E. M. Carreira
Laboratorium für Organische Chemie, ETH Hönggerberg
8093 Zürich (Switzerland)
Fax: (+41) 1-632-1328
E-mail: carreira@org.chem.ethz.ch

[**] This research was supported by the Swiss National Science Foundation and F. Hoffmann-LaRoche AG.

Supporting information for this article is available on the WWW under http://www.angewandte.org or from the author.

 © 2005 Wiley-VCH Verlag GmbH & Co. KGaA, Weinheim DOI: 10.1002/anie.200500172

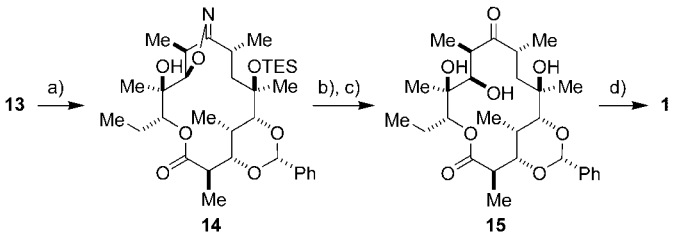


Scheme 2. Conditions: a) i) *t*BuOCl, CH_2Cl_2, −78 °C, 1.5 h, ii) *i*PrOH, EtMgBr, **3**, CH_2Cl_2, 0 °C→RT, 86%, (d.r. > 99:1); b) TEMPO (15 mol%), NaOCl, KBr (10 mol%), pH 8.6 buffer, CH_2Cl_2, 0 °C, 1 h, 93%; c) $PrPPh_3Br$, *t*BuLi, THF, −78 °C→RT, 15 h, 78%, (*Z*:*E* 33:1); d) $(DHQD)_2PHAL$ (20 mol%), $K_3[Fe(CN)_6]$, $MeSO_3NH_2$, K_2CO_3, $K_2OsO_4{\cdot}2H_2O$, *t*BuOH/H_2O, 0 °C, 2.5 h, 81% (d.r. 96:4); e) HF·py:py (1:3), 0 °C, 3 h, 80%; f) TEMPO (15 mol%), NaOCl, KBr (10 mol%), pH 8.6 buffer, CH_2Cl_2, 0 °C, 30 min; g) $NaClO_2$, 2-methyl-2-butene, pH 3.8 buffer, *t*BuOH, 0 °C, 30 min, 83% (over 2 steps). py = pyridine, $(DHQD)_2PHAL$ = dihydroquinidine phthalazine ligand. R = TES.

dation (TEMPO/NaOCl, $NaClO_2$, 83% yield) completed the synthesis of erythronolide A seco acid **13**.

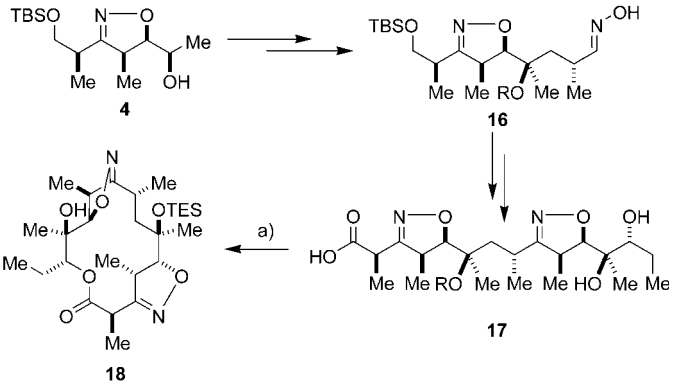
At the outset of this project, it was far from certain whether the cyclization could be successfully executed with the isoxazoline carboxylic acid **13**. The classic work of Woodward on the total synthesis of erythromycin A underscores the sensitivity of related macrolactonizations of carboxylic acids to the constellation of protecting groups.[16] On the basis of modeling, we hypothesized that an isoxazoline bridging C9–C11 would lead to a favorable conformation of **13** and facilitate macrolactonization. Indeed, following a modified Yamaguchi protocol,[17] the desired macrolactone was isolated in 78% yield without detection of any other cyclization by-products (Scheme 3). Deprotection of the triethylsilyl ether and subsequent N–O bond cleavage (Raney-Ni, AcOH) provided **15** in 93% yield, thus completing the formal total synthesis of erythronolide A. Treatment of **15** with $Pd(OAc)_2$ for 6 h under an atmosphere of H_2 produced erythronolide A. Its ^1H and ^{13}C NMR spectra as well as melting point and optical rotation are identical with those of naturally derived erythronolide A.[18]

An important aspect of this cycloaddition strategy would be the ability to access nonnatural polyketides. This approach



Scheme 3. Conditions: a) i)2,4,6-$Cl_3C_6H_2COCl$, NEt_3, THF, 0 °C, 30 min; ii) DMAP, toluene, 50 °C, 4 h, 78%; b) HF·NEt_3, NEt_3, CH_3CN, RT, 64 h, > 99%; c) Raney-Ni (W2), AcOH, H_2, EtOH, RT, 20 min, 93%; d) $Pd(OAc)_2$, MeOH, H_2, RT, 6 h, 40%. DMAP = 4-*N*,*N*-dimethylaminopyridine.

would extend the methodology beyond an aldol-equivalent strategy to one that could provide unusual analogues not directly accessible either through genetic engineering or traditional synthetic methods. A number of erythromycin analogues investigated in the pharmaceutical industry are heterocyclic derivatives (bridging C9–C11, for example) prepared from the natural product.[19] We thus became interested in the generation of nonnatural analogues such as **18** (Scheme 4). In a similar reaction sequence as described above, isoxazoline **4** could easily be converted to oxime **16** and subsequently to carboxylic acid **17**. Under modified Yamaguchi conditions, we obtained macrolactone **18** in 60% yield. Since the nitrile oxide and allylic alcohol partners can be varied readily, this strategy enables an approach to a plethora of



Scheme 4. Conditions: a) i) 2,4,6-$Cl_3C_6H_2COCl$, NEt_3, THF, 0 °C, 30 min; ii) DMAP, toluene, 50 °C, 4 h, 60%.

derivatives that may exhibit useful properties and allow the development of new antibiotics against multiresistant bacterial strains.

In summary, we have reported a stereoselective total synthesis of erythronolide A, whose focal points are two Mg^{II}-mediated cycloadditions of nitrile oxides, making this the shortest synthesis of erythronolide A to date: 21 linear steps, 4% overall yield. These accomplishments establish this methodology as a powerful tool for the synthesis of polyketide natural products. The isoxazoline serves as a robust protecting group for β-hydroxyketones that can be cleaved at a late stage of the synthesis within a densely functionalized structure. Moreover, the isoxazoline proved suitable for the delicate macrolactonization of erythronolide A seco acid **13**. Of broader significance, the strategy, beyond its use as an aldol equivalent process, opens up new possibilities for the preparation of nonnatural analogues.

Received: January 17, 2005
Published online: May 20, 2005

 © 2005 Wiley-VCH Verlag GmbH & Co. KGaA, Weinheim

Keywords: asymmetric synthesis · cycloaddition · erythronolides · macrolactonization · nitrile oxides

[1] J. M. McGuire, R. L. Bunch, R. C. Anderson, H. E. Boaz, E. H. Flynn, H. M. Powell, J. W. Smith, *Antibiot. Chemother.* **1952**, *2*, 281.

[2] The first total synthesis of an erythronolide analogue was reported in 1978: E. J. Corey, E. J. Trybulski, L. S. Melvin, Jr., K. C. Nicolaou, J. A. Secrist, R. Lett, J. R. Sheldrake, D. J. Brunell, M. F. Haslanger, S. Kim, S.-e. Yoo, *J. Am. Chem. Soc.* **1978**, *100*, 4618; E. J. Corey, E. J. Trybulski, L. S. Melvin, Jr., K. C. Nicolaou, J. A. Secrist, R. Lett, J. R. Sheldrake, D. J. Brunell, M. F. Haslanger, S. Kim, S.-e. Yoo, *J. Am. Chem. Soc.* **1978**, *100*, 4620.

[3] For reviews on early synthetic work, see: a) I. Paterson, M. M. Mansuri, *Tetrahedron* **1985**, *41*, 3569; b) J. Mulzer, *Angew. Chem.* **1991**, *103*; *Angew. Chem. Int. Ed. Engl.* **1991**, *30*, 1452.

[4] For recent studies on the syntheses of erythromycins and erythronolides, see: a) R. Stürmer, K. Ritter, R. W. Hoffmann, *Angew. Chem.* **1993**, *105*, 112; *Angew. Chem. Int. Ed. Engl.* **1993**, *32*, 101; b) S. F. Martin, T. Hida, P. R. Kym, M. Loft, A. Hodgson, *J. Am. Chem. Soc.* **1997**, *119*, 3193; c) D. A. Evans, A. S. Kim, R. Metternich, V. J. Novack, *J. Am. Chem. Soc.* **1998**, *120*, 5921; d) P. J. Hergenrother, A. Hodgson, A. S. Judd, W.-C. Lee, S. F. Martin, *Angew. Chem.* **2003**, *115*, 3400; *Angew. Chem. Int. Ed.* **2003**, 3278; e) Z.-H. Peng, K. A. Woerpel, *J. Am. Chem. Soc.* **2003**, *125*, 6018.

[5] a) J. W. Bode, N. Fraefel, D. Muri, E. M. Carreira, *Angew. Chem.* **2001**, *113*, 2128; *Angew. Chem. Int. Ed.* **2001**, *40*, 2082; b) for comprehensive reviews on cycloadditions of nitrile oxides, see: P. Caramella, P. Grünanger in *1,3-Dipolar Cycloaddition Chemistry*, *Vol. 1* (Ed.: A. Padwa), Wiley-Interscience, New York, **1984**, pp. 292–392; C. J. Easton, C. M. M. Hughes, G. P. Savage, G. W. Simpson, *Adv. Heterocycl. Chem.* **1994**, *60*, 261; c) for applications of cycloadditions of nitrile oxides in the synthesis of heterocycles and natural products, see: "Synthetic Applications of 1,3-Dipolar Cycloaddition Chemistry Toward Heterocycles and Natural Products" by V. Jäger, P. A. Colinas in *The Chemistry of Heterocyclic Compounds*, *Vol. 59* (Eds.: A. Padwa, W. H. Pearson), Wiley, New York, **2002**, pp. 361–472.

[6] Oxime **2** was prepared in three steps from (*S*)-methyl-3-hydroxyisobutyrate, which is available for less than 1 € per gram from Mitsubishi Rayon Co., Ltd. We would like to thank Mitsubishi Rayon Co. for a generous gift of (*S*)-methyl-3-hydroxyisobutyrate.

[7] a) Several preparations of chiral olefin **3** have been reported; for our purposes it was prepared from enantiomerically pure 2-hydroxy-3-pentyne, itself prepared by the method of R. Noyori, *J. Am. Chem. Soc.* **1997**, *119*, 8738; b) for another procedure, see: O. Hamed, P. M. Henry, *Organometallics* **1997**, *16*, 4903.

[8] W. P Griffith, S. V. Ley, G. P. Whitecomb, A. D. White, *J. Chem. Soc. Chem. Commun.* **1987**, 1625.

[9] Compound **6** was prepared from the corresponding bromide by lithium–halogen exchange with *t*BuLi and subsequent transmetalation with $MgBr_2$; the bromide is available in three steps from (*S*)-methyl-3-hydroxyisobutyrate: P. M. Smith, E. J. Thomas, *J. Chem. Soc. Perkin Trans. 1* **1998**, 3541.

[10] a) D. P. Curran, *J. Am. Chem. Soc.* **1983**, *105*, 5826; b) D. P. Curran, S. A. Scanga, C. J. Fenk, *J. Org. Chem.* **1984**, *49*, 3474.

[11] a) Y. Ito, M. Yamaguchi, *Tetrahedron Lett.* **1983**, *24*, 5385; b) T. Nakata, Y. Tani, M. Hatozaki, T. Oishi, *Chem. Pharm. Bull.* **1984**, *32*, 1411; c) D. A. Evans, M. D. Ennis, and T. Le, N. Mandel, G. Mandel, *J. Am. Chem. Soc.* **1984**, *106*, 1154.

[12] G. Wittig, U. Schöllkopf, *Chem. Ber.* **1954**, *87*, 1318.

[13] Substrate-directed dihydroxylation on a similar system proved troublesome; no diastereoselectivity was observed but the yield was excellent: S. D. Burke, F. J. Schoenen, M. S. Nair, *Tetrahedron Lett.* **1987**, *28*, 4143.

[14] For recent reviews on Sharpless asymmetric dihydroxylations, see: a) H. C. Kolb, M. S. VanNieuwenhze, K. B. Sharpless, *Chem. Rev.* **1994**, *94*, 2483; b) R. A. Johnson, K. B. Sharpless in *Catalytic Asymmetric Synthesis* (Ed.: I. Ojima), VCH, New York, **2000**, pp. 357.

[15] On a similar system, selective deprotection of the tertiary hydroxy group was observed under acidic conditions (dichloroacetic acid, MeOH, 0 °C).

[16] Woodward's early investigation revealed a 9-(*S*)-hydroxy group, protected as a cyclic acetal, ideal for a successful lactonization of the carboxylic acid: a) R. B. Woodward, E. Logusch, K. P. Nambiar, K. Sakan, D. E. Ward, B.-W. Au-Yeung, P. Balaram, L. J. Browne, P. J. Card, C. H. Chen, R. B. Chênevert, A. Fliri, K. Frobel, H.-J. Gais, D. G. Garratt, K. Hayakawa, W. Heggie, D. P. Hesson, D. Hoppe, I. Hoppe, J. A. Hyatt, D. Ikeda, P. A. Jacobi, K. S. Kim, Y. Kobuke, K. Kojima, K. Krowicki, V. J. Lee, T. Leutert, S. Malchenko, J. Martens, R. S. Matthews, B. S. Ong, J. B. Press, T. V. Rajan Babu, G. Rousseau, H. M. Sauter, M. Suzuki, K. Tatsuta, L. M. Tolbert, E. A. Truesdale, I. Uchida, Y. Ueda, T. Uyehara, A. T. Vasella, W. C. Vladechick, P. A. Wade, R. M. Williams, H. N.-C. Wong, *J. Am. Chem. Soc.* **1981**, *103*, 3210; b) R. B. Woodward, E. Logusch, K. P. Nambiar, K. Sakan, D. E. Ward, B.-W. Au-Yeung, P. Balaram, L. J. Browne, P. J. Card, C. H. Chen, R. B. Chênevert, A. Fliri, K. Frobel, H.-J. Gais, D. G. Garratt, K. Hayakawa, W. Heggie, D. P. Hesson, D. Hoppe, I. Hoppe, J. A. Hyatt, D. Ikeda, P. A. Jacobi, K. S. Kim, Y. Kobuke, K. Kojima, K. Krowicki, V. J. Lee, T. Leutert, S. Malchenko, J. Martens, R. S. Matthews, B. S. Ong, J. B. Press, T. V. Rajan Babu, G. Rousseau, H. M. Sauter, M. Suzuki, K. Tatsuta, L. M. Tolbert, E. A. Truesdale, I. Uchida, Y. Ueda, T. Uyehara, A. T. Vasella, W. C. Vladechick, P. A. Wade, R. M. Williams, H. N.-C. Wong, *J. Am. Chem. Soc.* **1981**, *103*, 3213; R. B. Woodward, E. Logusch, K. P. Nambiar, K. Sakan, D. E. Ward, B.-W. Au-Yeung, P. Balaram, L. J. Browne, P. J. Card, C. H. Chen, R. B. Chênevert, A. Fliri, K. Frobel, H.-J. Gais, D. G. Garratt, K. Hayakawa, W. Heggie, D. P. Hesson, D. Hoppe, I. Hoppe, J. A. Hyatt, D. Ikeda, P. A. Jacobi, K. S. Kim, Y. Kobuke, K. Kojima, K. Krowicki, V. J. Lee, T. Leutert, S. Malchenko, J. Martens, R. S. Matthews, B. S. Ong, J. B. Press, T. V. Rajan Babu, G. Rousseau, H. M. Sauter, M. Suzuki, K. Tatsuta, L. M. Tolbert, E. A. Truesdale, I. Uchida, Y. Ueda, T. Uyehara, A. T. Vasella, W. C. Vladechick, P. A. Wade, R. M. Williams, H. N.-C. Wong, *J. Am. Chem. Soc.* **1981**, *103*, 3215.

[17] a) J. Inanaga, K. Hirata, H. Saeki, T. Katsuki, M. Yamaguchi, *Bull. Chem. Soc. Jpn.* **1979**, *52*, 1989; studies in the context of erythronolide macrolactoniziation: Y. Sakurai, M. Hikota, K. Horita, O. Yonemitsu, *Chem. Pharm. Bull.* **1992**, *40*, 2540.

[18] a) Formation of erythromycin A oxime, see: A. M. Costa, J. Vilarrasa, *Tetrahedron Lett.* **2000**, *41*, 3371; b) Glycoside cleavage, see: R. A. LeMahieu, M. Carson, R. W. Kirstead, *J. Antibiot.* **1975**, *28*, 704; c) Regeneration of the ketone, see: R. A. LeMahieu, M. Carson, R. W. Kierstead, L. M. Fern, *J. Med. Chem.* **1974**, *17*, 953.

[19] For recent modifications, see, for example: a) Y. Watanabe, T. Adachi, T. Asaka, M. Kashimura, S. Morimoto, *Heterocycles* **1990**, *31*, 2121; b) R. L. Elliott, D. Pireh, G. Griesgraber, A. M. Nilius, P. J. Ewing, M. H. Bui, P. M. Raney, R. K. Flamm, K. Kim, R. F. Henry, D. T. W. Chu, J. J. Plattner, Y. S. Or, *J. Med. Chem.* **1998**, *41*, 1651; c) T. Tanikawa, T. Asaka, M. Kashimura, K. Suzuki, H. Sugiyama, M. Sato, K. Kameo, S. Morimoto, A. Nishida, *J. Med. Chem.* **2003**, *46*, 2706; d) M. C. Hsu, A. J. Junia, A. R. Haight, W. Zhang, *J. Org. Chem.* **2004**, *69*, 3907.

 © 2005 Wiley-VCH Verlag GmbH & Co. KGaA, Weinheim

Asymmetric Synthesis

Acetylenic Allenophanes: An Asymmetric Synthesis of a Bis(alleno)-bis(butadiynyl)-*meta*-cyclophane**

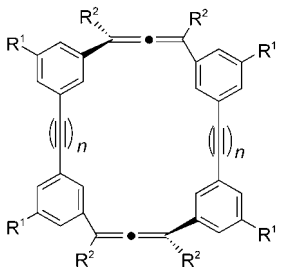
*Matthew D. Clay and Alex G. Fallis**

We have an ongoing interest in the design and synthesis of novel cyclophanes, many of which contain a twisted conformation that imparts helical chirality[1] to the assembled molecule.[2] This helical chirality is a consequence of the number, type, and combination of unsaturated linkages present in these molecules. The synthesis and design of cyclophanes[3] and cage compounds with high carbon content in novel shapes and supramolecular geometries[4] continues to be a topic of current interest.

Allenes are a unique family of organic molecules because of their diverse chemistry, axial chirality, and synthetic versatility,[5] and so investigations into allene-containing natural products and their total syntheses continue to increase.[6] Furthermore, medical applications for these compounds include employing them as inactivators of monoamine oxidase.[7]

In contrast, cyclophanes that have only allene bridges (termed allenophanes)[8] have received little attention and the only reported example was prepared as a mixture of diastereomers.[8] A related family of cyclophanes comprises structures that contain both allene and acetylene bridges. These acetylenic allenophanes should also possess interesting properties. Herein, we report the first asymmetric synthesis of an acetylenic allenophane that contains two allene bridges. This compound appears to be the first cyclophane of this general class.

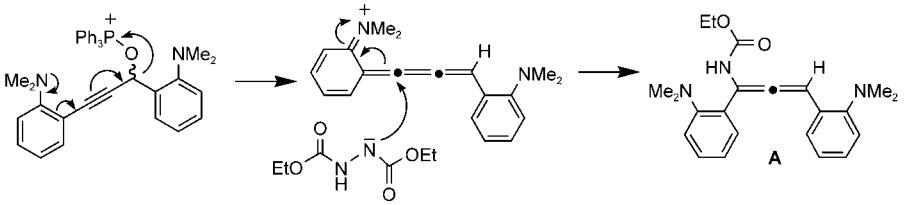
The general structure of an acetylenic allenophane is depicted in Scheme 1. The R^1 substituents aid solubility: the absence of similar groups in the previously prepared allenophane[8] limited its solubility and prevented a full investigation into its properties. The R^2 substituents may be hydrogen atoms or alkyl groups, depending on the method selected to synthesize the allene moiety. The number of acetylene bridges may also be varied.



Scheme 1. An acetylenic allenophane.

We devised a strategy to an acetylenic allenophane related to **16** based on the dimerization of desilylated **15** (see Scheme 4). We[9a] and others[9b] observed previously that the separation of the alkyne termini dictates whether the intra- or intermolecular product dominates. Molecular modeling studies have strongly suggested that the intermolecular product is favored when the termini separation is greater than 7 Å.[9c] In the case of **15**, the calculated alkyne separation of 8.87 Å[10] indicated that the intramolecular product **16** should be preferred.

We initially examined the allene preparation used by Myers and Zheng for the synthesis of an allenophane in which R^2 groups are hydrogen atoms (Scheme 1).[11] This asymmetric method had the advantage that the allene precursor, a secondary propargyl alcohol, was readily available through the addition of an acetylide to an aldehyde.[12] Initially, *ortho*-amino substituents at the aryl ring were chosen to aid solubility, but this idea had to be abandoned because electron donation from the lone pair of electrons on the nitrogen atom in the *ortho*-amino substituent leads to the formation of cumulene-type intermediates during allene formation (Scheme 2), and so *tert*-butyl groups were selected instead.



Scheme 2. Proposed mechanism for the formation of allene **A** because of *ortho*-amino aryl substituents.

Unfortunately, the procedure of Myers and Zheng afforded a disappointing yield of 18%.

An attractive alternative for the generation of asymmetric allenes employs an S_N2' addition of an organocuprate to a propargyl acetate.[13] This method allows fully substituted allenes to be synthesized, but requires the asymmetric synthesis of a tertiary propargyl alcohol. Reported methods for the preparation of this species are limited to examples that utilize the asymmetric addition of a zinc acetylide to a ketone[14] or the asymmetric addition of an alkyl zinc to a ketone.[15] Unfortunately, the asymmetric addition of dimethylzinc to the ketone precusor of **13** failed (see Scheme 4).

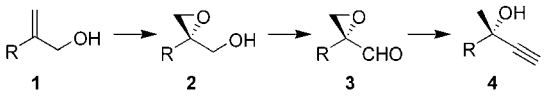
[*] M. D. Clay, Prof. Dr. A. G. Fallis
Department of Chemistry
University of Ottawa
10 Marie Curie, Ottawa, Ontario, K1N 6N5 (Canada)
Fax: (+1) 613-562-5170
E-mail: afallis@science.uottawa.ca

[**] We are grateful to the National Sciences and Engineering Research Council of Canada (NSERC) for financial support of this research. We thank H. Foucault and L. Barriault (University of Ottawa) for assistance with the molecular modeling studies. M.D.C. also thanks the NSERC, OGS, and University of Ottawa for graduate scholarships.

 DOI: 10.1002/anie.200500484 © 2005 Wiley-VCH Verlag GmbH & Co. KGaA, Weinheim

Similarly, the combination of the zinc acetylide to the appropriate acetophenone to generate **13** directly was also unsuccessful. This failure was likely due to the steric encumbrance of the *tert*-butyl solubilizing groups as well as the inherent poor electrophilicity of the ketones employed. Consequently, a new strategy was developed to construct these tertiary propargyl alcohols.

We designed a method in which the requisite stereogenic centers could be installed by using a Sharpless asymmetric epoxidation (Scheme 3). Oxidation of epoxy alcohol **2** should

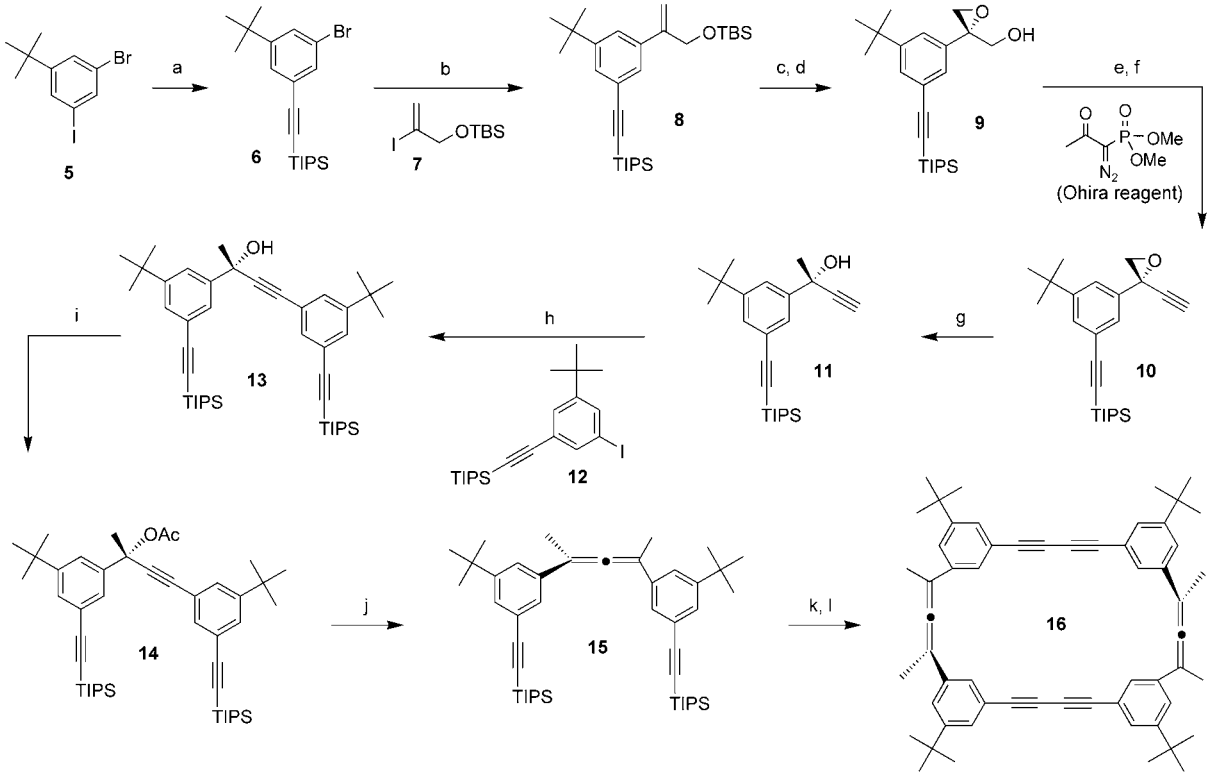


Scheme 3. An asymmetric synthetic route to tertiary propargyl alcohols.

afford the desired aldehyde **3**, which upon exposure to the reagent developed by Ohira[16] would give an epoxy alkyne that could undergo ring opening with a suitable hydride reagent to yield the desired tertiary propargyl alcohol **4**. The synthetic pathway that was developed is given in Scheme 4.

A Sonogashira coupling between 1-bromo-3-iodo-5-*tert*-butylbenzene (**5**)[17] and (triisopropylsilyl)acetylene smoothly generated aryl bromide **6** in 99% yield. A lithium–halogen exchange followed by quenching of the resulting anion with zinc bromide generated an organozinc intermediate, which was coupled with vinyl iodide **7**[18] to generate the *tert*-butyldimethylsilyl (TBS) ether **8**, also in 99% yield. Selective cleavage of the TBS group followed by Sharpless asymmetric epoxidation of the allylic alcohol provided the allylic epoxy alcohol **9** in 93% yield (88% *ee*).[19] Initially, the ring opening of **9** was examined with various aluminum hydride reagents. In each case, the epoxide was cleaved readily, however, despite a literature precedent[20] the resulting diol was partially racemized. This occurred presumably through a Payne rearrangement[21] of the epoxy alcohol. Therefore, the ring opening of the epoxide was postponed until a later stage in the synthesis.

Oxidation of **9** with the Dess–Martin periodinane gave an aldehyde in 89% yield, which was subsequently converted into a terminal alkyne with the Ohira reagent (93%). The epoxide in **10** was opened cleanly on exposure to L-selectride to provide tertiary propargyl alcohol **11**, and no lowering of enantiomeric excess was detected (HPLC analysis). This sequence for the conversion of an epoxide into a tertiary



Scheme 4. Synthesis of acetylenic allenophane **16**. Reagents and conditions: a) (triisopropylsilyl)acetylene, $[PdCl_2(PPh_3)_2]$, CuI, Et_3N, THF, RT, 16 h (99%); b) 1. **6**, *t*BuLi, THF, −78°C, 5 min; 2. $ZnBr_2$, THF, −78→0°C, 30 min; 3. **7**, $[Pd(PPh_3)_4]$, THF, RT, 16 h, (99%); c) 10% HCl, THF, RT, 4 h (79%); d) $[Ti(O\mathit{i}Pr)_4]$, L-DIPT, *t*BuOOH, 4-Å molecular sieves, CH_2Cl_2, −50→20°C, 16 h (93%, 88% *ee*); e) Dess–Martin periodinane, CH_2Cl_2, RT, 30 min (89%); f) Ohira reagent, K_2CO_3, MeOH, 0°C→RT, 90 min (93%); g) L-selectride, THF, 0°C, 10 min (88%); h) **12**, $[PdCl_2(PPh_3)_2]$, CuI, Et_3N, THF, RT, 16 h (51%); i) Ac_2O, DMAP, pyridine, CH_2Cl_2, RT, 24 h (85%); j) CH_3MgBr, LiBr, CuI, THF, 0°C, 2 h (74%); k) TBAF, THF, 0°C, 10 min (98%); l) addition of **15** to a solution of $Cu(OAc)_2$ in pyridine/diethyl ether (3:1) over 6 h, RT, total time: 8 h (40%). L-DIPT = diisopropyl L-tartrate, L-selectride = lithium tri-*sec*-butylborohydride, DMAP = 4-dimethylaminopyridine, TBAF = tetrabutylammonium fluoride, TIPS = triisopropylsilyl, Ac = acetyl.

 © 2005 Wiley-VCH Verlag GmbH & Co. KGaA, Weinheim

propargyl alcohol was easily completed within one day in an overall yield of 73%. A Sonogashira reaction between **11** and aryl iodide **12** (prepared through a lithium–halogen exchange of **6** followed by quenching with iodine) generated the propargyl alcohol **13** in 51% yield. A modification of the standard Sonogashira coupling conditions failed to increase the yield.[22]

Acetylization of **13** with acetic anhydride gave acetate **14** in 85% yield. As anticipated, (*S*)-allene **15** was formed through the addition of **14** to the organocuprate generated from a mixture of CH_3MgBr, LiBr, and CuI (74% yield). Removal of the triisopropylsilyl groups with TBAF generated the terminal bisalkyne **15** in 98% yield with 83% *ee*. This indicated that there was minimal racemization during generation of the allene. The slow addition of (*S*)-**15** to a solution of $Cu(OAc)_2$ in pyridine and diethyl ether afforded the desired (*S*,*S*)-acetylenic allenophane **16** in 40% yield. The desilylation–dimerization sequence could also be conducted in a one-pot procedure, but the isolation of **16** was more difficult because of the presence of several highly fluorescent impurities. Unfortunately, crystals of **16** suitable for X-ray crystallographic studies could not be obtained; however, molecular modeling studies revealed the unique conformation of this cyclophane:[23] Figure 1 a illustrates the chirality of **16**, whereas Figure 1 b reveals its helical nature.

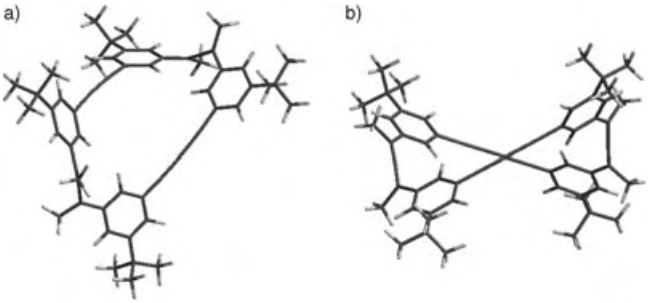


Figure 1. Molecular models of **16**: a) stereochemical configuration and b) helical arrangement.

The UV/Vis absorption and circular dichroism (CD) spectra of **16** in a solution of chloroform were recorded and are illustrated in Figures 2 and 3, respectively. There are very few reported examples of UV/Vis and CD spectra of cyclic

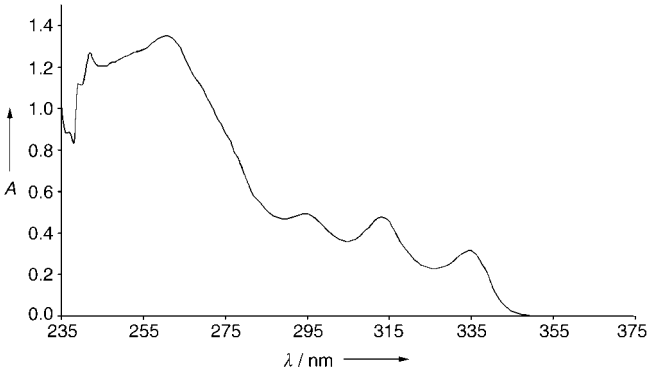


Figure 2. UV/Vis absorption spectrum of **16**.

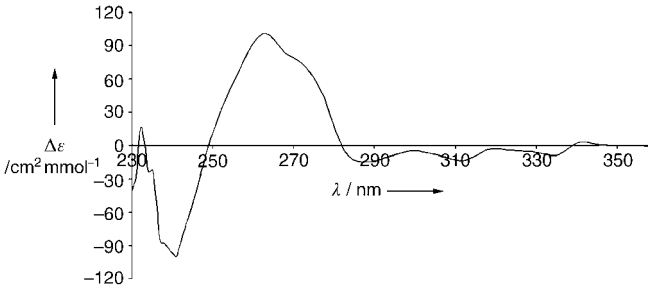


Figure 3. CD spectrum of **16**.

allenes with which to compare the spectra of our acetylenic allenophane.[24] Nevertheless, the typical "fingerprint" pattern for acetylenes with bands at 295, 313, and 335 nm is apparent in the UV/Vis spectrum. Major signals at 263 and 270 (sh) nm were observed in the CD spectrum that may have arisen from the through-space interactions of the phenyl rings.

In conclusion, a novel single-enantiomer acetylenic allenophane **16** has been synthesized by a series of palladium- and copper-mediated coupling reactions. A new protocol was developed that allowed the stereochemistry of the allene to be controlled by the use of a Sharpless asymmetric epoxidation and a tertiary α-hydroxyethyne intermediate. We are currently investigating the scope and synthetic utility of this reaction sequence for other targets.

Received: February 8, 2005
Published online: May 20, 2005

Keywords: alkynes · allenes · asymmetric epoxidation · cyclophanes · diynes

[1] For some examples of helical chirality in cyclophanes, see: a) R. Boese, A. J. Matzger, K. P. C. Vollhardt, *J. Am. Chem. Soc.* **1997**, *119*, 2052; b) M. M. Haley, M. L. Bell, S. C. Brand, D. B. Kimball, J. J. Pak, W. B. Wan, *Tetrahedron Lett.* **1997**, *38*, 7483; c) M. J. Marsella, I. T. Kim, F. Tham, *J. Am. Chem. Soc.* **2000**, *122*, 974.

[2] a) M. A. Romero, A. G. Fallis, *Tetrahedron Lett.* **1994**, *35*, 4711; b) S. K. Collins, G. P. A. Yap, A. G. Fallis, *Angew. Chem.* ***2000***, *112*, 393; *Angew. Chem. Int. Ed.* **2000**, *39*, 385; c) S. K. Collins, G. P. A. Yap, A. G. Fallis, *Org. Lett.* **2000**, *2*, 3185; d) S. K. Collins, G. P. A. Yap, A. G. Fallis, *Org. Lett.* **2002**, *4*, 11; e) M. A. Heuft, A. G. Fallis, *Angew. Chem.* **2002**, *114*, 4720; *Angew. Chem. Int. Ed.* **2002**, *41*, 4520; f) M. A. Heuft, S. K. Collins, A. G. Fallis, *Org. Lett.* **2003**, *5*, 1911.

[3] a) F. Diederich, *Cyclophanes*, Royal Society of Chemistry, Cambridge, UK, **1991**; b) F. Vögtle, *Cyclophane Chemistry*, Wiley, New York, **1993**; c) Y. Tobe, *Top. Curr. Chem.* **1994**, *172*, 1; d) J. Schulz, F. Vögtle, *Top. Curr. Chem.* **1994**, *172*, 41; e) G. J. Bodwell, *Angew. Chem.* **1996**, *108*, 2221; *Angew. Chem. Int. Ed. Engl.* **1996**, *35*, 2085; f) A. de Meijere, B. König, *Synlett* **1997**, 1221.

[4] a) *Modern Acetylene Chemistry* (Eds.: P. J. Stang, F. Diederich), Wiley-VCH, Weinheim, **1995**; b) B. König, *Top. Curr. Chem.* **1998**, *196*, 92; c) T. Tsuji in *Adv. Strained Interesting Org. Mol.*, *Vol. 7* (Ed.: B. Halton), JAI, Greenwich, CT, **1999**, pp. 103; d) G. J. Bodwell, T. Satou, *Angew. Chem.* **2002**, *114*, 4175; *Angew. Chem. Int. Ed.* **2002**, *41*, 4003; e) C. Grave, A. D. Schlüter, *Eur. J. Org. Chem.* **2002**, 3075.

 © 2005 Wiley-VCH Verlag GmbH & Co. KGaA, Weinheim

[5] a) R. Zimmer, C. U. Dinesh, E. Nandanan, F. A. Khan, *Chem. Rev.* **2000**, *100*, 3067; b) J. A. Marshall, *Chem. Rev.* **1996**, *96*, 3067; c) *Modern Allene Chemistry* (Eds.: N. Krause, A. S. K. Hashmi), Wiley-VCH, Weinheim, **2004**.

[6] A. Hoffmann-Roder, N. Krause, *Angew. Chem.* **2004**, *116*, 1216; *Angew. Chem. Int. Ed.* **2004**, *43*, 1196.

[7] R. A. Smith, R. L. White, A. Krantz, *J. Med. Chem.* **1988**, *31*, 1558.

[8] S. Thorand, F. Vögtle, N. Krause, *Angew. Chem.* ***1999***, *111*, 3899; *Angew. Chem. Int. Ed.* **1999**, *38*, 3721.

[9] a) S. K. Collins, PhD Thesis, University of Ottawa, **2001**; b) M. A. Heuft, PhD Thesis, University of Ottawa, **2003**; c) Y. Tobe, J. Kishi, I. Ohki, M. Sonoda, *J. Org. Chem.* **2003**, *68*, 3330; d) A. G. Fallis, *Synlett* **2004**, 2249.

[10] Semiempirical AM1 calculations were performed by using the Cerius^2–Dmol^3 Molecular Modeling Suite from Molecular Simulations Inc. of San Diego, CA (1999) and by using the methods in: M. Dewar, W. Thiel, *J. Am. Chem. Soc.* **1977**, *99*, 4499.

[11] A. G. Myers, B. Zheng, *J. Am. Chem. Soc.* **1996**, *118*, 4492.

[12] For a review, see: L. Pu, *Tetrahedron* **2003**, *59*, 9873.

[13] T. L. Macdonald, D. R. Reagan, *J. Org. Chem.* **1980**, *45*, 4740.

[14] a) G. Lu, X. Li, X. Jia, W. L. Chan, A. S. C. Chan, *Angew. Chem.* **2003**, *115*, 5211; *Angew. Chem. Int. Ed.* **2003**, *42*, 5057; b) P. G. Cozzi, *Angew. Chem.* **2003**, *115*, 3001; *Angew. Chem. Int. Ed.* **2003**, *42*, 2895.

[15] a) D. J. Ramón, M. Yus, *Angew. Chem.* **2004**, *116*, 286; *Angew. Chem. Int. Ed.* **2004**, *43*, 284; b) S.-J. Jeon, P. J. Walsh, *J. Am. Chem. Soc.* **2003**, *125*, 9544.

[16] a) S. Ohira, *Synth. Commun.* **1989**, *19*, 561; b) S. Müller, B. Liepold, G. J. Roth, H. J. Bestmann, *Synlett* **1996**, 521; c) G. J. Roth, B. Liepold, S. Müller, H. J. Bestmann, *Synthesis* **2004**, 59.

[17] S. Höger, A.-D. Meckenstock, H. Pellen, *J. Org. Chem.* **1997**, *62*, 4556.

[18] Synthesized by protection of the corresponding alcohol with TBS, see: S. Irifune, T. Kibayashi, Y. Ishii, M. Ogawa, *Synthesis* **1988**, 366.

[19] The enantiomeric excess was determined using a chiralcel OD-H column, eluent: hexane/*i*PrOH (99:1), 0.8 mL min^{-1}, t_R(major): 12.00 min, t_R(minor): 12.75 min; absolute configuration was inferred from a literature precedent, see: K. A. Jørgensen, R. A. Wheeler, R. Hoffmann, *J. Am. Chem. Soc.* **1987**, *109*, 3240.

[20] a) W. Adam, M. Braun, A. Griesbeck, V. Lucchini, E. Staab, B. Will, *J. Am. Chem. Soc.* **1989**, *111*, 203; b) V. Capriati, S. Florio, R. Luisi, A. Salomone, *Org. Lett.* **2002**, *4*, 2445.

[21] G. B. Payne, *J. Org. Chem.* **1962**, *27*, 3819.

[22] a) A. Elangovan, Y.-H. Wang, T.-I. Ho, *Org. Lett.* **2003**, *5*, 1841; b) W. P. Gallagher, R. E. Maleczka, Jr., *J. Org. Chem.* **2003**, *68*, 6775.

[23] Semiempirical AM1 calculations were performed by using a PC Spartan Pro (v. 1.03) program from Wavefunction, Inc. of Irvine, CA (2000).

[24] For CD spectra of cyclic allenes, see: C. Zelder, N. Krause, *Eur. J. Org. Chem.* **2004**, 3968.

Homogeneous Catalysis

Ru-Catalyzed Anti-Markovnikov Addition of Amides to Alkynes: A Regio- and Stereoselective Synthesis of Enamides**

Lukas J. Gooßen, Jan E. Rauhaus, and Guojun Deng*

The enamide group is an important substructure that is often found in natural products[1] and synthetic drugs that have, amongst others, sedative,[2] cytotoxic,[3] or anti-inflammatory[4] properties. Moreover, they are versatile synthetic intermediates that can serve as substrates for polymerizations,[5] [4+2] cycloadditions,[6,7] cross-coupling reactions,[8] Heck olefinations,[9] halogenations,[8] enantioselective additions,[10] or asymmetric hydrogenations.[11] However, a regio- and stereoselective construction of enamide substructures is not at all trivial. Traditional syntheses—for example, from carbonyl compounds and amides[12] or from hydroxylamines and acetic anhydride[13]—require harsh conditions and yield mixtures of *E*/*Z* products. Metal-catalyzed coupling reactions of vinyl halides,[14] vinyl triflates,[15] or vinyl ethers[16] proceed under milder conditions but suffer from the limited availability of these substrates.

In our opinion, a catalytic addition of amides to alkynes would be an ideal synthetic entry to enamides, since it would use readily available starting materials and be inherently atom-economic (Scheme 1). Related addition reactions of carboxylates,[17] water,[18] and amines[19] are well-established.[20] However, to the best of our knowledge, there is only one reported protocol in the literature for a catalytic hydroamidation reaction of terminal alkynes:[21] Watanabe et al. found that in the presence of Ru_3CO_{12}/trialkylphosphane catalysts, a very limited range of formanilides and acetanilides can be added to 1-hexyne, albeit at extremely high temperatures (180 °C) and under pressure.[22] Clearly, much more effective catalyst systems are required to allow an application of this reaction in organic synthesis.

To identify a catalyst system for the desired hydroamidation reaction, we chose the reaction of 1-hexyne (**1a**) with 2-pyrrolidinone (**2a**) as a model system and investigated the catalytic activity of several ruthenium complexes under various conditions (Scheme 2, Table 1). As anticipated, no

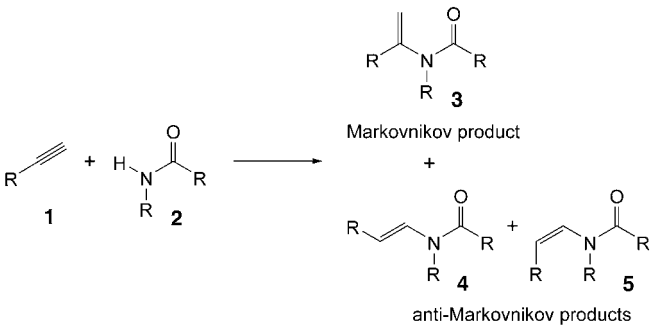
[*] Dr. L. J. Gooßen,[+] J. E. Rauhaus, G. Deng
Max-Planck-Institut für Kohlenforschung
Kaiser-Wilhelm-Platz 1, 45470 Mülheim an der Ruhr (Germany)
E-mail: goossen@oc.rwth-aachen.de

[+] New address:
Institut für Organische Chemie
Rheinisch-Westfälische Technische Hochschule Aachen
Professor Pirlet Str. 1, 52074 Aachen (Germany)
Fax: (+49) 241-80-93663

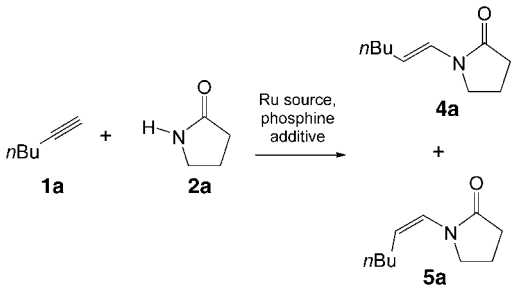
[**] We thank Prof. Dr. H.-J. Altenbach for helpful discussions, Martina Eckardt for technical assistance, Prof. Dr. M. T. Reetz for generous support and constant encouragement, and the DFG, the FCI, and the BMBF for financial support.

Supporting information for this article is available on the WWW under http://www.angewandte.org or from the author.

 © 2005 Wiley-VCH Verlag GmbH & Co. KGaA, Weinheim DOI: 10.1002/anie.200462844



Scheme 1. Addition of amides to terminal alkynes.



Scheme 2. Addition of 2-pyrrolidinone to 1-hexyne.

enamide products were observed in the presence of the literature systems[21c,22] at ambient pressure and a temperature of only 100 °C (entries 1 and 2). In contrast, several other ruthenium sources, although inactive themselves (entries 2–5), displayed noticeable catalytic activity when combined with tri-*n*-butylphosphane (entries 6–10). In all cases, the anti-Markovnikov products **4a** and **5a** were formed regioselectively. However, a significant stereoselectivity ($E/Z > 10{:}1$) was observed only for 1,5-cyclooctadienebis(2-methallyl)ruthenium [Ru(methallyl)$_2$(cod)]; with all other ruthenium sources, **4a** and **5a** were formed in almost equal amounts. The reaction of [Ru(methallyl)$_2$(cod)] with monodentate phosphanes leads to the formation of isolable bis(2-methallyl)bis(phosphane)ruthenium(II) complexes, which show the same reactivity as the mixtures prepared in situ (entry 16).

Among all the ligands investigated, tri-*n*-butylphosphane gave the highest *E* selectivity in combination with [Ru(methallyl)$_2$(cod)] (entries 10–15). Triarylphosphanes were less effective, and use of the chelating phosphane bis(dicyclohexylphosphanyl)methane ($Cy_2PCH_2PCy_2$) even led to a reversal of the stereoselectivity in favor of the *Z* product (entry 12).

As in our recently disclosed protocol for the anti-Markovnikov addition of carboxylic acids to alkynes,[17c] the addition of pyridine derivatives (2 equiv with respect to ruthenium) strongly enhanced the catalyst performance; other additives had no beneficial effects (entries 17–22). 4-(*N*,*N*-Dimethylamino)pyridine (DMAP), in particular, led to a significant increase in both the activity and the stereoselectivity of the [Ru(methallyl)$_2$(cod)]/P*n*Bu$_3$ catalyst system, and allowed the synthesis of **4a** in almost quantitative yield with an *E*/*Z* selectivity of 28:1 (entry 22). Gratifyingly,

Table 1: Optimization of reaction conditions for Scheme 2.[a]

Entry	Ru source	Ligand	Additive	Yield [%]	**4a**/**5a**[b]
1	$[Ru_3(CO)_{12}]$	P*n*Bu$_3$	–	0	nd
2	$RuCl_3 \cdot H_2O$	–	–	0	nd
3	[Ru(acac)$_3$]	–	–	0	nd
4	$[Ru_3(CO)_{12}]$	–	–	0	nd
5	$[\{RuCl_2(p\text{-cymene})\}_2]$	–	–	0	nd
6	$RuCl_3 \cdot H_2O$	P*n*Bu$_3$	–	79	1:1
7	[Ru(acac)$_3$]	P*n*Bu$_3$	–	0	nd
8	$[\{RuCl_2(p\text{-cymene})\}_2]$	P*n*Bu$_3$	–	95	1:1
9	$[RuCl_2(cod)]$	P*n*Bu$_3$	–	92	1:1
10	[Ru(methallyl)$_2$(cod)]	P*n*Bu$_3$	–	67	11:1
11	[Ru(methallyl)$_2$(cod)]	PCy_3	–	25	3:1
12	[Ru(methallyl)$_2$(cod)]	$Cy_2PCH_2PCy_2$	–	30	1:2
13	[Ru(methallyl)$_2$(cod)]	P(1-Np)$_3$	–	0	nd
14	[Ru(methallyl)$_2$(cod)]	P(*p*-FC$_6$H$_4$)$_3$	–	85	3:1
15	[Ru(methallyl)$_2$(cod)]	PPh_3	–	62	2:1
16	[Ru(methallyl)$_2$(PPh$_3$)$_2$]	–	–	66	2:1
17	[Ru(methallyl)$_2$(cod)]	P*n*Bu$_3$	$AgNO_3$	0	nd
18	[Ru(methallyl)$_2$(cod)]	P*n*Bu$_3$	NaO*t*Bu	52	9:1
19	[Ru(methallyl)$_2$(cod)]	P*n*Bu$_3$	NEt_3	61	5:2
20	[Ru(methallyl)$_2$(cod)]	P*n*Bu$_3$	DABCO	50	5:1
21	[Ru(methallyl)$_2$(cod)]	P*n*Bu$_3$	pyridine	95	19:1
22	[Ru(methallyl)$_2$(cod)]	P*n*Bu$_3$	DMAP	93	28:1
23	[Ru(methallyl)$_2$(cod)]	$Cy_2PCH_2PCy_2$	DMAP	<5	nd
24	[Ru(methallyl)$_2$(cod)]	P*n*Bu$_3$	DMAP/H_2O[c]	86	21:1
25[d]	[Ru(methallyl)$_2$(cod)]	P*n*Bu$_3$	DMAP	88	28:1
26[e]	[Ru(methallyl)$_2$(cod)]	P*n*Bu$_3$	DMAP	84	33:1
27	[Ru(methallyl)$_2$(cod)]	$Cy_2PCH_2PCy_2$	H_2O[c]	75	1:5
28	[Ru(methallyl)$_2$(cod)]	$Cy_2PCH_2PCy_2$	H_2O[f]	98	1:5

[a] Conditions: pyrrolidinone (1.0 mmol), 1-hexyne (2.0 mmol), ruthenium source (0.02 mmol), ligand (0.06 mmol; or 0.03 mmol for chelating ligands), additive (0.04 mmol), toluene (3 mL), 100 °C, 15 h. The yields and selectivities were determined by GC using *n*-tetradecane as the internal standard. Abbreviations: acac = acetylacetonate; Np = naphthyl; DABCO = 1,4-diazabicyclo[2.2.2]octane. [b] nd = not determined. [c] 0.5 mmol H_2O; [d] The reaction vessel was briefly purged with air. [e] 1.2 mmol 1-hexyne. [f] 8-mmol H_2O.

the presence of air and moisture had only a minor influence on the yields and selectivities of this optimized reaction protocol (entries 22, 24, and 25).

Since *Z* enamides are of similar synthetic importance but particularly hard to synthesize,[23] we next set out to identify a complementary *Z*-selective hydroamidation catalyst. Starting with the [Ru(methallyl)$_2$(cod)]/$Cy_2PCH_2PCy_2$ system, which had already shown some *Z* selectivity (entry 12), we again studied the influence of additives. Interestingly, this catalyst was completely inhibited by the addition of DMAP (entry 23), while other bases and additives had only a minor influence on the reaction outcome. Only the addition of small quantities of water increased both its activity and *Z* selectivity, such that **5a** also became accessible in excellent yield (99 %, $Z/E = 5{:}1$; entries 27 and 28).

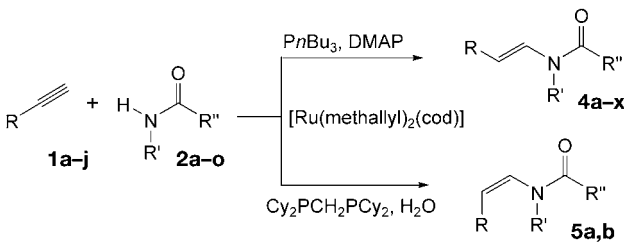
To make up for losses due to oligomerization and evaporation, the alkyne is best used in a slight excess of at least 1.2 equivalents (entries 22 and 26).

Currently, we can only speculate about the exact reaction mechanism; more in-depth investigations are underway. The *Z*-selective protocol is likely to follow the mechanism

 © 2005 Wiley-VCH Verlag GmbH & Co. KGaA, Weinheim

proposed for the addition of carboxylic acids to alkynes,[17] but it is difficult to pinpoint the origin of the reversal of selectivity when adding monodentate phosphanes and DMAP. A conceivable mechanism for the *E*-selective protocol might involve oxidative addition of the N–H bond to the ruthenium, followed by insertion of the alkyne into the resultant metal–nitrogen bond, and reductive elimination of the enamide product. On the other hand, the two mechanisms may mainly differ in concerted against stepwise addition of the nucleophile and the proton.[17a,b]

To investigate the scope of this new hydroamidation protocol, we applied it to the addition of a broad variety of nitrogen nucleophiles to several terminal alkynes (Scheme 3).

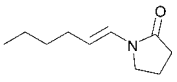
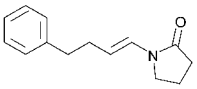
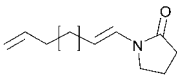
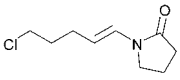
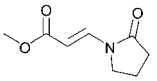
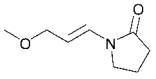
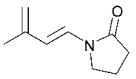
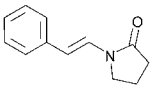
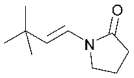
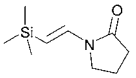
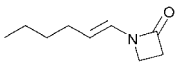
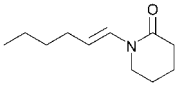
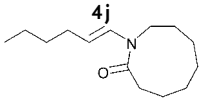
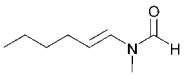
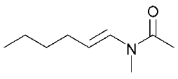
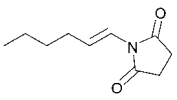
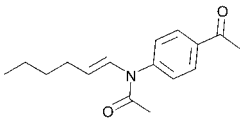
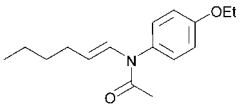
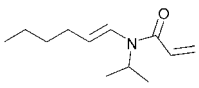
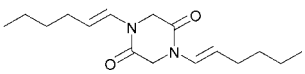
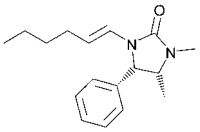
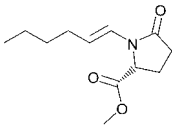
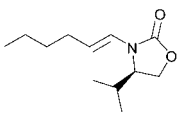
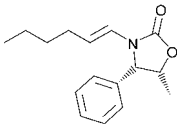


Scheme 3. Addition of N–H compounds to terminal alkynes.

Table 2 demonstrates the impressive scope of the *E*-selective reaction. Various alkynes were successfully converted into enamides, among them phenylacetylene, acetylenecarboxylic esters, trimethylsilylacetylene, and even conjugated enynes. The trimethylsilyl-enamides obtained should be attractive substrates for further coupling reactions, and the dienamides for hetero-Diels–Alder reactions.

Besides lactams, various secondary amides, anilides, ureas, bislactams, carbamates, and even chiral auxiliaries for subsequent cycloaddition reactions[7] can be used as the N–H-

Table 2: Substrate scope of the hydroamidation reaction (Scheme 3).[a]

Product	Yield [%] (ratio **4**/**5**)	Product	Yield [%] (ratio **4**/**5**)	Product	Yield [%] (ratio **4**/**5**)
 **4a**	95 (28:1) 99 (1:5)[b]	 **4b**	97 (30:1) 92 (1:8)[b]	 **4c**	99 (30:1)
 **4d**	81 (30:1)	 **4e**	99 (30:1)	 **4f**	93 (8:1)
 **4g**	98 (24:1)	 **4h**	99 (30:1)	 **4i**	99 (30:1)
 **4j**	69 (3:1)	 **4k**	70 (2:1)	 **4l**	94 (30:1)
 **4m**	86 (30:1)	 **4n**	83 (30:1)	 **4o**	84 (3:1)
 **4p**	12 (1:2)	 **4q**	33 (30:1)	 **4r**	94 (30:1)
 **4s**	38 (30:1)	 **4t**	99 (30:1)	 **4u**	99 (23:1)
 **4v**	96 (6:1)	 **4w**	97 (30:1)	 **4x**	84 (24:1)

[a] Conditions: amide (1.0 mmol), alkyne (2.0 mmol), [Ru(methallyl)$_2$(cod)] (0.02 mmol), P*n*Bu$_3$ (0.06 mmol), DMAP (0.04 mmol), toluene (3 mL), 100 °C, 15 h; yields refer to isomeric mixtures of isolated products. [b] Complementary conditions: amide (1.0 mmol), alkyne (2.0 mmol), [Ru(methallyl)$_2$(cod)] (0.02 mmol), $Cy_2PCH_2PCy_2$ (0.03 mmol), water (8.0 mmol), toluene (3.0 mL), 100 °C, 15 h.

 © 2005 Wiley-VCH Verlag GmbH & Co. KGaA, Weinheim

coupling partner. The reaction proceeds smoothly even in the presence of sensitive functional groups such as esters, ethers, ketones, halides, or silanes. For most substrates, the *E* products were obtained in an isomeric ratio greater than 20:1, and only imides gave only moderate yields and selectivities; primary amides could not be converted.

The *Z*-selective protocol was also successfully applied to selected substrates (Table 2, first row). Although this protocol does not yet reach the selectivity of its *E*-selective counterpart, the examples **5a** and **5b** demonstrate that the stereoselectivity of the reaction can indeed be inverted by modifying the ligand system.

In summary, a ruthenium-catalyzed reaction has been developed that allows, for the first time, the anti-Markovnikov addition of secondary amides, anilides, lactams, ureas, bislactams, and carbamates to terminal alkynes. Two complementary protocols have been identified that provide stereoselective synthetic entries to either the *E* or the *Z* isomers. Due to the mild reaction conditions, the excellent availability of the starting materials, and the ideal atom economy, this new transformation is well-suited for applications in synthetic organic chemistry and drug discovery.

Experimental Section

4a: An oven-dried flask was charged with [Ru(methallyl)$_2$(cod)] (6.4 mg, 0.02 mmol) and DMAP (4.99 mg, 0.04 mmol), and flushed with argon. Subsequently, P*n*Bu$_3$ (15 μL, 0.06 mmol), 2-pyrrolidinone (**2a**; 85.1 mg, 1 mmol), 1-hexyne (**1a**; 229 μL, 2.0 mmol), and dry toluene (3.0 mL) were added with a syringe. The resulting green solution was stirred for 15 h at 100 °C, then poured into an aqueous $NaHCO_3$ solution (30 mL). The resulting mixture was extracted repeatedly with 20 mL portions of ethyl acetate, the combined organic layers were washed with water and brine, dried with $MgSO_4$, and filtered, and the volatiles were removed in vacuo. The residue was purified by column chromatography (SiO_2, ethyl acetate/hexanes 3:1) to yield **4a** (158.9 mg, 95 % yield, 97 % isomeric purity) as a colorless oil.

^{1}H NMR (300.1 MHz, $CDCl_3$): $\delta = 6.86$ (d, $^3J = 14.7$ Hz, 1H), 4.92 (dt, $^3J = 14.7$ Hz, 7.2 Hz, 1H), 3.48 (t, $^3J = 7.2$ Hz, 2H), 2.46 (t, $^3J = 8.1$ Hz, 2H), 2.01–2.14 (m, 4H), 1.24–1.39 (m, 4H), 0.88 ppm (t, $^3J = 7.2$ Hz, 3H); ^{13}C NMR (75.5 MHz, $CDCl_3$): $\delta = 172.2$, 123.6, 112.5, 45.3, 32.3, 31.3, 29.7, 22.1, 17.4, 13.9 ppm; MS (EI, 70 eV): *m*/*z* (%): 167 (20), 124 (100) $[M]^+$, 86 (23), 69 (12), 41 (21); HRMS (EI): calcd for $C_{10}H_{17}NO$: 167.131014; found: 167.130871.

The experiments in Table 2 were carried out analogously. All products were purified by column chromatography and characterized by NMR spectroscopy and standard/high-resolution mass spectrometry.

Received: December 7, 2004
Revised: March 24, 2005
Published online: May 27, 2005

Keywords: alkynes · amides · enamides · homogeneous catalysis · hydroamidation · ruthenium

[1] L. Yet, *Chem. Rev.* **2003**, *103*, 4283 – 4306.
[2] Y. N. Han, G.-Y. Kim, H. K. Han, B. H. Han, *Arch. Pharmacol. Res.* **1993**, *16*, 289.
[3] S. G. Toske, P. R. Jensen, C. A. Kaufman, W. Fenical, *Tetrahedron* **1998**, *54*, 13459 – 13466.
[4] D. Davyt, W. Entz, R. Fernandez, R. Mariezcurrena, A. W. Mombru, J. Saldana, L. Dominguez, J. Coll, E. Manta, *J. Nat. Prod.* **1998**, *61*, 1560 – 1563.
[5] "*N*-Vinylamide polymers": D. H. Lorenz, *Encycl. Polym. Sci. Technol.* **1971**, *14*, 239 – 251.
[6] a) A. R. Katritzky, B. Rachwal, S. Rachwal, *J. Org. Chem.* **1995**, *60*, 3993 – 4001; b) A. Charles, M. B. Smith, *J. Org. Chem.* **1988**, *53*, 1161 – 1167; c) L. E. Overman, L. A. Clizbe, *J. Am. Chem. Soc.* **1976**, *98*, 2352 – 2354.
[7] C. Gaulon, R. Dhal, T. Chapin, V. Maisonneuve, G. Dujardin, *J. Org. Chem.* **2004**, *69*, 4192 – 4202.
[8] G. J. Roff, R. C. Lloyd, N. J. Turner, *J. Am. Chem. Soc.* **2004**, *126*, 4098 – 4099.
[9] C. E. Wilians, C. A. Mulder, J. G. de Vries, H. M. de Vries, *J. Organomet. Chem.* **2003**, *687*, 494 – 497.
[10] R. Matsubara, Y. Nakamura, S. Kobayashi, *Angew. Chem.* **2004**, *116*, 1711 – 1713; *Angew. Chem. Int. Ed.* **2004**, *43*, 1679 – 1681.
[11] a) T. Sell, A. Meiswinkel, G. Mehler, M. T. Reetz, *Tetrahedron Lett.* **2002**, *43*, 7941 – 7943; b) M. van den Berg, A. J. Minnaard, R. M. Haak, M. Leeman, E. P. Schudde, A. Meetsma, B. L. Feringa, H. M. de Vries, E. P. Maljaars, C. E. Wilians, D. Hyett, A. F. Boogers, J. W. Hendricks, J. G. de Vries, *Adv. Synth. Catal.* **2003**, *345*, 308 – 323.
[12] W. Adam, S. G. Bosio, N. J. Turro, *J. Org. Chem.* **2004**, *69*, 1704 – 1715.
[13] M. J. Burk, G. Casy, N. B. Johnson, *J. Org. Chem.* **1998**, *63*, 6084 – 6098.
[14] X. Pa, Q. Cai, D. Ma, *Org. Lett.* **2004**, *6*, 1809 – 1812.
[15] J. Wallace, D. J. Klauber, C. Chen, R. P. Volante, *Org. Lett.* **2003**, *5*, 4749 – 4752.
[16] J. L. Brice, J. E. Meerdink, S. Stahl, *Org. Lett.* **2004**, *6*, 1845 – 1848.
[17] a) H. Doucet, Z. Kabouche, C. Bruneau, P. H. Dixneuf, *J. Organomet. Chem.* **1997**, *551*, 151 – 157; b) T. Mitsudo, Y. Hori, Y. Watanabe, *J. Org. Chem.* **1985**, *50*, 1566 – 1568; c) L. J. Gooßen, J. Paetzold, *Chem. Commun.* **2003**, 706 – 707.
[18] a) M. Bassetti, B. Floris, *J. Chem. Soc. Perkin Trans. 2* **1988**, 227 – 233; b) T. Suzuki, T. Makoto, y. Wakatsuki, *Org. Lett.* **2001**, *3*, 735 – 737.
[19] a) F. Pholki, S. Doye, *Chem. Soc. Rev.* **2003**, *32*, 104 – 114; b) M. Beller, J. Seayad, A. Tillack, H. Jiao, *Angew. Chem.* **2004**, *116*, 3448 – 3479*Angew. Chem. Int. Ed.* **2004**, *43*, 3368 – 3398.
[20] For a recent review, see: F. Alonso, I. P. Beletskaya, M. Yus, *Chem. Rev.* **2004**, *104*, 3079 – 3159.
[21] a) For related reactions with acetylene, see: W. Reppe, *Justus Liebigs Ann. Chem.* **1956**, *601*, 81 – 138; b) Rohm&Haas Co., US 2806847, **1955**; Rohm&Haas Co. , US 2606848, **1956** [*Chem. Abstr.* **1958**, *52*, 16059]; c) M. Heider, J. Henkelmann, T. Ruel (BASF AG), DE 4333237, **1995** [*Chem. Abstr.* **1995**, *123*, 229254].
[22] T. Kondo, A. Tanaka, S. Kotachi, Y. Watanabe, *J. Chem. Soc. Chem. Commun.* **1995**, 413 – 414.
[23] C. Brehm, Y. Cancho-Grande, A. Fürstner, *Org. Lett.* **2001**, *3*, 3955 – 3957.

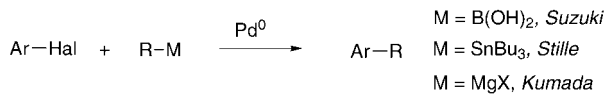
 © 2005 Wiley-VCH Verlag GmbH & Co. KGaA, Weinheim

C–H Activation

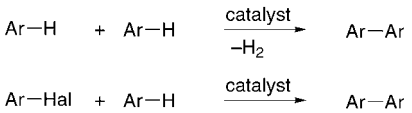
Anilide *ortho*-Arylation by Using C–H Activation Methodology**

Olafs Daugulis and Vladimir G. Zaitsev*

With few exceptions, the current methodology for biaryl formation utilizes functionalization on both components of the coupling process (Scheme 1).[1] Ideally, one would like to



Both coupling components must be functionalized.
Current investigations use substrates where Hal = Cl.



C–H Activation - one or no functionalized coupling components - use of the C–H bond as a functional group

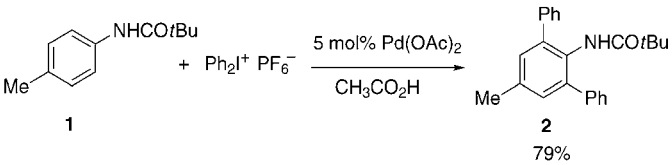
Scheme 1. C–X bond activation versus C–H bond activation.

selectively and efficiently couple two C–H bonds to give the corresponding product (Scheme 1). From a thermodynamic point of view, however, this latter process is quite often unfavorable (for example, the coupling of benzene to give biphenyl and hydrogen is unfavorable by 13.8 kJ mol^{-1}).[2] Given the potentially large number of C–H bonds in both reactants, it is also problematic to achieve the desired regioselectivity of coupling.

The R–X coupling with R–H is viable, but this variation has not been extensively investigated. Phenols and heterocycles have been *ortho*-arylated with aryl bromides through Pd^0–Pd^{II} catalytic cycles.[3] Benzanilides have been *ortho*-arylated on the benzoyl moiety under similar conditions.[4] Simple arenes may be arylated with aryl iodides under Ir catalysis, and *ortho*-arylation of aromatic ketones and imines by using Ru catalysis has been shown.[5] A few other examples of coupling reactions between Ar–H and Ar–Hal have been reported, mostly proceeding through a Pd^0–Pd^{II} catalytic cycle.[6]

Tremont, Liebeskind and co-workers have shown that anilide and aromatic imine coupling with alkyl iodides is promoted by Pd^{II}.[7] This alkylation is mechanistically distinct from the processes described above since it proceeds either through a σ-bond methathesis pathway or a Pd^{II}–Pd^{IV} couple.[7a] Inspired by this work, we have investigated the Pd-catalyzed arylation of arenes containing *ortho*-directing groups, in the hope of developing a general method for arene *ortho*-arylation under C–H activation conditions. We report herein the Pd-catalyzed *ortho*-arylation of anilides. 2,6-Diarylanilines are useful for the synthesis of ligands employed in Brookhart-type transition-metal-catalyzed polymerizations and currently are synthesized only from highly functionalized starting materials.[8]

The screening reactions were performed with respect to the arylating agent and the solvent. Reaction of 4-methylpivalanilide (**1**) with 4-methylphenyldiazonium tetrafluoroborate gave only minor amounts of coupling product under the tested conditions in a variety of solvents. Arylation of **1** with the commercially available $Ph_2I^+PF_6^-$ was successful in acetic acid and allowed the isolation of the diphenylated product **2** in 79% yield (Scheme 2; Table 1, entry 12).[9]



1 **2** 79%

Scheme 2. Amide arylation with iodonium salts.

Unfortunately, diphenyliodonium salts are the only ones commercially available, thus limiting the scope of this reaction. In addition, these salts are very expensive and have to be used in excess for complete conversion into the product.

We were pleased to find out that the combination of aryl iodides and AgOAc is effective in catalytically arylating the anilides by using palladium acetate. The reaction proceeds well in acetic acid, but the fastest rates were observed in trifluoroacetic acid and thus further investigations were carried out in this solvent.

A number of anilides could be arylated by using this methodology (Table 1). Generally, the pivaloyl derivatives gave the cleanest reactions; however, acetamides (entry 11) are also compatible with the reaction conditions. In this case more optimization is needed due to a competitive side reaction.[10] The reaction is highly tolerant with respect to substituents on the anilide: any halogenes, including iodine (entries 4, 9), are tolerated. The reaction is also compatible with bromo substituents on the aryl iodide (entries 2, 5). This allows construction of scaffolds that could be functionalized further by using conventional Pd^0 coupling processes. Ester groups are also tolerated (entries 7, 8). The use of *meta*-substituted anilides results in the selective addition of one aryl

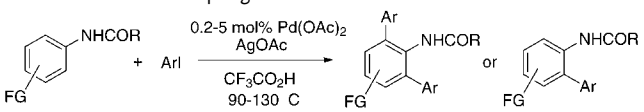
[*] Prof. Dr. O. Daugulis, Dr. V. G. Zaitsev
Department of Chemistry, University of Houston
Houston, TX 77204 (USA)
Fax: (+1) 713-743-2709
E-mail: olafs@uh.edu

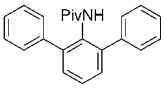
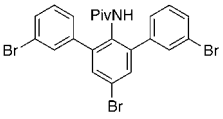
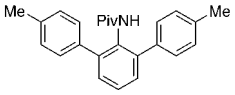
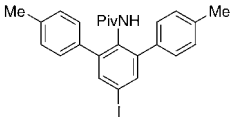
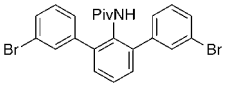
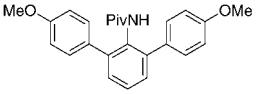
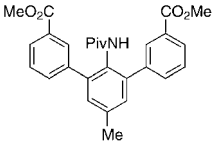
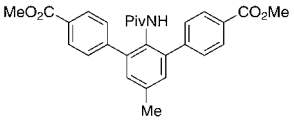
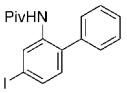
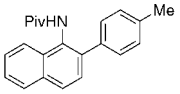
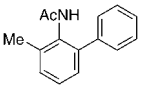
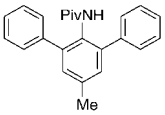
[**] This work was supported by the Welch Foundation and the University of Houston Small Grants Program. The authors are grateful to Prof. Maurice Brookhart (University of North Carolina, Chapel Hill, NC) for helpful comments.

Supporting Information for this article is available on the WWW under http://www.angewandte.org or from the author.

 © 2005 Wiley-VCH Verlag GmbH & Co. KGaA, Weinheim DOI: 10.1002/anie.200500589

Table 1: Iodoarene coupling with amides[a]



Entry	Amide FG	Ar	Product	Yield [%]
1	H	C_6H_5		91
2	4-Br	3-Br-C_6H_4		95
3	H	4-Me-C_6H_4		95
4	4-I	4-Me-C_6H_4		92
5	H	3-Br-C_6H_4		55
6	H	4-MeO-C_6H_4		67
7	4-Me	3-MeO_2C-C_6H_4		85
8	4-Me	4-MeO_2C-C_6H_4		96
9	3-I	C_6H_5		83
10	[b]	4-Me-C_6H_4		62
11	[c]	C_6H_5		76
12	4-Me	[d]		79

[a] Substrate (1 equiv), ArI (2–9 equiv), AgOAc (1 equiv per coupled Ar), $Pd(OAc)_2$ (0.2–5 mol%). In entries 1–10 and 12 R = *t*Bu, in entry 11 R = Me. Yields are given for isolated products. See the Experimental Section and Supporting Information for details. [b] 1-Naphthyl-*N*-pivalamide. [c] 2-Methylacetanilide. [d] $Ph_2I^+PF_6^-$ was used instead of ArI, with CH_3CO_2H as the solvent, and no AgOAc was added.

group (entry 9). High turnover numbers have been achieved: Entry 3 was run with 0.2 mol% Pd and complete conversion (according to GC) was observed, a result indicating a turnover number of 1000. This is a remarkably high turnover number for a C–H activation process.[11]

At this point only a speculative discussion about the reaction mechanism is possible. Qualitatively, the reactions are faster for ArI containing electron-donating groups, a result which sets this process apart from the conventional Pd-catalyzed couplings.[12] As expected for an electrophilic C–H activation process, the reactions are faster for anilides possessing donor substituents.[13] It has been shown that diaryliodonium trifluoromethanesulfonates can transfer Ar^+ to nitrogen-ligated Pd^{II}, thereby leading to the formation of unstable Pd^{IV} species that decompose through reductive elimination pathways.[14] This finding of Canty and co-workers may be relevant to the mechanism of this arylation procedure; however, at this point a σ-bond metathesis pathway can not be ruled out.

Finally, we include a note regarding the use of silver salts in this coupling process: the silver acetate price per mole is about twice that of the price of cesium carbonate, a base widely used for Pd-catalyzed coupling reactions. However, in many cases several equivalents of Cs_2CO_3 are used for the reactions, as opposed to the one equivalent of AgOAc per introduced aryl group for this method.

In conclusion, we have developed a new anilide arylation process based on C–H activation. The method is highly tolerant to functional groups and allows the presence of any halogens on the anilide moiety and bromo substituents on the aryl iodide. Up to 1000 turnovers have been demonstrated for this reaction. Recently, we have verified that the reaction developed here is quite general and allows for the arylation of other arenes containing *ortho*-directing groups. 2-Arylpyridines and imines derived from substituted benzaldehydes can be arylated using this methodology. The results of these latter investigations will be published separately.

Experimental Section

General considerations: The coupling reactions were performed without special precautions in 2-dram screw-cap vials. Flash chromatography was performed by using 60-Å silica gel (Sorbent Technologies) or acidic, Brockmann I, aluminum oxide (Aldrich). GC analyses were performed on a Shimadzu GC-2010 chromatograph equipped with a Restek column (Rtx-5, 15 m, 0.25 mm inner diameter). The ^1H and ^{13}C NMR spectra were recorded on a GE QE-300 spectrometer by using the residual solvent peak as a reference. IR spectra were obtained by using a ThermoNicolet Avatar 370 FT-IR instrument. Melting points were measured on a Mel-Temp apparatus and are uncorrected. Elemental analyses were performed by Atlantic Microlab Inc. of Norcross, GA.

2,6-Di(4-methylphenyl)pivalanilide (Table 1, entry 3): A solution of pivalanilide (0.53 g, 3.0 mmol), 4-iodotoluene (3.30 g, 15.0 mmol), palladium acetate (1.3 mg, 0.006 mmol), and silver acetate (1.00 g, 6.0 mmol) in trifluoroacetic acid (TFA; 2 mL) in a 2-dram screw-cap vial was heated at 90 °C for 3 days. At that point, the conversion was observed by GC analysis to be >99%. During this time, a dark-yellow precipitate was formed and the supernatant became clear dark red. The reaction mixture was diluted with toluene (30 mL), the solution was decanted, and the precipitate was washed with toluene (2 × 5 mL). The combined organic solutions were evaporated under reduced pressure and the residue was purified by flash chromatography on silica gel (toluene, then dichloromethane/toluene (1:1)) to give the product as a white solid (1.02 g, 95%): m.p. 239–240 °C

 © 2005 Wiley-VCH Verlag GmbH & Co. KGaA, Weinheim

(pentane); $R_f = 0.35$ (dichloromethane/pentane (1:1)); ^{1}H NMR ($CDCl_3$): $\delta = 0.87$ (s, 9H), 2.37 (s, 6H), 6.74 (br s, 1H), 7.17 (d, $J =$ 7.8 Hz, 4H), 7.25 (d, $J = 7.8$ Hz, 4H), 7.25–7.40 ppm (m, 3H); ^{13}C NMR ($CDCl_3$): $\delta = 21.2$, 27.1, 38.7, 127.1, 128.6, 128.7, 129.5, 131.6, 136.7, 136.8, 140.6, 176.3 ppm; FT-IR: $\tilde{\nu} = 1642$ (C=O), 3250 cm^{-1} (N–H); elemental analysis: calcd (%) for $C_{25}H_{27}NO$: C 83.99, H 7.61, N 3.92; found: C 83.47, H 7.64, N 4.00.

Silver iodide (1.37 g, 5.82 mmol) obtained after drying the precipitate in vacuo and in the dark dissolved completely in 28–30% ammonia (100 mL).

2,6-Di(3′-bromophenyl)-4-bromopivalanilide (Table 1, entry 2): A solution of 3-bromoiodobenzene (130 μL, 1.0 mmol), 4-bromopivalanilide[15] (64 mg, 0.25 mmol), palladium acetate (1.5 mg, 0.007 mmol), and silver acetate (87 mg, 0.5 mmol) in TFA (0.5 mL) was heated at 120 °C for 2 h. Workup as above followed by purification by flash chromatography (toluene, then dichloromethane) afforded the product as an off-white solid (135 mg, 95%): m.p. 206–207 °C (colorless crystals, from pentane); $R_f = 0.35$ (dichloromethane/pentane (1:2)); ^{1}H NMR ($CDCl_3$): $\delta = 0.90$ (s, 9H), 6.66 (br s, 1H), 7.20–7.30 (m, 4H), 7.40–7.55 ppm (m, 6H); ^{13}C NMR ($CDCl_3$): $\delta = 27.1$, 38.9, 121.0, 122.0, 127.5, 129.9, 130.8, 130.9, 131.5, 132.6, 140.1, 141.4, 176.7 ppm; FT-IR: $\tilde{\nu} = 1639$ (C=O), 3280 cm^{-1} (N–H); elemental analysis: calcd (%) for $C_{23}H_{20}Br_3NO$: C 48.80, H 3.56, N 2.47; found: C 48.91, H 3.48, N 2.54.

Received: February 17, 2005
Published online: May 24, 2005

Keywords: biaryls · C–C coupling · C–H activation · homogeneous catalysis · palladium

[1] a) J. Hassan, M. Sévignon, C. Gozzi, E. Schulz, M. Lemaire, *Chem. Rev.* **2002**, *102*, 1359; b) E. J.-G. Anctil, V. Snieckus, *J. Organomet. Chem.* **2002**, *653*, 150.

[2] R. Dasgupta, B. R. Maiti, *Ind. Eng. Chem. Process Des. Dev.* **1986**, *25*, 381.

[3] a) T. Satoh, T. Itaya, M. Miura, M. Nomura, *Chem. Lett.* **1996**, 826; b) T. Satoh, Y. Kawamura, M. Miura, M. Nomura, *Angew. Chem.* **1997**, *109*, 1820; *Angew. Chem. Int. Ed. Engl.* **1997**, *36*, 1740; ; c) T. Okazawa, T. Satoh, M. Miura, M. Nomura, *J. Am. Chem. Soc.* **2002**, *124*, 5286; d) B. S. Lane, D. Sames, *Org. Lett.* **2004**, *6*, 2897; e) B. Sezen, D. Sames, *J. Am. Chem. Soc.* **2004**, *126*, 13244; f) C.-H. Park, V. Ryabova, I. V. Seregin, A. W. Sromek, V. Gevorgyan, *Org. Lett.* **2004**, *6*, 1159; g) phenol *ortho*-arylation by Rh catalysis: R. B. Bedford, S. J. Coles, M. B. Hursthouse, M. E. Limmert, *Angew. Chem.* **2003**, *115*, 116; *Angew. Chem. Int. Ed.* **2003**, *42*, 112.

[4] a) Y. Kametani, T. Satoh, M. Miura, M. Nomura, *Tetrahedron Lett.* **2000**, *41*, 2655; intramolecular anilide arylation/alkylation reactions: b) E. J. Hennessy, S. L. Buchwald, *J. Am. Chem. Soc.* **2003**, *125*, 12084; c) T. Harayama, T. Akiyama, Y. Nakano, H. Nishioka, H. Abe, Y. Takeuchi, *Chem. Pharm. Bull.* **2002**, *50*, 519.

[5] Ir: a) K.-i. Fujita, M. Nonogawa, R. Yamaguchi, *Chem. Commun.* **2004**, 1926; Ru: b) F. Kakiuchi, S. Kan, K. Igi, N. Chatani, S. Murai, *J. Am. Chem. Soc.* **2003**, *125*, 1698; c) S. Oi, S. Fukita, N. Hirata, N. Watanuki, S. Miyano, Y. Inoue, *Org. Lett.* **2001**, *3*, 2579; cooperative Ru–Pd catalysis: d) S. Ko, B. Kang, S. Chang, *Angew. Chem.* **2005**, *117*, 459; *Angew. Chem. Int. Ed.* **2005**, *44*, 455.

[6] a) G. Dyker, *Angew. Chem.* **1994**, *106*, 117; *Angew. Chem. Int. Ed. Engl.* **1994**, *33*, 103; b) Q. Huang, A. Fazio, G. Dai, M. A. Campo, R. C. Larock, *J. Am. Chem. Soc.* **2004**, *126*, 7460; c) M. Lafrance, N. Blaquière, K. Fagnou, *Chem. Commun.* **2004**, 2874; d) an example with a Pd^{II}–Pd^{IV} cycle: F. Faccini, E. Motti, M. Catellani, *J. Am. Chem. Soc.* **2004**, *126*, 78.

[7] a) S. J. Tremont, H. U. Rahman, *J. Am. Chem. Soc.* **1984**, *106*, 5759; b) J. S. McCallum, J. R. Gasdaska, L. S. Liebeskind, S. J. Tremont, *Tetrahedron Lett.* **1989**, *30*, 4085.

[8] M. Schmid, R. Eberhardt, M. Klinga, M. Leskelae, B. Rieger, *Organometallics* **2001**, *20*, 2321.

[9] M. Xia, Z. Chen, *Synth. Commun.* **2000**, *30*, 531.

[10] Presumably, *N*-arylation is more favorable for the sterically more accessible acetyl derivatives.

[11] Turnover number = 762: M. Dams, D. E. De Vos, S. Celen, P. A. Jacobs, *Angew. Chem.* **2003**, *115*, 3636; *Angew. Chem. Int. Ed.* **2003**, *42*, 3512.

[12] J. K. Stille, K. S. Y. Lau, *Acc. Chem. Res.* **1977**, *10*, 434.

[13] a) H. Horino, N. Inoue, *J. Org. Chem.* **1981**, *46*, 4416; b) A. D. Ryabov, I. K. Sakodinskaya, A. K. Yatsimirskii, *J. Organomet. Chem.* **1991**, *406*, 309.

[14] A. J. Canty, J. Patel, T. Rodemann, J. H. Ryan, B. W. Skelton, A. H. White, *Organometallics* **2004**, *23*, 3466.

[15] M. J. S. Dewar, J. M. W. Scott, *J. Chem. Soc.* **1957**, 1445.

 © 2005 Wiley-VCH Verlag GmbH & Co. KGaA, Weinheim

Polyoxometalates

Molecular Recognition of Basic Fibroblast Growth Factor by Polyoxometalates**

*Qiang Wu, Ju Wang, Ling Zhang, An Hong, and Jinsong Ren**

The inhibition of angiogenesis-promoting factors such as fibroblast growth factor is considered to be a potential treatment for cancers, and has become an active area of research pursued with intense interest.[1] Two major targets of pharmacologic therapies are vascular endothelial growth factor (VEGF) and basic fibroblast growth factor (bFGF). bFGF is a globular single-chain heparin-binding polypeptide synthesized by different cell types. The 3D structure of the 18-kDa bFGF has been recently elucidated by X-ray crystallography.[2] bFGF consists entirely of β-sheet structure, which includes a threefold repeat of a four-stranded antiparallel β

[*] Q. Wu, Prof. Dr. J. Ren
Subdivision of Biological Inorganic Chemistry
Key Laboratory of Rare Earth Chemistry and Physics
Changchun Institute of Applied Chemistry
Chinese Academy of Sciences
Changchun, 130022 (China)
Fax: (+86) 431-526-2656
E-mail: jren@ciac.jl.cn
J. Wang, L. Zhang, Prof. A. Hong
Bioengineering Institute, Jinan University
Guangzhou 510632 (China)

[**] We thank the Distinguished Young Scholars of China and of Jilin province and the Distinguished Talent Program from the Chinese Academy of Sciences for financial support of this work. We also thank Dr. Georges M. Halpern and Terry T. Takahashi for their helpful comments.

Supporting information for this article is available on the WWW under http://www.angewandte.org or from the author.

 © 2005 Wiley-VCH Verlag GmbH & Co. KGaA, Weinheim DOI: 10.1002/anie.200500108

meander. It has been detected in a wide variety of normal and malignant tissues and is known to play key roles in the development, growth, and disease states in almost every organ system.[3] Ligands that recognize and bind bFGF may disrupt its interaction with endothelial cell-surface receptors such as heparan sulfate proteoglycans (HSPGs) and fibroblast growth factor receptors (FGFRs), and would represent a new class of potential therapeutic agent.

Much effort is underway in the development of drugs that inhibit bFGF-induced angiogenesis. The potential use of exogenous heparin analogues as inhibitors of angiogenesis, such as suramin,[4] pentosan polysulfate (PPS),[5] sulfonated derivatives of distamycin A,[6] and carboxylated compounds[7] have become the focus of several research groups. Suramin and PPS[8] have been evaluated in patients with various tumors, including Kaposi's sarcoma (KS), yet very large doses of these compounds are required to show activity, and their efficacy is limited by anticoagulant side effects. However, minor structural changes to suramin have resulted in a significant decrease in toxicity without loss of activity.[9]

This result was clear incentive for the design of novel compounds with high efficacy and low toxicity. Early transition metal oxygen anion clusters (polyoxometalates, or POMs) were explored as a different class of therapeutic agent. Unlike the flexible organic polysulfonated polyanionic heparin-based compounds, POMs are inorganic polyoxygen polyanions with fairly rigid cagelike structures.[10] POMs have been attractive for their promising antiviral, antitumor activities for more than a decade.[11] Based on cell-culture assays, enzymatic activities in vitro, and molecular modeling studies, POMs have regained considerable interest in recent years as a result of their remarkable interactions with HIV-1 reverse transcriptase (RT) and HIV-1 protease (P), as demonstrated by Hill, Pope, and co-workers.[12,13] Recently, it was reported that the POM $K_5SiCoW_{11}O_{39}$ could affect the mitogenic activity of bFGF,[14] yet little is known about the POM–bFGF interaction. Herein, we describe the recognition and binding of several POMs to bFGF. These POMs represent promising leads for the design of new compounds that might recognize bFGF, and which may represent potentially new avenues for the design and synthesis of new types of inhibitors of tumor angiogenesis.

Three representative POMs, the Keggin ($K_6SiNiW_{11}O_{39}$), the Wells–Dawson (α-$K_8P_2NiW_{17}O_{61}(H_2O)$), and the trivacant Keggin-derived sandwich ($K_{10}P_2Zn_4(H_2O)_2W_{18}O_{68}$) structures were selected for the present study. These ligands, whose basic anion backbones are illustrated in Figure 1, are hydrolytically stable under physiological conditions and vary in size and charge. The Keggin structure is ≈ 11.5 Å in diameter with six negative charges, the Wells–Dawson structure is $\approx 11.5 \times 15$ Å with eight negative charges, and the Keggin-derived sandwich structure is $\approx 11.5 \times 18.0$ Å with ten negative charges. The direct interaction between bFGF and POMs was first demonstrated by fluorescence, ultraviolet absorption, and circular dichroism measurements. bFGF was excited at 275 nm and its fluorescence was monitored at 303 nm in phosphate-buffered saline (PBS), pH 7.4 at 20 °C. The fluorescence intensity of bFGF was strongly quenched with an increase in the amount of POM. The titration reached

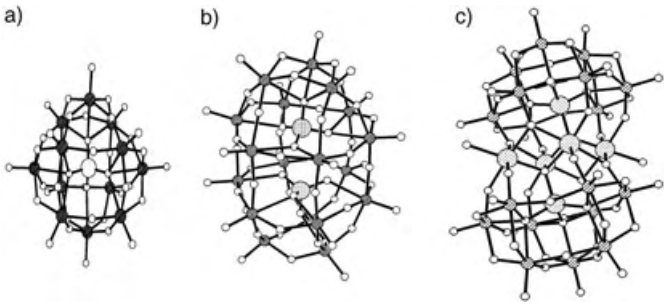


Figure 1. Basic anion backbone drawings of the three polyoxometalates: a) the Keggin structure, $[SiNiW_{11}O_{39}]^{6-}$; b) the Wells–Dawson structure, $[P_2NiW_{17}O_{61}(H_2O)]^{8-}$; and c) the trivacant Keggin-derived sandwich structure, $[P_2Zn_4(H_2O)_2W_{18}O_{68}]^{10-}$.

a clear end point at a molar ratio of 1:1 for all compounds, which permitted a direct measurement of the interaction stoichiometry. Nonlinear least-squares fits of the data yielded apparent binding constants (K_{app}) of 3.0, 5.0, and $5.7 \times 10^6\,M^{-1}$ for the Keggin-, the Wells-Dawson-, and the sandwich-type POMs, respectively.

A number of heparin analogues that bind bFGF have various effects on the thermal stability of bFGF. Heparin and sucrose octasulfate, for example, enhance the stability of bFGF to thermal denaturation.[15] Conversely, sulfonated distamycin A derivatives destabilize the protein.[6] To determine the effect of POMs on the thermal stability of bFGF, we used temperature-dependent circular dichroism (CD) at various wavelengths to investigate the melting of the complex. Under the ionic-strength conditions described herein, bFGF alone has a thermal melting temperature (T_m) of 59 °C. Figure 2 shows that upon addition of POM at a molar ratio of 1:1, bFGF was stabilized by 9, 12, and 20 °C for the Keggin, Wells–Dawson and sandwich structures, respectively. The results of the CD experiments demonstrate that the conformation of bFGF underwent a dramatic change in the presence of POMs which manifests mainly in a decrease in the band intensity at 204 nm (Figure 3). In comparison, Wells–

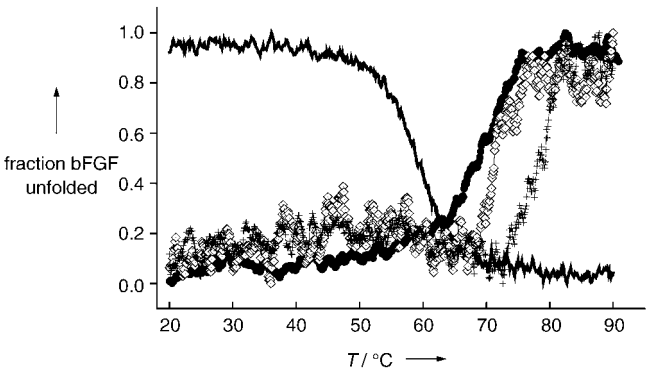


Figure 2. CD melting profiles of bFGF in the absence (——) and presence of Keggin (●), Wells–Dawson (◇), and Keggin-derived sandwich (+) compounds; POM/protein ratio = 1:1, and [bFGF] = 5 μM; solution conditions: NaCl (150 mM), PBS buffer (20 mM, pH 7.4); spectra were measured at $\lambda = 203$ or 229 nm and the temperature was raised in increments of 1 °C min^{-1} from 20 to 90 °C.

 © 2005 Wiley-VCH Verlag GmbH & Co. KGaA, Weinheim

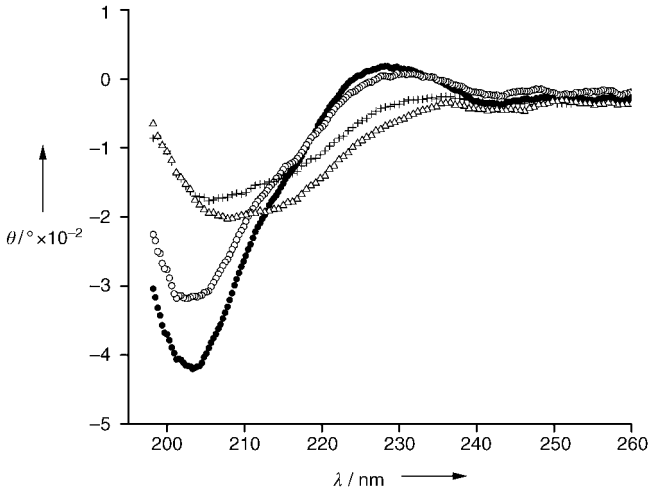


Figure 3. CD spectra of bFGF acquired at 20°C in the absence (●) and presence of Keggin (○), Wells–Dawson (△), and Keggin-derived sandwich (+) compounds. All experimental conditions and concentrations were the same as those described for Figure 2. The spectra were recorded as an average of three scans from 195 to 260 nm.

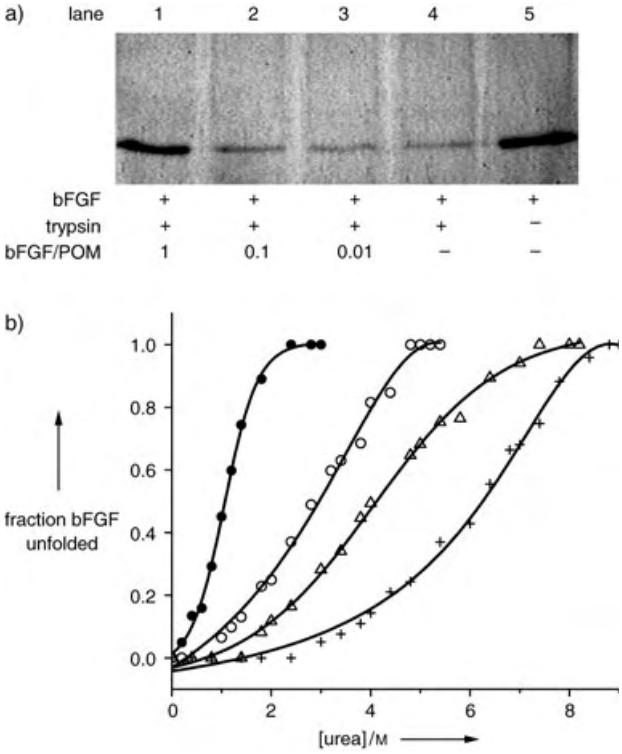


Figure 4. a) SDS-PAGE analysis of the effect of POMs on tryptic digests of bFGF: bFGF (10 μL, 4.8 μM) was incubated at 37°C for 3 h with trypsin (1 μg in 1 μL of 0.1 N HCl) in the absence or presence of increasing concentrations of the Keggin-type POMs. At the end of the reaction, all samples were supplemented with SDS-PAGE reducing sample buffer, heated at 100°C for 2 min, and subjected to SDS-PAGE (15%), after which the gels were stained with Coomassie blue. b) Fluorescence profiles of urea-induced bFGF denaturation in the absence (●) and presence of equimolar Keggin (○), Wells–Dawson (+), and Keggin-derived sandwich (△) compounds. All samples were incubated at 4°C for 48–72 h prior to analysis to ensure equilibrium had been established. The fluorescence data were collected at 20°C with a bFGF concentration of 1 μM and were presented as the fraction of unfolded bFGF. These experiments were performed in 100 mM PBS buffer, pH 7.0.

Dawson and sandwich-type POMs exerted a much more significant effect on bFGF with an approximate twofold loss in the CD signal and a marked red-shift of the minimum band. The direct interaction of POMs with bFGF was confirmed by their ability to protect bFGF from trypsin digestion; all compounds protected bFGF from protelytic cleavage. Figure 4a shows a digestion experiment with bFGF in the absence and presence of Keggin-type POMs. This protective effect was dose-dependent, and complete inhibition was observed at molar ratio of 1:1. Similar observations have been reported for the interaction of bFGF with heparin and its analogues.[16] To our knowledge, this is the first example of an enzyme or protein stabilized by a POM compound.

The binding of POMs to bFGF induced conformational changes, affected the whole structure of the protein, and had a stabilizing effect relative to free protein; all this was further verified by the effect of POMs on urea-mediated denaturation of bFGF. In the absence of POMs, the midpoint of urea-induced unfolding was observed at a urea concentration of 1.0 M (Figure 4b). Upon the addition of POMs at a molar ratio of 1:1, the unfolding transition of bFGF shifted to notably higher urea concentrations. The large shift in the transition midpoint suggests that POMs bind tightly to bFGF, which strongly supports the binding studies and thermal denaturation experiments discussed above. It should be noted that the degree of POM-based stabilization is highly dependent on the structure of the POM compound employed. The fluorescence titration, CD, and thermal unfolding studies demonstrated the varied effects of the different POM structures.

It was reported that the ability of heparin and its analogues to stabilize aFGF (acidic fibroblast growth factor) against denaturation in urea was diminished if the number of charges on these compounds was decreased.[17] In contrast to this trend, the Wells–Dawson-type POM has fewer charges than the sandwich-type POM, but exhibited the strongest stabilization of bFGF against urea-mediated unfolding. Previous studies have shown that the size, charge, and composition of POMs may all be interrelated in the inhibition of viral absorption/fusion and the inhibition of viral polymerase activity in a cell- or kinetics-based assay.[18] Modeling studies of POMs with HIV-1 P and HIV-1 RT determined that POMs exhibit reasonable steric fits in the substrate binding sites of these enzymes.[12,13]

Our results support these previous reports, and suggest that the structure of POMs might play a key role in the recognition and binding to bFGF. The POM compound $K_8ZnNiW_{11}O_{39}$ was generated through substitution of the central Si atom of the Keggin structure with Zn. It maintains the size of the smaller Keggin-type POM, but contains the same number of charges as the Wells–Dawson structure. Thermal denaturation and CD conformation studies indicate that it elicits similar effects upon the binding of bFGF as does the Keggin structure (data not shown). Whereas the exact mode of binding is not yet clear, the potential structure

 © 2005 Wiley-VCH Verlag GmbH & Co. KGaA, Weinheim

relevance is unambiguous. One issue that needs to be addressed is the stability of the Keggin and Wells–Dawson anions in dilute aqueous solution. Although it is not easy to quantify the stability of these compounds experimentally, an approximate calculation can be made.[19] At the most commonly used concentration of 5 μM employed for the experiments reported herein, the Keggin anion remains intact, and the Wells–Dawson structure could experience a Ni cation loss of ≈30%. Both anionic compounds could lose a certain amount of the Ni cation upon further dilution. As a consequence, the lacunary anions might also react in a manner similar to that of the Ni derivatives. Further studies are therefore required to elucidate this point as well as the structural basis for the molecular recognition of bFGF by the compounds discussed herein, but these issues are beyond the scope of this brief communication.

The identification of the specific bFGF binding site of POMs is essential for the understanding of their biological function. Unlike heparin and its analogues, POMs are fairly rigid, cagelike structures coated with oxygen atoms bearing partial negative charges; the binding modes of POMs may therefore be different from the organic polyanions. For example, the Hill and co-workers recently demonstrated that POMs function not by binding to the active site of HIV-1 P, but by binding to a cationic pocket of lysine residues on the outer surface of the flaps that cover the active site.[13] This led us to explore the binding site of POMs on bFGF; the cationic heparin-binding cleft of bFGF was decided as a good candidate target site.[20] Competition assays were first used to verify that the putative POM binding site on bFGF is at or near the cationic pocket of the previously described heparin-binding site. The fluorescent polyanion suramin, a polysulfonated naphthylurea compound, is a common chaotropic agent. It is known to inhibit a large number of important enzymes[21] and to block the activity of several growth factors, one of which is bFGF.[22] A comprehensive analysis of the interaction of suramin with the growth factor has shown that suramin caused nonspecific and irreversible protein aggregation with a stoichiometry that depends on drug concentration. Furthermore, suramin was found to bind at or near the heparin binding site of bFGF, and the fluorescence intensity was strongly enhanced upon binding bFGF.[23] The addition of POMs to the bFGF–suramin complex resulted in a progressive decrease of suramin fluorescence intensity (Supporting Information), which suggests that POMs can displace the drug from the bFGF. This observation implies that both suramin and POMs compete for the same binding site.

We subsequently constructed the C78S–C96S double mutant of bFGF and studied its interaction with POMs. Fluorescence titration studies showed that POMs also form a 1:1 stoichiometric complex with the mutant bFGF with similar affinities. The apparent binding constants of the POM–mutant bFGF complexes were found to be three to fivefold less than the corresponding complexes with wild-type bFGF. At a 1:1 molar ratio, the POMs showed no effect on the thermal denaturation profiles of the mutant bFGF, except for a slight increase in T_m (2 °C) for the sandwich-type complex. Although the change of local microenvironment could not be ruled out with the substitution of cysteine by serine residues, the overall conformation of the mutant bFGF was identical to that of the wild-type as monitored by CD studies and X-ray crystallography.[6] CD data showed that the Wells–Dawson and sandwich structures caused a compatible conformational change of mutant bFGF, whereas the Keggin-type showed no effect (data not shown). These results indicate that the replacement of Cys 78 and Cys 96 considerably affects the interaction of the protein with POMs. Among the four cysteine residues in bFGF, Cys 34 is completely buried and Cys 101 is partly buried within the folded peptide chain. Only Cys 78 and Cys 96 can be modified by thiolation or carboxymethylation.[13,24] Under nondenaturing conditions with the 5,5′-dithiobis(2-nitrobenzoic acid) (DTNB) method,[25] direct thiol titration studies revealed two free SH groups in the absence of POMs, and one free SH group in the presence of POMs, which indicates that POMs bind near one of the two, and subsequently prevent the protein from the thiol-mediated disulfide exchange reaction with the DTNB reagent. Cysteines 78 and 96 are located on opposing surfaces of the protein, and Cys 96 is known to be in the vicinity of the cationic pocket of the heparin binding site.[6,20] The competition study, the cysteine mutation data, and the thiol titration studies all strongly suggest that POMs bind in the vicinity of the heparin binding region of bFGF, whereas the exact binding site awaits high-resolution structural analysis of bFGF–POM complexes.

The design of synthetic molecules that can bind to a protein and block biologically important protein–protein interactions remains a major challenge. The results of the experiments described herein have identified a new structural family of bFGF-binding ligands. The unique structure of POMs may play a key role in the recognition and binding to the protein. The development of POMs as selective FGF binders may be limited, as many derivatives have little or no hydrolytic stability at physiologically relevant pH values and some POMs exhibit toxicity. However, the versatility of the POM compounds render them attractive, because many of the properties that dictate their utility, including elemental composition, structure, charge density, redox potential, acidity, and solubility can be controlled synthetically to varying degrees. Furthermore, a number of new POMs with hydrolytic stability at physiologically relevant pH values have been synthesized recently, and the toxicity problems exhibited by some POMs are considerably smaller or nonexistent in the second generation of POM-based chemotherapeutic agents. The data reported herein show promise for the development of new types of selective binders of fibroblast growth factors. Although we have just begun to address the issue of antiangiogenic activity, preliminary studies of POMs have shown an inhibition effect similar to that caused by heparin; further investigations of these points are currently underway.

Received: January 12, 2005
Revised: March 10, 2005
Published online: May 27, 2005

Keywords: angiogenesis · antitumor agents · growth factors · polyoxometalates · protein folding

 © 2005 Wiley-VCH Verlag GmbH & Co. KGaA, Weinheim

[1] a) J. Folkman, *N. Engl. J. Med.* **1971**, *285*, 1182 – 1186; b) A. Wellstein, F. Czubayko, *Breast Cancer Res. Treat.* **1996**, *38*, 109 – 119; c) J. Folkman, *Nat. Med.* **1995**, *1*, 27 – 31; d) A. Gagliardi, H. Hadd, D. C. Collins, *Cancer Res.* **1992**, *52*, 5073 – 5075; e) E. A. Kruger, P. H. Duray, D. K. Price, J. M. Pluda, W. D. Fig, *Semina. Oncol.* **2001**, *28*, 570 – 576; f) J. Sun, M. A. Blaskovich, R. K. Jain, F. Delarue, D. Paris, S. Brem, M. Wotoczek-Obadia, Q. Lin, D. Coppola, K. Choi, M. Mullan, A. D. Hamilton, S. M. Sebti, *Cancer Res.* **2004**, *64*, 3586 – 3592.

[2] a) J. Zhang, L. S. Cousens, P. J. Barr, S. R. Sprang, *Proc. Natl. Acad. Sci. USA* **1991**, *88*, 3446 – 3450; b) X. Zhu, H. Komiya, A. Chirino, S. Faham, G. M. Fox, T. Arakawa, B. T. Hsu, D. C. Rees, *Science* **1991**, *251*, 90 – 93; c) A. E. Eriksson, L. S. Cousens, L. H. Weaver, B. W. Mattews, *Proc. Natl. Acad. Sci. USA* **1991**, 88, 3441 – 3445; d) A. E. Eriksson, L. S. Cousens, B. Matthews, *Protein Sci.* **1993**, *2*, 1274 – 1284.

[3] a) W. H. Burgess, T. Maciag, *Annu. Rev. Biochem.* **1989**, *58*, 575 – 606; b) A. Yayon, M. Klasbrun, J. D. Esko, P. Leder, D. M. Ornitz, *Cell* **1991**, *64*, 841 – 848; c) D. M. Ornitz, A. B. Herr, M. Nilsson, J. Westman, C. M. Svahn, G. Waksman, *Science* **1995**, *268*, 432 – 436; d) S. Faham, R. E. Hileman, J. R. Fromm, R. J. Lindhardt, D. C. Rees, *Science* **1996**, *271*, 1116 – 1120; e) G. Venkataraman, V. Sasisekaharan, A. B. Herr, D. M. Ornitz, G. Waksman, C. L. Cooney, R. Langer, R. Sasisekharan, *Proc. Natl. Acad. Sci. USA* **1996**, *93*, 845 – 850; f) A. N. Plotnikov, J. Schlessinger, S. R. Hubbard, M. Mohammadi, *Cell* **1999**, *98*, 641 – 650.

[4] a) S. Takano, S. Gately, M. E. Neville, W. F. Herblin, J. L. Gross, H. Engelhard, M. Perricone, K. Eidsvoog, S. Brem, *Cancer Res.* **1994**, *54*, 2654 – 2660; b) P. S. Braddock, D. E. Hu, T. P. D. Fan, I. J. Stratford, A. L. Harris, R. Bicknell, *Br. J. Cancer.* **1994**, *69*, 890 – 898; c) F. Manetti, F. Corelli, M. Botta, *Curr. Pharm. Des.* **2000**, *6*, 1897 – 1924.

[5] G. Maier, M. E. Lippman, A. J. Wellstein, *J. Natl. Cancer Inst.* **1992**, *84*, 1716 – 1724.

[6] a) M. Zamai, V. R. Caiolfa, D. Pines, E. Pines, A. H. Parola, *Biophys. J.* **1998**, *75*, 672 – 682; b) M. Zamai, C. Hariharan, D. Pines, M. Safran, A. Yayon, V. R. Caiolfa, R. Cohen-Luria, E. Pines, A. H. Parola, *Biophys. J.* **2002**, *82*, 2652 – 2664.

[7] H. Q. Miao, D. M. Ornitz, E. Aingorn, S. A. Ben-Sasson, I. J. Vlodavsky, *Clin. Invest.* **1997**, *99*, 1565 – 1575.

[8] a) H. Kuyu, W. R. Lee, R. Bare, M. C. Hall, F. M. Torti, *Ann. Oncol.* **1999**, *10*, 891 – 898; b) G. Schwartsmann, E. Sprinz, L. Kalakun, N. Yamagushi, E. Sander, I. Grivicich, R. Koya, D. R. Mans, *Tumori* **1996**, *82*, 360 – 363.

[9] A. Firsching, P. Nickel, P. Mora, B. Allolio, *Cancer Res.* **1995**, *55*, 4957 – 4961.

[10] M. T. Pope, A. Müller, *Angew. Chem.* **1991**, *103*, 56 – 70; *Angew. Chem. Int. Ed. Engl.* **1991**, *30*, 34 – 48.

[11] a) Y. Take, Y. Tokutake, Y. Inouye, T. Yoshida, T. A. Yamamoto, T. Yamase, S. Nakamura, *Antiviral Res.* **1991**, *15*, 113 – 124; b) D. A. Judd, R. F. Schinazi, C. L. Hill, *Antiviral Chem. Chemother.* **1994**, *5*, 410 – 414; c) J. T. Rhule, C. L. Hill, D. A. Judd, R. F. Schinazi, *Chem. Rev.* **1998**, *98*, 327 – 357.

[12] a) C. L. Hill, D. A. Judd, J. Tang, J. Nettles, R. F. Schinazi, *Antiviral Res.* **1991**, *34*, A43; b) S. G. Sarafianos, U. Kortz, M. T. Pope, M. J. Modak, *Biochem. J.* **1996**, *319*, 619 – 626.

[13] D. A. Judd, J. H. Nettles, N. Nevins, J. P. Snyder, D. C. Liotta, J. Tang, J. Ermolieff, R. F. Schinazi, C. L. Hill, *J. Am. Chem. Soc.* **2001**, *123*, 886 – 897.

[14] L. W. Sun, Q. Wu, N. Liu, C. Yang, L. Y. Liu, Z. Q. Liu, D. Q. Zhao, *Chem. Lett.* **2004**. *33*, 298 – 299.

[15] a) T. Kajio, K. Kawahara, K. Kato, *FEBS Lett.* **1992**, *306*, 243 – 246; b) S. J. Prestrelski, G. M. Fox, T. Arakawa, *Arch. Biochem. Biophys.* **1992**, *293*, 314 – 319; c) T. Arakawa, J. Wen, J. S. Philo, *J. Protein Chem.* **1993**, *12*, 689 – 693.

[16] D. Coltrni, M. Rusnati, G. Zoppetti, P. Oreste, A. Isaccia, L. Bergonzoni, M. Presta, *Eur. J. Biochem.* **1993**, *214*, 51 – 58.

[17] C. J. Burke, D. B. Volkin, H. Mach, C. Russell Middaugh, *Biochemistry* **1993**, *32*, 6419 – 6426.

[18] a) S. Shigeta, S. Mori, J. Watanable, M. Bata, A. M. Khenkin, C. L. Hill, R. F. Schinazi, *Antiviral Chem. Chemother.* **1995**, *6*, 114 – 122; b) S. Shigeta, S. Mori, J. Watanable, Y. Yamase, R. F. Schinazi, *Antiviral Chem. Chemother.* **1996**, *7*, 346 – 352.

[19] R. Contant, J. P. Ciabrini, *J. Chem. Res. Synop.* **1982**, 50 – 51.

[20] a) A. E. Eriksson, L. S. Cousens, B. W. Matthews, *Protein Sci.* **1993**, *2*, 1274 – 1284; b) A. E. Eriksson, L. S. Cousens, L. H. Weaver, B. W. Matthews, *Proc. Natl. Acad. Sci. USA* **1991**, *88*, 3441 – 3445.

[21] a) K. Ono, H. Nakane, M. Fukushima, *Eur. J. Biochem.* **1988**, *172*, 349 – 353; b) Y. Moriyama, N. Nelson, *FEBS Lett.* **1988**, *234*, 383 – 386; c) S. J. Butler, E. C. Kelly, F. R. McKenzy, S. B. Guild, M. J. Wakelam, G. Milligan, *Biochem. J.* **1988**, *251*, 201 – 205.

[22] a) D. B. Rifkin, D. J. Moscatelli, *J. Cell Biol.* **1989**, *109*, 1 – 6; b) J. Folkman, M. Klagsbrun, J. Sasse, M. Wadzinsky, D. Ingber, I. A. Vlodavsky, *Am. J. Pathol.* **1988**, *130*, 393 – 400; c) M. Klagsbrun, J. Sasse, R. Sullivan, J. A. Smith, *Proc. Natl. Acad. Sci. USA* **1986**, *83*, 2448 – 2452; d) A. Hayek, F. L. Culler, G. M. Beattie, A. D. Lopez, P. Luevas, A. Baird, *Biochem. Biophys. Res. Commun.* **1987**, *147*, 876 – 880.

[23] C. R. Middaugh, H. Mach, C. J. Burke, D. B. Volkin, J. M. Dabora, P. K. Tsai, M. W. Bruner, J. A. Ryan, K. E. Marfia, *Biochemistry* **1992**, *31*, 9016 – 9024.

[24] a) J. Zhang, L. S. Cousens, P. J. Barr, S. R. Sprang, *Proc. Natl. Acad. Sci. USA* **1991**, *88*,3446 – 3450; b) P. Caccia, G. Nitti, O. Cletini, P. Pucci, M. Ruoppolo, F. Bertolero, B. Valsasina, F. Roletto, C. Cristiani, G. Cauet, *Eur. J. Biochem.* **1992**, *204*, 649 – 655; c) S. A. Thompson, *J. Biol. Chem.* **1992**, *267*, 2269 – 2273.

[25] P. W. Riddles, R. L. Blakeley, B. Zerner, *Methods Enzymol.* **1983**, *9*, 49 – 60.

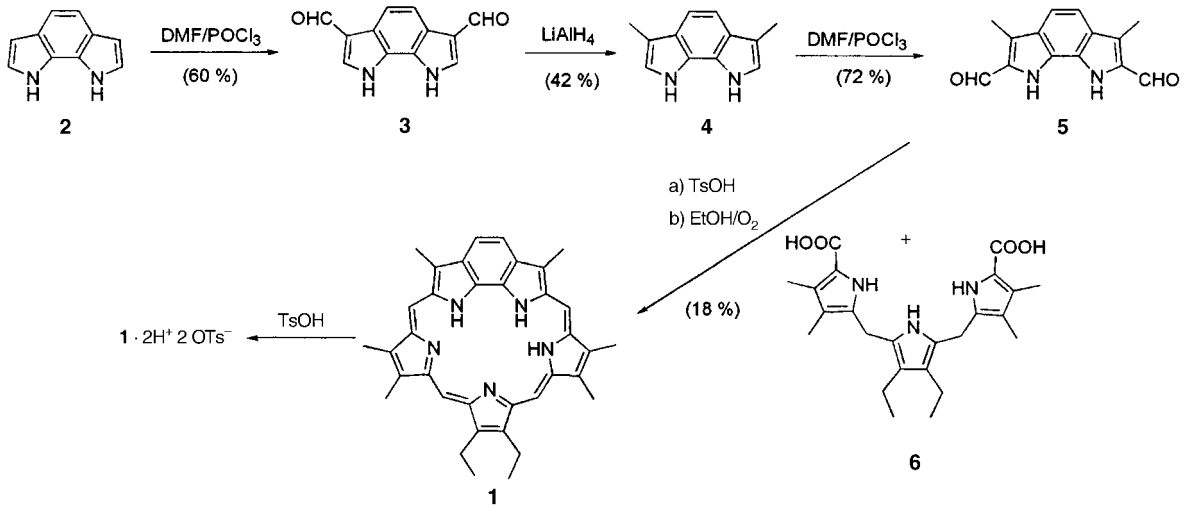
Sapphyrins

A Benzodipyrrole-Derived Sapphyrin**

*Pradeepta K Panda, Young-Jin Kang, and Chang-Hee Lee**

The discovery of expanded porphyrins has broadened the scope of porphyrin-related research. Since the first report of expanded porphyrins, namely a pentapyrrolic aromatic macrocycle referred to as sapphyrin,[1] various other oligopyrrole macrocycles including pentaphyrins, hexaphyrins, and rubyrins have been synthesized and characterized.[2] However, sapphyrins remain among the best studied of all the expanded porphyrins. For instance, they have been studied as hosts for anions[3,4] and as potential photosensitizers for photodynamic therapy,[5] and owing to their unique electronic features, which are exhibited in their narrow absorption bands, sapphyrins have also attracted interest as possible nonlinear optical materials. The synthesis and anion-binding properties of sapphyrins have been reviewed recently.[6] The most common synthesis of sapphyrins is the so-called 3+2 approach reported by Broadhurst et al.,[1] and this approach has successfully been employed to obtain a range of alkyl- and *meso*-substituted sapphyrins.[7–12] A less common but equally attractive approach is the so-called 4+1 approach, which relies on the use of a tetrapyrrolic precursor and formylpyrroles.[8,13,14] Despite these and other efforts, there has apparently been no report of a sapphyrin that imposes intrinsic conformational restriction on its pentapyrrolic core. In this light, we report here the synthesis and spectroscopic properties of what we believe is the first benzodipyrrole-derived sapphyrin system, **1**. As the corresponding benzo-extended sapphyrins[15] were found to exhibit red-shifted absorption bands, it was considered likely that the use of a benzodipyrrole unit such as **3** would provide another means of fine-tuning the electronic properties of sapphyrins.

Sapphyrin **1** was synthesized through a typical 3+2 condensation from the key precursors, diformylbenzodipyrrole derivative **5** and tripyrromethane dicarboxylic acid **6**. As shown in Scheme 1, 3,6-diformylbenzodipyyrole **3** was



Scheme 1. Synthesis of sapphyrin **1**. DMF = *N*,*N*-dimethylformamide, TsOH = *p*-toluenesulfonic acid.

obtained by a Vilsmeier–Haack reaction of benzodipyrrole (**2**),[16] which upon reduction with $LiAlH_4$ yielded 3,6-dimethylbenzodipyrrole (**4**). A further Vilsmeier–Haack reaction of this intermediate afforded the required dialdehyde **5** in 72% yield. Tripyrromethane dicarboxylic acid **6** was synthesized easily according to a reported procedure.[17] Acid-catalyzed condensation of benzodipyrrole derivative **5** and tripyrromethane dicarboxylic acid **6** followed by air oxidation provided the desired fused sapphyrin **1** in 18% yield. A higher yield was expected as a result of the conformational restriction imposed by the fused dipyrrole moiety, but the isolated yield of **1** was rather low. Intermediate **5** proved to be less reactive than simple dipyrroles, and this lack of reactivity is thought to account, in part, for the low isolated yield of the sapphyrin product.[18] Sapphyrin **1** was characterized by standard spectroscopic methods, as well as single-crystal X-ray diffraction studies. The salt $\mathbf{1}\cdot 2H^+2OTs$ (OTs = *p*-

[*] Dr. P. K. Panda, Prof. C.-H. Lee
Department of Chemistry
Kangwon National University
Chun-Chon 200-701 (Korea)
Fax: (+82) 33-253-7582
E-mail: chhlee@kangwon.ac.kr
Prof. Y.-J. Kang
Department of Science Education
Kangwon National University
Chun-Chon 200-701 (Korea)

[**] This work was supported by a grant from the Vascular System Research Center (VSRC) at KNU, and the Basic Research Program from the Korea Science and Engineering Foundation (R05-2003-000-11220-0). NMR and mass spectra were recorded at the Central Instrumentation Facility in KNU.

Supporting information for this article, including synthetic methods, and spectral and X-ray crystallographic data, is available on the WWW under http://www.angewandte.org or from the author.

 DOI: 10.1002/anie.200500944 © 2005 Wiley-VCH Verlag GmbH & Co. KGaA, Weinheim

$CH_3C_6H_4SO_3^-$ (tosylate)) was easily obtained by shaking a solution of **1** in dichloromethane with aqueous *p*-toluenesulfonic acid.

The ^{1}H NMR spectrum of the free-base sapphyrin **1** revealed three broadened signals at $\delta = -0.87$, -1.30, and -2.46 ppm for the inner NH protons which indicates that inner NH protons reside unsymmetrically as shown in Scheme 1. On the other hand, the ditosylate salt **1**·2 H$^+$2 OTs showed distinctive resonances at $\delta = -3.65$, -3.78, and -4.79 ppm, with a respective ratio of integration of 2:1:2, which indicates C_{2v} symmetry for the diprotonated salt. The signals for the aromatic protons of *p*-toluenesulfonic acid appear as broad singlets at $\delta = 5.44$ and 2.59 ppm and indicate a strong diamagnetic influence from the sapphyrin.

Diffraction-grade crystals of **1**·2 H$^+$2 OTs were obtained by the slow diffusion of hexane into a solution of the salt in chloroform. X-ray crystal structure analysis revealed the presence of one molecule of chloroform in the unit cell[19] and also showed that the oxygen atoms on one of the tosylate groups (upper) were disordered. As shown in Figure 1, the two oxygen atoms on the upper tosylate group are bound to three pyrrolic NH groups, with O–N distances of 2.830 (O1–N2), 2.932 (O1–N3), and 2.962 Å (O2–N5), while only a single oxygen atom (O1′) from the lower tosylate group is bound to the three NH groups at N1, N2, and N4 with respective O–N distances of 2.881, 2.927, and 2.838 Å. Presumably as a result of these interactions with the anions and possible steric congestion between the five inner N–H groups, the pyrrole ring that bears N5 is tilted upward relative to the mean plane of the macrocycle. This behavior is most unusual for a β-alkyl-substituted sapphyrin.

The pyrrole–tosylate N–O distances range from 2.838 to 2.962 Å and are well within the range expected for effective hydrogen-bonding interactions. Further analysis of the 3D packing structure indicated that two tosylate groups are located between two sapphyrin molecules. The two tosylate anions lie slip-stacked one above the other in an antiparallel manner with the sulfonate groups pointing outwards to minimize electronic repulsion between them (see Figure 2). The distance between the uppermost hydrogen atom (H50) of the methyl group of the lower tosylate group and carbon atom C49 at the 4-position of the benzene ring in the upper tosylate is 2.941 Å.

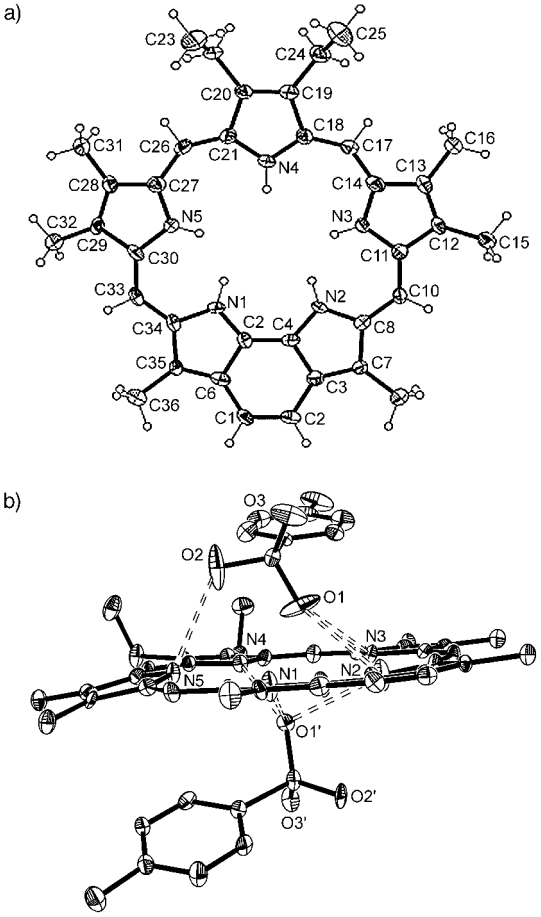


Figure 1. ORTEP views of the sapphyrin di-*p*-toluenesulfonic acid salt, **1**·2 H$^+$2 OTs$^-$. a) Top view with the tosylate groups omitted for clarity, and b) side view showing the unsymmetrical nature of the hydrogen-bonding interactions between the two anions and the protonated macrocycle.

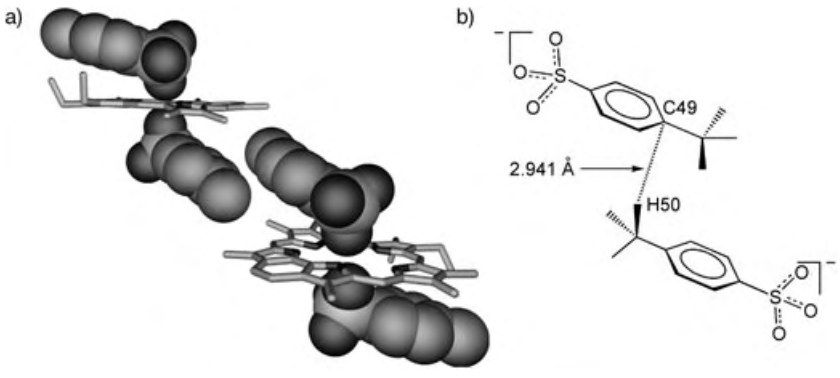


Figure 2. a) Arrangement of two diprotonated sapphyrin molecules (stick representations; C light gray, N dark gray) and their respective tosylate anions (space-filling representation; sulfonate oxygen atoms are shaded darker than S and C atoms) within the crystal structure. b) The two tosylate anions located between the two sapphyrins are packed antiparallel, with a distance of 2.941 Å separating atom C49 (*C*–C) of one OTs moiety and H50 (tolyl H_2C–*H*) of the other.

The absorption spectra of free-base **1** and its ditosylate salt **1**·2 H$^+$2 OTs are shown in Figure 3. Sapphyrin **1** shows a Soret-like band at 466 nm, whereas the Soret-like band is slightly red-shifted and appears at 469 nm in the salt **1**·2 H$^+$2 OTs. The bands are also red-shifted relative to the values of 457 and 456 nm reported for decaalkylsapphyrin and its diprotonated form, respectively.[20] The strongest absorbing Q-band in free-base form **1** appears at 727 nm, whereas for the salt **1**·2 H$^+$2 OTs the major Q-band at 703 nm is accompanied by a weaker band at 748 nm. The Q-bands are also significantly red-shifted relative to those of decaalkylsapphyrin.[14a] The Q-bands for **1** and its diprotonated salt are relatively less intense than those for other diprotonated

 © 2005 Wiley-VCH Verlag GmbH & Co. KGaA, Weinheim

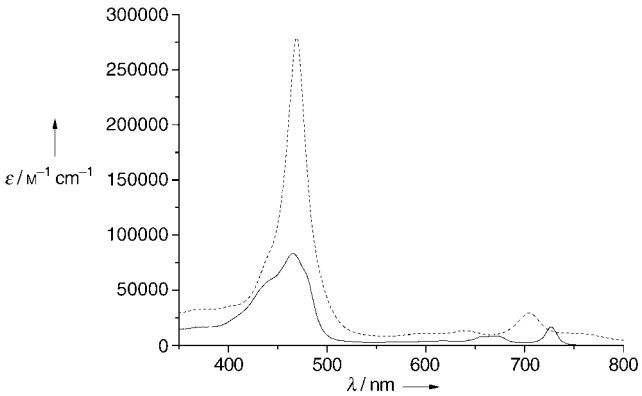


Figure 3. UV/Vis spectra of sapphyrin **1** (——; 1.99×10^{-5} M in $CHCl_3$ with 1% Et_3N) and **1**·2 H^+2 OTs^- (-----; 6.79×10^{-5} M in $CHCl_3$).

sapphyrin species. The absorption spectrum of the dichloride salt of **1**, which was obtained by Sessler's method,[18,20] was compared directly with the spectra of some benzo-extended sapphyrins.[15] From the results obtained (data not shown), it appears that incorporation of the benzene ring directly into the sapphyrin, as in **1**, has a stronger effect on the electronic properties of the molecule than in benzo-extended analogues by extension of the overall π-electron conjugation (aromaticity) through the use of the diene part of the fused benzene unit.

In conclusion, we have introduced a new member to the family of extended porphyrins, a pyrrole-fused sapphyrin. The diprotonated benzodipyrrole-bridged sapphyrin **1** is slightly buckled presumably from a combination of conformational restriction about the fused benzodipyrrole moiety and through steric interactions between the five inner amine groups. Currently, we are exploring further extensions of this theme, for instance, by targeting the replacement of the dipyrrole moiety with other aromatic and heteroaromatic subunits.

Received: March 15, 2005
Published online: May 27, 2005

Keywords: aromaticity · fused-ring systems · macrocycles · nitrogen heterocycles · porphyrinoids

[1] M. J. Broadhurst, R. Grigg, A. W. Johnson, *Chem. Commun.* **1969**, 23 – 24.
[2] a) H. Rexhausen, A. Gossauer, *J. Chem. Soc. Chem. Commun.* **1983**, 275; b) R. Charriére, T. A. Jenny, H. Rexhausen, A. Gossauer, *Heterocycles* **1993**, *36*, 1561 – 1575; c) J. L. Sessler, T. Morishima, V. Lynch, *Angew. Chem.* **1991**, *103*, 1018 – 1020; *Angew. Chem. Int. Ed. Engl.* **1991**, *30*, 977 – 980; d) M. G. P. M. S. Neves, R. M. Martins, A. C. Tomé, A. J. D. Silvestre, A. M. S. Silva, V. Félix, M. G. B. Drew, J. A. S. Cavaleiro, *Chem. Commun.* **1999**, 285 – 386; e) J.-Y. Shin, H. Furuta, K. Yoza, S. Igarashi, A. Osuka, *J. Am. Chem. Soc.* **2001**, *123*, 7190 – 7191.
[3] J. L. Sessler, M. Cyr, V. Lynch, E. McGhee, J. Ibers, *J. Am. Chem. Soc.* **1990**, *112*, 2810 – 2813.
[4] V. Kral, H. Furuta, K. Shreder, V. Lynch, J. L. Sessler, *J. Am. Chem. Soc.* **1996**, *118*, 1595 – 1607.
[5] B. G. Maiya, M. Cyr, A. Harriman, J. L. Sessler, *J. Phys. Chem.* **1990**, *94*, 3597 – 3601.
[6] J. L. Sessler, J. M. Davis, *Acc. Chem. Res.* **2001**, *34*, 989 – 997.
[7] M. J. Broadhurst, R. Grigg, A. W. Johnson, *J. Chem. Soc. Perkin Trans. 1* **1972**, 2111 – 2116.
[8] V. J. Bauer, D. L. Clive, J. D. Dolphin, J. B. Paine III, F. L. Harris, M. M. King, J. Loder, S. W. C. Wang, R. B. Woodward, *J. Am. Chem. Soc.* **1983**, *105*, 6429 – 6436.
[9] C. Bruckner, E. D. Sternberg, R. W. Boyle, D. Dolphin, *Chem. Commun.* **1997**, 1689 – 1690.
[10] A. Srinivasan, S. Mahajan, S. K. Pushpan, M. Ravikumar, T. K. Chandrashekar, *Tetrahedron Lett.* **1998**, *39*, 1961 – 1964.
[11] A. Srinivasan, S. K. Pushpan, M. R. Kumar, S. Mahajan, T. K. Chandrashekar, R. Roy, P. Ramamurthy, *J. Chem. Soc. Perkin Trans. 2* **1999**, 64, 961 – 968.
[12] A. Srinivasan, V. G. Anand, S. J. Narayanan, S. K. Pushpan, M. R. Kumar, T. K. Chandrashekar, K. I. Sugiura, Y. Sakata, *J. Org. Chem.* **1999**, *64*, 8693 – 8697.
[13] R. Paolesse, S. Licoccia, M. Spagnoli, T. Boschi, R. G. Khoury, K. M. Smith, *J. Org. Chem.* **1997**, *62*, 5133 – 5137.
[14] a) D. T. Richter, T. D. Lash, *J. Am. Chem. Soc.* **1998**, *120*, 9965 – 9966; b) D. T. Richter, T. D. Lash, *Tetrahedron Lett.* **1999**, *40*, 6735 – 6738; c) D. T. Richter, T. D. Lash, *J. Org. Chem.* **2004**, *69*, **8842 – 8850**.
[15] N. Ono, K. Kuroki, E. Watanabe, N. Ochi, H. Uno, *Heterocycles* **2004**, *62*, 365 – 373.
[16] A. Berlin, S. Bradamante, R. Ferraccioli, G. A. Pagani, F. Sannicolo, *J. Chem. Soc. Chem. Commun.* **1987**, 1176 – 1177.
[17] J. L. Sessler, M. R. Johnson, V. Lynch, *J. Org. Chem.* **1987**, *52*, 4394 – 4397.
[18] Spectroscopic data for free-base **1**: ^{1}H NMR (400 MHz, $CDCl_3$, 25 °C, TMS): $\delta = 10.64$ (brs, 2H), 10.49 (brs, 2H), 8.86 (s, 2H), 4.42 (m, 4H), 4.32 (s, 6H), 3.80 (s, 6H), 3.77 (s, 6H), 2.03 (t, 6H), −0.87 (brs, 1H), −1.30 (brs, 1H), −2.46 ppm (brs, 1H); FAB-MS *m/z* calcd for $C_{36}H_{37}N_5$: 539.30; found: 540.30 [$M+1$]; UV/Vis (1% Et_3N in $CHCl_3$): λ_{max} (logε) = 466 (4.92), 618 (3.59), 667 (3.92), 727 nm (4.22).
[19] Crystal data for **1**·2 H^+2 OTs^-: $C_{51}H_{54}Cl_3N_5O_6S_2$, triclinic, space group *P*-1, $a = 10.2266(8)$ Å, $b = 12.7492(10)$ Å, $c = 19.9972(16)$ Å, $\alpha = 108.042(2)°$, $\beta = 95.074(2)°$, $\gamma = 102.586(2)°$, $V = 2385.1(3)$ Å^3, $T = 173(2)$ K, $Z = 2$, GOF on $F^2 = 0.853$, R_1 ($I > 2\sigma(I)$) = 0.0646, $wR_2 = 0.1298$. The crystal was attached to glass fibers and mounted on a Bruker SMART diffractometer equipped with graphite monochromated $Mo_{K\alpha}$ ($\lambda = 0.71073$ Å) radiation, operating at 50 kV and 30 mA, and a CCD detector; 45 frames of two-dimensional diffraction images were collected and processed to obtain the cell parameters and orientation matrix. All data collections were performed at 173(2) K. The data collection 2θ range is 2.18–52.04°. No significant decay was observed during the data collection. The raw data were processed to give structure factors by using the SAINT program. The structure was solved by direct methods and refined by full-matrix least-squares against F^2 for all data by using SHELXTL software (version 5.14).[21] All non-hydrogen atoms were anisotropically refined. All other hydrogen atoms were included in their calculated positions and refined by using a riding model. CCDC 268397 contains the supplementary crystallographic data for this paper. These data can be obtained free of charge from the Cambridge Crystallographic Data Centre via www.ccdc.cam.ac.uk/data_request/cif.
[20] J. L. Sessler, M. Cyr, A. K. Burrell, *Tetrahedron* **1992**, *48*, 9661 – 9672.
[21] SHELXTL NT Crystal Structure Analysis Package, Version 5.14; Bruker AXS, Analytical X-ray System, Madison, WI, **1999**.

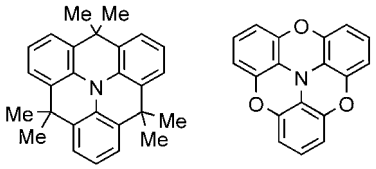
 © 2005 Wiley-VCH Verlag GmbH & Co. KGaA, Weinheim

Heterocyclic Chemistry

2,2′:6′,2″:6″,6-Trioxytriphenylamine: Synthesis and Properties of the Radical Cation and Neutral Species**

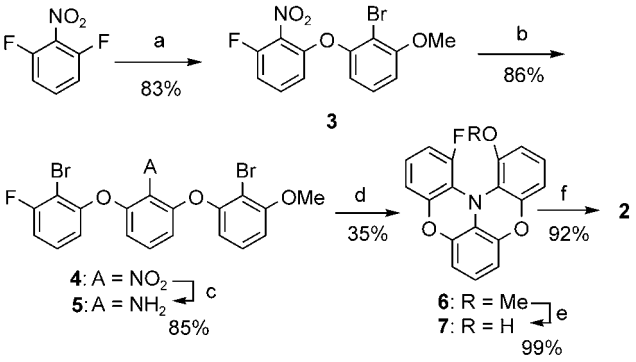
*Masato Kuratsu, Masatoshi Kozaki, and Keiji Okada**

A planar stable triphenylamine radical cation is a fascinating π-electron system that is potentially applicable to electronic and magnetic materials. Hellwinkel and co-workers synthesized an interesting compound **1**,[1] from which the radical cation **1**$^{\bullet+}$ was generated in concentrated sulfuric acid[1a] or by oxidation with lead tetraacetate in trifluoroacetic acid.[1c] The triphenylamine framework of **1**$^{\bullet+}$ is most likely planar. The dimethylmethylene bridges contribute to its stabilization; however, they disrupt the CT-type intermolecular interaction that is crucial for the construction of electronic and magnetic materials. To overcome this disadvantage and to improve stability, we designed a synthetic route to the new oxygen-bridged analogue **2**.[2,3] Quite recently, Livant and co-workers described a product fraction showing a molecular ion of $m/z =$ 287 in the thermolysis of tris(2,6-dimethoxyphenyl)amine. They assumed the structure **2** for the MS peak. However, the compound showed no NMR spectroscopic signal.[4] Herein, we report the preparation, structures, and properties of the neutral **2** and the radical cation **2**$^{\bullet+}$.



1 **2**

The synthesis of **2** is outlined in Scheme 1. Sequential aromatic nucleophilic substitution reactions of 2,6-difluoronitrobenzene with 2-bromo-3-methoxyphenolate and then with 2-bromo-3-fluorophenolate gave **4** (71% yield in two steps). The reduction of **4** proceeded selectively in the presence of *p*-bromophenol (10 equiv) to avoid a competing reduction of aromatic bromide. Intramolecular cyclization of **5** was performed under Pd^0-mediated cross-coupling reaction conditions[5] to afford **6** in 35% yield. Treatment of **6** with BBr_3 gave **7** in good yield. Intramolecular nucleophilic



Scheme 1. Reaction conditions: a) 2-bromo-3-methoxyphenol, NaH/DMSO, 130°C; b) 2-bromo-3-fluorophenol, NaH/DMSO, 130°C; c) hydrazine hydrate, Pd/C, *p*-bromophenol/ethanol, reflux; d) NaO*t*Bu, [Pd(dba)$_2$], P(*t*Bu)$_3$/toluene, reflux; e) BBr_3/CH_2Cl_2, −78°C→room temperature; f) K_2CO_3/DMF, room temperature. dba = *trans*,*trans*-dibenzylideneacetone.

substitution of **7** in DMF with K_2CO_3 as a base proceeded efficiently under remarkably mild conditions to give the desired compound **2** in good yield. Compound **2** had a reversible oxidation wave at +0.59 V versus SCE in DMF (SCE = saturated calomel electrode). The chemical oxidation of **2** was performed by using tris(*p*-bromophenyl)aminium hexafluorophosphate as an oxidant in methylene chloride. The salt **2**$^{\bullet+}\cdot PF_6^-$ can be recrystallized from acetonitrile/diethyl ether.

Figure 1 shows the molecular structures determined by X-ray crystallographic analysis of **2** and **2**$^{\bullet+}$.[6] The neutral compound **2** has a shallow bowl structure, whereas the radical

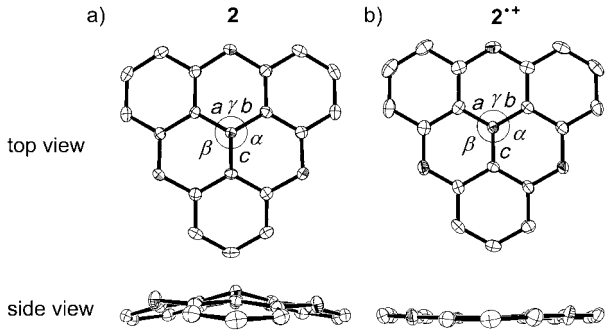


Figure 1. Molecular structures of **2** and **2**$^{\bullet+}$ drawn at 50% ellipsoid level; hydrogen atoms are removed for clarity. Selected bond lengths [Å] and angles [°]. a) For **2** measured at 123 K: $a = 1.408(2)$, $b = 1.403(3)$, $c = 1.412(3)$; $\alpha = 115.3(2)$, $\beta = 115.6(2)$, $\gamma = 115.7(2)$. b) For **2**$^{\bullet+}$ measured at 113 K: $a = 1.376(3)$, $b = 1.377(3)$, $c = 1.378(3)$; $\alpha = 120.1(2)$, $\beta = 119.9(2)$, $\gamma = 120.0(2)$.

cation **2**$^{\bullet+}$ has a planar structure. The C–N bond lengths become shorter and the C-N-C bond angles approach 120° in the radical cation **2**$^{\bullet+}$. The bond-length difference is in qualitative accordance with the HOMO shape of **2**; that is, the C–N and C–O bonds have an antibonding nature in the HOMO.

Triphenylamine radical cations without *para* substituents are generally unstable because of the large spin densities of

[*] M. Kuratsu, Dr. M. Kozaki, Prof. K. Okada
Graduate School of Science, Osaka City University
Sugimoto, Sumiyoshi-ku, Osaka 558-8585 (Japan)
Fax: (+81) 6-6690-2709
E-mail: okadak@sci.osaka-cu.ac.jp

[**] This work was partially supported by a research fund from Chisso Corporation, Japan. We thank Professor Stephen F. Nelsen for valuable discussions.

Supporting information for this article is available on the WWW under http://www.angewandte.org or from the author.

 © 2005 Wiley-VCH Verlag GmbH & Co. KGaA, Weinheim DOI: 10.1002/anie.200500397

the *para* positions.[7] For $\mathbf{2}^{\bullet+}$, neither dimerization tendency in the crystal structure nor oxygenation under aerated conditions in solution was observed. The spin delocalization in a whole molecule involving the oxygen atoms (phenoxazine radical cation structure) contributes to the stability of $\mathbf{2}^{\bullet+}$. The radical cation $\mathbf{2}^{\bullet+}$ exhibited a well-resolved EPR spectrum. The hyperfine coupling constants for $\mathbf{2}^{\bullet+}$ ($g = 2.0031$, $a_N = 0.90$, $a_{H_p} = 0.26$, and $a_{H_m} = 0.06$ mT) in butyronitrile at room temperature were slightly smaller than those for $\mathbf{1}^{\bullet+}$ ($g = 2.0027$, $a_N = 0.95$, $a_{H_p} = 0.30$, and $a_{H_m} = 0.07$ mT).[1c] The smaller spin density values for $\mathbf{2}^{\bullet+}$ are clearly related to the positive spin density of the oxygen atoms. The calculated spin-density map and values are shown in Figure 2.[8]

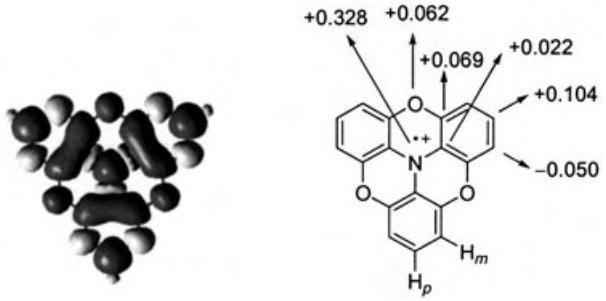


Figure 2. The spin-density map (black: positive spin, white: negative spin) and values (UB3LYP/6-31G*) for $\mathbf{2}^{\bullet+}$.

The radical cation $\mathbf{2}^{\bullet+}$ had broad absorptions in the visible region ($\lambda = 709$ and 785 nm, Figure 3). These absorptions can be related to the electronic transitions from the occupied

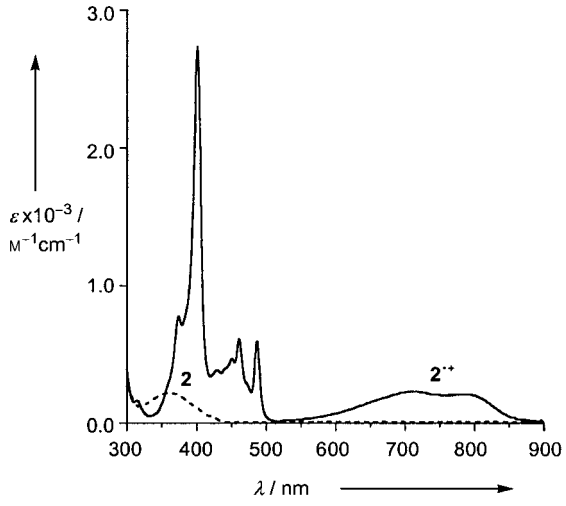


Figure 3. UV/Vis absorptions of **2** (-----) and $\mathbf{2}^{\bullet+}$ (——) in dichloromethane.

MOs delocalized on the outer electron-rich trioxytris(1,3-phenylene) moieties to the delocalized unoccupied orbital involving the nitrogen cation. The theoretical calculation (TD-DFT/6-31G*) roughly reproduced this situation ($\lambda_{calcd} = 729$ nm as a degenerate transition with the main contribution ($\approx 90\,\%$) of HOMO-1(β), HOMO(β)→LUMO(β) (oscillator strength of 0.01 in both cases); Figure 4).[8,9] The observed absorptions with a rather broad slope in the region of 500–700 nm can be attributed to vibrational fine structure of the degenerate band. The peak separation of 1370 cm^{-1} is close to that observed for the 10-phenylphenoxazine radical cation (1270 cm^{-1}).

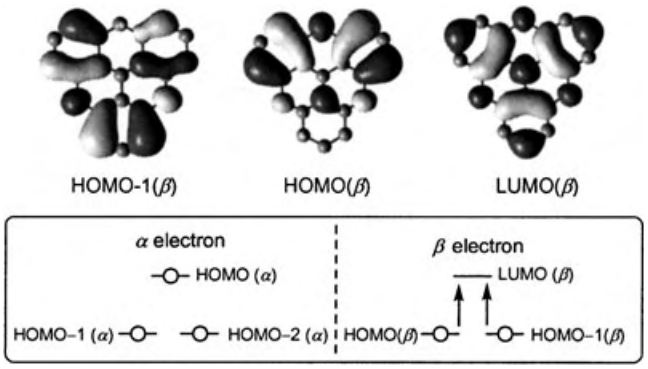


Figure 4. MOs and the energy diagram (UHF) of $\mathbf{2}^{\bullet+}$.

These studies clearly establish that 1) the neutral compound **2** is a good electron donor with a shallow bowl structure and 2) the radical cation $\mathbf{2}^{\bullet+}$ is a highly stable planar species. Moreover, the neutral compound **2** can form stable CT complexes with several electron acceptors, suggesting applicability to electronic and magnetic materials. We are particularly interested in forthcoming projects to follow up this work. The introduction of stable radicals at the *para* positions followed by the formation of CT complexes with electron acceptors would provide a magnetic CT-salt material.[10] Furthermore, the small geometrical change between the neutral and radical cation states may allow photostimulated phase transition to the photoconductive state $\mathbf{2}_2^{\bullet+}$.[11] The preparation of such materials is in progress.

Experimental Section

The synthesis of compounds **2**–**7** and the EPR spectrum for $\mathbf{2}^{\bullet+}$ with its simulation are described in the Supporting Information.

$\mathbf{2}^{\bullet+}\cdot PF_6^-$: Compound **2** (25.0 mg, 0.0870 mmol) was dissolved in dichloromethane (20 mL). A solution of tris(*p*-bromophenyl)aminium hexafluorophosphate (54.8 mg, 0.0874 mmol in CH_2Cl_2 (10 mL)) was added dropwise at room temperature with stirring in a glove box. After 30 min, the solvent was evaporated under vacuum and the crude product was recrystallized from acetonitrile/diethyl ether to give $\mathbf{2}^{\bullet+}$ as deep green plates (29.4 mg, 78 %); m.p. $\approx 278.0\,^{\circ}C$ (decomp). MS: *m*/*z* (%): FAB^+ (*m*-NBA) 287 (100) [$C_{18}H_9NO_3^+$], FAB^- (*m*-NBA) 145 (100) [PF_6^-]. Elemental analysis calcd (%) for $\mathbf{2}^{\bullet+}\cdot PF_6^-$ ($C_{18}H_9F_6NO_3P$): C 50.02, H 2.10, N 3.24; found: C 50.12, H 2.00, N 3.21.

Received: February 2, 2005
Published online: May 31, 2005

Keywords: amines · EPR spectroscopy · heterocycles · oxidation · radical ions

 © 2005 Wiley-VCH Verlag GmbH & Co. KGaA, Weinheim

[1] a) D. Hellwinkel, M. Melan, *Chem. Ber.* **1974**, *107*, 616–626; b) D. Hellwinkel, M. Melan, *Chem. Ber.* **1971**, *104*, 1001–1016; c) S. Bamberger, D. Hellwinkel, F. A. Neugebauer, *Chem. Ber.* **1975**, *108*, 2416–2421; d) D. Hellwinkel, W. Schmidt, *Chem. Ber.* **1980**, *113*, 358–384; e) J. E. Field, D. Venkataraman, *Chem. Mater.* **2002**, *14*, 962–964.

[2] M. Kuratsu, M. Kozaki, K. Okada, *Chem. Lett.* **2004**, *33*, 1174–1175.

[3] A bowl-shaped trioxatriphenylphosphine analogue has been reported: a) F. C. Krebs, P. S. Larsen, J. Larsen, C. S. Jacobsen, C. Boutton, N. Thorup, *J. Am. Chem. Soc.* **1997**, *119*, 1208–1216; b) G. K. H. Madsen, F. C. Krebs, B. Lebech, F. K. Larsen, *Chem. Eur. J.* **2000**, *6*, 1797–1804.

[4] P. D. Livant, D. J. D. Northcott, Y. Shen, T. R. Webb, *J. Org. Chem.* **2004**, *69*, 6564–6571.

[5] J. F. Hartwig, M. Kawatsura, S. I. Hauck, K. H. Shaughnessy, L. M. Alcazar-Roman, *J. Org. Chem.* **1999**, *64*, 5575–5580.

[6] Crystallographic data for **2**: crystal size $0.40\times0.30\times0.20$ mm, monoclinic, space group $P2_1$ (#4), $a=10.0772(13)$ Å, $b=6.8136(6)$ Å, $c=10.0712(13)$ Å, $\beta=119.964(4)°$, $V=599.08(12)$ Å^3, $Z=2$, $\rho_{calcd}=1.592$ g cm^{-3}, $2\theta_{max}=55.0°$, $Mo_{K\alpha}$ radiation (0.71070 Å), $T=123$ K, $\mu=1.10$ cm^{-1}, $T_{min}=0.977$, $T_{max}=0.989$, 4450 measured reflections, 1412 unique reflections, 1367 observed reflections ($I>-10\sigma$, all data), 208 parameters, $R_1(I>2\sigma)=0.035$, $R_w(I>2\sigma)=0.044$, GOF = 1.004; Crystallographic data for $\mathbf{2}^{\bullet+}\cdot PF_6^-$: crystal size $0.30\times0.20\times0.10$ mm, orthorhombic, space group *Pbca* (#61), $a=15.5415(10)$ Å, $b=13.4237(8)$ Å, $c=15.5653(10)$ Å, $V=3247.3(4)$ Å^3, $Z=8$, $\rho_{calcd}=1.768$ g cm^{-3}, $2\theta_{max}=55.0°$, $Mo_{K\alpha}$ radiation (0.71070 Å), $T=113$ K, $\mu=2.58$ cm^{-1}, $T_{min}=0.953$, $T_{max}=0.980$, 25720 measured reflections, 3708 unique reflections, 2763 observed reflections ($I>-10\sigma$, all data), 271 parameters, $R_1(I>2\sigma)=0.043$, $R_w(I>2\sigma)=0.047$, GOF = 1.030. CCDC 262144 (**2**) and CCDC 262145 ($\mathbf{2}^{\bullet+}$) contain the supplementary crystallographic data for this paper. These data can be obtained free of charge from the Cambridge Crystallographic Data Centre via www.ccdc.cam.ac.uk/data_request/cif.

[7] E. T. Seo, R. F. Nelson, J. M. Fritsch, L. S. Marcoux, D. W. Leedy, R. N. Adams, *J. Am. Chem. Soc.* **1966**, *88*, 3498–3503.

[8] The calculation was performed at the optimized geometry starting from the X-ray crystallographic structure with the Gaussian 03 program package.

[9] A better λ_{calc} value (753 nm) was obtained by using the NCG methodology with B3LYP/6-31G*: S. F. Nelsen, A. E. Konradsson, J. P. Telo, *J. Am. Chem. Soc.* **2005**, *127*, 920–925, and references therein.

[10] S. Hiraoka, T. Okamoto, M. Kozaki, D. Shiomi, K. Sato, T. Takui, *J. Am. Chem. Soc.* **2004**, *126*, 58–59.

[11] M. Chollet, L. Guerin, N. Uchida, S. Fukaya, H. Shimoda, T. Ishikawa, K. Matsuda, T. Hasegawa, A. Ota, H. Yamochi, G. Saito, R. Tazaki, S. Adachi, S. Koshihara, *Science* **2005**, *307*, 86–89.

 © 2005 Wiley-VCH Verlag GmbH & Co. KGaA, Weinheim

Tumor Imaging Agents

A Labeled Neutral Endopeptidase Inhibitor as a Potential Tool for Tumor Diagnosis and Prognosis**

Olivier Raguin, Marie-Claude Fournié-Zaluski, Anthony Romieu, André Pèlegrin, François Chatelet, Didier Pélaprat, Jacques Barbet, Bernard P. Roques, and Anne Gruaz-Guyon**

Scintigraphy with labeled somatostatin analogues and positron-emission tomography (PET) with ^{18}F-labeled 2-deoxy-2-fluoro-D-glucose (^{18}F-FDG) have greatly improved the diagnosis and staging of numerous tumors with somatostatin-receptor-subtype overexpression or active glucose metabolism, respectively. This entailed the development of numerous radiolabeled peptides that target other receptors overexpressed by tumors that do not accumulate somatostatin analogues or ^{18}F-FDG.[1,2] Proteolytic enzymes expressed on many cancer cells are also potential targets for radiopharmaceuticals. Recently ^{18}F- or ^{11}C-labeled inhibitors of metalloproteinase-2 (MMP-2), which is expressed in a variety of malignant tumors, have been proposed for use in PET.[3,4]

Neutral endopeptidase (NEP, CD10, CALLA, enkephalinase, neprylisin, EC 3.4.24.11) is a membrane-bound zinc metallopeptidase that interrupts cell signaling by degradation

[*] Dr. A. Romieu, Prof. B. P. Roques
INSERM U266
Université Paris V René Descartes
4 avenue de l'Observatoire, 75006 Paris (France)
Fax: (+33) 1-4326-6918
E-mail: roques@pharmacie.univ-paris5.fr

Dr. O. Raguin,[+] Dr. D. Pélaprat,[+] Dr. A. Gruaz-Guyon[+]
EA 3512, Faculté de Médecine Xavier Bichat
BP416, 16 rue Henri Huchard, 75870 Paris cedex 18 (France)
Fax: (+33) 1-4485-6306
E-mail: gruaz@bichat.inserm.fr

Prof. M.-C. Fournié-Zaluski
Pharmaleads
4 avenue de l'Observatoire, 75270 Paris cedex 06 (France)

Dr. A. Pèlegrin[+]
INSERM EMI 0227, Université Montpellier 1
CRLCC Val d'Aurelle
Centre de Recherche en Cancérologie
34298 Montpellier cedex 5 (France)

Prof. F. Chatelet
UFR Saint-Antoine, Université Paris VI Pierre et Marie Curie
27 rue Chaligny, 75012 Paris (France)

Dr. J. Barbet[+]
INSERM U601, Université de Nantes
Institut de Biologie
9 quai Moncousu, 44093 Nantes cedex 01 (France)

[+] These authors are members of the CNRS GDR 2352, Immunociblage des tumeurs, Marseille, France.

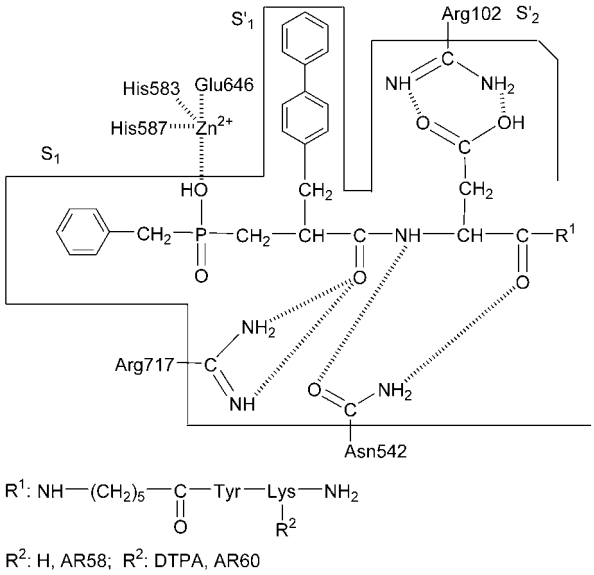
[**] We thank the French Ligue Nationale Contre le Cancer for awarding a research fellowship to O.R.

Supporting Information for this article is available on the WWW under http://www.angewandte.org or from the author.

 © 2005 Wiley-VCH Verlag GmbH & Co. KGaA, Weinheim DOI: 10.1002/anie.200500700

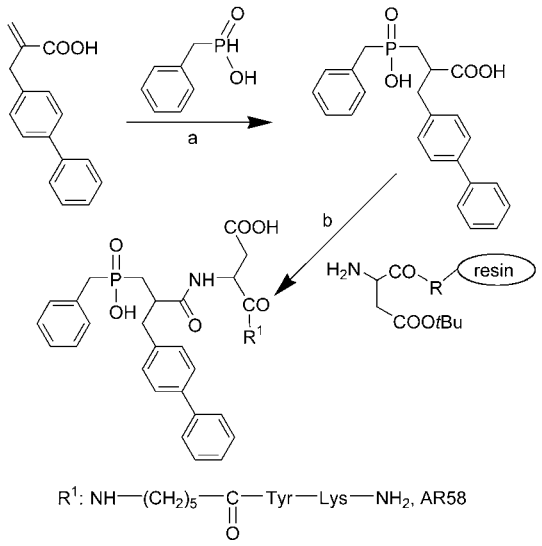
of numerous physiologically active peptides.[5,6] NEP is expressed in a large variety of tissues including the brain, kidney, and lung,[7] but it is also overexpressed in various types of hematological tumors, particularly acute lymphoblastic leukemia[8] and some lymphomas, as well as in solid tumors such as melanoma,[9] colonic, pancreatic, and prostatic adenocarcinomas.[10] Presence, or absence, of NEP expression has been proposed as a prognostic indicator, depending on the tumor type.[11–17] In addition, lack of NEP expression in a prostatic carcinoma may predict decreased androgen sensitivity and a poorer response to hormonal deprivation therapy.[18,19] A noninvasive scintigraphic technique imaging tumor-cell accumulation of a labeled NEP inhibitor could be an interesting diagnosis and/or prognosis tool.

Structure–activity relationship studies of NEP inhibitors,[6] site-directed mutagenesis experiments,[6,20,21] and crystallographic studies of enzyme–inhibitor complexes further elucidated the interactions that stabilize substrates or inhibitors in the NEP active site. Potent inhibition of NEP is obtained with compounds containing a strong zinc ligand as a phosphinic group, a hydrophobic moiety interacting with the S'_1 subsite of the enzyme,[22] hydrogen-bonding donor and acceptor groups for binding with Asn542 and Arg717, and a carboxylate function for Arg102 recognition (Scheme 1).



Scheme 1. Model of NEP active-site recognition by the phosphinic inhibitors AR58 and AR60 proposed from the crystallographic data reported by Oefner et al.[24]

Based on these findings, we designed novel compounds with a biphenylmethyl group and an aspartic acid unit to interact with the S'_1 and S'_2 subsites, respectively, and a benzyl moiety bearing a phosphinyl group as zinc ligand (Scheme 1). A 6-aminohexanoic acid was introduced as a spacer and its carboxylate moiety was coupled to a dipeptide amide Tyr-Lys-NH_2, with the tyrosine residue allowing labeling with iodine isotopes. The chelating agent diethylenetriaminepentaacetic acid (DTPA) was introduced on the ε NH_2 group of the lysine to allow labeling with metal radioisotopes. The peptide part of the molecule was synthesized by solid-phase methods and the phosphinic moiety, prepared independently by liquid-phase synthesis, was incorporated onto the peptidyl resin by a classical coupling step (Scheme 2, see the Supporting Information).



Scheme 2. Synthesis of the NEP inhibitor AR58. a) Bis(trimethylsilyl)-acetamide, 70°C; b) BOP, DIEA, NMP, solid-phase peptide synthesis then cleavage from the MBHA resin and final deprotection of the side chains of the amino acid residues (*tert*-butyl ether: Tyr, *tert*-butyl ester: Asp, *N-tert*-butoxycarbonyl: Lys) by trifluoroacetic acid to form R^1 and the desired product. BOP = 1-benzotriazolyloxytris(dimethylamino)-phosphonium hexafluorophosphate, DIEA = diisopropylethylamine, NMP = *N*-methyl-pyrrolidone, MBHA = 4-methyl-benzhydrylamine.

As the phosphinic moiety was synthesized as a mixture of enantiomers, the inhibitor was obtained as a mixture of two stereoisomers, which were separated by C18 reversed-phase HPLC. The first eluted isomer exhibited the best inhibitory potency: AR58-1 had an inhibition constant of $K_i = (3.6 \pm 0.1) \times 10^{-8}$ M, versus $K_i = (6.7 \pm 0.4) \times 10^{-7}$ M for the second eluted isomer (AR58-2).

High specific activities were obtained by labeling the DTPA-substituted derivative of AR58-1, referred to as AR60, with ^{111}In ((191 ± 20) MBq nmol^{-1}). The AR60 equilibrium binding-affinity constant ($(1.1 \pm 0.1) \times 10^8$ M^{-1}) was determined by competition binding experiments (Figure 1) on a human Burkitt lymphoma cell line (Ramos cells), in which NEP expression was confirmed by fluorescence-activated cell sorter (FACS) analysis (see the Supporting Information). This result suggests that coupling to DTPA does not significantly lower affinity. The number of NEP binding sites per Ramos cell (2.6×10^4–5.7×10^4) was in the same range as that already determined from equilibrium binding experiments of ^{125}I-labeled anti-CD10 antibody (2.1×10^4–7.5×10^4).[23]

A significant specific binding of ^{111}In-labeled AR60 to tissues of the kidneys (mainly the cortical zone), lungs, liver, and small intestine, but not of muscle, heart, stomach (not shown), and colon, was demonstrated by in vitro autoradiography studies (Figure 2), in agreement with NEP expression already described in these organs.[7] This labeled inhibitor

 © 2005 Wiley-VCH Verlag GmbH & Co. KGaA, Weinheim

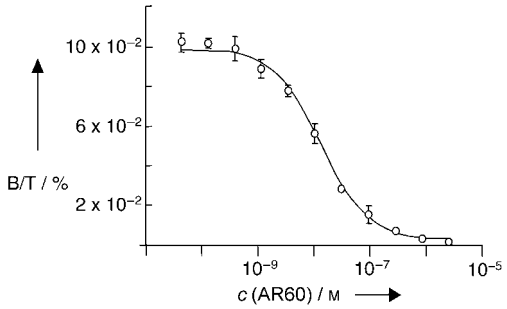


Figure 1. Typical competition binding curve between ^{111}In-labeled and unlabeled AR60. Trace amounts of ^{111}In-labeled AR60 were incubated with Ramos cells in the presence of increasing concentrations of AR60 saturated with nonradioactive indium. (The curve was generated by computer simulation with the Equilibrium Expert software.[25]) The fraction of radioactivity associated to the cells (bound/total (B/T) in %) was counted. The mean values from triplicate determinations are plotted. Bars give standard deviation values except those that were smaller than the points as plotted.

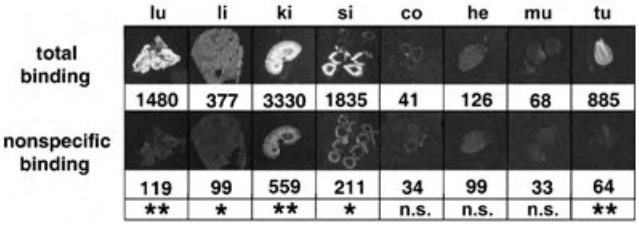


Figure 2. Autoradiogram of ^{111}In-AR60 binding to tissue sections (lu = lungs, li = liver, sp = spleen, ki = kidneys, si = small intestine, co = colon, he = heart, mu = muscle) from healthy BALB/c mice and intravenous grafts of Ramos cells to SCID mice (tu = tumor). Top: total binding. Bottom: nonspecific binding evaluated on adjacent sections in the presence of an excess (10^{-6} M) of AR58-1. Binding quantification, expressed in arbitrary activity units per surface unit, is indicated on each image. The Student t test was used to evaluate the significance of the results (*: statistical probability value $p < 0.05$; **: $p < 0.01$; n.s.: not significant).

bound specifically to sections of Ramos cell grafts to SCID mice.

We then investigated the in vivo biodistribution of ^{111}In-AR60 three and six hours after intravenous injection to healthy BALB/c mice (Figure 3). A fast blood clearance of ^{111}In-AR60 was observed, as assessed by the low residual blood radioactivity six hours after injection. Activity uptake was observed primarily in the kidneys and to a lesser extent in the lungs, liver, and colon. Since about 92% of the colon activity was associated with the stools, activity uptake in this organ was related to biliary excretion of ^{111}In-AR60. A low activity accumulation of < 1% of the injected dose per gram was observed in other organs six hours after injection. ^{111}In-AR60 stability in vivo was high since more than 70% was recovered intact in the serum 1 h after injection.

Coinjection of ^{111}In-AR60 (10 pmol) and a large excess of unlabeled Thiorphan (790 nmol), a specific NEP inhibitor, considerably reduced organ activity in the lungs, adrenal tissues, and kidneys, a result indicating uptake specificity in these organs (mean D values ± (standard error of the mean; s.e.m.) in the absence versus in the presence of thiorphan as

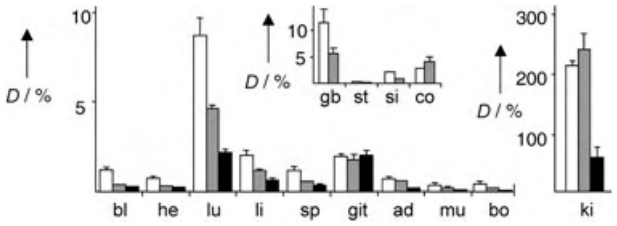


Figure 3. Biodistribution studies of ^{111}In-AR60 in healthy BALB/c mice. Mice were sacrificed, after an intravenous injection of only ^{111}In-AR60 (10 pmol in 150 μL of phosphate-buffered saline (PBS)) at 3 h (white bars) or 6 h (gray bars) or at 6 h in the presence of excess thiorphan (790 nmol, black bars). Tissue radioactivity is expressed as the percentage of injected dose per g of tissue (D, mean value ± standard error of the mean (s.e.m.), number of animals: 5 at 3 h, 4 at 6 h). Injected doses were corrected by subtraction of noninjected and subcutaneously injected material. Additional abbreviations to Figure 2: bl = blood, sp = spleen, git = gastrointestinal tract, ad = adrenal tissues, bo = bone, gb = gall bladder, st = stomach.

well as the p values: lungs: 4.60 ± 0.93 versus 2.17 ± 0.31, $p < 0.05$; adrenal tissues: 0.60 ± 0.08 versus 0.21 ± 0.03, $p < 0.01$; kidneys: 234 ± 56 versus 56 ± 33, $p < 0.01$;). Liver labeling was low and no significant difference was observed in the presence of thiorphan. These results are consistent with the rapid decrease of liver activity and the absence of gut activity through uptake of a tritiated NEP inhibitor, facts which suggest that several tissues are inaccessible to intravenously injected inhibitors thanks to the presence of functional barriers.[7]

^{111}In-AR60 uptake in tumors evaluated in SCID mice intravenously grafted with Ramos human Burkitt lymphoma cells was high ((10.3 ± 2.4) D, with a range of 21.8–3.5 D, 4.5 h after injection). Since in this model disseminated tumor-cell grafts occur in different organs, normal tissue uptakes were evaluated in healthy SCID mice. Tumor to normal tissue uptake ratios were high for the brain (144 ± 30, not shown), heart, stomach, blood, adrenal tissues, liver, spleen, and small intestine. Lower targeting contrasts were obtained for other organs, with values of around 3 for the colon, muscle, and bone, 1.4 ± 0.3 for the lungs, and 0.06 ± 0.01 for the kidneys (Figure 4).

Since the tumor to normal tissue uptake ratio is the key for isotopic tumor imaging, ^{111}In-AR60 should provide good contrast images except for tumors located on or near organs with high NEP expression, such as the kidneys and lungs. In

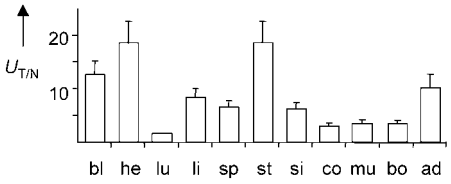


Figure 4. Tumor to normal tissue uptake ratios $U_{T/N}$ of ^{111}In-AR60 in SCID mice intravenously grafted with Ramos cells. Four animals were given ^{111}In-AR60 (10 pmol in 150 μL of PBS) by intravenous injection. Blood, organs, and tumor masses were collected and counted for radioactivity 4.5 h later. Tumor involvement of macroscopically suspect specimens was confirmed by histological analysis. Injected doses were corrected for losses as described in the legend to Figure 3. Since the graft is disseminated, results are expressed as the ratio between tumor uptake (10 samples) and mean organ uptake in nongrafted mice (mean value of $U_{T/N}$ ± (s.e.m.)).

 © 2005 Wiley-VCH Verlag GmbH & Co. KGaA, Weinheim

some organs of tumor-bearing mice, with no macroscopic tumor involvement, activity uptake was greater than the mean uptake of corresponding organs of nongrafted mice. Histological analysis revealed tumor involvement in four of these samples, two brain samples with values of 0.78 and 0.57 *D* versus (0.07 ± 0.03) *D* in ungrafted mice and two adrenal tissue samples with values of 1.91 and 9.33 *D* versus (1.07 ± 0.39) *D* in ungrafted mice. These results further demonstrated the specificity of tumor uptake of ^{111}In-AR60.

In conclusion, the fast plasma clearance, the elevated tumor labeling, and the low nonspecific uptake of ^{111}In-labeled NEP ligand AR60 in normal organs provide high uptake ratios between tumor and normal organs except for the kidneys and lungs, which express high NEP levels. Noninvasive scintigraphic imaging of NEP expression with this compound may be a potential tool for the diagnosis and/or prognosis of different tumor types.

Received: February 24, 2005
Published online: May 31, 2005

Keywords: imaging agents · metalloenzymes · peptidomimetics · radiopharmaceuticals · tumor targeting

[1] D. Kwekkeboom, E. P. Krenning, M. de Jong, *J. Nucl. Med.* **2000**, *41*, 1704.
[2] M. De Jong, D. Kwekkeboom, R. Valkema, E. P. Krenning, *Eur. J. Nucl. Med. Mol. Imaging* **2003**, *30*, 463.
[3] S. Furumoto, K. Takashima, K. Kubota, T. Ido, R. Iwata, H. Fukuda, *Nucl. Med. Biol.* **2003**, *30*, 119.
[4] Q. H. Zheng, X. Fei, T. R. DeGrado, J. Q. Wang, K. L. Stone, T. D. Martinez, D. J. Gay, W. L. Baity, B. H. Mock, B. E. Glick-Wilson, M. L. Sullivan, K. D. Miller, G. W. Sledge, G. D. Hutchins, *Nucl. Med. Biol.* **2003**, *30*, 753.
[5] B. Malfroy, J. P. Swerts, A. Guyon, B. P. Roques, J. C. Schwartz, *Nature* **1978**, *276*, 523.
[6] B. P. Roques, F. Noble, V. Dauge, M. C. Fournie-Zaluski, A. Beaumont, *Pharmacol. Rev.* **1993**, *45*, 87.
[7] N. Sales, I. Dutriez, B. Maziere, M. Ottaviani, B. P. Roques, *Regul. Pept.* **1991**, *33*, 209.
[8] M. A. Shipp, J. Vijayaraghavan, E. V. Schmidt, E. L. Masteller, L. D'Adamio, L. B. Hersh, E. L. Reinherz, *Proc. Natl. Acad. Sci. USA* **1989**, *86*, 297.
[9] S. Carrel, L. Zografos, M. Schreyer, D. Rimoldi, *Melanoma Res.* **1993**, *3*, 319.
[10] P. Chu, D. A. Arber, *Am. J. Clin. Pathol.* **2000**, *113*, 374.
[11] M. Ponzoni, A. J. Ferreri, G. Pruneri, B. Pozzi, S. Dell'Oro, A. Pigni, G. Pinotti, E. Villa, M. Freschi, G. Viale, C. Capella, *Int. J. Cancer* **2003**, *106*, 288.
[12] T. Tokuhara, M. Adachi, H. Hashida, H. Ishida, T. Taki, M. Higashiyama, K. Kodama, S. Tachibana, S. Sasaki, M. Miyake, *Jpn. J. Thorac. Cardiovasc. Surg.* **2001**, *49*, 489.
[13] K. Iwaya, H. Ogawa, M. Izumi, M. Kuroda, K. Mukai, *Virchows Arch.* **2002**, *440*, 589.
[14] S. N. Gaidukova, L. A. Sivak, *Lik. Sprava* **2002**, 47.
[15] J. H. Go, W. I. Yang, H. J. Ree, *Arch. Pathol. Lab. Med.* **2002**, *126*, 956.
[16] P. Uherova, C. W. Ross, B. Schnitzer, T. P. Singleton, W. G. Finn, *Am. J. Clin. Pathol.* **2001**, *115*, 582.
[17] J. P. Vannier, M. C. Bene, G. C. Faure, C. Bastard, R. Garand, A. Bernard, *Br. J. Haematol.* **1989**, *72*, 156.
[18] S. J. Freedland, D. B. Seligson, A. Y. Liu, A. J. Pantuck, S. H. Paik, S. Horvath, J. A. Wieder, A. Zisman, D. Nguyen, C. L. Tso, A. V. Palotie, A. S. Belldegrun, *Prostate* **2003**, *55*, 71.
[19] C. N. Papandreou, B. Usmani, Y. Geng, T. Bogenrieder, R. Freeman, S. Wilk, C. L. Finstad, V. E. Reuter, C. T. Powell, D. Scheinberg, C. Magill, H. I. Scher, A. P. Albino, D. M. Nanus, *Nat. Med.* **1998**, *4*, 50.
[20] N. Dion, P. Cohen, P. Crine, G. Boileau, *FEBS Lett.* **1997**, *411*, 140.
[21] A. Devault, V. Sales, C. Nault, A. Beaumont, B. Roques, P. Crine, G. Boileau, *FEBS Lett.* **1988**, *231*, 54.
[22] I. Schechter, A. Berger, *Biochem. Biophys. Res. Commun.* **1967**, *27*, 157.
[23] M. Hillairet de Boisferon, O. Raguin, M. Dussaillant, W. Rostene, J. Barbet, A. Gruaz-Guyon, *Bioconjugate Chem.* **2000**, *11*, 452.
[24] C. Oefner, B. P. Roques, M. C. Fournie-Zaluski, G. E. Dale, *Acta Crystallogr. D Biol. Crystallogr.* **2004**, *60*, 392.
[25] O. Raguin, A. Gruaz-Guyon, J. Barbet, *Anal. Biochem.* **2002**, *310*, 1.

 © 2005 Wiley-VCH Verlag GmbH & Co. KGaA, Weinheim

Drug Design

Polymer Therapeutics Designed for a Combination Therapy of Hormone-Dependent Cancer**

María J. Vicent, Francesca Greco, Robert I. Nicholson, Alison Paul, Peter C Griffiths, and Ruth Duncan**

Over the last decade, polymer therapeutics have emerged as first-generation nanomedicines.[1] The term polymer therapeutics was coined to include water-soluble polymers that are polymeric drugs,[2] hybrid polymer–drug[1,3] and polymer–protein conjugates,[4] polymeric micelles that contain cova-

[*] Dr. M. J. Vicent,[+] F. Greco, Prof. Dr. R. Duncan
Centre for Polymer Therapeutics
Welsh School of Pharmacy, Cardiff University
King Edward VII Avenue, Redwood Building, CF10 3XF Cardiff (UK)
Fax: (+44) 292-087-4536
E-mail: mjvicent@ochoa.fib.es

Prof. Dr. R. I. Nicholson
Tenovus Centre for Cancer Research
Welsh School of Pharmacy, Cardiff University
King Edward VII Avenue, Redwood Building, CF10 3XF Cardiff (UK)

Dr. A. Paul, Dr. P. C. Griffiths
School of Chemistry, Cardiff University
Cardiff CF10 3TB (UK)

[+] Present address:
Centro de Investigación Principe Felipe, FVIB
Medicinal Chemistry Unit
Av. Autopista del Saler 16, E-46013 Valencia (Spain)

[**] We thank the Marie Curie Individual Fellowship, Contract No. HPMF-CT-2002-01555 (M.J.V.), the Tenovus Research Centre, and the Centre for Polymer Therapeutics, Cardiff University (F.G.) for financial support. We also thank Richard K. Heenan and Stephen M. King from the ISIS facility, Rutherford Appleton Laboratories, Chilton, Didcot, Oxforshire (UK) for their help in the SANS data interpretation and the CCLRC and EPSRC for allocation of neutron-beam time.

Supporting information for this article is available on the WWW under http://www.angewandte.org or from the author.

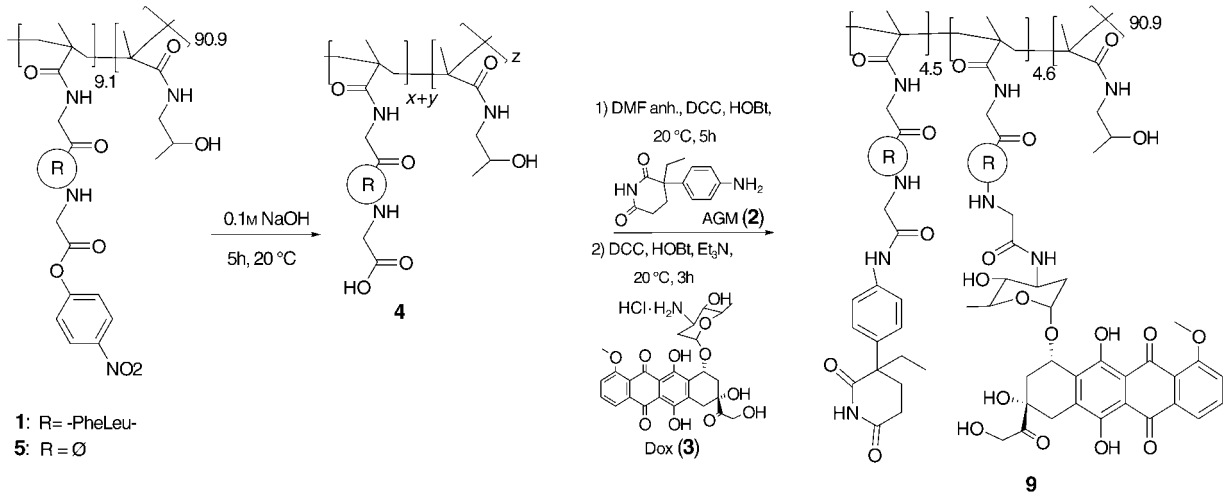
 DOI: 10.1002/anie.200462960 © 2005 Wiley-VCH Verlag GmbH & Co. KGaA, Weinheim

lently bound drug,[5] and multicomponent polyplexes used as nonviral vectors[6] to deliver genes and proteins into the cytosolic compartment of the cell. Of particular relevance to this study are those polymer–drug conjugates now finding acceptance as a new class of antitumor agents.[1,3,6] Polymer conjugates have distinct advantages over conventional chemotherapy. These include 1) passive tumor targeting owing to the enhanced permeability and retention (EPR) effect, a phenomenon that arises from the hyperpermeability of angiogenic tumor blood vessels,[7] 2) lower toxicity of bound drug,[8] and 3) after cellular uptake by the endocytic route, the potential to bypass mechanisms of drug resistance, including p-glycoprotein-mediated multidrug resistance (MDR).[9] So far, only conjugates derived from polyethyleneglycol (PEG),[10] polyglutamic acid (PGA),[11] polysaccharides,[12] and *N*-(2-hydroxypropyl)methacrylamide (HPMA) copolymer conjugates[13] have progressed to clinical trials. The HPMA copolymer–doxorubicin (Dox) conjugate PK1 (also named FCE28068) was the first synthetic polymer conjugate to enter Phase I trials in 1994.[8] Since then, HPMA copolymer conjugates with established chemotherapy drugs (such as taxol, platinates, or camptothecins)[6,13] and two gamma-camera imaging agents derived from HPMA copolymer have also progressed to clinical testing. Conjugates are now being synthesized to contain experimental drugs[14] and drugs directed towards new therapeutic targets (e.g. antiangiogenic HPMA copolymer–TNP470[15]). Further developments in this field include chemotherapy with two-step polymer–drug combinations (e.g. polymer-directed enzyme prodrug therapy (PDEPT)[16]).

The aim of this study was to design a polymer conjugate that would for the first time combine endocrine therapy and chemotherapy with the hope of eliciting improved antitumor activity in breast cancer. Arrival of the selective oestrogen receptor antagonist tamoxifen led to a 28% reduction in mortality of breast cancer patients at 5 years.[17] Even so, the prognosis for patients with metastatic breast cancer is still poor, the survival rate at 5 years being $<20\%$. The mixed antagonist/agonist activity of tamoxifen and the acquired resistance that can develop over time limit its therapeutic potential.[18] To circumvent this problem, there has been growing interest in the use of aromatase inhibitors. They prevent estrogen biosynthesis by inhibiting P450 aromatase present in normal tissue and in breast-cancer cells of postmenopausal women (77% of the new cases of breast cancer diagnosed each year).[19] Recent clinical trials in these patients showed that the aromatase inhibitors letrozole and anastrozole were more effective in treating estrogen receptor positive breast cancer than tamoxifen.[20]

In our case, we hypothesized that the combination of endocrine therapy and chemotherapy by simultaneous attachment to the same polymer would bring significant advantages. The combination could be administered as a single dose; benefits would be the manufacture of a single conjugate and improved patient compliance. After EPR-mediated targeting, the arrival of both pendant drugs within the tumor cells at the same time is guaranteed. It also provides the opportunity to tailor polymer–drug linkers to impart different rates of drug release for each compound, thus allowing agents to act synergistically. As HPMA copolymer–Dox has already shown activity in chemotherapy refractory breast-cancer patients[8] and this polymer has proven clinical safety, HPMA was chosen as the polymeric carrier (**1** and **5**), and the anthracycline antibiotic Dox (**3**) (widely used as a first-line treatment for breast cancer) was selected as the model chemotherapeutic. The first-generation aromatase inhibitor, aminoglutethimide (AGM; **2**), was chosen as the endocrine model.

A library of conjugates **6**–**11** was synthesized to contain Dox, AGM, or both drugs attached to the same polymeric chain (Scheme 1, Table 1, Supporting Information). HPMA copolymer intermediates ($M_w \approx 20\,000$–$25\,000\ g\,mol^{-1}$; $M_w/M_n = 1.3$–1.5) were used that contained either the tetrapeptide linker Gly–Phe–Leu–Gly (known to be cleaved by lysosomal thiol-dependent protease cathepsin B to release Dox)[6,13] or a Gly–Gly linker (known to be nondegradable and as such to provide a reference control for biological experiments). First, conjugates were prepared by aminolysis of polymeric intermediates in which the C-terminus of the



Scheme 1. Synthesis of HPMA copolymer-AGM-Dox conjugate (**9′**) using DCC coupling reactions. DMF = *N*,*N*-dimethylformamide, DCC = 1,3-dicyclohexylcarbodiimide, HOBt = 1-hydroxybenzotriazole.

 © 2005 Wiley-VCH Verlag GmbH & Co. KGaA, Weinheim

Table 1: Characteristics of the HPMA copolymer conjugates.

	Conjugate	Side-chain content [mol%]	Total drug [% w/w][a]		Free drug [% total drug][a]		Rg (±0.3) [nm][d]
			AGM	DOX	AGM	DOX	
6[b]	HPMA copolymer–GFLG–AGM	5	6.2	–	0.75	–	ND
6′[c]	HPMA copolymer–GFLG–AGM	5	6.0	–	0.58	–	7.9
7[b]	HPMA copolymer–GFLG–AGM	10	5.1	–	0.25	–	ND
7′[c]	HPMA copolymer–GFLG–AGM	10	10.4	–	0.59	–	16.5
8[b]	HPMA copolymer–GG–AGM	5	3.4	–	1.17	–	ND
8′[c]	HPMA copolymer–GG–AGM	5	5.4	–	0.61	–	4.1
9[b]	HPMA copolymer–GFLG–AGM–Dox	10	3.1	4.2	0.60	0.10	ND
9′[c]	HPMA copolymer–GFLG–AGM-Dox	10	5.4	7.2	0.73	0.23	12.8
10[b]	HPMA copolymer–GFLG–Dox	5	–	6.6	–	0.39	7.7
11[b]	HPMA copolymer–GFLG–Dox	10	–	14.1	–	0.78	12.4

[a] Total drug and free drug content determined by HPLC. Free drug content expressed as a percentage of total drug. [b] Conjugates synthesized by aminolysis (see supporting information). [c] Conjugates synthesized by DCC coupling (see Supporting Information). [d] Determined by SANS. Fit to a Gaussian coil with Schultz polydispersity. Polydispersity considered 1.3 in all cases. ND = not determined.

peptide side-chains were esterified with *p*-nitrophenol.[21] The lower reactivity of the aromatic amine of AGM, however, favored the use of DCC-mediated coupling. The improved yield of conjugation was particularly noticeable when AGM was bound to the polymeric precursor containing pendant side chains (10 mol%) (Table 1). FTIR and NMR spectroscopy confirmed the identity of the product, and NOE measurements verified the covalent binding of AGM (see Supporting Information). These observations were consistent with previous NOESY and TOCSY experiments, which established the structure of HPMA copolymer–Dox.[22]

Accurate characterization of the bioactive content of any polymer–drug conjugate destined for biological or clinical testing is essential. It is well known that the extinction coefficient of a bound drug can change significantly upon conjugation.[23] In this instance, measurement of the total and free Dox was straightforward, and a validated HPLC method was used.[24] For example, the Dox content of conjugate **9′** was 7.2% w/w (free Dox < 0.8% w/w total drug) (Table 1). The AGM content was more difficult to determine. Values were obtained either by UV/Vis spectroscopy with an *N*-Gly-AGM (**13**) derivative as standard or by an indirect HPLC method established to quantify residual AGM left after reaction (Table 1 and Supporting Information). Overall, the AGM content of the conjugates was in the range 3.1–10.4% w/w (free AGM content < 1.2% w/w total AGM) and in conjugate **9′** it was 5.4% w/w (Table 1). The molecular weight of the conjugates was in the range $M_w \approx 25\,000$–$30\,000\ g\,mol^{-1}$.

It has been postulated that polymer–drug conjugates exist in solution as unimolecular micelles and that conformation is influenced by drug loading. At present, however, there is almost no direct physical evidence to support this hypothesis.[25] We have recently demonstrated the value of small-angle neutron scattering (SANS) in providing insight into the solution conformation of polymer therapeutics, particularly in relation to the pH-triggered conformational change of endosomolytic polymers.[26] SANS was used in this case for the first time to define conjugate structure in solution (Table 1 and Supporting Information). The Gaussian coil model for polymer conformation showed the best fit to the raw scattering data. Whereas HPMA copolymer–GFLG–Dox (**10**) and HPMA copolymer–GFLG–AGM (5 mol%) (**6′**) conjugates prepared from the same polymeric intermediate had similar Rg (radius of gyration) values (7.7 and 7.9 nm, respectively; truly nano-sized medicines), an increase in the side-chain content to 10 mol% led to an increase in Rg to 16.5 nm for the AGM conjugate **7′**, but only to 12.5 nm for the Dox conjugate (**11**). Interestingly the HPMA copolymer–GFLG–AGM–Dox conjugate **9′** also displayed an Rg value of 12.8 nm. This might be explained by the tendency of Dox to display π–π stacking, thus leading to the formation of more-compact unimolecular micelles. It is clear that polymer–drug conjugate conformation is affected by both the drug loading and chemical nature of the drug.

Effective functioning of polymer–drug conjugates relies on 1) the stability of the polymer–drug linker in the circulatory system and, after arrival in the tumor tissue and cellular uptake by endocytosis, 2) lysosomal enzyme cleavage of the linker to release the active drug. All the HPMA copolymer conjugates were completely stable in buffer alone, as was the HPMA copolymer–GG–AGM (**8′**) in the presence of isolated rat liver lysosomal enzymes (Figure 1c and Supporting Information). However, in the presence of lysosomal enzymes, Dox and AGM were released from conjugates containing the Gly–Phe–Leu–Gly linker. The drug-release profile displayed marked differences depending on conjugate composition. For conjugates **10** and **11**, Dox release began immediately after addition of enzyme (Figure 1b) and was linear with time; it was apparent that the lower the Dox loading (cf. **10** and **11**) the greater the drug release after 5 h (see Supporting Information). This is in agreement with the solution conformation predicted by SANS (Table 1). Enzyme accessibility would be limited by a more compact coil structure. AGM release (conjugates **6** and **7**) also showed dependence on drug loading with a lower initial release for the highest loading (**7**) (Figure 1a). After 30 min, however, AGM liberation from **7** accelerated and release from **6** started to plateau (see supplementary information for comparison at 5 h).

When incubated with lysosomal enzymes, the conjugate containing both AGM and Dox as the combination (**9′**)

 © 2005 Wiley-VCH Verlag GmbH & Co. KGaA, Weinheim

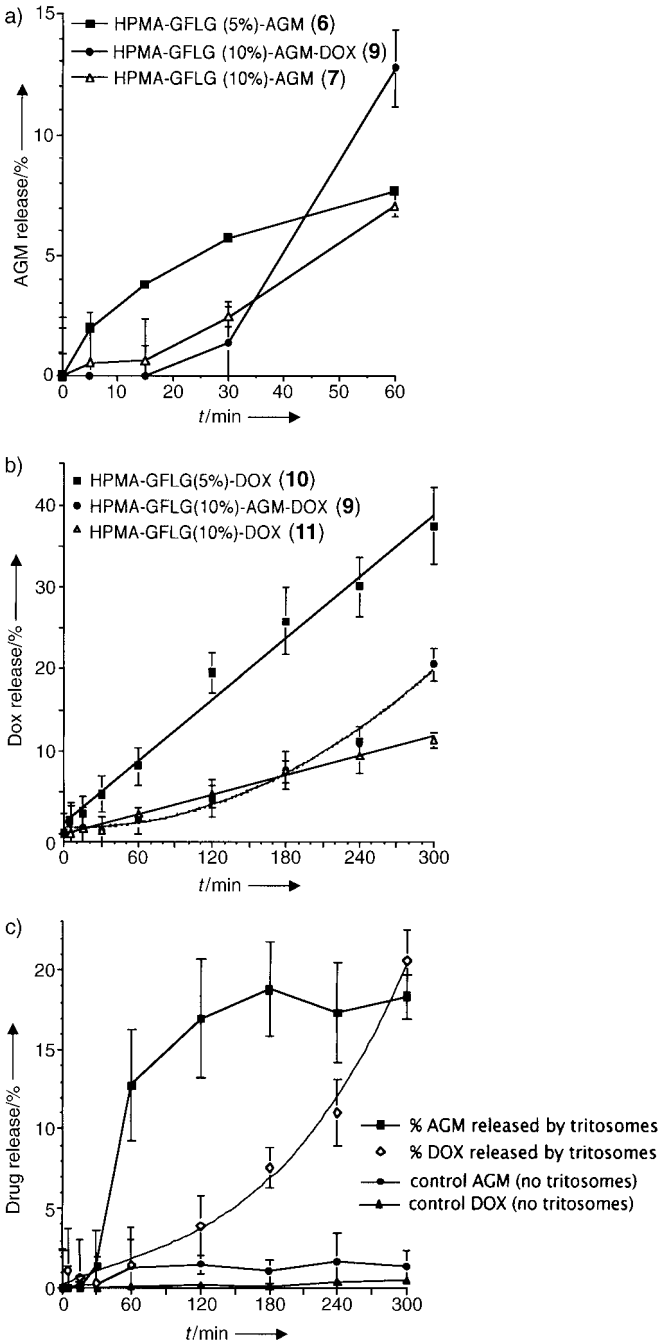


Figure 1. Liberation of Dox or AGM from HPMA copolymer conjugates during incubation with rat liver lysosomal enzymes (tritosomes). Release of a) AGM, b) Dox, and c) Dox and AGM from the HPMA copolymer–GFLG–AGM–Dox conjugate (**9′**). In all cases, drug release is expressed as a percentage of the total drug bound, and data represent the mean ± SEM ($n=4$). In specific cases, the release of drug in the absence of enzymes (control) is also shown.

displayed different profiles of drug liberation (Figure 1c) in comparison with that seen for the single-drug-pendant conjugates (at both 5 and 10 mol % loading). Both Dox and AGM release show a marked lag phase with little release over the first 30 min. However, after this time, AGM release was enhanced relative to **6** and **7**, and the Dox release rate was initially slower but then returned to that seen for **10**. The dynamic and complex geometry of this unimolecular micelle structure determines enzyme access leading to these complex release kinetics. To investigate how the release profile would translate into cytotoxicity, a human estrogen-dependent breast-cancer cell line MCF-7 and the aromatase-transfected derivative MCF-7ca were used (Figure 2 and Supporting Information). As expected, as a result of its slow rate of cellular uptake by endocytosis and the relatively prolonged duration needed for drug liberation, HPMA copolymer–GFLG–Dox (**10**) was much less active than free Dox (**3**). For example, their IC_{50} values against the MCF-7 cell line were >150 μM and 0.74 μM Dox-equivalents, respectively. Neither the HPMA copolymer–GFLG–AGM (**6′**), nor individual mixtures of drug conjugates bearing AGM (**6′**) or Dox (**10**) caused an elevation in cytotoxicity in either cell line MCF-7 or MCF-7ca (see Supporting Information).

In contrast, when AGM and DOX were covalently linked to the same polymeric backbone, that is, in conjugate **9′**, the in vitro cytotoxicity was significantly greater than seen for **10**, **3**, or **6′** against MCF-7 cells. The enhanced cytotoxicity of **9′** was even more evident for the aromatase expressing MCF-7ca cells (see Figure 2 and Supporting Information). The IC_{50} values obtained for MCF-7ca cells incubated with **3**, **6′**, or **9′** were 5238 μM, >1377 μM, and 40.9 μM AGM-equivalents, respectively. Conjugate **9′** displayed approximately tenfold enhancement in cytoxicity in the aromatase cell line, irrespective of whether the data are expressed in terms of Dox- or AGM-equivalents Although it is necessary to understand the precise molecular mechanism of action of these novel conjugates better, it has been reported that aromatase inhibitors can also promote apoptosis, so they may potentiate Dox cytotoxicity in this way.[19]

To conclude, the HPMA copolymer–GFLG–AGM–Dox conjugate (**9**) is the first polymer therapeutic to combine chemotherapy and endocrine therapy. The fact that AGM and Dox can act synergistically to produced markedly enhanced cytotoxicity in vitro relative to that of the HPMA copolymer–GFLG–Dox conjugate (**10**) (PK1), which has already shown activity in breast-cancer patients clinically, underlines the potential importance of this polymer–drug combination. It should be emphasized that mixtures of polymer conjugates containing only AGM or only Dox did not show synergistic benefit. The studies reported confirm cellular uptake of conjugate by endocytosis (verified by flow cytometry as shown in Figure 2b and in the Supporting Information), and also demonstrate the requirement of lysosomal thiol-dependent protease degradation of the polymer–drug linker to liberate drug and thus promote cytotoxicity. All the components (HPMA copolymers, Dox and AGM) are well established clinically, so further preclinical studies are warranted to establish the antitumor potential of this novel anticancer strategy in vivo. The observation that HPMA copolymer conjugates displayed lower hemolytic activity (10 % release at 1 h; $p<0.001$) than Dox (**3**) (92 % hemoglobin release at 1 h) (see Supporting Information) establishes the suitability for intravenous administration. Tailoring of the linker structure and drug loading within this novel nano-sized medicine (Rg in solution of 12.8 nm) may further optimize the drug-release

 © 2005 Wiley-VCH Verlag GmbH & Co. KGaA, Weinheim

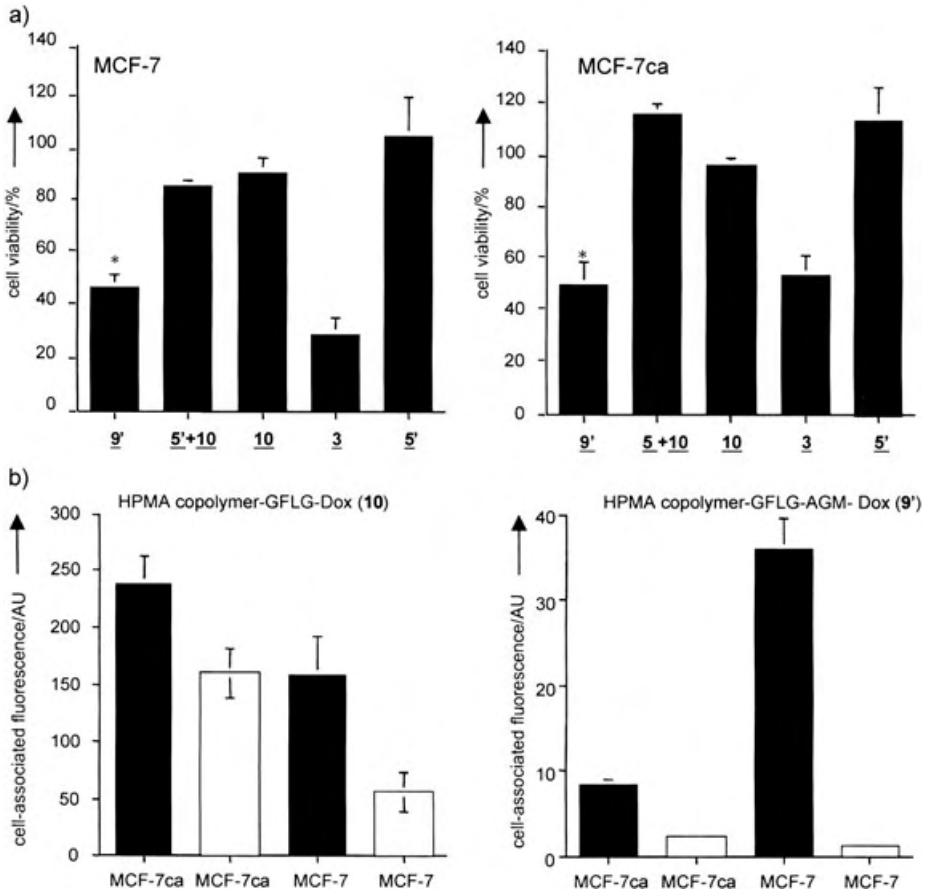


Figure 2. a) Cytotoxicity of Dox and HPMA copolymer conjugates against MCF-7 and MCF-7ca cell lines at the IC_{50} value (0.08 mg mL^{-1} and 0.009 mg mL^{-1} Dox-equivalents, respectively) in the presence of 10^{-9} M estradiol. Measured by MTT assay after 72 h incubation. Data are expressed as mean ± SEM ($n = 3$). The asterisk* indicates statistical significance ($P < 0.05$). b) Cell-associated fluorescence at 37 °C (total association, ■) and 4 °C (external binding, □) of PK1 and HPMA copolymer–AGM–Dox conjugate in MCF-7 and MCF-7ca cells after 1 h. Data are expressed as mean ± SEM ($n = 6$).

profile and cytotoxicity. Ongoing studies to define the precise molecular mechanisms of conjugate action will be used to steer the choice of chemistry used to achieve optimal release kinetics.

Received: December 16, 2004
Revised: March 15, 2005
Published online: May 24, 2005

Keywords: antitumor agents · drug delivery · drug design · polymers · tumor targeting

[1] R. Duncan, *Nat. Rev. Drug Discovery* **2003**, *2*, 347 – 360.
[2] W. H. Mandeville, D. I. Goldberg, *Curr. Pharm. Des.* **1997**, *3*, 15 – 28.
[3] a) H. Ringsdorf, *J. Polym. Sci. Polym. Symp.* **1975**, *51*, 35 – 53; b) R. Duncan, J. Kopecek, *Adv. Polym. Sci.* **1984**, 57, 51 – 101.
[4] J. M. Harris, R. B. Chess, *Nat. Rev. Drug Discovery* **2003**, *2*, 214 – 221.
[5] a) M. Yokoyama, M. Miyauchi, N. Yamada, T. Okano, Y. Sakurai, K. Kataoka, S. Inoue, *J. Controlled Release* **1990**, *11*, 269 – 278; b) Y. Bae, S. Fukushima, A. Harada, K. Kataoka, *Angew. Chem.* **2003**, *115*, 4788 – 4791; *Angew. Chem. Int. Ed.* **2003**, *42*, 4641 – 4643.
[6] a) R. Duncan, *Handbook of Anticancer Drug Development* (Eds.: D. Budman, H. Calvert, E. Rowinsky), Lippincott Williams & Wilkins, Baltimore, **2003**, pp. 239 – 260; b) J. W. Singer, B. Baker, P. de Vries, A. Kumar, S. Shaffer, E. Vawter, *Adv. Exp. Med. Biol.* **2003**, *519*, 81 – 99; c) J. W. Singer, B. Baker, P. de Vries, A. Kumar, S. Shaffer, E. Vawter, M. Bolton, P. Garzone, *Polymer Drugs in the Clinical Stage, Advantages and Prospects* (Eds.: H. Maeda, A. Kabanov, K. Kataoka, T. Okano), Kluwer/Plenum, New York, **2003**, pp. 81 – 95.
[7] a) Y. Matsamura, H. Maeda, *Cancer Res.* **1986**, *46*, 6387 – 6392; b) L. W. Seymour, K. Ulbrich, P. S. Steyger, M. Brerenton, V. Subr, J. Strohalm, R. Duncan, *Br. J. Cancer* **1994**, *70*, 636 – 641; c) F. M. Muggia, *Clin. Cancer Res.* **1999**, *5*, 7 – 8; d) H. Maeda, J. Wu, T. Sawa, Y. Matsumura, K. Hori, *J. Controlled Release* **2000**, *65*, 271 – 284.
[8] P. A. Vasey, S. B. Kaye, R. Morrison, C. Twelves, P. Wilson, R. Duncan, A. H. Thomson, L. S. Murray, T. E. Hilditch, T. Murray, S. Burtles, D. Fraier, E. Frigerio, J. Cassidy, *Clin. Cancer Res.* **1999**, *5*, 83 – 94.
[9] T. Minko, P. Kopeckova, V. Pozharov, J. Kopecek, *J. Controlled Release* **1998**, *54*, 223 – 233.
[10] R. B. Greenwald, Y. H. Chloe, McGuire, C. D. Conover, *Adv. Drug Delivery Rev.* **2003**, *55*, 217 – 250.
[11] C. Li, D-F. Yu, R. A. Newman, F. Cabral, C. Stephens, N. R. Hunter, L. Milas, S. Wallace, *Cancer Res.* **1998**, *58*, 2404 – 2409.
[12] D. Hreczuk-Hirst, D. Chicco, L. German, R. Duncan, *Int. J. Pharm.* **2001**, *230*, 57 – 66.
[13] R. Duncan in *Polymeric Drug Delivery Systems* (Ed.: G. S. Kwon), Marcel Dekker, New York, **2005**, pp. 1 – 92.
[14] a) F. Searle, S. Gac-Breton, R. Keane, S. Dimitrijevic, S. Brocchini, R. Duncan, *Bioconjugate Chem.* **2001**, *12*, 711 – 718; b) Y. Kasuya, Z-R. Lu, P. Kopeckova, S. E. Tabibi, J. Kopecek, *Pharm. Res.* **2002**, *19*, 115 – 123; c) L. Varticovski, Z. R. Lu, K. Mitchell, I. De Aos, J. Kopecek, *J. Controlled Release* **2001**, *74*, 275 – 281; d) M. J. Vicent, S. Manzanaro, J. A. De la Fuente, R. Duncan, *J. Drug Targeting* **2004**, *12*, 503 – 515.
[15] R. Satchi-Fainaro, M. Puder, J. W. Davies, H. T. Tran, D. A. Sampson, A. K. Greene, G. Corfas, J. Folkman, *Nat. Med.* **2004**, *10*, 225 – 261.
[16] a) R. Satchi-Fainaro, T. A. Connors, R. Duncan, *Br. J. Cancer* **2001**, *85*, 1070 – 1076; b) R. Satchi-Fainaro, H. Hailu, J. W. Davies, C. Summerford, R. Duncan, *Bioconjugate Chem.* **2003**, *14*, 797 – 804.
[17] V. C. Jordan, *Nat. Rev. Drug Discovery* **2003**, *2*, 206 – 213; Early Breast Cancer Trialist Group: *Lancet* **998**, *351*, 1451 – 1467.

 © 2005 Wiley-VCH Verlag GmbH & Co. KGaA, Weinheim

[18] a) M. P. Coleman, *Breast Cancer Res.* **1999**, *1*, 22–26; b) F. Cummings, *Clin. Ther.* **2002**, *24*, Suppl. C: C3–25.
[19] S. R. D. Johnston, M. Dowsett, *Nat. Rev. Cancer* **2003**, *3*, 821–831.
[20] P. E. Goss, K. Strasser, *Drugs* **2002**, 62, 957–966.
[21] a) P. Rejmanova, J. Labsky, J. Kopecek, *Makromol. Chem.* **1977**, *178*, 2159–2168; b) J. Kopecek, P. Rejmavova, J. Strohalm, K. Ulbrich, B. Rihova, V. Chytry, R. Duncan, J. B. Lloyd, British Patent Appl. 8500209 (4.1.85), **1985**.
[22] V. Pincioli, V. Rizzo, F. Angelucci, M. Tato, A. Vigevani, *Magn. Reson. Chem.* **1997**, *35*, 2–8.
[23] E. Configliacchi, G. Razzano, V. Rizzo, A. Vigevani, *J. Pharm. Biomed. Anal.* **1996**, *15*, 123–129.
[24] L. W. Seymour, K. Ulbrich, S. R. Wedge, I. C. Hume, J. Strohalm, R. Duncan, *Br. J. Cancer* **1991**, *63*, 859–866.
[25] R. Mendichi, V. Rizzo, M. Gigli, A. G. Schieroni, *Bioconjugate Chem.* **2002**, *13*, 1253–1258.
[26] K.-W. Wan, B. Malgesini, I. Verpili, P. Ferruti, P. C. Griffiths, A. Paul, A. C. Hann, R. Duncan, *Biomacromolecules* **2004**, *5*, 1102–1109.

 © 2005 Wiley-VCH Verlag GmbH & Co. KGaA, Weinheim

Supported Catalysts

A Collaborative Effect between Gold and a Support Induces the Selective Oxidation of Alcohols**

Alberto Abad, Patricia Concepción, Avelino Corma, and Hermenegildo García*

The selective oxidation of alcohols is one of the most challenging reactions in green chemistry.[1–4] An ideal green oxidation process should involve a highly active and selective recyclable catalyst that is able to work at atmospheric pressure in the presence of oxygen and the absence of solvents and bases.[5] Stoichiometric oxidations using transition metal compounds or sulfoxides (Swern oxidation) are still commonly used, despite the formation of a large amount of undesirable products. Several homogeneous Pd-, Cu-, or Ru-based catalysts are able to perform the selective oxidation of alcohols, but they require the use of organic solvents or high oxygen pressure.[6–11]

From the point of view of heterogeneous catalysis, probably the best system has been reported recently by Kaneda et al.,[12] where a palladium-containing apatite is able to oxidize alcohols at atmospheric oxygen pressure even in the absence of solvents. Mizuno et al.[13,14] have described a ruthenium-containing solid catalyst that is able to selectively produce carbonyl compounds from alcohols in the presence of oxygen at atmospheric pressure. Other solid catalysts based on hydrotalcites,[15] apatites and mixed oxides,[16] or supported Pt and Pd[17,18] have also been studied.

Small-crystal-size gold supported on inorganic oxides or active carbon has recently attracted considerable attention since these catalysts are able to promote the selective oxidation of alcohols.[19–25] Taking into account that inorganic oxides contain some sites that are able to oxidize alcohols stoichiometrically, it appeared to us that a new concept of catalyst could be put forward if these stoichiometric sites can be converted into catalytic sites by introducing a solid co-catalyst that facilitates the reoxidation of the intermediate metal hydrides to water and the original inorganic oxide. To prove this concept we selected cerium oxide, which contains stoichiometric oxidation sites of alcohols, and cationic gold, which is a metal that transfers hydrides reversibly.

In particular, the combination[26] of small-crystal-size gold (2–5 nm) and nanocrystalline ceria ($\approx$5 nm) turned out to give a highly active, selective, and recyclable catalyst for the oxidation of alcohols into aldehydes and ketones with high turnover numbers (TON) and frequencies (TOF) using oxygen at atmospheric pressure as oxidant in the absence of solvent and base.

Pure, nanocrystalline cerium oxide contains sites that are able to perform the oxidation of alcohols in a stoichiometric manner. Indeed, when IR experiments were carried out in situ by adsorbing 2-propanol on nanocrystalline cerium oxide (see Supporting Information), two IR bands associated with cerium alkoxide appeared; the growth of a band attributable to cerium hydride, was also observed. The appearance of a carbonyl band indicates that acetone was formed at the same time as the cerium hydride. Upon subsequent introduction of O_2 into the IR cell at room temperature, the band due to cerium hydride remained unaltered and the formation of water was not observed. These experiments show that cerium oxide alone is able to perform one reaction cycle, but the reduced cerium is stable in the presence of physisorbed O_2 and the catalytic cycle is not closed.

When gold nanoparticles were deposited onto the nanocrystalline cerium oxide (see Supporting Information for the detailed preparation procedure), the XPS spectrum of the Au 4f7/2 core level shows three bands (see Supporting Information), which correspond to Au^{3+}, Au^{+}, and Au^{0}.[27] The presence of cationic gold was also confirmed by the IR band of adsorbed CO (see Supporting Information).[28] These results can be rationalized by assuming that the gold nanoparticles formed on the $Au\subset CeO_2$ catalyst (see HRTEM images in the Supporting Information) interact with the nanometric ceria surface, which stabilizes the positive oxidation states of gold[26,29,30] by creating Ce^{3+} and oxygen-deficient sites in the ceria.

When the anaerobic oxidation of 2-propanol on $Au\subset CeO_2$ was monitored in situ by IR spectroscopy (see Supporting Information) in the same way as with pure nanocrystalline CeO_2, the IR bands of the cerium alkoxide

[*] A. Abad, Dr. P. Concepción, Prof. A. Corma, Prof. H. García
Instituto de Tecnología Química (CSIC-UPV)
Universidad Politécnica de Valencia
Avda. de los Naranjos s/n. 46022 Valencia (Spain)
Fax: (+34) 96-387-7809
E-mail: acorma@itq.upv.es

[**] The authors thank CICYT (MAT 2003-07945-C02-01) and AURICAT (HPRN-CT-2002-00174) for financial support.

Supporting information for this article is available on the WWW under http://www.angewandte.org or from the author.

 © 2005 Wiley-VCH Verlag GmbH & Co. KGaA, Weinheim DOI: 10.1002/anie.200500382

and hydride were again observed, and acetone was also formed. However, when O_2 was subsequently introduced the metal hydride disappeared and water was formed, contrary to what occurred with CeO_2. At this point the cerium oxide is therefore ready to perform another catalytic cycle.

After these spectroscopic studies, Au⊂CeO_2 was tested as a solid catalyst for the selective aerobic oxidation of a large variety of alcohols. The reactions were performed in a magnetically stirred, glass batch reactor in the absence of solvent and base at 80 °C, with O_2 at atmospheric pressure. In other cases the oxidations were also performed in basic water (see Supporting Information for experimental details). High conversions and selectivities were obtained with short reaction times (Table 1).

The benefit of using nanoparticles of CeO_2 as a support for the gold becomes obvious when comparing the activity (TOF) of Au⊂CeO_2 with the activities of Au supported on conventional CeO_2 (Au/CeO_2), Au/carbon (Au/C) (see Supporting Information for experimental details of the preparation), Au/TiO_2, and Au/Fe_2O_3 (these two last catalysts were supplied by the International Gold Council; Figure 1).[31] Note that Au⊂CeO_2 is active for the oxidation of alcohols in the absence of solvent and base, conditions under which most other supported gold catalysts are inefficient.[5] For instance, Au/C does not catalyze oxidation reactions in the absence of base and water.

Secondary alcohols can be oxidized with essentially complete conversion and high selectivities on Au⊂CeO_2 in the absence of solvent, and benzylic or allylic alcohols are selectively oxidized to the corresponding unsaturated aldehydes, although longer reaction times are required. Aliphatic primary alcohols are more reluctant to undergo oxidation in the absence of solvent. Notably, they give predominantly the corresponding ester with high selectivity, accompanied by lesser amounts of the aldehyde. We have found that esters are directly formed via the hemiacetal, which is detectable by ^{1}H NMR spectroscopy,

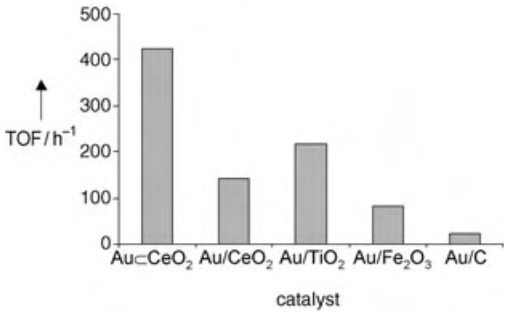
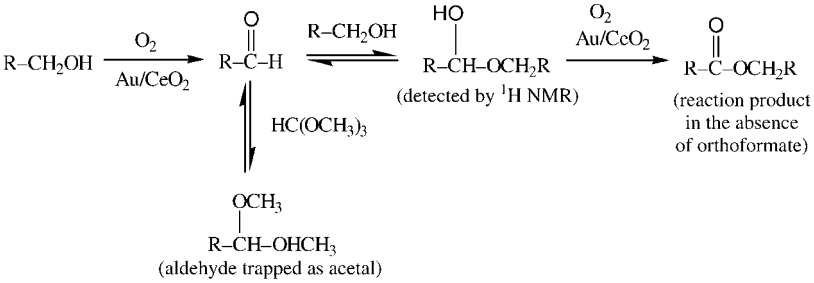


Figure 1. Turnover frequencies for the oxidation of 3-octanol, given as the ratio of moles of 3-octanone per mole of Au per hour, measured at $t = 10$ min (see Table 1 for reaction conditions).

as indicated in Scheme 1. Indeed, we have seen that the introduction of trimethyl orthoformate, which acts as a scavenger for aldehydes, into the reaction mixture gives the dimethyl acetal of the aldehyde with very high selectivity and completely inhibits the formation of the ester. Note that Au⊂CeO_2 is also very active for the oxidation of alcohols in basic aqueous solution. In this case pH plays an important role, with the TOF decreasing upon lowering the pH. In basic aqueous solution, the oxidation of primary alcohols gives the carboxylic acids rather than the esters.



Scheme 1. Reaction route proposed for the formation of esters in the oxidation of primary alcohols.

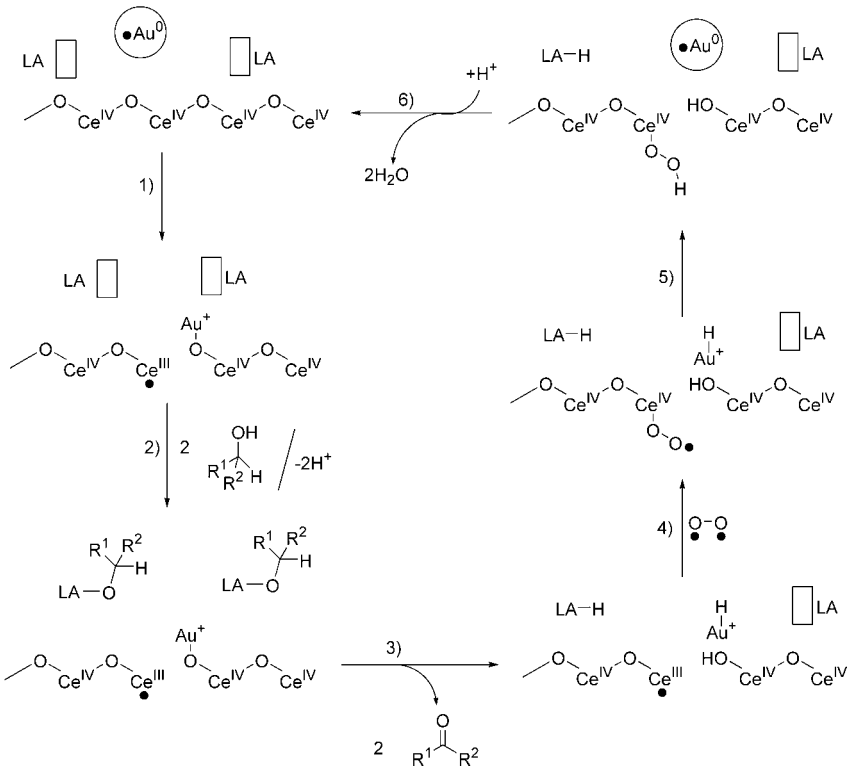
Table 1: Aerobic alcohol oxidation catalyzed by Au⊂CeO_2.[a]

Entry	Substrate	t [h]	Conversion [%]	Product	Selectivity [%]
1[b]	3-octanol	3.5	97	3-octanone	>99
2[c]	3-octanol	2.5	89	3-octanone	96
3[b]	2-phenylethanol	2.5	92	acetophenone	97
4[b]	2,6-dimethylcyclohexanol	2.5	78	2,6-dimethylcyclohexanone	94
5[b]	1-octen-3-ol	3.5	80	1-octen-3-one	>99
6[b]	cinnamyl alcohol	7	66	cinnamaldehyde	73
7[b]	3,4-dimethoxybenzyl alcohol	7	73	3,4-dimethoxybenzaldehyde	83
8[b]	3-phenyl-1-propanol	6	70	3-phenylpropyl 3-phenylpropanoate	98
9[d]	vanillin alcohol	2	96	vanillin	98
10[d]	2-hydroxybenzyl alcohol	2	>99	2-hydroxybenzaldehyde	87
11[d]	3,4-dimethoxybenzyl alcohol	2	>99	3,4-dimethoxybenzylic acid	>99
12[d]	cinnamyl alcohol	3	>99	cinnamylic acid	98
13[e]	*n*-hexanol	10	>99	hexanoic acid	>99
14[d]	2-phenylethanol	5	>99	acetophenone	51

[a] Conversion and selectivity were determined by GC using nonane and nitrobenzene as external standards. [b] Substrate (4.85 mmol), Au⊂CeO_2 (0.5 mol%), 353 K, $p = 1$ atm O_2 (flow: 25 mL min^{-1}). [c] As [b], but TEMPO (2,2,6,6-tetramethylpiperidine oxide; 4 equiv with respect to Au) was added. [d] Substrate (0.4 mmol), Au⊂CeO_2 (0.66 mol%), H_2O (5 mL), Na_2CO_3 (0.3 g), 323 K, $p = 1$ atm O_2 (flow: 25 mL m^{-1}). [e] Substrate (1 mmol), Au⊂CeO_2 (0.25 mol%), H_2O (5 mL), Na_2CO_3 (0.71 g), 373 K, $p = 25$ atm (synthetic air).

 © 2005 Wiley-VCH Verlag GmbH & Co. KGaA, Weinheim

On the basis of the Au⊂CeO_2 characterization and IR study, a reasonable mechanism for the catalytic reaction is depicted in Scheme 2. According to this mechanism, the interaction between gold and ceria will give rise to an important population of positively charged gold and Ce^{3+} species (detectable by XPS; step 1). The alcohol or the corresponding alkoxide will then react with the Lewis acid sites of Au⊂CeO_2 to give a metal alkoxide (step 2), which subsequently undergoes a rapid hydride transfer from C–H to Ce^{3+} and Au^+ to give the ketone and Ce–H (indicated as LA–H in Scheme 2) and Au–H (as observed by IR spectroscopy; step 3). Upon admission of oxygen into the system and coordination to the oxygen-deficient sites of ceria, formation of cerium-coordinated superoxide (Ce–OO•) species occurs (step 4).[32] These superoxide species evolve into cerium hydroperoxide by hydrogen abstraction from Au–H (step 5), and are responsible for the formation, after reduction of Ce^{IV}, of the initial Au^+ species. The absence of gold would render this step impossible and lead to a depletion of Ce^{III}. This mechanism is compatible with the lack of influence of an excess of TEMPO in the reaction (see footnote [e] in Table 1), since TEMPO is not able to quench oxygen-centered radicals.



Scheme 2. Proposed mechanism for the oxidation of alcohols in the presence of Au⊂CeO_2 as the catalyst. LA = Lewis acid.

Kaneda et al. have reported recently that Pd supported on hydroxyapatite is the most active solid catalyst, with a turnover number of 236000 and a TOF of 9800 h^{-1}.[12] We have been able to reproduce these results. Under the reported conditions our catalyst gives a TOF of 12500 h^{-1} for the conversion of 1-phenylethanol into acetophenone at 160 °C, with greater than 99 % selectivity for the desired product. The catalyst is fully recyclable after filtering and washing (NaOH 0.5 M), with a TON of 250000 after three recycles. This shows that gold, which was previously believed to be of little catalytic interest, can become an interesting oxidation catalyst when combined with the right support.

In conclusion, we have shown that gold nanoparticles transform nanocrystalline cerium oxide from a stoichiometric oxidant into a catalytic material for the selective oxidation of primary and secondary alcohols to aldehydes and ketones in the presence of oxygen at atmospheric pressure, with high TOFs and selectivities observed. This catalyst makes the process interesting from both an economic and environmental point of view.

Received: February 1, 2005
Published online: May 25, 2005

Keywords: alcohols · gold · nanoparticles · oxidation · supported catalysts

[1] R. P. Viswanath, *Catalysis* **2002**, 227.
[2] R. A. Sheldon in *Catalytic Oxidation* (Eds.: R. A. Sheldon, R. A. van Santen), World Scientific Publishing, Singapore, **1995**, p. 239.
[3] T. Mallat, A. Baiker, *Catal. Today* **2000**, *57*, 1.
[4] R. A. Sheldon, I. W. C. E. Arends, G. J. ten Brink, A. Dijksman, *Acc. Chem. Res.* **2002**, *35*, 774.
[5] T. Mallat, A. Baiker, *Chem. Rev.* **2004**, *104*, 3037.
[6] A. Hanyu, E. Takezawa, S. Sakaguchi, I. Ishii, *Tetrahedron Lett.* **1998**, *39*, 5557.
[7] I. E. Marko, P. R. Giles, M. Tsukazaki, S. M. Brown, C. J. Urch, *Science* **1996**, *274*, 2044.
[8] T. Nishimura, T. Onoue, K. Ohe, S. Uemura, *Tetrahedron Lett.* **1998**, *39*, 6011.
[9] T. Iwasawa, M. Tokunaga, Y. Obora, Y. Tsuji, *J. Am. Chem. Soc.* **2004**, *126*, 6554.
[10] A. Dijksman, A. Marino-Gonzalez, A. Mairata i Payeras, I. W. C. E. Arends, R. A. Sheldon, *J. Am. Chem. Soc.* **2001**, *123*, 6826.
[11] G. J. ten Brink, I. W. C. E. Arends, R. A. Sheldon, *Science* **2000**, *287*, 1636.
[12] K. Mori, T. Hara, T. Mizugaki, K. Ebitani, K. Kaneda, *J. Am. Chem. Soc.* **2004**, *126*, 10657.
[13] K. Yamaguchi, N. Mizuno, *Angew. Chem.* **2002**, *114*, 4720; *Angew. Chem. Int. Ed.* **2002**, *41*, 4538.
[14] K. Yamaguchi, N. Mizuno, *Chem. Eur. J.* **2003**, *9*, 4353.
[15] B. M. Choudary, M. Lakshmi Kantam, A. Rahman, C. Venkat Reddy, K. Koteswara Rao, *Angew. Chem.* **2001**, *113*, 785; *Angew. Chem. Int. Ed.* **2001**, *40*, 763.
[16] M. Matsumoto, N. Watanabe, *J. Org. Chem.* **1984**, *49*, 3435.
[17] T. Mallat, A. Baiker, *Catal. Today* **1994**, *19*, 247.
[18] T. Nishimura, N. Kakiuchi, M. Inoue, S. Uemura, *Chem. Commun.* **2000**, 1245.
[19] S. Biella, M. Rossi, *Chem. Commun.* **2003**, 378.
[20] L. Prati, M. Rossi, *J. Catal.* **1998**, *176*, 552.
[21] C. Milone, R. Ingoglia, A. Pistone, G. Neri, S. Galvagno, *Catal. Lett.* **2003**, *87*, 201.
[22] S. Biella, L. Prati, M. Rossi, *Inorg. Chim. Acta* **2003**, *349*, 253.

 © 2005 Wiley-VCH Verlag GmbH & Co. KGaA, Weinheim

[23] S. Carretin, P. McMorn, P. Johnston, K. Griffin, G. J. Hutchings, *Chem. Commun.* **2002**, 696.
[24] S. Carretin, P. McMorn, P. Johnston, K. Griffin, C. Kiely, G. C. Attard, G. J. Hutchings, *Top. Catal.* **2004**, *27*, 131.
[25] S. Biella, L. Prati, M. Rossi, *J. Catal.* **2002**, *206*, 242.
[26] S. Carretin, P. Concepcion, A. Corma, J. M. Lopez Nieto, *Angew. Chem.* **2004**, *116*, 2592; *Angew. Chem. Int. Ed.* **2004**, *43*, 2538.
[27] Q. F. H. Saltsburg, M. Stephanopoulus, *Science* **2003**, *301*, 935.
[28] G. Martra, L. Prati, C. Manfredotti, S. Biella, M. Rossi, S. Coluccia, *J. Phys. Chem. B* **2003**, *107*, 5453.
[29] R. J. Davis, *Science* **2003**, *301*, 926.
[30] J. Guzman, B. C. Gates, *Angew. Chem.* **2003**, *115*, 714; *Angew. Chem. Int. Ed.* **2003**, *42*, 690.
[31] Gold reference catalysts, *Gold Bull.* **2003**, *36*, 1.
[32] V. V. Pushkarev, V. I. Kovalchuk, J. L. D'Itri, *J. Phys. Chem. B* **2004**, *108*, 5341.

 © 2005 Wiley-VCH Verlag GmbH & Co. KGaA, Weinheim

Spin Crossover

One Shot Laser Pulse Induced Reversible Spin Transition in the Spin-Crossover Complex $[Fe(C_4H_4N_2)\{Pt(CN)_4\}]$ at Room Temperature**

*Sébastien Bonhommeau, Gábor Molnár, Ana Galet, Antoine Zwick, José-Antonio Real, John J. McGarvey, and Azzedine Bousseksou**

The use of light is one of the most promising ways to reversibly control various physical properties of organic and metal-organic compounds and opens up the possibility for the generation of new information storage devices.[1,2] Among these materials, iron(II) spin-crossover complexes are particularly interesting as they are known to exhibit a light-induced low-spin (LS) to high-spin (HS) transition.[3] However, this light-induced excited spin state trapping (LIESST) phenomenon is only efficient at cryogenic temperatures (typically below 50 K) because at higher temperatures the photo-induced HS state relaxes rapidly to the ground state. This is a serious limitation for the development of optical switches based on spin-crossover materials.

A possible approach to overcome this problem consists of working within the thermal hysteresis loop, in which the metastable HS or LS states have "infinite" lifetimes.[4] Such hysteresis phenomena have been found in many spin-crossover solids and can be related to long-range elastic interactions between the spin-state-changing molecules.[5] It should be emphasized that the hysteresis loop can be fine-tuned by chemical methods to situate it around room temperature.[6] The first light-induced LS→HS transition in the hysteresis region was recently observed by means of optical reflectivity when an 8-ns laser pulse was applied at 170 K to $[Fe(pm\text{-}bia)_2(NCS)_2]$ (pm-bia = *N*-2′-pyridylmethylene-4-aminobiphenyl), but the reverse phenomenon could not be detected.[2a] Herein, we report spectroscopic evidence for a bi-directional, light-induced spin transition at room temperature in $[Fe(pyrazine)\{Pt(CN)_4\}]$ (Figure 1) by applying a one-shot laser pulse of irradiation.

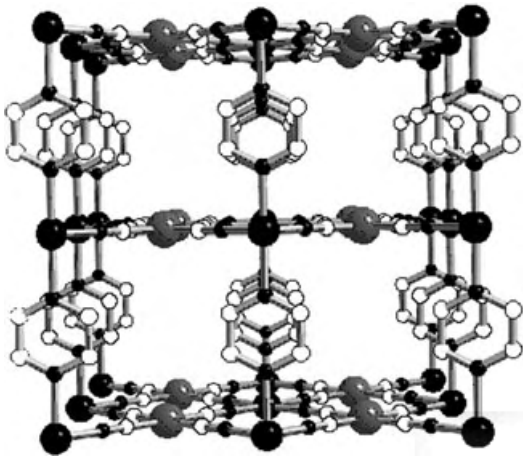


Figure 1. Schematic structure of $[Fe(pyrazine)\{Pt(CN)_4\}]$.

The synthesis of a hydrated form of the above-mentioned compound has been reported elsewhere.[7] Subsequent research has demonstrated that the spin-crossover behavior of this hydrated form ($[Fe(pyrazine)\{Pt(CN)_4\}]\cdot n H_2O$; $n \approx 2$–3) depends dramatically on the water content. Thermogravimetric analysis revealed that heating the sample at 420 K for 30 minutes is necessary to remove the water of crystallization. The dehydrated form $[Fe(pyrazine)\{Pt(CN)_4\}]$ exhibits "improved" spin-crossover behavior in that the transition becomes complete and is centered at room temperature. Moreover, the hysteresis loop becomes wider, square-shaped, and reproducible over several cycles. This compound preserves its spin state (HS or LS) for several months if it is kept in a dry atmosphere at room temperature (295 K).

Figure 2 shows the temperature dependence of the $\chi_M T$ value (χ_M is the molar magnetic susceptibility) for

[*] S. Bonhommeau, Dr. G. Molnár, Dr. A. Bousseksou
Laboratoire de Chimie de Coordination
CNRS UPR-8241
205, Route de Narbonne, 31077 Toulouse Cedex (France)
Fax: (+33) 5-6155-3003
E-mail: boussek@lcc-toulouse.fr
S. Bonhommeau, Dr. A. Zwick
Laboratoire de Physique des Solides de Toulouse
CNRS UMR-5477
Université de Toulouse III
31062 Toulouse Cedex (France)
Prof. J. J. McGarvey
School of Chemistry
Queen's University Belfast
Belfast BT9 5AG (UK)
A. Galet, Prof. J.-A. Real
Departament de Quimica Inorganica
Institut de Ciència Molecular
Universitat de València
Doctor Moliner 50, 46100 Burjassot, Valencia (Spain)

[**] Financial support is acknowledged from the Spanish DGICYT (CTQ 2004-03456/BQU), from Invest Northern Ireland (grant no. RTD COE 40), and the Paul Sabatier University (ATUPS and BQR/2004).

 DOI: 10.1002/anie.200500717 © 2005 Wiley-VCH Verlag GmbH & Co. KGaA, Weinheim

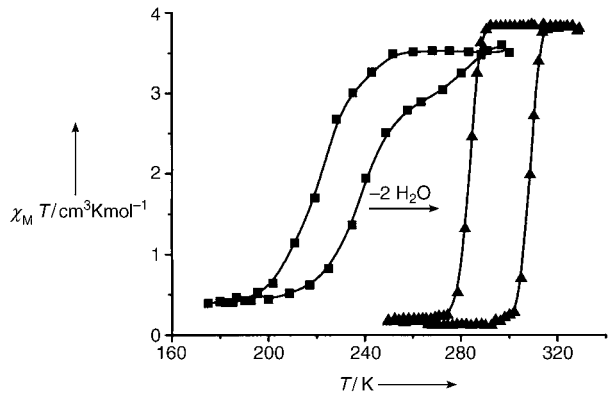


Figure 2. Graph of $\chi_M T$ versus T for [Fe(pyrazine){Pt(CN)$_4$}] in the cooling and heating modes before and after thermal treatment at 430 K.

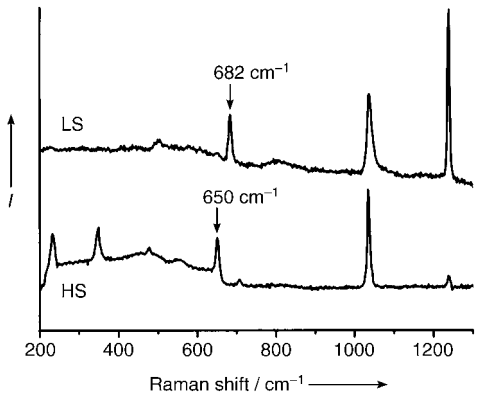


Figure 3. Raman spectra of [Fe(pyrazine){Pt(CN)$_4$}] in the HS and the LS states recorded in the 200–1300 cm^{-1} frequency range at 295 K and 265 K, respectively. Selected Raman marker bands are shown at 650 cm^{-1} (HS) and 682 cm^{-1} (LS). The intensity I on the y axis is given in arbitrary units.

[Fe(pyrazine){Pt(CN)$_4$}] before and after heating to 430 K. This figure demonstrates the dramatic improvement in the spin-crossover characteristics following the thermal dehydration treatment described earlier. The value of $\chi_M T$ for the dehydrated form at 330 K is 3.81 cm^3 K mol^{-1}; this value is consistent with the iron(II) ion being in the HS state ($S = 2$). Upon cooling the sample, the value of $\chi_M T$ remains constant down to about 292 K but then undergoes a sharp decrease that is characteristic of a first-order spin transition. The $\chi_M T$ value drops to 0.16 cm^3 K mol^{-1} at around 270 K, thus indicating that the spin transition is virtually complete. The heating mode reveals the occurrence of a thermal hysteresis with a hysteresis loop that is 24 K wide. The change in the spin state was also confirmed by Mössbauer spectroscopy. The Mössbauer spectrum recorded at 300 K (in the cooling mode) consists of a single doublet with quadrupole splitting (1.159(5) mm s^{-1}) and isomer shift (1.047(3) mm s^{-1}) values typical of Fe^{II} ions in the HS state. A new doublet appears at 80 K with smaller quadrupole splitting (0.306(4) mm s^{-1}) and lower isomer shift (0.439(2) mm s^{-1}) values, as expected for the LS state ($S = 0$) of Fe^{II} ions. The change in the spin state is also accompanied by a marked color change: pale orange for the HS state and deep red for the LS state.

Raman spectra of [Fe(pyrazine){Pt(CN)$_4$}] in the pure HS and LS states were recorded between 200 and 1300 cm^{-1} (Figure 3). In agreement with our previous observations on this family of complexes,[8] the Raman spectra are markedly different, which is in line with the change in the spin state, and several "marker bands" can be chosen to follow the spin transition. For example, peaks around 349 and 233 cm^{-1} (assigned to Pt-CN bending and Fe-N stretching modes, respectively) are associated with the HS state and the feature at 1238 cm^{-1} exhibits a significant increase in intensity in going from the HS to the LS state. However, the most relevant "marker band" near 650 cm^{-1}, previously assigned to an in-plane bending mode of the pyrazine ring,[8] is fairly intense in both spin states and exhibits a well-resolved frequency shift from 650 cm^{-1} (HS) to 682 cm^{-1} (LS).

A pulsed Nd:YAG laser enables the application of 8 ns pulses ($\lambda = 532$ nm) with pulse energies of about 1 mJ at the sample (spot size = 0.4 mm^2) in the ascending and descending branches of the hysteresis loop. Figure 4 exhibits the proportion of HS iron(II) ions before and after the one-shot laser pulse irradiation, as evaluated from the intensities of the Raman peaks. Raman spectra recorded in the 620–720 cm^{-1} frequency range before and after the application of the pulses are also presented in the insets of Figure 4. These spectra, as well as the color change observed just after excitation with light, prove clearly that a single laser pulse ensures both a LS→HS and a HS→LS transition, depending on the position in the hysteresis loop. Thermal effects arising from laser irradiation (either pump or probe beams) must be carefully checked for these light-induced changes to be fully interpreted. In any case, however, laser heating can induce only the LS→HS transition. Therefore, the observed light-induced HS→LS transition proves irrefutably that a simple heating effect cannot play any role here.

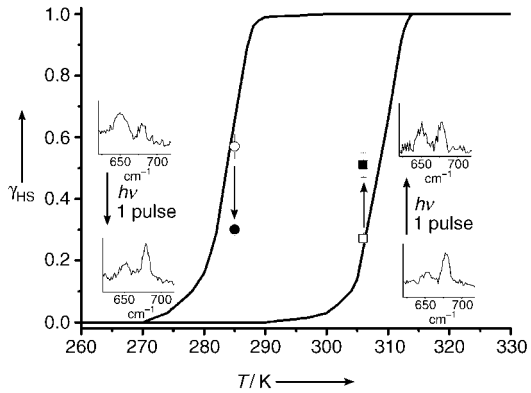


Figure 4. Proportion of HS iron(II) ions before and after a one-shot laser pulse of irradiation on the ascending and descending branches of the hysteresis loop of [Fe(pyrazine){Pt(CN)$_4$}]. The insets show the Raman spectra recorded before and after irradiation.

The observed change in the spin state appears to be incomplete: only around 20% of the iron ions are apparently converted from one state to the other in the single-pulse experiment. However, the absorption spectra of the compound indicate that the penetration depths of the pump laser (532 nm) and the probe laser (785 nm) are rather different.[9]

 © 2005 Wiley-VCH Verlag GmbH & Co. KGaA, Weinheim

In fact, the latter probes a volume that is larger than that irradiated by the green pulse. In other words, the ratio of the Raman peak intensities underestimates the real photoconversion efficiency and can therefore be used only to confirm the change in the spin state and to compare the relative efficiency of the laser pulses as a function of the number of pulses, pulse energy, etc. It should be noted that we could not obtain any useful Raman spectra using a green (514.5 nm) continuous wave laser because of laser heating effects.

A one-shot excitation triggers at least a partial spin conversion. We have therefore studied the effect of applying additional laser pulses and found that while the second pulse increases the spin conversion (to ca. 40% HS), subsequent pulses do not have any measurable additional effect on the HS/LS ratio. The conversion efficiency was also studied at different points around the wide hysteresis loop of [Fe(pyrazine){Pt(CN)$_4$}] which correspond to distinct stability regions for the LS and the HS states (Figure 5). The HS state

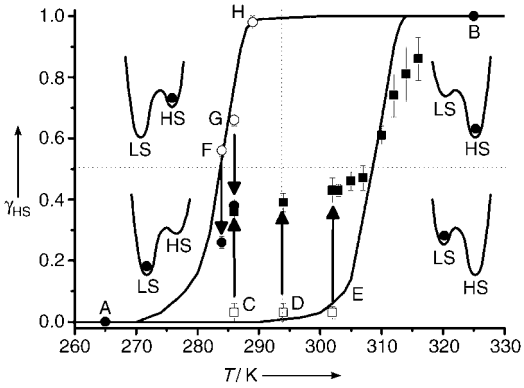


Figure 5. Proportion of HS iron(II) ions before and after irradiation with 10 laser pulses on points A–H of the hysteresis loop of [Fe(pyrazine){Pt(CN)$_4$}]. Points obtained by heating following irradiation at point E are also presented. Schematic diagrams of the free energy with minima corresponding to the LS and HS states at the respective temperatures are drawn in each part of the graph delimited by the two dotted lines. The intensity *I* on the *y* axis is given in arbitrary units.

is the ground state at high temperatures (point B) while the LS state becomes the stable form at low temperatures (points A and C). At points E and D (F, G, and H) the system is in the metastable LS (HS) state. Raman spectra were collected at each point before and after the application of 10 successive laser pulses. The Raman signals at points C, D, and E (Figure 6, points C, D, and E) for the irradiated region clearly demonstrate the appearance of the HS state following the pulsed irradiation, while at points F and G (Figure 6, points F and G) the fraction of the LS state increases. In contrast, we could not observe any irradiation effects at points A, B, and H (Figure 6, point H). As far as points A and B are concerned, this observation is clearly related to the fact that they are situated outside the hysteresis region. On the other hand, the absence of any effect at point H is probably related to the lower optical density of the HS state (relative to the LS form)[10] and the different energy barriers (compared to points F and G).

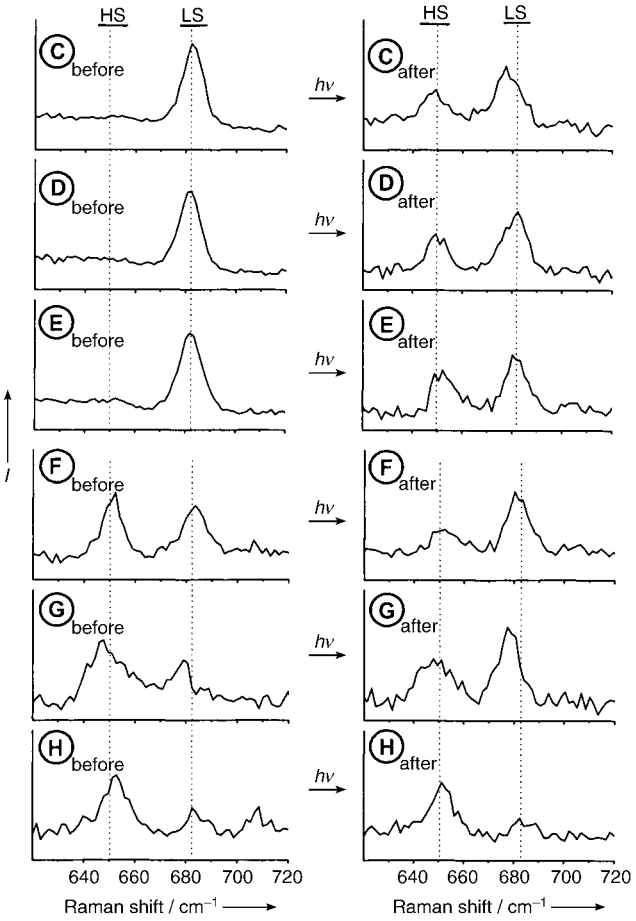


Figure 6. Selected Raman spectra of [Fe(pyrazine){Pt(CN)$_4$}] at points C–H on the hysteresis loop. These Raman spectra were recorded before and after 10 successive laser pulses.

The HS fractions, evaluated before and after an irradiation sequence of 10 pulses, are shown in Figure 5. First of all it should be noted that—within the experimental limits of accuracy—the same final state (ca. 40% HS) was reached from points C, D, and E, thus also confirming the absence of significant heating effects in the LS→HS transition. It appears also that the HS→LS transition can be obtained only in the descending branch (from an initial HS fraction of 0.7) of the hysteresis, which is in contrast with the findings for the LS→HS transition which was observed even in the stability domain for the LS state (point C). Figure 5 also shows data obtained by heating the sample following irradiation at point E. The photoinduced fraction of the HS state does not change within the hysteresis loop. With further heating it follows a similar evolution to that determined by magnetic measurements. This result reveals also that the intensities of the Raman peaks give a fairly reasonable approximation for the HS fraction in the zone irradiated by the laser pulses.

In considering the mechanism of the observed pulsed-laser-induced change in the spin state, we refer to the general concept of photoinduced phase transitions.[1a,b] The phase transition between the two spin states cannot occur thermally in the hysteresis region, because of the existence of a free

 © 2005 Wiley-VCH Verlag GmbH & Co. KGaA, Weinheim

energy barrier. However, photoexcitation may induce local transformation of the microscopic state of the system. The photoexcited species relaxes rapidly to the initial state when there is a weak excitation density. On the other hand, if the photoexcitation density exceeds a threshold it can lead to the formation of a nucleus of the second phase, which is stabilized by the lattice distortions accompanying the change in the spin state. Such photoinduced phase transitions are always cooperative and highly nonlinear phenomena, because the efficiency is not simply proportional to the total absorbed energy, and a threshold effect on the light intensity exists.

An interesting feature of the photoswitching phenomena observed in [Fe(pyrazine){Pt(CN)$_4$}] is that both the LS→HS and the HS→LS transitions can be triggered by the same irradiation wavelength. Such an unusual effect has also been reported by Liu et al.[2c] for a Prussian blue analogue. These authors took the observation as evidence for the so-called "domino effect": namely that the generation of a small amount of HS (LS) excited species in the LS (HS) lattice initiates the complete transformation of this latter into the second phase. We believe, however, that the effect can be explained more readily by the simple fact that the optical absorption bands of the HS and LS forms overlap at 532 nm. Since the color of the sample is very different in the two spin states, one can anticipate that there exists an excitation photon energy, which induces the LS→HS or the HS→LS transition selectively in this compound.

In conclusion, we have demonstrated by a spectroscopic method that a bi-directional, photoinduced spin transition can be brought about when applying a nanosecond laser pulse to [Fe(pyrazine){Pt(CN)$_4$}]. This phenomenon can be interpreted as a photoinduced structural-phase transformation. Since this transition occurs around room temperature over a wide range of bistability and involves magnetization and color changes as well, it opens up interesting perspectives for applications in memory devices and optical switches. A more detailed study of the dependence of the photoconversion efficiency on the excitation wavelength and pulse energy, as well as a dynamic study, are, however, necessary to find the optimal working conditions as well as to probe more thoroughly the physical mechanisms involved.

Experimental Section

Variable-temperature magnetic susceptibility measurements were carried out between 300 and 1.8 K on the polycrystalline sample (20 mg) using a Quantum Design MPMS2 SQUID magnetometer operated at 0.5 T. The magnetometer was calibrated with $(NH_4)_2Mn(SO_4)_2{\cdot}12H_2O$. Experimental susceptibilities were corrected for diamagnetism of the constituent atoms by the use of Pascal's constants.

A Spectra Physics Nd/YAG, model GCR3, pulsed laser operating at 532 nm was used to irradiate the polycrystalline sample with pulses of 8 ns duration. CW Raman spectra were collected from the irradiated region in a backscattering geometry before and after applying the laser pulse. Raman scattering was excited at 785 nm by means of a Ti-sapphire laser (Spectra Physics, model 3900S) pumped by an Ar^+ laser (Spectra Physics, model 2060A). The Rayleigh scattering was removed by a holographic notch filter and Raman spectra were recorded with a thermoelectrically cooled CCD detector (Andor Technology, Model DV430-FI) coupled to a Jobin–Yvon spectrograph (model HR640) equipped with a grating containing 300 grooves per mm. The spectral resolution at a slit width of 100 μm was around 7 cm^{-1}. Raman spectra were recorded between 200 and 1300 cm^{-1} with acquisition times of about 3 min. A cylindrical lens was inserted in the beam pathway to reduce the incident power density of the pump and probe beams, which traversed the same optical path close to the sample. CW beam power at the sample was then fixed at 5 mW on a spot size of about 0.4 mm^2, while the energy of each laser pulse on the sample was 1 mJ at the same spot. Under these conditions the experiments could be repeated many times on the same sample without degrading it. The sample temperature was controlled using a Linkam THMS600 liquid-nitrogen cryostage.

Received: February 25, 2005
Published online: May 13, 2005

Keywords: iron · phase transitions · photophysics · Raman spectroscopy · spin crossover

[1] a) *Photoinduced Phase Transitions* (Ed.: K. Nasu), World Scientific Publishing, Singapore, **2004**; b) K. Nasu, H. Ping, H. Mizouchi, *J. Phys. Condens. Matter* **2001**, *13*, 693; c) P. Gütlich, Y. Garcia, T. Woike, *Coord. Chem. Rev.* **2001**, *219*, 839; d) O. Sato, T. Iyoda, A. Fujishima, K. Hashimoto, *Science* **1996**, *272*, 704; e) M. Irie, *Chem. Rev.* **2000**, *100*, 1685; f) T. Tayagaki, K. Tanaka, *Phys. Rev. Lett.* **2001**, *86*, 2886.

[2] a) E. Freysz, S. Montant, S. Létard, J.-F. Létard, *Chem. Phys. Lett.* **2004**, *394*, 318; b) S. Koshihara, Y. Tokura, K. Takeda, T. Koda, *Phys. Rev. Lett.* **1992**, *68*, 1148; c) H. W. Liu, K. Matsuda, Z. Z. Gu, K. Takahashi, A. L. Cui, R. Nakajima, A. Fujishima, O. Sato, *Phys. Rev. Lett.* **2003**, *90*, 167403; d) H. Matsuzaki, W. Fujita, K. Awaga, H. Okamoto, *Phys. Rev. Lett.* **2003**, *91*, 017403; e) N. Huby, L. Guérin, E. Collet, L. Toupet, J.-C. Ameline, H. Cailleau, T. Roisnel, T. Tayagaki, K. Tanaka, *Phys. Rev. B* **2004**, *69*, 020101; f) E. Collet, M.-H. Lemée-Cailleau, M. Buron-Le Cointe, H. Cailleau, M. Wulff, T. Luty, S. Koshihara, M. Meyer, L. Toupet, P. Rabiller, S. Techert, *Science* **2003**, *300*, 612.

[3] a) A. Hauser, *Top. Curr. Chem.* **2004**, *234*, 155; b) C. Brady, J. J. McGarvey, J. K. McCusker, H. Toftlund, D. N. Hendrickson, *Top. Curr. Chem.* **2004**, *235*, 1.

[4] A. Bousseksou, G. Molnár, G. Matouzenko, *Eur. J. Inorg. Chem.* **2004**, 4353.

[5] H. Spiering, *Top. Curr. Chem.* **2004**, *235*, 171.

[6] O. Kahn, C. J. Martinez, *Science* **1998**, *279*, 44.

[7] V. Niel, J. M. Martínez-Agudo, M. C. Muñoz, A. B. Gaspar, J.-A. Real, *Inorg. Chem.* **2001**, *40*, 3838.

[8] a) G. Molnár, V. Niel, A. B. Gaspar, J.-A. Real, A. Zwick, A. Bousseksou, J. J. McGarvey, *J. Phys. Chem. B* **2002**, *106*, 9701; b) G. Molnár, V. Niel, J.-A. Real, L. Dubrovinsky, A. Bousseksou, J. J. Mc-Garvey, *J. Phys. Chem. B* **2003**, *107*, 3149.

[9] Unfortunately, we were unable to grow crystals to carry out optical density measurements and therefore the penetration depths could not be determined precisely. In practice, the "Raman sampling depth" and the "photoexcitation depth" should be compared. The latter depends not only on the absorption coefficient of the sample, but also on many other parameters such as the threshold photoexcitation density for the phase transition, while the former is determined by the collection optics, in addition to the sample's own optical properties (for example, diffuse scattering). Any quantitative analysis would be feasible only for a very thin film of the sample. To obtain an approximate idea at least of the beam penetration at different wavelengths we have carried out diffuse reflectance measurements on the HS and LS states at 295 K using an integration sphere and a teflon reference sample. These show that the optical density of the LS state at 532 nm is about twice

 © 2005 Wiley-VCH Verlag GmbH & Co. KGaA, Weinheim

that in the HS state, while at 785 nm it is 2 times (6 times) smaller than at 532 nm for the HS (LS) state.

[10] The key quantity here is the excitation photon density but its calculation requires the assumption that the total photon flux of the 532 nm pulse is absorbed uniformly within the sample. For our relatively thick and diffuse scattering samples this assumption would be invalid.

 © 2005 Wiley-VCH Verlag GmbH & Co. KGaA, Weinheim

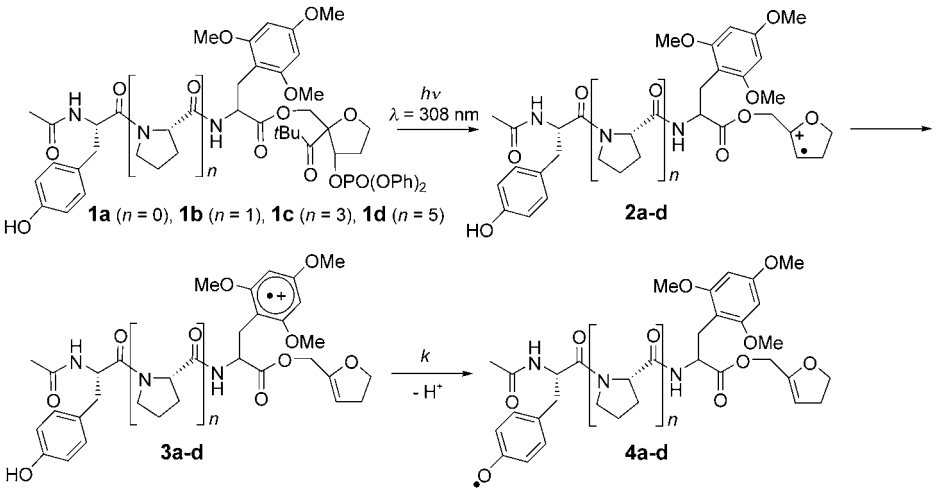
Electron Transfer in Peptides

Multistep Electron Transfer in Oligopeptides: Direct Observation of Radical Cation Intermediates**

Bernd Giese, Matthias Napp, Olivier Jacques, Hassen Boudebous, Alexander M. Taylor, and Jakob Wirz*

For the transport of electrons or electron holes over long distances, nature often uses DNA double strands or proteins. With DNA, experiments[1] and calculations[2] have clearly shown that these processes can occur by a hopping mechanism, where the charge transport takes place in a multistep reaction.[3] Purines act as carriers of positive charge[4] ("electron-hole transport"), and pyrimidines are carriers of negative charge[5] ("excess-electron transport"). A similar hopping model was also applied to explain long-distance charge transport through proteins.[6] Hopping is especially favored if the amino acids carry side chains that can be easily oxidized (tyrosine, tryptophan, and histidine). For instance, a multistep electron-hole transport cascade involving three tryptophan units was proposed for the photoactivation process in the enzyme photolyase.[6a] Presumably, not only tryptophan but also tyrosine and histidine are involved in the mechanism of radical initiation in ribonucleotide reductase, where an electron hole is transported over a distance of 35 Å.[6e] In these systems, transient intermediates occurring in the multistep charge transport have not yet been detected, and it is not clear whether the electron transfer is best described as proceeding through space or through the peptide bonds.[7]

In order to examine electron-hole transport in peptides, we synthesized the series of model systems **1a–d** bearing three different redox sites, that is, a modified tetrahydrofuran as a charge-injection system,[8] 2,4,6-trimethoxyphenylalanine[9] as an intermediate charge carrier, and tyrosine as a final electron donor. An oligoproline spacer of variable length ($n = 0, 1, 3, 5$) was chosen to separate the tyrosine residue from the 2,4,6-trimethoxyphenylalanine moiety. As is known from related studies of electron-hole transfer in DNA, irradiation of the pivaloylated tetrahydrofuran unit in compounds like **1a–d** will generate the dihydrofuranosyl radical cations, **2a–d**, through Norrish α cleavage and subsequent β elimination of the phosphate leaving group.[10] These radical cations have



Scheme 1. Mechanism for the photolysis of **1a–d** and the subsequent electron-transfer reactions.

strong oxidizing properties[11] and can oxidize the neighboring 2,4,6-trimethoxyphenylalanine side chain (Scheme 1).[12]

Compounds **1a–d** were dissolved in acetonitrile/water (3:1) and irradiated with 308-nm pulses from a XeCl excimer laser,[13] which allowed selective excitation of the pivaloyl chromophore. The transient absorption spectra observed after a delay of 50 ns with respect to the laser pulse indicated the presence of radical cations **3a–d** with an absorption maximum at 550 nm (Figure 1a shows the spectrum for system **1c** as a typical example).[14,15] This signal decayed

[*] Prof. Dr. B. Giese, Dr. M. Napp, Dr. O. Jacques, A. M. Taylor
Department of Chemistry, University of Basel
St. Johanns-Ring 19, 4056 Basel (Switzerland)
Fax: (+41) 61-267-1105
E-mail: bernd.giese@unibas.ch
Dipl.-Chem. H. Boudebous, Prof. Dr. J. Wirz
Department of Chemistry, University of Basel
Klingelbergstrasse 80, 4056 Basel (Switzerland)

[**] This work was supported by the Swiss National Science Foundation.

Supporting Information for this article is available on the WWW under http://www.angewandte.org or from the author.

 DOI: 10.1002/anie.200500391 © 2005 Wiley-VCH Verlag GmbH & Co. KGaA, Weinheim

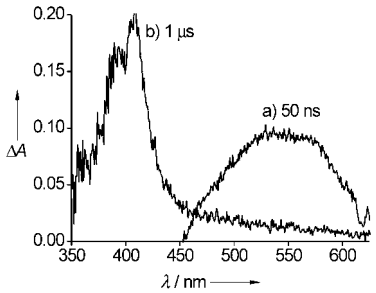


Figure 1. Transient absorption spectra observed after a delay of a) 50 ns and b) 1 μs with respect to the irradiation of **1c** in degassed acetonitrile/water (3:1) at a concentration of 8 mM.

within 1 μs and was replaced by the characteristic signal of the tyrosyl radical with a maximum absorbance at 410 nm (Figure 1b).[16]

Kinetic traces of the absorbance decay at 550 nm and of the growth observed at 410 nm obeyed the first-order rate law well, and the rate constants determined by least-squares fitting at the two wavelengths were the same within the limits of error. A typical example is shown in Figure 2.

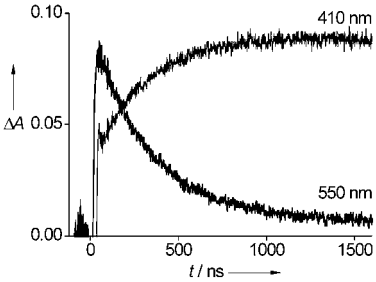


Figure 2. Kinetic traces of the transient absorptions at 410 and 550 nm for **1c** (7 mM) in degassed acetonitrile/water (3:1). The decay rate constant at 550 nm is $3.1(\pm0.2)\times10^6\ s^{-1}$ and the absorbance growth constant at 410 nm is $3.5(\pm0.3)\times10^6\ s^{-1}$.

However, the rate constants observed with model peptides **1a–d** increased linearly with the concentration of these compounds. This pointed to competition of intra- and intermolecular electron transfer. The slopes of these plots correspond to the intermolecular rate contributions k_{inter}, and the values so obtained ($k_{inter}\approx4\times10^8\ M^{-1}s^{-1}$) agree well with the rate constants of diffusion expected for compounds of this size. The intramolecular contributions, namely the rate constants k_{intra}, for electron transfer from the tyrosine side chain to the 2,4,6-trimethoxyphenylalanine radical cation moiety (**3a–d**→**4a–d**) were determined from the intercepts (Table 1).[17]

The rate constants k_{intra} (Table 1) decrease by a factor of only about two when the spacer between the aromatic redox centers is elongated by addition of two proline units (compare **1b** with **1c** and **1c** with **1d**). For an electron transfer through the peptide bonds one would expect a rate decrease of about 500 for two additional proline units.[18] This indicates that the electron transfer does not proceed by a through-bond mechanism. We attribute the small influence of additional proline spacers upon the k_{intra} value to the conformational flexibility of the aromatic amino acids.[19] The rate does increase considerably when the proline spacer is absent, as in **1a**, where the aromatic side chains are in close contact with each other.

Table 1: Rate constants for intramolecular (k_{intra}) and intermolecular (k_{inter}) electron transfer, determined from the intercepts and slopes of rate-versus-concentration plots. The number of proline units between the aromatic side chains is given by n, and σ_l is the length of the through-bond pathway, based on the number of covalent bonds between the aromatic redox centers.[6f]

	n	k_{intra} [s^{-1}]	k_{inter} [$M^{-1}s^{-1}$]	σ_l [Å]
1a	0	$8.6(\pm0.6)\times10^6$	$\leq5\times10^8$	9.8
1b	1	$1.1(\pm0.1)\times10^6$	$4.3(\pm0.4)\times10^8$	14.0
1c	3	$5.1(\pm0.3)\times10^5$	$3.0(\pm0.1)\times10^8$	22.4
1d	5	$2.8(\pm0.3)\times10^5$	$3.2(\pm0.1)\times10^8$	30.8

The radical cation of 1,3,5-trimethoxybenzene[12] should not be capable of oxidizing phenol to the phenol radical cation (oxidation potential $E_{ox}(PhOH/PhOH^{\bullet+})=1.50$ V versus a NHE).[20] But oxidation of phenol to the phenoxy radical in aqueous solution (pH 7) has a much lower potential of $E_{ox}(PhOH/PhO^{\bullet})=0.86$ V versus a NHE.[21] Thus, oxidation of tyrosine in the systems **3a–d** can easily occur, if the electron transfer is coupled with proton transfer to the solvent. We measured a kinetic deuterium isotope effect k_H/k_D of 1.8(±0.2).[22] This value is in good agreement with the isotope effect of 2.0–2.5 for the oxidation of tyrosine by a ruthenium–tris(bipyridine) complex in aqueous media, where a proton-coupled electron transfer occurs.[23]

In summary, electron-hole transport in peptide radical cations **3a–d** occurs by a hopping mechanism between the aromatic side chains of the amino acids, which is similar to the long-distance hole transport through DNA.[1–4]

Received: February 1, 2005
Published online: May 25, 2005

Keywords: charge transport · electron transfer · flash photolysis · peptides · radicals

[1] E. Meggers, M. E. Michel-Beyerle, B. Giese, *J. Am. Chem. Soc.* **1998**, *120*, 12950.
[2] J. Jortner, M. Bixon, T. Langenbacher, M. E. Michel-Beyerle, *Proc. Natl. Acad. Sci. USA* **1998**, *95*, 12759.
[3] Recent reviews: "Long-Range Charge Transfer in DNA": *Top. Curr. Chem.* **2004**, *236* and *237*.
[4] B. Giese, J. Amaudrut, A.-K. Köhler, M. Spormann, S. Wessely, *Nature* **2001**, *412*, 318.
[5] a) S. Breeger, U. Hennecke, T. Carell, *J. Am. Chem. Soc.* **2004**, *126*, 1302; b) T. Ito, S. E. Rokita, *Angew. Chem.* **2004**, *116*, 1875; *Angew. Chem. Int. Ed.* **2004**, *43*, 1839.
[6] a) C. Aubert, M. H. Vos, P. Mathis, A. P. M. Eker, K. Brettel, *Nature* **2000**, *405*, 586; b) J. R. Winkler, *Curr. Opin. Chem. Biol.* **2000**, *4*, 192; c) E. G. Petrov, V. May, *J. Phys. Chem. A* **2001**, *105*, 10176; d) C. C. Page, C. C. Moser, P. L. Dutton, *Curr. Opin. Chem. Biol.* **2003**, *7*, 551; e) J. Stubbe, D. G. Nocera, C. S. Yee, M. C. Y. Chang, *Chem. Rev.* **2003**, *103*, 2167; f) H. B. Gray, J. R. Winkler, *Q. Rev. Biophys.* **2003**, *36*, 341; g) T. Morita, S. Kimura, *J. Am. Chem. Soc.* **2003**, *125*, 8732.

 © 2005 Wiley-VCH Verlag GmbH & Co. KGaA, Weinheim

[7] The question of whether the electron travels through the peptide bonds by a bridge-mediated superexchange mechanism or by a hopping process has been the subject of several investigations: a) A. K. Mishra, R. Chandrasekar, M. Faraggi, M. H. Klapper, *J. Am. Chem. Soc.* **1994**, *116*, 1414; b) K. Bobrowski, J. Poznanski, J. Holcman, K. L. Wierzchowski, *J. Phys. Chem. B* **1999**, *103*, 10316; c) R. A. Malak, Z. Gao, J. F. Wishart, S. S. Isied, *J. Am. Chem. Soc.* **2004**, *126*, 13888; d) K. Yanagisawa, T. Morita, S. Kimura, *J. Am. Chem. Soc.* **2004**, *126*, 12780; e) F. Polo, S. Antonello, F. Formaggio, C. Toniolo, F. Maran, *J. Am. Chem. Soc.* **2005**, *127*, 492.

[8] The synthesis of the charge-injecting system was performed following procedures reported earlier: a) R. Glatthar, M. Spichty, A. Gugger, R. Batra, W. Damm, M. Mohr, H. Zipse, B. Giese, *Tetrahedron* **2000**, *56*, 4117; b) A. Marx, P. Erdmann, M. Senn, S. Körner, T. Jungo, M. Petretta, P. Imwinkelried, A. Dussy, K. J. Kulicke, L. Macko, M. Zehnder, B. Giese, *Helv. Chim. Acta* **1996**, *79*, 1980. (See the Supporting Information for further details.)

[9] We used the racemate: D. Dauzonne, R. Royer, *Synthesis* **1987**, 399.

[10] A. Gugger, R. Batra, P. Rzadek, G. Rist, B. Giese, *J. Am. Chem. Soc.* **1997**, *119*, 8740.

[11] When 2,3-dihydrofuran is used as a simple model system, the reduction potentials of radical cations like **2a–d** are estimated to be larger than 1.27 V versus a normal hydrogen electrode (NHE): K. Bernhard, J. Geimer, M. Canle-Lopez, J. Reynisson, D. Beckert, R. Gleiter, S. Steenken, *Chem. Eur. J.* **2001**, *7*, 4640.

[12] The half-wave oxidation potential of 1,3,5-trimethoxybenzene is 1.25 V versus a NHE: A. Zweig, W. G. Hodgson, W. H. Jura, *J. Am. Chem. Soc.* **1964**, *86*, 4124.

[13] Solutions of **1a–d** (0.3–8 mM) were degassed in a quartz cell of 4.5-cm path length and irradiated with laser pulses (Lambda-Physik COMPex 205, $\lambda = 308$ nm, pulse width of 25 ns, 100–150 mJ per pulse) at RT (22–24 °C). An iStar 720 ICCD camera (Andor) was used for the detection of transient absorption spectra. Transient kinetics were recorded with a 1P28 photomultiplier (Hamamatsu). For a detailed description, see: a) J. Wirz, *Pure Appl. Chem.* **1984**, *56*, 1289; b) E. Leyva, M. S. Platz, G. Persy, J. Wirz, *J. Am. Chem. Soc.* **1986**, *108*, 3783; c) S. Gerber, J. Wirz, *EPA Newsl.* **1989**, *36*, 19.

[14] P. O'Neill, S. Steenken, D. Schulte-Frohlinde, *J. Phys. Chem.* **1975**, *79*, 2773.

[15] The transient absorption spectrum recorded after oxidation of *N*-acetyl-2,4,6-trimethoxyphenylalanine methyl ester (**5**) by photosensitized electron transfer with 1,4-dicyanonaphthalene as a sensitizer and biphenyl as a codonor is similar to the spectrum shown in Figure 1a (see the Supporting Information). Furthermore, a compound with the pivaloylated tetrahydrofuran unit directly connected to *N*-acetyl-2,4,6-trimethoxyphenylalanine was synthesized (**6**). Laser flash photolysis of this compound again gave a spectrum that was practically identical to the one shown in Figure 1a (see the Supporting Information).

[16] K. M. Bansal, R. W. Fessenden, *Radiat. Res.* **1976**, *67*, 1.

[17] The irradiations were carried out at concentrations of 0.3–8 mM, which provided k_{intra} values from the intercepts of rate-versus-concentration plots with a standard error of about 10% (see the Supporting Information). The decay of the radical cation of 2,4,6-trimethoxyphenylalanine in the absence of tyrosine was much slower (dissociation constant $k_d = 1.1 \cdot 10^4\ s^{-1}$) than the intramolecular electron-transfer reaction **3a–d**→**4a–d** ($k_{intra} = 0.28 \times 10^6$–$8.6 \times 10^6\ s^{-1}$). These intramolecular rates are 10–100 times faster than the observed electron-transfer rates between a tryptophan radical cation and tyrosine.[7a,b] This is in accord with the higher oxidation potential (E_{ox}) of trimethoxyphenylalanine[12] compared to tryptophan ($E_{ox} = 1.02$ V versus a NHE).[21]

[18] By addition of two proline units, the length of the through-bond pathway (σ_l, 1.4 Å times the number of covalent bonds in the effective path) is increased by 8.4 Å. With a distance-decay constant of $\beta = 0.73\ Å^{-1}$, the k_{intra} value is expected to drop by a factor of about 500: D. R. Casimiro, L. L. Wong, J. L. Colon, T. E. Zewert, J. H. Richard, I.-J. Chang, J. R. Winkler, H. B. Gray, *J. Am. Chem. Soc.* **1993**, *115*, 1485.

[19] By using ^{1}H-NOESY experiments in [D_3]acetonitrile, conformation studies of **1c** were performed. The proline spacer adopts the all-*trans* conformation in about 80%. Subsequent molecular-modeling analysis (with the MakroModel 7.2 program) of compounds **1a–d** in a fixed all-*trans* conformation revealed that, due to the conformational flexibility of the aromatic side chains, different distances exist between the redox centers.

[20] S. Canonica, B. Hellrung, J. Wirz, *J. Phys. Chem. A* **2000**, *104*, 1226.

[21] A. Harriman, *J. Phys. Chem.* **1987**, *91*, 6102.

[22] The rate of intramolecular electron transfer in compound **1c** (acetonitrile/D_2O (3:1)) is $2.9(\pm 0.2) \times 10^5\ s^{-1}$.

[23] M. Sjödin, S. Styring, B. Åkermark, L. Sun, L. Hammarström, *Philos. Trans. R. Soc. London Ser. B* **2002**, *357*, 1471.

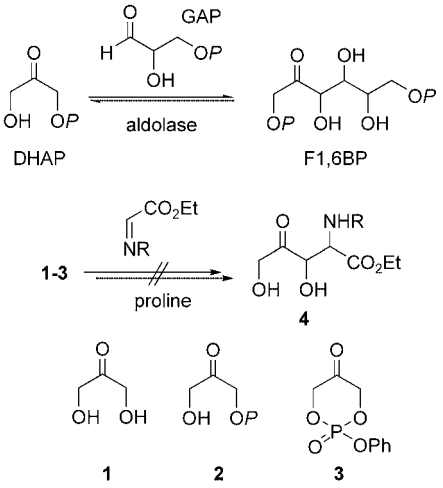
 © 2005 Wiley-VCH Verlag GmbH & Co. KGaA, Weinheim

Organocatalysis

Dihydroxyacetone in Amino Acid Catalyzed Mannich-Type Reactions**

Bernhard Westermann and Christiane Neuhaus*

After lying in obscurity for more than 40 years, proline-catalyzed carbonyl reactions have been studied intensively in recent years.[1] Although Martens and co-workers pointed out the enormous potential of these reactions in a Review in 1982, they did not attract significant interest until the studies of List, Barbas, MacMillan, Jørgensen, and others were published.[2] Proline-catalyzed reactions could possibly explain the origin of prebiotic aldol and Mannich products and thus the stereoselective synthesis of carbohydrates. During glycolysis and gluconeogenesis, an aldolase-catalyzed aldol reaction of two C_3 building blocks, 3-glyceraldehyde phosphate (GAP), and dihydroxyacetone phosphate (DHAP) takes place (Scheme 1).[3]



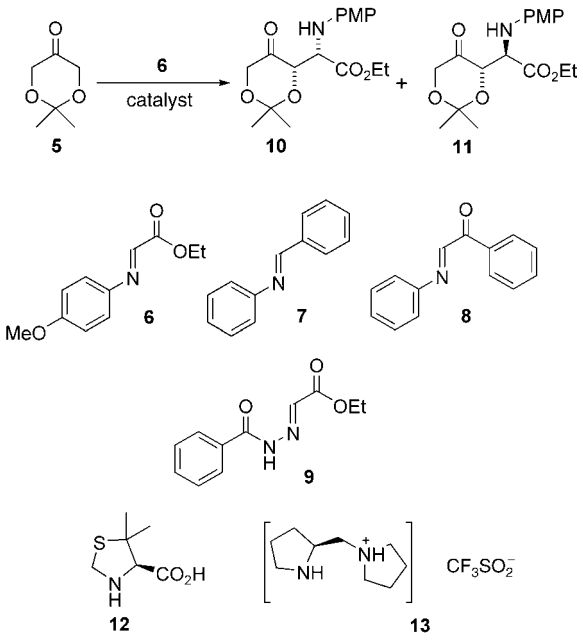
Scheme 1. Dihydroxyacetone and phosphorylated derivatives in aldol and Mannich reactions.

Despite the enormous number of publications dealing with organocatalytic carbonyl reactions, only a few examples can be found in which dihydroxyacetone (DHA, **1**) was used as the C_3 methylene compound in aldol reactions towards carbohydrate precursors.[4,5] Mannich and Mannich-type reactions of DHA are, to the best of our knowledge, unknown.[6] These reactions would offer a very simple approach to azasugar and aminosugar derivatives, which are of considerable biological interest owing to their glycosidase-inhibiting and aminoglycoside-mimicking properties.[7] As a multistep sequence is generally required in the synthesis of these compounds, a simple approach is highly desirable.

Herein we report the use of protected dihydroxyacetone and various imines in Mannich reactions. In this context, we present 2,2,2-trifluoroethanol (TFE) as a highly suitable solvent and describe the application of microwave irradiation to accelerate organocatalytic reactions.[8]

In contrast to hydroxyacetone no reaction could be observed with DHA (**1**) under the conditions provided by List and by Cordova and co-workers (L-proline (30 mol%), DMSO, room temperature).[9] Therefore, we used phosphate-protected dihydroxyacetone derivatives **2** and **3** in preliminary reactions.[10] Unfortunately, no reaction occurred between imine **6** and the methylene compound (Schemes 1 and 2).[11] Subsequently, we used the acetonide **5** of dihydroxyacetone which can easily be synthesized in large amounts in two steps. Acetonide **5** was previous employed in diastereo- and enantioselective aldol reactions as a DHA equivalent.[12] Besides the distinct reactivity, we assumed that a very compact, bicyclic transition state would result with this cyclic ketone, thus leading to high diastereoselectivities.

In the first experiment it could be shown that the desired products **10** (*syn*) und **11** (*anti*) were formed by using protected DHA **5** and imine **6** in the presence of racemic proline (30 mol%) (Scheme 2; Table 1, entry 1 (91:9 d.r.)). Further experiments with L-proline led to identical diastereomeric ratios; the enantioselectivity (82% *ee*) was satisfying.[13] Whereas solvents such as acetonitrile, toluene, and ionic liquids (Table 1, entries 4–6) did not result in notable improvements in stereoselectivites, very polar solvents such as formamide and TFE led to excellent diastereo- and enantioselectivities (Table 1, entries 7, 8). The use of TFE



Scheme 2. Catalyzed Mannich reactions. The reaction conditions are given in Table 1; PMP = *p*-methoxyphenyl.

[*] Prof. Dr. B. Westermann, Dipl.-Chem.-Ing. C. Neuhaus
Leibniz Institute of Plant Biochemistry
Department of Bioorganic Chemistry
Weinberg 3, 06120 Halle (Saale) (Germany)
Fax: (+49) 345-5582-1309
E-mail: Bernhard.Westermann@ipb-halle.de

[**] The authors are grateful to Dr. M. Lange, Girindus AG (Halle) for helpful discussions.

 DOI: 10.1002/anie.200500297 © 2005 Wiley-VCH Verlag GmbH & Co. KGaA, Weinheim

Table 1: Results of the Mannich reaction with **5** and **6** (see Scheme 2).

Entry	Catalyst	Conc. [mol%]	Solvent[a]	*t* [h]	*T* [°C]	Yield [%][b]	d.r.[c]	*ee* [%][d]
1	D,L-proline	30	DMSO	20	RT	46	91:9	–
2	L-proline	30	DMSO	20	RT	37	91:9	82
3	L-proline	30	H_2O	96	RT	34	93:7	34
4	L-proline	30	acetonitrile	40	RT	52	93:7	80
5	L-proline	30	toluene	40	RT	52	92:8	42
6	L-proline	30	$BMIMBF_4$	40	RT	39	89:11	n.d.
7	L-proline	30	formamide	20	RT	54	95:5	96
8	L-proline	30	TFE	20	RT	72	97:3	99
9	L-proline	30	TFE/H_2O (95:5)	20	RT	76	95:5	96
10	L-proline	30	TFE/H_2O (90:10)	20	RT	76	95:5	95
11	L-proline	20	TFE	20	RT	68	96:4	99
12	L-proline	10	TFE	20	RT	75	95:5	95
13	L-proline	5	TFE	20	RT	70	93:7	91
14	L-proline	30	TFE	20	0	44	97:3	97
15	L-proline	30	TFE	20	−20	36	96:4	97
16	DMTC (**12**)	30	TFE	40	RT	28	86:14	n.d.
17	diamine (**13**)	30	TFE			no reaction		

[a] $BMIMBF_4$ = 1-butyl-3-methylimidazolium tetrafluoroborate; TFE = 2,2,2-trifluoroethanol. [b] Yields of isolated products. [c] d.r. determined by GC–MS. [d] *ee* determined by HPLC (Chiralcel OD-H); n.d.: not determined.

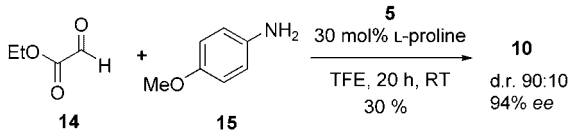
allowed the isolation of the product in 72% yield with reproducible diastereoselectivity (97:3 d.r.) and enantioselectivity (99% *ee*). A slight decrease in the selectivities (95:5 d.r. and 96/95% *ee* (Table 1, entries 9, 10) was observed in TFE/H_2O solvent mixtures (95:5; 90:10). To decrease the amount of proline, we ran further experiments in TFE with decreasing concentrations of catalyst (Table 1, entries 11–13). We proved that the amount of catalyst could be decreased significantly. Only at 5 mol% of L-proline did the stereoselectivity decrease quite drastically. Temperature effects were not observed (Table 1, entries 14, 15).

Other proline-derived catalysts proved to be unsuitable. L-5,5-Dimethylthiazolidine-4-carboxylic acid (DMTC; **12**) resulted in poor selectivities. No reaction occurred in the presence of (*S*)-1-(2-pyrrolidinylmethyl)pyrroline triflate (**13**) (Table 1, entries 16, 17). Disappointingly, imines **7** and **8** and hydrazone **9**[14] did not react with **5**.

One disadvantage of many proline-catalyzed reactions is the long reaction time. We therefore tried to accelerate the reaction under the action of microwaves. The results of the microwave-assisted organocatalytic Mannich reactions are listed in Table 2. Consistent with the previously observed results, TFE was once again the solvent of choice. After only 10 min **10** was obtained in 72% yield with high diastereo- (90:10 d.r.) and enantioselectivities (95% *ee*). A decrease in the irradiating power led to a lower yield, although the selectivities remained the same. The use of DMSO or formamide as solvent led to a significant decrease in the yield and diastereoselectivity.[15]

The Mannich-type reaction could also be carried out as a three-component process (Scheme 3). The reaction of glyoxylate **14**, *p*-anisidine (**15**), and **5** yielded **10** in 30% yield with selectivities comparable with those of the two-component reaction.

The relative configuration of all the products was determined by NMR spectroscopy. The *syn* conformation of the main diastereomer can be concluded based on the ^3J coupling constant (CHO-CHN) of 2.3 Hz and on NOE interactions.[16] This is consistent with results from other Mannich-type reactions. Therefore, it is possible to assume the same transition state proposed by Cordova.[6]



Scheme 3. Three-component reaction to **10**.

In conclusion nitrogen-containing carbohydrate derivatives were obtained with very good stereoselectivities from DHA derivatives. Furthermore it is possible to improve existing protocols (shorter reaction times, less catalyst) by using 2,2,2-trifluoroethanol as solvent and microwave-assisted procedure.[17]

Table 2: Results of the microwave-assisted Mannich reaction of **5** and **6** in the presence of L-proline (30 mol%).[a]

Solvent	*t* [min]	*E* [W][b]	Yield [%][c]	d.r.[d]	*ee* [%][e]
TFE	5	300	63	89:11	94
TFE	10	300	72	90:10	94
TFE	10	100	64	90:10	95
DMSO	10	300	18	92:8	n.d.
formamide	5	300	40	83:17	n.d.
formamide	10	300	38	80:20	n.d.

[a] All reactions were carried out in sealed 10-mL tubes. [b] Maximal irradiated power. [c] Yields of isolated products. [d] Determined by GC–MS. [e] Determined by HPLC (Chiralcel OD-H).

Experimental Section

Solvent (1 mL) and L-proline (35 mg, 0.3 mmol) were stirred at room temperature for 3 min, before **5** (130 mg, 1.0 mmol) was added. After 15 min **6** (207 mg, 1.0 mmol) was added. The reaction mixture was stirred for 20 h. A saturated solution of NH_4Cl (1.0 mL) was added, and the mixture was extracted with ethyl acetate (2 × 15 mL). The combined organic extracts were dried with Na_2SO_4, filtered, and concentrated. The residue was purified by column chromatography through silica gel (petroleum ether/ethyl acetate 3:1) to give the product **10** as an oil. R_f = 0.8 (petroleum ether/ethyl acetate 3:2); HPLC (Daicel Chiralcel OD-H, hexane/2-propanol 90:10, 1.0 mL min^{-1}, λ = 254 nm); $[\alpha]_D^{20} = -107.0$ (c = 0.2, ethyl acetate); ^{1}H NMR ($CDCl_3$, 300 MHz): δ = 1.24 (t, ^3J = 7.1 Hz, 3H; Me), 1.44 (s, 3H; Me), 1.49 (s, 3H; Me), 3.73 (s, 3H; Me), 4.02 (d, ^2J = 16.5 Hz, 1H; CH*H*, 5-H), 4.13 (dq, J = 7.1, 10.8 Hz, 1H; O*CH*$_2$CH$_3$), 4.24 (dq, J = 7.1, 10.8 Hz, 1H; O*CH*$_2$CH$_3$), 4.30 (dd, J_1 = 1.6 Hz, J = 16.5 Hz, 1H; CH*H*, 5-H), 4.59 (d, J = 2,3 Hz, 1H; 2-H), 4.74 (dd, J = 1.6, 2.3 Hz, 1H; 3-H), 6.7–6.8 ppm (m, 4H; Ar-H); ^{13}C NMR ($CDCl_3$, 75.5 MHz): δ = 14.2 (q), 23.3 (q), 24.2 (q), 55.5 (q), 58.8 (d), 61.5 (t), 67.0 (t), 76.4

 © 2005 Wiley-VCH Verlag GmbH & Co. KGaA, Weinheim

(d), 100.7 (s), 114.5 (d, 2C), 116.8 (d, 2C), 140.7 (s), 153.3 (s), 171.1 (s), 206.0 ppm (s); HRMS [M+Na^+]: 337.1423 (calcd), 337.1427 (found).

Received: January 26, 2005
Published online: May 24, 2005

Keywords: asymmetric synthesis · Mannich reaction · microwave irradiation · organocatalysis · proline

[1] P. I. Dalko, L. Moisan, *Angew. Chem.* **2004**, *116*, 5248; *Angew. Chem. Int. Ed.* **2004**, *43*, 5138.
[2] K. Drauz, A. Kleemann, J. Martens, *Angew. Chem.* **1982**, *94*, 590; *Angew. Chem. Int. Ed. Engl.* ***1982***, *21*, 584; today's significance of organocatalysis is outlined in special issues of *Acc. Chem. Res.* **2004**, *37*(8) and *Adv. Synth. Catal.* **2004**, *346*(9–10).
[3] Chemical application of aldolases: "Enolates, Organocatalysis, Biocatalysis and Natural Product Synthesis:" W. D. Fessner in *Modern Aldol Reactions*, *Vol. 1* (Ed.: R. Mahrwald), Wiley-VCH, Weinheim, **2004**, p. 201, and references therein.
[4] A. Cordova, W. Notz, C. F. Barbas, *Chem. Commun.* **2002**, 3024.
[5] W. Notz, B. List, *J. Am. Chem. Soc.* **2000**, *122*, 7386.
[6] A. Cordova, *Acc. Chem. Res.* **2004**, *37*, 102.
[7] N. Asano, *Glycobiology* **2003**, *13*, 93R ; A. Vasella, G. J. Davies, M. Böhm, *Curr. Opin. Chem. Biol.* **2002**, *6*, 619.
[8] O. Kappe, *Angew. Chem.* **2004**, *116*, 6408; *Angew. Chem. Int. Ed.* ***2004***, *43*, 6250; in the described experiments a microwave Emrys Optimizer was used.
[9] B. List, *Synlett* **2001**, 1675; A. Cordova, W. Notz, G. Zhong, J. M. Betancort, C. F. Barbas III, *J. Am. Chem. Soc.* **2002**, *124*, 1844.
[10] E. L. Ferroni, V. DiTella, N. Ghanayem, R. Jeske, C. Jodlowski, N. O'Connell, J. Styrsky, R. Svoboda, A. Venkataraman, B. M. Winkler, *J. Org. Chem.* **1999**, *64*, 4943; S. Goswami, A. K. Adak, *Tetrahedron Lett.* **2002**, *43*, 503.
[11] Strictly speaking it is a Mannich-type reaction.
[12] For a review, see: D. Enders, M. Voith, A. Lenzen, *Angew. Chem.* **2005**, *117*, 1330; *Angew. Chem. Int. Ed.* ***2005***, *44*, 5138; M. Majewski, P. Nowak, *J. Org. Chem.* **2000**, *65*, 5152; K. S. Kim, S. D. Hong, *Tetrahedron Lett.* **2000**, *41*, 5909; D. Enders, M. Voith, *Synthesis* **2002**, 1775.
[13] The diastereoselectivities were determined by GC–MS, the enantioselectivities by HPLC: Daicel Chiralcel OD-H.
[14] K. L. Yamada, M. Shibasaki, S. J. Harwood, H. Gröger, *Angew. Chem.* **1999**, *111*, 3805; *Angew. Chem. Int. Ed.* ***1999***, *38*, 3713.
[15] A comparative experiment at 60 °C (oil bath, atmospheric pressure, 30 mol % L-proline, TFE) afforded **10** with a complete turnover after 30 min (67 % yield, 90:10 d.r., 91 % *ee*).
[16] T. Murakami, K. Taguchi, *Tetrahedron* **1999**, *55*, 989.
[17] After submission of the manuscript, the use of **5** in proline-catalyzed aldol reactions was described: D. Enders, C. Grondal, *Angew. Chem.* **2005**, *117*, 1235; *Angew. Chem. Int. Ed.* **2005**, *44*, 1210.

 © 2005 Wiley-VCH Verlag GmbH & Co. KGaA, Weinheim

Amino Sugars

Asymmetric Synthesis of Selectively Protected Amino Sugars and Derivatives by a Direct Organocatalytic Mannich Reaction**

Dieter Enders, Christoph Grondal, Marianna Vrettou, and Gerhard Raabe*

In the classic Mannich reaction the corresponding β-aminocarbonyl compounds are formed from formaldehyde, an amine, and an enolizable carbonyl component.[1] These so-called Mannich bases have found broad applications as synthetic building blocks,[2] most importantly in the preparation of natural products and biologically active compounds.[3] The main disadvantage of the classic Mannich reaction has been the lack of stereocontrol and the formation of by-products. As a result, the development of more selective and particularly diastereo- and enantioselective protocols for this important C–C bond-forming reaction has been of substantial interest. In 1985 our research group, in cooperation with Steglich et al., disclosed for the first time a procedure for a stereoselective Mannich reaction, by which enamines together with acyliminoacetates could be transformed into diastereo- and enantiomerically pure α-amino-γ-keto esters.[4] Later on we developed a first practical procedure for the regio- and enantioselective α-aminomethylation of ketones with the assistance of a directing silyl group at the α-position to the carbonyl group.[5]

Interest in catalytic asymmetric variants of the Mannich reaction has grown considerably in recent years. The application of both metal-containing and metal-free catalysts has led to a breakthrough in accomplishing diastereo- and enantioselective Mannich reactions.[6] Although very low loadings of sophisticated chiral metal-based catalysts can be employed and lead to excellent yields as well as diastereo- and enantioselectivities,[7] more generous loadings of readily available metal-free organocatalysts are often preferentially used.

Special notice should be taken of the proline-catalyzed three-component Mannich reaction developed by List et al.[8] In this highly developed organocatalytic method, enolizable aldehydes and ketones are treated with in situ generated imines to afford the corresponding Mannich products with good to excellent stereoselectivities.[9] Barbas and his co-workers independently used this strategy for the direct

[*] Prof. Dr. D. Enders, Dipl.-Chem. C. Grondal, Dr. M. Vrettou, Prof. Dr. G. Raabe
Institut für Organische Chemie, RWTH Aachen
Landoltweg 1, 52074 Aachen (Germany)
Fax: (+49) 241-809–2127
E-mail: enders@rwth-aachen.de

[**] This work was supported by the Deutsche Forschungsgemeinschaft (Schwerpunktprogramm Organokatalyse) and the Fonds der Chemischen Industrie (Kekulé fellowship for C.G.). We thank Degussa AG, BASF AG, Bayer AG, and Wacker Chemie for the donation of chemicals.

 DOI: 10.1002/anie.200500810 © 2005 Wiley-VCH Verlag GmbH & Co. KGaA, Weinheim

asymmetric synthesis of α-amino acids by employing preformed iminoglyoxylates.[10]

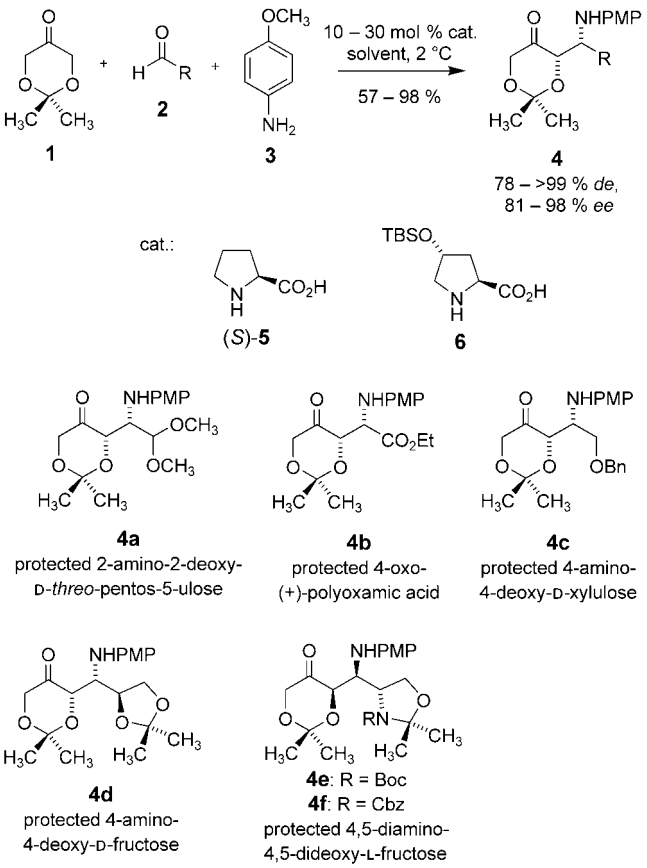
Recently, we reported a direct, organocatalytic de novo synthesis of carbohydrates. Starting from the dihydroxyacetone equivalent 2,2-dimethyl-1,3-dioxan-5-one (**1**),[11] various protected carbohydrates and amino sugars could be assembled in one step by a highly diastereo- and enantioselective proline-catalyzed aldol reaction.[12]

Carbohydrates are of great significance because of their diverse biological activities and application as synthetic building blocks and chiral auxiliaries.[13] Amino sugars are a class of carbohydrates, in which one or more hydroxy functions are replaced by amino groups. They are found as parts of glycoproteins, glycolipids, aminoglycosides, and many biologically active secondary metabolites containing free, methylated, or acetylated amino group.[14] The substitution of a hydroxy function by an amino group may alter the properties of the sugar significantly, for example, its hydrogen bonding properties, solubility, and charge. Consequently, amino sugars play important physiological roles in many glycoconjugates and are of interest for the development of new drugs.[15] There are numerous approaches for the synthesis of amino sugars. Most of them are based on naturally occurring carbohydrates and involve several protecting group manipulations as well as oxidation–reduction steps.[16] Alternatively, a linear synthetic sequence is used, but generally many reaction steps are required.[17]

Based on our organocatalytic $[C_3+C_x]$ concept for the direct synthesis of carbohydrates, we report here the successful development of a diastereo- and enantioselective Mannich variant that paves the way to selectively protected amino sugars and their derivatives.[18a] Initially, the (*S*)-proline-catalyzed three-component Mannich reaction of **1** with dimethoxyacetaldehyde (**2a**) and *para*-anisidine (**3**), as the amine component, was achieved. Thus, in the presence of 30 mol% proline in DMF at 2°C we obtained the Mannich product **4a** in 91% yield and excellent stereoselectivities (>99% *de*, 98% *ee* determined by HPLC; see Scheme 1). After recrystallization from heptane/2-propanol (9:1) **4a** could be obtained in practically diastereo- and enantiomerically pure form. Analogous conditions employed for the α-branched aldehydes **2d–g** and aldehyde **2b** also led to very good yields and selectivities; however, in the case of **2g** slightly superior results were obtained when acetonitrile and catalyst **6** were used (see Table 1). In contrast to the results of Barbas et al. aldehyde **2b** could also be used in the three-component reaction without prior isolation of the iminoglyoxylate.[18b]

In the case of linear aldehydes such as **2c** and the aromatic aldehydes **2h** and **2i** the results obtained under the above reaction conditions were not as good. Following extensive optimization of the reaction conditions we were able to verify the following general tendencies for these reactions.

1) The optimal reaction temperature was found to be between 2°C and ambient temperature. Apart from the expected decrease of the reaction rate at lower temperatures, we also observed a decline in the diastereo- and enantioselectivity, which may point to an isoinversion effect.[19]



Scheme 1. Organocatalytic asymmetric three-component Mannich reaction of dioxanone **1** with different aldehydes **2** and the amine **3**. R groups are defined in Table 1. PMP = *para*-methoxyphenyl, TBS = *tert*-butyldimethylsilyl, Bn = benzyl, Boc = *tert*-butoxycarbonyl, Cbz = benzyloxycarbonyl.

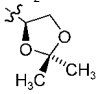
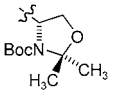
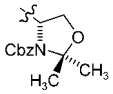
2) The addition of 1–10 equivalents of water led to an increase of the stereoselectivity independent of the solvent employed, although depending on the solvent, a decrease in the reaction reate could be observed.
3) The use of catalyst **6** generally led to an enhancement of the reaction rate, due to its superior solubility properties, and also the stereoselectivity subject to the solvent.
4) When catalyst **6** is employed, the addition of water has again a positive effect on the stereoselectivity.

In the case of the (*S*)-proline-catalyzed reaction of **2c**, we found that *N*-methylpyrrolidinone (NMP) accompanied by the addition of 3 equiv of water yielded the best results (94% yield, 60% *de*, 82% *ee*). Substitution of proline and NMP by catalyst **6** and acetonitrile, respectively, accompanied by the addition of 5 equiv of water afforded **4c** in 77% yield and greatly improved the selectivities (88% *de*, 96% *ee*). Similar observations were made in the case of aromatic aldehydes **2h** and **2i**.

In our initial report of the proline-catalyzed aldol reaction of **1**, we were able to show that in the case of NBoc- or NCbz-protected, (*S*)-configured enantiomerically pure Garner aldehydes **2e** and **f** (*S*)-proline is the appropriate catalyst. Analogous investigations of the Mannich reactions showed

 © 2005 Wiley-VCH Verlag GmbH & Co. KGaA, Weinheim

Table 1: Catalyzed asymmetric three-component Mannich reaction of dioxanone **1** with the aldehydes **2** and the amine **3** to give the products **4** (see Scheme 1).[a]

2/4	R	Cat. (mol%)	Yield [%][b]	Solvent	H_2O [equiv]	*de* [%][c]	*ee* [%][d]
a	$CH(OCH_3)_2$	(*S*)-**5** (30)	91	DMF	4	>99[d]	98
	$CH(OCH_3)_2$	**6** (20)	98	DMF	4	>99[d]	93
b	CO_2Et	(*S*)-**5** (10)	91	DMF	3	≥96	98
	CO_2Et	**6** (20)	94	DMF	–	≥96	95
c	CH_2OBn	(*S*)-**5** (30)	94	NMP	3	60[d]	82
	CH_2OBn	**6** (20)	77	CH_3CN	5	88[d]	96
d		(*S*)-**5** (30)	57	DMF	–	80 (≥96)[e]	≥98[f]
e		(*R*)-**5** (30)	67	DMF	–	≥96	≥96[f]
f		(*R*)-**5** (30)	63	DMF	–	≥96	≥96[f]
g		(*S*)-**5** (30)	83	CH_3CN	–	86	≥96[f]
		6 (20)	85	CH_3CN	–	≥96	≥96[f]
h		(*S*)-**5** (10)	67	NMP	–	≥96	51
		6 (20)	70	NMP	3	≥96	81
i		(*S*)-**5** (30)	75	DMF	2	60[d]	67
		6 (20)	96	CH_3CN	5	78[d]	87

[a] General reaction conditions : 0.77 mmol dioxanone **1**, 0.38 mmol aldehyde **2**, 0.42 mmol *para*-anisidine (**3**), 10–30 mol% catalyst, 1 mL solvent, 2 °C, 2–5 d. [b] Yields of **4** after flash chromatography on silica gel. [c] Determined by ^1H and ^{13}C NMR spectroscopy. [d] Determined by HPLC on chiral stationary phases (Daicel chiralpak AD, Daicel chiralcel OD). [e] After flash chromatography on silica gel. [f] Based on the *ee* value of the corresponding aldehyde **2**.

that when (*S*)-proline is used, only traces of the desired products could be isolated, whereas the (*R*)-proline-catalyzed reaction provided the Mannich products in good yields and virtually stereoisomerically pure (**4e**: 67%, ≤96% *de*, ≤96% *ee*; **4f**: 63%, 96% *de*, 96% *ee*). These results may support the suggestion that the proline-catalyzed Mannich reaction could facilitate kinetic resolutions of **1** with sterically demanding α-substituted aldehydes. Accordingly, (*R*)-proline should be the appropriate catalyst in the case of (*S*)-configurated, α-substituted aldehydes and (*S*)-proline for the application of (*R*)-configurated, α-substituted aldehydes. This was corroborated by the Mannich reaction of **1** with **2d** and **2g** and with (*S*)-proline as the catalyst (Table 1). As is evident from Scheme 1, the Mannich products **4a**–**f** constitute different selectively protected amino sugars and their derivatives, which could either be transformed to the corresponding amino sugars or used as synthetic building blocks, for example, **4a**. This organocatalysis can also be carried out smoothly on a multigram scale without any adverse effects on the yield and stereoselectivity (89% yield, ≤96% *de*, ≤96% *ee*), as exemplified by the reaction of **1** with **2a** and **3** to give **4a**.

The *syn* configuration of the Mannich products **4** was confirmed both by NOE measurements and an X-ray crystal structural analysis[20] on **4a** (Figure 1). These results are consistent with the transition-state model proposed by List et al. for the proline-catalyzed Mannich reaction. The stated absolute configurations are consistent with this model (Figure 2).

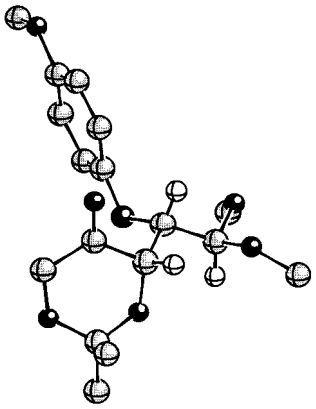


Figure 1. Crystal structure of **4a**.[20]

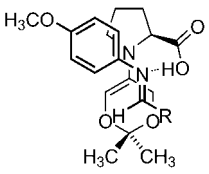
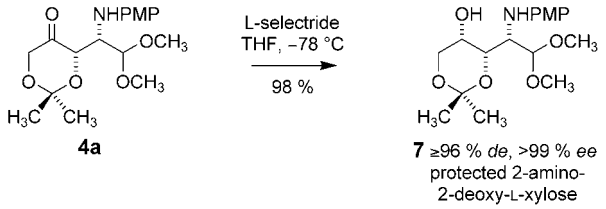


Figure 2. Transition-state model proposed by List et al.

The Mannich products **4** described here could be transformed into the corresponding β-amino alcohols by reduction of the keto function, which was successfully demonstrated in the

 © 2005 Wiley-VCH Verlag GmbH & Co. KGaA, Weinheim

case of **4a**. Thus, the reduction of **4a** with L-selectride proceeded at −78 °C with high stereocontrol to yield the all-*syn*-configured β-amino alcohol **7**, which in its protected form belongs to the class of the biologically very important 2-amino-2-deoxy sugars (Scheme 2).[17c,21] Furthermore, the polyoxamic acids are directly available from **4b** by reduction of the keto function.[22] They are integral parts of the polyoxines and also occur in isolated form in nature, and have attracted interest due to their biological activity.[23]



Scheme 2. Diastereoselective reduction of **4a** to **7** with L-selectride.

The efficient asymmetric catalytic method we have described here starting from simple and commercially available compounds provides a viable alternative to the conventional, relatively elaborate, and less flexible methods for the synthesis of amino sugars. Our protocol facilitates the synthesis of different amino pentoses and hexoses with high diversity in only one to two steps.

Experimental Section

Unless otherwise stated, all chemicals are commercially available and were used without further purification with the exception of aldehyde **2g**[24] and catalyst **6**.[25] All new compounds were fully characterized (IR, NMR, MS, elemental analysis, optical rotation, melting point).

4a: In a 100-mL round-bottomed flask a 60 % aqueous solution of **2a** (2.6 g, 15 mmol) was dissolved together with **3** (2.04 g, 16.5 mmol) and (*S*)-proline (519 mg, 4.5 mmol) in DMF (55 mL) at 2 °C. The solution was stirred for 30 min before **1** (2 g, 15 mmol) was added, and the mixture was stored for 5 days at 2 °C. The reaction was quenched with pH 7 buffer (50 mL) and the mixture stirred for 15 min at ambient temperature. After extraction of the aqueous phase with ethyl acetate (3 × 75 mL), the combined organic layers were dried over Na_2SO_4, concentrated, and purified by column chromatography using silica gel (diethyl ether/pentane, 1:2). The product **4a** (4.53 g, 89 %) was obtained as a pale yellow solid, which was recrystallized from heptane/2-propanol (9:1) to afford colorless crystals. M.p. 78–80 °C. $[\alpha]_D^{23} = -83.3$ ($c = 0.98$ in $CHCl_3$); IR ($CHCl_3$): $\tilde{\nu} = 3375$ (w), 2990 (m), 2938 (m), 2833 (m), 1748 (s), 1617 (s), 1515 (s), 1462 (m), 1378 (m), 1232 (s), 1123 (m), 1094 (m), 1040 (m), 977 (m), 889 (m), 824 (m), 757 (s), 527 cm^{-1} (s); ^1H NMR (400 MHz, C_6D_6): $\delta = 1.27$ (s, 3H, CCH_3), 1.29 (s, 3H, CCH_3), 3.02 (s, 3H, OCH_3), 3.16 (s, 3H, OCH_3), 3.55 (s, 3H, OCH_3), 3.76 (d, $J = 16.4$ Hz, 1H, CH_2), 3.94 (dd, $J = 16.4$ Hz, $J = 1.4$ Hz, 1H, CH_2), 4.38 (dd, $J = 6.6$ Hz, $J = 1.6$ Hz, 1H, *CH*) 4.44 (d, $J = 6.6$ Hz, 1H, $CH(OCH_3)_2$), 4.68 (br, 1H, *CH*), 6.75 ppm (*app*-s, 4H, Ar); ^{13}C NMR (100 MHz, C_6D_6): $\delta = 23.0$ (CH_3), 24.3 (CH_3), 53.3 (OCH_3), 54.5 (OCH_3), 54.9 (OCH_3), 56.3 (*CH*), 66.9 (CH_2), 75.1 (*CH*), 100.1 ($C(CH_3)_2$), 104.4 ($CH(OCH_3)_2$), 114.6 (*CH*), 115.9 (*CH*), 141.7 (*C*), 152.8 (*C*), 207.2 ppm (*CO*); MS (EI, 70 eV): *m*/*z* (%): 338.8 (11) [M^+], 263.9 (10) [$M^+ - C_3H_7O_2$], 217.9 (100) [$M^+ - C_7H_7NO$], 209.9 (16) [$M^+ - C_6H_9O_3$], 177.9 (68) [$C_{10}H_{12}NO_2^+$], 135.9 (17) [$C_8H_9NO^+$], 74.9 (31) [$C_6H_4^+$]; HPLC (Daicel OD, heptane/iPrOH 95/5, flow rate 0.8 mL min^{-1}, major isomer: $t_R =$ 11.86 min; minor isomer: $t_R = 8.78$ min; elemental analysis (%): calcd for $C_{17}H_{25}NO_6$: C 60.16, H 7.42, N 4.13; found: C 60.04, H 7.61, N 4.05.

Received: March 4, 2005
Published online: May 27, 2005

Keywords: amino sugars · asymmetric synthesis · dihydroxyacetone · Mannich reaction · organocatalysis

[1] C. Mannich, W. Krösche, *Arch. Pharm.* **1912**, *250*, 647–667.
[2] a) M. Arend, B. Westermann, N. Risch, *Angew. Chem.* **1998**, *110*, 1096–1122; *Angew. Chem. Int. Ed.* **1998**, *37*, 1044–1070; b) S. Kobayashi, H. Ishitani, *Chem. Rev.* **1999**, *99*, 1069–1094.
[3] a) P. Traxler, U. Trinks, E. Buchdunger, H. Mett, T. Meyer, M. Müller, U. Regenass, J. Rösel, N. Lydon, *J. Med. Chem.* **1995**, *38*, 2441–2448; b) J. R. Dimmock, K. K. Sidhu, M. Chen, R. S. Reid, T. M. Allen, G. Y. Kao, G. A. Truitt, *Eur. J. Med. Chem.* **1993**, *36*, 2243–2252; c) A. Kleemann, J. Engel in *Pharmazeutische Wirkstoffe: Synthese, Patente, Anwendungen* (Eds.: H. Sucker, P. Fuchs), Thieme, Stuttgart, **1982**.
[4] R. Kober, K. Papadopoulos, W. Miltz, D. Enders, W. Steglich, H. Reuter, H. Puff, *Tetrahedron* **1985**, *41*, 1693–1701.
[5] a) D. Enders, D. Ward, J. Adam, G. Raabe, *Angew. Chem.* **1996**, *108*, 1059–1062; *Angew. Chem. Int. Ed. Engl.* **1996**, *35*, 981–985; b) D. Enders, S. Oberbörsch, J. Adam, *Synlett* **2000**, 644–646; c) D. Enders, S. Oberbörsch, *Synlett* **2002**, 471–473; d) D. Enders, J. Adam, S. Oberbörsch, D. Ward, *Synthesis* **2002**, 2737–2748.
[6] a) A. Cordova, *Acc. Chem. Res.* **2004**, *37*, 102–112; b) *Asymmetric Organocatalysis* (Eds.: A. Berkessel, H. Gröger), Wiley-VCH, Weinheim, **2005**; c) S. Kobayashi, M. Ueno in *Comprehensive Asymmetric Catalysis Supplement I* (Eds.: E. N. Jacobsen, A. Pfaltz, H. Yamamoto), Springer, Berlin, **2003**, chap. 29.5.
[7] a) B. M. Trost, L. R. Terrell, *J. Am. Chem. Soc.* **2003**, *125*, 338–339; b) T. Ollevier, E. Nadeau, *J. Org. Chem.* **2004**, *69*, 9292–9295; c) S. Matsunaga, T. Yoshida, H. Morimoto, N. Kumagai, M. Shibasaki, *J. Am. Chem. Soc.* **2004**, *126*, 8777–8785; d) Y. Hamashima, N. Sasamoto, D. Hotta, H. Somei, N. Umebayashi, M. Sodeoka, *Angew. Chem.* **2005**, *117*, 1549–1553; *Angew. Chem. Int. Ed.* **2005**, *44*, 1525–1529.
[8] a) B. List, *J. Am. Chem. Soc.* **2000**, *122*, 9336–9337; b) B. List, P. Pojarliev, W. T. Biller, H. J. Martin, *J. Am. Chem. Soc.* **2002**, *124*, 827–833.
[9] a) W. Notz, K. Sakthivel, T. Bui, G. Zhong, C. F. Barbas III, *Tetrahedron Lett.* **2001**, *42*, 199–201; b) K. Juhl, N. Gathergood, K. A. Jørgensen, *Angew. Chem.* **2001**, *113*, 3083–3085; *Angew. Chem. Int. Ed.* **2001**, *40*, 2995–2997; c) Y. Hayashi, W. Tsuboi, I. Ashimine, T. Urushima, M. Shoji, K. Sakai, *Angew. Chem.* **2003**, *115*, 3805–3808; *Angew. Chem. Int. Ed.* **2003**, *42*, 3677–3680; d) W. Zhuang, S. Saaby, K. A. Jørgensen, *Angew. Chem.* **2004**, *116*, 4576–4578; *Angew. Chem. Int. Ed.* **2004**, *43*, 4476–4478; e) A. Münch, B. Wendt, M. Christmann, *Synlett* **2004**, 2751–2755; f) I. Ibrahem, J. Casas, A. Córdova, *Angew. Chem.* **2004**, *116*, 6690–6693; *Angew. Chem. Int. Ed.* **2004**, *43*, 6528–6531; g) A. J. A. Cobb, D. M. Shaw, D. A. Longbottom, J. B. Gold, S. V. Ley, *Org. Biomol. Chem.* **2005**, *3*, 84–96.
[10] a) A. Córdova, W. Notz, G. Zhong, J. M. Betancort, C. F. Barbas III, *J. Am. Chem. Soc.* **2002**, *124*, 1842–1843; b) A. Córdova, S.-I. Watanabe, F. Tanaka, W. Notz, C. F. Barbas III, *J. Am. Chem. Soc.* **2002**, *124*, 1866–1867.
[11] For a review see: D. Enders, M. Voith, A. Lenzen, *Angew. Chem.* **2005**, *117*, 1330–1351; *Angew. Chem. Int. Ed.* **2005**, *44*, 1304–1325.
[12] a) D. Enders, C. Grondal, *Angew. Chem.* **2005**, *117*, 1235–1238; *Angew. Chem. Int. Ed.* **2005**, *44*, 1210–1212; b) Two direct organocatalytic carbohydrate syntheses starting from **1** were

 © 2005 Wiley-VCH Verlag GmbH & Co. KGaA, Weinheim

later published independently: J. T. Suri, D. B. Ramachary, C. F. Barbas III, *Org. Lett.* **2005**, *7*, 1383 – 1385; I. Ibrahem, A. Cordova, *Tetrahedron Lett.* **2005**, *46*, 3363 – 3367.

[13] a) A. Varki, *Glycobiology* **1993**, *3*, 97 – 130; b) *Carbohydrate Mimics* (Eds.: Y. Chapleur), Wiley-VCH, Weinheim, **1998**; c) M. Sznaidman in *Bioorganic Chemistry: Carbohydrates* (Eds.: S. M. Hecht), Oxford University Press, New York, **1999**, pp. 1 – 56; d) K. M. Koeller, C.-H. Wong, *Chem. Rev.* **2000**, *100*, 4465 – 4493; e) K. C. Nicolaou, H. J. Mitchell, *Angew. Chem.* **2001**, *113*, 1625 – 1672; *Angew. Chem. Int. Ed.* **2001**, *40*, 1576 – 1624; f) S. Hanessian, *Total Synthesis of Natural Products: The "Chiron" Approach*, Pergamon, Oxford, **1983**; g) H. Kunz, K. Rück, *Angew. Chem.* **1993**, *105*, 355 – 377; *Angew. Chem. Int. Ed. Engl.* **1993**, *32*, 336 – 358.

[14] a) *Carbohydrate Based Drug Discovery* (Eds.: C.-H. Wong), Wiley-VCH, Weinheim, **2003**, chap. 26.3; b) A. C. Weymouth-Wilson, *Nat. Prod. Rep.* **1997**, *14*, 99 – 110.

[15] *Carbohydrate Based Drug Discovery* (Ed.: C.-H. Wong), Wiley-VCH, Weinheim, **2003**, chap. 24.

[16] a) G. A. Winterfeld, R. R. Schmidt, *Angew. Chem.* **2001**, *113*, 2718 – 2721; *Angew. Chem. Int. Ed.* **2001**, *40*, 2654 – 2657; b) C.-W. T. Chang, T. Clark, M. Ngaara, *Tetrahedron Lett.* **2001**, *42*, 6797 – 6801; c) J. Wang, L. Li, D. Tuttle, J. Y. Takemoto, C.-W. T. Chang, *Org. Lett.* **2002**, *4*, 3997 – 4000; d) N. Barroca, R. R. Schmidt, *Org. Lett.* **2004**, *6*, 1551 – 1554.

[17] a) M. P. Sibi, J. Lu, J. Edwards, *J. Org. Chem.* **1997**, *62*, 5864 – 5872; b) K. C. Nicolaou, P. S. Baran, Y.-L. Zhong, J. A. Vega, *Angew. Chem.* **2000**, *112*, 2625 – 2629; *Angew. Chem. Int. Ed.* **2000**, *39*, 2525 – 2529; c) L. Ermolenko, N. A. Sasaki, P. Potier, *J. Chem. Soc. Perkin Trans. 1* **2000**, 2465 – 2473; d) D. A. Evans, E. Hu, J. S. Tedrow, *Org. Lett.* **2001**, *3*, 3133 – 3136; e) H. Lu, Z. Su, L. Song, P. S. Mariano, *J. Org. Chem.* **2002**, *67*, 3525 – 3528.

[18] a) Very recently the (*S*)-proline-catalyzed synthesis of β-amino-α-oxyaldehydes was reported: I. Ibrahem, A. Córdova, *Tetrahedron Lett.* **2005**, *46*, 2839 – 2843; b) After we had submitted this manuscript, the editors drew our attention to work carried out independently on the (*S*)-proline-catalyzed Mannich reaction of **1** with **2b** and **3**: B. Westermann, C. Neuhaus, *Angew. Chem.* **2005**, DOI: 10.1002/ange200500297; *Angew. Chem. Int. Ed.* **2005**, DOI: 10.1002/anie200500297.

[19] H. Buschmann, H. D. Scharf, N. Hoffmann, P. Esser, *Angew. Chem.* **1991**, *103*, 480 – 518; *Angew. Chem. Int. Ed. Engl.* **1991**, *30*, 477 – 515.

[20] CCDC 265324 contains the supplementary crystallographic data for this paper. These data can be obtained free of charge from the Cambridge Crystallographic Data Centre via www.ccdc.cam.ac.uk/data_request/cif.

[21] For details on the biological relevance of 2-amino-2-deoxy sugars, see: I. V. Pelyvás, C. Monneret, P. Herczegh, *Synthetic Aspects of Aminodeoxy Sugars of Antibiotics*, Springer, Berlin, **1988**.

[22] We will report shortly in detail on the synthesis of the polyoxamic acids.

[23] a) B. M. Trost, A. C. Krueger, R. C. Bunt, J. Zambrano, *J. Am. Chem. Soc.* **1996**, *118*, 6520 – 6521; b) A. Tarrade, P. Dauban, R. H. Dodd, *J. Org. Chem.* **2003**, *68*, 9521 – 9524; c) S. Raghavan, S. C. Joseph, *Tetrahedron Lett.* **2003**, *44*, 6713 – 6715.

[24] H. Ohtake, Y. Imada, S.-I. Murakashi, *Bull. Chem. Soc. Jpn.* **1999**, *72*, 2737 – 2754.

[25] D. R. Langley, D. E. Thurston, *J. Org. Chem.* **1987**, *52*, 91 – 97.

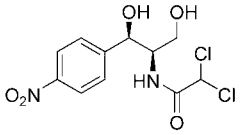
 © 2005 Wiley-VCH Verlag GmbH & Co. KGaA, Weinheim

Enzyme Catalysis

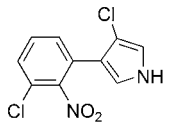
Sequential Enzymatic Oxidation of Aminoarenes to Nitroarenes via Hydroxylamines**

*Robert Winkler and Christian Hertweck**

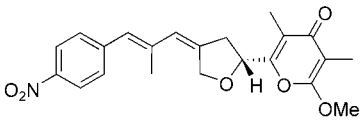
Aromatic nitro groups are relatively rare structural elements in natural products, but are found in diverse types of natural products, most of which are endowed with important biological properties. Prominent examples of bacterial nitroaryl metabolites include the potent antibiotic chloramphenicol (**1**),[1] the antifungal agent pyrrolnitrin (**2**),[2] and the cytostatic, *p*-nitrobenzoate-derived polyketide aureothin (**3**).[3,4] The nitrophenanthrene derivative aristolochic acid C (**4**) is the causative agent for "Chinese herbs nephropathy"[5] and 2-



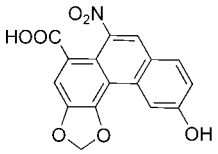
1



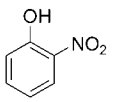
2



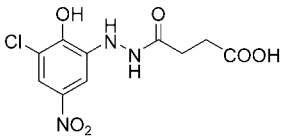
3



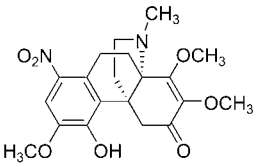
4



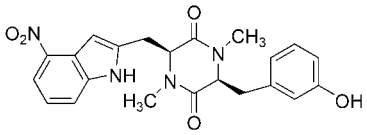
5



6



7



8

[*] R. Winkler, C. Hertweck
Leibniz Institute for Natural Products Research and Infection Biology, HKI
Beutenbergstrasse 11a, 07745 Jena (Germany)
Fax: (+49) 3641-656-705
E-mail: christian.hertweck@hki-jena.de

[**] We thank the Deutsche Forschungsgemeinschaft for financial support in the priority program SPP1152 "Evolution of Metabolic Diversity" (HE 3469/2) and A. Perner for MS measurements.

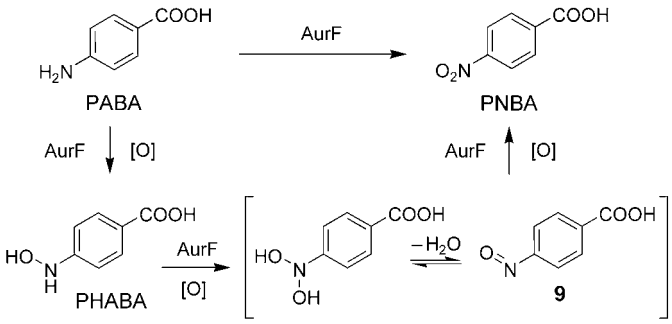
 DOI: 10.1002/anie.200500365 © 2005 Wiley-VCH Verlag GmbH & Co. KGaA, Weinheim

nitrophenol (**5**) is a well-studied component of the aggregation–attachment pheromone of ticks. The fungal nitroaryl compound stephanosporin (**6**) is the precursor of 2-chloro-4-nitrophenol.[6] Important examples of natural nonaromatic nitro compounds are nitropropionic acid[7] and the bacterial signal metabolite hormaomycin.[8,9]

Surprisingly, the biosynthesis of aromatic nitro groups is understood only to a small extent. One possible pathway involves aromatic substitution of nitro groups, as is the case for the unusual nitro alkaloid 1-nitroaknadinine (**7**) from *Stephania sutchuenensis*, which occurs simultaneously with the non-nitrated alkaloid. The proposed biosynthetic nitration step was mimicked in vitro with HNO_3.[10] More recently, it was reported that a NO synthase (NOS) takes part in the nitration of the diketopiperazine thaxtomin (**8**), a phytotoxin produced by the plant pathogen *Streptomyces turgidiscabies*.[11] Additional studies revealed that tryptophan is regioselectively nitrated by a complex of *Deinococcus radiodurans* NOS and Trp–tRNA synthetase.[12]

Despite these important findings, it appears that biosynthesis of the vast majority of aromatic nitro compounds proceeds by an alternate route: the enzymatic oxidation of primary amines.[1,13–15] In their studies with ^{18}O labeling and ^{15}N NMR spectroscopy, Baxter and co-workers revealed that both oxygen atoms of the fungal metabolite nitropropionate are derived from molecular oxygen.[7,16]

Conceivably, *N*-oxygenation could proceed in three steps via hydroxylamine and nitroso intermediates (Scheme 1), or both oxygen atoms could be introduced simultaneously by a



Scheme 1. Proposed biosynthetic pathway from PABA to PNBA via *p*-hydroxylaminobenzoate (PHABA).

dioxygenase, yet no direct evidence for either hypothesis has been given. The only existing studies on enzymatic nitro group formation have been carried out with haloperoxidases. These are not genuine N-oxygenases; they catalyze the oxidation of amino groups only under very specific, non-natural in-vitro conditions through the formation of reactive peroxo species, with excess H_2O_2 and/or in the absence of halide ions.[17–19] Furthermore, haloperoxidases such as CPO-P are not naturally involved in the biosynthesis of nitro compounds, as has been revealed by the analysis genes responsible for pyrrolnitrin biosynthesis.[13,20]

We recently cloned the N-oxygenase gene *aurF* from the gene cluster encoding aureothin biosynthesis in *Streptomyces thioluteus*.[21] Inactivation and complementation studies revealed that AurF plays a crucial role in the formation of the novel polyketide synthase starter unit *p*-nitrobenzoate (PNBA) from *p*-aminobenzoate (PABA),[14] and that the involvement of the cytochrome P_{450} monooxygenase AurH in *N*-oxygenation can be ruled out.[22] Furthermore, *aurF*-deficient null mutant permitted mutasynthesis of the aureothin derivative, aureonitrile.[23] Aside of PrnD from the pyrrolnitrin pathway in *Pseudomonas pyrrocinia*,[13] AurF is only the second known N-oxygenase involved in the biosynthesis of a nitro-group-containing metabolite. Whereas PrnD shows a clear Rieske motif, AurF appears to represent a novel type of oxygenase, as it does not share any of the known conserved oxidoreductase motifs (such as those for cofactor binding, for example).

A PABA-to-PNBA oxidation assay with AurF appeared as an ideal model system for gaining a deeper insight into nitro group formation. Although the expression of AurF was successful, all attempts to promote an in-vitro oxygenation failed, probably the result of a missing and yet unknown cofactor. It was reported earlier that cell-free extracts of *S. thioluteus* are unable to carry out *N*-oxygenation.[24] For this reason, *aurF* was expressed in the heterologous host *S. lividans*, and the oxygenation was performed as a whole-cell assay. Comparison of the whole-cell activities of recombinant and wild-type strains[24] implies that the heterologously produced AurF exhibits a slightly lower conversion rate, albeit in the same order of magnitude as that of the native enzyme. However, as all attempts at genetic manipulation of the wild-type *S. thioluteus* have failed, this functional vector–host system represents a valuable and flexible model system. A host strain of *S. lividans* containing the empty vector and phosphate buffer were used as negative controls in all experiments.

The putative PABA-derived hydroxylamine and nitroso arene intermediates are known to be highly reactive and unstable compounds. Therefore, the rapid and manipulation-free isolation and analysis of the corresponding benzoates from aqueous solution was a challenge. To avoid the extraction of labile intermediates, an at-line detection method was established analogously to a protocol for the analysis of acylated anilines from human whole blood.[25] The supernatant of centrifuged samples (1 mL) was loaded directly onto a RESOURCE RPC-18 column and eluted with a gradient of aqueous Na_2HPO_4-buffered acetonitrile/methanol. The method was thoroughly validated, and a very low detection limit (signal/noise ratio 3:1) for PABA (0.4 $\mu g\,mL^{-1}$) and PNBA (0.6 $\mu g\,mL^{-1}$) was detected with UV/Vis spectroscopy at $\lambda = 280$ nm. With this setup, the course of the oxygenation reaction (PNBA formation and PABA consumption) was observed. First, the *N*-oxygenation reaction was relatively slow (> 12 h to reach completion). Second, LC analyses revealed the simultaneous formation of an intermediate with PNBA production. Its shorter retention time relative to PABA and the UV/Vis spectrum suggested that this intermediate could be *p*-hydroxylaminobenzoic acid (PHABA; Figure 1).

Comparison with an authentic PHABA reference, prepared from PNBA with zinc and ammonium chloride in aqueous NaOH solution,[26] unequivocally confirmed this

 © 2005 Wiley-VCH Verlag GmbH & Co. KGaA, Weinheim

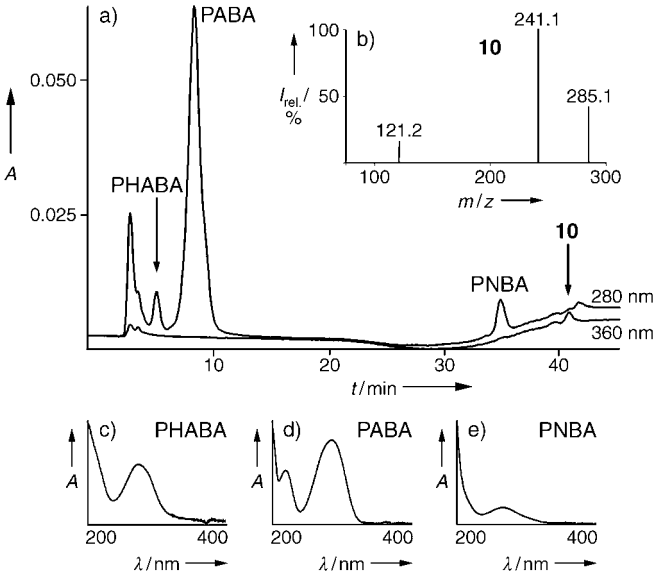


Figure 1. a) Chromatogram of PABA oxidation assay after 5 h; insets: b) MS–MS data for **10**; UV/Vis spectra for c) PHABA; d) PABA; e) PNBA.

finding. Moreover, synthetic PHABA was readily transformed into PNBA when administered to the AurF-producing strain, whereas the control strain was not capable of this transformation. This result shows that not only the first monooxygenation step, but also the second oxygen transfer is catalyzed by AurF. In fact, PNBA formed from exogenously supplied PHABA is produced approximately fivefold faster than it is formed from PABA (Figure 2). This result provides

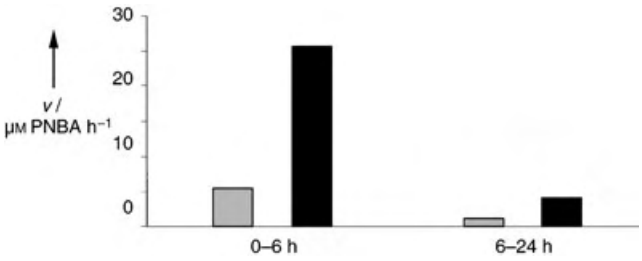


Figure 2. Rate of PNBA formation v with PABA or PHABA as substrates; ■ PNBA from PABA, ■ PNBA from PHABA.

the strongest evidence that PHABA is indeed a true intermediate in nitro group formation and that the N-oxygenation catalyzed by AurF occurs in a stepwise manner. Furthermore, the first oxygenation reaction to hydroxylamine appears to be the rate-limiting step for the overall reaction in vivo.

To gain deeper insight into the course and stoichiometry of the *N*-oxygenation reaction, the fates of PABA, PHABA, and PNBA were monitored by LC (Figure 3). Under starvation conditions (A), the biotransformation of PABA to PNBA clearly predominates. The concentrations of both hydroxylamine and PNBA increase while the concentration of PABA decreases; the sum of all three remains constant. After three

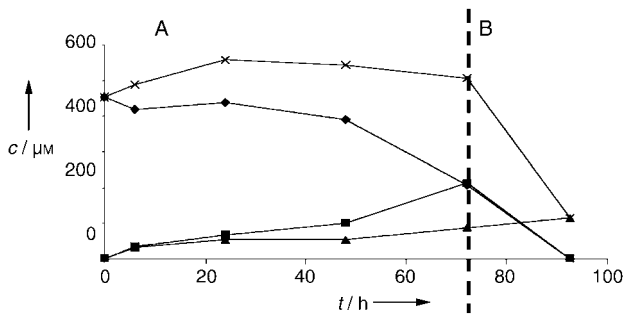
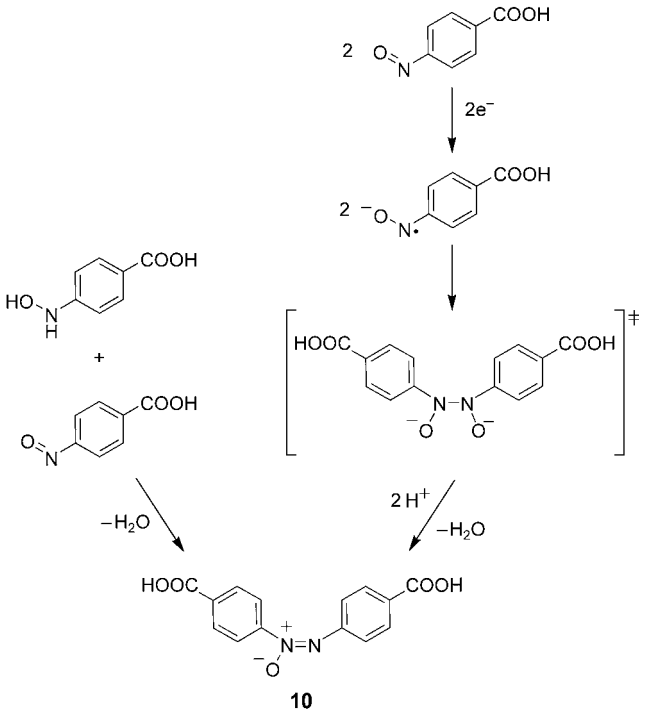


Figure 3. Stoichiometry of the *N*-oxygenation reaction. Time-dependent concentrations of PABA, PHABA, and PNBA under A) starvation conditions (secondary metabolism predominates) and B) growth (primary metabolism predominates); ◆ PABA, ■ PHABA, ▲ PNBA, × sum.

days, however, before all exogenously supplied PABA is converted into PNBA, cell lysis with concomitant release of new substrates initiates the continuation of cell division and growth. At this stage (B), primary metabolism sets in with predominant consumption of PABA for the biosynthesis of folic acid. This finding is in full accord with our earlier observation that feeding PABA to a growing culture (log phase) results in a significant decrease in the transformation of PABA into PNBA.[27] Moreover, the same phenomenon, the initiation of near-complete PABA consumption after three days, was observed in a control experiment with the strain lacking the *aurF* gene. Contrary to this, the formation of PNBA is detectable in cells expressing *aurF* even without supplemented PABA, which indicates that PABA is withdrawn from primary metabolism. Crosstalk between primary and secondary metabolism takes place as a result of the dual role of PABA as precursor for the polyketide synthase starter unit PNBA as well as for folic acid. Furthermore, the course and exact stoichiometry of the reaction under starvation conditions strongly support the key role of PHABA in nitro group formation.

Despite the high sensitivity of the analytical method, the proposed nitroso intermediate **9** (see Scheme 1), which resulted from the subsequent oxygen transfer to PHABA, could not be detected in the medium. The absence of a free nitroso intermediate in the reaction mixture may be rationalized by the rapid and possibly spontaneous turnover to the nitro compound. However, at $\lambda = 360$ nm it was possible to identify small amounts of another metabolite that derived from administered PABA and PHABA, respectively, which implies the intermediacy of a nitroso compound. MSn analyses and comparison with a synthetic sample proved that this novel metabolite is identical to azoxybenzol-4,4′-dicarboxylic acid (**10**). According to a number of mechanistic investigations, azoxybenzene derivatives are formed by the condensation of hydroxylamines with nitroso compounds, or by the dimerization of nitrosobenzenes (Scheme 2).[17,28,29] In both cases, nitroso benzoate intermediates are involved. However, it was also possible to observe the nonenzymatic formation of **10** from synthetic PHABA in phosphate buffer which seems to result from a spontaneous oxidation of PHABA under aerobic conditions. Nonetheless, the kinetic data clearly show that AurF also promotes the oxidation of

 © 2005 Wiley-VCH Verlag GmbH & Co. KGaA, Weinheim



Scheme 2. Formation of azoxy compound **10** from PHABA.

PHABA to PNBA. Interestingly, **10** was previously identified as a metabolite of the insect parasitic zygomycete *Entomophthora virulenta*.[30,31] The detection of **10** as a by-product in PABA oxidation thus not only supports the existence of PHABA, but also provides the first model for the biosynthesis of this unusual fungal azoxy metabolite.

Many speculations have been made on the biosynthesis of nitro compounds from amines,[15] yet until now, no hard evidence has been reported. Through the extraction-free at-line detection of PHABA, and by successful transformation of synthetic PHABA to PNBA, we provide herein the first direct evidence for a stepwise oxidation of aromatic amines to nitro groups via *p*-hydroxylamine as a key intermediate. Our results clearly demonstrate that AurF is a monooxygenase, which not only catalyzes the formation of hydroxylamine, but also the subsequent oxidation to the aromatic nitro group, presumably through the same catalytic mechanism (Scheme 1). Thus, regarding the intermediates, the sequential N-oxygenation by AurF represents the reverse of the stepwise enzymatic reduction of nitroaromatic compounds, as in the case of biodegradation of TNT.[32]

Experimental Section

Strains and cultivation: For heterologous expression, *aurF* was amplified by PCR from cosmid pHJ48, cloned into the expression vector pWHM4* downstream of the constitutive ermE* promoter. The resulting plasmid, pRW01, was introduced into *Streptomyces lividans* ZX1. A strain containing only the plasmid, but not the AurF-encoding insert, *S. lividans* ZX1/pWHM4*, was used as control. Both strains were stored as glycerol cell banks at −80 °C. A cell bank volume of 1 mL was used to inoculate 100 mL soy 2G medium (soy flour (15 g L^{-1}), glucose (15 g L^{-1}), NaCl (5 g L^{-1}), $CaCO_3$ (1 g L^{-1}), KH_2PO_4 (0.3 g L^{-1}), pH adjusted to 6.9 prior to sterilization) containing thiostrepton (25 μg mL^{-1}). Growth proceeded for 3 days at 28 °C in a 500-mL Erlenmeyer flask on a rotary shaker at 180 rpm. Seed culture (10 mL) was grown in 1-L Erlenmeyer flasks containing 250 mL Bö 6 (glucose (20 g L^{-1}), oatmeal (20 g L^{-1}), yeast extract (3 g L^{-1}), NaCl (3 g L^{-1}), $CaCO_3$ (3 g L^{-1}), $FeSO_4 \cdot 7H_2O$ (0.57 g L^{-1}), $MnCl_2 \cdot 4H_2O$ (0.6 g L^{-1})) containing thiostrepton (25 μg mL^{-1}) for 4 days at 28 °C on a rotary shaker at 180 rpm.

The deduced amino acid sequence of AurF has been deposited under accession number CAE 02601 at EMBL/GenBank.

N-Oxygenation assay: Culture broth of *S. lividans* ZX1/pRW01 was filtered through MN640 filter paper, and portions of wet cell mass (20 g) were resuspended in 500-mL Erlenmeyer flasks with 100 mL PBS ($Na_2HPO_4 \cdot 2H_20$ (1.44 g L^{-1}), KH_2PO_4 (0.24 g L^{-1}), NaCl (8.00 g L^{-1}), KCl (0.20 g L^{-1})), pH 7. After shaking for 15 min on a rotary shaker at 28 °C and 180 rpm, blank samples were taken, and substrates were added from a stock solution ($\approx$20 mg mL^{-1}) in methanol to yield a final concentration of 0.07 mg mL^{-1}. The enzymatic reaction was measured "at-line" by chromatographic determination of PABA, PHABA, and PNBA from 1-mL samples. Additional samples were frozen at −20 °C for later analysis.

LC Measurement of PABA, PHABA, PNBA: LC analysis was performed on an ÄKTAexplorer system equipped with a RESOURCE RPC-18 column (3 mL, Amersham Biosciences). Samples (1 mL) were centrifuged for 1 min at 12500 rcf and the supernatant was subsequently injected into a 100-μL sample loop through a 0.22-μm PES syringe filter. The chromatography method starts with 5 CV eluent A (CV = column volume), followed by a gradient of 5 CV from 0 to 100 % eluent B, and finally 5 CV eluent B, each with a flow rate of 2 mL min^{-1}. Eluent A consists of acetonitrile (12 % *v*/*v*) in Na_2HPO_4 (10 mM), pH 3; eluent B is methanol. This methanol gradient is essential for the elution of PNBA, and also permits the detection of more hydrophobic compounds. UV/Vis absorption was monitored at $\lambda = 280$, 325, and 360 nm. These detection wavelengths are based on results from previous UV/Vis scans of possible substrates and products. Peaks were identified and quantified by comparison with external reference standards. Peak fractionation was used to isolate 4,4-diazoxybenzoate for MS–MS analysis.

Received: January 31, 2005
Revised: March 23, 2005
Published online: June 1, 2005

Keywords: azoxides · enzyme catalysis · natural products · nitro compounds · oxygenases

[1] J. He, N. Magarvey, M. Piraee, L. C. Vining, *Microbiology* **2001**, *147*, 2817.
[2] K. Arima, H. Imanaka, M. Kousaka, A. Fukuda, G. Tamura, *Agric. Biol. Chem.* **1964**, *28*, 575.
[3] Y. Hirata, H. Nakata, K. Yamada, K. Okuhara, T. Naito, *Tetrahedron* **1961**, 252.
[4] R. Cardillo, C. Fuganti, D. Ghiringhelli, D. Giangrasso, P. Grasselli, *Tetrahedron Lett.* **1972**, 4875.
[5] J. P. Cosyns, *Drug Saf.* **2003**, *26*, 33.
[6] M. Lang, P. Spiteller, V. Hellwig, W. Steglich, *Angew. Chem.* **2001**, *113*, 1749; *Angew. Chem. Int. Ed.* **2001**, *40*, 1704.
[7] R. L. Baxter, A. B. Hanley, H. W. S. Chan, S. L. Greenwood, E. M. Abbot, I. J. McFarlane, K. Milne, *J. Chem. Soc. Perkin Trans. 1* **1992**, 2495.
[8] E. Rössner, A. Zeeck, W. A. König, *Angew. Chem.* **1990**, *102*, 84; *Angew. Chem. Int. Ed. Engl.* **1990**, *29*, 64.
[9] M. Brandl, S. I. Kozhushkov, B. D. Zlatopolskiy, P. Alvermann, B. Geers, A. Zeeck, A. de Meijere, *Eur. J. Org. Chem.* **2004**, 123.
[10] X. K. Wang, Y. R. Zhao, T. F. Zhao, S. Lai, C. T. Che, *Phytochemistry* **1994**, *35*, 263.

 © 2005 Wiley-VCH Verlag GmbH & Co. KGaA, Weinheim

[11] J. A. Kers, M. J. Wach, S. B. Krasnoff, J. Widom, K. D. Cameron, R. A. Bukhalid, D. M. Gibson, B. R. Crane, R. Loria, *Nature* **2004**, *429*, 79.
[12] M. R. Buddha, T. Tao, R. J. Parry, B. R. Crane, *J. Biol. Chem.* **2004**, *279*, 49567.
[13] S. Kirner, P. E. Hammer, D. S. Hill, A. Altmann, I. Fischer, L. J. Weislo, M. Lanahan, K.-H. van Pee, J. M. Ligon, *J. Bacteriol.* **1998**, *180*, 1939.
[14] J. He, C. Hertweck, *J. Am. Chem. Soc.* **2004**, *126*, 3694.
[15] W. Steglich, B. Fugmann, S. Lang-Fugmann, *Römpp Encyclopedia of Natural Products*, Georg Thieme, Stuttgart, **2002**.
[16] R. L. Baxter, S. L. Greenwood, *J. Chem. Soc. Chem. Commun.* **1986**, 175.
[17] N. Itoh, N. Morinaga, T. Kouzai, *Biochem. Mol. Biol. Int.* **1993**, *29*, 785.
[18] M. D. Corbett, B. R. Chipko, A. O. Batchelor, *Biochem. J.* **1980**, *187*, 893.
[19] S. Kirner, K.-H. van Pee, *Angew. Chem.* **1994**, *106*, 346; *Angew. Chem. Int. Ed. Engl.* **1994**, *33*, 352.
[20] S. Kirner, S. Krauss, G. Sury, T. Lam, J. M. Ligon, K.-H. van Pee, *Microbiology* **1996**, *142*, 2129.
[21] J. He, C. Hertweck, *Chem. Biol.* **2003**, *10*, 1225.
[22] J. He, M. Müller, C. Hertweck, *J. Am. Chem. Soc.* **2004**, *126*, 16742.
[23] M. Ziehl, J. He, H.-M. Dahse, C. Hertweck, *Angew. Chem.* **2005**, *117*, 1226; *Angew. Chem. Int. Ed.* **2005**, *44*, 1202.
[24] S. Kawai, K. Kobayashi, T. Oshima, F. Egami, *Arch. Biochem. Biophys.* **1965**, *112*, 537.
[25] R. M. Lindsay, A. M. McLaren, J. D. Baty, *J. Chromatogr.* **1988**, *433*, 292.
[26] H. Bauer, S. M. Rosenthal, *J. Am. Chem. Soc.* **1944**, *66*, 611.
[27] R. Winkler, C. Hertweck, unpublished results.
[28] G. A. Russel, E. J. Geels, *J. Am. Chem. Soc.* **1965**, *87*, 122.
[29] I. K. Kim, J. Whang, *J. Korean Chem. Soc.* **1976**, *20*, 56.
[30] N. Claydon, J. F. Grove, *J. Chem. Soc. Perkin Trans. 1* **1978**, 171.
[31] N. Claydon, *J. Invertebr. Pathol.* **1978**, *32*, 319.
[32] N. G. McGormick, F. E. Feeherry, H. S. Levinson, *Appl. Environ. Microbiol.* **1976**, *31*, 949.

 © 2005 Wiley-VCH Verlag GmbH & Co. KGaA, Weinheim

Crystal Engineering

Crystalline, Porous Microspheres Made from Amino Acids by Using Polymer-Induced Liquid Precursor Phases**

Sebastian Wohlrab, Helmut Cölfen, and Markus Antonietti*

Control of the crystallization processes is one of the most important techniques in applied colloid chemistry. With a controlled preparation of crystallites of defined size, the kinetic aspects of solubility (e.g. of pharmaceuticals), crystal superstructures, texture-controlled flow properties, filling degrees, and mechanical properties can be influenced. A high reproducibility of the chosen procedure is necessary to ensure the quality of industrial products.

As nucleation and growth are very sensitive processes, crystallization is usually controlled by addition of nucleation agents, stabilizers, or other ternary components. The use of special cosolvents,[1] low molecular additives, surfactants, and functional polymers is regularly reported (for recent reviews, see refs. [2–4]). Recent progress in the field of morphosynthesis indicates that there are non-classical pathways of crystallization via colloidal intermediates and subsequent mesoscale transformation.[3,5–7] In this process, crystalline structures are constructed by assembly and/or transformation from larger units (instead of by the addition of single molecules). Both Addadi et al.[8] and Cölfen and Mann[3] reviewed independently the role of amorphous nanoparticles in bio- and biomimetic mineralization. The experimental verification and role of similar intermediates in the size-directed formation of $CaCO_3$ particles is a question of industrial relevance.[9,10] Taden et al. analyzed a model system based on dye nanodroplets and found extraordinarily ordered dye crystals formed by mesoscale transformation.[7] Such colloidal intermediates are a manifestation of the Ostwald rule of stages, which describes structural growth in the practically relevant kinetic control limit.[11]

High-concentration liquid intermediates seem to be especially promising for rapid crystallization leading to objects with a controlled outer shape. Gower et al. were the first to describe the fine droplets of a polymer-induced liquid precursor phase (PILP) for a $CaCO_3$/polypeptide system,[12,13] the subsequent crystallization of which leads to bent, corrugated, and curved crystal superstructures. A special feature of

[*] Dr. S. Wohlrab, Dr. H. Cölfen, Prof. Dr. M. Antonietti
Max-Planck-Institute of Colloids and Interfaces
Department of Colloid Chemistry
Research Campus Golm, 14424 Potsdam (Germany)
Fax: (+49) 331-567-9502
E-mail: coelfen@mpikg.mpg.de

[**] The support of this work by the Max-Planck-Society is gratefully acknowledged. We thank Mrs. M. Barth for experimental assistance. Dr. Helmut Schlaad is acknowledged for the help with interpreting the ^{1}H NMR spectroscopy results.

Supporting information for this article is available on the WWW under http://www.angewandte.org or from the author.

 DOI: 10.1002/anie.200462467 © 2005 Wiley-VCH Verlag GmbH & Co. KGaA, Weinheim

the PILP phases is that they allow easy morphosynthesis of novel, biorelevant mineral structures through the shaping of a liquid on the micrometer scale so that crystallization occurs without requiring mass transport over longer distances.[14,15]

Herein we extend this approach to polar organic molecules by studying the formation of PILP phases consisting of charged amino acids and oppositely charged polyelectrolytes in ethanol/water mixtures. While addition of ethanol to an aqueous solution of the pure amino acid leads to well shaped single crystals, stable PILP microdroplets are formed spontaneously by adding an oppositely charged polyelectrolyte to the starting solution. These precursor phases can subsequently be crystallized to build novel crystalline porous microspheres of the component amino acids.

The method presented herein is an addition to the available approaches for the preparation of porous microspheres, such as solvothermal methods,[16] sol–gel methods,[17] preparation in commercially available microspherical silica gels,[18] the use of microemulsion droplets as liquid templates to prepare hollow inorganic microspheres,[16,19–21] and dynamic emulsification of oil droplets containing metal oxide precursors which through a reaction at the oil–water interface give porous star-shaped shells.[22]

Amino acids are practically insoluble in organic media, so their aqueous solutions undergo fast crystallization upon addition of a water-miscible organic solvent.[23] The charged amino acids employed, glutamic acid, aspartic acid, lysine, and histidine, crystallize according to this general scheme. Figure 1a shows the result of a default experiment with D,L-glutamic acid, and is representative for the other amino acids. Irregular elongated crystals with a size of 50 to 400 μm are obtained. As a result of the very fast precipitation process, no defined crystal faces or well-shaped edges are formed, although the macroscopic facetted crystal implies a single-crystalline nature.

A completely different behavior is obtained by addition of different amounts of branched polyethyleneimine (PEI, $M_w = 600\ g\,mol^{-1}$) corresponding to polymer:amino acid mass ratios of approximately 2:1, 1:1, 1:2, and 1:10 to the D,L-glutamic acid starting solution. The addition of ethanol results in turbidity, but no precipitation of crystals. Light microscopy investigations indicate the formation of amorphous liquid droplets (Figure 1b), similar to the PILP phases reported by Gower.[12–15]

Owing to their size and the small refractive index differences to the surrounding solvent, the existence of a PILP-phase is sometimes hard to observe. Anionic or cationic dyes, which interact with the polymers in the PILP phase, can be used for staining, such as the anionic dye amaranth for the PILP of D,L-glutamic acid and polyethyleneimine. Amaranth is highly soluble in ethanol and in water, but in the charged PILP-phase it acts as an ionophile leading to high extraction rates.

The process is illustrated in Figure 2. A 0.01 wt% amaranth solution in ethanol (I, red solution) is added to a D,L-glutamic acid solution (II, $10\ g\,L^{-1}$, clear solution) with 1 wt% PEI_{600}. A turbid pink emulsion is formed, and microscopy reveals liquidlike red droplets in a transparent medium. Centrifugation (3500 rpm for 30 min) of the emulsion results in a phase-separated binary system, where the dyed PILP forms a liquid viscous phase at the bottom (Figure 2c). This phase is very viscous as demonstrated in Figure 2d and subsequent crystallization leads to an imprint

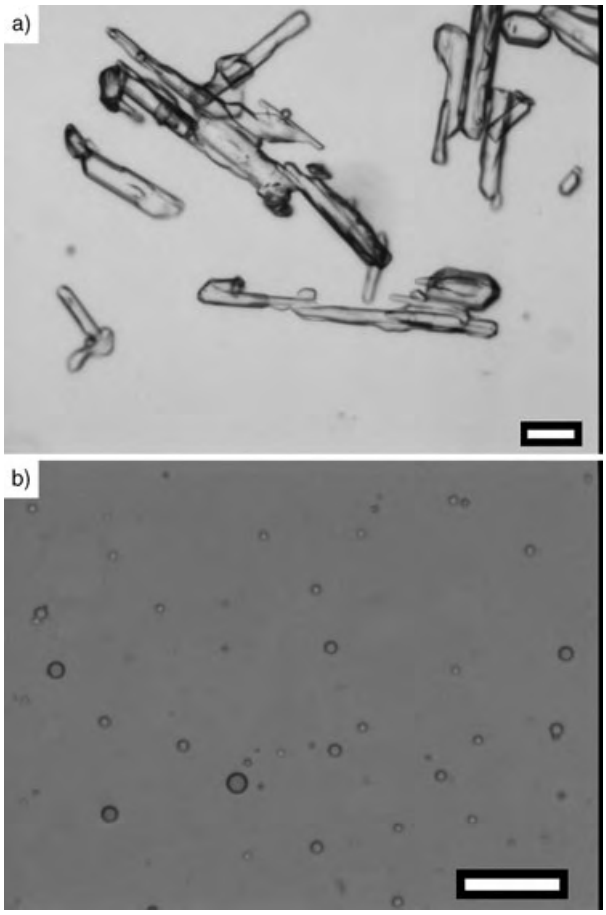


Figure 1. a) D,L-glutamic acid crystals made by precipitation crystallization after adding 10 mL ethanol to 1 mL of a saturated solution (at 20 °C) of D,L-glutamic acid, b) PILP formation under the same conditions in the presence of 1 wt% PEI ($M_w = 600\ g\,mol^{-1}$). Scale bars a) 50 μm, b) 20 μm.

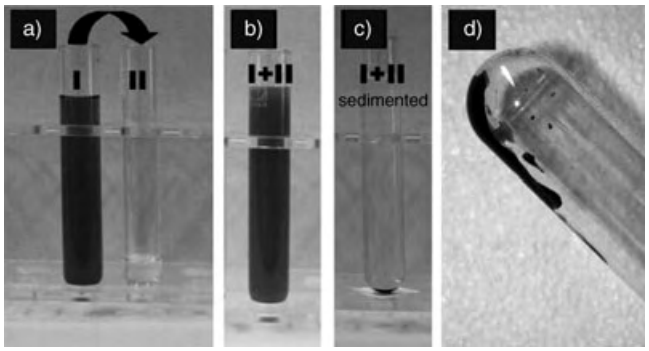


Figure 2. a) I contains ethanol + 0.01% amaranth, II contains $10\ g\,L^{-1}$ D,L-glutamic acid + 1% PEI_{600}, b) PILP formation after mixing of I and II, c) forced sedimentation and demixing by centrifugation (3500 rpm min^{-1}; 30 min) d) colored highly viscous PILP after centrifugation.

 © 2005 Wiley-VCH Verlag GmbH & Co. KGaA, Weinheim

of the centrifuge tube, the opposite side of the crystal has a microporous appearance (see Supporting Information). This experiment clearly demonstrates the existence of a liquid amino acid and polymer-rich phase in chemical equilibrium with its environment.

The droplets consist of amino acid bound to the polymer with a certain amount of water, while a surface excess of the charged polymers stabilizes the droplets. FTIR and ^{1}H NMR spectroscopic analyses qualitatively revealed a high amount of protonated PEI in the D,L-glutamic acid PILPs but through quantitative ^{1}H NMR spectroscopic analysis it was not possible to determine the exact concentration (data not shown). According to the altered ^{1}H NMR chemical shifts for all D,L-glutamic acid signals, the entire D,L-glutamic acid in the PILP interacts with PEI, thus indicating electrostatic as well as hydrogen-bonding interactions exist. This result was also supported by the FTIR data and pH dependent experiments (data not shown). For all polymer/amino acid pairs at different mass ratios, investigations indicate the formation of PILPs in the range of 1 to 5 μm. The PILPs have a long time stability (several months), but vanish immediately when the surrounding ethanol is evaporated. Experimental parameters, such as mode of mixing, stirring (at 0, 400, 1200 rpm), or ageing, had no influence on the particle size distribution.

To investigate the interacting forces and in particular the influence of charge, the zeta potentials of pure D,L-glutamic acid crystals where measured. Additionally, PEI_{600} was added to the crystals in a crystal:polymer ratio of 1:1 to give a reference value for polymer-coated colloids. While crystals of D,L-glutamic acid show a negative zeta potential of around −19 mV, crystals with adsorbed PEI have a positive potential of around 27 mV (Figure 3).

All PILPs made of D,L-glutamic acid and PEI_{600} gave a positive zeta potential of around 18 mV, indicating that the droplets are indeed electrostatically stabilized by an outer excess layer of adsorbed PEI. This finding also reflects the high PEI amount in the PILPs found by FTIR and ^{1}H NMR spectroscopy.

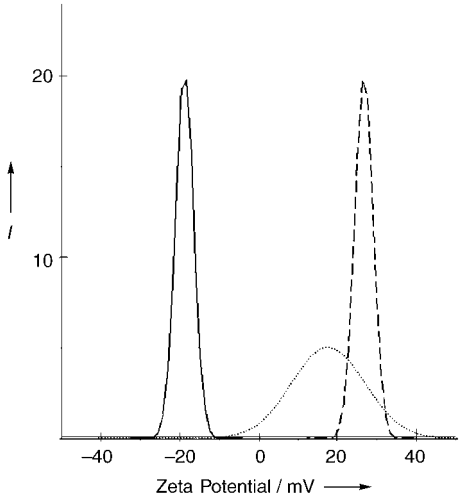


Figure 3. Zeta potentials for different particles: pure D,L-glutamic acid crystals (——); D,L-glutamic acid crystals plus PEI_{600} (– – –); positive zeta potential of a PILP made of D,L-glutamic acid and PEI_{600} (••••).

The three other polyelectrolyte/amino acid pairs examined also show comparable PILP formation. For the basic amino acids L-lysine and L-histidine, polyacrylic acid, PAA_{2000} ($M_w = 2000\ g\,mol^{-1}$), was employed to form the PILPs. Crystallization does not occur in any of the systems containing a low amount of amino acid and a high amount of polymer. A charge-coupled complex between the polyelectrolyte and the amino acid counterions is presumably inhibited from crystallizing, very similar to many structures formed by ionic self assembly.[24]

To promote crystallization from the PILPs, the amino acid concentration and thus the driving force towards crystallization has to be increased, while keeping the polymer concentration at the former level. The high amino acid concentrations of 10 wt% can only be realized by dissolving the amino acid at 60 °C, the PILPs formed at this temperature are then slowly cooled to room temperature to drive crystallization. As shown by light and polarized-light microscopy, the PILP is still liquid directly after cooling. However, after 1 h crystallization is underway for all amino acid/polymer pairs and concentrations, and within 24 h, the vast majority of droplets have crystallized, but a certain amount of PILP droplets are still present. After one week the crystallization process is completed. The resulting crystalline superstructures are spherical and have diameters between 10–100 μm.

The final crystalline structures are therefore much larger than the primary droplets. It is meanwhile a quite common observation that the colloidal stability is lowered throughout the crystallization process, and that the first-formed structures grow by attraction and aggregation of the primary amorphous species.[3,7] Figure 4a shows the light-microscopy image of the so-formed spherical crystal superstructures of D,L-glutamic acid. The typical spherical shape is a superstructure made of primary nanocrystals which in polarization microscopy results in the so called "Brewster cross" (Figure 4b).[25] This result indicates at a perfect radial alignment of the nanocrystals.

Scanning electron microscopy (SEM) investigations reveal that the spherical superstructure is porous, with the primary nanocrystals having a platelet like appearance with a diameter of 200 nm and thickness of 10–20 nm (Figure 4c and d). As D,L-glutamic acid usually crystallizes as needles, this shape speaks for a morphology control provided by the cationic polyelectrolyte, which stabilizes a distinct face. A double hydrophilic block copolymer was recently reported to exert a similar influence on the crystallization of D,L-alanine.[26] To learn more about the microparticle composition, we performed FTIR experiments, these indicated a negligible amount of PEI in the D,L-glutamic acid microcrystals (data not shown). These results were confirmed by ^{1}H NMR spectroscopy data (data not shown) which revealed a low amount of protonated PEI around the ^{1}H NMR detection limit in the microparticles. Wide-angle X-ray scattering (WAXS) revealed domain sizes of D,L-glutamic acid monohydrate > 100 nm for all directions except along the [232] axis which was found to be 20 nm in agreement with the nanoplate thickness in Figure 4d. The formation of these exposed and initially negatively charged (Cerius^2 calculation, not shown) nanoplatelet (232) faces maybe the result of face-selective polymer adsorption. This idea is supported by

 © 2005 Wiley-VCH Verlag GmbH & Co. KGaA, Weinheim

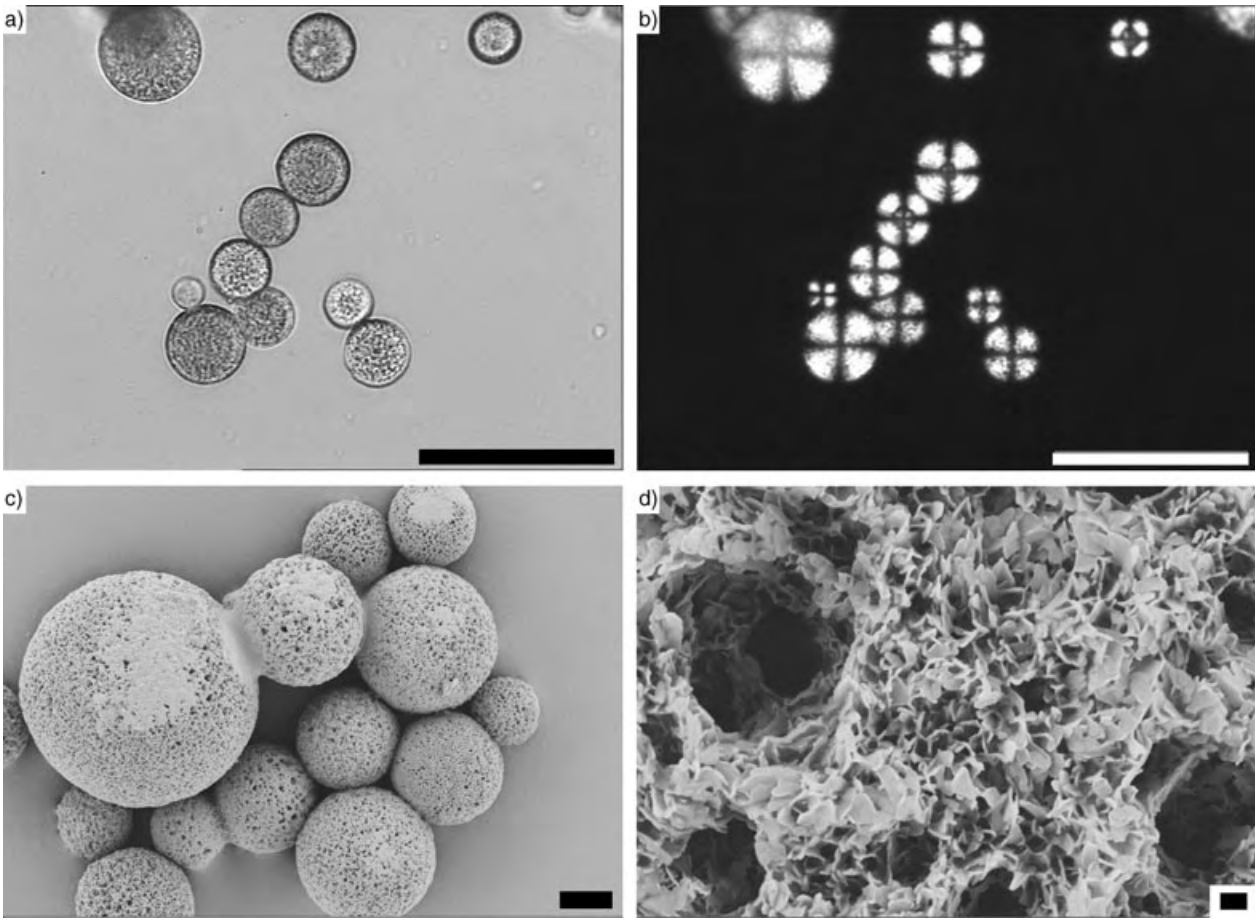


Figure 4. D,L-glutamic acid crystals through growth from a concentrated PILP precursor phase. The PILP formation was induced by adding 10 mL ethanol to 1 mL of a saturated solution (at 60 °C) of D,L-glutamic acid in the presence of 1 wt% PEI ($M_w = 600\ g\,mol^{-1}$), a) light microscopy, b) polarized light microscopy, c) SEM overview of some crystalline superstructures indicating porosity, d) SEM image with a higher magnification to resolve the pore architecture and the construction principle of the spheres. Scale bars: a,b) 100 μm, c) 10 μm, d) 200 nm.

^{1}H NMR spectroscopy which revealed a notable portion of D,L-glutamic acid with a different chemical shift to the pure crystal. This difference was also found in the PILP and indicates interaction with cationic PEI (data not shown).

The porous character is a memory of the excess water and polyelectrolyte in the parent PILP droplets. Therefore it is important to dry the crystals at 50 °C under vacuum to ensure a water-free product. The porosity is then determined by nitrogen sorption experiments using the BET method. For the samples prepared with polymer concentrations of ≤ 1 wt%, a BET-surface area of approximately 13 $m^2\,g^{-1}$ is found which is independent of the initial PILP droplet size. An estimate of the surface area based on the SEM images would result in slightly higher values and suggests the possibility that parts of the structural core are not accessible. BET measurements for L-lysine particles reveal a specific surface of 17 $m^2\,g^{-1}$, very similar to the value for the D,L-glutamic acid.

In the case of the basic amino acids, crystallization again leads to spherical aggregates of smaller crystals (Figure 5). In this case, we have chosen to use the chiral L-enantiomorphs. Again they show a completely different growth pattern to that of the corresponding pure solutions (default experiments shown in the insets of Figure 5), that is, the added polyacrylic acid also modifies the morphology of the primary nanocrystals. Flat crystals, with a thickness of around 50 nm (L-histidine) and about 30 nm (L-lysine), come together to form porous spherical particles with high surface areas. The platelets however have larger lateral extensions than in the D,L-glutamic acid case, resulting in a snowball-like morphology of the final crystalline superstructures. Again, it is interesting to see that the crystals are—whenever possible—radially aligned, so that the distance between the platelets can be seen.

The aspartic acid is effectively blocked from crystallization by the PEI coordination even at elevated concentrations, this is because of its low solubility in water (4 $g\,L^{-1}$ at 20 °C compared to 10 $g\,L^{-1}$ for D,L-glutamic acid at 20 °C), thus other conditions have to be explored for this system.

In conclusion, precipitation of charged amino acids in the presence of oppositely charged polyelectrolytes leads in all the examined cases to rather unusual colloidal structures, the resulting liquid droplets are made of the corresponding amino acid complexes in water. At lower supersaturations these supramolecular "water-in-ethanol" emulsions are stable against crystallization and Ostwald ripening for several months. This prolonged stability against crystallization is

 © 2005 Wiley-VCH Verlag GmbH & Co. KGaA, Weinheim

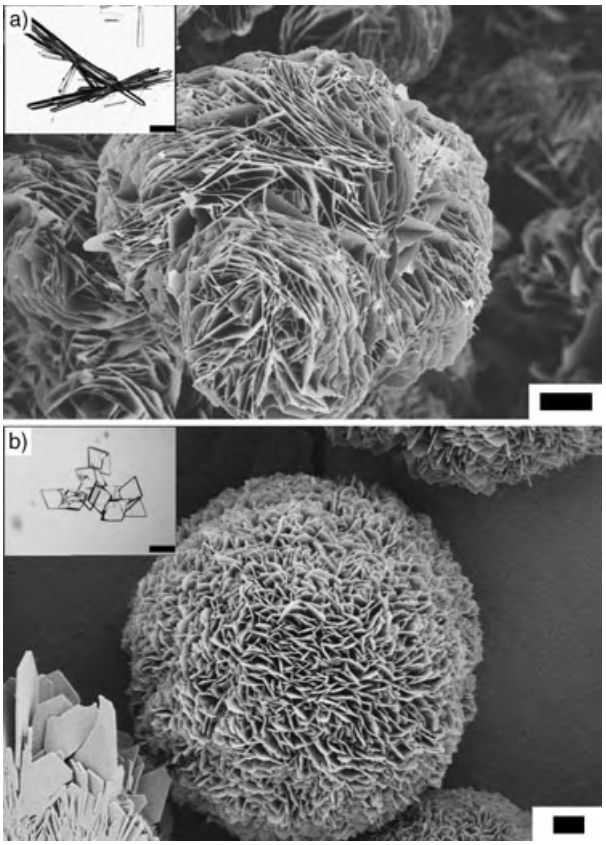


Figure 5. SEM images of a) L-histidine (scale bar 20 μm), b) L-lysine (scale bar 3 μm) crystal superstructures formed through growth from their PILPs. Insets: light micrographs of the default experiments of the as-prepared crystals precipitated without polymer (scale bars 250 μm).

most likely a result of the organic molecule crystals used which have a lower lattice energy than the inorganic ionic crystals investigated previously.[13–15] A kinetic effect can not be ruled out. By increasing the amino acid concentration, it is possible to use this polymer-induced liquid precursor state as a basis for crystallization. After some days, spherical, porous crystal superstructures with 10–100 μm diameter and a radial alignment of the primary nanocrystals are obtained. If the crystallization is repeated in 0.1N HCl or 0.1N NaOH, the electrostatic influence of the polymer on the resulting structures can be revealed. Although PILPs were obtained in every case, porous microcrystals were only obtained at acidic to neutral pH values for the acidic D,L-glutamic acid, and neutral to basic pH values for the basic L-histidine and L-lysine.

The described crystallization can also be understood as a special case of the crystallization by "drowning-out", "salting out", or "solventing out".[27] During protein crystallization similar effects can be observed when "liquid protein" phases are built.[28] While this effect is undesirable during protein crystallization, application of such precursors for crystal morphogenesis is very promising. Since the crystallization proceeds by the Ostwald rule of stages, including a liquid precursor step, the drowning-out process now becomes more attractive for crystal engineering. By using liquid intermediates for further crystallization, it is possible to direct the crystallization into desired morphologies or crystalline coatings,[13] as well as into micro- and nanostructures made of polar organic molecules. The particles have in addition an appropriate size, shape, and porosity for chromatographic applications, where beads made of the enantio-pure amino acids are especially promising.

Experimental Section

All polymers and amino acids were purchased from Aldrich (purity: 99% for D,L-glutamic acid, 98% for L-histidine and D,L-aspartic acid, and >97% for L-lysine), and used without further purification. Double distilled water was used for the preparation of the solutions. As the precipitation agent, HPLC grade ethanol (Merck) was used.

PILP formation: The oppositely charged polymer (0.1, 0.5, 1.0, and 2.0 wt% with respect to the water amount) was added to a solution of the amino acid (1 mL, 1 wt%; or in case of a lower solubility product, the saturated solution) at 20°C in double distilled water. Branched polyethyleneimine (PEI_{600}; $M_w = 600\ g\,mol^{-1}$) was used as the oppositely charged polymer for the negatively charged amino acids D,L-glutamic acid (isoelectric point (IEP) = pH 4.20) and D,L-aspartic acid (IEP = pH 4.25). Polyacrylic acid (PAA_{2000}; $M_w = 2000\ g\,mol^{-1}$) was employed to form PILPs of the positively charged amino acids L-lysine (IEP = pH 8.88) and L-histidine (IEP = pH 6.78). Ethanol (10 mL) was added to this mixture with stirring. The developed PILP phases could be observed by light microscopy as droplets with a diameter of 1–5 μm, depending on mechanical agitation. These low-concentration PILPs are stable for at least 6 months, both against crystallization and colloidal agglomeration.

Crystallization from the PILPs: To stimulate crystallization from the PILPs, the concentration of amino acid has to be increased, which was done by elevating the temperature to 60°C. The oppositely charged polymers (0.1, 0.5, 1.0, and 2.0 wt%) were added to the solution of the amino acid (1 mL of a 10 wt% solution, or in case of a lower solubility, the saturated solution) in double distilled water. Ethanol (10 mL) was added with stirring and the solution was allowed to cool to room temperature. Liquid PILP droplets could be observed, that crystallized within 24 h as indicated by light microscopy. The crystals were isolated from the fluid and washed three times with ethanol, then dried at 50°C under vacuum.

Light microscopy, polarized light microscopy, and high-resolution scanning electron microscopy (HRSEM) were applied to all samples. Light microscopy in solution establishes that the SEM micrographs show real structures and not drying artifacts resulting from the sample preparation. The SEM measurements were performed on a LEO 1550 GEMINI. Light microscopy images were taken in solution with an Olympus BX50 microscope. BET isotherms were measured with a Micromeretics Tristar 3000. Zeta potentials were measured with a Zetasizer HS3000 (Malvern), which determines the zeta potential from the speed of the particle movement in an electric field. Crystal and PILP containing dispersions in ethanol with and without PEI_{600} were investigated according to the conditions of the crystallization experiment.

Received: October 29, 2004
Revised: March 19, 2005
Published online: June 1, 2005

Keywords: amino acids · crystal engineering · glutamic acid · porous microsphere · superstructures

[1] M. Lahav, L. Leiserowitz, *Chem. Eng. Sci.* **2001**, *56*, 2245–2253.
[2] L. A. Estroff, A. D. Hamilton, *Chem. Mater.* **2001**, *13*, 3227–3235.

 © 2005 Wiley-VCH Verlag GmbH & Co. KGaA, Weinheim

[3] H. Cölfen, S. Mann, *Angew. Chem.* **2003**, *115*, 2452 – 2468; *Angew. Chem. Int. Ed.* **2003**, *42*, 2350 – 2365.
[4] F. C. Meldrum, *Int. Mater. Rev.* **2003**, *48*, 187 – 224.
[5] N. Jongen, P. Bowen, J. Lemaître, J. C. Valmalette, H. Hofmann, *J. Colloid Interface Sci.* **2000**, *226*, 189 – 198.
[6] R. L. Penn, J. F. Banfield, *Geochim. Cosmochim. Acta* **1999**, *63*, 1549 – 1557.
[7] A. Taden, K. Landfester, M. Antonietti, *Langmuir* **2004**, *20*, 957 – 961.
[8] L. Addadi, S. Raz, S. Weiner, *Adv. Mater.* **2003**, *15*, 959 – 970.
[9] D. Horn, J. Rieger, *Angew. Chem.* **2001**, *113*, 4460 – 4492; *Angew. Chem. Int. Ed.* **2001**, *40*, 4331 – 4361.
[10] J. Rieger, *Tenside Surfactants Deterg.* **2002**, *39*, 221 – 225.
[11] W. Ostwald, *Z. Phys. Chem.* **1897**, *22*, 289 – 330.
[12] L. A. Gower, D. A. Tirrell, *J. Cryst. Growth* **1998**, *191*, 153 – 160.
[13] L. B. Gower, D. J. Odom, *J. Cryst. Growth* **2000**, *210*, 719 – 734.
[14] M. J. Olszta, E. P. Douglas, L. B. Gower, *Calcif. Tissue Int.* **2003**, *72*, 583 – 591.
[15] M. J. Olszta, D. J. Odom, E. P. Douglas, L. B. Gower, *Connect. Tissue Res. Suppl. 1* **2003**, *44*, 326 – 334.
[16] H. Hu, B. Yang, X. Liu, R. Zhang, Y. Qian, *Inorg. Chem. Commun.* **2004**, *7*, 563 – 565.
[17] B. Zhang, B. Chen, K. Shi, S. He, X. Liu, Z. Du, *Appl. Catal. B* **2003**, *40*, 253 – 258.
[18] Y. Tsurita, M. Nogami, *J. Ceram. Soc. Jpn.* **2001**, *109*, 992 – 999.
[19] D. Walsh, B. Lebeau, S. Mann, *Adv. Mater.* **1999**, *11*, 324 – 328.
[20] D. Walsh, S. Mann, *Nature* **1995**, *377*, 320 – 323.
[21] S. Schacht, Q. Huo, I. G. Voigt-Martin, G. D. Stucky, F. Schüth, *Science* **1996**, *273*, 768 – 771.
[22] D. Volkmer, S. Tugulu, M. Fricke, T. Nielsen, *Angew. Chem.* **2003**, *115*, 60 – 64; *Angew. Chem. Int. Ed.* **2003**, *42*, 58 – 61.
[23] R. C. Weast, *CRC Handbook of Chemistry and Physics*, 65th ed., CRC, Boca Raton, FL, **1984/85**.
[24] C. F. J. Faul, M. Antonietti, *Adv. Mater.* **2003**, *15*, 673 – 683.
[25] H. Freund, *Handbuch der Mikroskopie in der Technik*, Umschauverlag, Frankfurt a.M., **1957**.
[26] S. Wohlrab, N. Pinna, M. Antonietti, H. Cölfen, *Chem. Eur. J.* **2005**, 11, 2903 – 2913.
[27] J. W. Mullin, *Crystallisation*, Butterworth Heinemann, Woburn, **2001**, p. 333.
[28] Y. G. Kuznetsov, A. J. Malkin, A. McPherson, *J. Cryst. Growth* **2001**, *232*, 30 – 39.

 © 2005 Wiley-VCH Verlag GmbH & Co. KGaA, Weinheim

Enantiomer Separation

Modified Linear Dextrins ("Acyclodextrins") as New Chiral Selectors for the Gas-Chromatographic Separation of Enantiomers**

*Giuseppe Sicoli, Zhengjin Jiang, Laszlo Jicsinsky, and Volker Schurig**

In memory of József Szejtli

Cyclodextrins (CDs) modified by alkylation, acylation, and silylation represent versatile chiral stationary phases (CSPs) for the gas-chromatographic separation of enantiomers.[1] Typically, they are dissolved in semipolar polysiloxanes[2a] or linked chemically to polydimethylsiloxane (Chirasil-Dex).[2b] The mechanism of enantiomer recognition is still not well understood, and the role of the CD cavity is unclear in cases were enantioselectivity is low, as it is in most reported cases ($\alpha < 1.1$).[1a] We therefore conjectured that the existence of a cavity may not be a prerequisite to chirality recognition in cyclodextrins. This has now been borne out by employing linear dextrins ("acyclodextrins") as a new generation of carbohydrate-based chiral selectors for the gas-chromatographic separation of enantiomers.

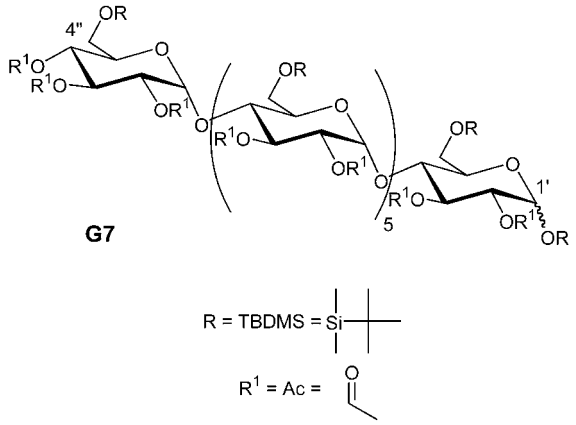
Despite the well-known propensity of cyclodextrins to include various organic compounds in their cavities,[3] it seems plausible to consider the ability of modified linear oligosaccharides as selectors for enantioselective chromatography since helical conformations may act as "semicavities" and suitable functionalities may be present. Previously, per-*n*-pentylated amylose[4a] and amylose tris(*n*-butylcarbamate)[4b] were employed for chiral separations by GC, albeit with limited enantioselectivity. Moreover, the ability of native acyclic α-1,4-linked dextrin (i.e. maltoheptaose) to form molecular complexes and its use for chiral separation by capillary zone electrophoresis has been demonstrated,[5a] for example, for racemic 1,12-dimethylbenzo[*c*]phenanthrene-5,8-dicarboxylic acid.[5b] Even with modified cyclodextrins, NMR studies in solution have shown that interactions of the outer surface play an important role in the chiral-recognition process.[6]

[*] G. Sicoli, Dr. Z. Jiang, Prof. Dr. V. Schurig
Institute of Organic Chemistry
University of Tübingen
Auf der Morgenstelle 18, 72076 Tübingen (Germany)
Fax: (+49) 7071-297-6257
E-mail: volker.schurig@uni-tuebingen.de
Dr. Z. Jiang
King's College, Department of Pharmacy
Micro Separations Group, Frankling-Wilkins Building
Stamford Street 150, SE19NN London (UK)
Dr. L. Jicsinsky
CYCLOLAB Ltd.
Illatos út 7, 1097 Budapest (Hungary)

[**] This work was supported by the Graduate College "Chemistry in Interphases" of the German Research Council.

 © 2005 Wiley-VCH Verlag GmbH & Co. KGaA, Weinheim DOI: 10.1002/anie.200500509

Herein, we compare the enantioselectivity of the versatile cyclic chiral selector heptakis(2,3-di-*O*-acetyl-6-*O*-*tert*-butyldimethylsilyl)-β-cyclodextrin (**CD7**)[7] with that of the acyclic dextrin counterpart heptakis[(1′-*O*,6-*O*)-*tert*-butyldimethylsilyl-(2,3-di-*O*,4″-*O*)-acetyl)]-maltoheptaose (**G7**, G = glucose), which was for the first time subjected to a two-step derivatization procedure that is well established for cyclic oligosaccharides.[8] Thus, maltoheptaose was first etherified with *tert*-butyldimethylsilyl chloride (TBDMSCl) at the primary hydroxy sites and then esterified with acetic anhydride at the secondary hydroxy sites. Spectroscopic evidence indicated that the derivatization of the terminal 1′,4″-hydroxy groups mainly leads to the 1′-*O*-TBDMS/4″-*O*-acetyl derivative. The linear selector **G7** was dissolved in the polysiloxane PS86, and a fused-silica capillary column (20 m × 0.25 mm i.d.) was coated according to the static method.[2a]



The new selector is capable of separating derivatized α-amino acid enantiomers. Thus, the racemic *N*-trifluoroacetyl-*O*-*methyl* esters of α-amino acids could be separated on both **CD7** and on the analogous linear dextrin counterpart **G7** with optimized temperature programming (Figure 1). Under isothermal conditions (Table 1) cyclic **CD7** exhibits a higher enantioseparation factor α than acyclic **G7**. The retention factors *k*′ of the enantiomers are quite different for **CD7** and **G7**, and the elution order is reversed for *tert*-butyl leucine and norvaline (Table 1). In all separations, D enantiomers are eluted after L enantiomers. More intriguing differences are observed for the separation of the racemic *N*-trifluoroacetyl-*O*-*ethyl* esters of α-amino acids (Table 2). Whereas the enantioselectivity is higher for alanine (Ala) on cyclic **CD7** than on acyclic **G7**, only the two diastereomers of isoleucine (IsoLeu) are separated on cyclic **CD7**. However, they are further resolved into enantiomers on acyclic **G7** (Figure 2a). Norvaline (Norval, Figure 2b) and serine (Ser, Figure 2c) can be separated on acyclic **G7** but not on cyclic **CD7**. Further differences in the retention factor *k*′ and enantioseparation factor α are evident from Table 2.

The role of molecular inclusion cannot be ignored in examples of extreme enantioselectivities that vary with the size of the cavity. For example, the unusually high enantioseparation factor of $\alpha = 4.08$ was observed for racemic 2-(fluoromethoxy)-3-methoxy-1,1,1,3,3-pentafluoropropane

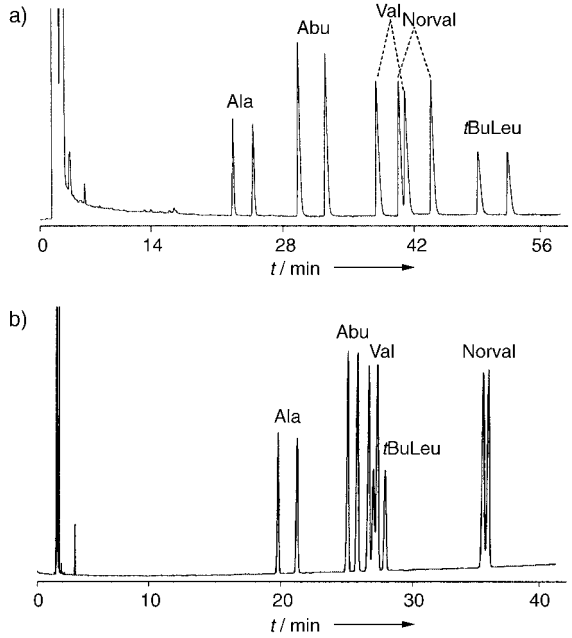


Figure 1. Gas-chromatographic separation of racemic *N*-trifluoroacetyl-*O*-methyl esters of α-amino acids on **CD7** (a) and on **G7** (b); in each case the dextrin is 20% (w/w) in PS86. Columns: 20 m × 0.25 mm i.d. fused-silica capillary, film thickness 0.25 μm. For (a): carrier gas: 0.8 bar hydrogen; oven temperature: 90 °C (5 min), temperature program to 120 °C, 0.5 K min^{-1}. For (b): carrier gas: 0.5 bar hydrogen; oven temperature: 80 °C (5 min), temperature program to 120 °C, 0.5 K min^{-1}.

Table 1: Retention factor *k*′ (first eluted enantiomer), enantioseparation factor α, and resolution factor R_s for *N*-trifluoroacetyl-*O*-methyl esters of some α-amino acids.[a]

	CD7			G7		
	k′	α	R_s	*k*′	α	R_s
Ala	10.2	1.18	5.59	9.9	1.10	5.21
2-Abu	16.9	1.23	4.69	14.2	1.04	2.44
Val	28.4	1.09	1.75	15.6	1.04	2.02
Norval	34.1	1.14	2.65	15.9	1.05	2.75
*t*BuLeu	51.1	1.25	12.8	24.8	1.02	1.25

[a] Experimental conditions: 85 °C (isothermal), 0.6 bar H_2.

Table 2: Retention factor *k*′ (first eluted enantiomer), enantioseparation factor α, and resolution factor R_s for *N*-trifluoroacetyl-*O*-ethyl esters of some α-amino acids.

	CD7				G7		
	k′	α	R_s		*k*′	α	R_s
Ala[a]	26.4	1.60	13.6		10.0	1.08	4.17
IsoLeu[a]	14.3	1.00	–		27.0	1.02	1.25
	16.7	1.00	–		28.3	1.02	1.04
Thr[a]	52.9	1.34	8.50		24.6	1.02	0.94
Norval[a]	21.7	1.00	–		24.9	1.01	0.84
Val[a]	11.7	1.08	1.60		16.6	1.03	1.70
Pro[b]	20.1	1.16	6.64		39.4	1.02	1.83
Ser[b]	27.3	1.00	–		25.3	1.06	3.03
Leu[b]	15.5	1.01	0.51		20.2	1.00	–
Asp[c]	37.8	1.03	1.15	44.2	1.03	2.08	
Met[d]	143.8	1.04	1.66		45.7	1.00	–

[a] Experimental conditions: 90 °C (isothermal), 0.6 bar H_2. [b] 100 °C (isothermal), 0.8 bar H_2. [c] 110 °C (isothermal), 0.6 bar H_2. [d] 120 °C (isothermal), 0.6 bar H_2.

 © 2005 Wiley-VCH Verlag GmbH & Co. KGaA, Weinheim

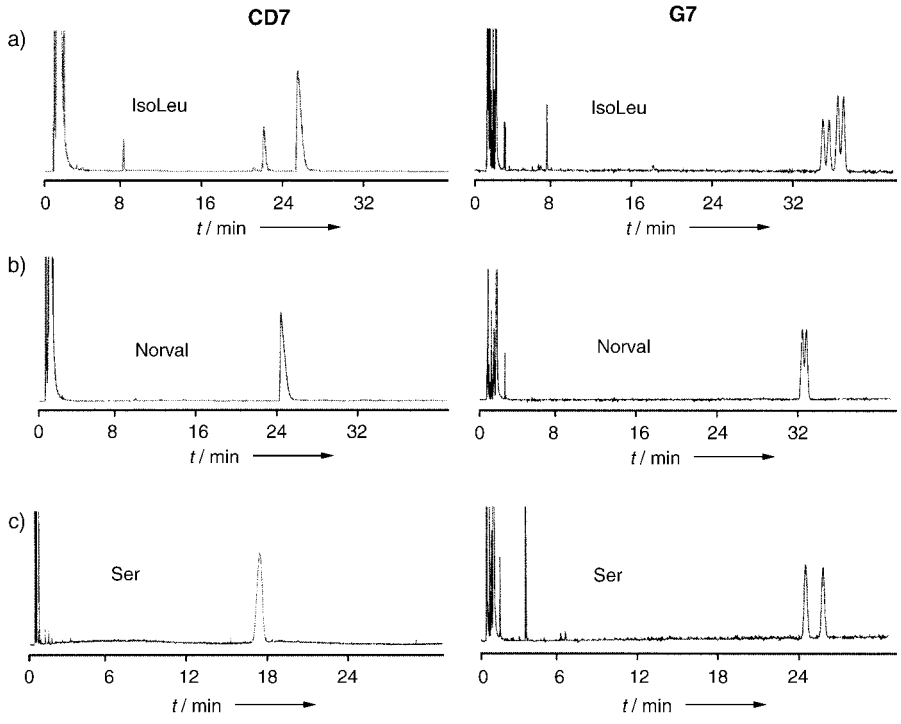


Figure 2. Gas-chromatographic separation of racemic *N*-trifluoroacetyl-*O*-ethyl esters of α-amino acids on **CD7** (left) and on **G7** (right); in each case the dextrin is 20% (w/w) in PS86. Columns: 20 m × 0.25 mm i.d. fused-silica capillary, film thickness 0.25 μm. For other experimental conditions, see Table 2.

("compound B", a decomposition product of the narcotic sevoflurane) on **CD7** (Figure 3a). The separation factor drops to $\alpha = 2.70$ for the γ-cyclodextrin analogue **CD8** and to $\alpha = 1$ (no enantiomeric discrimination) for the α-cyclodextrin analogue **CD6** (Table 3). Surprisingly, the separation of "compound B" occurs also on **G7**, although with reduced enantioselectivity (Figure 3b). Whereas a remarkable difference of enantioselectivity is observed for **CD7** and **CD8**, no such difference is discerned for **G7** and **G8** (Table 3). More interestingly, enantioselectivity is displayed by acyclic **G7** and **G8** but not by cyclic **CD6** (Table 3).

In conclusion, derivatized linear dextrins ("acyclodextrins") represent a new class of carbohydrate-based selectors for gas-chromatographic separation of enantiomers. Comparisons between **G7** and **CD7** indicate that acyclodextrins are useful for investigations of the role of molecular inclusion. Besides *N*-trifluoracetyl amino acid esters, other racemates such as lactones, alcohols, diols, and amides are also amenable to enantiomeric separation by **G7**. Current trials are concerned with the influence on the number of glucose entities in the linear dextrins for enantiorecognition.

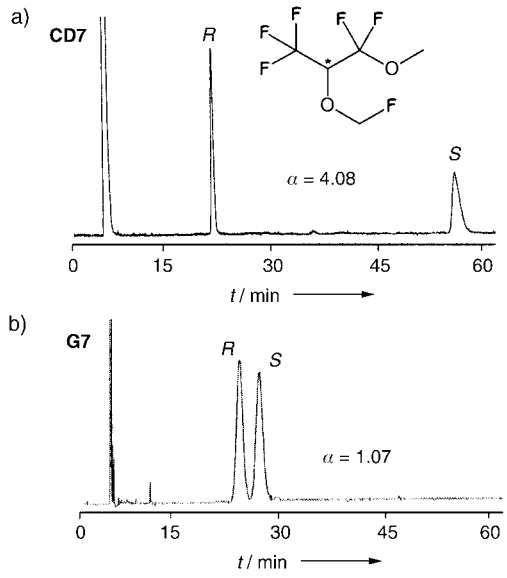


Figure 3. Gas-chromatographic separation of racemic 2-(fluoromethoxy)-3-methoxy-1,1,1,3,3-pentafluoropropane ("compound B") on **CD7** (a) and on **G7** (b); in each case the dextrin is 20% (w/w) in PS86. Columns: 20 m × 0.25 mm i.d. fused-silica capillary, film thickness 0.25 μm. Carrier gas: 0.3 bar; oven temperature: 30 °C.

Table 3: Enantioseparation factor α of "compound B" on modified cyclic and acyclic dextrins.[a,b]

CSP	CD6	CD7	CD8	G7	G8
α	1.00	4.08	2.70	1.07	1.06

[a] In each case the dextrin is 20% (w/w) in PS86. [b] Columns: 20 m × 0.25 mm i.d. fused-silica capillary, film thickness 0.25 μm, carrier gas 0.3 bar hydrogen, oven temperature 30 °C.

Experimental Section

Gas-chromatographic experiments were carried out on an HP 5890 gas chromatograph equipped with a flame ionization detector operated at 250 °C. The carrier gas was hydrogen (99.996%) (Messer-Griesheim, Frankfurt, Germany), which was used without further purification. The splitting ratio at the injector (held at 220 °C) was set to 1:100. Retention times were determined using a Shimadzu C-R6A data processor (Kyoto, Japan). *tert*-Butyldimethylsilyl chloride (TBDMSCl) and acetic anhydride were purchased from Aldrich.

Heptakis[(1′-*O*,6-*O*)-*tert*-butyldimethylsilyl]-maltoheptaose: Dry maltoheptaose (1 g, 0.87 mmol) was dissolved with vigorous stirring in anhydrous pyridine (15 mL). The solution was cooled in an ice bath, and a solution of TBDMSCl (1.6 g, 10.6 mmol) in anhydrous pyridine (20 mL) was then added dropwise over 4 h. Cooling was continued a further 2 h before the solution was allowed to warm to room temperature. After a further 12 h at RT, the solvent was removed under reduced pressure to give a white solid, which was taken up in CH_2Cl_2 (30 mL). The CH_2Cl_2 phase was washed with an aqueous solution of $KHSO_4$ (20 mL, 1M) to remove any residual pyridine and then with saturated aqueous NaCl solution. The CH_2Cl_2 layer was recovered and concentrated to dryness. Yield: 1.61 g (85%). The product was used without further purification. A mixture of three silylated linear dextrins was present (with 7 (M^1), 8 (M^2), and 9 (M^3)

 © 2005 Wiley-VCH Verlag GmbH & Co. KGaA, Weinheim

tert-butyldimethylsilyl substituents), as confirmed by mass-spectrometric analysis (ESI-MS): *m*/*z* 993 $[M_1+2Na]^{2+}$, 1056 $[M_2+2Na]^{2+}$, 1113 $[M_3+2Na]^{2+}$. From the elemental analysis it is evident that the main species (95%) is the linear oligosaccharide as its octa-*tert*-butyldimethylsilyl ether. Elemental analysis (%) calculated for $C_{90}H_{184}O_{36}Si_8$: C 52.29, H 8.97; found: C 52.20, H 9.35.

Heptakis[(1′-*O*,6-*O*)-*tert*-butyldimethylsilyl-(2,3-di-*O*,4″-*O*)-acetyl]-maltoheptaose (**G7**): Crude heptakis[(1′-*O*, 6-*O*)-*tert*-butyldimethylsilyl]-maltoheptaose (1.5 g) were dissolved in anhydrous pyridine (20 mL) and acetic anhydride (18 mL). The solution was stirred for 5 h at 100 °C and then concentrated. The remainder of the solvents were removed by coevaporation with toluene. Column chromatography of the residue eluting with toluene/ethanol (95:5 v/v) afforded amorphous **G7**. After acetylation of the hydroxy groups at the 2- and 3-positions, the structure of the mixed acetyl/TBDMS selector was elucidated by ^1H and ^{13}C NMR spectroscopy. The main species (95%) of the mixture showed a terminal silyl ether group on the reducing terminus C1 and a terminal acetyl ester group on the nonreducing terminus C4. ESI-MS: *m*/*z*: 1365 $[M+2Na]^{2+}$ (main species). Elemental analysis (%) calculated for $C_{120}H_{214}O_{51}Si_8$: C 53.43, H 8.00; found: C 53.35, H 8.17.

Received: February 10, 2005
Published online: May 25, 2005

Keywords: chiral stationary phases · cyclodextrins · enantiomer separation · gas chromatography · linear dextrins

[1] a) V. Schurig, H.-P. Nowotny, *Angew. Chem.* **1990**, *102*, 969 – 986; *Angew. Chem. Int. Ed. Engl.* **1990**, *29*, 939 – 1076; b) W. A. König, *Enantioselective Gas Chromatography with Modified Cyclodextrins*, Hüthig, Heidelberg, **1992**; c) W. A. König, *TrAC Trends Anal. Chem.* **1993**, *12*, 130 – 137; d) V. Schurig, *TrAC Trends Anal. Chem.* **2002**, *21*, 647 – 661.

[2] a) V. Schurig, H.-P. Nowotny, *J. Chromatogr.* **1988**, *441*, 155 – 163; b) H. Cousin, J. C. Combret, O. Trapp, V. Peulon-Agasse, X. Pannecoucke, L. Banspach, G. Trapp, Z. Jiang, V. Schurig, *Eur. J. Org. Chem.* **2003**, 3273 – 3287.

[3] H. J. Schneider, F. Racket, V. Rüdiger, *Chem. Rev.* **1998**, *98*, 1755 – 1785.

[4] a) V. Schurig, H.-P. Nowotny, M. Schleimer, D. Schmalzing, *J. High Resolut. Chromatogr.* **1989**, *12*, 549 – 551; b) V. Schurig, J. Zhu, V. Muschalek, *Chromatographia* **1993**, *35*, 237 – 240.

[5] a) K. Kano, K. Minami, K. Horiguchi, T. Ishimura, M. Kodera *J. Chromatogr. A* **1995**, *694*, 307 – 313; b) K. Kano, S. Negi, R. Takaoka, H. Kamo, T. Kitae, M. Yamaguchi, H. Okubo, M. Hirama, *Chem. Lett.* **1997**, 715 – 716.

[6] G. Uccello-Barretta, L. Ferri, F. Balzano, P. Salvadori, *Eur. J. Org. Chem.* **2003**, 1741 – 1748.

[7] A. Dietrich, B. Maas, V. Karl, P. Kreis, D. Lehmann, B. Weber, A. Mosandl, *J. High Resolut. Chromatogr.* **1992**, *15*, 176 – 179.

[8] a) K. Takeo, H. Mitoh, K. Uemura, *Carbohydr. Res.* **1989**, *187*, 203 – 221; b) A. R. Khan, P. Forgo, K. J. Stine, V. T. D'Souza, *Chem. Rev.* **1998**, *98*, 1977 – 1996.

 © 2005 Wiley-VCH Verlag GmbH & Co. KGaA, Weinheim

Catalyst Recycling

"Catalyst-on-a-Tape"—Teflon: A New Delivery and Recovery Method for Homogeneous Fluorous Catalysts**

*Long V. Dinh and J. A. Gladysz**

There are intense efforts to develop new or improved strategies for recovering homogeneous molecular catalysts.[1] Many of these approaches are bi- or multiphasic in nature, and one particularly innovative method involves catalysts that are derivatized with $(CH_2)_m(CF_2)_{n-1}CF_3$ ($(CH_2)_mR_{fn}$) moieties or fluorous "ponytails".[2,3] The initial applications of this now-familiar technique utilized perfluoroalkane solvents for recovery. However, the relatively high costs of such fluorous solvents, and other factors, pose limitations for industrial applications.

Second-generation methods eliminated the fluorous solvent by exploiting the temperature-dependent solubilities of fluorous catalysts in common organic solvents.[4,5] Appropriately designed fluorous molecules are soluble only at elevated temperatures, and essentially insoluble at low temperatures. Such a thermomorphic character allows homogeneous catalysis at the high-temperature limit, and catalyst recovery by a simple liquid/solid-phase separation at the low-temperature limit. The presence of an insoluble fluorous support can be beneficial, for example, when small quantities are involved. Initial efforts have involved Teflon shavings[4] and fluorous silica gel.[6–8]

We sought to expand the range of catalysts and fluorous supports that could be applied in such methods, and report herein a surprisingly effective procedure involving common commercial Teflon tape. This approach provides not only a convenient means of catalyst recovery, but also of catalyst delivery. From an engineering standpoint, tapes offer a variety of unique attributes, and it is reasonable to extrapolate that meshes and/or reactor parts, such as liners or stirring assemblies, could be fabricated with similar properties.

As a test reaction, we selected the ketone hydrosilylation shown in Figure 1, which in earlier work was catalyzed by the fluorous rhodium complexes **1**-R_{f6} and **1**-R_{f8} in a liquid/liquid biphase system comprising an organic and a fluorous solvent.[9] The red-orange compounds **1**-R_{f6} and **1**-R_{f8} have very little or no solubility in organic solvents at room temperature.[10] However, their solubilities increase markedly with

[*] Dr. L. V. Dinh, Prof. Dr. J. A. Gladysz
Institut für Organische Chemie
Friedrich-Alexander-Universität Erlangen-Nürnberg
Henkestrasse 42, 91054 Erlangen (Germany)
Fax: (+49) 9131-85-26865
E-mail: gladysz@organik.uni-erlangen.de

[**] We thank the Bundesministerium für Bildung und Forschung (BMBF) for support, Prof. Dr. A. Behr and Dr. R. Roll (University of Dortmund) for rhodium measurements, and Prof. Dr. D. Curran (University of Pittsburgh) for helpful discussions.

Supporting information for this article is available on the WWW under http://www.angewandte.org or from the author.

 DOI: 10.1002/anie.200500237 © 2005 Wiley-VCH Verlag GmbH & Co. KGaA, Weinheim

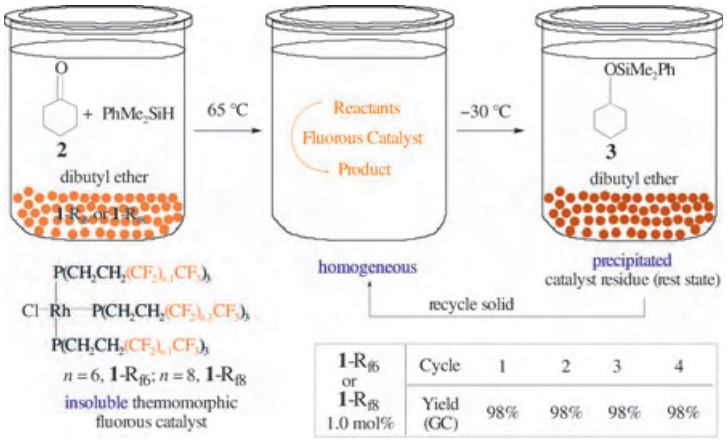


Figure 1. Recycling of a thermomorphic fluorous rhodium hydrosilylation catalyst by liquid/solid phase separation.

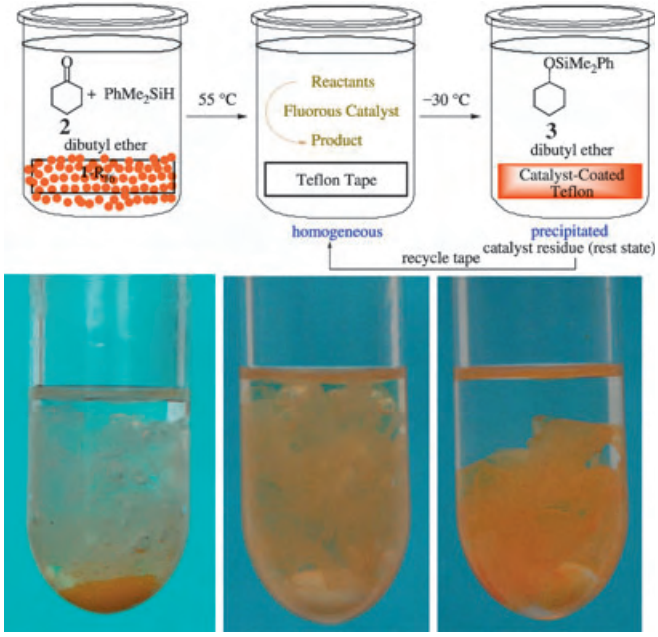


Figure 2. Recycling of a thermomorphic fluorous rhodium hydrosilylation catalyst using Teflon tape.

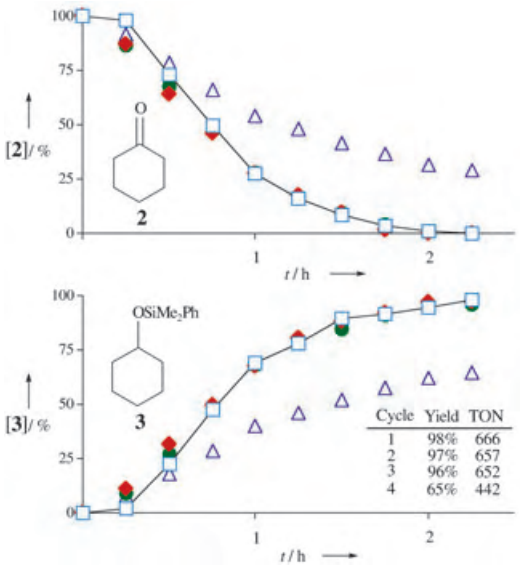


Figure 3. Reaction profile for four cycles under the conditions given in Figure 2: □ Cycle 1 ◆ Cycle 2 ● Cycle 3 △ Cycle 4. Top: decrease (%) in **2** with time, bottom: increase (%) in **3** with time. TON = turnover number.

temperature. Several features make this catalyst system a particularly challenging test for recovery by precipitation. For example, a variety of rest states are possible (e.g., various {Rh(H)(SiR_3)} or {Rh(OR′)(SiR_3)} species), each with unique solubility properties.[11] Also, the first cycle exhibits an induction period,[9] indicating some fundamental alteration of the catalyst precursor.

The solvent dibutyl ether was selected due to its extended liquid range (b.p. 142 °C). A solution of cyclohexanone (**2**; 0.53 M), $PhMe_2SiH$ (1.2 equiv), and a GC standard was treated with **1**-R_{f6} (1 mol %), and warmed to 65 °C, achieving homogeneous conditions.[12] After 8 h, the mixture was cooled to room temperature. GC analysis showed a 98 % yield of the silyl ether **3**. A brown-red catalyst residue slowly precipitated over several hours, and no color remained in the product-containing supernatant solution. To speed up this process, samples were transferred to a freezer (−30 °C); the supernatant solutions were then removed by syringe. The residue was washed twice with cold dibutyl ether and charged with fresh reactants. The cycle was repeated three additional times, each giving a 98 % yield of **3**.

Supports were sought that would facilitate the recovery of lower catalyst loadings. Thus, a similar sequence was conducted with **1**-R_{f6} (0.15 mol %), but in the presence of Teflon tape (thickness/width 0.0075/12 mm). For this system, homogeneous conditions could be achieved at 55 °C. Photographs of a typical sequence are shown in Figure 2. The white tape became lightly colored during the reaction, and orange-red when the sample was cooled. Enthalpic interactions between perfluoroalkyl segments are very small. Hence, it is noteworthy that the catalyst rest-state phase separates onto the tape, as opposed to giving a second solid phase. Interestingly, the Teflon stirring bar remained white.

GC analysis as above indicated a 97 % yield of **3**. In an identical reaction the concentrations of **2** and **3** were assayed at 15 min intervals over four cycles. Data are summarized in Figure 3. As in earlier work,[9] the first cycle exhibited an induction period. Retention of activity was excellent in the second and third cycles, but there was substantial loss in the fourth. In view of the similar rates of the first three cycles, this loss of activity can be attributed to catalyst deactivation, as opposed to leaching or some intrinsic problem with the recycling method.

Leaching was probed in two ways. First, the dibutyl ether supernatants from the first three cycles of the experiments shown in Figure 3 were combined, a fluorine-containing standard added, and a ^{19}F NMR spectrum recorded. The chemical shifts of the $-(CF_2)_5CF_3$ signals are independent of the remote substituent, and integration indicated a "total pony-tail leaching" corresponding to 11.4 % of the phosphine

 © 2005 Wiley-VCH Verlag GmbH & Co. KGaA, Weinheim

ligands of **1**-R_{f6}. Since the active and resting states of the catalyst probably involve only two phosphine ligands, some extraction is not surprising. Second, the supernatant from the first cycle was analyzed for rhodium by AAS-ICP (atom absorption spectrometry with inductively coupled plasma). An average of three determinations indicated leaching corresponding to 0.57% of the original charge. The second cycle gave a value of 5.3%.

One procedural refinement would be to precoat the catalyst on the Teflon tape. When coating is uniform, this would allow low loadings to be delivered by length as opposed to mass measurements. Accordingly, two $50 \times 12 \times 0.0075$ mm strips of tape were added to a solution of **1**-R_{f6} (0.013 g, 0.0039 mmol) in $CF_3C_6F_{11}$ (1.0 mL). The solvent was removed under an inert gas stream to give a yellowish catalyst-coated tape. This tape was applied in a three-cycle sequence and gave yield results similar to those in Figure 3. Photographs are supplied in the Supporting Information.

When catalysts are recycled as solid residues, it is important to exclude impurities that may "piggyback", such as metal particles, as the active species. This situation was probed in two ways. First, the tape was removed after a first cycle, rinsed with cold dibutyl ether, and transferred to a new vessel. A second charge of **2** and dibutyl ether was added, but not the $PhMe_2SiH$. The sample was warmed to 55°C, the now-off-white tape "fished out", and $PhMe_2SiH$ added. The rate profile was similar to the first cycle (ca. 20% slower at higher conversions), consistent with predominant homogeneous catalysis by desorbed fluorous species. Second, the second cycle of a sequence was conducted in the presence of elemental mercury (Hg:Rh 500:1), which inhibits catalysis by metal particles.[13] However, the rate profile was the same as a sequence in the absence of mercury (see Supporting Information).

Hydrosilylations of 2-octanone, acetophenone, and benzophenone to the corresponding ethers have been conducted under identical conditions. As summarized in the Supporting Information, similar results are obtained, albeit with up to 20% activity loss in the third cycle. The basis for this somewhat diminished performance is under study and further details will be provided in a full paper.

In summary, the above data constitute, to our knowledge, the first catalyst recycling method involving common Teflon tape. Attractive interactions between the fluorous domains of the catalyst and the tape are clearly operative. However, other forms of Teflon—such as used to coat stir bars—are ineffective, and additional work is needed to identify the optimum morphologies.[14] There are also tantalizing possibilities with other fluoropolymers, as well as for fabricating reactors or components thereof that could efficiently release and recapture thermomorphic fluorous catalysts as a function of temperature. Furthermore, precoated "catalyst-on-a-tape" systems offer many advantages for delivery alone, such as the introduction of low loadings without recourse to a balance or the tedious preparation of standard solutions. Finally, the slightly different solubility profiles of **1**-R_{f6} and **1**-R_{f8}[12] nicely illustrate how physical properties of fluorous compounds can be engineered to optimally fit a particular application or reaction condition.

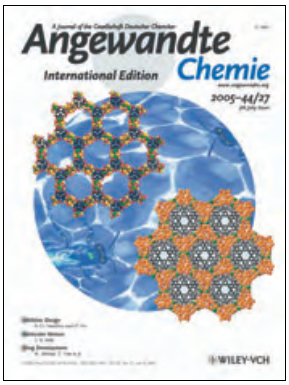
Received: January 21, 2005
Published online: May 18, 2005

Keywords: fluorine · homogeneous catalysis · hydrosilylation · rhodium · Teflon

[1] *Chem. Rev.* **2002**, *102*, Special Issue (pp. 3215–3892) on "Recoverable Catalysts and Reagents" (J. A. Gladysz, issue Editor).
[2] I. T. Horváth, *Acc. Chem. Res.* **1998**, *31*, 641.
[3] *Handbook of Fluorous Chemistry* (Eds.: J. A. Gladysz, D. P. Curran, I. T. Horváth), Wiley-VCH, Weinheim, **2004**.
[4] a) M. Wende, R. Meier, J. A. Gladysz, *J. Am. Chem. Soc.* **2001**, *123*, 11490; b) M. Wende, J. A. Gladysz, *J. Am. Chem. Soc.* **2003**, *125*, 5861.
[5] a) K. Ishihara, S. Kondo, H. Yamamoto, *Synlett* **2001**, 1371; b) K. Ishihara, A. Hasegawa, H. Yamamoto, *Synlett* **2002**, 1299; c) K. Mikami, Y. Mikami, H. Matsuzawa, Y. Matsumoto, J. Nishikido, F. Yamamoto, H. Nakajima, *Tetrahedron* **2002**, *58*, 4015; d) J. Otera, *Acc. Chem. Res.* **2004**, *37*, 288, and references therein; e) G. Maayan, R. H. Fish, R. Neumann, *Org. Lett.* **2003**, *5*, 3547.
[6] a) C. C. Tzschucke, C. Markert, H. Glatz, W. Bannwarth, *Angew. Chem.* **2002**, *114*, 4678; *Angew. Chem. Int. Ed.* **2002**, *41*, 4500; b) A. Biffis, M. Braga, M. Basato, *Adv. Synth. Catal.* **2004**, *346*, 451, and references therein.
[7] For related approaches involving fluorous catalysts, see a) O. Yamazaki, X. Hao, A. Yoshida, J. Nishikido, *Tetrahedron Lett.* **2003**, *44*, 8791; b) C. D. Ablan, J. P. Hallett, K. N. West, R. S. Jones, C. A. Eckert, C. L. Liotta, P. G. Jessop, *Chem. Commun.* **2003**, 2972.
[8] For another recent approach to catalyst recovery by precipitation, see V. K. Dioumaev, R. M. Bullock, *Nature* **2003**, *424*, 530.
[9] a) L. V. Dinh, J. A. Gladysz, *Tetrahedron Lett.* **1999**, *40*, 8995; b) L. V. Dinh, J. A. Gladysz, *New J. Chem.* **2005**, *29*, 173.
[10] J. J. J. Juliette, D. Rutherford, I. T. Horváth, J. A. Gladysz, *J. Am. Chem. Soc.* **1999**, *121*, 2696.
[11] For further discussion of this point, see Chapter 4 of reference [3] and J. A. Gladysz, *Pure Appl. Chem.* **2001**, *73*, 1319.
[12] When **1**-R_{f8} is employed in the reaction shown in Figure 1, identical yields are obtained. However, some catalyst (rest state) precipitates during the reaction, presumably as a result of the decreasing polarity of the solution as the product ether is formed. For a related phenomenon, see ref. [8]. Also, **1**-R_{f8} does not completely dissolve in dibutyl ether at 55°C at the concentrations and loadings (1.00–0.15 mol%) used.
[13] J. A. Widegren, R. G. Finke, *J. Mol. Catal. A* **2003**, *198*, 317.
[14] A reviewer has stressed that absorption isotherms and surface area measurements can provide much insight regarding the mode of catalyst attachment. Although these experiments are beyond the scope of this preliminary communication, such data are planned for a later full paper.

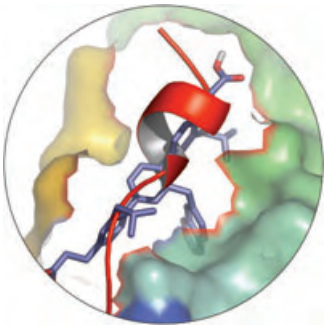
 © 2005 Wiley-VCH Verlag GmbH & Co. KGaA, Weinheim

Cover Picture

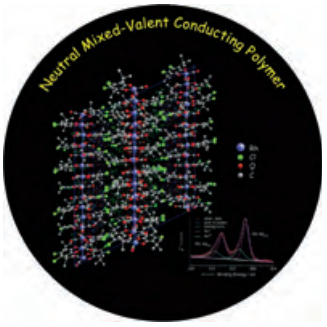


Wolfgang Schmitt,* Jonathan P. Hill, M. Paula Juanico, Andrea Caneschi, Ferdinando Costantino, Christopher E. Anson, and Annie K. Powell*

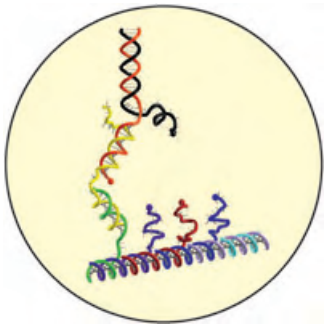
Busy bees may also find the honeycomb networks shown in the cover picture attractive. The networks are based on dinuclear Fe^{III} subunits, aminocarboxylic acid ligands, and potassium counterions. The properties of the hydrophobic organic ligands strongly influence the structure of the hydrophilic inorganic zone which in turn affects the overall structure of the supramolecular assemblies. For more information on this approach see the Communication by W. Schmitt, A. K. Powell, and co-workers on page 4187 ff.



Inhibitor Design
Modulators of protein–protein interactions are promising drug candidates in pharmaceutical research. In their Review on pp. 4130 ff., A. D. Hamilton and H. Yin discuss current strategies in combinatorial searches and in the rational design of such compounds.



Conducting Materials
In their Communication on page 4164 ff. M. Mitsumi, K. Toriumi, et al. report the spectroscopic and crystallographic properties of a highly conductive mixed-valence rhodium(I,II) semiquinonato/catecholato complex.



Molecular Motors
Synthetic DNA-based molecules based on the example of Kinesin are capable of moving across a surface in a particular direction. This topic is explored in the Highlight by T. R. Kelly on page 4124 ff.

Contents

VIP *The following Communications have been judged by at least two referees to be "very important papers" and will be published online at www.angewandte.org soon:*

*F. Studt, F. Tuczek**
Energetics and Mechanism of a Room Temperature Catalytic Synthesis of Ammonia (Schrock Cycle): Comparison with Biological Nitrogen Fixation

H. Zhu, J. Chai, H. Fan, H. W. Roesky, C. He, V. Jancik, H.-G. Schmidt, M. Noltemeyer, W. A. Merrill, P. P. Power*
A Stable Aluminacyclopropene LAl(η^2-C_2H_2) and Its End-On Azide Insertion to an Aluminaazacyclobutene

D. Loffreda, F. Delbecq, F. Vigné, P. Sautet*
Catalytic Hydrogenation of Unsaturated Aldehydes on Pt (111): Understanding the Selectivity from First-Principles Calculations

*C. Schaefer, G. C. Fu**
Catalytic Asymmetric Couplings of Ketenes with Aldehydes to Generate Enol Esters

M. Capdevila, J. Domènech, A. Pagani, L. Tío, L. Villarreal, S. Atrian*
Zn and Cd Metallothionein Recombinant Species from the Most Diverse Phyla May Contain Sulfide (S^{2-}) Ligands

*R. Shintani, W.-L. Duan, T. Nagano, A. Okada, T. Hayashi**
Chiral Phosphine–Olefin Bidentate Ligands in Asymmetric Catalysis: Rhodium-Catalyzed Asymmetric 1,4-Addition of Aryl Boronic Acids to Maleimides

Web Sites

http://www.pherobase.com/	Many Promising Smells	S. Schulz ____ 4118

Books

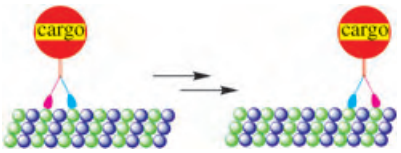
Synthetic Organic Photochemistry	Axel G. Griesbeck, Jochen Mattay	*reviewed by D. Döpp* ____ 4120
Handbook of Fluorous Chemistry	John A. Gladysz, Dennis P. Curran, István Horváth	*reviewed by G. Haufe* ____ 4121

Highlights

Molecular Motors

T. R. Kelly* ____ 4124 – 4127

Molecular Motors: Synthetic DNA-Based Walkers Inspired by Kinesin



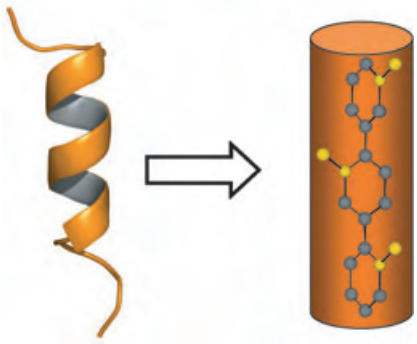
Molecules that walk the walk! As Confucius reputedly said, "a journey of a thousand miles begins with a single step". Three related strategies that offer initial answers to the challenging design problem of how to control motion across a surface at the molecular scale are highlighted (see diagram).

Reviews

Inhibitor Design

H. Yin, A. D. Hamilton* ____ 4130 – 4163

Strategies for Targeting Protein–Protein Interactions With Synthetic Agents



Small-molecule modulators of protein–protein interactions possess significant potential as novel therapeutic compounds. An overview of the strategies for obtaining compounds that disrupt protein–protein interactions is presented. The state of the art in the rational design of mimetics that reproduce the structures and functions of their natural targets is also discussed (see scheme).

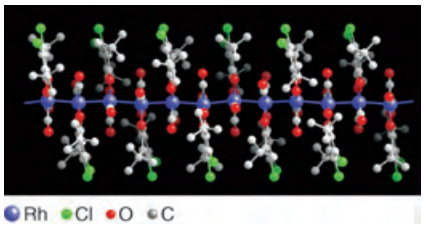
Communications

Conducting Materials

M. Mitsumi,* H. Goto, S. Umebayashi, Y. Ozawa, M. Kobayashi, T. Yokoyama, H. Tanaka, S. Kuroda, K. Toriumi* _____ 4164 – 4168

A Neutral Mixed-Valent Conducting Polymer Formed by Electron Transfer between Metal d and Ligand π Orbitals

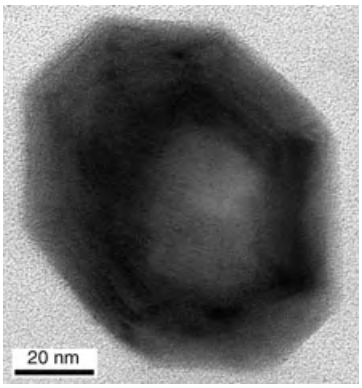
Frontier-orbital design aided in the preparation of the novel neutral linear chain rhodium(I,II) complex $[Rh(3,6\text{-dbdiox-}4,5\text{-}Cl_2)(CO)_2]_\infty$ (see picture), in which the mixed-valent state is formed by electron transfer between metal d and semiquinonate π* orbitals (3,6-dbdiox-4,5-Cl_2: semiquinonate or catecholate of 3,6-di-*tert*-butyl-4,5-dichloro-1,2-benzoquinone). This compound exhibits high conductivity (17–34 $S\,cm^{-1}$) at room temperature in spite of its being a neutral molecule.



Cesium Oxide Nanoparticles

A. Albu-Yaron, T. Arad, R. Popovitz-Biro, M. Bar-Sadan, Y. Prior, M. Jansen, R. Tenne* _____ 4169 – 4172

Preparation and Structural Characterization of Stable Cs_2O Closed-Cage Structures



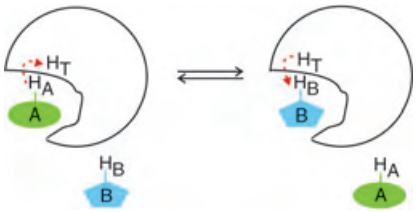
Fullerene-like Cs_2O nanoparticles were prepared by laser ablation of 3R-Cs_2O powder in evacuated quartz ampoules. The Cs_2O closed cages, such as the faceted nanoparticle shown in the picture, are remarkably stable as compared with the corresponding extremely unstable but technically important bulk compound, which makes them potentially useful in applications involving cesium oxide coatings, for example, photoemissive devices and catalytic converters.

Pharmacophore Mapping

V. M. Sánchez-Pedregal, M. Reese, J. Meiler, M. J. J. Blommers, C. Griesinger,* T. Carlomagno* _____ 4172 – 4175

The INPHARMA Method: Protein-Mediated Interligand NOEs for Pharmacophore Mapping

Orientation of a ligand: The first observation of interligand NOEs between two competitive ligands A and B binding consecutively and not simultaneously to the same target is reported for baccatin III and epothilone A in the presence of tubulin. Such effects, which are mediated by spin diffusion through protein protons (see scheme), could be used to determine the relative orientation of competitive ligands in the receptor binding pocket.



For the USA and Canada:
ANGEWANDTE CHEMIE International Edition (ISSN 1433-7851) is published weekly by Wiley-VCH PO Box 191161, D 69451 Weinheim, Germany. Air freight and mailing in the USA by Publications Expediting Inc. 200 Meacham Ave., Elmont, NY 11003. Periodicals postage paid at Jamaica NY 11431. US POSTMASTER: send address changes to *Angewandte Chemie*, Wiley-VCH, 111 River Street, Hoboken, NJ 07030. Annual subscription price for institutions: US$ 4948.00/4498.00 (valid for print and electronic / print or electronic delivery); for individuals who are personal members of a national chemical society, or whose institution already subscribes, or who are retired or self-employed consultants, print only: US$ 394.00. Postage and handling charges included. All Wiley-VCH prices are exclusive VAT.

 © 2005 Wiley-VCH Verlag GmbH & Co. KGaA, Weinheim

The best in chemistry –

for more than a hundred years



A Journal of the Gesellschaft Deutscher Chemiker

Angewandte
International Edition **Chemie**

www.angewandte.org

1888: ***The beginning of a success story***

Constant Innovations

1962: *First issue of the International Edition*
1976: *Graphical abstracts*
1979: *Cover pictures*
1988: *Centenary of Angewandte*
1989: *Routine use of color*
1991: *New section: Highlights*
1992: *Computerized editorial tracking system*
1995: *Internet service for readers*
1998: *Regular press service; full-text online*
2000: *New section: Essays; EarlyView: Communications available online ahead of the printed version*
2001: *New section: Minireviews*
2002: *Online submission of manuscripts*
2003: *Weekly publication; new section: News; new layout*
2004: *Backfiles (1962-1997); ManuscriptXpress: Online system for authors and referees*



Angewandte's advisors...

Wolfgang A. Herrmann
Technische Universität München

»**Angewandte Chemie** is at home in Germany and successful in the world. This journal has developed as the international community of chemists has grown together. Today, **Angewandte** is of central importance for modern chemists. It is the only journal I afford not to hurry through in the office – it's my "home is my castle journal"!«

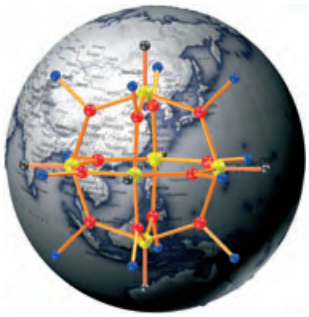
Angewandte Chemie International Edition *is a journal of the German Chemical Society (GDCh)*

GDCh

WILEY InterScience® DISCOVER SOMETHING GREAT

WILEY-VCH

1998/1506_gu

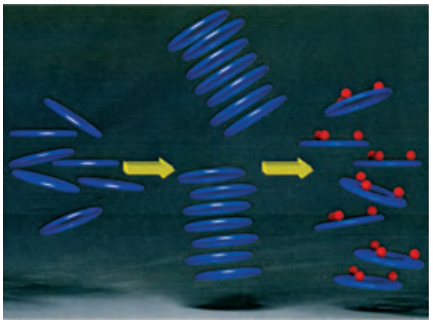


Globular configuration: a microporous coordination polymer based on a dodecanuclear copper(I) cluster (picture: C black, Cu red, N blue, S yellow) as a twelve-connected node, was synthesized by a simultaneous redox, sulfurization, and self-assembly reaction under solvothermal conditions. The synthesis provides a model reaction to simulate the transformation of inorganic sulfur into organic sulfur.

Topological Networks

D. Li,* T. Wu, X.-P. Zhou, R. Zhou, X.-C. Huang ——— **4175 – 4178**

Twelve-Connected Net with Face-Centered Cubic Topology: A Coordination Polymer Based on $[Cu_{12}(\mu_4\text{-}SCH_3)_6]^{6+}$ Clusters and CN^- Linkers

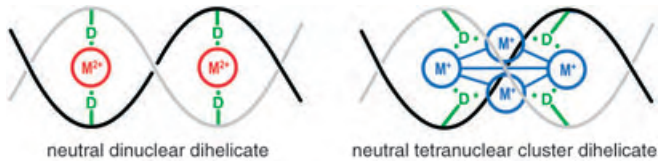


Fluorescence switching: Multimetallic fluorescent macrocycles aggregate into supramolecular assemblies on changing the solvent from THF to CH_2Cl_2. Coordinating bases (e.g., pyridine) cause deaggregation of these assemblies and result in a large enhancement of the fluorescence (see schematic representation of the organization of the macrocycles in THF (left), in CH_2Cl_2 (middle), and after addition of pyridine (right)).

Supramolecular Chemistry

C. T. L. Ma, M. J. MacLachlan* ——— **4178 – 4182**

Supramolecular Assembly and Coordination-Assisted Deaggregation of Multimetallic Macrocycles



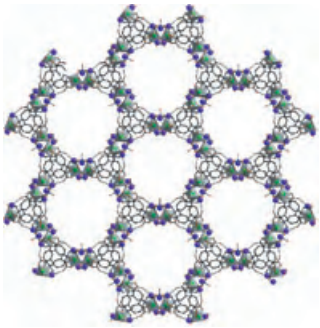
Self control! A potentially dianionic helicand ligand is used to exert control over the assembly of metal complexes into common helical structures or supramolecular clusters depending on the oxidation state of the metal (see scheme).

In the tetranuclear cluster dihelicates, a polyhedron of metal ions is the helical axis. The metal cluster in these complexes is stabilized by two soft donor atoms in the ligand.

Supramolecular Chemistry

M. R. Bermejo,* A. M. González-Noya, R. M. Pedrido, M. J. Romero, M. Vázquez ——— **4182 – 4187**

Route to Cluster Helicates



Emptying the honeycomb: Hybrid organic–inorganic coordination assemblies are synthesized using modified aminocarboxylic acid ligands as the structure-directing agents. The structure of the networks varies ranging from a lamellar motif through a densely packed hexagonal array, to an open-framework hexagonal assembly (see structure).

Hybrid Compounds

W. Schmitt,* J. P. Hill, M. P. Juanico, A. Caneschi, F. Costantino, C. E. Anson, A. K. Powell* ——— **4187 – 4192**

Supramolecular Coordination Assemblies of Dinuclear Fe^{III} Complexes

 © 2005 Wiley-VCH Verlag GmbH & Co. KGaA, Weinheim

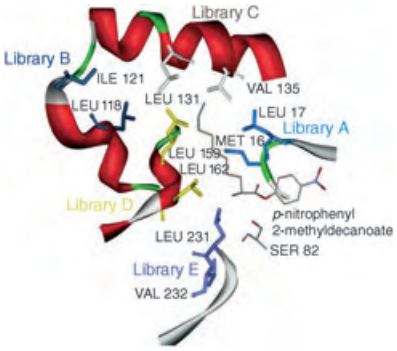
Contents

Directed Evolution

M. T. Reetz,* M. Bocola, J. D. Carballeira, D. Zha, A. Vogel _____ **4192 – 4196**

Expanding the Range of Substrate Acceptance of Enzymes: Combinatorial Active-Site Saturation Test

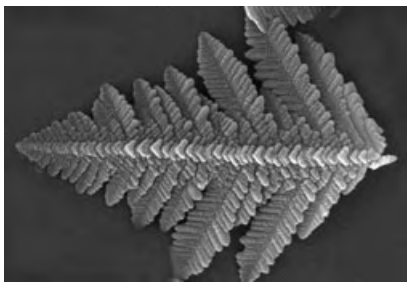
CASTing for success: The traditional problem of expanding the range of substrate acceptance of enzymes can be solved by creating focused libraries of mutants resulting from randomization of pairs of properly chosen amino acids around the active site (see example with the lipase from *Pseudomonas aeruginosa*, amino acid pairs are shown in the same color). CAST = combinatorial active-site saturation test.



Fractal Iron Oxide

M. Cao, T. Liu, S. Gao, G. Sun, X. Wu, C. Hu,* Z. L. Wang* _____ **4197 – 4201**

Single-Crystal Dendritic Micro-Pines of Magnetic α-Fe_2O_3: Large-Scale Synthesis, Formation Mechanism, and Properties

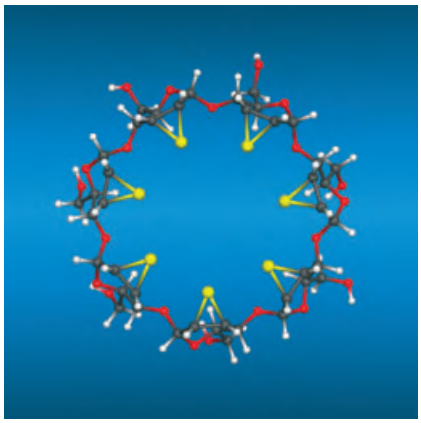


Fractal hematite dendrites with structures resembling pine trees (see picture) were obtained by hydrothermal treatment of $K_3[Fe(CN)_6]$. They are formed by a novel process in which fast growth along six crystallographically equivalent directions forms dendritic or snowflakelike single-crystal structures, which differs from the mechanisms reported for other fractal structures.

Non-Natural Cyclodextrins

M. Fukudome, T. Shiratani, S. Immel, Y. Nogami, D.-Q. Yuan, K. Fujita* _____ **4201 – 4204**

Synthesis of a Cycloallin Derivative from β-Cyclodextrin: Heptakis(2,3-dideoxy-2,3-epithio)-β-cycloallin

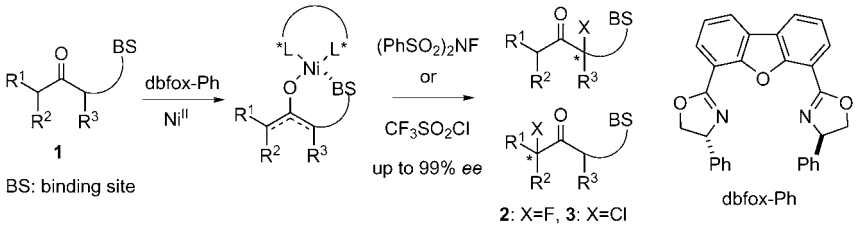


Made from sugar: Heptakis(2,3-dideoxy-2,3-epithio)-β-cycloallin has been synthesized in a one-pot procedure from a β-cyclodextrin derivative. Molecular modeling studies suggest that the structure of the cycloallin is inverted relative to that of regular cyclodextrins, with the sulfur atoms of the epithio groups pointing inwards to form the narrower aperture (see model; S yellow, O red, C gray, H white).

Drug Development

N. Shibata,* J. Kohno, K. Takai, T. Ishimaru, S. Nakamura, T. Toru,* S. Kanemasa _____ **4204 – 4207**

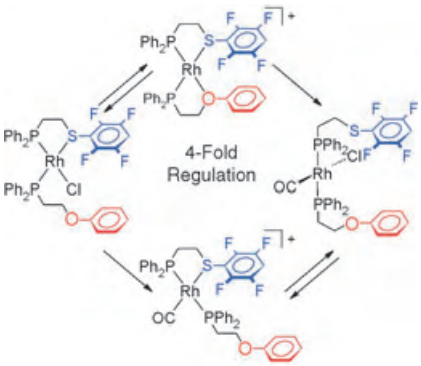
Highly Enantioselective Catalytic Fluorination and Chlorination Reactions of Carbonyl Compounds Capable of Two-Point Binding



New tools in drug development: The catalytic enantioselective fluorination and chlorination reactions of carbonyl compounds containing an additional binding site (see scheme) proceed with extremely high enantioselectivity and require low catalyst loadings (2–10 mol% dbfox-Ph/Ni^{II}). Asymmetric amplification is also observed in these enantioselective halogenations.

 © 2005 Wiley-VCH Verlag GmbH & Co. KGaA, Weinheim

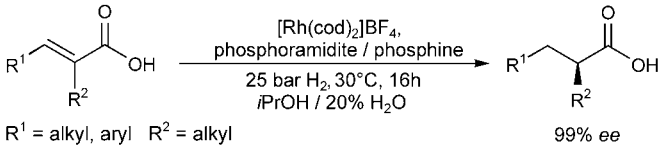
A halide-induced ligand rearrangement around a Rh^{I} center can be used for the preparation of heteroligated tweezer-type complexes. By using a variety of P,S- and P,O-hemilabile ligands, the complexes can be interconverted between four different Rh^{I}-coordination environments (see scheme).



Coordination Chemistry

A. M. Brown, M. V. Ovchinnikov, C. A. Mirkin* ——— 4207 – 4209

Heteroligated Rh^{I} Tweezer Complexes



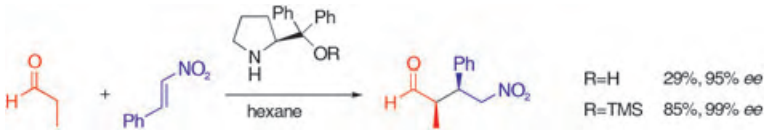
Mixing it up: A catalytic system based on a mixed-ligand approach has been developed for the rhodium-catalyzed asymmetric hydrogenation of cinnamic acid derivatives (see scheme, cod = cycloocta-1,5-diene). It is the first time that a catalyst complex based on a heterocombination of a chiral and an achiral monodentate ligand gives dramatically higher enantioselectivity (up to 99%) than any of the corresponding homocomplexes.

Asymmetric Catalysis

R. Hoen, J. A. F. Boogers, H. Bernsmann, A. J. Minnaard,* A. Meetsma, T. D. Tiemersma-Wegman, A. H. M. de Vries, J. G. de Vries,* B. L. Feringa* ——— 4209 – 4212

Achiral Ligands Dramatically Enhance Rate and Enantioselectivity in the Rh/Phosphoramidite-Catalyzed Hydrogenation of α,β-Disubstituted Unsaturated Acids

---



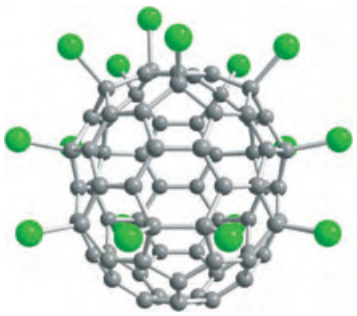
The direct, catalytic, asymmetric Michael addition of aldehydes to nitroolefins in the presence of a chiral diphenylprolinol silyl ether organocatalyst is described (see scheme). The desired 1,4-addition products were obtained in nearly optically pure form in good yield with high *syn* diastereoselectivity. TMS = trimethylsilyl.

Organocatalysis

Y. Hayashi,* H. Gotoh, T. Hayashi, M. Shoji ——— 4212 – 4215

Diphenylprolinol Silyl Ethers as Efficient Organocatalysts for the Asymmetric Michael Reaction of Aldehydes and Nitroalkenes

---



Tales of the unexpected: The [70]fullerene chloride $C_{70}Cl_{16}$ resulted from the reaction of [70]fullerene with a mixture of Br_2 and $TiCl_4$. A single-crystal X-ray crystallographic study revealed the presence of two isomers of $C_{70}Cl_{16}$, both containing a belt of ten chlorine atoms around the equator and a skew pyramidal cap of six chlorine atoms on the pole of the $C_{70}Cl_{16}$ molecule (see picture).

Fullerenes

S. I. Troyanov,* A. A. Popov 4215 – 4218

A [70]Fullerene Chloride, $C_{70}Cl_{16}$, Obtained by the Attempted Bromination of C_{70} in $TiCl_4$

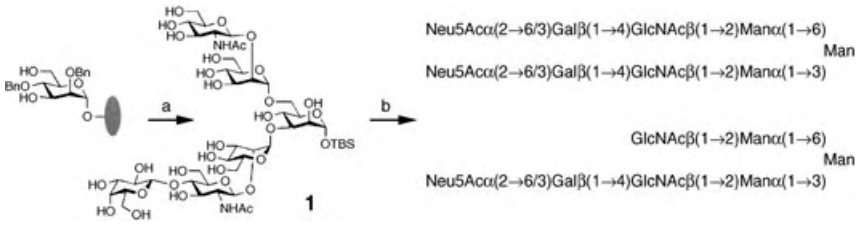
 © 2005 Wiley-VCH Verlag GmbH & Co. KGaA, Weinheim

Contents

Carbohydrate Chemistry

S. Hanashima, S. Manabe, Y. Ito* ——— 4218 – 4224

Divergent Synthesis of Sialylated Glycan Chains: Combined Use of Polymer Support, Resin Capture–Release, and Chemoenzymatic Strategies

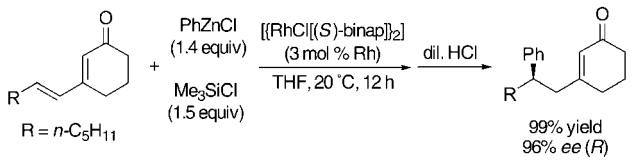


Carbo loading! The synthesis of α(2,3)- or α(2,6)-sialylated biantennary glycans is possible with a new approach. The common precursor **1** was synthesized with a soluble polymer support strategy (a) in combination with a resin capture–release protocol. Hexasaccharide **1** can then be diverged to various polysaccharides by enzymatic glycosylation (b). Bn = benzyl, TBS = *tert*-butyldimethylsilyl.

Asymmetric Catalysis

T. Hayashi,* S. Yamamoto, N. Tokunaga ——— 4224 – 4227

Rhodium-Catalyzed Asymmetric 1,6-Addition of Aryl Zinc Reagents to Dienones

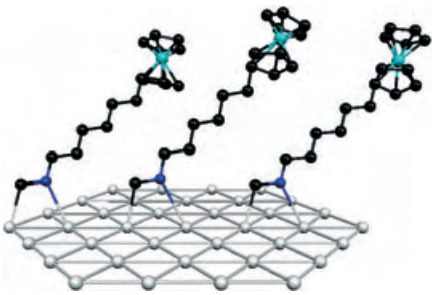


A highly enantioselective methodology allows the preparation of α,β-unsaturated ketones that contain a new stereogenic center at the C5 position. This approach is realized through the title reaction in the presence of chlorotrimethylsilane as a Lewis acid and a rhodium/(*S*)-binap complex as the catalyst followed by acidic hydrolysis (see scheme). binap = 2,2′-bis(diphenylphosphanyl)-1,1′-binaphthyl.

Molecular Devices

Y. Lee, G. M. Morales, L. Yu* ——— 4228 – 4231

Self-Assembled Monolayers of Isocyanides on Nickel Electrodes

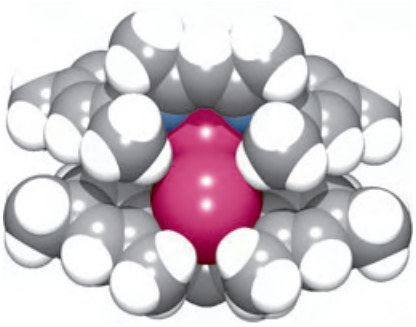


Alligator clip on a nickel electrode: Monolayers of ferrocenyl-terminated isocyanides are strongly chemisorbed on nickel surfaces (see picture). The nickel–isocyanide interaction has a parallel binding mode, and the monolayers have higher thermal stability in boiling ethanol than thiol monolayers on gold. The nickel–isocyanide monolayers could be useful in molecular electronics.

Metal–Metal Interactions

M. S. Hill,* P. B. Hitchcock, R. Pongtavornpinyo ——— 4231 – 4235

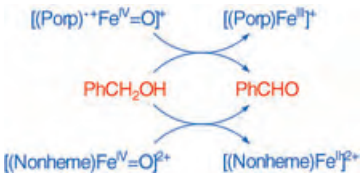
Dimerization of Indanediyl Fragments: An Alkene Analogue for Group 13?



A β-diketiminate complex of indium, $[In\{N(2,4,6\text{-}Me_3C_6H_2)C(Me)\}_2CH]$, dimerizes in the solid state (see space-filling model) to provide an indium species that is formally isoelectronic to the historically significant bis(stannane)diyls. A direct In–In bond is formed yielding a centrosymmetric dimer that possesses approximate C_{2h} symmetry with a mutual *trans*-bent orientation of the N-chelating ligands.

© 2005 Wiley-VCH Verlag GmbH & Co. KGaA, Weinheim

Iron-mediated oxidation: High-valent iron(IV)–oxo complexes of heme and nonheme ligands are generated in situ and are used in mechanistic studies of alcohol oxidation (see scheme). It is proposed that the oxidation of alcohols occurs by an α-CH hydrogen atom abstraction followed by electron transfer. Porp = porphyrin.

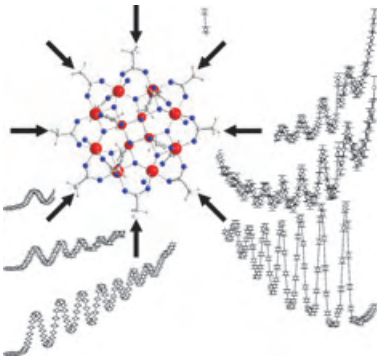


Reaction Mechanisms

N. Y. Oh, Y. Suh, M. J. Park, M. S. Seo, J. Kim,* W. Nam* ——— **4235 – 4239**

Mechanistic Insight into Alcohol Oxidation by High-Valent Iron–Oxo Complexes of Heme and Nonheme Ligands

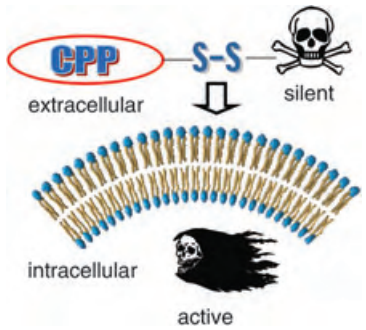
The pressure-dependence of the zero-field splitting of the $S = 10$ ground state of the single-molecule magnet Mn_{12}-acetate was studied by inelastic neutron scattering (INS) at hydrostatic pressures up to 12 kbar (see picture). The anisotropy increases with increasing pressure, and a pressure-dependent minority species of Mn_{12}-acetate was observed. The increased anisotropy arises from increases in the single-ion anisotropy of the Mn^{3+} building blocks.



Single-Molecule Magnets

A. Sieber, R. Bircher, O. Waldmann, G. Carver, G. Chaboussant, H. Mutka, H.-U. Güdel* ——— **4239 – 4242**

Effect of Pressure on the Magnetic Anisotropy in the Single-Molecule Magnet Mn_{12}-Acetate: An Inelastic Neutron Scattering Study



Ricin, diphtheria toxin, and other cytotoxic proteins are two-component systems which contain a carrier protein that biochemically silences the activity of the appended "warhead" protein until it is delivered into the cell. A cell-penetrating peptide (CPP) has been used in an analogous fashion (see picture) to suppress the activity of a PTP1B inhibitor that becomes activated by cleavage of the disulfide bridge upon cellular entry.

Drug Delivery

S.-Y. Lee, F. Liang, X.-L. Guo, L. Xie, S. M. Cahill, M. Blumenstein, H. Yang, D. S. Lawrence,* Z.-Y. Zhang* ——— **4242 – 4244**

Design, Construction, and Intracellular Activation of an Intramolecularly Self-Silenced Signal Transduction Inhibitor



The ins and outs of peptides: The internalization efficiencies of three cell-penetrating peptides (CPPs; penetratin, $(Arg)_9$, and Tat_{48-59}) have been measured by MALDI-TOF MS (see scheme). The method leads to direct detection of the CPPs and allows unambiguous discrimination between membrane-bound and internalized CPP. Furthermore, the cellular uptake efficiencies of several CPPs can be compared in a single experiment.

Analytical Methods

F. Burlina,* S. Sagan, G. Bolbach, G. Chassaing ——— **4244 – 4247**

Quantification of the Cellular Uptake of Cell-Penetrating Peptides by MALDI-TOF Mass Spectrometry

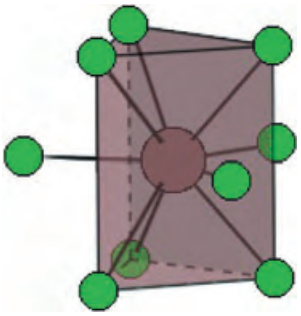
 © 2005 Wiley-VCH Verlag GmbH & Co. KGaA, Weinheim

Contents

Metal Nitrides

P. Kroll,* T. Schröter, M. Peters _____ 4249 – 4254

Prediction of Novel Phases of Tantalum(V) Nitride and Tungsten(VI) Nitride That Can Be Synthesized under High Pressure and High Temperature

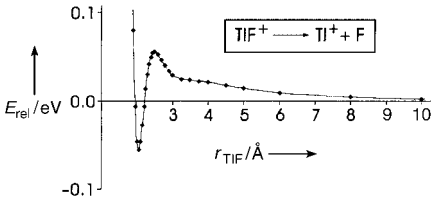


A combination of quantum-chemical and thermochemical calculations leads to the prediction of novel polymorphs of Ta_3N_5 and WN_2. Based on thermochemical data the fugacity of nitrogen at very high pressures is estimated which facilitates a detailed assessment of the synthesis conditions. The modifications of Ta_3N_5-II and WN_2-II have metal centers the are eight- and nine-fold coordinate (see picture: red W, green N).

Gas-Phase Reactions

D. Schröder,* C. van Wüllen,* H. Schwarz, T. M. Klapötke _____ 4254 – 4257

Stability of Gaseous Thallium Monofluoride as TlF^0, TlF^+, and TlF^{2+}

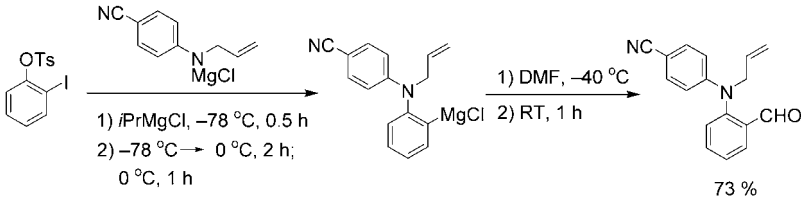


Probing a shallow minimum with a sledgehammer can be said to characterize the present experimental studies, which reveal the existence of thallium fluoride in three different charge states. High-level theory provides a quantitative description of the redox energetics of $TlF^{0/+/2+}$ (see picture: potential curve for TlF^+).

Arene Functionalization

W. Lin, I. Sapountzis, P. Knochel* _____ 4258 – 4261

Preparation of Functionalized Aryl Magnesium Reagents by the Addition of Magnesium Aryl Thiolates and Amides to Arynes

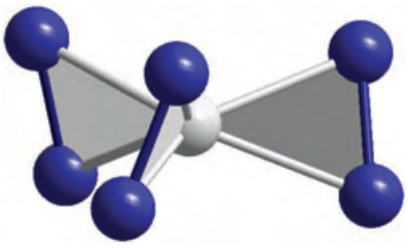


Reactive arynes, which are readily generated by the reaction of *ortho*-iodoarylsulfonates with *i*PrMgCl, undergo the smooth addition of various magnesium nucleophiles like magnesium thiolates, selenides, and amides. In all cases the resulting functionalized aryl magnesium species can be trapped by an electrophile leading to highly functionalized aromatic compounds (see scheme).

Oxygen-Rich Compounds

G. Stößer, H. Schnöckel* _____ 4261 – 4264

The Molecules AlO_2, $Al(O_2)_2$, and $Al(O_2)_3$: Experimental and Quantum-Chemical Investigations on the Oxidation of Aluminum Atoms



On the route to alumina, oxygen-rich oxides such as $Al(O_2)_3$ (see picture) are detected spectroscopically during the stepwise oxidation of aluminum atoms and confirmed structurally by quantum-chemical calculations.

 © 2005 Wiley-VCH Verlag GmbH & Co. KGaA, Weinheim

Looking for outstanding employees?

Do you need another expert for your excellent team?
... Chemists, PhD Students, Managers, Professors, Sales Representatives...

Place an advert in the printed version and have it made available online for 1 month, free of charge!

Angewandte Chemie International Edition
Advertising Sales Department: Marion Schulz
Phone: 0 62 01 - 60 65 65
Fax: 0 62 01 - 60 65 50
E-Mail: MSchulz@wiley-vch.de

Service

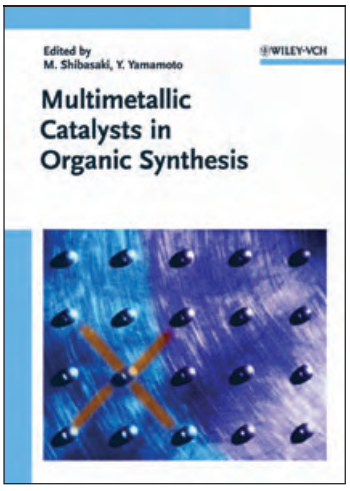
Vacancies ____ *4265*

Keywords ____ *4266*

Authors ____ *4267*

Preview ____ *4269*

Unique – New - Fascinating



2004. XV, 295 pages, 173 figures, 66 tables. Hardcover.
ISBN 3-527-30828-8
€ 129.- /£ 90.- /US$ 185.-

MASAKATSU SHIBASAKI and YOSHINORI YAMAMOTO, (eds.)

Multimetallic Catalysts in Organic Synthesis

The reference comprehensively covers this hot topic presenting the information hitherto scattered throughout smaller reviews or single book chapters to provide an introduction to this rapidly expanding field.
In ten chapters, the international team of expert authors treats asymmetric syntheses, new transformations, and organometallic reactions using homo- and hetero-bimetallic catalysts. Written for advanced researchers, this very timely publication is of significant benefit to organic and organometallic chemists in both academia and industry.

15710411_kn

Register now for the free
WILEY-VCH Newsletter!
www.wiley-vch.de/home/pas

WILEY-VCH • P.O. Box 10 11 61 • D-69451 Weinheim, Germany
Fax: +49 (0) 62 01 - 60 61 84
e-mail: service@wiley-vch.de • http://www.wiley-vch.de

WILEY-VCH

 © 2005 Wiley-VCH Verlag GmbH & Co. KGaA, Weinheim

Molecular Motors

Molecular Motors: Synthetic DNA-Based Walkers Inspired by Kinesin**

*T. Ross Kelly**

Keywords:
bioorganic chemistry · DNA · molecular devices · nanotechnology

The field of molecular devices has stimulated much research during the last two decades.[1] Over the past several years, increasing attention has focused on the construction of synthetic molecular motors, and both rotary and linear motors have been observed with "organic"[2–9] and DNA-based[10–16] systems. Biology is rich with molecular motors (flagella, muscles, cilia, etc.),[17] and until 2004 only biology provided examples of processive molecular motors in which a motor molecule moves across a surface. Kinesin is the prototypical processive biological motor,[18] although others such as DNA polymerases also exist. Fueled by ATP, kinesin "walks" along a microtubule as illustrated by the cartoons in Figure 1. A key feature of the kinesin system is that the direction of movement is controlled. The challenge of controlling directionality is perhaps best illustrated by considering the situation halfway between Figure 1b and 1c: If the kinesin is attached by only the turquoise-colored foot, and the nearest binding sites for a pink foot are identical (one to the left, to give Figure 1a, and one to the right, to give Figure 1d), how is unidirectional movement accomplished? Nature has clearly found a solution with kinesin, but to solve the issue of directionality in a synthetic device is probably the most challenging part of the problem. Four papers published in 2004[19–22] provide the first steps toward meeting this challenge. All of these use DNA-based systems.

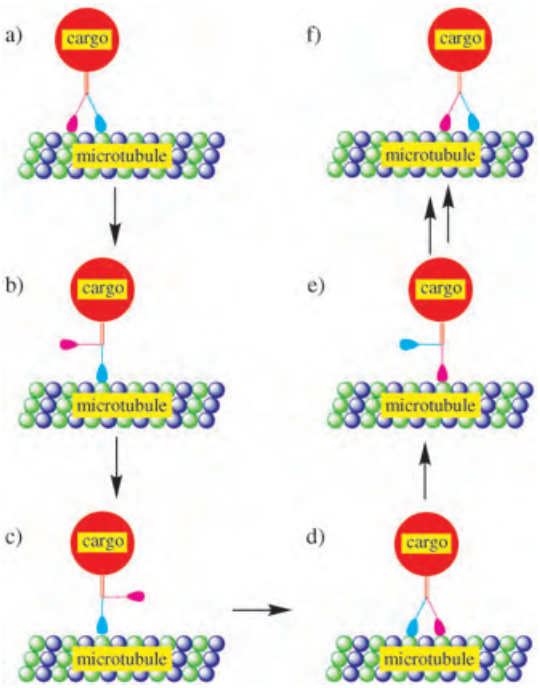


Figure 1. Schematic representation of kinesin (carrying cargo) "walking" along a microtubule.

The specifics of the four reports vary, but in essence the association/dissociation processes are driven by the hybridization of complementary single strands of DNA to form double helices, sometimes with the simultaneous cleavage of a second double helix. The second law of thermodynamics requires the expenditure of energy to achieve unidirectional motion.[23] All four systems utilize chemical energy to accomplish movement; the first three are powered by the free energy released during the course of base-pairing and double-helix formation, while the fourth is impelled primarily by the energetics of ATP hydrolysis.

Progress in this area of molecular motors was first reported by Sherman and Seeman.[19] Their concept is illustrated in Figure 2 and consists of several all-DNA components including a "footpath" (dark blue), two "legs" (brown, connected to each other by three flexible linkers) that bear single-stranded "feet" (foot 1 (F1) pink, foot 2 (F2) orange), and "footholds" (FH) A (turquoise) and B (green). Both *movement* and *standing still* are achieved by using two families of single-stranded DNA fuel strands designated as "unset" and "set" strands. Set strands join single-stranded segments by hybridizing with them, but can be removed by the addition of unset strands for which they have greater affinity. A foot attaches to a foothold when a set strand that is complementary to both is added to the solution. Complementary strand sections are shown in Figure 2 with the same color. Thus, when the pink and turquoise set strand labeled "SS 1A" is present as in Figure 2a, it connects foot 1 of the biped to foothold A as shown.

Each set strand has an eight-base overhang or "toehold" that is not complementary to any of the feet or footholds (it is colored gray in Figure 2a). The toehold allows the set strand to be

[*] Prof. T. R. Kelly
Department of Chemistry
Merkert Chemistry Center
Boston College
Chestnut Hill, MA 02467 (USA)
Fax: (+1) 617-552-2705
E-mail: ross.kelly@bc.edu

[**] We thank the National Institutes of Health (grant GM56262) for support of our work on molecular motors.

 © 2005 Wiley-VCH Verlag GmbH & Co. KGaA, Weinheim DOI: 10.1002/anie.200500568

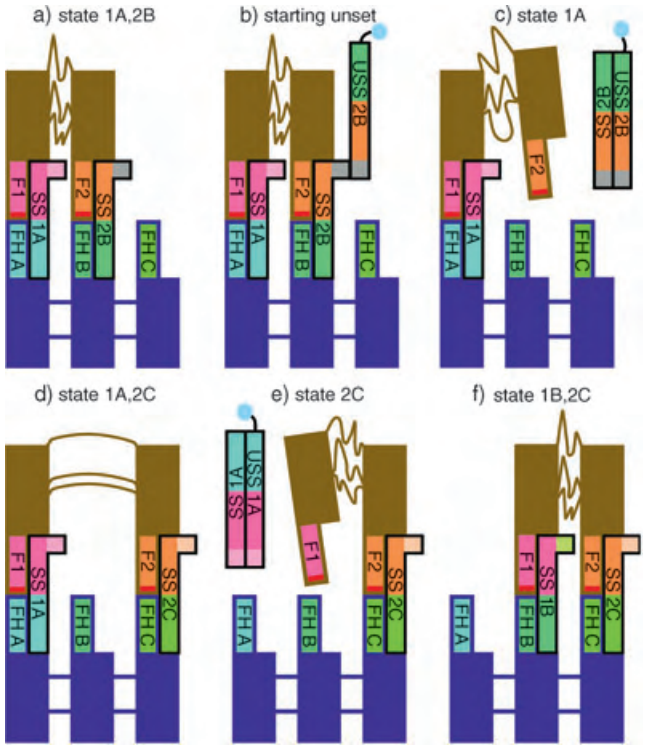


Figure 2. Conceptual representation of the operation of the Sherman–Seeman[19] biped walking device (see text for details). Matching colors indicate complementary sequences between strands; SS = set strand, USS = unset strand, F = foot, and FH = foothold. Panels (b) and (c) depict unset strand 2B first attaching to the toehold section of set strand 2B (drawn in gray) and then removing it to set foot 2 free. The set/unset complex in panel (c) can, if desired, then be removed by complexing the biotin group (depicted as a light blue circle) with streptavidin-coated magnetic beads. (Reproduced with permission of the authors.)

removed by the unset strand (Figure 2b, c). The sequences of each foot, foothold, and toehold are represented in the cartoons by unique colors. Detailed sequences are provided in Figure 3.

Figure 2a shows state 1A,2B of the system: In this state, foot 1 is set to foothold A, and foot 2 is set to foothold B. The biped is initially prepared in this state. For the biped to take a step, foot 2 first needs to be released from foothold B, as shown in Figure 2b and c. To start, unset strand 2B is introduced into the solution. It binds to the toehold of set strand 2B (Figure 2b) and subsequent branch migration results in the complete hybridization of set strand 2B with unset strand 2B. The resulting state shown in Figure 2c leaves foot 2 connected to the footpath only indirectly through the flexible linkers to foot 1 and set strand 1A. Once foot 2 has been freed from foothold B, it is free to be set back down either on foothold B, which would return the system to state 1A,2B, or on foothold C, which would move the system to state 1A,2C, as shown in Figure 2d. Note that the flexible linkers need to extend across foothold B to reach from foothold A to foothold C. Starting with state 1A,2C (Figure 2d) similar unset and set operations can be used to move foot 1 from foothold A to foothold B to bring the system to state 1B,2C, as shown in Figure 2f. The total distance traveled by the biped relative to the footpath during this step is approximately the 2-nm width of one DNA helical domain.

At present the range of the Sherman–Seeman walker is limited to one or two steps. Notably, it moves in a so-called inchworm fashion, with one foot always trailing the other. Until recently, it was not known if kinesin itself locomotes by an inchworm or hand-over-hand (foot-over-foot) mode. The inchworm motif has now been disproven[18] for kinesin (but not for inchworms).

Shin and Pierce[20] have taken Sherman and Seeman's work a step further by demonstrating a processive bipedal DNA nanomotor that moves by advancing the trailing foot to the lead at each step, as shown in Figure 4. As noted in the introduction, directionality is a crucial issue and especially difficult if only two feet and two kinds of footholds are used. The Shin–Pierce system uses two

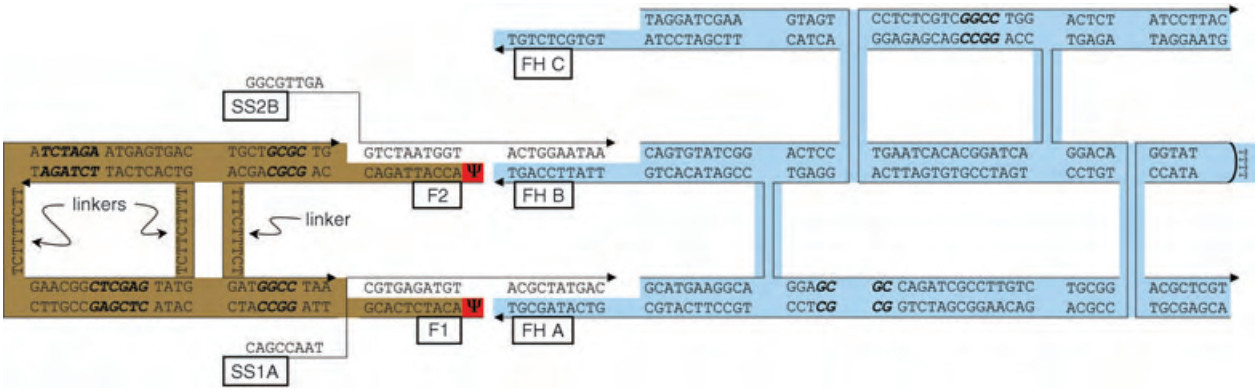


Figure 3. DNA base sequence corresponding to Figure 2a rotated 90° counterclockwise relative to Figure 2a, with SS = set strand, F = foot, and FH = foothold. (Reproduced with permission of the authors.)

 © 2005 Wiley-VCH Verlag GmbH & Co. KGaA, Weinheim

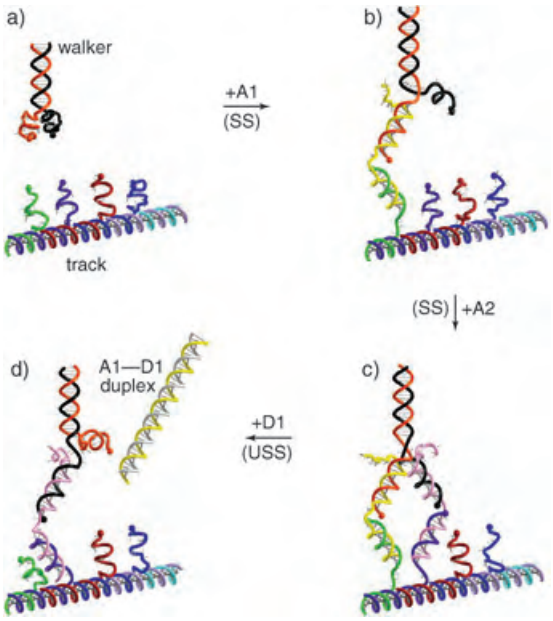


Figure 4. Schematic of the locomotion of the Shin–Pierce walker[20] (see text for details). The diagrams depict a) unbound walker, b) walker attached to branch 1, c) walker attached to branches 1 and 2, and d) walker released from branch 1 to yield DNA duplex waste. A and D denote attachment (set, SS) and detachment (unset, USS) strands, respectively. (Reproduced with permission of the authors.)

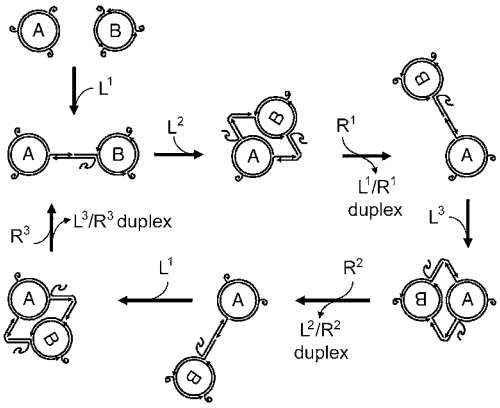


Figure 5. Rolling around a circle (or two meshed gears) following the design of Tian and Mao.[21] L = linker (set) strands, R = removal (unset) strands. (Figure courtesy of C. Mao.)

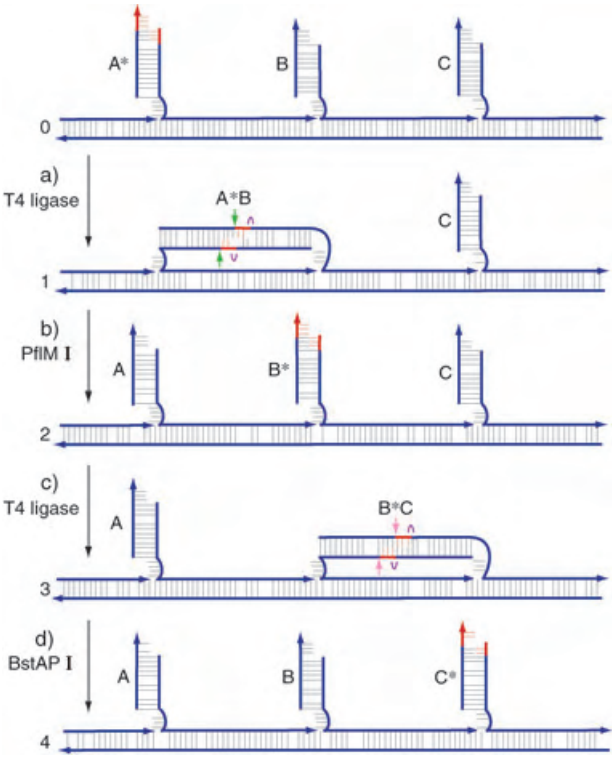


Figure 6. Operation of the device by Yan, Turberfield, Reif, and co-workers[22] (see text for details). The green and pink arrows indicate the sites of restriction; the purple ∩/∪ symbols show where ligation occurs. (Reproduced with permission of the authors.)

feet and four footholds and succeeds in efficiently achieving directionality. Their system comprises four components: a walker, a track, attachment fuel (i.e. "set") strands (A), and detachment (i.e. "unset") strands (D). The walker consists of two partially complementary oligonucleotides, with two single-stranded legs (feet) joined by a double-stranded helix. The track, which is constructed of six oligonucleotides, has four protruding single-stranded branches (footholds) separated by 15-base-pair scaffold helices. Neighboring branches run in opposite directions, so spacings of 1.5 helical turns place all branches on the same side of the track at approximately 5 nm apart (Figure 4a).

As shown in Figure 4, the walker strides along a track under the external control of A and D strands. An A set strand (yellow in the first instance) specifically anchors the orange leg of the walker to the green branch (foothold) by forming double helices with the corresponding leg and foothold. Single-stranded hinges adjacent to either end of these helices provide flexibility for adopting different conformations that depend on the fuel species that are present. When both legs are bound to the track, the trailing leg is released (Figure 4, c→d) by using a D unset strand that nucleates with the perfectly complementary A1 strand at a 10-base overhang (toehold) and then undergoes a strand-displacement reaction to produce duplex waste and to free the walker leg for the next step. Although Figure 4 does not show it, by appropriate additions of A and D strands, the walker is able to traverse the track from one end to the other and back, with full directional control.

A conceptually similar approach, except that movement is around a circular track, was reported by Tian and Mao[21] and is summarized in Figure 5.

A third strategy was recently described by Yan, Turberfield, Reif, and co-workers.[22] In this case, the walker, a six-nucleotide fragment colored red and indicated by * in Figure 6, moves along a DNA track, but it is more like a bucket being passed along a bucket brigade (or a crowd surfer being transported across a mosh pit). Here too, the process is unidirectional, but instead of using set and unset strands, T4 ligase accomplishes the set function and creates, at the same time, a recognition site for restriction endonucleases (PflM I, BstAP I)

 © 2005 Wiley-VCH Verlag GmbH & Co. KGaA, Weinheim

that subsequently operate in place of unset strands.

As shown in Figure 6, the self-assembled track contains three anchorages at which the walker (the red six-nucleotide fragment) can be bound. Each anchorage consists of a double-stranded segment with a three-nucleotide single-strand overhang ("sticky end"). At each step the ligand is ligated (e.g. 0→1) to the next anchorage, then cut (1→2) from the previous one by the restriction endonuclease. Each ligation creates a new restriction site, and each cut destroys the previous restriction site. The motion of the walker is unidirectional: the product of ligation between two neighboring anchorages can only be cleaved such that the walker moves onto the downstream anchorage (A*B and B*C can only be cut such that the walker is left attached to B and C, respectively). In effect, the system burns its bridges behind it as the six-nucleotide bundle tumbles down the track. Two idling steps are possible: B* can be religated to A and regenerated by restriction with PflM I; similarly, C* can be religated to B and regenerated with BstAP I. However, these idling steps neither reverse nor block the overall unidirectional motion of the walker. Once B* has been ligated to C, the walker can never return to A. It should be possible to extend the motion of the walker beyond three anchorages.

The sequence of events in Figure 6, unlike those discussed in the context of Figures 2–5, is said to be "autonomous," because once the walker (A*), the track (with its anchorages), and the three enzymes (T4 ligase and the restriction endonucleases PflM I and BstAP I) are mixed at the beginning, all the events (0→4) in Figure 6 occur without further external intervention.

The four papers highlighted above offer ingenious responses to a challenging design problem. Much remains to be done before a practical synthetic solution to transporting cargo across surfaces is achieved. But, as Confucius reputedly said, a journey of a thousand miles begins with a single step. With the walkers described above, the journey has begun.

Published online: June 2, 2005

[1] For complementary reviews, see: a) C. M. Niemeyer, M. Adler, *Angew. Chem.* **2002**, *114*, 3933–3937; *Angew. Chem. Int. Ed.* **2002**, *41*, 3779–3783; b) V. Balzani, M. Ventura, A. Credi, *Molecular Devices and Machines*, Wiley-VCH, Weinheim, **2003**.

[2] a) T. R. Kelly, H. De Silva, R. A. Silva, *Nature* **1999**, *400*, 150–152; b) T. R. Kelly, R. A. Silva, H. De Silva, S. Jasmin, Y. Zhao, *J. Am. Chem. Soc.* **2000**, *122*, 6935–6949; c) T. R. Kelly, *Acc. Chem. Res.* **2001**, *34*, 514–522; d) T. R. Kelly, M. Cavero, Y. Zhao, *Org. Lett.* **2001**, *3*, 3895–3898; e) T. R. Kelly, M. Cavero, *Org. Lett.* **2002**, *4*, 2653–2656.

[3] a) N. Koumura, R. W. J. Zijlstra, R. A. van Delden, N. Harada, B. L. Feringa, *Nature* **1999**, *400*, 152–154; b) B. L. Feringa, *Acc. Chem. Res.* **2001**, *34*, 504–513; c) R. A. van Delden, N. Koumura, N. Harada, B. L. Feringa, *Proc. Natl. Acad. Sci. USA* **2002**, *99*, 4945–4949; d) N. Koumura, E. M. Geertsema, M. B. van Gelder, A. Meetsma, B. L. Feringa, *J. Am. Chem. Soc.* **2002**, *124*, 5037–5051; e) M. K. J. ter Wiel, R. A. van Delden, A. Meetsma, B. L. Feringa, *J. Am. Chem. Soc.* **2003**, *125*, 15076–15086.

[4] a) R. A. Bissell, E. Córdova, A. E. Kaifer, J. F. Stoddart, *Nature* **1994**, *369*, 133–137; b) M.-V. Martínez-Díaz, N. Spencer, J. F. Stoddart, *Angew. Chem.* **1997**, *109*, 1991–1994; *Angew. Chem. Int. Ed. Engl.* **1997**, *36*, 1904–1907; c) V. Balzani, A. Credi, F. M. Raymo, J. F. Stoddart, *Angew. Chem.* **2000**, *112*, 3484–3530; *Angew. Chem. Int. Ed.* **2000**, *39*, 3349–3391; d) T. J. Huang, H.-R. Tseng, L. Sha, W. Lu, B. Brough, A. H. Flood, B.-D. Yu, P. C. Celestre, J. P. Chang, J. F. Stoddart, C.-M. Ho, *Nano Lett.* **2004**, *4*, 2065–2071.

[5] a) M. C. Jimenez, C. Dietrich-Buchecker, J.-P. Sauvage, *Angew. Chem.* **2000**, *112*, 3422–3425; *Angew. Chem. Int. Ed.* **2000**, *39*, 3284–3287; b) J.-P. Collin, C. Dietrich-Buchecker, P. Gavina, M. C. Jimenez-Molero, J.-P. Sauvage, *Acc. Chem. Res.* **2001**, *34*, 477–487; c) C. Dietrich-Buchecker, M. C. Jimenez-Molero, V. Sartor, J.-P. Sauvage, *Pure Appl. Chem.* **2003**, *75*, 1383–1393.

[6] a) A. M. Brouwer, C. Frochot, F. G. Gatti, D. A. Leigh, L. Mottier, F. Paolucci, S. Roffia, G. W. H. Wurpel, *Science* **2001**, *291*, 2124–2128; b) D. A. Leigh, J. K. Y. Wong, F. Dehez, F. Zerbetto, *Nature* **2003**, *424*, 174–179; c) J. V. Hernández, E. R. Kay, D. A. Leigh, *Science* **2004**, *306*, 1532–1537.

[7] X. Zheng, M. E. Mulcahy, D. Horinek, F. Galeotti, T. F. Magnera, J. Michl, *J. Am. Chem. Soc.* **2004**, *126*, 4540–4542.

[8] M. F. Hawthorne, J. I. Zink, J. M. Skelton, M. J. Bayer, C. Liu, E. Livshits, R. Baer, D. Neuhauser, *Science* **2004**, *303*, 1849–1851.

[9] For a recent review, see: C. P. Mandl, B. König, *Angew. Chem.* **2004**, *116*, 1650–1652; *Angew. Chem. Int. Ed.* **2004**, *43*, 1622–1624.

[10] a) C. Mao, W. Sun, Z. Shen, N. C. Seeman, *Nature* **1999**, *397*, 144–146; b) H. Yan, X. Zhang, Z. Shen, N. C. Seeman, *Nature* **2002**, *415*, 62–65.

[11] a) B. Yurke, A. J. Turberfield, A. P. Mills, Jr., F. C. Simmel, J. L. Neumann, *Nature* **2000**, *406*, 605–608; b) A. J. Turberfield, J. C. Mitchell, B. Yurke, A. P. Mills, Jr., M. I. Blakely, F. C. Simmel, *Phys. Rev. Lett.* **2003**, *90*, 118102.

[12] J. J. Li, W. Tan, *Nano Lett.* **2002**, *2*, 315–318.

[13] P. Alberti, J. Mergny, *Proc. Natl. Acad. Sci. USA* **2003**, *100*, 1569–1573.

[14] L. Feng, S. H. Park, J. H. Reif, H. Yan, *Angew. Chem.* **2003**, *115*, 4478–4482; *Angew. Chem. Int. Ed.* **2003**, *42*, 4342–4346.

[15] Y. Chen, M. Wang, C. Mao, *Angew. Chem.* **2004**, *116*, 3638–3641; *Angew. Chem. Int. Ed.* **2004**, *43*, 3554–3557.

[16] a) W. U. Dittmer, F. C. Simmel, *Nano Lett.* **2004**, *4*, 689–691; b) W. U. Dittmer, A. Reuter, F. C. Simmel, *Angew. Chem.* **2004**, *116*, 3634–3637; *Angew. Chem. Int. Ed.* **2004**, *43*, 3550–3553.

[17] For an overview, see: *Molecular Motors* (Ed.: M. Schliwa), Wiley-VCH, Weinheim, **2003**.

[18] For leading references, see: a) C. L. Asbury, A, N. Fehr, S. M. Block, *Science* **2003**, *302*, 2130–2134; b) A. Yildiz, M. Tomishige, R. D. Vale, P. R. Selvin, *Science* **2004**, *303*, 676–678.

[19] W. B. Sherman, N. C. Seeman, *Nano Lett.* **2004**, *4*, 1203–1207; for an important correction, see: W. B. Sherman, N. C. Seeman, *Nano Lett.* **2004**, *4*, 1801.

[20] J.-S. Shin, N. A. Pierce, *J. Am. Chem. Soc.* **2004**, *126*, 10834–10835.

[21] Y. Tian, C. Mao, *J. Am. Chem. Soc.* **2004**, *126*, 11410–11411.

[22] P. Yin, H. Yan, X. G. Daniell, A. J. Turberfield, J. H. Reif, *Angew. Chem.* **2004**, *116*, 5014–5019; *Angew. Chem. Int. Ed.* **2004**, *43*, 4906–4911.

[23] A. P. Davis, *Angew. Chem.* **1998**, *110*, 953–954; *Angew. Chem. Int. Ed.* **1998**, *37*, 909–910.

 © 2005 Wiley-VCH Verlag GmbH & Co. KGaA, Weinheim

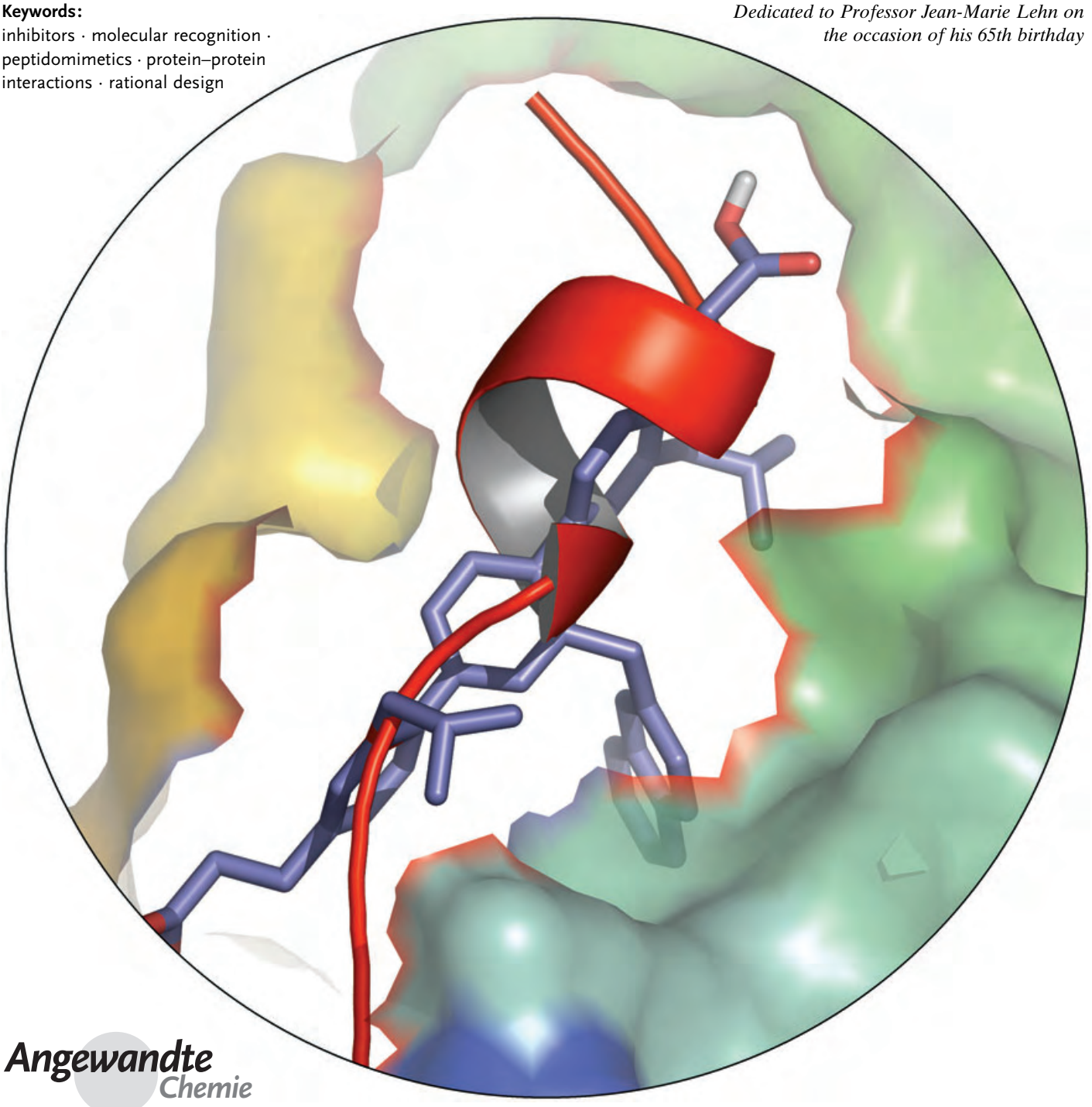
Inhibitor Design

Strategies for Targeting Protein–Protein Interactions With Synthetic Agents

*Hang Yin and Andrew D. Hamilton**

Keywords:
inhibitors · molecular recognition · peptidomimetics · protein–protein interactions · rational design

Dedicated to Professor Jean-Marie Lehn on the occasion of his 65th birthday



Angewandte Chemie

 © 2005 Wiley-VCH Verlag GmbH & Co. KGaA, Weinheim DOI: 10.1002/anie.200461786

The development of small-molecule modulators of protein–protein interactions is a formidable goal, albeit one that possesses significant potential for the discovery of novel therapeutics. Despite the daunting challenges, a variety of examples exists for the inhibition of two large protein partners with low-molecular-weight ligands. This review discusses the strategies for targeting protein–protein interactions and the state of the art in the rational design of molecules that mimic the structures and functions of their natural targets.

From the Contents

1. Introduction 4131
2. Key Features of Protein–Protein Associations Relevant to Inhibitor Design 4131
3. Strategies for the Recognition of Protein Exterior Surfaces 4133
4. Synthetic Modulators of Protein–Protein Interactions from Chemical Libraries 4137
5. Synthetic Inhibitors of Protein–Protein Interactions from Rational Design 4150
6. Summary and Outlook 4156

1. Introduction

The pharmaceutical industry is largely built on the skills of organic chemists—with occasional assistance from Nature—in the identification of small molecules (MW < 750 Da) that inhibit a given target (proteins, DNA, etc.) but that also retain optimized pharmacokinetic and oral absorption properties. The completion of the human genome sequence is clearly a landmark achievement which, in theory, should reveal all the targets available for drug development. In the spirit of Herbert Hoover ("*a chicken in every pot and a car in every garage*"), Stuart Schreiber has thrown out the challenge "*… to identify a small-molecule partner for every gene product*".[1]

There is little doubt that the enterprise of designing small molecules to fit enzyme active sites has been remarkably successful. The problem of identifying enzyme inhibitors is simplified by the nature of enzyme active sites. Most often the catalytic domain is made up of multiple recognition sites that are contained within a well-defined cleft or cavity, shielded from solvent to some extent. As the dominant interactions in an enzyme active site include hydrogen bonding, salt bridges, and electrostatic forces, "druglike" molecules that contain various hydrophilic motifs and hydrogen-bond donors and receptors often work well. Furthermore, native substrates can provide effective templates for inhibitor design. Finally, biological assays for the potency of enzyme inhibitors are generally straightforward, as they are based on the modification of enzyme activity.

In contrast, the development of small-molecule modulators of protein–protein interactions has been widely regarded as a formidable goal, albeit one that possesses significant potential for the discovery of novel therapeutics. Approaches for the disruption of protein–protein interactions are limited by the following key aspects: 1) natural proteinaceous ligands do not provide direct links to the design of small molecules, and the key interacting residues are often unclear; 2) large interfacial areas, typically $\approx 1600\ \text{Å}^2$ of buried surface (around 170 atoms) are involved in forming protein–protein interfaces, which poses a serious challenge for any small molecule to be competitive; 3) the binding regions of protein partners are often noncontiguous and thus cannot be mimicked by simple synthetic peptides; 4) selectivity in targeting an individual protein is difficult, as many protein–protein interfaces are relatively featureless; 5) few "druglike" small molecules have been identified from library screening as effective disruptors of protein–protein interactions; and 6) biological assays cannot necessarily follow enzyme activity, and in many cases activity must be detected through more challenging techniques that monitor binding directly (for example, calorimetry or surface plasmon resonance).

Despite these daunting challenges, there is a variety of examples of the inhibition of two large protein partners with low-molecular-weight ligands. A number of recent reviews have addressed this topic,[2–8] so our goal herein is to provide an overview of the strategies for targeting protein–protein interactions and the state of the art in the rational design of mimetics that reproduce the structures and functions of their natural targets.

2. Key Features of Protein–Protein Associations Relevant to Inhibitor Design

2.1. "Hot Spots" of Binding Energy

In a milestone analysis by Clackson and Wells, the binding energy of the complex between human growth hormone (hGH) and the extracellular domain of its first-bound receptor (hGHbp) could be ascribed to a small and complementary set of interfacial residues.[9] This suggested that the critical domain of one protein partner might be mimicked by relatively simple small molecules. The technique of alanine scanning (in which the interfacial residues are mutated to alanine systematically to determine the change in binding free energy) was used to detect which residues constituted the key binding region (or functional epitope, which also became known as the "hot spot"). Cunningham and Wells found that eight out of 31 side chains on the binding surface of hGH

[*] Dr. H. Yin, Prof. Dr. A. D. Hamilton
Department of Chemistry, Yale University
P.O. Box 208107, New Haven, CT 06520-8107 (USA)
Fax: (+1) 203-432-6144
E-mail: andrew.hamilton@yale.edu

 DOI: 10.1002/anie.200461786 © 2005 Wiley-VCH Verlag GmbH & Co. KGaA, Weinheim

accounted for approximately 85% of the binding energy, whereas half of the residues make no substantial contributions to the interaction.[10] On the side of hGHbp, Trp 104 and Trp 69 dominated the binding interface with each contributing over -4.5 kcal mol^{-1} in binding energy to the total energy of the hGH–hGHbp complex formation of -12.3 kcal mol^{-1} (Figure 1).

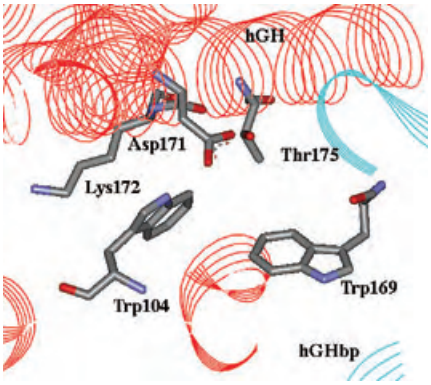


Figure 1. The hGH/hGHbp interface (key binding residues are shown in stick representation).

Extensive work has been done since then to further underpin the concept of hot spots in protein–protein interactions.[11] Bogan and Thorn examined 2325 alanine mutants for which changes in the free energy of binding have been measured, and showed that the energetic contributions of the individual side chains did not correlate with their buried surfaces.[12] In several cases, a set of energetically unimportant contacts surrounded the hot spot, and appeared to occlude bulk-solvent access in the manner of an O-ring. Certain amino acid residues, particularly tryptophan (21%), arginine (13%), and tyrosine (12%) appear more frequently in hot spots (that is, they contribute more than 2 kcal mol^{-1} to a given binding interaction) than others such as leucine, methionine, serine, threonine, and valine, each of which account for less than 3% of all hot-spot residues.[13] Tryptophan, arginine, and tyrosine residues are also found more frequently in the protein interfaces, with 3.91, 2.47, and 2.29-fold enrichment in hot-spot areas, respectively. An enrichment of tyrosine and tryptophan and a discrimination against valine, isoleucine, and leucine have also been reported in antibody complementarity-determining region (CDR) sequences.[14] Padlan proposed that the enrichment of these aromatic amino acid residues is a result of their contribution to the binding energy through hydrophobic effects without a large entropic penalty, as they have fewer rotatable bonds.

Recent developments in bioinformatics have provided insight into the analysis of protein–protein interfaces and have helped the detection of hot spots. A wealth of data on alanine mutations in various protein–protein complexes is available and has assisted in the design of small molecules to modulate their interactions.[15] Alternatives for the detection of hot-spot regions include computational tools that generate combinatorial libraries of functional epitopes and identify recurring sets of residues in the epitope.[16] By this method the spatial arrangement of key structural motifs at protein–protein interfaces has been efficiently detected. Ben-Tal and co-workers have developed an algorithm (Rate4Site; http://consurf.tau.ac.il) for the identification of functional interfaces based on the evolutionary relations among homologous proteins reflected in phylogenetic trees.[17] By using the tree topology and branch lengths corresponding to the evolutionary relationships between two proteins, the method accurately predicted a homodimer interface of a hypothetical protein Mj0577 that was also confirmed under X-ray crystallographic analysis.

2.2. Enthalpy, Entropy, and Heat Capacity

In an excellent in-depth review, Stites addressed the thermodynamic aspects of protein–protein association and the relative importance of enthalpy, entropy, and heat-capacity effects in stabilizing complex formation.[7] The most important parameter is the association constant, which is determined by the free-energy difference (ΔG) between the associated and unassociated states of the proteins. This determines the concentration at which the protein complex is formed in significant quantity.



Hang Yin is currently a postdoctoral associate with Prof. William F. DeGrado at the University of Pennsylvania School of Medicine. In 2004, he completed his PhD with Prof. Andrew D. Hamilton at Yale University from research in synthetic agents as α-helical mimetics that target protein–protein interactions. Prior to that, he completed his BS degree in Chemistry at Peking University.



Andrew D. Hamilton is currently the Provost, Benjamin Silliman Professor of Chemistry, and Professor of Molecular Biophysics and Biochemistry at Yale University. He received his undergraduate education at the University of Exeter. In 1974, he moved to the University of British Columbia, and then to Cambridge University where he received his PhD in 1980 for work on porphyrin chemistry with Prof. Sir Alan Battersby. After postdoctoral research with Prof. Jean-Marie Lehn, he was appointed to an Assistant Professorship in Chemistry at Princeton University. In 1988, he moved to the University of Pittsburgh, where in 1992 he became Professor of Chemistry, and in 1994, Chair of the Chemistry Department. In 1997, he moved to his present position at Yale University.

 © 2005 Wiley-VCH Verlag GmbH & Co. KGaA, Weinheim

It is widely accepted that the hydrophobic effect dominates the change in heat capacity (ΔC_p) for protein folding and binding.[18] However, Stites pointed out that there is no clear correlation between ΔH or ΔS and the values of ΔG and ΔC_p, despite the previous assertion that protein–protein interactions are driven by either enthalpic or entropic processes.[19] He also concluded that hydrophobic interactions generally provide the key driving force for protein–protein complex formation. Other alternatives, such as electrostatic effects, can also play an important role in protein association in certain cases.[20] The amount of polar and nonpolar surface buried in a protein–protein interaction does not often correlate well with its ΔC_p value.[21] A possible explanation for this is the large number of buried water molecules at the interface; water of this type may have a lower heat capacity than bulk solvent and is probably responsible for the large change in ΔC_p for many protein–protein interactions.

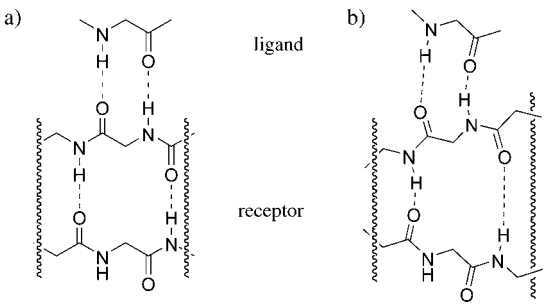
Cochran has argued that despite the large interacting surfaces and high binding energies of protein association, small molecular antagonists can be identified that have competitive binding affinities.[6] The driving force for disruption derives either from enthalpy-favored protein stabilization or entropy-favored ligand exchange.

2.3. Positively and Negatively Cooperative Interactions

Williams et al. proposed that the thermodynamic parameters for protein–protein associations have more complex origins.[22] They analyzed the cooperativity of protein–ligand interactions and suggested that the binding energy can derive in part from changes occurring within the receptor proteins.[22–25] These findings have implications for protein–protein interactions, as the binding between two proteins is not simply a function of the properties of the interacting surface regions; it is also a function of how these interactions modify the internal structure of the protein.

A binding event is defined as positively cooperative with respect to a second interaction if its affinity is increased in the presence of that second interaction. Conversely, a binding event is negatively cooperative if its affinity is decreased in the presence of that second interaction (Scheme 1). The general expectation for a positively cooperative binding event is the tightening of protein structure with a resulting gain in enthalpy and loss in entropy. An example is the formation of the biotin–streptavidin complex ($\Delta H = -134\ \mathrm{kJ\,mol^{-1}}$ and $T\Delta S = -57\ \mathrm{kJ\,mol^{-1}}$ at 25 °C).[26] During a positively cooperative binding event, the ligand decreases the dynamic motion of the residues with which it interacts directly. As noncovalent bonding is opposed by the kinetic energy of motion, these residues, in turn, form more stable bonds with adjacent residues. This effect propagates and results in a more efficient packing of the whole protein.[24]

In negatively cooperative ligand binding the interacting partners become more dynamic, with an associated loss in enthalpy and gain in entropy.[25] Williams et al. showed that O_2 binds to hemoglobin in a negatively cooperative manner.[24] The optimal binding of O_2 is incompatible with the geometry present in the tense (T) state. Analogous to Scheme 1b, the ligand distorts the structure of the receptor, which forces a loosening of the hemoglobin tetramer through breakage of inter-subunit salt bridges, and converts the protein to the relaxed (R) state.[27]



Scheme 1. Structural models for a) positive and b) negative cooperativity; the lower pair of hydrogen bonds is within a protein receptor and the upper pair of hydrogen bonds is formed upon the binding of a peptide ligand.

3. Strategies for the Recognition of Protein Exterior Surfaces

Each protein has a unique exterior surface composed of charged, hydrophobic, and hydrophilic domains. Protein surfaces are critical in mediating protein–ligand and protein–protein interactions in a variety of biological processes, such as cell proliferation, growth, and differentiation. Therefore, synthetic molecules that match both the electrostatic and structural features of the protein target are expected to bind to the exterior surface and disrupt protein–protein interactions. Such possibilities could offer an innovative and systematic approach to regulating biological processes.[28]

3.1. Recognition of Protein Surfaces: Biological Strategies

3.1.1. Artificial Antibodies

Many uses of antibodies in chemistry and medicine require a single defined molecular specificity in the form of monoclonal antibodies (MAbs).[29] Earlier efforts have been focused on the humanization of antibodies derived from rodent MAbs to overcome the problems of immunogenicity and inefficient secondary immune function that frequently beset clinical use.[30] Humanized antibodies are created by transplanting the CDR loops from the rodent to the human antibody constant regions. The functional antibody fragments are then secreted from *E. coli*.[31]

Monoclonal antibodies that block the interaction between interleukin 2 (IL-2) and its receptor (IL-2R) represent a successful example of targeting protein–protein interactions in immunotherapy.[32] Mouse antibodies against IL-2R (anti-Tac) have been used to inhibit graft-versus-host disease (GVHD) and to suppress autoimmune disorders in rodents.[33,34] In clinical trials, anti-Tac has ameliorated steroid-resistant GVHD. Jones et al. humanized anti-Tac by combining the CDR from rodent antibodies with constant

 © 2005 Wiley-VCH Verlag GmbH & Co. KGaA, Weinheim

and framework regions from human antibodies, thus minimizing xenogenic elements.[35] Queen et al. and Junghans et al. produced a humanized version of anti-Tac that retains the murine CDR along with virtually all of the remainder of the molecule from human immunoglobulin G1κ (IgG1κ).[36]

Some strategies have been employed to improve the efficacy of immunotherapy. One is through the modification of a natural toxin to kill cells that express the MAb-recognized antigen. Lorberboum-Galski et al. deleted the cell-recognition domain I of the single-chain *Pseudomonas* exotoxin (PE) to create the modified toxin PE40.[37] The chimeric protein IL-2–PE40 was able to inhibit protein synthesis in tumor cell lines that express IL-2R, leading to cell death. However, large protein toxins are immunogenic and provide only a narrow therapeutic window before the host develops antitoxin antibodies. Radiolabeled MAbs were developed as alternative immunoconjugates for the delivery of cytotoxic agents to target cells.[38] Waldmann used ^{90}Yb-labeled anti-Tac antibodies to treat patients with adult T-cell leukemia (ATL); 11 of 17 treated patients underwent a partial (9) or complete (2) remission.[33] Thus, the anti-Tac antibody armed with a radionuclide provides an effective therapy for leukemias expressing IL-2R.

3.1.2. Miniature Proteins

Despite the success of protein engineering in the generation of functional antibody fragments, alternative smaller and more compact protein frameworks are still desirable for several reasons:[39] 1) higher theoretical affinities can be expected for structured proteins because of the smaller loss in entropy upon binding;[40] 2) the interpretation of the interaction at the interface is simplified if the overall structure of the parent protein is preserved; 3) a higher proteolytic stability can be expected for a folded protein than a random peptide, making it more suitable for recombinant production; 4) a constrained scaffold has the potential to effectively present hydrophobic residues which might be buried in a peptide format; 5) the binding activity of a domain rather than a peptide is more likely to be maintained when produced by fusion to a different protein or domain.

Rather than designing such presentation scaffolds de novo, many groups have recruited naturally existing proteins or domains for further engineering. To date, a number of native or engineered protein scaffolds, such as β barrels,[41] α-helix bundles,[42] and zinc-finger motifs,[43] have been used to construct artificial binding molecules.

Schepartz and co-workers have developed a general solution called "protein grafting", in which the functional epitope is grafted into a rigid miniature protein scaffold. This method, often used in combination with molecular evolution, can be used to identify miniature proteins with high affinity and specificity for protein and nucleic acid targets.[44] A recent application of this approach was in the identification of high-affinity ligands for the KIX domain of the transcriptional coactivator protein (CBP).[45] The complex between the CBP KIX domain and the kinase-inducible activation domain (KID) of the transcription factor CREB represents a challenging target, as the KID-binding cleft on the surface of the KIX domain is shallow and is more reminiscent of a solvent-exposed protein surface than a typical α-helix-binding groove.[46] Hydrophobic interactions contribute significantly to the free energy of KID^{P}–KIX complex formation; the side chains at *i*, *i*+3, *i*+4, and *i*+7 positions (Tyr 134, Ile 137, Leu 138, and Leu 141, respectively) on the same face of the helical region of the CREB KID domain interact with the surface of KIX. These key residues were grafted onto the solvent-exposed α-helical face of the small yet stable protein, avian pancreatic polypeptide (aPP).[47] The resulting phosphopeptide PPKID4^{P} (G**PSQPTYP**GDDAPVRRLS^{P}F-FYILLDLYLDAPGVC, S^{P} = phosphoserine), containing the additional functional epitope (shown in bold), exhibited high affinity ($K_d = 562 \pm 41$ nM). The grafted protein also showed a higher preference for CBP KIX than for carbonic anhydrase (CA; $K_d = 106 \pm 12$ μM), which also binds hydrophobic ligands, and calmodulin (CaM; $K_d = 52 \pm 12$ μM), whose native ligand, smooth muscle myosin light-chain kinase (smMLCK) also adopts an α-helical conformation with the key binding residues at the *i*, *i*+3, *i*+7 positions (Trp800, Thr803, and Val807, respectively).[48–50]

Vita and co-workers reported the rational design of miniature proteins that reproduce the CDR2-like region of CD4, which interacts with the envelope protein of HIV-1.[51–53] This strategy is based on the scorpion charybdotoxin as a scaffold.[54,55] Charybdotoxin is a compact protein (37 amino acids) composed of an antiparallel triple-stranded β sheet and a short α helix, stabilized by three disulfide bonds in the interior core (Figure 2b).[56,57] Such geometry is adopted by all known scorpion toxins,[56,58] regardless of size, amino acid sequence, or function (blockage of K^+, Na^+, or Cl^- ion channels, etc.),[59] which indicates that this motif readily permits sequence adoption. As this scorpion toxin contains most of the structural elements commonly found in protein

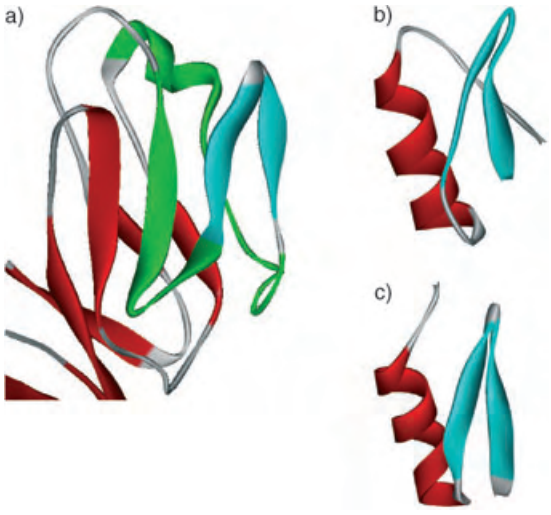


Figure 2. Structural comparison between a) CD4 and b) scorpion charybdotoxin and c) scyllatoxin. The region of residues 25–64 of CD4 (green) binds gp120. The CDR2-like loop of residues 36–47 (cyan) was transferred to charybdotoxin or scyllatoxin, each of which contain a solvent-exposed β hairpin loop (also shown in cyan), structurally similar to the CDR2-like loop.

 © 2005 Wiley-VCH Verlag GmbH & Co. KGaA, Weinheim

structure (α helix, β sheet, β turn, and loops), it is an attractive scaffold for protein grafting on which functional amino acid sequences can be incorporated. The cell-surface protein CD4 binds to the envelope glycoprotein gp120, which plays important roles in determining HIV virus tropism and cell infection.[60] A protruding β hairpin, the CDR2-like loop of CD4 (Figure 2a), is centered on the CD4–gp120 interface to form an antiparallel β sheet with the β15 strand of gp120.[61] The chimeric miniature protein, CD4M, based on the charybdotoxin scaffold (Figure 2b) yet with the key amino acid residues of CD4, inhibited the binding of gp120 to CD4 with an IC_{50} value of 20 μM.[55]

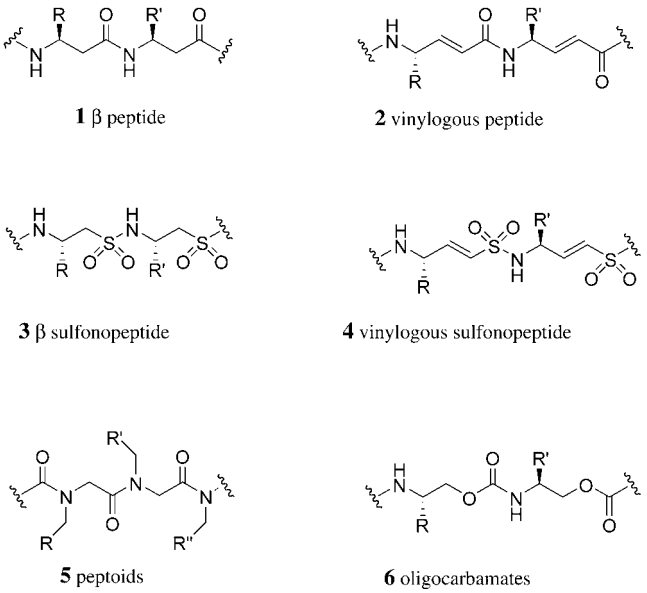
With scyllatoxin, another scorpion toxin scaffold, Vita et al. observed additional miniature proteins as potent inhibitors of the CD4–gp120 interaction.[52] Scyllatoxin (Figure 2c) is a 31-residue protein with a double-stranded β sheet (residues 18–29) that is structurally similar to the CDR2-like loop of CD4.[52] It is slightly shorter than charybdotoxin and has no N-terminal β strand. It has a shorter loop joining the helix to the first β strand, which allows full access of the β hairpin of the toxin to a large-molecule probe and makes it a better host structure for the CDR2-like loop of CD4. A chimeric protein based on the scyllatoxin scaffold, CD4M9, showed improved potency in disrupting the CD4–gp120 interaction with an IC_{50} value of 0.4 μM, 100-fold higher than that of native CD4. In a later report, the interacting face of CD4M9 was optimized to produce a potent miniature CD4 (CD4M33, $IC_{50} = 4.0$ nM) with genuine CD4-like properties. CD4M33 also exhibited strong antiviral activity in blocking HIV-1 cell–cell fusions at low nanomolar concentrations.[53]

3.1.3. Functional Oligonucleotides

Analogous to peptide libraries, the generation and selection of oligonucleotides (aptamers) that bind specific ligands has been widely used for the development of pharmaceutical reagents and diagnostic assays.[62] Since the systematic evolution of ligands by exponential enrichment (SELEX) method was first reported in 1990,[63] numerous modifications of this technology have greatly expanded its potential.[64] Modified nucleotides have been introduced into selection experiments, resulting in the isolation of aptamers that are surprisingly stable in vivo. For example, nuclease-resistant nucleic acid ligands with high potency ($K_i = 100$ pM) for vascular endothelial growth factor (VEGF) were identified from RNA aptamer libraries.[65] Anti-HIV reverse transcriptase (HIV-RT) aptamers selected from a single-stranded DNA pool bound to the enzyme with K_i values as low as 1 nM.[66] Both RNA and modified RNA aptamers selected to bind basic fibroblast growth factor (bFGF) can successfully inhibit bFGF binding to cell-surface receptors at concentrations as low as 1 nM.[67] The antithrombin single-stranded DNA aptamers can block blood clotting in vivo.[68] The folding patterns of these selected aptamers are surprisingly diverse, and contain secondary structure elements such as G-quartets, stem-loops and pseudoknots.[69]

3.1.4. Unnatural Biopolymers

The intrinsic susceptibility of peptides and nucleotides to enzyme degradation makes alternative well-folded scaffolds desirable. Thus, peptide-like or nucleotide-like biopolymers, such as β peptides, β sulfonopeptides, peptoids, oligocarbamates and PNA, have been under intense investigation (Scheme 2).[70] For example, Seebach and co-workers



Scheme 2. Unnatural biopolymers with properties that are similar to peptides.

reported a small cyclo-β-tetrapeptide that mimics the natural hormone somatostatin and displays biological activity and micromolar affinity for human receptors.[71] Schreiber and co-workers examined the conformational properties of small vinylogous peptides.[72] Gennari et al. examined the folding of oligosulfonamides (β-sulfonopeptides and vinylogous sulfonopeptides).[73] Peptoids, one of the first unnatural oligomers developed for pharmaceutical and combinatorial applications, were found to adopt conformations in water when chiral side chains were appended onto amide nitrogens.[74] A family of oligocarbamates were reported by Schultz and co-workers to bind MAb 20D6.3 with IC_{50} values between 60 and 180 nM, although their structural preferences were not clear.[75]

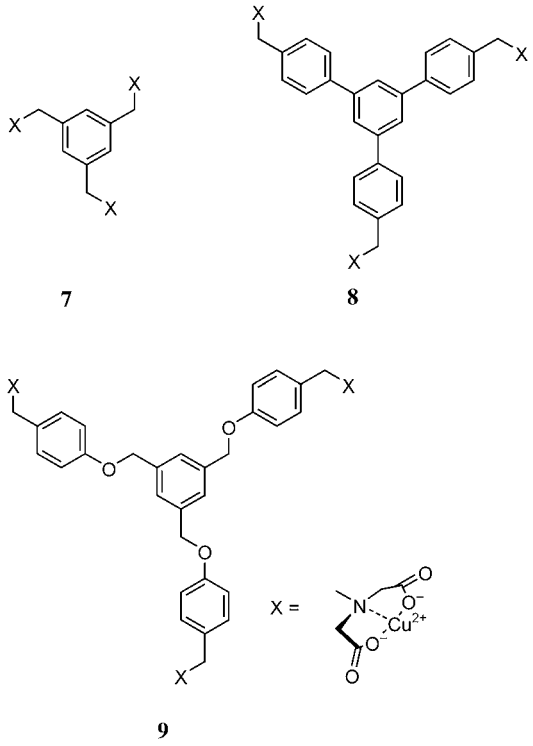
3.2. Recognition of Protein Surfaces: Chemical Strategies

3.2.1. Recognition of the Surface of Carbonic Anhydrase by Cu^{II} Complexes

The surface of a protein offers an array of charged, polar, aliphatic and aromatic groups that can be targeted by surface-recognition agents. For example, the imidazole group of histidine is a potential target site, as it coordinates strongly to transition metals. Mallik and co-workers described the design, synthesis, and protein-binding properties of molecules that contain three Cu^{2+}–iminodiacetate arms (Cu^{2+}-IDA) sepa-

 © 2005 Wiley-VCH Verlag GmbH & Co. KGaA, Weinheim

rated by aromatic linkers (Scheme 3).[48] The potential advantage of this strategy is that the metal–ligand interactions are stronger in water than other noncovalent forces, and thus complementary interactions can lead to tight and selective

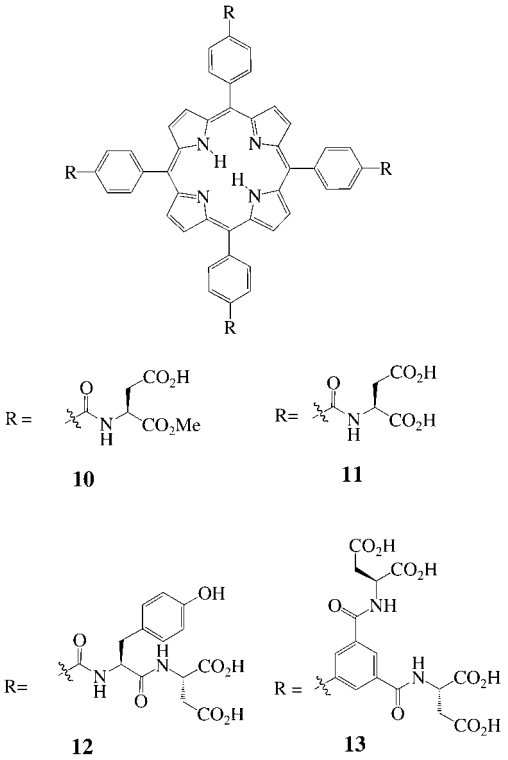


Scheme 3. Cu^{2+}-IDA-containing molecules that target the surface of carbonic anhydrase.

binding. Compound **8** was observed to bind to bovine erythrocyte carbonic anhydrase (CA), a protein with six surface histidine residues and a binding constant (K_a) of $3 \times 10^5\,M^{-1}$. With the copper cation removed, the ligand portion of **8** alone did not bind CA. Compound **7**, with a shorter spacer between the Cu^{2+}–IDA arms, and **9**, which is more flexible, both showed weaker binding to CA (**7**: $K_a = 7.5 \times 10^4\,M^{-1}$; **9**: $K_a = 3.3 \times 10^4\,M^{-1}$). Interestingly, the weaker binding of **7** is primarily due to a less-favorable ΔH, which suggests a poorer geometric fit between **7** and the histidine groups of CA. The more flexible **9** has a more favorable enthalpic contribution than **8**, yet a significantly larger unfavorable entropy term ($-T\Delta S$) which leads to weaker overall binding. Furthermore, **8** preferably binds CA over chicken egg albumin, which also contains six surface histidine residues but with a different spatial orientation. (Compounds **7** and **9** were much less selective in this regard.) These findings indicate the importance of geometric accessibility and preorganization of the copper arms relative to the target histidine groups for high binding affinity and selectivity.

3.2.2. *Surface Recognition of Cytochrome c*

Cytochrome c (Cytc) from horse heart is an electron-transport protein with a high isoelectric point (pI 10).[76] The exposed surface of the heme edge is surrounded by a series of cationic residues which constitute a distinct binding domain for various protein partners, such as cytochrome oxidase and cytochrome c reductase. These interactions are highly sensitive to modifications of the surface lysine residues, which indicates a strong dependence on electrostatic interactions.[77] Jain and Hamilton demonstrated that this surface can be recognized by receptors designed with tetraphenylporphyrin (TPP) as a scaffold bearing various amino acid and peptide derivatives on its periphery (Scheme 4).[78]



Scheme 4. TPP derivatives for the recognition of the exterior surface of cytochrome c.

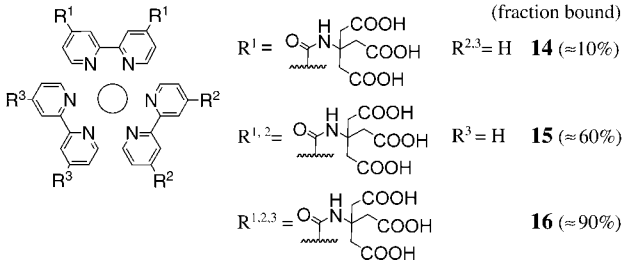
A convenient fluorescence-quenching assay permitted facile measurement of the dissociation constants of a range of derivatives. Porphyrin **12**, with a Tyr–Asp dipeptide residue on each phenyl ring, bound tightly to Cytc with a K_d value of 20 nM. Comparison of K_d values for a series of TPP derivatives showed that affinity is significantly increased through the addition of anionic residues to the porphyrin core, as octaanionic **11** showed an approximate sixfold increase in affinity ($K_d = 160$ nM) over tetraanionic **10** ($K_d =$ 900 nM). Thermodynamic parameters for **11** and the ionic-strength-dependence data of the binding interaction of **11** and **12** are similar to those of cytochrome c peroxidase, a native Cytc partner, which suggests that the molecular surfaces of **11** and **12** may mimic part of the binding domain of Cytc peroxidase. Tetrabiphenylporphyrin-based receptor **13**, which has a larger hydrophobic core and 16 charges on its periphery, exhibited the strongest affinity with a K_d value of 0.67 nM.[79] Compound **13** showed good selectivity in binding to Cytc in comparison with the closely related protein cytochrome c_{551}

 © 2005 Wiley-VCH Verlag GmbH & Co. KGaA, Weinheim

($K_d = 180$ nM) and ferredoxin ($K_d = 17$ μM), which suggests that complementary charge and size are required for strong binding.

The effects of TPP derivatives on protein folding were also studied. The thermal denaturation profile of Cytc in the presence and absence of the TPP-based receptors at pH 7.4 was traced with circular dichroism (CD) spectroscopy. The melting point (T_m) of Cytc dropped from 85 °C to 64 °C in the presence of receptor **12**. The copper porphyrin dimer of **12** also induced the unfolding of Cytc with 2:1 stoichiometry under physiologically relevant conditions and accelerated its rate of proteolytic degradation.[80]

Hamachi and co-workers employed a related design concept for the recognition of Cytc.[81] A $[Ru(bpy)_3]$ complex with carboxylate groups on its periphery was shown to form a complex with Cytc selectively over myoglobin, horseradish peroxidase, and cytochrome b_{562}. This approach offers the advantage of the templating function of metal, with which molecular assembly can be carried out in a stepwise ligation of the individual bipyridine units. With this synthetic strategy, a series of unsymmetrically substituted receptors were prepared; compound **16** (Scheme 5), the most symmetrical

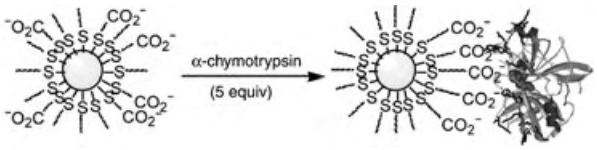


Scheme 5. $[Ru(bpy)_3]$ complexes that recognize the surface of cytochrome c.

compound, showed the strongest binding. However, investigation of the photoreduction of Cytc catalyzed by these complexes showed **15** to be the most efficient catalyst. This effect was attributed to a balance between the binding of the Ru complexes and accessibility to the sacrificial reducing agent.

3.2.3. Inhibition of Chymotrypsin with Nanoparticle Receptors

Rotello and co-workers developed mixed-monolayer-protected gold clusters (MMPCs) functionalized with terminal anionic groups for recognition of the positively charged surface of α chymotrypsin (ChT) (Scheme 6).[82] They found that the enzyme was inhibited by a two-step mechanism that comprised a fast, reversible inhibition step followed by a slower, irreversible process. The interaction was shown to be very efficient with a K_i^{app} value of 10.4 ± 1.3 nM and a stoichiometry of five protein molecules to one MMPC. This process was selective for ChT in comparison with elastase, β galactosidase, and cellular retinoic binding protein, demonstrating the effectiveness of the designed electrostatic interactions. Dynamic light scattering (DLS) data showed that the inhibition proceeds without MMPC aggregation. Furthermore, the minimum at 202 nm in the CD spectrum (a result of high β-sheet content) underwent a time-dependent increase and a shift to lower wavelength, indicating a conformational change toward random coil and a loss of native secondary structure.



Scheme 6. Recognition of the surface of α chymotrypsin by a nanoparticle receptor.

In a subsequent publication, the authors demonstrated with DLS that the addition of cationic surfactants results in the release of ChT from the surface of the anionic gold nanoparticles.[83] In an effort to retain the native structure upon protein binding, the same group incorporated oligo(ethylene glycol) (OEG) groups onto the monolayer-protected nanoparticles.[84] CD and fluorescence anisotropy measurements indicated that the protein regained a high degree of structural integrity. ChT was also released under elevated ionic strength with full enzymatic activity, suggesting a complete restoration of the native structure.

These examples demonstrate that molecules designed to recognize protein surfaces can also dramatically affect the native conformation of the target protein. Much work remains to evaluate the mechanisms of these processes and to establish if they are medicinally viable. Similarly, it should be possible to identify molecules that enhance protein folding through stabilization of the native state.

4. Synthetic Modulators of Protein–Protein Interactions from Chemical Libraries

On the basis of bioinformatics analysis, there are predicted to be ≈6500 promising targets—receptors, enzymes, and ion channels—for the design of novel pharmaceutical agents.[85] This number increases dramatically, however, if protein–protein interactions are also considered as drug targets. The key is to find strategies that will effectively and reliably lead to molecules with acceptable pharmacokinetic properties that disrupt protein–protein contacts. High-throughput data-generation techniques, including microarray analysis, combinatorial chemical library preparation, and computational (in silico) screening methods have become essential in the search for protein–protein disruptors. If structural information on a certain target is not available, then screening is arguably the most efficient method to search for synthetic antagonists of protein–protein interactions as drug candidates.

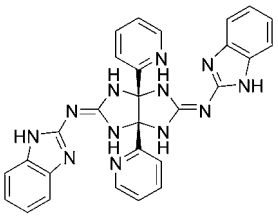
4.1. Agonists of Protein–Protein Interactions

4.1.1. Small Nonpeptide Mimetics of G-CSF

The granulocyte colony-stimulating factor (G-CSF) is a polypeptide growth factor that regulates the production of

 © 2005 Wiley-VCH Verlag GmbH & Co. KGaA, Weinheim

neutrophilic granulocytes, which serve as the foundation for host defense systems.[86] When G-CSF binds to its receptor (G-CSFr), it triggers receptor homodimerization, which results in the activation of protein tyrosine kinases JAK1 and JAK2.[87,88] The JAK kinases then phosphorylate receptor-associated proteins, such as the signal transduction and activators of transcription (STAT) proteins, thereby regulating transcription.[87,89] Compound **17** (Scheme 7) was identified from a high-throughput cell-based screen as an agonist of the G-CSF protein with 30% efficacy in a luciferase assay.[90] Like G-CSF, **17** caused tyrosine phosphorylation of both JAK1 and JAK2 as well as of G-CSFr, but not the interleukin-3 (IL-3) receptor, indicating specific recognition of the target. Both G-CSF and **17** induced tyrosine phosphorylation of STAT3 and STAT5. The time course for STAT activation in response to **17** is similar to that to G-CSF.



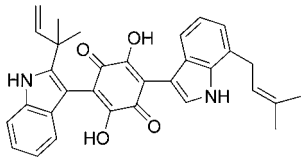
17 SB 247464

Scheme 7. The G-CSFr agonist **17** (SB 247464).

Further studies showed that **17** stimulates primary murine bone marrow cells to form granulocytic colonies and elevates peripheral blood neutrophil counts in mice. The collective data demonstrated that **17** acts as a mimetic of G-CSF to activate G-CSF receptors by targeting a different domain of G-CSFr.

4.1.2. An Agonist of Insulin Receptor Tyrosine Kinase with Antidiabetic Activity in Vivo

A natural product, L-783,281 (**18**; Scheme 8), from a fungal extract was identified as an agonist of the human insulin receptor tyrosine kinase (IRTK).[91] The development of orally active small-molecule mimetics of insulin is a major challenge in medicinal chemistry. Insulin binds to the extracellular α subunits of its receptor and causes conformational changes that lead to the stimulation of tyrosine kinase activity and autophosphorylation of the membrane-spanning β units.[92] Compound **18** was selected from a 50000-compound library including synthetic compounds and natural products. Compound **18** induced 50% of the maximal effect of insulin on IRTK activity at low concentration (3–6 μM). The in vivo efficacy of **18** was tested in mice, and elicited a significant decrease in blood glucose levels.

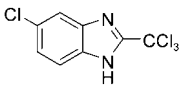


18 L-783,281

Scheme 8. Insulin mimetic **18** (L-783,281) that induces activation of IRTK.

4.1.3. Small-Molecule Switches for the hGH–hGHbp Interaction

Schultz and co-workers reported the regulation of human growth hormone (hGH) and the extracellular domain of the hGH receptor (hGHbp) through a two-step process.[93] First, two residues, Thr175 of hGH and Trp104 of hGHbp were mutated to glycine, creating a cavity on the hGH–hGHbp interface. In the second step, a library of small molecules was screened; compound E8 (**19**, Scheme 9) was identified as a ligand that complements the defective interface. The binding affinity of E8 was quantified with surface plasmon resonance. The binding affinity of the mutant hormone for the mutant receptor increased by more than 1000-fold in the presence of 100 μM E8 relative to the control in the absence of E8. JAK2 phosphorylation assays showed that the mitogenic signaling pathway through the hGH receptor is stimulated only in the presence of the mutant hormone and 50 μM E8. Dose-dependent proliferation of IL-3-dependent promyeloid cells (FDC-P1) further confirmed that E8 gates mitogenic signaling through the mutant hGH–hGHbp complex ($EC_{50} = 10$ nM). The combined results indicated that E8 not only mediates binding of the mutant hormone but also switches on the signal transduction pathway.



19 E8

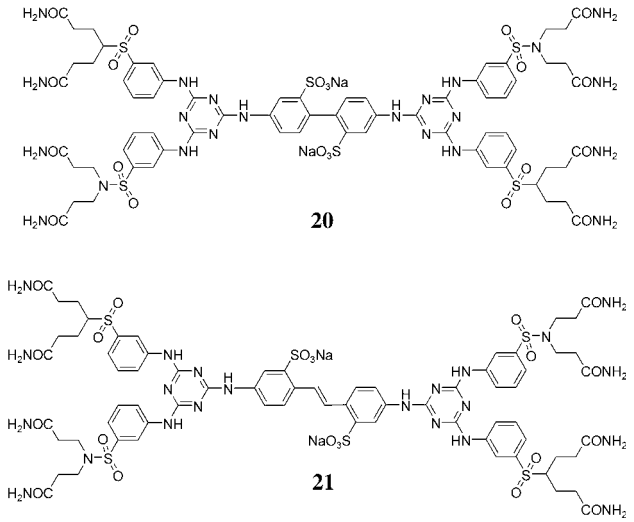
Scheme 9. The ligand **19** (E8) complements the defective hGH–hGHbp interface in the complex of Thr175 Gly hGH and Trp104 Gly hGHbp.

4.2. Inhibitors Identified from Solution- and Solid-Phase Screening

4.2.1. Bistriazine Derivatives that Disrupt Multimer Assembly of RS Virus Fusion Protein

Human respiratory syncytial virus (RSV) is one of the leading causes of lower respiratory tract infection in children and infants and is an important cause of community-acquired respiratory infection among hospitalized adults.[94] The 70K viral fusion glycoprotein (F) of human RSV forms homotetramers and mediates viral fusion.[95] By screening a 20000-compound library with a whole-cell-based assay, a group from Wyeth–Ayerst Research identified a series bistriazine derivatives with biphenyl **20** or stilbene **21** linkers (Scheme 10) that disrupt viral fusion.[96] These inhibitors target RSV(F), which functions in an oligomeric state on the virion surface. In particular, the bistriazine inhibitors selectively block the assembly of the fusion protein F without affecting other surface glycoproteins. The disruption involves destabilization of the bioactive multimeric state of the F protein and a decrease in its fusion capacity. Compound **20** binds tightly to

 © 2005 Wiley-VCH Verlag GmbH & Co. KGaA, Weinheim



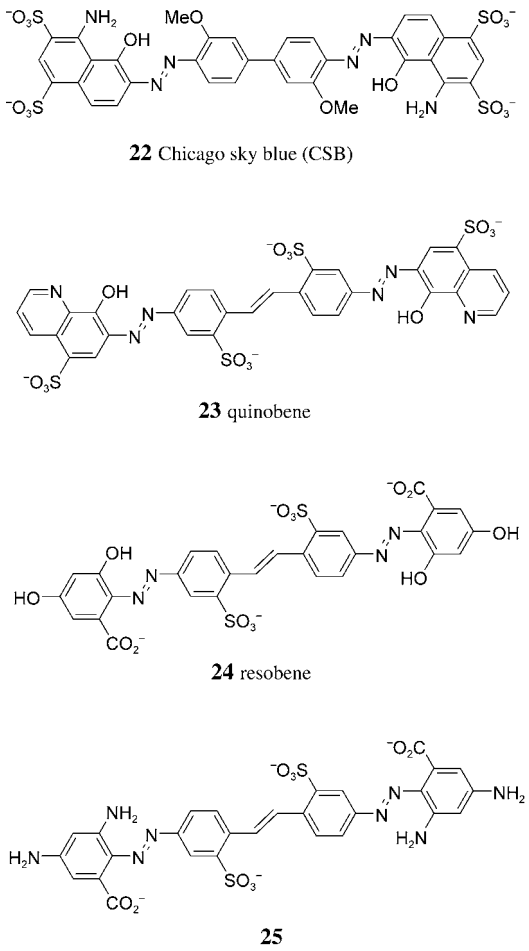
Scheme 10. Bistriazine compounds that inhibit the multimer assembly of RS virus fusion proteins.

F protein with an IC_{50} value of 0.15 μM, and **21** with an even more potent IC_{50} value of 0.05 μM.

Structure–activity relationship studies of these bistriazine derivatives indicated the importance of the negatively charged core and the rigidity around the central unit. One proposal was that the inhibitor interacts with F protein through multivalent hydrogen bonds to terminal amide groups. The authors also took advantage of the intrinsic fluorescence of **20** and **21** to show that the inhibitors bind directly to the F protein. Several of these agents are currently undergoing clinical trials as potential prophylactic drugs against RSV.[97]

4.2.2. *Bisazobenzene and Bisazonaphthalene Derivatives as Anti-HIV-1 Agents through the Disruption of Gp120–CD4 Fusion*

The treatment of human immunodeficiency virus type 1 (HIV-1) remains an area of great interest in clinical research. The third variable domain (V3 loop) of the HIV-1 gp120 exterior envelope glycoprotein interacts with the β-chemokine receptors CCR3 and CCR5, which in turn facilitates viral infection.[98] The active sites of coreceptors CXCR4 and CCR5 are exposed upon binding of CD4 to gp120, which results in virus/coreceptor binding and subsequent fusion of the viral particle with the cell. The processes of viral attachment and virus–cell fusion are critical therapeutic targets. This has been established by the recent success of the T-20 peptide of Trimeris, which itself, however, has been an impetus for the discovery of nonpeptide antagonists.[99] In an antiviral drug screen conducted by the National Cancer Institute (NCI), Chicago Sky Blue (CSB; **22;** Scheme 11), a naphthalene sulfonic acid dye, was identified as an active inhibitor of HIV activity through the disruption of the gp120–CD4 interaction.[100] Although this compound was active in vitro ($IC_{50} = 4.8$ μM), the azobenzidine core was metabolized to carcinogenic aromatic amines, preventing continued development.

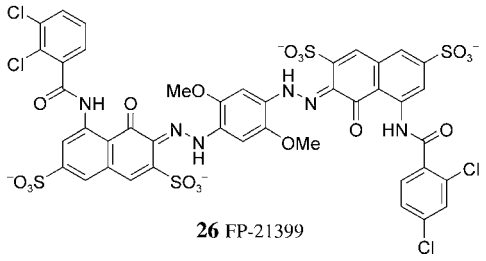


Scheme 11. Bisazobenzene- and bisazonaphthalene-based synthetic inhibitors of the gp120–CD4 interaction.

Further screening of CSB analogues resulted in the identification of compounds such as **23**–**25** (Scheme 11), in which the biphenyl core was replaced with stilbene to avoid degradation.[101] Compounds **23** (quinobene) and **24** (resobene) showed moderate disruption of the gp120–CD4 interaction with IC_{50} values of 1.3 μM and 1.4 μM, respectively, whereas **25** was markedly less potent ($IC_{50} = 31$ μM). As the molecular target of these compounds was unknown in the early phase of the study, more recent experiments have shown that resobene (**24**) interacts with the V3 domain of gp120 rather than binding to CD4. The principal neutralizing domain of the V3 loop is rich in hydrophobic and cationic residues, and it is likely that the correct orientation and composition of anionic and electron-rich heteroatoms in conjunction with the aromatic character of these compounds is important for V3 binding. Resobene, which possesses the best pharmacological profile, has been suggested as a possible topical microbicide in preventing HIV transmission.[102]

An independent screening effort by Lexigen led to the discovery of FP-21399 (**26**; Scheme 12) as a disruptor of the interaction between gp120 and antibodies directed against the V3 loop.[103] FP-21399 inhibits gp120-mediated spreading of T-cell-topic strains and interacts in a specific manner with the HIV-1 gp120–gp41 complex during virus entry.[104] Ono and

 © 2005 Wiley-VCH Verlag GmbH & Co. KGaA, Weinheim



26 FP-21399

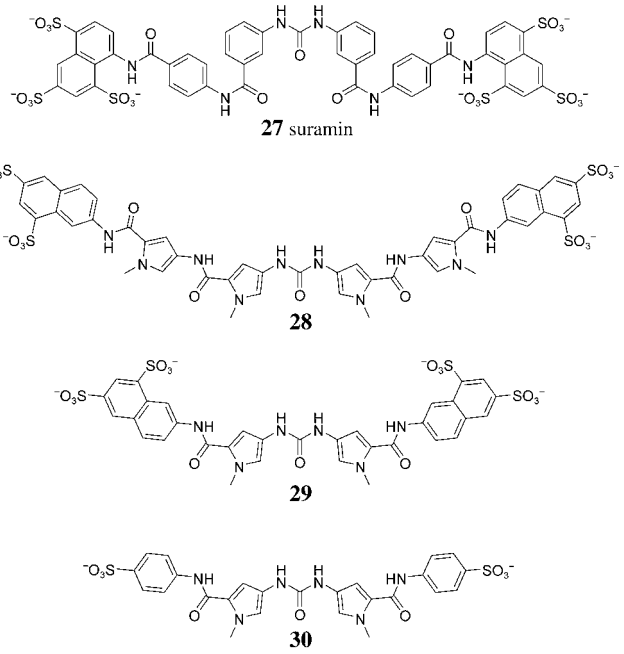
Scheme 12. FP-21399.

co-workers showed that FP-21399 mediates membrane fusion at concentrations as low as 1 $\mu g\,mL^{-1}$. Animal studies showed that FP-21399 decreases the infected population of mice from 71 % (control) to 21–13 % at a dosage of 10–50 $mg\,kg^{-1}$. FP-21399 is currently under phase-II clinical trials as a potential anti-HIV drug that operates through the disruption of viral fusion.[105] These approaches towards molecules that bock HIV viral fusion have provided excellent examples of the identification of synthetic ligands from a chemical library that disrupt protein–protein interactions.

4.2.3. Bisnaphthalene Sulfonates and Cationic Porphyrins as Anti-FGF Agents

Fibroblast growth factors (FGF) have been detected in a variety of cell types and are implicated in the progress of cell differentiation and development, including mitosis and angiogenesis. There are at least 19 members in the FGF family; among them, FGF-1 (acidic FGF) and FGF-2 (basic FGF) are regarded as the most important growth factors that bind to heparin sulfate proteoglycans.[106] X-ray crystallographic studies showed that FGF-2 proteins take up a β-trefoil structure with a central cavity ringed by hydrophobic residues that are conserved in all FGF family proteins.[107,108] Mutagenesis studies on FGF-2, supported by X-ray crystallography, have identified separate functional domains for heparin and receptor binding (Figure 3).[107,109]

Suramin (**27**; Scheme 13) a prototype growth factor antagonist, was found to disrupt the interaction between FGF-2 and FGFR (FGF protein receptor) in various cell lines. However, the development of suramin into a viable drug has been hampered by its high toxicity and lack of selectivity. For example, Takano et al. showed that the administration of suramin leads to tumor enhancement, possibly due to its immunosuppressive activity.[110] Gagliardi et al. conducted a detailed structure–activity relationship of 70 oligo-anionic analogues of suramin by measuring the ability of each to inhibit angiogenesis in a chick egg chorioallantoic membrane (CAM) assay.[111] Of the 70 analogues, compound **30** (Scheme 13) had antiangiogenic activities similar to suramin, and an additional seven compounds showed significantly stronger potency than suramin. All of the seven analogues were based on the naphthalenetrisulfonic acid scaffold and contained urea groups. The authors concluded that the presence of the naphthalene sulfonate groups and the correct number of rigid spacers between them is crucial for maintaining activity. Based on such observations, Manetti et al. attempted to optimize the pharmacological profile of suramin without compromising its affinity by synthesizing heterocyclic suramin analogues such as compound **28**.[112] In comparison with **27**, the congeners generally have a lower number of sulfonic groups either on the α- or β-aminonaphthalene moieties to modulate the binding to plasma proteins, whereas the benzene rings are replaced by pyrrole and pyrazole. These compounds possess better toxicity profiles than suramin and are more promising anti-FGF agents. Structure–activity relationship studies showed that compound **29**, which lacks a pyrrole spacer on either side, and **30**, in which the naphthalene sulfonate groups are missing, were less active than **28**. One of the low-energy conformations of **28**, obtained by molecular modeling, is a crescent shape in which all NH groups are directed toward the same face. A model of this conformation interacting with the FGF surface showed excellent electrostatic and geometric complementarity, cor-



27 suramin

28

29

30

Scheme 13. Bisnaphthalene sulfonate-based anti-FGF agents.

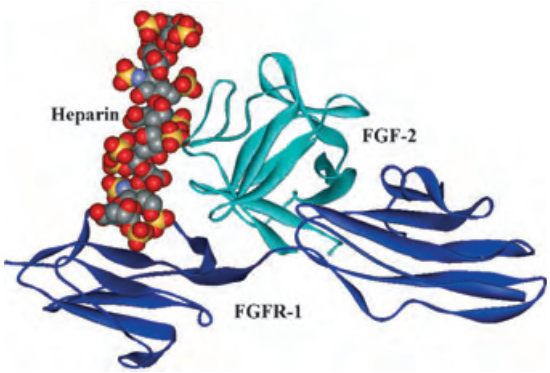
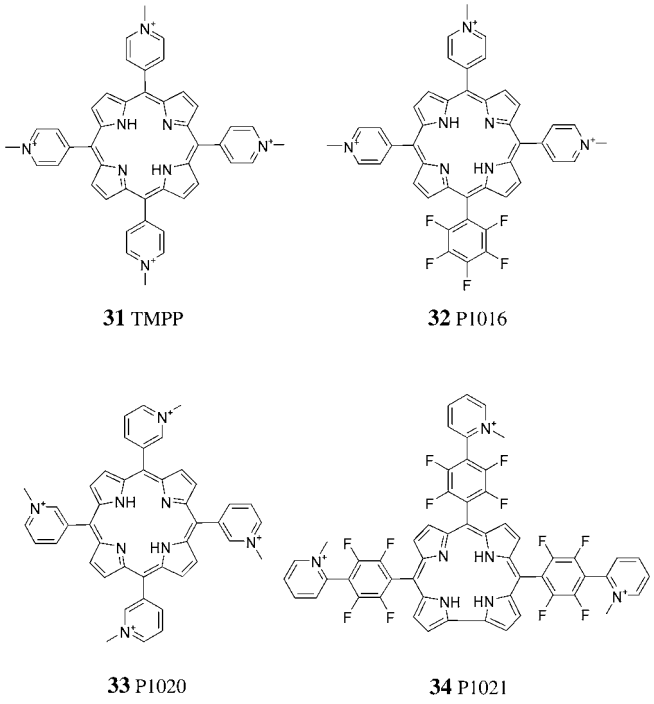


Figure 3. X-ray crystal structure of a ternary complex of FGF-2 (cyan), FGFR-1 (blue) and a heparin hexamer (UAP-SGN-IDU-SGN-IDU-SGN; CPK representation).

 © 2005 Wiley-VCH Verlag GmbH & Co. KGaA, Weinheim

relating well with structure–activity relationships observed experimentally. Further biophysical characterization by Zamai and co-workers with fluorescence anisotropy partially validated this model by confirming a 1:1 stoichiometry for the binding of **28** to FGF ($K_d = 0.127$ μM).[113] The interaction was reversible through the addition of heparin which suggests that **28** binds to the heparin-binding domain of FGF, as was suggested in the modeled structure. Moreover, single and double lysine mutants K128Q ($K_d = 1.23$ μM) and K128Q-K138Q ($K_d = 5.12$ μM) showed much weaker binding, which indicates the importance of the cationic side chains in complex formation.

Yayon and co-workers reported the disruption of the FGF-2–FGFR interaction with synthetic compounds based on a porphyrin scaffold (Scheme 14).[114] The cationic tetra-(methylpyridinium)porphyrin (TMPP) **31** was initially iden-



31 TMPP **32** P1016

33 P1020 **34** P1021

Scheme 14. FGF inhibitors based on the TMPP scaffold.

tified from high-throughput screening. Further studies indicated that TMPP is able to block the binding of ^{125}I-labeled FGF to FGFR with an IC_{50} value of 1 μM. TMPP also showed some affinity for VEGF and was able to block its interaction with VEGFR ($IC_{50} = 10$ μM). Furthermore EGF, which is not a heparin-binding or heparin-dependent growth factor, was not inhibited in binding to its receptor tyrosine kinase by TMPP. This selectivity suggests that interfering with heparin binding might play a key role in the inhibitory effect of TMPP.

Several analogues of **31** were prepared and similarly measured for their ability to disrupt the FGF-2–FGFR complex. Interestingly, the unsymmetrical compound **32**, in which the charged *N*-methylpyridinium group was replaced with a neutral *N*-pentafluorophenyl group, showed a 50-fold higher potency in vitro ($IC_{50} = 20$ nM) than TMPP. Compound **33**, with an *N*-methyl-3-pyridinium modification, is 10-fold less active than TMPP, indicating that the position of the charges is important. As compound **32**, in contrast to TMPP (**31**), was completely inactive in vivo in the suppression of the metastasis of Lewis lung carcinoma, other derivatives with high efficacy in vivo and in vitro were sought. Compound **34**, a corrole derivative with three positive charges as in **32** and with the same side chains as in **33**, seemed to be the most balanced agent. The in vitro activity of **34** was 10-fold higher ($IC_{50} = 100$ nM) than that of TMPP, and the corresponding in vivo activity was also improved. Compound **34** inhibited tumor metastasis at a concentration fivefold lower than that of TMPP.

The exact mechanism of inhibition is unclear at this stage. Beyond the demonstration of disrupting the heparin–FGF-2–FGFR ternary complex, there has been no further characterization of the direct binding of **34** with FGF-2 or FGFR. In light of the binding capacity of oligo-anionic compounds such as suramin and its analogues, it is unlikely that these cationic porphyrins bind to FGF at the same site; this would potentially leave other molecular surfaces involved in the bioactive ternary complex available as therapeutic targets.

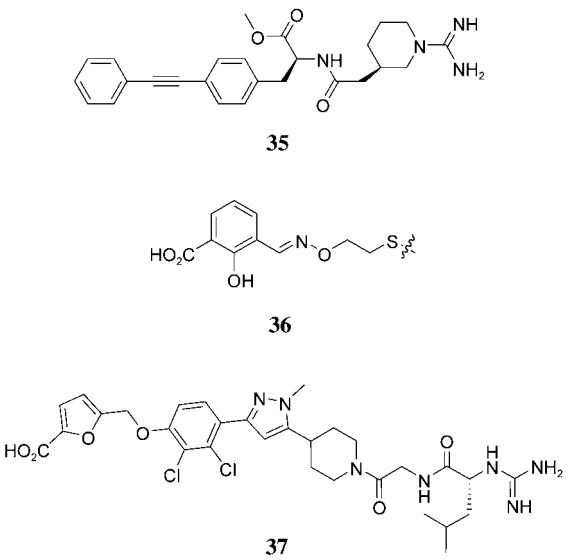
4.2.4. Inhibitors of the IL-2–IL-2Rα Interaction

The development of a synthetic antagonist for IL-2 binding to the α subunit of its receptor (IL-2Rα) is an interesting example of the combination of rational design, library screening, and sheer good fortune. IL-2 triggers T-cell proliferation by recognition of a heterotrimeric (α, β, and γ subunits) receptor complex on the T-cell surface.[32] X-ray crystallographic analysis showed that IL-2 is a four-helix bundle, and site-directed mutagenesis identified residues in the AB loop (K35, K38, T41, F42, K43, and Y45) and in the B helix (E61 and L72) as critical for the formation of the IL-2–IL-2Rα complex.[115] Previous studies have shown that monoclonal antibodies against IL-2R (anti-Tac) are effective immunosuppressive agents[32,116] which emphasizes the potential advantage of low-molecular-weight ligands that are able to disrupt the binding of IL-2 to IL-2Rα.

Research at Hoffmann–LaRoche reported that the synthetic inhibitor **35** (Scheme 15) was able to disrupt the IL-2–IL-2Rα interaction.[117] Compound **35** was designed to mimic the R38–F42 region of IL-2 through an acylphenylalanine group to emulate residues R38 and F42 in their contact with the IL-2Rα receptor. Compound **35** and its enantiomer were prepared and evaluated with a scintillation proximity competitive binding assay. A moderate affinity of **35** to disrupt the IL-2–IL-2Rα complex was observed ($IC_{50} = 3$ μM at pH 7.4), whereas the opposite enantiomer was inactive. In comparison, IL-2 gave an IC_{50} value of 13 nM. However, ^{15}N-HSQC NMR experiments showed that **35** actually inhibits the IL-2–IL-2Rα association by binding to IL-2 instead of IL-2Rα.[118] Nonetheless, **35** exemplifies a designed low-molecular-weight compound that mimics a discontinuous protein surface epitope, and represents the first well-characterized nonpeptide inhibitor of a cytokine–cytokine-receptor interaction.

A research group from Sunesis recently reported small-molecule IL-2 inhibitors with improved potency.[119] Their

 © 2005 Wiley-VCH Verlag GmbH & Co. KGaA, Weinheim



Scheme 15. Synthetic antagonists of the formation of the IL-2–IL-2Rα complex.

approach involved the identification of synthetic fragments with modest affinity for protein surfaces by using a novel "tether" technique (Figure 4).[120] This method involves link-

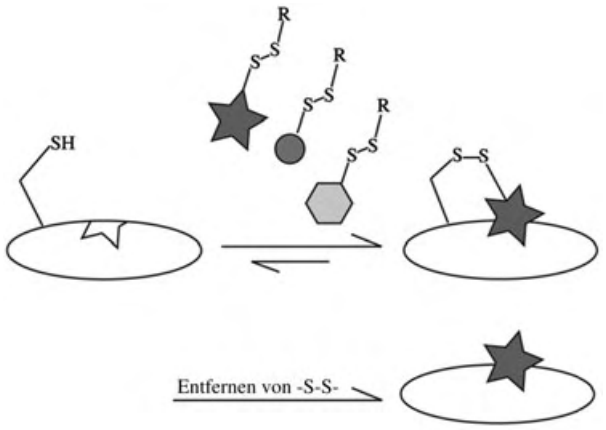


Figure 4. Principle of the "tether" method for the detection of lead compounds that recognize a specific site on the protein surface.

ing a library of thiol-functionalized fragments with cysteine-containing or modified proteins under reducing conditions. The resulting equilibrium exchange process favors fragments that make contact with the protein surface in addition to the disulfide bond. The identity of the favored and thus enriched fragment can then be determined by mass spectrometry. This method allows not only the screening of large fragment libraries, but also the probing of different regions of the protein by changing the location of the cysteine groups. Two or more fragments that bind to different regions of the protein with modest affinity can then be potentially linked to form a tight-binding inhibitor.

Braisted and co-workers applied the tether method to screen a library for IL-2 inhibitors. A series of fragments, such as **36**, were detected as hits by the mutant proteins.[119] Statistical analysis of these fragments indicated that the mutants Y31C and L72C preferentially select for small aromatic carboxylic acids. A focus set of 20 compounds then was prepared with the addition of carboxylic acid analogues to **36**. Eight of the 20 compounds inhibited IL-2–IL-2Rα binding at submicromolar concentrations, showing 5 to 50-fold improvement in potency over the lead. Analogue **37** showed the strongest binding with an IC_{50} value of 60 nM. A stoichiometry of 1:1 for **37** binding to IL-2 was confirmed by surface plasmon resonance (SPR). Further studies showed both **35** and **37** bind to a "hot spot" region on IL-2,[121] which is revealed through a conformational change that, in turn, is initiated upon binding of the small-molecule ligand. This study demonstrates how screening of a guided library is a useful alternative to structure-based, rational design in the search for inhibitors of protein–protein interactions. The structure-based design relies on X-ray crystallographic or NMR solution structures to identify rigid, well-defined pockets, whereas the fragment-assembly methods have advantages in targeting protein surfaces with adaptable or dynamic regions.

4.2.5. An Antagonist of the EPO–EPOR Interaction that Induces EPOR Dimerization

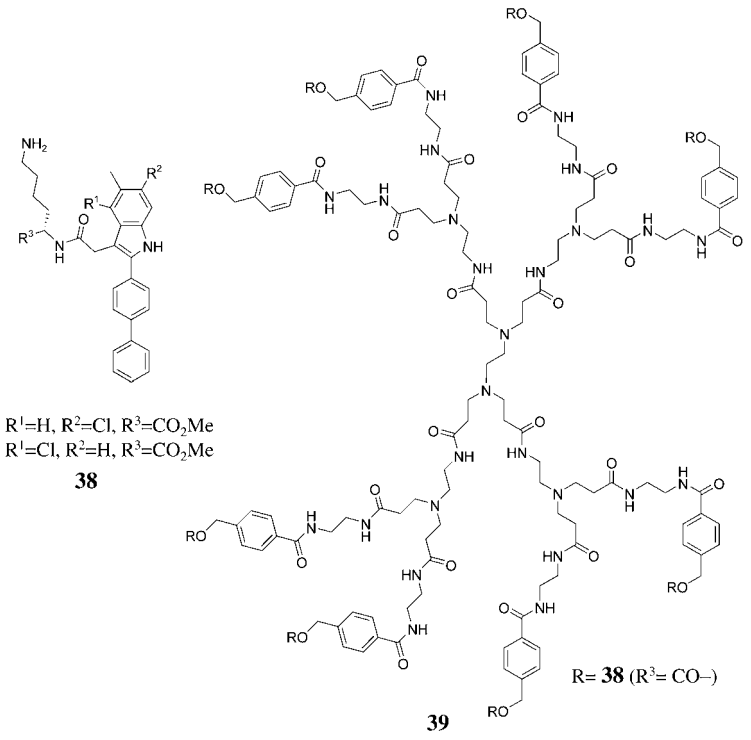
Erythropoietin (EPO) binds EPO receptors (EPOR) on red blood cells and regulates the proliferation and differentiation of erythroid progenitor cells.[122] Upon EPO binding, EPOR dimerizes, which in turn triggers a variety of biological responses. The original purpose of the work reported by Qureshi et al. was to use small molecules to mimic the functional EPO protein and to induce EPOR dimerization. Instead, an antagonist of the EPO–EPOR interaction was identified through a preliminary screen of the Merck chemical library (compound **38**; present as two regioisomers; Scheme 16).[123] The ability of **38** to block the EPO–EPOR interaction was detected with a radiolabeling/binding assay, and an IC_{50} value of 59.5 ± 1.1 μM was determined.

A branched compound, **39**, with eight units of **38**, was more potent ($IC_{50} = 4.4 \pm 1.9$ μM) and induced EPOR dimerization. In analogy to natural EPO, **39** was able to activate a STAT-dependent luciferase reporter gene in BAF cells expressing human EPOR. It also supported the proliferation of EPOR-expressed tumor cell lines and differentiated human progenitor cells into colonies or erythrocytic lineage. These results demonstrate that **38** is a weak antagonist of the EPO–EPOR interaction, whereas compound **39**, with several identical binding domains, may act as an activator of EPOR.

4.2.6 A Low-Molecular-Weight Modulator of the N-Type Calcium Channel

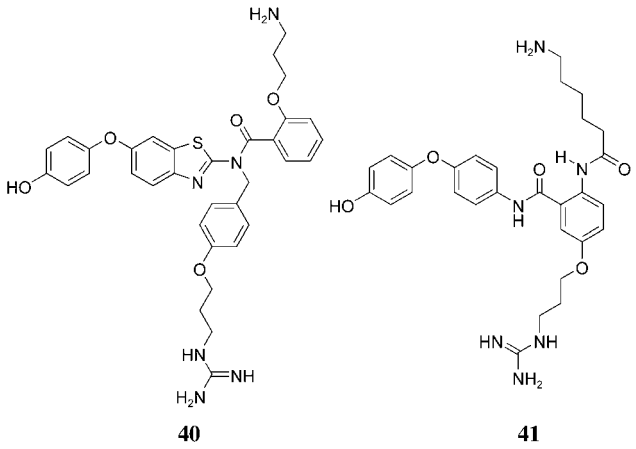
The N-type calcium channel is a critical protein for the process of neurotransmitter release in the central and peripheral nervous system.[124] The protein subunit assembly within the calcium channel is essential to its biological function, and previous work has shown that calcium channel activity can be mediated by modulation of the interaction

 © 2005 Wiley-VCH Verlag GmbH & Co. KGaA, Weinheim



Scheme 16. Synthetic antagonists of EPO–EPOR complex formation.

among its subunits.[125] Computational modeling was used to design mimetics of the discontinuous three-residue pharmacophore of ω-conotoxin GVIA, a native ligand of voltage-gated N-type calcium channels.[126] Benzothiazole derivative **40** (Scheme 17) was selected to mimic the K2 and Y13 C^{α}–C^{β}



Scheme 17. Inhibitors of the N-type calcium channel.

bond vector based on the computational modeling prediction. Further optimization of the design led to anthranilamide **41** with more conformational flexibility. Moderate affinities for functional blocking of the N-type calcium channel were observed (**40**, $IC_{50} = 98\ \mu M$; **41**, $IC_{50} = 68\ \mu M$).

4.2.7. Allosteric Inhibitors of iNOS Dimerization

The mammalian nitric oxide synthase (NOS) isoforms are homodimeric proteins that catalyze NADPH-dependent oxidation of L-arginine to nitric oxide (NO) and L-citrulline.[127] Crystallographic structures of the three NOS isoforms (eNOS, nNOS, and iNOS) have revealed that they share a catalytic heme domain that is highly conserved in the immediate vicinity of the heme active site.[128] As the NOS isoforms are only active as homodimers,[129] synthetic agents that disrupt the dimerization of the subunits would have broad therapeutic potential in iNOS-mediated pathologies.

A research group from Berlex Bioscience reported highly potent and selective pyrimidine-imidazole-based inhibitors identified from a screen of an 8649-compound library prepared on a solid-phase support in three combinatorial steps.[130] A cell-based iNOS activity assay was conducted to measure the production of the NO· radical species, and identified 53 compounds as preliminary leads, accounting for 0.6% of the library. The binding mode of one of the most potent compounds **42** ($K_i = 2.2$ nM) was further characterized by X-ray crystallography (Figure 5). The crystal structure reveals

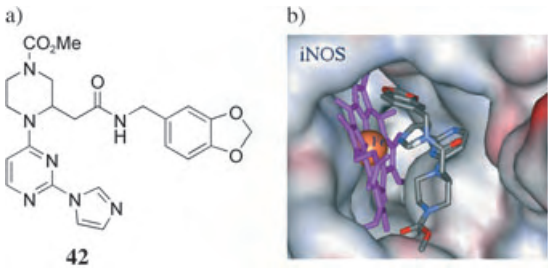


Figure 5. a) Pyrimidine-imidazole-based Inhibitor of iNOS; b) Crystal structure of the inhibitor–iNOS complex shows that **42** coordinates with the heme.

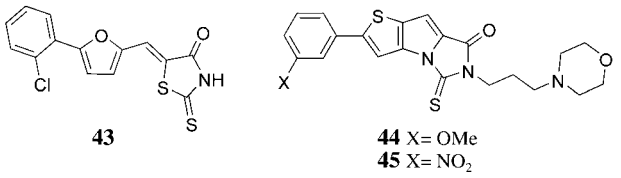
that **42** occupies the arginine-binding site of the iNOS oxygenase domain and directly coordinates to the heme. Helix 7a (not shown) of iNOS, as well as the critical arginine-binding residue Glu 371, are displaced upon the binding of **42**, and the induced disorder disturbs the interface of the dimer, thus inhibiting the dimerization through an allosteric effect. This study represents a relatively rare case in which the inhibitory mode of a low-molecular-weight ligand of protein–protein interactions was fully characterized, shedding light on the design of small-molecule antagonists.

4.2.8. Photochemically Enhanced Inhibitors of the TNF-α–TNFRc1 Interaction

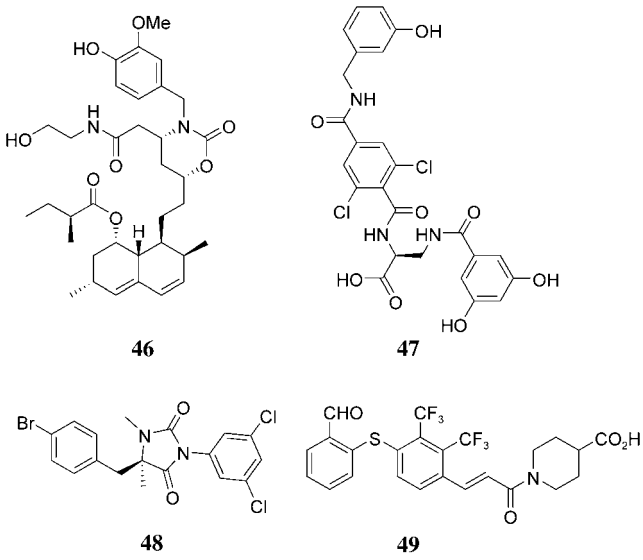
A research group from DuPont reported a group of photochemically enhanced low-molecular-weight inhibitors of tumor necrosis factor alpha (TNF-α),[131] a pleiotropic

 © 2005 Wiley-VCH Verlag GmbH & Co. KGaA, Weinheim

cytokine involved in inflammation.[132] A preliminary screen identified **43** (Scheme 18) as a lead with moderate potency in disrupting the binding of TNF-α to its native receptor TNFRc1 ($IC_{50} = 2.9$ μM). Structure–activity relationship studies showed that replacement of the internal heterocyclic sulfur atom improves binding, and the optimized compounds **44** and **45** showed IC_{50} values of 50 nM and 270 nM, respectively. More interestingly, **43** exhibited an impressive 2000-fold selectivity in blocking the TNF-α–TNFRc1 interaction over that with the other receptor TNFRc2. Compound **44** had an IC_{50} value of 600 nM for inhibiting the TNF-induced phosphorylation of Iκ-B in Ramos cells and was not cytotoxic at concentrations up to 100 μM. An X-ray crystal structure showed that **45** covalently binds to the backbone nitrogen atom of A62 of TNFRc1, suggesting it functions by blocking interactions between the exposed Tyr-containing β turn of the native ligands and the region near A62 of TNFRc1. A key feature of these rhodamine thiocarbonyl-based TNF-α inhibitors is that they are light dependent, as it appears that **45** binds reversibly in the dark and irreversibly upon irradiation. The authors proposed a mechanism in which the inhibitors bind reversibly to TNRFc1 with weak affinity and then covalently modify the receptors through a photochemical reaction.



Scheme 18. Photochemically enhanced TNF-α inhibitors.



Scheme 19. Synthetic inhibitors of the ICAM-1–LFA-1 interaction (see Table 1).

Table 1: Inhibitors of ICAM-1–LFA-1 complex formation (see Scheme 19).

Entry	Source	Affinity in Vitro	Inhibition of Cell Adhesion	I domain binding
46[235,245]	Novartis	$IC_{50} = 40$ nM	$IC_{50} = 0.4$ μM	+
47[235]	Genentech	$IC_{50} = 20$ nM		–
48[246]	Boehringer Ingelheim	$K_d = 26$ nM	$IC_{50} = 2.6$ μM	+
49[247]	Abbott Laboratories	$IC_{50} = 5$ nM	$IC_{50} = 0.1$ nM	+

4.2.9. *Inhibitors of the ICAM-1–LFA-1 Interaction*

Integrins make up a large family of cell-surface receptor proteins that mediate the mechanical and chemical signals of the extracellular matrix (ECM) by signaling through the cell membrane.[133] Many integrin signals converge on cell-cycle regulation and modulate such cellular processes as proliferation and differentiation. Functional integrins are heterodimeric proteins consisting of two transmembrane glycoprotein subunits, α and β, that share homology and noncovalently interact with each other. Each α/β combination has its own binding specificity and signaling properties.

The interaction between leukocyte-function-associated antigen-1 (LFA-1) and intracellular adhesion molecule-1 (ICAM-1) has drawn considerable attention owing to its essential role in the regulation of immune and inflammatory responses.[134] LFA-1 forms a complex with ICAM-1 by inserting into the I domain between β sheets 2 and 3 of a seven-bladed putative β-propeller region on the α_L subunit.[135] Recently, several research groups have reported low-molecular-weight inhibitors of ICAM-1–LFA-1 interactions from screening efforts (see Scheme 19 and Table 1).

4.2.10. *Mediators of the Cell-Signaling Pathway from Solution-Phase Combinatorial Libraries*

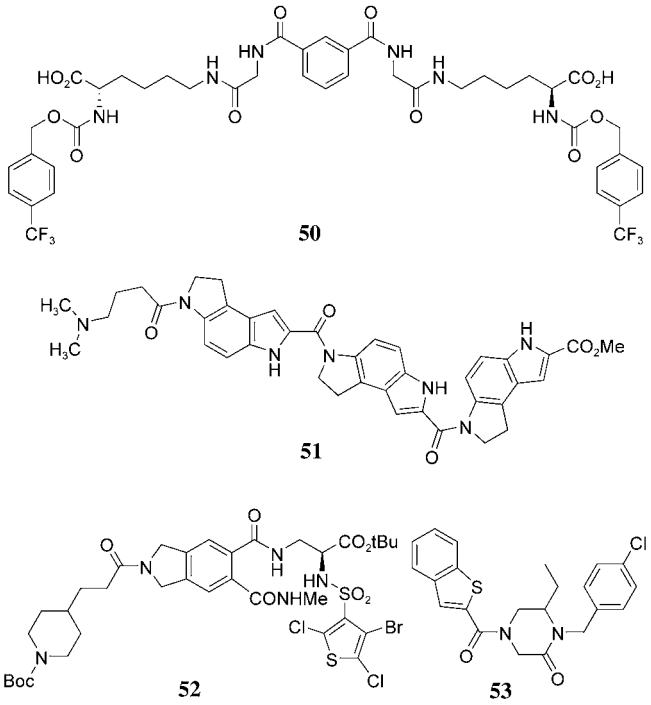
The solution-phase preparation of combinatorial libraries developed in the research group of Boger has had an important impact on the study of low-molecular-weight modulators of cellular signaling through the inhibition, promotion, and mimicking of protein–protein interactions.[3] The advantage of solution-phase synthesis of combinatorial libraries is that significantly larger quantities can be prepared than is possible with solid-phase techniques. This allows the repeated use of library members without the need for resynthesis. The simplicity of the chemistry makes it applicable to a wide range of library designs. Boger et al. selected several targets in signal transduction pathways, wherein protein–protein interactions play key roles at distinct stages for modulating cellular signaling.[3] Table 2 summarizes the targets, screening methods, and compounds detected with their effectiveness in inhibition (see also Scheme 20). More extensive discussions are available elsewhere.[2–4]

4.2.11. *Antagonists of MDM2 that Induce p53 Accumulation*

p53 is a transcription factor found in a mutated state in approximately 50% of human tumors.[136] The overexpression

Table 2: Synthetic mediators of cell signaling pathways identified from screening solution-phase combinatorial libraries (see Scheme 20).

Target Interaction	Screening Method	Inhibitor	IC_{50} [μM]	Inhibitory Effect
MMP-2–$\alpha_v\beta_3$	ELISA	**50**	1.0	antiangiogenic agents[248]
Paxillin–α_4	ELISA	**51**	0.3	inhibition of cell migration
c-Myc–Max	FRET	**52**	20	inhibition of c-Myc-induced oncogenic transformation[249]
LEF-1–β catenin	reporter assay	**53**	4	inhibition of LEF-1–β-catenin-mediated gene transcription

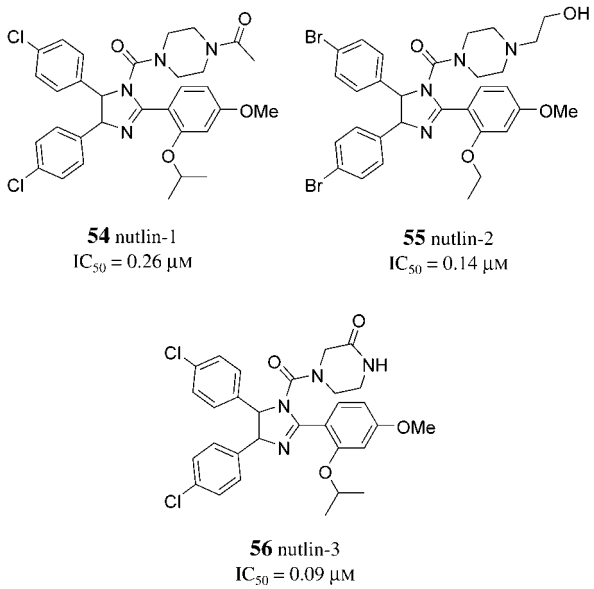


Scheme 20. Mediators of cell-signaling pathways.

of wild-type p53 induces a large number of downstream genes that lead to cell-cycle arrest or apoptosis. In unstressed normal cells, p53 is present at very low levels, resulting from its rapid degradation through the ubiquitin-dependent proteasome pathway. A research group at Pfizer identified small molecules that stabilize p53 by inhibiting its ubiquitination which thus induce apoptosis of human cancer cells.[137]

The oncoprotein mouse double minute 2 (MDM2) regulates p53 turnover by promoting its ubiquitination.[138] The overexpression of MDM2 abolishes the ability of p53 to induce cell-cycle arrest and apoptosis.[139] In about 40–60% of human osteogenic sarcomas and about 30% of soft-tissue sarcomas, MDM2 is overexpressed, implicating its involvement in the development of these tumors.[140] Therefore, the overexpression of MDM2 plays a key role in the tolerance of wild-type p53, making it an attractive target for the development of potential antitumor agents. Recently, several approaches were taken to modulate the p53–MDM2 interaction. Chen et al. showed that inhibition of MDM2 expression by antisense oligonucleotides resulted in the activation of p53, leading to growth arrest or apoptosis.[141] Blaydes et al. inhibited the binding of p53 to MDM2 through microinjection of the 3G5 anti-MDM2 antibody; this led to activated cellular p53 function.[142] García-Echeverría et al. reported that a hexapeptide representing residues 18–23 of p53 is the minimum-binding epitope for HDM2 (the human analogue of MDM2) recognition. The hexapeptide blocked HDM2 interaction with p53 with an IC_{50} value of 700 μM. A 13-residue peptide from the region of residues 16–28 of p53 displayed even more potent binding (IC_{50} = 8.7 μM).[143] Robinson and co-workers recently reported a group of α-helical mimetics based on a β-hairpin scaffold as antagonists of p53–MDM2 binding.[144] These studies provide a proof-of-concept for the activation of p53 by targeting MDM2, but the various oligonucleotides, antibodies, and polypeptides are not suitable for studies in vivo, emphasizing the need for small-molecule inhibitors.

A research group at Roche has recently reported a series of low-molecular-weight antagonists of MDM2 that cause the accumulation of p53 in cellular assays.[145] Three *cis*-imidazoline analogues **54**–**56** (Nutlins; Scheme 21) were identified in



Scheme 21. *cis*-Imidazoline-based MDM2 inhibitors.

a preliminary screen by using surface plasmon resonance (IC_{50} = 90–260 nM). The binding modes of these inhibitors were determined by X-ray crystallography. The imidazoline scaffold reproduces features of the helical backbone of the p53 peptide and directs the side chains to the pockets on MDM2 that are normally occupied by residues Phe19, Trp23, and Leu26 of p53 (Figure 6). The halogen atoms on the phenyl groups filled the Trp23 pocket and enhanced binding, consistent with a previous result that the p53 peptide with a 6-Cl-Trp23 mutant showed stronger affinity for MDM2.[146]

 © 2005 Wiley-VCH Verlag GmbH & Co. KGaA, Weinheim

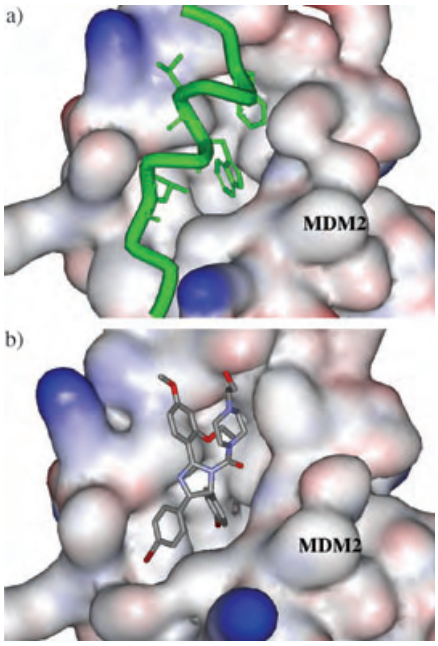


Figure 6. X-ray crystallographic structures of a) the p53–MDM2 complex; b) the **55**–MDM2 complex.

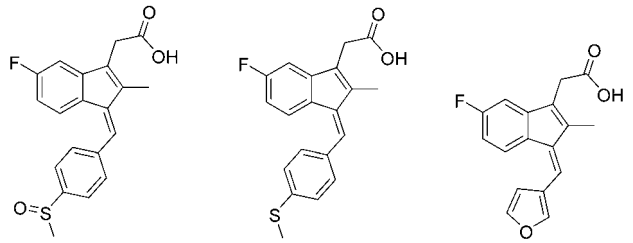
Nutlin-1 (**54**) induced the accumulation of p53 as well as the downstream cyclin-dependent kinase inhibitor $p21^{waf1/Cip1}$ and MDM2 in HCT116 and RKO tumor cells. For cells in which p53 is mutated or deleted, no accumulation of MDM2 or p21 was detected despite the high basal levels of p53. These results indicate that wild-type p53 accumulates in cells treated with **54**, leading to an elevation in the levels of MDM2 and p21 proteins in a manner that is consistent with activation by the p53 pathway. An alternative possibility that the imidazoline derivatives induce p53 accumulation by means of DNA damage was ruled out, as the phosphorylation of serine residues normally caused by DNA-damaging reagents was not observed. Further investigation showed that **56** induced apoptosis in cancer cells with wild-type p53. Animal studies demonstrate that **56** is effective in decreasing tumor volume in nude mice (200 mg kg^{-1} twice a day) over a 20-day period with tolerable toxicity.

As the most recent examples of small-molecule inhibitors of the p53–HDM2 interaction, Hamilton and co-workers reported terphenyl-based helical mimics of p53 that target the HDM2 protein.[147] Issaeva et al. reported a small molecule, RITA (reaction of p53 and induction of tumor cell apoptosis), that binds to p53 and induces its accumulation in tumor cells by disrupting the p53–HDM2 interaction.[148]

4.2.12. *Inhibitors of the Ras–Raf Interaction*

There has been considerable interest in the identification of small-molecule agents that modulate the activity of the Ras family of GTPases, as these proteins play a vital role in growth-factor-activated cell proliferation, differentiation, and survival.[149] The signaling pathway that passes through Raf (a downstream effector of Ras), mitogen-activated protein kinase kinase (MEK), and extracellular signal-regulated kinase (ERK) is necessary for Ras-regulated cellular proliferation.[150]

Müller, Waldmann, and co-workers identified a series of synthetic compounds from a cell-based assay that were able to disrupt the Ras–Raf interaction.[151] The Müller research group had previously reported that the metabolite **58** of the nonsteroidal anti-inflammatory drug (NSAID) sulindac (**57**) (Scheme 22) is able to interfere with the Ras pathway,



57 Sulindac **58** **59**

Scheme 22. Structures of sulindac and its analogues that disrupt Ras–Raf binding.

although its molecular target has yet to be identified.[152] Phenotype-based screening of a library containing 188 sulindac analogues, prepared by solid-phase synthesis, generated 23 lead compounds. All of these derivatives had the ability to induce reversion of the transformed phenotype of the Madine–Darby canine kidney (MDCK)-F3 cells and to induce apoptosis. Four compounds were shown to disrupt the Ras–Raf interaction. The most active compound **59** blocked the Ras–Raf interaction with an IC_{50} value of 30 μM in vitro and an IC_{50} value of 10 μM in the cellular cytotoxicity assay.

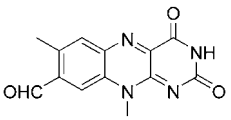
An alternative approach for the identification of small-molecule inhibitors of Ras–Raf-1 binding was reported by Tamanoi and co-workers,[153] with a previously developed dual-bait two-hybrid system.[154] A library of 73400 compounds was screened for the ability to block the interaction of DBD-H-Ras and full-length AD-Raf-1 expressed in SKY54 cells. From this, 3009 compounds were found to have a growth-inhibitory effect. From these leads, 708 compounds induced a phenotype of decreased growth and β-galactosidase activity with some degree of selectivity for H-Ras–Raf-1, versus the negative control on plates. Further evaluation allowed the selection of 38 compounds that showed a clear decrease in β-galactosidase activity at 30 μM in SKY54 cells expressing DBD-H-Ras and AD-Raf-1. A serum response element (SRE)-luciferase assay was used as a secondary screen to determine the ability of the 38 compounds to inhibit the Ras-induced transcriptional activation through SRE and AP-1 sites from the c-fos promoter.[155] MCP1 ($C_{29}H_{27}ClN_2O_3$; M_r 487; structure not available), which has an excellent profile in the primary two-hybrid assay, showed robust dose response in CHO cells and the ability to inhibit H-Ras (V-12)-induced AP-1 activation in HEK293 cells. An alternative mechanism by which the MCP compounds indirectly disrupt Ras–Raf by inhibition of Hsp90 and destabilization of the structurally fragile Raf-1 was ruled out,[156] because MCP1 did not decrease the level of endogenous Raf-1 upon 40 h incubation

 © 2005 Wiley-VCH Verlag GmbH & Co. KGaA, Weinheim

in HT1080 cells. MCP1 also inhibited Ras-induced Raf-1 activation in HEK293 cells, Raf-1 and MPK1 activities in HT1080 fibrosarcoma cells, and epidermal growth factor-induced Raf-1 activation in A549 lung carcinoma cells.

4.2.13. *An Antagonist of Nerve Growth Factor*

A research group at Hoffmann–LaRoche reported a low-molecular-weight antagonist of nerve growth factor (NGF) with good selectivity.[157] NGF is a homodimer protein that binds to two neurotrophin ligands with different domains: $p75^{NTR}$, a nonselective receptor of the tumor necrosis factor (TNF) superfamily, and $p140^{Trk}$ (TrkA), a tyrosine kinase receptor that mediates the trophic effects of NGF.[158] In cells that express both NGF receptors, TrkA activity is modulated by $p75^{NTR}$.[159] If cells lack TrkA expression, $p75^{NTR}$ triggers apoptosis by binding to NGF.[160] Niederhauser et al. have reported that Ro 08-2750 (**60**; Scheme 23) selectively inhibits the binding of NGF to $p75^{NTR}$ over TrkA.[157] The inhibitory potency of Ro 08-2750 was determined in a cell-based competition assay with radiolabeled NGF protein. Compound **60** is effective in blocking the NGF interaction with $p75^{NTR}$ with an IC_{50} value in the lower micromolar region. Furthermore, 10-nM Ro 08-2750 completely rescued cells from NGF-induced apoptosis, indicating that the inhibitor disrupts the formation of the NGF–$p75^{NTR}$ complex, whereas no toxic effect was observed. The authors proposed that Ro 08-2750 causes a conformational change in NGF over time, as the inhibition is time-dependent. However, Arkin and Wells argued that the dependence could be the result of covalent binding; therefore, further clarification of the inhibitory mechanism is necessary.[8]



60 Ro 08-2750

Scheme 23. The NGF inhibitor Ro 08-2750.

4.2.14. *Antagonists of the Immune Regulatory Protein B7.1*

Erbe et al. reported low-molecular-weight compounds that inhibit the binding of CD28 and CTLA4 to human B7.1,[161] a T-cell surface protein that plays a critical role in the activation of native T cells.[162] Signaling through CD28 augments the T-cell response, whereas CTLA4 signaling attenuates it.[163] The crystal structure of the B7.1–CTLA4 complex revealed that CTLA4 dimers and B7.1 dimers pack in a periodic arrangement (Figure 7a).[164] Figure 7b shows that the ^{99}MYPPPY^{104} loop of CTLA4 is buried in a shallow depression of the B7.1 surface, indicating a high degree of shape complementarity. Two compounds, **61** ($IC_{50} = 30$ nM) and **62** ($IC_{50} = 60$ nM), were identified as inhibitors of the B7.1–CD28 interaction in high-throughput screening assays (Scheme 24). These two compounds bind to the same site within the N-terminal domain of human B7.1, which is not present in the homologous protein B7.2 or mouse B7.1. This imparts high selectivity of the inhibition of human B7.1 over its analogues. Structure–activity relationship studies identified a dihydrodipyrazolopyridinone derivative **63** as the most potent inhibitor for the B7.1–CD28 interaction ($IC_{50} = 4$ nM).[165]

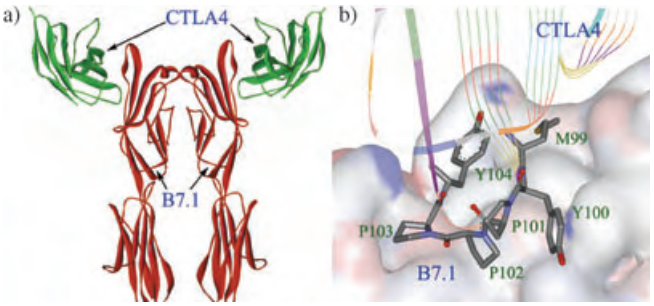
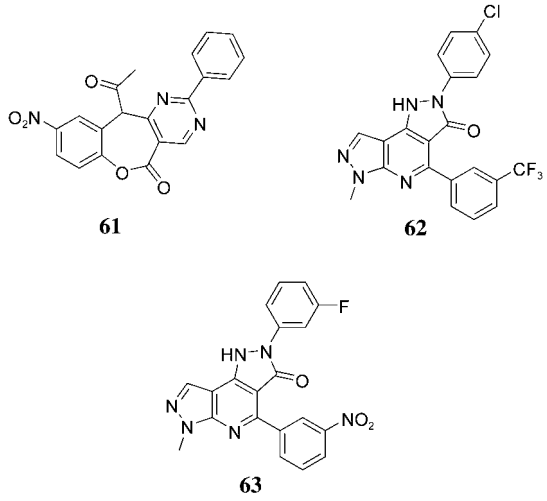


Figure 7. a) Overview of the B7.1–CTLA4 complex: CTLA4 and B7.1 pack in a periodic arrangement in which bivalent CTLA4 homodimers bridge bivalent B7.1 homodimers; b) close-up view of the B7.1–CTLA4 interface.



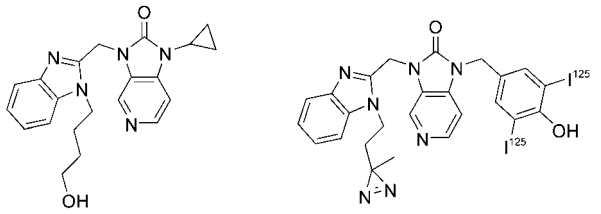
61 **62** **63**

Scheme 24. Inhibitors of the human B7.1 protein.

4.2.15. *A Photoaffinity-Labeled Inhibitor of the RSV Fusion Protein*

The transient hexameric helical bundle involved in viral entry into cells is an important target that has been the focus of many recent studies. Although small-molecule inhibitors of the HIV gp41 glycoprotein and other viral fusion proteins have been ardently sought,[166,167] no well-characterized inhibitors of that type have been found. A research group from Bristol-Myers Squibb recently used photoaffinity labeling to determine the binding site of a previously reported inhibitor, **64**, on the respiratory syncytial virus (RSV) fusion protein (Scheme 25).[168] A photolabeled analogue, **65**, was found to attach to Tyr 198 in the hydrophobic cavity on the N-terminal heptad repeat (HR-N) trimer of the RSV fusion machinery. Molecular dynamics (MD) simulations were then employed to predict the orientation of **65** within the binding cleft. The photoaffinity labeling method provides a general means to study the binding modes for inhibitors that target protein–protein interfaces.

 © 2005 Wiley-VCH Verlag GmbH & Co. KGaA, Weinheim



64 BMS-433771 **65** [^{125}I]-BMS-356188

Scheme 25. Small-molecule inhibitors of the RSV fusion protein.

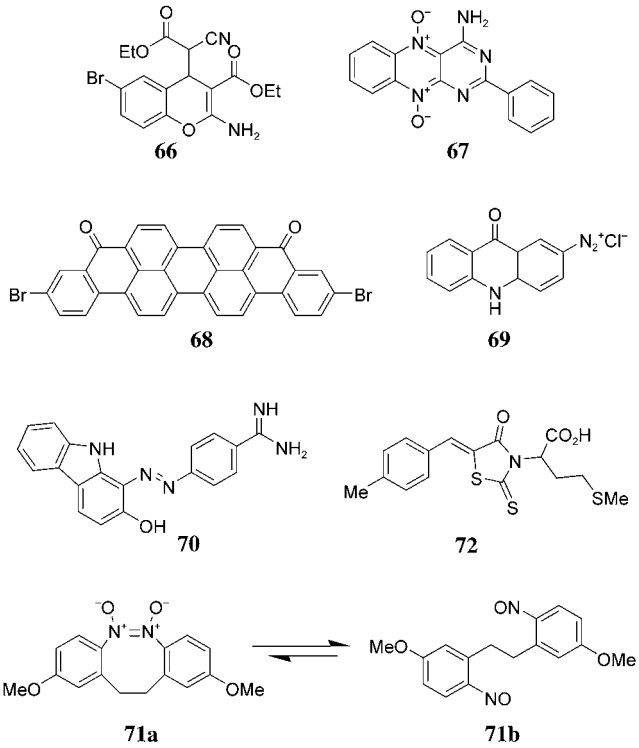
4.3. Computer-Aided Screening for Low-Molecular-Weight Inhibitors of Protein–Protein Interactions

Major advances in high-throughput screening technologies in recent years have made it possible to assay up to 100 000 compounds a day. Such screens could be made even more efficient if the size of the target pool were decreased. Screening compound libraries in silico beforehand can decrease the number of compounds actually synthesized and tested. The operations can be categorized as diversity- and structure-based designs. Diversity-based designs are used to select a focused library from a larger library while maintaining the diverse character of the full-range library.[169] A variety of computational methods based on compound similarity clustering, gridlike partitioning of chemical space, and the application of genetic algorithms are used in screening large libraries to generate focused libraries.[170] Whereas diversity-based design is the method of choice if no structural information is available, structure-based methods use prior information of the target structure to assist the design and selection of the leads with 3D complementarity to the target binding site and provide a higher hit rate than the diversity design.[171] Although in-silico screening technology has been used in many studies to aid the discovery of new enzyme inhibitors for indications such as AIDS and parasitic infections, the use of this technology to search for inhibitors of protein–protein interactions remains a largely underexplored area.[172] Some progress has been made in the establishment of computer-aided screening and design as a general approach to search for inhibitors of protein–protein interactions.[173,174]

4.3.1. Inhibitors of Antiapoptotic Bcl-2 Proteins

Proteins in the Bcl-2 family play a critical role in determining the fate of a cell through the process of apoptosis.[175] Many oncogenic mutations, particularly those of p53, result in defects in DNA-damage-induced apoptosis through a Bcl-2-dependent mechanism.[176] Furthermore, the overexpression of Bcl-2 can inhibit the potency of many currently available anticancer drugs by blocking the apoptotic pathway.[177] Therefore, agents that directly mimic the death-promoting BH3 domain of the pro-apoptotic subfamily of Bcl-2 proteins are of potential therapeutic value.[178]

Several research groups have used in-silico screening to assist in the search for low-molecular-weight inhibitors of Bcl-2 and Bcl-x_L (Scheme 26 and Table 3).[179] Huang and co-workers presented one of the first approaches in computer-



Scheme 26. Inhibitors of Bcl-2 (Bcl-x_L) from virtual library screening.

Table 3: Inhibitors of Bcl-2 (Bcl-x_L) discovered with in silico screening techniques (see Scheme 26).

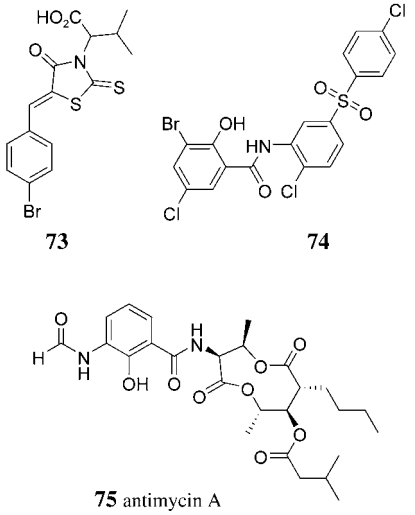
Compound	Target	IC_{50} [μM]	Docking Program	Library (Size)	Size of Focused Library
66[180]	Bcl-2	9	DOCK 3.5	MDL/ACD 3D (193 833)	28
67[181]	Bcl-2	1.6 ± 0.1	DOCK	NCI (208 876)	35
68[181]	Bcl-2	7.7 ± 4.5			
69[181]	Bcl-2	10.4 ± 1.2			
70[181]	Bcl-2	5.8 ± 2.2			
71[181]	Bcl-2 (Bcl-x_L)	10.4 (7)			
72[182]	Bcl-x_L	8.5 ± 0.6	TreeDock	Chemnavigator, Chembridge (93)	3

aided screening to narrow a large commercial library into a focused target group.[180] A 3D structure of the Bcl-2 protein derived from the NMR solution structure of the Bcl-x_L–Bak complex was used as the virtual target for 193 833 compounds from the MDL/ACD 3D database (Molecular Design). The computational docking experiments with DOCK 3.5 were carried out on 1000 compounds selected by their scoring function in shape complementarity, which relates to the attractive van der Waals energy. A filter of the preliminary candidates generated 53 compounds, of which 28 were chosen for synthesis and testing, reflecting a wide chemical diversity.

 © 2005 Wiley-VCH Verlag GmbH & Co. KGaA, Weinheim

Compound **66** showed moderate potency in disrupting the Bcl-2–Bak dimerization ($IC_{50} = 9\ \mu M$) and was able to induce apoptosis in HL-60 cells by caspase activation. Compound **66** represents the first reported antagonist of the Bcl-2–Bak complex identified with de-novo computer-aided design. In a similar fashion, Enyedy et al. identified five synthetic compounds (**67**–**71**) that disrupt the interaction between Bcl-2 (Bcl-x_L) and the Bak peptide with IC_{50} values at the low μM level.[181] Lugovskoy et al. combined the structural and computational approaches to preselect 93 compounds that possess good spatial agreement with a previous lead by using structural interface mapping and exhaustive computational interaction analysis techniques.[182] Analogue **72** was selected from the virtual screening and showed a similar affinity to that of the initial lead compound.

In addition to the in-silico approach, traditional screening methods have also been employed to identify inhibitors of Bcl-2 (Bcl-x_L) proteins. Detgerev et al. screened a commercial library (ChemBridge) of 16320 compounds and identified three compounds that disrupt the Bcl-x_L–Bak interaction (Scheme 27) with IC_{50} values in the low μM range.[183] A ^{15}N-



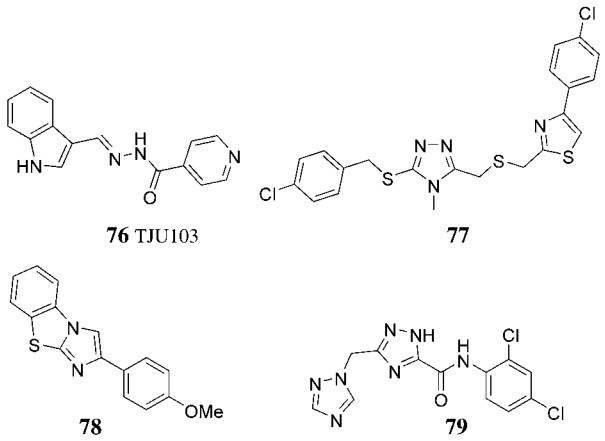
Scheme 27. Inhibitors of Bcl-x_L from wet screening.

HSQC NMR analysis showed that the synthetic inhibitors target the hydrophobic cleft where the BH3 domain binds on the surface of Bcl-x_L, and this was further confirmed with a NOESY experiment, which indicated direct contact between **73** and the residues Tyr65 and Phe107. Compound **73** was able to induce apoptosis in JK cells with overexpressed Bcl-x_L, suggesting the potential therapeutic application of **73** as an antitumor agent.

Antimycin A (**75**; Scheme 27), an inhibitor of mitochondrial electron transfer, was found to antagonize Bak binding to Bcl-x_L and to induce mitochondrial swelling.[2,179,184]

4.3.2. *Nonpeptide CD4 Inhibitors*

Protein–protein interactions among the proteins of the immunoglobulin superfamily (IgSF) play an important role in the mediation of cell-surface recognition.[185] The glycoprotein CD4 is expressed on the surface of helper T cells and functions as a coreceptor for stabilizing the interactions of T-cell receptors with antigens presented by the MHC class II molecule expressed on antigen-presenting cells.[186] CD4 binds to nonpolymorphic regions of the MHC class II β2 domain,[187] resulting in the co-oligomerization of CD4, MHC class II, and the T-cell receptor to initiate signaling in T cells. Huang and co-workers used computer-based screening to search a commercially available library of 150000 small organic compounds with the program DOCK 3.5.[173] After two rounds of virtual screening, 41 compounds were selected and tested in human mixed lymphocyte reactions. From the large library, four compounds were found to have inhibitory effects on alloreactive T-cell proliferation (Scheme 28). Among them, TJU103 (**76**) was the most promising lead for prolonging the median survival time of allograft mice to 52 days (in comparison with 20 days for the untreated control group).



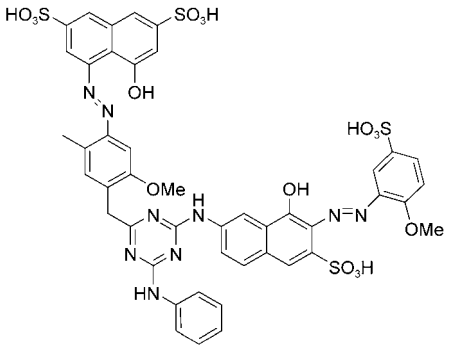
Scheme 28. CD4 inhibitors from in-silico screening.

4.3.3. *Disruptors of the Hexameric Helical Bundle of gp41*

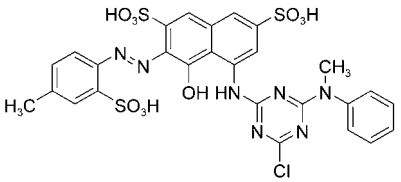
Debnath and co-workers improved the structure-based virtual screening with the DOCK suite of programs,[188] by using a force-field scoring method instead of shape-based scoring. This approach takes into account the interactions between the surrounding charged groups of the targeted hydrophobic cleft and the ionic groups in the potential inhibitors, thus improving the reliability of the docking results. The method was employed in the search for compounds that target the core region of gp41 of the HIV-1 virus. This has become an attractive target in light of the limitations in the use of inhibitors toward HIV-1 reverse transcriptase (HIV-1 RT) and HIV-1 protease.[189] A database of 20000 small organic molecules was screened, and the 200 top-scoring compounds were selected for inspection with visualization techniques for direct ranking.[190] Sixteen compounds from the screening process were prepared; their ability to disrupt the hexameric helical bundle formed through the gp41 N36–C34 complex was tested in vitro using an ELISA assay. Of these

 © 2005 Wiley-VCH Verlag GmbH & Co. KGaA, Weinheim

compounds, **80** and **81** (Scheme 29) showed potent activity with IC_{50} values of 0.73 μg mL^{-1} and 3.18 μg mL^{-1}, respectively. Assays of the active compounds in vivo demonstrated that both **80** and **81** inhibit HIV-1-mediated cell fusion and the cytopathic effect (CPE). The validation of the in-silico screening method was confirmed, as **80** and **81** were ranked first and third in the computational scoring and showed the most potent activity in the assay.



80 ADS-J1



81 ADS-J2

Scheme 29. Small-molecule inhibitors targeted to the core structure of the HIV-1 glycoprotein gp41.

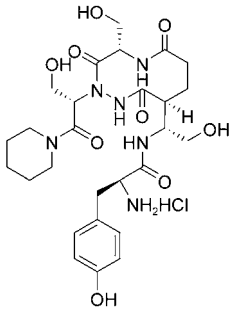
5. Synthetic Inhibitors of Protein–Protein Interactions from Rational Design

Information from biology can aid the design of synthetic molecules with features that structurally and functionally mimic the complementarity-determining region (CDR) of targeted proteins. With the assistance of X-ray crystallography, NMR spectroscopy, and computational simulation, chemists can manipulate biological processes with small synthetic agents through the recognition of protein surfaces or the disruption of protein–protein interactions. For example, by using NMR-based screening, Hajduk et al. determined that certain motifs (e.g. biphenyls) are more likely to be used as a template for the discovery and design of therapeutics with high affinity and specificity for a broad range of protein targets.[191] Many designed inhibitors also have very rigid structures to prevent hydrophobic collapse. Although this theoretical and empirical insight facilitates rational design, the engineering of small molecules to target particular protein–protein interactions remains a major challenge.

5.1. Rational Design of Synthetic Inhibitors that Recognize the Exterior Surfaces of Proteins

5.1.1. A Synthetic Inhibitor that Mimics the Complementarity-Determining Region of MAb 87.92.6

Through structural information and computational modeling, Saragovi et al. pioneered the design of small-molecule antagonists of protein–protein interactions.[192] Their target was the monoclonal antibody MAb 87.92.6, which recognizes the reovirus type 3 cellular receptor (Reo3R). Previous work had shown that cyclic peptide analogues of the second CDR of MAb 87.92.6 successfully block the interaction of MAb 87.92.6 and Reo3R.[193] However, the proteinaceous nature of the peptide analogues prevented further development as a result of their poor solubility, limited blood-brain barrier permeability, and susceptibility to proteolysis. For this reason the 87.1-mimetic **82** (Scheme 30) was designed and synthesized to mimic the second CDR of MAb 87.92.6. This synthetic inhibitor showed good solubility in water, making it permeable to the blood-brain barrier. Binding assays showed that immobilized **82** specifically binds to MAb 9BG5 (a native partner of MAb 87.92.6) with a 14-fold stronger affinity than the negative control. Compound **82** can competitively block the binding of MAb 9BG5 to VLSH, a dimeric peptide derived from the second CDR of MAb 87.92.6, in a dose-dependent fashion. Cellular studies demonstrated that **82** inhibits concanavalin A (Con A)-induced T-cell proliferation of splenocytes in a dose-dependent manner, as did the VLA5 peptide and the intact MAb 87.92.6. On the other hand, the peptide analogue and a CD4 mimetic (a reverse-turn mimetic derived from residues 41–54 of human CD4) were inactive in the same assay system. These data suggested that **82** inhibits cell proliferation by mediating the Reo3R receptor.



82 87.1-mimetic

Scheme 30. Structure of 87.1-mimetic as mimetic of the complementarity-determining region of monoclonal antibody 87.92.6.

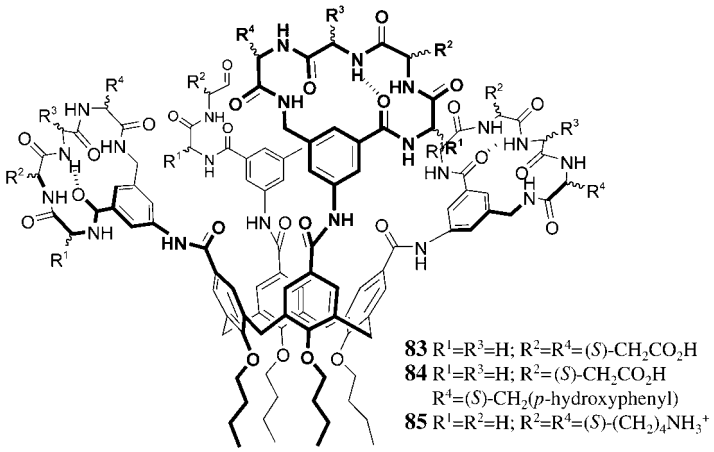
5.1.2. Calix[4]arene-Based Inhibitors of PDGF and Cytochrome c

Calix[4]arene has been widely used in supramolecular chemistry as a result of its well-defined shape and ease of synthesis.[194] Sebti and Hamilton reported the use of calix[4]-arene derivatives as synthetic reagents for the recognition of protein surfaces.[195] The basis of this design was threefold: 1) the relatively large binding area (> 400 Å^2) of calix[4]arene provided a promising scaffold for mimicking the interacting region of an antibody–antigen interface; 2) modular design and stepwise functionalization of the upper rim of calix[4]-arene facilitates efficient diversity-oriented synthesis of inhibitors; 3) the flexibility of the calix[4]arene scaffold facilitates the recognition of a dynamic surface in an "induced-fit" mechanism.

 © 2005 Wiley-VCH Verlag GmbH & Co. KGaA, Weinheim

There are four positions on the upper rim of calix[4]arenes that can be used to attach different recognition domains. Varying both the nature and the symmetry of the substituents on the rim can be used to increase the diversity of the family. As protein surfaces are intrinsically unsymmetrical, the ability to prepare inhibitors with a complementary and unsymmetrical distribution of charge and hydrophobicity should greatly improve their selectivity.

Platelet-derived growth factor (PDGF) is a potent inducer of growth and motility such as cell proliferation, angiogenesis, wound healing, and chemotaxis.[196] PDGF binds to its cell-surface receptor, PDGFR, resulting in dimerization, receptor autophosphorylation, and recruitment of tumor cells.[197] Overexpression of PDGFR is observed in many carcinomas, and some cancer patients have high serum levels of PDGF.[198] These elevated levels of PDGFR in cancer patients also correlate with poor response to chemotherapy and shorter survival times. Hamilton and co-workers studied the surface recognition of PDGF by synthetic agents that are able to disrupt its interaction with PDGFR and thereby elicit antitumor and anti-angiogenesis effects.[199] PDGF-BB is a homodimer of two proteins that consist of two β strands with three intramolecular disulfide bridges. The three surface loops connecting the strands are clustered at one end of the elongated dimer upon dimerization. Mutational analyses indicates that the key binding regions are in these loop regions. These regions are rich in cationic and hydrophobic residues; the recognition strategy based on hydrophobic and electrostatic complementarity could be applied to this domain. Molecules **83–85** (Scheme 31), in which multiple



83 R^1=R^3=H; R^2=R^4=(*S*)-CH_2CO_2H
84 R^1=R^3=H; R^2=(*S*)-CH_2CO_2H
R^4=(*S*)-CH_2(*p*-hydroxyphenyl)
85 R^1=R^2=H; R^2=R^4=(*S*)-$(CH_2)_4NH_3^+$

Scheme 31. Artificial inhibitors based on functionalized calix[4]arene derivatives.

recognition elements are projected on the same face of a calix[4]arene scaffold, were evaluated as antagonists against PDGF-induced PDGFR autophosphorylation and MAP kinase activation in NIH3T3 cells. These assays identified a strong dependence on the loop sequence projected by the calix[4]arene core to obtain high inhibitory activity. Cationic derivative **85** ($IC_{50}=50\ \mu M$) had only modest potency, whereas all anionic derivatives, including **83**, were moderately active ($IC_{50}<10\ \mu M$). The inhibitory effect was strongest for **84**, a derivative containing a Gly-Asp-Gly-Tyr cyclic peptide sequence, with a remarkably low IC_{50} value of 250 nM. Compound **84** directly interacts with PDGF as shown by gel-shift analysis, suggesting that inhibition was likely a result of **84** binding directly to PDGF. Compound **84** was also able to displace ^{125}I-PDGF from PDGFR in a dose-dependent manner, indicating that its binding led to the disruption of the PDGF–PDGFR interaction. Cell-based studies showed that **84** possesses potent antitumor and anti-angiogenic properties against human tumors in nude mice and it is currently being evaluated in further biological studies.

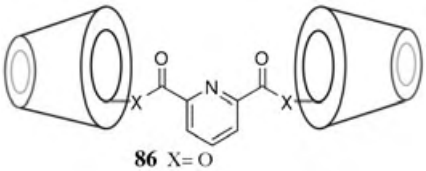
Another application of calix[4]arene **83** in the disruption of protein–protein interactions was reported by Wei and co-workers.[200] Synthetic receptor **83** was found to block cytochrome c (Cytc) binding to cytochrome c peroxidase (CytcP) in a fluorescence titration assay. Compound **83** replaced CytcP to efficiently form a Cytc–**83** complex in a binding ratio of 1:1 and with a K_a value of $10^8\ M^{-1}$. Further investigation also showed that the complex of Cytc–Apaf-1, a critical intermediate in the apoptosis pathway,[201] could be disrupted upon the addition of **83** at an antagonist/complex ratio of about 200:1.

5.1.3. *β-Cyclodextrin Dimers as Disruptors of Lactate Dehydrogenase and Citrate Synthase Aggregates*

Breslow and co-workers reported that β-cyclodextrin (CD) dimers can selectively inhibit the assembly of individual protein subunits into multiprotein aggregates, such as the formation of citrate synthase (CS) dimers and L-lactate dehydrogenase (LDH) tetramers.[202] Protein interfaces of this type often contain defined hydrophobic patches. The disruption strategy was therefore to construct cyclodextrin dimers separated by appropriate spacers. Cyclodextrins had previously been shown to form tight complexes with hydrophobic side chains of polypeptides and were therefore expected to block protein assembly by interacting with the hydrophobic side chains in the interfacial regions.[203]

Eleven CD dimers with a variety of linkers and CD-cavity orientations were designed and synthesized. The ability of these analogues to disrupt protein multimerization were assayed by monitoring enzyme activity. Of a group of enzymes tested, only CS and LDH were vulnerable to inhibition, whereas sorbitol dehydrogenase, adenosine deaminase, D-galactose dehydrogenase and phosphohexose isomerase were not affected at CD dimer concentrations as high as 480 μM. Compounds with β or α cyclodextrin groups oriented with their cavities facing away from the spacer core were inactive, and neither were the compounds with ether linkages separating the cyclodextrin groups. However, compounds **86** and **87**, in which β-cyclodextrin dimers are respectively separated by either pyridyl diesters or diamides, selectively disrupted the aggregation of LDH ($IC_{50}=140\ \mu M$) and CS ($IC_{50}=30\ \mu M$) (scheme 32). As a negative control, the authors showed that β cyclodextrin and pyridine dicarboxylate alone were not active, indicating the special requirement of a correctly spaced β-cyclodextrin dimer for the disruption

 © 2005 Wiley-VCH Verlag GmbH & Co. KGaA, Weinheim



Scheme 32. Cyclodextrin dimers as inhibitors of protein subunit aggregation.

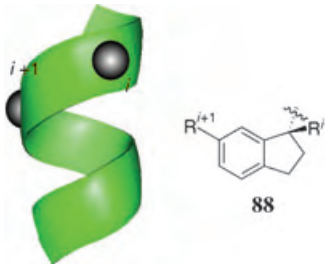
of LDH and CS. Although the exact origin of protein selectivity and the precise mode of disruption is still unclear, there are several aromatic side chains on the surface of LDH and CS where the cyclodextrin dimers could potentially bind.

5.2. Low-Molecular-Weight Agents as Structural and Functional Mimetics of Protein Secondary Structures

A logical progression from the use of constrained peptides as inhibitors of protein–protein interactions is to use easily accessible synthetic molecules to mimic the surfaces of constrained peptides. Such approaches offer the advantage of improved biostability, lower molecular weight, and in some cases better bioavailability. Synthetic molecules that adopt various well-defined secondary structures are well-documented;[72,73,75,204] the focus of this section is on low-molecular-weight compounds that disrupt protein–protein interactions by mimicking the structural features of different protein secondary structures.

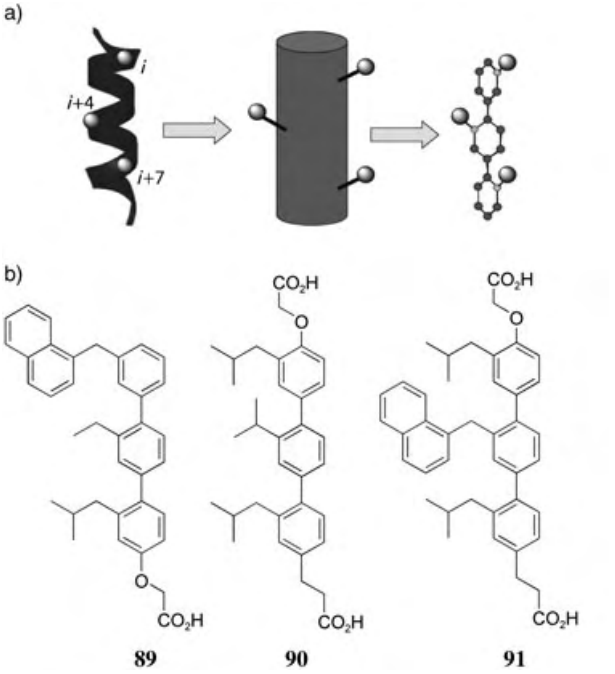
5.2.1. α-Helix Mimetics

Several synthetic mimetics of α-helical surface binding domains have been reported. The pioneering work of Horwell et al. showed that 1,6-disubstituted indanes **88** present functionality in a similar spatial arrangement to the *i* and *i*+1 residues of an α helix (Scheme 33).[205] Derivatives with large hydrophobic peptide side chains (Phe-Phe and Trp-Phe) were found to bind to the tachykinin receptors NK1, NK2, and NK3 with micromolar affinities. These mimetics do not cover a large enough surface to sufficiently represent an α-helical mimetic. However, they demonstrate nicely the potential of using nonpeptide scaffolds to present critical recognition functionality in a suitable spatial orientation for binding to a target protein.



Scheme 33. The indane template that mimics the *i* and *i*+1 positions of an α helix.

Hamilton and co-workers recently reported that a terphenyl scaffold could reasonably mimic the surface of an α-helical peptide in which the 3,2′,2″-substituents on the phenyl rings present functionality in a spatial orientation that mimics the *i*, *i*+3(4) and *i*+7 residues on an α helix (Scheme 34a).



Scheme 34. a) Rational design of terphenyl-based α-helical mimetics; b) terphenyl-based inhibitors.

This strategy was first employed in the design of an inhibitor of the interaction between calmodulin (CaM) and small muscle myosin light chain kinase (smMLCK).[49] Mutational studies on the sequence of a 20-mer fragment from smMLCK revealed critical roles for residues Trp 800, Thr 803, and Val 807. A helical peptide derived from the plasma membrane calcium pump protein C20W that binds to the same region of CaM as smMLCK also indicates a critical role for hydrophobic residues at these positions. For synthetic simplicity, indole was changed to naphthalene for the tryptophan side chain, and the threonine hydroxy group was removed, leading to a designed ligand **89** (Scheme 34b). The binding of **89** to CaM was demonstrated with affinity chromatography. This ligand also inhibited the CaM-mediated activation of 3′,5′-phosphodiesterase (PDE), which is believed to bind CaM at the same site employed by smMLCK. Terphenyl **89** competed with smMLCK peptide with an IC_{50} value of 9 nM.

It was shown subsequently that appropriately designed terphenyl scaffolds can disrupt the assembly of the hexameric gp41 core that leads to HIV-1 viral particle fusion with host cells.[167] Terphenyl derivatives can be designed to mimic the hydrophobic functionality at the *i*, *i*+4 and *i*+7 residues of the α-helical heptad repeat regions of the C- and N-terminal peptides. These synthetic helix mimetics disrupt the binding of the C-terminal peptides to the trimeric N-terminal core and prevent HIV-1 entry into host cells. Derivative **90** was found

 © 2005 Wiley-VCH Verlag GmbH & Co. KGaA, Weinheim

to disrupt a model system composed of two peptides (N36 and C34) from the N- and C-heptad repeat regions which form a stable six-helix bundle analogous to the gp41 core (Figure 8). Circular dichroism (CD) spectroscopy demonstrated that the

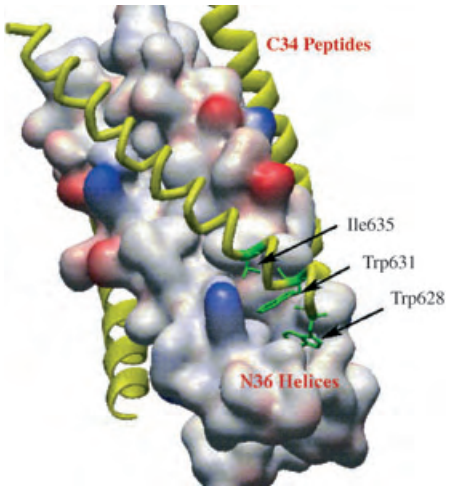


Figure 8. Crystal Structure of the gp41 fusion active center C34 (residues 628–661, represented as helical tubes) in complex with N36 (residues 546–581) The complex arises by inserting the side chains of Trp 628, Trp 631 and Ile 635 into a hydrophobic cleft on the protein surface.

C34 peptide forms a random coil on its own in solution while the N36 peptide forms concentration-dependent aggregates. Titration of compound **90** into a PBS-buffered solution of this model system resulted in a decrease of the CD signal at 222 and 208 nm, corresponding to a decrease in helicity of the hexameric bundle; the decrease saturates at three equivalents of terphenyl. The T_m value of the N36 core in the presence of excess **90** is significantly lower than that of the gp41 core, and resembles that of the N36 region alone, which suggests that the terphenyl competes for the C34 binding site. The electrostatic and hydrophobic features of **90** were found to be critical for this behavior, as terphenyls with positively charged groups and no alkyl substituents had little effect on the behavior of the gp41 core as monitored by CD. An ELISA experiment with an antibody that binds to the N36–C34 helix bundle, but not the individual peptides, demonstrated that **90** disrupted the formation of the hexameric bundle with an IC_{50} value of $13.18 \pm 2.54\ \mu g\,mL^{-1}$ whereas a dye-transfer fusion assay indicated that **90** inhibited HIV-1-mediated cell–cell fusion with an IC_{50} value of $15.70 \pm 1.30\ \mu g\,mL^{-1}$.

This α-helix mimetic strategy was used for the design of an inhibitor of the anti-apoptotic protein Bcl-x_L.[206] A current strategy for inhibiting Bcl-x_L function is to block the Bak-recognition site on Bcl-x_L, thereby disrupting the protein–protein contact. A Bcl-x_L–Bak complex structure determined by NMR spectroscopy shows that a helical region of Bak (residues 72–87, $K_d = 340$ nM) binds to a hydrophobic cleft on the surface of Bcl-x_L.[207] Furthermore, the crucial residues for binding were shown by alanine scanning to be Val 74, Leu 78, Ile 81, and Ile 85, which project from the *i*, *i*+4, *i*+7 and *i*+11 positions along one face of the helix (Figure 9). A series of terphenyl derivatives were prepared with different sequences and substitution patterns on the 3,2′,2″-positions, and fluorescence polarization was employed to monitor their interactions with the target protein. The assay demonstrated that

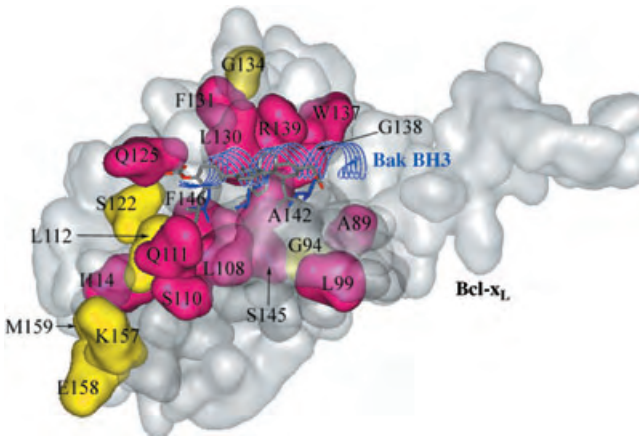
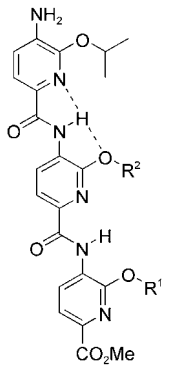


Figure 9. Results of the ^{15}N-HSQC experiment with ^{15}N-lalbeled Bcl-x_L. The residues that show chemical-shift changes in the presence of **91** (green) are highlighted. The most probable conformation of inhibitor **91**, predicted from a computational docking simulation, has been superimposed on the helical Bak BH3 domain (blue) for comparison.

terphenyl **91** with two carboxylates and the substituent sequence isobutyl, 1-naphthylmethylene, isobutyl was a potent inhibitor ($K_i = 114$ nM). The specificity was confirmed by scrambling the sequence of the three key substituents, which produced a 30-fold decrease in K_i. Similarly, the removal of the two carboxylate groups or their replacement by positively charged groups led to a loss of activity. HSQC NMR experiments with **91** indicated that these terphenyl derivatives target the hydrophobic cleft on the surface of Bcl-x_L known to interact with Bak.

An alternative design for mimicking the binding surface of α helices based on an oligo-amide foldamer was subsequently elaborated by Hamilton and co-workers.[208] The anticipated foldamer conformation is depicted in Scheme 35 and results from the constraint of intramolecular hydrogen bonds between the amide hydrogen atoms and the pyridine nitrogen atoms, in addition to the disfavored interaction that would occur between the amide carbonyl group and the nitrogen atom of the pyridine in an alternative conformation. Further conformational biasing is induced by a hydrogen bond between the amide -NH group and the oxygen atom of the alkoxy binding functionality. The intramolecularly hydrogen-bonded conformation was confirmed in the solid state by crystallography, which further revealed that the alkoxy side chains were tilted at 45° to maximize interaction of the lone pair on the oxygen atom

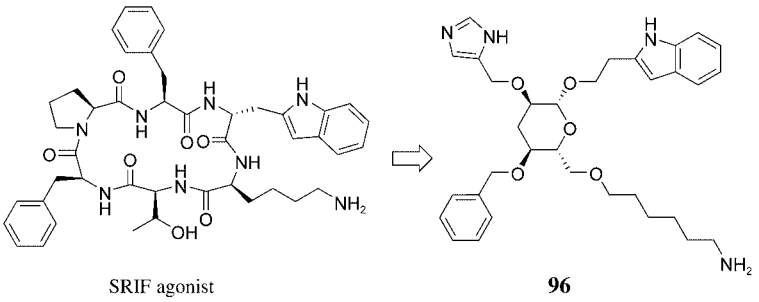


92 $R^1 = R^2 = i$Pr
93 $R^1 = i$Pr; R^2 = Bn
94 $R^1 = R^2$ = Bn

Scheme 35. α-Helical mimetics based on oligo-amide foldamers; Bn = benzyl.

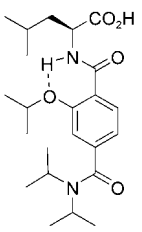
 © 2005 Wiley-VCH Verlag GmbH & Co. KGaA, Weinheim

with the amide -NH group. The foldamer was tested as a proteomimetic antagonist of Bak to disrupt its interaction with Bcl-x_L. The in vitro assay identified three inhibitors of the interaction, **92–94**, with K_i values of 2.3, 9.8, and 1.6 μM, respectively, whereas the foldamers with trisbenzyloxy and trismethoxy groups demonstrated weaker activities and a requirement for some size matching and sequence specificity between the protein and the mimetic.



Scheme 37. β-D-Glucose-based nonpeptide peptidomimetics of somatostatin (SRIF).

Most recently, Hamilton and co-workers reported a group of novel synthetic helical mimetics based on a terephthalamide scaffold.[209] The backbone of the terphenyl was reduced to a much simpler terephthalamide, as in **95** (Scheme 36), while the spatial arrangement of the projected side chains was maintained. The flanking phenyl rings of the terphenyl backbone were replaced by two functionalized carboxamide groups, which retain the planar geometry of the phenyl rings, due to the restricted rotation of the amide bonds. The intramolecular hydrogen bond between the amide -NH and the alkoxy oxygen atom of **95** ensures that the 2-isopropoxy group and the upper isobutyl side chain are positioned on the same side of the terephthalamide group. A fluorescence polarization assay was once again used to monitor release of the fluorescently labeled Bak peptide from Bcl-x_L and sub-micromolar affinities were observed ($K_i = 0.78$ μM). Treatment of human HEK293 cells with the terephthalamide derivatives resulted in disruption of the Bcl-x_L–Bak interaction in whole cells. HSQC experiments with ^{15}N-labeled Bcl-x_L suggested that terephthalamide and the Bak BH3 peptide target the same area on the Bcl-x_L exterior surface, confirming that terephthalamide is a successful alternative scaffold to terphenyl as an α-helical mimetic.



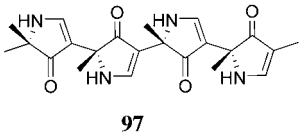
Scheme 36. Terephthalamide-based α-helical mimetic.

5.2.2. *β-Turn Mimetics*

Hirschmann, Smith, and co-workers have made many important contributions to the development of nonpeptide peptidomimetics. For example, they reported a mimetic of the cyclic peptide somatostatin (SRIF) with a D-glucose scaffold, **96** (Scheme 37).[210] Carbohydrates represent an attractive approach to mimicking β turns, as they impose an appropriate projection of several side chains and are relatively rigid. The shape and substitution pattern of D-glucose was found to best present the Trp, Lys, and Phe side chains. A radiolabeling/binding assay showed that **96** completely displaced ^{125}I-CGP23996 from the SRIF receptor on membranes from cerebral cortex, pituitary, and AtT-20 cells with an IC_{50} value of 1.9 μM.

Further peptidomimetic approaches of this type include β-D-glucose-based mimetics for somatostatin (SRIF)[211] and antagonists for substance P (NK-1),[212] pyrrolinone-based renin inhibitors,[213] HIV-1 protease inhibitors,[214,215] pyrrolinone-based matrix metalloprotease inhibitors,[216] competent nonpeptide hybrid ligands for the human class II MHC protein HLA-DR1,[217] and azepine-based cryptophycin mimetics.[218]

Smith, Hirschmann, and co-workers elaborated a pyrrolinone-based mimetic of the β-strand/β-sheet and/or β-turn conformations of peptides[215,217,219] in which all of the key recognition features (side chains and hydrogen-bond donors/acceptors) are faithfully represented within a low-molecular-weight nonpeptide analogue based on pyrrolinone **97** (Scheme 38). This design has been applied to the development of antagonists of HIV-1 protease and more recently to mimics of MHC class II protein substrate.[214,217]



Scheme 38. Polypyrrolinone-based β-turn peptidomimetics.

Rebek and colleagues reported a low-molecular-weight β-loop mimetic that disrupts the interaction between the type I interleukin-1 receptor (IL-1RI) and the adapter protein MyD88.[220] The IL-1R superfamily and the Toll-like receptor (TLR), which share a conserved Toll/IL-1R/resistance (TIR) domain,[221] are critical to both innate and adaptive immunity for host defense.[222] IL-1 monomers act as proinflammatory mediators through dimerization and recruitment of the putative adapter protein MyD88, which also contains a TIR domain,[223,224] through homotypic binding of the TIR domain between IL-1RI and MyD88.[224,225] Xu et al. previously determined the crystal structure of the TIR domains of human TLR1 and TLR2 (Figure 10) and elucidated the structural basis of the TIR–TIR interaction between IL-1RI and MyD88.[226] The protruding BB loop was proposed to be critical for complex formation, as mutations at almost every position in this region led to a significant decrease in the signaling activity of the receptors.

Rebek and co-workers prepared an analogue of the central three-residue sequence of the BB loop **98** which mimics the (F/Y)-(V/L/I)-(P/G) residues (Scheme 39) and studied its ability to disrupt the IL-1RI–MyD88 interaction. Compound **98** attenuated the IL-1β-mediated activation of

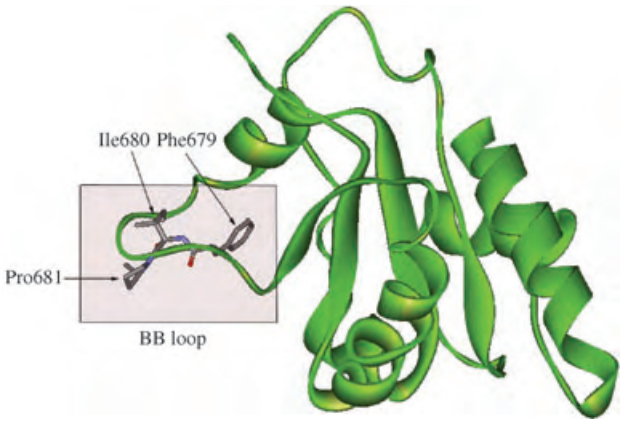
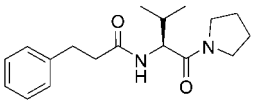


Figure 10. Crystal structure of the TIR domain with the BB loop bracketed.



98

Scheme 39. Low-molecular-weight mimetic **98** of the BB loop.

p38 MAP kinase at micromolar concentrations. Sandwich ELISA assays demonstrated that **98** prevents IL-1β-mediated IL-1RI–MyD88 association in EL4 cells. The specificity of **98** to disrupt the association of IL-1RI and MyD88 was confirmed by the fact that **98** did not affect other members of the Toll receptor superfamily (TLR1–10).

5.2.3. *β-Strand/β-Sheet Mimetics*

The β strand is a linear or saw-toothed peptide structural element that can form β sheets, which account for over 30% of all protein secondary structure. In the last decade, small-molecule β-strand/β-sheet mimetics and their applications, as in the development of protease inhibitors,[227] have been reported.[228] However, the examples of synthetic agents that mimic β strands and β sheets and disrupt large protein–protein interactions are still scarce.

Integrins are a receptor protein family involved in a variety of cellular functions such as wound healing, cell differentiation, homing of tumor cells, and apoptosis. Functional integrins are heterodimeric aggregates consisting of α- and β-transmembrane glycoprotein subunits that are non-covalently bound and share homology. Corbett et al. identified potent and selective $\alpha_v\beta_3$-integrin antagonists from screening a library prepared by solid-phase synthesis.[229] Nicolaou and co-workers applied scaffold **96** to mimic the cyclopeptide cRGDFV sequence that inhibits integrin–ligand interactions.[230]

ICAM proteins 1, 2, and 3 interact with LFA-1 (the integrin $\alpha_L\beta_2$, CD11a/CD18) and mediate the adhesion, extravasation, migration, and proliferation of lymphocytes.[231] An epitope consisting of the amino acids Glu34, Lys39, Met64, Tyr66, Asn68, and Gln73, located on the opposite side of an antiparallel β-sheet within the first domain of ICAM-1, was identified as essential for its interaction with LFA-1 (Figure 11).[232]

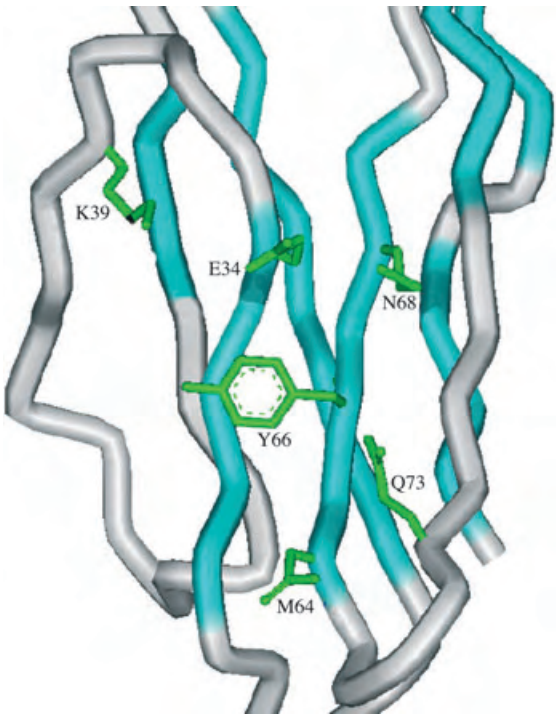
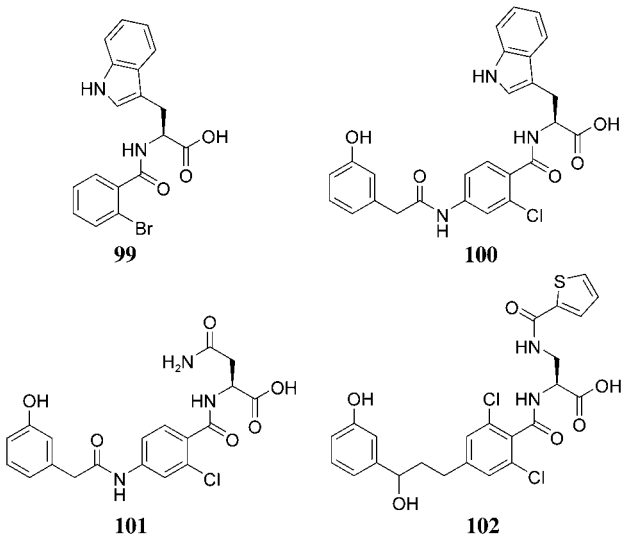


Figure 11. The discontinuous binding epitope of ICAM-1 (shown in green).

One of the greatest challenges in the design of small-molecule proteomimetics for the inhibition of protein–protein interactions is that the interacting units are often widely spread. To transfer all of the interacting functionality of a target protein to a designed synthetic compound remains a major challenge. A research group at Genentech presented an elegant approach in which the native ligand of the targeted receptor is used as the lead and small-molecule antagonists are identified through chemical diversity exploration.[233] Kistrin, a disintegrin protein containing an RGD sequence, was found to disrupt the LFA-1 and ICAM-1 interaction in vitro by mimicking the critical interacting residues from ICAM-1. The peptide sequence H_2N-CGY$^{(m)}$DMPC-COOH (Y$^{(m)}$ = *meta*-tyrosine), which has a similar potency for the disruption of the ICAM-1–LFA-1 interaction, was selected as a lead in the design of synthetic inhibitors.

Compound **100** (Scheme 40), from a related program with an IC_{50} value of 1.6 μM, was modified with a *meta*-phenol group to mimic the Y$^{(m)}$ residue in the peptide lead and gave a 30-fold improvement in the ELISA assay. Compound **100** was then subdivided into five modules and modifications were made within each module for further optimization. This exploration of chemical diversity generated **101**, which represents a minimal display of the epitope with high potency (IC_{50} = 3.7 nM), and **102**, one of the best combinations of the molecular modules (IC_{50} = 1.4 nM). An MLR assay showed that compound **102** antagonizes ICAM-1 by binding LFA-1

 © 2005 Wiley-VCH Verlag GmbH & Co. KGaA, Weinheim



Scheme 40. Synthetic inhibitors that disrupt the LFA-1–ICAM-1 interaction.

and mediates lymphocyte proliferation and adhesion in vitro. Compounds **99–102** emerged from consideration of the discontinuous ICAM-1 epitope with five residues spanning three different β-strands across the face of a protein, through the lead compound kistrin and consequently the H_2N-CGY$^{(m)}$DMPC-COOH peptide. However, there has been ongoing debate about whether these compounds indeed function as ICAM-1 mimetics.[234] Springer and co-workers argued that this group of compounds are not ICAM-1 mimetics as they do not bind either to the α_L or α_M I domain as ICAM-1 does, but perturb binding of MAb to the β_2 I-like domain that does not participate directly in binding ICAM-1.[234,235]

FtsZ, a homologue of eukaryotic tubulins, is an essential component of the septal rings that mediate cell division in Gram-negative bacteria.[236] Z-interacting protein A (ZipA) is a 36.4-kDa membrane-anchored protein that is recruited to the septal ring at a very early stage of the cell-division cycle by the formation of a complex with FtsZ. Some cell division can be interrupted by disruption of the ZipA–FtsZ interaction; this protein–protein interface has become a possible target for the development of new antibiotics. X-ray crystallography and NMR spectroscopic analyses revealed that FtsZ binds to a broad and predominantly hydrophobic surface area on the solvent-exposed side of a β sheet on ZipA (Figure 12).[237] Upon binding, the 17-residue FtsZ peptide (^{367}KEPDYLDI-PAFLRKQAD^{383}) adopts an extended β-strand conformation in the region of residues 367–373 followed by an α-helical domain from positions 374 to 383. Direct interatomic contacts are made between 11 ZipA amino acid residues and seven FtsZ residues in the span between residues 370 and 381.

A group at Wyeth Research recently reported the design of small-molecule inhibitors of ZipA–FtsZ interactions based on key residues of the protein–protein interface.[238] Compounds **103–105** (Scheme 41) showed only weak inhibition in the fluorescence polarization assays ($IC_{50} = 1.17$, 2.06, and 2.75 mM, respectively).[239] X-ray crystallographic analysis showed that **103** and **104** essentially recognize the same

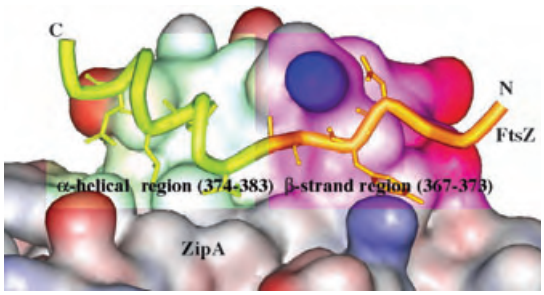
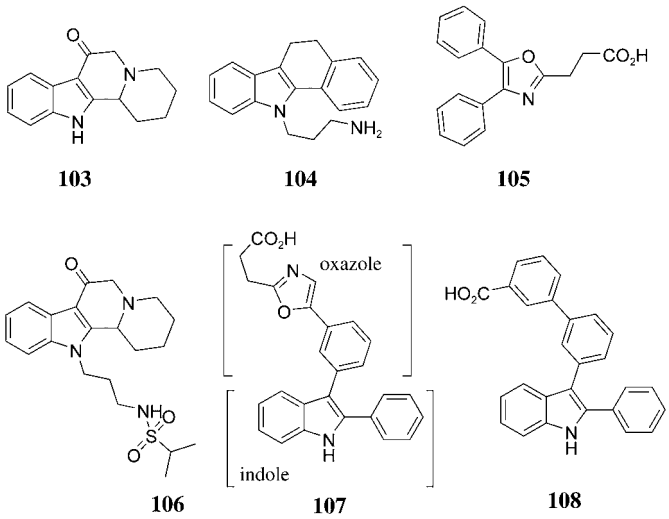


Figure 12. The ZipA–FtsZ interface (residues 367–383). FtsZ peptide (tube representation) binds to a hydrophobic pocket on the ZipA surface as an extended β strand (residues 367–373) followed by an α helix (residues 374–383).



Scheme 41. Synthetic inhibitors that disrupt the ZipA–FtsZ interaction.

binding site, whereas **105** and **106** occupy a distinct region on the surface of ZipA. The indole rings in **103** and **104** recognize the lipophilic pocket, whereas **105** binds to a hydrophilic region. Based on the structural information provided by the lead, the chimeric molecule **107**, which combines the structural features of both the indole and oxazole motifs, was designed. The most potent inhibitor **108**, an analogue of the chimera (Scheme 41), gave an IC_{50} value of 192 μM to disrupt ZipA-FtsZ binding. The target site of the inhibitors was confirmed by 2D ^{15}N-HSQC experiments.

6. Summary and Outlook

Recent examples of synthetic agents that disrupt protein–protein interactions have been reviewed. Most of these agents were identified from the screening of chemical libraries or from structure-based rational design. In the next a few years, emerging techniques have the potential to revolutionize the approach and to provide more efficient means for compound library preparation and evaluation. With a range of combinatorial synthetic methods, libraries containing many thou-

 © 2005 Wiley-VCH Verlag GmbH & Co. KGaA, Weinheim

sands of compounds can be readily prepared for screening.[3,4] Applications of mass spectrometry, NMR spectroscopy, and nanotechnology in high-throughput screening have greatly enhanced our ability to identify small molecules that disrupt protein–protein interactions.[240] Novel techniques such as the "tether" method (Section 4.2.4) make it possible to identify lead compounds with only weak to modest potency.[120] These compounds then offer the possibility of fragment reassembly, leading to highly potent inhibitors. Benkovic and co-workers recently reported a novel methodology of genetic selection to identify small-molecule antagonists of protein–protein interactions by using whole cells as reporters, thus bypassing the inherent limitation of in vitro analysis.[241]

Synthetic agents identified from high-throughput screening serve as valuable leads for structure–activity relationship (SAR) studies aimed toward higher potency or retention of binding affinity with improved bioavailability. Pharmacophore models derived from SAR are then required to be confirmed with further binding mode studies. The integration of biology into chemistry with strategies such as phenotype screening, have expanded our intellectual horizon.[151] As biological molecules often act on multiple targets simultaneously (for example, Danial et al. recently reported that Bcl-2 family proteins also play roles in metabolic pathways aside of apoptosis),[242] it seems likely that our model of single targets for highly selective small molecules may be outmoded. Akin to the way in which people have been practicing herbal medicine over millennia, modern scientists now are beginning to identify active compounds in living organisms prior to the identification of their targets.

Rational approaches, on the other hand, involve the design and synthesis of molecules that deliberately incorporate functional groups in a complementary manner to that of protein targets. The design of these mimetics is based on the features presented on protein surfaces, such as clusters of hydrophobic groups, electrostatic domains, and metal-coordinating groups. The selectivity and generality of inhibitors developed by this strategy in the context of numerous other protein targets remains to be determined. Protein surface recognition is greatly complicated by the high degeneracy of the exterior functionalities presented by different proteins. Most rational designs described herein have attempted to assign geometric, electrostatic, and hydrophobic complementarity requirements for recognition. In some cases, this evaluation was extended to the measurement of target selectivity through indirect (in vivo toxicity) or limited (selectivity among a small set of related proteins) techniques. These efforts are important initial steps toward improved affinity and selectivity. Computer-aided rational design is a very promising approach in the search for synthetic agents that target protein–protein interfaces. Enhanced selectivity remains the major challenge in the design of molecules that target protein exterior surfaces. However, as our understanding of surface mobility and functionality increases, coupled with more accurate computational analysis, designs will improve in potency and selectivity.

Large organic molecules ($MW > 750$ Da) are generally problematic as viable drug candidates.[199,243] The disadvantage of large molecules is primarily ascribed to their deviation from Lipinski's rules.[244] However, these agents may be particularly valuable for cases in which protein surfaces do not possess clear binding sites that may allow high affinity association with small molecules. For some proteins in which "epitope transfer" to small molecules is challenging, large synthetic agents may offer a pharmacological proof-of-principle that can be potentially minimized or modified to a viable drug candidate. This seems especially likely for cases in which the compounds are originally designed to allow facile structural modifications. Some large molecules have already been evaluated under clinical trials to have limited toxicity and moderate pharmacological profiles, indicating that a large size may not always be disadvantageous. It is also encouraging that other large molecules like antibodies and peptides have all yielded successful drugs. Polymers and nanoparticles represent other promising fields that can produce synthetic agents that modulate protein–protein interactions.

Without question, the use of synthetic agents to disrupt protein–protein interactions will increase over the next decade. After all, the opportunities provided to chemists by Nature are almost limitless.

We thank the National Institutes of Health (GM35208 and GM69850) for financial support of the work described in this review that was carried out in our laboratories.

Received: August 25, 2004
Revised: December 24, 2004
Published online: June 14, 2005

[1] S. L. Schreiber, *Bioorg. Med. Chem.* **1998**, *6*, 1127.
[2] T. Berg, *Angew. Chem.* **2003**, *115*, 2566; *Angew. Chem. Int. Ed.* **2003**, *42*, 2462.
[3] D. L. Boger, J. Desharnais, K. Capps, *Angew. Chem.* **2003**, *115*, 4270; *Angew. Chem. Int. Ed.* **2003**, *42*, 4138.
[4] D. L. Boger, *Bioorg. Med. Chem.* **2003**, *11*, 1607.
[5] P. L. Toogood, *J. Med. Chem.* **2002**, *45*, 1543; A. G. Cochran, *Curr. Opin. Chem. Biol.* **2001**, *5*, 654; T. R. Gadek, J. B. Nicholas, *Biochem. Pharmacol.* **2003**, *65*, 1; A. V. Veselovsky, Y. D. Ivanov, A. S. Ivanov, A. I. Archakov, P. Lewi, P. Janssen, *J. Mol. Recognit.* **2002**, *15*, 405.
[6] A. G. Cochran, *Chem. Biol.* **2000**, *7*, R85.
[7] W. E. Stites, *Chem. Rev.* **1997**, *97*, 1233.
[8] M. R. Arkin, J. A. Wells, *Nat. Rev. Drug Discovery* **2004**, *3*, 301.
[9] T. Clackson, J. A. Wells, *Science* **1995**, *267*, 383.
[10] B. C. Cunningham, J. A. Wells, *J. Mol. Biol.* **1993**, *234*, 554.
[11] W. L. DeLano, *Curr. Opin. Struct. Biol.* **2002**, *12*, 14.
[12] A. A. Bogan, K. S. Thorn, *J. Mol. Biol.* **1998**, *280*, 1.
[13] B. Y. Ma, T. Elkayam, H. Wolfson, R. Nussinov, *Proc. Natl. Acad. Sci. USA* **2003**, *100*, 5772.
[14] E. A. Padlan, *Proteins Struct. Funct. Genet.* **1990**, *7*, 112.
[15] K. S. Thorn, A. A. Bogan, *Bioinformatics* **2001**, *17*, 284.
[16] N. Leibowitz, Z. Y. Fligelman, R. Nussinov, H. J. Wolfson, *Proteins Struct. Funct. Genet.* **2001**, *43*, 235; B. Y. Ma, H. J. Wolfson, R. Nussinov, *Curr. Opin. Struct. Biol.* **2001**, *11*, 364.
[17] F. Glaser, T. Pupko, I. Paz, R. E. Bell, D. Bechor-Shental, E. Martz, N. Ben-Tal, *Bioinformatics* **2003**, *19*, 163; R. E. Bell, N. Ben-Tal, *Comp. Funct. Genomics* **2003**, *4*, 420.
[18] P. L. Privalov, S. J. Gill, *Adv. Protein Chem.* **1988**, *41*, 191; J. M. Sturtevant, *Proc. Natl. Acad. Sci. USA* **1977**, *74*, 2236.
[19] G. Weber, *J. Phys. Chem.* **1993**, *97*, 7108; G. I. Makhatadze, P. L. Privalov, *Adv. Protein Chem.* **1995**, *48*, 307.

 © 2005 Wiley-VCH Verlag GmbH & Co. KGaA, Weinheim

[20] G. C. Kresheck, L. B. Vitello, J. E. Erman, *Biochemistry* **1995**, *34*, 8398.
[21] T. N. Bhat, G. A. Bentley, G. Boulot, M. I. Greene, D. Tello, W. Dallacqua, H. Souchon, F. P. Schwarz, R. A. Mariuzza, R. J. Poljak, *Proc. Natl. Acad. Sci. USA* **1994**, *91*, 1089.
[22] D. H. Williams, A. J. Maguire, W. Tsuzuki, M. S. Westwell, *Science* **1998**, *280*, 711.
[23] D. H. Williams, E. Stephens, M. Zhou, *Chem. Commun.* **2003**, 1973.
[24] D. H. Williams, E. Stephens, M. Zhou, *J. Mol. Biol.* **2003**, *329*, 389.
[25] D. H. Williams, C. T. Calderone, D. P. O'Brien, R. Zerella, *Chem. Commun.* **2002**, 1266.
[26] M. R. Eftink, A. C. Anusiem, R. L. Biltonen, *Biochemistry* **1983**, *22*, 3884.
[27] M. F. Perutz, A. J. Wilkinson, M. Paoli, G. G. Dodson, *Annu. Rev. Biophys. Biomol. Struct.* **1998**, *27*, 1.
[28] C. A. Janeway, Jr., P. D. Travers, M. J. Walport, J. D. Capra, *Immunobiology: the Immune System in Health and Disease, 3rd ed.*, Garland, New York, **1997**.
[29] W. Dall'Acqua, P. Carter, *Curr. Opin. Struct. Biol.* **1998**, *8*, 443; T. J. Vaughan, J. K. Osbourn, P. R. Tempest, *Nat. Biotechnol.* **1998**, *16*, 535.
[30] G. Winter, W. J. Harris, *Trends Pharmacol. Sci.* **1993**, *14*, 139.
[31] A. Skerra, A. Pluckthun, *Science* **1988**, *240*, 1038; M. Better, C. P. Chang, R. R. Robinson, A. H. Horwitz, *Science* **1988**, *240*, 1041.
[32] T. A. Waldmann, *Immunol. Today* **1993**, *14*, 264.
[33] T. A. Waldmann, *Science* **1986**, *232*, 727.
[34] T. B. Strom, V. R. Kelley, T. G. Woodworth, J. R. Murphy, *Immunol. Rev.* **1992**, *129*, 131; T. Diamantstein, H. Osawa, *Immunol. Rev.* **1986**, *92*, 5; R. L. Kirkman, L. V. Barrett, G. N. Gaulton, V. E. Kelley, A. Ythier, T. B. Strom, *J. Exp. Med.* **1985**, *162*, 358.
[35] P. T. Jones, P. H. Dear, J. Foote, M. S. Neuberger, G. Winter, *Nature* **1986**, *321*, 522.
[36] R. P. Junghans, T. A. Waldmann, N. F. Landolfi, N. M. Avdalovic, W. P. Schneider, C. Queen, *Cancer Res.* **1990**, *50*, 1495; C. Queen, W. P. Schneider, H. E. Selick, P. W. Payne, N. F. Landolfi, J. F. Duncan, N. M. Avdalovic, M. Levitt, R. P. Junghans, T. A. Waldmann, *Proc. Natl. Acad. Sci. USA* **1989**, *86*, 10029.
[37] H. Lorberboum-Galski, R. W. Kozak, T. A. Waldmann, P. Bailon, D. J. P. Fitzgerald, I. Pastan, *J. Biol. Chem.* **1988**, *263*, 18650.
[38] R. W. Kozak, A. Raubitschek, S. Mirzadeh, M. W. Brechbiel, R. Junghaus, O. A. Gansow, T. A. Waldmann, *Cancer Res.* **1989**, *49*, 2639; R. W. Kozak, R. W. Atcher, O. A. Gansow, A. M. Friedman, J. J. Hines, T. A. Waldmann, *Proc. Natl. Acad. Sci. USA* **1986**, *83*, 474.
[39] P. A. Nygren, M. Uhlen, *Curr. Opin. Struct. Biol.* **1997**, *7*, 463.
[40] R. C. Ladner, *Trends Biotechnol.* **1995**, *13*, 426.
[41] F. Martin, C. Toniatti, A. L. Salvati, S. Venturini, G. Ciliberto, R. Cortese, M. Sollazzo, *EMBO J.* **1994**, *13*, 5303; F. Martin, C. Toniatti, A. L. Salvati, G. Ciliberto, R. Cortese, M. Sollazzo, *J. Mol. Biol.* **1996**, *255*, 86; S. J. McConnell, R. H. Hoess, *J. Mol. Biol.* **1995**, *250*, 460.
[42] J. Ku, P. G. Schultz, *Proc. Natl. Acad. Sci. USA* **1995**, *92*, 6552; K. Nord, E. Gunneriusson, J. Ringdahl, S. Stahl, M. Uhlen, P. A. Nygren, *Nat. Biotechnol.* **1997**, *15*, 772.
[43] Y. Choo, A. Klug, *Curr. Opin. Biotechnol.* **1995**, *6*, 431.
[44] J. W. Chin, A. Schepartz, *Angew. Chem.* **2001**, *113*, 3922; *Angew. Chem. Int. Ed.* **2001**, *40*, 3806; J. W. Chin, R. M. Grotzfeld, M. A. Fabian, A. Schepartz, *Bioorg. Med. Chem. Lett.* **2001**, *11*, 1501; J. W. Chin, A. Schepartz, *J. Am. Chem. Soc.* **2001**, *123*, 2929; N. J. Zondlo, A. Schepartz, *J. Am. Chem. Soc.* **1999**, *121*, 6938; J. K. Montclare, A. Schepartz, *J. Am. Chem. Soc.* **2003**, *125*, 3416.
[45] S. E. Rutledge, H. M. Volkman, A. Schepartz, *J. Am. Chem. Soc.* **2003**, *125*, 14336.
[46] I. Radhakrishnan, G. C. Perez Alvarado, D. Parker, H. J. Dyson, M. R. Montminy, P. E. Wright, *Cell* **1997**, *91*, 741.
[47] I. Glover, I. Haneef, J. Pitts, S. Wood, D. Moss, I. Tickle, T. Blundell, *Biopolymers* **1983**, *22*, 293.
[48] M. A. Fazal, B. C. Roy, S. G. Sun, S. Mallik, K. R. Rodgers, *J. Am. Chem. Soc.* **2001**, *123*, 6283.
[49] B. P. Orner, J. T. Ernst, A. D. Hamilton, *J. Am. Chem. Soc.* **2001**, *123*, 5382.
[50] W. E. Meador, A. R. Means, F. A. Quiocho, *Science* **1992**, *257*, 1251.
[51] E. Drakopoulou, J. Vizzavona, C. Vita, *Lett. Pept. Sci.* **1998**, *5*, 241.
[52] C. Vita, E. Drakopoulou, J. Vizzavona, S. Rochette, L. Martin, A. Menez, C. Roumestand, Y. S. Yang, L. Ylisastigui, A. Benjouad, J. C. Gluckman, *Proc. Natl. Acad. Sci. USA* **1999**, *96*, 13091.
[53] L. Martin, F. Stricher, D. Misse, F. Sironi, M. Pugniere, P. Barthe, R. Prado-Gotor, I. Freulon, X. Magne, C. Roumestand, A. Menez, P. Lusso, F. Veas, C. Vita, *Nat. Biotechnol.* **2003**, *21*, 71.
[54] C. Vita, C. Roumestand, F. Toma, A. Menez, *Proc. Natl. Acad. Sci. USA* **1995**, *92*, 6404.
[55] E. Drakopoulou, S. Zinn-Justin, M. Guenneugues, B. Gilquin, A. Menez, C. Vita, *J. Biol. Chem.* **1996**, *271*, 11979.
[56] F. Bontems, B. Gilquin, C. Roumestand, A. Menez, F. Toma, *Biochemistry* **1992**, *31*, 7756.
[57] C. Vita, F. Bontems, F. Bouet, M. Tauc, P. Poujeol, H. Vatanpour, A. L. Harvey, A. Menez, F. Toma, *Eur. J. Biochem.* **1993**, *217*, 157.
[58] F. Bontems, C. Roumestand, P. Boyot, B. Gilquin, Y. Doljansky, A. Menez, F. Toma, *Eur. J. Biochem.* **1991**, *196*, 19; F. Bontems, C. Roumestand, B. Gilquin, A. Menez, F. Toma, *Science* **1991**, *254*, 1521.
[59] F. Dreyer, *Rev. Physiol. Biochem. Pharmacol.* **1990**, *115*, 93; P. N. Strong, *Pharmacol. Ther.* **1990**, *46*, 137.
[60] R. W. Sweet, A. Truneh, W. A. Hendrickson, *Curr. Opin. Biotechnol.* **1991**, *2*, 622; D. J. Capon, R. H. R. Ward, *Annu. Rev. Immunol.* **1991**, *9*, 649.
[61] P. D. Kwong, R. Wyatt, J. Robinson, R. W. Sweet, J. Sodroski, W. A. Hendrickson, *Nature* **1998**, *393*, 648.
[62] S. E. Osborne, I. Matsumura, A. D. Ellington, *Curr. Opin. Chem. Biol.* **1997**, *1*, 5.
[63] C. Tuerk, L. Gold, *Science* **1990**, *249*, 505; A. D. Ellington, J. W. Szostak, *Nature* **1990**, *346*, 818.
[64] S. E. Osborne, A. D. Ellington, *Chem. Rev.* **1997**, *97*, 349.
[65] L. S. Green, D. Jellinek, C. Bell, L. A. Beebe, B. D. Feistner, S. C. Gill, F. M. Jucker, N. Janjic, *Chem. Biol.* **1995**, *2*, 683.
[66] D. J. Schneider, J. Feigon, Z. Hostomsky, L. Gold, *Biochemistry* **1995**, *34*, 9599.
[67] D. Jellinek, L. S. Green, C. Bell, C. K. Lynott, N. Gill, C. Vargeese, G. Kirschenheuter, D. P. C. McGee, P. Abesinghe, W. A. Pieken, R. Shapiro, D. B. Rifkin, D. Moscatelli, N. Janjic, *Biochemistry* **1995**, *34*, 11363; D. Jellinek, C. K. Lynott, D. B. Rifkin, N. Janjic, *Proc. Natl. Acad. Sci. USA* **1993**, *90*, 11227.
[68] L. C. Bock, L. C. Griffin, J. A. Latham, E. H. Vermaas, J. J. Toole, *Nature* **1992**, *355*, 564; L. C. Griffin, G. F. Tidmarsh, L. C. Bock, J. J. Toole, L. L. K. Leung, *Blood* **1993**, *81*, 3271.
[69] R. R. Breaker, *Curr. Opin. Chem. Biol.* **1997**, *1*, 26; N. J. Jing, M. E. Hogan, *J. Biol. Chem.* **1998**, *273*, 34992; D. J. Patel, *Curr. Opin. Chem. Biol.* **1997**, *1*, 32.
[70] S. H. Gellman, *Acc. Chem. Res.* **1998**, *31*, 173.
[71] K. Gademann, M. Ernst, D. Hoyer, D. Seebach, *Angew. Chem.* **1999**, *111*, 1302; *Angew. Chem. Int. Ed.* **1999**, *38*, 1223.
[72] M. Hagihara, N. J. Anthony, T. J. Stout, J. Clardy, S. L. Schreiber, *J. Am. Chem. Soc.* **1992**, *114*, 6568.

 © 2005 Wiley-VCH Verlag GmbH & Co. KGaA, Weinheim

[73] C. Gennari, B. Salom, D. Potenza, A. Williams, *Angew. Chem.* **1994**, *106*, 2181; *Angew. Chem. Int. Ed. Engl.* **1994**, *33*, 2067; M. Gude, U. Piarulli, D. Potenza, B. Salom, C. Gennari, *Tetrahedron Lett.* **1996**, *37*, 8589.
[74] K. Kirshenbaum, A. E. Barron, R. A. Goldsmith, P. Armand, E. K. Bradley, K. T. V. Truong, K. A. Dill, F. E. Cohen, R. N. Zuckermann, *Proc. Natl. Acad. Sci. USA* **1998**, *95*, 4303; P. Armand, K. Kirshenbaum, R. A. Goldsmith, S. Farr-Jones, A. E. Barron, K. T. V. Truong, K. A. Dill, D. F. Mierke, F. E. Cohen, R. N. Zuckermann, E. K. Bradley, *Proc. Natl. Acad. Sci. USA* **1998**, *95*, 4309.
[75] C. Y. Cho, E. J. Moran, S. R. Cherry, J. C. Stephans, S. P. A. Fodor, C. L. Adams, A. Sundaram, J. W. Jacobs, P. G. Schultz, *Science* **1993**, *261*, 1303.
[76] R. A. Scott, A. G. Mauk, *Cytochrome c: A Multidisciplinary Approach*, University Science Books, Sausalito, **1996**.
[77] W. H. Koppenol, E. Margoliash, *J. Biol. Chem.* **1982**, *257*, 4426.
[78] R. K. Jain, A. D. Hamilton, *Org. Lett.* **2000**, *2*, 1721.
[79] T. Aya, A. D. Hamilton, *Bioorg. Med. Chem. Lett.* **2003**, *13*, 2651.
[80] A. J. Wilson, K. Groves, R. K. Jain, H. S. Park, A. D. Hamilton, *J. Am. Chem. Soc.* **2003**, *125*, 4420; K. Groves, A. J. Wilson, A. D. Hamilton, *J. Am. Chem. Soc.* **2004**, *126*, 12833.
[81] H. Takashima, S. Shinkai, I. Hamachi, *Chem. Commun.* **1999**, 2345.
[82] N. O. Fischer, C. M. McIntosh, J. M. Simard, V. M. Rotello, *Proc. Natl. Acad. Sci. USA* **2002**, *99*, 5018.
[83] N. O. Fischer, A. Verma, C. M. Goodman, J. M. Simard, V. M. Rotello, *J. Am. Chem. Soc.* **2003**, *125*, 13387.
[84] R. Hong, N. O. Fischer, A. Verma, C. M. Goodman, T. Emrick, V. M. Rotello, *J. Am. Chem. Soc.* **2004**, *126*, 739.
[85] G. C. Terstappen, A. Reggiani, *Trends Pharmacol. Sci.* **2001**, *22*, 23.
[86] G. D. Demetri, J. D. Griffin, *Blood* **1991**, *78*, 2791.
[87] J. N. Ihle, B. A. Witthuhn, F. W. Quelle, K. Yamamoto, O. Silvennoinen, *Annu. Rev. Immunol.* **1995**, *13*, 369.
[88] K. Shimoda, J. Feng, H. Murakami, S. Nagata, D. Watling, N. C. Rogers, G. R. Stark, I. M. Kerr, J. N. Ihle, *Blood* **1997**, *90*, 597; S. S. Tian, P. Tapley, C. Sincich, R. B. Stein, J. Rosen, P. Lamb, *Blood* **1996**, *88*, 4435.
[89] C. Schindler, J. E. Darnell, *Annu. Rev. Biochem.* **1995**, *64*, 621.
[90] S. S. Tian, P. Lamb, A. G. King, S. G. Miller, L. Kessler, J. I. Luengo, L. Averill, R. K. Johnson, J. G. Gleason, L. M. Pelus, S. B. Dillon, J. Rosen, *Science* **1998**, *281*, 257.
[91] B. Zhang, G. Salituro, D. Szalkowski, Z. H. Li, Y. Zhang, I. Royo, D. Vilella, M. T. Diez, F. Pelaez, C. Ruby, R. L. Kendall, X. Z. Mao, P. Griffin, J. Calaycay, J. R. Zierath, J. V. Heck, R. G. Smith, D. E. Moller, *Science* **1999**, *284*, 974.
[92] S. R. Hubbard, *EMBO J.* **1997**, *16*, 5572.
[93] Z. H. Guo, D. M. Zhou, P. G. Schultz, *Science* **2000**, *288*, 2042.
[94] S. F. Dowell, L. J. Anderson, H. E. Gary, D. D. Erdman, J. F. Plouffe, T. M. File, B. J. Marston, R. F. Breiman, *J. Infect. Dis.* **1996**, *174*, 456.
[95] P. L. Collins, G. Mottet, *J. Gen. Virol.* **1991**, *72*, 3095.
[96] W. D. Ding, B. Mitsner, G. Krishnamurthy, A. Aulabaugh, C. D. Hess, J. Zaccardi, M. Cutler, B. Feld, A. Gazumyan, Y. Raifeld, A. Nikitenko, S. A. Lang, Y. Gluzman, B. O'Hara, G. A. Ellestad, *J. Med. Chem.* **1998**, *41*, 2671.
[97] A. A. Nikitenko, Y. E. Raifeld, T. Z. Wang, *Bioorg. Med. Chem. Lett.* **2001**, *11*, 1041; W. J. Weiss, T. Murphy, M. E. Lynch, J. Frye, A. Buklan, B. Gray, E. Lenoy, S. Mitelman, J. O'Connell, S. Quartuccio, C. Huntley, *J. Med. Primatol.* **2003**, *32*, 82; V. Razinkov, C. Huntley, G. Ellestad, G. Krishnamurthy, *Antiviral Res.* **2002**, *55*, 189; V. Razinkov, A. Gazumyan, A. Nikitenko, G. Ellestad, G. Krishnamurthy, *Chem. Biol.* **2001**, *8*, 645.
[98] H. Choe, M. Farzan, Y. Sun, N. Sullivan, B. Rollins, P. D. Ponath, L. J. Wu, C. R. Mackay, G. LaRosa, W. Newman, N. Gerard, C. Gerard, J. Sodroski, *Cell* **1996**, *85*, 1135.
[99] S. B. Jiang, Q. Zhao, A. K. Debnath, *Curr. Pharm. Des.* **2002**, *8*, 563.
[100] D. J. Clanton, R. A. Moran, J. B. McMahon, O. S. Weislow, R. W. Buckheit, M. G. Hollingshead, V. Ciminale, B. K. Felber, G. N. Pavlakis, J. P. Bader, *J. Acquired Immune Defic. Syndr.* **1992**, *5*, 771.
[101] P. Mohan, M. F. Wong, S. Verma, P. P. Huang, A. Wickramasinghe, M. Baba, *J. Med. Chem.* **1993**, *36*, 4130.
[102] S. M. Halliday, C. Lackman Smith, J. P. Bader, W. G. Rice, D. J. Clanton, L. H. Zalkow, R. W. Buckheit, *Antiviral Res.* **1996**, *33*, 41.
[103] M. Ono, Y. Wada, Y. M. Wu, R. Nemori, Y. Jinbo, H. Wang, K. M. Lo, N. Yamaguchi, B. Brunkhorst, H. Otomo, J. Wesolowski, J. C. Way, I. Itoh, S. Gillies, L. B. Chen, *Nat. Biotechnol.* **1997**, *15*, 343.
[104] J. L. Zhang, H. Choe, B. J. Dezube, M. Farzan, P. L. Sharma, X. C. Zhou, L. B. Chen, M. Ono, S. Gillies, Y. M. Wu, J. G. Sodroski, C. S. Crumpacker, *Virology* **1998**, *244*, 530.
[105] B. J. Dezube, T. A. Dahl, T. K. Wong, B. Chapman, M. Ono, N. Yamaguchi, S. D. Gillies, L. B. Chen, C. S. Crumpacker, *J. Infect. Dis.* **2000**, *182*, 607.
[106] W. H. Burgess, T. Maciag, *Annu. Rev. Biochem.* **1989**, *58*, 575.
[107] A. E. Eriksson, L. S. Cousens, B. W. Matthews, *Protein Sci.* **1993**, *2*, 1274.
[108] K. Ogura, K. Nagata, H. Hatanaka, H. Habuchi, K. Kimata, S. Tate, M. W. Ravera, M. Jaye, J. Schlessinger, F. Inagaki, *J. Biomol. NMR* **1999**, *13*, 11.
[109] A. Baird, D. Schubert, N. Ling, R. Guillemin, *Proc. Natl. Acad. Sci. USA* **1988**, *85*, 2324; X. Zhu, H. Komiya, A. Chirino, S. Faham, G. M. Fox, T. Arakawa, B. T. Hsu, D. C. Rees, *Science* **1991**, *251*, 90; B. A. Springer, M. W. Pantoliano, F. A. Barbera, P. L. Gunyuzlu, L. D. Thompson, W. F. Herblin, S. A. Rosenfeld, G. W. Book, *J. Biol. Chem.* **1994**, *269*, 26879; L. Y. Li, M. Safran, D. Aviezer, P. Bohlen, A. P. Seddon, A. Yayon, *Biochemistry* **1994**, *33*, 10999; L. D. Thompson, M. W. Pantoliano, B. A. Springer, *Biochemistry* **1994**, *33*, 3831.
[110] S. Takano, S. Gately, M. E. Neville, W. F. Herblin, J. L. Gross, H. Engelhard, M. Perricone, K. Eidsvoog, S. Brem, *Cancer Res.* **1994**, *54*, 2654.
[111] A. R. T. Gagliardi, M. Kassack, A. Kreimeyer, G. Muller, P. Nickel, D. C. Collins, *Cancer Chemother. Pharmacol.* **1998**, *41*, 117.
[112] F. Manetti, V. Cappello, M. Botta, F. Corelli, N. Mongelli, G. Biasoli, A. L. Borgia, M. Ciomei, *Bioorg. Med. Chem.* **1998**, *6*, 947.
[113] M. Zamai, C. Hariharan, D. Pines, M. Safran, A. Yayon, V. R. Caiolfa, R. Cohen-Luria, E. Pines, A. H. Parola, *Biophys. J.* **2002**, *82*, 2652.
[114] D. Aviezer, S. Cotton, M. David, A. Segev, N. Khaselev, N. Galili, Z. Gross, A. Yayon, *Cancer Res.* **2000**, *60*, 2973.
[115] B. J. Brandhuber, T. Boone, W. C. Kenney, D. B. McKay, *Science* **1987**, *238*, 1707; K. Sauve, M. Nachman, C. Spence, P. Bailon, E. Campbell, W. H. Tsien, J. A. Kondas, J. Hakimi, G. Ju, *Proc. Natl. Acad. Sci. USA* **1991**, *88*, 4636.
[116] F. Vincenti, M. Lantz, J. Birnbaum, M. Garovoy, D. Mould, J. Hakimi, K. Nieforth, S. Light, *Transplantation* **1997**, *63*, 33.
[117] J. W. Tilley, L. Chen, D. C. Fry, S. D. Emerson, G. D. Powers, D. Biondi, T. Varnell, R. Trilles, R. Guthrie, F. Mennona, G. Kaplan, R. A. LeMahieu, M. Carson, R. J. Han, C. M. Liu, R. Palermo, G. Ju, *J. Am. Chem. Soc.* **1997**, *119*, 7589.
[118] S. D. Emerson, R. Palermo, C. M. Liu, J. W. Tilley, L. Chen, W. Danho, V. S. Madison, D. N. Greeley, G. Ju, D. C. Fry, *Protein Sci.* **2003**, *12*, 811.

 © 2005 Wiley-VCH Verlag GmbH & Co. KGaA, Weinheim

[119] A. C. Braisted, J. D. Oslob, W. L. Delano, J. Hyde, R. S. McDowell, N. Waal, C. Yu, M. R. Arkin, B. C. Raimundo, *J. Am. Chem. Soc.* **2003**, *125*, 3714.
[120] D. A. Erlanson, A. C. Braisted, D. R. Raphael, M. Randal, R. M. Stroud, E. M. Gordon, J. A. Wells, *Proc. Natl. Acad. Sci. USA* **2000**, *97*, 9367.
[121] J. T. Nguyen, J. A. Wells, *Proc. Natl. Acad. Sci. USA* **2003**, *100*, 7533.
[122] S. B. Krantz, *Blood* **1991**, *77*, 419.
[123] S. A. Qureshi, R. M. Kim, Z. Konteatis, D. E. Biazzo, H. Motamedi, R. Rodrigues, J. A. Boice, J. R. Calaycay, M. A. Bednarek, P. Griffin, Y. D. Gao, K. Chapman, D. F. Mark, *Proc. Natl. Acad. Sci. USA* **1999**, *96*, 12156.
[124] K. Dunlap, J. I. Luebke, T. J. Turner, *Trends Neurosci.* **1995**, *18*, 89; R. Newcomb, A. Palma, *Brain Res.* **1994**, *638*, 95.
[125] D. Walker, D. Bichet, K. P. Campbell, M. De Waard, *J. Biol. Chem.* **1998**, *273*, 2361; G. W. Zamponi, E. Bourinet, D. Nelson, J. Nargeot, T. P. Snutch, *Nature* **1997**, *385*, 442.
[126] J. B. Baell, S. A. Forsyth, R. W. Gable, R. S. Norton, R. J. Mulder, *J. Comput.-Aided Mol. Des.* **2001**, *15*, 1119.
[127] B. S. S. Masters, K. McMillan, E. A. Sheta, J. S. Nishimura, L. J. Roman, P. Martasek, *FASEB J.* **1996**, *10*, 552; O. W. Griffith, D. J. Stuehr, *Annu. Rev. Physiol.* **1995**, *57*, 707.
[128] H. Y. Li, C. S. Raman, C. B. Glaser, E. Blasko, T. A. Young, J. F. Parkinson, M. Whitlow, T. L. Poulos, *J. Biol. Chem.* **1999**, *274*, 21276; T. O. Fischmann, A. Hruza, X. D. Niu, J. D. Fossetta, C. A. Lunn, E. Dolphin, A. J. Prongay, P. Reichert, D. J. Lundell, S. K. Narula, P. C. Weber, *Nat. Struct. Biol.* **1999**, *6*, 233; B. R. Crane, A. S. Arvai, D. K. Ghosh, C. Q. Wu, E. D. Getzoff, D. J. Stuehr, J. A. Tainer, *Science* **1998**, *279*, 2121.
[129] K. J. Baek, B. A. Thiel, S. Lucas, D. J. Stuehr, *J. Biol. Chem.* **1993**, *268*, 21120; P. Klatt, S. Pfeiffer, B. M. List, D. Lehner, O. Glatter, H. P. Bachinger, E. R. Werner, K. Schmidt, B. Mayer, *J. Biol. Chem.* **1996**, *271*, 7336; I. Rodriguez Crespo, N. C. Gerber, P. R. O. de Montellano, *J. Biol. Chem.* **1996**, *271*, 11462.
[130] K. McMillan, M. Adler, D. S. Auld, J. J. Baldwin, E. Blasko, L. J. Browne, D. Chelsky, D. Davey, R. E. Dolle, K. A. Eagen, S. Erickson, R. I. Feldman, C. B. Glaser, C. Mallari, M. M. Morrissey, M. H. J. Ohlmeyer, C. H. Pan, J. F. Parkinson, G. B. Phillips, M. A. Polokoff, N. H. Sigal, R. Vergona, M. Whitlow, T. A. Young, J. J. Devlin, *Proc. Natl. Acad. Sci. USA* **2000**, *97*, 1506; E. Blasko, C. B. Glaser, J. J. Devlin, W. Xia, R. I. Feldman, M. A. Polokoff, G. B. Phillips, M. Whitlow, D. S. Auld, K. McMillan, S. Ghosh, D. J. Stuehr, J. F. Parkinson, *J. Biol. Chem.* **2002**, *277*, 295.
[131] P. H. Carter, P. A. Scherle, J. A. Muckelbauer, M. E. Voss, R. Q. Liu, L. A. Thompson, A. J. Tebben, K. A. Solomon, Y. C. Lo, Z. Li, P. Strzemienski, G. J. Yang, N. Falahatpisheh, M. Xu, Z. R. Wu, N. A. Farrow, K. Ramnarayan, J. Wang, D. Rideout, V. Yalamoori, P. Domaille, D. J. Underwood, J. M. Trzaskos, S. M. Friedman, R. C. Newton, C. P. Decicco, *Proc. Natl. Acad. Sci. USA* **2001**, *98*, 11879.
[132] G. Kollias, E. Douni, G. Kassiotis, D. Kontoyiannis, *Immunol. Rev.* **1999**, *169*, 175.
[133] F. G. Giancotti, E. Ruoslahti, *Science* **1999**, *285*, 1028.
[134] R. Vazeux, P. A. Hoffman, J. K. Tomita, E. S. Dickinson, R. L. Jasman, T. St. John, W. M. Gallatin, *Nature* **1992**, *360*, 485; T. A. Springer, *Nature* **1990**, *346*, 425; C. G. Gahmberg, *Curr. Opin. Cell Biol.* **1997**, *9*, 643.
[135] C. C. Huang, T. A. Springer, *Proc. Natl. Acad. Sci. USA* **1997**, *94*, 3162.
[136] M. Hollstein, K. Rice, M. S. Greenblatt, T. Soussi, R. Fuchs, T. Sorlie, E. Hovig, B. Smithsorensen, R. Montesano, C. C. Harris, *Nucleic Acids Res.* **1994**, *22*, 3551.
[137] W. G. Wang, R. Takimoto, F. Rastinejad, W. S. El-Deiry, *Mol. Cell. Biol.* **2003**, *23*, 2171; R. Takimoto, W. G. Wang, D. T. Dicker, F. Rastinejad, J. Lyssikatos, W. S. El-Deiry, *Cancer Biol. Ther.* **2002**, *1*, 47; B. A. Foster, H. A. Coffey, M. J. Morin, F. Rastinejad, *Science* **1999**, *286*, 2507.
[138] Y. Haupt, R. Maya, A. Kazaz, M. Oren, *Nature* **1997**, *387*, 296; R. Honda, H. Tanaka, H. Yasuda, *FEBS Lett.* **1997**, *420*, 25; M. H. G. Kubbutat, S. N. Jones, K. H. Vousden, *Nature* **1997**, *387*, 299.
[139] J. D. Chen, X. W. Wu, J. Y. Lin, A. J. Levine, *Mol. Cell. Biol.* **1996**, *16*, 2445.
[140] J. D. Oliner, J. A. Pietenpol, S. Thiagalingam, J. Gvuris, K. W. Kinzler, B. Vogelstein, *Nature* **1993**, *362*, 857; C. Cordoncardo, E. Latres, M. Drobnjak, M. R. Oliva, D. Pollack, J. M. Woodruff, V. Marechal, J. D. Chen, M. F. Brennan, A. J. Levine, *Cancer Res.* **1994**, *54*, 794.
[141] L. H. Chen, S. Agrawal, W. Q. Zhou, R. W. Zhang, J. D. Chen, *Proc. Natl. Acad. Sci. USA* **1998**, *95*, 195; L. H. Chen, W. G. Lu, S. H. Agrawal, W. Q. Zhou, R. W. Zhang, J. D. Chen, *Mol. Med.* **1999**, *5*, 21.
[142] J. P. Blaydes, V. Gire, J. M. Rowson, D. Wynford Thomas, *Oncogene* **1997**, *14*, 1859.
[143] C. Garcia-Echeverria, P. Chene, M. J. J. Blommers, P. Furet, *J. Med. Chem.* **2000**, *43*, 3205.
[144] R. Fasan, R. L. A. Dias, K. Moehle, O. Zerbe, J. W. Vrijbloed, D. Obrecht, J. A. Robinson, *Angew. Chem.* **2004**, *116*, 2161; *Angew. Chem. Int. Ed.* **2004**, *43*, 2109.
[145] L. T. Vassilev, B. T. Vu, B. Graves, D. Carvajal, F. Podlaski, Z. Filipovic, N. Kong, U. Kammlott, C. Lukacs, C. Klein, N. Fotouhi, E. A. Liu, *Science* **2004**, *303*, 844.
[146] C. Garcia-Echeverria, P. Chene, M. J. J. Blommers, P. Furet, *J. Med. Chem.* **2000**, *43*, 3205.
[147] H. Yin, G. I. Lee, H. S. Park, G. A. Payne, J. M. Rodriguez, S. M. Sebti, A. D. Hamilton, *Angew. Chem.* **2005**, *117*, 2764; *Angew. Chem. Int. Ed.* **2005**, *44*, 2704.
[148] N. Issaeva, P. Bozko, E. M. , M. Protopopova, L. G. G. C. Verhoef, M. Masucci, A. Pramanik, G. Sellvanova, *Nat. Med.* **2004**, *10*, 1321.
[149] D. R. Lowy, B. M. Willumsen, *Annu. Rev. Biochem.* **1993**, *62*, 851; D. Bar-Sagi, *Mol. Cell. Biol.* **2001**, *21*, 1441.
[150] J. M. Shields, K. Pruitt, A. McFall, A. Shaub, C. J. Der, *Trends Cell Biol.* **2000**, *10*, 147.
[151] O. Muller, E. Gourzoulidou, M. Carpintero, I. M. Karaguni, A. Langerak, C. Herrmann, T. Moroy, L. Klein-Hitpass, H. Waldmann, *Angew. Chem.* **2004**, *116*, 456; *Angew. Chem. Int. Ed.* **2004**, *43*, 450; H. Waldmann, I. M. Karaguni, M. Carpintero, E. Gourzoulidou, C. Herrmann, C. Brockmann, H. Oschkinat, O. Muller, *Angew. Chem.* **2004**, *116*, 460; *Angew. Chem. Int. Ed.* **2004**, *43*, 454.
[152] I. M. Karaguni, P. Herter, P. Debruyne, S. Chtarbova, A. Kasprzynski, U. Herbrand, M. R. Ahmadian, K. H. Glusenkamp, G. Winde, M. Mareel, T. Moroy, O. Muller, *Cancer Res.* **2002**, *62*, 1718; C. Herrmann, C. Block, C. Geisen, K. Haas, C. Weber, G. Winde, T. Moroy, O. Muller, *Oncogene* **1998**, *17*, 1769.
[153] J. Kato-Stankiewicz, I. Hakimi, G. Zhi, J. Zhang, I. Serebriiskii, L. Guo, H. Edamatsu, H. Koide, S. Menon, R. Eckl, S. Sakamuri, Y. C. Lu, Q. Z. Chen, S. Agarwal, W. R. Baumbach, E. A. Golemis, F. Tamanoi, V. Khazak, *Proc. Natl. Acad. Sci. USA* **2002**, *99*, 14398.
[154] I. Serebriiskii, V. Khazak, E. A. Golemis, *J. Biol. Chem.* **1999**, *274*, 17080; I. G. Serebriiskii, O. V. Mitina, J. Chernoff, E. A. Golemis, *Regul. Eff. Small Gtpases F* **2001**, 332, 277.
[155] C. S. Hill, R. Marais, S. John, J. Wynne, S. Dalton, R. Treisman, *Cell* **1993**, *73*, 395.
[156] S. Soga, T. Kozawa, H. Narumi, S. Akinaga, K. Irie, K. Matsumoto, S. V. Sharma, H. Nakano, T. Mizukami, M. Hara, *J. Biol. Chem.* **1998**, *273*, 822.
[157] O. Niederhauser, M. Mangold, R. Schubenel, E. A. Kusznir, D. Schmidt, C. Hertel, *J. Neurosci. Res.* **2000**, *61*, 263.

 © 2005 Wiley-VCH Verlag GmbH & Co. KGaA, Weinheim

[158] M. Barbacid, *J. Neurobiol.* **1994**, *25*, 1386.
[159] P. Kahle, P. A. Barker, E. M. Shooter, C. Hertel, *J. Neurosci. Res.* **1994**, *38*, 599.
[160] J. M. Frade, A. Rodriguez Tebar, Y. A. Barde, *Nature* **1996**, *383*, 166.
[161] D. V. Erbe, S. Wang, Y. Z. Xing, J. F. Tobin, *J. Biol. Chem.* **2002**, *277*, 7363.
[162] E. A. Greenfield, K. A. Nguyen, V. K. Kuchroo, *Crit. Rev. Immunol.* **1998**, *18*, 389; D. J. Lenschow, T. L. Walunas, J. A. Bluestone, *Annu. Rev. Immunol.* **1996**, *14*, 233.
[163] F. A. Harding, J. G. McArthur, J. A. Gross, D. H. Raulet, J. P. Allison, *Nature* **1992**, *356*, 607; T. L. Walunas, D. J. Lenschow, C. Y. Bakker, P. S. Linsley, G. J. Freeman, J. M. Green, C. B. Thompson, J. A. Bluestone, *Immunity* **1994**, *1*, 405; P. Waterhouse, J. M. Penninger, E. Timms, A. Wakeham, A. Shahinian, K. P. Lee, C. B. Thompson, H. Griesser, T. W. Mak, *Science* **1995**, *270*, 985.
[164] C. C. Stamper, Y. Zhang, J. F. Tobin, D. V. Erbe, S. Ikemizu, S. J. Davis, M. L. Stahl, J. Seehra, W. S. Somers, L. Mosyak, *Nature* **2001**, *410*, 608.
[165] N. J. Green, J. Xiang, J. Chen, L. R. Chen, A. M. Davies, D. Erbe, S. Tam, J. F. Tobin, *Bioorg. Med. Chem.* **2003**, *11*, 2991.
[166] S. B. Jiang, A. K. Debnath, *Biochem. Biophys. Res. Commun.* **2000**, *270*, 153; M. Ferrer, T. M. Kapoor, T. Strassmaier, W. Weissenhorn, J. J. Skehel, D. Oprian, S. L. Schreiber, D. C. Wiley, S. C. Harrison, *Nat. Struct. Biol.* **1999**, *6*, 953.
[167] J. T. Ernst, O. Kutzki, A. K. Debnath, S. Jiang, H. Lu, A. D. Hamilton, *Angew. Chem.* **2001**, *113*, 288; *Angew. Chem. Int. Ed.* **2001**, *40*, 278.
[168] C. Cianci, D. R. Langley, D. D. Dischino, Y. Sun, K.-L. Yu, A. Stanley, J. Roach, Z. Li, R. Dalterio, R. Colonno, N. A. Meanwell, M. Krystal, *Proc. Natl. Acad. Sci. USA* **2004**, *101*, 15046.
[169] D. Gorse, R. Lahana, *Curr. Opin. Chem. Biol.* **2000**, *4*, 287.
[170] J. H. Van Drie, M. S. Lajiness, *Drug Discovery Today* **1998**, *3*, 274.
[171] E. K. Kick, D. C. Roe, A. G. Skillman, G. C. Liu, T. J. A. Ewing, Y. X. Sun, I. D. Kuntz, J. A. Ellman, *Chem. Biol.* **1997**, *4*, 297.
[172] C. S. Ring, E. Sun, J. H. McKerrow, G. K. Lee, P. J. Rosenthal, I. D. Kuntz, F. E. Cohen, *Proc. Natl. Acad. Sci. USA* **1993**, *90*, 3583; I. D. Kuntz, *Science* **1992**, *257*, 1078.
[173] S. Li, J. M. Gao, T. Satoh, T. M. Friedman, A. E. Edling, U. Koch, S. Choksi, X. B. Han, R. Korngold, Z. W. Huang, *Proc. Natl. Acad. Sci. USA* **1997**, *94*, 73.
[174] Z. W. Huang, S. N. Li, R. Korngold, *Biopolymers* **1997**, *43*, 367.
[175] J. C. Reed, *Nature* **1997**, *387*, 773; J. M. Adams, S. Cory, *Science* **1998**, *281*, 1322.
[176] E. R. Fearon, B. Vogelstein, *Cell* **1990**, *61*, 759; T. G. Graeber, C. Osmanian, T. Jacks, D. E. Housman, C. J. Koch, S. W. Lowe, A. J. Giaccia, *Nature* **1996**, *379*, 88.
[177] A. Strasser, D. C. S. Huang, D. L. Vaux, *Biochim. Biophys. Acta* **1997**, *1333*, F151.
[178] J. M. Adams, S. Cory, *Trends Biochem. Sci.* **2001**, *26*, 61.
[179] J. B. Baell, D. C. S. Huang, *Biochem. Pharmacol.* **2002**, *64*, 851.
[180] J. L. Wang, D. X. Liu, Z. J. Zhang, S. M. Shan, X. B. Han, S. M. Srinivasula, C. M. Croce, E. S. Alnemri, Z. W. Huang, *Proc. Natl. Acad. Sci. USA* **2000**, *97*, 7124.
[181] I. J. Enyedy, Y. Ling, K. Nacro, Y. Tomita, X. H. Wu, Y. Y. Cao, R. B. Guo, B. H. Li, X. F. Zhu, Y. Huang, Y. Q. Long, P. P. Roller, D. J. Yang, S. M. Wang, *J. Med. Chem.* **2001**, *44*, 4313.
[182] A. A. Lugovskoy, A. I. Degterev, A. F. Fahmy, P. Zhou, J. D. Gross, J. Y. Yuan, G. Wagner, *J. Am. Chem. Soc.* **2002**, *124*, 1234.
[183] A. Degterev, A. Lugovskoy, M. Cardone, B. Mulley, G. Wagner, T. Mitchison, J. Y. Yuan, *Nat. Cell Biol.* **2001**, *3*, 173.
[184] S. P. Tzung, K. M. Kim, G. Basanez, C. D. Giedt, J. Simon, J. Zimmerberg, K. Y. J. Zhang, D. M. Hockenbery, *Nat. Cell Biol.* **2001**, *3*, 183.
[185] Z. W. Huang, S. Li, R. Korngold, *Med. Chem. Res.* **1997**, *7*, 137; A. F. Williams, A. N. Barclay, *Annu. Rev. Immunol.* **1988**, *6*, 381; L. M. Amzel, R. J. Poljak, *Annu. Rev. Biochem.* **1979**, *48*, 961.
[186] M. C. Miceli, J. R. Parnes, *Adv. Immunol.* **1993**, *53*, 59.
[187] R. Konig, L. Y. Huang, R. N. Germain, *Nature* **1992**, *356*, 796.
[188] A. K. Debnath, L. Radigan, S. B. Jiang, *J. Med. Chem.* **1999**, *42*, 3203.
[189] H. F. Gunthard, J. K. Wong, C. C. Ignacio, J. C. Guatelli, N. L. Riggs, D. V. Havlir, D. D. Richman, *J. Virol.* **1998**, *72*, 2422; J. K. Wong, H. F. Gunthard, D. V. Havlir, Z. Q. Zhang, A. T. Haase, C. C. Ignacio, S. Kwok, E. Emini, D. D. Richman, *Proc. Natl. Acad. Sci. USA* **1997**, *94*, 12574; C. C. J. Carpenter, M. A. Fischl, S. M. Hammer, M. S. Hirsch, D. M. Jacobsen, D. A. Katzenstein, J. S. G. Montaner, D. D. Richman, M. S. Saag, R. T. Schooley, M. A. Thompson, S. Vella, P. G. Yeni, P. A. Volberding, *JAMA-J. Med. Assoc.* **1998**, *280*, 78.
[190] D. A. Gschwend, W. Sirawaraporn, D. V. Santi, I. D. Kuntz, *Proteins Struct. Funct. Genet.* **1997**, *29*, 59; C. S. Ring, E. Sun, J. H. McKerrow, G. K. Lee, P. J. Rosenthal, I. D. Kuntz, F. E. Cohen, *Proc. Natl. Acad. Sci. USA* **1993**, *90*, 3583.
[191] P. J. Hajduk, M. Bures, J. Praestgaard, S. W. Fesik, *J. Med. Chem.* **2000**, *43*, 3443.
[192] H. U. Saragovi, D. Fitzpatrick, A. Raktabutr, H. Nakanishi, M. Kahn, M. I. Greene, *Science* **1991**, *253*, 792.
[193] W. V. Williams, T. Kieberemmons, J. Vonfeldt, M. I. Greene, D. B. Weiner, *J. Biol. Chem.* **1991**, *266*, 5182.
[194] V. Bohmer, *Angew. Chem.* **1995**, *107*, 785; *Angew. Chem. Int. Ed. Engl.* **1995**, *34*, 713.
[195] S. M. Sebti, A. D. Hamilton, *Oncogene* **2000**, *19*, 6566.
[196] C. H. Heldin, A. Ostman, L. Ronnstrand, *Biochim. Biophys. Acta* **1998**, *1378*, F79.
[197] A. Kazlauskas, J. A. Cooper, *Cell* **1989**, *58*, 1121; E. J. Lowenstein, R. J. Daly, A. G. Batzer, W. Li, B. Margolis, R. Lammers, A. Ullrich, E. Y. Skolnik, D. Barsagi, J. Schlessinger, *Cell* **1992**, *70*, 431.
[198] K. Forsberg, I. Valyinagy, C. H. Heldin, M. Herlyn, B. Westermark, *Proc. Natl. Acad. Sci. USA* **1993**, *90*, 393; E. J. Battegay, J. Rupp, L. Iruelaarispe, E. H. Sage, M. Pech, *J. Cell Biol.* **1994**, *125*, 917; R. Kumar, J. Yoneda, C. D. Bucana, I. J. Fidler, *Int. J. Oncol.* **1998**, *12*, 749; R. Thommen, R. Humar, G. Misevic, M. S. Pepper, A. W. A. Hahn, M. John, E. J. Battegay, *J. Cell. Biochem.* **1997**, *64*, 403.
[199] M. A. Blaskovich, Q. Lin, F. L. Delarue, J. Sun, H. S. Park, D. Coppola, A. D. Hamilton, S. M. Sebti, *Nat. Biotechnol.* **2000**, *18*, 1065.
[200] Y. Wei, G. L. McLendon, A. D. Hamilton, M. A. Case, C. B. Purring, Q. Lin, H. S. Park, C. S. Lee, T. N. Yu, *Chem. Commun.* **2001**, 1580.
[201] C. Purring, H. Zou, X. D. Wang, G. McLendon, *J. Am. Chem. Soc.* **1999**, *121*, 7435; P. Li, D. Nijhawan, I. Budihardjo, S. M. Srinivasula, M. Ahmad, E. S. Alnemri, X. D. Wang, *Cell* **1997**, *91*, 479; H. Zou, W. J. Henzel, X. S. Liu, A. Lutschg, X. D. Wang, *Cell* **1997**, *90*, 405.
[202] D. K. Leung, Z. W. Yang, R. Breslow, *Proc. Natl. Acad. Sci. USA* **2000**, *97*, 5050.
[203] R. Breslow, Z. W. Yang, R. Ching, G. Trojandt, F. Odobel, *J. Am. Chem. Soc.* **1998**, *120*, 3536; M. Maletic, H. Wennemers, D. Q. McDonald, R. Breslow, W. C. Still, *Angew. Chem.* **1996**, *108*, 1594; *Angew. Chem. Int. Ed. Engl.* **1996**, *35*, 1490.
[204] Y. Hamuro, S. J. Geib, A. D. Hamilton, *J. Am. Chem. Soc.* **1996**, *118*, 7529; J. S. Nowick, S. Mahrus, E. M. Smith, J. W. Ziller, *J. Am. Chem. Soc.* **1996**, *118*, 1066; R. S. Lokey, B. L. Iverson,

 © 2005 Wiley-VCH Verlag GmbH & Co. KGaA, Weinheim

Nature **1995**, *375*, 303; T. J. Murray, S. C. Zimmerman, *J. Am. Chem. Soc.* **1992**, *114*, 4010.
[205] D. Horwell, M. Pritchard, J. Raphy, G. Ratcliffe, *Immunopharmacology* **1996**, *33*, 68; D. C. Horwell, W. Howson, G. S. Ratcliffe, H. M. G. Willems, *Bioorg. Med. Chem.* **1996**, *4*, 33.
[206] O. Kutzki, H. S. Park, J. T. Ernst, B. P. Orner, H. Yin, A. D. Hamilton, *J. Am. Chem. Soc.* **2002**, *124*, 11838.
[207] M. Sattler, H. Liang, D. Nettesheim, R. P. Meadows, J. E. Harlan, M. Eberstadt, H. S. Yoon, S. B. Shuker, B. S. Chang, A. J. Minn, C. B. Thompson, S. W. Fesik, *Science* **1997**, *275*, 983.
[208] J. T. Ernst, J. Becerril, H. S. Park, H. Yin, A. D. Hamilton, *Angew. Chem.* **2003**, *115*, 553; *Angew. Chem. Int. Ed.* **2003**, *42*, 535.
[209] H. Yin, A. D. Hamilton, *Bioorg. Med. Chem. Lett.* **2004**, *14*, 1375; H. Yin, G. I. Lee, K. A. Sedey, J. M. Rodriguez, H. G. Wang, S. M. Sebti, A. D. Hamilton, *J. Am. Chem. Soc.* **2005**, *127*, 5463.
[210] R. Hirschmann, K. C. Nicolaou, S. Pietranico, J. Salvino, E. M. Leahy, P. A. Sprengeler, G. Furst, A. B. Smith, C. D. Strader, M. A. Cascieri, M. R. Candelore, C. Donaldson, W. Vale, L. Maechler, *J. Am. Chem. Soc.* **1992**, *114*, 9217.
[211] R. Hirschmann, K. C. Nicolaou, S. Pietranico, E. M. Leahy, J. Salvino, B. Arison, M. A. Cichy, P. G. Spoors, W. C. Shakespeare, P. A. Sprengeler, P. Hamley, A. B. Smith, T. Reisine, K. Raynor, L. Maechler, C. Donaldson, W. Vale, R. M. Freidinger, M. R. Cascieri, C. D. Strader, *J. Am. Chem. Soc.* **1993**, *115*, 12550; J. Liu, D. J. Underwood, M. A. Cascieri, S. P. Rohrer, L. D. Cantin, G. Chicchi, A. B. Smith, R. Hirschmann, *J. Med. Chem.* **2000**, *43*, 3827.
[212] R. Hirschmann, J. Hynes, M. A. Cichy-Knight, R. D. van Rijn, P. A. Sprengeler, P. G. Spoors, W. C. Shakespeare, S. Pietranico-Cole, J. Barbosa, J. Liu, W. Q. Yao, S. Rohrer, A. B. Smith, *J. Med. Chem.* **1998**, *41*, 1382.
[213] A. B. Smith, R. Hirschmann, A. Pasternak, R. Akaishi, M. C. Guzman, D. R. Jones, T. P. Keenan, P. A. Sprengeler, P. L. Darke, E. A. Emini, M. K. Holloway, W. A. Schleif, *J. Med. Chem.* **1994**, *37*, 215.
[214] A. B. Smith, R. Hirschmann, A. Pasternak, W. Q. Yao, P. A. Sprengeler, M. K. Holloway, L. C. Kuo, Z. G. Chen, P. L. Darke, W. A. Schleif, *J. Med. Chem.* **1997**, *40*, 2440; P. V. Murphy, J. L. O'Brien, L. J. Gorey-Feret, A. B. Smith, *Tetrahedron* **2003**, *59*, 2259; P. V. Murphy, J. L. O'Brien, L. J. Gorey-Feret, A. B. Smith, *Bioorg. Med. Chem. Lett.* **2002**, *12*, 1763.
[215] A. B. Smith, L. D. Cantin, A. Pasternak, L. Guise-Zawacki, W. Q. Yao, A. K. Charnley, J. Barbosa, P. A. Sprengeler, R. Hirschmann, S. Munshi, D. B. Olsen, W. A. Schleif, L. C. Kuo, *J. Med. Chem.* **2003**, *46*, 1831.
[216] A. B. Smith, T. Nittoli, P. A. Sprengeler, J. J. W. Duan, R. Q. Liu, R. F. Hirschmann, *Org. Lett.* **2000**, *2*, 3809.
[217] A. B. Smith, A. B. Benowitz, P. A. Sprengeler, J. Barbosa, M. C. Guzman, R. Hirschmann, E. J. Schweiger, D. R. Bolin, Z. Nagy, R. M. Campbell, D. C. Cox, G. L. Olson, *J. Am. Chem. Soc.* **1999**, *121*, 9286.
[218] A. B. Smith, Y. S. Cho, G. R. Pettit, R. Hirschmann, *Tetrahedron* **2003**, *59*, 6991.
[219] A. B. Smith, W. Y. Wang, P. A. Sprengeler, R. Hirschmann, *J. Am. Chem. Soc.* **2000**, *122*, 11037; A. B. Smith, H. Liu, R. Hirschmann, *Org. Lett.* **2000**, *2*, 2037; A. B. Smith, T. P. Keenan, R. C. Holcomb, P. A. Sprengeler, M. C. Guzman, J. L. Wood, P. J. Carroll, R. Hirschmann, *J. Am. Chem. Soc.* **1992**, *114*, 10672; A. B. Smith, M. C. Guzman, P. A. Sprengeler, T. P. Keenan, R. C. Holcomb, J. L. Wood, P. J. Carroll, R. Hirschmann, *J. Am. Chem. Soc.* **1994**, *116*, 9947.
[220] T. Bartfai, M. M. Behrens, S. Gaidarova, J. Pemberton, A. Shivanyuk, J. Rebek, *Proc. Natl. Acad. Sci. USA* **2003**, *100*, 7971.
[221] N. J. Gay, F. J. Keith, *Nature* **1991**, *351*, 355; D. S. Schneider, K. L. Hudson, T. Y. Lin, K. V. Anderson, *Genes Dev.* **1991**, *5*, 797.
[222] J. A. Hoffmann, F. C. Kafatos, C. A. Janeway, R. A. B. Ezekowitz, *Science* **1999**, *284*, 1313; E. B. Kopp, R. Medzhitov, *Curr. Opin. Immunol.* **1999**, *11*, 13; K. V. Anderson, *Curr. Opin. Immunol.* **2000**, *12*, 13.
[223] D. M. Underhill, A. Ozinsky, A. M. Hajjar, A. Stevens, C. B. Wilson, M. Bassetti, A. Aderem, *Nature* **1999**, *401*, 811; M. Muzio, J. Ni, P. Feng, V. M. Dixit, *Science* **1997**, *278*, 1612; H. Wesche, W. J. Henzel, W. Shillinglaw, S. Li, Z. D. Cao, *Immunity* **1997**, *7*, 837; K. Burns, F. Martinon, C. Esslinger, H. Pahl, P. Schneider, J. L. Bodmer, F. Di Marco, L. French, J. Tschopp, *J. Biol. Chem.* **1998**, *273*, 12203.
[224] R. Medzhitov, P. Preston-Hurlburt, E. Kopp, A. Stadlen, C. Q. Chen, S. Ghosh, C. A. Janeway, *Mol. Cell* **1998**, *2*, 253.
[225] K. A. Lord, B. Hoffmanliebermann, D. A. Liebermann, *Oncogene* **1990**, *5*, 1095.
[226] Y. W. Xu, X. Tao, B. H. Shen, T. Horng, R. Medzhitov, J. L. Manley, L. Tong, *Nature* **2000**, *408*, 111.
[227] M. L. West, D. P. Fairlie, *Trends Pharmacol. Sci.* **1995**, *16*, 67; D. Leung, G. Abbenante, D. P. Fairlie, *J. Med. Chem.* **2000**, *43*, 305.
[228] W. A. Loughlin, J. D. Tyndall, M. P. Glenn, D. P. Fairlie, *Chem. Rev.* **2004**, *104*, 6085.
[229] J. W. Corbett, N. R. Graciani, S. A. Mousa, W. F. DeGrado, *Bioorg. Med. Chem. Lett.* **1997**, *7*, 1371.
[230] K. C. Nicolaou, J. I. Trujillo, K. Chibale, *Tetrahedron* **1997**, *53*, 8751.
[231] R. W. McMurray, *Semin. Arthritis Rheum.* **1996**, *26*, 215; N. Oppenheimer Marks, P. E. Lipsky, *Clin. Immunol. Immunopathol.* **1996**, *79*, 203.
[232] J. M. Casasnovas, T. Stehle, J. H. Liu, J. H. Wang, T. A. Springer, *Proc. Natl. Acad. Sci. USA* **1998**, *95*, 4134.
[233] T. R. Gadek, D. J. Burdick, R. S. McDowell, M. S. Stanley, J. C. Marsters, K. J. Paris, D. A. Oare, M. E. Reynolds, C. Ladner, K. A. Zioncheck, W. P. Lee, P. Gribling, M. S. Dennis, N. J. Skelton, D. B. Tumas, K. R. Clark, S. M. Keating, M. H. Beresini, J. W. Tilley, L. G. Presta, S. C. Bodary, *Science* **2002**, *295*, 1086.
[234] J. Takagi, T. A. Springer, *Immunol. Rev.* **2002**, *186*, 141.
[235] K. Welzenbach, U. Hommel, G. Weitz-Schmidt, *J. Biol. Chem.* **2002**, *277*, 10590.
[236] Z. Liu, A. Mukherjee, J. Lutkenhaus, *Mol. Microbiol.* **1999**, *31*, 1853; C. A. Hale, P. A. J. de Boer, *J. Bacteriol.* **1999**, *181*, 167; C. A. Hale, P. A. J. de Boer, *Cell* **1997**, *88*, 175.
[237] L. Mosyak, Y. Zhang, E. Glasfeld, S. Haney, M. Stahl, J. Seehra, W. S. Somers, *EMBO J.* **2000**, *19*, 3179; F. J. Moy, E. Glasfeld, L. Mosyak, R. Powers, *Biochemistry* **2000**, *39*, 9146; F. J. Moy, E. Glasfeld, R. Powers, *J. Biomol. NMR* **2000**, *17*, 275.
[238] A. G. Sutherland, J. Alvarez, W. D. Ding, K. W. Foreman, C. H. Kenny, P. Labthavikul, L. Mosyak, P. J. Petersen, T. S. Rush, A. Ruzin, D. H. H. Tsao, K. L. Wheless, *Org. Biomol. Chem.* **2003**, *1*, 4138.
[239] C. H. Kenny, W. D. Ding, K. Kelleher, S. Benard, E. G. Dushin, A. G. Sutherland, L. Mosyak, R. Kriz, G. Ellestad, *Anal. Biochem.* **2003**, *323*, 224.
[240] K. B. Lee, S. J. Park, C. A. Mirkin, J. C. Smith, M. Mrksich, *Science* **2002**, *295*, 1702; C. A. Lepre, J. M. Moore, J. W. Peng, *Chem. Rev.* **2004**, *104*, 3641.
[241] A. R. Horswill, S. N. Savinov, S. J. Benkovic, *Proc. Natl. Acad. Sci. USA* **2004**, *101*, 15591.
[242] N. N. Danial, C. F. Gramm, L. Scorrano, C. Y. Zhang, S. Krauss, A. M. Ranger, S. R. Datta, M. E. Greenberg, L. J. Licklider, B. B. Lowell, S. P. Gygi, S. J. Korsmeyer, *Nature* **2003**, *424*, 952.
[243] A. P. Li, *Drug Discovery Today* **2001**, *6*, 357.
[244] C. A. Lipinski, F. Lombardo, B. W. Dominy, P. J. Feeney, *Adv. Drug Delivery Rev.* **1997**, *23*, 3.

 © 2005 Wiley-VCH Verlag GmbH & Co. KGaA, Weinheim

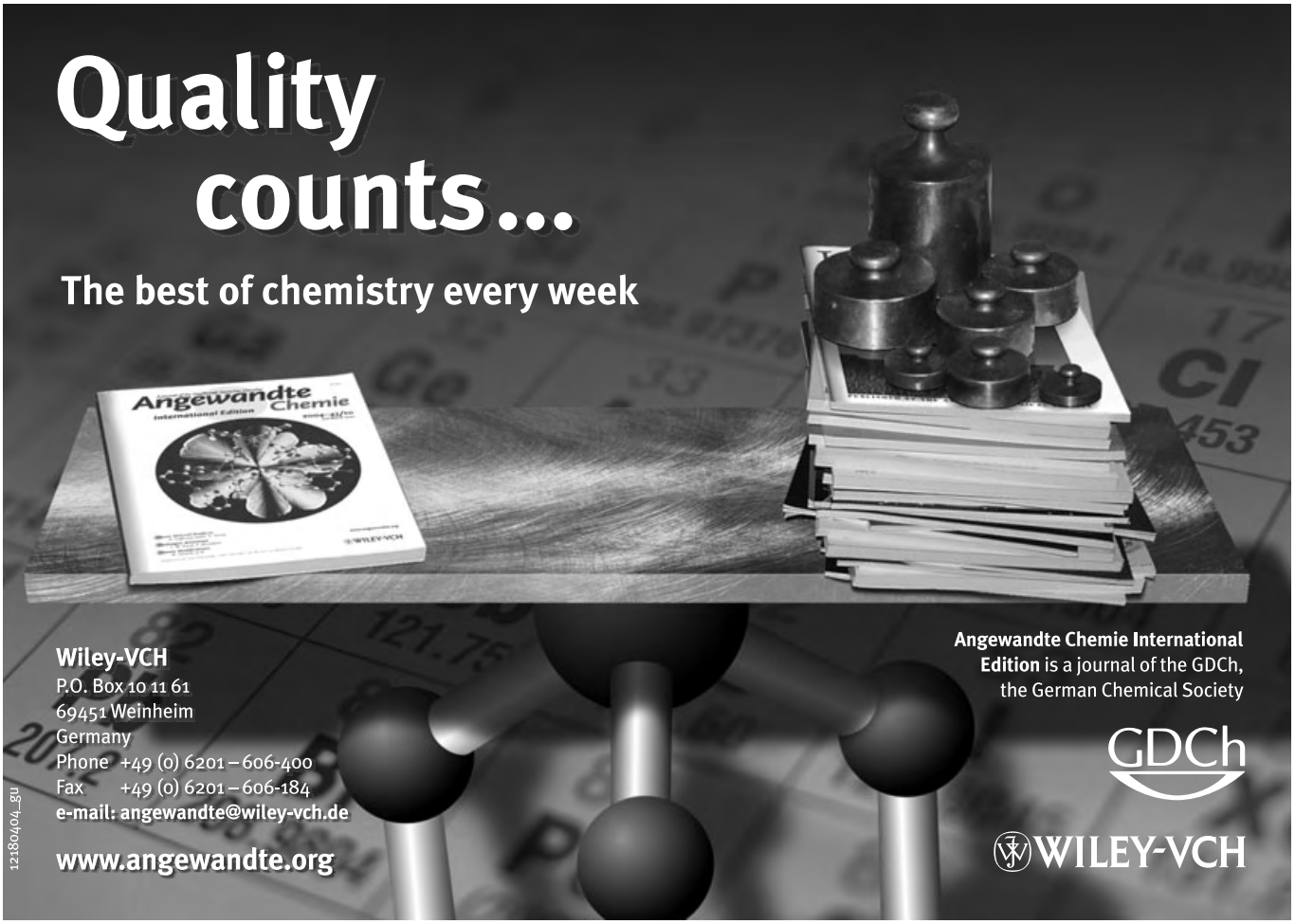
[245] J. Kallen, K. Welzenbach, P. Ramage, D. Geyl, R. Kriwacki, G. Legge, S. Cottens, G. Weitz-Schmidt, U. Hommel, *J. Mol. Biol.* **1999**, *292*, 1.

[246] K. Last-Barney, W. Davidson, M. Cardozo, L. L. Frye, C. A. Grygon, J. L. Hopkins, D. D. Jeanfavre, S. Pav, C. G. Qian, J. M. Stevenson, L. Tong, R. Zindell, T. A. Kelly, *J. Am. Chem. Soc.* **2001**, *123*, 5643; T. A. Kelly, D. D. Jeanfavre, D. W. McNeil, J. R. Woska, P. L. Reilly, E. A. Mainolfi, K. M. Kishimoto, G. H. Nabozny, R. Zinter, B. J. Bormann, R. Rothlein, *J. Immunol.* **1999**, *163*, 5173.

[247] Z. H. Pei, Z. L. Xin, G. Liu, Y. H. Li, E. B. Reilly, N. L. Lubbers, J. R. Huth, J. T. Link, T. W. von Geldern, B. F. Cox, S. Leitza, Y. Gao, K. C. Marsh, P. DeVries, G. F. Okasinski, *J. Med. Chem.* **2001**, *44*, 2913; G. Liu, J. R. Huth, E. T. Olejniczak, R. Mendoza, P. DeVries, S. Leitza, E. B. Reilly, G. F. Okasinski, S. W. Fesik, T. W. von Geldern, *J. Med. Chem.* **2001**, *44*, 1202; G. Liu, J. T. Link, Z. H. Pei, E. B. Reilly, S. Leitza, B. Nguyen, K. C. Marsh, G. F. Okasinski, T. W. von Geldern, M. Ormes, K. Fowler, M. Gallatin, *J. Med. Chem.* **2000**, *43*, 4025; M. Winn, E. B. Reilly, G. Liu, J. R. Huth, H. S. Jae, J. Freeman, Z. H. Pei, Z. L. Xin, J. Lynch, J. Kester, T. W. von Geldern, S. Leitza, P. DeVries, R. Dickinson, D. Mussatto, G. F. Okasinski, *J. Med. Chem.* **2001**, *44*, 4393.

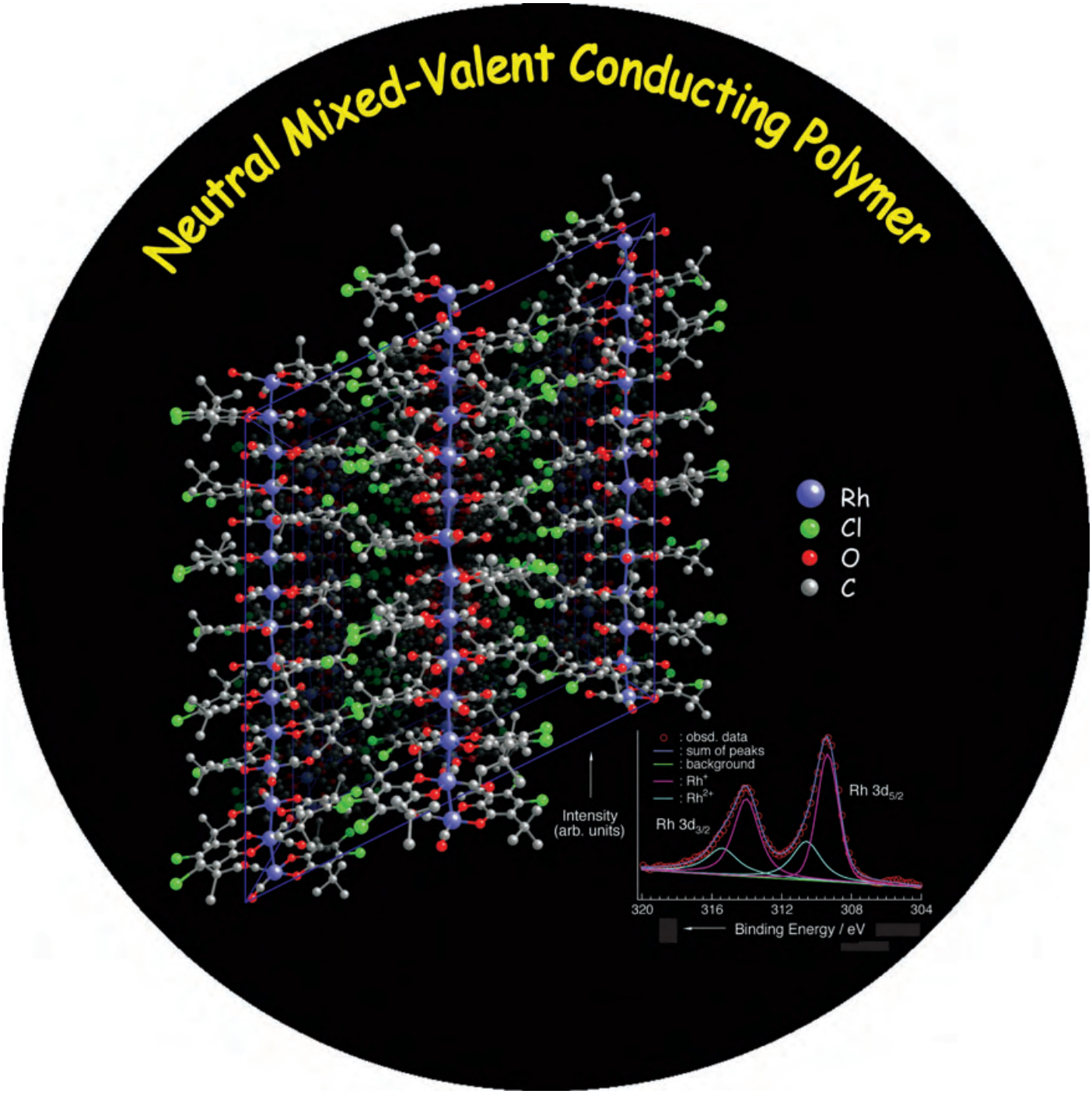
[248] P. C. Brooks, S. Stromblad, L. C. Sanders, T. L. von Schalscha, R. T. Aimes, W. G. Stetler Stevenson, J. P. Quigley, D. A. Cheresh, *Cell* **1996**, *85*, 683.

[249] R. Dallafavera, M. Bregni, J. Erikson, D. Patterson, R. C. Gallo, C. M. Croce, *Proc. Natl. Acad. Sci. USA* **1982**, *79*, 7824; A. Gerbitz, J. Mautner, C. Geltinger, K. Hortnagel, B. Christoph, H. Asenbauer, G. Klobeck, A. Polack, G. W. Bornkamm, *Oncogene* **1999**, *18*, 1745.



 © 2005 Wiley-VCH Verlag GmbH & Co. KGaA, Weinheim

Communications



The spectroscopic and X-ray crystallographic properties of a highly conductive neutral mixed-valence rhodium(I,II) semiquinonato/catecholato complex in which the mixed-valence states are formed by electron transfer between rhodium d and semiquinonate π^* orbitals are reported by M. Mitsumi, K. Toriumi et al. in the Communication on the following pages.

 © 2005 Wiley-VCH Verlag GmbH & Co. KGaA, Weinheim DOI: 10.1002/anie.200501189

Conducting Materials

A Neutral Mixed-Valent Conducting Polymer Formed by Electron Transfer between Metal d and Ligand π Orbitals**

Minoru Mitsumi, Hidekazu Goto, Shunsuke Umebayashi, Yoshiki Ozawa, Mototada Kobayashi, Toshihiko Yokoyama, Hisaaki Tanaka, Shin-ichi Kuroda, and Koshiro Toriumi**

Recently, conducting systems that consist of a single-component molecule have attracted much attention.[1–3] These studies should develop basic technology for molecular electronic devices. Kobayashi and co-workers reported that a crystal of $[Ni(tmdt)_2]_\infty$ (tmdt = trimethylenetetrathiafulvalenedithiolate) is a single-component molecular metal with a 3D π band, which was designed on the basis of a very small HOMO–LUMO gap and crossing bands formed by the HOMO and LUMO.[1] On the other hand, many directly bonded infinite M–M chain compounds have been prepared, but a single-component molecular conductor with a metal-containing backbone has yet to be reported.[4,5]

When building such a material by the bottom-up method, frontier-orbital engineering is very important for obtaining the desired physical properties and/or functionalities. Redox-active dioxolene derivatives can create redox isomers of benzoquinone (BQ), semiquinonate ($SQ^{\bullet-}$), and catecholate (cat^{2-}) by two sequential one-electron transfers. Several transition-metal complexes that contain these dioxolene ligands have very close energy levels between the frontier orbitals of the metal d and dioxolene ligand π orbitals, and intramolecular electron transfer occurs between the metal and the ligand in a thermal equilibrium known as valence tautomerism.[6] On the other hand, the rhodium(I) semiquinonato complex $[Rh(3,6\text{-dbsq})(CO)_2]_\infty$ (3,6-dbsq = 3,6-di-*tert*-butyl-1,2-benzosemiquinonate) was reported to form a linear-chain structure with a direct Rh–Rh interaction.[7] Although this compound does not show valence tautomerism, the energy levels of the electron-rich rhodium(I) core and the electron-deficient semiquinonato ligand are considered to be relatively close. If the energy level of the ligand $\pi^*(SQ^{\bullet-})$ orbital can be adjusted to be close to or the same as the energy level of the 1D d band, which is comprised of metal d_{z^2} orbitals, a rhodium(I,II) semiquinonato/catecholato mixed-valent state would be achieved by intramolecular electron transfer between metal and ligand (Figure 1). This approach

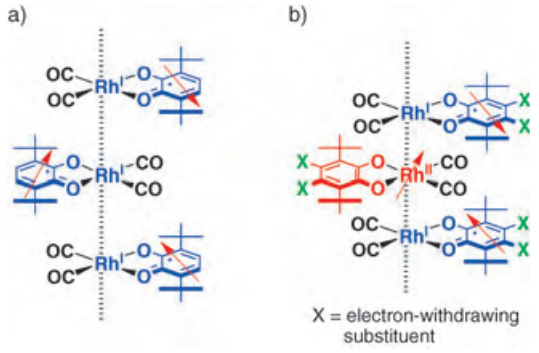


Figure 1. a) Stacking of $\{Rh^+\text{-}SQ^{\bullet-}\}$ units in $[Rh(3,6\text{-dbsq})(CO)_2]_\infty$. b) Mixed stack of $\{Rh^+\text{-}SQ^{\bullet-}\}$ and $\{Rh^{2+}\text{-}cat^{2-}\}$ units.

may be a fundamental methodology for the development of novel neutral mixed-valent conducting polymers with metal-containing backbones based on metal complexes. Recently, we successfully controlled the energy level of the frontier orbitals in the metal complex by chemically modifying the ligand. Electron transfer was realized between metals and ligands, and a mixed-valent state of the directly bonded infinite M–M chain was ascertained.

Herein, we report the synthesis, crystal structure, and electronic properties of the novel linear-chain mixed-valent rhodium(I,II) semiquinonato/catecholato complex $[Rh(3,6\text{-dbdiox-4,5-}Cl_2)(CO)_2]_\infty$ (**1**), in which 3,6-dbdiox-4,5-Cl_2 indicates the 3,6-di-*tert*-butyl-4,5-dichloro-1,2-benzosemiquinonate (3,6-dbsq-4,5-$Cl_2^{\bullet-}$) or 3,6-di-*tert*-butyl-4,5-dichlorocatecholate (3,6-dbcat-4,5-Cl_2^{2-}) state. This compound is the first example of a neutral mixed-valent conducting polymer with a metal-containing backbone in which the mixed-valent state is formed by electron transfer between metal d and ligand π* orbitals.

Black needle crystals of **1** were obtained by a redox reaction of $[Rh_4(CO)_{12}]$ with 3,6-di-*tert*-butyl-4,5-dichloro-1,2-benzoquinone[8] in *n*-pentane.[9]

The X-ray photoelectron spectrum (XPS) of **1** exhibits broad Rh $3d_{5/2}$ and $3d_{3/2}$ signals compared to the spectrum of the rhodium(I) complex $[Rh(3,6\text{-dbsq})(CO)_2]_\infty$. The signals of **1** are well resolved into Rh^+ $3d_{5/2,3/2}$ and Rh^{2+} $3d_{5/2,3/2}$ doublets (Figure 2), which clearly reveal that **1** exists in the mixed-valent state composed of Rh^+ and Rh^{2+} on the rapid XPS timescale (ca. 10^{-17} s).[10] Furthermore, the intensity ratios of the Rh^+ $3d_{5/2}$/Rh^{2+} $3d_{5/2}$ and Rh^+ $3d_{3/2}$/Rh^{2+} $3d_{3/2}$ doublets are 2:1(±0.1). This suggests that the formal oxidation state of

[*] Dr. M. Mitsumi, H. Goto, S. Umebayashi, Prof. Dr. Y. Ozawa, Prof. Dr. M. Kobayashi, Prof. Dr. K. Toriumi
Department of Material Science
Graduate School of Material Science
University of Hyogo
3-2-1 Kouto, Kamigori-cho, Ako-gun, Hyogo 678-1297 (Japan)
Fax: (+81) 791-58-0154
E-mail: mitsumi@sci.u-hyogo.ac.jp
toriumi@sci.u-hyogo.ac.jp
Prof. Dr. T. Yokoyama
Institute for Molecular Science
Myodaiji, Okazaki 444-8585 (Japan)
Dr. H. Tanaka, Prof. Dr. S. Kuroda
Department of Applied Physics
Nagoya University
Nagoya 464-8603 (Japan)

[**] This work was supported by a Grant-in-Aid for Young Scientists (No. 15750055) from the Ministry of Education, Culture, Sports, Science and Technology, Japan and a Grant-in-Aid for Scientific Research from the Hyogo Prefecture.

Supporting information for this article is available on the WWW under http://www.angewandte.org or from the author.

 © 2005 Wiley-VCH Verlag GmbH & Co. KGaA, Weinheim

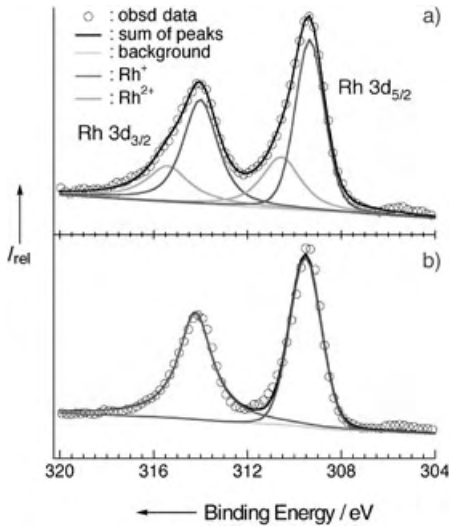


Figure 2. Rh $3d_{5/2}$ and Rh $3d_{3/2}$ core-level spectra for a) **1** and b) [Rh(3,6-dbsq)$(CO)_2]_\infty$. obsd = observed

rhodium is approximately $Rh^{1.33+}$ and the [Rh^{I}(3,6-dbsq-4,5-Cl_2)$(CO)_2$]/[Rh^{II}(3,6-dbcat-4,5-Cl_2)$(CO)_2$] ratio is nearly 2:1.

X-ray crystal structure analysis of **1** was performed at 302 and 56 K with synchrotron radiation (see the Experimental Section). Compound **1** crystallizes in the monoclinic space group *C*2/*c* at both temperatures. It consists solely of neutral linear chains of [Rh(3,6-dbdiox-4,5-Cl_2)$(CO)_2$] molecules, which form trimeric units in the linear chain at 302 K (Figure 3a). The Rh–Rh distances in the trimers (2.8685(2) and 2.8629(2) Å) are about 0.03 Å shorter than the Rh–Rh distances between them (2.8942(3) and 2.8984(3) Å). These Rh–Rh distances are approximately 0.4 Å shorter than those of Rh^+ complex [Rh(3,6-dbsq)$(CO)_2]_\infty$ (3.252(4) and 3.304(5) Å)[7] and are similar to those of $Rh^{1.5+}$ complex [{Rh$(MeCN)_4$}$(BF_4)_{1.5}]_\infty$ (2.8442(8) and 2.9277(8) Å).[12] The formation of the trimer is consistent with the formal oxidation state of $Rh^{1.33+}$ estimated from the XPS spectrum. The structural data also strongly suggests that **1** has a rhodium(I,II) mixed-valent state. The overlap of the complex molecules can be classified into two modes (Figure 3b), in which the dioxolene ligands do not directly overlap. These overlap modes alternate in the linear chain. At 56 K, the trimers in the linear chain are dimerized by shortening the Rh1–Rh1* bond to form hexameric units (Figure 4). The Rh–Rh distances in

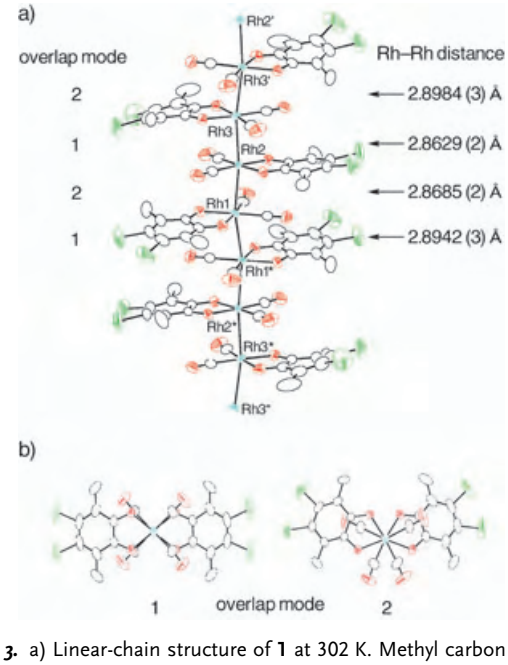


Figure 3. a) Linear-chain structure of **1** at 302 K. Methyl carbon atoms of the *t*Bu groups are omitted for clarity. b) Two overlap modes of the complex molecules.

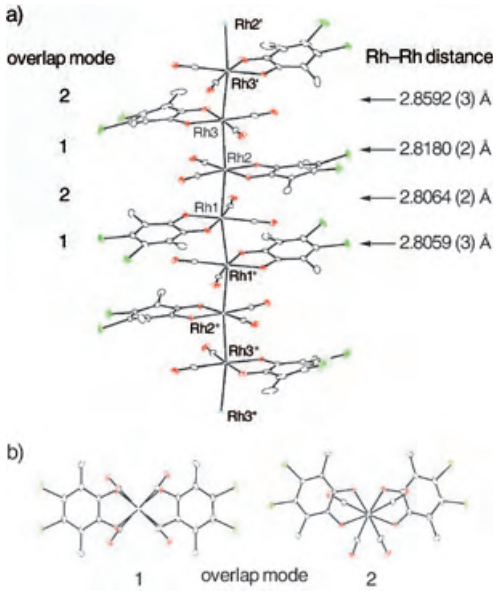


Figure 4. a) Linear chain structure of **1** at 56 K. Methyl carbon atoms of the *t*Bu groups are omitted for clarity. b) Two overlap modes of the complex molecules.

the hexamer are 2.8059(3)–2.8180(2) Å, while the Rh–Rh distance between hexamers is 2.8592(3) Å. The observed dimerization of trimers in the 1D chain originates from Peierls distortion associated with the pairing of unpaired electrons in the d_{z^2} orbitals of Rh^{2+} ions.[13] In the crystal structures at 302 and 56 K, no notable conformational change is observed. The C–C and C–O bond lengths of each dioxolene ligand exist in the boundary region of the semiquinonate and catecholate forms, respectively. These structural features indicate that the dioxolene ligands are either charge-localized and structurally disordered or charge-delocalized. Therefore, it is impossible to determine the oxidation state of each dioxolene ligand from the C–C and C–O bond lengths.

Figure 5 shows electronic absorption spectra of **1** in the solid state and in solution with CH_2Cl_2, and those of [Rh(3,6-dbsq)$(CO)_2]_\infty$ are shown for reference. In the solid state, [Rh(3,6-dbsq)$(CO)_2]_\infty$ shows a relatively intense absorption at 6700 cm^{-1}, which is assigned to the absorption associated with the band structure formed by d_{z^2} orbitals along the linear chain.[7] The dominant feature of the absorption spectrum of **1** in the solid state is an intense, broad absorption band that extends from 15000 cm^{-1} to the IR region. This broad

 © 2005 Wiley-VCH Verlag GmbH & Co. KGaA, Weinheim

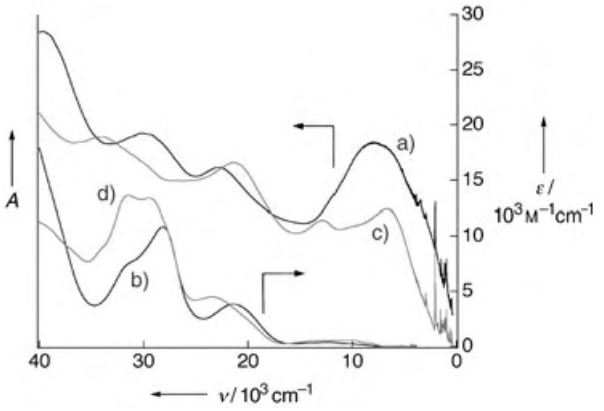


Figure 5. Electronic absorption spectra of **1** in the solid state (KBr pellet) (a) and in solution with CH_2Cl_2 (b) and of $[Rh(3,6\text{-dbsq})(CO)_2]_\infty$ in the solid state (KBr pellet) (c) and in solution with CH_2Cl_2 (d).

absorption band probably consists of several overlapping bands, including the intervalence charge-transfer transitions of $Rh^{2+}\leftarrow Rh^{+}$ and/or $\pi^*(SQ^{\bullet-})\leftarrow\pi^*(Cat^{2-})$[14] along with the absorption associated with the band structure formed by d_{z^2} orbitals, as observed in $[Rh(3,6\text{-dbsq})(CO)_2]_\infty$. On the other hand, the absorption spectrum of a solution of **1** in CH_2Cl_2 is quite similar to that observed for $[Rh(3,6\text{-dbsq})(CO)_2]_\infty$ in the same solvent, and this indicates that **1** exists as a discrete rhodium(I) semiquinonato complex in solution with CH_2Cl_2.

Single-crystal electrical resistivity ρ of **1** along the 1D chain direction was measured in the temperature range 80–300 K by a four-probe technique (Figure 6). Compound **1** shows significant electrical conductivity ($\sigma = 17$–$34\ S\,cm^{-1}$) at room temperature in spite of its neutral molecular character. This high electrical conductivity also clearly demonstrates that the rhodium atoms in **1** are in the mixed-valent state. The temperature dependence of the electrical conductivity confirms semiconducting behavior, and the activation energies E_a in the high- and low-temperature regions are 114 meV (300–179 K) and 64.4 meV (154–80 K), respectively. The increase in resistivity with decreasing temperature is attributable to dimerization of the trimers. The resistivity of **1** shows significant hysteresis in the temperature range of 161–275 K, but the origin of the hysteresis is unclear.

The effective magnetic moment μ_{eff} of **1** at 300 K is 1.61 μ_B, which is smaller than the theoretical value of 1.73 μ_B for a paramagnetic isolated spin of $S = 1/2$ (see the Supporting Information).[15] The μ_{eff} value gradually decreases down to 208 K, shows a rounded hump around 208–172 K, and then decreases to 1.22 μ_B at 5.0 K. This value is slightly smaller than that of 1.41 μ_B expected when two Rh^{2+} spins become a spin singlet and only four semiquinonato spins exist as magnetically isolated spins in a hexamer unit. The Weiss constants θ, based on the equation $\chi_M = C/(T-\theta)$, are −59 K (300–208 K) and −21.6 K (176–52 K), which suggest an antiferromagnetic interaction between the unpaired spins. This complicated magnetic behavior is attributed to either a Rh^{2+} ion or a semiquinonato ligand in the rhodium complex unit with a spin of $S = 1/2$.

The electronic structure of **1** can be estimated from these experimental results as follows: At room temperature, the 1D

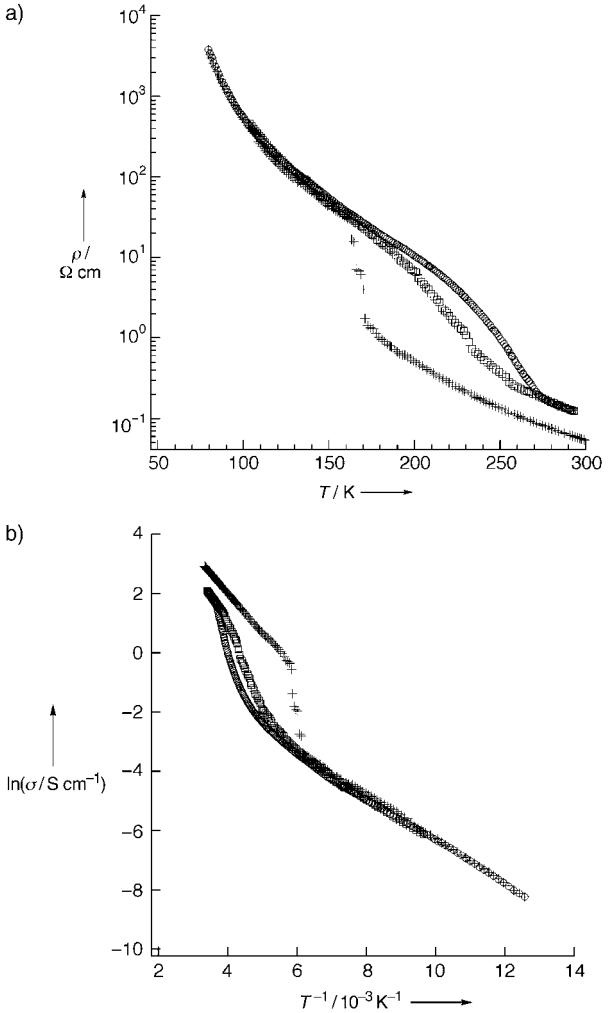


Figure 6. a) Temperature dependence of electrical resistivity ρ of **1** measured along the 1D chain direction: 1st cooling (+), 1st heating (○), 2nd cooling (□). b) Temperature dependence of electrical conductivity σ of **1**.

band formed by the d_{z^2} orbitals of **1** has one unpaired electron per trimer and exhibits significant conductivity. As the temperature is lowered, the trimers dimerize and the unpaired electrons pair, which lowers the conductivity.

In conclusion, we have reported the first neutral linear-chain mixed-valent rhodium(I,II) semiquinonato/catecholato complex **1**, in which the mixed-valent state is realized by electron transfer between metal d and semiquinonate π^* orbitals. This compound exhibits high conductivity (17–34 $S\,cm^{-1}$) at room temperature in spite of its being a neutral molecule. Tuning of the energy levels between the metal d and ligand π orbitals would be expected to facilitate the control of electron transfer between metal and ligand by external factors, such as light, heat, and/or pressure. Therefore, this research offers opportunities for the development of novel neutral conducting polymers based on metal complexes in which the solid-state properties could be changed by metal–ligand electron transfer induced by such external fields. Further investigations are currently underway to produce a variety of the mixed-valent rhodium(I,II) semiquinonato/catecholato compounds by using frontier-orbital control.

 © 2005 Wiley-VCH Verlag GmbH & Co. KGaA, Weinheim

Experimental Section

1 was prepared by a procedure similar to a literature method.[9] $[Rh_4(CO)_{12}]$ (54 mg, 0.072 mmol) and 3,6-di-*tert*-butyl-4,5-dichloro-1,2-benzoquinone[8] (96 mg, 0.33 mmol) were dissolved in *n*-pentane at 35 °C. After slowly cooling to −5 °C, black needle crystals of **1** separated from the solution. These crystals were collected by filtration and washed with *n*-pentane: yield 75 mg (58 %). Elemental analysis (%) calcd for $C_{16}H_{18}Cl_2O_4Rh$: C 42.88, H 4.05, Cl 15.82; found: C 42.68, H 3.97, Cl 15.64; UV/Vis/NIR (KBr pellet): λ_{max} = 251, 334, 439, 1270 nm; UV/Vis/NIR (CH_2Cl_2): λ_{max} (ε_M) = 317 (sh, 7460), 356 (10800), 468 (3830), 818 (378), 990 (sh, 238), 1160 nm (sh, 119).

X-ray crystallography for **1**: A single crystal was mounted on a carbon fiber attached to a closed-cycle helium cryostat. Data were collected at 302 and 56 K, under vacuum to measure reflection intensity accurately by reducing air-scattering background, with synchrotron radiation (20.03 keV (λ = 0.6188 Å) at 302 K and 21.99 keV (λ = 0.5638 Å) at 56 K) and a MAC Science low-temperature vacuum X-ray camera equipped with an imaging plate (IP) area detector in the BL02B1 beamline at SPring-8. The frames were indexed and the reflections integrated with DENZO and subsequently scaled with SCALEPACK.[16a] An empirical correction for absorption anisotropy was applied to all intensity data by using PLATON-MULABS.[16b] The structure was solved by direct methods (SIR97)[17a] and refined by full-matrix least-squares techniques on F^2 (SHELXL-97).[17b] All non-hydrogen atoms were anisotropically refined, while all hydrogen atoms were placed at their idealized positions but not refined. All calculations were performed with the teXsan crystallographic software package.[17c]

Crystal data for **1** at 302 K: $C_{16}H_{18}Cl_2O_4Rh$, M_r = 448.13, black needles, 0.330 × 0.065 × 0.020 mm, monoclinic, space group *C*2/*c*, *a* = 31.696(1), *b* = 11.142(1), *c* = 34.317(1) Å, β = 116.030(1)°, *V* = 10890.0(11) Å^3, *Z* = 24, ρ_{calcd} = 1.640 g cm^{-3}, *F*(000) = 5400, μ(0.6188 Å) = 0.803 mm^{-1}, $2\theta_{max}$ = 52.46°. 15811 reflections were measured, of which 10533 were unique (R_{int} = 0.0399). *wR*2 = 0.1001, *S* = 0.921 (all data), *R*1 = 0.0363 (10533 reflections with $I > 2\sigma(I)$), 622 parameters, min./max. residual electron density −1.080/0.821 e A^{-3}, min./max. transmission 0.94227/0.95022.

Crystal data for **1** at 56 K: $C_{16}H_{18}Cl_2O_4Rh$, M_r = 448.13, black needles, 0.300 × 0.075 × 0.045 mm, monoclinic, space group *C*2/*c*, *a* = 31.644(1), *b* = 10.990(1), *c* = 33.683(1) Å, β = 116.373(1)°, *V* = 10494.7(11) Å^3, *Z* = 24, ρ_{calcd} = 1.702 g cm^{-3}, *F*(000) = 5400, μ(0.5638 Å) = 0.632 mm^{-1}, $2\theta_{max}$ = 60.46°. 28574 reflections were measured, of which 22583 were unique (R_{int} = 0.0312). *wR*2 = 0.1282, *S* = 1.056 (all data), *R*1 = 0.0473 (22583 reflections with $I > 2\sigma(I)$), 622 parameters, min./max. residual electron density −2.640/5.151 e A^{-3}, min./max. transmission 0.91585/0.97378. CCDC-267426 and -267427 contain the supplementary crystallographic data for this paper. These data can be obtained free of charge from the Cambridge Crystallographic Data Centre via www.ccdc.cam.ac.uk/data_request/cif.

XPS data were obtained on a VG ESCALAB 220i-XL spectrometer equipped with nonmonochromatized $Mg_{K\alpha}$ radiation (1253.6 eV). The carbon 1s binding energy (284.6 eV) was used to calibrate the binding energy. Curve-fitting analysis was performed with the iterative least-squares computer program XPSPEAK41 by using a combination of Gaussian and Lorentzian line shapes. Direct-current electrical conductivity measurements were made on several single crystals of **1** by using a four-probe technique. Magnetic susceptibility of **1** was measured with a Quantum Design MPMS-5SH SQUID magnetometer.

Keywords: conducting materials · electron transfer · frontier orbital engineering · mixed-valent compounds · rhodium

[1] H. Tanaka, Y. Okano, H. Kobayashi, W. Suzuki, A. Kobayashi, *Science* **2001**, *291*, 285 – 287.

[2] M. E. Itkis, X. Chi, A. W. Cordes, R. C. Haddon, *Science* **2002**, *296*, 1443 – 1445.

[3] R. Llusar, S. Uriel, C. Vicent, J. M. Clemente-Juan, E. Coronado, C. J. Gómez-García, B. Braïda, E. Canadell, *J. Am. Chem. Soc.* **2004**, *126*, 12076 – 12083.

[4] a) *Extended Linear Chain Compounds*, *Vols. 1–3* (Ed.: J. S. Miller), Plenum, New York, **1982**, and references therein; b) "Mixed-Valence Compounds": H. J. Keller, *NATO ASI Ser. Ser. C* **1980**, *58*, 387 – 411; c) "Chemistry and Physics of One-Dimensional Metals": P. Day, *NATO ASI Ser. Ser. B* **1977**, *25*, 197 – 223.

[5] J. K. Bera, K. R. Dunbar, *Angew. Chem.* **2002**, *114*, 4633 – 4637; *Angew. Chem. Int. Ed.* **2002**, *41*, 4453 – 4457, and references therein.

[6] C. G. Pierpont, *Coord. Chem. Rev.* **2001**, *216–217*, 99 – 125.

[7] C. W. Lange, M. Földeàki, V. I. Nevodchikov, V. K. Cherkasov, G. A. Abakumov, C. G. Pierpont, *J. Am. Chem. Soc.* **1992**, *114*, 4220 – 4222.

[8] V. A. Garnov, V. I. Nevodchikov, G. A. Abakumov, V. K. Cherkasov, L. G. Abakumova, Yu. A. Kurskii, *Izv. Akad. Nauk SSSR Ser. Khim.* **1985**, 2793 – 2794.

[9] M. Mitsumi, S. Umebayashi, Y. Ozawa, M. Tadokoro, H. Kawamura, K. Toriumi, *Chem. Lett.* **2004**, *33*, 970 – 971.

[10] The valence states of the metal atoms in $[K_2\{Pt(CN)_4\}Br_{0.3}\cdot 3H_2O]_\infty$ (KCP(Br)),[11a] $[(2,5\text{-dMe-dcnqi})_2Cu]_\infty$ (2,5-dMe-dcnqi = 2,5-dimethyl-*N*,*N*′-dicyanoquinonediimine),[11b] and $[Pt_2(EtCS_2)_4I]_\infty$[11c] in the metallic state are observed not as an average valence state, but as a mixed-valent state on the rapid XPS timescale.

[11] a) G. A. Sawatzky, E. Antonides, *J. Phys. Colloq.* **1976**, C4 – 117–123; b) I. H. Inoue, A. Kakizaki, H. Namatame, A. Fujimori, A. Kobayashi, R. Kato, H. Kobayashi, *Phys. Rev. B* **1992**, *45*, 5828 – 5833; c) M. Mitsumi, T. Murase, H. Kishida, T. Yoshinari, Y. Ozawa, K. Toriumi, T. Sonoyama, H. Kitagawa, T. Mitani, *J. Am. Chem. Soc.* **2001**, *123*, 11179 – 11192.

[12] M. E. Prater, L. E. Pence, R. Clérac, G. M. Finniss, C. Campana, P. Auban-Senzier, D. Jérome, E. Canadell, K. R. Dunbar, *J. Am. Chem. Soc.* **1999**, *121*, 8005 – 8016.

[13] In the X-ray diffraction experiment on **1** at 56 K with synchrotron radiation, neither diffuse scattering nor satellite reflections that correspond to lattice modulation could be observed.

[14] H.-C. Chang, K. Mochizuki, S. Kitagawa, *Inorg. Chem.* **2002**, *41*, 4444 – 4452.

[15] We also measured the temperature dependence of the powder EPR spectra (*T* = 280–4 K) to reveal the spin states of Rh^{2+} and semiquinonato ligand; however, EPR signals with the intensity expected from the magnetic susceptibility could not be detected as the EPR signals are considerably broadened because of the very short spin–lattice relaxation time.

[16] a) Z. Otwinowski, W. Minor, *Methods Enzymol.* **1997**, *276*, 307 – 326; b) PLATON, A. L. Spek, *J. Appl. Crystallogr.* **2003**, *36*, 7 – 13.

[17] a) SIR97: A. Altomare, M. C. Burla, M. Camalli, G. L. Cascarano, C. Giacovazzo, A. Guagliardi, A. G. G. Moliterni, G. Polidori, R. Spagna, *J. Appl. Crystallogr.* **1999**, *32*, 115 – 119; b) G. M. Sheldrick, SHELXL-97, University of Göttingen, Göttingen, Germany, **1997**; c) Crystal Structure Analysis Package, Molecular Structure Corporation, **1985**, **1999**.

Received: April 5, 2005
Published online: June 14, 2005

 © 2005 Wiley-VCH Verlag GmbH & Co. KGaA, Weinheim

Cesium Oxide Nanoparticles

Preparation and Structural Characterization of Stable Cs_2O Closed-Cage Structures**

*Ana Albu-Yaron, Talmon Arad, Ronit Popovitz-Biro, Maya Bar-Sadan, Yehiam Prior, Martin Jansen, and Reshef Tenne**

Films of cesium oxides with a Cs to O ratio of about 2:1 (in addition to Ag) and approximately monolayer dimensions are widely utilized, for example, on the surface of S-1 photocathodes,[1] negative electron affinity (NEA) devices,[2] and also discharge lamps, television cameras, and lasers. These films reduce the work function of the electrode and thereby increase the electron emission current and long-wavelength response of these devices.[1,2] Particular emphasis has been placed on the study of $Cs_{1+x}O$ for applications in catalytic converters[3,4] and optical fibers. The structure of these surface layers deposited on photoemissive and NEA devices has proved difficult to resolve and interpret, partly due to the thinness of the film and the pronounced instability of Cs_2O. Furthermore, as these films are highly reactive and thin, they are damaged or destroyed by short exposure to low vacuum. This stringent vacuum requirement increases the difficulty and expense of their manufacture and handling and prevents applications that require periodic atmospheric exposure. Enhancing the stability of these films is a long-standing goal.

The complex Cs–O phase diagram[5] has been investigated in the past. Although the synthesis of various oxides of cesium was reported already in the early 1900s, the actual structural characterization of Cs_2O and Cs_3O was described only 50 years later.[6,7] Cs_2O crystallizes in the 3R anti-$CdCl_2$ structure (PDF #09-0104)[8a,b] and is the only known binary alkali metal oxide with a layered structure. This suggests that a much more stable Cs_2O configuration should exist. Kinetic stabilization could be achieved by forming a closed-cage fullerene-like (*IF*) structure, which is the subject of the present report. These structures do not expose the highly reactive (*hk*0) prismatic faces, as the strong and reactive bonds of the cesium and oxygen atoms at the edges of the layers are canceled out by the inherently closed nature, and only rather weak interactions between adjacent Cs-O-Cs triple layers across the van der Waals gap actually occur. Moreover, *IF* including nanotubes[9] of various other layered compounds, such as WS_2[10,11] and BN,[12] were shown to have unusual mechanical, optical, and electronic properties that arise mainly from their highly curved surfaces, shape, and size. The extensive potential of WS_2 *IF* as superior solid lubricants[13] and impact-resistant materials[14] has already been confirmed.

Here we report the synthesis of closed-cage (fullerene-like *IF*) Cs_2O nanoparticles and their structural characterization by HRTEM. We attempted the synthesis using a variant of laser ablation in a rather unusual setup (Figure 1 a).

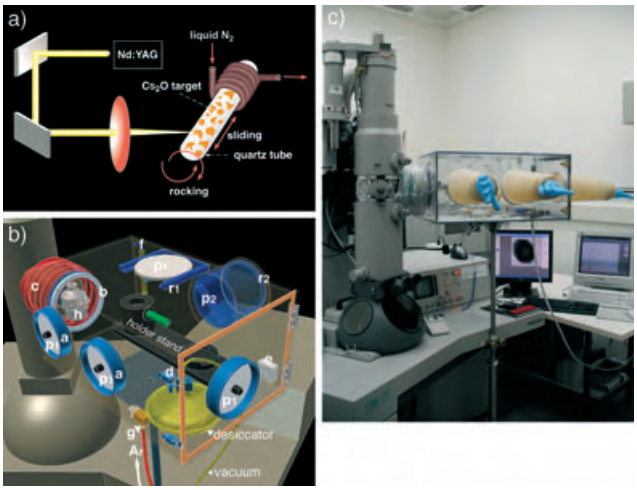


Figure 1. a) Experimental setup for laser ablation. b) Schematic of the environmental chamber. c) Image of the CM120 TEM with the environmental chamber attached to the CompuStage entry.

Moreover, a homebuilt argon-purged environmental chamber (Figure 1 b,c), tightly attached to the entry of the transmission electron microscope (TEM), has been designed and developed to overcome the tremendous experimental difficulties in manipulating Cs_2O. The synthesized nanoparticles exhibit remarkable stability not only under the electron beam of the microscope but also, to a certain extent, even when exposed temporarily to air, and this makes them potentially useful in developing new photoemissive and NEA devices.

3R-Cs_2O powder[15] (Figure 2) served as a precursor in the present work. Subsequent laser ablation of the powder while sealed in evacuated quartz ampoules led to the desired closed-cage nanoparticles of Cs_2O. Unfortunately, the production yields of the fullerene-like Cs_2O structures were too low to permit XRD characterization so far. Figure 3 a and b show two examples of closed-cage nested nanoparticles of Cs_2O typically observed in the laser-ablated material. While that shown in Figure 3 a is faceted, the layers of the *IF*-Cs_2O nanoparticles shown in Figure 3 b are evenly folded to form quasi-spherical, closed nanoparticles. Here, each fringe represents a molecular sheet of Cs_2O. The interlayer distance

[*] Dr. A. Albu-Yaron, Dr. R. Popovitz-Biro, M. Bar-Sadan, Prof. R. Tenne
Department of Materials and Interfaces
Weizmann Institute of Science
Rehovot 76100 (Israel)
Fax: (+972) 8-934-4138
E-mail: reshef.tenne@weizmann.ac.il
T. Arad
Electron Microscopy Unit
Weizmann Institute of Science
Rehovot 76100 (Israel)
Prof. Y. Prior
Department of Chemical Physics
Weizmann Institute of Science
Rehovot 76100 (Israel)
Prof. Dr. M. Jansen
Max-Planck-Institut für Festkörperforschung
Heisenbergstrasse 1, Stuttgart (Germany)

[**] The authors thank Mr. C. Mühle for the preparation of the samples.

 DOI: 10.1002/anie.200500356 © 2005 Wiley-VCH Verlag GmbH & Co. KGaA, Weinheim

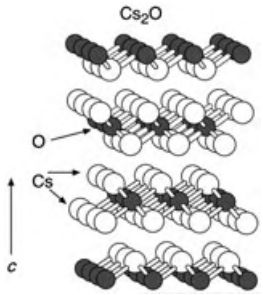


Figure 2. The structure of the Cs_2O precursor.

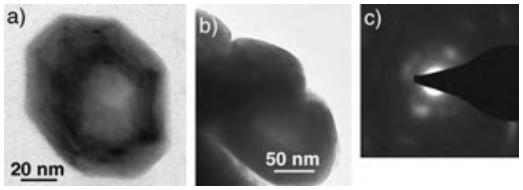


Figure 3. TEM images of typical closed-cage nested *IF*-Cs_2O nanoparticles obtained by laser ablation of 3R-Cs_2O powder precursor: a) faceted Cs_2O *IF* nanoparticle of approximately 70–90 nm in size, b) quasi-spherical *IF* nanoparticles of approximately 70–140 nm in diameter. All particles have at least 30 layers. c) SAED pattern of the nanoparticle in (a). Here reflections from both (00l) and (*hk*0) planes can be seen.

between the Cs_2O fringes is 6.35 Å. The faceted nanoparticle in Figure 3a is about 70–90 nm in size, while the quasi-spherical nanoparticles shown in Figure 3b are about 70–140 nm in diameter and consist of at least 30 layers. Although the nanoparticle cores appear quite dark, the somewhat brighter contrast suggests that they are hollow in the center. The folded and closed nature of both nanoparticles was verified by tilting experiments. Selected-area electron diffraction (SAED) from the nanoparticle in Figure 3a, which is shown in Figure 3c, exhibits the reflections of both (00l) and the hexagonal pattern of the (*hk*0) planes at any tilt angle and confirms the closed nature[10,11] of *IF*-CsO_2. Energy dispersive X-ray analysis (EDS) showed that only cesium and oxygen were present in the nanoparticle with an approximate 2:1 ratio.

Figure 4a shows an enlarged view of part of the faceted polyhedral Cs_2O nanoparticle shown in Figure 3a. A computer simulation of the magnified image is overlaid on the lattice image in Figure 4b. Note the good agreement between the simulated and experimentally observed image. A line profile of the framed area in Figure 4a, shown in Figure 4c, confirms the interlayer spacing of 6.37 Å, which agrees very well with the value of $^1/_3\,c$ of Cs_2O. The fast Fourier transform (FFT) of the framed region in Figure 4a is shown in Figure 4d, and the distance calculated therefrom (6.35 Å) also agrees with $^1/_3\,c$ of Cs_2O. The *IF*-Cs_2O nanoparticles were found to be very stable under the electron beam of the TEM, while TEM analysis of the surrounding amorphous or platelet bulk Cs_2O starting material, also present in these samples, was particularly difficult due to their instability and outgassing

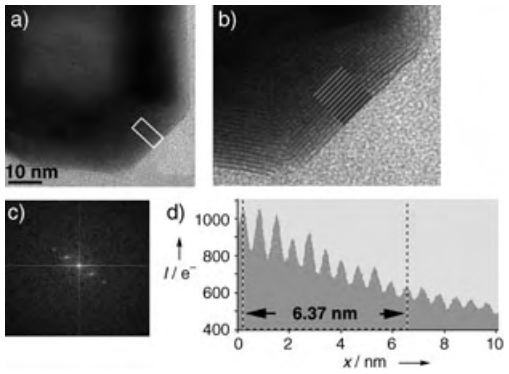


Figure 4. a) An enlarged view of part of a faceted Cs_2O nanoparticle. b) Higher magnification of the *IF*-Cs_2O nanoparticle displayed in a) with a computer simulation of the image overlaid on the lattice image. Note the good agreement between the simulated and experimentally observed images. c) FFT of the framed area in (a). d) Line profile of the framed area in (a) showing an interlayer spacing of 6.37 Å.

under the electron beam. More strikingly, when the grid bearing the specimen was taken out and reinserted into the TEM after a few minutes in the ambient atmosphere, almost no damage occurred to the inspected fullerene-like Cs_2O *IF* nanoparticles, while the surrounding Cs_2O material had deteriorated rapidly.

Subsequent HRTEM experiments on a grid transferred from the TEM and analyzed after roughly 1 h in the ambient laboratory atmosphere (Figure 5a), revealed that the pristine Cs_2O nanoparticle with fullerene-like structure was only partially damaged. The overall shape of this fullerene-like

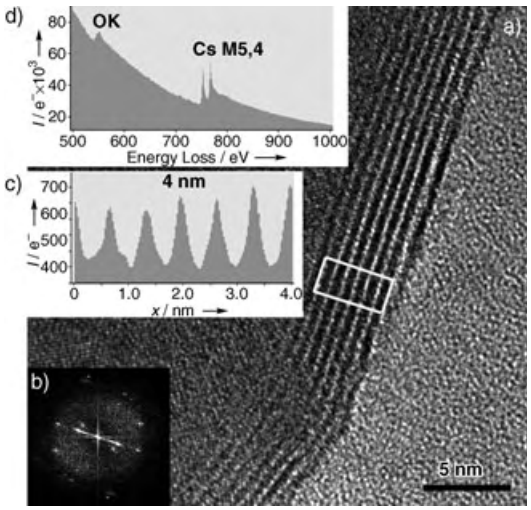


Figure 5. Higher magnification image of a faceted *IF*-Cs_2O nanoparticle, analyzed first in the CM120 TEM and then transferred to the HRTEM following about 1 h of exposure to ambient atmosphere. a) Region of the nanoparticle exhibiting reduced number of layers as compared to the 30 or more layers of a typical pristine nanoparticle (see Figures 3 and 4). The layer spacings, obtained from the respective FFT in (b) and the line profile in (c) from the framed areas in (a) is 6.8 Å in this part. The EELS spectrum in (d) exhibits only Cs and O in a ratio of less than 2:1.

 © 2005 Wiley-VCH Verlag GmbH & Co. KGaA, Weinheim

nanoparticle changed from a faceted structure, like in Figure 3a, to a more spherical topology; starting from the kinks between the facets, exfoliation and amorphization of the outer molecular Cs_2O sheets took place and advanced progressively inwards. Careful inspection of this nanoparticle revealed that the number of perfectly closed molecular layers decreased from about 30 to 8, and most of the Cs_2O layers (ca. 20) were only partially ruptured. The interlayer distance increased from about 6.4 Å in the pristine nanoparticle to 6.8 Å (Figure 5b,c) and in some places even to 8.5 Å (not shown), likely due to intercalation of water. In general, however, the inner layers of the *IF*-Cs_2O nanoparticles were found to be undamaged and exhibited smaller expansion.

Electron energy loss spectroscopy (EELS) and imaging with the Gatan imaging filter (GIF) revealed only Cs and O (excess oxygen; Figure 5d), while GIF analysis of the surrounding amorphous material (not shown), revealed Cs, O, and C. These results, together with the above TEM observations, imply that the amorphous and platelet materials on the grid react vigorously with ambient CO_2 to form cesium carbonate, while the *IF* nanoparticles react slowly with water, which could be possibly removed by mild heat treatment or prolonged evacuation in the HRTEM column. In keeping with previous observations on alkali-metal-doped WS_2 and MoS_2 nanoparticles,[16] water uptake into the van der Waals gap between the layers is common in layered compounds. Furthermore, in analogy to intercalated *IF*-WS_2,[16] evidence for some time-dependent recovery of the damaged nanoparticles, accompanied by rounding of its initial polyhedral shape, was observed after a few days in the high vacuum of the HRTEM. The partially recovered Cs_2O layers were less faceted than the original ones. These observations indicate that, in contrast to the presently used cesium oxide films in photocathodes, which are irreversibly damaged under low vacuum, the *IF* nanoparticles, if damaged, could possibly be recovered by mild heating under vacuum.

The presence of the closed Cs-O-Cs hexagonal planes in the *IF*-Cs_2O structures clearly enhances the stability of the material in ambient atmosphere. The inert van der Waals surface of the closed nanoparticles presents a diffusion barrier to the intercalation process, which leads to a sequential and therefore slower hydrolytic attack on the layers in these structures. In contrast, the existence of dangling bonds at the prismatic edges on the periphery of the Cs_2O quasi-two-dimensional planar structures explains the high reactivity of amorphous or platelet powder. Therefore, the formation of closed-cage *IF*-Cs_2O nanostructures induces kinetic stabilization of the material and accounts for its intrinsically low reactivity.

The synthesis of *IF*-Cs_2O has led to a new member of the fullerene-like family of otherwise extremely unstable but important materials. The unprecedented relative stability of the *IF*-Cs_2O nanoparticles synthesized here, both under the electron beam and in air, is very encouraging and suggests that once larger amounts of pure *IF* nanoparticles have been synthesized and fully characterized, their beneficial effect on lowering the work function and photoemission from various surfaces could be directly evaluated and fully exploited in NEA, photoemissive, and other devices. The action of other metals, such as silver and bismuth, that are known to enhance the quantum yield of photocathodes may in fact be related to their possible catalytic effect in the synthesis of *IF*-Cs_2O nanoparticles. Theoretical work is underway to elucidate the electronic structure of these nanoparticles. Previous studies on various semiconducting nanotubes[17,18] indicated that while quantum-size effects are of lesser importance in closed-cage nanostructures, folding of the molecular sheets reduces the energy gap and makes the nanotubes more conductive, and this could favorably affect their thermionic and photoemission.

Experimental Section

The 3R-Cs_2O powder precursor in the present work was synthesized by reaction of measured amounts of cesium metal and oxygen at 180 °C for 3 d.[15] The product was subsequently sealed in evacuated quartz ampoules. The orange-tinted powder was characterized by XRD and Raman spectroscopy.[8a,b] The Raman peak at $\tilde{\nu} = 103\ cm^{-1}$ can be assigned to the A_{1g} mode.[8a]

Cs_2O powder precursor in a vacuum-sealed quartz ampoule was ablated with a pulsed Nd:YAG laser; the beam was manually scanned so as to impinge on a new position. Cooling with liquid N_2 vapor was performed through a copper tube in the form of a helical coil, which wrapped part of the ampoule surface. Figure 1a shows the experimental arrangement. During ablation, a deeply colored powder accumulated on the walls of the cooled side of the quartz ampoule.

Further manipulations were performed in a specially designed and built environmental cell attached as a matching counterpart to the CompuStage entry of the TEM, operating under a flow of Ar of purity > 99.99 % and without any modification of the microscope or of the sample holder; it allowed safe preparation, mounting, handling, and introduction into the microscope of the specimen grid without exposure to the ambient atmosphere. Figure 1b shows a schematic of the environmental chamber; Figure 1c is an overview of the installation of the chamber attached to the CM120 TEM column. The quartz ampoule was broken inside the chamber, and a small amount of the laser-ablated material transferred onto a gold grid for mounting into the TEM. The environmental chamber was operated with both the room-temperature and the cryo holders of the CM120 TEM. A completely different system, which only excludes air during insertion of the grid into the microscope, has been previously reported.[19]

The following microscopes were used: a TEM-Philips CM120 (120 kV) with EDS system (EDAX Phoenix) and a field-emission gun high-resolution TEM (HRTEM) model FEI Tecnai F-30 (300 kV). A Gatan imaging filter (GIF) was used for for electron energy loss spectroscopy (EELS) and for elemental mapping. Fast Fourier transform (FFT) of the high-resolution images was obtained by Digital Micrograph software (Gatan). The computer simulation was performed with the software MacTempas. The following parameters were used for the simulation: thickness 35 nm; defocus of −30 nm.

Received: January 30, 2005
Revised: March 22, 2005
Published online: June 3, 2005

Keywords: cage compounds · cesium · electron microscopy · nanostructures · oxides

[1] A. H. Sommer, *Photoemissive Materials*, Krieger, Huntington, **1980**, p. 132–166, pp. 167–174.
[2] W. E. Pickett, *Phys. Rev. Lett.* **1994**, *73*, 1664–1667.

 © 2005 Wiley-VCH Verlag GmbH & Co. KGaA, Weinheim

[3] Z. You, I. Balint, K.-I. Aika, *Appl. Catal. B* **2004**, *53*, 233 – 244.
[4] B. A. A. L. van Setten, C. G. M. Spitters, J. Bremmer, A. M. M. Mulders, M. Makkee, J. A. Molijn, *Appl. Catal. B* **2003**, *42*, 337 – 347.
[5] A. Simon in *Structure and Bonding*, *Vol. 36* (Eds.: J. D. Dunitz, J. B. Goodenough, P. Hemmerich, J. A. Ibers, C. K. Jørgensen, J. B. Neilands, D. Reinem, R. G. P. Williams), Springer, New York, **1979**, pp. 81 – 127.
[6] K. R. Tsai, P. M. Harris, E. N. Lassettre, *J. Phys. Chem.* **1956**, *60*, 338 – 344.
[7] K. R. Tsai, P. M. Harris, E. N. Lassettre, *J. Phys. Chem.* **1956**, *60*, 345 – 347.
[8] a) A. Band, A. Albu-Yaron, T. Livne, H. Cohen, Y. Feldman, L. Shimon, R. Popovitz-Biro, V. Lyahovitskaya, R. Tenne, *J. Phys. Chem. B* **2004**, *108*, 12360 – 12367; b) S. Gemming, G. Seifert, C. Mühle, M. Jansen, A. Albu-Yaron, T. Arad, R. Tenne, *J. Solid State Chem.* **2005**, *178*, 1190 – 1196.
[9] C. N. R. Rao, M. Nath, *Dalton Trans.* **2003**, 1 – 25.
[10] R. Tenne, L. Margulis, M. Genut, G. Hodes, *Nature* **1992**, *360*, 444 – 446.
[11] L. Margulis, G. Salitra, R. Tenne, M. Talianker, *Nature* **1993**, *365*, 113 – 114.
[12] N. G. Chopra, J. Luyken, K. Cherry, V. H. Crespi, M. L. Cohen, S. G. Louie, A. Zettl, *Science* **1995**, *269*, 966 – 967.
[13] L. Rapoport, Yu. Bilik, Y. Feldman, M. Homyonfer, S. R. Cohen, R. Tenne, *Nature* **1997**,*387*, 791 – 793.
[14] Y. Q. Zhu, T. Sekine, K. S. Brigatti, S. Firth, R. Tenne, R. Rosentsveig, H. W. Kroto, D. R. M. Walton, *J. Am. Chem. Soc.* **2003**,*125*, 1329 – 1333.
[15] G. Brauer, *Handbuch der Präparativen Anorganischen Chemie*, *Vol. 2*, Enke, Stuttgart, **1978**, p. 938.
[16] A. Zak, Y. Feldman, V. Lyakhovitskaya, G. Leitus, R. Popovitz-Biro, E. Wachtel, H. Cohen, S. Reich, R. Tenne, *J. Am. Chem. Soc.* **2002**, *124*, 4747 – 4758.
[17] G. Seifert, H. Terrones, M. Terrones, M. Jungnickel, T. Frauenheim, *Phys. Rev. Lett.* **2000**, *85*, 146 – 149.
[18] I. Cabria, J. W. Mintmire, *Europhys. Lett.* **2004**, 65, 82 – 88.
[19] P. O. Jeitschko, A. Simon, R. Ramlau, Hj. Mattausch, *Z. Anorg. Allg. Chem.* **1997**, *623*, 1447 – 1454.

 © 2005 Wiley-VCH Verlag GmbH & Co. KGaA, Weinheim

Pharmacophore Mapping

The INPHARMA Method: Protein-Mediated Interligand NOEs for Pharmacophore Mapping**

Víctor M. Sánchez-Pedregal, Marcel Reese, Jens Meiler, Marcel J. J. Blommers, Christian Griesinger, and Teresa Carlomagno**

In structure-based drug design, the relative orientation of two competitive ligands A and B in the receptor binding pocket plays a central role in the design of high-affinity drug candidates from weakly bound lead compounds. In this communication we report on the observation of interligand spin-diffusion-mediated transferred-NOE data, which have the potential to be used for the determination of the relative orientation of two competitive ligands in the receptor binding pocket. In many cases, the orientation of one ligand in the binding pocket is known, for example, from crystallography or fluorescence resonance energy transfer (FRET) data. In these cases it is desirable to develop a methodology that allows the determination of a unique binding mode and pharmacophore model for a second competitive ligand. We anticipate that the interligand transferred NOEs described here could provide the experimental basis for a methodology that is applicable to any combination of ligands weakly bound to a common receptor.

The conformation of a ligand in the binding pocket of a macromolecular receptor can be accessed by NMR spectroscopy in solution by two approaches. If the molecular weight of the complex is of the order of 50 kDa or smaller and $^{13}C/^{15}N$-labeled receptor can be produced in vitro, a detailed three-dimensional picture of the ligand and of its interactions with the receptor binding pocket can be obtained with standard NMR spectroscopy methods.[1] However, in other cases the macromolecular receptor is too large for NMR studies in solution or it cannot be synthesized in vitro to introduce NMR-active isotopes. In these instances, NMR spectroscopy

[*] Dr. V. M. Sánchez-Pedregal, M. Reese, Prof. Dr. C. Griesinger, Dr. T. Carlomagno
Max-Planck-Institut für Biophysikalische Chemie
Am Fassberg 11, 37077 Göttingen (Germany)
Fax: (+49) 551-201-2202
E-mail: cigr@nmr.mpibpc.mpg.de
taco@nmr.mpibpc.mpg.de

Dr. J. Meiler
University of Washington
BOX 357350, Seattle WA 98195 (USA)

Dr. M. J. J. Blommers
Core Technologies
Novartis Pharma AG
P.O. Box, 4002 Basel (Switzerland)

[**] This work was supported by the Max-Planck-Gesellschaft, the Deutsche Forschungsgemeinschaft (grant: GRK 782), the European Union (Marie Curie fellowship to V.M.S.-P.), and the Fonds der Chemischen Industrie (to C.G.).

Supporting Information for this article is available on the WWW under http://www.angewandte.org or from the author.

 © 2005 Wiley-VCH Verlag GmbH & Co. KGaA, Weinheim DOI: 10.1002/anie.200500503

can be applied to determine the receptor-bound conformation of the ligand, provided the rate constant for the dissociation of the complex (k_{off}) is much larger than the relaxation constants of the ligand in the complex and the difference between the resonance frequencies of the free and bound ligand forms (a fast-exchange regime). Under this condition, which implies a dissociation constant (K_d) value in the low micromolar to millimolar range, information on the ligand structure is derived from transferred NOEs (tr-NOE)[2] and transferred cross-correlated relaxation rates (tr-CCRR).[3,4] The determination of the receptor-bound conformation of the ligand leaves open the question of its orientation in the receptor binding pocket.

The relative orientation of two competitive ligands weakly bound to a common receptor could be determined by the simple and novel approach that we propose here. A NOESY spectrum of a mixture of the two ligands in the presence of the common receptor is recorded. Under the fast-exchange condition described above, and provided that the two ligands A and B bind competitively to the macromolecular receptor T, intermolecular tr-NOE peaks between the two ligands A and B can be observed in the NOESY spectrum. A NOE peak between a proton H_A of ligand A and a proton H_B of ligand B in the presence of the receptor T originates from spin diffusion involving a proton H_T of the receptor. During the NOESY mixing time, ligand A binds to receptor T and H_A transfers its magnetization to H_T (Figure 1). The complex AT

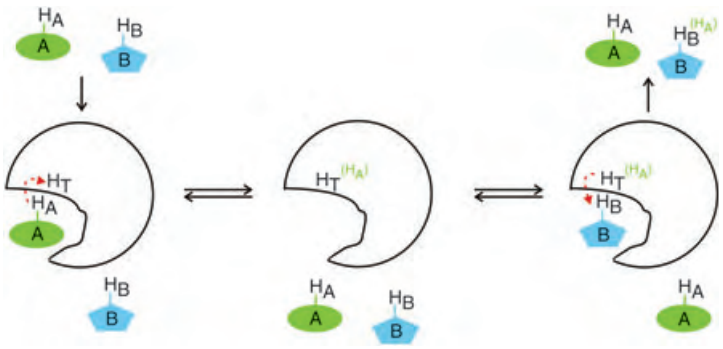


Figure 1. Schematic representation of the principle of the interligand NOEs observed between two competitive ligands A (in green) and B (in blue), which bind consecutively to the same target receptor T. For details see text.

then dissociates and ligand B binds to receptor T. The magnetization of H_A, which had been transferred to H_T, can now be transferred to H_B; this results in an intermolecular peak H_A–H_B. Clearly, this peak can only exist if both H_A and H_B are close to H_T in the AT and BT complexes, respectively. Therefore, a number of such intermolecular NOE peaks will describe the relative orientation of the two ligands in the receptor binding pocket. Such interligand NOEs have never been observed so far and should not be mistaken for the interligand NOEs that occur for two ligands binding simultaneously in adjacent or partially overlapping binding pockets.[5] Here, the two ligands A and B are never either close in space or bound to the protein simultaneously; instead, the two ligands bind to the protein competitively and consecutively and the observed NOEs are a consequence of spin diffusion mediated by the protons of the protein.

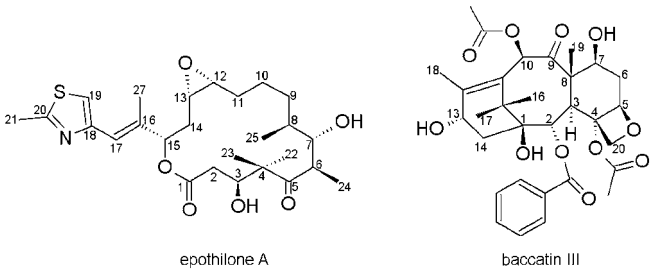
If the orientation of ligand A in the binding pocket of receptor T is known, the possible binding modes of ligand B, resulting from docking calculations, could be ranked by evaluating their compatibility with the experimental interligand NOEs. The expected H_A–H_B intermolecular NOEs could be computed for each orientation of ligand B in the BT complex and compared with the experimental ones. The structures that give rise to intermolecular NOEs in good agreement with the experimental ones would be retained, while the others would be rejected. Work along these lines is currently being carried out in our laboratory to develop a computer program for the evaluation of interligand NOEs by using the full-relaxation-matrix approach.[6] A qualitative interpretation of the interligand NOEs, based on the simplified model shown in Figure 1, should not be attempted, as spin diffusion among protein protons can generate intermolecular NOEs between ligands that are in contact with nonneighboring sites of the protein binding pocket. The interligand NOEs should be interpreted exclusively with the help of theoretical calculations by using the full-relaxation-matrix approach. We call this approach INPHARMA (interligand NOE for pharmacophore mapping).

Herein, we show for the first time that such interligand NOEs can be observed. Our system is a mixture of the protein tubulin and two of its ligands. Tubulin is the target of several drugs that interfere either positively or negatively with the tubulin polymerization process. Disturbing microtubule dynamics and, therefore, the cell-division process represents one of the major therapeutic strategies against human solid tumors. Among the small organic molecules that promote tubulin polymerization, paclitaxel is routinely used in hospitals to treat mammalian and ovarian carcinomas. Epothilone and discodermolide,[7] which compete with paclitaxel for the same binding pocket,[8] are more potent than paclitaxel in the promotion of tubulin polymerization and will most likely enter the pharmaceutical market in the next decade. Two low-resolution structures of Zn-induced tubulin sheets stabilized by paclitaxel and epothilone, respectively, have become available by electron crystallography.[9,10]

Recently, thanks to a combination of tr-NOE and tr-CCRR data, we determined the structure of epothilone A (Epo A) weakly bound to soluble tubulin.[11] The tubulin-bound structure of Epo A determined by NMR spectroscopy[11] is not in agreement with the tubulin-bound conformation of Epo A determined by electron crystallography,[10] a fact suggesting that the binding mode of epothilone to tubulin can be dependent on the protein state. Therefore, it is relevant to investigate the binding mode of Epo A to soluble tubulin, namely in conditions that are as close as possible to the physiological ones.

We applied the INPHARMA method to a mixture of epothilone A and baccatin III[12] in the presence of tubulin. The complex Epo A–tubulin is only transiently formed during the mixing time of a NOESY experiment and tr-NOEs can be observed for a 100:1 mixture of Epo A and tubulin, thereby

 © 2005 Wiley-VCH Verlag GmbH & Co. KGaA, Weinheim



making the system suitable for application of the INPHARMA method (epothilone A = ligand B; tubulin = target T). A model of the complex of tubulin with paclitaxel is available by electron crystallography. Unfortunately, paclitaxel is poorly soluble in water and therefore not suitable for NMR studies in solution. However, the precursor of paclitaxel, baccatin III, which lacks the C13 side chain, is water soluble, binds to tubulin in a transiently formed complex, and delivers tr-NOEs. Thus, although the biological activity of baccatin III is lower than that of paclitaxel, we chose baccatin III as ligand A for our experiments. To confirm that baccatin binds in the same pocket as paclitaxel, namely, that it competes with epothilone for the taxane-binding pocket, we evaluated the change in the tr-NOE rates of baccatin in the presence of tubulin upon addition of epothilone. For a concentration ratio of epothilone A/baccatin of 0.67:1, the tr-NOE rates of baccatin decrease to 60 % of their original value, a result confirming that the two ligands compete for the same binding pocket with a similar K_d value.

We recorded NOESY experiments at different mixing times (20, 40, 70, 100, and 200 ms) for a mixture of epothilone A (0.6 mM), baccatin III (0.6 mM), and tubulin (12 μM) in D_2O. Intermolecular NOE cross-peaks between the aromatic protons of baccatin III and several methyl groups of Epo A are clearly observable in the section of the NOESY spectrum recorded at a mixing time of 70 ms and shown in Figure 2.

19 intermolecular NOE peaks can already be observed in the NOESY spectrum with a mixing time of 40 ms. The build-up curves of the intensities of six of these NOE peaks (Figure 3) show the characteristic damped-parabolic shape for spin-diffusion-mediated NOEs. Additional intermolecular NOEs become visible after 100 ms or at higher mixing times. As a control, we recorded a NOESY spectrum of the mixture of Epo A and baccatin III in the absence of tubulin with a mixing time of 400 ms; this spectrum showed no intermolecular NOEs. Thus, we can conclude that the intermolecular NOEs between Epo A and baccatin III, observed in presence of tubulin, are mediated by protons of tubulin. We are in the process of developing a full-relaxation-matrix analysis of the observed interligand NOEs to determine the binding mode of epothilone to soluble tubulin, with the assumption that baccatin III binds tubulin with the same pharmacophore as paclitaxel.

Herein, we have reported the first observation of protein-mediated NOEs between two ligands that bind competitively and consecutively to the same target molecule. The inter-

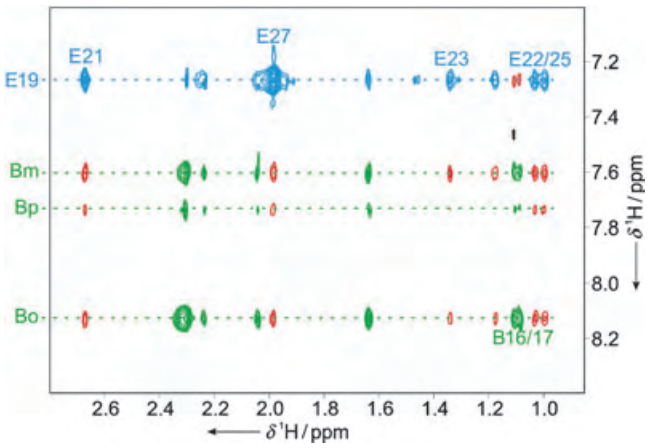


Figure 2. NOESY spectrum of a mixture of tubulin, epothilone A, and baccatin III with concentrations of 12 μM, 0.6 mM, and 0.6 mM, respectively. The spectrum was acquired on a 900-MHz spectrometer equipped with a cryoprobe with a mixing time of 70 ms. The blue and green peaks are intramolecular transferred NOE peaks of epothilone A and baccatin III, respectively. The red peaks represent the interligand transferred NOEs mediated by the protein protons. The numbering of the atoms corresponds to that shown in the compound structures for epothilone A (E) and baccatin III (B). Bm, Bo, and Bp indicate the protons in the *meta*, *ortho*, and *para* positions of the benzene ring of baccatin III, respectively.

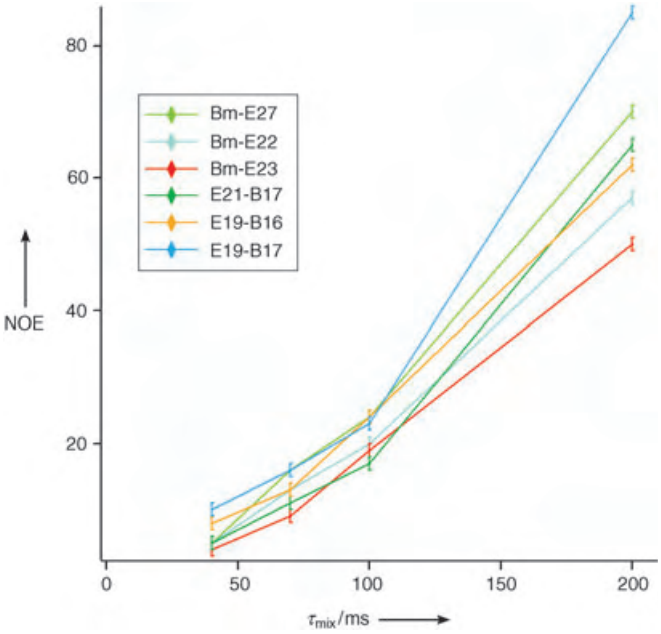


Figure 3. Build-up curves of 6 out of the 19 most intense interligand tr-NOE cross-peaks. The typical damped-parabolic behavior can be observed for all peaks, thereby confirming that the interligand NOEs arise from spin diffusion mediated by the protein protons.

ligand NOEs observed by us should not be confused with the interligand NOEs already reported in the literature,[13] where the two ligands bind simultaneously to the target. Our INPHARMA methodology could be used to distinguish among different binding modes of a ligand to a macro-

 © 2005 Wiley-VCH Verlag GmbH & Co. KGaA, Weinheim

molecular target, if the binding mode of a second competitive ligand is known. This novel approach should be particularly attractive for the pharmaceutical industry, where there is a strong need for the rapid determination of the binding epitope of different ligands to a common target.

Received: February 9, 2005
Revised: April 14, 2005
Published online: June 1, 2005

Keywords: drug design · epothilones · ligand interactions · NMR spectroscopy · pharmacophore mapping

[1] J. Cavanagh, W. J. Fairbrother, A. G. Palmer, N. J. Skelton, *Protein NMR Spectroscopy*, Academic Press, London, **1996**.
[2] F. Ni, *Prog. Nucl. Magn. Reson. Spectrosc.* **1994**, *26*, 517.
[3] T. Carlomagno, I. C. Felli, M. Czech, R. Fischer, M. Sprinzl, C. Griesinger, *J. Am. Chem. Soc.* **1999**, *121*, 1945.
[4] M. J. J. Blommers, W. Stark, C. E. Jones, D. Head, C. E. Owen, W. Jahnke, *J. Am. Chem. Soc.* **1999**, *121*, 1949.
[5] R. E. London, *J. Magn. Reson.* **1999**, *141*, 301.
[6] R. E. London, M. E. Perlman, D. G. Davis, *J. Magn. Reson.* **1992**, *97*, 79.
[7] L. F. He, G. A. Orr, S. B. Horwitz, *Drug Discovery Today* **2001**, *6*, 1153.
[8] J. Kowalski, P. Giannakakou, E. Hamel, *J. Biol. Chem.* **1997**, *272*, 2534.
[9] E. Nogales, S. G. Wolf, K. H. Downing, *Nature* **1998**, *391*, 199.
[10] J. H. Nettles, H. L. Li, B. Cornett, J. M. Krahn, J. P. Snyder, K. H. Downing, *Science* **2004**, *305*, 866.
[11] T. Carlomagno, M. J. J. Blommers, J. Meiler, W. Jahnke, T. Schupp, F. Petersen, D. Schinzer, K. H. Altmann, C. Griesinger, *Angew. Chem.* **2003**, *115*, 2615; *Angew. Chem. Int. Ed.* **2003**, *42*, 2511.
[12] L. F. He, P. G. F. Jagtap, D. G. I. Kingston, H. J. Shen, G. A. Orr, S. B. Horwitz, *Biochemistry* **2000**, *39*, 3972.
[13] B. Becattini, S. Sareth, D. Y. Zhai, K. J. Crowell, M. Leone, J. C. Reed, M. Pellecchia, *Chem. Biol.* **2004**, *11*, 1107.

 © 2005 Wiley-VCH Verlag GmbH & Co. KGaA, Weinheim

Topological Networks

Twelve-Connected Net with Face-Centered Cubic Topology: A Coordination Polymer Based on $[Cu_{12}(\mu_4\text{-}SCH_3)_6]^{6+}$ Clusters and CN^- Linkers**

Dan Li, Tao Wu, Xiao-Ping Zhou, Rui Zhou, and Xiao-Chun Huang*

In recent years, the analysis of topological networks of metal–organic coordination polymers has been a topical area of research in crystal engineering, not only as an important tool for simplifying complicated supramolecular coordination polymers, but also in the rational design of some functional materials with unique properties.[1–3] Considerable effort has been invested in the characterization and design of such coordination polymers.[4] O'Keeffe et al. identified five regular nets, one quasiregular net, and fourteen semiregular three-periodic nets by transitivity *pqrs*.[5] Of these nets, the face-centered cubic net (fcu) is the only quasiregular net with transitivity 1112, which exhibits the highest coordination number (12). It has been suggested that among the numerous topological nets, the most important and plausible targets for designed synthesis are those with "simple, high-symmetry" structures.[6] Although many coordination polymers with different topological networks containing 3~8-connected nodes are known,[7] synthetically prepared examples of higher connected and higher symmetry nets, such as fcu, have not been reported to date.

Significant interest has also arisen in organic and coordination chemistry for the design and synthesis of novel coordination polymers with ligands generated in situ.[8] We have previously reported[9] the reaction of CuSCN with acetonitrile and methanol under solvothermal conditions, which yielded a novel 3D polymeric photoluminescent complex, $\{[Cu(\mu_3\text{-}SCH_3)_2(CN)]_2[Cu_{10}(\mu_3\text{-}SCH_3)_4(\mu_4\text{-}SCH_3)_2]\}_n$, in which the methyl mercaptide is generated in situ. The complex contains dodecanuclear copper(I) clusters, which can be rationalized in terms of an α-Po simple cubic net (pcu), by defining the decanuclear copper cluster $[Cu_{10}(\mu_3\text{-}SCH_3)_4(\mu_4\text{-}SCH_3)_2]$ as a node and $[Cu(\mu_3\text{-}SCH_3)_2(CN)]$ as a

[*] Prof. Dr. D. Li, T. Wu, X.-P. Zhou, Dr. X.-C. Huang
Department of Chemistry, Shantou University
Shantou, Guangdong 515063 (P. R. China)
Fax: (+86) 754-290—2767
E-mail: dli@stu.edu.cn
R. Zhou
Department of Chemistry, Medical College,
Shantou University
Shantou, Guangdong 515063 (P. R. China)

[**] This work was supported by the National Natural Science Foundation of China (No. 29901004 and 20271031) and the Natural Science Foundation of Guangdong Province of China (No. 021240). Acknowledgment is also made to Dr. Nick Bampos of the Department of Chemistry, University of Cambridge for proofreading the manuscript prior to publication.

Supporting information for this article is available on the WWW under http://www.angewandte.org or from the author.

 DOI: 10.1002/anie.200500290 © 2005 Wiley-VCH Verlag GmbH & Co. KGaA, Weinheim

linker. In our ongoing research, we have found that the complex can also be obtained by reaction of $Cu(NO_3)_2 \cdot 3H_2O$ or $Cu(CH_3COO)_2 \cdot 2H_2O$ and NaSCN in the presence of acetonitrile and methanol under the same solvothermal conditions (140 °C). Interestingly, when the reaction temperature was increased to 160 °C, a very different product, namely, $[Cu_{12}(\mu_4\text{-}SCH_3)_6(CN)_6]_n \cdot 2H_2O$ (**1**), was obtained in low yield. This compound is very stable in air at ambient temperature, and relatively insoluble in common solvents.

X-ray single-crystal analysis[10] revealed that the crystal structure of **1** is composed of a 3D neutral microporous framework based on the highly symmetrical, spherical dodecanuclear copper(I) cluster $[Cu_{12}(\mu_4\text{-}SCH_3)_6]^{6+}$ connected by CN^- ligands and guest water molecules, with space group $Fm\bar{3}m$. The basic spherical unit (Figure 1) contains a centrosymmetric Cu_{12} cubo-octahedron, involving a regular octahedron of sulfur atoms with each edge bridged by a CuX unit (X = C or N) from the CN^- ligand. All methyl groups point outwards. Three mutually perpendicular, coplanar, eight-membered Cu_4S_4 rings intersect at the sulfur atoms to generate an globular configuration. Each Cu^I center lies in a planar and trigonal coordination sphere and binds to two bridging μ_4-SCH_3 ligands and to one N or C atom of the CN^- ligand (S–Cu 2.2284(17), Cu–X 1.889(15), C–N 1.17(3) Å, S-Cu-S 127.1(2), S-Cu-X 116.44(12)°). The coordination environment of all the sulfur atoms in μ_4 bridging mode is a square-pyramidal $CSCu_4$ unit, with one carbon atom at the apex and four copper atoms in the equatorial plane. The C–S bond lengths are all 1.81(2) Å, similar to those in other mercaptanes.[11] While μ_2- and μ_3-thiolate bridging modes are relatively common, symmetric μ_4-thiolates remain scarce.[11] Three adjacent Cu^I atoms bridged by three sulfur atoms form an equilateral triangle with a Cu···Cu distance of 2.987(2) Å that indicates a weak Cu···Cu interaction. The corresponding bond angles and lengths are equal, and thus an ideal 32-face polyhedron results: eight equilateral triangles and 24 isosceles triangles (see Supporting Information).

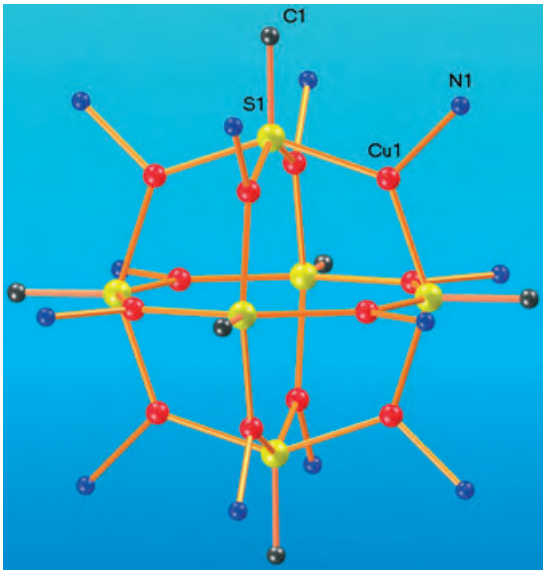


Figure 1. Structure of the basic globular $Cu_{12}(SCH_3)_6(CN)_6$ unit with a center of symmetry at the center of the S_6 cage; hydrogen atoms are omitted for clarity.

A polymer $[Cu_{13}Cl_{13}(SCH_2CH_2NH_3)_6 \cdot H_2O]_n$ containing $(Cu_{12}S_6)$ clusters with a similar globular configuration has been previously reported[11a] in which the corresponding bond angles and lengths in each cluster are non-equivalent, for example, Cu–S bond lengths range from 2.221 to 2.300 Å. In this complex, $^-SCH_2CH_2NH_3^+$ is a neutral ligand, and the clusters act as 4-connected nodes linked by CuCl subunits and chloride ions to form a 2D framework. In contrast, each $[Cu_{12}(\mu_4\text{-}SCH_3)_6]^{6+}$ unit in complex **1**, which has higher symmetry, is connected to twelve adjacent clusters by twelve cyanide ions to give a 3D microporous supramolecular framework (Figure 2). Approximately 20.3 % of the crystal volume is occupied by free water molecules with a volume of about 748.1 $Å^3$ in each cell unit.

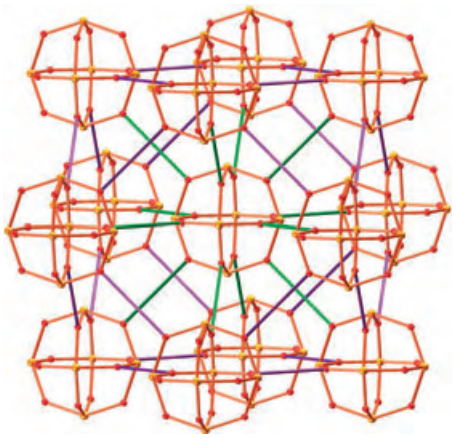


Figure 2. The site of each $Cu_{12}S_6$ cluster in the cell unit.

The 3D framework can be rationalized as a face-centered cubic net (fcu) with Schläfli symbol $(3^{24}4^{36}5^6)$ by assigning the dodecanuclear copper(I) cluster $[Cu_{12}(\mu_4\text{-}SCH_3)_6]^{6+}$ as a node and the CN^- ligand as a linker (Figure 3), in accordance with the quasiregular net structure defined by O'Keeffe. In each

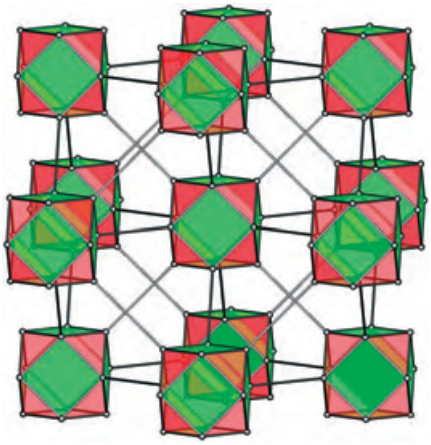


Figure 3. The 3D, 12-connected augmented fcu topological network.

 © 2005 Wiley-VCH Verlag GmbH & Co. KGaA, Weinheim

cell unit, the central node or the center of the central cluster is located at (0.5, 0.5, 0.5), and the other adjacent twelve nodes are located at the center of each edge of the cube, respectively (Figure 2). Eight water molecules occupy the center of the tetrahedron. The distance from the center of each spherical unit to adjacent units is $a/\sqrt{2}$ (10.918 Å), and each spherical unit resides at a crystallographic inversion center. To the best of our knowledge, this is the first fcu topological network observed in coordination polymers, and represents the highest connected topology of any known coordination network.

Thermogravimetric analysis of **1** showed that the structural skeleton remains stable up to 190 °C (see Supporting Information). Initial loss of guest water molecules is followed by the abrupt loss of organic components (CH_3 and CN) from 190 to 275 °C (found weight loss 21.9%, calcd 22.8%; see Supporting Information).

Another interesting feature of **1** is the in situ generation of SCH_3^- and CN^- ligands. We have previously shown that the sulfur atom in SCH_3^- originates from SCN^- and the methyl group from methanol rather than acetonitrile.[9] In an attempt to understand the mechanism for the transformation of inorganic sulfur into organic sulfur, we identified the following experimental phenomena: 1) the colorless residual solution has a characteristically pungent smell and quickly becomes green after the reactor is opened to air; this indicates reduction of Cu^{2+} to Cu^+ and production of CH_3SH or H_2S in the reactions; 2) yellow α-CuSCN single crystals and yellow S_8 single crystals were found in the residual solid in two analogous reactions.[12] Even though it cannot be found in the present reactions, we assume that H_2S acts indirectly as the sulfurization reagent, which is generated by the reaction of S with H_2O, and which can then react with CH_3OH to form SCH_3^-. Possibly, S from the decomposition of SCN^- and CuSCN from redox reaction of Cu^{2+} and SCN^- are two important intermediates in the present reactions. Moreover, it is likely that the frameworks of the two complexes were determined by the reaction temperature. The precise mechanism and the effect of the temperature on the reactions warrant further investigation.

In conclusion, a novel microporous polymer containing a face-centered cubic (fcu) topological network with the highest connectivity, based on a dodecanuclear copper(I) cluster as a twelve-connected node, was synthesized by a simultaneous redox, sulfurization, and self-assembly reaction under solvothermal conditions. The concept of using a cluster as a building block to construct high-connectivity networks is therefore feasible, and the reactions confirm the transformation of inorganic into organic sulfur. The result provides a new avenue for designing and generating new solid-state materials based on networks of high-coordinate nodes linked by bridging ligands.

Experimental Section

1: A mixture of $Cu(NO_3)_2{\cdot}3H_2O$ (0.241 g, 1.0 mmol), NaSCN (0.081 g, 1.0 mmol), methanol (5.0 mL), and acetonitrile (5.0 mL) was stirred for 1 min in air, then transferred and sealed in a 25 mL teflon-lined reactor, which was heated in an oven to 160 °C for 72 h and then cooled to room temperature at a rate of 5 °C h^{-1}. Yellow cubic crystals were obtained in 4.5% yield based on $Cu(NO_3)_2{\cdot}3H_2O$.

Elemental analysis (%) calcd for **1** ($C_{12}H_{22}Cu_{12}N_6O_2S_6$): H 1.79, C 11.65, N 6.79%; found: H 1.82, C 11.59, N 6.82%; IR (KBr, cm^{-1}): 2920s, 2825w, 2127s, 1418m, 1305m, 957s, 689w, 645m, 463w.

Received: January 25, 2005
Revised: April 17, 2005
Published online: June 1, 2005

Keywords: cluster compounds · copper · S ligands · solvothermal synthesis · topological networks

[1] a) B. Moulton, M. J. Zaworotko, *Chem. Rev.* **2001**, *101*, 1629–1658; b) M. Eddaoudi, D. B. Moler, H.-L. Li, B. Chen, T. M. Reineke, M. O'Keeffe, O. M. Yaghi, *Acc. Chem. Res.* **2001**, *34*, 319–330; c) P. J. Hagrman, D. Hagrman, J. Zubieta, *Angew. Chem.* **1999**, *111*, 2798–2848; *Angew. Chem. Int. Ed.* **1999**, *38*, 2639–2684; d) S. R. Batten, R. Robson, *Angew. Chem.* **1998**, *110*, 1558–1595; *Angew. Chem. Int. Ed.* **1998**, *37*, 1460–1494.

[2] a) B. F. Abrahams, S. R. Batten, M. J. Grannas, H. Hamit, B. F. Hoskins, R. Robson, *Angew. Chem.* **1999**, *111*, 1538–1540; *Angew. Chem. Int. Ed.* **1999**, *38*, 1475–1477; b) B. F. Abrahams, P. A. Jackson, R. Robson, *Angew. Chem.* **1998**, *110*, 2801–2804; *Angew. Chem. Int. Ed.* **1998**, *37*, 2656–2659; c) L. Carlucci, G. Ciani, D. M. Proserpio, S. Rizzato, *Chem. Commun.* **2001**, 1198–1199; d) J.-C. Dai, X.-T. Wu, Z.-Y. Fu, S.-M. Hu, W.-X. Du, C.-P. Cui, L.-M. Wu, H.-H. Zhang, R.-Q. Sun, *Chem. Commun.* **2002**, 12- 13.

[3] a) L. Carlucci, G. Ciani, P. Macchi, D. M. Proserpio, *Chem. Commun.* **1998**, 1837- 1838; b) M. Eddaoudi, J. Kim, M. O'Keeffe, O. M. Yaghi, *J. Am. Chem. Soc.* **2002**, *124*, 376–377; c) T.-Y. Niu, X.-Q. Wang, A. J. Jacobson, *Angew. Chem.* **1999**, *111*, 2059–2062; *Angew. Chem. Int. Ed.* **1999**, *38*, 1934–1937; d) S. A. Barnett, A. J. Blake, N. R. Champness, C. Wilson, *Chem. Commun.* **2002**, 1640–1641; e) B. Rather, B. Moulton, R. D. B. Walsh, M. J. Zaworotko, *Chem. Commun.* **2002**, 694–695; f) L. Carlucci, N. Cozzi, G. Ciani, M. Moret, D. M. Proserpio, S. Rizzato, *Chem. Commun.* **2002**, 1354–1355; g) B. Moulton, H. Abourahma, M. W. Bradner, J.-J. Lu, G. J. McManus, M. J. Zaworotko, *Chem. Commun.* **2003**, 1342–1343; h) S. Banfi, L. Carlucci, E. Caruso, G. Ciani, D. M. Proserpio, *Cryst. Growth Des.* **2004**, *4*, 29–32.

[4] a) R. M. Barrer, H. Villiger, *Z. Kristallogr.* **1969**, *128*, 352–370; b) A. F. Wells, *Three-Dimensional Nets and Polyhedra*, Wiley, New York, **1977**; c) A. F. Wells, *Further Studies of Three-Dimensional Nets*, *Am. Crystallogr. Assoc. Monogr.* **1979**, No. 8; d) S. J. Chung, T. Hahn, W. E. Klee, *Acta Crystallogr. Sect. A* **1985**, 40, 42–50; e) J. V. Smith, *Chem. Rev.* **1988**, *88*, 149–182; f) D. E. Akporiaye, G. D. Price, *Zeolites* **1989**, *9*, 23–32; g) M. O'Keeffe, *Z. Kristallogr.* **1991**, *196*, 21–37; h) M. O'Keeffe, *Acta Crystallogr. Sect. A* **1992**, 48, 670–673; i) M. O'Keeffe, *Acta Crystallogr. Sect. A* **1995**, 51, 916–920; j) M. O'Keeffe, N. E. Brese, *Acta Crystallogr. Sect. A* **1992**, 48, 663–669; k) O. Delgado Friedrichs, A. W. M. Dress, D. H. Huson, J. Klinowsky, A. L. Mackay, *Nature* **1999**, *400*, 644–647; l) O. Delgado Friedrichs, D. H. Huson, *Discrete Comput. Geom.* **2000**, *4*, 279–292.

[5] a) O. Delgado Friedrichs, M. O'Keeffe, O. M. Yaghi, *Acta Crystallogr. Sect. A* **2003**, 59, 22–27; b) O. Delgado Friedrichs, M. O'Keeffe, O. M. Yaghi, *Acta Crystallogr. Sect. A* **2003**, 59, 515–525.

[6] a) M. O'Keeffe, M. Eddaoudi, H.-L. Li, T. Reineke, O. M. Yaghi, *J. Solid State Chem.* **2000**, *152*, 3–20; b) O. M. Yaghi, M. O'Keeffe, N. W. Ockwig, H. K. Chae, M. Eddaoudi, J. Kim, *Nature* **2003**, *423*, 705–714.

 © 2005 Wiley-VCH Verlag GmbH & Co. KGaA, Weinheim

[7] a) R. J. Hill, D.-L. Long, M. S. Turvey, A. J. Blake, N. R. Champness, P. Hubberstey, C. Wilson, M. Schröder, *Chem. Commun.* **2004**, 1792 – 1793; b) J. U. Schutze, R. Eckhardt, R. D. Fischer, D. C. Apperley, N. A. Davies, R. K. Harris, *J. Organomet. Chem.* **1997**, *534*, 187 – 194; c) S. M. F. Lo, S. S. Y. Chui, L. Y. Shek, Z. Y. Lin, X. X. Zhan, G. H. Wen, I. D. Williams, *J. Am. Chem. Soc.* **2000**, *122*, 6293 – 6294; d) D.-L. Long, A. J. Blake, N. R. Champness, C. Wilson, M. Schröder, *Angew. Chem.* **2001**, *113*, 2509 – 2513; *Angew. Chem. Int. Ed.* **2001**, *40*, 2444 – 2447; e) D.-L. Long, R. J. Hill, A. J. Blake, N. R. Champness, P. Hubberstey, D. M. Proserpio, C. Wilson, M. Schröder, *Angew. Chem.* **2004**, *116*, 1887 – 1890; *Angew. Chem. Int. Ed.* **2004**, *43*, 1851 – 1854; f) L. Pan, H. Liu, X. Lei, X. Huang, D. H. Olson, N. J. Turro, J. Li, *Angew. Chem.* **2003**, *115*, 560 – 564; *Angew. Chem. Int. Ed.* **2003**, *42*, 542 – 546; g) Q. Fang, X. Shi, G. Wu, G. Tian, G. Zhu, R. Wang, S. Qiu, *J. Solid State Chem.* **2003**, *176*, 1 – 4; h) B. Moulton, J.-J. Lu, R. Hajndl, S. Hariharan, M. J. Zaworotko, *Angew. Chem.* **2002**, *114*, 2945 – 2948; *Angew. Chem. Int. Ed.* **2002**, *41*, 2821 – 2824; i) G. J. McManus, Z.-Q. Wang, M. J. Zaworotko, *Cryst. Growth Des.* **2004**, *4*, 11 – 13.

[8] a) E. C. Constable, *Metals and Ligand Reactivity*, VCH, Weinheim, **1996**; b) R. A. Michelin, M. Mozzon, R. Bertani, *Coord. Chem. Rev.* **1996**, 147, 299 – 338; c) V. Y. Kukushkin, A. J. L. Pombeiro, *Chem. Rev.* **2002**, *102*, 1771 – 1802; d) J.-P. Zhang, S.-L. Zheng, X.-C. Huang, X.-M. Chen, *Angew. Chem.* **2004**, *116*, 208 – 211; *Angew. Chem. Int. Ed.* **2004**, *43*, 206 – 209; e) Z. P. Demko, K. B. Sharpless, *Angew. Chem.* **2002**, *114*, 2214 – 2217; *Angew. Chem. Int. Ed.* **2002**, *41*, 2110 – 2113; f) J.-K. Cheng, Y.-G. Yao, J. Zhang, Z.-J. Li, Z.-W. Cai, X.-Y. Zhang, Z.-N. Chen, Y.-B. Chen, Y. Kang, Y.-Y. Qin, Y.-H. Wen, *J. Am. Chem. Soc.* **2004**, *126*, 7796 – 7797.

[9] D. Li, T. Wu, *Inorg. Chem.* **2005**, *44*, 1175 – 1177.

[10] Crystal data for **1**: $C_{12}H_{22}Cu_{12}N_6O_2S_6$, cubic, space group $Fm\bar{3}m$ (no. 225), $M_r = 1237.20$, $a = 15.4410(19)$, $b = 15.4410(19)$, $c = 15.4410(19)$ Å, $\alpha = \beta = \gamma = 90°$, $V = 3681.5(8)$ Å^3, $Z = 4$, $\rho_{calcd} = 2.232$ g cm^{-3}, $\mu = 7.137$ mm^{-1}, $F(000) = 2384$, $T = 296(2)$ K; $R1 = 0.0634$, $wR2 = 0.1897$ for all data. Data collection was performed on a Bruker Smart Apex CCD diffractometer ($Mo_{K\alpha}$ radiation, $\lambda = 0.71073$ Å) by using frames of 0.3° oscillation ($4.56 \leq 2\theta \leq 50°$). The structure was solved by direct methods, and all non-hydrogen atoms were subjected to anisotropic refinement by full-matrix least-squares methods on F^2 by using the SHELXTL program.[13] The hydrogen atoms were generated geometrically.

[11] a) R. V. Parish, Z. Salehi, R. G. Pritchard, *Angew. Chem.* **1997**, *109*, 276 – 278; *Angew. Chem. Int. Ed. Engl.* **1997**, *36*, 251 – 253; b) R. G. Pritchard, R. V. Parish, Z. Salehi, *J. Chem. Soc. Dalton Trans.* **1999**, 243 – 250; c) W.-P. Su, R. Cao, M.-C. Hong, J.-T. Chen, J.-X. Lu, *Chem. Commun.* **1998**, 1389 – 1340; d) Z. Salehi, R. V. Parish, R. Z. Pritchard, *J. Chem. Soc. Dalton Trans.* **1997**, 4241 – 4246; e) G. W. Adamson, N. A. Bell, H. M. M. Shearer, *Acta Crystallogr. Sect. B* **1982**, 38, 462 – 465; f) M. D. Janssen, A. L. Spek, D. M. Grove, G. van Koten, *J. Am. Chem. Soc.* **1996**, *118*, 4081 – 4084.

[12] Heating a mixture of $CuSO_4$, CH_3CN, and CH_3OH in a sealed reactor at 180 °C gave yellow single crystals of α-CuSCN (crystal data at 293 K: orthorhombic, $a = 7.2535(6)$, $b = 6.6842(6)$, $c = 11.0466(9)$ Å, $V = 535.58(8)$ Å^3). Heating a mixture of $Cu(NO_3)_2 \cdot 3H_2O$, NaSCN, CH_3OH, and *m*-phenylenediacetonitrile in a sealed reactor at 180 °C gave pale yellow crystals of S_8 (crystal data at 293 K: orthorhombic, $a = 10.4612(10)$, $b = 12.8619(12)$, $c = 24.486(2)$ Å, $V = 3294.7(5)$ Å^3).

[13] G. M. Sheldrick, SHELXTL 6.10, Bruker Analytical Instrumentation, Madison, Wisconsin, USA, **2000**.

 © 2005 Wiley-VCH Verlag GmbH & Co. KGaA, Weinheim

Supramolecular Chemistry

Supramolecular Assembly and Coordination-Assisted Deaggregation of Multimetallic Macrocycles**

*Cecily Tsz Lui Ma and Mark J. MacLachlan**

One of the most important objectives in supramolecular chemistry is the self-assembly of molecular building blocks into well-defined architectures.[1] The remarkable functions of self-assembled structures in biological systems has resulted in considerable effort being devoted to the development of new materials that employ this concept. Examples include catalysts,[2] organic nanotubes,[3] supramolecular polymers,[4] and chemical sensors.[5]

Aggregation of rigid, shape-persistent macrocycles has become a topic of growing interest.[6] Conjugated phenylacetylene macrocycles (PAMs), for example, show solvent- and concentration-dependent aggregation that is mediated by π–π interactions between the macrocycles and leads to nanotubular assemblies.[7] Such aggregation, however, is usually weak and depends strongly on the substituents of the macrocycles for organization.[8] Stronger forces, such as hydrogen-bonding interactions, have been used to aggregate cyclic D,L-peptides and urea macrocycles.[9] In these systems, solvents containing hydrogen-bond donors or acceptors may decrease aggregation.[10] The use of coordination chemistry to assemble shape-persistent macrocycles is an underdeveloped area.

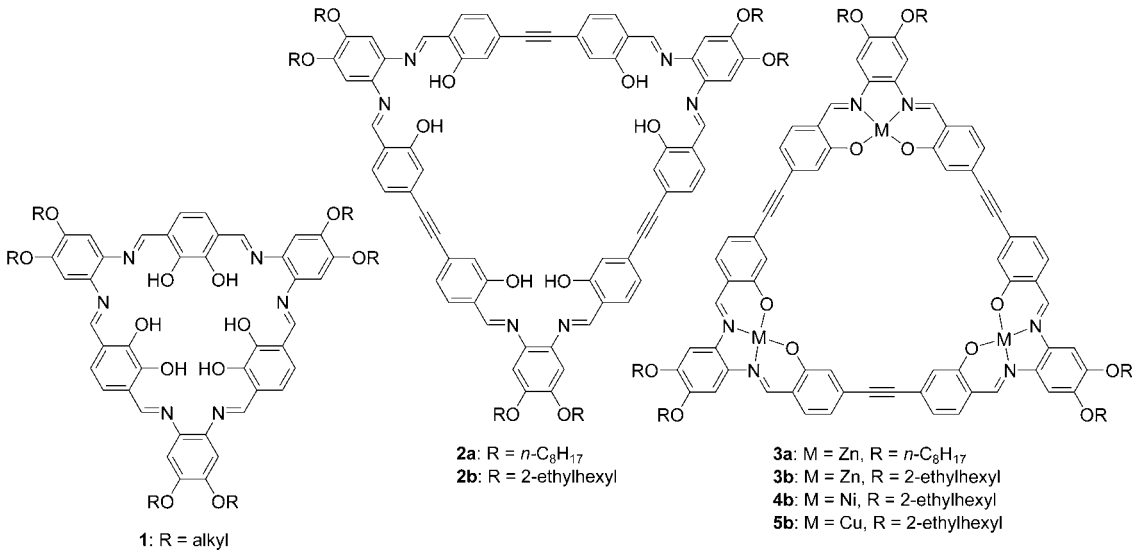
We recently reported the synthesis of small macrocycles **1** containing Schiff bases with the intention of studying their self-assembly.[11] However, these macrocycles have only a very small cavity in the center and would not yield significant porosity if stacked. A larger, conjugated macrocycle **2a** containing Schiff bases (Scheme 1) is readily prepared in high yield without the use of a template.[12,13] This macrocycle may react with transition-metal salts to form trimetalated macrocycles, in which the metals are incorporated into the tetradentate (N_2O_2) binding sites. Herein, we report our findings on the surprising aggregation behavior of these large, shape-persistent metallomacrocycles in solution. The metal center plays an important role in mediating the assembly of the macrocycles. Furthermore, we demonstrate coordination-assisted deaggregation of the metallomacrocycles, a mechanism that may form the basis of new chemical sensors.

[*] C. T. L. Ma, Prof. M. J. MacLachlan
Department of Chemistry
University of British Columbia
2036 Main Mall, Vancouver, BC V6T1Z1 (Canada)
Fax: (+1) 604-822-2847
E-mail: mmaclach@chem.ubc.ca

[**] We thank the UBC and NSERC of Canada (Discovery Grant) for funding. C.T.L.M. thanks the NSERC for a PGSA graduate fellowship award and Alfred Leung and Jonathan Chong for technical assistance.

Supporting information for this article is available on the WWW under http://www.angewandte.org or from the author.

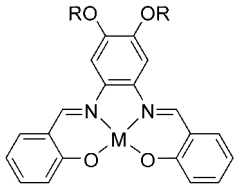
 © 2005 Wiley-VCH Verlag GmbH & Co. KGaA, Weinheim DOI: 10.1002/anie.200500058



Scheme 1. Conjugated macrocycles **1**–**5**.

Metalation of **2a** with Zn^{II} salts afforded metallomacrocycle **3a**. Macrocycles with branched 2-ethylhexyloxy substituents **2b**–**5b** were also prepared to give enhanced solubility. MALDI-TOF mass-spectrometric analysis of metallomacrocycles **3**–**5** verified their composition. In addition to the molecular ion, signals corresponding to the protonated dimer were also observed. In the case of **3a**, significant aggregation was observed, as signals for ions of up to $[(\mathbf{3a})_9]^+$ were present in the spectrum (see the Supporting Information). The intensity of the signal that arose from the aggregates was very large only in the case of **3a**.

^{1}H NMR spectroscopic analysis of **3a** showed that it aggregates in solution. In [D$_8$]THF, sharp signals are displayed, all of which can be assigned to the macrocycle, including the imine resonance at $\delta = 8.85$ ppm. The resonances broaden as the ratio of CD_2Cl_2/[D$_8$]THF is increased such that the aromatic groups are no longer visible (Figure 1). This effect is attributed to a significant decrease in the T_2 relaxation time, caused by the formation of large aggregates.[14] Well-defined oligomeric structures (e.g., dimers) would be expected to give rise to sharp signals, but our results indicate that larger aggregates are present. The resonances associated with the macrocycle are completely diminished in CD_2Cl_2, whereas those for the alkoxy side groups are broad. Broadening has been observed in the aggregation of PAMs in highly polar solvents.[6c,15] For comparison, **2** and the monometalated compound **6** do not aggregate at similar concentrations in THF or CH_2Cl_2.



Self-association can have a large effect on the optical properties of macrocycles in solution. To investigate further the aggregation behavior of the macrocycles, we undertook UV/Vis and fluorescence spectroscopic studies of macrocycles **3**–**5** in mixtures of CH_2Cl_2/THF of different compositions at constant concentration (Figure 2a,b). Metallomacrocycles **4b** (M = Ni^{II}) and **5b** (M = Cu^{II}) both show UV/Vis spectra with several well-defined absorption features. Moreover, there is virtually no difference between the spectra recorded in THF and in CH_2Cl_2. The spectra of zinc macrocycles **3a** and **3b** in THF appear to be very similar to those of macrocycles **4b** and **5b**, with several distinct features observed. However, as the ratio of CH_2Cl_2/THF increases, the UV/Vis spectra for **3a** and **3b** undergo a dramatic change that leads to broad, featureless absorption spectra in CH_2Cl_2.

Metallomacrocycle **3a** is fluorescent in THF ($\phi = 0.86\,\%$), with signals at 558 and 596 nm (Figure 2b). The signals are red-shifted and diminish in intensity on changing the solvent from THF to CH_2Cl_2, thus leading to a broad emission for **3a** in CH_2Cl_2 that is similar to that arising from an excited-state complex (excimer) and that shows no vibrational fine structure. Metallomacrocycle **3b** with peripheral 2-ethylhexyloxy substituents behaves similarly to **3a**, which has unbranched alkyl substituents.

The optical properties for **3a** were examined in a range of solvents with varying dielectric constants (Figure 2c). In a coordinating solvent (e.g., THF, dimethyl sulfoxide (DMSO),

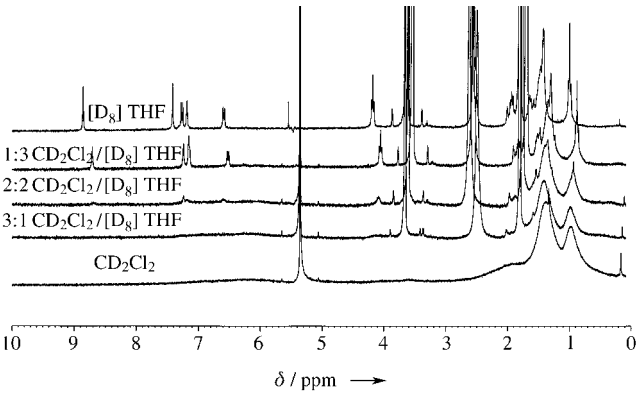


Figure 1. ^{1}H NMR spectra of **3a** in various mixtures of CD_2Cl_2/[D$_8$]THF ([**3a**] = ca. 6×10^{-4} M for all of the spectra).

 © 2005 Wiley-VCH Verlag GmbH & Co. KGaA, Weinheim

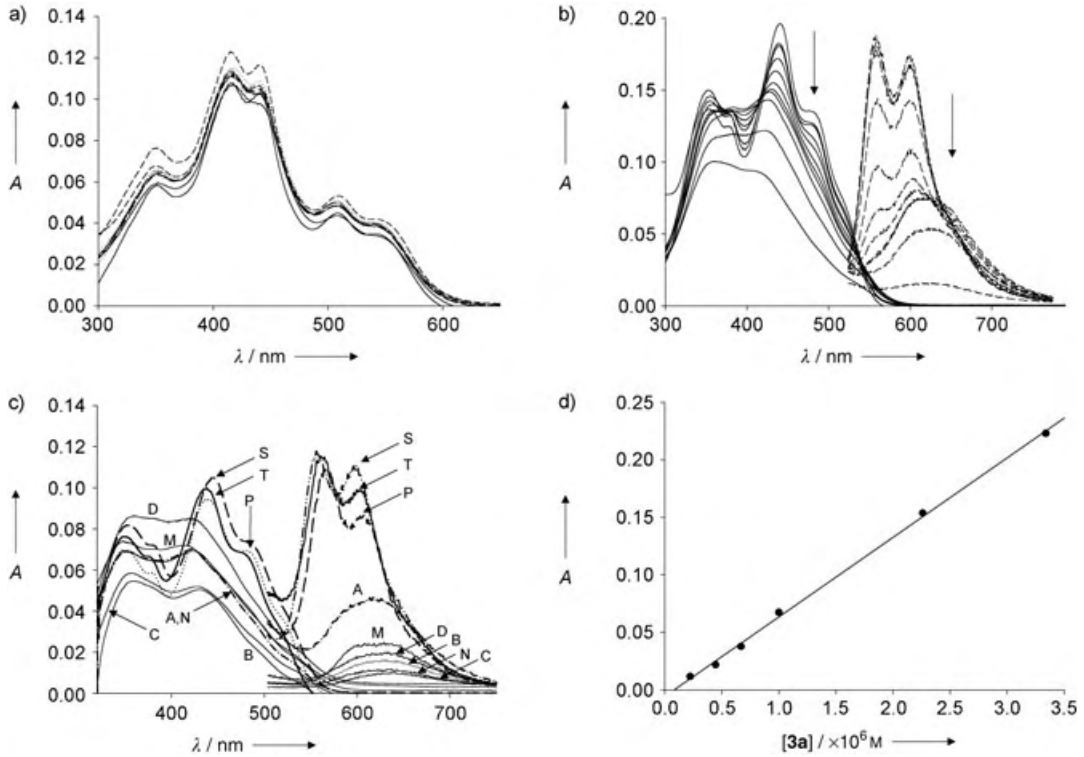


Figure 2. a) UV/Vis spectra of **4b** in various mixtures of CH_2Cl_2/THF (1:0–0:1 in 10% increments); [**4b**] = 9.0×10^{-7} M. b) UV/Vis and fluorescence spectra of **3a** in CH_2Cl_2/THF with the same solvent compositions; the arrows indicate the direction of the increasing CH_2Cl_2/THF ratio. c) UV/Vis and fluorescence spectra of **3a** in various solvents (T: THF, S: DMSO, P: pyridine, A: acetone, B: benzene, D: dichloromethane, M: methanol, C: cyclohexane, N: acetonitrile). d) Graph of absorbance (*A*) at 380 nm as a function of concentration (M) of **3a**.

and pyridine), the absorption spectrum shows well-defined features and the macrocycle fluoresces with two signals near to approximately 560 and 600 nm. In a weakly or noncoordinating solvent (e.g., acetone, methanol, dichloromethane, benzene, acetonitrile, and cyclohexane), the absorption spectrum is broad and nearly featureless and the emission spectrum is broad and red-shifted. The broad absorption spectra and the lack of any dependence on the dielectric constant corroborate the notion that the aggregation is a ground-state effect, and not because of excimers.

These results indicate that **3a** is aggregated at concentrations as low as 10^{-6} or 10^{-7} M in most noncoordinating solvents. Furthermore, a plot of absorbance versus concentration is linear with little concentration dependence on the aggregation (Figure 2d). A reliable equilibrium constant from the system could not be extracted, but it is estimated that K_{assoc} must be greater than 10^7.[16] Given that the macrocycle is electron rich, we were surprised that π–π interactions between the macrocycles would be significant at low concentration in a solvent such as CH_2Cl_2, in which **3a** is soluble.[8] Since **3a** aggregates in MeOH, it is unlikely that hydrogen-bonding interactions are an important factor for assembly. It is also surprising that **3a** aggregates in benzene, in which π–π interactions with the solvent are expected to compete with π–π interactions of the macrocycle, thus suppressing assembly. Moreover, if π–π interactions were solely responsible for the assembly, macrocycles containing Schiff bases and Cu^{II} and Ni^{II} centers are anticipated to be flat with square-planar geometry at the metal and would show a stronger tendency than Zn^{II} macrocycles to aggregate. These results suggest that the aggregation of the macrocycles involve a further interaction, namely, a Zn···O interaction between the macrocycles to maintain a coordination number of five at the Zn^{II} center. The fifth coordination site is occupied by a solvent molecule in coordinating solvents, but the coordination of phenolic oxygen atoms to the zinc centers is involved in the assembly. The coordination of phenolic oxygen atoms to metal centers in salen-type zinc complexes has been observed in the solid state.[17]

The addition of the paramagnetic Cu^{II} metallomacrocycle **5b** to a solution of the Zn^{II} metallomacrocycle **3b** in CH_2Cl_2 led to only a small degree of fluorescence quenching, but did not disrupt the aggregated state of **3b**, as observed by fluorescence and UV/Vis spectroscopies. This outcome indicates that **3b** prefers to interact with other macrocycles of the same type rather than forming dimers with **5b**, which further supports a Zn···O interaction between the macrocycles. If **5b** interacted with the aggregates of **3b**, the paramagnetic Cu^{II} centers would be expected to quench the fluorescence of the zinc metallomacrocycles.

In contrast to the negligible effects of nonpolar solvents on aggregation, coordinating solvents, such as THF and pyridine, readily interrupted the aggregation of **3a** and **3b**. To prove that coordination was the important interaction, **3a** was treated with pyridine and lutidine (Figure 3a,b). UV/Vis and fluorescence spectroscopic analysis showed that **3a** deaggre-

 © 2005 Wiley-VCH Verlag GmbH & Co. KGaA, Weinheim

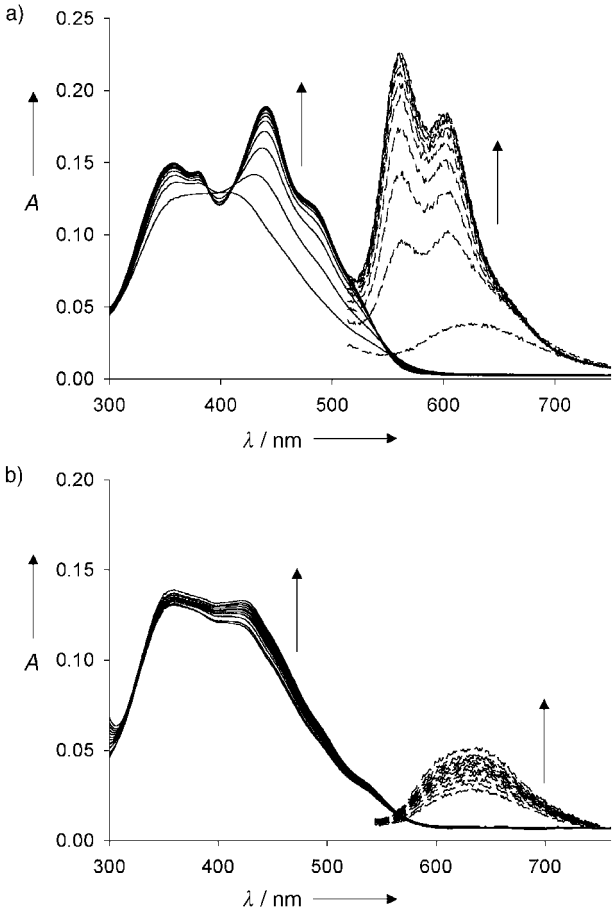


Figure 3. UV/Vis and fluorescence spectra of **3a** titrated with a) pyridine (3.6×10^{-3}–0.020 M; step size: 1.81×10^{-3} M) and b) lutidine (1.26×10^{-3}–0.014 M; step size: 1.26×10^{-3} M; [**3a**] = 1.8×10^{-6} M). The arrows indicate the direction of the increasing concentration of the base.

gates with the addition of pyridine. With lutidine, however, which is more basic but unable to coordinate to the metal centers, the macrocycle remained aggregated.[18] The absence of an isosbestic point in the titration of **3a** with pyridine is consistent with multiple metal centers being coordinated.

The aggregation behavior of **3a** and **3b** is illustrated in Figure 4. The molecules are not aggregated in THF but on changing the solvent to CH_2Cl_2 or benzene aggregate into supramolecular assemblies. We do not know for certain whether the assemblies are tubular, but it seems likely since the aggregation is dominant even at a concentration of 10^{-7} M. Although other possibilities cannot be ruled out, a tubular assembly would maximize interactions between the macrocycles. Addition of a molecule that can coordinate to the macrocycles results in deaggregation and replenished luminescence. These assemblies may serve as the basis of a new model for chemically sensing coordinating bases, in which the mechanism involves deaggregation of the supramolecular assembly.

To test this mechanism as the basis of a chemical sensor, we titrated the macrocycle assembly of **3a** in CH_2Cl_2 with quinuclidine. The fluorescence increased rapidly after

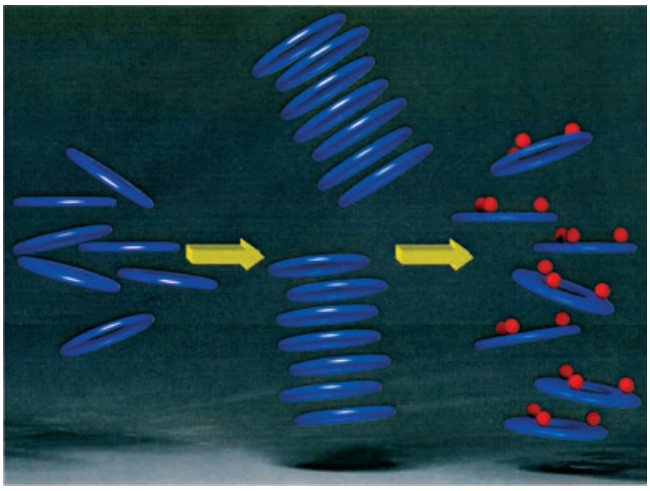


Figure 4. Illustration of aggregation and coordination-assisted deaggregation of multimetallic macrocycles. Left: macrocycles (blue) in THF. Middle: macrocycles aggregated when in CH_2Cl_2. Right: macrocyclic assemblies deaggregate after treatment with a coordinating ligand (red spheres).

30 equivalents of quinuclidine were added, with a total fluorescence increase of 100% at 575 nm. The deaggregation was confirmed by ^{1}H NMR spectroscopic analysis. Although the ^{1}H NMR spectrum of **3a** in CD_2Cl_2 is broadened by aggregation, the spectrum displays the sharp signals expected for **3a** on addition of only three–six equivalents of quinuclidine. Thus, the deaggregation of the macrocyclic assemblies generates a turn-on signal for sensing coordinating bases, such as quinuclidine. This approach is a new method of chemical sensing that may be exploited for sensing molecules of biological relevance.

In summary, we have observed the strong aggregation of metallomacrocycles containing Schiff bases in solution that appears to be facilitated by Zn···O interactions between the macrocycles. The optical and fluorescent properties of the macrocyclic assemblies undergo significant changes when treated with coordinating bases that cause deaggregation of the supramolecular assemblies. These results suggest a new chemical method for control over the assembly of nanostructures from shape-persistent macrocycles. Future work will involve the use of bidentate ligands (e.g., 1,4-pyrazine) to form supramolecular nanotubes.

Received: January 7, 2005
Revised: April 14, 2004
Published online: June 8, 2005

Keywords: metallacycles · Schiff bases · self-assembly · sensors · supramolecular chemistry

[1] For recent examples of self-assembled architectures, see: a) F. Würthner, S. Yao, U. Beginn, *Angew. Chem.* **2003**, *115*, 3368–3371; *Angew. Chem. Int. Ed.* **2003**, *42*, 3247–3250; b) E. R. Zubarev, M. U. Pralle, E. D. Sone, S. I. Stupp, *Adv. Mater.* **2002**, *14*, 198–203; c) S. Park, J.-H. Lim, S.-W. Chung, C. A. Mirkin, *Science* **2004**, *303*, 348–351; d) A. Petitjean, H. Nierengarten, A.

 © 2005 Wiley-VCH Verlag GmbH & Co. KGaA, Weinheim

Dorsselaer, J.-M. Lehn, *Angew. Chem.* **2004**, *116*, 3781 – 3785; *Angew. Chem. Int. Ed.* **2004**, *43*, 3695 – 3699.
[2] a) S. Litvinchuk, G. Bollot, J. Mareda, A. Som, D. Ronan, M. R. Shah, P. Perrottet, N. Sakai, S. Matile, *J. Am. Chem. Soc.* **2004**, *126*, 10067 – 10075; b) G. Süss-Fink, M. Faure, T. R. Ward, *Angew. Chem.* **2002**, *114*, 105 – 108; *Angew. Chem. Int. Ed.* **2002**, *41*, 99 – 101.
[3] D. T. Bong, T. D. Clark, J. R. Granja, M. R. Ghadiri, *Angew. Chem.* **2001**, *113*, 1016 – 1041; *Angew. Chem. Int. Ed.* **2001**, *40*, 988 – 1011.
[4] a) O. Ikkala, G. Brinke, *Chem. Commun.* **2004**, 2131 – 2137; b) H. Xu, D. M. Rudkevich, *Chem. Eur. J.* **2004**, *10*, 5432 – 5442; c) Y. Zhou, D. Yan, *Angew. Chem.* **2004**, *116*, 5004 – 5007; *Angew. Chem. Int. Ed.* **2004**, *43*, 4896 – 4899; d) J. J. L. M. Cornelissen, M. Fischer, N. A. J. M. Sommerdijk, R. J. M. Nolte, *Science* **1998**, *280*, 1427 – 1430.
[5] a) A. Tsuda, S. Sakamoto, K. Yamaguchi, T. Aida, *J. Am. Chem. Soc.* **2003**, *125*, 15722 – 15723; b) S.-S. Sun, A. J. Lees, *Coord. Chem. Rev.* **2002**, *230*, 171 – 192; c) M. J. E. Resendiz, J. C. Noveron, H. Disteldorf, S. Fischer, P. J. Stang, *Org. Lett.* **2004**, *6*, 651 – 653.
[6] a) S. Höger, K. Bonrad, A. Mourran, U. Beginn, M. Möller, *J. Am. Chem. Soc.* **2001**, *123*, 5651 – 5659; b) J. Zhang, J. S. Moore, *J. Am. Chem. Soc.* **1992**, *114*, 9701 – 9702; c) Y. Tobe, N. Utsumi, K. Kawabata, A. Nagano, K. Adachi, S. Araki, M. Sonoda, K. Hirose, K. Naemura, *J. Am. Chem. Soc.* **2002**, *124*, 5350 – 5364; d) S. Höger, *J. Polym. Sci. Part A* **1999**, *37*, 2685 – 2698; e) M. M. Haley, *Top. Curr. Chem.* **1999**, *201*, 81 – 130; f) C. Grave, A. D. Schlüter, *Eur. J. Org. Chem.* **2002**, 3075 – 3098.
[7] S. Lahiri, J. L. Thompson, J. S. Moore, *J. Am. Chem. Soc.* **2000**, *122*, 11315 – 11319.
[8] A. S. Shetty, J. Zhang, J. S. Moore, *J. Am. Chem. Soc.* **1996**, *118*, 1019 – 1027.
[9] a) L. S. Shimizu, A. D. Hughes, M. D. Smith, M. J. Davis, B. P. Zhang, H. C. Zur Loye, K. D. Shimizu, *J. Am. Chem. Soc.* **2003**, *125*, 14972 – 14973; b) M. R. Ghadiri, J. R. Granja, R. A. Milligan, D. E. McRee, N. Khazanovich, *Nature* **1993**, *366*, 324 – 327.
[10] J. C. Adrian, C. S. Wilcox, *J. Am. Chem. Soc.* **1991**, *113*, 678 – 680.
[11] A. J. Gallant, M. J. MacLachlan, *Angew. Chem.* **2003**, *115*, 5465 – 5468; *Angew. Chem. Int. Ed.* **2003**, *42*, 5307 – 5310.
[12] C. Ma, A. Lo, A. Abdolmaleki, M. J. MacLachlan, *Org. Lett.* **2004**, *6*, 3841 – 3844.
[13] For recent examples of macrocycles containing Schiff bases, see: a) J. L. Sessler, J. M. Veauthier, W.-S. Cho, V. M. Lynch, *Inorg. Chem.* **2004**, *43*, 1220 – 1228; b) C. V. Depree, U. Beckmann, K. Heslop, S. Brooker, *Dalton Trans.* **2003**, 3071 – 3081; c) S. Akine, D. Hashimoto, T. Saiki, T. Nabeshima, *Tetrahedron Lett.* **2004**, *45*, 4225 – 4227; d) J. Gao, J. H. Reibenspies, R. A. Zingaro, F. R. Woolley, A. E. Martell, A. Clearfield, *Inorg. Chem.* **2005**, *44*, 232 – 241.
[14] H. Evertsson, S. Nilsson, C. J. Welch, L.-O. Sundelöf, *Langmuir* **1998**, *14*, 6403 – 6408.
[15] D. Zhao, J. S. Moore, *J. Org. Chem.* **2002**, *67*, 3548 – 3554.
[16] This equilibrium constant was estimated on the assumption that the concentration of the free macrocycle was $< 10^{-7}$ M when the total concentration of macrocycle was 10^{-6} M; see the Supporting Information.
[17] a) J. Reglinski, S. Morris, D. E. Stevenson, *Polyhedron* **2002**, *21*, 2175 – 2182; b) S. Akine, T. Taniguchi, T. Nabeshima, *Inorg. Chem.* **2004**, *43*, 6142 – 6144.
[18] A small increase in fluorescence (but no wavelength shift) may result from the neutralization of a trace of residual acid in the solution or the change in the dielectric constant of the solvent.

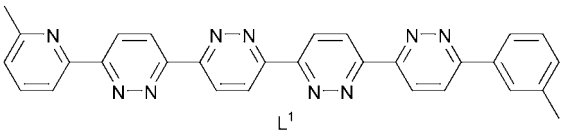
 © 2005 Wiley-VCH Verlag GmbH & Co. KGaA, Weinheim

Supramolecular Chemistry

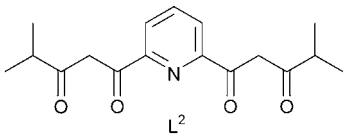
Route to Cluster Helicates**

Manuel R. Bermejo, Ana M. González-Noya, Rosa M. Pedrido, María J. Romero, and Miguel Vázquez*

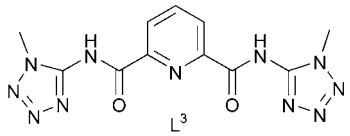
Most supramolecular helicates contain either two or three metal centers, whereas those with four or more remain relatively uncommon.[1,2] Strategies for the construction of metallohelicates with high nuclearity use long organic ligand strands or guest molecules as templating agents, and thus some linear[3] and circular helicates[4] have been reported. In contrast, there are very few examples of discrete multimetallic helicates in which the metal centers are disposed in a polyhedral mode: the pentatopic ligand L^1 forms a quadruply



L^1



L^2



L^3

stranded helicate[5] $[Ag_{10}L^1_4]^{10+}$, and related ligands L^2 and L^3 form bis(triple-helical) metal complexes with six ligand strands wrapped around the $[M_8O_2]^{12+}$ metaloxo clusters ($M = Zn^{II}$, Cd^{II}, and Mn^{II}).[6] These helicates are complex

[*] Prof. M. R. Bermejo, Dr. A. M. González-Noya, Dr. R. M. Pedrido, M. J. Romero, Dr. M. Vázquez[+]
Departamento de Química Inorgánica
Facultade de Química
Universidade de Santiago de Compostela
15782 Santiago de Compostela (Spain)
Fax: (+34) 981-528-073
E-mail: qimb45@usc.es

[+] Present address:
Departamento de Química Inorgánica
Facultade de Química, Universidade de Vigo
36310 Vigo (Spain)

[**] M.R.B. thanks the Xunta de Galicia (PGIDIT03PXI20901PR and PGIDIT04PXIC20902PR) and the Ministerio de Educación y Ciencia of Spain (BQU2003-00167) for financial support. M.V. thanks the Xunta de Galicia for support under the "Isidro Parga Pondal Program". We thank Dr. M. Eugenio Vázquez Sentís (Universidade de Santiago de Compostela) for fruitful discussions and continuing interest in this work.

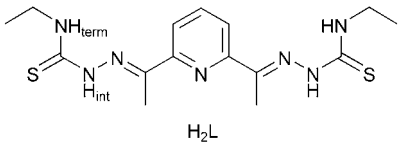
Supporting information for this article is available on the WWW under http://www.angewandte.org or from the author.

 © 2005 Wiley-VCH Verlag GmbH & Co. KGaA, Weinheim DOI: 10.1002/anie.200500840

polystranded architectures that do not display metal–metal interactions.

Helicates are being used in the construction of novel materials, devices, and machines with programmed properties and functions, such as luminescence,[7] DNA binding,[8] chirality,[9] magnetic exchange,[3,10] anion binding,[11] metal-ion translocation,[12] or electrochemical structural rearrangement.[13] However, all these possible applications could undergo remarkable development if the extremely important biological, physical, and chemical properties of cluster compounds were considered.[14] Unfortunately, there are no efficient synthetic routes to "cluster helicates".

Herein, we report the first strategy to construct cluster compounds with a helical arrangement of ligands around the central metal core, that is, "cluster helicates". In particular, we describe the use of a ligand that potentially has a dianionic and helicand character and is equipped with two soft donor atoms, which allow the helicate assembly to be controlled through selection of the oxidation state of the metal centers. We therefore designed bis(4-ethyl-3-thiosemicarbazone)-2,6-diacetylpyridine (H_2L) as such a ligand (int = internal, term = terminal), which contains two soft sulfur donor atoms so that it would be an effective moiety to support the self-assembly of metal(II) dinuclear dihelicate complexes.[15] We recently reported the anion-binding properties of this ligand, and its application to the selective colorimetric recognition of fluoride anions in organic solvents.[16]



H_2L

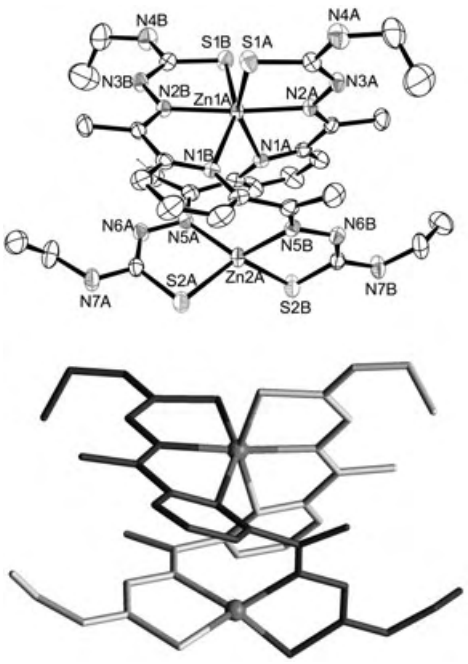


Figure 1. Top: Molecular structure of dihelicate complex $[Zn_2(L)_2]$ (**1**), with the two strands of L labeled as A and B. Thermal ellipsoids are drawn at the 40% probability level, carbon atoms are shown as unshaded ellipsoids, and hydrogen atoms have been omitted for clarity. Bottom: Ball-and-stick representation of **1**, with the two strands of L highlighted in light gray (A) and dark gray (B).

The next step in the study was the preparation of metal(II) dinuclear dihelicate derivatives containing H_2L. Our experience with this class of complex and the absence of hard donor atoms in the main body of H_2L led us to use Cu^{II} and Zn^{II} ions to prepare these complexes. Electrochemical oxidation[17] of a zinc plate in a conducting solution of H_2L in acetonitrile afforded a yellow solution, from which a pale yellow solid precipitated on concentration. The ESI mass spectrum and elemental analysis of this material are consistent with the formation of the neutral dimeric species $[Zn_2(L)_2]$, which arises from the double deprotonation of H_2L in the electrochemical cell. This complex was also characterized by IR spectroscopy (see Supporting Information).

Recrystallization of this yellow precipitate from acetonitrile by slow evaporation afforded pale yellow crystals of complex **1**, from which its molecular structure was determined by X-ray crystallography (Figure 1).[18,19] Its structure reveals the formation of the common [6+4] double-stranded dihelicate $[Zn_2(L)_2]$ (**1**). A racemic mixture of both enantiomers is observed in the unit cell. One Zn^{II} center is tetracoordinated in a tetrahedral mode by two imine nitrogen atoms and two thiolate sulfur atoms from two different ligands. The other Zn^{II} ion is hexacoordinated in a distorted octahedral mode by two pyridine nitrogen atoms, two imine nitrogen atoms, and two thiolate sulfur atoms. This coordination is achieved by symmetrical intertwining of the two ligand strands along the helical axis (Zn···Zn: 4.26 Å). This behavior is quite similar to that found by us in a zinc(II) dinuclear dihelicate complex containing a similar thiosemicarbazone ligand.[15]

The copper(II) derivative was obtained by treatment of H_2L with copper(II) perchlorate in hot acetonitrile. A dark brown solid was isolated and identified as the discrete complex $[Cu_2(L)_2]\cdot 2\,CH_3CN$ (**2**), which was characterized by elemental analysis, IR spectroscopy, ESI mass spectrometry, and magnetic moment measurements (see Supporting Information). Unfortunately, it was impossible to obtain single crystals suitable for X-ray diffraction studies. However, it is expected that **2** has a double-helical arrangement of ligands around the metal centers as it is structurally analogous to **1**.

Once the ability of H_2L to form dinuclear dihelicate complexes with Cu^{II} and Zn^{II} centers was established, we explored the possibility of increasing the nuclearity of these dinuclear dihelicates to obtain neutral dihelical species with a stoichiometry of M_4L_2 by substitution of the divalent metal centers by metal(I) ions (Figure 2).

It is known that all pure substances fulfill the principle of electroneutrality, and as H_2L has a tendency to form metal complexes in its doubly deprotonated form, two dianionic ligand units can be coordinated by four metal(I) ions to form a neutral $[M_4L_2]$ complex. We believe that the presence of the coordinatively versatile thiolate donor atoms in H_2L is

 © 2005 Wiley-VCH Verlag GmbH & Co. KGaA, Weinheim

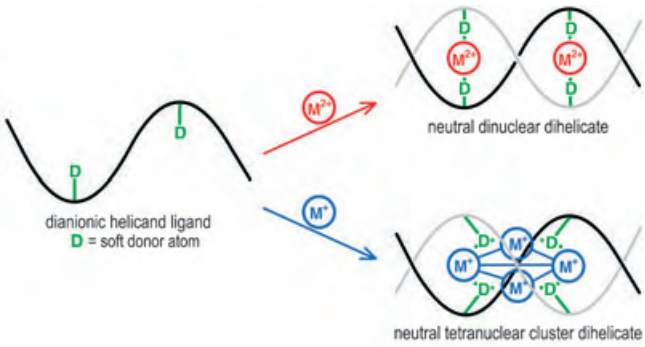


Figure 2. Schematic representation of our synthetic approach to the assembly of "cluster helicates": The substitution of divalent metal centers by metal(I) ions and the use of a dianionic and helicand ligand that contains two soft donor atoms, which can act both as terminal or bridging coordination points depending of the hardness/softness of the metal centers they bind, are the factors that make stabilization of this novel supramolecular motif possible.

essential in satisfying the coordination requirements of the four metal(I) ions and then in stabilizing the $[M_4L_2]$ cluster. Furthermore, these thiolate atoms can act either as terminal or bridging coordination points depending on the degree of hardness/softness of the metal centers to which they bind: as the hardness of the metal ion increases, the tendency of the thiolate sulfur atom to act as a μ_1 donor increases. Therefore, monothiolate ligands that act as μ_2 or μ_3 bridges between soft acids are very common in transition-metal chemistry.[20] Moreover, the ability of thiourea sulfur atoms to act as bridges between either Cu^I or Ag^I ions in the formation of high-nuclearity $[M_6L_6]$ cluster complexes has been recently reported by Dilworth and co-workers.[21] Finally, if two L^{2-} units can stabilize a neutral $[M_4L_2]$ complex, we expect that this $[M_4L_2]$ complex will have a double-helical microarchitecture, since H_2L can form dihelicates. Therefore, we expect H_2L, which potentially has dianionic and helicand character, to be a good building block for the construction of tetranuclear cluster dihelicates.

Treatment of H_2L with $[Cu(CH_3CN)_4]PF_6$ in hot acetonitrile and recrystallization of the resulting brown solid from acetonitrile afforded single crystals of $[Cu_4(L)_2]\cdot 4\,CH_3CN$ (**3**), which were studied by X-ray diffraction.[22] This complex was further characterized by IR spectroscopy and ESI mass spectrometry (see Supporting Information). In the ESI mass spectrum, a base peak corresponding to $[Cu_4(L)_2+H]^+$ was observed, thus confirming that the [4+2] complex is the main species in solution.

ORTEP and ball-and-stick representations of the structure of **3** are shown in Figure 3 (selected bond angles and distances are given in the Supporting Information). The structure comprises four Cu^I ions and two doubly deprotonated thiosemicarbazone ligands and is solvated with four molecules of acetonitrile. Each Cu^I center occupies a three-coordinate distorted trigonal environment, in which they are bound by two thiolate sulfur atoms from different ligands and one imine nitrogen atom. Thus, both ligands act as bis-bidentate N_2S_2 donors. The pyridine nitrogen atoms of the two

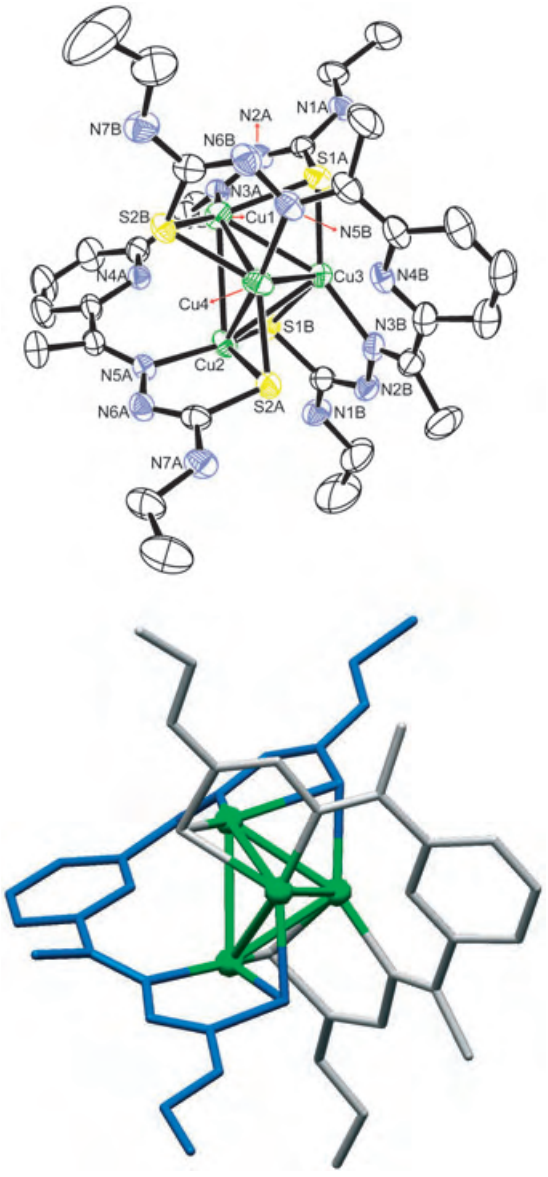


Figure 3. Top: Molecular structure of the neutral tetranuclear cluster helicate complex $[Cu_4(L)_2]\cdot 4\,CH_3CN$ (**3**), with the two strands of L labeled as A and B. Thermal ellipsoids are drawn at the 40% probability level, carbon atoms are shown as unshaded ellipsoids, and hydrogen atoms and solvent molecules have been omitted for clarity. Bottom: Ball-and-stick representation of **3**, with the two strands of L colored in blue (A) and gray (B), and the Cu_4 core shown in green.

L^{2-} units remain uncoordinated. The distortion from an ideal trigonal geometry at all the Cu^I centers is shown by the angles between the nitrogen, copper, and sulfur atoms, which range from 83.95° to 146.73° (see Supporting Information).

The four metal centers form a $\{Cu_4S_4\}$ central core, with each thiolate sulfur atom bridging two Cu^I ions. The two ligands span the tetrahedral core of metal centers and intertwine to give a double-helix structure. A racemic mixture of both enantiomers is observed in the unit cell. The double deprotonation of the ligand on coordination is evident from the observed bond lengths in the cluster (see Supporting

 © 2005 Wiley-VCH Verlag GmbH & Co. KGaA, Weinheim

Information). The C_{thio}–S_{thio} bond lengths increased from 1.656–1.668 Å in H_2L to 1.764–1.771 Å in **3** while the N_{int}–C_{thio} bond lengths decreased from 1.367–1.368 Å to 1.282–1.294 Å, thus indicating that the N_{int}=C_{thio}–S_{thio} resonance form predominates in the complex. This assumption is confirmed by the C_{thio}–N_{term} bond lengths in **3** (1.346–1.366 Å), as they indicate the single nature of the bonds.

The four Cu^I ions in this unique neutral dihelicate are located in the vertex of a distorted tetrahedron. This distortion is clearly revealed by the Cu···Cu distances. Interestingly, the distances between the "bridged" Cu^I ions are shorter (2.672–2.706 Å) than those between the "unbridged" Cu^I ions (2.881–2.883 Å). Currently, there is extended controversy over the existence of Cu···Cu interactions in Cu^I cores, such as those found in the present case.[23] The distances between the metal centers are close to the sum of the van der Waals radii for two copper atoms (2.80 Å)[24] and are in agreement with the proposed existence of Cu···Cu interactions.[25] These interactions would mean that the coordination number of the Cu^I ions in **3** should increase from 3 to 6.

To confirm our approach to the preparation of cluster dihelicates, we synthesized another metal(I) derivative using this ligand. Electrochemical oxidation of a silver plate in a conducting solution of H_2L in acetonitrile yielded a yellow solution from which a yellow solid precipitated upon concentration. Recrystallization of this solid from dimethyl sulfoxide (DMSO) afforded single crystals of $[Ag_4(L)_2]\cdot 4\,DMSO$ (**4**), which were characterized by X-ray diffraction.[26] This complex was also characterized by IR spectroscopy and ESI mass spectrometry (see Supporting Information): the ESI mass spectrum showed a base signal corresponding to $[Ag_4(L)_2 + H]^+$, thus confirming the presence of **4** in solution.

ORTEP and ball-and-stick representations of **4** are shown in Figure 4 (selected bond angles and distances are given in the Supporting Information). The asymmetric unit of this complex comprises two doubly deprotonated ligands, four Ag^I ions, and four unbound DMSO molecules. The Ag^I complex has a similar connectivity to the Cu^I analogue **3**, with the two ligands wrapped around the tetranuclear central Ag^I core to give a double-stranded helical structure. The trigonal coordination geometries of the four metal centers are very distorted, as illustrated by the range of angles between the N, S, and Ag atoms (75.94°–157.45°). Moreover, the C_{thio}–S_{thio} bond lengths are in the range of 1.754–1.774 Å, the N_{int}–C_{thio} bond lengths lie in the range 1.267–1.321 Å, and the C_{thio}–N_{term} bond lengths lie in the range 1.302–1.382 Å, thus indicating a less regular geometry in this complex relative to the Cu^I analogue. Both left- and right-handed helicates are present in the unit cell at 50% occupancy.

The four Ag^I ions form a distorted tetrahedron (Figure 5). The intermetallic Ag···Ag distances range from 2.909 to 3.086 Å between the sulfur-bridged Ag^I ions and from 3.219 to 3.235 Å between the unbridged Ag^I ions. All these distances are significantly shorter than the sum of the van der Waals radii for two silver atoms (van der Waals radius for Ag = 3.44 Å)[24] and may suggest the existence of metal–metal interactions.[27] The possible existence of these interactions implies that the coordination number of the Ag^I ions in **4**

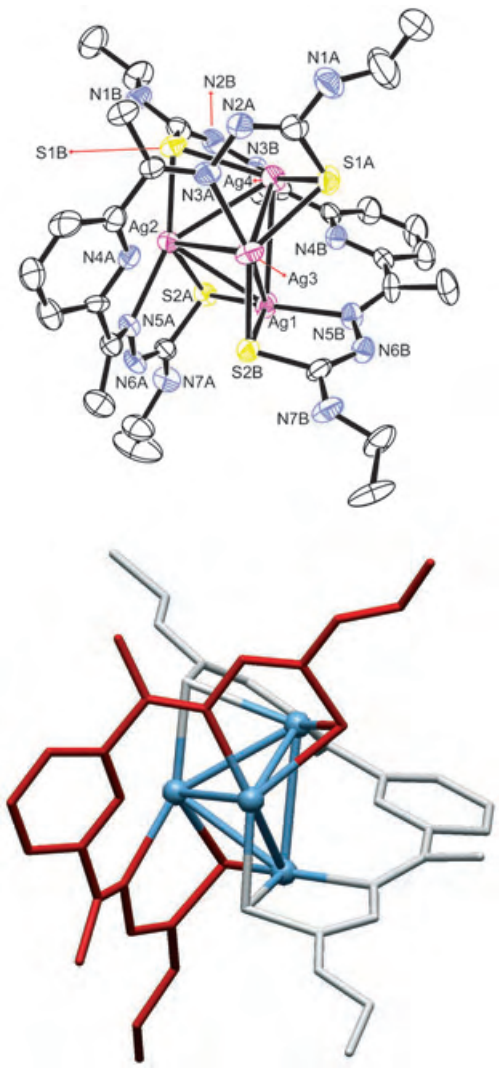


Figure 4. Top: Molecular structure of the neutral tetranuclear cluster helicate complex $[Ag_4(L)_2]\cdot 4\,DMSO$ (**4**), with the two strands of L labeled as A and B. Thermal ellipsoids are drawn at the 40% probability level, carbon atoms are shown as unshaded ellipsoids, and hydrogen atoms and solvent molecules have been omitted for clarity. Bottom: Ball-and-stick representation of **4**, with the two strands of L colored in red (A) and light gray (B), and the Ag_4 core shown in light blue.

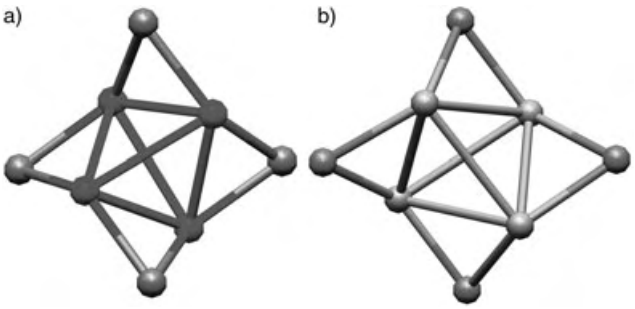


Figure 5. Ball-and-stick representation of the central $\{M_4S_4\}$ core of a) $[Cu_4(L)_2]\cdot 4\,CH_3CN$ (**3**) and b) $[Ag_4(L)_2]\cdot 4\,DMSO$ (**4**).

 © 2005 Wiley-VCH Verlag GmbH & Co. KGaA, Weinheim

should increase from 3 to 6, which is unusual for this metal ion.

To our knowledge, complexes **3** and **4** are the first examples of double-stranded helicates in which the helical axis is composed of a polyhedron of metal ions. Moreover, there are few reports of structurally characterized copper(I) thiosemicarbazone complexes[21,28] and, surprisingly, the structure of only one silver(I) thiosemicarbazone complex has been determined,[21] although the stoichiometries of these coordination compounds were first reported in the early 1980s.[29]

In conclusion, we have prepared dinuclear dihelicates and tetranuclear cluster dihelicates and demonstrated that self-assembly of their building blocks can be controlled. This control can be achieved by using a dianionic helicand ligand that is equipped with two soft donor atoms and by selection of the oxidation state of the metal centers. We believe that this synthetic approach could provide new perspectives on the preparation of complex, stable, and reproducible metallosupramolecular architectures with high nuclearity and programmed properties. Our synthetic approach to the preparation of "cluster helicates" seems to be extendable to other systems, as our ongoing research has produced new examples of metal(I) tetranuclear cluster dihelicate complexes using different bis(thiosemicarbazone) ligands.

Received: March 7, 2005
Published online: June 1, 2005

Keywords: copper · helical structures · self-assembly · silver · zinc

[1] a) J.-M. Lehn, *Supramolecular Chemistry—Concepts and Perspectives*, Wiley-VCH, Weinheim, **1995**; b) E. C. Constable in *Comprehensive Supramolecular Chemistry*, *Vol. 9* (Eds.: J. L. Atwood, J. E. D. Davies, J.-M. Lehn, D. D. MacNicol, F. Vögtle), Pergamon, Oxford, **1996**, p. 213; c) C. Piguet, G. Bernardinelli, G. Hopfgartner, *Chem. Rev.* **1997**, *97*, 2005; d) M. Albrecht, *Chem. Rev.* **2001**, *101*, 3457; e) R. M. Yeh, A. V. Davis, K. N. Raymond in *Comprehensive Coordination Chemistry II*, *Vol. 7* (Eds.: J. A. McCleverty, T. J. Meyer), Elsevier, Oxford, **2004**, p. 327; f) M. J. Hannon, L. J. Childs, *Supramol. Chem.* **2004**, *16*, 7; g) M. Albrecht, I. Jansera, R. Fröhlich, *Chem. Commun.* **2005**, 157.

[2] a) J. Sanmartín, M. R. Bermejo, A. M. García-Deibe, O. Piro, E. E. Castellano, *Chem. Commun.* **1999**, 1953; b) M. R. Bermejo, R. Pedrido, A. M. González-Noya, M. J. Romero, M. Vázquez, L. Sorace, *New J. Chem.* **2003**, *26*, 1753.

[3] a) S.-M. Peng, C.-C. Wang, Y.-L. Jang, Y.-H. Chen, F.-Y. Li, C. Y. Mou, M.-K. Leung, *J. Magn. Mater.* **2000**, *209*, 80; b) V. Maurizot, G. Linti, I. Huc, *Chem. Commun.* **2004**, 924.

[4] a) B. Hasenknopf, J.-M. Lehn, N. Boumediene, A. Dupont-Gervais, A. Van Dorsselaer, B. Kneisel, D. Fenske, *J. Am. Chem. Soc.* **1997**, *119*, 10956; b) P. L. Jones, K. J. Byrom, J. C. Jeffery, J. A. McCleverty, M. D. Ward, *Chem. Commun.* **1997**, 1361.

[5] P. N. W. Baxter, J.-M. Lehn, G. Baum, D. Fenske, *Chem. Eur. J.* **2000**, *6*, 4510.

[6] R. W. Saalfrank, N. Löw, S. Trummer, G. M. Sheldrick, M. Teichert, D. Stalke, *Eur. J. Inorg. Chem.* **1998**, 559.

[7] M. Elhabiri, R. Scopelliti, J.-C. Bünzli, C. Piguet, *J. Am. Chem. Soc.* **1999**, *121*, 10747.

[8] M. J. Hannon, V. Moreno, M. J. Prieto, E. Moldrheim, E. Sletten, I. Meistermann, C. J. Isaac, K. J. Sanders, A. Rodger, *Angew. Chem.* **2001**, *113*, 903; *Angew. Chem. Int. Ed.* **2001**, *40*, 880.

[9] R. Prabaharan, N. C. Fletcher, M. Nieuwenhuyzen, *J. Chem. Soc. Dalton Trans.* **2002**, 602.

[10] M. Vázquez, A. Taglietti, D. Gatteschi, L. Sorace, C. Sangregorio, A. M. González, M. Maneiro, R. Pedrido, M. R. Bermejo, *Chem. Commun.* **2003**, 1840.

[11] J. Keegan, P. E. Kruger, M. Nieuwenhuyzen, J. O'Brien, N. Martin, *Chem. Commun.* **2001**, 2092.

[12] D. Kalny, M. Elhabiri, T. Moav, A. Vaskevich, I. Rubinstein, A. Shanzer, A.-M. Albrecht-Gary, *Chem. Commun.* **2002**, 1426.

[13] V. Amendola, L. Fabbrizzi, P. Pallavicini, E. Sartirana, A. Taglietti, *Inorg. Chem.* **2003**, *42*, 1632.

[14] a) D. Gatteschi, O. Kahn, J. S. Miller, F. Palacio, *Magnetic Molecular Materials*, Reidel, Dordrecht, **1991**; b) *Catalysis by Di- and Polynuclear Metal Cluster Complexes* (Eds.: R. D. Adams, F. A. Cotton), Wiley-VCH, New York, **1998**; c) *Metal Clusters in Chemistry*, *Vol. 1–3* (Eds.: P. Braunstein, L. A. Oro, P. R. Raithby), Wiley-VCH, New York, **1999**; d) *Metal Sites in Proteins and Models*, *Vol. 1–3* (Eds.: H. A. O. Hill, P. J. Sadler, A. J. Thomson), Springer, Berlin, **1999**.

[15] R. Pedrido, M. R. Bermejo, M. J. Romero, M. Vázquez, A. M. González-Noya, M. Maneiro, M. J. Rodríguez, M. I. Fernández, *Dalton Trans.* **2005**, 572.

[16] M. Vázquez, L. Fabbrizzi, A. Taglietti, R. Pedrido, A. M. Gónzález-Noya, M. R. Bermejo, *Angew. Chem.* **2004**, *116*, 1996; *Angew. Chem. Int. Ed.* **2004**, *43*, 1962.

[17] a) M. Vázquez, M. R. Bermejo, M. Fondo, A. M. González, J. Mahía, L. Sorace, D. Gatteschi, *Eur. J. Inorg. Chem.* **2001**, 1863; b) R. Pedrido, M. R. Bermejo, A. M. García-Deibe, A. M. González-Noya, M. Maneiro, M. Vázquez, *Eur. J. Inorg. Chem.* **2003**, 3193.

[18] Crystal structure analysis of **1**: X-ray diffraction data were collected from a yellow prismatic crystal ($\approx 0.35 \times 0.20 \times 0.20\ mm^3$) by means of a Smart CCD-1000 BRUKER diffractometer using graphite-monochromatized $Mo_{K\alpha}$ radiation ($\lambda = 0.71073$ Å) from a fine-focus sealed-tube source. Crystal data for $C_{30}H_{42}N_{14}S_4Zn_2$: $M_r = 857.76$, $T = 298(2)$ K, monoclinic $C2/c$, $a = 16.6419(8)$, $b = 15.9953(8)$, $c = 15.1626(7)$ Å, $\beta = 109.7820(10)°$, $V = 3798.0(3)$ Å^3, $Z = 4$, $\rho_{calcd} = 1.500\ g\,cm^{-3}$, $\mu = 1.526\ mm^{-1}$, 12634 measured reflections, 4524 independent reflections ($R_{int} = 0.0475$), 4524 independent reflections with $I_O > 2\sigma(I_O)$, 231 parameters refined, GOF = 1.077, $R_1 = 0.0482$ ($I_O > 2\sigma(I_O)$) and 0.0876 (for all data), $R_{2w} = 0.0840$ ($I_O > 2\sigma(I_O)$) and 0.0961 (for all data), max./min. residual electron density 0.350/-0.551 e Å^{-3}.[26b]

[19] G. M. Sheldrick, SHELX-97 (SHELXS-97 and SHELXL-97), Programs for Crystal Structure Analyses, University of Göttingen, Germany, **1998**.

[20] a) I. Dance, *Polyhedron* **1986**, *5*, 1037; b) K. L. Tang, X. L. Jin, Y. Q. Tang, *Reviews on Heteroatom Chemistry* (Ed.: S. Oae), MYU, Tokyo, **1996**, *15*, 83; c) D. Fenske, C. Persau, S. Dehnen, C. E. Anson, *Angew. Chem.* **2004**, *116*, 309; *Angew. Chem. Int. Ed.* **2004**, *43*, 305.

[21] L. J. Ashfield, A. R. Cowley, J. R. Dilworth, P. S. Donnelly, *Inorg. Chem.* **2004**, *43*, 4121.

[22] Crystal structure analysis of **3**: X-ray diffraction data were collected from a brown prismatic crystal ($\approx 0.48 \times 0.32 \times 0.19\ mm^3$) by means of a Smart CCD-1000 BRUKER diffractometer using graphite-monochromatized $Mo_{K\alpha}$ radiation ($\lambda = 0.71073$ Å) from a fine-focus sealed-tube source. Crystal data for $C_{38}Cu_4H_{54}N_{18}S_4$: $M_r = 1145.40$, $T = 293$ (2) K, monoclinic $P2(1)/c$, $a = 22.509(5)$, $b = 15.037(3)$, $c = 16.051(3)$ Å, $\beta = 108.143(4)°$, $V = 5162.8(18)$ Å^3, $Z = 4$, $\rho_{calcd} = 1.368\ g\,cm^{-3}$, $\mu = 1.827\ mm^{-1}$, 31220 measured reflections, 10535 independent reflections ($R_{int} = 0.0471$), 10535 independent reflections with $I_O > 2\sigma(I_O)$,

 © 2005 Wiley-VCH Verlag GmbH & Co. KGaA, Weinheim

557 parameters refined, GOF = 1.006, $R_1 = 0.0529$ ($I_O > 2\sigma(I_O)$) and 0.1187 (for all data), $R_{2w} = 0.1777$ ($I_O > 2\sigma(I_O)$) and 0.2147 (for all data), max./min. residual electron density 0.946/ −0.544 e Å^{-3}.[26b]

[23] P. Abraham, A. G. Samuelsen, J. Chandrasekhar, *Inorg. Chem.* **1993**, *32*, 6107.

[24] *Inorganic Chemistry: Principles of Structure and Reactivity*, *4th ed.* (Eds.: J. E. Huheey, E. A. Keiter, R. L. Keiter), Harper Collins College Publishers, New York, **1993**.

[25] a) Y. Cheng, T. J. Emge, J. G. Brennan, *Inorg. Chem.* **1996**, *35*, 7339; b) M. Faulhaber, M. Driess, K. Merz, *Chem. Commun.* **1998**, 1887.

[26] a) Crystal structure analysis of **4**: X-ray diffraction data were collected from a yellow prismatic crystal ($\approx 0.46 \times 0.30 \times 0.18$ mm^3) by means of a Smart CCD-1000 BRUKER diffractometer using graphite-monochromatized $Mo_{K\alpha}$ radiation ($\lambda = 0.71073$ Å) from a fine-focus sealed-tube source. Crystal data for $Ag_4C_{38}H_{66}N_{14}O_4S_8$: $M_r = 1471.01$, $T = 293$ (2) K, monoclinic $P2(1)/c$, $a = 22.910(5)$, $b = 15.600(3)$, $c = 16.550(3)$ Å, $\beta = 107.74(3)°$, $V = 5633.6(19)$ Å^3, $Z = 4$, $\rho_{calc} = 1.711$ g cm^{-3}, $\mu = 1.706$ mm^{-1}, 15892 measured reflections, 8169 independent reflections ($R_{int} = 0.0452$), 8169 independent reflections with $I_O > 2\sigma(I_O)$, 616 parameters refined, GOF = 1.092, $R_1 = 0.0680$ ($I_O > 2\sigma(I_O)$) and 0.1041 (for all data), $R_{2w} = 0.2057$ ($I_O > 2\sigma(I_O)$) and 0.2342 (for all data), max./min. residual electron density 1.401/−0.879 e Å^{-3}. All the crystal structures were solved by direct methods and refined by full-matrix least-square procedures on F^2 using SHELX-97 software.[19] All non-hydrogen atoms were refined anisotropically. All hydrogen atoms were included in the model at calculated positions. b) CCDC 265393 (**1**), 265394 (**3**), and 265395 (**4**) contain the supplementary crystallographic data for this paper. These data can be obtained free of charge from the Cambridge Crystallographic Data Centre via www.ccdc.cam.ac.uk/data_request/cif.

[27] a) Q.-M. Wang, T. C. W. Mak, *J. Am. Chem. Soc.* **2001**, *123*, 7594; b) Q.-M. Wang, T. C. W. Mak, *Chem. Commun.* **2002**, 2682.

[28] A. R. Cowley, J. R. Dilworth, P. S. Donnelly, E. Labisbal, A. Sousa, *J. Am. Chem. Soc.* **2002**, *124*, 5270.

[29] K. K. Aravindakshan, C. G. R. Nair, *Indian J. Chem. Sect. A* **1981**, *20*, 684.

 © 2005 Wiley-VCH Verlag GmbH & Co. KGaA, Weinheim

Hybrid Compounds

Supramolecular Coordination Assemblies of Dinuclear Fe^{III} Complexes**

Wolfgang Schmitt, Jonathan P. Hill, M. Paula Juanico, Andrea Caneschi, Ferdinando Costantino, Christopher E. Anson, and Annie K. Powell**

Dedicated to Professor Rüdiger Kniep on the occasion of his 60th birthday

Construction of 3D architectures as well as molecular recognition processes are regarded as key aspects of modern supramolecular chemistry.[1] The ability to produce hierarchically ordered structures by the self-assembly of oligomeric subunits is of importance for potential applications.[2] This self-assembly requires a detailed knowledge of the competing structure-directing forces present within the reaction systems. Furthermore, it requires the ability to tune these interactions by consideration of steric restrictions and the nature and specific affinities of the chemical components.

Hybrid organic–inorganic coordination assemblies represent a distinct class of supramolecular compound whose preparation is currently a very active area in chemical and materials research.[3] Hybrid organic–inorganic materials present a means for customizing physical and chemical properties by reducing dimensionality and by influencing the devolution pattern of classical inorganic materials within their crystal structures. One strategy for the synthesis of such

[*] Dr. W. Schmitt, Dr. J. P. Hill, Dr. M. P. Juanico, Dr. C. E. Anson, Prof. Dr. A. K. Powell
Institut für Anorganische Chemie
Universität Karlsruhe
Engesserstrasse Geb. 30.45, 76128 Karlsruhe (Germany)
Fax: (+49) 721-608-8142
E-mail: schmitt.wolfgang@nims.go.jp
powell@chemie.uni-karlsruhe.de

Dr. W. Schmitt, Dr. J. P. Hill
National Institute for Materials Science
ICYS Department
Tsukuba, 1-1 Namiki, Ibaraki 305 0044 (Japan)
Fax: (+81) 29-860-4708

Prof. Dr. A. Caneschi, F. Costantino
Dipartimento di Chimica and
UdR INSTM di Firenze
Polo Scientifico
Via della Lastruccia 3, 50019 Sesto Fiorentino (Fi) (Italy)

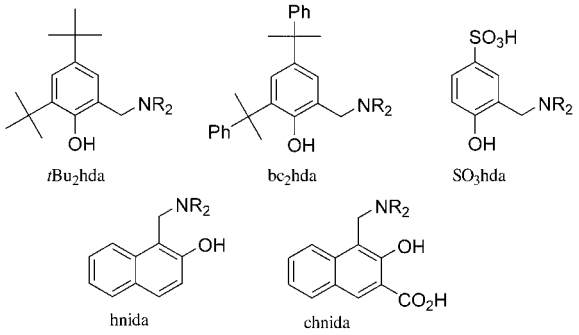
[**] This work was supported by the DFG "Center for Functional Nanostructures (CFN)", the Special Coordination Funds for Promoting Science and Technology from MEXT, Japan through ICYS Fellowships (W.S. and J.P.H.) and the EU-FP6 RTN QUEMOLNA and NOE MAGMANET (A.K.P., M.P.J., A.C., F.C.). Structural studies have been performed under the approval of the Photon Factory Program Advisory Committee (Proposal 04G238). We are grateful to T. Sasaki for assistance with TEM measurements.

Supporting information for this article (magnetic data for **5**, representative TGA data, additional presentations of the crystal structures) is available on the WWW under http://www.angewandte.org or from the author.

 DOI: 10.1002/anie.200500516 © 2005 Wiley-VCH Verlag GmbH & Co. KGaA, Weinheim

structures makes use of rigid organic complexing agents. By using metal atoms, oligonuclear complexes or clusters, and organic components with distinct morphologies as building blocks it is hoped to control the self-assembly process.[4] Using this approach it is not only possible to reconstruct classical inorganic structures but also to overcome the geometrical limitations of the classical aluminosilicates resulting in materials with unprecedented porosity. Construction of multidimensional M-O-M frameworks has been demonstrated to produce materials supporting cooperative effects in their inorganic regions and can also lead to improved thermal stability.[5] Careful selection of metal ions and ligands and consideration of their preferred coordination modes and geometries allows the construction of crystalline architectures containing 1D, 2D, and 3D M-O-M frameworks and a systematic investigation of their chemophysical properties.[5,6]

Herein we describe a concept for synthesis of hybrid organic–inorganic compounds where the shape and functionality of aromatic ligands determine the dimensions and architecture of the inorganic regions of the resulting hybrid materials. Our work emphasizes the structure-directing effects of iminodiacetic acid substituted phenols and similar naphthol derivatives (Scheme 1). These multidentate complexing agents contain hydrophilic and hydrophobic moieties



Scheme 1. The protonated organic ligands obtained by Mannich reaction on the appropriate phenol or naphthol; R = CH_2COOH.

and react with Fe^{III} salts to give dinuclear complexes where the transition-metal ions are doubly bridged by combinations of hydroxo-, oxo-, and carbonate groups. The resulting complexes, which form through hydrolysis reactions in the presence of specific amounts of water, can be described by the general formulae $[Fe_2(\mu\text{-}OH)(\mu\text{-}CO_3)L_2]^{3-}$, $[Fe_2(\mu\text{-}O)(\mu\text{-}CO_3)L_2]^{4-/6-}$, or $[Fe_2(\mu\text{-}CO_3)_2L_2]^{4-}$. The fixation of atmospheric CO_2 by transition-metal ions is now well-established.[7] Alkali counterions are bound to the negatively charged Fe^{III} complexes through the carboxylate groups and other O-donors. They are further linked to each other by water molecules forming supramolecular coordination assemblies. The hydrophilic/hydrophobic character of the reaction systems favors the formation of cross-linked structures in which self-assembling processes organize vast areas of different polarities.

The hydrolysis reactions in the presence of the tetradentate ligand tBu_2hda led to the crystallization of **1**.

$K_3[Fe_2(\mu\text{-}OH)(\mu\text{-}CO_3)(tBu_2hda)_2]\cdot 3H_2O\cdot EtOH$ **1**

The long Fe–O bond lengths of 2.002(3) and 2.007(4) Å to the bridging oxygen atom confirm the identity of this bridging ligand as a hydroxo group; the hydrogen atom could be located and refined in the crystal structure. This compound forms a two dimensional lamellar structure with potassium ions in the *ab* plane connected to the dinuclear Fe^{III} complexes above and below this plane while the organic residues of the Fe^{III} complexes point in the direction of the crystallographic *c* axis. In this direction the 2D layers bind to each other through weak induced dipole interactions forming organic regions approximately 11.5 Å thick. Similarly in **2**, the ligand hnida stabilizes a layered structure with organic and inorganic layers parallel to the crystallographic *bc* plane.

$K_4[Fe_2(\mu\text{-}O)(\mu\text{-}CO_3)(hnida)_2]\cdot 6H_2O\cdot 2EtOH$ **2**

The Fe^{III} centers of the dinuclear complex in **2** are doubly bridged by a carbonate anion and an oxo ligand, which has significantly shorter bonds (both 1.81 Å) to the Fe^{III} centers than the corresponding hydroxo group in **1**. This oxygen also coordinates to two K^+ ions resulting in a distorted tetrahedral $Fe_2(\mu_4\text{-}O)K_2$ geometry. Figure 1 shows the dinuclear Fe^{III} subunits in **1** and **2** and the layered arrangements of hydrophobic and hydrophilic moieties. It is noteworthy that in **2** the dinuclear subunit straddles the hydrophilic layer while in **1** both organic ligand moieties of a given $[Fe_2(\mu\text{-}OH)(\mu\text{-}CO_3)(tBu_2hda)_2]^{3-}$ unit are accommodated in the same hydrophobic layer.

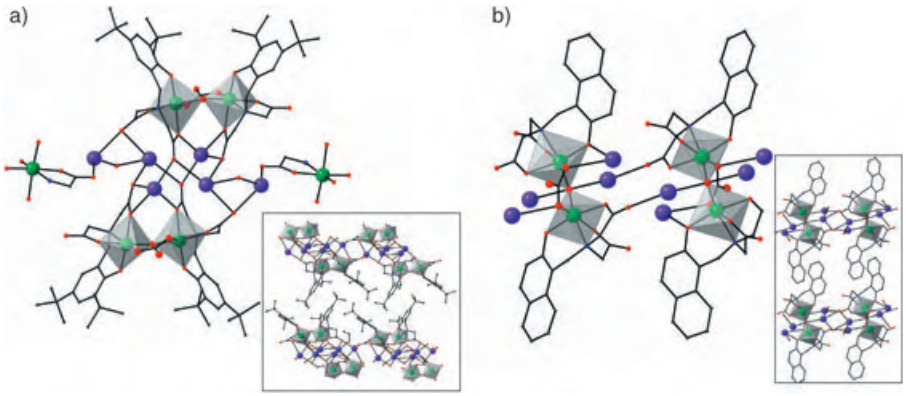


Figure 1. a) Layered arrangement of dinuclear Fe^{III} complexes in **1**. Inset: section of the structure of **1** viewed along the crystallographic *a*-axis. b) Structure of **2** illustrating the straddling of the hydrophilic layer by the dinuclear subunit. Inset: section of the structure of **2** viewed along the crystallographic *a*-axis. Hydrogen atoms and solvent molecules are omitted for clarity; Fe green, O red, N blue, K purple, C dark gray; coordination polyhedra of the Fe centers are shown in gray.

 © 2005 Wiley-VCH Verlag GmbH & Co. KGaA, Weinheim

Modification of the tBu$_2$hda ligand by substitution of the *tert*-butyl groups with α,α-dimethylbenzyl groups increases the hydrophobicity of the complexing agent. The compound **3** crystallizes from aqueous systems containing the bc$_2$hda ligand, and dipole–dipole and dipole–cation interactions favor a layered structure similar to **1**. However, **3** has the additional feature of a π-bound potassium ion which is trapped within the hydrophobic part made up of the α,α-dimethylbenzyl groups (Figure 2).[8] This motif is attracting

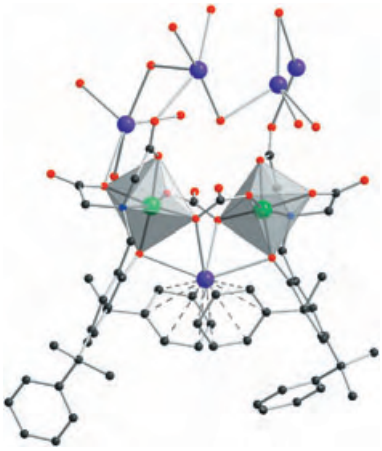


Figure 2. Coordination geometry of the Fe^{III} centers and the cation–π binding of potassium ions in complex **3**. Color code: Fe green, O red, N blue, K purple, C dark gray. Hydrogen atoms and solvent molecules are omitted for clarity.

interest because of its importance in protein dynamics although the near absence of structural evidence has made it difficult to visualize cation–π interactions involving alkali metal cations.[9]

$K_3[Fe_2(\mu\text{-}CO_3)_2(bc_2hda)_2] \cdot 3\,H_2O \cdot EtOH$ **3**

The π-binding of the potassium cation in **3** prompted us to consider further alterations to the ligand. Thus, we chose to introduce carboxylate or sulfonate groups, either of which can be placed at various positions on the ligand. We considered that these functional groups would influence the inorganic structural motif of the coordination assemblies and could create 2D or 3D networks. Introduction of a carboxy group at the 3-position of the naphthyl ring of (2-hydroxynaphthyl)-methylene iminodiacetic acid (hnida) gives the chnida ligand, which stabilizes another novel structural motif. In the resulting compound **4**, the dinuclear Fe^{III} complexes are arranged so that the polar oxo, carbonate, and carboxylate groups together with the water-bridged K$^+$ ions build a honeycomb structure containing channels running parallel to the crystallographic *c*-axis. Each dinuclear unit penetrates a honeycomb wall with the Fe···Fe axis approximately perpendicular to the *c* axis, whereas the naphthalene moieties of the two ligands project into adjacent channels of the lattice, where the naphthalene mean planes make angles of 40.7 and 51.4° to the *c* axis.

$K_6[Fe_2(\mu\text{-}O)(\mu\text{-}CO_3)(chnida)_2] \cdot 13.5\,H_2O$ **4**

The resulting hydrophobic channels are approximately 14 Å in diameter. In the chnida ligand, the carboxy group is positioned adjacent to the phenolic OH group maximizing the amphiphilicity of the ligand. As before, this enables complexes with this ligand to pack into a structure where hydrophobic and hydrophilic regions are segregated. However, in the structure of **4** it is almost as though the bilayer arrangement seen for **1**–**3** has been rolled up, leading to channels which contain the naphthyl residues (Figure 3 a).

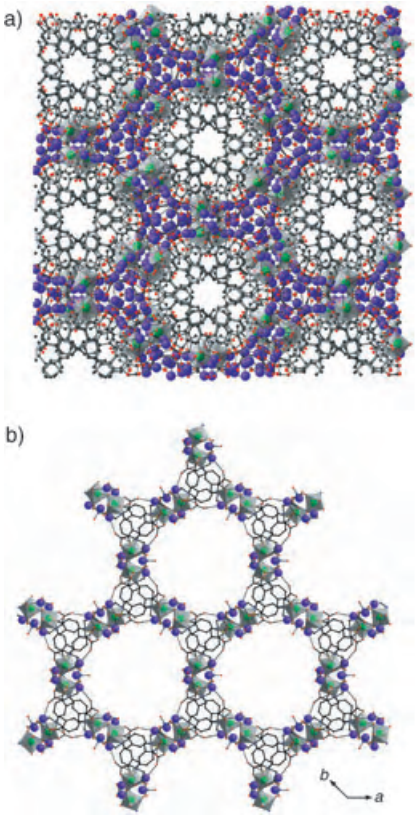


Figure 3. a) Honeycomb structural motif in **4**. Inorganic and organic parts form parallel nanosized channels which run along the crystallographic *c*-axis and which are filled with naphthyl moieties (view in [001] direction). b) Open framework structure in **5** viewed along the crystallographic *c*-axis. Hydrogen atoms, solvent molecules, and one disordered K$^+$ counterion are omitted for clarity; Fe green, O red, N blue, K purple, C dark gray.

This structure is the direct consequence of the introduction of the carboxy group adjacent to the phenolic OH group. This carboxy group does not coordinate to Fe^{III} ions but interacts only with the potassium counterions.

In addition to the single-crystal X-ray structure analysis, we performed high resolution transmission electron microscopy (HRTEM) on powdered samples of **4** to characterize the extended structure of the compound further. Although crystals of **4** are very sensitive to electron-beam-induced damage it was possible to observe areas displaying the expected honeycomb pattern, in good agreement with the crystal structure determination (Figure 4).

 © 2005 Wiley-VCH Verlag GmbH & Co. KGaA, Weinheim

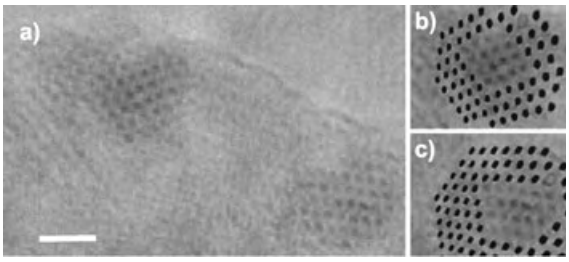


Figure 4. a) TEM image of **4** distinguishing the organic (dark) and inorganic (light) areas (scale bar 10 nm). b), c) Overlay of organic regions of the (110) plane of crystal structure on TEM image. Dot array was generated from the *hkl* file and adjusted for perspective.

To encourage the formation of materials containing pores or empty channels where the organic ligand is incorporated into an extended framework structure, we introduced a sulfonic acid group in the position *para* to the phenolic hydroxy group of the hda ligand so that the dinuclear unit could pillar between hydrophilic regions of supramolecular structures. This strategy yielded **5** in which five of the potassium cations are strongly bound by the oxo, carbonate, and carboxylate groups around the Fe_2 unit. Each ligand sulfonate group binds to the K^+ counterions of a neighboring dinuclear complex. In the resulting coordination assembly, the dinuclear complexes and K^+ ions form the walls of an open framework honeycomb motif, where the Fe_2 units are aligned within, rather than through the walls, as was found for **4**.

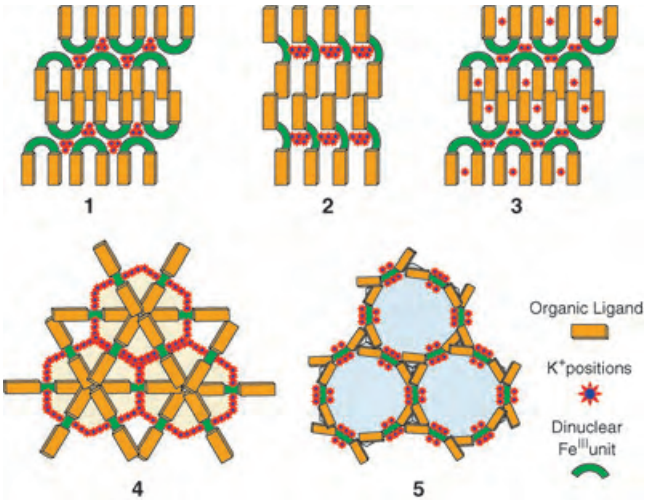
$K_6[Fe_2(\mu\text{-}O)(\mu\text{-}CO_3)(SO_3hda)_2]\cdot 11\,H_2O\cdot 9\,MeOH$ **5**

The aromatic rings of the dinuclear subunits are stacked about the threefold screw (3_2) axes which coincide with the vertices of this hexagonal structure (Figure 3b). The open framework structure has channels with cross-sectional diameter of approximately 9 Å, which contain water, methanol, and the disordered sixth potassium ion. Recently, other hybrid coordination assemblies have attracted interest as new catalytic materials[5e,10] or separation media.[2d,11] Compound **5** is a good example of the application of our concept in the synthesis of closely related compounds and it seems reasonable to expect the tailoring of channel geometry by variation of the dimensions and functionality of the ligand.

Magnetic susceptibility studies show that the dinuclear Fe^{III} units in these compounds are, as expected, fairly strongly antiferromagnetically coupled, presumably with the coupling transmitted through the μ-oxo bridge.[12] As an example, for compound **5** the room temperature χT value is 1.25 $cm^3\,K\,mol^{-1}$ per dinuclear unit (for two uncoupled Fe^{III} ions the value is $\chi T_{theor} = 8.75\ cm^3\,K\,mol^{-1}$) and decreases steeply on lowering the temperature. It then remains constant, but not zero, between 35 and 5 K as a result of the presence of a small amount of paramagnetic impurity (confirmed by magnetization experiments). The data can be reproduced quantitatively using a van Vleck law for a dimer of coupled $S = 5/2$ ions with the best fit for $J = -173 \pm 2\ cm^{-1}$ and allowing for the presence of less than 3% paramagnetic impurity (for full details see the Supporting Information).

The thermogravimetric analyses (TGA) reveal that the coordination assemblies decompose by initial solvent loss (below 150 °C) followed by degradation of the organic ligand at temperatures between 250 and 350 °C. The loss of the structural integrity is accompanied by the formation of potassium oxide and iron oxides. Weight losses at higher temperatures can be attributed to the solid-state reactions of this mixture forming different phases of potassium iron oxides. A detailed account of thermolysis and pyrolysis of the complexes and the structure of the decomposition products will be reported elsewhere. However, it is noteworthy that in the case of **1** we were able to identify $KFeO_2$ and the K-β-ferrite $K_xFe_{22}O_{34}$ ($x = 2$–4)[13] as the main products using X-ray diffraction (XRD) analysis of samples thermolyzed at different, increasing temperatures. $KFeO_2$ and $K_xFe_{22}O_{34}$ ($x = 2$–4) are the only thermodynamically stable ternary compounds in the K_2O-Fe_2O_3 system and usually form by reaction of Fe_2O_3 or Fe_3O_4 with K_2CO_3 or K_2O.[14] Recent work has suggested that the active state of the industrially used Fe_2O_3 dehydrogenation catalyst for the production of styrene from ethylbenzene consists of the $KFeO_2$ and $K_xFe_{22}O_{34}$ ($x = 2$–4) oxides.[15] Since the production of styrene is one of the most important industrial processes and reaches a production level of 20×10^6 tons/year,[16] nanostructured materials containing these oxides are of industrial interest.

In summary, our studies demonstrate that hydroxybenzyl iminodiacetic acid ligands can be used to prepare an unprecedented type of hybrid organic–inorganic network by self-assembly of the dinuclear doubly bridged Fe^{III} subunits and their potassium counterions, resulting in a variety of 3D architectures which are summarized in Scheme 2. The structure of the inorganic hydrophilic zone is strongly influenced by the shape and functionality of the organic ligand providing a means of controlling different motifs of supramolecular coordination assemblies. Selection of the ligand structure and polarity can result in crystalline materials where the packing of hydrophilic and hydrophobic portions differs from a simple bilayer arrangement. This approach has allowed formation of a dense hexagonal array (using the chnida ligand) and a



Scheme 2. Pictograms of structural motifs in the supramolecular coordination networks.

 © 2005 Wiley-VCH Verlag GmbH & Co. KGaA, Weinheim

hexagonal open-framework structure containing cylindrical voids (using the SO_3hda ligand). Thermal decomposition of these and similar aggregates, which contain distinct areas of polarity and structure, can lead to unusual oxides whose structures and compositions depend on those of the precursor compound. In particular, we are seeking to prepare nanostructured mixed transition metal oxides whose properties may depart from those prepared by other techniques.

Experimental Section

All ligands were prepared by Mannich reaction between the appropriate phenol or naphthol, iminodiacetic acid and aqueous formaldehyde.[17]

1: Complex **1** was prepared by the reaction of Na_2tBu_2hda (0.198 g, 0.5 mmol) with $Fe(NO_3)_3{\cdot}9H_2O$ (0.202, 0.5 mmol) in a mixture of methanol (20 mL) and ethanol (95%; 30 mL) and subsequent slow addition of (2 M; 1 mL KOH) to the stirred reaction mixture. Blue-purple crystals of **1** were grown by slow evaporation of the ethanol solution. Yield: 72% based on $Fe(NO_3)_3{\cdot}9H_2O$. Elemental analysis (%) calcd for $C_{41}Fe_2H_{63}K_3N_2O_{17}$, which corresponds to the crystallographically determined formula minus one water: C 45.39, H 5.85, N 2.58; found: C 45.66, H 6.41, N 2.83. FTIR: $\tilde{\nu}$ = 3679 (m), 3435 (s, br), 2955 (s), 2868 (w), 2814 (w), 1631 (vs), 1471 (m), 1440 (w), 1413 (w), 1375 (s), 1329 (m), 1308 (m), 1263 (m), 1243 (m), 1207 (m), 1171 (m), 1125 (m), 1085 (w), 1036 (s), 1008 (w), 980 (w), 961 (w), 916 (m) 892 (w), 875 (m) cm^{-1}.

2: Complex **2** was prepared by the reaction of hnida (0.08 g, 0.28 mmol) with $FeCl_3{\cdot}6H_2O$ (0.135 g, 0.5 mmol) in ethanol (95%, 30 mL) in the presence of potassium hydrogen carbonate (0.63 g, 6.3 mmol). Water (3 mL) was then added to assist the dissolution of the potassium hydrogen carbonate. Red-purple crystals of **2** were grown by slow evaporation of the solvent. Yield: 32% based on hnida. Elemental analysis (%) calcd for $C_{35}Fe_2H_{48}K_4N_2O_{22}$: C 37.64, H 4.33, N 2.51; found: C 37.31, H 4.22, N 2.57. FTIR: $\tilde{\nu}$ = 3557 (w), 3417 (s, br), 2967 (w), 2918 (w), 1598 (vs), 1507 (m), 1484 (m), 1460 (s), 1430 (m), 1398 (s), 1363 (s), 1309 (m), 1289 (sh), 1275 (s), 1243 (w), 1224 (w), 1174 (w), 1162 (w), 1144 (w), 1120 (w), 1099 (w), 1071 (m), 1046 (m), 1021 (m), 980 (w), 969 (w), 919 (m), 899 (w), 876 (w), 858 (m), 827 (m), 783 (w), 737 (s), 646 (m), 556 (m), 503 (m), 484 (m) cm^{-1}.

3: Complex **3** was prepared as reported previously.[8]

4: Complex **4** was prepared by the reaction of chnida (0.08 g, 0.24 mmol) with $FeCl_3{\cdot}6H_2O$ (0.135 g, 0.5 mmol) in a mixture of methanol (30 mL) and ethanol (95%; 20 mL) and subsequent slow addition of KOH (2 M; 2 mL) to the stirred reaction mixture. Red crystals of **4** were grown by slow evaporation of the solution. Yield: 36% based on chnida. FTIR: $\tilde{\nu}$ = 3412 (s), 3070 (sh), 2924 (w), 1621 (vs), 1597 (sh), 1558 (sh), 1500 (m), 1447 (m), 1428 (w), 1395 (s), 1365 (sh), 1291 (w), 1272 (m), 1210 (m), 1173 (w), 1154 (w), 1125 (w), 1097 (m), 1049 (w), 1024 (w), 978 (m), 930 (w), 906 (m), 862 (m), 815 (m), 743 (s) cm^{-1}.

5: Complex **5** was prepared by the dissolving of SO_3hda (0.08 g, 0.24 mmol) with $FeCl_3{\cdot}6H_2O$ (0.135 g, 0.5 mmol) in methanol (30 mL) and ethanol (95%; 20 mL) and subsequent slow addition of KOH (2 M; 2 mL) to the stirred reaction mixture. Red-brown crystals of **5** were grown by slow evaporation of the ethanol solution. Yield: 10–20% based on SO_3hda. FTIR: $\tilde{\nu}$ = 3475(br), 2576(m), 1610(s), 1480(s), 1385(s), 1295(s), 1213(s), 1183(s), 1132(s), 1104(s), 1034(s), 977(w), 934(w), 861(w), 794(w), 746(w) cm^{-1}.

Crystallographic data: Data measured on a STOE IPDS diffractometer for **1** and **2** or on a Bruker SMART Apex diffractometer for **4** and **5** at 200 K using graphite-monochromated $Mo_{K\alpha}$ radiation. The structure of **3** has been reported by us previously.[8] Structure solution by direct methods and full-matrix refinement against F^2 (all data) using SHELXTL.[18] Non-hydrogen atoms refined with anisotropic temperature factors apart from some disordered solvent molecules. The hydroxo hydrogen atom in **1** was located and refined, all organic ligand hydrogen atoms were placed in calculated positions. CCDC 262829–262832 contain the supplementary crystallographic data for this paper. These data can be obtained free of charge from the Cambridge Crystallographic Data Centre via www.ccdc.cam.ac.uk/data_request/cif.

1: $C_{41}H_{65}Fe_2K_3N_2O_{18}$, 1102.95 $g\,mol^{-1}$, purple-blue block 0.3 × 0.25 × 0.2 mm, T = 200 K, triclinic, $P\bar{1}$, a = 9.7594(8), b = 13.8993(11), c = 18.7162(16) Å, α = 97.662(10)°, β = 100.012(10)°, γ = 93.350(9)°, V = 2469.2(4) $Å^3$, Z = 2, $F(000)$ = 1156, ρ_{calcd} = 1.483 $Mg\,m^{-3}$, $\mu(Mo_{K\alpha})$ = 0.913 mm^{-1}, 16248 reflections measured ($2\theta_{max}$ = 52.0°), of which 9003 unique (R_{int} = 0.0897). 314 parameters, wR_2 = 0.1474, S = 0.921 (all data), R_1 (3984 data with $I > 2\sigma(I)$) = 0.0606.

2: $C_{35}H_{48}Fe_2K_4N_2O_{22}$, 1116.85 $g\,mol^{-1}$, purple block 0.25 × 0.2 × 0.15 mm, T = 200 K, triclinic, $P\bar{1}$, a = 8.6793(7), b = 15.1432(11), c = 17.9198(15) Å, α = 88.492(9), β = 76.093(9), γ = 74.962(9)°, V = 2206.3(3) $Å^3$, Z = 2, $F(000)$ = 1152, ρ_{calcd} = 1.681 $Mg\,m^{-3}$, $\mu(Mo_{K\alpha})$ = 1.121 mm^{-1}, 14611 reflections measured ($2\theta_{max}$ = 52.3°) of which 8112 unique (R_{int} = 0.0279). 625 parameters, wR_2 = 0.1202, S = 0.975 (all data), R_1 (5298 data with $I > 2\sigma(I)$) = 0.0690.

4: $C_{33}H_{49}Fe_2K_6N_2O_{31.5}$, 1324.04 $g\,mol^{-1}$, red cuboctahedron 0.2 × 0.2 × 0.2 mm, T = 200 K, rhombohedral, $R\bar{3}c$, a = 35.3692(10), c = 43.3010(18) Å, V = 46911(3) $Å^3$, Z = 36, $F(000)$ = 2444, ρ_{calcd} = 1.687 $Mg\,m^{-3}$, $\mu(Mo_{K\alpha})$ = 1.132 mm^{-1}, 63861 reflections measured ($2\theta_{max}$ = 52.0°) of which 10213 unique (R_{int} = 0.0798). 741 parameters, wR_2 = 0.4287, S = 1.348 (all data), R_1 (5085 with $I > 2\sigma(I)$) = 0.1294. Several crystals were investigated, and all gave a well-defined rhombohedral cell with systematic absences for $\bar{R}3c$. Structure solution readily gave the Fe_2 dinuclear complex and one or two of the K^+ counterions. However, refinement invariably resulted in high temperature factors for the atoms of the dinuclear unit, and indicated that all but one of the K^+ ions, and all the framework and lattice waters, were badly disordered, resulting in the high R-factors. Twinned refinement[19] in appropriate lower-symmetry rhombohedral or C-centered monoclinic space groups did not improve matters, and the problem is clearly one of disorder rather than (pseudo-)merohedral twinning. The final structure obtained, however, clearly establishes the formulation and the nature of the packing.

5: $C_{32}H_{76}Fe_2K_6N_2O_{40}S_2$, 1539.37 $g\,mol^{-1}$, red-brown prismatic needle 0.40 × 0.18 × 0.18 mm, T = 200 K, trigonal, space group $P3_221$, a = 20.8830(6), c = 12.4648(6) Å, V = 4707.6(3) $Å^3$, Z = 3, $F(000)$ = 2400, ρ_{calcd} = 1.629 $Mg\,m^{-3}$, $\mu(Mo_{K\alpha})$ = 1.026 mm^{-1}, 23724 reflections measured, of which 7108 unique (R_{int} = 0.0440). 332 parameters, wR_2 = 0.1551, S = 1.001 (all data), R_1 = 0.0561 (6232 data with $I > 2\sigma(I)$). One K^+ counterion was 50:50 disordered against a water molecule. One lattice MeOH molecule per asymmetric unit (two per dimer) could be located and refined, but the residual volume is consistent with an overall formulation with seven MeOH per dinuclear unit. Loss of these solvent molecules is facile on removal of crystals from the mother liquor.

Magnetism: The magnetic susceptibility of a polycrystalline powder of **5** was measured between 2 and 300 K with applied magnetic fields of 0.1 and 1 T using a Cryogenic S600 SQUID magnetometer. Data were corrected for the magnetism of the sample holder which was determined separately in the same temperature range and field, and the underlying diamagnetism of the sample was estimated from Pascal's constants. Magnetization measurements were performed on the same sample at 2.7 K with field up to 6.0 T.

Thermogravimetric analysis was performed under flowing N_2 and in a temperature range of 25–1000 °C using Rigaku ThermoPlus TG 8120 or Netzsch STA 409C instruments.

TEM studies were carried out on a JEOL FX2000. The sample was ground to a powder and placed on copper mesh for TEM analysis

 © 2005 Wiley-VCH Verlag GmbH & Co. KGaA, Weinheim

(Accelerating voltage: 200 kV). Calibration was performed using a MoS_2 standard.

Received: February 10, 2005
Published online: June 14, 2005

Keywords: bridging ligands · coordination modes · crystal engineering · iron · supramolecular chemistry

[1] a) *Comprehensive Supramolecular Chemistry*, *Vols. 1–11* (Eds.: J.-M. Lehn, J. L. Atwood, J. E. D. Davis, D. D. MacNicol, F. Vögtle), Pergamon, Oxford, **1990–1996**; b) J.-M. Lehn, *Supramolecular Chemistry: Concepts and Perspectives*, VCH, Weinheim, **1995**.

[2] a) M. Eddaoudi, J. Kim, N. Rosi, D. Vodak, J. Wachter, M. O'Keeffe, O. M. Yaghi, *Science* **2002**, *295*, 469–472; b) N. L. Rosi, J. Eckert, M. Eddaoudi, D. T. Vodak, J. Kim, M. O'Keeffe, O. M. Yaghi, *Science* **2003**, *300*, 1127–1129; c) G. Férey, M. Latroche, C. Serre, F. Millange, T. Loiseau, A. Percheron-Guégan, *Chem. Commun.* **2003**, 2976–2977; d) D. N. Dybtsev, H. Chun, S. H. Yoon, D. Kim, K. Kim, *J. Am. Chem. Soc.* **2004**, *126*, 32–33; e) M. Fujita, Y.-J. Kwon, S. Washizu, K. Ogura, *J. Am. Chem. Soc.* **1994**, *116*, 1151–1152; f) J. S. Seo, D. Wand, H. Lee, S. I. Jun, J. Oh, Y. Jeon, K. Kim, *Nature* **2000**, *404*, 982–986.

[3] a) R. Robson, *J. Chem. Soc. Dalton Trans.* **2000**, 3735–3744; b) M. Fujita, K. Umemoto, M. Yoshizawa, N. Fujita, T. Kusukawa, K. Biradha, *Chem. Commun.* **2001**, 509–518; c) M. Fujita, *Chem. Soc. Rev.* **1998**, *27*, 417–425; d) M. Eddaoudi, D. B. Moler, H. L. Li, B. L. Chen, T. M. Reineke, M. O'Keeffe, O. M. Yaghi, *Acc. Chem. Res.* **2001**, *34*, 319–330; e) S. R. Seidel, P. J. Stang, *Acc. Chem. Res.* **2002**, *35*, 972–983; f) B. Olenyuk, A. Fechtenkötter, P. J. Stang, *J. Chem. Soc. Dalton Trans.* **1998**, 1707–1728; g) G. F. Swiegers, T. J. Malefetse, *Chem. Rev.* **2000**, *100*, 3483–3537; h) D. J. Price, A. K. Powell, P. T. Wood, *Dalton Trans.* **2003**, *12*, 2478–2482; i) S. O. H. Gutschke, D. J. Price, A. K. Powell, P. T. Wood, *Eur. J. Inorg. Chem.* **2001**, 2739–2741.

[4] a) O. M. Yaghi, M. O'Keeffe, N. W. Ockwig, H. K. Chae, M. Eddaoudi, J. Kim, *Nature* **2003**, *423*, 705–714; b) O. M. Yaghi, H. Li, *Angew. Chem.* **1995**, *107*, 232–234; *Angew. Chem. Int. Ed. Engl.* **1995**, *34*, 207–209; c) D. N. Dybtsev, H. Chun, K. Kim, *Angew. Chem.* **2004**, *116*, 5143–5146; *Angew. Chem. Int. Ed.* **2004**, *43*, 5033–5036.

[5] a) C. Livage, C. Egger, G. Férey, *Chem. Mater.* **2001**, *13*, 410; b) C. Livage, C. Egger, G. Férey, *Chem. Mater.* **1999**, *11*, 1546; c) D. J. Price, S. Tripp, A. K. Powell, P. T. Wood, *Chem. Eur. J.* **2001**, *7*, 200–208; d) S. O. H. Gutschke, D. J. Price, A. K. Powell, P. T. Wood, *Angew. Chem.* **2001**, *113*, 1974–1977; *Angew. Chem. Int. Ed.* **2001**, *40*, 1920–1923; e) N. Guillou, Q. M. Gao, P. M. Forster, J. S. Chang, S. E. Park, G. Férey, A. K. Cheetham, *Angew. Chem.* **2001**, *113*, 2913–2916; *Angew. Chem. Int. Ed.* **2001**, *40*, 2831–2834.

[6] a) P. M. Forster, P. M. Thomas, A. K. Cheetham, *Chem. Mater.* **2002**, *14*, 17–20; b) P. M. Forster, A. K. Cheetham, *Angew. Chem.* **2002**, *114*, 475–477; *Angew. Chem. Int. Ed.* **2002**, *41*, 457–459.

[7] See for example: a) B. Kersting, *Angew. Chem.* **2001**, *113*, 4110–4112; *Angew. Chem. Int. Ed.* **2001**, *40*, 3987–3990; b) W. Schmitt, C. E. Anson, R. Sessoli, M. van Veen, A. K. Powell, *J. Inorg. Biochem.* **2002**, *91*, 173–189; c) W. Schmitt, P. A. Jordan, R. K. Henderson, G. R. Moore, C. E. Anson and A. K. Powell, *Coord. Chem. Rev.* **2002**, *228*, 115–126; d) S. Laborda, R. Clérac, C. E. Anson, A. K. Powell, *Inorg. Chem.* **2004**, *43*, 5931–5943; e) F. Bramsen, A. D. Bond, C. J. McKenzie, R. G. Hazell, B. Moubaraki, K. S. Murray, *Chem. Eur. J.* **2005**, *11*, 825–831.

[8] W. Schmitt, C. E. Anson, J. P. Hill, A. K. Powell, *J. Am. Chem. Soc.* **2003**, *125*, 11142–11143.

[9] a) J. C. Ma, D. A. Dougherty, *Chem. Rev.* **1997**, *97*, 1303–1324; b) G. W. Gokel, L. J. Barbour, R. Ferdani, J. Hu, *Acc. Chem. Res.* **2002**, *35*, 878–886; c) G. W. Gokel, *Chem. Commun.* **2003**, 2847–2852.

[10] a) J. S. Seo, D. Wand, H. Lee, S. I. Jun, J. Oh, Y. Jeon, K. Kim, *Nature* **2000**, *404*, 982–986; b) M. Fujita, Y.-J. Kwon, S. Washizu, K. Ogura, *J. Am. Chem. Soc.* **1994**, *116*, 1151–1152.

[11] D. Bradshaw, T. J. Prior, E. J. Cussen, J. B. Claridge, M. J. Rosseinsky, *J. Am. Chem. Soc.* **2004**, *126*, 6106–6114.

[12] a) O. Kahn, *Molecular Magnetism*, Wiley-VCH, New York, **1993**; b) H. Weihe, H. U. Güdel, *J. Am. Chem. Soc.* **1997**, *119*, 6539–6543.

[13] All potassium β-ferrite $K_xFe_{22}O_{34}$ ($x = 2$–4) structures are hexagonal and are composed of spinel blocks separated by layers of potassium ions. Depending on the potassium ion content (x), variation in the packing of the spinel units gives a different lattice constant c (23.8 or 35.9 Å with $a = b = 5.9$ Å). In this case the best simulation of the XRD pattern are obtained with $c = 35.9$ Å confirming $x = 4$.[12a]

[14] a) Y. Joseph, G. Ketteler, C. Kuhrs, W. Ranke, W. Weiss, R. Schlögl, *Phys. Chem. Chem. Phys.* **2001**, *3*, 4141–4153; b) G. Ketteler, W. Ranke, R. Schlögl, *J. Catal.* **2002**, *212*, 104–111.

[15] P. G. Menon, B. Delmon in *Handbook of Heterogeneous Catalysis*, *Vol. 1* (Eds.: G. Ertl, H. Knözinger, J. Weitkamp), VCH, Weinheim, **1997**, p. 101.

[16] W. P. Addiego, W. Liu, T. Boger, *Catal. Today* **2001**, *69*, 25–31.

[17] V. Temkina, M. N. Rusina, G. F. Yaroschenko, M. Z. Branzburg, L. M. Timakova, N. M. Dyatlova, *Zh. Obshch. Khim.* **1975**, *45*, 1564–1570.

[18] G. M. Sheldrick, SHELXTL-NT, 5.1, Bruker Analytical X-ray Systems, Madison, WI, **1997**.

[19] a) R. Herbst-Irmer, G. M. Sheldrick, *Acta Crystallogr. Sect. B* **1998**, *54*, 443–449; b) R. Herbst-Irmer, G. M. Sheldrick, *Acta Crystallogr. Sect. B* **2002**, *58*, 477–481.

 © 2005 Wiley-VCH Verlag GmbH & Co. KGaA, Weinheim

Directed Evolution

Expanding the Range of Substrate Acceptance of Enzymes: Combinatorial Active-Site Saturation Test**

Manfred T. Reetz, Marco Bocola, José Daniel Carballeira, Dongxing Zha, and Andreas Vogel*

Directed evolution of proteins has emerged as a powerful tool to enhance the stability, activity, and selectivity of enzymes.[1] It involves the proper combination of random gene mutagenesis, expression of thousands of mutant enzymes, and high-

[*] Prof. Dr. M. T. Reetz, Dr. M. Bocola, Dr. J. D. Carballeira, Dr. D. Zha, Dr. A. Vogel
Max-Planck-Institut für Kohlenforschung
Kaiser-Wilhelm-Platz 1, 45470 Mülheim/Ruhr (Germany)
Fax: (+49) 208-306-2985
E-mail: reetz@mpi-muelheim.mpg.de

[**] This work was supported by the Fonds der Chemischen Industrie and the Deutsche Forschungsgemeinschaft (Schwerpunkt 1170).

 © 2005 Wiley-VCH Verlag GmbH & Co. KGaA, Weinheim DOI: 10.1002/anie.200500767

throughput screening.[2] Since structural and mechanistic information is not necessary, the process is fundamentally different from so-called rational design based on site-specific mutagenesis.[3] We have previously applied directed evolution to the creation of enantioselective lipases,[4] epoxide hydrolases,[5] and monooxygenases,[6] and other groups have contributed in this field as well.[1,7] The combination of rational design and random mutagenesis at defined positions in the form of focused libraries[1] has also been employed with the aim of enhancing ligand binding,[8] increasing catalytic activity,[1,9] or influencing enantioselectivity.[4b,10]

A major limitation in exploiting enzymes as catalysts in synthetic organic chemistry is the often encountered limited degree of substrate acceptance.[11] Especially in industrial applications, "methods are desired that have a broad substrate spectrum".[11a] In addition to the use of libraries focusing on a predefined region[1,9] of an enzyme, directed evolution through such standard techniques as the error-prone polymerase chain reaction (epPCR), saturation mutagenesis, and/or DNA shuffling can in principle be employed to solve this problem,[1] and successful cases with regard to nonaccepted substrates have been reported.[1,9,12]

Herein, we describe a method for expanding the scope of substrate acceptance of a given enzyme with the aim of including a wide range of structurally different compounds. Two straightforward steps are required: the design and the generation of relatively small focused libraries of enzyme mutants produced by randomization at several sets of two spatially close amino acid positions around the active site. The choice of two amino acids which are spatially close to one another allows for potential synergistic conformational effects arising from side-chain orientations, an unpredictable phenomenon which cannot be brought about by single-site saturation mutagenesis.[13] The optimal choice of the respective pairs of amino acids is guided by the 3D structure of the wild-type (WT) enzyme with a bound substrate. Geometric inspection allows the definition of sites at which the side chains of the individual amino acids in each pair point toward the binding site of the WT enzyme. On the basis of the secondary structure of an enzyme,[14] it is clear that, for a given pair of spatially as close as possible amino acids in which the side chains point in the direction of the binding site, the following geometric relation pertains: If one member of the pair occurs in the protein sequence at position n, then the second one is found at a sequence of (n+1) in a loop, (n+2) in a β sheet, (n+3) in a 3_{10} helix, and (n+4) in an α helix (Figure 1).[15]

Complete randomization at each pair is then performed in a process that we call the combinatorial active-site saturation test (CAST). Our strategy constitutes a practical compromise between conventional saturation mutagenesis at single sites and simultaneous randomization at multiple sites by using large cassettes. It ensures an appreciable degree of structural diversity and therefore a reasonable chance of finding useful catalysts arising from the $20^2 = 400$ theoretically different mutants in each library, a number which corresponds to $32^2 = 1024$ different codons when using NNK degeneracy (N: any nucleotide; K: G or T).[1] This is in contrast to the limited structural variation of the 20 expected single mutants

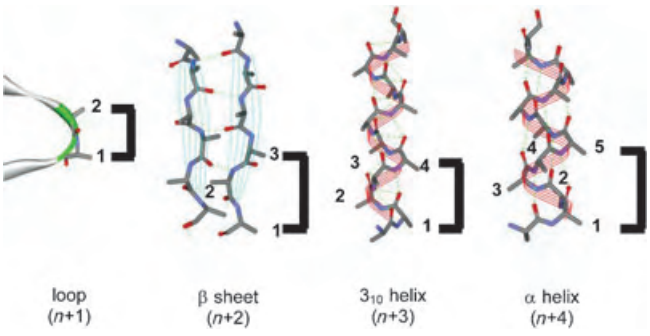


Figure 1. Structural guides in designing libraries of mutant enzymes for CASTing according to the secondary structure of proteins.

(32 codons) in the case of randomization at only single sites,[1,16] a value which may limit the probability of discovering hits. The second important feature of the CAST approach is the limited screening effort. To achieve 95% probability of mutant coverage in the case of randomization at two amino acid positions, about 3000 clones need to be screened (oversampling).[17] In contrast, a focused cassette involving simultaneous randomization at four amino acid sites,[4b] for example, produces theoretically a library of 160000 different mutants, a number requiring $32^4 = 1048576$ codons. This would require a huge screening effort comprising $> 3 \times 10^6$ clones for 95% coverage.[17] Although screening only a small fraction of such a focused library can actually lead to the discovery of positive hits,[4b,10a,10c] the overall process entails uncertainty with respect to the statistical possibility of missing positive mutants.

In a model study, we applied CASTing to expand the substrate acceptance of the lipase from *Pseudomonas aeruginosa*[18] as a catalyst in the hydrolysis of carboxylic acid esters.[4,19] In doing this, one can focus either on the carboxylic acid part or on the alcohol part of the ester (or both). The WT enzyme catalyzes the hydrolysis of triglycerides or fatty acid esters such as palmitic acid *p*-nitrophenyl ester but not of more sterically demanding substrates; not even benzoic acid esters are accepted. Since this constitutes a particularly difficult problem, we focused CASTing on this part of the enzyme. The lipase consists of 285 amino acids, with Ser 82 being the site at which the rate-determining formation of the intermediate oxyanion occurs.[18]

Upon applying the above guidelines (Figure 1) to the crystal structure of the lipase from *Pseudomonas aeruginosa*, solved by Dijkstra et al. in 2000[20] and partially reproduced in Figure 2, the following amino acid pairs were defined: Met 16/Leu 17, Leu 118/Ile 121, Leu 131/Val 135, Leu 159/Leu 162, and Leu 231/Val 232. Five libraries, A–E, respectively, were then created separately by complete saturation, that is, simultaneous radomization at each pair.

About 3000 bacterial colonies from each of the five libraries were harvested on agar plates by a colony picker and deposited in the deep wells of microtiter plates containing Luria–Bertani broth. Following growth of the bacteria and expression of the enzyme, aliquot portions of the lipase-containing supernatants were used to catalyze the hydrolysis of a set of 11 structurally different esters **1**–**11**. In all cases the

 © 2005 Wiley-VCH Verlag GmbH & Co. KGaA, Weinheim

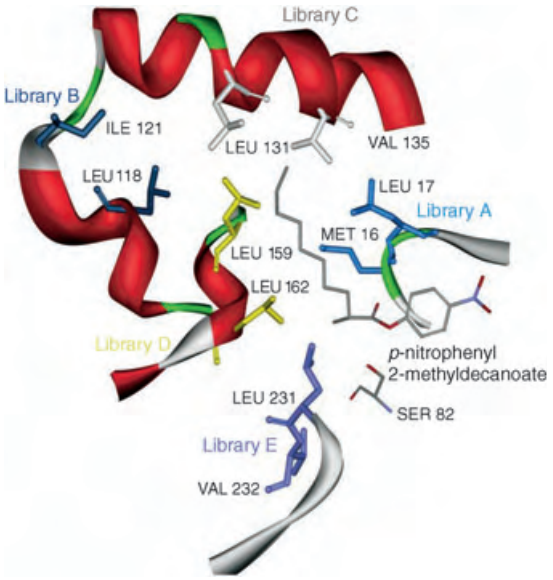
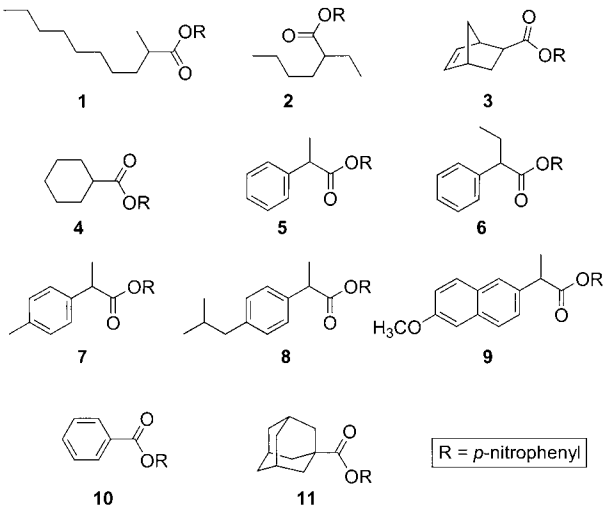


Figure 2. CASTing of the lipase from *Pseudomonas aeruginosa* leading to the construction of five libraries of mutants (A–E) produced by simultaneous randomization at two amino acid sites. (For illustrative purposes, the binding of substrate **1** is shown.)



p-nitrophenyl ester was chosen because the hydrolysis would liberate *p*-nitrophenol which can be monitored easily by UV/Vis spectroscopy.[2,4] A standard UV/Vis plate reader was used to record each reaction rate as measured by the time-resolved appearance of the *p*-nitrophenolate absorption peak at 405 nm (8 min per 96- or 384-well microtiter plate). Parts of the data were checked by GC, and the agreement was found to be excellent. The overall effort in studying the required 165 000 reactions (5 libraries × 3000 clones × 11 substrates) is actually limited, because the process of gene mutagenesis, gene expression, and harvesting of mutants needs to be performed only once.

The results of this multisubstrate screening are remarkable in several respects. Only a part of the data is shown here. Mutants were identified that catalyze the hydrolysis of substrates **1**–**11**; these substrates are either not accepted at all by the WT enzyme or the mutants were found to be considerably more active than the WT enzyme. Figure 3 summarizes the relative reaction rates of WT- and mutant-catalyzed hydrolyses.[21] The eight most important hits (mutants ACA5, A16D8, A2D3, D1A12, D1B10, D1C4, D1F8, and D1E1) originate from libraries A or D, with the latter providing the majority of improved mutants.

The data show that for each substrate, **1**–**11**, one or more mutants were found which lead to a pronounced increase in hydrolysis rate. This means that broad substrate acceptance

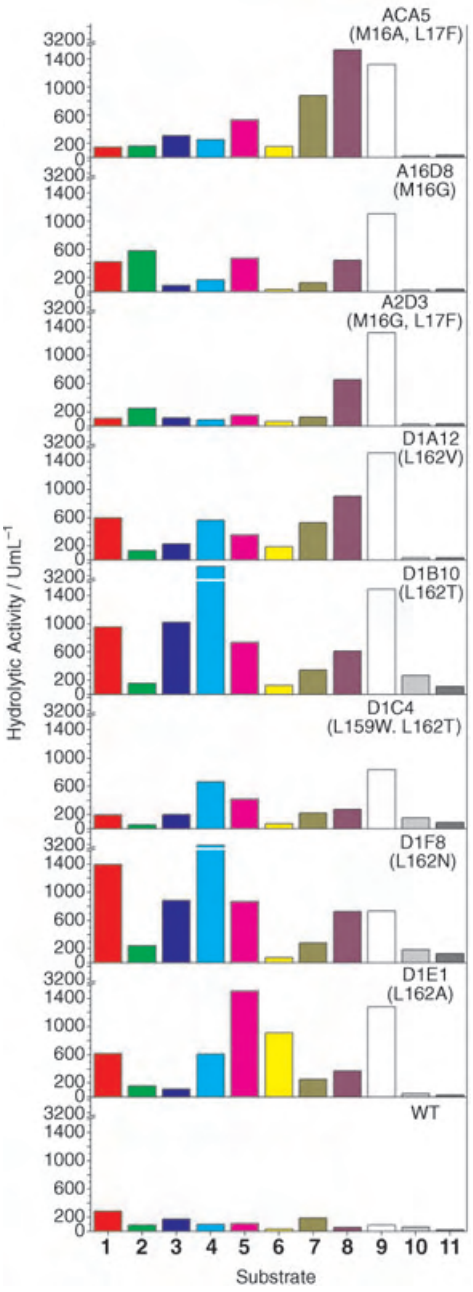


Figure 3. Substrate profiles of lipase variants produced by CASTing. Hydrolytic activities of selected mutants and the WT enzyme were measured photometrically in a continuous assay by following the absorbance at 405 nm for 8 min in a microtiter plate.

 © 2005 Wiley-VCH Verlag GmbH & Co. KGaA, Weinheim

has been achieved. Even such bulky substrates as the Naproxen ester **9** are hydrolyzed rapidly, in this case by at least six different mutants. In contrast, the lipase from *Candida rugosa* shows much lower low activity as do other commercial lipases.[22] The adamantyl carboxylic acid ester **11** is a special case. It is not accepted by the WT enzyme, a result that contrasts with the catalytic effect of mutants D1B10, D1C4, and D1F8, which lead to clearly detectable, although low, turnover. In this case further improvement is necessary.

The eight mutants identified by the screening process were sequenced.[23] Again, the results are remarkable. Firstly, in three cases the mutants are characterized by two amino acid substitutions, whereas in five cases single mutations are involved (Table 1). Some of the largest effects are observed in

Table 1: Active mutants of the lipase from *Pseudomonas aeruginosa* created by CASTing.

Mutant	Library[a]	Mutations
ACA5	A	Met16Ala, Leu17Phe
A16D8	A	Met16Gly
A2D3	A	Met16Gly, Leu17Phe
D1A12	D	Leu162Val
D1B10	D	Leu162Thr
D1C4	D	Leu159Trp, Leu162Thr
D1F8	D	Leu162Asn
D1E1	D	Leu162Ala

[a] Library A: simultaneous randomization at Met16 and Leu17; Library D: simultaneous randomization at Leu159 and Leu162; see Figure 2.

the double mutants, which would not have been discovered by conventional saturation mutagenesis. Moreover, the simple expectation that the introduction of a sterically smaller amino acid creates more space for a bulky substrate to fit properly is not fulfilled in all cases, a fact making a detailed interpretation of such subtle effects difficult at this time. The mutation Leu17Phe, which occurs in two different mutants, is an example. It is also interesting to note that amino acid 162 is a particularly sensitive hot spot (Table 1), in line with the results of earlier directed-evolution studies.[4] We conclude that CASTing is a practical first step in a directed-evolution project with the aim of expanding the range of substrate acceptance. Further improvements can be envisioned in an evolutionary sense by recasting, by combining the mutations of two hits, or by applying the usual mutagenesis methods, such as epPCR or DNA shuffling, which cover the whole gene.[1]

Finally, we note that several of the substrates are chiral, which means that kinetic resolution of the racemates is relevant. Although we have not (yet) performed systematic studies regarding this point, it appears that CASTing can indeed be used to evolve enantioselectivity as well, which is not surprising. For example, mutant D1A12 catalyzes the hydrolytic kinetic resolution of ester **6** with a selectivity factor of $E = 20 \pm 5$ and mutant ACA5 performs the same reaction with $E = 25 \pm 5$, both in favor of the *S* substrate. The WT enzyme does not accept this substrate to any appreciable extent, which means that enantioselectivity could not be measured reliably.

In summary, a practical method (CAST) for solving the long-standing problem of wide substrate acceptance of enzymes has been developed. CASTing combines the features of rational design and combinatorial amino acid randomization at focused sites. It is different from previous focused libraries[1,9] in that a complete set of pairs of amino acids around the bound substrate is considered. This enables the systematic creation of relatively small libraries of mutants, the screening of which by currently available assays leads to positive hits and consequently to the identification of the critical regions around the active site that are crucial for substrate acceptance. We believe that the method can also be considered when attempting to improve the catalytic profile of enzymes in general, for example, in the enhancement of activity and perhaps stability, as well as regio- and stereoselectivity. It is also relevant when attempting to convert a given enzyme into a different type of catalyst.[12] Therefore, CASTing may well constitute a useful alternative to the usual epPCR as the initial step in directed-evolution studies.

Received: March 2, 2005
Revised: April 15, 2005
Published online: June 1, 2005

Keywords: directed evolution · enzymes · lipases · protein engineering · substrate acceptance

[1] a) K. A. Powell, S. W. Ramer, S. B. del Cardayré, W. P. C. Stemmer, M. B. Tobin, P. F. Longchamp, G. W. Huisman, *Angew. Chem.* **2001**, *113*, 4068–4080; *Angew. Chem. Int. Ed.* **2001**, *40*, 3948–3959; b) F. H. Arnold, G. Georgiou, *Directed Enzyme Evolution: Screening and Selection Methods*, *Vol. 230*, Humana Press, Totowa, NJ, **2003**; c) S. Brakmann, K. Johnsson, *Directed Molecular Evolution of Proteins (or How to Improve Enzymes for Biocatalysis)*, Wiley-VCH, Weinheim, **2002**; d) A. Svendsen, *Enzyme Functionality—Design, Engineering, and Screening*, Marcel Dekker, New York, **2004**; e) S. Brakmann, A. Schwienhorst, *Evolutionary Methods in Biotechnology (Clever Tricks for Directed Evolution)*, Wiley-VCH, Weinheim, **2004**.

[2] a) M. T. Reetz, *Angew. Chem.* **2001**, *113*, 292–320; *Angew. Chem. Int. Ed.* **2001**, *40*, 284–310; b) M. T. Reetz in reference [1d], pp. 559–598; c) D. Wahler, J.-L. Reymond, *Curr. Opin. Biotechnol.* **2001**, *12*, 535–544.

[3] Review: F. Cedrone, A. Menez, E. Quemeneur, *Curr. Opin. Struct. Biol.* **2000**, *10*, 405–410.

[4] a) M. T. Reetz, A. Zonta, K. Schimossek, K. Liebeton, K.-E. Jaeger, *Angew. Chem.* **1997**, *109*, 2961–2963; *Angew. Chem. Int. Ed. Engl.* **1997**, *36*, 2830–2832; b) M. T. Reetz, S. Wilensek, D. Zha, K.-E. Jaeger, *Angew. Chem.* **2001**, *113*, 3701–3703; *Angew. Chem. Int. Ed.* **2001**, *40*, 3589–3591; c) M. T. Reetz, *Tetrahedron* **2002**, *58*, 6595–6602; d) M. Bocola, N. Otte, K.-E. Jaeger, M. T. Reetz, W. Thiel, *ChemBioChem* **2004**, *5*, 214–223; e) M. T. Reetz, *Proc. Natl. Acad. Sci. USA* **2004**, *101*, 5716–5722.

[5] a) M. T. Reetz, C. Torre, A. Eipper, R. Lohmer, M. Hermes, B. Brunner, A. Maichele, M. Bocola, M. Arand, A. Cronin, Y. Genzel, A. Archelas, R. Furstoss, *Org. Lett.* **2004**, *6*, 177–180; b) F. Cedrone, S. Niel, S. Roca, T. Bhatnagar, N. Ait-Abdelkader, C. Torre, H. Krumm, A. Maichele, M. T. Reetz, J. C. Baratti, *Biocatal. Biotransform.* **2003**, *21*, 357–364.

 © 2005 Wiley-VCH Verlag GmbH & Co. KGaA, Weinheim

[6] a) M. T. Reetz, B. Brunner, T. Schneider, F. Schulz, C. M. Clouthier, M. M. Kayser, *Angew. Chem.* **2004**, *116*, 4167 – 4170; *Angew. Chem. Int. Ed.* **2004**, *43*, 4075 – 4078; b) M. T. Reetz, F. Daligault, B. Brunner, H. Hinrichs, A. Deege, *Angew. Chem.* **2004**, *116*, 4170 – 4173; *Angew. Chem. Int. Ed.* **2004**, *43*, 4078 – 4081.

[7] Reviews: references [4c,e]; "Changing the Enantioselectivity of Enzymes by Directed Evolution": M. T. Reetz, *Methods Enzymol.* **2004**, *388*, 238 – 256; N. J. Turner, *Trends Biotechnol.* **2003**, *21*, 474 – 478.

[8] a) S. Schlehuber, A. Skerra, *Biophys. Chem.* **2002**, *96*, 213 – 228; b) A. Knappik, L. Ge, A. Honegger, P. Pack, M. Fischer, G. Wellnhofer, A. Hoess, J. Wölle, A. Plückthun, B. Virnekäs, *J. Mol. Biol.* **2000**, *296*, 57 – 86.

[9] Examples: a) L. B. Evnin, J. R. Vásquez, C. S. Craik, *Proc. Natl. Acad. Sci. USA* **1990**, *87*, 6659 – 6663; b) J. Yang, Y. Koga, H. Nakano, T. Yamane, *Protein Eng.* **2002**, *15*, 147 – 152; c) E. Whittle, J. Shanklin, *J. Biol. Chem.* **2001**, *276*, 21500 – 21505; d) A. R. Schmitzer, F. Lépine, J. N. Pelletier, *Protein Eng. Des. Sel.* **2004**, *17*, 809 – 819; e) C. M. Hill, W.-S. Li, J. B. Thoden, H. M. Holden, F. M. Raushel, *J. Am. Chem. Soc.* **2003**, *125*, 8990 – 8991; f) F. Brühlmann, W. Chen, *Biotechnol. Bioeng.* **1999**, *63*, 544 – 551; g) E. M. Gabor, D. B. Janssen, *Protein Eng. Des. Sel.* **2004**, *17*, 571 – 579; h) J. Yang, Y. Koga, H. Nakano, T. Yamane, *Protein Eng.* **2002**, *15*, 147 – 152; i) S. V. Taylor, P. Kast, D. Hilvert, *Angew. Chem.* **2001**, *113*, 3408 – 3436; *Angew. Chem. Int. Ed.* **2001**, *40*, 3310 – 3335.

[10] a) M. Chen-Goodspeed, M. A. Sogorb, F. Wu, S.-B. Hong, F. M. Raushel, *Biochemistry* **2001**, *40*, 1325 – 1331; b) "Directed Evolution of Enantioselective Enzymes as Catalysts in the Production of Chiral Pharmaceuticals": M. T. Reetz in *Pharmacochemistry Library*, *Vol. 32 (Trends in Drug Research III)* (Ed.: H. van der Goot), Elsevier, Amsterdam, **2002**, pp. 27 – 37; c) Y. Koga, K. Kato, H. Nakano, T. Yamane, *J. Mol. Biol.* **2003**, *331*, 585 – 592; d) S. Park, K. L. Morley, G. P. Horsman, M. Holmquist, K. Hult, R. J. Kazlauskas, *Chem. Biol.* **2005**, *12*, 45 – 54.

[11] a) M. Breuer, K. Ditrich, T. Habicher, B. Hauer, M. Keßeler, R. Stürmer, T. Zelinski, *Angew. Chem.* **2004**, *116*, 806 – 843; *Angew. Chem. Int. Ed.* **2004**, *43*, 788 – 824; b) K. Drauz, H. Waldmann, *Enzyme Catalysis in Organic Synthesis: A Comprehensive Handbook*, *Vol. I–III*, 2nd ed., Wiley-VCH, Weinheim, **2002**; c) K. Faber, *Biotransformations in Organic Chemistry*, 4th ed., Springer, Berlin, **2000**; d) A. Schmid, J. S. Dordick, B. Hauer, A. Kiener, M. Wubbolts, B. Witholt, *Nature* **2001**, *409*, 258 – 268.

[12] Discussions of enzyme promiscuity, plasticity, and so-called moonlighting: a) A. Aharoni, L. Gaidukov, O. Khersonsky, S. McQ Gould, C. Roodveldt, D. S. Tawfik, *Nat. Genet.* **2005**, *37*, 73 – 76; b) S. Raillard, A. Krebber, Y. Chen, J. E. Ness, E. Bermudez, R. Trinidad, R. Fullem, C. Davis, M. Welch, J. Seffernick, L. P. Wackett, W. P. C. Stemmer, J. Minshull, *Chem. Biol.* **2001**, *8*, 891 – 898; c) P. J. O'Brien, D. Herschlag, *Chem. Biol.* **1999**, *6*, R91 – R105; d) S. D. Copley, *Curr. Opin. Chem. Biol.* **2003**, *7*, 265 – 272; e) U. T. Bornscheuer, R. J. Kazlauskas, *Angew. Chem.* **2004**, *116*, 6156 – 6165; *Angew. Chem. Int. Ed.* ***2004***, *43*, 6032 – 6040.

[13] The randomization at two amino acids which are not spatially close to each other yet have side chains pointing toward the active site (for example, in two different libraries) may of course also be considered.

[14] a) A. Fersht, *Structure and Mechanism in Protein Science*, W. H. Freeman, New York, **1999**; b) R. A. Copeland, *Enzymes*, Wiley-VCH, Weinheim, **2000**.

[15] These guidelines are derived from ideal secondary structural units. If in a given case the latter are not ideal, as, for example, in a kinked helix, then additional positions need to be considered. In the case of a kinked helix, for example, it may be a sequentially neighboring amino acid (n+1). It is mandatory to include such structural aspects when designing combinatorial active-site saturation test libraries, that is, the shape of the binding pocket serves as a guide.

[16] Examples: a) G. DeSantis, K. Wong, B. Farwell, K. Chatman, Z. Zhu, G. Tomlinson, H. Huang, X. Tan, L. Bibbs, P. Chen, K. Kretz, M. J. Burk, *J. Am. Chem. Soc.* **2003**, *125*, 11476 – 11477; b) S. A. Funke, A. Eipper, M. T. Reetz, N. Otte, W. Thiel, G. van Pouderoyen, B. W. Dijkstra, K.-E. Jaeger, T. Eggert, *Biocatal. Biotransform.* **2003**, *21*, 67 – 73; c) R. Georgescu, G. Bandara, L. Sun in *Directed Evolution Library Creation* (Eds.: F. H. Arnold, G. Georgiou), Humana Press, Totowa, NJ, **2003**, pp. 75 – 89.

[17] For this calculation we used the traditional statistical method; see, for example: M. S. Warren, S. J. Benkovic, *Protein Eng.* **1997**, *10*, 63 – 68, and references therein.

[18] a) K.-E. Jaeger, B. Schneidinger, K. Liebeton, D. Haas, M. T. Reetz, S. Philippou, G. Gerritse, S. Ransac, B. W. Dijkstra in *Molecular Biology and Biotechnological Application* (Eds.: T. Nakazawa, K. Furukawa, D. Haas, S. Silver), ASM Press, Washington, **1996**, pp. 319 – 339; b) K.-E. Jaeger, K. Liebeton, A. Zonta, K. Schimossek, M. T. Reetz, *Appl. Microbiol. Biotechnol.* **1996**, *46*, 99 – 105.

[19] We thank K.-E. Jaeger for providing the lipase-expression system.[18]

[20] M. Nardini, D. A. Lang, K. Liebeton, K.-E. Jaeger, B. W. Dijkstra, *J. Biol. Chem.* **2000**, *275*, 31219 – 31225.

[21] Because of the instability of the lipase from *Pseudomonas aeruginosa*,[18] it was not possible to purify mutants and to perform detailed kinetic studies. A previous kinetic study was performed by using the supernatants and assuming similar amounts of enzyme expressed and secreted (M. T. Reetz, S. Wilensek, unpublished results; see also: M. T. Reetz, *Tetrahedron* **2002**, *58*, 6595 – 6602). To lend support to this assumption, we measured the lipase activity towards the "natural" compound palmitic acid *p*-nitrophenyl ester as a reference substrate. All of the mutants of the present study showed similar activities towards this reference substrate but slightly lower activities relative to the WT enzyme. Therefore, the low activities of the WT enzyme towards the different substrates in Figure 3 are not because of a lower expression rate. This was confirmed by sodium dodecylsulfate PAGE analysis. This means that the profiles of the mutants reflect inherent activity enhancements.

[22] A comparative study encompassing various substrates and lipases is underway, as are CASTing experiments on commercially available lipases that have higher thermal stability than the lipase from *Pseudomonas aeruginosa*.

[23] None of the variants contain additional mutations because of the PCR.

Fractal Iron Oxide

Single-Crystal Dendritic Micro-Pines of Magnetic α-Fe_2O_3: Large-Scale Synthesis, Formation Mechanism, and Properties**

Minhua Cao, Tianfu Liu, Song Gao, Genban Sun, Xinglong Wu, Changwen Hu, and Zhong Lin Wang**

Hierarchical self-assembly of nanoscale building blocks (nanoclusters, nanowires, nanobelts, and nanotubes) is a technique for building functional electronic and photonic nanodevices.[1,2] Fractal structures are common in nature across all length scales, from self-assembled molecules, to the shapes of coastlines, to the distribution of galaxies, and even to the 3D shapes of clouds. On the nanoscale, dendritic fractals are one type of hyperbranched structure which are generally formed by hierarchical self-assembly under non-equilibrium conditions.[3,4] Investigation of hierarchically self-assembled fractal patterns in chemical systems has shown that the distinct size, shape, and chemical functionality of such structures make them promising candidates for the design and fabrication of new functional nanomaterials,[5] but it is challenging to develop simple and novel synthetic approaches for building hierarchically self-assembled fractal architectures of various systems.

[*] Dr. M. Cao, X. Wu, Prof. C. Hu
Institute of Polyoxometalate Chemistry
Northeast Normal University
Changchun, 130024 (P. R. China)
Fax: (+86) 10-6282-8869
E-mail: huchw@nenu.edu.cn
Dr. T. Liu, G. Sun, Prof. C. Hu
The Institute for Chemical Physics
Beijing Institute of Technology
Beijing, 100081 (P. R. China)
and
Department of Chemistry
Beijing Institute of Technology
Beijing, 100081 (P. R. China)
E-mail: cwhu@bit.edu.cn
Prof. Z. L. Wang
School of Materials Science and Engineering
Georgia Institute of Technology
Atlanta, GA 30332-0245 (USA)
Fax: (+1) 404-894-8008
E-mail: zhong.wang@mse.gatech.edu
Prof. S. Gao
State Key Laboratory of Rare Earth Materials Chemistry and Applications
College of Chemistry and Molecular Engineering
Peking University
Beijing, 100871 (P. R. China)

[**] This work was supported by the Natural Science Foundation Council of China (NSFC) (No. 20271007, No. 20331010, No. 90406002, and No. 20401005), by the Specialized Research Fund for the Doctoral Program of Higher Education (SRFDP, No. 20030007014), and by Jilin Distinguished Young Scholars Program and the Natural Science Young Foundation of Northeast Normal University.

Magnetic nanomaterials have been the subject of increasing interest due to their physical properties and technological applications.[6–8] In the past few years, research has focused primarily on zero- and one-dimensional (1D) magnetic nanomaterials such as magnetic metals, alloys, and metal oxides and has led to substantial advances including the assembly of 2D or 3D superlattices from spherical nanoparticles or nanorods.[9–14] However, to the best of our knowledge, the hierarchical self-assembly of magnetic nanomaterials has not been reported. Here we present the spontaneous, large-scale, hierarchical self-assembly of dendritic nanostructures of magnetic Fe_2O_3 (so-called micro-pine structure). The α-Fe_2O_3 micron-pine dendrites were synthesized by hydrothermal reaction of $K_3[Fe(CN)_6]$ in aqueous solution at suitable temperatures. The method is based on the weak dissociation of $[Fe(CN)_6]^{3-}$ ions under hydrothermal conditions. The resulting structures display exquisite fractal features, which morphologically resemble a type of pine tree. The structure was formed as a result of fast growth along six crystallographically equivalent directions, and this process is different from the reported formation mechanism of general fractal structures. The magnetic properties of the nanostructure show a lower Morin transition temperature of 216 K. The reported structures could have important applications in biomedical science and magnetism.

The micro-pines were synthesized on a large scale and in high purity. Figure 1 shows typical SEM images of α-Fe_2O_3 micro-pine dendrites obtained with a $K_3[Fe(CN)_6]$ concentration of 0.015 M at 140 °C. The low-magnification image in Figure 1a shows that the product consists almost entirely of such dendritic structures, and this indicates the high yield and good uniformity achieved with this approach. The high-magnification images in Figure 1b and c show the morphology of a single dendrite in two opposite directions. They reveal a clear and well-defined dendritic fractal structure with a pronounced trunk consisting of corrugations and highly ordered branches distributed on both sides of the trunk. Figure 1d shows striking periodic corrugated structures on the trunk of a single dendrite. The lengths of the dendrite trunks are 3–5 μm, and those of the branch trunk range from 50 nm to 1.5 μm. Note that the protrusion direction of the dendrite trunk and those of the branches are opposite, as is clearly shown by the SEM images (Figure 1b and c), and all dendrites have similar structure. The micro-pine dendrites were shown by powder XRD (Figure 1e) to consist of pure α-Fe_2O_3 phase (hematite), which has a rhombohedral structure with lattice parameters of $a = 0.50355$ and $c = 1.3747$ nm. The XRD peaks are labeled by using the three- and four-index systems, as for hexagonal nanostructure. The four-index system facilitates the discussion below.

The phase composition is further supported by the room-temperature Mössbauer spectrum (Figure 1f), which shows a single sextet with an isomeric shift of 0.44 mm s^{-1}, a quadrupole splitting of -0.23 mm s^{-1}, and a hyperfine field of 516.8 KOe and thus provides clear evidence for the presence of α-Fe_2O_3 rather than γ-Fe_2O_3 or Fe_3O_4.[15] Moreover, the results of many experiments show that this approach has excellent reproducibility, and the resulting structures are

 DOI: 10.1002/anie.200500448 © 2005 Wiley-VCH Verlag GmbH & Co. KGaA, Weinheim

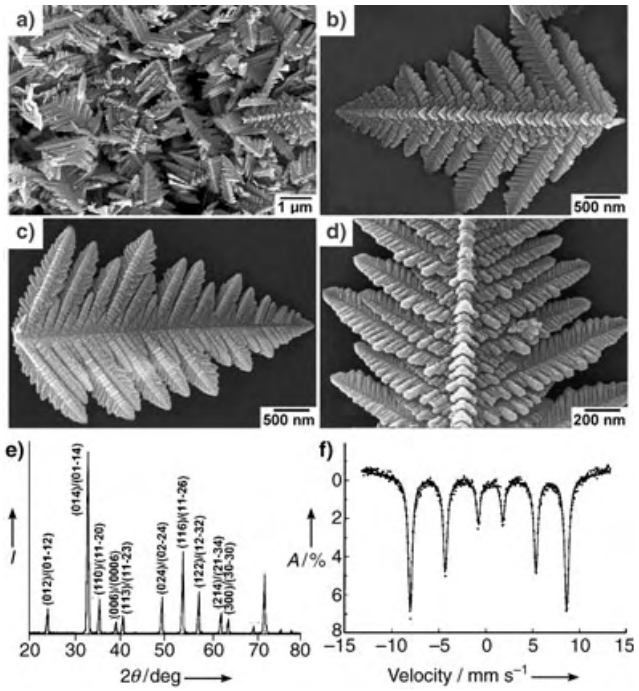


Figure 1. Electron microscopy images and chemical characterization of α-Fe_2O_3 fractals synthesized with a $K_3[Fe(CN)_6]$ concentration of 0.015 M at 140 °C. a) Low-magnification SEM image of fractals showing the high yield and good uniformity. b) SEM image of a single α-Fe_2O_3 fractal taken from one side. c) SEM image of a single α-Fe_2O_3 fractal taken from the other side. d) A higher magnification image of a single α-Fe_2O_3 fractal showing striking periodic corrugated structures on the main trunk. e) XRD pattern of the sample confirming formation of a pure α-Fe_2O_3 phase. *I* = intensity. f) Mössbauer spectrum of the sample recorded at room temperature. *A* = absorption.

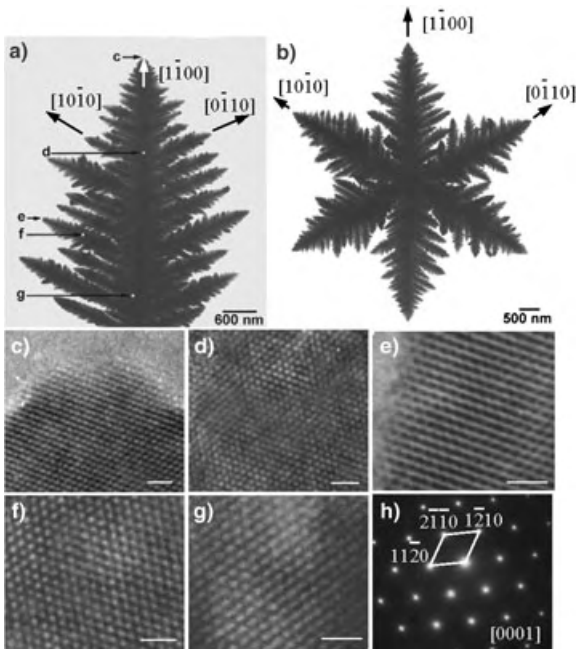


Figure 2. TEM images of the same α-Fe_2O_3 fractals as shown in Figure 1. a) Image of a fractal exhibiting hyperbranches. b) TEM image of a sixfold-symmetric dendritic structure. c–g) High-resolution TEM images recorded in different regions of the dendritic structure in (a) showing the well-defined single-crystalline nature of the entire dendritic structure (scale bar: 1 nm). h) Electron diffraction pattern recorded from the entire dendritic structure in (a) which also shows the single-crystalline nature of the entire dendritic structure.

highly stable, without morphological or compositional change over several months when stored in air.

The dendrite micro-pines have a single-crystalline structure. Figure 2a shows a TEM image of a micro-pine. The TEM observations revealed that the micro-pine dendrites occasionally show a sixfold-symmetric structure (Figure 2b), like a snowflake. Further structural characterization of the dendrite was carried out by high-resolution TEM (HRTEM). Figure 2c–g show HRTEM images taken from the areas labeled c–g in Figure 2a; they respectively show the lattice structures at the tip of the dendrite, the trunk of the dendrite, the tip of the dendrite branch, the trunk of the dendrite branch, and the junction between the trunk of the dendrite and that of the dendrite branch. They all show clear lattice fringes that indicate single-crystallinity of the entire dendrite structure. The lattice spacing of 2.5177 Å between adjacent lattice planes in each of these images corresponds to the distance between two $\{11\bar{2}0\}$ crystal planes. The selected-area electron diffraction (SAED) pattern (Figure 2g) taken from the entire dendrite clearly shows a single-crystalline structure. The diffraction pattern indicates that the dendrite is oriented along [0001] with the three branches along $[10\bar{1}0]$ (or [100]), $[1\bar{1}00]$ (or $[1\bar{1}0]$), and $[0\bar{1}10]$ (or $[0\bar{1}0]$) (Figure 2a). Thus, the sixfold-symmetric structure shown in Figure 2b is a result of growth along $\pm[10\bar{1}0]$, $\pm[1\bar{1}00]$, and $\pm[0\bar{1}10]$.

The reaction temperature and the concentration of $K_3[Fe(CN)_6]$ significantly affect the morphology of the product. For example, when the temperature was increased from 140 to 200 °C while keeping the concentration of $K_3[Fe(CN)_6]$ constant at 0.015 M, the morphology of the sample changed continuously from hyperbranched dendrites at 140 °C (Figure 3a) to slightly branched dendrites at 170 °C (Figure 3b), and finally nanorod-branched dendrites at 200 °C (Figure 3c), somewhat similar to ZnO nanowire comb structures.[16] The reaction temperature must be higher than 140 °C, otherwise the reaction is very slow. When the concentration of $K_3[Fe(CN)_6]$ was varied between 0.005 and 0.025 M while maintaining a constant reaction temperature of 140 °C, α-Fe_2O_3 micro-pine dendrites such as that shown in Figure 2a were the major product. However, on gradually increasing the concentration of $K_3[Fe(CN)_6]$ while maintaining the reaction temperature at 140 °C, a continuous transition from thin to thick nanorod-branched dendrites was observed. Figure 3d–f show TEM images of samples that were synthesized at concentrations of $K_3[Fe(CN)_6]$ of 0.04, 0.06, and 0.1 M, respectively. The higher the concentration of $K_3[Fe(CN)_6]$, the thicker the nanorod branches of the dendrites. These results suggest that it is possible to control and tune the shape of α-Fe_2O_3 dendritic nanostructures by controlling the kinetic parameters of the reaction process, that is, temperature and concentration.

The formation of the dendrites could be explained by the model proposed in Figure 4. From the crystal structure, $\langle 10\bar{1}0 \rangle$ are six equivalent directions. For reasons of spatial confine-

 © 2005 Wiley-VCH Verlag GmbH & Co. KGaA, Weinheim

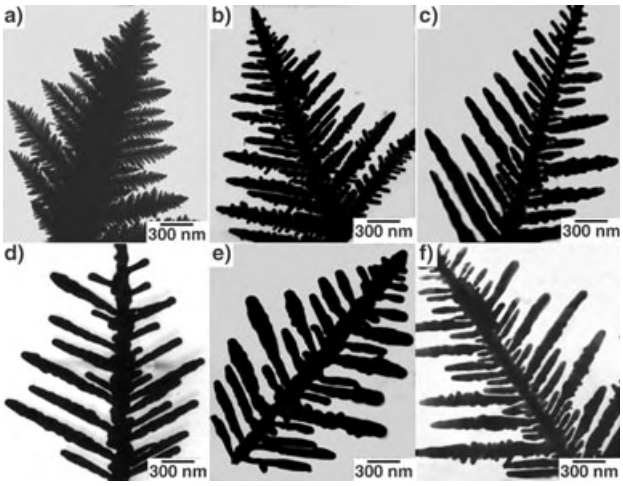


Figure 3. Evolution of crystal shape under different reaction conditions. a–c) TEM images of α-Fe_2O_3 dendrites obtained with a concentration of $K_3[Fe(CN)_6]$ of 0.01 M and reaction temperatures of 140, 170, and 200 °C, respectively. d–f) TEM images of α-Fe_2O_3 dendrites obtained at a reaction temperature of 140 °C and concentrations of $K_3[Fe(CN)_6]$ of 0.04, 0.06, and 0.1 M, respectively.

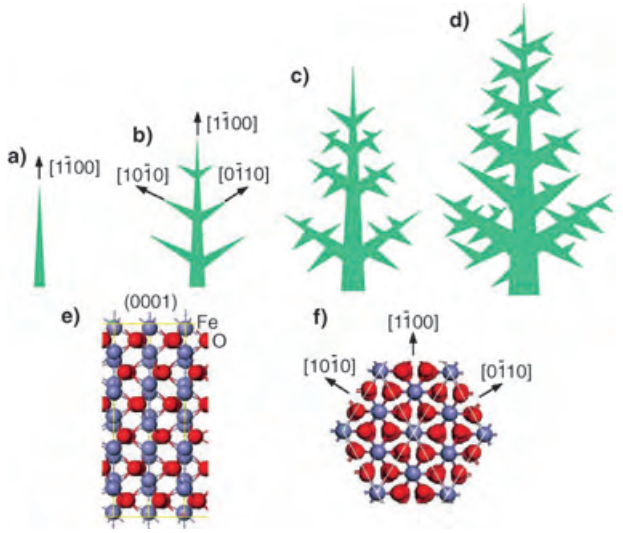


Figure 4. Proposed formation process of the micro-pine dendrite structure by fast growth along the six crystallographically equivalent directions $\langle 10\bar{1}0\rangle$.

ment, one of the directions, for example, $[1\bar{1}00]$, initiates fast growth, and formation of a needle is possible if the growth along $[1\bar{1}00]$ is much faster than along the other directions (Figure 4a). Subsequent growth along the other two crystallographically equivalent directions, $[10\bar{1}0]$ and $[0\bar{1}10]$, leads to the formation of main and possibly symmetric branches on both sides (Figure 4b). As growth continues, each side branch can initiate growth along $\pm[0\bar{1}10]$ and $\pm[10\bar{1}0]$ to form minibranches (Figure 4c). With further growth, all of the branches become thicker and finally interconnected (Figure 4d), and form the micro-pine dendrite structure observed in Figure 1. If growth is symmetric along the six crystallographically equivalent directions $\langle 10\bar{1}0\rangle$, a sixfold-symmetric "snowflake" structure would be formed (see Figure 2b).

To understand the reasons why the six $\langle 10\bar{1}0\rangle$ directions are the directions of fastest growth, we start from the crystal structure of hematite. Figure 4e shows a projection of the crystal structure along $[2\bar{1}\bar{1}0]$, which is parallel to the *c* plane. It is apparent that the Fe^{3+} and O^{2-} ions are arranged alternatively parallel to the *c* plane, which is thus terminated with either Fe^{3+} or O^{2-} and has a net ionic charge on the surface (so-called polar surface). Therefore, during synthesis in solution, the *c* plane will be immediately covered by adsorbing molecules to neutralize the ionic charges, which also terminate growth along [0001]. Therefore, the possible structure is a platelet parallel to the (0001) plane. On the other hand, the six crystallographically equivalent planes $\{2\bar{1}\bar{1}0\}/\{10\bar{1}0\}$ are neutral surfaces and are the most typical low-energy facets for a hexagonal crystal lattice (Figure 4f). Growth parallel to the *c* plane tends to enlarge the surfaces of $\{2\bar{1}\bar{1}0\}/\{10\bar{1}0\}$ and leads to the formation of side branches that are dominated by $\{2\bar{1}\bar{1}0\}$ and $\{10\bar{1}0\}$ surfaces.

The magnetic behavior of α-Fe_2O_3 dendritic micro-pines, which is of importance for practical applications, was investigated for the sample obtained with a $K_3[Fe(CN)_6]$ concentration of 0.015 M at 140 °C (Figure 1). The variable-temperature (5–300 K) magnetic susceptibility (Figure 5a) displays the characteristic behavior for α-Fe_2O_3 but with a lower

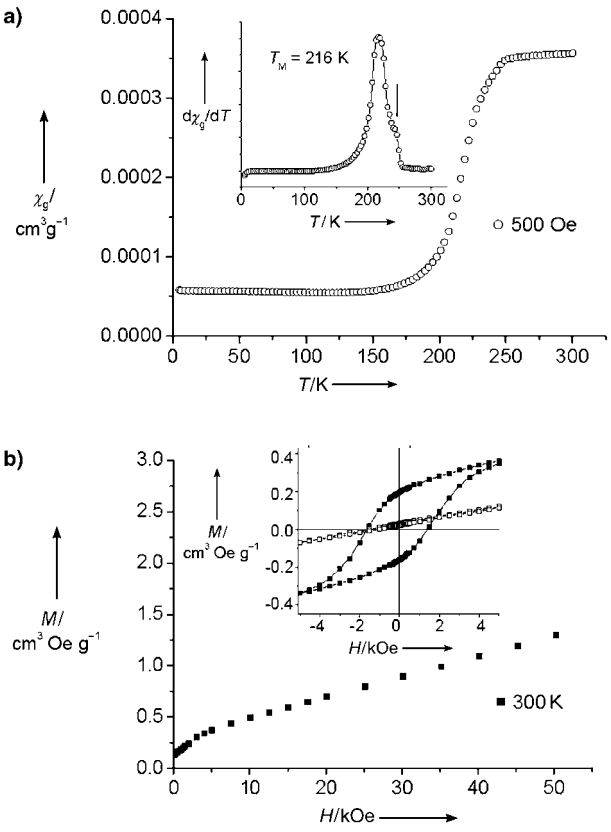


Figure 5. Magnetic measurements for the sample prepared with a $K_3[Fe(CN)_6]$ concentration of 0.015 M at 140 °C. a) Temperature dependence of magnetic susceptibility. b) Field dependence of magnetization at 5 (□) and 300 K (■).

 © 2005 Wiley-VCH Verlag GmbH & Co. KGaA, Weinheim

Morin transition temperature T_M of 216 K, which is determined by the sharp peak in the $d\chi_g/dT$ curve. Normally bulk hematite has the Morin transition from the low-temperature antiferromagnetic phase to a weakly ferromagnetic phase at 260 K, and it was documented that annealing led to an increase in T_M for small-sized hematite.[17] The decrease in T_M here may result from some lattice strain and defects in the dendrites obtained by low-temperature hydrothermal synthesis. Superparamagnetic phenomena were not found for the sample, since the sizes of the branch trunk are rather large (50 nm to 1.5 μm) compared to the single-domain size of hematite. The shoulder around 243 K in the $d\chi_g/dT$ curve may indicate the presence of a larger trunk with higher T_M. The field dependence of the magnetization at 300 and 5 K (Figure 5b) confirm the antiferromagnetic state at low temperature and weak ferromagnetism above T_M. The coercive force at 300 K of 1510 Oe is larger than that of 1080 Oe for spherical hematite with a diameter of 160 nm, which might be due to the shape anisotropy of the dendrites.[17]

We recently employed a soft-templating route for fabricating well-crystallized 1D nanostructures based on self-assembly of surfactants and inorganic precursors.[18–20] However, the disadvantage of this method is that the presence of the surfactants can easily result in the formation of byproducts, which may limit their applications. In the present study, we emphasize the role of the $K_3[Fe(CN)_6]$ complex as a single precursor in the synthesis of nanomaterials. $K_3[Fe(CN)_6]$ plays a crucial role in the formation of dendritic fractal structures; if other iron sources such as $FeCl_3$, $Fe(NO_3)_3$, and $Fe_2(SO_4)_3$, are used, even under the same reaction conditions, only particles are observed instead of micro-pine dendrites. $[Fe(CN)_6]^{3-}$ ions are very stable ($K_s = 1.0 \times 10^{42}$) in aqueous solution at room temperature, and almost no free Fe^{3+} ions can be detected. However, in our case, we believe that α-Fe_2O_3 formation proceeds through three steps [Eq. (1)] under the hydrothermal conditions: first, $[Fe(CN)_6]^{3-}$ ions dissociate slowly into Fe^{3+} ions; second, the Fe^{3+} ions are subsequently hydrolyzed in aqueous solution to form FeOOH or $Fe(OH)_3$; and finally, the resulting FeOOH or $Fe(OH)_3$ decompose into α-Fe_2O_3. This growth process might be determined by the first step because of the weak dissociation tendency of $[Fe(CN)_6]^{3-}$ ions [Eq. (1)].

$$[Fe(CN)_6]^{3-} \rightleftharpoons Fe^{3+} \rightarrow FeOOH/Fe(OH)_3 \rightarrow \alpha\text{-}Fe_2O_3 \quad (1)$$

Dendritic fractals of several materials have been found and investigated.[21–27] It is generally accepted that fractal aggregation arises in situations far from thermodynamic equilibrium where high driving forces lead to the generation of rough crystallites and random association.[24] In the past few years the model known as diffusion-limited aggregation (DLA) has been successfully developed to interpret this ramified growth of different systems controlled by diffusive processes.[28] In our system, the formation of micro-pine dendrites of α-Fe_2O_3 is a new growth process in which fast growth along six crystallographically equivalent directions forms single-crystal dendrites or snowflakelike structures.

We have described a distinct type of hierarchical α-Fe_2O_3 micro-pine dendrite. Formation of such structures requires a suitable iron complex precursor that slowly dissociates to yield Fe^{3+} ions under the hydrothermal conditions. Our experimental method also provides a simple and facile route for the preparation of α-Fe_2O_3 nanostructures, which could have important applications in biomedical science due to the biodegradability of iron oxide. It could also be a general approach for the large-scale, high-purity growth of dendritic fractal structures of a wide range of materials.

Experimental Section

α-Fe_2O_3 micro-pine dendrites were synthesized by hydrothermal reaction of $K_3[Fe(CN)_6]$ in aqueous solutions at suitable temperatures. In a typical synthesis, $K_3[Fe(CN)_6]$ was dissolved in distilled water to form a clear solution of a certain concentration, which was placed in a Teflon-sealed autoclave and maintained at a given temperature for 2 d. The red product was isolated by centrifugation, repeatedly washed with distilled water and absolute ethanol, and dried at 50 °C in air. The concentration of $K_3[Fe(CN)_6]$ was varied in the range from 0.005 to 0.1 M, and the reaction temperature from 140 to 200 °C.

X-ray diffraction (XRD) was performed on a Japan Rigaku D/max γA X-ray diffractometer with graphite-monochromatized $Cu_{K\alpha}$ radiation ($\lambda = 0.154178$ nm). A JEOL JEM-2010F transmission electron microscope operating at 200 kV accelerating voltage was used for TEM (transmission electron microscopy) analysis. Scanning electron microscopy (SEM) was performed with an Amray 1910FE microscope. The Mössbauer spectrum was recorded on a conventional Mössbauer spectrometer with a room-temperature ^{57}Co source (Rh matrix) in transmission geometry. Magnetic measurements were performed on a Quantum Design MPMS-XL5 SQUID magnetometer.

Received: February 6, 2005
Published online: June 7, 2005

Keywords: fractals · hydrothermal synthesis · iron oxides · magnetic properties · nanostructures

[1] R. L. Whetten, J. T. Khoury, M. M. Alvarez, S. Murthy, I. Vezmar, Z. L. Wang, C. C. Cleveland, W. D. Luedtke, U. Landman, *Adv. Mater.* **1996**, *8*, 428.
[2] S. Sun, C. B. Murray, D. Weller, L. Folks, A. Moser, *Science* **2000**, *287*, 1989.
[3] a) I. Lisiecki, P. A. Albouy, M. P. Pileni, *Adv. Mater.* **2003**, *15*, 712; b) T. A. Witten, Jr., L. M. Sander, *Phys. Rev. Lett.* **1981**, *47*, 351.
[4] P. Meakin, *Phys. Rev. Lett.* **1983**, *51*, 1119.
[5] P. D. Yang, T. Deng, D. Y. Zhao, P. Y. Feng, D. Pine, B. F. Chmelka, G. M. Whitesides, G. D. Stucky, *Science* **1998**, *282*, 2244.
[6] D. Zitoun, M. Respaud, M. C. Fromen, M. J. Casanove, P. Lecante, C. Amiens, B. Chaudret, *Phys. Rev. Lett.* **2002**, *89*, 37203.
[7] X. G. Wen, S. H. Wang, Y. Ding, Z. L. Wang, S. H. Yang, *J. Phys. Chem. B* **2005**, *109*, 215.
[8] E. V. Shevchenko, D. V. Talapin, H. Schnablegger, A. Kornowski, O. Festin, P. Svedlindh, M. Haase, H. Weller, *J. Am. Chem. Soc.* **2003**, *125*, 9090.
[9] a) L. Q. Xu, W. Q. Zhang, Y. W. Ding, Y. Y. Peng, S. Y. Zhang, W. C. Yu, Y. T. Qian, *J. Phys. Chem. B* **2004**, *108*, 10859; b) S. J.

 © 2005 Wiley-VCH Verlag GmbH & Co. KGaA, Weinheim

Park, S. Kim, S. Lee, Z. G. Khim, K. Char, T. Hyeon, *J. Am. Chem. Soc.* **2000**, *122*, 8581.
[10] a) V. F. Puntes, K. M. Krishan, A. P. Alivisatos, *Science* **2001**, *291*, 2115; b) V. F. Puntes, D. Zanchet, C. K. Erdonmez, A. P. Alivisatos, *J. Am. Chem. Soc.* **2002**, *124*, 12874.
[11] a) F. Dumestre, B. Chaudret, C. Amiens, M. Respaud, P. Fejes, P. Renaud, P. Zurcher, *Angew. Chem.* **2003**, *115*, 5371; *Angew. Chem. Int. Ed.* **2003**, *42*, 5213; b) F. Dumestre, B. Chaudret, C. Amiens, M. C. Fromen, M. J. Casanove, M. Respaud, P. Zurcher, *Angew. Chem.* **2002**, *114*, 4462; *Angew. Chem. Int. Ed.* **2002**, *41*, 4286.
[12] N. Cordente, M. Respaud, F. Senocq, M. J. Casanove, C. Amiens, B. Chaudret, *Nano Lett.* **2001**, *1*, 565.
[13] J. Park, B. Koo, Y. Hwang, C. Bae, K. An, J. G. Park, H. M. Park, T. Hyeon, *Angew. Chem.* **2004**, *116*, 2332; *Angew. Chem. Int. Ed.* **2004**, *43*, 2282.
[14] a) E. V. Shevchenko, D. V. Talapin, A. L. Rogach, A. Kornowski, M. Haase, H. Weller, *J. Am. Chem. Soc.* **2002**, *124*, 11480; b) E. V. Shevchenko, D. V. Talapin, H. Schnablegger, A. Kornowski, O. Festin, P. Svedlindh, M. Haase, H. Weller, *J. Am. Chem. Soc.* **2003**, *125*, 9090.
[15] R. M. Cornell, U. Schwertmann, *The Iron Oxides*, VCH, Weinheim, **1996**.
[16] Z. L. Wang, X. Y. Kong, J. M. Zuo, *Phys. Rev. Lett.* **2003**, *91*, 185502.
[17] T. P. Raming, A. J. A. Winnubst, A. C. M. van Kats, A. P. Philipse, *J. Colloid Interface Sci.* **2002**, *249*, 346.
[18] a) M. H. Cao, C. W. Hu, G. Peng, Y. J. Qi, E. B. Wang, *J. Am. Chem. Soc.* **2003**, *125*, 4982; b) M. H. Cao, C. W. Hu, E. B. Wang, *J. Am. Chem. Soc.* **2003**, *125*, 11196.
[19] M. H. Cao, Y. H. Wang, C. X. Guo, Y. J. Qi, C. W. Hu, *Langmuir* **2004**, *20*, 4784.
[20] a) M. H. Cao, C. W. Hu, Y. H. Wang, Y. H. Guo, C. X. Guo, E. B. Wang, *Chem. Commun.* **2003**, 1884; b) G. B. Sun, M. H. Cao, Y. H. Wang, C. W. Hu, L. Ren, K. L. Huang, *Chem. Commun.* **2005**, 1740.
[21] a) S. T. Selvan, *Chem. Commun.* **1998**, 351; b) X. Q. Wang, K. Naka, H. Itoh, S. Park, Y. Chujo, *Chem. Commun.* **2002**, 1300.
[22] a) J. P. Xiao, Y. Xie, R. Tang, M. Chen, X. B. Tian, *Adv. Mater.* **2001**, *13*, 1887; b) Y. Zhou, S. H. Yu, C. Y. Wang, X. G. Li, Y. R. Zhu, Z. Y. Chen, *Adv. Mater.* **1999**, *11*, 850.
[23] M. Wang, S. Zhong, X. B. Yin, J. M. Zhu, R. W. Peng, Y. Wang, K. Q. Zhang, N. B. Ming, *Phys. Rev. Lett.* **2001**, *86*, 3827.
[24] M. Wang, X. Y. Liu, C. S. Strom, P. Bennema, W. Enckevort, N. B. Ming, *Phys. Rev. Lett.* **1998**, *80*, 3089.
[25] J. Zhu, S. Liu, O. Palchik, Y. Koltypin, A. Gedanken, *Langmuir* **2000**, *16*, 6396.
[26] a) Z. G. R. Tian, J. Liu, J. A. Voigt, H. F. Xu, M. J. Mcdermott, *Nano Lett.* **2003**, *3*, 89; b) A. Parfenov, I. Gryczynski, J. Malicka, C. D. Geddes, J. R. Lakowicz, *J. Phys. Chem. B* **2003**, *107*, 8829.
[27] Q. Peng, Y. J. Dong, Z. X. Deng, Y. D. Li, *Inorg. Chem.* **2002**, *41*, 5249.
[28] a) R. R. Brady, R. C. Ball, *Nature* **1984**, *309*, 225; b) M. Wang, N. B. Ming, *J. Phys. Chem. B* **1993**, *48*, 3825.

 © 2005 Wiley-VCH Verlag GmbH & Co. KGaA, Weinheim

Non-Natural Cyclodextrins

Synthesis of a Cycloallin Derivative from β-Cyclodextrin: Heptakis(2,3-dideoxy-2,3-epithio)-β-cycloallin**

*Makoto Fukudome, Tomonori Shiratani, Stefan Immel, Yasuyoshi Nogami, De-Qi Yuan, and Kahee Fujita**

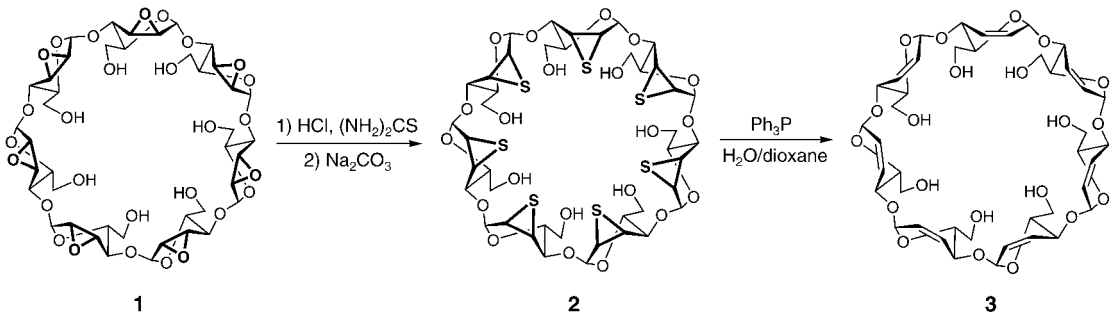
Macrocyclic molecules that comprise several subunits in a circular array exhibit novel functions that are otherwise not observed in the individual units. Many host molecules that consist of several identical functional subunits, such as cyclodextrins, cyclophanes, and their related natural and artificial macrocycles, have been prepared by enzymatic or synthetic methods and have developed the concept of artificial molecular recognition and catalysis.[1] Cyclodextrins, in particular, have been the leading compounds from the initial stage of this research. Despite extensive studies on the functionalization of cyclodextrins for diverse purposes such as the development of artificial receptors and enzymes, their modification has been limited mostly to their primary hydroxy groups while secondary sites have received much less attention.[2] Moreover, successful studies on complete modifications at the secondary sites are rare as the modifications on 2-OH or 3-OH do not proceed selectively and are accompanied inevitably by products of either over- or under-modification. Only per(3,6-anhydro)-[3] and per(2-*O*-tosyl)-cyclodextrins,[4] per(2,3-anhydro)-cyclomannins **1** (see Scheme 1),[4,5] cycloaltrins,[6] per(3-amino-3-deoxy)-β-cycloaltrin,[7] and per(3-deoxy)-cyclomannins[8] are available by the selective modifications of cyclodextrins at the present time. However, to the best of our knowledge, the preparation of a cycloallin family has not been studied as yet.

Here, we report the first successful one-pot preparation of a novel type of cycloallin derivative, **2**, from cyclomannin derivative **1**, which itself is obtained in three steps from β-cyclodextrin (Scheme 1). The synthesis is as simple as heating an aqueous acidic solution of **1** at 90 °C for 30 min followed by stirring at room temperature under alkaline conditions. It is quite astonishing that these simple reaction conditions not only ensure a complete conversion of the seven epoxide

[*] M. Fukudome, Prof. Dr. D.-Q. Yuan, Prof. Dr. K. Fujita
Department of Molecular Medicinal Sciences
Graduate School of Biomedical Sciences
Nagasaki University
Nagasaki 852-8521 (Japan)
Fax: (+81) 95-819-2423
E-mail: fujita@net.nagasaki-u.ac.jp
Dr. T. Shiratani, Prof. Dr. Y. Nogami
Daiichi College of Pharmaceutical Sciences
Fukuoka 815-8511 (Japan)
Dr. S. Immel
Clemems Schöpf-Institute of Organic Chemistry and Biochemistry
Technical University of Darmstadt
64287 Darmstadt (Germany)

[**] The authors are grateful to Japan Maize Products Co. Ltd. for a generous gift of cyclodextrins.

 DOI: 10.1002/anie.200462678 © 2005 Wiley-VCH Verlag GmbH & Co. KGaA, Weinheim



Scheme 1. Preparation of **2** from a cyclodextrin and its conversion into olefin **3**.

residues to episulfides but also guarantee the inversion of configuration at all the subunits, as revealed by the structural analysis of **2**.

The assignment of the NMR signals of **2** (Figure 1) relied on ^{1}H,^{1}H and ^{1}H,^{13}C COSY NMR spectra and indicates that **2** consists of 2,3-dideoxy-2,3-epithioallopyranose units. The

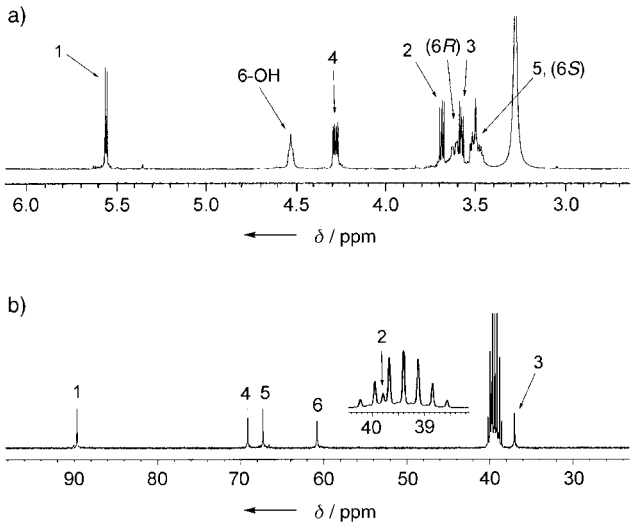
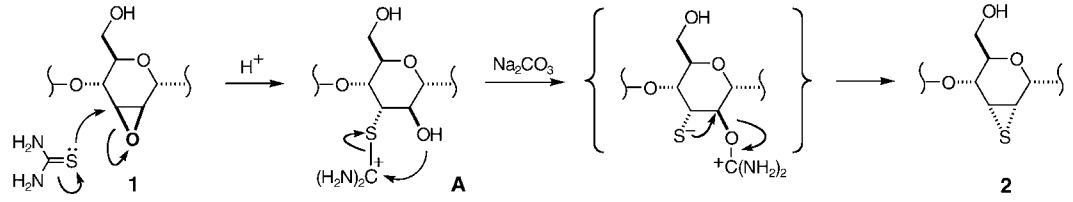


Figure 1. a) ^{1}H and b) ^{13}C NMR spectra of **2** measured in [D_6]DMSO.

remarkable upfield shifts of signals for both C-2 and C-3 ($\Delta\delta_{C2} = 8.9$ ppm and $\Delta\delta_{C3} = 16.1$ ppm relative to the corresponding signals for **1** suggest the replacement of all the oxygen atoms of the epoxide by sulfur substituents. The time-of-flight (TOF) mass spectrum of **2** showed a parent-ion peak for $[M+Na^+]$ at $m/z = 1143$, which is consistent with the molecular ion of **2** and strongly supports the above structural assignment.

The large coupling constant $J_{1,2} = 5.0$ Hz implies that the epithio groups are of allo-type rather than manno-type, after previous reports that $J_{1,2} = 4.4$ and 0 Hz for methyl 2,3-dideoxy-2,3-epithio-4,6-di-*O*-methyl-α-D-alloside or -mannoside, respectively.[9] Moreover, when the chemical shifts of C-2 and C-3 are compared with the corresponding values for mono-alloepoxy-β-cyclodextrin, the upfield shifts of $\Delta\delta_{C2} = 17.4$ ppm and $\Delta\delta_{C3} = 16.1$ ppm are similar in magnitude. However, such similarity in the upfield shifts is not observed in comparison with mono-mannoepoxy-β-cyclodextrin, $\Delta\delta_{C2} = 10.3$ ppm and $\Delta\delta_{C3} = 17.9$ ppm, which again supports the proposed allo structure of **2**. Thus, compound **2** is assigned as per(2,3-dideoxy-2,3-epithio)-β-cycloallin. The coupling constant $J_{4,5} = 8.9$ Hz indicates that the 2,3-anhydro-2,3-epithioalloses have an $^OH_5$ conformation[10] rather than the ^5H_O conformation, and the structure of **2** is expected to be as shown in Scheme 1.

A plausible mechanism for the transformation of **1** to **2** is depicted in Scheme 2. On the basis of the known reaction behavior of mannoepoxide rings in cyclodextrins,[2] the conversion of **1** into **2** is believed to be initiated by the nucleophilic ring opening of epoxide residues with thiourea as the nucleophile. Under basic conditions, transfer of $(NH_2)_2C^+$ from 3-S to 2-O and subsequent intramolecular substitution of 2-$OC^+(NH_2)_2$ by 3-S^- take place to generate the episulfide residues. Formation of thioureidoaltropyranoside residues was confirmed by monitoring the progress of the reaction by TLC (silica gel, *n*PrOH/EtOAc/H_2O = 7:7:5 by volume). The appearance of a new spot with a retention factor $R_f \approx 0$ was noted which is much lower than the R_f values for both **1** ($R_f = 0.7$) and the final product **2** ($R_f = 0.6$). The thioureidoaltropyranosides seem to be stable under acidic conditions until all the epoxide residues are transformed, and TOF-MS analysis of the reaction mixture clearly demonstrated a base peak at $m/z = 1540$, which is consistent with $[M-7]$ of perthioureido intermediate **A**. As soon as the reaction mixture was basified



Scheme 2. Plausible reaction mechanism for the formation of **2**.

 © 2005 Wiley-VCH Verlag GmbH & Co. KGaA, Weinheim

at room temperature, TLC analysis of the mixture revealed that the spot with $R_f = 0.6$ became more intense while that at $R_f = 0$ disappeared completely.

Molecular modeling studies were carried out to elucidate the 3D structure of **2** which is of pivotal importance in molecular design and recognition. As shown in Figure 2, all of the 2,3-epithioalloside units adopt $^{O}H_5$ conformations with Cremer–Pople ring-puckering parameters $Q = 0.504(5)$ Å, $\nu = 51.0(3)°$, and $\phi = 338(1)°$. The "straitjacket" effect of the 2,3-epithio rings enforces mean values of about 0.2° for the torsion angle about C1-C2-C3-C4 by forcing the pyranoside rings into this rigid conformation. Almost identical pyranoside geometries were also found in the solid-state structures of methyl 2,3-anhydro-4,6-bis(*O*-*p*-bromobenzyl)-α-D-mannopyranoside and its allo isomer[11] as well as per-2,3-anhydro-α-cyclomannin.[12]

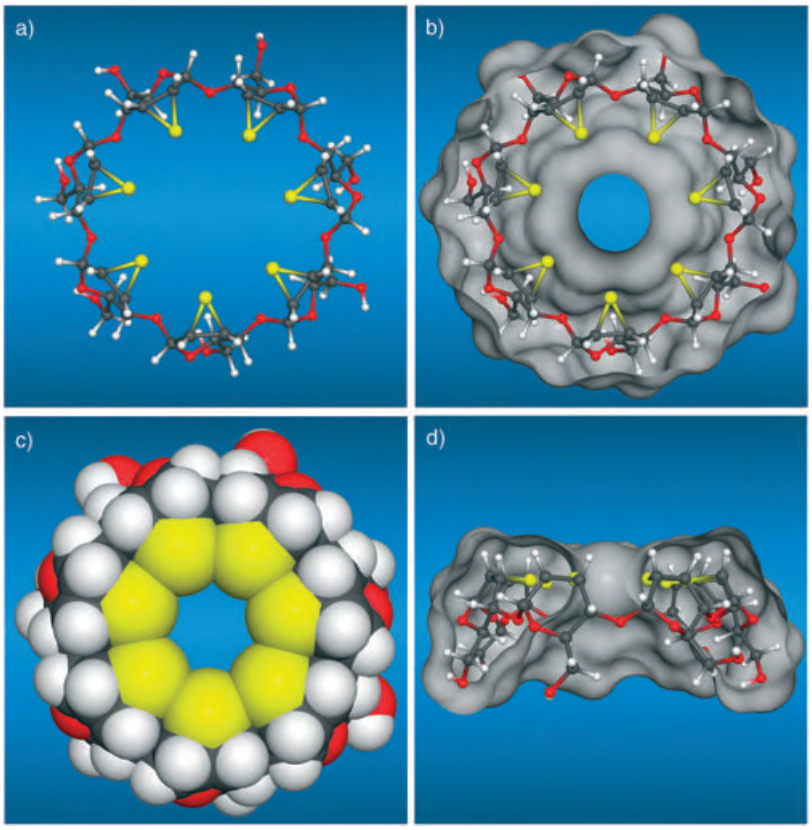


Figure 2. Molecular models of **2** displaying the arrangement of the inward pointing sulfur atoms and the reversed cavity shape of the macrocycle. (Left column (a, c): ball-and-stick and CPK-type models; right column (b, d): half-opened contact surface representations with models superimposed).

Corey–Pauling–Koltun (CPK) models and contact surface[13] representations reveal that the epithioalloside units of **2** are arranged to form a cavity whose shape is reversed from that of cyclodextrins; that is, the side on which the primary 6-OH groups reside is much wider than the other side (top side). The epithio rings are situated on the top side, parallel to the mean ring plane of the molecule, with the sulfur atoms pointing inwards and forming a circle with a radius of 3.7 Å (based on the atom positions). This arrangement of sulfur atoms substantially narrows the top side of the aperture to an inner width of about 3 Å only (diameter of the surface opening).

The unique 3D structure of **2** is of particular interest in molecular recognition. Furthermore, its seven episulfide rings make it a promising candidate for molecular recognition as well as further functionalization. As an example, thiirane **2** was converted quantitatively into the corresponding olefin species **3** simply by heating an alkaline solution of **2** in the presence of triphenylphosphine for a couple of hours. The TOF mass spectrum of **3** showed a parent-ion peak for $[M+Na^+]$ at $m/z = 919$. Seven different carbon atoms and eight different hydrogen atoms were recognized in the ^{13}C and ^{1}H NMR spectra, respectively, of **3**, consistent with C_7 symmetry. The large downfield shifts of resonances for atoms C-2 ($\delta = 127.0$ ppm), C-3 ($\delta = 130.0$ ppm), H-2 ($\delta = 5.76$ ppm), and H-3 ($\delta = 5.86$ ppm) suggest an olefinic structure.[2a]

In summary, we have reported the first successful synthesis of an epithio-β-cycloallin, which is an important intermediate in the functionalization of cyclodextrins and may equally serve as an artificial host molecule for molecular recognition.

Experimental Section

2: A solution of HCl (0.1M, 2 mL) containing **1** (29 mg, 0.029 mmol) and thiourea (720 mg, 9.3 mmol) was stirred at 90 °C for 30 min and then cooled down with a cold water bath. Sodium carbonate (28 mg, 0.26 mmol) and CH_3CN (0.9 mL) were added, and the solution was stirred at room temperature for 4 h. The solution was neutralized with HCl (1M), then diluted with 20% aq. EtOH (120 mL), and filtered through a cellulose acetate membrane (3 μm). The filtrate was purified by chromatography on a Lobar column (RP 18, size B) using initially an eluent of 20% aq. EtOH (500 mL) and then a gradient from 30% to 70% aq. EtOH (500 mL for each) to give **2** (18 mg, 56%); m.p.: 210 °C; $[\alpha]_D^{23} = +175.9$ ($c = 0.0433$ in 50% aq. ethanol); ^{1}H NMR (500 MHz, [D$_6$]DMSO, 35 °C, TMS): $\delta = 5.56$ (d, ^3J(H,H) = 5.0 Hz, 7H; H1), 4.54 (t, ^3J(H,H) = ca. 6.0 Hz, 7H; 6-OH), 4.28 (dd, ^3J(H,H) = 4.4, 8.9 Hz, 7H; H4), 3.69 (dd, ^3J(H,H) = 5.0, 6.6 Hz, 7H; H2), 3.62 (dd, ^3J(H,H) = ca. 5.5, ca. 10.5 Hz, 7H; 6R-H), 3.58 (dd, ^3J(H,H) = ca. 4.6, ca. 6.6 Hz, 7H; H3), 3.53–3.47 ppm (m, 14H; H5 and 6S-H); ^{13}C NMR (125 MHz, [D$_6$]DMSO, 35 °C, TMS): $\delta = 89.8$ (C1), 69.3 (C4), 67.4 (C5), 60.9 (C6), 39.8 (C2), 37.0 ppm (C3); TOF MS: $m/z = 1143$ $[M+Na^+]$.

3: Thiirane (**2**; 38 mg), sodium bicarbonate (8 mg), and triphenylphosphine (290 mg) were dissolved in aqueous dioxane (80% by volume, 3 mL), and the resultant solution was stirred at 95 °C for 170 min. After evaporation of the solvent, the residue was dissolved in water (70 mL), filtered through a membrane, and purified by chromatographey on a Lobar column (RP 18, size B) with a gradient elution from 40% to 80% aq. CH_3OH (500 mL for each) to give **3** (30 mg, 98%); m.p.: 188 °C; $[\alpha]_D^{25} = +105.5$ ($c = 0.133$ in 75% aq. methanol); ^{1}H NMR (500 MHz, [D$_6$]DMSO, 35 °C, TMS): $\delta = 5.86$ (dd, ^3J(H,H) = 1.4, 10.0 Hz, 7H; H3), 5.76 (ddd, ^3J(H,H) = 1.6, 3.0,

 © 2005 Wiley-VCH Verlag GmbH & Co. KGaA, Weinheim

10.0 Hz, 7H; H2), 5.12 (d, ^3J(H,H) = 3.0 Hz, 7H; H1), 4.62 (s, 7H; 6-OH), 4.15 (dd, ^3J(H,H) = 1.4, 8.9 Hz, 7H; H4), 3.80–3.71 (m, 14H; H5 and 6R-H), 3.68 ppm (dd, ^3J(H,H) = ca. 5.3, ca. 12 Hz, 7H; 6S-H); ^{13}C NMR (125 MHz, [D$_6$]DMSO, 35 °C, TMS): δ = 61.1 (C6), 69.7 (C4), 71.7 (C5), 93.3 (C1), 127.0 (C2), 130.0 ppm (C3); TOF MS: m/z = 919 [M+Na$^+$].

Molecular models and graphics were generated using the *MolArch*$^+$ program.[14]

Received: November 20, 2004
Revised: March 22, 2005
Published online: June 8, 2005

Keywords: cyclic oligosaccharides · cycloallin · cyclodextrins · episulfides

[1] Cyclodextrins: Special Issue, *Chem. Rev.* **1998**, *5*; *Comprehensive Supramolecular Chemistry*, Pergamon, Oxford, **1996**; F. W. Lichtenthaler, S. Immel, *J. Inclusion Phenom. Mol. Recognit. Chem.* **1996**, *25*, 3–16; *Monographs in Supramolecular Chemistry*, The Royal Society of Chemistry, **1994**.

[2] a) D.-Q. Yuan, T. Tahara, W.-H. Chen, Y. Okabe, C. Yang, Y. Yagi, Y. Nogami, M. Fukudome, K. Fujita, *J. Org. Chem.* **2003**, *68*, 9456–9466; b) A. R. Khan, P. Forgo, K. J. Stine, V. T. D'Souza, *Chem. Rev.* **1998**, *98*, 1977–1996.

[3] A. Gadelle, J. Defaye, *Angew. Chem.* **1991**, *103*, 94–95; *Angew. Chem. Int. Ed. Engl.* **1991**, *30*, 78–80; P. R. Ashton, P. Ellwood, I. Staton, J. F. Stoddart, *Angew. Chem.* **1991**, *103*, 96–97; *Angew. Chem. Int. Ed. Engl.* **1991**, *30*, 80–81; H. Yamamura, K. Fujita, *Chem. Pharm. Bull.* **1991**, *39*, 2505–2508.

[4] P. Zhang, A. W. Coleman, *Supramol. Chem.* **1993**, *2*, 255–263.

[5] A. W. Coleman, P. Zhang, C-C. Ling, J. Mahuteau, H. Parrot-Lopez, M. Miocque, *Supramol. Chem.* **1992**, *1*, 11–14; A. R. Kahn, L. Barton, V. T. D'Souza, *J. Chem. Soc. Chem. Commun.* **1992**, 1112–1114.

[6] K. Fujita, H. Shimada, K. Ohta, Y. Nogami, K. Nasu, T. Koga, *Angew. Chem.* **1995**, *107*, 1783–1784; *Angew. Chem. Int. Ed. Engl.* **1995**, *34*, 1621–1622; Y. Nogami, K. Nasu, T. Koga, K. Ohta, K. Fujita, S. Immel, H. J. Lindner, G. E. Schmitt, F. W. Lichtenthaler, *Angew. Chem.* **1997**, *109*, 1987–1991; *Angew. Chem. Int. Ed. Engl.* **1997**, *36*, 1899–1902.

[7] A. R. Kahn, W. Tong, V. T. D'Souza, *Supramol. Chem.* **1995**, *4*, 243–246.

[8] C. Yang, D.-Q. Yuan, Y. Nogami, K. Fujita, *Tetrahedron Lett.* **2003**, *44*, 4641–4644; H. J. Lindner, F. W. Lichtenthaler, K. Fujita, C. Yang, D.-Q. Yuan, Y. Nogami, *Acta Crystallogr. Sect. E* **2003**, *59*, 387–389.

[9] M. V. Jesudason, L. N. Owen, *J. Chem. Soc. Perkin Trans. 1* **1974**, 2019–2024.

[10] G. A. Jeffrey, J. H. Yates, *Carbohydr. Res.* **1979**, *74*, 319–322. In the $^0H_5$, $^5H_0$ nomenclature, H denotes half-chair conformations with the Cremer–Pople ring-puckering parameters at $\Theta = 30°$ and $\phi = (30 + n\pi/3)°$.

[11] X. Wu, F. Kong, D. Lu, G. Li, *Carbohydr. Res.* **1992**, *235*, 163.

[12] S. Immel, K. Fujita, H. J. Lindner, Y. Nogami, F. W. Lichtenthaler, *Chem. Eur. J.* **2000**, *6*, 2327–2333; S. Immel, F. W. Lichtenthaler, H. J. Lindner, K. Fujita, M. Fukudome, Y. Nogami, *Tetrahedron: Asymmetry* **2000**, *11*, 27–36.

[13] M. L. Connolly, *Science* **1983**, *221*, 709–713.

[14] S. Immel, *MolArch*$^+$*—MOLecular ARCHitecture Modeling Program* v7.70, Technical University of Darmstadt, Germany, **2005**; http://caramel.oc.chemie.tu-darmstadt.de/immel/.

 © 2005 Wiley-VCH Verlag GmbH & Co. KGaA, Weinheim

Drug Development

Highly Enantioselective Catalytic Fluorination and Chlorination Reactions of Carbonyl Compounds Capable of Two-Point Binding**

Norio Shibata, Junji Kohno, Kazumi Takai, Takehisa Ishimaru, Shuichi Nakamura, Takeshi Toru,* and Shuji Kanemasa*

The enantioselective electrophilic halogenation of carbonyl compounds represents one of the best established strategies for the construction of chiral C–X bonds in organic chemistry.[1] The resulting chiral halo compounds, especially fluorine-containing chiral organic molecules, are very fascinating in the field of medicinal chemistry.[2] The unique hydrophobic, space-filling, and electronic properties of a fluorine atom can make substrates with C–F bonds useful candidates for drug development. Next to fluorination, enantioselective chlorination is also an important topic with regard to some aspects of pharmaceuticals.[3] Although recent rapid advances in the methodology of enantioselective halogenations have made great contributions in these fields,[4–6] more efficient and more flexible methods are required. In this paper we describe highly enantioselective fluorination and chlorination reactions of carbonyl compounds that are capable of two-point binding. Both of the halogenations are catalyzed by the catalyst dbfox-Ph/Ni^{II} with very high enantioselectivity up to 99% *ee*. Furthermore, we also present the first significant examples of asymmetric amplification in enantioselective halogenations starting with the catalyst at 45% enantiopurity to afford the halogenated compounds with significantly increased *ee* values of $>90\%$.

We initiated the study of asymmetric fluorination reaction of β-keto esters **1a–g**, since α-fluorinated β-keto esters such as telithromycin have attractive antibiotic activity.[7] Recently, we found that chiral Cu^{II} and Ni^{II} complexes of phenyl-bis(oxazoline) (box-Ph) effectively catalyze the enantioselec-

[*] Prof. Dr. N. Shibata, Prof. Dr. T. Toru
Department of Applied Chemistry
Graduate School of Engineering, Nagoya Institute of Technology
Gokiso, Showa-ku, Nagoya 466-8555 (Japan)
Fax: (+81) 52-735-5442
E-mail: nozshiba@nitech.ac.jp
toru@nitech.ac.jp

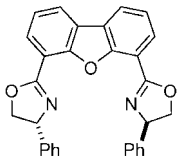
Prof. Dr. S. Kanemasa
Institute for Materials Chemistry and Engineering
Kyushu University
6-1 Kasugakoen, Kasuga 816-8580 (Japan)

J. Kohno, K. Takai, T. Ishimaru, Dr. S. Nakamura
Department of Applied Chemistry
Graduate School of Engineering, Nagoya Institute of Technology
Gokiso, Showa-ku, Nagoya 466-8555 (Japan)

[**] This work was supported in part by the Japan Science & Technology (JST) Agency, Innovation Plaza Tokai. We also thank Dr. Akihiro Ishii of Central Glass Co., Ltd. for a gift of CF_3SO_2Cl.

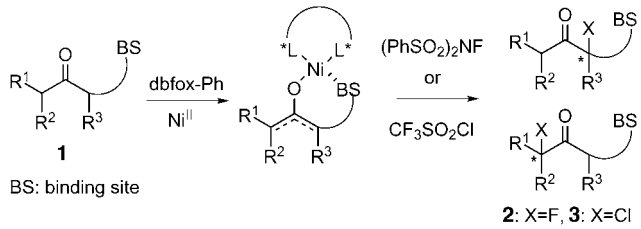
Supporting information for this article is available on the WWW under http://www.angewandte.org or from the author.

 © 2005 Wiley-VCH Verlag GmbH & Co. KGaA, Weinheim DOI: 10.1002/anie.200501041



dbfox-Ph

tive fluorination of β-keto esters with *N*-fluorobenzenesulfonimide (NFSI); however, the enantioselectivity was not high enough.[6d] In previous works by one of us, the dbfox-Ph ligand was highly effective in asymmetric Diels–Alder and Michael addition reactions.[8] Thus we turned to this ligand to improve the fluorination reaction. A solution of **1a** in CH_2Cl_2 was treated with 1.2 equiv of NFSI in the presence of a catalytic amount of dbfox-Ph/$Ni(ClO_4)_2{\cdot}6H_2O$ at room temperature to afford the α-fluoro compound **2a** in high yield with an extremely high enantioselectivity (Scheme 1; Table 1, entry 1, 99% *ee*). The ester **1a** proved to be the ideal yardstick to measure our results, as it has been studied by many investigators under a variety of conditions for enantioselective fluorinations.[4–6]

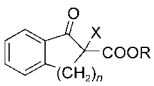
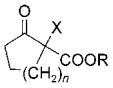
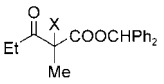
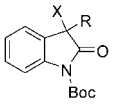
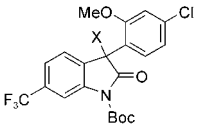
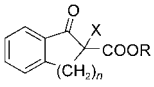


Scheme 1. Enantioselective halogenations of substrates capable of two-point binding using dbfox-Ph/Ni^{II} with NFSI or CF_3SO_2Cl.

The scope of the fluorination of a series of β-keto esters **1b–g** was investigated; we found that the dbfox-Ph/Ni^{II} catalyst exhibits excellent enantioselectivity as well (Table 1, entries 2–7). In most cases, our fluorination was more enantioselective than the reported procedures owing to the remarkable control of the enantioface of enolates by the dbfox-Ph/Ni^{II} complex.[9] It is notable that catalyst loading can be reduced to 2 mol% without loss of enantioselectivity (entries 1 and 11).

To demonstrate the further synthetic utility of this dbfox-Ph/Ni^{II} fluorination system, we tested other substrates capable of two-point binding. Pharmaceutically important fluorooxindoles[10] **2h–j** were selected as target molecules. Although we reported the enantioselective synthesis of fluorooxindoles using a combination of cinchona alkaloids and Selectfluor,[6c] no catalytic enantioselective method has been described. Under similar reaction conditions, a significant degree of enantioselectivity has been obtained irrespective of the substrates used (Table 1, entries 8–10). It is noted that fluorooxindole **2j** was converted into MaxiPost,[6c,10] an effective opener of maxi-K channels, by cleavage of the Boc group. This is the first example of a catalytic enantioselective preparation of MaxiPost.

Table 1: Enantioselective fluorination of **1** (X = H) to give **2** (X = F).[a]

Entry	Substrate **1** (X = H) Product **2** (X = F)		*t* [h]	Yield [%]	*ee* [%]
1		**a**: R = *t*Bu, *n* = 1	3	76	99 (*S*)
2		**b**: R = Ad, *n* = 1	2	71	99
3		**c**: R = L-Men, *n* = 1	2	66	99
4		**d**: Ad, *n* = 2	3	88	95
5		**e**: *t*Bu, *n* = 1	2	84	93
6		**f**: *t*Bu, *n* = 2	2	86	99
7[b]		**g**	18	75	83
8[c,d]		**h**: Me	35	73	93
9[c]		**i**: Ph	5	72	96
10[c]		**j**	14	71	93 (*S*)
11[e]		**a**: R = *t*Bu, *n* = 1	6	93	99 (*S*)

[a] Reaction conditions: A solution of **1** (1.0 equiv), NFSI (1.2 equiv), dbfox-Ph (0.11 equiv), and $Ni(ClO_4)_2{\cdot}6H_2O$ (0.1 equiv) in CH_2Cl_2 was stirred in the presence of 4-Å molecular sieves at room temperature unless otherwise noted. Enantiomeric excess was determined by chiral HPLC analysis. See the Supporting Information for details. Abbreviations: L-Men = L-menthyl, Ad = 1-adamantyl. [b] The reaction was carried out at 0°C. [c] $Ni(OAc)_2{\cdot}4H_2O$ (0.1 equiv) was used instead of $Ni(ClO_4)_2{\cdot}6H_2O$. [d] Enantiomeric excess was determined after cleavage of the Boc group. [e] dbfox-Ph (0.02 equiv) and $Ni(ClO_4)_2{\cdot}6H_2O$ (0.02 equiv) were used.

Highly enantioselective chlorinations of ketones, acid halides, and aldehydes have been reported; however, asymmetric chlorination of β-keto esters has relatively low enantioselectivity.[5] In addition, no enantioselective syntheses of α-chlorooxindoles, which are potentially important in medicinal chemistry, have been reported.[11] We were pleased to find that our dbfox-Ph/Ni^{II} system was also effective for the asymmetric chlorination of a series of substrates including β-keto esters **1a–d** and oxindoles **1i** and **1j** (Table 2). The substrates were chlorinated smoothly with CF_3SO_2Cl under our optimized conditions to produce **3a–d, 3i**, and **3j** with high enantioselectivity. Chlorooxindole **3j** can be converted to BMS225113, a pharmaceutically important chlorooxindole.[11] It is highly noted that CF_3SO_2Cl as a chlorinating agent is essential to achieve high enantioselectivity, since *N*-chlorosuccimide (NCS) under the same conditions provided poorer results (entry 2 vs entry 3).

 © 2005 Wiley-VCH Verlag GmbH & Co. KGaA, Weinheim

Table 2: Enantioselective chlorination of **1** (X = H) to give **3** (X = Cl).[a]

Entry	**1**	R	**3**	*t* [h]	Yield [%]	*ee* [%]
1	**1a**	*t*Bu	**3a**	10	72	97
2	**1b**	Ad	**3b**	17	85	97
3[b]	**1b**	Ad	**3b**	3	85	54
4	**1c**	L-Men	**3c**	9	66	94
5	**1d**	Ad	**3d**	45	61 (71)[d]	98
6[c]	**1i**	Ph	**3i**	20	93	61
7[c]	**1j**	–	**3j**	17	93	60

[a] Reaction conditions: **1** (1.0 equiv), CF_3SO_2Cl (1.2 equiv), dbfox-Ph (0.11 equiv), and $Ni(ClO_4)_2 \cdot 6H_2O$ (0.1 equiv) were stirred in CH_2Cl_2 in the presence of 4-Å molecular sieves at room temperature unless otherwise noted. Enantioselectivity was determined by chiral HPLC analysis. See the Supporting Information for details. [b] NCS was used instead of CF_3SO_2Cl. [c] $Ni(OAc)_2 \cdot 4H_2O$ was used instead of $Ni(ClO_4)_2 \cdot 6H_2O$. *t*BuOMe was used as a solvent. [d] Conversion yield.

We finally examined experiments of chiral amplification[12,13] in the halogenations on our systems. Fluorinations of **1a** with NFSI were carried out in the presence of $Ni(ClO_4)_2 \cdot 6H_2O$ and dbfox-Ph, enantiopurities of which were varied from 11% to 60%. Figure 1 shows the relationship

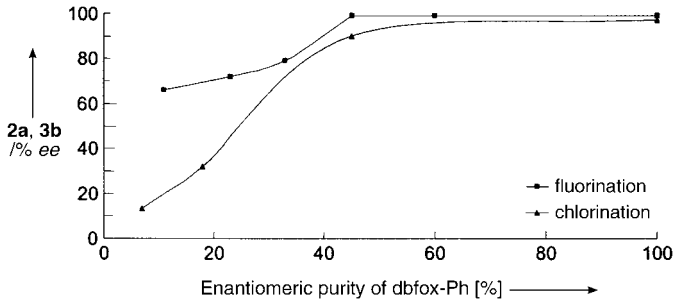


Figure 1. Chiral amplification in the halogenations of **1a**,**b** with NFSI or CF_3SO_2Cl catalyzed by dbfox-Ph/$Ni(ClO_4)_2 \cdot 6H_2O$.

between the enantiomeric purity of the dbfox-Ph ligand used and the enantioselectivity observed for **2a** when the molar ratio of dbfox-Ph to $Ni(ClO_4)_2 \cdot 6H_2O$ was 1.1:1 and the catalyst loading was 10 mol%. When the dbfox-Ph ligand had *ee* values of 45% and 11%, **2a** was obtained with 99% and 66% *ee*, respectively. A similar positive nonlinear effect of chiral amplification was also observed in the chlorination of **1b** with CF_3SO_2Cl under the same conditions, and dbfox-Ph with >45% enantiopurity was required to obtain the enantioenriched products **3b** with >90% *ee*.

In conclusion, the catalytic enantioselective fluorination and chlorination reactions of carbonyl compounds structurally capable of two-point binding were achieved with extremely high enantioselectivity by the use of the dbfox-Ph[14]/Ni^{II} complex. In addition, this system led to not only the first catalytic enantioselective synthesis of MaxiPost and BMS225113, but also the first observation of asymmetric amplification in halogenation reactions of β-keto esters.[13] We assumed octahedral complexes coordinated with a water molecule for **1a**/dbfox-Ph/Ni^{II}, **1j**/ dbfox -Ph/Ni^{II} optimized using MM2 in the light of the X-ray structure of the dbfox-Ph/Ni^{II} complex (Figure 2).[8] In these complexes, one of the faces

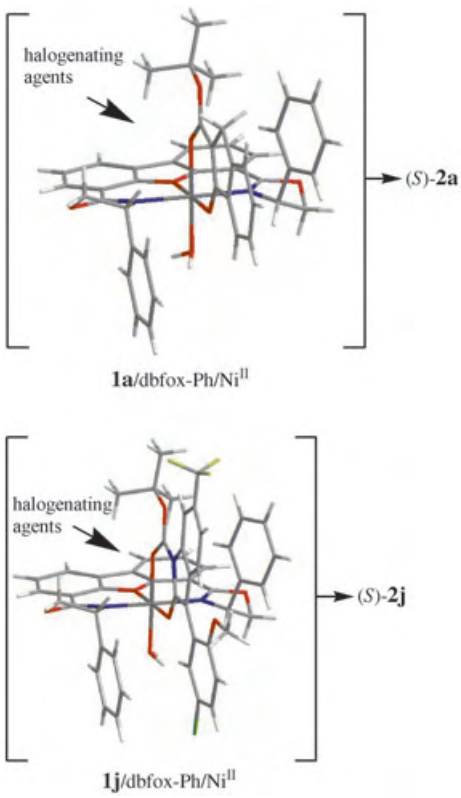


Figure 2. Optimized structures of the complexes of **1a**/dbfox-Ph/Ni^{II} and **1j**/dbfox-Ph/Ni^{II}.

is covered so efficiently that the halogenating agents approach from the *Si* face of the substrates. The details are now under investigation.

Received: March 22, 2005
Published online: June 8, 2005

Keywords: asymmetric amplification · asymmetric synthesis · enantioselectivity · fluorination · halogenation

[1] a) H. Ibrahim, A. Togni, *Chem. Commun.* **2004**, 1147; b) J.-A. Ma, D. Cahard, *Chem. Rev.* **2004**, *104*, 6119; c) K. Muñiz, *Angew. Chem.* **2001**, *113*, 1701; *Angew. Chem. Int. Ed.* **2001**, *40*, 1653; d) S. France, A. Weatherwax, T. Lectka, *Eur. J. Org. Chem.* **2005**, *3*, 475.

[2] a) *Biomedical Aspects of Fluorine Chemistry* (Eds.: R. Filler, Y. Kobayashi), Kodansha/Elsevier Biomedical, Tokyo, **1982**; b) "Biomedical Frontiers of Fluorine Chemistry": *ACS Symp. Ser.* **1996**, 639; c) J. T. Welch, *Tetrahedron* **1987**, *43*, 3123.

[3] *The Chemistry of α-Haloketones, α-Haloaldehydes, α-Haloimines* (Eds.: N. D. Kimpe, R. Verhe), Wiley, New York, **1990**.

[4] a) L. Hintermann, A. Togni, *Angew. Chem.* **2000**, *112*, 4530; *Angew. Chem. Int. Ed.* **2000**, *39*, 4359; b) S. Piana, I. Devillers, A. Togni, U. Rothlisberger, *Angew. Chem.* **2002**, *114*, 1021; *Angew. Chem. Int. Ed.* **2002**, *41*, 979; c) D. Cahard, C. Audouard, J.-C. Plaquevent, N. Roques, *Org. Lett.* **2000**, *2*, 3699; d) B. Mohar, J. Baudoux, J.-C. Plaquevent, D. Cahard, *Angew. Chem.* **2001**, *113*, 4339; *Angew. Chem. Int. Ed.* **2001**, *40*, 4214; e) D. Y. Kim, E. J. Park, *Org. Lett.* **2002**, *4*, 545; f) Y. Hamashima, K. Yagi, H. Takano, L. Tamas, M. Sodeoka, *J. Am. Chem. Soc.* **2002**, *124*, 14530; g) B. Greedy, J. M. Paris, T. Vidal, V. Gouverneur,

 © 2005 Wiley-VCH Verlag GmbH & Co. KGaA, Weinheim

Angew. Chem. **2003**, *115*, 3413; *Angew. Chem. Int. Ed.* **2003**, *42*, 3291; h) J.-A. Ma, D. Cahard, *Tetrahedron: Asymmetry* **2004**, *15*, 1007; i) F. A. Davis, P. Zhou, C. K. Murphy, G. Sundarababu, H. Qi, W. Han, R. M. Przeslawski, B.-C. Chen, P. Carroll, *J. Org. Chem.* **1998**, *63*, 2273.

[5] a) L. Hintermann, A. Togni, *Helv. Chim. Acta* **2000**, *83*, 2425; b) H. Wack, A. E. Taggi, A. M. Hafez, W. J. Drury III, T. Lectka, *J. Am. Chem. Soc.* **2001**, *123*, 1531; c) M. Marigo, N. Kumaragurubaran, K. A. Jørgensen, *Chem. Eur. J.* **2004**, *10*, 2133; d) M. P. Brochu, S. P. Brown, D. W. C. MacMillan, *J. Am. Chem. Soc.* **2004**, *126*, 4108; e) N. Halland, A. Braunton, S. Bachmann, M. Marigo, K. A. Jørgensen, *J. Am. Chem. Soc.* **2004**, *126*, 4790; f) Y. Zhang, K. Shibatomi, H. Yamamoto, *J. Am. Chem. Soc.* **2004**, *126*, 15038; g) A. M. Hafez, A. E. Taggi, H. Wack, J. Esterbrook, T. Lectka, *Org. Lett.* **2001**, *3*, 2049; h) S. France, H. Wack, A. E. Taggi, A. M. Hafez, T. R. Wagerle, M. H. Shah, C. L. Dusich, T. Lectka, *J. Am. Chem. Soc.* **2004**, *126*, 4245.

[6] a) N. Shibata, E. Suzuki, Y. Takeuchi, *J. Am. Chem. Soc.* **2000**, *122*, 10728; b) N. Shibata, E. Suzuki, T. Asahi, M. Shiro, *J. Am. Chem. Soc.* **2001**, *123*, 7001; c) N. Shibata, T. Ishimaru, E. Suzuki, K. L. Kirk, *J. Org. Chem.* **2003**, *68*, 2494; d) N. Shibata, T. Ishimaru, T. Nagai, J. Kohno, T. Toru, *Synlett* **2004**, 1703; e) N. Shibata, T. Ishimaru, M. Nakamura, T. Toru, *Synlett* **2004**, 2509; f) N. Shibata, T. Tarui, Y. Doi, K. L. Kirk, *Angew. Chem.* **2001**, *113*, 4593; *Angew. Chem. Int. Ed.* **2001**, *40*, 4461.

[7] A. Denis, F. Bretin, C. Fromentin, A. Bonnet, G. Piltan, A. Bonnefoy, C. Agouridas, *Bioorg. Med. Chem. Lett.* **2000**, *10*, 2019.

[8] a) S. Kanemasa, Y. Oderaotoshi, S. Sakaguchi, H. Yamamoto, J. Tanaka, E. Wada, D. P. Curran, *J. Am. Chem. Soc.* **1998**, *120*, 3074; b) S. Kanemasa, Y. Oderaotoshi, *J. Synth. Org. Chem. Jpn.* **1998**, 368; c) K. Itoh, S. Kanemasa, *J. Am. Chem. Soc.* **2002**, *124*, 13394.

[9] The fluorination reaction occurred with high enantioselectivity for the substrates containing sterically bulky substituents located on the ester side. For the β-keto esters **1** with methyl or cyclohexyl ester groups, slightly lower enantioselectivities were obtained (R = Me, 65% *ee*; R = *c*C_6H_{11}, 91% *ee*).

[10] V. K. Gribkoff, J. E. Starrett, Jr., S. I. Dworetzky, P. Hewawasam, C. G. Boissard, D. A. Cook, S. W. Frantz, K. Heman, J. R. Hibbard, K. Huston, G. Johnson, B. S. Krishnan, G. G. Kinney, L. A. Lombardo, N. A. Meanwell, P. B. Molinoff, R. A. Myers, S. L. Moon, A. Ortiz, L. Pajor, R. L. Pieschl, D. J. Post-Munson, L. J. Signor, N. Srinivas, M. T. Taber, G. Thalody, J. T. Trojnacki, H. Wiener, K. Yeleswaram. S. Yeola, *Nat. Med.* **2001**, *7*, 471.

[11] V. K. Gribkoff, D. J. Post-Munson, S. W. Yeola, C. G. Boissard, P. Hewawasam, WO 2002030868.

[12] *Comprehensive Asymmetric Catalysis* (Eds.: E. R. Jacobsen, A. Pfaltz, H. Yamamoto), Springer, Berlin, **1999**.

[13] For asymmetric amplification of the dbfox-Ph/Ni^{II} catalyst in the Diels–Alder reaction, see ref. [8a].

[14] Just before submission of this manuscript, a report on dbfox/Zn^{II}-catalyzed halogenations appeared. L. Bernardi, K. A. Jørgensen, *Chem. Commun.* **2005**, 1324.

 © 2005 Wiley-VCH Verlag GmbH & Co. KGaA, Weinheim

Coordination Chemistry

Heteroligated Rh^I Tweezer Complexes**

*Aaron M. Brown, Maxim V. Ovchinnikov, and Chad A. Mirkin**

The unique combination of the coordination geometry of transition-metal centers with the structural and geometric properties of organic ligands provides the basis for the synthesis and design of metallosupramolecular complexes[1] and metal–organic frameworks.[2] Indeed, the ability to incorporate multiple types of building blocks (namely, metal centers and ligands) into metallosupramolecular structures is a key requirement for the rational tailoring of their structural and electronic properties. Currently, the impetus for this research is shifting away from the synthesis of structurally complex and aesthetically pleasing structures towards the preparation of functional metallosupramolecular entities with preprogrammed catalytic and molecular-sensing properties.[3] We have previously demonstrated that tweezer-type salen-containing (salen = *N*,*N*′-bis(salicylidene)cyclohexyldiamine) complexes have improved catalytic rates and selectivities relative to the corresponding bimetallic macrocyclic analogues.[3b,c] These results motivated us to develop a general synthesis of "heteroligated" tweezer-type complexes.

Recently, we reported a novel halide-induced ligand-rearrangement process that was observed in multimetallic Rh^I metallomacrocycles and which results in the formation of two- and three-dimensional complexes that contain heteroligated coordination environments.[4] Herein, we report a general high-yielding methodology for the preparation and postsynthetic modification of heteroligated monometallic Rh^I tweezer-type complexes (Scheme 1). This methodology is based on a unique reaction that allows the preparation of condensed complexes **4b–f** which contain two distinct phosphine-substituted ligands or heteroligated systems that can undergo stepwise substitution reactions with Cl^- ions and/or CO to result in four unique geometries with respect to the orientation of each S- or O-appended aromatic group.

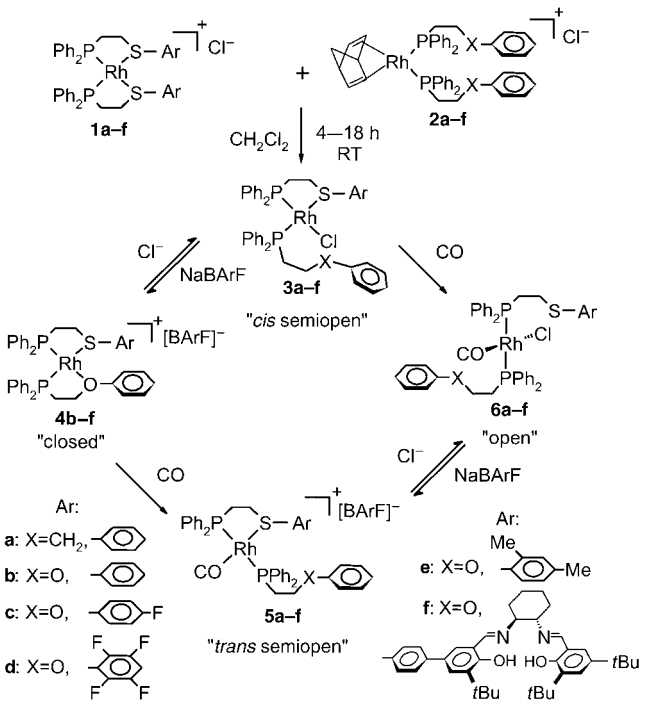
The neutral heteroligated "semiopen" tweezer complexes **3a–f** were synthesized in one step from stoichiometric amounts of the corresponding hemilabile ligands $Ph_2P(CH_2)_2SAr$ (Ar = aryl), $Ph_2P(CH_2)_2XC_6H_5$ (X = O, CH_2), and $[\{RhCl(nbd)\}_2]$ (nbd = norbornadiene) in CH_2Cl_2. Initially, the kinetic products **1a–f,** which have *cis*-thioether and *cis*-phosphine ligands around a Rh^I center, and **2a–f**, which have nbd and *cis*-phosphine ligands around a Rh^I center, are

[*] A. M. Brown, M. V. Ovchinnikov, Prof. C. A. Mirkin
Department of Chemistry and the Institute for Nanotechnology
2145 Sheridan Road
Evanston, IL 60208-3113 (USA)
Fax: (1) 847-467-5123
E-mail: chadnano@northwestern.edu

[**] C.A.M. acknowledges the NSF and AFOSR for support of this work.

Supporting information for this article is available on the WWW under http://www.angewandte.org or from the author.

 DOI: 10.1002/anie.200500689 © 2005 Wiley-VCH Verlag GmbH & Co. KGaA, Weinheim



Scheme 1. Synthesis of the heteroligated Rh^{I} tweezer complexes **3a–f**, and the stepwise synthesis of closed complexes **4b–f**, neutral *cis* semiopen complexes **3a–f**, cationic *trans* semiopen complexes **5a–f**, and open tweezer complexes **6a–f**. BArF = $B[3,5\text{-}(CF_3)_2C_6H_3]_4^-$

formed, but convert over 18 h into the semiopen neutral complexes **3a–f** (Scheme 1). Elemental analysis, ^{1}H, ^{19}F, and ^{31}P NMR spectroscopic, and ESIMS data are in full agreement with the proposed formulations. For example, complex **3b** exhibits highly diagnostic resonances in its $^{31}P\{^{1}H\}$ NMR spectrum at $\delta = 73.61$ ppm (dd, J(Rh-P) = 185 Hz, J(P-P) = 41 Hz), which corresponds to the P center of the η^2-P,S chelating ligand, and $\delta = 30.1$ ppm (dd, J(Rh-P) = 168 Hz, J(P-P) = 41 Hz), which corresponds to the P center of the η^1-P,O ligand.[4,5] Further evidence for the formation of these neutral complexes was obtained from a single-crystal X-ray study of complex **3e** (Figure 1).[6] The Rh^{I} center in **3e** exhibits a square-planar geometry with Cl1-Rh1-P2 and Cl1-Rh1-S1 angles of 87.8 and 86.8°, respectively.

The rate of these conversions was also studied by ^{31}P NMR spectroscopy at 25 °C in CD_2Cl_2, and the corresponding half-lives of the reactions were measured (**3a**: $t_{1/2}$ = 180 min, **3b**: 95 min, **3c**: 65 min, **3d**: 40 min, **3e**: 152 min, **3f**: 95 min; 20 mM [{RhCl(nbd)}$_2$]). These rates appear to be inversely proportional to the electron density of the aryl groups tethered to the S atom: As the electron density of the aryl subsitutent in the P,S ligand decreases, the Rh–S bonds in **1** weaken and the rate of the formation of **3** increases. This trend in the reaction rates reflects the increase in the strength of the Rh–S bond as a function of the increase in electron density of the aromatic group appended to the S atom.

The reversible abstraction of Cl^- ions from **3b–f** with one equivalent of NaBArF results in the clean formation of condensed cationic complexes **4b–f** in which the Rh^{I} center coordinates to the O atom. All the data obtained are

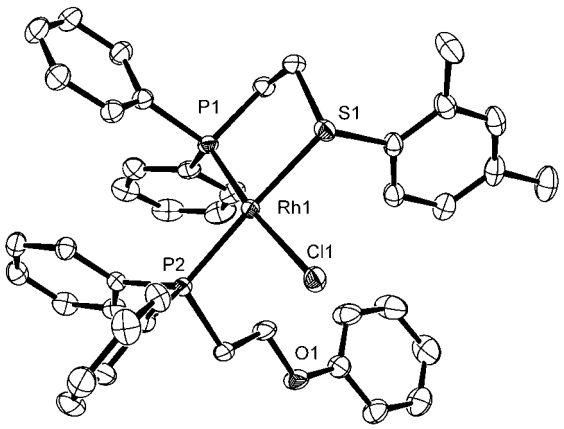


Figure 1. ORTEP diagram of **3e** ($C_{42}H_{42}ClOP_2RhS$) with thermal ellipsoids set at 50% probability. Hydrogen atoms and solvent molecules have been omitted for clarity.[6]

consistent with the proposed formulations. For example, complex **4b** exhibits highly diagnostic resonances in its $^{31}P\{^{1}H\}$ NMR spectrum at $\delta = 73.5$ ppm (dd, J(Rh-P) = 200 Hz, J(P-P) = 41 Hz) and $\delta = 51.8$ ppm (dd, J(Rh-P) = 168 Hz, J(P-P) = 41 Hz), which are characteristic of P centers in a coordination environment in which a Rh^{I} center has *cis*-phosphine, *cis*-thioether, and ether ligands. Furthermore, a signal at m/z 731.2 is observed in its ESIMS spectra that corresponds to a $[C_{40}H_{38}P_2S_2Rh]^+$ ion. Complexes **4b–f** react with stoichiometric quantities of benzyltriethyl ammonium chloride in CH_2Cl_2 to regenerate the corresponding chloride-ligated semiopen complexes **3b–f**. Abstraction of the Cl^- ion from **3a** results in a mixture of products because there is no O atom to which the Rh^{I} center can coordinate. However, the addition of one equivalent of benzyltriethylammonium chloride in solution or excess CO to **4a** in CH_2Cl_2 results in the formation of complexes **3a** or **5a**, respectively.

The addition of CO to complexes **4b–f** selectively cleaves the Rh–O bond and results in the formation of cationic semiopen tweezer-type complexes **5b–f**, in which the P atoms are *trans* to one another. Again, all the data collected are consistent with the proposed formulations. For example, semiopen complex **5b** exhibits resonances in its $^{31}P\{^{1}H\}$ NMR spectrum at $\delta = 63.1$ ppm (dd, J(Rh-P) = 116 Hz, J(P-P) = 268 Hz), which corresponds to a P center coordinated to a Rh^{I} center with phosphine and thioether ligands, and $\delta =$ 19.2 ppm (dd, J(Rh-P) = 121 Hz, J(P-P) = 268 Hz), which corresponds to a P center coordinated to a Rh^{I} center with phosphine and CO ligands. Alternatively, complexes **5a–f** may also be synthesized from complexes **6a–f** and stoichiometric quantities of NaBArF in diethyl ether. In this case, the lack of an O atom in **6a** does not affect the abstraction of the Cl^- ion and results in the clean formation of **5a**.

The neutral open complexes **6a–f** are synthesized from **5a–f** and stoichiometric quantities of benzyltriethylammonium chloride in CH_2Cl_2. Alternatively, the addition of CO to complexes **3a–f** cleaves the Rh–S bonds and results in the fully open tweezers **6a–f** in which the phosphines are *trans* to one another, thus resulting in further separation of the phosphine substituents. Each of these complexes exhibits

 © 2005 Wiley-VCH Verlag GmbH & Co. KGaA, Weinheim

overlapping doublets of doublets in their $^{31}P\{^1H\}$ NMR spectra at approximately $\delta = 24$ ppm, which corresponds to two inequivalent phosphines.

The Cl^- ion is an integral component in these transformations. For example, the independently synthesized intermediate Rh^I complexes **1b** and **2b** were stirred together for 18 hours and the semiopen complex **3b** was formed. However, this reaction was repeated with the BF_4^- salt instead of the chloride salt and resulted in no ligand rearrangement, as determined by ^{31}P NMR spectroscopy.

The interconversion between complexes **3**–**6** allows the spatial separation between the aryl groups and the overall flexibility of these complexes to be systematically controlled (Scheme 1). The synthetic approach described herein is amenable to the inclusion of a variety of aromatic groups, including free-base salen functionalities, as demonstrated in **3f**–**6f**. With this approach, we now have the ability to synthesize designer catalytic intramolecular systems, which could be used to incorporate a catalytic functionality into one arm of a tweezer and add a separate cocatalyst, activator, or enantioselectivity-influencing agent on the other arm, with a precise control over spatial separation and flexibility. These types of structures are becoming important as allosteric catalysts[3b,c] and sensors,[3a] and the ability to modulate their properties through this type of chemistry will help researchers to finetune the reactivity of these complexes.

Received: February 23, 2005
Published online: June 7, 2005

Keywords: coordination modes · nanostructures · supramolecular chemistry · synthetic methods · transition metals

[1] a) S. Leininger, B. Olenyuk, P. J. Stang, *Chem. Rev.* **2000**, *100*, 853 – 908; b) S. R. Seidel, P. J. Stang, *Acc. Chem. Res.* **2002**, *35*, 972 – 983; c) M. Fujita, *Acc. Chem. Res.* **1999**, *32*, 53 – 61; B. Kesanli, W. Lin, *Coord. Chem. Rev.* **2003**, *246*, 305 – 326; d) E. Lindner, S. Pautz, M. Haustein, *Coord. Chem. Rev.* **1996**, *155*, 145 – 162; e) B. J. Holliday, C. A. Mirkin, *Angew. Chem.* **2001**, *113*, 2076 – 2097; *Angew. Chem. Int. Ed.* **2001**, *40*, 2022 – 2043; f) F. A. Cotton, C. Lin, C. A. Murillo, *Acc. Chem. Res.* **2001**, *34*, 759 – 771; g) G. F. Swiegers, T. J. Malefetse, *Chem. Rev.* **2000**, *100*, 3483 – 3538; h) J. W. Lee, S. Samal, N. Selvapalam, H. J. Kim, K. Kim, *Acc. Chem. Res.* **2003**, *36*, 621 – 630.

[2] N. L. Rosi, J. Eckert, M. Eddaoudi, D. T. Vodak, J. Kim, J. M. O'Keeffe, O. M. Yaghi, *Science* **2003**, *300*, 1127 – 1130; O. Ohmori, M. Fujita, *Chem. Commun.* **2004**, 1586 – 1587.

[3] a) N. C. Gianneschi, S. T. Nguyen, C. A. Mirkin, *J. Am. Chem. Soc.* **2005**, *127*, 1644 – 1645, and references therein; b) N. C. Gianneschi, S.-H. Cho, S. T. Nguyen, C. A. Mirkin, *Angew. Chem.* **2004**, *116*, 5619 – 5623; *Angew. Chem. Int. Ed.* **2004**, *43*, 5503 – 5507, and references therein; c) N. C. Gianneschi, P. A. Bertin, S. T. Nguyen, C. A. Mirkin, L. N. Zakharov, A. L. Rheingold, *J. Am. Chem. Soc.* **2003**, *125*, 10508 – 10509; d) B. J. Holliday, J. R. Farrell, C. A. Mirkin, K.-C. Lam, A. L. Rheingold, *J. Am. Chem. Soc.* **1999**, *121*, 6316 – 6317; e) J. Hua, W. Lin, *Org. Lett.* **2004**, *6*, 861 – 864; f) N. Fujita, K. Biradha, M. Fujita, S. Sakamoto, K. Yamaguchi, *Angew. Chem.* **2001**, *113*, 1768 – 1771; *Angew. Chem. Int. Ed.* **2001**, *40*, 1718 – 1721; g) M. Yoshizawa, S. Miyagi, M. Kawano, K. Ishiguro, M. Fujita, *J. Am. Chem. Soc.* **2004**, *126*, 9172 – 9173.

[4] A. M. Brown, M. V. Ovchinnikov, C. L. Stern, C. A. Mirkin, *J. Am. Chem. Soc.* **2004**, *126*, 14316 – 14317.

[5] C. Bonuzzi, M. Bressan, F. Morandini, A. Morvillo, *Inorg. Chim. Acta* **1988**, *154*, 41 – 43.

[6] Crystal data for **3e**: $C_{42}H_{42}ClOP_2RhS$: Monoclinic space group $P21/c$, $a = 9.7234(9)$, $b = 18.5595(2)$, $c = 21.697(2)$ Å, $\alpha = 90.00$, $\beta = 102.686(2)$, $\gamma = 90°$, $V = 3819.9(6)$ Å^3, $Z = 4$, $T = 153$ K, $2\theta_{max} = 57.84°$, $Mo_{K\alpha}\lambda = 0.71073$ Å, $R1 = 0.0318$ (for 8061 reflections with $I > 2\sigma(I)$) $wR2 = 0.0787$ and $S = 1.070$ for 434 parameters and 9263 unique reflections. Further details on the crystal structure investigations may be obtained from the Fachinformationszentrum Karlsruhe, 76344 Eggenstein-Leopoldshafen, Germany (fax: (+49) 7247-808-666; e-mail: crysdata@fiz-karlsruhe.de) on quoting the depository number CSD-415095.

 © 2005 Wiley-VCH Verlag GmbH & Co. KGaA, Weinheim

Asymmetric Catalysis

Achiral Ligands Dramatically Enhance Rate and Enantioselectivity in the Rh/Phosphoramidite-Catalyzed Hydrogenation of α,β-Disubstituted Unsaturated Acids**

Rob Hoen, Jeroen A. F. Boogers, Heiko Bernsmann, Adriaan J. Minnaard, Auke Meetsma, Theodora D. Tiemersma-Wegman, André H. M. de Vries, Johannes G. de Vries,* and Ben L. Feringa**

In 2000, three research groups demonstrated that the widely held view that chiral bidentate ligands are necessary to achieve high enantioselectivity in rhodium-catalyzed hydrogenations needs revision. Monodentate phosphonites,[1a] phosphites[1b] and phosphoramidites[1c] proved to be highly versatile ligands for this important transformation and afforded excellent enantioselectivities for a broad range of substrates.

[*] R. Hoen, Dr. H. Bernsmann, Dr. A. J. Minnaard, A. Meetsma, T. D. Tiemersma-Wegman, Prof. Dr. B. L. Feringa
Department of Organic Chemistry
Stratingh Institute
University of Groningen
Nijenborgh 4, 9747 AG Groningen (The Netherlands)
Fax: (+31) 50-363-4296
E-mail: a.j.minnaard@rug.nl
b.l.feringa@rug.nl

Dr. J. A. F. Boogers, Dr. A. H. M. de Vries, Prof. Dr. J. G. de Vries
DSM Pharma Chemicals-Advanced Synthesis
Catalysis and Development
P.O. Box 18, 6160 Geleen (The Netherlands)
Fax: (+31) 46-476-7604
E-mail: hans-jg.vries-de@dsm.com

[**] We thank A. Kiewiet for carrying out the mass spectrometric analysis. Financial support from the NRSC-C, NWO-CW, EU Combicat Program, and EET is gratefully acknowledged.

Supporting information for this article (results of ligand screening and general experimental methods) is available on the WWW under http://www.angewandte.org or from the author.

 DOI: 10.1002/anie.200500784 © 2005 Wiley-VCH Verlag GmbH & Co. KGaA, Weinheim

Recently it has been shown that mixtures of chiral monodentate ligands improve the enantioselectivity and reactivity in several cases.[2] This new strategy has been employed in rhodium-catalyzed asymmetric hydrogenations[2,3] and in rhodium-catalyzed additions of boronic acid.[4] By using this mixed-ligand approach and exploiting the fact that the structure of monodentate ligands can be varied easily enables a large number of different catalytic complexes to be screened for a variety of reactions. Reetz and co-workers have also introduced a variation of this mixed-ligand approach using a combination of chiral and achiral ligands.[3a] So far, however, beneficial influences observed for mixed-ligand systems are limited to a mixture of two chiral monodentate ligands.

Herein, we report a mixed-ligand approach in which a combination of a chiral monodentate phosphoramidite and an achiral monodentate phosphine ligand gives for the first time drastic improvement resulting in high, and in some cases unprecedented, enantioselectivities compared to known bidentate ligands and (combinations of) chiral monodentate ligands in the rhodium-catalyzed hydrogenation of disubstituted acrylic acids.

Our efforts focused on chiral dihydrocinnamic acid derivatives, which are key intermediates in the synthesis of several bioactive compounds, including renin inhibitors,[5] γ-secretase inhibitors,[6] enkephalinase inhibitors,[7] endothelin receptor antagonists,[8] and opioid antagonists.[9]

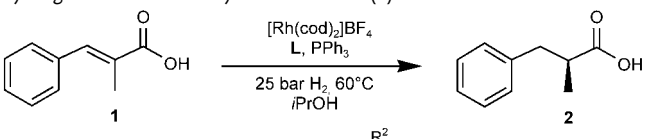
An initial screening of several mixtures of monodentate phosphoramidites and other phosphorus ligands in the rhodium-catalyzed asymmetric hydrogenation of α-methylcinnamic acid (**1**) showed that the heterocombination of a chiral phosphoramidite with an achiral triphenylphosphine gave a dramatic increase in conversion and in enantioselectivity, compared to the corresponding homocomplexes (Table 1).

For example the use of **L1c** in combination with triphenylphosphine resulted in an enhancement of the conversion from 76 to 100% and the *ee* value from 0 to 63% (entries 5 and 6). It was observed that phosphoramidites based on 3,3′-dimethyl-2,2′-dihydroxy-1,1′-binaphthyl (3,3′-dimethylbinol) gave distinctly higher *ee* values than the phosphoramidites based on binol (entries 1–8 versus 9–16, Table 1). Piperidine-based phosphoramidite **L2c**[10] further improved the enantioselectivities. The addition of triphenylphosphine in the presence of the catalyst based on **L2c** resulted in a remarkable increase in the *ee* value from 2 to 85% (entries 13 and 14).

A screening of different phosphines was performed after further optimization of the solvent, temperature, pressure, and ligand ratio.[11] A variety of achiral alkyl phosphines and substituted aryl phosphines were tested in the rhodium-catalyzed asymmetric hydrogenation of α-methylcinnamic acid (**1**) using **L2c** (Table 2).

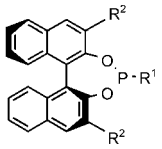
Substitution at the *ortho* position of triphenylphosphine increased the *ee* value significantly (entries 2 and 3), whereas substitution at the *meta* or *para* position had hardly any influence on the enantioselectivity (compare entries 2, 4, 5, 8,

Table 1: Screening of phosphoramidites in the rhodium-catalyzed asymmetric hydrogenation of α-methylcinnamic acid (**1**)[a,b]



1 **2**

L1a $R^1 = NMe_2$, R^2 = H
L1b R^1 = morpholine, R^2 = H
L1c R^1 = piperidine, R^2 = H
L1d R^1 = (*R*)-α-methylbenzylamine, R^2 = H

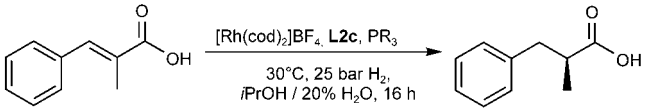


L2a $R^1 = NMe_2$, R^2 = Me
L2b R^1 = morpholine, R^2 = Me
L2c R^1 = piperidine, R^2 = Me
L2d R^1 = pyrrolidine, R^2 = Me

Entry	Ligand	Conversion [%]	*ee*[c,d] [%]
1	**L1a**	43	8
2	**L1a** + PPh_3	100	43
3	**L1b**	72	0
4	**L1b** + PPh_3	100	55
5	**L1c**	76	0
6	**L1c** + PPh_3	100	63
7	**L1d**	91	0
8	**L1d** + PPh_3	100	37
9	**L2a**	91	10
10	**L2a** + PPh_3	100	80
11	**L2b**	82	3
12	**L2b** + PPh_3	100	80
13	**L2c**	81	2
14	**L2c** + PPh_3	100	85
15	**L2d**	86	16
16	**L2d** + PPh_3	100	76

[a] Reaction conditions: 1 mmol substrate in 4 mL solvent with 0.01 mmol $[Rh(cod)_2]BF_4$ (cod = cycloocta-1,5-diene), 0.02 mmol phosphoramidite and 0.01 mmol PPh_3. [b] Reactions were carried out for 5 h. [c] *ee* values were determined by GC on a chiral stationary phase (see Supporting Information). [d] In all cases the *R* enantiomer of the ligand gave the *S* enantiomer of the product.

Table 2: Screening of achiral phosphines in the rhodium-catalyzed asymmetric hydrogenation of α-methylcinnamic acid (**1**)[a,b]



1 **2**

Entry	R	*ee*[c,d] [%]	TOF [mol mol^{-1} h^{-1}]
1	–	16[e]	2
2	Ph (**P1**)	88	46
3	*o*-tolyl (**P2**)	97	33
4	*m*-tolyl (**P3**)	87	69
5	*p*-tolyl (**P4**)	86	61
6	xylyl (**P5**)	89	92
7	mesityl (**P6**)	33[f]	3
8	*m*-ClPh (**P7**)	89	46
9	*p*-ClPh (**P8**)	90	18
10	cyclohexyl (**P9**)	87	28
11	*n*-butyl (**P10**)	67	17
12	*tert*-butyl (**P11**)	13[g]	2

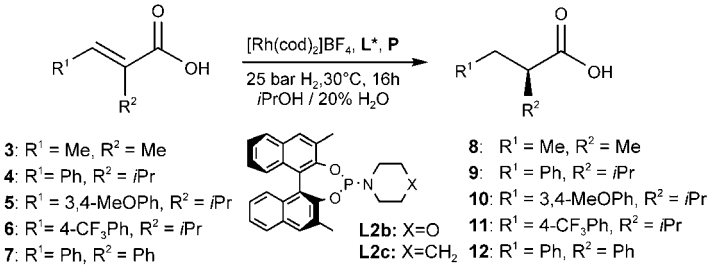
[a] Reaction conditions: 1 mmol substrate in 4 mL solvent with 0.01 mmol $[Rh(cod)_2]BF_4$, 0.02 mmol phosphoramidite and 0.01 mmol PR_3. [b] Reactions were carried out for 16 h. [c] *ee* values were determined by GC on a chiral stationary phase (see Supporting Information), full conversion. [d] In all cases the *R* enantiomer of the ligand gave the *S* enantiomer of the product. [e] 34% conversion. [f] 55% conversion. [g] 39% conversion.

 © 2005 Wiley-VCH Verlag GmbH & Co. KGaA, Weinheim

and 9). Linear or branched alkyl phosphines resulted in a decrease in the rate and enantioselectivity compared to tricyclohexylphosphine **P9** (entries 10–12). Electron-donating or -withdrawing substituents on the aryl phosphines had no influence on the *ee* value (compare entries 2 with 4 and 5 as well as 8 and 9). While reactions were in general complete after 2 h, incomplete conversions were obtained with the sterically hindered phosphines **P6** and **P11** after 16 h (entries 7 and 12). In these cases, not only did the rate of the hydrogenations decrease, but the enantioselectivities also dropped dramatically.

Next the hydrogenation of a number of disubstituted acrylic acids was studied (Table 3). In all cases, full conversion

Table 3: Rhodium-catalyzed asymmetric hydrogenation of substituted acrylic acids[a],[b]



Entry	Substrate	Product	Ligand	Phosphine	*ee*[c,d] [%]
1	**3**	**8**	**L2b**	**P3**	87
2	**4**	**9**	**L2c**	**P2**	99[e]
3	**5**	**10**	**L2c**	**P1**	92
4	**6**	**11**	**L2c**	**P3**	95
5[f]	**7**	**12**	**L2c**	**P2**	95

[a] Reaction conditions: 1 mmol substrate in 4 mL solvent with 0.01 mmol $[Rh(cod)_2]BF_4$, 0.02 mmol phosphoramidite and 0.01 mmol PPh_3. [b] Reactions were carried out for 16 h. [c] *ee* values were determined by GC or HPLC on chiral stationary phases, full conversion was obtained unless indicated otherwise. [d] In all cases the *S* enantiomer of the ligand gave the *S* enantiomer of the product.[15] [e] Conversion 98%. [f] Reaction was performed at 60°C.

of the substrates was obtained with high to excellent *ee* values. The enantioselectivity is higher when R^1 is an aromatic group than when R^1 is an alkyl group, as in tiglic acid (**3**, compare entry 3 of Table 2 with entry 1 of Table 3). Electron-donating as well as electron-withdrawing substituents at the aromatic moiety had little effect on the enantioselectivity (entry 3 versus 4, Table 3). The size of R^2 also has little influence on the enantioselectivities. Enantiomeric excesses of $\geq 97\%$ for **2** and **9** could be obtained by fine-tuning of the phosphine–phosphoramidite combination (entry 3 of Table 2 and entry 2 of Table 3).

On the basis of preliminary NMR experiments it can be concluded that the formation of a heterocomplex comprising one chiral phosphoramidite and one achiral phosphine bound to the Rh center is the predominant factor for the remarkable selectivity enhancement and high activity. The formation of a homocomplex comprising two achiral phosphines bound to the Rh center causes a non-asymmetric catalytic reaction. Using a 2:1 ratio of phosphoramidite:phosphine suppresses the formation of the latter homocomplex.

The enantioselectivities obtained here for products **2** and **12** exceed or are comparable to reported values for rhodium-catalyzed and ruthenium-catalyzed hydrogenations using chiral bidentate ligands.[5a,12,13] With the exception of five Ru complexes based on bidentate phosphine ligands, which hydrogenate substrate **3** with $\geq 95\%$ *ee*,[12f,13b,13c,14] the present system belongs to the most selective so far reported.

In conclusion, a new catalytic system, based on a mixed-ligand approach, has been developed for the rhodium-catalyzed asymmetric hydrogenation of cinnamic acid derivatives with *ee* values up to 99%. Easy variation of the chiral and achiral monodentate ligands makes it possible to screen a variety of catalytic systems in a short time. It has been shown for the first time that a catalyst complex based on a heterocombination of a chiral and an achiral monodentate ligand gives dramatically higher enantioselectivity than any of the corresponding homocomplexes.

Received: March 3, 2005
Published online: June 1, 2005

Keywords: asymmetric catalysis · hydrogenation · ligand effects · phosphines · rhodium

[1] a) C. Claver, E. Fernandez, A. Gillon, K. Heslop, D. J. Hyett, A. Martorell, A. G. Orpen, P. G. Pringle, *Chem. Commun.* **2000**, 961; b) M. T. Reetz, G. Mehler, *Angew. Chem.* **2000**, *112*, 4047; *Angew. Chem. Int. Ed.* **2000**, *39*, 3889; c) M. Van den Berg, A. J. Minnaard, E. P. Schudde, J. Van Esch, A. H. M. de Vries, J. G. de Vries, B. L. Feringa, *J. Am. Chem. Soc.* **2000**, *122*, 11539.

[2] a) M. T. Reetz, T. Sell, A. Meiswinkel, G. Mehler, *Angew. Chem.* **2003**, *115*, 814; *Angew. Chem. Int. Ed.* **2003**, *42*, 790; b) D. Peña, A. J. Minnaard, J. A. F. Boogers, A. H. M. de Vries, J. G. de Vries, B. L. Feringa, *Org. Biomol. Chem.* **2003**, *1*, 1087.

[3] a) M. T. Reetz, G. Mehler, *Tetrahedron Lett.* **2003**, *44*, 4593; b) M. T. Reetz, *Chim. Oggi* **2003**, *21*, 5; c) M. T. Reetz, G. Mehler, A. Meiswinkel, *Tetrahedron: Asymmetry* **2004**, *15*, 2165; d) M. T. Reetz, X. Li, *Tetrahedron* **2004**, *60*, 9709; e) M. T. Reetz, X. Li, *Angew. Chem.* **2005**, *117*, in press; *Angew. Chem. Int. Ed.* **2005**, in press.

[4] a) A. Duursma, R. Hoen, J. Schuppan, R. Hulst, A. J. Minnaard, B. L. Feringa, *Org. Lett.* **2003**, *5*, 3111; b) A. Duursma, J.-G. Boiteau, L. Lefort, J. A. F. Boogers, A. H. M. de Vries, J. G. de Vries, A. J. Minnaard, B. L. Feringa, *J. Org. Chem.* **2004**, *69*, 8045.

[5] a) T. Sturm, W. Weissensteiner, F. Spindler, *Adv. Synth. Catal.* **2003**, *345*, 160; b) Y. Yuasa, Y. Yuasa, H. Tsuruta, *Can. J. Chem.* **1998**, *76*, 1304; c) A. Dondoni, G. De Lathauwer, D. Perrone, *Tetrahedron Lett.* **2001**, *42*, 4819.

[6] a) I. Churcher, K. Ashton, J. W. Butcher, E. E. Clarke, H. D. L. Harrison, A. P. Owens, M. R. Teall, S. Williams, J. D. Wrigley, *Bioorg. Med. Chem. Lett.* **2003**, *13*, 179; b) A. P. Owens, A. Nadin, A. C. Talbot, E. E. Clarke, T. Harrison, H. D. Lewis, M. Reilly, J. D. J. Wrigley, J. Castro, *Bioorg. Med. Chem. Lett.* **2003**, *13*, 4143.

[7] Y. Yuasa, Y. Yuasa, H. Tsuruta, *Aust. J. Chem.* **1998**, *51*, 511.

 © 2005 Wiley-VCH Verlag GmbH & Co. KGaA, Weinheim

[8] M. L. Bray, D. Gorbacheva, H. Jahansouz, M. J. Kaufman, K. Ishikawa, N. Harada, K. Suzuki, *Chem. Pharm. Bull.* **2001**, *49*, 1.
[9] a) Y. Lu, T. M.-D. Nguyen, G. Weltrowska, I. Berezowska, C. Lemieux, N. N. Chung, P. W. Schiller, *J. Med. Chem.* **2001**, *44*, 3048; b) Y. Lu, G. Weltrowska, C. Lemieux, N. N. Chung, P. W. Schiller, *Bioorg. Med. Chem. Lett.* **2001**, *11*, 323.
[10] The beneficial effect of piperidine as the amine moiety in phosphoramidite **L1c** was also observed in other hydrogenations: H. Bernsmann, M. van den Berg, R. Hoen, G. Mehler, M. T. Reetz, A. J. Minnaard, J. G. de Vries, B. L. Feringa, *J. Org. Chem.* **2005**, *70*, 943.
[11] Optimized conditions for high enantioselectivities are: solvent, *i*PrOH/H_2O (20%,) 25 bar H_2 pressure, 30°C, and a 2:1 ratio of phosphoramidite and phosphine.
[12] For compound **2** see: a) I. Yamada, M. Ohkouchi, M. Yamaguchi, T. J. Yamagishi, *J. Chem. Soc. Perkin Trans. 1* **1997**, 1869; b) T. Uemura, X. Zhang, K Matsumura, N. Sayo, H. Kumobayashi, T. Ohta, K. Nozaki, H. Takaya, *J. Org. Chem.* **1996**, *61*, 5510; c) F. Spindler, C. Malan, M. Lotz, M. Kesselgruber, U. Pittelkow, A. Rivas-Nass, O. Briel, H.-U. Blaser, *Tetrahedron: Asymmetry* **2004**, *15*, 2299; d) F. Maienza, F. Santoro, F. Spindler, C. Malan, A. Mezzetti, *Tetrahedron: Asymmetry* **2002**, *13*, 1817; e) I. Yamada, M. Yamaguchi, T. Yamagishi, *Tetrahedron: Asymmetry* **1996**, *7*, 3339; f) X. Cheng, Q. Zhang, J.-H. Xie, L.-X. Wang, Q.-L Zhou, *Angew. Chem.* **2005**, *117*, 1142; *Angew. Chem. Int. Ed.* **2005**, *44*, 1118.
[13] For compound **12** see: a) M. D. Jones, R. Raja, J. M. Thomas, B. F. G. Johnson, D. W. Lewis, J. Rouzad, K. D. M. Harris, *Angew. Chem.* **2003**, *115*, 4462; *Angew. Chem. Int. Ed.* **2003**, *42*, 4326; b) J. Rouzad, M. D. Jones, R. Raja, B. F. G. Johnson, J. M. Thomas, M. J. Duer, *Helv. Chim. Acta* **2003**, *86*, 1753.
[14] a) C. J. A. Daley, J. A. Wiles, S. H. Bergens, *Can. J. Chem.* **1998**, *76*, 1447; b) J. P. Genêt, C. Pinel, V. Ratovelomanana-Vidal, S. Mallart, X. Pfister, L. Bischoff, M. C. Caño de Andrade, S. Darses, C. Galopin, J. A. Laffitte, *Tetrahedron: Asymmetry* **1994**, *5*, 675.
[15] The absolute configuration of **11** was confirmed by X-ray analysis of the corresponding α-methylbenzylamine derivative. The absolute configurations of **9** and **10** were assigned by analogy (see Supporting Information).

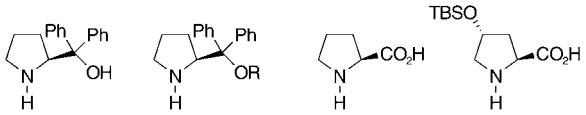
 © 2005 Wiley-VCH Verlag GmbH & Co. KGaA, Weinheim

Organocatalysis

Diphenylprolinol Silyl Ethers as Efficient Organocatalysts for the Asymmetric Michael Reaction of Aldehydes and Nitroalkenes**

Yujiro Hayashi, Hiroaki Gotoh, Takaaki Hayashi, and Mitsuru Shoji*

A subtle change in catalyst structure can sometimes improve catalytic activity dramatically, as we found in our recent study on α-aminoxylation, tandem O-nitroso aldol/Michael reactions, and Mannich reactions catalyzed by the siloxyproline **4**, a highly active proline surrogate (Scheme 1).[1] The simple



1 **2a** R = TMS **2b** R = TES **2c** R = TBS **3** **4**

Scheme 1. Organocatalysts examined in this study. TMS = trimethylsilyl, TES = triethylsilyl, TBS = *tert*-butyldimethylsilyl.

introduction of a siloxy group into the proline structure leads to an increase in the catalytic activity, thus allowing a decrease in catalyst loading and shorter reaction times, without compromising the enantioselectivity, and is accompanied by broadening of the substrate scope. This higher activity can be attributed to the increased solubility of **4** in organic solvents. The fact that the substitution of a hydroxy group for a siloxy group can dramatically affect catalytic activity prompted us to investigate other catalytic systems, and these investigations led us to the diphenylprolinol silyl ether **2**. The parent diphenyl-2-pyrrolidinemethanol (**1**, diphenylprolinol), a commercially available amino alcohol developed by Corey and co-workers, has proved to be a very useful ligand for asymmetric synthesis: *B*-alkylated oxazaborodine is a useful catalyst for the CBS reduction,[2] while an effective, asymmetric Lewis acid catalyst prepared from *B*-aryl oxazaborodine and a Brønsted acid promotes the Diels–Alder reaction of a broad range of substrates with excellent enantioselectiv-

[*] Prof. Dr. Y. Hayashi, H. Gotoh, T. Hayashi, Dr. M. Shoji
Department of Industrial Chemistry
Faculty of Engineering, Tokyo University of Science
Kagurazaka, Shinjuku-ku, Tokyo 162-8601 (Japan)
Fax: (+81) 3-5261-4631
E-mail: hayashi@ci.kagu.tus.ac.jp

[**] We thank Prof. K. Saigo and Dr. Y. Ishida (The University of Tokyo) for the use of a high-pressure mercury lamp. This work was partially supported by a Grand-in-Aid for Scientific Research on Priority Area (A): "Creation of Biologically Functional Molecules", from the Ministry of Education, Culture, Sports, Science, and Technology of Japan.

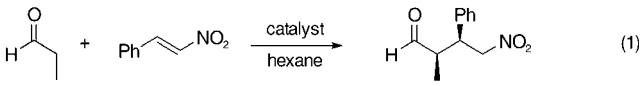
Supporting information for this article is available on the WWW under http://www.angewandte.org or from the author.

 © 2005 Wiley-VCH Verlag GmbH & Co. KGaA, Weinheim DOI: 10.1002/anie.200500599

ity[3] and also catalyzes asymmetric cyanosilylation.[4] Herein we disclose another synthetically useful feature of diphenylprolinol (**1**), the silyl ethers **2** of which were found to be exceptionally effective in the asymmetric catalysis of the Michael reaction of aldehydes and nitroalkenes.[5]

The Michael reaction of a carbon nucleophile with a nitroalkene[6] is one useful synthetic method for the preparation of nitroalkanes, which are versatile synthetic intermediates owing to the various possible transformations of the nitro group into other useful functional groups. The need for environmentally friendly and metal-free reactions has led recently to great progress in the organocatalyst-mediated Michael addition to nitroalkenes: Asymmetric Michael reactions of malonates and β-ketoesters as nucleophiles are promoted by a cinchona-alkaloid derivative[7] and a bifunctional thiourea catalyst.[8] The reactions of ketones and aldehydes as nucleophiles are catalyzed by proline,[9] pyrrolidinyltetrazole,[10] aminomethylpyrrolidine,[11] and 2,2′-bipyrrolidine.[12] Kotsuki and co-workers have developed an excellent Michael reaction of ketones with a pyrrolidine catalyst that includes pyridine as the conjugate base.[13] Recently, Wang et al. reported a highly enantio- and diastereoselective Michael reaction of aldehydes, although the catalyst loading was high (20 mol%) and an alkyl-substituted nitroalkene was a poor Michael acceptor (22% *ee*).[14] The development of more-effective asymmetric catalysts in terms of both enantioselectivity and substrate scope is desirable.

The Michael reaction of propanal and nitrostyrene was selected as a model [Eq. (1), Table 1]. The first catalyst



(1)

Table 1: The effect of the catalyst in the Michael reaction of propanal and nitrostyrene.

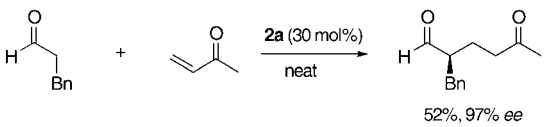
Entry	Catalyst (mol%)	*T* [°C]	*t* [h]	Yield [%][a]	*syn*/*anti*[b]	*ee* [%][c]
1	**3** (20)	0	24	44	97:3	28
2	**4** (20)	0	24	25	92:8	75
3	**1** (20)	23	24	29	86:14	95
4	**2a** (10)	23	1	82	85:15	99
5	**2a** (10)	0	5	85	94:6	99
6	**2a** (5)	23	38	85	96:4	99
7	**2b** (10)	0	22	72	93:7	99
8	**2c** (10)	0	27	80	95:5	99

[a] Yield of isolated product. [b] Determined by ^{1}H NMR spectroscopy (400 MHz). [c] The *ee* values were determined by HPLC analysis on a chiral phase (chiralcel OD-H).

examined, proline (**3**), led to a low yield and low enantioselectivity (Table 1, entry 1). Higher enantioselectivity (75% *ee*) was observed with the siloxyproline **4**, but the yield was poor (Table 1, entry 2). Although excellent enantioselectivity (95% *ee*) was observed when diphenylprolinol (**1**) was employed, the progress of the reaction was slow, and the yield was unsatisfactory (29%) even after 24 h (Table 1, entry 3). The reactivity of the catalyst was increased dramatically, along with the enantioselectivity, when the hydroxy group in **1** was exchanged for a siloxy group. That is, the reaction was complete within 1 h at room temperature in the presence of the diphenyl siloxy proline **2a**, and the adduct was afforded in good yield (82%) and with increased enantioselectivity (99% *ee*; Table 1, entry 4). When the reaction was performed at a lower temperature (0°C), the adduct was obtained in nearly optically pure form (99% *ee*), in good yield, and also with high diastereoselectivity (*syn*/*anti* 94:6; Table 1, entry 5). The catalyst loading can be reduced to 5 mol% without compromising the enantioselectivity, but the reaction must then be carried out at room temperature, and a longer reaction time is needed. Not only the TMS-substituted compound **2a**, but also the TES and TBS derivatives **2b** and **2c** are excellent catalysts; however, the reaction becomes slower as the silyl substituent becomes bulkier. As excellent results had been obtained with the model system, the generality of the reaction was examined in detail, with the results summarized in Table 2.

The reaction has broad applicability with respect to both the Michael acceptor and the donor; the adducts were obtained in nearly optically pure form (99% *ee*) and with excellent *syn* diastereoselectivity in most of the cases examined. Both aryl- and alkyl-substituted nitroalkenes are excellent Michael acceptors: Not only phenyl, but also electron-rich and electron-deficient aryl groups and heteroaromatic substituents can be present on the nitroalkene. Alkyl-substituted nitroalkenes, such as 1-nitro-1-hexene and 2-cyclohexyl-1-nitroethene, are also excellent Michael acceptors (Table 2, entries 5 and 6). Not only propanal, but also other linear aldehydes, such as *n*-butanal and *n*-pentanal (Table 2, entries 9 and 10), and branched aldehydes, such as isovaleraldehyde (Table 2, entries 7 and 8), can be employed successfully as the Michael donor, again to afford the adducts in nearly optically pure form. In the reaction of (*Z*)-nitrostyrene[15] with propanal, the same high levels of diastereo- and enantioselectivity were observed as those found in the reaction of the *E* isomer (Table 2, entries 1 and 11). In this reaction, the rapid isomerization of (*Z*)-nitrostyrene to the corresponding *E* isomer was observed by TLC. This method also has its limitations, however: Isobutyraldehyde was found to be a poor nucleophile; in its reaction with nitrostyrene the product was afforded with only moderate enantioselectivity (68% *ee*; Table 2, entry 12). The β,β′-disubstituted nitroolefin (*E*)-2-methyl-2-phenyl-1-nitroethene was found to be a poor Michael acceptor, with the desired adduct formed in low yield.

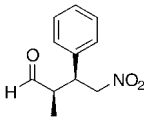
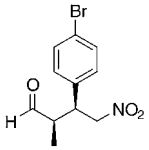
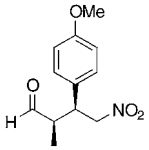
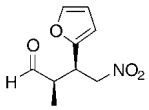
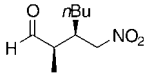
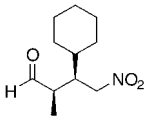
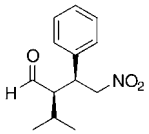
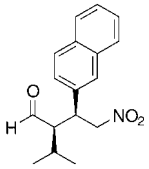
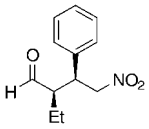
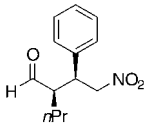
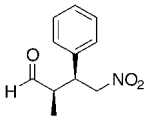
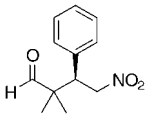
A preliminary study showed that not only nitroalkenes, but also α,β-unsaturated ketones can be employed as the Michael acceptor: 3-Phenylpropanal reacted with methyl vinyl ketone in the presence of **2a** to afford the Michael adduct[16] in 52% yield and with 97% *ee* [Eq. (2); Bn = benzyl].



(2)

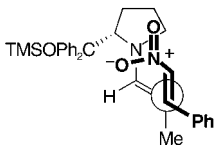
 © 2005 Wiley-VCH Verlag GmbH & Co. KGaA, Weinheim

Table 2: Catalytic asymmetric Michael reaction of aldehydes and nitroalkenes.

Entry	Catalyst loading [mol%]	Product	*T* [°C]	*t* [h]	Yield [%][a]	*syn*/*anti*[b]	*ee* [%][c]
1	10		0	5	85	94:6	99
2	10		0	1	72	95:5	99
3	10		0	5	80	95:5	99
4	10		0	5	81	94:6	99
5	10		0	25	52	84:16	99
6	20		23	48	56	96:4	99
7	20		23	46	72	93:7	99
8	20		23	24	77	94:6	99
9	10		0	48	66	93:7	99
10	10		0	48	74	95:5	99
11[d]	10		0	5	84	96:4	99
12	20		23	96	85	–	68

[a] Yield of isolated product. [b] Determined by ^{1}H NMR spectroscopy (400 MHz). [c] The *ee* values were determined by HPLC analysis on a chiral phase (chiralpak AS-H, IA, AD-H, and chiralcel OD-H). [d] (*Z*)-Nitrostyrene was used as the Michael acceptor.

The higher reactivity of **2** relative to that of the parent compound **1** can be attributed to effective formation of the corresponding enamine without generation of the aminal, which would be formed in the case of diphenylprolinol (**1**).[5] The high diastereoselectivities and excellent enantioselectivities can be explained as follows: The *anti* enamine, with its double bond oriented away from the diphenylsiloxymethyl group, would be formed selectively and would react with nitrostyrene via an acyclic synclinal transition state proposed by Seebach and Golinski,[17] as shown in Scheme 2. In this model, an electrostatic interaction between nitro group and the nitrogen atom of the enamine would be operating.[12c] The bulky diphenylsiloxymethyl group on the pyrrolidine ring would play two important roles towards the excellent enantioselectivity: promotion of the selective formation of the *anti* enamine and selective shielding of the *Re* face of the enamine double bond.



Scheme 2. Transition-state model.

In summary, with the development of a highly enantioselective Michael reaction of aldehydes and nitroalkenes we have shown that silylation of the prolinol **1** can dramatically improve its catalytic activity. This reaction has several noteworthy features: 1) The catalyst **2** is easily prepared from commercially available diphenylprolinol in a single step, 2) a broad range of Michael acceptors (nitroalkenes) and Michael donors (aldehydes) can be used, and 3) the adducts were obtained in nearly optically pure form in almost all cases examined.

Experimental Section

Typical experimental procedure: Propanal (0.75 mL, 10 mmol) was added to a solution of nitrostyrene (154 mg, 1.0 mmol) and **2a** (34 mg, 0.1 mmol) in hexane (1.0 mL) at 0 °C. After the reaction mixture had been stirred for 5 h at that temperature, the reaction was quenched by the addition of aqueous 1N HCl. Organic materials were extracted three times with AcOEt, and the combined organic phases were dried (Na_2SO_4), concentrated, and purified by preparatory TLC (chloroform) to afford the Michael adduct (183 mg, 85%) as a clear oil: *syn*/*anti* 94:6 (by ^{1}H NMR spectroscopy of the crude mixture), 99% *ee* (by HPLC on a chiral phase: chiralcel OD-H column, $\lambda = 254$ nm, *i*PrOH/hexane 1:10, 1.0 mL min^{-1}; $t_R = 14.5$ min (minor), 19.7 min (major)).[11a]

Received: February 17, 2005
Revised: April 19, 2005
Published online: June 1, 2005

Keywords: asymmetric catalysis · diphenylprolinol · Michael addition · nitroalkenes · organocatalysis

[1] Y. Hayashi, J. Yamaguchi, K. Hibino, T. Sumiya, T. Urushima, M. Shoji, D. Hashizume, H. Koshino, *Adv. Synth. Catal.* **2004**, *346*, 1435.

[2] a) E. J. Corey, R. K. Bakshi, S. Shibata, *J. Am. Chem. Soc.* **1987**, *109*, 5551; b) E. J. Corey, R. K. Bakshi, S. Shibata, C.-P. Chen, V. K. Singh, *J. Am. Chem. Soc.* **1987**, *109*, 7925; c) C. J. Hetal,

 © 2005 Wiley-VCH Verlag GmbH & Co. KGaA, Weinheim

P. A. Magriotis, E. J. Corey, *J. Am. Chem. Soc.* **1996**, *118*, 10938. CBS is an abbreviation of Corey–Bakshi–Shibata.
[3] a) Q.-Y. Hu, G. Zhou, E. J. Corey, *J. Am. Chem. Soc.* **2004**, *126*, 13708, and references therein; b) for a Review, see: E. J. Corey, *Angew. Chem.* **2002**, *114*, 1724; *Angew. Chem. Int. Ed.* **2002**, *41*, 1650.
[4] D. H. Ryu, E. J. Corey, *J. Am. Chem. Soc.* **2004**, *126*, 8106.
[5] During the preparation of this manuscript, **2** was reported to be an excellent catalyst for the α sulfenylation of aldehydes: M. Marigo, T. C. Wabnitz, D. Fielenbach, K. A. Jørgensen, *Angew. Chem.* **2005**, *117*, 804; *Angew. Chem. Int. Ed.* **2005**, *44*, 794.
[6] For an excellent review, see: O. M. Berner, L. Tedeschi, D. Enders, *Eur. J. Org. Chem.* **2002**, 1877.
[7] H. Li, Y. Wang, L. Tang, L. Deng, *J. Am. Chem. Soc.* **2004**, *126*, 9906.
[8] a) T. Okino, Y. Hoashi, Y. Takemoto, *J. Am. Chem. Soc.* **2003**, *125*, 12672; b) T. Okino, Y. Hoashi, T. Furukawa, X. Xu, Y. Takemoto, *J. Am. Chem. Soc.* **2005**, *127*, 119.
[9] a) B. List, P. Pojarliev, H. J. Martin, *Org. Lett.* **2001**, *3*, 2423; b) K. Sakthivel, W. Notz, T. Bui, C. F. Barbas III, *J. Am. Chem. Soc.* **2001**, *123*, 5260; c) D. Enders, A. Seki, *Synlett* **2002**, 26.
[10] a) A. J. A. Cobb, D. A. Longbottom, D. M. Shaw, S. V. Ley, *Chem. Commun.* **2004**, 1808; b) A. J. A. Cobb, D. M. Shaw, D. A. Longbottom, J. B. Gold, S. V. Ley, *Org. Biomol. Chem.* **2005**, *3*, 84.
[11] a) J. M. Betancort, C. F. Barbas III, *Org. Lett.* **2001**, *3*, 3737; b) N. Mase, R. Thayumanavan, F. Tanaka, C. F. Barbas III, *Org. Lett.* **2004**, *6*, 2527; c) J. M. Betancort, K. Sakthivel, R. Thayumanavan, F. Tanaka, C. F. Barbas III, *Synthesis* **2004**, 1509; d) for a review, see: W. Notz, F. Tanaka, C. F. Barbas III, *Acc. Chem. Res.* **2004**, *37*, 580.
[12] a) A. Alexakis, O. Andrey, *Org. Lett.* **2002**, *4*, 3611; b) O. Andrey, A. Alexakis, G. Bernardinelli, *Org. Lett.* **2003**, *5*, 2559; c) O. Andrey, A. Alexakis, A. Tomassini, G. Bernardinelli, *Adv. Synth. Catal.* **2004**, *346*, 1147.
[13] T. Ishii, S. Fujioka, Y. Sekiguchi, H. Kotsuki, *J. Am. Chem. Soc.* **2004**, *126*, 9558.
[14] W. Wang, J. Wang, H. Li, *Angew. Chem.* **2005**, *117*, 1393; *Angew. Chem. Int. Ed.* **2005**, *44*, 1369.
[15] T. Ohwada, T. Ohta, K. Shudo, *J. Am. Chem. Soc.* **1986**, *108*, 3029.
[16] P. Melchiorre, K. A. Jørgensen, *J. Org. Chem.* **2003**, *68*, 4151.
[17] D. Seebach, J. Golinski, *Helv. Chim. Acta* **1981**, *64*, 1413.

 © 2005 Wiley-VCH Verlag GmbH & Co. KGaA, Weinheim

Fullerenes

A [70]Fullerene Chloride, $C_{70}Cl_{16}$, Obtained by the Attempted Bromination of C_{70} in $TiCl_4$**

Sergey I. Troyanov and Alexey A. Popov*

The use of liquid inorganic chlorides as chlorinating agents for fullerenes resulted recently in the synthesis of several new chlorofullerenes. In addition to $C_{60}Cl_6$, which was obtained many years ago and investigated by ^{13}C NMR and IR spectroscopy,[1] four highly chlorinated [60]fullerenes, $C_{60}Cl_{24}$,[2] $C_{60}Cl_{28}$,[3] and two isomers of $C_{60}Cl_{30}$,[3,4] have been prepared and characterized by means of single-crystal X-ray crystallography and IR spectroscopy. The application of this method to the chlorination of C_{70} produced a highly chlorinated fullerene, $C_{70}Cl_{28}$, which, according to the single-crystal X-ray crystallographic study, comprised three isomers with similar structures.[5] Earlier, $C_{70}Cl_{10}$ was prepared by treating C_{70} with ICl in benzene; its addition pattern has been deduced from ^{13}C NMR spectroscopic analysis,[6a] substitution reactions,[6b] and theoretical modeling studies.[6c] Thus, the chlorination of the fullerenes under mild conditions results in "lower" chlorides, whereas the use of strong chlorinating agents at elevated temperatures produces "higher" chlorides of both [60]- and [70]fullerenes. These results raise the question as to whether "missing" intermediate chlorides could be obtained by variation of the reactants and/or reaction conditions.

Herein, we report the synthesis of such an intermediate chloride of [70]fullerene, $C_{70}Cl_{16}$, and its characterization by single-crystal X-ray crystallography, IR spectroscopy, and DFT calculations. Notably, the new fullerene chloride was obtained during an attempt to brominate C_{70} in $TiCl_4$. Typically, neat bromine (0.5 mL) was added to a solution of C_{70} (30 mg) in $TiCl_4$ (2.0 mL) in a glass ampoule. The ampoule was evacuated on cooling and sealed. A yellow crystalline precipitate formed after heating the mixture at 60–80 °C for 1–2 days. Work-up consisted of distilling off the bromine and excess $TiCl_4$ into a second section of the sealed ampoule by cooling it with liquid nitrogen. Alternatively, the ampoule was opened and the mixture was poured into 15% HCl. The yellow precipitate so formed was washed with dilute HCl and then water before removal by filtration and drying at 50 °C for

[*] Prof. Dr. S. I. Troyanov, Dr. A. A. Popov
Chemistry Department
Moscow State University
119992 Moscow, Leninskie Gory (Russia)
Fax: (+7) 95-939-1240
E-mail: troyanov@thermo.chem.msu.ru

[**] This work was partially supported by the Russian Foundation for Basic Research (03-03-32855 and 03-03-32179). The authors are grateful to A. P. Turnbull (BESSY, Berlin, Germany) for his help with the reduction of the diffraction data, and N. V. Chelovskaya (Moscow State University, Russia) and M. Feist (Humboldt Universität Berlin, Germany) for thermoanalytical measurements.

Supporting information for this article is available on the WWW under http://www.angewandte.org or from the author.

 DOI: 10.1002/anie.200500476 © 2005 Wiley-VCH Verlag GmbH & Co. KGaA, Weinheim

several hours. The product was stable in air for many months. Thermal decomposition occurs between 240 and 360 °C (a typical temperature range for fullerene chlorides[7]) with the evolution of chlorine and small amounts of bromine, as monitored by mass spectrometric analysis of the evolved gases.

The crystal-structure determination revealed the product had a composition of $C_{70}Cl_{16}\cdot 0.5\,Br_2$ (**1**).[8] The molecular structure of $C_{70}Cl_{16}$ shows a remarkable combination of a chlorine belt around the equator and a skew pyramidal chlorine cap at one of the poles (Figures 1 and 2). The same

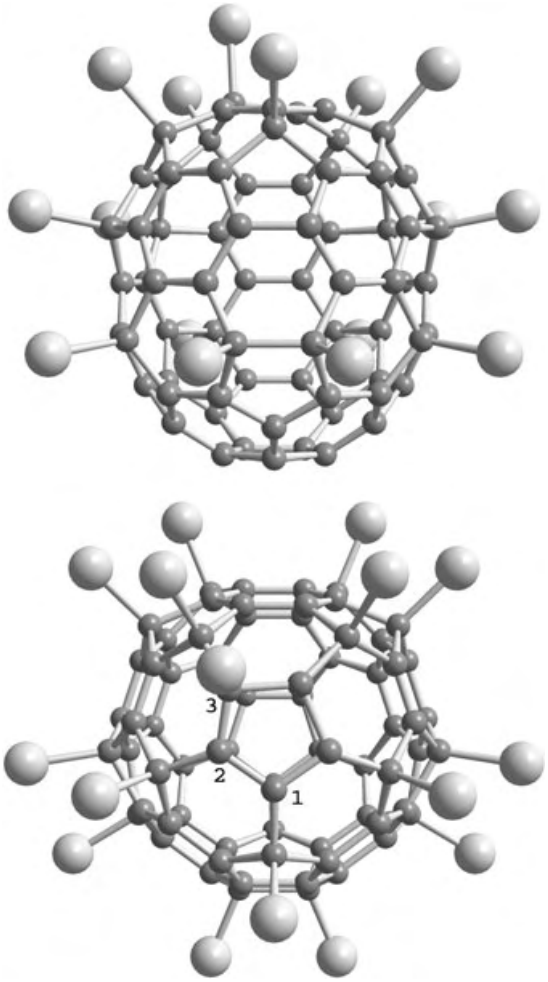


Figure 1. Side and top views of the C_1 isomer of $C_{70}Cl_{16}$.

belt of ten halogen atoms (Cl5–Cl9 in **1**) with nine 1,4 and one 1,2 X···X contacts is also present in $C_{70}Cl_{10}$[6] and $C_{70}Br_{10}$,[9] whereas a X_{10} belt without a 1,2 contact was reported recently for the $C_{70}(OO\mathit{t}Bu)_{10}$ derivative.[10] The combination of a skew pyramidal cap of six halogen atoms (Cl1–Cl4) with a cyclopentadiene fragment in the pentagon is characteristic of $C_{60}X_6$ structures with X being Cl[1] or Br.[11] A similar fragment was found in the $C_{70}(OO\mathit{t}Bu)_6$ derivative, but not on the top pentagon.[10] Both enantiomeric $C_{70}Cl_{16}$ molecules with C_1 symmetry are present in the crystal of **1**; their overlapping results in overall C_s symmetry with statistically disordered C3

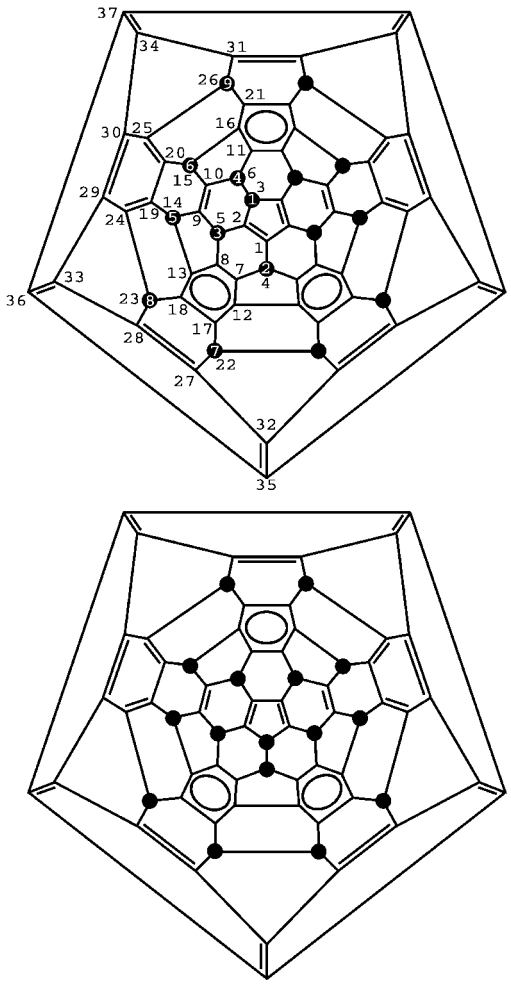


Figure 2. Schlegel diagrams for the experimentally observed C_1 (top) and C_s (bottom) isomers of $C_{70}Cl_{16}$ showing the labeling scheme for the independent C and Cl atoms. An alternative labeling with contiguous numbering for the whole molecules is given in the Supporting Information.

and Cl1 atoms. A comparison of the experimental and calculated[12] IR spectra demonstrates their close similarity (Figure 3), thus suggesting the high purity of $C_{70}Cl_{16}$ in compound **1**.

Another compound (**2**) obtained when the reaction was carried out with a larger amount of bromine had a composition of $C_{70}Cl_{16}\cdot 3\,Br_2$ according to the single-crystal X-ray analysis.[8] In spite of the poor crystal quality, the X-ray crystallographic study of **2** has unambiguously revealed the presence of two isomers of $C_{70}Cl_{16}$, namely, those with chlorinated positions at C1 (C_s) and C3 (C_1), in a ratio of approximately 3:4 (Figure 2). The IR spectrum of **2** was virtually identical to that of **1**.

Averaged experimental C–C bond lengths in **1** correspond satisfactorily to those calculated at the PBE/TZ2P level of theory.[12] The longest bond (C22–C22a) between sp^3 carbon atoms is 1.65 Å (calcd: 1.64 Å), while sp^2–sp^3 C–C bonds are shorter with an averaged value of 1.51 Å (calcd: 1.51 Å). Two independent six-membered isolated (C11-C16-C21-C21a-C16a-C11a) and nearly isolated (C7-C8-C13-C18-C17-C12)

 © 2005 Wiley-VCH Verlag GmbH & Co. KGaA, Weinheim

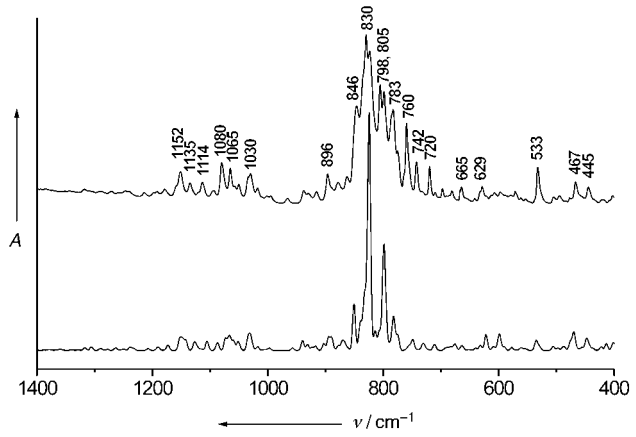


Figure 3. Experimental IR spectrum (above) of (**1**) and calculated one for C_1-$C_{70}Cl_{16}$ (below) using force-field scaling factors found for the $C_{60}Cl_{24}$ molecule.[2]

aromatic rings are characterized by averaged C–C bond lengths of 1.39 Å (calcd: 1.40 Å). Finally, there are two isolated double C–C bonds with an average bond length of 1.34 Å (calcd: 1.34 Å). Bond lengths in the chlorinated cap region are distorted as a result of disorder in the crystal. The average C–Cl (Cl2–Cl9) bond has a length of 1.85 Å, whereas the apparent effective position of C3 (between two actual positions in each enantiomer) results in a strongly elongated C3···Cl1 distance (2.04 Å).

DFT calculations performed at the PBE/TZ2P level revealed that three isomers of $C_{70}Cl_{16}$ with different positions of the chlorinated carbon atoms in the cyclopentadiene ring on the cap are essentially isoenergetic with the relative energies of 0 (for C1), 2.8 (C3), and 7.6 kJ mol^{-1} (C2).[13] Alternative $C_{70}Cl_{16}$ structures with a cap of six chlorine atoms on the opposite pole of the cage were found to be 33–40 kJ mol^{-1} less favorable; this result may be attributed to the presence of only two benzenoid rings in their addition patterns compared to three such rings in the synthesized isomers.

It is known from our recent investigation of the bromination of [70]fullerene that even the use of liquid bromine does not result in the addition of more than ten Br atoms to the [70]fullerene cage.[9] Therefore, the formation of $C_{70}Cl_{16}$ can not be explained by two successive steps, such as bromination to give $C_{70}Br_{16}$ and halogen exchange. $TiCl_4$ itself can not chlorinate C_{70}; the solvate $C_{70}\cdot 2\,TiCl_4$ has been isolated from a solution of C_{70} in $TiCl_4$ and characterized by single-crystal X-ray crystallography.[14] Although the mechanism of the [70]fullerene chlorination by the mixture of Br_2 and $TiCl_4$ remains unclear, it can be assumed that the formation of the chloride higher than $C_{70}Cl_{10}$ results from the high Lewis acidity of $TiCl_4$. The formation of Br^+ or BrCl species in Br_2/Lewis acid systems is known to promote the electrophilic bromochlorination of olefins.[15] Clearly, $TiCl_4$ also participates in a Br/Cl exchange that results in the thermodynamically more stable chloride. The exclusive formation of chlorides as the reaction products is documented, for example, for the system $Br_2/SbCl_5$/norbornene.[16] However, bromination of C_{70} with Br_2 in molten $TiBr_4$ produced only $C_{70}Br_{10}$, possibly because of the absence of BrCl molecules in this system.

Alternatively, the reaction may proceed through a radical mechanism involving the addition of Br$^\bullet$ with subsequent Br/Cl exchange. In this case, the formation of $C_{70}Cl_{16}$ can be rationalized with a simple kinetic model,[17] when it is assumed that addition occurs in turn to the sites of maximum free valence in closed-shell molecules and of maximum spin density in the radicals; furthermore, 1,2-addition of a bulky addend (Br or Cl) is avoided unless it is necessary to quench the radical. This model successfully explains the formation of $C_{60}X_6$ and $C_{70}X_{10}$ isomers by the radical addition of bulky groups to C_{60} and C_{70}.[17] We have found by using bond orders from extended Hückel calculations that the most reactive site in $C_{70}X_{10}$ (X = Br or Cl) is C4. Further addition occurs in the sequence C5-C6-C5a-C6a until the radical $C_{70}X^{\cdot}_{15}$ is formed. The maximum spin density in $C_{70}X^{\cdot}_{15}$ is located on C1 (0.38), C3 (0.20), and C3a (0.20), whereas the spin density on the C2 and C2a sites is only 0.03. Thus, both energetic and kinetic considerations favor the experimentally observed isomers of $C_{70}Cl_{16}$.

In summary, the reaction between C_{70} and a $Br_2/TiCl_4$ mixture resulted in the isolation of the new chlorofullerene $C_{70}Cl_{16}$. X-ray crystallography elucidated the structure of two $C_{70}Cl_{16}$ isomers, which are the most stable according to theoretical calculations. Formation of these isomers was also rationalized from kinetic considerations based on the Hückel theory. This new reaction represents a promising synthetic approach for the preparation of chlorofullerenes with a level of addition that lies between that of the "lower" and "higher" fullerene chlorides.

Received: February 8, 2005
Published online: June 1, 2005

Keywords: chlorination · density functional calculations · fullerenes · halogen exchange · structure elucidation

[1] P. R. Birkett, A. G. Avent, A. D. Darwish, H. W. Kroto, R. Taylor, D. R. M. Walton, *J. Chem. Soc. Chem. Commun.* **1993**, 1230.
[2] N. B. Shustova, A. A. Popov, L. N. Sidorov, A. P. Turnbull, E. Kemnitz, S. I. Troyanov, *Chem. Commun.* **2005**, 1411.
[3] S. I. Troyanov, N. B. Shustova, A. A. Popov, L. N. Sidorov, E. Kemnitz, *Angew. Chem.* **2005**, *117*, 436; *Angew. Chem. Int. Ed.* **2005**, *44*, 432.
[4] P. A. Troshin, R. N. Lyubovskaya, I. N. Ioffe, N. B. Shustova, E. Kemnitz, S. I. Troyanov, *Angew. Chem.* **2005**, *117*, 238; *Angew. Chem. Int. Ed.* **2005**, *44*, 234.
[5] S. I. Troyanov, N. B. Shustova, I. N. Ioffe, A. P. Turnbull, E. Kemnitz, *Chem. Commun.* **2005**, 72.
[6] a) P. R. Birkett, A. G. Avent, A. D. Darwish, H. W. Kroto, R. Taylor, D. R. M. Walton, *J. Chem. Soc. Perkin Trans. 2* **1997**, 457; b) H. Al-Matar, A. K. Abdul-Sada, A. G. Avent, P. W. Fowler, P. B. Hitchcock, K. M. Rogers, R. Taylor, *J. Chem. Soc. Perkin Trans. 2* **2002**, 53; c) S. J. Austin, P. W. Fowler, J. P. B. Sandall, P. R. Birkett, A. G. Avent, A. D. Darwish, H. W. Kroto, R. Taylor, D. R. M. Walton, *J. Chem. Soc. Perkin Trans. 2* **1995**, 1027.
[7] S. I. Troyanov, N. B. Shustova, A. A. Popov, M. Feist, E. Kemnitz, *Russ. J. Inorg. Chem.* **2004**, *49*, 1303.

 © 2005 Wiley-VCH Verlag GmbH & Co. KGaA, Weinheim

[8] Data collection for crystals of $C_{70}Cl_{16}\cdot 0.5\,Br_2$ (**1**) and $C_{70}Cl_{16}\cdot 3\,Br_2$ (**2**) was performed on a MAR345 image plate at 100 K using synchrotron radiation on the BESSY storage ring (PSF BL14.2 of the Free University of Berlin, Germany). **1**: hexagonal, space group $P6_3/m$, $a = 21.631(2)$, $c = 19.019(2)$ Å, $V = 7707(1)$ Å^3, $Z = 6$; reflections collected 17141, independent 2701. Structure solution with SHELXS-97. The final anisotropic LS refinement (SHELXL-97) with 423 parameters converged to $wR_2 = 0.128$ and $R_1 = 0.052$. **2**: orthorhombic, space group $Ama2$, $a = 18.743(1)$, $b = 24.595(2)$, $c = 13.117(1)$ Å, $V = 6046.7(7)$ Å^3, $Z = 4$; reflections collected 9015, independent 2885. Anisotropic LS refinement with 476 parameters gave the final values of $wR_2 = 0.213$ and $R_1 = 0.088$. CCDC-261277 and -261278 contain the supplementary crystallographic data for this paper. These data can be obtained free of charge from The Cambridge Crystallographic Data Centre via www.ccdc.cam.ac.uk/data_request/cif.

[9] S. I. Troyanov, A. A. Popov, N. I. Denisenko, O. V. Boltalina, E. Kemnitz, *Angew. Chem.* **2003**, *115*, 2497; *Angew. Chem. Int. Ed.* **2003**, *42*, 2395.

[10] Z. Xiao, F. Wang, S. Huang, L. Gan, J. Zhou, G. Yuan, M. Lu, J. Pan, *J. Org. Chem.* **2005**, *70*, 2060.

[11] a) P. R. Birkett, P. B. Hitchcock, H. W. Kroto, R. Taylor, D. R. M. Walton, *Nature* **1992**, *357*, 479; b) S. I. Troyanov, P. A. Troshin, O. V. Boltalina, E. Kemnitz, *Fullerenes Nanotubes Carbon Nanostructures* **2003**, *11*, 61; c) P. A. Troshin, E. Kemnitz, S. I. Troyanov, *Russ. Chem. Bull.* **2004**, *113*, 2675.

[12] DFT calculations of molecular structures and IR spectra were performed with the PRIRODA package (D. N. Laikov, *Chem. Phys. Lett.* **1997**, *281*, 151) using the PBE functional (J. P. Perdew, K. Burke, M. Ernzerhof, *Phys. Rev. Lett.* **1996**, *77*, 3865) and TZ2P-quality basis set.

[13] Point energy B3LYP/cc-pVTZ(-f) calculations performed on the PBE/TZ2P geometry have also shown that the C_s isomer (C1) is only 4.8 kJ mol^{-1} more stable than the C_1 isomer (C3).

[14] S. I. Troyanov, *Russ. J. Inorg. Chem.* **2001**, *46*, 1612 .

[15] S. Uemura, A. Onoe, M. Okano, *Bull. Chem. Soc. Jpn.* **1974**, *47*, 143.

[16] N. V. Zyk, E. K. Beloglazkina, V. S. Tyurin, Yu. K. Grishin, *Russ. Chem. Bull.* **1998**, *107*, 2290.

[17] K. M. Rogers, P. W. Fowler, *Chem. Commun.* **1999**, 2357.

 © 2005 Wiley-VCH Verlag GmbH & Co. KGaA, Weinheim

Carbohydrate Chemistry

Divergent Synthesis of Sialylated Glycan Chains: Combined Use of Polymer Support, Resin Capture–Release, and Chemoenzymatic Strategies**

*Shinya Hanashima, Shino Manabe, and Yukishige Ito**

As key constituents of cell-surface glycoproteins and glycosphingolipids, sialic acid containing glycan chains are involved in a variety of important physiological events such as cell–cell recognition, adhesion, and signal transduction.[1] It has been reported that the increased levels of sialic acid and sialyltransferase expression in tumor cells are closely related to their metastatic potential and malignancy progression.[2] Sialic acid residues of cell-surface glycoconjugates are also recognized by virulent proteins such as influenza virus hemagglutinins, which initiate the viral invasion into the host cell cytoplasm.[3] In cell-mediated immunity, the rolling of leukocytes is dependent on the levels of endothelial sialic acid.[4] Modulation of the recognition events exerted by sialylated glycans, therefore, seems promising for therapeutic purposes.[5]

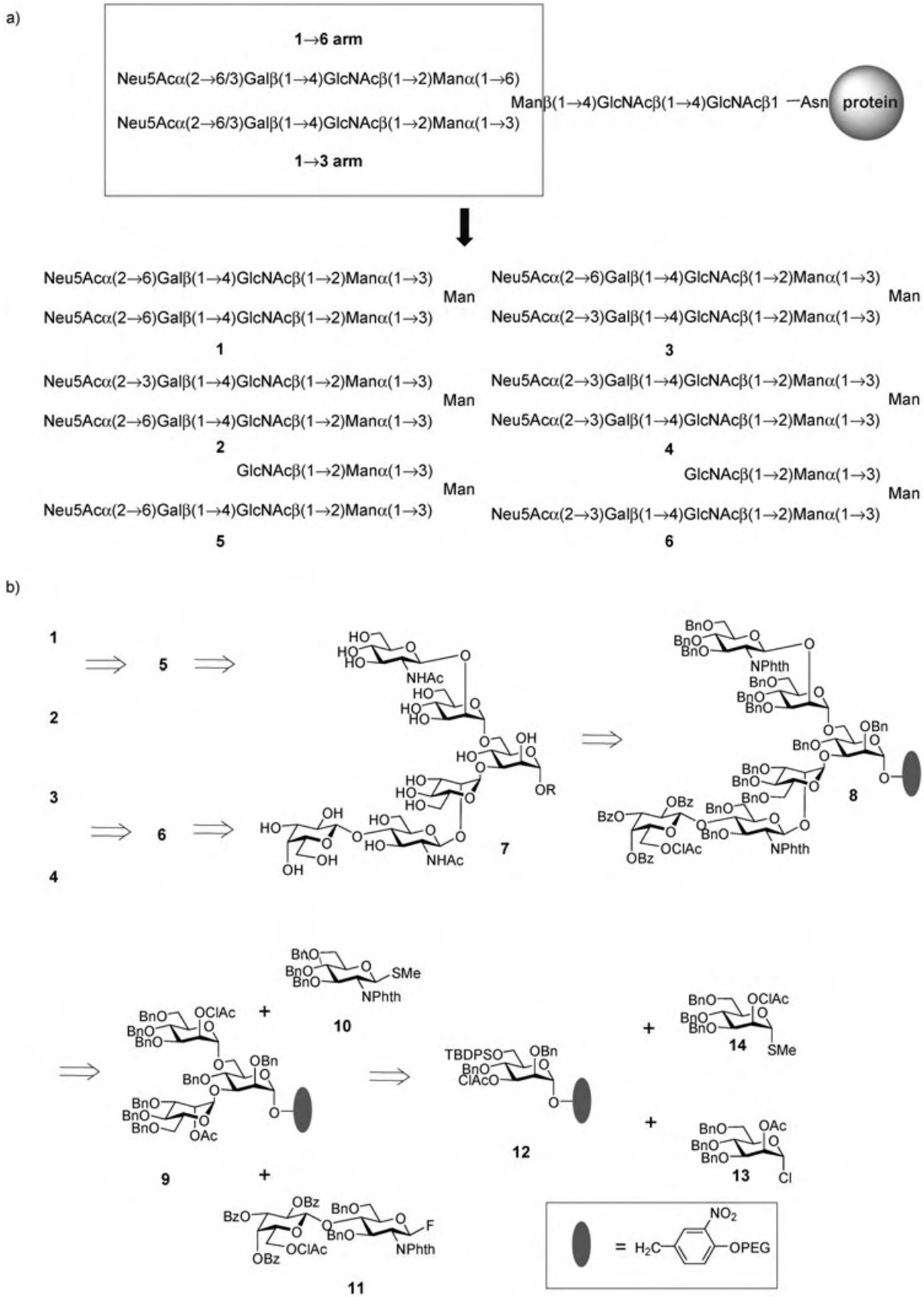
Among the types of glycoprotein structures, asparagine-linked complex-type oligosaccharides (*N*-glycans) are most prominent[6] in terms of diversity as well as complexity. These *N*-glycans are often terminated with a sialic acid (Neu5Ac) residue attached to a penultimate galactose (Gal) moiety through an α(2,3) or α(2,6) linkage (Scheme 1 a). The synthesis of sialylated *N*-glycans has been reported by several groups.[7] Most notably, Unverzagt and co-workers developed chemoenzymatic routes to afford a variety of biantennary glycans.[7d,e,8] More recently, Kajihara and co-workers reported the systematic preparation of biantennary complex-type glycans and glycopeptides, starting from glycopeptides that are isolated from egg yolks as the common

[*] Dr. Y. Ito
RIKEN (The Institute of Physical and Chemical Research)
2-1 Hirosawa, Wako, Saitama 351-0198 (Japan)
and
CREST, Japan Science and Technology Agency (JST)
Kawaguchi, Saitama 332-1102 (Japan)
Fax: (+81) 48-482-4680
E-mail: yukito@riken.jp
Dr. S. Hanashima
RIKEN (The Institute of Physical and Chemical Research)
2-1 Hirosawa, Wako, Saitama 351-0198 (Japan)
Dr. S. Manabe
RIKEN and PRESTO, JST (Japan)

[**] This work was partly supported by the Special Postdoctoral Researchers Program at RIKEN and by a Grant-in-Aid for Young Scientists (B) (16710165) from the Ministry of Education, Science, Culture, Sports, and Technology in Japan (to S.H.). We thank Dr. Teiji Chihara and his staff for elemental analyses, and Ms. Tamiko Chijimatsu for NMR measurements. We thank Ms. Akemi Takahashi for her technical assistance.

Supporting information for this article is available on the WWW under http://www.angewandte.org or from the author.

 © 2005 Wiley-VCH Verlag GmbH & Co. KGaA, Weinheim DOI: 10.1002/anie.200500777



Scheme 1. a) Structures of sialylated complex-type *N*-glycans; b) retrosynthetic analysis for polysaccharides **1**–**6**. Bn = benzyl, Bz = benzoyl, Gal = galactose, GlcNAc = *N*-acetylglucosamine, Man = mannose, Neu5Ac = sialic acid, PEG = poly(ethylene glycol), Phth = phthalyl, TBDPS = *tert*-butyldiphenylsilyl.

 © 2005 Wiley-VCH Verlag GmbH & Co. KGaA, Weinheim

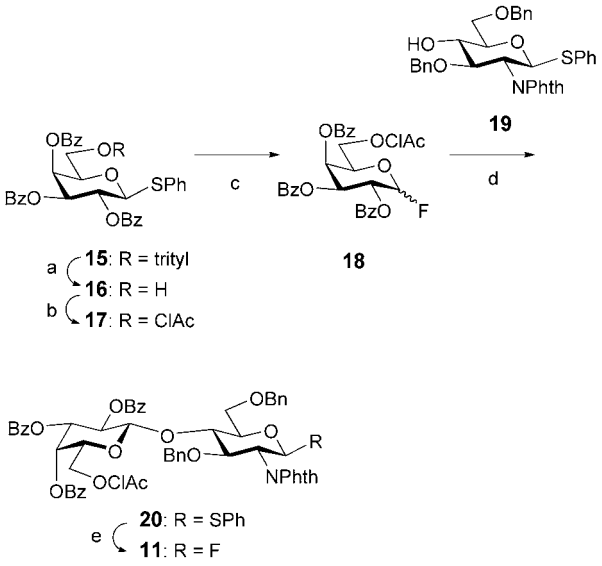
precursor.[9] In terms of chemical synthesis, the preparation of (2,6)-[7a] and (2,3)-linked disialylated *N*-glycans[7b] have been reported.

Polymer-supported synthesis is considered to be a promising technology that should facilitate, and ultimately automate, the synthesis of oligosaccharides. To date, however, there are only a few reported syntheses of branched complex structures such as sialylated *N*-glycans.[10] As part of our efforts to develop methodologies for the efficient construction of glycan chains based on soluble polymer-support technology,[11] we set out to synthesize disialylated compounds **1**–**4** as well as monosialylated saccharides **5** and **6** in a divergent manner. Low molecular weight (average $M_W \approx 750$) monomethyl polyethylene glycol (PEG) was chosen as the polymer support. For purification, the PEG-supported product can be adsorbed on silica gel, washed to remove the non-PEG supported materials (e.g. excess donor), and then retrieved by elution with polar solvents.[11e] With a unique resin capture–release purification, which uses a chloroacetyl group as the purification handle, fully assembled oligomers can be distinguished from shorter products. A nitro-modified Wang-resin-type linker, which has been shown to endure most of the typical glycosylation conditions,[12] was used.

The synthetic plan for the preparation of target glycans **1**–**6** is depicted in Scheme 1b. With hexasaccharide **7** as the common precursor, the scheme involves the use of glycosyltransferases to introduce the terminal Neu5Ac residues and penultimate Gal of the (1,6) branch. An initial glycosylation with either (2,6)- or (2,3)-sialyltransferase should provide monosialylated heptasaccharide **5** or **6**, which can then serve as substrates of sequential galactosylation–sialylation to afford **1**–**4**. Thus, simply by changing the type of glycosyltransferase, all positional isomers of $Neu5Ac_2Gal_2GlcNAc_2$-Man_3, **1** (2,6/2,6), **2** (2,3/2,6), **3** (2,6/2,3), and **4** (2,3/2,3), as well as monosialylated **5** and **6**, can be prepared from the single precursor **7**. Compound **8** was designed as a protected hexasaccharide that would be assembled from Man_3 **9**, GlcNAc **10**, and LacNAc **11** derivatives.

As shown in Scheme 2, lactosamine fluoride **11** was prepared from galactosyl donor **15**[13] and glucosamine component **19**.[14] Removal of the trityl group of **15** afforded **16**, which was reprotected with a chloroacetyl (ClAc) group to give **17**. Conversion of the phenylthio group to fluoride was carried out by using *N*-bromosuccinimide (NBS) and diethylaminosulfur trifluoride (DAST)[15] to afford **18** in nearly quantitative yield ($\alpha/\beta = 46{:}54$). Coupling with **19** was then conducted through activation with $[Cp_2HfCl_2]$ and AgOTf[16] in toluene to afford **20**, which was then converted into fluoride **11**.

The synthesis of the trimannose core is depicted in Scheme 3. Phenylthiomannoside **21**[17] was silylated and chloroacetylated to give **22** in 93% yield. The nitro-modified Wang-resin-type linker was introduced with **23**[18] under activation with *N*-iodosuccinimide (NIS) and triflic acid (TfOH),[19] to afford **24** in 92% yield. Removal of the allyl group afforded phenol **25**, to which PEG was introduced under standard Mitsunobu conditions to provide **12**. Following the selective deprotection with hydrazinedithiocarbonate (HDTC),[20] the resultant **26** was glycosylated sequentially



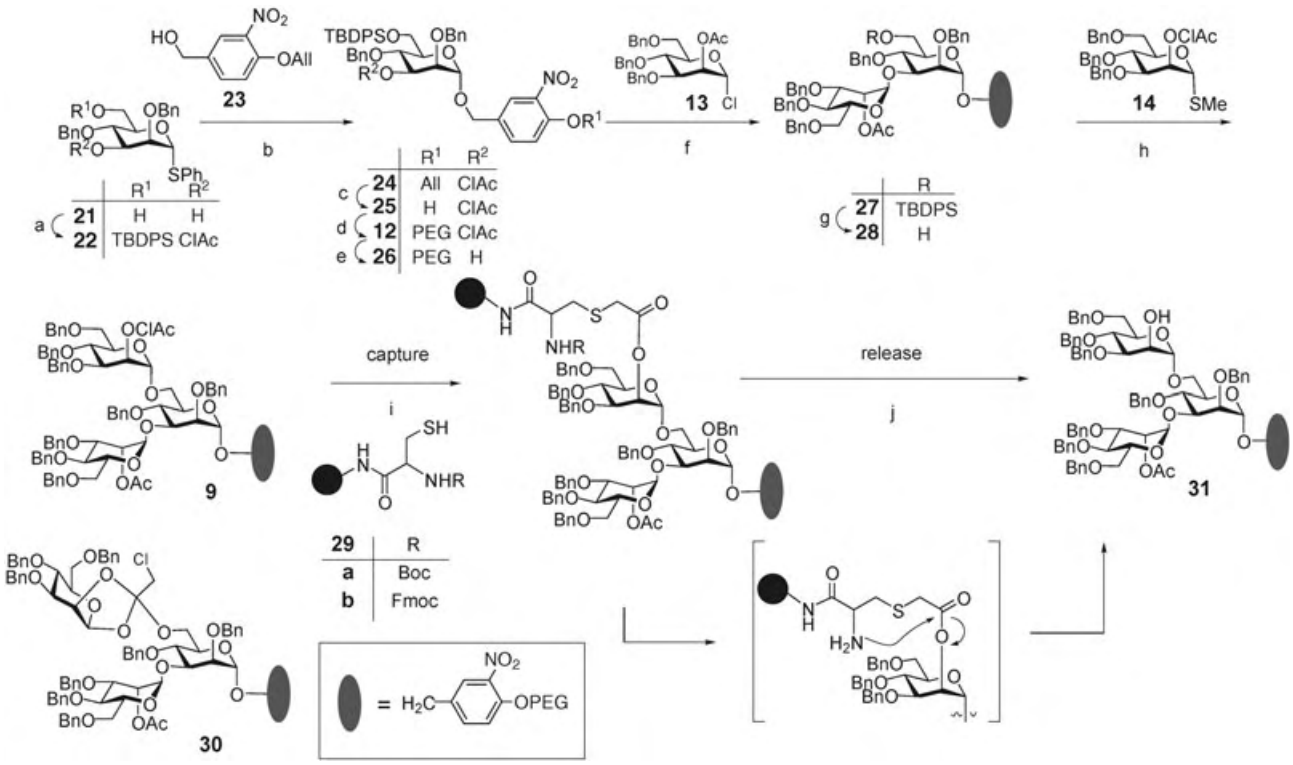
Scheme 2. Reagents and conditions: a) TFA, Et_3SiH, CH_2Cl_2, −40 °C, 96%; b) $(ClAc)_2O$, pyridine, CH_2Cl_2, 96%; c) NBS, DAST, CH_2Cl_2, 98%; d) AgOTf, $[Cp_2HfCl_2]$, molecular sieves (4 Å), toluene, 45 °C, 85%; e) NBS, DAST, CH_2Cl_2, 84%. TFA = trifluoroacetic acid, Cp = cyclopentadienyl.

with 2-*O*-Ac- and 2-*O*-ClAc-protected donors **13** and **14**. The initial glycosylation with chloride **13**[21] proceeded smoothly under standard conditions to afford disaccharide **27** with excellent purity in 98% yield,[22] then desilylation produced **28**. Subsequent glycosylation with methylthiomannoside **14**,[11d] when conducted through activation with NIS and TMSOTf (0.2–0.4 equiv) in CH_2Cl_2 (−20 °C), gave a mixture of the desired product **9** [$\delta_H = 5.18$ (d, $J = 1.7$ Hz), 4.99 ppm (d, $J = 1.7$ Hz)] and the corresponding orthoester **30** [$\delta_H =$ 5.25 (d, $J = 2.4$ Hz), 5.19 ppm (s)] in variable ratios (1:5–1:0.7). In contrast, the use of a stoichiometric amount of TfOH with NIS at low temperatures drastically suppressed formation of the orthoester and provided **9** as the major product. Capture–release purification was then carried out by using Merrifield resin loaded with *N*-protected (Boc or Fmoc) Cys (**29a**,**b**)[11d] in the presence of excess iPr_2NEt to specifically capture **9**. We found that Boc-protected **29a** was more expedient than the Fmoc-protected **29b** for the chemoselective reaction. Notably, orthoester **30** did not react under these conditions and remained in the solution phase, along with unreacted **9**. Removal of the Boc group was carried out with 10% TFA in CH_2Cl_2. Treatment with 10% piperidine in THF initiated the cyclo-release to afford product **31** (60% overall yield from **12**).

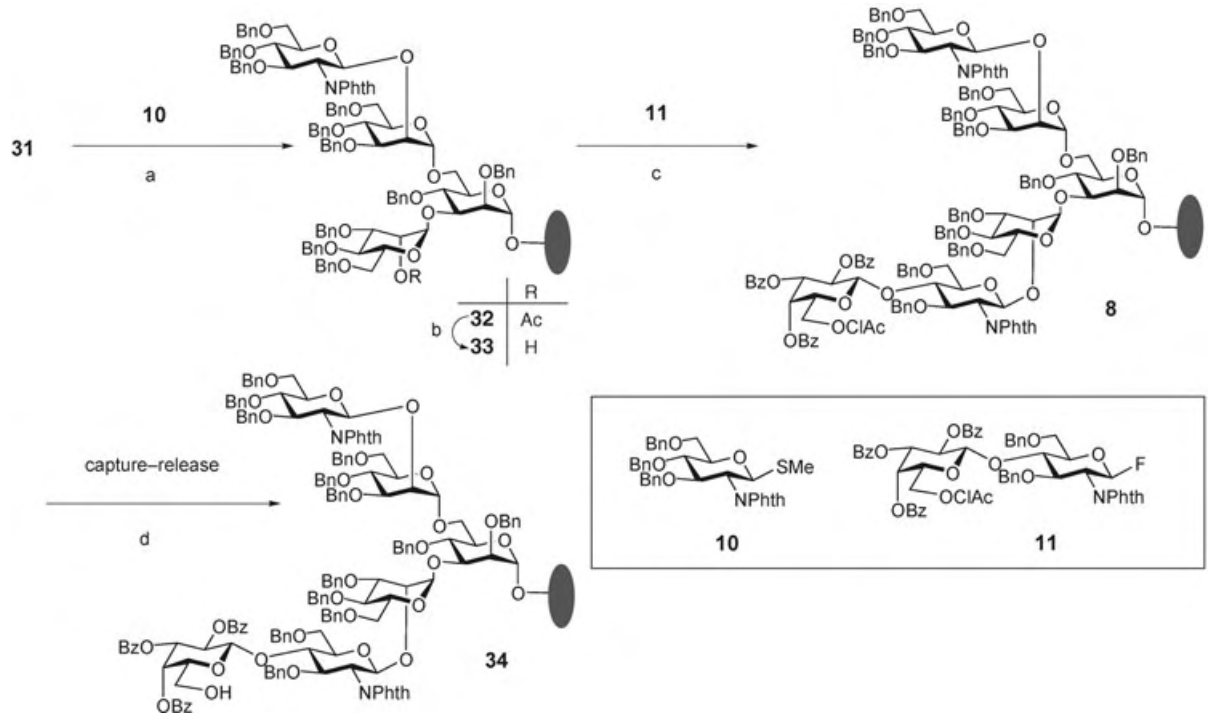
The construction of hexasaccharide **8** is shown in Scheme 4. For the elongation of the α(1,6) branch, thioglycoside **10**[23] was used as the donor to afford **32**,[22] which was deacetylated to give **33**. Reaction with LacNAc donor **11** with $[Cp_2HfCl_2]$ and AgOTf gave hexasaccharide **8** in 92% yield, which was subjected to the same capture–release purification used for **31** to afford **34** in 81% yield (from **31**).

Cleavage from the linker and global deprotection are depicted in Scheme 5. After acetylation of **34**, the nitro group was reduced to an amine function by using $Mo(CO)_6$.[24]

 © 2005 Wiley-VCH Verlag GmbH & Co. KGaA, Weinheim

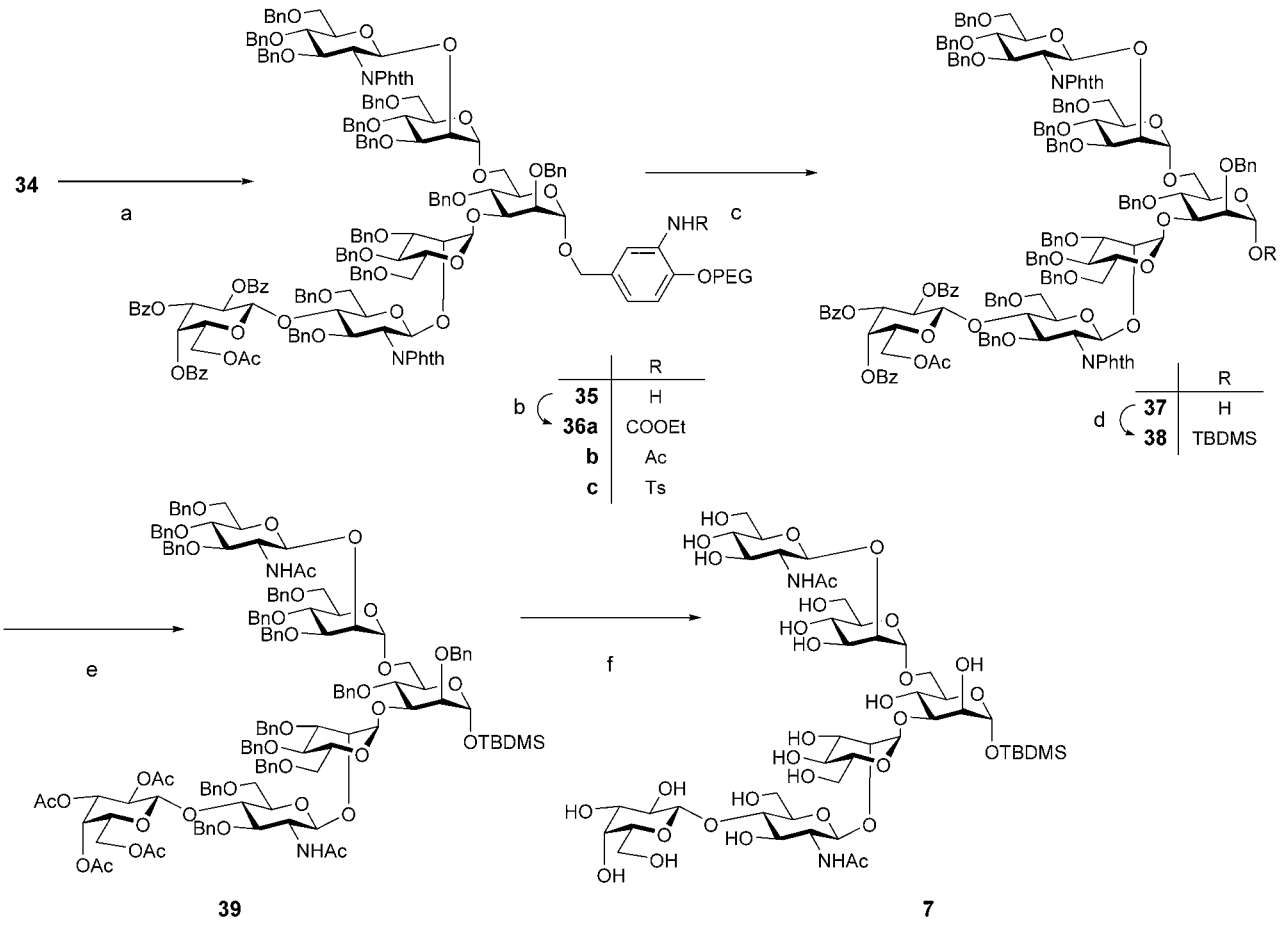


Scheme 3. Reagents and conditions: a) 1) TBDPSCl, DMAP, Et_3N, DMF; 2) $(ClAc)_2O$, pyridine, CH_2Cl_2, 93%; b) NIS, TfOH, molecular sieves (4 Å), CH_2Cl_2, 4°C, 92%; c) $[Pd(PPh_3)_4]$, Et_3SiH, AcOH, toluene, 98%; d) HO-PEG-OMe, DEAD, Ph_3P, THF, 94%; e) HDTC (0.42 M), CH_3CN, 98%; f) **13**, AgOTf, CH_2Cl_2, molecular sieves (4 Å), −20→0°C, 98%; g) HF-pyridine, THF, 98%; h) **14**, NIS, TfOH, molecular sieves (4 Å), −40°C, 94%; i) iPr_2NEt, CH_3CN/CH_2Cl_2; j) 1) 10% TFA in CH_2Cl_2, 2) 10% piperidine, THF, 60% from **12**. All = allyl, DEAD = diethyl azodicarboxylate, DMAP = 4-(*N*,*N*-dimethylamino)pyridine, DMF = dimethylformamide.



Scheme 4. Reagents and conditions: a) **10**, NIS, TfOH, molecular sieves (4 Å), CH_2Cl_2, −10→0°C, 92%; b) NaOMe (0.05 M) in MeOH/THF, 96%; c) **11**, AgOTf, $[Cp_2HfCl_2]$, toluene, molecular sieves (4 Å), −20→0°C, 92%; d) 1) **29**, iPr_2NEt, DMF, 80°C, 2) TFA (10%) in CH_2Cl_2, 3) piperidine (10%) in THF, 88% from **31**.

 © 2005 Wiley-VCH Verlag GmbH & Co. KGaA, Weinheim



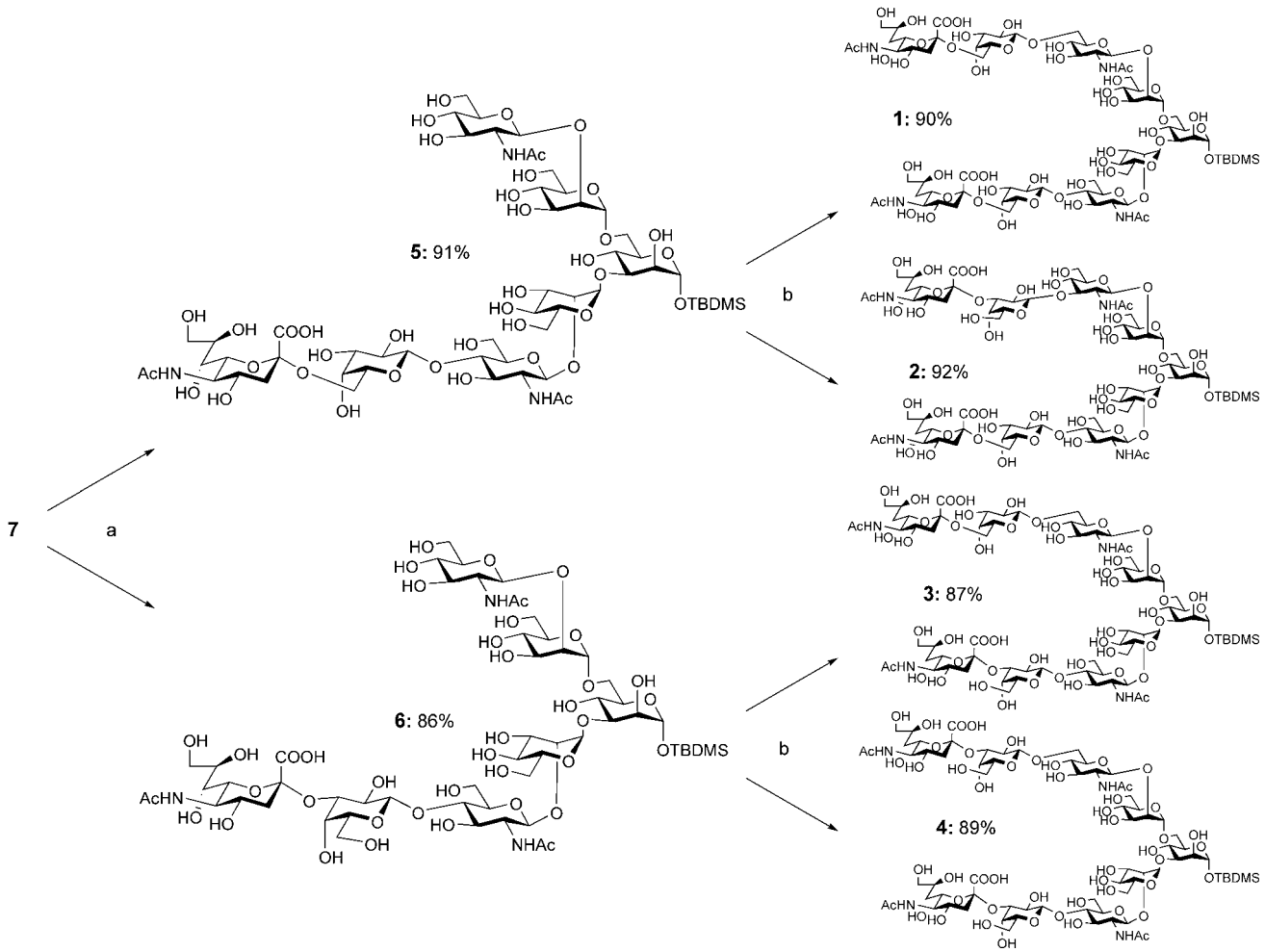
Scheme 5. Reagents and conditions: a) 1) Ac_2O, pyridine, 2) $Mo(CO)_6$, EtOH, dichloroethane; b) EtOCOCl, iPr_2NEt, CH_2Cl_2; c) TFA (15%) in CH_2Cl_2, 88%; d) BTBSA, TBAF (0.05 equiv) in THF-NMP; e) 1) ethylenediamine, *n*BuOH, 95°C; 2) Ac_2O, pyridine, 56%; f) 1) NaOMe (0.05 M) in MeOH, 93%; 2) $Pd(OH)_2/C$ (20%), MeOH, H_2O, 92%. Ts = tosyl.

Amine **35** was then converted into ethyl carbamate **36a**, then treated with 15% TFA in CH_2Cl_2 to give **37** in 88% yield (from **34**). Interestingly, the corresponding acetyl **36b** and tosyl **36c** derivatives were more resistant to cleavage under these conditions. The liberated hydroxy group was protected as a *tert*-butyldimethylsilyl (TBDMS) ether with *N*,*O*-bis(*tert*-butyldimethylsilyl)acetamide (BTBSA) and a catalytic amount of tetrabutylammonium fluoride (TBAF)[25] in *N*-methylpyrrolidinone (NMP) to yield **38**. Following conversion of the phthalimide **38** to the acetamide **39**, the acetyl and benzyl groups were removed to afford **7**.

As several types of sialyltransferases are commercially available, and chemical sialylation is technically demanding, enzymatic glycosylation is an attractive strategy for the preparation of oligosaccharides that contain sialic acids.[26] Hexasaccharide **7** possesses a terminal LacNAc residue, which is an excellent substrate for sialyltransferases. In fact, **7** was smoothly converted into **5** and **6** with α(2,6)-*N*-sialyltransferase (EC 2.4.99.1, Toyobo) and α(2,3)-*N*-sialyltransferase (EC 2.4.99.5, Calbiochem), respectively, then subjected to sequential galactosylation/sialylation[27] to afford **1**–**4** (Scheme 6). As an example, heptasaccharide **5** was treated with β(1,4)-galactosyltransferase (EC 2.4.1.22, Toyobo) and UDP-galactose in $MnCl_2$ containing a cacodylate buffer; upon completion of the galactose transfer, α(2,6)- or α(2,3)-sialyltransferase and CMP-Neu5Ac were added to the reaction mixture to give nonasaccharides **1** and **2** in quantitative yields (CMP = cytidine-5′-monophosphoryl). Similarly, heptasaccharide **6** was used to afford nonasaccharides **3** and **4** in high yields. During the enzymatic transformations, the TBDMS group served as a hydrophobic tag that allowed product isolation by using reversed-phase solid-phase extraction cartridges.[28]

In summary, the α(2,3)- or α(2,6)-sialylated biantennary glycans **1**–**6**, which correspond to the branched portions of typical complex-type *N*-glycans, were systematically synthesized with a polymer–resin hybrid strategy and enzymatic glycosylation. By using low molecular weight (average $M_W \approx 750$) monomethyl polyethylene glycol as the polymer support, the purification procedures were simple and involved only loading on silica gel, washing to remove the non-PEG-supported materials (e.g. excess donor), then eluting with polar solvents. Introduction of sialic acid on the nonreducing ends, and of the penultimate galactose moiety on the (1,6) branch was successful with commercially available glycosyltransferases and the appropriate sugar nucleotides. The common precursor **7** was synthesized by using a soluble polymer support strategy, in which Merrifield resin loaded

 © 2005 Wiley-VCH Verlag GmbH & Co. KGaA, Weinheim



Scheme 6. Enzymatic transformations of **7** to **1**–**6**: a) α2,6- or α2,3-sialyltransferase, CMP-Neu5Ac, alkaline phosphatase, BSA, cacodylate buffer (50 mM); b) 1) β1,4-galactosyltransferase, UDP-galactose, BSA, alkaline phosphatase, $MnCl_2$, cacodylate buffer (50 mM); 2) α2,6- or α2,3-sialyltransferase, CMP-Neu5Ac. UDP = uridine diphosphate.

with Boc-Cys was used for the capture–release protocol to facilitate product purification. Hexasaccharide **7** was diverged to monosialylated **5** and **6** and disialylated **1**–**4** saccharides by enzymatic glycosylation with α(2,3)- or α(2,6)-sialyltransferase and β(1,4)-galactosyltransferase.

Received: March 3, 2005
Published online: June 1, 2005

Keywords: carbohydrates · glycoproteins · glycosylation · oligosaccharides · sialic acids

[1] T. Angata, A. Varki, *Chem. Rev.* **2002**, *102*, 439–469.
[2] Y. J. Kim, A. Varki, *Glycoconjugate J.* **1997**, *14*, 569–576.
[3] a) W. Weis, J. H. Brown, S. Cusak, J. C. Paulson, J. J. Skehel, D. C. Wiley, *Nature* **1988**, *333*, 426–431; b) N. K. Sauter, J. E. Hanson, G. D. Glick, J. H. Brown, R. L. Crowther, S.-J. Park, J. J. Skehel, D. C. Wiley, *Biochemistry* **1992**, *31*, 9609–9620.
[4] R. Kannagi, *Curr. Opin. Struct. Biol.* **2002**, *12*, 599–608.
[5] For an example, see: K.-Y. Lee, H. G. Kim, M. R. Hwang, J. I. Chae, J. M. Yang, Y. C. Lee, Y. K. Choo, Y. I. Lee, S.-S. Lee, S.-I. Do, *J. Biol. Chem.* **2002**, *277*, 49341–49351.
[6] a) A. Kobata, *Acc. Chem. Res.* **1993**, *26*, 319–324; b) R. A. Dwek, *Chem. Rev.* **1996**, *96*, 683–720.
[7] a) T. Ogawa, M. Sugimoto, T. Kitajima, *Tetrahedron Lett.* **1986**, *27*, 5739–5742; b) J. Seifert, M. Lergenmüller, Y. Ito, *Angew. Chem.* **2000**, *112*, 541–544; *Angew. Chem. Int. Ed.* **2000**, *39*, 531–534; c) X. Wu, M. Grathwohl, R. R. Schmidt, *Angew. Chem.* **2002**, *114*, 4664–4668; *Angew. Chem. Int. Ed.* **2002**, *41*, 4489–4493; d) C. Unverzagt, *Carbohydr. Res.* **1998**, 305, 423–431; e) I. Prahl, C. Unverzagt *Angew. Chem.* **2002**, *114*, 4434–4437; *Angew. Chem. Int. Ed.* **2002**, *41*, 4259–4262.
[8] C. Unverzagt, S. Andre, J. Seifert, S. Kojima, C. Fink, G. Srikrishna, H. Freeze, K. Kayser, H.-J. Gabius, *J. Med. Chem.* **2002**, *45*, 478–491.
[9] a) K. Fukae, N. Yamamoto, Y. Hatakeyama, Y. Kajihara, *Glycoconjugate J.* **2004**, *21*, 243–250; b) Y. Kajihara, Y. Suzuki, N. Yamamoto, K. Sasaki, T. Sakakibara, L. R. Juneja, *Chem. Eur. J.* **2004**, *10*, 971–985.
[10] P. H. Seeberger, W.-C. Hasse, *Chem. Rev.* **2000**, *100*, 4349–4394.
[11] a) H. Ando, S. Manabe, Y. Nakahara, Y. Ito, *J. Am. Chem. Soc.* **2001**, *123*, 3848–3849; b) H. Ando, S. Manabe, Y. Nakahara, Y. Ito, *Angew. Chem.* **2001**, *113*, 4861–4864; *Angew. Chem. Int. Ed.* **2001**, *40*, 4725–4728; c) Y. Ito, S. Manabe, *Chem. Eur. J.* **2002**, *8*, 3076–3084; d) S. Hanashima, S. Manabe, Y. Ito, *Synlett* **2003**, 979–982; e) L. Jiang, R. C. Hartley, T.-H. Chan, *Chem. Commun.* **1996**, 2193–2194.

 © 2005 Wiley-VCH Verlag GmbH & Co. KGaA, Weinheim

[12] a) S. Manabe, Y. Nakahara, Y. Ito, *Synlett* **2000**, 1241 – 1244; b) X. Wu, M. Grathwohl, R. R. Schmidt, *Org. Lett.* **2001**, *3*, 747 – 750; c) H. Ohno, H. Tanaka, T. Takahashi, *Synlett* **2004**, 508 – 511.
[13] a) Synthesis of **15** is described in the Supporting Information; b) R. J. Ferrier, R. H. Furneaux, *Carbohydr. Res.* **1976**, *52*, 63 – 68.
[14] O. Kanie, Y. Ito, T. Ogawa, *J. Am. Chem. Soc.* **1994**, *116*, 12073 – 12074.
[15] K. C. Nicolaou, R. E. Dolle, D. P. Papahatjis, J. L. Randall, *J. Am. Chem. Soc.* **1984**, *106*, 4189 – 4192.
[16] a) T. Matsumoto, H. Maeta, K. Suzuki, G. Tsuchihashi, *Tetrahedron Lett.* **1988**, *29*, 3567 – 3570; b) K. Suzuki, H. Maeta, T. Suzuki, T. Matsumoto, *Tetrahedron Lett.* **1989**, *30*, 6789 – 6882.
[17] I. Matsuo, M. Isomura, T. Miyazaki, T. Sakakibara, K. Ajisaka, *Carbohydr. Res.* **1998**, *305*, 401 – 413.
[18] For preparation, see the Supporting Information.
[19] P. Konradsson, U. E. Udodong, B. Fraser-Reid, *Tetrahedron Lett.* **1990**, *31*, 1331.
[20] C. A. A. van Boeckel, T. Beetz, *Tetrahedron Lett.* **1983**, *24*, 3775 – 3778.
[21] F. Yamazaki, S. Sato, T. Nukada, Y. Ito, T. Ogawa, *Carbohydr. Res.* **1990**, *201*, 31 – 50.
[22] Although capture–release purification was not conducted in these cases, complete glycosylation was confirmed by ^{1}H NMR spectroscopy.
[23] A. Dan, Y. Ito, T. Ogawa, *Carbohydr. Lett.* **1996**, *1*, 469 – 474.
[24] S. Iyer, G. M. Kulkarni, *Synth. Commun.* **2004**, *34*, 721 – 725.
[25] D. A. Johnson, L. M. Taubner, *Tetrahedron Lett.* **1996**, *37*, 605 – 608.
[26] Y. Ito, J. J. Gaudino, J. C. Paulson, *Pure Appl. Chem.* **1993**, *65*, 753 – 762.
[27] C. Unverzagt, H. Kunz, J. C. Paulson, *J. Am. Chem. Soc.* **1990**, *112*, 9308 – 9309.
[28] M. M. Palcic, L. D. Heeze, M. Pierce, O. Hindsgaul, *Glycoconjugate J.* **1988**, *5*, 49 – 63; P. Stangier, M. Palcic, D. Bundle, *Carbohydr. Res.* **1995**, *267*, 153 – 159; Y. Ito, J. C. Paulson, *J. Am. Chem. Soc.* **1993**, *115*, 1603 – 1604.

 © 2005 Wiley-VCH Verlag GmbH & Co. KGaA, Weinheim

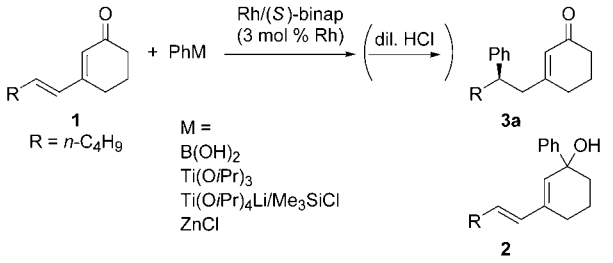
Asymmetric Catalysis

Rhodium-Catalyzed Asymmetric 1,6-Addition of Aryl Zinc Reagents to Dienones**

Tamio Hayashi, Shohei Yamamoto, and Norihito Tokunaga*

The catalytic asymmetric 1,4-addition of organometallic reagents to electron-deficient olefins is one of the most important methods of forming stereogenic centers in carbon–carbon bond-forming reactions.[1] In this field, attention has focused on asymmetric 1,4-additions catalyzed by copper,[2,3] rhodium,[4–8] palladium,[9] and nickel[10] complexes. On the other hand, asymmetric 1,6-addition to extended conjugate systems has developed less rapidly.[11] Although several reports have appeared on diastereoselective 1,6-additions,[12] the use of a chiral catalyst for this asymmetric transformation remains to be studied. Herein, we report the first example of a catalytic asymmetric 1,6-addition to 2,4-dien-1-ones, in which a stereogenic center at the C5 position is also formed; this reaction is realized by a rhodium-catalyzed addition of aryl zinc reagents to dienones in the presence of chlorotrimethylsilane.

To investigate conjugate addition to 3-((*E*)-hexenyl)-2-cyclohexenone (**1**), several phenyl organometallic reagents that had been successfully used in rhodium-catalyzed asymmetric 1,4-addition reactions to electron-deficient alkenes[4–7] were examined for their reactivity and selectivity (Scheme 1 and Table 1). When the reaction was carried out with phenylboronic acid under reaction conditions that have been shown to be very efficient for asymmetric 1,4-additions



Scheme 1. Rhodium-catalyzed addition of phenyl organometallic reagents (PhM) to dienone **1**.

[*] Prof. T. Hayashi, S. Yamamoto, N. Tokunaga
Department of Chemistry
Graduate School of Science, Kyoto University
Sakyo, Kyoto 606-8502 (Japan)
Fax: (+81) 75-753-3988
E-mail: thayashi@kuchem.kyoto-u.ac.jp

[**] This work was supported in part by a Grant-in-Aid for Scientific Research from the Ministry of Education, Culture, Sports, Science, and Technology, Japan (21 COE on Kyoto University Alliance for Chemistry). N.T. thanks the Japanese Society for the Promotion of Science for the award of a fellowship for graduate students.

Supporting information for this article is available on the WWW under http://www.angewandte.org or from the author.

 © 2005 Wiley-VCH Verlag GmbH & Co. KGaA, Weinheim DOI: 10.1002/anie.200500678

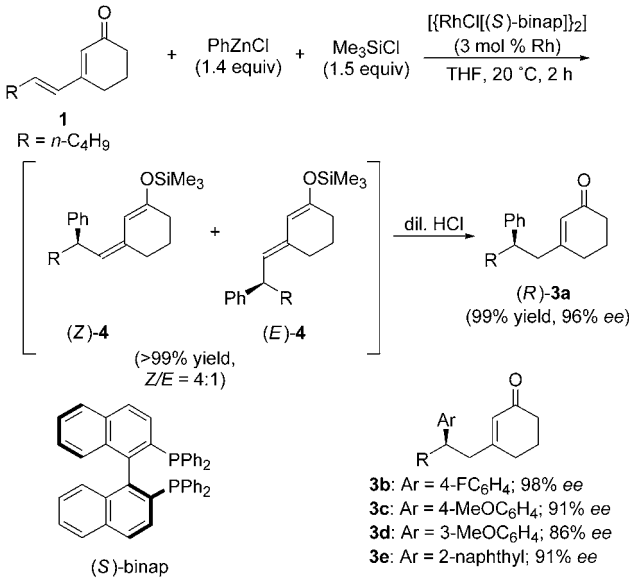
Table 1: Rhodium-catalyzed asymmetric 1,6-addition to **1** forming products **3a–e**.[a]

Entry	PhM (equiv)	Conditions[b]	Yield [%][c]	*ee* [%][d]
1	$PhB(OH)_2$ (2.5)	A	0[e]	–
2	$PhTi(OiPr)_3$ (1.6)	B	0[f]	–
3	$PhTi(OiPr)_4Li/Me_3SiCl$ (1.5/2.0)	C	78 (**3a**)	88
4	PhZnCl[g] (1.4)	D	18 (**3a**)	96
5	$PhZnCl$[g]$/Me_3SiCl$ (1.4/1.5)	D	99 (**3a**)	96
6	$PhZnX$[h]$/Me_3SiCl$ (1.4/1.5)	D	94 (**3a**)	94
7	$4\text{-}FC_6H_4ZnX$[h]$/Me_3SiCl$ (1.4/1.5)	D	90 (**3b**)	98
8	$4\text{-}MeOC_6H_4ZnCl$[g]$/Me_3SiCl$ (1.4/1.5)	D	94 (**3c**)	91
9	$3\text{-}MeOC_6H_4ZnCl$[h]$/Me_3SiCl$ (1.4/1.5)	D	86 (**3d**)	86
10	2-naphthylZnCl[h]$/Me_3SiCl$ (1.4/1.5)	D	85 (**3e**)	91

[a] The reactions were carried out with 0.30 mmol of **1** in the presence of 3 mol% of the rhodium catalyst. [b] Conditions A: [{Rh(OH)[(*S*)-binap]}$_2$], dioxane/H_2O (10:1), 50°C, 3 h. Conditions B: [{Rh(OH)[(*S*)-binap]}$_2$], THF, 30°C, 1 h; hydrolysis with dilute HCl. Conditions C: [{RhCl[(*S*)-binap]}$_2$], THF, 20°C, 0.5 h; hydrolysis with dilute HCl. Conditions D: [{RhCl[(*S*)-binap]}$_2$], THF, 20°C, 2 h; hydrolysis with dilute HCl. [c] Yield of product isolated by column chromatography on silica gel (hexane/ethyl acetate, 4:1). [d] Determined by HPLC analysis with a chiral stationary-phase column (chiralpak OJ: hexane/2-propanol, 95:5); *ee* value for *R* enantiomer. [e] Dienone **1** was recovered. [f] A 1,2-addition product **2** was formed in 70% yield. [g] Generated from ArLi and $ZnCl_2$. [h] Generated from ArMgBr and $ZnCl_2$.

(3 mol% (Rh) of [{Rh(OH)[(*S*)-binap]}$_2$] (binap = 2,2′-bis-(diphenylphosphanyl)-1,1′-binaphthyl) as the catalyst in dioxane/H_2O (10:1) at 50°C for 3 h),[5b] the starting dienone **1** was recovered quantitatively (Table 1, entry 1). The use of the phenyltitanium reagent $PhTi(OiPr)_3$ in the presence of [{Rh(OH)[(*S*)-binap]}$_2$] in THF at 30°C, which gives titanium enolates as 1,4-addition products with high enantioselectivities from α,β-unsaturated ketones,[6a] does not react in the same way with the present substrate **1**. Instead, titanium reagent reacted to give the tertiary alcohol **2** (70% yield; Table 1, entry 2) by a noncatalyzed 1,2-addition. The lithium titanate reagent $PhTi(OiPr)_4Li$ (1.5 equiv), used in the presence of chlorotrimethylsilane (2.0 equiv) and [{RhCl[(*S*)-binap]}$_2$] (3 mol% Rh) in THF at 20°C, proved more promising.[6c] The 1,6-addition product (*R*)-3-(2-phenylhexyl)-2-cyclohexenone (**3a**) was afforded after acidic hydrolysis in 78% yield and with 88% *ee* (Table 1, entry 3). The zinc reagent PhZnCl (1.4 equiv), which has been recently found to be more efficient than boron or titanium reagents in rhodium-catalyzed asymmetric 1,4-addition reactions to enones,[7] gave the 1,6-addition product **3a** with higher enantioselectivity (96% *ee* (*R*)), although its yield was as low as 18% (Table 1, entry 4).

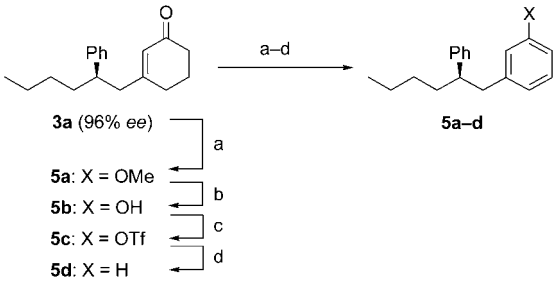
We have found, therefore, that chlorotrimethylsilane greatly accelerates[13] the rhodium-catalyzed 1,6-addition of aryl zinc reagents to dienone **1**. Thus, **1** was treated with PhZnCl (1.4 equiv; generated from PhLi and $ZnCl_2$ in THF) in the presence of chlorotrimethylsilane (1.5 equiv) and [{RhCl[(*S*)-binap]}$_2$] (3 mol% Rh) in THF at 20°C for 2 h, and the phenylation product (*R*)-**3a** was obtained in a quantitative yield with 96% *ee* after acidic hydrolysis (Scheme 2; Table 1, entry 5). The 1,6-addition product before hydrolysis was a 1,3-dienyl silyl ether **4** (*Z*/*E* = 4:1). The high yield of the addition product may be ascribed to the



Scheme 2. Rhodium-catalyzed asymmetric 1,6-addition of ArZnCl to dienone **1** in the presence of Me_3SiCl.

activation of **1** by the chlorosilane acting as a Lewis acid,[13] which accelerates the addition of **1** to a phenylrhodium species in the catalytic cycle (see below). The asymmetric addition of aryl zinc reagents generated from $4\text{-}FC_6H_4MgBr$, $4\text{-}MeOC_6H_4Li$, $3\text{-}MeOC_6H_4MgBr$, and 2-naphthylMgBr also gave the corresponding 1,6-addition products **3b–e**, respectively, in high yields and with high enantioselectivities (Table 1, entries 7–10). The formation of any 1,4- or 1,2-addition products was not detected in the reaction of **1** under the current conditions.

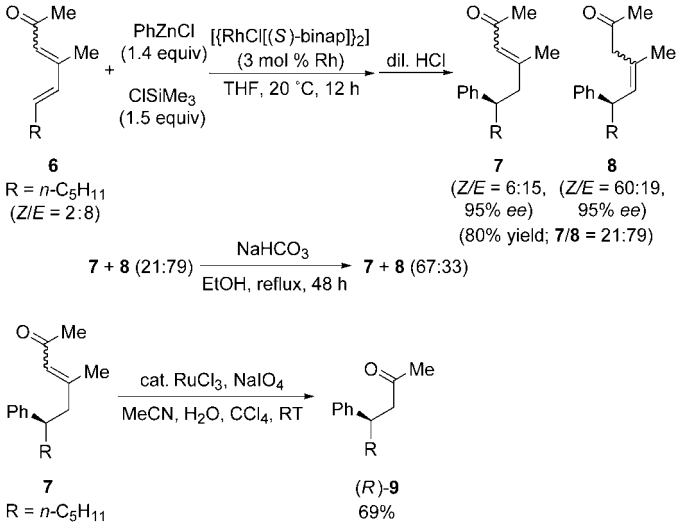
The absolute configuration of the 1,6-addition product **3a** was determined to be *R* after its conversion into (*R*)-1,2-diphenylhexane[14] (**5d**). The key step in the synthetic pathway to **5d** is the oxidation of the cyclohexenone moiety in **3a** into the methoxyphenyl group in **5a** (Scheme 3).[15]



Scheme 3. Determination of the absolute configuration of the 1,6-addition product **3a**. a) I_2, MeOH, reflux (99%); b) BBr_3, CH_2Cl_2, room temperature (90%); c) Tf_2O, pyridine, $ClCH_2CH_2Cl$, room temperature (99%); d) H_2, Pd/C, EtOH, $EtN(iPr)_2$, room temperature (86%). Tf = trifluoromethanesulfonyl.

 © 2005 Wiley-VCH Verlag GmbH & Co. KGaA, Weinheim

The treatment of the linear dienone 4-methylundeca-3,5-dien-2-one (**6**) with PhZnCl and chlorotrimethylsilane in the presence of the Rh/(*S*)-binap (3 mol% Rh) catalytic system also proceeded with perfect 1,6-selectivity to give the phenylation product in high yield (Scheme 4). Hydrolysis with

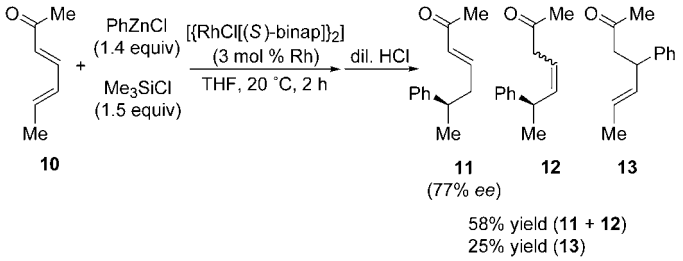


Scheme 4. Rhodium-catalyzed asymmetric 1,6-addition of PhZnCl to dienone **6** in the presence of Me_3SiCl.

hydrochloric acid afforded α,β-unsaturated ketone **7** and β,γ-unsaturated ketone **8** as a mixture of olefinic isomers in a ratio of 21:79. Treatment of the mixture with sodium bicarbonate in ethanol at reflux for 48 h shifted the ratio of **7**/**8** to 67:33. Both **7** and **8** were found to be *R* enantiomers in 95% *ee*. The configuration was determined by correlation with (*R*)-3-phenylnonen-2-one[5a] ((*R*)-**9**), which was obtained by oxidative cleavage of the double bond in **7**.

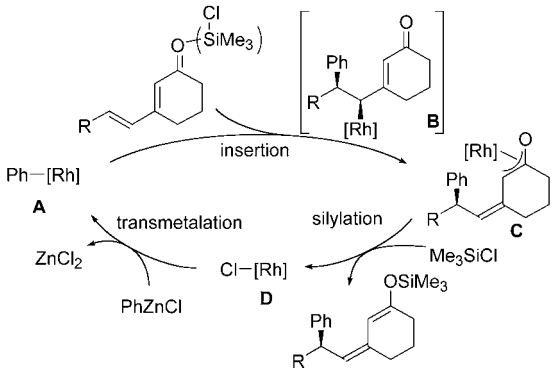
The selectivity of the 1,6-addition was not as high in the reaction of hepta-3,5-dien-2-one (**10**); the 1,4-addition product was formed as a by-product because **10** lacks a substituent at the β position. Thus, the addition of PhZnCl to **10** in the presence of chlorotrimethylsilane under similar conditions gave the 1,6-addition products **11** (77% *ee*) and **12** in a combined yield of 58% together with the 1,4-addition product **13** in 25% yield (Scheme 5).

The catalytic cycle proposed for the rhodium-catalyzed 1,4-addition of aryl titanates in the presence of chlorotrimethylsilane[6c] can be applied to the 1,6-addition of aryl zinc



Scheme 5. Rhodium-catalyzed asymmetric addition of PhZnCl to dienone **10** in the presence of Me_3SiCl.

reagents (Scheme 6), as this mechanism involves the reaction of an oxo-π-allyl rhodium intermediate with chlorosilane to afford a chlororhodium complex and a silyl enolate as the product. With a dienone as the substrate, insertion of its γ,δ-double bond into the phenyl–rhodium bond in **A** is slow

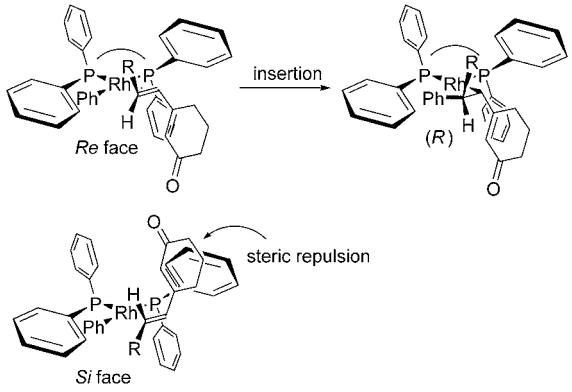


Scheme 6. The catalytic cycle for the rhodium-catalyzed 1,6-addition reaction. [Rh] = [Rh{(*S*)-binap}].

compared with the insertion of the α,β-double bond of an α,β-unsaturated ketone; therefore, insertion of the dienone γ,δ-double bond takes place more smoothly with the assistance of a chlorosilane as a Lewis acid. An alkyl rhodium intermediate **B** is formed by the insertion reaction and undergoes isomerization to a thermodynamically stable oxo-π-allyl rhodium complex **C**. A silylation reaction of **C** with chlorotrimethylsilane yields a chlororhodium species **D** and a silyl dienyl ether as the 1,6-addition product. Transmetalation between **D** and PhZnCl regenerates the phenylrhodium species **A**.

The absolute configuration *R* of the 1,6-addition product **3**, obtained with (*S*)-binap as a chiral ligand, was rationalized by using the stereochemical pathway shown in Scheme 7. At the insertion step, coordination of the γ,δ-double bond at the *Re* face is more favorable than coordination at the *Si* face because of the steric repulsions between one of the phenyl rings of the binap ligand and the cyclohexene moiety.

In summary, catalytic asymmetric 1,6-additions to 2,4-dien-1-ones has been realized with up to 98% *ee* using a chiral



Scheme 7. The stereochemical pathway in the rhodium-catalyzed asymmetric 1,6-addition reaction.

 © 2005 Wiley-VCH Verlag GmbH & Co. KGaA, Weinheim

bisphosphine/rhodium catalyst, aryl zinc reagents, and a chlorosilane. Further studies on the scope and limitations of this new catalytic asymmetric carbon–carbon bond-forming reaction are underway.

Received: February 23, 2005
Published online: June 1, 2005

Keywords: 1,6-addition · asymmetric catalysis · organometallic reagents · rhodium · zinc

[1] For recent reviews on catalytic asymmetric 1,4-addition reactions, see: a) N. Krause, A. Hoffmann-Roder, *Synthesis* **2001**, 171; b) M. P. Sibi, S. Manyem, *Tetrahedron* **2000**, *56*, 8033; c) K. Tomioka, Y. Nagaoka in *Comprehensive Asymmetric Catalysis*, *Vol. 3* (Eds.: E. N. Jacobsen, A. Pfaltz, H. Yamamoto), Springer, Berlin, **1999**, chap. 31.1; d) M. Kanai, M. Shibasaki in *Catalytic Asymmetric Synthesis*, *2nd ed.* (Ed.: I. Ojima), Wiley, New York, **2000**, p. 569.

[2] For selected reviews on enantioselective copper-catalyzed conjugate addition, see: a) A. Alexakis, C. Benhaim, *Eur. J. Org. Chem.* **2002**, 3221; b) B. L. Feringa, R. Naasz, R. Imbos, L. A. Arnold, *Modern Organocopper Chemistry* (Ed.: N. Krause), Wiley-VCH, Weinheim, **2002**, p. 224; c) B. L. Feringa, *Acc. Chem. Res.* **2000**, *33*, 346.

[3] For recent examples, see: a) L. A. Arnold, R. Naasz, A. J. Minnaard, B. L. Feringa, *J. Am. Chem. Soc.* **2001**, *123*, 5841; b) C. A. Luchaco-Cullis, A. H. Hoveyda, *J. Am. Chem. Soc.* **2002**, *124*, 8192; c) S. J. Degrado, H. Mizutani, A. H. Hoveyda, *J. Am. Chem. Soc.* **2002**, *124*, 13362; d) A. Duursma, A. J. Minnaard, B. L. Feringa, *J. Am. Chem. Soc.* **2003**, *125*, 3700; e) A. W. Hird, A. H. Hoveyda, *Angew. Chem.* **2003**, *115*, 1314; *Angew. Chem. Int. Ed.* **2003**, *42*, 1276; f) K. Agapiou, D. F. Cauble, M. J. Krische, *J. Am. Chem. Soc.* **2004**, *126*, 4528.

[4] For reviews, see: a) T. Hayashi, *Synlett* **2001**, 879; b) K. Fagnou, M. Lautens, *Chem. Rev.* **2003**, *103*, 169; c) T. Hayashi, K. Yamasaki, *Chem. Rev.* **2003**, *103*, 2829; d) T. Hayashi, *Bull. Chem. Soc. Jpn.* **2004**, *77*, 13.

[5] For organoboron reagents, see: a) Y. Takaya, M. Ogasawara, T. Hayashi, M. Sakai, N. Miyaura, *J. Am. Chem. Soc.* **1998**, *120*, 5579; b) T. Hayashi, M. Takahashi, Y. Takaya, M. Ogasawara, *J. Am. Chem. Soc.* **2002**, *124*, 5052; c) T. Hayashi, K. Ueyama, N. Tokunaga, K. Yoshida, *J. Am. Chem. Soc.* **2003**, *125*, 11508; d) R. Shintani, K. Ueyama, I. Yamada, T. Hayashi, *Org. Lett.* **2004**, *6*, 3425; e) S. Sakuma, M. Sakai, R. Itooka, N. Miyaura, *J. Org. Chem.* **2000**, *65*, 5951; f) S. Sakuma, N. Miyaura, *J. Org. Chem.* **2001**, *66*, 8944; g) M. Kuriyama, K. Tomioka, *Tetrahedron Lett.* **2001**, *42*, 921; h) M. Kuriyama, K. Nagai, K.-i. Yamada, Y. Miwa, T. Taga, K. Tomioka, *J. Am. Chem. Soc.* **2002**, *124*, 8932; i) M. T. Reetz, D. Moulin, A. Gosberg, *Org. Lett.* **2001**, *3*, 4083; j) R. Amengual, V. Michelet, J.-P. Genêt, *Synlett* **2002**, 1791; k) M. Pucheault, S. Darses, J.-P. Genêt, *Tetrahedron Lett.* **2002**, *43*, 6155; l) M. Pucheault, S. Darses, J.-P. Genêt, *Eur. J. Org. Chem.* **2002**, 3552; m) R. Itooka, Y. Iguchi, N. Miyaura, *J. Org. Chem.* **2003**, *68*, 6000; n) J.-G. Boiteau, R. Imbos, A. J. Minnaard, B. L. Feringa, *Org. Lett.* **2003**, *5*, 681; J.-G. Boiteau, R. Imbos, A. J. Minnaard, B. L. Feringa, *Org. Lett.* **2003**, *5*, 1385; o) Q. , Shi, L. Xu, X. Li, X. Jia, R. Wang, T. T.-L. Au-Yeung, A. S. C. Chan, T. Hayashi, R. Cao, M. Hong, *Tetrahedron Lett.* **2003**, *44*, 6505; p) Y. Iguchi, R. Itooka, N. Miyaura, *Synlett* **2003**, 1040; q) J.-G. Boiteau, A. J. Minnaard, B. L. Feringa, *J. Org. Chem.* **2003**, *68*, 9481; r) Y. Ma, C. Song, C. Ma, Z. Sun, Q. Chai, M. B. Andrus, *Angew. Chem.* **2003**, *115*, 6051; *Angew. Chem. Int. Ed.* **2003**, *42*, 5871; s) C. Defieber, J.-F. Paquin, S. Serna, E. M. Carreira, *Org. Lett.* **2004**, *6*, 3873; t) L. Navarre, S. Darses, J.-P. Genêt, *Angew. Chem.* **2004**, *116*, 737; *Angew. Chem. Int. Ed.* **2004**, *43*, 719; u) M. Pucheault, V. Michaut, S. Darses, J.-P. Genêt, *Tetrahedron Lett.* **2004**, *45*, 4729; v) A. Duursma, J.-G. Boiteau, L. Lefort, J. A. F. Boogers, A. H. M. De Vries, J. G. De Vries, A. J. Minnaard, B. L. Feringa, *J. Org. Chem.* **2004**, *69*, 8045; w) K. M. Belyk, C. D. Beguin, M. Palucki, N. Grinberg, J. DaSilva, D. Askin, N. Yasuda, *Tetrahedron Lett.* **2004**, *45*, 3265; x) P. Mauleon, J. C. Carretero, *Org. Lett.* **2004**, *6*, 3195; y) R. J. Moss, K. J. Wadsworth, C. J. Chapman, C. G. Frost, *Chem. Commun.* **2004**, 1984; z) B. M. Bocknack, L.-C. Wang, M. J. Krische, *Proc. Natl. Acad. Sci. USA* **2004**, *101*, 5421.

[6] For organotitanium reagents, see: a) T. Hayashi, N. Tokunaga, K. Yoshida, J. W. Han, *J. Am. Chem. Soc.* **2002**, *124*, 12102; b) K. Yoshida, T. Hayashi, *J. Am. Chem. Soc.* **2003**, *125*, 2872; c) N. Tokunaga, K. Yoshida, T. Hayashi, *Proc. Natl. Acad. Sci. USA* **2004**, *101*, 5445.

[7] For organozinc reagents, see: R. Shintani, N. Tokunaga, H. Doi, T. Hayashi, *J. Am. Chem. Soc.* **2004**, *126*, 6240.

[8] Other organometallic reagents: for silicon, see: a) S. Oi, A. Taira, Y. Honma, Y. Inoue, *Org. Lett.* **2003**, *5*, 97; b) Y. Otomaru, T. Hayashi, *Tetrahedron: Asymmetry* **2004**, *15*, 2647; for zirconium, see: c) S. Oi, T. Sato, Y. Inoue, *Tetrahedron Lett.* **2004**, *45*, 5051.

[9] T. Nishikata, Y. Yamamoto, N. Miyaura, *Chem. Commun.* **2004**, 1822.

[10] For a recent example, see: Y.-S. Kwak, E. J. Corey, *Org. Lett.* **2004**, *6*, 3385.

[11] A rhodium-catalyzed asymmetric 1,6-addition to 3-alkynyl-2-en-1-ones that affords axially chiral allenes has been reported: T. Hayashi, N. Tokunaga, K. Inoue, *Org. Lett.* **2004**, *6*, 305.

[12] For organocopper reagents, see: a) J. A. Marshall, H. Roebke, *J. Org. Chem.* **1966**, *31*, 3109; b) J. A. Marshall, R. A. Ruden, L. K. Hirsch, M. Phillippe, *Tetrahedron Lett.* **1971**, *12*, 3795; c) N. Krause, *J. Org. Chem.* **1992**, *57*, 3509; d) N. Krause, S. Thorand, *Inorg. Chim. Acta* **1999**, *296*, 1; e) M. Uerdingen, N. Krause, *Tetrahedron* **2000**, *56*, 2799; for an iron-catalyzed reaction, see: f) K. Fukuhara, H. Urabe, *Tetrahedron Lett.* **2005**, *46*, 603.

[13] For the acceleration of a 1,4-addition reaction of organocuprates by chlorotrimethylsilane, see: a) E. J. Corey, N. W. Boaz, *Tetrahedron Lett.* **1985**, *26*, 6015; b) E. J. Corey, N. W. Boaz, *Tetrahedron Lett.* **1985**, *26*, 6019.

[14] S. Norsikian, I. Marek, S. Klein, J. F. Poisson, J. F. Normant, *Chem. Eur. J.* **1999**, *5*, 2055; $[\alpha]_D^{20} = -70$ ($c = 1.1$, Et_2O).

[15] A. S. Kotnis, *Tetrahedron Lett.* **1990**, *31*, 481.

 © 2005 Wiley-VCH Verlag GmbH & Co. KGaA, Weinheim

Molecular Devices

Self-Assembled Monolayers of Isocyanides on Nickel Electrodes**

*Youngu Lee, Gustavo M. Morales, and Luping Yu**

Self-assembled monolayers (SAMs) of thiols on Au(111) surfaces have been examined extensively in recent years as a platform for surface science. They have been used in a number of applications in the areas of molecular electronics and surface-property modulation.[1] In molecular electronics, SAMs of thiol on a gold substrate have been particularly useful in controlling the placement and orientation of molecular electronic components such as wires, diodes, switches, and memories. In the design of molecular electronic components, appropriate interfaces between molecules and electrodes are as crucial as the active organic molecules. To be useful, these interfaces should possess low impedance and high stability. The mismatch between the Fermi level of the electrodes and either the HOMO or LUMO level of the adsorbent molecule generally induces a contact barrier which is the source of contact impedances.[2] So far, the thiol–gold linkage has been mainly considered for composing molecular electronic devices. Gold has an advantage over other surfaces for SAM formation because of its intrinsic inertness in air and high conductivity. However, there are still several limitations of gold surfaces as the electrode for practical molecular electronic applications. Theoretical calculations predicted that the combination of sulfur and gold yields one of the highest contact barriers for charge transport.[3] It is also well-known that SAMs of thiols on gold are thermally unstable.[4] Furthermore, the stochastic behavior of thiols on gold electrodes that results from the breakage of the adsorbent molecule–metal contact have also been observed.[5] The high diffusion mobility of gold atoms makes them less attractive for practical applications because of the limited lifetime of the devices.[6] Therefore, it is meaningful to develop a new combination of chemical linkage groups—alligator clips—and metal electrodes.

Current semiconductor technology employs nickel, tungsten, and their silicon alloys as electrodes for microelectronic devices. In addition, the ferromagnetic character of Ni presents the possibility of expanding the application of such electrodes to spintronic devices.[7] Although there are various reports about the thiol–nickel interaction,[8] the thiol–nickel junction is not as good as the thiol–gold junction for molecular electronic applications. Therefore, it is necessary to develop new alligator clips for Ni substrates. According to theoretical calculations, the isocyanide–nickel junction has significant advantages over the thiol–gold junction and others because of its low charge-transport barriers.[3] There have been several examples of SAMs generated from isocyanides on Au,[9] Pt,[10] Pd,[11] Ag,[9b,12] and Cr.[13] However, the isocyanide–nickel interaction has not yet been explored except for vacuum-evaporated methyl isocyanide (CH_3NC) on Ni(100) and Ni(111) surfaces.[14]

Herein, we report the synthesis of ferrocenylalkyl isocyanides and their assembly on polycrystalline Ni surfaces. The ferrocenyl moiety was introduced as a messenger for convenient characterization of monolayers by electrochemical methods to evaluate the surface coverage and thermal stability of SAMs.[15] Additionally, the conformation and binding mode of isocyanide on Ni surfaces, which were characterized by reflection–absorption infrared (RAIR) spectroscopy, are discussed.

We synthesized the ferrocenyl-terminated isocyanide molecules **5** to test their ability to chemisorb on Ni surfaces. In addition to isocyanides, several ferrocenyl-terminated molecules containing reactive functional groups that can potentially chemisorb on Ni surfaces, such as cyanide (**6**), isothiocyanate (**7**), diselenide (**9**), and thiol (**10**), were synthesized (Scheme 1). Polycrystalline Ni surfaces were used as substrates for monolayer formation. Ni surfaces were pretreated by electrochemical reduction (−1.3 V vs. Ag/AgCl, 3 M NaCl) in an aqueous solution of $HClO_4$ (1 M) for 20 minutes prior to use, since Ni is easily oxidized on exposure to air.[8]

The molecular packing and surface coverage of the monolayers were assessed by cyclic voltammetry. Figure 1 shows cyclic voltammograms (CVs) obtained after electrochemically reduced Ni electrodes had been immersed in 0.01 M ethanolic solutions of **5**, **9**, and **10** for 48 hours. Oxidation and reduction peaks were observed at +0.47 and +0.44 V, which correspond to the oxidation and reduction of the ferrocene moiety.[15] However, Ni surfaces immersed for 48 hours in solutions of ferrocenyl-terminated molecules containing azide (**2**), amine (**3**), cyanide (**6**), and isothiocyanate (**7**) functional groups gave featureless CVs similar to those of bare electrodes. These results indicate that **5**, **9**, and **10** were successfully chemisorbed on the electrochemically reduced nickel surfaces. The charge density obtained for SAMs of **5**, **9**, and **10** are clearly different, and they follow the order of isocyanide > thiol > diselenide.

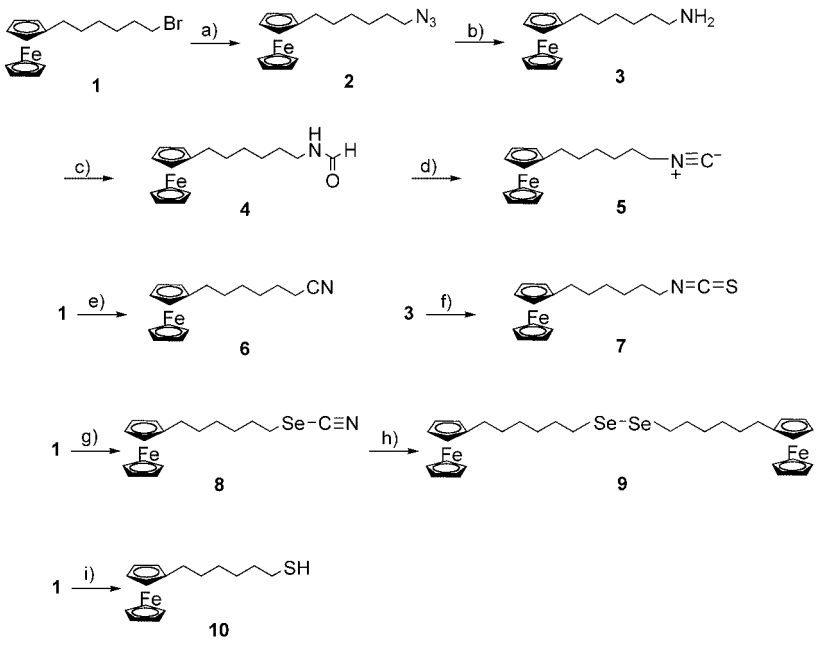
The surface coverage was calculated from the area of ferrocene redox peaks, by assuming that the surface has zero roughness and all chemisorbed molecules are electrochemically active. A surface coverage of 1×10^{-9} mol cm^{-2} was obtained from the electrodes modified by a 0.01 M ethanolic solution of **5**. This value is approximately two times larger than the reported value for a well-packed monolayer of ferrocenyl alkylthiols on gold ($4.6–8 \times 10^{-10}$ mol cm^{-2}).[15] The discrepancy for the Ni surface may arise from the rough morphology of Ni surfaces compared to that of gold (see the Supporting Information).

[*] Y. Lee, G. M. Morales, Prof. L. Yu
Department of Chemistry and James Franck Institute
The University of Chicago
5735 South Ellis Avenue, Chicago, IL 60637 (USA)
Fax: (+1) 773-702-0805
E-mail: lupingyu@midway.uchicago.edu

[**] This research was supported by the National Science Foundation, the NSF MRSEC program at the University of Chicago, AFOSR, and the UC-Argonne Nanoscience Consortium.

Supporting information for this article is available on the WWW under http://www.angewandte.org or from the author.

 © 2005 Wiley-VCH Verlag GmbH & Co. KGaA, Weinheim DOI: 10.1002/anie.200500942



Scheme 1. Synthesis of ferrocenyl-terminated molecules containing various functional groups. a) NaN_3, DMF, RT, 12 h, 92%; b) lithium aluminum hydride, Et_2O, RT, 2 h, 80%; c) ethyl formate, reflux, 18 h, 93%; d) $POCl_3$, triethylamine, THF, 0°C, 2 h, 60%; e) NaCN, DMF, RT, 12 h, 95%; f) di-2-pyridyl thionocarbonate, CH_2Cl_2, RT, 1 h, 81%; g) KSeCN, CH_3CN, 0°C to RT, 30 min, 92%; h) NaH, DMF, RT, 24 h, 66%; i) thiourea, EtOH, reflux, 18 h and then KOH, reflux, 2 h, 60%.

suggests that chemisorbed monolayers are chemically and thermodynamically stable under the given experimental conditions.

When Ni surfaces not treated reductively were used, the surface coverage was 1.9×10^{-10} mol cm^{-2}, five times lower than that of the electrochemically reduced Ni surfaces. The surface coverage of the monolayer on the nonreduced Ni surfaces decreased by over 50% of the original value after 100 repetitive scans at 0.1 V s^{-1}. The instability of the monolayers on nonreduced Ni surfaces may be a result of the weak interaction from the physisorption of isocyanides on nickel oxide rather than chemisorption.

Figure 2 shows the CVs of electrochemically reduced Ni electrodes modified with **5** at different scan rates. The peak splitting ($\Delta E_p = E_p^{ox} - E_p^{red}$) increased with increasing scan rate and was larger than that obtained under the same conditions for a monolayer of **5** on polycrystalline gold (data not shown). These phenomena are not consistent with the theory for a reversible redox couple confined to a surface.[16] However, ΔE_p approaches zero at low scan rates, as

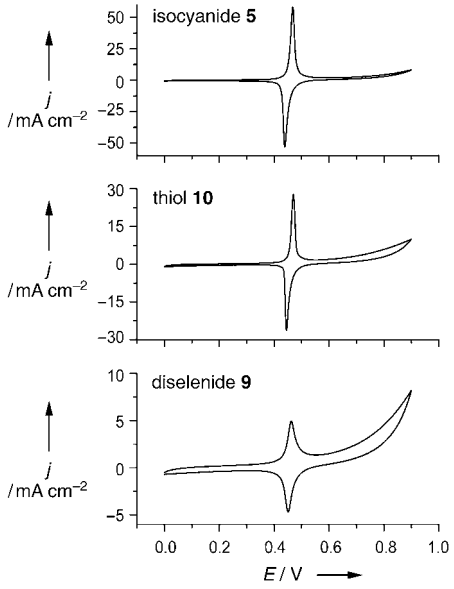


Figure 1. Cyclic voltammograms of monolayers of isocyanide **5**, diselenide **9**, and thiol **10** self-assembled on electrochemically reduced nickel surfaces. Electrolyte: 0.1 M nBu_4NPF_6 in THF. Scan rate: 0.01 V s^{-1}.

The electrochemical responses of monolayers of **5** were shown to be stable when subjected to repetitive cycling at different sweep rates. Only a small loss (5%) in the surface coverage was observed after 100 cycles at 0.2 V s^{-1}. Notably, surface coverage decreased by only 12% when monolayers of **5** were sonicated in THF for 10 minutes. This observation

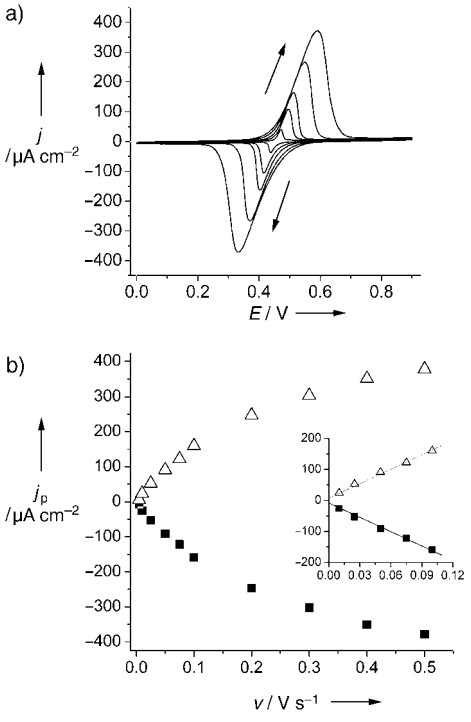


Figure 2. a) Cyclic voltammograms of an electrochemically reduced nickel electrode modified with a monolayer of isocyanide **5**. Electrolyte: 0.1 M nBu_4NPF_6 in THF. Scan rate: 0.01, 0.05, 0.1, 0.25, and 0.5 V s^{-1}. b) Plot of current density versus scan rate (△ oxidation, ■ reduction) for a monolayer of isocyanide **5** at an electrochemically reduced nickel surface and recorded in 0.1 M nBu_4NPF_6/THF. Inset: enlargement of the low-scan-rate region; the line is intended to guide the eye.

 © 2005 Wiley-VCH Verlag GmbH & Co. KGaA, Weinheim

expected for a reversible surface-confined redox couple. This behavior can be attributed to a slow electron transfer rate on the timescale of the experiment, where at low scan rates the redox centers remain nearly at equilibrium with the electrode surface.

Another important piece of evidence for a surface-confined faradaic reaction is the linearity between the peak current (J_p) and the scan rate (ν), as expressed by Equation (1).[16]

$$j_p = \frac{I_p}{A} = \frac{n^2F^2\Gamma\nu}{4RT} \quad (1)$$

The plot of anodic and cathodic current density against the scan rate is nearly linear at low scan rates, which indicates the existence of a surface-confined faradaic reaction (inset in Figure 2b). At faster scan rates, a deviation from the linearity was observed which is common for slow-electron-transfer kinetics (Figure 2). Along with previous CV results, this electrochemical behavior confirms the fact that a monolayer of **5** was formed on Ni surfaces.

Reflection–absorption infrared (RAIR) spectroscopy has been used to investigate the chemisorption and binding mode of SAMs on various metal surfaces.[15] Figure 3 shows the

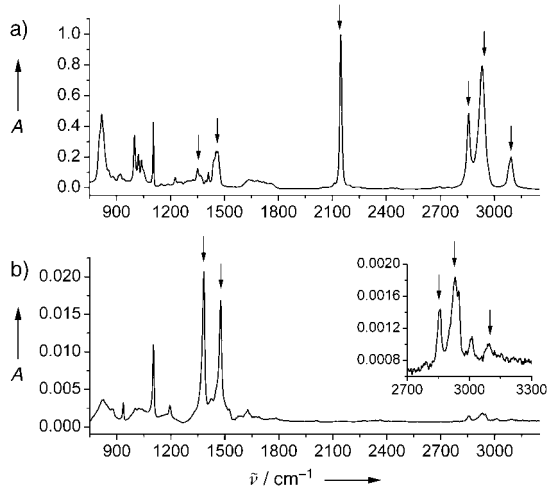


Figure 3. FTIR spectra of **5**: a) transmission on a KBr plate and b) RAIR spectra of a self-assembled monolayer on a nickel surface.

transmission (a) and RAIR (b) spectra for **5** on a KBr plate and a Ni surface, respectively. In the transmission mode, the characteristic peaks of the hydrocarbon chain and ferrocene unit of **5** appear at 2932 (C–H symmetric stretching), 2855 (C–H asymmetric stretching), 3093 (C–H stretching in ferrocene), 1464 (C–C stretching from the substituted ferrocene), and 1350 cm^{-1} (C–H bending from the substituted ferrocene; Figure 3a). These peaks are also observed in the RAIR spectrum (Figure 3b). This result clearly shows the formation of monolayers of **5** on Ni surfaces. In addition, the binding mode of isocyanides on Ni surfaces was deduced from the RAIR spectrum. While a strong peak for isocyanide stretching is observed in the transmission spectrum at 2147 cm^{-1}, the RAIR spectrum on nickel does not show the corresponding peak. In contrast, the isocyanide stretching peak of the monolayers of **5** on gold occurs at 2213 cm^{-1}. This result is in agreement with previous reports of isocyanides on gold, and the peak has been assigned to the absorption of isocyanide bonded to the metal surface through the carbon atom of the isocyanide.[9] Considering the surface selection rules for RAIR spectroscopy,[17] the absence of an isocyanide stretching peak in the RAIR spectrum suggests that the chemisorbed isocyanides are bonded through both their carbon and nitrogen atoms, and that they adopt a position parallel to the surface. This observation is consistent with previous studies of methyl isocyanide on Ni surfaces.[14a]

We examined the thermal stability by immersing Ni electrodes modified with **5** into boiling ethanol (78 °C).[18] The surface coverage (Γ) of the monolayers of **5** was monitored by cyclic voltammetry as a function of boiling time (Figure 4).

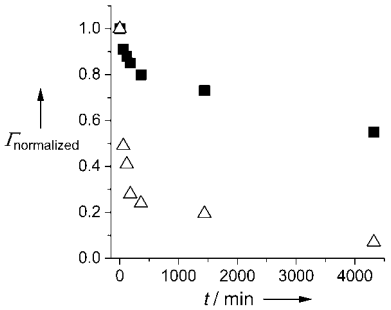


Figure 4. Thermal stability profiles of nickel–isocyanide **5** (■) and gold–thiol **10** (△) as a function of time in boiling ethanol (78 °C).

After three days in boiling ethanol, the surface coverage decreased by about 50%. Notably, SAMs of **10** on a gold surface lost over 50% of their surface coverage after one hour in boiling ethanol. The nickel–isocyanide interaction in the present study clearly shows higher thermal stability than the gold–thiol interaction. The peak shape and position in the voltammograms before and after the heating process are constant, which indicates that this experimental condition does not lead to decomposition of the isocyanide compounds on the surface.

In conclusion, ferrocenyl-terminated isocyanides were synthesized and tested for surface reaction with Ni substrates. SAMs generated from isocyanides on Ni surfaces were characterized by cyclic voltammetry and RAIR spectroscopy. It was found that SAMs of isocyanides on Ni surfaces have a parallel binding mode and high thermal stability in boiling ethanol. The results indicate the presence of strong chemisorption between isocyanides and the metallic Ni surface. This work is an indication that molecular electronic components with isocyanide groups should be synthesized so that they can be immobilized on substrates more relevant to industrial standards.

 © 2005 Wiley-VCH Verlag GmbH & Co. KGaA, Weinheim

Experimental Section

Experimental details for the synthesis of all compounds, monolayer preparation, cyclic voltammetry, FTIR spectroscopy, and AFM measurements can be found in the Supporting Information.

Received: March 15, 2005
Published online: June 2, 2005

Keywords: chemisorption · molecular devices · monolayers · nickel · self-assembly

[1] a) *Thin Films: Self-Assembled Monolayers of Thiols* (Ed.: A. Ulman), Academic Press, San Diego, **1998**; b) Y. Xia, G. M. Whitesides, *Angew. Chem.* **1998**, *110*, 568 – 594; *Angew. Chem. Int. Ed.* **1998**, *37*, 550 – 575.
[2] S. Datta, W. Tian, S. Hong, R. Reifenberger, J. I. Henderson, C. P. Kubiak, *Phys. Rev. Lett.* **1997**, *79*, 2530 – 2533.
[3] J. M. Seminario, C. E. De La Cruz, P. A. Derosa, *J. Am. Chem. Soc.* **2001**, *123*, 5616 – 5617.
[4] a) E. Delamarche, B. Michel, H. Kang, C. Gerber, *Langmuir* **1994**, *10*, 4103 – 4108; b) J. B. Schlenoff, M. Li, H. Ly, *J. Am. Chem. Soc.* **1995**, *117*, 12528 – 12536.
[5] G. K. Ramachandran, T. J. Hopson, A. M. Rawlett, L. A. Nagahara, A. Primak, S. M. Lindsay, *Science* **2003**, *300*, 1413 – 1416.
[6] N. B. Zhitenev, A. Erbe, Z. Bao, *Phys. Rev. Lett.* **2004**, *92*, 186805.
[7] a) Z. H. Xiong, D. Wu, Z. Valy Vardeny, J. Shi, *Nature* **2004**, *427*, 821 – 824.
[8] a) Z. Mekhalif, F. Laffineur, N. Couturier, J. Delhalle, *Langmuir* **2003**, *19*, 637 – 645; b) S. M. Kane, D. R. Huntley, J. L. Gland, *J. Phys. Chem. B* **2001**, *105*, 9548 – 9556; c) S. M. Kane, J. L. Gland, *Surf. Sci.* **2000**, *468*, 101 – 108; d) Z. Mekhalif, A. Lazarescu, L. Hevesi, J.-J. Pireaux, J. Delhalle, *J. Mater. Chem.* **1998**, *8*, 545 – 551.
[9] a) K. L. Murphy, W. T. Tysoe, D. W. Bennett, *Langmuir* **2004**, *20*, 1732 – 1738; b) J. I. Henderson, S. Feng, T. Bein, C. P. Kubiak, *Langmuir* **2000**, *16*, 6183 – 6187; c) A. C. Ontko, R. J. Angelici, *Langmuir* **1998**, *14*, 3071 – 3078.
[10] a) D. Bong, I. Tam, R. Breslow, *J. Am. Chem. Soc.* **2004**, *126*, 11796 – 11797; b) M. Geissler, J. Chen, Y. Xia, *Langmuir* **2004**, *20*, 6993 – 6997.
[11] K. Murphy, S. Azad, D. W. Bennett, W. T. Tysoe, *Surf. Sci.* **2000**, *467*, 1 – 9.
[12] H. S. Han, S. W. Han, S. W. Joo, K. Kim, *Langmuir* **1999**, *15*, 6868 – 6874.
[13] O. Clot, M. O. Wolf, *Langmuir* **1999**, *15*, 8549 – 8551.
[14] a) C. M. Friend, J. Stein, E. L. Muetterties, *J. Am. Chem. Soc.* **1981**, *103*, 767 – 772; b) C. M. Friend, E. L. Muetterties, J. Gland, *J. Phys. Chem.* **1981**, *85*, 3256 – 3262.
[15] H. O. Finklea, *Electroanalytical Chemistry*, *Vol. 19* (Eds.: A. J. Bard, I. Rubinstein), Marcel Dekker, New York, **1998**.
[16] A. J. Bard, R. Faulkner, *Electrochemical Methods*, Wiley, New York, **1980**.
[17] R. G. Greenler, *J. Chem. Phys.* **1966**, *44*, 310 – 315.
[18] F. Bensebaa, T. H. Ellis, A. Badia, R. B. Lennox, *Langmuir* **1998**, *14*, 2361 – 2367.

 © 2005 Wiley-VCH Verlag GmbH & Co. KGaA, Weinheim

Metal–Metal Interactions

Dimerization of Indanediyl Fragments: An Alkene Analogue for Group 13?**

Michael S. Hill, Peter B. Hitchcock, and Ruti Pongtavornpinyo*

The occasionally vexed question of the potential for homonuclear multiple bonding between the heavier elements of Groups 13 and 14 continues to provoke intense interest.[1] For the wide-ranging family of Group 14 derivatives in this category, a lineage that culminated in the recent synthesis of the long-sought silicon alkyne analogue, 1,1,4,4-tetrakis[bis-(trimethylsilyl)methyl]-1,4-diisopropyl-2-tetrasilyne,[2] may be traced directly to the seminal discovery of the dimeric stannanediyl [{[$(Me_3Si)_2HC]_2Sn$}$_2$] by Lappert and co-workers.[3] All possible alkene and alkyne analogues based on a link between two Group 14 centers have since been prepared.[4] The structures of these R_2EER_2 and REER (E = Group 14 element) complexes substantiate an incremental decrease in the strength of any π-bonded component on transition from the respective planar D_{2h} and linear $D_{\infty h}$ structures. More pronounced *trans*-bent (C_{2h}) configurations (defined by the out-of-plane angle δ) are observed as the group is descended, alongside an increasing tendency of the R_2EER_2 species to dissociate to monomeric forms in solution. These observations have been attributed to the increasing stability of the lone pair of electrons in the *n*s orbital with increasing atomic number and the formation of polarized donor–acceptor interactions between the metal centers. A complementary molecular-orbital description ascribes increased nonbonding (or even antibonding) character to the b_u highest unoccupied molecular orbital (HOMO), through σ^* mixing, with increasing principal quantum number of the valence orbitals of E.[1,4]

Similar questions of multiple bond order in respect to Group 13 species have been especially problematic. The claim by Robinson and co-workers[5] of a triple-bond interaction between the Ga centers of the reduced species [$Na_2(GaC_6H_3$2,6-trip$)_2$] (trip = 2,4,6-*i*$Pr_3C_6H_2$) provoked vigorous debate,[5–13] while the subsequent work of Power and co-workers has highlighted as many contrasts as similarities within complexes maintaining contacts between formally low-valent heavier Group 13 and 14 elements.[14–16]

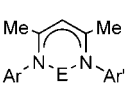
[*] Dr. M. S. Hill, R. Pongtavornpinyo
Department of Chemistry
Imperial College London
Exhibition Road, South Kensington
London SW7 2AZ (UK)
Fax: (+44) 207-594-5804
E-mail: mike.hill@imperial.ac.uk

Dr. P. B. Hitchcock
School of Chemistry
University of Sussex
Brighton, BN1 9QJ (UK)

[**] We thank the Royal Society for the provision of a University Research Fellowship (M.S.H.).

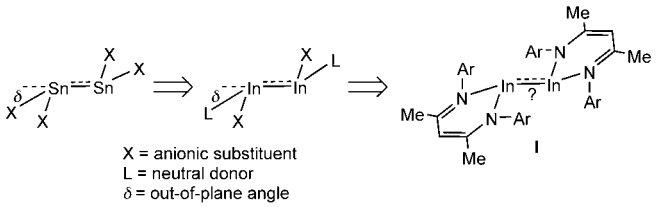
 DOI: 10.1002/anie.200500764 © 2005 Wiley-VCH Verlag GmbH & Co. KGaA, Weinheim

Our entry point was provided by the syntheses of the monovalent indium and thallium β-diketiminate derivatives **1** and **2**, respectively.[17] These compounds exist as well-sepa-



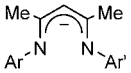
1: Ar = Ar' = 2,6-*i*Pr$_2$C$_6$H$_3$, E = In
2: Ar = Ar' = 2,6-*i*Pr$_2$C$_6$H$_3$, E = Tl
3: Ar = Ar' = 2,6-*i*Pr$_2$C$_6$H$_3$, E = Ga
4: Ar = Ar' = 2,6-*i*Pr$_2$C$_6$H$_3$, E = Al
5: Ar = 2,6-*i*Pr$_2$C$_6$H$_3$, Ar' =2-CH$_3$OC$_6$H$_4$, E = In
6: Ar = Ar' = 2,4,6-Me$_3$C$_6$H$_3$, E = In

rated singlet "carbene analogues" and are isostructural to the previously reported gallium and aluminum complexes, **3** and **4**, respectively.[18,19] It has been observed that variation of the overall steric demands of the bulky terphenyl ligands in combination with a low-valent gallium or indium center results in either monomeric or metal–metal-bonded species, the nuclearity of which is dictated by the size and topology of the stabilizing ligand system.[16,20] Although investigations by us suggested that an ability to isolate the two-coordinate species **1**–**4** was chiefly a product of the kinetic stability imparted by the bulky *N*-aryl 2,6-diisopropylphenyl (dipp) substituents,[17–19] we reasoned that use of substituents with decreased steric demands would similarly promote the formation of compounds with higher nuclearity. A particularly appealing target was the dimeric species, illustrated as the localized enamideimine form **I**, which may be considered as essentially isoelectronic to the stannanediyl discovered by Lappert and co-workers and other dimeric stannanediyls (Scheme 1).



Scheme 1. Generalized Sn=Sn and In=In complexes and target dimeric species **I**.

Known anions **II** and **III** were selected to provide an incremental decrease in the steric demands of the supporting ligand environment.[21] The appropriate β-imino amine pre-



II: Ar = 2,6-*i*Pr$_2$C$_6$H$_3$, Ar' = 2-CH$_3$OC$_6$H$_4$
III: Ar = Ar' = 2,4,6-Me$_3$C$_6$H$_2$

cursor was used in a synthetic route identical to that employed in the synthesis of **1**, providing facile access to In^{I} derivatives supported by **II** and **III**. Although the THF reaction solutions were somewhat photo- and thermally sensitive to depositing indium metal, rapid workup and crystallization in the dark from hexane at 5 °C provided yellow crystals of the desired In^{I} derivatives **5** and **6**. In common with the behavior of **1**, both compounds begin to decompose immediately on dissolution in aromatic solvents. Prompt acquisition of ^{1}H and ^{13}C NMR spectra in [D$_6$]benzene, however, enabled collection of data that were consistent with C_s- and C_2-symmetric structures for **5** and **6**, respectively. This solution lability to reductive decomposition has thus far restricted a thorough assessment of the nature of these species in solution. However, our appraisal of the strength of the In–In interactions present in the solid state (see below) and the analysis of Power and co-workers of the unique neutral Group 13 dimers [(2,6-dippC$_6$H$_3$M)$_2$] (M = Ga, In)[14,16] indicate that it is unlikely that anything other than transient In–In interactions persist in solution.[22]

Although crystalline samples of both complexes may be successfully manipulated for crystallographic purposes, both compounds darken because of the separation of metallic indium over the course of several days, even when stored at low temperature under N$_2$ and in the dark. These difficulties notwithstanding, the molecular structures of both compounds were determined by single-crystal X-ray diffraction studies. Although the data for **5** were of a poor quality, the structure, in common with our previously reported indium complexes bearing dipp substituents at both nitrogen donor centers, was unambiguously monomeric and contained no short In–In interactions (Figure 1). It is apparent that the presence of a single dipp group is sufficient to prevent any well-defined intermolecular contact.

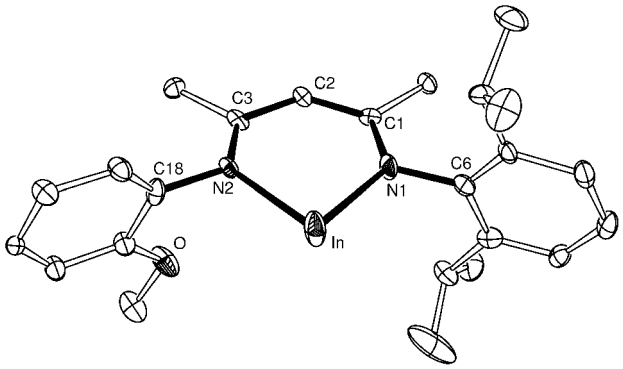


Figure 1. Structure of **5** (ORTEP plot, ellipsoids are set at 20% probability; H atoms are omitted for clarity). Selected bond lengths [Å] and angles [°]: In-N1 2.277(10), In-N2 2.257(9), N1-C1 1.339(16), N1-C6 1.461(18), N2-C3 1.318(15), N2-C18 1.453(15), C1-C2 1.389(18), C2-C3 1.414(17); N1-In-N2 82.6(4), In-N1-C1 128.0(8), In-N2-C3 129.0(7), N1-C1-C2 125.1(10), C1-C2-C3 129.5(13), C2-C3-N2 125.3(12).

Further X-ray analysis of **6** provided high-quality data and revealed that replacement of both of the dipp substituents of **1** by mesityl permits dimerization through the formation of a direct In–In bond. The centrosymmetric dimer possesses approximate C_{2h} symmetry with a mutual *trans*-bent orientation of the N-chelated ligands (Figure 2). It is notable, therefore, that **6** provides the first example of a neutral dimeric Group 13 species that is formally isoelectronic to the historically significant bis(stannane)diyls. The space-filling models shown in Figure 3 emphasize the efficient encapsulation of the In–In bond axis provided by the *N*-mesityl substituents of the chelate ligands within the dimeric arrange-

 © 2005 Wiley-VCH Verlag GmbH & Co. KGaA, Weinheim

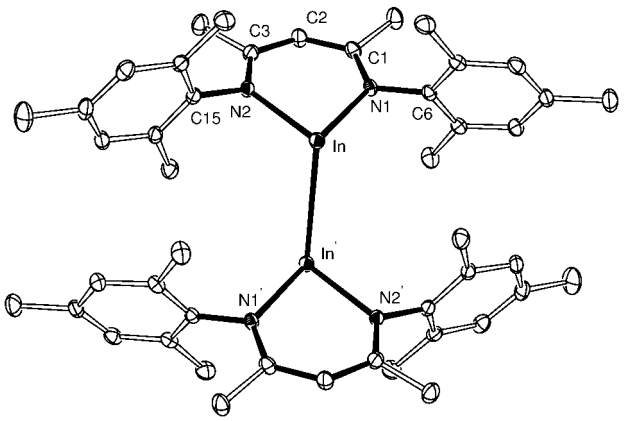


Figure 2. Structure of **6** (ORTEP plot, ellipsoids are set at 25% probability; H atoms are omitted for clarity). Selected bond lengths [Å] and angles [°]: In-N1 2.262(2), In-N2 2.256(2), In-In′ 3.1967(4), N1-C1 1.336(3), N1-C6 1.435(3), N2-C3 1.327(3), N2-C15 1.435(3), C1-C2 1.394(4), C2-C3 1.397(4); N1-In-N2 83.15(8), N1-In-In′ 110.65(6), N2-In-In′ 107.88(6), In-N1-C1 127.68(19), In-N2-C3 128.73(19), N1-C1-C2 125.1(3), C1-C2-C3 130.2(3), C2-C3-N2 124.4(3).

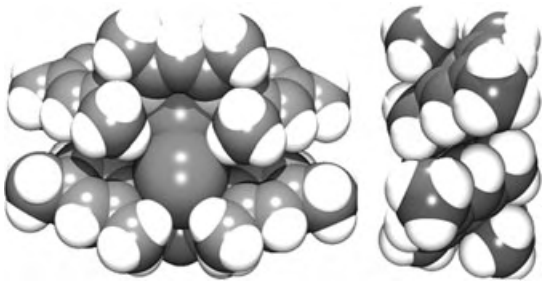


Figure 3. Space-filling (POVRAY) illustrations of **6** showing the kinetic protection of the In–In bond.

ment. The In–In distance in **6** (3.1967(4) Å) is significantly longer than that observed in the dimeric terphenyl derivative $[(2,6\text{-dipp}C_6H_3In)_2]$ (2.9786(5) Å).[16] Irrespective of the precise details of the bonding, this elongation can be interpreted in a straightforward manner as a consequence of the increased overall coordination number of the individual indium centers in **6** (three compared to two). This view is given further credence by the observation that the only other known In^I dimer features pentahapto coordination with a pentabenzylcyclopentadienyl anion and a very weak In···In interaction of 3.631(2) Å.[23] The In–In distance in **6** also lies well above the range established for typical In–In single bonds, such as those within the β-diketiminato disproportionation product $[\{\{HC[CMeN(dipp)]_2\}InCl\}_2]$ (2.8343(7) Å) and the three-coordinate indium centers of $[\{(2,4,6\text{-}i\text{Pr}_3C_6H_2)_2In\}_2]$ (2.775(2) Å), both of which feature formally divalent indium.[24,25] The β-diketiminato chelate structure is effectively planar (root-mean-square deviation of the In-N1-C1-C2-C3-N2 plane: 0.03 Å) with the result that the *trans*-bent configuration may be accurately defined by the In′-In-C2 angle of 113.02°. This represents an out-of-plane angle of 66.98° and indicates that dimerization occurs with a significantly greater degree of pyramidalization (with respect to a planar alkene-like D_{2h} structure) than that observed in the majority of homoleptic stannylenes of the general formula R_2SnSnR_2 (typically $\delta = 30$–$45°$).[1]

Dimerization has little effect on the local environment around the indium center provided by the chelated β-diketiminato ligand. The N1-In-N2 angle (83.15(8)°) is similar to the angles observed in the mononuclear compounds **1** and **5** (81.12(10) and 82.6(4)°, respectively), whereas the In–N1 and In–N2 bond lengths (2.262(2) and 2.256(2) Å, respectively) are actually the shortest observed for any indium(I) β-diketiminato chelate.[17] This latter, somewhat counterintuitive, feature occurs despite the increased coordination number of the indium centers and may be an illustration of the decreased steric demands of the chelated ligands and intrasubstituent repulsion.

We undertook DFT calculations on the dimeric model complex $[\{In[N(H)C(H)]_2CH\}_2]$ by using the B3LYP DFT and LANL2DZ pseudo potentials (and basis set) implemented in Gaussian 03.[26] The bond lengths and angles with regard to the two indium-containing fragments of the fully optimized structures are, in general, within 2% of the experimentally determined parameters. The In–In distance for the model system is, however, somewhat overestimated at 3.388 Å, as is the degree of *trans* bending indicated by the out-of-plane angle of 77.69°. The calculated molecular orbitals of this model compound do, however, reveal a qualitative insight into the In–In bonding present within **6** and provide a cogent comparison to bonding models developed for related Group 13 and 14 species. The frontier molecular-orbital diagram is presented in Figure 4 and illustrates that the

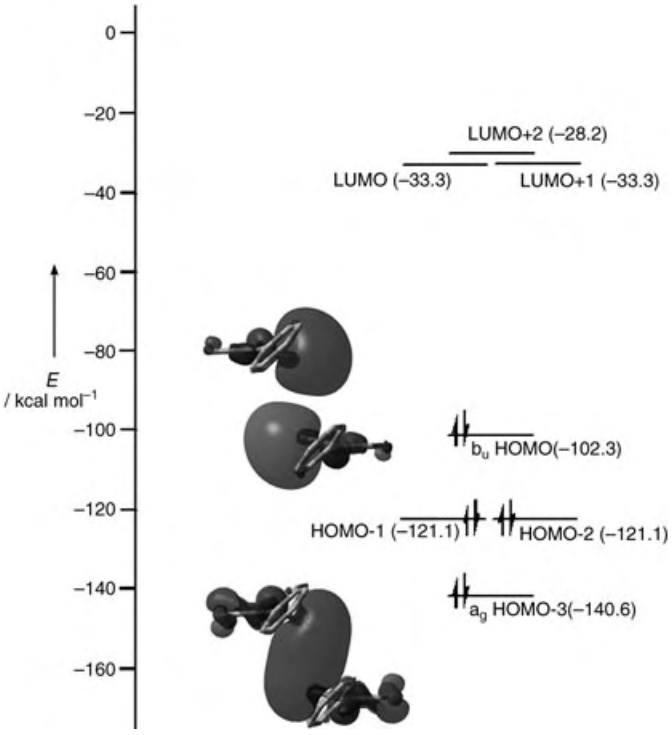


Figure 4. Calculated (B3LYP/LANDZ) frontier molecular-orbital diagram for $[\{In[(N(H)C(H)]_2CH\}_2]$ illustrating the b_u HOMO and a_g HOMO-3. LUMO = lowest unoccupied molecular orbital.

 © 2005 Wiley-VCH Verlag GmbH & Co. KGaA, Weinheim

HOMO is a b_u orbital that is nonbonding with regard to In–In contact. The degenerate HOMO-1 and -2 provide a level of π overlap between the indium centers and the nitrogen donor atoms of the chelated ligands. The HOMO-3 is an In–In σ-bonding orbital of A_g symmetry. This a_g orbital thus provides the primary bonding interaction between the metal centers. This view of the metal–metal bonding within **6** is qualitatively similar to that which has been evinced for alkene analogues of the heavier Group 14 elements and some multiply bonded gallium species.[1,9–13,27] The b_u HOMO in these cases has been variously interpreted as a "slipped" π bond or as possessing lone-pair or even antibonding character. Experimental and theoretical studies of heavier Group 14 R_2EER_2 species indicate that, despite increased lone-pair character with increased atomic mass of E, the π-bonding b_u HOMO acts to provide a minor augmentation of the overall bonding interaction between the metal centers.[1] A similar rationale has been applied to the recently completed series of REER derivatives.[4] The data presented herein and the somewhat limited literature precedents highlight some notable contrasts within Group 13. The experimental data indicate that In–In bonding with π character within **6** is feeble at best, or indeed destructive. A further calculation based on the separation of $[\{In[(N(H)C(H)]_2CH\}_2]$ into two singlet indanediyl fragments provided a bond-dissociation energy of only 2 kcal mol^{-1}. This extremely low value is commensurate with values calculated (ca. 3 kcal mol^{-1}) for the separation of the two {InH} fragments of $[In_2H_2]$ and suggests that the notion of "multiple bonding" within molecules such as **6** is fallacious if the only expectation is an augmentation of the overall bond strength.[28] The weakness of the Ga–Ga bonding within the neutral complex $[\{(2,6\text{-dipp})_2C_6H_3Ga\}_2]$ was similarly attributed to the large energy difference between the lone pair on the singlet Ga^{I} center and the p orbitals.[14] This situation is likely to be exacerbated in the current case by N–In π interactions within the planar β-diketiminato chelates and indicates that the "multiple bonding" present within **6** actually represents an overall bond order of less than unity. This view of the HOMO within homonuclear bonding in Group 13 elements has been emphasized previously by calculations carried out on the hypothetical cationic species $[MeGaGaMe]^+$.[11] In this case, removal of an electron from the b_u HOMO of [MeGaGaMe] caused a decrease of approximately 0.2 Å in the computed Ga–Ga bond length. Preliminary calculations on the $[\{In[(N(H)C(H)]_2CH\}_2]^+$ species indicated a similar and pronounced contraction of the In–In bond length to approximately 3 Å and highlighted the fact that the b_u HOMO may also possess antibonding character. Experiments to assess the validity of this hypothesis and further studies on the reactivity of these unusual species are in progress.

Experimental Section

5: Precooled THF (20 mL) was added at −78 °C to a rapidly stirred mixture of **II**-H (0.45 g, 1.25 mmol), InI (0.30 g, 1.25 mmol), and $KN(SiMe_3)_2$ (0.24 g, 1.25 mmol) in the absence of light. The reaction mixture was stirred for 3 h and allowed to warm to room temperature to produce a gray slurry. Volatiles were removed and the gray solid residue extracted with hexane (25 mL). Filtration, concentration to approximately 10 mL, and storage at 5 °C afforded bright yellow crystals suitable for X-ray analysis (0.29 g, 49 %). Elemental analysis calcd (%) for $C_{24}H_{31}InN_2O$: C 60.26, H 6.55, N 5.86; found: C 62.26, H 5.47, N 5.42 (partially decomposed in transit); ^{1}H NMR (270 MHz, [D$_6$]benzene, 25 °C): $\delta = 1.14$ (d, 6H, $^3J_{HH} = 6.9$ Hz; $CH(CH_3)_2$), 1.21 (d, 6H, $^3J_{HH} = 6.9$ Hz; $CH(CH_3)_2$), 1.75 (s, 3H; CCH_3), 1.90 (s, 3H; CCH_3), 3.20 (m, 2H, $^3J_{HH} = 6.9$ Hz; $CH(CH_3)_2$), 3.25 (s, 3H; OCH_3), 5.06 (s, 1H; C*H*), 6.50 (d, 1H; Ar*H*), 6.88–6.96 (m, 2H; Ar*H*), 7.15–7.16 ppm (m, 4H; Ar*H*); ^{13}C{^{1}H} NMR (125.8 MHz, [D$_6$]benzene): $\delta = 23.8$ ($CH(CH_3)_2$), 25.7 (CCH_3), 28.2 ($CH(CH_3)_2$), 28.6 (*C*H-$(CH_2)_2$), 55.1 (OCH_3), 98.7 (γ-*C*H), 111.8, 121.3, 123.3, 123.9, 124.5, 125.2, 125.5, 125.8, 126.7, (ArH) 142.3 (*o*-*C*(dipp)), 145.2 (*i*-C(dipp)), 155.6 (*i*-Ar-2-OCH_3), 163.6 (*C*N), 163.9 ppm (*C*N).

6: This compound was made by the same general method employing **III**-H (0.69 g, 2.07 mmol), InI (0.50 g, 2.07 mmol), and $KN(SiMe_3)_2$ (0.42 g, 2.10 mmol) to afford pale yellow rectangular crystals suitable for X-ray analysis (0.42 g, 45 %). Elemental analysis (%) calcd for $C_{46}H_{58}In_2N_4$: C 61.62, H 6.53, N 6.25; found: C 61.68, H 6.47, N 6.18; ^{1}H NMR (500 MHz, [D$_6$]benzene, 25 °C): $\delta = 1.59$ (s, 6H; CCH_3), 2.03 (s, 12H; *o*-CH_3), 2.12 (s, 6H; *p*-CH_3), 4.92 (s, 1H; C*H*), 6.76 ppm (s, 4H; *m*-Ar*H*); ^{13}C{^{1}H} NMR (125.8 MHz, [D$_6$]benzene): $\delta = 19.3$ (*o*-CH_3), 20.9 (*p*-CH_3), 23.6 (CCH_3), 98.2 (γ-*C*H), 129.5 (*m*-ArH), 133.4 (*p*-Ar), 137.4 (*o*-Ar), 146.0 (*i*-Ar), 163.4 ppm (*C*N).

Data for the X-ray structural analyses of **5** and **6** were collected on a KappaCCD diffractometer ($\lambda(Mo_{K\alpha}) = 0.71073$ Å), solved by direct methods (SHELXS-97), and refined against all F^2 using SHELXL-97) with non-hydrogen atoms anisotropic and hydrogen atoms in riding mode. An absorption correction (MULTISCAN) was applied. For **5**, the diffraction was weak and limited in extent. Crystallographic data for **5** ($C_{24}H_{31}InN_2O$) at 173(2) K: $M_r = 478.33$, crystal dimensions $0.25 \times 0.10 \times 0.05$ mm^3, orthorhombic, space group $P2_12_12$ (no. 18), $a = 11.6183(8)$, $b = 22.8982(14)$, $c = 8.7686(6)$ Å, $V = 2332.8(3)$ Å^3, $Z = 4$, $\rho_{calcd} = 1.36$ Mg m^{-3}, $\mu = 1.03$ mm^{-1}; of 10481 reflections measured ($3.41 < \theta < 23.26°$), 3304 were independent ($R_{int} = 0.067$); $wR2 = 0.253$ (all data), $R1 = 0.100$ (for 2765 reflections with $I > 2\sigma(I)$), 254 parameters, GOF = 1.114. Crystallographic data for **6** ($C_{46}H_{58}In_2N_4$) at 173(2) K: $M_r = 896.6$, crystal dimensions $0.10 \times 0.10 \times 0.05$ mm^3, triclinic, space group $P\bar{1}$ (no. 2), $a = 8.6847(3)$, $b = 9.9683(3)$, $c = 13.5822(5)$ Å, $\alpha = 71.003(2)$, $\beta = 82.758(2)$, $\gamma = 81.907(2)°$, $V = 1096.67(6)$ Å^3, $Z = 1$, $\rho_{calcd} = 1.36$ Mg m^{-3}, $\mu = 1.09$ mm^{-1}; of 17033 reflections measured ($3.54 < \theta < 26.06°$), 4316 were independent ($R_{int} = 0.053$); $wR2 = 0.072$ (all data), $R1 = 0.031$ (for 3783 reflections with $I > 2\sigma(I)$), 241 parameters, GOF = 1.031. CCDC-264672 and -264673 (**5** and **6**) contain the supplementary crystallographic data for this paper. These data can be obtained free of charge from the Cambridge Crystallographic Data Centre via www.ccdc.cam.ac.uk/data_request/cif.

Received: March 1, 2005
Published online: June 2, 2005

Keywords: carbenoids · Group 13 elements · indium · metal–metal interactions · multiple bonds

[1] a) P. P. Power, *Chem. Rev.* **1999**, *99*, 3463; b) P. P. Power, *J. Chem. Soc. Dalton Trans.* **1998**, 2939.
[2] A. Sekiguchi, R. Kinjo, M. Ichinohe, *Science* **2004**, *305*, 1755.
[3] a) P. J. Davidson, M. F. Lappert, *J. Chem. Soc. Chem. Commun.* **1973**, 317; b) D. E. Goldberg, D. H. Harris, M. F. Lappert, K. M. Thomas, *J. Chem. Soc. Chem. Commun.* **1976**, 261; c) D. E. Goldberg, P. B. Hitchcock, M. F. Lappert, K. M. Thomas, A. J. Thorne, T. Fjeldberg, A. Haarland, B. E. R. Schilling, *J. Chem. Soc. Dalton Trans.* **1986**, 2387.
[4] For a review of REER structure and bonding, see: P. P. Power, *Chem. Commun.* **2003**, 2091.

 © 2005 Wiley-VCH Verlag GmbH & Co. KGaA, Weinheim

[5] a) J. Su, X.-W. Li, C. Crittendon, G. H. Robinson, *J. Am. Chem. Soc.* **1997**, *119*, 5471; b) G. H. Robinson, *Acc. Chem. Res.* **1999**, *32*, 773.
[6] K. W. Klinkhammer, *Angew. Chem.* **1997**, *109*, 2414; *Angew. Chem. Int. Ed.* **1997**, *109*, 2414.
[7] Y. Xie, R. S. Grev, J. Cu, H. F. Schaefer, P. von R. Schleyer, J. Su, X.-W. Li, G. H. Robinson, *J. Am. Chem. Soc.* **1998**, *120*, 3773.
[8] I. Bytheway, Z. Lin, *J. Am. Chem. Soc.* **1998**, *120*, 12133.
[9] Y. Xie, H. F. Schaefer, G. H. Robinson, *Chem. Phys. Lett.* **2000**, *317*, 174.
[10] F. A. Cotton, A. H. Cowley, X. Feng, *J. Am. Chem. Soc.* **1998**, *120*, 1795.
[11] T. L. Allen, W. H. Fink, P. P. Power, *J. Chem. Soc. Dalton Trans.* **2000**, 407.
[12] A. J. Bridgeman, L. R. Ireland, *Polyhedron* **2001**, *20*, 2841.
[13] N. Takagi, M. W. Schmidt, S. Nagase, *Organometallics* **2001**, *20*, 1646.
[14] N. J. Hardman, R. J. Wright, A. D. Phillips, P. P. Power, *Angew. Chem.* **2002**, *114*, 2966; *Angew. Chem. Int. Ed.* **2002**, *41*, 2842.
[15] N. J. Hardman, R. J. Wright, A. D. Phillips, P. P. Power, *J. Am. Chem. Soc.* **2003**, *125*, 2667.
[16] R. J. Wright, A. D. Phillips, N. J. Hardman, P. P. Power, *J. Am. Chem. Soc.* **2002**, *124*, 8538.
[17] a) M. S. Hill, P. B. Hitchcock, *Chem. Commun.* **2004**, 1818; b) M. S. Hill, P. B. Hitchcock, R. Pongtavornpinyo, *Dalton Trans.* **2005**, 273.
[18] C. Cui, H. W. Roesky, H. G. Schmidt, M. Noltemeyer, H. Hao, F. Cimpoesu, *Angew. Chem.* **2000**, *112*, 4444; *Angew. Chem. Int. Ed.* **2000**, *39*, 4274.
[19] N. J. Hardman, B. E. Eichler, P. P. Power, *Chem. Commun.* **2000**, 1991.
[20] a) S. T. Haubrich, P. P. Power, *J. Am. Chem. Soc.* **1998**, *120*, 2202; b) B. E. Eichler, N. J. Hardman, P. P. Power, *Angew. Chem.* **2000**, *112*, 391; *Angew. Chem. Int. Ed.* **2000**, *39*, 383.
[21] A. P. Dove, V. C. Gibson, E. L. Marshall, A. J. P. White, D. J. Williams, *Dalton Trans.* **2004**, 570.
[22] Tris(trialkylsilyl)methyl derivatives of indium(I) exist as weakly bonded tetrahedral aggregates in the solid state, and in solution this nuclearity is maintained unless very sterically demanding silyl substituents are employed; see: W. Uhl, A. Janschak, W. Saak, M. Kaupp, R. Wartchow, *Organometallics* **1998**, *17*, 5009.
[23] H. Schumann, C. Janiak, F. Görlitz, J. Loebel, A. Dietrich, *J. Organomet. Chem.* **1989**, *363*, 243.
[24] M. Stender, P. P. Power, *Polyhedron* **2002**, *21*, 525.
[25] P. J. Brothers, K. Hübler, U. Hübler, B. C. Noll, M. J. Olmstead, P. P. Power, *Angew. Chem.* **1996**, *108*, 2528; *Angew. Chem. Int. Ed. Engl.* **1996**, *35*, 2355.
[26] Gaussian 03 (Revision C.02), M. J. Frisch, G. W. Trucks, H. B. Schlegel, G. E. Scuseria, M. A. Robb, J. R. Cheeseman, J. A. Montgomery, Jr., T. Vreven, K. N. Kudin, J. C. Burant, J. M. Millam, S. S. Iyengar, J. Tomasi, V. Barone, B. Mennucci, M. Cossi, G. Scalmani, N. Rega, G. A. Petersson, H. Nakatsuji, M. Hada, M. Ehara, K. Toyota, R. Fukuda, J. Hasegawa, M. Ishida, T. Nakajima, Y. Honda, O. Kitao, H. Nakai, M. Klene, X. Li, J. E. Knox, H. P. Hratchian, J. B. Cross, C. Adamo, J. Jaramillo, R. Gomperts, R. E. Stratmann, O. Yazyev, A. J. Austin, R. Cammi, C. Pomelli, J. W. Ochterski, P. Y. Ayala, K. Morokuma, G. A. Voth, P. Salvador, J. J. Dannenberg, V. G. Zakrzewski, S. Dapprich, A. D. Daniels, M. C. Strain, O. Farkas, D. K. Malick, A. D. Rabuck, K. Raghavachari, J. B. Foresman, J. V. Ortiz, Q. Cui, A. G. Baboul, S. Clifford, J. Cioslowski, B. B. Stefanov, G. Liu, A. Liashenko, P. Piskorz, I. Komaromi, R. L. Martin, D. J. Fox, T. Keith, M. A. Al-Laham, C. Y. Peng, A. Nanayakkara, M. Challacombe, P. M. W. Gill, B. Johnson, W. Chen, M. W. Wong, C. Gonzalez, J. A. Pople, Gaussian, Inc., Pittsburgh, PA, **2004**; the input coordinates were based on the data from the X-ray structure of **6**, and the validity of the optimized structure as a true energy minimum was confirmed by the absence of any imaginary frequencies within the computed vibrational spectrum.
[27] P. P. Power, *Struct. Bonding (Berlin)* **2002**, *103*, 57.
[28] a) G. Treboux, J.-C. Barthelat, *J. Am. Chem. Soc.* **1993**, *115*, 4870; b) H.-G. Himmel, L. Manceron, A. J. Downs, P. Pullumbi, *Angew. Chem.* **2002**, *114*, 829; *Angew. Chem. Int. Ed.* **2002**, *41*, 796.

 © 2005 Wiley-VCH Verlag GmbH & Co. KGaA, Weinheim

Reaction Mechanisms

Mechanistic Insight into Alcohol Oxidation by High-Valent Iron–Oxo Complexes of Heme and Nonheme Ligands**

Na Young Oh, Yumi Suh, Mi Joo Park, Mi Sook Seo, Jinheung Kim, and Wonwoo Nam**

High-valent iron–oxo species are frequently invoked as the key intermediates in the catalytic oxidation of organic substrates by heme and nonheme iron mono-oxygenases.[1,2] In the case of heme-containing enzymes such as cytochromes P450, oxoiron(IV) porphyrin π-cation radicals have been proposed as active oxidants that effect a number of oxidation reactions, which include alkane hydroxylation, olefin epoxidation, and alcohol oxidation.[1] Indeed, a number of synthetic oxoiron(IV) porphyrin π-cation radicals have been prepared and used in mechanistic studies of alkane hydroxylation and olefin epoxidation.[3] In mononuclear nonheme iron enzymes, oxoiron(IV) intermediates have been unveiled very recently in enzymatic and biomimetic reactions.[4–6] The mononuclear nonheme oxoiron(IV) species have been well-characterized with various spectroscopic techniques and with X-ray crystallography and were shown to be active in a variety of oxidation reactions such as alkane hydroxylation, olefin epoxidation, and the oxidation of sulfides and PPh_3.[4–6]

The oxidation of alcohols to the corresponding carbonyl compounds is an important chemical process in industrial and

[*] N. Y. Oh,[+] Y. Suh,[+] M. J. Park, Dr. M. S. Seo, Prof. Dr. J. Kim, Prof. Dr. W. Nam
Department of Chemistry
Division of Nano Sciences and Center for Biomimetic Systems
Ewha Womans University
Seoul 120-750 (Korea)
Fax: (+82) 2-3277-4441
E-mail: jinheung@ewha.ac.kr
wwnam@ewha.ac.kr

[+] These authors contributed equally to this work.

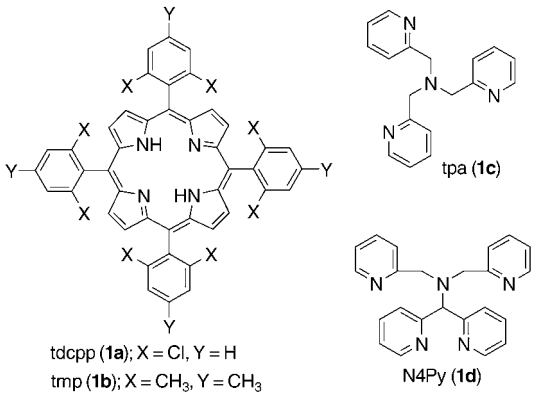
[**] This research was supported by the Ministry of Science and Technology of Korea through Creative Research Initiative Program.

Supporting information for this article is available on the WWW under http://www.angewandte.org or from the author.

 DOI: 10.1002/anie.200500623 © 2005 Wiley-VCH Verlag GmbH & Co. KGaA, Weinheim

biological reactions.[7,8] Thus, tremendous effort has been devoted to developing environmentally benign catalysis and bioinspired oxidation reactions. In the latter case, the oxidation of alcohols by synthetic copper complexes has been intensively investigated as chemical models of galactose oxidase (GOase).[9,10] It has been also shown that cytochromes P450 and their model compounds are able to catalyze the oxidation of alcohols,[11,12] although mechanistic details of iron-complex-mediated alcohol oxidation have never been investigated with in situ generated intermediates of oxoiron(IV) porphyrin π-cation radicals. In the present work, we carried out alcohol oxidation reactions with spectroscopically well characterized oxoiron(IV) porphyrin π-cation radicals, $[(tdcpp)^{\bullet+}Fe^{IV}{=}O]^{+}$ (**1a**) and $[(tmp)^{\bullet+}Fe^{IV}{=}O]^{+}$ (**1b**),[13] and mononuclear nonheme oxoiron(IV) complexes, $[(tpa)Fe^{IV}{=}O]^{2+}$ (**1c**)[5b] and $[(N4Py)Fe^{IV}{=}O]^{2+}$ (**1d**)[5c] (see Scheme 1 for structures of heme and nonheme ligands).[14] To the best of our knowledge, this study provides the first mechanistic details of alcohol oxidation with oxoiron(IV) complexes generated in situ, which bear heme and nonheme ligands.

The high-valent iron–oxo complexes were prepared by using reported methods (see Supporting Information), and kinetic studies with benzyl alcohol were performed at different temperatures due to the different reactivity of the oxoiron(IV) complexes in the oxidation reactions; reaction temperatures were −100 °C for **1a**, −60 °C for **1b**, −40 °C for **1c**, and 0 °C for **1d**. Upon adding 25 equivalents of benzyl alcohol to the solutions of **1**, the intermediates reverted back to the starting iron complexes and showed pseudo-first-order decay as monitored by a UV/Vis spectrophotometer (see Figure 1a for **1d** and Supporting Information for **1a–c**). Pseudo-first-order fitting of the kinetic data allowed us to determine k_{obs} values for the reactions of **1a–d** (Table 1; k_{obs} is the observed rate constant), and product analysis of the resulting solutions with HPLC and GC revealed that benzaldehyde was produced with high yields in all of the reactions (> 70 % based on the intermediates generated; Scheme 2).



Scheme 1. Structures of heme and nonheme ligands of the iron complexes **1a–d** used in this study.

The pseudo-first-order rate constants increased proportionally with benzyl alcohol concentration, thus leading us to determine second-order rate constants (see Table 1, Figure 1b, and Supporting Information). We then determined activation enthalpy, entropy, and Gibbs energy ($\Delta H^{\neq}$, $\Delta S^{\neq}$,

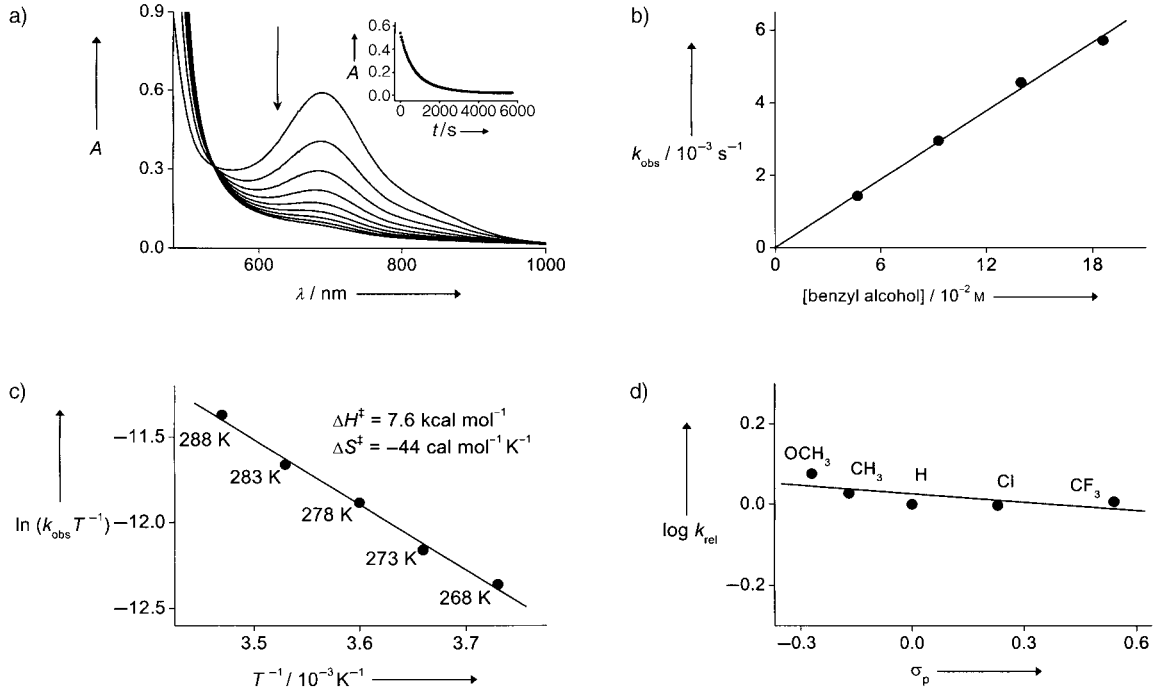


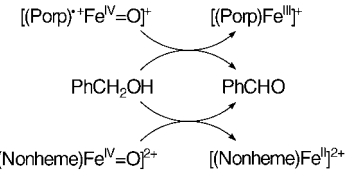
Figure 1. Reactions of **1d** with benzyl alcohols at 0 °C. a) UV/Vis spectral changes of **1d** (2 mM) upon addition of 25 equivalents of benzyl alcohol (50 mM, interval 300 s, A = absorbance). Inset shows absorbance traces monitored at 695 nm. b) Plot of k_{obs} against the concentration of benzyl alcohol to determine a second-order rate constant. c) Plot of first-order rate constants against $1/T$ to determine activation parameters. d) Hammett plot of $\log k_{rel}$ against substituent constants σ_p of benzyl alcohols. The k_{rel} values were calculated by dividing k_{obs} of *para*-X-benzyl alcohol by k_{obs} of benzyl alcohol.

 © 2005 Wiley-VCH Verlag GmbH & Co. KGaA, Weinheim

Table 1: Kinetic parameters determined in the oxidation of benzyl alcohol by oxoiron(IV) complexes of heme and nonheme ligands.[a]

Intermediate[b]	T [°C]	k_{obs} [10^{-3} s^{-1}]	k_2 [10^{-1} M^{-1} s^{-1}][c]	$\Delta G^{\neq}$ [kcal mol^{-1}][d]	k_H/k_D[e]	ρ[f]
1a	−100	6.9 ± 0.3	1.7 ± 0.2	11 ± 1	21 ± 3	−0.39
1b	−60	3.5 ± 0.2	0.84 ± 0.03	16 ± 2	> 20 [g]	−0.43
1c	−40	5.5 ± 0.3	1.2 ± 0.1	16 ± 2	58 ± 5	−0.06
1d	0	1.4 ± 0.1	0.31 ± 0.02	20 ± 2	48 ± 4	−0.07

[a] See Supporting Information for detailed reaction procedures. [b] Intermediates were prepared as described in the Supporting Information. [c] k_2 is the second-order rate constant, see Figure 1b and Supporting Information. [d] Data of $\Delta H^{\neq}$ and $\Delta S^{\neq}$ are reported in Figure 1c and Supporting Information. [e] Data of k_H and k_D are listed in Supporting Information; k_H is the rate constant obtained with $C_6H_5CH_2OH$, k_D is the rate constant obtained with $C_6D_5CD_2OH$. [f] See Figure 1d and Supporting Information. ρ = Hammett reaction constant. [g] The k_D value was similar to the natural decay of **1b**, which indicates that the k_H/k_D value should be greater than that reported. See the k_D value and the rate of natural decay of **1b** in Supporting Information.

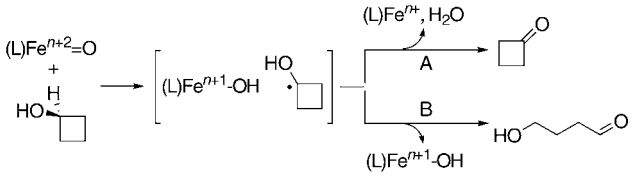


Scheme 2. Oxidation of benzyl alcohol by high-valent iron–oxo complexes of heme and nonheme ligands.

and $\Delta G^{\neq}$) for the benzyl alcohol oxidation with **1** by plotting first-order-rate constants determined at different temperatures against $1/T$ (see Table 1, Figure 1c, and Supporting Information). Taking into consideration that the reactions were performed at different temperatures, we find the kinetic and activation parameters indicate that the relative reactivities of oxoiron(IV) complexes are in the order of **1a** > **1b** > **1c** > **1d**. The greater reactivity of oxoiron(IV) porphyrin π-cation radicals compared to nonheme oxoiron(IV) complexes is rationalized with the higher oxidation state of the iron center in oxoiron(IV) porphyrin π-cation radicals (i.e., the formal oxidation states of Fe^{V} and Fe^{IV} in oxoiron(IV) porphyrin π-cation radical and nonheme oxoiron(IV) species, respectively).[15] In the case of oxoiron(IV) porphyrin π-cation radicals, it has been well documented that the reactivity of electron-deficient iron porphyrins is greater than that of electron-rich iron porphyrins.[16] It has been also shown that the reactivity of nonheme oxoiron(IV) species is dependent on the ligand architecture,[5a–c] and the results presented herein demonstrate that **1c** is more reactive than **1d** in alcohol oxidation.

The kinetics of benzyl alcohol oxidation have also been measured with [D_7]-deuterated benzyl alcohol ($C_6D_5CD_2OH$) to investigate the C–H kinetic isotope effect (KIE). The KIE values determined were large in all of the reactions (see Table 1 and Supporting Information), and such large KIE values have also been observed in GOase[17] and its models[10a,c,18] as well as in the oxidation of benzyl alcohol by high-valent ruthenium-oxo complexes[19] and hydrogen atom abstraction reactions by the iron(IV) intermediates of mono-iron Taurine/α-Ketoglutarate Dioxygenase (TauD)[4b] and diiron methane monooxygenase enzymes.[20] The large, non-classical KIE values indicate that heme and nonheme oxoiron intermediates activate alcohols exclusively by hydrogen atom abstraction from the α-CH of benzyl alcohol and that C–H bond cleavage is the rate-determining step in the alcohol oxidation.[10a,c,17–19] Consistent with this mechanism, studies with *para*-substituted benzyl alcohols reveal that the reaction rates are not greatly influenced by the electron-withdrawing and electron-donating ability of the *para* substituents and that plotting the rates as a function of σ_p of the substituents affords small Hammett ρ values (see Table 1, Figure 1d, and Supporting Information). It is of interest to note that Hammett ρ values obtained in the reactions of GOase and its model compounds are small (e.g., ≈ −0.1)[17,18] and that the Hammett ρ values of synthetic oxoiron(IV) porphyrin π-cation radicals, **1a** and **1b**, are similar to those reported in cytochrome P450 enzymes (e.g., ≈ −0.4).[11]

We then studied cyclobutanol oxidation with the oxoiron(IV) species, as the substrate has been often used as a mechanistic probe to distinguish a one-electron versus a two-electron process in alcohol oxidation by high-valent transition-metal oxidants.[21] For example, if cyclobutanone is produced predominantly, then the reaction occurs by hydrogen atom abstraction followed by an electron transfer (i.e., a two-electron process, see Scheme 3, pathway A). If a carbon



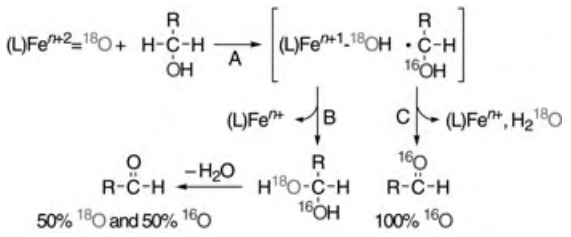
Scheme 3. Oxidation of cyclobutanol by heme and nonheme oxoiron(IV) complexes.

radical formed by hydrogen atom abstraction of cyclobutanol escapes from the solvent cage, a ring-opened product, 4-hydroxybutyraldehyde, is formed (Scheme 3, pathway B).[21a] In the present study, when the oxidation of cyclobutanol was carried out with two oxoiron(IV) complexes, **1a** and **1c**, we found that cyclobutanone was formed exclusively (80–90% yields; see Supporting Information), thus demonstrating that the alcohol oxidation by heme and nonheme oxoiron(IV) complexes proceeds by a two-electron process (Scheme 3, pathway A). A similar observation was reported in the oxidation of cyclobutanol by $Fe^{IV}O^{2+}$ in aqueous solution.[21a]

Finally, the oxidation of benzyl alcohol was carried out with an ^{18}O-labeled oxoiron(IV) complex, $[(N4Py)Fe^{IV}{=}^{18}O]^{2+}$ ([^{18}O]**1d**), to understand whether the final step of the alcohol oxidation is the dehydration of a *gem*-diol intermediate or hydride transfer in the solvent cage to yield a carbonyl

 © 2005 Wiley-VCH Verlag GmbH & Co. KGaA, Weinheim

product (Scheme 4). We therefore prepared [^{18}O]**1d** by treating [(N4Py)Fe^{IV}=O]$^{2+}$ with $H_2{}^{18}O$ and checked the percentage of the ^{18}O isotope in [^{18}O]**1d** with electrospray ionization mass spectrometry (80% ^{18}O in [^{18}O]**1d**, see



Scheme 4. Proposed mechanism for the oxidation of alcohol by heme and nonheme oxoiron(IV) complexes.

Supporting Information).[22] Upon addition of 25 equivalents of benzyl alcohol to the solution of [^{18}O]**1d**, the intermediate reverted back to the starting [Fe^{II}(N4Py)]$^{2+}$, and product analysis with GC–MS revealed that ca. 5% of the oxygen in the benzaldehyde product derived from the oxoiron(IV) species. A control experiment, carried out by incubating benzaldehyde in $H_2{}^{18}O$ under the identical conditions, showed ca. 6% incorporation of the ^{18}O isotope from $H_2{}^{18}O$ in benzaldehyde due to solvent exchange. Based on the observation that the oxygen atom in the aldehyde product does not derive from the oxoiron(IV) complex, we conclude that the benzaldehyde product is formed by hydride transfer (Scheme 4, pathway C), not by a *gem*-diol dehydration (Scheme 4, pathway B).[21a,23]

In summary, we have reported the first example of alcohol oxidation by mononuclear nonheme oxoiron(IV) complexes. We have also reported mechanistic details of alcohol oxidation that have been investigated with in situ generated high-valent iron–oxo complexes of heme and nonheme ligands. The reactivity of heme and nonheme oxoiron(IV) complexes has been briefly compared as well. Finally, we have proposed a plausible mechanism for alcohol oxidation by heme and nonheme oxoiron(IV) intermediates, in which the oxidation of alcohols occurs by an α-CH hydrogen atom abstraction followed by electron transfer (Scheme 4, pathways A and C).

Received: February 21, 2005
Published online: June 2, 2005

Keywords: alcohols · enzyme models · iron · oxidation · reaction mechanisms

[1] a) B. Meunier, S. P. de Visser, S. Shaik, *Chem. Rev.* **2004**, *104*, 3947; b) W. Nam, Y. O. Ryu, W. J. Song, *J. Biol. Inorg. Chem.* **2004**, *9*, 654; c) S. Shaik, S. P. de Visser, D. Kumar, *J. Biol. Inorg. Chem.* **2004**, *9*, 661; d) J. T. Groves, *Proc. Natl. Acad. Sci. USA* **2003**, *100*, 3569; e) P. R. Ortiz de Montellano, J. J. De Voss, *Nat. Prod. Rep.* **2002**, *19*, 477; f) M. Sono, M. P. Roach, E. D. Coulter, J. H. Dawson, *Chem. Rev.* **1996**, *96*, 2841.

[2] a) A. S. Borovik, *Acc. Chem. Res.* **2005**, *38*, 54; b) M. Costas, M. P. Mehn, M. P. Jensen, L. Que, Jr., *Chem. Rev.* **2004**, *104*, 939; c) C. He, Y. Mishina, *Curr. Opin. Chem. Biol.* **2004**, *8*, 201; d) L. D. Slep, F. Neese, *Angew. Chem.* **2003**, *115*, 3048; *Angew. Chem. Int. Ed.* **2003**, *42*, 2942; e) E. I. Solomon, T. C. Brunold, M. I. Davis, J. N. Kemsley, S.-K. Lee, N. Lehnert, F. Neese, A. J. Skulan, Y.-S. Yang, J. Zhou, *Chem. Rev.* **2000**, *100*, 235.

[3] a) J. T. Groves, R. C. Haushalter, M. Nakamura, T. E. Nemo, B. J. Evans, *J. Am. Chem. Soc.* **1981**, *103*, 2884; b) Z. Gross, S. Nimri, *Inorg. Chem.* **1994**, *33*, 1731; c) Y. M. Goh, W. Nam, *Inorg. Chem.* **1999**, *38*, 914; d) W. Nam, S.-E. Park, I. K. Lim, M. H. Lim, J. Hong, J. Kim, *J. Am. Chem. Soc.* **2003**, *125*, 14674.

[4] a) J. C. Price, E. W. Barr, B. Tirupati, J. M. Bollinger, Jr., C. Krebs, *Biochemistry* **2003**, *42*, 7497; b) J. C. Price, E. W. Barr, T. E. Glass, C. Krebs, J. M. Bollinger, Jr., *J. Am. Chem. Soc.* **2003**, *125*, 13008; c) D. A. Proshlyakov, T. F. Henshaw, G. R. Monterosso, M. J. Ryle, R. P. Hausinger, *J. Am. Chem. Soc.* **2004**, *126*, 1022; d) P. J. Riggs-Gelasco, J. C. Price, R. B. Guyer, J. H. Brehm, E. W. Barr, J. M. Bollinger, Jr., C. Krebs, *J. Am. Chem. Soc.* **2004**, *126*, 8108.

[5] a) J.-U. Rohde, J.-H. In, M. H. Lim, W. W. Brennessel, M. R. Bukowski, A. Stubna, E. Münck, W. Nam, L. Que, Jr., *Science* **2003**, *299*, 1037; b) M. H. Lim, J.-U. Rohde, A. Stubna, M. R. Bukowski, M. Costas, R. Y. N. Ho, E. Münck, W. Nam, L. Que, Jr., *Proc. Natl. Acad. Sci. USA.* **2003**, *100*, 3665; c) J. Kaizer, E. J. Klinker, N. Y. Oh, J.-U. Rohde, W. J. Song, A. Stubna, J. Kim, E. Münck, W. Nam, L. Que, Jr., *J. Am. Chem. Soc.* **2004**, *126*, 472; d) A. Decker, J.-U. Rohde, L. Que, Jr., E. I. Solomon, *J. Am. Chem. Soc.* **2004**, *126*, 5378; e) J.-U. Rohde, S. Torelli, X. Shan, M. H. Lim, E. J. Klinker, J. Kaizer, K. Chen, W. Nam, L. Que, Jr., *J. Am. Chem. Soc.* **2004**, *126*, 16750; f) C. V. Sastri, M. S. Seo, M. J. Park, K. M. Kim, W. Nam, *Chem. Commun.* **2005**, 1405; g) S. O. Kim, C. V. Sastri, M. S. Seo, J. Kim, W. Nam, *J. Am. Chem. Soc.* **2005**, *127*, 4178.

[6] a) V. Balland, M.-F. Charlot, F. Banse, J.-J. Girerd, T. A. Mattioli, E. Bill, J.-F. Bartoli, P. Battioni, D. Mansuy, *Eur. J. Inorg. Chem.* **2004**, 301; b) T. A. van den Berg, J. W. de Boer, W. R. Browne, G. Roelfes, B. L. Feringa, *Chem. Commun.* **2004**, 2550; c) C. A. Grapperhaus, B. Mienert, E. Bill, T. Weyhermüller, K. Wieghardt, *Inorg. Chem.* **2000**, *39*, 5306.

[7] a) S. S. Stahl, *Angew. Chem.* **2004**, *116*, 3480; *Angew. Chem. Int. Ed.* **2004**, *43*, 3400; b) R. A. Sheldon, I. W. C. E. Arends, G.-J. T. Brink, A. Dijksman, *Acc. Chem. Res.* **2002**, *35*, 774.

[8] J. W. Whittaker, *Chem. Rev.* **2003**, *103*, 2347.

[9] a) T. D. P. Stack, *Dalton Trans.* **2003**, 1881; b) B. A. Jazdzewski, W. B. Tolman, *Coord. Chem. Rev.* **2000**, *200–202*, 633; c) S. Itoh, M. Taki, S. Fukuzumi, *Coord. Chem. Rev.* **2000**, *198*, 3.

[10] a) R. C. Pratt, T. D. P. Stack, *J. Am. Chem. Soc.* **2003**, *125*, 8716; b) F. Thomas, G. Gellon, I. Gautier-Luneau, E. Saint-Aman, J.-L. Pierre, *Angew. Chem.* **2002**, *114*, 3173; *Angew. Chem. Int. Ed.* **2002**, *41*, 3047; c) P. Chaudhuri, M. Hess, J. Müller, K. Hildenbrand, E. Bill, T. Weyhermüller, K. Wieghardt, *J. Am. Chem. Soc.* **1999**, *121*, 9599; d) S. Itoh, M. Taki, S. Takayama, S. Nagatomo, T. Kitagawa, N. Sakurada, R. Arakawa, S. Fukuzumi, *Angew. Chem.* **1999**, *111*, 2944; *Angew. Chem. Int. Ed.* **1999**, *38*, 2774.

[11] A. D. N. Vaz, M. J. Coon, *Biochemistry* **1994**, *33*, 6442.

[12] J. H. Han, S.-K. Yoo, J. S. Seo, S. J. Hong, S. K. Kim, C. Kim, *Dalton Trans.* **2005**, 402.

[13] T. Wolter, W. Meyer-Klaucke, M. Müther, D. Mandon, H. Winkler, A. X. Trautwein, R. Weiss, *J. Inorg. Biochem.* **2000**, *78*, 117.

[14] Abbreviations used: tdcpp = *meso*-tetrakis(2,6-dichlorophenyl)-porphinato dianion, tmp = *meso*-tetramesitylporphinato dianion, N4Py = *N*,*N*-bis(2-pyridylmethyl)-*N*-bis(2-pyridyl)methylamine, tpa = tris(2-pyridylmethyl)amine.

[15] A. Decker, E. I. Solomon, *Angew. Chem.* **2005**, *117*, 2292; *Angew. Chem. Int. Ed.* **2005**, *44*, 2252.

[16] D. Dolphin, T. G. Traylor, L. Y. Xie, *Acc. Chem. Res.* **1997**, *30*, 251, and references therein.

 © 2005 Wiley-VCH Verlag GmbH & Co. KGaA, Weinheim

[17] M. M. Whittaker, J. W. Whittaker, *Biochemistry* **2001**, *40*, 7140, and references therein.
[18] Y. Wang, J. L. DuBois, B. Hedman, K. O. Hodgson, T. D. P. Stack, *Science* **1998**, *279*, 537.
[19] L. Roecker, T. J. Meyer, *J. Am. Chem. Soc.* **1987**, *109*, 746.
[20] J. C. Nesheim, J. D. Lipscomb, *Biochemistry* **1996**, *35*, 10240.
[21] a) O. Pestovsky, A. Bakac, *J. Am. Chem. Soc.* **2004**, *126*, 13757; b) D. G. Lee, T. Chen, *J. Org. Chem.* **1991**, *56*, 5341; c) J. Rocek, A. E. Radkowsky, *J. Am. Chem. Soc.* **1973**, *95*, 7123.
[22] M. S. Seo, J.-H. In, S. O. Kim, N. Y. Oh, J. Hong, J. Kim, L. Que, Jr., W. Nam, *Angew. Chem.* **2004**, *116*, 2471; *Angew. Chem. Int. Ed.* **2004**, *43*, 2417.
[23] M. S. Thompson, T. J. Meyer, *J. Am. Chem. Soc.* **1982**, *104*, 4106.

 © 2005 Wiley-VCH Verlag GmbH & Co. KGaA, Weinheim

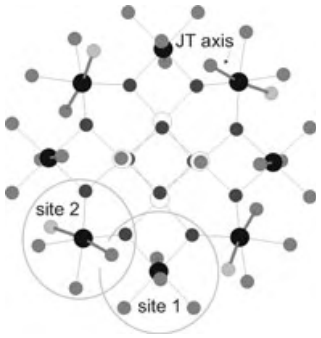


Figure 1. Structure of the core of Mn_{12}-acetate (view along the S_4 axis). For clarity only the first coordination sphere of the Mn ions is drawn. The single-ion Jahn–Teller (JT) axes are represented by thick bonds. Mn^{4+}: white, Mn^{3+}: black, μ_3-O^{2-}: dark gray, OAc: medium gray, H_2O: light gray. The two specific sites 1 and 2 are used in the data analysis and discussion.

Single-Molecule Magnets

Effect of Pressure on the Magnetic Anisotropy in the Single-Molecule Magnet Mn_{12}-Acetate: An Inelastic Neutron Scattering Study**

*Andreas Sieber, Roland Bircher, Oliver Waldmann, Graham Carver, Grégory Chaboussant, Hannu Mutka, and Hans-Ulrich Güdel**

Mn_{12}-acetate is the prototype of a class of polynuclear transition metal complexes known as single-molecule magnets (SMMs). These spin clusters exhibit new phenomena such as slow relaxation and quantum tunneling of magnetization (QTM) at low temperature,[1,2] and this discovery, about a decade ago, triggered a flurry of interdisciplinary research in physics and chemistry. Mn_{12}-acetate was the first SMM discovered, and its properties have been thoroughly studied by many different techniques. As shown in Figure 1, it is composed of a tetrahedral core of oxygen-coordinated Mn^{4+} ions, which are surrounded by a ring of eight Mn^{3+} ions with oxo and acetate coordination.[3] Dominant antiferromagnetic interactions between the Mn^{4+} and Mn^{3+} ions lead to an $S = 10$ ground state.[4] The Mn^{3+} coordination environment is Jahn–Teller-distorted; the elongated Mn–O bonds are emphasized in Figure 1. The concerted action of the resulting Mn^{3+} single-ion anisotropies leads to an overall easy-axis-type anisotropy of the $S = 10$ cluster ground state, which can be expressed by Equation (1).

$$\hat{H}_{ZFS} = D[\hat{S}_z^2 - {}^1/_3 S(S+1)] + B_4^0 \hat{O}_4^0$$
where
$$\hat{O}_4^0 = 35\hat{S}_z^4 - 30S(S+1)\hat{S}_z^2 + 25\hat{S}_z^2 - 6S(S+1) + 3S^2(S+1)^2 \quad (1)$$

As a result the $S = 10$ ground state splits in zero field into eleven $\pm M_S$ sublevels, of which $M_S = \pm 10$ are lowest in energy. An energy barrier between the plus and minus M_S sublevels is thus built up (Figure 2). Inelastic neutron scattering (INS), for which $\Delta M_S = \pm 1$ transitions are allowed, is eminently suited for the direct measurement of this splitting pattern in zero field.[5] The physical properties of Mn_{12}-acetate can be tuned by chemical variation[6,7] or by physical perturbations such as an external magnetic field or pressure.[8,9] Here we report the first spectroscopic study of the anisotropy splitting of Mn_{12}-acetate under hydrostatic pressure up to 12 kbar. From magnetization experiments it was earlier concluded that the anisotropy barrier increases with increasing pressure.[8] From the observed acceleration of the

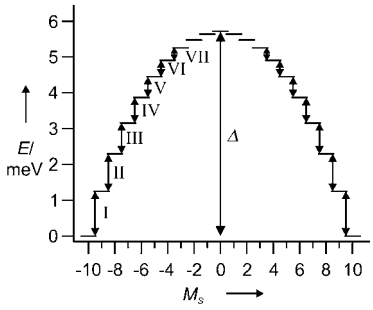


Figure 2. Axial anisotropy splitting and energy barrier Δ of the $S = 10$ ground state. The double arrows correspond to the observed $\Delta M_S = \pm 1$ INS transitions.

[*] A. Sieber, R. Bircher, O. Waldmann, G. Carver, Prof. H.-U. Güdel
Department of Chemistry and Biochemistry
University of Bern
3000 Bern 9 (Switzerland)
Fax: (+41) 31-631-4399
E-mail: hans-ulrich.guedel@iac.unibe.ch
G. Chaboussant
Laboratoire Léon Brillouin (LLB-CNRS-CEA)
CEA Saclay
91191 Gif-sur-Yvette Cedex (France)
H. Mutka
Institut Laue-Langevin
6 rue Jules Horowitz, BP 156, 38042 Grenoble Cedex 9 (France)

[**] This work was financially supported by the Swiss National Science Foundation (NFP 47) and the European Union (TMR Quemolna MRTN-CT-2003-504880).

Supporting information for this article is available on the WWW under http://www.angewandte.org or from the author.

 DOI: 10.1002/anie.200500171 © 2005 Wiley-VCH Verlag GmbH & Co. KGaA, Weinheim

magnetization relaxation it was further postulated that pressure induces partial conversion of the normal, slow-relaxing (SR) Mn_{12}-acetate molecules into a faster relaxing (FR) species.[9] Since INS allows the identification and quantitative characterization of individual species, we expect to clarify and quantify these points, which are important for understanding the mechanism and structural origin of slow magnetic relaxation in Mn_{12}-acetate.

Figure 3 shows the relevant section of the 2.5 K INS spectrum of a fully deuterated sample of Mn_{12}-acetate for the full accessible pressure range, measured on IN5 at the ILL in Grenoble. At 2.5 K the only allowed INS transition is $M_S = \pm 10$ to ± 9. Besides the major peak I around 1.25 meV, we observe a weaker peak *I* around 0.92 meV. The intensity ratio of the two peaks is clearly pressure dependent, and we assign the weak peak to a minority species. Its fraction increases from 3.8% at ambient pressure to 11.1% at 5 kbar, and this conversion is reversible. Above 6 kbar the minority peak is no longer observable in our spectra, most likely due to inhomogeneous broadening and the lower signal-to-noise ratio in the high-pressure clamp cells. Furthermore, a shift of the INS peak positions to higher energies with increasing pressure is evident for both species. Figure 4 shows the pressure dependence of the INS spectrum at 23 K. At this temperature all levels are thermally populated and seven transitions (labeled I to VII in Figure 4) within the zero-field split (ZFS) $S = 10$ ground state are observed. The 5 kbar pattern was measured at four temperatures from 2.5 K to 23 K, and this allowed the peaks originating from the two different species to be identified (cf. Supporting Information). The pressure dependent peak positions of the majority and minority species are listed in Tables S1 and S2, respectively, in the Supporting Information.

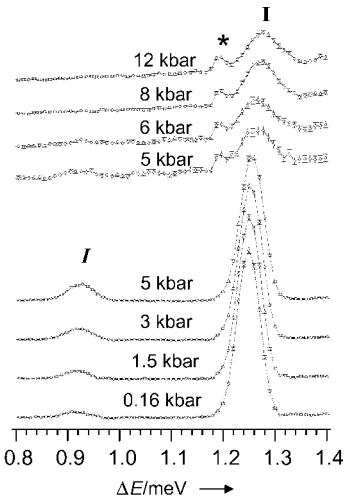


Figure 3. INS spectra at 2.5 K of Mn_{12}-acetate for the indicated pressures. The spectra correspond to the sum of all the scattering angles and are normalized to the elastic intensity. The upper four spectra were obtained with the clamp cells. The lower signal-to-noise ratios in the clamp-cell data originate from the higher background. The labels I and *I* refer to the $\pm 10 \rightarrow \pm 9$ transition (Figure 2) of the majority and minority species, respectively. The asterisk marks a spurion.

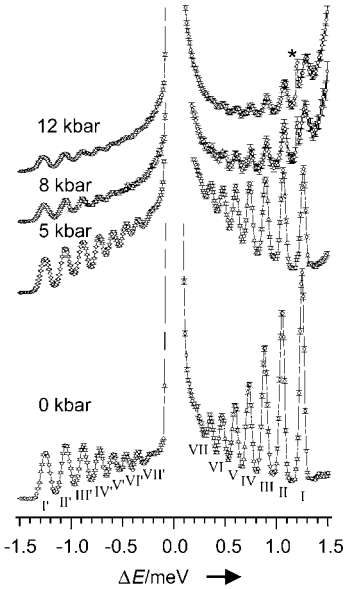


Figure 4. INS spectra at 23 K of Mn_{12}-acetate for the indicated pressures. The spectra correspond to the sum of all the scattering angles and are normalized to the elastic intensity. The lower signal-to-noise ratios at 8 and 12 kbar originate from the higher background of the clamp cells. The labeling of the peaks corresponds to the scheme adopted in Figure 2. The data at ambient pressure are taken from ref. [5]. The asterisk marks a spurion.

It is straightforward to assign the majority species in our INS spectra to the normal, SR Mn_{12}-acetate molecules with the structure shown in Figure 1. The minority species with a significantly smaller anisotropy is assigned to a FR isomer with a different structure. The observed fraction of 3.8% at ambient pressure is in good agreement with the value of 5% derived from ac susceptibility measurements.[10]

For ambient pressure the ZFS of the majority species has been studied previously in great detail by INS with higher instrumental resolution.[5] In addition to the D and B_4^0 parameters in Equation (1), it was possible to quantify two higher order terms which lead to deviations from the pattern in Figure 2. In the present study we concentrate on transitions I–IV, and these are essentially unaffected by the higher order terms and are sufficient to determine both D and B_4^0 accurately. The results of least-squares fits of the eigenvalues of Equation (1) to the experimental energies are given in Tables S1 and S2 in the Supporting Information. The variation of D as a function of pressure for both species is shown in Figure 5. In analogy to other Mn_{12} systems,[6,7] we assume an $S = 10$ ground state for the minority species, which is in good agreement with our INS data. The pressure dependence of D of the SR species is in good agreement with the values given in ref. [8]. The 2.1% increase in $|D|$ between ambient pressure and 12 kbar is significant. B_4^0 is pressure-independent within experimental accuracy, and thus this parameter was kept constant in the analysis.

D in Equation (1) can be related to the anisotropy of the individual Mn^{3+} ions by Equation (2) where the projection

$$D = 2 \sum_{i=1}^{2} a_i D_{Mn^{3+},i} (3 \cos^2 \alpha_i - 1) \qquad (2)$$

 © 2005 Wiley-VCH Verlag GmbH & Co. KGaA, Weinheim

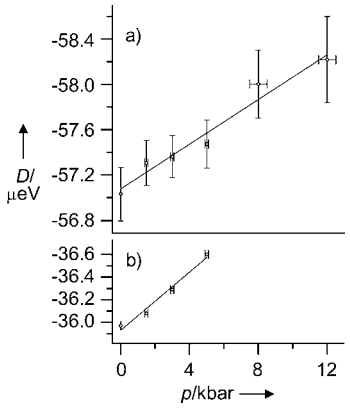


Figure 5. Variation of D as a function of hydrostatic pressure for a) the majority species and b) the minority species.

coefficient $a_i = 0.02845$[3] and α_i is the projection angle of the respective single-ion anisotropy axis (Jahn–Teller axis) on the cluster-anisotropy axis (S_4 axis). The two distinct Mn^{3+} sites with $i = 1$ and 2 (Figure 1) have values of $\alpha_1 = 11°$ and $\alpha_2 = 37°$, respectively, and thus contribute differently to D. In a recent pressure study of another SMM containing Mn^{3+}, $[Mn_4O_3Br(OAc)_3(dbm)_3]$ (dbm = dibenzoylmethane) or Mn_4 in short, $|D|$ was found to decrease by 3.8% between ambient pressure and 12 kbar.[11] This was ascribed to a tilting of the Jahn–Teller axes under pressure, which leads to a decrease in the $(3\cos^2\alpha_i - 1)$ factor in Equation (2). The situation is different in Mn_{12}-acetate, where the observed increase in $|D|$ can be explained by an increase in $|D_{Mn^{3+},i}|$. Using the angular overlap model (AOM) as in ref. [12] and assuming the same compressibility for all Mn^{3+}–O bonds ($d_{12\,kbar}/d_{0\,kbar} = 0.9975$),[11] we can calculate the pressure dependence of $D_{Mn^{3+},i}$ by scaling the AOM parameters with the Mn–O distances. Assuming constant α_i in Equation (2) (isotropic compression), we calculate an increase in $|D|$ of 2.2% between ambient pressure and 12 kbar. The excellent agreement with the experimental value of 2.1% is fortuitous, but the calculation clearly reveals that an increase in the single-ion anisotropy under pressure can explain the observed pressure dependence. As seen in Figure 5b, $|D|$ increases about twice as strongly with pressure in the minority species, but here, too, the main effect is an increase in single-ion anisotropies with increasing pressure.

For a number of Mn_{12}-acetate derivatives FR minority species have been identified and studied in detail. In all cases the activation energy for the magnetization relaxation Δ_{rel} is reduced by about 40% compared to the SR species, but with regard to the anisotropy barrier Δ (Figure 2), two different groups can be distinguished. In the first group the reduction of Δ is about an order of magnitude smaller than the reduction of Δ_{rel}.[6] This is ascribed to a switching of the Jahn–Teller axis of one of the Mn^{3+} ions on site 2 towards the μ_3-oxo bridge (Figure 1). In the second group the reduction of Δ is similar to that of Δ_{rel},[7] and a rather unusual coordination geometry (compressed octahedron) at one Mn^{3+} ion on site 2 was proposed. From our INS data we derive $\Delta = 5.75$ and 3.7 meV at ambient pressure for the SR and FR species, respectively. The reduction of Δ is thus similar to the reduction of the relaxation barrier from $\Delta_{rel} = 5.6$ meV for the SR to $\Delta_{rel} = 3.5$ meV for the FR species.[13] This would place Mn_{12}-acetate in the second group, but additional structural information on the FR species in Mn_{12}-acetate would be desirable.

High-resolution INS allows the simultaneous direct measurement of the anisotropy splitting and its pressure dependence in the $S = 10$ ground state of the two molecular species in Mn_{12}-acetate. From the INS data we clearly see a transformation of the SR into the FR species under pressure. The axial anisotropy of both species increases with increasing pressure, in striking contrast to the situation found in Mn_4, for which a decrease is observed. Apparently, there are no general rules for the pressure dependence of the axial anisotropy in SMMs, though we could provide a consistent explanation for both Mn_{12}-acetate and Mn_4.

Experimental Section

A fully deuterated, polycrystalline sample of Mn_{12}-acetate was synthesized according to ref. [14].

INS measurements were performed on the high-resolution time-of-flight spectrometer IN5 at the Institut Laue-Langevin in Grenoble, France. A neutron wavelength of $\lambda_i = 5.9$ Å (FWHM = 57 μeV) was used. Data treatment involved the calibration of the detectors with a vanadium spectrum. The time-of-flight to energy conversion and data reduction were performed with the standard program INX at the ILL.

A standard ILL continuously loaded high-pressure He gas cell, loaded with 4.3 g of Mn_{12}-acetate, was used for pressures $p = 0.16(1)$, 1.5(1), 3.0(1), and 5.0(1) kbar. For $p = 5.0(5)$, 6.0(5), and 8.0(5) kbar the standard ILL 10 kbar high-pressure clamp cell (0.6 g sample) and for $p = 12.0(5)$ kbar the standard ILL 15 kbar high-pressure clamp cell (0.4 g sample) were used with FC-75 (fluorinated hydrocarbon, 3M) as pressure-transmitting medium. An ILL orange cryostat was used for cooling.

Received: January 17, 2005
Revised: March 30, 2005
Published online: June 7, 2006

Keywords: high-pressure chemistry · inelastic neutron scattering · Jahn–Teller distortion · magnetic properties · manganese

[1] R. Sessoli, D. Gatteschi, A. Caneschi, M. A. Novak, *Nature* **1993**, *365*, 141 – 143.
[2] D. Gatteschi, R. Sessoli, *Angew. Chem.* **2003**, *115*, 278 – 309; *Angew. Chem. Int. Ed.* **2003**, *42*, 268 – 297.
[3] A. Cornia, R. Sessoli, L. Sorace, D. Gatteschi, A. L. Barra, C. Daiguebonne, *Phys. Rev. Lett.* **2002**, *89*, 257201.
[4] G. Chaboussant, A. Sieber, S. Ochsenbein, H.-U. Güdel, M. Murrie, A. Honecker, N. Fukushima, B. Normand, *Phys. Rev. B* **2004**, *70*, 104422.
[5] R. Bircher, G. Chaboussant, A. Sieber, H.-U. Güdel, H. Mutka, *Phys. Rev. B* **2004**, 70, 212413.
[6] S. M. J. Aubin, Z. Sun, E. M. Rumberger, D. N. Hendrickson, G. Christou, *J. Appl. Phys.* **2002**, *91*, 7158 – 7160.
[7] K. Takeda, K. Awaga, T. Inabe, A. Yamaguchi, H. Ishimoto, T. Tomita, H. Mitamura, T. Goto, N. Mori, H. Nojiri, *Phys. Rev. B* **2002**, *65*, 094424.
[8] Y. Murata, K. Takeda, T. Sekine, M. Ogata, K. Awaga, *J. Phys. Soc. Jpn.* **1998**, *67*, 3014 – 3017.
[9] Y. Suzuki, K. Takeda, K. Awaga, *Phys. Rev. B* **2003**, *67*, 132402.

 © 2005 Wiley-VCH Verlag GmbH & Co. KGaA, Weinheim

[10] M. Evangelisti, J. Bartolomé, *J. Magn. Magn. Mater.* **2000**, *221*, 99–102.
[11] A. Sieber, G. Chaboussant, R. Bircher, C. Boskovic, H.-U. Güdel, G. Christou, H. Mutka, *Phys. Rev. B* **2004**, *70*, 172413.
[12] D. Gatteschi, L. Sorace, *J. Solid State Chem.* **2001**, *159*, 253–261.
[13] B. Barbara, L. Thomas, F. Lionti, I. Chiorescu, A. Sulpice, *J. Magn. Magn. Mater.* **1999**, *200*, 167–181.
[14] T. Lis, *Acta Crystallogr. Sect. B* **1980**, *36*, 2042–2046.

 © 2005 Wiley-VCH Verlag GmbH & Co. KGaA, Weinheim

Drug Delivery

Design, Construction, and Intracellular Activation of an Intramolecularly Self-Silenced Signal Transduction Inhibitor**

Seung-Yub Lee, Fubo Liang, Xiao-Ling Guo, Laiping Xie, Sean M. Cahill, Michael Blumenstein, Heyi Yang, David S. Lawrence, and Zhong-Yin Zhang**

The AB protein toxins are among the most potent and lethal cell death inducing agents known. This protein family includes such notorious cytotoxins as ricin, and the cholera, diphtheria, tetanus, and botulinum toxins.[1] These, and related family members, share a variety of structural and mechanistic motifs. The A polypeptide acts on a specific intracellular target in a fashion that compromises cellular viability. By contrast, the B moiety serves as a transporter that delivers the A component to the intracellular environment. In addition, the B polypeptide is typically conjoined to the A moiety through a disulfide bridge, which suppresses the biological activity of the latter. However, upon intracellular reduction of the disulfide, the A protein is released into its fully activated state.

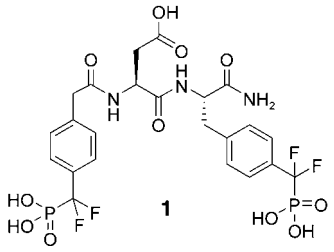
[*] Dr. S.-Y. Lee, Dr. S. M. Cahill, Prof. D. S. Lawrence
Department of Biochemistry
Albert Einstein College of Medicine
1300 Morris Park Avenue, Bronx, NY 10461 (USA)
Fax: (+1) 718-430-8565
E-mail: dlawrenc@aecom.yu.edu
Dr. F. Liang, X.-L. Guo, Dr. L. Xie, Dr. H. Yang, Prof. Z.-Y. Zhang
Department of Molecular Pharmacology
Albert Einstein College of Medicine
1300 Morris Park Avenue, Bronx, NY 10461 (USA)
Fax: (+1) 718-430-8922
E-mail: zyzhang@aecom.yu.edu
Dr. M. Blumenstein
Department of Chemistry
Hunter College and
the Graduate School of the City University of New York
New York, NY 10021 (USA)

[**] This work was supported by NIH Grants DK68447 and CA095019, and the G. Harold and Leila Y. Mathers Charitable Foundation. Z.-Y.Z. is an Irma T. Hirschl Career Scientist.

Supporting information for this article is available on the WWW under http://www.angewandte.org or from the author.

It occurred to us that the AB protein toxin mechanism by which a highly toxic, but membrane-impermeable, protein is delivered to a cell in an inert form might prove applicable to other inhibitory agents as well. We describe herein a strategy that employs a cell-penetrating peptide (CPP)[2] to 1) suppress the activity of an appended inhibitor, 2) deliver the membrane-impermeable inhibitor to the intracellular environment, and, once inside the cell, 3) release the inhibitor in its active form.

We previously described the protein tyrosine phosphatase (PTP) 1B inhibitor **1**.[3] This species is the most potent

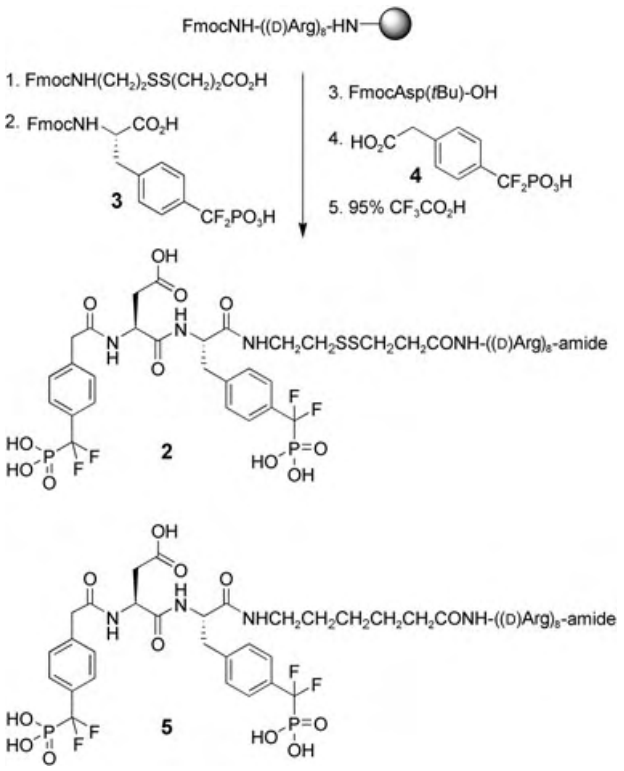


1

(inhibitory constant, $K_i = 2.4$ nM) and selective PTP1B inhibitor (1000–10000-fold versus a panel of phosphatases) reported to date. The negatively charged aryldifluorophosphonate functional groups participate in key active-site and near-active-site interactions that are responsible for the high PTP1B potency displayed by **1**.[4] Not surprisingly, the negatively charged inhibitor is not cell-permeable.[5] We anticipated that a cell-permeable derivative of **1** could be prepared by coupling it to the CPP ((D)-Arg)$_8$ moiety to generate **2** (Scheme 1). Polycationic CPPs are widely used to transport cargo through cell membranes.[2] However, we also expected that electrostatic interactions between the positively charged CPP and the negatively charged cargo might have the desirable effect of suppressing inhibitory efficacy. Consequently, effective inhibition of PTP1B, a cytoplasmically oriented endoplasmic reticulum (ER)-embedded protein,[6] should only transpire upon release of the cargo from the CPP and only if release occurs within a PTP1B-available region of the cell. By contrast, a corresponding construct that lacks the disulfide bridge (**5**) should be unable to effectively inhibit PTP1B.

Compound **2** was directly prepared on the Rink resin by sequential coupling of eight (D)-Fmoc-Arg(Pbf) residues (Pbf = 2,2,4,6,7-pentamethyldihydrobenzofuran-5-sulfonyl), FmocNH$(CH_2)_2SS(CH_2)_2CO_2H$, compound **3**, Fmoc-Asp-(*t*Bu)OH, and compound **4** (Scheme 1).[7] Simultaneous deprotection and cleavage mediated by CF_3CO_2H furnished **2**. Compound **2** is an extraordinarily ineffective inhibitor of PTP1B, with a K_i value (8.2 μM) that is three orders of magnitude lower than that of **1**. This appears to be a consequence of intramolecular interactions between the PTP1B-directed portion of **2** and its disulfide-linked ((D)-Arg)$_8$ appendage. NMR experiments under aqueous conditions confirm that the key active-site-directed aryldifluorophosphonate moiety is engaged in through-space interactions with the ((D)-Arg)$_8$ cell-permeabilizing sequence (see Supporting Information). Furthermore, the intramolecular nature

 © 2005 Wiley-VCH Verlag GmbH & Co. KGaA, Weinheim DOI: 10.1002/anie.200462004



Scheme 1. Solid-phase synthesis of the CPP-S-S-(PTB1-B inhibitor) constructs **2** and **5**. Peptides were prepared on the Rink amide resin by using 9-fluorenylmethoxycarbonyl (Fmoc)-protected amino acids and a standard coupling protocol involving 1-hydroxybenzotriazole/2-(1*H*-benzotriazol-1-yl)-1,1,3,3-tetramethyluronium hexafluorophosphate/*N*-methylmorpholine for the activation of acids.

enhancements in IRβ and IRS-1 phosphotyrosine levels have been reported with a PTP1B inhibitor.[5]

We performed an analogous study using a Chinese hamster oocyte (CHO) cell line transfected with an expression plasmid encoding human IR (CHO/HIRc). We previously found that compound **1** has no effect on IRβ and IRS-1 phosphotyrosine levels in this cell line, since its five negative charges render it membrane-impermeable.[5] The CHO/HIRc cell line was exposed to compounds **2** and **5** over a selected range of concentrations for 1 h and subsequently treated either with or without insulin (10 nM) for 10 min. Cell lysates were then resolved by SDS-PAGE, electrotransferred to nitrocellulose membranes, and probed with anti-pTyr antibody (Figure 1). Compound **5** has no effect on IRβ or IRS-1

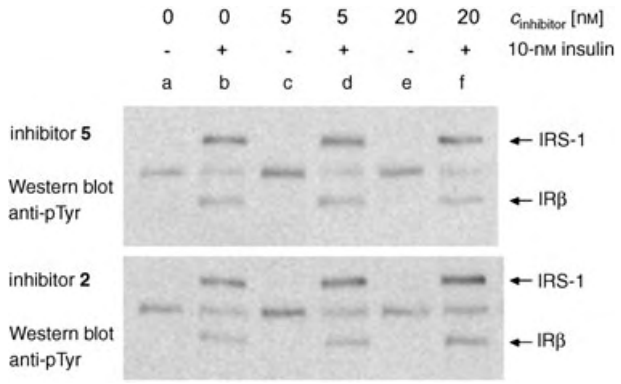


Figure 1. Effect of PTP1B inhibitors **5** (upper gel) and **2** (lower gel) on the tyrosine phosphorylation status of IRS-1 and IRβ. Lane a (no inhibitor, without insulin); lane b (no inhibitor, with insulin); lane c (5-nM **5** and **2**, without insulin); lane d (5-nM **5** and **2**, with insulin); lane e (20-nM **5** and **2**, without insulin); lane f (20-nM **5** and **2**, with insulin).

of this interaction is confirmed by the fact that the inhibitory efficacy of free **1** is not affected by added $((D)\text{-Arg})_8$ (at concentrations up to 20 μM). Finally, the masking effect of the positively charged permeabilizing sequence is due to electrostatic interactions, since a corresponding cell-permeable fatty-acid-derivatized PTP1B inhibitor is fully active.[5]

The disulfide bridge present in **2** is absent in the otherwise structurally equivalent derivative **5**. Compound **5** was synthesized in a fashion analogous to that outlined in Scheme 1 with the exception that $FmocNH(CH_2)_5CO_2H$ was employed in step 1. As expected, both compounds **2** and **5** ($K_i = 9.0$ μM) are equally poor PTP1B inhibitors under nonreducing conditions.

We determined the cellular effects of compounds **2** and **5** on insulin signaling to assess the efficacy of the delivery strategy mimicking AB protein toxins. Insulin-mediated activation of the insulin receptor (IR) produces a wide array of cellular responses, including enhanced phosphorylation of the insulin receptor β (IRβ) subunit and the insulin receptor substrate-1 (IRS-1). Previous studies have demonstrated that PTP1B serves as a negative regulator of the insulin-activated signaling pathways by catalyzing the dephosphorylation of IRβ and IRS-1.[5] For example, the antisense-mediated reduction of PTP1B in rat hepatoma cells generates a 2.3-fold and 1.5-fold increase in IRβ and IRS-1 phosphotyrosine levels, respectively.[8] In addition, significant phosphotyrosine levels, even at concentrations as high as 100 nM (data not shown). This is not surprising given that the latter concentration is 90 times lower than the in vitro K_i of **5**. By contrast, even at 5 nM, compound **2** enhances the phosphotyrosine content of IRβ and IRS-1 1.7- and 1.4-fold, respectively. An even more pronounced effect is observed at 20 nM (2.4- and 2.2-fold, respectively). These concentrations are nearly three orders of magnitude lower than the K_i value displayed by **2** under nonreducing conditions in vitro. These results are consistent with the notion that the disulfide bridge linking the PTP1B inhibitory component ($K_i = 2.4$ nM) with the CPP has been cleaved and that the liberated inhibitor has ready access to the cytoplasmically oriented protein target.

In summary, we have shown that a CPP module can be used to biochemically silence the biological activity of appended cargo.[9] This property, which is a characteristic feature of AB protein toxins, should restrict the desired biological effect to the targeted intracellular environment. We are currently investigating the scope of this approach as well as the utility of compound **2** for the treatment of diabetes and obesity.[10]

Received: September 15, 2004
Revised: March 7, 2005
Published online: June 2, 2005

 © 2005 Wiley-VCH Verlag GmbH & Co. KGaA, Weinheim

Keywords: drug delivery · inhibitors · peptides · prodrugs · signal transduction

[1] P. O. Falnes, K. Sandvig, *Curr. Opin. Cell Biol.* **2000**, *12*, 407.
[2] P. Lundberg, U. Langel, *J. Mol. Recognit.* **2003**, *16*, 227.
[3] K. Shen, Y. F. Keng, L. Wu, X. L. Guo, D. S. Lawrence, Z. Y. Zhang, *J. Biol. Chem.* **2001**, *276*, 47311.
[4] J. P. Sun, A. A. Fedorov, S. Y. Lee, X. L. Guo, K. Shen, D. S. Lawrence, S. C. Almo, Z. Y. Zhang, *J. Biol. Chem.* **2003**, *278*, 12406.
[5] L. Xie, S. Y. Lee, J. N. Andersen, S. Waters, K. Shen, X. L. Guo, N. P. Moller, J. M. Olefsky, D. S. Lawrence, Z. Y. Zhang, *Biochemistry* **2003**, *42*, 12792.
[6] J. V. Frangioni, P. H. Beahm, V. Shifrin, C. A. Jost, B. G. Neel, *Cell* **1992**, *68*, 545.
[7] See Supporting Information for details concerning the synthesis and characterization of compounds **2** and **5**, IRβ and IRS-1 phosphorylation status, and cell-culture studies.
[8] J. E. Clampit, J. L. Meuth, H. T. Smith, R. M. Reilly, M. R. Jirousek, J. M. Trevillyan, C. M. Rondinone, *Biochem. Biophys. Res. Commun.* **2003**, *300*, 261.
[9] While this manuscript was under review, a paper appeared describing a similar strategy: T. Jiang, E. S. Olson, Q. T. Nguyen, M. Roy, P. A. Jennings, R. Y. Tsien, *Proc. Natl. Acad. Sci. USA* **2004**, *101*, 17867.
[10] Z. Y. Zhang, S. Y. Lee, *Expert Opin. Invest. Drugs* **2003**, *12*, 223.

 © 2005 Wiley-VCH Verlag GmbH & Co. KGaA, Weinheim

Analytical Methods

Quantification of the Cellular Uptake of Cell-Penetrating Peptides by MALDI-TOF Mass Spectrometry**

Fabienne Burlina, Sandrine Sagan, Gérard Bolbach, and Gérard Chassaing*

Cell-penetrating peptides (CPPs) are widely used to deliver biologically active molecules into cells.[1] We have successfully applied matrix-assisted laser desorption/ionization time-of-flight mass spectrometry (MALDI-TOF MS) to the quantification of cellular uptake of CPPs. Penetratin, which corresponds to residues 43 to 58 of the *Antennapedia* homeodomain, was one of the first small CPPs to be discovered a decade ago.[2] Many others were identified soon after: Tat-derived peptides,[3] nuclear localization sequences,[4] transportan,[5] model amphipatic peptides,[6] polybasic peptides,[7,8] amphipathic proline-rich peptides,[9] and β peptides.[10] Many studies concerning the cellular uptake efficiencies of these CPPs have been reported, most of them based on the quantification of a radioactive or a fluorescent reporter group.[11] Only one example of direct CPP quantification has been reported, based on HPLC analysis of fluorescent CPPs.[12] The results strongly differ from one study to another. For example, the ratio between intracellular and extracellular concentrations of penetratin ranges from 0.6:1.0[13] to 95.0:1.0.[14] Discrepancies observed between studies can be explained by the use of different cell types and cell treatments (fixed or unfixed cells), different methods of detection, interference of the reporter group, or inaccurate distinction between internalized and membrane-associated peptides. In some of the studies the fraction of CPP bound to the external surface of the cells is removed by washing or by enzymatic digestion.[11] In other cases discrimination between internalized and membrane-bound peptide is achieved by chemical modification of the non-internalized peptide[12] or by the use of a reduction-sensitive fluorophore.[15] We report here a novel method based on MALDI-TOF MS to measure the concentration of internalized peptide and its application to the study of three widely used CPPs: penetratin, Tat_{48-59}, and $(Arg)_9$. The concept is outlined in Figure 1.

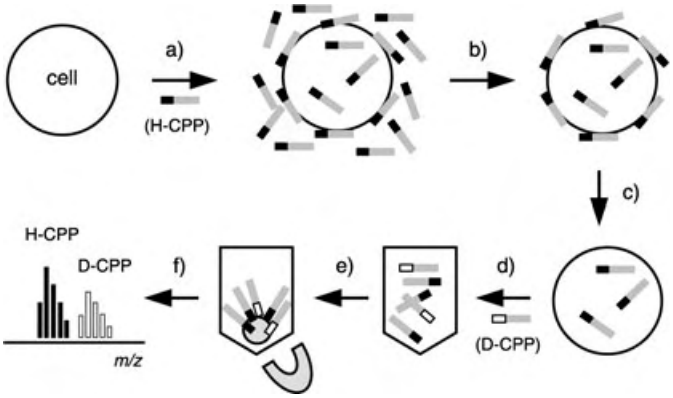


Figure 1. Quantification of CPP cellular uptake by MALDI-TOF MS. a) Cells are incubated with biotinylated non-deuterated CPP (H-CPP). b) Cells are washed. c) Membrane-bound CPP is digested by trypsin then trypsin inhibitor is added. d) A known and appropriate amount of internal standard (biotinylated deuterated CPP, D-CPP) is added, cell lysis is performed in 0.3% triton X100 and 1 M NaCl, and the sample is heated for 15 min at 100°C. e) Biotinylated peptides are captured by streptavidin-coated magnetic beads. f) Beads are washed and analyzed by MALDI-TOF MS. The ratio between the $[M+H]^+$ signal areas of H-CPP and D-CPP yields the absolute amount of internalized peptide.

Peptide quantification by MALDI-TOF MS can only be achieved by using the same peptide labeled with a stable isotope as an internal standard. Both peptides have identical chemical structure and exhibit the same efficiencies of desorption/ionization and detection. The relative intensity of the peptides $[M+H]^+$ signals therefore corresponds to the relative proportion of the peptides in the sample.[16,17] We

[*] Dr. F. Burlina, Dr. S. Sagan, Dr. G. Bolbach, Dr. G. Chassaing
UMR CNRS 7613
Synthèse, Structure et Fonction de Molécules Bioactives
Université Pierre et Marie Curie
4 place Jussieu, 75252 Paris cedex 05 (France)
Fax: (+33) 144-273-843
E-mail: burlina@ccr.jussieu.fr

[**] We thank Dr. Alain Prochiantz and Dr. Alain Joliot for fruitful discussions. We are also grateful to Dr. John Offer and Dr. Florian Toepert for their critical comments on the manuscript.

Supporting information for this article is available on the WWW under http://www.angewandte.org or from the author.

 © 2005 Wiley-VCH Verlag GmbH & Co. KGaA, Weinheim DOI: 10.1002/anie.200500477

have previously reported a method to directly analyze by MALDI-TOF MS biotinylated peptides that were extracted from a complex mixture using streptavidin-coated magnetic beads.[18] We have now combined this technique with isotopic labeling to quantify cellular uptake of CPPs. The process of capturing the CPPs on beads enables concentration of the internalized CPP and its purification from cell lysate before MALDI-TOF MS analysis. This step is essential to facilitate detection of very small amounts of internalized CPP and also to allow distinction between the CPPs and endogenous peptides having the same molecular weight. The use of MALDI-TOF MS gives the advantage of direct detection of the peptide. Therefore, discrimination between internalized and membrane-bound peptide can be easily achieved by submitting the non-internalized peptide to a chemical or an enzymatic treatment that modifies its molecular weight. Intracellular degradation of the CPPs can also be studied. Finally, the simultaneous comparison of the cellular uptake efficiencies of several CPPs can be performed as long as the peptides have different molecular weights.

The CPPs used in this study were functionalized on their N-terminus with biotin and an isotopic tag composed either of four non-deuterated glycine residues (H-CPP, internalized) or four deuterated glycine residues (D-CPP, internal standard). The internalization experiments were performed following the protocol described in Figure 1 (see also the Supporting Information). The internal standard was submitted to the whole process of cell lysis and internalized CPP extraction to enable any degradation artefacts to be detected. Indeed this process allows the fast distinction between intracellular degradation of CPP (only H-CPP digests would be detected) and degradation of CPP occurring during sample preparation (the same H-CPP and D-CPP digests would be detected) by MALDI-TOF MS (see the Supporting Information). The conditions used for cell lysis and peptide capture were found to be particularly critical for the accuracy of the quantification. Indeed, the lysate may contain molecules that exhibit affinity for the CPPs and may thus hamper their capture by streptavidin-coated magnetic beads. This situation may lead to discrimination during capture between the internalized CPP and the internal standard since both peptides have not necessarily been exposed to the same interactions. Nucleic acids in particular were found to perturb the peptide extraction process. This problem could be overcome by treating the lysate with nucleases before peptide capture or by performing the capture in the presence of high salt concentrations. However, degradation of both the internalized peptide and the internal standard was then observed. This effect was possibly a result of the release of lysosomal enzymes during cell lysis. The addition of protease inhibitors during the whole process of peptide extraction was not sufficient to completely block degradation; this was only achieved by directly heating the cells in the lysis solution at 100 °C for 15 minutes and maintaining the samples at 4 °C for the rest of the extraction process (see the Supporting Information). In addition to protease denaturation, this heating step enables both the internal standard and the internalized CPP to associate to the same extent with lysate components and to be subsequently captured on streptavidin-coated magnetic beads with the same efficiency. After capture of the biotinylated peptides, lysate components were easily removed by using the protocol described previously for washing the beads.[18] The peptides associated with the beads were then mixed with the matrix α-cyano-4-hydroxycinnamic acid, deposited directly on the MALDI-TOF plate, and then analyzed. Spectra were averaged for statistical sampling from a few hundred laser shots recorded on different spots of the deposit. The acquisition of $[M+H]^+$ signals with the natural isotopic distribution for both H-CPP and D-CPP was the indication of a valid statistical sampling (Figure 2a and Supporting Information). The areas of the H-CPP and D-CPP $[M+H]^+$ signals, including all the isotopes, were used for the quantification. Quantification was more precise when H-CPP and D-CPP signals had similar intensities because the signal/noise ratio was then comparable for both peptides. In practice, the amount of internalized H-CPP was first evaluated by adding various known quantities of D-CPP to samples containing the internalized peptide. Quantification was then found to be feasible with our mass spectrometer for H-CPP/D-CPP signals ratios ranging from 0.2:1 to 5:1. The experiment was repeated, with the amount of D-CPP adjusted to get a signal ratio close to 1:1. Quantifications performed on different deposits of the same biological sample gave highly reproducible results (±5% variation).

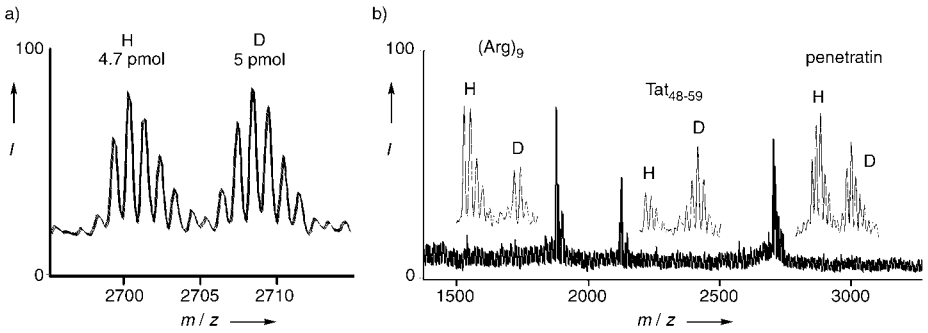


Figure 2. MALDI-TOF mass spectra obtained for internalization of a) penetratin and b) a mixture of penetratin (biotin-GGGG-RQIKIWFQNRRMKWKK-NH_2), Tat_{48-59} (biotin-GGGG-RKKRRQRRRPPQ-NH_2), and $(Arg)_9$ (biotin-GGGG-RRRRRRRRR-NH_2). H and D correspond to the $[M+H]^+$ peaks of the internalized CPPs and the internal standards, respectively.

By using this protocol we measured the intracellular concentrations of penetratin, Tat_{48-59}, and $(Arg)_9$. Each experiment was carried out by incubating 10^6 Chinese hamster ovary (CHO) cells (corresponding to a total intracellular volume of 1.5 μL) for 75 minutes at 37 °C with the CPP (7.5 μM). The highest intracellular concentration was found for $(Arg)_9$ corresponding to 4.5 ± 1 μM (average concentration ± standard deviation (± SD), $n = 10$) followed by penetratin (3.5 ± 0.8 μM, $n = 12$) and Tat_{48-59} (0.7 ± 0.2 μM, $n =$

 © 2005 Wiley-VCH Verlag GmbH & Co. KGaA, Weinheim

10; Figures 2a and 3a). H-CPPs digests corresponding exclusively to cleavage at the C-terminus of basic residues were occasionally observed with low abundance. These species were likely formed by the trypsin treatment used to digest the membrane-bound H-CPP and not completely eliminated during the subsequent washing step (Figure 1). In contrast to other CPP uptake assays our mass spectrometry approach allowed the facile distinction between these false positives and the peptide fraction that was actually internalized. No other digestion products were detected (see the Supporting Information for full mass spectra). The trypsin treatment was omitted in another set of experiments aimed at evaluating the affinities of the CPPs for the cellular membrane. Depending on the CPP, the amount corresponding to the sum of internalized and membrane-bound peptide was 5 to 60 times higher than the amount of internalized peptide (Figure 3b). These results stress the importance of the trypsin digestion step combined with direct quantification of the CPP to accurately discriminate extracellular membrane-bound peptide from internalized peptide. They also show that the efficiency of CPP internalization is not directly linked to membrane affinity. Finally, the amount of internalized CPPs was measured when the cells were incubated with a mixture of the three CPPs (7.5 μM each; Figures 2b and 3a). No cell lysis during incubation was observed. The relative internalization efficiencies of the CPPs were found to be equivalent to those calculated from the single CPP incubation experiments, but lower amounts of internalized peptide were measured (Figure 3a). These data show that no competition occurs between the three CPPs and suggest that a limited number of internalization domains are available. Experiments using CPP mixtures are more applicable for screening than for absolute quantification of cellular uptake. Indeed, saturation phenomena can occur as observed with the CPP mixture used in this study. Other CPP mixtures may also lead to competition between individual peptides. Furthermore, low-intensity signals may be observed in the MALDI-TOF mass spectra for CPPs that are the most poorly internalized.

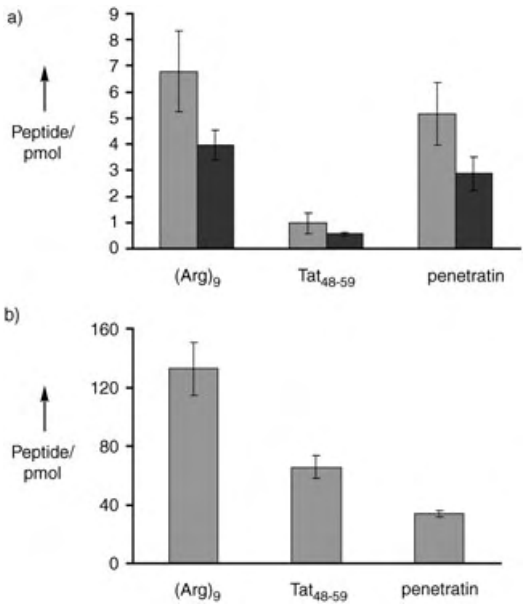


Figure 3. a) Amount of intact internalized CPP. Gray and black bars correspond to incubation of 10^6 CHO cells with each CPP independently or a mixture of the three CPPs, respectively. Each data is the average result of at least three independent experiments performed in duplicates or triplicates (±SD). Comparison of the mean differences between intracellular amounts of the three CPPs was performed with the Welch t test (populations with unequal SD) and was found significant ($p = 0.016$) between penetratin and $(Arg)_9$ and very significant ($p < 0.0001$) between penetratin or $(Arg)_9$ and Tat_{48-59}. b) Total amount of membrane-bound and internalized CPP. Data correspond to incubation of 10^6 CHO cells with each CPP independently.

In contrast to the majority of data reported in the literature for penetratin, Tat-derived peptides, and $(Arg)_9$, the intracellular CPP concentration was found in this study to be lower than the extracellular CPP concentration. Some of the high values of internalized CPP reported in the literature are likely explained by an incomplete elimination of the fraction of membrane-bound peptide. Results that closely match the ones determined in this study were obtained by fluorescence correlation microscopy, which allows unambiguous discrimination between extracellular and intracellular CPP.[13]

The detailed analysis of intracellular degradation of CPPs by using MALDI-TOF MS has been reported before.[19,20] However, compared to the method used, our procedure offers the advantage of allowing distinction between degradation occurring during sample preparation and actual intracellular degradation, with the internal standard (D-CPP) serving as a control (see the Supporting Information).

In conclusion, the method presented here enables direct quantification of CPP with unambiguous discrimination between membrane-bound and intracellular CPP. It is the first method described that allows direct comparison of internalization efficiencies using mixtures of CPPs. It is simple to use, fast, and yields highly reproducible results. The process of sample analysis on the MALDI-TOF plate lends itself to automation for the high-throughput screening of CPP libraries. The present method will provide a reliable and efficient tool for the design and optimization of new CPPs and for the study of their internalization mechanisms.

Received: February 8, 2005
Published online: June 1, 2005

Keywords: analytical methods · drug delivery · isotopic labeling · mass spectrometry · peptides

[1] A. Joliot, A. Prochiantz, *Nat. Cell Biol.* **2004**, *6*, 189–196.
[2] D. Derossi, A. H. Joliot, G. Chassaing, A. Prochiantz, *J. Biol. Chem.* **1994**, *269*, 10444–10450.
[3] E. Vivès, P. Brodin, B. Lebleu, *J. Biol. Chem.* **1997**, *272*, 16010–16017.
[4] A. D. Ragin, R. A. Morgan, J. Chmielewski, *Chem. Biol.* **2002**, *8*, 943–948.
[5] M. Pooga, M. Hällbrink, M. Zorko, Ü. Langel, *FASEB J.* **1998**, *12*, 67–77.
[6] A. Scheller, B. Wiesner, M. Melzig, M. Bienert, J. Oehlke, *Eur. J. Biochem.* **2000**, *267*, 6043–6049.

 © 2005 Wiley-VCH Verlag GmbH & Co. KGaA, Weinheim

[7] J. B. Rothbard, E. Kreider, C. L. VanDeusen, L. Wright, B. L. Wylie, P. A. Wender, *J. Med. Chem.* **2002**, *45*, 3612 – 3618.
[8] S. Futaki, T. Suzuki, W. Ohashi, T. Yagami, S. Tanaka, K. Ueda, Y. Sugiura, *J. Biol. Chem.* **2001**, *276*, 5836 – 5840.
[9] J. Fernández-Carneado, M. J. Kogan, S. Castel, E. Giralt, *Angew. Chem.* **2004**, *116*, 1847 – 1850; *Angew. Chem. Int. Ed.* **2004**, *43*, 1811 – 1814.
[10] N. Umezawa, M. A. Gelman, M. C. Haigis, R. T. Raines, S. H. Gellman, *J. Am. Chem. Soc.* **2002**, *124*, 368 – 369.
[11] M. Lindgren, M. Hällbrink, Ü. Langel in *Cell-penetrating peptides Processes and applications* (Ed.: Ü. Langel), CRC, Boca Raton, FL, **2002**, pp. 263 – 275.
[12] J. Oehlke, A. Scheller, B. Wiesner, E. Krause, M. Beyermann, E. Klauschenz, M. Melzig, M. Bienert, *Biochim. Biophys. Acta* **1998**, *1414*, 127 – 139.
[13] R. Fischer, T. Waizenegger, K. Köhler, R. Brock, *Biochim. Biophys. Acta* **2002**, *1564*, 365 – 374.
[14] M. E. Lindgren, M. M. Hällbrink, A. M. Elmquist, Ü. Langel, *Biochem. J.* **2004**, *377*, 69 – 76.
[15] G. Drin, M. Mazel, P. Clair, D. Mathieu, M. Kaczorek, J. Temsamani, *Eur. J. Biochem.* **2001**, *268*, 1304 – 1314.
[16] J. Gobom, K.-O. Kraeuter, R. Persson, H. Steen, P. Roepstorff, R. Ekman, *Anal. Chem.* **2000**, *72*, 3320 – 3326.
[17] Y. Lu, P. Bottari, F. Turecek, R. Aebersold, M. H. Gelb, *Anal. Chem.* **2004**, *76*, 4104 – 4111.
[18] a) S. Girault, G. Chassaing, J.-C. Blais, A. Brunot, G. Bolbach, *Anal. Chem.* **1996**, *68*, 2122 – 2126; b) S. Girault, S. Sagan, G. Bolbach, S. Lavielle, G. Chassaing, *Eur. J. Biochem.* **1996**, *240*, 215 – 222.
[19] A. Elmquist, Ü. Langel, *Biol. Chem.* **2003**, *384*, 387 – 393.
[20] R. Fischer, K. Köhler, M. Fotin-Mleczek, R. Brock, *J. Biol. Chem.* **2004**, *279*, 12625—12635.

 © 2005 Wiley-VCH Verlag GmbH & Co. KGaA, Weinheim

Metal Nitrides

Prediction of Novel Phases of Tantalum(V) Nitride and Tungsten(VI) Nitride That Can Be Synthesized under High Pressure and High Temperature

Peter Kroll, Timon Schröter, and Martina Peters*

The recent chemical syntheses of novel nitride compounds under high-pressure/high-temperature conditions is based on advances in instrumentation of diamond anvil cells and multi-anvil cells.[1–3] Spinel-type γ-Si_3N_4 is formed at pressures above 15 GPa and temperatures exceeding 2000 K,[4] the isotypic γ-Ge_3N_4 at pressures above 12 GPa and temperatures about 1000–1200 °C.[5] γ-P_3N_5 forms at 11 GPa and 1500 °C.[6] Hf_3N_4, for which no modification existed before, has been synthesized at 2800 K and 18 GPa and adopts the Th_3P_4-type structure. An isotypic Zr_3N_4 forms at pressures between 15.6 and 18 GPa and temperatures between 2500 and 3000 K.[7] PtN with sphalerite-type structure, the first binary nitride of the noble metals group, has been synthesized above 50 GPa and temperatures exceeding 2000 K.[8] Most recently, polymeric nitrogen with cubic structure was synthesized at temperatures above 2000 K and pressures above 110 GPa.[9] While this pure nitride compound deteriorated on expansion (reduction in pressure), all the novel binary nitrides could be quenched to ambient conditions. Some of them have or are proposed to have outstanding mechanical,[10] optical,[9] or electronic[11] properties. Herein we investigate the possible preparation of novel nitrides of tantalum and tungsten, predict the crystal structures of Ta_3N_5-II, WN_2-I, and WN_2-II, and estimate the range of pressure and temperature necessary to synthesize these new phase modifications.

The binary Ta–N system displays a rich crystal chemistry, ranging from solid solutions of nitrogen in close-packed tantalum, over compounds with a composition of approximately 1:1, and several nitrogen-rich phases up to Ta_3N_5, the most nitrogen rich tantalum(V) nitride.[12] Just recently, a new tantalum nitride with composition Ta_2N_3 adopting a bixbyite-type structure has been synthesized by plasma-enhanced chemical vapor deposition methods.[13] Our computation of the crystal structure of the experimentally observed orthorhombic modification of Ta_3N_5 with space group *Cmcm* is in excellent agreement with experimental[14,15] and recent theoretical data.[16,17] The volume of this ground-state structure, which exhibits two kinds of distorted $\{TaN_6\}$ octahedra, is 104.28 Å^3 per Ta_3N_5 unit. In search of high-pressure modifications of Ta_3N_5 we found three candidates with a denser packing of atoms and a higher average tantalum–nitrogen coordination, thus fulfilling the pressure-coordination rule:[18] A Sm_2SnS_5-type structure that contains both six- and eight-fold coordinate tantalum,[19] a U_3Se_5-type that has seven- and eight-fold coordinate tantalum,[20] and the most promising candidate we found is isostructural to U_3Te_5.[21] The orthorhombic structure of this modification (space group *Pnma*) comprises three different tantalum atoms in the unit cell, each in eighth-fold coordination to nitrogen (Figure 1). This

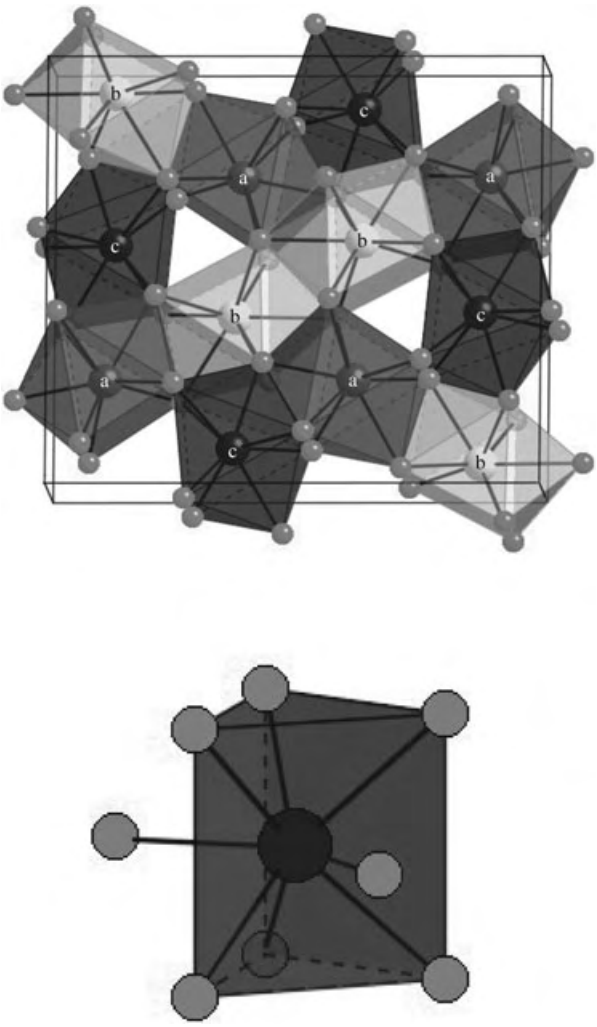


Figure 1. The U_3Te_5-type structure of Ta_3N_5-II. Top: a polyhedral view of the structure which contains three different Ta atoms (a–c: a unit cell is outlined). Bottom: A representative bicapped trigonal-prismatic environment of Ta (large circle, N small circles).

situation is similar to the coordination of hafnium in cubic Hf_3N_4, which is build up by $\{HfN_8\}$ bisdisphenoids.[7] The $\{TaN_8\}$ polyhedra, however, are bicapped trigonal prisms. The energy difference of the U_3Te_5-type polymorph of Ta_3N_5 relative to the ground state *Cmcm* structure is +1.36 eV per Ta_3N_5 unit, its volume is 78.40 Å^3 per Ta_3N_5, indicating a contraction by almost 26 %.[22]

The results of our energy–volume computations and the corresponding enthalpy–pressure phase diagram of Ta_3N_5 are shown in Figure 2. Accordingly, the *Cmcm* ground-state structure is the most stable modification of Ta_3N_5 up to 9 GPa. Above this pressure the U_3Te_5-type is favored. The

[*] P. Kroll, T. Schröter, M. Peters
Institut für Anorganische Chemie
Rheinisch-Westfälische Technische Hochschule Aachen (RWTH)
Landoltweg 1, 52056 Aachen (Germany)
Fax: (+49) 241-809-2288
E-mail: peter.kroll@ac.rwth-aachen.de

 DOI: 10.1002/anie.200462980 © 2005 Wiley-VCH Verlag GmbH & Co. KGaA, Weinheim

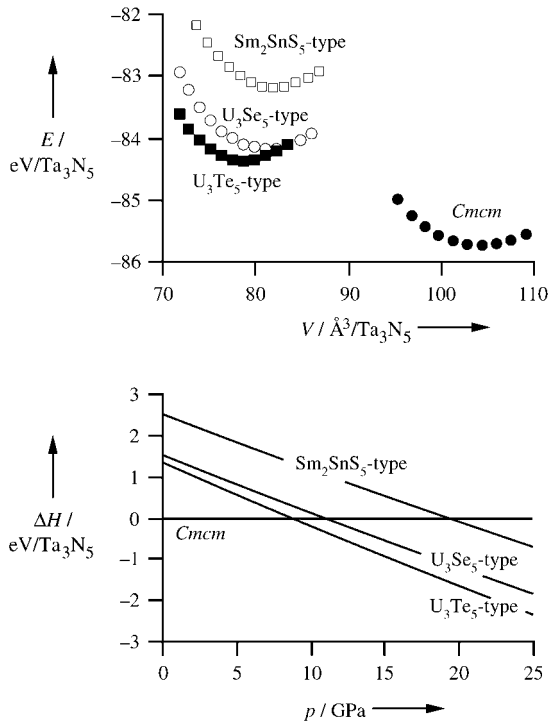


Figure 2. Energy–volume (*E*–*V*) diagram (top) and enthalpy–pressure (Δ*H*-*p*) diagram (bottom) for different phases of Ta_3N_5.

U_3Se_5- and Sm_2SnS_5-types will surpass the ground state for stability above 11 and 19 GPa, respectively, but will not outperform the U_3Te_5-type. Neglecting further entropy contributions to the free enthalpy ΔG (that is, $\Delta G \approx \Delta H$) we predict the formation of a new high-pressure modification, Ta_3N_5-II, from the ground-state structure Ta_3N_5-I at about 9 GPa. This transition will take place, because entropy differences between solid-state compounds, though present and contributing to the free enthalpy ΔG, are typically small in comparison to the much larger variation of ΔH within a few GPa of pressure (see the Methods Section for definition of ΔH).

To date, WN_2 has not been synthesized in crystalline form. For a long time is has been speculated that it would adopt a fluorite-type structure,[23] but no binary nitride of tungsten(VI) paralleling the oxide WO_3 has been produced. Nitrogen-rich WN_x thin films, with x approaching 2, however, can be produced by low-temperature deposition methods.[24,25] Our calculations suggest that WN_2, if it exists in crystalline form, may adopt the monoclinic structure of baddeleyite (m-ZrO_2, space group $P2_1/c$).[26] In this case the tungsten atoms are seven-fold coordinate in a monocapped trigonal prismatic arrangement of nitrogen atoms. We found three more seven-coordinate structures with a similar tungsten environment that are close in energy.[27] The monoclinic modification of WN_2-I ($V = 31.39$ Å^3/WN_2), however, has the lowest energy.[28] It competes with a six-coordinate brookite-type structure
(+0.07 eV/WN_2), which has a significantly larger volume of 36.13 Å^3/WN_2. Our calculations give no indication of fluorite- or pyrite-type structures appearing at high pressures. The most likely candidate we find for a high-pressure phase of WN_2 is a cotunnite-type (α-$PbCl_2$ (C23), space group *Pnma*[29]) modification. If adopted, tungsten will be nine-fold coordinated by nitrogen atoms (Figure 3). The {WN_9}

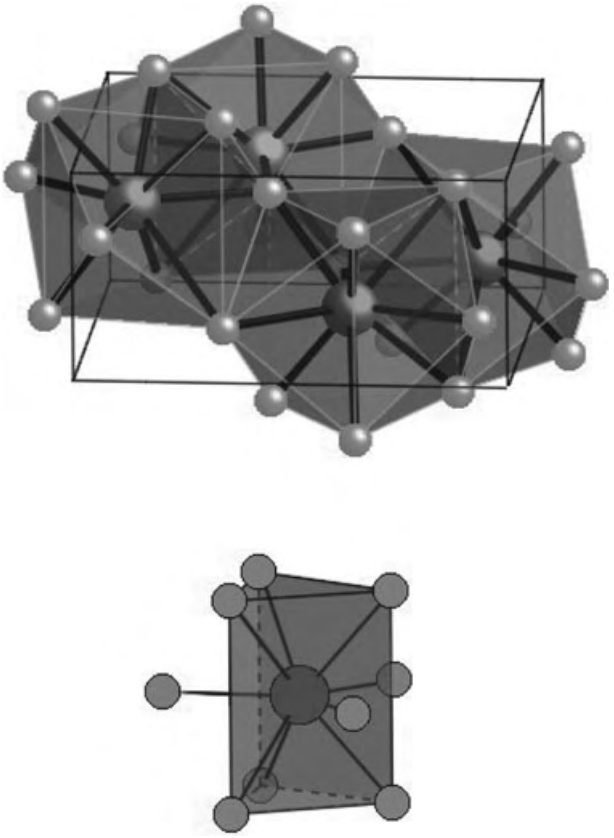


Figure 3. Cotunnite-type structure of WN_2. Top: a polyhedral view of the structure (a unit cell is outlined). Bottom: the tricapped trigonal prism {WN_9} environment (large circle W, smaller circles N).

polyhedra are tricapped trigonal prisms. The structure is more than 13% denser ($V = 27.29$ Å^3/WN_2), its energy is 0.78 eV/WN_2 higher than the proposed monoclinic ground state.[30] Energy–volume and enthalpy–pressure phase diagrams of WN_2 are displayed in Figure 4. The baddeleyite-type is the most stable modification of WN_2 up to a pressure of 34 GPa. Above this pressure it will transform into the cotunnite-type of WN_2-II.

How may the high-pressure phases of Ta_3N_5 and WN_2 be realized? In principle it is possible to start with a sample of Ta_3N_5-I and compress it to enforce its transformation into Ta_3N_5-II. Synthesizing the high-pressure phase of WN_2-II may follow a similar plan, however an amorphous sample of appropriate composition must be used. A chemical synthesis in the diamond anvil cell will start with metal platelets or cold-pressed powder pellets of the mononitrides (TaN or WN) as precursors. These are embedded in liquid nitrogen, which will act as the pressure medium, and then squeezed to the desired pressure. The starting materials are electrical conductors and can be heated with laser radiation to activate the transformation. However, it is possible that the solid nitride

 © 2005 Wiley-VCH Verlag GmbH & Co. KGaA, Weinheim

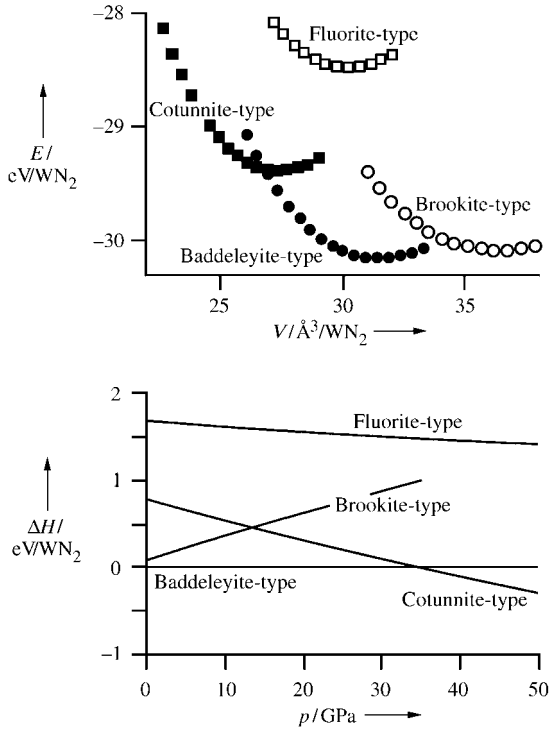


Figure 4. Energy–volume (*E*–*V*) diagram (top) and enthalpy–pressure (Δ*H*–*p*) diagram (bottom) for different phases of WN_2. The brookite-type WN_2 becomes mechanically unstable above 35 GPa.

compounds may decompose under development of nitrogen. For instance, Ta_3N_5 starts to decompose into TaN and nitrogen gas through a series of phases of intermediate composition at about 1000 °C at ambient pressure.[31,32]

Predicting the chemical synthesis of the new high-pressure phases, therefore, necessitates evaluating the equilibrium of the reaction $3\,TaN + N_2 \rightleftharpoons Ta_3N_5$ and $WN + \frac{1}{2}N_2 \rightleftharpoons WN_2$ as a function of pressure and temperature. To achieve this, we first calculate the enthalpy of formation ΔH as a function of pressure within density functional theory (DFT) at zero Kelvin. The phases of the products have been identified already, leaving just those of the starting materials to be found. We found the CoSn-type of ε-TaN as the phase of TaN with lowest enthalpy at ambient pressure. We compute its transition into the WC-type of ϑ-TaN to occur at about 8 GPa. This compares to shock-compression results, in which ε-TaN transforms to ϑ-TaN between 1 and 3 GPa below 1800 °C, but into a highly defective δ-TaN (NaCl-type) above 1800 °C at similar pressures.[34,33] Our choice of a reference phase of nitrogen was the ε-phase of N_2.[11] Computations for zero Kelvin suggest polymeric nitrogen may form at pressures above 55 GPa. Experimentally its formation in the cubic phase is observed at temperatures above 2.000 K and pressures above 110 GPa.[9] From this information we determine ΔH to be negative for both the formation of Ta_3N_5-I (-1.46 eV/Ta_3N_5) and Ta_3N_5-II (-0.10 eV/Ta_3N_5).

We proceed in a similar way for the tungsten–nitrogen system. A NiAs-type is identified as the ground-state structure of WN. We find no further modification of WN becoming more favorable up to 100 GPa. Our calculations then show that WN_2-I forms exothermically, $\Delta H = -0.24$ eV/WN_2. WN_2-II, on the other hand, has a positive ΔH value of $+0.53$ eV/WN_2. It requires a substantial pressure, we estimate 4 GPa, to stabilize this phase against decomposition.[35] Note that ΔH of WN_2-I, taken per atom (!), is significantly smaller than ΔH of Ta_3N_5-I. This result might indicate the difficulties in synthesizing crystalline WN_2 at ambient conditions.

At elevated temperatures the formation of gaseous nitrogen will contribute most to the free enthalpy of formation, ΔG, while the difference in entropy between the solid-state compounds contributes significantly less.[36] Therefore, we can use Equation (1) as a first order approximation to ΔG. With $\Delta_{sol}H(p)$ already determined, the free enthalpy of a gaseous species as a function of pressure and temperature is given by Equation (2) with f the fugacity of nitrogen.

$$\Delta G(p,T) = \Delta_{sol}H(p) + \Delta_{gas}G(p,T) \quad (1)$$

$$\Delta_{gas}G(p,T) = \Delta_{gas}G^0(p = 1\,\text{bar},T) + RT\,\ln\left(f/(1\,\text{bar})\right) \quad (2)$$

The first term on the right side of Equation (2), $\Delta_{gas}G^0(p{=}1\,\text{bar},T)$, is known for nitrogen to very high precision for the range 300–4000 K and tabulated in thermochemical tables.[37] The replacement of pressure by fugacity in the second term of the equation is mandatory even at moderate pressures to describe the deviation of nitrogen from ideal gas behavior. Pressure p and fugacity f are related through $f = \gamma p$, with γ the fugacity coefficient. If $\gamma = 1$, the gas has ideal behavior. A comprehensive collection of experimental data about nitrogen properties from the freezing line up to 2000 K and for pressures up to 1 GPa has been compiled by Jacobsen et al.[38] To approximate γ beyond this regime we propose two extrapolations: a conservative estimate and a more liberal expansion of γ. They provide the lower and upper boundary for the fugacity of nitrogen at high pressures. Details of both expansions are given in the Methods Section. Figure 5 shows both extrapolations used in this work in comparison to the virial expansion of Unland et al., which is based on experimental data, but valid only up to 2 GPa.[39] A value of $\ln\gamma = 20$ corresponding to a fugacity 10^6 times larger than the pressure should not come as a surprise, because it matches the measured properties of nitrogen at, for example, 300 K and 2 GPa.[38]

In Figure 6 shows the calculated phase boundary between mononitride and fully oxidized metal nitride in the pressure–temperature (p,T) phase diagrams of Ta-N and W-N. Accordingly, at 2800 K we predict the formation of Ta_3N_5-II in a diamond anvil cell at pressures above 17 GPa or above 25 GPa, depending upon which extrapolation of $\ln\gamma$ is applied. Similarly, WN_2-II can be synthesized above 31 or above 55 GPa at this temperature. Up to 34 GPa, however, WN_2-I is still favored over WN_2-II and, hence, will form instead. Once the novel high-pressure modifications have formed, they may be stabilized kinetically against transformation into the ground-state structures by a rapid quench. For WN_2-II its probable decomposition into WN and nitrogen provides an additional challenge.[40] Treating nitrogen as an ideal gas (setting $f = p$, $\ln\gamma = 1$) in the calculations yields a

 © 2005 Wiley-VCH Verlag GmbH & Co. KGaA, Weinheim

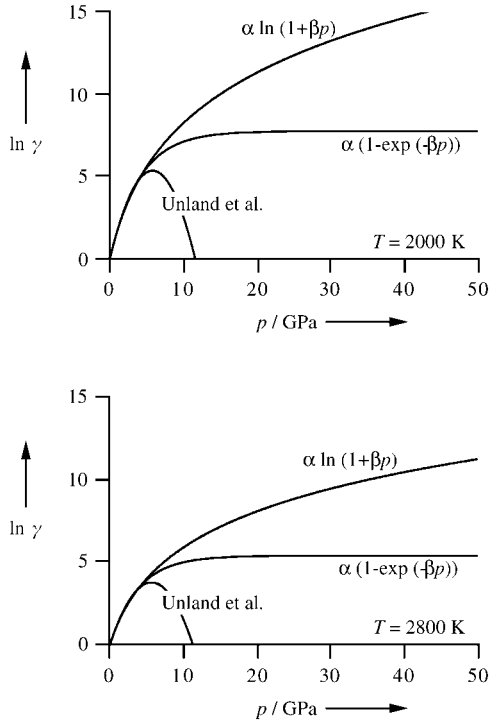


Figure 5. Plot of the logarithm of the fugacity coefficient ln γ as a function of pressure for both extrapolations used in this work in comparison to the virial expansion of Unland et al. The temperatures are typical for recent high-pressure experiments.[6,7] The (physically unrealistic) decrease of the fugacity coefficient at higher pressures in the virial expansion of Unland et al. is due to the functional form used.

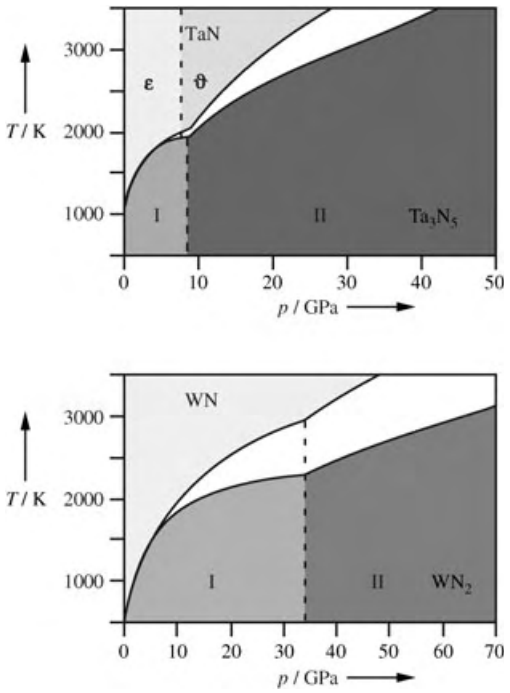


Figure 6. Phase boundary between TaN and Ta_3N_5 in the tantalum–nitrogen pressure–temperature phase diagram (top) and between WN and WN_2 in the tungsten–nitrogen pressure–temperature phase diagram (bottom). In both figures, the lower full line corresponds to the conservative expansion, the upper full line marks the more liberal estimate for the fugacity of nitrogen. Dashed lines separate phases of same composition. Gray shades indicate regions in which the respective phase is thermodynamically stable. The uncolored (white) region is the uncertainty range between the conservative and liberal expansion.

formation pressure of 44 GPa for Ta_3N_5-II at 2800 K, while WN_2-II will not form below 100 GPa. If we compare these results with our previous estimate of 22 GPa for the pressure of formation of Hf_3N_4 at this temperature[41] we notice the trend of increasing pressure needed to fully oxidize the metal when going from Group IV to Group V to Group VI. This trend can be expected for the experiment as well: Hf_3N_4 in fact forms at 18 GPa at 2800 K, which corroborates the substantial difference between fugacity and pressure.[7]

What properties may we expect from the new phases? If synthesized, the novel high-pressure phases Ta_3N_5-II and WN_2-II will not be transparent. A band-structure calculation reveals them as metallic conductors, despite the simple electron counting scheme of Ta^{+5} or W^{+6} together with N^{3-}, which leads us to expect a semiconductor. The ground-state structures, however, do have a band gap: 1.4 eV for Ta_3N_5-I and 0.4 eV for WN_2-I. The novel phases are very low-compressible materials. We calculate the bulk modulus B_0 of Ta_3N_5-II to be 378 GPa, that of the *Cmcm* ground state Ta_3N_5-I to be 265 GPa, WN_2-I has a B_0 of 318 GPa and WN_2-II of 408 GPa. These values exceed those of the high-pressure phases of spinel silicon nitride, γ-Si_3N_4 (300 GPa), and cubic hafnium nitride, Hf_3N_4 (283 GPa).[4,11]

The high-pressure modifications also show trend of increasing metal–nitrogen bond length with increasing coordination, termed the coordination–distance paradoxon.[42] The average Ta–N bond length is 2.10 Å (range: 1.96–2.28 Å) in Ta_3N_5-I, and increases about 5% to an average of 2.21 Å (range: 2.05–2.31 Å) in Ta_3N_5-II. The average W–N bond length in WN_2-I is 2.09 Å (1.87–2.22 Å), and increases to 2.19 Å (2.06–2.42 Å) in WN_2-II. This trend manifests itself in a decrease of the wave number of the principle Raman-active vibrational mode. It shifts from 900 cm^{-1} to 830 cm^{-1} in the Ta_3N_5-I to Ta_3N_5-II transition, and from 968 cm^{-1} to 797 cm^{-1} in the WN_2-I to WN_2-II transition.

In summary, we predict the novel modifications Ta_3N_5-II, WN_2-I, and WN_2-II that should be accessible by chemical synthesis at high pressures. Our assessment of the Ta–N and W–N phase diagrams is based on a combination of quantum-chemical calculations of crystal phases at high pressures and thermochemical calculations using proposed empirical relations for the fugacity of nitrogen. The *Cmcm* modification Ta_3N_5-I will undergo a structural transition into Ta_3N_5-II at 9 GPa. Using nitrogen as both pressure medium and reactant Ta_3N_5-II can be synthesized from the mononitride at pressures above 17 and 25 GPa at 2800 K. WN_2-II becomes accessible above 31 and 55 GPa at this temperature. If synthesized, this modification comprises unique $\{WN_9\}$-tricapped trigonal prisms, the highest W–N coordination in crystal chemistry. The high-pressure modifications exhibit very high bulk moduli, 378 GPa for Ta_3N_5-II and 408 GPa for WN_2-II. We conclude that nitrogen can be activated by such pressures and is capable of oxidizing tungsten to its highest oxidation state,

 © 2005 Wiley-VCH Verlag GmbH & Co. KGaA, Weinheim

tungsten(VI). Investigation of the phase diagrams of Ta–N and W–N will give further substantial information on the fugacity of nitrogen at very high pressures.

Experimental Section

Our computations of crystal structures are based on density functional theory as implemented in the Vienna Ab Initio Simulation Package (VASP).[43–46] We employ the generalized gradient approximation (GGA) to compute energy differences and band structures, and rely on Blöchls projector augmented wave (PAW) method.[47,48] The local density approximation (LDA) is used for comparison and to compute the elastic properties and vibrational spectra. The pseudopotentials of the metal atoms include the d-electrons as valence states. Cut-off energy (500 eV) for the expansion of the wave function into plane waves and k-point sampling scheme are chosen to ensure that all structures are well-converged to better than 1 meV per atom. The application of pressure to the crystal structures is simulated by reducing the volume of the unit cell. With the constraint of constant volume, all other structural parameters (atomic positions and lattice parameter) are optimized and the energy calculated. This results in a energy–volume (E–V) diagram, which can be fitted with common equations of state (EOS) to access the bulk modulus B_0 and its pressure derivative B'. We calculate the pressure p by numerical differentiation of a spline fit to the E–V data and get the enthalpy H from $H = E + pV$. It is good practice to give the enthalpy difference ΔH relative to a reference (ground state) structure.

The extrapolation of the fugacity of nitrogen is based on the thermochemical data compiled by Jacobsen et al.[38] and the corresponding six-parameter virial expansion of $\ln \gamma$ by Unland et al.[39] We started with a linear extrapolation of $\ln\gamma$ for pressures beyond 3 GPa. This approach corresponds to that of Ma et al.,[49] but leads to much too unrealistic values for $\ln \gamma$. The more modest functional forms we choose are motivated by simplicity and reasonable high-pressure behavior. They have been fitted with the virial expansion and adjusted to reproduce the pressure of formation of Hf_3N_4 and Zr_3N_4. In particular, the conservative estimate is given by $\ln\gamma_l = \alpha_l(T)\,(1-\exp(-\beta_l(T)\,p))$, with virial expansions for both $\alpha_l = \alpha_1/T + \alpha_2/T^2 + \alpha_3/T^3$ and $\beta_l = \beta_0 + \beta_1/T + \beta_2/T^2$. Coefficients are: $\alpha_1 = 14.0707$, $\alpha_2 = 2.40815$, $\alpha_3 = 0.86685$, $\beta_0 = 0.29775$, $\beta_1 = -0.09503$, $\beta_2 = 0.00996$. The more liberal estimate is given by $\ln\gamma_h = \alpha_h/T\,\ln(1+\beta_h p)$. Coefficients are: $\alpha_h = 10.4583$, $\beta_h = 0.3879$. In both expansions the temperature T is given in units of 1000 K and the pressure p in GPa.

Received: December 17, 2004
Revised: February 18, 2005
Published online: June 6, 2005

Keywords: density functional calculations · nitrides · phase diagrams · tantalum · tungsten

[1] P. F. McMillan, *Chem. Commun.* **2003**, 919–923.
[2] R. Boehler, *Rev. Geophys.* **2000**, *38*, 221–245.
[3] V. V. Struzhkin, R. J. Hemley, H.-K. Mao, Y. A. Timofeev, M. I. Eremets, *Hyperfine Interact.* **2000**, *128*, 323–343.
[4] A. Zerr, G. Miehe, G. Serghiou, M. Schwarz, E. Kroke, R. Riedel, H. Fueß, P. Kroll, R. Böhler, *Nature* **1999**, *400*, 340–342.
[5] K. Leinenweber, M. O'Keeffe, M. Somayazulu, H. Hubert, P. F. McMillan, G. H. Wolf, *Chem. Eur. J.* **1999**, *5*, 3076–3078.
[6] K. Landskron, H. Huppertz, J. Senker, W. Schnick, *Angew. Chem.* **2001**, *113*, 2713–2716; *Angew. Chem. Int. Ed.* **2001**, *40*, 2643–2645.
[7] A. Zerr, G. Miehe, R. Riedel, *Nat. Mater.* **2003**, *2*, 185–189.
[8] E. Gregoryanz, C. Sanloup, M. Somayazulu, J. Badro, G. Fiquet, H. K. Mao, R. J. Hemley, *Nat. Mater.* **2004**, *3*, 294–297.
[9] M. I. Eremets, A. G. Gavriliuk, I. A. Trojan, D. A. Dzivenko, R. Boehler, *Nat. Mater.* **2004**, *3*, 558–563.
[10] A. Zerr, M. Kempf, M. Schwarz, E. Kroke, M. Göken, R. Riedel, *J. Am. Ceram. Soc.* **2002**, *85*, 86–90.
[11] P. Kroll, *Phys. Rev. Lett.* **2003**, *90*, 125501.
[12] H. O. Pierson, *Handbook of Refractory Carbides and Nitrides: Properties, Characteristics, and Applications*, Noyes Publictions, Westwood, **1996**.
[13] A. Y. Ganin, L. Kienle, G. V. Vajenine, *Eur. J. Inorg. Chem.* **2004**, 3233–3239.
[14] J. Strähle, *Z. Anorg. Allg. Chem.* **1973**, *402*, 47–57.
[15] N. E. Brese, M. O'Keeffe, P. Rauch, F. J. DiSalvo, *Acta Crystallogr. Sect. C* **1991**, *47*, 2229–2294.
[16] C. M. Fang, E. Orhan, G. A. de Wijs, H. T. Hintzen, R. A. de Groot, R. Marchand, J. Y. Saillard, G. de With, *J. Mater. Chem.* **2001**, *11*, 1248–1252.
[17] We obtain: Ta_3N_5, space group *Cmcm* (63), $Z = 4$, $a = 3.9053$, $b = 10.3208$, $c = 10.3488$ Å; Ta(1) 4 *c*, 0.0000,0.1978,0.2500; Ta(2) 4 *c*, 0.0000,0.1333,0.5596; N(1) 4 *c*, 0.0000,0.7634,0.2500; N(2) 8 *f*, 0.0000,0.0470,0.1194; N(3) 8 *f*, 0.0000,0.3086,0.0738.
[18] A. Neuhaus, *Chimia* **1964**, *18*, 93–103.
[19] M. Julien-Pouzol, S. Jaulmes, *Acta Crystallogr. Sect. B* **1979**, *35*, 2672–2674.
[20] P. T. Moseley, D. Brown, B. Whittaker, *Acta Crystallogr. Sect. B* **1972**, *28*, 1816–1821.
[21] O. Tougait, M. Potel, H. Noel, *J. Solid State Chem.* **1998**, *139*, 356–361.
[22] We obtain: Ta_3N_5, space group *Pnma* (62), $Z = 4$, $a = 10.9982$, $b = 2.9681$, $c = 9.6070$ Å; Ta(1) 4 *c*, 0.1260,0.2500,0.4096; Ta(2) 4 *c*, 0.3671,0.2500,0.5773; Ta(3) 4 *c*, 0.3835,0.2500,0.2513; N(1) 4 *c*, 0.0245,0.2500,0.6093; N(2) 4 *c*, 0.0687,0.2500,0.2047; N(3) 4 *c*, 0.2616,0.2500,0.7773; N(4) 4 *c*, 0.2849,0.2500,0.0468; N(5) 4 *c*, 0.5746,0.2500,0.5800.
[23] R. J. Meyer, F. Peters, L. Gmelin, E. Pietsch, M. Becke-Goehring, *Gmelins Handbuch der Anorganischen Chemie*, 8th ed., system 54, Verlag Chemie, Berlin, **1933**, p. 153.
[24] C. W. Lee, Y. T. Kim, S.-K. Min, *Appl. Phys. Lett.* **1993**, *62*, 3312–3314.
[25] P.-C. Jiang, J. S. Chen, *J. Vac. Sci. Technol. A* **2001**, *21*, 616–621.
[26] D. McCullough, K. N. Trueblood, *Acta Crystallogr.* **1959**, *12*, 507–511.
[27] Space groups in each case are orthorhombic: *Pca* 2_1, and two times *Pbc*a. The structures are distinguishable through the connectivity pattern between layers build up by seven-coordinate W centers and four-coordinate N atoms. One *Pbca* variant is related to the brookite-type by a small (displacement) translation of half of the anions.
[28] We obtain: WN_2, space group $P\,2_1/c$ (14), $Z = 4$, $a = 4.9249$, $b = 4.9688$, $c = 5.1989$ Å, $\beta = 99.196°$; W(1) 4 *e*, 0.2861,0.0630,0.2203; N(1) 4 *e*, 0.5706,0.2609,0.0208; N(2) 4 *e*, 0.0656,0.3266,0.3390.
[29] P. P. Ewald, C. Hermann, *Strukturberichte Vol. 2*, Akademische Verlagsgesellschaft, Leipzig, **1931**, p. 16.
[30] We obtain: WN_2, space group *Pnma* (62), $Z = 4$, $a = 5.4424$, $b = 3.1508$, $c = 6.3658$ Å; W(1) 4 *c*, 0.2393,0.2500,0.1217; N(1) 4 *c*, 0.4716,0.2500,0.8466; N(2) 4 *c*, 0.3613,0.2500,0.4275.
[31] J.-C. Gilles, *C. R. Seances Acad. Sci. Ser. C* **1968**, *266*, 546–547.
[32] R. Niewa, private communication.
[33] T. Mashimo, S. Tashiroa, M. Nishidaa, K. Miyahara, E. Eto, *Physica B* **1997**, *239*, 13–15.
[34] G. Brauer, A. Skokan, A. Neuhaus, E. Mohr, *Monatsh. Chem.* **1972**, *103*, 794–798.
[35] Structures with a metal-atom coordination of more than six gain enthalpy relative to the mononitride and nitrogen with increasing pressure. The situation is not so straight forward for Ta_3N_5-I, which exhibits a maximum of ΔH at 10 GPa.
[36] The critical point of N_2 is at about 126 K and 3.44 MPa. Thus for most of the pressure–temperature regime we address herein

 © 2005 Wiley-VCH Verlag GmbH & Co. KGaA, Weinheim

there is no difference between gaseous and liquid state of nitrogen.
[37] M. W. Chase, *JANAF-Thermochemical Tables* **1998**, 9.
[38] R. T. Jacobsen, R. B. Stewart, M. Jahangiri, *J. Phys. Chem. Ref. Data* **1986**, *15*, 735 – 909.
[39] J. Unland, B. Onderka, A. Davydov, R. Schmid-Fetzer, *J. Cryst. Growth* **2003**, *256*, 33 – 51.
[40] It takes about 4 GPa at 0 K, or 8 GPa at 1000 K, to stabilize WN_2-II against decomposition into the mononitride and nitrogen. WN_2-II, however, is mechanically stable towards distortions, as investigated by computing the elastic constants.
[41] P. Kroll, *J. Phys. Condens. Matter* **2004**, *16*, S1235-S1244.
[42] W. Kleber, K.-Th. Wilke, *Krist. Tech.* **1969**, *4*, 165 – 199.
[43] G. Kresse, J. Hafner, *Phys. Rev. B* **1993**, *47*, 558 – 561.
[44] G. Kresse, J. Hafner, *Phys. Rev. B* **1994**, *49*, 14251 – 14269.
[45] G. Kresse, J. Furthmüller, *Comput. Mater. Sci.* **1996**, *6*, 15 – 50.
[46] G. Kresse, J. Furthmüller, *Phys. Rev. B* **1996**, *54*, 11169 – 11186.
[47] P. E. Blöchl, *Phys. Rev. B* **1994**, *50*, 17953 – 17979.
[48] G. Kresse, D. Joubert, *Phys. Rev. B* **1999**, *59*, 1758 – 1775.
[49] X. Ma, C. Li, F. Wang, W. Zhang, *CALPHAD* **2003**, *27*, 383 – 388.

 © 2005 Wiley-VCH Verlag GmbH & Co. KGaA, Weinheim

Gas-Phase Reactions

Stability of Gaseous Thallium Monofluoride as TlF^0, TlF^+, and TlF^{2+}**

Detlef Schröder, Christoph van Wüllen,* Helmut Schwarz, and Thomas M. Klapötke*

Dedicated to Professor Konrad Seppelt

As the most electronegative element, fluorine forms rather strong bonds with many elements, including metals. Accordingly, fluorine allows formation of the highest valences in the molecular compounds of several elements, for example, CoF_3, AgF_2, IrF_7, PtF_6, and AuF_5. Similarly, several multiply charged metal atoms form stronger bonds to fluorine than to any other element,[1] and even the triply charged diatomic metal fluorides TiF^{3+} and UF^{3+} are known.[2,3] However, there exist some notable exceptions such as gold(I) fluoride, which remained elusive until 1994,[4] while AuCl, AuBr, and AuI were well-characterized more than a century ago. The corresponding diatomic ion AuF^+ has a bond energy of only 0.8 eV,[5] whereas the heavier analogue gold iodide ion AuI^+ has a much stronger bond (ca. 2.6 eV).[6] Three major factors contribute to the comparably weak Au–F bonding in the cation: 1) the unfavorable overlap between the 6s orbital of gold and the $2p_\sigma$ orbital of fluorine, 2) the small polarizability of fluorine, and 3) the relativistically lowered energy of the gold 6s orbital which disfavors the ionic bonding preferred in fluorine compounds.[7]

Herein, we report a combined experimental and theoretical investigation on the stability of thallium monofluoride in different charge states $TlF^{0/+/2+}$.[8] The TlF^{2+} dication is of particular interest because the $6s^15d^{10}$ ground state of Tl^{2+} corresponds to the configuration of the neutral gold atom while the positive charge is expected to weaken the Tl–F bond and may even lead to Coulomb explosion into the singly charged atomic ions. Accordingly, the question arises about the existence and, if so, the stability of TlF^{2+} in the gas phase. It turns out, however, that the deceptively simple monocation TlF^+ poses an even bigger challenge for both experiment and theory.

Neutral thallium(I) fluoride is a colorless, hygroscopic solid. Upon heating to about 200 °C, TlF evaporates in high vacuum (10^{-6} mbar). Electron ionization (EI, 70 eV) of gaseous neutral TlF affords the following cationic species (relative abundances in brackets): TlF^+ (2%), Tl^+ (100%), TlF^{2+} (1%), and Tl^{2+} (6%); in addition, some minor signals arising from EI of the neutral dimer Tl_2F_2 are observed.[10] Considering that neutral TlF is used as a precursor,[11] the weakness of the molecular ion signal for TlF^+ upon EI indicates either an intrinsic instability of the cation or unfavorable Franck–Condon overlaps between neutral and monocationic $TlF^{0/+}$. Consistent with the argument of intrinsic instability, the mass-selected TlF^+ ion undergoes a pronounced unimolecular decomposition to afford atomic Tl^+ according to Equation (1) accompanied by a small kinetic energy release (KER) of (10 ± 4) meV.[12]

$$TlF^+ \rightarrow Tl^+ + F \qquad (1)$$

In the approximately 2-m long field-free region of the sector-field mass spectrometer used,[8,9] a fraction of about 15% of the incident TlF^+ ions entering this region undergoes metastable-ion decay, which corresponds to a unimolecular rate constant in the order of $10^4\ s^{-1}$. For a diatomic species having just one degree of freedom, the sheer magnitude of this value may appear surprising because metastable-ion decay usually only applies to a fraction between 0.1 and 1% of the incident ions.[13] We return to this aspect later in the discussion.

Upon collision of mass-selected TlF^+ ions (which have 8 keV kinetic energy) with oxygen, dissociation to afford Tl^+ prevails. Despite the large collision energy, charge stripping (CS)[14] to afford the dications TlF^{2+} and Tl^{2+} is rather inefficient; only at highest sensitivity is a small signal for TlF^{2+} observed.[15] Compared to other metal–fluoride cations for which medium to intense dication signals are formed upon CS,[2,3,16] this observation implies that either dissociation of TlF^+ is particularly facile, that the formation of TlF^{2+} is very

[*] Dr. D. Schröder, Prof. Dr. C. van Wüllen, Prof. Dr. H. Schwarz
Institut für Chemie
Technische Universität Berlin
Strasse des 17. Juni 135, 10623 Berlin (Germany)
Fax: (+49) 30-314-21102
E-mail: detlef.schroeder@tu-berlin.de
christoph.vanwullen@tu-berlin.de
Prof. Dr. T. M. Klapötke
Lehrstuhl für Anorganische Chemie
Universität München
Butenandtstrasse 5–13, 81377 München (Germany)

[**] Financial support by the Deutsche Forschungsgemeinschaft, the European Commission (MCInet), and the Fonds der Chemischen Industrie is acknowledged.

 © 2005 Wiley-VCH Verlag GmbH & Co. KGaA, Weinheim DOI: 10.1002/anie.200461334

energy-demanding, or that TlF^{2+} undergoes rapid dissociation. Further, a composite peak is found for the Tl^+ fragment, where the abundant, narrow component is due to the process in Equation (1) and a weak, broader component can be attributed to the occurrence of charge separation according to Equation (2).[17] Thus facile dissociations of both TlF^+ and TlF^{2+} are implied.

$$TlF^{2+} \rightarrow Tl^+ + F^+ \qquad (2)$$

Unlike TlF^+, the mass-selected dication TlF^{2+} undergoes minimal unimolecular decay (< 0.1% of the incident beam), just as expected for a diatomic species in the μs regime.[13] Upon collision of mass-selected TlF^{2+} with O_2 as collision gas, fragmentation to $Tl^{2+} + F$ as well as charge exchange to afford TlF^+ and subsequently $Tl^+ + F$ are observed (Figure 1). Note that the charge-exchange products unambiguously prove

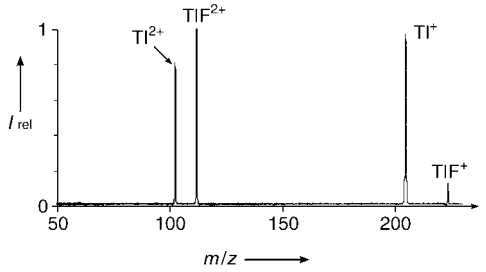


Figure 1. Charge-exchange spectrum (collision gas: O_2, 80% T) of mass-selected TlF^{2+}. Note that the precursor dication appears in the middle of the spectrum and is off-scale.

that a dication has been mass-selected in the experiment because product ions with m/z values larger than that of the parent ion can only be detected for precursor ions with $z > 1$. Quite unusual for such a charge-exchange experiment is, however, the low abundance of the TlF^+ monocation, again suggesting that dissociation of the singly charged species is facile. In spite of this feature, the experimental data presented so far still demonstrate that TlF can exist not only as a neutral compound but also in its singly and doubly charged cation states.

Further insight into the energetics of $TlF^{0/+/2+}$ is gained by high-level ab initio calculations (Table 1).[18,21] Neutral TlF ($^1\Sigma$) with $r = 2.09$ Å and $\tilde{\nu} = 472\ cm^{-1}$ is located in a deep potential-energy well with a computed dissociation energy of $D_0 = 4.57$ eV at 0 K[21] which nicely matches the experimental values available (exp. 4.58 eV).[22] In marked contrast to the substantial binding in the neutral species, the computed bond energy for the ground state of the monocation TlF^+ ($^2\Sigma$) with $r = 2.05$ Å and $\tilde{\nu} = 349\ cm^{-1}$ is only $D_0 = 0.02$ eV. Consistent with the corresponding Born–Haber cycle, the ionization energy $IE(TlF) = 10.54$ eV (exp. 10.52 eV[23]) is 4.55 eV larger than $IE(Tl) = 5.99$ eV (exp. 6.11 eV[24]). Near the minimum,

Table 1: Total energies of $TlF^{0/+/2+}$, the relevant dissociation asymptotes, and the corresponding properties derived from them.

Species	RCCSD(T)	MR-AQCC	Property[a][b]	Experiment
Tl (^{2}P)	−171.972828	−171.952973		
Tl^+ (^{1}S)	−171.776110	−171.759799	$IE(Tl) = 5.99$ eV	6.11 eV[c]
Tl^{+*} (^{3}P)		−171.500409	$E_{ex} = 6.09$ eV[d]	6.13 eV[c]
Tl^{2+} (^{2}S)	−171.033119	−171.019725	$IE(Tl^+) = 20.22$ eV	20.43 eV[c]
Tl^{3+} (^{1}S)	−169.946212		$IE(Tl^{2+}) = 29.58$ eV	29.83 eV[c]
TlF ($^1\Sigma$)	−271.818959		D_0(Tl-F) = 4.57 eV	4.58 eV[e]
TlF^+ ($^2\Sigma$)		−271.406636	$D_0(Tl^+\text{-F}) = 0.02$ eV[d]	0.16 eV[f][g]
			IE(TlF) = 10.54 eV[h]	10.52 eV[e]
TlF^{+*} ($^2\Sigma$)		−271.275686	$E_{ex}(TlF^+) = 3.65$ eV[d]	
TlF^{2+} ($^1\Sigma$)	−270.730202		$D_0(Tl^{2+}\text{-F}) = 1.16$ eV	
			$IE(TlF^+) = 19.08$ eV[d]	19.7 ± 1.1 eV[i]
F^- (^{1}S)	−99.777073	−99.762934	EA(F) = 3.36 eV	3.40 eV[g]
F (^{2}P)	−99.652718	−99.646514		
F^+ (^{3}P)	−99.015109	−99.012100	IE(F) = 17.35 eV	17.42 eV[g]

[a] Values derived from RCCSD(T) calculations unless stated otherwise. [b] Ref. [21]. [c] Taken from ref. [24]. [d] Derived from MR-AQCC values. [e] Ref. [22] [f] Derived from the difference of the appearance energies from TlF^+ and Tl^+ upon photoionization of gaseous TlF with an experimental error of 0.05 eV. Note further that the appearance of Tl^+ may be shifted to energies slightly higher than the adiabatic value owing to the 0.1 eV barrier discussed in the text. [g] Taken from ref. [23]. [h] Derived from the combined RCCSD(T) and MR-AQCC values, see Figure 2. [i] This work; see ref. [15].

the bonding in TlF^+ can be described as a mixture of the mostly repulsive interaction of the quasi-closed shell Tl^+ (^{1}S) with F (^{2}P) and ionic contributions from the Tl^{2+} (^{2}S) + F^- (^{1}S) asymptote. With respect to the unusually low D_0 value of TlF^+, the dissociation into ground-state Tl^+ (^{1}S) + F (^{2}P) was considered in more detail.

As shown in Figure 2, the ion dissociation of TlF^+ is associated with a very modest barrier of only about 0.1 eV (precisely, 897 cm^{-1}) at a Tl–F distance of $r = 2.5$ Å. To assess

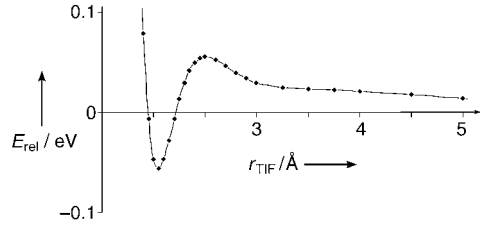


Figure 2. Computed potential-energy curve (in eV) of diatomic TlF^+.

whether or not the computed potential-energy curve is compatible with the experimentally observed metastable state of TlF^+ formed upon ionization, the one-dimensional vibrational Schrödinger equation of TlF^+ was solved. A bound vibrational state TlF^+ ($\nu = 0$) is located 173 cm^{-1} above the minimum, and two metastable states or resonances TlF^+ ($\nu = 1$) and TlF^+ ($\nu = 2$) are situated 479 cm^{-1} and 733 cm^{-1}, respectively, above the minimum. Starting from a Boltzmann distribution ($T = 500$ K) of the vibrational states of neutral TlF and assuming that EI occurs as a vertical process, the Franck–Condon factors suggest that upon ionization the bound state TlF^+ ($\nu = 0$) and the metastable states with $\nu = 1$ and $\nu = 2$ are populated with probabilities of 65, 24, and 6%, respectively; the remaining percentage directly ionizes into

 © 2005 Wiley-VCH Verlag GmbH & Co. KGaA, Weinheim

the continuum states which decay within a few vibrational periods.

The decay rates of the metastable states can be estimated within the semiclassical approximation which goes back to the seminal description of nuclear α-decay by Gamow.[25] For TlF^+ ($v=2$), a lifetime of 7 ns is thus estimated, while the lifetime of TlF^+ ($v=1$) is very large, because the energy level is only slightly above the dissociation asymptote. For the $v=2$ resonance, also a fully quantum mechanical wave-packet propagation was performed for a period of 60 ns which led to an exponential decay of TlF^+ ($v=2$) with a lifetime of 26 ns, which is consistent with the semiclassical estimate. While these values have been obtained for the rotational ground state ($J=0$), the preferentially populated rotational level at $T=500$ K is around $J=27$ and 33% of the molecules occupy rotational levels above $J=40$ and 25% above $J=45$. If the centrifugal potential corresponding to J values between 40 and 45 is added to the calculated potential-energy curve, the minimum is shifted upwards with respect to the dissociation asymptote by approximately 0.05 eV. Even more important is that the barrier height is reduced by about 15%. As a consequence, the $v=2$ resonance vanishes and the semiclassical estimate for the lifetime of $v=1$ decreases to 2×10^{-4} s for $J=40$ and 9×10^{-6} s for $J=45$. The observed metastable decay thus most likely corresponds to the decay of a rotationally excited quasi-stationary vibrational state ($v=1$), for which both the population based on the Franck–Condon factors and the decay rate are in reasonable agreement with the experimental results.

The dication TlF^{2+} ($^1\Sigma$) with $r=1.95$ Å and $\tilde{\nu}=498$ cm^{-1} is located 19.08 eV above ground state TlF^+ ($^2\Sigma$). As a consequence of the large *IE*, TlF^{2+} is a metastable dication for which decomposition with charge separation into $Tl^+ + F^+$ [Eq. (2)] is exothermic by 1.71 eV. Nevertheless, a Coulomb barrier kinetically stabilizes the dication, thereby allowing its mass spectrometric detection. Using the computed TlF^{2+} curve in conjunction with Coulomb's law, the crossing is estimated to occur at an interatomic distance of about 5 Å. From these theoretical results, the redox chemistry of $TlF^{0/+/2+}$ can be described quantitatively (Figure 3). Furthermore, note that the similar Tl–F distances in the ground states of TlF, TlF^+, and TlF^{2+} discount particularly unfavorable Franck–Condon effects in the vertical electron-transfer processes.

Given the rather weakly bound monocationic species, possible low-lying excited states of TlF^+ were considered as an alternative explanation for the observed TlF^+ species. The lowest lying excited state TlF^{+*} ($^2\Sigma$) with $r=2.20$ Å and $\tilde{\nu}=517$ cm^{-1} is located 3.65 eV above ground state TlF^+ ($^2\Sigma$). The bonding in TlF^{+*} ($^2\Sigma$) arises from the $Tl^+(^3P)+F(^2P)$ asymptote, that is, the covalent coupling of atomic fluorine and the first excited state of the metal cation, Tl^+ (^3P), which has a $6s^16p^1$ configuration and $E_{ex}=7.06$ eV (exp. 7.10 eV). The excited state TlF^{+*} ($^2\Sigma$) is located in a deep well with respect to the associated dissociation asymptote, yet is also some 3.7 eV above ground state asymptote for $Tl^+(^1S)+F(^2P)$. Thus, formation of TlF^{+*} ($^2\Sigma$) might offer an explanation for the long-lived TlF^+ molecular ion formed upon EI. Nevertheless, the experimental observations themselves disfavor this line of reasoning. If TlF^{+*} ($^2\Sigma$) were the major component of the mass-selected TlF^+ beam, its unimolecular dissociation which occurs on the μs timescale must lead to the atomic fragments in their ground state, that is, $Tl^+(^1S)+F(^2P)$, which would in turn requires the release of approximately 3.7 eV because neither Tl^+ nor F have excited states in this energy region.[24] However, the measured KER of the Tl^+ fragment is rather small. Failure to observe a significant amount of photons emitted during the ion beam's passage of the off-axis photomultiplier in the third field-free region of the instrument[8,26,27] discounts the alternative option of a radiative transition. Furthermore, even though the dication signal obtained upon CS of TlF^+ is rather weak, the *IE*(TlF^+) $\approx 19.7\pm1.1$ eV determined in energy-resolved experiments[15] is consistent with ground state TlF^+ serving as the precursor, whereas TlF^{+*} would require a significantly lower amount of energy of dication formation and should have a larger cross section.

In conclusion, diatomic TlF can exist in the three different charge states 0, +1, and +2. The neutral state shows tight binding, the monocation resides in a very shallow well, and the dication even is metastable with respect to Coulomb explosion, though the dication is kinetically stabilized. Perhaps surprising is that electron ionization of neutral TlF as well as charge exchange of metastable TlF^{2+}, both commonly considered as "harsh" methods, do allow the generation of ground state TlF^+, although this diatomic species can only survive in the lowest vibrational levels. As we have pointed out in a previous case,[28] this apparent paradox is directly associated with the small size of the system. For a polyatomic species with a large density of states, these "harsh" methods as well as the thermal energy of the precursor are very unlikely to support a well of only about 0.1 eV depth in the μs timeframe. In contrast, for small species, diatomic molecules in particular, there is a finite possibility that the rovibrational ground states might be populated despite the large energies involved in the experiments. Hence, the assumption that mass spectrometric experiments with ions having keV energies cannot sample very weakly bound species[29] is somewhat too general, and reconsideration of this aspect might be useful to resolve some current discrepancies.[30]

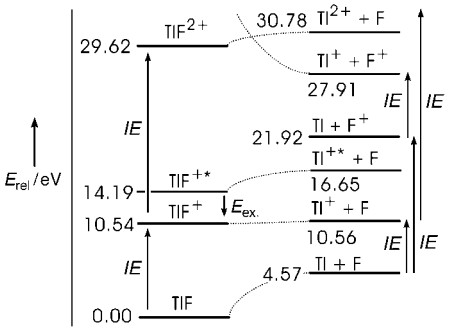


Figure 3. Computed redox energetics of $TlF^{0/+/2+}$ (adiabatic values in eV).

Received: July 16, 2004
Revised: March 14, 2005
Published online: June 7, 2005

 © 2005 Wiley-VCH Verlag GmbH & Co. KGaA, Weinheim

Keywords: Ab initio calculations · charge transfer · Coulomb explosion · mass spectrometry · metastable ions · thallium fluoride

[1] D. Schröder, H. Schwarz, *J. Phys. Chem. A* **1999**, *103*, 7385.

[2] D. Schröder, J. N. Harvey, H. Schwarz, *J. Phys. Chem. A* **1998**, *102*, 3639.

[3] D. Schröder, M. Diefenbach, T. M. Klapötke, H. Schwarz, *Angew. Chem.* **1999**, *111*, 206; *Angew. Chem. Int. Ed.* **1999**, *38*, 137.

[4] a) D. Schröder, J. Hrušák, I. C. Tornieporth-Oetting, T. M. Klapötke, H. Schwarz, *Angew. Chem.* **1994**, *106*, 223; *Angew. Chem. Int. Ed. Engl.* **1994**, *33*, 212; b) P. Schwerdtfeger, J. S. McFeaters, R. L. Stephens, M. J. Liddell, M. Dolg, B. A. Hess, *Chem. Phys. Lett.* **1994**, *218*, 362; c) M. Iliaš, P. Furdik, M. Urban, *J. Phys. Chem. A* **1998**, *102*, 5263; d) C. J. Evans, M. C. L. Gerry, *J. Am. Chem. Soc.* **2000**, *122*, 1560; e) S. Andreev, J. J. BelBruno, *Chem. Phys. Lett.* **2000**, *329*, 490.

[5] P. Schwerdtfeger, J. S. McFeaters, M. J. Liddell, J. Hrušák, H. Schwarz, *J. Chem. Phys.* **1995**, *103*, 245.

[6] R. Brown, P. Schwerdtfeger, D. Schröder, H. Schwarz, *J. Am. Soc. Mass Spectrom.* **2002**, *13*, 485.

[7] a) H. Schwarz, *Angew. Chem.* **2003**, *115*, 4580; *Angew. Chem. Int. Ed.* **2003**, *42*, 4442; b) P. Pyykkö, *Angew. Chem.* **2004**, *116*, 4512; *Angew. Chem. Int. Ed.* **2004**, *43*, 4412.

[8] The experiments were performed with a modified VG ZAB/HF/AMD 604 four-sector mass spectrometer of BEBE configuration (B stands for magnetic and E for electric sector).[9] The ions of interest were generated by electron ionization (EI, 70 eV) of anhydrous TlF. The ions accelerated by a potential of 8 kV were mass-selected using B(1)/E(1), and the respective mass spectra were recorded by scanning B(2). For collisional activation, helium was used as collision gas at 80% transmission (T). In the charge stripping (CS) and charge-exchange (CE) experiments,[1] oxygen was used throughout as the collision gas (80% T). Energy-resolved CS was performed with B(1)-only mass-selected ions. The attempt to detect photons emitted from metastable TlF^+ was conducted as follows: At a mass-resolution of $m/\Delta m = 2000$, the total ion current of TlF^+ in the mass region m/z 220 to 226 was measured by scanning B(1) and monitoring the cations using the off-axis detector mounted behind E(1). Next, the deflector electrode which directs the ions on the detector was switched off. If photons were emitted during the passage of the TlF^+ beam in the vicinity of the detector, these should give rise to signals at the correct m/z values of the two Tl isotopes in the B(1) scan. Even though the detector was set to maximal sensitivity, no photons could be observed.

[9] C. A. Schalley, D. Schröder, H. Schwarz, *Int. J. Mass Spectrom. Ion Processes* **1996**, *153*, 173.

[10] See also: a) E. Murad, D. L. Hildenbrand, R. P. Main, *J. Chem. Phys.* **1966**, *45*, 263; b) F. J. Kenesha, D. Cubicciotti, *J. Phys. Chem.* **1967**, *71*, 1958; c) J. Berkowitz, T. A. Walter, *J. Chem. Phys.* **1968**, *49*, 1184.

[11] While we cannot strictly exclude that the dimeric ions $Tl_2F_n^+$ ($n = 1, 2$; see ref. [10]) may serve as precursor of the TlF^+ species formed, the low pressures applied in the ion source as well as the favorable Franck–Condon factors for the ionization of neutral TlF into low-lying cation states (see text) discount the need to include this issue in the further discussion.

[12] Ion dissociation owing to collisional activation by background gases was found to be negligible.

[13] R. G. Cooks, J. H. Beynon, R. M. Caprioli, G. R. Lester, *Metastable Ions*, Elsevier, Amsterdam, **1973**.

[14] R. G. Cooks, J. H. Beynon, J. F. Litton, *Org. Mass Spectrom.* **1975**, *10*, 503, and references therein.

[15] The signal is too weak for an accurate determination of the energy demand of the CS process; only a crude value of $IE(TlF^+) \approx Q_{min} = 19.7 \pm 1.1$ eV can be extracted from experiment.

[16] a) P. Dai, S. McCullough-Catalano, M. Bolton, A. D. Jones, C. B. Lebrilla, *Int. J. Mass Spectrom. Ion Processes* **1995**, *144*, 67; b) C. Heinemann, D. Schröder, H. Schwarz, *J. Phys. Chem.* **1995**, *99*, 16195.

[17] From the distance between the peak maxima of the broad component, a KER of about (3 ± 1) eV can be estimated for Coulomb explosion of TlF^{2+} according to Equation (2).

[18] The calculations were performed using the MOLPRO[19] ab initio program at the RCCSD(T) and MR-AQCC levels. For thallium, we used a scalar-relativistic small-core ECP replacing 60 core electrons ([Kr]4d104f14 core) together with a 12s12p9d3f2g basis contracted to 6s6p4d3f2g.[20] For fluorine, the aug-cc-pVQZ basis set has been used. The 5s and 5p orbitals of thallium and the 1s orbital of fluorine were left uncorrelated. The MR-AQCC calculations use a reference CASSCF wave function with 13 active orbitals (full valence space covering the Tl 5d/6s/6p and F 2s/2p atomic orbitals).

[19] MOLPRO (version 2002.3) is a package of ab initio programs written by H.-J. Werner, P. J. Knowles, M. Schütz, R. Lindh, P. Celani, T. Korona, G. Rauhut, F. R. Manby, R. D. Amos, A. Bernhardsson, A. Berning, D. L. Cooper, M. J. O. Deegan, A. J. Dobbyn, F. Eckert, C. Hampel, G. Hetzer, A. W. Lloyd, S. J. McNicholas, W. Meyer, M. E. Mura, A. Nicklaß, P. Palmieri, R. Pitzer, U. Schumann, H. Stoll, A. J. Stone, R. Tarroni, T. Thorsteinsson.

[20] B. Metz, M. Schweizer, H. Stoll, M. Dolg, W. Liu, *Theor. Chem. Acc.* **2000**, *104*.

[21] All energies given include zero-point vibrational corrections and an asymptotic atomic spin–orbit correction to account for the spin–orbit coupling in Tl, Tl^+ (6s6p, ^3P), F, and F^+ which shift the state-averaged atomic asymptotes lower by 0.644, 0.967, 0.017, and 0.021 eV, respectively.

[22] For a discussion of several values, see ref. [10b].

[23] Taken from: NIST Standard Reference Database #69, National Institute of Standards, Gaithersburg, 2003, see: http://webbook.nist.gov/chemistry/.

[24] Taken from: NIST Atomic Spectra Database, NIST Standard Reference Database #78, National Institute of Standards, Gaithersburg, **2004**; see: http://physics.nist.gov/cgi-bin/AtData/main_asd.

[25] G. Gamow, *Z. Phys.* **1928**, *51*, 204.

[26] Here, we assume release of a single photon with $E_{h\nu} = 3.7$ eV; the emission of two or more photons with $\Sigma E_{h\nu,i} = 3.7$ eV might escape detection.

[27] To our knowledge, there is no precedent of this particular experiment. However, photon emission upon collisional activation has already been observed in sector instruments, see: a) J. L. Holmes, P. M. Mayer, A. A. Mommers, *J. Am. Chem. Soc.* **1991**, *113*, 9405; b) J. L. Holmes, P. M. Mayer, A. A. Mommers, *Int. J. Mass Spectrom. Ion Processes* **1994**, *135*, 213; c) J. L. Holmes, P. M. Mayer, *J. Mass Spectrom.* **1995**, *30*, 52.

[28] D. Schröder, J. N. Harvey, M. Aschi, H. Schwarz, *J. Chem. Phys.* **1998**, *108*, 8446.

[29] a) F. Cacace, G. de Petris, M. Rosi, A. Troiani, *Chem. Eur. J.* **2002**, *8*, 3653; b) F. Cacace, G. de Petris, M. Rosi, A. Troiani, *Chem. Eur. J.* **2002**, *8*, 5684.

[30] One example for such a controversy is the recent mass spectrometric detection of neutral N_4; see: E. E. Rennie, P. M. Mayer, *J. Chem. Phys.* **2004**, *120*, 10561, and references therein.

 © 2005 Wiley-VCH Verlag GmbH & Co. KGaA, Weinheim

Arene Functionalization

Preparation of Functionalized Aryl Magnesium Reagents by the Addition of Magnesium Aryl Thiolates and Amides to Arynes**

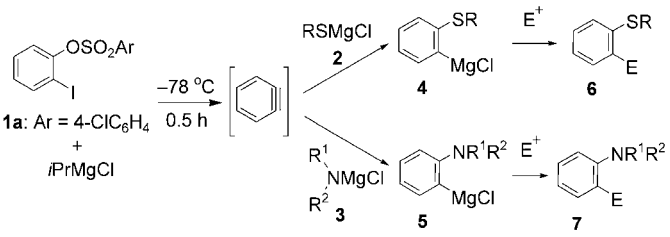
*Wenwei Lin, Ioannis Sapountzis, and Paul Knochel**

Dedicated to Professor Reinhard W. Hoffmann

The functionalization of arenes is an important synthetic task.[1] A potential approach is the addition reaction of nucleophiles to intermediate arynes.[2] The addition of heteroatom–metal bonds (Nu–Met; Nu = OR, NR_2, SR, PR_2) to alkynes is usually a difficult process due to the high energy of the Nu–Met bond and to the high nucleophilicity of the resulting C–Met bond of the adduct, which is prone to undergo polymerization and other side reactions.[3] In the presence of a catalytic amount of a metal catalyst, various heteroatom–hydrogen bonds can be added to triple bonds.[3,4] However, in this case, the reactivity of the C–Met bond of the adduct cannot be exploited. By using a very reactive alkyne, such as an aryne,[5] the addition of nucleophiles should be facilitated and should afford useful arylmetal complexes, which should react with various electrophiles. Although the addition of various nitrogen nucleophiles to arynes has been reported,[5,6] the successful trapping of the intermediates with electrophiles has been reported in only a few cases.[7]

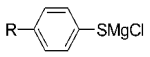
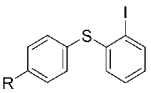
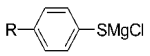
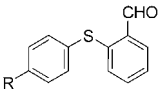
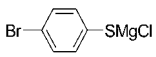
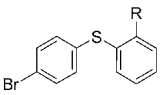
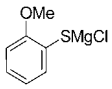
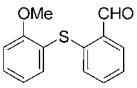
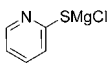
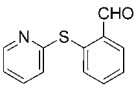
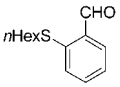
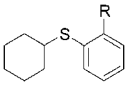
Recently we have described a new preparation of polyfunctional arynes by the elimination of 2-magnesiated diaryl sulfonates prepared from the corresponding iodides of type **1**.[8] Herein, we report the selective addition of magnesiated thiols and amines of types **2** and **3** to arynes generated by our previous procedure, providing 2-thio- and 2-amino-substituted aryl magnesium species of types **4** and **5**, respectively (Scheme 1). In contrast to previous methods,[2,5d,6] these aryl magnesium reagents can be trapped by a range of electrophiles giving rise to thioethers of type **6** and arylamines of type **7** (Table 1 and Table 2).

Thus, the addition of *i*PrMgCl (2.0 equiv) to thiophenol (1.0 equiv) in THF (−78 °C, 10 min) followed by the addition of 2-iodophenyl 4-chlorobenzenesulfonate (**1a**) (1.0 equiv; −78 °C, 0.5 h) and subsequent warming to 0 °C within 10 min led to the benzyne-addition product **4a**, which, upon quenching with iodine in THF at −78 °C, provided 2-iodophenyl



Scheme 1. Preparation of aryl thioethers and aryl amines by addition reactions to benzyne.

Table 1: Synthesis of thioethers of type **6** by the addition of magnesium thiolates **2** to benzyne followed by the trapping of the intermediate Grignard reagent **4** with an electrophile (see Scheme 1).

Entry	2	Electrophile	6	Yield [%][a]
1	PhSMgCl (**2a**)	I_2	 **6a**	83
				
2	**2b**: R = F	I_2	**6b**: R = F	90
3	**2c**: R = Cl	I_2	**6c**: R = Cl	84
4	**2d**: R = Br	I_2	**6d**: R = Br	82
				
5	**2b**	DMF	**6e**: R = F	78
6	**2c**	DMF	**6f**: R = Cl	73
7	**2d**	DMF	**6g**: R = Br	75
				
8	**2d**	EtCOCl	**6h**: R = COEt	90
9	**2d**	PhCOCl	**6i**: R = COPh	88
10	**2d**	PhCHO	**6j**: R = CH(OH)Ph	85
11	 **2e**	DMF	 **6k**	80
12	 **2f**	DMF	 **6l**	82
13	*n*-HexSMgCl (**2g**)	DMF	 **6m**	67
				
14	*c*-HexSMgCl (**2h**)	DMF	**6n**: R = CHO	73
15	**2h**	PhCOCl	**6o**: R = COPh	83

[a] Yield of isolated, analytically pure product.

[*] Dipl.-Chem. W. Lin, Dr. I. Sapountzis, Prof. Dr. P. Knochel
Ludwig-Maximilians-Universität München
Department Chemie und Biochemie
Butenandtstrasse 5–13, Haus F, 81377 München (Germany)
Fax: (+49) 89-2180-77680
E-mail: paul.knochel@cup.uni-muenchen.de

[**] We thank the Fonds der Chemischen Industrie, the Deutsche Forschungsgemeinschaft (DFG), and Merck Research Laboratories (MSD) for financial support, as well as Chemetall GmbH (Frankfurt) and BASF AG (Ludwigshafen) for generous gifts of chemicals. I.S. thanks Sanofi-Aventis (Frankfurt) for a fellowship.

Supporting information for this article is available on the WWW under http://www.angewandte.org or from the author.

 © 2005 Wiley-VCH Verlag GmbH & Co. KGaA, Weinheim DOI: 10.1002/anie.200500443

phenyl sulfide (**6a**) in 83% yield (entry 1, Table 1). Various substituted thiophenolates, such as **2b–d**, reacted as well affording after iodolysis the 2-iodophenyl thioethers **6b–d** in 82–90% yield (entries 2–4).

Similarly, the intermediate Grignard reagents were formylated with DMF (2.5 equiv, −40°C to RT, 1 h) leading to aldehydes **6e–g** in 73–78% yield (entries 5–7, Table 1). Acid chlorides (in the presence of CuCN·2 LiCl) and aldehydes were also excellent trapping agents, leading to ketones **6h–i** and to the benzylic alcohol **6j**, respectively, in 85–90% yield (entries 8–10). The *ortho*-substituted magnesium thiolate **2e** (entry 11) and the heterocyclic thiolate **2f** (entry 12) both underwent the addition reaction followed by formylation with DMF giving rise to **6k** (80% yield) and **6l** (82% yield), respectively. Aliphatic thiolates, such as **2g** and **2h**, added to benzyne under the same reaction conditions affording the functionalized alkyl aryl thioethers **6m–o** in 67–83% yield (entries 13–15).

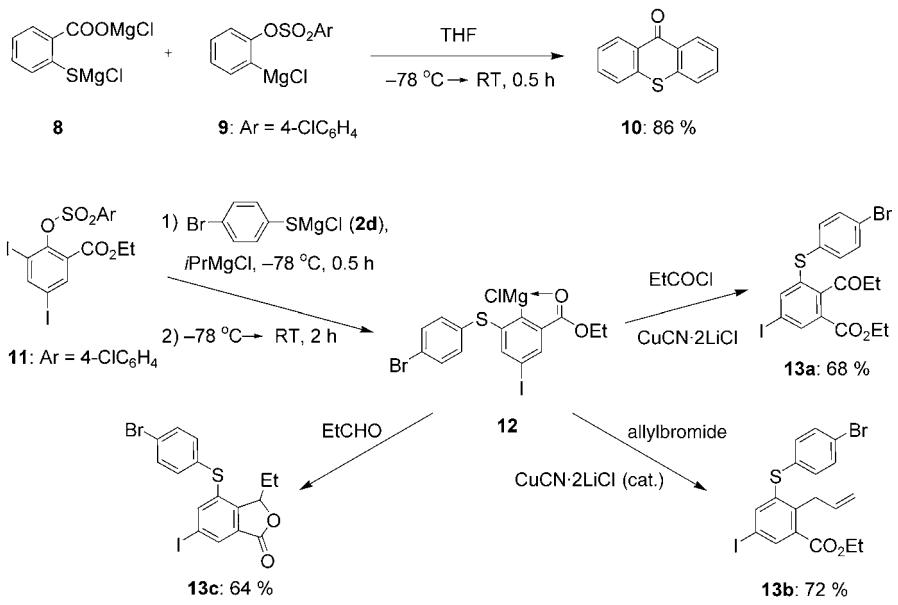
The high strain of the generated aryne ensures a smooth addition and excellent functional-group compatibility. Thus, the reaction of the magnesium thiolate **8**, bearing a carboxy group in position 2, with the 2-magnesiated benzenesulfonate **9** provided the desired addition aryl magnesium species, which reacted intramolecularly with the carbonyl group in *ortho*-position leading to thioxanthone (**10**) in 86% yield (Scheme 2).

Interestingly, functionalized arynes displayed remarkable regioselectivity in the addition step. Thus, the polyfunctional sulfonate **11** was selectively magnesiated in the α-position to the sulfonate group (inductive activation of the *ortho*-carbon–iodine bond), and its reaction with the magnesium thiolate **2d** provided only the magnesium reagent **12**, which was stabilized by chelation. Its reaction with various electrophiles, like an acid chloride, allyl bromide in the presence of CuCN·2 LiCl, or an aldehyde, furnished the tetrasubstituted thioethers **13a–c** in 64–72% yield (Scheme 2).

Remarkably, all the previous reactions involved the conversion of the magnesium–sulfur bond of **2** into the magnesium–carbon bond in **4**. We have also examined the addition of a magnesium amide of type **3** to benzyne; this results in the conversion of a nitrogen–magnesium bond to a carbon–magnesium bond in the product **5** (Scheme 1). Thus, the reaction of magnesiated *N*-methylaniline (**3a**) with the 2-magnesiated benzenesulfonate **9** provided the desired addition product of type **5** (−78°C, 30 min, then 0°C for 10 min). After the addition of CuCN·2 LiCl and allyl bromide, the desired product **7a** was obtained in 83% yield (entry 1, Table 2). Typical electrophiles, such as benzoyl chloride, benzaldehyde, and DMF, reacted similarly furnishing the diarylamines **7b–d** in 74–85% yield (entries 2–4). Related phenyl-substituted secondary magnesium amides, such as **3b** and **3c** (entries 5–7), reacted in a similar way leading to the benzaldehyde **7e** (71% yield) and the indolines **7f** and **7g** (62–66% yield), respectively. The bulky aliphatic amide *i*Pr_2NMgCl (**3d**) was less prone to add to benzyne, and the desired product **7h** (after formylation) was obtained only in 25% yield (entry 8). Interestingly, a functionalized magnesium amide, such as **3e**, underwent the benzyne addition providing a polyfunctional aryl magnesium species, which was efficiently trapped with DMF and EtCOCl according to our standard procedure furnishing the tertiary amines **7i** (73% yield, entry 9) and **7j** (76% yield, entry 10), respectively.

During this study, we realized that the rate of addition to the aryne strongly depended on the nucleophilicity of the magnesium reagent (Nu–MgX) as noted previously by Huisgen.[5a] Thus, whereas magnesium amides are basic reagents, magnesium thiolates are more nucleophilic and therefore add more readily.[9] We anticipated that highly nucleophilic reagents, like phenylselenyl magnesium chloride **14**, would react well with benzyne. Preliminary experiments confirmed this hypothesis. Thus, the addition of **14** to **9** lead via the magnesiated intermediate **16**[10] to the products **15a** (85% yield) and **15b** (87% yield) under standard conditions (Scheme 3).

In summary, we have developed a general procedure for the thio-(seleno-) and aminomagnesiation of arynes. The resulting aryl magnesium species can be trapped with numerous electrophiles in contrast to most previously reported addition reactions. Further extensions utilizing other nucleophiles are currently underway in our laboratories.



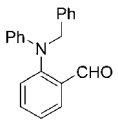
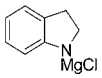
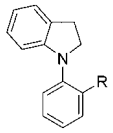
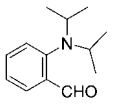
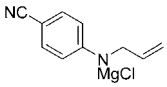
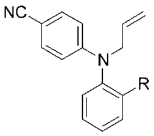
Scheme 2. Preparation of polyfunctional thioethers using the addition of magnesium thiolates to arynes.

Experimental Section

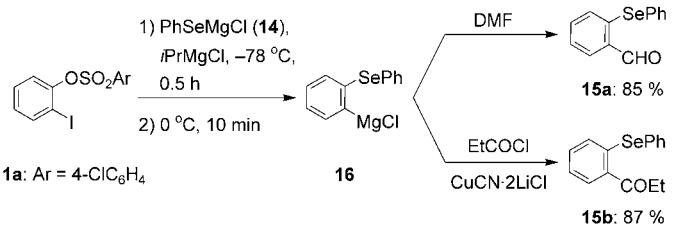
Typical procedure: Preparation of **6g**: A dry and argon-flushed 25-mL Schlenk flask, equipped with a magnetic stirring bar and a septum, was charged with a solution of 4-bromothiophenol (190 mg, 1.0 mmol) in dry THF (3 mL). This solution was cooled to −78°C, *i*PrMgCl (1.88 mL, 2.0 equiv, 1.07 M in THF) was

 © 2005 Wiley-VCH Verlag GmbH & Co. KGaA, Weinheim

Table 2: Synthesis of tertiary amines of type **7** by the addition of magnesium amides **3** to benzyne followed by the trapping of the intermediate Grignard reagent **5** with an electrophile.

Entry	3	Electrophile	7	Yield [%][a]
				
1	Ph(Me)NMgCl (**3a**)		**7a**: R = allyl	83
2		PhCOCl	**7b**: R = COPh	85
3		PhCHO	**7c**: R = CH(OH)OPh	80
4		DMF	**7d**: R = CHO	74
5	Ph(Bn)NMgCl (**3b**)	DMF	 **7e**	71
				
6	**3c**		**7f**: R = allyl	66
7	**3c**	EtCOCl	**7g**: R = COEt	62
8	 **3d**	DMF	 **7h**	25
				
9	**3e**	DMF	**7i**: R = CHO	73
10	**3e**	EtCOCl	**7j**: R = COEt	76

[a] Yield of isolated, analytically pure product.



Scheme 3. Preparation of aryl selenoethers by addition reactions to benzyne.

added dropwise, and the reaction mixture was stirred for 10 min. A solution of **1a** (394 mg, 1.0 mmol) in dry THF (2 mL) was added, and the reaction mixture was stirred vigorously for 30 min at the same temperature. The resulting mixture was immediately warmed to 0 °C and stirred for 10 min. Then the reaction mixture was cooled to −40 °C, and DMF (0.20 mL, 2.5 equiv) was added. Thereafter, the reaction mixture was warmed to room temperature and stirred for 1 h. The reaction was quenched with sat. aq. NH_4Cl solution and extracted with CH_2Cl_2 (3 × 40 mL). The combined organic phases were dried over anhydrous Na_2SO_4 and filtered, and the solvent was removed by evaporation in vacuo. Purification by flash chromatography (*n*-pentane/diethyl ether 20:1) furnished the thioether **6g** as a yellow solid (220 mg, 75 %).

Preparation of **7d**: A dry and argon-flushed 25-mL Schlenk flask, equipped with a magnetic stirring bar and a septum, was charged with a solution of *N*-methylaniline (107 mg, 1.0 mmol) in dry THF (3 mL). This solution was cooled to −20 °C, *i*PrMgCl (0.94 mL, 1.0 equiv, 1.07 M in THF) was added dropwise, and the reaction mixture was stirred for 30 min. The reaction mixture was cooled to −78 °C, and *i*PrMgCl (0.94 mL, 1.0 equiv, 1.07 M in THF) was added. A solution of **1a** (394 mg, 1.0 mmol) in dry THF (2 mL) was added, and the reaction mixture was stirred vigorously for 30 min at the same temperature. The resulting mixture was immediately warmed to 0 °C and stirred for 10 min. Then, the reaction mixture was cooled to −40 °C, and DMF (0.20 mL, 2.5 equiv) was added. Thereafter, the reaction mixture was warmed to room temperature and stirred for 1 h. The reaction was quenched with sat. aq. NH_4Cl solution and extracted with CH_2Cl_2 (3 × 40 mL). The combined organic phases were dried over anhydrous Na_2SO_4 and filtered, and the solvent was removed by evaporation in vacuo. Purification by flash chromatography (*n*-pentane/diethyl ether 250:1) furnished the amino aldehyde **7d** as a yellow oil (156 mg, 74 %).

Received: February 5, 2005
Published online: June 7, 2005

Keywords: amination · arynes · Grignard reagents · heterocycles · thioethers

[1] a) M. C. Whisler, S. MacNeil, V. Snieckus, P. Beak, *Angew. Chem.* **2004**, *116*, 2256; *Angew. Chem. Int. Ed.* **2004**, *43*, 2206; b) B. Chauder, L. Green, V. Snieckus, *Pure Appl. Chem.* **1999**, *71*, 1521; c) V. Snieckus, *Chem. Rev.* **1990**, *90*, 879.

[2] H. Pelissier, M. Santelli, *Tetrahedron* **2003**, *59*, 701.

[3] a) R. Taube in *Applied Homogeneous Catalysis with Organometallic Compounds* (Eds.: B. Cornils, W. A. Herrmann), Wiley-VCH, New York, **1996**, p. 507–520; b) T. E. Müller, M. Beller in *Transition Metals for Organic Synthesis* (Eds.: M. Beller, C. Bolm), Wiley-VCH, Weinheim, **1998**, p. 316–330; c) T. E. Müller, M. Beller, *Chem. Rev.* **1998**, *98*, 675.

[4] a) J. H. Teles, S. Brode, M. Chabanas, *Angew. Chem.* **1998**, *110*, 1475; *Angew. Chem. Int. Ed.* **1998**, *37*, 1415; b) M. Beller, M. Eichberger, H. Trauthwein, *Angew. Chem.* **1997**, *109*, 2306–2308; *Angew. Chem. Int. Ed. Engl.* **1997**, *36*, 2225; c) M. Beller, C. Breindl, T. H. Riermeier, M. Eichberger, H. Trauthwein, *Angew. Chem.* **1998**, *110*, 3571; *Angew. Chem. Int. Ed.* **1998**, *37*, 3389; d) G. A. Molander, J. A. C. Romero, *Chem. Rev.* **2002**, *102*, 2161; e) M. Nobis, B. Driessen-Hoelscher, *Angew. Chem.* **2001**, *113*, 4105; *Angew. Chem. Int. Ed.* **2001**, *40*, 3983; f) F. Pohki, S. Doye, *Chem. Soc. Rev.* **2003**, *32*, 104; g) P. W. Roesky, T. E. Mueller, *Angew. Chem.* **2003**, *115*, 2812; *Angew. Chem. Int. Ed.* **2003**, *42*, 2708; h) S. Doye, *Synlett* **2004**, 1653.

[5] For excellent reviews, see: a) J. Sauer, R. Huisgen, *Angew. Chem.* **1960**, *72*, 294; b) R. W. Hoffmann, *Dehydrobenzene and*

Cycloalkynes, Academic Press, New York **1967**; c) L. Castedo, E. Guitian in *Studies in Natural Products Chemistry*, *Vol. 3*, *Part B* (Ed.: Atta-ur-Rahman), Elsevier, Amsterdam, **1989**, p. 417; d) S. V. Kessar *in Comprehensive Organic Synthesis*, *Vol. 4* (Eds.: B. M. Trost, I. Fleming, H. F. Semmelhack), Pergamon, Oxford, **1991**, S. 483; e) R. F. C. Brown, F. W. Eastwood, *Synlett* **1993**, 9; f) W. Sander, *Acc. Chem. Res.* **1999**, *32*, 669; g) T. Hamura, Y. Ibusuki, K. Sato, T. Matsumoto, Y. Osamura, K. Suzuki, *Org. Lett.* **2003**, *5*, 3551; h) T. Hosoya, T. Hamura, Y. Kuriyama, M. Miyamaoto, T. Matsumoto, K. Suzuki, *Synlett* **2000**, 520; i) T. Hosoya, E. Takashiro, T. Matsumoto, K. Suzuki, *J. Am. Chem. Soc.* **1994**, *116*, 1004; j) M. Beller, C. Breindl, T. H. Riermeier, A. Tillack, *J. Org. Chem.* **2001**, *66*, 1403; k) P. Maurin, M. Ibrahim-Ouali, M. Santelli, *Tetrahedron Lett.* **2001**, *42*, 8147; l) Z. Liu, R. C. Larock, *Org. Lett.* **2003**, *5*, 4673; m) H. Yoshida, Y. Honda, E. Shirakawa, T. Hiyama, *Chem. Commun.* **2001**, 1880; n) H. Yoshida, E. Shirakawa, Y. Honda, T. Hiyama, *Angew. Chem.* **2002**, *114*, 3381; *Angew. Chem. Int. Ed.* **2002**, *41*, 3247; o) D. Peña, S. Escudero, D. Pérez, E. Guitián, L. Castedo, *Angew. Chem.* **1998**, *110*, 2804; *Angew. Chem. Int. Ed.* **1998**, *37*, 2659; p) J.-M. Becht, A. Gissot, A. Wagner, C. Mioskowski, *Chem. Eur. J.* **2003**, *9*, 3209; q) Z. Liu, R. C. Larock, *Org. Lett.* **2004**, *6*, 99.

[6] a) B. Jamart-Gregoire, C. Leger, P. Caubère, *Tetrahedron Lett.* **1990**, *31*, 7599; b) S. Tripathy, R. LeBlanc, T. Durst, *Org. Lett.* **1999**, *1*, 1973; c) M. Paz, C. Saa, E. Guitian, L. Castedo, J. M. Saa, *Heterocycles* **1993**, *36*, 1217; d) I. Fleming, M. Woolias, *J. Chem. Soc. Perkin Trans. 1* **1979**, 827.

[7] a) A. I. Meyers, P. D. Pansegrau, *J. Chem. Soc. Chem. Commun.* **1985**, 690; b) P. Beak, A. I. Meyers, *Acc. Chem. Res.* **1986**, *19*, 356.

[8] I. Sapountzis, W. Lin, M. Fischer, P. Knochel, *Angew. Chem.* **2004**, *116*, 4464; *Angew. Chem. Int. Ed.* **2004**, *43*, 4364.

[9] Low steric hindrance is also essential for an efficient addition reaction, since bulky amides add significantly less efficiently.

[10] A. Krief, T. Van Wemmel, M. Redon, W. Dumont, C. Delmotte, *Angew. Chem.* **1999**, *111*, 2389; *Angew. Chem. Int. Ed.* **1999**, *38*, 2245.

 © 2005 Wiley-VCH Verlag GmbH & Co. KGaA, Weinheim

Oxygen-Rich Compounds

The Molecules AlO_2, $Al(O_2)_2$, and $Al(O_2)_3$: Experimental and Quantum-Chemical Investigations on the Oxidation of Aluminum Atoms**

*Gregor Stößer and Hansgeorg Schnöckel**

Dedicated to Professor Klaus Krogmann on the occasion of his 80th birthday

We have already mentioned the significance of peroxo- and hyperoxo complexes with unusual spin states as intermediates in oxidation processes in biology and synthetic chemistry when we reported the oxidation of AlX molecules with O_2 under matrix-isolation conditions.[1][2] The reactions of metal atoms with oxygen discussed herein also prove to be complex, since electrons are taken up stepwise by the O_2 molecules with retention of symmetry and spin rules ($O_2 \rightarrow O_2^- \rightarrow O_2^{2-}$). On the preparative scale, this process results exclusively cleavage of the O–O bond and the formation of O^{2-} ions; with metal cations these ions form particularly stable oxides, such as Al_2O_3. To investigate the primary steps of this reaction we have treated aluminum atoms with an increasing excess of O_2 in the matrix-gas argon under matrix-isolation conditions and have obtained the molecules AlO_2 (**1**), $Al(O_2)_2$ (**2**), and $Al(O_2)_3$ (**3**). These result are reported herein, while details of the spectra and the results of quantum-chemical calculations are given in the Supporting Information.

The formation of C_{2v} symmetrical AlO_2 (**1**) in solid argon from aluminum atoms with approximately 0.1 % O_2 has been reported elsewhere.[3]. In our experiments, and in agreement with the literature, we have observed the symmetrical AlO_2 vibration in the IR spectrum at 496 cm^{-1} and measured its $^{16}O/^{18}O$ shifts.[4] A new band at 1070 cm^{-1} is observed at higher O_2 concentrations in argon gas (1–3 %) after reaction of aluminum atoms, again in agreement with the literature.[5] $^{16}O/^{18}O$ substitution experiments indicate that this new band belongs to a species with four equivalent oxygen atoms.[6] As will be shown below, this species is $Al(O_2)_2$ (**2**), which is assigned the structure (D_{2d} symmetry) illustrated in Figure 1. At still higher O_2 concentrations in the matrix and finally in pure solid O_2 a band at 688 cm^{-1} is observed in the IR spectrum. This band shifts to 671 cm^{-1} in $^{18}O_2$ enriched O_2 and occurs at 679 cm^{-1} in the presence of $^{16}O/^{18}O$ species.[7] Since,

[*] Dr. G. Stößer, Prof. Dr. H. Schnöckel
Institut für Anorganische Chemie
Universität Karlsruhe (TH)
Engesserstrasse 15, Geb. 30.45, 76128 Karlsruhe (Germany)
Fax: (+49) 721-608-4854
E-mail: hansgeorg.schnoeckel@chemie.uni-karlsruhe.de

[**] This work was supported by the Deutsche Forschungsgemeinschaft and the Fonds der Chemischen Industrie. We thank Prof. Dr. Wim Klopper for his help with the quantum-chemical calculations and Priv.-Doz. Dr. Dr. Hans-Jörg Himmel for valuable suggestions.

Supporting information for this article is available on the WWW under http://www.angewandte.org or from the author.

 DOI: 10.1002/anie.200500512 © 2005 Wiley-VCH Verlag GmbH & Co. KGaA, Weinheim

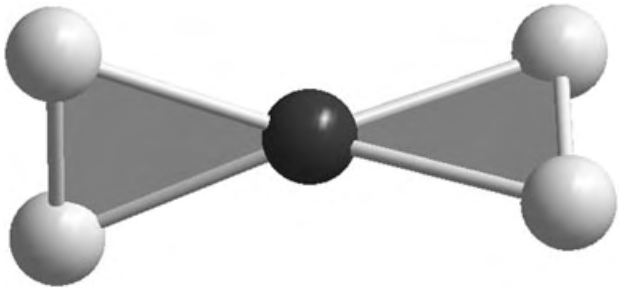


Figure 1. Minimum structure of $Al(O_2)_2$ (**2**) calculated with B3LYP/TZVPP (see Table 1).

under identical conditions, a new band appears at 1065 cm^{-1} in the Raman spectrum,[8] we have assigned these two intense bands as well as a weak signal in the Raman spectrum at 406 cm^{-1} to the molecule $Al(O_2)_3$ (**3**), whose calculated molecular structure (D_3 symmetry)is illustrated in Figure 2.

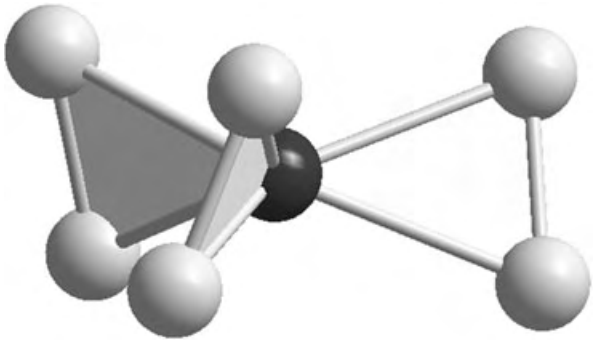


Figure 2. Minimum structure von $Al(O_2)_3$ (**3**) calculated with B3LYP/TZVPP (see Table 1).

To confirm the assignment of the cited vibrational frequencies to molecules **1**, **2**, and **3** extensive quantum-chemical calculations were carried out; these gave the Al–O and O–O distances and force constants listed in Table 1.

Table 1: Distances r [pm] and force constants f [N m^{-1}] of AlO_2 (**1**), $Al(O_2)_2$ (**2**), and $Al(O_2)_3$ (**3**) calculated with B3LYP/TZVPP.

	r_{Al-O}	r_{O-O}	f_{Al-O_2}	f_{O-O}
1	195	134	210	648
2	175	148	386	473
3	185	136	353	632

The special bond properties in **1**, its stability, and the kinetics of the conversion of its different isomers have been reported in detail recently.[9] We have been able to confirm these results according to which the observed C_{2v} hyperoxide **1** has a stability similar to that of the linear $D_{\infty h}$ isomer. Presumably the energy barrier between the two species is very high so that in our spectra only the somewhat less stable (according to calculation[9]) C_{2v} isomer is observed.[10]

For **2**, the D_{2d} isomer shown in Figure 1 is approximately 55 kJ mol^{-1} more stable than a molecule with D_{2h} symmetry. The other isomers (C_{4v} and T_d) also lie energetically much higher (266 and 329 kJ mol^{-1}, respectively). Although only one band is observed for **2**, the assignment seems to be correct since five $^{16}O/^{18}O$ shifts were observed for this band which are in very good agreement with those calculated, and indicates that there are four equivalent oxygen atoms in this molecule. Moreover, this interpretation is plausible since the bands assigned to **2** appear after the formation of **1** and prior to the formation of **3**. The special bonding situation in **2** arises because in the highest singly occupied molecular orbital (SOMO; $1a_2$, Figure 3) one electron must be shared by both

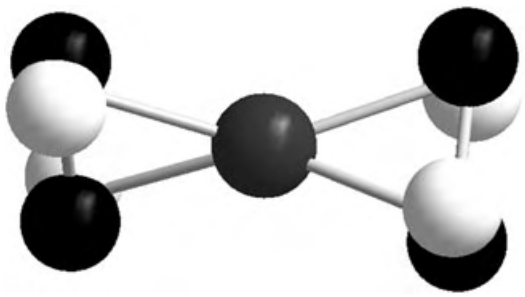


Figure 3. Graphical representation of the SOMO ($1a_2$) of $Al(O_2)_2$ (**2**).

O_2 groups, that is, compared to neutral O_2, each O_2 group is weakened because it carries an additional 1.5 electrons. Hence **2** may not be described as $O_2^-Al^{3+}O_2^{2-}$ (that is, as hyperoxide with an additional peroxo group). Thus it appears plausible that the O–O bond in **2** is weaker and the Al–O bond stronger than in **1**.

Unlike the unusual bonding relationships in **2**, those in **3** appear analogous to the bonding relationships in the recently described $XAl(O_2)_2$ species (X = F, Cl, Br),[1] which means that in **3** there are three O_2^- groups attached to the Al^{3+} ion by interactions that are predominantly ionic in character. This situation becomes especially clear through the absence of vibrational coupling between the three O_2 vibrations, since almost identical frequencies of 1158 and 1154 cm^{-1} are calculated for the E and A_1 vibrations. In this respect, as well as with the O–O and Al–O distances and also the force constants, the expected parallels to the $XAl(O_2)_2$ species emerge. The unusual spin situation in the $XAl(O_2)_2$ compounds (triplet electronic ground states) becomes even more unusual in **3** for which a quartet ground state is found. To our knowledge this is unique for molecular compounds free of transition metals.[11] Admittedly, the energy difference between the doublet and quartet states is very small. This finding and the absence of stabilization in **3** from a Jahn–Teller distortion also provide support for an essentially ionic bonding mode. In spite of the unusual bonding situations in **1**, **2**, and **3** a consistent picture emerges for the three compounds:

The following distances and force constants were calculated for the isolated ions O_2^- and O_2^{2-}: O_2^- 135 pm, 660 N m^{-1} and O_2^{2-} 163 pm, 190 N m^{-1}.[1] In comparison the force constants determined from the observed frequencies for

 © 2005 Wiley-VCH Verlag GmbH & Co. KGaA, Weinheim

1, **2**, and **3** and the calculated distances confirm that in **1** and **3** (as with the $XAl(O_2)_2$ species) the hyperoxide ions are essentially ionically bonded to the positively charged Al centers. In **2**, in agreement with the electronic situation, the O_2 bond is clearly elongated, similar to the bond an O_2^{2-} ion. On the other hand, the Al–O bond also clearly lengthens in the order $\mathbf{2} < \mathbf{3} < \mathbf{1}$, which correlates very well with the calculated Al-O_2 force constants (Table 1). These findings are illustrated in Figure 3 for the special bonding situation of compound **2**. For compound **3** and **1** this bond lengthening may be attributed to the reduced formal charge at the Al center (Al^{1+} in **1** and Al^{3+} in **3**).

The energetic ordering of the three hypervalent compounds is shown in Figure 4 and emerges from experimental

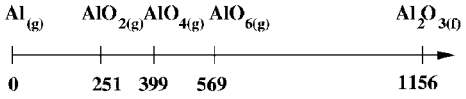


Figure 4. Energy scheme [kJ mol^{-1}] for the stepwise exothermic oxidation of Al atoms with O_2.

thermodynamic data[12] and the quantum-mechanical results obtained in this work. Relative to 1 mol aluminum atoms, in the stepwise formation of **1**, **2**, and **3** more energy is released than for any other molecular Al_xO_y compound.[13] Nevertheless, the $Al(O_2)_n$ ($n = 1, 2, 3$) molecules described herein are certainly only obtainable in measurable quantities under matrix conditions, since the formation of alumina from $Al(O_2)_3$ is favored by 587 kJ mol^{-1}

The results on the oxidation of aluminum atoms with excess O_2 reported herein demonstrate the complexity of such apparently trivial reactions. On the other hand, this process is an extreme situation, in the reverse case, that is, the reaction of excess aluminum atoms with few O_2 molecules is a more realistic model when it comes to the investigation of the primary products of oxidation, for example, on aluminum surfaces. This problem is at the center of current gas-phase investigations of Al_n clusters and their oxidation by O_2, reactions which are being studied with the aid of FT mass spectroscopy.[14]

Experimental section

A detailed description of the experimental construction used may be found in ref. [15]. Aluminum was evaporated in high vacuum (10^{-7} mbar) at 1400 K from a resistance-heated boron nitride cell and cocondensed with the matrix gas (Ar/O_2) for 2 h onto a copper block cooled to 10 K with a "closed cycle" cryostat (Leybold LB510). Each hour approximately 150 μg Al and 50 mmol matrix gas were evaporated. Isotope substitution experiments were carried out with $^{18}O_2$, a 1:1 mixture of $^{16}O_2/^{18}O_2$, and a 1:2:1 mixture of $^{16}O_2/^{16}O^{18}O/^{18}O_2$. The IR and Raman spectra were recorded immediately after sample deposition. The following chemicals were used in the matrix reactions: Al (Merck, 99.9999 %), Ar (Messer 99.999 %), $^{16}O_2$ (Messer 99.9998 %), $^{18}O_2$ (Linde 99.9998 %, isotopic purity 99 %).

The IR spectra were taken with Bruker (Karlsruhe) FTIR spectrometers, types 113v and 66v. DTGS and MCT detectors were used, the resolution was 1 cm^{-1}. Raman spectra were taken with a Dilor grating spectrometer, type 800. The Raman vibrations were excited with a argon ion laser (Coherent), the selected wave length was 458 nm.

The quantum-chemical DFT calculations (functional B3-LYP)[16] were carried out with the Turbomole program package.[17] The ab initio calculations were carried out at the CASSCF level with Dalton,[18] Gaussian 98[19] was used for calculation of the CCSD(T) energies. TZVPP basis sets were used for all calculations.[20]

Received: February 10, 2005
Published online: June 1, 2005

Keywords: ab initio calculations · aluminum oxides · matrix isolation · oxidation · Raman spectroscopy

[1] a) J. Bahlo, H.-J. Himmel, H. Schnöckel, *Angew. Chem.* **2001**, *113*, 4820; *Angew. Chem. Int. Ed.* **2001**, *40*, 4696; b) J. Bahlo, H.-J. Himmel, H. Schnöckel, *Inorg. Chem.* **2002**, *41*, 2678; J. Bahlo, H.-J. Himmel, H. Schnöckel, *Inorg. Chem.* **2002**, *41*, 4488.

[2] a) M. Moskovits, G. A. Ozin, *Cryochemistry*, Wiley, New York, **1976**; b) B. Meyer, *Low Temperature Spectroscopy*, American Elsevier, New York, **1971**; c) H. E. Hallam, *Vibrational Spectroscopy of Trapped Species*, Wiley, London, **1973**.

[3] a) L. V. Serebrennikov, S. B. Osin, A. A. Mal'tsev, *J. Mol. Struct.* **1982**, *81*, 25; b) S. M. Sonchik, L. Andrews, K. D. Carlson, *J. Phys. Chem.* **1983**, *87*, 2004; c) I. L. Rozhanskii, L. V. Serebrennikov, A. F. Shevel'kov, *Zh. Fiz. Khim.* **1990**, *64*, 521; d) L. Andrews, T. R. Burkholder, J. T. Yustein, *J. Phys. Chem.* **1992**, *96*, 10182.

[4] The following frequencies were detected in the IR spectrum for the isotopologues of AlO_2 (cm^{-1}): $Al^{16}O_2$ 496.4, $Al^{16}O^{18}O$ 488.6, $Al^{18}O_2$ 480.1.

[5] L. V. Serebrennikov, A. A. Mal'tsev, *Vestn. Mosk. Univ. Ser. 2 Khim.* **1985**, *26*(2), 137.

[6] The following frequencies were detected in the IR spectrum for the isotopologues of $Al(O_2)_2$ (cm^{-1}): $Al^{16}O_4$ 1070.2, $Al^{16}O_3{}^{18}O$ 1062.4, $Al^{16}O_2{}^{18}O_2$ 1054.1, $Al(^{16}O^{18}O)_2$ 1055.6, $Al^{16}O^{18}O_3$ 1043.9, $Al^{18}O_4$ 1035.4.

[7] This experimental observation is in agreement with the results of earlier work, although in the earlier work no conclusive explanation could be made: L. Andrews, T. R. Burkholder, J. T. Yustein, *J. Phys. Chem.* **1992**, *96*, 10182.

[8] The following frequencies of the different isotopologues were observed in Raman (a) and IR spectra (b) (cm^{-1}): a) $Al(^{16}O_2)_3$ 1065, $Al(^{16}O/^{18}O)_3$ 1035, $Al(^{18}O_2)_3$ 1005; b) $Al(^{16}O_2)_3$ 686.4, $Al(^{16}O_2)_2(^{18}O_2)$ 681.3, $Al(^{16}O_2)(^{18}O_2)_2$ 675.1, $Al(^{18}O_2)_3$ 670.7; in experiments with a 1:2:1 mixture of $^{16}O_2/^{16}O^{18}O/^{18}O_2$ broad bands appear at 685, 679, and 672 cm^{-1} which arise from the superimposition of ten different isotopologues.

[9] M. V. Pak, M. S. Gordon, *J. Phys. Chem.* **2003**, *118*(10), 4471.

[10] In contrast, with the homologous species GaO_2, the photolytically induced (254 nm) isomerization of the C_{2v} structure to the $D_{\infty h}$ structure with an activation barrier of about 300 kJ mol^{-1} is readily observed: A. Köhn, B. Gaertner, H. Himmel, *Chem. Eur. J.* **2005**, in press.

[11] E. C. Brown, W. T. Borden, *J. Phys. Chem. A* **2002**, *106*, 2963.

[12] "NIST-JANAF Thermochemical Tables, Fourth Edition": a) M. W. Chase, Jr., *J. Phys. Chem. Ref. Data Monogr.* **1989**, 9; b) National Institute of Standards Web Based Chemical Data, http://webbook.nist.gov/chemistry/.

[13] G. Stößer, Dissertation, Universität Karlsruhe, **2004**.

[14] R. Burgert, H. Schnöckel, unpublished results.

[15] H. Schnöckel, S. Schunck, *Chem. Unserer Zeit* **1987**, *21*, 73.

[16] C. Lee, W. Yang, R. G. Parr, *Phys. Rev. B* **1988**, *37*, 785.

[17] a) R. Ahlrichs, M. Bär, M. Häser, H. Horn, C. Kölmel, *Chem. Phys. Lett.* **1989**, *162*, 165; b) http://www.turbomole.com.

 © 2005 Wiley-VCH Verlag GmbH & Co. KGaA, Weinheim

[18] a) Dalton, a molecular electronic structure program, Release 1.2 (2001), T. Helgaker, H. J. Aa. Jensen, P. Joergensen, J. Olsen, K. Ruud, H. Aagren, A. A. Auer, K. L. Bak, V. Bakken, O. Christiansen, S. Coriani, P. Dahle, E. K. Dalskov, T. Enevoldsen, B. Fernandez, C. Haettig, K. Hald, A. Halkier, H. Heiberg, H. Hettema, D. Jonsson, S. Kirpekar, W. Klopper, R. Kobayashi, H. Koch, K. V. Mikkelsen, P. Norman, M. J. Packer, T. B. Pedersen, T. A. Ruden, P. Salek, A. Sanchez, T. Saue, S. P. A. Sauer, B. Schimmelpfennig, K. O. Sylvester-Hvid, P. R. Taylor, O. Vahtras.

[19] Gaussian 98 (Revision A.11), M. J. Frisch, G. W. Trucks, H. B. Schlegel, G. E. Scuseria, M. A. Robb, J. R. Cheeseman, V. G. Zakrzewski, J. A. Montgomery, Jr., R. E. Stratmann, J. C. Burant, S. Dapprich, J. M. Millam, A. D. Daniels, K. N. Kudin, M. C. Strain, O. Farkas, J. Tomasi, V. Barone, M. Cossi, R. Cammi, B. Mennucci, C. Pomelli, C. Adamo, S. Clifford, J. Ochterski, G. A. Petersson, P. Y. Ayala, Q. Cui, K. Morokuma, P. Salvador, J. J. Dannenberg, D. K. Malick, A. D. Rabuck, K. Raghavachari, J. B. Foresman, J. Cioslowski, J. V. Ortiz, A. G. Baboul, B. B. Stefanov, G. Liu, A. Liashenko, P. Piskorz, I. Komaromi, R. Gomperts, R. L. Martin, D. J. Fox, T. Keith, M. A. Al-Laham, C. Y. Peng, A. Nanayakkara, M. Challacombe, P. M. W. Gill, B. Johnson, W. Chen, M. W. Wong, J. L. Andres, C. Gonzalez, M. Head-Gordon, E. S. Replogle, and J. A. Pople, Gaussian, Inc., Pittsburgh, PA, **2001**.

[20] A. Schäfer, C. Huber, R. Ahlrichs, *J. Chem. Phys.* **1994**, *100*, 5829.

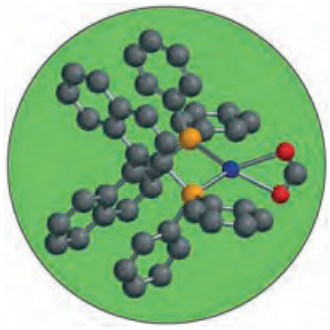
 © 2005 Wiley-VCH Verlag GmbH & Co. KGaA, Weinheim

Cover Picture

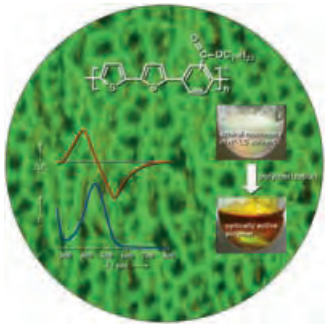


Donna G. Blackmond*

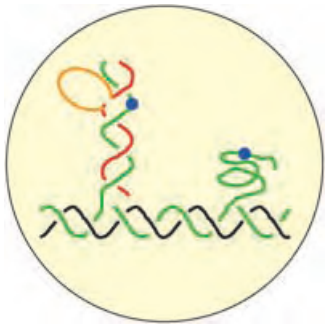
The London Eye moves continuously even as passengers embark and disembark, serving as both a backdrop and a metaphor for a steady-state catalytic cycle. The theme of the Review by D. G. Blackmond on page 4302 ff. is the mechanistic study of complex catalytic reactions using reaction progress kinetic analysis. A new set of graphical tools are described that are based on reaction monitoring in situ with simple data manipulations. Photo: ArtoftheState.co.uk.



Asymmetric Catalysis
In his Minireview on page 4292 ff., J. M. Janey provides a synopsis of catalytic, enantioselective α amination and α oxygenation reactions of carbonyl compounds which provide access to important enantiomerically pure building blocks such as α-amino acids.



Liquid Crystals as Solvents
Polymerization of an achiral monomer in an inert chiral nematic liquid-crystal medium leads to optically active polybithiophene derivatives. K. Akagi and H. Goto discuss this phenomenon in their Communication on page 4322 ff.



DNA Motors
In their Communications on pages 4355 ff. and 4358 ff., C. Mao et al. and J. Bath et al., respectively, describe DNA devices that move along well-defined tracks by means of enzyme-assisted cleavage and a strand-displacement strategy.

Contents

VIP *The following Communications have been judged by at least two referees to be "very important papers" and will be published online at www.angewandte.org soon:*

*F. Studt, F. Tuczek**
Energetics and Mechanism of a Room Temperature Catalytic Synthesis of Ammonia (Schrock Cycle): Comparison with Biological Nitrogen Fixation

H. Zhu, J. Chai, H. Fan, H. W. Roesky, C. He, V. Jancik, H.-G. Schmidt, M. Noltemeyer, W. A. Merrill, P. P. Power*
A Stable Aluminacyclopropene LAl(η^2-C_2H_2) and Its End-On Azide Insertion to an Aluminaazacyclobutene

D. Loffreda, F. Delbecq, F. Vigné, P. Sautet*
Catalytic Hydrogenation of Unsaturated Aldehydes on Pt (111): Understanding the Selectivity from First-Principles Calculations

*C. Schaefer, G. C. Fu**
Catalytic Asymmetric Couplings of Ketenes with Aldehydes to Generate Enol Esters

M. Capdevila, J. Domènech, A. Pagani, L. Tío, L. Villarreal, S. Atrian*
Zn and Cd Metallothionein Recombinant Species from the Most Diverse Phyla May Contain Sulfide (S^{2-}) Ligands

*R. Shintani, W.-L. Duan, T. Nagano, A. Okada, T. Hayashi**
Chiral Phosphine–Olefin Bidentate Ligands in Asymmetric Catalysis: Rhodium-Catalyzed Asymmetric 1,4-Addition of Aryl Boronic Acids to Maleimides

News

Carbohydrates: R. R. Schmidt Awarded ____ **4284**

Catalysis: H. Kagan Receives Prize **4284**

Organometallic Chemistry: L. Oro Honored ____ **4284**

Books

Asymmetric Organocatalysis — Albrecht Berkessel, Harald Gröger — *reviewed by M. J. Krische* ____ **4285**

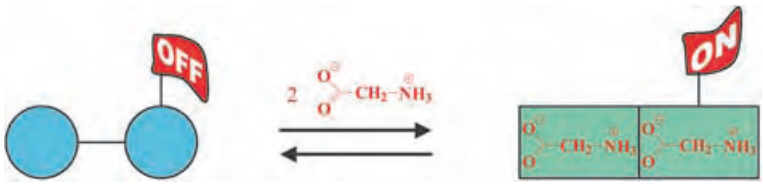
Analytical Chemistry — Robert Kellner, Jean-Michel Mermet, Matthias Otto, Miguel Valcárel, H. Michael Widmer — *reviewed by J. Bettmer* ____ **4286**

Highlights

Gene Regulation

B. Kräutler* ____ **4288 – 4290**

A High-Precision Switch on an RNA Message



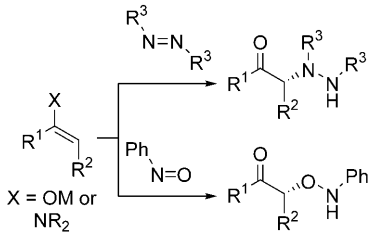
The glycine-dependent riboswitch is a high-precision molecular RNA switch to control the use of glycine as a "fuel" (in energy-yielding catabolism) or as a "chemical" (in anabolism and protein biosynthesis).

Minireviews

Synthetic Methods

J. M. Janey* ____ **4292 – 4300**

Recent Advances in Catalytic, Enantioselective α Aminations and α Oxygenations of Carbonyl Compounds



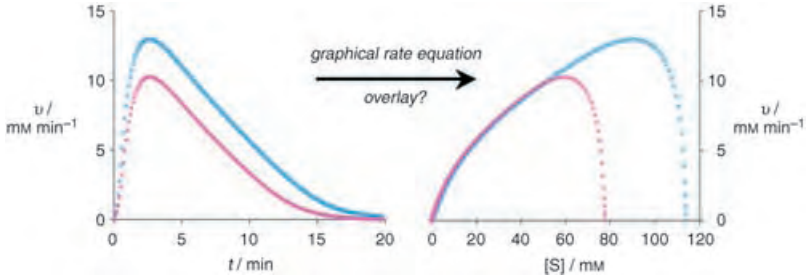
Chiral Lewis acids and Lewis bases catalyze the α amination and the α oxygenation of aldehydes, ketones, and esters (see scheme). This is a powerful way to directly introduce a heteroatom adjacent to a carbonyl group, and this reaction provides access to important enantiomerically pure building blocks such as α-amino acids.

Reviews

Reaction Kinetics

D. G. Blackmond* _____ 4302 – 4320

Reaction Progress Kinetic Analysis: A Powerful Methodology for Mechanistic Studies of Complex Catalytic Reactions



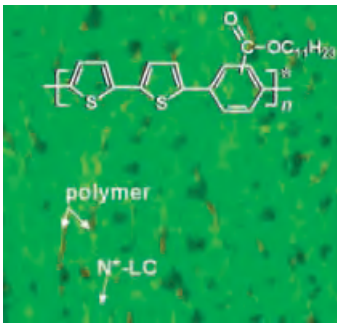
Intuitive and precise: Kinetic measurements are often considered time-intensive and routine studies required to determine concentration dependences and help distinguish between different proposed reaction mechanisms. This Review describes step by step how this can be achieved from a minimal number of experiments with the help of intuitive "graphical rate equations" (see picture) without prior mechanistic knowledge of a catalytic reaction cycle.

Communications

Chiral Polymerization

H. Goto, K. Akagi* _____ 4322 – 4328

Optically Active Conjugated Polymers Prepared from Achiral Monomers by Polycondensation in a Chiral Nematic Solvent

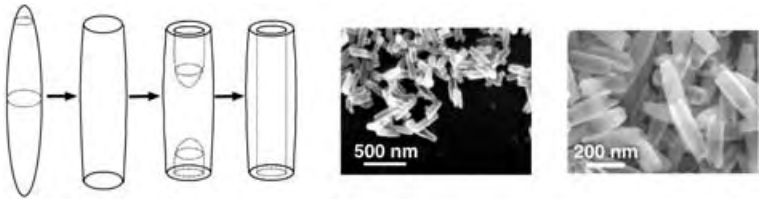


Contagious chirality: A chiral polymer (see image) was obtained from the polycondensation of an achiral monomer by using a chiral nematic liquid crystal (N*-LC) as an inert reaction solvent. The chirality of the polymer is thought to derive from the asymmetry produced by the chiral medium during polymerization.

Iron Oxide Nanotubes

C.-J. Jia, L.-D. Sun,* Z.-G. Yan, L.-P. You, F. Luo, X.-D. Han, Y.-C. Pang, Z. Zhang, C.-H. Yan* _____ 4328 – 4333

Single-Crystalline Iron Oxide Nanotubes



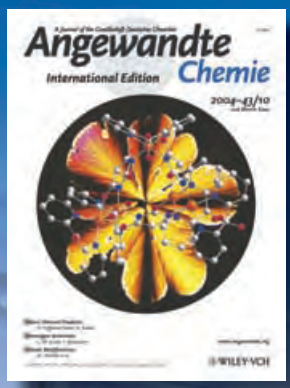
Phosphate ions play a crucial role not only for the formation of the spindlelike precursors of the single-crystalline hematite nanotubes that were synthesized by a facile hydrothermal method. They are also important for the adsorption and coordination effects. The mechanism of tube formation was deduced through EM observations as a coordination-assisted dissolution process (see picture).

For the USA and Canada:
ANGEWANDTE CHEMIE International Edition (ISSN 1433-7851) is published weekly by Wiley-VCH PO Box 191161, D 69451 Weinheim, Germany. Air freight and mailing in the USA by Publications Expediting Inc. 200 Meacham Ave., Elmont, NY 11003. Periodicals postage paid at Jamaica NY 11431. US POSTMASTER: send address changes to *Angewandte Chemie*, Wiley-VCH, 111 River Street, Hoboken, NJ 07030. Annual subscription price for institutions: US$ 4948.00/4498.00 (valid for print and electronic / print or electronic delivery); for individuals who are personal members of a national chemical society, or whose institution already subscribes, or who are retired or self-employed consultants, print only: US$ 394.00. Postage and handling charges included. All Wiley-VCH prices are exclusive VAT.

 © 2005 Wiley-VCH Verlag GmbH & Co. KGaA, Weinheim

The best in chemistry –

for more than a hundred years



A Journal of the Gesellschaft Deutscher Chemiker

Angewandte
International Edition **Chemie**

www.angewandte.org

1888: ***The beginning of a success story***

Constant Innovations

1962: *First issue of the International Edition*
1976: *Graphical abstracts*
1979: *Cover pictures*
1988: *Centenary of Angewandte*
1989: *Routine use of color*
1991: *New section: Highlights*
1992: *Computerized editorial tracking system*
1995: *Internet service for readers*
1998: *Regular press service; full-text online*
2000: *New section: Essays; EarlyView: Communications available online ahead of the printed version*
2001: *New section: Minireviews*
2002: *Online submission of manuscripts*
2003: *Weekly publication; new section: News; new layout*
2004: *Backfiles (1962-1997); ManuscriptXpress: Online system for authors and referees*



Angewandte's advisors...

Seiji Shinkai
Kyushu University, Fukuoka

» ***Angewandte Chemie*** *is my favorite journal and I am honored to serve on its International Advisory Board. The research essence of an article can be understood rapidly because text and illustrations are finely harmonized. Furthermore, the high quality contents, which have a strong impact, are published very quickly.* «

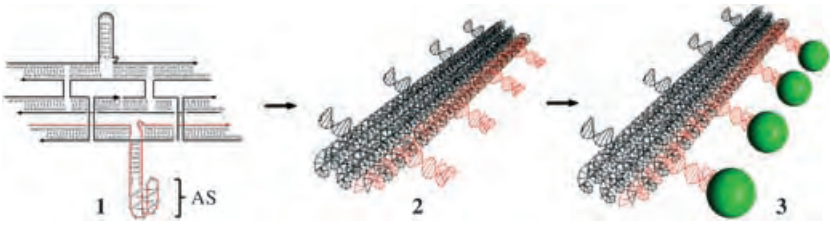
Angewandte Chemie International Edition *is a journal of the German Chemical Society (GDCh)*

GDCh

WILEY InterScience® DISCOVER SOMETHING GREAT

WILEY-VCH

1190140_gu



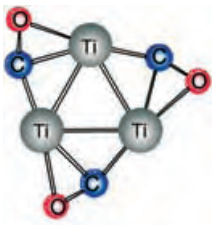
Lined up nicely: The self-assembly of proteins on rationally designed nanostructures into periodic linear arrays has been demonstrated. Triple-crossover DNA tiles **1** containing an aptamer sequence (AS) to which thrombin specifically binds can form linear arrays **2**. These direct the ultimate positioning of thrombin proteins (green spheres) in **3.** This system should facilitate the construction of other such programmable nanoscale protein arrays.

Protein Nanoarrays

Y. Liu, C. Lin, H. Li, H. Yan* **4333 – 4338**

Aptamer-Directed Self-Assembly of Protein Arrays on a DNA Nanostructure

---



cyclo-$Ti_3[\eta^2(\mu_2\text{-C, O})]_3$

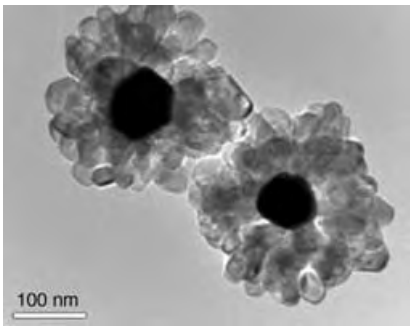
A windmill-like trititanium cluster with side-on-bonded CO ligands (see picture), which may have antiaromatic character, was revealed by FTIR spectroscopy and DFT calculations. It is generated, along with other side-on-bonded mono- and polycarbonyl di- and trititanium clusters, in the reaction of laser-ablated Ti atoms with CO in a solid argon matrix.

Cluster Compounds

Q. Xu,* L. Jiang, N. Tsumori **4338 – 4342**

cyclo-$Ti_3[\eta^2(\mu_2\text{-C,O})]_3$: A Side-on-Bonded Polycarbonyl Titanium Cluster with Potentially Antiaromatic Character

---



Reactor core: Hollow core–shell Au–TiO_2 nanocomposites can be prepared by a wet chemical method to form reactors that contain a catalyst core with a shell that is permeable to reactants. The core can be enlarged, and modification of the synthesis produces flowerlike nanostructures (see picture). Catalytic reactions in both the gaseous and liquid phase can be conducted in this type of photosensitized metal–semiconductor nanoreactor.

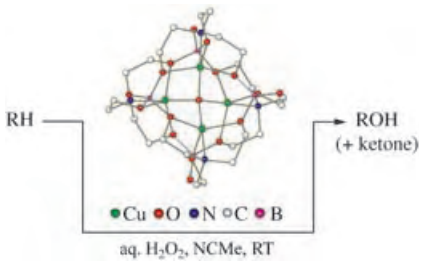
Nanoreactors

J. Li, H. C. Zeng* **4342 – 4345**

Size Tuning, Functionalization, and Reactivation of Au in TiO_2 Nanoreactors

---

Rich activity from a few coppers: Di-, tri-, tetra-, and polynuclear copper triethanolamine complexes are easily prepared and are selective and efficient catalysts for alkane peroxidative oxidation under mild conditions (see picture).



Alkane Activation

A. M. Kirillov, M. N. Kopylovich, M. V. Kirillova, M. Haukka, M. F. C. G. da Silva, A. J. L. Pombeiro* **4345 – 4349**

Multinuclear Copper Triethanolamine Complexes as Selective Catalysts for the Peroxidative Oxidation of Alkanes under Mild Conditions

 © 2005 Wiley-VCH Verlag GmbH & Co. KGaA, Weinheim

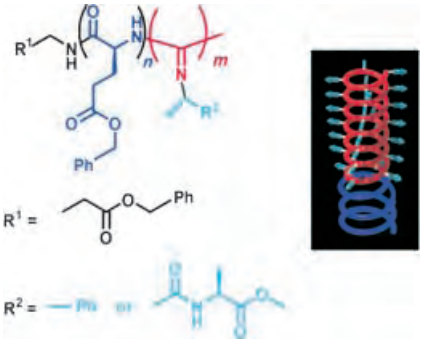
Contents

Copolymer Synthesis

A. Kros,* W. Jesse, G. A. Metselaar, J. J. L. M. Cornelissen* ____ **4349 – 4352**

Synthesis and Self-Assembly of Rod–Rod Hybrid Poly(γ-benzyl L-glutamate)-*block*-Polyisocyanide Copolymers

Connecting rods: Rigid rod–rod block copolymers are synthesized from peptide and polyisocyanide blocks (see picture: blue = poly(γ-benzyl L-glutamate); red = poly(methylbenzyl isocyanide) or poly-(L-isocyanoalanyl-L-alanine methyl ester). The polyisocyanide helix has side arms organized in a parallel β-sheet (light blue). Some copolymers self-assemble into ordered layers of hollow capsules.

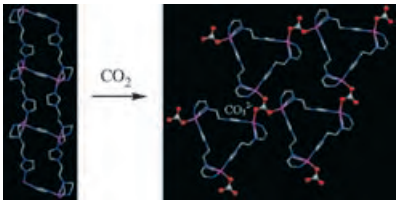


Carbon Dioxide Fixation

L.-Y. Kong, Z.-H. Zhang, H.-F. Zhu, H. Kawaguchi, T.-a. Okamura, M. Doi, Q. Chu, W.-Y. Sun,* N. Ueyama ____ **4352 – 4355**

Copper(II) and Zinc(II) Complexes Can Fix Atmospheric Carbon Dioxide

Carbonato bridges from atmospheric carbon dioxide: The copper(II) and zinc(II) complexes of the novel imidazole-containing polyamine ligand N^1-(2-aminoethyl)-N^1-(2-imidazolethyl)ethane-1,2-diamine are found to fix carbon dioxide by hydration to μ_3-carbonate ligands. This is revealed by IR and solid-state ^{13}C NMR spectroscopic and X-ray crystallographic studies of the two-dimensional complexes (see picture).



Molecular Devices

Y. Tian, Y. He, Y. Chen, P. Yin, C. Mao* ____ **4355 – 4358**

A DNAzyme That Walks Processively and Autonomously along a One-Dimensional Track

Inching its way forward: A DNA nanodevice is presented which can autonomously and processively move on a well-defined track with a 7-nm step size. The moving principle integrates DNAzyme activity and a strand-displacement strategy, which resembles the behavior of a caterpillar eating its way through a row of plants (see picture).

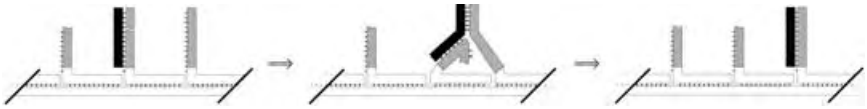


Molecular Devices

J. Bath,* S. J. Green, A. J. Turberfield ____ **4358 – 4361**

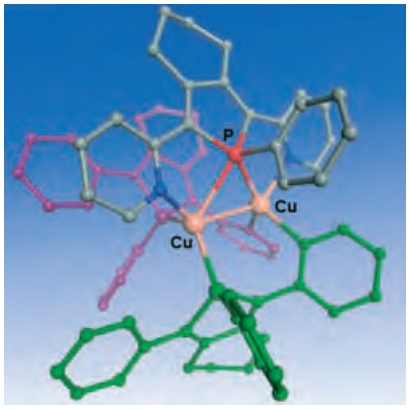
A Free-Running DNA Motor Powered by a Nicking Enzyme

DNA burns its bridges: A unidirectional molecular motor that moves an oligonucleotide cargo along a self-assembled track is powered by restriction endonuclease hydrolysis of the phosphodiester backbone (see scheme). Damage caused to the track by the restriction enzyme prevents the cargo from stepping backwards and therefore imposes directionality.



 © 2005 Wiley-VCH Verlag GmbH & Co. KGaA, Weinheim

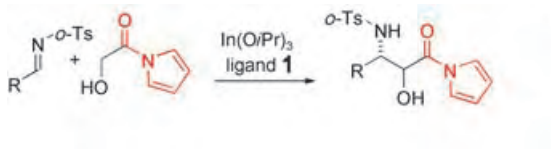
Newcomers in the family: Pd–Pt heterobimetallic and Cu–Cu homobimetallic species (see picture) bearing bridging phosphane ligands are reported. Their structural arrangement reveals a continuum between semi-bridging and bridging coordination modes.

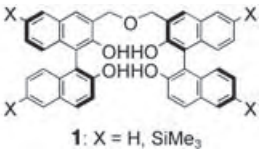


Coordination Modes

F. Leca, C. Lescop, E. Rodriguez-Sanz, K. Costuas, J.-F. Halet, R. Réau* ——— **4362 – 4365**

Bridging Phosphanes: Exotic or Versatile Binucleating Ligands?





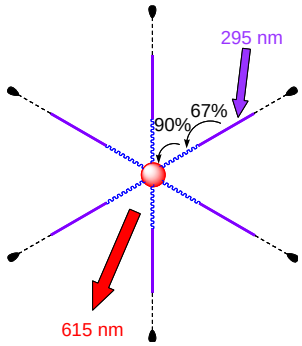
Stretching the limits of the Mannich reaction: A new indium–binol catalyst was used to generate the enolate of the ester-equivalent donor in situ (see scheme). The donor, an *N*-acylpyrrole, has many similarities to an aromatic ketone, in particular the enolates should have the same coordination mode. Versatile β-amino-α-hydroxy carboxylic acid derivatives were obtained in high yield and *ee* values.

Asymmetric Mannich Reaction

S. Harada, S. Handa, S. Matsunaga,* M. Shibasaki* ——— **4365 – 4368**

Direct Catalytic Asymmetric Mannich-Type Reactions of *N*-(2-Hydroxyacetyl)-pyrrole as an Ester-Equivalent Donor

---



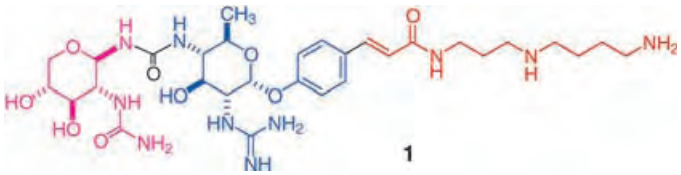
A star in the making: Star-shaped block copolymers have been synthesized by reversible addition–fragmentation chain-transfer (RAFT) polymerization to obtain light-harvesting systems with an energy gradient from the periphery to the core. Excitation-energy transfer in the block copolymers occurs through an energy cascade from the excited acenaphthenyl units to the coumarin chromophores and hence to the Ru^{II} complex core (red sphere: see picture).

Light-Harvesting Polymers

M. Chen, K. P. Ghiggino,* S. H. Thang, G. J. Wilson ——— **4368 – 4372**

Star-Shaped Light-Harvesting Polymers Incorporating an Energy Cascade

---



A three-fragment coupling strategy afforded the antibiotic glycocinnasperimicin D (**1**). The convergent total synthesis features a Heck reaction to form the cinnamoyl glycoside, the [3,3] sigmatropic rearrangement of an allyl cyanate for the stereoselective synthesis of the allyl amine, and the coupling of a glycosyl isocyanate with an amino sugar for the construction of the urea glycoside linkage.

Amino Sugar Synthesis

T. Nishiyama, M. Isobe, Y. Ichikawa* ——— **4372 – 4375**

Total Synthesis of Glycocinnasperimicin D

 © 2005 Wiley-VCH Verlag GmbH & Co. KGaA, Weinheim

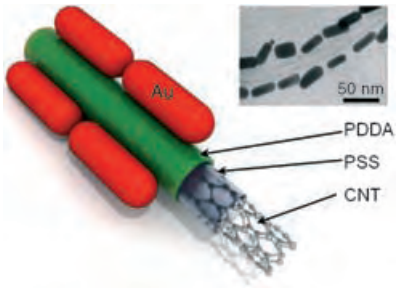
Contents

Nanostructures

M. A. Correa-Duarte, J. Pérez-Juste, A. Sánchez-Iglesias, M. Giersig, L. M. Liz-Marzán* ——— **4375 – 4378**

Aligning Au Nanorods by Using Carbon Nanotubes as Templates

With strings attached: Gold nanorods undergo uniform electrostatic assembly on multiwall carbon nanotubes (MWNTs) to form strings of rods with end-to-end contacts (see picture, PSS = polystyrene sulfonate, PDDA = poly(diallyldimethyl)-ammonium chloride). This arrangement results in uniaxial plasmon coupling, and the polarization-dependent optical response has been used to monitor the degree of alignment of carbon nanotubes within polymer films.

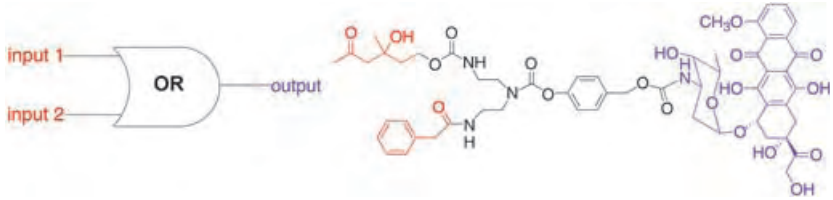


Prodrug Activation

R. J. Amir, M. Popkov, R. A. Lerner, C. F. Barbas III, D. Shabat* . **4378 – 4381**

Prodrug Activation Gated by a Molecular "OR" Logic Trigger

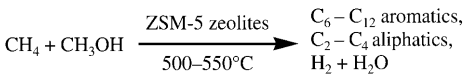
Molecules that define logic: A molecular "OR" logic gate trigger has been demonstrated by masking a functional group in a doxorubicin prodrug with a linker that contains two cleavable substrates (input). The prodrug molecule was activated by two different enzymes to release the parent drug (see scheme; input red; output (drug) blue).



Hydrocarbon Chemistry

V. R. Choudhary,* K. C. Mondal, S. A. R. Mulla ——— **4381 – 4385**

Simultaneous Conversion of Methane and Methanol into Gasoline over Bifunctional Ga-, Zn-, In-, and/or Mo-Modified ZSM-5 Zeolites

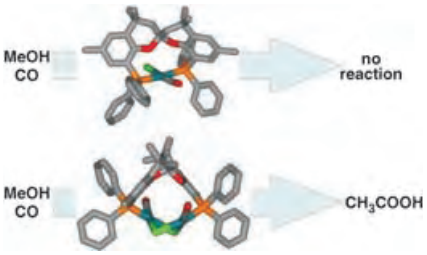


Gasoline from methane: Methane can be activated nonoxidatively and converted into higher hydrocarbons over bifunctional zeolite catalysts at low temperatures ($\leq 600\,^{\circ}C$; see scheme). The amount of methane converted per mole of methanol by this process can meet or even exceed 1 mol. This approach could potentially lead to an economically feasible technology for the commercial conversion of methane into liquid hydrocarbons.

Homogeneous Catalysis

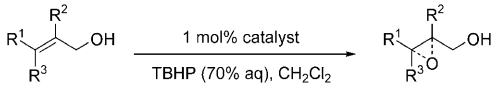
Z. Freixa,* P. C. J. Kamer, M. Lutz, A. L. Spek, P. W. N. M. van Leeuwen ——— **4385 – 4388**

Activity of SPANphos Rhodium Dimers in Methanol Carbonylation



Contrary to earlier speculation, mononuclear rhodium species that contain *trans* diphosphines, such as SPANphos, are inactive towards the oxidative addition of methyl iodide, whereas the corresponding dinuclear species are very reactive. Thus, the active species in methanol carbonylation is most likely the dimeric system (see scheme; P orange, O red, Rh blue, Cl green).

 © 2005 Wiley-VCH Verlag GmbH & Co. KGaA, Weinheim

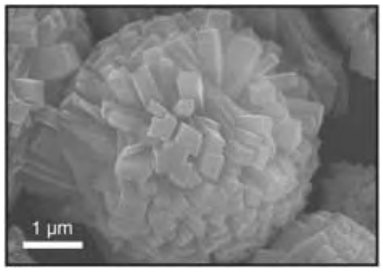


Bishydroxamic acid derivatives are used as ligands for a vanadium catalyst in the preparation of epoxy alcohols (see scheme). The methodology uses aqueous *tert*-butyl hydroperoxide (TBHP) as an achiral oxidant, low catalyst loading, low reaction temperatures (0 °C to room temperature), and simple workup procedures. The reaction is applied to the kinetic resolution of a secondary allylic alcohol and the preparation of small epoxy alcohols. R^1, R^2, R^3: alkyl, aryl, H.

Asymmetric Catalysis

W. Zhang, A. Basak, Y. Kosugi, Y. Hoshino, H. Yamamoto* ——— **4389 – 4391**

Enantioselective Epoxidation of Allylic Alcohols by a Chiral Complex of Vanadium: An Effective Controller System and a Rational Mechanistic Model



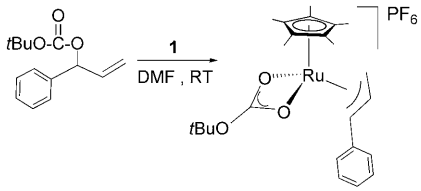
"**Hedgehog" or "nest"** microspheres of V_2O_5 are formed when nanorods of V_2O_5 are synthesized in a mediated polyol process. When the concentration of the starting material is low, a nest shape is preferred, whereas a high concentration of $[V(acac)_3]$ affords hedgehog-shaped microspheres (see picture). The V_2O_5 microspheres exhibit remarkable electrochemical properties when used as the cathode material in a lithium-ion battery.

Battery Materials

A.-M. Cao, J.-S. Hu, H.-P. Liang, L.-J. Wan* ——— **4391 – 4395**

Self-Assembled Vanadium Pentoxide (V_2O_5) Hollow Microspheres from Nanorods and Their Application in Lithium-Ion Batteries

Branching out: A previously unrecognized ruthenium carbonate intermediate is formed during the reaction of an allylic *tert*-butoxycarbonate with the ruthenium complex $[Ru(Cp^*)(CH_3CN)_3]PF_6$ (**1**; see scheme). The isolatable carbonate–allyl complex functions very effectively as an allylic alkylation catalyst. These results provide new insights into the mechanism of this ruthenium-catalyzed reaction.

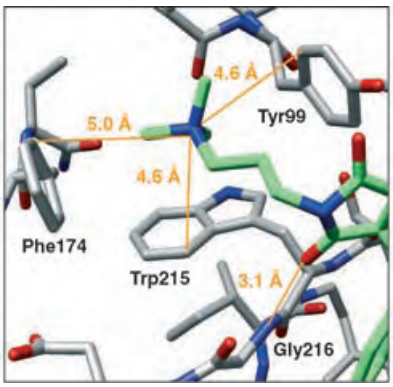


Homogeneous Catalysis

R. Hermatschweiler, I. Fernández, F. Breher, P. S. Pregosin,* L. F. Veiros, M. J. Calhorda ——— **4397 – 4400**

Ruthenium-Catalyzed Allylic Alkylation Reactions: Carbonate-Based Catalysts and Intermediates

The aromatic box formed by the side chains Phe174, Tyr99, and Trp215 in the S4-pocket of Factor Xa is a very effective onium binding site (see picture; red O, blue N, green C_{ligand}, gray $C_{protein}$). The free enthalpy increment for cation–π interactions between quaternary ammonium ions and aromatic groups in this box is determined to be $\Delta\Delta G = 2.8$ kcal mol^{-1}. Database searches reveal that similar cation binding sites are not uncommon in biological systems.



Molecular Recognition

K. Schärer, M. Morgenthaler, R. Paulini, U. Obst-Sander, D. W. Banner,* D. Schlatter, J. Benz, M. Stihle, F. Diederich* ——— **4400 – 4404**

Quantification of Cation–π Interactions in Protein–Ligand Complexes: Crystal-Structure Analysis of Factor Xa Bound to a Quaternary Ammonium Ion Ligand

 © 2005 Wiley-VCH Verlag GmbH & Co. KGaA, Weinheim

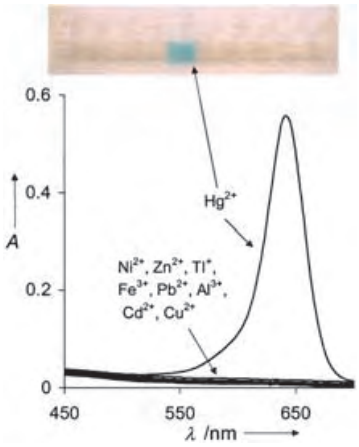
Contents

Analytical Chemistry

J. V. Ros-Lis, M. D. Marcos, R. Mártinez-Máñez,* K. Rurack,* J. Soto ——— **4405 – 4407**

A Regenerative Chemodosimeter Based on Metal-Induced Dye Formation for the Highly Selective and Sensitive Optical Determination of Hg^{2+} Ions

Into the blue: Hg^{2+}-ion-triggered formation of a brightly fluorescent squaraine dye is used as a novel approach for the design of highly selective and sensitive chromofluorogenic probes for the analysis of Hg^{2+} ions down to concentrations below 2 ppb (see picture). Through the adsorption of the sensor on a solid support a prototype reusable test strip is also generated.



WILEY InterScience®
DISCOVER SOMETHING GREAT

"Hot Papers" are chosen by the Editors for their importance in a rapidly evolving field of high current interest. A preview with the graphical abstracts of these articles can be found on the *Angewandte Chemie* homepage in Wiley InterScience at www.angewandte.org.

All articles in *Angewandte Chemie* are published online up to several weeks ahead of print. They are found under the "EarlyView" link on the journal's homepage in Wiley InterScience.

Service

Keywords ——— *4408*

Authors ——— *4409*

Preview ——— *4411*

Corrigendum

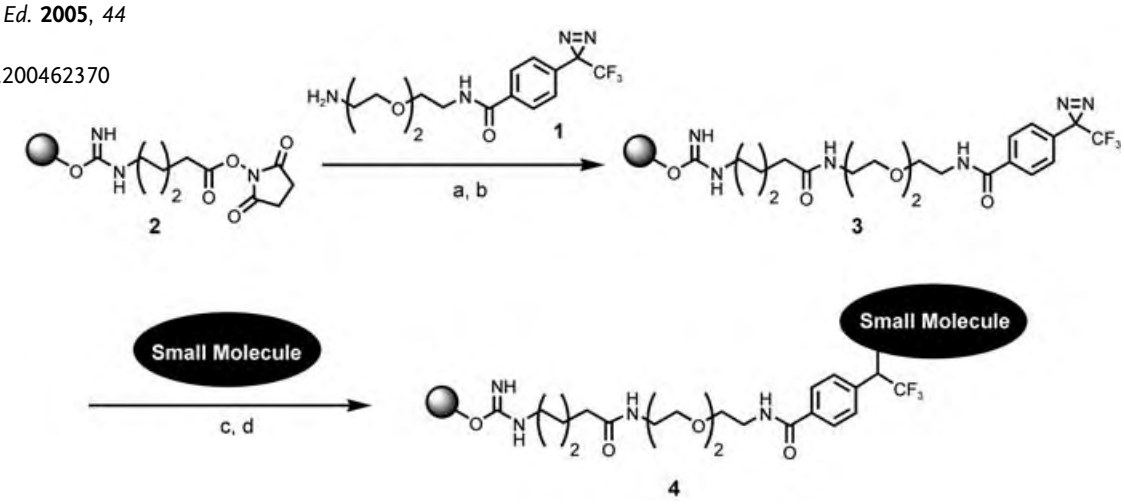
Photo-Cross-Linked Small-Molecule Affinity Matrix for Facilitating Forward and Reverse Chemical Genetics

N. Kanoh, K. Honda, S. Simizu, M. Muroi, H. Osada* ——— **3559–3562**

Angew. Chem. Int. Ed. **2005**, *44*

DOI 10.1002/anie.200462370

In this communication, the structure of activated CH agarose 4B beads (**2**), which were purchased from Amersham Bioscience, and the following structures (**3** and **4**) in Scheme 1 were rendered incorrectly; the correct structures are shown. The authors apologize for this oversight.





Awarded...

R. R. Schmidt Receives Haworth Lectureship

Richard R. Schmidt (Universität Konstanz, Germany) is the winner of the 2005 Haworth Memorial Lectureship, which is awarded every two years by the Royal Society of Chemistry. The award is given in recognition of researchers who have made significant contributions to the field of carbohydrate chemistry. A silver medal and £500 are part of the prize. Schmidt completed his PhD studies under the direction of R. Gompper at the University of Stuttgart in 1962. His postdoctoral research was carried out in the research group of F. M. Huennekens at Scripps Research Institute in La Jolla in 1965–66. In 1969 he returned to the University of Stuttgart, where he held a professorship until 1975. Since that year he has been professor of chemistry and biochemistry at the University of Konstanz, today as professor emeritus.



R. R. Schmidt

Schmidt's research is focused on finding and improving strategies for the synthesis of biologically important oligosaccharides with the trichloroacetimidate method, which he developed. His work also involves quinone methides, polar 1,4-cycloadditions, heterocyclic 8π-electron systems, and nucleosides. His research group's efforts in the generation of carbohydrate arrays on glass slides recently appeared in *ChemBioChem*.[1] Schmidt was a member of the advisory boards of *Liebigs Annalen der Chemie* and the *European Journal of Organic Chemistry* from 1994 to 2004.

H. Kagan Receives Bower Award

Henri B. Kagan (Université Paris-Sud, France) was given the US$250000 Bower Award for Science Achievement from the Franklin Institute in Philadelphia for his outstanding work in the area of asymmetric synthesis. His achievements include the first asymmetric synthesis with circularly polarized light, the first description of a chiral "homogenous" solid-phase catalyst, and the synthesis of DIOP, a chiral bidentate diphosphine ligand which has had a significant impact in the development of asymmetric catalysis. He recently reported the in situ formation of a chiral heterobimetallic catalyst for the addition of trimethylsilyl cyanide to benzaldehyde in *Angewandte Chemie*.[2a] Kagan is a member of the academic advisory board for *Advanced Synthesis & Catalysis*, in which he recently published a review of multisubstrate screening of asymmetric catalysts.[2b]



H. Kagan

Kagan studied chemistry in Paris and received his PhD in 1960 after working with J. Jacques at the Collège de France. Afterward he joined the research group of A. Horeau at the same institution, and also worked for a year with T. Mabry at the University of Texas in Austin. In 1967 he became assistant professor at the Université Paris-Sud in Orsay, and assumed full professorship in 1973. Before retiring emeritus, he was a professor at the Institut Universitaire de France from 1993 to 1999. Kagan has been a corresponding member of the French Academy of Sciences since 1978 and a full member since 1991. He is the recipient of numerous prizes, including the August Wilhelm von Hofmann Medal of the GDCh, the Wolf Prize, and the Nagoya Medal.

L. Oro Honored

The Université de Rennes 1 in France has given Luis A. Oro (Universidad Zaragoza, Spain) an honorary doctorate in recognition of his achievements in organometallic chemistry (particularly with the transition metals rhodium, iridium, ruthenium, and osmium) and in catalysis (hydration, hydrosilylation, and C–H bond activation). The honorary title is also reflective of the healthy Spanish-French relationship in science. Oro is already a foreign member of the French Academy of Sciences.



L. Oro

Oro received his PhD in 1970 at the University of Zaragoza. Following postdoctoral work at Cambridge University, he accepted successive positions at the University of Zaragoza, the University of Madrid (Complutense), and the University of Santander. In 1982 he returned to the University of Zaragoza as professor of inorganic chemistry. Oro is the president of the Real Sociedad Española de Química, member of the advisory board for the *European Journal of Inorganic Chemistry*, and joint editor of a multivolume handbook of metal clusters.[3a] His research group recently reported on oxygen activation and the formation of a doubly oxygen-bridged dirhodium complex in *Angewandte Chemie*.[3b]

[1] M. B. Biskup, J. U. Müller, R. Weingart, R. R. Schmidt, *ChemBioChem* **2005**, *6*, 1007.

[2] a) Y. N. Belokon, M. North, V. I. Maleev, N. V. Voskoboev, M. A. Moskalenko, A. S. Peregudov, A. V. Dmitriev, N. S. Ikonnikov, H. B. Kagan, *Angew. Chem.* **2004**, *116*, 4177; *Angew. Chem. Int. Ed.* **2004**, *43*, 4085, b) T. Satyanarayana, H. B. Kagan, *Adv. Synth. Catal.* **2005**, *347*, 737.

[3] a) P. Braunstein, L. A. Oro, P. R. Raithby (Eds.), *Metal Clusters in Chemistry*, Wiley-VCH, Weinheim, **1999**, b) C. Tejel, M. A. Ciriano, E. Sola, M. Pilar - del Río, G. Ríos-Moreno, F. J. Lahoz, L. A. Oro, *Angew. Chem.* **2005**, *117*, 3331; *Angew. Chem. Int. Ed.* **2005**, *44*, 3267.

 © 2005 Wiley-VCH Verlag GmbH & Co. KGaA, Weinheim DOI: 10.1002/anie.200502045

Gene Regulation

A High-Precision Switch on an RNA Message**

*Bernhard Kräutler**

Keywords:
amino acids · catabolism · gene regulation · molecular switches · RNA

In the classic view, (oligo)ribonucleotides (RNA) are molecular vehicles in high-fidelity transmission systems, through which genetic information is realized by protein expression.[1] In cellular organisms, messenger RNA (mRNA) represents a transcript of the DNA with coding and noncoding regions, and can be classified as a "conditional" molecular message: the downstream fate of the transcribed message depends on cellular constituents, and is subject to further expressional control either at the stage of its own transcription (as nascent RNA) or during translation.

Recent work has uncovered a previously unrecognized function of RNA as a regulatory component in gene expression. Direct interactions between natural RNA molecules and low molecular weight compounds were shown by Breaker and co-workers to provide a new mechanism of genetic control in metabolite-sensitive "riboswitches".[2,3] Such riboswitches contain conserved sequences and are found in the 5′-untranslated (noncoding) region of the mRNA. By an allosteric effect, the binding of a metabolite induces a switch in the DNA-transcribed mRNA between "on" and "off" states, which control subsequent processing events of the coded message. Metabolite binding riboswitches therefore adapt gene expression efficiently and directly to the molecular contents of the cell. Although they are particularly widespread among bacteria, they are not restricted to prokaryotes, but are used in eukaryotes as well.[4]

The discovery of the group of glycine-dependent bacterial riboswitches provided evidence of Nature's capacity for even more exquisite RNA-engineering:[5] glycine-dependent riboswitches represent a new type of riboswitch that consists of a tandem of two glycine-binding RNA motifs (see Figure 1 for a representation of the tandem motifs from *Bacillus subtilis*). These conserved RNA motifs, which encompass about 100–120 nucleotides each, are separated by a short stretch of RNA. The glycine-dependent riboswitches are part of the 5′-untranslated region of the *gcvT* operon, which codes for proteins that degrade glycine for energy production. In the mRNA from *B. subtilis*, the downstream (3′ direction) glycine-binding motif (aptamer II) of the tandem encompasses a putative intrinsic transcription terminator motif. In the absence of glycine, the latter is "off" and continued transcription of the message is terminated (and hence the eventual expression of the proteins involved in glycine catabolism as well). These riboswitches bind glycine at concentrations of 10–

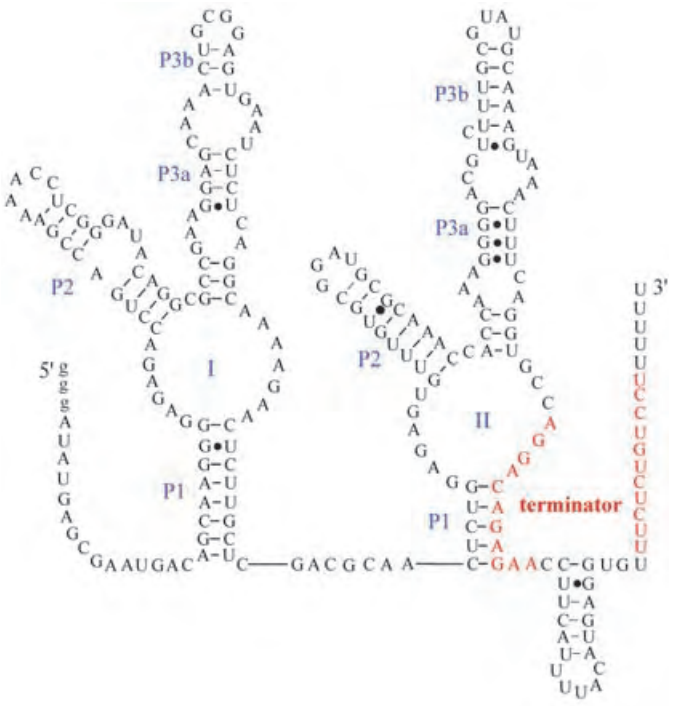


Figure 1. The glycine-binding tandem RNA motif of *Bacillus subtilis*. Hypothetical base-paired elements are indicated (P1–P3) as is the putative terminator sequence (red), rendered here in the "on" state, permitting further RNA transcription (adapted from Ref.[5]).

[*] Prof. Dr. B. Kräutler
Institute of Organic Chemistry
Innrain 52a
and
Center for Molecular Biosciences
Leopold Franzens University, Innsbruck
6020 Innsbruck (Austria)
Fax: (+43) 512-507-2892
E-mail: bernhard.kraeutler@uibk.ac.at

[**] This work was supported by the Austrian National Science Foundation (FWF, project no. P13595) and by the European Union (project EU-HPRN-CT-2002-00195).

 © 2005 Wiley-VCH Verlag GmbH & Co. KGaA, Weinheim DOI: 10.1002/anie.200500774

100 μM and with remarkable selectivity for their small molecular target, which consists of only 10 atoms. Both of the glycine aptamer motifs must be occupied by their target for disruption of the putative terminator hairpin and to bring the riboswitch into the "on" state. The tandem arrangement imparts the system with full sensitivity to glycine binding in a "digital" manner and in a narrow concentration range. Indeed, the tandem motif is highly selective and is able to discriminate very efficiently for other low molecular weight compounds, such as the glycine homologue, alanine and related amino acids.[5] These findings in vitro were shown to have relevance in vivo: when incorporated into the *B. subtilis* genome, a fusion construct coding for the glycine riboswitch upstream of a β-galactosidase reporter gene showed full transcriptional control by glycine (on the expression of β-galactosidase in this modified bacterium).

Cooperativity in glycine binding the two tandem binding motifs was studied with several RNA constructs based on the glycine binding riboswitch of *Vibrio cholerae*. With a method termed "inline probing" (which reveals metabolite-induced changes in RNA structure by monitoring alterations in the levels of spontaneous RNA cleavage) the aptamer tandem of *V. cholerae* was found to respond to glycine in the narrow concentration range of 10–100 μM, whereas a corresponding experiment with a single glycine-binding motif showed the same effect in a concentration range tenfold greater. The decrease in the dynamic range with the tandem arrangement is indicative of a significant cooperative effect for which a Hill coefficient of 1.64 was determined. Binding of glycine at one site was deduced to lead to concomitant restructuring of both binding motifs and was estimated to increase binding affinity at the other site by about 100- to 1000-fold.

The cooperative tandem glycine riboswitches thus hold a crucial regulatory position in the metabolism of these prokaryotes, which they switch precisely depending on the availability of glycine. When this simple amino acid is abundant, the glycine-bound "on"-state dominates, and proteins that are involved in the breakdown of glycine for energy (one of the major uses of glycine) are expressed (Figure 2).[1] Outside this pathway, glycine remains available as a basic anabolic component to be used primarily in amino acid biosynthesis. These microorganisms clearly depend on precise molecular sensors for the economic use of glycine: this natural "chemical" is required first of all for biosynthesis; when available in high concentration, it can also serve as a "fuel".

Cooperative binding of the small molecule glycine to the glycine riboswitches thus provides prokaryotic cells with a high-precision instrument for shifting from (exclusive) anabolic to (additional) catabolic uses of glycine. Studies of hemoglobin provided the first insight into the crucial fine-tuning of a multi-subunit enzyme and helped to uncover cooperativity in ligand binding.[1] The discovery of the glycine riboswitches shows that such cooperativity is not monopolized by proteins, but is a strategy naturally used by other modular biomolecules as well (as is the case for the noncoding regions of mRNA). Indeed, earlier work by Breaker and co-workers with artificially evolved RNA has already provided a remarkable precedence for the observation of "cooperativity" in the binding of small molecules by RNA.[6]

Whereas the structural basis for the observed cooperativity of the tandem glycine riboswitches remains to be elucidated, pioneering structural studies have provided initial insight into the intricate modes of highly selective molecular recognition by the conserved "aptamer"-regions of riboswitches. Recent crystallographic[7] and NMR spectroscopic[8] studies of adenine- and guanine-sensing mRNAs revealed the structural basis for the use of oligonucleotides in the recognition of small molecules. This work confirmed that the binding site corresponds to the central bulge of the aptamers, as had been expected from the results of mutational studies.[9] The exquisite selectivity was

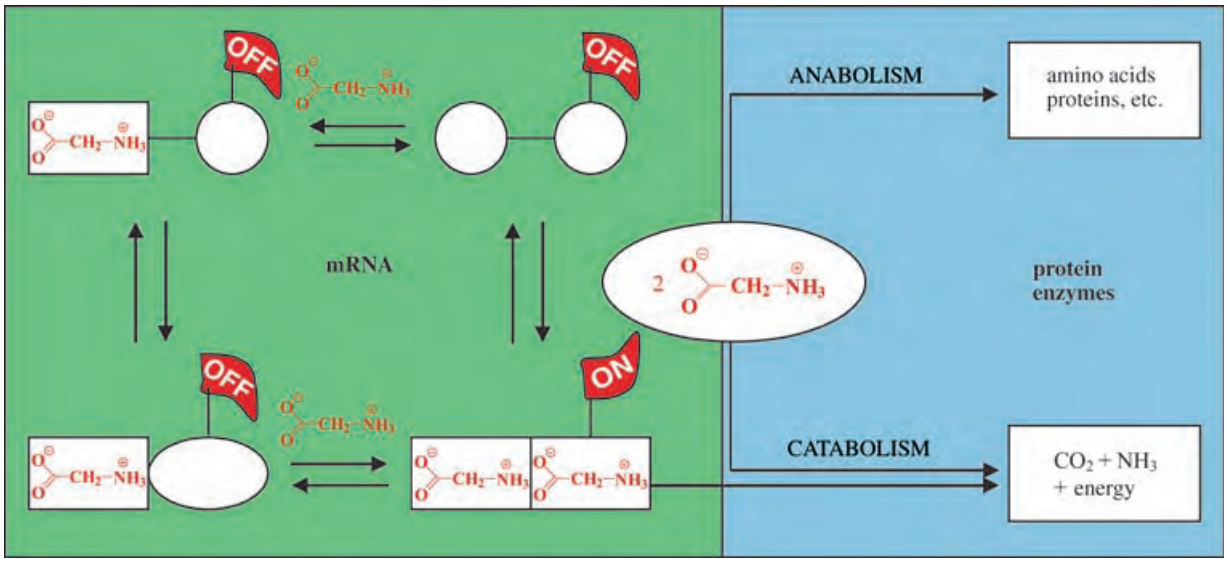


Figure 2. The glycine-dependent riboswitch, a crucial element in the regulation of glycine metabolism and subject to cooperative binding of glycine in a tandem motif.

 © 2005 Wiley-VCH Verlag GmbH & Co. KGaA, Weinheim

shown to result from specific hydrogen bonding with a strategically situated RNA base. In previous experiments in vitro, various oligomeric RNAs ("aptamers") had been already prepared which were able to recognize and selectively bind small molecules with high affinity.[10] These studies, the discovery of self-splicing RNA and natural ribozymes,[11] more recent experiments on artificial ribozymes[12] and on *retro*-riboswitches[13] promise to expand our general knowledge on the intriguing functional diversity of RNA.[14]

Published online: June 9, 2005

[1] *Lehninger Principles of Biochemistry* (Eds.: D. L. Nelson, M. M. Cox), 3rd ed., Worth Publishers, New York, **2000**.

[2] a) A. Nahvi, N. Sudarsan, M. S. Ebert, X. Zou, K. L. Brown, R. R. Breaker, *Chem. Biol.* **2002**, *9*, 1043–1049; b) W. C. Winkler, R. R. Breaker, *ChemBioChem* **2003**, *4*, 1024–1032.

[3] W. C. Winkler, A. Nahvi, A Roth, J. A. Collins, R. R. Breaker, *Nature* **2004**, *428*, 281–286.

[4] M. Famulok, *Science* **2004**, *306*, 233–234.

[5] M. Mandal, M. Lee, J. E. Barrick, Z. Weinberg, G. M. Emilsson, W. L. Ruzzo, R. R. Breaker, *Science* **2004**, *306*, 275–279.

[6] A. M. Jose, G. A. Soukup, R. R. Breaker, *Nucleic Acids Res.* **2001**, *29*, 1631–1637.

[7] a) A. Serganov, Y.-R. Yuan, O. Pikovskaya, A. Polonskaia, L. Malinina, A. T. Phan, C. Hoebartner, R. Micura, R. R. Breaker, D. J. Patel, *Chem. Biol.* **2004**, *11*, 1729–1741; b) R. B. Batey, S. D. Gilbert, R. K. Montagne, *Nature* **2004**, *432*, 411–415.

[8] J. Noeske, C. Richter, M. A. Grundl, H. R. Nasiri, H. Schwalbe, J. Wöhnert, *Proc. Natl. Acad. Sci. USA* **2005**, *102*, 1372–1377.

[9] M. Mandal, R. R. Breaker, *Nat. Struct. Mol. Biol.* **2004**, *11*, 29–35.

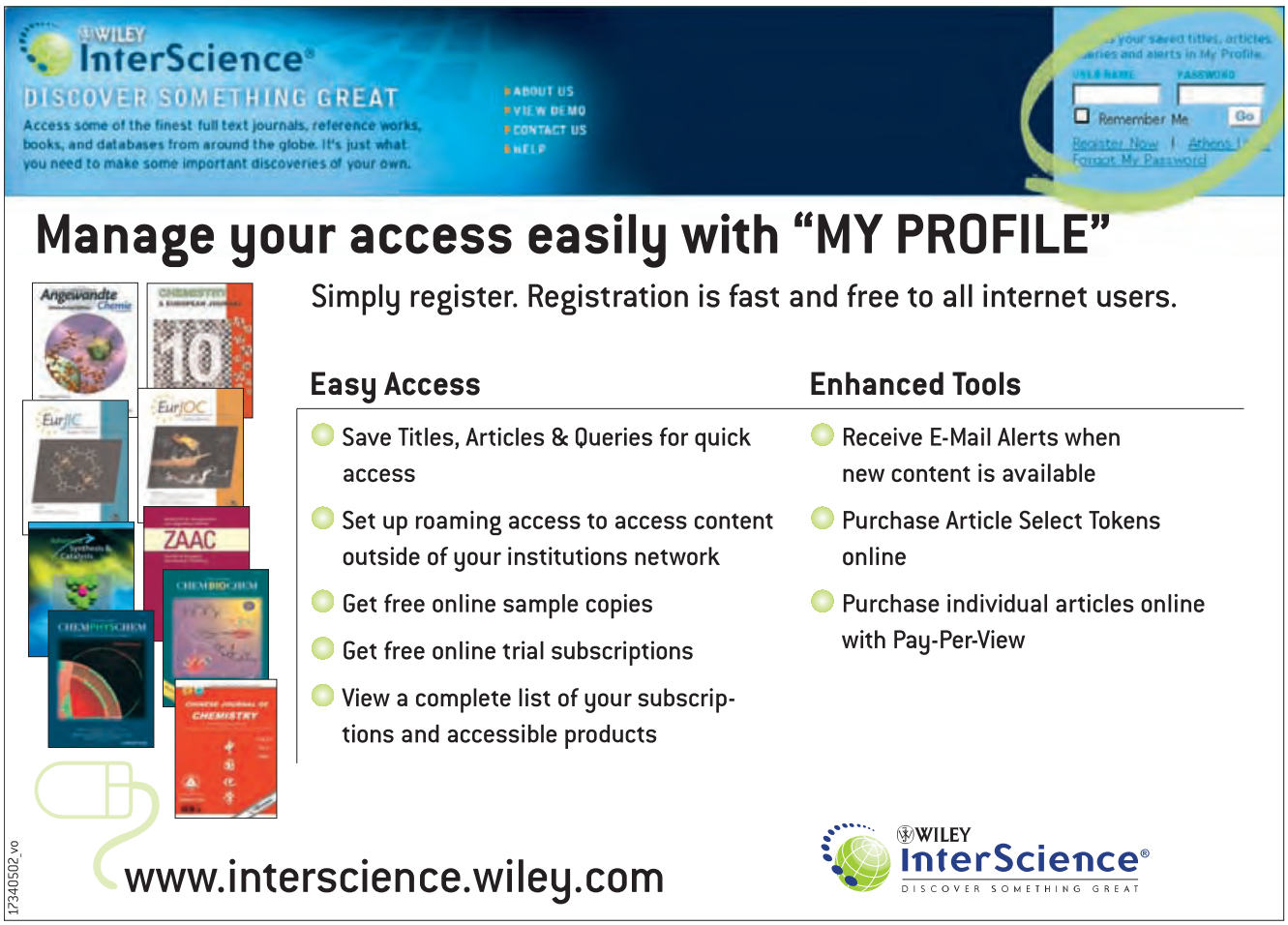
[10] a) J. R. Lorsch, J. W. Szostak, *Biochemistry* **1994**, *33*, 973–982; b) M. Famulok, A. Jenne, *Curr. Opin. Chem. Biol.* **1998**, *2*, 320–327; c) D. Sussman, J. C. Nix, C. Wilson, *Nat. Struct. Biol.* **2000**, *7*, 53–57.

[11] T. R. Cech, *Biochem. Soc. Trans.* **2002**, *30*, 1162–1166.

[12] F. Joyce, *Nature* **2002**, *418*, 214–221.

[13] S. Gschösser, K. Gruber, C. Kratky, C. Eichmüller, B. Kräutler, *Angew. Chem.* **2005**, *117*, 2324–2328; *Angew. Chem. Int. Ed.* **2005**, *44*, 2284–2288.

[14] *The RNA World* (Eds.: R. F. Gesteland, T. R. Cech, J. F. Atkins), Cold Spring Harbor Laboratory Press, Cold Spring Harbor, **1999**.



Synthetic Methods

Recent Advances in Catalytic, Enantioselective α Aminations and α Oxygenations of Carbonyl Compounds**

*Jacob M. Janey**

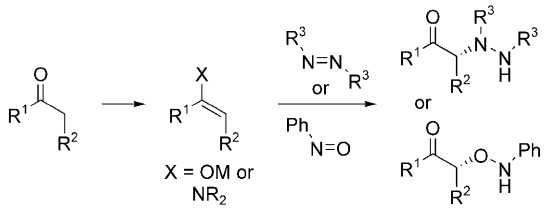
Keywords:
amination · asymmetric catalysis · Lewis acids · organocatalysis · synthetic methods

The direct introduction of either a nitrogen or oxygen atom adjacent to a carbonyl group in a catalytic, enantioselective manner using both chiral Lewis acid and Lewis base catalysis has been described recently. The enantiomerically enriched products of these reactions, such as α-amino acids, represent fundamental building blocks for the construction of complex natural products and other important bioactive molecules. This Minireview provides a synopsis of this ever-growing field and highlights some of the challenges that still remain.

1. Introduction

The literature concerning α amination[1] and α oxygenation[2] of ketones, aldehydes, and esters contains many examples of nonstereoselective and auxiliary-controlled methodologies. The more prominent, well-established methods of enantioselective α oxygenation include the use of Davis oxaziridine,[3] Sharpless dihydroxylation of enol ethers,[4] manganese–salen epoxidation of enol ethers,[5] and Shi epoxidation of enol ethers.[6] It is only rather recently that direct catalytic, asymmetric variants have been reported.[7] This review will focus only upon these contemporary aminations and oxygenations, although it should be noted that the catalytic, asymmetric α halogenation of carbonyls may also serve as an alternative entry to enantioenriched α-amino and α-hydroxy carbonyls.[8]

The basic reaction manifold consists of an enolate (or enamine) reacting with an electrophilic nitrogen or oxygen atom (Scheme 1). The enolate may either be preformed (such as a silyl enol ether) or generated in situ through "soft" enolization involving a Lewis acidic metal and a base. Enamines are also competent nucleophiles and form from the reversible condensation between an aldehyde or ketone and a secondary amine. The heteroatom electrophile is either an azodicarboxylate for aminations, or nitrosobenzene for both oxygenation and amination reactions, depending upon the reaction conditions.



Scheme 1. General reactivity pattern.

The reactions can be catalyzed by either chiral Lewis acids or Lewis bases. For Lewis acid catalysis, there are two modes for activation and stereochemical induction (Figure 1). The chiral Lewis acid metal complex may generate a chiral metal enolate (**A**) by either "soft" enolization of the carbonyl or by transmetalation of a preformed enolate. The chiral Lewis acid

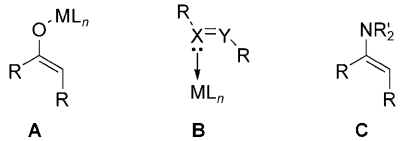


Figure 1. Modes for catalyst activation.

[*] Dr. J. M. Janey
Department of Process Research
Merck Research Laboratories
Merck & Co., Inc.
P.O. Box 2000
Rahway, NJ 07065 (USA)
Fax: (+1) 732-594-5170
E-mail: jacob_janey@merck.com

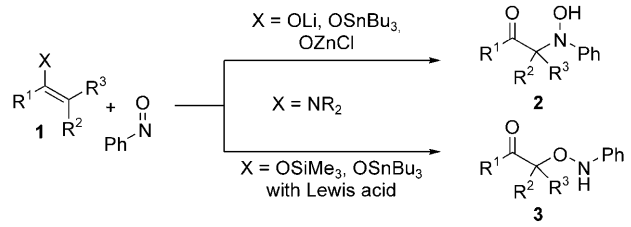
[**] The author would like to thank Prof. Hisashi Yamamoto (University of Chicago) for helpful discussions.

 © 2005 Wiley-VCH Verlag GmbH & Co. KGaA, Weinheim DOI: 10.1002/anie.200462314

may also serve to activate the electrophile by coordination to either an oxygen or nitrogen lone pair (**B**). It is also possible that the Lewis acid complex plays both roles at once by forming a metal enolate, which may then bind to and activate the electrophile. Chiral Lewis bases catalyze these reactions by the reversible formation of a chiral enamine (**C**). The asymmetry is then transferred upon reaction between this enamine and the electrophile, followed by imine hydrolysis of the product, which allows for catalyst turnover.

2. α Oxygenations Catalyzed by Chiral Lewis Acids

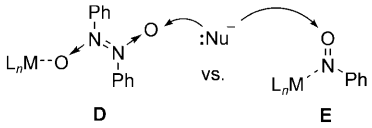
In recent years a growing number of reports have detailed the use of nitrosobenzene as a versatile electrophile for catalytic enantioselective nucleophilic additions. Nitrosobenzene can best be thought of as the nitrogen equivalent of an aldehyde in terms of reactivity and, as such, displays many of the same reactivity patterns, although with some unique and obvious deviations. Of particular note is the proclivity for nitrosobenzene to undergo nucleophilic attack at either oxygen or nitrogen. As depicted in Scheme 2, depending



Scheme 2. Divergent regioselectivity in reactions with nitrosobenzene.

upon the nature of the enolate and presence or absence of a catalyst, either the α-oxygenated or α-aminated product may emerge.[9]

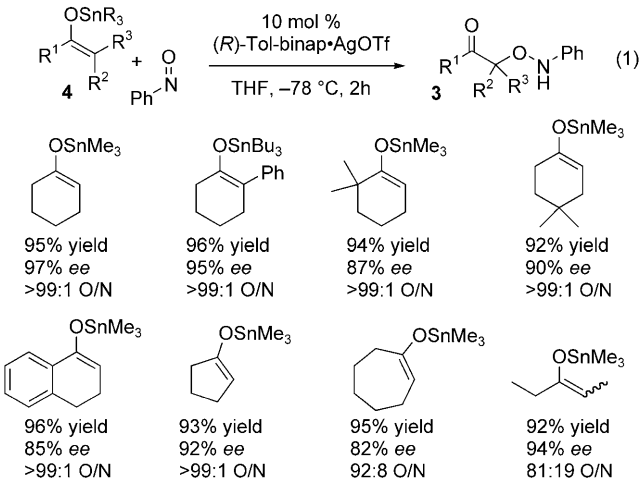
Hisashi Yamamoto and co-workers have extensively explored this "nitroso-aldol" reaction and report that tin(IV), lithium, and zinc(II) enolates, in the absence of any Lewis acid catalyst, give predominantly the aminated product **2**.[9b] In addition, morpholine-derived enamines may also generate **2**.[10] By contrast, silyl enol ethers and tin(IV) enolates in the presence of a Lewis acid give mainly the α-oxygenated product **3**. This divergent reactivity pattern is explained by the facile formation of a nitrosobenzene dimer **D** in the presence of a Lewis acid (Scheme 3). Coordination of a metal at one oxygen then favors nucleophilic attack at the other. Yamamoto et al. also considered the nitrogen coordination in monomer **E**, but ancillary evidence argues against this mode



Scheme 3. Possible modes of nucleophilic attack: a complex of the dimer (**D**) versus a complex of the monomeric nitrosobenzene (**E**).

of activation. Upon addition of Lewis acid they detected the dimer by in situ IR spectroscopy, and also a peak in the ESI mass spectra corresponded to a Lewis acid coordinated to the dimer. It should be noted that this cannot rule out monomer **E** as the actual kinetically active species in the reaction pathway. In addition to the divergent reactivity of enol ethers observed with Lewis acids, enamines may also exhibit such behavior. For example, morpholine-derived enamines give predominantly **2**, whereas pyrrolidine enamines give mainly **3**.[11] Although no explanation for this selectivity has been posited, it is known that enamines derived from pyrrolidine are orders of magnitude more nucleophilic than those from morpholine.[12]

The first Lewis acid catalyzed, enantioselective addition to nitrosobenzene was reported by Yamamoto and co-workers [Eq. (1)].[13] They report that silver(I)–binap complexes effectively catalyze the enantioselective reaction between tin(IV) enolates **4** and nitrosobenzene giving the α-oxygenated carbonyl **3** with excellent regio- and enantioselectivity for a variety of cyclic ketones (Scheme 4). Although the N–O bond



(1)

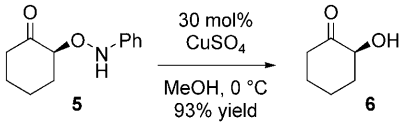
Scheme 4. α Oxygenation of tin(IV) enolates catalyzed by a silver(I)–binap complex.

of **5** is easily cleaved under a variety of hydrogenation conditions, Yamamoto et al. report that catalytic copper(II) sulfate in methanol rapidly gives the free alcohol **6** with no racemization [Eq. (2)].



Jacob Janey was born in Minnesota in 1976. He received his BS degree in chemistry from the University of Chicago in 1998, where he worked in the laboratory of Viresh H. Rawal. In 2003 he earned a PhD in organic chemistry from Harvard University under the guidance of David A. Evans. His thesis dealt with the development and application of chiral Lewis acids for ketene cycloadditions and Suga–Ibata oxazole aldol reactions. He is currently a Senior Research Chemist in the Department of Process Research at Merck & Co., Inc.

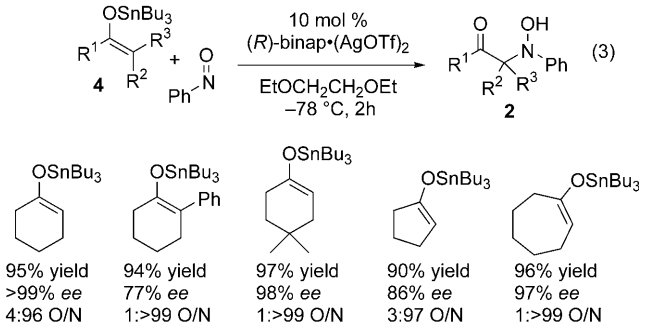
 © 2005 Wiley-VCH Verlag GmbH & Co. KGaA, Weinheim



5 6 (2)

3. α Aminations Catalyzed by Chiral Lewis Acids

The O selectivity of reactions with nitrosobenzene can be completely reversed, as reported recently by Yamamoto and co-workers.[14] They detail conditions under which tin(IV) enolates **4** react with nitrosobenzene to give almost exclusively the α-amino product **2** in a catalytic, enantioselective manner [Eq. (3)]. As shown in Scheme 5, a range of cyclic



Scheme 5. α Amination of tin(IV) enolates catalyzed by a Ag_2^I-binap complex.

tin(IV) enolates react with nitrosobenzene giving **2** with uniformly high levels of both N selectivity and enantioselectivity when conducted in the presence of 10 mol% of a preformed catalyst composed of a 2:1 mixture of silver(I) triflate and (*R*)-binap. This catalyst also showed pronounced solvent effects with THF giving predominantly the oxygenated product, albeit with little enantioselectivity. For aminations, the optimal solvent was found to be ethylene glycol diethyl ether. The reactions in other diether solvents were equally N selective, although the enantioselectivity was moderate at best.

Although no model has been offered to explain why the 1:1 complex of silver(I) and binap is O selective while the 2:1 complex is N selective and gives product **2**, X-ray structures of the 1:2, 1:1, and 2:1 silver(I)–binap complexes were reported.[14] In the 2:1 structure, each phosphine of binap is coordinated to a separate Ag^I center; one of the metal centers also bears two triflates and the other bears two water molecules (Figure 2). In contrast, the 1:1 complex has a tetragonal Ag^I center bound in a chelate by both phosphines of binap in addition to the coordinated counterion (Figure 3). Based on these structures it is not immediately apparent what factors govern O versus N selectivity, as solvent appears to play an important role in this regard.

Azodicarboxylates also serve as ready electrophiles for the Lewis acid catalyzed amination reaction. In a seminal paper on this topic, David A. Evans and Scott G. Nelson[15] reported that a chiral magnesium Lewis acid complex **8** in the presence of a complimentary base will enolize aryl-substitut-

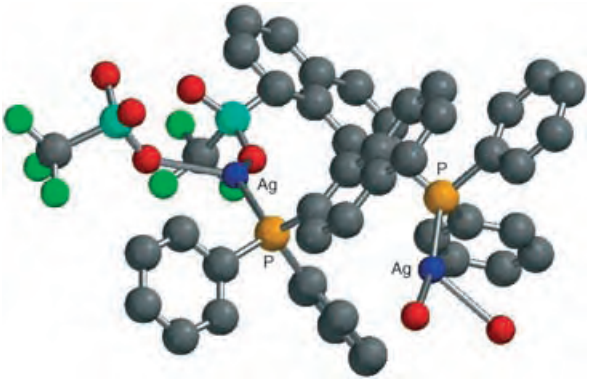


Figure 2. X-ray structure of [{Ag(OTf)}$_2${μ-(*R*)-binap}{Ag(H_2O)$_2$}]. O red, S turquoise, F green.

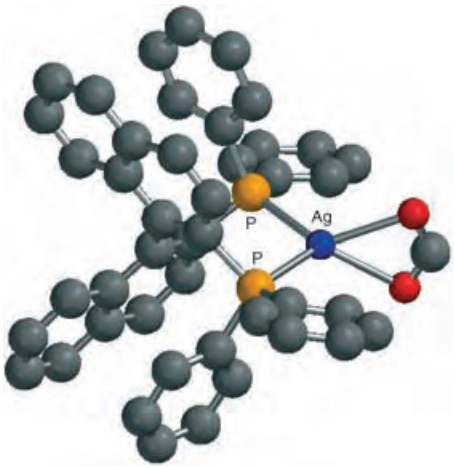


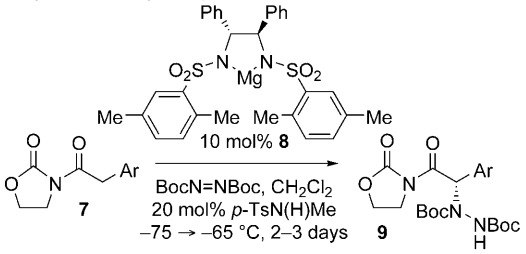
Figure 3. X-ray structure of [Ag($OCOCF_3$){(*R*)-binap}]. The CF_3 group was not localized.[14]

ed carboximides **7**, which are then aminated by di-*tert*-butyl azodicarboxylate [Eq. (4)]. As shown in Table 1, the catalyst provides the expected α-amino acid derivatives **9** with excellent levels of enantioselectivity and yield. The enantiomeric purity can be upgraded with a single recrystallization. It is postulated that the azodicarboxylate acts as the base for the soft enolization between Mg^{II} and **7**. A kinetic investigation indicates that the *N*-methyl-*p*-toluenesulfonamide additive acts as a weak acid to protonate the hydrazide conjugate from the Mg^{II} complex, allowing for liberation of the catalyst. The sense of asymmetric induction was rationalized based upon a chelated tetrahedral magnesium enolate where the C_2-symmetric chiral backbone of the bis(sulfonamide) ligand gears the aryl substituents to shield one face of the bound enolate.

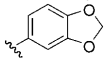
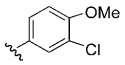
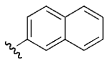
Chiral C_2-symmetric copper(II) bis(oxazoline) Lewis acids also are capable of effecting a "soft" enolization–amination reaction [Eq. (5)].[16] The reaction proceeds quite well for a variety of α-keto esters **10** and dibenzyl azodicarboxylates catalyzed by **11** (Table 2). Since the products **12** were quite prone to racemization, the crude reaction mixture was immediately treated with L-selectride. The reaction most likely proceeds through a complex in which the distorted square-planar Cu^{II} center is chelated to the α-keto ester

 © 2005 Wiley-VCH Verlag GmbH & Co. KGaA, Weinheim

Table 1: α Amination of carboximides catalyzed by a magnesium bis(sulfonamide) complex.[a]

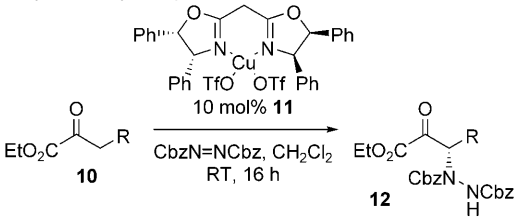


(4)

Entry	Ar	Yield [%]	*ee* [%]
1	Ph	92	86
2	4-F-C_6H_4	97	90
3	4-MeO-C_6H_4	93	86
4		85	82
5		84	80
6		87	82

[a] Boc = *tert*-butyloxycarbonyl, Ts = toluenesulfonyl.

Table 2: α Amination of α-keto esters catalyzed by a copper(II)–bis(oxazoline) complex.[a]



(5)

Entry	R	Yield [%]	*ee* [%]
1	Bn	55	77
2	Me	45	90
3	pentyl	63	93
4	allyl	62	93
5	but-3-enyl	52	92
6	*i*Bu	53	96
7	*i*Pr	78	95
8	(*c*-hexyl)methyl	54	96

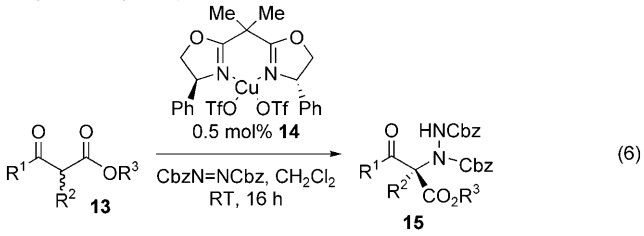
[a] Bn = benzyl, Cbz = benzyloxycarbonyl, Tf = trifluoromethanesulfonyl.

enolate. The sense of asymmetric induction can be rationalized by electrophilic attack of the azodicarboxylate onto the less hindered face of the copper(II) enolate.

This type of amination reaction was extended to β-keto ester substrates (**13**) as well [Eq. (6)].[17] Once again, a C_2-symmetric copper(II)–bis(oxazoline) complex, **14**, was found to be the optimal catalyst with very low loadings (0.5 mol%). The catalyst shows exceptional levels of selectivity for a variety of cyclic and acyclic keto esters (Table 3). The proposed mechanism and model for stereoinduction is similar to that previously described: the chelating ability of the substrate explains the high levels of enantioselectivity.

Lewis acid activation of the azodicarboxylate electrophile has also been reported by Evans and co-workers.[18] They

Table 3: α Amination of β-keto esters catalyzed by a copper(II)–bis(oxazoline) complex.

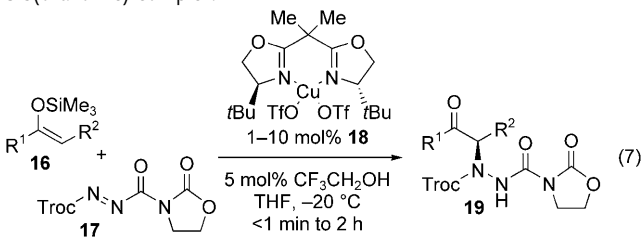


(6)

Entry	R^1	R^2	R^3	Yield [%]	*ee* [%]
1	Me	Me	Et	91	96
2	Et	Me	Et	98	98
3	Ph	Me	Et	81	87
4	*i*Pr	Me	*t*Bu	89	98
5	Bn	Me	*t*Bu	79	98
6	Me	allyl	*t*Bu	80	98
7	Me	Me	*t*Bu	86	98
8	$(CH_2)_3$		Et	96	99
9	$(CH_2)_4$		Et	96	99
10	$(CH_2)_5$		Et	70	99

synthesized the azodicarboxylate derivative **17**, which is capable of forming a chelate with the Cu^{II} complex **18** [Eq. (7)]. This reacts cleanly with a variety of silyl enol ethers **16** giving aminated products **19** with uniform high selectivities and yields (Table 4). Cyclic silyl enol ethers **20** are also good nucleophiles for this transformation (Scheme 6). The key to efficient catalyst turnover in this reaction was found to be the addition of CF_3CH_2OH. This alcohol additive serves to break down a hetero-Diels–Alder intermediate that binds strongly to the Cu^{II} catalyst. The rationale for the observed stereoselectivity is consistent with that seen for other reactions catalyzed by copper(II)–bis(oxazoline) complexes.[19]

Table 4: α Amination of enolsilanes catalyzed by a copper(II)–bis(oxazoline) complex.[a]

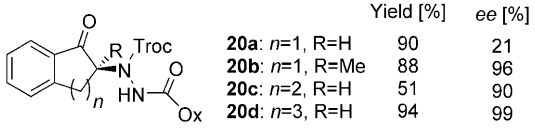


(7)

Entry	R^1	R^2	Yield [%]	*ee* [%]
1	Ph	Me	95	99
2	4-MeO-C_6H_4	Me	96	99
3	6-MeO-Nap	Me	96	99
4	Ph	Et	93	98
5	Ph	allyl	92	97
6	Ph	*i*Bu	92	98
7	Ph	*i*Pr	86	99
8	4-MeO-C_6H_4	*t*Bu	84	98
9	4-MeO-C_6H_4	Bn	88	91
10	4-MeO-C_6H_4	Ph	95	91
11	pyrrolyl	Me	93	98
12	pyrrolyl	allyl	73	98
13	pyrrolyl	*i*Pr	65	99

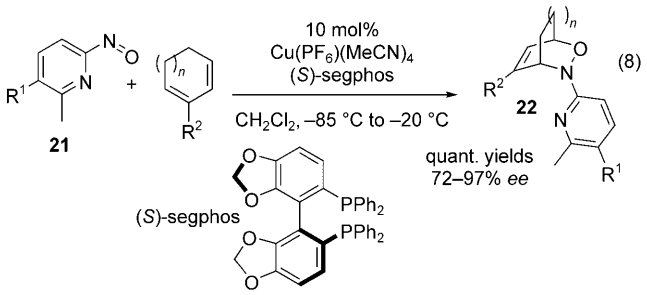
[a] Troc = 2,2,2-trichloroethoxycarbonyl.

 © 2005 Wiley-VCH Verlag GmbH & Co. KGaA, Weinheim



Scheme 6. α Aminations of cyclic silyl enol ethers. Ox = 2-oxazolidinone, Troc = 2,2,2-trichloroethoxycarbonyl.

Although not directly related to the aforementioned topics, Yamamoto et al. have also explored the use of arylnitroso compounds as heterodienophiles in the Diels–Alder reaction of various cyclic dienes [Eq. (8)].[20] They



(8)

report quantitative yields and excellent enantioselectivity for forming cycloadduct **22** when they use a chiral Lewis acid catalyst composed of a copper(I) hexafluorophosphate salt and the axially chiral bisphosphine (*S*)-segphos. The key to this reaction is the use of 2-nitrosopyridines **21**, as these are capable of forming a five-membered chelate with the chiral Cu^{I} catalyst. This provides a high level of organization in the transition state, thus leading to exceptional levels of stereoselectivity. The reported model to explain the stereochemical outcome of this Diels–Alder reaction with (*S*)-binap as a ligand assumes a tetrahedral Cu^{I} center with a "filled" first and third quadrant according to the mnemonic developed by Noyori (Figure 4).[21] Cycloadduct **22** can be transformed over a five-step sequence in 48% overall yield to a fully protected 1,4-amino alcohol.

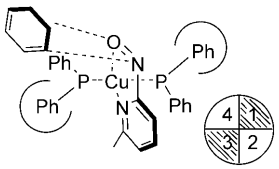
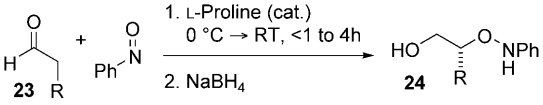


Figure 4. Transition-state model for the hetero-Diels–Alder reaction catalyzed by copper(I)–(*S*)-binap.

4. α Oxygenations Catalyzed by Chiral Lewis Bases

Many of the aforementioned amination and oxygenation reactions relied upon pregenerated, stable metal enolates as reaction partners, but as stated in the introduction, enamines are also known to react cleanly with nitrosobenzene. Given this precedent and the burgeoning literature concerning catalysis of the aldol reaction by chiral Lewis bases by means of reversible formation of enamines, a series of reports have appeared recently which detail the use of proline to catalyze the addition of simple aldehydes and ketones to nitrosobenzene. The primary advantage of this approach is that it avoids the added step of first forming a metal enolate; in addition, proline catalysis tolerates benign reaction conditions (ambient temperature and atmosphere, wet solvents). The first reports of this methodology all appeared within three months of each other from the laboratories of Guofu Zhong, David W. C. MacMillan, and Yujiro Hayashi, and differ only in choice of solvent and the substrates examined.[22] As shown in Equation (9), enolizable aldehydes **23** with varying degrees of branching and functionality react quite well with nitrosobenzene in the presence of catalytic amounts of L-proline. Since the initial α-alkoxy aldehydes produced are oligomeric, subsequent reduction with $NaBH_4$ is necessary to give diol **24**. Table 5 shows that a variety of aldehydes, from bulky ones

Table 5: α Oxygenation of enolizable aldehydes catalyzed by L-proline.



(9)

Entry	R	Solv.	L-Proline [mol%]	Yield [%]	*ee* [%]
1	Me	$CHCl_3$	5	88	97
2	*n*Bu	$CHCl_3$	5	79	98
3	*i*Pr	$CHCl_3$	5	85	99
4	$CH_2CH{=}CH_2$	$CHCl_3$	5	80	99
5	Bn	$CHCl_3$	5	95	97
6	Ph	$CHCl_3$	5	60	99
7	$(CH_2)_2OTIPS$[a]	$CHCl_3$	5	76	98
8	(*N*-methylindol-3-yl)methyl	$CHCl_3$	5	83	98
9	*n*Pr	DMSO	20	71	99
10	$CH_2{=}CHCH_2CH_2$	DMSO	20	73	99
11	$BnOCH_2$	DMSO	20	54	99
12	$BocNH(CH_2)_4$	DMSO	20	61	94
13	Et	CH_3CN	30	87	99

TIPS = triisopropylsilyl.

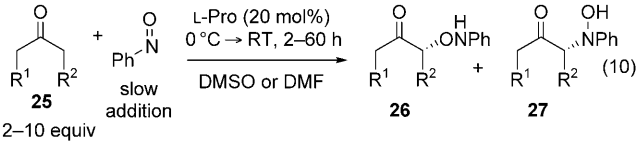
(Table 5, entry 3) to aldehydes containing other functional groups (entries 7, 8, 11, and 12), are well tolerated and produce the expected diol with excellent enantioselectivity and moderate-to-high yields. MacMillan and co-workers report that chloroform is the best solvent in terms of catalyst efficiency. They found that L-proline loadings could be dropped to 1 mol% with little loss in reaction efficiency. In other recent reports photochemically generated singlet oxygen was used as an electrophile for this transformation, albeit with moderate enantioselectivity.[23]

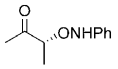
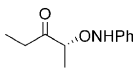
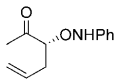
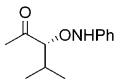
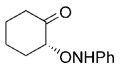
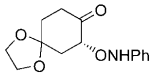
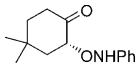
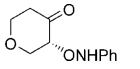
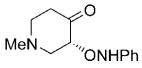
Ketones have proven to be more challenging substrates for this reaction.[24] Besides their diminished ability to reversibly form enamines with proline, they have two enolizable carbon atoms, which may compromise chemoselectivity in the oxygenation reaction. To avoid this complication, a large excess (2–10 equiv) of ketone **25** is often used and nitrosobenzene is added slowly with a syringe pump

 © 2005 Wiley-VCH Verlag GmbH & Co. KGaA, Weinheim

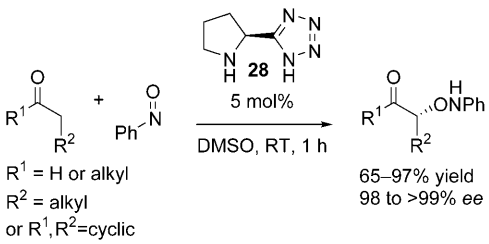
[Eq. (10)]. This protocol prevents the formation of any C_2-symmetric diaddition products and cleanly gives **26**, although in the case of acyclic ketones (Table 6, entries 1–4) minor amounts of the regioisomer **27** arising from N addition are

Table 6: α Oxygenation of ketones catalyzed by L-proline.

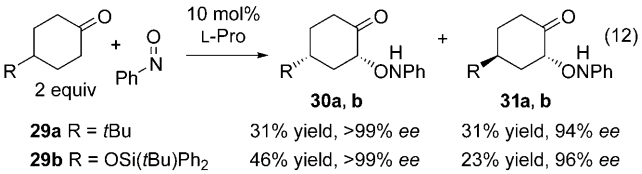


Entry	Product **26**	**26**/**27**	Yield [%]	*ee* [%]
1		81:19	93	>99
2		98:2	66	99
3		88:22	87	>99
4		90:10	64	>99
5		>99:1	91	>99
6		>99:1	96	>99
7		>99:1	84	>99
8		>99:1	53	96
9		>99:1	44	99

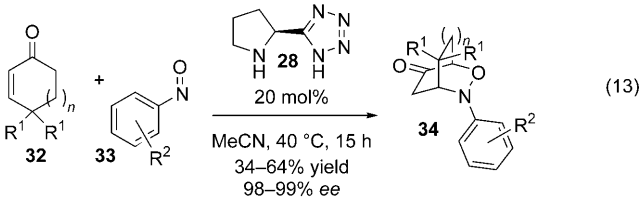
formed. It is also interesting to note that in the case of nonsymmetric ketones, such as entries 1, 3, and 4, it is the more substituted carbon that undergoes reaction with nitrosobenzene. Cyclic ketones (entries 5–9) are excellent substrates, giving **26** with complete regio- and stereoselectivity regardless of any substitution at the 4-position. In addition, Yamamoto et al. have described a more efficient proline–tetrazole catalyst **28**, which mediates the oxygenation of both aldehydes and ketones in high yields (65–97%) and enantioselectivities [Eq. (11)].[11] Shorter reaction times, lower catalyst loadings, and faster addition times of nitrosobenzene were reported with catalyst **28**.



The proline-catalyzed reaction has also been applied to the desymmetrization of *meso* ketones **29a** and **29b** [Eq. (12)].[24b] The degree of catalyst control is very high as both the *cis* (**30a**,**b**) and *trans* ketones (**31a**,**b**) are produced with high *ee*.



An interesting extension to this chemistry is the hetero-Diels–Alder reaction between cyclic enones and nitrosobenzene catalyzed by chiral Lewis bases.[25] A variety of 2-cyclohexene-1-ones **32** react with nitrosobenzenes **33** catalyzed by proline tetrazole **28** giving cycloadducts **34** with moderate yields and very high enantioselectivity [Eq. (13)].



This reaction appears to be insensitive to substituents at the 4-position of enones **32** and nitrosobenzene **33**. Although formally a hetero-Diels–Alder reaction, this appears to be a more stepwise process. After a typical nitroso-aldol reaction, the nitrogen undergoes a conjugate addition to the enone double bond to give the cycloadduct **34**. Attempts at reversing the regioselectivity of this reaction with silver(I) Lewis acids were unsuccessful as the oxygen is reluctant to add in a conjugate manner to the enone.

The purported mechanism of this proline-catalyzed nitroso-aldol reaction is similar to that of the proline-catalyzed aldol reaction (Figure 5).[26] The proline enamine is believed to form an organized six-membered chairlike transition state with nitrosobenzene. A hydrogen bond between the nitrogen of nitrosobenzene and the acid functionality of proline accounts for the observed facial bias. According to calculations performed by Houk and co-workers, the O-*syn* transition state, which leads to the observed major enantiomer, is favored by 3.3 kcal mol^{-1} over the O-*anti* transition state. A

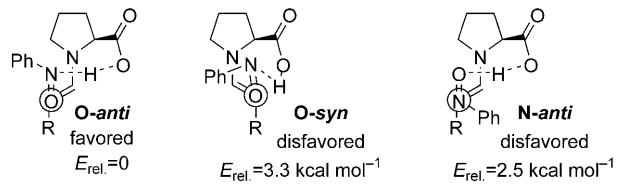


Figure 5. Possible transition state in the reaction of a proline enamine with nitrosobenzene.

 © 2005 Wiley-VCH Verlag GmbH & Co. KGaA, Weinheim

competing pathway that is only 2.5 kcal mol^{-1} higher in energy proceeds via the N-*anti* transition state, which gives rise to the undesired α-aminated product. Although the observed selectivities lend support to this model to explain the stereoinduction, kinetic data suggests a more complex catalytic cycle.[27] A calorimetric analysis of the reaction kinetics clearly indicates a selectivity-enhancing autoinductive process in which the rate and *ee* of the reaction increase with each cycle of the catalytic species. This implies that a product–proline adduct of some sort (either an enamine or hydrogen-bonded species) gives rise to an improved catalyst over the original, sparingly soluble proline.

5. α Aminations Catalyzed by Chiral Lewis Bases

To date, there have been no reported organocatalytic reactions of nitrosobenzene that give the product resulting from attack at nitrogen as the major product, other than the single example of a stoichiometric morpholine enamine giving the N adduct.[10] Instead, K. A. Jørgensen et al. as well as Benjamin List have reported that proline catalyzes the amination of aldehydes and ketone with azodicarboxylates (Table 7).[28] These reactions proceed with moderate-to-excellent yields and high enantioselectivity, and appear to be quite general for a variety of aldehydes and azodicarboxylates. There have also been reports that α,α-disubstituted aldehydes are competent substrates, although selectivities are moderate at best.[29]

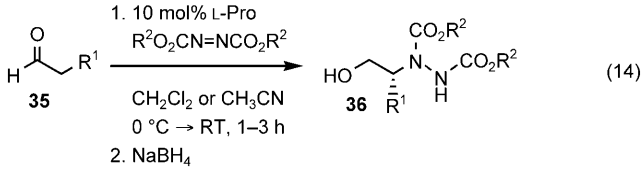
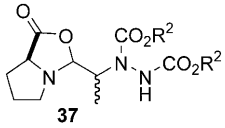


Table 7: α Amination of enolizable aldehydes catalyzed by L-proline.

Entry	R^1	R^2	Yield [%]	*ee* [%]
1	Me	Et	67	93
2	Et	Et	77	95
3	*i*Pr	Et	83	93
4	*t*Bu	Et	57	91
5	allyl	Et	92	93
6	Bn	Et	68	89
7	*i*Pr	Bn	99	96
8	*n*Pr	Bn	93	95
9	*n*Bu	Bn	94	97
10	Me	Bn	97	95
11	Bn	Bn	95	95

The mechanism for this transformation exhibits very interesting and dramatic kinetics.[30] An examination of this reaction using calorimetry reveals both a nonlinear effect and an accelerating reaction rate, which is a hallmark of an autocatalytic reaction wherein the *ee* is amplified after each catalytic cycle. It was found that adding product to the reaction mixture accelerated the reaction. In addition, premixing proline and the product gave a new catalyst (or precatalyst) species which led to a much improved reaction rate. The authors characterized an oxazolidinone (**37**) that leads to this acceleration. Although the exact role and mechanism of this "improved" catalyst is not yet known, it may serve as a solublized proline species that can enter the catalytic cycle immediately, as solid proline is only slightly soluble in organic solvents such as chloroform. It has also been proposed that the origin of autocatalysis may be the improved solubility of proline through hydrogen-bonding interactions with a matched product molecule.[30b]



A recent contribution to this area was made by K. A. Jørgensen and co-workers who report that a quinidine-derived alkaloid (β-isocupreidine, β-ICD) serves as an efficient catalyst for the α amination of α-cyanoacetates and β-dicarbonyl compounds [Eq. (15)].[31] This highly efficient reaction proceeds with 5 mol% β-ICD to give the expected product with excellent levels of enantioselectivity for a variety of aryl-substituted α-cyanoacetates and a few β-dicarbonyl compounds (Table 8 and Scheme 7). No mechanistic scenarios were offered, although given the high acidity of the substrates and the basic nature of the catalyst, an enolate with a chiral ammonium (β-ICD-H$^+$) counterion is a likely intermediate.

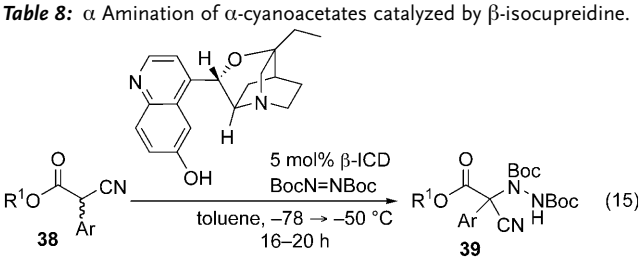
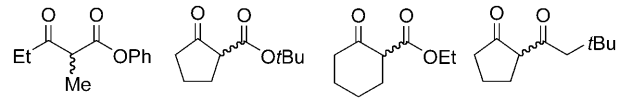


Table 8: α Amination of α-cyanoacetates catalyzed by β-isocupreidine.

Entry	Ar	Yield [%]	*ee* [%]
1	Ph	99	>98
2	2-F-C_6H_4	99	98
3	3-Me-C_6H_4	99	97
4	4-Cl-C_6H_4	99	98
5	4-NO_2-C_6H_4	99	91
6	4-MeO-C_6H_4	95	89
7	2-naphthyl	99	98
8	2-thienyl	99	97



Scheme 7. α Amination of β-dicarbonyl compounds.

6. Summary and Outlook

The catalytic, asymmetric α amination and α oxygenation of carbonyl compounds represents a valuable advance in synthetic methodology. Although much progress has been made in developing this chemistry, many challenges and

 © 2005 Wiley-VCH Verlag GmbH & Co. KGaA, Weinheim

questions still remain. A deeper understanding of the mechanism and the factors that govern O versus N selectivity with nitroso compounds will allow for innovation in catalyst design and make this methodology a robust and efficient way to access valuable, enantiopure building blocks with broad applicatione to the synthesis of biologically important molecules. In addition, more convenient electrophilic sources of nitrogen and oxygen along with broadened and general substrate scope would be a welcome advance. This area is developing at a rapid pace and surely further progress in both catalyst design and mechanistic insight will be forthcoming.

Received: October 14, 2004
Published online: June 9, 2005

[1] For reviews on electrophilic amination, see: a) G. Boche in *Stereoselective Synthesis*, *Vol. 9* (Eds.: G. Helmchen, R. W. Hoffmann, J. Mulzer, E. Schaumann), Thieme, Stuttgart, **1996**, pp. 5133 – 5157; b) C. Greck, J. P. Genet, *Synlett* **1997**, 741 – 748; for diastereoselective aminations, see: c) D. A. Evans, T. C. Britton, R. L. Dorow, J. F. Dellaria, *J. Am. Chem. Soc.* **1986**, *108*, 6395 – 6397; d) D. A. Evans, T. C. Britton, R. L. Dorrow, J. F. Dellaria, *Tetrahedron* **1988**, *44*, 5525 – 5540; e) L. A. Trimble, J. C. Vederas, *J. Am. Chem. Soc.* **1986**, *108*, 6397 – 6399; f) C. Gennari, L. Colombo, G. Bertolini, *J. Am. Chem. Soc.* **1986**, *108*, 6394 – 6395; g) W. Oppolzer, O. Tamura, G. Sundarababu, M. Signer, *J. Am. Chem. Soc.* **1992**, *114*, 5900 – 5902; h) J. M. Harris, R. McDonald, J. C. Vederas, *J. Chem. Soc. Perkin Trans. 1* **1996**, 2669 – 2674.

[2] For leading references, see: a) R. M. Moriarty, B. A. Berglund, R. Penmasta, *Tetrahedron Lett.* **1992**, *33*, 6065 – 6068; b) T. Shono, Y. Matsamura, K. Inoue, F. Iwasaki, *J. Chem. Soc. Perkin Trans. 1* **1986**, 73 – 77; c) G. Tsuchihashi, K. Maniwa, S. Iiuchijama, *J. Am. Chem. Soc.* **1974**, *96*, 4280 – 4283.

[3] F. A. Davis, C. Bang-Chi, *Chem. Rev.* **1992**, *92*, 919 – 934.

[4] a) K. Morikawa, J. Park, P. G. Andersson, T. Hashiyama, K. B. Sharpless, *J. Am. Chem. Soc.* **1993**, *115*, 8463 – 8464; b) T. Hashiyama, K. Morikawa, K. B. Sharpless, *J. Org. Chem.* **1992**, *57*, 5067 – 5068; for a Sharpless epoxidation route, see: c) A. Paju, T. Kanger, T. Pehk, M. Lopp, *Tetrahedron: Asymmetry* **2002**, *13*, 7321 – 7326.

[5] a) W. Adam, R. T. Fell, V. R. Stegmann, C. R. Saha-Möller, *J. Am. Chem. Soc.* **1996**, *118*, 708 – 714; b) W. Adam, R. T. Fell, C. Mock-Knoblauch, C. R. Saha-Möller, *Tetrahedron Lett.* **1996**, *37*, 6531 – 6534; c) T. Fukuda, T. Katsuki, *Tetrahedron Lett.* **1996**, *37*, 4389 – 4392; d) D. R. Reddy, E. R. Thornton, *J. Chem. Soc. Chem. Commun.* **1992**, 172 – 173.

[6] a) Y. Zhu, Y. Tu, H. Yu, Y. Shi, *Tetrahedron Lett.* **1998**, *39*, 7819 – 7822; b) W. Adam, R. T. Fell, C. R. Saha-Möller, C. Zhao, *Tetrahedron: Asymmetry* **1998**, *9*, 397 – 401.

[7] For recent reviews, see: a) P. Merino, T. Tejero, *Angew. Chem.* **2004**, *116*, 3055 – 3058; *Angew. Chem. Int. Ed.* **2004**, *43*, 2995 – 2997; b) R. O. Duthaler, *Angew. Chem.* **2003**, *115*, 1005 – 1008; *Angew. Chem. Int. Ed.* **2003**, *42*, 975 – 978.

[8] a) H. Wack, A. E. Taggi, A. M. Hafez, W. J. Drury III, T. Lectka, *J. Am. Chem. Soc.* **2001**, *123*, 1531 – 1532; b) S. France, H. Wack, A. E. Taggi, A. M. Hafez, T. R. Wagerle, M. H. Shah, C. L. Dusich, T. Lectka, *J. Am. Chem. Soc.* **2004**, *126*, 4245 – 4255; c) M. Marigo, N. Kumaragurubaran, K. A. Jørgensen, *Chem. Eur. J.* **2004**, *10*, 2133 – 2137; d) L. Hintermann, A. Togni, *Helv. Chim. Acta* **2000**, *83*, 2425 – 2435; for Lewis base catalyzed variants, see: e) M. Marigo, S. Bachmann, N. Halland, A. Braunton, K. A. Jørgensen, *Angew. Chem.* **2004**, *116*, 5623 – 5626; *Angew. Chem. Int. Ed.* **2004**, *43*, 5507 – 5510; f) M. P. Brochu, S. P. Brown, D. W. C. MacMillan, *J. Am. Chem. Soc.* **2004**, *126*, 4108 – 4109; g) N. Halland, A. Braunton, S. Bachmann, M. Marigo, K. A. Jørgensen, *J. Am. Chem. Soc.* **2004**, *126*, 4790 – 4791; for catalytic asymmetric fluorinations, see: h) L. Hintermann, A. Togni, *Angew. Chem.* **2000**, *112*, 4530 – 4533; *Angew. Chem. Int. Ed.* **2000**, *39*, 4359 – 4362; i) R. Frantz, L. Hintermann, M. Perseghini, D. Broggini, A. Togni, *Org. Lett.* **2003**, *5*, 1709 – 1712; j) D. Y. Kim, E. J. Park, *Org. Lett.* **2002**, *4*, 545 – 547; k) Y. Hamashima, K. Yagi, H. Takano, L. Tamás, M. Sodeoka, *J. Am. Chem. Soc.* **2002**, *124*, 14530 – 14531.

[9] a) N. Momiyama, H. Yamamoto, *Angew. Chem.* **2002**, *114*, 3112 – 3114; *Angew. Chem. Int. Ed.* **2002**, *41*, 2986 – 2988; b) N. Momiyama, H. Yamamoto, *Org. Lett.* **2002**, *4*, 3579 – 3582.

[10] J. W. Lewis, P. L. Myers, J. L. Ormerod, *J. Chem. Soc. Perkin Trans. 1* **1972**, *20*, 2521 – 2524.

[11] N. Momiyama, H. Torii, S. Saito, H. Yamamoto, *Proc. Natl. Acad. Sci. USA* **2004**, *101*, 5374 – 5378.

[12] B. Kempf, N. Hampel, A. R. Ofial, H. Mayr, *Chem. Eur. J.* **2003**, *9*, 2209 – 2218.

[13] N. Momiyama, H. Yamamoto, *J. Am. Chem. Soc.* **2003**, *125*, 6038 – 6039.

[14] N. Momiyama, H. Yamamoto, *J. Am. Chem. Soc.* **2004**, *126*, 5360 – 5361.

[15] D. A. Evans, S. G. Nelson, *J. Am. Chem. Soc.* **1997**, *119*, 6452 – 6453.

[16] K. Juhl, K. A. Jørgensen, *J. Am. Chem. Soc.* **2002**, *124*, 2420 – 2421.

[17] M. Marigo, K. Juhl, K. A. Jørgensen, *Angew. Chem.* **2003**, *115*, 1405 – 1407; *Angew. Chem. Int. Ed.* **2003**, *42*, 1367 – 1369.

[18] D. A. Evans, D. S. Johnson, *Org. Lett.* **1999**, *1*, 595 – 598.

[19] J. S. Johnson, D. A. Evans, *Acc. Chem. Res.* **2000**, *33*, 325 – 335.

[20] Y. Yamamoto, H. Yamamoto, *J. Am. Chem. Soc.* **2004**, *126*, 4128 – 4129.

[21] M. Kitamura, M. Tsukamoto, Y. Bessho, M. Yoshimura, U. Kobs, M. Widhalm, R. Noyori, *J. Am. Chem. Soc.* **2002**, *124*, 6649 – 6667.

[22] a) G. Zhong, *Angew. Chem.* **2003**, *115*, 4379 – 4382; *Angew. Chem. Int. Ed.* **2003**, *42*, 4247 – 4250; b) S. P. Brown, M. P. Brochu, C. J. Sinz, D. W. C. MacMillan, *J. Am. Chem. Soc.* **2003**, *125*, 10808 – 10809; c) Y. Hayashi, J. Yamaguchi, K. Hibino, M. Shoji, *Tetrahedron Lett.* **2003**, *44*, 8293 – 8296.

[23] A. Córdova, H. Sundén, M. Engqvist, I. Ibrahem, J. Casas, *J. Am. Chem. Soc.* **2004**, *126*, 8914 – 8915.

[24] a) A. Bøgevig, H. Sundén, A. Córdova, *Angew. Chem.* **2004**, *116*, 1129 – 1132; *Angew. Chem. Int. Ed.* **2004**, *43*, 1109 – 1112; b) A. Córdova, H. Sundén, A. Bøgevig, M. Johansson, F. Himo, *Chem. Eur. J.* **2004**, *10*, 3673 – 3684; c) Y. Hayashi, J. Yamaguchi, T. Sumiya, M. Shoji, *Angew. Chem.* **2004**, *116*, 1132 – 1135; *Angew. Chem. Int. Ed.* **2004**, *43*, 1112 – 1115.

[25] Y. Yamamoto, N. Momiyama, H. Yamamoto, *J. Am. Chem. Soc.* **2004**, *126*, 5962 – 5963.

[26] a) P. Ha-Yeon, K. N. Houk, *J. Am. Chem. Soc.* **2004**, *126*, 13912 – 13913; for selected reviews of proline catalysis and mechanisms, see; b) P. I. Dalko, L. Moisan, *Angew. Chem.* **2004**, *116*, 5248 – 5286; *Angew. Chem. Int. Ed.* **2004**, *43*, 5138 – 5175; c) C. Allemann, R. Gordillo, F. R. Clemente, P. H.-Y. Cheong, K. N. Houk, *Acc. Chem. Res.* **2004**, *37*, 558 – 569; d) B. List, *Acc. Chem. Res.* **2004**, *37*, 548 – 557; e) B. List, *Synlett* **2001**, 1675 – 1686; f) P. I. Dalko, L. Moisan, *Angew. Chem.* **2001**, *113*, 3840 – 3864; *Angew. Chem. Int. Ed.* **2001**, *40*, 3726 – 3748; g) M. Movassaghi, E. N. Jacobsen, *Science* **2002**, *298*, 1904 – 1905.

[27] S. P. Mathew, H. Iwamura, D. G. Blackmond, *Angew. Chem.* **2004**, *116*, 3379 – 3383; *Angew. Chem. Int. Ed.* **2004**, *43*, 3317 – 3321.

[28] a) A. Bøgevig, K. Juhl, N. Kumaragurubaran, W. Zhuang, K. A. Jørgensen, *Angew. Chem.* **2002**, *114*, 1868 – 1871; *Angew. Chem.*

 © 2005 Wiley-VCH Verlag GmbH & Co. KGaA, Weinheim

Int. Ed. **2002**, *41*, 1790 – 1793; b) B. List, *J. Am. Chem. Soc.* **2002**, *124*, 5656 – 5657.

[29] H. Vogt, S. Vanderheiden, S. Bräse, *Chem. Commun.* **2003**, 2448 – 2449.

[30] a) H. Iwamura, S. P. Mathew, D. G. Blackmond, *J. Am. Chem. Soc.* **2004**, *126*, 11770 – 11771; b) H. Iwamura, D. H. Wells, S. P. Mathew, M. Klussmann, A. Armstrong, D. G. Blackmond, *J. Am. Chem. Soc.* **2004**, 126, 16312—16313.

[31] S. Saaby, M. Bella, K. A. Jørgensen, *J. Am. Chem. Soc.* **2004**, *126*, 8120 – 8121.

Life's Simple Pleasures!



13280407_gu

No need to waste precious time looking for the right information – Register now for the free **Wiley-VCH Alerting Service.**

It's simple – and it's fast.

To receive regular news per e-mail tailored precisely to your needs and interests, just fill in the registration form at **www.wiley-vch.de/home/pas/**

WILEY-VCH

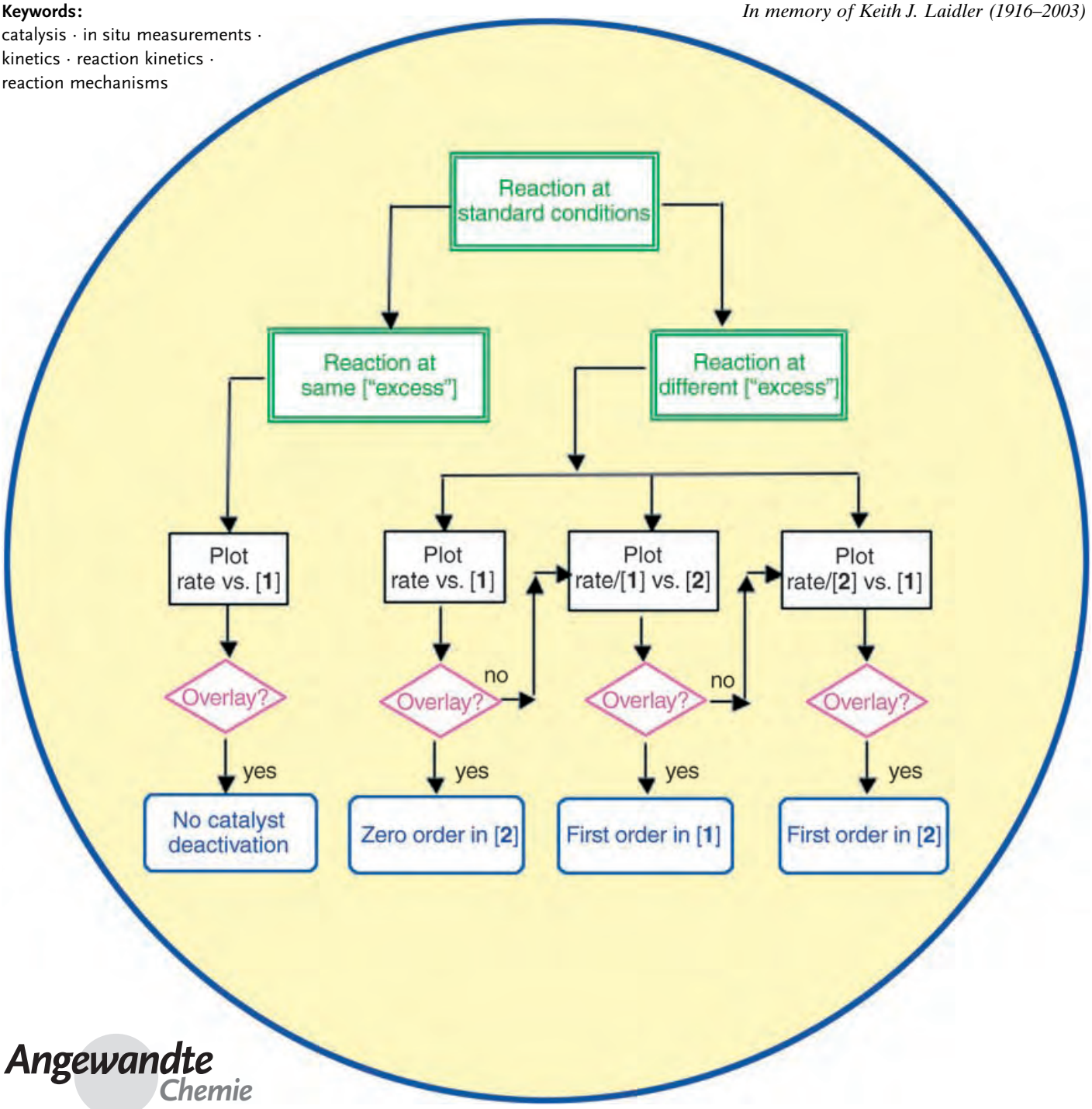
Reaction Kinetics

Reaction Progress Kinetic Analysis: A Powerful Methodology for Mechanistic Studies of Complex Catalytic Reactions

*Donna G. Blackmond**

Keywords:
catalysis · in situ measurements · kinetics · reaction kinetics · reaction mechanisms

In memory of Keith J. Laidler (1916–2003)



 © 2005 Wiley-VCH Verlag GmbH & Co. KGaA, Weinheim DOI: 10.1002/anie.200462544

Reaction progress kinetic analysis to obtain a comprehensive picture of complex catalytic reaction behavior is described. This methodology employs in situ measurements and simple manipulations to construct a series of graphical rate equations that enable analysis of the reaction to be accomplished from a minimal number of experiments. Such an analysis helps to describe the driving forces of a reaction and may be used to help distinguish between different proposed mechanistic models. This Review describes the procedure for undertaking such analysis for any new reaction under study.

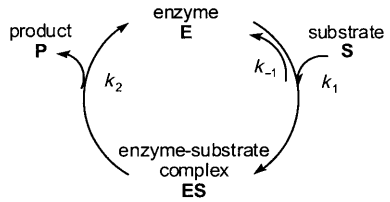
From the Contents

1. Introduction 4303
2. Reaction Progress Kinetic Analysis: Definition 4304
3. Getting Started 4304
4. A Simple Example of High-Throughput Kinetics 4307
5. Dealing with Added Complexity 4309
6. Graphical Tools for Reactions with Two Substrates: Dissecting the Reaction-Rate Expression 4310
7. Interrogating the Data 4311
8. A Flow Chart for Kinetic Analysis of Catalytic Reaction Systems 4318
9. Summary 4318

1. Introduction

Kinetic investigations of multistep organic reactions form a critical part of fundamental mechanistic studies as well as being indispensable to practical applications of organic synthesis. Such studies are aimed at providing a better understanding of reaction pathways by giving concentration dependences of reacting components as well as rate and equilibrium constants pertaining to elementary steps in the reaction network. Analysis of experimental data in multistep catalytic reactions is complicated, however, by the complexity of the reaction rate laws characteristic of these reactions, and therefore simplified means of representing the kinetic data are often sought.

One of the most important examples of such a simplifying tool is the double-reciprocal plot developed by Lineweaver and Burk. The original paper outlining this approach[1] has become the most-cited paper in the history of the *Journal of the American Chemical Society*[2] and offers a straightforward means of linearizing enzymatic reaction rates (Scheme 1)



Scheme 1. Catalytic reaction cycle for a simple enzyme-catalyzed reaction.

given by the Michaelis–Menten Equation [Eq. (1), υ = reaction rate (in M min^{-1}), υ_{max} = maximum reaction rate (in M min^{-1}), [S] = substrate concentration (in M), K_{MM} = Michaelis constant (in M)].[3] The Lineweaver–Burk Equation [Eq. (2)] turns the Michaelis–Menten Equation upside down;

$$\upsilon = \frac{\upsilon_{max}[S]}{K_{MM} + [S]} \quad (1)$$

$$\frac{1}{\upsilon} = \frac{1}{\upsilon_{max}} + \frac{K_{MM}}{\upsilon_{max}}\frac{1}{[S]} \quad (2)$$

this simple but powerful operation created an enabling graphical tool for several generations of chemists trying to make sense of experimental kinetic data in both enzymatic and nonenzymatic catalytic systems (Figure 1).[4]

Today, 70 years since the Lineweaver–Burk Equation was developed, dramatic advances both in experimental measurement techniques and in computer analysis tools provide far more accurate methods for extracting kinetic parameters in reaction systems. Reaction progress kinetic analysis is a methodology that makes use of the voluminous data sets that are now readily obtained from continuous monitoring of the entire course of a reaction. This analysis has permitted the development of a new set of enabling graphical tools that we have termed "graphical rate equations" for a new generation of chemists. Reaction progress kinetic analysis gives the same information provided by classical kinetic approaches with only a fraction of the number of separate experiments. In addition, monitoring the time evolution of the reaction can yield significant further clues about issues that can be problematic in classical experimental approaches, such as catalyst activation and deactivation, as well as substrate and product inhibition or acceleration.[5]

In its most comprehensive form, reaction progress kinetic analysis uses detailed kinetic modeling to assess quantitatively the relative likelihood of different proposed reaction

[*] Prof. D. G. Blackmond
Department of Chemistry
Imperial College
London SW7 2AZ (UK)
Fax: (+44) 020-7594-5804
E-mail: d.blackmond@imperial.ac.uk

 DOI: 10.1002/anie.200462544 © 2005 Wiley-VCH Verlag GmbH & Co. KGaA, Weinheim

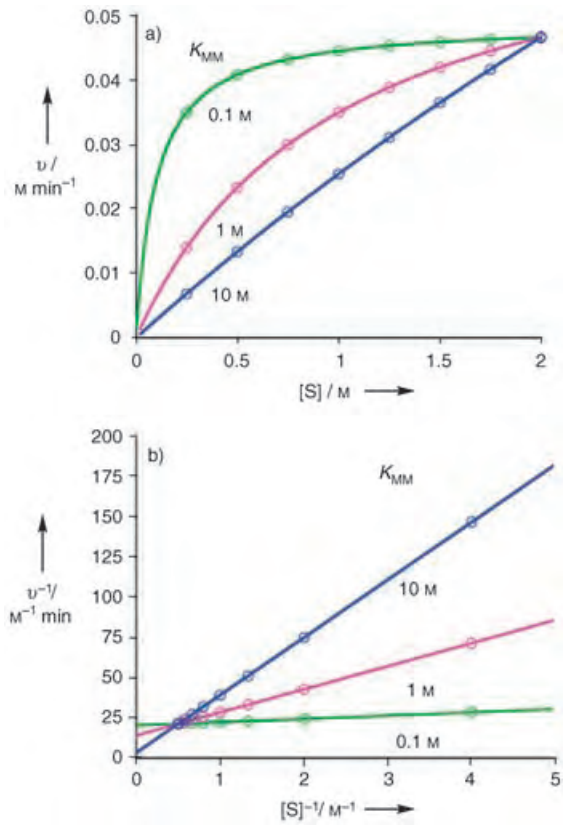


Figure 1. Plots of a) the Michaelis–Menten Equation [Eq. (1)] and b) the Lineweaver–Burk Equation [Eq. (2)] to describe the reaction mechanism shown in Scheme 1 for different values of υ_{max} and K_{MM}.

mechanisms. At the other end of the spectrum, monitoring reaction progress can provide a rapid, qualitative "fingerprint" of reaction behavior for streamlining practical exploitation of new chemistry as well as offering general insights useful for further mechanistic study. In the middle lies a graphical approach where simple manipulations applied to a series of seemingly inscrutable experimental kinetic profiles allow the "interrogation" of the data to yield a wealth of mechanistic information, while requiring only minimal mathematical prowess on the part of the analyst.

The level at which reaction progress kinetic analysis is carried out in any particular example will ultimately reflect a balance between the depth of information desired, the complexity of the reaction under study, the quality of the measured data, and the time commitment of the analyst. This Review gives an introducion to reaction progress kinetic analysis through topical experimental examples from my research group. Special emphasis will be placed on the intermediate level of data "interrogation" to help demonstrate the power of modern experimental techniques in rapid and comprehensive kinetic analysis and to illustrate the accessibility and intuitive value of this graphical approach.



Donna G. Blackmond is a Professor in the Departments of Chemistry as well as Chemical Engineering and Chemical Technology at Imperial College (Chair of Catalysis). Previously she held appointments at the University of Hull, the Max-Planck-Institut für Kohlenforschung, the University of Pittsburgh, and Merck & Co, Inc. She was recently awarded the Arthur C. Cope Scholar Award from the American Chemical Society. Her research interests are focussed on the kinetics of organic reactions with application in pharmaceutical processes.

2. Reaction Progress Kinetic Analysis: Definition

Reaction progress kinetic analysis is faster, requires fewer experiments, can provide enhanced mechanistic detail, and is arguably more accurate than classical kinetic techniques. Why, then, have these methods not yet become common practice in studies of organic reactions? The answer to this question lies, I believe, in our general difficulty in relating the mathematics of a reaction rate law to the molecular story unfolding within a catalytic reaction system. Kinetics conjures up images of experimental drudgery, mathematical manipulations, and logarithmic graphs; chemists prefer to spend their time devising novel transformations in the laboratory. What is not generally made evident in our training in kinetics is that, rather than being a rote and rather detached method of "dotting the i's and crossing the t's" undertaken only after a mechanistic supposition has been all but confirmed by other work, kinetics and its concomitant mathematics are critical tools that can help predict how molecules undergo transformations. Furthermore, these tools can be applied each and every time a reaction is carried out—without altering the conditions under which the reaction is typically performed.

Kinetics is one of several languages for describing chemical events. Other possibilities include drawing out a reaction mechanism or construction of an energy diagram. The fact that the study of kinetics presents a "language barrier" to many chemists reflects the different ways reactions are viewed. To a synthetic chemist, a chemical reaction is characterized by the singular verdict of its outcome: yield and selectivity at the end of the reaction event are registered as numbers in a table. From a kinetic perspective, a chemical reaction is a journey narrated by the reaction rate law. While reaction progress is evident in an energy diagram with its "reaction coordinate" axis, surprisingly few chemists realize that they may envision kinetic graphs in this way. Where classical kinetic approaches provide only a bare summary of the journey that the molecules have undertaken, reaction progress kinetic analysis allows much more to be learnt by following the molecules on their journey.

3. Getting Started

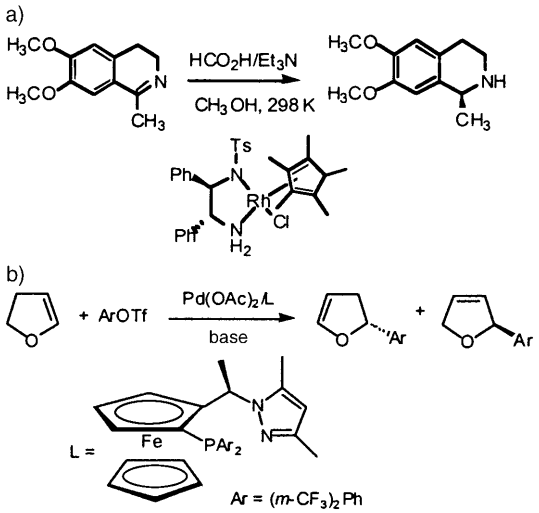
The two key components required for carrying out reaction progress kinetic analysis are: 1) an in situ method of continuous and accurate experimental data collection and 2) a computational means for manipulating the data (typically a PC with a spreadsheet program, perhaps supplemented by a commercial curve-fitting package). Data collection may be

 © 2005 Wiley-VCH Verlag GmbH & Co. KGaA, Weinheim

carried out by using any method that provides an adequate and accurate response (both in signal strength and in time resolution) that is related in a known way to reaction turnover. Understanding the ways in which we manipulate the data we obtain requires that a few words are first said about the different ways in which kinetic data can be measured.

3.1. Integral Measurements

Kinetic methods that rely on a relationship between the measurable parameter and species concentration are called integral measurements because concentration is proportional to the integral of the reaction rate. For example, FTIR spectroscopic studies that follow particular vibrations of reactant or product molecules and also incorporate a chemometric analysis relate the signal intensity to temporal reactant or product concentrations (Table 1, left column). The reaction rate is obtained by differentiating the experimental concentration versus time data. Thus, with integral methods, rate is termed a "processed" parameter to the "primary" parameter of concentration or conversion of the substrate. Typically, some method of smoothing the concentration data is applied before calculating the rate to minimize the noise inherent in the derivative process.[6]



Scheme 2. Examples of reactions monitored using integral (a; see Figure 2a) and differential (b, see Figure 2b) measurements of reaction progress.

Table 1: Integral and differential measurements of reaction progress.

FTIR spectroscopy as an example of an integral measurement[a]	Reaction calorimetry as an example of a differential measurement[b]
$A = \varepsilon b c$	$\dot{q} = \Delta H_{rxn} \times \text{volume} \times \text{rate}$
$\text{rate} = \frac{dc}{dt}$	
$\text{conversion} = 1 - \frac{A}{A_0}$	$\text{conversion} = \int_{t=0}^{t=t} q(t)dt \,/\, \int_{t=0}^{t=t(\text{end})} q(t)dt$
measured parameter: conversion	measured parameter: reaction rate
processed parameter: reaction rate	processed parameter: conversion

[a] A = absorbance, c = concentration, ε = extinction coefficient, b = cell path length. [b] $\dot{q}$ = reactant heat flow, ΔH_{rxn} = heat of reaction.

3.2. Differential Measurements

Methods that measure reaction rate directly are termed differential or derivative measurements (Table 1, right column). These methods include reaction calorimetry, which measures the instantaneous heat flow of the reaction. The reaction rate is related to the heat flow q through the thermodynamic heat of reaction ΔH_{rxn}. In this case the rate is the primary measured parameter, while concentration or conversion (the processed parameters) is proportional to the integral of the rate versus the time.

3.3. A "Graphical Rate Equation"

The reaction shown in Scheme 2a is an example in which the reaction progress was monitored by using an integral method (Figure 2a).[7] Another example in which a differential method (Figure 2b) was used is the reaction shown in Scheme 2b.[8] The graphs in Figure 2 reflect the way data are collected, with time as the x-axis. However, viewing reaction progress as a function of time is not the best way to extract kinetic information from a reaction. Con-

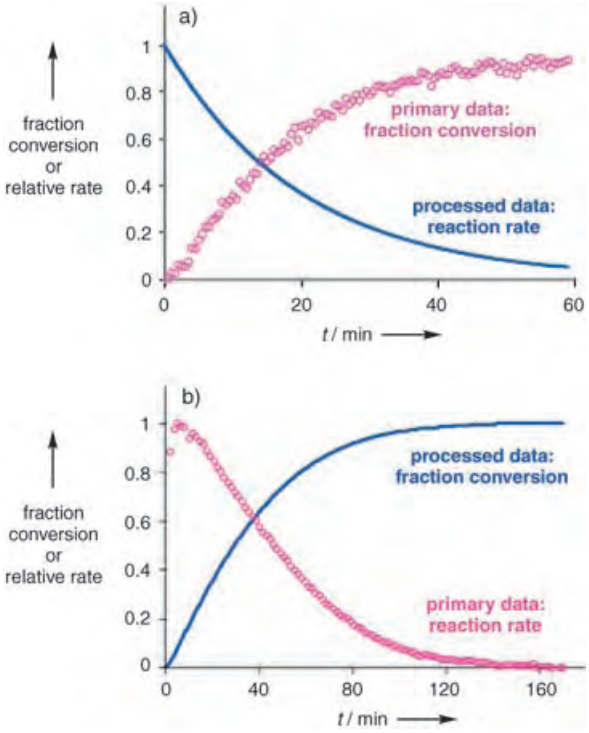


Figure 2. a) Integral (see Scheme 2a) and b) differential (see Scheme 2b) methods for monitoring reaction progress.

 © 2005 Wiley-VCH Verlag GmbH & Co. KGaA, Weinheim

sider the Michaelis–Menten rate expression [Eq. (1)] used to describe the simple mechanism shown in Scheme 1. We can see that time appears only implicitly in this expression. Instead, as with all reaction-rate expressions, the Michaelis–Menten Equation defines a relationship between *rate* and *substrate concentration*. This is where it is useful to combine the two ways in which reaction progress data are described. For any given reaction, the differential measurement can be plotted as the *y*-axis and the integral measurement as the *x*-axis, thus leaving time out of the picture. The resulting plot is termed a "graphical rate equation". Figure 3 shows such plots of rate versus substrate concentration for the two examples of Figure 2.

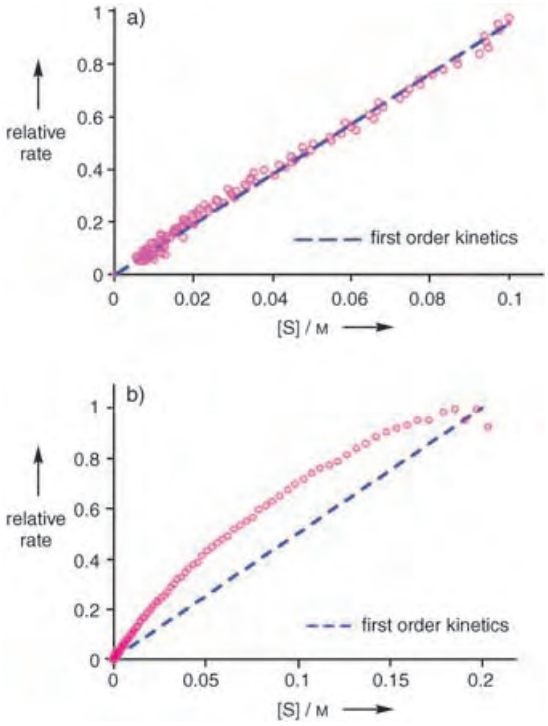


Figure 3. "Graphical rate equations" constructed from the data in Figure 2a and b.

Either concentration or conversion can be used as the "integral method" *x*-axis in these plots. The fraction conversion x of the limiting substrate S is related to the concentration of the substrate by Equation (3).

$$[S] = [S]_0\,(1-x) \tag{3}$$

$$v = \frac{d[S]}{dt} = -[S]_0\,\frac{dx}{dt}$$

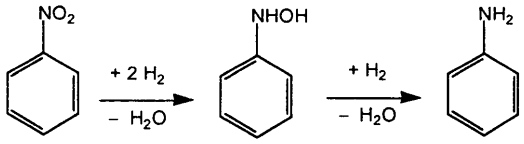
Although fraction conversion is often preferred, comparisons on this basis can be misleading, because a given value for fraction converted represents different substrate concentrations for experiments carried out at different initial concentrations of the limiting substrate. Notice also that plotting concentration as the *x*-axis means that the reaction progresses from right to left, because substrate concentration decreases over the course of the reaction.

The graphical rate equation is a powerful tool for probing concentration dependences. For example, the straight-line relationship in Figure 3a shows that the asymmetric transfer hydrogenation of Scheme 2a exhibits overall first-order kinetics in the concentration of the imine substrate. The curvature in the graphical rate equation in Figure 3b suggests a more complex relationship must be used to describe the enantioselective Heck coupling of Scheme 2b.

The key to the success of this graphical tool lies in the accurate construction of the graphical rate equation by obtaining sufficient high-quality data over the course of the reaction. This highlights the importance of accurate, rapid-response in situ measurement tools in reaction progress kinetic analysis.

3.4. Two (or More) In Situ Techniques are Better than One

Facile access to a range of in situ monitoring techniques makes it possible in many cases today to employ more than one such technique simultaneously. Monitoring a reaction by several orthogonal techniques[9]—methods that rely on different properties of a reacting system to monitor its progress—is a good way of checking that the desired reaction is indeed being followed. A multitechnique approach can also provide valuable mechanistic information that one technique used alone might miss. The reaction shown in Scheme 3 and the



Scheme 3. Room-temperature hydrogenation of nitrobenzene at normal pressure using a Pd/carbon catalyst (see Figure 4).

corresponding analysis shown in Figure 4 are shown as an example.[10] Hydrogenation of nitro substituents on aromatic rings using heterogeneous catalysts is a common transforma-

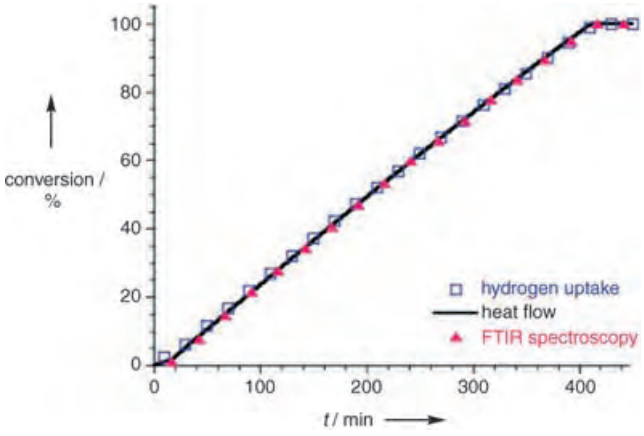


Figure 4. Reaction progress of the Pd/carbon-catalyzed hydrogenation of nitrobenzene shown in Scheme 3 as monitored by three different in situ techniques.

 © 2005 Wiley-VCH Verlag GmbH & Co. KGaA, Weinheim

tion in the pharmaceutical industry. The conversion of nitrobenzene, shown in Figure 4, into aniline using Pd/C is monitored by three separate in situ methods that monitor different properties of the reaction under study: FTIR spectroscopy follows the disappearance of the nitro group in the starting material; hydrogen uptake monitors the stepwise stoichiometry of the hydrogenation; and reaction calorimetry measures the thermodynamic heats in all steps of this highly exothermic reaction. Figure 4 shows clearly that the three methods are in excellent agreement. This result demonstrates that the kinetic data are accurately following the reaction in question and that any potential contribution from side reactions may be safely neglected.

Note that no discrepancy is observed between a method following the decay of the starting material and one monitoring the stoichiometry of the hydrogen uptake, although the hydrogen uptake profile differs for the first and second steps in Scheme 3. From this information it can be proposed that intermediate species, such as hydroxylamine, do not build up in solution over the course of the reaction, since all three techniques give identical information about the global reaction stoichiometry. Thus, in this case, the use of these three methods also offers additional mechanistic insight.

3.5. Calibrating the In Situ Measurement

Whatever the method or methods used to follow the progress of the reaction, it is vitally important to verify that the measurement indeed correlates with the turnover of substrate molecules to product. In most cases it is not feasible to compare the reaction progress profile with three separate measurement techniques as in the previous example. More routinely, calibration of the in situ technique is accomplished by periodic sampling of the reaction mixture over time and employing a known analytical method of assessing concentration. Figure 5 shows a comparison of conversion versus time determined from GC analysis of discrete samples and from the reaction heat flow for the example shown in Scheme 4, the copper-free Sonogashira coupling of bromoacetophenone with phenylacetylene using $[Pd(PtBu_3)_2]$ as catalyst.[11,12] Although discrete analytical sampling alone seldom provides the quantity of data required for reaction progress kinetic analysis, it serves as a check on the veracity of the in situ technique used for monitoring the reaction progress.[13]

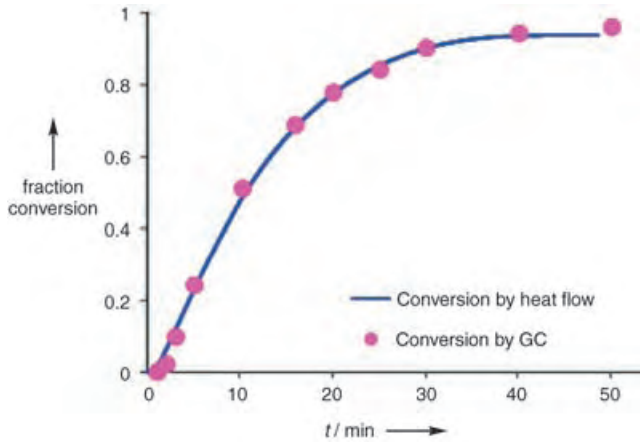
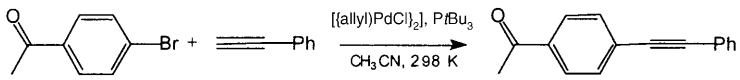


Figure 5. Fraction converted versus time for the reaction shown in Scheme 4 as monitored by reaction calorimetry and verified by GC analysis.



Scheme 4. Sonogashira coupling of an aryl bromide with phenylacetylene using a zero-valent Pd phosphine catalyst (see Figure 5).

3.6. Caveats

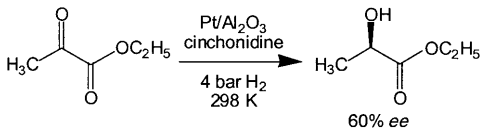
The principles and the graphical tools developed here for reaction progress kinetic analysis owe a large debt to a long history of graphical approaches in enzyme catalysis that are beyond the scope of this Review. Curve-fitting and simulation approaches as well as widely available commercial software packages that determine rate constants will not be the focus of this Review. The fact that these approaches are available but not routinely used by synthetic organic chemists studying chemical catalytic systems provides a strong rationale for the development of the approach described here.

The rate equations developed in this Review are based on the steady-state approximation. Reaction progress kinetic analysis may also be applied (with certain caveats) to stoichiometric reactions; however, this extension of the methodology is beyond the scope of the present Review. The parallel reaction cycles of asymmetric catalytic reactions are not treated here, although the simple reaction schemes given may be easily extended to these systems.

Illustrating the graphical approach described here required access to data sets for manipulation, and hence all of the data and examples discussed come from work carried out in my research group or in collaborative efforts. These data are used here without attempts at detailed mechanistic interpetation; interested readers can refer to the published papers.

4. A Simple Example of "High-Throughput Kinetics"

The asymmetric hydrogenation reaction depicted in Scheme 5 and carried out in two different solvents is used as an introductory illustration of kinetic analysis of the progress of the reaction.[14] Reaction progress, determined by an integral (Figure 6a) and by a differential (Figure 6b)



Scheme 5. Asymmetric hydrogenation of ethyl pyruvate mediated by cinchona-modified Pt/Al_2O_3.

 © 2005 Wiley-VCH Verlag GmbH & Co. KGaA, Weinheim

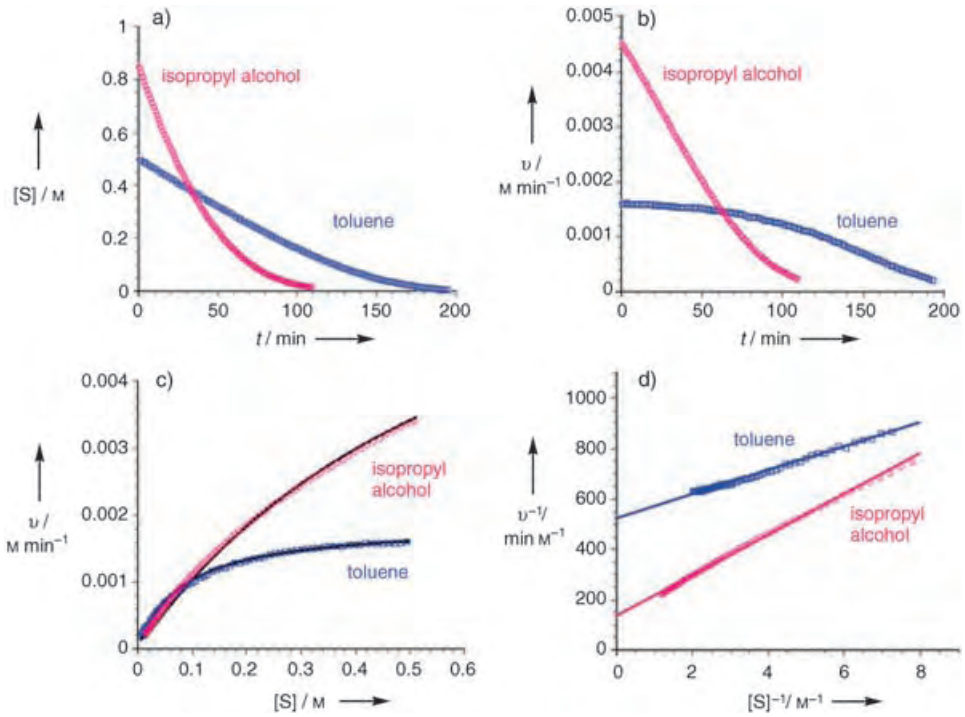


Figure 6. Kinetic analysis (by differential and integral methods) of the hydrogenation reaction shown in Scheme 5 carried out in two different solvents: a) Substrate concentration versus time (integral method). b) Reaction rate versus time (differential method). c) Rate versus substrate concentration; a fit to Equation (1) gives $\upsilon_{max} = 0.008 \pm 0.33\%$ M min^{-1}, $K_{MM} = 0.684 \pm 0.56\%$ M^{-1} (isopropyl alcohol) and $\upsilon_{max} = 0.002 \pm 0.07\%$ M min^{-1}, $K_{MM} = 0.083 \pm 0.23\%$ M^{-1} (toluene). d) Reciprocal rate versus reciprocal substrate (Lineweaver–Burk plot); a fit to Equation (2) gives $\upsilon_{max} = 0.007 \pm 0.90\%$ M min^{-1}, $K_{MM} = 0.600 \pm 1.32\%$ M^{-1} (isopropyl alcohol) and $\upsilon_{max} = 0.002 \pm 0.12\%$ M min^{-1}, $K_{MM} = 0.091 \pm 0.34\%$ M^{-1} (toluene).

method, is plotted as a function of time.[15] This example shows how the progress curves can be used to obtain both a *qualitative* comparison of the reaction's features in the two solvents as well as a *quantitative* analysis of kinetic parameters. The important point about monitoring reaction progress is that, in a single experiment, kinetic data can be obtained not only at the initial concentration of the reactant but also at every concentration between this value and that at the reaction's end. Thus, continuous monitoring of reaction progress is akin to carrying out hundreds of separate initial rate experiments.

The qualitative approach allows some information to be gained before a reaction mechanism is proposed. The temporal data of Figure 6a and 6b show that the reaction is slower in toluene and appears to exhibit a greater degree of "flatness" in the progress curve relative to that in isopropyl alcohol. This observation suggests that the reaction exhibits less-positive-order kinetics in toluene than in isopropyl alcohol. Such a conclusion is even easier to reach by looking at the graphical rate equation of Figure 6c, which is constructed by combining Figure 6a and b. The closer the data are to a horizontal line, the closer the reaction is to zero-order kinetics. Thus, the reaction seems to be not-quite zero order when carried out in toluene, and not-quite first order when carried out in isopropyl alcohol.

Possible reaction mechanisms for kinetic modeling of the data need to be considered if a more quantitative approach is to be used. A good place to start for a constant-pressure hydrogenation reaction is the simple Michaelis–Menten mechanism shown in Scheme 1, with the rate constant k_2 replaced by a pseudo-first-order constant that incorporates the constant hydrogen concentration. The qualitative observations made above are indeed borne out quantitatively by the Michaelis–Menten kinetic model of Scheme 1 and Equation (1). Figure 6c shows that an excellent fit to Equation (1) is obtained for reactions in both solvents and give statistically significant values of the kinetic parameters. These parameters show that the value of K_{MM} in toluene is nearly one order of magnitude lower than it is in isopropyl alcohol. Since K_{MM} is related to the inverse of the binding constant,[16] this result suggests that much stronger catalyst–substrate binding occurs in toluene, thus confirming the pseudo-zero-order form of Equation (1) for the reaction in toluene. In isopropyl alcohol, the Michaelis–Menten Equation cannot be simplified to an integer order, thus resulting in a reaction order that lies between 0 and 1, with its value changing with [S].

These same reaction progress data may also be plotted in the time-honored Lineweaver–Burk double reciprocal plot as in Figure 6d, which shows similar values for the kinetic parameters with similar standard deviations. One advantage of the "straight-line" approach of Figure 6d is that slopes and intercepts can be extracted easily without resorting to a curve-fitting program. One drawback is that the relative values of K_{MM} in the two solvents are intuitively less easy to visualize from double-reciprocal plots of Figure 6d than they are from the direct "graphical rate equation" plots of Figure 6c.

 © 2005 Wiley-VCH Verlag GmbH & Co. KGaA, Weinheim

The most important message to take away from this example is that, in this simple case, one single experiment is all that is mathematically required to develop a quantitative kinetic model of the reaction at a given pressure and temperature. The reason for this is because the experiment contained in essence hundreds of separate initial rate measurements at different substrate concentrations. In comparison to the days of labor that the classical kinetic approach would require, this is very high-throughput kinetic analysis indeed.

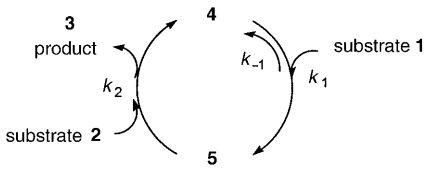
5. Dealing with Added Complexity

The example from the previous section (Scheme 5 and Figure 6) gives a sense of the ease with which a mechanistic model can be developed and tested by monitoring the reaction progress even in a single experiment, and it demonstrates both qualitative and quantitative approaches to reaction progress kinetic analysis. Furthermore, it illustrates the value of the "graphical rate equation" (the plot of rate versus concentration) as a visual aid in assessing concentration dependences. However, most reactions are mechanistically and experimentally much more complicated than this example.

5.1. Reactions with Two Substrates: Beyond the Lineweaver–Burk Plot

The reaction system in Scheme 1 represents the simplest case of a catalytic reaction mechanism, which in practice applies to only a very few cases—including decompositions and isomerizations, or, as already shown, hydrogenations under constant pressure. Typically, however, chemists are more interested in putting molecules together, and thus most reactions of interest will involve at least two reactant species. This means that, under synthetically relevant conditions, two separate reactant concentrations will change simultaneously over the course of the reaction.

Scheme 6 shows how the simple reaction system of Scheme 1 is modified for the case where a second substrate



Scheme 6. Mechanism for a simple reaction with two substrates and one intermediate species.

2 adds to the catalytic intermediate species **5** formed from the binding of the first substrate **1** to catalyst **4** to form the product **3**. The rate expression for this case can be written in the same form as the Michaelis–Menten relationship of Equation (1) to give Equation (4).

$$\upsilon = \frac{\upsilon_{max}\,[\mathbf{1}]}{K_{MM} + [\mathbf{1}]} \tag{4}$$

$$\upsilon_{max} = k_2\,[\mathbf{2}][\mathbf{4}]_{total},\; K_{MM} = \frac{k_{-1} + k_2\,[\mathbf{2}]}{k_1}$$

It can be seen that the kinetic parameters υ_{max} and K_{MM} have now become more complex. They are no longer constants, but instead they each incorporate a dependence on the concentration of the second substrate. A Lineweaver–Burk plot for a two-substrate reaction must be constructed from a series of experiments in which the concentration of the substrate [**2**] is held constant. It is important to emphasize that the constants obtained from this plot are only valid at that particular concentration of the second substrate. This limits the information that can be extracted from these parameters; for example, the magnitude of K_{MM} will no longer be easily related to the strength of binding of the substrate to the catalyst.

K_{MM} can be generalized—that is, the value of K_{MM} can be related back to values of the elementary step rate constants—by using a classical kinetic approach in which not one, but a series of Lineweaver–Burk plots are constructed at different constant values of [**2**]. This process will provide the relationship between K_{MM} and [**2**] that is needed to determine k_1, k_{-1}, and k_2 individually. Since each data point on each Lineweaver–Burk plot represents a separate experiment, it is clear that the classical kinetic approach to reactions involving two substrates involves even more work than it does for experiments with only one substrate.

5.2. Defining the Reaction ["Excess"]

Reaction progress kinetic analysis can help in the streamlining of the approach described above for reactions with two substrates. If the Michaelis–Menten form of the kinetic parameters is dismissed and the rate equation written out instead in terms of the elementary step rate constants, the relationship in Equation (5a) and (5b) is obtained.

$$\upsilon = \frac{k_1 k_2\,[\mathbf{1}]\,[\mathbf{2}]\,[\mathbf{4}]_{total}}{k_{-1} + k_1\,[\mathbf{1}] + k_2\,[\mathbf{2}]} \tag{5a}$$

$$\upsilon = \frac{a\,[\mathbf{1}]\,[\mathbf{2}]\,[\mathbf{4}]_{total}}{1 + b\,[\mathbf{1}] + c\,[\mathbf{2}]} \tag{5b}$$

$$a = \frac{k_1}{k_{-1}}\,k_2,\; b = \frac{k_1}{k_{-1}},\; c = \frac{k_2}{k_{-1}}$$

Equation (5b) divides both the numerator and denominator by the constant k_{-1} to give the rate equation in what is called the "one-plus" form.[17] These equations reveal that for reactions with two substrates the idea of an integer reaction order in either substrate will be at best an approximation: [**1**] and [**2**] appear in additive terms in the denominator as well as being multiplied together in the numerator. Reaction progress data can help make sense of this complex situation, without constraining one concentration to remain constant; instead conditions are employed where both [**1**] and [**2**] change over the course of the reaction.

 © 2005 Wiley-VCH Verlag GmbH & Co. KGaA, Weinheim

Although [**1**] and [**2**] both change with time, the manner in which they change is linked to the reaction stoichiometry. For the reaction shown in Scheme 6, this stoichiometric "rule" says that each time one molecule of **1** is converted into one molecule of product **3**, one molecule of **2** is necessarily also converted. Here we define a parameter called the ["excess"], which is equal to the difference in the initial concentrations of the two substrates [Eq. (6)].[18]

$$[\mathbf{2}] = [\mathbf{2}]_0 - [\mathbf{1}]_0 + [\mathbf{1}] \;\Rightarrow\; [\mathbf{2}] = [\text{"excess"}] + [\mathbf{1}] \qquad (6)$$

This parameter ["excess"] has units, the same units as [**1**] and [**2**] (typically M or mM). The ["excess"] need not be a large number—such as the familiar tenfold excess used in classical kinetic experiments to approximate zero-order conditions in one substrate. The ["excess"] may be a positive number, a negative number, or zero ([“excess”] = 0 for equimolar conditions). A few important points to emphasize about this parameter ["excess"] include:

- ["excess"] gives the difference between the initial concentrations of the two substrates.
- ["excess"] does not change as the reaction progresses (for constant volume reactions).
- ["excess"] is *not* identical to either the number of equivalents or to a percentage excess concentration, both of which do change as the reaction progresses.

One of the key features of reaction progress kinetic analysis is that reactions can be carried out using synthetically relevant conditions. A synthetically reasonable value for the excess of one substrate over the other is employed, thus avoiding the synthetically unreasonable tenfold concentration differences typical of the "pseudo-zero-order" classical kinetic approach.

5.3. How ["Excess"] Helps to Streamline Kinetic Analysis

If the stoichiometric relationship of Equation (6) is substituted into the rate expression Equation (5b), the resulting rate equation is given by Equation (7). For a given set of conditions, the quantities $[\mathbf{4}]_{total}$ and ["excess"] are constant, and k_1, k_{-1}, and k_2 are constants, thus leaving [**1**] as the only variable.

$$v = a' \frac{[\text{"excess"}]\,[\mathbf{1}] + [\mathbf{1}]^2}{1 + b'\,[\mathbf{1}]}\,[\mathbf{4}]_{total} \qquad (7)$$

$$a' = \frac{k_1 k_2}{k_{-1} + k_2\,[\text{"excess"}]},\; b' = \frac{k_1 + k_2}{k_{-1} + k_2\,[\text{"excess"}]}$$

Writing the rate expression in this form highlights how the parameter ["excess"] helps deal with the conundrum of having two concentrations changing at once. Equation (7) shows that there is no need to carry out reactions where the concentration of one substrate is artificially fixed at a pseudoconstant high value over the course of the reaction. As long as the ["excess"] is known, then monitoring the concentration of *one* substrate as the reaction progresses allows the kinetics of reactions with two substrates to be assessed. And because the concentrations of each reactant need not be fixed in turn for a series of experiments probing the other substrate's concentration dependence, this process cuts down significantly on the total number of experiments that must be carried out in order to complete the kinetic analysis of a reaction.

Equation (7) allows us to illustrate two important ways in which we use the variable ["excess"] in kinetic analysis, as outlined in the next two sections.

5.3.1. Experiments Eploying the Same ["Excess"]

First, suppose several experiments are carried out with the same ["excess"] but different starting concentrations of **1** and **2**. Equation (7) illustrates that this is equivalent to carrying out the same experiment from two different starting points. This possibility becomes useful to probe reactions for complexities such as product inhibition or catalyst deactivation (see Section 7.1.2).

5.3.2. Experiments with Different ["Excess"]

Equation (7) shows that there are only two independent adjustable parameters in this rate equation, a' and b', while the reaction mechanism has three independent rate constants, k_1, k_{-1}, and k_2. This situation is analogous to having two simultaneous algebraic equations containing three unknowns, for which an infinite number of solutions exists. Suppose, however, that several experiments are carried out with different ["excess"] values. Collecting data from reactions with at least two different ["excess"] values gives an extra equation and allows a unique solution to be obtained for all three rate constants. This becomes especially important when different mechanistic models are to be tested (Sections 7.4 and 7.5).

6. Graphical Tools for Reactions with Two Substrates: Dissecting the Reaction-Rate Expression

The dependence of the reaction rate on [**1**] in Equation (7) is complex, with second-order and first-order polynomials in [**1**] appearing in the numerator and denominator, respectively. Since [**1**] and [**2**] are associated with the parameter ["excess"], it is often easier in practice to return to the rate equation in the form of Equation (5b), where both [**1**] and [**2**] appear explicitly. In this section some limiting cases of this rate equation are probed.

The denominator of Equation (5b) is comprised of three terms: one is a constant (simply the number 1) and the other two terms contain reactant concentrations [**1**] and [**2**], each multiplied by constants. It is this complexity that makes the concentration dependences of [**1**] and [**2**] nonstraightforward. The key to relating this equation to the species shown in the reaction mechanism (Scheme 6) is to probe which, if any, of the three terms in the denominator dominates the other two.

 © 2005 Wiley-VCH Verlag GmbH & Co. KGaA, Weinheim

Table 2: Limiting cases of the rate expression given in Equation (5b) for the catalytic reaction in Scheme 6.

Dominating species (Scheme 6)	Dominating term in denominator of Eq. (5b)	Observed rate equation
5	b	$v = k_2[\mathbf{2}][\mathbf{4}]_{total}$ (8)
4	c	$v = k_1[\mathbf{1}][\mathbf{4}]_{total}$ (9)
none	all terms contribute	$v = \frac{\frac{k_1}{k_{-1}} k_2 [\mathbf{1}][\mathbf{2}][\mathbf{4}]_{total}}{1+\frac{k_1}{k_{-1}}[\mathbf{1}]+\frac{k_2}{k_{-1}}[\mathbf{2}]}$ (5b)

The various limiting forms of this equation are discussed below and are summarized in Table 2.

Note that the ratio given by the constant b in Equation (5b) is the equilibrium constant for the binding of substrate **1** and hence gives information about the concentration of the catalyst intermediate species **5**. If the term containing b outweighs the other denominator terms, the intermediate species **5** dominates and the slow step will be the reaction consuming this intermediate. This limiting situation is commonly termed "saturation kinetics" in species **1**. The rate equation in this case simplifies to that of Equation (8) in Table 2. A case of saturation kinetics for a reaction with only one substrate was shown in the introductory example of Section 4.0 and one for a reaction with two substrates will be shown in Section 7.2.

The constant c gives the ratio of rate constants for the two reactions of intermediate species **5:** forward to yield product **3** versus backward to reform substrate **1**. If c is large, then intermediate **5** does not build up to a significant concentration. In this case the formation of the intermediate **5** will be rate-limiting, and the unbound catalyst species **4** will be the "resting state" of the catalyst. Equation (9) in Table 2 describes this case, with an example given in Section 7.3.

It is also possible that none of the terms in the denominator dominate the rate expression. This situation is equivalent to saying that the reaction doesn't have a rate-limiting step—a circumstance more common than is typically considered; it simply means that the catalyst exists in significant amounts in both forms **4** and **5** in the system rather than opting for one particular resting state. In this case it is necessary to use the full rate Equation (5b), without simplification of the denominator, to describe the reaction (see Section 7.5).

The observed kinetics will be dictated by the reaction involving the catalytic species that dominates, as summarized in Table 2. It can be seen from this discussion that observation of integer reaction orders in catalytic reactions can hide a wealth of mechanistic information. The next few examples will demonstrate how reaction progress data can be used to help discern which, if any, of these limiting cases are applicable to the reaction under study. While we start from the form of equation (5), we will see again how the parameter ["excess"], which defines the relationship between substrates **1** and **2**, can help us gather significant mechanistic detail from a minimal number of experiments.

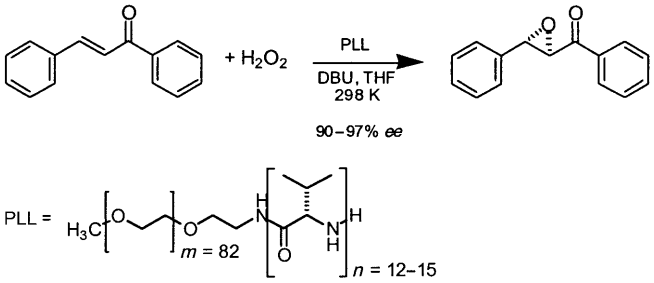
7. "Interrogating" the Data

The ["excess"] relationship allows a set of data pairs of ([**2**], time) points to be compiled with the data from the reaction analysis, that is, with ([**1**], time) and (rate, time) data pairs. Armed with these data, it is now possible to start constructing graphical rate equations for reactions with two substrates. A number of examples below highlight how these data can give information about catalyst behavior. It should be noted that all of the kinetic treatment described here is designed for use in experiments that are carried out under isothermal conditions where the reaction under study is dominant (that is, there are minimal side reactions).

7.1. Catalyst Instabilities

7.1.1. Induction Periods

An important consideration that is often neglected in classical kinetic approaches is the problem of induction periods in catalytic reactions. Transient behavior at the beginning of a reaction is common in chemical catalysis where reactions are often initiated by addition of a catalyst precursor, rather than a catalyst in its active form. Even when the catalyst itself is in its active form, there may be other considerations that cause data obtained at the very outset of the reaction to be suspect. The example in Scheme 7



Scheme 7. Epoxidation of chalcone by H_2O_2 in the presence of the catalyst PLL (MeO-poly(ethylene glycol)-poly-(L-leucine); see Figure 7). DBU = 1,8-diazabicyclo[5.4.0]unde-7-ene.

illustrates this for the Julià–Colonna epoxidation of 1,3-diphenylpropenone (chalcone).[19] The reaction rate versus time curve (Figure 7) shows that the rate rises for the first few minutes of the reaction, before decreasing with time in the manner expected for a reaction exhibiting positive-order kinetics in substrate concentration.[20] The inset in Figure 7 shows a plot of the graphical rate equation in the form of reaction rate versus fraction conversion of the chalcone substrate and shows that the reaction reaches about 20% conversion before the rate profile assumes positive-order kinetics. During the initial few minutes of reaction, the measured values of rate will vary dramatically with even small increments in time. For example, an initial rate measurement taken at 30 seconds would differ by a factor of 50% from one taken at 60 seconds. Such transient behavior might never be

 © 2005 Wiley-VCH Verlag GmbH & Co. KGaA, Weinheim

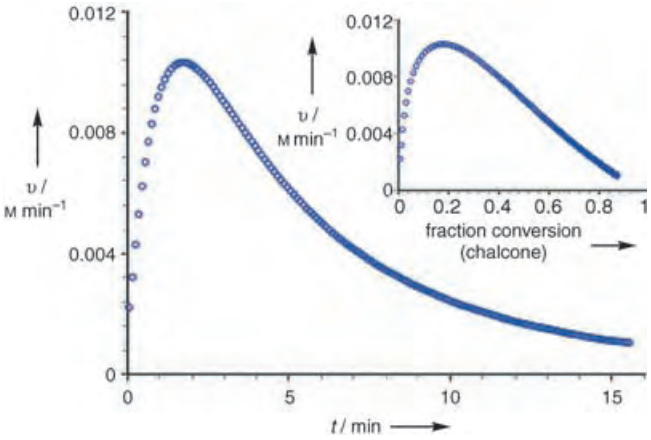
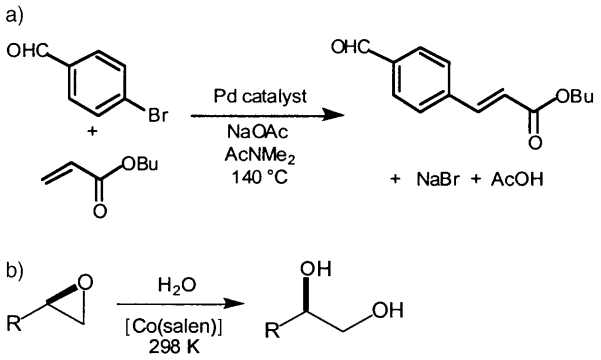


Figure 7. Reaction rate versus time profile for the epoxidation of chalcone with H_2O_2 (see scheme 7).



Scheme 8. a) Heck coupling of aryl bromides. b) Hydrolytic epoxide ring opening.

detected, and misleading interpretation of kinetic data might result, if reaction-progress analysis was not available.

The potential complications of induction periods can easily be overcome when kinetic data are obtained using an in situ method for monitoring reaction progress. Most often it is the steady-state characteristics of the reaction that are of interest for our kinetic analysis. Since the reaction rate and the concentrations of the reactants are known at every point in the reaction, the data obtained during the induction period can simply be discarded and the analysis carried out by selecting only the portion of the reaction that exhibits steady-state behavior. This is what has been done in the examples in the following sections, both for graphical data "interrogation" and for detailed kinetic modeling studies.[21]

7.1.2. *Catalyst Deactivation and Product Inhibition*

A source of additional complexity in catalytic reactions arises in cases where the catalyst deactivates over time, or where the concentration of the active catalyst can be altered over the course of the reaction by substrate or product inhibition. These issues are often cited in support of the practice of carrying out initial rate measurements, to remove time-dependent properties of the reaction from consideration. Such practice may in some cases provide an ideal picture of the kinetics of the reaction; however, this picture can be quite misleading in the practical world, where reactions necessarily are carried out from beginning to end.

One of the most powerful features of reaction progress kinetic analysis is that it allows us to account for the influence of such time-dependent processes, rather than simply ignoring them. Consider the two reactions shown in Scheme 8a and 8b, for which reaction progress data are plotted in the graphical rate equation form in Figure 8a[22] and 8b,[23] respectively. Palladium-catalyzed Heck couplings of aryl halides (Scheme 8a) are commercially important carbon–carbon bond-forming reactions that are often plagued by catalyst deactivation.[24] Epoxide ring opening catalyzed by a cobalt–salen complex, as performed by Jacobsen and co-workers, offers a strikingly efficient method for the kinetic resolution of racemic epoxides (Scheme 8b).[25] These reactions are more complex than our introductory hydrogenation example, because in each case two substrate concentrations change simultaneously over the course of the reaction.

The issue of catalyst deactivation can be probed for the two reactions by carrying out two separate reactions with different starting concentrations of species **1** and **2**, but identical values of the ["excess"]. As explained in Section 5.3, two such experiments represent an identical reaction started from two different places. Thus, choosing any concentration value on either of the plots in Figure 8a and b gives data that correspond to experiments that are identical except for two things: 1) the reaction with a higher initial concentration (red curve) contains more product than that with a lower initial concentration (blue curve); and 2) the catalyst for the reaction with a higher initial concentration has completed more turnovers. By comparing the curves for the reaction progress under these conditions, it is possible to address both the influence of the presence of product and the possibility of catalyst deactivation slowing the reaction over time.

Figure 8a shows that the two curves (reaction rate versus [ArX]) fall exactly on top of one another, thus confirming that neither the presence of product nor the "extra work" done by the catalyst in the reaction shown in red had any influence on the reaction kinetics. We will return to this example later to discuss the interesting "bend" in the curves toward the end of the reaction. For now, however, it has been shown how two simple experiments effectively tell us that neither catalyst deactivation nor product inhibition is a factor in this Heck reaction.

The reaction shown in Figure 8b tells a different story. For a given epoxide concentration, a slightly higher rate was observed in the reaction indicated by the blue curve (lower initial concentration) compared to that shown in red (higher initial concentration). This result suggests that either product inhibition or catalyst deactivation influences the reaction. In this case, further experiments are required to establish which of the two effects is responsible for the lowered rate. For example, reaction product could be added to the mixture at the outset of a reaction under the conditions shown by the blue curve, and the effect on the resulting graphical rate equation observed: namely, do the new data fall on top of the blue curve, or do they fall on top of the red curve? If the curve with addition of product overlays with the blue curve, then it

 © 2005 Wiley-VCH Verlag GmbH & Co. KGaA, Weinheim

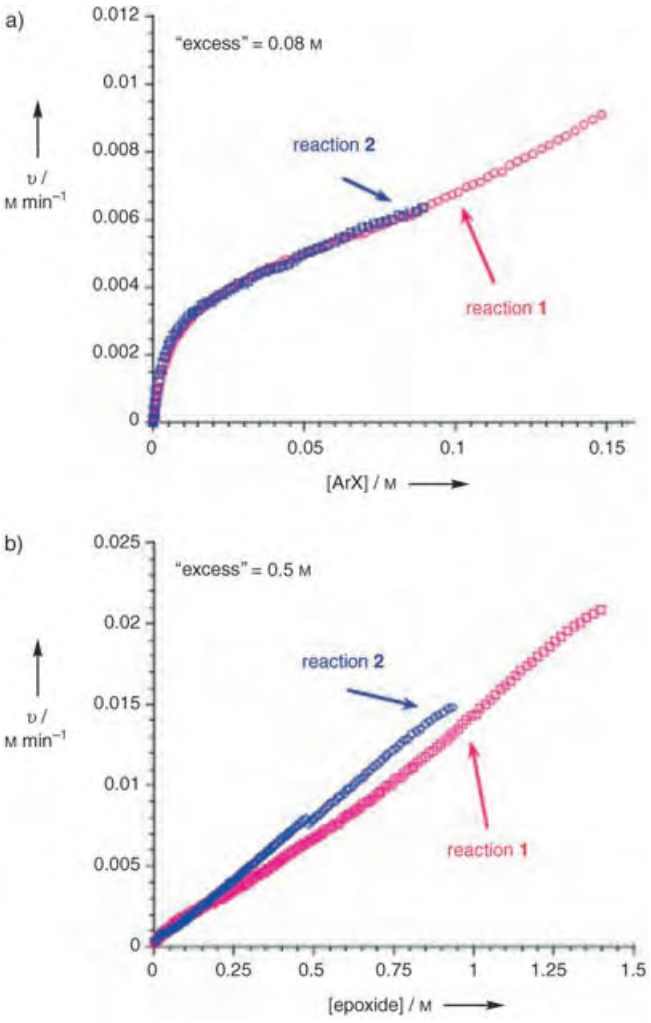


Figure 8. Probing catalyst deactivation by carrying out two reactions at the same ["excess"] but different initial substrate concentrations. a) Heck coupling using a C-N palladacycle catalyst (0.0002 M); red curve: $[ArX]_0 = 0.16$ M, $[olefin]_0 = 0.24$ M; blue curve: $[ArX]_0 = 0.12$ M, $[olefin]_0 = 0.20$ M; b) epoxide ring opening with 2 mol% [Co(salen)]; red curve: $[epoxide]_0 = 1.5$ M, $[H_2O]_0 = 2$ M; blue curve: $[epoxide]_0 = 1$ M, $[H_2O]_0 = 1.5$ M.

can be concluded that catalyst deactivation and not product inhibition is responsible—this is what was found for the reaction shown in Scheme 8b. Further experiments suggested that such deactivation was significant only at the unusually high water:epoxide ratios used in these experiments. Since the hydrolytic kinetic resolution is typically carried out at 0.55 equivalents of water (compared to the 1.3–1.5 equivalents used here), it could be concluded that catalyst deactivation would not be a factor under synthetically relevant conditions.[26]

The example shown in Figure 8b brings up an important consideration in comparing reaction progress kinetic analysis to classical kinetic approaches. Kinetic behavior may be altered when reactions are carried out under conditions significantly removed from those of practical application, as is often the case in classical kinetic approaches in which pseudoconstant concentrations of one reactant is used. The consequences of this practice of removing the catalytic reaction system from its "natural environment" are seldom addressed. Our goal is to employ the conditions under which we plan to run a reaction and allow reaction progress kinetics to help us understand how our reaction works. Kinetic analysis that studies the reacting system in its natural state provides a truer account of the journey taken by the reaction.

These two illustrations have shown how reaction progress kinetic analysis can make use of two simple experiments with identical ["excess"] to address the questions of catalyst deactivation and product inhibition. Adding a third experiment to the list (that of product addition at the start of the reaction) can generally settle these issues definitively for a given system under a given range of conditions. Initial rate measurements leave these questions unanswered; however—especially since the experimental protocol is disarmingly straightforward—it makes sense not to avoid looking for the answers.

7.2. Saturation Kinetics in a Reaction with Two Substrates

Returning to the Heck coupling example of Figure 8a, we turn our attention to the unusual bend observed in the rate curves at high conversion. This unusual shape is also evident when the data are plotted in the time domain, as in Figure 9a,[27] where in addition to the data from Figure 8a, a third reaction carried out at a different ["excess"] value is shown. For most of the reaction, the curve of rate versus [ArX] in Figure 8a is a straight line suggestive of first-order kinetics; however, this line has a non-zero y-intercept ($y = mx + b$ instead of $y = mx$). The parameter ["excess"] can be used to explain this. From the initial reactant concentrations, it can be seen that the aryl bromide is the limiting reactant in all three cases in Figure 9a. If the rate was first order in [ArX] (or [**1**]), the graphical rate equation should have had a y-intercept of zero. However, if the reaction is first order in [olefin] (or [**2**]), then the rate is given by Equation (10):

$$v = k[\mathbf{2}] = k([\text{"excess"}] + [\mathbf{1}]) \tag{10}$$

$$\text{slope} = k$$

$$y\text{–intercept} = k[\text{"excess"}]$$

This result suggests that the Heck reaction under study fits the limiting condition of Equation (8) in Table 2 and describes "saturation kinetics" in [ArX]. The resting state of the catalyst is species **5**, that is, the oxidative addition complex with the substrate. Note that the condition of saturation in a reaction with two substrates is revealed by a linear rate versus concentration curve (overall first-order kinetics), while for a reaction with only one substrate, saturation gives a horizontal line (overall zero-order kinetics) on the same plot.

This result can be corroborated with another form of the graphical rate equation. The simplified rate expression of Equation (8) is divided on both sides by the concentration of the olefin [**2**] to give Equation (11), in which the variables that are functions of time (v and [**2**]) appear as a quotient on the

 © 2005 Wiley-VCH Verlag GmbH & Co. KGaA, Weinheim

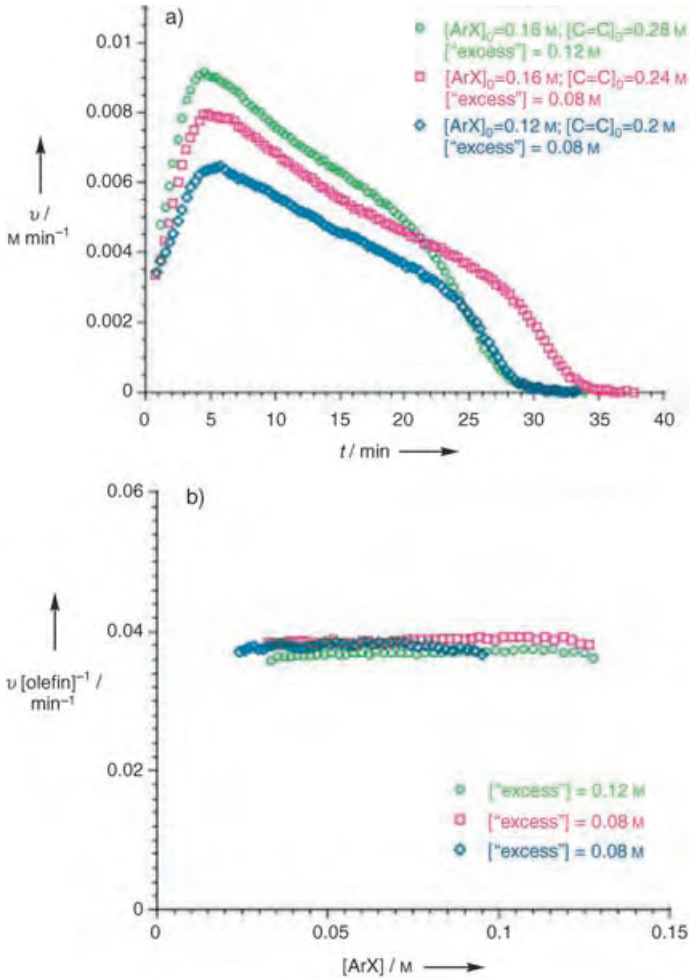


Figure 9. a) Primary data of reaction rate versus time for the Heck coupling in Scheme 8a (C,N palladacycle catalyst) carried out under three different sets of initial substrate conditions. b) A variation of the graphical rate equation for the Heck coupling derived from Figure 8a and 9a. The reaction rate divided by the corresponding olefin concentration is plotted versus aryl halide concentration [see Eq. (11)].

left side of the equation, while the quantities on the right side are constants.

$$\frac{v(t)}{[\mathbf{2}](t)} = k_2\,[\mathbf{4}]_{\text{total}} = \text{constant} \qquad (11)$$

A graphical rate equation can be made according to Equation (11) with our data from the three reactions shown in Figure 9a. This is achieved by dividing each row of a column of rate data points by its corresponding olefin concentration; Equation (11) says that a horizontal straight line could be obtained when this function is plotted versus [**1**] or [**2**] for experiments carried out at any ["excess"] value (Figure 9b).

It is evident from Figures 8, 9a, and 9b that three simple reaction experiments and two graphical rate equations have given extensive detail concerning the mechanism of this Heck coupling reaction. These plots reveal that the system suffers from neither catalyst deactivation nor product inhibition and it exhibits pseudozero order (saturation) kinetics in [ArX] and first-order kinetics in [olefin]. Such efficient mechanistic analysis from so few experiments was possible only because of the voluminous reaction progress data available for constructing the graphical rate equations.

7.3. Free Catalyst as the Resting State

Reactions following the simple mechanism in Scheme 6 can look deceptively different from one another when carried out under different conditions: changing the substrates, the catalyst, the reaction temperature, or even the relative substrate concentrations can shift the resting state of the catalyst in the cycle and thus change the observed substrate concentration dependences. An example illustrating this reconsiders this Heck reaction, but now employing the $[Pd(PtBu)_3)_2]$ catalyst that Littke and Fu have shown to be active under mild conditions.[28] Plotting the standard graphical rate equation of rate versus [ArX] for three reactions carried out at two different ["excess"] values gives a first-order relationship for rate versus [ArX], with a *y*-intercept at zero (Figure 10).[29] This result suggests that the reaction obeys the limiting form of Equation (9) (Table 2) and that the unbound catalyst is the resting state in the reaction. This indicates that the rate-limiting step is the formation of the oxidative addition Pd complex, while the addition and insertion of the olefin proceeds much faster. It can also be seen from the two experiments carried out at the same ["excess"] value that catalyst deactivation is not a problem for this catalyst under the conditions employed. Comparing Figures 10 and 8a illustrates how differently two different Pd catalysts can behave even in the same reaction.

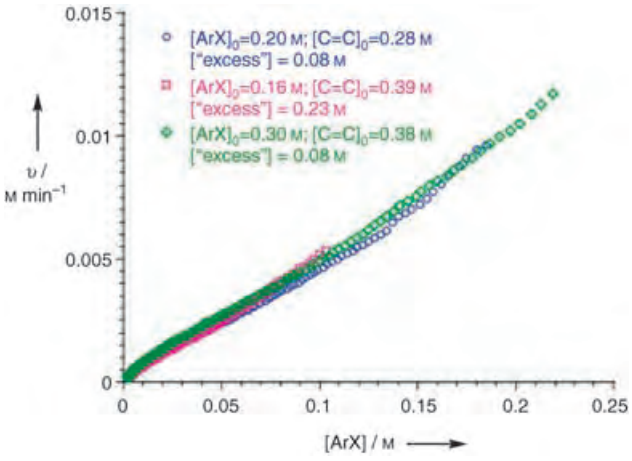


Figure 10. Standard graphical rate of reaction [Eq. (9)] for the Heck coupling shown in Scheme 8a using $[Pd(PtBu_3)_2]$ as the catalyst; the reaction was carried out at three different sets of initial concentrations of the reactants.

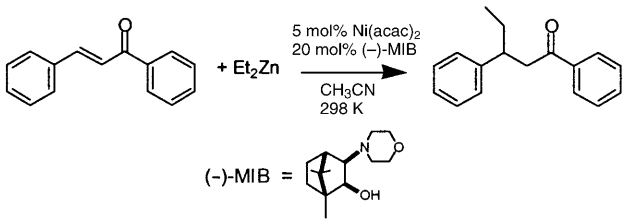
7.4. An Ambiguous Case of Catalyst Resting State

These examples have highlighted two limiting cases of the resting state of the catalyst shown in Table 2 for the reaction system of Scheme 6 with two substrates, demonstrating how

 © 2005 Wiley-VCH Verlag GmbH & Co. KGaA, Weinheim

reaction progress kinetic analysis can help in obtaining a rapid and comprehensive picture of the reaction's concentration driving forces in both cases. Reaction progress kinetic analysis can also help to sort out mechanistic details efficiently for more complicated cases that fall in between these two limits.

The reaction shown in Scheme 9,[30] the conjugate addition of diethylzinc to chalcone mediated by chiral amino alcohols



Scheme 9. Alkylation of chalcone with diethylzinc using $Ni(acac)_2$ and (−)-MIB ((2*S*)-(−)-3-*exo*-morpholinoisoborneol) as a chiral ligand (see Figure 11).

in the presence of a Ni complex, involves a complex mix of reagents. The active catalyst species itself is formed in situ, and much conjecture has been put forward about the reaction mechanism, with complicated dependences of the rate and selectivity on various reaction variables.[31] This would be a formidable test case for reaction progress kinetic analysis. The most important aspects are considered here, a detailed interpretation will be reported separately.[32]

7.4.1. *Failure of the Standard Graphical Rate Equation*

In the terminology of Scheme 6, [chalcone] can be represented by [**1**] and [Et_2Zn] by [**2**]. Three reaction progress curves of this reaction at two different ["excess"] values are shown in Figure 11 as a function of time.[33] Note that the reaction exhibits an induction period, thus suggesting that rate data at conversions less than about 20% will not give a reliable picture of the steady-state catalytic cycle. At conversions higher than this, the reaction appears to be well-behaved, and our analysis will focus on this region. Further details about the relationship between rate and reactant concentrations cannot easily be discerned from the raw reaction rate versus time data. Therefore the next step is to plot graphical rate equations.

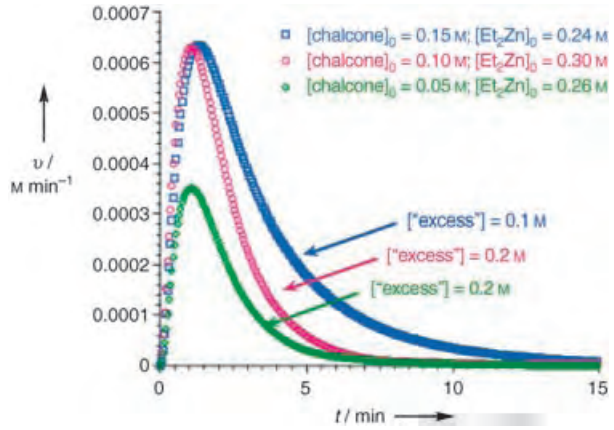


Figure 11. Primary data (reaction rate versus time) for the dialkylzinc alkylation of chalcone (see Scheme 9). The reaction was carried out under three different sets of initial substrate concentrations.

The standard graphical rate equation of rate versus [**1**] is shown in Figure 12a. The curves for the two reactions with the same value of ["excess"] fall on top of each other, which indicates that product inhibition or catalyst deactivation is not a factor in this reaction. However, the third reaction, carried out at different initial concentrations of both chalcone and diethylzinc, as well as at a different value of ["excess"], doesn't fall nicely on the other two. Indeed, it is difficult to determine any useful relationship between the substrate and the reaction rate from these plots. In this situation, the best thing to do is to try plotting other forms of the graphical rate equation.

7.4.2. *Trying Other Graphical Rate Equations: Do the Curves "Overlay"?*

New graphical rate equations can be made by "normalizing" the rate law in Equation (5b) in different ways. For instance, the rate can be divided by each substrate concentration in turn to provide a new function to plot against the other substrate concentration. This procedure gave Figure 9b in the example of the palladium-catalyzed Heck coupling, where all three curves fell on top of each other in a horizontal straight line which indicated zero-order kinetics (Section 7.2). In that case, this result was not unexpected, because it was predicted by Equation (11). In most new reactions, as in the current example, the shape of curves given by developing new graphical rate equations will not be known a priori. What is sought, then, in making these plots is a relationship – whether a straight line or some other function – that produces curves that fall on top of one another; the questions is, therefore, do the curves "overlay"?

Figure 12b and c show the plots of the graphical rate equations where the general rate equation has been divided first by the concentration of chalcone [**1**] [Eq. (12)], and then by diethylzinc [**2**] [Eq. (13)].

$$\frac{v}{[\mathbf{1}]} = \frac{a\,[\mathbf{2}]\,[\mathbf{4}]_{total}}{1 + b\,[\mathbf{1}] + c\,[\mathbf{2}]} \tag{12}$$

$$\frac{v}{[\mathbf{2}]} = \frac{a\,[\mathbf{1}]\,[\mathbf{4}]_{total}}{1 + b\,[\mathbf{1}] + c\,[\mathbf{2}]} \tag{13}$$

Both equations still appear to be complex. Indeed the plot in Figure 12b doesn't help to deconvolute the picture, because the curves don't overlay when plotted. This observation indicates that unlike the previous Heck examples, the order in [**1**] is not a simple integer; the *b* term in the denominator is not negligible in this case.

However, the curves do overlay when the data is plotted according to Equation (13). This result indicates that the data plotted according to Equation (13) versus [**1**] are independent of [**2**], since at any given [**1**] value one of the three runs has a value of [**2**] that is different from the others. This means that

 © 2005 Wiley-VCH Verlag GmbH & Co. KGaA, Weinheim

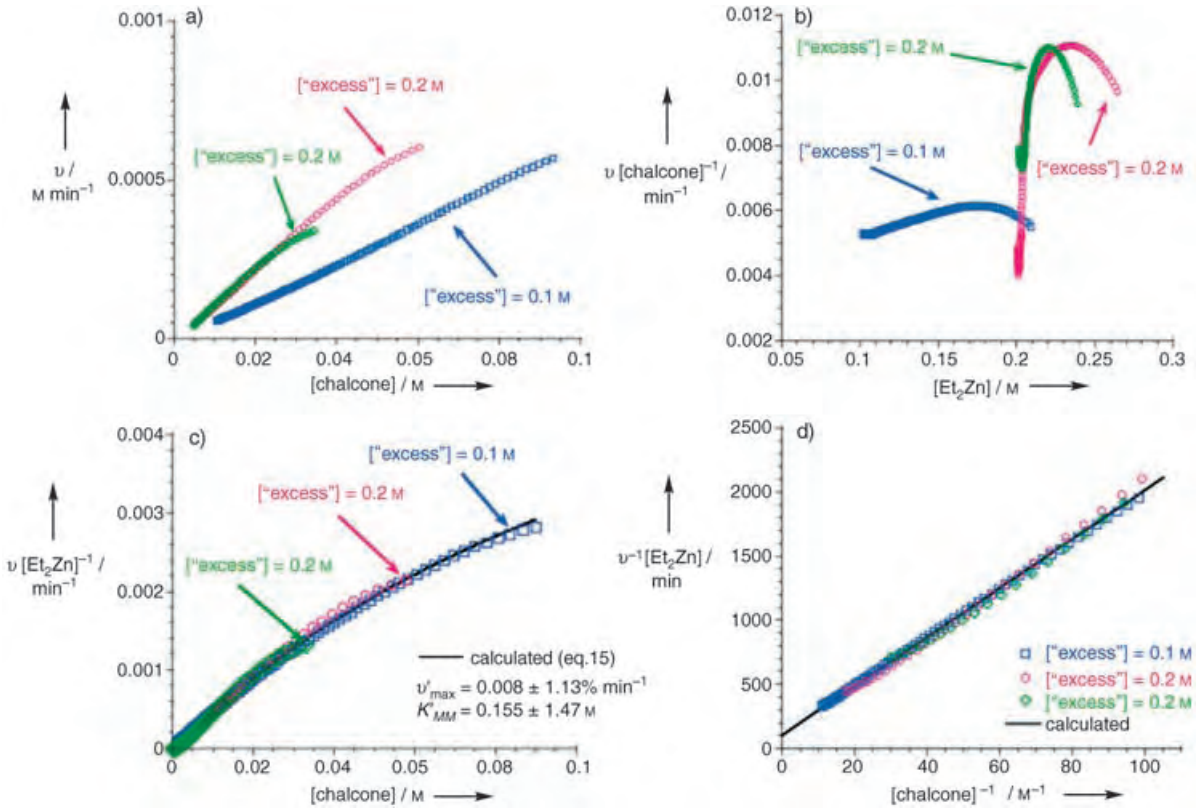


Figure 12. Graphical rate equations for the alkylation of chalcone with dialkylzinc as in Scheme 9 constructed from the primary data given in Figure 11. a) Standard graphical rate equation rate versus [**1**]. b) v/[**1**] versus [**2**]. c) v/[**2**] versus [**1**]; the solid line represents the curve fit to the modified Michaelis–Menten Equation [Eq. (15)]. d) Lineweaver–Burk plot showing the experimental data and the fit calculated according to the inverse form of Equation (15).

the right side of Equation (13) can't contain [**2**], and therefore the term c[**2**] must be small compared to the other terms. Thus Equation (13) can be simplified to Equation (14).

$$\frac{v}{[\mathbf{2}]} = \frac{a\,[\mathbf{1}]\,[\mathbf{4}]_{total}}{1 + b\,[\mathbf{1}]} \tag{14}$$

$$\frac{k_2}{k_{-1}}\,[\mathbf{2}] \ll \frac{k_1}{k_{-1}}\,[\mathbf{1}]$$

$$\frac{k_2}{k_{-1}}\,[\mathbf{2}] \ll 1$$

Equation (14) and its graphical version in Figure 12c show that this reaction exhibits overall first-order kinetics in the concentration of diethylzinc [**2**] and a saturation kinetics expression in the concentration of chalcone [**1**]. Since the plots in Figure 12c do not show a horizontal straight line, as they did in the Heck reaction (Figure 9), it can be deduced that the condition of saturation in [**1**] has not been reached under the concentrations of these conjugate addition reactions.

7.4.3. *Quantifying the Results of the Data Interrogation*

These graphical conclusions can be quantified just as in the asymmetric hydrogenation example of Figure 6 (Section 4). Equation (14) can be written in a Michaelis–Menten form [Eq. (15)] and a simple curve-fitting program applied

$$v' = \frac{v'_{max}\,[\mathbf{1}]}{K'_{MM} + [\mathbf{1}]} \tag{15}$$

$$v' = \text{“normalized rate”} = \frac{v}{[\mathbf{2}]}$$

$$v'_{max} = k_1\,k_2\,[\mathbf{4}]_{total}$$

$$K'_{MM} = \frac{k_{-1}}{k_1}$$

fitting the data in Figure 12c to Equation (15) yields the values for v_{max} and K_{MM} that are shown in the Figure.[34] Note that excellent standard deviations were obtained in these values based on the data from just three separate experiments.

The straight-line approach could instead be used with the same data by inverting Equation (15). The Lineweaver–Burk plot constructed from the same three experiments is shown in Figure 12d. The same quantitative information is available from the plot in this form.

To obtain the information on this plot from a classical kinetic approach would have required a much greater experimental effort. It would have been necessary to complete at least two separate Lineweaver–Burk plots in which data was included from two sets of reactions carried out at two different (constant) values of [**2**] while varying [**1**]. At the very

 © 2005 Wiley-VCH Verlag GmbH & Co. KGaA, Weinheim

least, about half a dozen reactions in each set would have been needed. Reaction progress kinetic analysis allows the total number of experiments to be cut by a factor of four.

7.4.4. Turnover Frequency: Reaction Order in [Catalyst]

The reaction mechanism of Scheme 6 predicts that reaction rate will be proportional to the concentration of the catalyst. Although there are notable exceptions, most catalytic reactions do exhibit first-order behavior in the catalyst concentration. A graphical rate equation can be developed to confirm the relationship by dividing the general rate expression of Equation (5b) (reaction with two substrates) by the total catalyst concentration $[\mathbf{4}]_{total}$ [Eq. (16)]. This expression for the rate normalized by catalyst concentration is also referred to as the turnover frequency (TOF).[35]

$$\frac{\upsilon}{[\mathbf{4}]_{total}} = \mathrm{TOF} = \frac{a\,[\mathbf{1}]\,[\mathbf{2}]}{1 + b\,[\mathbf{1}] + c\,[\mathbf{2}]} \qquad (16)$$

Any two or more reactions carried out using the same ["excess"] but different catalyst concentrations may now be investigated and TOF plotted versus [**1**] (for example, chalcone). If the curves fall on top of one another, the reaction is first order in the catalyst concentration. Note that catalyst concentration is a constant for the entire reaction, and TOF is calculated by dividing each rate data point by this constant number; this is in contrast to the other graphical rate equations where each data point for the rate was divided by a quantity ([**1**] or [**2**]) that changes over the course of the reaction.

Figure 13 shows the TOF versus [chalcone] plots for two reactions shown in Scheme 9 carried out at the same ["excess"] and different concentrations of the catalyst precursor (Ni salt). Since the curves fall on top of one another, the reaction is first order in [Ni]. Note that constructing the graphical rate equation and determining the order in [catalyst] by this method requires no information about the reaction orders in [**1**] and [**2**]. As long as TOF is plotted for reactions with the same ["excess"], the key to this plot is not the shape of the profile but simply whether the curves fall on top of one another.

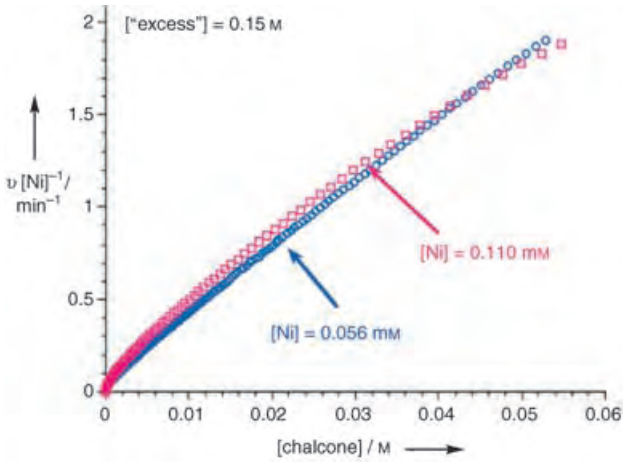


Figure 13. Graphical rate equation for turnover frequency as in Equation (16) for data from the reaction shown in Scheme 9.

7.5. Complex Cases

In some reactions with two substrates it may be found that none of the plots of graphical rate equations result in all the curves falling on top of one another. What this means is that neither substrate exhibits an integer order and both substrate concentration terms in the denominator of the rate expression Equation (5b) make a noticeable contribution to the overall rate expression. The catalyst is almost evenly distributed between its free state **4** and intermediate **5** so that that the reaction does not exhibit a definitive rate-limiting step or resting state.[36] In such cases, the failure of the graphical approach to produce curves that overlay suggests that detailed kinetic modeling studies must be carried out to determine the values of the rate constants in the system.

7.6. Other Reaction Mechanisms

Although the discussion in this section focuses on a simple reaction with two substrates (Scheme 6), a similar approach may be applied in constructing graphical rate equations for more complicated reactions.[37] The method allows the rapid assessment of whether the concentration dependences in a particular reaction system obey simple or complex forms. Indeed, in most cases a simple series of a half-dozen separate reaction-progress experiments are all that is required to assess concentration dependences of the two substrates and the catalyst, while assessing whether the reaction exhibits catalyst deactivation or product inhibition are also important features of the reaction.

7.7. Lessons Learned

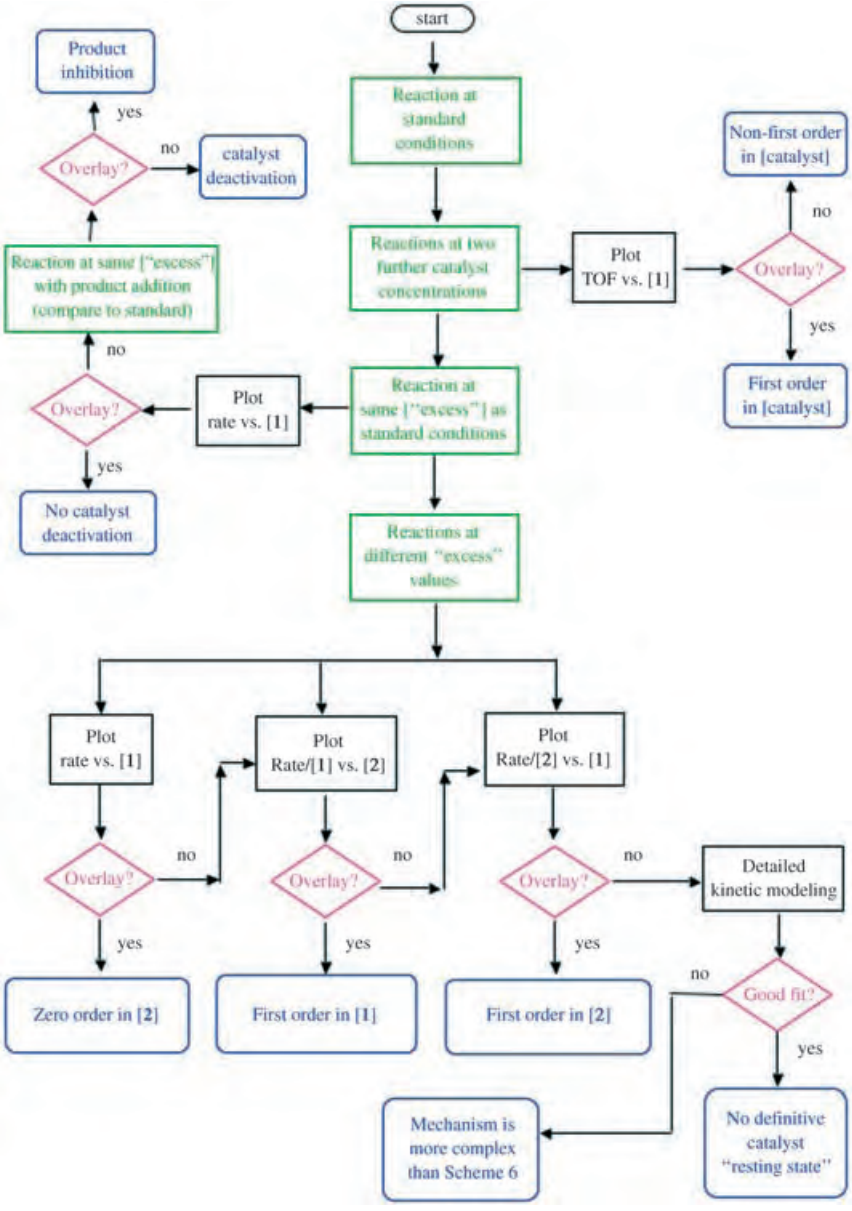
These examples illustrate several important points about reaction progress kinetic analysis. 1) Access to powerful in situ experimental tools enables new experimental protocols to be devised to collect accurate and plentiful data sets to streamline the data collection portion of the task. Understanding how the data are going to be manipulated also contributes to optimizing our experimental design. 2) Kinetics may be used to deconvolute a reaction system and even to propose new mechanistic possibilities. 3) The straightforward experimental effort and data manipulation of reaction progress kinetic analysis allows kinetics to be used at the outset of a mechanistic investigation rather than simply to confirm a mechanistic proposal.

The relationships found from the data interrogation do not depend on the mechanism shown in Scheme 6. The trends observed can be used to indicate the direction of other potential schemes, thus carrying out kinetic studies as a first—instead of a last—resort is good advice for the study of any new reaction.

 © 2005 Wiley-VCH Verlag GmbH & Co. KGaA, Weinheim

8. A Flow Chart for Kinetic Analysis of Catalytic Reaction Systems

A summary of what has been demonstrated in the examples discussed above can be illustrated by making a flow chart for the kinetic analysis of a reaction with two substrates hypothesized to follow the reaction mechanism shown in Scheme 6. Even with no proposed reaction mechanism in mind, this simple system can be used as the starting point, and the steps described in Scheme 10 can act as a guide to tackling kinetic analysis of any new reaction system. The experiments listed in the flow chart follow those described in the examples in this Review.



Scheme 10. Flow chart for carrying out kinetic analysis of a reaction with two substrates. The green boxes indicate experiments to be carried out, black boxes indicate plots to be constructed, magenta boxes are query points for determining whether manipulation of the data results in overlay between curves from reactions carried out under different conditions.

The analysis begins with the choice of a set of reaction conditions for the first experiment, including initial concentrations of substrates **1** and **2**, and catalyst concentration, at a fixed temperature that will remain constant through the series of experiments. This experiment will serve as the "standard conditions", and the experiments that follow will involve alterations in one or more of these conditions. Next the reactions can be carried out at two catalyst concentrations that are different from the standard conditions, and the graphical rate equation is plotted as turnover frequency (TOF) versus [**1**]. This helps us ascertain the order in the catalyst concentration. If the reaction is not first order in the catalyst concentration, then the simple mechanism of Scheme 1 is an imperfect description of all of the activities of the catalyst.

Next, at least one further experiment is carried out with the same value of ["excess"] as our standard conditions but different values of starting concentrations of **1** and **2**. A plot of these data in the form of the graphical rate equation of rate versus [**1**] will show whether or not the curves overlay. If they do, then catalyst deactivation or product inhibition is not a feature of these reactions. If they don't, further experiments are carried out with product addition to distinguish product inhibition from catalyst deactivation.

In the next step further reactions are carried out at values of ["excess"] different from that of the standard conditions. With these data, various graphical rate equations described in Section 7 can be tried. The goal is to find out if the data overlay in any of the different forms of the graphical rate equation and helps in determining whether the reaction exhibits simple integer order, or if it exhibits saturation kinetics in one or both of the two substrates.

If none of these plots result in overlay between the different experiments, then it is known that either the catalyst does not exhibit a definitive resting state in the mechanism of Scheme 6, or that the reaction mechanism itself is more complex. In this case, other measures must be used, including detailed quantitative kinetic modeling of the mechanism and other proposed mechanisms.

9. Summary

This Review has endeavored to illustrate the ways in which accurate in situ reaction progress data coupled with simple data manipulations can help to illuminate aspects of catalytic behavior. Particular focus has been placed on a graphical approach involving simple manipulations that aims to keep the situation close to the "story" of the molecules on their reaction pathway, without straying too far into the mathematical wilderness of quantitative kinetics. Reaction profiles hold a

 © 2005 Wiley-VCH Verlag GmbH & Co. KGaA, Weinheim

wealth of mechanistic information that we are challenged to reveal; it is hoped that the ideas discussed here will inspire chemists to begin to demand more from the data that are now so easily obtainable through in situ techniques.

Contributions to the experimental work presented here from co-workers and collaborators cited in the references are gratefully acknowledged. Valuable discussions with and/or a critical reading of the manuscript by the following people are gratefully acknowledged: Prof. Stephen L. Buchwald, Eric Strieter, Prof. Eric N. Jacobsen, Prof. Andreas Pfaltz, Dr. Suju P. Mathew, Hiroshi Iwamura, Dr. Joel le Bars, Prof. Stanley M. Roberts, Dr. Emma Emanuelsson, Dr. Martin Klussmann, Dr. David H. Wells, Jr., Dr. Frederic G. Buono, Prof. William Tolman, Dr. Brian G. Cox, Dr. Steve Eyley, Dr. Marijan Stefinovic, Dr. Yongkui Sun, Dr. Thorsten Rosner, Lars P. C. Nielsen, Prof. Michael J. Krische, Prof. Robert. G. Bergman, and Prof. Athel Cornish-Bowden. Research funding from the EPSRC/DTI ("From Micrograms to Multikilos"), the Max-Planck-Gesellschaft Sonderprogramm zur Förderung hervorragender Wissenschaftlerrinnen, Pfizer Global Research, Merck Research Laboratories, AstraZeneca, Mitsubishi Pharma, and Mettler-Toledo Autochem is gratefully acknowledged.

Received: November 8, 2004

[1] H. Lineweaver, D. Burk, *J. Am. Chem. Soc.* **1934**, *56*, 658.
[2] *Chem. Eng. News* **2003**, *81*, 25.
[3] L. Michaelis, M. Menten, *Biochem. Z.* **1913**, *49*, 1333.
[4] The Michaelis Menten rate law was conceived first by Victor Henri (V. Henri, *C. R. Hebd. Seances Acad. Sci.* **1902**, *135*, 916). A linearized form of the Michaelis–Menten Equation was published by Hanes two years before the Lineweaver–Burk paper[1] (C. S. Hanes, *Biochem. J.* **1932**, *26*, 1406). The Lineweaver–Burk and other related graphical methods are covered in detail in enzyme kinetics textbooks. For an especially lucid discussion of both the history and the use of graphical methods in general and the opportunities and limitations of such methods, see A. Cornish-Bowden, *Enzyme Kinetics*, 3rd ed., Portland, London, **2004**.
[5] Extensive graphical methods have been developed, primarily for studying enzyme kinetics, for consideration of reaction complexities such as product inhibition by using a classical kinetic approach, which entailed a concomitant increase in the number of required experiments. The textbook cited in Ref. [4] provides an excellent background to these methods.
[6] Rate may be calculated from (concentration, time) data sets by fitting the data to an arbitrary function (e.g., a 9th order polynomial) and then differentiating this function to obtain (rate, time) data. Care must be taken to insure that the fit is accurate to obtain an accurate rate profile.
[7] M. Ropic, D. G. Blackmond, unpublished results.
[8] T. Rosner, M. Baumann, A. Togni, D. G. Blackmond, unpublished results.
[9] S. Eyley, personal communication.
[10] J. LeBars, D. G. Blackmond, unpublished results.
[11] J. S. Mathew, D. G. Blackmond, unpublished results.
[12] A. Soheili, J. Albaneze-Walker, J. A. Murry, P. G. Dormer, D. L. Hughes, *Org. Lett.* **2003**, *5*, 4191.
[13] The use of a corroborating technique also helps check the validity of the method when the question of complications other than side reactions arises. For example, the extent of contribution to the overall signal from physical processes such as heat of mixing or heat of precipitation may be quantified by using reaction calorimetry, while by using FTIR spectroscopy the possibility of an inhomogeneous solution layer adjacent to the IR window may be explored.
[14] For a review, see: M. Studer, H.-U. Blaser, *Adv. Synth. Catal.* **2003**, *345*, 45.
[15] F. Bohnen, A. Gomez, D. G. Blackmond, unpublished results.
[16] If k_2 is small compared to k_{-1}, the Michaelis parameter K_{MM} in Equation (1) is identical to the inverse of the binding constant $K_1 = k_1/k_{-1}$.
[17] F. G. Helfferich, *Kinetics of Homogeneous Multi-Step Reactions*, Elsevier, Amsterdam, **2001**, chap 7.2.
[18] The concentration of **2** is strictly given by: [**2**] = ["excess"] + [**1**] + [**5**]; however, [**5**] may be neglected under typical catalytic conditions where [**5**] $\ll$ [**1**] and [**5**] $\ll$ ["excess"]. This consideration helps to set a lower limit on ["excess"]. In general, practical values of ["excess"] should be at least an order of magnitude greater than the catalyst concentration.
[19] a) S. Colonna, H. Molinari, S. Banfi, S. Juliá, J. Masana, A. Alvarez, *Tetrahedron* **1983**, *39*, 1635; b) S. Banfi, S. Colonna, H. Molinari, S. Juliá, J. Guixer, *Tetrahedron* **1984**, *40*, 5207, and references therein; c) R. W. Flood, T. P. Geller, S. A. Petty, S. M. Roberts, J. Skidmore, M. Volk, *Org. Lett.* **2001**, *3*, 683.
[20] S. P. Mathew, S. Gunathilagan, D. G. Blackmond, unpublished results.
[21] The graphical tools described here may only be used where the steady-state approximation applies. For many catalytic reactions this rules out data at the very start of the reaction if an induction period is present (see Section 7.1.1). By definition, the steady-state approximation breaks down for the last few turnovers of the reaction, where the concentration of the catalytic intermediate species approaches that of the substrates being consumed and the parameter ["excess"] is no longer constant (see discussion in Ref. [18]). These graphical tools are generally recommended for use on reaction progress data between 15 and 85% conversion of the limiting substrate.
[22] Figure 8a was redrawn in a different form from T. Rosner, J. LeBars, A. Pfaltz, D. G. Blackmond, *J. Am. Chem. Soc.* **2001**, *123*, 1848.
[23] J. LeBars, C. P. Stevenson, E. N. Jacobsen, D. G. Blackmond, unpublished results.
[24] Reviews: R. F. Heck, *Org. React.* **1982**, *27*, 345–390; A. de Meijere, F. E. Meyer, *Angew. Chem.* **1994**, *106*, 2473–2506; *Angew. Chem. Int. Ed. Engl.* **1994**, *33*, 2379–2411; W. Cabri, I. Candiani, *Acc. Chem. Res.* **1995**, *28*, 2–7.
[25] a) M. Tokunaga, J. F. Larrow, F. Kakiuchi, E. N. Jacobsen, *Science* **1997**, *277*, 936; b) J. M. Keith, J. F. Larrow, E. N. Jacobsen, *Adv. Synth. Catal.* **2001**, *343*, 109.
[26] For a detailed kinetic analysis of this reaction, see L. P. C. N. Nielsen, C. P. Stevenson, D. G. Blackmond, E. N. Jacobsen, *J. Am. Chem. Soc.* **2004**, *126*, 1360.
[27] Figure 9a was constructed from the data in: T. Rosner, J. LeBars, A. Pfaltz, D. G. Blackmond, *J. Am. Chem. Soc.* **2001**, *123*, 1848.
[28] A. F. Littke, G. C. Fu, *J.Am. Chem. Soc.* **2001**, *123*, 6989.
[29] C. Ellis, D. G. Blackmond, unpublished results.
[30] The high *ee* value achieved in this reaction justifies the simplification of the treatment to include only one catalytic cycle.
[31] a) A. H. M. deVries, J. F. G. A. Jansen, B. L. Feringa, *Tetrahedron* **1994**, *50*, 4479; b) C. Bolm, M. Ewald, M. Felder, *Chem. Ber.* **1992**, *125*, 1205.
[32] H. Iwamura, F. G. Buono, D. G. Blackmond, unpublished results.
[33] H. Iwamura, F. G. Buono, D. G. Blackmond, unpublished results.
[34] The data were fit using the Solver program in Excel. Statistical analysis was performed using Solvstat.xls, a macro program for

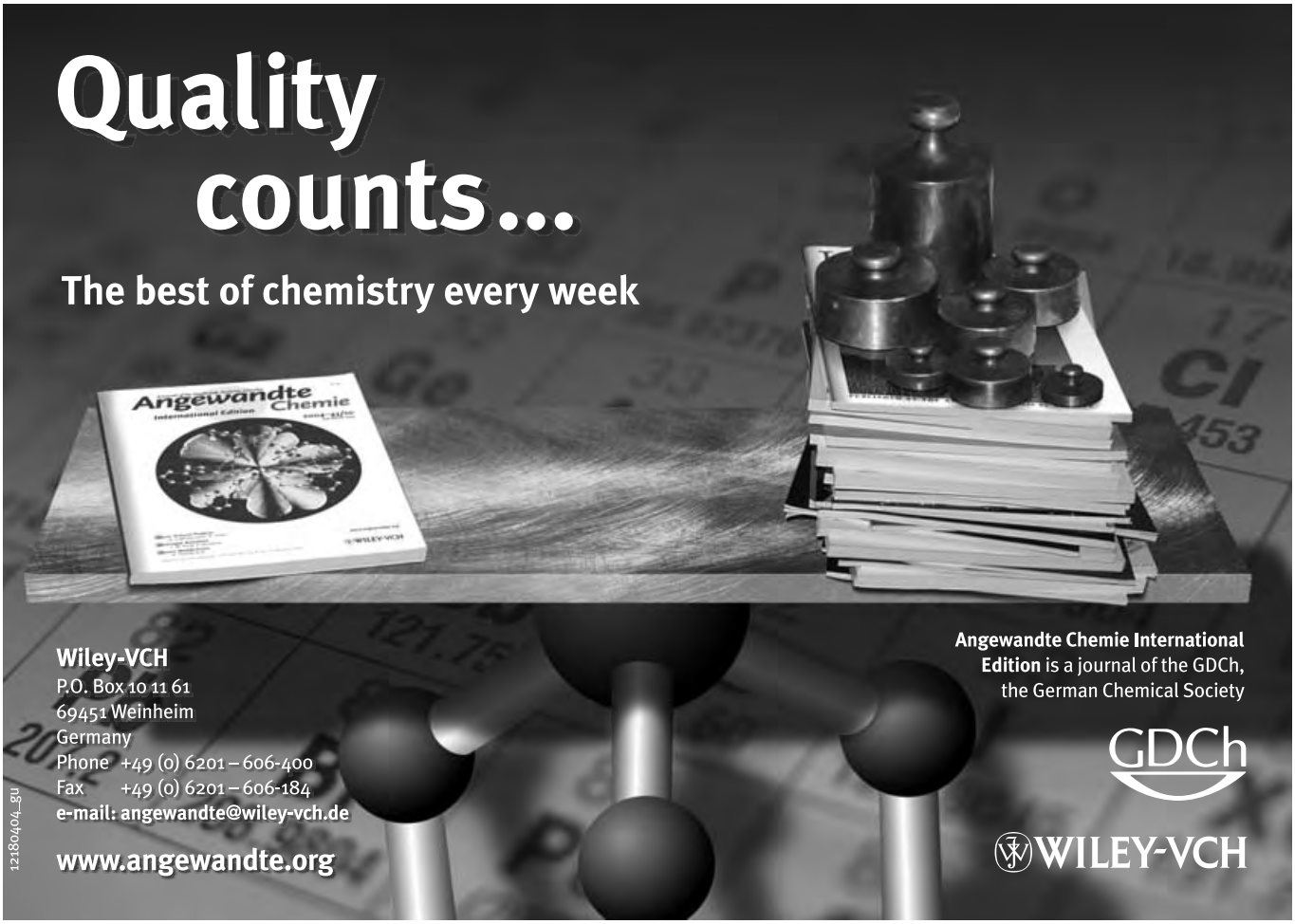
 © 2005 Wiley-VCH Verlag GmbH & Co. KGaA, Weinheim

use with Excel that is available with E. J. Billo, *Excel for Chemists*, Wiley-VCH, New York, **2001**.

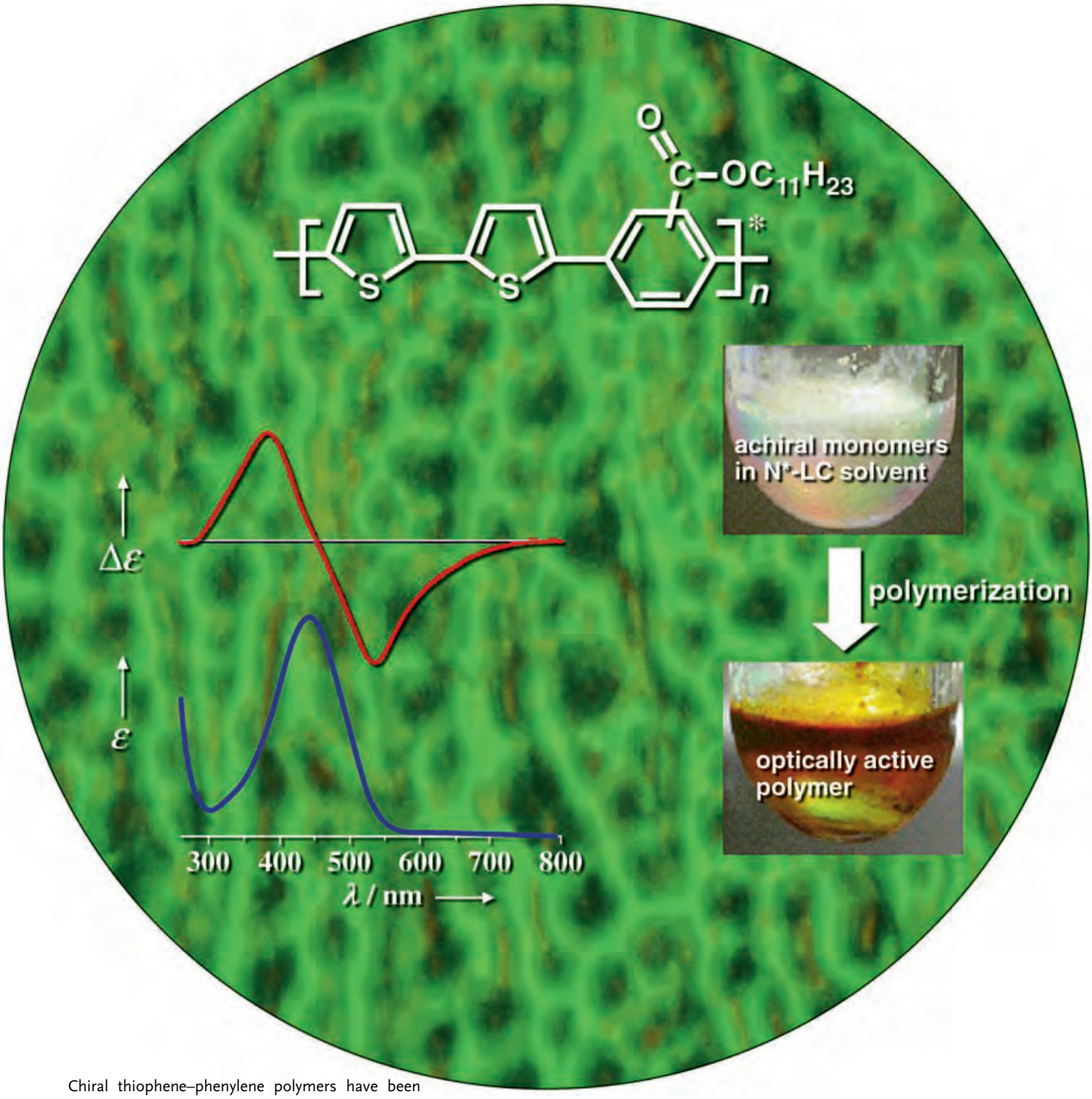
[35] The left side of Equation (16) has the units of inverse time, and therefore it appears the turnover frequency should have no concentration dependence. A closer examination reveals that the units of TOF are: $\text{M(substrate)} \times \text{M(catalyst)}^{-1} \times \text{time}^{-1}$. While the units of molarity cancel these are, in reality, molarities of two different substances. The right hand side of Equation (16) shows clearly that TOF exhibits a concentration dependence.

[36] For a lucid discussion of the concept of the rate-limiting step, see K. J. Laidler, *J. Chem. Educ.* **1988**, *65*, 250.

[37] For examples of kinetic modeling studies of reactions exhibiting more complex mechanisms, see: a) T. Rosner, P. J. Sears, W. A. Nugent, D. G. Blackmond, *Org. Lett.* **2000**, *2*, 2511; b) D. G. Blackmond, C. R. McMillan, S. Ramdeehul, A. Schorm, J. M. Brown, *J. Am. Chem. Soc.* **2001**, *123*, 10103; c) F. G. Buono, P. J. Walsh, D. G. Blackmond, *J. Am. Chem. Soc.* **2002**, *124*, 13652; also see Ref. [26].



Communications



Chiral thiophene–phenylene polymers have been prepared from achiral monomers by a Stille polycondensation reaction using a chiral nematic liquid crystal as solvent. The chirality of the polymers is thought to derive from the asymmetry produced by the chiral liquid-crystalline medium during polymerization. For more details, see the Communication by H. Goto and K. Akagi on the following pages.

 © 2005 Wiley-VCH Verlag GmbH & Co. KGaA, Weinheim DOI: 10.1002/anie.200462859

Chiral Polymerization

Optically Active Conjugated Polymers Prepared from Achiral Monomers by Polycondensation in a Chiral Nematic Solvent**

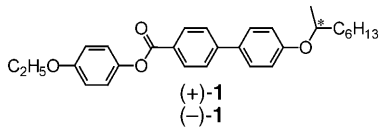
*Hiromasa Goto and Kazuo Akagi**

Asymmetric synthesis is one of the most intriguing research fields in chemistry. Methods for obtaining optically active compounds, such as enantioselective syntheses,[1] asymmetric autocatalytic reactions,[2] asymmetric autoinductions,[3] asymmetric transformations,[4] as well as absolute asymmetric reactions,[5] have been extensively studied. Many approaches to produce stable optically active polymers have also been proposed, such as the introduction of a bulky substituent to a vinyl polymer[6] or an optically active substituent to the polymer side chain,[7] and the induction of chiroptical properties.[8] The synthesis of chiral polymers in an isotropic organic solvent such as tetrahydrofuran (THF), benzene, or diethyl ether requires the use of a chiral monomer or a chiral catalyst.

Liquid crystals are unique in that they exhibit both crystal-like birefringence and fluid behavior. Chiral nematic liquid crystals (N*-LCs) have a quasi-layer structure in which the director of each layer is gradually rotated to produce helicity over several layers. Although liquid crystals exhibit fluid behavior, the crystal-like structural order of N*-LCs can effectively provide chiral order in the propagating step of a polymerization reaction, in contrast to chiral isotropic liquids. However, polymerization reactions performed in liquid-crystal media have received little attention as the liquid-crystalline phase is generally lost upon the addition of a non-liquid-crystal compound.

Helical polyacetylenes with chiroptical properties have been synthesized by using a N*-LC as the reaction medium.[9] The helical polyacetylene prepared in this way exhibited relatively stable chirality as a result of its insolubility and infusibility. In the case of chiral polybithiophene, which was prepared from achiral bithiophene by electrochemical polymerization in a N*-LC electrolyte, the polymer displayed a split Cotton effect in circular dichroism (CD) spectroscopy as well as optically active electrochromism.[10a] N*-LCs are thus considered to provide an effective chiral environment for the control of polycondensation reactions.[10] Herein, we report the use of a nematic liquid crystal as an asymmetric solvent for chiral polymerization and that successful polymerization is dependent on careful consideration of the affinity of the monomer for the N*-LC as well as its solubility therein. We selected a monomer that displays a good affinity for chiral nematic liquid crystals and prepared a stable N*-LC that is suitable for the polycondensation reaction of aromatic compounds and exhibits a chiral nematic phase at around 90 °C as the reaction solvent. The addition of the monomer and the production of the resulting polymer do not affect the liquid crystallinity of the N*-LC reaction medium in this system.

Chiral nematic liquid-crystalline compounds (+)-**1** and (−)-**1**, which comprise a three-ring core with optically active



(+)-**1**
(−)-**1**

terminal alkyl groups, were prepared as the chiral solvents for the polycondensation reactions. The chiral nematic liquid-crystal phase of these compounds is stable over a wide temperature range and remains stable upon the addition of aromatic compounds such as dibromobenzene and dibromothiophene. The phase-transition behavior of these compounds was determined by differential scanning calorimetry and polarizing optical microscopy (POM) as K 97 (72) N* 135 (133) BP (134) Iso* (K = crystal, N* = chiral nematic, BP = blue phase, Iso* = isotropic; parentheses denote the transition temperature in the cooling process). Both (+)-**1** and (−)-**1** exhibit a frustrated platelet texture of a blue phase and the oily streak texture of a chiral nematic liquid-crystal phase, as observed by POM (see Figure 1 a, b). Generally, high shear stress breaks the helical structure of the N*-LC to result in a nematic phase with no helical structure. However, chiral

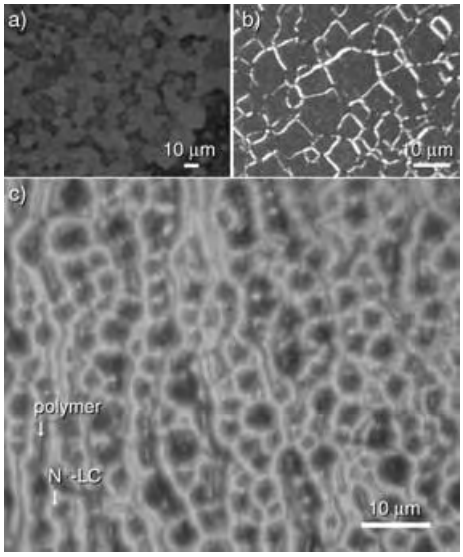


Figure 1. Polarized optical microscopy images: a) Platelet texture of cubic blue phase of (+)-**1** at 134 °C; b) oily streak texture of chiral nematic phase of (+)-**1** at 120 °C; c) presence of polymer mass, (−)-**P2**, and matrix N*-LC (oily streaks) in the reaction mixture at 93 °C after reaction for 24 h.

[*] Dr. H. Goto, Prof. Dr. K. Akagi
Tsukuba Research Center for Interdisciplinary Materials Science (TIMS)
Institute of Materials Science
University of Tsukuba
Tsukuba, Ibaraki 305-8573 (Japan)
Fax: (+81) 29-855-7440
E-mail: akagi@ims.tsukuba.ac.jp

[**] This work was supported by Grants-in-Aid for Scientific Research from the Ministry of Education, Culture, Sports, Science, and Technology, Japan.

 © 2005 Wiley-VCH Verlag GmbH & Co. KGaA, Weinheim

nematic liquid crystallinity was confirmed to be maintained under stirring at 80 rpm using a Teflon-coated 1-cm magnetic stirrer bar in a 1.7-cm-diameter Schlenk flask.

Two types of chiral polymer were synthesized in this study: 1) a polymer with chiral substituents prepared in an isotropic organic solvent (THF) and 2) a polymer with no chiral substituents prepared in a chiral nematic liquid crystal as solvent. The syntheses of the polymers through a C–C bond-forming Stille polycondensation reaction are shown in Scheme 1. Brominated chiral benzene derivatives **3** were treated with bis(trimethyltin)-substituted bithiophene derivative **2** in THF under an argon atmosphere in the presence of $[Pd(PPh_3)_4]$ as catalyst. After 24 h reaction, the mixture was washed with methanol and then acetone to afford the aromatic conjugated polymers with chiral substituents, (+)-**P1** (from **2** and (+)-**3**) and (−)-**P1** (from **2** and (−)-**3**).

Polymerization in the chiral nematic medium was performed by placing 1 g of **1** ((+)-**1** or (−)-**1**) in a small Schlenk flask under argon flow at 93 °C. Iridescence was confirmed due to the selective reflection of light, then **2** (0.1 g, 0.2 mmol) was added and dissolved in the medium. Achiral 2,5-dibromobenzoic acid undecyl ester (**4**; 87 mg, 0.2 mmol) was then added to the mixture and stirred at exactly 80 rpm for 30 min before the addition of a catalytic amount of $[Pd(PPh_3)_4]$ (3 mg, 0.0026 mmol) to initiate the polycondensation. Stirring was continued at 80 rpm to preserve the chiral nematic liquid crystallinity, and the temperature was maintained at exactly 93 °C during the course of the reaction. Chiral nematic liquid crystallinity was confirmed by monitoring the selective reflection of the mixture during the course of the reaction. Although the transition temperature of the chiral nematic liquid-crystalline phase may be depressed by the introduction of "impurities", namely the monomer, catalyst, or the resulting polymer, this mixture was confirmed to maintain its chiral nematic liquid-crystalline phase at 93 °C. After 24 h reaction, the visible selective reflection of the N*-LC in the reaction flask again confirmed that the chiral nematic liquid-crystalline phase was maintained in the mixture. The mixture in the Schlenk flask also gave rise to a fluorescent emission from the presence of a fluorescent polymeric product in the N*-LC solvent. Figure 1c shows the POM image of the reaction mixture at 93 °C. Polymer fractions of higher molecular weight which were insoluble in the N*-LC medium were observed as insoluble orange masses surrounded by the oily streak texture of the N*-LC.

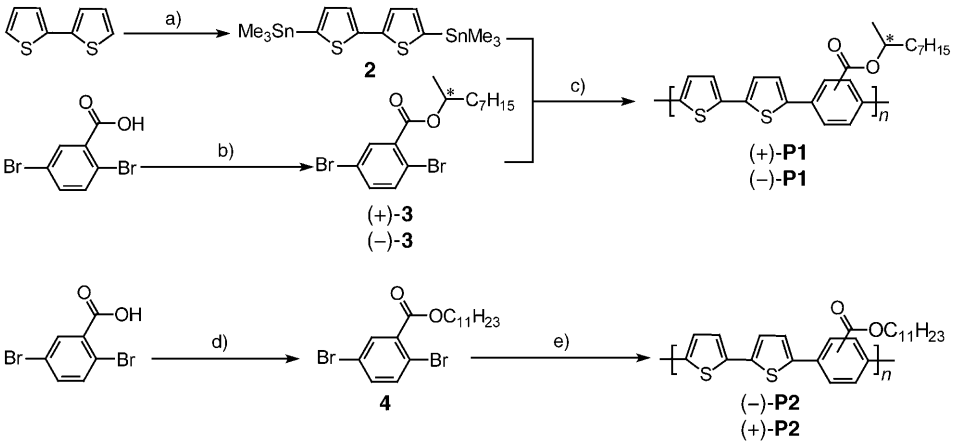
The reaction mixture was allowed to cool to room temperature and then dissolved in a minimal amount of THF, then the solution was poured into a large volume of acetone to dissolve and completely remove **1** (N*-LC) and the fractions of low molecular weight. The product, which was insoluble in acetone, was further washed in acetone and then methanol to leave a red solid that was soluble in THF and $CHCl_3$. The polymers prepared in media (−)-**1** and (+)-**1** are abbreviated (+)-**P2** and (−)-**P2**, respectively. The directions of optical rotation of the polymers were the opposite of those of the N*-LC solvent used.

The results of both sets of polymerization reactions are summarized in Table 1. The number-average molecular weights of (+)-**P1** and (−)-**P1** are 3500 and 3200, respectively, while those of (+)-**P2** and (−)-**P2** are 7000 and 6100, respectively. The quantum efficiency (Φ) of both polymers in $CHCl_3$ was determined as 23 %.

Table 1: Results of polymerization experiments.

Polymer	Monomer	Solvent	Yield [%]	M_n[a]	M_w[b]	MWD[c]	DP[d]	Φ [%][e]
(+)-**P1**	**2**, (+)-**3**	THF	71	3500	4900	1.4	8 (24)	23
(−)-**P1**	**2**, (−)-**3**	THF	75	3200	4700	1.4	8 (24)	23
(+)-**P2**	**2**, **4**	(−)-**1**	86	7000	12500	1.8	16 (48)	23
(−)-**P2**	**2**, **4**	(+)-**1**	85	6100	9200	1.5	14 (42)	23

[a] Number-average molecular weight evaluated relative to a polystyrene (PS) standard. [b] Molecular weight evaluated relative to PS standard. [c] Molecular weight distribution relative to PS standard. [d] Degree of polymerization relative to PS standard. [e] Fluorescence quantum yield evaluated using quinine sulfate in 1.0 M sulfuric acid as standard.



Scheme 1. Synthetic routes to the polymers. a) *n*BuLi, THF, then Me_3SnCl; b) (+)- or (−)-nonanol, DEAD, PPh_3, THF; c) $[Pd(PPh_3)_4]$, THF; d) $C_{11}H_{23}OH$, DEAD, PPh_3, THF; e) **2**, $[Pd(PPh_3)_4]$, (+)-**1** or (−)-**1**. DEAD = diethyl azodicarboxylate, * = stereogenic center.

 © 2005 Wiley-VCH Verlag GmbH & Co. KGaA, Weinheim

Figure 2 shows the UV/Vis absorption and CD spectra of solutions of the polymers in $CHCl_3$. Polymers (+)-**P1** and (−)-**P1** exhibit maxima (λ_{max}) at 418 nm in the UV/Vis spectrum and CD signals in the region that correspond to the

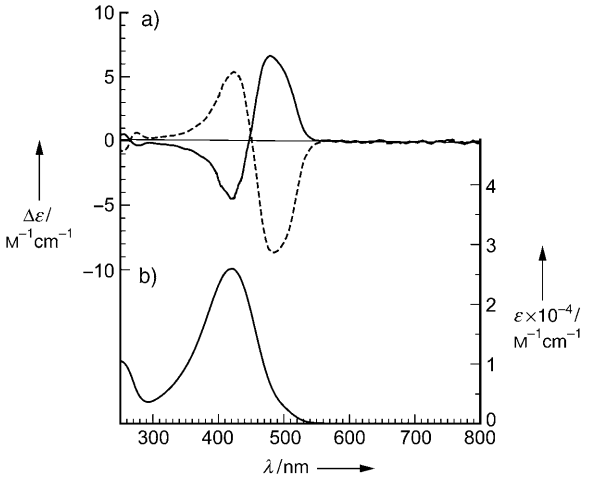


Figure 2. a) Circular dichroism and b) UV/Vis absorption spectra of (+)-**P1** (——) and (−)-**P1** (----) in $CHCl_3$.

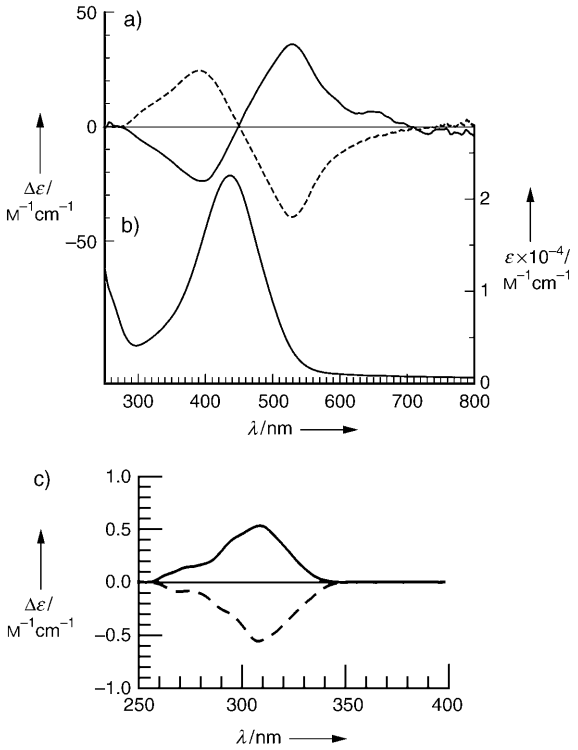


Figure 3. a) CD and b) UV/Vis spectra of (+)-**P2** (——) and (−)-**P2** (----) in $CHCl_3$. c) CD spectra of N*-LC solvents (+)-**1** (——) and (−)-**1** (----) measured as solutions in $CHCl_3$.

conjugated double bonds of the polymer main chain. They also display mirror-image, exciton-coupled, Davydov-split CD signals at two exciton levels. This splitting is not detected by absorption spectroscopy which indicates an interchain origin of the optical activity and suggests that the polymer has helical interchain organization. Such chiral aggregation of the polymer main chains bears a resemblance to the form of the N*-LC.[7b] Polymer (+)-**P1** displays a positive first and negative second Cotton effect, whereas (−)-**P1** exhibits a negative first and a positive second Cotton effect. This result indicates that the transition moments of (+)-**P1** and (−)-**P1** are clockwise and counterclockwise, respectively.[11] The polymers with chiral substituents have a stable optical activity which is attributable to a stabilization of the chiral structure of the polymer main chain by the ester groups.

Polymers (+)-**P2** and (−)-**P2**, which were prepared in the N*-LC solvent, display absorbance maxima at 436 nm that tail off toward 800 nm. The CD bands at 380 and 530 nm of solutions of the polymers in $CHCl_3$ are assigned to the bisignate exciton-coupled band associated with the absorption band at 436 nm, and a similar bisignate Cotton effect as seen for **P1** is observed (Figure 3). This result indicates that the transition moments of (+)-**P2** and (−)-**P2** are also oriented clockwise and counterclockwise, respectively. The CD spectrum of (−)-**P2** in THF has almost the same shape as that of (−)-**P2** in chloroform. The expected mirror-image relationship between (+)-**P2** and (−)-**P2** is not caused by the chiral compound that was employed as the solvent in this case because the Cotton effect of **1** is only observed at shorter wavelengths ((+)-**1**: CD ($CHCl_3$): λ_{max} ($\Delta\varepsilon$) = 308 nm (+0.53 $M^{-1}cm^{-1}$); (−)-**1**, CD ($CHCl_3$): λ_{max} ($\Delta\varepsilon$) = 308 nm (−0.55 $M^{-1}cm^{-1}$)).

The polymers **P2** prepared in the N*-LC medium have an optically active structure in isotropic solution. The chiral structure developed during polymerization was preserved even after dissolution and washing, probably as a result of the steric hindrance of the ester groups at the 2-position of the benzene rings which stabilizes the chiral structure of the polymer. To examine the origin of chirality of the polymer, a model compound of low molecular weight was prepared by a Stille reaction. 5-Trimethylstannyl-2,2′-bithiophene[12] and compound **4** were coupled in the same manner as in the preparation of (−)-**P2** to yield the bithiophene–phenylene–bithiophene compound **P3**. This model polymer exhibited no Cotton effect in the CD spectrum which implies that the axial chirality of **P3** was not produced by the N*-LC reaction medium. Thus, the optical activity of **P2** may be derived from chiral aggregation, not axial chirality. However, the optical activity of **P2** may alternatively be caused by a polymer effect such as small changes in one direction in the dihedral angle between repeat monomer units, which would also produce a Cotton effect. Also, high optical rotations in chloroform are obtained for (−)-**P2** ($[\alpha]_D^{20} = -910.1°$) and (+)-**P2** ($[\alpha]_D^{20} = 762.5°$) relative to the lower molecular weight polymers (−)-**P1** ($[\alpha]_D^{20} = -71.8°$) and (+)-**P1** ($[\alpha]_D^{20} = 88.4°$). This result suggests that the polymer effect is important in this system. Although the origin of the Cotton effect cannot be clarified completely on the basis of the results for **P3**, which exhibits neither polymer effects nor aggregation, the experimental results strongly imply that the chirality of **P2** derives from chiral aggregation rather than the helical structure of the main chain (axial chirality). However, in the helical aggregation state of the polymer, several hierarchical levels of chiral structure are plausible, including helical main-chain confor-

 © 2005 Wiley-VCH Verlag GmbH & Co. KGaA, Weinheim

mations. In this case, the main chain plays a role of a virtual chiral axis.[7b]

Polymers (+)-**P1** and (−)-**P1** exhibit circularly polarized luminescence (CPL) at 500 nm in solution in chloroform, with g_{em} values of -1.1×10^{-3} and $+8.6\times10^{-4}$ at an excitation wavelength $\lambda_{ex}=380$ nm. The degree of circular polarization in the emission is defined by $g_{em}=(I_L-I_R)/[(I_L+I_R)/2]=\Delta I/I=V_{AC}/V_{DC}$, in which I denotes the intensity, subscripts L and R denote left and right, respectively, and V_{DC} and V_{AC} are the values of measured fluorescence and CPL, respectively. Polymers (+)-**P1** and (−)-**P1** display photoluminescence (PL) at 540 nm and CPL centered at 556 nm. Solutions in $CHCl_3$ of (+)-**P2** and (−)-**P2** prepared in the chiral nematic liquid-crystal medium display bisignate and opposite CPL signs ($\lambda_{ex}=380$ nm): $g_{em}=+3.17\times10^{-3}$ (at 620 nm) for (+)-**P2** and $g_{em}=-2.40\times10^{-3}$ (at 620 nm) for (−)-**P2**, as shown in Figure 4. Polymerization under vigorous stirring at 200 rpm

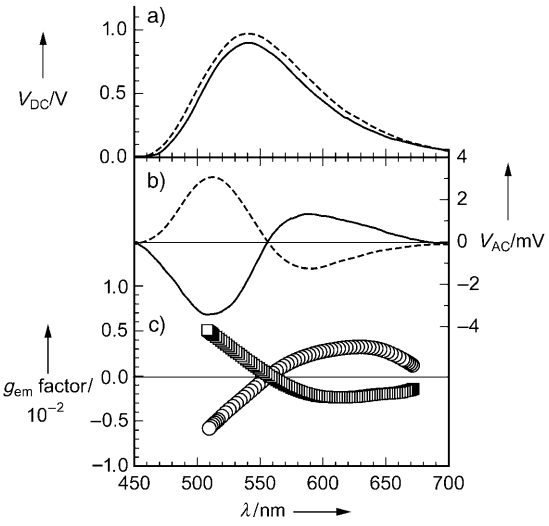


Figure 4. a) PL and b) CPL spectra, and c) g_{em} factors of (+)-**P2** (——, ○) and (−)-**P2** (-----, □) in $CHCl_3$.

produced polymers that exhibit no Cotton effect in CD measurements, which is attributable to the loss of the helical structure of the chiral nematic liquid-crystalline phase as a result of excessive shear stress and growth of the polymer in the nonhelical medium. Green et al. showed that chiral solvents such as (*R*)-2-chlorohexane can transfer chirality to the poly(*n*-hexylisocyanate) main chain of an otherwise achiral polymer.[13] In the present experiments, the chiral structure of the polymer could not be produced when the reaction solvent was in an isotropic or nonhelical state. This is probably a result of the fact that the chirality-inducing property of solvent **1** in the nonhelical state is insufficient to induce chiral aggregation of **P2**, whereas the solvent in a chiral nematic liquid-crystalline mesophase with helical architecture effectively affords a polymer with chiral structure during the polymerization process.

Heating of the chiral compounds should result in racemization as a result of the random rotation of polymer main chains and a loss of chiral aggregation. To examine this process, (−)-**P1** and (−)-**P2** were heated in cumene, a solvent of high boiling point. Optical spectra were recorded after the samples had been heated once to 150 °C and then allowed to cool to 25 °C. Heat treatment of (−)-**P1** at 150 °C for 15 min under an argon atmosphere resulted in a weakening, but not complete disappearance, of the Cotton effect. On the other hand, the intensities of the absorption bands of the polymer increased with heating, accompanied by a shift of the maxima to longer wavelengths and an increase in ε values. Figure 5

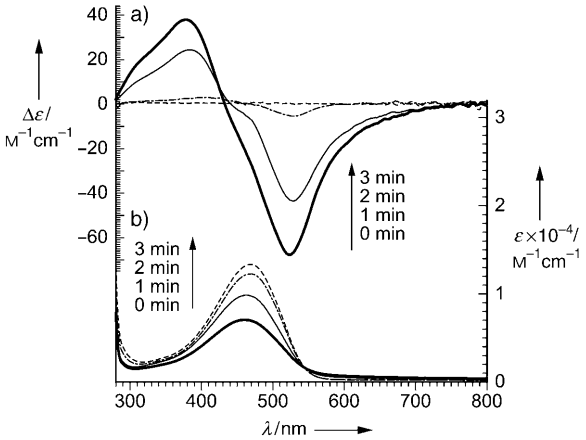


Figure 5. a) CD spectra and b) UV/Vis absorption spectra of (−)-**P2** after heating in cumene for 0, 1, 2, and 3 minutes at 150 °C. These spectra were recorded at 25 °C.

shows the UV/Vis and CD spectra of (−)-**P2** in cumene under an argon atmosphere before and after heat treatment. Heating the sample at 150 °C for 3 min can be seen to cause a shift of the absorption maxima from $\lambda=458$ to 469 nm and an increase in ε (but decrease in $\Delta\varepsilon$), along with a shift of the CD peaks to longer wavelengths. The heated sample of (−)-**P2** no longer displayed a Cotton effect, although the UV/Vis absorption intensities increased. This result is thought to reflect deaggregation of the polymer, free rotation of the main chain, and a decrease in the average dihedral angle in the main chain during heating. Random rotation of the monomer repeat unit along the polymer main chain as a result of heating is considered to improve the average coplanarity of the polymer measured at 25 °C and increase the effective conjugation length, which leads to an increase in the absorption intensity and a red shift of the absorption peaks. The change in the CD intensities of the annealed polymer in cumene is irreversible.

Figure 6 shows the PL and CPL spectra and g_{em} factors for (−)-**P2** before and after heating, with the spectra for (−)-**P2** in $CHCl_3$ shown for reference (thick line). The minima and maxima in the PL spectrum of the polymer in solution in cumene occured at longer wavelengths than in solution in $CHCl_3$, and heating reduced the intensity of the CPL. The emission peaks (minima/maxima) in the CPL spectrum also shifted slightly to longer wavelengths upon heat treatment. The g_{em} factors of (−)-**P2** also decreased upon heating. Heat treatment of (−)-**P2** at 150 °C for 3 min resulted in the loss of the CPL signal, although the polymer exhibited photoluminescence. This CPL result is suggestive of deaggregation of

 © 2005 Wiley-VCH Verlag GmbH & Co. KGaA, Weinheim

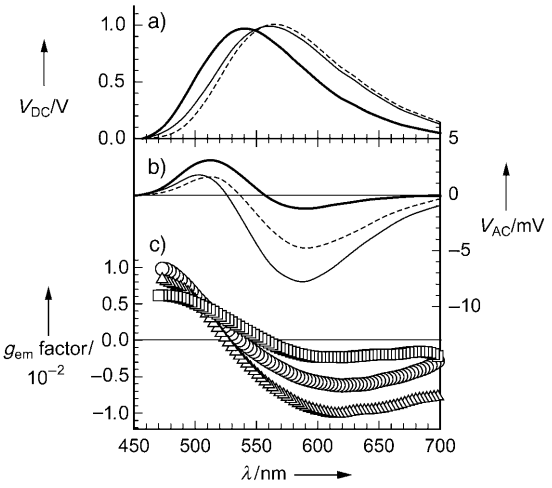


Figure 6. a) PL and b) CPL spectra, and c) g_{em} values of (−)-**P2** in $CHCl_3$ (unheated; bold line, □), in cumene (before heating; ——, △), and in cumene after heating at 150 °C for 1 min (-----, ○). These spectra were obtained at 25 °C.

the polymer and swelling in the solvent upon heating. The chirality of the polymers (+)-**P2** and (−)-**P2**, which contain no chiral substituents, is thus considered to derive from the asymmetry produced by the chiral liquid-crystal medium during polymerization. No chiral molecules reacted with the monomer during the polymerization process, and the N*-LC employed as a solvent functioned only as the reaction medium. In general, the synthesis of chiral polymers requires the introduction of a chiral substituent or the use of a chiral catalyst. The present N*-LC medium thus provides a molecular matrix with central chirality for polymerization, and growth of the polymer in this three-dimensional chiral medium results in the chiral aggregation. The chiral nematic liquid-crystal phase has a chiral helical superstructure with a long helical pitch (> 400 nm), and the small twist angle between quasi-layers of the liquid crystal at the molecular level produces a strong Cotton effect in the CD and CPL spectra of the resultant polymers. The polymerization mechanism has an affinity with the so-called "sergeant-and-soldier" system,[14] as the small asymmetric environment within the quasi-layers of the N*-LC gives consistent optical activity in the resultant polymers. In other words, the "asymmetric field effect" induces the chirality of the polymer aggregation.

In summary, a reaction medium comprised of a chiral nematic liquid crystal leads to chiral aggregation of the conjugated polymer product (as observed by CPL) during the polymerization process, and the aggregation is maintained after visual dissolution of the polymer in chloroform or THF. As enzymes (proteins) form specific stereostructures in which the spacing of the folded protein main chains produce a spatially asymmetric reaction field, the approach proposed in this study may provide a model for biological reactions such as the synthesis of biomolecules in asymmetric environments in living organisms. The results of this study also demonstrate the utility of the chemistry of reaction media.

Experimental Section

All experiments were performed under an argon atmosphere using Schlenk/vacuum line techniques. Tetrahydrofuran (THF), ethanol, acetone, and ether were distilled prior to use. High purity chloroform (Wako) was used without purification for optical measurements of the polymers. ^{1}H NMR spectra were measured in $CDCl_3$ using a Bruker AV-600 FT-NMR spectrometer. Chemical shifts are represented in parts per million downfield from tetramethylsilane (TMS) as an internal standard. Infrared spectra were measured with a JASCO FT-IR 550 spectrometer as KBr disks. Optical absorption spectra were measured in quartz cells at room temperature using a HITACHI U-2000 spectrometer. CD spectra were obtained with a JASCO J-720 spectrometer. PL and CPL measurements of the polymers were performed with a JASCO CPL 200S spectrometer. Phase-transition temperatures were determined using a TA Instrument Q-100 differential scanning calorimeter with a constant heating/cooling rate of 10 °C min^{-1}, and texture observations were made using a Nikon ECLIPS E400 POL polarizing microscope equipped with a Linkam TM 600PM heating/cooling stage. Temperature calibration of the heating stage was carried out by using DSC. The molecular weights of polymers were determined by gel permeation chromatography on a Shodex A-80 M column with a JASCO HPLC 870 UV detector using THF, with the instrument calibrated with a polystyrene standard.

Received: December 9, 2004
Revised: February 22, 2005
Published online: June 1, 2005

Keywords: chirality · circular dichroism · circularly polarized luminescence · liquid crystals · polymerization

[1] a) N. Cramer, S. Laschat, A. Baro, H. Schwalbe, C. Richter, *Angew. Chem.* **2005**, *117*, 831 – 833; *Angew. Chem. Int. Ed.* **2005**, *44*, 820 – 822; b) V. Athawale, M. Athawale, N. Manjrekar, *J. Polym. Mater.* **2004**, *21*, 305 – 313; c) P. S. Baran, J. M. Richter, D. W. Lin, *Angew. Chem.* **2005**, *117*, 615 – 618; *Angew. Chem. Int. Ed.* **2005**, *44*, 609 – 612; d) M. M. Ahmed, B. P. Berry, T. J. Hunter, D. J. Tomcik, G. A. O'Doherty, *Org. Lett.* **2005**, *7*, 745 – 748; e) C. Naeslund, S. Ghirmai, S. Sjoeberg, *Tetrahedron* **2005**, *61*, 1181 – 1186; f) K. Tanaka, G. Nishida, A. Wada, K. Noguchi, *Angew. Chem.* **2004**, *116*, 6672 – 6674; *Angew. Chem. Int. Ed.* **2004**, *43*, 6510 – 6512; g) A. J. Boydell, V. Vinader, B. Linclau, *Angew. Chem.* **2004**, 116, 5795 – 5797; *Angew. Chem. Int. Ed.* **2004**, *43*, 5677 – 5679; h) M. Rivero, I. Alonso, J. C. Carretero, *Chem. Eur. J.* **2004**, *10*, 5443 – 5459; i) D. G. Gillingham, O. Kataoka, S. B. Garber, A. H. Hoveyda, H. Amir, *J. Am. Chem. Soc.* **2004**, *126*, 12288 – 12290; j) K. Fuji, T. Morimoto, K. Tsutsumi, K. Kakiuchi, Kiyomi, *Tetrahedron Lett.* **2004**, *45*, 9163 – 9166; k) A. Cordova, *Chem. Eur. J.* **2004**, *10*, 1987 – 1997; l) A. H. Hoveyda, *Stimul. Concepts Chem.* **2000**, 145 – 160.

[2] a) H. Wynberg, *J. Macromol. Sci. A* **1989**, *26*, 1033 – 1041; b) K. Soai, I. Sato, *Organomet. News* **2003**, 4, 138 – 141; c) T. Shibata, T. Hayase, J. Yamamoto, K. Soai, *Tetrahedron: Asymmetry* **1997**, *8*, 1717 – 1719.

[3] a) L. Shengjian, J. Yaozhong, M. Aiqiao, Y. Guishu, *J. Chem. Soc. Perkin Trans. 1* **1993**, 885 – 886; b) A. H. Alberts, H. Wynberg, *J. Am. Chem. Soc.* **1989**, *111*, 7265 – 7266; c) K. Soai, Y. Inoue, T. Takahashi, T, Shibata, *Tetrahedron* **1996**, *52*, 13355 – 13362.

[4] a) C. Cimarelli, A. Mazzanti, G. Palmieri, E. Volpini, *J. Org. Chem.* **2001**, *66*, 4759 – 4765; b) B. M. Matute, J.-E. Baeckvall, *J. Org. Chem.* **2004**, *69*, 9191 – 9195; c) S. Miniere, V. Reboul, P. Metzner, M. Fochi, B.-F. Bonini, *Tetrahedron: Asymmetry* **2004**, *15*, 3275 – 3280; d) O. Hamelin, J. Pecaut, M. Fontecave, *Chem. Eur. J.* **2004**, *10*, 2548 – 2554; e) P. Jakubec, D. Berkes, F.

 © 2005 Wiley-VCH Verlag GmbH & Co. KGaA, Weinheim

Povazanec, *Tetrahedron Lett.* **2004**, *45*, 4755 – 4758; f) M. Edin, J. Steinreiber, J.-E. Baeckvall, *Proc. Natl. Acad. Sci. USA* **2004**, *101*, 5761 – 5766.
[5] a) C. M. Chung, M. Hasegawa, *J. Am. Chem. Soc.* **1991**, *113*, 7311 – 7316; b) R. Bielski, M. Tencer, *Can. J. Chem.* **2003**, *81*, 1029 – 1037; c) L. Addadi, J. van Mill, M. Lahav, *J. Am. Chem. Soc.* **1982**, *104*, 3422 – 3429.
[6] Y. Okamoto, T. Nakano, *Chem. Rev.* **1994**, *94*, 349 – 372.
[7] a) S. Yorozuya, I. Osaka, A. Nakamura, Y. Inoue, K. Akagi, *Synth. Met.* **2003**, *135–136*, 93 – 94; b) B. M. W. Langeveld-Voss, R. A. J. Janssen, E. W. Meijer, *J. Mol. Struct. (THEOCHEM)* **2000**, *521*, 285 – 301; c) K. Giseop, T. Masuda, *J. Polym. Sci. Part A* **2001**, *39*, 71 – 77; d) H. Goto, K. Akagi, *Synth. Met.* **2001**, *119*, 165 – 166; e) H. Tang, M. Fujiki, T. Sato, *Macromolecules* **2002**, *35*, 6439 – 6445.
[8] a) S. Su, N. Kuramoto, *Macromolecules* **2001**, *34*, 7249 – 7256; b) E. Yashima, Y. Maeda, Y. Okamoto. *Chem. Lett.* **1996**, 955 – 956.
[9] a) K. Akagi, G. Piao, S. Kaneko, K. Sakamaki, H. Shirakawa, M. Kyotani, *Science* **1998**, *282*, 1683 – 1686; b) H. Shirakawa, *Curr. Appl. Phys.* **2001**, *1*, 88 – 89; c) G. Piao, N. Kawamura, K. Akagi, H. Shirakawa, M. Kyotani, *Polym. Adv. Technol.* **2000**, *11*, 826 – 829.
[10] a) H. Goto, K. Akagi, *Macromolecules* **2005**, *38*, 1091 – 1098; b) H. Goto, K. Akagi, *Macromol. Rapid Commun.* **2004**, *25*, 1482 – 1486; c) H. Goto, K. Akagi, Jpn. Pat. 362 979, **2002** [*Chem. Abstr.* **2003**, *139*, 344169]; d) H. Goto, K. Akagi, *Book Abstr. Int. Conf. Sci. Technol. Synth. Met*. (*ICSM) 2002* (Shanghai, China) **2002**, p. 17.
[11] a) N. Berova, K. Nakanishi in *Circular Dichroism: Principles and Applications*, *2nd ed.* (Eds.: N. Berova, K. Nakanishi, R. W. Woody), Wiley-VCH, New York, **2000**, pp. 337 – 382; b) S. F. Mason, *Molecular Optical Activity and the Chiral Discriminations*, Cambridge University Press, Cambridge **1982**.
[12] a) L. Groenendaal, M. J. Bruining, E. H. J. Hendrickx, A. Persoons, J. A. J. M. Vekemans, E. E. Havinga, E. W. Meijer, *Chem. Mater.* **1998**, *10*, 226 – 234; b) O. Henze, D. Parker, W. J. Feast, *J. Mater. Chem.* **2003**, *13*, 1269 – 1273.
[13] M. M. Green, N. C. Peterson, T. Sato, A. Teramoto, R. Cook, S. Lifson, *Science* **1995**, *268*, 1860 – 1866.
[14] a) L J. Prins; P. Timmerman, D. N. Reinhoudt, *J. Am. Chem. Soc.* **2001**, *123*, 10153 – 10163; b) B. M. W. Langeveld-Voss, R. J. M. Waterval, R. A. J. Janssen, E. W. Meijer, *Macromolecules* **1999**, *32*, 227 – 230; c) M. M. Green, M. P. Reidy, R. J. Johnson, G, Darling, D. J. O'Leary, G. Willson, *J. Am. Chem. Soc.* **1989**, *111*, 6452 – 6454; d) A. Saxena, G. Guo, M. Fujiki, Y. Yang, A. Ohira, K. Okoshi, M. Naito, *Macromolecules* **2004**, *37*, 3081 – 3083; e) N. Reinhoudt, M. C. Calama, *Science* **2002**, *295*, 2403 – 2406.

 © 2005 Wiley-VCH Verlag GmbH & Co. KGaA, Weinheim

Iron Oxide Nanotubes

Single-Crystalline Iron Oxide Nanotubes**

Chun-Jiang Jia, Ling-Dong Sun, Zheng-Guang Yan, Li-Ping You, Feng Luo, Xiao-Dong Han, Yu-Cheng Pang, Ze Zhang, and Chun-Hua Yan**

In recent years considerable attention has been focused on one-dimensional nanostructured materials owing to their unique physical properties and potential applications in sensors, magnetics, electric transportation, optics, and even as building blocks for nanoscale devices.[1] In particular, much effort has been devoted to the controllable synthesis of inorganic nanotubes since the discovery of carbon nanotubes in 1991.[2] The synthesis of a number of tubular materials from two-dimensional layered precursors at elevated temperatures, based on a "rolling-up" mechanism, has been reported,[3] such as BN, V_2O_5, WS_2, and $NiCl_2$. With the development of soft-chemistry synthetic methods, a low-temperature solution approach provides a facile method to produce nanotubes of lamellar compounds,[4] for example InS, Bi, and $Cu(OH)_2$. Nanotubes made from other materials,[5] such as Si, ZnS, Eu_2O_3, and GaN, which do not possess 2D layered structures, have also been prepared by employing various templates. However, except for a few examples,[5a,d] the template-assisted method has proved to be unsuitable for the formation of single-crystalline nanotubes. A mild solution strategy has been used[6] to obtain single-crystalline hexagonal prismatic Te nanotubes, but it is difficult to extend this method to the formation of other three-dimensional materials. It is therefore still a challenge to extend the fabrication of single-crystalline tubular nanostructures from lamellar to 3D materials.

Hematite (α-Fe_2O_3), the most stable iron oxide under ambient conditions, is widely used in catalysts,[7] pigments,[8] sensors,[9] and as the raw material for the synthesis of

[*] C.-J. Jia, Prof. Dr. L.-D. Sun, Z.-G. Yan, F. Luo, Y.-C. Pang, Prof. Dr. C.-H. Yan
State Key Lab of Rare Earth Materials Chemistry and Applications
PKU-HKU Joint Lab in Rare Earth Materials and Bioinorganic Chemistry
Peking University
Beijing 100871 (China)
Fax: (+86) 10-62754179
E-mail: sun@pku.edu.cn
yan@pku.edu.cn

Prof. L.-P. You
Electron Microscopy Laboratory
Peking University
Beijing 100871 (China)

Prof. Dr. X.-D. Han, Prof. Dr. Z. Zhang
Institute of Microstructure & Properties of Advanced Materials
Beijing University of Technology
Beijing 100022 (China)

[**] Grants-in-aid from NSFC (nos. 10374006, 20221101, and 20423005) and MOST of China (no. 2002CB613500) are gratefully acknowledged.

Supporting information for this article is available on the WWW under http://www.angewandte.org or from the author.

 © 2005 Wiley-VCH Verlag GmbH & Co. KGaA, Weinheim DOI: 10.1002/anie.200463038

maghemite (γ-Fe_2O_3), which is of great importance as a ferro fluid and in magnetic recording materials. Because of its excellent properties, much attention has been directed to the controlled synthesis of hematite particles. For example, Matijevic and co-workers[10] have prepared monodispersed hematite particles by forced hydrolysis of ferric ions in solution, and Kallay et al.[11] and Sugimoto et al.[12] have synthesized hematite particles with controllable shape and size by a sol–gel method. Recently, much research has been focused on the synthesis of 1D nanostructures, including nanorods,[13] nanowires,[14] nanobelts[15] of hematite, and nanotubes of magnetite,[16] owing to their potential applications in various fields. Herein, we report a rational synthesis of single-crystalline hematite nanotubes by a convenient hydrothermal method, and demonstrate a feasible, large-scale, and controllable synthesis of single-crystalline Fe_2O_3 nanostructures. A mechanism for the formation of tubular-structured hematite is proposed in accordance with the morphology investigations carried out by electron microscopy. Different from the mechanism of formation of other inorganic nanotubes reported previously, these hematite nanotubes are formed by a coordination-assisted dissolution process. The presence of phosphate ions is the crucial factor that induces the formation of a tubular structure, which results from the selective adsorption of phosphate ions on the surfaces of hematite particles and their ability to coordinate with ferric ions. Single-crystalline maghemite nanotubes are also obtained by a reduction and re-oxidation process with hematite nanotubes as precursors. This approach not only enriches iron oxide chemistry, but also provides a new strategy to synthesize single-crystalline nanotubes of non-lamellar-structured materials, which could be applicable to the synthesis of other inorganic tubular nanostructures.

The hematite products were synthesized by a solution-phase approach. In a typical experimental procedure, the nanotubes were obtained by the hydrothermal treatment of an $FeCl_3$ solution (0.02 M) in the presence of $NH_4H_2PO_4$ (7.2×10^{-4} M) at 220 °C for 48 h. The morphology of the typical hematite nanotubes obtained was studied by electron microscopy. Figure 1a shows an SEM image of the as-synthesized hematite nanotubes, with a magnified image shown in the inset. The product consists almost entirely of nanotubes with outer diameters of 90–110 nm, inner diameters of 40–80 nm, and lengths of 250–400 nm. Some of the nanotubes have one end open with the other end closed. The phase purity of the products was examined by X-ray diffraction (Figure 1b). All the peaks can be well-indexed to a pure corundum structure (space group $R\bar{3}c$) of hematite (JCPDS: 33-0664).

To provide further insight into the nanostructures of the tubes, analytical TEM investigations were also performed. Figure 2a shows an STEM image of a single hematite tube collected with a high angle annular dark field detector (HAADF) attached to a TEM. The sidewalls of the hematite nanotubes in the STEM images appear brighter as a result of the relatively large number of atoms relative to the other parts of the nanotubes. The compositional line profiles (Figure 2b) probed by energy-dispersive X-ray spectroscopy (EDS) exhibit well-correlated iron and oxygen signals across the tube walls (the arrow in Figure 2a). Figure 2c shows a typical HRTEM image of a single hematite nanotube, and the inset of this figure shows the low-resolution TEM image. The clear lattice image indicates the high crystallinity and single-crystalline nature of the hematite nanotubes. A lattice spacing of 0.460 nm for the (003) planes of the rhombohedral hematite structure along the nanotube can be readily

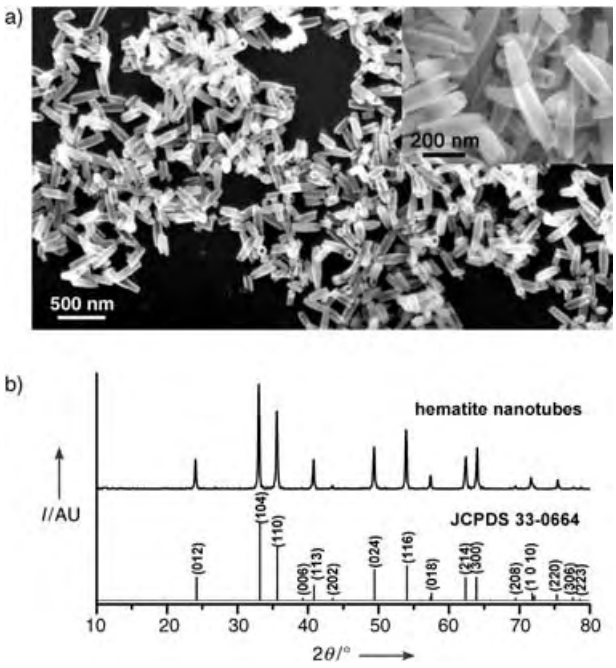


Figure 1. a) Hematite nanotubes imaged with SEM (inset: magnified view) and b) XRD pattern of the hematite nanotubes.

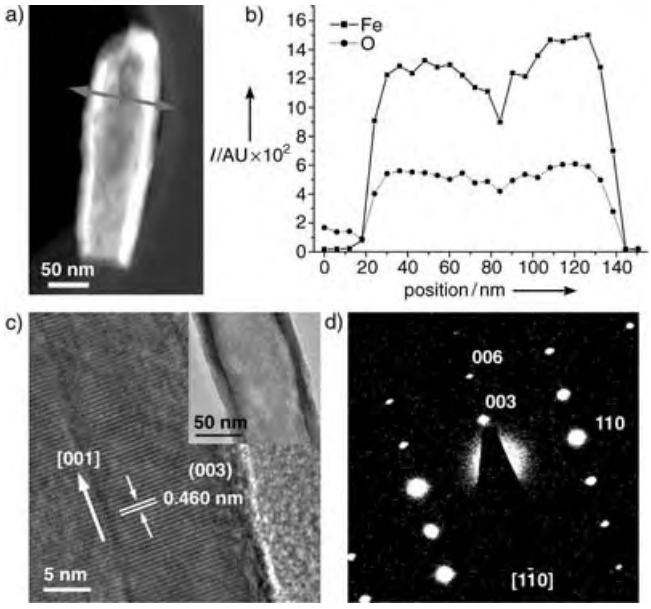


Figure 2. a) STEM image of a single nanotube; b) compositional line profiles across the tube probed by EDS along the line in part a); c) HRTEM image; d) SAED pattern of the single nanotube shown in the inset of part c).

 © 2005 Wiley-VCH Verlag GmbH & Co. KGaA, Weinheim

resolved. The selective-area electron diffraction (SAED) (Figure 2d) and HRTEM analyses reveal that the nanotubes grow along [001] (*c* axis). The (003) reflection shown in Figure 2d is often forbidden in the corundum structure of hematite, as shown in the XRD patterns (see Figure 1b). We suppose that the observation of the (003) reflection by ED is the result of a double-diffraction effect due to the strong electron scattering.[17]

For a complete view of the formation process of the hematite nanotubes and their growth mechanism, a detailed time-dependent morphology evolution study was conducted at 220 °C (Figure 3a–d). The product obtained after 2 h

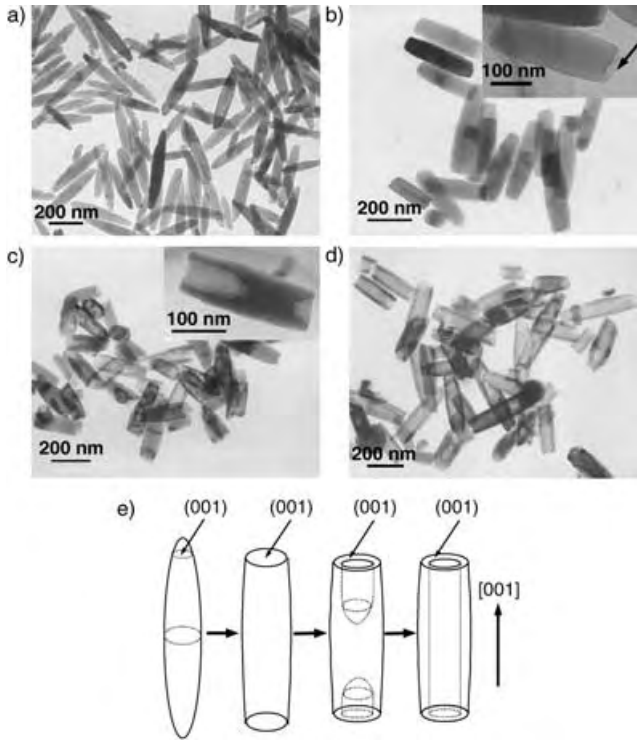


Figure 3. Morphology evolution of the hematite nanotubes with reaction time: TEM images of the products obtained at 220 °C after a) 2 h, b) 8 h, c) 12 h, and d) 48 h; e) schematic illustration of the tube-formation process.

contains spindlelike particles with a diameter of 60–70 nm and a length of 350–450 nm, as has been extensively observed in forced hydrolysis processes.[10,18] Prolonging the reaction time to 8 h gave nanorods with a diameter of about 100 nm and a length of 250–400 nm. The tips of these rods are concave, as can be observed in the inset of Figure 3b. A mixture of rodlike, tubular, and semitubular (inset of Figure 3c) nanostructures was formed after longer reaction times (12 h, Figure 3c). For reaction times of 48 h (Figure 3d), the product consists predominantly of nanotubes that are completely hollow. XRD analysis confirmed the hematite phase of all the above products. HRTEM and SAED analysis of the hematite nanorods and tubes formed at different stages (see Supporting Information) showed that they all grow along the [001] direction, which is consistent with the preferential growth direction of the spindles.

Based on the above time-dependent morphology evolution evidence, the formation process of the nanotubes can be proposed as occurring by "dissolution" of the spindlelike precursors from the tips toward the interior along the long axis, via rodlike nanocrystals and semi-nanotubes, until hollow tubes are formed (Figure 3e). The driving force is the high activity of the sharp spindle tips, which are easily attacked by the protons in acidic solution (pH 1.8). Notably, only part of the interior is dissolved during the formation of hematite nanotubes, and the dissolution is not uniform from spindle to spindle and even for a single spindle (see Figure 3b,c). Furthermore, the diameter of the final nanotubes is larger and the surface is smoother than those of the spindlelike precursors, which indicates that recrystallization on the surface also accompanies the "dissolution" process. This process is similar to that occurring in ZnO, which "etches" from the center of the hexagonal disks to form hexagonal rings.[19]

Although the formation process of the nanotubes has been deduced, the intrinsic cause of the shape transformation from spindle to tube is still unclear. The growth control of hematite nanocrystals by the adsorption of phosphate ions has been extensively studied.[10,18] Our investigations show that phosphate adsorption on the hematite surface takes place, and that these adsorbed phosphate ions cannot be removed by washing (Supporting Information).[20] The adsorption behavior of anions on oxides and hydroxides depends on the surface properties, particularly the surface hydroxy group configuration.[21] The adsorption of phosphate on hematite occurs by reaction with the singly coordinated surface hydroxy groups to form a monodentate or bidentate inner-sphere complex.[22] A hematite crystal has a rhombohedrally centered hexagonal structure of the corundum type with a close-packed lattice in which two thirds of the octahedral sites are occupied by Fe^{3+} ions (see Figure 4a). In a typical crystal unit, each Fe atom is surrounded by six O atoms, whereas each O atom is bound to four Fe atoms. Due to these characteristics of the corundum structure, the surface hydroxy group configuration of the various crystal faces of hematite is quite different.[21] For (001) planes (see Figure 4b), the surface hydroxy functions are all doubly coordinated, whereas for other planes that commonly occur at the surface of natural and artificial hematite crystals, such as the (100), (110), (012), and (104) planes, singly coordinated surface hydroxy groups are present. Therefore, the adsorption capacities and affinities for phosphate to hematite are much lower for the (001) planes than for the others,[22a] and the adsorbed phosphate will protect them from further reaction. Although previous studies[23] have shown that dissolution of hematite does not appear to take place preferentially at specific crystal faces, the selective adsorption of phosphate ions on the crystal planes parallel to the *c* axis other than (001) favors the dissolution along the *c* axis and causes the hematite tube to grow in the [001] direction.

Besides the selective adsorption of phosphate ions at different faces, the coordination effect of phosphate ions with Fe^{3+} ions is another important aspect in the formation of

 © 2005 Wiley-VCH Verlag GmbH & Co. KGaA, Weinheim

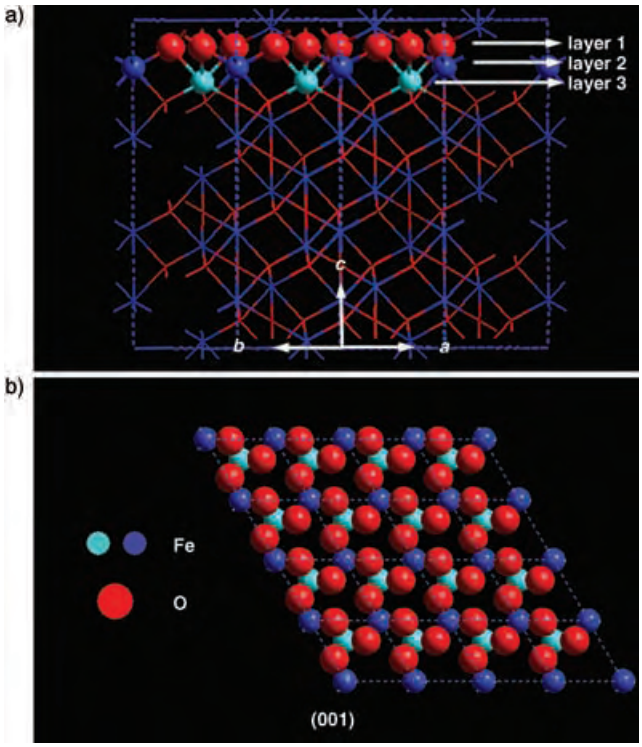


Figure 4. Schematic structures of hematite: a) crystal structure projection on the (110) plane: the repeating elemental sequence is $(O,Fe,Fe)_n$ along the *c* axis; b) crystal structure projection on the O-terminated (001) plane, in which O atoms are all doubly coordinated by Fe atoms. Compared with other planes, the adsorption capacities and affinities for phosphate are much lower for (001) owing to the absence of singly coordinated hydroxy groups.

nanotubes. As for the "dissolution" of the hematite particles, the following reactions take place:

$$Fe_2O_3 + 6\,H^+ \rightarrow 2\,Fe^{3+} + 3\,H_2O \quad (1)$$

$$Fe^{3+} + x\,H_2PO_4^- \rightarrow [Fe(H_2PO_4)_x]^{3-x} \quad (2)$$

The formation of $[Fe(H_2PO_4)_x]^{3-x}$ [Eq. (2)] forces Equation (1) toward the right-hand side and speeds up the dissolution of the hematite particles. Based on the two roles played by phosphate ions during the reaction, we have proposed a coordination-assisted dissolution process for the hematite tube formation during hydrothermal treatment of the spindle precursors in the presence of phosphate ions (see Figure 3e).

Experiments to determine the parameters, other than the reaction time, that are also important for the formation of the nanotubes were carried out. For example, their formation at temperatures lower than 220 °C is not favored as spindle nanocrystals dominate at 180 °C and only a few nanotubes form at 200 °C (Supporting Information). The phosphate ions are essential for the formation of spindlelike hematite, which is the precursor for the formation of the tubular structure. Furthermore, the concentration of phosphate ions should be maintained for the coordination-assisted dissolution process to proceed. If the concentration of phosphate ions is lower than 6.5×10^{-4} M, nanorods or only a few nanotubes are obtained instead of large amounts of nanotubes. On the other hand, a relatively large phosphate ion concentration ($> 1.0 \times 10^{-3}$ M) destroys the tubes. Under basic conditions only solid particles are obtained, and the mediation effect of phosphate ions is weak. Moreover, tubular structures are not formed due to the lack of spindle precursors, and the high pH value does not favor the dissolution. Other ions that coordinate to Fe^{3+}, like SO_4^{2-}, also lead to the "dissolution" of the spindle precursors and formation of the final tubular product. Studies on the formation of other kinds of hematite nanostructures, based on this dissolution process, are still in progress.

Maghemite, and especially its nanostructures,[24] are scientifically interesting and technologically important as a type of magnetic material. We were able to obtain maghemite nanotubes by a reduction and re-oxidation process starting with the hematite nanotubes as precursors. Figure 5a shows an SEM image of the maghemite nanotubes obtained. Compared with the corresponding hematite precursors, the size, tubular structure, and the single-crystal nature are perfectly maintained for maghemite. The XRD patterns of the maghemite nanotubes are shown in Figure 5b; all of them can be well indexed to a pure spinel structure of maghemite

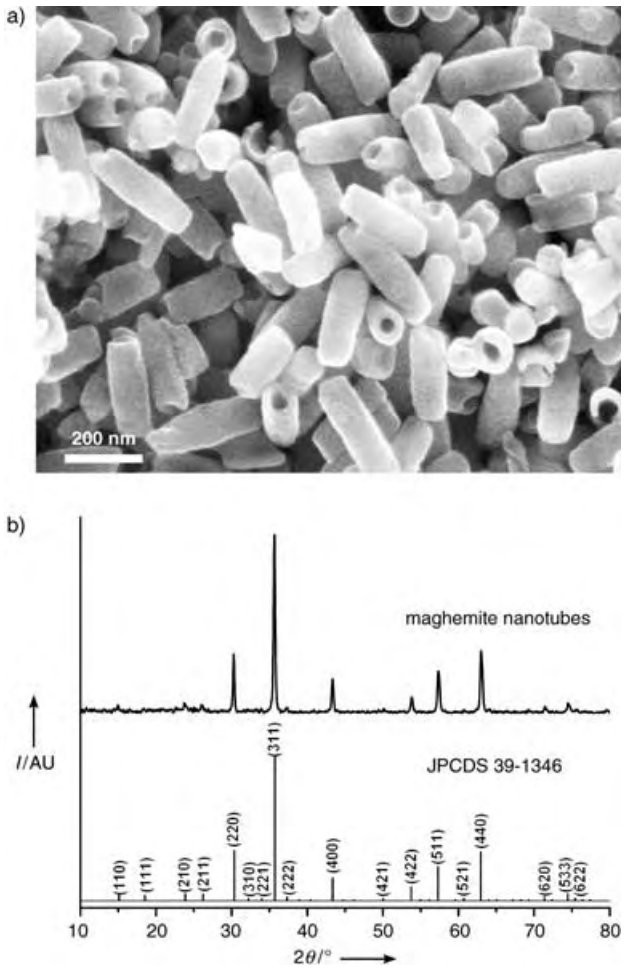


Figure 5. a) SEM image and b) XRD pattern of the maghemite nanotubes.

 © 2005 Wiley-VCH Verlag GmbH & Co. KGaA, Weinheim

(JCPDS: 39-1346). The sharp peaks confirm the high crystallinity of the products. A study of the magnetic properties of these maghemite nanotubes is still in progress. Both the hematite and maghemite nanotubes provide novel structures for magnetism studies and also have potential applications for the design of novel complex structures[25] and as carriers in biomagnetic sensors, nanomedicine, and catalysis.

In summary, single-crystalline hematite nanotubes have been fabricated by a facile, one-step hydrothermal method. Various experimental conditions, including temperature, additives, pH value, and reaction time for the growth of hematite nanocrystals were investigated. Based on the evidence of electron microscope images, the formation mechanism of tubular-structured hematite has been proposed as a coordination-assisted dissolution process. The presence of phosphate ions in this process is crucial because of their different adsorption ability on the different crystal planes of hematite and a coordination effect with Fe^{3+}, which induces the preferential dissolution of the hematite spindle precursors along the long axis from the tips down to the interior. Maghemite nanotubes have also been obtained in a reduction and re-oxidation processes of these hematite precursors. These results not only enrich the tubular nanostructures of inorganic compounds, but also provide a new strategy to synthesize single-crystalline nanotubes of nonlamellar-structured materials, which could be applicable to the synthesis of other inorganic tubular nanostructures.

Experimental Section

The hematite nanotubes were fabricated by hydrothermal treatment of a mixture of $FeCl_3$ and $NH_4H_2PO_4$ solutions. In a typical experimental procedure, 3.20 mL of aqueous $FeCl_3$ solution (0.5 M) and 2.88 mL of aqueous $NH_4H_2PO_4$ solution (0.02 M) were mixed with vigorous stirring. Distilled water was then added to a final volume of 80 mL. After stirring for ten minutes, the mixture was transferred into a Teflon-lined stainless-steel autoclave with a capacity of 100 mL for hydrothermal treatment at 220 °C for 48 h. After the autoclave had cooled down to room temperature naturally, the precipitate was separated by centrifugation, washed with distilled water and absolute ethanol, and dried under vacuum at 80 °C. The parameters that are essential for the tube formation were studied by varying temperature, concentration of $NH_4H_2PO_4$, pH value, and the reaction time.

Maghemite nanotubes were obtained by a reduction and re-oxidation of the hematite nanotube precursors. The dried hematite powders were annealed in a furnace at 360 °C under a continuous hydrogen gas flow for 5 h. Then, the gas flow was stopped, the powder exposed to air, and the furnace temperature decreased to 240 °C over 2 h.

The powder XRD patterns were recorded with a Rigaku D/MAX-2000 diffractometer using Cu K_α radiation ($\lambda = 1.5418$ Å). SEM images were obtained with a DB-235 focused ion beam (FIB) system. TEM images were recorded with a JEOL 200CX transmission electron microscope at a working voltage of 160 kV. HRTEM, EDS, and STEM were performed with a Philips Tecnai F30 FEG-TEM operating at 300 kV. IR spectra were obtained with a Nicolet Magna 750 FTIR spectrometer at a resolution of 4 cm^{-1} with a Nic-Plan IR microscope.

Received: December 22, 2004
Published online: June 15, 2005

Keywords: hematite · hydrothermal synthesis · iron · materials science · nanotubes

[1] a) J. T. Hu, T. W. Odom, C. M. Lieber, *Acc. Chem. Res.* **1999**, *32*, 435; b) G. R. Patzke, F. Krumeich, R. Nesper, *Angew. Chem.* **2002**, *114*, 2554; *Angew. Chem. Int. Ed.* **2002**, *41*, 2446; c) F. Favier, E. C. Walter, M. P. Zach, T. Benter, R. M. Penner, *Science* **2001**, *293*, 2227; d) Y. N. Xia, P. D. Yang, Y. G. Sun, Y. Y. Wu, B. Mayers, B. Gates, Y. D. Yin, F. Kim, Y. Q. Yan, *Adv. Mater.* **2003**, *15*, 353; e) Y. C. Sui, R. Skomski, K. D. Sorge, D. J. Sellmyer, *Appl. Phys. Lett.* **2004**, *84*, 1525.
[2] S. Iijima, *Nature* **1991**, *354*, 56.
[3] a) N. G. Chopra, R. J. Luyken, K. Cherrey, V. H. Crespi, M. L. Cohen, S. G. Louie, A. Zettl, *Science* **1995**, *269*, 966; b) P. M. Ajayan, O. Stephan, P. Redlich, C. Colliex, *Nature* **1995**, *375*, 564; c) R. Tenne, L. Margulis, M. Genut, G. Hodes, *Nature* **1992**, *360*, 444; d) Y. R. Hacohen, E. Grunbaum, R. Tenne, J. Sloan, J. L. Hutchison, *Nature* **1998**, *395*, 336.
[4] a) J. A. Hollingsworth, D. M. Poojary, A. Clearfield, W. E. Buhro, *J. Am. Chem. Soc.* **2000**, *122*, 3562; b) Y. D. Li, J. W. Wang, Z. X. Deng, Y. Y. Wu, X. M. Sun, D. P. Yu, P. D. Yang, *J. Am. Chem. Soc.* **2001**, *123*, 9904; c) W. X. Zhang, X. G. Wen, S. H. Yang, Y. Berta, Z. L. Wang, *Adv. Mater.* **2003**, *15*, 822.
[5] a) J. Q. Hu, Y. Bando, Z. W. Liu, J. H. Zhan, D. Golberg, T. Sekiguchi, *Angew. Chem.* **2004**, *116*, 65; *Angew. Chem. Int. Ed.* **2004**, *43*, 63; b) X. D. Wang, P. X. Gao, J. Li, C. J. Summers, Z. L. Wang, *Adv. Mater.* **2002**, *14*, 1732; c) G. S. Wu, L. D. Zhang, B. C. Cheng, T. Xie, X. Y. Yuan, *J. Am. Chem. Soc.* **2004**, *126*, 5976; d) J. Goldberger, R. R. He, Y. F. Zhang, S. W. Lee, H. Q. Yan, H. J. Choi, P. D. Yang, *Nature* **2003**, *424*, 599.
[6] B. Mayers, Y. N. Xia, *Adv. Mater.* **2002**, *14*, 279.
[7] A. S. S. Brown, J. S. J. Hargreaves, B. Rijniersce, *Catal. Lett.* **1998**, *53*, 7.
[8] R. M. Cornell, U. Schwertmann, *The Iron Oxides. Structure, Properties, Reactions, Occurrence and Uses*, VCH, Weinheim, **1996**, p. 464.
[9] H. T. Sun, C. Cantalini, M. Faccio, M. Pelino, M. Catalano, L. Tapfer, *J. Am. Ceram. Soc.* **1996**, *79*, 927.
[10] M. Ozaki, S. Kratohvil, E. Matijevic, *J. Colloid Interface Sci.* **1984**, *102*, 146.
[11] N. Kallay, I. Fischer, E. Matijevic, *Colloids Surf.* **1985**, *13*, 145.
[12] T. Sugimoto, K. Sakata, *J. Colloid Interface Sci.* **1992**, *152*, 587.
[13] L. Vayssieres, N. Beermann, S.-E. Lindquist, A. Hagfeldt, *Chem. Mater.* **2001**, *13*, 233.
[14] a) Y. Y. Fu, J. Chen, H. Zhang, *Chem. Phys. Lett.* **2001**, *350*, 491; b) Y. J. Xiong, Z. Q. Li, X. X. Li, B. Hu, Y. Xie, *Inorg. Chem.* **2004**, *43*, 6540.
[15] X. G. Wen, S. H. Wang, Y. Ding, Z. L. Wang, S. H. Yang, *J. Phys. Chem. B* **2005**, *109*, 215.
[16] Z. Q. Liu, D. H. Zhang, S. Han, C. Li, B. Lei, W. G. Lu, J. Y. Fang, C. W. Zhou, *J. Am. Chem. Soc.* **2005**, *127*, 6.
[17] P. Hirsch, A. Howie, R. B. Nicholson, D. W. Pashley, M. J. Whelan, *Electron Microscopy of Thin Crystals*, Robert E. Krieger, Huntington, New York, **1977**, p. 117.
[18] a) T. Sugimoto, A. Muramatsu, K. Sakata, D. J. Shindo, *J. Colloid Interface Sci.* **1993**, *158*, 420; b) M. Ocaña, M. P. Morales, C. J. Serna, *J. Colloid Interface Sci.* **1995**, *171*, 85.
[19] F. Li, Y. Ding, P. X. Gao, X. Q. Xin, Z. L. Wang, *Angew. Chem.* **2004**, *116*, 5350; *Angew. Chem. Int. Ed.* **2004**, *43*, 5238.
[20] N. J. Reeves, S. Mann, *J. Chem. Soc. Faraday Trans.* **1991**, *87*, 3875.
[21] V. Barrón, J. Torrent, *J. Colloid Interface Sci.* **1996**, *177*, 407.
[22] a) X. Huang, *J. Colloid Interface Sci.* **2004**, *271*, 296; b) M. I. Tejedor-Tejedor, M. A. Anderson, *Langmuir* **1990**, *6*, 602; c) J. D. Russell, R. L. Parfitt, A. R. Fraser, V. C. Farmer, *Nature* **1974**, *248*, 220.

 © 2005 Wiley-VCH Verlag GmbH & Co. KGaA, Weinheim

[23] R. M. Cornell, R. Giovanoli, *Clay Miner.* **1993**, *28*, 223.
[24] a) S. J. Park, S. Kim, S. Lee, Z. G. Khim, K. Char, T. Hyeon, *J. Am. Chem. Soc.* **2000**, *122*, 8581; b) K. Woo, H. J. Lee, J. P. Ahn, Y. S. Park, *Adv. Mater.* **2003**, *15*, 1761; c) P. Tartaj, T. Gonzalez-Carreno, C. J. Serna, *Adv. Mater.* **2004**, *16*, 529.
[25] a) Y. Kusano, M. Fukuhara, T. Fujii, J. Takada, R. Murakami, A. Doi, L. Anthony, Y. Ikeda, M. Takano, *Chem. Mater.* **2004**, *16*, 3641; b) P. Ball, *Nature* **2004**, *431*, 524.

 © 2005 Wiley-VCH Verlag GmbH & Co. KGaA, Weinheim

Protein Nanoarrays

Aptamer-Directed Self-Assembly of Protein Arrays on a DNA Nanostructure**

*Yan Liu, Chenxiang Lin, Hanying Li, and Hao Yan**

DNA-based self-assembly[1] represents a versatile system for nanoscale construction due largely to the well-characterized conformation of DNA and its predictability in the formation of base pairs. The methodology of DNA self-assembly begins with the chemical synthesis of single-stranded DNA molecules that self-assemble into branched DNA motifs, known as tiles. DNA tiles can carry sticky ends that are complementary to the sticky ends of other DNA tiles; this facilitates continued assembly of the tiles into DNA lattices. Substantial progress has been made in recent years with DNA nanostructures in the construction of patterned arrays.[2–13] One promising application of DNA-based self-assembly is the use of self-assembled DNA nanostructures to direct the assembly of other macromolecular components such as proteins. DNA-templated protein arrays with predictable control at the nanometer scale could lead to single-molecule detection in proteomics studies. Individual proteins placed at unique locations on the nanoarray could be detected with single-molecule imaging techniques such as recognition imaging, in which specific antibodies are attached to the scanning probe cantilever.[14] Niemeyer has also pointed out another interesting application of precisely controlled protein assemblies in the construction of spatially well-defined multienzyme constructs.[15]

The noncovalent streptavidin–biotin interaction has been the most-explored method in the creation of streptavidin molecule networks through the modification of DNA oligonucleotides with biotin.[6,16–19] However, this method is limited in that only one type of protein–ligand interaction is present. Although other proteins can be fused with streptavidin by protein engineering, it is a tedious process, and the function of the proteins and the biotin-binding capacity of streptavidin may both be affected by the fusion. The covalent linkage of proteins to nucleic acids often relies on the use of heterobispecific cross-linkers,[20] and involves multistep chemical coupling and purification steps. Another method to covalently link proteins to oligonucleotides uses recombinant protein engineering to incorporate a cysteine residue into the protein to allow subsequent coupling to thiolated oligonucleotides by disulfide linkages.[21–23] Although attachment through covalent bonds would be ideal, the process for this has not yet been automated. To realize the potential of self-assembled DNA templates in the construction of protein nanoarrays, there is an immediate need to develop programmable methods in which DNA nanostructures are used to direct the assembly of any protein of interest.

Aptamers are DNA or RNA molecules that can be selected from random pools based on their ability to bind other molecules. Aptamers have been selected to bind other nucleic acids, proteins, small organic compounds, and even entire organisms.[24–27] Aptamers that exhibit sub-nanomolar affinities for a wide range of protein targets have been identified.[27,28] It is possible to generate a virtually unlimited number of specific ligand–aptamer pairs, so that each class of spatially displayed aptamer will interact with high affinity to its specific ligand. Cox and Ellington have reported the identification of new aptamer sequences through an automated systematic evolution of ligands by exponential enrichment (SELEX) process.[25]

Herein, we demonstrate the first use of selective DNA aptamer binding as a robust platform to link proteins to periodic sites of a self-assembled DNA array. The system employs three components: 1) a rationally designed DNA nanostructure that self-assembles into highly ordered spatial lattices by virtue of specific annealing of complementary sticky ends; 2) a DNA-docking site containing an aptamer sequence which tethers the protein of interest to the DNA lattice; and 3) the protein to be displayed on a self-assembled DNA lattice.

The DNA aptamer-directed self-assembled protein nanoarray possesses the following advantageous features: 1) the DNA tiling self-assembly is programmable: a rich set of DNA tiles and lattices with various geometries and patterns can be generated by altering the tiling design and sticky-end associations;[2–13] 2) the DNA tiles and aptamers are compatible with each other, as they are both composed of oligonucleotides; 3) new protein-binding aptamers can be generated with automated processes; 4) DNA nanostructure-displayed aptamers are not just limited to proteins, but can be extended to bind other ligand types.

To demonstrate this system, we chose the thrombin-binding aptamer (TBA). TBA is a well-characterized 15-base DNA aptamer with a consensus sequence of d(GGTTGGTGTGGTTGG) that folds into a unimolecular guanine quadruplex and binds thrombin with nanomolar affinity.[29] Thrombin is a multifunctional serine protease that

[*] Dr. Y. Liu, C. Lin, H. Li, Prof. Dr. H. Yan
Department of Chemistry and
Biochemistry & Biodesign Institute
Arizona State University
Tempe, AZ 85287 (USA)
Fax: (+1) 480-965-2747
E-mail: hao.yan@asu.edu

[**] This work was supported by grants from NSF (CCF-0453686, CCF-0453685) and a research grant from the Biodesign Institute at ASU to H.Y. We thank Prof. Andrew Ellington, Prof. Thomas H. LaBean, and Prof. Daniel Kenan for helpful discussions.

Supporting information for this article is available on the WWW under http://www.angewandte.org or from the author.

 DOI: 10.1002/anie.200501089 © 2005 Wiley-VCH Verlag GmbH & Co. KGaA, Weinheim

recognizes multiple macromolecular substrates and plays a key role in both coagulation and anticoagulation.

Figure 1 illustrates the use of a triple-crossover (TX) DNA tile as the template to direct the assembly of an aptamer and its subsequent organization of proteins into 1D periodic arrays. The TX tile shown is similar to another developed previously,[3,19] except that it has two DNA hairpin loops: one protrudes outward in the plane of the tile and contains the

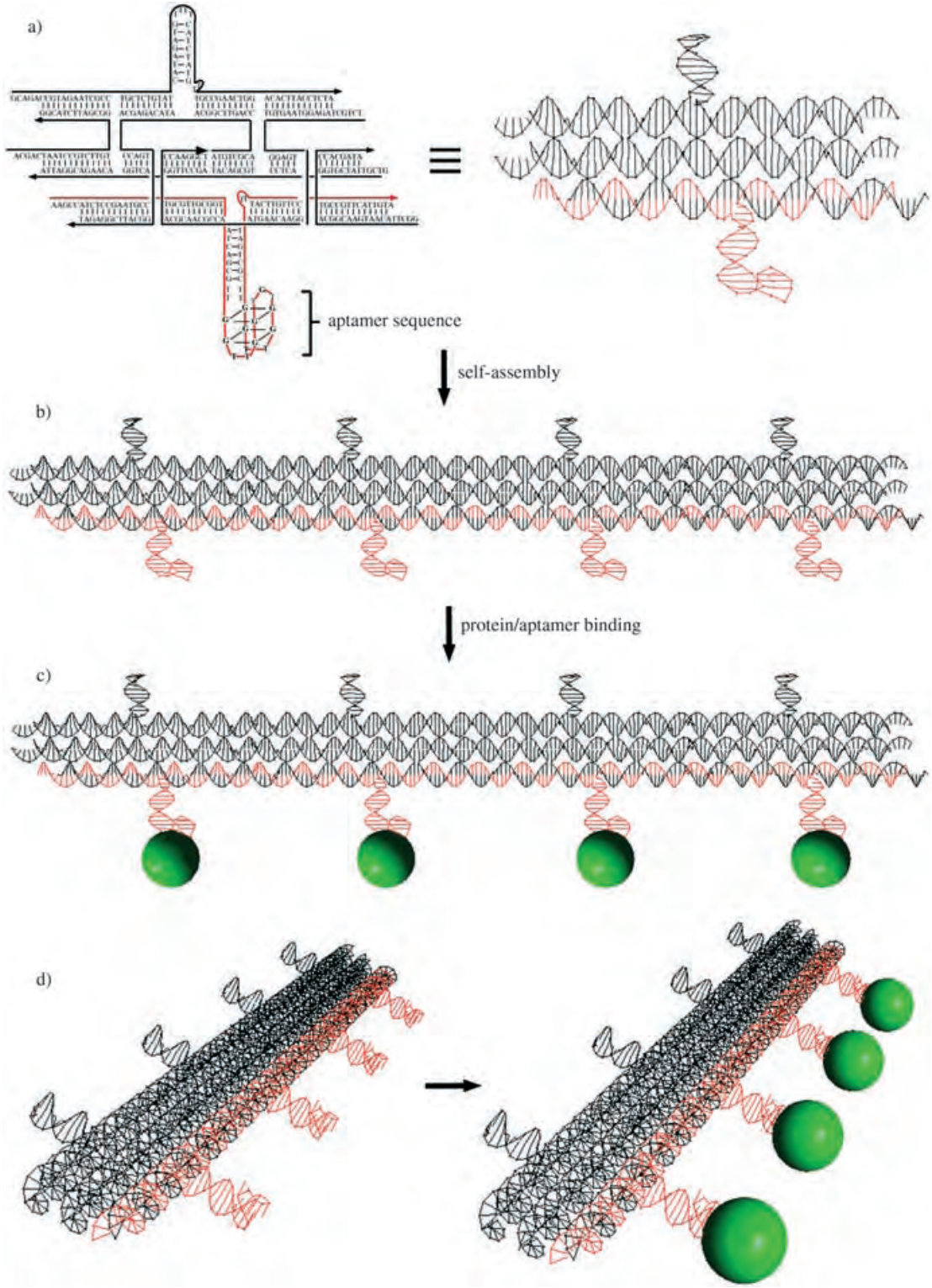


Figure 1. Aptamer-directed self-assembly of thrombin protein on a triple crossover DNA tile: a) DNA strand structure and sequence used for the self-assembly, the red strand contains the thrombin-binding aptamer sequence, which is illustrated as a G-quadruplex structure; b) the TX tiles self-assemble into linear DNA nanoarrays, in which the spacing between adjacent aptamer loops corresponds to five helical DNA turns: ≈17 nm; c) binding of thrombin (green spheres) to aptamers on the linear array leads to linear protein arrays; d) 3D rendering of the aptamer-directed self-assembly of the protein array.

 © 2005 Wiley-VCH Verlag GmbH & Co. KGaA, Weinheim

aptamer sequence (in red) at the end of the stem, the other loop serves as a control; it also protrudes out of the TX tile, but does not contain the aptamer sequence. The length of the stem is arbitrary and can be adjusted as needed to place the target binding molecules in the desired positions and rotational orientations. In general, aptamers can be extended from the tile lattice regardless of their specific secondary structures. Furthermore, the DNA lattice may contain an arbitrary number of different tiles if necessary, so that the aptamers that bind proteins can be placed at every tile, every other tile, every third tile, and so on. Notably, various protein-binding tiles within the lattice may potentially be engineered to display different proteins at defined positions and orientations by virtue of the different possible combinations of aptamers and target ligands. Together, the DNA nanostructure and aptamers constitute a versatile and novel platform for the nanoarchitecture of proteins and synthetic molecules.

The dimensions of the three components used in this study are summarized below. The TX tile is approximately $6 \times 17 \times 2$ nm^3 as illustrated in Figure 1 a. The DNA aptamer stem loop is approximately 2 nm in helical diameter. A stem of 9 bp ($l \approx 3$ nm) was included to allow enough space for the thrombin to bind the aptamer. Thrombin has a molecular weight of ≈ 37 kDa, and a spherical diameter of about 3 nm.[30] Other larger target macromolecules could also be accommodated onto the lattice by varying the dimension of the tiles and the length of the stems. The TX tile self-assembles in $1 \times$ TAE/Mg^{2+} buffer (Experimental Section) into a linear array of TBA units with a periodic distance of ≈ 17 nm between two adjacent aptamers (Figure 1 b). The self-assembly of the DNA linear array is then followed by the addition of thrombin protein to the solution. Binding of thrombin to its aptamer results in a periodic linear array of thrombin molecules, illustrated by the green spheres in Figure 1 c. Figure 1 d gives a 3D view of the aptamer-directed self-assembly of thrombin protein on the 1D TX array.

Both AFM and gel electrophoresis experiments were used to demonstrate aptamer-directed self-assembly. Following formation of the 1D TX array and subsequent binding of thrombin, the preparations were examined by AFM. Figure 2 a shows an AFM height profile of the linear TX arrays before the addition of thrombin protein. Figures 2 b–d show the protein nanoarrays that result from the binding of thrombin to the periodic aptamer sites on the linear TX array. With its diameter of ≈ 3 nm, thrombin binding to the aptamer sequences generates topographical features on the mica surface that are higher than those of bare TX arrays; these are observed as regularly spaced brighter spots at the aptamer locations. The AFM images of Figures 2 b–d clearly demonstrate the regular spacing of the thrombin molecules templated on the linear TX arrays. The average distance measured between pairs of adjacent thrombin molecules along a given TX array is $\approx 18 \pm 1$ nm (Figure 3, profile 1), which is in good agreement with the designed parameters of five helical DNA turns between each adjacent aptamer pair. AFM measurements show that thrombin molecules have an average height of $\approx 2.7 \pm 0.3$ nm (Figure 3, profiles 3–6), in comparison with a height of $\approx 1.7 \pm 0.2$ nm measured across

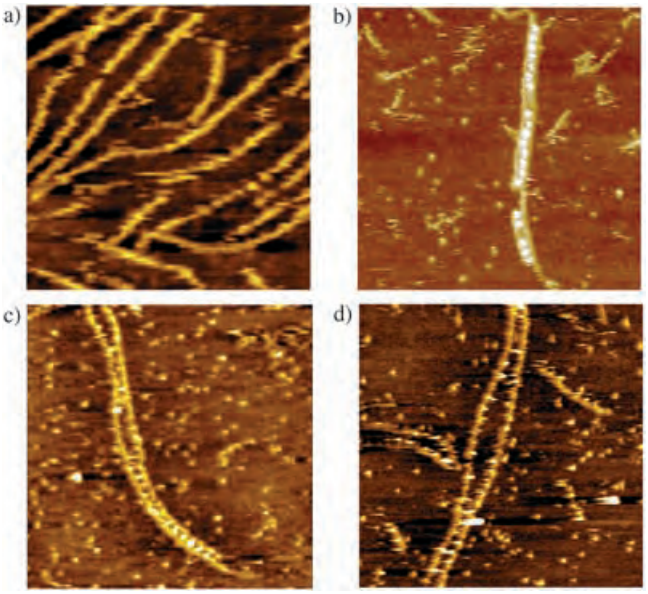


Figure 2. AFM images of the aptamer-directed self-assembly of thrombin protein linear arrays: a) 1D TX tile array with aptamer sequences prior to thrombin protein binding; b)–d) AFM images after binding of thrombin to the TX array; brighter spots correspond to thrombin proteins. Each image shows 500×500 nm^2.

the DNA segment on the array (Figure 3, profile 2). This further confirms that the periodic bumps in the lattice result from the binding of thrombin to the DNA tiles. (More distance and height profiles are available in the Supporting Information.)

Interestingly, upon binding with thrombin, the TX linear array has an inclination to form a parallel pair with the proteins sandwiched inside. One possible explanation is that each protein binds with two aptamers which brings two opposing TX tiles together. A second possibility is that the protein dimerizes under the experimental conditions, and each monomer in the dimer binds with an aptamer on the opposite side of the TX tiles, thus creating the parallel pair of the TX linear array. We believe the latter explanation is most relevant, and this conclusion is supported by several important observations: first, the average center-to-center distance between the parallel pair of DNA linear arrays is 22 ± 1 nm (Figure 3, profile 2). The width of the TX tile is ≈ 6 nm, the hairpin loop including the aptamer sequence on each TX tile is about 4–5 nm, and therefore the protein structure in the center should have a span of ≈ 7–8 nm. This spacing is consistent with the hypothesis of two protein molecules separating the DNA arrays. Secondly, some loosely bound TX pairs were also observed with alternating, closely parallel, separated sections (Figures 2 c and d). Upon careful examination of the separated parts, proteins were observed to be bound on one side but not on the other. This indicates that the linkage between the two parallel linear DNA arrays is not through a single protein molecule, but through a protein dimer. Upon examination of the X-ray crystal structure of the thrombin–aptamer complex, each thrombin molecule is observed to have two possible binding sites for the different locations of the aptamer.[30] Specifically, the G8-T9-G10

 © 2005 Wiley-VCH Verlag GmbH & Co. KGaA, Weinheim

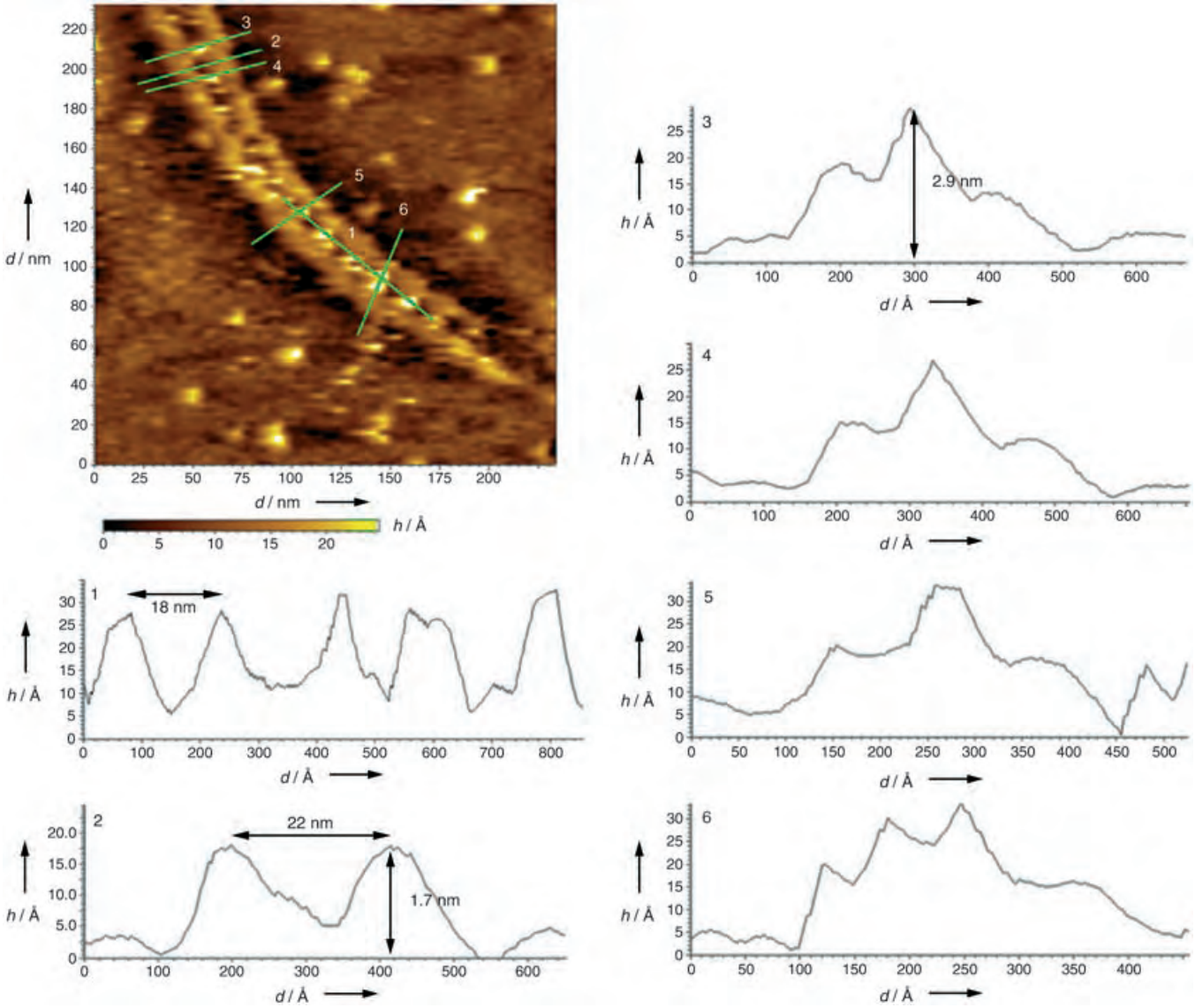


Figure 3. Analysis of the AFM data in Figure 2c (magnified): lines and numbers in the image correspond to the cross sections of the image shown in profiles 1 to 6. The periodicity of the protein molecules in the array is clearly shown (lateral distance ≈17–19 nm). The parallel pairing of the TX linear arrays show protein molecules sandwiched in between that are higher (2.5–3 nm), than the DNA tiles (≈1.7 nm). Profile 6 clearly shows two loosely bound thrombin molecules resolved by AFM. The average distance between the linear DNA arrays is ≈22 nm.

region of the aptamer binds the fibrinogen-binding site (Arg75 and Arg77), and the T13-G14-G15 region binds to the heparin-binding site (Arg101, Arg233, Lys236, Trp237, and Lys240) through both ion pairing (negatively charged phosphate on the DNA backbone with the positively charged amino acid residues on the protein) and hydrogen bonding.[30] In the crystal structure of the complex, the aptamer is squeezed in between two thrombin molecules and concurrently, one thrombin protein has two aptamer-binding sites. Although the site of primary bimolecular interaction in solution is not clear, we propose that both sites in both the aptamer and protein molecules are involved, and the dimerization of thrombin is induced by aptamer binding. Owing to the limit of AFM resolution, the geometry of dimer formation is not clear. It is possible that the two opposing TX arrays can assume parallel or antiparallel alignments.

The model proposed above is further evidenced by analysis with nondenaturing polyacrylamide gel electrophoresis. Figure 4 shows a gel image that demonstrates the concentration dependence of TX aptamer–protein binding. The sticky ends of the TX tiles were removed to allow the formation of single tile complex monomers, which are able to migrate in the gel. The isoelectric point (pI) of thrombin is 7.5, close to the pH value of the buffer. Therefore, the protein alone barely migrates in the gel. However, if bound to the negatively charged TX tile, the thrombin–aptamer complex can migrate in the gel, albeit slower than TX tile alone. Stains-all was used for gel imaging; as the protein is neutral in charge, it is not stained with the positively charged dye, whereas the DNA is well-stained.

The gel image shows that with an increase in protein concentration, at least two slower-migrating bands show up in

 © 2005 Wiley-VCH Verlag GmbH & Co. KGaA, Weinheim

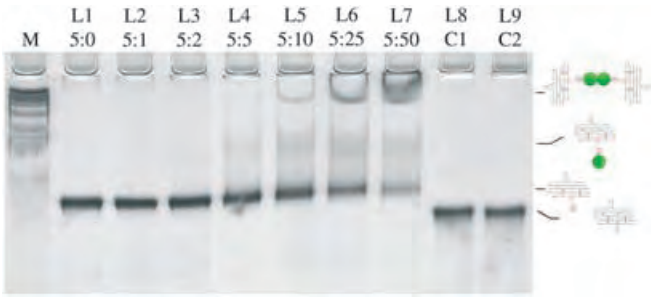


Figure 4. Nondenaturing gel electrophoresis of TX tile and TX aptamer–protein complexes. The polyacrylamide gel (10%) in 1×TAE/Mg^{2+} buffer was run at constant current (25 mA) for 48 h at 4°C. The gel was stained with Stains-all (0.1%) and destained by exposure to white light. Lane M: 100-bp DNA ladder; lane L1: TX tile alone; lanes L2–L7: consistent quantity of TX tiles (10 pmol) but an increasing amount of thrombin from 2 to 100 pmol. DNA/protein ratios are indicated for each lane. Lane L8 contains the control TX molecule without the aptamer sequence; L9 contains a mixture of the control TX and thrombin at a molar ratio of 5:10. The assignments of the bands are indicated schematically on the right-hand side.

the lane, and the intensity distribution of the bands within the lane shifts toward the slower-migrating bands. At a molar ratio of 5:1 TX tile/thrombin, the first slower-migrating band initially appears, the intensity of which increases and then levels off at a tile/protein ratio of 5:10. At a molar ratio of about 5:10, another even slower-migrating band appears; its intensity increases steadily up to the ratio of 5:50. If the aptamer–protein interaction is a one-to-one stoichiometry, only one slower-migrating band would be expected to appear. The appearance of the second slower band and its relative position in the gel indicate that this is a dimer of the TX DNA molecule with one or two protein molecules sandwiched in between. If only one protein molecule were present between each TX pair, the intensity of this band relative to the first slower-migrating band would be expected to decrease with an increase in protein concentration, yet the opposite trend is observed. We therefore conclude that two protein molecules are sandwiched between two opposing TX tiles, as indicated by the schematic representation to the right of the gel image. Lanes 8 and 9 are the controls: lane 8 contains the TX molecule without the aptamer sequence (strand structure and sequence shown in Supporting Information); it migrates slightly faster than the TX assembly with the aptamer sequence in the lane 2. Lane 9 contains a 5:10 molar ratio of the control TX tile used in lane 8 and thrombin. No slower-migrating bands are evident, which indicates that nonspecific interactions are not present between the protein and the TX tile in which the aptamer is absent. It is also notable that the fast-migrating bands show a backward shift in the lanes with the high protein concentrations, whereas the middle bands smear forward. This can be explained through an unstable interaction between the TX aptamer and the thrombin molecule in the 1:1 complex; such complexes formed in solution may break down under gel conditions. To obtain good band separation, the polyacrylamide gel (10%) was run for 48 h. The thrombin–aptamer interaction is governed not by covalent bonds, but by dynamic equilibrium. It is possible that during the long gel-running time, some complex dissociation occurs. This would result in the DNA aptamer band running in the front, but hindered, as observed, and the 1:1 protein–aptamer complex running in the middle, yet smeared.

On the other hand, the 2:2 complex (the slowest-migrating band) is apparently more stable. This phenomenon is consistent with the observation that at a molar ratio of 5:10, AFM images show that aptamers on the DNA array are mostly occupied by thrombin. Overall, dimer formation as evidenced by gel electrophoresis is consistent with the AFM imaging results.

In summary, we have demonstrated the incorporation of aptamer sequences into a rationally designed DNA nanostructure, and have successfully used the aptamer-bearing DNA nanostructure for the directed assembly of thrombin protein arrays. The results clearly show that the thrombin-binding aptamer still functions as the protein-binding moiety upon incorporation into a complex DNA nanostructure. This is encouraging, as it will open up future opportunities for the construction of nanoscale protein arrays in a programmable fashion.

The DNA tiles could be easily modified to accommodate other aptamer sequences in the construction of 2D or 3D protein arrays. Precisely controlled organization of protein molecules onto periodic 2D DNA lattices would give insight into protein structure with 2D cryoelectron diffraction microscopy. However, the ultimate resolution for obtaining structural information from spatially organized proteins will depend on the flexibility of the orientation, and the conformation of the aptamers on the DNA tiles. A recent development by Simmel and co-workers[31] involved a combination of the aptamer-directed self-assembly system with the use of fuel DNA strands to control the binding and release of thrombin proteins. In this way, the pattern of the protein nanoarray could be efficiently tuned. Also, the incorporation of previously developed DNA nanoactuators[32] into the aptamer-directed protein array would permit a change in the relative positions of proteins in real time, which could enable the study of proximity effects of protein–protein interactions. Indeed, the DNA-directed self-assembly of proteins can be used for the direct visualization of protein–protein interactions, as the spatial resolution of such interactions is greatly amplified by the patterning of the DNA structure.

Experimental Section

All DNA strands used for the work reported herein are listed in the Supporting Information. The DNA sequences were designed with the SEQUIN program.[33] DNA strands were commercially synthesized (Integrated DNA Technologies, Inc.) and purified by denaturing gel electrophoresis. Thrombin from human plasma (freeze-dried from a sodium citrate buffer) and Stains-all were purchased from Sigma-Aldrich. The TX tile complex and DNA array were formed by mixing equal quantities of each strand designed in the complex or lattice unit at a concentration of 1 μM (as estimated by OD_{260}) in 1×TAE/Mg^{2+} buffer (Tris, 40 mM; acetic acid, 20 mM; EDTA, 2 mM; and magnesium acetate, 12.5 mM; pH 8.0). The mixture was cooled slowly from 90°C to 20°C. Thrombin was reconstituted into aqueous solution by adding ultrapure water to a final protein concentration of ≈10 μM.

 © 2005 Wiley-VCH Verlag GmbH & Co. KGaA, Weinheim

Nondenaturing gel electrophoresis: TX tiles were mixed with thrombin at different concentration ratios and left at room temperature for 30 min to establish binding equilibrium. Sampling aliquots were loaded onto a nondenaturing polyacrylamide gel (10%), and run at 4°C for 48 h at a constant current of 25 mA. A solution of Stains-all (0.1%) in water/formamide (45:55, v/v) was used to stain the gel. The gel was destained by exposure to white light, and the gel image was collected with a scanner.

AFM imaging: DNA lattice samples (5 μL, ≈30 nM) were dropped onto freshly cleaved mica (Ted Pella, Inc.) and left to adsorb to the surface for 3 min. Buffer (1 × TAE/Mg^{2+}) in volumes of either 30 μL or 400 μL was then added to the drops on the mica. Imaging was performed in a fluid cell in tapping mode on a Multimode NanoScope IIIa (Digital Instruments) or a Pico-Plus AFM (Molecular Imaging) with NP-S tips (Veeco, Inc.). The 3D structure of the TX tile was drawn with Strata 3D software.

Received: March 26, 2005
Published online: June 9, 2005

Keywords: DNA structures · nanostructures · protein arrays · scanning probe microscopy · self-assembly

[1] N. C. Seeman, *Nature* **2003**, *421*, 427.
[2] E. Winfree, F. Liu, L. A. Wenzler, N. C. Seeman, *Nature* **1998**, *394*, 539.
[3] T. H. Labean, H. Yan, J. Kopatsch, F. R. Liu, E. Winfree, J. H. Reif, N. C. Seeman, *J. Am. Chem. Soc.* **2000**, *122*, 1848.
[4] C. D. Mao, W. Q. Sun, N. C. Seeman, *J. Am. Chem. Soc.* **1999**, *121*, 5437.
[5] R. Sha, F. Liu, D. P. Millar, N. C. Seeman, *Chem. Biol.* **2000**, *7*, 743.
[6] H. Yan, S. H. Park, G. Finkelstein, J. H. Reif, T. H. LaBean, *Science* **2003**, *301*, 1882.
[7] H. Yan, T. H. LaBean, L. P. Feng, J. H. Reif, *Proc. Natl. Acad. Sci. USA* **2003**, *100*, 8103.
[8] P. W. K. Rothemund, N. Papadakis, E. Winfree, *PLoS Biology* **2004**, *2*, 2041.
[9] P. W. K. Rothemund, A. Ekani-Nkodo, N. Papadakis, A. Kumar, D. K. Fygenson, E. Winfree, *J. Am. Chem. Soc.* **2004**, *126*, 16344.
[10] B. Q. Ding, R. J. Sha, N. C. Seeman, *J. Am. Chem. Soc.* **2004**, *126*, 10230.
[11] J. C. Mitchell, J. R. Harris, J. Malo, J. Bath, A. J. Turberfield, *J. Am. Chem. Soc.* **2004**, *126*, 16342.
[12] D. Liu, S. H. Park, J. H. Reif, T. H. LaBean, *Proc. Natl. Acad. Sci. USA* **2004**, *101*, 717.
[13] N. Chelyapov, Y. Brun, M. Gopalkrishnan, D. Reishus, B. Shaw, L. Adleman, *J. Am. Chem. Soc.* **2004**, *126*, 13924.
[14] C. Stroh, H. Wang, R. Bash, B. Ashcroft, J. Nelson, H. Gruber, D. Lohr, S. M. Lindsay, P. Hinterdorfer, *Proc. Natl. Acad. Sci. USA* **2004**, *101*, 12503.
[15] C. M. Niemeyer in *Nanobiotechnology: Concepts, Applications and Perspectives*, (Eds.: C. M. Niemeyer, C. A. Mirkin), Wiley-VCH, Weinheim, **2004**, 227.
[16] C. M. Niemeyer, M. Adler, S. Gao, L. Chi, *Bioconjugate Chem.* **2001**, *12*, 364.
[17] C. M. Niemeyer, M. Adler, S. Gao, L. Chi, *J. Biomol. Struct. Dyn.* **2002**, *20*, 223.
[18] C. M. Niemeyer, M. Adler, B. Pignataro, S. Lenhert, S. Gao, L. Chi, H. Fuchs, D. Blohm, *Nucleic Acids Res.* **1999**, *27*, 4553.
[19] H. Y. Li, S. H. Park, J. H. Reif, T. H. LaBean, H. Yan, *J. Am. Chem. Soc.* **2004**, *126*, 418.
[20] C. M. Niemeyer, T. Sano, C. L. Smith, C. R. Cantor, *Nucleic Acids Res.* **1994**, *22*, 5530.
[21] D. R. Corey, P. G. Schultz, *Science* **1987**, *238*, 1401.
[22] S. Howorka, S. Cheley, H. Bayley, *Nat. Biotechnol.* **2001**, *19*, 636.
[23] R. B. Fong, Z. L. Ding, C. J. Long, A. S. Hoffman, P. S. Stayton, *Bioconjugate Chem.* **1999**, *10*, 720.
[24] E. N. Brody, M. C. Willis, J. D. Smith, S. Jayasena, D. Zichi, L. Gold, *Mol. Diagn.* **1999**, *4*, 381.
[25] J. C. Cox, A. D. Ellington, *Bioorg. Med. Chem.* **2001**, *9*, 2525.
[26] R. C. Conrad, L. Giver, Y. Tian, A. D. Ellington, *Comb. Chem.* **1996**, *267*, 336.
[27] W. Xu, A. D. Ellington, *Proc. Natl. Acad. Sci. USA* **1996**, *93*, 7475.
[28] D. E. Tsai, D. J. Kenan, J. D. Keene, *Proc. Natl. Acad. Sci. USA* **1992**, *89*, 8864.
[29] R. F. Macaya, P. Schultze, F. W. Smith, J. A. Roe, J. Feigon, *Proc. Natl. Acad. Sci. USA* **1993**, *90*, 3745.
[30] K. Padmanabhan, K. P. Padmanabhan, J. D. Ferrara, J. E. Sadler, a. Tulinsky, *J. Biol. Chem.* **1993**, *268*, 17651.
[31] W. U. Dittmer, A. Reuter, F. C. Simmel, *Angew. Chem.* **2004**, *116*, 3634; *Angew. Chem. Int. Ed.* **2004**, *43*, 3550.
[32] L. P. Feng, S. H. Park, J. H. Reif, H. Yan, *Angew. Chem.* **2003**, *115*, 4478; *Angew. Chem. Int. Ed.* **2003**, *42*, 4342.
[33] N. C. Seeman, *J. Biomol. Struct. Dyn.* **1990**, *8*, 573.

 © 2005 Wiley-VCH Verlag GmbH & Co. KGaA, Weinheim

Cluster Compounds

cyclo-$Ti_3[\eta^2(\mu_2\text{-}C,O)]_3$: A Side-on-Bonded Polycarbonyl Titanium Cluster with Potentially Antiaromatic Character**

Qiang Xu, Ling Jiang, and Nobuko Tsumori*

Carbon monoxide, one of the most important ligands in transition-metal chemistry from an academic and industrial viewpoint, is well known to coordinate only in the direction from the C atom to metal(s), forming terminal or bridging metal–CO bonds, in the known metal carbonyls,[1] with very few exceptions for chemisorbed CO on some transition metal

[*] Prof. Dr. Q. Xu, L. Jiang
National Institute of Advanced Industrial Science and Technology (AIST)
Ikeda, Osaka 563-8577 (Japan)
and
Graduate School of Science and Technology
Kobe University
Nada Ku, Kobe, Hyogo 657-8501 (Japan)
Fax: (+81) 72-751-9629
E-mail: q.xu@aist.go.jp
Dr. N. Tsumori
National Institute of Advanced Industrial Science and Technology (AIST)
Ikeda, Osaka 563-8577 (Japan)
and
Toyama National College of Technology
13 Hongo-machi, Toyama, 939-8630 (Japan)

[**] We gratefully thank Dr. K. Ohta for helpful discussion and the referees for valuable comments and suggestions, and acknowledge AIST and Kobe University for financial support.

Supporting information for this article is available on the WWW under http://www.angewandte.org or from the author.

 © 2005 Wiley-VCH Verlag GmbH & Co. KGaA, Weinheim DOI: 10.1002/anie.200500364

surfaces[2] and so-called four-electron-donor CO in a limited number of organometallic complexes.[3] The recently reported $Sc_2[\eta^2(\mu_2\text{-C,O})]$ is a simple homoleptic metal carbonyl with only a single side-on-bonded CO ligand,[4] whereas there has been no report thus far of a side-on-bonded polycarbonyl metal cluster. Here we report the generation, IR spectroscopic characterization, and theoretical investigation of side-on-bonded mono- and polycarbonyl titanium clusters $Ti_2(CO)_n$ ($n=1$, 2) and $Ti_3(CO)_n$ ($n=1$–3). In particular, calculations revealed the novel planar, CO side-on-bonded windmill-like *cyclo*-$Ti_3[\eta^2(\mu_2\text{-C,O})]_3$ molecule, which may have antiaromatic character.

Matrix-isolated $Ti_2(CO)_n$ ($n=1, 2$) and $Ti_3(CO)_n$ ($n=1$–3) molecules were produced by codeposition of laser-ablated Ti atoms with CO in excess argon at 7 K and were investigated by FTIR spectroscopy.[5] Recent studies, with the aid of an isotopic substitution technique, have shown that a combination of matrix-isolation IR spectroscopy and quantum chemical calculations is a powerful tool for investigating the spectrum, structure, and bonding of novel species.[6,7] The IR spectra as a function of changes in CO concentrations and laser energy are of particular interest here. At high CO concentration (0.20%) and low laser energy (4 mJ/pulse), only mononuclear species $Ti(CO)_n$ ($n=1$–6) with IR absorptions in the 1740–2040 cm^{-1} region were observed as the reaction products on sample annealing,[8] which have been previously identified.[9] At lower CO concentration (0.05%) and higher laser power (12 mJ/pulse), these mononuclear species almost disappeared, while new absorptions appeared in the 1160–1420 cm^{-1} region on sample annealing, which disappeared after broadband irradiation and did not recover upon further annealing (Figure 1 and Table 1).[8] Note that these new bands were only observed with lower CO concentration and higher laser energy than those for the mononuclear Ti carbonyls, that is, these new products involve more than one Ti atom. Since doping with CCl_4 as an electron scavenger had no effect on these bands, the products are neutral (Figure 1).

On the basis of the growth/decay characteristics as a function of changes in experimental conditions (Figure 1 and ref. [8]), the bands in the 1160–1420 cm^{-1} region can be grouped into five species. All of the absorptions exhibit the isotopic $^{12}C^{16}O/^{13}C^{16}O$ and $^{12}C^{16}O/^{12}C^{18}O$ frequency ratios characteristic of C–O stretching vibrations, but their ν_{C-O} values are anomalously lower than for terminal or bridging CO (Table 1 and Table 2). They are therefore attributed to Ti cluster carbonyls containing only side-on-bonded CO ligand(s) with extremely weakened C–O bonding, as observed for $Sc_2[\eta^2(\mu_2\text{-C,O})]$.[4] The absorptions at 1297.8 cm^{-1} (trapping sites: 1304.2 and 1293.5 cm^{-1}) and at 1253.3 cm^{-1} respectively split into doublets for the mixed $^{12}C^{16}O+^{13}C^{16}O$ and $^{12}C^{16}O+^{12}C^{18}O$ samples (Figure 2), and this indicates that only one CO subunit is involved in each molecule;[10] the former is assigned to Ti_2CO and the latter to Ti_3CO on the basis of the stepwise annealing behavior (Figure 1). The absorptions at 1334.3 cm^{-1} (site: 1324.8 cm^{-1}) and at 1189.9 cm^{-1} (sites: 1185.0 and 1181.7 cm^{-1}) respectively split into triplets with approxi-

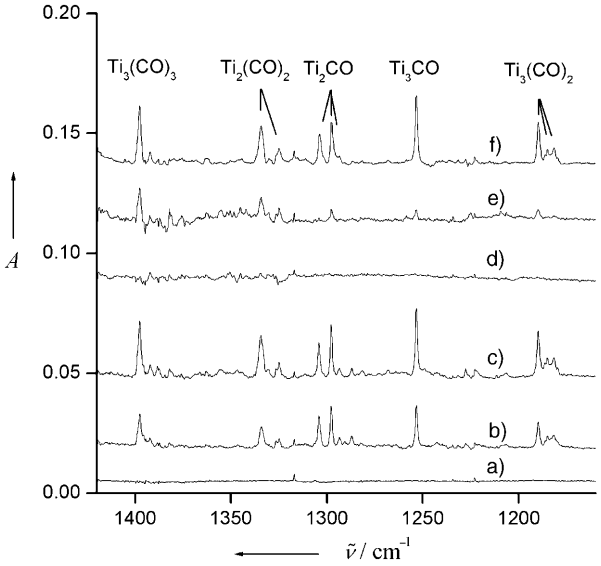


Figure 1. IR spectra in the 1420–1160 cm^{-1} region for laser-ablated Ti atoms codeposited with 0.05% CO in argon at 7 K: a) after 60 min of sample deposition, b) after annealing to 30 K, c) after annealing to 34 K, d) after 20 min of broadband irradiation, e) after annealing to 36 K, f) after doping with 0.01% CCl_4 and annealing to 34 K.

Table 1: IR absorptions [cm^{-1}] observed from codeposition of laser-ablated Ti atoms with CO in an excess of argon at 7 K.

$^{12}C^{16}O$	$^{13}C^{16}O$	$^{12}C^{18}O$	$^{12}C^{16}O+^{13}C^{16}O$	$^{12}C^{16}O+^{12}C^{18}O$	Assignment
1397.6	1365.1	1368.7	1397.6, 1388.7, 1380.6, 1365.1	1397.6, 1388.4, 1381.8, 1368.5	$Ti_3(CO)_3$
1334.3	1303.4	1307.4	1334.3, 1315.8, 1303.8	1334.2, 1318.5, 1307.0	$Ti_2(CO)_2$
1324.8	1294.2	1298.8			$Ti_2(CO)_2$ site
1304.2	1274.2	1277.6	1304.2, 1274.4	1304.0, 1277.6	Ti_2CO site
1297.8	1268.2	1271.4	1297.7, 1268.3	1297.7, 1271.4	Ti_2CO
1293.5	1264.4	1267.5	1293.3, 1264.2	1293.3, 1267.2	Ti_2CO site
1253.3	1224.8	1228.8	1253.3, 1224.8	1253.4, 1228.7	Ti_3CO
1189.9	1162.2	1165.2	1190.0, 1172.8, 1164.1 (1231.5)	1189.9, 1173.6, 1165.0 (1235.1)	$Ti_3(CO)_2$
1185.0	1157.3	1159.7			$Ti_3(CO)_2$ site
1181.7	1154.2	1157.2			$Ti_3(CO)_2$ site

Table 2: Comparison of observed and calculated isotopic frequency ratios of the reaction products.

Molecule	Mode	$^{12}C^{16}O/^{13}C^{16}O$			$^{12}C^{16}O/^{12}C^{18}O$		
		obsd	BP86	B3LYP	obsd	BP86	B3LYP
Ti_2CO	C–O str.	1.0233	1.0238	1.0237	1.0208	1.0222	1.0223
$Ti_2(CO)_2$	C–O asym. str.	1.0237	1.0239	1.0236	1.0206	1.0217	1.0223
Ti_3CO	C–O str.	1.0233	1.0241	1.0236	1.0199	1.0217	1.0225
$Ti_3(CO)_2$	C–O asym. str.	1.0238	1.0240	1.0237	1.0212	1.0219	1.0225
$Ti_3(CO)_3$	C–O asym. str.	1.0238	1.0261	1.0240	1.0211	1.0238	1.0217

 © 2005 Wiley-VCH Verlag GmbH & Co. KGaA, Weinheim

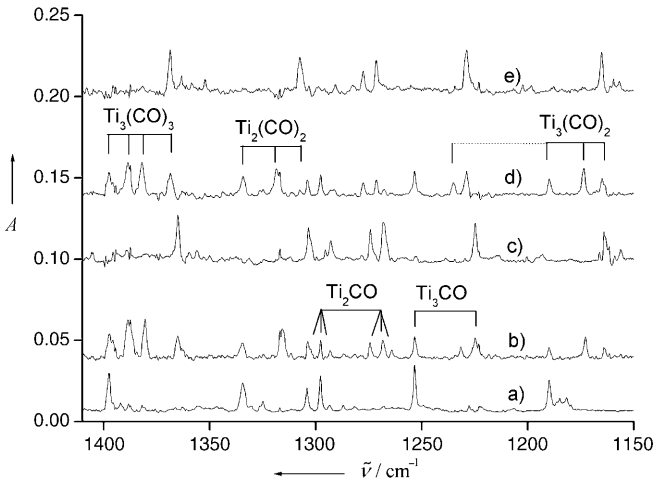


Figure 2. IR spectra in the 1420–1150 cm^{-1} region for laser-ablated Ti atoms codeposited with isotopic CO in Ar for 60 min at 7 K, followed by annealing to 34 K. a) 0.05% $^{12}C^{16}O$, b) 0.025% $^{12}C^{16}O$ + 0.025% $^{13}C^{16}O$, c) 0.05% $^{13}C^{16}O$, d) 0.025% $^{12}C^{16}O$ + 0.025% $^{12}C^{18}O$, e) 0.05% $^{12}C^{18}O$.

mately 1:2:1 relative intensities in the mixed-isotope experiments (Figure 2), that is, each mode involves two equivalent CO ligands;[10] we assign the former to the asymmetric C–O stretching of $Ti_2(CO)_2$, and the latter to $Ti_3(CO)_2$. The splitting of the highest absorption at 1397.6 cm^{-1} into a quadruplet in the mixed-isotope experiments suggests the involvement of three CO subunits.[10] Quantum chemical calculations (vide infra) indicate that this species is preferably assigned to $Ti_3(CO)_3$ rather than to $Ti_2(CO)_3$. For species containing two or three CO ligands, symmetric C–O stretching modes should be observed due to the reduced symmetry of the isotopically mixed species. The symmetric C–O stretching for each isotopomer of $Ti_2(^{12}C^{16}O)(^{13}C^{16}O)$ and $Ti_2(^{12}C^{16}O)(^{12}C^{18}O)$ overlapped with $Ti_3(CO)_3$ absorptions, and the symmetric C–O stretching modes in the mixed-isotope spectra for $Ti_3(CO)_3$ were too weak to be observed, as predicted by DFT calculations,[8] whereas an additional blue-shifted absorption was observed for the symmetric C–O stretching mode for each isotopomer of $Ti_3(^{12}C^{16}O)(^{13}C^{16}O)$ and $Ti_3(^{12}C^{16}O)(^{12}C^{18}O)$ (Table 1). With 0.05% CO all five species were observed, whereas only the CO-poorer and Ti-richer species, Ti_2CO and Ti_3CO, survived on further lowering the CO concentration to 0.02%.[8]

Density functional calculations, performed at the BP86/6-311++G(d,p) and B3LYP/6-311++G(d,p) levels[11] for the possible isomers of $Ti_2(CO)_n$ ($n=1$, 2) and $Ti_3(CO)_n$ ($n=1$–3), provide strong support to the above assignments and insight into structures and bonding. The trial calculations to test reliability gave ν_{C-O} values for linear quintet TiCO of 1889.0 (BP86) and 1971.2 cm^{-1} (B3LYP), close to the experimental value (1855.2 cm^{-1}) with scale factors (obsd/calcd frequency ratios) of 0.982 and 0.941, respectively, in good agreement with previous reports ($\nu_{C-O}=1854.4$ cm^{-1} in solid argon, 1920.0 cm^{-1} in solid neon).[9] Hereafter, mainly BP86 results are presented for discussion. The calculations show that the planar $Ti_2[\eta^2(\mu_2\text{-}C,O)]$ (**1**) molecule with a single side-on-bonded CO ligand, similar to $Sc_2[\eta^2(\mu_2\text{-}C,O)]$,[4] and the planar $Ti_2[\eta^2(\mu_2\text{-}C,O)]_2$ (**2**) molecule with two side-on-bonded CO units (Figure 3) nicely match the experimental vibrational frequencies, relative absorption intensities, and isotopic shifts for $Ti_2(CO)$ and $Ti_2(CO)_2$, respectively. The ν_{C-O} values of **1** and **2** are predicted to be 1330.9 and 1332.6 cm^{-1} (B_2), respectively, in good agreement with observations (1297.8 and 1334.3 cm^{-1}), whereas the symmetric C–O stretching mode (A_1) of **2** exhibits a much lower intensity than the antisymmetric B_2 mode (Table S1 in Supporting Information), consistent with the absence of this A_1 absorption in the IR spectra. The calculated $^{12}C^{16}O/^{13}C^{16}O$ ($^{12}C^{16}O/^{12}C^{18}O$) frequency ratios of **1** and **2** are 1.0238 (1.0222) and 1.0239 (1.0217), respectively, in accord with the observed values of 1.0233 (1.0208) and 1.0237 (1.0206) (Table 2). Our

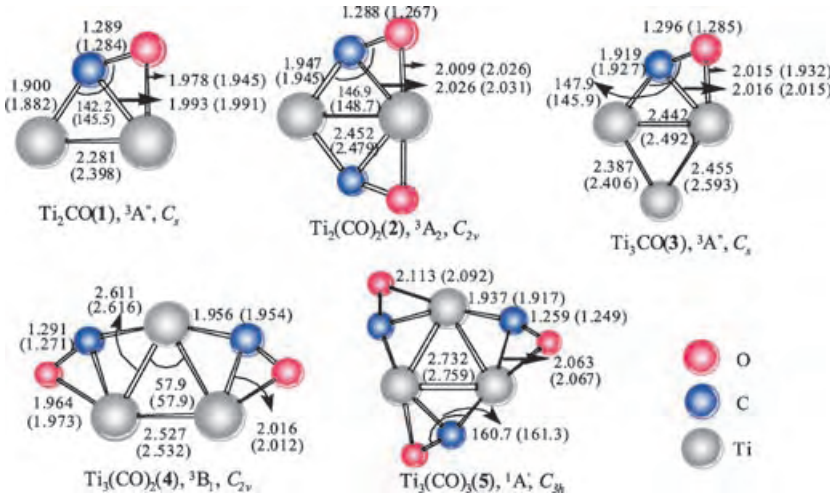


Figure 3. Optimized structures (bond lengths in Å, bond angles in degrees), electronic ground states, and point groups of the reaction products calculated at the BP86/6-311++G(d,p) and B3LYP/6-311++G(d,p) (in parentheses) levels.

BP86 calculations predict that **1** ($^3A''$, C_s, $R_{C-O}=1.289$ Å, $\nu_{C-O}=1330.9$ cm^{-1}) has a structure similar to but smaller R_{C-O} and higher ν_{C-O} than those of the analogous $Sc_2[\eta^2(\mu_2\text{-}C,O)]$ ($^1A'$, C_s, 1.320 Å, 1237.6 cm^{-1}).[4] The R_{C-O} value of **1** is larger than that of $OTi(\eta^2\text{-}CO)$ (1.246 Å).[12] In comparison with **1**, **2** [$^3A_2$, C_{2v}, 1.288 Å, 1332.6 cm^{-1} (B_2)] is predicted to have longer Ti–Ti, Ti–C, and Ti–O bonds but almost the same R_{C-O}.

For a trititanium cluster, a side-on-bonded CO ligand may have two possible coordination forms: $\eta^2(\mu_3\text{-}C,\mu_2\text{-}O)$ and $\eta^2(\mu_2\text{-}C,O)$. Our BP86 calculations show that the *cyclo*-$Ti_3[\eta^2(\mu_3\text{-}C,\mu_2\text{-}O)]$ ($^3A'$, C_s, 1.364 Å, 1099.5 cm^{-1}) and *cyclo*-$Ti_3[\eta^2(\mu_3\text{-}C,\mu_2\text{-}O)]_2$ ($^1A'$, C_{2v}, 1.371 Å, 1064.2 cm^{-1}) molecules do not fit the observations, as their calculated ν_{C-O} values are much lower than the observed frequencies for $Ti_3(CO)$ (1253.3 cm^{-1}) and $Ti_3(CO)_2$ (1189.9 cm^{-1}). Calculations at

 © 2005 Wiley-VCH Verlag GmbH & Co. KGaA, Weinheim

the same level show that the planar *cyclo*-$Ti_3[\eta^2(\mu_2\text{-C,O})]$ (**3**) molecule ($^3A''$, C_s, 1.296 Å, 1302.7 cm^{-1}) and the planar *cyclo*-$Ti_3[\eta^2(\mu_2\text{-C,O})]_2$ (**4**) molecule [$^3B_1$, C_{2v}, 1.291 Å, 1316.0 cm^{-1} (B_2)] (Figure 3) fit the experimental results well (Tables 1 and 2).[8] For **4**, the calculated symmetric C–O stretching mode (A_1, 1359.8 cm^{-1}, 45 km mol^{-1}) has an intensity much lower than the antisymmetric one (B_2, 1316.0 cm^{-1}, 731 km mol^{-1}) (Table S1 in Supporting Information), in agreement with the absence of this A_1 absorption in the IR spectra. By comparing **1** with **3** and **2** with **4**, it is found that addition of the third Ti atom to Ti_2 to form a triangular Ti_3 cluster leads to the lengthening of C–O bonds, which corresponds to weakening of the C–O bond and therefore to lower ν_{C-O}, in agreement with the observations.

As a Ti cluster carrying three side-on-bonded CO ligands should be considered for the 1397.6 cm^{-1} absorption, we first performed BP86 calculations on possible isomers of $Ti_2(CO)_3$, which predict that its most stable isomer ($^3A_1$, C_{3v}) exhibits IR absorptions at 1432.1 and 1357.7 cm^{-1} with intensities of 152 and 502(×2) km mol^{-1}, respectively. The prediction does not match the observation of a single IR absorption at 1397.6 cm^{-1}, and this leads to the conclusion that $Ti_2(CO)_3$ should be excluded. Calculations at the same level revealed that the planar *cyclo*-$Ti_3[\eta^2(\mu_2\text{-C,O})]_3$ (**5**) molecule having a $^1A_1$ ground state with C_{3h} symmetry (Figure 3) nicely fits the observations for this tricarbonyl species (scale factor 0.967). Species **5** [$^1A_1$, C_{3h}, 1445.9 cm^{-1} (E′)] consists of an equilateral Ti_3 triangle with $R_{Ti-Ti} = 2.732$ Å, much longer than in the naked Ti_3 cluster[13] or in **3** or **4**, and three equivalent side-on-bonded CO units with $R_{C-O} = 1.259$ Å, the shortest among $Ti_3(CO)_n$ ($n = 1$–3), forming a planar windmill-like molecule. It lies 44.55 kcal mol^{-1} lower in energy than the planar CO-bridged *cyclo*-$Ti_3(\mu\text{-CO})_3$ molecule with D_{3h} symmetry, which has three imaginary vibrational frequencies. In addition, the cyclic $Ti_3(CO)_3$ isomer with terminally bonded CO ligands and D_{3h} symmetry exhibits no geometry convergence, and the removal of symmetry restrictions in the optimization procedure results in a nonplanar structure with C_1 symmetry [$\nu_{C-O} = 1500.5$ (734), 1450.9 (464), and 1108.2 cm^{-1} (119 km mol^{-1})], which lies 14.75 kcal mol^{-1} higher in energy than **5**. We also performed DFT calculations on other electronic states for the planar C_{3h} *cyclo*-$Ti_3[\eta^2(\mu_2\text{-C,O})]_3$ molecule and found that the triplet state exhibits no geometry convergence, and the relative triplet energy at the singlet geometry is predicted to be 9.37 kcal mol^{-1} higher. Species **5** has an $\ldots(a')^2(e')^4(e')^4(a')^2(a'')^2(e'')^4$ electronic configuration; the doubly degenerate HOMO consists of the π orbitals localized on the Ti-C-Ti subunits, and the HOMO−1 is the delocalized π orbital mainly involving the Ti_3C_3 unit (Figure 4). It is noted that the LUMO is quite low in energy (HOMO–LUMO energy gap: 13.81 kcal mol^{-1}).

Interestingly, theoretical examination of **5** reveals that this molecule may have antiaromatic character. Recently, aromaticity[14,15] has been extended by gas-phase observations to main-group metal clusters such as Al_4^{2-}, Al_4^{4-}, Si_4^{2+}, Si_4, Si_4^{2-}, Sn_6^{2-}, and Hg_4^{6-}, which have stimulated several theoretical investigations and heated discussions.[16] One of the useful approaches to the characterization of aromaticity and antiaromaticity is analysis of the nucleus-independent chemical shift (NICS) on the basis of the magnetic criterion, in which a negative NICS corresponds to aromaticity and a positive NICS to antiaromaticity.[17] Calculations on **5** at the gauge-including atomic orbital (GIAO) BP86/6-311++G(d,p) level show that the NICSs at the Ti_3 ring center and 1 Å above are 23.4 and 14.8, respectively, and thus indicate significant antiaromaticity. The corresponding values for benzene calculated at the same level are −7.7 and −10.1. Further calculations to clarify the source of the NICS value of **5** by way of current density plots and dissected NICS data are in progress and will be reported in a subsequent full paper.

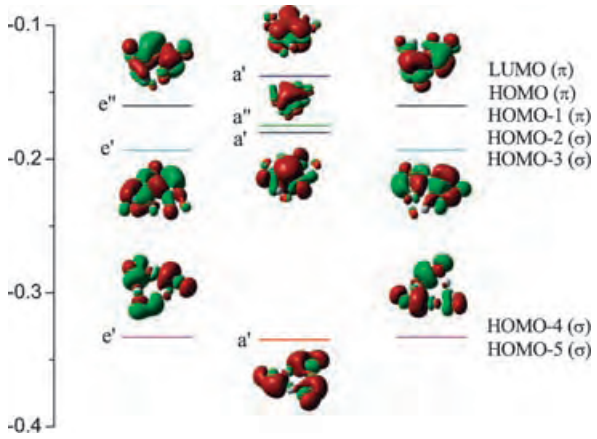


Figure 4. Molecular orbital pictures of singlet *cyclo*-$Ti_3[\eta^2(\mu_2\text{-C,O})]_3$ showing the LUMO and the HOMOs down to the fifth valence molecular orbital from the HOMO. HOMO, HOMO−3, and HOMO−4 each consist of degenerate pairs, both of which are shown here.

In summary, FTIR spectroscopy and calculations revealed the novel planar windmill-like *cyclo*-$Ti_3[\eta^2(\mu_2\text{-C,O})]_3$ molecule exhibiting antiaromatic character as a new example of transition metal cluster compounds having aromaticity or antiaromaticity. This molecule is generated, along with other side-on-bonded mono- and polycarbonyl di- and trititanium clusters, from the reaction of laser-ablated Ti atoms with CO in a solid argon matrix. All of these molecules show unusually low C–O stretching frequencies and thus represent a new class of metal carbonyls with extremely weakened C–O bonding. It is possible that further development in the concept of aromaticity and antiaromaticity in transition-metal systems, through matrix-isolation and theoretical investigations, will lead to the discovery of new classes of compounds or new insights into the electronic structures and chemical bonding of transition-metal cluster compounds.

Experimental Section

Matrix-isolation IR spectroscopy: The experimental setup for laser ablation and matrix-isolation IR spectroscopy was similar to those in previous reports.[5] Briefly, Ti atoms ablated with the Nd:YAG laser fundamental (1064 nm, 10 Hz repetition rate) were codeposited with CO in excess argon onto a CsI window at 7 K. IR spectra were recorded on a BIO-RAD FTS-6000e spectrometer at 0.5 cm^{-1} resolution by using a liquid-nitrogen-cooled HgCdTe (MCT) detector for the range of 5000–400 cm^{-1}. Samples were annealed at different temperatures and subjected to broadband irradiation ($\lambda > 250$ nm) from a high-pressure mercury arc lamp (Ushio, 100 W).

 © 2005 Wiley-VCH Verlag GmbH & Co. KGaA, Weinheim

Calculations: DFT calculations were performed to predict the structures and vibrational frequencies of the observed reaction products with the Gaussian 03 program.[11] The BP86 density functional was used with 6-311++G(d,p) basis sets for C and O atoms, and the all-electron set of Wachters and Hay as modified by Gaussian 03 for Ti atoms. Geometries were fully optimized and vibrational frequencies were calculated with analytical second derivatives. Previous investigations have shown that the use of BP86 can provide reliable information for titanium carbonyls, such as IR frequencies, relative absorption intensities, and isotopic shifts.[9] For comparison, calculations were also performed with the hybrid B3LYP functional. Molecular orbitals were generated with GaussView.

Received: January 31, 2005
Revised: April 21, 2005
Published online: June 9, 2005

Keywords: antiaromaticity · cluster compounds · density functional calculations · IR spectroscopy · matrix isolation

[1] F. A. Cotton, G. Wilkinson, *Advanced Inorganic Chemistry*, 4th ed., Wiley, New York, **1980**, p. 1049.
[2] D. W. Moon, S. L. Bernasek, D. J. Dwyer, J. L. Gland, *J. Am. Chem. Soc.* **1985**, *107*, 4363; N. D. Sinn, T. E. Madey, *Phys. Rev. Lett.* **1984**, *53*, 2481; F. M. Hoffmann, R. A. de Paola, *Phys. Rev. Lett.* **1984**, *52*, 1697.
[3] F. A. Cotton, *Prog. Inorg. Chem.* **1976**, *21*, 1, and references therein; F. A. Cotton, B. A. Frenz, L. Kruczynski, *J. Am. Chem. Soc.* **1973**, *95*, 951; M. Manassero, M. Sansoni, G. Longoni, *J. Chem. Soc. Chem. Commun.* **1976**, 919; W. A. Herrmann, H. Biersack, M. L. Ziegler, K. Weidenhammer, R. Siegel, D. Rehder, *J. Am. Chem. Soc.* **1981**, *103*, 1692; R. Colton, M. J. McCormick, *Coord. Chem. Rev.* **1980**, *31*, 1.
[4] L. Jiang, Q. Xu, *J. Am. Chem. Soc.* **2005**, *127*, 42.
[5] T. R. Burkholder, L. Andrews, *J. Chem. Phys.* **1991**, *95*, 8697; M. F. Zhou, N. Tsumori, L. Andrews, Q. Xu, *J. Phys. Chem. A* **2003**, *107*, 2458; L. Jiang, Q. Xu, *J. Chem. Phys.* **2005**, *122*, 034505.
[6] M. F. Zhou, L. Andrews, C. W. Bauschlicher, Jr., *Chem. Rev.* **2001**, *101*, 1931; J. Li, B. E. Bursten, B. Y. Liang, L. Andrews, *Science* **2002**, *295*, 2242; L. Andrews, X. F. Wang, *Science* **2003**, *299*, 2049.
[7] M. F. Zhou, N. Tsumori, Z. H. Li, K. N. Fan, L. Andrews, Q. Xu, *J. Am. Chem. Soc.* **2002**, *124*, 12936; M. F. Zhou, Q. Xu, Z. X. Wang, P. von R. Schleyer, *J. Am. Chem. Soc.* **2002**, *124*, 14854.
[8] See Supporting Information.
[9] G. V. Chertihin, L. Andrews, *J. Am. Chem. Soc.* **1995**, *117*, 1595; M. F. Zhou, L. Andrews, *J. Phys. Chem. A* **1999**, *103*, 5259; R. Busby, W. Klotzbücher, G. A. Ozin, *Inorg. Chem.* **1977**, *16*, 822.
[10] J. H. Darling, J. S. Ogden, *J. Chem. Soc. Dalton Trans.* **1972**, 2496.
[11] Gaussian 03 (Revision B.04), M. J. Frisch, G. W. Trucks, H. B. Schlegel, G. E. Scuseria, M. A. Robb, J. R. Cheeseman, J. A. Montgomery, Jr., T. Vreven, K. N. Kudin, J. C. Burant, J. M. Millam, S. S. Iyengar, J. Tomasi, V. Barone, B. Mennucci, M. Cossi, G. Scalmani, N. Rega, G. A. Petersson, H. Nakatsuji, M. Hada, M. Ehara, K. Toyota, R. Fukuda, J. Hasegawa, M. Ishida, T. Nakajima, Y. Honda, O. Kitao, H. Nakai, M. Klene, X. Li, J. E. Knox, H. P. Hratchian, J. B. Cross, C. Adamo, J. Jaramillo, R. Gomperts, R. E. Stratmann, O. Yazyev, A. J. Austin, R. Cammi, C. Pomelli, J. W. Ochterski, P. Y. Ayala, K. Morokuma, G. A. Voth, P. Salvador, J. J. Dannenberg, V. G. Zakrzewski, S. Dapprich, A. D. Daniels, M. C. Strain, O. Farkas, D. K. Malick, A. D. Rabuck, K. Raghavachari, J. B. Foresman, J. V. Ortiz, Q. Cui, A. G. Baboul, S. Clifford, J. Cioslowski, B. B. Stefanov, G. Liu, A. Liashenko, P. Piskorz, I. Komaromi, R. L. Martin, D. J. Fox, T. Keith, M. A. Al-Laham, C. Y. Peng, A. Nanayakkara, M. Challacombe, P. M. W. Gill, B. Johnson, W. Chen, M. W. Wong, C. Gonzalez, J. A. Pople, Gaussian, Inc., Pittsburgh, PA, **2003**.
[12] M. F. Zhou, L. Andrews, *J. Phys. Chem. A* **1999**, *103*, 2066.
[13] M. Castro, S. R. Liu, H. J. Zhai, L. S. Wang, *J. Chem. Phys.* **2003**, *118*, 2116.
[14] Thematic Issue on Aromaticity (Guest Ed.: P. von R. Schleyer), *Chem. Rev.* **2001**, *101*(5).
[15] P. J. Garratt, *Aromaticity*, Wiley, New York, **1986**; V. J. Minkin, M. N. Glukhovtsev, B. Y. Simkin, *Aromaticity and Antiaromaticity; Electronic and Structural Aspects*, Wiley, New York, **1994**.
[16] X. Li, A. E. Kuznetsov, H. F. Zhang, A. I. Boldyrev, L. S. Wang, *Science* **2001**, *291*, 859; Z. F. Chen, C. Corminboeuf, T. Heine, J. Bohmann, P. von R. Schleyer, *J. Am. Chem. Soc.* **2003**, *125*, 13930; A. E. Kuznetsov, K. A. Birch, A. I. Boldyrev, X. Li, A. I. Zhai, L. S. Wang, *Science* **2003**, *300*, 622; A. E. Kuznetsov, J. D. Corbett, L. S. Wang, A. I. Boldyrev, *Angew. Chem.* **2001**, *113*, 3473; *Angew. Chem. Int. Ed.* **2001**, *40*, 3369; H. J. Zhai, A. E. Kuznetsov, A. I. Boldyrev, L. S. Wang, *ChemPhysChem* **2004**, *5*, 1885.
[17] P. von R. Schleyer, C. Maerker, A. Dransfeld, H. Jiao, N. J. R. van Eikema Hommes, *J. Am. Chem. Soc.* **1996**, *118*, 6317; P. von R. Schleyer, H. Jiao, N. J. R. van Eikema Hommes, V. G. Malkin, O. L. Malkina, *J. Am. Chem. Soc.* **1997**, *119*, 12669.

 © 2005 Wiley-VCH Verlag GmbH & Co. KGaA, Weinheim

Nanoreactors

Size Tuning, Functionalization, and Reactivation of Au in TiO_2 Nanoreactors**

*Jing Li and Hua Chun Zeng**

Over the past few years, there have been a significant number of new methods developed for the fabrication of core–shell structures ranging from multiphase semiconductors to metal–metal oxide nanocomposites.[1–10] Recently, the engineering of movable cores inside hollow shells has also been achieved with a silica template method and a Kirkendall-type diffusion process.[6,10] If the shell is permeable to reactants, this new type of core–shell nanostructure can be considered in a wider sense as a tiny reactor containing a movable catalyst core. As regards their applications, hydrogenation of ethylene (C_2H_4) has been conducted in Pt–CoO hollow core–shell nanostructures, and the heterogeneous catalytic activity of Pt cores has been demonstrated in the gas phase.[10] To carry out a

[*] J. Li, Prof. Dr. H. C. Zeng
Department of Chemical and Biomolecular Engineering
Faculty of Engineering
National University of Singapore
10 Kent Ridge Crescent, Singapore 119260 (Singapore)
Fax: (+65)6779-1936
E-mail: chezhc@nus.edu.sg

[**] The authors gratefully acknowledge the financial support of the Ministry of Education, Singapore.

Supporting information for this article is available on the WWW under http://www.angewandte.org or from the author.

 © 2005 Wiley-VCH Verlag GmbH & Co. KGaA, Weinheim DOI: 10.1002/anie.200500394

wider range of chemical reactions under both gaseous and liquid conditions, we note that multifunctional core–shell nanoreactors may be required in this emerging area of research. Apart from its normal role of container, for instance, a reactor (shell) itself should also be able to participate in certain chemical processes. Furthermore, a synthetic flexibility in size manipulation, functionalization, and reactivation of the catalyst (core) in a confined environment is yet to be demonstrated. Herein, we report that hollow Au–TiO_2 core–shell nanocomposites can be synthesized by using a wet chemical approach. Encouragingly, our synthetic method offers the flexibility to investigate the aforementioned exploratory subjects. In addition to the synthetic fabrication of Au–TiO_2 nanostructures, the photocatalytic activity of the core–shell nanoreactors was elucidated by desorption and/or decomposition of anchored organic molecules on the metallic cores under UV irradiation.

To test the above conceptual schemes, we conducted a series of experiments. The schematic flowchart in Figure 1

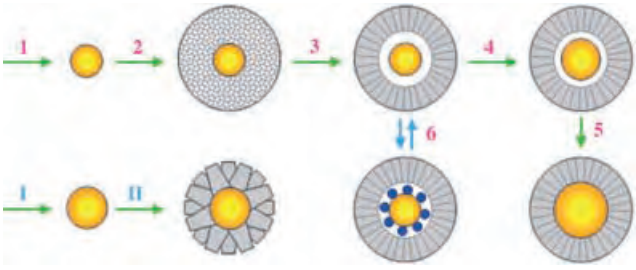


Figure 1. Schematic illustration of the three different processes investigated: fabrication of Au–TiO_2 nanoreactor and size tuning of core catalyst (steps 1–5); preparation of flowerlike Au–TiO_2 core–shell structure (steps I and II); and inclusion/removal of ionic or molecular species in an Au–TiO_2 nanoreactor (reversible steps 6). Gold cores are represented in orange/yellow, anatase TiO_2 shells in gray, and surface-anchored species in blue. Projected lines in products of steps 3–6 indicate the channels formed perpendicularly to the central space of the reactor.

illustrates some major process steps in aqueous media: 1) formation of metallic cores; 2) aggregation of TiO_2 nanocrystallites around a single metallic core; 3) evacuation of central TiO_2 crystallites by Ostwald ripening; and 4) and 5) manipulation of the metal core (that is, growth of the inside metal) to a desired size.

Figure 2 shows TEM images of the Au–TiO_2 nanoreactors fabricated through steps 1–3. For each discrete Au–TiO_2 core–shell structure, the Au catalyst core (50–150 nm) and a hollow interior can be clearly observed. The crystallites located in the central part of the TiO_2 spheres were removed during the synthesis.[11] Thus, it is understandable that intercrystallite channels must exist between the inner and outer spaces, through which ionic and/or molecular species can be transferred into or out of the nanoreactor. In addition to adjustable shell thickness and void volume through Ostwald ripening,[11,12] the size of the catalytic core can be further tuned within the nanoreactor (steps 3 and 4). In such a size manipulation, gold nutrients ($HAuCl_4$; see the Supporting Information) were first introduced into the vacant space

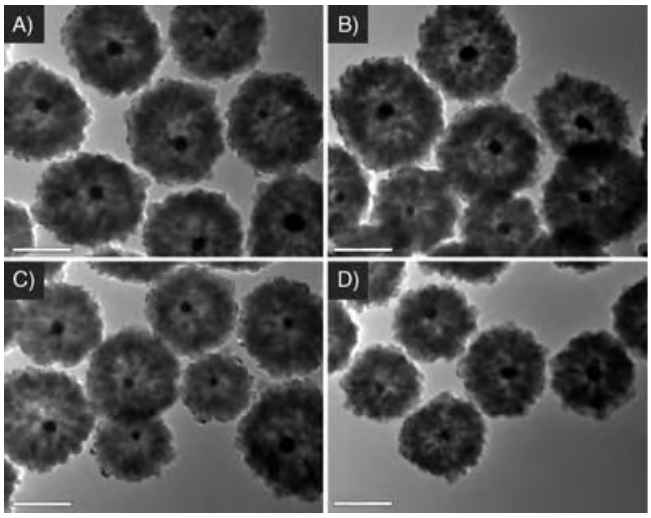


Figure 2. A)–D) TEM images of Au–TiO_2 core–shell nanoreactors with a central vacant space (prepared in step 3 of Figure 1). Experimental conditions: $HAuCl_4$ (3.1 mL, 0.32 mM) + sodium citrate solution (0.1 mL, 0.01 M) + TiF_4 (2.0 mL, 0.04 M) + H_2O to a total volume of 30.0 mL; at 180 °C for 48 h. All bar scales: 500 nm.

of the nanoreactor, and the $HAuCl_4$-soaked Au–TiO_2 nanoreactors were then placed in a solution of cetyltrimethylammonium bromide (CTAB) and ascorbic acid. It is believed that a slow interdiffusion between the $HAuCl_4$ inside the nanoreactor and the CTAB/ascorbic acid solution outside the nanoreactor would ensure a slow growth of Au cores while preventing TiO_2 shells from direct metal deposition. Furthermore, with the introduction of CTAB surfactant better-faceted Au cores can also be attained. Figure 3 shows Au–TiO_2 nanoreactors after core enlargement (Au: 150–250 nm). If $HAuCl_4$ and CTAB/ascorbic acid were premixed in the outside bulk solution, however, small Au nanoparticles would also be deposited on the outer surface of TiO_2 in addition to

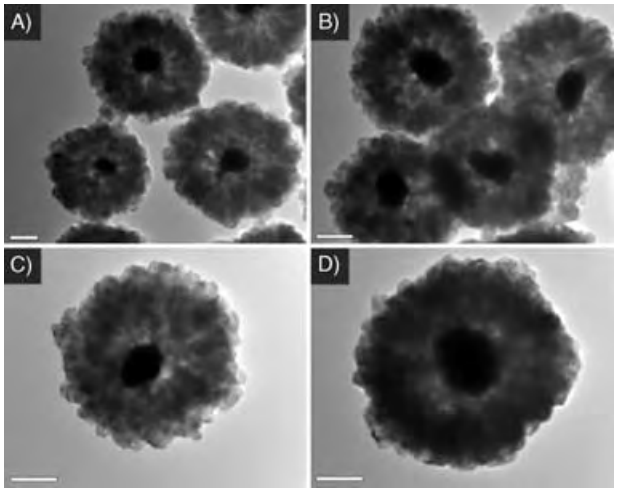


Figure 3. A)–D) TEM images of Au–TiO_2 core–shell nanoreactors after enlargement of Au cores (prepared in step 4 of Figure 1). A size-tuning experiment was carried out (see the Supporting Information); the pristine Au–TiO_2 core–shell nanoreactors used in this core tuning were those of Figure 2. All bar scales: 200 nm.

 © 2005 Wiley-VCH Verlag GmbH & Co. KGaA, Weinheim

the desired core growth. In such a case, the vacant space can be filled up entirely (step 5, Figure 1; see the Supporting Information), which once again confirms the availability of communicable channels between the interior space of reactors and the exterior environment.

X-ray diffraction (XRD) investigations show that all the prepared Au–TiO_2 composite samples contain both face-centered cubic Au (space group (SG): $Fm\bar{3}m$, $a_0 = 4.078$ Å, JCPDS card No. 4-0784; see the Supporting Information) and tetragonal anatase TiO_2 (SG: $I4_1/amd$, $a_0 = 3.7852$ Å and $c_0 = 9.5139$ Å, JCPDS card No. 21-1272; see the Supporting Information). The chemical compositions of these metal–metal oxide nanocomposites were further confirmed by energy-dispersive X-ray spectroscopy (EDX). It was clearly shown that the content of Au in the size-tuned Au–TiO_2 nanoreactors increased in accordance with the enlargement of the Au cores, as evidenced in EDX elemental profiles (see the Supporting Information).

The present approach also permits other types of synthetic architecture. For example, on adding ascorbic acid to the synthesis mixture, well-faceted and much larger anatase TiO_2 crystallites were formed, which gave rise to a flowerlike Au–TiO_2 core–shell structure (steps I and II, Figure 1; see the Supporting Information). As detailed in Figure 4, the TiO_2 shell comprises only a small number of crystallites that are single-crystalline and elongated along the ⟨001⟩ directions.[11] In this case, it is likely that the ascorbic acid molecules would adsorb preferentially on certain crystal planes of TiO_2 crystallites during hydrothermal Ostwald ripening, thus resulting in larger building blocks from which the TiO_2 shell is formed. Nonetheless, this type of metal–metal oxide nanocomposite would be still very useful for new applications, such as storage of photogenerated electrons where no interior space is required.[13]

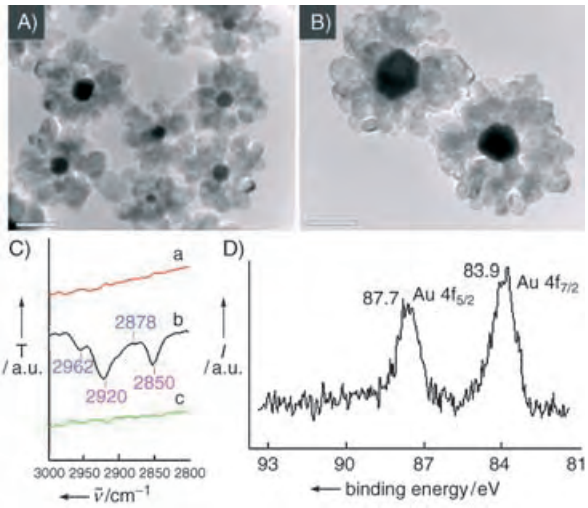


Figure 4. A, B) TEM images of flowerlike Au–TiO_2 core–shell structures (prepared in step II of Figure 1, see the Supporting Information); bar scales: 100 nm. C) FTIR spectra: a: clean Au–TiO_2; b: $C_{12}H_{25}SH$-adsorbed Au–TiO_2; and c: removal of $C_{12}H_{25}SH$ from b under UV irradiation. D) XPS spectrum of Au 4f measured for the Au–TiO_2 core–shell nanoreactors (Figure 2) after photocatalytic decomposition/desorption of adsorbed $C_{12}H_{25}SH$ molecules.

The catalytic Au cores can still be functionalized to meet targeted applications. For example, surface hydrophobicity or hydrophilicity can be attained by the introduction of alkane chains or carboxylic groups, respectively, to the Au core. Here, as a simple illustration, the straight-chain aliphatic thiol $C_{12}H_{25}SH$ was anchored on the Au surface (reversible steps 6, Figure 1). The Fourier-transform infrared (FTIR) spectra of Figure 4C show that the asymmetric and symmetric vibrational modes of C–H are located at 2920 and 2850 cm^{-1} ($\nu_{as}(CH_2)$ and $\nu_s(CH_2)$) and weaker modes at 2962 and 2878 cm^{-1} ($\nu_{as}(CH_3)$ and $\nu_s(CH_3)$), respectively, in the $C_{12}H_{25}SH$ adsorbed samples (see the Supporting Information), which indicates an all-*trans* conformation for the molecules.[14] Interestingly, after UV irradiation ($\lambda = 254$ nm, 15 h) the thiolate anions were desorbed and/or decomposed, as confirmed with both FTIR (Figure 4C) and X-ray photoelectron spectroscopy (XPS; see the Supporting Information). The Au^0 (binding energies at 87.7 and 83.9 eV, Au 4$f_{5/2}$ and 4$f_{7/2}$; Figure 4D) and TiO_2 (binding energies at 464.1 and 458.4 eV, Ti 2$p_{1/2}$ and 2$p_{3/2}$; see the Supporting Information) phases are clearly observed, whereas the signals for S over the binding energy range 160.0–170.0 eV are absent (see the Supporting Information).[14,15] This XPS observation indicates that the Au cores became clean again after removal of the anchored thiolate anions. In this process, the photogenerated holes in the valance band are likely to be responsible for the organic molecular oxidation (including the solvent used, ethanol;[16] see the Supporting Information), whereas the photogenerated electrons may transfer to the metallic core and induce reductive desorption of anionic sulfur species ($-S^{\delta-}$) from the Au surface. The reversibility of this process could be very useful for sulfur-poisoned metal catalyst regeneration in actual applications. It should also be recognized that unlike the normal Au–oxide nanocomposites (for example, Au–TiO_2) reported in literature,[17] the composite nanoreactors fabricated in the present work possess an additional function of screening reactants as a result of the presence of membrane-like shells. With this new structural feature (that is, inorganic membrane reactors), only chemical species permeable through the shell channels can access the catalytic metal cores and thus undergo metal-catalyzed reactions. In this regard, effective control of pore structure and channel size as well as chemical modification (inorganic and/or organic anchoring) of channel walls for the reactor shells would become immediate research tasks in future selective reactions. To further develop the nanoreactors, it is anticipated that higher catalytic activity could be attained with even smaller metal nanoparticles. Current research efforts are directed toward the size reduction of the reactor as well as chemical compatibility between the prepared solid materials (reactors) and solution constituents (reactants, products, and solvent media which form the reaction environment), although further exploitation appears to be challenging.

In summary, the preparation, size manipulation, functionalization, photocatalytic reactions, and reactivation of gold nanoparticles inside Au–TiO_2 nanoreactors have been dem-

 © 2005 Wiley-VCH Verlag GmbH & Co. KGaA, Weinheim

onstrated. The current approach offers a method for the synthetic fabrication of complex nanocomposites with high process flexibility. Many other catalytic reactions, in both the gaseous and liquid phase, can be conducted in this type of photosensitized metal–semiconductor nanoreactor. It is believed that higher catalytic activity and selectivity can be achieved when metal cores are trimmed down to even smaller sizes and the channel structure of the shell is better controlled.

Experimental Section

The synthesis of Au–TiO_2 core–shell nanoreactors involves a number of process steps (Figure 1). For the preparation of the starting Au-core nanoparticles, $HAuCl_4$ (3.0–4.0 mL, 0.2–0.6 mM) was mixed with sodium citrate solution (0.075–0.40 mL, 0.01M). After the solution was stirred for 3–4 h at room temperature (that is, after forming Au-seed nanoparticles, step 1, Figure 1), TiF_4 (1.0–2.0 mL, 0.04 M) and deionized water were added sequentially to a total volume of 30.0 mL. The mixture was then transferred to a Teflon-lined stainless-steel autoclave, and the hydrothermal reaction was conducted at 180 °C for 48 h in an electric oven. During this process, anatase TiO_2 crystallites were aggregated on the surface of Au cores, followed by evacuation of central TiO_2 crystallites (steps 2 and 3, Figure 1). Experiments for tuning Au cores inside TiO_2 nanoreactors were also carried out with two different methods (steps 4 and 5, Figure 1; see the Supporting Information). Flowerlike Au–TiO_2 core–shell structures without central voids (steps I and II, Figure 1) were synthesized with three different methods by varying the reagent concentrations, reaction temperature, and process time (see the Supporting Information). Adsorption and photon-assisted removal of adsorbed dodecanethiol ($C_{12}H_{25}SH$) on the interior Au cores were also conducted (see Supporting Information). The crystallographic structures of the products were determined by X-ray diffraction (XRD; Shimadzu XRD-6000, $Cu_{K\alpha}$). The spatial, morphological, and compositional studies were carried out with field-emission scanning electron microscopy and energy-dispersive X-ray spectroscopy (FESEM/EDX, JSM-6700F), transmission electron microscopy (TEM; JEM-2010F), Fourier-transform infrared spectroscopy (FTIR, KBr method; Bio-Rad FTS 135), and X-ray photoelectron spectroscopy (XPS; AXIS-Hsi, Kratos Analytical).[18,19]

Received: February 2, 2005
Published online: June 13, 2005

Keywords: gold · nanoreactors · nanostructures · photocatalysis

[1] W. Schärtl, *Adv. Mater.* **2000**, *12*, 1899 – 1908.
[2] F. Caruso, *Adv. Mater.* **2001**, *13*, 11 – 22.
[3] C.-J. Zhong, M. M. Maye, *Adv. Mater.* **2001**, *13*, 1507 – 1511.
[4] N. S. Sobal, U. Ebels, H. Möhwald, M. Giersig, *J. Phys. Chem. B* **2003**, *107*, 7351 – 7354.
[5] P. Mulvaney, L. M. Liz-Marzan, M. Giersig, T. Ung, *J. Mater. Chem.* **2000**, *10*, 1259 – 1270.
[6] K. Kamata, Y. Lu, Y. Xia, *J. Am. Chem. Soc.* **2003**, *125*, 2384 – 2385.
[7] Z. Yang, Z. Niu, Y. Lu, Z. Hu, C. C. Han, *Angew. Chem.* **2003**, *115*, 4333 – 4335; *Angew. Chem. Int. Ed.* **2003**, *42*, 1943 – 1945.
[8] H. Gu, R. Zheng, X. Zhang, B. Xu, *J. Am. Chem. Soc.* **2004**, *126*, 5664 – 5665.
[9] P. F. Noble, O. J. Cayre, R. G. Alargova, O. D. Velev, V. N. Paunov, *J. Am. Chem. Soc.* **2004**, *126*, 8092 – 8093.
[10] Y. Yin, R. M. Rioux, C. K. Erdonmez, S. Hughes, G. A. Somorjai, A. P. Alivisatos, *Science* **2004**, *304*, 711 – 714.
[11] H. G. Yang, H. C. Zeng, *J. Phys. Chem. B* **2004**, *108*, 3492 – 3495.
[12] B. Liu, H. C. Zeng, *Small* **2005**, *1*, 566 – 571.
[13] T. Hirakawa, P. V. Kamat, *Langmuir* **2004**, *20*, 5645 – 5647.
[14] Y.-S. Shon, S. M. Gross, B. Dawson, M. Porter, R. W. Murray, *Langmuir* **2000**, *16*, 6555 – 6561.
[15] J. Lukkari, M. Meretoja, I. Kartio, K. Laajalehto, M. Rajamäki, M. Lindström, J. Kankare, *Langmuir* **1999**, *15*, 3529 – 3537.
[16] H. Tada, T. Soejima, S. Ito, H. Kobayashi, *J. Am. Chem. Soc.* **2004**, *126*, 15952 – 15953.
[17] V. Subramanian, E. E. Wolf, P. V. Kamat, *J. Am. Chem. Soc.* **2004**, *126*, 4943 – 4950.
[18] H. G. Yang, H. C. Zeng, *Angew. Chem.* **2004**, *116*, 5318 – 5321; *Angew. Chem. Int. Ed.* **2004**, *43*, 5206 – 5209.
[19] B. Liu, H. C. Zeng, *J. Am. Chem. Soc.* **2004**, *126*, 16744 – 16746.

 © 2005 Wiley-VCH Verlag GmbH & Co. KGaA, Weinheim

Alkane Activation

Multinuclear Copper Triethanolamine Complexes as Selective Catalysts for the Peroxidative Oxidation of Alkanes under Mild Conditions**

*Alexander M. Kirillov, Maximilian N. Kopylovich, Marina V. Kirillova, Matti Haukka, M. Fátima C. Guedes da Silva, and Armando J. L. Pombeiro**

Copper species are widely found in nature and are present in many enzymes as di-, tri- or polynuclear Cu centers that catalyze selectively various oxidation reactions.[1] These reactions include the poorly characterized particulate methane monooxygenase (pMMO), which is present in methanotrophs, wherein a tri- or multinuclear Cu cluster catalyzes alkane hydroxylation and alkene epoxidation.[1f–i] Although increasing attention has been paid to the design of Cu complexes with polydentate ligands as models of copper oxidases[1a,b,2] and some mononuclear compounds have been

[*] A. M. Kirillov, Dr. M. N. Kopylovich, M. V. Kirillova, Dr. M. F. C. G. da Silva, Prof. A. J. L. Pombeiro
Centro de Química Estrutural
Complexo I
Instituto Superior Técnico
Av. Rovisco Pais, 1049-001, Lisbon (Portugal)
Fax: (+351) 21-846-4455
E-mail: pombeiro@ist.utl.pt

Dr. M. Haukka
Department of Chemistry
University of Joensuu
P.O. Box 111, FIN-80101, Joensuu (Finland)

[**] This work has been partially supported by the Fundação para a Ciência e a Tecnologia and its POCTI programme (FEDER funded) (project POCTI/QUI/43415/2001), Portugal, and by a Human Resources and Mobility Marie-Curie Research Training Network (AQUACHEM project, CMTN-CT-2003-503864).

Supporting information for this article is available on the WWW under http://www.angewandte.org or from the author.

 DOI: 10.1002/anie.200500585 © 2005 Wiley-VCH Verlag GmbH & Co. KGaA, Weinheim

recognized as catalysts for alkane oxidation,[3] the use of multicopper complexes for such reactions still remains an unexplored area of research. Our main aims are to find a simple synthetic method to generate multinuclear copper complexes with *N*,*O*-polydentate ligands and to investigate the catalytic activity of these complexes for the oxidation of alkanes under mild conditions, thus extending our interest of alkane functionalization catalyzed by biologically inspired complexes from vanadium compounds, such as synthetic amavadine and its models, to copper complexes.[4]

As a polydentate ligand, we chose an ethanolamine as it is cheap, commercially available, environmentally tolerable, is of a recognized synthetic significance,[5] and its Cu complexes have not yet been applied to alkane functionalization. Cyclohexane and methane were tested as the main substrates in view of the biological interest of the latter and the significance of the oxidized products of both starting materials, that is, cyclohexanol/cyclohexanone (manufacture of adipic acid, Nylon-6,6′ and polyamide-6) from cyclohexane[6] and methanol or other oxidized species, from methane. Attempts have been made to develop processes that have advantages (e.g., higher efficiency, selectivity, simplicity, and use of milder conditions)[7] over commercial processes.[6,7a] However, of the mononuclear Cu^{I} and Cu^{II} complexes tested as catalysts for cyclohexane oxidation,[3] most provide modest yields and low selectivity,[3b,e,f] require expensive[3f,i] and environmentally unfriendly[3g] reagents and various additives,[3g,i] and/or involve complicated syntheses.[3b–d,f–i] Although the catalytic oxidation of methane under relatively mild conditions is currently a matter of a high interest,[8] reported Cu catalysts are scant and have little activity. [9]

Herein we report the easy generation and characterization of copper(II) triethanolamine (H_3tea) complexes that adopt dimeric ($[Cu_2(H_2tea)_2(C_6H_5COO)_2]\cdot 2H_2O$; **1**), trimeric ($[Cu_3(H_2tea)_2(4\text{-}OC_6H_4COO)_2(H_2O)]\cdot 4H_2O$; **2**), tetrameric ($[O\subset Cu_4(tea)_4(BOH)_4][BF_4]_2$; **3**) and polymeric structures ($[Cu_2(H_2tea)_2\{\mu\text{-}C_6H_4(COO)_2\text{-}1,4\}]_n\cdot 2n\,H_2O$; **4**) and show that they are highly selective and active catalysts for the oxidation of alkanes. The addition of different types of aromatic carboxylates or $Na[BF_4]$ to an aqueous blue solution of $Cu(NO_3)_2$, H_3tea, and NaOH provides the formation at room temperature of Cu complexes of diverse nuclearity. Hence, by adding benzoic acid, 4-hydroxybenzoic acid, $Na[BF_4]$, or terephthalic acid one obtains compounds **1**, **2**, **3**, or **4**, respectively, which are isolated as crystalline solids in good yields (76–91%) and characterized by IR and FABMS spectroscopies, elemental analysis, and X-ray crystallography (preparation procedures and characterization details are provided as Supporting Information).[10]

The molecular structure of **1** (Figure 1a) consists of centrosymmetric binuclear fragments, $[Cu_2(H_2tea)_2]^{2+}$, which are stabilized by two monodentate benzoate ligands. Each Cu center has a distorted tetragonal bipyramidal geometry and each H_2tea molecule acts as a tetradentate ligand with one bridging alkoxo group. The equatorial plane is defined by the two bridging alkoxo oxygen atoms of the H_2tea ligands, one amino nitrogen atom and one carboxylate oxygen atom.

The molecular structure of **2** (Figure 1b) consists of three metal atoms that are clustered by two oxygen bridges of two triethanolamine ligands and two carboxylate groups; the central Cu atom is an inversion center. Each lateral Cu atom is coordinated by one H_2tea ligand and the distorted square-

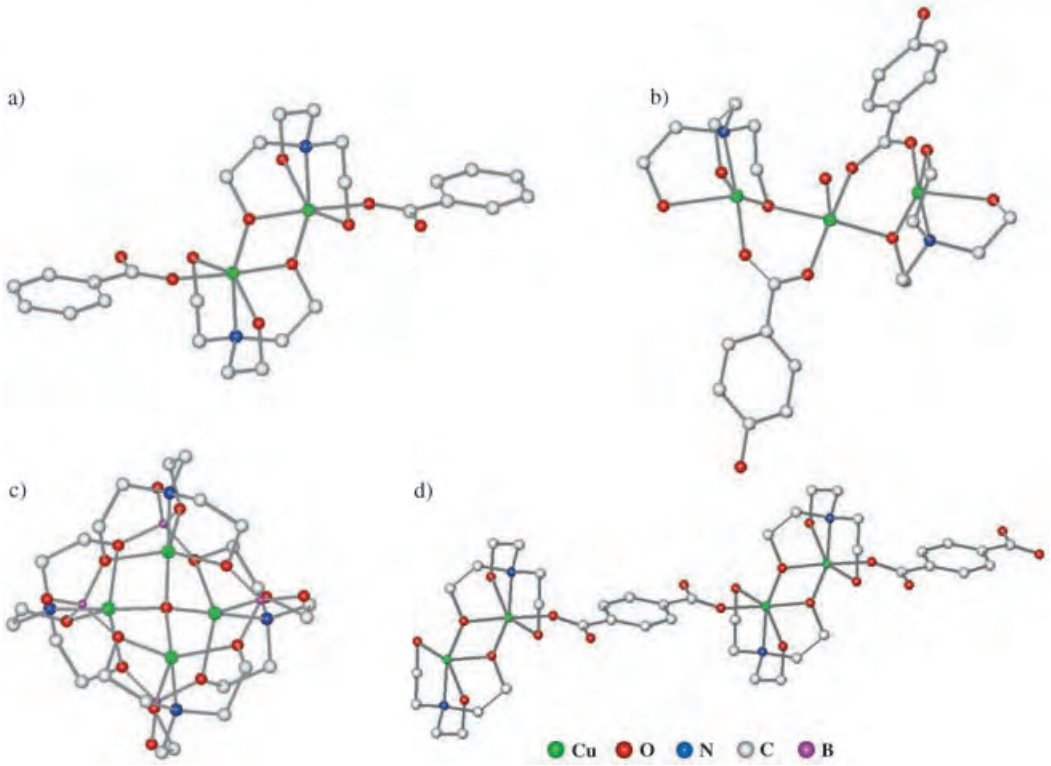


Figure 1. Ball-and-stick representation of the molecular structures of complexes **1** (a), **2** (b), $\mathbf{3}^{2+}$ (c), **4** (d) (only two dinuclear repeating units are shown). Solvent molecules, counterions, and hydrogen atoms are omitted for clarity.

 © 2005 Wiley-VCH Verlag GmbH & Co. KGaA, Weinheim

pyramidal geometry is completed by one carboxylate oxygen atom. The pentacoordinated central Cu atom binds with one water molecule (Cu–O 2.452(3) Å) that is involved in a hydrogen-bonding network with non-coordinated water molecules (see the Supporting Information). The overall positive charge is compensated by the deprotonation of OH groups on the substituted benzoate ligands. Although H_3tea as a tetradentate ligand has been extensively used to prepare polynuclear complexes,[5a,b] to our knowledge, compound **2** is the first example of a trinuclear complex with such a ligand.

Complex **3** (Figure 1c) is composed of two metallacrown ether centrosymmetric subunits $[O\subset Cu_4(tea)_4(BOH)_4]^{2+}$ and four BF_4^- counterions per unit cell, which are linked by hydrogen bonds (see the Supporting Information). Each subunit is present in the crystal as a cyclic Cu^{II} complex, in which an oxygen atom (μ_4-O) is encapsulated in the center. Four practically equivalent copper atoms (Cu–Cu separations of 3.066(3)–3.196(3) Å) are located in the corners of an almost regular tetragon. The copper pentacoordination comprises one N and three O atoms of a deprotonated triethanolamine molecule and the μ_4-O center. Eight μ_3-O centers, two from each tea ligand, are linked to four B–OH groups (formed by an unusual conversion from $[BF_4]^-$ in alkali medium), which leads to additional tetragon stabilization.

Copper(II), H_3tea, and terephthalic acid are involved in the formation of the 1D coordination polymer **4** (Figure 1d), which is constructed from unsymmetrical binuclear nodes $[Cu_2(H_2tea)_2]^{2+}$ (Cu–Cu separation of 2.905(3) Å), which has a structure similar to that of **1** and linear-type spacers. The parallel chains are arranged in neighboring layers (see the Supporting Information).

All these complexes are catalyst precursors for the oxidation of cyclohexane to cyclohexanol and cyclohexanone in acetonitrile by hydrogen peroxide in acidic medium (liquid biphasic catalysis) at room temperature (Table 1). The tri- and tetranuclear complexes **2** and **3** have evident labile sites and exhibit the highest activity with overall yields (based on cycloalkane) of up to 32% (see entries 3, 7, and 11) for a typical acid-to-catalyst molar ratio of 10:1, whereas the other complexes, **1** and **4**, required a higher amount of acid, which is conceivably to promote unsaturation of the metal centers upon ligand protonation. Turnover numbers (TONs, moles of product/mole of complex) of about 360–380 can be reached for a sufficiently high ratio of alkane to catalyst (6400).

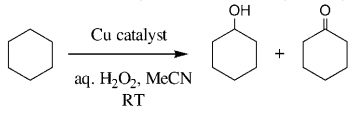
Complexes **2** and **3** can also catalyze the peroxidative oxidation of gaseous alkanes such as methane and ethane, although less effectively than in the case of cyclohexane. For example, methanol (TON = 47, 2.2% yield) and ethanol (TON = 23, 2.1% yield) are obtained from CH_4 and C_2H_6, respectively, with catalyst **3** at 40 °C at an alkane pressure of 30 atm, a H_2O_2:catalyst molar ratio of 1000, and a HNO_3:catalyst molar ratio of 20. The use of O_2 instead of H_2O_2 results in a marked decrease in the activity which, nevertheless, can still be catalytic (e.g., TON = 4 for oxidation of methane to methanol with catalyst **3** and $p(O_2) = 2$ atm, the other conditions being similar to those given above).

The activity is dependent on the molar ratio of the peroxide to catalyst (compare entries 3–7 for **2** and entries 8–12 for **3**). Typically for cyclohexane reactions of 6 h, ratios of peroxide to catalyst ranging from 200:1 to 400:1 led to the best yields. Very high selectivity towards the formation of cyclohexanol and cyclohexanone was exhibited by these systems as no traces of any by-products were detected by GC or GC–MS analyses of the final reaction mixtures. The remarkable activity of our copper complexes is even higher than those found in amavadine and related vanadium catalysts for the same reaction.[4b] Based on mass, our Cu complexes appear to exhibit an activity that is comparable to or even higher than that of pMMO (17 nmol of ethanol per min mg of catalyst **3**; 34 nmol of methanol per min mg of catalyst **3**; or 97 nmol of cyclohexanol and cyclohexanone per min mg of catalyst **2** averaged over the reaction time versus 12–17 nmol of ethanol per min mg of protein for the enzymatic hydroxylation of ethane,[1g] which is a particularly favorable substrate).

The relevance of polydentate *N*,*O*-triethanolaminate ligands is evident in view of the much lower activity of a simple copper salt such as $Cu(NO_3)_2$ under the same reaction conditions (3–5% yield, TON ≈ 1, entries 15, 16, in the case of cyclohexane oxidation; or 0.06% yield, TON = 0.6 for the methane oxidation). This is conceivably associated with the involvement of those ligands (upon decoordination of an N or O atom) in proton-transfer steps for example among H_2O_2, oxo, and/or peroxo ligands, as suggested for some vanadium catalysts that may require particular N, O additives as cocatalysts.[4,7c,11]

The above alkane reactions appear to proceed mainly by mechanisms that involve both carbon-centered and oxygen-

Table 1: Peroxidative oxidation of cyclohexane catalyzed by complexes **1**–**4**.[a]



Entry	Catalyst	$n(H_2O_2)$/ n(catalyst)	t [h]	Yield [%][b]		
				Cyclohexanol	Cyclohexanone	Total[c]
1	**1**	200	6	5.0	7.2	12.2
2	**1**	400	6	6.0	9.4	15.4
3	**2**	200	6	19.9	10.6	30.5
4	**2**	400	6	7.9	6.8	14.7
5[d]	**2**	200	72	19.3	6.3	25.6
6[d]	**2**	400	72	20.3	9.0	29.3
7[d]	**2**	800	72	16.7	14.9	31.6
8	**3**	200	6	15.4	11.8	27.2
9	**3**	400	6	14.2	8.9	23.1
10[d]	**3**	200	72	20.6	6.5	27.1
11[d]	**3**	400	72	20.8	9.8	30.6
12[d]	**3**	800	72	13.5	10.5	24.0
13	**4**	200	6	6.5	5.8	12.3
14	**4**	400	6	7.0	8.6	15.6
15	$Cu(NO_3)_2$[e]	200	6	1.1	2.1	3.2
16	$Cu(NO_3)_2$[e]	400	6	1.6	3.8	5.4

[a] Reaction conditions: catalyst (0.025 mmol), H_2O_2 (2.50–10.00 mmol), C_6H_{12} (0.63 mmol). Full experimental details are provided in the Supporting Information. [b] Moles of product/100 moles of cyclohexane. [c] Cyclohexanol + cyclohexanone. [d] Catalyst (0.0125 mmol). [e] For comparative purposes.

 © 2005 Wiley-VCH Verlag GmbH & Co. KGaA, Weinheim

centered radicals (the former upon homolysis of an alkane C–H bond) as very pronounced decreases in product yields occur when the reactions are carried out in the presence of either a carbon-radical trap such as $CBrCl_3$ or TEMPO (2,2,6,6-tetramethylpiperidin-1-oxyl) (use of the former almost completely suppresses the formation of cyclohexanol and cyclohexanone when used in excess relative to the alkane, whereas the latter leads to around 60% suppression of activity for a stoichiometric amount in relation to the alkane)[12] or an oxygen-radical trap such as Ph_2NH (activity suppression of ca. 90% for a stoichiometric amount relative to H_2O_2). BHT (2,6-di-*tert*-butyl-4-methylphenol) has a lower inhibition effect, commonly below 50%.[12]

Competitive nonradical pathways can probably occur through either 1) electrophilic attack from an oxidized metal (metal-peroxo or metal-oxo) centre to an alkane C–H bond with heterolytic cleavage of this bond to give an organocopper intermediate (R^- abstraction) as proposed[6a,8c,8g] for other metals, or 2) a concerted mechanism involving a direct insertion of an activated electrophilic oxygen atom, for example, a bridging oxygen atom, into an alkane C–H bond or through a pairwise process with C–H addition to two oxygen-atoms, as suggested for biological alkane hydroxylation by pMMO.[1g]

The higher activity of catalysts **2** and **3** might be accounted for by: 1) their lower coordination number (they are five-coordinate, whereas the others are six-coordinate); 2) the presence of a labile ligand (H_2O); 3) the expected higher stability of the multinuclear structures that have relatively close copper atoms supported by various bridging ligands (in the other complexes, only μ-ethoxy-type bridges are involved in the coordination to Cu atoms at a close distance). The last feature (3) agrees with the isolation after the reaction of the tetranuclear catalyst **3**, which maintains its high activity for further catalytic assays. Moreover, it is also consistent with the proposed involvement of three or four Cu atoms in a xylyl hydroxylation reaction in which a (μ-1,1-hydroperoxide) dicopper intermediate is further activated by a second dicopper center that acts as a Lewis acid thus promoting the electrophilic character of the hydroperoxide towards the substrate.[2e,13]

In conclusion, we have found a simple and convenient route for the formation of novel di-, tri-, tetra-, and polynuclear copper triethanolamine complexes, which can be easily prepared in high yields by using cheap, commercially available, and environmentally tolerable reagents. We have also opened up the possibility of applying such copper complexes as highly selective and active catalyst precursors for single-pot alkane oxidation at room temperature with an environmentally friendly oxidant (H_2O_2 that produces only water as by-product) towards the establishment of a powerful copper-based alkane oxidation system, which mimics pMMO and has some advantages over the current industrial synthetic processes for alcohols and ketones.

Received: February 16, 2005
Revised: April 20, 2005
Published online: June 8, 2005

Keywords: alkanes · biphasic catalysis · C–H activation · copper · oxidation

[1] a) S. Itoh in *Comprehensive Coordination Chemistry*, *Vol. 8* (Eds.: J. A. McCleverty, T. J. Meyer, L. Que, W. B. Tolman), 2nd ed., Elsevier, Dordrecht, **2003**, chap. 8.15, pp. 369–393; b) D. H. Lee in *Comprehensive Coordination Chemistry*, *Vol. 8* (Eds.: J. A. McCleverty, T. J. Meyer, L. Que, W. B. Tolman), 2nd ed., Elsevier, Dordrecht, **2003**, chap. 8.17, pp. 437–457; c) J. J. R. Fraústo da Silva, R. J. P. Williams, *The Biological Chemistry of the Elements*, Oxford University Press, Oxford, **2001**; d) E. I. Solomon, U. M. Sundaram, T. E. Machonkin, *Chem. Rev.* **1996**, *96*, 2563; e) J. P. Klinman, *Chem. Rev.* **1996**, *96*, 2541; f) M. Ayala, E. Torres, *Appl. Catal. A* **2004**, *272*, 1; g) S. J. Elliot, M. Zhu, L. Tso, H.-H. T. Nguyen, J. H.-K. Yip, S. I. Chan, *J. Am. Chem. Soc.* **1997**, *119*, 9949; h) R. L. Lieberman, A. C. Rosenzweig, *Crit. Rev. Biochem. Mol. Biol.* **2004**, *39*, 147; i) R. L. Lieberman, A. C. Rosenzweig, *Nature* **2005**, *434*, 177.

[2] a) P. Gamez, P. G. Aubel, W. L. Driessen, J. Reedijk, *Chem. Soc. Rev.* **2001**, *30*, 376; b) K. D. Karlin, A. D. Zuberbühler in *Bioinorganic Catalysis* (Eds.: J. Reedijk, E. Bouwman), 2nd ed., Dekker, New York, **1999**, pp. 469–534; c) M. C. Mimmi, M. Gullotti, L. Santagostini, G. Battaini, E. Monzani, R. Pagliarin, G. Zoppellaro, L. Casella, *Dalton Trans.* **2004**, 2192; d) L. M. Mirica, X. Ottenwaelder, T. D. P. Stack, *Chem. Rev.* **2004**, *104*, 1013; e) E. A. Lewis, W. B. Tolman, *Chem. Rev.* **2004**, *104*, 1047.

[3] a) G. B. Shul'pin, J. Gradinaru, Y. N. Kozlov, *Org. Biomol. Chem.* **2003**, *1*, 3611; b) R. S. da Cruz, J. M. D. E. Silva, U. Arnold, M. S. Sercheli, U. Schuchardt, *J. Braz. Chem. Soc.* **2002**, *13*, 170; c) T. Ohta, T. Tachiyama, K. Yoshizawa, T. Yamabe, T. Uchida, T. Kitagawa, *Inorg. Chem.* **2000**, *39*, 4358; d) S. Velusamy, T. Punniyamurthy, *Tetrahedron Lett.* **2003**, *44*, 8955; e) U. Schuchardt, R. Pereira, M. Rufo, *J. Mol. Catal. A* **1998**, *135*, 257; f) R. Raja, P. Ratnasamy, *Catal. Lett.* **1997**, *48*, 1; g) D. H. R. Barton, S. D. Beviere, W. Chavasiri, E. Csuhai, D. Doller, *Tetrahedron* **1992**, *48*, 2895; h) T. Okuno, S. Ohba, Y. Nishida, *Polyhedron* **1997**, *16*, 3765; i) N. Komiya, T. Naota, Y. Oda, S. I. Murahashi, *J. Mol. Catal. A.* **1997**, *117*, 21.

[4] a) P. M. Reis, J. A. L. Silva, A. F. Palavra, J. J. R. F. da Silva, T. Kitamura, Y. Fujiwara, A. J. L. Pombeiro, *Angew. Chem.* **2003**, *115*, 845; *Angew. Chem. Int. Ed.* **2003**, *42*, 821; b) P. M. Reis, J. A. L. Silva, J. J. R. F. da Silva, A. J. L. Pombeiro, *Chem. Commun.* **2000**, 1845.

[5] a) A. Singh, R. C. Mehrotra, *Coord. Chem. Rev.* **2004**, *248*, 101; b) J. G. Verkade, *Acc. Chem. Res.* **1993**, *26*, 483; c) R. W. Saalfrank, I. Bernt, F. Hampel, *Angew. Chem.* **2001**, *113*, 1745; *Angew. Chem. Int. Ed.* **2001**, *40*, 1700; d) W. Plass, A. Pohlmann, J. Rautengarten, *Angew. Chem.* **2001**, *113*, 4333; *Angew. Chem. Int. Ed.* **2001**, *40*, 4207; e) F. T. Chen, D. F. Li, S. Gao, X. Y. Wang, Y. Z. Li, L. M. Zheng, W. X. Tang, *Dalton Trans.* **2003**, 3283; f) R. W. Saalfrank, I. Bernt, F. Hampel, A. Scheurer, T. Nakajima, S. H. Z. Huma, F. W. Heinemann, M. Schmidtmann, A. Müller, *Polyhedron* **2003**, *22*, 2985; g) V. Tudor, G. Marin, V. Kravtsov, Yu. A. Simonov, J. Lipkowski, M. Brezeanu, M. Andruh, *Inorg. Chim. Acta* **2003**, *353*, 35; h) V. G. Makhankova, O. Yu. Vassilyeva, V. N. Kokozay, B. W. Skelton, J. Reedijk, G. A. Van Albada, L. Sorace, D. Gatteschi, *New J. Chem.* **2001**, *25*, 685; i) K. H. Whitmire, J. C. Hutchison, A. Gardberg, C. Edwards, *Inorg. Chim. Acta* **1999**, *294*, 153; j) H. Oshio, Y. Saito, T. Ito, *Angew. Chem.* **1997**, *109*, 2689; *Angew. Chem. Int. Ed. Engl.* **1997**, *36*, 2673.

[6] a) A. E. Shilov, G. B. Shul'pin, *Activation and Catalytic Reactions of Saturated Hydrocarbons in the Presence of Metal Complexes*, Kluwer, Dordrecht, **2000**; b) R. Whyman, *Applied Organometallic Chemistry and Catalysis*, Oxford University Press, Oxford, **2001**.

 © 2005 Wiley-VCH Verlag GmbH & Co. KGaA, Weinheim

[7] For reviews see: a) U. Schuchardt, D. Cardoso, R. Sercheli, R. Pereira, R. S. da Cruz, M. C. Guerreiro, D. Mandelli, E. V. Spinace, E. L. Pires, *Appl. Catal. A* **2001**, *211*, 1; b) J. M. Bregeault, *Dalton Trans.* **2003**, 3289; c) G. B. Shul'pin, *J. Mol. Catal. A* **2002**, *189*, 39; d) G. B. Shul'pin, G. V. Nizova, Y. N. Kozlov, I. G. Pechenkina, *New J. Chem.* **2002**, *26*, 1238; e) U. Schuchardt, W. A. Carvalho, E. V. Spinace, *Synlett* **1993**, *10*, 713.

[8] a) G. B. Shul'pin, G. V. Nizova, Y. N. Kozlov, L. G. Cuervo, G. Süss-Fink, *Adv. Synth. Catal.* **2004**, *346*, 317; b) I. Bar-Nahum, A. M. Khenkin, R. Neumann, *J. Am. Chem. Soc.* **2004**, *126*, 10236; c) R. A. Periana, G. Bhalla, W. J. Tenn, K. J. H. Young, X. Y. Liu, O. Mironov, C. J. Jones, V. R. Ziatdinov, *J. Mol. Catal. A* **2004**, *220*, 7; d) Q. Zhang, D. He, Q. Zhu, *J. Nat. Gas Chem.* **2003**, *12*, 81; e) M. Muehlhofer, T. Strassner, W. H. Herrmann, *Angew. Chem.* **2002**, *114*, 1817; *Angew. Chem. Int. Ed.* **2002**, *41*, 1745; f) D. Wolf, *Angew. Chem.* **1998**, *110*, 3545; *Angew. Chem. Int. Ed.* **1998**, *37*, 3351; g) C. Jia, T. Kitamura, Y. Fujiwara, *Acc. Chem. Res.* **2001**, *34*, 633.

[9] a) A. O. Kuzmin, G. L. Elizarova, L. G. Matvienko, E. R. Salivanova, V. N. Parmon, *Mendeleev Commun.* **1998**, 210; b) E. D. Park, Y.-S. Hwang, C. W. Lee, J. S. Lee, *Appl. Catal. A* **2003**, *247*, 269.

[10] X-ray crystal-structure analyses: **1**: $C_{13}H_{21}CuNO_6$, $M_r = 350.85$, monoclinic, $P21/n{:}b2$, crystal size $0.66 \times 0.43 \times 0.25\ mm^3$, $a = 7.556(5)$, $b = 26.922(5)$, $c = 8.014(5)$ Å, $\alpha = 90.046(5)$, $\beta = 111.070(5)$, $\gamma = 89.980(5)°$, $V = 1521.2(14)$ Å^3, $T = 293(2)$ K, $Z = 4$, $\rho_{calcd} = 1.523\ Mg\,m^{-3}$, $\mu = 1.461\ mm^{-1}$, $F(000) = 724$, max/min transm. = 0.7115/0.4456, $\Theta = 1.51$–$25.08°$; 5318 reflections observed, 2680 unique ($R_{int} = 0.1244$); $R1 = 0.0583$, $wR2 = 0.1467$ ($I > 2\sigma(I)$), $R1 = 0.0908$, $wR2 = 0.1663$ (all data), largest difference peak and hole: 1.137/−0.803 e Å^{-3}. **2**: $C_{52}H_{90}Cu_6N_4O_{34}$, $M_r = 1696.52$, monoclinic, $C2/c$, crystal size $0.14 \times 0.09 \times 0.05\ mm^3$, $a = 20.1793(4)$, $b = 11.2602(2)$, $c = 16.1429(2)$ Å, $\alpha = \gamma = 90$, $\beta = 116.5880(10)°$, $V = 3280.13(10)$ Å^3, $T = 100(2)$ K, $Z = 2$, $\rho_{calcd} = 1.718\ Mg\,m^{-3}$, $\mu = 2.007\ mm^{-1}$, $F(000) = 1752$, max/min transm. = 0.34702/0.30557, $\Theta = 3.11$–$26.36°$, 20924 reflections observed, 3341 unique ($R_{int} = 0.0383$); $R1 = 0.0338$, $wR2 = 0.0895$ ($I > 2\sigma(I)$), $R1 = 0.0380$, $wR2 = 0.0927$ (all data), largest difference peak and hole: 2.021/−0.869 e Å^{-3}. **3**: $C_{24}H_{52}B_6Cu_4F_8N_4O_{17}$, $M_r = 1139.72$, triclinic, $\bar{P}1$, crystal size $0.32 \times 0.27 \times 0.25\ mm^3$, $a = 12.1081(3)$, $b = 18.4078(4)$, $c = 18.6603(5)$ Å, $\alpha = 98.928(2)$, $\beta = 100.5170(10)$, $\gamma = 101.041(2)°$, $V = 3934.82(17)$ Å^3, $T = 100(2)$ K, $Z = 4$, $\rho_{calcd} = 1.924\ Mg\,m^{-3}$, $\mu = 2.248\ mm^{-1}$, $F(000) = 2312$, max/min transm. = 0.6001/0.5305, $\Theta = 3.06$–$26.00°$; 47993 reflections observed, 15132 unique ($R_{int} = 0.0384$); $R1 = 0.0495$, $wR2 = 0.1203$ ($I > 2\sigma(I)$), $R1 = 0.0726$, $wR2 = 0.1376$ (all data), largest difference peak and hole: 1.929/−0.761 e Å^{-3}. **4**: $C_{10}H_{18}CuNO_6$ $M_r = 311.79$, triclinic, $\bar{P}1$, crystal size $0.26 \times 0.18 \times 0.11\ mm^3$, $a = 7.4983(8)$, $b = 7.9730(6)$, $c = 10.8652(13)$ Å, $\alpha = 84.071(8)$, $\beta = 89.669(8)$, $\gamma = 70.382(6)°$, $V = 608.30(11)$ Å^3, $T = 100(2)$ K, $Z = 2$, $\rho_{calcd} = 1.702\ Mg\,m^{-3}$, $\mu = 1.815\ mm^{-1}$, $F(000) = 324$, max/min transm. = 0.8212/0.6448, $\Theta = 2.73$–$27.50°$; 6244 reflections observed, 2748 unique ($R_{int} = 0.0174$); $R1 = 0.0251$, $wR2 = 0.0576$ [$I > 2\sigma(I)$], $R1 = 0.0315$, $wR2 = 0.0601$ (all data), largest difference peak and hole: 0.468/−0.354 e Å^{-3}. CCDC 259925 (**1**), 259926 (**2**), 259927 (**3**), and 259928 (**4**) contain the supplementary crystallographic data for this paper. These data can be obtained free of charge from The Cambridge Crystallographic Data Centre via www.ccdc.cam.ac.uk/data_request/cif.

[11] G. B. Shul'pin, Y. N. Kozlov, G. V. Nizova, G. Süss-Fink, S. Stanislas, A. Kitaygorodskiy, V. S. Kulikova, *J. Chem. Soc. Perkin Trans. 2* **2001**, 1351.

[12] L. M. Slaughter, J. P. Collman, T. A. Eberspacher, J. I. Brauman, *Inorg. Chem.* **2004**, *43*, 5198.

[13] R. W. Cruse, S. Kaderli, C. J. Meyer, A. D. Zuberbühler, K. D. Karlin, *J. Am. Chem. Soc.* **1988**, *110*, 5020.

 © 2005 Wiley-VCH Verlag GmbH & Co. KGaA, Weinheim

Copolymer Synthesis

Synthesis and Self-Assembly of Rod–Rod Hybrid Poly(γ-benzyl L-glutamate)-*block*-Polyisocyanide Copolymers**

Alexander Kros, Wim Jesse, Gerald A. Metselaar, and Jeroen J. L. M. Cornelissen**

Dedicated to Professor Roeland J. M. Nolte on the occasion of his 60th birthday

The synthesis and self-assembly of rod–rod block copolymers is still a pristine area in the field of polymer chemistry.[1,2] Nevertheless, it promises applications, for example, as biosensors, scaffolds for tissue engineering, and materials with new properties.[3] To our knowledge only two publications on rod–rod block copolymers have been published till now. Deming and co-workers synthesized polyleucine–poly(hydroxylated glutamate), which formed large vesicular systems in water.[4] This block copolymer was prepared by an elegant method developed by this group for the living polymerization of *N*-carboxy anhydrides of amino acids (NCAs) using a 2,2′-bipyridylnickel(0)(1,5-cyclooctadiene) [Ni(bpy)(cod)] complex as the catalyst.[5] This synthetic method enabled not only the preparation of the above system but also of a host of block polypeptides.[6] The synthesis and self-assembly of hybrid block copolymers containing a π-conjugated polymer and peptide segment was described by Jenekhe and Kong.[7] Upon changing the secondary conformation (that is, helix versus coil) of the peptide segment in a polyfluorene–poly(γ-benzyl glutamate), different types of nanosized assemblies were observed.

Cornelissen and co-workers studied the polymerization and self-assembly of isocyanopeptide polymers[8] and rod–coil block copolymers containing this peptidomimetic segment.[9] These peptide-derived polyisocyanides have unique properties that result from the intramolecular β-sheetlike hydrogen-

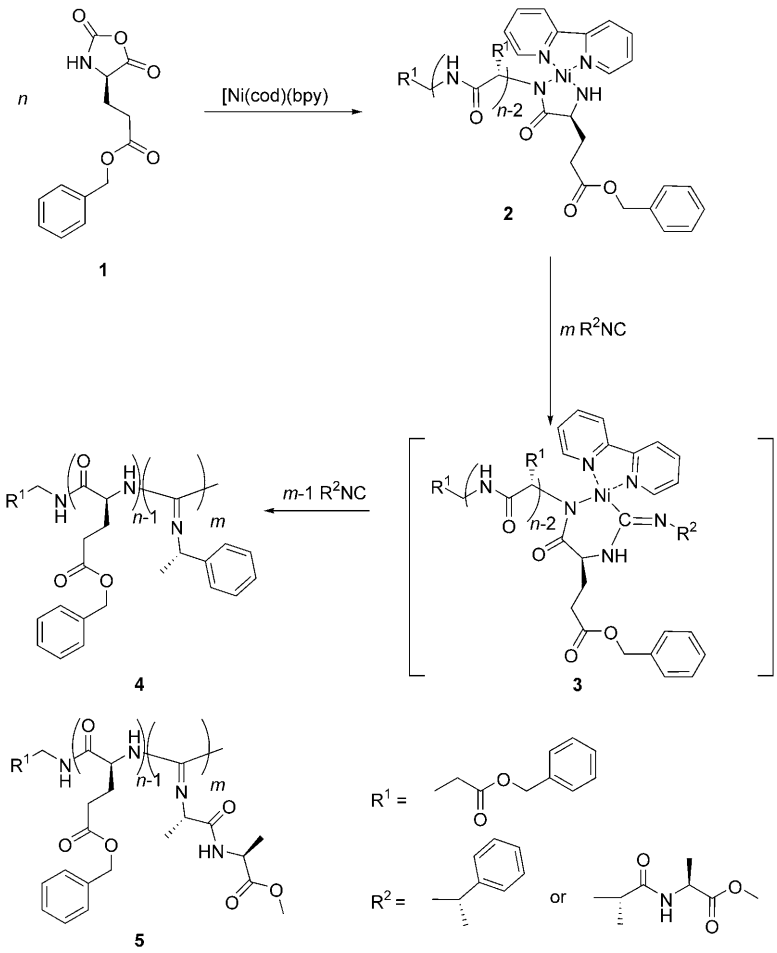
[*] Dr. A. Kros, W. Jesse
Department of Soft Matter Chemistry
Leiden Institute of Chemistry
Leiden University
PO Box 9502, 2300RA Leiden (The Netherlands)
Fax: (+31) 71-527-4397
E-mail: a.kros@chem.leidenuniv.nl
G. A. Metselaar, Dr. J. J. L. M. Cornelissen
Department of Organic Chemistry
Institute for Molecules and Materials
Radboud University Nijmegen
Toernooiveld 1, 6525ED Nijmegen (The Netherlands)
Fax: (+31) 24-365-2929
E-mail: j.cornelissen@science.ru.nl

[**] The Council for the Chemical Sciences of the Netherlands Organization for Scientific Research is acknowledged for Veni Innovative Research Grants to A.K. and J.J.L.M.C. We are grateful to Prof. Hans Fraaije and Dr. P. Budzelaar for stimulating discussions.

Supporting information for this article is available on the WWW under http://www.angewandte.org or from the author.

 DOI: 10.1002/anie.200500877 © 2005 Wiley-VCH Verlag GmbH & Co. KGaA, Weinheim

bonding arrays formed between the polymer side arms. The resultant macromolecules are stiffer than DNA, as determined by atomic force microscopy (AFM) studies.[10] The polymerization of isocyanides using nickel salts as a catalyst has been studied in Nolte's research group for several years.[11] From these investigations it was postulated that the polymerization of the isocyanide monomers occurs via a so-called "merry-go-round" mechanism around the central nickel atom resulting in a 4_1 (four repeat units per turn) helix, which is formed as the kinetic product. We have investigated the possibility of using the living polymerization catalyst developed by Deming,[5] which is formed by the action of NCAs on [Ni(bpy)(cod)],[5] as a catalyst for the polymerization of isocyanides. A catalyst that can be applied to two different monomers has great potential, as it allows the synthesis of a whole new class of rod–rod block copolymers with multiple structural motifs (for example, an α-helical peptide segment combined with a β-helical polyisocyanopeptide segment) and consequently unique properties. Herein, we describe the synthesis and self-assembly of hybrid block copolymers composed of a poly(γ-benzyl L-glutamate) block (PBLG) and two different polyisocyanide blocks, namely, poly((*S*)-(−)-α-methylbenzyl isocyanide) (PMBI) and poly(L-isocyanoalanyl-L-alanine methyl ester) (L,L-PIAA).



Scheme 1. Synthesis of PBLG-*block*-PMBI (**4**) and PBLG-*block*-L,L-PIAA (**5**) by a combination of *N*-carboxyanhydride ring-opening and isocyanide polymerization.

The diblock copolymers were synthesized by the nickel-catalyzed living polymerization of γ-benzyl L-glutamate *N*-carboxyanhydride (Bn-Glu NCA, **1**) according to the procedure of Deming and co-workers (Scheme 1),[5,6] followed by the addition of (*S*)-(−)-α-methylbenzyl isocyanide (MBI) or L-isocyanoalanyl-L-alanine methyl ester (L,L-IAA) to the reaction mixture. Upon addition of the isocyanide to the PBLG homopolymer with the active nickel complex still attached (intermediate **2**, Scheme 1),[5] a color change from red to yellow was observed, which indicated an alteration in the coordination sphere of the metal. From previous studies by Deming and co-workers[12] it is known that the N-terminus of the growing polypeptide chain can be terminated when **2** is treated with an electrophile. An isocyanide coordinated to a nickel(II) center is an electrophilic species. We therefore expect that the coordinated primary amine is able to react with an incoming isocyanide, likely through the temporary formation of a five-coordinate complex,[13] to yield a carbene-like initiator complex for the isocyanide polymerization.[9,11] This polymerization subsequently commences through the coordination of free monomers to the formally nickel(II) center (possibly helped by the partial dissociation of the bpy ligand) and their insertion in the growing polyisocyanide chain. More detailed experiments to elucidate the precise polymerization mechanism are currently in progress.

During polymerization of the L,L-IAA monomer, gelation of the reaction mixture was observed within minutes after addition of the isocyanide, which indicates its rapid polymerization and the formation of high-molecular-weight material. After workup, block copolymers free from residual homopolymers were isolated by selective solvent extractions. The block copolymers were characterized by ^{1}H NMR, FTIR, and CD spectroscopy and gel permeation chromatography (GPC; see the Supporting Information for details).

PBLG and the copolymers were first studied by GPC in THF, which provided direct evidence of the formation of the block copolymers. PBLG aggregates in this solvent, and thus gives rise to a broad peak.[14] The resultant block copolymer had a smaller elution volume, which indicates a higher molecular weight than the PBLG homopolymer. However, the rigid nature of the copolymers prevented calibration with standards such as polystyrene. The polymers were subsequently studied in 0.1 M LiBr in DMF at 65 °C. While PBLG is completely soluble without any aggregation in this solvent, the block copolymers did not dissolve, thus indicating the absence of any residual homopolymer. GPC analysis at 65 °C in this solvent provided the molecular weight parameters of the PBLG block isolated from a sample taken before addition of the isocyanide monomers, which allows the determination of the degree of polymerization of the block copolymers by ^{1}H NMR spectroscopy (Table 1). The degree of polymeri-

 © 2005 Wiley-VCH Verlag GmbH & Co. KGaA, Weinheim

Table 1: Molecular weight data for PBLG-*block*-polyisocyanide polymers.

Entry	Polymer	PBLG segment[a] [kg mol^{-1}]	DP[b]	PBLG[a] M_w/M_n	Block ratio[c] (DP[b])	Polyisocyanide[d] [kg mol^{-1}]	Block copolymer[d] [kg mol^{-1}]
1	PBLG-*block*-PMBI	30	146	1.30	0.89 (130)	17	47
2	PBLG-*block*-PMBI	25	122	1.20	1.27 (155)	26	52
3	PBLG-*block*-L,L-PIAA	35	170	1.43	7.3 (1244)	229	264
4	PBLG-*block*-L,L-PIAA	46	225	1.47	5.2 (1163)	214	260

[a] Molecular weight data were obtained by GPC at 65 °C by using 0.1 M LiBr in DMF as the solvent and polystyrene standards. [b] Degree of polymerization. [c] Determined by integration of the ^{1}H NMR spectrum measured in $CDCl_3$ or CD_2Cl_2. [d] Determined by using GPC data of the PBLG block and ^{1}H NMR data of the block copolymer.

zation (DP) of the polyisocyanide block was determined by analysis of the integrals of the protons of the methyl groups in the case of L,L-PIAA, or the phenyl group in the case of PMBI, relative to the benzylic protons of the PBLG segment. Further evidence for the formation of block copolymers came from AFM studies. A relatively short contour length was observed for the polypeptide homopolymer upon deposition of the sample on mica (not shown), while significantly longer individual polymer chains could be visualized for the block copolymers (Figure 1).



Figure 1. AFM image of isolated PBLG-*block*-L,L-PIAA strands. The sample was prepared from a 0.01 g L^{-1} polymer solution in $CHCl_3$.

FTIR spectroscopic studies were carried out on films cast from a suitable solvent. A selection of the IR vibrations is given in Table 2. The PBLG homopolymer adopts a typical α-helical structure as is evident from the amide I and amide II positions. No indications were found for β-sheet secondary structures. The block copolymers showed a shoulder ($\tilde{\nu}$ = 1614 cm^{-1}) on the amide I vibration, indicative of an imine IR vibration. In the case of PBLG-*block*-PMBI, an amide I vibration was observed at 1650 cm^{-1}, showing the stability of the α-helical PBLG. A shift was observed in PBLG-*block*-L,L-PIAA, which indicates that a mixture of the PBLG α-helix and the β-sheet of L,L-PIAA was present.

Table 2: Selected IR spectroscopic data [cm^{-1}].

Polymer	$\tilde{\nu}_{\text{amide I}}$	$\tilde{\nu}_{\text{amide II}}$	$\tilde{\nu}_{\text{amide A}}$
PBLG	1650.0	1548.0	3292.0
L,L-PIAA	1657.0	1532.0	3276.0
PBLG-*block*-L,L-PIAA	1654.0	1530.3	3270.5
PBLG-*block*-PMBI	1650.0	1548.0	3291.0

CD analysis confirmed the existence of conformationally ordered block copolymers, in agreement with the FTIR studies. The helical structure of the PBLG segment gave a double minimum at 222 and 210 nm. Furthermore, the chiral polyisocyanopeptide displayed a single Cotton effect centered around ≈315 nm, which is typical for the n–π* transition of the C=N chromophores in these materials.[8] Together the FTIR and CD spectra revealed that the PBLG-*block*-L,L-PIAA has three secondary structural motifs within one macromolecule, that is, an α-helical polypeptide segment and a polyisocyanide helix with side arms organized in a parallel β-sheet, which to our knowledge is unprecedented.

Preliminary self-assembly studies were performed in organic solutions. The formation of spherical objects was observed upon fast drying of a solution of PBLG-*block*-L,L-PIAA (Figure 2). Confocal laser scanning microscopy revealed that these objects were actually polymersomes with a uniform diameter of 7.5 μm (standard deviation of 0.9 μm).[15] Slow evaporation resulted in the formation of closed films, which suggests that the polymersomes are a kinetically trapped architecture. Polarized optical microscopy studies showed that the polymers were aligned and confirmed that the polymersomes were hollow (Figure 2). However, PBLG-*block*-PMBI was unable to assemble into spheres and only formed a continuous film. The absence of the stabilizing hydrogen-bonding array along the polymeric backbone of the polyisocyanide segment in this block copolymer will likely result in a less well-defined helix, which in return will affect the self-organizing properties of the macromolecule.[3] This finding may explain why no defined aggregates are formed from PBLG-*block*-PMBI under the applied conditions.

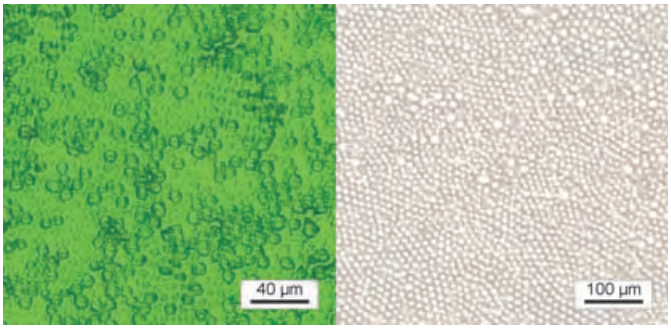


Figure 2. Confocal laser scanning (left) and optical microscope (right) images showing the typical morphologies of PBLG-*block*-L,L-PIAA. The sample was prepared by spreading drops of dilute chloroform solutions (1 mg mL^{-1}) on glass slides.

In summary, we have found a route to synthesize rigid rod–rod block copolymers comprising a peptide block and a

 © 2005 Wiley-VCH Verlag GmbH & Co. KGaA, Weinheim

polyisocyanide block. These compounds assemble upon drying into ordered layers of hollow capsules with potential applications in the fields of therapeutics or biomaterials. All protected amino acids and isocyanides are in principle compatible with the block copolymer synthesis, which allows a wealth of hybrid materials to be synthesized. As the secondary structure of the polymer segments can be controlled, for example, during the synthesis or by external stimuli, it is expected that aggregate formation can also be controlled.[4,9] In-depth investigations of the self-assembly of the block copolymers and the polymerization mechanism are in progress.

Received: March 9, 2005
Published online: June 20, 2005

Keywords: block copolymers · peptides · self-assembly · vesicles

[1] For examples of self-assembling coil–coil diblock copolymers, see: a) D. E. Discher, A. Eisenberg, *Science* **2002**, *297*, 967 – 973, and references therein; b) N. S. Cameron, M. K. Corbierre, A. Eisenberg, *Can. J. Chem.* **1999**, *77*, 1311 – 1326.
[2] For examples of self-assembling rod–coil diblock copolymers, see: a) S. A. Jenekhe, X. L. Chen, *Science* **1998**, *279*, 1903 – 1907; b) S. A. Jenekhe, X. L. Chen, *Science* **1999**, *283*, 372 – 375; c) M. Muthukumar, C. K. Ober, E. L. Thomas, *Science* **1997**, *277*, 1225 – 1231; d) F. Chécot, S. Lecommandoux, Y. Gnanou, H.-A. Klok, *Angew. Chem.* **2002**, *114*, 1395 – 1399; *Angew. Chem. Int. Ed.* **2002**, *41*, 1339 – 1343.
[3] R. A. L. Jones, *Nat. Mater.* **2004**, *3*, 209 – 210.
[4] E. G. Bellomo, M. D. Wyrsta, L. Pakstis, D. J. Pochan, T. J. Deming, *Nat. Mater.* **2004**, *3*, 244 – 248.
[5] a) T. J. Deming, *Nature* **1997**, *390*, 386 – 389; b) T. J. Deming, S. A. Curtin, *J. Am. Chem. Soc.* **2000**, *122*, 5710 – 5717.
[6] a) J. N. Cha, G. D. Stucky, D. E. Morse, T. J. Deming, *Nature* **2000**, *403*, 289 – 292; b) A. P. Nowak, V. Breedveld, L. Pakstis, B. Ozbas, D. J. Pine, D. Pochan, T. J. Deming, *Nature* **2002**, *417*, 424 – 428.
[7] X. Kong, S. A. Jenekhe, *Macromolecules* **2004**, *37*, 8180 – 8183.
[8] J. J. L. M. Cornelissen, J. J. J. M. Donners, R. de Gelder, W. S. Graswinckel, G. A. Metselaar, A. E. Rowan, N. A. J. M. Sommerdijk, R. J. M. Nolte, *Science* **2001**, *293*, 676 – 680.
[9] a) J. J. L. M. Cornelissen, M. Fischer, N. A. J. M. Sommerdijk, R. J. M. Nolte, *Science* **1998**, *280*, 1427 – 1430; b) D. M. Vriezema, A. Kros, R. de Gelder, J. J. L. M. Cornelissen, A. E. Rowan, R. J. M. Nolte, *Macromolecules* **2004**, *37*, 4736 – 4739.
[10] P. Samorì, C. Ecker, I. Gossl, P. A. J. de Witte, J. J. L. M. Cornelissen, G. A. Metselaar, M. B. J. Otten, A. E. Rowan, R. J. M. Nolte, J. P. Rabe, *Macromolecules* **2002**, *35*, 5290 – 5294.
[11] J. J. L. M. Cornelissen, A. E. Rowan, R. J. M. Nolte, N. A. J. M. Sommerdijk, *Chem. Rev.* **2001**, *101*, 4039 – 4070.
[12] K. R. Brzezinska, S. A. Curtin, T. J. Deming, *Macromolecules* **2002**, *35*, 2970 – 2976.
[13] A comparable insertion mechanism for isoelectronic CO has been postulated based both on experimental and theoretical studies. See: a) C. S. Shultz, J. M. DeSimone, M. Brookhart, *J. Am. Chem. Soc.* **2001**, *123*, 9172 – 9173; b) F. De Angelis, A. Sgamellotti, N. Re, *Organometallics* **2002**, *21*, 2036 – 2040.
[14] H. Block, *Poly(γ-benzyl L-glutamate) and Other Glutamic Acid Containing Polymers*, Gordon & Breach, New York, **1983**, p. 59.
[15] Large polymersomes were also observed upon assembly of rod–coil diblock copolymers; see ref. [2a].

 © 2005 Wiley-VCH Verlag GmbH & Co. KGaA, Weinheim

Carbon Dioxide Fixation

Copper(II) and Zinc(II) Complexes Can Fix Atmospheric Carbon Dioxide**

Ling-Yan Kong, Zheng-Hua Zhang, Hui-Fang Zhu, Hiroyuki Kawaguchi, Taka-aki Okamura, Mototsugu Doi, Qian Chu, Wei-Yin Sun, and Norikazu Ueyama*

In the past few decades various zinc(II) complexes with polyamine ligands have been synthesized as models of zinc(II)-containing enzymes, in particular carbonic anhydrase.[1] From these studies, zinc(II) and zinc(II)-bound hydroxides have been demonstrated to play important roles in the hydrolysis of the substrates. However, zinc(II)–polyamine complexes that can fix carbon dioxide have not been reported until recently.[2]

The chemical fixation and activation of carbon dioxide has drawn long-standing interest as excess CO_2 is an atmospheric pollutant and also because CO_2 could be used as an attractive C_1 feedstock for the preparation of useful carbon-containing compounds by the reaction of CO_2 with metal complexes.[3] So far, a great deal of research has been performed on the coordination chemistry of CO_2 and its hydration products HCO_3^- and CO_3^{2-}.[4]

The focus of our attention is the reaction of imidazole-containing ligands with a variety of metal salts.[5] Previous studies have shown that the nature of the organic ligand is crucial for determining the structure and properties of metal complexes.[6] Following this approach, we prepared a new ligand L (Scheme 1) by incorporation of an imidazole group into a polyamine ligand and report herein its copper(II) and zinc(II) complexes, which contain a network formed with the aid of CO_3^{2-}.

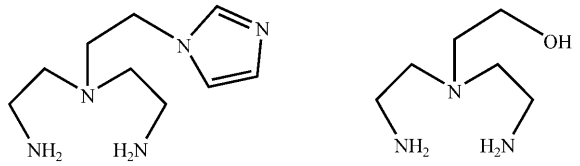
Treatment of a mixture of L and $M(ClO_4)_2{\cdot}6H_2O$ (M = Cu, Zn) with imidazole at pH 9 in air gave the complexes $[M_3(L)_3(\mu_3\text{-}CO_3)](ClO_4)_4{\cdot}n\,CH_3CN$ (**1a**: M = Cu, $n = 3$; **1b**:

[*] L.-Y. Kong, Z.-H. Zhang, Dr. H.-F. Zhu, Q. Chu, Prof. Dr. W.-Y. Sun
Coordination Chemistry Institute
State Key Laboratory of Coordination Chemistry
Nanjing University, Nanjing 210093 (China)
Fax: (+86) 25-8331-4502
E-mail: sunwy@nju.edu.cn
Dr. H. Kawaguchi
Coordination Chemistry Laboratories
Institute for Molecular Science
Okazaki, Aichi 444-8585 (Japan)
Dr. T.-a. Okamura, M. Doi, Prof. Dr. N. Ueyama
Department of Macromolecular Science
Graduate School of Science
Osaka University
Toyonaka, Osaka 560 (Japan)

[**] This work was supported by the National Natural Science Foundation of China (grant no. 20231020) and the National Science Fund for Distinguished Young Scholars (grant no. 20425101).

Supporting information for this article is available on the WWW under http://www.angewandte.org or from the author.

 © 2005 Wiley-VCH Verlag GmbH & Co. KGaA, Weinheim DOI: 10.1002/anie.200500587



Scheme 1. Structures of ligands L and L0.

M = Zn, $n = 1$) by slow evaporation. Subsequent crystallographic studies confirmed that **1a** and **1b** have the same framework structure, although they crystallize in a hexagonal unit cell with space group $P6_3$ and a trigonal unit cell with space group $P3c1$, respectively.[7] No imidazole or imidazolate group is found in the complex; instead, a carbonate anion is present. Complex **1b** can also be obtained by treatment of L with $Zn(ClO_4)_2 \cdot 6H_2O$ at pH 9 without addition of imidazole.

As illustrated in Figure 1a, each metal atom is coordinated by four N atoms from two different ligands L, and, in turn, each ligand L links two metal centers through its N donor atoms. It is noteworthy that three metal atoms and three ligands L form a trigonal M_3L_3 21-membered ring with a metal–metal separation of 9.24 Å in **1a** and 9.15 Å in **1b**. These trigonal rings are further linked by the μ_3-CO_3^{2-} anions through their three O atoms to generate a 2D network structure (Figure 1b). Thus, each metal center is pentacoordinated with a distorted trigonal-bipyramidal geometry. To the best of our knowledge, this is the first example of a polymeric carbonate complex with supramolecular use of a polyamine ligand containing an imidazole group, although di-, tri-, and tetranuclear zinc(II) carbonate complexes are known.[8] The cationic layers of **1a** and **1b** are packed in an ABAB fashion along the *c* axis to form trigonal channels filled with acetonitrile molecules. The perchlorate anions are located between the cationic layers.

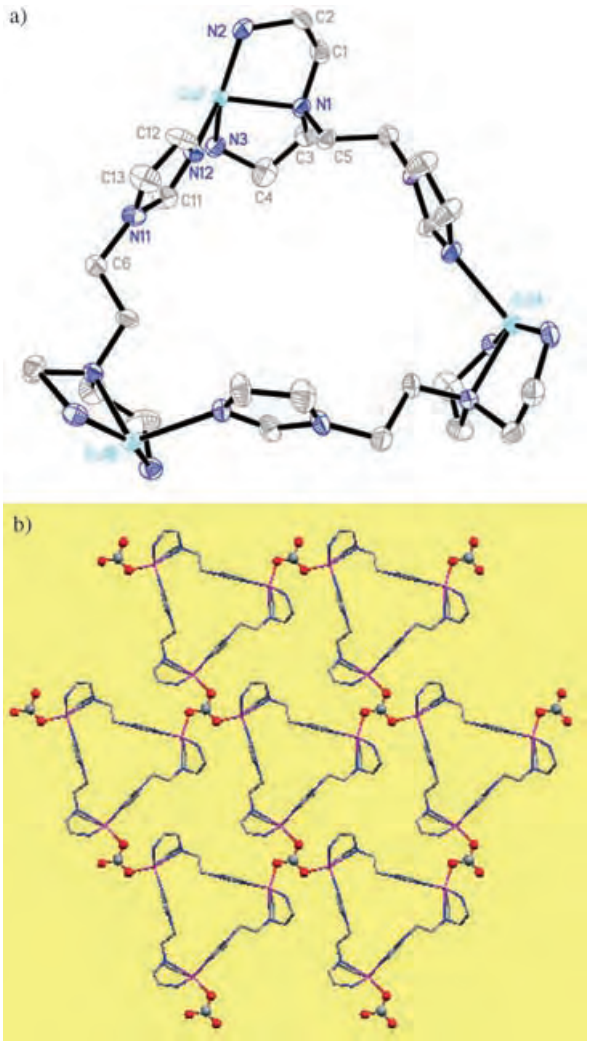


Figure 1. ORTEP drawing of a) the trigonal M_3L_3 structure of **1a**, with thermal ellipsoids at the 50% probability level, and b) the 2D network linked by carbonate anions.

To determine the origin of the carbonate ligands in **1a** and **1b**, the same reactions of L and imidazole with metal perchlorate salts were carried out under an inert atmosphere (Ar or N_2); the zinc(II) complex $[Zn_2(L)_2(im)](ClO_4)_3 \cdot 2CH_3CN \cdot 0.5H_2O$ (**2**; im = imidazolate anion) was successfully isolated and characterized. A single-crystal X-ray analysis[9] revealed that complex **2** features an infinite 1D ladder structure in which the imidazolate units act as the rungs (Figure 2). Each zinc(II) center has a slightly distorted

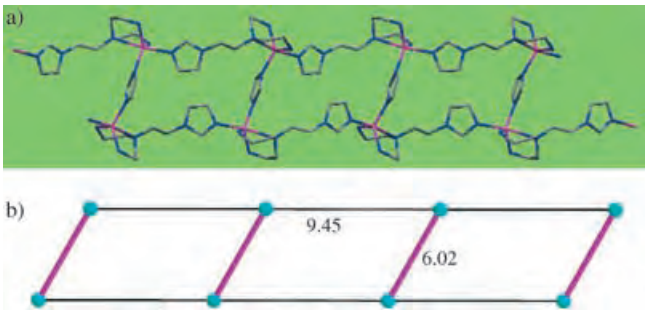


Figure 2. a) 1D ladder structure of **2**. b) The simplified ladder of **2**, where the ligands L and the imidazole units are presented by thin (black) and thick (violet) lines, respectively, and the solid balls denote zinc(II) centers.

trigonal-bipyramidal geometry which is the same as that in **1b**, except that the N atoms of the imidazolate ligands in **2** replace the O atoms of the carbonate ligands in **1b**. Similar to **1b**, each ligand L bridges two zinc(II) centers and each metal atom links two ligands L, although in this case to give an infinite 1D chain structure (Figure 2a) rather than an M_3L_3 ring (see Figure 1a). The imidazolate groups link zinc(II) centers from two 1D chains to form a noninterpenetrating 1D ladder structure (Figure 2a). The Zn···Zn distances in the ladder are 6.02 Å along the rungs and 9.45 Å along the side-rails (Figure 2b). The 1D ladders are linked together by hydrogen bonds with the perchlorate anions, and the voids between the ladders are filled with CH_3CN molecules.

The existence of the carbonate ligands in **1a** and **1b**, and the reaction of **2** with CO_2, were further investigated by IR and NMR spectroscopy. The IR spectra of **1a**, **1b**, and **2** were measured in the solid state. Strong carbonate-related vibra-

 © 2005 Wiley-VCH Verlag GmbH & Co. KGaA, Weinheim

tions are observed at 1440 cm^{-1} in **1a** and at 1457 cm^{-1} in **1b**.[10,11] The presence of carbonate ligands in **1b** was further confirmed by the solid-state ^{13}C NMR spectrum. As shown in Figure 3, a peak at $\delta = 167.9$ ppm is observed in the ^{13}C NMR spectrum of **1b**, which can be assigned to the coordinated

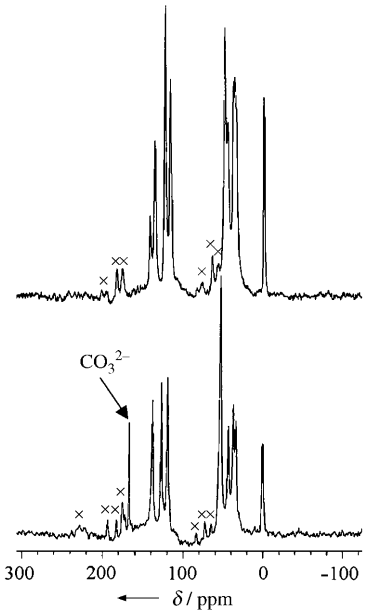


Figure 3. Solid-state ^{13}C NMR spectra of **1b** (bottom) and **2** (top). Peaks labeled with × are spinning sidebands.

carbonate ligand. Complex **2** was found to be stable in the solid state since no IR spectral changes were observed after three weeks of exposure of powdered **2** to the air.[11] However, in solution, the ^1H NMR spectra in CD_3CN/D_2O (2:1) show that **2** reacts with CO_2 quickly.[11] The reaction product of **2** with CO_2 in solution is **1b**, as confirmed by recrystallization of **2** from an aqueous acetonitrile solution in air by slow evaporation.[12]

These results clearly show that the carbonate anion in **1a** and **1b** comes from the hydration of atmospheric carbon dioxide, therefore the copper(II) and zinc(II) complexes of L can fix carbon dioxide. It should be noted that the introduction of the imidazole group into the ligand L plays a crucial role in fixing the CO_2, since the polyamine ligand L0 (see Scheme 1), which contains a hydroxy group, reacts with zinc(II) perchlorate hexahydrate in air to give mono- and dinuclear zinc(II) complexes without absorption of carbon dioxide.[13] In addition, the anion was found to strongly influence the formation of the infinite framework.[14]

Experimental Section

Synthesis of L: The amino groups of L0 were protected by reaction of L0 with phthalic anhydride. The amine-protected L0 (35 g, 0.086 mol) was brominated by slow addition of freshly distilled PBr_3 (7.5 mL) under N_2 in the temperature range 95–100 °C. The pure brominated product (10 g, 0.021 mol), well-ground K_2CO_3 (7.1 g, 0.051 mol), and imidazole (2.9 g, 0.042 mol) in dry dimethylformamide (50 mL) were stirred for 8 h at 100 °C. After cooling to room temperature, the solution was poured into saturated brine (100 mL) and extracted with ethyl acetate to give *N*-(2-imidazolylethyl)-*N*-bis(2-phthalimidoethyl)amine. Deprotection of the amino groups was carried out by treatment with hydrazine to give ligand L·4 HCl. Total yield from L0: ca. 20%, m.p. 192 °C.

Synthesis of **1a**: The reaction was carried out in an open vessel equipped with a magnetic stirrer at room temperature. A solution of $Cu(ClO_4)_2 \cdot 6H_2O$ (42.0 mg, 0.11 mmol) in water (2 mL) was added to an aqueous solution (2 mL) of L·4 HCl (38.9 mg, 0.11 mmol) at pH 8 (adjusted by addition of 0.5 M NaOH), and the pH value of the solution was then adjusted to 9 by further addition of 0.5 M NaOH. An aqueous solution (1.5 mL) of imidazole (7.7 mg, 0.11 mmol) was then added and the mixture stirred. The resulting colorless precipitate was dissolved by addition of acetonitrile (ca. 5 mL) to the mixture. Colorless crystals of **1a** were obtained, in about 50% yield, by slow evaporation of the filtrate over two or three days. $C_{34}H_{66}N_{18}O_{19}Cl_4Cu_3$: calcd. C 29.95, H 4.88, N 18.49; found C 29.72, H 4.84, N 18.43.

Synthesis of **1b**: This compound was obtained by the same procedure as described for **1a** but with $Zn(ClO_4)_2 \cdot 6H_2O$ (42.2 mg, 0.11 mmol) instead of $Cu(ClO_4)_2 \cdot 6H_2O$. Yield: ca. 60%. $C_{30}H_{60}N_{16}O_{19}Cl_4Zn_3$: calcd. C 28.00, H 4.70, N 17.42; found C 28.10, H 4.80, N 17.48.

Synthesis of **2**: This complex was synthesized following the same procedure as that for **1b** except that the reaction was carried out under an argon atmosphere at room temperature. The yield was ca. 50%. $C_{21}H_{42}N_{12}O_{12.5}Cl_3Zn_2$ (noncoordinated CH_3CN was lost upon drying) calcd. C 28.03, H 4.70, N 18.68; found C 27.77, H 4.63, N 18.65.

Crystallographic analyses: Crystallographic data for complex **1a** were collected with a Rigaku RAXIS-RAPID Imaging Plate diffractometer at 200 K, using graphite-monochromated $Mo_{K\alpha}$ radiation ($\lambda = 0.7107$ Å). The structure was solved by direct methods with SIR92 and expanded using Fourier techniques. The collection of crystallographic data for complexes **1b** and **2** was carried out on a Rigaku Mercury or a Saturn CCD area detector at 173 and 123 K, respectively, using graphite-monochromated $Mo_{K\alpha}$ radiation ($\lambda = 0.7107$ Å). The structure of **1b** was solved by Patterson methods with DIRDIF99 PATTY and that of **2** was solved by direct methods with SIR97 and expanded using Fourier techniques. All non-hydrogen atoms were refined anisotropically by the full-matrix least-squares method. The hydrogen atoms, except those of the water molecules, were generated geometrically. CCDC-263621 (**1a**), -263622 (**1b**), and -263623 (**2**) contain the supplementary crystallographic data for this paper. These data can be obtained free of charge from the Cambridge Crystallographic Data Centre via www.ccdc.cam.ac.uk/data_request/cif.

Received: February 17, 2005
Revised: April 21, 2005
Published online: June 17, 2005

Keywords: carbon dioxide fixation · copper · networks · NMR spectroscopy · zinc

[1] For recent reviews, see: a) G. Parkin, *Chem. Rev.* **2004**, *104*, 699–767; b) E. Kimura, *Acc. Chem. Res.* **2001**, *34*, 171–179; c) H. Vahrenkamp, *Acc. Chem. Res.* **1999**, *32*, 589–596.

[2] A copper(II) complex containing a polyamine moiety was recently reported to have CO_2-fixation properties: E. García-España, P. Gaviña, J. Latorre, C. Soriano, B. Verdejo, *J. Am. Chem. Soc.* **2004**, *126*, 5082–5083.

[3] a) W. Leitner, *Coord. Chem. Rev.* **1996**, *153*, 257–284; b) X. L. Yin, J. R. Moss, *Coord. Chem. Rev.* **1999**, *181*, 27–59; c) D. A. Palmer, R. van Eldik, *Chem. Rev.* **1983**, *83*, 651–731; d) D.

 © 2005 Wiley-VCH Verlag GmbH & Co. KGaA, Weinheim

Belli Dell'Amico, F. Calderazzo, L. Labella, F. Marchetti, G. Pampaloni, *Chem. Rev.* **2003**, *103*, 3857 – 3897.

[4] For some examples of carbonato–metal and bicarbonato–metal complexes, see: a) A. N. Acharya, A. Das, A. C. Dash, *Adv. Inorg. Chem.* **2004**, *55*, 127 – 199; b) Z. W. Mao, G. Liehr, R. van Eldik, *J. Am. Chem. Soc.* **2000**, *122*, 4839 – 4840; c) J. C. Kim, J. H. Cho, H. Kim, A. J. Lough, *Chem. Commun.* **2004**, 1796 – 1797; d) D. S. Marlin, M. M. Olmstead, P. K. Mascharak, *Inorg. Chem.* **2004**, *43*, 1681 – 1687.

[5] See, for example: a) J. Fan, L. Gan, H. Kawaguchi, W.-Y. Sun, K.-B. Yu, W.-X. Tang, *Chem. Eur. J.* **2003**, *9*, 3965 – 3973; b) J. Fan, H.-F. Zhu, T. Okamura, W.-Y. Sun, W.-X. Tang, N. Ueyama, *Chem. Eur. J.* **2003**, *9*, 4724 – 4731; c) J. Fan, H.-F. Zhu, T. Okamura, W.-Y. Sun, W. X. Tang, N. Ueyama, *Inorg. Chem.* **2003**, *42*, 158 – 162; d) J. Fan, W.-Y. Sun, T. Okamura, W. X. Tang, N. Ueyama, *Inorg. Chem.* **2003**, *42*, 3168 – 3175; e) S.-Y. Wan, J. Fan, T. Okamura, H.-F. Zhu, X.-M. Ouyang, W.-Y. Sun, N. Ueyama, *Chem. Commun.* **2002**, 2520 – 2521.

[6] For some recent reviews, see: a) S. Kitagawa, R. Kitaura, S. Noro, *Angew. Chem.* **2004**, *116*, 2388 – 2430; *Angew. Chem. Int. Ed.* **2004**, *43*, 2334 – 2375; b) S. R. Seidel, P. J. Stang, *Acc. Chem. Res.* **2002**, *35*, 972 – 983.

[7] Crystal data for **1a**: $C_{34}H_{66}N_{18}O_{19}Cl_4Cu_3$, crystal size: $0.30\times0.30\times0.25\ mm^3$, hexagonal, space group $P6_3$, $a=b=13.668(9)$, $c=17.200(15)$ Å, $V=2782(4)$ Å^3, $Z=2$, $\rho_{calcd}=1.627\ g\,cm^{-3}$, $\mu=1.413\ mm^{-1}$, $T=200$ K. 4253 Reflections and 257 parameters were used for the full-matrix, least-squares refinement on F^2. $R1=0.0324$ ($I>2\sigma(I)$), $wR2=0.0545$ (all data). Crystal data for **1b**: $C_{30}H_{60}N_{16}O_{19}Cl_4Zn_3$, crystal size: $0.20\times0.20\times0.15\ mm^3$, trigonal, $P3c1$, $a=b=13.664(7)$, $c=16.696(11)$ Å, $V=2699.6(3)$ Å^3, $Z=2$, $\rho_{calcd}=1.583\ g\,cm^{-3}$, $\mu=1.601\ mm^{-1}$, $T=173$ K. The final refinement on F^2 gave $R1=0.057$ ($I>2\sigma(I)$), $wR2=0.1650$ (all data) using 3910 observed reflections.

[8] For examples of di-, tri-, and tetranuclear zinc(II) carbonate complexes, see: a) F. Meyer, P. Rutsch, *Chem. Commun.* **1998**, 1037 – 1038; b) R. A. Allred, L. H. McAlexander, A. M. Arif, L. Berreau, *Inorg. Chem.* **2002**, *41*, 6790 – 6801; c) A. Trösch, H. Vahrenkamp, *Inorg. Chem.* **2001**, *40*, 2305 – 2311; d) M. Döring, M. Ciesielski, O. Walter, H. Görls, *Eur. J. Inorg. Chem.* **2002**, 1615 – 1621; e) M. Fondo, A. M. García-Deibe, M. R. Bermejo, J. Sanmartín, A. L. Llamas-Saiz, *J. Chem. Soc. Dalton Trans.* **2002**, 4746 – 4750; f) M. Fondo, A. M. García-Deibe, N. Ocampo, J. Sanmartín, M. R. Bermejo, *Dalton Trans.* **2004**, 2135 – 2141.

[9] Crystal data of **2**: $C_{25}H_{48}N_{14}O_{12.5}Cl_3Zn_2$, crystal size: $0.10\times0.10\times0.08\ mm^3$, triclinic, $P\bar{1}$, $a=10.805(5)$, $b=11.222(5)$, $c=18.333(6)$ Å, $\alpha=75.22(1)$, $\beta=72.94(1)$, $\gamma=86.46(2)°$, $V=2054.5(14)$ Å^3, $Z=2$, $\rho_{calcd}=1.587\ g\,cm^{-3}$, $\mu=1.436\ mm^{-1}$, $T=123$ K. The final refinement on F^2 gave $R1=0.085$ ($I>2\sigma(I)$), $wR2=0.236$ (all data) using 4238 observed reflections.

[10] a) A. Schrodt, A. Neubrand, R. van Eldik, *Inorg. Chem.* **1997**, *36*, 4579 – 4584; b) M. Kato, T. Ito, *Inorg. Chem.* **1985**, *24*, 504 – 508.

[11] See the Supporting Information for the IR and ^{1}H NMR spectra.

[12] X-ray structural analysis confirmed that the recrystallization product of **2** from aqueous acetonitrile solution is **1b**.

[13] J. Xia, Y. Xu, S. A. Li, W. Y. Sun, K. B. Yu, W. X. Tang, *Inorg. Chem.* **2001**, *40*, 2394 – 2401.

[14] For example, when $M(NO_3)_2{\cdot}4H_2O$ (M = Cu, Zn) was treated with ligand L under the same conditions as for the preparation of complexes **1a** and **1b**, the IR spectra of the reaction products showed no carbonate-related vibrations, which means that no carbon dioxide has been absorbed.

 © 2005 Wiley-VCH Verlag GmbH & Co. KGaA, Weinheim

Molecular Devices

A DNAzyme That Walks Processively and Autonomously along a One-Dimensional Track**

*Ye Tian, Yu He, Yi Chen, Peng Yin, and Chengde Mao**

Herein, we report a DNA nanodevice that autonomously and processively moves along a DNA track. The motion mechanism of this DNA device is reminiscent of that of single-headed myosins I, a family of cellular protein motors.[1] The DNA device contains a DNA enzyme (DNAzyme) that constantly extracts chemical energy from its substrate molecules (RNA) and uses this energy to fuel the motion of the DNA device.

Nanomachines have potential applications in smart materials, sensors, and optoelectronic devices.[2] Many approaches have been explored to develop such nanomachines. By taking advantage of a rich body of knowledge of DNA biophysics, various DNA nanomachines have been rationally designed and built based on conformational changes.[3] The motions include opening/closure, extension/contraction, and rotation. More complex nanomechanical devices, such as walkers and gears, have also been demonstrated.[3l,m,o] However, such devices need human intervention for each step of their motions. The DNA structures change only once when the conditions of the solution are changed or a DNA strand is added. These DNA devices are in sharp contrast with cellular protein motors and manmade machines at the macroscale, both of which can continuously work without human interference.

An autonomous DNA motor has recently been reported[3k,n]—here we refer to "autonomous" as being self-contained and not requiring human interference or other external active components such as protein enzymes. The motor performs an extremely simple motion: open and close. In a related, autonomous system, a DNA fragment could be continuously translocated along one direction by natural proteins (a combination of a DNA ligase and two restriction endonucleases).[3o] Logically, we wondered if it is possible to construct a more sophisticated, self-contained autonomous motor that could constantly walk or rotate. Herein, we demonstrate that such a machine is feasible.

The walking mechanism of the new system integrates DNAzyme activity and a strand-displacement strategy (Figure 1). The system consists of a walker and a track: The walker is a 10–23 DNAzyme, **E**,[4] which is a DNA molecule that can cleave RNA with sequence specificity (Figure 1A).

[*] Y. Tian, Y. He, Y. Chen, P. Yin, Prof. C. Mao
Department of Chemistry, Purdue University
West Lafayette, Indiana 47907 (USA)
Fax: (+1) 765-494-0239
E-mail: mao@purdue.edu

[**] This work was supported by the NSF (EIA-0323452), DARPA/DSO (MDA 972-03-1-0020), and Purdue University (a startup fund).

Supporting information for this article is available on the WWW under http://www.angewandte.org or from the author.

 DOI: 10.1002/anie.200500703 © 2005 Wiley-VCH Verlag GmbH & Co. KGaA, Weinheim

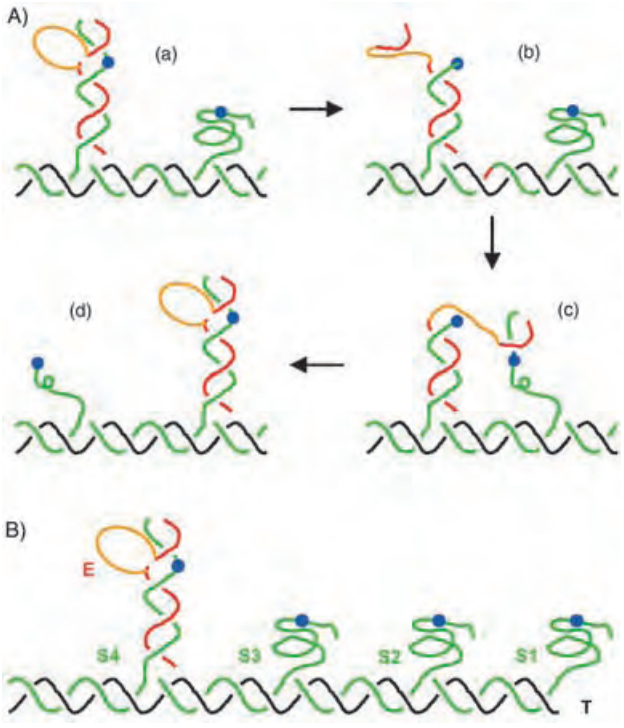


Figure 1. Scheme of a walking DNAzyme and its track. A) The walking principle. B) A construction where the walking DNAzyme is at one end of its track. Black lines: template (**T**); green lines: substrate (**S**); red/yellow lines: a 10–23 DNAzyme (red), with the catalytic core highlighted (yellow); blue dots indicate the bonds to be cleaved by the DNAzyme.

The 10–23 DNAzyme is the 23rd clone after the 10th round of selection in an experiment performed in vitro.[4] The track is a regular, linear array of RNA substrate, **S**. The 10–23 DNAzyme contains a catalytic core and two recognition arms that can bind to a RNA substrate through Watson–Crick base-pairing (Figure 1 A (a)). The two arms are asymmetrical by design: one arm is 7 bases long and the other is 15 bases long. When the RNA substrate is cleaved, the short fragment (7-base) dissociates from the DNAzyme and the long fragment (16-base), in contrast, remains stably associated with the DNAzyme under the experimental condition (b). After the short RNA fragment dissociates, the short arm of the DNAzyme becomes unpaired and can search for other complementary single strands. The RNA substrate next to the enzyme base-pairs with the short recognition arm of the DNAzyme (c). The resulting short duplex is stable as a result of intracomplex hybridization. Following this hybridization, a strand replacement occurs through branch migration, whereby the intact RNA substrate replaces the cleaved RNA fragment to result in a more stable, longer, pseudocontinuous DNA duplex (d). In this process, the DNAzyme moves from one RNA substrate to the next RNA substrate. The process can be repeated such that the DNAzyme moves continuously. Thus, the DNAzyme autonomously and processively moves along the track.

Herein, DNA–RNA chimeras were used as the substrate **S**. In the chimeras, only the two residues that flanked the bond to be cleaved were RNA residues, while all other residues were DNA. Such chimeras could be cleaved efficiently by the DNAzyme, but were more stable than RNA. Each **S** strand contained two segments: one for enzyme recognition and the other as a positional tag. A single template strand, **T**, could base-pair with the positional tags and organize four substrates (**S1**, **S2**, **S3**, and **S4**) into a regular, one-dimensional substrate array to constitute the track (Figure 1 B). The spacings between any two neighboring substrates was two helical turns (7 nm).

The overall DNA construct was stable. We assembled the DNA structure in a stepwise fashion and then analyzed all complexes by native polyacrylamide gel electrophoresis (PAGE, Figure 2). Each complex appeared as a single band with expected mobility which suggests that each combination of DNA strands led to the formation of a stable complex.

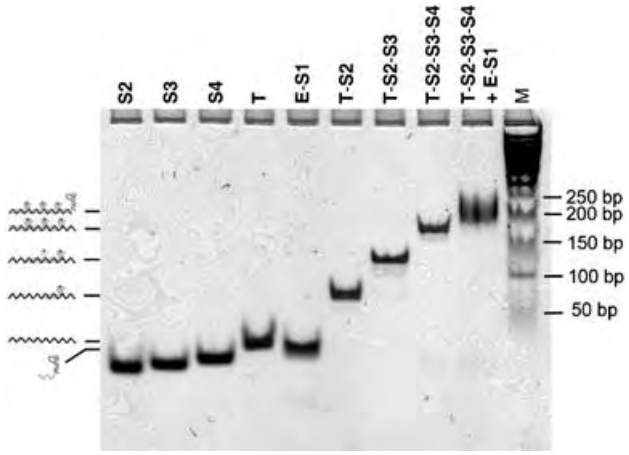


Figure 2. Native PAGE analysis of the DNA complexes. Lane M contains a series of DNA size markers (M = marker; bp = base pair).

The DNAzyme can walk in either direction, **S1**→**S4** or **S4**→**S1** (Figure 1 B). The movement of the DNAzyme was demonstrated by monitoring the differential behaviors of substrate cleavage (Figure 3). When the DNAzyme walks from **S1** to **S4**, the cleavage of the substrate would be in the time order of **S1**–**S2**–**S3**–**S4**, with **S1** cleaved initially and **S4** cleaved last of all. We performed an experiment to confirm this, with separate preparation of complexes **T**-**S2**-**S3**-**S4** and **E**-**S1** and then mixed the two complexes at 22 °C to form an intact track with the DNAzyme at **S1** (Figure 3). Upon mixing, the movement started. The DNAzyme moved from **S1** to **S2** to **S3** and finally to **S4**. This movement was accompanied by sequential cleavage of the substrate. Thus, the order of the substrate cleavage reflects the movement of the DNAzyme. Figure 3 A clearly shows that the digestion order is **S1**, **S2**, **S3**, and **S4**, which is consistent with the design. Note that a substantial population of **S1** was likely to be cleaved before or during association of complex **E**-**S1** with complex **T**-**S2**-**S3**-**S4**.

To further confirm this observation, we performed a similar experiment at 22 °C, but changed the movement to the opposite direction, **S4**→**S1**. Clearly, the order of cleavage reversed (Figure 3 B). When the walking process was performed at 37 °C in both directions, similar orders of substrate

 © 2005 Wiley-VCH Verlag GmbH & Co. KGaA, Weinheim

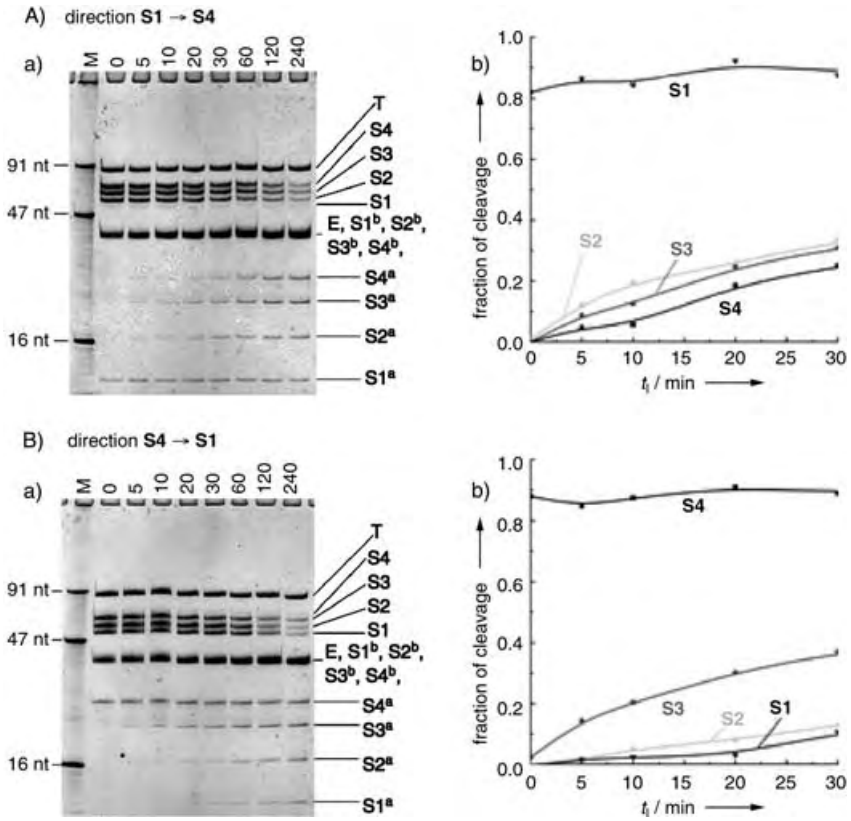


Figure 3. Denaturing PAGE monitoring the movement of the DNAzyme at 22 °C in the directions **S1**→**S4** (A) and **S4**→**S1** (B): a) gel images as a function of incubation time, t_i (lanes M contain three single-stranded DNA size markers; nt = nucleotide (bases); superscripts a and b denote short and long cleaved substrate fragments, respectively); b) quantification of the differential substrate cleavage.

cleavage were observed to those seen at 22 °C, but the process occurred faster at the higher temperature (see Supporting Information). When these walking experiments were repeated (at both temperatures and in both directions), exactly the same orders of substrate cleavage were observed (see Supporting Information).

To exclude the possibility that DNAzyme dissociates from the track after cleaving each substrate, we performed a control experiment (Figure 4). The DNAzyme and substrate

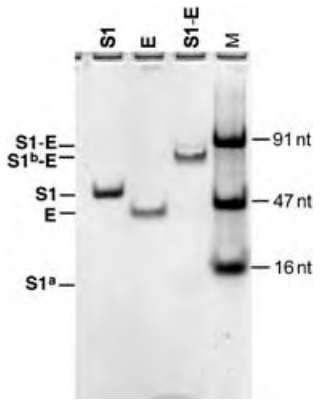


Figure 4. Native PAGE shows that complex **E-S**^{b} is stable, and no dissociation can be observed. Lane M contains three single-stranded DNA size markers.

(or the long cleaved substrate fragment) formed stable complexes under a native condition. The complexes migrated much slower than either the DNAzyme or the substrate alone by native PAGE, and no dissociation was observed. Thus, we confirmed that the DNAzyme did not dissociate from the track and that the movement was processive. In another control experiment, one substrate (**S4**) was incubated with the DNAzyme for two hours, and then another substrate (**S1**) was added to the solution. Upon addition of **S1**, aliquots of the mixture were withdrawn at various time intervals and the enzyme activity was quenched by addition of an excess of EDTA to remove free Mg^{2+}, an essential cofactor of the DNAzyme. The samples were then analyzed by both denaturing and native PAGE, which showed that **S4** was almost completely cleaved, while **S1** underwent almost no cleavage (see Supporting Information). This experiment confirmed that the enzyme could migrate from one substrate to another much more efficiently when both substrates were located along one track than when the substrates were in different complexes.

In conclusion, we have developed a DNA nanodevice that can autonomously move along an engineered track. In similar fashion to a cellular protein motor, it consumes chemical energy for autonomous motion. However, the current DNA device destroys its track when it walks, so the track is not reuseable. Relative to protein motors, the current DNA device moves extremely slowly. On the other hand, cellular protein motors move along straight protein tracks, whereas our engineered DNA system is much more versatile. It is conceivable to engineer tracks to allow a DNA device to move in a more complicated geometry—for example, smooth curves and sharp turns. Other questions that remain include: Can we develop a system with a reuseable track? Can we directly visualize the movement? Can the DNA device transport any cargo? Our next objective is to address these challenges.

Experimental Section

Oligonucleotides: All oligonucleotides were designed with a computer program SEQUIN[5] and purchased from Integrated DNA Technologies (IDT), Inc. Strand **E**: 5′-AGT GCT GAT TCG GAC AGG CTA GCT ACA ACG AGA GTG AC-3′; Strand **T**: 5′-ACC ATC TGT GGC ATA GCA GCG AGT ATC TAA CGC ATG GAA GCG TCG ATC TTG AGC ATT GGA GCG GCA ATC TCC TGC ATC ATC GCG-3′; Strand **S1**: 5′-TTT TTG TCA CTC rArUG TCC GAA TCA GCA CTT TCG CGA TGA TGC AGG AGA TTG C-3′; Strand **S2**: 5′-TTT TTT TTT TGT CAC TCrA rUGT CCG AAT CAG CAC TTT CGC GAT GAT GCA GGA GAT TGC-3′; Strand **S3**: 5′-TTT TTT TTT TTT TTT GTC ACT CrArU GTC

 © 2005 Wiley-VCH Verlag GmbH & Co. KGaA, Weinheim

CGA ATC AGC ACT TTC GCT TCC ATG CGT TAG ATA CT-3′; Strand **S4**: 5′-TTT TTT TTT TTT TTT TTT TTG TCA CTC rArUG TCC GAA TCA GCA CTT TCG CTG CTA TGC CAC AGA TGG T-3′.

Formation of the Walking System: 1) For the system in which the DNAzyme moved from **S1** to **S4**, the two parts (strands **E** and **S1** (part A); strands **T**, **S2**, **S3**, and **S4** (part B)) were prepared separately. For each part, 1.0 μM DNA strands were combined in an equimolar ratio in TAE/Mg^{2+} (TAE = Tris–acetate–EDTA; EDTA = ethylenediamine tetraacetic acid) buffer, which contained Tris buffer (40 mM, pH 8.0), acetic acid (20 mM), EDTA (2 mM), and $Mg(OAc)_2$ (12.5 mM). Parts A and B were formed by quickly cooling the DNA solution from 95 °C to 22 °C over 10 min. 2) For the system in which the DNAzyme moved from **S4** to **S1**, part A consisted of strands **E** and **S4** while part B consisted of strands **T**, **S1**, **S2**, and **S3**.

DNAzyme Walking: An equimolar ratio of parts A and B was mixed and then incubated at 22 °C or 37 °C to start the movement. At various time intervals during the experiment, a 10-μL aliquot was taken out and the reaction was quenched by the addition of a solution of EDTA (2 μL, 0.1 M) and formamide (6 μL), then the mixture was left on dry ice. All samples were then analyzed by denaturing PAGE.

Denaturing PAGE: Gels contained 20% polyacrylamide (acrylamide/bisacrylamide, 19:1) and urea (8.3 M) and were run at 55 °C. Tris–borate–EDTA (TBE) buffer, which comprised Tris (89 mm, pH 8.0), boric acid (89 mm), and EDTA (2 mm), was used as the separation buffer. Gels were run on a Hoefer SE 600 electrophoresis unit at 600 V (constant voltage).

Native PAGE: Gels contained 6–12% acrylamide (19:1, acrylamide:bisacrylamide) and TAE/Mg^{2+} buffer. 1 μL of a solution of tracking dye, which contained TAE/Mg^{2+}, 50% glycerol, and 0.2% each of Bromophenol Blue and Xylene Cyanol FF, was added to each sample (0.3 μg DNA in 10 μL of TAE/Mg^{-2+}). Gels were run on an FB VE-10–1 vertical electrophoresis system at 120 V (constant voltage) at 4 °C. Gels were stained with Stains-All (0.01% Stains-All from Sigma, 45% formamide) and then scanned.

Quantification of Reaction: Upon completion of electrophoresis, the gels were stained with Stains-All dye (Sigma) and the images were scanned into a computer as jpeg files. With the image files, each band was estimated using OptiQuant (Packard), an image analysis and processing software.

Received: February 24, 2005
Revised: March 29, 2005
Published online: June 9, 2005

Keywords: bioorganic chemistry · DNA · enzymes · molecular devices · nanotechnology

[1] J. A. Hammer, *Trends Cell Biol.* **1991**, *1*, 50.
[2] a) R. K. Soong, G. D. Bachand, H. P. Neves, A. G. Olkhovets, H. G. Craighead, C. D. Montemagno, *Science* **2000**, *290*, 1555; b) C. P. Collier, G. Mattersteig, E. W. Wong, Y. Luo, K. Beverly, J. Sampaio, F. M. Raymo, J. F. Stoddart, J. R. Heath, *Science* **2000**, *289*, 1172; c) A. M. Brouwer, C. Frochot, F. G. Gatti, D. A. Leigh, L. Mottier, F. Paolucci, S. Roffia, G. W. H. Wurpel, *Science* **2001**, *291*, 2124; d) D. A. Leigh, J. K. Y. Wong, F. Dehez, F. Zerbetto, *Nature* **2003**, *424*, 174; e) N. Koumura, R. W. J. Zijlstra, R. A. van Delden, N. Harada, B. Feringa, *Nature* **1999**, *401*, 152; f) H. G. Craighead, *Science* **2000**, *290*, 1532.
[3] a) C. Mao, W. Sun, Z. Shen, N. C. Seeman, *Nature* **1999**, *397*, 144; b) B. Yurke, A. J. Turberfield, A. P. Mills, F. C. Simmel, J. L. Neumann, *Nature* **2000**, *406*, 605; c) H. Yan, X. Zhang, Z. Shen, N. C. Seeman, *Nature* **2002**, *415*, 62; d) J. J. Li, W. Tan, *Nano Lett.* **2002**, *2*, 315; e) F. C. Simmel, B. Yurke, *Appl. Phys. Lett.* **2002**, *80*, 883; f) P. Alberti, J. Mergny, *Proc. Natl. Acad. Sci. USA* **2003**, *100*, 1569; g) A. J. Turberfield, J. C. Mitchell, B. Yurke, A. P. Mills, Jr., M. I. Blakey, F. C. Simmel, *Phys. Rev. Lett.* **2003**, *90*, 118102; h) L. Feng, S. H. Park, J. H. Reif, H. Yan, *Angew. Chem.* **2003**, *115*, 4478; *Angew. Chem. Int. Ed.* **2003**, *42*, 4342; i) D. Liu, S. Balasubramanian, *Angew. Chem.* **2003**, *115*, 5912; *Angew. Chem. Int. Ed.* **2003**, *42*, 5734; j) W. U. Dittmer, A. Reuter, F. C. Simmel, *Angew. Chem.* **2004**, *116*, 3634; *Angew. Chem. Int. Ed.* **2004**, *43*, 3550; k) Y. Chen, M. Wang, C. Mao, *Angew. Chem.* **2004**, *116*, 3638; *Angew. Chem. Int. Ed.* **2004**, *43*, 3554; l) W. Sherman, N. C. Seeman, *Nano Lett.* **2004**, *4*, 1203; m) J.-S. Shin, N. A. Pierce, *J. Am. Chem. Soc.* **2004**, *126*, 10834; n) Y. Chen, C. Mao, *J. Am. Chem. Soc.* **2004**, *126*, 8626; o) Y. Tian, C. Mao, *J. Am. Chem. Soc.* **2004**, *126*, 11410; p) P. Yin, H. Yan, X. G. Daniell, A. J. Turberfield, J. H. Reif, *Angew. Chem.* **2004**, *116*, 5014; *Angew. Chem. Int. Ed.* **2004**, *43*, 4906; q) W. Shen, M. F. Bruist, S. D. Goodman, N. C. Seeman, *Angew. Chem.* **2004**, *116*, 4854; *Angew. Chem. Int. Ed.* **2004**, *43*, 4750; r) W. U. Dittmer, F. C. Simmel, *Nano Lett.* **2004**, *4*, 689; s) M. Brucale, G. Zuccheri, B. Samori, *Org. Biomol. Chem.* **2005**, *3*, 575.
[4] S. W. Santoro, G. F. Joyce, *Proc. Natl. Acad. Sci. USA* **1997**, *94*, 4262.
[5] N. C. Seeman, *J. Biomol. Struct. Dyn.* **1990**, *8*, 573.
[6] While attending the workshop "*Engineering a DNA World*" at Caltech in January 2005, we became aware that Prof. M. N. Stojanovic at Columbia University was working on a related system.

 © 2005 Wiley-VCH Verlag GmbH & Co. KGaA, Weinheim

Molecular Devices

A Free-Running DNA Motor Powered by a Nicking Enzyme**

Jonathan Bath, Simon J. Green, and Andrew J. Turberfield*

Herein, we present a simple linear motor, built from DNA and a restriction enzyme, which moves a DNA cargo in discrete steps along a DNA track. Movement is powered by a nicking enzyme that cuts the track. Damage to the track in the wake of the cargo imposes directionality.

The specificity of base-pairing, the rigidity of short segments of the double helix, and the flexibility of single-stranded segments make DNA an ideal material for construction of nanometer-sized mechanical devices.[1–7] Such devices can generate forces of the order of picoNewtons,[2] in the same range as the forces developed by single-molecule

[*] Dr. J. Bath, S. J. Green, Prof. A. J. Turberfield
University of Oxford
Department of Physics
Clarendon Laboratory
Parks Road, Oxford OX1 3PU (UK)
Fax: (+44) 1865-272-400
E-mail: j.bath1@physics.ox.ac.uk

[**] This work was supported by the MoD and by the UK research councils BBSRC, EPSRC, and MRC through the UK Bionanotechnology IRC.

Supporting information for this article is available on the WWW under http://www.angewandte.org or from the author.

 © 2005 Wiley-VCH Verlag GmbH & Co. KGaA, Weinheim DOI: 10.1002/anie.200501262

protein motors.[8,9] A typical device relies on the binding of a fuel strand of DNA to trigger a conformational change. The device can be restored to its initial conformation by subsequent addition of a reset strand that strips the fuel strand from the device. The operation of these devices can be coupled to stepwise movement along a track.[10,11] There is interest in designing free-running devices that operate continuously while the supply of fuel lasts. One approach is to design a secondary structure to slow the conversion of DNA fuel into waste unless catalyzed, and to couple the catalysis of fuel to the operation of a device.[12] Another approach is to use the hydrolysis of the phosphodiester backbone of DNA[6] or a combination of DNA and ATP hydrolysis.[7] We have used the hydrolysis of DNA, catalyzed by a restriction enzyme, as the energy source for our motor. Autonomous, directional motion is achieved by making DNA cleavage conditional on the state of our device. The device moves a cargo stepwise along a one-dimensional track; damage caused to the track by the restriction enzyme prevents the cargo from stepping backwards and therefore imposes directionality—a "burnt bridges" mechanism.[13]

A suitable track is a rigid self-assembled structure with many identical single-stranded stators attached periodically along its length. Motion is driven by cleavage of the stators by the restriction endonuclease N.BbvC IB (New England Biolabs). N.BbvC IB binds to double-stranded DNA at a specific 7-bp (bp = base pair) recognition sequence and catalyzes cleavage of the DNA backbone of one strand only to introduce a nick at a precisely determined position. This nicking property has been specifically engineered by modification of the naturally occurring heterodimeric enzyme BbvC I.[14] The cargo is an oligonucleotide that can hybridize to any one of the stators. It is only when the cargo is hybridized to a stator that N.BbvC IB can cut the stator to release a short fragment of the stator and promote movement of the cargo onto the next stator along the track.

Figure 1 shows one step of the motor. In our experiments, the stators are 24-nt (nt = nucleotide) sequences attached to a double-stranded track every 21 bp (7 nm) by a 3-nt flexible linker. Stators are attached at the 3′ end and, when hybridized with the cargo, can be cut by N.BbvC IB at 8 nt from the 5′ end. The melting temperature of the 8-nt stator fragment generated by cutting is calculated to be between 13 °C and 20 °C, well below the operating temperature of the motor (37 °C). Figure 1 a shows the cargo bound to stator S_i. Cutting by N.BbvC IB releases an 8-nt fragment of the stator and promotes movement of the cargo onto an adjacent stator. Release of the short stator fragment leaves the cargo with an 8-nt single-stranded overhang that can bind to the intact stator S_{i+1}, initiating an energetically favorable step to S_{i+1} (Figure 1 b). The backwards step to S_{i-1} is strongly inhibited because S_{i-1}, which was cut in the previous step, lacks the 8-nt section that is complementary to the exposed overhang of the cargo. The step from S_{i+1} to S_i is a simple branch-migration reaction. The initial part of this reaction involves a random walk of the branch point that marks the junction between sections of the cargo bound to the competing stators S_i and S_{i+1}. For each base pair broken between cargo and S_i, a base pair can be formed between cargo and S_{i+1}. However, the lengths of the tethers that hold the stators to the rigid track limit this process, and stepping to S_{i+1} requires thermally activated, spontaneous dissociation of the last 3–6 nucleotides of the cargo from S_i. After spontaneous dissociation of the last few nucleotides, the cargo arrives at S_{i+1} (Figure 1 c) and the operational cycle is complete.

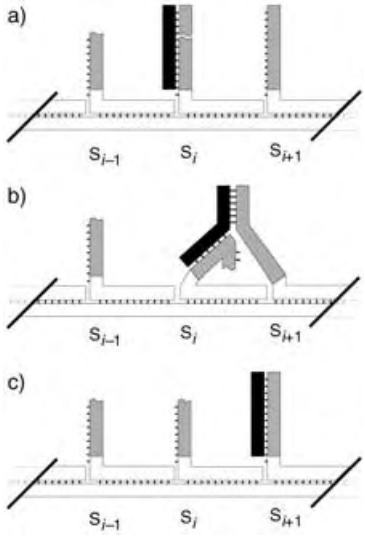


Figure 1. Design of a linear motor powered by a nicking enzyme. DNA strands are represented as black and gray ribbons, with black lines indicating base pairs. The track is an array of periodically spaced single-stranded stators. The cargo (black ribbon) is an oligonucleotide that can bind to any one of the stators. a) The cargo is bound to stator S_i which enables enzyme N.BbvC IB to cut the stator and release a short stator fragment and to leave the cargo with a single-stranded overhang free to bind to the adjacent stator S_{i+1}. The cargo cannot bind to S_{i-1} which was cut in the previous step. b) The cargo then steps onto S_{i+1} by a simple branch-migration reaction. For each base pair broken between cargo and S_i, a base pair can be formed between cargo and S_{i+1}. The tethers that hold the stators to the rigid track limit this process, and stepping to S_{i+1} requires spontaneous dissociation of the last few nucleotides of the cargo from S_i. c) Upon dissociation, the cargo is bound to S_{i+1} and the operational cycle is complete.

Our test track is composed of three stators, S_{1-3} (Figure 2 a, Table 1). The cargo is labeled at the 5′ end with the nonfluorescent quencher, Iowa Black. The track is labeled with Cy3 and Cy5 cyanine dyes, which are arranged such that when the cargo is bound to S_2 the signal from Cy3 is quenched and when the cargo is bound to S_3 the signal from Cy5 is quenched. The test track incorporates modifications to stators S_1 and S_3. The interaction between the cargo and S_1 spans 2 nt more than the interaction between the cargo and either S_2 or S_3 which ensures that the cargo binds more stably to S_1 than to either of the other stators: ΔG°_{37} is calculated to be -30.4, -27.1, and $-23.6\ \mathrm{kcal\,mol^{-1}}$ for binding to S_1, S_2, and S_3 respectively.[15] At equilibrium, under our experimental conditions, we calculate that the cargo is distributed between the stators S_1, S_2, and S_3 in a ratio of 94:6:$\ll$1. This distribution allows us to prepare the track with the cargo bound predominantly to S_1. The complex that forms between S_3 and the cargo contains a single mismatch within the N.BbvC IB recognition site that renders S_3 resistant to cutting.

 © 2005 Wiley-VCH Verlag GmbH & Co. KGaA, Weinheim

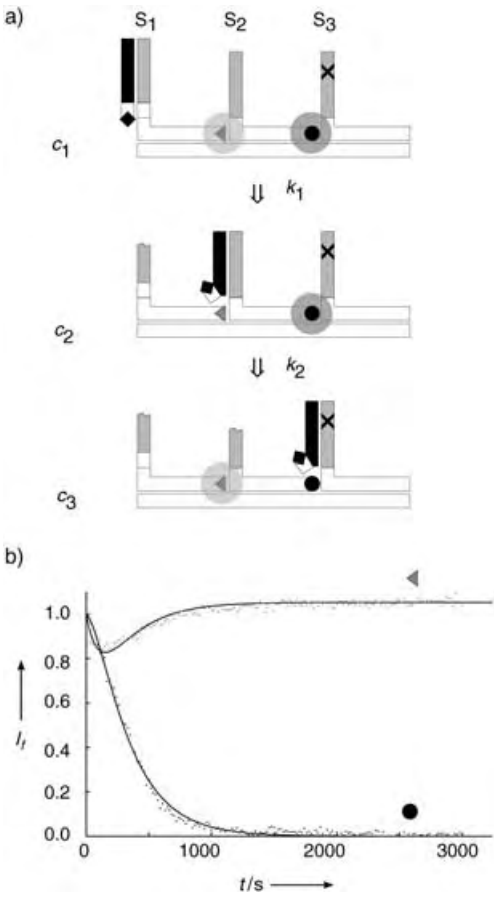


Figure 2. Operation of a linear motor powered by a nicking enzyme. a) The five strands of DNA used to assemble the test track are represented as ribbons. The black square represents the quencher Iowa Black carried by the cargo; as the cargo steps along the track, its position can be determined from the fluorescence signal of the two reporter fluorophores, Cy3 (gray triangle) and Cy5 (black circle). b) Normalized fluorescence intensities (I_f) from Cy3 (gray triangle) and Cy5 (black circle) showing the movement of the cargo when the motor was incubated with N.BbvC IB at 37 °C. The solid lines show the fit to a simple model described in the text. Fluorescence from Cy3 is transiently quenched when the cargo resides on S_2; fluorescence from Cy5 is permanently quenched when the cargo arrives at S_3.

This ensures that when the cargo reaches the "mismatch" stator S_3 it is trapped and the motor stops.

The test track was prepared by self-assembly followed by purification by polyacrylamide gel electrophoresis (PAGE) as described in the Supporting Information. To test the operation of the motor, a purified track with cargo on S_1 at a concentration of approximately 8 nM was incubated at 37 °C. Movement of the cargo from S_1 was triggered by the addition of N.BbvC IB in approximately eightfold excess relative to the concentration of the track. The position of the cargo on the track was measured by recording the fluorescence signals from Cy3 and Cy5 (Figure 2b). Quenching of the signal from Cy3 indicates that the cargo is bound to S_2; quenching of the signal from Cy5 indicates that the cargo is bound to S_3. As the cargo moves from S_1 to S_2 and then to S_3 there is a transient reduction in the signal from Cy3 corresponding to the state in which the cargo is bound to S_2. The signal from Cy5 is permanently quenched when the cargo arrives at S_3.

The movement of cargo along the test track can be modeled with two first-order rate constants—k_1, for stepping between S_1 and S_2; and k_2, for stepping between S_2 and S_3—according to Equation (1), where $c_i(t)$ is the fraction of stator i occupied by the cargo at time t.

$$\begin{aligned}\frac{dc_1(t)}{dt} &= -k_1\, c_1(t)\\ \frac{dc_2(t)}{dt} &= k_1\, c_1(t) - k_2\, c_2(t)\\ \frac{dc_3(t)}{dt} &= k_2\, c_2(t)\end{aligned} \qquad (1)$$

We have assumed that the cargo moves along a track (rather than between tracks), that it cannot hop directly from S_1 to S_3, and that the probability of a backward step is negligible. The relationships between the fluorescence intensities of Cy3 and Cy5 and the fractions c_2 and c_3 are described in the Supporting Information. The data can be fitted very well by this simple model (solid lines in Figure 2b) by using values of 0.003 s^{-1} and 0.009 s^{-1} for k_1 and k_2, respectively, to give a cargo speed of the order of 0.1 nm s^{-1}.

We performed a control experiment in which an excess of free stator is able to compete with track-bound stators for hybridization to the cargo. At a 100-fold excess of competitor, we could still see changes in the fluorescence of Cy3 and Cy5 that are characteristic of stepping of the cargo along the track. We conclude that movement of the cargo between tracks is not significant at the concentration of track used during normal operation of the motor (see Supporting Information).

Direct stepping from S_1 to S_3 is unlikely. For S_1 to approach closer to S_3 than to S_2 would require a bend of the track at S_2 of more than 120°. The fit to the data is not improved by the addition of a third rate constant corresponding to stepping of the cargo directly from S_1 to S_3 which suggests that the cargo does step sequentially along the track.

Table 1: DNA strands.

Strand	Modification	Sequence
cargo	5′-(Iowa Black)	CGATGTTAGTTGG**GCTGAGG**TTCGAT
S_1	3′-Cy3	ATCGAA**CC/TCAGC**CCAACTAACATCGTTTCCGTCTTTAATGCCTTTCTGT
S_2	3′-Cy5	ATCGAA**CC/TCAGC**CCAACTAACATTTTCCGGTAGTGCGCTATATCCGT
S_3	none	ATCGAA**CT⋆TCAGC**CCAACTAACATTTTCCGTATTTGTGCGTCAAGAGT
track	none	ACTCTTGACGCACAAATACGGACGGATATAGCGCACTACCGGACAGAAAGGCATTAAAGACGG

The N.BbvC IB recognition site is shown in bold; / indicates the position at which N.BbvC IB cuts; ⋆ indicates the single nucleotide change that prevents N.BbvC IB from cutting.

 © 2005 Wiley-VCH Verlag GmbH & Co. KGaA, Weinheim

The probability of a backwards step from an intact stator to a cut stator is negligible as the free energy change is extremely large: $\Delta G^{\circ}_{37} = 10.3\ \text{kcal mol}^{-1} \approx 17\,RT$. We expect the probability of a backwards step between cut stators to be similar to that of a forwards step from an uncut stator: both processes involve blunt-strand exchange—that is, exchange without a toehold[16]—whose rates depend weakly on the length of the strand.[17] The system has been designed to ensure that both of these processes are much less probable than a forwards step from a cut to an intact stator: the cargo has an 8-nt single-stranded toehold that can bind only to an intact stator to initiate strand displacement. Such toeholds greatly increase the rate of strand displacement.[16]

Stepping requires spontaneous dissociation of the last 3–6 nucleotides of the cargo (Figure 1b). S_1 has two extra nucleotides that hybridize to the proximal end of the cargo, so stepping from S_1 to S_2 requires the spontaneous dissociation of approximately one nucleotide more than stepping from S_2 to S_3. The difference in activation energy between the two steps may account for the threefold difference in the rate constants, k_1 and k_2.

The rate at which N.BbvC IB cuts its substrate has been measured as $0.17\ \text{s}^{-1}$,[18] which is much faster than the rate at which the cargo moves along the track: motion of the cargo along the track without first cutting it can therefore be neglected. Dissociation of the 8-nt stator fragment once this has been released by the enzyme is also fast: the melting temperature of this fragment is well below the operating temperature of the device, and the dissociation rate, once the fragment has been released by the enzyme, is estimated to be $> 0.01\ \text{s}^{-1}$.[19] The rate-limiting step is either the release of product by N.BbvC IB or stepping from the cut stator to the intact stator. In a control experiment in which there was competition between free (not track-bound) stators for binding to the cargo, we have shown that in the presence of an excess of N.BbvC IB the stepping rate between stators is proportional to the concentration of competing stators (see Supporting Information). Extrapolation to the effective stator concentration on the track (see Supporting Information) gives an estimate of the order of magnitude of the stepping rate of $0.01\ \text{s}^{-1}$, which is of the same order as that measured. In contrast, the rate constant for stepping from a truncated (precut) stator is four orders of magnitude higher (see Supporting Information). We tentatively conclude that the release of product by N.BbvC IB is the rate-limiting step,[18] although the fact that k_1 and k_2 are different suggests that the spontaneous dissociation of the last few nucleotides of the cargo may also play a role.

The results presented here demonstrate the design, construction, and operation of a directional linear DNA motor driven by an enzyme that nicks DNA. The motor can be halted at a desired location by a simple modification to the track. This nanometer-scale motor moves at a speed of order $0.1\ \text{nm s}^{-1}$ along a self-assembled track.

Received: April 11, 2005
Published online: June 15, 2005

Keywords: DNA · enzymes · molecular devices · nanostructures · self-assembly

[1] C. Mao, W. Sun, Z, Shen, N. C. Seeman, *Nature* **1999**, *397*, 144–146.
[2] B. Yurke, A. J. Turberfield, A. P. Mills, Jr., F. C. Simmel, J. L. Neumann, *Nature* **2000**, *406*, 605–608.
[3] J. J. Li, W. Tan, *Nano Lett.* **2002**, *2*, 315–318.
[4] H. Yan, X. Zhang, Z. Shen, N. C. Seeman, *Nature* **2002**, *415*, 62–65.
[5] P. Alberti, J.-L. Mergny, *Proc. Natl. Acad. Sci. USA* **2003**, *100*, 1569–1573.
[6] Y. Chen, M. Wang, C. Mao, *Angew. Chem.* **2004**, *116*, 3638–3641; *Angew. Chem. Int. Ed.*, **2004**, *43*, 3554–3557.
[7] P. Yin, H. Yan, X. G. Daniell, A. J. Turberfield, J. H. Reif, *Angew. Chem.* **2004**, *116*, 5014–5019; *Angew. Chem. Int. Ed.* **2004**, *43*, 4906–4911.
[8] K. Svoboda, C. F. Schmidt, B. J. Schnapp, S. M. Block, *Nature* **1993**, *365*, 721–727.
[9] J. T. Finer, R. M. Simmons, J. A. Spudich, *Nature* **1994**, *368*, 113–119.
[10] W. B. Sherman, N. C. Seeman, *Nano Lett.* **2004**, *4*, 1203–1207.
[11] J.-S. Shin, N. A. Pierce, *J. Am. Chem. Soc.* **2004**, *126*, 10834–10835.
[12] A. J. Turberfield, J. C. Mitchell, B. Yurke, A. P. Mills, Jr., M. I. Blakey, F. C. Simmel, *Phys. Rev. Lett.* **2003**, *90*, 118102.
[13] J. Mai, I. M. Sokolov, A. Blumen, *Phys. Rev. E* **2001**, *64*, 011102.
[14] D. Heiter, K. D. Lunnen, G. G. Wilson, *J. Mol. Biol.* **2005**, *348*, 631–640.
[15] J. SantaLucia, Jr., *Proc. Natl. Acad. Sci. USA* **1998**, *95*, 1460–1465.
[16] B. Yurke, A. P. Mills, Jr., *Genetic Programming and Evolvable Machines* **2003**, *4*, 111–122.
[17] L. P. Reynaldo, A. V. Vologodskii, B. P. Neri, V. I. Lyamichev, *J. Mol. Biol.* **2000**, *297*, 511–520.
[18] S. R. W. Bellamy, S. E. Milsom, D. J. Scott, L. E. Daniels, G. G. Wilson, S. E. Halford, *J. Mol. Biol.* **2005**, *348*, 641–653.
[19] L. Morrison, L. M. Stols, *Biochemistry* **1993**, *32*, 3095–3904.

 © 2005 Wiley-VCH Verlag GmbH & Co. KGaA, Weinheim

Coordination Modes

Bridging Phosphanes: Exotic or Versatile Binucleating Ligands?**

*François Leca, Christophe Lescop, Elena Rodriguez-Sanz, Karine Costuas, Jean-François Halet, and Régis Réau**

The recent discovery that tertiary phosphanes PR_3 can act as bridging ligands[1] (**A**, Figure 1) was a breakthrough in coordination chemistry,[2] since binucleating ligands potentially allow the synthesis of di- and polynuclear complexes that are of great interest in many fields, such as catalysis, bioinorganic chemistry, and materials sciences.[3] Up to now, only two types of binuclear compounds bearing symmetrically bridging phosphanes are known (Rh^{I}[1] (**C**) and Pd^{I}[4] homodimers (**D**), Figure 1). In order to establish phosphanes as versatile binucleating ligands, it is necessary to show that they can effectively stabilize other dinuclear fragments, and that they possess properties typical of well-established bridging ligands.[3] In this paper we describe the synthesis and characterization in the solid state of the first heterobimetallic complex and the first copper(I) homodimers bearing bridging phosphane ligands. Furthermore, we show that there is a continuum between symmetrically bridging (**A**) and semi-bridging (**B**)[5] coordination modes (Figure 1), a key structural feature analogous to that observed for CO,[6] which is the archetypal bridging ligand.

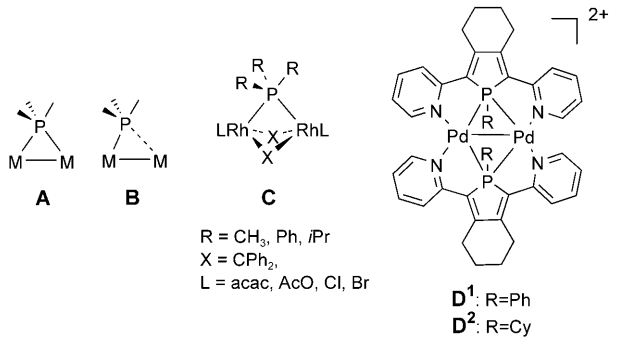
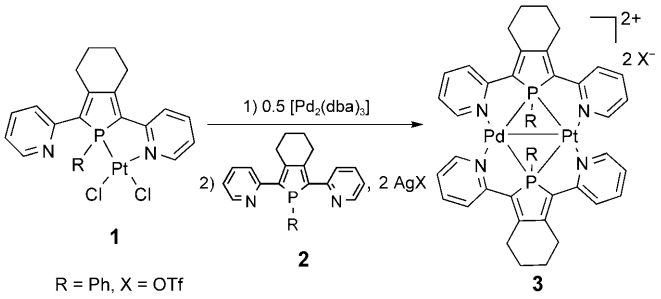


Figure 1. Bridging (**A**) and semi-bridging (**B**) coordination modes for phosphanes, and complexes **C** and **D** bearing bridging phosphanes. acac = acetylacetonate; Cy = cyclohexyl.

We have synthesized a heteronuclear Pd–Pt analog of complex $\mathbf{D^1}$ (Figure 1) by a stepwise method, which allows the sequential introduction of the metal centers.[4b] Treatment of Pt^{II} complex **1** with Pd^0, 2,5-bis(2-pyridyl)phosphole (**2**),[7] and two equivalents of AgOTf gave derivative **3**, which was isolated as an air-stable red powder (69% yield, Scheme 1).



Scheme 1. Synthesis of Pd^{I}–Pt^{I} heterodimer **3**.

High-resolution mass spectrometry data and elemental analyses are consistent with the proposed formula. Between room temperature and 173 K, the $^{31}P\{^1H\}$ NMR spectrum of **3** consists of a sharp singlet at $\delta = 49.9$ ppm ($^1J_{PPt} = 2113.5$ Hz). As expected, two sets of signals are present for the pyridyl groups in the $^{13}C\{^1H\}$ NMR spectrum.[8] It is noteworthy that heterobimetallic **3** is stable in CH_2Cl_2 solution for days; no signals corresponding to the Pd^{I} dimer $\mathbf{D^1}$ ($^{31}P\{^1H\}$ NMR: $\delta =$ 69.9 ppm) or to the corresponding, hitherto-unknown Pt^{I} dimer are observed.

The proposed structure of **3** was confirmed by an X-ray diffraction study (Figure 2).[8] The dication of **3** contains two square-planar metal centers capped by two 2,5-bis(2-pyridyl)phosphole ligands acting as six-electron μ-1κN:1,2κP:2κN donors. The geometric parameters of the 2,5-bis(2-pyridyl)-phosphole ligands are almost identical for **3** and the corresponding homometallic Pd^{I} dimer $\mathbf{D^1}$.[4] The metal–metal distance in **3** (2.7851(9) Å) is fairly long compared to typical Pd^{I}–Pt^{I} single bond lengths,[9] but is similar to that measured for the dipalladium complexes **D** (2.767(1)–2.787(1) Å).[4] The dication of **3** has a crystallographic center of symmetry at the midpoint of the metal–metal bond, which induces an equal occupancy of the Pd and Pt atoms at the two metal positions.[10] The metal–nitrogen bond lengths in **3** and $\mathbf{D^1}$ are essentially equal, although the geometry of the M_2P_2 core differs: for the homobimetallic complex $\mathbf{D^1}$ the P atoms bridge the two Pd^{I} centers symmetrically (Δ(μ-P–Pd) = 0.009(4) Å),[4] and the M_2P_2 core forms a diamond shape (**E** in Figure 2; $M^1 = M^2 = Pd$), whereas in the heterodimer **3** each μ-P atom binds the two metal centers nonsymmetrically (Δ(μ-P–M) = 0.083(3) Å) and the M_2P_2 core adopts a dis-

[*] Dr. F. Leca, Dr. C. Lescop, E. Rodriguez-Sanz, Prof. R. Réau
UMR 6509
CNRS-Université de Rennes 1
Institut de Chimie
35042 Rennes Cedex (France)
Fax: (+33) 2-2323-6939
E-mail: regis.reau@univ-rennes1.fr
Dr. K. Costuas, Dr. J.-F. Halet
UMR 6511
CNRS-Université de Rennes 1
Institut de Chimie
35042 Rennes Cedex (France)

[**] This work was supported by the Ministère de l'Education Nationale, de la Recherche et de la Technologie, the Centre National de la Recherche Scientifique, and the Institut Universitaire de France. K.C. and J.-F.H. thank the Institut de Développement et des Ressources en Informatique Scientifique (IDRIS-CNRS) of Orsay, France, for use of their computing facilities.

Supporting information for this article is available on the WWW under http://www.angewandte.org or from the author.

 © 2005 Wiley-VCH Verlag GmbH & Co. KGaA, Weinheim DOI: 10.1002/anie.200500529

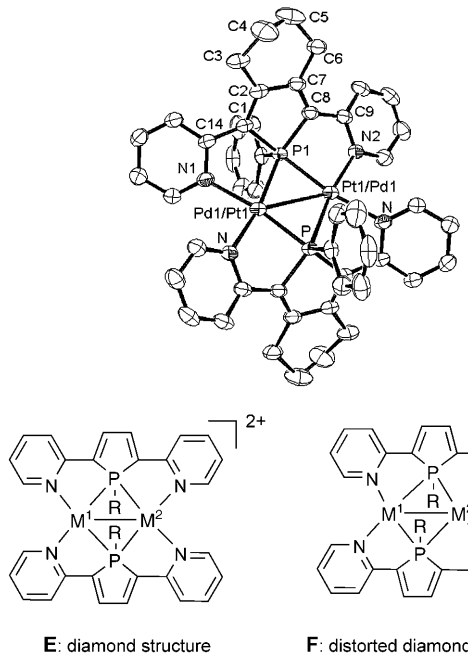
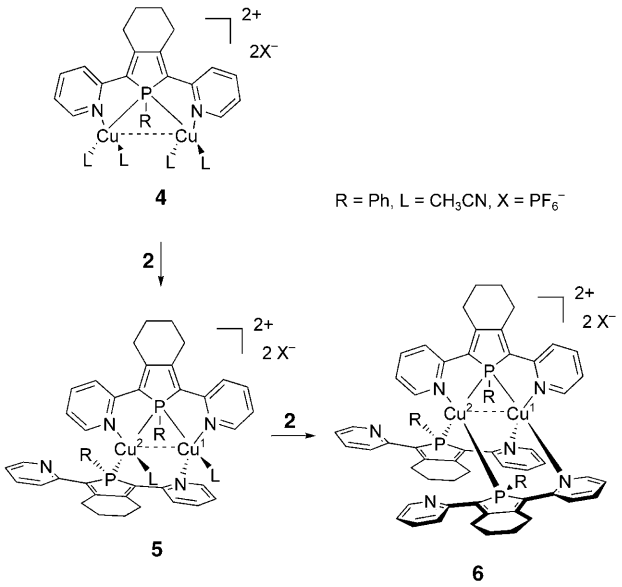


Figure 2. Molecular structure of the cation of complex **3** in the solid state (hydrogen atoms have been omitted for clarity; thermal ellipsoids at 50% probability). Selected bond lengths [Å]: P1–M1 2.3923(14), P1–M2 2.3091(15), N1–M1 2.160(5), N2–M2 2.142(4).

torted diamond shape (**F** in Figure 2; $M^1 = Pd$, $M^2 = Pt$). Hence, in spite of the tridentate coordination mode of the N,P,N-ligand **2**, the P atom can adopt a nonsymmetrical coordination mode. In fact, the μ-P centers of heterobimetallic **3** adopt a geometry that is intermediate between a symmetrically bridging (**A**) and a semi-bridging (**B**) coordination mode (Figure 1). This result suggests that there is no substantial discontinuity between these two coordination modes for μ-PR_3 ligands. In order to verify such a hypothesis, density functional theory calculations were carried out.[8]

The structure of heterobimetallic **3** was first optimized without symmetry constraints. The resulting structural arrangement matches the experimental structure with good accuracy.[8] The two phosphorus atoms are bound asymmetrically to the metal centers ($\Delta(\mu\text{-P}-\text{M}) \approx 0.09$ Å), which gives rise to the experimentally observed distorted diamond structure **F**. Geometry optimization of **3** by imposing a C_2 symmetry axis containing the metal atoms leads to the diamond structure **E.** Interestingly, the energy of **E** is very close to that of **F** ($\Delta E = 0.5$ kcal mol^{-1}).[11] Analogous results were obtained for the homometallic compound $\mathbf{D}^1$: for example, the energies of structures **E** and **F** are almost the same ($\Delta E = 1.1$ kcal mol^{-1}). Obviously, there is a shallow and broad energy minimum around the symmetrical bridging position of the phosphorus atoms in this kind of complex. In other words, there is little energy cost for a bridging P center to move from a symmetrical to a substantially nonsymmetrical bridging position. Tiny changes such as the metal's electronic requirements, the environment about the metal, and/or the crystal packing can be invoked as the cause of the differences in structure between conformers **E** and **F**.

This conclusion was nicely confirmed by synthesis of a novel series of homobimetallic complexes in which two Cu^I atoms are tethered by a bridging phosphole. The reaction of di(2-pyridyl)phosphole (**2**) with $[Cu(CH_3CN)_4]PF_6$ (1:2 ratio) in CH_2Cl_2 at room temperature gives the dimetalated complex **4** (Scheme 2), which was isolated as an air-stable powder



Scheme 2. Synthesis of Cu^I dimers **4**–**6**.

in 95% yield. In its ^{31}P NMR spectrum, besides the PF_6 signal ($\delta = -143.2$ ppm, $J_{P,F} = 704.1$ Hz), a singlet is observed at $\delta = -0.1$ ppm. Integration of the ^1H NMR spectrum suggests that **4** contains one di(2-pyridyl)phosphole and four acetonitrile ligands; the simple $^{13}C\{^1H\}$ NMR spectrum is in favor of a symmetric structure.[8] An X-ray diffraction study[8] revealed that compound **4** has the structure $[Cu_2(\mathbf{2})(CH_3CN)_4](PF_6)_2$ (Figure 3), in which two Cu^I atoms are capped by a 2,5-bis(2-pyridyl)phosphole ligand acting, again, as a six-electron μ-1κN:1,2κP:2κN donor. The Cu^I atoms have a distorted tetrahedral geometry due to the bite angle of the P,N-chelate

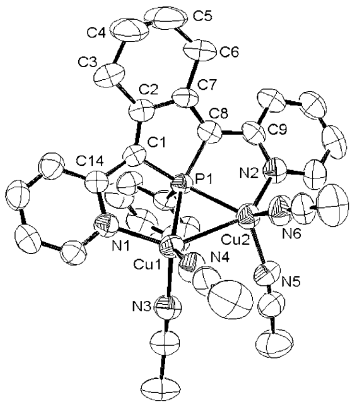


Figure 3. Molecular structure of the cation of complex **4** in the solid state (hydrogen atoms have been omitted for clarity; thermal ellipsoids at 50% probability).

 © 2005 Wiley-VCH Verlag GmbH & Co. KGaA, Weinheim

(N1-Cu1-P1 = 85.29(12)°; N2-Cu2-P1 = 85.55(14)°), with a short intermetallic distance (2.568(10) Å).[12] The two Cu–N(pyridine) bond lengths are equal and the P atom adopts an almost symmetrical coordination mode ($\Delta(\mu\text{-P–Cu}) = 0.010(2)$ Å; Table 1). Derivative **4** is the first complex in which two d^{10}-metal centers are bridged by a phosphane donor, and where two metals are held together by one bridging phosphane and no other supporting ligands (**C** is triply bridged and **D** is doubly bridged, Figure 1). These results suggest that bridging phosphane ligands are able to stabilize a large variety of bimetallic complexes and confirm that "*there is no inherent thermodynamic instability associated with this bonding situation*".[2a]

Table 1: Selected bond lengths [Å] for complexes **4**–**6**.

	4	**5**	**6**
Cu1–P1[a]	2.324(1)	2.293(1)	2.265(1)
Cu2–P1[a]	2.314(1)	2.387(1)	2.560(1)
Cu1–N1[a]	2.040(4)	2.047(4)	2.147(5)
Cu2–N2[a]	2.041(5)	2.043(4)	2.052(5)
Cu2–P2[b]	–	2.250(1)	2.299(1)
Cu2–P3[b]	–	–	2.296(1)
Cu1···Cu2	2.568(1)	2.5552(8)	2.6204(9)

[a] P1, N1, and N2 belong to the μ-1κN:1,2κP:2κN ligand; [b] P2 and P3 are the nonbridging P atoms.

The acetonitrile ligands of **4** can be displaced in CH_2Cl_2 solution by one or two equivalents of phosphole **2** to give complexes **5** (85% yield) and **6** (81% yield), respectively, which can be isolated as air-stable powders (Scheme 2).[8] An X-ray diffraction study[8] revealed that these dicationic Cu^I dimers still feature one 2,5-bis(2-pyridyl)phosphole ligand acting as a μ-1κN:1,2κP:2κN donor. The fact that the bridging coordination mode of the P center is retained upon addition of **2** to complex **4** highlights the robustness of bridging phosphanes as binucleating ligands. The tetrahedral geometry of the Cu^I atoms in **5** prevents the formation of a doubly bridged structure of type **D** (Figure 1), which requires square-planar metal centers. The dinuclear fragment of complexes **5** and **6** is bridged by one or two additional 1κP:2κN-chelates **2** (Scheme 2), respectively, the $Cu^I\cdots Cu^I$ separation being hardly perturbed with respect to that of complex **4** (Table 1). Note that the arrangement of the P,N-ligands in **6** (Scheme 2), which leads to two Cu atoms with either a "high-P" or "high-N" environment, is probably due to steric factors.

The series **4**–**6** gives the unique opportunity to study the evolution of the bridging coordination mode of a phosphane upon decreasing the local symmetry of the bimetallic core. It is striking to observe that the difference between the two μ-P–Cu distances increases continuously on going from **4** to **6** ($\Delta(\mu\text{-P–Cu})$: **4**, 0.010(2) Å; **5**, 0.094(2) Å ; **6**, 0.295(2) Å). The value of $\Delta(\mu\text{-P–M})$ found in complex **6** is typical for semi-bridged phosphanes,[5] with the longest P–Cu bond length always being observed for Cu2 (Scheme 2), which has a "high-P" environment (Table 1). Once again, the P atom of the N,P,N-pincer **2** can adopt a nonsymmetric bridging geometry. Moreover, these structural data confirm experimentally that there is no substantial discontinuity between symmetrical bridging (**A**) and semi-bridging (**B**) coordination modes for μ-PR_3 ligands (Figure 1). It is thus likely that these two coordination modes are shallow and broad minima on a flat potential energy surface. This situation is reminiscent of that of CO, the prototypical bridging ligand, and is a clue to understanding many of their key properties (e.g. fluxional behavior, bonding modes).[2a,3d,6]

These results show that chelates featuring bridging phosphanes are versatile binucleating ligands and that phosphanes have now to be considered as standard bridging ligands. The development of the robust Cu^I dimers **4** and **5** as building blocks for supramolecular architectures is under active investigation.

Received: February 10, 2005
Published online: June 8, 2005

Keywords: bridging ligands · copper · heterometallic complexes · phosphine ligands · phosphole

[1] a) T. Pechmann, C. D. Brandt, H. Werner, *Angew. Chem.* **2000**, *112*, 4069; *Angew. Chem. Int. Ed.* **2000**, *39*, 3909; b) T. Pechmann, C. D. Brandt, C. Röger, H. Werner, *Angew. Chem.* **2002**, *114*, 2398; *Angew. Chem. Int. Ed.* **2002**, *41*, 2301; c) T. Pechmann, C. D. Brandt, H. Werner, *Chem. Commun.* **2003**, 1136; d) T. Pechmann, C. D. Brandt, H. Werner, *Chem. Eur. J.* **2004**, *10*, 728; e) T. Pechmann, C. D. Brandt, H. Werner, *Dalton Trans.* **2004**, 959.

[2] a) P. Braunstein, N. M. Boag, *Angew. Chem.* **2001**, *113*, 2493; *Angew. Chem. Int. Ed.* **2001**, *40*, 2427; b) H. Werner, *Angew. Chem.* **2004**, *116*, 956; *Angew. Chem. Int. Ed.* **2004**, *43*, 938.

[3] a) A. L. Gavrilova, B. Bornich, *Chem. Rev.* **2004**, *104*, 349; b) P. Braunstein, J. Rose in *Catalysis by Di- and Polynuclear Metal Cluster Complexes* (Eds.: R. D. Adams, F. A. Cotton), VCH, New York, **1998**; c) N. Wheatley, P. Kalck, *Chem. Rev.* **1999**, *99*, 3379; d) *Metal Clusters in Chemistry* (Eds.: P. Braunstein, L. A. Oro, P. R. Raithby), Wiley-VCH, New York, **1999**; e) E. C. Carson, S. J. Lippard, *J. Am. Chem. Soc.* **2004**, *126*, 3415; f) M. Ochiai, Y.-S. Lin, J. Yamada, H. Misawa, S. Arai, K. Matsumoto, *J. Am. Chem. Soc.* **2004**, *126*, 2539; g) E. Goto, R. A. Begum, S. Zhan, T. Tanase, K. Tanigaki, K. Sakai, *Angew. Chem.* **2004**, *116*, 5139; *Angew. Chem. Int. Ed.* **2004**, *43*, 5029.

[4] a) M. Sauthier, B. Le Guennic, V. Deborde, L. Toupet, J.-F. Halet, R. Réau, *Angew. Chem.* **2001**, *113*, 234; *Angew. Chem. Int. Ed.* **2001**, *40*, 228; b) F. Leca, M. Sauthier, V. Deborde, L. Toupet, R. Réau, *Chem. Eur. J.* **2003**, *9*, 3785.

[5] a) P. Leoni, F. Marchette, L. Marchetti, V. Passarelli, *Chem. Commun.* **2004**, 2346; b) P. H. M. Budzelaar, P. W. N. M. van - Leeuwen, C. F. Roobeek, A. G. Orpen, *Organometallics* **1992**, *11*, 23; c) T. Murahashi, T. Otani, T. Okuno, H. Kurosawa, *Angew. Chem.* **2000**, *112*, 547; *Angew. Chem. Int. Ed.* **2000**, *39*, 537; d) P. Leoni, M. Pasquali, A. Fortunelli, G. Germano, A. Albinati, *J. Am. Chem. Soc.* **1998**, *120*, 9564.

[6] a) P. Macchi, L. Garlaschelli, A. Sironi, *J. Am. Chem. Soc.* **2002**, *124*, 14173; b) A. Sironi in *Metal Clusters in Chemistry* (Eds.: P. Braunstein, L. A. Oro, P. R. Raithby), Wiley-VCH, New York, **1999**, p. 397; c) A. G. Orpen, *Chem. Rev.* **1993**, *93*, 191; d) Y. Xie, H. F. Schaefer III, R. B. King, *J. Am. Chem. Soc.* **2000**, *122*, 8746; e) I. S. Ignatey, H. F. Schaefer III, R. B. King, S. T. Brown, *J. Am. Chem. Soc.* **2000**, *122*, 1989.

[7] C. Hay, M. Hissler, C. Fischmeister, J. Rault-Berthelot, L. Toupet, L. Nyulaszi, R. Réau, *Chem. Eur. J.* **2001**, *7*, 4222.

[8] The Supporting Information includes NMR spectra (^1H and ^{13}C), mass spectra, and elemental analysis results for **3**, **4**, **5**, and **6**,

 © 2005 Wiley-VCH Verlag GmbH & Co. KGaA, Weinheim

along with ORTEP views of the cations of complexes **5** and **6**, details of the X-ray crystal structure determinations, and theoretical calculations. CCDC-262841 (**3**), -262842 (**4**), -262843 (**5**), and -262844 (**6**) contain the supplementary crystallographic data for this paper. These data can be obtained free of charge from the Cambridge Crystallographic Data Centre via www.ccdc.cam.ac.uk/data_request/cif.

[9] M. Tanabe, T. Yamada, K. Osakada, *Organometallics* **2003**, *22*, 2190.

[10] The two structures in which the Pd and Pt atoms are localized either at the M^1 or M^2 position are enantiomers. Hence, the equal occupancy of the two sites by a Pd or a Pt atom does not affect the coordinates of the P and N centers.

[11] This difference in energy is at the limit of accuracy of the method used. Moreover, structures **E** and **F** have similar HOMO–LUMO gaps (**E**: 1.553 eV; **F**: 1.556 eV).

[12] For a theoretical study of $[Cu_2(\mu\text{-}PH_3)_2(PH_3)_4]^{2+}$ see: P. A. Alemany, S. Alvarez, *Inorg. Chem.* **1992**, *31*, 4266. For recent papers on $Cu^I\cdots Cu^I$ interactions see: M. A. Carvajal, S. Alvarez, J. J. Novoa, *Chem. Eur. J.* **2004**, *10*, 2117; A. Vega, J.-Y. Saillard, *Inorg. Chem.* **2004**, *43*, 4012; S. Masaoka, D. Tanaka, Y. Nakanishi, S. Kitagawa, *Angew. Chem.* **2004**, *116*, 2584; *Angew. Chem. Int. Ed.* **2004**, *43*, 2530.

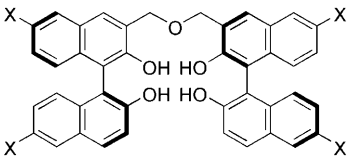
 © 2005 Wiley-VCH Verlag GmbH & Co. KGaA, Weinheim

Asymmetric Mannich Reaction

Direct Catalytic Asymmetric Mannich-Type Reactions of *N*-(2-Hydroxyacetyl)pyrrole as an Ester-Equivalent Donor**

Shinji Harada, Shinya Handa, Shigeki Matsunaga, and Masakatsu Shibasaki**

The catalytic in situ generation of metal enolates and enamines from donor substrates in asymmetric carbon–carbon bond-forming reactions has recently received much attention.[1] Although tremendous progress has been made in this area in the last five years with various metal catalysts and organocatalysts,[2] room for improvement remains. For example, in metal catalysis, the donor substrates are mostly limited to ketones.[3,4] The use of donor substrates with the oxidation state of carboxylic acid is still a formidable task since the pK_a value of the α proton in carboxylic acid derivatives is much higher than that in ketones. A few landmark studies addressing this issue were recently reported.[5] In particular, Evans et al. achieved a highly enantioselective aldol reaction utilizing *N*-acyl thiazolidinethione donors and a chiral Ni catalyst.[5a] The reaction proceeded with excellent yield and selectivity; however, stoichiometric amounts of the silylating reagent and amine base were required to facilitate catalyst turnover. The development of a suitable ester-equivalent donor and/or a new asymmetric catalyst to achieve both high enantioselectivity and conversion without additional stoichiometric reagents is desirable. Herein, we report that an *N*-acylpyrrole moiety is an effective achiral template for the in situ generation of metal enolates. New complexes composed of In(O*i*Pr)$_3$ and (*S*,*S*)-linked-binol **1** were used to catalyze the



X=H: (*S*,*S*)-linked-binol **1a**
X=$(CH_3)_3$Si: (*S*,*S*)-6,6',6'',6'''-TMS-linked-binol **1b**

asymmetric Mannich-type reaction of *N*-(2-hydroxyacetyl)-pyrrole and *ortho*-tosylimines, which proceeded through simple proton transfer to give β-amino-α-hydroxy carboxylic acid derivatives in high enantioselectivity (91–98% *ee*, major diastereomer) and good yield (65–98%).

We selected *N*-acylpyrrole as a donor substrate for investigation and as an achiral template for the following reasons. Evans et al. reported the unique properties of *N*-acylpyrrole.[6] We subsequently demonstrated the utility of the *N*-acylpyrrole moiety as an ester surrogate in catalytic asymmetric conjugate additions, in which an α,β-unsaturated *N*-acylpyrrole substrate was used as an activated, monodentate electrophile.[7] Because the lone pair on the nitrogen atom in the pyrrole ring is delocalized in an aromatic system, the properties of the carbonyl group are similar to those of a phenyl ketone. We supposed that *N*-acylpyrrole would also be useful as an ester-equivalent donor because the aromaticity would assist enolate formation. Since the coordination mode of the *N*-acylpyrrole donor is similar to that of an aromatic ketone, the chiral environment optimized for ketone donors would be applicable for *N*-acylpyrrole. Based on our previous report that the complex Et_2Zn/linked-binol **1a** is suitable for the formation of an enolate from an aromatic hydroxyketone,[2c] we used *N*-(2-hydroxyacetyl)pyrrole **2** (Figure 1) and complexes composed of a metal and linked-binol **1a** in the preliminary evaluations of the potential of the *N*-acylpyrrole moiety for the catalytic in situ generation of metal enolates.

The results of the initial screening in the Mannich-type reaction with **2** are shown in Table 1. When the Et_2Zn/**1a**

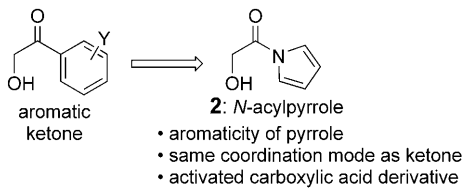


Figure 1. Structure and properties of *N*-acylpyrrole (**2**).

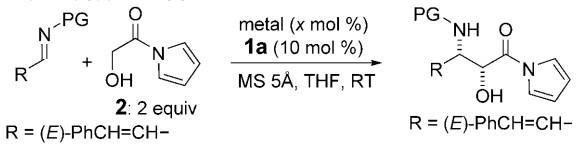
[*] S. Harada, S. Handa, Dr. S. Matsunaga, Prof. Dr. M. Shibasaki
Graduate School of Pharmaceutical Sciences
The University of Tokyo
Hongo, Bunkyo-ku, Tokyo 113-0033 (Japan)
Fax: (+81) 3-5684-5206
E-mail: smatsuna@mol.f.u-tokyo.ac.jp
mshibasa@mol.f.u-tokyo.ac.jp

[**] This work was supported by a Grant-in-Aid for Specially Promoted Research and a Grant-in-Aid for Encouragement of Young Scientists (B) (for S.M.) from JSPS and MEXT.

Supporting information for this article is available on the WWW under http://www.angewandte.org or from the author.

 DOI: 10.1002/anie.200501180 © 2005 Wiley-VCH Verlag GmbH & Co. KGaA, Weinheim

Table 1: Direct catalytic asymmetric Mannich-type reaction of *N*-(2-hydroxyacetyl)pyrrole (**2**).[a]



2: 2 equiv
R = (*E*)-PhCH=CH–
PG = *p*-Ts: **3a**, *o*-Ts: **4a**
R = (*E*)-PhCH=CH–

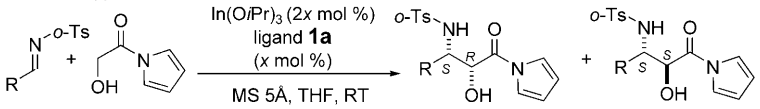
Entry	Imine	Metal (*x* mol %)	Prod.	*t* [h]	Yield [%]	*syn*/*anti*	*ee* [%]
1	**3a**	Et_2Zn (40)	**5a**	96	11	40:60	–
2	**3a**	$In(OiPr)_3$ (20)	**5a**	96	61	86:14	93
3	**4a**	$In(OiPr)_3$ (20)	**6a**	96	94	91:9	96

[a] PG = protecting group, MS 5Å = molecular sieves 5 Å, RT = room temperature.

complex was used for *para*-tosylimine **3a**, a Mannich adduct was obtained in only low yield (Table 1, entry 1, 11%), probably due to the low Brønsted basicity of the Zn catalyst in the formation of the zinc enolate from **2**. Screening of other metal sources revealed that $In(OiPr)_3$ was the most effective.[16] When a 2:1 complex of $In(OiPr)_3$ and **1a** was used, the reaction of **2** and **3a** in THF proceeded at room temperature to give the Mannich adduct in 61% yield and 93% *ee* (Table 1, entry 2). The reaction of *ortho*-tosylimine **4a** under the same conditions gave **6a** with improved yield (94%), diastereoselectivity (*syn*/*anti* = 91:9), and enantioselectivity (96% *ee* (*syn*); Table 1, entry 3).[8,9] In this reaction, we assumed that either an indium alkoxide or an indium phenoxide functions as a Brønsted base and deprotonates **2** at the α position to form the indium enolate in situ. Although there are many reports on Lewis acidic indium catalysts ($In(OTf)_3$, $InCl_3$, $InBr_3$, etc.),[10] the Brønsted basic property of indium chiral catalysis was utilized for the first time in organic synthesis. Furthermore, the present reaction using an α-hydroxy-substituted donor complements the reports by Evans and Shair,[5] in which α-alkyl-substituted donors were used.[11]

The substrate scope of the present reaction is summarized in Tables 2 and 3. The diastereomeric ratio depended on the imines used. As shown in Table 2, alkenyl imines **4a–d** afforded *syn* adducts in good diastereoselectivity (88:12–91:9) and high enantioselectivity (93–97% *ee* (*syn*) Table 2, entries 1–4). The *syn* selectivity of the reactions of imines **4e** and **4f**, which have an unsubstituted and *para*-substituted aromatic ring, respectively, was only modest (Table 2, entries 5 and 6).[12] At present, this reaction with the In-$(OiPr)_3$/(*S*,*S*)-linked-binol complex is limited to sp^2-hybridized imines; however, subsequent functionalization of the C–C double bond in the Mannich adducts obtained from alkenyl imines **4a–d** can afford β-alkyl-substituted β-amino-α-hydroxy carboxylic acid derivatives (see below). Further trials to expand the substrate scope of the reaction to aliphatic imines are ongoing. On the other hand, imines **4g–k**, which contain *ortho*-substituted aromatic rings, and cyclopropyl imine **4l** gave products with *anti* selectivity[8] in high *ee* (92–98% *ee*, *anti*; Table 3). Both electron-withdrawing (Cl, Br) and electron-donating substituents (Me, MeO) on the aromatic ring were applicable. For less reactive substrates, an increased amount of the chiral ligand (15 mol%) was required to obtain products in good yield (Table 3, entries 1, 2, and 5–7). Use of a modified linked-binol ligand **1b** resulted

Table 2: Mannich-type reaction of imines **4a–f** with **2**.

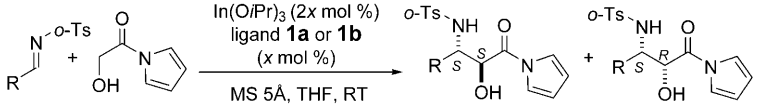


4a–f **2**: 2 equiv *syn*-**6a–f** *anti*-**6a–f**

Entry	**4**, R	Lig. **1a** [*x* mol %]	Prod.	*t* [h]	Yield [%]	d.r. *syn*/*anti*	*ee* [%] *syn*, *anti*
1	**4a**, (*E*)-PhCH=CH-	10	**6a**	96	94[a]	91:9	96, 83
2	**4b**, (*E*)-*p*-tol-CH=CH-	10	**6b**	97	86[a]	89:11	95, 76
3	**4c**, (*E*)-*p*-Cl-C_6H_4-CH=CH-	10	**6c**	97	79[a]	88: 12	93, 71
4	**4d**, (*E*)-2-furyl-CH=CH-	10	**6d**	99	80	90:10	97, 81
5	**4e**, Ph	10	**6e**	111	98	61:39	91, 91
6	**4f**, *p*-Cl-C_6H_4-	10	**6f**	89	97	59:41	96, 94

[a] Yield of isolated product after conversion into the corresponding benzoate.

Table 3: Mannich-type reaction of **4g–l** with **2**.



4g–l **2**: 2 equiv *anti*-**6g–l** *syn*-**6g–l**

Entry	**4**, R	Ligand (*x* mol %)	Prod.	*t* [h]	Yield [%]	d.r. *anti*/*syn*	*ee* [%] *anti*, *syn*
1	**4g**, 1-naphthyl	**1a** (15)	**6g**	99	86	72:28	90, 87
2	**4g**, 1-naphthyl	**1b** (15)	**6g**	99	87	77:23	94, 89
3	**4h**, *o*-Cl-C_6H_4	**1a** (10)	**6h**	76	87	83:17	93, 81
4	**4i**, *o*-Br-C_6H_4	**1a** (10)	**6i**	89	68	86:14	95, 90[a]
5	**4j**, *o*-Me-C_6H_4	**1a** (15)	**6j**	92	76	76:24	93, 85[a]
6	**4k**, *o*-MeO-C_6H_4	**1a** (15)	**6k**	93	70	77:23	89, 81
7	**4k**, *o*-MeO-C_6H_4	**1b** (15)	**6k**	93	74	77:23	92, 86
8	**4l**, cyclopropyl	**1a** (10)	**6l**	65	83	63:37	96, 91
9	**4l**, cyclopropyl	**1b** (10)	**6l**	65	86	75:25	98, 90

[a] The enantiomeric excess was determined after conversion of the product into the triethylsilyl ether.

 © 2005 Wiley-VCH Verlag GmbH & Co. KGaA, Weinheim

in slightly better stereoselectivity in some cases (Table 3, entries 1, 6, and 8 vs. 2, 7, and 9).

In all entries in Tables 2 and 3, the *syn* and the *anti* adducts were obtained with the same absolute configuration at the β position (*S*), implying that selection of the imine enantioface is identical.[8] Proposed models of the acyclic *anti*-periplanar transition state are shown in Figure 2. Imines **4a–f**

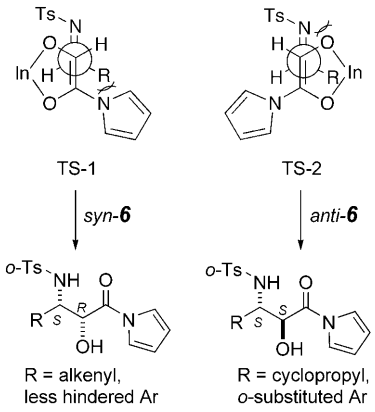
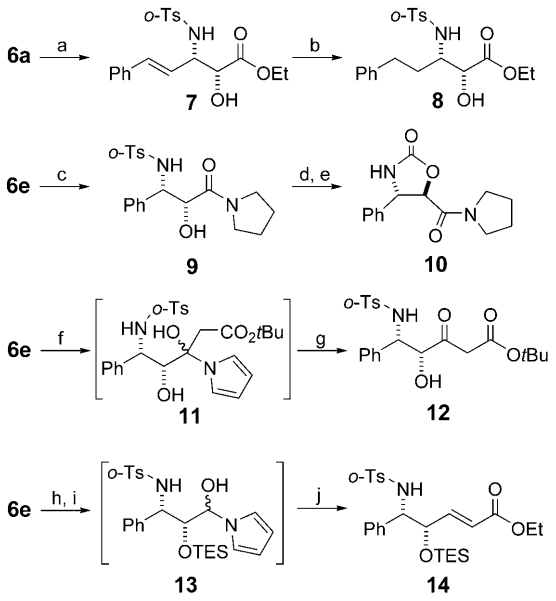


Figure 2. Postulated transition-state model of Mannich-type reactions.

with a planar configuration would favor the TS-1 to minimize *gauche* interactions. On the other hand, imines **4g–l** have a twisted configuration due to steric (**4g–k**) and stereoelectronic (**4l**) effects. Thus, steric repulsion between imine substituents R and the pyrrole ring of the indium enolate would become more predominant, and the *anti*-periplanar TS-2 would be more favorable than TS-1. For a more precise understanding of the diastereoselectivity evidenced in Table 2 and Table 3 and the effects of the modified ligand **1b**, further mechanistic studies including clarification of the structure of the complex of $In(OiPr)_3$ and (*S*,*S*)-linked-binol **1** are required.

Finally, the utility of the *N*-acylpyrrole unit as an ester surrogate was demonstrated through several transformations of Mannich adducts (Scheme 1).[13] The *N*-acylpyrrole unit of **6a** was readily transformed into an ethyl ester unit by treatment with NaOEt at room temperature for 5 min, affording **7** in quantitative yield. Hydrogenation of the C–C double bond in **7** gave **8** in 92% yield, which corresponds to the β-amino-α-hydroxy ester accessible from an aliphatic imine. Substitution with amine also proceeded smoothly. Amide **9** was obtained in quantitative yield by the treatment of Mannich adduct **6e** with pyrrolidine and DBU at 40 °C for 1 h. Neither epimerization nor racemization was observed during substitution. After conversion of **9** into the cyclic carbamate (94% yield), the *o*-Ts group was removed under mild reduction conditions (Mg powder, room temperature, 20 min)[14] to give **10** in 81% yield. In addition to substitution reactions with alcohols and amines, reaction of **6e** with a lithium enolate followed by treatment with DBU provided keto ester **12** in 62% yield. Protection with a triethylsilyl (TES) group followed by reduction with $LiBH_4$ afforded the pyrrole carbinol **13** as a stable intermediate. Under Masamune–Roush conditions,[15] the aldehyde moiety was generated in situ from the crude pyrrole carbinol **13**, and the α,β-unsaturated ester **14** was obtained in 67% yield (in two steps from the TES-protected Mannich adduct).



Scheme 1. Transformations of Mannich adducts. Reaction conditions: a) NaOEt, EtOH, 0 °C→RT, 5 min, quant. yield; b) Pd/C, H_2, MeOH, RT, 30 min, 92%; c) pyrrolidine, DBU, THF, 40 °C, 1 h, quant. yield; d) triphosgene, py, CH_2Cl_2, −78 °C→RT, 1 h, 94%; e) Mg powder, MeOH, RT, 20 min, 81%; f) LDA, *t*Bu acetate, THF, −78 °C, 10 min; g) DBU, CH_2Cl_2, RT, 5 min, 62% (2 steps); h) TESCl, imidazole, DMF, 0 °C, 30 min, 87%; i) $LiBH_4$, THF, RT, 30 min; j) $(EtO)_2P(O)CH_2CO_2Et$, LiCl, DBU, CH_3CN, RT, 7 h, 67% (2 steps). DBU = 1,8-diazabicyclo-[5.4.0]undec-7-ene, py = pyridine.

In summary, we have demonstrated the utility of *N*-acylpyrrole **2** as an ester-equivalent donor in a direct Mannich-type reaction. A catalytic amount of a chiral complex composed of $In(OiPr)_3$ and the (*S*,*S*)-linked-binol **1** was effective in generating the indium enolate in situ from **2**. The reaction is formally a simple proton transfer, and high enantioselectivity (up to 98% *ee*) was achieved at ambient temperature. Mechanistic studies of indium catalysis, trials to improve the unsatisfactory reaction rate and diastereoselectivity, and further application of the *N*-acylpyrrole moiety as an ester-equivalent donor in other reactions are ongoing.

Received: April 4, 2005
Published online: June 7, 2005

Keywords: amino alcohols · asymmetric catalysis · indium · Mannich reaction · pyrroles

[1] A review of the direct Mannich reaction: a) A. Córdova, *Acc. Chem. Res.* **2004**, *37*, 102; a review of the direct aldol reaction: b) B. Alcaide, P. Almendros, *Eur. J. Org. Chem.* **2002**, 1595.

[2] Selected examples of direct Mannich reactions using unmodified ketones and/or aldehydes as donors: with metal catalysts: a) K. Juhl, N. Gathergood, K. A. Jørgensen, *Angew. Chem.* **2001**, *113*, 3083; *Angew. Chem. Int. Ed.* **2001**, *40*, 2995; b) B. M. Trost, L. R. Terrell, *J. Am. Chem. Soc.* **2003**, *125*, 338; c) S. Matsunaga, N.

 © 2005 Wiley-VCH Verlag GmbH & Co. KGaA, Weinheim

Kumagai, S. Harada, M. Shibasaki, *J. Am. Chem. Soc.* **2003**, *125*, 4712, and references therein; with organocatalysts: d) B. List, *J. Am. Chem. Soc.* **2000**, *122*, 9336; e) W. Notz, K. Sakthivel, T. Bui, G. Zhong, C. F. Barbas III, *Tetrahedron Lett.* **2001**, *42*, 199; f) B. List, P. Pojarliev, W. T. Biller, H. J. Martin, *J. Am. Chem. Soc.* **2002**, *124*, 827; g) A. Córdova, W. Notz, G. Zhong, J. M. Betancort, C. F. Barbas III, *J. Am. Chem. Soc.* **2002**, *124*, 1842; h) A. Córdova, S.-i. Watanabe, F. Tanaka, W. Notz, C. F. Barbas III, *J. Am. Chem. Soc.* **2002**, *124*, 1866; i) Y. Hayashi, W. Tsuboi, I. Ashimine, T. Urushima, M. Shoji, K. Sakai, *Angew. Chem.* **2003**, *115*, 3805; *Angew. Chem. Int. Ed.* **2003**, *42*, 3677; j) W. Zhuang, S. Saaby, K. A. Jørgensen, *Angew. Chem.* **2004**, *116*, 4576; *Angew. Chem. Int. Ed.* **2004**, *43*, 4476; k) D. Uraguchi, M. Terada, *J. Am. Chem. Soc.* **2004**, *126*, 5356, and references therein. For other related examples, see reviews in ref. [1].

[3] See refs [1] and [2a–c]; see also a) N. Yoshikawa, Y. M. A. Yamada, J. Das, H. Sasai, M. Shibasaki, *J. Am. Chem. Soc.* **1999**, *121*, 4168; b) B. M. Trost, H. Ito, *J. Am. Chem. Soc.* **2000**, *122*, 12003; c) N. Kumagai, S. Matsunaga, T. Kinoshita, S. Harada, S. Okada, S. Sakamoto, K. Yamaguchi, M. Shibasaki, *J. Am. Chem. Soc.* **2003**, *125*, 2169.

[4] For exceptional examples in Mannich-type reactions using readily enolizable substrates with the oxidation state of carboxylic acid, see: with glycine Schiff base as a donor: a) T. Ooi, M. Kameda, J. Fujii, K. Maruoka, *Org. Lett.* **2004**, *6*, 2397; b) L. Bernardi, R. G. Gothelf, R. G. Hazell, K. A. Jørgensen, *J. Org. Chem.* **2003**, *68*, 2583; with malonates and ketoesters as donors: c) M. Marigo, A. Kjærsgaard, K. Juhl, N. Gathergood, K. A. Jørgensen, *Chem. Eur. J.* **2003**, *9*, 2359; d) Y. Hamashima, N. Sasamoto, D. Hotta, H. Somei, N. Umebayashi, M. Sodeoka, *Angew. Chem.* **2005**, *117*, 1549; *Angew. Chem. Int. Ed.* **2005**, *44*, 1525.

[5] Asymmetric aldol reactions: a) D. A. Evans, C. W. Downey, J. L. Hubbs, *J. Am. Chem. Soc.* **2003**, *125*, 8706; b) Y. Suto, N. Kumagai, S. Matsunaga, M. Kanai, M. Shibasaki, *Org. Lett.* **2003**, *5*, 3147; diastereoselective aldol reactions: c) D. A. Evans, J. S. Tedrow, J. T. Shaw, C. W. Downey, *J. Am. Chem. Soc.* **2002**, *124*, 392; d) D. A. Evans, C. W. Downey, J. T. Shaw, J. S. Tedrow, *Org. Lett.* **2002**, *4*, 1127; racemic aldol reactions: e) G. Lalic, A. D. Aloise, M. D. Shair, *J. Am. Chem. Soc.* **2003**, *125*, 2852; f) N. Kumagai, S. Matsunaga, M. Shibasaki, *J. Am. Chem. Soc.* **2004**, *126*, 13632.

[6] a) D. A. Evans, G. Borg, K. A. Scheidt, *Angew. Chem.* **2002**, *114*, 3320; *Angew. Chem. Int. Ed.* **2002**, *41*, 3188; for the application of *N*-acylpyrrole as a donor after conversion into enol silane, see: b) D. A. Evans, D. S. Johnson, *Org. Lett.* **1999**, *1*, 595; c) D. A. Evans, K. A. Scheidt, J. N. Johnston, M. C. Willis, *J. Am. Chem. Soc.* **2001**, *123*, 4480.

[7] For the use of an α,β-unsaturated *N*-acylpyrrole as an electrophile, see: a) S. Matsunaga, T. Kinoshita, S. Okada, S. Harada, M. Shibasaki, *J. Am. Chem. Soc.* **2004**, *126*, 7559; b) T. Kinoshita, S. Okada, S. Matsunaga, Park, S.-R. *Angew. Chem.* **2003**, *115*, 4828; *Angew. Chem. Int. Ed.* **2003**, *42*, 4680; c) T. Mita, K. Sasaki, M. Kanai, M. Shibasaki, *J. Am. Chem. Soc.* **2005**, *127*, 514.

[8] For the determination of relative and absolute configurations of Mannich adducts **6a–l**, see the Supporting Information.

[9] The addition of MS 5 Å had beneficial effects on the reaction rate but did not affect the enantiomeric excess. Similar effects of molecular sieves were observed in related reactions using zinc catalysts and hydroxy ketones as donors; see, a) S. Harada, N. Kumagai, T. Kinoshita, S. Matsunaga, M. Shibasaki, *J. Am. Chem. Soc.* **2003**, *125*, 2582; b) S. Matsunaga, T. Yoshida, H. Morimoto, N. Kumagai, M. Shibasaki, *J. Am. Chem. Soc.* **2004**, *126*, 8777, and references therein; see also, refs [2b,c and 3b,c].

[10] Reviews: a) B. C. Ranu, *Eur. J. Org. Chem.* **2000**, 2347; b) J. Podlech, T. C. Maier, *Synthesis*, **2003**, 633.

[11] After submission of this manuscript, an excellent organocatalytic Mannich reaction using α-oxyaldehydes was reported, see: a) I. Ibrahem, A. Córdova, *Tetrahedron Lett.* **2005**, *46*, 2839; α-oxyaldehydes were also used as donors in organocatalytic aldol (dimerization) reactions, see: b) A. B. Northrup, I. K. Mangion, F. Hettche, D. W. C. MacMillan, *Angew. Chem.* **2004**, *116*, 2204; *Angew. Chem. Int. Ed.* **2004**, *43*, 2152; c) J. Casas, M. Engqvist, I. Ibrahem, B. Kaynak, A. Córdova, *Angew. Chem.* **2005**, *117*, 1367; *Angew. Chem. Int. Ed.* **2005**, *44*, 1343, and references therein; for related recent work using α-oxyketones as donors, see also: d) D. Enders, C. Grondal, M. Vrettou, G. Raabe, *Angew. Chem.* **2005**, *117*, in press; *Angew. Chem. Int. Ed.* **2005**, *44*, in press; for other examples using α-oxyketones, see refs [1, 2], and references therein.

[12] The diastereoselectivity of the reaction with the imine from benzaldehyde was improved by using the bulkier 2,4,6-triisopropylbenzenesulfonyl imine (*syn*/*anti* = 78:22, *syn*: 95% ee); however, reactivity decreased significantly (27% yield).

[13] For conversion of *N*-acylpyrrole units, see refs [6, 7], and references therein.

[14] For the removal of Ts group using Mg powder, see ref. [2a]; see, also: B. Nyasse, L. Grehn, U. Ragnarsson, *Chem. Commun.* **1997**, 1017.

[15] a) M. A. Blanchette, W. Choy, J. T. Davis, A. P. Essefeld, S. Masamune, W. R. Roush, T. Sakai, *Tetrahedron Lett.* **1984**, *25*, 2183; b) D. J. Dixon, M. S. Scott, C. A. Luckhurst, *Synlett* **2003**, 2317.

[16] Note added in proof: since submission of this manuscript we have found that $In(OiPr)_3$ can be purchased from Kojundo Chemical lab (sales@kojundo.co.jp).

 © 2005 Wiley-VCH Verlag GmbH & Co. KGaA, Weinheim

Light-Harvesting Polymers

Star-Shaped Light-Harvesting Polymers Incorporating an Energy Cascade**

Ming Chen, Kenneth P. Ghiggino, San H. Thang, and Gerard J. Wilson*

The photosynthetic apparatus of both photosynthetic bacteria and higher plants involves a reaction center surrounded by intricate arrays of pigments that form an energy gradient for efficient light collection.[1] Artificial systems that can mimic this remarkable natural process have attracted great interest. Among them, polymers used to simulate the process are known as "light-harvesting" or "antenna" polymers.[2] Owing

[*] Dr. M. Chen, Prof. K. P. Ghiggino
School of Chemistry, University of Melbourne
Victoria 3010 (Australia)
Fax: (+61) 3-9347-5180
E-mail: ghiggino@unimelb.edu.au
Dr. S. H. Thang, Dr. G. J. Wilson
CSIRO Molecular Science
Bag 10, Clayton South, Victoria 3169 (Australia)

[**] We thank the Australian Research Council for financial support of this work under the Discovery Grant program. The provision of a David Hay Award to M.C. by the Faculty of Science at The University of Melbourne is acknowledged.

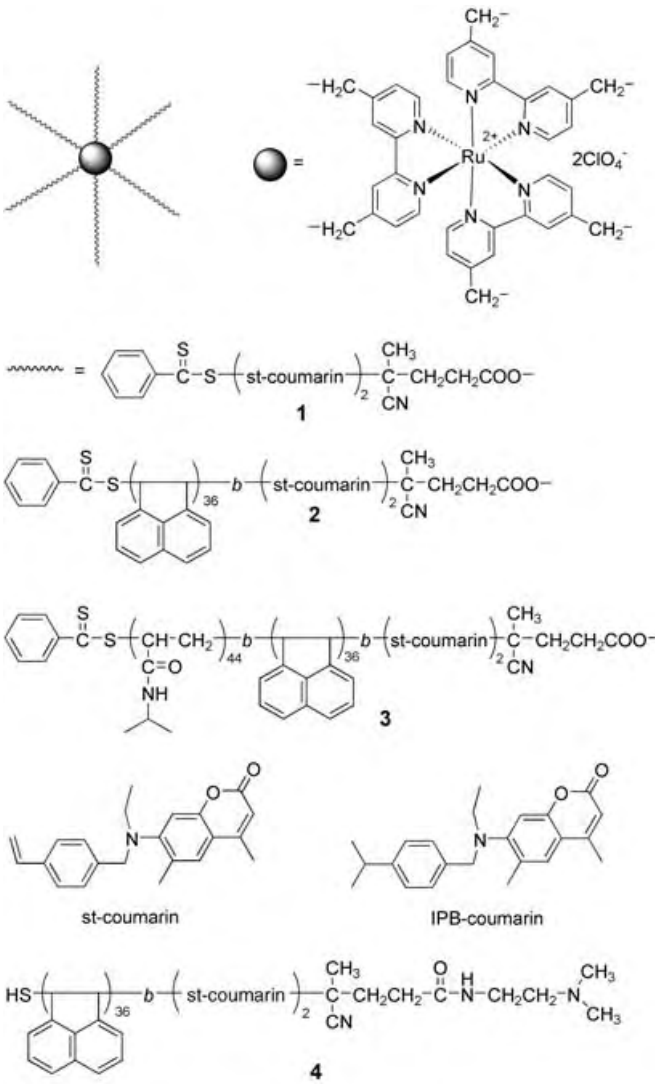
 © 2005 Wiley-VCH Verlag GmbH & Co. KGaA, Weinheim DOI: 10.1002/anie.200462796

to their structural features, multiarmed star-shaped polymers are particularly attractive as artificial light-harvesting systems.[3] Compared with linear light-harvesting polymers, the condensed packing of chromophores around a central energy-trap core will lower the average donor–acceptor distance, thus leading to a faster rate and higher efficiency of energy transfer.[4] Star-shaped polymers with an encapsulated lumophore core may also have potential uses in molecular-scale optoelectronics, photonics, security devices, luminescence-based sensors, and other emerging areas of technology.[5] A tetrahedral starlike arrangement of chromophores has previously been shown to exhibit advantages for collection of diffuse light through exciton interactions.[6] Dendritic light-harvesting systems that exhibit cascade-energy-transfer behavior have also been reported recently.[7] However, the multistep syntheses required for such systems have so far limited their widespread application and there remains a need for simpler synthetic strategies to create light-harvesting arrays.

During the last two decades, controlled/living radical polymerization has emerged as one of the most effective synthetic routes to well-defined polymers.[8] Among them, reversible addition–fragmentation chain-transfer (RAFT) polymerization appears to be one of the most efficient and could potentially be applied to any classical radical system.[9] The RAFT process involves performing a conventional radical polymerization in the presence of certain thiocarbonylthio compounds (S=C(Z)-SR), so-called RAFT agents. Light-harvesting polymers with defined properties can be synthesized by RAFT polymerization with specially functionalized RAFT agents.[3,10] We report herein the synthesis by RAFT methods of well-defined star-shaped light-harvesting block copolymers that contain an energy cascade of chromophores from the periphery to the core.

Hexa(dithiobenzoate)-functionalized Ru^{II} tris(bipyridine) (Ru-hexa-RAFT) was synthesized as previously reported.[3] It was used to control the polymerization of a styrene-functionalized coumarin monomer (st-coumarin).[11] The resulting star-shaped polymer **1** has an average length of two st-coumarin repeat units in each arm. Polymer **1** was subsequently used as a macro-RAFT agent to control the polymerization of acenaphthylene to obtain the star-shaped diblock copolymer **2** with a narrow polydispersity and an average length of 36 acenaphthenyl repeat units in each arm. The ratio of the acenaphthenyl to coumarin chromophores in each arm of polymer **2** was designed to provide selective excitation of acenaphthenyl units of this polymer at 295 nm. To avoid the competing quenching effect of the dithiobenzoyl groups on excited chromophores observed previously,[3,10] a triblock copolymer, **3**, with an average length of 44 *N*-isopropylacrylamide (NIPAM) repeat units in each arm was similarly synthesized by using polymer **2** as the macro-RAFT agent and NIPAM monomer.

The numbers of st-coumarin, acenaphthenyl, and NIPAM repeating units in the polymers are calculated based on gravimetric determinations. These values agreed with compositions determined spectrophotometrically by comparing the absorption spectra of the polymers with the corresponding model compounds. The agreement obtained indicates that



incorporating the chromophores in the polymer does not perturb their absorption spectra, that is, there is no evidence for ground-state electronic interactions between chromophores. This observation has also been reported in previous work on related polymers.[3,10] The composition of polymer **1** was also characterized by NMR spectroscopy. The block copolymers **2** and **3** displayed narrow molecular-weight distributions by gel permeation chromatography (GPC).

To investigate the energy-transfer process between acenaphthenyl and coumarin units in the star-shaped polymers, a linear block copolymer, **4**, was synthesized through hydrolysis of the star-shaped diblock copolymer **2** with an amine.[12]

Acenaphthene, a 4-isopropylbenzyl-functionalized coumarin compound (IPB-coumarin), tris(bipyridine) Ru^{II} dichloride, and 4-cyano-4-((thiobenzoyl)sulfanyl)pentanoic acid[3] were selected as model compounds to characterize the electronic interaction between the photoexcited donor chromophore with the ground-state acceptor. Energy transfer between an electronically excited donor and ground-state acceptor is commonly described by the induced dipole–dipole (Förster) mechanism.[13] The strength of the electronic interaction is characterized by the Förster critical transfer distance determined from the spectroscopic and photophys-

 © 2005 Wiley-VCH Verlag GmbH & Co. KGaA, Weinheim

ical properties of the donor and acceptor and defined as the distance at which the rate of energy transfer equals the rate of other excited-state relaxation processes of the donor. Assuming an orientation factor (κ^2) equal to 2/3 (corresponding to a random distribution of transition dipole orientations), we calculated the Förster critical distances between these chromophores in degassed dichloromethane solutions as shown in Table 1.

Table 1: The Förster critical transfer distances (R_0 [Å]) between relevant chromophores in degassed dichloromethane solution.

	Acenaphthenyl	Coumarin	Ru^{II} complex	Dithiobenzoyl
acenaphthenyl	13.7	29.2	23.2	24.6
coumarin	29.2	13.0	39.7	16.0
Ru^{II} complex	23.2	39.7	NA	NA
dithiobenzoyl	24.6	16.0	NA	NA

The Förster critical transfer distance between acenaphthenyl and coumarin chromophores (29.2 Å) exceeds that for the acenaphthenyl and Ru^{II} complex moieties (23.2 Å). Owing to the polymer structure, the interchromophoric distance between acenaphthenyl and coumarin units can be expected to be smaller than that between the acenaphthenyl units and the Ru^{II} complex core in the star-shaped block copolymers. Thus, the rate of energy transfer from excited acenaphthenyl molecules to the coumarin units should be faster than that between the excited acenaphthenyl molecules and Ru^{II} complex cores, thus leading to a sequential energy-transfer process.

A comparison of the absorption and emission spectra from degassed dichloromethane solutions of the polymers is shown in Figure 1. Photoexcitation of acenaphthenyl units in the linear polymer **4** at 295 nm, in which absorption is almost exclusively (> 95 %) due to the acenaphthenyl donor, results in fluorescence being predominantly emitted from the coumarin acceptor at 440 nm. After the Ru^{II} core has been introduced into the star-shaped polymers, the coumarin emission is dramatically quenched, whereas significant emission from the Ru^{II} complex core is observed at 615 nm in polymers **2** and **3**. It should be noted that emission from the star-shaped polymers at 415 nm arises largely from acenaphthenyl excimers.[14] Figure 1 also shows that removal of the competing quenching effect of the dithiobenzoyl end groups in the triblock copolymer **3** increases the efficiency of the energy transfer from acenaphthenyl units to the Ru^{II} moieties.

The excitation spectrum of **4**, monitored at 435 nm, contains a major contribution attributable to acenaphthenyl chromophore absorption at 295 nm, which confirms that energy transfer occurs. By comparing the excitation spectrum with the normalized absorption spectrum,[15] the efficiency of energy transfer from the acenaphthenyl to coumarin units in this linear polymer was determined to be 67 %.

When the Ru^{II} complex emission is monitored at 615 nm, the excitation spectra of **2** and **3** exhibit major contributions due to the absorption of coumarin chromophores at 345 nm and acenaphthenyl chromophores at 295 nm. The efficiencies of energy transfer from coumarin units to the Ru^{II} complex

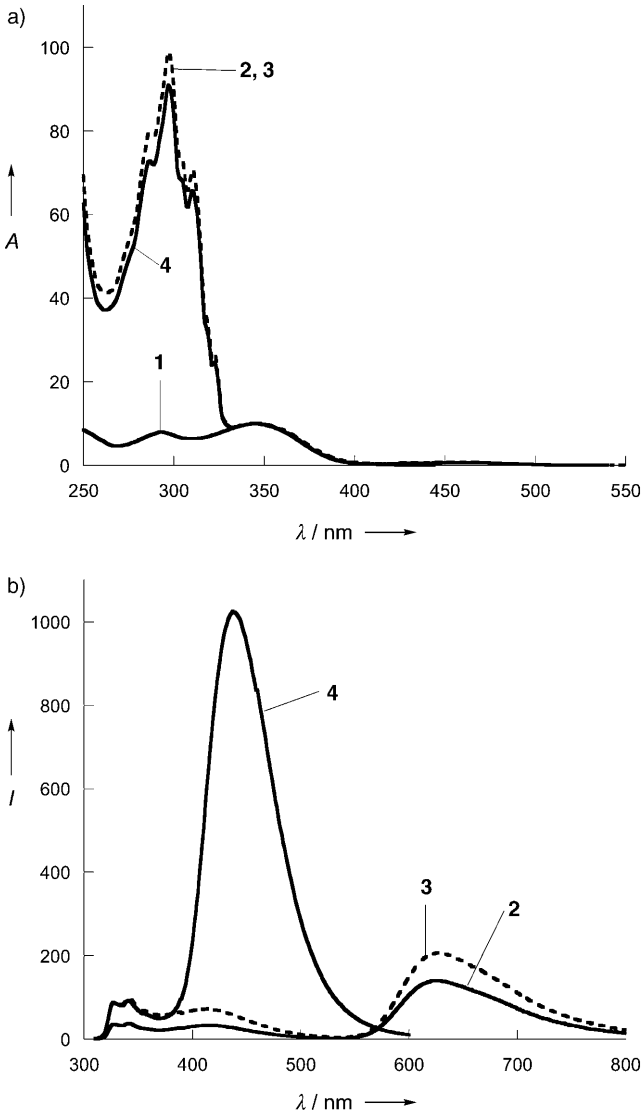


Figure 1. a) Absorption (normalized at $\lambda = 350$ nm) and b) luminescence spectra of polymers **1**–**4** in dichloromethane. For luminescence measurements, all degassed solutions have the same absorbance at the excitation wavelength of 295 nm. Fluorescence in **1** is totally quenched by the adjacent dithiobenzoyl end group.

core, determined as described above, in both star-shaped polymers are 90 %. This is a consequence of the relatively large R_0 (39.7 Å) and short donor-to-acceptor separations. The efficiencies from acenaphthenyl to the Ru^{II} complex core in polymers **2** and **3** are 47 % and 62 %, respectively. The higher efficiency in **3** relative to **2** is the result of a decrease in the competing dithiobenzoyl quenching effect that results from insertion of the photo-inactive NIPAM spacers in the triblock copolymer.

The excited acenaphthenyl units can conceivably pass their excitation energy to the Ru^{II} complex core either in a stepwise cascade fashion through coumarin sequences or by a direct one-step energy-transfer process. In the present case, we believe that the former path is favored for the following reason: Energy transfer between excited acenaphthenyl and coumarin units is kinetically favored as a result of the larger

 © 2005 Wiley-VCH Verlag GmbH & Co. KGaA, Weinheim

Förster critical distance and shorter interchromophoric distance in comparison with those of excited acenaphthenyl units and the Ru^{II} core. This conclusion is also supported by the measured energy-transfer efficiencies. The efficiency of energy transfer from the acenaphthenyl to coumarin units is 67% in the linear model polymer, **4**. The transfer efficiency from coumarin units to the Ru^{II} core is 90%. Hence, the theoretical efficiency for the overall energy-transfer process from acenaphthenyl to the Ru^{II} complex through a cascade route in **3** can be expected to be 60% (i.e., $67 \times 90\%$), which agrees well with the measured value, 62%. The sequence of the energy-transfer processes is depicted schematically in Figure 2.

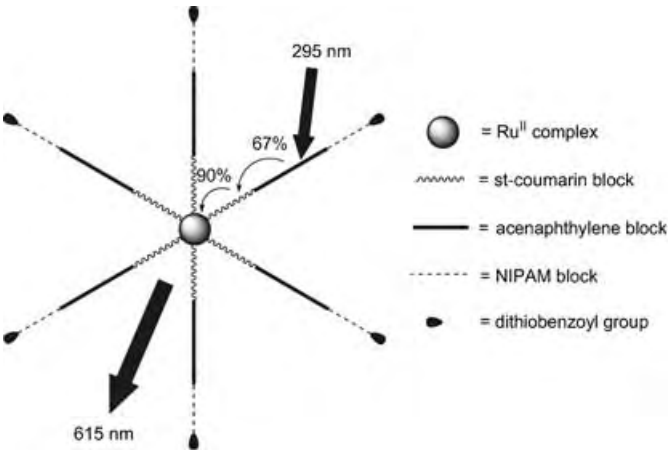


Figure 2. Schematic representation of the energy-transfer processes within the star-shaped block copolymer **3**.

In conclusion, star-shaped block copolymers have been synthesized to obtain light-harvesting systems with an energy gradient from the periphery to the core. Photophysical data suggest that the transfer of excitation energy in the block copolymers occurs mainly through a stepwise energy cascade from the initially excited acenaphthenyl units to the coumarin chromophores and hence to the Ru^{II} complex core.

Experimental Section

Solutions for luminescence measurements were degassed by multiple freeze–pump–thaw cycles at $\approx 10^{-6}$ torr. Emission and excitation spectra were recorded on a Varian Cary Eclipse fluorometer and were corrected for the wavelength dependence of the sensitivity of the detector and the output of the excitation light source by using a calibrated standard lamp source. Molecular-weight determinations were performed in THF at 25 °C with a Waters GPC instrument with a refractive-index detector. Molecular weights are reported as linear polystyrene equivalents.

IPB-coumarin: A mixture of coumarin-2 (0.20 g, 0.92 mmol; Exciton, laser grade), 4-ispropyl benzyl chloride (0.17 g, 1.01 mmol), K_2CO_3 (0.38 g, 2.67 mmol), KI (0.05 g, 0.28 mmol) in CH_3CN (10 mL) was stirred under nitrogen at 85 °C for 24 h. Purification was performed with column chromatography on silica gel (Kieselgel-60, 70–230 mesh) with a mixture of ethyl acetate and *n*-hexane in a ratio of 1:4 as eluent. Yield: 0.25 g, 78%. ^{1}H NMR (200 MHz, $CDCl_3$): $\delta =$ 1.03 (t, 3H, $J = 6.94$ Hz), 1.21 (s, 3H), 1.24 (s, 3H), 2.37 (b, 3H), 2.41 (b, 3H), 2.87 (m, 1H), 3.05 (q, 2H, $J = 6.94$, 14.25 Hz), 4.16 (s, 2H), 6.11 (b, 1H), 6.92(s, 1H), 7.10–7.26(m, 4H), 7.35 ppm (s, 1H). UV/Vis (DCM): λ_{max} ($\log \varepsilon$): 347 (4.16).

1: A mixture of Ru-hexa-RAFT[3] (30 mg, 11.9 μmol), 2,2′-azobis(isobutyronitrile) (AIBN; 0.5 mg, 3.7 μmol), st-coumarin (477 mg, 1.43 mmol) and solvent (1 mL, acetonitrile/chlorobenzene = 1:2, *v*/*v*) was degassed through three freeze–pump–thaw cycles, sealed under vacuum, and heated at 70 °C for 8 h. The polymer was purified by precipitation into MeOH (20 mL). Yield: 78 mg (10%). $\bar{M}_n$ (by calculation) = 6500; $\bar{M}_n$ (by ^{1}H NMR spectroscopy) = 6200; $\bar{M}_n$ (by UV/Vis spectroscopy) = 6500; $\bar{M}_n$ is the number-average molecular weight.

2: Polymer **2** was prepared from polymer **1** (17 mg, 2.6 μmol equivalent Ru-hexa-RAFT), AIBN (0.5 mg, 3.7 μmol), acenaphthylene (474 mg, 3.12 mmol) and chlorobenzene (1 mL) at 70 °C for 16 h. Yield: 120 mg (18%). $\bar{M}_n$ (by calculation) = 39300; $\bar{M}_n$ (by UV/Vis) = 43000; $\bar{M}_n$ (by GPC) = 5300, $\bar{M}_w/\bar{M}_n$ (by GPC) = 1.13; $\bar{M}_w$ is the weight-average molecular weight.

3: Polymer **3** was prepared from polymer **2** (40 mg, 0.9 μmol equivalent Ru-hexa-RAFT), AIBN (0.5 mg, 3.7 μmol), NIPAM (49 mg, 432 mmol) and solvent (1 mL, acetonitrile/chlorobenzene = 1:1, *v*/*v*) at 70 °C for 16 h. Yield: 67 mg (55%). $\bar{M}_n$ (by calculation) = 69100; $\bar{M}_n$ (by GPC) = 3700, $\bar{M}_w/\bar{M}_n$ (by GPC) = 1.16.[16]

4: Polymer **4** was prepared from the hydrolysis of polymer **2** (40 mg) by using *N*,*N*-dimethylethylenediamine (0.5 mL) in chlorobenzene (1 mL) under nitrogen. Yield: 30 mg (75%). $\bar{M}_n$ (by calculation) = 6100; $\bar{M}_n$ (by GPC) = 7100, $\bar{M}_w/\bar{M}_n$ (by GPC) = 1.21.

Received: December 3, 2004
Revised: March 18, 2005
Published online: June 3, 2005

Keywords: block copolymers · chromophores · light harvesting · luminescence · ruthenium

[1] a) G. McDermott, S. M. Prince, A. A. Freer, A. M. Hawthornthwaite-Lawless, M. Z. Papiz, R. J. Cogdell, N. W. Isaacs, *Nature* **1995**, *374*, 517; b) R. J. Cogdell, N. W. Isaacs, A. A. Freer, T. D. Howard, A. T. Gardiner, S. M. Prince, M. Z. Papiz, *FEBS Lett.* **2003**, *555*, 35; c) V. Sundström, T. Pullerits, R. van Grondelle, *J. Phys. Chem. B* **1999**, *103*, 2327.

[2] a) J. S. Aspler, C. E. Hoyle, J. E. Guillet, *Macromolecules* **1978**, *11*, 925; b) J. E. Guillet, *Polymer Photophysics and Photochemistry*, Cambridge University Press, Cambridge, **1985**; c) S. E. Webber, *Chem. Rev.* **1990**, *90*, 1469.

[3] M. Chen, K. P. Ghiggino, A. Launikonis, A. W. H. Mau, E. Rizzardo, W. H. F. Sasse, S. H. Thang, G. J. Wilson, *J. Mater. Chem.* **2003**, *13*, 2696.

[4] A. Bar-Haim, J. Klafter, *J. Phys. Chem. B* **1998**, *102*, 1662.

[5] a) S. Hecht, J. M. J. Fréchet, *Angew. Chem.* **2001**, *113*, 76; *Angew. Chem. Int. Ed.* **2001**, *40*, 74; b) V. Balzani, A. Credi, M. Venturi, *Molecular Devices and Machines—A Journey into the Nano World*, Wiley-VCH, Weinheim, **2003**; c) M.-S. Choi, T. Yamazaki, I. Yamazaki, T. Aida, *Angew. Chem.* **2004**, *116*, 152; *Angew. Chem. Int. Ed.* **2004**, *43*, 150; d) K. Kuriki, Y. Koike, Y. Okamoto, *Chem. Rev.* **2002**, *102*, 2347; e) M. A. Baldo, D. F. O'Brien, Y. You, A. Shoustikov, S. Sibley, M. E. Thompson, S. R. Forrest, *Nature* **1998**, *395*, 151; f) A. P. H. J. Schenning, E. Peeters, E. W. Meijer, *J. Am. Chem. Soc.* **2000**, *122*, 4489.

[6] H. Langhals, C. Wagner, R. Ismal, *New J. Chem.* **2001**, *25*, 1047.

[7] a) C. Devadoss, P. Bharathi, J. S. Moore, *J. Am. Chem. Soc.* **1996**, *118*, 9635; b) T. Weil, E. Reuther, K. Müllen, *Angew. Chem.* **2002**, *114*, 1980; *Angew. Chem. Int. Ed.* **2002**, *41*, 1900; c) J. M. Serin, D. W. Brousmiche, J. M. J. Fréchet, *Chem. Commun.* **2002**, 2605.

[8] a) "Controlled Radical Polymerization": *ACS Symp. Ser.* **1998**, *685* (Ed.: K. Matyjaszewski); b) "Controlled/Living Radical

 © 2005 Wiley-VCH Verlag GmbH & Co. KGaA, Weinheim

Polymerization: Progress in ATRP, NMP, and RAFT": *ACS Symp. Ser.* **2000**, *768* (Ed.: K. Matyjaszewski); c) "Advances in Controlled/Living Radical Polymerization": *ACS Symp. Ser.* **2003**, *854* (Ed.: K. Matyjaszewski)

[9] a) T. P. Le, G. Moad, E. Rizzardo, S. H. Thang, PCT Int. Appl. WO 98/01478 [*Chem. Abstr.* **1998**, *128*, 115390]; b) J. Chiefari, Y. K. Chong, F. Ercole, J. Krstina, J. Jeffery, T. Le, R. T. A. Mayadunne, G. F. Meijs, C. L. Moad, G. Moad, E. Rizzardo, S. H. Thang, *Macromolecules* **1998**, *31*, 5559.

[10] a) M. Chen, K. P. Ghiggino, A. W. H. Mau, E. Rizzardo, S. H. Thang, G. J. Wilson, *Chem. Commun.* **2002**, 2276; b) M. Chen, K. P. Ghiggino, A. W. H. Mau, E. Rizzardo, W. H. F. Sasse, S. H. Thang, G. J. Wilson, *Macromolecules* **2004**, *37*, 5479.

[11] A. Adronov, D. R. Robello, J. M. J. Fréchet, *J. Polym. Sci. A* **2001**, *39*, 1366.

[12] K. A. Latif, M. Y. Ali, *Tetrahedron* **1970**, *26*, 4247.

[13] Th. Förster, *Ann. Phys.* **1948**, *2*, 55.

[14] K. P. Ghiggino, T. A. Smith, *Prog. React. Kinet.* **1993**, *18*, 375.

[15] F. Bai, C. H. Chang, S. E. Webber, *Macromolecules* **1986**, *19*, 2484.

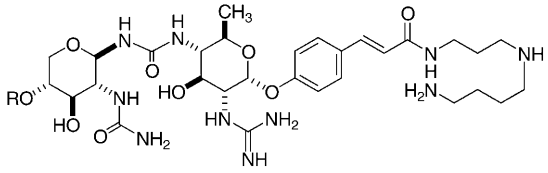
[16] There might be additional specific interactions between the amphiphilic copolymer **3** and the column packing and/or the solvent, which leads to an unreasonably low molecular weight value. Similar unusual GPC behavior of NIPAM polymers has also been reported previously: a) X. Y. Wu, R. H. Pelton, K. C. Tam, D. R. Woods, A. E. Hamielec, *J. Polym. Sci. Part A* **1993**, *31*, 957; b) H. G. Schild, *Prog. Polym. Sci.* **1992**, *17*, 163; c) F. Ganachaud, M. J. Monteiro, R. G. Gilbert, M-A. Dourges, S. H. Thang, E. Rizzardo, *Macromolecules* **2000**, *33*, 6738.

Amino Sugar Synthesis

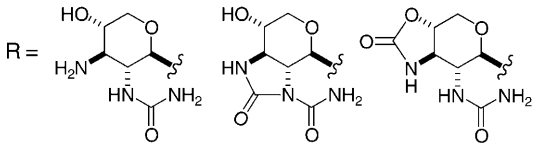
Total Synthesis of Glycocinnasperimicin D**

*Taihei Nishiyama, Minoru Isobe, and Yoshiyasu Ichikawa**

Glycocinnasperimicin D (**1**) was isolated from the fermentation broth of the producing strain (*Nocardia*), and its structure was elucidated by spectroscopic studies by Umezawa and his co-workers.[1] This molecule belongs to a family of glycocinnamoylspermidine antibiotics which also includes LL-BM123β (**2**), LL-BM123γ_1 (**3**), and LL-BM123γ_2 (**4**); these members contain three different types of unusual amino sugars.[2,3] Glycocinnasperimicin D contains the two highly functionalized amino sugars: 2-ureidopentose (left) and 2-guanidino-4-ureido-6-deoxy-α-D-glucopyranose (right) with the *p*-cinnamoylspermidine aglycone. Moreover, these two unusual amino sugars are joined through a unique glycosyl urea linkage.



glycocinnasperimicin D (**1**): R = H



LL-BM123β (**2**) LL-BM123γ_1 (**3**) LL-BM123γ_2 (**4**)

The amino sugar antibiotic **1** is of special interest because of its broad-spectrum activity against Gram-negative organisms; however, the natural product was no longer available as a result of mutation of the *Nocardia* strain.[4] Its intriguing structural features, coupled with its unique biological activity and the lack of availability from natural sources, encouraged us to explore the synthesis of this molecule. We report herein the first total synthesis of glycocinnasperimicin D (**1**).

It is evident that the construction of the urea glycoside in the presence of a variety of nitrogen-containing functional groups constitutes the major challenge in the total synthesis of **1**. Recently, we developed a new approach to the synthesis of urea glycosides which involves the reaction of a highly reactive glycosyl isocyanate with amines.[5] It was envisaged that our protocol could be applied to the synthesis of **1** as represented in the retrosynthetic analysis shown in Scheme 1. Oxidation of the glycosyl isonitrile **7** could generate the glycosyl isocyanate **5**, which would react with the amino sugar **6** at the position indicated. The amino sugar **6** could be obtained by the Heck reaction of the iodophenyl glycoside **8** with the acrylamide **9**, which contains the spermidine moiety. We anticipated that this convergent tactic for the synthesis of the cinnamoyl glycoside would avoid the problems associated with the glycosidation of a poorly nucleophilic phenol bearing an electron-withdrawing substituent.[6]

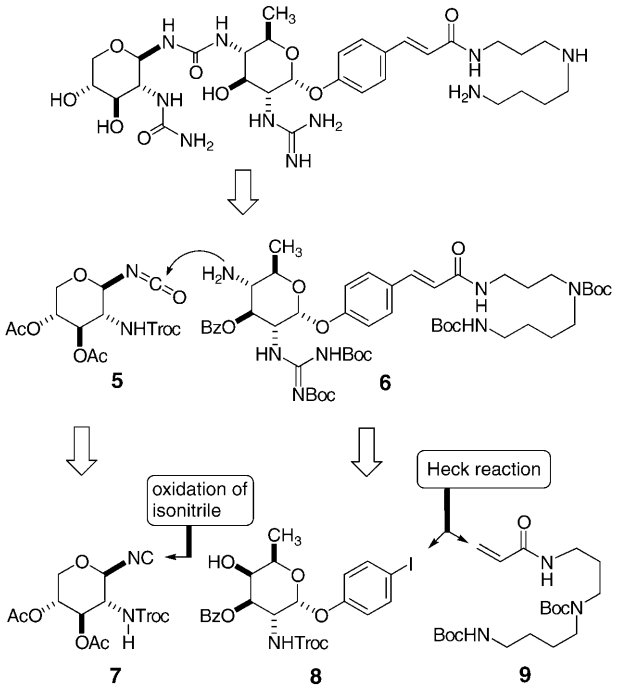
The synthesis of the left-hand amino sugar in the form of **7** began with the stereoselective synthesis of an allyl amine on the basis of a protocol developed recently by our research group[7] (Scheme 2). Thus, the enantioselective addition of diethylzinc to the α,β-unsaturated aldehyde **10** in the presence of the Soai catalyst **11**[8] proceeded smoothly to afford the allylic alcohol **12** in 79% yield and with high diastereoselec-

[*] Prof. Dr. Y. Ichikawa
Faculty of Science
Kochi University
Akebono-cho, Kochi 780-8520 (Japan)
Fax: (+81) 88-844-8359
E-mail: ichikawa@cc.kochi-u.ac.jp
T. Nishiyama, Prof. Dr. M. Isobe
Laboratory of Organic Chemistry
School of Bioagricultural Sciences, Nagoya University
Chikusa, Nagoya 464-8601 (Japan)

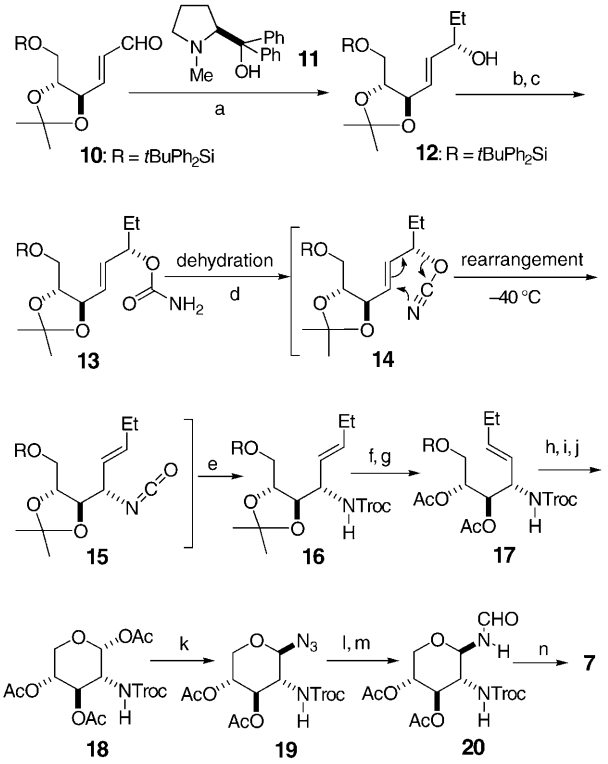
[**] We thank Dr. Yoshikazu Takahashi (Microbial Chemistry Research Center) for cellulose TLC analysis, antimicrobial assays, and valuable discussions about glycocinnasperimicin D. The authors are grateful for Grants-in-Aid for Scientific Research from the Ministry of Education, Science, Sports, and Culture of Japan for financial support.

Supporting information for this article is available on the WWW under http://www.angewandte.org or from the author.

 © 2005 Wiley-VCH Verlag GmbH & Co. KGaA, Weinheim DOI: 10.1002/anie.200500892



Scheme 1. Retrosynthetic analysis of glycocinnasperimicin D.



Scheme 2. Synthesis of the left-hand amino sugar moiety: a) Et_2Zn, cyclohexane, 0 °C→RT (79%); b) CCl_3CONCO, CH_2Cl_2; c) aqueous K_2CO_3, MeOH (93% over two steps); d) PPh_3, CBr_4, Et_3N, CH_2Cl_2, −40 °C; e) CCl_3CH_2OH, room temperature, overnight (82% over two steps); f) $FeCl_3{\cdot}6H_2O$, $CHCl_3$; g) Ac_2O, pyridine (80%); h) HF·pyridine, THF; i) O_3, CH_2Cl_2, Me_2S; j) Ac_2O, DMAP, pyridine (71% over three steps); k) $TMSN_3$, $SnCl_4$, CH_2Cl_2, (86%); l) PPh_3, THF, H_2O; m) AcOCHO (72% over two steps); n) PPh_3, CBr_4, Et_3N, CH_2Cl_2, (85%). DMAP = 4-dimethylaminopyridine, TMS = trimethylsilyl, Troc = 2,2,2-trichloroethoxycarbonyl.

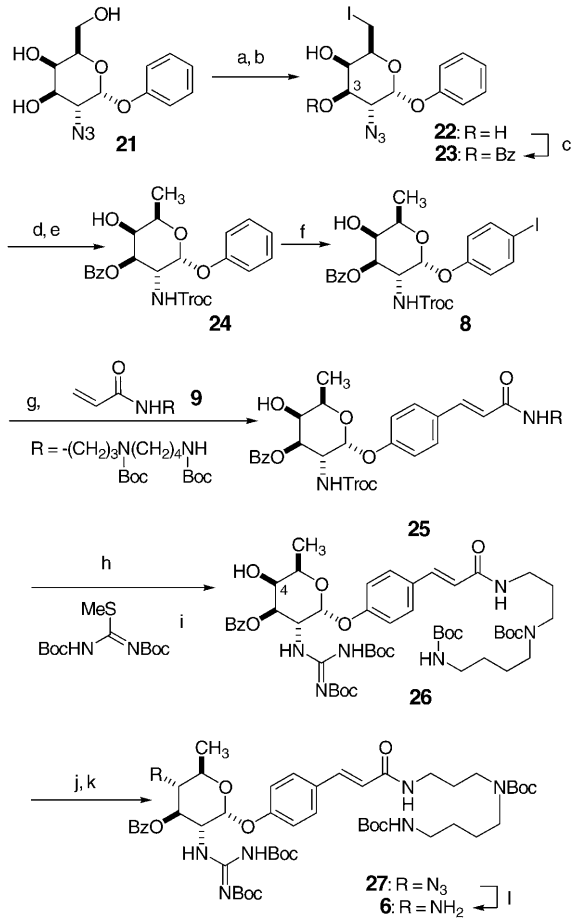
tivity (15:1, checked by ^1H NMR spectroscopic analysis of the corresponding acetates). The allylic alcohol **12** was then transformed into the allyl carbamate **13** by treatment with trichloroacetyl isocyanate followed by hydrolysis with potassium carbonate in aqueous methanol. Upon dehydration of the carbamate **13** with triphenylphosphane, carbon tetrabromide, and triethylamine at −40 °C, the resulting allyl cyanate **14** underwent a spontaneous [3,3] sigmatropic rearrangement to afford the allyl isocyanate **15** with a high degree of 1,3-chirality.[9] Subsequent trapping of **15** with 2,2,2-trichloroethanol gave the Troc carbamate **16** in 82% yield from **13**.[10]

Hydrolysis of the isopropylidene ketal in **16** was more problematic than we had initially anticipated; the acetonide **16** was subjected to a number of deprotection protocols without success, possibly as a result of silyl-group migration to the adjacent hydroxy groups. Fortunately, Lewis acid catalyzed deprotection with ferric chloride hexahydrate ($FeCl_3{\cdot}6H_2O$) was found to be successful.[11] After treatment of **16** with $FeCl_3{\cdot}6H_2O$ in chloroform followed by workup, the resulting mixture was treated immediately with acetic anhydride and pyridine to prevent silyl-group migration. The required acetate **17** was obtained in acceptable yield (80% based on the consumed starting material) along with recovered **16** (23%). Careful cleavage of the *tert*-butyldiphenylsilyl ether **17** (HF·pyridine, THF)[12] followed by oxidative cleavage of the alkene (O_3, CH_2Cl_2, −78 °C) gave the corresponding lactol, which was subsequently treated with acetic anhydride and pyridine to furnish predominantly the α-*O*-acetyl glycoside **18** in 71% yield over three steps. Treatment of **18** with trimethylsilyl azide in the presence of tin(VI) chloride furnished the β-glycosyl azide **19** exclusively (86%).[13] The isonitrile group at the anomeric position was constructed in a three-step sequence by 1) Staudinger reaction of the glycosyl azide **19**, 2) formylation of the resulting iminophosphorane with acetic formic anhydride (72% yield over two steps), and 3) dehydration of the formamide **20** by the modified Appel procedure[14] to afford the isonitrile glycoside **7** (85% yield).

The synthesis of the right-hand amino sugar in the form of **6** commenced with the α-phenyl 2-azido-D-galactoside **21**,[15] which was prepared from D-galactal in a four-step sequence (Scheme 3). Tosylation of the primary alcohol in **21** followed by displacement with iodide anion gave the iodide **22** in 73% yield over two steps. After selective protection of the equatorial hydroxy group at C3 in **22** as a benzoate group (93% yield), reductive hydrogenolysis of the iodide **23** was carried out with concomitant reduction of the azide group. Subsequent protection of the resulting amine as its Troc carbamate gave the 6-deoxypyranose **24** in 81% yield.[16]

The cinnamic spermidine amide attached to the amino sugar was constructed from the phenyl glycoside **24** by a two-step protocol. Thus, treatment of **24** with ceric ammonium nitrate (CAN) and an iodine salt (nBu_4NI) in acetonitrile at 70 °C furnished the iodophenyl galactoside **8** in 86% yield.[17] The Heck reaction of **8** with acrylamide **9** proceeded smoothly to furnish the cinnamoyl galactoside **25** in 73% yield. Cleavage of the Troc carbamate in **25** (Zn, AcOH, THF) followed by treatment of the resulting amine with *N*,*N*-di-(*tert*-butoxycarbonyl)-*S*-methylisothiourea and mercuric

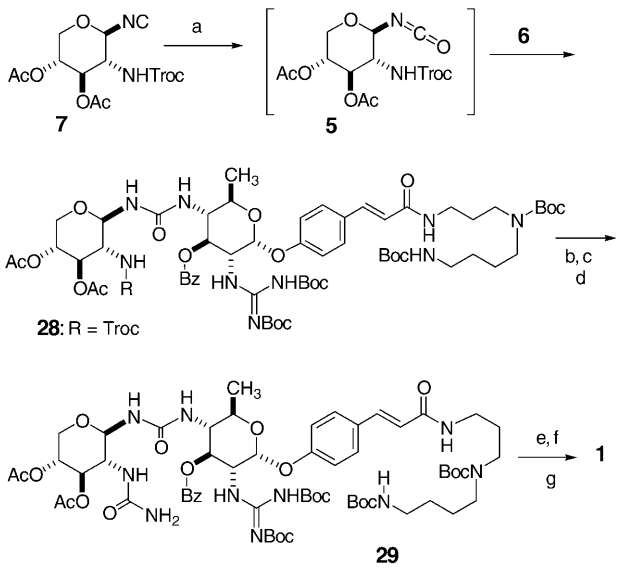
 © 2005 Wiley-VCH Verlag GmbH & Co. KGaA, Weinheim



Scheme 3. Synthesis of the right-hand amino sugar unit: a) TsCl, pyridine (81%); b) NaI, nBu_4NI, DME (91%); c) BzCl, pyridine (93%); d) H_2, Pd-C (5%), Et_3N, EtOH; e) TrocCl, pyridine (81% over two steps); f) nBu_4NI, CAN, CH_3CN (86%); g) $Pd(OAc)_2$, P(*o*-Tol)$_3$, Et_3N, CH_3CN, 70°C (73%); h) Zn, AcOH, THF; i) $HgCl_2$, Et_3N, DMF (72% over two steps); j) Tf_2O, pyridine, CH_2Cl_2; k) NaN_3, DMF (73% over two steps); l) $HS(CH_2)_3SH$, Et_3N, MeOH (73%). Boc = *tert*-butoxycarbonyl, Bz = benzoyl, DME = dimethoxyethane, DMF = *N*,*N*-dimethylformamide, Tf = trifluoromethanesulfonyl, Tol = tolyl.

chloride in DMF afforded the bis(Boc)-protected guanidine **26** in 72% yield for the two steps.[18] The amino group at C4 was introduced by S_N2 displacement of a triflate with azide anion; thus the hydroxyl group in **26** was transformed into the corresponding triflate, and the rather unstable product was subjected immediately to treatment with sodium azide in DMF to furnish **27** in 73% yield over two steps. Whereas reduction of the azide group in **27** with PPh_3, $SnCl_2$,[19] nBu_3SnH,[20] or H_2/Pd-C[21] was unsuccessful, careful treatment with propanedithiol and triethylamine in MeOH[22] furnished the amino sugar **6** in 73% yield to set the stage for the coupling reaction.

With both key amino sugars **6** and **7** in hand, we next investigated their coupling to construct the urea glycosyl linkage (Scheme 4). In the event, oxidation of the isonitrile **7** with pyridine *N*-oxide in the presence of 3-Å molecular sieves and a catalytic amount of iodine in acetonitrile generated the isocyanate **5**,[5] which was treated directly with the amino



Scheme 4. Final coupling and completion of the synthesis of glycocinnasperimicin D (**1**): a) pyridine *N*-oxide, I_2 (cat.), 3-Å molecular sieves, CH_3CN (85% for **28**); b) Zn, AcOH, THF; c) CCl_3CONCO, CH_2Cl_2; d) Et_3N, MeOH (77% over two steps); e) TFA, CH_2Cl_2; f) 28% aqueous NH_3, CH_3OH; g) HPLC purification, lyophilization (23%). TFA = trifluoroacetic acid.

sugar **6**. Gratifyingly, this procedure gave the desired coupling product **28** in good yield (85%). Removal of the Troc group in **28** and subsequent treatment of the resulting amine with trichloroacetyl isocyanate, followed by methanolysis, gave the fully protected glycocinnasperimicin D **29** in 77% yield. Finally, removal of the Boc group in **29** with trifluoroacetic acid and subsequent cleavage of the benzoyl and two acetyl groups in a mixture of aqueous ammonia and methanol yielded glycocinnasperimicin D (**1**). To our delight, careful and laborious purification by HPLC provided pure synthetic material **1** (23% yield, isolated as the hydrochloride), the spectral data (^1H NMR, ^{13}C NMR, HRMS), TLC behavior, and antimicrobial activity of which were in good agreement with those of the natural glycocinnasperimicin D.

In conclusion, the first total synthesis of glycocinnasperimicin D (**1**) has been carried out by a convergent route on the basis of a three-fragment coupling strategy. Our synthesis features a Heck reaction to form the cinnamoyl glycoside, the stereoselective formation of an allyl amine by the [3,3] sigmatropic rearrangement of an allyl cyanate, and the construction of the urea glycoside by the coupling of a glycosyl isocyanate with an amino sugar. In particular, the oxidation of an isonitrile glycoside afforded a highly reactive isocyanate glycoside, which was key to the crucial coupling step.

Received: March 10, 2005
Published online: June 14, 2005

Keywords: amino sugars · antibiotics · natural products · sigmatropic rearrangement · total synthesis

 © 2005 Wiley-VCH Verlag GmbH & Co. KGaA, Weinheim

[1] K. Dobashi, K. Nagaoka, Y. Watanabe, M. Nishida, M. Hamada, H. Naganawa, T. Takita, T. Takeuchi, H. Umezawa, *J. Antibiot.* **1985**, 1166.

[2] a) G. A. Ellestad, D. B. Cosulich, R. W. Broschard, J. H. Martin, M. P. Kunstmann, G. O. Morton, J. E. Lancaster, W. Fulmor, F. M. Lovell, *J. Am. Chem. Soc.* **1978**, *100*, 2515; b) S. H. L. Chiu, R. Fiala, R. Kennett, L. Wozniak, M. W. Bullock, *J. Antibiot.* **1984**, 1000; c) H.-R. Tsou, R. R. Fiala, P. C. Mowery, M. W. Bullock, *J. Antibiot.* **1984**, 1382.

[3] For synthetic studies of glycocinnamoylspermidine antibiotics, see: a) K. Araki, K. Miyazawa, H. Hashimoto, J. Yoshimura, *Tetrahedron Lett.* **1982**, *23*, 1705; b) K. Araki, H. Hashimoto, J. Yoshimura, *Carbohydr. Res.* **1982**, *109*, 143; c) K. Araki, M. Kawa, K. Miyazawa, H. Hashimoto, J. Yoshimura, *Bull. Chem. Soc. Jpn.* **1986**, *59*, 3137.

[4] Personal communication from Dr. H. Naganawa and Dr. Y. Takahashi.

[5] a) Y. Ichikawa, T. Nishiyama, M. Isobe, *Synlett* **2000**, 1253; b) Y. Ichikawa, T. Nishiyama, M. Isobe, *J. Org. Chem.* **2001**, *66*, 4200.

[6] T. Nishiyama, Y. Ichikawa, M. Isobe, *Synlett* **2004**, 89.

[7] a) Y. Ichikawa, T. Ito, T. Nishiyama, M. Isobe, *Synlett* **2003**, 1034; b) Y. Ichikawa, T. Ito, M. Isobe, *Eur. J. Org. Chem.* **2005**, 1949.

[8] K. Soai, A. Ookawa, T. Kaba, K. Ogawa, *J. Am. Chem. Soc.* **1987**, *109*, 7111.

[9] For representative examples of the allylic cyanate-to-isocyanate rearrangement, see: a) C. Christophersen, A. Holm, *Acta Chem. Scand.* **1970**, *24*, 1512; b) L. E. Overman, M. Kakimoto, *J. Org. Chem.* **1978**, *43*, 4564; c) Y. Ichikawa, *Synlett* **1991**, 238; d) K. Banert, S. Groth, *Angew. Chem.* **1992**, *104*, 865; *Angew. Chem. Int. Ed. Engl.* **1992**, *31*, 866.

[10] a) Y. Ichikawa, K. Tsuboi, M. Isobe, *J. Chem. Soc. Perkin Trans. 1* **1994**, 2791; b) Y. Ichikawa, M. Osada, I. Ohtani, M. Isobe, *J. Chem. Soc. Perkin Trans. 1* **1997**, 1449.

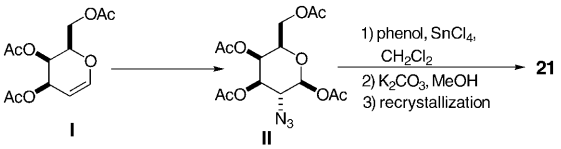
[11] K. S. Kim, Y. H. Song, B. H. Lee, C. S. Hahn, *J. Org. Chem.* **1986**, *51*, 404.

[12] D. A. Evans, S. W. Kaldor, T. K. Jones, J. Clardy, T. J. Stout, *J. Am. Chem. Soc.* **1990**, *112*, 7001.

[13] H. Paulson, Z. Gyorgydeak, M. Friedman, *Chem. Ber.* **1974**, *107*, 1568.

[14] a) Y. Ichikawa, *J. Chem. Soc. Perkin Trans. 1* **1992**, 2135; b) I. A. O'Neil in *Comprehensive Organic Functional Group Transformations*, *Vol. 3* (Eds.: A. Katritzky, O. Meth-Cohn, C. W. Ress), Pergamon, Oxford, **1995**, pp. 696.

[15] Multigram quantities of the phenyl glycoside **21** were readily obtained in 51% yield from D-galactal by the following three-step synthesis: 1) azidonitration of the D-galactal **I** followed by acetolysis to give **II** (see: R. U. Lemieux, R. M. Ratcliffe, *Can. J. Chem.* **1979**, *57*, 1244), 2) Lewis acid catalyzed glycosylation of **II** with phenol (86%, α/β 4:1), and 3) deprotection of the acetyl groups and purification of the resulting triol by recrystallization.



[16] For recent examples of C6 deoxygenation, see: A. Medgyes, E. Farkas, A. Liptak, V. Pozsgay, *Tetrahedron* **1997**, *53*, 4159.

[17] T. Sugiyama, *Bull. Chem. Soc. Jpn.* **1981**, *54*, 2847.

[18] Z. X. Guo, A. N. Cammidge, D. Horwell, *Synth. Commun.* **2000**, *30*, 2933.

[19] S. N. Maiti, J. Beres, M. P. Singh, R. G. Micetich, *Tetrahedron Lett.* **1986**, *27*, 1423.

[20] H. H. Wasserman, K. R. Brunner, J. D. Buynak, C. G. Carter, T. Oku, R. P. Robinson, *J. Am. Chem. Soc.* **1985**, *107*, 519.

[21] E. J. Corey, K. C. Nicolaou, R. D. Balanson, Y. Machida, *Synthesis* **1975**, 590.

[22] H. Bayley, D. N. Stadring, J. R. Knowles, *Tetrahedron Lett.* **1978**, *19*, 3633.

 © 2005 Wiley-VCH Verlag GmbH & Co. KGaA, Weinheim

Nanostructures

Aligning Au Nanorods by Using Carbon Nanotubes as Templates**

*Miguel A. Correa-Duarte, Jorge Pérez-Juste, Ana Sánchez-Iglesias, Michael Giersig, and Luis M. Liz-Marzán**

One of the most exciting challenges in modern chemistry and materials science is the manipulation and assembly at the nanoscale.[1] This is particularly interesting since the properties of the nanomaterials are dependent on their aggregation state, and thus collective properties are in general different from the properties of single nanoparticles.[2] A clear example of such sensitivity to aggregation and interparticle distance is found in metal nanoparticles, which display peculiar optical properties as a result of surface plasmon resonance phenomena.[3] The resonance conditions depend on a number of parameters, such as particle size and shape, surface charge, and the nature of the dielectric environment, but also on interparticle coupling when the separation is small.[4] Furthermore, the formation of anisotropic nanoparticles and assemblies provides a new way to control the optical response through the selective excitation of longitudinal or transverse plasmon modes by polarized light.[5]

The formation of strings of metal nanoparticles in general,[6–8] and metal nanorods in particular,[9,10] has recently attracted a great deal of attention, since such assemblies have

[*] Dr. M. A. Correa-Duarte, Dr. J. Pérez-Juste, A. Sánchez-Iglesias, Prof. L. M. Liz-Marzán
Departamento de Química Física
Universidade de Vigo
36310 Vigo (Spain)
Fax: (+34) 986-812-556
E-mail: lmarzan@uvigo.es
Prof. M. Giersig
Center of Advanced European Studies and Research (CAESAR)
Ludwig-Erhard-Allee 2, 53175 Bonn (Germany)

[**] We are grateful to Dr. I. Pastoriza-Santos (Univ. Vigo) for performing zeta potential measurements, B. Rodríguez-González for assistance with TEM measurements, and to Nanolab Inc. for supplying MWNT samples. Financial support from the Spanish Xunta de Galicia (project no. PGIDIT03TMT30101PR) and Ministerio de Educación y Ciencia/FEDER (project MAT2004-02991) are gratefully acknowledged.

Supporting information for this article is available on the WWW under http://www.angewandte.org or from the author.

 DOI: 10.1002/anie.200500581 © 2005 Wiley-VCH Verlag GmbH & Co. KGaA, Weinheim

potential uses as waveguides that would allow the miniaturization of devices below the diffraction limit[11] and as catalytic motors.[12]

Herein we present the formation of strings of Au nanorods by using multiwall carbon nanotubes (MWNTs) as templates. The use of MWNTs to template the assembly of aligned nanoparticles is not new,[8] but this is the first example in which the nanorods are assembled with a preferential stringlike alignment. The resulting nanocomposites show broadened absorption bands, as a result of end-to-end plasmon coupling between neighboring nanorods. Additionally, the nanorods can serve as a label to monitor the alignment of carbon nanotubes within polymer films, as demonstrated through optical absorption measurements on stretched poly(vinyl alcohol) (PVA) films loaded with the nanocomposite arrays.

The formation of the aligned composites is based in the polyelectrolyte layer-by-layer (LBL) approach,[13,14] which has been recently applied to assemble silica-coated gold nanoparticles on MWNTs.[8] Gold nanorods were synthesized by the seed-mediated procedure recently published by Nikoobakht and El-Sayed,[15] and the surfactant (cetyl trimethylammonium bromide, CTAB) was exchanged with poly(vinylpyrrolidone) (PVP) to clean the colloid (remove excess surfactant) and reverse the surface charge.[16] Prior to the assembly of nanorods, the MWNTs were wrapped with a negatively charged polyelectrolyte (polystyrene sulfonate, PSS), followed by electrostatic assembly of a positively charged polyelectrolyte (poly(diallyldimethyl) ammonium chloride, PDDA). PSS has been shown to adsorb on MWNTs as a result of suppression of the hydrophobic surface.[17] Once this first (charged) monolayer had been deposited, the standard LBL procedure could be applied.

Figure 1 shows TEM images of Au nanorods assembled on MWNTs at various magnifications. The low-magnification image (Figure 1 a) shows that the assembly is extremely uniform over long distances in the whole sample, while the higher magnification images (Figure 1 b,c) show the high degree of alignment of the nanorods, which in general form stripes, though defects (rods with different orientation) are also observed. It is interesting to note that there is a clear tendency for the particles to align in stripes on opposite sides of the MWNTs, rather than uniformly covering the surface (even though a large excess of nanorods was used) and aiming to achieve maximum coverage. Similar images were obtained for the assembly of nanorods with different aspect ratios of the same carbon nanotubes. The reason for not achieving a full coverage of the MWNTs is related to the anisotropic surface potential of the nanorods. It has been recently shown[18] that the potential decays more rapidly in areas with larger curvature (near the tips) so that the approach of a like-charged object (in this case another nanorod) is more favorable towards the tip than the side, thus favoring a stringlike conformation. It could be argued that such a chainlike structure is derived from the drying process on the TEM grid, which would imply some sort of rearrangement of the nanorods on the MWNTs. This is, however, rather unlikely since the electrostatic interactions involved are relatively strong and thus diffusion of the rods on the MWNT surface is restricted. Additionally, the optical properties in solution (see below) point toward uniaxial plasmon coupling, which would not be expected for a random distribution of nanorods on the nanotubes.

This aligned structure is reminescent of that recently reported by Kamat and co-workers[10] in which mercaptopropionic acid was used as a linker molecule. The optical effect derived from such an alignment is described[10] as uniaxial plasmon coupling, and is reflected in the disappearance of the longitudinal plasmon band and the appearance of a new, broader band centered at longer wavelengths. The same effect is observed during the formation of the anisotropic nanocomposite colloids reported here, as shown in Figure 2, where UV/Vis spectra of the precursor nanorods and the final nanorod–MWNT assemblies are displayed for nanorods with various aspect ratios. The variation in the aspect ratio allows precise tuning of the position of the longitudinal plasmon band of the nanorods, and in all three cases the spectra measured after assembly show broader and red-shifted bands, which reflect the uniaxial plasmon coupling between neighboring nanorods.

Since the longitudinal and transverse surface plasmon modes can be selectively excited by using light polarized with the electric field parallel or perpendicular, respectively, to the long axis of the rods, the oriented assembly of nanorods on the surface of the carbon nanotubes can in principle be used as a sensor of the alignment of the nanotubes themselves; this property is of high relevance for reinforcement applications.[19] We have tested this possibility through the preparation of thin films of the gold nanorod–MWNT composites dispersed in poly(vinyl alcohol) (PVA) thin films. The process

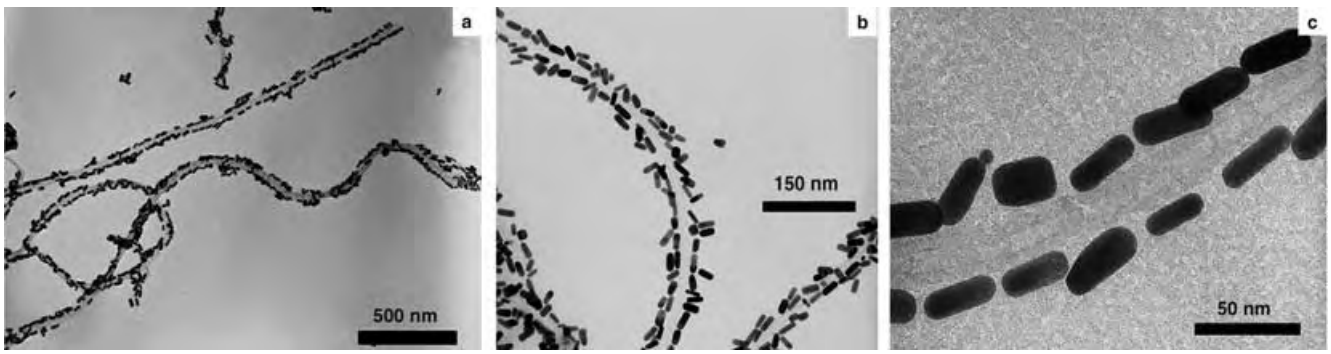


Figure 1. TEM images of Au nanorods (average aspect ratio 2.94), assembled on MWNTs (average diameter 30 nm) at various magnifications.

 © 2005 Wiley-VCH Verlag GmbH & Co. KGaA, Weinheim

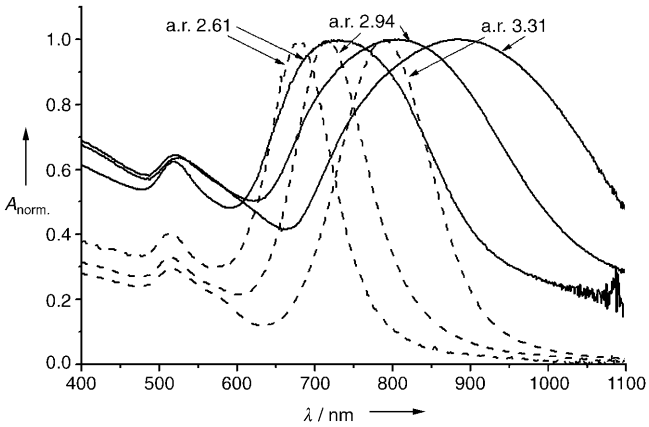


Figure 2. UV/Vis spectra of aqueous dispersions of individual Au nanorods (dashed lines) and nanorods attached on MWNTs (solid lines). The average aspect ratios (a.r.) of the nanorods are indicated.

consisted simply of drying a colloid in the presence of dissolved PVA; this approach has been successfully used by other research groups with silver spheres[20] as well as gold and silver nanorods.[5,21,22] Once the film has been completely dried, alignment is obtained through gently heating and stretching the nanocomposite polymer film. In the case of Au and Ag nanorods, the elongation of the polymer molecules[23] drives the alignment of the small particles toward a preferential direction. We wondered whether the much longer and flexible carbon nanotubes would also get aligned as a result of the stretching of the polymer; this is a very interesting feature for applications in plastic reinforcement. This question was answered by examination of the UV/Vis spectra (Figure 3). The solid black line corresponds to the freshly dried polymer film. Since the nanotubes are randomly oriented, the shape of the spectrum basically coincides with that of the aqueous dispersion, with both plasmon bands clearly visible. Both bands are still visible after stretching the sample (——) since unpolarized light can excite both resonances, irrespective of the nanoparticle orientation. The only difference here is that the longitudinal band is narrower, thus indicating a lower degree of interaction when the nanorod–nanotube composites are pulled and separated from each other. However, the most interesting aspect and definitive indication that a high degree of orientation has been achieved within the film is provided by the spectra of the stretched film obtained using polarized light. The transverse resonance band is fully suppressed and only the longitudinal one is observed when the polarization is parallel to the long axis (•••••, 0°). Conversely, the longitudinal band is suppressed and only the transverse mode is excited when the film is illuminated with light polarized perpendicular to the long axis (–•–•, 90°). Such a result can only be obtained if the nanorods (and in turn the nanotubes) display a well-defined preferential orientation within the film. TEM experiments on this sort of system involve ultramicrotoming of the film and are thus extremely laborious and time consuming, especially when the loading of the CNTs is low, since various experiments are required to actually find the particles. It is however possible (see inset of Figure 3), and this confirms the spectroscopic indication that the nanorods are preferentially oriented within the film.

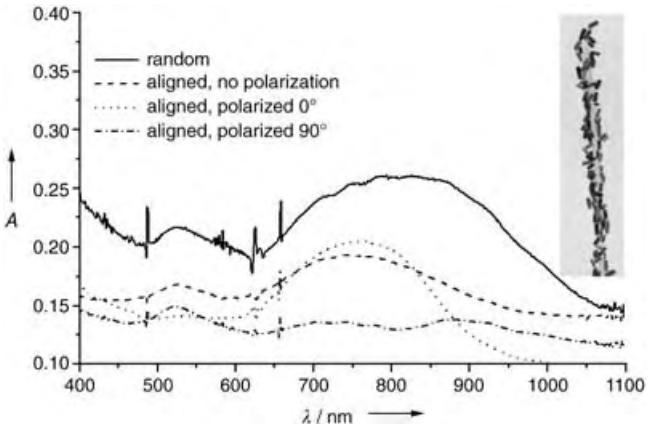


Figure 3. UV/Vis spectra of Au nanorod/MWNT nanocomposites dispersed in a PVA film before (-----) and after (——) stretching. Spectra of the stretched film using polarized light (•••••: 0°; –•–•: 90°) are also shown. The aspect ratio of the rods is 2.94. The inset shows a TEM image of a stretched Au/CNT composite in PVA.

In summary, we have demonstrated the uniform electrostatic assembly of gold nanorods on multiwall carbon nanotubes in such a way that the rods form strings with end-to-end contacts. Such a morphology results in uniaxial plasmon coupling, but can be used to monitor the degree of alignment of carbon nanotubes within polymer films or other nanostructured systems.

Received: February 16, 2005
Published online: June 14, 2005

Keywords: colloids · gold · nanorods · nanostructures · nanotubes

[1] *Nanoparticles: Building Blocks for* Nanotechnology (Ed.: V. Rotello), Kluwer, New York, **2004**.
[2] A. P. Alivisatos, *Science* **1996**, *271*, 933.
[3] U. Kreibig, U. Vollmer, *Optical Properties of Metal Clusters*, Springer, Berlin, **1996**.
[4] L. M. Liz-Marzán, P. Mulvaney, *J. Phys. Chem. B* **2003**, *107*, 7312.
[5] B. M. I. van der Zande, L. Pages, R. A. M. Hikmet, A. Van - Blaaderen, *J. Phys. Chem. B* **1999**, *103*, 5761.
[6] S. Fullam, D. Cottell, H. Rensmo, D. Fitzmaurice, *Adv. Mater.* **2000**, *12*, 1430.
[7] M. Giersig, I. Pastoriza-Santos, L. M. Liz-Marzán, *J. Mater. Chem.* **2004**, *14*, 607.
[8] M. A. Correa-Duarte, N. Sobal, L. M. Liz-Marzán, M. Giersig, *Adv. Mater.* **2004**, *16*, 2179.
[9] K. K. Caswell, J. N. Wilson, U. H. F. Bunz, C. J. Murphy, *J. Am. Chem. Soc.* **2003**, *125*, 13914.
[10] K. G. Thomas, S. Barazzouk, B. I. Ipe, S. T. S. Joseph, P. V. Kamat, *J. Phys. Chem. B* **2004**, *108*, 13066.
[11] S. A. Maier, M. L. Brongersma, P. G. Kik, H. A. Atwater, *Phys. Rev. B* **2002**, *65*, 193408.
[12] W. F. Paxton, K. C. Kistler, C. C. Olmeda, A. Sen, S. K. St. Angelo, Y. Cao, T. E. Mallouk, P. E. Lammert, V. H. Crespi, *J. Am. Chem. Soc.* **2004**, *126*, 13424.
[13] N. A. Kotov, I. Dekany, J. H. Fendler, *J. Phys. Chem.* **1995**, *99*, 13065.

 © 2005 Wiley-VCH Verlag GmbH & Co. KGaA, Weinheim

[14] F. Caruso, R. A. Caruso, H. Möhwald, *Science* **1998**, *282*, 1111.
[15] B. Nikoobakht, M. A. El-Sayed, *Chem. Mater.* **2003**, *15*, 1957.
[16] A zeta potential value of −20 mV for PVP-modified Au nanorods was measured with a Malvern Zetasizer 2000 instrument.
[17] M. J. O'Connel, P. Boul, L. M. Ericson, C. Huffman, Y. Wang, E. Haroz, C. Kuper, J. Tour, K. D. Ausman, R. E. Smalley, *Chem. Phys. Lett.* **2001**, *342*, 265.
[18] J. Pérez-Juste, L. M. Liz-Marzán, S. Carnie, D. Y. C. Chan, P. Mulvaney, *Adv. Funct. Mater.* **2004**, *14*, 571.
[19] D. M. Guldi, A. Mamedov, T. Crisp, N. A. Kotov, A. Hirsch, M. Prato, *J. Phys. Chem. B* **2004**, *108*, 8770.
[20] Y. Dirix, C. Bastiaansen, W. Caseri, P. Smith, *Adv. Mater.* **1999**, *11*, 223.
[21] O. Wilson, G. J. Wilson, P. Mulvaney, *Adv. Mater.* **2002**, *14*, 1000.
[22] J. Pérez-Juste, B. Rodríguez-González, P. Mulvaney, L. M. Liz-Marzán, *Adv. Funct. Mater.* **2005**, in press.
[23] D. Fornasiero, F. Grieser, *Chem. Phys. Lett.* **1987**, *139*, 103.

 © 2005 Wiley-VCH Verlag GmbH & Co. KGaA, Weinheim

Prodrug Activation

Prodrug Activation Gated by a Molecular "OR" Logic Trigger**

*Roey J. Amir, Mikhail Popkov, Richard A. Lerner, Carlos F. Barbas III, and Doron Shabat**

Molecular logic gates are increasingly important in attributing chemical reactivity to molecular devices.[1–5] Specific input signals of basic logic gates can be programmed into single molecules that generate readable output signals, such as fluorescence[6] or UV/Vis light.[7] Here we show that the release of an active drug molecule through a prodrug activation process is a viable output signal. The term "prodrug" is used to indicate that a chemical derivatization has been applied to alter the physicochemical properties of a drug.[8,9] The prodrug is converted into the active drug in vivo by metabolic processes or environmental conditions. Masking of a functional group in a targeted drug with a simple linker which contains two moieties that can be cleaved by different mechanisms can generate a molecular "OR" logic gate trigger. The gate is activated upon a cleavage signal from either of the two input ports. The signal will be translated into a bond cleavage that releases the active drug molecule.

Several anticancer prodrugs have been designed for selective activation in malignant tissues by a specific enzyme secreted within the proximity of the tumor.[10] A prodrug with a molecular "OR" logic gate triggering device could potentially target two different cancerous tissues with different enzyme-expression patterns. There are several examples for enzymes that are present in elevated levels in malignant tissues.[11] The substrates of two of these enzymes could be introduced in the molecular "OR" logic trigger to generate an agent for dual-prodrug monotherapy. Prodrug strategies are sometimes based on the assumption that a particular enzyme is elevated in the tumor tissues and that activation of a prodrug in the tumor tissue will result in a significantly improved therapeutic index. While there is much evidence for overexpression of particular enzymes in tumors, consistent patterns of expression are elusive. Consequently, attempts to develop drugs activated by tumor-specific enzymes in general have not been very successful. Prodrugs with two modes of activation could offer an advantage over single-triggered prodrugs, particularly in circumstances where two different enzymes are present in elevated levels in various regions of the tumor. Herein, we report the design, synthesis, and bioactivation of a molecular "OR" logic trigger which is used to activate a prodrug with dual susceptibility to enzymatic activity.

Classical "OR" logic gates have two input ports and one output port.[12] An activating signal, which operates on either one of the input ports, activates the output signal of the gate (Figure 1). Obviously, positive input signals from both input ports should also activate the gate.

Diethylenetriamine has previously been introduced in a multitriggering mechanism[13] and is used as a linker in the construction of the molecular "OR" logic trigger. The central secondary amine is attached to a drug molecule while the two primary amines are linked to different enzymatic substrates (triggers 1 and 2). The enzymatic cleavage of either one of the substrates generates a free-amine intermediate (intermediate 1 or 2) that initiates an intracyclization reaction to release the free drug unit (Figure 2).

To provide a proof of concept for the "OR" triggering release mechanism suggested in Figure 2, we prepared **1**, which contains two different enzymatic substrates and 4-nitrophenol, as a model compound that represents a potential drug. The two substrates were a phenylacetamide moiety, which is the substrate for penicillin G amidase[14] (PGA), and a retro-aldol retro-Michael substrate that is cleaved by catalytic antibody (Ab) 38C2.[15–17] According to the proposed pathway presented in Figure 3, cleavage by antibody 38C2 or by PGA should catalyze the formation of intermediates **2** or **3**, respectively, and subsequent intracyclization will release 4-nitrophenol.

The "OR" logic trigger substrate **1** was incubated with either antibody 38C2 or PGA in phosphate-buffered saline (PBS) solution (pH 7.4) at 37 °C. The formation of 4-nitro-

[*] R. J. Amir, Dr. D. Shabat
Department of Organic Chemistry
School of Chemistry, Faculty of Exact Sciences
Tel Aviv University
Tel Aviv 69978 (Israel)
Fax: (+972) 3-640-9293
E-mail: chdoron@post.tau.ac.il
Dr. M. Popkov, Prof. R. A. Lerner, Prof. C. F. Barbas III
The Skaggs Institute for Chemical Biology
Departments of Molecular Biology and Chemistry
The Scripps Research Institute
10550 North Torrey Pines Road
La Jolla, CA 92037 (USA)

[**] R.J.A. and M.P. contributed equally to this work. D.S. thanks the Israel Science Foundation for financial support.

Supporting information for this article is available on the WWW under http://www.angewandte.org or from the author.

 © 2005 Wiley-VCH Verlag GmbH & Co. KGaA, Weinheim DOI: 10.1002/anie.200500842

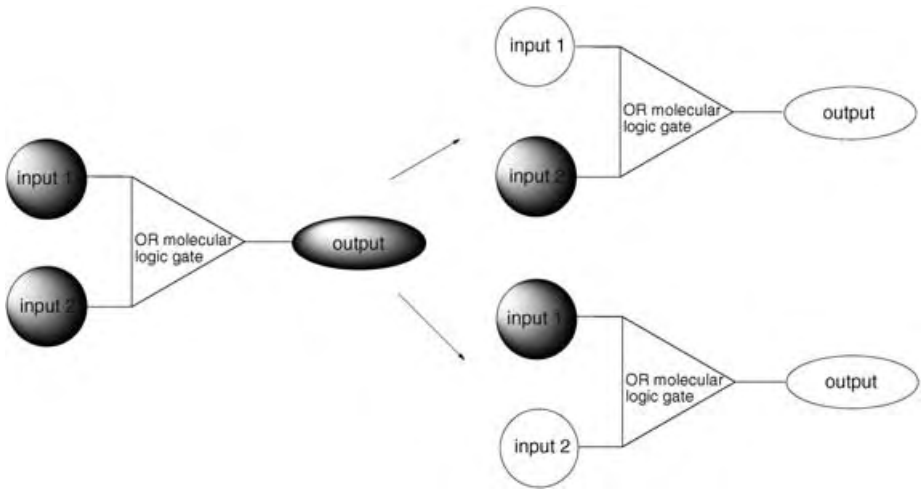


Figure 1. Schematic illustration of an "OR" molecular logic gate. Activation of the gate is indicated by a color change from black to white.

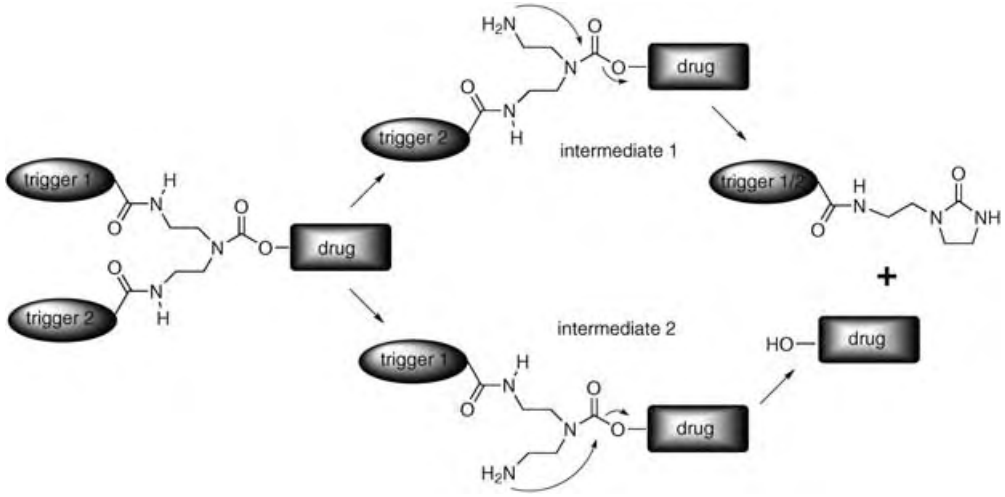


Figure 2. Diethylenetriamine as an "OR" molecular logic trigger.

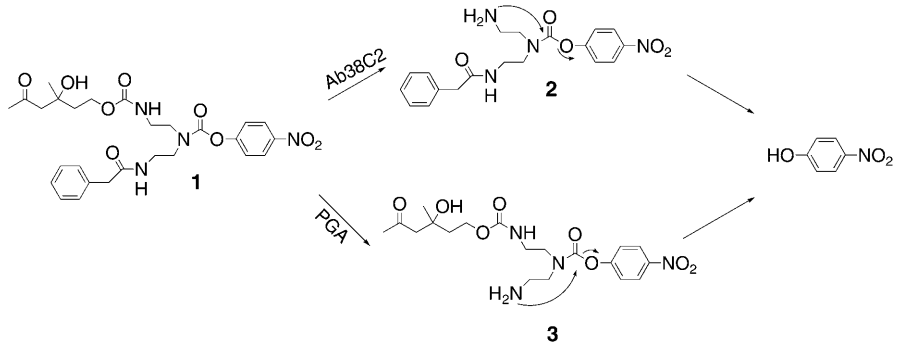


Figure 3. Activation of a molecular "OR" logic trigger by a dual-triggering mechanism with PGA or catalytic antibody (Ab) 38C2.

phenol was monitored by UV/Vis spectroscopy at a wavelength of 405 nm. Figure 4 clearly shows that either the enzyme or the catalytic antibody initiates the activation of compound **1** to release 4-nitrophenol. The reaction was faster with PGA than with antibody 38C2. No release was observed when the substrate was incubated in buffer alone.

Next, we prepared an actual prodrug (pro-Dox) by equipping the "OR" molecular logic trigger with the anticancer drug doxorubicin (Dox). 4-Hydroxybenzyl alcohol was used as a linker between the amino group of Dox and diethylenetriamine (Figure 5). As with the model compound, the two substrates were a phenylacetamide and a retro-aldol retro-Michael substrate. Cleavage by either antibody 38C2 or PGA should result in removal of the 4-hydroxybenzyl alcohol and release of free Dox (through 1,6-elimination).

The prodrug was incubated with either PGA or catalytic antibody 38C2, and the release of free Dox was monitored by reverse-phase HPLC. The HPLC chromatograms in Figure 6 show that upon incubation of PGA (Figure 6a) or antibody 38C2 (Figure 6b) with pro-Dox, intermediates 1 and 2 (shown in Figure 2) were generated and intracyclization liberated the active drug Dox. No release of the drug was observed in the absence of PGA or the antibody.

The "OR" logic gate prodrug was assessed in cell growth inhibition assays. We evaluated the ability of the prodrugs to inhibit cell proliferation in the presence of PGA or catalytic antibody 38C2 using two different cell lines: the human T-lineage acute lymphoblastic leukemia (ALL) cell line MOLT-3 and the human erythroleukemia cell line HEL. The data are shown graphically in Figure 7, and the results are summarized in Table 1. Both PGA and antibody 38C2 could activate the prodrug pro-Dox, and cell growth was inhibited with IC_{50} values close to that of the parent drug.

 © 2005 Wiley-VCH Verlag GmbH & Co. KGaA, Weinheim

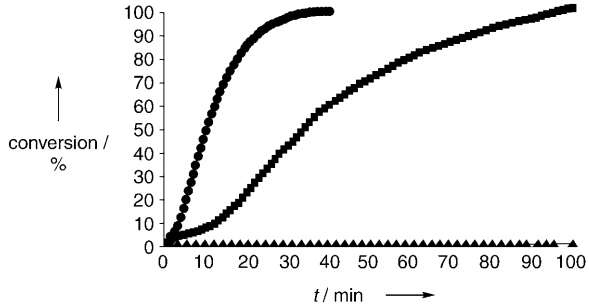


Figure 4. UV/Vis Absorbance at $\lambda = 405$ nm as a function of time in the activation of "OR" molecular logic trigger **1**. ● = **1** + PGA, ■ = **1** + Ab38C2, ▲ = **1** in PBS (pH 7.4). Concentration of substrate is 500 μM; concentrations of PGA or Ab38C2 are 50 μM each.

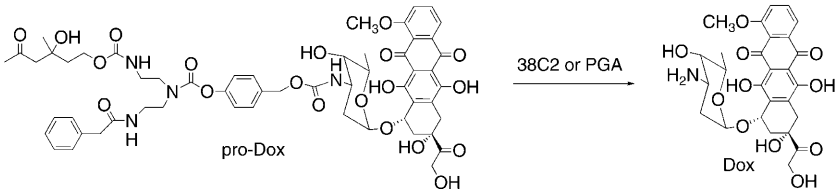


Figure 5. Activation of doxorubicin prodrug by a molecular "OR" logic trigger with antibody 38C2 or PGA.

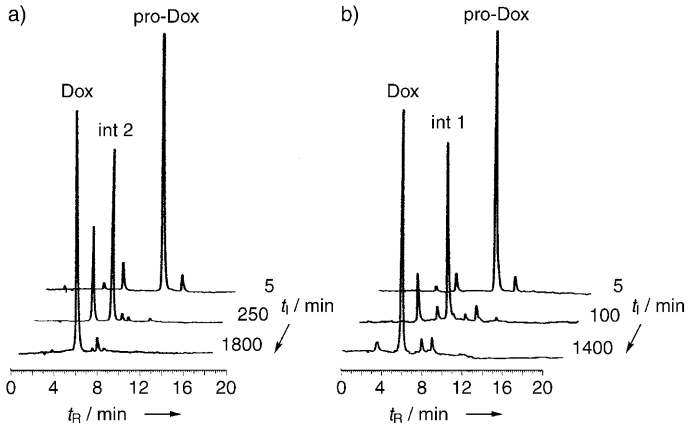


Figure 6. Reverse-phase HPLC chromatograms of a) pro-Dox (70 μM) with PGA (4 μM) in PBS (pH 7.4) and b) pro-Dox (70 μM) with catalytic antibody 38C2 (20 μM) in PBS (pH 7.4). t_R = retention time; t_I = incubation time.

Table 1: IC_{50} values from cell growth inhibition assays.

Drug/Prodrug	IC_{50} [nM]	
	MOLT-3 cells	HEL cells
Dox	3.0	20
pro-Dox	80	200
pro-Dox/38C2	6.5	24
pro-Dox/PGA	7.0	28

A prodrug with a molecular "OR" logic trigger substrate could be used as an efficient tool to evaluate the catalytic activity of the triggering enzymes. In fact, the system allows a direct comparison to be performed between the activities of PGA and antibody 38C2 by using the same prodrug molecule. We used a fixed concentration of the pro-Dox compound (50 nM) and varying concentrations of antibody 38C2 or PGA. The results in Figure 8 show that PGA was about 50-fold more

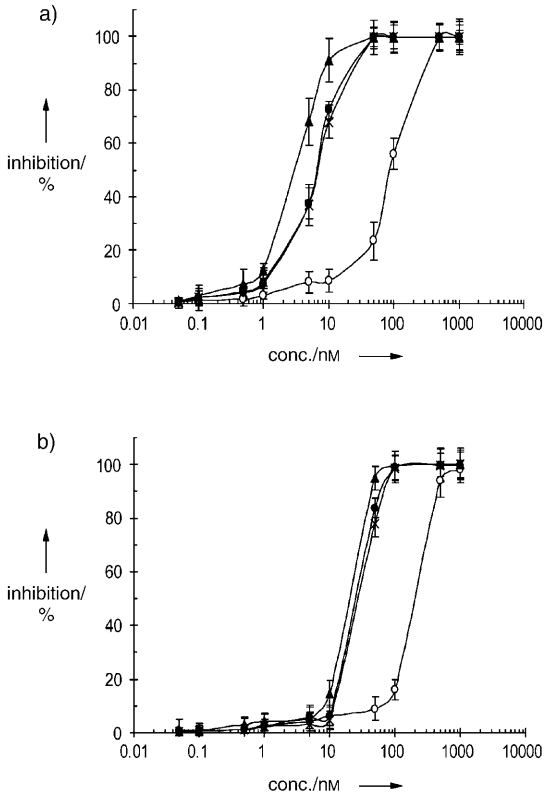


Figure 7. Growth inhibition activity of pro-Dox in the presence and absence of antibody 38C2 and PGA. The growth response of leukemia cell lines MOLT-3 (a) and HEL (b) cells to incubation (72 h) with increasing concentrations of the prodrug in the presence and absence of 38C2 catalytic antibody (1 μM; ●) or PGA (1 μM; ×) was analyzed by using a standard ^3H thymidine proliferation assay. Dox (▲) and pro-Dox (○) were also evaluated. Data points and error bars represent mean values ± standard deviation, respectively.

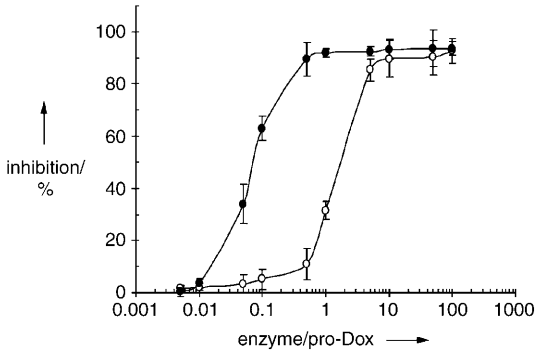


Figure 8. Growth inhibition of HEL cells in the presence of pro-Dox (50 nM) and increasing concentrations of antibody 38C2 (○) or PGA (●), shown as the ratio of enzyme to pro-Dox. Data points and error bars represent mean values ± standard deviation, respectively.

 © 2005 Wiley-VCH Verlag GmbH & Co. KGaA, Weinheim

active in growth inhibition of HEL cells than antibody 38C2. Similar results were obtained with MOLT-3 cells (data not shown).

In summary, we have designed and synthesized a molecular "OR" logic trigger operated by two different enzymes. The "smart" linker that is used to mask the doxorubicin amine functionality acts as a dual-input "OR" logic trigger. The input signals are enzymatic cleavages by antibody 38C2 or penicillin G amidase, and the output is the release of the active drug. Our current efforts are focused on the design and synthesis of prodrugs that are activated with a molecular "AND" logic trigger.

Received: March 7, 2005
Published online: June 8, 2005

Keywords: catalytic antibodies · drug delivery · enzymes · logic gates · prodrugs

[1] A. P. de Silva, N. D. McClenaghan, *J. Am. Chem. Soc.* **2000**, *122*, 3965.
[2] A. P. de Silva, N. D. McClenaghan, *Chem. Eur. J.* **2004**, *10*, 574.
[3] K. L. Kompa, R. D. Levine, *Proc. Natl. Acad. Sci. USA* **2001**, *98*, 410.
[4] S. Sivan, S. Tuchman, N. Lotan, *Biosystems* **2003**, *70*, 21.
[5] S. Uchiyama, N. Kawai, A. P. de Silva, K. Iwai, *J. Am. Chem. Soc.* **2004**, *126*, 3032.
[6] J. M. Montenegro, E. Perez-Inestrosa, D. Collado, Y. Vida, R. Suau, *Org. Lett.* **2004**, *6*, 2353.
[7] S. Giordani, F. M. Raymo, *Org. Lett.* **2003**, *5*, 3559.
[8] K. Haba, M. Popkov, M. Shamis, R. A. Lerner, C. F. Barbas, 3rd, D. Shabat, *Angew. Chem.* **2005**, *117*, 726; *Angew. Chem. Int. Ed.* **2005**, *44*, 716.
[9] M. Shamis, H. N. Lode, D. Shabat, *J. Am. Chem. Soc.* **2004**, *126*, 1726.
[10] F. M. de Groot, E. W. Damen, H. W. Scheeren, *Curr. Med. Chem.* **2001**, *8*, 1093.
[11] L. Devy, F. M. de Groot, S. Blacher, A. Hajitou, P. H. Beusker, H. W. Scheeren, J. M. Foidart, A. Noel, *FASEB J.* **2004**, *18*, 565.
[12] G. McSkimming, J. H. R. Tucker, H. Bouas-Laurent, J.-P. Desvergne, *Angew. Chem.* **2000**, *112*, 2251; *Angew. Chem. Int. Ed.* **2000**, *39*, 2167.
[13] R. J. Amir, D. Shabat, *Chem. Commun.* **2004**, 1614.
[14] G. S. Bignami, P. D. Senter, P. G. Grothaus, K. J. Fischer, T. Humphreys, P. M. Wallace, *Cancer Res.* **1992**, *52*, 5759.
[15] D. Shabat, H. N. Lode, U. Pertl, R. A. Reisfeld, C. Rader, R. A. Lerner, C. F. Barbas III, *Proc. Natl. Acad. Sci. USA* **2001**, *98*, 7528.
[16] D. Shabat, C. Rader, B. List, R. A. Lerner, C. F. Barbas III, *Proc. Natl. Acad. Sci. USA* **1999**, *96*, 6925.
[17] J. Wagner, R. A. Lerner, C. F. Barbas III, *Science* **1995**, *270*, 1797.

 © 2005 Wiley-VCH Verlag GmbH & Co. KGaA, Weinheim

Hydrocarbon Chemistry

Simultaneous Conversion of Methane and Methanol into Gasoline over Bifunctional Ga-, Zn-, In-, and/or Mo-Modified ZSM-5 Zeolites**

Vasant R. Choudhary, Kartick C. Mondal, and Shafeek A. R. Mulla*

In response to increased energy demands, worldwide efforts have been made over the past 2–3 decades to develop alternative methods for the conversion of methane (a main constituent of natural gas, coal-bed gas, and biogas) into value-added products. These include ethylene (by oxidative coupling of methane),[1–3] syngas (by partial oxidation with or without simultaneous steam- and/or CO_2-mediated methane reformation),[4–8] and gasoline/liquid hydrocarbon fuels[9–14] that involve either oxidative[1–10] or nonoxidative[11–15] methane activation. As methane and carbon dioxide are key greenhouse gases responsible for global warming, the current industrial practice of emission and/or flaring of produced methane will be banned in the near future. The methane produced in remote places must therefore be converted into easily transportable energy sources like liquid hydrocarbon fuels at the sites of methane production. The most important approach for the transformation of methane into liquid hydrocarbons is the well-established and already commercially proven route:[16] methane→syngas→methanol→gasoline, based on the methanol-to-gasoline (MTG) process developed by Mobil.[16–18] In 1985, Mobil successfully operated a commercial plant in New Zealand for MTG conversions. However, its operation had to be discontinued as a result of unfavorable process economics.[18–20] The cost of the syngas production step (by steam reforming) is about twice the cost of the MTG production step.

The MTG process could become economically viable if it were possible to convert a significant portion of the methane into gasoline without the intermediate steps of conversion into syngas and methanol. Herein, we show that this very difficult goal can be met through the nonoxidative activation of methane and its simultaneous conversion with methanol into gasoline-range hydrocarbons over bifunctional Ga-, In-, Zn-, and/or Mo-modified ZSM-5 type zeolites that have both dehydrogenation and acid functions. We also show that the amount of methane converted can be equimolar to the amount of methanol converted in this novel process, depend-

[*] Dr. V. R. Choudhary, K. C. Mondal, S. A. R. Mulla
Chemical Engineering and Process Development Division
National Chemical Laboratory
Pune - 411 008 (India)
Fax: (+91) 20-2589-3041
E-mail: vrc@ems.ncl.res.in

[**] K.C.M. thanks the University Grant Commission, New Delhi for a Senior Research Fellowship. The authors are grateful to Dr. O. G. B. Nambiar and his research group for their help with GC–MS analysis.

Supporting information for this article is available on the WWW under http://www.angewandte.org or from the author.

 DOI: 10.1002/anie.200500694 © 2005 Wiley-VCH Verlag GmbH & Co. KGaA, Weinheim

ing on the specific conditions. The conversion of methane to higher hydrocarbons was confirmed by using ^{13}C-labeled methanol and analysis of the reaction products by GC–MS. This work has the potential to revolutionize the methane-to-liquid hydrocarbons (MTL) conversion technology through the modified MTG process of Mobil.

The results in Figure 1, Figure 2, and Table 1 clearly indicate that methane is nonoxidatively activated and converted at low temperature (< 600 °C) during methanol conversion over the bifunctional zeolite catalysts. However, methane is not activated/converted over H-ZSM-5; instead, it is produced in appreciable quantity (Figure 2). The simultaneous conversion of methane results in a significant change in the hydrocarbon product distribution relative to that of the conventional MTG process. Furthermore, the formation of individual $C_{\geq 2}$ hydrocarbons is increased markedly, as shown in Figure 1 and Table 1. The liquid hydrocarbons formed are mainly C_{7-12} aromatic compounds. The formation of benzene (the presence of which is undesirable because of its toxicity) was very small. In the absence of methane, an appreciable amount of methane is produced in the aromatization of methanol. Therefore, the presence of methane as a co-reactant in our process is beneficial, as the aromatization of methanol results in no net formation of methane. It is of great practical interest that the amount of methane converted per mole of methanol in the feed could meet or exceed 1 mol, depending on the process temperature and methane/methanol ratio in the feed (Figure 2). The required methanol itself can be produced from methane through a well-established technology ($CH_4 \rightarrow$syngas$\rightarrow$methanol). Similarly, methane can also be activated and converted over bifunctional zeolite catalysts during the aromatization of other organic oxygenates, such as ethanol (which can be produced from renewable sources) and dimethyl ether (produced directly from syngas). Notably, Figure 1 illustrates that the hydrocarbon product distribution in the aromatization process presented herein is strongly influenced by the bifunctional zeolite, the oxygenate (methanol, ethanol, or dimethyl ether) used in the process, and the presence of methane in the feed. However, such strong influences are not observed in the aromatization of oxygenates over the monofunctional (acidic) zeolite (H-ZSM-5).

The H-GaAl-ZSM-5 (which is highly acidic and contains finely dispersed gallium oxide species) performs much better than the catalyst prepared through external impregnation of either the gallium, zinc, indium, or molybdenum oxide species on H-ZSM-5. However, the performance of the molybdenum, gallium, and indium oxide-impregnated H-ZSM-5 was

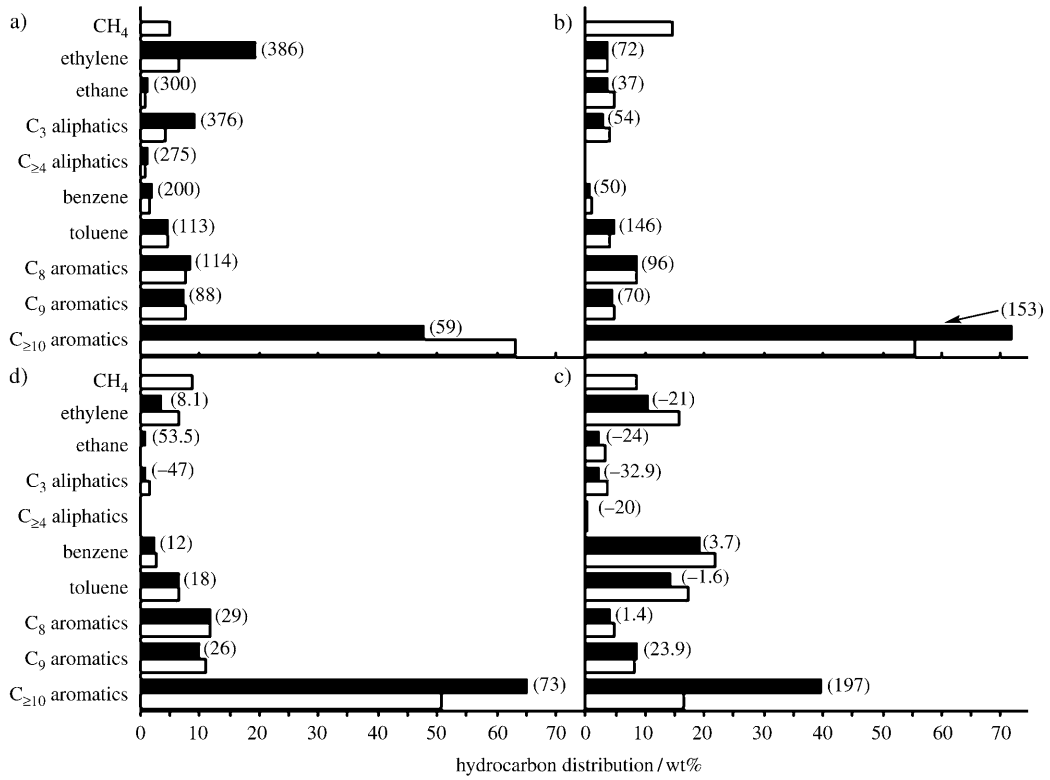


Figure 1. Distribution of hydrocarbons formed in the aromatization of a) methanol over H-GaAl-ZSM-5 at 550 °C, b) methanol over Mo-Zn/H-ZSM-5 at 500 °C, c) ethanol over H-GaAl-ZSM-5 at 625 °C, and d) dimethyl ether (DME) over H-GaAl-ZSM-5 at 550 °C in the presence (solid bars) and absence (open bars) of methane. $CH_4/(CH_3OH$ or DME$) = 15.0{:}1$, $CH_4/C_2H_5OH = 10{:}1$, $CH_4/N_2 = 8.5{:}1$, and gas hourly space velocity (GHSV), measured at 0 °C and 1 atm $= 1050\ cm^3\,g^{-1}\,h^{-1}$. Values in round brackets correspond to the percentage increase in the formation of a particular hydrocarbon as a result of the presence of methane. The conversion of methanol, ethanol, or DME was 100%. In the presence of oxygenate, the amount of methane converted was 0.96 and 1.19 mol/mol CH_3OH for H-GaAl-ZSM-5 and Mo-Zn/H-ZSM-5, respectively, and 0.8 and 0.94 mol/mol CH_3CH_2OH and DME, respectively. In continuous operation for 7 h, both catalysts showed no significant change in catalytic activity for methane conversion.

 © 2005 Wiley-VCH Verlag GmbH & Co. KGaA, Weinheim

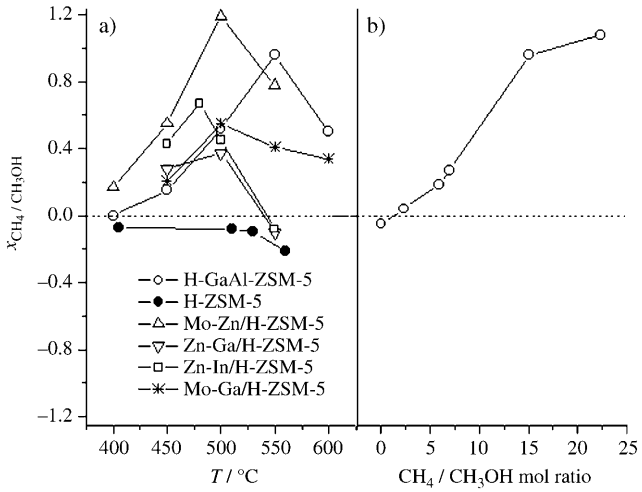


Figure 2. a) Moles of methane converted per mole of methanol (X_{CH_4/CH_3OH}) in the simultaneous aromatization of methane and methanol over H-GaAl-ZSM-5 and H-ZSM-5 ($CH_4/CH_3OH = 15:1$, $CH_4/N_2 = 8.5:1$, GHSV = 1050 $cm^3 g^{-1} h^{-1}$); Mo-Zn/H-ZSM-5 ($CH_4/CH_3OH = 14.1:1$, $CH_4/N_2 = 8.5:1$, GHSV = 1050 $cm^3 g^{-1} h^{-1}$); Zn-In/H-ZSM-5 ($CH_4/CH_3OH = 12.72$, $CH_4/N_2 = 8.5:1$, GHSV = 1200 $cm^3 g^{-1} h^{-1}$); Mo-Ga/H-ZSM-5 ($CH_4/CH_3OH = 13.75:1$, $CH_4/N_2 = 7.3:1$, GHSV = 1200 $cm^3 g^{-1} h^{-1}$); and Zn-Ga/H-ZSM-5 ($CH_4/CH_3OH = 5.9:1$, $CH_4/N_2 = 7.2:1$, GHSV = 1200 $cm^3 g^{-1} h^{-1}$). b) Effect of the ratio of CH_4/CH_3OH in the feed on moles of methane converted per mole of methanol in the simultaneous aromatization of methane and methanol over H-GaAl-ZSM-5 at 550 °C ($CH_4/N_2 = 8.5:1$, GHSV = 1050 $cm^3 g^{-1} h^{-1}$). Methanol conversion in all cases was 100 %.

Table 1: Influence of methane on the process formation of C_{2-12} hydrocarbons with H-GaAl-ZSM-5 and Mo-Zn/H-ZSM-5 zeolite catalysts.

Reaction conditions			X_{CH_4/CH_3OH}[a]	Δ (C_2–C_{12} hydrocarbons) [%][b]
T [°C]	CH_4/CH_3OH [mol ratio]	GHSV [$cm^3 g^{-1} h^{-1}$]		
		catalyst: H-GaAl-ZSM-5		
500	15.0:1	1050	0.52	49
550	15.0:1	1050	0.96	108
550	7.0:1	1050	0.27	31.8
550	15.0:1	2100	0.79	83
		catalyst: Mo-Zn/H-ZSM-5		
450	14.1:1	1050	0.55	53
500	14.1:1	1050	1.19	126
550	14.1:1	1050	0.78	77
500	7.1:1	1050	0.29	30
500	14.1:1	2100	0.55	47

[a] Moles methane converted per mole methanol. [b] Increase due to the presence of methane.

improved appreciably after the addition of zinc oxide to the catalyst. The catalytically active Mo-containing species may be Mo_2C and/or MoO_xC_y.[21]

Low-temperature (≤ 600 °C) conversion of methane to aromatic hydrocarbons is not thermodynamically feasible, as $\Delta G > 33.4\ kJ\,mol^{-1}_{carbon}$. However, if this conversion is carried out in the presence of methanol over the bifunctional zeolite catalysts, which have strong protic acid and dehydrogenation sites, it becomes thermodynamically favorable as a result of the simultaneous conversion of methane and methanol. (For example, $\Delta G = -8.8$, -15.5, and $-22.2\ kJ\,mol^{-1}$ at 400, 500, and 600 °C, respectively, for one mole of methane converted per mole of methanol.)

In the absence of methanol and/or the absence of bifunctional sites on the zeolite catalyst, there was no conversion of methane. The negative values observed for the ratio of (methane converted)/(methanol converted) with the H-ZSM-5 zeolite (Figure 2a) and in the absence of methane (Figure 2b) indicates the net formation of methane to a significant extent. An temperature optimum is observed for obtaining the highest ratio of (methane converted)/(methanol converted), which depends on the bifunctional zeolite used (Figure 2a). This can be explained by the expected competition between the formation of methane from methanol by cracking reactions (which have a higher rate at higher temperature) and the activation/conversion of methane, which has a lower rate at lower temperature. The ratio of (methane converted)/(methanol converted) is, however, increased markedly with an increase in the methane/methanol ratio in the feed (Figure 2b).

The activation and conversion of methane in the process was confirmed by using ^{13}C-labeled methanol and analysis of the aromatic hydrocarbons formed by GC–MS. The MS data of toluene and xylene produced in the presence and absence of methane in the feed are compared in Figure 3. The mass spectra clearly reveal the formation of unlabeled toluene (formed from methane alone) and partially labeled aromatic compounds (formed from both methane and methanol) in the aromatization of $^{13}CH_3OH$ over the H-GaAl-ZSM-5 and Zn-In/H-ZSM-5 catalysts in the presence of methane. Methane appears to act as an alkylating agent in the formation of methylbenzenes and methylnaphthalenes. Indeed, upon passing a mixture of methane and benzene ($CH_4/C_6H_6 = 12.5:1$) over the H-GaAl-ZSM-5 zeolite at 550 °C, the alkylation of benzene was observed in the formation of toluene and xylenes in significant quantity (with 1.0 % conversion of benzene).

We propose the following mechanism for the activation and conversion of methane during the aromatization of methanol over the bifunctional zeolite catalysts Z, which have strong Brønsted acid sites and nonframework gallium, zinc, and/or indium oxide species, with or without Mo_2C or MoO_xC_y species as dehydrogenation sites in the zeolite channels.

Methanol aromatization [Eq. (1)]:

$$Z^-H^+ + CH_3OH \rightleftharpoons Z^-[CH_3OH_2]^+ \mathbf{I} \rightarrow Z^-H^+ + H_2O + C_{1-12}\,\text{hydrocarbons} \quad (1)$$

 © 2005 Wiley-VCH Verlag GmbH & Co. KGaA, Weinheim

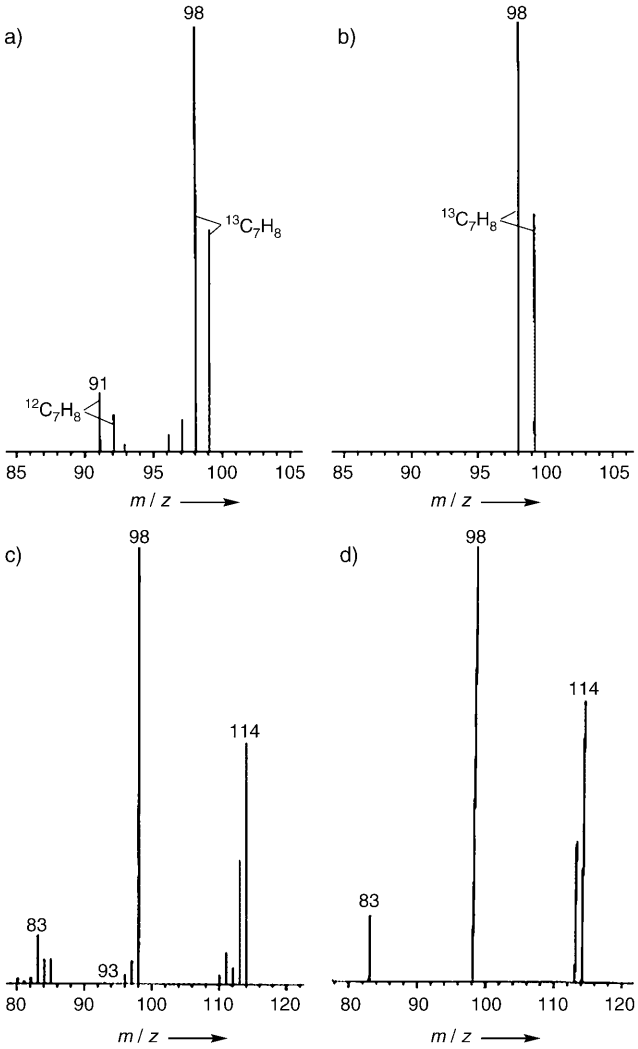
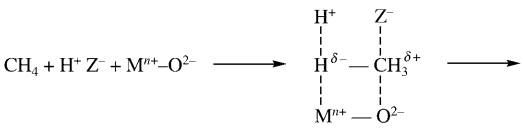


Figure 3. GC–MS spectra of toluene and xylene formed in the aromatization of ^{13}C-labeled methanol ($^{13}CH_3OH$) over the H-GaAl-ZSM-5 zeolite in the presence and absence of methane under identical conditions (at 550 °C and GHSV = 1050 $cm^3 g^{-1} h^{-1}$). Reaction conditions: a) $CH_4/^{13}CH_3OH = 14.7:1$, $CH_4/N_2 = 7.3:1$, toluene, $t_{ret} = 4.56$ min; b) $CH_4/^{13}CH_3OH = 0:1$, $N_2/^{13}CH_3OH = 16.7:1$ toluene, $t_{ret} = 4.56$ min; c) $CH_4/^{13}CH_3OH = 14.7:1$, $CH_4/N_2 = 7.3:1$, xylene, $t_{ret} = 7.68$ min; d) $CH_4/^{13}CH_3OH = 0:1$, $N_2/^{13}CH_3OH = 16.7:1$ xylene, $t_{ret} = 7.68$ min. t_{ret} = retention time.

Methane activation and conversion (M = Ga, Zn, or In; X = Mo_2C or MoO_xC_y species) [Eq. (2)–(7)]:



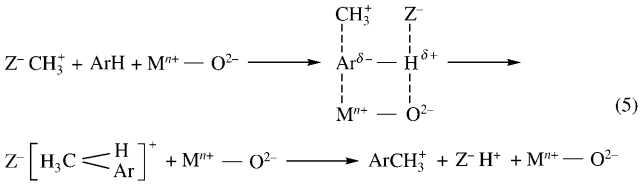
(2)



$$Z^- CH_3^+ \rightarrow Z^- H^+ + CH_2 \quad (3)$$

$$2\,CH_2 \rightarrow C_2H_4 \quad (4)$$

(Z⁻H⁺+Mn−O₂⁻; oligomerization, aromatization; aliphatics, aromatics and H₂)



(5)

$$X + Z^- CH_3^+ \rightarrow XCH_2 + Z^- H^+ \quad (6)$$

$$2\,XCH_2 \rightarrow 2\,X + C_2H_4 \quad (7)$$

Methane is activated mostly as a result of the combined action of the metal oxide species and zeolitic protons, both present at the channel intersections in close proximity to each other. Our earlier studies on the alkane and alkene aromatization over Ga-modified ZSM-5 zeolites also revealed that the zeolitic protons and nonframework gallium oxide species work in cooperation with each other.[22] Methyl cations are likely to be produced through the formation of pentacoordinated carbocations **II**, similar to that proposed earlier by Olah.[23] As no methane conversion is observed in the absence of methanol and/or the bifunctional sites, activation of the H–CH_3 bond and formation of the pentacoordinated carbocations **II** are expected to be facilitated by the nonframework metal oxide species in the presence of oxonium cations **I** and/or carbenium ions formed from the olefins produced from methanol.

The highly unstable methyl cations are expected to be stabilized by the zeolitic framework negative charge (Z^-) as $Z^-CH_3^+$. The role of the metal oxide/carbide species (gallium, indium, and zinc oxides, MoC_2 or MoO_xC_y species) present at the zeolite channel intersections in close proximity to the zeolite protons is not only to facilitate the methane activation but also to facilitate recombination of hydrogen adatoms[24] formed during the C–H bond activation [Eq. (2)]. One mole of H_2 (which appears in the products) is produced per mole of methane activated. The mechanism explains the observed direct conversion of methane into toluene and incorporation of ^{12}C from methane into the aromatics produced from $^{13}CH_3OH$. A very high concentration of methane relative to that of higher hydrocarbons (and consequently relative to methanol) is essential for the formation of a significant amount of methyl cations [by Eq. (2)] and/or pentacoordinated carbocations **II**. This is consistent with the observations; the methane converted per mole of methanol converted is increased markedly with an increase in the methane/methanol ratio in the feed (Table 1, Figure 2b).

Methanol aromatization is highly exothermic ($\Delta H_r \approx -264$ kJ mol^{-1} (*m*-xylene)), and this is one of the major concerns about the MTG process of Mobil. However, in our process, the simultaneous endothermic conversion of methane and exothermic aromatization of methanol over the same catalyst are coupled, which renders the process highly energy efficient. It also eliminates the possibility of process runaway. The other important advantages of this process are: 1) the oxygenate additive (methanol or dimethyl ether) in the methane feed can be produced from methane itself through a well-established technology (methane→syngas→methanol or dimethyl ether); 2) the conversion of the additive is

 © 2005 Wiley-VCH Verlag GmbH & Co. KGaA, Weinheim

complete (100%); 3) methane converted per mole of additive can be close to 1.0, hence the requirement of the additive is much smaller than that of the previous process involving higher hydrocarbons as the additive.[11–14] The process of high-temperature (>700°C) methane aromatization over Mo/H-ZSM-5 catalysts[21] is not technically feasible, as the catalyst is deactivated very rapidly. Because of the above highly attractive features, the process presented herein is expected to be much more feasible commercially. Further development of the bifunctional zeolite catalysts and optimization of the process conditions should lead to an economically feasible MTL technology which would not only eliminate the flaring of methane and associated natural gases but which would also satisfy increasing energy demands.

Experimental Section

A mixture of methanol (or ^{13}C-labeled methanol) vapors and premixed methane–N_2 (molar ratio $CH_4/N_2 = 8.5$) gas from a cylinder was passed over bifunctional Ga-, In-, Zn- and/or Mo-modified ZSM-5 (H-GaAl-ZSM-5 (Si/Al = 49.6, Si/Ga = 15.3, nonframework Ga = 0.65 mmol g^{-1}), Mo (2%)–Zn (2%)/H-ZSM-5, Zn (2%)–In (2%)/H-ZSM-5, Mo (2%)–Ga (2%)/H-ZSM-5, and Zn (2.3%)–Ga (2.4%)/H-ZSM-5) zeolite catalysts[25,26] in a tubular quartz reactor[11,26] at different reaction conditions. Before reaction, the Mo-containing catalyst was pretreated by passing a mixture of CH_4–H_2 (6% H_2) over it at 550°C for 4 h, whereas the other catalysts were pretreated in the presence of N_2 under similar conditions. The reaction products were analyzed by GC with thermal conductivity and flame ionization detectors connected in series, or by GC–MS. Methane conversion was determined by using nitrogen as an internal standard: (% CH_4 converted) = $\{[(CH_4/N_2)_{feed} - (CH_4/N_2)_{products}]/(CH_4/N_2)_{feed}\} \times 100$. In all runs, 100% conversion of methanol to hydrocarbons and water was observed. The formation of carbon monoxide in the methanol conversion in the presence or absence of methane was negligible. Furthermore, no formation of carbon monoxide was detected upon passing a mixture of methane and steam over the bifunctional zeolite catalyst at 550°C.

Received: February 24, 2005
Published online: June 13, 2005

Keywords: gallium · heterogeneuos catalysis · methane activation · molybdenum · zeolites

[1] T. Ito, J. H. Lunsford, *Nature* **1985**, *314*, 721.
[2] J. H. Lunsford, *Angew. Chem.* **1995**, *107*, 1059; *Angew. Chem. Int. Ed. Engl.* **1995**, *34*, 970.
[3] L. Mleczko, M. Baerns, *Fuel Process. Technol.* **1995**, *42*, 217.
[4] A. T. Ashcroft, A. K. Cheetham, J. S. Foord, M. L. H. Green, C. P. Grey, A. J. Murrell, P. D. F. Vernon, *Nature* **1990**, *344*, 319.
[5] V. R. Choudhary, A. S. Mamman, S. D. Sansare, *Angew. Chem.* **1992**, *104*, 1273; *Angew. Chem. Int. Ed. Engl.* **1992**, *31*, 1189.
[6] D. A. Hickman, L. D. Schmidt, *Science* **1993**, *259*, 343.
[7] V. R. Choudhary, A. M. Rajput, B. Prabhakar, *Angew. Chem.* **1994**, *106*, 2179; *Angew. Chem. Int. Ed. Engl.* **1994**, *33*, 2104.
[8] V. R. Choudhary, B. S. Uphade, A. S. Mamman, A. M. Rajput, US Patent 6293979, **2001**.
[9] V. R. Choudhary, S. D. Sansare, S. T. Chaudhari, US Patent 5336825, **1994**.
[10] V. R. Choudhary, S. D. Sansare, A. M. Rajput, US Patent 5306854, **1994**.
[11] V. R. Choudhary, A. K. Kinage, T. V. Choudhary, *Science* **1997**, *275*, 1286.
[12] O. A. Anunziata, G. V. G. Mercado, L. B. Pierella, *Catal. Lett.* **2003**, *87*, 167.
[13] T. Baba, H. Sawada, *Phys. Chem. Chem. Phys.* **2003**, *5*, 3919.
[14] T. Baba, Y. Abe, *Appl. Catal. A* **2003**, *250*, 265.
[15] T. V. Choudhary, A. E. Aksoylu, D. W. Goodman, *Catal. Rev.* **2003**, *45*, 151.
[16] S. L. Meisel, J. P. McCullough, C. H. Lechthaler, P. B. Weisz, *Chemtech* **1976**, 89.
[17] C. D. Chang, J. C. W. Kuo, W. H. Lang, S. M. Jacob, J. J. Wise, A. J. Silvestri, *Ind. Eng. Chem. Process Des. Dev.* **1978**, *17*, 255.
[18] J. Haggin, *Chem. Eng. News* **1987**, *65*(25), 22.
[19] J. Haggin, *Chem. Eng. News* **1987**, *65*(22), 22.
[20] J. H. Lunsford, *Catal. Today* **1990**, *6*, 235.
[21] Y. Xu, X. Bao, L. Lin, *J. Catal.* **2003**, *216*, 386.
[22] V. R. Choudhary, S. A. R. Mulla, S. Banerjee, *Microporous Mesoporous Mater.* **2001**, *47*, 253; V. R. Choudhary, S. A. R. Mulla, S. Banerjee, *Microporous Mesoporous Mater.* **2003**, *57*, 317.
[23] G. A. Olah, *Angew. Chem.* **1995**, *107*, 1519; *Angew. Chem. Int. Ed. Engl.* **1995**, *34*, 1393.
[24] E. Iglesia, D. G. Burton, J. A. Biscardi, M. J. L. Gines, S. L. Soled, *Catal. Today* **1997**, *38*, 339.
[25] The H-GaAl-ZSM-5, Mo (2%)–Zn (2%)/H-ZSM-5, Zn (2%)–In (2%)/H-ZSM-5, Mo (2%)–Ga (2%)/H-ZSM-5, and Zn (2.3%)–Ga (2.4%)/H-ZSM-5 zeolite catalysts were prepared by impregnating H-ZSM-5 (Si/Al = 20, Na/Al < 0.01) with required quantities of the respective metal nitrates or ammonium heptamolybdate, and calcination at 550°C for 4 h.
[26] V. R. Choudhary, A. K. Kinage, T. V. Choudhary, *Appl. Catal.* **1997**, *162*, 239.

 © 2005 Wiley-VCH Verlag GmbH & Co. KGaA, Weinheim

Homogeneous Catalysis

Activity of SPANphos Rhodium Dimers in Methanol Carbonylation**

Zoraida Freixa, Paul C. J. Kamer, Martin Lutz, Anthony L. Spek, and Piet W. N. M. van Leeuwen*

Oxidative addition to organometallic compounds is one of the key elementary steps in many catalytic processes. For this reason, the reaction has been extensively studied, and in the

[*] Dr. Z. Freixa
Institute of Chemical Research of Catalonia (ICIQ)
Avda. Països Catalans s/n., Tarragona (Spain)
Fax: (+34) 97792-0221
E-mail: zfreixa@iciq.es

Dr. P. C. J. Kamer, Prof. P. W. N. M. van Leeuwen
Van't Hoff Institute for Molecular Sciences
University of Amsterdam
Nieuwe Achtergracht 166, Amsterdam (The Netherlands)
Fax: (+31) 20525-5406

Dr. M. Lutz, Prof. Dr. A. L. Spek
Bijvoet Center for Biomolecular Research
Department of Crystal and Structural Chemistry
Utrecht University
Padualaan 8, 3584 CH Utrecht (The Netherlands)

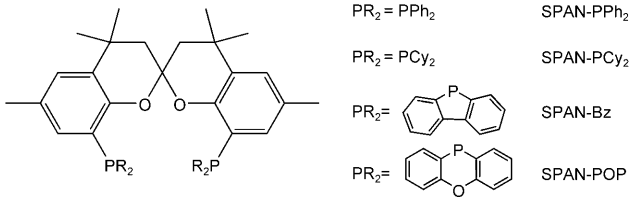
[**] Dr. Gisela Colet and Dr. Lluís Solà from the Research Support Area of ICIQ are kindly acknowledged for the help on the use of the React IR 4000 spectrometer.

 DOI: 10.1002/anie.200500226 © 2005 Wiley-VCH Verlag GmbH & Co. KGaA, Weinheim

last few years many publications have appeared concerning its implication to ligand-promoted methanol carbonylation.[1] It is commonly accepted that the rate-limiting step of this reaction is precisely the oxidative addition of MeI to a square planar d^8 complex. This reaction is thought to proceed by an S_N2 mechanism. Accordingly, many groups have been working on the acceleration of the overall catalytic reaction by using ligands that increase the electronic density on the metal center as well as stabilizing the ligand through chelation to make it resistant to the harsh conditions of the process.[2] Recent breakthroughs on this topic concern the use of benzoic acid-based flexible *trans*-chelating diphosphines and the use of bis(imino)carbazolide ligands recently reported by Haynes and co-workers, which, to our knowledge, led to the fastest systems published until now.[3,4]

Herein we report on SPANphos mononuclear rhodium complexes, which, even though they resemble the commonly accepted catalyst precursor for methanol carbonylation with phosphine ligands, do not undergo oxidative addition with methyl iodide. As an alternative, we present unprecedented reactivity of SPANphos dinuclear complexes and its implication to the reaction mechanism of the carbonylation of methanol.

Recently, our group reported a *trans*-spanning diphosphine ligand (SPANphos, Scheme 1)[5] for which crystal structures of its mono- and dinuclear rhodium chloro carbonyl



Scheme 1. The SPAN-diphosphine family. Cy = cyclohexyl

complexes have been characterized by X-ray diffraction (Figure 1).[6] These systems are closely related to the those published by Süss-Fink and co-workers and the dinuclear SPANphos rhodium compound resembles the bis-acyl complexes isolated at the end of the reaction by that group.[3] These binuclear complexes, which are formed by the elimination of phosphine, were considered to be inactive but act as a reservoir to the mononuclear, putative catalyst.[3]

Inspired by these results, we considered using complexes of SPANphos ligands, which is a truly *trans*-chelating diphosphine family that cannot *cis* coordinate, as a catalyst for methanol carbonylation. The results obtained showed that SPAN-diphosphines are very active catalyst for this reaction (Table 1). The TOF obtained compare well with those reported by Süss-Fink and co-workers for other *trans*-chelating diphosphine ligands under the same catalytic conditions.[3] In their report, the catalytic cycle is proposed to proceed through a mononuclear species that contains diphosphine ligands in a *trans* disposition.[3]

When a MeOH/rhodium ratio of about 10000:1 was used (Table 1 entries 6–11), high activities were still observed. These results can be considered as an indication that the

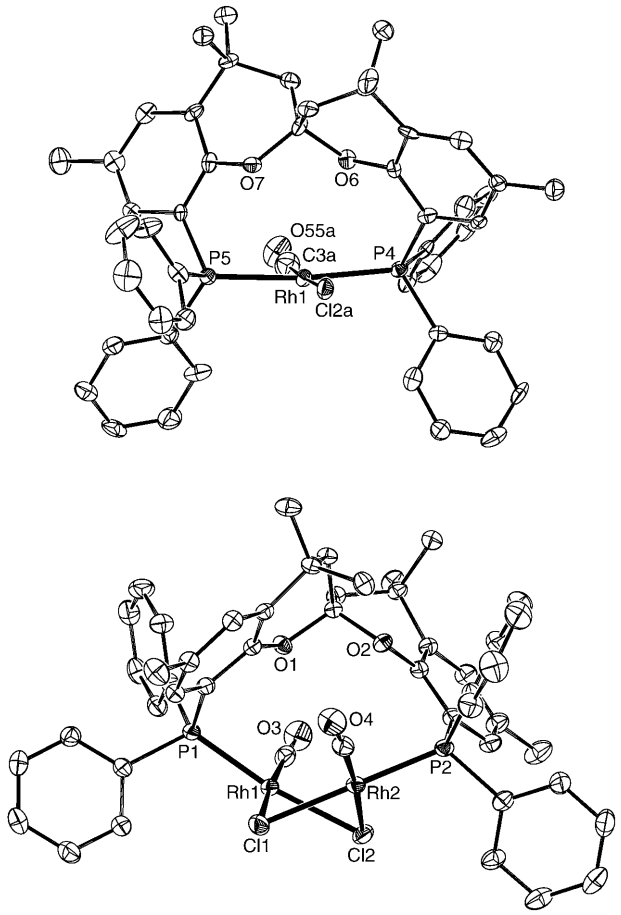


Figure 1. Upper: Displacement ellipsoid plot (50% probability level) of [RhCl(SPAN-PPh_2)(CO)] (**1**). The Cl and CO groups are substitutionally disordered; only the major configuration is shown. Hydrogen atoms are omitted for clarity. Lower: Displacement ellipsoid plot (50% probability level) of [$Rh_2(\mu\text{-}Cl)_2$(SPAN-PPh_2)$(CO)_2$] (**2**). Hydrogen atoms and disordered CH_2Cl_2 solvent molecules have been omitted for clarity.

Table 1: Methanol carbonylation with Rh catalyst and SPAN-diphosphine ligands.[a]

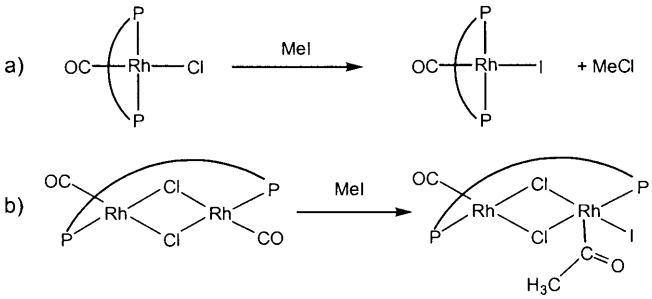
Entry	Ligand[b]	Conv. [%]	*t* [h]	TON[c]	TOF[d]
1[e]	no ligand	20	0.25	190	762
2[e]	SPAN-PPh_2	93	1	902	902
3[e]	SPAN-PCy_2	86	0.67	831	1247
4[e]	SPAN-Bz	84	0.67	817	1225
5[e]	SPAN-POP	79	0.3	766	2299
6[f]	no ligand	no conv.	1.5	0	0
7[f]	SPAN-PPh_2	11.3	1.5	1093	728
8[f]	SPAN-PCy_2	9.1	1.5	880	586
9[f]	SPAN-Bz	9.1	1.5	880	586
10[f]	SPAN-POP	7.5	1.5	725	483
11[f,g]	SPAN-POP	14.3	1.5	2764[g]	1842[g]

[a] Conditions: $T = 150\,^{\circ}C$, P(at 22 °C) = 22 bar of CO, 700 rpm, [{Rh(μ-Cl)$(CO)_2$}$_2$] 28 μmol, ligand/Rh = 1. [b] PPh_2, PCy_2, Bz, and POP refer to the substitution of the phosphorous atom (see Scheme 1). [c] TON = turnover number (in mol conversion per mol Rh). [d] TOF = turnover frequency (in mol conversion per mol Rh per h). [e] MeOH/MeI/H_2O/Rh = 967:100:682:1. [f] MeOH/MeI/H_2O/Rh = 9670:1000:6820:1. [g] Dimeric [$Rh_2(\mu\text{-}Cl)_2$(SPAN-POP)$(CO)_2$], ligand/Rh = 1:2, TON in mol conversion per mol Rh_2, TOF in mol conversion per mol Rh_2 per h.

 © 2005 Wiley-VCH Verlag GmbH & Co. KGaA, Weinheim

observed activity cannot be just attributed to a medium effect caused by phosphine quaternization taking place during the reaction.

Surprisingly, the study of the rate of the oxidative addition of MeI to the mononuclear [ClRh(SPAN-PPh_2)(CO)] (**1**) rendered no rhodium(III) methyl or acetyl compounds, not even after 24 h in pure MeI. Only [RhI(SPAN-PPh_2)(CO)], which arises from halide metathesis, was isolated at the end of the reaction (Scheme 2, reaction a). A previously reported



Scheme 2. a) Reaction of **1** with MeI. b) Reaction of **2** with MeI and the proposed structure for the resulting acyl compound; configuration at the Rh center is unclear.

example of halide exchange instead of oxidative addition was found for a *cis* coordinated mixed P,S-bidentate ferrocenyl ligand.[7] A crystal structure examination of the corresponding [RhCl(CO)(L)] complex showed that one face of the square planar complex is blocked by the ferrocenyl moiety of the ligand backbone, thus inhibiting MeI addition.[7] Both of these cases can be considered as an extreme situation of the extensively studied steric effects on the rate of MeI oxidative addition.[1c,8]

When dimeric [Rh_2(μ-Cl)$_2$(SPAN-POP)$(CO)_2$] was tested as a catalyst for methanol carbonylation (Table 1, entry 11) the results obtained showed that this catalyst is nearly four times more active than the corresponding mononuclear compound (entry 10). These results, together with the fact that when using other *trans*-spanning diphosphines dinuclear structures were isolated at the end of the reaction,[3] brought us to consider a different approach: the activity observed in the case of *trans*-spanning diphosphine ligands should perhaps be attributed to a dinuclear species rather than to the mononuclear species, [RhX(*trans*-P-P)(CO)] (X = Cl, I). To prove this hypothesis, we studied the rate of MeI oxidative addition to the dinuclear compound **2** (Scheme 2, reaction b). The results obtained showed that the oxidative addition to this dimetal species is only ten times slower compared to the most active catalyst reported until now (Figure 2),[4] but it constitutes the most active phosphine-based catalyst. In the IR spectrum of the reaction, the fact that the band at 1981 cm^{-1} decays but does not disappear at the end of the reaction suggests that the migration, and probably also the oxidative addition, occurs only at one of the two rhodium centers. The addition of MeI at only one of the two metallic centers of a rhodium dimer to render a Rh^{I}–Rh^{III} monoacyl species is not unprecedented. Similar reactivity, at much lower reaction rates, has already been reported by Oro and

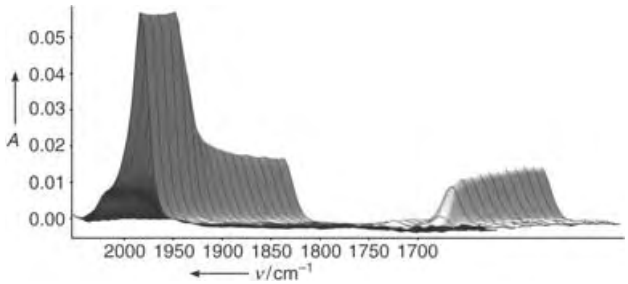


Figure 2. IR decay curves/surface for oxidative addition of MeI to **2** at 283 K. [MeI] = 1.6 M (1 spectrum per minute).

co-workers for dinuclear Rh complexes with diamido bridging ligands.[9] Simultaneous NMR spectroscopy experiments performed on reaction mixtures and GC–MS analysis of reaction products are consistent with this hypothesis.

Kinetic studies by using in situ FTIR have been performed on the reaction of MeI with the dinuclear compound **2**, which showed that the reaction is first order with respect to both MeI and **2**. From the pseudo first-order constants obtained over a range of MeI concentrations and temperatures, the activation parameters ($\Delta H^{\neq} = 32.15\ kJ\,mol^{-1}$, $\Delta S^{\neq} = -163.73\ J\,mol^{-1}\,K^{-1}$) were calculated. These values are in concordance with those previously reported for this reaction with mononuclear complexes.[1c,4,8a,8b]

We conclude that *trans*-spanning diphosphine ligands form mononuclear rhodium compounds that are inactive for the oxidative addition of methyl iodide. The lack of reactivity as established for SPAN-diphosphines should be attributed to one face of the square-planar compound being completely blocked by the backbone of the ligand. Consequently, the activity observed with mononuclear systems as precursors for MeOH carbonylation is most likely to arise from dinuclear species formed by partial dissociation of the ligand. A complete catalytic cycle that involves dinuclear species should be considered. These dimetal compounds showed an unprecedented activity for MeI oxidative addition, and also for MeOH carbonylation, and constitute one of the fastest systems reported until now.

Experimental Section

SPAN-diphosphines were synthesized according to a modified reported procedure published for the diphenyl phosphine derivative.[5]

Compounds **1** and **2** were synthesized in Schlenk tubes by mixing the appropriate quantities of SPAN-PPh_2 and [Rh_2(μ-Cl)$_2$$(CO)_4$], dissolving the mixtures in degassed CH_2Cl_2, passing the resulting solutions through celite, and removing the solvent by evaporation. Yields were quantitative. Suitable crystals for X-ray diffraction were grown by slow diffusion of pentane into CH_2Cl_2 solutions of the rhodium complexes.

1: ^{1}H NMR (400 MHz, 298 K, CD_2Cl_2, TMS): $\delta = 1.22$ (s, 3H, CH_3), 1.24 (s, 3H, CH_3), 1.31 (s, 6H, CH_3), 1.77 (d, $J = 13.8$ Hz, 1H, CH_2), 1.86 (d, $J = 13.8$ Hz, 1H, CH_2), 1.96 (s, 3H, CH_3), 2.00 (s, 3H, CH_3), 2.45 (d, $J = 13.8$ Hz, 1H, CH_2), 2.49 (d, $J = 13.8$ Hz, 1H, CH_2), 6.23 (dd, $J = 9.6$, $J = 1.6$ Hz, 1H, CH_{arom}), 6.40 (dd, $J = 9.6$, $J = 1.6$ Hz, 1H, CH_{arom}), 7.01 (d, $J = 1.6$ Hz, 1H, CH_{arom}), 7.02 (d, $J = 1.6$ Hz, 1H, CH_{arom}), 7.15–7.45 (m, 16H, CH_{arom}), 7.72 (dd, $J = 9.6$, $J = 8.4$ Hz, 1H, CH_{arom}), 7.84 ppm (dd, $J = 9.6$, $J = 8.4$ Hz, 1H, CH_{arom}); ^{13}C NMR

 © 2005 Wiley-VCH Verlag GmbH & Co. KGaA, Weinheim

(100 MHz, 298 K, TMS): $\delta = 21.4$ (CH_3), 21.5 (CH_3), 29.3 (CH_3), 29.5 (CH_3), 30.6 (CH_3), 30.8 (CH_3), 47.9 (CH_2), 48.1 (CH_2), 86.3 (C), 86.5 (C), 117.2 (C), 127–138 ppm (C_{arom}); ^{31}P NMR (162 MHz, 298 K): $\delta =$ 22.29 (dd, $J = 365.4$, $J = 132.0$ Hz), 26.50 ppm (dd, $J = 365.4$, $J =$ 132.0 Hz); MS [M−Cl].

2: ^{1}H NMR(400 MHz, 298 K, CD_2Cl_2, TMS): $\delta = 0.73$ (s, 3H, CH_3), 1.18 (s, 3H, CH_3), 1.70 (d, $J = 14.4$ Hz, 1H, CH_2), 2.00 (s, 3H, CH_3), 2.10 (d, $J = 14.4$ Hz, 1H, CH_2), 6.28 (dd, $J = 12.0$, $J = 1.6$ Hz, 1H, CH_{arom}), 7.05 (d, $J = 1.5$ Hz, 1H, CH_{arom}), 7.15–7.35 (m, 8H, CH_{arom}), 7.73 ppm (dd, $J = 11.6$, $J = 7.6$ Hz, 1H, CH_{arom}); ^{13}C NMR (100 MHz, 298 K, TMS): $\delta = 21.1$ (CH_3), 29.5 (CH_3), 31.0 (d, CH_3, $J =$ 20.6 Hz), 50.462 (CH_2), 102.5 (C), 117.2 (C), 128–137 ppm (C_{arom}); ^{31}P NMR (162 MHz, 298 K): $\delta = 45.88$ ppm (d, $J = 178.16$ Hz); MS [M−Cl], [M−2Cl].

Catalytic experiments: In a typical experiment 29.3 mL of a mixture MeOH/H_2O was placed in a 100-mL Hastelloy autoclave. The autoclave was then pressurized to 10 bar of carbon monoxide and heated to 150 °C with vigorous stirring (700 rpm). When the reaction temperature was reached and had stabilized, a solution of [$Rh_2Cl_2(CO)_4$] and the appropriate quantity of the corresponding ligand in MeI were added through a liquid injection port and the autoclave was pressurized to the desired reaction pressure. Pressure was maintained constant during the reaction by feeding gas from a 1-L autoclave pressurized with over 60 bar of carbon monoxide. After the required reaction time, the autoclave was cooled to room temperature. The solution was analyzed by NMR spectroscopy to determine the selectivity. The conversion was calculated from gas consumption of the reservoir autoclave.

Kinetic experiments: Kinetic measurements for the reaction of **1** or **2** with MeI in CH_2Cl_2 were performed in situ by using a React IR 4000 from Mettler Toledo equipped with a diamond probe. A solution that contained the corresponding rhodium compound in distilled CH_2Cl_2 was placed in the sample vessel under an argon atmosphere. The temperature was fixed by using a thermostat jacket. When the desired temperature was achieved and remained constant, freshly distilled MeI was added by using a syringe. The IR spectra were scanned in the region 400–2200 cm^{-1} and saved at regular time intervals (usually 10 s) under computer control.

Received: January 20, 2005
Published online: June 8, 2005

Keywords: carbonylation · homogeneous catalysis · phosphine ligands · rhodium

[1] a) E. Daura-Oller, P. J. M. Poblet, C. Bo, *Dalton Trans.* **2003**, 92–98; b) M. Sharma, N. Kumari, P. Das, P. Chutia, D. K. Dutta, *J. Mol. Catal. A* **2002**, *188*, 25–35; c) H. C. Martin, N. H. James, J. Aitken, J. A. Gaunt, H. Adams, A. Haynes, *Organometallics* **2003**, *22*, 4451–4458; d) V. Chauby, J.-C. Daran, C. S.-L. Berre, F. Malbosc, P. Kalck, O. D. Gonzalez, C. E. Haslam, A. Haynes, *Inorg. Chem.* **2002**, *41*, 3280–3290; e) M. Bassetti, A. Capone, L. Mastrofrancesco, M. Salamote, *Organometallics* **2003**, *22*, 2535–2538.

[2] a) C.-A. Carraz, E. J. Ditzel, A. G. Orpen, D. D. Ellis, P. G. Pringle, G. J. Sunley, *Chem. Commun.* **2000**, 1277–1278; b) D. K. Dutta, J. D. Woollins, A. M. Z. Slawin, D. Konwar, P. Das, M. Sharma, P. Bhattacharyya, S. M. Aucota, *Dalton Trans.* **2003**, 2674–2679; c) J. Rankin, A. D. Poole, A. C. Benyei, D. J. Cole-Hamilton, *Chem. Commun.* **1997**, 1835–1836; d) J. Rankin, A. C. Benyei, A. D. Poole, D. J. Cole-Hamilton, *J. Chem. Soc. Dalton Trans.* **199**9, 3771–3782.

[3] a) C. M. Thomas, R. Mafua, B. Therrien, E. Rusanov, H. Stoeckli-Evans, G. Süss-Fink, *Chem. Eur. J.* **2002**, *8*, 3343–3352; b) C. M. Thomas, G. Süss-Fink, *Coord. Chem. Rev.* **2003**, *243*, 125–142.

[4] J. A. Gaunt, V. C. Gibson, A. Haynes, S. K. Spitzmesser, A. J. P. White, D. J. Williams, *Organometallics* **2004**, *23*, 1015–1023.

[5] Z. Freixa, M. S. Beentjes, G. D. Batema, C. B. Dieleman, G. P. F. van Strijdonck, J. N. H. Reek, P. C. J. Kamer, J. Fraanje, K. Goubitz, P. W. N. M. van Leeuwen, *Angew. Chem.* **2003**, *115*, 1322–1325; *Angew. Chem. Int. Ed.* **2003**, *42*, 1284–1287.

[6] a) Crystal structure determinations: X-ray intensities were measured on a Nonius KappaCCD diffractometer with a rotating anode (graphite monochromator, $\lambda = 0.71073$ Å) at 150 K. The structures were solved with direct methods (SHELXS-97)[6b] and refined with SHELXL-97[6b] against F^2 of all reflections. Structure calculations and checking were performed with the PLATON program.[6c] Compound **1**: $C_{48}H_{46}ClO_3P_2Rh$, $M_r = 871.15$, yellow needles, $0.18 \times 0.12 \times 0.06$ mm^3, orthorhombic, $Pna2_1$ (no. 33), $a =$ 17.271(2), $b = 13.1760(12)$, $c = 17.5576(18)$ Å, $V = 3995.4(7)$ Å^3. $Z = 4$, $\rho_{calcd} = 1.448$ g cm^{-3}. A total of 50605 reflections were measured of which 7749 were unique. The crystal appeared to be cracked into two fragments with a rotation of 4° approximately about the a axis. The structure was thus refined as a general twin of two domains with a twin fraction of 0.284(2). The CO and Cl ligands were substitutionally disordered to each other in a ratio of 0.62:0.38, respectively; 524 parameters, 4 restraints; R values: $R1$ ($I > 2\sigma(I)$): 0.0566, $wR2$ (all refl.) = 0.1096; Flack x parameter −0.06(4); $S = 1.080$. Compound **2**: $C_{49}H_{46}Cl_2O_4P_2Rh_2 \cdot 2CH_2Cl_2$, $M_r = 1207.37$, orange plates, $0.35 \times 0.33 \times 0.12$ mm^3, monoclinic, $P2_1/c$ (no. 14), $a = 19.7446(1)$, $b = 14.4777(1)$, $c = 19.2880(1)$ Å, $\beta = 110.1247(2)°$, $V = 5176.97(5)$ Å^3. $Z = 4$, $\rho_{calcd} = 1.549$ g cm^{-3}. A total of 79995 reflections were measured of which 11842 were unique. The CH_2Cl_2 solvent molecules were disordered; 620 parameters, 69 restraints; R values: $R1$ ($I > 2\sigma(I)$): 0.0279, $wR2$ (all refl.) = 0.0747; $S = 1.043$. CCDC-260236 (**1**) and -260237 (**2**) contain the supplementary crystallographic data for this paper. These data can be obtained free of charge from the Cambridge Crystallographic Data Centre via www.ccdc.cam.ac.uk/data_request/cif; b) G. M. Sheldrick, SHELXS-97 and SHELXL-97, programs for crystal structure solution and refinement, University of Göttingen, Germany, **1997**; c) A. L. Spek, *J. Appl. Crystallogr.* **2003**, *36*, 7–13.

[7] R. Broussier, M. Laly, P. Perron, B. Gautheron, I. E. Nifant'ev, J. A. K. Howard, L. G. Kuz'mina, P. Kalck, *J. Organomet. Chem.* **1999**, *587*, 104–112.

[8] a) L. Gonsalvi, J. A. Gaunt, H. Adams, A. Castro, G. J. Sunley, A. Haynes, *Organometallics* **2003**, *22*, 1047–1054; b) L. Gonsalvi, H. Adams, G. J. Sunley, E. Ditzel, A. Haynes, *J. Am. Chem. Soc.* **2002**, *124*, 13597–13612; c) L. Cavallo, M. Solà, *J. Am. Chem. Soc.* **2001**, *123*, 12294–12302; d) L. Gonsalvi, H. Adams, G. J. Sunley, E. Ditzel, A. Haynes, *J. Am. Chem. Soc.* **1999**, *121*, 11233–11234.

[9] M. V. Jiménez, E. Sola, M. A. Egea, A. Huet, A. C. Francisco, F. J. Lahoz, L. Oro, *Inorg. Chem.* **2000**, *39*, 4868–4878.

 © 2005 Wiley-VCH Verlag GmbH & Co. KGaA, Weinheim

Asymmetric Catalysis

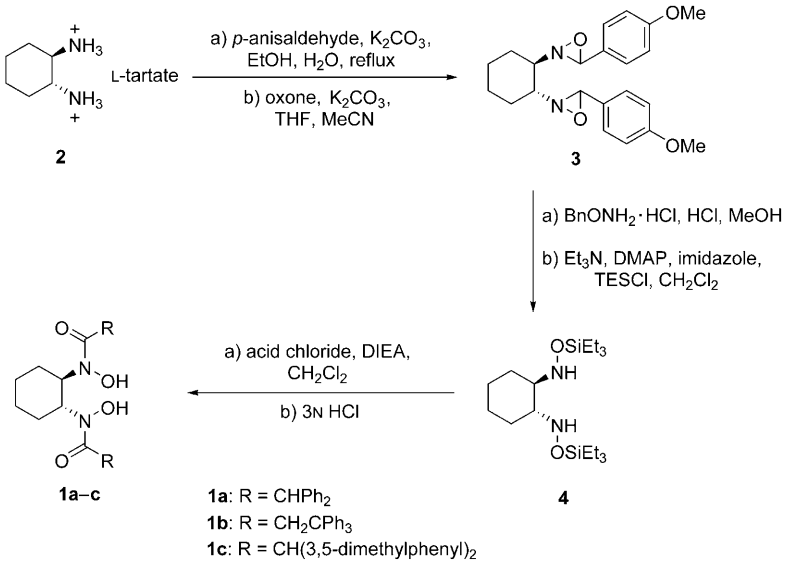
Enantioselective Epoxidation of Allylic Alcohols by a Chiral Complex of Vanadium: An Effective Controller System and a Rational Mechanistic Model**

*Wei Zhang, Arindrajit Basak, Yuji Kosugi, Yujiro Hoshino, and Hisashi Yamamoto**

The asymmetric epoxidation of allylic alcohols by metal catalysts,[1] though a widely used synthetic method, could gain even more practical applications if the following were realized: 1) employment of a ligand designed to achieve high enantioselectivity for *Z* olefins, 2) catalyst loading of less than 1 mol%, 3) reaction temperatures of 0°C to room temperature over a shorter time, 4) use of aqueous *tert*-butyl hydroperoxide (TBHP) as an achiral oxidant instead of anhydrous TBHP, and 5) simple workup procedures for small epoxy alcohols. Many important improvements have been made to the methodology developed by Sharpless and co-workers for the titanium tartarate catalyzed asymmetric epoxidation.[2–4] Nonetheless, each of these approaches fails to fulfil the above criteria.[1–5] Herein, we report our recent progress on all five fronts.

Recently, we developed a series of hydroxamic acid ligands and demonstrated that they were effective for the vanadium-catalyzed asymmetric epoxidation of allylic alcohols.[6,7] These results suggested that several structural features of the hydroxamic acid significantly enhanced the rate and enantioselectivity of the reaction. However, the ligand deceleration effect was still observed in these cases.[6–8] To exclude this effect, we planned to design a new C_2-symmetric bishydroxamic acid **1** that incorporated the following features: 1) an additional binding site with which **1** can chelate as a bidentate ligand to the metal center to complete the generation of a chiral vanadium/ligand complex more efficiently than the monohydroxamic acid and 2) an R group of the amide in **1** that is sufficiently large so the oxygen atom of the carbonyl group is directed towards the cyclohexane ring to minimize steric interaction and restrict its coordination with the metal center. Furthermore, the attachment of additional ligands to the vanadium center will also be restricted because of steric reasons. Thus, doubly or triply coordinated species, which are believed to be inactive, should not be generated from the bishydroxamic acid ligand, and consequently a ligand deceleration effect within the vanadium/**1** catalytic system should not be problematic.[8]

We devised a synthetic protocol for **1** from a readily available diamine tartrate salt (Scheme 1) so that the veracity of our hypothesis could be proved.[9] These reaction sequences can be carried out with satisfactory yields and without any purification to provide **4**, from which we have prepared an array of diverse ligands **1a–c**.



2 3 4 1a–c

Scheme 1. Preparation of bishydroxamic acid. DIEA = *N*,*N*-diisopropylethylamine, Bn = benzyl, DMAP = 4-dimethylaminopyridine, TESCl = triethylsilyl chloride.

As expected, the use of a complex of vanadium with ligand **1** provided epoxy alcohols both in good yields with high enantioselectivities (Table 1).[9] The catalyst **5a**, derived from vanadium and **1a**, invariably induced excellent enantioselectivities during the epoxidation of *trans*-disubstituted and -trisubstituted allylic alcohols. The most gratifying aspect of this catalytic system was the excellent enantioselectivity observed during the epoxidation of *cis*-substituted allylic alcohols with catalyst **5b**, which was derived from vanadium and **1b.** It is of note that 1) the slow reactivity of some substrates were surmounted by performing the epoxidation at 0°C or room temperature without significant loss of enantioselectivity, 2) the catalyst loading could be as low as 0.2 mol%, 3) all the reactions were performed in air and in the presence of aqueous TBHP; the use of anhydrous TBHP increased neither the yield nor the enantioselectivity.[9] Also as expected, the negative effect of a dynamic ligand exchange was not observed in the vanadium/bishydroxamic acid catalytic system. The high reactivity of the vanadium/ligand complex was maintained, even if the ratio of ligand/vanadium was increased to more than 3:1.[9]

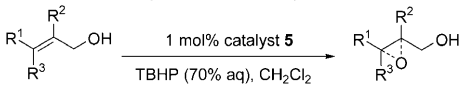
[*] W. Zhang, Dr. A. Basak, Dr. Y. Hoshino, Prof. Dr. H. Yamamoto
Department of Chemistry
The University of Chicago
5735 South Ellis Avenue, Chicago, IL 60637 (USA)
Fax: (+1) 773-702-0805
E-mail: yamamoto@uchicago.edu
Y. Kosugi
Graduate School of Engineering
Nagoya University, Furo-cho
Chikusa, Nagoya 464-8603 (Japan)

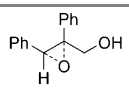
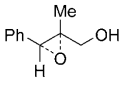
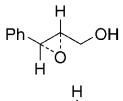
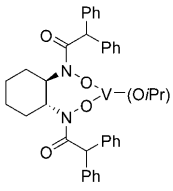
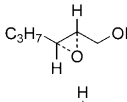
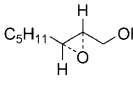
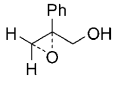
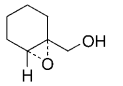
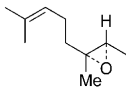
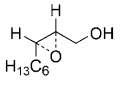
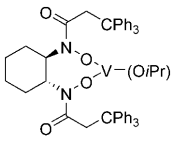
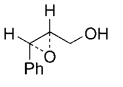
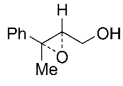
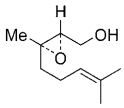
[**] Support of this work by the SORST project of the Japan Science and Technology Agency (JST), the National Institutes of Health (NIH; GM068433-01), and a starter grant from the University of Chicago is gratefully acknowledged.

Supporting information for this article is available on the WWW under http://www.angewandte.org or from the author.

 DOI: 10.1002/anie.200500938 © 2005 Wiley-VCH Verlag GmbH & Co. KGaA, Weinheim

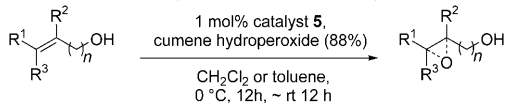
Table 1: Enantioselective epoxidation of allylic alcohols

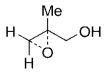
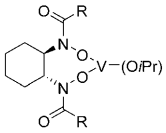
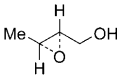
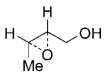
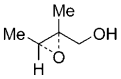
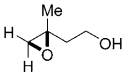


Catalyst	Product	*T* [°C]	*t* [h]	Yield [%]	*ee* [%]
		−20	48	91	97
		−20	48	84	97
		−20	60	53	97
 **5a**		−20	72	56	95
		−20	72	51	95
		0	48	73	95
		−20	48	79	95
		−20	48	68	95[a]
		0	72	60	95
 **5b**		−20	120	24	97
		−20	48	64	96
		−20	48	62	95

[a] Catalyst was **5c**.

Table 2: Enantioselective epoxidation of small allylic alcohols



	Catalyst	Product	Yield [%]	*ee* [%]
	5c		78	97
 **5a–c**	**5a**		50	93
	5b		71	92
	5a		68	95
	5c		73	94

To explain the reaction enantioselectivity, we have proposed a possible intermediate during the epoxidation[10] (Figure 1). If **1a** is divided into four sections, as indicated by the circle in Figure 1, it is seen that the second and fourth quadrants of **1a** (corresponding to the shaded sections) are more crowded than the first and third quadrants (corresponding to the unshaded quarters) because of the structural features of the chiral cyclohexyl bishydroxamic acid (Figure 1a), especially when the vanadium center is introduced. $[VO(OiPr)_3]$ coordinates with **1a** by displacement of two *i*PrOH units with two hydroxy groups from the bishydroxamic acid (Figure 1b). Another *i*PrOH unit of $[VO(OiPr)_3]$ is then displaced by TBHP, which occupies the less-crowded third quadrant. Finally, when the allylic alcohol forms, it will coordinate with the vanadium center through its oxygen atom from the top. During the reaction, the oxygen atom of TBHP is spiro overlapped with the olefin and attacks it from the bottom. Steric bulk at the α position of the carboxylate group, which is greater in the case of **1a**, plays an important role and is suitable for *trans*-substituted allylic alcohols as the sub-

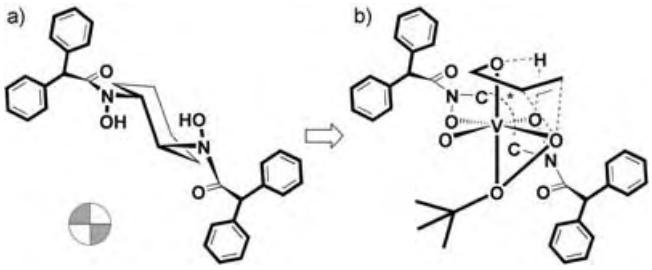
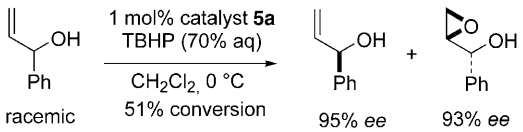


Figure 1. Postulated model of the epoxidation of allylic alcohols catalyzed by the vanadium/**1a** complex. a) Chiral cyclohexyl bishydroxamic acid **1a** and b) the proposed reaction intermediate. The circle represents the division of the bishydroxamic acid into quarters to explain its stereochemistry. The shaded sections of the circle represent the parts of the bishydroxamic acid in bold.

This method was applied to the asymmetric synthesis of small epoxy alcohols, which is a long-standing problem in asymmetric oxidation. Thus, after the reaction, the product was extracted with water to give the enantiopure epoxy alcohols (Table 2).[2,9]

Finally, the method was also applied to the kinetic resolution of a secondary allylic alcohol. As expected, both the epoxy alcohol and the allylic alcohol were isolated with high enantioselectivities [Eq. (1)].[9]



(1)

 © 2005 Wiley-VCH Verlag GmbH & Co. KGaA, Weinheim

strate. On the other hand, the additional flexibility of **1b** allows the *cis*-substituted allylic alcohols enough space to fit into the chiral pocket, thus resulting in high selectivity.

In conclusion, we have developed a new catalytic system for the asymmetric epoxidation of allylic alcohols. Investigations into the mechanism and further applications of bishydroxamic acid ligands in asymmetric catalysis is in progress.

Experimental Section

Representative experimental procedure: $[VO(OiPr)_3]$ (0.0025 mL, 0.0104 mmol) was added to a solution of **1a** (11.2 mg, 0.0210 mmol) in CH_2Cl_2 or toluene (1 mL), and the reaction mixture was stirred for 1 h at RT. The resulting solution was cooled to 0 °C, and 70 % aqueous TBHP (0.22 mL, 1.59 mmol) and α-phenylcinnamyl alcohol (220 mg, 1.05 mmol) were added. The mixture was stirred at the same temperature for 12 h. The process of epoxidation was monitored by TLC. Saturated aqueous Na_2SO_3 was added, and the reaction mixture was stirred for 1 h at 0 °C. The reaction mixture was then allowed to warm to RT, extracted with Et_2O, dried over Na_2SO_4, and concentrated under reduced pressure. The remaining residue was purified by flash column chromatography on silica gel to provide the epoxy alcohol (93 %, 94 % *ee*). Determination of the *ee* values of the epoxy alcohols is provided in the Supporting Information.

Received: March 14, 2005
Published online: June 8, 2005

Keywords: asymmetric catalysis · chirality · epoxidation · ligand design · vanadium

[1] For recent reviews, see: a) K. A. Jørgensen, *Chem. Rev.* **1989**, *89*, 431 – 458; b) A. Pfenninger, *Synthesis* **1986**, 89 – 116.
[2] Y. Gao, R. M. Hanson, J. M. Klunder, S. Y. Ko, H. Masamune, K. B. Sharpless, *J. Am. Chem. Soc.* **1987**, *109*, 5765 – 5780.
[3] For a recent report on chiral vanadium catalysts for epoxidation, see: a) C. Bolm, T. Kuhn, *Synlett* **2000**, 899 – 901; b) B. Traber, Y. G. Jung, T. K. Park, J. I. Hong, *Bull. Korean Chem. Soc.* **2001**, *22*, 547 – 548; c) H. L. Wu, B. J. Uang, *Tetrahedron: Asymmetry* **2002**, *13*, 2625 – 2628.
[4] For recent reports on achiral metal catalysts and chiral oxidants, see: a) W. Adam, P. L. Alsters, R. Neumann, C. R. Saha-Möller, D. Seebach, A. K. Beck, R. Zhang, *J. Org. Chem.* **2003**, *68*, 8222 – 8231; b) W. Adam, A. K. Beck, A. Pichota, C. R. Saha-Möller, D. Seebach, N. Vogl, R. Zhang, *Tetrahedron: Asymmetry* **2003**, *14*, 1355 – 1361; c) W. Adam, P. L. Alsters, R. Neumann, C. R. Saha-Möller, D. Seebach, R. Zhang, *Org. Lett.* **2003**, *5*, 725 – 728.
[5] For recent reviews on vanadium, see: a) T. Hirao, *Chem. Rev.* **1997**, *97*, 2707 – 2724; b) C. Bolm, *Coord. Chem. Rev.* **2003**, *237*, 245 – 256.
[6] a) N. Murase, Y. Hoshino, M. Oishi, H. Yamamoto, *J. Org. Chem.* **1999**, *64*, 338 – 339; b) Y. Hoshino, N. Murase, M. Oishi, H. Yamamoto, *Bull. Chem. Soc. Jpn.* **2000**, *73*, 1653 – 1658.
[7] Y. Hoshino, H. Yamamoto, *J. Am. Chem. Soc.* **2000**, *122*, 10452 – 10453.
[8] D. J. Berrisford, C. Bolm, K. B. Sharpless, *Angew. Chem.* **1995**, *107*, 1159 – 1171; *Angew. Chem. Int. Ed. Engl.* **1995**, *34*, 1059 – 1070.
[9] See the Supporting Information for detailed experimental procedures.
[10] For a mechanistic study on an oxidation mediated by a vanadium/hydroxamic acid system, see: a) K. P. Bryliakov, E. P. Talsi, *Kinet. Catal.* **2003**, *44*, 334 – 346; b) K. P. Bryliakov, E. P. Talsi, T. Kühn, C. Bolm, *New J. Chem.* **2003**, *27*, 609 – 614.

 © 2005 Wiley-VCH Verlag GmbH & Co. KGaA, Weinheim

Battery Materials

Self-Assembled Vanadium Pentoxide (V_2O_5) Hollow Microspheres from Nanorods and Their Application in Lithium-Ion Batteries**

*An-Min Cao, Jin-Song Hu, Han-Pu Liang, and Li-Jun Wan**

Self-assembled structures with highly specific morphology and novel properties are of great interest to chemists and materials scientists. As a result of rapid advancements in synthetic strategies, highly organized building blocks of metals,[1] semiconductors,[2] copolymers,[3] organic–inorganic hybrid materials,[4] and biominerals[5] have been synthesized by using various methods. However, controlled organization into curved structures from rodlike building blocks remains a challenge. Such a capability is attractive to scientists not only because of its importance in understanding the concept of self-assembly with artifial building blocks but also for its great application potential.[6–9] Vanadium pentoxide (V_2O_5) has been extensively studied as a well-known transition-metal oxide. Various nanostructures of V_2O_5,[10] such as nanotubes, nanowires, nanofibers, nanobelts, nanorods, and mesoporous structures have already been synthesized by a variety of methods, including reverse-micelle transition, sol–gel process, hydrothermal treatment, and electrochemical deposition. Nanostructured V_2O_5 has potential application in the fields of lithium-ion batteries,[10c,d,11] actuators,[10f] catalysis,[12] and sensors.[13] To our knowledge, hollow microspherical V_2O_5 has not been reported until now although such a structure has long been a focus of research.[14]

Herein, we describe a facile method to self-assemble V_2O_5 nanorods into microspheres. A mediated polyol process was adopted to prepare hollow microspherical V_2O_5, in which ethylene glycol (EG) is treated with a metal salt in the presence of poly(vinylpyrrolidone) (PVP). Such a method was previously used to obtain metal nanoparticles, nanowires (EG as a reductant),[15] and oxide nanowires (EG as a ligand).[16] We now present its use, for the first time, to synthesize hollow microspheres of V_2O_5. Using vanadium(III) acetylacetonate (acac) as the metal-ion source, we have synthesized hollow microspheres with nanorods on their surface; moreover, the morphologies of such nanorods are

[*] A.-M. Cao, J.-S. Hu, H.-P. Liang, Prof. Dr. L.-J. Wan
Institute of Chemistry
Chinese Academy of Sciences (CAS)
Beijing 100080 (China)
Fax: (+86) 106-255-8934
E-mail: wanlijun@iccas.ac.cn

[**] This work was supported by the National Natural Science Foundation of China (No. 20025308, 20177025, 10028408, and 20121301), the National Key Project on Basic Research (Grant G2000077501). The Chinese Academy of Sciences is gratefully acknowledged. The authors thank Dr. Li Jiang at Schlumberger Doll Research (USA) for his help with the writing of the manuscript.

Supporting information for this article is available on the WWW under http://www.angewandte.org or from the author.

 DOI: 10.1002/anie.200500946 © 2005 Wiley-VCH Verlag GmbH & Co. KGaA, Weinheim

readily tunable. The as-prepared vanadium hollow microspheres can be calcined into crystalline V_2O_5 without changing their morphologies. These V_2O_5 products exhibit improved electrochemical properties when they are used as cathode material in lithium-ion batteries and show good application potential.

Briefly, PVP was mixed with $[V(acac)_3]$ in a solution of EG at room temperature and normal pressure then heated at 140 °C for about 100 min, which led to the eventual formation of vanadium precursors with different structures. It is worth noting that PVP had a great influence on the morphologies of the synthesized vanadium precursors. In the absence of PVP, nanorods mainly form, the aspect ratios and diameters of which are tunable. Figure 1a shows such nanorods with

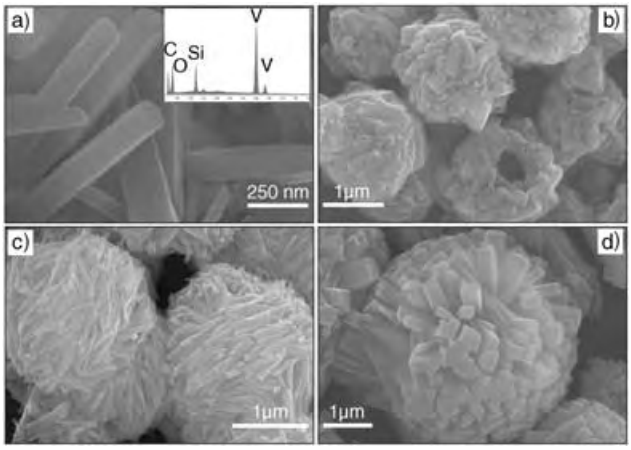


Figure 1. a) SEM image of the vanadium precursor prepared with 6 mM $[V(acac)_3]$ and no PVP. The inset shows the EDX pattern of the rod. b–d) SEM images of the microspheres synthesized with different concentrations of $[V(acac)_3]$ at 6 mM (b), 18 mM (c), and 42 mM (d), while the concentration of PVP was constant at 0.14 mM.

diameters of about 200 nm and lengths up to 2 μm at a concentration of 6 mM $[V(acac)_3]$. The energy-disperse X-ray (EDX) spectroscopic analysis (inset in Figure 1a) of the nanorods shows their chemical composition correlating well to that of the vanadium precursor. Upon the introduction of 0.14 mM of PVP, uniform hollow microspheres formed in large quantity, the morphology of which could be readily regulated by changing the concentration of $[V(acac)_3]$. At a concentration of 6 mM $[V(acac)_3]$, the rods are relatively short and circle around to form the spherical shell just taking the shape of a nest (Figure 1b). A broken sphere in the lower part of Figure 1b clearly shows the hollow feature of the sphere. At a concentration of 18 mM $[V(acac)_3]$, these nanorods become longer and have a higher packing density as shown in Figure 1c. At a concentration of 42 mM $[V(acac)_3]$, these nanorods eventually self-align perpendicular to the spherical surface and emanate from the center rather like the spines of a hedgehog (Figure 1d).

After the preparation of the precursors, we investigated the effect of calcination on the crystallization and morphology of the hollow microspheres. Subsequent calcination at 500 °C over 2 h did not change the individual morphologies of these vanadium precursors. Figure 2a shows a representative SEM image of a calcined V_2O_5 sample, which shows that the structure of the hollow microspheres was preserved. The sample was prepared under the same conditions as those

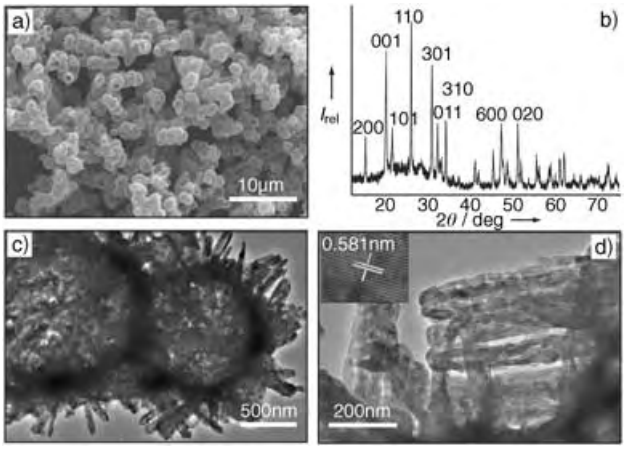


Figure 2. a) SEM image, b) XRD pattern, and c) low and d) high magnification TEM images of the calcinated V_2O_5 hollow microspheres. The inset in Figure 2d is a high-resolution TEM (HRTEM) picture taken from the edge of a nanorod surface.

applied to generate the samples shown in Figure 1c. The following characterizations are all based on this sample unless otherwise noted. Figure 2b shows a wide-angle XRD pattern of this calcined sample, which can be indexed as the orthogonal symmetry of V_2O_5 (space group: *Pmmn* (59), $a = 11.516$, $b = 3.566$, $c = 3.777$ Å; JCPDS card no. 41–1426), thus demonstrating the presence of crystalline V_2O_5. The TEM image in Figure 2c further affirms that the calcined V_2O_5 superstructures are indeed hollow microspheres with nanorods pointing out from the surface. The presence of nanorods can be clearly seen in Figure 2d. In a high-resolution TEM (HRTEM) image taken from the edge of a nanorod (inset of Figure 2d), the lattice fringes are clearly visible with a spacing of 0.581 nm, which is in good agreement with the spacing of the (200) planes of V_2O_5 (JCPDS card no. 41–1426).

Time-dependent experiments were performed to gain insight into the formation process of such vanadium precursors. Products were collected at different stages from the reaction mixture once the precipitate had began to appear in solution, and their morphologies were subjected to SEM investigation. As shown in Figure 3, when a sample was taken immediately after the formation of precipitate ($t = 0$ min), the collected product comprised microspheres with smooth surfaces (Figure 3a); after ten minutes, the surfaces of the samples were found to be rougher (Figure 3b). Nanorods formed over the following 20 minutes (Figure 3c), which were evidently very stable in solution as such their highly ordered superstructure remained unchanged with subsequent heating for over an hour (Figure 3d).

Ethylene glycol has been established as a cross-linking reagent.[16,17] Xia and co-workers proposed that two key steps are involved in producing nanowires: 1) coordination of EG

 © 2005 Wiley-VCH Verlag GmbH & Co. KGaA, Weinheim

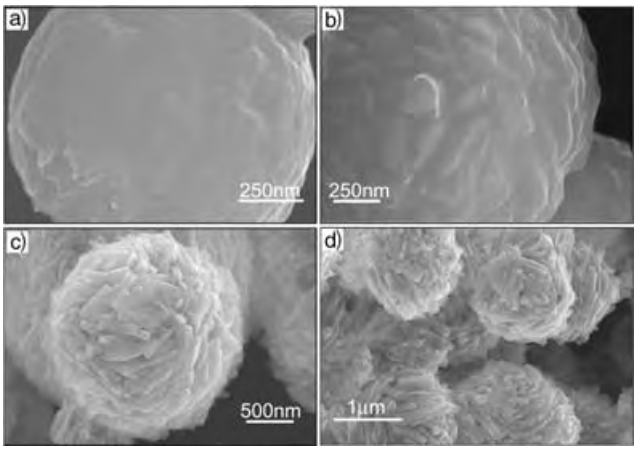


Figure 3. SEM images of the samples collected at different stages after the precipitate appeared in the clear solution: a) 0, b) 10, c) 30, and d) 90 min.

to the central metal ion to form a metal glycolate and 2) subsequent oligomerization.[16] Such a mechanism may be adapted to explain the formation of rodlike vanadium precursors. The XRD pattern (see the Supporting Information) of the vanadium precursor shows its crystalline nature with characteristically strong peaks around 10°, which is a feature of the coordination and oligomerization processes in EG.[16] FTIR spectra (see the Supporting Information) show the gradual displacement of the acac ligands with EG. The C–OH vibration at 1056 cm^{-1} together with the CH_2 band at 2939 and 2877 cm^{-1} in the final product increases at the expense of the characteristically strong bands of C=O in $[V(acac)_3]$ at 1566 and 1527 cm^{-1}. This result indicates that EG has completely replaced acac in a similar way to that proposed by Xia and co-workers.[16]It is evident that PVP plays a completely different role to that reported in the polyol process.[15,16] The introduction of PVP is crucial in obtaining uniform hollow microspheres because of the template effect of the polymer. As the vinyl group is hydrophobic and carbonyl group is hydrophilic, PVP also functions as a surfactant in an EG solution. Indeed, hollow structures have already been synthesized with PVP as the template.[18] A probable mechanism for the evolution of such structures is presented in Figure 4. PVP forms spherical micelles in EG with the carbonyl groups on the outside. The acac ligand of $[V(acac)_3]$ is gradually replaced by EG to form vanadium glycolates, which are easily adsorbed onto the micelle surface through their

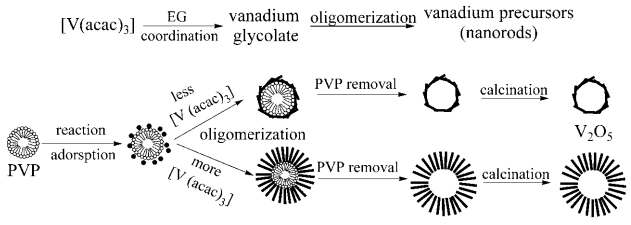


Figure 4. Schematic illustration of the evolution of V_2O_5 hollow microspheres.

abundant hydroxy groups. Nanorods form and grow as the oligomerization of vanadium glycolates proceeds. These rods are flat on the surface at relatively low abundance but gradually turn and pack more tightly as the concentration of $[V(acac)_3]$ increases. Finally, they are perpendicular to the surface because of a spherical hindrance effect. Hollow spheres retain their geometry even after PVP is removed. Considering the abundant carbonyl and hydroxy groups in the system and because PVP is known to be a hydrogen-bonding acceptor,[3a,19] we believe the key factors affecting this self-assembly process are hydrogen bonding and the requirement that the "grafted" nanorods pack effectively. The exact role of PVP in the polyol process has long been an issue of debate,[16,18] and extensive work is underway towards its further clarification.

Cyclic voltammetry was used to investigate the electrochemical behavior of the highly ordered superstructures. Figure 5a shows the cyclic voltammograms (CVs) of V_2O_5

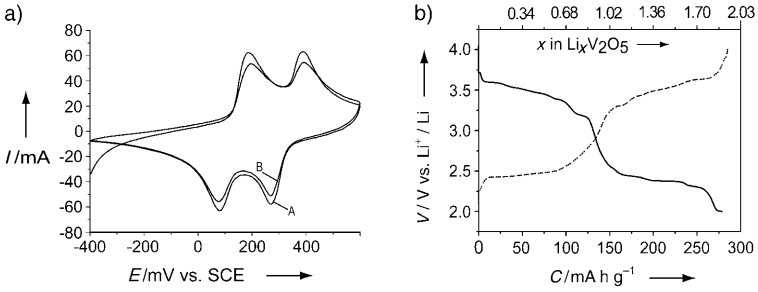


Figure 5. a) Cyclic voltammograms of V_2O_5 microspheres obtained at a scan rate of 10 $mV s^{-1}$. The first scan is indicated by curve A and after 15 cycles by curve B. b) The third charge(dash–dot line)–discharge(solid line) profile with a current rate of *C*/5.

hollow microspheres. Curve A (Figure 5a) is the first scan and B is the scan after 15 cycles. In the potential region from −400 to 600 mV, two sets of peaks can be seen at 80 and 270 mV. These peaks have been attributed to two successive electrochemical processes [Eq. (1) and (2)]:[11a–c]

$$V_2O_5 + {}^1/_2\,Li^+ + {}^1/_2\,e^- \rightleftharpoons Li_{0.5}V_2O_5 \quad (1)$$

$$Li_{0.5}V_2O_5 + {}^1/_2\,Li^+ + {}^1/_2\,e^- \rightleftharpoons LiV_2O_5 \quad (2)$$

In the first reduction peak at 270 mV, only a fraction of the V^{5+} ions is reduced to V^{4+} ions. The remaining V^{5+} ions are reduced to V^{4+} ions in the second peak at 80 mV.[11b] The reverse reactions take place as indicated by the two corresponding oxidation peaks. With the electrochemical reaction, different phases of $Li_xV_2O_5$ are formed. From the binary phase diagram of V_2O_5–$Li_xV_2O_5$, we determined that the cathodic peaks at 80 and 270 mV correspond to the phase transformations from α-V_2O_5 to ε-V_2O_5, and ε-V_2O_5 to δ-V_2O_5, respectively.[11d,e]

The charge–discharge capability of the microspheres was investigated by using V_2O_5 as the cathode in a lithium-ion battery. Figure 5b is the profile of a third charge–discharge cycle. The capacity was as high as 286.4 $mA h g^{-1}$ while the

 © 2005 Wiley-VCH Verlag GmbH & Co. KGaA, Weinheim

charge–discharge efficiency was up to 97.2% in the potential range from 2.0 to 4.0 V. These results show that V_2O_5 might be very good cathode material.[10c,d,11] The V_2O_5 samples with different morphologies (from nest-shaped to hedgehog-shaped) were tested for their electrochemical performances; they exhibited similar CV characteristics and had a variation of capacity in the Li-ion battery of less than 7 mA h g^{-1} (≈2%).

After the electrochemical investigation had been performed, the morphologies of the V_2O_5 samples were reinvestigated by TEM. The results showed that the structure of the hollow microspheres and nanorods remained unchanged.

The correlations among structure, composition, morphology of V_2O_5, and its electrochemical properties in the lithium-ion battery have been well studied by other researchers.[10c,d] In our system, the hollow microspheres together with the porous and rugged nanorods that have interconnected nanoparticles are favorable in reducing the diffusion distance of the solid-state lithium ion. Thus, the intercalation and extraction processes are of much higher efficiency, the kinetic performance of the lithium-ion battery is better, and therefore a higher capacity can be achieved.

In summary, we have developed a mediated polyol process to synthesize V_2O_5 with highly ordered superstructures, in which nanoparticles interconnect to form nanorods, and these rods circle around to form hollow microspheres. The protocol represents a substantial simplification over more conventional methods such as electrostatic spray or thermal evaporation. The physical state of the nanorods on the surface can be varied by changing the concentration of $[V(acac)_3]$ and the formed microspheres can adopt different shapes that range from nest-like to hedgehog-like. The prepared V_2O_5 exhibits desirable electrochemical properties such as high capacity and remarkable reversibility when it is used as cathode material in a lithium-ion battery.

Experimental Section

Preparation of V_2O_5 hollow microspheres: In a typical synthesis, $[V(acac)_3]$ (0.3 g, 18 mM; Aldrich) and PVP (0.4 g, 0.14 mM; $\bar{M}_w$ = 58000; ACROS Organics) were added to ethylene glycol (48 mL; Beijing Chemical Reagent Ltd.) to give a cloudy solution. The mixture was stirred with a magnetic stirrer bar and heated to 140°C. The cloudy mixture turned clear after 20 min and became opaque again after 70 min, indicating the formation of vanadium precursor. The solution was heated for another 30 min to ensure the formation of the composite structure before being allowed to cool to room temperature. The products were washed and separated by centrifugation–redispersion cycles with alcohol. These vanadium precursor was calcined at 500°C for 2 h to obtain crystalline orthogonal V_2O_5.

Characterization: Products were characterized by XRD, (Rigaku Dmax/rb diffractometer with $Cu_{K\alpha}$ radiation, $\lambda = 0.1542$ nm, 40 kV, 100 mA), TEM (Philips TECNAI-20), SEM (Hitachi S-4300F), and by FTIR (Bruker Tensor 27).

CV measurements were conducted by using an electrochemical cell with a three-electrode configuration. The working electrode was a glassy carbon disk of 3 mm in diameter, polished with Al_2O_3 paste, and washed ultrasonically in Millipore water. The experiment was carried out in an $LiClO_4$–propylene carbonate (Li–PC, 1M) solution with a standard calomel electrode (SCE) as the reference electrode and a Pt counter electrode with an EG&G instrument (model 273, Princeton Applied Research). Electrochemical discharge–charge behavior was investigated directly in coin cells assembled in an argon-filled glove box. The cell was made from a lithium anode and a cathode that was a mixture of V_2O_5 (80%), graphite/carbon black (12%), and teflon (8%). The cathode was separated from the anode by an insulator sheet. The electrolyte reservoir was made from $LiPF_6$ (1M) in a mixture of ethylene carbonate/dimethyl carbonate/dimethoxy ethane 1:1:1 (w/w).

Received: March 15, 2005
Published online: June 8, 2005

Keywords: cyclic voltammetry · lithium batteries · nanostructures · self-assembly · vanadates

[1] a) G. Kaltenpoth, M. Himmelhaus, L. Slansky, F. Caruso, M. Grunze, *Adv. Mater.* **2003**, *15*, 1113; b) H. Zeng, J. Li, J. Liu, Z. Wang, S. Sun, *Nature* **2002**, *420*, 395.
[2] a) J. Yuan, K. Laubernds, Q. Zhang, S. L. Suib, *J. Am. Chem. Soc.* **2003**, *125*, 4966; b) M. Yada, C. Taniguchi, T. Torikai, T. Watari, S. Furuta, H. Katsuki, *Adv. Mater.* **2004**, *16*, 1448; c) H. Fan, K. Yang, D. M. Boye, T. Sigmon, K. J. Malloy, H. Xu, G. P. López, C. J. Brinker, *Science* **2004**, *304*, 567; d) P. Gao, Z. Wang, *J. Am. Chem. Soc.* **2003**, *125*, 11299; e) J. Hu, L. Ren, Y. Guo, H. Liang, A. Cao, L. Wan, C. Bai, *Angew. Chem.* **2005**, *117*, 1295; *Angew. Chem. Int. Ed.* **2005**, *44*, 1269.
[3] a) S. A. Jenekhe, X. L. Chen, *Science* **1998**, *279*, 1903; b) O. Ikkala, G. T. Brinke, *Science* **2002**, *295*, 2407; c) H. Duan, M. Kuang, J. Wang, D. Chen, M. Jiang, *J. Phys. Chem. B* **2004**, *108*, 550.
[4] J. Du, Y. Chen, *Angew. Chem.* **2004**, *43*, 5194; *Angew. Chem. Int. Ed.* **2004**, *43*, 5084.
[5] W. Shenton, D. Pum, U. B. Sleytr, S. Mann, *Nature* **1997**, *389*, 585.
[6] G. A. Ozin, *Can. J. Chem.* **1999**, *77*, 2001.
[7] S. Park, J.-H. Lim, S.-W. Chung, C. A. Mirkin, *Science* **2004**, *303*, 348.
[8] a) P. F. Noble, O. J. Cayre, R. G. Alargova, O. D. Velev, V. N. Paunov, *J. Am. Chem. Soc.* **2004**, *126*, 8092; b) A. D. Dinsmore, M. F. Hsu, M. G. Nikolaides, M. Marquez, A. R. Bausch, D. A. Weitz, *Science* **2002**, *298*, 1006.
[9] a) E. Hosono, S. Fujihara, K. Kakiuchi, H. Imai, *J. Am. Chem. Soc.* **2004**, *126*, 7790; b) B. Liu, H. C. Zeng, *J. Am. Chem. Soc.* **2004**, *126*, 8124.
[10] a) H.-J. Muhr, F. Krumeich, U. P. Schönholzer, F. Bieri, M. Niederberger, L. J. Gauckler, R. Nesper, *Adv. Mater.* **2000**, *12*, 231; b) N. Pinna, U. Wild, J. Urban, R. Schlögl, *Adv. Mater.* **2003**, *15*, 329; c) K. Takahashi, S. J. Limmer, Y. Wang, G. Cao, *J. Phys. Chem. B* **2004**, *108*, 9795; d) P. Liu, S.-H. Lee, C. E. Tracy, Y. Yan, J. A. Turner, *Adv. Mater.* **2002**, *14*, 27; e) J. Liu, X. Wang, Q. Peng, Y. Li, *Adv. Mater.* **2005**, *17*, 764; f) G. Gu, M. Schmid, P.-W. Chiu, A. Minett, J. Fraysse, G.-T. Kim, S. Roth, M. Kozlov, E. Munoz, R. H. Baughman, *Nat. Mater.* **2003**, *2*, 316; g) N. Pinna, M. Willinger, K. Weiss, J. Urban, R. Schlögl, *Nano Lett.* **2003**, *3*, 1131.
[11] a) A. Tranchant, R. Messina, J. Perichon, *J. Electroanal. Chem.* **1980**, *113*, 225; b) M. Benmoussa, A. Outzourhit, A. Bennouna, E. L. Ameziane, *Thin Solid Films* **2002**, *405*, 11; c) Y.-T. Kim, S. Gopukumar, K.-B. Kim, B.-W. Cho, *J. Power Sources* **2003**, *117*, 110; d) J. M. Cocciantelli, M. Ménétrier, C. Delmas, J. P. Doumerc, M. Pouchard, M. Broussely, J. Labat, *Solid State Ionics* **1995**, *78*, 143; e) D. W. Murphy, P. A. Christian, F. J. Disalvo, J. V. Waszczak, *Inorg. Chem.* **1979**, *18*, 2800.
[12] M. Ponzi, C. Duschatzky, A. Carrascull, E. Ponzi, *Appl. Catal. A* **1998**, *169*, 373.
[13] J. Livage, *Chem. Mater.* **1991**, *3*, 578.
[14] a) F. Caruso, R. A. Caruso, H. Möhwald, *Science* **1998**, *282*, 1111; b) X. Sun, Y. Li, *Angew. Chem.* **2004**, *116*, 3915; *Angew. Chem.*

 © 2005 Wiley-VCH Verlag GmbH & Co. KGaA, Weinheim

Int. Ed. **2004**, *43*, 3827; c) Q. Peng, Y. Dong, Y. Li, *Angew. Chem.* **2003**, *115*, 3135; *Angew. Chem. Int. Ed.* **2003**, *42*, 3027.

[15] a) Y. Sun, Y. Xia, *Adv. Mater.* **2002**, *14*, 833; b) F. Kim, S. Connor, H. Song, T. Kuykendall, P. Yang, *Angew. Chem.* **2004**, *116*, 3759; *Angew. Chem. Int. Ed.* **2004**, *43*, 3673; c) J. Chen, T. Herricks, M. Geissler, Y. Xia, *J. Am. Chem. Soc.* **2004**, *126*, 10854; d) B. Wiley, T. Herricks, Y. Sun, Y. Xia, *Nano Lett.* **2004**, *4*, 1733; e) Y. Gao, P. Jiang, D. F. Liu, H. J. Yuan, X. Q. Yan, Z. P. Zhou, J. X. Wang, L. Song, L. F. Liu, W. Y. Zhou, G. Wang, C. Y. Wang, S. S. Xie, J. M. Zhang, D. Y. Shen, *J. Phys. Chem. B* **2004**, *108*, 12877.

[16] a) X. Jiang, Y. Wang, T. Herricks, Y. Xia, *J. Mater. Chem.* **2004**, *14*, 695; b) Y. Wang, X. Jiang, Y. Xia, *J. Am. Chem. Soc.* **2003**, *125*, 16176.

[17] T. C. Mo, S. Y. Chen, *Ferroelectrics* **2001**, *259*, 305.

[18] a) J.-H. Park, C. Oh, S.-I. Shin, S.-K. Moon, S.-G. Oh, *J. Colloid Interface Sci.* **2003**, *266*, 107; b) G. Xi, Y. Peng, L. Xu, M. Zhang, W. Yu, Y. Qian, *Inorg. Chem. Commun.* **2004**, *7*, 607.

[19] a) L. Wang, S. Cui, Z. Wang, X. Zhang, *Langmuir* **2000**, *16*, 10490; b) S. W. Kuo, F. C. Chang, *Macromolecules* **2001**, *34*, 5224; c) Y. Zhang, Y. Guan, S. Yang, J. Xu, C. C. Han, *Adv. Mater.* **2003**, *15*, 832.

 © 2005 Wiley-VCH Verlag GmbH & Co. KGaA, Weinheim

Homogeneous Catalysis

Ruthenium-Catalyzed Allylic Alkylation Reactions: Carbonate-Based Catalysts and Intermediates**

René Hermatschweiler, Ignacio Fernández, Frank Breher, Paul S. Pregosin, Luis F. Veiros, and Maria José Calhorda*

Transition-metal-catalyzed allylic alkylation reactions continue to attract attention. This chemistry can be accomplished using a variety of (primarily) late-transition-metal complexes[1–3] and affords high yields of product. In contrast to palladium(II)-catalyzed allylic alkylation reactions,[1] which often afford the linear (less substituted) product, the use of ruthenium-based catalysts affords primarily branched organic products; that is, the nucleophile prefers to attack at the more substituted carbon,[4] immediately adjacent to the phenyl group [Eq. (1) $Cp^* = C_5Me_5$; X = halide or carbonate].

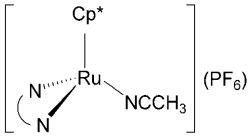
$$PhCH{=}CHCH_2X + Nu^- \xrightarrow[\text{DMF or acetone}]{[Ru(Cp^*)(CH_3CN)_3]PF_6} PhCH(Nu)CH{=}CH_2 + X^- \quad (1)$$

Trost et al.[4] have shown that the cationic tris(nitrile) complex $[Ru(Cp^*)(CH_3CN)_3]PF_6$ (**1**), is an excellent catalyst for the chemistry shown in Equation (1) and that carbonate is the preferred leaving group, X, in terms of the observed regioselectivity.[4] Bruneau et al.[5] have recently reported that the bipyridine derivatives, **2**, are also efficient catalysts. Further, we note that conventional wisdom suggests that an oxidative addition mechanism is operating in this allylation chemistry,[4,6,7] although no explanation for the role of the anion (chloride or carbonate) has been forthcoming.

[*] R. Hermatschweiler, Dr. I. Fernández, Dr. F. Breher, Prof. Dr. P. S. Pregosin
Laboratory of Inorganic Chemistry
ETHZ, Hönggerberg
8093 Zürich (Switzerland)
Fax: (+41) 44-633-1071
E-mail: pregosin@inorg.chem.ethz.ch
Prof. Dr. L. F. Veiros
Centro de Química Estrutural
Complexo I, Instituto Superior Técnico
Av. Rovisco Pais 1, 1049-001 Lisbon (Portugal)
Prof. M. J. Calhorda
Departamento de Química e Bioquímica
Faculdade de Ciências
Universidade de Lisboa, 1749-016 Lisbon (Portugal)

[**] P.S.P. thanks the Swiss National Science Foundation, the "Bundesamt für Bildung und Wissenschaft", and the ETHZ for financial support. I.F. thanks the Junta de Andalucía for a research contract. We also thank Johnson Matthey for the loan of precious metals. We acknowledge the COST working group D24/0014/02.

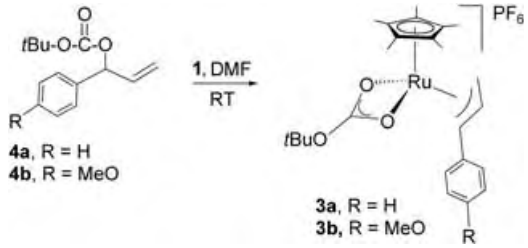
Supporting information for this article (computational details, the corresponding list of references, and the atomic coordinates for the optimized structures) is available on the WWW under http://www.angewandte.org or from the author.



2 (N,N = bipyridine or phenanthroline)

We have recently reported[8] that the source of the observed high branched-to-linear regioselectivity (when X = Cl), has an electronic origin. These findings are based on X-ray crystallography and NMR spectroscopy data, together with DFT calculations. In an extension of this study we show herein that a) the carbonate anion can remain in the coordination sphere of the ruthenium and b) an isolated, well characterized Ru^{IV} allyl carbonate complex is a better catalyst than **1**.

Reaction of the branched *tert*-butyl carbonates **4a** and **4b** (Scheme 1) with **1** in DMF at ambient temperature affords the Ru^{IV} cationic complexes **3a** and **3b**, respectively, in excellent yield.[9]



Scheme 1. Synthesis of the new carbonate complexes, **3a** (R = H) and **3b** (R = OMe).

The solid-state structure[10] of **3b** (Figure 1) reveals the expected distorted piano-stool arrangement of the various ligands in this coordinatively saturated complex. The *tert*-butyl carbonate ligand clearly coordinates in a bidentate fashion through two oxygen atoms, and the allyl ligand shows an *endo* configuration such that the phenyl substituent is remote to the bulky Cp* ligand. Thus the oxidative addition affords the monocationic carbonate and not the bis(acetonitrile) dicationic complex.

The characteristic chemical shifts in the ^1H and ^{13}C NMR spectra[9] of pure **3a** have been recorded and compared to the analogous data from the in situ measurement involving stoichiometric amounts of **1** and the branched *tert*-butyl carbonate. These results show that **3a** is formed immediately on mixing, which indicates that a) the oxidative addition is not likely to be the rate-determining step in the catalysis and b) the isolated carbonate complex is not formed during the work-up procedure.

The reaction between a DMF solution of **3a** and one equivalent of the dimethyl malonate anion (DMM) leads to the formation of a mixture of branched and linear organic products [Eq. (2)]. This reaction shows **3a** to be reactive towards nucleophiles.

$$\mathbf{3a} \xrightarrow[\text{DMF}]{\text{DMM anion (1 equiv)}} \text{organic products, branched-to linear ratio = 70:30} \quad (2)$$

 DOI: 10.1002/anie.200500967 © 2005 Wiley-VCH Verlag GmbH & Co. KGaA, Weinheim

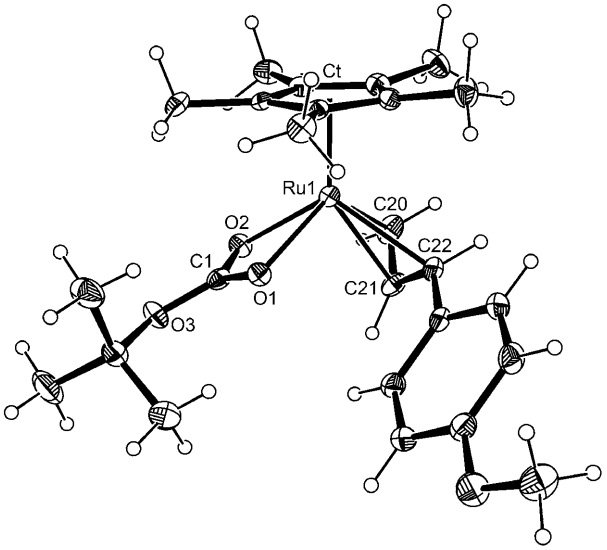
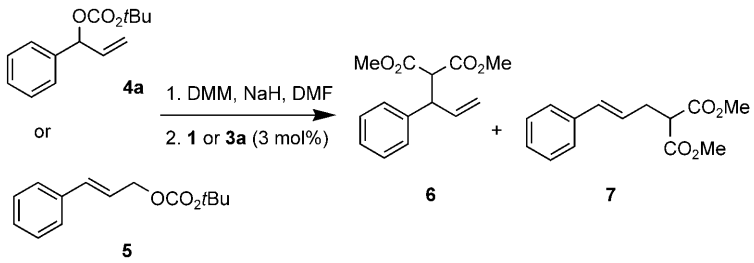


Figure 1. Molecular structure for the cation of **3b**. Thermal ellipsoids are set at 30% probability. The PF_6^- ion has been omitted for clarity. Selected bond lengths [pm] and angles [°]: Ru1-O1 214.8(3), Ru1-O2 211.6(3), Ru1-C20 216.2(5), Ru1-C21 213.7(5), Ru1-C22 230.3(5), Ru1-Ct 183.8(5), C1-O1 126.0(6), C1-O2 127.1(6), C1-O3 131.1(6); O1-C1-O2 117.9(4), O1-C1-O3 125.9(5), O2-C1-O3 116.2(4), C20-C21-C22 116.5(5); $\phi = 32.4°$; Ct = centroid of the Cp* ligand; ϕ is the intersection of the planes described by Ru1, O1, C1, O2 and the atoms of the five-membered Cp* ring.

We have used complex **3a** as a catalyst for the allylic alkylation reaction with dimethyl malonate (Scheme 2, Table 1). With the branched carbonate, **4a**, the reaction was



Scheme 2. Alkylation of branched and linear carbonates by dimethyl malonate/NaH with **1** or **3a** as the catalyst (see Table 1).

25-times faster with complex **3a** than with **1**. Using the linear substrate **5**, the reaction with complex **3a** is only a factor of two faster than **1**.

Table 1: Yields and regioselectivities of the alkylation of **4a** and **5** by dimethyl malonate (see Scheme 2).

Catalyst	Substrate	*t* [min]	Yield [%]	**6**/**7**[a]
1	**5**	40	98	90:10
3a	**5**	20	96	90:10
1	**4a**	25	98	90:10
3a	**4a**	1	97	90:10

[a] The ratio **6**/**7** (branched/linear) was determined by ^{1}H NMR spectroscopy.

We believe the difference between the reactivity of **4a** and **5** is related to the differing stabilities of the η^6-arene complexes formed by these substrates under the reaction conditions.[11] These results suggest that, not only is **3a** a relevant structure in the catalytic cycle, but that the presence of the nitrile ligands in solution, when using catalyst **1**, slows the reaction in Equation (1), presumably as these ligands compete with the olefin for a position on the ruthenium center. We note that for the complexes **2**, Bruneau reports reaction times of around 16 h at ambient temperature whereas with **3a** the reactions are complete within a few minutes.

DFT calculations[12] were carried out on model complexes, where the Cp* ligand was replaced by Cp ($Cp = C_5H_5$), and the *tert*-butyl substituent by a methyl group. Three isomers were considered, namely, an analogue of allyl/carbonates **3a** and **3b**, $[Ru(Cp)\{OC(OMe)O\}(\eta^3\text{-}PhCHCHCH_2)]^+$ (**3′**), and the two ruthenium η^6-arene complexes, **8** (derived from coordination of the linear carbonate, **5**) and **9** (derived from coordination of the branched carbonate **4**). The three optimized structures are represented in Figure 2. The calculated geometry of the carbonate complex **3′** compares well with the experimentally determined structure of **3b** (Figure 1)

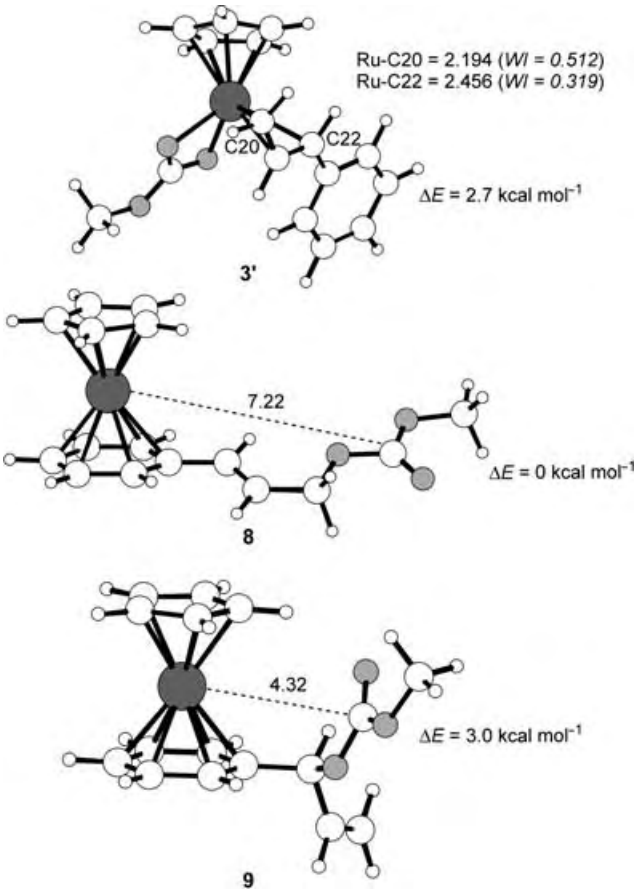


Figure 2. Optimized geometries (B3LYP) of the allyl/carbonate, **3′** and the η^6-arene complexes, **8** (linear carbonate) and **9** (branched carbonate. The Ru and the O atoms are gray and relevant distances [Å], Wiberg indices (italics), and the relative energies of the three isomers are indicated.

 © 2005 Wiley-VCH Verlag GmbH & Co. KGaA, Weinheim

with maximum and mean absolute deviations of 0.15 and 0.07 Å, respectively, for the interatomic distances of the metal coordination sphere.

The coordination of the allyl ligand in **3′** is distorted, and is similar to what was observed for $[Ru(Cp^*)Cl(CH_3CN)(\eta^3\text{-}PhCHCHCH_2)]^+$.[8] The bond length from the metal center to the allyl carbon atom C22 adjacent to the phenyl group is 0.26 Å longer than the corresponding distance to the methylene allyl carbon atom C20. This Ru–C22 distance reflects a weaker bond, as shown by the Wiberg indices (Figure 2), and supported by natural population analysis (NPA) charges[12] (−0.32 for C20 and −0.08 for C22) indicative of a less efficient back-donation from the metal to C22.

Interestingly, both the charges calculated for the allylic carbon atoms and the nature of the LUMO of **3′**, with a larger contribution from C22 than from C20 (Figure 3), are in agreement with the observed preference of nucleophilic attack on C22 and the experimentally observed regioselectivity of the reaction.

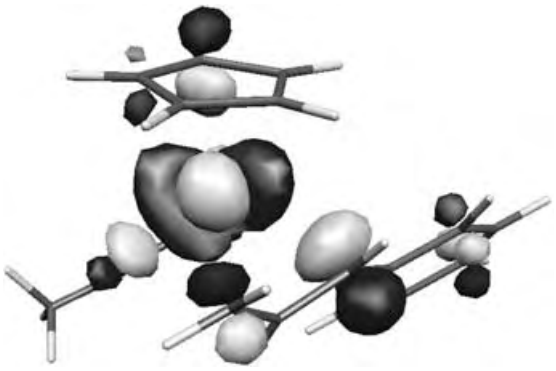


Figure 3. LUMO of **3′**, showing a large contribution from C22 of the allyl ligand.

The calculated relative energies of the isomeric η^6-arene complexes **8** and **9** (Figure 2) indicate that the linear carbonate, **8**, forms a complex which is 3.0 kcal mol^{-1} more stable than the branched analogue, **9**, corroborating the observed differences in reactivity for the corresponding substrates **4a** and **5**. In addition, the geometrical features of the two species might also play a role in the course of the reaction. For the isomer with the branched substrate, **9**, the carbonate group is considerably closer to the metal than in the linear carbonate analogue, **8**. The formation of the allyl/carbonate complex **3′** should hence be considerably easier for **9** than **8**, in agreement with the differences in observed reaction rates. An η^6-arene complex with the branched carbonate could not be detected experimentally.[11]

In conclusion, we have shown that the carbonate anion coordinates to the ruthenium atom, yielding a previously unknown reaction intermediate in the allylic alkylation catalytic sequence. Moreover, when isolated, this ruthenium carbonate species serves as a new, even more efficient catalyst than the reported nitrile complexes, presumably because its use does not lead to the presence of competing ligands in the reaction mixture.

Received: March 16, 2005
Published online: June 16, 2005

Keywords: allylic alkylation · carbonate complex · density functional calculations · ruthenium · structure elucidation

[1] B. M. Trost, M. L. Crawley, *Chem. Rev.* **2003**, *103*, 2921; B. M. Trost, D. L. van Vranken, *Chem. Rev.* **1996**, *96*, 395; H. Tye, *J. Chem. Soc. Perkin Trans. 1* **2000**, 275; L. F. Tietze, H. Ila, P. Bell. *Chem. Rev.* **2004**, *104*, 3453; O. Reiser, *Angew. Chem.* **1993**, *105*, 576; *Angew. Chem. Int. Ed. Engl.* **1993**, *32*, 547.

[2] B. M. Trost, I. Hachiya, *J. Am. Chem. Soc.* **1998**, *120*, 1104; B. M. Trost, N. G. Andersen, *J. Am. Chem. Soc.* **2002**, *124*, 14320.

[3] D. A. Evans, J. D. Nelson, *Tetrahedron Lett.* **1998**, *39*, 1725; D. A. Evans, J. D. Nelson, *J. Am. Chem. Soc.* **1998**, *120*, 5581.

[4] B. M. Trost, P. L. Fraisse, Z. T. Ball, *Angew. Chem.* **2002**, *114*, 1101; *Angew. Chem. Int. Ed.* **2002**, *41*, 1059; B. M. Trost, C. M. Older, *Organometallics* **2002**, *21*, 2544; S. W. Zhang, T. Mitsudo, T. Kondo, Y. Watanabe, *J. Organomet. Chem.* **1993**, *450*, 197–207.

[5] M. D. Mbaye, B. Demerseman, J. L. Renaud, L. Toupet, C. Bruneau, *Angew. Chem.* **2003**, *115*, 5220; *Angew. Chem. Int. Ed.* **2003**, *42*, 5066.

[6] T. Kondo, H. Ono, N. Satake, T. Mitsudo, Y. Watanabe, *Organometallics* **1995**, *14*, 1945; H. Kondo, Y. Yamaguchi, H. Nagashima, *Chem. Commun.* **2000**, 1075.

[7] K. Onitsuka, Y. Ajioka, Y. Matsushima, S. Takahashi, *Organometallics* **2001**, *20*, 3274; Y. Matsushima, K. Onitsuka, S. Takahashi, *Organometallics* **2004**, *23*, 3763.

[8] R. Hermatschweiler, I. Fernández, P. S. Pregosin, E. J. Watson, A. Albinati, S. Rizzato, L. F. Veiros, M. J. Calhorda, *Organometallics* **2005**, *24*, 1809.

[9] Synthesis of **3a**. $[RuCp^*(CH_3CN)_3]PF_6$ (64 mg, 0.128 mmol) and **4a** (30 mg, 0.128 mmol) were stirred in DMF (3 mL) for 30 min at room temperature. The solution volume was reduced in vacuum and diethyl ether was added precipitating an orange-brown powder. The solid was washed with diethyl ether and dried under vacuum to yield 74 mg (94%) of the crude product. ^{1}H NMR (500 mHz, [D$_7$]DMF, 298 K): $\delta = 1.53$ (9H), 1.72 (15H), 3.52 (1H, $J = 10$ Hz), 4.66 (1H, $J = 6.5$ Hz), 5.11 (1H, $J = 11.0$ Hz), 6.36 (1H, $J = 11.0$, 10.0, 6.5 Hz), 7.42 (2H, $J = 7.7$, 7.3 Hz), 7.62 (1H, $J = 7.7$ Hz), 7.74 ppm (2H, $J = 7.3$ Hz); ^{13}C NMR (126 mHz, [D$_7$]DMF, 298 K): $\delta = 8.8$ (CH_3), 28.2 (CH_3), 65.8 (H_2C_{allyl}), 85.9 (C), 90.2 (HC_{allyl}), 99.9 (HC_{allyl}), 107.2 (C), 129.2 (HCAr), 130.5 (HCAr), 130.8 (HCAr), 135.2 (C_{ipso}), 164.4 ppm (CO_3). Elemental analysis (%) calcd for $C_{24}H_{33}O_3F_6PRu$: C 46.83, H 5.40; found: C 46.15, H 5.25. ESI MS: 471.2 [M^+], 427.2 [M^+-CO_2], 371.2, 353.2 [$M^+-C_5H_9O_3$, $M^+-C_9H_9$]. Synthesis of **3b**. $[RuCp^*(CH_3CN)_3]PF_6$ (55 mg, 0.110 mmol) and **4b** (29 mg, 0.110 mmol) were stirred in DMF (3 mL) for 30 min at room temperature. The solution volume was reduced in vacuum and diethyl ether was added precipitating an orange-red powder. The solid was washed with diethyl ether and dried under vacuum to yield 67 mg (95%) of the crude product. ^{1}H NMR (500 mHz, [D$_7$]DMF, 298 K): $\delta = 1.53$ (9H), 1.70 (15H), 3.50 (1H, $J = 9.6$ Hz), 4.61 (1H, $J = 6.4$ Hz), 5.21 (1H, $J = 11.1$ Hz), 6.20 (1H, $J = 11.1$, 9.6, 6.4 Hz), 7.00 (2H, $J = 8.6$ Hz), 7.71 ppm (2H, $J = 8.6$ Hz); ^{13}C NMR(126 mHz, [D$_7$]DMF, 298 K): $\delta = 8.8$ (CH_3), 28.3 (CH_3), 55.7 (OCH_3), 65.3 (H_2C_{allyl}), 85.7 (C), 93.2 (HC_{allyl}), 98.6 (HC_{allyl}), 106.3 (C), 114.8 (HCAr), 127.1 (C_{ipso}), 132.8 (HCAr), 162.0 (C_{ipso}), 164.3 ppm (CO_3). Elemental analysis (%) calcd for $C_{25}H_{35}O_4F_6PRu$: C

 © 2005 Wiley-VCH Verlag GmbH & Co. KGaA, Weinheim

46.51, H 5.46; found: C 46.31, H 5.40. ESI MS: 501.1 [M^+], 457.2 [M^+-CO_2], 401.1, 383.1 [$M^+-C_5H_9O_3$), 353.3 [$M^+-C_{10}H_{11}O$]. Catalysis: Dimethyl malonate (76 μL, 0.65 mmol) and NaH (26 mg, 0.64 mmol, 60 % dispersion in mineral oil) were stirred in DMF (1.5 mL) for 30 min at room temperature, after which time the carbonate **4a** or **5** (0.21 mmol) and the catalyst **1** or **3a** (0.02 mmol, 3 mol %) were added. The resulting solution was stirred at room temperature (see Table 1 for reaction times) and then diluted with diethyl ether and water (ca. 10 mL). After three extractions with diethyl ether, the combined organic extracts were washed with water and brine, dried over $MgSO_4$,and concentrated. The crude product was purified by chromatography on silica gel (hexane/ethyl acetate 6/1). The branched/linear ratio was determined by ^{1}H NMR spectroscopy.

[10] Crystal structure of **3b**: Orange single crystals were obtained from a CH_2Cl_2 solution of **3b** which was layered with *n*-pentane; $C_{25}H_{35}F_6O_4PRu$, orthorhombic, space group *Pbca*; $a = 11.030(1)$, $b = 21.378(2)$, $c = 23.626(2)$ Å; $V = 5570.9(7)$ Å^3; $Z = 8$; $\rho_{calcd} = 1.539$ Mg m^{-3}; crystal dimensions $0.58 \times 0.23 \times 0.13$ mm; diffractometer Bruker SMART Apex; $Mo_{K\alpha}$ radiation, 200 K, $2\Theta_{max} = 49.42°$; 41 497 reflections, 4749 independent ($R_{int} = 0.0451$), direct methods; empirical absorption correction SADABS (v. 2.03); refinement against full matrix (versus F^2) with SHELXTL (v. 6.12) and SHELXL-97, 343 parameters, $R1 = 0.0596$ and w$R2$ (all data) = 0.1231, max./min. residual electron density 0.877/ −1.067 e Å^{-3}. The hydrogen atoms were placed in idealized positions and included as riding atoms. CCDC-265478 (**3b**) contains the supplementary crystallographic data for this paper. These data can be obtained free of charge from the Cambridge Crystallographic Data Centre via www.ccdc.cam.ac.uk/data_request/cif.

[11] Starting from substrate **5**, several 18-electron η^6-arene Ru^{II} complexes of the type, [Ru(Cp*)(η^6-$RC_6H_4CH{=}CHCH_2OC$(O-*t*Bu)O)]PF_6 where R is a *para* substituent can be isolated. This type of arene complex is well known, see *Organometallics* (Eds.: C. Elschenbroich, A. Salzer), 2nd ed., VCH, Weinheim, **1992**, pp. 356–357. However, for the analogous reactions using branched carbonate **4**, the oxidative addition reaction is too rapid for us to isolate the η^6-arene complex.

[12] DFT calculations were performed with the Gaussian 98 software package using the B3LYP hybrid functional. The basis set used for the geometry optimizations (VDZP) included a standard LanL2DZ augmented with a polarization function for Ru and 4-31G(d) for the other atoms. Single point energies were calculated for the optimized complexes using the same functional and a VTZP basis set: SDD with a polarization function for Ru and 6-311G(d,p) for the remaining elements. The atomic charges and Wiberg indices resulted from a Natural Population Analysis (NPA). Computational details and the corresponding list of references are given in the Supporting Information.

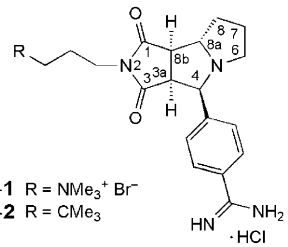
 © 2005 Wiley-VCH Verlag GmbH & Co. KGaA, Weinheim

Molecular Recognition

Quantification of Cation–π Interactions in Protein–Ligand Complexes: Crystal-Structure Analysis of Factor Xa Bound to a Quaternary Ammonium Ion Ligand**

Kaspar Schärer, Martin Morgenthaler, Ralph Paulini, Ulrike Obst-Sander, David W. Banner, Daniel Schlatter, Jörg Benz, Martine Stihle, and François Diederich**

In our molecular recognition studies, aimed at quantifying the energetics of individual protein–ligand interactions,[1] we became interested in exploring cation–π interactions[2,3] in the D-pocket of thrombin, a central serine protease in the blood coagulation cascade. The bottom of this hydrophobic pocket is lined by the indole residue of Trp215 (Figure 1), an aromatic amino acid side chain frequently involved in cation–π interactions in biological systems.[4] To probe this interaction, we prepared the tricyclic inhibitors[5] (±)-**1** and (±)-**2**, predicted by computer modeling[6] to position a quaternary ammonium ion and an uncharged *tert*-butyl group above the indole ring of Trp215.



(±)-**1** R = NMe_3^+ Br^-
(±)-**2** R = CMe_3

The synthesis of (±)-**1** started with the 1,3-dipolar cycloaddition between maleimide **3**, aldehyde **4**, and L-proline (**5**) to give (±)-**6**, which was transformed into amidinium salt (±)-**7** using a Pinner-reaction (Scheme 1, for full experimen-

[*] Dr. U. Obst-Sander, Dr. D. W. Banner, Dr. D. Schlatter, Dr. J. Benz, M. Stihle
Pharma Division
Präklinische Forschung
F. Hoffmann-La Roche AG
4070 Basel (Schweiz)
E-mail: david.banner@roche.com
Dr. K. Schärer, M. Morgenthaler, R. Paulini, Prof. Dr. F. Diederich
Laboratorium für Organische Chemie
ETH Hönggerberg
HCI, 8093 Zürich (Switzerland)
Fax: (+41) 1-632-1109
E-mail: diederich@org.chem.ethz.ch

[**] This work was supported by a grant from the ETH Research Council and by F. Hoffmann-La Roche, Basel. We thank Olivier Kuster, Dr. Thomas Tschopp, and Dr. Alain Gast for the biological assays as well as Dr. Michael Hennig for his support of this work.

Supporting information for this article is available on the WWW under http://www.angewandte.org or from the author.

 © 2005 Wiley-VCH Verlag GmbH & Co. KGaA, Weinheim DOI: 10.1002/anie.200500883

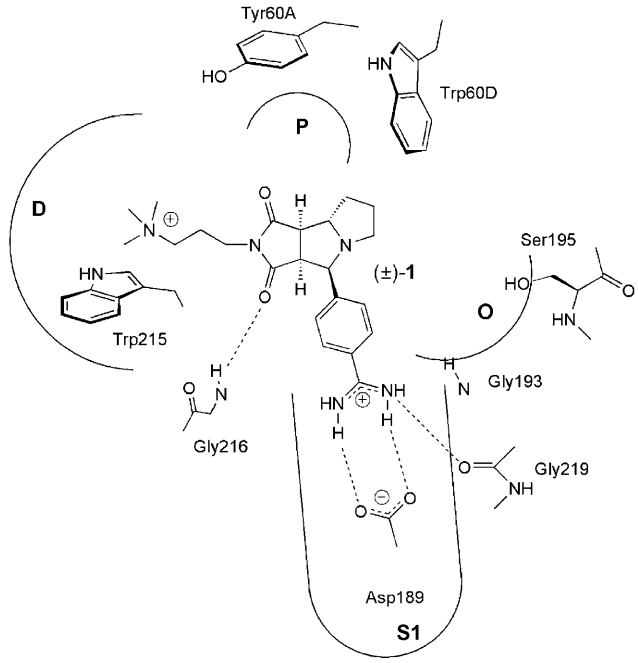
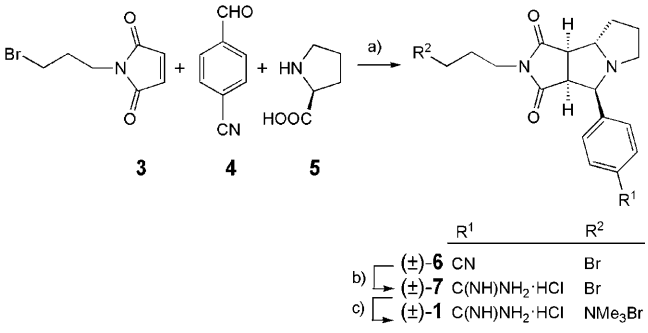


Figure 1. Schematic representation of the binding mode of the designed inhibitor (±)-**1** in the active site of thrombin. Only the 3a*S*,4*R*,8a*S*,8b*R* configured enantiomer is predicted to bind.[5] Reference inhibitor (±)-**2** is predicted by computer modeling to adopt a similar binding mode.



Scheme 1. Synthesis of inhibitor (±)-**1**. a) MeCN, 80 °C, 32%; b) 1. HCl, MeOH, $CHCl_3$, 4 °C; 2. NH_4Cl, MeOH, H_2O, 65 °C, 60%; c) Me_3N, MeOH, RT, 90%.

tal details, see Supporting Information). Nucleophilic substitution with Me_3N subsequently afforded (±)-**1**. The synthesis of reference compound (±)-**2** followed a similar route (see Supporting Information).

The activities of inhibitors (±)-**1** and (±)-**2** were tested, as previously described,[7] towards thrombin, the digestive enzyme trypsin, and two other serine proteases from the blood coagulation cascade, Factor VIIa and Factor Xa (Table 1), representing targets in the treatment of thrombotic diseases.[8] No inhibition of Factor VIIa was observed within the limits of the assay, and the binding of both ligands to trypsin was of similar, moderate strength. In contrast, their affinities against thrombin and Factor Xa differ greatly.

The onium ion inhibitor (±)-**1** showed a much lower activity ($K_i = 7.76$ μM) towards thrombin than the reference

Table 1: Activities (inhibition constants K_i [μM]) of inhibitors (±)-**1** and (±)-**2**.

Inhibitor	K_i [μM]			
	thrombin	trypsin	Factor VIIa	Factor Xa
(±)-**1**	7.76	10.5	> 69[a]	0.28
(±)-**2**	0.13	7.1	> 69[a]	29

[a] Upper limit of the assay.

compound (±)-**2** ($K_i = 0.13$ μM). According to molecular modeling,[6] the large difference in activity (K_i(**1**)/K_i(**2**) = 60 and $\Delta\Delta G = 2.5$ kcal mol^{-1} in favor of the *tert*-butyl inhibitor) cannot be explained by different binding geometries of the two imide-N substituents in the hydrophobic D-pocket.[5] Rather, the data suggest that cation–π interactions between the onium ion of (±)-**1** and a single indole residue (of Trp215) are not very effective and cannot compensate the costs of desolvation of the ionic residue upon incorporation into the D-pocket. Such desolvation costs do not occur in the complexation of a *tert*-butyl residue, and (±)-**2** binds with an affinity similar to that of other inhibitors of this class, which direct large aliphatic residues into the D-pocket.[9a]

In contrast, inhibitor (±)-**1** shows good activity towards Factor Xa ($K_i = 0.28$ μM) while the activity of reference compound (±)-**2** is very low ($K_i = 29$ μM). Thus, towards Factor Xa, the difference in activities (K_i(**2**)/K_i(**1**) = 100, $\Delta\Delta G = 2.8$ kcal mol^{-1}) is even more distinctive than in thrombine but in the opposite sense, favoring onium ion recognition.[10] Again, modeling suggested nearly identical binding modes for both inhibitors. To elucidate the origin of the strong complexation of the onium ion, the X-ray crystal structure of (±)-**1**, co-crystallized with Factor Xa, was measured at a resolution of 1.64 Å (Figure 2).[11]

In the structure, the 3a*S*,4*R*,8a*S*,8b*R* configured enantiomer of (±)-**1** (*ent*-**1**) adopts a binding geometry at the active site of Factor Xa similar to that predicted for the related serine protease thrombin.[9b] The phenylamidinium residue is incorporated in the S1 pocket, and interacts with the carboxylate side chain of Asp189 (*d*(N···O) 3.2 and 3.3 Å), and the "lower" imide-C=O unit undergoes hydrogen bonding to the backbone-NH group of Gly216 (*d*(O···N 3.1 Å). The tricyclic scaffold of *ent*-**1** occupies the central cavity of Factor Xa (Figure 2b).

As expected from computer modeling, the quaternary ammonium ion of *ent*-**1** binds in the S4-pocket of Factor Xa, which is lined by Trp215, Tyr99, and Phe174. The three side chains form an "aromatic box", with the onium ion located in its center. The shortest distances between the N^+ center and closest C atoms of the surrounding aromatic rings are nearly ideal (4.6 to 5.0 Å, Figure 2a) for strong cation–π interactions (see below).

A survey of the literature shows that the S4-pocket of Factor Xa has indeed been filled many times by basic residues. Examples are 4-amino-substituted pyridines, piperazines, pyrrolidines, amidines and phenylamidines, imidazoles and imidazolines, and benzylamines.[12] We presume that the positively charged residues occupy the cation binding site in the aromatic box in their protonated form. The occupation of

 © 2005 Wiley-VCH Verlag GmbH & Co. KGaA, Weinheim

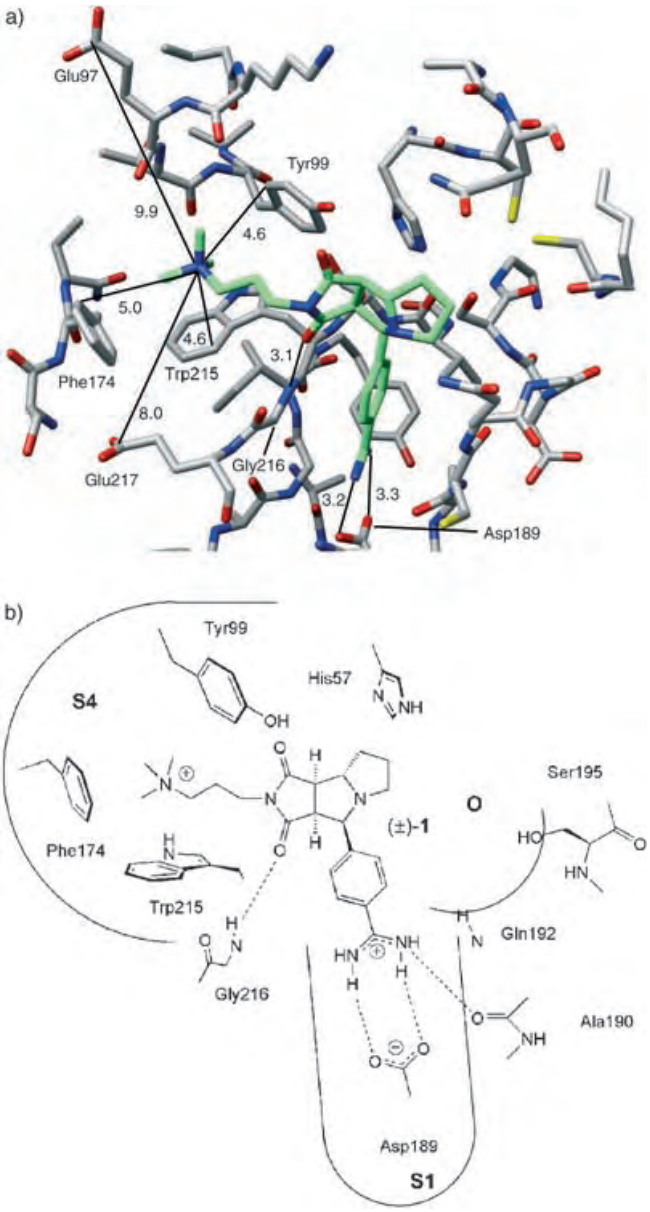


Figure 2. a) Binding mode of inhibitor (3a*S*,4*R*,8a*S*,8b*R*)-**1** in the active site of Factor Xa according to X-ray crystal-structure analysis. Interatomic distances are in Å. Shortest distances between onium ion methyl carbon atoms and carbon atoms of the aromatic box are 3.9 Å (to Tyr 99), 3.9 Å (to Phe 174), and 3.6 Å (to Trp 215); red O, blue N, yellow S, green C_{ligand}, gray $C_{protein}$, b) Schematic representation of the complex between Factor Xa and the active enantiomer of (±)-**1**.

the S4-pocket by an *N*,*N*,*N*-trimethylanilinium residue has also been reported.[13]

In some complexes, the side chains of Glu 97 or Glu 217 in Factor Xa undergo weak ion pairing with phenylamidinium ions occupying the S4-pocket.[12a,13] However, in the large majority of cases, the two carboxylate groups are located at positions remote from the cationic site and are oriented towards the solvent, as seen in the complex of Factor Xa with *ent*-**1** ($d(N\cdots CO_2^-)_{Glu\,97}$ 9.9 Å, $d(N\cdots CO_2^-)_{Glu217}$ 8.0 Å). Thus, Coulombic interactions with the two carboxylate groups are not at the origin of the preference of the S4-pocket for cationic residues.

From these results a new interpretation arises concerning the special feature of this pocket to accept basic residues: in their protonated form, these residues undergo efficient cation–π interactions with the aromatic box formed by Tyr 99, Trp 215, and Phe 174. The difference in binding free enthalpy of $\Delta\Delta G = 2.8$ kcal mol^{-1} favoring (±)-**1** over (±)-**2** corresponds to an averaged value of about 0.9 kcal mol^{-1} per aromatic ring. This value is in accordance with those reported for cation–π interactions with individual aromatic rings.[14] Despite the large free enthalpy increment for the interaction with a single aromatic ring, the results obtained in this work for the D-pocket of thrombin suggest that efficient cation–π interactions require the "solvation" of the cation by several aromatic rings.

Inspired by these results, we performed Protein Data Bank (PDB) searches[15] to identify similar aromatic boxes for the complexation of ammonium ions. Figure 3 shows examples for quaternary ammonium ions bound to different proteins. Figure 3a depicts the already mentioned trimethylanilinium residue in the S4-pocket of Factor Xa (PDB-code: 1LPK).[13] The distances of the N^+ center to the three aromatic rings are very close to those found in our study. Figure 3b features histone H3 permethylated at Lys 27 in the polycomb chromodomain of *Drosophila* (1PFB),[16] while Figure 3c shows an N,N-dimethylated proline in the periplasmic ligand binding protein ProX from *E. Coli* (1R9Q).[17] At least one of the three side chains forming the aromatic boxes shown in Figure 3a–c is a Trp residue. The orientation of the cationic center is always close to the normals passing through the centroids of the aromatic planes which provides for optimal interactions with the π systems. Figure 3d shows a box of four aromatic side-chains from human phosphatidylcholine transfer protein complexed with the choline moiety of its substrate

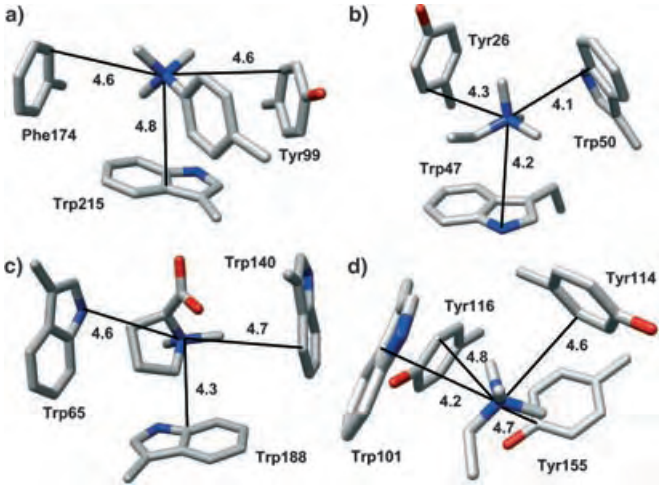


Figure 3. Examples from PDB searches showing quaternary ammonium ions bound in the S4-pocket of Factor Xa (a) and in similar aromatic boxes of other proteins (b–d). The shortest ligand–protein distances are indicated in Å; red O, blue N, gray C. PDB-codes: a) 1LPK, b) 1PFB, c) 1R9Q, d) 1LN3. See text for details.

 © 2005 Wiley-VCH Verlag GmbH & Co. KGaA, Weinheim

(1LN3).[18] Similar to the previous structures, the cationic center is located near the centroid normals of the π systems of Trp 101 and Tyr 155. In contrast, the ring planes of Tyr 114 and Tyr 116 are slightly twisted. Their normals are not oriented perfectly towards the cation. Apparently, in this example, the loss of interactions caused by the twisted orientation of these side-chains is compensated by the presence of a fourth aromatic residue. In all the structures shown in Figure 3 the shortest distances between the N^+ center and the aromatic side chains are between 4–5 Å ($d(N^+\cdots C_{arom})$), which seems to be the optimal separation for quaternary ammonium ion–π interactions. For further examples of quaternary ammonium ions in aromatic boxes, see Figures 5–9 in the Supporting Information.

The PDB search was extended to protonated tertiary ammonium ions complexed in aromatic boxes within proteins (Figure 4). Again, the cations are close to the centroid normals of the aromatic rings. An additional interesting feature is the presence of a hydrogen bond formed on the open side of the aromatic box between R_3NH^+ and an acceptor residue of the protein, which results in additional stabilization. This hydrogen bonding is sometimes mediated by a water molecule. Examples are the structure of a (protonated) tertiary amine inhibitor bound to oxidosqualene cyclase (Figure 4a; 1H37),[19] the complex of a protonated N,N-dimethylated lysine residue of a histone in the HP1 chromodomain of *Drosophila* (Figure 4b; 1KNA),[20] the complex of morphine in the antibody 9B1 (Figure 4c; 1Q0Y),[21] and the complex of nicotine in a nicotinic ACh receptor (Figure 4d; 1UW6).[22] Similarly, some of the protonated onium ions in the S4-pocket of Factor Xa not only interact with the aromatic box but also form hydrogen bonds to neighboring polar residues or H_2O molecules.[12a,f] Interestingly, protonated secondary ammonium ions are not found in such arrangements, presumably because of high desolvation costs.

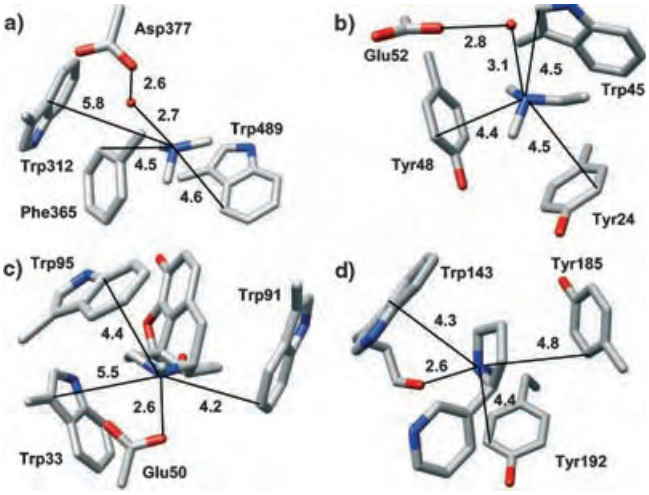


Figure 4. Examples from PDB searches showing protonated tertiary ammonium ions bound in aromatic boxes. The shortest ligand–protein distances are indicated in Å; red O, blue N, gray C. PDB-codes: a) 1H37, b) 1KNA, c) 1Q0Y, d) 1UW6.

Cation–π interactions are also seen in crystal packings of small molecules, although steric factors and the requirements of a dense crystal packing in these cases prevent the formation of aromatic boxes. A search of the Cambridge Structural Database (CSD) for close contacts between tetraalkylammonium ions and arene units furnished 22 examples, seven of which displayed a second close contact to another aromatic residue.[23] As in the case of the protein examples, cations were located close to the centroid normals of the arene systems. A selection of examples is included in Figure 10 in the Supporting Information.

In conclusion, we have shown by biological assays and protein crystallography that the aromatic box formed by the side chains of Phe 174, Tyr 99, and Trp 215 in the S4-pocket of Factor Xa is a very effective onium binding site. By comparing the affinity of the quaternary ammonium ion receptor (±)-**1** to that of the *tert*-butyl derivative (±)-**2**, the free enthalpy increment for cation–π interactions in this box was determined as $\Delta\Delta G = 2.8\ kcal\,mol^{-1}$. PDB searches revealed the more general occurrence of similar cation binding sites in biological systems; hence the observations made in this investigation should provide useful guidance in lead design and optimization.

Received: March 9, 2005
Published online: June 13, 2005

Keywords: cation–pi interactions · Factor Xa · inhibitors · molecular recognition · thrombin

[1] F. Hof, F. Diederich, *Chem. Commun.* **2004**, 477–480.
[2] a) N. Zacharias, D. A. Dougherty, *Trends Pharmacol. Sci.* **2002**, *23*, 281–287; b) J. C. Ma, D. A. Dougherty, *Chem. Rev.* **1997**, *97*, 1303–1324; c) D. A. Dougherty, *Science* **1996**, *271*, 163–168; d) D. A. Dougherty, D. A. Stauffer, *Science* **1990**, *250*, 1558–1560.
[3] For a recent review, see: E. A. Meyer, R. K. Castellano, F. Diederich, *Angew. Chem.* **2003**, *115*, 1244–1287; *Angew. Chem. Int. Ed.* **2003**, *42*, 1210–1250.
[4] P. Gallivan, D. A. Dougherty, *Proc. Natl. Acad. Sci. USA* **1999**, *96*, 9459–9464.
[5] Members of this class of inhibitors show nearly identical binding geometries in the structurally well-defined active site of thrombin; see: a) K. Schärer, M. Morgenthaler, P. Seiler, F. Diederich, *Helv. Chim. Acta* **2004**, *87*, 2517–2538; b) J. A. Olsen, D. W. Banner, P. Seiler, U. Obst-Sander, A. D'Arcy, M. Stihle, K. Müller, F. Diederich, *Angew. Chem.* **2003**, *115*, 2611–2615; *Angew. Chem. Int. Ed.* **2003**, *42*, 2507–2511; c) U. Obst, D. W. Banner, L. Weber, F. Diederich, *Chem. Biol.* **1997**, *4*, 287–295.
[6] a) P. R. Gerber, K. Müller, *J. Comput.-Aided Mol. Des.* **1995**, *9*, 252–268; b) Gerber Molecular Design (http://www.moloc.ch).
[7] For thrombin: K. Hilpert, J. Ackermann, D. W. Banner, A. Gast, K. Gubernator, P. Hadvary, L. Labler, K. Müller, G. Schmid, T. B. Tschopp, H. van de Waterbeemd, *J. Med. Chem.* **1994**, *37*, 3889–3901. For Factor Xa: Kinetic enzyme inhibition test exposing a chromogenic substrate (S) (S-2222 $K_m = 316\ \mu M$) at 200 μM to human Factor Xa (3 nM) in microtiter plates at room temperature in the presence of buffer pH 7.8 (2-[4-(2-hydroxyethyl)-1-piperazinyl] ethanesulfonic acid (HEPES) 100 mM, NaCl 140 mM, poly(ethylene glycol) $M_w = 6000$ (PEG 6000) 0.1%, Tween 80 0.2%), or various concentrations of inhibitor. The K_i-value is calculated $[K_i = IC_{50}/(1+(S/K_m))]$ from the IC_{50}

 © 2005 Wiley-VCH Verlag GmbH & Co. KGaA, Weinheim

determined graphically from a dose-response curve of the inhibitor.

[8] E. W. Davie, K. Fujikawa, W. Kisiel, *Biochemistry* **1991**, *30*, 10363 – 10370.

[9] a) U. Obst, P. Betschmann, C. Lerner, P. Seiler, F. Diederich, V. Gramlich, L. Weber, D. W. Banner, P. Schönholzer, *Helv. Chim. Acta* **2000**, *83*, 855 – 909; b) Only the enantiomer *ent*-**1** which has the same absolute configuration required for thrombin binding is bound by Factor Xa. For a study of enantiomerically pure tricyclic thrombin inhibitors, see refs. [5a] and [5c].

[10] D. Monnaie, D. Arosio, N. Griffon, T. Rose, A. R. Rezaie, E. Di Cera, *Biochemistry* **2000**, *39*, 5349 – 5354.

[11] For protein expression and purification, see the Supporting Information. Crystallization and structure determination: A solution of short-form Factor Xa (15 mg mL^{-1}) was incubated overnight with ligand (3.8 mM) prior to crystallization. The protein–ligand complex was mixed with an equal volume of crystallization buffer (0.2 M NH_4OAc, 0.1 M 2-[2,2′-bis(hydroxylethyl)amino]-2-hydroxymethyl-1,3-propanediol(Bis-Tris) pH 5.5, and 25% PEG 3350) in microbatch mode. Crystals appeared after a week and grew to full size within two weeks. Before data collection, crystals were transferred to crystallization buffer supplemented with 20% glycerol and flash-frozen in liquid N_2. Diffraction data were measured on a Bruker FR591 X-ray generator, with 0.2 mm focus, run at 50 kV/60 mA and equipped with an Osmic focusing monochromator and an Oxford Cryostream cooler run at 100 K. The Marresearch345 (dtb) image plate detector was placed 110 mm from the crystal and scanned with 0.15 mm pixel size. Exposure times were 600 s for 0.5° frames. Data from 262 frames were processed to 1.62 Å resolution using XDS (W. Kabsch, *J. Appl. Crystallogr.* **1993**, *26*, 795 – 800). Space group $P2_12_12_1$; unit cell dimensions $a=48.84$, $b=71.67$, and $c=72.75$ Å. For 163433 measured reflections 32725 were independent, R factor 6.1% (37.4% in the outermost shell, 1.62–1.71 Å), with completeness 98.7% (97.1%) and I/σ 15.5 (4.3). Data reduction used the CCP4 package ("The CCP4 Suite: Programs for Protein Crystallography" *Acta Crystallogr. Sect. D* **1994**, *50*, 760–763). The structure was solved by molecular replacement using 1c5m.pdb as model. Model building with Moloc[6] and refinement with Refmac5 (G. N. Murshudov, A. A. Vagin, E. J. Dodson, *Acta Crystallogr. Sect. D* **1997**, *53*, 240 – 255) to 1.64 Å resolution gave final overall crystallographic R factors of 20.4% (observed) and 23.7% (total), with values in the outer shell (1.64–1.68 Å) of 28.6% and 29.7%, respectively, for 2421 atoms, including one Na^+ ion and 276 H_2O molecules. The inhibitor density is very clear. Coordinates have been deposited with the Protein Data Bank, PDB-code: 2bok.

[12] For selected crystal structures, see: a) S. Maignan, J.-P. Guilloteau, Y. M. Choi-Sledeski, M. R. Becker, W. R. Ewing, H. W. Pauls, A. P. Spada, V. Mikol, *J. Med. Chem.* **2003**, *46*, 685 – 690 (PDB-codes: 1NFU, 1NFW, 1NFX, 1NFY); b) H. Nishida, Y. Miyazaki, T. Mukaihira, F. Saitoh, M. Fukui, K. Harada, M. Itoh, A. Muraoka, T. Matsusue, A. Okamoto, Y. Hosaka, M. Matsumotu, S. Ohnishi, H. Mochizuki, *Chem. Pharm. Bull.* **2002**, *50*, 1187 – 1194 (PDB-codes: 1IQE, 1IQF, 1IQG, 1IQH, 1IQI, 1IQJ, 1IQK, 1IQL, 1IQM, 1IQN); c) S. Maignan, J.-P. Guilloteau, S. Pouzieux, Y. M. Choi-Sledeski, M. R. Becker, S. I. Klein, W. R. Ewing, H. W. Pauls, A. P. Spada, V. Mikol, *J. Med. Chem.* **2000**, *43*, 3226 – 3232 (PDB-codes: 1F0R, 1F0S, 1EZQ); d) M. Adler, D. D. Davey, G. B. Phillips, S.-H. Kim, J. Jancarik, G. Rumennik, D. R. Light, M. Whitlow, *Biochemistry* **2000**, *39*, 12534 – 12542 (PDB-code 1FJS); e) K. Kamata, H. Kawamoto, T. Honma, T. Iwama, S.-H. Kim, *Proc. Natl. Acad. Sci. USA* **1998**, *95*, 6630 – 6635 (PDB-code: 1XKA); f) H. Brandstetter, A. Kühne, W. Bode, R. Huber, W. von der Saal, K. Wirthensohn, R. A. Engh, *J. Biol. Chem.* **1996**, *271*, 29988 – 29992 (PDB-code: 1FAX); g) A positively charged residue placed in the D-pocket (thrombin) or S4-pocket (Factor Xa) of the enzymes was predicted to increase inhibitor selectivity for Factor Xa over thrombin in a computational GRID/CPCA analysis of the corresponding enzyme active sites. However, in contrast to the results of the computational study, the binding data for (±)-**2** suggest that the analogous introduction of uncharged hydrophobic groups leads to selective inhibitors of thrombin rather than Factor Xa; M. A. Kastenholz, M. Pastor, G. Cruciani, T. Fox, *J. Med. Chem.* **2000**, *43*, 3033 – 3044.

[13] H. Matter, E. Defossa, U. Heinelt, P.-M. Blohm, D. Schneider, A. Müller, S. Herok, H. Schreuder, A. Liesum, V. Brachvogel, P. Lönze, A. Walser, F. Al-Obeidi, P. Wildgoose, *J. Med. Chem.* **2002**, *45*, 2749 – 2769 (PDB-codes: 1LPG, 1LPK).

[14] For the energetics of cation–π interactions, see: a) refs. [2–4]; b) D. L. Beene, G. S. Brandt, W. Zhong, N. M. Zacharias, H. A. Lester, D. A. Dougherty, *Biochemistry* **2002**, *41*, 10262 – 10269.

[15] a) M. Hendlich, A. Bergner, J. Günther, G. Klebe, *J. Mol. Biol.* **2003**, *326*, 607 – 620; b) J. Günther, A. Bergner, M. Hendlich, G. Klebe, *J. Mol. Biol.* **2003**, *326*, 621 – 636. PDB searches were performed using Relibase 1.2.1 (March 2003). All database entries containing ligands possessing quaternary ammonium ions (263 structures), tertiary (1024 structures), and secondary (1594 structures) amines were retrieved together with their binding sites and examined by visual inspection. Molecular graphics images were produced using the UCSF Chimera package from the Computer Graphics Laboratory, University of California, San Francisco (supported by NIH P41RR-01081). http://www.cgl.ucsf.edu/chimera E. F. Pettersen, T. D. Goddard, C. C. Huang, G. S. Couch, D. M. Greenblatt, E. C. Meng, T. E. Ferrin, *J. Comput. Chem.* **2004**, *25*, 1605 – 1612.

[16] J. Min, Y. Zhang, R.-M. Xu, *Genes Dev.* **2003**, *17*, 1823 – 1828. PDB-code: 1PFB.

[17] A. Schiefner, J. Breed, L. Bösser, S. Kneipl, J. Gade, G. Holtmann, K. Diederichs, W. Welte, E. Bremer, *J. Biol. Chem.* **2004**, *279*, 5588 – 5596. PDB-code: 1R9Q.

[18] S. L. Roderick, W. W. Chan, D. S. Agate, L. R. Olsen, M. W. Vetting, K. R. Rajashankar, D. E. Cohen, *Nat. Struct. Biol.* **2002**, *9*, 507 – 511. PDB-code: 1LN3.

[19] A. Lenhart, D. J. Reinert, J. D. Aebi, H. Dehmlow, O. H. Morand, G. E. Schulz, *J. Med. Chem.* **2003**, *46*, 2083 – 2092. PDB-code: 1H37.

[20] S. A. Jacobs, S. Khorasanizadeh, *Science* **2002**, *295*, 2080 – 2083. PDB-code: 1KNA.

[21] E. Pozharski, M. A. Wilson, A. Hewagama, A. B. Shanafelt, G. Petsko, D. Ringe, *J. Mol. Biol.* **2004**, *337*, 691 – 697. PDB-code: 1Q0Y.

[22] P. H. N. Celie, S. E. van Rossum-Fikkert, W. J. van Dijk, K. Brejc, A. B. Smit, T. K. Sixma, *Neuron* **2004**, *41*, 907 – 914. PDB-code: 1UW6.

[23] F. H. Allen, *Acta Crystallogr. Sect. B* **2002**, *58*, 380 – 388. The CSD search was performed using a distance constraint for the distance d between ammonium N atom and the centroid of the aromatic ring of $3.5\text{ Å} < d < 5.5\text{ Å}$. Hits were limited to structures containing no errors or partial disorders, excluding polymeric, powder, or organometallic compounds.

Analytical Chemistry

A Regenerative Chemodosimeter Based on Metal-Induced Dye Formation for the Highly Selective and Sensitive Optical Determination of Hg^{2+} Ions**

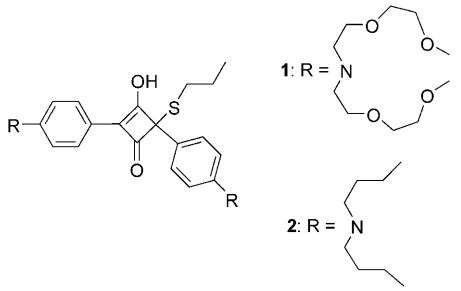
José V. Ros-Lis, M. Dolores Marcos, Ramón Mártinez-Máñez, Knut Rurack,* and Juan Soto*

The Hg^{2+} ion is one of the environmentally most important metal ions whose toxicity, even at very low concentrations, has long been recognized and is a problem of primary concern.[1] Moreover, despite a reduction of its industrial use as a result of stricter regulations, high concentrations of mercury are still present in many environmental compartments and it can still be found in many products of daily life such as paints, electronic equipment, and batteries.[2] Accordingly, the need for analytical methods for the sensitive and selective determination of mercury is of topical interest, especially in situations where conventional techniques are not appropriate, for instance in many on-site or in situ analyses and for rapid screening applications. In these fields, optical and electrochemical sensing devices play a leading role, in particular utilizing molecular probes that generate and transduce an analytical signal as a response to the binding event.[3] Although several examples of redox-active,[4] fluorogenic,[5] and chromogenic[6] chemosensors for Hg^{2+} ions have been reported recently, the combined "binding site and signaling subunit" approach that is commonly used with such probes often harbors disadvantages for analysis in realistic media. Many signaling units suffer through the strong hydrogen-bonding ability of water, fluoroionophores often undergo unspecific fluorescence quenching upon binding to heavy-metal ions, and the number of Hg^{2+}-ion-selective receptors is limited.

A particularly attractive alternative presented herein are chemodosimeters that indicate an analyte through a specific chemical reaction between dosimeter molecule and target species, leading to the formation of a fluorescent or colored product.[7,8] A disadvantage of dosimeters, however, is that the reactions are mostly irreversible and thus provide only single-use assays.

To take advantage of the favorable features of chemodosimeters and also reuse them, it is necessary to install a procedure that allows the molecular reporter to be regenerated. We thus designed a method where the indicator dye is passivated first in a chemical addition reaction with a small organic compound, the "spectroscopic inhibitor" that "switches off" the color and fluorescence of the indicator. This addition product is the chemodosimeter. The target ion then reacts with the inhibitor, liberating the dye, that is, signaling is accomplished by "metal-induced dye release" methods. With the proper choice of dye scaffold and passivation reaction, it should thus be possible to generate drastic chromo- and fluorogenic changes that result in a true "switching-on" behavior rather than a modulation of already existing signals or minor shifts of absorption or emission bands.

We have applied this newly designed procedure to the selective analysis of Hg^{2+} ions. The method is based on the thiophilic affinity of the Hg^{2+} ion and its reactivity with 2,4-bis(4-dialkylaminophenyl)-3-hydroxy-4-alkylsulfanylcyclobut-2-enone (APC) derivatives. As we have recently shown, APC derivatives can be elegantly obtained by a simple reaction of squaraines—the indicator dye—with thiols, the inhibitor.[9] A representative compound (**1**) is shown in Scheme 1. Compound **1** contains two independent subchromophores that are electronically separated and chemically bound through an sp^3-hybridized carbon atom. Accordingly, **1** shows two overlapping bands in the UV spectral region; one at approximately 265 nm which is characteristic for the dialkylanilino moiety and a second, 1.3-fold more intensive band centered at around 305 nm (Figure 1). The latter band can be ascribed to the dialkylaminophenylhydroxycyclobut-2-enone (PC) group. Quantum chemical calculations at the semiempirical level are in agreement with the experimental results and reveal the existence of two independent transitions of moderate oscillator strength, the HOMO–LUMO transition that is located on the PC fragment and the energetically higher-lying HOMO-1–LUMO + 1 transition localized on the anilino group.



Scheme 1. Derivatives **1** and **2**.

Addition of Hg^{2+} ions to solutions of **1** results in a dramatic change of color owing to the appearance of a new

[*] J. V. Ros-Lis, Dr. M. D. Marcos, Prof. R. Mártinez-Máñez, Dr. J. Soto
Centro de Investigación en Química Molecular Aplicada
Departamento de Química
Universidad Politécnica de Valencia
Camino de Vera s/n, 46071 Valencia (Spain)
Fax: (+34) 96-387-9349
E-mail: rmaez@qim.upv.es
Dr. K. Rurack
Div. I.3
Bundesanstalt für Materialforschung und -prüfung (BAM)
Richard-Willstätter-Strasse 11, 12489 Berlin (Germany)
Fax: (+49) 30-8104-5005
E-mail: knut.rurack@bam.de

[**] We thank the Ministerio de Ciencia y Tecnología (projects REN2002-04237-C02-01 and MAT2003-08568-C03-02) for support. J.V.R.L. also thanks the Ministerio de Educación, Cultura y Deporte for a Doctoral Fellowship.

Supporting information for this article is available on the WWW under http://www.angewandte.org or from the author.

 DOI: 10.1002/anie.200500583 © 2005 Wiley-VCH Verlag GmbH & Co. KGaA, Weinheim

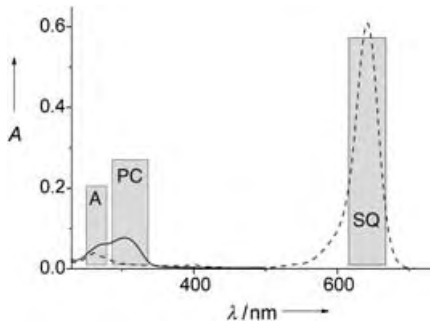
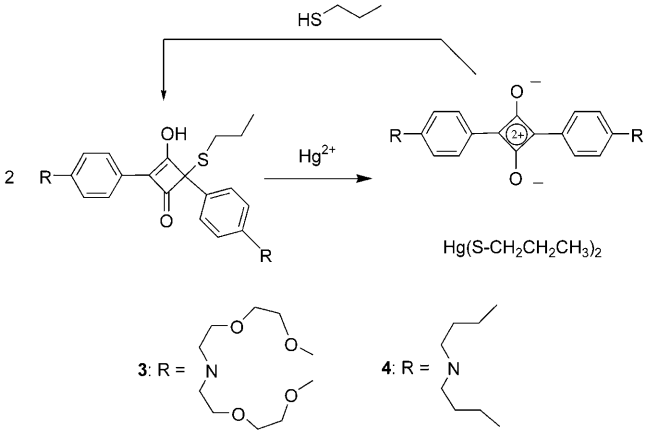


Figure 1. Absorption spectra of **1** (——) and **3** (-----) in water/acetonitrile (4:1 v/v), before and after the reaction of **1** with Hg^{2+} ions. The gray bars denote the region of absorption of the single chromophores: A = anilino moiety (this band is also present as a higher transition in **3**), PC = aminophenylhydroxycyclobut-2-enone group and SQ = squaraine.

and intense absorption band at 642 nm that is typical for a squaraine dye (Figure 1).[9,10] This Hg^{2+}-ion triggered formation of squaraines is shown in Scheme 2. The reaction product



Scheme 2. The analytical cycle: Hg^{2+}-ion-induced formation of **3** and **4** and regeneration of **1** and **2** by reaction with propanethiol.

3 has a comparatively large molar absorptivity ($\lg\varepsilon = 5.05$) and a moderately high fluorescence quantum yield ($\Phi_f = 0.023$) in water/acetonitrile (4:1). This dual chromo- and fluorogenic sensing of Hg^{2+} ions is remarkable as both absorption and emission are found at the red end of the visible spectral window where usually the interference arising from matrix absorption or autofluorescence is negligible. Moreover, this dramatic hyper- and bathochromic shift upon mercury-induced transformation of **1** into **3** allows for straightforward "naked-eye" monitoring of the Hg^{2+}-ion-detection process.[11]

To optimize the method, different pH ranges were tested and a basic pH (9.6, buffered with 2-(cyclohexylamino)ethanesulfonic acid (CHES) 0.01M) was found to yield the best performance of the chromofluorogenic dosimeter. Furthermore, these studies revealed that a maximum signal can be observed at a molar ratio of **1**/Hg^{2+} = 2:1, suggesting the formation of $Hg(SR)_2$ species (see Scheme 2).

As the coordination with thiols is not an exclusive feature of mercury, the reactivity of **1** in the presence of other metal ions was studied. In a typical experiment, up to 10 equivalents of Hg^{2+}, Cu^{2+}, Fe^{3+}, Pb^{2+}, Ni^{2+}, Cd^{2+}, Zn^{2+}, Al^{3+}, and Tl^{+} were added to a solution of **1** in water/acetonitrile (4:1, $c_1 = 6\times10^{-6}$ M, pH 9.6, CHES 0.01M). The results are shown in Figure 2. There is a remarkably selective development of

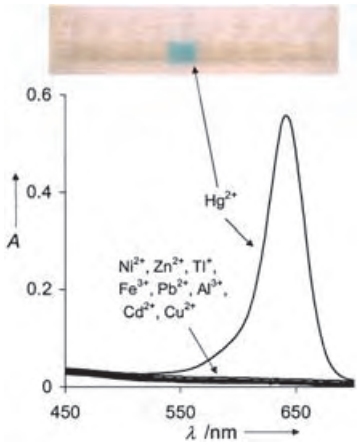


Figure 2. Absorption spectra of **1** (6×10^{-6} M) in water/acetonitrile (4:1 v/v, pH 9.6, CHES 0.01 M) upon addition of 0.5 equivalents of various metal ions. In the photograph, from left to right: Ni^{2+}, Zn^{2+}, Tl^{+}, Fe^{3+}, Hg^{2+}, Pb^{2+}, Al^{3+}, Cd^{2+}, Cu^{2+}, and no metal ion.

the blue color only in the presence of Hg^{2+}, while the other potential competitors remain entirely silent. This chromogenic indication reaction allows Hg^{2+} ions to be detected down to 20 ppb by using a conventional spectrophotometer and standard conditions (such as 10-mm cells).

Despite the inherent interest of the colorimetric response, fluorometric methods can reach much lower detection limits with very low-cost and widely used instrumentation. Considering the high brightness (the product of ε and Φ_f) of squaraine dyes, the present system should be ideal for use in conjunction with fluorescence detection. Thus, similar studies to those described above were performed with $c_1 = 1\times10^{-7}$ M on a conventional fluorometer. Figure 3 shows the fluorescence titration spectra of **1** with Hg^{2+} ions, revealing that the

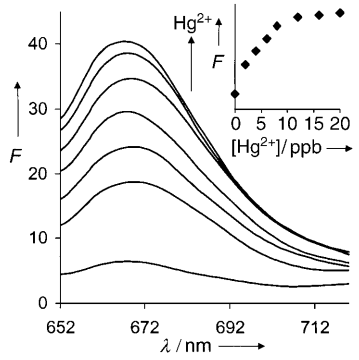


Figure 3. Fluorescence titration spectra of **1** (10^{-7} M) with Hg^{2+} ions in water/acetonitrile (4:1 v/v, pH 9.6, CHES 0.01 M, $\lambda_{exc} = 642$ nm). The inset shows the titration curve obtained from the emission intensities at 670 nm.

 © 2005 Wiley-VCH Verlag GmbH & Co. KGaA, Weinheim

detection of less than 2 ppb of Hg^{2+}, which is the U.S. Environmental Protection Agency's limit for drinking water, is clearly possible by the Hg^{2+}-ion-induced release of the highly fluorescent squaraine **3**.

Motivated by these favorable features of the solution-based chemistry, we took a step towards the use of metal-triggered reactions for in situ sensing and rapid screening applications. For this purpose, the APC derivative **2** (Scheme 1) containing hydrophobic *n*-butyl chains was prepared and adsorbed on powdered silica. The butyl chains offer the required hydrophobicity to prevent the leaching of the dye in aqueous samples. This rather simple method allowed an accurate control of the amount of dye that is physisorbed onto the solid. The loading is a key parameter for fluorometric applications as too high loadings can easily lead to self-quenching for dyes with narrow, intense, and weakly Stokes-shifted absorption and fluorescence spectra.

In a series of experiments we found that a suitably sensitive solid able to show dual chromofluorogenic signaling should typically contain **2** in a concentration of 10^{-6} mmol g^{-1}. The powder was then fixed on a polyethyleneterephthalate film for a first prototype of a dip-stick assay that was tested by simply dipping the films into aqueous samples containing Hg^{2+} ions. Once the sticks come into contact with the sample solutions, the solid turns blue ($\lambda_{abs} = 642$ nm) and begins to fluoresce ($\lambda_{em} = 670$ nm). The response time is on the order of a few seconds and the behavior is consistent with the reaction shown in Scheme 2. Compound **2** reacts with the mercuric ion to give the corresponding squaraine derivative **4** that remains adsorbed on the solid, resulting in a chromo- and fluorogenic "switching-on" process indicative of the presence of Hg^{2+} ions. Finally, having accomplished the reaction, the chemical reaction described above[9] can be used to regenerate the chemodosimetrical solid quantitatively with propanethiol (Scheme 2). Upon addition of the "spectroscopic inhibitor", the conjugation in the squaraine is interrupted and the color immediately turns from blue back to colorless; the device is ready for the next cycle (see the Supporting Information).

In summary, we have designed a highly selective and sensitive dual chromofluorogenic chemodosimeter system for the determination of Hg^{2+} ions in aqueous environments using a very simple and specific reaction, that is, Hg^{2+}-triggered formation of a squaraine dye. The method allows the selective detection of Hg^{2+} ions below 2 ppb in aqueous solutions, shows a fluorescence enhancement, and displays a very large shift in absorption with the development of a blue color from colorless solutions. The possibility to adsorb or anchor the probe on suitable supports allowed prototypes of reusable dip-stick assays to be designed for rapid screening for the target analyte. Additionally, we believe that this procedure, based on guest-induced dye release methods using suitable dye scaffoldings and passivation reactions, might be of interest as a new route for the design of new and improved regenerative sensor molecules for the rapid colorimetric screening of a number of other target guests.

Received: February 16, 2005
Revised: April 8, 2005
Published online: June 9, 2005

Keywords: chemodosimeter · dyes · fluorometric analysis · mercury · spectrophotometric analysis

[1] a) L. Magos, *Met. Ions Biol. Syst.* **1997**, *34*, 321–370; b) M. F. Wolfe, S. Schwarzbach, R. A. Sulaiman, *Environ. Toxicol. Chem.* **1998**, *17*, 146–160.

[2] a) Q. R. Wang, D. Kim, D. D. Dionysiou, G. A. Sorial, D. Timberlake, *Environ. Pollut.* **2004**, *131*, 323–336; b) G. M. Dias, G. C. Edwards, *Hum. Ecol. Risk Assess.* **2003**, *9*, 699–721.

[3] For recent examples on sensing devices for Hg^{2+} ions see: a) I. Murkovic, O. S. Wolfbeis, *Sens. Actuators B* **1997**, *39*, 246–251; b) X.-B. Zhang, C.-C. Guo, Z.-Z. Li, G.-L. Shen, R.-Q. Yu, *Anal. Chem.* **2002**, *74*, 821–825; c) A. Safavi, M. Bagheri, *Sens. Actuators B* **2004**, *99*, 608–612.

[4] a) J. M. Lloris, R. Martínez-Máñez, T. Pardo, J. Soto, M. E. Padilla-Tosta, *Chem. Commun.* **1998**, 837–838; b) J. M. Lloris, R. Martínez-Máñez, M. E. Padilla-Tosta, T. Pardo, J. Soto, P. D. Beer, J. Cadman, D. K. Smith, *J. Chem. Soc. Dalton Trans.* **1999**, 2359–2369.

[5] For recent examples see: a) X. Guo, X. Qian, L. Jia, *J. Am. Chem. Soc.* **2004**, *126*, 2272–2273; b) S. Y. Moon, N. R. Cha, Y. H. Kim, S. Chang, *J. Org. Chem.* **2004**, *69*, 181–183; c) E. M. Nolan, S. J. Lippard, *J. Am. Chem. Soc.* **2003**, *125*, 14270–14271.

[6] For recent examples see: a) J. V. Ros-Lis, R. Martínez-Máñez, K. Rurack, F. Sancenón, J. Soto, M. Spieles, *Inorg. Chem.* **2004**, *43*, 5183–5185; b) E. Palomares, R. Vilar, J. R. Durrant, *Chem. Commun.* **2004**, 362–363; c) A. B. Descalzo, R. Martínez-Máñez, R. Radeglia, K. Rurack, J. Soto, *J. Am. Chem. Soc.* **2003**, *125*, 3418–3419.

[7] For metal ions see a) V. Dujols, F. Ford, A. W. Czarnik, *J. Am. Chem. Soc.* **1997**, *119*, 7386–7387; b) M.-Y. Chae, A. W. Czarnik, *J. Am. Chem. Soc.* **1992**, *114*, 9704–9705; For other analytes see c) T.-H. Kim, T. M. Swager, *Angew. Chem.* **2003**, *115*, 4951–4954; *Angew. Chem. Int. Ed.* **2003**, *42*, 4803–4806; d) C. A. Roeschlaub, N. L. Maidwell, R. Rezai, P. G. Sammes, *Chem. Commun.* **1999**, 1637–1638.

[8] A related class of sensor molecules are chromo- and fluoro-reactands where analyte and probe usually undergo a (reversible or irreversible) condensation reaction: a) G. J. Mohr, *Chem. Eur. J.* **2004**, *10*, 1082–1090; b) F. Tanaka, N. Mase, C. F. Barbas, *Chem. Commun.* **2004**, 1762–1763; Alternatively, analytes can trigger the reversible formation of a colored or fluorescent product: c) F. Sancenón, R. Martínez-Máñez, M. A. Miranda, M. J. Seguí, J. Soto, *Angew. Chem.* **2003**, *115*, 671–674; *Angew. Chem. Int. Ed.* **2003**, *42*, 647–650; d) F. Sancenón, A. B. Descalzo, R. Martínez-Máñez, M. A. Miranda, J. Soto, *Angew. Chem.* **2001**, *113*, 2710–2713; *Angew. Chem. Int. Ed.* **2001**, *40*, 2640–2643.

[9] J. V. Ros-Lis, B. García, D. Jiménez, R. Martínez-Máñez, F. Sancenón, J. Soto, F. Gonzalvo, M. C. Valldecabres, *J. Am. Chem. Soc.* **2004**, *126*, 4064–4065.

[10] a) S. Das, K. G. Thomas, K. J. Thomas, P. V. Kamat, M. V. George, *J. Phys. Chem.* **1994**, *98*, 9291–9296; b) C. Cornelissen-Gude, W. Rettig, R. Lapouyade, *J. Phys. Chem. A* **1997**, *101*, 9673–9677.

[11] The ethoxyethyl substituents at the amino nitrogen of **1** and **3** were employed to increase the solubility of the compounds in aqueous solution. The moiety itself does not respond to the metal ions tested in this work in a classical fluoroionophore-type fashion.

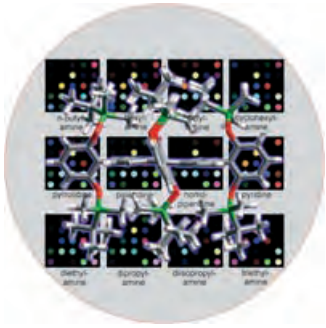
 © 2005 Wiley-VCH Verlag GmbH & Co. KGaA, Weinheim

Cover Picture

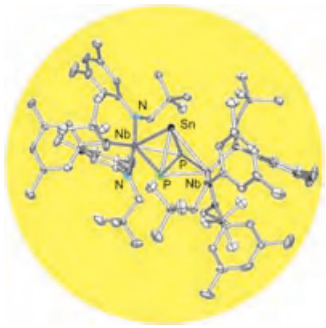


K. C. Nicolaou,* Paul G. Bulger, and David Sarlah

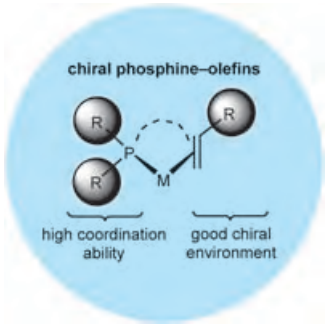
A powerful combination of two synthetic methods has advanced the art of organic synthesis like few other reactions. In their Reviews on page 4442 ff. and 4490 ff. K. C. Nicolaou and co-workers illustrate how palladium-catalyzed cross-couplings and metathesis-based reactions, respectively, have blossomed into powerful tools for carbon–carbon bond formation in the total synthesis of natural products.



Sensors
Selective discrimination between closely related amines can be achieved by a molecular recognition process that generates a colorimetric "signature" for each compound. This method is described by K. S. Suslick and co-workers in their Communication on page 4528 ff.



Coordination Chemistry
Dinuclear complexes with bridging {*cyclo*-EP_2}-units are formed from a niobium phosphide anion and divalent Group 14 salts. C. C. Cummins and J. S. Figueroa describe the structures of these compounds in their Communication on page 4592 ff.



Asymmetric Catalysis
In their Communication on page. 4611 ff. T. Hayashi et al. describe rhodium complexes with bidentate chiral phosphine–olefin ligands that are highly efficient catalysts for the enantioselective 1,4-addition of aryl boronic acids to maleimides.

Contents

The following Communications have been judged by at least two referees to be "very important papers" and will be published online at www.angewandte.org soon:

*V. Lavallo, Y. Canac, C. Präsang, B. Donnadieu, G. Bertrand**
Stable Cyclic (Alkyl)(amino)carbenes as Rigid or Flexible, Bulky, Electron-Rich Ligands for Transition-Metal Catalysts

S. Aime, D. Delli Castelli, E. Terreno*
Highly Sensitive MRI-CEST Agents using Liposomes (LIPOCEST)

H. Braunschweig, K. Radacki, D. Rais, D. Scheschkewitz*
A T-Shaped Platinum(II) Boryl Complex as the Precursor to a Base-Stabilized Borylene of Platinum

X. Liang, D. Fu, R. Liu,* Q. Zhang, T. Y. Zhang, X. Hu**
Highly Efficient $NaNO_2$-Catalyzed Destruction of Trichlorophenol using Molecular Oxygen

*P. Maire, T. Büttner, F. Breher, P. Le Floch, H. Grützmacher**
Heterolytic Hydrogen Splitting with Novel Rhodium(I) Amides

D. Banser, M. Schnell, J.-U. Grabow, E. J. Cocinero, A. Lesarri, J. L. Alonso*
The Internuclear Potential, Electronic Structure, and Chemical Bond of Tellurium Selenide

Web Sites

http://molmovdb.org/	Proteins in Motion	D. Heinz,* W.-D. Schubert ——— **4428**

Books

Nanofabrication Towards Biomedical Applications	Challa S. S. R. Kumar, Josef Hormes, Carola Leuschner	*reviewed by E. Katz* ——— **4429**
Side Reactions in Organic Synthesis	Florencio Zaragoza-Dörwald	*reviewed by M. A. Sierra* ——— **4430**

Highlights

Medicinal Chemistry

T. Larsen, A. Link* ——— **4432 – 4434**

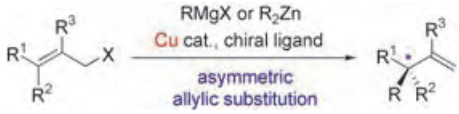
A Timely Reassessment of Early Prediction in the Bioavailability of Orally Administered Drugs

Rule of thumb: Deciding the fate of drug candidates after an estimate of oral bioavailability depends on how heavily the selection parameters are applied. A retrospective analysis of medications on the market has shown that lipophilicity, percent polar surface area, and the number of H-bond donors are properties that have remained relatively constant over the years, and are clearly the most important physicochemical determinants.

Asymmetric Synthesis

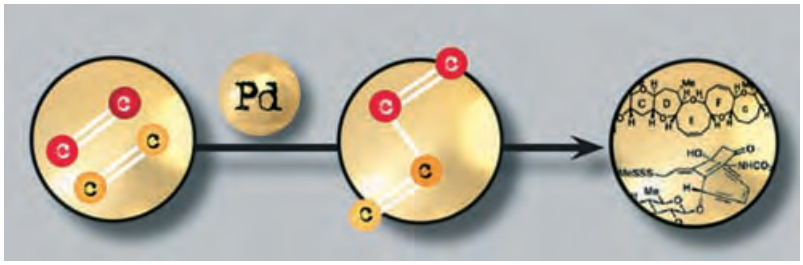
H. Yorimitsu,* K. Oshima* - **4435 – 4439**

Recent Progress in Asymmetric Allylic Substitutions Catalyzed by Chiral Copper Complexes



Copper complements palladium as a catalyst of asymmetric allylic substitutions (see scheme). Palladium catalysis requires soft nucleophiles to ensure high stereo- and regioselectivity, whereas hard nucleophiles such as Grignard and organozinc reagents may be used under copper catalysis. Vast progress during the last decade reveals the promising future of copper catalysis in this asymmetric transformation.

Reviews

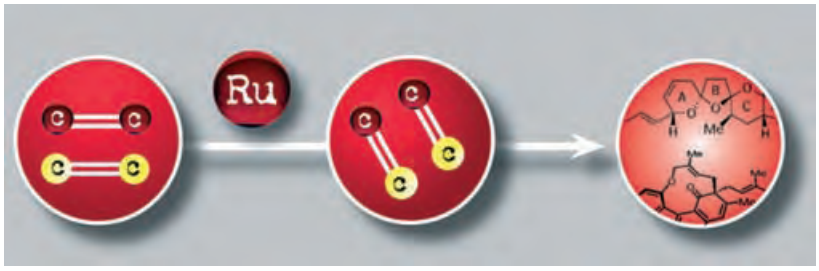


The virtues of the palladium-catalyzed cross-coupling reactions come alive in this stimulating Review article as the authors highlight a number of total syntheses featuring these important carbon–carbon bond-forming reactions.

Synthetic Methods

K. C. Nicolaou,* P. G. Bulger, D. Sarlah ——— **4442 – 4489**

Palladium-Catalyzed Cross-Coupling Reactions in Total Synthesis



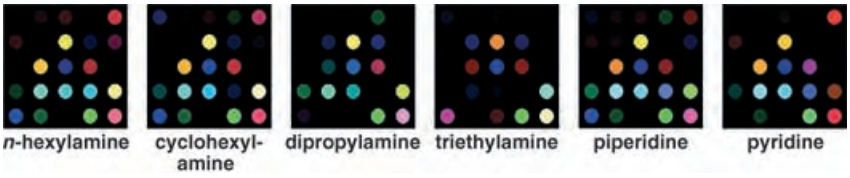
The benefits of metathesis reactions (alkene, enyne, and alkyne) are made apparent in this stimulating Review article. The authors highlight a number of total syntheses featuring these important carbon–carbon bond-forming reactions.

Synthethic Methods

K. C. Nicolaou,* P. G. Bulger, D. Sarlah ——— **4490 – 4527**

Metathesis Reactions in Total Synthesis

Communications



Seeing smells: Highly selective discrimination between closely related amines has been demonstrated by using an array of chemoresponsive dyes (see picture). Hierarchical classification of amines based on their colorimetric response is successful and matches that expected from qualitative structural and electronic considerations. High sensitivity (ca. 100 ppbv) has been shown for the detection and discrimination of amines.

Sensors

N. A. Rakow, A. Sen, M. C. Janzen, J. B. Ponder, K. S. Suslick* ___ **4528 – 4532**

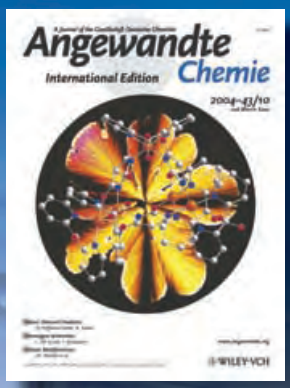
Molecular Recognition and Discrimination of Amines with a Colorimetric Array

For the USA and Canada:
ANGEWANDTE CHEMIE International Edition (ISSN 1433-7851) is published weekly by Wiley-VCH PO Box 191161, D 69451 Weinheim, Germany. Air freight and mailing in the USA by Publications Expediting Inc. 200 Meacham Ave., Elmont, NY 11003. Periodicals postage paid at Jamaica NY 11431. US POSTMASTER: send address changes to *Angewandte Chemie*, Wiley-VCH, 111 River Street, Hoboken, NJ 07030. Annual subscription price for institutions: US$ 4948.00/4498.00 (valid for print and electronic / print or electronic delivery); for individuals who are personal members of a national chemical society, or whose institution already subscribes, or who are retired or self-employed consultants, print only: US$ 394.00. Postage and handling charges included. All Wiley-VCH prices are exclusive VAT.

 © 2005 Wiley-VCH Verlag GmbH & Co. KGaA, Weinheim

The best in chemistry –

for more than a hundred years



A Journal of the Gesellschaft Deutscher Chemiker

Angewandte International Edition **Chemie**

www.angewandte.org

1888: ***The beginning of a success story***

Constant Innovations

1962: *First issue of the International Edition*
1976: *Graphical abstracts*
1979: *Cover pictures*
1988: *Centenary of Angewandte*
1989: *Routine use of color*
1991: *New section: Highlights*
1992: *Computerized editorial tracking system*
1995: *Internet service for readers*
1998: *Regular press service; full-text online*
2000: *New section: Essays; EarlyView: Communications available online ahead of the printed version*
2001: *New section: Minireviews*
2002: *Online submission of manuscripts*
2003: *Weekly publication; new section: News; new layout*
2004: *Backfiles (1962-1997); ManuscriptXpress: Online system for authors and referees*



Angewandte's advisors...

Ulrich Stilz
Aventis, Frankfurt/Main

» With its interdisciplinary and international orientation ***Angewandte Chemie*** *has set the benchmark for publishing innovative results. The editorial team is acknowledged for the success of this renowned journal, that provides scientists with a unique forum, in which to discuss their discoveries. «*

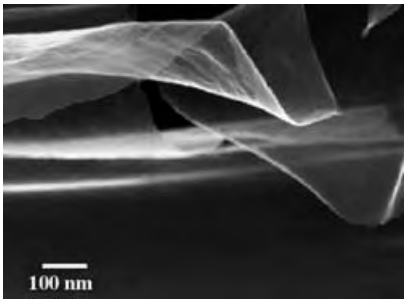
Angewandte Chemie International Edition *is a journal of the German Chemical Society (GDCh)*

GDCh

WILEY InterScience® DISCOVER SOMETHING GREAT

WILEY-VCH

11981404_gu

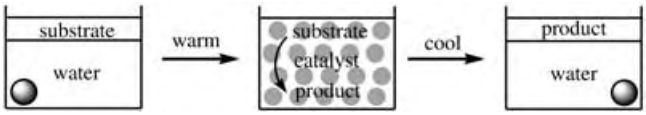


Complete removal of interstitial water molecules from various foam films of amphiphilic compounds results in self-standing bilayer membranes. The dried foam films (DFFs) in the micrometer to submicrometer range (see picture) are stable even under ultrahigh-vacuum conditions and at temperatures higher than 100 °C.

Dried Foam Films

J. Jin, J. Huang, I. Ichinose* **4532 – 4535**

Dried Foam Films: Self-Standing, Water-Free, Reversed Bilayers of Amphiphilic Compounds

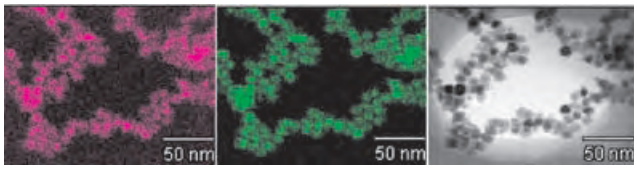


A new concept for catalytic reactions in aqueous media is demonstrated by using a temperature-responsive polymer support, poly(*N*-alkylacrylamide), which is converted into a catalyst by assembly with phosphotungstic acid. At high temperature, the catalyst is highly active in the oxidation of alcohols with H_2O_2 owing to the formation of emulsions, whereas the product and catalyst are easily separated at low temperature (see scheme).

Green Chemisty

H. Hamamoto, Y. Suzuki, Y. M. A. Yamada, H. Tabata, H. Takahashi, S. Ikegami* **4536 – 4538**

A Recyclable Catalytic System Based on a Temperature-Responsive Catalyst

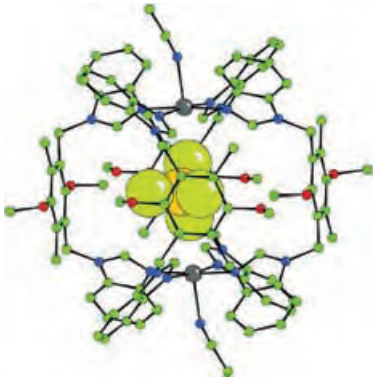


Cores to celebrate: At 370 °C, Pt@Cu core–shell nanoparticles rapidly alloy but the reciprocal core–shell nanoparticles, Cu@Pt (see STEM images, left: Cu spectral map; middle: Pt spectral map; right: bright-field image), are kinetically stabilized and show high activity and selectivity for NO reduction.

Heterogeneous Catalysis

S. Zhou, B. Varughese, B. Eichhorn,* G. Jackson, K. McIlwrath **4539 – 4543**

Pt–Cu Core–Shell and Alloy Nanoparticles for Heterogeneous NO_x Reduction: Anomalous Stability and Reactivity of a Core–Shell Nanostructure



Stuck in the middle: Supramolecular host–guest cages of general formula $[BF_4 \subset (RCN)_2Co_2L_4](BF_4)_3$ with L being a di(benzimidazole)-1,4-phenylene derivative (R = Me, Et, Ph) have been prepared. An encapsulated BF_4^- anion (B yellow, F pale green; see structure) is locked firmly inside the cage and plays a pivotal role as a template around which the Co^{II} ions (gray) and L ligands (ball-and-stick representation) self-assemble.

Host–Guest Chemistry

H. Amouri,* L. Mimassi, M. N. Rager, B. E. Mann, C. Guyard-Duhayon, L. Raehm **4543 – 4546**

Host–Guest Interactions: Design Strategy and Structure of an Unusual Cobalt Cage That Encapsulates a Tetrafluoroborate Anion

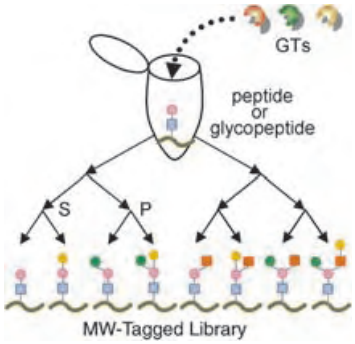
 © 2005 Wiley-VCH Verlag GmbH & Co. KGaA, Weinheim

Contents

Combinatorial Chemistry

H. Ito, A. Kameyama, T. Sato, K. Kiyohara, Y. Nakahara, H. Narimatsu* **4547 – 4549**

Molecular-Weight-Tagged Glycopeptide Library: Efficient Construction and Applications

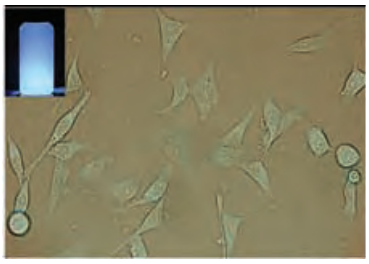


Generation of diversity: An oligosaccharide library can be constructed from glycopeptides by repeating incomplete glycosyltransferse (GTs) reactions in a single tube (see picture). Each product has a different molecular weight (MW). Therefore, the structure of each component in the library can be identified immediately by mass spectrometry alone. The differently colored shapes in the picture symbolize different glycosyl residues.

Imaging Agents

J. H. Warner, A. Hoshino, K. Yamamoto, R. D. Tilley* **4550 – 4554**

Water-Soluble Photoluminescent Silicon Quantum Dots

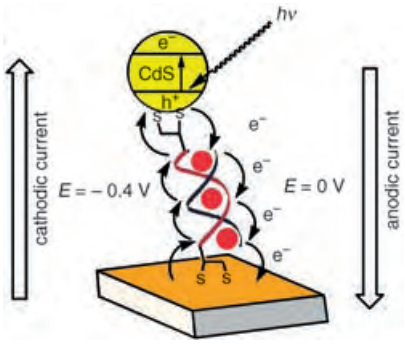


Strong photoluminescence in the blue region of the visible spectrum was observed for a dispersion of allylamine-capped silicon quantum dots in water. Their ease of synthesis and optical properties make them excellent candidates for biomedical applications, as demonstrated by their incorporation inside the cytosol of HeLa cells (see microscopy image, the inset shows the fluorescence from the silicon quantum dots on excitation with UV light).

Electrochemistry

R. Gill, F. Patolsky, E. Katz, I. Willner* **4554 – 4557**

Electrochemical Control of the Photocurrent Direction in Intercalated DNA/CdS Nanoparticle Systems

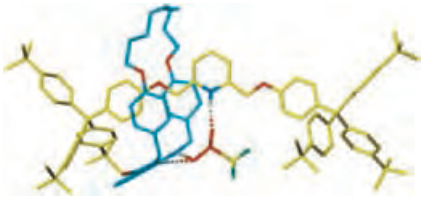


A change in direction: The photocurrent generated by CdS nanoparticles attached by means of a double-stranded DNA linker to a gold electrode is reversibly switched between the anodic or cathodic direction (see graphic) depending on the redox state of the methylene blue intercalator.

Supramolecular Chemistry

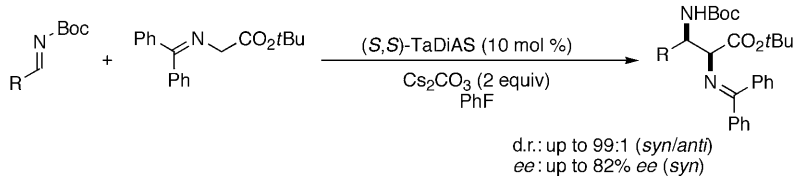
D. A. Leigh,* P. J. Lusby, A. M. Z. Slawin, D. B. Walker **4557 – 4564**

Rare and Diverse Binding Modes Introduced through Mechanical Bonding



Any which way, but not loose: A range of diverse noncovalent binding interactions are observed with a [2]rotaxane (see structure) and a [2]catenane that are not found with similar but not mechanically interlocked fragments. (C (macrocycle) turquoise, other C atoms yellow, O red, N blue, H gray, F green, S orange.)

 © 2005 Wiley-VCH Verlag GmbH & Co. KGaA, Weinheim

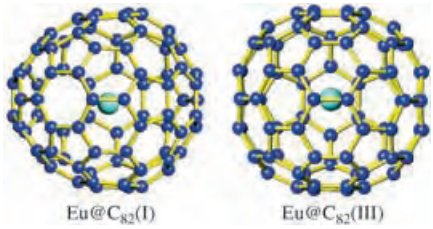


Optically active α,β-diamino acids are prepared under asymmetric phase-transfer reaction conditions from a glycine Schiff base and N-protected imines with a tartrate-derived diammonium salt (TaDiAS) as the phase-transfer catalyst (see scheme; Boc = *tert*-butoxycarbonyl). Chemoselective deprotection of the N atoms allows straightforward transformations of the α,β-diamino acid products to be carried out.

Phase-Transfer Catalysis

A. Okada, T. Shibuguchi, T. Ohshima,*
H. Masu, K. Yamaguchi,
M. Shibasaki* _____ **4564 – 4567**

Enantio- and Diastereoselective Catalytic Mannich-Type Reaction of a Glycine Schiff Base Using a Chiral Two-Center Phase-Transfer Catalyst

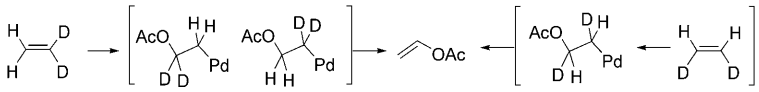


A question of symmetry: Unlike other mono-metallofullerenes, the cage structures of Eu@C_{82} (isomers I and III) have been shown to have C_s (no. 6) and C_{2v} symmetry, respectively, by the maximum entropy method using synchrotron X-ray powder diffraction data. In both isomers (see structures) the Eu ion (turquoise) is located near the top of the carbon cage adjacent to a C–C double bond.

Structure Elucidation

B.-Y. Sun, T. Sugai, E. Nishibori, K. Iwata,
M. Sakata, M. Takata,
H. Shinohara* _____ **4568 – 4571**

An Anomalous Endohedral Structure of Eu@C_{82} Metallofullerenes

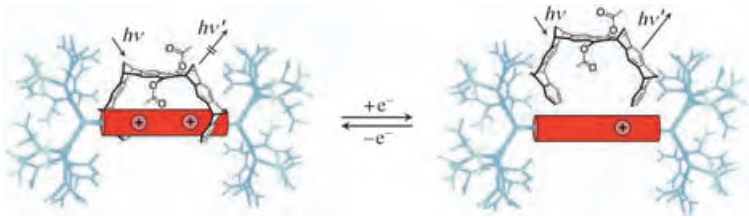


Finding the right pathway: Reaction of isotopomers of ethylene with acetate species (see scheme) adsorbed on a Pd(111) surface in ultrahigh vacuum has shown that vinyl acetate is produced by insertion of ethylene into the acetate species to form an acetoxyethyl intermediate, which decomposes by β-hydride elimination to yield vinyl acetate.

Reaction Mechanisms

D. Stacchiola, F. Calaza, L. Burkholder,
A. W. Schwabacher, M. Neurock,
W. T. Tysoe* _____ **4572 – 4574**

Elucidation of the Reaction Mechanism for the Palladium-Catalyzed Synthesis of Vinyl Acetate



A large guest for a small host: The tweezering process about the bipyridinium core of a dendrimer by a molecular tweezer (see picture) has been studied electrochemically and by fluorescence spectroscopy and is found to be quite similar to the threading/dethreading processes observed with wire-type bipyridinium-based units and ring-shaped molecules.

Host–Guest Chemistry

V. Balzani,* P. Ceroni, C. Giansante,
V. Vicinelli, F.-G. Klärner,* C. Verhaelen,
F. Vögtle,* U. Hahn _____ **4574 – 4578**

Tweezering the Core of a Dendrimer: A Photophysical and Electrochemical Study

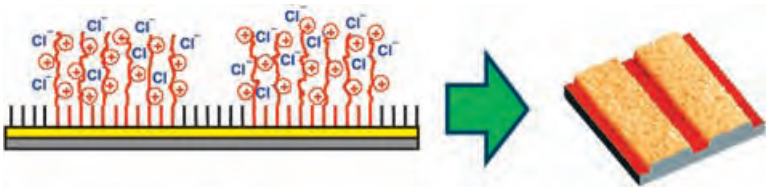
 © 2005 Wiley-VCH Verlag GmbH & Co. KGaA, Weinheim

Contents

Nanotechnology

S. Moya, O. Azzaroni, T. Farhan, V. L. Osborne, W. T. S. Huck* ——— **4578 – 4581**

Locking and Unlocking of Polyelectrolyte Brushes: Toward the Fabrication of Chemically Controlled Nanoactuators



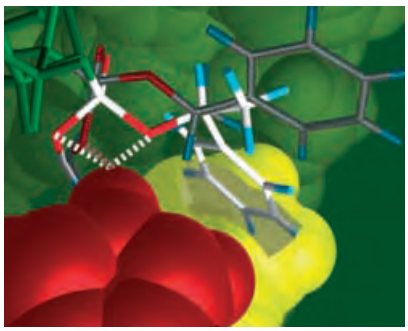
Polymer brushwork: The collapse of polyelectrolyte brushes in salt solutions combined with binding interactions and ion-size-exclusion effects is used in the design of smart polymer surfaces that can be switched between permanently collapsed or extended states with different surface properties (see picture)—a step toward the use of surface-confined polyelectrolytes as nanoactuators.

Protein Engineering

A. O. Magnusson, M. Takwa, A. Hamberg, K. Hult* ——— **4582 – 4585**

An *S*-Selective Lipase Was Created by Rational Redesign and the Enantioselectivity Increased with Temperature

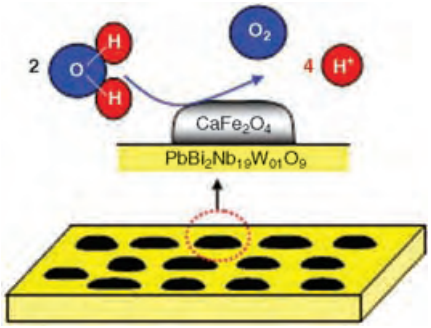
Higher activity with larger pockets: The figure shows a superposition of intermediates that occur in acyl transfer to (*S*)-1-phenylethanol catalyzed by *Candida antarctica* lipase B (CALB). Wild-type CALB cannot accomodate the phenyl group (gray) in the stereospecificity pocket and form all of the catalytically essential H bonds. The Trp 104 Ala mutation liberates the volume in yellow, the *S* enantiomer is easily fitted, and the specificity constant increases by a factor of 130 000.



Photocatalysis with Visible Light

H. G. Kim, P. H. Borse, W. Choi, J. S. Lee* ——— **4585 – 4589**

Photocatalytic Nanodiodes for Visible-Light Photocatalysis



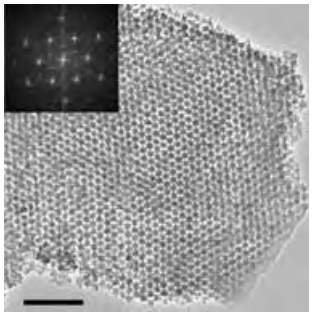
Oxidative decomposition of toxic pollutants (such as acetaldehyde and isopropyl alcohol), decomposition of water, and photocurrent generation can all be achieved with visible light. Nano-islands of p-type $CaFe_2O_4$ interfacing with bulk n-type $PbBi_2Nb_{1.9}W_{0.1}O_9$ (shown) form photocatalytic nanodiodes that demonstrate high stability and high activity for such applications.

Mesoporous Films

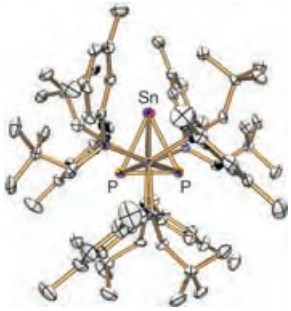
M. Kuemmel, D. Grosso, C. Boissière, B. Smarsly, T. Brezesinski, P. A. Albouy, H. Amenitsch, C. Sanchez* ——— **4589 – 4592**

Thermally Stable Nanocrystalline γ-Alumina Layers with Highly Ordered 3D Mesoporosity

Feature film: Mesoporous alumina thin films synthesized with a polymeric template have more than 50% porosity, a narrow pore-size distribution, high accessibility, and high thermal stability up to 900°C. The inorganic network is composed of sintered nanocrystalline γ-Al_2O_3 particles, and the pores are ellipsoidal with a face-centered cubic mesostructure (see image).



Divalent Group 14 salts react with the $[Na(thf)_x]^+$ derivative of the terminal niobium phosphide anion $[P{\equiv}Nb\{N(Np)Ar\}_3]^-$ (Np = neopentyl, Ar = 3,5-$Me_2C_6H_3$) to give complexes of the form $[(\mu_2{:}\eta^3,\eta^3\text{-}cyclo\text{-}EP_2)\{Nb[N(Np)Ar]_3\}_2]$ (E = Ge, Sn, and Pb; see structure). The bridging {*cyclo*-EP_2} units in these complexes can be considered as neutral 2π-electron three-membered rings that are isolobal to the cyclopropenium ion.

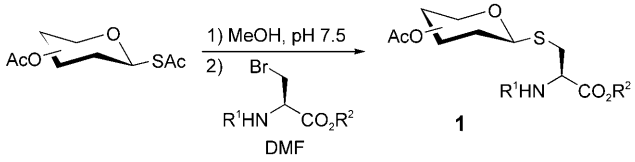


Bridging Ligands

J. S. Figueroa, C. C. Cummins* ——— 4592 – 4596

Triatomic EP_2 Triangles (E = Ge, Sn, Pb) as $\mu_2{:}\eta^3,\eta^3$-Bridging Ligands

---

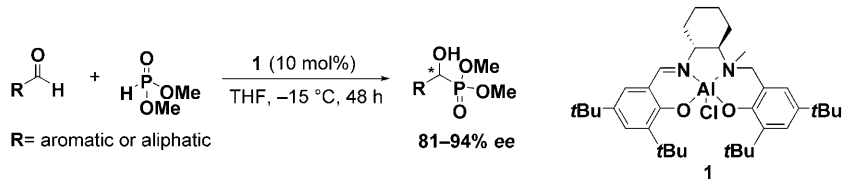


A high-yield one-pot synthesis of S-linked glycosyl amino acids **1** has been developed (see scheme; DMF = dimethyl formamide) and used in the solid-phase synthesis of S-linked glycopeptides. This approach has been shown to be efficient for the synthesis of various S-linked glycosyl amino acid building blocks.

Glycopeptide Synthesis

D. A. Thayer, H. N. Yu, M. C. Galan, C.-H. Wong* ——— 4596 – 4599

A General Strategy toward S-Linked Glycopeptides



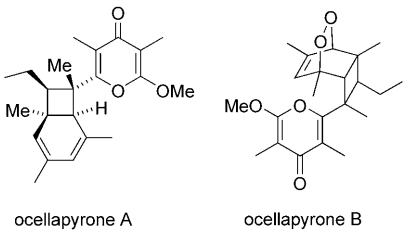
Quite universally: The chiral trigonal-bipyramidal Al(salalen) complex **1** was synthesized and found to be an efficient catalyst for enantioselective hydrophosphonylation of various aldehydes with dimethyl phosphite (see scheme). This is the first example where a molecular catalyst can be applied to the reactions of both aromatic and aliphatic aldehydes with enantioselectivities greater than 80% *ee*.

Asymmetric Catalysis

B. Saito, T. Katsuki* ——— 4600 – 4602

Synthesis of an Optically Active C_1-Symmetric Al(salalen) Complex and Its Application to the Catalytic Hydrophosphonylation of Aldehydes

---



A natural product anticipated through total synthesis! Ocellapyrone A was obtained in the laboratory several months before the structure of this unusual natural product (see scheme) was reported. An isomerization/8π–6π electrocyclization cascade was used for the formation of the natural product from a polyene precursor. The synthesis of ocellapyrone B from a diastereomer of ocellapyrone A was also performed.

Natural Products Synthesis

A. K. Miller, D. Trauner* ——— 4602 – 4606

Mining the Tetraene Manifold: Total Synthesis of Complex Pyrones from *Placobranchus ocellatus*

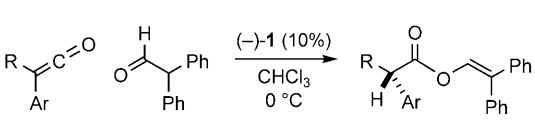
 © 2005 Wiley-VCH Verlag GmbH & Co. KGaA, Weinheim

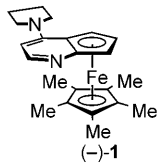
Contents

Asymmetric Catalysis

C. Schaefer, G. C. Fu* ____ **4606 – 4608**

Catalytic Asymmetric Couplings of Ketenes with Aldehydes To Generate Enol Esters



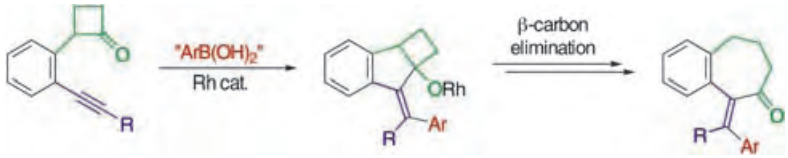


With a little help from the ferrocenyl catalyst ((–)-**1**), a wide array of α-arylalkanoic acid derivatives can be produced from the catalytic asymmetric coupling of ketenes with aldehydes (see scheme). The enol esters are readily transformed into other useful families of compounds such as carboxylic acids and alcohols.

Organic Synthesis

T. Matsuda, M. Makino, M. Murakami* ____ **4608 – 4611**

Synthesis of Seven-Membered-Ring Ketones by Arylative Ring Expansion of Alkyne-Substituted Cyclobutanones

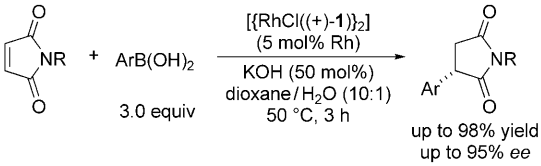


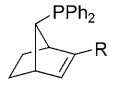
Ever-increasing circles: Seven-membered-ring ketones are constructed by a rhodium(I)-catalyzed arylative ring-expansion reaction of alkyne-substituted aryl cyclobutanones, in which two C–C bond-forming and one C–C bond-cleaving events occur consecutively (see scheme).

Addition Reactions

R. Shintani, W.-L. Duan, T. Nagano, A. Okada, T. Hayashi* ____ **4611 – 4614**

Chiral Phosphine–Olefin Bidentate Ligands in Asymmetric Catalysis: Rhodium-Catalyzed Asymmetric 1,4-Addition of Aryl Boronic Acids to Maleimides



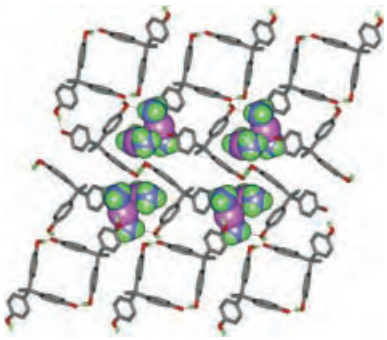


Two is better than one: Novel chiral phosphine–olefin ligands **1a** and **1b** act as bidentate ligands with some transition metals and have proved to be highly effective in the rhodium-catalyzed asymmetric 1,4-addition of aryl boronic acids to maleimides with high enantioselectivity (see scheme).

Host–Guest Systems

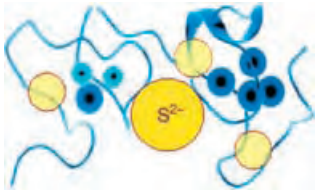
S.-L. Zheng,* M. Messerschmidt, P. Coppens* ____ **4614 – 4617**

An Unstable Ligand-Unsupported Cu^{I} Dimer Stabilized in a Supramolecular Framework



A stable environment: A $[Cu(NH_3)_2]_2^{2+}$ dimer with weak cuprophilicity is stabilized in the cavities of a supramolecular framework (see structure). This Cu^{I} dimer is otherwise unstable, so stabilization within a supramolecular matrix offers an unprecedented opportunity for systematic studies of the isolated dimeric species, either in the ground state or the excited state.

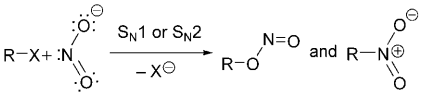
A sulfide surprise: The analysis of Zn^{II}–, Cd^{II}–, and Cu^{I}–MT recombinant preparations of metallothioneins (MTs) from many organisms provides clear evidence that sulfide ions are present in nearly all their physiologically stable Zn^{II}–MT and Cd^{II}–MT complexes (see picture), but in none of the Cu^{I}–MT species. The features of the MT complexes are in good correlation with those reported for plant and yeast Zn^{II}– or Cd^{II}–γ-glutamyl peptides.



Bioinorganic Chemistry

M. Capdevila,* J. Domènech, A. Pagani, L. Tío, L. Villarreal, S. Atrian **4618 – 4622**

Zn– and Cd–Metallothionein Recombinant Species from the Most Diverse Phyla May Contain Sulfide (S^{2-}) Ligands

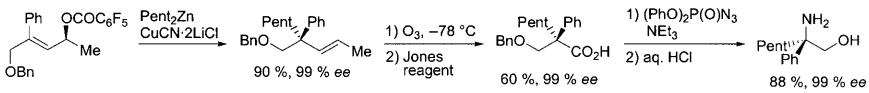


Lost control: The rationalization of the ambident reactivity of NO_2^- by the change between charge control to orbital control has to be revised. S_N1-type reactions of carbocations with NO_2^- give kinetically controlled product mixtures only when these reactions proceed without activation energy (diffusion control). Activation-controlled S_N1 alkylations are reversible and lead to the thermodynamically more stable nitro compounds.

Ambident Anions

A. A. Tishkov, U. Schmidhammer, S. Roth, E. Riedle, H. Mayr* **4623 – 4626**

Ambident Reactivity of the Nitrite Ion Revisited



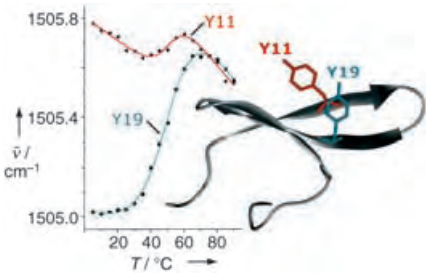
Trisubstituted allylic pentafluorobenzoates react with diorganozinc reagents in the presence of CuCN·2 LiCl to provide alkenes bearing a chiral quaternary center in α position (> 95 % *ee*). These alkenes are readily converted into chiral tertiary alcohols or into chiral amino alcohols by a straightforward sequence of ozonolysis followed by Curtius rearrangement (see scheme).

Asymmetric Synthesis

H. Leuser, S. Perrone, F. Liron, F. F. Kneisel, P. Knochel* **4627 – 4631**

Highly Enantioselective Preparation of Tertiary Alcohols and Amines by Copper-Mediated Diastereoselective Allylic S_N2' Substitutions

Launching a probe: Introducing individual tyrosine residues labeled with ^{13}C at the C4 position of the phenol ring (Y11 and Y19 in the picture) shifts the resulting tyrosine IR band to lower frequencies. This opens the door to the simultaneous monitoring of local conformational changes in different regions of proteins by IR spectroscopy, as demonstrated with a chemically synthesized analogue of a WW domain.



Protein Folding

S. Tremmel,* M. Beyermann, H. Oschkinat, M. Bienert, D. Naumann, H. Fabian* **4631 – 4635**

^{13}C-Labeled Tyrosine Residues as Local IR Probes for Monitoring Conformational Changes in Peptides and Proteins

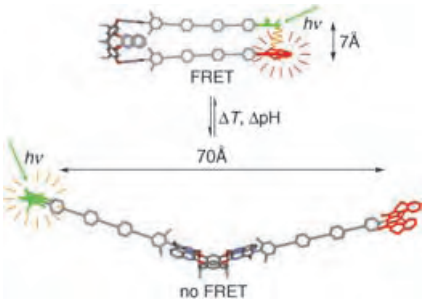
 © 2005 Wiley-VCH Verlag GmbH & Co. KGaA, Weinheim

Contents

Molecular Devices

V. A. Azov, A. Schlegel, F. Diederich* ——— **4635 – 4638**

Geometrically Precisely Defined Multinanometer Expansion/Contraction Motions in a Resorcin[4]arene Cavitand Based Molecular Switch



A molecular switch based on a resorcin-[4]arene cavitand undergoes reversibly very large, geometrically precisely defined molecular motion (see picture). Controlled switching between the contracted (linear extension ≈7 Å) and the expanded (linear extension ≈7 nm) states is induced by pH or temperature changes and was observed by ^{1}H NMR spectroscopy and fluorescence resonance energy transfer (FRET).

The issues for July 2005 appeared online on the following dates
Issue 25: June 10 · Issue 26: June 17 · Issue 27: June 23 · Issue 28: July 4

Sources

Product and Company Directory

You can start the entry for your company in "Sources" in any issue of *Angewandte Chemie*.

If you would like more information, please do not hesitate to contact us.

Wiley-VCH Verlag – Advertising Department
Tel.: 0 62 01 - 60 65 65
Fax: 0 62 01 - 60 65 50
E-Mail: MSchulz@wiley-vch.de

Service

Keywords ——— *4640*

Authors ——— *4641*

Angewandte's Sister Journals ——— *4642 – 4643*

Vacancies ——— *A42*

Preview ——— *4645*

Medicinal Chemistry

A Timely Reassessment of Early Prediction in the Bioavailability of Orally Administered Drugs

*Tim Larsen and Andreas Link**

Keywords:
hydrogen bonds · lipophilicity · medicinal chemistry · metabolism · structure–activity relationships

The rapid and efficient biopharmaceutical classification of compounds under investigation is a major focus of the pharmaceutical industry.[1] The reasons for failure during and after the discovery and development of novel chemical entities (NCEs) are multifactorial. Whereas a lack of efficacy associated with improper validation of biological targets or delays at the product portfolio level are not directly linked to the drug candidate itself, many of the reasons for the failure of a candidate can be traced back to the structure of the molecule. For instance, pharmacokinetics, animal toxicity, and the observation of adverse effects in humans are all inextricably linked to the chemical structure of the drug. Therefore, the selection of the right compound to enter clinical development is critical. Medicinal chemists have responded to this turn toward higher quality through the implementation of studies in absorption, distribution, metabolism, elimination, and safety into the discovery process.

In this context, the seminal retrospective analysis of drug properties associated with oral bioavailability performed by Lipinski and co-workers at Pfizer in 1997 fell on fertile ground.[2] The derived rule of thumb ("Rule of Five") rapidly became an important factor in the decrease of failures in early drug development projects.

Despite the practical value of this study on the prediction of good oral absorptivity for a drug candidate based on a number of simple properties, the opportunities and needs for predictive ADMET (adsorption, distribution, metabolism, excretion, toxicology) have never been greater.[1] Over the seven years in which Lipinski's Rule of Five has been applied, its descriptive power has also revealed some shortcomings. The overly rigorous selection of drug candidates to fit the rule may be analogous to the evil deeds of Damastes, also known as Procrustes, the legendary robber of ancient Attica who lived in the area of Eleusis. Nicknamed "the stretcher", he captured passing travelers to fit them in one of his two beds. Short travelers were placed on a long bed, and their limbs were stretched until they fit properly. Tall people were placed on a small bed; extremities that hung over the edge were amputated. This bloody amusement was put to a stop by the hero Theseus, who finally killed Procrustes (Figure 1).[3] In a manner perhaps a little less heroic than that of Theseus, several research groups have tried to counteract the overly rigorous or even erroneous application of the practical "Rule of Five". Many useful refinements have



Figure 1. Procrustes (Damastes), who captured travelers and brutally altered their body size to fit the bed in which they lay (upper right), was killed by Theseus. The center picture shows Theseus and the Minotaur; further deeds in the circle: Sinis, Phaia, Cercyon, Procrustes, Skiron, Marathonian Taurus (see cover picture *Angew. Chem. Int. Ed.* **2002**, *41*, issue 15). Kylix: 440–430 BC, E 84, Copyright British Museum, London.

[*] T. Larsen, Prof. Dr. A. Link
Lehrstuhl für Pharmazeutische/
Medizinische Chemie
Ernst-Moritz-Arndt-Universität Greifswald
Friedrich-Ludwig-Jahn-Strasse 17
17487 Greifswald (Germany)
Fax: (+49) 3834-86-4895
E-mail: link@pharmazie.uni-greifswald.de

 © 2005 Wiley-VCH Verlag GmbH & Co. KGaA, Weinheim DOI: 10.1002/anie.200462888

been proposed as a result, including the suggestion of additional parameters such as percent polar surface area (PSA), cyclicity, and the number of rotatable bonds present.[4–6]

In an examination of the physicochemical properties of 1100 drug candidates in the data records of former SmithKline Beecham Pharmaceuticals, Veber et al. showed that the molecular weight cut-off at $M_r = 500$ alone does not significantly distinguish compounds with poor oral bioavailability from those with acceptable values.[6] Whereas this result is in full accordance with Lipinski's "Rule of Five", it was found that for this special case only two new criteria for a high probability of good oral bioavailability were sufficient instead of the established four. First, there must be 10 or fewer rotatable bonds and second, the polar surface area must be equal to or less than 140 Å^2 (or alternatively, 12 or fewer H-bond donors and acceptors).

This helpful suggestion to decrease the number of selection parameters which was derived from a biased proprietary data set was misinterpreted as the invention of two additional and broadly applicable selection criteria. The expansion of a rule of thumb usually waters down the basic concept and leads to a loss of practical value. Hence, it was argued that increasing the number of progression criteria on discovery projects could aid in the identification of quality compounds, but at the same time, it would also increase the complexity of the discovery process and thus slow it down. As a result, patent lifetimes would decrease, costs would increase, and there would be a drop in competitiveness in an aggressively competitive field.[1]

Therefore, instead of amendments, Leeson and Davis suggest a re-evaluation of the individual share of the parameters clog P (calculated logarithm of the partition coefficient in 1-octanol/water as a measurement of lipophilicity), molecular size expressed as M_r, and the number of H-bond acceptors and donors over time.[7] The resulting question is: Are there any time-related differences in the physical properties of orally available drugs? Vieth et al. observed no meaningful correlation between the year of launch (in the U.S. between 1982 and 2002) and target class, M_r, or lipophilicity for oral drugs.[8]

The study by Leeson and Davis revealed that drugs developed and marketed prior to 1983 have characteristics that differ significantly from newer NCEs. In a related study by Wenlock et al., drugs in various phases of clinical development were analyzed. The results showed that the mean molecular weight of compounds in the earlier phases of development was significantly higher than that of candidates in later phases of development and marketed drugs. Similar trends were observed for the characteristics of the number of H-bond acceptors and rotatable bonds present. Furthermore, it was shown that the more lipophilic compounds tended to be discontinued prior to phase III trials. These results highlight the well-known phenomenon that during lead optimization, molecules tend to get larger, more complex, more lipophilic, and so on. This issue has already been clarified by Teague et al. through the highly original concept of "lead-likeness".[9] Subsequently, Wenlock et al. demonstrated that the recognized resorption-limiting factors are not historical artifacts but are under physiological control.[10]

The investigation of Leeson and Davis sought to identify the physical properties that showed a historical shift between drugs developed before 1983 and newer drugs. Therefore, two sets were chosen: the first group contained drugs launched prior to 1983 (864 compounds) and the other collection contained drugs launched between 1983 and 2002 (329 compounds). The mean values of lipophilicity, percent polar surface area, and numbers of H-bond donors did not change over the years. Hence, these are probably the most important physical properties for oral bioavailability, which is related to an underlying requirement for effective membrane permeability.

Hydrogen-bond donors may therefore be more important than acceptors in this respect. This interpretation deserves comment in current models of membrane permeability and should be taken into account in real and virtual data bases, genetic algorithms, and fuzzy logic approaches.

On the one hand, it is necessary for the associated hydrogen-bonded water molecules to dissociate for sufficient membrane permeability; on the other hand, the drug candidate requires adequate solubility in lipids. Cell penetration and absorption are highly dependent on the ability to form hydrogen bonds as well as on drug size and lipophilicity. As medicinal chemists realize intuitively, there is an important and unchanging need to adjust the balance of polar versus nonpolar properties to allow sufficient gastrointestinal absorption.[7] Abraham et al. cast doubt on the assertion that the moderately hydrophilic solvent 1-octanol is an ideal model of the hydrophobic core of the membrane phospholipid bilayer.[11]

The first experimental detection of a low-polarity alkane-like region at the 1-octanol/water interface was reported recently.[12] The implications of this phenomenon that has been termed "grease wall" for the partitioning of drugs in 1-octanol/water mixtures await further investigation. Concentrations of lipophilic compounds at this interface might resemble accumulation in cell membranes. However, the estimation of the balance of polar versus nonpolar properties with the established 1-octanol/water partition coefficients (and the derived values of log P) is far from trivial. The reason that log P values nevertheless add a substantial share to predictive power lies in their considerable redundancy with respect to the other criteria discussed.

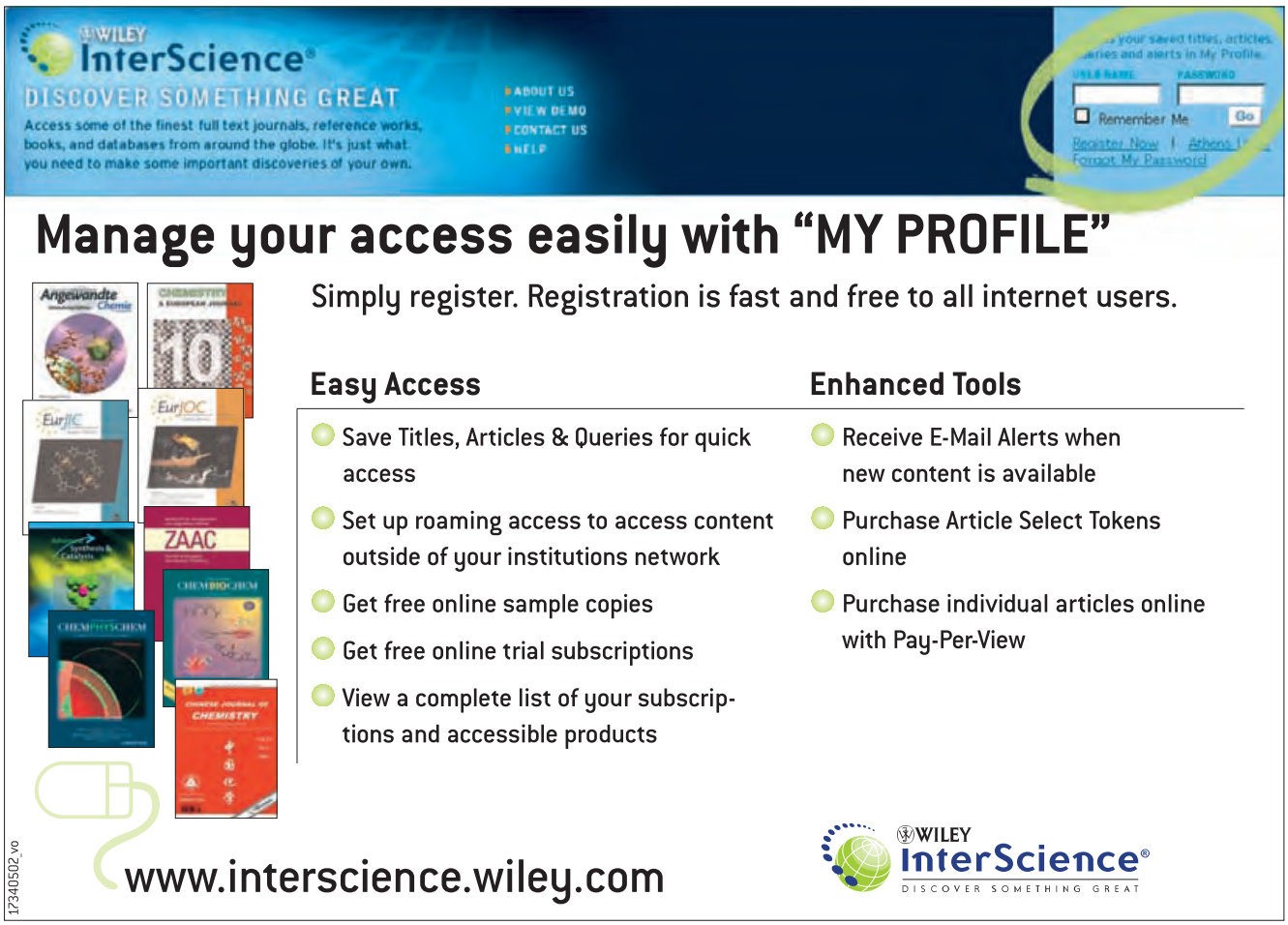
To date, in silico ADMET modeling is both a hot topic and difficult prospect.[13] Taking this insight into account, Lipinski's Rule of Five will maintain its value as a simple but highly practicable rule of thumb for years. With the results of Leeson and Davis taken into consideration, medicinal chemists may be rewarded with a robustness and prediction power higher than those derived from present methods.

Published online: June 28, 2005

[1] A. M. Davis, R. J. Riley, *Curr. Opin. Chem. Biol.* **2004**, *8*, 378–386.
[2] C. A. Lipinski, F. Lombardo, B. W. Dominy, P. J. Feeney, *Adv. Drug Delivery Rev.* **1997**, *46*, 3–25.
[3] Ovid, *Metamorphoses*, *Liber VII*.
[4] C. A. Bergstrom, M. Strafford, L. Lazorova, A. Avdeef, K. Luthman, P. Ar-

 © 2005 Wiley-VCH Verlag GmbH & Co. KGaA, Weinheim

tursson, *J. Med. Chem.* **2003**, *46*, 558–570.
[5] J. Xu, *J. Med. Chem.* **2002**, *45*, 5311–5320.
[6] D. F. Veber, S. R. Johnson, H. Y. Cheng, B. R. Smith, K. W. Ward, K. D. Kopple, *J. Med. Chem.* **2002**, *45*, 2615–2623.
[7] P. D. Leeson, A. M. Davis, *J. Med. Chem.* **2004**, *47*, 6338–6348.
[8] M. Vieth, M. G. Siegel, R. E. Higgs, I. A. Watson, D. H. Robertson, K. A. Savin, G. L. Durst, P. A. Hipskind, *J. Med. Chem.* **2004**, *47*, 224–232.
[9] S. J. Teague, A. M. Davis, P. D. Leeson, T. Oprea, *Angew. Chem.* **1999**, *111*, 3962–3967; *Angew. Chem. Int. Ed.* **1999**, *38*, 3743–3748.
[10] M. C. Wenlock, R. P. Austin, P. Barton, A. M. Davis, P. D. Leeson, *J. Med. Chem.* **2003**, *46*, 1250–1256.
[11] M. H. Abraham, H. S. Chadha, G. S. Whiting, R. C. Mitchell, *J. Pharm. Sci.* **1994**, *83*, 1085–1100.
[12] W. H. Steel, R. A. Walker, *Nature* **2003**, *424*, 296–299.
[13] T. R. Stouch, J. R. Kenyon, S. R. Johnson, X. Q. Chen, A. Doweyko, Y. Li, *J. Comput.-Aided Mol. Des.* **2003**, *17*, 83–92.



 © 2005 Wiley-VCH Verlag GmbH & Co. KGaA, Weinheim

Asymmetric Synthesis

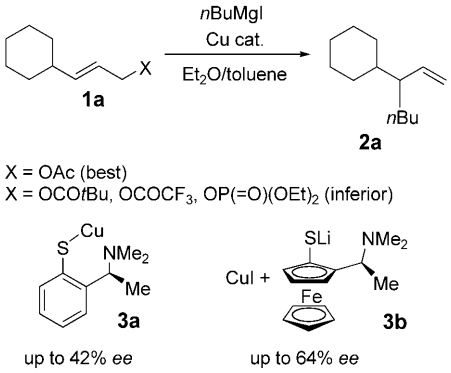
Recent Progress in Asymmetric Allylic Substitutions Catalyzed by Chiral Copper Complexes

Hideki Yorimitsu and Koichiro Oshima**

Keywords:
allylic substitution · asymmetric synthesis · copper · Grignard reagents · organozinc reagents

Allylic substitutions (also known as allylic alkylations) are among the most important carbon–carbon bond-forming reactions in organic synthesis. Palladium-catalyzed allylic substitutions and their asymmetric version have been extensively studied and widely used in a variety of total syntheses.[1] Palladium catalysis mostly requires soft nucleophiles such as malonate carbanions for high stereo- and regioselectivity. On the other hand, copper catalysis allows the use of hard nucleophiles including Grignard and organozinc reagents, thus being complementary to palladium catalysis. Moreover, copper-catalyzed substitution reactions usually proceed with high S_N2' regioselectivity, which guarantees the creation of stereogenic centers. Despite its promising potential, copper-catalyzed allylic substitution reactions had fallen behind, especially with regards to the development of asymmetric reactions.[2] However, since the first report on asymmetric allylic substitutions catalyzed by a chiral copper complex appeared in 1995,[3] remarkable progress in the development of copper-catalyzed asymmetric reactions has been made.

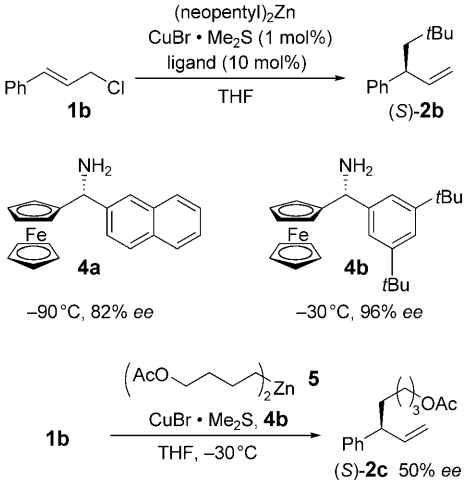
Bäckvall, van Koten, and co-workers reported that chiral arenethiolatocopper(I) **3a** catalyzed the asymmetric allylic substitution of allylic acetate with



Scheme 1.

butylmagnesium reagent (Scheme 1).[3] Their contribution is quite important not only because it reported the first copper-catalyzed asymmetric allylic substitution but also as the inherent difficulty of this asymmetric transformation was pointed out. The enantiomeric excess of the product heavily depended on many factors including the coordinating ability of the leaving group in the allylic substrates, the temperature, and the method of addition of the substrate and the Grignard reagent. The reactions of butylmagnesium iodide with **1a** (X = OAc) catalyzed by **3a** at 0 °C and at 20 °C showed similar enantioselectivities (29 % *ee* and 31 % *ee*, respectively). A lower temperature of −20 °C adversely affected the enantioselectivity (7 % *ee*). Simultaneous addition of the substrate and the Grignard reagent to a solution of **3a** provided the product with 42 % *ee*. Their observations underscored the difficulty in generating a unique transition state that leads to high enantioselectivity; there appeared to be several species present in the reaction mixture. Bäckvall and co-workers recently obtained the highest *ee* value (64 % *ee*) for the reaction of **1a** with butylmagnesium iodide in the presence of ferrocenethiolatocopper(I) **3b**.[4] Even with this latest ligand **3b**, fine tuning of the solvent, temperature, and method of addition was required.

A breakthrough in copper-catalyzed asymmetric allylic substitutions came in 1999,[5] when Dübner and Knochel focused on dialkylzinc as an alkyl source (Scheme 2). To attain a high enantioselectivity, the system required a high ratio of ligand to copper, very low temperatures, and the presence of bulky alkyl groups on zinc. For instance, the reaction of cinnamyl chloride with dineopentylzinc under catalysis by CuBr·Me_2S/**4a** (1:10) at −90 °C afforded (*S*)-**2b** with 82 % *ee*. Note, no enantioselectivity was observed when alkylzinc chloride, RZnCl, was used instead of



Scheme 2.

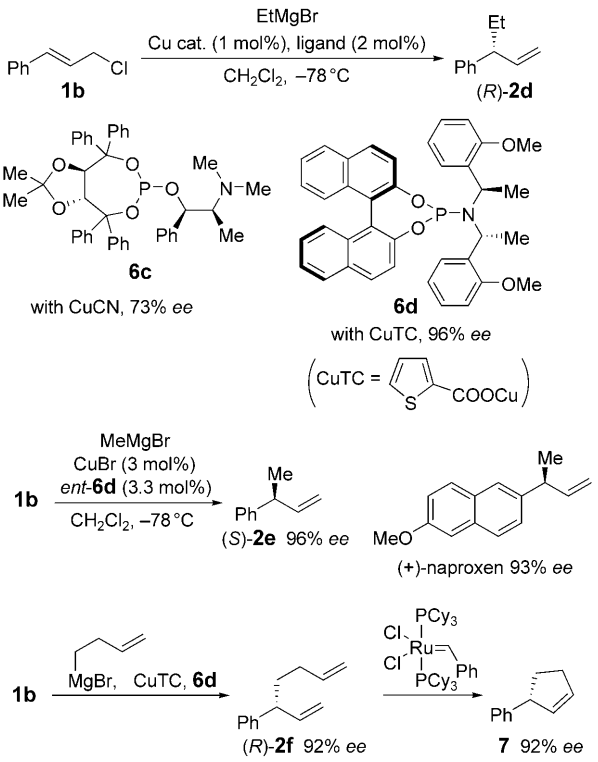
[*] Dr. H. Yorimitsu, Prof. Dr. K. Oshima
Department of Material Chemistry
Graduate School of Engineering
Kyoto University
Kyoto-daigaku Katsura
Nishikyo-ku, Kyoto 615-8510 (Japan)
Fax: (+81) 75-383-2438
E-mail:
yori@orgrxn.mbox.media.kyoto-u.ac.jp
oshima@orgrxn.mbox.media.kyoto-u.ac.jp

DOI: 10.1002/anie.200500653
© 2005 Wiley-VCH Verlag GmbH & Co. KGaA, Weinheim

dialkylzinc, R_2Zn (see Woodward's work[6]). Later, ligand **4b** proved to be more effective in this reaction to provide **2b** with 96% *ee*. However, dineopentylzinc still gave the best results. The use of linear dialkylzincs such as dipentylzinc and functionalized dialkylzinc **5** afforded the corresponding products with approximately 44–65% *ee*. Despite the necessity of bulky alkyl groups, the work of Dübner and Knochel contributed to the accelerated development of copper-catalyzed asymmetric allylic substitution reactions.

Highly enantioselective allylic substitutions with linear alkylzinc reagents remained a major challenge, but then Feringa and co-workers proposed chiral phosphoramidite ligands as the solution (Scheme 3).[7] Treatment of cinnamyl bromide with diethylzinc in the presence of $CuBr{\cdot}Me_2S$ coupled with phosphoramidite **6a** in diglyme at −40 °C afforded **2d** with 77% *ee*. Importantly, the enantiomeric excess increased as the reaction proceeded, and it was rationalized that different catalytic species are present at the early stage of the reaction. Further extensive screening of chiral phosphoramidites revealed that **6b** led to improved enantioselectivities.

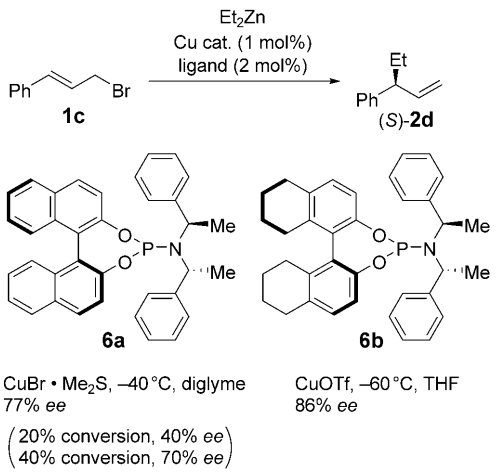
Independently, Alexakis and co-workers developed a system similar to that reported by Feringa for the reaction of Grignard reagents (Scheme 4).[8] As Bäckvall and van Koten also noted, enantioselectivity as well as regioselectivity were functions of many variables, even with the aid of chiral phosphite ligand **6c**. Very recently, a highly effective phosphoramidite ligand **6d** was developed that provided (*R*)-**2d** with high enantioselectivity. This ligand was also suitable for asymmetric allylic substitutions with diethylzinc (91% *ee*, starting from cinnamyl bromide, −40 °C) and with methylmagnesium bromide (96% *ee*). The highly enantioselective methylation was applied to the formal synthesis of (+)-naproxen. Asymmetric substitution with 3-butenyl Grignard reagent followed by ring-closing metathesis in one pot yielded chiral cyclopentene **7**, a new chiral synthon (Scheme 4). At present, this is the most efficient asymmetric allylic substitution reported with a Grignard reagent.



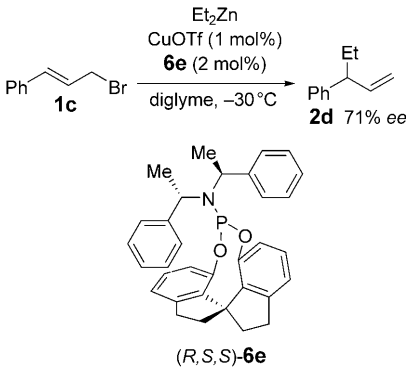
Scheme 4. Cy = cyclohexyl.

Zhou and co-workers devised original chiral spiro phosphoramidite and phosphite ligands and applied them to asymmetric allylic substitution reactions (Scheme 5).[9] Enantiomeric excess of the products was generally moderate. They successfully obtained a single crystal of a copper complex from $CuBr{\cdot}Me_2S$ and a spiro phosphoramidite ligand, L, which was similar to **6e**. X-ray crystallographic analysis disclosed the dimeric structure of $[\{CuBrL_2\}_2]$. Furthermore, the optimal Cu/ligand ratio for the reaction was shown to be 1:2. Although the actual shapes of the active species and the transition state are still not clear, these observations are nonetheless quite informative.

Hoveyda and co-workers developed various peptide-based chiral ligands for asymmetric allylic substitution reactions under copper catalysis (Scheme 6).[10] Through the synthesis and analysis of a library of ligands, the modularity of these ligands could be utilized for the improvement of the efficiency, regioselectivity, and stereoselectivity of the reaction. Dipeptide ligands **8** permitted access to the asymmetric syntheses of quaternary carbon atoms and α-alkyl-β,γ-unsaturated esters starting from allylic phosphates such as **1d**–**1f** (Scheme 6). The reactions were applied to the syntheses of a natural product, (*R*)-(−)-sporochnol, and the topoisomerase II inhibitor, (*R*)-(−)-elenic acid. With the state-of-the-art ligand **8c**, efficient addition of the alkyl reagent to trisubstituted aliphatic, not aromatic, substrates to deliver quaternary carbon centers (from **1f** to **2g**, for instance; see Scheme 6) was

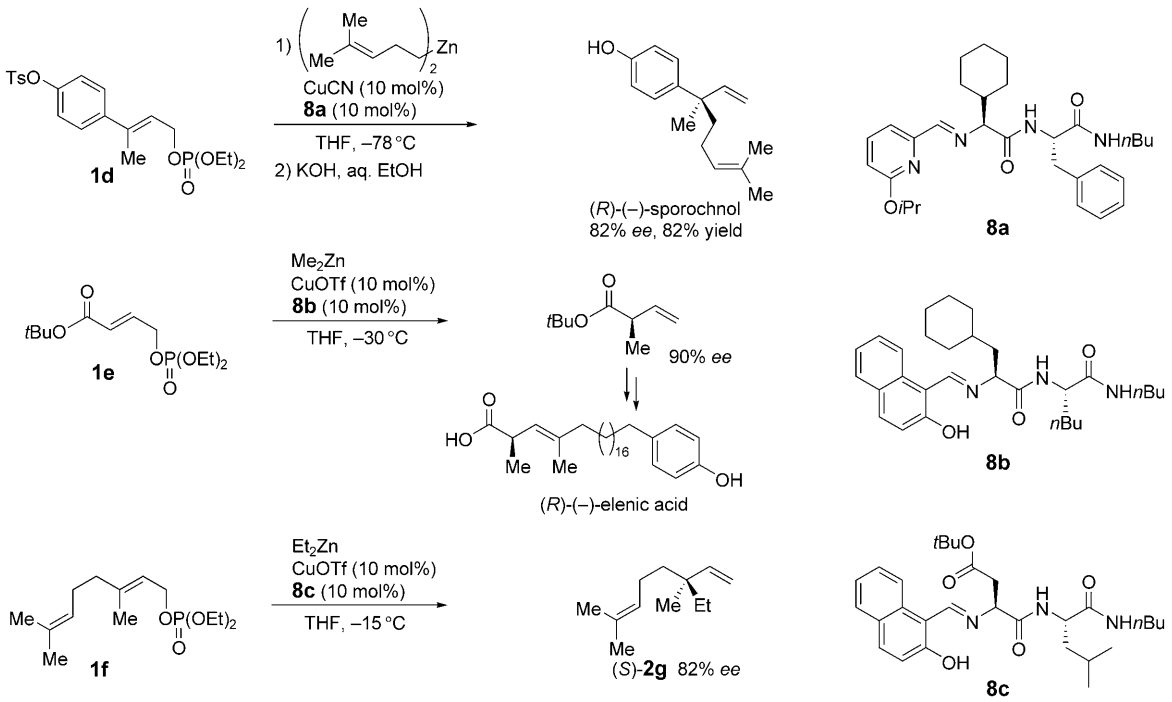


Scheme 3. Diglyme = diethyleneglycol dimethyl ether, Tf = trifluoromethanesulfonyl.



Scheme 5.

 © 2005 Wiley-VCH Verlag GmbH & Co. KGaA, Weinheim

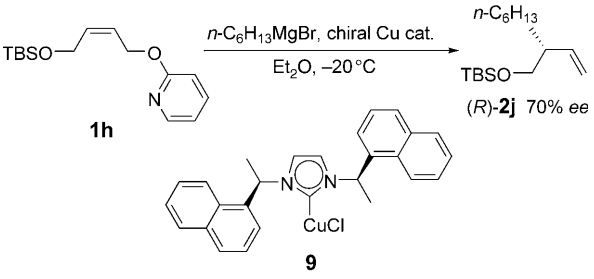


Scheme 6. Ts = *p*-toluenesulfonyl.

observed. Furthermore, the authors proposed a plausible working model through extensive screening of peptide ligands.

Piarulli, Gennari, and co-workers applied their own library of Schiff bases to the asymmetric desymmetrization of *meso* cyclic allylic bis(diethylphosphates) with organozinc reagents (Scheme 7).[11] Although only the reactions of a 4-cyclopentene-1,3-diol derivative gave satisfactory results, ligands **8d** and **8e** exhibited high efficiencies. Interestingly, in the case of asymmetric phenylation, selective transfer of the phenyl group from a mixed organozinc reagent ($2\,Ph_2Zn + Me_2Zn$) furnished the phenylated product with good enantioselectivity.

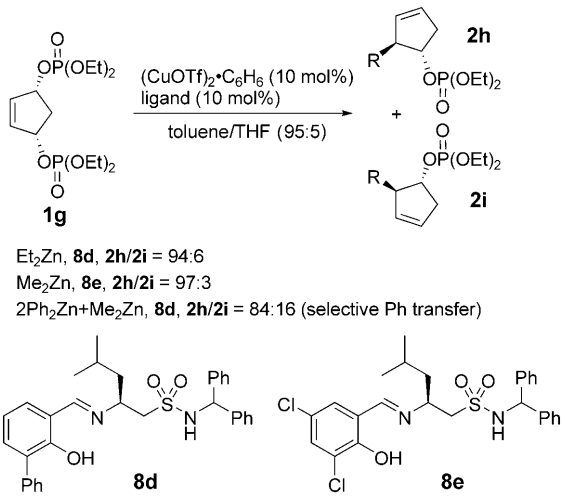
Okamoto and co-workers used C_2-symmetric carbene–copper complexes for asymmetric allylic substitution reactions (Scheme 8).[12] Sterically demanding **9** gave the highest *ee* values. The 2-pyridyloxy group of **1h** as well as the acetoxy group were good leaving groups. Although a moderate level of *ee* was obtained in preliminary results, the use of readily modifiable carbene ligands merits further investigation.



Scheme 8. TBS = *tert*-butyldimethylsilyl.

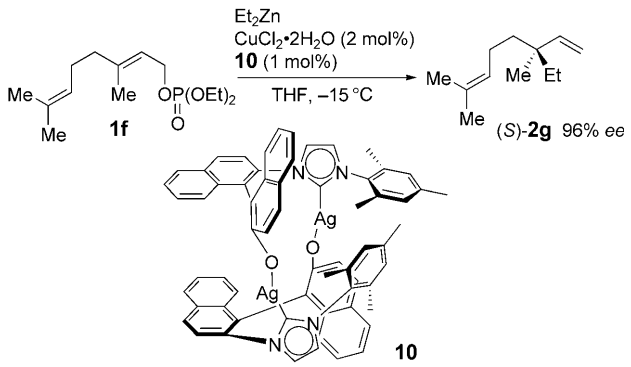
Hoveyda and co-workers have developed new bidentate carbene-based chiral ligands for efficient copper-catalyzed asymmetric allylic substitutions (Scheme 9).[13] Dinuclear silver complex **10** underwent facile ligand exchange with copper salts to generate highly effective chiral copper complexes. The catalyst loading was significantly lower than required with Schiff base ligands such as **8c**, and a higher extent of asymmetric induction in the alkylation of trisubstituted olefins than that obtained in Scheme 6 was noted. An advantage of the system is that air- and moisture-insensitive $CuCl_2 \cdot 2\,H_2O$ can catalyze the asymmetric reactions.

Woodward and co-workers examined the asymmetric allylic substitution of 2-halomethylcinnamate derivatives (Scheme 10),[14] which are attractive substrates as they are readily prepared on a large scale in two steps through Morita–Baylis–Hillman chemistry. The first generation BINOL (BINOL = 2,2′-binaphthol) catalyst **11** delivered the

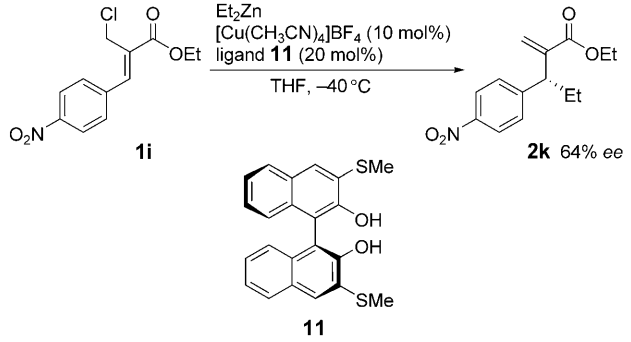


Scheme 7. Ph = phenyl.

 © 2005 Wiley-VCH Verlag GmbH & Co. KGaA, Weinheim



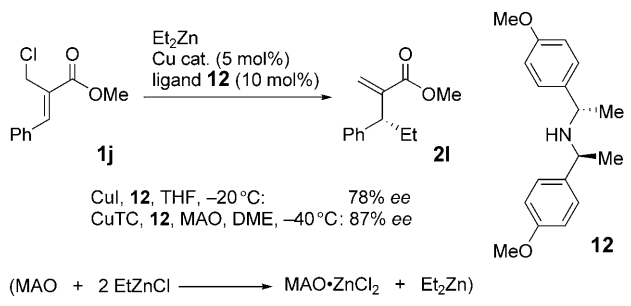
Scheme 9.



Scheme 10.

corresponding products with up to 64% *ee*. Other BINOL-type ligands exhibited lower enantioselectivities, and the system resisted further optimization. Very recently, Woodward and co-workers identified chiral secondary amines as alternative ligands for the asymmetric conversion of 2-halomethylcinnamates (Scheme 11).[6] The C_2-symmetric di(1-arylethyl)amine skeleton was indispensable for efficient stereoselection. By means of high-throughput screening, 4-methoxy-substituted ligand **12** appeared to be the optimal ligand.

During the high-throughput screening of ligands, Woodward and co-workers noticed that free amines such as **12** were always superior to their corresponding hydrochloride salts (Scheme 11). Moreover, kinetic studies revealed that the enantioselectivity of the reaction decreased as the reaction proceeded. Also, as observed by Dübner and Knochel,[5] the deliberate use of ethylzinc chloride instead of diethylzinc also led to poorer enantioselectivity. It was hence expected that removal of EtZnCl, which was gradually formed during the reaction, would enhance the enantioselectivity. To this end, they decided to exploit the zinc Schlenk equilibrium with the aid of methylaluminoxane (MAO). Indeed, the addition of MAO resulted in the anticipated increase in enantioselectivity. After further optimization, they attained up to 87% *ee* (CuTC (copper(I) thiophene-2-carboxylate), **12**, MAO, DME; Scheme 11). Although the difference in the enantiomeric excess in the absence and presence of MAO was not so large, the use of the zinc Schlenk equilibrium is attractive and applicable to other reactions.[15] The report by Woodward and co-workers lacks detailed investigation on the zinc Schlenk equilibrium that featured in their reaction. Thus, further mechanistic studies and more-efficient systems are awaited.



Scheme 11. DME = 1,2-dimethoxyethane.

Copper salts are generally cheaper than those of palladium. More significant advantages are that copper-catalyzed allylic substitutions normally proceed with high S_N2' regioselectivity and that copper catalysis allows the use of hard nucleophiles. Further extension of the scope of organometallic reagents may lead to considerably complex chiral organic molecules: for instance, the use of arylmetal reagents has not been well exploited. Although an increasing number of copper-catalyzed asymmetric allylic substitutions have emerged, little attention has been paid to their mechanistic aspects. Identification of the active species in such reactions is also still in its infancy. On the basis of experimental and theoretical studies on simpler systems,[16] profound mechanistic understanding of the enantioselection should open the door to more diverse copper-catalyzed asymmetric allylic substitutions.

Published online: June 9, 2005

[1] a) J. Tsuji, *Acc. Chem. Res.* **1969**, *2*, 144–152; b) J. Tsuji, I. Minami, *Acc. Chem. Res.* **1987**, *20*, 140–145; c) B. M. Trost, *Tetrahedron* **1977**, *33*, 2615–2649; d) B. M. Trost, D. L. Van Vranken, *Chem. Rev.* **1996**, *96*, 395–422; e) B. M. Trost, M. L. Crawley, *Chem. Rev.* **2003**, *103*, 2921–2943.

[2] For reviews, see: a) R. M. Magid, *Tetrahedron* **1980**, *36*, 1901–1930; b) B. H. Lipshutz, S. Sengupta, *Org. React.* **1992**, *41*, 135–631; c) A. S. E. Karlström, J.-E. Bäckvall in *Modern Organocopper Chemistry* (Ed.: N. Krause), Wiley-VCH, Weinheim, **2002**, pp. 259–288; For copper-catalyzed S_N2' reactions of

 © 2005 Wiley-VCH Verlag GmbH & Co. KGaA, Weinheim

vinyl epoxides, see: d) M. Pineschi, *New J. Chem.* **2004**, *28*, 657 – 665; For copper-catalyzed reactions with soft nucleophiles, see: e) Y. Kanda, O. Onomura, T. Maki, Y. Matsumura, *Chirality* **2003**, *15*, 89 – 94.

[3] M. van Klaveren, E. S. M. Persson, A. del Villar, D. M. Grove, J.-E. Bäckvall, G. van Koten, *Tetrahedron Lett.* **1995**, *36*, 3059 – 3062.

[4] a) A. S. E. Karlström, F. F. Huerta, G. J. Meuzelaar, J.-E. Bäckvall, *Synlett* **2001**, 923 – 926; b) G. J. Meuzelaar, A. S. E. Karlström, M. van Klaveren, E. S. M. Persson, A. del Villar, J.-E. Bäckvall, G. van Koten, *Tetrahedron* **2000**, *56*, 2895 – 2903.

[5] a) F. Dübner, P. Knochel, *Angew. Chem.* **1999**, *111*, 391 – 393; *Angew. Chem. Int. Ed.* **1999**, *38*, 379 – 381; ; b) F. Dübner, P. Knochel, *Tetrahedron Lett.* **2000**, *41*, 9233 – 9237.

[6] P. J. Goldsmith, S. J. Teat, S. Woodward, *Angew. Chem.* **2005**, *117*, 2275 – 2277; *Angew. Chem. Int. Ed.* **2005**, *44*, 2235 – 2237.

[7] a) H. Malda, A. W. van Zijl, L. A. Arnold, B. L. Feringa, *Org. Lett.* **2001**, *3*, 1169 – 1171; b) A. W. van Zijl, L. A. Arnold, A. J. Minnaard, B. L. Feringa, *Adv. Synth. Catal.* **2004**, *346*, 413 – 420.

[8] a) A. Alexakis, C. Malan, L. Lea, C. Benhaim, X. Fournioux, *Synlett* **2001**, 927 – 930; b) A. Alexakis, K. Croset, *Org. Lett.* **2002**, *4*, 4147 – 4149; c) K. Tissot-Croset, D. Polet, A. Alexakis, *Angew. Chem.* **2004**, *116*, 2480 – 2482; *Angew. Chem. Int. Ed.* **2004**, *43*, 2426 – 2428; d) K. Tissot-Croset, A. Alexakis, *Tetrahedron Lett.* **2004**, *45*, 7375 – 7378.

[9] W.-J. Shi, L.-X. Wang, Y. Fu, S.-F. Zhu, Q.-L. Zhou, *Tetrahedron: Asymmetry* **2003**, *14*, 3867 – 3872.

[10] a) C. A. Luchaco-Cullis, H. Mizutani, K. E. Murphy, A. H. Hoveyda, *Angew. Chem.* **2001**, *113*, 1504 – 1508; *Angew. Chem. Int. Ed.* **2001**, *40*, 1456 – 1460; b) K. E. Murphy, A. H. Hoveyda, *J. Am. Chem. Soc.* **2003**, *125*, 4690 – 4691; c) M. A. Kacprzynski, A. H. Hoveyda, *J. Am. Chem. Soc.* **2004**, *126*, 10676 – 10681; d) K. E. Murphy, A. H. Hoveyda, *Org. Lett.* **2005**, *7*, 1255 – 1258.

[11] a) U. Piarulli, P. Daubos, C. Claverie, M. Roux, C. Gennari, *Angew. Chem.* **2003**, *115*, 244 – 246; *Angew. Chem. Int. Ed.* **2003**, *42*, 234 – 236; ; b) S. Ongeri, U. Piarulli, M. Roux, C. Monti, C. Gennari, *Helv. Chim. Acta* **2002**, *85*, 3388 – 3399.

[12] S. Tominaga, Y. Oi, T. Kato, D. K. An, S. Okamoto, *Tetrahedron Lett.* **2004**, *45*, 5585 – 5588.

[13] A. O. Larsen, W. Leu, C. N. Oberhuber, J. E. Campbell, A. H. Hoveyda, *J. Am. Chem. Soc.* **2004**, *126*, 11130 – 11131.

[14] C. Börner, J. Gimeno, S. Gladiali, P. J. Goldsmith, D. Ramazzotti, S. Woodward, *Chem. Commun.* **2000**, 2433 – 2434.

[15] For further details on the zinc Schlenk equilibrium in modern organic synthesis, see: a) S. Matsubara, Y. Yamamoto, K. Utimoto, *Synlett* **1999**, 1471 – 1473; b) S. E. Denmark, S. P. O'Connor, *J. Org. Chem.* **1997**, *62*, 3390 – 3401; c) Y. Mori, M. Seki, *Tetrahedron Lett.* **2004**, *45*, 7343 – 7345; d) P. Knochel, R. D. Singer, *Chem. Rev.* **1993**, *93*, 2117 – 2188.

[16] a) E. Nakamura, S. Mori, *Angew. Chem.* **2000**, *112*, 3902 – 3924; *Angew. Chem. Int. Ed.* **2000**, *39*, 3750 – 3771; b) E. Nakamura, M. Yamanaka, N. Yoshikai, S. Mori, *Angew. Chem.* **2000**, *112*, 1989 – 1992; *Angew. Chem. Int. Ed.* **2001**, *40*, 1935 – 1938; c) M. Yamanaka, S. Kato, E. Nakamura, *J. Am. Chem. Soc.* **2004**, *126*, 6287 – 6293; d) W. Nakanishi, M. Yamanaka, E. Nakamura, *J. Am. Chem. Soc.* **2005**, *127*, 1446 – 1453; e) N. Kinoshita, K. H. Marx, K. Tanaka, K. Tsubaki, T. Kawabata, N. Yoshikai, E. Nakamura, K. Fuji, *J. Org. Chem.* **2004**, *69*, 7960 – 7964; f) S. Mori, E. Nakamura in *Modern Organocopper Chemistry* (Ed.: N. Krause), Wiley-VCH, Weinheim, **2002**, pp. 315 – 346; g) A. S. E. Karlström, J.-E. Bäckvall, *Chem. Eur. J.* **2001**, *7*, 1981 – 1989; h) A. E. Dorigo, J. Wanner, P. v. R. Schleyer, *Angew. Chem.* **1995**, *107*, 492 – 494; *Angew. Chem. Int. Ed. Engl.* **1995**, *34*, 476 – 478.

 © 2005 Wiley-VCH Verlag GmbH & Co. KGaA, Weinheim

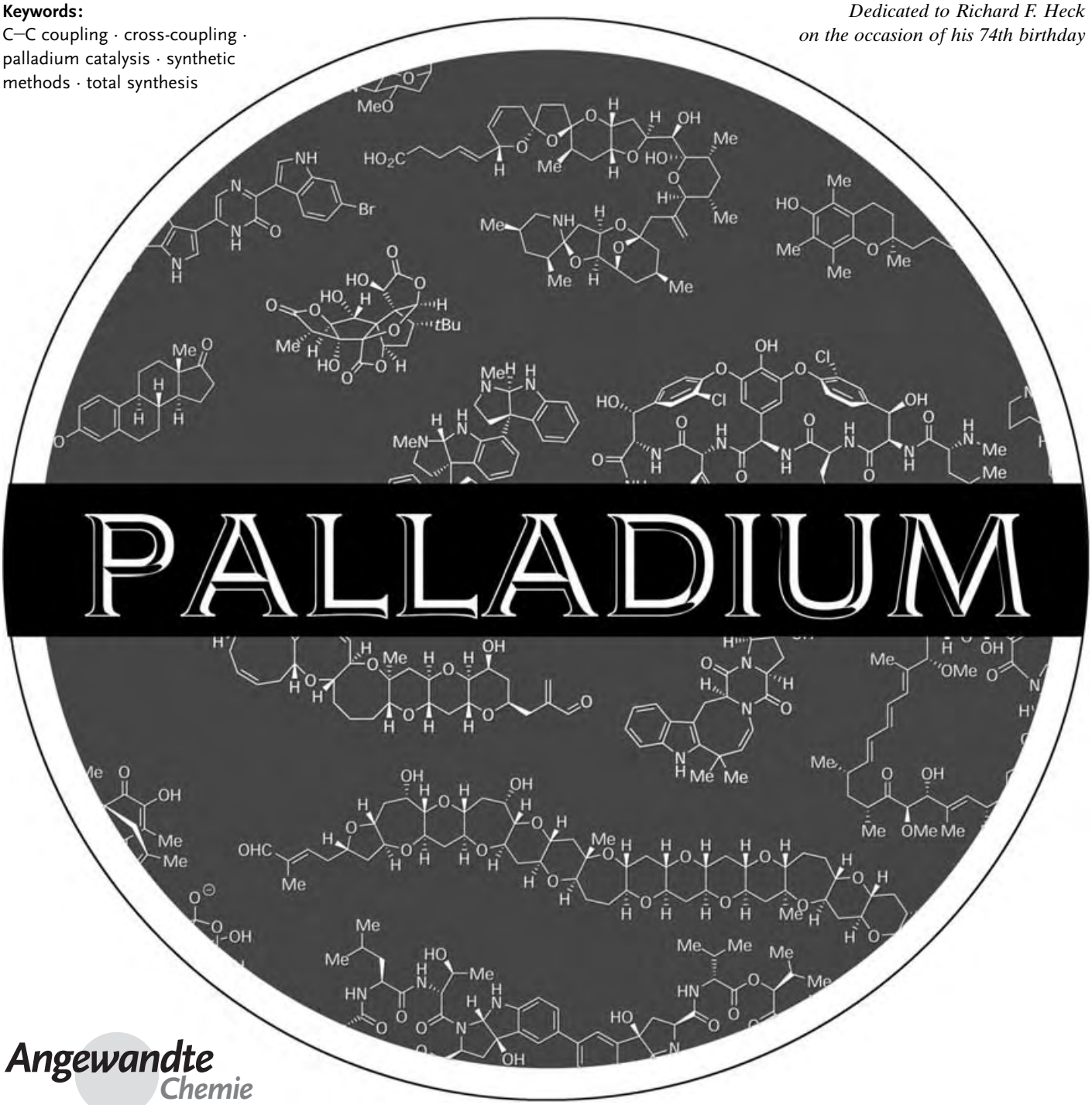
Synthetic Methods

Palladium-Catalyzed Cross-Coupling Reactions in Total Synthesis

K. C. Nicolaou, Paul G. Bulger, and David Sarlah*

Keywords:
C–C coupling · cross-coupling · palladium catalysis · synthetic methods · total synthesis

Dedicated to Richard F. Heck on the occasion of his 74th birthday



 © 2005 Wiley-VCH Verlag GmbH & Co. KGaA, Weinheim DOI: 10.1002/anie.200500368

In studying the evolution of organic chemistry and grasping its essence, one comes quickly to the conclusion that no other type of reaction plays as large a role in shaping this domain of science than carbon–carbon bond-forming reactions. The Grignard, Diels–Alder, and Wittig reactions are but three prominent examples of such processes, and are among those which have undeniably exercised decisive roles in the last century in the emergence of chemical synthesis as we know it today. In the last quarter of the 20th century, a new family of carbon–carbon bond-forming reactions based on transition-metal catalysts evolved as powerful tools in synthesis. Among them, the palladium-catalyzed cross-coupling reactions are the most prominent. In this Review, highlights of a number of selected syntheses are discussed. The examples chosen demonstrate the enormous power of these processes in the art of total synthesis and underscore their future potential in chemical synthesis.

From the Contents

1. Introduction	4443
2. The Heck Reaction	4445
3. The Stille Reaction	4452
4. The Suzuki Reaction	4458
5. The Sonogashira Reaction	4468
6. The Tsuji–Trost Reaction	4473
7. The Negishi Reaction	4478
8. Summary and Outlook	4481

1. Introduction

Ever since the first laboratory construction of a carbon–carbon bond by Kolbe in his historic synthesis of acetic acid in 1845, carbon–carbon bond-forming reactions have played an enormously decisive and important role in shaping chemical synthesis. Aldol- and Grignard-type reactions, the Diels–Alder and related pericyclic processes, and the Wittig and related reactions are but a few examples of such processes that have advanced our ability to construct increasingly complex carbon frameworks and, thus, enabled the syntheses of a myriad of organic compounds. In the last quarter of the 20th century, a new paradigm for carbon–carbon bond formation has emerged that has enhanced considerably the prowess of synthetic organic chemists to assemble complex molecular frameworks and has changed the way we think about synthesis. Based on transition-metal catalysis, this newly acquired ability to forge carbon–carbon bonds between or within functionalized and sensitive substrates provided new opportunities, particularly in total synthesis but also in medicinal and process chemistry as well as in chemical biology and nanotechnology.

Prominent among these processes are the palladium-catalyzed carbon–carbon bond-forming reactions. Because the historical, mechanistic, theoretical, and practical aspects of these processes have been amply discussed,[1] in this Review we focus only on selected applications of the most commonly applied palladium-catalyzed carbon–carbon bond-forming reactions in total synthesis, namely, the Heck, Stille, Suzuki, Sonogashira, Tsuji–Trost, and the Negishi reactions, with particular emphasis on the pioneering as well as some of the most recent and exciting examples. In doing so, we hope to illustrate the tremendous enabling ability of these modern synthetic tools.

The Heck reaction can be broadly defined as the palladium-catalyzed coupling of alkenyl or aryl (sp^2) halides or triflates with alkenes (Scheme 1) to yield products which formally result from the substitution of a hydrogen atom in the alkene coupling partner. The first examples of this reaction as we would recognize it today were reported independently by Mizoroki (1971)[2] and, in an improved form, by Heck (1972).[3] However, it would prove to be more than a decade before the broader applicability of this transformation began to be investigated by the wider synthetic organic community. The development of catalytic asymmetric Heck reactions in the late 1980s led to a further resurgence of interest in this field.[4] The Heck reaction now stands as a remarkably robust and efficient method for carbon–carbon bond formation, particularly in the generation of tertiary and quaternary stereocenters and intramolecular ring formation, and remains a flourishing area of research. Significantly, it inspired important variations that, with time, have assumed their own names, identities, and place in total synthesis.

The palladium-catalyzed cross-coupling of organic electrophiles with vinyl organotin compounds is today known as the Stille reaction (Scheme 1),[5] after the late Professor J. K. Stille who pioneered (1978)[6] and subsequently developed[7] this reaction, although the seeds of discovery were sown earlier by Kosugi and his group, who published the first reports of transition-metal-catalyzed carbon-carbon bond-forming reactions with organotin compounds a year earlier.[8,9] Nearly 30 years later the Stille reaction remains one of

[*] Prof. Dr. K. C. Nicolaou, Dr. P. G. Bulger, D. Sarlah
Department of Chemistry
and The Skaggs Institute for Chemical Biology
The Scripps Research Institute
10550 North Torrey Pines Road, La Jolla, CA 92037 (USA)
Fax: (+1) 858-784-2469
E-mail: kcn@scripps.edu
and
Department of Chemistry and Biochemistry
University of California San Diego
9500 Gilman Drive, La Jolla, CA 92093 (USA)

 DOI: 10.1002/anie.200500368 © 2005 Wiley-VCH Verlag GmbH & Co. KGaA, Weinheim

the most widely applied palladium-catalyzed carbon–carbon bond-forming reactions, in large part due to typically mild reaction conditions, the ease of preparation of a wide range of coupling partners, and the tolerance of a wide variety of sensitive functionalities in this transformation. In particular, the number of ingenious and daring applications of Stille couplings in the challenging proving ground of total synthesis bears testament to the faith placed in the robustness and versatility of this reaction by practitioners of this art. Notably, the Stille reaction can be viewed as a variation of the Heck reaction in which a hydrogen atom is replaced by a tin-bearing substituent.[10]

Another extraordinarily useful palladium-catalyzed carbon–carbon bond-forming reaction involves the palladium-mediated coupling of organic electrophiles, such as aryl or alkenyl halides and triflates, with organoboron compounds in the presence of a base (Scheme 1),[11] a process known today as the Suzuki reaction. The first examples of this protocol were reported by the Suzuki group in 1979[12]



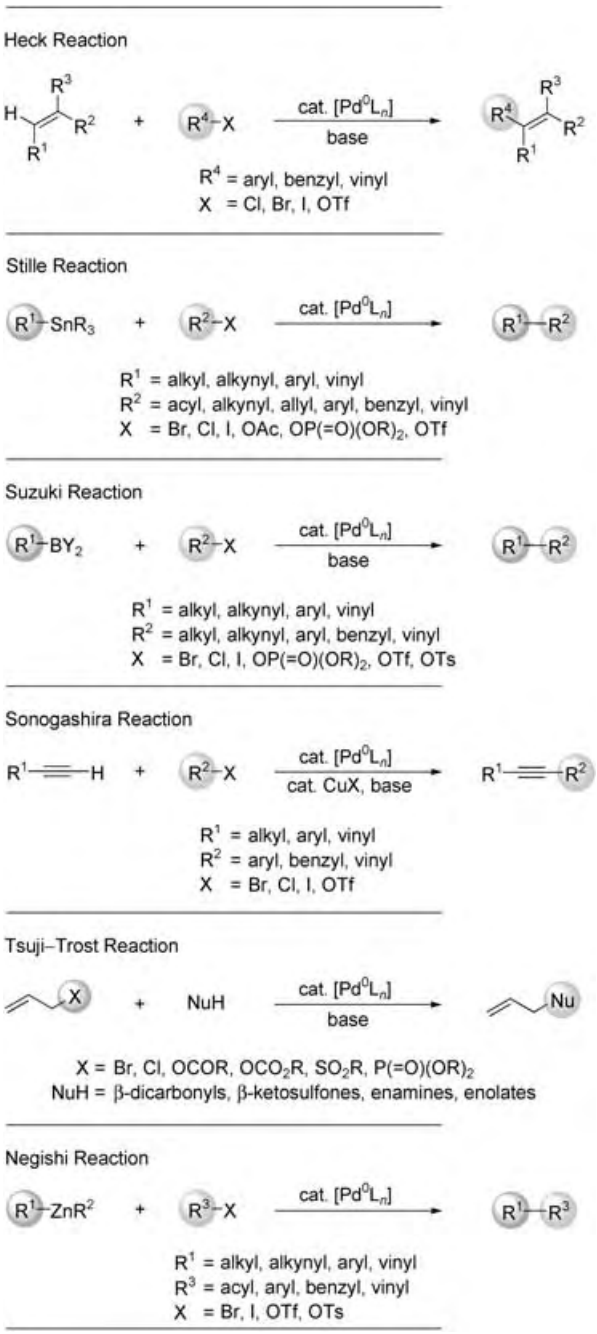
K. C. Nicolaou was born in Cyprus and educated in the UK and USA. He is Chairman of the Department of Chemistry at The Scripps Research Institute where he holds the Darlene Shiley Chair in Chemistry and the Aline W. and L. S. Skaggs Professorship in Chemical Biology. He is also Professor of Chemistry at the University of California, San Diego. His impact on chemistry, biology and medicine flows from contributions to chemical synthesis, which are described in numerous publications and patents.



Paul G. Bulger was born in London (UK) in 1978. He received his M.Chem in 2000 from the University of Oxford, where he completed his Part II project under Dr. Mark G. Moloney. He obtained his D.Phil in chemistry in 2003 for research conducted under Professor Sir Jack E. Baldwin. In the fall of 2003, he joined Professor K. C. Nicolaou's group as a postdoctoral researcher. His research interests encompass reaction mechanism and design and their application to complex natural product synthesis and chemical biology.



David Sarlah was born in Celje, Slovenia in 1983. He is currently student in the Faculty of Chemistry and Chemical Technology, University of Ljubljana (Slovenia). Since 2001, he has been a research assistant at the Laboratory of Organic and Medicinal Chemistry at the National Institute of Chemistry (Slovenia) where he carried out research on asymmetric catalysis under the direction of Dr. B. Mohar. During the summer of 2004, he was engaged in total synthesis endeavors as a member of the azaspiracid team under Professor K. C. Nicolaou.



Scheme 1. The most commonly utilized palladium-catalyzed cross-coupling reactions.

although, again, the inspiration or the seeds of this development can be found in earlier work by others, in this case the groups of Heck (1973)[13] and Negishi (1977).[14] The ensuing quarter of a century saw remarkable developments in the field. Amongst its manifold applications, the Suzuki reaction is particularly useful as a method for the construction of conjugated dienes and higher polyene systems of high stereoisomeric purity, as well as of biaryl and related systems. Furthermore, tremendous progress has been made in the development of Suzuki coupling reactions of unactivated

 © 2005 Wiley-VCH Verlag GmbH & Co. KGaA, Weinheim

alkyl halides, enabling $C(sp^2)$–$C(sp^3)$ and even $C(sp^3)$–$C(sp^3)$ bond-forming processes.[15,16] The ease of preparation of organoboron compounds (e.g. aryl, vinyl, alkyl) and their relative stability to air and water, combined with the relatively mild conditions for the reaction as well as the formation of nontoxic by-products, makes the Suzuki reaction a valuable addition to the armory of the synthetic organic chemist. Indeed, it has become one of the most reliable and widely applied palladium-catalyzed cross-coupling reactions in total synthesis, where it has found a prominent role.[17] It is, again, worth mentioning that the Suzuki reaction may be considered as a variation of the Heck reaction, in which a boron-containing group replaces a hydrogen atom in the olefinic partner of the cross-coupling.

The palladium-catalyzed coupling of terminal alkynes with vinyl or aryl halides was first reported independently and simultaneously by the groups of Cassar[18] and Heck[19] in 1975. A few months later, Sonogashira and co-workers demonstrated that, in many cases, this cross-coupling reaction could be accelerated by the addition of cocatalytic Cu^I salts to the reaction mixture.[20,21] This protocol, which has become known as the Sonogashira reaction, can be viewed as both an alkyne version of the Heck reaction and an application of palladium catalysis to the venerable Stephens–Castro reaction (the coupling of vinyl or aryl halides with stoichiometric amounts of copper(I) acetylides).[22] The Sonogashira reaction provides a valuable method for the synthesis of conjugated acetylenic systems, which are used in a diverse array of important applications from natural products and pharmaceuticals to designed molecules of interest in biotechnology and nanotechnology. Interestingly, the utility of the "copper-free" Sonogashira protocol (i.e. the original Cassar–Heck version of this reaction) has subsequently been "rediscovered" independently by a number of other researchers in recent years.[23]

The palladium-catalyzed nucleophilic substitution of allylic compounds, known as the Tsuji–Trost reaction (Scheme 1), is arguably one of the most synthetically useful carbon–carbon bond-forming reactions to emerge in the last quarter of the previous century.[24] Allyl acetates are by far the most commonly employed electrophiles, and soft anions such as those derived from β-dicarbonyl compounds are most routinely used as the nucleophilic coupling partner. However, a wide variety of substrate combinations is possible, which gives the reaction an exceptionally broad scope. The development of the palladium-catalyzed asymmetric allylic alkylation reaction over the last decade has considerably increased the enabling nature of this transformation.[25] A notable feature of the allylic alkylation reaction is its net reaction at sp^3-hybridized carbon atom centers, a feature common among the palladium-catalyzed coupling reactions only to the Fu modification of the Suzuki reaction. The asymmetric allylic alkylation reaction now provides a powerful method for ring formation, 1,3-chirality transfer, desymmetrization of *meso* substrates, the resolution of racemic compounds, and a plethora of other applications.

Historically, the use of organozinc reagents as the nucleophilic component in palladium-catalyzed cross-coupling reactions, known as the Negishi coupling (Scheme 1), actually predates the development of both the organostannane- (Stille, 1978)[6] and organoborane-based (Suzuki, 1979)[12] procedures, with the first such examples being reported in 1977.[26] Nevertheless, the rapid and widespread embracement of the latter two protocols by synthetic chemists during the 1980s led to the potential of organozinc reagents in cross-coupling processes being relatively underappreciated and underutilized during this time, particularly in total synthesis. However, recent years have witnessed a resurgent interest in the development and application of organozinc-mediated cross-couplings, largely fueled by the recognition that these reagents offer complementary modes of reactivity to those of the less electropositive metals species (e.g. B and Sn). Organozinc reagents exhibit a very high intrinsic reactivity in palladium-catalyzed cross-coupling reactions, which combined with the availability of a number of procedures for their preparation and their relatively low toxicity, makes the Negishi coupling an exceedingly useful alternative to other cross-coupling procedures, as well as constituting an important method for carbon–carbon bond formation in its own right.[27]

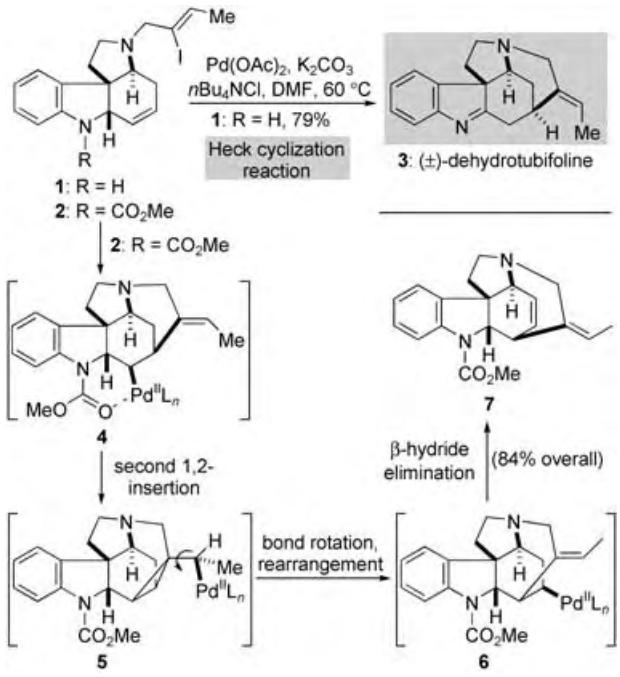
In the following sections, we discuss the contributions of these palladium-catalyzed carbon–carbon bond-forming reactions to the art and science of total synthesis and the new thinking that they have precipitated in the field.

2. The Heck Reaction

Total synthesis has benefited enormously from the Heck reaction, which has been widely applied in both its intermolecular and intramolecular variants.[28–30] The enabling attributes of this remarkable reaction manifest themselves in a plethora of ways, including appendage attachments, polyene construction, fragment couplings, and ring-closure reactions. In this section, we highlight a few examples that demonstrate the elegance and effectiveness of strategies based on the Heck reaction as the key step.

Among alkaloid total syntheses employing the Heck reaction, that of dehydrotubifoline (**3**) by Rawal and co-workers stands out (Scheme 2).[31] In this instance the palladium-catalyzed process was used to forge the final carbon–carbon bond and cast the final ring of the polycyclic structure of the target in 79% yield (**1**→**3**, Scheme 2). This effective operation, involving a 6-*exo*-palladation followed by β-hydride elimination and tautomerization of the resulting enamine species, would seem simple enough and certainly predictable, until one considers the different outcome observed with the corresponding *N*-carbomethoxy cyclization substrate **2**. In that initial attempt, the researchers noticed the exclusive formation of the unexpected compound **7**, the apparent product of a 7-*endo*-cyclopalladation reaction, in 84% yield. Moreover, close scrutiny of the spectroscopic data of pentacyclic compound **7** revealed that inversion of geometry of the exocyclic double bond had occurred, an outcome inconsistent with a direct 7-*endo* mode of ring closure. The proposed mechanistic explanation for the formation of **7** is both intriguing and illuminating. Thus, under the Jeffery modification[32] of the Heck conditions

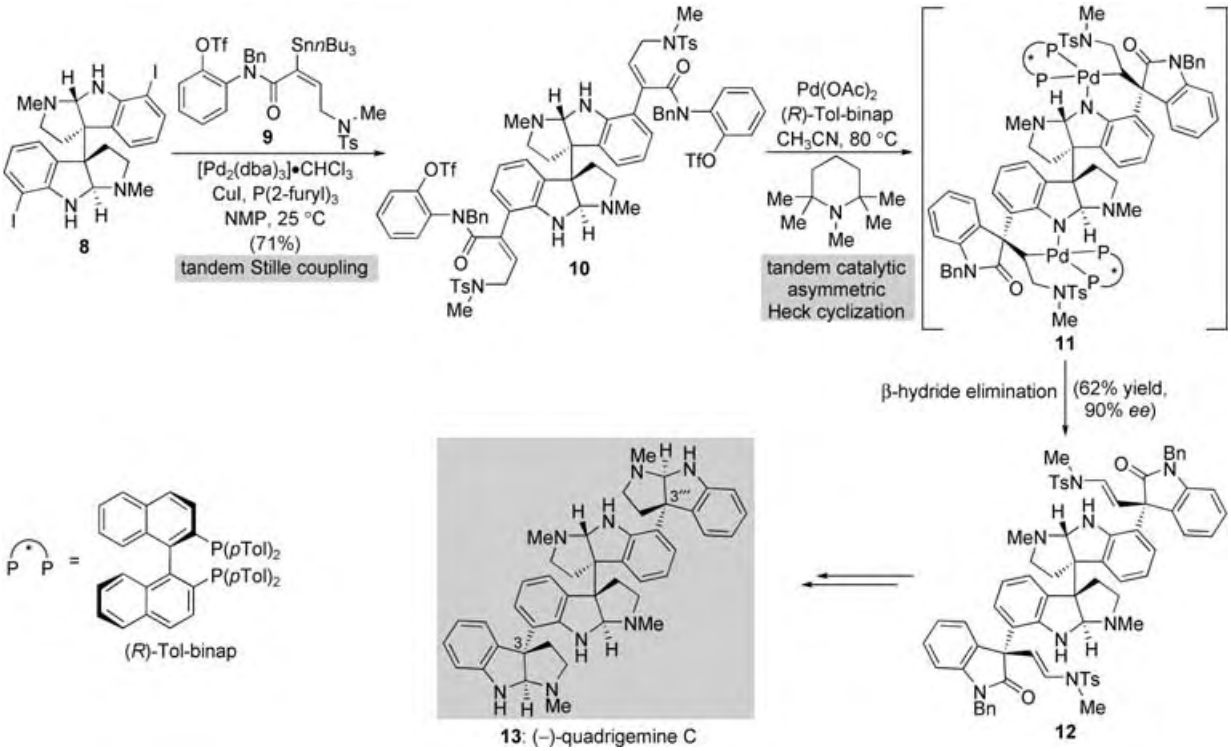
 © 2005 Wiley-VCH Verlag GmbH & Co. KGaA, Weinheim



Scheme 2. Intramolecular Heck reactions in the total synthesis of (±)-dehydrotubifoline (**3**) (Rawal et al., 1993).[31]

($Pd(OAc)_2$ cat., K_2CO_3, nBu_4NCl, DMF, 60 °C), the expected 6-*endo* cyclization occurs to yield initially σ-alkyl–palladium species **4** which, due to stabilization by intramolecular carbamate complexation, is prevented from undergoing a normally facile *syn*-β-hydride elimination, despite the presence of a β-hydrogen atom.[33] Instead, this intermediate is sufficiently long-lived to undergo a second cyclopalladation to form the cyclopropylmethyl palladium complex **5**, which is forced by steric congestion to undergo a 120° rotation about the σ bond. This then allows the proper alignment required for fragmentation of the other cyclopropane bond to give palladium complex **6**, which is no longer stabilized by carbamate complexation and undergoes the anticipated β-hydride elimination to provide the observed product **7**. Based on these mechanistic considerations, the Rawal group subjected the "carbamate-free" substrate **1** to the same reaction conditions realizing, much to their delight, the formation of the natural product dehydrotubifoline (**3**). This case serves to illustrate the fact that the "normal" mechanistic pathways of metal-catalyzed processes may be diverted, in certain cases, by the judicious placement of coordinating groups within the employed substrates.[34]

Palladium-catalyzed reactions abound in the spectacular synthesis of quadrigemine C (**13**, Scheme 3), a tetrameric member of the polypyrrolidinoindoline alkaloid family, by Overman and co-workers.[35] Noting that the quaternary C3 and C3‴ stereocenters within the target molecule **13** have the same absolute configuration, these researchers applied catalytic asymmetric Heck reactions[4] to effect the desymmetrization of an advanced *meso* intermediate **10**, formation of the two peripheral indoline residues, and installation of the final two quaternary stereocenters in a single step. This remarkable double cyclization (**10**→**11**→**12**) was preceded by another highly effective palladium-catalyzed carbon–carbon bond-forming reaction, namely a Stille coupling, which was used to assemble the required precursor **10** from its constituent

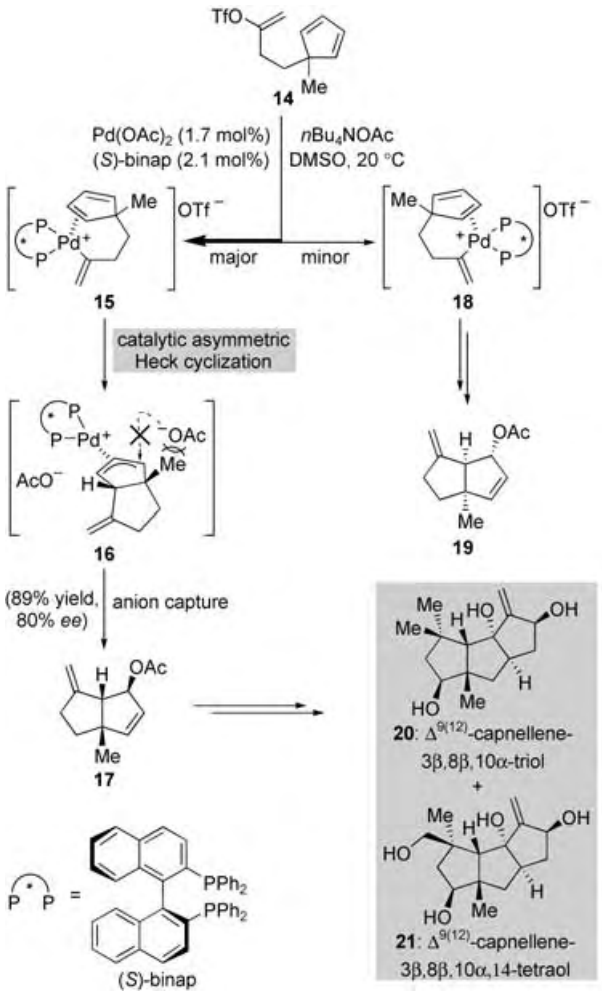


Scheme 3. Sequential tandem Stille couplings and asymmetric intramolecular Heck reactions in the enantioselective synthesis of (−)-quadrigemine C (**13**) (Overman et al., 2002).[35]

 © 2005 Wiley-VCH Verlag GmbH & Co. KGaA, Weinheim

fragments, bisaromatic iodide **8** and stannane **9**. Thus, following assembly of **10** from **8** and **9** under Farina conditions[36] (note the selectivity of the cross-coupling of the vinyl stannane moiety with the aryl iodide groups in the presence of the aryl triflate groups, owing to the higher reactivity of aryl iodides relative to the corresponding triflates towards oxidative addition to Pd^0 species),[37] the crucial asymmetric Heck reaction was induced by treatment with $Pd(OAc)_2$ (100 mol%, precatalyst), (*R*)-Tol-binap (200 mol%, ligand), and 1,2,2,6,6-pentamethylpiperidine (base) in acetonitrile at 80°C to yield decacyclic system **12** in 62% yield with 90% *ee*, together with another two undesired stereoisomeric products in a combined yield of 21%. A few more steps then converted the advanced intermediate **12** into the targeted natural product **13** in good overall yield. This accomplishment stands as a powerful testament to the power of modern synthetic methods, most notably the catalytic asymmetric Heck reaction, to construct quaternary stereocenters[38,39] and crowded bonds.

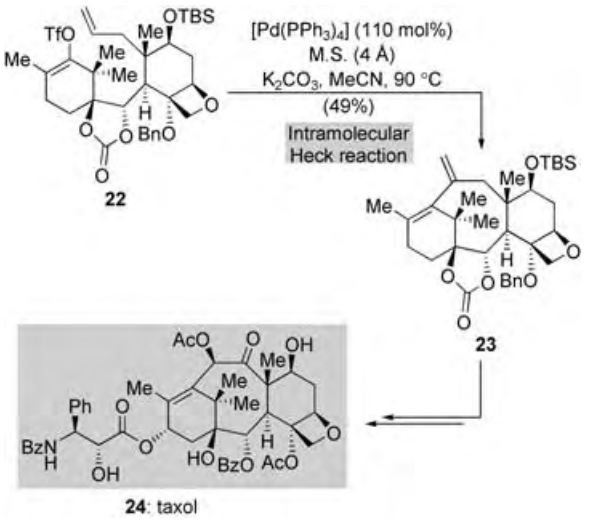
These workers were not alone in developing the asymmetric Heck reaction. Shibasaki and his group also made pioneering contributions to the field at about the same time. Indeed, it was the Overman and the Shibasaki groups that independently reported the first examples of asymmetric Heck reactions in 1989.[40,41] The Shibasaki group applied their chemistry to the catalytic asymmetric synthesis of vernolepin and, subsequently, compound **17**, a key intermediate in the total synthesis of the complex triquinane sesquiterpenes $\Delta^{9(12)}$-capnellene-3β,8β,10α-triol (**20**) and $\Delta^{9(12)}$-capnellene-3β,8β,10α,14-tetraol (**21**), by making use of an asymmetric Heck reaction/anion-capture cascade sequence (Scheme 4).[42] Thus, starting with the prochiral vinyl triflate **14**, the team was able to prepare the diquinane derivative **17** in 89% yield with 80% *ee* by treatment with catalytic amounts of $Pd(OAc)_2$ (1.7 mol%) in the presence of (*S*)-binap (2.1 mol%) and nBu_4NOAc in DMSO at 20°C. The reaction presumably proceeds through a mechanism involving oxidative addition of the vinyl triflate to the initially formed Pd^0–binap complex, followed by coordination of the resulting vinyl–Pd^{II} species to, potentially, either enantiotopic double bond of the cyclopentadienyl system to give intermediates **15** or **18**. Intermediate **15** enjoys much less steric congestion as a result of the chiral environment created around the Pd^{II} ion than does intermediate **18** and is, therefore, energetically favored; rearrangement of **15** through 1,2-insertion of the coordinated alkene into the Pd–C(vinyl) σ bond is then followed by a rapid σ→π shift to generate the π-allylpalladium species **16**. Trapping of the latter intermediate with an acetate ion derived from nBu_4NOAc, whose presence proved to be essential for the reaction to occur, proceeded in both a regio- (attack at the least-hindered terminus of the π-allyl system) and stereocontrolled (attack from the face opposite to palladium) manner, leading to the key building block, diquinane **17**. Elaboration of this intermediate, and others like it, allowed the formal total syntheses of both natural products **20** and **21**. In addition to these pioneering examples, asymmetric Heck reactions have been successfully employed in several other total syntheses of a structurally diverse range of natural products, including alkaloids, terpenoids, and polyketides. For a fuller coverage of this topic, the reader is referred to a recently published review.[4a]



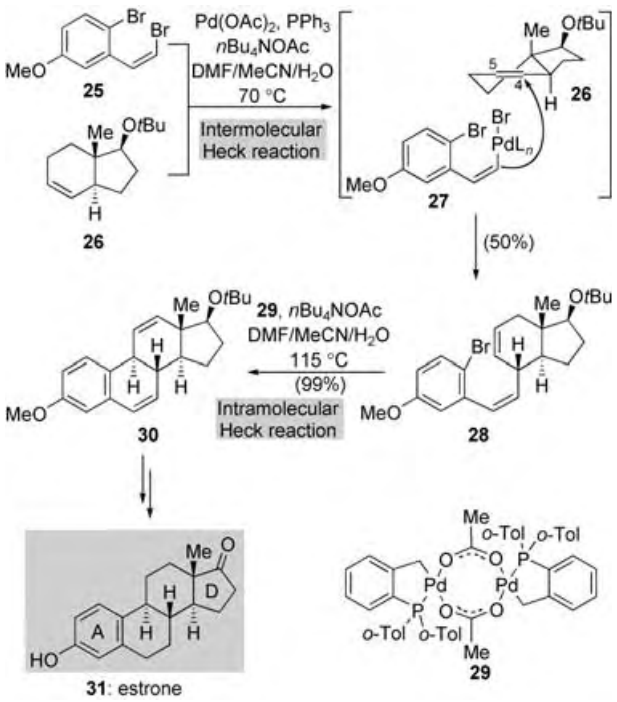
Scheme 4. Use of a catalytic asymmetric intramolecular Heck reaction to generate a key intermediate (**17**) in the total synthesis of $\Delta^{9(12)}$-capnellene-3β,8β,10α-triol (**20**) and $\Delta^{9(12)}$-capnellene-3β,8β,10α,14-tetraol (**21**) (Shibasaki et al., 1989).[42]

It can be seen from the previous two examples that, besides the customary halide species, the corresponding aryl and vinyl triflates also make excellent electrophilic coupling partners in the Heck reaction. One of the most breathtaking applications of vinyl triflates in the intramolecular Heck reaction was in the construction of the core tricyclic ABC ring system of taxol (**24**) by Danishefsky and co-workers, en route to their total synthesis of this famous natural product (Scheme 5).[43] The intramolecular cyclization of the cyclohexene moiety of triflate **22** onto the pendant terminal alkene was brought about by treatment with $[Pd(PPh_3)_4]$ and K_2CO_3 in refluxing MeCN, thus effecting the closure of the central eight-membered ring to generate the tetracyclic product **23** in 49% yield. It was found to be necessary to add a stoichiometric amount of the palladium "catalyst" in several portions over the course of the reaction to ensure its completion. Nonetheless, this transformation is astonishing for several reasons, not the least of which are the remarkable steric

 © 2005 Wiley-VCH Verlag GmbH & Co. KGaA, Weinheim



Scheme 5. The intramolecular Heck cyclization of an enol triflate in the total synthesis of Taxol (**24**) (Danishefsky et al., 1995).[43]



Scheme 6. Sequential inter- and intramolecular Heck reactions in the enantioselective total synthesis of estrone (**31**) (Tietze et al., 1998).[50]

hindrance at the junction of ring closure that had to be overcome and the strained nature of the product thus formed, which contains a tetrasubstituted bridgehead double bond. Furthermore, the delicate oxetane ring was retained intact, together with the rest of the sensitive functionality, illustrating the mildness of this ring-closure method. The success of this reaction must be, in no small part, due to the presence of the cyclic carbonate 1,2-diol-protecting group. This protecting group restricts the rotational degrees of freedom available to the precursor **22**, thus making the ring closure less entropically unfavorable.[44]

Steroid research can be regarded as one of the triumphs of 20th century science, from the story of their structure elucidation to their manifold pharmaceutical applications. No less significant is the impact this field has had on organic synthesis by providing inspiration for the development and application of a rich collection of novel synthetic methods.[45] Classic examples include the development of Robinson-type annulations,[46] the biomimetic olefin-cation cyclizations, as suggested by the Eschenmoser–Stork hypothesis[47] and pioneered by Johnson and his group,[48] and the cobalt-mediated alkyne cyclotrimerization/*ortho*-quinodimethane strategies introduced by Vollhardt and co-workers.[49]

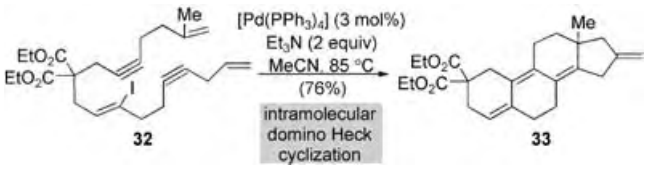
An alternative approach to the steroid skeleton, based on palladium-catalyzed Heck reactions, has more recently been introduced by Tietze and his group and is exemplified by an elegant, enantioselective total synthesis of the female sex hormone estrone (**31**, Scheme 6).[50] The cornerstone of this strategy relies on the generation of the steroid ring B by the fusion of the functionalized aromatic compound **25** onto the enantiopure hydrindene derivative **26**[51] through consecutive inter- and intramolecular Heck reactions. Specifically, these researchers discovered that treatment of a mixture of **25** and **26** with catalytic amounts of $Pd(OAc)_2$ and PPh_3 in the presence of nBu_4NOAc in a mixed $DMF/MeCN/H_2O$ solvent system at 70 °C led to the selective formation of the intermolecular Heck reaction product **28**; when the latter was treated with a catalytic amount of the novel palladacycle **29**[52] in the same solvent system, but at a slightly higher temperature (115 °C), the desired intramolecular ring closure was effected, generating the estrone core structure **30** in quantitative yield. A few more steps then completed what amounted to a concise total synthesis of the natural product.

The overall conversion of **25** and **26** into tetracyclic structure **30** is indeed a remarkable transformation, several aspects of which warrant further discussion. First, it will be noted that the initial union of **25** and **26** involves selective reaction at the vinyl bromide moiety of compound **25**. The researchers expected this selectivity based on earlier investigative work which uncovered subtle reactivity differences between the two halogen atoms in dihalides such as **25**: the vinyl–bromine bond was found to be more susceptible to oxidative addition to Pd^0 complexes than the corresponding aryl–bromine bond. Second, whereas the diastereoselectivity of the 1,2-insertion of Pd^{II} complex **27** into the double bond of hydrindene **26** could be confidently predicted on the basis of approach of the complex to the less sterically hindered face of the double bond, the regioselectivity of the insertion would, at first glance, appear to be questionable at best. Fortuitously, the sole regioisomeric product of the reaction was, indeed, the desired one, and in a case of a rationalization after the event, it was proposed that the selectivity was due to stereoelectronic effects in the transition state for 1,2-insertion. Finally, palladacycle **29** was found to be uniquely effective in catalyzing the intramolecular Heck reaction, with more-conventional catalyst systems proving to be much less efficient. Even more impressively, it was subsequently found that the direct conversion of **25** and **26** into tetracyclic

 © 2005 Wiley-VCH Verlag GmbH & Co. KGaA, Weinheim

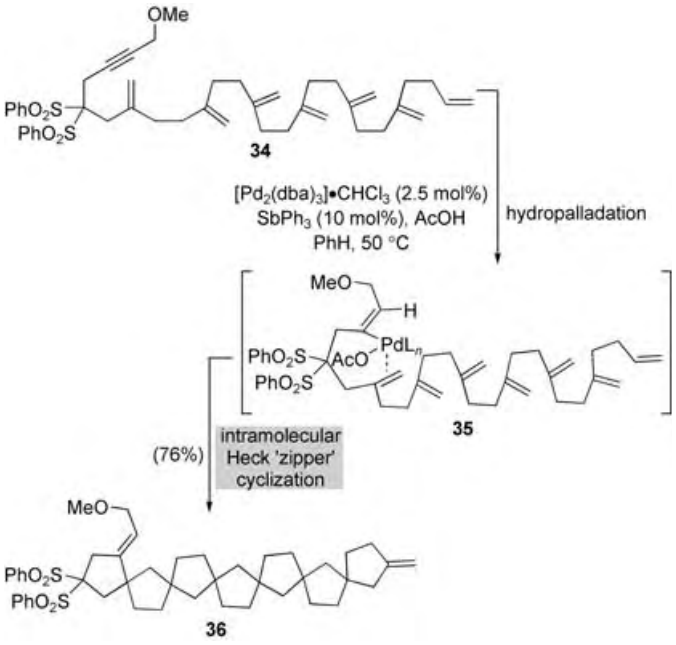
compound **30**, in a domino reaction without the need for isolation of intermediate **28**, could be effected by treatment of a mixture of the two starting materials with catalyst **29**, although the overall yield (35%) was slightly lower than that of the two-step process.

A famous and equally stunning application of the domino intramolecular Heck reaction can be found in the formation of the steroidal ring framework in compound **33** in a single operation from the polyunsaturated acyclic precursor molecule **32** (Scheme 7).[53] It was Negishi and co-workers who



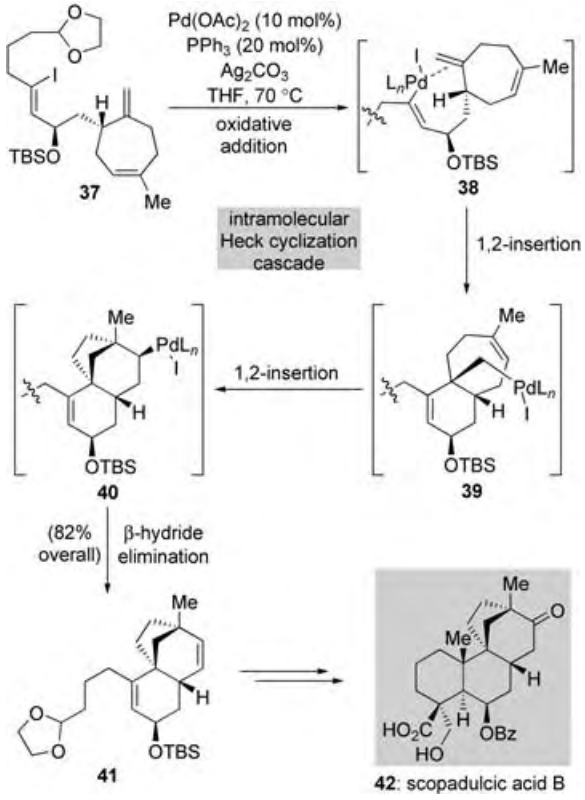
Scheme 7. A palladium-catalyzed "zipper" tetracyclization approach to steroidal skeletons (Negishi et al., 1990).[53]

demonstrated this transformation by treatment of iodide **32** with $[Pd(PPh_3)_4]$ catalyst (3 mol%) in the presence of triethylamine in refluxing acetonitrile. This reaction involves a series of consecutive carbopalladations that lead to the regiocontrolled formation of four new carbon–carbon bonds and four carbocyclic rings, ultimately generating polycycle **33** in an impressive 76% overall yield. Not to be outdone, the Trost group subsequently reported even more spectacular examples of intramolecular Heck-type polycyclization processes. These studies are exemplified by the hydridopalladium acetate catalyzed formation of the intriguing heptacyclic structure **36** in a single operation from the open-chain precursor **34** (Scheme 8).[54] Such cascade cyclization processes, colorfully termed "zipper reactions", provide efficient and economical means of generating polycyclic molecular complexity from simple acyclic materials in a manner that would have been impossible before the advent of palladium-catalyzed carbon–carbon bond-forming reactions, and are illustrative of the enabling power of this methodology.[55,56]



Scheme 8. A hydridopalladium acetate-catalyzed "zipper" polycyclization (Trost and Shi, 1991).[54]

An application of a palladium-catalyzed polyene cyclization reaction in the context of total synthesis can be found in the pioneering approach of the Overman group towards the synthesis of the scopadulcic acid family of diterpenes.[57] In this highly inventive strategy, it was reasoned by the group that the three of the four rings of the formidable tetracyclic structure of the target products, including the sterically congested bridged bicyclic system and two of the three quaternary stereocenters, could be fashioned from a simple monocyclic precursor and in a single step through a palladium-catalyzed intramolecular Heck cyclization cascade process. The realization of this hypothesis in practice is illustrated by the total synthesis of scopadulcic acid B (**42**), as shown in Scheme 9, in which the substituted cycloheptene **37** was converted into tricyclic compound **41** in one step. This cascade was triggered by the addition of $Pd(OAc)_2$ (10 mol%), PPh_3 (20 mol%), and Ag_2CO_3 to a refluxing solution of iodide **37** in THF. The initial oxidative addition into the carbon-iodine bond generated intermediate **38** with retention of configuration. This was followed by the first intramolecular cyclization to generate alkylpalladium(II) intermediate **39**, which was unable to exit the catalytic cycle

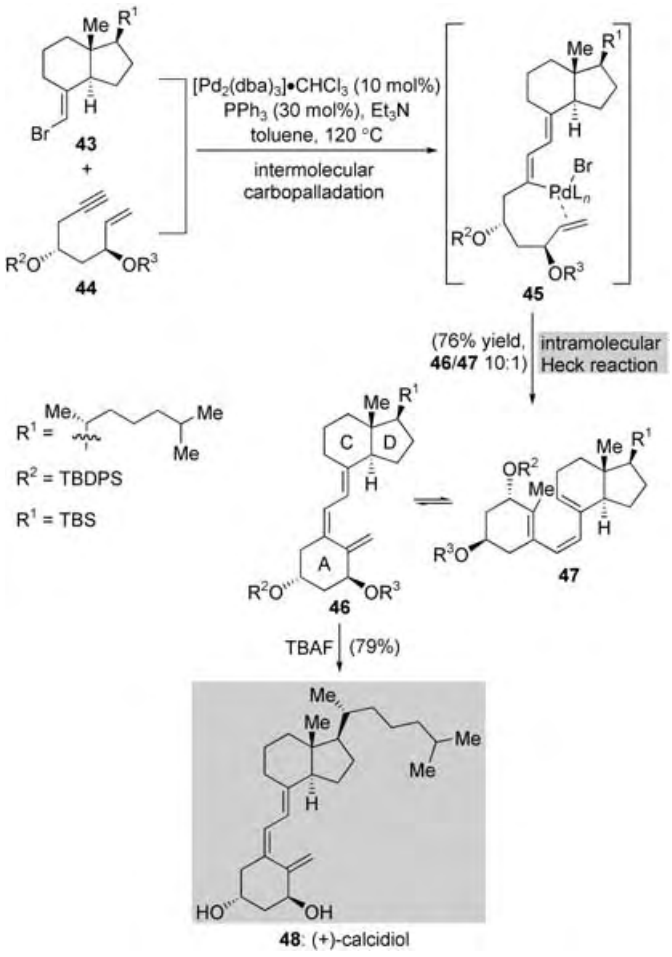


Scheme 9. A sequential intramolecular Heck cyclization approach to the total synthesis of scopadulcic acid B (**42**) (Overman et al., 1993).[57]

 © 2005 Wiley-VCH Verlag GmbH & Co. KGaA, Weinheim

by β-hydride elimination owing to the absence of any suitably disposed hydrogen atoms and thus underwent the second 1,2-insertion reaction into the trisubstituted alkene conveniently located within bonding distance. The resulting species **40**, having exhausted its possibilities for intramolecular carbon–carbon bond formation, finally succumbed to β-hydride elimination to afford the isolated product **41**. Each of these steps proceeded with remarkable efficiency and selectivity: tricyclic compound **41** was isolated in 82% yield as a single stereoisomer! This intermediate could then be elaborated in a number of steps, which included the fusion of the final carbocyclic ring onto the tricyclic system, to complete the total synthesis of scopadulcic acid B (**42**). This synthesis provides further evidence for the utility of the Heck reaction in the construction of sterically crowded systems and quaternary stereocenters through cascade processes.

The Trost group has reported an interesting addition to the menagerie of methods documented for the preparation of the clinically important 1α-hydroxyvitamin D (calcidiol) and its analogues,[58] in a convergent strategy based on a palladium-catalyzed cascade reaction (Scheme 10).[59,60] Thus, the addition of a mixture of bromide **43** and enyne **44** to a heated solution of $[Pd_2(dba)_3]\cdot CHCl_3$ (10 mol%) and PPh_3 (30 mol%) in toluene/Et_3N (1:1 v/v) initiated a sequence involving the oxidative addition of the carbon–bromine bond of vinyl halide **43** to Pd^0 followed by chemoselective intermolecular carbopalladation of the alkyne moiety of compound **44** to yield intermediate **45**. The latter was suitably arranged to undergo a subsequent regioselective intramolecular Heck reaction to form the final carbon–carbon bond of the product. The net result of this reaction sequence was the attachment of the CD-ring fragment, formation of ring A, and creation of the requisite triene system in a single operation! The desired product **46** was in fact isolated as a 10:1 mixture with the isomeric triene **47**. It was shown that this triene mixture derives from a thermal equilibration, by means of a 1,7-sigmatropic hydrogen shift, of the initially formed product **46** under the reaction conditions. Separation of the minor product component **47** and subsequent thermal reequilibration increased the overall yield of the desired triene **46** to 76%. Removal of the two silyl protecting groups then completed the total synthesis of (+)-calcidiol (**48**).[61]

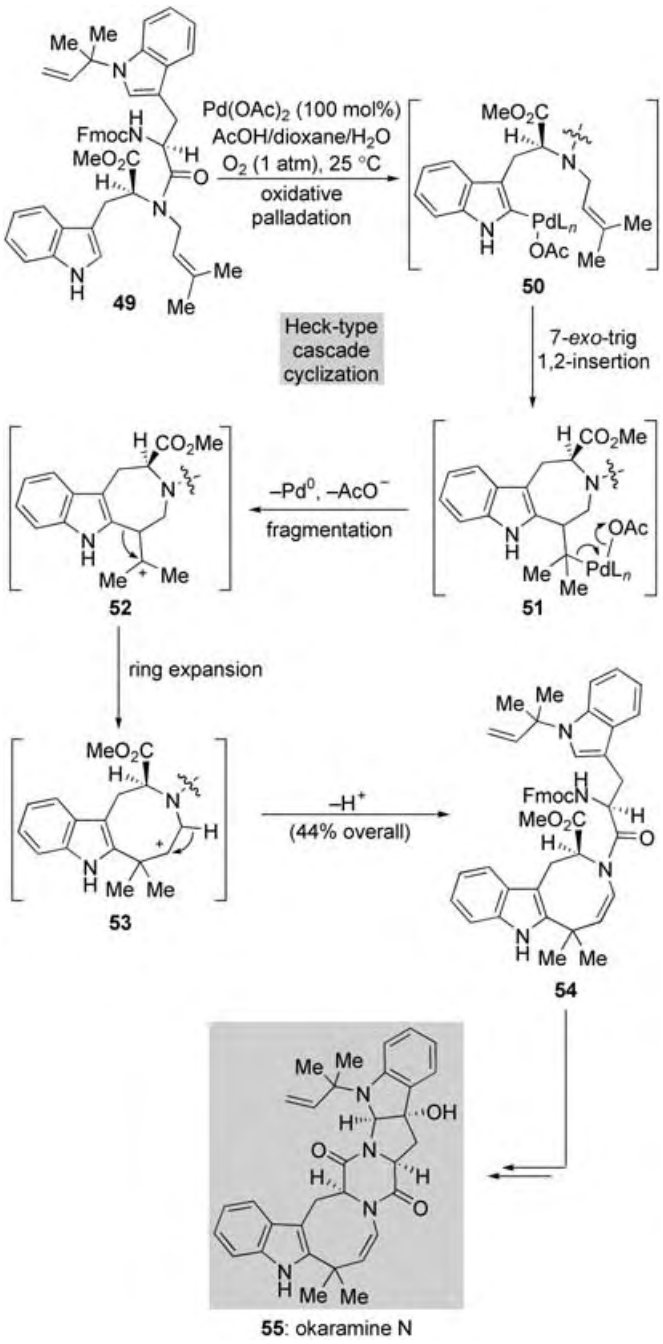


Scheme 10. A tandem intermolecular carbopalladation/intramolecular Heck cyclization approach to the synthesis of (+)-calcidiol (**48**) (Trost et al., 1992).[59]

The versatility of the Heck reaction is such that it is continually finding applications in novel carbon–carbon bond-forming processes, seemingly limited only by the ingenuity of the practitioner. As one recent example, we highlight the masterful synthesis of okaramine N (**55**, Scheme 11) by the Corey group.[62] In this instance, one of the key issues facing the researchers was the formation of the eight-membered medium ring, a motif often notoriously difficult to construct by traditional cyclization methods owing to a combination of enthalpic and entropic factors.[63,64] Nevertheless, the team surmised that it would, in fact, be possible to generate this ring system in a single step from an appropriately substituted acyclic precursor by employing palladium chemistry. Indeed, as shown in Scheme 11, it was found that treatment of indole **49** with $Pd(OAc)_2$ (100 mol%) in an AcOH/dioxane/H_2O solvent system under O_2 (1 atm) at ambient temperature led to the direct formation of pentacyclic compound **54** in reasonable yield (44%).

The visual relationship between the starting material **49** and the product **54** obscures the fact that the proposed mechanism of the reaction linking the two is, in reality, comprised of five distinct transformations, none of which is the apparent 8-*endo* mode of ring closure. Indeed, it may not be readily apparent how the reaction is initiated since, unlike all the other examples discussed so far, there is no carbon–halogen (or triflate) bond within the starting material **49** into which a Pd^0 species can insert. In fact, the first step in the mechanism proposed for this remarkable transformation is the selective and direct palladation of the unprotected indole unit, in the presence of the other *N*-prenylated indole motif, at C2 to generate indolyl–palladium(II) intermediate **50**.[65] Once formed, this palladated species can then undergo the expected 7-*exo*-trig 1,2-insertion to generate the next intermediate in the sequence, namely η^1-alkyl–palladium(II) species **51**. At this point the course of the reaction diverges from that which would, at first inspection, appear to be the most likely outcome. Despite the presence of no fewer than seven appropriately located hydrogen atoms, compound **51** does not undergo β-hydride elimination, but instead suffers a heterolytic fragmentation to generate tertiary carbocation **52**.

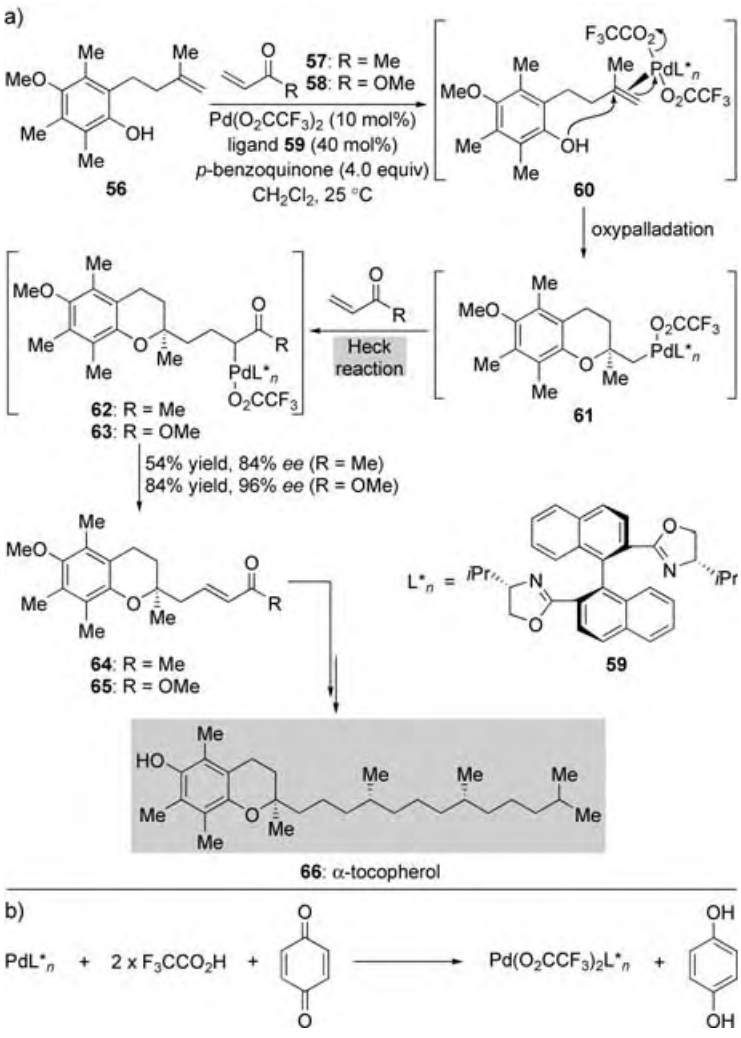
 © 2005 Wiley-VCH Verlag GmbH & Co. KGaA, Weinheim



Scheme 11. Use of a novel Heck-type cascade cyclization to furnish an 8-membered ring in the synthesis of okaramine N (**55**) (Corey et al., 2003).[62]

Selective migration of the most-electron-rich group (i.e. the β-(2-indolyl) group) then results in ring expansion to furnish the eight-membered ring system **53**, rapidly followed by loss of a proton to yield the observed product **54**. The researchers' faith in the viability of this whole process was won by earlier model studies that demonstrated its aptitude for the formation of similar systems;[66] nonetheless, its application in the complex setting described here was certainly not without risk, a risk which ultimately paid off handsomely. Critical to the success of this venture was the employment of an $AcOH/H_2O$ solvent system; in the absence of acetic acid, no cyclization occurred, whilst omission of water resulted in the near exclusive formation of seven-membered-ring cyclization products. The direct, selective C–H bond functionalization of the indole nucleus represents a particularly exciting aspect of this methodology.[67] However, such procedures have generally required stoichiometric amounts of palladium(II) salts, which from a practical and economic standpoint, limits their use somewhat, particularly on a large scale. Recently though, the Stoltz group reported protocols for the aerobic oxidative annulation of indoles through C–H bond functionalization that are truly catalytic in palladium and which would thus appear to hold great potential for future development.[68]

The Tietze group recently reported a novel palladium-catalyzed domino reaction for the synthesis of the vitamin E family of tocopherols and tocotrienols (Scheme 12a). This process combines sequential intramolecular enantioselective oxypalladation and intermolecular Heck reactions to rapidly assemble the chiral chroman framework of these biologically and commercially important antioxidant molecules.[69] Treat-

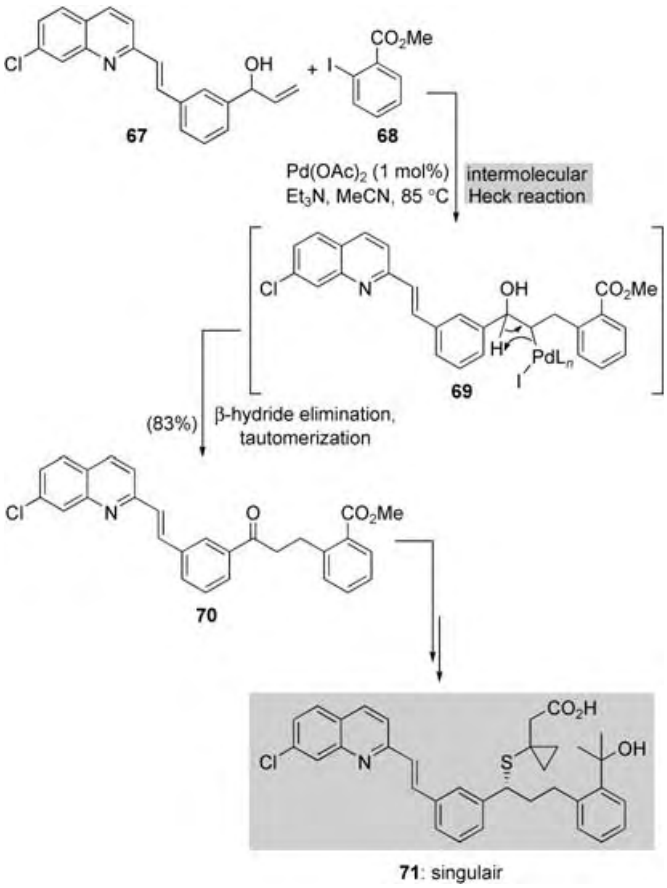


Scheme 12. a) A palladium-catalyzed enantioselective domino reaction in the synthesis of α-tocopherol (**66**); b) regeneration of the catalytically active Pd^{II} species from a Pd^0 complex (Tietze et al., 2005).[69]

 © 2005 Wiley-VCH Verlag GmbH & Co. KGaA, Weinheim

ment of readily available alkene **56** with $Pd(O_2CCF_3)_2$ (10 mol%), ligand **59** (40 mol%), *p*-benzoquinone (4.0 equiv), and either methyl vinyl ketone (**57**) or methyl acrylate (**58**), in CH_2Cl_2 at ambient temperature triggers a series of events that lead to the corresponding products **64** (R = Me) or **65** (R = OMe) in good to excellent yield and with excellent enantioselectivity. The sequence presumably begins with the enantiofacial coordination of the chiral ligated Pd^{II} complex, generated from $Pd(O_2CCF_3)_2$ and the enantiomerically pure ligand **59**, to the 1,1-disubstituted alkene, yielding intermediate **60**. This coordination of Pd^{II} to the π system renders the alkene moiety susceptible to nucleophilic attack, thus enabling the intramolecular cyclization of the free phenolic hydroxy group to generate σ-alkyl–palladium(II) species **61**. Unable to undergo the customary β-hydride elimination, intermediate **61** is sufficiently long-lived to be intercepted by either **57** or **58** in an intermolecular Heck reaction process to afford the observed products **64** or **65**, respectively. Notably, the final β-hydride elimination from intermediates **62** and **63** concomitantly generates a Pd^0 species, whereas it is a Pd^{II} complex that is required, in this case, to initiate the domino reaction. Thus, to avoid the use of stoichiometric amounts of $Pd(O_2CCF_3)_2$, a method needed to be found for the reoxidation of Pd^0 to Pd^{II} in situ, and indeed this was the role played by *p*-benzoquinone (Scheme 12b). The functionalized side chains introduced in the intermolecular Heck reaction provided a sufficient handle for the elaboration of either **64** or **65** into α-tocopherol (**66**), the member of the vitamin E family with the most pronounced biological activity.

The impact of palladium-catalyzed coupling reactions has been felt in a number of fields outside academic research laboratories, particularly in the pharmaceutical industry. Palladium-catalyzed carbon–carbon bond-forming reactions have provided chemists with new avenues for the design, synthesis, optimization, and manufacture of therapeutic agents, and, as such, have dramatically benefited humanity.[70,71] One such example is found in the synthesis of singulair (**71**, Scheme 13), a selective leukotriene receptor antagonist marketed by Merck for the prophylaxis and chronic treatment of asthma. An intermolecular Heck reaction was utilized to couple the two key fragments;[72] treatment of a mixture of allylic alcohol **67** and aromatic iodide **68** with triethylamine and a low catalyst loading (1 mol% of $Pd(OAc)_2$) in refluxing acetonitrile, notably in the absence of any additional ligands for palladium, led to the formation of ketone **70** in 83% yield.[72] Isolation of ketone **70** on a large scale by direct crystallization of the product from the reaction mixture proved to be remarkably facile. The selective formation of ketone **70** in this reaction is the result of β-hydride elimination from the initially formed alkyl–palladium(II) intermediate **69** occurring regioselectively towards the hydroxy substituent as shown, to give an enol species that subsequently tautomerizes to the observed ketone **70**. The formation of carbonyl compounds in such a manner is the usual fate of allylic alcohols when subjected to the Heck reaction[73] and, therefore, this process constitutes a useful alternative to the traditional 1,4-conjugate addition reactions for the construction of such systems.

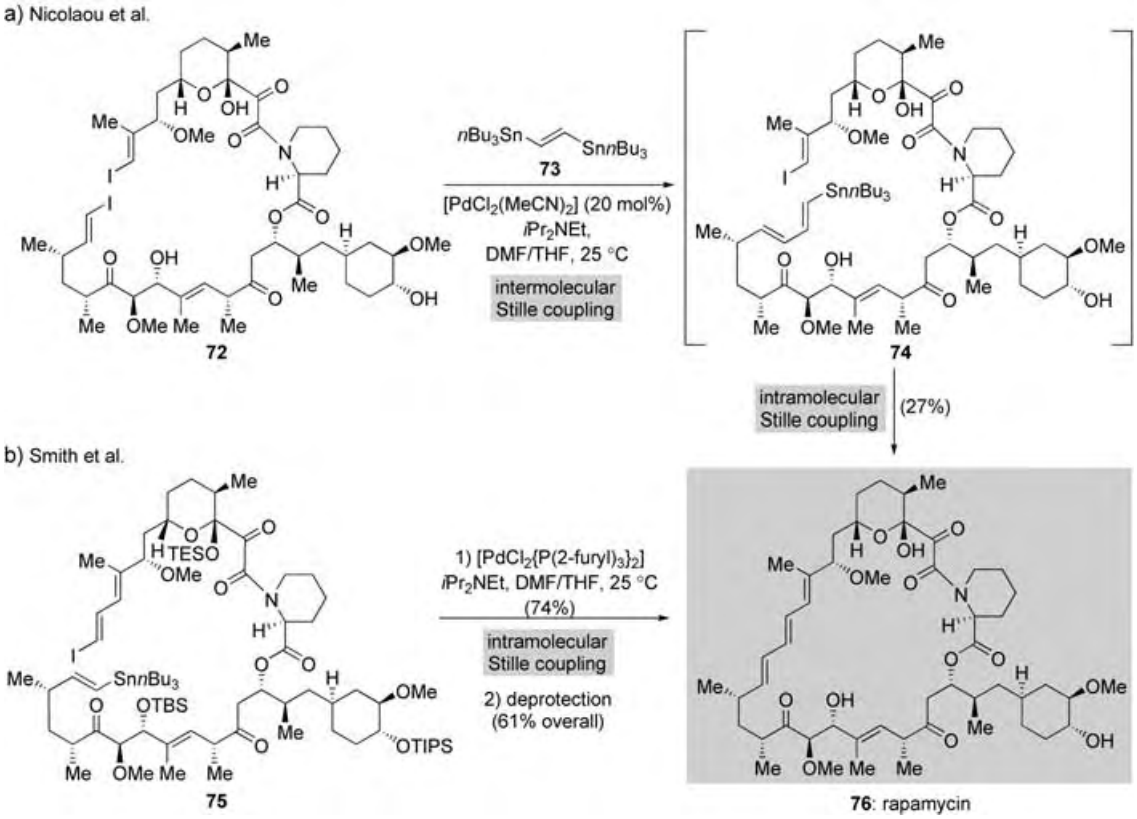


Scheme 13. The use of an intermolecular Heck reaction in the commercial synthesis of Singulair (**71**) (Merck, 1993).[72]

3. The Stille Reaction

In addition to being a powerful intermolecular carbon–carbon bond-forming process, the Stille reaction has found widespread use in the generation of cyclic structures. The first examples of the intramolecular Stille reaction, reported by Piers and co-workers in 1985,[74] were concerned with the generation of five- and six-membered rings. However, it was not long before the utility of this process for the generation of a wider variety of ring sizes, macrocyclic systems in particular, was demonstrated.[75] Today, the Stille reaction constitutes a reliable and often-used method for the construction of carbocyclic and heterocyclic rings, be they common, medium or large.[76] A striking example of this type of reaction is the pioneering stitching-cyclization reaction applied by the Nicolaou group to construct rapamycin (**76**) from the bis(vinyl iodide) precursor **72** and *trans*-1,2-distannyl ethylene **73** (Scheme 14a).[77] The final step of the total synthesis of rapamycin involved a double Stille coupling process and proceeded from the naked (no protecting groups) precursor **72**, under the influence of $[PdCl_2(MeCN)_2]$ (20 mol%) and iPr_2NEt as a dilute solution in DMF/THF at ambient temperature, presumably through the intermediacy of iodostannane **74**. Thus, in one fell swoop, the 29-membered macrocyclic ring of rapamycin, with its *all-trans* triene system,

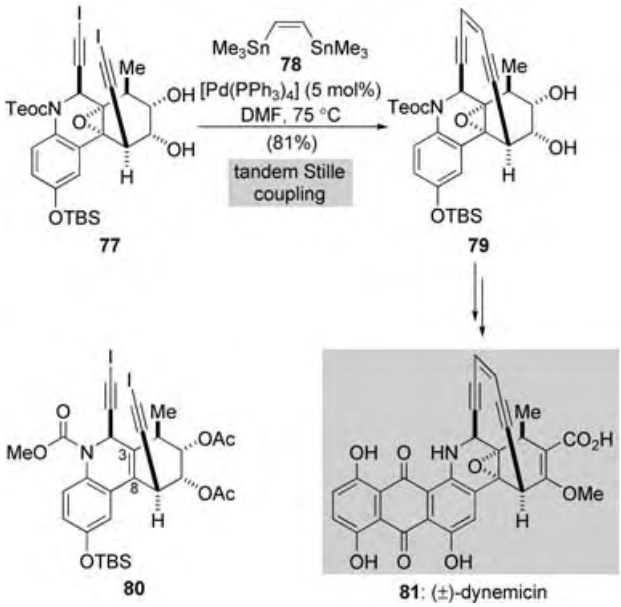
 © 2005 Wiley-VCH Verlag GmbH & Co. KGaA, Weinheim



Scheme 14. Approaches to the total synthesis of rapamycin (**76**). a) A "stitching cyclization" to complete the total synthesis (Nicolaou and co-workers, 1993);[77] b) an intramolecular Stille macrocyclization approach (Smith et al., 1995).[78]

was installed from an acyclic precursor and without the need for any protection/deprotection operations. The success of this macrocyclization reaction undoubtedly relies, to no small measure, on the templating effect of the palladium center, which brings the two ends of the chain into the requisite close proximity for bond formation. A variation of this strategy was subsequently employed by Smith and co-workers in their elegant total synthesis of rapamycin,[78] in this case involving acyclic precursor **75** (Scheme 14b).[79,80]

Another spectacular "stitching-cyclization" reaction involving a double Stille reaction was subsequently employed in the total synthesis of the enediyne anticancer antibiotic dynemicin (**81**) by Danishefsky and co-workers (Scheme 15).[81] The bis(iodoalkyne) substrate **77** reacted smoothly with *cis*-1,2-distannyl ethylene (**78**) in the presence of catalytic amounts of $[Pd(PPh_3)_4]$ in a dilute solution in DMF at 75 °C to afford the highly strained 10-membered-ring enediyne intermediate **79** in a remarkable 81% yield, with this pivotal intermediate thence being converted through a multistep sequence into the target molecule. Interestingly, when the structurally related olefin **80** (with a C3–C8 double bond instead of an epoxide moiety) was subjected to the same reaction conditions, none of the corresponding cyclized enediyne product was obtained. This observation highlights the importance of seemingly subtle conformational effects on the outcome of the process, with these factors often proving crucial to the success or failure of a given cross-coupling reaction.[82]

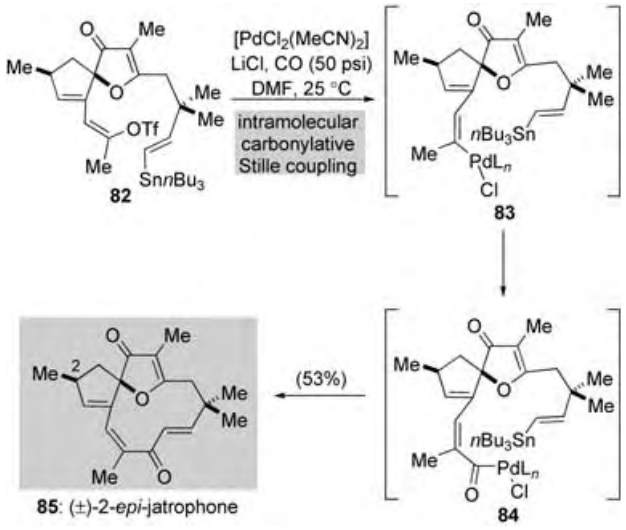


Scheme 15. A "stitching cyclization" route to the enediyne core in the total synthesis of dynemicin (**81**) (Danishefsky et al., 1996).[81]

In a beautiful example of the application of a carbonylative Stille coupling, the Stille–Hegedus group formed the 11-membered ring of 2-*epi*-jatrophone (**85**) by exposing vinyl triflate **82** to a catalytic amount of $[PdCl_2(MeCN)_2]$ and LiCl

 © 2005 Wiley-VCH Verlag GmbH & Co. KGaA, Weinheim

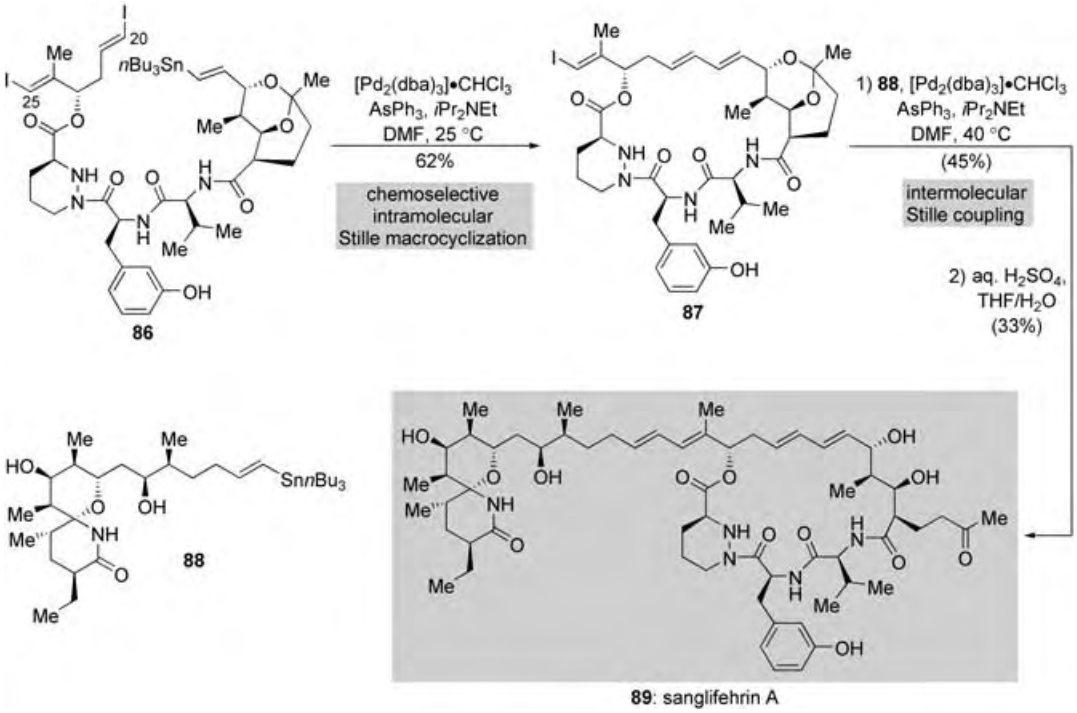
in DMF under a carbon monoxide atmosphere (50 psi) as shown in Scheme 16.[83,84] The mechanism of this impressive reaction, the final step in the total synthesis, presumably involves oxidative addition of a palladium(0) species into the



Scheme 16. The use of an intramolecular carbonylative Stille coupling to complete the synthesis of (±)-2-*epi*-jatrophone (**85**) (Stille et al., 1990).[83]

vinyl triflate C–O bond (**82**→**83**) followed by CO insertion to generate acylpalladium(II) intermediate **84**, and, finally, an intramolecular coupling to yield the observed product **85**. This transformation accomplishes the formation of two carbon–carbon bonds, the incorporation of the final carbon atom of the molecular framework, and the generation of the macrocyclic ring in a single operation—impressive indeed! It is worth recalling here that the carbonylative Stille coupling serves well as an alternative to Stille couplings of acid chlorides, especially when the latter intermediates are either not available or too labile to be used.

The remarkable level of control, in both a chemoselective and stereoselective sense, that is possible in executing Stille reactions is nicely illustrated by our total synthesis of the novel immunosuppressant agent sanglifehrin A (**89**, Scheme 17) by the Nicolaou group.[85] The cornerstone of the devised synthetic strategy was the proposed late-stage chemoselective Stille macrocyclization of bis(vinyl iodide) precursor **86** to generate the 22-membered ring intermediate **87** (Scheme 17), to which the complex spirolactam side chain would be appended through a second Stille coupling process. It was anticipated that participation of the less-hindered vinyl iodide group at C20 in the crucial macrocyclization reaction would be more favored over that involving the other vinyl iodide at C25, thus leading to the desired 22-membered ring, in preference to the alternative 21-membered macrocycle. In the event, this rather daring maneuver paid dividends, as it was found that treatment of a dilute solution of **86** in DMF with $[Pd_2(dba)_3]\cdot CHCl_3$ (15 mol%), $AsPh_3$ (60 mol%), and iPr_2NEt at ambient temperature led to the exclusive formation of the desired sanglifehrin cyclic intermediate **87** in 62% yield. A subsequent intermolecular Stille reaction between vinyl iodide **87** and alkenyl stannane **88** completed the carbon framework of the targeted natural product, which was finally unveiled by rupture of the acetal protecting group under aqueous acidic conditions. A second total synthesis of sanglifehrin A (**89**) was subsequently reported by the Paquette group, who also employed a Stille coupling reaction

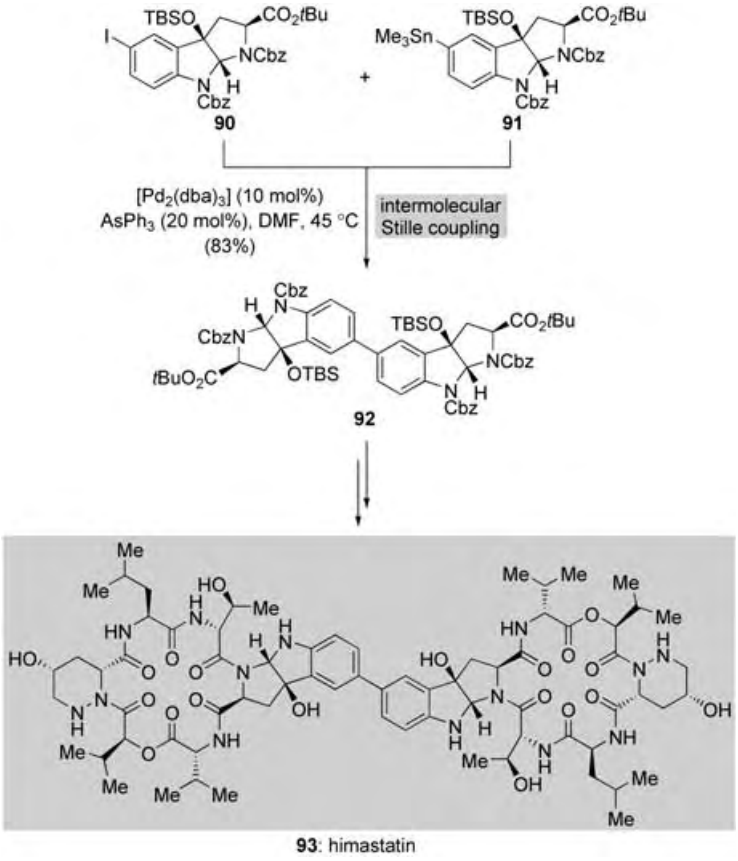


Scheme 17. Chemoselective intra- and intermolecular Stille couplings in the total synthesis of sanglifehrin A (**89**) (Nicolaou et al., 1999).[85]

 © 2005 Wiley-VCH Verlag GmbH & Co. KGaA, Weinheim

between the same two fully elaborated fragments **87** and **88** followed by cleavage of the acetal protecting group as the final synthetic steps.[86] In this case, however, the key macrocyclization step en route to vinyl iodide **87** involved the lactonization of an appropriately substituted seco-acid. Notably, once again the presence of unprotected functionalities such as amino, hydroxy, and secondary amide was tolerated under these palladium-catalyzed reaction conditions, thus underscoring the mildness of such protocols.

The use of transition metals in the formation of aryl–aryl bonds dates back to the beginning of the last century, with the discovery of the copper-promoted reductive coupling of aromatic halides (Ullmann reaction).[87] Whilst vast improvements in such copper-based protocols have been and continue to be made,[88] it was not until the advent of, at first, nickel-promoted and, subsequently, palladium-catalyzed carbon–carbon bond-formation methods that aryl–aryl coupling processes would assume the broad scope and generality that they enjoy today. The Stille reaction ranks among the most synthetically useful of the palladium-catalyzed processes for aryl–aryl bond formation, although arguably to a lesser extent than does the Suzuki reaction (see Section 4), and has found widespread use in this task.[89] An illustrative example of the utility of this transformation can be found in the total synthesis of himastatin (**93**, Scheme 18), a structurally intricate actinomycete metabolite with potent antibacterial and antitumor properties, by Danishefsky and Kamenecka.[90]



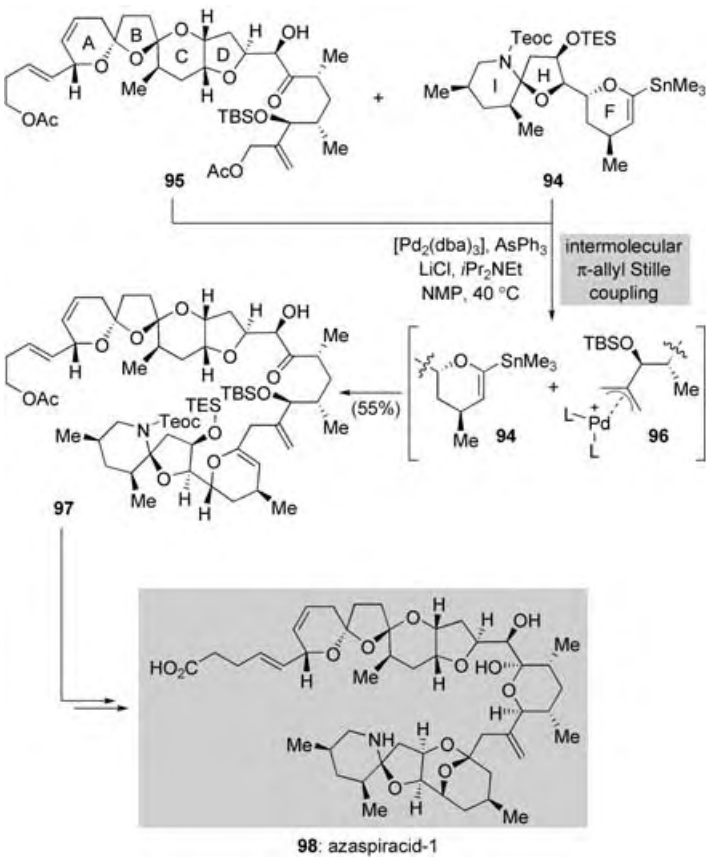
Scheme 18. Formation of an aryl-aryl linkage through a Stille coupling in the total synthesis of himastatin (**93**) (Danishefsky and Kamenecka, 1998).[90]

Smooth coupling between aryl iodide **90** and aryl stannane **91** was induced by treatment with catalytic amounts of $[Pd_2(dba)_3]$ (10 mol%) and $AsPh_3$ (20 mol%) in warm DMF to forge the key carbon–carbon bond between the two central indolyl moieties in an impressive 83% yield. Importantly, these reaction conditions were found to be compatible with the sensitive pyrroloindoline core present within both coupling partners **90** and **91**, which allowed the advancement of intermediate **92** through a number of steps to the targeted natural product. It is important to note that, although aryl iodides, bromides, and triflates are by far the most commonly used electrophilic coupling partners in this context with aryl stannanes, there have been extensive efforts at developing viable coupling conditions with the corresponding cheaper and often more readily available (but also far less reactive) aryl chlorides.[91,92]

The examples of Stille reactions discussed so far have focused on $C(sp^2)$–$C(sp^2)$ couplings, that is, between vinyl or aryl halides or triflates and vinyl or aryl organostannanes, which necessarily result in the formation of diene (or higher polyene) systems. However, the use of allylic halides allows formal $C(sp^2)$–$C(sp^3)$ couplings and broadens considerably both the scope of the Stille reaction and the structural diversity of the products that can be formed. This so-called π-allyl Stille coupling reaction provides a reliable and general method for the synthesis of "skipped" 1,4-diene systems. An important development in Stille reaction methodology was the discovery by the Stille–Hegedus group that the more readily available corresponding allylic acetates could be coaxed, under appropriate reaction conditions, into functioning as viable electrophiles for palladium-catalyzed coupling reactions with organostannanes.[93] An example of this type of reaction in the construction of complex natural products can be found in the recent total synthesis and structure elucidation of the marine toxin azaspiracid-1 by the Nicolaou group.[94] As shown in Scheme 19, addition of the vinyl stannane FHI-ring intermediate **94** to a mixture of the allylic acetate ABCD-ring intermediate **95**, LiCl, iPr_2NEt, and catalytic amounts of $[Pd_2(dba)_3]$ and $AsPh_3$ in NMP at 40 °C led to smooth coupling of the two fragments, presumably through the intermediacy of π-allyl–palladium complex **96**, to generate compound **97**. The latter advanced intermediate was elaborated into **98**, the spectroscopic data of which were shown to be identical to those of the natural product, thus solving the mystery and intrigue surrounding the structural identity of one of Nature's most remarkable natural products.

An intramolecular variant of the π-allyl Stille coupling was employed in the elegant total synthesis of the originally proposed structure of amphidinolide A by Pattenden and Lam (Scheme 20).[95,96] In this tour de force of Stille chemistry, an intermolecular coupling reaction between bis(stannane) **99** and vinyl iodide **100** was used to assemble the cyclization precursor **101**. Removal of the silyl protecting groups gave tetraol **102**, which was

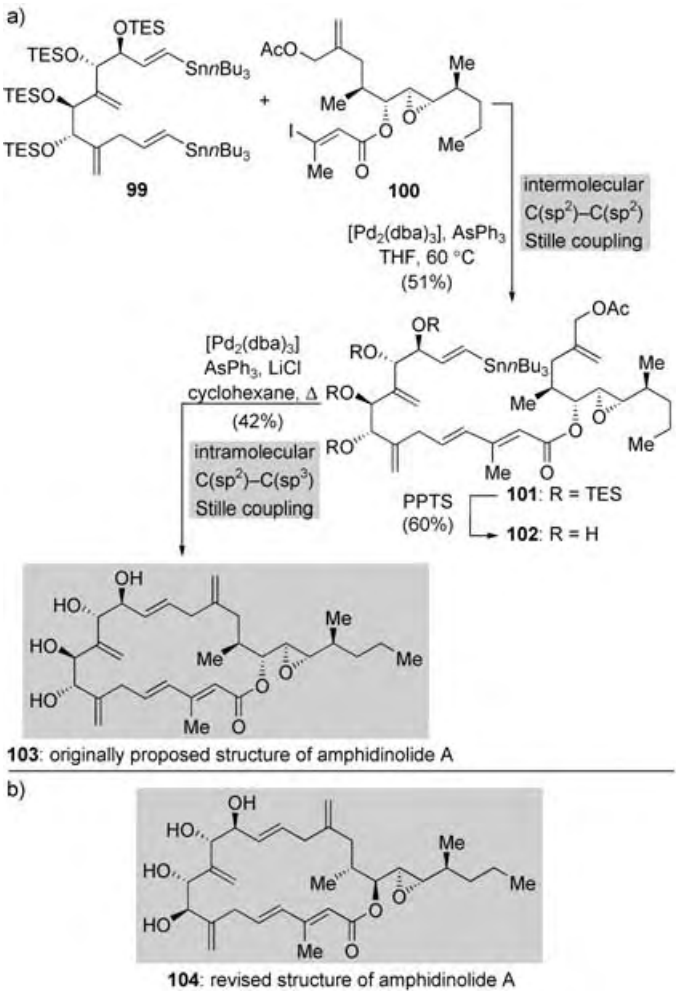
 © 2005 Wiley-VCH Verlag GmbH & Co. KGaA, Weinheim



Scheme 19. The use of a fragment-coupling π-allyl Stille coupling in the synthesis of azaspiracid-1 (**98**) (Nicolaou et al., 2004).[94]

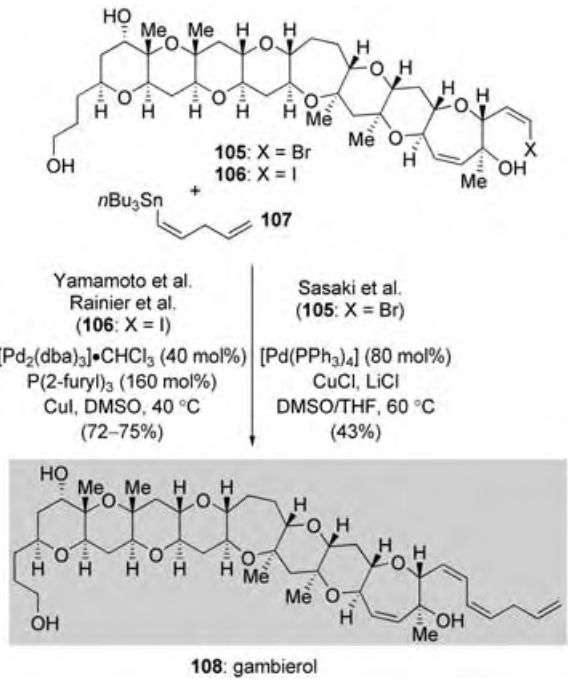
treated with catalytic amounts of $[Pd_2(dba)_3]$ and $AsPh_3$ to effect the desired π-allyl–palladium-mediated macrocyclization. The selectivity of the initial coupling between **99** and **100** is particularly noteworthy in view of the number of products that could potentially be formed in this step. Thus, the exclusive formation of the single desired product **101** is the result of discrimination not only between the two stannane units in **99**, but also between the vinyl iodide and allylic acetate moieties embedded within the coupling partner **100**. Thus, remarkably, under the particular conditions employed, coupling is only observed between the less-hindered stannane group in **99** and the more-reactive vinyl iodide group in **100**. Much to the researchers' chagrin, however, the spectroscopic data of the final compound **103** did not match those of the natural product, thus suggesting that the proposed configuration at one or more stereogenic centers was incorrect. Two more years would elapse before the ambiguity surrounding the structure of amphidinolide A was finally resolved, through further chemical synthesis studies by the Trost group (see structure **104**, Scheme 20).[97,98]

In addition to intramolecular cyclization reactions and fragment-coupling processes, the Stille reaction is also a powerful method for effecting appendage attachments. The utility of this protocol is dramatically manifested in the total syntheses of gambierol (**108**, Scheme 21) by the Sasaki[99] and Yamamoto groups.[100] Both groups employed a Stille reaction in the final step of their respective syntheses to append the delicate triene-containing side chain onto a fully elaborated, protecting-group-free polycyclic ether precursor. The Sasaki group coupled stannane **107** with vinyl bromide **105**, while Yamamoto and co-workers utilized the corresponding vinyl iodide **106**. Although there were significant differences in the reaction conditions employed by the two groups, in both cases the presence of cocatalytic Cu^I salts was necessary to facilitate the transmetalation event and, hence, allow the reactions to proceed at acceptable rates. In both cases, the coupling product was formed with the expected retention of the geometry of the alkene, and the overall efficiency of these processes is quite remarkable, given both the steric encumbrance around the coupling site and the sheer size and complexity of the vinyl halides **105** and **106**. Interestingly, this appendage attachment was postponed by both teams until the last step out of necessity rather than choice. While similar couplings could be effected by both groups without undue difficulty at earlier stages in their syntheses (on compounds related to **105** or **106**, but in which the hydroxy functional groups were protected), the sensitivity of the resulting triene systems thwarted all attempts at the successful liberation of

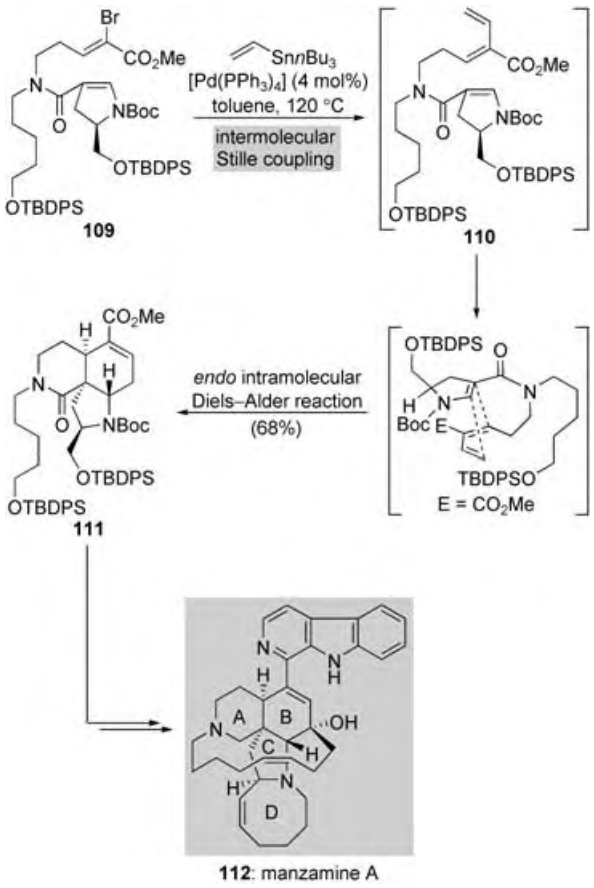


Scheme 20. a) Sequential $C(sp^2)$–$C(sp^2)$ and $C(sp^2)$–$C(sp^3)$ Stille couplings in the synthesis of the structure originally proposed for amphidinolide A (**103**) (Pattenden and Lam, 2002);[95] b) revised structure of amphidinolide A (**104**) (Trost and Harrington, 2004).[97]

 © 2005 Wiley-VCH Verlag GmbH & Co. KGaA, Weinheim



Scheme 21. Appendage of the triene-containing side chain to complete the total synthesis of gambierol (**108**) (Sasaki et al., 2002; Yamamoto and et al.; 2003, Rainier et al., 2004).[99–101]



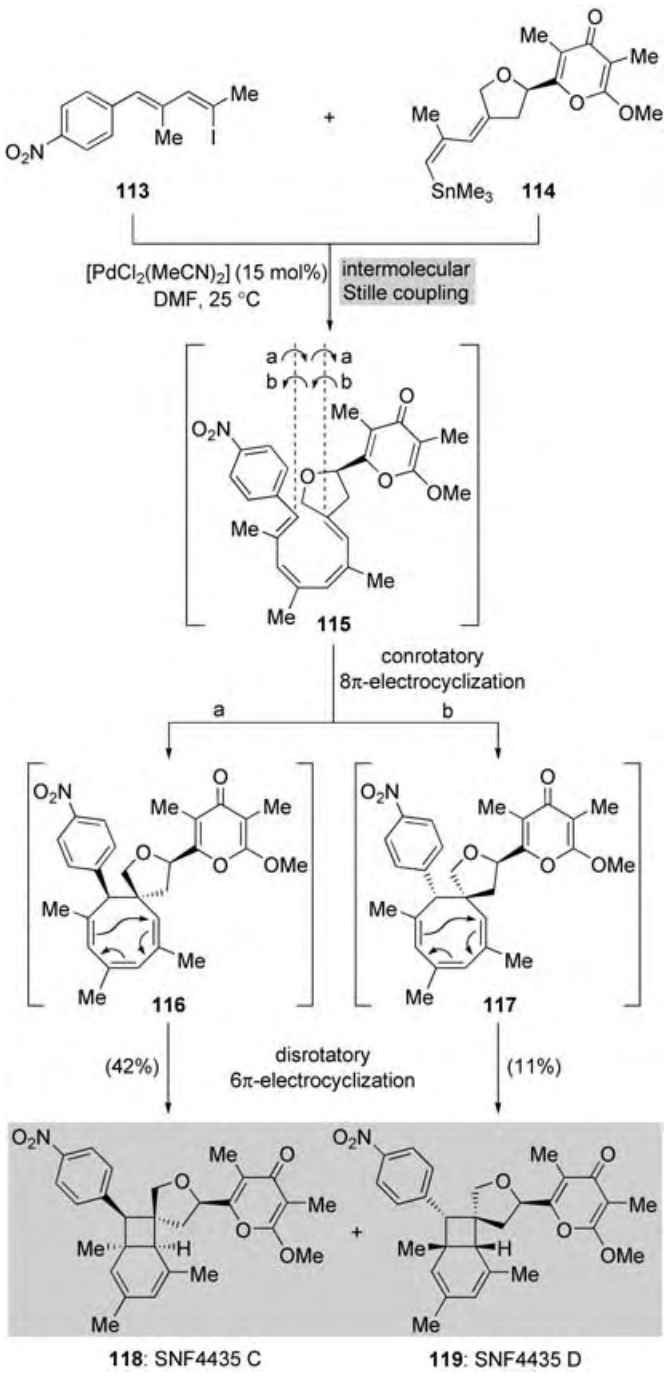
Scheme 22. A tandem intermolecular Stille coupling/intramolecular Diels–Alder approach to the tricyclic core structure of manzamine A (**112**) (Martin et al., 1999).[102]

the said functionality, which, incidentally, highlights once again the sometimes fickle nature of protecting groups in total synthesis. Most recently, Rainier and co-workers have also reported a novel total synthesis of gambierol (**108**).[101] These researchers made use of the conditions employed by the Yamamoto group to install the unsaturated side chain through a Stille reaction, a transformation that was again left until the very end of the synthetic sequence and which, in this case, proceeded in 75% yield.

An extremely useful application of the Stille reaction involves the generation of transient intermediates that can react further, typically in an intramolecular fashion, to produce often dramatic increases in structural complexity in a single operation. Owing to the usually mild conditions of the Stille reaction, intermediates that would otherwise be too fleeting or unstable to be isolated can be produced cleanly and rapidly for subsequent transformations, thus giving rise to powerful cascade sequences. An elegant example of this strategy can be found in the total synthesis of the marine-sponge-derived alkaloid manzamine A (**112**, Scheme 22), by Martin and co-workers, whereby a novel Stille coupling/intramolecular Diels–Alder cascade sequence was employed to furnish the tricyclic core structure of the target molecule.[102,103] Thus, as shown in Scheme 22, treatment of vinyl bromide **109** with vinyl(tri-*n*-butyltin) and a catalytic amount of $[Pd(PPh_3)_4]$ in refluxing toluene initially effected an intermolecular Stille reaction to afford diene **110**, which was suitably disposed to then undergo an *endo*-selective intramolecular Diels–Alder cycloaddition to afford tricyclic compound **111** in 68% yield as a single stereoisomer. In this remarkable transformation, the first notable example of the application of such a cascade process in total synthesis,[104] three new carbon–carbon bonds and three new stereocenters are formed in a single operation, with the relative and absolute stereochemistry of the product **111** being defined by the lone stereocenter in the vinyl bromide starting material **109**.

A number of alternative reaction pathways, besides [4+2] cycloadditions, can be envisaged for the polyene systems generated through Stille fragment-coupling reactions. One such approach that has received considerable attention recently is the development of Stille coupling/electrocyclization cascade processes that provide a rapid entry into polycyclic compounds with high stereospecificity from simple precursor coupling partners. As an astounding example of this principle, we highlight here the recent total syntheses by Parker and Lim[105] of SNF4435 C (**118**) and SNF4435 D (**119**, Scheme 23), two immunosuppressant agents isolated from a culture broth of *Streptomyces spectabilis*.[106] The bicyclo[4.2.0]octadiene core structure of these intriguing natural products bears a striking resemblance to that of the endiandric acids,[107] for which a biosynthetic pathway involving an electrocyclization reaction cascade had been proposed by Black and co-workers[108] and subsequently demonstrated experimentally by the Nicolaou group more than 20 years ago.[109] Therefore, by analogy, it was postulated that the SNF compounds arise through sequential conrotatory

 © 2005 Wiley-VCH Verlag GmbH & Co. KGaA, Weinheim



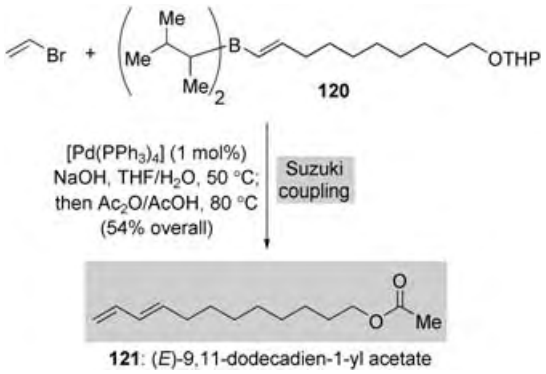
Scheme 23. A tandem Stille fragment coupling/electrocyclization cascade sequence in the total synthesis of SNF4435 C (**118**) and SNF4435 D (**119**) (Parker and Lim, 2004).[105]

8π- and disrotatory 6π-electrocyclizations of the fully elaborated *Z*,*Z*,*Z*,*E*-tetraene **115**, as shown in Scheme 23.[110] The total synthesis of the natural products by Parker and Lim, following this biomimetic strategy, involved as the pivotal step the union of vinyl iodide **113** and vinyl stannane **114** in DMF at room temperature, under the influence of catalytic amounts of $[PdCl_2(MeCN)_2]$, to generate stereoselectively the putative tetraene intermediate **115**. The latter intermediate spontaneously underwent the desired electrocyclization cascade to afford directly a mixture of the target molecules SNF4435 C (**118**) and SNF4435 D (**119**) in 42 and 11 % yields, respectively.[111,112] Interestingly, the ratio of synthetic **118**/**119** produced in this manner (4:1) is not too different from that of the natural products found in Nature (2.3:1). Coupled with the observation that the electrocyclization cascade occurs under ambient laboratory conditions, this result lends credence to the suggestion that this step in the biosynthesis of these compounds is not enzyme-catalyzed.

As we conclude this discussion of the Stille reaction in total synthesis, it is worth mentioning an interesting development in the evolution of metal-mediated cross-coupling reactions of organostannanes with organic electrophiles. Many researchers have reaped the rewards from the beneficial effect of cocatalytic Cu^I salts in accelerating the rate of stubborn Stille coupling reactions, a phenomenon first reported in 1990.[36b] More recently, however, the Liebeskind group pioneered a "palladium-free" Stille reaction protocol in which the coupling of the organostannane and organohalide components is mediated by stoichiometric amounts of Cu^I thiophene carboxylate (CuTC) and proceeds rapidly at or below room temperature.[113] This methodology offers the synthetic chemist a complementary and useful alternative to the traditional palladium-catalyzed Stille coupling processes.[114,115]

4. The Suzuki Reaction

The first application of this cross-coupling reaction in natural products synthesis was reported by Rossi and coworkers in 1981, less than two years after the seminal publications by the Suzuki group,[12] detailing an expedient synthesis of (*E*)-9,11-dodecadien-1-yl acetate (**121**), an insect sex pheromone isolated from *Diparopsis castanea*.[116] Thus, as illustrated in Scheme 24, the targeted compound was prepared by means of the palladium-catalyzed coupling reaction between vinyl borane (*E*)-**120** and vinyl bromide, followed by treatment of the resulting crude product mixture with acetic anhydride in acetic acid to effect the direct conversion of the tetrahydropyranyl protecting group into the corresponding acetate. Although certainly modest by today's standards, this, and other similar early applications demonstrated, for the first

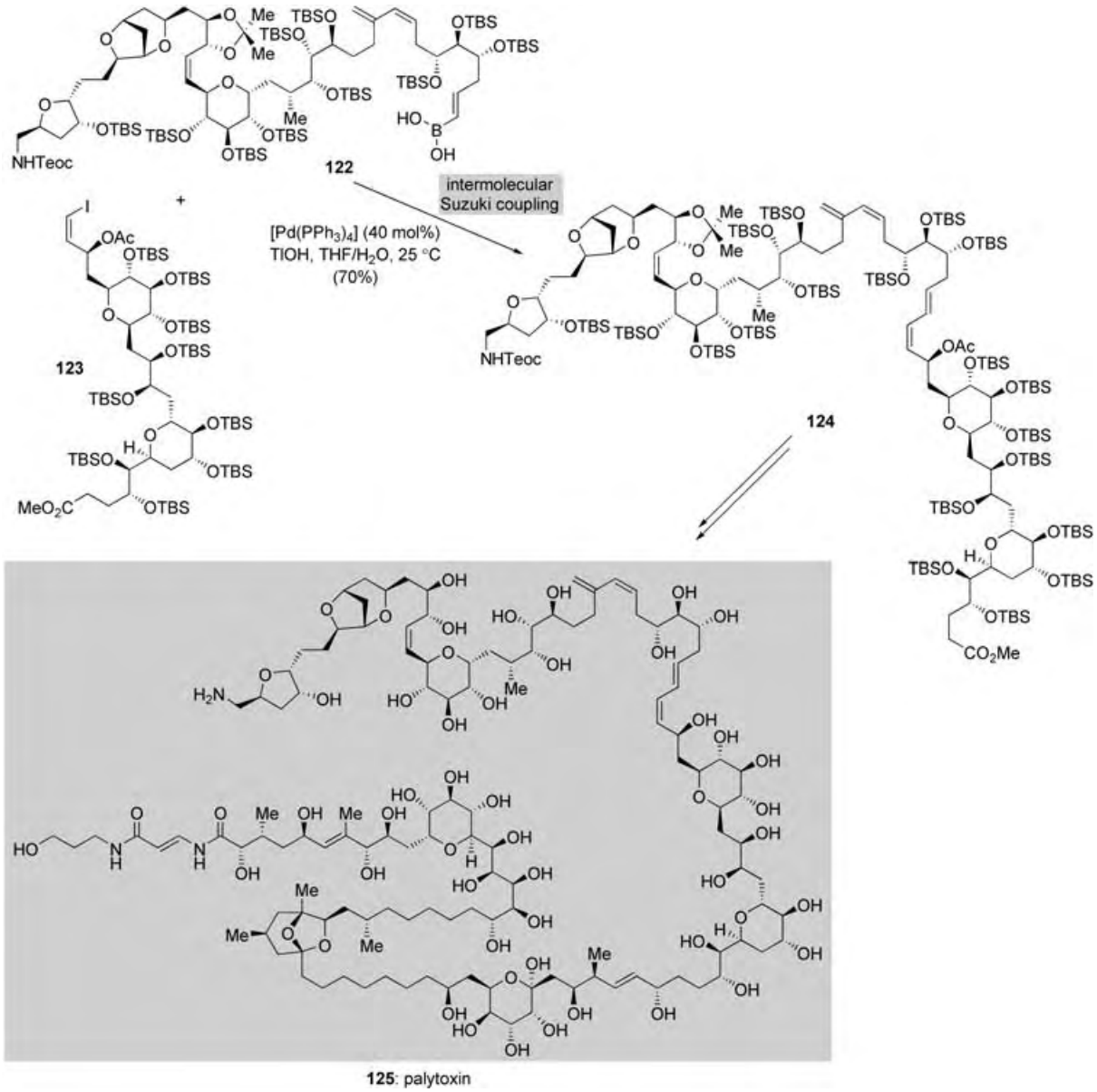


Scheme 24. The first application of a Suzuki reaction in a total synthesis, that of the insect pheromone **121** (Rossi et al., 1981).[116]

 © 2005 Wiley-VCH Verlag GmbH & Co. KGaA, Weinheim

time, the potential of such palladium-catalyzed cross-coupling reactions for the synthesis of diene systems under mild conditions, in good yield, and with a high stereospecificity—often lacking in the traditional olefination methods available at the time. Indeed, it was ground-breaking work such as this that paved the way for the remarkable developments in the field that would be forthcoming over the next quarter of a century. It is certainly instructive to compare this early example with the more-recent applications of the Suzuki reaction highlighted in order to more fully appreciate the degree to which the field has flourished in the intervening years.

One of the most remarkable applications of the Suzuki reaction in natural products synthesis is found in the synthesis of palytoxin (**125**, Scheme 25) by Kishi and co-workers.[117] This Herculean feat holds a special place in the history of total synthesis in that palytoxin is the largest secondary metabolite synthesized to date, in terms of both molecular weight and number of stereocenters.[118] Of no less significance is the fact that, as is often the case with total synthesis, this mammoth endeavor led to the discovery and development of a number of synthetically useful reactions and protocols, among which was a refinement of the conditions of the Suzuki coupling. The researchers' initial efforts at effecting the union of advanced intermediates **122** and **123** (Scheme 25) under conventional Suzuki coupling conditions were met with frustrating failure; thus, forced by necessity, the team proceeded to investigate methods for increasing the rate of the reaction. Eventually, a synthetic roadblock was turned into an avenue of discovery, as it was found that the use of TlOH as the base had a pronounced effect,[119] to the extent that the desired coupling between **122** and **123** occurred rapidly at ambient temperature upon treatment with a substoichiometric amount of $[Pd(PPh_3)_4]$ (40 mol%) in

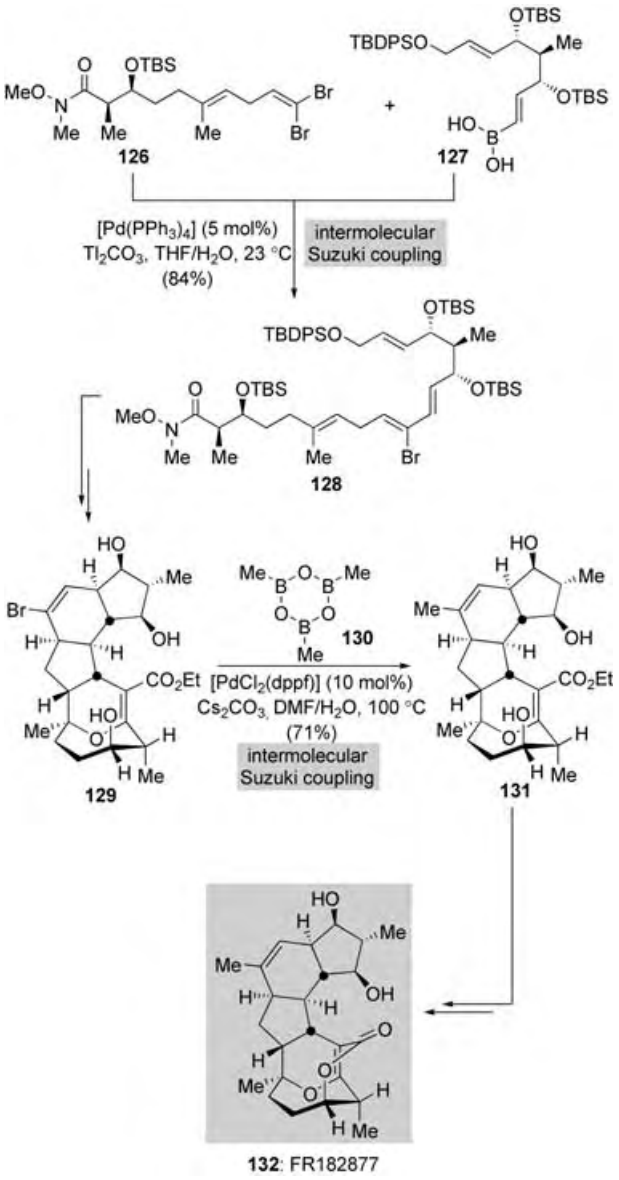


Scheme 25. Use of a thallium base in a fragment-coupling Suzuki reaction towards the total synthesis of palytoxin (**125**) (Kishi et al., 1994).[117]

 © 2005 Wiley-VCH Verlag GmbH & Co. KGaA, Weinheim

aqueous THF. The product **124** was then elaborated in a series of operations to complete the total synthesis of palytoxin.

The use of thallium bases in Suzuki coupling reactions has since often proved to be superior to many other procedures, particularly with sensitive substrates that would otherwise be labile under prolonged exposure to basic conditions.[120] Evans and Starr made use of this protocol in their recent total synthesis of (−)-FR182877 (**132**, Scheme 26),[121] a structurally and biologically remarkable hexacyclic natural product isolated from a *Streptomyces* species.[122] It was anticipated that the advanced acyclic intermediate **128** could be assembled through the selective Suzuki coupling of boronic acid **127** with the *E* vinyl bromide moiety in 1,1-dibromoolefin **126**. In practice, this coupling was first attempted by following a TlOEt-mediated procedure described by Roush and co-workers.[120] Although the desired product **128** was indeed obtained in 40% yield under these conditions, the reaction



Scheme 26. Suzuki reactions in the total synthesis of FR182877 (**132**) (Evans and Starr, 2002).[121]

was complicated by the unexpected formation of significant amounts (≈20%) of a by-product arising from the reaction of boronic acid **127** with both bromine moieties in dibromide **126**. A number of other bases were then screened, but these reactions were plagued by the formation of a myriad of by-products from competitive decomposition of the starting materials **126** and **127**. To the researchers' delight, however, they ultimately found that the use of Tl_2CO_3 translated to an improved selectivity for the desired coupling product **128** whilst maintaining a reasonable rate of reaction at room temperature and under the optimum coupling conditions ($[Pd(PPh_3)_4]$ (5 mol%), Tl_2CO_3, THF/H_2O 3:1, 23 °C). Compound **128** could be reliably produced in an excellent yield of 84%.

These tribulations serve as an important caveat not only for the Suzuki reaction but, indeed, for most transition-metal-catalyzed carbon–carbon bond-forming processes: a great deal of skill and persistence is often required to unearth the best experimental conditions for a given reaction and these conditions are often very substrate-dependent. Procedures for all types of bond-forming processes that are equally applicable and effective to all substrate types remain an elusive "Holy Grail" in transition-metal-based organic synthesis research. Notably, the selectivity of the formation of compound **128** in this case is due to the faster rate of oxidative addition of the *E* vinyl bromide moiety within the 1,1-dibromoolefin **126** to the Pd^0 species than that of the more sterically hindered *Z* vinyl bromide unit; this general phenomenon which has been employed extensively in natural product synthesis since the pioneering studies of Roush and Riva.[123] Having subsequently converted intermediate **128** into pentacyclic compound **129** through a beautifully orchestrated cascade sequence of transannular Diels–Alder reactions,[124,125] as first suggested by the insightful biosynthetic proposal of Sorensen and co-workers,[126] Evans and Starr were then faced with the task of replacing the remaining bromine atom in intermediate **129** with a methyl group. Again, it proved to be the Suzuki reaction that rose to the challenge. Thus, inspired by the earlier work of Gray and co-workers,[127] the required transformation was effected by treatment of bromide **129** with trimethylboroxine **130**, [$PdCl_2$-(dppf)] (10 mol%), and Cs_2CO_3 in aqueous DMF at 100 °C, yielding compound **131** in 71% yield. Crucially, not only was the presence of the vinylogous ester and the three unprotected hydroxy groups tolerated in this step, but also the delicate and highly strained "anti-Bredt" bridgehead olefin[128] emerged unscathed from the coupling reaction, underlining again the mildness of these protocols.

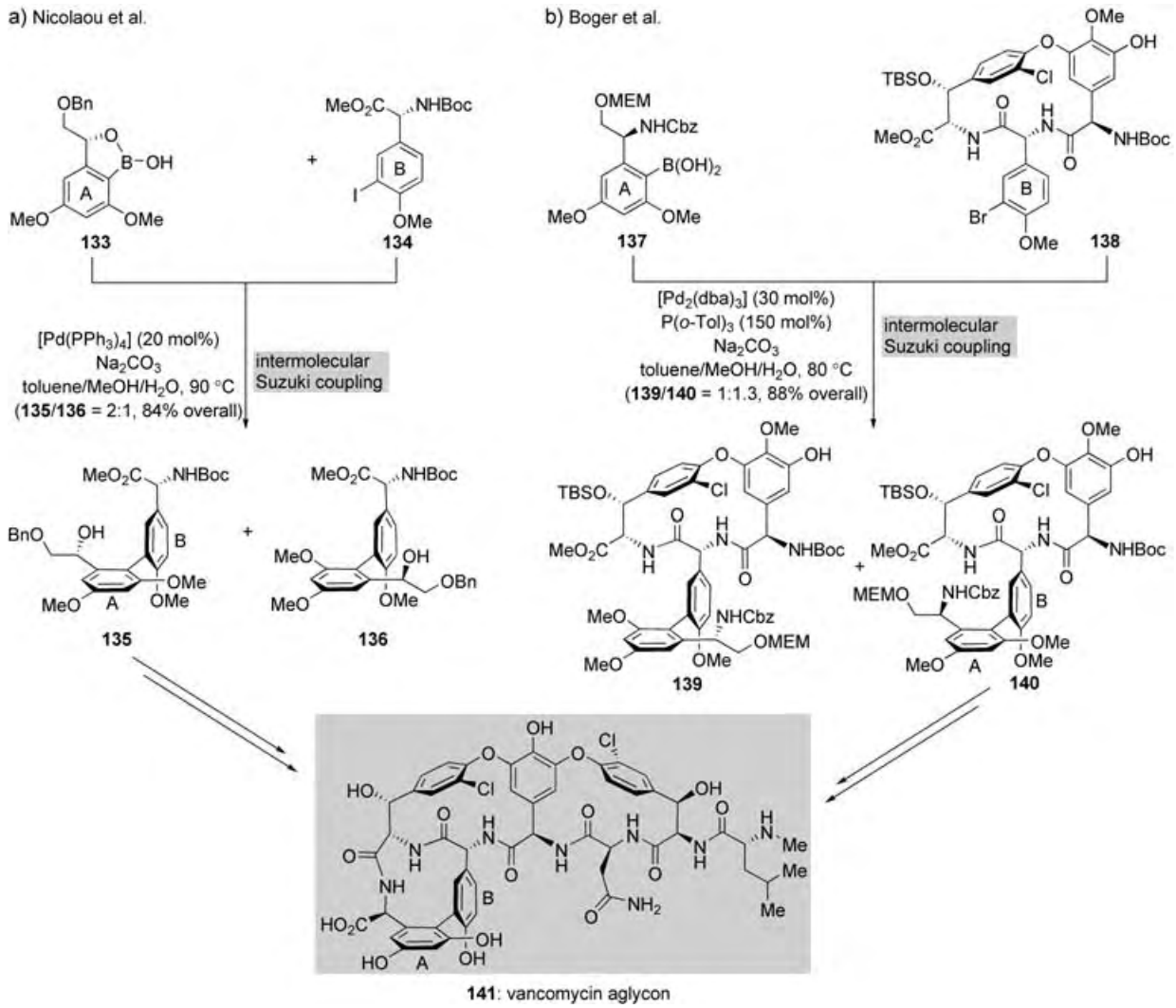
As touched upon in the previous section, the Suzuki reaction represents one of the, if not the most, widely used methods for aryl–aryl bond formation in modern organic synthesis. Given the ubiquitous occurrence of biaryl systems in a host of scientifically and economically important fields, from natural products to ligands for asymmetric catalysis, pharmaceutical compounds, and nanomaterials, extensive research efforts have recently been expended to develop further the utility and efficiency of the Suzuki reaction within this context. For the purposes of this Review, it is instructive to divide, somewhat arbitrarily, Suzuki aryl–aryl couplings

 © 2005 Wiley-VCH Verlag GmbH & Co. KGaA, Weinheim

into two categories: 1) those resulting in biphenyl-type systems, including binaphthyls, and 2) those leading to heteroatom-containing biaryls. Below we highlight selected examples of both categories in total synthesis.

Our first examples of the former category are found in the approaches to the total synthesis of the vancomycin aglycon (**141**, Scheme 27) described first by the Nicolaou group,[129] and subsequently by Boger and his group.[130] The carbon–carbon bond linking the aryl rings A and B would appear to be a prime candidate for formation through Suzuki coupling, and indeed this was the method adopted by both groups.[131] However, an additional degree of complexity which needed to be taken into consideration in planning such a procedure arises from the atropisomerism of the AB ring-coupled product which is enforced by the restricted rotation around the biaryl axis.[132] For instance, the protocol adopted by the Nicolaou group, involving the coupling of boronic acid **133** with iodide **134**, could potentially produce either or both atropisomeric products **135** and **136** (Scheme 27a), and it is not easy to gauge through cursory inspection which of the two compounds would predominate in such a reaction. As events transpired, under the optimum coupling conditions (Na_2CO_3 and $[Pd(PPh_3)_4]$ (20 mol%) in toluene/MeOH/H_2O (20:2:1) at 90 °C) the two stereoisomers **135** and **136** were formed in a 2:1 ratio and in 84% total yield. Gratifyingly, the major reaction product **135** was shown to have the configuration corresponding to that in the target aglycon and, following chromatographic separation from the undesired minor isomer **136**, was subsequently elaborated to complete the total synthesis.

In the strategy adopted by the Boger team, a Suzuki coupling between an A-ring boronic acid unit and a B-ring aromatic halide was also used to forge the crucial biaryl linkage; however, their approach differed conceptually in two respects from that employed by the Nicolaou group. First, a more elaborate B-ring halide **138** (Scheme 27b) was utilized in which the CD-ring bisaryl ether containing macrocycle was already incorporated. Second, it was anticipated that although the inherent axial stereoselectivity of the Suzuki coupling would not initially be controllable, a subsequent thermal equilibration of the atropisomeric products would, perhaps, yield the desired atropisomer preferentially. Indeed, the

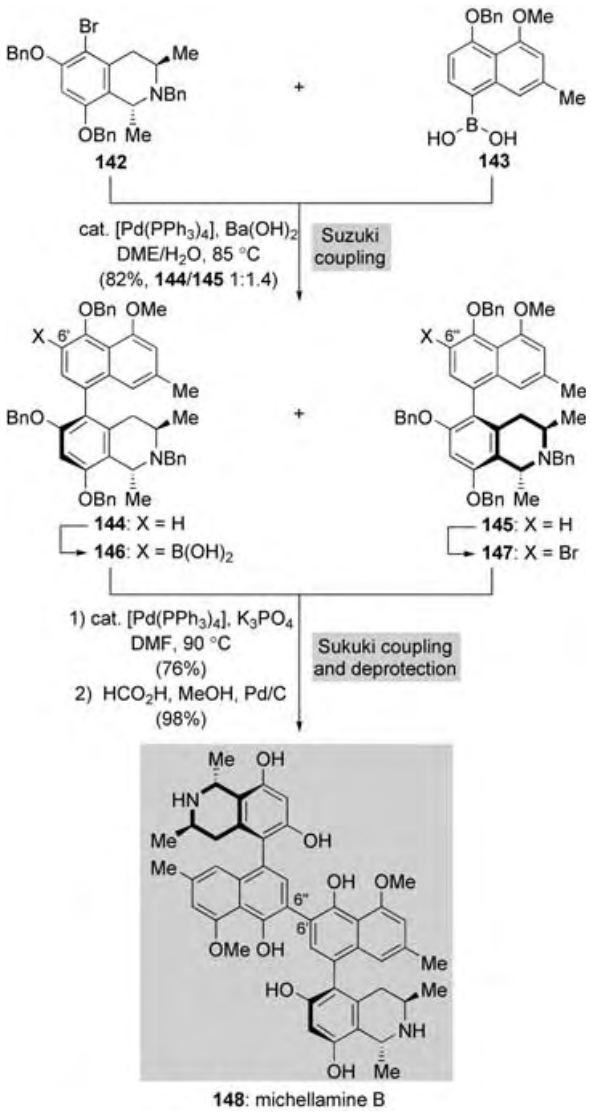


Scheme 27. Atropselective approaches to the AB-ring biaryl domain of vancomycin aglycon (**141**). a) Nicolaou et al. 1998;[129] b) Boger et al., 1999.[130]

 © 2005 Wiley-VCH Verlag GmbH & Co. KGaA, Weinheim

coupling of boronic acid **137** with bromide **138** yielded a nearly stereorandom mixture of the desired product **140** and the unwanted atropisomer **139** (**139**/**140** ≈ 1:1.3), although the overall yield for the process was again excellent (88%). Given the steric congestion and electron-rich nature of the coupling partners **137** and **138**, the overall efficiency of this Suzuki reaction is all the more remarkable. Key to its success was the use of the catalyst system derived from $[Pd_2(dba)_3]$ (30 mol%) and P(*o*-tolyl)$_3$ (150 mol%). At elevated reaction temperatures P(*o*-tolyl)$_3$ has often been found to be a superior ligand to the more traditional PPh_3 in such couplings. This is true particularly with organic electrophiles that prove recalcitrant towards oxidative addition to Pd^0, since the more bulky phosphine minimizes undesired quaternization of the phosphorus atom by the halide and also results in the formation of the more thermally stable 14-electron [Pd{P(*o*-tolyl)$_3$}$_2$] complexes.[133] After separation of the two products, it was found that the undesired component **139** could be thermally equilibrated upon heating to 120°C in chlorobenzene to provide a mixture of the two atropisomers that was now significantly enriched in the desired stereoisomer **140** (**139**/**140** ≈ 1:3). In this way, the axial selectivity of the Suzuki coupling could be controlled indirectly, with the majority of the material being channeled down the desired pathway. Note that the preexisting C-O-D bisaryl stereogenic axis was not affected by the conditions employed for the thermal equilibration of the AB-ring system in compound **139** owing to the significantly higher activation energy barrier to isomerization of the former unit (30.4 versus 25.1 kcal mol^{-1}).

As another example of the use of the Suzuki coupling to fashion atropisomeric systems, we consider the total synthesis of michellamine B (**148**, Scheme 28), a representative member of a class of homo- and heterodimeric alkaloid natural products that exhibit potent anti-HIV activity,[134] by Dawson and co-workers.[135] The coupling of enantiomerically pure bromotetrahydroisoquinoline **142** with naphthyl boronic acid **143** under the influence of $Ba(OH)_2$ and a catalytic amount of $[Pd(PPh_3)_4]$ in aqueous DME at 85°C yielded a nearly equimolar mixture of the two atropisomeric products **144** and **145** in a combined yield of 82%. The team's choice of the Suzuki reaction to effect this coupling was influenced to no small degree by the previously reported model studies of Hoye and Chen, who had demonstrated the clear superiority of this process over both the Stille reaction and the palladium-catalyzed cross-coupling of zinc derivatives for the union of similarly hindered and electron-rich aryl derivatives.[136] Although this step lacked atropselectivity, the researchers were able to turn this to their advantage on the basis of the configuration of the two coupling products **144** and **145** which corresponds exactly to that found in the "bottom" and "top" halves, respectively, of the targeted natural product. Thus, if a method could be found for joining intermediates **144** and **145** through their respective C6′ and C6″ positions (michellamine B numbering), an expeditious and stereospecific route to the complete michellamine B framework could be at hand. To the researchers' delight, compounds **144** and **145** could indeed be regioselectively converted into the corresponding boronic acid and bromo derivatives **146** and **147**, respectively, and another Suzuki coupling was then employed to effect their

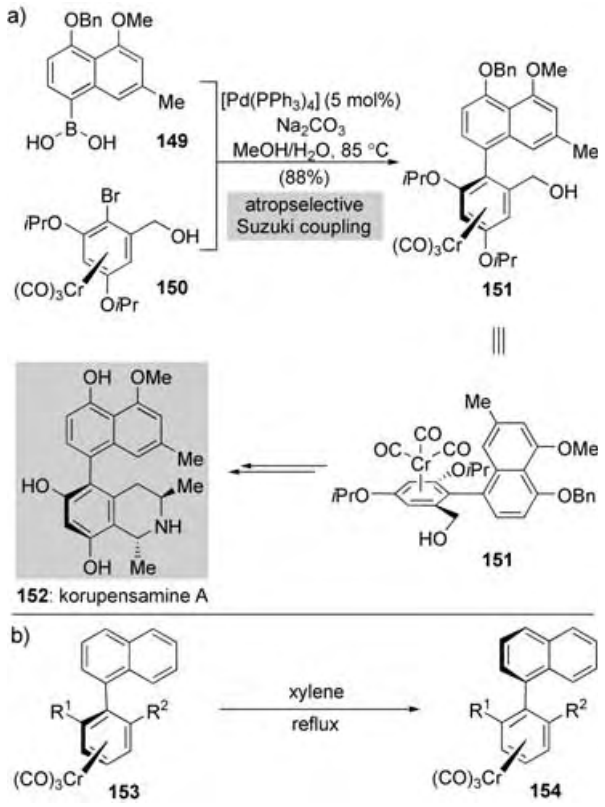


Scheme 28. Sequential Suzuki aryl-aryl couplings in the total synthesis of michellamine B (**148**) (Dawson et al., 1996).[135]

union. Removal of all eight benzyl protecting groups from the coupling product through standard procedures then yielded the targeted compound **148**.[137] The coupling of **146** and **147** was initially attempted under the conditions employed earlier in the synthesis, giving the product in 61% yield. However, it was subsequently discovered that the yield for this second merger could be increased to 76% under non-aqueous conditions (cat. $[Pd(PPh_3)_4]$, K_3PO_4, DMF, 90°C), which is somewhat surprising given not only the generally recognized tolerance of water, but also its often beneficial effect in the Suzuki reaction. Note that atropisomerism about the newly formed C6′–C6″ bond is not observed, as rotation about this bond is evidently not sufficiently hindered by the steric environment.

An interesting approach to this issue of atropisomerism in biaryl synthesis, championed in particular by the Uemura group, involves the use of planar chiral tricarbonyl-(arene)chromium complexes[138] in palladium-catalyzed cross-coupling reactions.[139] An illustrative example of this

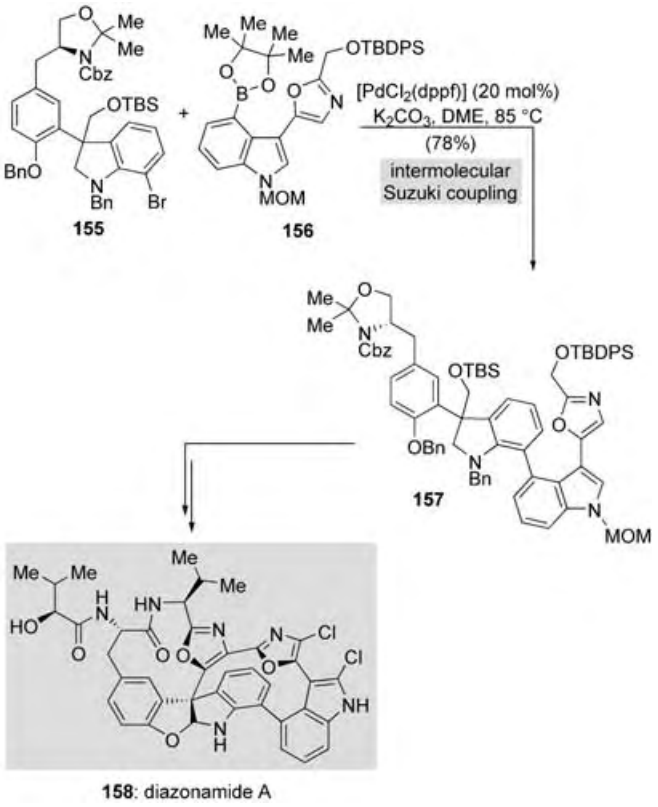
strategy is found in the synthesis of the alkaloid korupensamine A (**152**, Scheme 29),[140] a molecule that can be formally considered as the monomeric unit of the michellamine alkaloids alluded to above. Thus, as shown in Scheme 29a, the Suzuki coupling of naphthyl boronic acid **149** with enantiopure tricarbonylchromium-complexed aryl bromide **150** led to the smooth formation of biaryl system **151** in 88% yield and as a single stereoisomer. The sense of stereochemical induction in the formation of the atropisomeric biaryl axis in the product **151** is dictated by the preexisting chirality inherent in the starting tricarbonylchromium complex **150**, with the product shown in Scheme 29a having the same configuration as that found in korupensamine A (**152**). This result had, in fact, been anticipated by the research team on the basis of previous studies on similarly highly stereoselective cross-couplings, although the sense of stereochemical induction was found to be remarkably dependent on the nature of the *ortho*-substituent(s) on the tricarbonyl(arene)chromium complex.[141] Intermediate **151** was then elaborated to give the target molecule **152** in a series of steps that maintained the stereochemical integrity of the biaryl axis. Intriguingly, the coupling reaction (**149** + **150** → **151**) yields the less thermodynamically stable isomeric product, in which the axial configuration is such that the naphthyl ring is oriented in the same direction (*syn*) as the tricarbonylchromium unit, and hence suffers from severe steric interactions (as in **151**). To rationalize this counter-



Scheme 29. Atropselective Suzuki coupling of a planar chiral tricarbonyl(arene)chromium complex in the enantioselective synthesis of korupensamine A (**152**) (Uemura et al., 2000).[140]

intuitive phenomenon, it was proposed that isomer **151** represents the kinetic reaction product, which is not subsequently equilibrated to the thermodynamic isomer under the reaction conditions. It was also shown that a number of such kinetic coupling products could indeed be subsequently isomerized to generate the thermodynamically more stable *anti* atropisomers (i.e. **153** → **154**, Scheme 29b), thus enabling the selective formation of either biaryl atropisomer from a single chiral chromium complex. While these results are indeed impressive, the utility of this methodology is mitigated somewhat by the fact that the synthesis of the enantiopure (or enantioenriched) chiral chromium complexes is often far from trivial. Indeed, for all the enabling power of transition-metal-catalyzed reactions discussed herein, synthetic chemists are still singularly lacking truly general methods for the selective synthesis of biaryl atropisomers.

Nevertheless, despite these current limitations, the Suzuki reaction remains an extraordinarily effective and powerful method for aryl–aryl bond formation, particularly with sensitive, densely functionalized substrates and for the construction of sterically congested systems. A case in point is the second-generation synthesis of the revised structure[142] of diazonamide A, reported by the Nicolaou group in 2003.[143] As shown in Scheme 30, indoline bromide **155** and indole boronate ester **156** were successfully merged by employing a catalytic amount (20 mol%) of [$PdCl_2$(dppf)] in the presence of K_2CO_3 in anhydrous degassed DME at 85 °C. The advanced intermediate **157** contains all but one of the aromatic systems destined to be incorporated in the final target structure **158**,



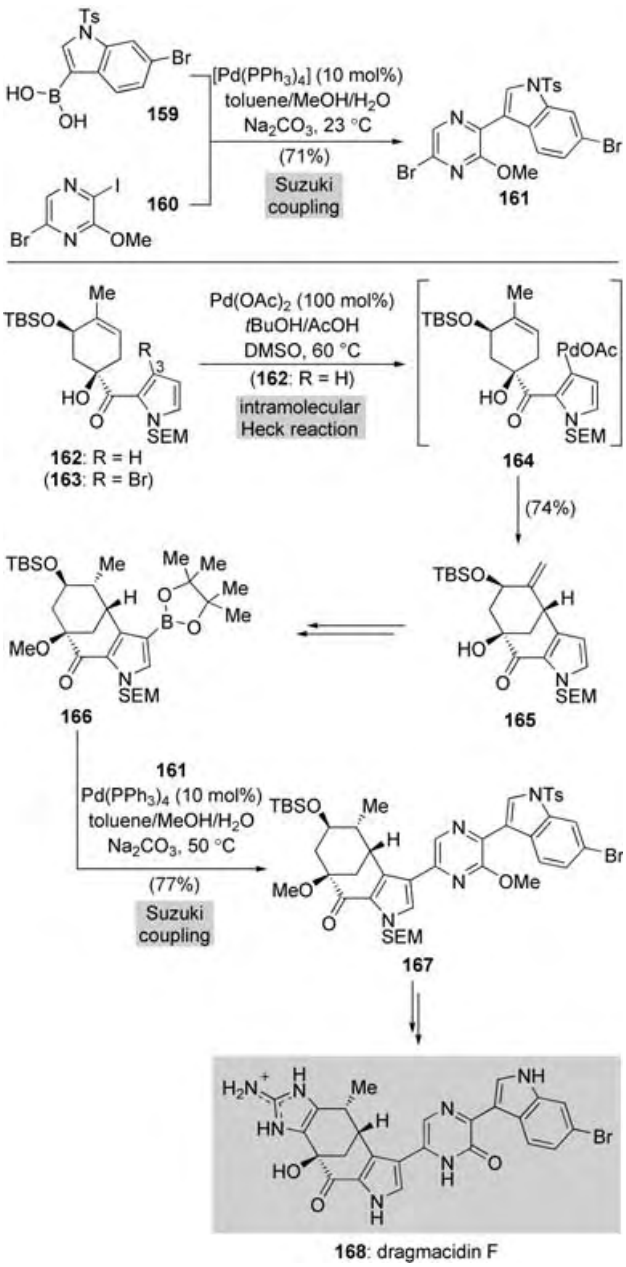
Scheme 30. Formation of a biaryl system through a Suzuki coupling in the total synthesis of diazonamide A (**158**) (Nicolaou et al., 2003).[143]

 © 2005 Wiley-VCH Verlag GmbH & Co. KGaA, Weinheim

thus illustrating both the degree of synthetic convergence (and hence efficiency) and the rapid increase in molecular complexity that are possible through the application of the Suzuki reaction and related processes.[144,145]

Palladium-catalyzed reactions have also revolutionized the synthesis of heteroatom-containing biaryl systems, with the Suzuki reaction being at the forefront of this new technology.[146] Over the last 25 years there has been a fundamental shift away from the generation of such motifs through iterative (and often cumbersome) heterocyclic ring syntheses by classical cyclization and dehydration reactions, towards the direct palladium-catalyzed union of preformed, and often fully functionalized, heterocycles.[147] As an illustrative example, such coupling reactions were used not once, but twice in the recent elegant synthesis of dragmacidin F (**168**, Scheme 31) by the Stoltz group.[148] In an exquisitely marshaled sequence of Suzuki coupling events, pyrazine derivative **160** was first coupled with indolyl boronic acid **159** to afford dibromide **161**, which was subsequently coupled with the advanced pyrrole boronate ester fragment **166** to complete a rapid synthesis of the core heptacyclic framework of the targeted natural product. The selectivity of these transformations is outstanding, with the required indolyl bromide unit surviving both transformations intact. This selectivity is the combined result of 1) the faster rate of oxidative addition of pyrazine carbon–halogen bonds to Pd^0 species than that of the corresponding benzenoid carbon–halogen bonds, and 2) the greater susceptibility of carbon–iodine bonds over the corresponding carbon–bromine bonds to oxidative addition. An important finding on the part of the researchers was that precise control of the temperature at which these couplings were conducted was essential to maintain the desired selectivity. Interestingly, the reason for the adoption of this Suzuki coupling strategy was that the team had been thwarted in their earlier attempts to generate similar polycyclic structures through the construction of the central pyrazine ring by classic cyclocondensation chemistry of advanced intermediates, owing to the recalcitrance of the reacting partners to undergo the required cyclization processes.[149] Palladium-mediated chemistry was also instrumental in permitting the synthesis of the pyrrole coupling partner **166**, in which a key carbon–carbon bond-forming step was the oxidative Heck cyclization of monosubstituted pyrrole precursor **162** to produce the congested pyrrole-fused bicyclic structure **165** in good yield and as a single regio- and stereoisomer. Although this transformation, of which we saw a related example in the synthesis of okaramine N (**55**; see Section 2, Scheme 11) described earlier, could not be made catalytic in palladium, it is nevertheless particularly remarkable in that it effects the C–H functionalization of the deactivated C3 position of the acyl pyrrole unit. Furthermore, this direct cyclization of compound **162** (R = H) was found to be superior in terms of both regioselectivity and overall yield to the intramolecular Heck reaction of the corresponding bromide **163** (R = Br).

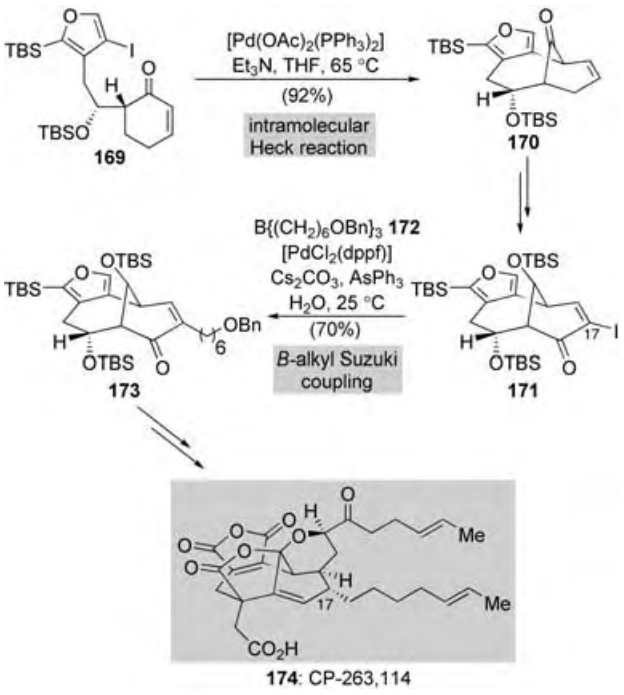
An important trend in the Suzuki reaction over the last 15 years has been the development and application of what have become known as *B*-alkyl Suzuki–Miyaura coupling reactions. In this process an alkyl group (i.e. sp^3-hybridized C atom), as opposed to the more traditionally used vinyl or aryl groups, is transferred from the organoborane component during the palladium-catalyzed coupling process with vinyl or aryl halides or triflates. Compared to the aforementioned $C(sp^3)$–$C(sp^2)$ Stille reactions,[150] *B*-alkyl Suzuki–Miyaura couplings have a much broader scope in that a potentially vast range of alkyl boranes (typically prepared through the regio- and chemoselective hydroboration of readily available alkene precursors and used in situ) can be employed in the reaction.[151] While the Suzuki coupling reactions illustrated so far in this section have been concerned with the assembly of diene systems and biaryl structural motifs, the *B*-alkyl Suzuki–Miyaura reaction is typically, though by no means always,



Scheme 31. Multiple use of palladium-catalyzed carbon–carbon bond-forming reactions in the total synthesis of dragmacidin F (**168**) (Stoltz et al., 2004).[148]

used for the stereoselective generation of isolated alkene units. The first examples of this process were reported by Miyaura and Suzuki in 1986;[152] since its pioneering application in the total synthesis of (+)-quadrilure in 1990 by the Mori group,[153] the *B*-alkyl Suzuki–Miyaura coupling has developed into a versatile and powerful tool in total synthesis.[154] In particular, and as we shall see below, this reaction has recently emerged as a viable alternative to the ring-closing-metathesis of olefins as a method for ring formation. In conjunction with this process, it is worth recalling here, that in an interesting reversal of reactivity, great progress has been made even more recently in the development of practical methods for the coupling of alkyl (i.e. sp^3) halides with vinyl and aryl (i.e. sp^2) organoboron species, which involve the reversal of reactivity of the two reactive ends of the coupling partners.[16]

During the course of their epic,[155] and ultimately successful[156] approach to the total synthesis of the architecturally unique nonadride natural products CP-225,917 and CP-263,114,[157] Danishefsky and co-workers employed a *B*-alkyl Suzuki–Miyaura coupling reaction to append a side chain at C17 of the functionalized tricyclic α-iodoenone **171** (Scheme 32). Thus, the treatment of **171** with trialkylborane **172** in the presence of Cs_2CO_3 and catalytic amounts of [$PdCl_2$(dppf)] and $AsPh_3$ in aqueous DMF led to smooth coupling, generating the alkylated product **173** in 70% yield. First introduced by Johnson and co-workers in 1993,[158] these particular coupling conditions have been found by many researchers to be quite mild and effective for the *B*-alkyl Suzuki–Miyaura reaction, and have subsequently found widespread use in its application. [$PdCl_2$(dppf)] is often shown to be the catalyst of choice for these couplings, as it has



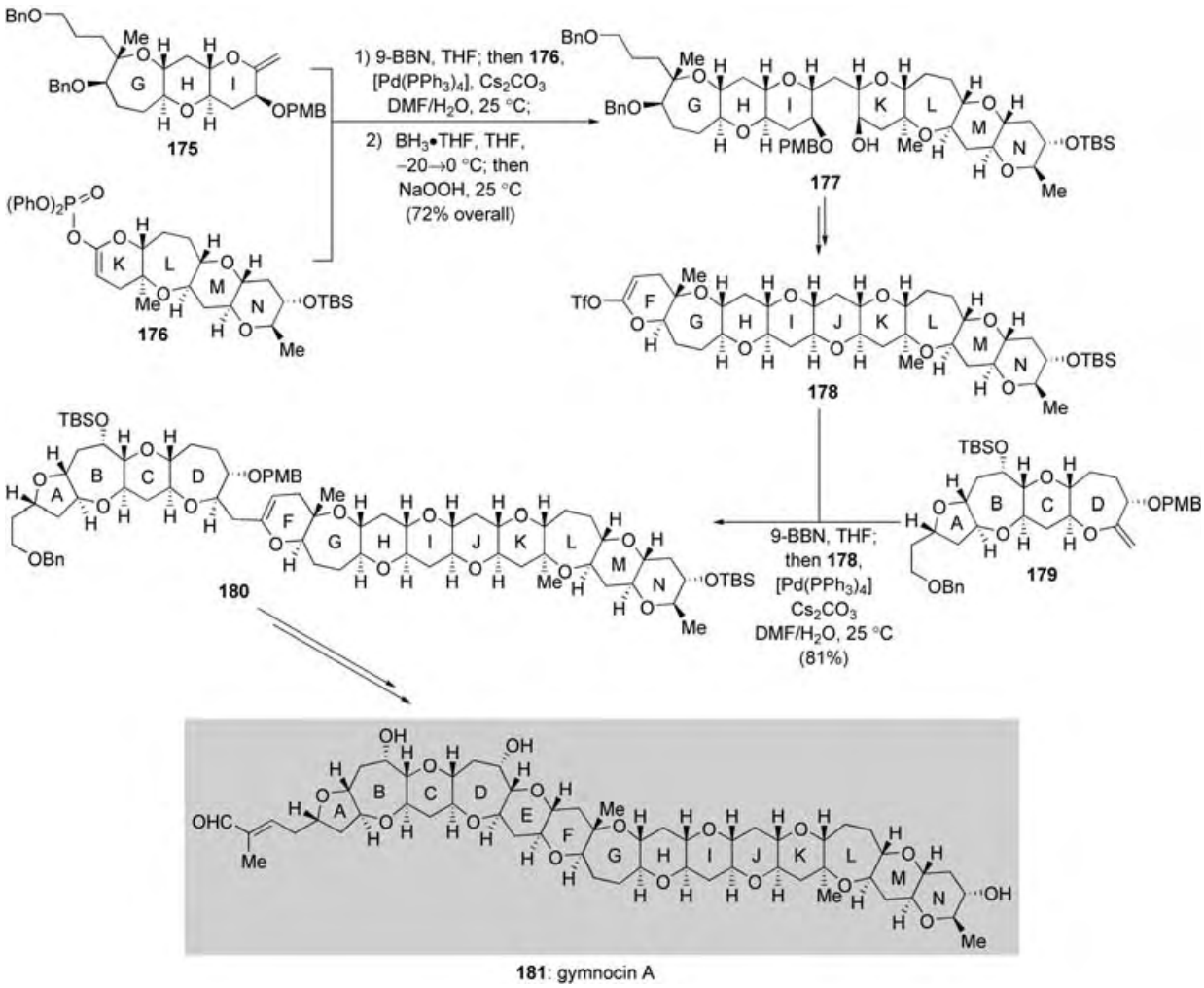
Scheme 32. Sequential intramolecular Heck and intermolecular *B*-alkyl Suzuki reactions in the total synthesis of CP-263,114 (**174**) (Danishefsky et al., 2000).[156]

been suggested that the rate of undesired β-hydride elimination from the transmetalated [Pd(dppf)(alkyl)(vinyl)] complex is slowed down by the presence of the large bidentate ligand,[159] whilst the rate of the product-forming reductive elimination is concurrently enhanced owing to the large bite angle of the ligand.[160] The α-iodo enone coupling partner **171** was prepared through a short sequence of reactions from tricyclic compound **170**, which was itself synthesized by another palladium-catalyzed bond-forming reaction, namely the intramolecular Heck cyclization of the *anti* aldol precursor **169** (Scheme 32). Exposure of compound **169** to a catalytic amount of [$Pd(OAc)_2(PPh_3)_2$] in THF in the presence of Et_3N at 65 °C led to clean, if somewhat slow (4 days were required for the completion of the reaction), cyclization to generate the desired tricyclic compound **170** in 92% yield. The remarkable regioselectivity of this reaction is noteworthy in view of the fact that coupling was observed exclusively between the furan ring and the α-carbon atom of the α,β-unsaturated system, with no trace of the alternative ring closure mode, that is, between the furan ring and the β-carbon atom. This selectivity is presumably a consequence of subtle, yet pivotal, differences between the molecular arrangements (and hence relative energies) required for the two different modes of 1,2-insertion, with the former (α-carbon attack) proving much more facile.

The power and utility of the *B*-alkyl Suzuki–Miyaura reaction in fragment-coupling processes is dramatically manifested in the recent total synthesis of gymnocin A,[161] a member of the polycyclic ether class of marine natural products associated with the notorious "red-tide" phenomena,[162,163] by Sasaki and Tsukano.[164,165] The salient features of the highly convergent synthetic strategy adopted by the Sasaki team are highlighted in Scheme 33. Thus, exocyclic enol ether **175** was subjected to a regio- and diastereoselective hydroboration with 9-BBN and, without purification, the resulting alkyl borane adduct was treated with cyclic ketene acetal phosphate **176** under Johnson conditions to afford, following the regio- and steroselective hydroboration/oxidation of the resulting trisubstituted enol ether, coupled product **177** in good overall yield (72%). Elaboration of the coupling product **177** then gave cyclic ketene acetal triflate **178**, which entered into the second key *B*-alkyl Suzuki–Miyaura fragment coupling reaction, this time with the alkyl borane species derived from hydroboration of the ABCD-ring exocyclic enol ether unit **179**, to give compound **180** in 81% yield. Intermediate **180** was then advanced further to complete the total synthesis of gymnocin A (**181**) in short order. Given the structural complexity and sheer size of the individual fragments, the remarkable efficiency of this second cross-coupling bears testament to the power and reliability of this process in total synthesis. The Sasaki group has developed this efficient approach to polyether construction, and through its application have accomplished the total synthesis of a number of other members of this class of marine natural products.[166]

The use of cyclic ketene acetal phosphates in palladium-catalyzed cross-coupling reactions was pioneered by the Nicolaou group,[167] who was subsequently the first to apply this methodology in the total synthesis of the polyether

 © 2005 Wiley-VCH Verlag GmbH & Co. KGaA, Weinheim

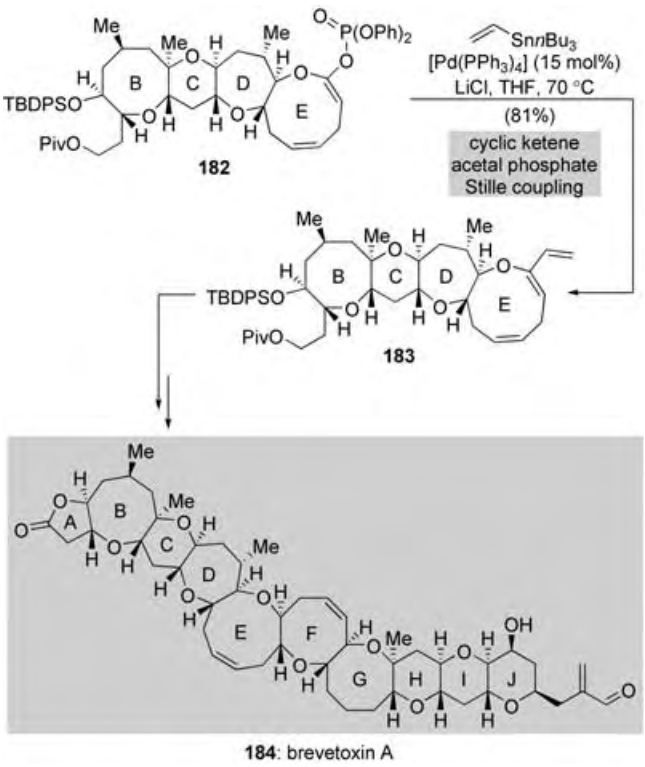


Scheme 33. Intermolecular *B*-alkyl Suzuki–Miyarua couplings in the total synthesis of gymnocin A (**181**) (Sasaki et al., 2003).[161]

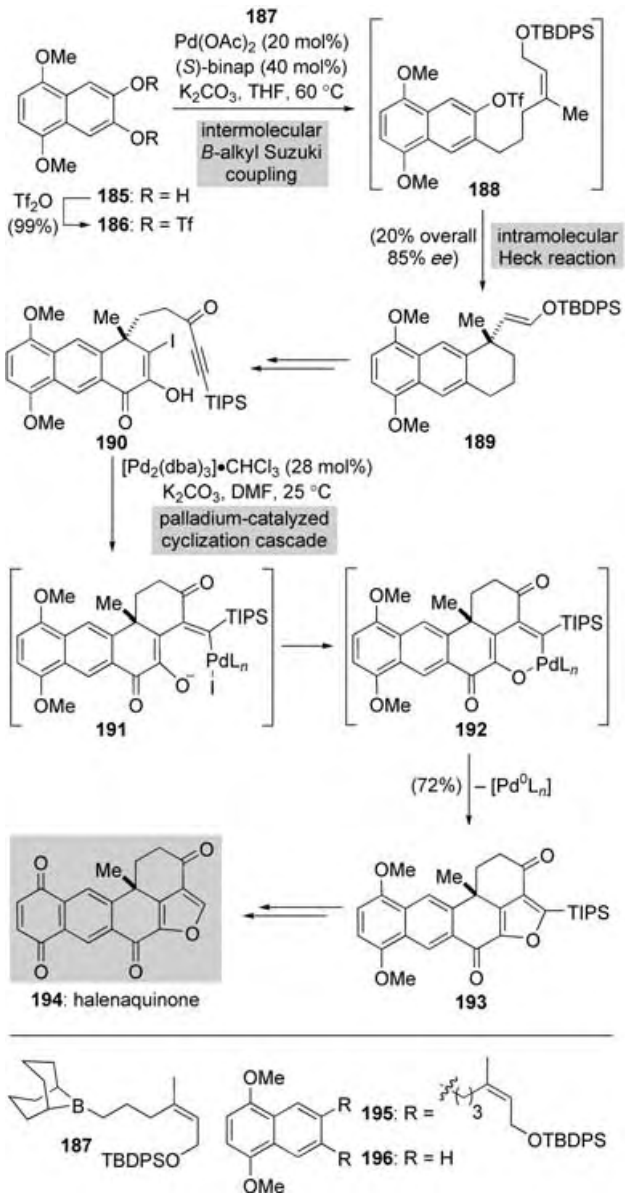
marine neurotoxin brevetoxin A (**184**, Scheme 34).[168] They later expanded the scope of this technology to encompass the corresponding cyclic aminal phosphates.[169] Cyclic ketene acetal (or aminal) phosphates, readily prepared from the corresponding lactones (or lactams) by treatment with a strong, non-nucleophilic base followed by quenching with diphenylphosphoryl chloride, smoothly enter into a variety of palladium-catalyzed carbon–carbon bond-forming reactions, including the Stille, Suzuki, and Sonogashira reactions, as well as into carbonylative processes. Furthermore, cyclic ketene acetal phosphates often prove to be superior substrates for these palladium-catalyzed reactions than the corresponding cyclic ketene acetal triflates, owing to the lower cost of the reagents involved in their preparation and their higher stability.[168,169]

Shibasaki and co-workers made use of a number of novel palladium-catalyzed transformations in their elegant synthetic approach to halenaquinone (**194**, Scheme 35) and related pentacyclic marine natural products.[170] The team had previously secured a somewhat arduous synthetic route from the symmetrical catechol derivative **185** to the advanced tricyclic compound **189** in which an intermolecular *B*-alkyl Suzuki–Miyaura coupling reaction and an intramolecular Heck cyclization were used as the carbon–carbon bond-forming steps between a number of protection/deprotection operations. They subsequently realized a significant upgrade in elegance and efficiency in their route to tricyclic system **189** through the application of an unprecedented intermolecular *B*-alkyl Suzuki–Miyaura coupling/intramolecular asymmetric Heck cyclization cascade sequence to fuse the six-membered ring to a symmetrical bis(triflate) precursor **186**, whilst concomitantly installing the benzylic quaternary stereocenter. The desired product **189** could indeed be formed in a single operation from bis(triflate) **186** by treatment with borane **187**,[171] K_2CO_3, and catalytic amounts of $Pd(OAc)_2$ (20 mol%) and (*S*)-binap (40 mol%) in THF at 60 °C. Tricyclic compound **189** was formed with good enantioselectivity (85% *ee*); however, the overall yield for this process was rather low (20%) and, despite the researchers' best efforts, could not be increased further. Major by-products in this reaction were identified as the reduced compound **196** and the double Suzuki coupling product **195**, with the propensity for formation of the latter likely being due to the generally lower rates of Heck reactions than those of Suzuki couplings. Intriguingly, it was found that the use of achiral ligands resulted in much better conversion into (racemic)

 © 2005 Wiley-VCH Verlag GmbH & Co. KGaA, Weinheim



Scheme 34. Pioneering use of cyclic ketene acetal phosphates as organic electrophiles in a palladium-catalyzed cross-coupling reaction, in the total synthesis of brevetoxin A (**184**) (Nicolaou et al., 1998).[168]



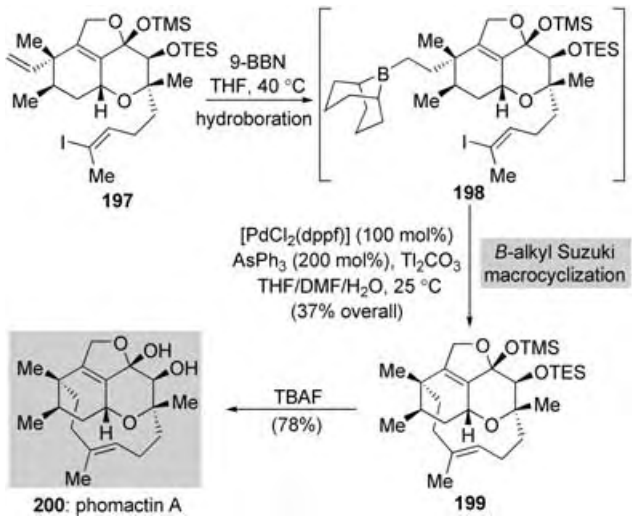
Scheme 35. Novel palladium-catalyzed cascade processes in the total synthesis of halenaquinone (**194**) (Shibasaki et al., 1996).[170]

tricyclic compound **189**. Thus, replacing the (*S*)-binap with $AsPh_3$ more than doubled the yield of this cascade process from 20 to 46%. After the elaboration of cyclization product **189** to give acetylenic ketone **190**, another novel palladium-catalyzed cyclization cascade reaction was employed to append the final two rings of the pentacyclic structure, including the highly substituted furan ring, in a single step to give diketone **193**.[172] A few more steps then completed the total synthesis of halenaquinone (**194**). Hence, two palladium-catalyzed reactions resulted in the creation of four new bonds (3 × C–C), three new rings, and, enantioselectively, a quaternary stereocenter.[173]

The intramolecular variant of the *B*-alkyl Suzuki–Miyaura reaction also proves to be a valuable, if still relatively uncharted and underutilized, addition to the repertoire of methods available to the synthetic chemist for ring construction. In particular, this intramolecular cross-coupling protocol allows for the highly regio- and stereocontrolled formation of endo- and exocyclic alkene systems of defined double-bond geometry, especially in the fusion of new rings to preexisting cyclic systems. Although the first such applications reported in 1989 were directed toward the construction of five- and six-membered ring systems,[174] more recently the potential of this reaction in the formation of a wider range of ring sizes, in synthetically useful yields, has begun to be tapped.

One of the most sophisticated applications in total synthesis of the intramolecular *B*-alkyl Suzuki–Miyaura coupling reaction to date was reported by Halcomb and his group, who employed it to forge the 12-membered macrocyclic ring of the terpenoid natural product phomactin A (**200**, Scheme 36).[175] Once the fully elaborated tricyclic precursor **197** had been prepared, the major remaining synthetic hurdle facing the team was the construction of the macrocycle in the presence of the other sensitive functionalities within the molecule, particularly the protected dihydroxyfuran motif. To their delight, they were able to effect the selective regiocontrolled (anti-Markovnikov addition) hydroboration of the terminal alkene in the presence of both the tri- and tetrasubstituted alkene systems upon treatment of compound **197** with 9-BBN in THF at 40 °C to afford the primary trialkyl borane intermediate **198**. Without purification, this intermediate was then slowly added to a mixture of $[PdCl_2(dppf)]$ (100 mol%), $AsPh_3$ (200 mol%), and Tl_2CO_3 in a THF/DMF/H_2O solvent system to afford the desired transannular macrocyclization product **199** in 37% yield. The

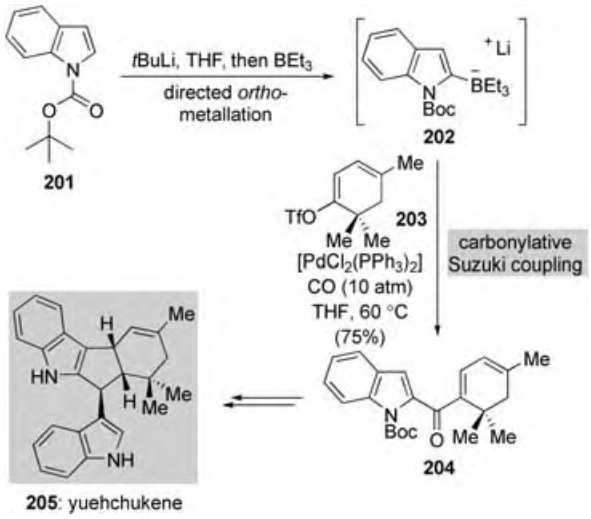
 © 2005 Wiley-VCH Verlag GmbH & Co. KGaA, Weinheim



Scheme 36. Use of the *B*-alkyl Suzuki–Miyarua coupling to effect a macrocyclization in the synthesis of phomactin A (**200**) (Halcomb and Mohr, 2003).[175]

subsequent unmasking of the two protected hydroxy groups then completed the total synthesis. Although the yield of this key cyclization is moderate at best, and a high "catalyst" loading is required, it nevertheless sets a new standard for such processes. Note that only the (desired) primary alkyl group is transferred from the boron atom (as its corresponding "ate" complex) during the transmetalation event in the catalytic cycle, owing to the much faster rate of transmetalation relative to that with the secondary alkyl groups on boron. Indeed, reports of synthetically useful *B*-alkyl Suzuki–Miyaura coupling reactions involving secondary alkyl borane species are scarce.[176] The researchers found that the choice of base was crucial to the efficiency of the reaction, and that the use of Tl_2CO_3 (rather than Cs_2CO_3 as in the original Johnson conditions) gave the best results. Presumably, the use of the thallium base increases the rate of the desired macrocyclization to a greater degree than it does the rates of competitive, undesired, intermolecular oligomerization pathways, a factor also influenced by the use of high dilution conditions.[177] The macrocyclization event was postponed until a late stage in the synthesis because of the anticipation that the rigid structure of the tricyclic core would bias the system towards the desired intramolecular process. As expected, the cyclized product **199** was formed exclusively as a single stereoisomer and with retention of configuration of the trisubstituted alkene moiety. This potential for control over olefin geometry in macrocyclization reactions compares favorably with that encountered in the corresponding ring-closing olefin-metathesis processes in which mixtures of isomers are often obtained and the stereochemical course of ring closure is generally not predictable. Thus, the intramolecular *B*-alkyl Suzuki–Miyaura coupling reaction offers a complementary approach to metathesis-based protocols.

In a similar manner to the carbonylative Stille reactions described earlier, the palladium-catalyzed, three-component cross-coupling of organic electrophiles, carbon monoxide, and organoborane compounds also provides an efficient means for the synthesis of unsymmetrical ketones from simpler precursor building blocks.[178] This procedure was applied as one of the key steps in an expedient synthesis of the bisindole alkaloid yuehchukene (**205**) by Ishikura and co-workers,[179] in which a carbonylative Suzuki reaction was used to assemble the 2-indolyl ketone intermediate **204** rapidly (Scheme 37).



Scheme 37. Three-component, carbonylative Suzuki coupling in the total synthesis of yuehchukene (**205**) (Ishikura et al., 1996).[179]

Directed *ortho*-metalation[180] of *N*-Boc-indole (**201**) followed by treatment with triethylborane led to the formation of lithiated "ate" complex **202**, which was not isolated but, instead, added directly to a solution of vinyl triflate **203** and a catalytic amount of $[PdCl_2(PPh_3)_2]$ in THF at 60 °C under a pressurized (10 atm) carbon monoxide atmosphere to effect the desired coupling in good overall yield. It will be noticed that, unlike the other examples of the Suzuki reaction highlighted so far, no additional base is required in the cross-coupling step, since the negatively charged, four-coordinate boron "ate" complex that is required to undergo the transmetalation step in the catalytic cycle is already present. The use of carbon monoxide under high (or at least greater than atmospheric) pressure has often been found to be a convenient method for suppressing a major side reaction sometimes encountered in carbonylative palladium-catalyzed reactions, namely the direct coupling of an organic electrophile and an organometallic component without carbon monoxide insertion.[181] A number of vinyl and aryl halides and triflates were shown to be viable coupling partners in this carbonylation process, enabling the synthesis of a variety of 2-indolyl ketone derivatives.[182] This method for the regioselective acylation at C2 of indoles is complementary to more traditional Friedel–Crafts-type acylations, which result in the preferential functionalization at C3.[183]

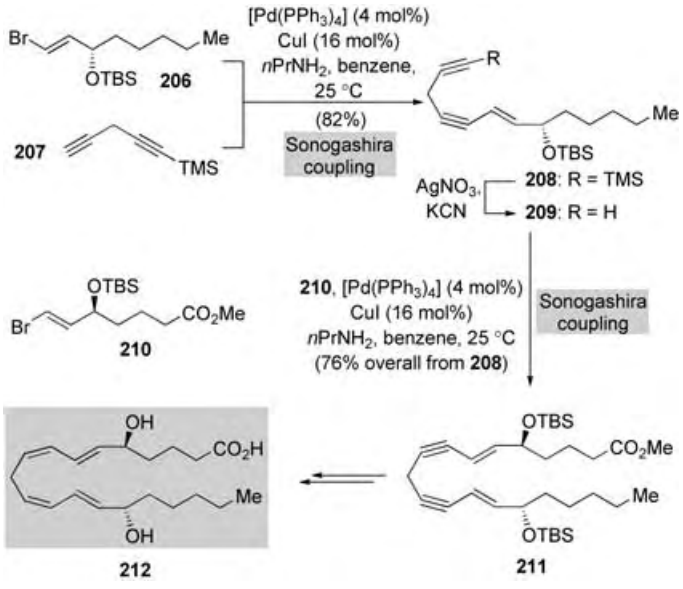
5. The Sonogashira Reaction

The Sonogashira reaction has emerged in recent years as one of the most general, reliable, and effective methods for

 © 2005 Wiley-VCH Verlag GmbH & Co. KGaA, Weinheim

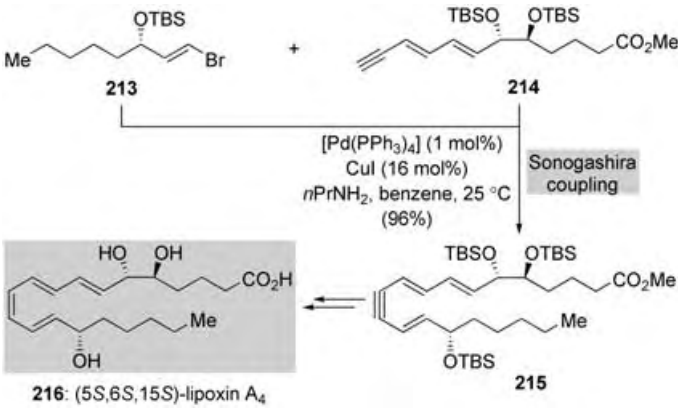
the synthesis of substituted alkynes.[184] The palladium-catalyzed coupling of a number of preformed metal acetylides (e.g. Zn,[185] Mg,[186] B,[187] Al,[188] and Sn[189] derivatives) with organic electrophiles also provides a useful access to substituted alkynes. Nevertheless, the Sonogashira protocol (employing cocatalytic Cu^I salts) is the most widely used of the palladium-catalyzed alkynylation methods, particularly in the context of total synthesis, largely owing to its broad applicability and convenience.

An early application of the Sonogashira reaction in total synthesis can be found in the generalized synthetic route to the biologically significant lipoxins and related eicosanoids pioneered by the Nicolaou group in the early 1980s. As an illustrative example, we highlight the stereospecific synthesis of (5*S*,15*S*)-dihydroxy-6,13-*trans*-8,11-*cis*-eicosatetraenoic acid (**212**),[190] an important metabolite of arachidonic acid. Besides securing the stereochemistry of the remote hydroxy-bearing stereogenic centers, the central problem in the synthesis of this and similar polyunsaturated compounds resides in the construction of an aliphatic chain that have double bonds of defined geometry in specified positions within the molecule. The solution devised by the Nicolaou group involved the stereospecific formation of the conjugated unsaturated systems through Sonogashira coupling reactions in which the acetylene components function as masked *Z*-alkene motifs. Thus, as illustrated in Scheme 38, the coupling of vinyl bromide (*E*)-**206** with the terminal alkyne **207** upon exposure to $[Pd(PPh_3)_4]$ (4 mol%), CuI (16 mol%), and nPrNH$_2$ (1.2 equiv) in benzene proceeded smoothly at room temperature to afford enediyne **208** in good yield. As expected, compound **208** was formed as a single geometric isomer, with the anticipated retention of configuration about the *E* double bond. After the liberation of the terminal acetylene to give compound **209**, a second Sonogashira reaction, this time with vinyl bromide **210** under the same coupling conditions gave bis(enyne) **211** as a single isomer and again in good yield. With the entire molecular framework of the target natural product thus rapidly assembled through this convergent and flexible approach, the few remaining synthetic steps required only selective hydrogenation of the two alkyne units, under Lindlar conditions, and removal of protecting groups.



Scheme 38. Sequential Sonogashira couplings in the total synthesis of **212** (Nicolaou and Webber, 1984).[190]

Variations on this general Sonogashira coupling theme allowed the synthesis of a number of other structurally and biosynthetically related eicosanoid natural products, including the lipoxin family of secondary metabolites. For example, (5*S*,6*S*,15*S*)-lipoxin A$_4$ (**216**) was readily obtained through the smooth union of the enantiomerically pure building blocks **213** and **214**, followed by standard Lindlar reduction and protecting-group cleavage procedures (Scheme 39).[191] A large number of isomeric lipoxin A[192] and lipoxin B[193] derivatives were produced by analogous routes, which enabled not only the identification and structure elucidation of a number of naturally occurring isomers of this series, but also provided meaningful quantities of materials for further biological investigations.[194]



Scheme 39. Application of a fragment-coupling Sonogashira reaction in the total synthesis of (5*S*,6*S*,15*S*)-lipoxin A$_4$ (**216**) (Nicolaou et al., 1985).[191]

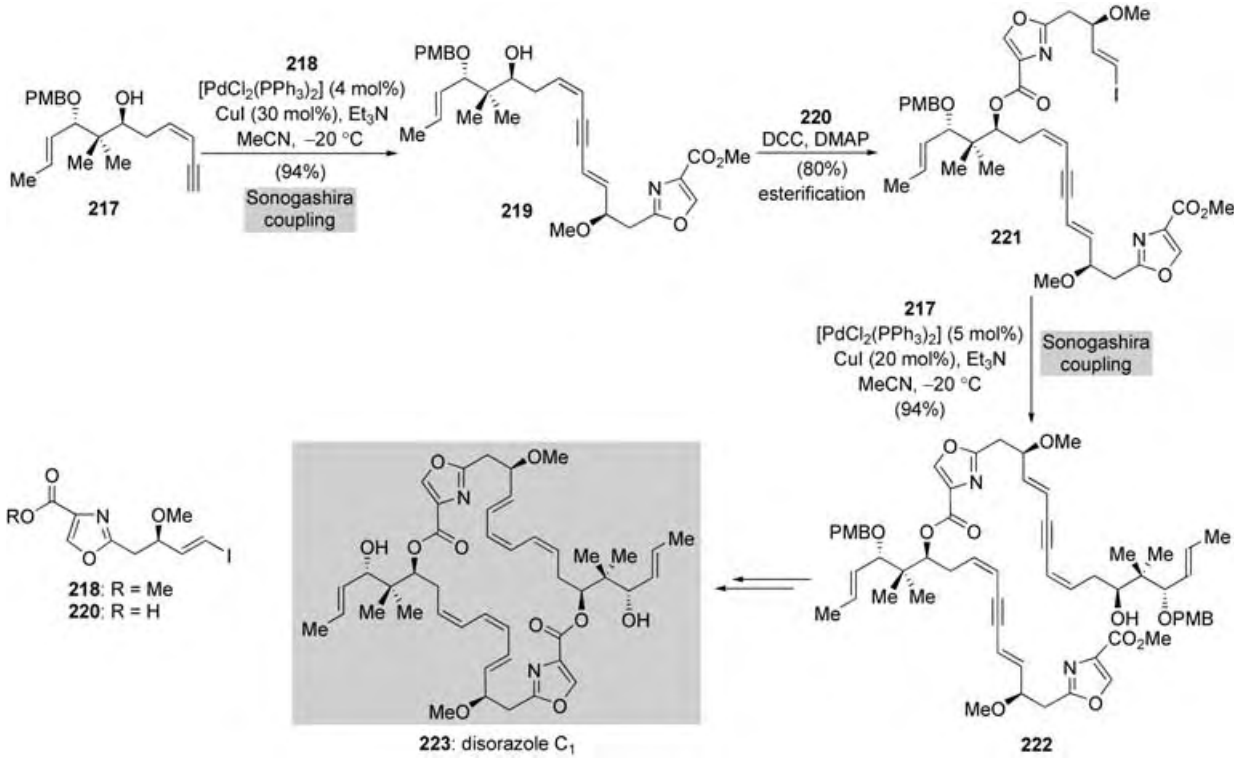
These instructive examples serve to highlight the fact that the Sonogashira reaction provides an important alternative to the Stille and Suzuki reactions for the stereoselective synthesis of polyene systems, by means of this two-step protocol of alkyne–alkene coupling followed by selective reduction of the triple bond. Such methodology proves to be of particular use when the organostannane or organoboron components, required for the Stille or Suzuki coupling reactions, respectively, are either unavailable or too unstable to be synthetically useful. It is important to note that both the corresponding *E*- and *Z*-alkene isomers can be readily prepared in a stereoselective fashion from the parent alkyne. Thus, whereas the *Z* alkenes are typically prepared by catalytic hydrogenation procedures, a number of routes are available for the synthesis of the corresponding *E* isomers;[195] the hydrosilylation protocols recently developed by the Fürstner[196] and Trost groups[197] are potentially convenient and chemoselective methods.

 © 2005 Wiley-VCH Verlag GmbH & Co. KGaA, Weinheim

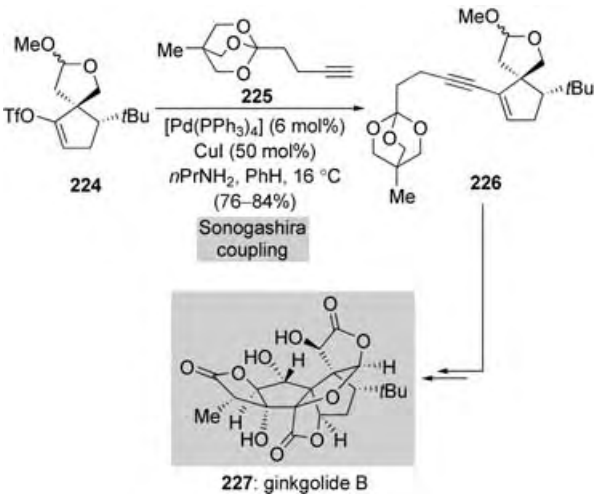
The power of the Sonogashira reaction in fragment-coupling processes is nicely illustrated in the synthesis of disorazole C_1 (**223**) by Wipf and Graham (Scheme 40).[198] Noting the symmetry elements inherent within the natural product, the team reasoned that the formidable molecular framework of their target could be broken down into just three relatively simple fragments that could be appropriately unified through the judicious employment of esterification, Sonogashira, and macrolactonization reactions. As shown in Scheme 40, the coupling of alkyne **217**, containing an unprotected secondary hydroxy group, with vinyl iodide **218** occurred rapidly in the presence of $[PdCl_2(PPh_3)_2]$ (4 mol%), CuI (30 mol%), and Et_3N in MeCN to yield the desired coupling product **219** in nearly quantitative yield. The secondary hydroxy group in compound **219** was then esterified with carboxylic acid **220** to give vinyl iodide **221**, onto which was appended another molecule of alkyne **217** through another high-yielding Sonogashira coupling. Hence, in only three operations, the entire carbon framework of the final target structure had been assembled under mild conditions and in a stereospecific manner from the simple starting materials **217**, **218**, and **220**, with no protecting-group manipulation required. A few more steps then completed the total synthesis, with the two sensitive *E*,*Z*,*Z*-triene systems being unveiled in the last step through the selective hydrogenation of the alkyne moieties facilitated by the Lindlar catalyst. Thus, as was the case in the synthesis of **212**, the alkyne unit serves a dual function in the synthesis: as a coupling handle for carbon–carbon bond formation and as a surrogate for a *Z* alkene, enabling the postponement of the unveiling of the latter, rather delicate structural motif until a late stage in the synthesis.

In a similar vein to the other palladium-catalyzed processes discussed so far, the finding that vinyl triflates (also known as enol triflates) are effective electrophiles in cross-couplings with terminal alkynes has significantly expanded the scope and utility of the Sonogashira reaction.[199] One of the first such applications in total synthesis, which indeed remains a prime example of this methodology in natural products synthesis, can be found in the masterful synthesis of ginkgolide B (**227**) by E. J. Corey and co-workers, reported in 1988.[200] In this true classic in total synthesis,[118] one of the key early steps was the formation of enyne **226** through the coupling of enol triflate **224** (derived from the corresponding ketone) with the orthoester-substituted terminal alkyne **225** (Scheme 41). The required transformation was induced by treatment of a mixture of the coupling partners **224** and **225** with a catalytic amount of $[Pd(PPh_3)_4]$ (6 mol%), a substoichiometric amount of CuI (50 mol%), and nPrNH$_2$ (excess) in toluene, providing the desired product **226** in yields between 76 and 84%.

One of the most common applications of the Sonogashira reaction in total synthesis is the incorporation of two-carbon alkyne motifs into synthetic intermediates, either as ring appendages or as a means of acyclic-chain elongation. (Trimethylsilyl)acetylene serves as a conveniently handled acetylene equivalent, with the added benefit that, because one terminus of the alkyne unit is blocked as the corresponding trimethylsilane, monocoupling products are observed exclusively. Such a reaction was applied by Isobe and co-workers at an early juncture in the course of their asymmetric total synthesis of tetrodotoxin,[201] the notorious puffer fish poison that has been called "one of Nature's great marvels".[202] Thus, (trimethylsilyl)acetylene was smoothly cou-

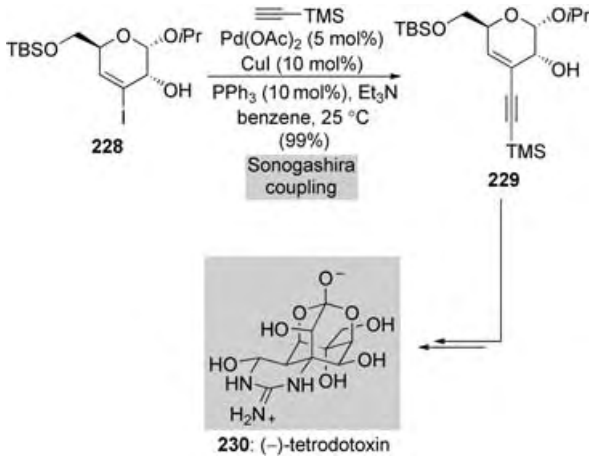


Scheme 40. Sequential use of fragment-coupling Sonogashira reactions in the total synthesis of disorazole C_1 (**223**) (Wipf and Graham, 2004).[198]



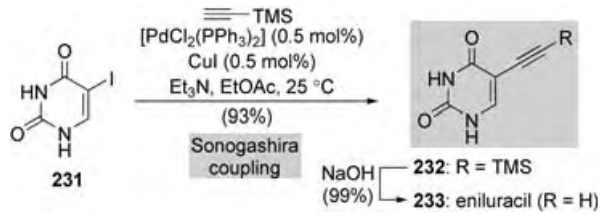
Scheme 41. Application of an enol triflate in a Sonogashira coupling in the total synthesis of ginkgolide B (**227**) (Corey et al., 1988).[200]

pled with vinyl iodide **228** upon exposure to catalytic amounts of $Pd(OAc)_2$ (5 mol%), PPh_3 (10 mol%), and CuI (10 mol%) in the presence of Et_3N in benzene at ambient temperature to afford enyne **229** in near-quantitative yield (Scheme 42). This product was then advanced through a number of steps to complete the total synthesis.



Scheme 42. Use of the Sonogashira reaction to introduce an ethynyl group in the enantioselective synthesis of (−)-tetrodotoxin (**230**) (Isobe et al., 2003).[201]

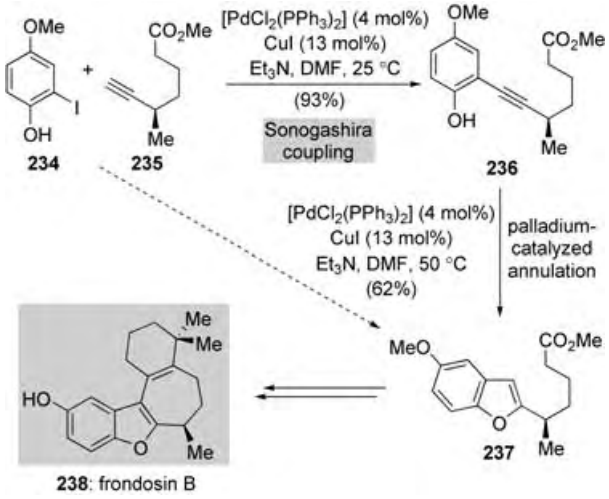
This protocol has also found industrial application, for example, in the concise synthesis of eniluracil (**233**, Scheme 43), a chemotoxic agent enhancer developed by GlaxoSmithKline and used for the treatment of breast and colorectal cancers.[203] In this synthesis, the coupling of 5-iodouracil (**231**) with (trimethylsilyl)acetylene proceeded in excellent yield and, on a large scale, in the presence of catalytic amounts of $[PdCl_2(PPh_3)_2]$ and CuI in EtOAc at ambient temperature. It was found that the catalyst loading of both the palladium complex and the copper salt could be lowered to a mere 0.5 mol% each while maintaining an acceptable reaction rate, with the resultant benefits of lower



Scheme 43. Use of the Sonogashira reaction to introduce an ethynyl group in the synthesis of eniluracil (**233**) (Glaxo SmithKline, 2001).[203]

reagent costs and minimal heavy-metal contamination in the process. The subsequent basic hydrolytic cleavage of the silyl protecting group to afford the target compound also proceeded smoothly and in nearly quantitative yield. Thus, this protocol provides a mild, safe, and high-yielding method for the introduction of an unsubstituted ethynyl fragment, thus offering a versatile alternative to the synthesis of such motifs through the standard homologation of aldehyde precursors.[204]

An interesting approach to the total synthesis of the interleukin-8 receptor antagonist frondosin B by employing palladium-catalyzed chemistry was reported by Danishefsky and co-workers.[205] The researchers proposed that a concise and convergent synthetic route to the pivotal benzofuran intermediate **237** could be secured through a heteroannulation reaction between *ortho*-iodophenol derivative **234** and terminal alkyne **235** (Scheme 44). This cascade process would involve the initial Sonogashira coupling between **234** and **235** to generate intermediate **236**, which would then undergo the required intramolecular cyclization in a process that was already known to be catalyzed by palladium salts.[206,207] While it was, indeed, found that this one-pot process could be effected to yield benzopyran **237** directly from **234** and **235**, such procedures were invariably plagued by numerous competing side reactions and decomposition pathways, to the detriment of the formation of the desired product **237**, which, even under optimum conditions, could be isolated only



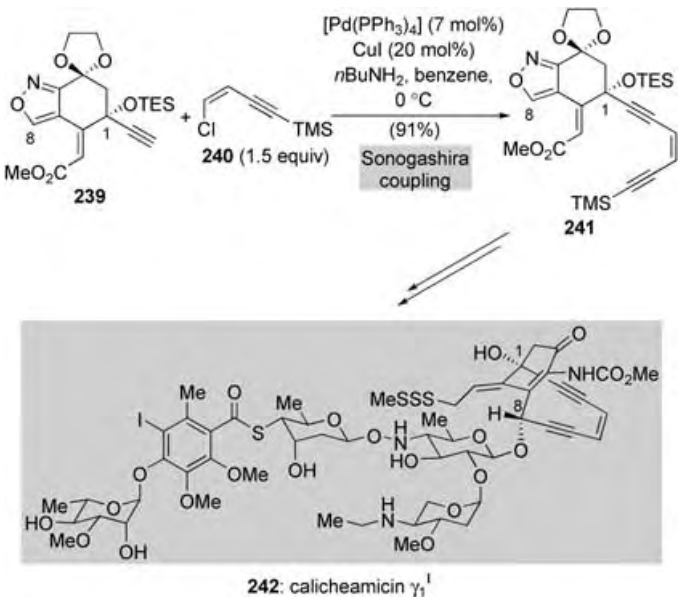
Scheme 44. Use of the Sonogashira reaction in a heteroannulation protocol in the total synthesis of frondosin B (**238**) (Danishefsky et al., 2001).[205]

 © 2005 Wiley-VCH Verlag GmbH & Co. KGaA, Weinheim

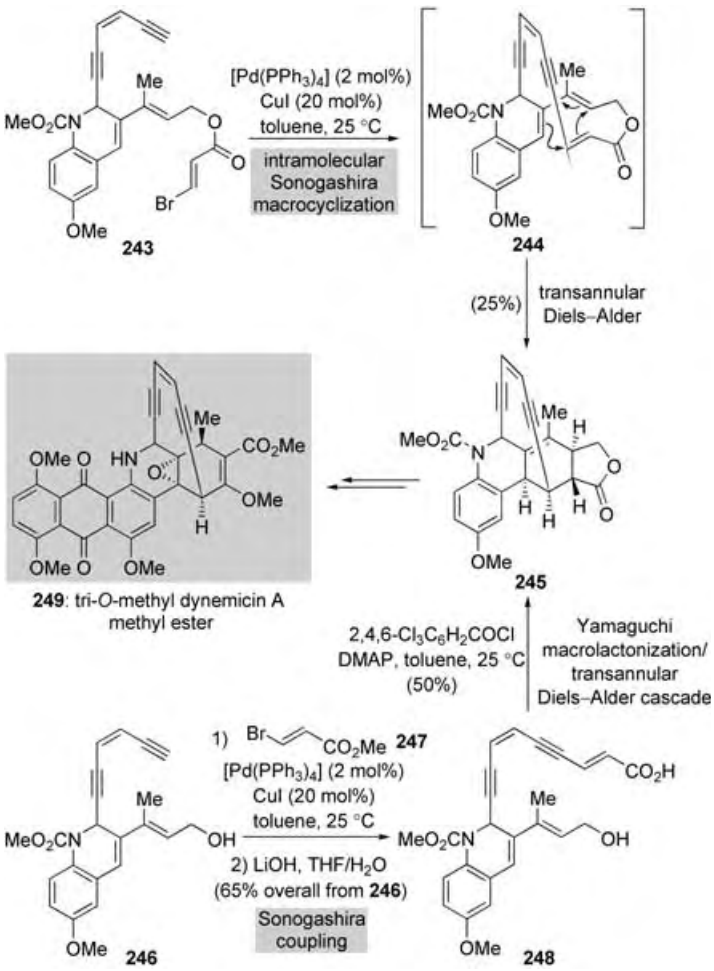
in modest yields (20–40%). To circumvent this dilemma, the researchers investigated the possibility of carrying out the Sonogashira coupling and heteroannulation reactions as separate, subsequent steps. Much to their delight, the coupling of **234** and **235** to give alkyne **236** proceeded in an excellent yield of 93% at room temperature under the influence of $[PdCl_2(PPh_3)_2]$ (4 mol%), CuI (13 mol%), and Et_3N (2.0 equiv) in DMF. The choice of base was found to influence the efficacy of this step dramatically; for example, replacement of Et_3N with piperidine lowered the yield of alkyne **236** to 74%. The isolated, purified alkyne **236** was resubjected to the same reaction conditions, except for the elevated temperature of 50 °C, to effect the smooth cyclization to give the sought-after benzofuran **237** in 62% yield. Both the initial coupling and the subsequent cyclization were found to occur without any erosion of stereochemical integrity of the resulting benzylic tertiary stereocenter.

Some of the most spectacular applications of the Sonogashira reaction can be found in synthetic approaches to various members of the enediyne class of antibiotics, as reported by numerous different groups.[208] The characteristic (*Z*)-1,5-diyne-3-ene motif contained within this family of natural products would appear to lend itself readily to assembly through palladium-catalyzed carbon–carbon bond-forming processes, and indeed has proven to be a significant testing ground for the Sonogashira coupling in total synthesis. We highlight but two of the many such elegant applications. The first of these is in the pioneering total synthesis of calicheamicin γ_1^I (**242**) by the Nicolaou group in 1992.[209] As illustrated in Scheme 45, the coupling of the densely functionalized cyclohexyl-substituted alkyne **239** with vinyl chloride **240** (itself prepared through the Sonogashira reaction of *cis*-1,2-dichloroethylene with trimethylsilyl acetylene) proceeded smoothly to afford the corresponding product **241** in 91% yield. Crucially, and as anticipated, this union occurred with retention of the *Z* geometry of the alkene coupling partner.

In contrast, Schreiber and co-workers made use of both inter- and intramolecular Sonogashira reactions in their captivating and highly inventive approach to the core molecular framework of dynemicin A.[210] The cornerstone of their synthetic strategy was the anticipation that macrocyclic lactone **244** (Scheme 46) could be coaxed into undergoing a transannular Diels–Alder reaction as shown to furnish the advanced pentacyclic intermediate **245**. Such an approach would differ fundamentally from previous approaches to the dynemicin skeleton in which the enediyne motif was appended onto a previously established tricyclic system (for an example see the approach by Danishefsky and co-workers, Section 3, Scheme 15).[211] The Schreiber group investigated the potential viability of two different strategies to the putative macrocyclic transannular Diels–Alder precursor **244**.



Scheme 45. Application of a Sonogashira coupling to generate the enediyne system in the total synthesis of calicheamicin γ_1^I (**242**) (Nicolaou et al., 1992).[209]



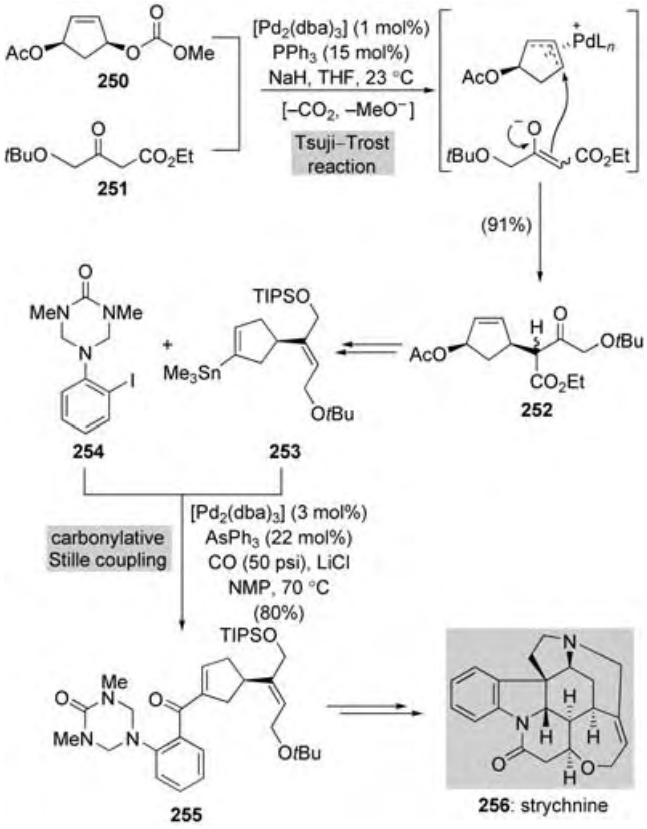
Scheme 46. Different uses of the Sonogashira coupling in cascade reactions en route to tri-*O*-methyl dynemicin A methyl ester (**249**) (Schreiber et al., 1993).[210]

In the first of these, it was proposed that the macrocyclic ring could be generated by the coupling of the terminal alkyne and the bromide-bearing vinyl carbon atom in ester **243** through a Sonogashira coupling reaction. However, to both their surprise and delight, when ester **243** was treated with [Pd(PPh_3)$_4$] (2 mol%) and CuI (20 mol%) in toluene, the sole isolable product was in fact found to be the Diels–Alder cycloadduct **245**, which had been formed as a single stereoisomer in 25% yield. In this amazing and unprecedented tandem Sonogashira/Diels–Alder reaction, three rings and four contiguous stereocenters were formed in a single operation and within 2 h at room temperature, presumably through the transient intermediacy of the expected macrocycle **244**. The second approach made use of an intermolecular Sonogashira coupling between enediyne **246** and bromoacrylate **247**, followed by basic hydrolysis of the resulting ester group, to generate the corresponding polyunsaturated carboxylic acid with complete retention of alkene geometry. When acid **248** was subjected to the Yamaguchi macrocyclization protocol,[212] cyclization to give lactone **244** was again spontaneously followed by the transannular Diels–Alder reaction at room temperature to generate the same pentacyclic intermediate **245**. Such cascade processes serve to highlight the utility and potential of the Sonogashira reaction in generating molecular complexity from much simpler precursor molecules.

6. The Tsuji–Trost Reaction

The alkylation of allylic substrates by stabilized nucleophiles is one of the most synthetically useful reactions catalyzed by palladium(0) complexes. From an historical perspective, this reaction reflects the first demonstration of a metalated species acting as an electrophile, providing a counterpoint to decades of research that had indicated that such entities only behaved as nucleophiles. On a more practical level, the Tsuji–Trost reaction, as this general process is known, typically proceeds under mild conditions, with (generally) high and predictable levels of chemo-, regio-, and stereoselectivity. The stoichiometric allylation of enolates with π-allyl–palladium complexes was first reported by the Tsuji group 40 years ago,[213] and subsequently developed into a catalytic reaction by Trost and co-workers.[25a] A wide range of allylic substrates undergo this reaction with a correspondingly wide range of carbanions, making this a versatile and important process for the formation of carbon–carbon bonds. Whilst the most commonly employed substrates for palladium-catalyzed allylic alkylation are allylic acetates, a variety of leaving groups also function effectively—these include halides, sulfonates, carbonates, carbamates, epoxides, and phosphates. As such, the Tsuji–Trost reaction has been widely embraced by synthetic chemists, and we can highlight but a few of the many elegant applications of this process here. It is important to recall that a wide variety of heteroatom nucleophiles (e.g. N, O, and S nucleophiles) also make excellent coupling partners in the Tsuji–Trost reaction; however, the utility of these processes are beyond the scope of this Review.

A classic and instructive example of the intermolecular Tsuji–Trost reaction can be found in the total synthesis of the naturally occurring enantiomer of strychnine (**256**, Scheme 47) by Overman and co-workers in 1993.[214] Com-



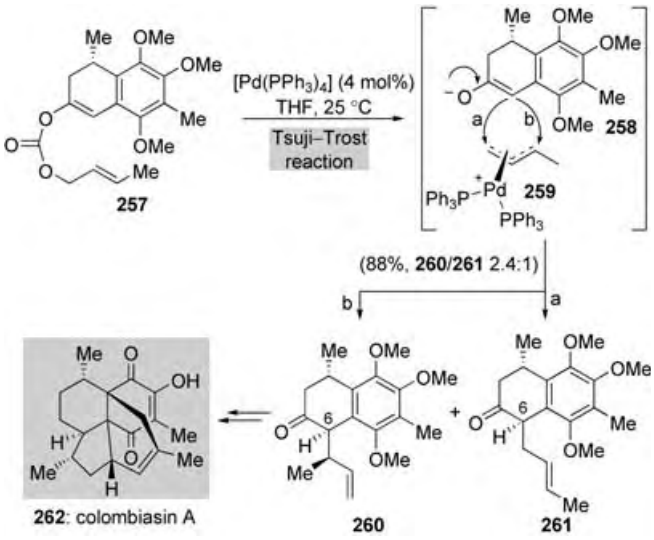
Scheme 47. Tsuji–Trost and carbonylative Stille coupling reactions in the total synthesis of strychnine (**256**) (Overman et al., 1993).[214]

prising only 24 skeletal atoms woven into a bewitching polycyclic structure, strychnine holds a special place in the annals of structure determination and natural product synthesis. However, following the landmark total synthesis of racemic strychnine by Woodward and co-workers in 1954,[215] enantioselective syntheses of this remarkable alkaloid would not be forthcoming for nearly 50 years, with the success of the Overman approach being, in a large part, due to the application of palladium-catalyzed reactions.[216] The first key step in the synthesis involved the allylation of acetoacetate derivative **251** (Scheme 47) with enantiopure allylic carbonate **250**, under the influence of [Pd_2(dba)$_3$] (1 mol%), PPh_3 (15 mol%), and NaH in THF at ambient temperature to furnish the *cis*-alkylated adduct **252** in 91% yield. Several features of this reaction merit further comment. First, the net stereochemical outcome of this reaction is the overall retention of the configuration at the leaving-group-bearing carbon atom, thus complementing normal S_N2 reactions, which proceed with inversion of configuration. As illustrated in Scheme 47, this is the consequence of two successive inversions at this center, and is a general feature of the Tsuji–Trost reactions of soft nucleophiles. Second, the regiochem-

© 2005 Wiley-VCH Verlag GmbH & Co. KGaA, Weinheim

istry of the alkylation is such that compound **252** is formed exclusively. In general, the regiochemical course of the alkylation of unsymmetrical allylic substrates is such that attack is favored at the less-substituted terminus; however, and as we shall see, this is somewhat dependent on the specific nature of the nucleophile, the electrophile, and the catalyst system. Although cyclopentene derivative **250** contains two potential leaving groups, namely the acetate and the carbonate units, the exclusive displacement of the latter was observed. This outcome had been anticipated on the basis of relevant precedent, which had demonstrated the higher reactivity of allylic carbonates in these processes than that of the corresponding acetates.[217] Finally, compound **252** was formed as a 1:1 mixture of epimers at the stereocenter adjacent to the ketone group, but this proved to be inconsequential as this mixture could be advanced to give stannane **253** as a single stereoisomer. A carbonylative Stille reaction was then employed to effect the linking of stannane **253** with aryl iodide **254** through a carbonyl bridge, affording tricyclic compound **255** in 80% yield. This intermediate was subsequently elaborated to complete the asymmetric total synthesis of (−)-strychnine.

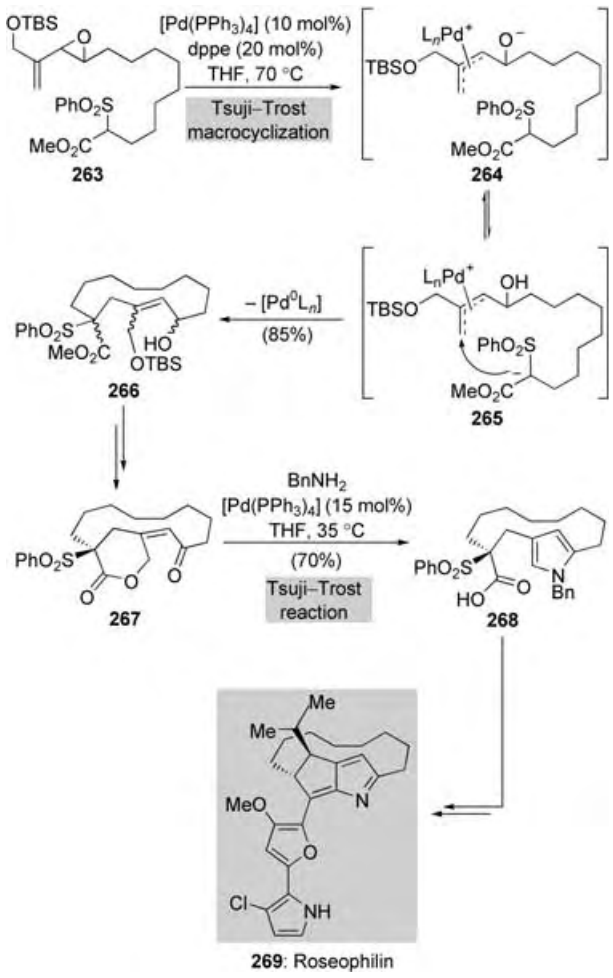
The pioneering total synthesis of the marine diterpenoid colombiasin A (**262**, Scheme 48) by the Nicolaou group in



Scheme 48. Regioselective Tsuji–Trost reaction of a crotyl enol carbonate precursor in the total synthesis of colombiasin A (**262**) (Nicolaou et al., 2001).[218]

2001[218] was the end result of the development of a number of synthetically useful techniques, foremost amongst them being the extension of the Tsuji–Trost allylation reaction to a new class of substrates as well as interesting observations regarding the regioselectivity of the addition of enolate nucleophiles to η^3-crotyl–palladium electrophilic complexes. The adopted synthetic plan called for the installation of the C6 side chain through a Tsuji–Trost reaction of an appropriately substituted crotyl enol carbonate precursor (i.e. **257**→**260**).[219] However, it was appreciated from the outset that there were a number of potential pitfalls associated with this novel transformation, not the least of which was the issue of the regioselectivity of the addition of enolate intermediate **258** to palladium complex **259**. Indeed, a substantial body of literature precedent suggested that addition would occur predominantly at the less-hindered terminus of the complex (path a) to generate the undesired regioisomeric product **261**. However, it was proposed that if the reaction conditions could be tailored such that electronic factors, rather than the customary steric effects, became the dominant factor in determining the regioselectivity of addition, then the reaction could indeed be coaxed into following the desired pathway (i.e. path b), as the site of greatest partial positive charge in the allylic domain of complex **259** resides at the secondary carbon atom terminus. Gratifyingly, it was found that exposure of enol carbonate **257** to $[Pd(PPh_3)_4]$ (4 mol%) in THF at ambient temperature led to the rapid formation of a mixture of the two regioisomeric products **260** and **261**, in a combined yield of 88%, in which the desired isomer predominated (**260**/**261** 2.4:1). The employment of PPh_3 as a ligand for palladium proved to be crucial in dictating this regiochemical outcome, as it presumably enabled the sufficient accumulation of partial positive charge character on the crotyl ligand in complex **259** to favor attack at the more-substituted carbon terminus. Indeed, it was observed that better σ-donor ligands (e.g. dppe or $P(OiPr)_3$), which would be expected to lower the cationic character of complex **259**, restored the "normal" regioselectivity, with the undesired product **261** predominating in these reactions. These groundbreaking results showed, for the first time in the context of complex molecule construction, that the regioselectivity of nucleophilic addition in the Tsuji–Trost reaction can, under appropriate conditions, be manipulated beyond mere steric control. Certainly, in this instance, it went against established doctrine. The regiochemistry issues notwithstanding, this allylation reaction was, in fact, extremely stereoselective, with both the undesired product **261** and, even more remarkably, the desired compound **260** being formed as single stereoisomers. This outcome presumably reflects the inherent influence of the remote methyl-group-bearing stereocenter in the starting material **257** on the allylation step.[220]

The intramolecular Tsuji–Trost reaction represents a powerful method for the formation of a broad spectrum of ring systems, be they carbocyclic or heterocyclic, small or large. An elegant example of the scope of this process is the total synthesis of the architecturally unique alkaloid roseophilin (**269**, Scheme 49) by Fürstner and Weintritt.[221,222] The central synthetic challenges confronting these researchers were the formation of both the azafulvene-type chromophore and the rather strained *ansa* 12-membered carbocyclic ring; the Tsuji–Trost reaction proved to be instrumental in addressing both these issues. Thus the initial formation of the macrocyclic ring was effected by the addition of a dilute solution of allylic epoxide **263** to catalytic amounts of $[Pd(PPh_3)_4]$ and dppe in refluxing THF to generate compound **266** in an impressive 85% yield (Scheme 49). As with the strychnine example described above, the reaction sequence was initiated by the selective oxidative addition of the more reactive unit of a bifunctional substrate to a palladium(0) species through the judicious modulation of leaving-group

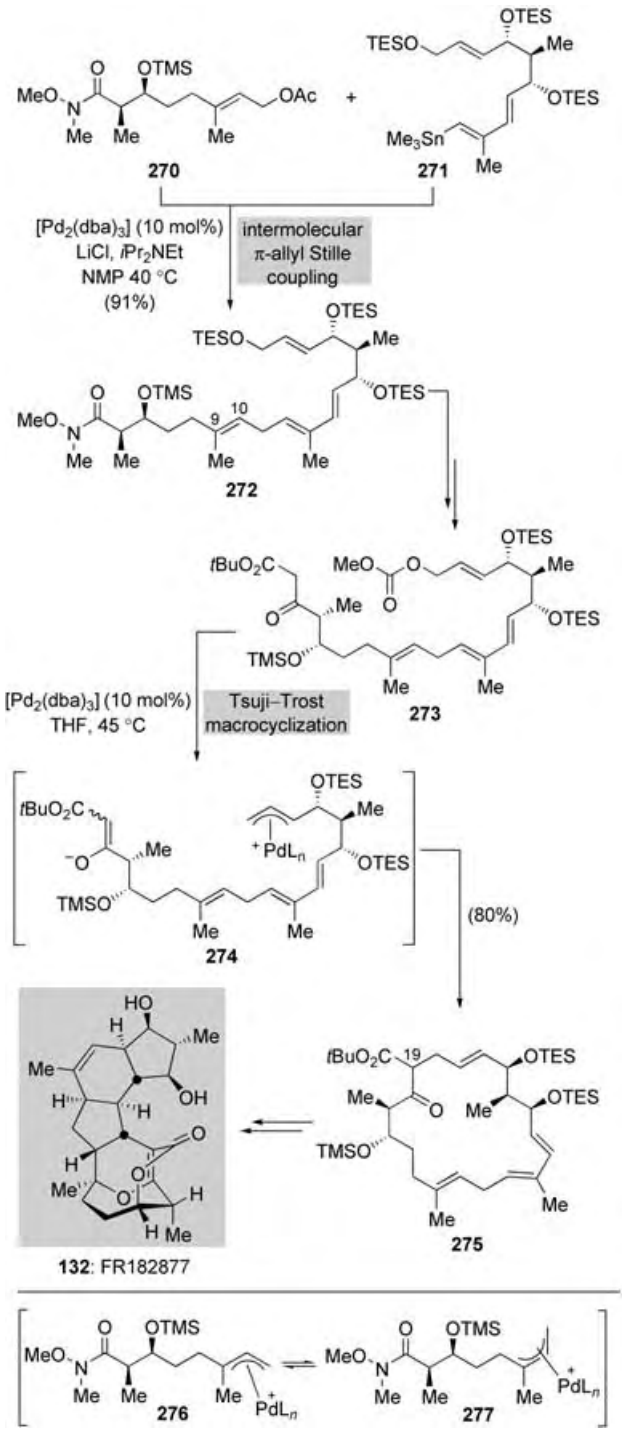


Scheme 49. Sequential use of Tsuji–Trost reactions in the total synthesis of roseophilin (**269**) (Fürstner and Weintritt, 1998).[221]

reactivity. Thus, in this case, the allylic epoxide moiety in compound **263** was opened selectively in the presence of the allylic silyl ether group, driven by the attendant release of ring strain, to generate the presumed alkoxide intermediate **264**. Following equilibration to generate the stabilized carbanion species **265**, macrocyclization can then occur at the less-hindered terminus of the π-allyl system to generate the observed product **266**. There was no inherent diastereoselectivity in this reaction, with the product **266** being formed as a mixture of all possible stereoisomers. This did not prove to be a hindrance as no tedious separation of the individual components was required, and all the isomers eventually converged into the one final target product. Note that the reaction proceeded under neutral conditions, with no external base needed in the reaction cocktail, which, in this case, is due to the generated alkoxide intermediate **264** being of sufficient basicity to deprotonate the β-sulfone ester group. High-dilution conditions were employed for this transformation to favor the desired macrocyclization over competing detrimental oligomerization processes. Following the elaboration of compound **266** to give lactone **267**, another Tsuji–Trost reaction was employed to generate the corresponding *meta*-pyrrolocyclophane **268**. This interesting palladium-catalyzed transformation, which again proceeds under mild neutral conditions, would appear to offer an appealing alternative to traditional acid-catalyzed condensation protocols for the formation of pyrrole ring systems from acyclic 1,4-diketones or their synthetic equivalents.[223]

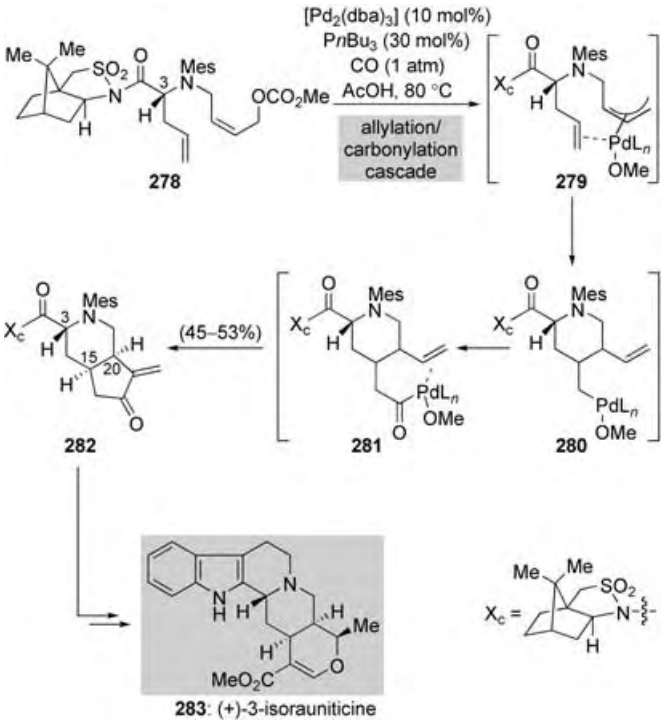
Brilliant use of π-allyl–palladium(II)-mediated bond-forming reactions was made by Sorensen and co-workers in their enantioselective total synthesis of the naturally occurring enantiomer of FR182877 (**132**).[224] The first of these couplings was the π-allyl Stille reaction between allylic acetate **270** and dienylstannane **271** to afford intermediate **272** as a single stereoisomer in 91% yield (Scheme 50). That this reaction proceeded as superbly as it did was only the result of extensive prior investigative work on the part of the researchers to optimize the coupling conditions. In particular, it was found that the dienylstannane component **271** was exquisitely sensitive to traces of acid,[225] with the consequent protodestannylation of this partner competing with its coupling to allylic acetate **270**. Fortunately, the simple addition of a mild amine base (iPr$_2$NEt) to the reaction medium was found to be sufficient to suppress the undesired protodestannylative destruction of **271** almost completely. Of equal benefit was the discovery that only at reaction temperatures at or below 40 °C could coupling product **272** be obtained as the desired stereoisomer. At higher temperatures, significant amounts of the corresponding C9–C10 *Z* isomer of coupling product **272** were obtained. The formation of the latter was likely due to the erosion of stereochemical integrity of the presumed initially formed reactive π-allyl–palladium intermediate **276**, through competing thermal equilibration, to give a mixture of isomeric complexes **276** and **277** prior to coupling with stannane **271**. Nevertheless, with a practical and highly convergent route to coupled intermediate **272** thus secured, this compound was rapidly advanced to generate allylic carbonate **273**, the precursor for the second pivotal palladium-catalyzed reaction in the sequence, namely a Tsuji–Trost macrocyclization. To the researchers' delight, cyclization of precursor **273** to give the sought-after macrocycle **275** proved to be both remarkably facile and efficient and could be effected by simply treating a moderately dilute solution (0.05 M) of the starting material (**273**) in THF with [Pd$_2$(dba)$_3$] (10 mol%) at 45 °C. In this manner, the cyclized product **275** could be cleanly obtained in 60–85% yield and, interestingly, as a single diastereoisomer (i.e. only one stereoisomer at the newly formed C19 stereogenic center was produced in the cyclization event). The success of this reaction is undoubtedly due to the shrewd employment of a methyl carbonate as the allylic activating group. Carbonate groups enable irreversible palladium oxidative addition under mild conditions, promoted by the expulsion of a molecule of CO_2 and an alkoxide anion (in this case methoxide). This alkoxide anion serves a dual purpose in that, as with the analogous case in the synthesis of roseophilin discussed above, it also functions to deprotonate the activated β-ketoester methylene moiety, thus enabling the required ring closure. These spectacular examples clearly illustrate the practical utility of palladium-catalyzed carbon–carbon bond-formation processes via electrophilic π-allyl intermediates in the construction of complex molecules.

 © 2005 Wiley-VCH Verlag GmbH & Co. KGaA, Weinheim



Scheme 50. Application of π-allyl Stille fragment-coupling and Tsuji–Trost macrocyclization reactions in the enantioselective synthesis of FR182877 (**132**) (Sorensen et al., 2003).[224]

The insertion of alkenes into π-allyl–palladium species is a key step in the carbocyclization of allylic electrophiles with alkenes, a process that represents a powerful method for the formation of five- and six-membered carbocyclic and heterocyclic ring systems.[226,227] The combination of palladium-catalyzed allylation and carbonylation reactions is especially attractive as it permits the (potentially stereoselective) formation of three carbon–carbon bonds plus the insertion of a ketone carbonyl group in a single step. The Oppolzer group has been one of the key pioneers and exponents of this methodology, the utility of which is magnificently demonstrated in their synthesis of the heteroyohimbine alkaloid 3-isorauniticine (**283**, Scheme 51).[228,229] Thus, the treatment of



Scheme 51. Application of an allylation/carbonylation cascade reaction in the enantioselective synthesis of 3-isorauniticine (**283**) (Oppolzer et al., 1991).[228]

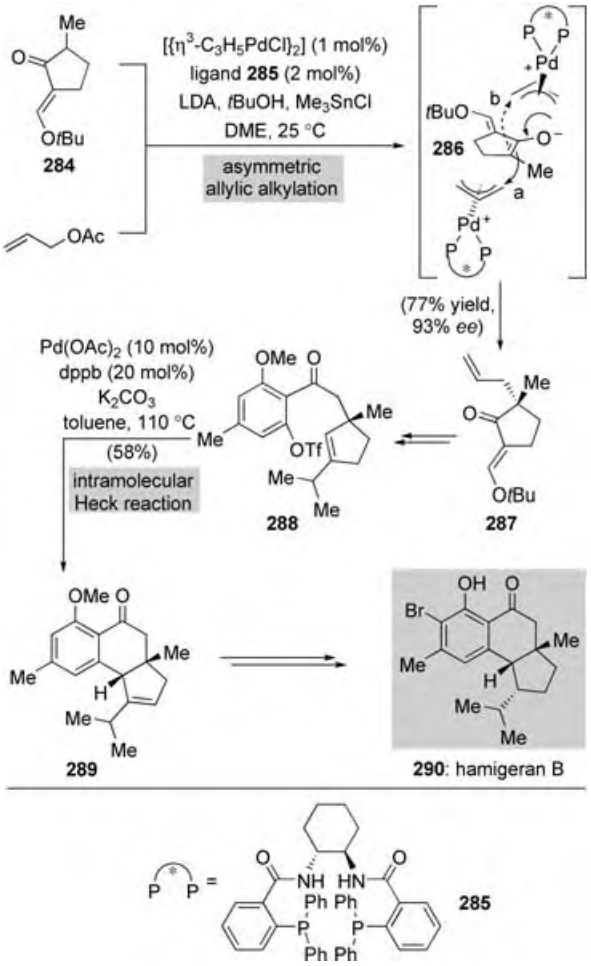
a solution of allylic carbonate **278** in AcOH with catalytic amounts of [Pd$_2$(dba)$_3$] (10 mol %) and P(nBu)$_3$ (30 mol %) at 80 °C under carbon monoxide (1 atm) initiated a highly orchestrated sequence of carbon–carbon bond-forming steps, which culminated in the diastereoselective construction of bicyclic enone **282** in reproducible yields of roughly 50 %. The first step in this sequence is the selective ionization of the allylic moiety within the starting material **278** by a Pd^0 complex, to generate π-allyl–palladium intermediate **279**. This species then undergoes a regioselective insertion into the pendant terminal alkene system (which in effect acts as the nucleophile to capture the electrophilic π-allyl–palladium complex) to form η^1-alkyl–palladium(II) intermediate **280**. This process can be formally considered as a suprafacial palladium-ene cyclization. The insertion of carbon monoxide into η^1-alkyl–palladium(II) intermediate **280** to generate the next intermediate **281** is evidently much faster than the undesired β-hydride elimination. Finally, acyl palladium(II) intermediate **281** undergoes a regioselective intramolecular Heck reaction to afford the observed product **282**. The overall yield for this process was, in fact, more impressive than the illustrated yield of 45–53 % would appear to indicate, as two minor stereoisomeric products, diastereoisomeric with

respect to **282** at the newly formed ring junction, were also formed in a combined yield of 25%. Thus, the preexisting C3 stereogenic center exerted a moderate influence on the diastereoselectivity of the cyclization cascade in generating the C15 and C20 stereocenters.

The development of procedures to induce asymmetry during palladium-catalyzed allylic alkylation reactions has dramatically enhanced the synthetic utility of this process.[230] Any discussion of the asymmetric allylic alkylation reaction is complicated somewhat by the fact that there are a number of different possible mechanisms of enantiodiscrimination, depending on the nature of the nucleophile and/or electrophile and at which point in the catalytic cycle the chiral elements are set. We can but highlight a few of the more commonly applied types of processes here. Nevertheless, the ability to generate stereochemical complexity from simpler (often achiral) starting materials by using only catalytic quantities of chiral ligands, and equally significantly, in a reliable, predictable, and selective fashion, has propelled the asymmetric allylic alkylation reaction to the forefront of modern synthetic methodology.[231]

While stabilized carbanions (e.g. those derived from β-ketoesters or malonate-type compounds) have traditionally been, and indeed continue to be, the most widely used carbon nucleophiles in the asymmetric allylic alkylation reaction,[232] there has been considerable interest in expanding the scope of this process to include a broader range of nucleophiles. The Trost group has been instrumental in pioneering the recent development of viable protocols for the asymmetric alkylation of ketone enolates,[233] arguably the most synthetically useful class of potential nucleophiles, and has applied this to an elegant synthesis of hamigeran B (**290**),[234] an antiviral metabolite isolated from the marine sponge *Hamigera tarangaensis*.[235] As shown in Scheme 52, the synthetic route adopted called for the early installation of the methyl-group-bearing quaternary stereocenter, and this was fashioned by the asymmetric alkylation of cyclic ketone **284**. Under the optimum conditions shown, the desired alkylated product was readily obtained in excellent yield (77%) and with remarkable enantiopurity (93% *ee*) at ambient temperature. The basis of the enantioselectivity of this alkylation resides in the differentiation between the prochiral faces of the nucleophile by the π-allyl complex. Evidently, the chiral environment created around the π-allyl–palladium complex by the bidentate ligand **285** is sufficient to direct the alkylation almost exclusively towards the "bottom" face of enolate intermediate **286**,[236] that is, path a is significantly favored over path b.

Following the elaboration of ketone **287** to give triflate **288**, it was envisaged that the final carbon–carbon bond could be forged by means of an intramolecular Heck reaction. Indeed, it was found that treatment of triflate **288** with $Pd(OAc)_2$ (10 mol%), dppb (20 mol%), and K_2CO_3 in refluxing toluene led to cyclization furnishing, stereoselectively, the desired *cis*-fused tricyclic compound **289** in 58% yield. Critical to the success of this venture was the employment of carbonate rather than tertiary amine bases, since the use of the latter led to simple hydrogenolysis of the triflate moiety without cyclization occurring. A few more steps then completed the total synthesis.[237] In the sense that the

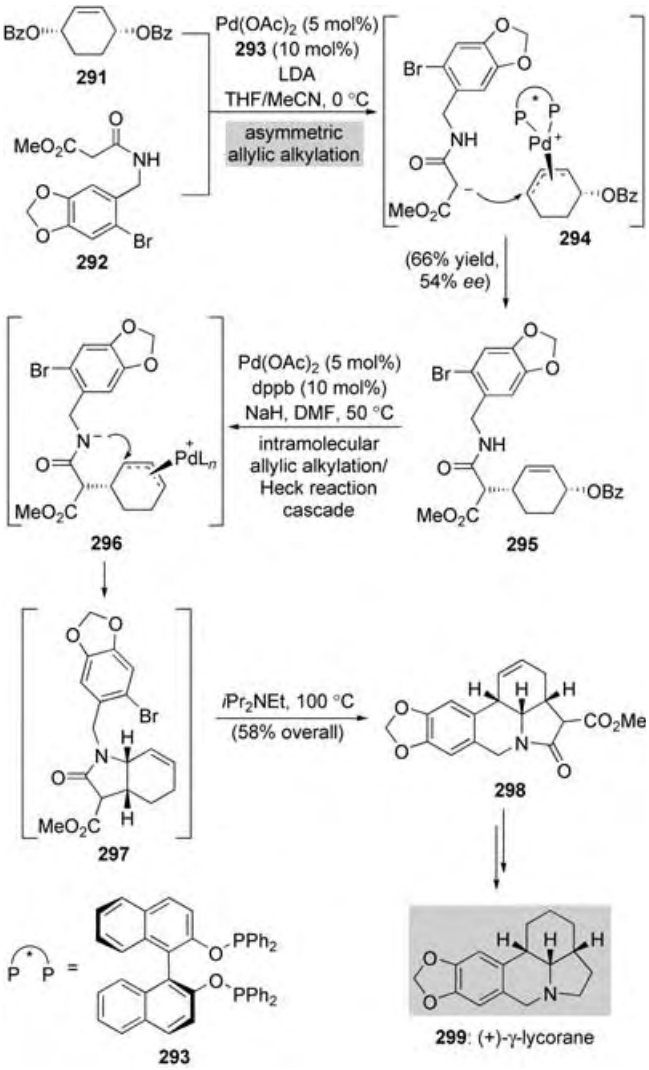


Scheme 52. Use of asymmetric allylic alkylation and intramolecular Heck reactions in the total synthesis of hamigeran B (**290**) (Trost et al., 2004).[234]

stereoselectivity of formation of the remaining two stereogenic centers in the final target molecule **290** was directed by the initially installed quaternary center, all the chiral elements in the final product were thus installed through the asymmetric allylic alkylation reaction.[238] Very recently, the Stoltz[239] and Trost groups[240] independently reported the extension of the palladium-catalyzed enantioselective allylation reaction to produce a broader range of ketone derivatives bearing quaternary stereocenters, through the asymmetric decarboxylative alkylation of the corresponding allyl enol carbonate precursors.

One of the most useful and widely applied classes of asymmetric π-allyl–palladium reactions is the catalytic desymmetrization of *meso* substrates. Readily available *meso*-2-alkene-1,4-diol derivatives, typically contained within cyclic structures, are the most commonly employed electrophilic substrates. As an example of such an application in total synthesis, we highlight the concise enantioselective construction of the alkaloid γ-lycorane (**299**) by Mori and coworkers in 1995 (Scheme 53).[241] The key fragment-coupling step in this synthesis was the desymmetrization of *meso* dibenzoate **291** with the carbanion derived from amide **292** (generated with LDA), induced by catalytic amounts of

 © 2005 Wiley-VCH Verlag GmbH & Co. KGaA, Weinheim



Scheme 53. Use of an asymmetric allylic alkylation reaction in the enantioselective total synthesis of (+)-γ-lycorane (**299**) (Mori et al., 1995).[241]

$Pd(OAc)_2$ (5 mol%) and chiral bis(phosphine) **293** (10 mol%). In this event, selective ionization of one of the two enantiotopic benzoate leaving groups, to generate π-allyl intermediate **294** preferentially, is induced by the chirality of the palladium–ligand complex and forms the basis of the asymmetric induction. Intermediate **294** is superficially similar to the π-allyl–palladium species we saw earlier in the course of the synthesis of strychnine (Scheme 47), and indeed the relative stereochemical outcome of both reactions is the same (i.e. net retention of configuration as the result of two subsequent inversions, nucleophilic attack at the less-hindered terminus of the π-allyl system). However, the two reactions differ fundamentally in how the absolute stereochemistry of the respective products **252** and **295** is introduced. In the present case, an achiral starting material **291** is converted into an enantioenriched product **295** through the action of a chiral, enantiomerically pure catalyst system, whilst in the synthesis of strychnine a chiral starting material **250** is converted into a chiral product **252** under the influence of an achiral catalyst system. It should be mentioned that the enantioselectivity of the alkylation to generate γ-lycorane intermediate **295** is, by modern standards, only moderate (54% *ee*). Indeed, asymmetric alkylations of similar substrates with newer generations of chiral ligands (e.g. **285**, Scheme 52) routinely proceed with greater than 95% *ee*.[242]

With the alkylated product **295** in hand, the remaining major obstacle separating the researchers' position from the final product was the task of fusing the remaining two rings of the natural product to the cyclohexene scaffold. In a masterful piece of synthetic planning, based on the recognition that intermediate **295** still retains an allylic ester moiety itself capable of undergoing a palladium-catalyzed nucleophilic displacement, the researchers reasoned that this task could be accomplished in a single operation directly from **295**, through the application of an unprecedented, intramolecular allylic alkylation/Heck reaction cascade sequence. Thus, treatment of amide **295** with $Pd(OAc)_2$ (5 mol%), dppb (10 mol%), and NaH in DMF at 50 °C triggered the initial intramolecular allylic alkylation to generate the presumed intermediate **297**, which upon the addition of iPr_2NEt followed by further heating to 100 °C, obligingly underwent the anticipated intramolecular Heck cyclization to afford pentacyclic compound **298** in 58% yield as a single diastereoisomer. Note that the regio- and stereochemical outcome of both the Heck and the (formal) S_N2' displacement steps were dictated solely by steric effects and constraints of the starting material **295**, hence the need for chiral ligands in this transformation was obviated. From this and the other examples discussed above, it is clear that the Tsuji–Trost reaction represents an extraordinarily useful method for carbon–carbon bond formation, yet it can be argued that the true potential of this process, in particular its asymmetric version, has only begun to be tapped.

7. The Negishi Reaction

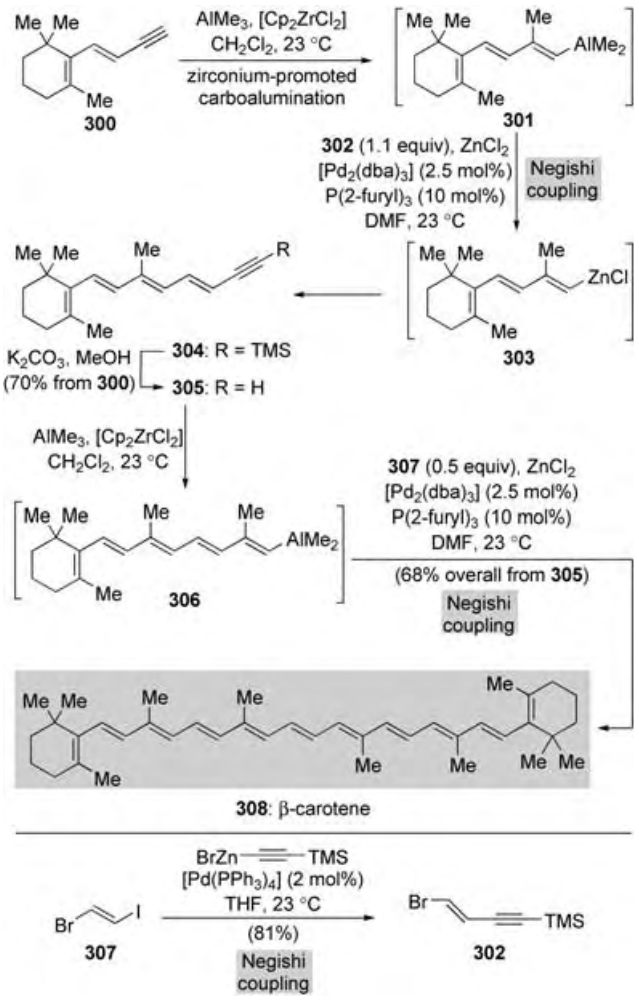
In the context of total synthesis, the Negishi coupling would appear to have been relatively underutilized, in particular having been overshadowed to a large extent by the developments in the Stille and Suzuki reactions. Nevertheless, recent years have seen renewed interest in the Negishi coupling which, in appropriate cases, is often the cross-coupling method of choice for a given synthetic task. The two classes of organozinc reagents that find most use in Negishi couplings are diorganozinc species (R_2Zn) and organozinc halides (RZnX). The latter, typically prepared either by the direct insertion of zinc (zinc dust) into organic halides or by transmetalation from other organometallic species, are particularly useful when functionalized zinc reagents are required.[243] Despite their only moderate reactivity towards many organic electrophiles, organozinc reagents are among the most reactive of nucleophilic species in palladium-catalyzed cross-coupling reactions, owing to their ability to undergo rapid transmetalation with transition-metal salts, most notably those of palladium. The Negishi reaction is particularly powerful when applied in an intermolecular context in fragment-coupling processes, often succeeding in

 © 2005 Wiley-VCH Verlag GmbH & Co. KGaA, Weinheim

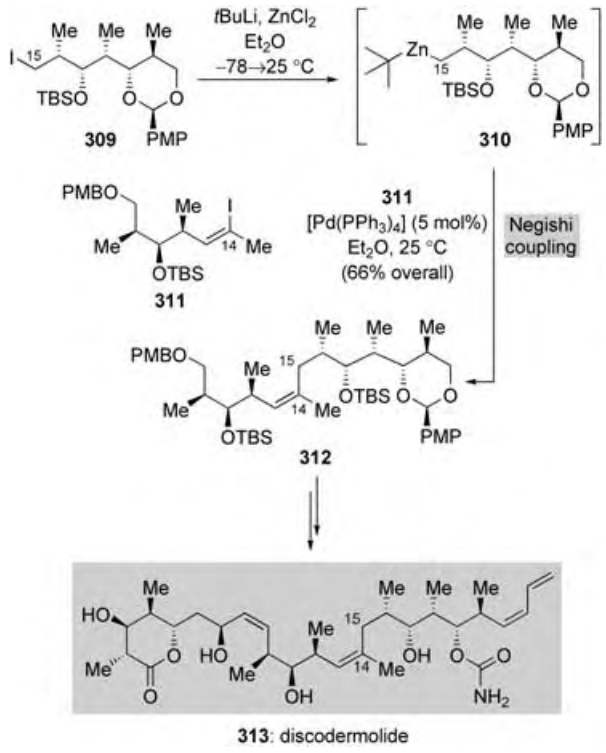
cases in which the corresponding Stille or Suzuki reactions founder. Alkyl–zinc reagents readily enter into the cross-coupling process, expanding the scope of the Negishi reaction beyond standard $C(sp^2)$–$C(sp^2)$ couplings. The major drawback of the Negishi coupling, at least by comparison with the Stille and Suzuki reactions, is the incompatibility of organozinc reagents with many common functional groups, together with their relative sensitivity towards oxygen and water.[244]

An elegant and instructive example of the utility of this coupling reaction to assemble conjugated polyene systems rapidly in high yield and with excellent stereoselectivity is the novel, general synthetic route to the carotenoids reported by the Negishi group.[245] As shown in Scheme 54 for the synthesis of β-carotene (**308**), the key feature of the researchers' approach was the regio- and stereoselective zirconium-catalyzed methylalumination of terminal alkyne precursors, followed by cross-coupling of the resulting vinyl alane intermediates with the appropriate vinyl halide electrophiles. These remarkable carbon–carbon bond-forming processes, each involving four different organometallic intermediates and three transmetalation processes (Zr→Al→Zn→Pd) proceed with remarkable overall efficiency and stereoselectivity, allowing the synthesis of the target molecule **308** in greater than 99% stereoisomeric purity and in only three operations from the starting alkyne **300**! This synthetic route would appear to compare favorably to traditional syntheses of carotenoids proceeding through the venerable Wittig or Horner–Wadsworth–Emmons reaction protocols, which are often plagued by low yields and the formation of stereoisomeric mixtures. Carbometalation (and, by extension, hydrometalation)/cross-coupling tandem processes of the type illustrated here are only made viable by the fast rate of the key transmetalation events to and from the zinc salt, as in its absence such coupling processes are often agonizingly lethargic. This principle of "double metal catalysis",[246] first introduced more than 25 years ago, offers considerable potential for the streamlining of synthetic processes.[247]

As a prime exemplar of both the utility of the Negishi reaction in fragment coupling reactions and the employment of alkyl zinc reagents in these processes to form $C(sp^2)$–$C(sp^3)$ bonds, we highlight here the gram-scale synthesis of the clinically relevant microtubule-stabilizing agent discodermolide (**313**, Scheme 55) by the Smith group.[248,249] In this approach, the two fragments **309** and **311** were coupled to forge the C14–C15 bond of the target product. Significantly, it was found that optimum results in this coupling reaction were obtained only when 3 equivalents of *t*BuLi were employed in the initial lithium–halogen exchange process; when the customary 2 equivalents were used, a 1:1 mixture of the iodide starting material **309** and the expected product **312** was obtained. This led to the proposal that, in this case, the mixed *tert*-butyl alkyl zinc intermediate **310** was in fact the reactive



Scheme 54. Negishi coupling reactions in the total synthesis of β-carotene (**308**) (Negishi and Xeng, 2001).[245]

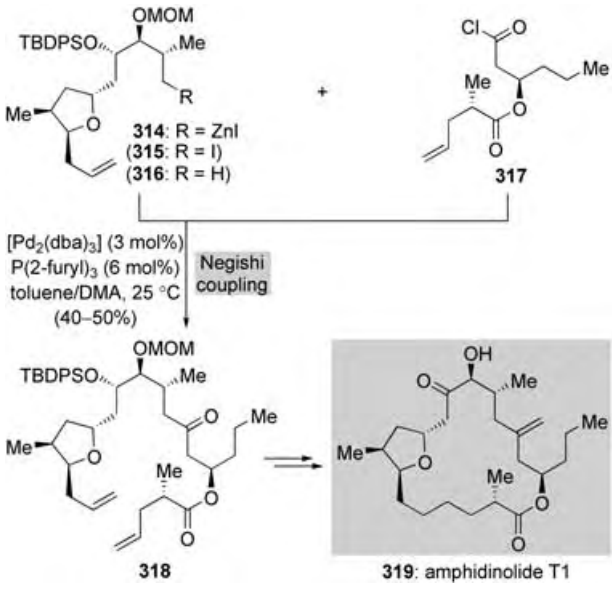


Scheme 55. Application of a Negishi fragment-coupling reaction in the enantioselective synthesis of discodermolide (**313**) (Smith et al., 2000).[248]

 © 2005 Wiley-VCH Verlag GmbH & Co. KGaA, Weinheim

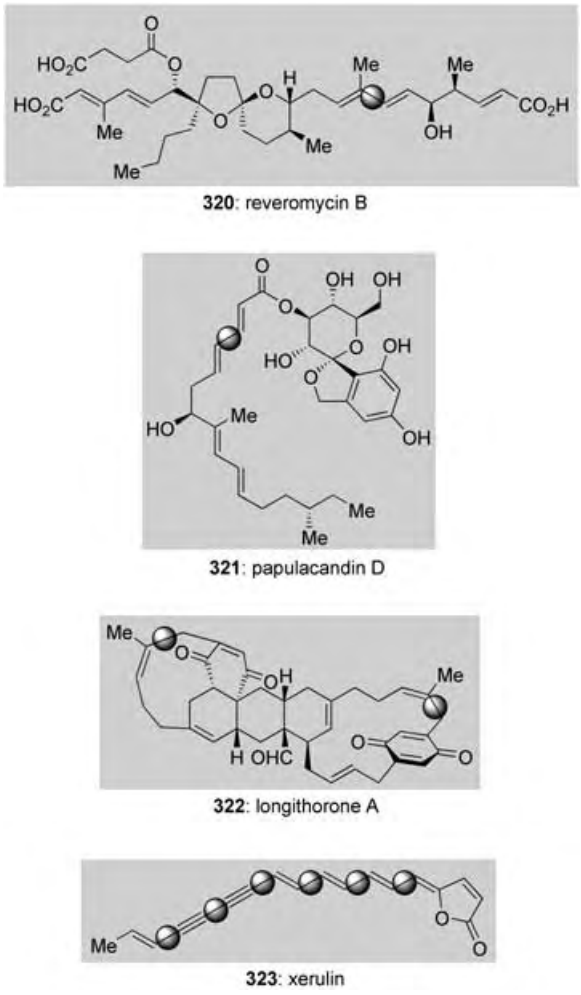
alkyl donor in the cross-coupling step (note then the selective transfer of the primary alkyl group from intermediate **310**), rather than the expected organozinc halide species (RZnI). The researchers also demonstrated the clear superiority of the Negishi protocol over both the palladium-catalyzed Grignard and *B*-alkyl Suzuki coupling, together with cuprate-based procedures, for the union of fragments **309** and **311**. Of no less significance, particularly from a material throughput point of view, was that the reaction proceeded efficiently when using a nearly equimolar ratio of the two coupling partners (**309**/**311** 1.1:1). In contrast, many cross-coupling reactions require a larger excess of one or the other coupling partner in order to proceed to completion, which can be particularly wasteful if it is a valuable, hard-won intermediate that has to be sacrificed in this manner.[250]

The palladium-catalyzed acylation of organozinc reagents with acid chlorides provides a convenient route to unsymmetrically substituted ketones.[251] Given the attenuated reactivity of organozinc compounds, overaddition of the reagent to the ketone product is not usually a troublesome issue in these reactions, which allows the production of a wide variety of alkyl, alkenyl, and aryl ketone systems in good yield and under mild conditions. One of the most elaborate examples of an acyl-Negishi coupling reported to date is that leading to the formation of ketone **318** (Scheme 56), an advanced intermediate in the synthesis of the marine-derived macrolide amphidinolide T1 (**319**) by Fürstner and co-workers.[252] Thus, after a considerable amount of experimentation, it was found that exposure of alkyl zinc iodide species **314** (R = ZnI), derived from the corresponding primary alkyl iodide (**315**, R = I) by treatment with a zinc/copper couple, to the enantiomerically pure acid chloride **317** in the presence of $[Pd_2(dba)_3]$ (3 mol%) and P(2-furyl)$_3$ (6 mol%) in a toluene/DMA mixed solvent system at ambient temperature led to coupling to give the desired ketone **318** in yields between 40 and 50%. Despite the researchers' best efforts, a significant amount (typically 20–30%) of the reduced compound **316** (R = H) was always also formed in this reaction. Nevertheless, sufficient quantities of the pivotal intermediate **318** could be secured by this route to enable the execution of the remaining few steps required to complete the total synthesis.



Scheme 56. Use of an acid chloride as the electrophile in the Negishi coupling in the total synthesis of amphidinolide T1 (**319**) (Fürstner et al., 2003).[252]

A selection of other architecturally intriguing natural products that have been the target of total syntheses involving Negishi couplings as key carbon–carbon bond-forming steps are highlighted in Scheme 57: reveromycin B (**320**) (Theodorakis and Drouet, 1999),[253] papulacandin D (**321**) (Barrett and co-workers, 1996),[254] longithorone A (**322**) (Shair and co-workers, 2002),[255] and xerulin (**323**) (Negishi and co-workers, 2000).[256] The carbon–carbon bond(s) formed in each case is(are) shown, and while such a cursory overview of the state of the art can neither be comprehensive nor do full justice to the remarkable developments in the field and the efforts of the many researchers involved who could not be acknowledged, it can hopefully serve to emphasize how the Negishi



Scheme 57. Selected examples of natural products syntheses employing Negishi reactions (the C–C bonds formed by this cross-coupling process are highlighted with circles): reveromycin B (**320**) (Theodorakis and Drouet, 1999),[253] papulacandin D (**321**) (Barrett et al., 1996),[254] longithorone A (**322**) (Shair et al., 2002),[255] and xerulin (**323**) (Negishi et al., 2000).[256]

 © 2005 Wiley-VCH Verlag GmbH & Co. KGaA, Weinheim

coupling reaction offers the synthetic chemist a plethora of opportunities for carbon–carbon bond-forming operations.

8. Summary and Outlook

As amply demonstrated above, total synthesis has benefited enormously from the palladium-catalyzed cross-coupling reactions that have emerged in the last few decades. These marvelous tools allow the artisans of this flagship discipline of chemical synthesis to flourish and produce some of the most stunning masterpieces in the history of total synthesis. To be sure, the ever-growing expansion of these carbon–carbon bond-forming reactions into new vistas will undoubtedly enable even more impressive accomplishments in the future.

Just as the Grignard, Diels–Alder, Wittig, and hydroboration reactions as well as asymmetric oxidation and hydrogenation of double bonds enabled quantum leaps in our ability to construct complex molecules in the laboratory, so do the carbon–carbon cross-coupling reactions. In particular, these processes do not require the preparation of reactive intermediates prior to the carbon–carbon bond-forming event. Rather, they proceed by activation of stable and readily available starting materials in situ and, therefore, are both more practical and often more efficient in terms of overall yield. And beyond these processes, and fortunately for synthetic chemists, who have been empowered so much by them, a new group of reactions catalyzed by transition metals have appeared on the horizon. These powerful processes are known collectively as metathesis reactions, and their impact in total synthesis is discussed in the following Review article.[257]

Abbreviations

9-BBN	9-borabicyclo[3.3.1]nonane
binap	2,2′-bis(diphenylphosphino)-1,1′-binaphthyl
Bn	benzyl
Boc	*tert*-butoxycarbonyl
Bz	benzoyl
Cbz	benzyloxycarbonyl
Cp	cyclopentadienyl
dba	dibenzylideneacetone
DCC	1,3-dicyclohexylcarbodiimide
DMA	*N*,*N*-dimethylacetamide
DMAP	4-dimethylaminopyridine
DME	ethylene glycol dimethyl ether
DMF	*N*,*N*-dimethylformamide
DMSO	dimethyl sulfoxide
dppb	1,4-bis(diphenylphosphino)butane
dppe	1,2-bis(diphenylphosphino)ethane
dppf	1,1′-bis(diphenylphosphino)ferrocene
Fmoc	9-fluorenylmethoxycarbonyl
LDA	lithium diisopropylamide
MOM	methoxymethyl
M.S.	molecular sieves
NMP	1-methyl-2-pyrrolidinone
Piv	pivaloyl
PMB	4-methoxybenzyl
PMP	4-methoxyphenyl
SEM	2-(trimethylsilyl)ethoxymethyl
TBAF	tetra-*n*-butylammonium fluoride
TBDPS	*tert*-butyldiphenylsilyl
TBS	*tert*-butyldimethylsilyl
Teoc	2-(trimethylsilyl)ethoxycarbonyl
TES	triethylsilyl
Tf	trifluoromethanesulfonyl
THP	2-tetrahydropyranyl
TIPS	triisopropylsilyl
TMS	trimethylsilyl
Ts	4-toluenesulfonyl

It is with enormous pride and great pleasure that we thank our collaborators whose names appear in the references cited and whose contributions made the described work so rewarding and enjoyable. We also acknowledge helpful discussions with Professor Phil S. Baran. We gratefully acknowledge the National Institutes of Health (USA), the Skaggs Institute for Chemical Biology, the George E. Hewitt Foundation, Amgen, Merck, Novartis, and Pfizer for supporting our research programs.

Received: January 31, 2005
Published online: June 30, 2005

[1] a) *Metal-Catalyzed Cross-Coupling Reactions*, *2nd ed.* (Eds.: A. de Meijere, F. Diederich), Wiley-VCH, Weinheim, **2004**; b) L. S. Hegedus, *Transition Metals in the Synthesis of Complex Organic Molecules*, *2nd ed.*, University Science Books, Sausalito, **1999**; c) *Handbook of Organopalladium Chemistry for Organic Synthesis* (Ed.: E. Negishi), Wiley Interscience, New York, **2002**; d) *Cross-Coupling Reactions: A Practical Guide* (Ed.: N. Miyaura), Springer, Berlin, **2002** (Series *Topics in Current Chemistry*, *No. 219*).

[2] T. Mizoroki, K. Mori, A. Ozaki, *Bull. Chem. Soc. Jpn.* **1971**, *44*, 581.

[3] R. F. Heck, J. P. Nolley, Jr., *J. Org. Chem.* **1972**, *37*, 2320–2322.

[4] For reviews of the asymmetric Heck reaction, see: a) A. B. Dounay, L. E. Overman, *Chem. Rev.* **2003**, *103*, 2945–2963; b) M. Shibasaki, D. J. B. Christopher, A. Kojima, *Tetrahedron* **1997**, *53*, 7371–7395; c) M. Shibasaki, E. M. Vogl, *J. Organomet. Chem.* **1999**, *576*, 1–15.

[5] For a comprehensive review of the Stille reaction up to the mid 1990s, see: V. Farina, V. Krishnamurthy, W. J. Scott, *Org. React.* **1997**, *50*, 1–652.

[6] a) D. Milstein, J. K. Stille, *J. Am. Chem. Soc.* **1978**, *100*, 3636–3638; b) D. Milstein, J. K. Stille, *J. Am. Chem. Soc.* **1979**, *101*, 4992–4998.

[7] J. K. Stille, *Angew. Chem.* **1986**, *98*, 504–520; *Angew. Chem. Int. Ed. Engl.* **1986**, *25*, 508–524.

[8] a) M. Kosugi, K. Sasazawa, Y. Shimizu, T. Migita, *Chem. Lett.* **1977**, 301–302; b) M. Kosugi, K. Sasazawa, T. Migita, *Chem. Lett.* **1977**, 1423–1424.

[9] For a brief genealogy of palladium-catalyzed cross-coupling reactions, see: E. Negishi, *J. Organomet. Chem.* **2002**, *653*, 34–40.

 © 2005 Wiley-VCH Verlag GmbH & Co. KGaA, Weinheim

[10] For a recent Review of the mechanisms of the Stille reaction, see P. Espinet, A. M. Echavarren, *Angew. Chem.* **2004**, *116*, 4808 – 4839; *Angew. Chem. Int. Ed.* **2004**, *43*, 4704 – 4734.
[11] For an early review of the Suzuki reaction, see A. Suzuki, *Acc. Chem. Res.* **1982**, *15*, 178 – 184.
[12] a) N. Miyaura, K. Yamada, A. Suzuki, *Tetrahedron Lett.* **1979**, *20*, 3437 – 3440; b) N. Miyaura, A. Suzuki, *J. Chem. Soc. Chem. Commun.* **1979**, 866 – 867.
[13] The Heck group reported, at a conference in November 1973, the coupling of (*Z*)- and (*E*)-1-hexenylboronic acids with methyl acrylate with stoichiometric amounts of $Pd(OAc)_2$ in Et_3N, resulting in carbon–carbon bond formation to afford methyl (*E*,*Z*)-2,4-nonadienoate and methyl (*E*,*E*)-2,4-nonadienoate, respectively: a) R. F. Heck in *Proceedings of the Robert A. Welch Foundation Conferences on Chemical Research XVII. Organic-Inorganic Reagents in Synthetic Chemistry* (Ed. W. O. Milligan), **1974**, p. 53–98; see also: b) H. A. Dieck, R. F. Heck, *J. Org. Chem.* **1975**, *40*, 1083 – 1090.
[14] Negishi reported, first at the 174th National Meeting of the American Chemical Society (New Orleans, March 1977), and then in a table within a chapter in a book published in 1978, an example of a coupling between an alkynyl borate species and an aryl iodide under palladium-catalyzed conditions: E. Negishi in *Aspects of Mechanism and Organometallic Chemistry* (Ed.: J. H. Brewster), Plenum, New York, **1978**, p. 285.
[15] For the first examples of alkyl–alkyl Suzuki cross-coupling reactions, see: T. Ishiyama, S. Abe, N. Miyaura, A. Suzuki, *Chem. Lett.* **1992**, 691 – 694.
[16] For more recent developments in the Suzuki coupling reactions of alkyl halides, see: a) J. Zhou, G. C. Fu, *J. Am. Chem. Soc.* **2004**, *126*, 1340 – 1341, and references therein; for a Review of catalysts for cross-coupling reactions with non-activated alkyl halides, see: b) A. C. Frisch, M. Beller, *Angew. Chem.* **2005**, *117*, 680 – 695; *Angew. Chem. Int. Ed.* **2005**, *44*, 674 – 688.
[17] N. Miyaura, A. Suzuki, *Chem. Rev.* **1995**, *95*, 2457 – 2483.
[18] L. Cassar, *J. Organomet. Chem.* **1975**, *93*, 253 – 259.
[19] H. A. Dieck, F. R. Heck, *J. Organomet. Chem.* **1975**, *93*, 259 – 263.
[20] K. Sonogashira, Y. Tohda, N. Hagihara, *Tetrahedron Lett.* **1975**, *16*, 4467 – 4470.
[21] For a brief historical overview of the development of the Sonogashira reaction, see: K. Sonogashira, *J. Organomet. Chem.* **2002**, *653*, 46 – 49.
[22] R. D. Stephens, C. E. Castro, *J. Org. Chem.* **1963**, *28*, 3313 – 3315.
[23] For examples of the "copper-free" Sonogashira protocol, see: a) M. Alami, F. Ferri, G. Linstrumelle, *Tetrahedron Lett.* **1993**, *34*, 6403 – 6406; b) J.-P. Genet, E. Blart, M. Savignac, *Synlett* **1992**, 715 – 717; c) C. Xu, E. Negishi, *Tetrahedron Lett.* **1999**, *40*, 431 – 434; "copper-free" Sonogashira protocols have also been developed with the intention of eliminating the possibility of copper-catalyzed oxidative dimerization of the alkyne component, which is often a deleterious competing side-reaction in Sonogashira processes; for selected examples, see: d) S. Urgaonkar, J. G. Verkade, *J. Org. Chem.* **2004**, *69*, 5752 – 5755; e) D. Gelman, S. L. Buchwald, *Angew. Chem.* **2003**, *115*, 6175 – 6178; *Angew. Chem. Int. Ed.* **2003**, *42*, 5993 – 5996.
[24] For early reviews of the Tsuji-Trost reaction, see a) B. M. Trost, *Acc. Chem. Res.* **1980**, *13*, 385 – 393; b) J. Tsuji, *Tetrahedron* **1986**, *42*, 4361 – 4401.
[25] For recent reviews of the palladium-catalyzed asymmetric alkylation reaction, see: a) B. M. Trost, M. L. Crawley, *Chem. Rev.* **2003**, *103*, 2921 – 2943; b) B. M. Trost, *J. Org. Chem.* **2004**, *69*, 5813 – 5837.
[26] a) E. Negishi, A. O. King, N. Okukado, *J. Org. Chem.* **1977**, *42*, 1821 – 1823; for a discussion, see: b) E. Negishi, *Acc. Chem. Res.* **1982**, *15*, 340 – 348.
[27] a) E. Erdik, *Tetrahedron* **1992**, *48*, 9577 – 9648; b) E. Negishi, T. Takahashi, S. Babu, D. E. Van Horn, N. Okukado, *J. Am. Chem. Soc.* **1987**, *109*, 2393 – 2401.
[28] For early reviews of the Heck reaction, see: a) R. F. Heck, *Acc. Chem. Res.* **1979**, *12*, 146 – 151; b) R. F. Heck, *Org. React.* **1982**, *27*, 345 – 390.
[29] For a more recent overview of the Heck reaction, see: I. P. Beletskaya, A. V. Cheprakov, *Chem. Rev.* **2000**, *100*, 3009 – 3066, and references therein.
[30] For reviews of the intramolecular Heck reaction, see: a) J. T. Link, *Org. React.* **2002**, *60*, 157 – 534; b) E. Negishi, C. Copéret, S. Ma, S.-Y. Liou, F. Liu, *Chem. Rev.* **1996**, *96*, 365 – 393.
[31] a) V. H. Rawal, C. Michoud, R. F. Monestel, *J. Am. Chem. Soc.* **1993**, *115*, 3030 – 3031; b) V. H. Rawal, C. Michoud, *J. Org. Chem.* **1993**, *58*, 5583 – 5584.
[32] T. Jeffery, *Tetrahedron Lett.* **1994**, *35*, 3051 – 3054.
[33] Z. Owczarczyk, F. Lamaty, E. J. Vawter, E. Negishi, *J. Am. Chem. Soc.* **1992**, *114*, 10091 – 10092.
[34] For other total syntheses of dehydrotubifoline, which incidentally all employ palladium- (or nickel)-catalyzed carbon–carbon bond-forming reactions, see: a) M. Mori, M. Nakanishi, D. Kajishima, Y. Sato, *J. Am. Chem. Soc.* **2003**, *125*, 9801 – 9807; b) M. Mori, M. Nakanishi, D. Kajishima, Y. Sato, *Org. Lett.* **2001**, *3*, 1913 – 1916; c) J. Bonjoch, D. Solé, J. Bosch, *J. Am. Chem. Soc.* **1995**, *117*, 11017 – 11018; d) S. R. Angle, J. M. Fevig, S. D. Knight, R. W. Marquis, Jr., L. E. Overman, *J. Am. Chem. Soc.* **1993**, *115*, 3966 – 3976; e) J. M. Fevig, R. W. Marquis, Jr., L. E. Overman, *J. Am. Chem. Soc.* **1991**, *113*, 5085 – 5086.
[35] A. D. Lebsack, J. T. Link, L. E. Overman, B. A. Stearns, *J. Am. Chem. Soc.* **2002**, *124*, 9008 – 9009.
[36] a) V. Farina, B. Krishnan, *J. Am. Chem. Soc.* **1991**, *113*, 9585 – 9593; b) L. S. Liebeskind, R. W. Fengl, *J. Org. Chem.* **1990**, *55*, 5359 – 5364; c) V. Farina, S. Kapadia, B. Krishnan, C. Wang, L. S. Liebeskind, *J. Org. Chem.* **1994**, *59*, 5905 – 5911.
[37] L. M. Alzacar-Roman, J. F. Hartwig, *Organometallics* **2002**, *21*, 491 – 502.
[38] For Reviews on the synthesis of quaternary stereocenters, see: a) J. Christoffers, A. Mann, *Angew. Chem.* **2001**, *113*, 4725 – 4732; *Angew. Chem. Int. Ed.* **2001**, *40*, 4591 – 4597; b) E. J. Corey, A. Guzman-Perez, *Angew. Chem.* **1998**, *110*, 402 – 415; *Angew. Chem. Int. Ed.* **1998**, *37*, 389 – 401.
[39] For a discussion of the synthesis of contiguous stereogenic quaternary carbon centers, see: E. A. Peterson, L. E. Overman, *Proc. Natl. Acad. Sci. USA* **2004**, *101*, 11943 – 11948.
[40] T. Sato, M. Sodeoka, M. Shibasaki, *J. Org. Chem.* **1989**, *54*, 4738 – 4739.
[41] N. E. Carpenter, D. J. Kucera, L. E. Overman, *J. Org. Chem.* **1989**, *54*, 5846 – 5848.
[42] a) K. Kagechika, M. Shibasaki, *J. Org. Chem.* **1991**, *56*, 4093 – 4094; b) K. Kagechika, T. Ohshima, M. Shibasaki, *Tetrahedron* **1993**, *49*, 1773 – 1782.
[43] a) S. J. Danishefsky, J. J. Masters, W. B. Young, J. T. Link, L. B. Snyder, T. V. Magee, D. K. Jung, R. C. A. Isaacs, W. G. Bornmann, C. A. Alaimo, C. A. Coburn, M. J. Di Grandi, *J. Am. Chem. Soc.* **1996**, *118*, 2843 – 2859; b) J. J. Masters, J. T. Link, L. B. Snyder, W. B. Young, S. J. Danishefsky, *Angew. Chem.* **1995**, *107*, 1886 – 1888; *Angew. Chem. Int. Ed. Engl.* **1995**, *34*, 1723 – 1726.
[44] For other total syntheses of taxol, see: a) K. C. Nicolaou, Z. Yang, J. J. Liu, H. Ueno, P. G. Nantermet, R. K. Guy, C. F. Claiborne, J. Renaud, E. A. Couladouros, K. Paulvannan, E. J. Sorensen, *Nature* **1994**, *367*, 630 – 634; b) K. C. Nicolaou, P. G. Nantermet, H. Ueno, R. K. Guy, E. A. Couladouros, E. J. Sorensen, *J. Am. Chem. Soc.* **1995**, *117*, 624 – 633; c) K. C. Nicolaou, J.-J. Liu, Z. Yang, H. Ueno, E. J. Sorensen, C. F. Claiborne, R. K. Guy, C.-K. Hwang, M. Nakada, P. G. Nanter-

met, *J. Am. Chem. Soc.* **1995**, *117*, 634 – 644; d) K. C. Nicolaou, Z. Yang, J.-J. Liu, P. G. Nantermet, C. F. Claiborne, J. Renaud, R. K. Guy, K. Shibayama, *J. Am. Chem. Soc.* **1995**, *117*, 645 – 652; e) K. C. Nicolaou, H. Ueno, J.-J. Liu, P. G. Nantermet, Z. Yang, J. Renaud, K. Paulvannan, R. Chadha, *J. Am. Chem. Soc.* **1995**, *117*, 653 – 659; f) R. A. Holton, C. Somoza, H.-B. Kim, F. Liang, R. J. Biediger, P. D. Boatman, M. Shindo, C. C. Smith, S. Kim, H. Nadizadeh, Y. Suzuki, C. Tao, P. Vu, S. Tang, P. Zhang, K. K. Murthi, L. N. Gentile, J. H. Liu, *J. Am. Chem. Soc.* **1994**, *116*, 1597 – 1598; g) R. A. Holton, H.-B. Kim, C. Somoza, F. Liang, R. J. Biediger, P. D. Boatman, M. Shindo, C. C. Smith, S. Kim, H. Nadizadeh, Y. Suzuki, C. Tao, P. Vu, S. Tang, P. Zhang, K. K. Murthi, L. N. Gentile, J. H. Liu, *J. Am. Chem. Soc.* **1994**, *116*, 1599 – 1600; h) P. A. Wender, N. F. Badham, S. P. Conway, P. A. Floreancig, T. E. Glass, C. Gränicher, J. B. Houze, J. Jänichen, D. Lee, D. G. Marquess, P. L. McGrane, W. Meng, T. P. Mucciaro, M. Mühlebach, M. G. Natchus, H. Paulsen, D. B. Rawlins, J. Satkofsky, A. J. Shuker, J. C. Sutton, R. E. Taylor, K. Tomooka, *J. Am. Chem. Soc.* **1997**, *119*, 2755 – 2756; i) P. A. Wender, N. F. Badham, S. P. Conway, P. E. Floreancig, T. E. Glass, J. B. Houze, N. E. Krauss, D. Lee, D. G. Marquess, P. L. McGrane, W. Meng, M. G. Natchus, A. J. Shuker, J. C. Sutton, R. E. Taylor, *J. Am. Chem. Soc.* **1997**, *119*, 2757 – 2758; j) K. Morihara, R. Hara, S. Kawahara, T. Nishimori, N. Nakamura, H. Kusama, I. Kuwajima, *J. Am. Chem. Soc.* **1998**, *120*, 12980 – 12981; k) T. Mukaiyama, I. Shiina, H. Iwadare, M. Saitoh, T. Nishimura, N. Ohkawa, H. Sakoh, K. Nishimura, Y. Tani, M. Hasegawa, K. Yamada, K. Saitoh, *Chem. Eur. J.* **1999**, *5*, 121 – 161.

[45] a) A. A. Akhrem, Y. A. Titov, *Total Steroid Synthesis*, Plenum, New York, **1970**; b) R. T. Blickenstaff, A. C. Ghosh, G. C. Wolf, *Total Synthesis of Steroids*, Academic Press, New York, **1974**.

[46] For a review of annulation methods, see: M. E. Jung, *Tetrahedron* **1976**, *32*, 3 – 31.

[47] a) G. Stork, A. W. Burgstahler, *J. Am. Chem. Soc.* **1955**, *77*, 5068 – 5077; b) A. Eschenmoser, L. Ruzicka, O. Jeger, D. Arigoni, *Helv. Chim. Acta* **1955**, *38*, 1890 – 1904; c) P. A. Stadler, A. Eschenmoser, H. Schinz, G. Stork, *Helv. Chim. Acta* **1957**, *40*, 2191 – 2198.

[48] See, for example, the total synthesis of progesterone by this method: a) W. S. Johnson, M. B. Gravestock, B. E. McCarry, *J. Am. Chem. Soc.* **1971**, *93*, 4332 – 4334; b) M. B. Gravestock, W. S. Johnson, B. E. McCarry, R. J. Parry, B. E. Ratcliffe, *J. Am. Chem. Soc.* **1978**, *100*, 4274 – 4282.

[49] a) R. L. Funk, K. P. C. Vollhardt, *J. Am. Chem. Soc.* **1980**, *102*, 5253 – 5261; b) R. L. Funk, K. P. C. Vollhardt, *J. Am. Chem. Soc.* **1979**, *101*, 215 – 217; c) R. L. Funk, K. P. C. Vollhardt, *J. Am. Chem. Soc.* **1977**, *99*, 5483 – 5484.

[50] L. F. Tietze, T. Nöbel, M. Spescha, *J. Am. Chem. Soc.* **1998**, *120*, 8971 – 8977.

[51] a) T. Mandai, T. Matsumoto, M. Kawada, J. Tsuji, *J. Org. Chem.* **1992**, *57*, 6090 – 6092; b) T. Mandai, T. Matsumoto, M. Kawada, J. Tsuji, *Tetrahedron* **1993**, *49*, 5483 – 5493; c) L. F. Tietze, P. S. V. Subba Rao, *Synlett* **1993**, 291 – 292.

[52] a) W. A. Herrmann, C. Brossmer, K. Öfele, C.-P. Reisinger, T. Priermeier, M. Beller, H. Fischer, *Angew. Chem.* **1995**, *107*, 1989 – 1992; *Angew. Chem. Int. Ed. Engl.* **1995**, *34*, 1844 – 1848; b) M. Beller, H. Fisher, W. A. Herrmann, K. Öfele, C. Brossmer, *Angew. Chem.* **1995**, *107*, 1992 – 1993; *Angew. Chem. Int. Ed. Engl.* **1995**, *34*, 1848 – 1849.

[53] Y. Zhang, G. Wu, G. Angel, E. Negishi, *J. Am. Chem. Soc.* **1990**, *112*, 8590 – 8592.

[54] a) B. M. Trost, Y. Shi, *J. Am. Chem. Soc.* **1991**, *113*, 701 – 703; b) B. M. Trost, *Angew. Chem.* **1995**, *107*, 285 – 307; *Angew. Chem. Int. Ed. Engl.* **1995**, *34*, 259 – 281.

[55] For reviews of domino reactions in organic synthesis, see a) L. F. Tietze, *Chem. Rev.* **1996**, *96*, 115 – 136; b) T.-L. Ho, *Tandem Organic Reactions*, Wiley, New York, **1992**; for a Review of the use of homogenous catalysis in atom-economical synthesis, see reference [54b].

[56] For other selected examples of "zipper" reactions, see: a) L. E. Overman, M. M. Abelman, D. J. Kucera, V. D. Tran, D. J. Ricca, *Pure Appl. Chem.* **1992**, *64*, 1813 – 1819; b) H. Henniges, F. E. Meyer, U. Schick, F. Funke, P. J. Parsons, A. de Meijere, *Tetrahedron* **1996**, *52*, 11545 – 11578; c) T. Sugihara, C. Coperet, Z. Owczarczyk, L. S. Harring, E. Negishi, *J. Am. Chem. Soc.* **1994**, *116*, 7923 – 7924; d) F. E. Meyer, H. Henniges, A. de Meijere, *Tetrahedron Lett.* **1992**, *33*, 8039 – 8042.

[57] a) L. E. Overman, D. J. Ricca, V. D. Tran, *J. Am. Chem. Soc.* **1993**, *115*, 2042 – 2044; b) D. J. Kucera, S. J. O'Connor, L. E. Overman, *J. Org. Chem.* **1993**, *58*, 5304 – 5306.

[58] H. F. DeLuca, H. K. Schnoes, *Annu. Rev. Biochem.* **1983**, *52*, 411 – 439.

[59] a) B. M. Trost, J. Dumas, *J. Am. Chem. Soc.* **1992**, *114*, 1924 – 1925; b) B. M. Trost, J. Dumas, M. Villa, *J. Am. Chem. Soc.* **1992**, *114*, 9836 – 9845.

[60] For an alternative synthesis of the vitamin D A-ring through intramolecular Heck cyclization, see: K. Nagasawa, Y. Zako, H. Ishihara, I. Shimizu, *Tetrahedron Lett.* **1991**, *32*, 4937 – 4940.

[61] For the recent application of this methodology in the synthesis of novel vitamin D analogues, see: A. Kittaka, Y. Suhara, H. Takayanagi, T. Fujishima, M. Kurihara, H. Takayama, *Org. Lett.* **2000**, *2*, 2619 – 2622.

[62] P. S. Baran, C. A. Guerrero, E. J. Corey, *J. Am. Chem. Soc.* **2003**, *125*, 5628 – 5629.

[63] For selected discussions of methods for the synthesis of eight-membered rings, see: a) M. E. Maier, *Angew. Chem.* **2000**, *112*, 2153 – 2157; *Angew. Chem. Int. Ed.* **2000**, *39*, 2073 – 2077; b) L. Yet, *Tetrahedron* **1999**, *55*, 9349 – 9403; c) G. A. Molander, *Acc. Chem. Res.* **1998**, *31*, 603 – 609; d) N. A. Petasis, M. A. Patane, *Tetrahedron* **1992**, *48*, 5757 – 5821; e) G. Illuminati, L. Mandolini, *Acc. Chem. Res.* **1981**, *14*, 95 – 102.

[64] For a review of medium ring nitrogen heterocycles, see P. A. Evans, A. B. Holmes, *Tetrahedron* **1991**, *47*, 9131 – 9166.

[65] For precedent of the direct palladation of indoles at C2, see: a) T. D. Cushing, J. F. Sanz-Cervera, R. M. Williams, *J. Am. Chem. Soc.* **1996**, *118*, 557 – 579; b) B. M. Trost, S. A. Godleski, J. P. Genet, *J. Am. Chem. Soc.* **1978**, *100*, 3930 – 3931.

[66] P. S. Baran, E. J. Corey, *J. Am. Chem. Soc.* **2002**, *124*, 7904 – 7905.

[67] For a review of Ru-, Rh-, and Pd-catalyzed carbon–carbon bond formation involving C–H activation, see: V. Ritleng, C. Sirlin, M. Pfeffer, *Chem. Rev.* **2002**, *102*, 1731 – 1769.

[68] E. M. Ferreira, B. M. Stoltz, *J. Am. Chem. Soc.* **2003**, *125*, 9578 – 9579.

[69] L. F. Tietze, K. M. Sommer, J. Zinngrebe, F. Stecker, *Angew. Chem.* **2005**, *117*, 262 – 264; *Angew. Chem. Int. Ed.* **2005**, *44*, 257 – 259.

[70] For a review of palladium-catalyzed cross-coupling reactions in the synthesis of pharmaceuticals, see: A. O. King, N. Yasuda, *Top. Organomet. Chem.* **2004**, *7*, 205 – 245.

[71] For a review of Heck arylations in the synthesis of pharmaceuticals, see: M. Prashad, *Top. Organomet. Chem.* **2004**, *7*, 181 – 203.

[72] a) M. Labelle, M. Belley, Y. Gareau, J. Y. Gauthier, D. Guay, R. Gordon, S. G. Grossman, T. R. Jones, Y. Leblanc, M. McAuliffe, C. McFarlane, P. Masson, K. M. Metters, N. Oiumet, D. H. Patrick, H. Piechuta, C. Rochette, N. Sawyer, Y. B. Xiang, C. B. Pickett, A. W. Ford-Hutchinson, R. J. Zamboni, R. N. Young, *Bioorg. Med. Chem. Lett.* **1995**, *5*, 283 – 288; b) A. O. King, E. G. Corley, R. K. Anderson, R. D. Larsen, T. R. Verhoeven, P. J. Reider, Y. B. Xiang, M. Belley, Y. Leblanc, M. Labelle, P. Prasit, R. J. Zamboni, *J. Org. Chem.* **1993**, *58*, 3731 – 3735; c) R. D. Larsen, E. G. Corley, A. O. King, J. D. Carroll, P. Davis,

 © 2005 Wiley-VCH Verlag GmbH & Co. KGaA, Weinheim

T. R. Verhoeven, P. J. Reider, M. Labelle, J. Y. Gauthier, Y. B. Xiang, R. J. Zamboni, *J. Org. Chem.* **1996**, *61*, 3398 – 3405.
[73] For studies on the generality of this phenomenon, see: T. Jeffery, *Tetrahedron Lett.* **1991**, *32*, 2121 – 2124.
[74] E. Piers, R. W. Friesen, B. A. Keay, *J. Chem. Soc. Chem. Commun.* **1985**, 809 – 810.
[75] For the first examples of macrocyclization by means of a Stille coupling, see: J. K. Stille, M. Tanaka, *J. Am. Chem. Soc.* **1987**, *109*, 3785 – 3786.
[76] M. A. J. Duncton, G. Pattenden, *J. Chem. Soc. Perkin Trans. 1* **1999**, 1235 – 1246.
[77] a) K. C. Nicolaou, T. K. Chakraborty, A. D. Piscopio, N. Minowa, P. Bertinato, *J. Am. Chem. Soc.* **1993**, *115*, 4419 – 4420; b) K. C. Nicolaou, A. D. Piscopio, P. Bertinato, T. K. Chakraborty, N. Minowa, K. Koide, *Chem. Eur. J.* **1995**, *1*, 318 – 333.
[78] A. B. Smith III, S. M. Condon, J. A. McCauley, J. L. Leazer, Jr., J. W. Leahy, R. E. Maleczka, Jr., *J. Am. Chem. Soc.* **1995**, *117*, 5407 – 5408.
[79] For other total syntheses of rapamycin, employing different macrocyclization strategies, see: a) D. Romo, S. D. Meyer, D. D. Johnson, S. L. Schreiber, *J. Am. Chem. Soc.* **1993**, *115*, 7906 – 7907; b) C. M. Hayward, D. Yohannes, S. J. Danishefsky, *J. Am. Chem. Soc.* **1993**, *115*, 9345 – 9346.
[80] For the application a related "stitching cyclization" to the synthesis of mycotrienol, see: C. E. Masse, M. Yang, J. Solomon, J. S. Panek, *J. Am. Chem. Soc.* **1998**, *120*, 4123 – 4134.
[81] a) M. D. Shair, T.-Y. Yoon, K. K. Mosny, T. C. Chou, S. J. Danishefsky, *J. Am. Chem. Soc.* **1996**, *118*, 9509 – 9525; b) M. D. Shair, T.-Y. Yoon, S. J. Danishefsky, *Angew. Chem.* **1995**, *107*, 1883 – 1885; *Angew. Chem. Int. Ed. Engl.* **1995**, *34*, 1721 – 1723; c) M. D. Shair, T. Yoon, S. J. Danishefsky, *J. Org. Chem.* **1994**, *59*, 3755 – 3757.
[82] For an alternative total synthesis of dynemicin A, see: A. G. Myers, N. J. Tom, M. E. Fraley, S. B. Cohen, D. J. Madar, *J. Am. Chem. Soc.* **1997**, *119*, 6072 – 6094.
[83] A. C. Gyorkos, J. K. Stille, L. S. Hegedus, *J. Am. Chem. Soc.* **1990**, *112*, 8465 – 8472.
[84] For the introduction of vinyl triflates as viable coupling partners in the Stille and carbonylative Stille reactions, see: a) W. J. Scott, G. T. Crisp, J. K. Stille, *J. Am. Chem. Soc.* **1984**, *106*, 4630 – 4632; b) G. T. Crisp, W. J. Scott, J. K. Stille, *J. Am. Chem. Soc.* **1984**, *106*, 7500 – 7506.
[85] a) K. C. Nicolaou, J. Xu, F. Murphy, S. Barluenga, O. Baudoin, H.-X. Wei, D. L. F. Gray, T. Ohshima, *Angew. Chem.* **1999**, *111*, 2599 – 2604; *Angew. Chem. Int. Ed.* **1999**, *38*, 2447 – 2451; b) K. C. Nicolaou, F. Murphy, S. Barluenga, T. Ohshima, H. Wei, J. Xu, D. L. F. Gray, O. Baudoin, *J. Am. Chem. Soc.* **2000**, *122*, 3830 – 3838.
[86] a) M. Duan, L. A. Paquette, *Angew. Chem.* **2001**, *113*, 3744 – 3748; *Angew. Chem. Int. Ed.* **2001**, *40*, 3632 – 3636; b) L. A. Paquette, M. Duan, I. Konetzki, C. Kempmann, *J. Am. Chem. Soc.* **2002**, *124*, 4257 – 4270.
[87] F. Ullmann, J. Bielecki, *Ber. Dtsch. Chem. Ges.* **1901**, *34*, 2174 – 2185.
[88] a) T. D. Nelson, R. D. Crouch, *Org. React.* **2004**, *63*, 265 – 555; b) M. Sainsbury, *Tetrahedron* **1980**, *36*, 3327 – 3359; c) P. E. Fanta, *Chem. Rev.* **1964**, *64*, 613 – 632.
[89] For recent reviews on aryl–aryl bond formation, with a particular emphasis on transition-metal-based processes, see: a) J. Hassan, M. Sévignon, C. Gozzi, E. Schulz, M. Lemaire, *Chem. Rev.* **2002**, *102*, 1359 – 1469; b) S. P. Stanforth, *Tetrahedron* **1998**, *54*, 263 – 303; c) G. Bringmann, R. Walter, R. Weinrich, *Angew. Chem.* **1990**, *102*, 1006 – 1020; *Angew. Chem. Int. Ed. Engl.* **1990**, *29*, 977 – 991.
[90] a) T. M. Kamenecka, S. J. Danishefsky, *Angew. Chem.* **1998**, *110*, 3164 – 3166; *Angew. Chem. Int. Ed.* **1998**, *37*, 2993 – 2995; b) T. M. Kamenecka, S. J. Danishefsky, *Angew. Chem.* **1998**, *110*, 3166 – 3168; *Angew. Chem. Int. Ed.* **1998**, *37*, 2995 – 2998; c) T. M. Kamenecka, S. J. Danishefsky, *Chem. Eur. J.* **2001**, *7*, 41 – 63.
[91] For a recent Review of palladium-catalyzed coupling reactions of aryl chlorides, see: A. F. Littke, G. C. Fu, *Angew. Chem.* **2002**, *114*, 4350 – 4386; *Angew. Chem. Int. Ed.* **2002**, *41*, 4176 – 4211.
[92] For a review of monoligated palladium species as catalysts in cross-coupling reactions, see: U. Christmann, R. Vilar, *Angew. Chem.* **2005**, *117*, 370 – 378; *Angew. Chem. Int. Ed.* **2005**, *44*, 366 – 374.
[93] L. Del Valle, J. K. Stille, L. S. Hegedus, *J. Org. Chem.* **1990**, *55*, 3019 – 3023.
[94] a) K. C. Nicolaou, S. Vyskocil, T. V. Koftis, Y. M. A. Yamada, T. Ling, D. Y.-K. Chen, W. Tang, G. Petrovic, M. O. Frederick, Y. Li, M. Satake, *Angew. Chem.* **2004**, *116*, 4412 – 4418; *Angew. Chem. Int. Ed.* **2004**, *43*, 4312 – 4318; b) K. C. Nicolaou, T. V. Koftis, S. Vyskocil, G. Petrovic, T. Ling, Y. M. A. Yamada, W. Tang, M. O. Frederick, *Angew. Chem.* **2004**, *116*, 4418 – 4424; *Angew. Chem. Int. Ed.* **2004**, *43*, 4318 – 4324.
[95] H. W. Lam, G. Pattenden, *Angew. Chem.* **2002**, *114*, 526 – 529; *Angew. Chem. Int. Ed.* **2002**, *41*, 508 – 511.
[96] For a discussion of the chemistry and biology of the amphidinolide family of natural products, see: J. Kobayashi, M. Tsuda, *Nat. Prod. Rep.* **2004**, *21*, 77 – 93, and references therein.
[97] B. M. Trost, P. E. Harrington, *J. Am. Chem. Soc.* **2004**, *126*, 5028 – 5029.
[98] In the period between the synthesis of amphidinolide A diastereoisomer **103** by the Pattenden group and the subsequent structure elucidation by the Trost group, stereoisomer **103** was also synthesized by the Maleczka group, who confirmed that the structure originally proposed for amphidinolide A needed to be revised: R. E. Maleczka, Jr., L. R. Terrell, F. Geng, J. S. Ward III, *Org. Lett.* **2002**, *4*, 2841 – 2844.
[99] H. Fuwa, N. Kainuma, K. Tachibana, M. Sasaki, *J. Am. Chem. Soc.* **2002**, *124*, 14983 – 14992, and references therein.
[100] a) I. Kadota, H. Takamura, K. Sato, A. Ohno, K. Matsuda, Y. Yamamoto, *J. Am. Chem. Soc.* **2003**, *125*, 46 – 47; b) I. Kadota, H. Takamura, K. Sato, A. Ohno, K. Matsuda, M. Satake, Y. Yamamoto, *J. Am. Chem. Soc.* **2003**, *125*, 11893 – 11899.
[101] H. W. B. Johnson, U. Majumder, J. D. Rainier, *J. Am. Chem. Soc.* **2005**, *127*, 848 – 849.
[102] a) S. F. Martin, J. M. Humphrey, A. Ali, M. C. Hillier, *J. Am. Chem. Soc.* **1999**, *121*, 866 – 867; b) J. M. Humphrey, Y. Liao, A. Ali, T. Rein, Y.-L. Wong, H.-J. Chen, A. K. Courtney, S. F. Martin, *J. Am. Chem. Soc.* **2002**, *124*, 8584 – 8592.
[103] For the first total synthesis of manzamine A, through a different approach, see: J. D. Winkler, J. M. Axten, *J. Am. Chem. Soc.* **1998**, *120*, 6425 – 6426.
[104] For other examples of tandem Stille/[4+2]-cycloaddition reactions, see: a) S. Bruckner, E. Abraham, P. Klotz, J. Suffert, *Org. Lett.* **2002**, *4*, 3391 – 3393; b) R. Skoda-Foeldes, G. Jeges, L. Kollar, J. Horvarth, Z. Tuba, *J. Org. Chem.* **1997**, *62*, 1326 – 1332.
[105] a) K. A. Parker, Y.-H. Lim, *J. Am. Chem. Soc.* **2004**, *126*, 15968 – 15969; for earlier model studies by the same group, see: b) K. A. Parker, Y.-H. Lim, *Org. Lett.* **2004**, *6*, 161 – 164.
[106] a) K. Kurosawa, K. Takahashi, E. Tsuda, *J. Antibiot.* **2001**, *54*, 541 – 547; b) K. Takahashi, E. Tsuda, K. Kurosawa, *J. Antibiot.* **2001**, *54*, 548 – 553.
[107] W. S. Bandaranayake, J. E. Banfield, D. St. C. Black, G. D. Fallon, B. M. Gatehouse, *J. Chem. Soc. Chem. Commun.* **1980**, 162 – 163.
[108] J. E. Banfield, D. St. C. Black, S. R. Johns, R. I. Willing, *Aust. J. Chem.* **1982**, *35*, 2247 – 2256, and references therein.

[109] a) K. C. Nicolaou, N. A. Petasis, R. E. Zipkin, J. Uenishi, *J. Am. Chem. Soc.* **1982**, *104*, 5555 – 5557; b) K. C. Nicolaou, N. A. Petasis, J. Uenishi, R. E. Zipkin, *J. Am. Chem. Soc.* **1982**, *104*, 5557 – 5558; c) K. C. Nicolaou, R. E. Zipkin, N. A. Petasis, *J. Am. Chem. Soc.* **1982**, *104*, 5558 – 5560; d) K. C. Nicolaou, N. A. Petasis, R. E. Zipkin, *J. Am. Chem. Soc.* **1982**, *104*, 5560 – 5562.

[110] C. M. Beaudry, D. Trauner, *Org. Lett.* **2002**, *4*, 2221 – 2224.

[111] For other biomimetic approaches to the synthesis of the SNF compounds, see: a) J. E. Moses, J. E. Baldwin, R. Marquez, R. M. Adlington, A. R. Cowley, *Org. Lett.* **2002**, *4*, 3731 – 3734; b) reference [110].

[112] For the application of a similar strategy towards the synthesis of vitamin A derivatives, see: P. Vogt, M. Schlageter, E. Widmer, *Tetrahedron Lett.* **1991**, *32*, 4115 – 4116.

[113] G. D. Allred, L. S. Liebeskind, *J. Am. Chem. Soc.* **1996**, *118*, 2748 – 2749.

[114] For an example of an application of this "palladium-free" Stille protocol in total synthesis, see reference [98].

[115] In a modification of the Suzuki reaction, a protocol for the palladium-catalyzed coupling of aryl and alkenyl iodides with boronic acids, mediated by CuTC in the absence of base, was subsequently reported by the Liebeskind group: C. Savarin, L. S. Liebeskind, *Org. Lett.* **2001**, *3*, 2149 – 2152.

[116] R. Rossi, A. Carpita, M. G. Quirici, *Tetrahedron* **1981**, *37*, 2617 – 2673.

[117] a) R. W. Armstrong, J.-M. Beau, S. H. Cheon, W. J. Christ, H. Fujioka, W.-H. Ham, L. D. Hawkins, H. Jin, S. H. Kang, Y. Kishi, M. J. Martinelli, W. J. McWhorter, Jr., M. Mizuno, M. Nakata, A. E. Stutz, F. X. Talamas, M. Taniguchi, J. A. Tino, K. Ueda, J.-I. Uenishi, J. B. White, M. Yonaga, *J. Am. Chem. Soc.* **1989**, *111*, 7525 – 7530; b) R. W. Armstrong, J.-M. Beau, S. H. Cheon, W. J. Christ, H. Fujioka, W.-H. Ham, L. D. Hawkins, H. Jin, S. H. Kang, Y. Kishi, M. J. Martinelli, W. J. McWhorter, Jr., M. Mizuno, M. Nakata, A. E. Stutz, F. X. Talamas, M. Taniguchi, J. A. Tino, K. Ueda, J.-I. Uenishi, J. B. White, M. Yonaga, *J. Am. Chem. Soc.* **1989**, *111*, 7530 – 7533; c) E. M. Suh, Y. Kishi, *J. Am. Chem. Soc.* **1994**, *116*, 11 205 – 11 206.

[118] a) K. C. Nicolaou, E. J. Sorensen, *Classics in Total Synthesis*, VCH, Weinheim, **1996**; b) K. C. Nicolaou, S. A. Snyder, *Classics in Total Synthesis II*, Wiley-VCH, Weinheim, **2003**.

[119] J.-I. Uenishi, J.-M. Beau, R. W. Armstrong, Y. Kishi, *J. Am. Chem. Soc.* **1987**, *109*, 4756 – 4758.

[120] TlOEt and Tl_2CO_3 are now commonly substituted for TlOH, as commercial sources of the latter have all but disappeared, and the reagent is unstable to both air and light; for a discussion, see: S. A. Frank, H. Chen, R. K. Kunz, M. J. Schnaderbeck, W. R. Roush, *Org. Lett.* **2000**, *2*, 2691 – 2694 , and references therein.

[121] a) D. A. Evans, J. T. Starr, *J. Am. Chem. Soc.* **2003**, *125*, 13 531 – 13 540; b) D. A. Evans, J. T. Starr, *Angew. Chem.* **2002**, *114*, 1865 – 1868; *Angew. Chem. Int. Ed.* **2002**, *41*, 1787 – 1790.

[122] a) H. Muramatsu, M. Miyauchi, B. Sato, S. Yoshimura, *40th Symposium on the Chemistry of Natural Products*, Fukuoka, Japan, **1998**, p. 487–492; b) B. Sato, H. Muramatsu, M. Miyauchi, Y. Hori, S. Takase, M. Hino, S. Hashimoto, H. Terano, *J. Antibiot.* **2000**, *53*, 123 – 130; c) B. Sato, H. Nakajima, Y. Hori, M. Hino, S. Hashimoto, H. Terano, *J. Antibiot.* **2000**, *53*, 204 – 206; d) S. Yoshimura, B. Sato, T. Kinoshita, S. Takase, H. Terano, *J. Antibiot.* **2000**, *53*, 615 – 622; e) S. Yoshimura, B. Sato, T. Kinoshita, S. Takase, H. Terano, *J. Antibiot.* **2002**, *55*, C1.

[123] W. R. Roush, R. Riva, *J. Org. Chem.* **1988**, *53*, 710 – 712.

[124] For a review of applications of transannular Diels–Alder strategies in total synthesis, see: E. Marsault, A. Toró, P. Nowak, P. Deslongchamps, *Tetrahedron* **2001**, *57*, 4243 – 4260.

[125] For a general Review of the Diels–Alder reaction in total synthesis, see: K. C. Nicolaou, S. A. Snyder, T. Montagnon, G. Vassilikogiannakis, *Angew. Chem.* **2002**, *114*, 1742 – 1773; *Angew. Chem. Int. Ed.* **2002**, *41*, 1668 – 1698.

[126] C. D. Vanderwal, D. A. Vosburg, S. Weiler, E. J. Sorensen, *Org. Lett.* **1999**, *1*, 645 – 648.

[127] M. Gray, I. P. Andrews, D. F. Hook, J. Kitteringham, M. Voyle, *Tetrahedron Lett.* **2000**, *41*, 6237 – 6240.

[128] For reviews on bridgehead olefins, see: a) P. M. Wagner, *Chem. Rev.* **1989**, *89*, 1067 – 1093; b) G. Köbrich, *Angew. Chem.* **1973**, *85*, 494 – 503; *Angew. Chem. Int. Ed. Engl.* **1973**, *12*, 464 – 473.

[129] a) K. C. Nicolaou, S. Natarajan, H. Li, N. F. Jain, R. Hughes, M. E. Solomon, J. M. Ramanjulu, C. N. C. Boddy, M. Takayanagi, *Angew. Chem.* **1998**, *110*, 2872 – 2878; *Angew. Chem. Int. Ed.* **1998**, *37*, 2708 – 2714; b) K. C. Nicolaou, N. F. Jain, S. Natarajan, R. Hughes, M. E. Solomon, H. Li, J. M. Ramanjulu, M. Takayanagi, A. E. Koumbis, T. Bando, *Angew. Chem.* **1998**, *110*, 2879 – 2881; *Angew. Chem. Int. Ed.* **1998**, *37*, 2714 – 2716; c) K. C. Nicolaou, M. Takayanagi, N. F. Jain, S. Natarajan, A. E. Koumbis, T. Bando, J. M. Ramanjulu, *Angew. Chem.* **1998**, *110*, 2881 – 2883; *Angew. Chem. Int. Ed.* **1998**, *37*, 2717 – 2719.

[130] D. L. Boger, S. Miyazaki, S. H. Kim, J. W. Hu, O. Loiseleur, S. L. Castle, *J. Am. Chem. Soc.* **1999**, *121*, 3226 – 3227.

[131] For an alternative total synthesis of the vancomycin aglycon by means of an oxidative coupling process to generate the AB-ring system, see: a) D. A. Evans, M. R. Wood, B. W. Trotter, T. I. Richardson, J. C. Barrow, J. L. Katz, *Angew. Chem.* **1998**, *110*, 2864 – 2868; *Angew. Chem. Int. Ed.* **1998**, *37*, 2700 – 2704; b) D. A. Evans, C. J. Dinsmore, P. S. Watson, M. R. Wood, T. I. Richardson, B. W. Trotter, J. L. Katz, *Angew. Chem.* **1998**, *110*, 2868 – 2872; *Angew. Chem. Int. Ed.* **1998**, *37*, 2704 – 2708.

[132] For a discussion of atropisomerism in the context of peptide antibiotics, see: P. Lloyd-Williams, E. Giralt, *Chem. Soc. Rev.* **2001**, *30*, 145 – 157.

[133] The 14-electron $[Pd^0L_n]$ intermediates are generally assumed to be the catalytically active species that undergo oxidative addition; however, oxidative addition of an aryl bromide to a 12-electron $[Pd\{P(o\text{-tolyl})_3\}]$ species has been reported: J. F. Hartwig, F. Paul, *J. Am. Chem. Soc.* **1995**, *117*, 5373 – 5374, and references therein.

[134] a) K. P. Manfredi, J. W. Blunt, J. H. Cardellina II, J. B. McMahon, L. L. Pannell, G. M. Cragg, M. R. Boyd, *J. Med. Chem.* **1991**, *34*, 3402 – 3405; b) M. R. Boyd, Y. F. Hallock, J. H. Cardellina II, K. P. Manfredi, J. W. Blunt, J. B. McMahon, R. W. Buckheit, Jr., G. Bringmann, M. Schäffer, G. M. Cragg, D. W. Thomas, J. G. Jato, *J. Med. Chem.* **1994**, *37*, 1740 – 1745.

[135] P. D. Hobbs, V. Upender, J. Liu, D. J. Pollart, D. W. Thomas, M. I. Dawson, *Chem. Commun.* **1996**, 923 – 924.

[136] a) T. R. Hoye, M. Chen, L. Mi, O. P. Priest, *Tetrahedron Lett.* **1994**, *35*, 8747 – 8750; b) T. R. Hoye, M. Chen, *J. Org. Chem.* **1996**, *61*, 7940 – 7942.

[137] This synthesis was the first to produce the final michellamine product as a single atropisomer; for other (nonstereoselective) syntheses and synthetic approaches to the michellamine alkaloids, see: a) G. Bringmann, S. Harmsen, J. Holenz, T. Geuder, R. Götz, P. A. Keller, R. Walter, Y. F. Hallock, J. H. Cardellina II, M. R. Boyd, *Tetrahedron* **1994**, *50*, 9643 – 9648; b) T. R. Kelly, A. Garcia, F. Lang, J. J. Walsh, K. V. Bhaskar, M. R. Boyd, R. Götz, P. A. Keller, R. Walter, G. Bringmann, *Tetrahedron Lett.* **1994**, *35*, 7621 – 7624; c) P. D. Hobbs, V. Upender, M. I. Dawson, *Synlett* **1997**, 965 – 967; d) reference [136].

[138] M. F. Semmelhack in *Comprehensive Orgnometallic Chemistry II*, *Vol. 12* (Eds.: E. W. Abel, F. G. A. Stone, G. Wilkinson), Pergamon, New York, **1995**, p. 979 – 1038.

[139] M. Uemura, *Top. Organomet. Chem.* **2004**, *7*, 129 – 156.

[140] T. Watanabe, M. Shakadou, M. Uemura, *Synlett* **2000**, 1141 – 1144.

 © 2005 Wiley-VCH Verlag GmbH & Co. KGaA, Weinheim

[141] K. Kamikawa, T. Watanabe, M. Uemura, *J. Org. Chem.* **1996**, *61*, 1375 – 1384.
[142] For the total synthesis of the originally proposed structure of diazonamide A and its subsequent structure revision, see: a) J. Li, S. Jeong, L. Esser, P. G. Harran, *Angew. Chem.* **2001**, *113*, 4901 – 4906; *Angew. Chem. Int. Ed.* **2001**, *40*, 4765 – 4770; b) J. Li, A. W. G. Burgett, L. Esser, C. Amezcua, P. G. Harran, *Angew. Chem.* **2001**, *113*, 4906 – 4909; *Angew. Chem. Int. Ed.* **2001**, *40*, 4770 – 4773.
[143] a) K. C. Nicolaou, P. B. Rao, J. Hao, M. V. Reddy, G. Rassias, X. Huang, D. Y.-K. Chen, S. A. Snyder, *Angew. Chem.* **2003**, *115*, 1795 – 1800; *Angew. Chem. Int. Ed.* **2003**, *42*, 1753 – 1758; b) K. C. Nicolaou, J. Hao, M. V. Reddy, P. B. Rao, G. Rassias, S. A. Snyder, X. Huang, D. Y.-K. Chen, W. E. Brenzovich, N. Giuseppone, P. Giannakakou, A. O'Brate, *J. Am. Chem. Soc.* **2004**, *126*, 12 897 – 12 906.
[144] For highlights of synthetic studies towards diazonamide A, see: a) T. Ritter, E. M. Carreira, *Angew. Chem.* **2002**, *114*, 2601 – 2606; *Angew. Chem. Int. Ed.* **2002**, *41*, 2489 – 2495; b) V. Wittmann, *Nachr. Chem.* **2002**, *50*, 477 – 482.
[145] For other total syntheses of the revised structure of diazonamide A, see: a) A. W. G. Burgett, Q. Li, Q. Wie, P. G. Harran, *Angew. Chem.* **2003**, *115*, 5111 – 5116; *Angew. Chem. Int. Ed.* **2003**, *42*, 4961 – 4966; b) K. C. Nicolaou, M. Bella, D. Y.-K. Chen, X. Huang, Y. Ling, S. A. Snyder, *Angew. Chem.* **2002**, *114*, 3645 – 3649; *Angew. Chem. Int. Ed.* **2002**, *41*, 3495 – 3499; c) K. C. Nicolaou, D. Y.-K. Chen, X. Huang, T. Ling, M. Bella, S. A. Snyder, *J. Am. Chem. Soc.* **2004**, *126*, 12 888 – 12 896.
[146] J. J. Li, G. W. Gribble, *Palladium in Heterocyclic Chemistry*, Pergamon, Oxford, **2000** (*Tetrahedron Organic Chemistry Series*, *Vol. 20*).
[147] Transition-metal-catalyzed intramolecular C–C and C–X bond-forming reactions leading to heterocyclic ring systems have also gained prominence: I. Nakamura, Y. Yamamoto, *Chem. Rev.* **2004**, *104*, 2127 – 2198, and references therein.
[148] N. K. Garg, D. D. Capsi, B. M. Stoltz, *J. Am. Chem. Soc.* **2004**, *126*, 9552 – 9553.
[149] N. K. Garg, R. Sarpong, B. M. Stoltz, *J. Am. Chem. Soc.* **2002**, *124*, 13 179 – 13 184.
[150] In comparison to π-allyl Stille couplings of allylic acetates (and other leaving groups), the palladium-catalyzed cross-coupling of allylic acetates with organoboranes has received much less attention; for examples and a discussion, see: G. Ortar, *Tetrahedron Lett.* **2003**, *44*, 4311 – 4314.
[151] "Coupling Reactions Between sp^3 and sp^2 Carbon Centers": K. Tamao in *Comprehensive Organic Synthesis*, *Vol. 3* (Eds.: B. M. Trost, I. Fleming), Pergamon, Oxford, **1991**, p. 435.
[152] N. Miyaura, T. Ishiyama, M. Ishikawa, A. Suzuki, *Tetrahedron Lett.* **1986**, *27*, 6369 – 6372.
[153] K. Mori, P. Puapoomchareon, *Liebigs Ann. Chem.* **1990**, 159 – 162.
[154] For an excellent Review of the development, mechanistic background, and applications of the *B*-alkyl Suzuki-Miyaura cross-coupling reaction, see S. R. Chemler, D. Trauner, S. J. Danishefsky, *Angew. Chem.* **2001**, *113*, 4676 – 4701; *Angew. Chem. Int. Ed.* **2001**, *40*, 4544 – 4568.
[155] a) O. Kwon, D.-S. Su, D. Meng, W. Deng, D. C. D'Amico, S. J. Danishefsky, *Angew. Chem.* **1998**, *110*, 1978 – 1981; *Angew. Chem. Int. Ed.* **1998**, *37*, 1877 – 1880; b) O. Kwon, D.-S. Su, D. Meng, W. Deng, D. C. D'Amico, S. J. Danishefsky, *Angew. Chem.* **1998**, *110*, 1981 – 1983; *Angew. Chem. Int. Ed.* **1998**, *37*, 1880 – 1882; c) D. Meng, S. J. Danishefsky, *Angew. Chem.* **1999**, *111*, 1582 – 1585; *Angew. Chem. Int. Ed.* **1999**, *38*, 1485 – 1488; d) D. Meng, Q. Tan, S. J. Danishefsky, *Angew. Chem.* **1999**, *111*, 3393 – 3397; *Angew. Chem. Int. Ed.* **1999**, *38*, 3197 – 3201.
[156] Q. Tan, S. J. Danishefsky, *Angew. Chem.* **2000**, *112*, 4683 – 4685; *Angew. Chem. Int. Ed.* **2000**, *39*, 4509 – 4511.
[157] For a comprehensive review of total syntheses of and synthetic approaches towards CP-225,917 and CP-263,114, see: D. A. Spiegel, J. T. Njardarson, I. M. McDonald, J. L. Wood, *Chem. Rev.* **2003**, *103*, 2691 – 2727.
[158] C. R. Johnson, M. P. Braun, *J. Am. Chem. Soc.* **1993**, *115*, 11 014 – 11 015.
[159] T. Hayashi, M. Konishi, Y. Kobori, M. Kumada, T. Higuchi, K. Hirotsu, *J. Am. Chem. Soc.* **1984**, *106*, 158 – 163.
[160] J. E. Marcone, K. G. Moloy, *J. Am. Chem. Soc.* **1998**, *120*, 8527 – 8528.
[161] For the isolation and structure elucidation of gymnocin A, see: M. Satake, M. Shoji, Y. Oshima, H. Naoki, T. Fujita, T. Yasumoto, *Tetrahedron Lett.* **2002**, *43*, 5829 – 5832.
[162] For reviews of the chemistry and biology of marine polycyclic ether toxins, see: a) M. Murata, T. Yasumoto, *Nat. Prod. Rep.* **2000**, *17*, 293 – 316; b) P. J. Scheuer, *Tetrahedron* **1994**, *50*, 3 – 18; c) T. Yasumoto, M. Murata, *Chem. Rev.* **1993**, *93*, 1897 – 1909.
[163] For reviews of synthetic approaches to polycyclic ether arrays, see: a) F. P. Marmsäter, F. G. West, *Chem. Eur. J.* **2002**, *8*, 4346 – 4353; b) Y. Mori, *Chem. Eur. J.* **1997**, *3*, 849 – 852; c) E. Alvarez, M.-L. Candenas, R. Pérez, J. L. Ravelo, J. D. Martin, *Chem. Rev.* **1995**, *95*, 1953 – 1980.
[164] a) C. Tsukano, M. Sasaki, *J. Am. Chem. Soc.* **2003**, *125*, 14 294 – 14 295; b) C. Tsukano, M. Ebine, M. Sasaki, *J. Am. Chem. Soc.* **2005**, *127*, 4326 – 4335.
[165] For earlier model studies by the same group, see: a) M. Sasaki, C. Tsukano, K. Tachibana, *Org. Lett.* **2002**, *4*, 1747 – 1750; b) M. Sasaki, C. Tsukano, L. Tachibana, *Tetrahedron Lett.* **2003**, *44*, 4351 – 4354.
[166] For a personalized account of the synthesis of polycyclic ethers by this Suzuki–Miyaura cross-coupling strategy, see: M. Sasaki, H. Fuwa, *Synlett* **2004**, 1851 – 1874.
[167] K. C. Nicolaou, G.-Q. Shi, J. L. Gunzner, P. Gärtner, Z. Yang, *J. Am. Chem. Soc.* **1997**, *119*, 5467 – 5468.
[168] a) K. C. Nicolaou, Z. Yang, G.-Q. Shi, J. L. Gunzner, K. A. Agrios, P. Gartner, *Nature* **1998**, *392*, 264 – 269; b) K. C. Nicolaou, M. E. Bunnage, D. G. McGarry, S. Shi, P. K. Somers, P. A. Wallace, X.-J. Chu, K. A. Agrios, J. L. Gunzner, Z. Yang, *Chem. Eur. J.* **1999**, *5*, 599 – 617; c) K. C. Nicolaou, P. A. Wallace, S. Shi, M. A. Ouellette, M. A. Bunnage, J. L. Gunzner, K. A. Agrios, G.-Q. Shi, P. Gärtner, Z. Yang, *Chem. Eur. J.* **1999**, *5*, 618 – 627; d) K. C. Nicolaou, G.-Q. Shi, J. L. Gunzner, P. Gärtner, P. A. Wallace, M. A. Ouellette, S. Shi, M. E. Bunnage, K. A. Agrios, C. A. Veale, C.-K. Hwang, J. Hutchinson, C. V. C. Prasad, W. G. Ogilvie, Z. Yang, *Chem. Eur. J.* **1999**, *5*, 628 – 645; e) K. C. Nicolaou, J. L. Gunzner, G.-Q. Shi, K. A. Agrios, P. Gärtner, Z. Yang, *Chem. Eur. J.* **1999**, *5*, 646 – 658.
[169] K. C. Nicolaou, K. Namoto, *Chem. Commun.* **1998**, 1757 – 1758.
[170] a) A. Kojima, T. Takemoto, M. Sodeoka, M. Shibasaki, *J. Org. Chem.* **1996**, *61*, 4876 – 4877; b) A. Kojima, T. Takemoto, M. Sodeoka, M. Shibasaki, *Synthesis* **1998**, 581 – 589.
[171] The reasoning behind the use of the *Z*-configured trisubstituted alkene motif in borane **187** was the recognition that *Z* alkenes consistently provide higher levels of enantioselectivity in asymmetric Heck reactions than do their *E*-disposed counterparts; for a similar example, see: T. Takemoto, M. Sodeoka, H. Sasai, M. Shibasaki, *J. Am. Chem. Soc.* **1993**, *115*, 8477 – 8478.
[172] Similar reactions for the preparation of indole and furan systems have been reported by Larock and co-workers, see: a) R. C. Larock, E. K. Yum, M. J. Doty, K. K. C. Sham, *J. Org. Chem.* **1995**, *60*, 3270 – 3271; b) R. C. Larock, E. K. Yum, M. D. Refvik, *J. Org. Chem.* **1998**, *63*, 7652 – 7662.
[173] A palladium-catalyzed domino reaction has also been employed in the total synthesis of the structurally related natural product (+)-xestoquinone, in this case an elegant tandem catalytic asymmetric Heck cyclization cascade: S. P.

Maddaford, N. G. Andersen, W. A. Cristofoli, B. A. Keay, *J. Am. Chem. Soc.* **1996**, *118*, 10766 – 10773.

[174] a) N. Miyaura, T. Ishiyama, H. Sasaki, M. Ishikawa, M. Satoh, A. Suzuki, *J. Am. Chem. Soc.* **1989**, *111*, 314 – 321. See also b) T. Oh-e, N. Miyaura, A. Suzuki, *J. Org. Chem.* **1993**, *58*, 2201 – 2208.

[175] a) P. J. Mohr, R. L. Halcomb, *J. Am. Chem. Soc.* **2003**, *125*, 1712 – 1713; b) N. C. Callan, R. L. Halcomb, *Org. Lett.* **2000**, *2*, 2687 – 2690.

[176] For examples of *B*-alkyl Suzuki–Miyaura coupling reactions involving secondary alkylborane species, see reference [174a].

[177] For model studies on the feasibility of the ring-closing *B*-alkyl Suzuki–Miyaura reaction in transannular macrocyclization, see: S. R. Chemler, S. J. Danishefsky, *Org. Lett.* **2000**, *2*, 2695 – 2698.

[178] a) T. Ishiyama, N. Miyaura, A. Suzuki, *Tetrahedron Lett.* **1991**, *32*, 6923 – 6926; b) T. Ishiyama, H. Kizaki, N. Miyaura, A. Suzuki, *Tetrahedron Lett.* **1993**, *34*, 7595 – 7598.

[179] M. Ishikura, K. Imaizumi, N. Katagiri, *Heterocycles* **2000**, *53*, 553 – 556.

[180] a) V. Snieckus, *Chem. Rev.* **1990**, *90*, 879 – 933; b) H. W. Gschwend, H. R. Rodriguez, *Org. React.* **1979**, *26*, 1 – 360.

[181] See for example a) M. Tanaka, *Tetrahedron Lett.* **1979**, *20*, 2601 – 2602; b) W. F. Goure, M. E. Wright, P. D. Davis, S. S. Labadie, J. K. Stille, *J. Am. Chem. Soc.* **1984**, *106*, 6417 – 6422.

[182] M. Ishikura, M. Terashima, *J. Org. Chem.* **1994**, *59*, 2634 – 2637.

[183] J. A. Joule, K. Mills, *Heterocyclic Chemistry*, *4th ed.*, Blackwell, Oxford, **2000**.

[184] For a review of palladium-catalyzed alkynylation reactions, see: E. Negishi, L. Anastasia, *Chem. Rev.* **2003**, *103*, 1979 – 2017.

[185] A. O. King, N. Okukado, E. Negishi, *J. Chem. Soc. Chem. Commun.* **1977**, 683 – 684.

[186] H. P. Dang, G. Linstrumelle, *Tetrahedron Lett.* **1978**, *19*, 191 – 194.

[187] J. A. Soderquist, K. Matos, A. Rane, J. Ramos, *Tetrahedron Lett.* **1995**, *36*, 2401 – 2402.

[188] K. Takai, K. Oshima, H. Nozaki, *Tetrahedron Lett.* **1980**, *21*, 2531 – 2534.

[189] J. K. Stille, J. H. Simpson, *J. Am. Chem. Soc.* **1987**, *109*, 2138 – 2152.

[190] K. C. Nicolaou, S. E. Webber, *J. Am. Chem. Soc.* **1984**, *106*, 5734 – 5736.

[191] K. C. Nicolaou, C. A. Veale, S. E. Webber, H. Katerinopoulos, *J. Am. Chem. Soc.* **1985**, *107*, 7515 – 7518.

[192] a) K. C. Nicolaou, S. E. Webber, *J. Chem. Soc. Chem. Commun.* **1986**, 1816 – 1817; b) B. E. Marron, R. A. Spanevello, M. E. Elisseou, C. N. Serhan, K. C. Nicolaou, *J. Org. Chem.* **1989**, *54*, 5522 – 5527; c) K. C. Nicolaou, B. E. Marron, C. A. Veale, S. E. Webber, C. N. Serhan, *J. Org. Chem.* **1989**, *54*, 5527 – 5535; d) K. C. Nicolaou, S. E. Webber, J. Ramphal, Y. Abe, *Angew. Chem.* **1987**, *99*, 1077 – 1080; *Angew. Chem. Int. Ed. Engl.* **1987**, *26*, 1019 – 1021.

[193] a) K. C. Nicolaou, S. E. Webber, *Synthesis* **1986**, 453 – 461; b) K. C. Nicolaou, S. E. Webber, *J. Chem. Soc. Chem. Commun.* **1985**, 297 – 298.

[194] For a review of the biosynthesis, biological properties, and chemical synthesis of lipoxins, see: K. C. Nicolaou, J. Y. Ramphal, N. A. Petasis, C. N. Serhan, *Angew. Chem.* **1991**, *103*, 1119 – 1135; *Angew. Chem. Int. Ed. Engl.* **1991**, *30*, 1100 – 1116.

[195] D. J. Pasto in *Comprehensive Organic Synthesis*, *Vol. 8* (Eds.: B. M. Trost, I. Fleming), Pergamon, Oxford, **1991**, p. 471.

[196] A. Fürstner, K. Radkowski, *Chem. Commun.* **2002**, 2182 – 2183.

[197] B. M. Trost, Z. T. Ball, T. Jöge, *J. Am. Chem. Soc.* **2002**, *124*, 7922 – 7923.

[198] P. Wipf, T. H. Graham, *J. Am. Chem. Soc.* **2004**, *126*, 15346 – 15347.

[199] For a review, see K. Sonogashira in *Handbook of Organopalladium Chemistry for Organic Synthesis* (Ed.: E. Negishi), Wiley, New York, **2002**, p. 493.

[200] E. J. Corey, M. Kang, M. C. Desai, A. K. Ghosh, I. N. Houpis, *J. Am. Chem. Soc.* **1988**, *110*, 649 – 651.

[201] N. Ohyabu, T. Nishikawa, M. Isobe, *J. Am. Chem. Soc.* **2003**, *125*, 8798 – 8805.

[202] A. Hinman, J. Du Bois, *J. Am. Chem. Soc.* **2003**, *125*, 11510 – 11511.

[203] J. W. B. Cooke, R. Bright, M. J. Coleman, K. P. Jenkins, *Org. Process Res. Dev.* **2001**, *5*, 383 – 386.

[204] a) S. Müller, B. Liepold, G. J. Roth, H. J. Bestmann, *Synlett* **1996**, 521 – 522; b) E. J. Corey, P. L. Fuchs, *Tetrahedron Lett.* **1972**, *13*, 3769 – 3772.

[205] M. Inoue, M. W. Carson, A. J. Frontier, S. J. Danishefsky, *J. Am. Chem. Soc.* **2001**, *123*, 1878 – 1889.

[206] For similar examples of this heteroannulation procedure, see: a) reference [172a]; b) M. Botta, V. Summa, F. Corelli, G. Di Petro, P. Lombardi, *Tetrahedron: Asymmetry* **1996**, *7*, 1263 – 1266, and references therein.

[207] For a review of the synthesis of heterocycles *via* palladium π-olefin and π-alkyne chemistry, see: G. Zeni, R. C. Larock, *Chem. Rev.* **2004**, *104*, 2285 – 2309.

[208] For reviews of the chemistry and biology of the enediynes, see: a) A. L. Smith, K. C. Nicolaou, *J. Med. Chem.* **1996**, *39*, 2103 – 2117; b) K. C. Nicolaou, A. L. Smith in *Modern Acetylene Chemistry* (Eds.: P. J. Stang, F. Diederich), VCH, Weinheim, **1995**, p. 203; c) K. C. Nicolaou, W.-M. Dai, *Angew. Chem.* **1991**, *103*, 1453 – 1483; *Angew. Chem. Int. Ed. Engl.* **1991**, *30*, 1387 – 1416.

[209] K. C. Nicolaou, C. W. Hummel, E. N. Pitsinos, M. Nakada, A. L. Smith, K. Shibayama, H. Saimoto, *J. Am. Chem. Soc.* **1992**, *114*, 10082 – 10084.

[210] a) J. Taunton, J. L. Wood, S. L. Schreiber, *J. Am. Chem. Soc.* **1993**, *115*, 10378 – 10379; b) J. L. Wood, J. A. Porco, Jr., J. Taunton, A. Y. Lee, J. Clardy, S. L. Schreiber, *J. Am. Chem. Soc.* **1992**, *114*, 5898 – 5900; c) H. Chikashita, J. A. Porco, Jr., T. J. Stout, J. Clardy, S. L. Schreiber, *J. Org. Chem.* **1991**, *56*, 1692 – 1694; d) J. A. Porco, Jr., F. J. Schoenen, T. J. Stout, J. Clardy, S. L. Schreiber, *J. Am. Chem. Soc.* **1990**, *112*, 7410 – 7411.

[211] For examples of other approaches to the dynemicin A skeleton, see references [81] and [82]; see also: a) K. C. Nicolaou, C.-K. Hwang, A. L. Smith, S. V. Wendeborn, *J. Am. Chem. Soc.* **1990**, *112*, 7416 – 7418; b) K. C. Nicolaou, A. L. Smith, S. V. Wendeborn, C.-K. Hwang, *J. Am. Chem. Soc.* **1991**, *113*, 3106 – 3144.

[212] J. Inanaga, K. Hirata, H. Saeki, T. Katsuki, M. Yamaguchi, *Bull. Chem. Soc. Jpn.* **1979**, *52*, 1989 – 1993.

[213] J. Tsuji, H. Takahashi, *Tetrahedron Lett.* **1965**, *6*, 4387 – 4388.

[214] a) S. D. Knight, L. E. Overman, G. Pairaudeau, *J. Am. Chem. Soc.* **1993**, *115*, 9293 – 9294; b) S. D. Knight, L. E. Overman, G. Pairaudeau, *J. Am. Chem. Soc.* **1995**, *117*, 5776 – 5788.

[215] a) R. B. Woodward, M. P. Cava, W. D. Ollis, A. Hunger, H. U. Daeniker, K. Schenker, *J. Am. Chem. Soc.* **1954**, *76*, 4749 – 4751; b) R. B. Woodward, M. P. Cava, W. D. Ollis, A. Hunger, H. U. Daeniker, K. Schenker, *Tetrahedron* **1963**, *19*, 247 – 288.

[216] For other total syntheses of strychnine, see: a) P. Magnus, M. Giles, R. Bonnert, C. S. Kim, L. McQuire, A. Merritt, N. Vicker, *J. Am. Chem. Soc.* **1992**, *114*, 4403 – 4405; b) P. Magnus, M. Giles, R. Bonnert, G. Johnson, L. McQuire, M. Deluca, A. Merritt, C. S. Kim, N. Vicker, *J. Am. Chem. Soc.* **1993**, *115*, 8116 – 8129; c) M. E. Kuehne, F. Xu, *J. Org. Chem.* **1993**, *58*, 7490 – 7494; d) M. E. Kuehne, F. Xu, *J. Org. Chem.* **1998**, *63*, 9427 – 9433; e) V. H. Rawal, S. Iwasa, *J. Org. Chem.* **1994**, *59*, 2685 – 2686; f) D. Solé, J. Bonjoch, S. García-Rubio, E. Peidró, J. Bosch, *Angew. Chem.* **1999**, *111*, 408 – 410; *Angew. Chem. Int. Ed.* **1999**, *38*, 395 – 397; g) D. Solé, J. Bonjoch, S. García-Rubio, E. Peidró, J. Bosch, *Chem. Eur. J.* **2000**, *6*, 655 – 665; h) M. J.

 © 2005 Wiley-VCH Verlag GmbH & Co. KGaA, Weinheim

Eichberg, R. L. Dorta, K. Lamottke, K. P. C. Vollhardt, *Org. Lett.* **2000**, *2*, 2479 – 2481; i) M. Ito, C. W. Cameron, M. Mortimore, J. B. Goh, S. F. Martin, *J. Am. Chem. Soc.* **2001**, *123*, 8003 – 8010; j) M. Nakanishi, M. Mori, *Angew. Chem.* **2002**, *114*, 2014 – 2016; *Angew. Chem. Int. Ed.* **2002**, *41*, 1934 – 1936; k) G. J. Bodwell, J. Li, *Angew. Chem.* **2002**, *114*, 3395 – 3396; *Angew. Chem. Int. Ed.* **2002**, *41*, 3261 – 3262; l) T. Ohshima, Y. Xu, R. Takita, S. Shimizu, D. Zhong, M. Shibasaki, *J. Am. Chem. Soc.* **2002**, *124*, 14546 – 14547; m) reference [29a]; n) Y. Kaburagi, H. Tokuyama, T. Fukuyama, *J. Am. Chem. Soc.* **2004**, *126*, 10246 – 10247; o) T. Ohshima, Y. Xu, R. Takita, M. Shibasaki, *Tetrahedron* **2004**, *60*, 9569 – 9588.

[217] J. Tsuji, I. Shimizu, I. Minami, Y. Ohashi, *Tetrahedron Lett.* **1982**, *23*, 4809 – 4812.

[218] a) K. C. Nicolaou, G. Vassilikogiannakis, W. Mägerlein, R. Kranich, *Angew. Chem.* **2001**, *113*, 2543 – 2547; *Angew. Chem. Int. Ed.* **2001**, *40*, 2482 – 2486; b) K. C. Nicolaou, G. Vassilikogiannakis, W. Mägerlein, R. Kranich, *Chem. Eur. J.* **2001**, *7*, 5359 – 5371.

[219] J. Tsuji, I. Minami, *Acc. Chem. Res.* **1987**, *20*, 140 – 145.

[220] For an alternative, equally elegant synthesis of colombiasin A, see: A. I. Kim, S. D. Rychnovsky, *Angew. Chem.* **2003**, *115*, 1305 – 1308; *Angew. Chem. Int. Ed.* **2003**, *42*, 1267 – 1270.

[221] a) A. Fürstner, H. Weintritt, *J. Am. Chem. Soc.* **1998**, *120*, 2817 – 2825; b) A. Fürstner, T. Gastner, H. Weintritt, *J. Org. Chem.* **1999**, *64*, 2361 – 2366.

[222] For a Review of the chemistry and biology of roseophilin, see: A. Fürstner, *Angew. Chem.* **2003**, *115*, 3706 – 3728; *Angew. Chem. Int. Ed.* **2003**, *42*, 3582 – 3603.

[223] For reviews of pyrrole synthesis, see: a) G. Balme, *Angew. Chem.* **2004**, *116*, 6396 – 6399; *Angew. Chem. Int. Ed.* **2004**, *43*, 6238 – 6241; b) V. F. Ferreira, M. C. B. V. De Souza, A. C. Cunha, L. O. R. Pereira, M. L. G. Ferreira, *Org. Prep. Proced. Int.* **2001**, *33*, 411 – 454; c) R. J. Sundberg in *Comprehensive Heterocyclic Chemistry, Vol. 2* (Eds.: A. R. Katritzky, C. W. Rees, E. F. V. Scriven), Pergamon, Oxford, **1996**, p. 119.

[224] a) D. A. Vosburg, C. D. Vanderwal, E. J. Sorensen, *J. Am. Chem. Soc.* **2002**, *124*, 4552 – 4553; b) C. D. Vanderwal, D. A. Vosburg, S. Weiler, E. J. Sorensen, *J. Am. Chem. Soc.* **2003**, *125*, 5393 – 5407.

[225] The proclivity of similar dienylstannane systems to undergo acid-promoted protodestannylation has been documented; for an example, see: J. Uenishi, R. Kawahama, A. Tanio, S. Wakabayashi, *J. Chem. Soc. Chem. Commun.* **1993**, 1438 – 1439.

[226] This type of palladium-catalyzed cyclization has been termed "metallo-ene-type" reactions; for a discussion, see: a) W. Oppolzer, B. Stammen, *Tetrahedron* **1997**, *53*, 3577 – 3586; for a Review of metallo-ene reactions in organic synthesis, see: b) W. Oppolzer, *Angew. Chem.* **1989**, *101*, 39 – 53; *Angew. Chem. Int. Ed. Engl.* **1989**, *28*, 38 – 52.

[227] For a review of the stereochemistry of palladium-catalyzed cyclization reactions involving π-allyl intermediates, including a discussion of the Tsuji-Trost and palladium-ene reactions, see: A. Heumann, M. Réglier, *Tetrahedron* **1995**, *51*, 975 – 1015.

[228] W. Oppolzer, H. Bienaymé, A. Genevois-Borella, *J. Am. Chem. Soc.* **1991**, *113*, 9660 – 9661.

[229] For an earlier application of a similar reaction by the same group, see: W. Oppolzer, J.-Z. Xu, C. Stone, *Helv. Chim. Acta* **1991**, *74*, 465 – 468.

[230] For recent reviews of the asymmetric allylic alkylation reaction, see reference [25]; for earlier reviews, see a) B. M. Trost, D. L. Van Vranken, *Chem. Rev.* **1996**, *96*, 395 – 422; b) M. Sawamura, Y. Ito, *Chem. Rev.* **1992**, *92*, 857 – 891; c) G. Consiglio, R. M. Waymouth, *Chem. Rev.* **1989**, *89*, 257 – 276.

[231] For a brief Review of palladium-catalyzed enantioselective allylic substitution in the synthesis of natural products, see: T. Graening, H.-G. Schmalz, *Angew. Chem.* **2003**, *115*, 2684 – 2688; *Angew. Chem. Int. Ed.* **2003**, *42*, 2580 – 2584.

[232] B. M. Trost, R. Radinov, E. M. Grenzer, *J. Am. Chem. Soc.* **1997**, *119*, 7879 – 7880.

[233] B. M. Trost, G. M. Schroeder, *J. Am. Chem. Soc.* **1999**, *121*, 6759 – 6760.

[234] B. M. Trost, C. Pissot-Soldermann, I. Chen, G. M. Schroeder, *J. Am. Chem. Soc.* **2004**, *126*, 4480 – 4481.

[235] K. D. Wellington, R. C. Cambie, P. S. Rutledge, P. R. Berquist, *J. Nat. Prod.* **2000**, *63*, 79 – 85.

[236] Although drawn for simplicity as the simple enolate **286**, the actual nature of the nucleophilic species in such ketone asymmetric alkylations is somewhat more involved; for a discussion, see reference [233].

[237] For other total syntheses of hamigeran B, see: a) K. C. Nicolaou, D. Gray, J. Tae, *Angew. Chem.* **2001**, *113*, 3787 – 3790; *Angew. Chem. Int. Ed.* **2001**, *40*, 3675 – 3678; b) K. C. Nicolaou, D. Gray, J. Tae, *Angew. Chem.* **2001**, *113*, 3791 – 3795; *Angew. Chem. Int. Ed.* **2001**, *40*, 3679 – 3683; c) D. L. J. Clive, J. Wang, *Angew. Chem.* **2003**, *115*, 3528 – 3531; *Angew. Chem. Int. Ed.* **2003**, *42*, 3406 – 3409; for a total synthesis of 6-*epi*-(−)-hamigeran B, see: d) G. Mehta, H. M. Shinde, *Tetrahedron Lett.* **2003**, *44*, 7049 – 7053.

[238] For the alkylation of oxindoles through this methodology, see: B. M. Trost, M. U. Frederiksen, *Angew. Chem.* **2005**, *117*, 312 – 314; *Angew. Chem. Int. Ed.* **2005**, *44*, 308 – 310.

[239] D. C. Behenna, B. M. Stoltz, *J. Am. Chem. Soc.* **2004**, *126*, 15044 – 15045.

[240] B. M. Trost, J. Xu, *J. Am. Chem. Soc.* **2005**, *127*, 2846 – 2847.

[241] H. Yoshizaki, H. Satoh, Y. Sato, S. Nukui, M. Shibasaki, M. Mori, *J. Org. Chem.* **1995**, *60*, 2016 – 2021.

[242] For a review, see: B. M. Trost, C. B. Lee in *Catalytic Asymmetric Synthesis, 2nd ed.* (Ed.: I. Ojima), Wiley-VCH, New York, **2000**, Ch. 8E, p. 503.

[243] For discussions of the preparation of polyfunctional organozinc reagents, see: a) P. Knochel, R. D. Singer, *Chem. Rev.* **1993**, *93*, 2117 – 2188; b) A. Boudier, L. O. Bromm, M. Lotz, P. Knochel, *Angew. Chem.* **2000**, *112*, 4584 – 4606; *Angew. Chem. Int. Ed.* **2000**, *39*, 4414 – 4435.

[244] For a synopsis of recent advances in the Negishi coupling, see: G. Lessene, *Aust. J. Chem.* **2004**, *57*, 107.

[245] F. Xeng, E. Negishi, *Org. Lett.* **2001**, *3*, 719 – 722.

[246] E. Negishi, N. Okukado, A. O. King, D. E. V. Horn, B. I. Spiegel, *J. Am. Chem. Soc.* **1978**, *100*, 2254 – 2256.

[247] This process of enyne carbometalation and subsequent palladium-catalyzed cross-coupling has been extended to allylic electrophiles; see: H. Matsushita, E. Negishi, *J. Am. Chem. Soc.* **1981**, *103*, 2882 – 2884.

[248] a) A. B. Smith III, T. J. Beauchamp, M. J. LaMarche, M. D. Kaufman, Y. Qiu, H. Arimoto, D. R. Jones, K. Kobayashi, *J. Am. Chem. Soc.* **2000**, *122*, 8654 – 8664; b) A. B. Smith III, M. D. Kaufman, T. J. Beauchamp, M. J. LaMarche, H. Arimoto, *Org. Lett.* **1999**, *1*, 1823 – 1826.

[249] a) For a review of the chemistry and biology of discodermolide, see: M. Kalesse, *ChemBioChem* **2000**, *1*, 171 – 175; b) for examples of other approaches to discodermolide, see: I. Paterson, G. J. Florence, *Eur. J. Org. Chem.* **2003**, 2193 – 2208.

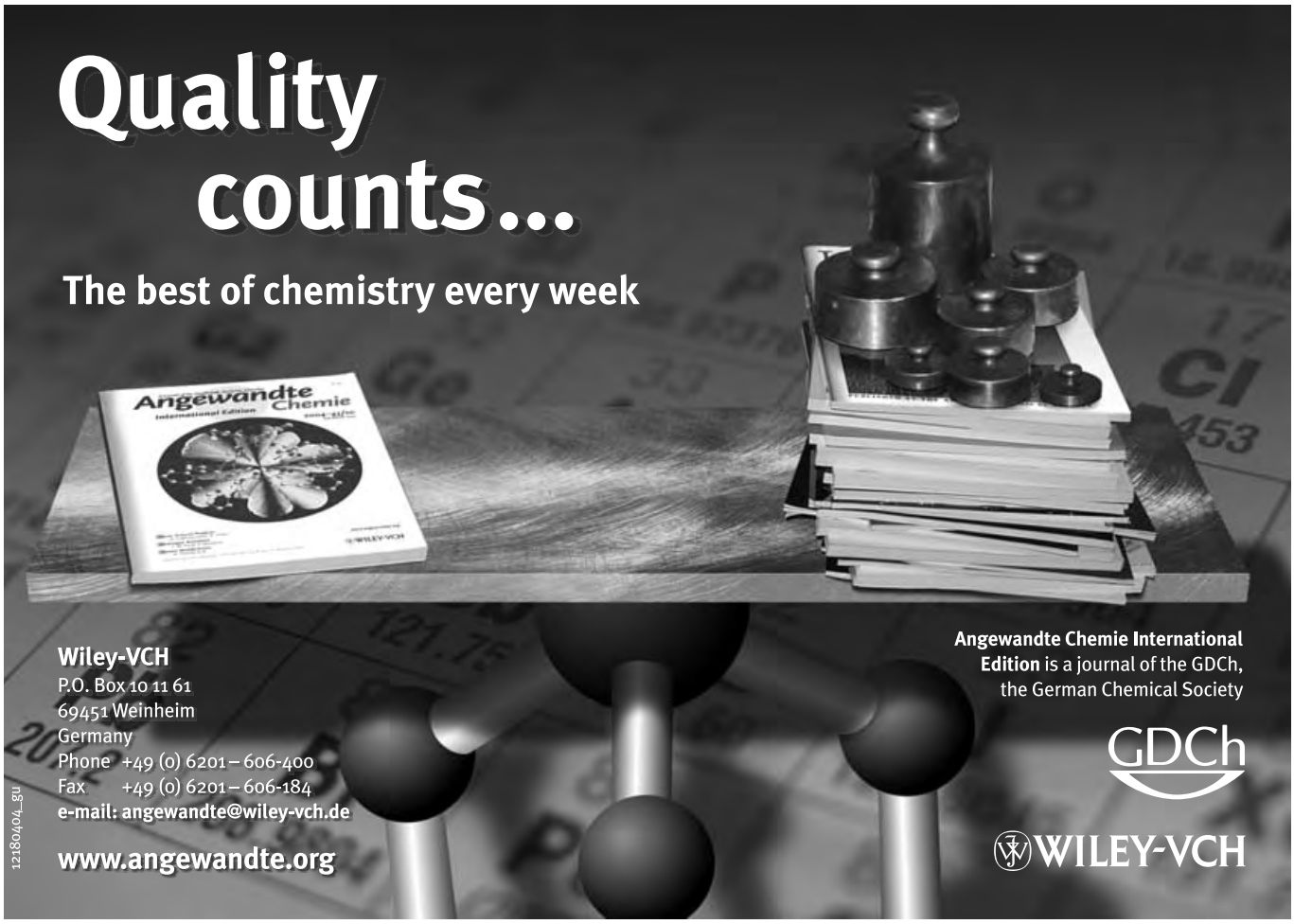
[250] In the synthesis of discodermolide by the Marshall group, a *B*-alkyl Suzuki–Miyarua fragment-coupling strategy was employed to form the C14–C15 bond, in which 2.2 equivalents of an alkyl iodide structurally related to **309** was required: J. A. Marshall, B. A. Johns, *J. Org. Chem.* **1998**, *63*, 7885 – 7892.

[251] E. Negishi, V. Bagheri, S. Chatterjee, F.-T. Luo, *Tetrahedron Lett.* **1983**, *24*, 5181 – 5184.

[252] C. Aïssa, R. Riveiros, J. Ragot, A. Fürstner, *J. Am. Chem. Soc.* **2003**, *125*, 15512 – 15520.

 © 2005 Wiley-VCH Verlag GmbH & Co. KGaA, Weinheim

[253] K. E. Drouet, E. A. Theodorakis, *J. Am. Chem. Soc.* **1999**, *121*, 456 – 457.
[254] A. G. M. Barrett, M. Peña, J. A. Willardsen, *J. Org. Chem.* **1996**, *61*, 1082 – 1100.
[255] M. E. Layton, C. A. Morales, M. D. Shair, *J. Am. Chem. Soc.* **2002**, *124*, 773 – 774.
[256] E. Negishi, A. Alimardanov, C. Xu, *Org. Lett.* **2000**, *2*, 65 – 67.
[257] See the following Review in this issue: K. C. Nicolaou, P. G. Bulger, D. Sarlah, *Angew. Chem.* **2005**, *117*, 4564–4601; *Angew. Chem. Int. Ed.* **2005**, *44*, 4490–4527.



 © 2005 Wiley-VCH Verlag GmbH & Co. KGaA, Weinheim

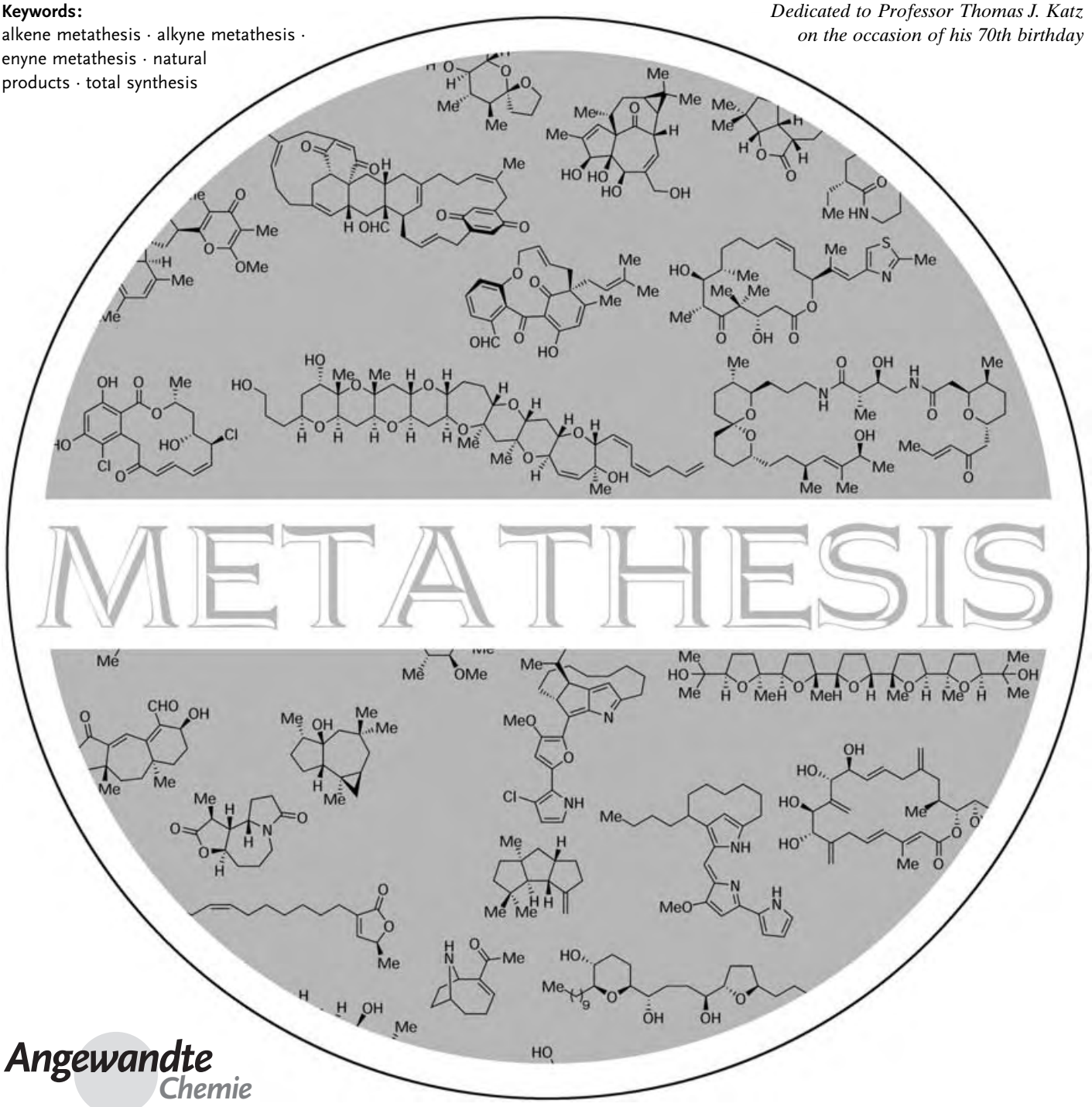
Synthethic Methods

Metathesis Reactions in Total Synthesis

K. C. Nicolaou, Paul G. Bulger, and David Sarlah*

Keywords:
alkene metathesis · alkyne metathesis · enyne metathesis · natural products · total synthesis

Dedicated to Professor Thomas J. Katz on the occasion of his 70th birthday



 © 2005 Wiley-VCH Verlag GmbH & Co. KGaA, Weinheim DOI: 10.1002/anie.200500369

With the exception of palladium-catalyzed cross-couplings, no other group of reactions has had such a profound impact on the formation of carbon–carbon bonds and the art of total synthesis in the last quarter of a century than the metathesis reactions of olefins, enynes, and alkynes. Herein, we highlight a number of selected examples of total syntheses in which such processes played a crucial role and which imparted to these endeavors certain elements of novelty, elegance, and efficiency. Judging from their short but impressive history, the influence of these reactions in chemical synthesis is destined to increase.

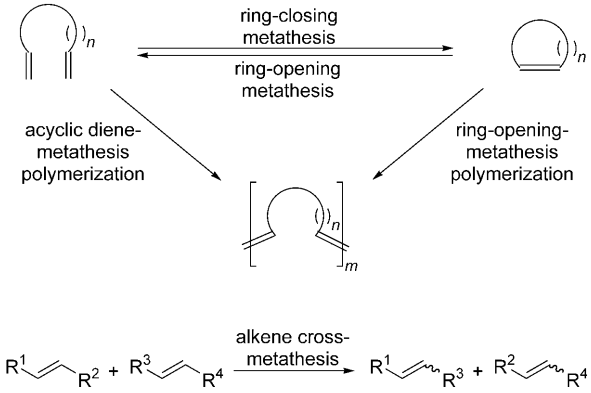
From the Contents

1. Introduction	4491
2. The Alkene-Metathesis Reaction	4493
3. The Enyne-Metathesis Reaction	4512
4. The Alkyne-Metathesis Reaction	4517
5. Summary and Outlook	4520

1. Introduction

Ever since the birth of the art of organic synthesis, as marked by Wöhler's synthesis of urea in 1828, progress in this field has, to a large degree, been dependent on our ability to construct carbon frameworks through carbon–carbon bond-forming reactions. The Grignard,[1] Diels–Alder,[2] and Wittig reactions[3] are three of the most prominent such processes that played decisive roles in shaping the science of chemical synthesis as we know it today. During the last quarter of the previous century, two more such reactions emerged as rivals to the aforementioned carbon–carbon bond-forming processes: the palladium-catalyzed cross-coupling reactions and those collectively known as metathesis reactions. As a most stringent test, total synthesis often serves as a measure of the power of a given reaction. Surveys of relevant applications of enabling reactions are, therefore, of importance in that they not only help to underscore the scope and generality of such processes in chemical synthesis, but they also serve to place into perspective that particular reaction within the field, and to inspire future improvements and new applications. In the preceding Review in this issue ("Palladium-Catalyzed Cross-Coupling Reactions in Total Synthesis"),[4] such a critical analysis was provided. The purpose of this Review is to do the same for the alkene, enyne, and alkyne metathesis reactions.[5]

Alkene metathesis, in all its various guises (Scheme 1), has arguably influenced and shaped the landscape of synthetic organic chemistry more than any other single process over the last 15 years.[6] The wealth of synthetic transformations that can be accomplished when this reaction is applied to appropriate substrates is astonishing, since the same catalyst (initiator) systems can promote several different types of reactions, depending on the substrates and reaction conditions employed. The history of alkene metathesis is a fascinating one, beginning with its serendipitous discovery nearly 50 years ago through to the design and application of the latest initiators available today.[7] The elucidation of the mechanistic pathway was, itself, the culmination of nearly two decades of extensive, if not collaborative or competitive, research by numerous groups, and the subject of lively debate in the literature during that period. The generally accepted mechanism of alkene metathesis was originally proposed by



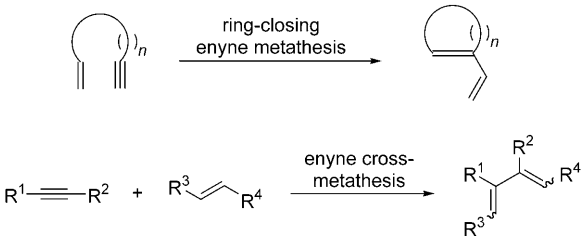
Scheme 1. The most commonly employed alkene-metathesis reactions in organic synthesis.

Hérisson and Chauvin in 1971,[8] with key experimental evidence for its validity subsequently being provided by the Casey,[9] Katz,[10] and Grubbs groups,[11] and invokes metal carbene intermediates as key propagating species in the catalytic cycle. From a practical viewpoint, a key milestone in the evolution of alkene metathesis was the demonstration by Katz and co-workers in 1976 that single-component, well-defined tungsten carbenes, for example $Ph_2C{=}W(CO)_5$, could initiate alkene metathesis without added coactivators.[12,13] This discovery ushered in the modern era of rational catalyst design, and after further development, the alkene-metathesis reaction has developed into one of the most powerful carbon–carbon bond-forming reactions currently available to the synthetic chemist.

[*] Prof. Dr. K. C. Nicolaou, Dr. P. G. Bulger, D. Sarlah
Department of Chemistry
and The Skaggs Institute for Chemical Biology
The Scripps Research Institute
10550 North Torrey Pines Road, La Jolla, CA 92037 (USA)
Fax: (+1) 858-784-2469
E-mail: kcn@scripps.edu
and
Department of Chemistry and Biochemistry
University of California San Diego
9500 Gilman Drive, La Jolla, CA 92093 (USA)

DOI: 10.1002/anie.200500369
© 2005 Wiley-VCH Verlag GmbH & Co. KGaA, Weinheim

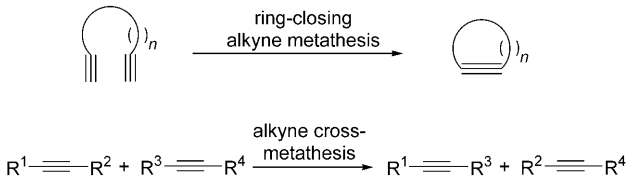
Although alkene metathesis constitutes, by far, the most widely utilized type of metathesis reaction, recent years have witnessed the discovery and development of a number of related processes employing a broader range of substrates. Prominent amongst these is the enyne-metathesis reaction, which involves the union of an alkene with an alkyne to form a 1,3-diene system (Scheme 2).[14] Unlike the corresponding



Scheme 2. Enyne-metathesis reactions in organic synthesis.

alkene-metathesis reactions, enyne metatheses are wholly atom economical (that is, no olefin-containing by-product is released during the process)[15] and are therefore driven by enthalpic rather than entropic factors, principally the stability of the conjugated diene system thus produced. Another distinction is that enyne metathesis can occur by any one of several independent mechanistic pathways, with the course of the reaction being dictated by whether metal carbene species or low-valent transition-metal complexes mediate the process, although the net outcome is (usually) the same. The enyne-metathesis reaction was discovered by Katz and his group, who reported the first examples of this process in 1985 in the presence of catalytic amounts of tungsten Fischer carbene complexes.[16] At the same time, these workers proposed the currently accepted mechanism for this type of process, invoking a sequence of [2+2] cycloaddition and cycloreversion steps involving metal carbene species, which closely parallels the mechanism of alkene metathesis. Subsequently, the Trost group documented the cycloisomerization of 1,*n*-enyne systems in the presence of palladium(II) complexes to generate 1,3-diene systems, which formally arise as the result of enyne ring-closing metathesis, yet proceed through non-carbenoid mechanistic pathways.[17] This type of transformation forms an important subset of a larger class of transition-metal-mediated reactions.[18–20] This transformation can also be effected by complexes of a number of other late transition metals, including ruthenium,[21] iridium,[22] and platinum.[23] Nevertheless, in terms of both scope and frequency of use, the metal carbene mediated reactions are the most widely employed among the enyne-metathesis processes.

Most recently, it has proven to be the turn of alkyne metathesis to emerge from the shadow of alkene metathesis and become a valuable addition to the armory of the synthetic chemist in its own right.[24] Unlike enyne metathesis, alkyne metathesis is a direct analogue of the alkene-metathesis reaction and involves the mutual exchange of alkylidyne units between two acetylene moieties (Scheme 3). Alkyne meta-



Scheme 3. Alkyne-metathesis reactions in organic synthesis.

thesis can be applied in both inter- and intramolecular contexts, although the application and development of these processes in the field of total synthesis is still very much in its infancy. The first examples of homogeneously catalyzed alkyne-metathesis reactions were reported by Mortreux and Blanchard in 1974,[25,26] with a mechanistic rationale (involving a Chauvin-type series of metal carbyne and metallacyclobutadiene intermediates as the propagating species) being put forward by Katz and McGinnis less than a year later.[10] As was the case with alkene metathesis, however, the acknowledgment that alkyne metathesis could serve as a synthetically useful tool in the construction of complex molecules would be postponed until the development of newer generations of more practical catalyst systems that could operate efficiently under mild conditions and in the presence of sensitive functionality. Breakthroughs in alkyne-metathesis chemistry within the last decade, largely spearheaded by the pioneering work of the Bunz and Fürstner groups, include the development of practical, selective ring-closing and intermolecular (cross) alkyne-metathesis versions. These processes are often complementary to the corresponding alkene-metathesis reactions and have propelled this field to the forefront of the emerging metathesis technology.



The impact of K. C. Nicolaou's career on chemistry, biology, and medicine flows from his contributions to chemical synthesis, which have been described in numerous publications and patents. His dedication to chemical education is reflected in his training of hundreds of graduate students and postdoctoral fellows. His Classics in Total Synthesis series, which he has co-authored with his students Erik J. Sorensen and Scott A. Snyder, are used around the world as a teaching tool and source of inspiration for students and practitioners of the art of chemical synthesis.



Paul G. Bulger was born in London (UK) in 1978. He received his M.Chem in 2000 from the University of Oxford, where he completed his Part II project under Dr. Mark G. Moloney. He obtained his D.Phil in chemistry in 2003 for research conducted under Professor Sir Jack E. Baldwin. In the fall of 2003, he joined Professor K. C. Nicolaou's group as a postdoctoral researcher. His research interests encompass reaction mechanism and design and their application to complex natural product synthesis and chemical biology.

 © 2005 Wiley-VCH Verlag GmbH & Co. KGaA, Weinheim

In this Review, we highlight a number of total syntheses that feature one or more of these transition-metal-catalyzed carbon–carbon bond-forming reactions, and we hope to underscore their power in chemical synthesis.[27]

2. The Alkene-Metathesis Reaction

The alkene-metathesis reaction is the most commonly employed of the metathesis-based carbon–carbon bond-forming reactions. In the context of total synthesis, it has been primarily the alkene ring-closing metathesis reaction and, more recently, the alkene cross-metathesis reaction that have found the most widespread and gainful use. The success of the alkene-metathesis reaction and the many stunning and ingenious situations in which it has been applied are largely due to the advent of today's readily available catalyst systems that display high activity and excellent functional-group tolerance. The three such catalysts most routinely used by organic chemists (all of which are commercially available) are shown in Figure 1. The molybdenum-based catalyst **1** was

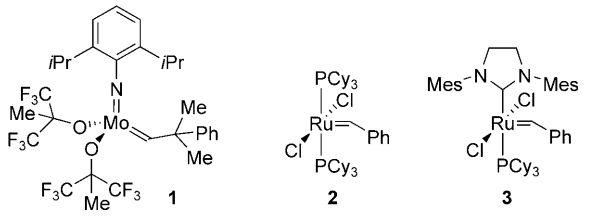


Figure 1. Commonly used alkene metathesis initiators (catalysts).

introduced by the Schrock group in 1990,[28] and represented the first real groundbreaking advance in catalyst design since the tungsten carbenes initially used by Katz and co-workers.[12] Catalyst **1** displays superb metathesis activity with a wide variety of alkene substrates, and is particularly useful for the formation of sterically crowded systems.[29] The singular drawback of catalyst **1** is its pronounced sensitivity to oxygen, moisture, and certain polar or protic functional groups owing to the electrophilicity of the high-oxidation-state transition-metal center.[30] Grubbs and co-workers subsequently introduced ruthenium-based carbene complexes,[31] initially optimized to **2**,[32] as general and practical metathesis catalysts.



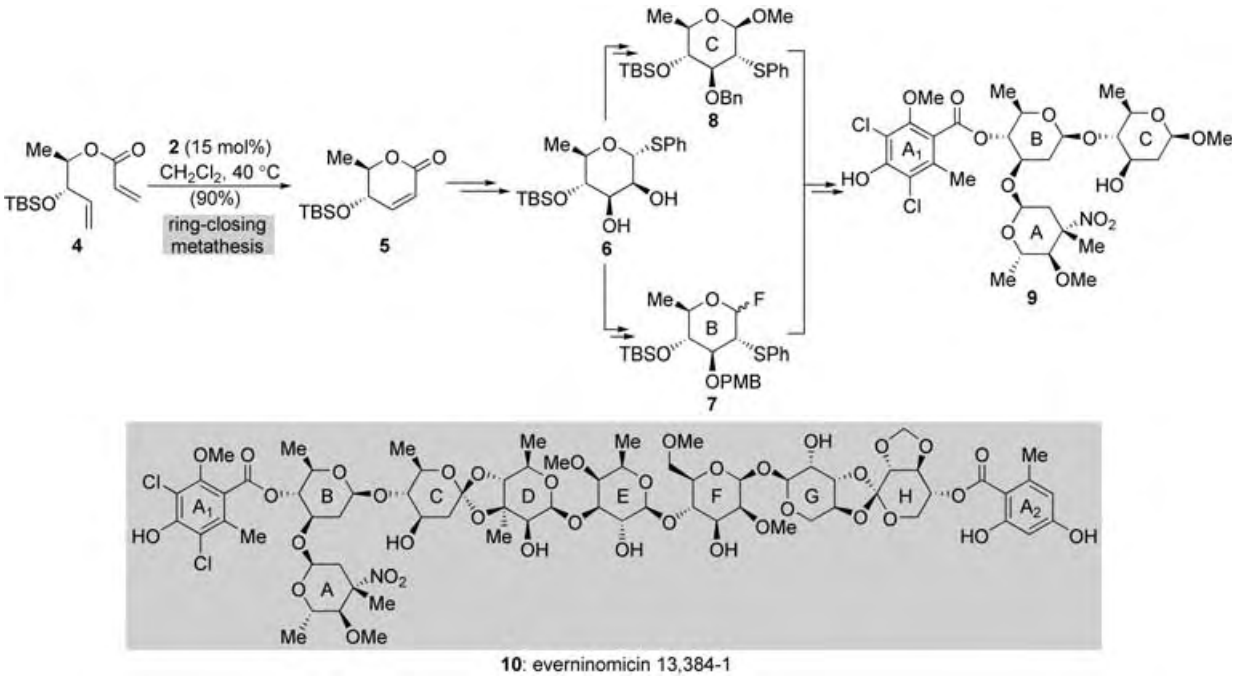
David Sarlah was born in Celje, Slovenia in 1983. He is currently student in the Faculty of Chemistry and Chemical Technology, University of Ljubljana (Slovenia). Since 2001, he has been a research assistant at the Laboratory of Organic and Medicinal Chemistry at the National Institute of Chemistry (Slovenia) where he carried out research on asymmetric catalysis under the direction of Dr. B. Mohar. During the summer of 2004, he was engaged in total synthesis endeavors as a member of the azaspiracid team under Professor K. C. Nicolaou.

Although less active than the Schrock molybdenum-based systems **1**, the "first-generation" Grubbs initiator **2** exhibits much greater functional-group tolerance and has opened up new vistas in synthetic applications, most notably in the total synthesis of complex products, both natural and designed. Recent developments in catalyst (re)design have focused largely on the specific tailoring of catalyst reactivity through modifications of the ancillary ligands bound to the ruthenium center. In particular, the replacement of one of the phosphine ligands in **2** with an N-heterocyclic carbene ligand,[33] as reported independently by several groups,[34,35] increases the catalytic activity, thermal stability, and functional-group tolerance of the complex. The "second-generation" catalyst **3** engenders metathesis reactions with particularly high levels of activity, in certain cases approaching that of the Schrock system **1**, and with a unique reactivity profile that nicely complements both earlier catalysts **1** and **2**.[36] Despite these advances, the search for increasingly efficient and selective metathesis catalysts continues unabated.[37] It should be mentioned that the complexes used in metathesis reactions are more accurately described as "initiators" rather than "catalysts", since they are generally not recovered unchanged at the end of the process. Nevertheless, the use of the term "catalyst" is so entrenched in the metathesis literature that, in this Review, we use both descriptors interchangeably, being mindful of the somewhat lax use of terminology that results.

2.1. Alkene Ring-Closing Metathesis

Alkene ring-closing metathesis has developed into one of the most powerful and reliable methods for ring formation. A seemingly limitless array of ring systems, be they common, medium or large, carbocyclic or heterocyclic,[38] can be fashioned by this tool, with the limits of its feasibility continually being probed and expanded. Alkene ring-closing metathesis reactions are now so routinely embedded within multistep target-oriented synthesis that the complexity of the target molecule can obscure possible connections to the metathesis event. A case in point is the early studies toward the synthesis of the ornate oligosaccharide antibiotic everninomicin 13,384-1 (**10**, Scheme 4) reported by the Nicolaou group.[39] In an effort to increase the degree of synthetic convergence, a strategy was sought that would enable the preparation of both the B- and C-ring carbohydrate building blocks from a common intermediate. Whilst the array of functionality present in these units in their final format (i.e. **10**) does not reveal any obvious metathesis disconnection, retrosynthetic analysis suggested that both **7** (B-ring) and **8** (C-ring) could likely be constructed from **6**, which in turn could be derived from α,β-unsaturated intermediate **5**. With simplification to this initial goal structure, the connection of these ring systems to metathesis becomes readily apparent. Indeed, the use of this metathesis-based strategy ultimately proved fruitful, as the complete tetracyclic $A_1B(A)C$-ring assembly (i.e. compound **9**) of the target compound **10** was synthesized following the alkene ring-closing metathesis of α,ω-diene **4** in the presence of the first-generation Grubbs ruthenium catalyst **2** (15 mol%, CH_2Cl_2, reflux, 90%

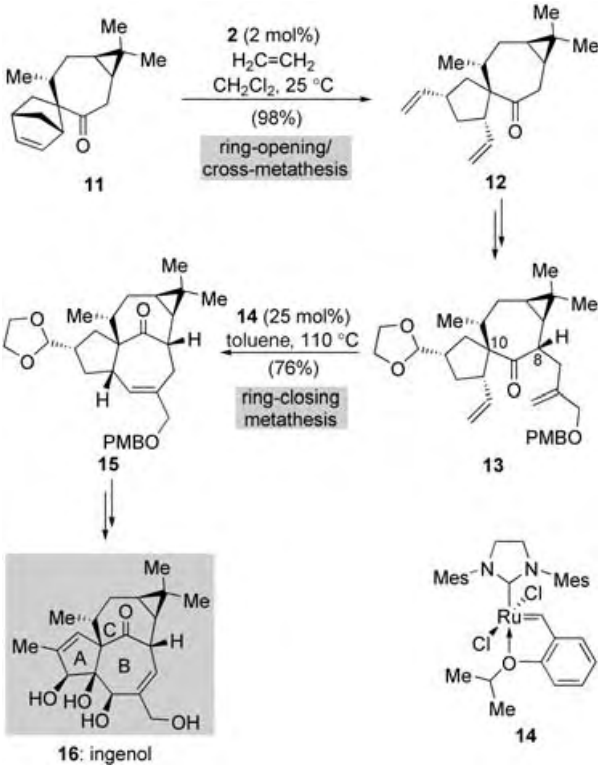
 © 2005 Wiley-VCH Verlag GmbH & Co. KGaA, Weinheim



Scheme 4. Ring-closing metathesis in the fashioning of the B- and C-ring carbohydrates of everninomicin $A_1B(A)C$-ring model system (**9**) (Nicolaou and co-workers, 1998).[39]

yield).[40] Although this ring-closing reaction would appear far from groundbreaking today, the use of metathesis in this situation engendered a particularly concise feature to this complex natural product that would have otherwise been challenging to achieve with equal efficiency.[41]

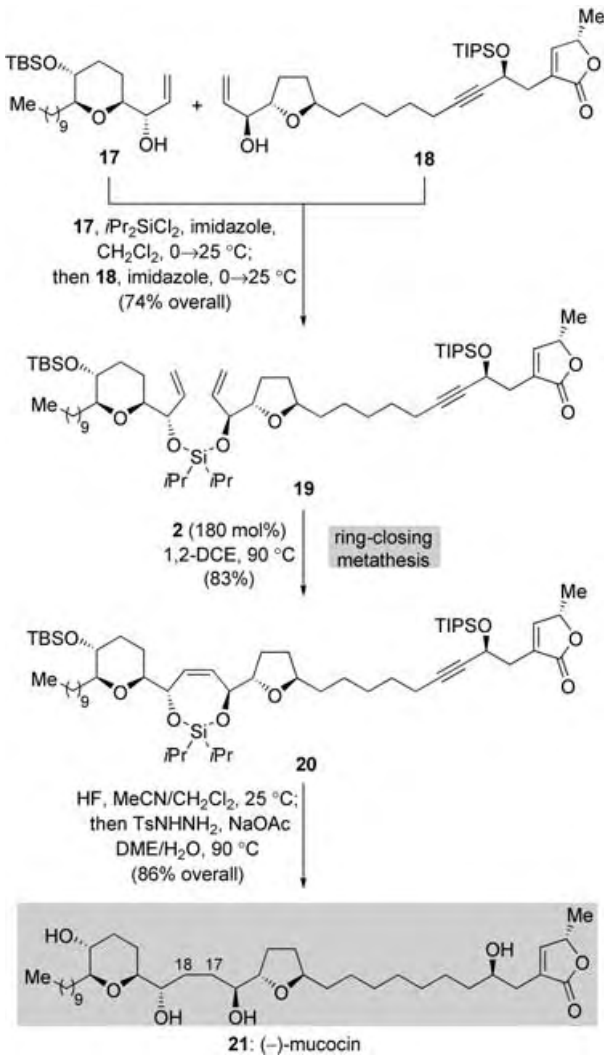
Brilliant use of olefin metathesis reactions in a complex setting was made by Wood and co-workers in their recent total synthesis of ingenol (**16**, Scheme 5).[42] The parent member of a large class of ingenane diterpenes, ingenol (**16**) has captivated the attention of synthetic chemists for more than 20 years.[43] The irresistible lure of this natural product is due partly to its promising biological activity,[44] but also to its rather remarkable polycyclic, highly oxygenated molecular architecture, the most distinctive feature of which is the strained "inside–outside" (*trans*) intrabridgehead stereochemistry of the bicyclic BC-ring system.[45] Indeed, the stereoselective synthesis of this motif has inspired several ingenious approaches, whilst at the same time proving to be the undoing of many more.[46,47] The Wood team proposed that it would be prudent to establish the stereochemical relationship between C8 and C10 before the formation of the BC-ring system, and that the latter task could be accomplished through a ring-closing-metathesis reaction (i.e. **13**→**15**). In an insightful piece of retrosynthetic analysis, they further proposed that **13** could, in turn, arise from diene **12**, the product of a ring-opening cross-metathesis reaction of the norbornene derivative **11**. Indeed, they found that the readily available, enantiomerically pure precursor **11** underwent smooth ring opening upon exposure to initiator **2** (2 mol%) under an ethylene atmosphere (1 atm) in CH_2Cl_2 at ambient temperature to afford diene **12** in nearly quantitative yield. Note that the alternative metathesis pathway available to precursor **11**, namely ring-opening-metathesis polymerization, was efficiently suppressed due to both the relatively high dilution conditions (initially 0.007 M in **11**) and the vast excess of (gaseous) ethylene employed.[48] Following the



Scheme 5. Ring-opening/cross-metathesis and ring-closing-metathesis reactions in the total synthesis of ingenol (**16**) (Wood and co-workers, 2004).[42]

uneventful advancement of diene **12** to give intermediate **13**, the stage was set for the pivotal ring-closing-metathesis reaction. While the team could take heart from previous model studies which had demonstrated the viability of related reactions,[49,50] its successful execution in the present case, and in such an elaborate setting, was by no means a foregone conclusion. To their delight, they found that the desired ring closure could, indeed, be effected in good yield (76%), provided that the novel "phosphine-free" catalyst **14** was employed. Introduced concomitantly and independently by the Hoveyda[51] and Blechert groups[52] in 2000, the cleverly designed complex **14** has proven itself to be a valuable alternative to the second-generation Grubbs catalyst **3** in ring-closing-metathesis processes, particularly in the formation of trisubstituted alkene systems. The incorporation of the cyclopentane A-ring into the cyclization precursor **13** was found to be essential for the formation of the strained BC-ring system by ring-closing metathesis to occur; it is presumed that the presence of this ring biases the conformation of the precursor such that the olefinic termini are in closer proximity and, thus, more amenable to undergo ring closure.[49] Whilst the "southern" portion of cyclized compound **15** looks relatively barren when compared with the targeted structure **16**, the trisubstituted allylic alcohol functionality concomitantly introduced into compound **15** during the metathesis event provided a sufficient handle for its ultimately victorious elaboration, over a number of steps, to the coveted final product **16**.[53]

An interesting development in the alkene-metathesis field has been the employment of temporary silicon-based tethers in ring-closing-metathesis reactions, the utility of which has been elegantly exemplified in the total synthesis of the antitumor agent (−)-mucocin (**21**, Scheme 6) by Evans and co-workers.[54] Although the target compound **21** contains three rings that would appear to be prime candidates for construction through ring-closing metathesis, it was, in fact, only the C17–C18 carbon–carbon bond that was forged by this methodology. While this linkage could conceivably be formed through a selective cross-metathesis reaction (see below) between precursors **17** and **18**, it may not, at first glance, be readily apparent how it could be derived from a ring-closing-metathesis event. A clue lies in the two secondary hydroxy groups flanking the two sides of the C17–C18 bond in the target compound. Thus, if precursors **17** and **18** were to be linked together through these hydroxy groups, formation of the C17–C18 bond would then entail an intramolecular as opposed to an intermolecular process. This could endow the reaction with not only entropic advantages, but also higher levels of chemo-, regio-, and stereoselectivity. Temporary silicon tethers have proven to be versatile disposable linkers in a myriad of applications,[55] and the present case represents an instructive addition to this repertoire.[56,57] Thus, as shown in Scheme 6, the mixed bis(alkoxy)silane was readily formed by treatment of allylic alcohol **17** with excess diisopropyldichlorosilane to afford the corresponding monoalkoxychlorosilane, followed by the removal of the excess silylating agent and addition of the second allylic alcohol **18**. The cyclization of the silicon-tethered diene **19**, which can also be viewed as a fragment-coupling reaction, then proceeded as planned upon exposure to ruthenium carbene **2** in refluxing 1,2-dichloroethane. Referring to complex **2** as a "catalyst" would in this case be something of a misnomer, since an excess (180 mol% with respect to **19**, added slowly as a solution in 1,2-dichloroethane over 34 h) was required to drive the reaction to completion. This requirement did not come as a complete surprise to the team, as they had previously shown that the construction of *trans*-1,4-silaketals through ring-closing metathesis was often quite a challenging event.[58] Nevertheless, the cyclized (or coupled) product **20** was obtained in good yield (83%) without any competing and undesired participation of either the alkyne or the butenolide groups. Having fulfilled their various purposes in an exemplary manner, the three silicon groups in compound **20** were then cleaved upon exposure to hydrofluoric acid, with a subsequent chemoselective reduction of both the alkyne and the C17–C18 alkene groups with diimide then unveiling the final product **21**.[59,60]

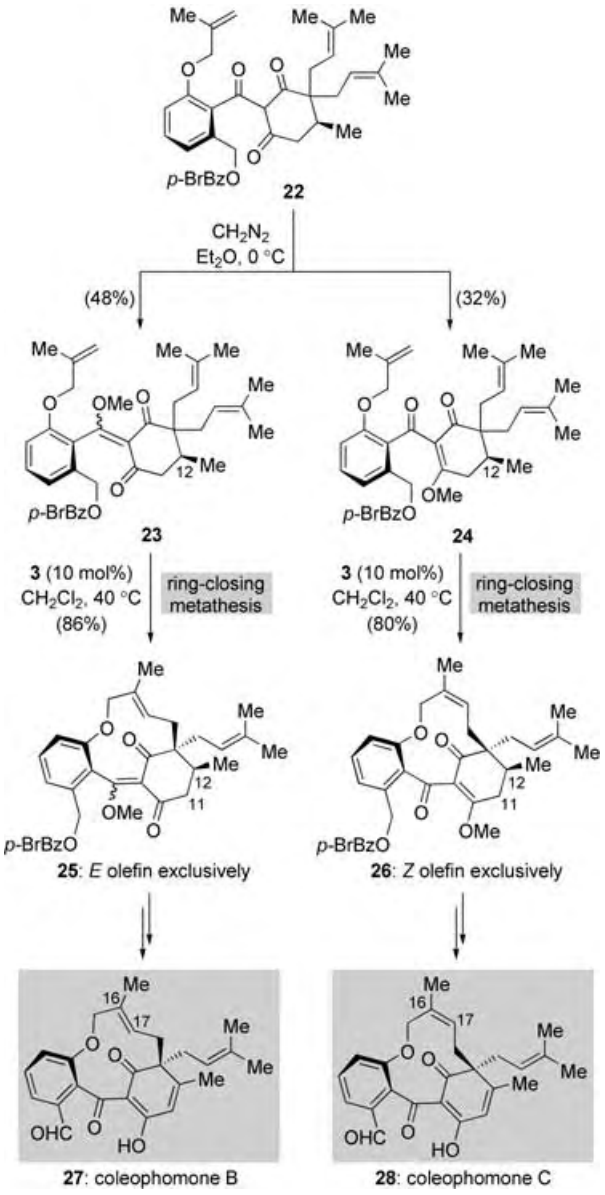


Scheme 6. Use of a temporary silicon tether to facilitate a ring-closing-metathesis reaction in the enantioselective total synthesis of (−)-mucocin (**21**) (Evans and co-workers, 2003).[54]

There also has been a burgeoning interest in recent years in the formation of medium-sized rings through ring-closing metathesis.[61] An unfortunate complicating factor in this

 © 2005 Wiley-VCH Verlag GmbH & Co. KGaA, Weinheim

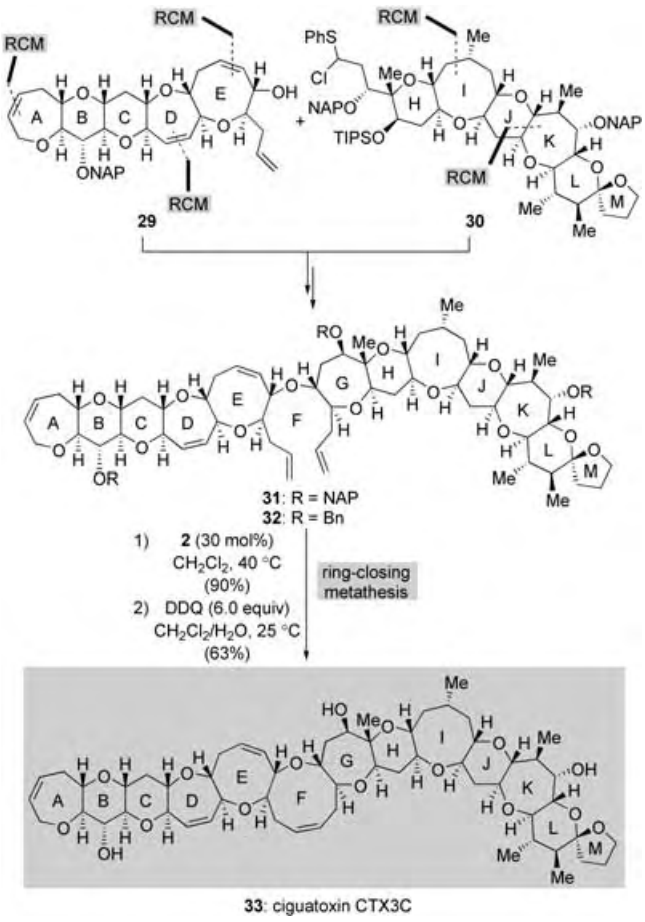
application is that, in addition to the difficulties inherent in the construction of medium-sized rings by any cyclization method, the ring strain present in medium-sized cycloalkenes renders them rather prone to the reverse metathesis processes, namely ring-opening metathesis or ring-opening-metathesis polymerization. A commonly employed tactic to circumvent this problem is the incorporation of some form of conformational constraint (be it cyclic or acyclic) into the cyclization precursor, in order to force (or at least encourage) it to adopt a conformation suitable for ring closure, as was applied in the synthesis of ingenol described above. Another such application is in the total synthesis of coleophomones B (**27**) and C (**28**, Scheme 7) by the Nicolaou group.[62] These two compounds differ only in the geometry of the C16–C17 alkene located within the *ansa* bridge, and while a metathesis-based strategy to fashion this motif would seem particularly appealing, its viability in practice would rest on the answers to two key questions: 1) Would the formation of a trisubstituted alkene system in such a rigid, strained setting by ring-closing metathesis, in fact, be feasible? 2) If so, what would be the stereoselectivity of the process? The latter factor, which could hardly be anticipated a priori, clearly stood as a critical element in reaching both **27** and **28**. As events transpired, it was found that both isomers **27** and **28** could be obtained in their pure geometrical forms in separate metathesis reactions simply through the subtle modification of a common advanced intermediate. The final strategy towards these natural products is illustrated in Scheme 7. Thus, having reached the advanced staging area represented by intermediate **22** (itself a poor metathesis substrate), the rather labile tricarbonyl moiety was "protected" by treatment with CH_2N_2. This step was nonselective and led to the formation of both **23** and **24**, which differ only in the site at which methylation occurred; however, this result proved critical to the success of the overall approach. Separate exposure of **23** and **24** to catalyst **3** (10 mol%) in CH_2Cl_2 at reflux effected the desired metathesis to form the corresponding 11-membered cycloalkene ring systems in good yield, but as singular (and different) geometrical isomers. Remarkably, whereas the cyclization of **23** furnished the *E*-alkene-containing product **25** as the sole isomer, ring-closure of **24** afforded the corresponding *Z*-geometric isomer **26** exclusively. Furthermore, these metathesis reactions were also superbly diastereoselective, in that only the prenyl group *cis* to the vicinal C12 methyl group participated in each ring-closure. In hindsight, this outcome is plausible in light of the fact that such a reactive conformation would place the remaining prenyl group *trans* to the C12 methyl group, an arrangement that would correspond to a more favorable equatorial conformation for both groups on the cyclohexane ring. A few cursory modifications involving the introduction of the final C11–C12 alkene and global deprotection then provided the natural products **27** and **28** from these advanced intermediates **25** and **26**, respectively.[63]



Scheme 7. Stereoselective ring-closing-metathesis reactions in the total synthesis of coleophomones B (**27**) and C (**28**) (Nicolaou and co-workers, 2002).[62]

No fewer than six alkene ring-closing-metathesis reactions were used by Hirama and co-workers in their epic total synthesis of ciguatoxin CTX3C (**33**, Scheme 8).[64] Their convergent approach to the daunting polycyclic framework of this remarkable marine metabolite called for the synthesis of two separate fragments **29** and **30**, which correspond to the ABCDE- and HIJKLM-ring domains, respectively, followed by their late-stage union and subsequent formation of the final two ether rings. In the event, alkene ring-closing metathesis was employed in a diverse variety of settings, not only to construct rings A, D, and E in fragment **29**, but also, and perhaps rather less obviously, to forge rings I and J in the complementary hexacyclic fragment **30**. The successful union of the two domains **29** and **30** was then followed by a short sequence of steps to arrive at the advanced intermediate **31**. At this juncture the team was tantalizingly close to the target molecule and needed only to form the final (and thirteenth!) ether ring and then to liberate the three protected secondary hydroxy groups. That the formation of this nine-membered ring was left until the very end of the synthesis bears

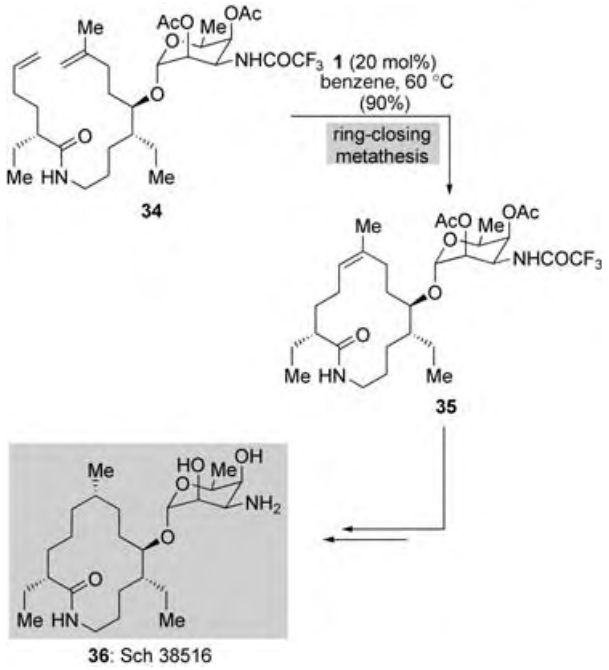
 © 2005 Wiley-VCH Verlag GmbH & Co. KGaA, Weinheim



Scheme 8. Multiple use of ring-closing-metathesis (RCM) reactions in the total synthesis of ciguatoxin CTX3C (**33**) (Hirama and co-workers, 2002).[64]

testament to the confidence placed by the team in the reliability of the ring-closing-metathesis reaction, trust which had no doubt been garnered in part by its successful implementation at many earlier points in the route. Indeed, it was found that the treatment of diene **31** with initiator **2** (30 mol %) in CH_2Cl_2 at reflux effected the desired cyclization in an astonishing yield of 90 %. Ironically, whereas the potentially troublesome formation of the nine-membered ring proceeded perfectly, it was, in fact, the final deprotection step that caused the team the most consternation. Originally, they had labored heroically to produce the corresponding tris(benzyl ether) **32**, which also underwent efficient ring-closing metathesis to form the corresponding nine-membered ring, only to witness the destruction of most of this precious material during its deprotection to afford the target product **33**, as this step could be achieved in a maximum yield of only 7 %. Thus, in their "second-generation" synthesis, the corresponding 2-naphthylmethyl ether protecting groups were employed, with it being anticipated (and, much to their relief, experimentally demonstrated) that the final deprotection event would proceed much more efficiently.[64b] Indeed, by changing the nature of the protecting groups, the efficiency of this final step was increased by nearly an order of magnitude, occurring in 63 % yield.

It could be argued that some of the most spectacular applications of alkene ring-closing metathesis have been in effecting macrocyclizations. Indeed, one of the first reported uses of a ring-closing-metathesis reaction in total synthesis was the remarkably efficient macrocyclization of diene **34** (Scheme 9), catalyzed by the Schrock molybdenum carbene **1**,

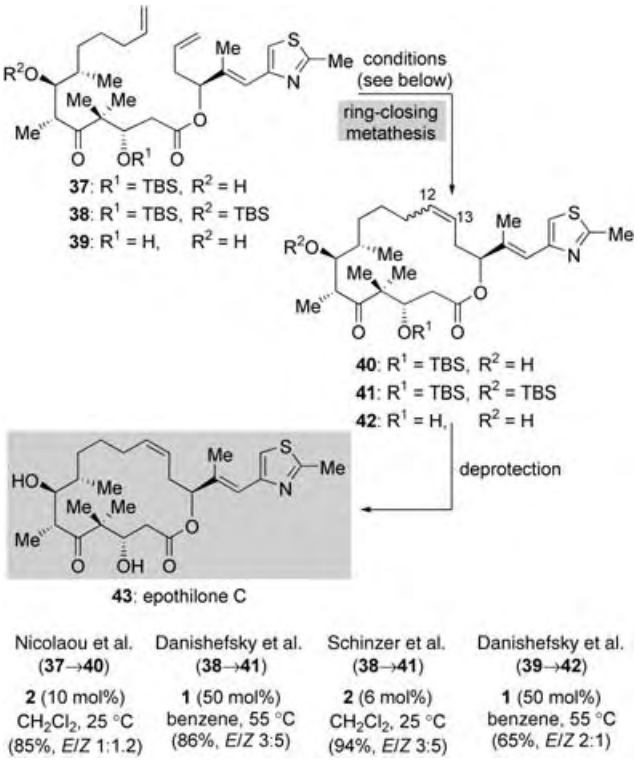


Scheme 9. Ring-closing metathesis in the total synthesis of Sch 38516 (**36**) (Hoveyda and co-workers, 1996).[65]

in the synthesis of the antifungal agent Sch 38516 (**36**) by the Hoveyda group.[65] Early applications such as this, which were admirably daring at the time and which are still noteworthy today, paved the way for more ambitious and challenging ring-closing-metathesis macrocyclizations, while at the same time providing insight into the essential parameters for successful macrocyclization.[66]

In particular, the first approaches to the total synthesis of epothilone C (**43**, Scheme 10) provided an early testing ground for ring-closing-metathesis macrocyclizations, and these studies served to highlight both the advantages and limitations of this methodology.[67] The first olefin-metathesis-based total synthesis of epothilone C (**43**) was reported by the Nicolaou group who, seeking to form the 16-membered macrocyclic ring by a route other than macrolactonization, anticipated that the power of ring-closing metathesis could potentially be employed to fashion the C12–C13 alkene in **40** from a precursor such as **37**. In those early days of the development of olefin metathesis in complex situations, however, several variables in the proposed transformation constituted unexplored territory in the metathesis landscape. Not only was the compatibility of the functionality in precursor **37**, in particular the unprotected hydroxy group and the thiazole unit, with the (then recently developed) ruthenium-based catalysts, such as **2**, questionable, but there were concerns over the stereochemical outcome of the

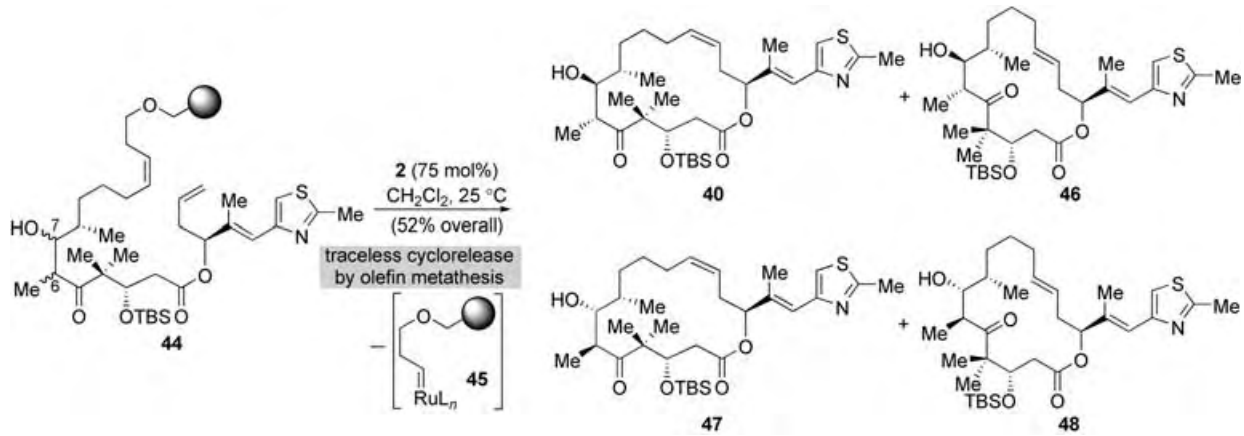
 © 2005 Wiley-VCH Verlag GmbH & Co. KGaA, Weinheim



Scheme 10. Ring-closing-metathesis reactions in the total synthesis of epothilone C (**43**) (Nicolaou and co-workers, 1997; Danishefsky and co-workers; 1997, Schinzer and co-workers, 1999).[68,69,71]

cyclization. Fortunately, these worries proved to be relatively unfounded, as exposure of **37** to the Grubbs catalyst **2** (10 mol%) in CH_2Cl_2 at ambient temperature for 20 h effected macrocyclization to **40**, which was obtained as a 1:1.2 mixture of *E*/*Z* isomers in 85% combined yield.[68] Standard cleavage of the lone silyl protecting group in **40** then afforded the targeted product **43**. While the team was amply satisfied with the overall conversion of **37** into **40**, they were nonetheless surprised to find the degree to which seemingly subtle modifications of the array of functionality situated on the backbone of the eventual macrocyclic system dictated the *E*/*Z* ratio of the resultant cycloalkene products. Parallel studies by both the Danishefsky[69,70] and the Schinzer groups,[71] in their explorations of the same type of ring-closing reaction, provided further evidence for this phenomenon. For example, the Danishefsky team showed that the stereoselectivity of the macrocyclization could be dramatically reversed, from being marginally *Z* selective (**38**→**41**) to displaying good *E* selectivity (**39**→**42**), simply by liberating the protected hydroxy groups prior to cyclization. In contrast, the comparable results obtained by the Schinzer group in their conversion of **38** into **41** and the Danishefsky group in their ring-closing metathesis of the same substrate indicates that, at least in this case, changing reaction parameters such as solvent, temperature, or even metathesis catalyst leads to the cycloalkene products in only a slightly altered ratio. In other situations this is often not the case, and changing these latter parameters can exert a drastic influence on *E*/*Z* selectivity.[72] Even though subsequent experimentation in numerous contexts has revealed that most metathesis-based macrocyclizations provide predominantly *E* alkenes,[73] the variability of these results should serve as a reminder that we still lack the ability to reliably predict (or achieve) product geometry for certain ring-closing-metathesis reactions in complex situations. Indeed, this sometimes unpredictable formation of stereoisomeric mixtures represents one of the few significant blots on the landscape of ring-closing-metathesis macrocyclization.

The Nicolaou group subsequently investigated solid-phase synthetic approaches to epothilone C (**43**), with the aim of applying metathesis technology in the context of combinatorial chemistry, in order to generate novel natural product analogues with which the molecular basis for the promising anticancer activity of the epothilones could be probed. To facilitate such screening of diverse epothilone-like structural congeners, these researchers sought to extend their original metathesis approach to generate libraries of analogues by utilizing the power of split-and-pool combinatorial synthesis.[74] In this regard, it was anticipated to fashion an intermediate such as **44** (Scheme 11), poised for a ring-closing-metathesis reaction, in which the tether between the epothilone scaffold and the solid support was appended to the



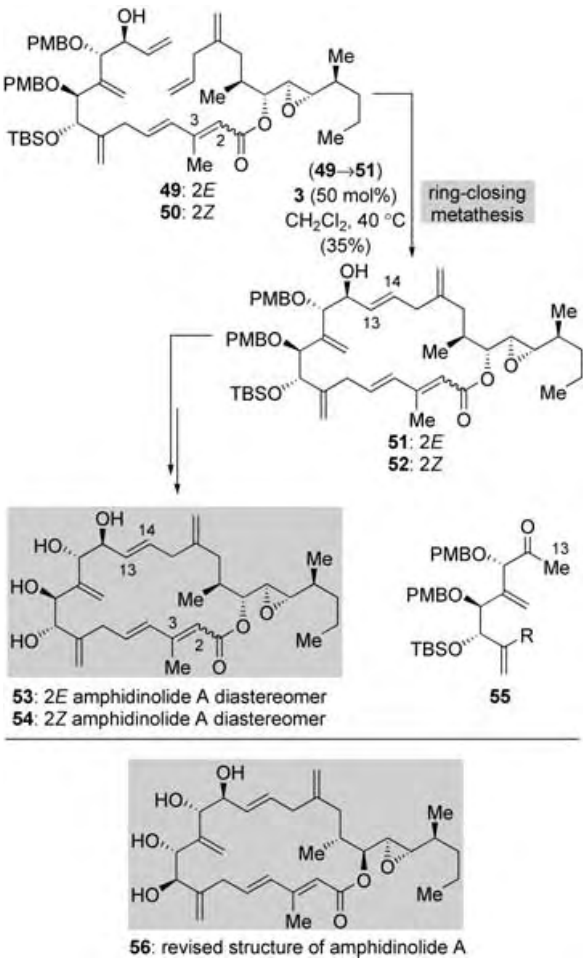
Scheme 11. Solid-phase synthesis of epothilone C and analogues through a ring-closing-metathesis cyclorelease strategy (Nicolaou and co-workers, 1997).[76]

 © 2005 Wiley-VCH Verlag GmbH & Co. KGaA, Weinheim

terminal position of one of the olefins that would ultimately participate in the key macrocycle-forming metathesis event. Although the increased steric hindrance imposed by incorporating the alkyl tether at this site could, conceivably, make metathesis more challenging to achieve, the benefits of linking in this manner would far outweigh any potential risk, as ring closure would be attended by traceless cleavage of the desired product from the resin, meaning that no remnants of the original tether that joined the epothilone scaffold to the polystyrene support would remain.[75] This result would be in contrast to most conventional solid-phase approaches, where some signature of the original tether (whether as a hydroxy group or other functional handle) usually remains following cleavage. Perhaps more significantly, appending the solid support in this mode would impart a safety feature to this cyclorelease strategy in that only material capable of undergoing metathesis would ultimately be freed from the resin. As such, any precursor that had not reacted properly during a step leading to **44** would remain attached, thereby ensuring that the products obtained from the metathesis reaction would not be contaminated with undesired by-products.

This strategy proved relatively easy to explore, with **44** being synthesized in short order. Following exposure of this intermediate to carbene initiator **2** in CH_2Cl_2 at ambient temperature, the desired metathesis-based cyclorelease was indeed effected in 52% overall yield over the course of 2 days.[76] However, the ruthenium complex is concomitantly "captured" by the resin during each cyclorelease event, hence the need for the high "catalyst" loading. At the end of this process, a mixture of four products, **40**, **46**, **47**, and **48**, was isolated. Their formation resulted from the anticipated lack of *Z*/*E* selectivity in the metathesis step combined with a 1:1 mixture of C6/C7 *syn* diastereomers within the starting material **44** from an earlier aldol addition. Fortunately, the polarity differences between these four compounds were sufficient to allow their separation by TLC or HPLC. Repetition of this sequence with novel building blocks then led to several hundred distinct analogues, whose biological screening established a clear structure–activity profile for the epothilones, ultimately paving the way for the rational design of novel epothilone-like structures with comparable or even higher antitumor activities than the parent natural product.

In the appropriate situations, however, ring-closing-metathesis macrocyclizations can proceed with excellent selectivity. One such example is found in the synthesis of the originally proposed structure of amphidinolide A (**53**, Scheme 12) by the Maleczka group in 2002.[77] Having arrived at the late-stage intermediate **49**, the team proposed to generate the macrocyclic ring and concomitantly install the C13–C14 1,2-disubstituted alkene through an alkene ring-closing-metathesis reaction. Given the array of alkene functionality contained within intermediate **49**, such a daring, late-stage metathesis step was not without obvious risks. The main question marks centered on the likelihood of actually being able to direct the reaction down the desired pathway, from amongst the plethora of metathesis opportunities available to the polyolefinic substrate, together with the degree of control of alkene geometry should the desired



Scheme 12. Ring-closing-metathesis reactions in the total synthesis of amphidinolide A stereoisomers (Maleczka and co-workers, 2002).[77]

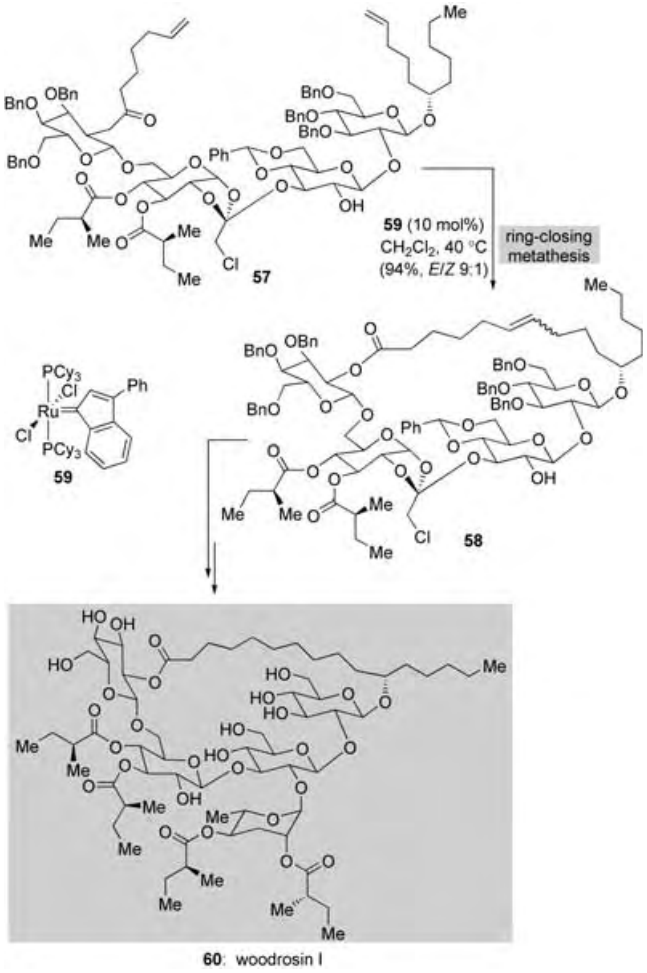
reaction indeed prove to be feasible. Much to their delight, the desired macrocyclization of **49** was effected by treatment of the substrate with the second-generation Grubbs ruthenium catalyst **3** in refluxing CH_2Cl_2. Although the ring closure occurred in only moderate yield (35%) and required a relatively high catalyst loading (50 mol%), no other metathesis products were observed. Furthermore, only the desired C13–C14 *E* isomer was formed. This ring closure had, in fact, first been attempted with the less reactive first-generation Grubbs ruthenium carbene **2** in the seemingly logical expectation that a less reactive metathesis catalyst would induce greater selectivity for the less hindered monosubstituted alkenes, and thus the desired C13–C14 metathesis. Surprisingly, exposure of substrate **49** to catalyst **2** merely truncated the allylic alcohol motif to generate the corresponding methyl ketone **55**.[78]

Unfortunately, the team's joy at effecting this macrocyclization was soon to be tempered by the realization that, following the straightforward deprotection of the cyclized product **51** to give the targeted compound **53**, their final product was not the same as natural amphidinolide A. In an effort to uncover the true identity of amphidinolide A, the team subsequently prepared a number of alternative stereoisomers of this structure. One of these compounds was the

 © 2005 Wiley-VCH Verlag GmbH & Co. KGaA, Weinheim

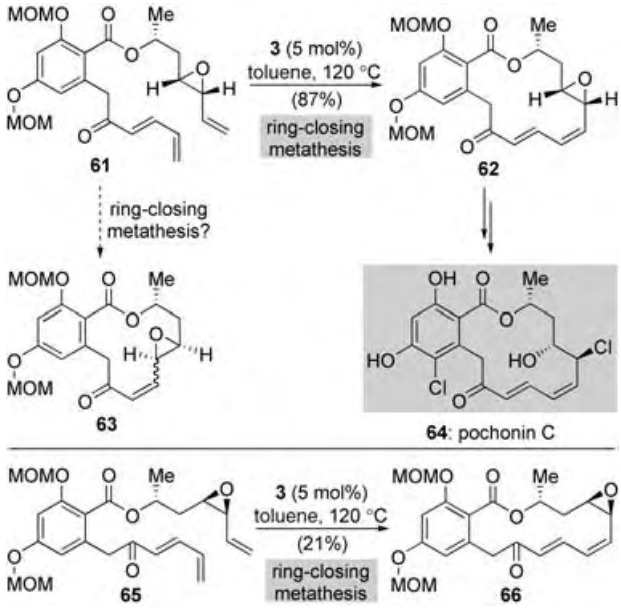
corresponding 2*Z* isomer **54**, which was synthesized through an analogous ring-closing-metathesis macrocyclization strategy. Interestingly, the ring closure of **50** to give **52** proved to be much more efficient proceeding in 88% yield (again with complete *E* selectivity) and requiring only 20 mol% of catalyst **3** to go to completion. This further illustrates the importance of substrate preorganization prior to ring closure. Despite the team's best efforts, however, the mystery surrounding the true structure of amphidinolide A would not be resolved for a further 2 years[79] when the Trost group would provide convincing evidence for its formulation being as compound **56**.[80,81]

In cases in which the stereochemical outcome of ring-closing metathesis is irrelevant (for example, when the resulting alkene system is hydrogenated to give the corresponding alkane), this methodology offers a particularly efficient and practical protocol for the formation of macrocyclic systems, and one which compares favorably with more-traditional methods of macrocyclization. A stunning example of the power of ring-closing metathesis to effect macrocyclization is the total synthesis of woodrosin I (**60**, Scheme 13) by the Fürstner group.[82,83] Having overcome a number of synthetic hurdles during the assembly of the oligosaccharide backbone present in precursor **57**, the team was gratified to find that the anticipated ring-closing-metathesis reaction proceeded smoothly upon exposure of this substrate to a 10 mol% loading of the novel phenylindenylidene complex **59** (championed by the Fürstner group as a useful alternative to the "first-generation" Grubbs catalyst **2**)[37d] in refluxing CH_2Cl_2. Macrocyclic product **58** was obtained in an astonishing yield of 94% (and as an inconsequential 9:1 mixture of *E*/*Z* isomers), with a short sequence of operations involving the hydrogenation of the newly formed alkene, attachment of the rhamnose moiety, and global deprotection, then completing this remarkable total synthesis.



Scheme 13. Ring-closing-metathesis macrocyclization in the total synthesis of woodrosin I (**60**) (Fürstner and co-workers, 2002).[82]

The applicability of ring-closing-metathesis reactions to form higher polyene systems (e.g. conjugated dienes and trienes) in macrocyclic rings has also come under close scrutiny in recent years. An instructive example of this is demonstrated in the total synthesis of pochonin C (**64**, Scheme 14), the most potent member of a small family of



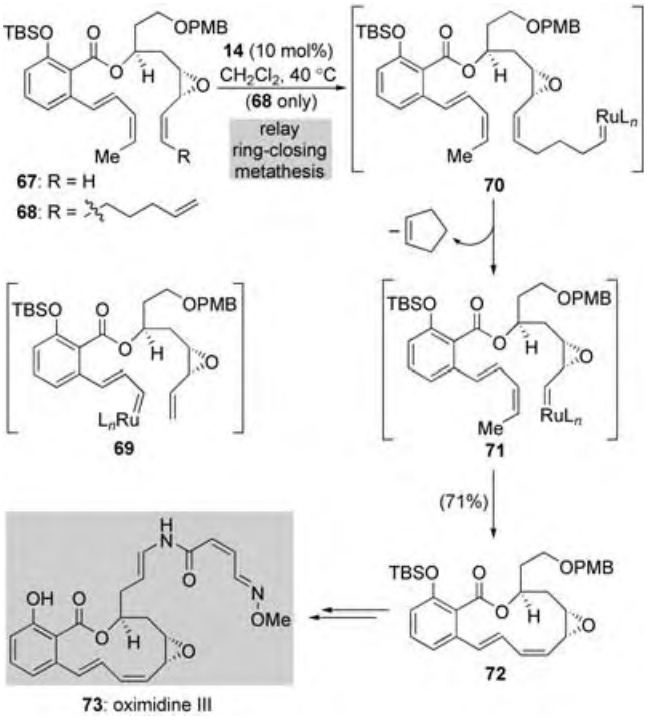
Scheme 14. Ring-closing metathesis to form a diene system in the total synthesis of pochonin C (**60**) (Winssinger and co-workers, 2004).[84]

novel antiviral natural products, reported by Winssinger and co-workers in 2004.[84] While a macrolactonization approach to the 14-membered ring present in the targeted compound **64** would certainly appear to be a viable strategy, these researchers were keen to investigate more modular approaches to the macrocyclic framework, and surmised that the characteristic *E*,*Z*-conjugated diene system could be formed through a ring-closing-metathesis reaction of triene **61**.[85] In addition to the customary questions regarding the stereochemical outcome (i.e. *E* vs. *Z*) of the macrocyclization event, in cases such as these there are also potential regioselectivity issues in that, depending on which double bond of the diene system is engaged in the metathesis event, either the desired diene product (e.g. **62**), or the truncated

 © 2005 Wiley-VCH Verlag GmbH & Co. KGaA, Weinheim

monoalkene product (e.g. **63**) could be formed.[86] Again, the outcome can be highly dependent on the reaction parameters, although the former regioselectivity pathway typically predominates. The Winssinger team found that exposure of triene **61** to the second-generation Grubbs catalyst **3** (5 mol%) in toluene at 120°C for 10 minutes (conditions previously developed by the Danishefsky group and shown to be particularly effective in related applications)[87] led to the formation of the required 14-membered ring product **62** as a single regio- and stereoisomer in 87% yield. From intermediate **62**, a few more steps were all that was required to complete the total synthesis of pochonin C (**64**). The influence of the epoxide configuration over the conformational organization of the open-chain metathesis precursor was made evident by the finding that the corresponding *cis*-epoxide **65** underwent metathesis-based ring closure in poor yield (21%), albeit again with excellent regio- and stereoselectivity.

The Porco group has applied the recently developed principle of "relay ring-closing metathesis"[88] to form the conjugated diene system contained within the macrolactone ring of oximidine III (**73**, Scheme 15).[89] Pioneered by the



Scheme 15. Relay ring-closing metathesis in the total synthesis of oximidine III (**73**) (Porco and co-workers, 2004).[89]

Hoye group,[90] relay ring-closing metathesis has been introduced as a means to enable otherwise sluggish (or entirely unsuccessful) ring-closing-metathesis reactions by moving the site of catalytic initiation away from points of steric hindrance and/or electronic deactivation within a precursor substrate. Thus, as is illustrated in Scheme 15, the addition of precursor **68** to a solution of the Hoveyda–Blechert catalyst **14** (10 mol%) in refluxing CH_2Cl_2 led to the formation of the desired macrocyclic product **72** in good yield (71%). The proposed mechanism of this transformation involves the initial reaction of the ruthenium carbene catalyst with the least hindered terminal double bond to generate carbene complex **70**. This intermediate can then undergo kinetically favorable ring-closing metathesis to extrude cyclopentene and generate the next intermediate **71**, which still contains a metal carbene species and which then undergoes macrocyclization to yield the observed product **72**. The clear superiority, in this instance, of the relay protocol over a conventional ring-closing-metathesis macrocyclization was demonstrated by the observation that when alkene **67** was subjected to the same metathesis conditions, the product **72** was formed in a meager yield of only 15%. In this case, the researchers proposed that the formation of carbene intermediate **69** from alkene **67** competed with the formation of intermediate **71**, with the former species **69** being a stabilized, unreactive ruthenium carbene which shuts down the catalytic cycle, resulting in the low yield. The conversion of precursor **68** into macrocyclic compound **72** was also found to be remarkably stereoselective, with the *E,Z*-diene system being formed exclusively. Having obtained the macrocyclic core of oximidine III (**73**) in this efficient manner, the team was able to manipulate the periphery to complete the total synthesis in a few more steps.[91]

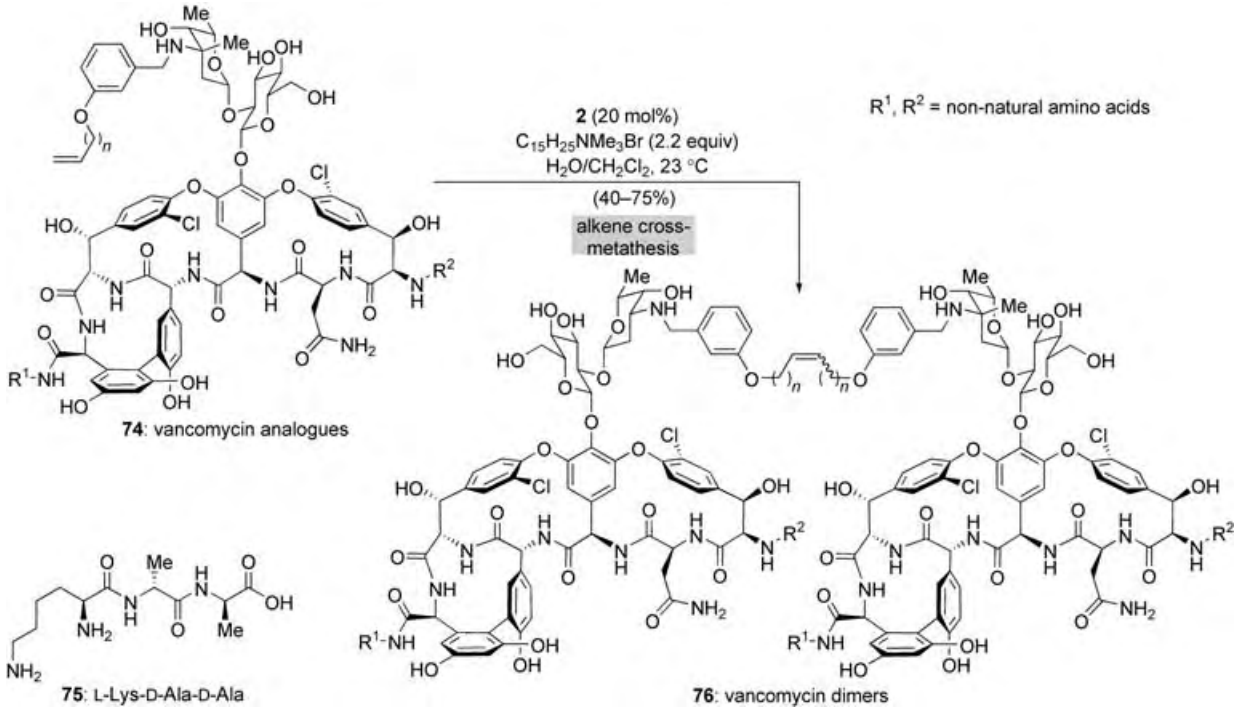
2.2. Alkene Cross-Metathesis

Alkene cross-metathesis has long been of great commercial importance to the industrial sector, but its transition to synthetically viable methodology in total synthesis has been a much more recent affair.[92] Alkene cross-metathesis represents a particularly appealing alternative to other transition-metal-mediated cross-coupling processes (e.g. the Stille or Suzuki reaction) in that readily available alkenes are employed, and no synthetic investment in the preparation of elaborated coupling partners (e.g. vinyl stannanes, vinyl halides, etc.) is required. Furthermore, the mild reaction conditions and functional-group tolerance of modern cross-metathesis often complements the more traditional olefination methods (e.g. the Wittig reaction). Despite its enormous potential for carbon–carbon bond formation, the widespread uptake of alkene cross-metathesis by synthetic chemists has lagged far behind that of the corresponding ring-closing processes. Indeed, until recently, many chemists' experience of cross-metathesis merely involved the unwanted formation of dimeric products arising from a disappointing ring-closing-metathesis event. The biggest challenge in cross-metathesis is the chemo- and stereoselective formation of the desired compound from amongst the myriad of potential reaction products. In this regard, it has been the recent advances in catalyst design, coupled with the development of empirical models for predicting the outcome of cross-metathesis reactions (largely due to the pioneering work of the Grubbs group),[93] that have emboldened chemists with the courage to commit their valuable intermediates to these processes. In return, they have been rewarded with new synthetic avenues and opportunities that were unthinkable even just a few years ago.

 © 2005 Wiley-VCH Verlag GmbH & Co. KGaA, Weinheim

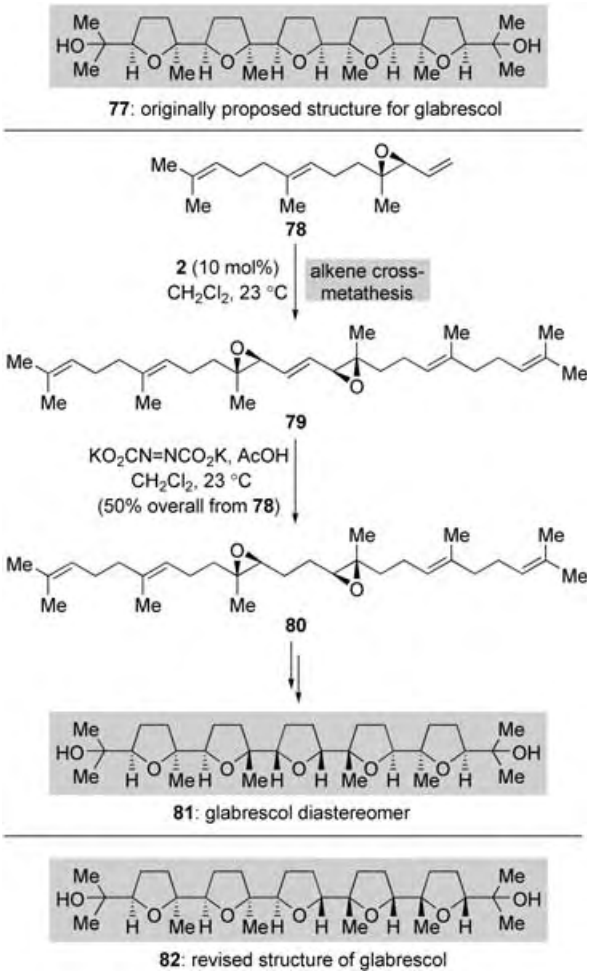
In the context of total synthesis, the applications of the olefin cross-metathesis reaction can be divided, somewhat arbitrarily, into two main classes: 1) chain-elongation processes, and 2) fragment-coupling reactions (including dimerization processes). As one example of the latter, we highlight the efforts of the Nicolaou group towards overcoming emerging bacterial resistance to vancomycin, the antibiotic currently considered to be the last line of defense against methicillin-resistant *Staphylococcus aureus* (MRSA).[94] The strategy entailed the use of alkene cross-metathesis reactions to effect the dimerization of vancomycin-type monomers such as **74** (Scheme 16) to give compounds of type **76**.[95,96] Indeed, during the past decade, several other clinically employed compounds have been dimerized, based on the notion that their biological activity would be enhanced.[97] Among several of the particularly noteworthy features of the developed cross-metathesis protocol to reach these agents (e.g. **76**), as shown in Scheme 16, was the employment of a phase-transfer agent ($C_{15}H_{25}NMe_3Br$) to encapsulate the ruthenium catalyst, and hence enable it to carry out its function in aqueous media at 23 °C. Because these reaction parameters are essentially ambient conditions, it was then decided to extend this initial homodimerization approach to include the selective formation of heterodimers by adding combinations of different substrates of type **74** in the presence of vancomycin's biological target, a terminal L-Lys-D-Ala-D-Ala peptide subunit **75**. Since it had already been established that two monomers of vancomycin could bind simultaneously (and reversibly) to this target through separate hydrogen-bonding networks,[98] this design assumed that those monomers within the collection of examined substrates that bound most tightly to this peptide chain would be captured by cross-metathesis as the corresponding dimer. As such, this approach should lead to the formation of highly active antibacterial agents. Upon execution of this target-accelerated combinatorial strategy, also referred to as dynamic combinatorial screening,[99] non-statistical distributions of dimers were formed. In each case, the compound with the greatest potency (based on synthesizing and testing all potential dimers separately) was the predominant product in each round of compound formation. Significantly, several of the agents prepared in this fashion by cross-metathesis demonstrated not only enhanced activity against MRSA relative to vancomycin, but also potency against several vancomycin-resistant bacterial strains.

Another dimerization-based cross-metathesis approach was employed by the Corey group in their quest to determine the correct structure of the polycyclic oxasqualenoid glabrescol.[100] The team had originally prepared compound **77** (Scheme 17), corresponding to the structure first proposed for the natural product, through a beautifully orchestrated biomimetic polyepoxide-cyclization strategy to fashion all five tetrahydrofuran rings in a single step and in a stereospecific fashion.[101,102] However, much to their dismay, the spectroscopic data of their synthetic material did not match that reported for the natural product.[103] The team was, therefore, faced with the task of having to synthesize a number of other possible stereoisomers, which could correspond to either the C_s- or C_2-symmetric nature of the natural product, before they could clear the ambiguity regarding the actual structure of glabrescol. One of the targeted stereoisomers was compound **81**, which, following their general polycyclization strategy, they hypothesized could be derived from bisepoxide **79**, the symmetrical nature of which lends itself to its preparation through a dimerization protocol.



Scheme 16. Dynamic combinatorial synthesis: the use of cross-metathesis to effect selective formation of vancomycin dimers (**76**) under ambient-like conditions in the presence of its biological target, L-Lys-D-Ala-D-Ala (Nicolaou and co-workers, 2001).[95]

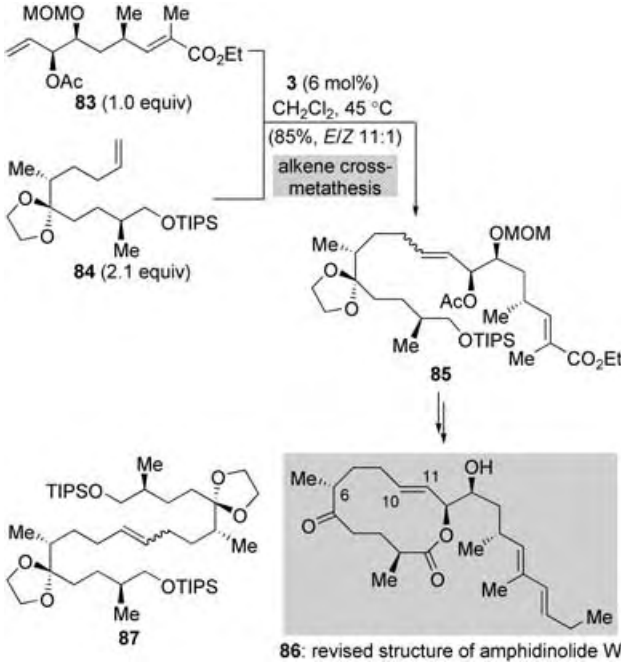
 © 2005 Wiley-VCH Verlag GmbH & Co. KGaA, Weinheim



Scheme 17. Dimerization through cross-metathesis in the total synthesis of a glabrescol diastereomer (**81**) (Corey and Xiong, 2000).[100]

Indeed, the team found that readily available epoxide **78** underwent selective cross-metathesis upon treatment with initiator **2** (10 mol%) in CH_2Cl_2 at ambient temperature to afford the coupled product **79**. Pleasingly, only the terminal alkene units participated in the metathesis event, with no interference from the more sterically hindered trisubstituted olefins. Furthermore, the reaction was also superbly stereoselective, with the *E*-isomeric product being formed exclusively, although in this context the stereoselectivity was irrelevant as the newly formed double bond was immediately reduced in the next step. The resulting product **79** was then elaborated to give the desired pentacyclic diol **81**. Unfortunately, the new synthetic material the team now had in their hands still did not correspond to natural glabrescol, and it would be only after a great deal of further synthetic effort that the true structure of the natural product would be revealed as **82**.[104–106]

An elegant example of the coupling of two different fragments by means of alkene cross-metathesis can be found in the total synthesis and structure revision of amphidinolide W (**86**, Scheme 18) by the Ghosh group.[81a] The strategy adopted by the researchers for the formation of the macrocyclic ring system involved the coupling of the two advanced

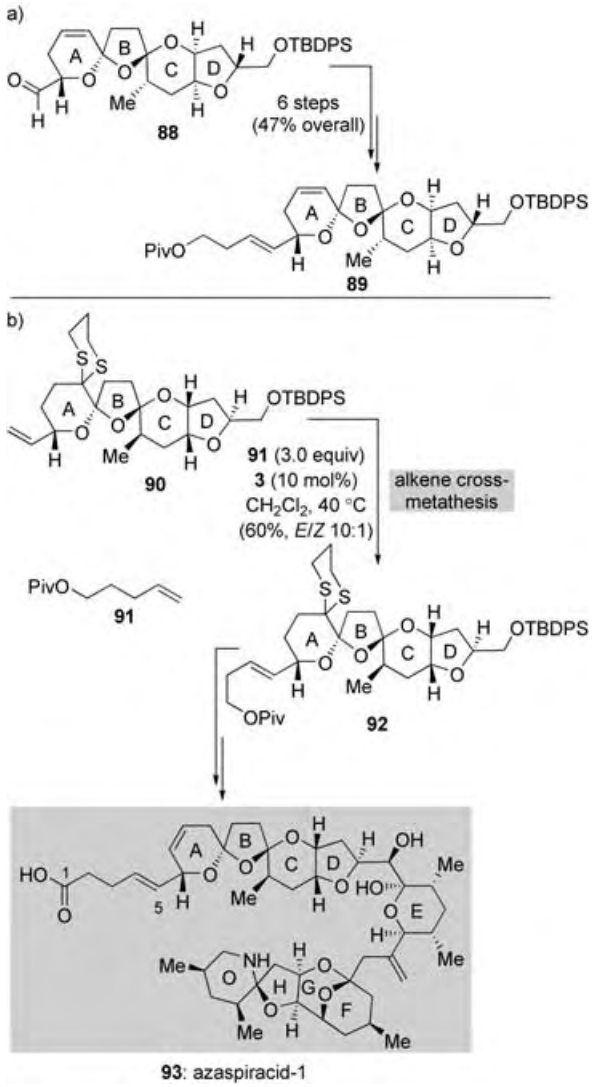


Scheme 18. Fragment coupling through cross-metathesis in the total synthesis of the revised structure of amphidinolide W (**86**) (Ghosh and co-workers, 2004).[81a]

intermediates **83** and **84** through alkene cross-metathesis (with the concomitant installation of the C10–C11 olefin), followed by a late-stage macrolactonization. To their delight, the cross-metathesis between **83** and **84** proceeded smoothly over the course of 15 h upon the addition of catalyst **3** (6 mol%) to a refluxing solution of the two components in CH_2Cl_2, affording the desired product **85** in excellent yield (85%) and with good *E* selectivity (*E*/*Z* 11:1). An excess of alkene **84** was required, as this substrate underwent competitive homodimerization to give compound **87** (which was itself inert to secondary metathesis reactions). Furthermore, it was found that the specific employment of an acetate protecting group for the allylic secondary hydroxy group in coupling partner **83** was required for optimum results. With an efficient, modular approach to compound **85** now at their disposal, the researchers were able to advance this key intermediate over a number of steps to complete the total synthesis of the revised structure **86** of the targeted natural product.[107]

Alkene cross-metathesis was efficiently used as a means of chain elongation in the recent enantioselective synthesis of the revised structure of azaspiracid-1 (**93**, Scheme 19) by the Nicolaou group.[108] Previously, in the course of their synthesis of the originally proposed structure of this remarkable marine neurotoxin (which was subsequently shown to be incorrect), the team employed a six-step sequence to append the C1–C5 unsaturated side chain onto the ABCD-ring intermediate **88** (Scheme 19a).[109] While each individual step proceeded smoothly and in high yield, the somewhat laborious nature of this sequence prompted the team to consider other, more direct methods for the incorporation of this motif. The presence of the 1,2-disubstituted double bond in this side

 © 2005 Wiley-VCH Verlag GmbH & Co. KGaA, Weinheim

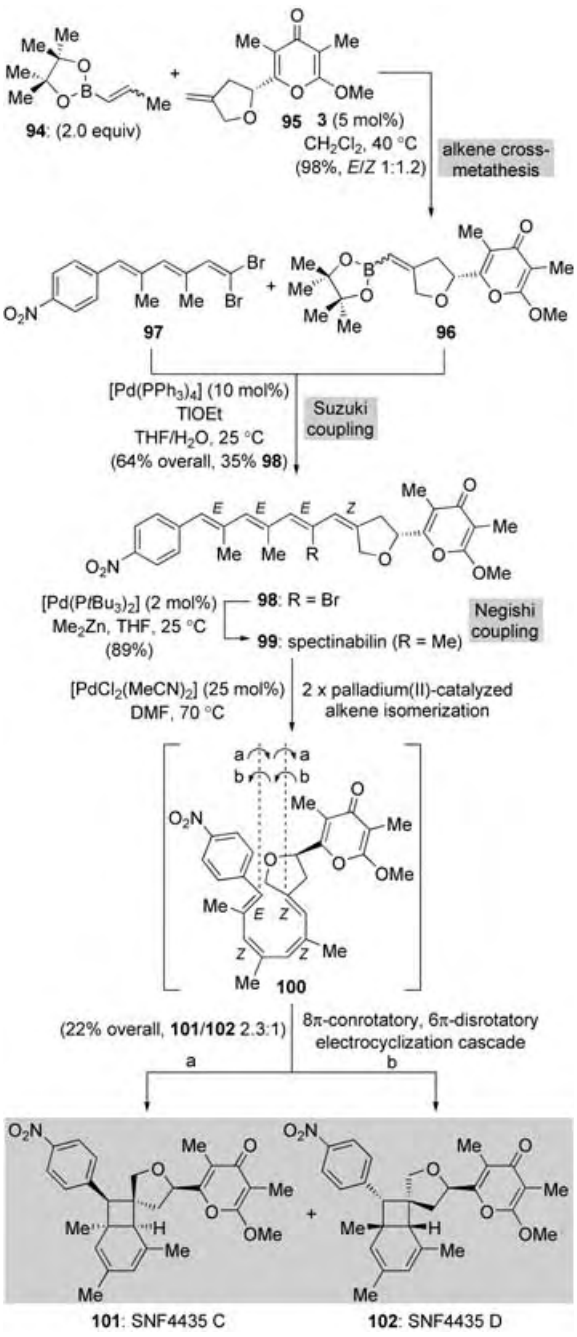


Scheme 19. Introduction of the C1–C5 side-chain in the total synthesis of azaspiracid-1: a) six-step route in the synthesis of the originally proposed structure; b) single-step alkene cross-metathesis approach in the synthesis of the revised structure **93** (Nicolaou and co-workers, 2004).[108]

chain invites the possibility of its construction in a single step through alkene cross-metathesis, and indeed this was the method adopted in the final drive towards the revised structure of the natural product. Thus, exposure of a mixture of tetracyclic compound **90** and the readily available alkene **91** (used in excess) in refluxing CH_2Cl_2 to the second-generation catalyst **3** (10 mol%) resulted in the formation of the desired product **92** in 60% yield and with good stereoselectivity (*E*/*Z* 10:1, isomers readily separable by column chromatography; Scheme 19b). Most of the mass balance of this reaction consisted of unconverted starting material **90**, which could be recovered and resubjected to the reaction conditions. After three cycles, the total yield of **92** was 95%, which represented a considerable increase in both efficiency and elegance over the original six-step route.[110] Notably, the dithiane functionality did not interfere with the cross-metathesis by sequestering the catalyst **3**, further illustrating the remarkable functional-group tolerance of this ruthenium complex.

An exceedingly useful characteristic of the cross-metathesis protocol for chain elongation is that it can be employed for the concomitant generation of functionalized reagents that can be engaged in subsequent reactions to produce further molecular complexity. This is particularly beneficial when it provides access to reagents that could not be readily obtained by other methods. A stunning example of this concept, which furthermore demonstrates both brilliance in synthetic planning and the phenomenal enabling ability of modern transition-metal-mediated cross-coupling reactions, is the biomimetic synthesis of the immunosuppressant agents SNF4435 C (**101**) and SNF4435 D (**102**, Scheme 20) by Baldwin and co-workers.[111] The bicyclo[4.2.0]octadiene core structure of these architecturally unique natural products has been proposed to arise through a sequential 8π-conrotatory/6π-disrotatory electrocyclization cascade of the *Z*,*Z*,*Z*,*E* tetraene precursor **100**.[112] The viability of this hypothesis was experimentally verified by Parker and Lim who, in the preparation of tetraene **100** through a fragment-coupling Stille reaction, observed its rapid and spontaneous rearrangement to generate a mixture of **101** and **102** in a ratio closely matching that of the compounds found in Nature.[113] Furthermore, related electrocyclization cascades had been proposed as key steps in the biosynthesis of the endiandric acids by Black and co-workers[114] and subsequently demonstrated experimentally by the Nicolaou group[115] more than two decades earlier. However, Baldwin and co-workers noted the striking similarity between tetraene **100** and spectinabilin (**99**), the latter being a known natural product isolated from the same producing species (*Streptomyces spectabilis*) more than 25 years earlier by Rinehart and co-workers.[116] Indeed, the two compounds differ only in the geometry of the two central double bonds in their respective tetraene systems, thus leading the Baldwin group to the intriguing proposal that a key intermediate in the biogenesis of SNF4435 C (**101**) and SNF4435 D (**102**) is, in fact, spectinabilin (**99**), which undergoes an initial double alkene isomerization to give *Z*,*Z*,*Z*,*E* tetraene **100**, followed by the electrocyclization cascade.[117] From a synthetic point of view, this proposal is appealing because it should, in principle, be easier to construct a *Z*,*E*,*E*,*E* tetraene system (as in **99**) than the corresponding *Z*,*Z*,*Z*,*E* motif (as in **100**). The issue would then become whether the double isomerization of spectinabilin (**99**) could be effected selectively. Much to their delight, the team found that this biosynthetic proposal could, indeed, be reduced to practice, and the key steps in the synthesis are illustrated in Scheme 20. Thus, following a protocol developed by Grubbs and Morrill,[118] the cross-metathesis of vinyl boronate **94** with disubstituted alkene **95** generated the corresponding product **96** in excellent yield, albeit with moderate stereoselectivity ($E/Z \approx 1{:}1.2$). This methodology offers a convenient approach for the preparation of synthetically useful vinyl boronate species, such as **96**, which would be inaccessible by more conventional means (e.g. hydroboration of alkynes).[119] The selective Suzuki coupling of boronate **96** (as a mixture of *E*/*Z* isomers) with the *E* vinyl bromide moiety in dibromide **97** occurred with retention of stereochemistry with respect to

 © 2005 Wiley-VCH Verlag GmbH & Co. KGaA, Weinheim

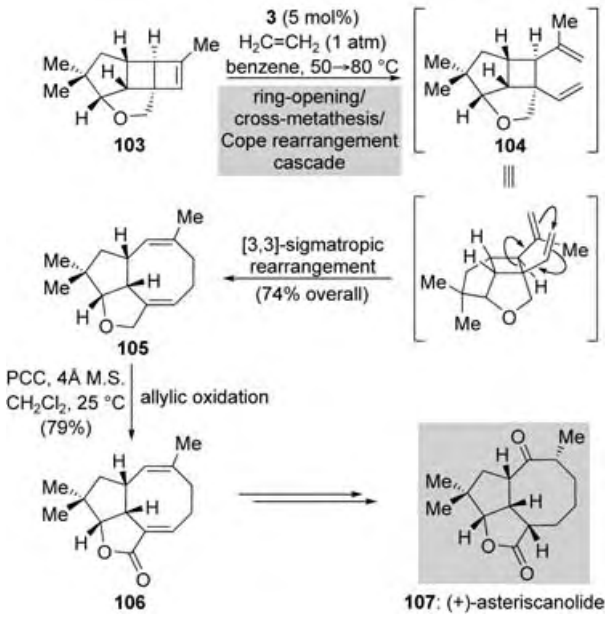


Scheme 20. Multiple use of transition-metal-catalyzed carbon–carbon bond-forming reactions in the total synthesis of SNF4435 C (**101**) and SNF4435 D (**102**) (Baldwin and co-workers, 2004).[111]

both coupling partners,[120] and was followed by separation of the resulting 1:1.2 mixture of stereoisomers to give the desired bromide **98** in 35% overall yield from **96**. A stereospecific Negishi coupling of bromide **98** with Me_2Zn, catalyzed by the commercially available 14-electron complex $[Pd(PtBu_3)_2]$,[121] then afforded spectinabilin (**99**). Finally, exposure of synthetic **99** to $[PdCl_2(MeCN)_2]$ (25 mol%) in DMF at 70°C initiated the novel isomerization/electrocyclization cascade, ultimately producing the target compounds **101** and **102** in a 2.3:1 ratio.[122] Although the overall yield for this cascade process was modest (22%), it nevertheless represents an important proof of principle. While the promotion of the initial double isomerization by a palladium(II) species can hardly be considered to be "biomimetic" in its own right, it is not unreasonable to speculate that Nature has her own complementary methods for effecting such a transformation. This remarkable total synthesis, in which all the key carbon–carbon bond-forming reactions employed transition-metal catalysis, stands as a powerful testament to the current state of the art of metathesis and cross-coupling reactions in contemporary organic synthesis.

2.3. Alkene Metathesis in Cascade Processes

The utility of alkene metathesis extends far beyond merely effecting individual ring-closing or cross-metathesis events, which necessarily generate only one new productive carbon–carbon linkage. The incorporation of metathesis steps into cascade processes has received a burgeoning level of attention in recent years, a trend that is likely to expand in the future, particularly in terms of combining metathesis with other reactions in the current synthetic repertoire. One such application is seen in the recent total synthesis of (+)-asteriscanolide (**107**, Scheme 21) by Limanto and Snapper,



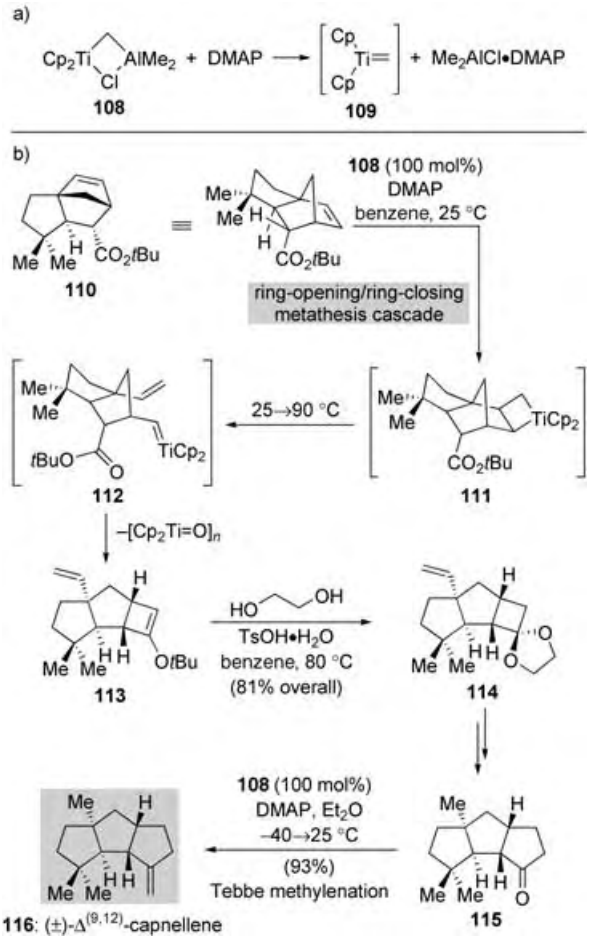
Scheme 21. A ring-opening/cross-metathesis/Cope rearrangement cascade in the enantioselective total synthesis of (+)-asteriscanolide (**107**) (Snapper and Limanto, 2000).[123]

which features the use of a novel ring-opening cross-metathesis/Cope rearrangement strategy to fashion the characteristic tricyclic core structure of the natural product.[123] The primary synthetic target was tricyclic lactone **106**, as this compound had previously been elaborated to the natural product by Wender and co-workers in their pioneering total synthesis of **107**.[124] Limanto and Snapper found that treatment of the highly strained cyclobutene **103** with catalyst **3** (5 mol%) in benzene under an ethylene atmosphere initially

 © 2005 Wiley-VCH Verlag GmbH & Co. KGaA, Weinheim

effected the selective ring-opening cross-metathesis to afford the presumed intermediate **104**, which under the reaction conditions underwent a [3,3]-sigmatropic rearrangement to yield tricyclic compound **105** in 74% overall yield. In this cleverly designed process, both the metathesis and Cope rearrangement steps enjoy the thermodynamic driving force provided by the relief of ring strain upon fragmentation of different four-membered rings. The uneventful allylic oxidation of product **105** then completed the concise synthesis of the desired lactone **106**, which was then converted into the natural product following the protocol of Wender and co-workers.[125] Cascade reactions that involve a metathesis step in combination with a number of other different transformations, including cycloadditions and Heck reactions,[126] have also been reported.

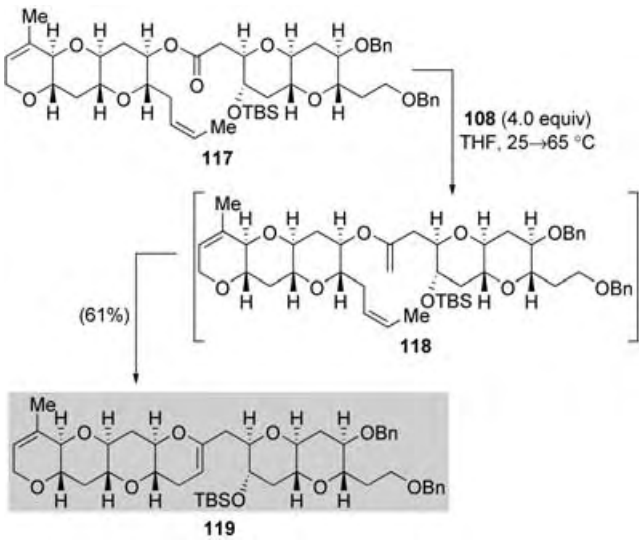
Alternative strategies involve the design of substrates that can undergo consecutive metathesis reactions in a single step. A beautiful early example of this type of protocol can be found in the expeditious synthesis of (±)-$\Delta^{(9,12)}$-capnellene (**116**, Scheme 22) by the Grubbs group,[127] also highlighting one of the rare applications of the Tebbe reagent (**108**) in a metathesis-based context in total synthesis. First introduced by Tebbe and co-workers in 1978,[128] titanocene complex **108** undergoes reversible elimination of Me_2AlCl (the latter can then be sequestered by a mild base, in this case DMAP) to generate the reactive titanium methylene intermediate **109** (Scheme 22a). For preparative purposes, intermediate **109** can undergo two main types of reaction: 1) olefination of organic carbonyl-containing compounds (including esters and amides) to give Wittig-type methylenated products[129] and 2) reaction with alkenes to form metallacycles that can be used as catalysts in alkene metathesis.[130] From an historical perspective, the reported metathesis activity of carbene **109** predates the development of both the molybdenum- and ruthenium-based catalysts such as **1**, **2**, and **3**.[131] However, the reactivity profile of carbene **109** is such that it reacts with almost all other functional groups in preference to alkenes, accounting for why it is currently widely employed to methylenate carbonyl compounds, but is not a popular catalyst to initiate the metathesis of complex molecules. In the present case, however, the combination of steric hindrance around the *tert*-butyl ester carbonyl group and the increased reactivity of the strained norbornene-type alkene inverts the usual reactivity pattern such that titanium carbene **109** reacts preferentially with the latter motif present in bridged bicyclic compound **110**, at ambient temperature, to afford metallacyclobutane **111** (Scheme 22b). The remarkable regioselectivity of this step had been anticipated by the workers on the basis of model studies and is likely the result of steric effects. Upon heating the solution of this newly formed intermediate to 90 °C, a productive cycloreversion ensued to form the new titanium carbene species **112**, which in a display of its alternate mode of reactivity, reacted with the proximal carbonyl group to afford the observed product **113**. Owing to the sensitivity of the cyclobutene enol ether, this product was immediately protected and isolated as the corresponding ketal **114**, in 81% overall yield from **110**. Although necessarily stoichiometric in the titanium complex **108**, this reaction nevertheless effected the high-yielding conversion of a readily available starting material into an advanced intermediate, which required only a few more steps to reach the targeted compound **116**. Interestingly, the last of these steps called for the methylenation of ketone **115** to give the corresponding exocyclic olefin; again, the use of the Tebbe reagent resulted in an excellent yield.[132,133]



Scheme 22. Titanium methylidene reagents: a) generation from the Tebbe reagent (**108**), b) use in a ring-opening-/ring-closing-metathesis cascade in the total synthesis of (±)-$\Delta^{(9,12)}$-capnellene (**116**) (Grubbs and Stille, 1986).[127]

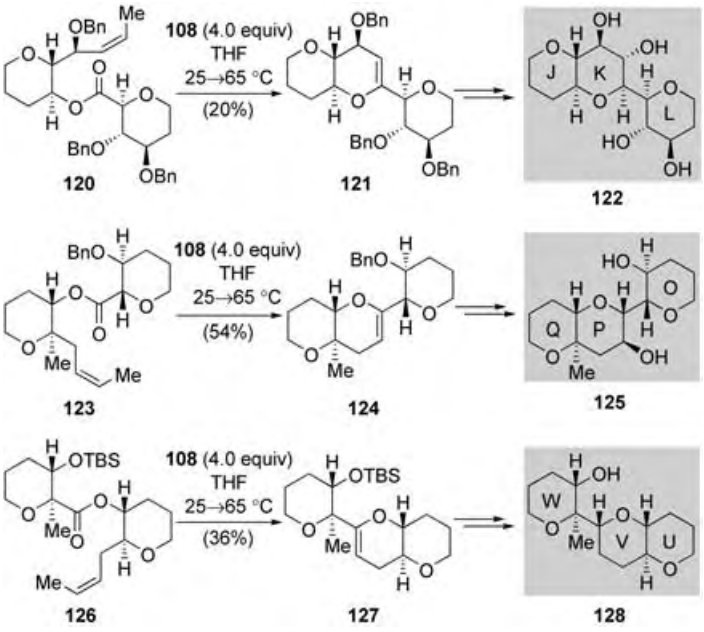
The Nicolaou group has developed a number of novel approaches to the synthesis of complex polyether frameworks through tandem metathesis reactions. One such protocol makes efficient use of the multifunctional reactivity of titanium carbene complexes as described above to effect tandem methylenation/alkene ring-closing metathesis, a representative example of which is illustrated in Scheme 23.[134] In this case, the sequence is believed to commence with the initial methylenation of the ester carbonyl group (i.e. **117**→**118**), based on the established general preference of this reagent to engage carbonyl functionalities before alkenes. With excess Tebbe reagent in solution, however, subsequent alkene metathesis between the newly generated alkene and its neighboring partner can ensue at elevated temperature (i.e. **118**→**119**). Since the initial disclosure of this transformation, the developed technology has been applied to several of the ring systems embedded within the structure of

 © 2005 Wiley-VCH Verlag GmbH & Co. KGaA, Weinheim

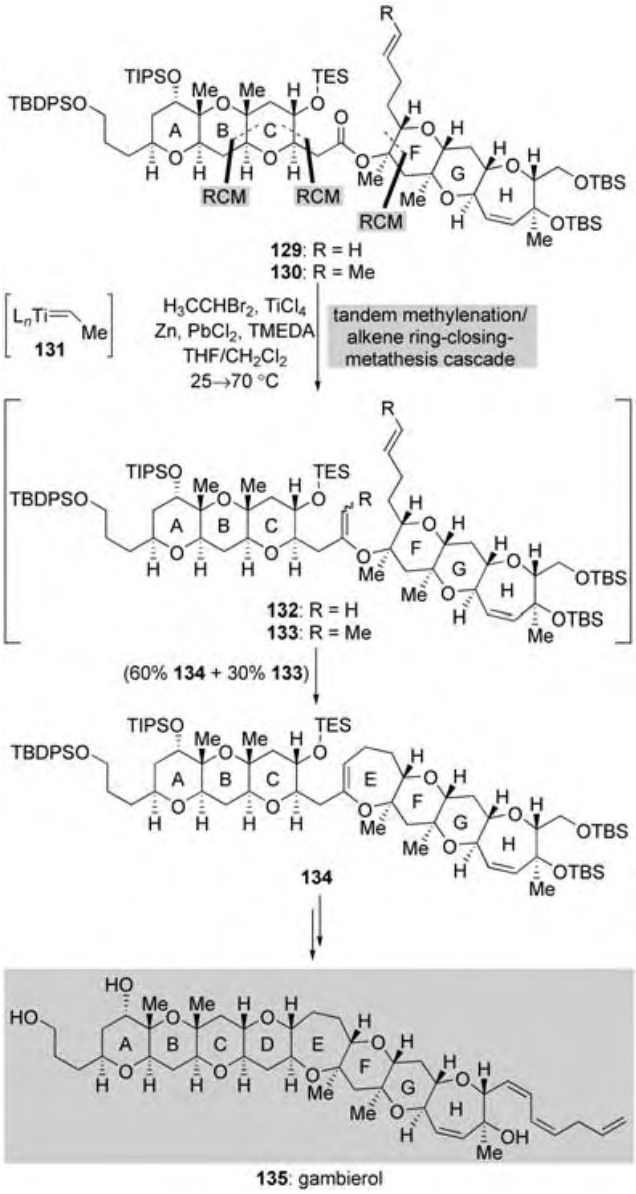


Scheme 23. The synthesis of complex polyether frameworks through tandem methylenation/ring-closing metathesis: proof-of-principle (Nicolaou and co-workers, 1996).[134]

the complex marine natural product maitotoxin (Scheme 24).[135] Rainier and co-workers subsequently made use of this type of tandem methylenation/ring-closing metathesis cascade sequence in their recent total synthesis of the polyether toxin gambierol (**135**, Scheme 25).[136] The convergent strategy adopted by these researchers initially called for the syntheses of separate ABC- and FGH-ring-containing fragments, followed by their union through an intermolecular esterification reaction. Ring-closing-metathesis reactions of enol ethers were instrumental in forging these subunits, used



Scheme 24. The synthesis of complex polyether frameworks through tandem methylenation/ring-closing metathesis: application to the JKL-, OPQ-, and UVW-ring systems of maitotoxin (Nicolaou and co-workers, 1996).[135] For the complete structure of maitotoxin, see reference [135].



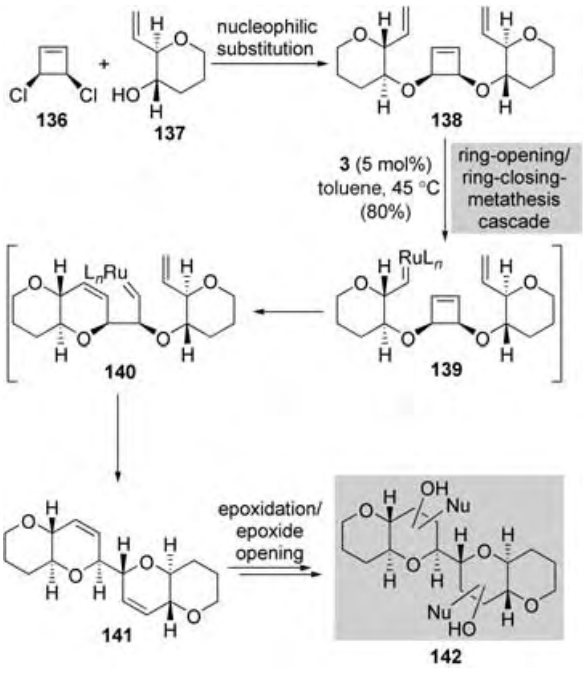
Scheme 25. The synthesis of complex polyether frameworks through tandem methylenation/ring-closing metathesis: application to the total synthesis of gambierol (**135**) (Rainier and co-workers, 2005).[136]

as they were to construct the B-, C-, and F-rings.[137] The fashioning of the F-ring by ring-closing metathesis was particularly noteworthy in light of the fact that it entailed the formation of a crowded tetrasubstituted alkene. Having arrived at the key hexacyclic intermediate **129**, the team had originally planned on closing the seven-membered E-ring to give compound **134** through a two-step process involving a Tebbe-type methylenation, which would generate enol ether **132**, followed by a separate ring-closing-metathesis event. Unfortunately, and to their dismay, they were unsuccessful in all their efforts at converting ester **129** into acyclic enol ether metathesis precursor **132** using the Takai–Utimoto titanium methylidene protocol.[138] Far from heralding the dismantlement of the synthetic

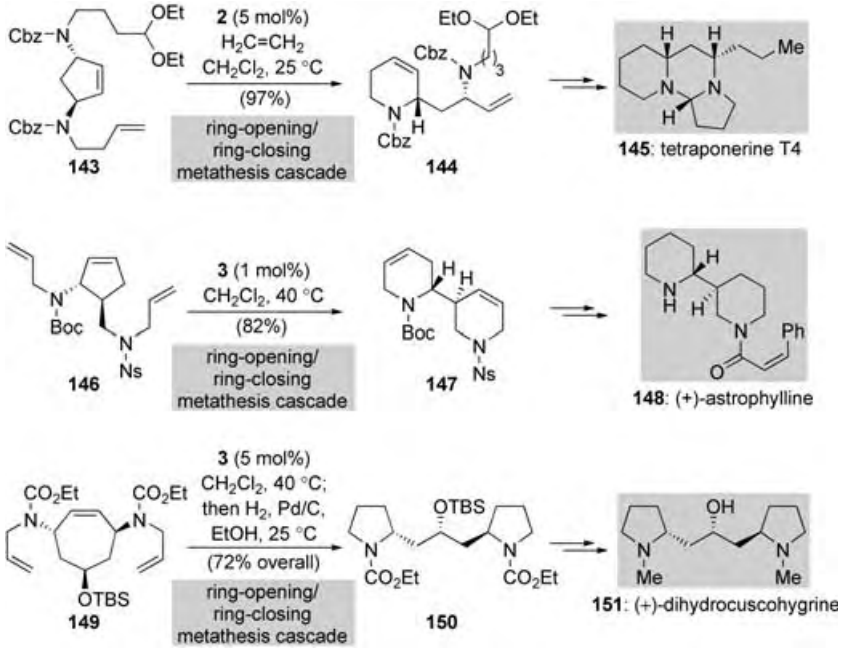
 © 2005 Wiley-VCH Verlag GmbH & Co. KGaA, Weinheim

route, this misfortune inspired the team to investigate other methods for effecting the olefination of this ester carbonyl group. Eventually, and after much experimentation, they made the serendipitous and joyful discovery that subjecting ester **130**, which bore a different alkene-containing side-chain, to the modified Takai–Utimoto conditions shown (ostensibly to generate the corresponding substituted enol ether **133** through the intermediacy of the titanium alkylidene **131**) led to the formation of cyclic enol ether **134** in 60% yield! Furthermore, the expected product **133** was also isolated as a side product in 30% yield, and independently subjected to a ring-closing-metathesis reaction in the presence of the second-generation Grubbs catalyst **3**, also to afford cyclic product **134** in a yield of 60%. Having bypassed this synthetic roadblock in an unexpected manner, these researchers were then able to complete the total synthesis in only a few more steps.[139]

Another protocol developed by the Nicolaou group makes use of a cyclobutene scaffold as a template for tandem metathesis reactions. Thus, as is shown in Scheme 26, treatment of readily available cyclobutene-1,2-diol derivative **138** with the second-generation ruthenium catalyst **3** (5 mol%) in toluene at 45°C effected its smooth conversion into the corresponding tetracyclic compound **141**, with complete transfer of chirality from the original cyclobutene ring to the newly formed pyran systems.[140] Interestingly, and despite close precedent for analogous metathesis reactions with less-hindered substrates,[141] the first-generation catalyst **2** failed to induce the desired reaction in the present case. An alternative mechanism involving initiation at the cyclobutene alkene unit cannot be excluded. It should be recalled that all the steps in the catalytic cycle (and thus, in principle, the overall transformation) are reversible. However, there is a powerful thermodynamic driving force in this type of process that benefits from both entropic (release of ethylene) and enthalpic (release of ring strain) factors. The utility of this cascade process was extended beyond ring formation by the fact that the diolefinic product **141** could be subjected to epoxidation and subsequent stereospecific epoxide-opening reactions with a variety of nucleophiles. Such a route constitutes rapid and flexible access to complex molecular frameworks, which could easily be modified to produce tailor-made intermediates for total synthesis, or compound libraries for biological screening. These types of cascade processes, which involve sequential ring-opening and ring-closing metathesis reactions, have been termed "ring-rearrangement metatheses". Their use in target-oriented synthesis has been championed in particular by the Blechert group, who has applied them to the elegant syntheses of a variety of structurally diverse alkaloid natural products, including tetraponerine T4 (**145**, Scheme 27),[142] (+)-astrophylline (**148**),[143] and (+)-dihydrocuscohygrine (**151**).[144]

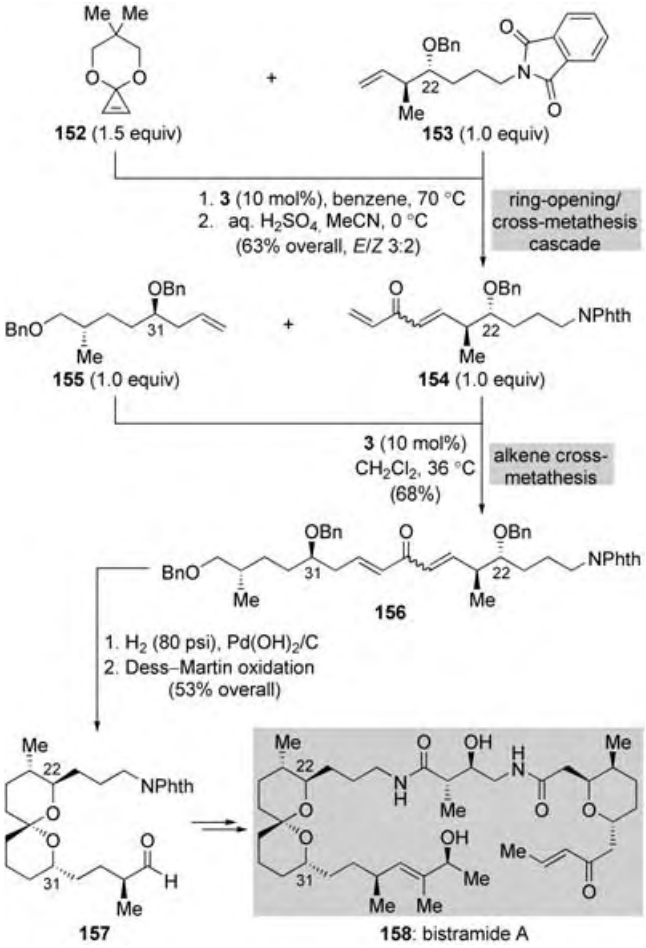


Scheme 26. A ring-opening-/ring-closing-metathesis cascade in the stereocontrolled synthesis of polyether frameworks (**142**) (Nicolaou and co-workers, 2001).[140]



Scheme 27. Ring-rearrangement metathesis reactions in the total syntheses of tetraponerine T4 (**145**), (+)-astrophylline (**148**), and (+)-dihydrocuscohygrine (**151**) (Blechert and co-workers, 2000, 2003, 2002).[142–144]

In a variation on this theme, a ring-opening/cross-metathesis cascade reaction featured prominently in the recent synthesis of the protein kinase C activator bistramide A (**158**,

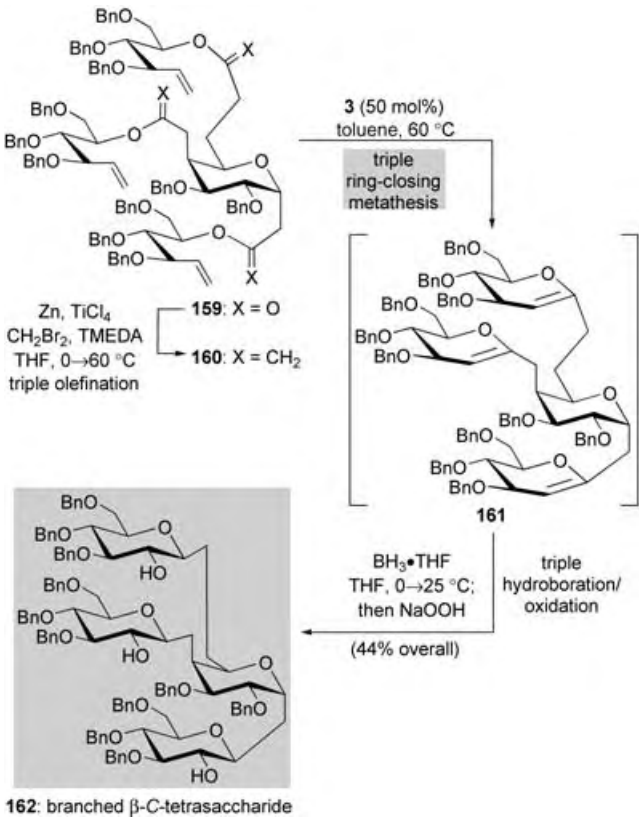


Scheme 28. Multiple use of alkene cross-metathesis reactions in the enantioselective total synthesis of bistramide A (**158**) (Kozmin and co-workers, 2004).[145]

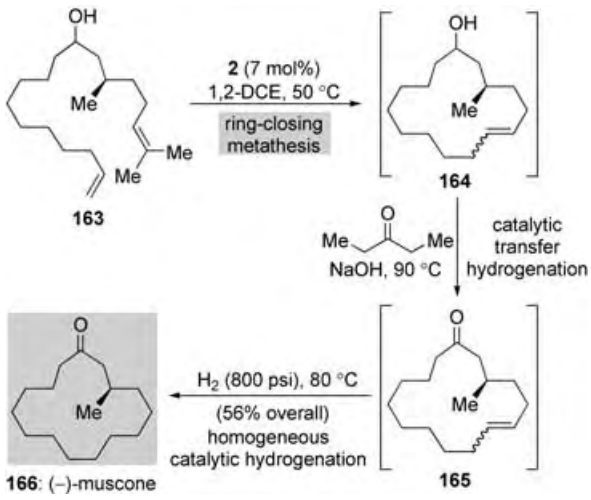
Scheme 28) by Kozmin and co-workers.[145] The first key carbon–carbon bond-forming reaction in their inventive approach to the spiroketal domain of the targeted product involved the treatment of a mixture of terminal alkene **153** and a slight excess (1.5 equiv) of cyclopropene acetal **152** with second-generation ruthenium catalyst **3** (10 mol%) in benzene at 60 °C to afford, after acidic hydrolysis of the crude product mixture to effect the cleavage of the acetal protecting group, divinyl ketone **154**. The stereoselectivity of this reaction was poor, with the product being formed as a 3:2 mixture of *E*/*Z* isomers, but fortunately this was irrelevant in the context of this synthesis (see below). This ring-opening/cross-metathesis cascade follows the same principles as illustrated earlier in the synthesis of (+)-asteriscanolide **107** (see Scheme 21), except that in this case a substituted alkene is employed as the coupling partner instead of ethylene. As with the corresponding cyclobutenes, cyclopropenes make excellent participants in ring-opening-metathesis processes owing to the enormous relief of ring strain. It should be noted that, unlike the ring-opening/ring-closing metathesis cascade described in Scheme 26, this particular type of tandem process is atom economical (i.e. no ethylene is released), and thus largely driven by enthalpic factors, which must overcome the negative entropic factors (i.e. two molecules being combined into one). The α,β-unsaturated system generated within product **154** readily lends itself to further manipulation, and indeed the very next step involved an intermolecular fragment-coupling/cross-metathesis reaction between **154** and alkene **155**, again catalyzed by ruthenium complex **3**, to afford the expected product **156** in 68% yield. Interestingly, the corresponding acetal obtained before the acidic hydrolysis step proved to be inert towards subsequent metathesis, which may also go some way towards explaining the exclusive formation of the mono-cross-coupled product in the first metathesis step. Although the stereoselectivity of this process was again irrelevant, only a single geometrical isomer (*E*) was generated at the new linkage. Significantly, this cross-metathesis proceeded efficiently, employing only 1 equivalent of each coupling partner, whereas many cross-metatheses require one of the components to be used in an (often large) excess. High-pressure hydrogenation of the stereoisomeric mixture of **156** effected the cleavage of the three benzyl protecting groups, saturation of the two disubstituted alkenes and concomitant stereoselective spiroketalization in one pot. Subsequent Dess–Martin oxidation of the resulting primary alcohol afforded aldehyde **157**. The team thus had a remarkably concise and efficient route to the key spiroketal fragment **157** from which they were able to complete the total synthesis of (+)-bistramide (**158**) in due course.

An area of alkene-metathesis chemistry that has been investigated by a number of researchers involves the use of double, triple, or even quadruple ring-closing-metathesis reactions to generate a variety of bicyclic, tricyclic, and tetracyclic ring systems in a single step from an appropriately substituted acyclic precursor.[146] A highlight of this methodology is the novel approach to branched β-*C*-tetrasaccharides developed by the Postema group, an example of which is illustrated in Scheme 29.[147] Thus, triester **159** was, following the methylenation protocol developed by Takai and co-workers,[138] converted into the corresponding hexaene **160**, which was then exposed to catalyst **3** (50 mol%, added in five portions over 2.5 h) in toluene at 60 °C to effect the desired triple ring-closing metathesis to form tris-glycal **161**. This latter intermediate was not isolated, but directly subjected to a regio- and stereoselective triple hydroboration/oxidation procedure to afford tetrasaccharide **162** in 44% overall yield from triester **159**. Although the catalyst loading may seem relatively high in this case, this reflects the fact that not only do three metathesis reactions have to be catalyzed, but also that ring-closing metathesis of electron-rich enol ethers is known to be more difficult than that of simple alkyl-substituted diene systems.[148,149] Notably, no competing macrocyclization or oligomerization processes were observed during the metathesis step. Strictly speaking, the actual metathesis events cannot be classified as a cascade process, since the individual ring-closures occur independently of each other. Nevertheless, the overall conversion of **159** into **162** represents a highly efficient gain in molecular complexity, involving nine independent transformations (each occurring with an average yield of 91%) and the formation of three new rings and six new stereogenic centers without the need for the purification of any of the intermediates. Through the judi-

 © 2005 Wiley-VCH Verlag GmbH & Co. KGaA, Weinheim



Scheme 29. A triple ring-closing-metathesis reaction in the synthesis of a novel branched β-*C*-tetrasaccharide (**162**) (Postema and Piper, 2004).[147]



Scheme 30. "Tandem catalysis" in the enantioselective synthesis of (−)-muscone (**166**) (Grubbs and co-workers, 2001).[152]

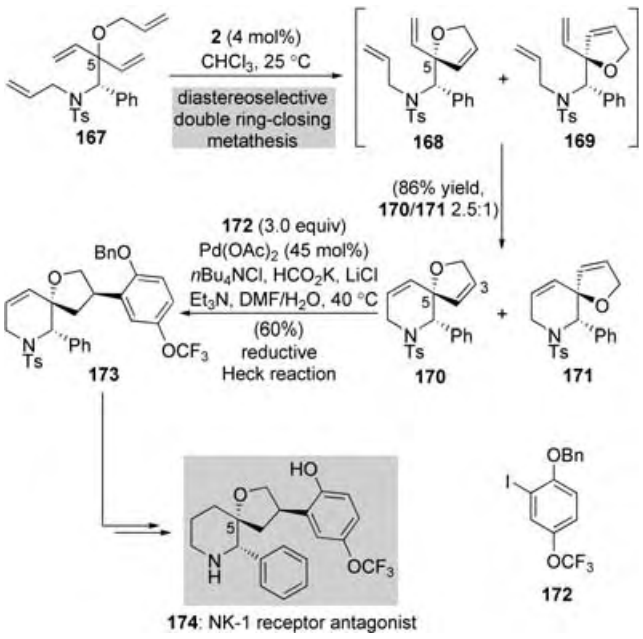
cious positioning of alkene units within a precursor molecule, a diverse array of annulated, spirocyclic, and polycyclic ring systems can be fashioned by employing multiple ring-closing metathesis reactions.

Our final example in this section highlights the multifarious uses of ruthenium carbene systems such as **2** and **3**. In addition to being versatile catalysts for metathesis reactions, complexes **2** and **3** have been shown to function also as effective precatalysts for a variety of unrelated transformations, including hydrogenation, radical addition, and the vinylation of terminal alkynes.[150,151] This broad spectrum of activity has been employed by Grubbs and co-workers in a remarkable synthesis of the fragrant natural product (−)-muscone (**166**, Scheme 30), whereby sequential alkene ring-closing metathesis, hydrogen transfer, and hydrogenation reactions were mediated in a one-pot process by complexes derived from a single ruthenium carbene species, namely complex **2**.[152] As illustrated in Scheme 30, this sequence began with the treatment of diene **163**, bearing an unprotected secondary hydroxy group, with initiator **2** (7 mol%) in 1,2-dichloroethane at 50 °C, which effected the desired ring-closing-metathesis reaction to initially afford macrocyclic alkene **164** as a mixture of geometrical isomers. Subsequent addition of 3-pentanone and NaOH to this solution followed by heating to reflux then initiated the ruthenium-catalyzed transfer dehydrogenation of alcohol **164**, formally transferring "H_2" from this intermediate to the 3-pentanone (which is used in excess to drive this reversible reaction in the desired direction) to afford macrocyclic ketone **165**. At this point the reaction mixture was transferred to a Parr hydrogenation apparatus, pressurized with H_2 gas (800 psi), and heated to 80 °C. Under these conditions, the ruthenium complex(es) present is converted into ruthenium hydride species, which function effectively to hydrogenate the 1,2-disubstituted alkene chemoselectively in the presence of the ketone carbonyl group. Only once this stage was complete was the reaction mixture worked up and purified to give the targeted product **166** in an overall yield of 56% for the three steps.[153] This approach to "tandem catalysis"[152] offers great potential for the streamlining of synthetic processes and will undoubtedly find many more exciting applications in target-oriented synthesis once its fuller scope is convincingly demonstrated.[154]

2.4. Diastereoselective and Enantioselective Alkene Metathesis

One of the frontiers of the alkene-metathesis reaction is its use in the generation of stereogenic centers within molecules. The two main methods that have been employed to achieve this process are: 1) diastereoselective ring-closing-metathesis reactions, with achiral metathesis catalysts, of systems containing pre-existing stereogenic centers and 2) enantioselective metathesis reactions of achiral substrates with chiral catalysts. An example of the former protocol is in the novel approach to the synthesis of selective NK-1 receptor antagonists (e.g. **174**, Scheme 31) developed by workers at Merck.[155,156] The spirocyclic core structure characteristic of this class of therapeutic agents had been previously synthesized in a stepwise manner, involving the fusion of the tetrahydrofuran ring onto a preexisting enantiomerically pure piperidine scaffold.[157] The Merck team was keen to investigate more direct and conceptually novel methods for the construction of this bicyclic template and found that this ring system could be formed in a single step from an acyclic precursor by using a diastereoselective double ring-closing-

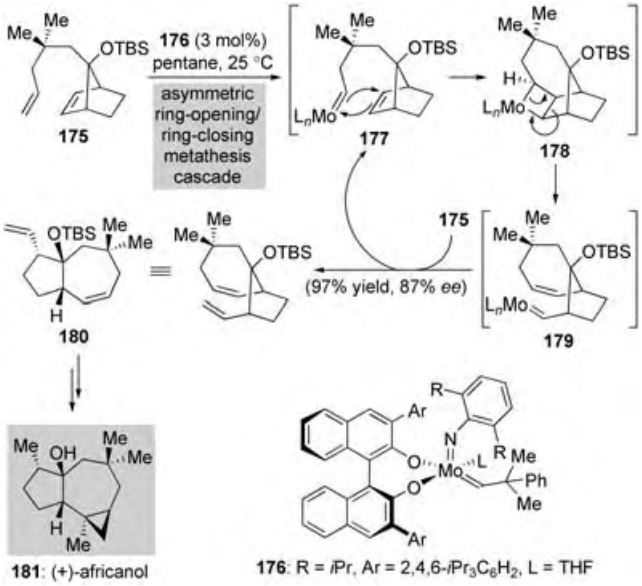
 © 2005 Wiley-VCH Verlag GmbH & Co. KGaA, Weinheim



Scheme 31. Diastereoselective double ring-closing metathesis and reductive Heck reactions in the synthesis of an NK-1 receptor antagonist **174** (Merck, 2001).[155]

metathesis reaction. Thus, as is shown in Scheme 31, treatment of the (*S*)-phenylglycine-derived tetraene **167** with the first-generation Grubbs catalyst **2** (4 mol%) in $CHCl_3$ at ambient temperature led to the formation of the two diastereoisomeric products **170** and **171** in a combined yield of 86% yield and with 70% diastereoselectivity. The major pathway for this reaction was believed to involve the initial formation of the five-membered ring to generate dihydrofuran intermediates **168** and **169**, which then undergo the second, slower ring closure. The diastereoselectivity of the overall process thus arises during the first stage, with the preferential cyclization of the *O*-allyl group onto one of the two diastereotopic C5 vinyl groups, dictated by the adjacent tertiary stereocenter. Following the separation of the major isomeric product **170** from the undesired component **171**, a remarkably chemo-, regio-, and stereoselective reductive Heck reaction was then employed to append the aromatic ring onto C3 of the dihydrofuran ring to give tricyclic compound **173**, which was converted, in two steps, into the final target structure **174**.

While undeniably elegant, there are a number of limitations associated with this type of diastereoselective metathesis process. Firstly, one or more stereogenic centers have to be incorporated into the precursor molecule at sites where they can influence the course of the reaction. More importantly, since the stereochemical course of the reaction is under substrate control, it is generally not possible to obtain selectively both possible diastereoisomeric products through modification of the reaction conditions. A more appealing approach in this regard would be to induce asymmetry in achiral molecules through the use of chiral metathesis catalysts since, in principle, one could obtain selectively either product stereoisomer through the use of the appropriate catalyst antipode. Collaborative efforts between the Schrock and Hoveyda groups have led to the development of such chiral molybdenum-based catalysts for catalytic asymmetric alkene metathesis. More recently, chiral ruthenium-based systems have been introduced by the Grubbs group;[158] however, to date, it is the corresponding molybdenum complexes that have been the most widely studied. Applications of this emerging methodology in total synthesis are still rare, and since catalytic asymmetric metathesis has recently been authoritatively reviewed,[159] the most recent example of this process in target-oriented synthesis may suffice to demonstrate its enormous potential. Thus, as illustrated in Scheme 32, Schrock, Hoveyda, and co-workers employed a



Scheme 32. An asymmetric ring-opening/ring-closing-metathesis cascade in the enantioselective synthesis of (+)-africanol (**181**) (Schrock, Hoveyda, and co-workers, 2004).[160]

novel asymmetric ring-opening-/ring-closing-metathesis cascade reaction to furnish the bicyclic core structure and prove the stereochemical identity of the sesquiterpenoid (+)-africanol (**181**).[160] Treatment of readily available diene **175** with the chiral molybdenum carbene initiator **176** in pentane at ambient temperature effected its conversion, over the course of 6 h, into the rearranged bicyclic structure **180**, which was formed in nearly quantitative yield (97%) and with good enantioselectivity (87% *ee*). Notably, this reaction could be carried out under highly concentrated conditions, with sufficient pentane being added just to dissolve the chiral catalyst, yet homodimeric products were not observed. This metathesis cascade effects the enantioselective desymmetrization of a *meso* precursor substrate **175**, the most commonly employed mode of asymmetric alkene metathesis. This cascade sequence gave the team an extremely rapid and enantioselective access to an advanced intermediate **180**, which contained most of the key structural features present in the natural product **181**. Thus, with intermediate **180** in hand, these researchers were able to complete their elegant total synthesis in only a few more steps.

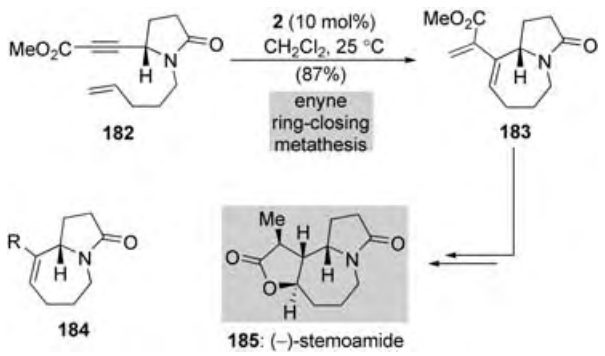
 © 2005 Wiley-VCH Verlag GmbH & Co. KGaA, Weinheim

3. The Enyne-Metathesis Reaction

The enyne-metathesis reaction is an extremely useful method for the construction of 1,3-diene systems, often in a stereoselective manner, from simpler precursor molecules under mild conditions. The synthetic value of this reaction is enhanced by the fact that, in addition to being a means to an end in itself, the 1,3-diene systems thus formed are themselves versatile synthetic intermediates that can undergo further selective transformations (e.g. cycloaddition reactions). The intramolecular (ring-closing) enyne-metathesis reaction is a particularly powerful method for the construction of ring systems, both carbocyclic and heterocyclic and, indeed, it is in this context that the reaction has found the most use. Intermolecular (cross-metathesis) reactions have been employed much less frequently owing to the perceived difficulties in achieving at least reasonable levels of selectivity; however, even in this case there have been tremendous advances in recent years. The most widely used initiators for enyne metathesis are the ruthenium carbene based catalyst precursors, which have been "borrowed" from the alkene-metathesis realm, but which serve equally admirably in this context and exhibit the by now familiar levels of high activity and functional-group tolerance in these processes as well.[161] Here we highlight some of the most elegant and instructive applications of the enyne-metathesis reaction in total synthesis.

3.1. Enyne Ring-Closing Metathesis

It was the Mori group who pioneered the use of ruthenium carbene complexes in enyne-metathesis chemistry, first demonstrating its applicability to the formation of five-, six-, and seven-membered nitrogen-containing heterocyclic rings in 1994.[162] Inspired by this achievement, it was not long before the same group also reported the first application of an enyne-metathesis reaction in a total synthesis, namely that of the tricyclic alkaloid (−)-stemoamide (**185**, Scheme 33) in 1996.[163] The team reasoned that, once a stereoselective route to bicyclic compound **183** had been secured, the resulting diene system would provide a convenient handle for the fusion of the third and final ring onto the structure,

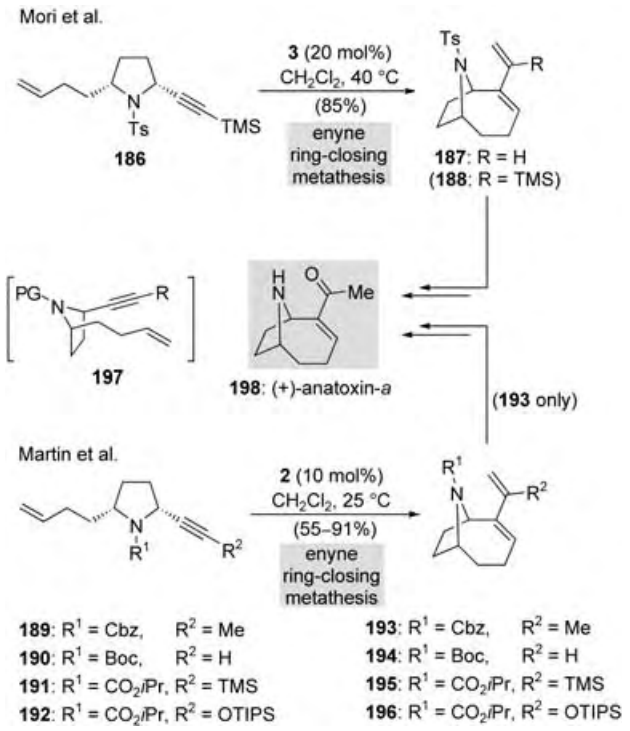


Scheme 33. Enyne ring-closing metathesis in the enantioselective synthesis of (−)-stemoamide (**185**) (Mori and Kinoshita, 1996).[163]

thus completing the total synthesis. The immediate issue then became the construction of bicyclic intermediate **183**, and it was proposed that this compound could, in turn, arise from the enyne ring-closing metathesis of precursor **182**. To their delight, the researchers found that this transformation could be effected by treatment of a solution of precursor **182** in CH_2Cl_2 with the first-generation Grubbs catalyst **2** (4 mol%) at ambient temperature, to furnish bicyclic product **183** in 87% yield and without any erosion of stereochemical integrity at the sensitive propargylic position. This reaction is all the more noteworthy in light of the researchers' previous experience of enyne ring-closing-metathesis reactions of alkyne systems bearing carboalkoxy substituents, namely that, while the cyclization itself is accelerated by the presence of the ester substituent, the resulting sensitive cross-conjugated product typically undergoes extensive decomposition during purification and is only isolated in low yields.[162] To rationalize the apparent discrepancy in the excellent yield of compound **183**, it was proposed that the diene system is forced, by steric effects, to adopt a nonplanar conformation in which conjugation between the two alkene π systems is minimal, thus protecting the system from the destruction that otherwise might have been expected to occur. With intermediate **183** then in hand, only a few more steps were required to arrive at the targeted product **185**.[164] Interestingly, the formation of a trisubstituted alkene system such as **184** (Scheme 33) through simple alkene metathesis in the presence of the ruthenium carbene catalysts available at the time (e.g. **2**) would have been exceedingly difficult, if not impossible, yet this was readily accomplished by means of enyne metathesis.

More recent applications of enyne metathesis in alkaloid total synthesis can be found in the concise routes to (+)-anatoxin-*a* (**198**, Scheme 34) developed independently and almost simultaneously by the groups of Martin[165] and Mori.[166] Despite its modest molecular weight, anatoxin-*a* has proven to be a particularly tempting target for synthetic chemists, due not only to its biological profile[167] but also to its unusual aza-bridged bicyclic structure, and has accordingly inspired a legion of elegant synthetic approaches.[168,169] The cornerstone of both groups' strategies was the employment of enyne ring-closing-metathesis reactions of readily available *cis*-2,5-disubstituted pyrrolidine precursors to assemble rapidly the bicyclic core framework, followed by the appropriate side-chain manipulation and amine-deprotection maneuvers required to complete the total synthesis. While the use of ring-closing olefin-metathesis reactions in the construction of bridged aza-bicyclic structures had been documented,[170] the formation of such systems through the corresponding enyne-metathesis processes represented uncharted terrain, which served to heighten the novelty associated with these proposed steps. In the event, both groups found that with the appropriate substrates the desired cyclizations could be effected with remarkable ease and efficiency. Martin and co-workers induced the cyclization of precursor **189** (R^1 = Cbz, R^2 = Me) by treatment with the second-generation Grubbs catalyst **3** (10 mol%) in CH_2Cl_2 at ambient temperature to afford bicyclic compound **193** in 87% yield. Selective oxidative cleavage of the less substituted double bond

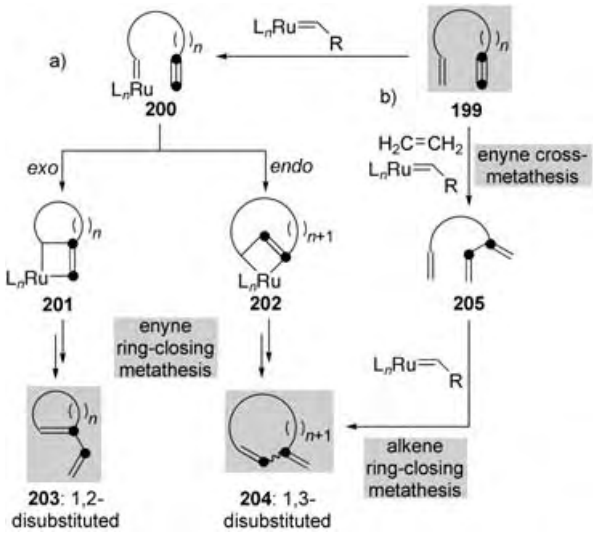
 © 2005 Wiley-VCH Verlag GmbH & Co. KGaA, Weinheim



Scheme 34. Enyne ring-closing-metathesis approaches to the total synthesis of (+)-anatoxin-*a* (**198**) (Martin and co-workers, 2004; Mori and co-workers, 2004).[165,166]

followed by removal of the Cbz group then yielded the target compound. The group had in fact previously shown that a variety of substituted alkynes, for example, **190**, **191**, and **192**, could undergo enyne ring-closing metathesis to generate the corresponding bicyclic systems **194**, **195**, and **196** in good yields. However, with the finishing line within tantalizing reach, the researchers were thwarted in their valiant efforts at converting any one of **194**, **195,** or **196** into the target compound **198**, and it was with only their fourth substrate **193** that the final synthetic hurdles could be surmounted. If nothing else, these tribulations illustrate the fact that synthetic routes almost invariably contain unexpected pitfalls, and that fortune favors the persistent! Mori and co-workers found that while the enyne metathesis of alkyne **186**, carried out in refluxing CH_2Cl_2 in the presence of catalyst **3** (20 mol%), did indeed yield the desired bicyclic skeleton, unexpected desilylation occurred during the reaction to generate diene **187** as the observed product. Much to the team's relief diene **187** could be elaborated also to give the coveted target compound, this time through a selective oxymercuration/alcohol oxidation sequence. The facile nature of these cyclization reactions in generating rather strained bicyclic systems provides further evidence for the beneficial effects of biasing substrates to adopt a conformation favorable to cyclization. In the present case, the potential $A^{1,3}$-strain between the N-protecting group and the *cis*-2,5-pyrrolidine ring substituents favors the diaxial conformer **197**.[171] Finally, it should be mentioned that the Aggarwal group has also utilized an analogous approach in their elegant synthesis of the related alkaloid (−)-ferruginine, employing an enyne ring-closing metathesis to construct the more constrained azabicyclo[3.2.1]octane core structure present in the natural product.[172]

The intramolecular enyne-metathesis reaction also offers a useful method for the synthesis of macrocyclic ring systems, albeit one much less utilized than the corresponding alkene ring-closing macrocyclizations. However, when applying enyne ring-closing metathesis reactions to the synthesis of large rings, a number of selectivity issues, absent in other metathesis processes, arise and need to be taken into careful consideration. These issues relate to the orientation of ring closure, and have been elegantly summarized by Lee and Hansen.[173] Thus, as shown in Scheme 35, the ruthenium



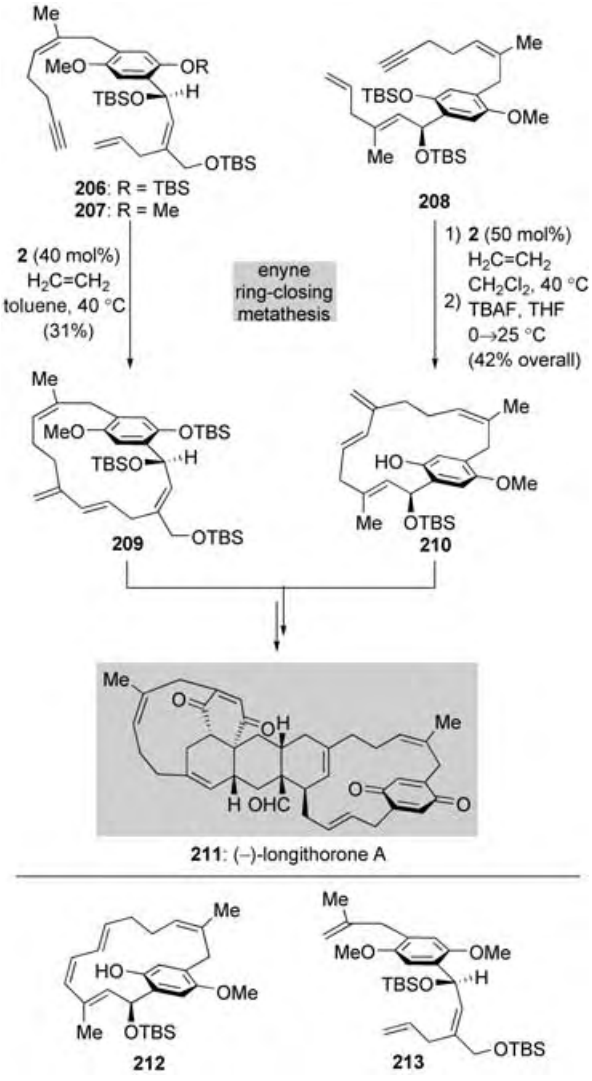
Scheme 35. Models for macrocyclization by enyne ring-closing metathesis: a) direct pathway; b) two-step enyne-cross-metathesis/alkene ring-closing-metathesis pathway (Lee and Hansen, 2003).[173]

carbene intermediate **200** generated from the starting enyne **199** can undergo two possible modes of ring closure, termed *exo* and *endo*, to generate the two different metallacyclobutene intermediates **201** and **202**, which subsequently yield the 1,2-disubstituted product **203** and 1,3-disubstituted product **204**, respectively. Furthermore, the *endo* mode of ring closure leads to products with an additional carbon atom within the ring relative to those derived from the *exo* mode. The mode of ring closure followed in any given case depends largely on the geometric constraints imposed by the tether linking the alkene and alkyne moieties. Thus, the formation of common- and medium-sized rings by enyne ring-closing metathesis is typically constrained to follow the *exo* path (as in the examples discussed above), whereas macrocyclizations generally follow the *endo* mode of ring closure owing to the increased flexibility of the tether. Another important factor to consider is that, following a seminal report by the Mori group,[174] enyne-metathesis macrocyclizations are generally conducted under an atmosphere of ethylene.[175] In these particular cases, the course of the macrocyclization is believed to be diverted away from that of a direct intramolecular

 © 2005 Wiley-VCH Verlag GmbH & Co. KGaA, Weinheim

enyne-metathesis reaction, which would be expected to be inherently slow owing to the low effective concentration of the reacting termini. Instead, a two-step process has been proposed involving an initial rapid intermolecular enyne cross-metathesis of the terminal alkyne unit with ethylene (a known process, see below) to generate a 2-substituted butadiene **205**, which subsequently undergoes a conventional intramolecular alkene ring-closing-metathesis reaction. Given the sensitivity of the ruthenium metathesis catalysts to steric effects, the less hindered terminal double bond of the butadiene moiety would be expected to be engaged selectively in the macrocyclization event to yield the formal *endo* enyne-metathesis product **204**, and indeed this is observed experimentally.[176]

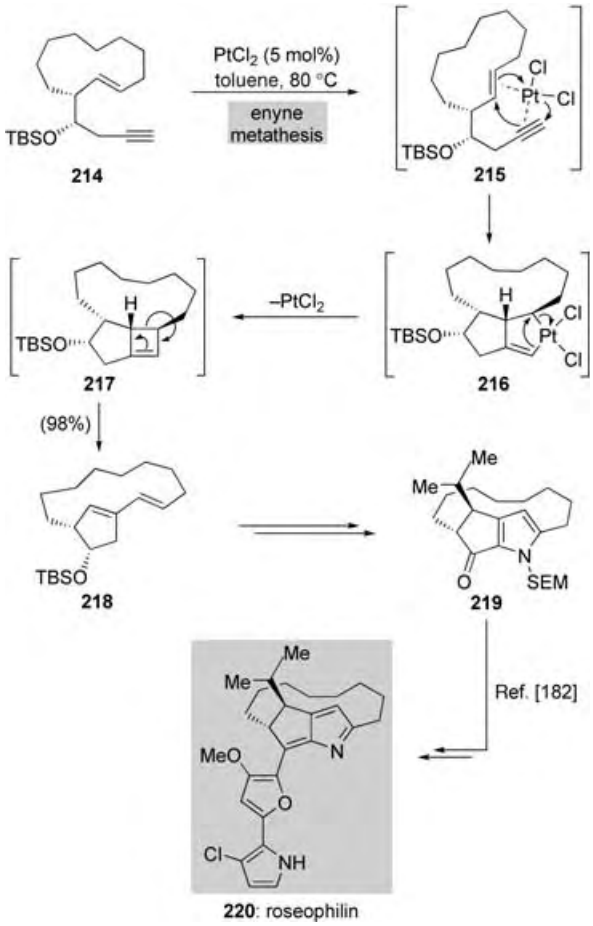
The regiochemical outcome of enyne-metathesis macrocyclizations certainly weighed heavily on the minds of Shair and co-workers as they embarked on their journey to complete the total synthesis of the marine natural product (−)-longithorone A (**211**, Scheme 36).[177] Inspired by the insightful biogenetic hypothesis of the Schmitz group,[178] the Shair team proposed to employ a beautifully choreographed sequence of inter- and intramolecular Diels–Alder reactions to assemble much of the imposing polycyclic architecture of this remarkable natural product. This then led them to conceive of macrocyclic compounds **209** and **210** as key synthetic intermediates, corresponding to the "left" and "right" halves of the natural product, respectively. On first inspection, the stereocontrolled synthesis of these "simpler" intermediates would still appear to be far from trivial. However, recognizing the characteristic 1,3-disubstituted butadiene system embedded within both compounds **209** and **210**, the team began to contemplate the exciting possibility of constructing both intermediates through enyne ring-closing-metathesis reactions of the respective precursors **206** and **208**. From the discussion above (see Scheme 35), one would be forgiven for thinking that this was a fairly routine assumption, but at the time enyne metathesis had never been applied to the synthesis of macrocycles, only to smaller rings, which had always resulted in the formation of the corresponding 1,2-disubstituted cyclic products. Eager to answer the question of 1,2- versus 1,3-disubstitution selectivity in enyne-metathesis macrocyclizations, the group performed some simple model studies, which showed for the first time that the desired 1,3-disubstituted diene systems could be obtained preferentially, if not exclusively, in the formation of larger rings. Emboldened by this breakthrough, the group set to work on the real system and arrived at intermediates **206** and **208** in short order. At this point, it will be noted that both **206** and **208** bear seemingly extraneous functionality, in the shape of benzylic hydroxy group derivatives, which is not present in the target product **211**. These substituents were, in fact, key to the planning of the macrocyclization reactions, as it was anticipated that these groups would gear the ring closures to produce selectively only the desired atropisomers of the cyclized products. Specifically, the potential steric interactions between the benzylic TBS ether groups and the phenolic hydroxy derivatives would, ideally, dictate that macrocyclization of compounds **206** and **208** occur selectively through the lower-energy conformers shown, thus generating the desired atropisomeric products.[179] In practice, the cyclization of enyne **208**, induced by treatment with catalyst **2** (50 mol%) in refluxing CH_2Cl_2 under ethylene atmosphere, proceeded with both excellent atropselectivity and *E*/*Z* selectivity to afford, after treatment of the crude product mixture with TBAF to effect the selective desilylation of the phenolic hydroxy group, the desired paracyclophane **210** in 42% overall yield. A significant by-product formed in this reaction was the unusual paracyclophane **212** in which a methylene group was lost during the macrocyclization.[180] In contrast, the macrocyclization of enyne **206** was both less atropselective (3:1) and less selective in the control of the endocyclic olefin geometry (*E*/*Z* 4.5:1); nevertheless, the desired product **209** could be produced reliably in yields averaging 31%. In the absence of an ethylene atmosphere, macrocyclization did not occur with either **206** or **208**; thus, it seems likely that both reactions proceed through the two-step process alluded to earlier. Interestingly, when the cyclization of precursor **207** was attempted in the presence of the more



Scheme 36. Enyne ring-closing-metathesis macrocyclizations in the enantioselective total synthesis of (−)-longithorone A (**211**) (Shair and co-workers, 2002).[177]

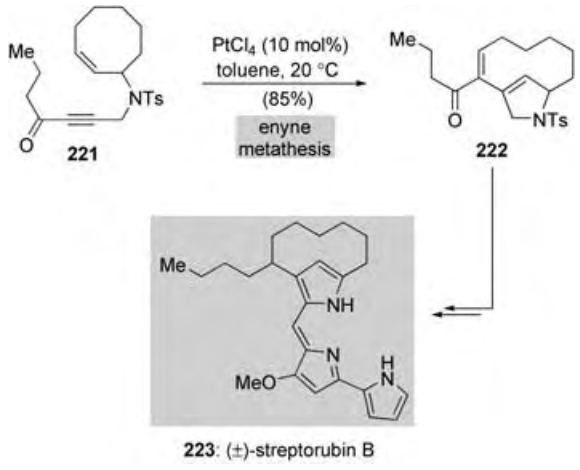
reactive ruthenium initiator **3**, the unexpected product **213** was obtained in which the alkyne-bearing side chain had been truncated, presumably resulting from the increased activity of this catalyst towards trisubstituted olefins. Having secured both the key intermediates **209** and **210**, the Shair group was then able to complete the total synthesis in only a few more steps. Significantly, the 1,3-diene systems formed in both intermediates **209** and **210** ultimately participated in the crucial biomimetic Diels–Alder reactions. This meritorious total synthesis is noteworthy not only for its pioneering applications of enyne metathesis in macrocyclizations, but also in that it sets a new "gold standard" for enyne-metathesis chemistry in general.

An important feature of the enyne-metathesis reaction is that, unlike the other metathesis processes we have discussed so far, the overall process can be mediated by catalysts other than metal carbene containing species, and in these cases the reaction can proceed by (one or more) entirely different mechanisms. An illustrative example can be found in the formal total synthesis of roseophilin (**220**, Scheme 37) by Trost and Doherty.[181,182] The treatment of enantiomerically pure enyne **214** with $PtCl_2$ (5 mol%) in toluene at 80°C initiated a sequence of events involving the formal cleavage of one and the formation of two carbon–carbon double bonds, expansion of a macrocyclic ring by two carbon atoms, and the



Scheme 37. $PtCl_2$-catalyzed enyne metathesis in the formal synthesis of roseophilin (**220**) (Trost and Doherty, 2000).[181]

installation of a bridgehead alkene moiety, ultimately leading to the formation of the bicyclic product **218** as a single stereoisomer in a remarkable yield of 98%! The 1,3-diene system in compound **218** then provided a handle for its elaboration into tricyclic compound **219**, an intermediate in the Fürstner group's pioneering total synthesis of roseophilin (**220**),[183] and thus the completion of the formal synthesis of the natural product. The mechanism proposed for this transformation invokes a platinum(II)⇄platinum(IV) manifold, involving the initial formation of the metallacyclopentene intermediate **216**, followed by reductive elimination to generate cyclobutene **217**, which under the conditions of the reaction undergoes conrotatory electrocyclic ring-opening (driven by the release of ring strain) to yield the observed product **218**. It has been shown that a wide range of electrophilic species, ranging from other transition-metal complexes (e.g. $[\{RuCl_2(CO)_3\}_2]$, $[IrCl(CO)_3]_n$, and various palladacycles) to simple Lewis and Brønsted acids that cannot undergo redox equilibria (e.g. $BF_3{\cdot}OEt_2$, $AlCl_3$, and HBF_4) are also effective catalysts for this type of transformation. In these cases, alternative mechanistic pathways have been proposed involving formal cationic intermediates.[184] These types of transformations have been termed "skeletal reorganizations" to differentiate them from the metal carbene mediated processes; however, they all fall under the banner of enyne metathesis since the net outcome is the same.[185] Semantics aside, these reactions offer a remarkably simple, atom-economical, and user-friendly method for generating molecular complexity by employing the most basic of catalyst systems. Another example of this type of enyne metathesis is in the synthesis of streptorubin B (**223**, Scheme 38) by the



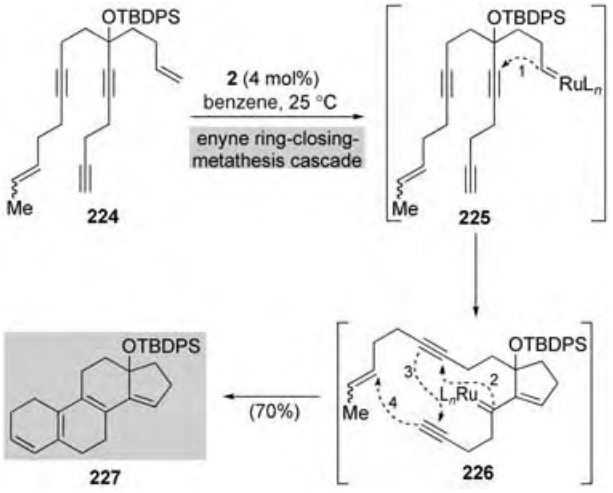
Scheme 38. $PtCl_4$-catalyzed enyne metathesis in the total synthesis of (±)-streptorubin B (**223**) (Fürstner and co-workers, 1998).[183a]

Fürstner group, in which the metathesis of enyne **221**, mediated by a catalytic amount of $PtCl_4$ (10 mol%), generated bicyclic pyrrolophane **222** in 85% yield.[183a] The same transformation could also be effected with $BF_3{\cdot}OEt_2$ or HBF_4 as catalysts, although the yield of the product was somewhat lower in these cases (64% and 57%, respectively).

 © 2005 Wiley-VCH Verlag GmbH & Co. KGaA, Weinheim

3.2. Enyne Metathesis in Cascade Processes

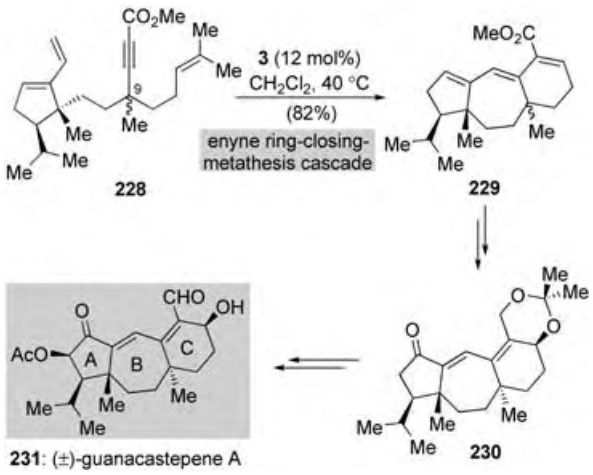
One of the most exciting and powerful applications of the enyne-metathesis reaction is its use in cascade processes to generate complex polycyclic structures from simpler precursor substrates. An enyne ring-closing-metathesis reaction initially generates a new metal carbene that can potentially be intercepted by another appropriately located olefin within the same molecule, resulting in a second intramolecular metathesis event to form another ring and a new metal carbene species, and so on. The first examples of tandem enyne metathesis were reported by Grubbs and co-workers,[186] with the same group subsequently reporting the instructive example highlighted in Scheme 39.[187] Thus, exposure of acyclic



Scheme 39. Use of a domino enyne ring-closing-metathesis sequence for the construction of a steroid-type polycycle **227** (Grubbs and co-workers, 1996).[187]

compound **224** to ruthenium catalyst **2** (4 mol%) in benzene at ambient temperature triggered a cascade sequence resulting in the regiocontrolled formation of four new carbon–carbon bonds and four new rings to afford the steroid-type compound **227** in 70% yield. The initiation of this highly orchestrated process presumably occurred with the insertion of the ruthenium alkylidene into the most (kinetically) reactive terminal alkene of the starting material **224** to generate **225**. The latter carbene species underwent enyne ring-closing metathesis with the proximal triple bond to generate the subsequent intermediate **226**, a substrate poised to react, in order, with the next three sites of unsaturation. Hence, each alkyne unit serves as a metathesis relay point, thus allowing the propagation of the polycyclization cascade until the terminating alkene ring-closing-metathesis event. Through the judicious positioning of unsaturation within an acyclic precursor molecule, one can envisage any possible number of multiple ring-forming processes.

The Hanna group made gainful use of this type of tandem ring-closing process in their recent formal synthesis of guanacastepene A (**231**, Scheme 40).[188] The first total synthesis of this novel tricyclic diterpene had been reported in 2002 by the Danishefsky group,[189] with a subsequent formal



Scheme 40. An enyne ring-closing-metathesis cascade in the formal synthesis of (±)-guanacastepene (**231**) (Hanna and co-workers, 2004).[188]

synthesis being reported by Snider and co-workers a year later.[190] Both of these two elegant syntheses adopted a stepwise approach to the construction of the tricyclic core structure, first fusing the seven-membered ring onto a pre-existing cyclopentane derivative, then at a later point installing the final six-membered ring (i.e. A→AB→ABC). In an unprecedented approach to this terpene skeleton, Hanna and co-workers surmised that it would be possible to generate the characteristic tricyclic ring system of guanacastepene A (**231**) in a single step from an appropriate monocyclic A-ring precursor through a tandem enyne ring-closing-metathesis reaction (i.e. A→ABC). Indeed, it was found that readily available ester **228** (as a 1:1 mixture of epimers at the C9 stereocenter) underwent the desired cyclization cascade upon treatment with the second-generation Grubbs catalyst (12 mol%) in refluxing CH_2Cl_2 to afford exclusively tricyclic compound **229** in 82% yield. The particular use of catalyst **3** was essential to the success of this transformation, as previous studies by the group had indicated that the less active ruthenium-based catalyst **2** was ineffective at promoting similar reactions.[191] The selectivity of this cascade process is quite remarkable, and is again due to the fact that the reaction had been "programmed" to initiate at a specific point in the precursor molecule **228**, namely the least hindered (and hence most kinetically reactive) terminal alkene, thus ensuring the correct regiochemical outcome. Equally important is the fact that the triene functionality concomitantly installed in the formation of intermediate **229** proved to be amenable enough to allow its elaboration to give ketone **230**, a late-stage intermediate in the Danishefsky team's original total synthesis of guanacastepene A (**231**), thus completing the formal synthesis of the natural product.[192]

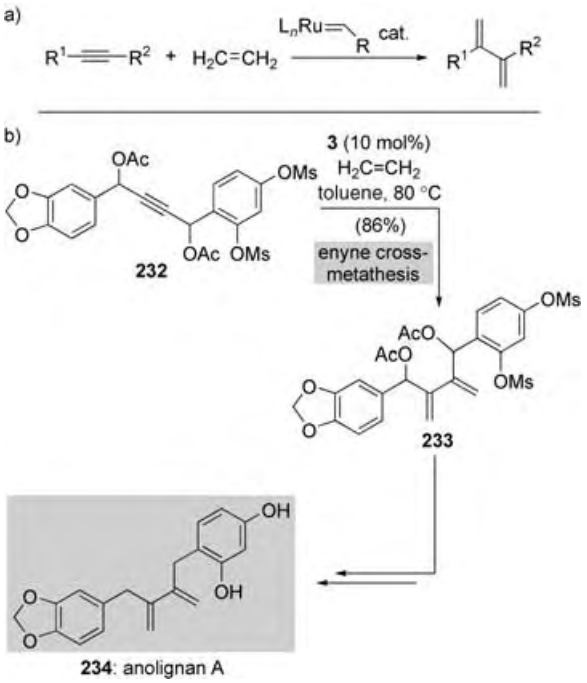
3.3. Enyne Cross-Metathesis

In comparison to the generally reliable, high-yielding, and selective intramolecular processes, intermolecular enyne metathesis (enyne cross-metathesis) has seen little use in

 © 2005 Wiley-VCH Verlag GmbH & Co. KGaA, Weinheim

the synthesis of complex molecules, despite its appealing potential for the formation of synthetically useful acyclic 1,3-diene systems in fragment-coupling processes.[193] The biggest problem in effecting intermolecular metathesis between an alkene and an alkyne is selectivity. Not only can three different types of intermolecular metatheses (alkene, alkyne, and enyne) potentially occur in these reactions, but the formation of stereoisomeric *E*/*Z* mixtures in the desired cross-metathesis diene product can also be a major problem. Currently, the success or failure of any given intermolecular enyne-metathesis reaction appears to be very substrate-dependent, and there is as yet no "working model" that can be used to predict the outcome of these reactions reliably.

The most common application of intermolecular enyne metathesis employs ethylene as the alkene component, and this provides a particularly convenient method for the production of 2,3-disubstituted butadiene systems (or 2-substituted butadienes in the case of terminal alkynes), an important and synthetically useful structural motif (Scheme 41 a). This protocol was introduced by the Mori group,



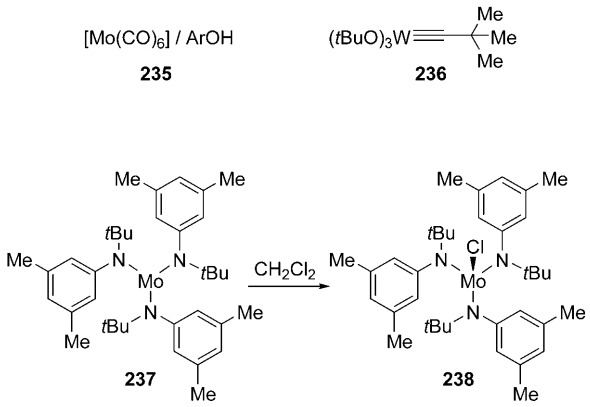
Scheme 41. Enyne cross-metathesis: a) generalized scheme; b) application to the total synthesis of anolignan A (**234**) (Mori and co-workers, 2002).[194a]

who subsequently applied it to an expedient synthesis of anolignan A (**234**, Scheme 41 b).[194] Thus, the cross-metathesis of internal alkyne **232** was induced by treatment with initiator **3** (10 mol%) in toluene at 80 °C under ethylene at atmospheric pressure to furnish butadiene **233** with the required regiochemistry and in 86% yield. A few more routine steps then completed the total synthesis. These cross-metathesis conditions were found to be more effective than those in the presence of the first-generation ruthenium catalyst **2** (10 mol%, CH_2Cl_2, 25 °C), which gave **233** in lower yield (65%). Indeed, heteroatom substitution at the propargylic position(s) of the alkyne coupling partner is(are) generally required to attain at least satisfactory yields when using catalyst **2** in this type of cross-metathesis, whereas the more active catalyst **3** is effective with a much wider range of terminal and internal alkynes.[195] Atmospheric pressure of ethylene is usually sufficient for these reactions, although the Diver group reported that certain sluggish cases can be accelerated by employing ethylene at elevated pressures.[196]

The first enyne-cross-metathesis reactions of substituted alkenes to afford acyclic 1,3-disubstituted butadiene systems were reported by the Blechert group in 1997.[197] The potential utility of these processes has since caught the attention of many researchers, who have developed their own improvements and applications,[198] including elegant cascade reactions.[199] Nevertheless, the first application of an enyne-cross-metathesis reaction with an alkene other than ethylene in a total synthesis remains an unfulfilled, yet eagerly anticipated, event[200] representing as it does one of the frontiers of enyne-metathesis chemistry.

4. The Alkyne-Metathesis Reaction

Despite the mechanistic parallels between alkyne metathesis and its more ubiquitous alkene-based sibling, the familiar carbene-type catalysts used most routinely in alkene metathesis (e.g. **1**, **2**, and **3**) do not catalyze the corresponding alkyne-metathesis reactions. Instead, this field has its own selected assortment of transition-metal-based catalyst systems, of which the most commonly employed three are illustrated in Scheme 42. The first of these is the classic



Scheme 42. Commonly used alkyne-metathesis initiators.

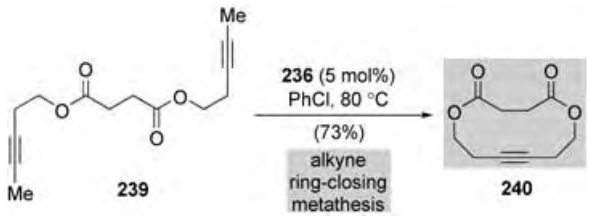
Mortreux system **235**[25] (later refined by Bunz and co-workers)[201] based on a mixture of $Mo(CO)_6$ and any one of a number of phenolic additives (e.g. 4-chlorophenol), which generates one or more not as yet well-defined catalytically active species in situ. The simplicity and user-friendly nature of this catalyst system is offset somewhat by its rather limited tolerance of polar functional groups and the elevated temperatures (ca. 140–150 °C) required to initiate and maintain

 © 2005 Wiley-VCH Verlag GmbH & Co. KGaA, Weinheim

catalytic activity. A major breakthrough in rational catalyst design for alkyne metathesis came with the development of well-defined tungsten alkylidyne complexes by the Schrock group, of which catalyst **236** is the most widely used.[202] Recently, the Fürstner group introduced the monochloro molybdenum complex **238** as a powerful precatalyst for alkyne metathesis; **238** is conveniently formed in situ by the activation of the corresponding trisamido complex **237** with CH_2Cl_2 as a chlorine source.[203–205] The tungsten and molybdenum complexes **236** and **238** complement each other nicely in terms of scope, activity, and functional-group tolerance, and typically perform more efficiently in advanced settings than do the Mortreux catalysts **235**.

4.1. Alkyne Ring-Closing Metathesis

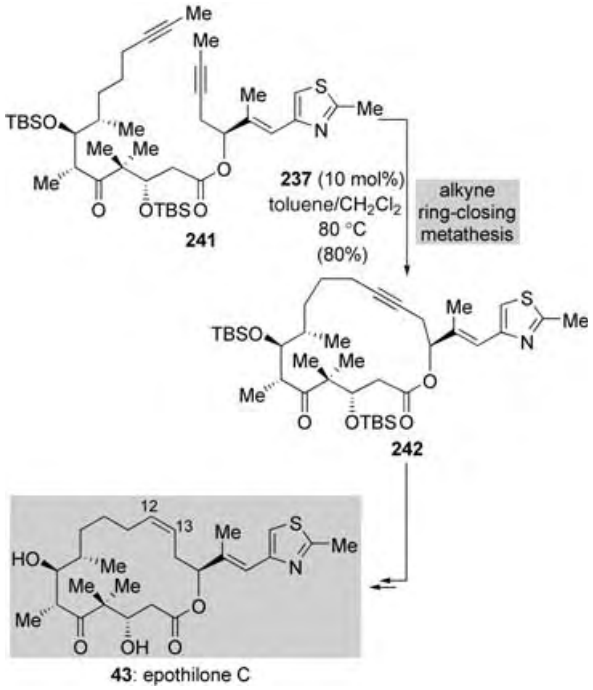
In the 20 or so years following its discovery, alkyne metathesis had found only sporadic and limited application in organic synthesis.[206] However, a groundbreaking report by the Fürstner group in 1998 detailing the first examples of alkyne ring-closing metathesis,[207,208] of which one is illustrated in Scheme 43, heralded a new era for this process. It is



Scheme 43. One of the first applications of alkyne ring-closing metathesis (Fürstner and Seidel, 1998).[207]

an indication of the rapid blossoming of the field that, even only a few years later, these first examples now appear extremely modest; nonetheless they remain highly instructive. Thus, the treatment of diyne **239** with a catalytic amount of the Schrock tungsten initiator **236** (5 mol%) in chlorobenzene at 80 °C led to smooth cyclization to generate the corresponding 12-membered cycloalkyne **240** in 73% yield. Several features of this reaction deserve further comment. First, terminal alkynes make poor substrates for alkyne-metathesis reactions as they deactivate the catalysts and are prone to polymerization. Thus, methyl-substituted alkynes are routinely employed, since not only are they sufficiently reactive, but the by-product (2-butyne), which has to be sacrificed, is volatile and easily removed. Secondly, systems smaller than 12-membered rings have not yet been formed in synthetically useful yields by alkyne ring-closing metathesis,[209] as a result of the geometric constraints of the alkyne unit and the resulting product strain; thus this process is restricted to macrocyclization reactions. Finally, an interesting and useful empirical observation is that alkyne ring-closing-metathesis reactions generally proceed even faster than those of the corresponding alkene ring-closing-metathesis macrocyclizations.

However, the real utility of alkyne ring-closing metathesis stems from the subsequent selective manipulations that are possible with the alkyne system thus formed. In particular, the combination of alkyne ring-closing metathesis followed by stereoselective partial reduction of the triple bond offers an efficient, though indirect, method for the preparation of macrocyclic alkenes of well-defined *E* or *Z* stereochemistry. As we have seen, alkene ring-closing-metathesis macrocyclization reactions are often plagued by the formation of geometrical isomers, with the product distribution often not being predictable and varying dramatically with seemingly subtle changes in precursor structure. This can often have disastrous consequences in terms of product isolation and yield, particularly if it occurs at a late stage in a multistep synthetic route. A case in point is the various approaches to the total synthesis of epothilone C **43** (see Scheme 10). Indeed, it is interesting to note that while three of the earliest total syntheses (those of the Nicolaou,[68] Danishefsky,[69] and Schinzer groups[71]) all employed successful, yet relatively nonstereoselective, alkene ring-closing-metathesis reactions to fashion the C12–C13 double bond; subsequent approaches have largely shied away from this protocol, employing instead more conventional olefination methods, which in this context allowed greater control of alkene stereochemistry.[210] Upon revisiting this problem, the Fürstner group postulated that the stereoselective formation of the coveted natural C12–C13 *Z* isomer of epothilone C could indeed be achieved by metathesis technology through the alkyne ring-closing metathesis of diyne **241** followed by hydrogenation in the presence of the Lindlar catalyst (Scheme 44). This system thus proved to be a significant testing ground for their nascent method. The team found that the desired macrocyclization could be effected in a pleasing 80% yield by treatment of substrate **241** with the

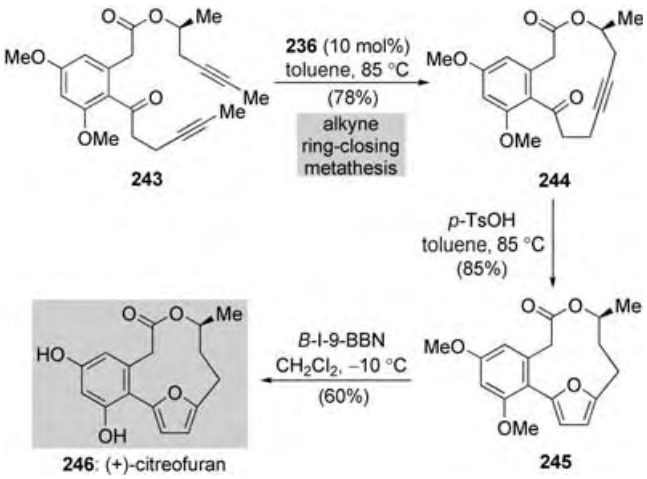


Scheme 44. Alkyne ring-closing metathesis in the total synthesis of epothilone C (**43**) (Fürstner and co-workers, 2001).[211]

 © 2005 Wiley-VCH Verlag GmbH & Co. KGaA, Weinheim

trisamido molybdenum catalyst precursor **237** (10 mol%) in a toluene/CH_2Cl_2 solvent mixture at 80 °C for 8 h.[211] Only two more steps, one of which involved the chemo- and stereoselective semi-hydrogenation of the triple bond under Lindlar conditions, were then required to unveil the target compound **43**.[203b] Notably, the catalyst system rigorously distinguishes between the (reactive) alkyne moieties and the preexisting double bond present in the precursor **241**; indeed, a useful feature of alkyne metathesis is that alkene systems are generally inert toward the catalysts. The particular choice of catalyst system in this case was important, owing to its tolerance of both the sulfur and basic nitrogen atoms of the thiazole ring, the presence of which would have been deleterious to the use of the Schrock catalyst **236**.

The Fürstner group has applied this alkyne ring-closing metathesis/Lindlar reduction protocol in the stereocontrolled synthesis of a number of other macrocyclic natural products,[212] thus demonstrating the versatility, broad applicability, and mildness of this method. It is important to also recall the recent development of novel mild procedures for the conversion of alkynes into the corresponding *E*-alkene systems.[213,214] However, given the synthetic versatility of the alkyne group, it is only appropriate that other ways to elaborate the cycloalkynes formed by alkyne ring-closing metathesis besides simple hydrogenation procedures have begun to be investigated. The first foray into this territory was recently documented in the enantioselective synthesis of (+)-citreofuran (**246**, Scheme 45). Although not readily apparent



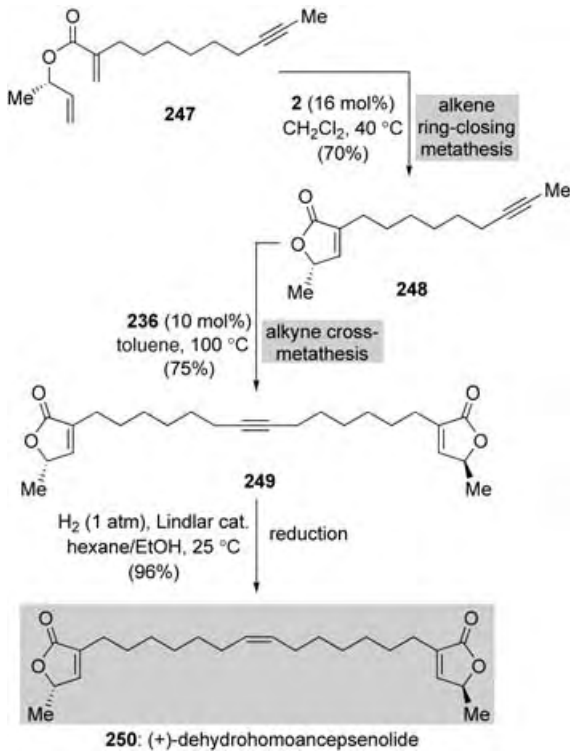
Scheme 45. Alkyne ring-closing metathesis in the enantioselective synthesis of (+)-citreofuran (**246**) (Fürstner and co-workers, 2003).[215]

from a cursory inspection of the molecular structure of **246**, an alkyne-metathesis reaction was used to forge the macrocyclic ring system and to provide a handle for the construction of the furan ring.[215] Thus, as shown in Scheme 45, the readily prepared diyne **243** underwent smooth macrocyclization within 1 hour upon the addition of tungsten alkylidyne catalyst **236** (10 mol%) to a solution of the substrate in toluene at 85 °C to afford the 12-membered bicyclic product **244** in 78% yield. The relative ease of this cyclization is likely to be due, in part, to the presence of the preexisting aromatic ring, which restricts the conformational degrees of freedom available to the starting material **243**. Concomitantly, all the elements required for the formation of the furan ring had been installed during the cyclization. Hence, exposure of cycloalkyne **244** to acidic conditions rendered the somewhat strained triple bond susceptible to nucleophilic attack by the neighboring ketone group, thus initiating a transannular cycloaromatization event that led to the formation of tricyclic compound **245**.[216] With the complete skeleton of the target compound thus formed, the uneventful liberation of the phenolic hydroxy groups was all that was required to complete this concise total synthesis.[217] Notably, there is a particular strategic advantage associated with this order of ring construction (i.e. macrocycle then furan), namely that while the tricyclic framework of the natural product is in fact somewhat strained, the bulk of this strain energy is introduced during the kinetically favorable formation of a five-membered ring. In the alternative scenario (i.e. furan then macrocycle), the extra enthalpic energy barrier would have to be overcome during the macrocyclization event, which is inherently less favorable owing to entropic factors.[218]

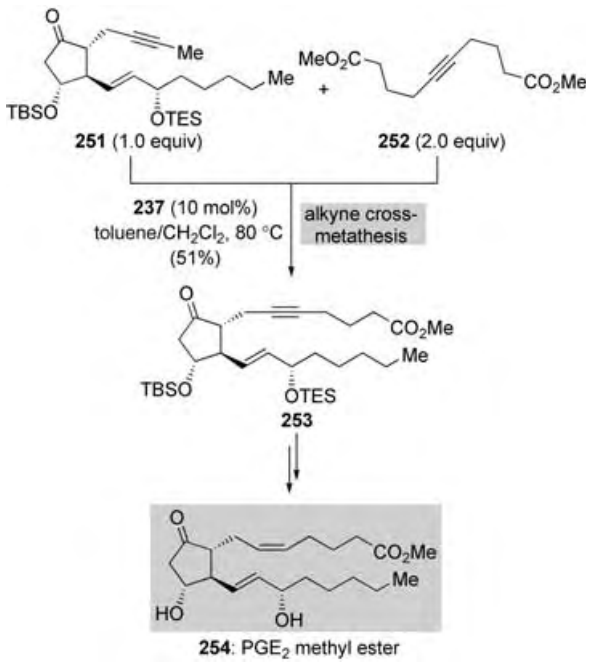
4.2. Alkyne Cross-Metathesis

Alkyne cross-metathesis also holds great potential for selective and efficient carbon–carbon bond formation. To date, the major use of alkyne cross-metathesis has been in acyclic diyne metathesis (ADIMET) polymerization reactions, particularly in the preparation of poly(*p*-phenyleneethynylene) (PPE) type conjugated organic polymers which have a number of potentially useful applications.[219] Recently, however, the first applications in natural products synthesis have emerged. As with the corresponding alkene cross-metathesis reactions, for the purposes of categorization it is convenient to divide alkyne cross-metathesis into two broad classes: dimerization reactions and chain elongation processes. An example of the former process, which also nicely illustrates the current state of the art of metathesis catalyst design, is found in the concise approach to (+)-dehydrohomoancepsenolide (**250**, Scheme 46) reported by Fürstner and Dierkes.[220] Given the C_2 symmetry of the deceptively simple looking structure of the target compound, a reasonable retrosynthetic scission would appear to involve the breaking of the central *Z*-configured alkene, which would be fashioned in a stereoselective manner through the alkyne cross-metathesis of butenolide **248** followed by hydrogenation in the presence of the Lindlar catalyst. The key step in the formation of butenolide **248** was itself proposed to involve a metathesis event, namely the alkene ring-closing-metathesis reaction of enoate **247**. Indeed, it was found that this initial transformation could be effected by treatment of enoate **247** with the first-generation Grubbs catalyst **2** (16 mol%) in CH_2Cl_2 at reflux for 24 h. This reaction was superbly chemoselective and no competing enyne-metathesis side reactions were observed, which was due only to the modulated reactivity of the catalyst employed as the more active second-generation catalyst **3** failed to distinguish rigorously between the alkyne and alkene moieties of the precursor **247**. Furthermore, no co-catalytic

 © 2005 Wiley-VCH Verlag GmbH & Co. KGaA, Weinheim



Scheme 46. Sequential alkene ring-closing-metathesis and alkyne-cross-metathesis reactions in the total synthesis of (+)-dehydrohomoancepsenolide (**250**) (Fürstner and Dierkes, 2000).[220]



Scheme 47. Alkyne cross-metathesis in the enantioselective synthesis of PGE_2 methyl ester (**254**) (Fürstner and co-workers, 2000).[222]

$Ti(OiPr)_4$ was required in this reaction, which is often not the case in ring-closing-metathesis reactions of similar substrates with the first-generation catalyst **2**.[221] Treatment of butenolide **248** with the Schrock catalyst **236** (10 mol%) in toluene at 100 °C effected its successful dimerization to give alkyne **249** in 75% yield, and a subsequent Lindlar hydrogenation completed the expedient total synthesis. The chemoselectivity was inverted in the second metathesis step; the catalyst employed this time selectively activated the triple bond at the expense of the alkene group. The lasting impact of this synthesis is its demonstration of the selectivity for different types of unsaturation within the same molecule that is now possible with the metathesis catalysts currently available.

The first examples of alkyne metathesis to effect chain elongation were also documented by the Fürstner group in their recent incursion into the field of prostaglandin synthesis.[222] As shown in Scheme 47, these researchers found that the selective cross-metathesis of cyclopentanone **251** (prepared through a three-component coupling reaction)[223] with an excess of symmetrical alkyne **252** could be achieved in the presence of complex **237** and CH_2Cl_2 (which serves as the activating agent) in toluene at 80 °C to provide the desired product **253** in 51% yield. No unwelcome side products derived through homodimerization of the starting material **251** were observed in this reaction, possibly as a result of steric effects. This transformation attests to both the excellent reactivity profile of the catalyst system, which again selectively engaged the alkyne units in the presence of both the alkene and the polar, coordinating ketone and ester groups, and the overall mildness of the method, leaving as it did the rather fragile β-hydroxyketone motif on the cyclopentane ring unscathed. While the synthetic potential of alkyne metathesis is undeniable, it will only be through its application in a wider variety of settings that a clearer picture of the generality and predictability of this process will emerge.[224]

5. Summary and Outlook

The emergence of metathesis reactions in chemical synthesis over the last few years has been rather dramatic. It has been delightful to review the field and highlight some of its most exciting applications in total synthesis. Indeed, the speed and imagination with which synthetic chemists have adopted the olefin-metathesis reaction and its siblings, the enyne- and alkyne-metathesis reactions, have been both remarkable and highly productive. Despite this progress, however, limitations do remain with these reactions. These shortcomings include the rather poor ability to predict and control the *E*/*Z* ratio of olefin products (except for small and common rings) and the rather large catalyst loading often necessary for reaction completion. Furthermore, more-efficient and practical chiral catalysts are needed to enable asymmetric processes.

Unquestionably, the early and stunning successes of these reactions will be followed by improvements in catalyst design that will overcome at least some of the above-mentioned problems and lead to even more spectacular applications. Furthermore, although the novelty of these reactions may wear off as time goes by, their power as tools in the minds and hands of creative synthetic chemists will always remain sharp as they attempt to solve more complex puzzles, whether posed by natural or designed molecules. It is also evident that

 © 2005 Wiley-VCH Verlag GmbH & Co. KGaA, Weinheim

metathesis reactions are beginning to rival the venerable and more-established palladium-catalyzed cross-coupling reactions[4] as means to construct carbon–carbon bonds and as enablers of total synthesis. Equally crystal clear is the fact that together these discoveries have revolutionized the way synthetic chemists go about their business these days.

Abbreviations

Ac	acetyl
B-I-9-BBN	9-iodo-9-borabicyclo[3.3.1]nonane
Bn	benzyl
Boc	*tert*-butoxycarbonyl
Cbz	benzyloxycarbonyl
Cp	cyclopentadienyl
Cy	cyclohexyl
1,2-DCE	1,2-dichloroethane
DDQ	2,3-dichloro-5,6-dicyano-1,4-benzoquinone
DMAP	4-dimethylaminopyridine
DME	ethylene glycol dimethyl ether
DMF	*N*,*N*-dimethylformamide
HPLC	high-pressure liquid chromatography
Mes	2,4,6-trimethylphenyl
MOM	methoxymethyl
Ms	methanesulfonyl
M.S.	molecular sieves
NAP	2-naphthylmethyl
Ns	4-nitrobenzenesulfonyl
*p*BrBz	4-bromobenzoyl
PCC	pyridinium chlorochromate
Phth	phthalimido
Piv	pivaloyl
PMB	4-methoxybenzyl
SEM	2-(trimethylsilyl)ethoxycarbonyl
TBAF	tetra-*n*-butylammonium fluoride
TBDPS	*tert*-butyldiphenylsilyl
TBS	*tert*-butyldimethylsilyl
TES	triethylsilyl
TIPS	triisopropylsilyl
TLC	thin-layer chromatography
TMEDA	*N*,*N*,*N*′,*N*′-tetramethylethylenediamine
TMS	trimethylsilyl
Ts	4-toluenesulfonyl

It is with enormous pride and great pleasure that we thank our collaborators whose names appear in the references cited and whose contributions made the described work so rewarding and enjoyable. We also acknowledge helpful discussions with Professor Phil S. Baran. We gratefully acknowledge the National Institutes of Health (USA), the Skaggs Institute for Chemical Biology, the George E. Hewitt Foundation, Amgen, Merck, Novartis, and Pfizer for supporting our research programs.

Received: January 31, 2005

[1] *Grignard Reagents: New Developments* (Ed.: H. G. Richey), Wiley, Chichester, **2000**, p. 418.
[2] For an overview of the utility of the Diels–Alder reaction in total synthesis, see: K. C. Nicolaou, S. A. Snyder, T. Montagnon, G. Vassilikogiannakis, *Angew. Chem.* **2002**, *114*, 1742–1773; *Angew. Chem. Int. Ed.* **2002**, *41*, 1668–1698.
[3] K. C. Nicolaou, M. W. Härter, J. L. Gunzner, A. Nadin, *Liebigs Ann./Recl.* **1997**, 1283–1301.
[4] K. C. Nicolaou, P. G. Bulger, D. Sarlah, *Angew. Chem.* **2005**, *117*, 4516–4563, *Angew. Chem. Int. Ed.* **2005**, *44*, 4442–4489, preceding Review article in this issue.
[5] For a comprehensive treatise of metathesis reactions and applications, see: *Handbook of Metathesis*, *Vols. 1, 2, 3* (Ed.: R. H. Grubbs), Wiley-VCH, Weinheim, **2003**, p. 1234.
[6] For reviews of the alkene-metathesis reaction, see: a) B. Schmidt, J. Hermanns, *Top. Organomet. Chem.* **2004**, *7*, 223–267; b) S. J. Connon, S. Blechert, *Top. Organomet. Chem.* **2004**, *7*, 93–124; c) A. Fürstner, *Angew. Chem.* **2000**, *112*, 3140–3172; *Angew. Chem. Int. Ed.* **2000**, *39*, 3012–3043; d) R. H. Grubbs, S. Chang, *Tetrahedron* **1998**, *54*, 4413–4450; for a review of olefin and enyne metathesis, see: J. Prunet, L. Grimauld, *Comprehensive Organic Functional Group Transformations II*, *Vol. 1* (Eds.: A. R. Katritzky, R. J. K. Taylor), Elsevier, Oxford, **2005**, pp. 669–722.
[7] a) K. J. Ivin, J. C. Mol, *Olefin Metathesis and Metathesis Polymerization*, Academic Press, San Diego, **1997**, p. 496; b) K. C. Nicolaou, S. A. Snyder, *Classics in Total Synthesis II*, Wiley-VCH, Weinheim, **2003**, pp. 166–172; c) T. M. Trnka, R. H. Grubbs, *Acc. Chem. Res.* **2001**, *34*, 18–29.
[8] J.-L. Hérisson, Y. Chauvin, *Makromol. Chem.* **1971**, *141*, 161–176.
[9] C. P. Casey, T. J. Burkhardt, *J. Am. Chem. Soc.* **1974**, *96*, 7808–7809.
[10] T. J. Katz, J. McGinnis, *J. Am. Chem. Soc.* **1975**, *97*, 1592–1594.
[11] a) R. H. Grubbs, P. L. Burk, D. D. Carr, *J. Am. Chem. Soc.* **1975**, *97*, 3265–3267; b) R. H. Grubbs, D. D. Carr, C. Hoppin, P. L. Burk, *J. Am. Chem. Soc.* **1976**, *98*, 3478–3483.
[12] a) J. McGinnis, T. J. Katz, S. Hurwitz, *J. Am. Chem. Soc.* **1976**, *98*, 605–606; b) T. J. Katz, J. McGinnis, C. Altus, *J. Am. Chem. Soc.* **1976**, *98*, 606–608; c) T. J. Katz, S. J. Lee, N. Acton, *Tetrahedron Lett.* **1976**, *17*, 4247–4250; d) T. J. Katz, N. Acton, *Tetrahedron Lett.* **1976**, *17*, 4251–4254; e) S. J. Lee, J. McGinnis, T. J. Katz, *J. Am. Chem. Soc.* **1976**, *98*, 7818–7819.
[13] T. J. Katz, *Angew. Chem.* **2005**, *117*, 3070–3079; *Angew. Chem. Int. Ed.* **2005**, *44*, 3010–3019.
[14] For specific reviews of the enyne-metathesis reaction, see: a) S. T. Diver, A. J. Giessert, *Chem. Rev.* **2004**, *104*, 1317–1382; b) C. S. Poulsen, R. Madsen, *Synthesis* **2003**, 1–18; c) M. Mori, *Top. Organomet. Chem.* **1998**, *1*, 133–154.
[15] B. M. Trost, *Acc. Chem. Res.* **2002**, *35*, 695–705.
[16] T. J. Katz, T. M. Sivavec, *J. Am. Chem. Soc.* **1985**, *107*, 737–738.
[17] a) B. M. Trost, G. J. Tanoury, *J. Am. Chem. Soc.* **1988**, *110*, 1636–1638; b) B. M. Trost, V. K. Chang, *Synthesis* **1993**, 824–832.
[18] More recently, analogous gallium(III)-catalyzed skeletal reorganizations of enynes have been reported: N. Chatani, H. Inoue, T. Kotsuma, S. Murai, *J. Am. Chem. Soc.* **2002**, *124*, 10294–10295.
[19] C. Aubert, O. Buisine, M. Malacria, *Chem. Rev.* **2002**, *102*, 813–814.
[20] For a review of transition-metal-catalyzed cycloisomerizations, see: B. M. Trost, M. J. Krische, *Synlett* **1998**, 1–18.
[21] N. Chatani, T. Morimoto, T. Muto, S. Murai, *J. Am. Chem. Soc.* **1994**, *116*, 6049–6050.
[22] N. Chatani, H. Inoue, T. Morimoto, T. Muto, S. Murai, *J. Org. Chem.* **2001**, *66*, 4433–4436.

 © 2005 Wiley-VCH Verlag GmbH & Co. KGaA, Weinheim

[23] a) N. Chatani, N. Furukawa, H. Sakurai, S. Murai, *Organometallics* **1996**, *15*, 901 – 903; b) A. Fürstner, F. Stelzer, H. Szillat, *J. Am. Chem. Soc.* **2001**, *123*, 11 863 – 11 869.
[24] For specific reviews of the alkyne-metathesis reaction, see: a) A. Fürstner, P. W. Davies, *Chem. Commun.* **2005**, 2307 – 2320; b) T. Lindel in *Organic Synthesis Highlights V* (Eds.: H.-G. Schmalz, T. Wirth), Wiley-VCH, Weinheim, **2003**, pp. 27 – 35; c) U. H. F. Bunz, L. Kloppenburg, *Angew. Chem.* **1999**, *111*, 503 – 505; *Angew. Chem. Int. Ed.* **1999**, *38*, 478 – 481.
[25] A. Mortreux, M. Blanchard, *J. Chem. Soc. Chem. Commun.* **1974**, 786 – 787.
[26] Heterogeneous catalysis of alkyne metathesis (at temperatures between 200 and 450 °C) had been documented earlier: F. Pennella, R. L. Banks, G. C. Bailey, *J. Chem. Soc. Chem. Commun.* **1968**, 1548 – 1549.
[27] J. Mulzer, E. Öhler, *Top. Organomet. Chem.* **2004**, *7*, 269 – 366.
[28] R. R. Schrock, J. S. Murdzek, G. C. Bazan, J. Robbins, M. DiMare, M. O'Regan, *J. Am. Chem. Soc.* **1990**, *112*, 3875 – 3886.
[29] For reviews of the use of molybdenum imido alkylidene catalysts in alkene metathesis, see: a) R. R. Schrock, A. H. Hoveyda, *Angew. Chem.* **2003**, *115*, 4740 – 4782; *Angew. Chem. Int. Ed.* **2003**, *42*, 4592 – 4633; b) R. R. Schrock, *Tetrahedron* **1999**, *55*, 8141 – 8153; c) R. R. Schrock, *Top. Organomet. Chem.* **1998**, *1*, 1 – 36.
[30] A well-defined rhenium(VII) alkene-metathesis catalyst was also developed by the Schrock group, but has not found widespread use: R. Toreki, R. R. Schrock, *J. Am. Chem. Soc.* **1990**, *112*, 2448 – 2449.
[31] S. T. Nguyen, L. K. Johnson, R. H. Grubbs, J. W. Ziller, *J. Am. Chem. Soc.* **1992**, *114*, 3974 – 3975.
[32] a) P. Schwab, M. B. France, J. W. Ziller, R. H. Grubbs, *Angew. Chem.* **1995**, *107*, 2179 – 2181; *Angew. Chem. Int. Ed. Engl.* **1995**, *34*, 2039 – 2041; b) P. Schwab, R. H. Grubbs, J. W. Ziller, *J. Am. Chem. Soc.* **1996**, *118*, 100 – 110.
[33] For reviews of the utility of *N*-heterocyclic carbene ligands in transition-metal catalysis, see: a) W. A. Herrmann, *Angew. Chem.* **2002**, *114*, 1342 – 1363; *Angew. Chem. Int. Ed.* **2002**, *41*, 1290 – 1309; b) W. A. Herrmann, C. Köcher, *Angew. Chem.* **1997**, *109*, 2257 – 2282; *Angew. Chem. Int. Ed. Engl.* **1997**, *36*, 2162 – 2187.
[34] a) T. Weskamp, F. J. Kohl, W. Hieringer, D. Gleich, W. A. Herrmann, *Angew. Chem.* **1999**, *111*, 2573 – 2576; *Angew. Chem. Int. Ed.* **1999**, *38*, 2416 – 2419; b) M. Scholl, T. M. Trnka, J. P. Morgan, R. H. Grubbs, *Tetrahedron Lett.* **1999**, *40*, 2247 – 2250; c) J. Huang, E. D. Stevens, S. P. Nolan, J. L. Petersen, *J. Am. Chem. Soc.* **1999**, *121*, 2674 – 2678; d) J. Huang, H.-J. Schanz, E. D. Stevens, S. P. Nolan, *Organometallics* **1999**, *18*, 5375 – 5380; e) L. Ackermann, A. Fürstner, T. Weskamp, F. J. Kohl, W. A. Herrmann, *Tetrahedron Lett.* **1999**, *40*, 4787 – 4790.
[35] These studies had been preceded by a pioneering report by the Herrmann group in which *both* phosphine ligands in the first-generation ruthenium complex were replaced with *N*-heterocyclic carbene ligands: T. Weskamp, W. C. Schattenmann, M. Spiegler, W. A. Herrmann, *Angew. Chem.* **1998**, *110*, 2631 – 2633; *Angew. Chem. Int. Ed.* **1998**, *37*, 2490 – 2493.
[36] M. Scholl, S. Ding, C. W. Lee, R. H. Grubbs, *Org. Lett.* **1999**, *1*, 953 – 956.
[37] For examples of the development of novel catalysts for metathesis, see: a) H. Wakamatsu, S. Blechert, *Angew. Chem.* **2002**, *114*, 2509 – 2511; *Angew. Chem. Int. Ed.* **2002**, *41*, 2403 – 2405; b) S. J. Connon, A. M. Dunne, S. Blechert, *Angew. Chem.* **2002**, *114*, 3989 – 3993; *Angew. Chem. Int. Ed.* **2002**, *41*, 3835 – 3838; c) J. J. Van Veldhuizen, S. B. Garber, J. S. Kingsbury, A. H. Hoveyda, *J. Am. Chem. Soc.* **2002**, *124*, 4954 – 4955; d) A. Fürstner, L. Ackermann, B. Gabor, R. Goddard, C. W. Lehmann, R. Mynott, F. Stelzer, O. R. Thiel, *Chem. Eur. J.* **2001**, *7*, 3236 – 3253.
[38] For a review of the synthesis of oxygen- and nitrogen-containing heterocycles by ring-closing metathesis, see: a) A. Deiters, S. F. Martin, *Chem. Rev.* **2004**, *104*, 2199 – 2238; for a review of the synthesis of phosphorus- and sulfur-containing heterocycles by ring-closing metathesis, see: b) M. D. McReynolds, J. M. Dougherty, P. R. Hanson, *Chem. Rev.* **2004**, *104*, 2239 – 2258; for a review of total syntheses of piperidine and pyrrolidine alkaloids with ring-closing metathesis as a key step, see: c) F.-X. Felpin, J. Lebreton, *Eur. J. Org. Chem.* **2003**, 3693 – 3712.
[39] K. C. Nicolaou, R. M. Rodríguez, H. J. Mitchell, F. L. van Delft, *Angew. Chem.* **1998**, *110*, 1975 – 1977; *Angew. Chem. Int. Ed.* **1998**, *37*, 1874 – 1876.
[40] For a review of the applications of alkene metathesis and related reactions in carbohydrate chemistry, see: R. Roy, S. K. Das, *Chem. Commun.* **2000**, 519 – 529.
[41] For the total synthesis of this complex oligosaccharide, see: a) K. C. Nicolaou, H. J. Mitchell, H. Suzuki, R. M. Rodriguez, O. Baudoin, K. C. Fylatakidou, *Angew. Chem.* **1999**, *111*, 3523 – 3528; *Angew. Chem. Int. Ed.* **1999**, *38*, 3334 – 3339; b) K. C. Nicolaou, R. M. Rodríguez, K. C. Fylaktakidou, H. Suzuki, H. J. Mitchell, *Angew. Chem.* **1999**, *111*, 3529 – 3534; *Angew. Chem. Int. Ed.* **1999**, *38*, 3340 – 3345; c) K. C. Nicolaou, H. J. Mitchell, R. M. Rodríguez, K. C. Fylaktakidou, H. Suzuki, *Angew. Chem.* **1999**, *111*, 3535 – 3540; *Angew. Chem. Int. Ed.* **1999**, *38*, 3345 – 3350; d) K. C. Nicolaou, R. M. Rodríguez, H. J. Mitchell, H. Suzuki, K. C. Fylaktakidou, O. Baudoin, F. L. van Delft, *Chem. Eur. J.* **2000**, *6*, 3095 – 3115; e) K. C. Nicolaou, H. J. Mitchell, K. C. Fylaktakidou, R. M. Rodríguez, H. Suzuki, *Chem. Eur. J.* **2000**, *6*, 3116 – 3148; f) K. C. Nicolaou, H. J. Mitchell, R. M. Rodríguez, K. C. Fylaktakidou, H. Suzuki, S. R. Conley, *Chem. Eur. J.* **2000**, *6*, 3149 – 3165.
[42] A. Nickel, T. Maruyama, H. Tang, P. D. Murphy, B. Greene, N. Yusuff, J. L. Wood, *J. Am. Chem. Soc.* **2004**, *126*, 16 300 – 16 301.
[43] S. Kim, J. Winkler, *Chem. Soc. Rev.* **1997**, *26*, 387 – 399.
[44] M. Blanco-Molina, G. C. Tron, A. Macho, C. Lucena, M. A. Calzado, E. Muñoz, G. Appendino, *Chem. Biol.* **2001**, *8*, 767 – 778, and references therein.
[45] For a review of inside–outside isomerism, see: R. W. Alder, S. P. East, *Chem. Rev.* **1992**, *92*, 2097 – 2111.
[46] For the successful construction of this bridgehead junction with the correct stereochemistry, see: a) J. H. Rigby, B. Bazin, J. H. Meyer, F. Mohammadi, *Org. Lett.* **2002**, *4*, 799 – 801; b) R. L. Funk, T. A. Olmstead, M. Parvez, J. B. Stallman, *J. Am. Chem. Soc.* **1993**, *115*, 5873 – 5875.
[47] For other total syntheses of ingenol, see: a) K. Tanino, K. Onuki, K. Asano, M. Miyashita, T. Nakamura, Y. Takahashi, I. Kuwajima, *J. Am. Chem. Soc.* **2003**, *125*, 1498 – 1500; b) J. D. Winkler, M. B. Rouse, M. F. Greaney, S. J. Harrison, Y. T. Jeon, *J. Am. Chem. Soc.* **2002**, *124*, 9726 – 9728; for a formal total synthesis, see: c) K. Watanabe, Y. Suzuki, K. Aoki, A. Sakakura, K. Suenaga, H. Kigoshi, *J. Org. Chem.* **2004**, *69*, 7802 – 7808.
[48] It is worth recalling that ring-opening-metathesis polymerization reactions are widely used in the industrial production of polymers of great commercial value. For examples, see: M. Schuster, S. Blechert, *Angew. Chem.* **1997**, *109*, 2124 – 2145; *Angew. Chem. Int. Ed. Engl.* **1997**, *36*, 2036 – 2056, and references therein.
[49] H. Tang, N. Yusuff, J. L. Wood, *Org. Lett.* **2001**, *3*, 1563 – 1566.
[50] A related metathesis-based approach to the ingenol ABC-ring core structure has also been reported: H. Kigoshi, Y. Suzuki, K. Aoki, D. Uemura, *Tetrahedron Lett.* **2000**, *41*, 3927 – 3930.
[51] S. B. Garber, J. S. Kingsbury, B. L. Gray, A. H. Hoveyda, *J. Am. Chem. Soc.* **2000**, *122*, 8168 – 8179.

 © 2005 Wiley-VCH Verlag GmbH & Co. KGaA, Weinheim

[52] S. Gessler, S. Randl, S. Blechert, *Tetrahedron Lett.* **2000**, *41*, 9973 – 9976.

[53] For a very recent approach to the "inside–outside" tetracyclic core structure of ingenol employing ring-closing metathesis, see: O. L. Epstein, J. K. Cha, *Angew. Chem.* **2005**, *117*, 123 – 125; *Angew. Chem. Int. Ed.* **2005**, *44*, 121 – 123.

[54] P. A. Evans, J. Cui, S. J. Gharpure, A. Polosukhin, H.-R. Zhang, *J. Am. Chem. Soc.* **2003**, *125*, 14702 – 14703.

[55] For reviews of the utility of temporary silicon tethers in organic synthesis, see: a) L. Fensterbank, M. Malacria, S. M. Sieburth, *Synthesis* **1997**, 813 – 854; b) M. Bols, T. Skrydstrup, *Chem. Rev.* **1995**, *95*, 1253 – 1277.

[56] The first application of a silicon-tethered ring-closing-metathesis reaction in a total synthesis had been disclosed the previous year by the Eustache group, in their elegant synthesis of attenol A: P. Van de Weghe, D. Aoun, J.-G. Boiteau, J. Eustache, *Org. Lett.* **2002**, *4*, 4105 – 4108.

[57] For other examples of silicon-tethered ring-closing-metathesis reactions, see: a) B. A. Harrison, G. L. Verdine, *Org. Lett.* **2001**, *3*, 2157 – 2159; b) S. E. Denmark, S.-M. Yang, *Org. Lett.* **2001**, *3*, 1749 – 1752; c) T. M. Gerash, M. Chytil, M. T. Didiuk, J. Y. Park, J. J. Urban, S. P. Nolan, G. L. Verdine, *Org. Lett.* **2000**, *2*, 3999 – 4000; d) A. Briot, M. Bujard, V. Gouverneur, S. P. Nolan, C. Mioskowski, *Org. Lett.* **2000**, *2*, 1517 – 1519; e) T. R. Hoye, M. A. Promo, *Tetrahedron Lett.* **1999**, *40*, 1429 – 1432; f) P. A. Evans, V. S. Murthy, *J. Org. Chem.* **1998**, *63*, 6768 – 6769; g) G. C. Fu, R. H. Grubbs, *J. Am. Chem. Soc.* **1992**, *114*, 7324 – 7325.

[58] P. A. Evans, J. Cui, G. P. Buffone, *Angew. Chem.* **2003**, *115*, 1776 – 1779; *Angew. Chem. Int. Ed.* **2003**, *42*, 1734 – 1737.

[59] For other total syntheses of mucocin, see: a) S. Takahashi, A. Kubota, T. Nakata, *Angew. Chem.* **2002**, *114*, 4945 – 4948; *Angew. Chem. Int. Ed.* **2002**, *41*, 4751 – 4754; b) S. Takahashi, T. Nakata, *J. Org. Chem.* **2002**, *67*, 5739 – 5752; c) S. Bäurle, S. Hoppen, U. Koert, *Angew. Chem.* **1999**, *111*, 1341 – 1344; *Angew. Chem. Int. Ed.* **1999**, *38*, 1263 – 1266; d) P. Neogi, T. Doundoulakis, A. Yazbak, S. C. Sinha, S. C. Sinha, E. Keinan, *J. Am. Chem. Soc.* **1998**, *120*, 11279 – 11284.

[60] Another temporary tether that has found use in ring-closing-metathesis applications is the ester linkage; for an example, see: G. L. Nattrass, E. Diez, M. M. McLachlan, D. J. Dixon, S. V. Ley, *Angew. Chem.* **2005**, *117*, 586 – 590; *Angew. Chem. Int. Ed.* **2005**, *44*, 580 – 584.

[61] For a Review of the synthesis of medium-sized rings by the ring-closing-metathesis reaction, see: M. E. Maier, *Angew. Chem.* **2000**, *112*, 2153 – 2157; *Angew. Chem. Int. Ed.* **2000**, *39*, 2073 – 2076.

[62] a) K. C. Nicolaou, G. Vassilikogiannakis, T. Montagnon, *Angew. Chem.* **2002**, *114*, 3410 – 3415; *Angew. Chem. Int. Ed.* **2002**, *41*, 3276 – 3281; b) G. Vassilikogiannakis, I. Margaros, M. Tofi, *Org. Lett.* **2004**, *6*, 205 – 208; c) K. C. Nicolaou, T. Montagnon, G. Vassilikogiannakis, C. J. N. Mathison, *J. Am. Chem. Soc.* **2005**, *127*, 8872 – 8888.

[63] A number of other ingenious concepts for controlling the stereochemical course of ring-closing-metathesis reactions to generate medium-sized ring systems have been developed; for selected examples, see: a) A. Fürstner, K. Radkowski, C. Wirtz, R. Goddard, C. W. Lehmann, R. Mynott, *J. Am. Chem. Soc.* **2002**, *124*, 7061 – 7069 (selective formation of either the *E* or *Z* isomer by exerting either kinetic or thermodynamic control, respectively, in the ring-closing-metathesis event); b) A. Ivkovic, R. Matovic, R. N. Saicic, *Org. Lett.* **2004**, *6*, 1221 – 1224 (a ring-closing-metathesis/Grob fragmentation strategy to afford *Z*-configured medium-sized cycloalkenes); c) E. A. Couladouros, A. P. Mihou, E. A. Bouzas, *Org. Lett.* **2004**, *6*, 977 – 980 (control of metathesis precursor conformation through the presence or absence of intramolecular hydrogen bonding, leading to *Z*- or *E*-configured cycloalkenes, respectively).

[64] a) M. Inoue, K. Miyazaki, H. Uehara, M. Maruyama, M. Hirama, *Proc. Natl. Acad. Sci. USA* **2004**, *101*, 12013 – 12018; b) M. Inoue, H. Uehara, M. Maruyama, M. Hirama, *Org. Lett.* **2002**, *4*, 4551 – 4554; c) M. Hirama, T. Oishi, H. Uehara, M. Inoue, M. Maruyama, H. Oguri, M. Satake, *Science* **2001**, *294*, 1904 – 1907.

[65] Z. Xu, C. W. Johnson, S. S. Salman, A. H. Hoveyda, *J. Am. Chem. Soc.* **1996**, *118*, 10926 – 10927.

[66] For a discussion of the parameters required for successful macrocyclization, see: A. Fürstner, G. Siedel, N. Kindler, *Tetrahedron* **1999**, *55*, 8215 – 8230.

[67] For a discussion of the chemistry, biology, and medicine of the epothilones, see: K. C. Nicolaou, A. Ritzén, K. Namoto, *Chem. Commun.* **2001**, 1523 – 1535, and references therein.

[68] a) Z. Yang, Y. He, D. Vourloumis, H. Vallberg, K. C. Nicolaou, *Angew. Chem.* **1997**, *109*, 170 – 173; *Angew. Chem. Int. Ed. Engl.* **1997**, *36*, 166 – 168; b) K. C. Nicolaou, Y. He, D. Vourloumis, H. Vallberg, F. Roschangar, F. Sarabia, S. Ninkovic, Z. Yang, J. I. Trujillo, *J. Am. Chem. Soc.* **1997**, *119*, 7960 – 7973.

[69] D. Meng, P. Bertinato, A. Balog, D.-S. Su, T. Kamenecka, E. J. Sorensen, S. J. Danishefsky, *J. Am. Chem. Soc.* **1997**, *119*, 10073 – 11092.

[70] The Danishefsky group had previously reported the first total synthesis of epothilone C, in which they employed a non-metathesis-based approach: A. Balog, D. Meng, T. Kamenecka, P. Bertinato, D.-S. Su, E. J. Sorensen, S. J. Danishefsky, *Angew. Chem.* **1996**, *108*, 2976 – 2978; *Angew. Chem. Int. Ed. Engl.* **1996**, *35*, 2801 – 2803.

[71] a) D. Schinzer, A. Limberg, A. Bauer, O. M. Böhm, M. Cordes, *Angew. Chem.* **1997**, *109*, 543 – 544; *Angew. Chem. Int. Ed. Engl.* **1997**, *36*, 523 – 524; b) D. Schinzer, A. Bauer, O. M. Böhm, A. Limberg, M. Cordes, *Chem. Eur. J.* **1999**, *5*, 2483 – 2491.

[72] For examples of variations in *E*/*Z* selectivity, see: J. Prunet, *Angew. Chem.* **2003**, *115*, 2932 – 2936; *Angew. Chem. Int. Ed.* **2003**, *42*, 2826 – 2830, and references therein.

[73] For examples and a discussion of this concept, see: A. Fürstner, T. Dierkes, O. R. Thiel, G. Blanda, *Chem. Eur. J.* **2001**, *7*, 5286 – 5298, and references therein.

[74] For general discussions of this topic, see: *Handbook of Combinatorial Chemistry: Drugs, Catalysts, Methods, Vols. 1, 2* (Eds.: K. C. Nicolaou, R. Hanko, W. Hartwig), Wiley-VCH, Weinheim, **2002**, p. 1114.

[75] For a discussion of the concepts of ring-closing metathesis applied to polymer-bound substrates, see: J.-U. Peters, S. Blechert, *Synlett* **1997**, 348 – 350.

[76] a) K. C. Nicolaou, N. Winssinger, J. Pastor, S. Ninkovic, F. Sarabia, Y. He, D. Vourloumis, Z. Yang, T. Li, P. Giannakakou, E. Hamel, *Nature* **1997**, *387*, 268 – 272; b) K. C. Nicolaou, D. Vourloumis, T. Li, J. Pastor, N. Winssinger, Y. He, S. Ninkovic, F. Sarabia, H. Vallberg, F. Roschangar, N. P. King, M. R. V. Finlay, P. Giannakakou, P. Verdier-Pinard, E. Hamel, *Angew. Chem.* **1997**, *109*, 2181 – 2187; *Angew. Chem. Int. Ed. Engl.* **1997**, *36*, 2097 – 2103.

[77] R. E. Maleczka, Jr., L. R. Terrell, F. Geng, J. S. Ward III, *Org. Lett.* **2002**, *4*, 2841 – 2844.

[78] A similar observation has been reported: T. R. Hoye, H. Zhao, *Org. Lett.* **1999**, *1*, 1123 – 1125.

[79] The originally proposed structure of amphidinolide A was also synthesized by the Pattenden and Trost groups at around the same time; both groups confirmed that it did not correspond to the natural product: a) H. W. Lam, G. Pattenden, *Angew. Chem.* **2002**, *114*, 526 – 529; *Angew. Chem. Int. Ed.* **2002**, *41*,

 © 2005 Wiley-VCH Verlag GmbH & Co. KGaA, Weinheim

508 – 511; b) B. M. Trost, J. D. Chisholm, S. A. Wrobleski, M. Jung, *J. Am. Chem. Soc.* **2002**, *124*, 12420 – 12421.
[80] B. M. Trost, P. E. Harrington, *J. Am. Chem. Soc.* **2004**, *126*, 5028 – 5029.
[81] For examples of the use of metathesis reactions in the total synthesis of other members of the amphidinolide family of natural products, see: a) A. K. Ghosh, G. Gong, *J. Am. Chem. Soc.* **2004**, *126*, 3704 – 3705; b) C. Aïssa, R. Riveiros, J. Ragot, A. Fürstner, *J. Am. Chem. Soc.* **2003**, *125*, 15512 – 15520; c) A. K. Ghosh, C. Liu, *J. Am. Chem. Soc.* **2003**, *125*, 2374 – 2375; d) A. Fürstner, C. Aïssa, R. Riveiros, J. Ragot, *Angew. Chem.* **2002**, *114*, 4958 – 4960; *Angew. Chem. Int. Ed.* **2002**, *41*, 4763 – 4766.
[82] a) A. Fürstner, F. Jeanjean, P. Razon, *Angew. Chem.* **2002**, *114*, 2203 – 2206; *Angew. Chem. Int. Ed.* **2002**, *41*, 2097 – 2101; b) A. Fürstner, F. Jeanjean, P. Razon, C. Wirtz, R. Mynott, *Chem. Eur. J.* **2003**, *9*, 307 – 319; c) A. Fürstner, F. Jeanjean, P. Razon, C. Wirtz, R. Mynott, *Chem. Eur. J.* **2003**, *9*, 320 – 326.
[83] For a review of the total synthesis and biological evaluation of macrocyclic glycolipids, see: A. Fürstner, *Eur. J. Org. Chem.* **2004**, 943 – 958.
[84] S. Barluenga, P. Lopez, E. Moulin, N. Winssinger, *Angew. Chem.* **2004**, *116*, 3549 – 3552; *Angew. Chem. Int. Ed.* **2004**, *43*, 3467 – 3470.
[85] Analogous ring-closing-metathesis approaches to the synthesis of the structurally related natural product radicicol had been documented: a) R. M. Garbaccio, S. J. Stachel, D. K. Baeschlin, S. J. Danishefsky, *J. Am. Chem. Soc.* **2001**, *123*, 10903 – 10908; b) Z.-Q. Yang, S. J. Danishefsky, *J. Am. Chem. Soc.* **2003**, *125*, 9602 – 9603.
[86] For examples of this general phenomenon of regioselectivity on the ring-closing-metathesis reactions of diene–ene systems, see: L. A. Paquette, K. Basu, J. C. Eppich, J. E. Hofferberth, *Helv. Chim. Acta* **2002**, *85*, 3033 – 3051.
[87] K. Yamamoto, K. Biswas, C. Gaul, S. J. Danishefsky, *Tetrahedron Lett.* **2003**, *44*, 3297 – 3299.
[88] For an excellent review of the principles and practice of relay ring-closing metathesis, see: D. J. Wallace, *Angew. Chem.* **2005**, *117*, 1946 – 1949; *Angew. Chem. Int. Ed.* **2005**, *44*, 1912 – 1915.
[89] X. Wang, E. J. Bowman, B. J. Bowman, J. A. Porco, Jr., *Angew. Chem.* **2004**, *116*, 3685 – 3689; *Angew. Chem. Int. Ed.* **2004**, *43*, 3601 – 3605.
[90] T. R. Hoye, C. S. Jeffrey, M. A. Tennakoon, J. Wang, H. Zhao, *J. Am. Chem. Soc.* **2004**, *126*, 10210 – 10211.
[91] For selected additional examples of diene–ene-metathesis reactions in natural product synthesis, see: a) G. Evano, J. V. Schaus, J. S. Panek, *Org. Lett.* **2004**, *6*, 525 – 528; b) K. Biswas, H. Lin, J. T. Njardarson, M. D. Chappell, T.-C. Chou, Y. Guan, W. P. Tong, L. He, S. B. Horwitz, S. J. Danishefsky, *J. Am. Chem. Soc.* **2002**, *124*, 9825 – 9832; c) C. A. Dvorak, W. D. Schmitz, D. J. Poon, D. C. Pryde, J. P. Lawson, R. A. Amos, A. I. Meyers, *Angew. Chem.* **2000**, *112*, 1730 – 1732; *Angew. Chem. Int. Ed.* **2000**, *39*, 1664 – 1666.
[92] For reviews of alkene cross-metathesis, see: a) S. J. Connon, S. Blechert, *Angew. Chem.* **2003**, *115*, 1944 – 1968; *Angew. Chem. Int. Ed.* **2003**, *42*, 1900 – 1923; b) S. E. Gibson, S. P. Keen, *Top. Organomet. Chem.* **1998**, *1*, 155 – 181.
[93] a) A. K. Chatterjee, T.-L. Choi, D. P. Sanders, R. H. Grubbs, *J. Am. Chem. Soc.* **2003**, *125*, 11360 – 11370; b) H. E. Blackwell, D. J. O'Leary, A. K. Chatterjee, R. A. Washenfelder, D. A. Bussmann, R. H. Grubbs, *J. Am. Chem. Soc.* **2000**, *122*, 58 – 71.
[94] For reviews of the glycopeptide antibiotics, see: a) K. C. Nicolaou, C. N. C. Boddy, S. Bräse, N. Winssinger, *Angew. Chem.* **1999**, *111*, 2230 – 2287; *Angew. Chem. Int. Ed.* **1999**, *38*, 2096 – 2152; b) D. H. Williams, B. Bardsley, *Angew. Chem.* **1999**, *111*, 1264 – 1286; *Angew. Chem. Int. Ed.* **1999**, *38*, 1172 – 1193.
[95] a) K. C. Nicolaou, S. Y. Cho, R. Hughes, N. Winssinger, C. Smethurst, H. Labischinski, R. Endermann, *Chem. Eur. J.* **2001**, *7*, 3798 – 3823; b) K. C. Nicolaou, R. Hughes, S. Y. Cho, N. Winssinger, H. Labischinski, R. Endermann, *Chem. Eur. J.* **2001**, *7*, 3824 – 3843.
[96] The Schreiber group pioneered this strategy of dimerization of biologically relevant compounds through alkene cross-metathesis in their synthesis of novel dimers of the immunosuppressant FK506: S. T. Diver, S. L. Schreiber, *J. Am. Chem. Soc.* **1997**, *119*, 5106 – 5109.
[97] For representative references, see: a) D. Bradley, *Drug Discovery Today* **2000**, *5*, 44 – 45; b) S. J. Sucheck, A. L. Wong, K. M. Koeller, D. D. Boehr, K. Draker, P. Sears, G. D. Wright, C.-H. Wong, *J. Am. Chem. Soc.* **2000**, *122*, 5230 – 5231; c) P. J. Loll, A. E. Bevivino, B. D. Korty, P. H. Axelsen, *J. Am. Chem. Soc.* **1997**, *119*, 1516 – 1522; d) J. P. Mackay, U. Gerhard, D. A. Beauregard, R. A. Maplestone, D. H. Williams, *J. Am. Chem. Soc.* **1994**, *116*, 4573 – 4580.
[98] a) D. H. Williams, A. J. Maguire, W. Tsuzuki, M. S. Westwell, *Science* **1998**, *280*, 711 – 714; b) J. P. Mackay, U. Gerhard, D. A. Beauregard, M. S. Westwell, M. S. Searle, D. H. Williams, *J. Am. Chem. Soc.* **1994**, *116*, 4581 – 4590; c) U. Gerhard, J. P. Mackay, R. A. Maplestone, D. H. Williams, *J. Am. Chem. Soc.* **1993**, *115*, 232 – 237.
[99] For an entry to this field, see the following papers and references therein: a) J.-M. Lehn, A. V. Eliseev, *Science* **2001**, *291*, 2331 – 2332; b) G. R. L. Cousins, R. L. E. Furlan, Y.-F. Ng, J. E. Redman, J. K. M. Sanders, *Angew. Chem.* **2001**, *113*, 437 – 442; *Angew. Chem. Int. Ed.* **2001**, *40*, 423 – 428; c) H. Hioki, W. C. Still, *J. Org. Chem.* **1998**, *63*, 904 – 905; d) T. Giger, M. Wigger, S. Audétat, S. A. Benner, *Synlett* **1998**, 688 – 691.
[100] a) Z. Xiong, E. J. Corey, *J. Am. Chem. Soc.* **2000**, *122*, 4831 – 4832; b) Z. Xiong, E. J. Corey, *J. Am. Chem. Soc.* **2000**, *122*, 9328 – 9329.
[101] For selected recent reviews of approaches in biomimetic synthesis, see: a) M. C. de la Torre, M. A. Sierra, *Angew. Chem.* **2003**, *115*, 162 – 184; *Angew. Chem. Int. Ed.* **2003**, *42*, 160 – 181; b) K. C. Nicolaou, T. Montagnon, S. A. Snyder, *Chem. Commun.* **2003**, 551 – 564; c) U. Scholz, E. Winterfeldt, *Nat. Prod. Rep.* **2000**, *17*, 349 – 366.
[102] For selected recent examples of biomimetic syntheses, see: a) B. Gerard, G. Jones II, J. A. Porco, Jr., *J. Am. Chem. Soc.* **2004**, *126*, 13620 – 13621; b) S. K. Bagal, R. M. Adlington, J. E. Baldwin, R. Marquez, *J. Org. Chem.* **2004**, *69*, 9100 – 9108; c) G. Vassilikogiannakis, M. Stratakis, *Angew. Chem.* **2003**, *115*, 5623 – 5626; *Angew. Chem. Int. Ed.* **2003**, *42*, 5465 – 5468; d) B. M. Trost, H. C. Shen, J.-P. Surivet, *Angew. Chem.* **2003**, *115*, 4073 – 4077; *Angew. Chem. Int. Ed.* **2003**, *42*, 3943 – 3947.
[103] The synthesis of compound **77** was reported by the Kodama group, who confirmed that it did not correspond to the natural product, soon after the initial disclosure by the Corey group: H. Hioki, C. Kanehara, Y. Ohnishi, Y. Umemori, H. Sakai, S. Yoshio, M. Matsushita, M. Kodama, *Angew. Chem.* **2000**, *112*, 2652 – 2654; *Angew. Chem. Int. Ed.* **2000**, *39*, 2552 – 2554.
[104] The total synthesis and structure revision of glabrescol was first reported by the Morimoto group, who had to prepare a similarly large number of incorrect stereoisomers, a few weeks prior to the corresponding disclosure by the Corey group: Y. Morimoto, T. Iwai, T. Kinoshita, *J. Am. Chem. Soc.* **2000**, *122*, 7124 – 7125.
[105] Molecular-modeling studies subsequently indicated that the originally proposed structure does not correspond to the most thermodynamically favorable form: B. R. Bellenie, J. M. Goodman, *Tetrahedron Lett.* **2001**, *42*, 7477 – 7479.
[106] The Smith group has reported an elegant total synthesis of (−)-cylindrocyclophanes A and F by employing a novel tandem alkene cross-metathesis dimerization/ring-closing-metathesis

 © 2005 Wiley-VCH Verlag GmbH & Co. KGaA, Weinheim

strategy: A. B. Smith, C. M. Adams, S. A. Kozmin, D. V. Paone, *J. Am. Chem. Soc.* **2001**, *123*, 5925 – 5937; for a discussion of this and other cross-metathesis strategies, see reference [7b], pp. 178–184.

[107] The structure originally proposed for amphidinolide W (**86**) was the 6*S* diastereoisomer, which was also synthesized by the Ghosh group and shown to be different from the natural product.

[108] a) K. C. Nicolaou, S. Vyskocil, T. V. Koftis, Y. M. A. Yamada, T. Ling, D. Y.-K. Chen, W. Tang, G. Petrovic, M. O. Frederick, Y. Li, M. Satake, *Angew. Chem.* **2004**, *116*, 4412 – 4418; *Angew. Chem. Int. Ed.* **2004**, *43*, 4312 – 4318; b) K. C. Nicolaou, T. V. Koftis, S. Vyskocil, G. Petrovic, T. Ling, Y. M. A. Yamada, W. Tang, M. O. Frederick, *Angew. Chem.* **2004**, *116*, 4418 – 4424; *Angew. Chem. Int. Ed.* **2004**, *43*, 4318 – 4324.

[109] a) K. C. Nicolaou, Y. Li, N. Uesaka, T. V. Koftis, S. Vyskocil, T. Ling, M. Govindasamy, W. Qian, F. Bernal, D. Y.-K. Chen, *Angew. Chem.* **2003**, *115*, 3771 – 3776; *Angew. Chem. Int. Ed.* **2003**, *42*, 3643 – 3648; b) K. C. Nicolaou, D. Y.-K. Chen, Y. Li, W. Qian, T. Ling, S. Vyskocil, T. V. Koftis, M. Govindasamy, N. Uesaka, *Angew. Chem.* **2003**, *115*, 3777 – 3781; *Angew. Chem. Int. Ed.* **2003**, *42*, 3649 – 3653.

[110] A somewhat similar cross-metathesis strategy proceeded much less efficiently in model studies towards the synthesis of ciguatoxin CTX: H. Oguri, S. Sasaki, T. Oishi, M. Hirama, *Tetrahedron Lett.* **1999**, *40*, 5405 – 5408.

[111] a) J. E. Baldwin, presented at The Scripps Research Institute, La Jolla, 6th December 2004; b) M. F. Jacobsen, J. E. Moses, R. M. Adlington, J. E. Baldwin, *Org. Lett.* **2005**, *7*, 2473 – 2476.

[112] See C. M. Beaudry, D. Trauner, *Org. Lett.* **2002**, *4*, 2221 – 2224, and references therein.

[113] K. A. Parker, Y.-H. Lim, *J. Am. Chem. Soc.* **2004**, *126*, 15968 – 15969.

[114] J. E. Banfield, D. St. C. Black, S. R. Johns, R. I. Willing, *Aust. J. Chem.* **1982**, *35*, 2247 – 2256, and references therein.

[115] a) K. C. Nicolaou, N. A. Petasis, R. E. Zipkin, J. Uenishi, *J. Am. Chem. Soc.* **1982**, *104*, 5555 – 5557; b) K. C. Nicolaou, N. A. Petasis, J. Uenishi, R. E. Zipkin, *J. Am. Chem. Soc.* **1982**, *104*, 5557 – 5558; c) K. C. Nicolaou, R. E. Zipkin, N. A. Petasis, *J. Am. Chem. Soc.* **1982**, *104*, 5558 – 5560; d) K. C. Nicolaou, N. A. Petasis, R. E. Zipkin, *J. Am. Chem. Soc.* **1982**, *104*, 5560 – 5562.

[116] K. Kakinuma, C. A. Hanson, K. L. Rinehart, Jr., *Tetrahedron* **1976**, *32*, 212 – 222.

[117] J. E. Moses, J. E. Baldwin, R. Marquez, R. M. Adlington, A. R. Cowley, *Org. Lett.* **2002**, *4*, 3731 – 3734.

[118] C. Morrill, R. H. Grubbs, *J. Org. Chem.* **2003**, *68*, 6031 – 6034.

[119] Danishefsky and co-workers applied similar methodology in the synthesis of Suzuki macrocyclization precursors of novel epothilone analogues: J. T. Njardarson, K. Biswas, S. J. Danishefsky, *Chem. Commun.* **2002**, *23*, 2759 – 2761.

[120] For the first application of a selective mono-cross-coupling reaction of a 1,1-dibromoalkene, see: W. R. Roush, R. Riva, *J. Org. Chem.* **1988**, *53*, 710 – 713.

[121] C. Dai, G. C. Fu, *J. Am. Chem. Soc.* **2001**, *123*, 2719 – 2724.

[122] For a discussion of the reasoning behind the particular choice of a palladium(II) species to effect this isomerization, see reference [117].

[123] J. Limanto, M. L. Snapper, *J. Am. Chem. Soc.* **2000**, *122*, 8071 – 8072.

[124] P. A. Wender, N. C. Ihle, C. R. D. Correia, *J. Am. Chem. Soc.* **1988**, *110*, 5904 – 5906.

[125] Two other total syntheses of asteriscanolide, both employing ring-closing-metathesis reactions to construct the eight-membered ring, have been reported: a) M. E. Krafft, Y. Y. Cheung, K. A. Abboud, *J. Org. Chem.* **2001**, *66*, 7443 – 7448; b) M. E. Krafft, Y. Y. Cheung, C. A. Juliano-Capucao, *Synthesis* **2000**, 1020 – 1026; c) L. A. Paquette, J. Tae, M. P. Arrington, A. H. Sadoun, *J. Am. Chem. Soc.* **2000**, *122*, 2742 – 2748.

[126] R. Grigg, M. York, *Tetrahedron Lett.* **2000**, *41*, 7255 – 7258, and references therein.

[127] J. R. Stille, R. H. Grubbs, *J. Am. Chem. Soc.* **1986**, *108*, 855 – 856.

[128] a) F. N. Tebbe, G. W. Parshall, G. S. Reddy, *J. Am. Chem. Soc.* **1978**, *100*, 3611 – 3613; b) F. N. Tebbe, G. W. Parshall, D. W. Ovenall, *J. Am. Chem. Soc.* **1979**, *101*, 5074 – 5075.

[129] K. A. Brown-Wensley, S. L. Buchwald, L. Cannizzo, L. Clawson, S. Ho, D. Meinhardt, J. R. Stille, D. Straus, R. H. Grubbs, *Pure Appl. Chem.* **1983**, *55*, 1733 – 1744.

[130] D. A. Straus, R. H. Grubbs, *J. Mol. Catal.* **1985**, *28*, 9 – 19.

[131] F. N. Tebbe, G. W. Parshall, D. W. Ovenall, *J. Am. Chem. Soc.* **1979**, *101*, 5074 – 5075.

[132] More recently, dimethyltitanocene has been introduced as a more easily handled equivalent of the Tebbe reagent: N. A. Petasis, S.-P. Lu, E. I. Bzowej, D.-K. Fu, J. P. Staszewski, I. Adritopoulou-Zanze, M. A. Petane, Y.-H. Hu, *Pure Appl. Chem.* **1996**, *68*, 667 – 670.

[133] The Lebel group has recently reported novel one-pot methylenation/ring-closing-metathesis protocols that employ sequential rhodium- and ruthenium-based catalysts: H. Lebel, V. Paquet, *J. Am. Chem. Soc.* **2004**, *126*, 11152 – 11153.

[134] K. C. Nicolaou, M. H. D. Postema, C. F. Claiborne, *J. Am. Chem. Soc.* **1996**, *118*, 1565 – 1566.

[135] K. C. Nicolaou, M. H. D. Postema, E. W. Yue, A. Nadin, *J. Am. Chem. Soc.* **1996**, *118*, 10335 – 10336.

[136] H. W. B. Johnson, U. Majumder, J. D. Rainier, *J. Am. Chem. Soc.* **2005**, *127*, 848 – 849.

[137] a) J. M. Cox, J. D. Rainier, *Org. Lett.* **2001**, *3*, 2919 – 2922; b) U. Majumder, J. M. Cox, J. D. Rainier, *Org. Lett.* **2003**, *5*, 913 – 916.

[138] K. Takai, T. Kakiuchi, Y. Kataoka, K. Utimoto, *J. Org. Chem.* **1994**, *59*, 2668 – 2670.

[139] For other total syntheses of gambierol, see: a) I. Kadota, H. Takamura, K. Sato, A. Ohno, K. Matsuda, Y. Yamamoto, *J. Am. Chem. Soc.* **2003**, *125*, 46 – 47; b) I. Kadota, H. Takamura, K. Sato, A. Ohno, K. Matsuda, M. Satake, Y. Yamamoto, *J. Am. Chem. Soc.* **2003**, *125*, 11893 – 11899; c) H. Fuwa, N. Kainuma, K. Tachibana, M. Sasaki, *J. Am. Chem. Soc.* **2002**, *124*, 14983 – 14992, and references therein.

[140] K. C. Nicolaou, J. A. Vega, G. Vassilikogiannakis, *Angew. Chem.* **2001**, *113*, 4573 – 4577; *Angew. Chem. Int. Ed.* **2001**, *40*, 4441 – 4445.

[141] W. J. Zuercher, M. Hashimoto, R. H. Grubbs, *J. Am. Chem. Soc.* **1996**, *118*, 6634 – 6640.

[142] R. Stragies, S. Blechert, *J. Am. Chem. Soc.* **2000**, *122*, 9584 – 9591.

[143] M. Schaudt, S. Blechert, *J. Org. Chem.* **2003**, *68*, 2913 – 2920.

[144] C. Stapper, S. Blechert, *J. Org. Chem.* **2002**, *67*, 6456 – 6460.

[145] A. V. Statsuk, D. Liu, S. A. Kozmin, *J. Am. Chem. Soc.* **2004**, *126*, 9546 – 9547.

[146] For examples, see: a) D. J. Wallace, *Tetrahedron Lett.* **2003**, *44*, 2145 – 2148; b) M.-P. Heck, C. Baylon, S. P. Nolan, C. Mioskowski, *Org. Lett.* **2001**, *3*, 1989 – 1991; c) S. Ma, B. Ni, *Org. Lett.* **2002**, *4*, 639 – 641; d) D. J. Wallace, C. J. Cowden, D. J. Kennedy, M. S. Ashwood, I. F. Cottrell, U.-H. Dolling, *Tetrahedron Lett.* **2000**, *41*, 2027 – 2029; e) B. Schmidt, H. Wilsemann, *J. Org. Chem.* **2000**, *65*, 5817 – 5822; f) D. J. Wallace, P. G. Bulger, D. J. Kennedy, M. S. Ashwood, I. F. Cottrell, U.-H. Dolling, *Synlett* **2001**, 357 – 360.

[147] J. L. Piper, M. H. D. Postema, *J. Org. Chem.* **2004**, *69*, 7395 – 7398.

[148] For example, see: J. Louie, R. H. Grubbs, *Organometallics* **2002**, *21*, 2153 – 2164.

[149] For the successful employment of enol ether ring-closing metathesis in the total syntheses of trilobolide, nortrilobolide,

 © 2005 Wiley-VCH Verlag GmbH & Co. KGaA, Weinheim

and thapsivillosin F, see: S. F. Oliver, K. Högenauer, O. Simic, A. Antonello, M. D. Smith, S. V. Ley, *Angew. Chem.* **2003**, *115*, 6178 – 6182; *Angew. Chem. Int. Ed.* **2003**, *42*, 5996 – 6000.

[150] a) B. Alcaide, P. Almendros, *Chem. Eur. J.* **2003**, *9*, 1258 – 1262, and references therein; b) B. Schmidt, *Eur. J. Org. Chem.* **2004**, 1865 – 1880, and references therein.

[151] It should be recalled that a number of useful non-metathesis-based carbon–carbon bond-forming reactions are catalyzed by other ruthenium complexes; for reviews, see: a) S. Dérien, F. Monnier, P. H. Dixneuf, *Top. Organomet. Chem.* **2004**, *7*, 1 – 44; b) B. Schmidt, *Angew. Chem.* **2003**, *115*, 5146 – 5149; *Angew. Chem. Int. Ed.* **2003**, *42*, 4996 – 4999; c) B. M. Trost, F. D. Toste, A. B. Pinkerton, *Chem. Rev.* **2001**, *101*, 2067 – 2096.

[152] J. Louie, C. W. Bielawski, R. H. Grubbs, *J. Am. Chem. Soc.* **2001**, *123*, 11312 – 11313.

[153] A related, but stepwise, metathesis-based approach to the synthesis of (−)-muscone has also been reported: a) V. P. Kamat, H. Hagiwara, T. Katsumi, T. Hoshi, T. Suzuki, M. Ando, *Tetrahedron* **2000**, *56*, 4397 – 4403; b) V. P. Kamat, H. Hagiwara, T. Suzuki, M. Ando, *J. Chem. Soc. Perkin Trans. 1* **1998**, 2253 – 2254.

[154] For a novel ring-closing tandem catalysis approach to the synthesis of (+)-muscopyridine, see: A. Fürstner, A. Leitner, *Angew. Chem.* **2003**, *115*, 320 – 323; *Angew. Chem. Int. Ed.* **2003**, *42*, 308 – 311.

[155] D. J. Wallace, J. M. Goodman, D. J. Kennedy, A. J. Davies, C. J. Cowden, M. S. Ashwood, I. F. Cottrell, U.-H. Dolling, P. J. Reider, *Org. Lett.* **2001**, *3*, 671 – 674.

[156] For the first examples of diastereoselective ring-closing-metathesis reactions, see: C. M. Huwe, J. Velder, S. Blechert, *Angew. Chem.* **1996**, *108*, 2542 – 2544; *Angew. Chem. Int. Ed. Engl.* **1996**, *35*, 2376 – 2378.

[157] J. J. Kulagowski, N. R. Curtis, C. J. Swain, B. J. Williams, *Org. Lett.* **2001**, *3*, 667 – 670.

[158] T. J. Seiders, D. W. Ward, R. H. Grubbs, *Org. Lett.* **2001**, *3*, 3225 – 3228.

[159] a) A. H. Hoveyda, R. R. Schrock in *Organic Synthesis Highlights V* (Eds.: H.-G. Schmalz, T. Wirth), Wiley-VCH, Weinheim, **2003**, pp. 210 – 229; b) A. H. Hoveyda, R. R. Schrock, *Chem. Eur. J.* **2001**, *7*, 945 – 950; see also A. H. Hoveyda, *Top. Organomet. Chem.* **1998**, *1*, 105 – 132.

[160] a) G. S. Weatherhead, G. A. Cortez, R. R. Schrock, A. H. Hoveyda, *Proc. Natl. Acad. Sci. USA* **2004**, *101*, 5805 – 5809; the first such application in total synthesis was in that of (+)-*endo*-brevicomin: b) S. D. Burke, N. Müller, C. M. Beaudry, *Org. Lett.* **1999**, *1*, 1827 – 1829.

[161] The Schrock-type molybdenum carbene based catalyst systems, although extremely active in alkene-metathesis reactions, have not found gainful use in the corresponding enyne-metathesis processes; for illustrative examples, see: a) M. P. Schramm, D. S. Reddy, S. A. Kozmin, *Angew. Chem.* **2001**, *113*, 4404 – 4407; *Angew. Chem. Int. Ed.* **2001**, *40*, 4274 – 4277; b) S.-H. Kim, W. J. Zuercher, N. B. Bowden, R. H. Grubbs, *J. Org. Chem.* **1996**, *61*, 1073 – 1081.

[162] A. Kinoshita, M. Mori, *Synlett* **1994**, 1020 – 1022.

[163] a) A. Kinoshita, M. Mori, *J. Org. Chem.* **1996**, *61*, 8356 – 8357; b) A. Kinoshita, M. Mori, *Heterocycles* **1997**, *46*, 287 – 299.

[164] For other total syntheses of stemoamide, see: a) M. P. Sibi, T. Subramanian, *Synlett* **2004**, 1211 – 1214; b) M. K. Gurjar, D. S. Reddy, *Tetrahedron Lett.* **2002**, *43*, 295 – 298; c) P. A. Jacobi, K. Lee, *J. Am. Chem. Soc.* **2000**, *122*, 4295 – 4303; d) D. R. Williams, J. P. Reddy, G. S. Amato, *Tetrahedron Lett.* **1994**, *35*, 6417 – 6420.

[165] a) J. B. Brenneman, R. Machauer, S. F. Martin, *Tetrahedron* **2004**, *60*, 7301 – 7314; b) J. B. Brenneman, S. F. Martin, *Org. Lett.* **2004**, *6*, 1329 – 1331.

[166] M. Mori, T. Tomita, Y. Kita, T. Kitamura, *Tetrahedron Lett.* **2004**, *45*, 4397 – 4399.

[167] P. Thomas, M. Stephens, G. Wilkie, M. Amar, G. G. Lunt, P. Whiting, T. Gallagher, E. Pereira, M. Alkondon, E. X. Alburquerque, S. J. Wannacott, *J. Neurochem.* **1993**, *60*, 2308 – 2311.

[168] For a review of synthetic approaches to and total syntheses of anatoxin-*a* up to mid-1996, see: H. L. Mansell, *Tetrahedron* **1996**, *52*, 6025 – 6061.

[169] For total syntheses of anatoxin-*a* since mid-1996, see: a) T. Wegge, S. Schwarz, G. Seitz, *Tetrahedron: Asymmetry* **2000**, *11*, 1405 – 1410; b) P. J. Parsons, N. P. Camp, N. Edwards, L. R. Sumoreeah, *Tetrahedron* **1999**, *55*, 309 – 315; c) V. K. Aggarwal, P. S. Humphries, A. Fenwick, *Angew. Chem.* **1999**, *111*, 2178 – 2180; *Angew. Chem. Int. Ed.* **1999**, *38*, 1985 – 1986; d) B. M. Trost, J. D. Oslob, *J. Am. Chem. Soc.* **1999**, *121*, 3057 – 3064; e) C.-Y. Oh, K.-S. Kim, W.-H. Ham, *Tetrahedron Lett.* **1998**, *39*, 2133 – 2136; f) P. J. Parsons, N. P. Camp, M. J. Underwood, D. M. Harvey, *Tetrahedron* **1996**, *52*, 11637 – 11642.

[170] For selected examples of the formation of bridged aza-bicyclic structures by ring-closing metathesis, see the relevant citations in reference [165b].

[171] For a review of allylic 1,3-strain as a controlling factor in stereoselective transformations, see: R. W. Hoffmann, *Chem. Rev.* **1989**, *89*, 1841 – 1860.

[172] V. K. Aggarwal, C. J. Astle, M. Roger-Evans, *Org. Lett.* **2004**, *6*, 1469 – 1471.

[173] a) E. C. Hansen, D. Lee, *J. Am. Chem. Soc.* **2004**, *126*, 15074 – 15080; b) E. C. Hansen, D. Lee, *J. Am. Chem. Soc.* **2003**, *125*, 9582 – 9583.

[174] M. Mori, N. Sakakibara, A. Kinoshita, *J. Org. Chem.* **1998**, *63*, 6082 – 6083.

[175] For examples of enyne-metathesis macrocyclizations under an atmosphere of ethylene, see: A. G. M. Barrett, A. J. Hennessy, R. L. Vezouet, P. A. Procopiou, P. W. Searle, S. Stefaniak, R. J. Upton, A. J. P. White, D. J. Williams, *J. Org. Chem.* **2004**, *69*, 1028 – 1037.

[176] Alternative reasons, including maintaining the reactivity of the catalyst, have been invoked for the beneficial effect of ethylene on ring-closing enyne-metathesis reactions to generate common- and medium-sized ring systems, since these reactions invariably still yield the corresponding 1,2-disubstituted cyclic products and are not believed to involve the two-step process; for a discussion, see reference [174].

[177] a) C. A. Morales, M. E. Layton, M. D. Shair, *Proc. Natl. Acad. Sci. USA* **2004**, *101*, 12036 – 12041; b) M. E. Layton, C. A. Morales, M. D. Shair, *J. Am. Chem. Soc.* **2002**, *124*, 773 – 775.

[178] a) X. Fu, M. B. Hossain, F. J. Schmitz, D. van der Helm, *J. Org. Chem.* **1997**, *62*, 3810 – 3819; b) X. Fu, M. B. Hossain, D. van der Helm, F. J. Schmitz, *J. Am. Chem. Soc.* **1994**, *116*, 12125 – 12126.

[179] For conceptually related uses of temporary directing groups to effect atropselective macrocyclizations in the synthesis of vancomycin, see: a) D. A. Evans, C. J. Dinsmore, P. S. Watson, M. R. Wood, T. I. Richardson, B. W. Trotter, J. L. Katz, *Angew. Chem.* **1998**, *110*, 2868 – 2872; *Angew. Chem. Int. Ed.* **1998**, *37*, 2704 – 2708; b) K. C. Nicolaou, C. N. C. Boddy, *J. Am. Chem. Soc.* **2002**, *124*, 10451 – 10455.

[180] A similar observation had been reported previously in a ring-closing alkene-metathesis reaction: D. Joe, L. E. Overman, *Tetrahedron Lett.* **1997**, *38*, 8635 – 8638.

[181] B. M. Trost, G. A. Doherty, *J. Am. Chem. Soc.* **2000**, *122*, 3801 – 3810.

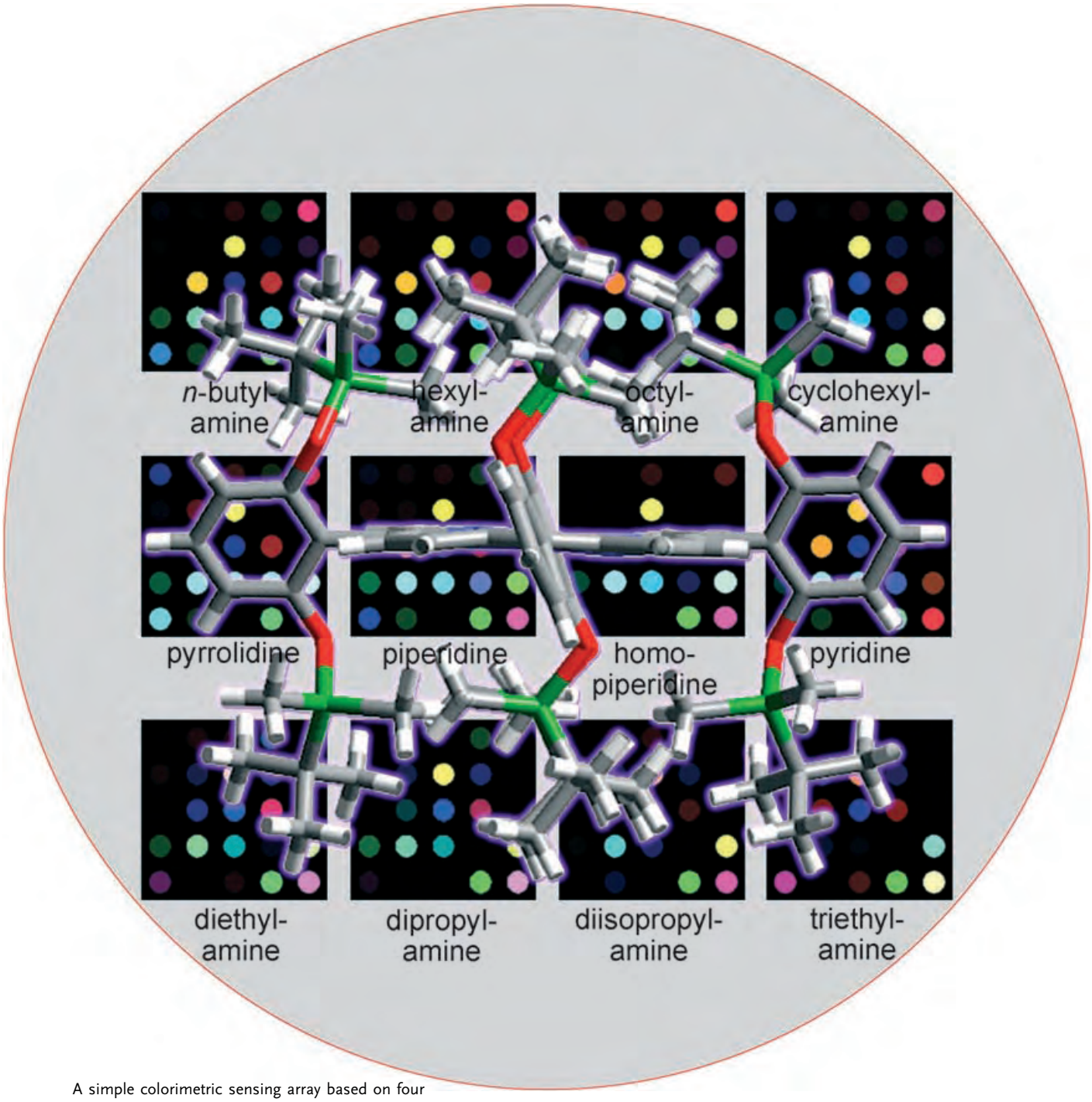
[182] For a Review of the chemistry and biology of roseophilin and the prodigiosin alkaloids, in which five different ring-closing-metathesis approaches to roseophilin are highlighted, see: A. Fürstner, *Angew. Chem.* **2003**, *115*, 3706 – 3728; *Angew. Chem. Int. Ed.* **2003**, *42*, 3582 – 3603.

 © 2005 Wiley-VCH Verlag GmbH & Co. KGaA, Weinheim

[183] a) A. Fürstner, H. Weintritt, *J. Am. Chem. Soc.* **1998**, *120*, 2817 – 2825; b) A. Fürstner, T. Gastner, H. Weintritt, *J. Org. Chem.* **1999**, *64*, 2361 – 2366.
[184] For a discussion of the plausible mechanistic pathways of these types of enyne-metathesis reactions, see: A. Fürstner, H. Szillat, B. Gabor, M. Mynott, *J. Am. Chem. Soc.* **1998**, *120*, 8305 – 8314, and references therein.
[185] For a discussion of the reorganization of enyne systems catalyzed by platinum salts, see: L. Añorbe, G. Domínguez, J. Pérez-Castells, *Chem. Eur. J.* **2004**, *10*, 4938 – 4943.
[186] a) S.-H. Kim, N. Bowden, R. H. Grubbs, *J. Am. Chem. Soc.* **1994**, *116*, 10801 – 10802; b) S.-H. Kim, W. J. Zuercher, N. B. Bowden, R. H. Grubbs, *J. Org. Chem.* **1996**, *61*, 1073 – 1081.
[187] W. J. Zuercher, M. Scholl, R. H. Grubbs, *J. Org. Chem.* **1998**, *63*, 4291 – 4298.
[188] F.-D. Boyer, I. Hanna, L. Ricard, *Org. Lett.* **2004**, *6*, 1817 – 1820.
[189] a) D. S. Tan, G. B. Dudley, S. J. Danishefsky, *Angew. Chem.* **2002**, *114*, 2289 – 2292; *Angew. Chem. Int. Ed.* **2002**, *41*, 2185 – 2188; b) S. Lin, G. B. Dudley, D. S. Tan, S. J. Danishefsky, *Angew. Chem.* **2002**, *114*, 2292 – 2295; *Angew. Chem. Int. Ed.* **2002**, *41*, 2188 – 2191.
[190] B. Shi, N. A. Hawryluk, B. B. Snider, *J. Org. Chem.* **2003**, *68*, 1030 – 1042.
[191] F.-D. Boyer, I. Hanna, *Tetrahedron Lett.* **2002**, *43*, 7569 – 7572.
[192] For the application of an enyne-metathesis cascade process in the synthesis of erythrocarine, see: K. Shimizu, M. Takimoto, M. Mori, *Org. Lett.* **2003**, *5*, 2323 – 2325.
[193] S. T. Diver, A. J. Giessert, *Synthesis* **2004**, 466 – 471.
[194] a) M. Mori, K. Tonogaki, N. Nishiguchi, *J. Org. Chem.* **2002**, *67*, 224 – 226; b) A. Kinoshita, N. Sakakibara, M. Mori, *J. Am. Chem. Soc.* **1997**, *119*, 12388 – 12389.
[195] K. Tonogaki, M. Mori, *Tetrahedron Lett.* **2002**, *43*, 2235 – 2238.
[196] J. A. Smulik, S. T. Diver, *J. Org. Chem.* **2000**, *65*, 1788 – 1792.
[197] R. Stragies, M. Schuster, S. Blechert, *Angew. Chem.* **1997**, *109*, 2629 – 2630; *Angew. Chem. Int. Ed. Engl.* **1997**, *36*, 2518 – 2520.
[198] For examples of enyne cross-metathesis of substituted alkenes, see: H.-Y. Lee, B. G. Kim, M. L. Snapper, *Org. Lett.* **2003**, *5*, 1855 – 1858, and references therein.
[199] For examples of enyne cross-metathesis in cascade processes, see: a) B. P. Peppers, S. T. Diver, *J. Am. Chem. Soc.* **2004**, *126*, 9524 – 9525; b) J. A. Smulik, S. T. Diver, *Tetrahedron Lett.* **2001**, *42*, 171 – 174; c) S. C. Schürer, S. Blechert, *Chem. Commun.* **1999**, 1203 – 1204.
[200] For studies towards the synthesis of the marine sponge metabolite mycothiazole A in which an enyne cross-metathesis reaction was employed to fashion a key 1,3-diene intermediate, see: S. Rodriguez-Conesa, P. Candal, C. Jiménez, J. Rodriguez, *Tetrahedron Lett.* **2001**, *42*, 6699 – 6702.
[201] a) L. Kloppenburg, D. Song, U. H. F. Bunz, *J. Am. Chem. Soc.* **1998**, *120*, 7973 – 7974; see also: b) K. Grela, J. Ignatowska, *Org. Lett.* **2002**, *4*, 3747 – 3749.
[202] a) R. R. Schrock, D. N. Clark, J. Sancho, J. H. Wengrovius, S. M. Rocklage, S. F. Pedersen, *Organometallics* **1982**, *1*, 1645 – 1651; the Schrock group were the first to report alkyne metathesis in the presence of a well-defined alkylidyne catalyst: b) J. H. Wengrovius, J. Sancho, R. R. Schrock, *J. Am. Chem. Soc.* **1981**, *103*, 3932 – 3934.
[203] a) A. Fürstner, C. Mathes, C. W. Lehmann, *J. Am. Chem. Soc.* **1999**, *121*, 9453 – 9454; b) A. Fürstner, C. Mathes, C. W. Lehmann, *Chem. Eur. J.* **2001**, *7*, 5299 – 5317.
[204] A related and potentially useful molybdenum-based catalyst for alkyne metathesis was introduced by the Cummins group at about the same time, although this has not yet found widespread use in organic synthesis: Y.-C. Tsai, P. L. Diaconescu, C. C. Cummins, *Organometallics* **2000**, *19*, 5260 – 5262.
[205] A recent modification of molybdenum catalyst precursor **237** for alkyne metathesis was recently described: W. Zhang, J. S. Moore, *J. Am. Chem. Soc.* **2004**, *126*, 12796.
[206] For examples of early applications of alkyne metathesis in organic synthesis, see: a) N. Kaneta, T. Hirai, M. Mori, *Chem. Lett.* **1995**, 627 – 628; b) N. Kaneta, K. Hikichi, S. Asaka, M. Uemura, M. Mori, *Chem. Lett.* **1995**, 1055 – 1056.
[207] A. Fürstner, G. Seidel, *Angew. Chem.* **1998**, *110*, 1758 – 1760; *Angew. Chem. Int. Ed.* **1998**, *37*, 1734 – 1736.
[208] A. Fürstner, O. Guth, A. Rumbo, G. Seidel, *J. Am. Chem. Soc.* **1999**, *121*, 11108 – 11113.
[209] An 11-membered ring could be formed in 45% yield by alkyne ring-closing metathesis; however, this was accompanied by the formation of the corresponding 22-membered cyclodimeric product in 40% yield.[203b]
[210] For reviews of epothilone syntheses, see: a) reference [67]; b) C. R. Harris, S. J. Danishefsky, *J. Org. Chem.* **1999**, *64*, 8434 – 8456; c) K. C. Nicolaou, F. Roschangar, D. Vourloumis, *Angew. Chem.* **1998**, *110*, 2120 – 2153; *Angew. Chem. Int. Ed.* **1998**, *37*, 2014 – 2045.
[211] A. Fürstner, C. Mathes, K. Grela, *Chem. Commun.* **2001**, 1057 – 1059.
[212] For further examples of the application of the alkyne ring-closing-metathesis/Lindlar reduction protocol in total synthesis, see: a) A. Fürstner, D. De Souza, L. Parra-Rapado, J. T. Jensen, *Angew. Chem.* **2003**, *115*, 5516 – 5518; *Angew. Chem. Int. Ed.* **2003**, *42*, 5358 – 5360; b) A. Fürstner, F. Stelzer, A. Rumbo, H. Krause, *Chem. Eur. J.* **2002**, *8*, 1856 – 1871; c) A. Fürstner, K. Radkowski, J. Grabowski, C. Wirtz, R. Mynott, *J. Org. Chem.* **2000**, *65*, 8758 – 8762.
[213] a) B. M. Trost, Z. T. Ball, T. Jöge, *J. Am. Chem. Soc.* **2002**, *124*, 7922 – 7923; b) F. Lacombe, K. Radkowski, G. Seidel, A. Fürstner, *Tetrahedron* **2004**, *60*, 7315 – 7324; c) A. Fürstner, K. Radkowski, *Chem. Commun.* **2002**, 2182 – 2183.
[214] For a Minireview of recent methods for the synthesis of *E*-alkene units in macrocyclic compounds, see reference [72].
[215] A. Fürstner, A.-S. Castanet, K. Radkowski, C. W. Lehmann, *J. Org. Chem.* **2003**, *68*, 1521 – 1528.
[216] For a review of regioselective syntheses of substituted furans, see: X. L. Hou, H. Y. Cheung, T. Y. Hon, P. L. Kwan, T. H. Lo, S. Y. Tong, H. N. C. Wong, *Tetrahedron* **1998**, *54*, 1955 – 2020.
[217] For a previous total synthesis of citreofuran, see: S. Lai, X. Gao, Y. Shizuri, S. Yamamura, *Chin. Chem. Lett.* **1994**, *5*, 481 – 484.
[218] For a discussion of this phenomenon as applied to related systems, see: J. A. Marshall, E. V. Van Devender, *J. Org. Chem.* **2001**, *66*, 8037 – 8041.
[219] a) U. H. F. Bunz in *Modern Arene Chemistry* (Ed.: D. Astruc), Wiley-VCH, Weinheim, **2002**, pp. 217 – 249; see also: b) W. Zhang, J. S. Moore, *Macromolecules* **2004**, *37*, 3973 – 3975, and references therein.
[220] A. Fürstner, T. Dierkes, *Org. Lett.* **2000**, *2*, 2463 – 2464.
[221] A. Fürstner, K. Langemann, *J. Am. Chem. Soc.* **1997**, *119*, 9130 – 9136.
[222] A. Fürstner, K. Grela, C. Mathes, C. W. Lehmann, *J. Am. Chem. Soc.* **2000**, *122*, 11799 – 11805.
[223] R. Noyori, M. Suzuki, *Angew. Chem.* **1984**, *96*, 854 – 883; *Angew. Chem. Int. Ed. Engl.* **1984**, *23*, 847 – 876.
[224] For an application of alkyne cross-metathesis in studies towards the total syntheses of (−)-terpestacin and siccanol by the Jamison group, see: J. Chan, T. F. Jamison, *J. Am. Chem. Soc.* **2004**, *126*, 10682 – 10691.

 © 2005 Wiley-VCH Verlag GmbH & Co. KGaA, Weinheim

Communications



A simple colorimetric sensing array based on four different types of molecular recognition allows the discrimination of functionalized organic vapors. Sensitivities well below 1 ppmv have been observed for amines and the technique even allows the discrimination of isomers. More about this approach can be found in the Communication by K. S. Suslick and co-workers on the following pages.

 © 2005 Wiley-VCH Verlag GmbH & Co. KGaA, Weinheim DOI: 10.1002/anie.200500939

Sensors

Molecular Recognition and Discrimination of Amines with a Colorimetric Array**

*Neal A. Rakow, Avijit Sen, Michael C. Janzen, Jennifer B. Ponder, and Kenneth S. Suslick**

Electronic nose technology for the generalized detection of volatile organic compounds (VOCs) has generally employed arrays of sensors based either on adsorption into a set of polymers or on oxidations at a set of heated metal oxides.[1,2] While such systems generally allow for distinction between analytes of different chemical functionality, the discrimination of compounds within a given chemical class remains a challenging goal. We have previously reported the colorimetric array detection of a wide range of odorants using a family of metalloporphyrins immobilized on reverse-phase silica[3] and on hydrophobic membranes.[4] Here we report the use of an expanded colorimetric array detector[4] that is capable of the highly sensitive and highly selective discrimination of amines.

Volatile amines are common by-products of rapidly growing cells. As a consequence, the human nose is well-adapted for the detection of amines, with sensitivities approximately 10^4 higher for these compounds than for most alkanes, alcohols, or ketones.[5] For example, cadaverine and putrescene are bacterial metabolic products relevant to food freshness,[6] isobutylamine is diagnostic of bacterial vaginosis,[7] and aniline and *o*-toluidine are biomarkers in lung cancer.[8] While sensitive detection of individual amine compounds has been previously reported,[9] the selective discrimination within a larger family of amines is not easily achieved. Previous approaches to selectively discriminate between amines include sensors based on molecular imprinting,[10,11] functionalized mesoporous silica,[12] and chromogenic reagents.[13] Amines span a wide range of molecular shapes, sizes, and electronic properties; molecular recognition of these compounds poses a unique scientific challenge with important technological consequences.

Molecular recognition relies on the ability to differentiate on the basis of the chemical properties of analytes. Four families of chemically responsive dyes were incorporated into a colorimetric sensor array (Figure 1 and see the Supporting Information) to probe a wide region of "chemical properties space": 1) a series of various metalated tetraphenylporphyrins was used to differentiate analytes on the basis of Lewis acid/base interactions (namely, metal-selective coordination); 2) bis-pocketed Zn porphyrins[14] were used to differentiate on the basis of the size and shape of the analyte; 3) pH acid/base indicators (for example, methyl red and Nile red) were used to differentiate on the basis of Brønsted basicity; and finally 4) highly solvatochromic dyes (for example, Reichardt's ET_{30} betaine dye) were used to indicate the polarity of the analyte. Both the dyes and substrate were chosen to be hydrophobic; as a consequence, changes in humidity over a wide range (10 to >95% relative humidity) do not affect either the initial color of the dyes or the response of the array to analyte vapors.

Responses to a set of very closely related analytes were recorded to provide a stringent test of the molecular recognition by this sensor array: specifically, 12 amines comprising linear, branched, and cyclic structures of similar molecular weight were chosen to provide subtle distinctions in electronic structure and molecular shape (Figure 2). As seen, each amine gives a unique color-difference map. The closest analyte pairs were, not surprisingly, *n*-butylamine and *n*-hexylamine. Even here, however, the array responses are distinct even by eye, and statistical comparisons shows that the variance (that is, the sum of the squares of the differences between the changes in red, green, and blue (RGB) values) among multiple runs of hexylamine is 4.5-fold less than the variance between *n*-hexylamine and *n*-butylamine.

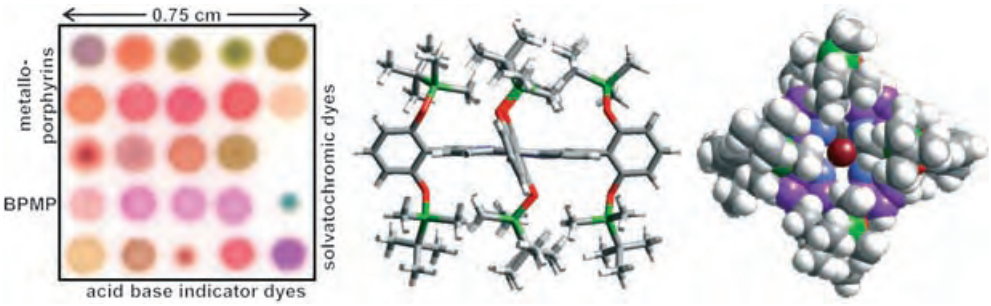


Figure 1. Colorimetric sensor array and the structure of the bis-pocket Zn porphyrin[9a] 5,10,15,20-tetrakis(2′,6′-bis(*tert*-butyldimethylsilyloxyl)phenyl)porphyrinatozinc(II), shown in framework side view (center) and space-filled top view (right). BPMP = bis-pocket metalloporphyrins.

[*] Dr. N. A. Rakow, Dr. A. Sen, Dr. M. C. Janzen, J. B. Ponder, Prof. K. S. Suslick
School of Chemical Sciences
University of Illinois at Urbana-Champaign
601 South Goodwin Avenue, Urbana, Illinois 61801 (USA)
Fax: (+1) 217-333-2685
E-mail: ksuslick@uiuc.edu

[**] This work was supported by the U.S. NIH (HL 25934) and in part by the U.S. DOE (DEFG02-91ER45439), through the Frederick Seitz Materials Research Laboratory at the University of Illinois at Urbana-Champaign. We gratefully thank Dr. W. B. McNamara III and the staff of ChemSensing, Inc. for their assistance in array printing.

Supporting information for this article is available on the WWW under http://www.angewandte.org or from the author.

 © 2005 Wiley-VCH Verlag GmbH & Co. KGaA, Weinheim

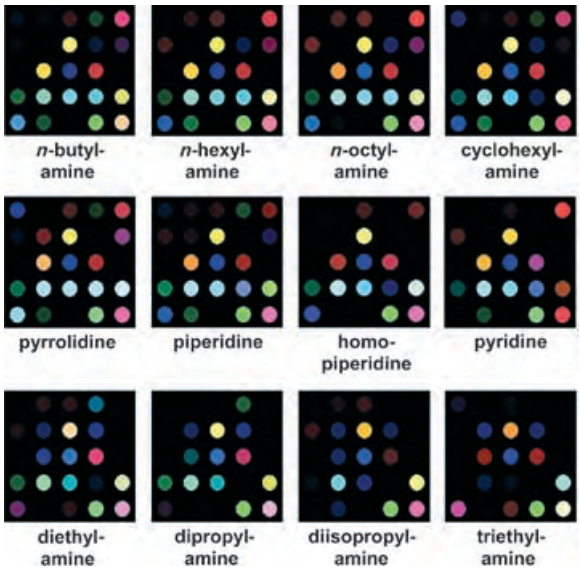


Figure 2. Color-difference maps for a family of 12 amines. Maps are generated from the absolute values of the differences of the red, green, and blue values of each dye spot before and after equilibration with the analytes; saturated analyte vapor at 20 °C. The images shown are in eight bit color expanded from five bit.

The images are digitally obtained and thus detailed statistical analysis of the difference maps is straightforward (all digital data and statistical analyses are provided as Supporting Information): each analyte is represented as a 72-dimensional vector (namely, the red, green, and blue difference values of 24 dyes). Principal component analysis (PCA) provides a quantitative evaluation of the analytical dispersion (that is, selectivity) of a technique based on its number of independent dimensions of discrimination.[11] Other techniques for electronic nose technology generally have very few independent dimensions (typically only two or three for 99% of the total discrimination, with a single dimension highly predominant (>90%)), and consequently only have very limited ability to discriminate between similar analytes.[2] In contrast, because the colorimetric dye array probes a wide range of intermolecular interactions, we observe a very high level of dispersion with the colorimetric dye array. When PCA is applied even to this family of closely related analytes, there are six dimensions necessary for 90% discrimination, eight for 95%, and ten for 99% (Figure 3).

A hierarchical cluster analysis[15] (HCA) was performed and a response dendrogram generated to examine the multivariate distances between the analyte responses in this 72-dimensional RGB color space (Figure 4). Remarkably, the dendrogram is consistent with the qualitative structural and electronic properties of the amines: the branched amines produce one cluster, linear amines another, the cyclic structures are tightly associated, and the lone aromatic amine (pyridine) separate from any of the other clusters. In contrast to prior electronic nose technologies, the colorimetric array is able to easily resolve very similar compounds and even structural isomers. For example, the C_6 amines (*n*-hexylamine, homopiperidine, dipropylamine, diisopropylamine, and triethylamine) have clearly distinct color patterns.

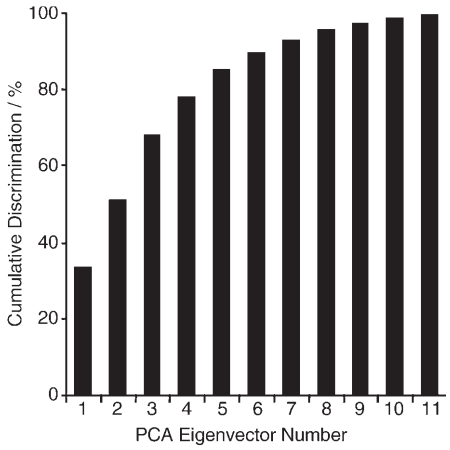


Figure 3. Principal component analysis from 12 very closely related amines shows that the 24-dye sensor array has a very high level of dispersion.

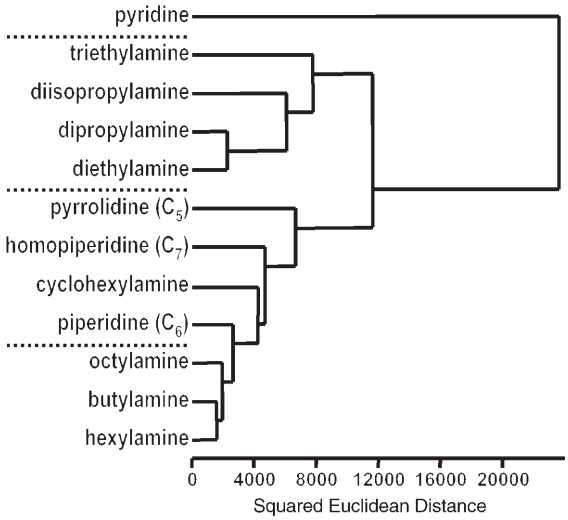


Figure 4. Dendrogram representation of the hierarchical cluster analysis of amines at their saturation vapor pressure from HCA (minimum variance).

The origin of this high level of discrimination lies in the broad range of chemical properties space being probed by the colorimetric array.

In addition to excellent analyte discrimination, high sensitivity to odorants is essential for practical applications. these amine analytes can be readily distinguished at concentrations well below 1 ppmv by using the array. Color-difference maps for a series of amines as a function of concentration are shown in Figure 5, where vivid and easily distinguishable responses are even seen at 600 ppbv. It is important to recognize that the same analyte at different concentrations gives different color change patterns: some dyes change color at low concentrations and then saturate, others do not begin to change until high concentrations. Quantitative analysis is therefore most easily accomplished by quantitative comparison to a library of analyte patterns at various concentrations (see the Supporting Information). Given the magnitude of the color changes observed at

 © 2005 Wiley-VCH Verlag GmbH & Co. KGaA, Weinheim

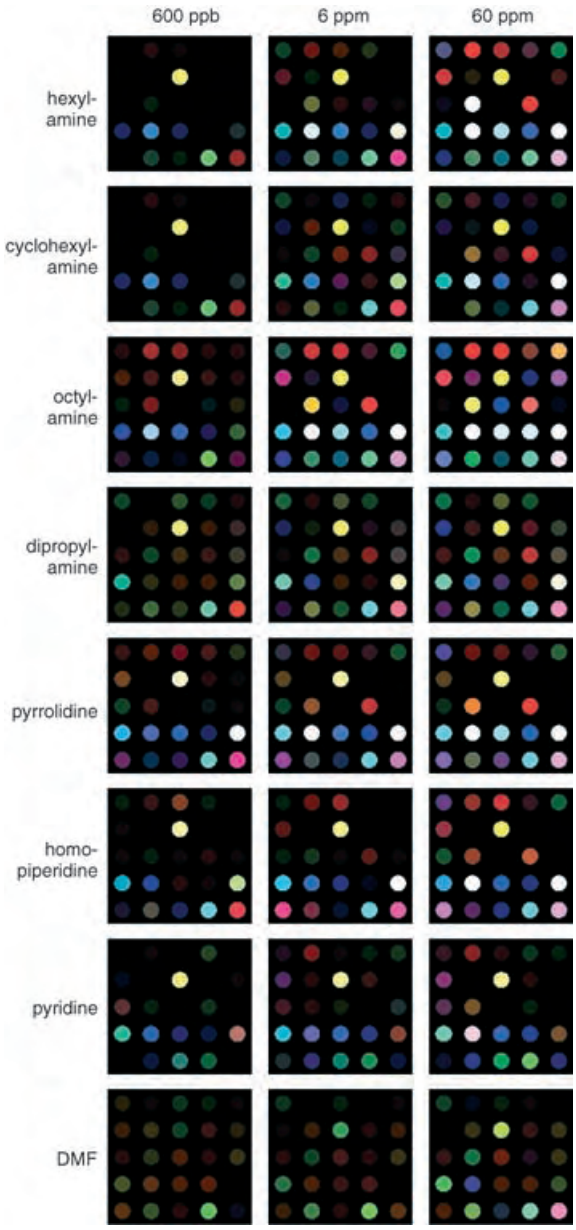


Figure 5. Color difference maps for a family of amines at 600 ppbv, 6 ppmv, and 60 ppmv at 20 °C. The images shown are in eight-bit color expanded from four bit.

600 ppbv, it is clear that detection at even lower concentrations is possible. Indeed, the limits of detection ($3 \times$ signal/noise) for several amines are well under 100 ppbv. Even GC-MS techniques typically achieve only 100 to 1000 ppbv sensitivities for such compounds in the absence of preconcentration. In many cases, these colorimetric arrays are in fact more sensitive than the human nose.[4,5] The origin of this high sensitivity to amines is based on strong and relatively specific interactions (for example, metal ligation): this is in marked contrast to previous electronic nose technologies that rely on weak, nonspecific interactions (for example, physical adsorption onto metal oxides or into polymers). Interestingly, it has been argued recently that the active site of many mammalian olfactory receptors are metalloproteins.[16]

A second 36-dye sensor array was designed without any bis-pocketed metalloporphyrins to test the role of bis-pocketed Zn porphyrins in selective differentiation between closely related amines. The new 36-dye sensor array contained various nonpocketed metalated tetraphenylporphyrins, pH acid/base indicators, and solvatochromic dyes. HCA of the response of 29 amines reveals a clustering of the aromatic and aliphatic amines into distinct branches. Class differentiation between primary, secondary, tertiary, and cyclic amines is reduced (see the Supporting Information), although there remains no possibility of confusion among individual amines. PCA shows our 36-dye array has an extraordinarily high level of dispersion: 11, 14, and 21 dimensions are required to define 90, 95, and 99% of the total variance, respectively.

In summary, we have demonstrated the facile discrimination of a range of functionalized organic vapors by using a simple colorimetric sensing array. Sensitivities well below 1 ppmv have been observed for amines, and in other work, thiols, phosphines, and carboxylic acids. Even distinction between isomeric amines is readily feasible by incorporating dyes that allow for distinction based on metal coordination, molecular size/shape, analyte acidity/basicity, and polarity.

Experimental Section

Methods: A 24-dye colorimetric array[3] composed of metalloporphyrins, free-base porphyrins, pH indicators, and solvatochromic dyes were spotted onto reverse-phase silica gel (Whatman KC2, 200 μm thickness, 350 $m^2 g^{-1}$ surface area) using 0.1 μL microcapillary tubes and employed for the analyses described herein (Figure 1 and see the Supporting Information). The 36-dye arrays used for data given in the Supporting Information were spotted on hydrophobic membranes and are commercially available from ChemSensing, Inc. (www.chemsensing.com, Array no. 031). Images were obtained at 1200 dots per inch in RGB color mode using an ordinary flatbed scanner (Epson Perfection 1200S). Color-difference maps were obtained from the scanned RGB images by digitally subtracting the image before exposure to analytes from the image after exposure, using a 314-pixel average from the center of each dye spot (thus avoiding subtraction artifacts at the periphery of the spots). Statistical analysis was performed with MVSP 3.1 (Kovach Co.). Gas streams containing the vapor of interest at known vapor pressure[17] were generated by flowing nitrogen through the neat liquid analyte in a thermostated, glass-fritted bubbler. To vary analyte concentrations, serial dilution in nitrogen using MKS digital mass-flow controllers was utilized. In all cases, full equilibration of the array by the analyte vapor was confirmed by monitoring images versus time. All liquid analytes were obtained from Aldrich or Fisher Scientific and used as received.

Received: March 14, 2005

Keywords: amines · dyes/pigments · metalloporphyrins · molecular recognition · sensors

[1] K. J. Albert, N. S. Lewis, C. L. Schauer, G. A. Sotzing, S. E. Stitzel, T. P. Vaid, D. R. Walt, *Chem. Rev.* **2000**, *100*, 2595.
[2] J. W. Gardner, P. N. Bartlett, *Electronic Noses: Principles and Applications*, Oxford University Press, New York, **1999**.
[3] N. A. Rakow, K. S. Suslick, *Nature* **2000**, *406*, 710.
[4] a) K. S. Suslick, N. A. Rakow, A. Sen, *Tetrahedron* **2004**, *60*, 11133; b) K. S. Suslick, *MRS Bull.* **2004**, *29*, 720.

 © 2005 Wiley-VCH Verlag GmbH & Co. KGaA, Weinheim

[5] M. Devos, F. Patte, J. Rouault, P. Laffort, L. J. Van Gemert, *Standardized Human Olfactory Thresholds*, Oxford University Press, New York, **1990**.
[6] a) M. T. Vecianánogues, A. Marinefont, M. C. Vidalcarou, *J. Agric. Food Chem.* **1997**, *45*, 2036; b) G. Nouadje, N. Simeon, F. Dedieu, M. Nertz, P. Puig, F. Couderc, *J. Chromatogr. A* **1997**, *789*, 109.
[7] H. Wolrath, R. Forsum, P. G. Larsson, H. Boren, *J. Clin. Microbiol.* **2001**, *39*(11), 4026.
[8] G. Preti, J. N. Labows, J. G Kostelc, S. Aldinger, R. Daniele, *J. Chromatogr. Biomed. Appl.* **1988**, *432*, 1.
[9] G. A. Sotzing, J. N. Phend, R. H. Grubbs, N. S. Lewis, *Chem. Mater.* **2000**, *12*, 593.
[10] E. Mertz, S. C. Zimmerman, *J. Am. Chem. Soc.* **2003**, *125*, 3424–3425.
[11] N. T. Greene, S. L. Morgan, K. D. Shimizu, *Chem. Commun.* **2004**, 1172.
[12] M. Comes, M. D. Marcos, R. Martinez-Manez, F. Sancenon, J. Soto, L. A. Villaescusa, P. Amoros, D. Beltran, *Adv. Mater.* **2004**, *16*, 1783.
[13] G. J. Mohr. *Chem. Eur. J.* **2004**, *10*, 1082.
[14] a) A. Sen, K. S. Suslick, *J. Am. Chem. Soc.* **2000**, *122*, 11565; b) P. Bhyrappa, J. K. Young, J. S. Moore, K. S. Suslick, *J. Am. Chem. Soc.* **1996**, *118*, 5708; c) P. Bhyrappa, G. Vaijayanthimala, K. S. Suslick, *J. Am. Chem. Soc.* **1999**, *121*, 262; d) S. C. Zimmerman, M. S. Wendland, N. A. Rakow, I. Zharov, K. S. Suslick, *Nature* **2002**, *418*, 399.
[15] K. R. Beebe, R. J. Pell, M. B. Seasholtz, *Chemometrics: A Practical Guide*, Wiley-Interscience, New York, **1998**.
[16] J. Wang, Z. Luthey-Schulten, K. S. Suslick, *Proc. Natl. Acad. Sci. USA* **2003**, *100*, 3035.
[17] C. L. Yaws, *Handbook of Vapor Pressure*, Gulf Publishing, Houston, **1994**.

Dried Foam Films

Dried Foam Films: Self-Standing, Water-Free, Reversed Bilayers of Amphiphilic Compounds**

*Jian Jin, Jianguo Huang, and Izumi Ichinose**

Foam films and lipid membranes are typical two-dimensional assemblies of amphiphiles with an inverse molecular arrangement.[1–3] In contrast to lipid membranes, which are spontaneously formed in water, foam films are formed in the air. Thin foam films are composed of a water layer sandwiched between two layers of amphiphiles that direct their hydrophobic moieties outwards.[4,5]

The first historical observation of thin foam films was probably made by Hooke as early as 1672. He reported the films as "holes in soap bubbles", as some parts of the colored bubbles turned black upon draining the water.[6] When interstitial water drains away, the foam film becomes much thinner than the wavelength of visible light and thus appears black as a result of the diminished reflection intensity.[7–9] Such films are named Black Films, and it is possible for the thickness of the water layer to be less than a few nanometers. Bélorgey and Benattar have reported that the thinnest film of ionic surfactant has only three hydration water molecules per counterion.[10] Thin foam films are usually formed in open frames placed in a sealed cell that is filled with saturated vapor, and the films are stable as long as water exists in the interstitial space.[11–14] However, they are so transient in ambient air that the interstitial water molecules have long been deemed to be indispensable to maintain the structure.[15] Herein, we report for the first time that some kinds of foam films exist even after being dried in ambient air. As illustrated in Figure 1, the dried foam films are formed by slowly evaporating the solution of amphiphilic compounds in the holes of substrates. The amphiphilic compounds spontaneously organize into a head-to-head arrangement with their hydrocarbon chains directed towards the air, and give self-standing reversed bilayers. The films form on porous substrates with micron to submicron pores and are stable under ultrahigh vacuum and at temperatures greater than 100 °C.

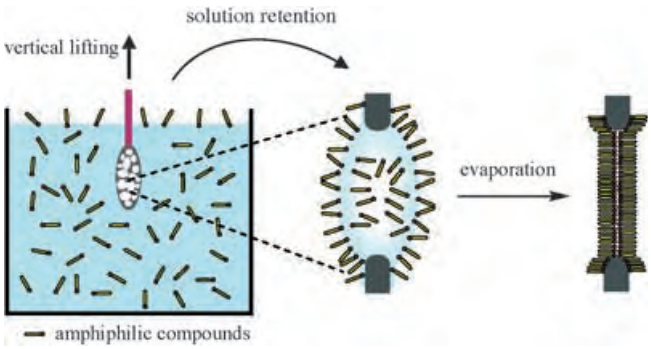


Figure 1. The formation of dried foam films; amphiphilic compounds in solution are illustrated in the monomeric dispersion in conditions below the critical micelle concentration (CMC).

A small amount of an 8.2 mM aqueous solution of dodecyltrimethylammonium bromide (DTAB, Figure 2A) was retained in the holes of the porous substrate by the vertical lifting method. Initially, a perforated polymer membrane on a 150-mesh microgrid (Figure 2B) was used as the substrate. The holes of a few micrometers in the polymer membrane are slightly hydrophobic and are therefore suitable for capturing small droplets of DTAB solution. The substrate was then allowed to stand for one hour in air at a humidity of between 40 and 50 %. The dried foam films obtained were too

[*] Dr. J. Jin, Dr. J. Huang, Dr. I. Ichinose
Advanced Materials Laboratory
National Institute for Materials Science (NIMS)
1-1 Namiki, Tsukuba, Ibaraki, 305-0044 (Japan)
Fax: (+81) 29-852-7449
E-mail: ichinose.izumi@nims.go.jp

[**] The authors acknowledge M.-P. Pileni and F. Papadimitrakopoulos for helpful discussions on the structural stability of dried foam films.

Supporting information for this article is available on the WWW under http://www.angewandte.org or from the author.

 © 2005 Wiley-VCH Verlag GmbH & Co. KGaA, Weinheim DOI: 10.1002/anie.200500036

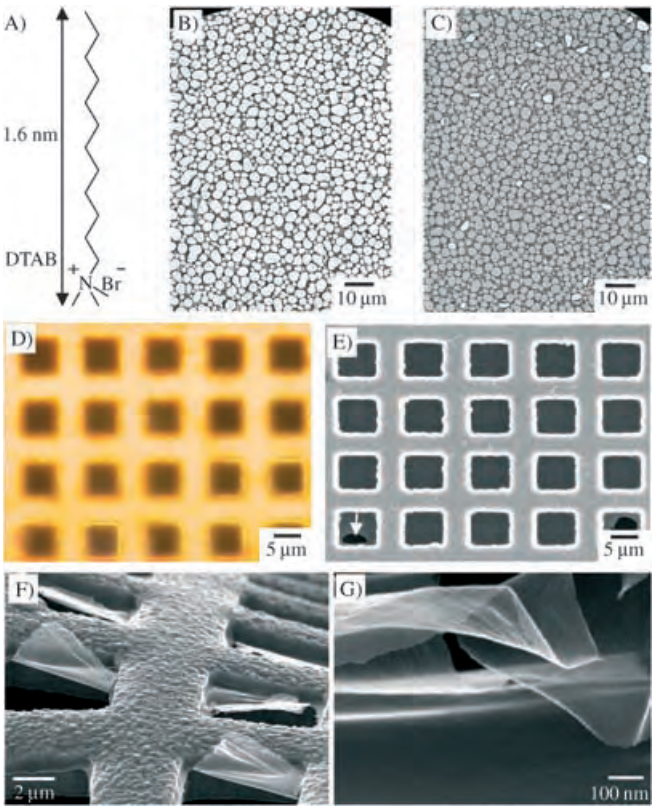


Figure 2. A) Molecular structure of DTAB; B) TEM image of a perforated polymer membrane on a 150-mesh microgrid; C) TEM image of DTAB films formed on the holes of the polymer membrane; D) confocal micrograph of DTAB films formed on a 2000-mesh copper grid; E) FE-SEM image of DTAB films formed on a 2000-mesh copper grid; F) cross-sectional FE-SEM image of DTAB films formed on a 2000-mesh copper grid; G) high-magnification of image in part F).

weak for the focused electron beam of a transmission electron microscope (TEM). However, this problem was successfully solved by coating the specimens with a thin layer of Pt nanoparticles by using a mild ion-sputter. As shown in Figure 2C, DTAB films uniformly cover the holes of the polymer membrane except for a few broken parts; the covered areas are dark because of the presence of the thin Pt layer. The films are extremely smooth and flat without any cracks. We then examined a 2000-mesh copper grid with 7-μm cells. Confocal microscopy, which has a detection limit close to 10 nm, is not useful for the observation of DTAB films owing to their thickness (Figure 2D). However, field-emission scanning electron microscopy (FE-SEM) gave a clear image of the films covering the holes of the copper grid (Figure 2E). Fully covered cells are easily distinguished from the cell; a black broken part is marked with an arrow. This sample was carefully torn and used for cross-sectional observation. As shown in Figure 2F, the film is flexible and prone to be warped by the electron beam when isolated from the wall of the copper grid. The film is transparent, which indicates that the film is thinner than the mean free-path of secondary electrons ($\approx$5 nm) in the SEM observation. By scrutinizing the edge of the film, the thickness was estimated to be 6.5 ± 1.0 nm. The total thickness of Pt layers on both sides of the film was calculated to be about 4.0 nm from the deposition parameters. Therefore, the net thickness of the DTAB film is 2.5 nm, which means that the film probably has a bilayer structure, as the molecular length of DTAB is 1.6 nm.

Many different types of amphiphilic compounds were employed for the preparation of dried foam films. For example, double-chain-type didodecyldimethylammonium bromide (DDAB), zwitterionic dodecylphosphocholine (D-PC), nonionic polyoxyethylene dodecyl ether (Brij-35), natural egg lecithin, and two alkylsilane compounds—octadecyltrimethoxysilane (C18-Si) and octadecyldimethyl(3-trimethoxysilylpropyl) ammonium chloride (C18-N-Si)—were examined. Their dried foam films are shown in Figure 3. DDAB, D-PC, C18-Si, and C18-N-Si gave uniform films on 2000-mesh copper grids. The C18-Si film was prepared from ethanol solution (8.2 mM) because of its low solubility in water. This means that water is not indispensable for the formation of dried foam films. Interestingly, the C18-N-Si film was stable enough to withstand a focused electron beam without Pt coating. This stabilization is probably caused by the hydrolysis of methoxysilane groups and the subsequent formation of a siloxane network.

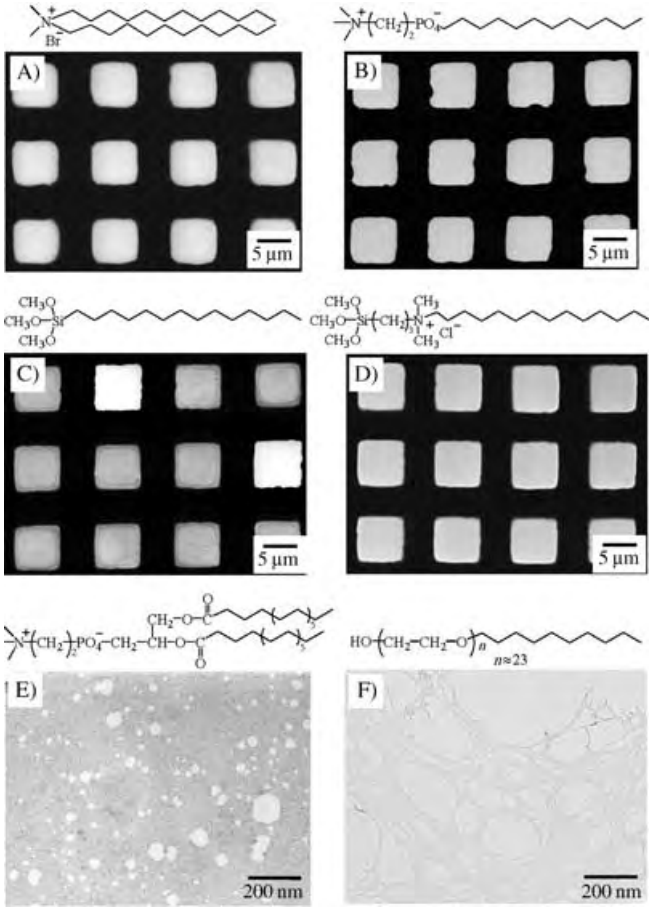


Figure 3. TEM images of the dried foam films of A) DDAB, B) D-PC, C) C18-Si, and D) C18-N-Si prepared on 2000-mesh copper grids; E) lecithin and F) Brij-35 films prepared on the holes of perforated polymer membranes. All films except C18-Si were prepared from aqueous solutions (8.2 mM) of the corresponding amphiphilic compounds.

 © 2005 Wiley-VCH Verlag GmbH & Co. KGaA, Weinheim

The lecithin and Brij-35 films are very different from the others. As shown in Figure 3E, many circular pores are observed for the lecithin film. It is known that this compound spontaneously forms vesicular assemblies known as liposomes, and such a structure might be reflected in the circular pores of the dried foam film. The film made of Brij-35 appears to be a torn plastic film (Figure 3F). Natural lipids and nonionic surfactants have been extensively studied by many researchers,[16–19] who have reported that stable and densely packed foam films are readily formed because of the weak electrostatic repulsion between the two monolayers.[17,18] However, these liquid foam films are subject to serious morphology changes after evaporation of the water layer.

In previous studies, the amount of interstitial water has been estimated by transmission FTIR spectroscopy[20,21] as the water layer gives a strong absorption peak in the range from 3200 to 3600 cm^{-1}. The sensitivity of FTIR measurements is very high, and it is possible to detect a water layer not less than 0.2 nm thick.[18] To confirm the disappearance of water from the dried foam films, we recorded FTIR measurements. As shown in Figure 4, the characteristic peaks of water are not

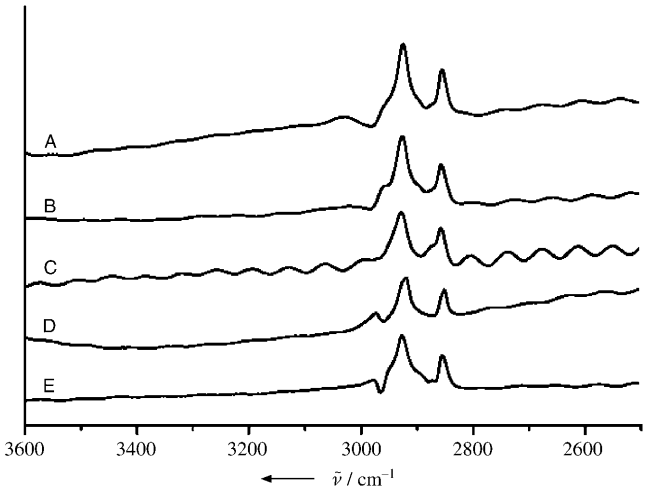


Figure 4. Transmission FTIR spectra of the dried foam films of A) DTAB, B) DDAB, C) D-PC, D) C18-Si, and E) C18-N-Si on porous alumina membranes.

detected at all. It is clear that all the dried foam films have no liquid water and, moreover, no fluidic properties of liquids. Being skeptics, we assumed that a trace amount of water of crystallization should remain in the films. However, we could not find any evidence for the existence of this water. For example, DTAB, which has a trimethylammonium group and a bromide ion in its hydrophilic moiety, cannot strongly bind water molecules by hydrogen bonding, coordination bonding etc. Furthermore, TEM and FE-SEM observations were conducted under high vacuum conditions (lower than 1×10^{-6} torr). In these cases, all the interstitial water should have completely evaporated. What is to be emphasized is the structural stability of the dried foam films. The existence of water or a hydration layer is not necessarily essential to maintain the self-standing reversed bilayer structure.

What is the role of alkyl chains in the structural stabilization of the reversed bilayer structure? In the crystalline state DTAB has an interdigitated bilayer structure. As the cross-section of the alkyl chain is smaller than that of the trimethylammonium group, this amphiphilic compound acquires stable molecular packing by inserting its alkyl chains from both sides of the bilayer. However, the reversed bilayer structure does not allow such interdigitation. If the alkyl chains in an all-*trans* conformation are closely packed in the reversed bilayer, they need to be highly tilted. However, such a molecular arrangement necessarily leads to many defects. We estimated the degree of conformational disorder of the alkyl chains from the FTIR spectra. Alkyl chains that have an all-*trans* conformation in the crystalline state give CH_2 stretching vibration bands near 2918 (ν_{as}) and 2848 cm^{-1} (ν_s). These bands are known to shift up to near 2927 (ν_{as}) and 2856 cm^{-1} (ν_s), respectively, when conformational disorder is induced in the alkyl chains.[22] The dried foam films of DTAB give absorption peaks at 2924.7 (ν_{as}) and 2855.3 cm^{-1} (ν_s). These peaks are significantly shifted to higher wavenumbers from the bands of ordered alkyl chains, thereby indicating that the alkyl chains in the DTAB film are very disordered at room temperature. Similar large shifts to higher wavenumbers were observed for all the dried foam films derived from charged amphiphilic compounds (see the Supporting Information), meaning that the alkyl chains in the films are never closely packed. We have shown that dried foam films are self-standing and that if the alkyl chains are disordered, the hydrophilic moieties have to contribute to the structural stabilization. As observed in the crystallographic analysis of CTAB, the trimethylammonium groups and bromide ions form into two-dimensional ionic sheets.[23] Such a structure might be what makes it possible to keep the film in suspension. The importance of hydrophilic moieties was supported by the following phenomenological facts: C18-N-Si gives films that are very stable against a focused electron beam, and zwitterionic D-PC forms uniform dried foam films. In contrast, nonionic Brij-35 and related surfactants give highly tattered films.

The thermal stability of dried foam films was analyzed statistically by monitoring the change of the surface coverage on a 150-mesh microgrid with increasing temperature. As shown in Figure 5, the coverage of DTAB films lies in a range from 93 to 98% from room temperature to 150°C. However, the coverage drastically decreases to 10% when the grid is heated at 160°C. That this change occurs at a temperature well above the boiling point of water strongly indicates that no water is present in the dried foam films. A bulk crystal of DTAB, in which the alkyl chains have an interdigitated structure, has a melting point of 246°C. The dried foam films that have loosely packed alkyl chains show a transition temperature about 90°C lower than this melting point. These temperatures are considerably higher than the phase transition temperatures of biolipids as the head-groups of biolipids are fully hydrated and their phase transition is generally caused by the disordering of the alkyl chains. What is important is that the coverage in Figure 5 declines sharply. This means that the dried foam films have high molecular cooperativity: if the alkyl chains are disordered, the hydrophilic moieties have to be in the crystalline state. This is probably the reason why the films have high thermal stability.

 © 2005 Wiley-VCH Verlag GmbH & Co. KGaA, Weinheim

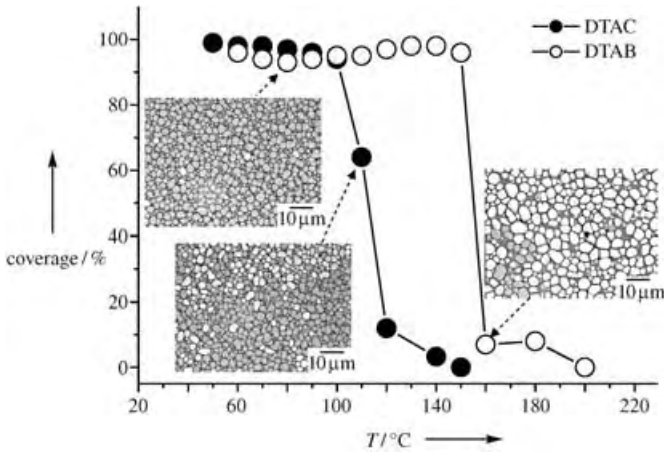


Figure 5. Temperature dependence of the coverage of DTAB and DTAC films.

The coverage of DTAC, which has a chloride ion as the counteranion of a trimethylammonium group, decreases greatly at a temperature about 40 °C lower than that of DTAB, thus showing that the thermal stability is very sensitive to the size of the counterion.[24]

Foam films have been known for more than three centuries and water has always been thought to be an essential component. However, we have found that water is not always indispensable on the micrometer scale as dried foam films are quite stable in the air, under vacuum, and even at high temperature.[25] These findings have immense potential for the design of nanoscale architectures. In fact, we have made it possible to combine a wet process for film formation and a dry process for metal coating. It is also possible to form free-standing films composed of metal oxides and polymers. These artificially organized thin films will contribute widely to various fields of chemistry.

Experimental Section

Materials. The 150-mesh microgrid and 2000-mesh copper grid were purchased from Oken, Japan. The former grid has a perforated polymer membrane, with the surface of the polymer membrane coated with thin glassy carbon to reinforce the pores of a few micrometers. The latter grid is made of pure copper and has regularly arranged square holes of 7 μm at an interval of 2000 per inch. The porous alumina membrane (Anodisc-25) with a pore size of 0.2 μm was purchased from Whatman and used as the substrate for FTIR measurements.

Pt Coating. TEM and FE-SEM specimens were often coated with a 2-nm-thick platinum layer by using a Hitachi E-1030 ion sputter. The coating was performed with a current density of 10 mA at room temperature under an argon pressure of 10 Pa or lower. The thickness was calibrated by using the quartz crystal microbalance technique. Under our experimental conditions, platinum nanoparticles of about 0.8 nm were uniformly deposited on the surfaces of any kind of dried foam film. The deposition did not have any effect on the film morphology. However, deposition of more than 10 nm of platinum was prone to disrupt the films, probably resulting from the high surface tension of the platinum layer.

Characterizations. TEM observations were made with a JEM-1010 (JEOL) instrument at an acceleration voltage of 100 kV. FE-SEM images were obtained with a Hitachi S-4800. The cross-sectional specimen was prepared by carefully tearing a 2000-mesh copper grid covered with dried foam films, followed by Pt coating in a vertical sample holder. FTIR spectra were obtained with a Bio-Rad Win-IR spectrometer. The sample was set in a chamber filled with dried nitrogen gas. Confocal laser microscopy images were obtained with an instrument from Lasertec (VL2000D). The coverage of dried foam films was calculated by counting the films remaining after heating for 15 min at a given temperature. The number of holes examined was higher than 600.

Received: January 5, 2005
Revised: May 6, 2005
Published online: June 24, 2005

Keywords: amphiphiles · foams · self-assembly · thin films

[1] K. Mysels, K. Shinoda, S. Frankel, *Soap Films*, Pergamon, New York, **1959**.
[2] E. Sackmann, *Science* **1996**, *271*, 43 – 48.
[3] H. T. Tien, R. H. Barish, L. Q. Gu, A. L. Ottova, *Anal. Sci.* **1998**, *14*, 3 – 18.
[4] A. Sheludko, *Adv. Colloid Interface Sci.* **1967**, *1*, 391 – 464.
[5] H. D. Yaros, J. Newman, C. J. Radke, *J. Colloid Interface Sci.* **2003**, *262*, 442 – 455.
[6] R. Hooke, *Communications to the Royal Society*, March **1672**, p. 28.
[7] I. Newton, *Opticks Book II*, *Part I*, Smith and Wotford, London, **1704**.
[8] E. Mileva, D. Exerowa, *Adv. Colloid Interface Sci.* **2003**, *100–102*, 547 – 562.
[9] D. Platikanov, H. Graf, A. Weiss, *Colloid Polym. Sci.* **1990**, *268*, 760 – 765.
[10] O. Bélorgey, J. J. Benattar, *Phys. Rev. Lett.* **1991**, *66*, 313 – 316.
[11] D. Sentenac, J. J. Benattar, *Phys. Rev. Lett.* **1998**, *81*, 160 – 163.
[12] E. Ruckenstein, M. Manciu, *Langmuir* **2002**, *18*, 2727 – 2736.
[13] N. Krasteva, R. Krustev, H. J. Müller, D. Vollhardt, H. Möhwald, *J. Phys. Chem. B* **2001**, *105*, 1185 – 1190.
[14] J. J. Benattar, Q. Shen, S. Bratskaya, V. Petkova, M. P. Krafft, B. Pucci, *Langmuir* **2004**, *20*, 1047 – 1050.
[15] J. T. G. Overbeek, *J. Phys. Chem.* **1960**, *64*, 1178 – 1183.
[16] N. Cuvillier, F. Millet, V. Petkova, M. Nedyalkov, J. J. Benattar, *Langmuir* **2000**, *16*, 5029 – 5035.
[17] F. Lhert, D. Blaudez, C. Heywang, J. M. Turlet, *Langmuir* **2002**, *18*, 512 – 518.
[18] C. Berger, B. Desbat, H. Kellay, J. M. Turlet, D. Blaudez, *Langmuir* **2003**, *19*, 1 – 5.
[19] R. M. Muruganathan, R. Krustev, N. Ikeda, H. J. Müller, *Langmuir* **2003**, *19*, 3062 – 3065.
[20] X. Du, Y. Liang, *Phys. Chem. Chem. Phys.* **2000**, *2*, 1515 – 1518.
[21] C. E. H. Berger, V. Bergeron, B. Desbat, D. Blaudez, H. Kellay, J. M. Turlet, *Langmuir* **2003**, *19*, 8615 – 8617.
[22] Z. Zhang, A. L. Verma, M. Yoneyama, K. Nakashima, K. Iriyama, Y. Ozaki, *Langmuir* **1997**, *13*, 4422 – 4427.
[23] H. Hirata, N. Iimura, *J. Pharm. Soc. Jpn.* **2001**, *121*, 403 – 421.
[24] The thermal stability of dried foam films is sensitive to the molecular structure of amphiphilic compounds, too. The dried foam films of D-PC and C18-N-Si disappeared near 160 and 180 °C, respectively. The higher thermal stability of the latter film must be because of the covalent bonding between the hydrophilic groups.
[25] We also found that C18-Si gave very stable films from the ethanol solution. Formation of dried foam films may not, therefore, be restricted to a dehydration mechanism. The molecular design of amphiphilic compounds will provide new types of self-standing films.

 © 2005 Wiley-VCH Verlag GmbH & Co. KGaA, Weinheim

Green Chemisty

A Recyclable Catalytic System Based on a Temperature-Responsive Catalyst**

*Hiromi Hamamoto, Yachiyo Suzuki, Yoichi M. A. Yamada, Hidetsugu Tabata, Hideyo Takahashi, and Shiro Ikegami**

In modern synthetic organic chemistry, the development of an efficient reagent or catalyst recycling system is regarded as one of the most important topics.[1] A great deal of effort has been invested in devising methodologies for this purpose. Although various types of recyclable catalytic systems have been explored by using solid reagents and catalysts, it is difficult to retain or raise their activities relative to those of their homogeneous counterparts. Recently, much attention has been focused on the creation of catalytic systems that exploit stimuli-responsive materials. The use of a biphasic system comprising ionic liquids or fluorous solvents and an organic solvent and that can be mixed by changing the temperature is a potential strategy (Figure 1 A).[2–4]

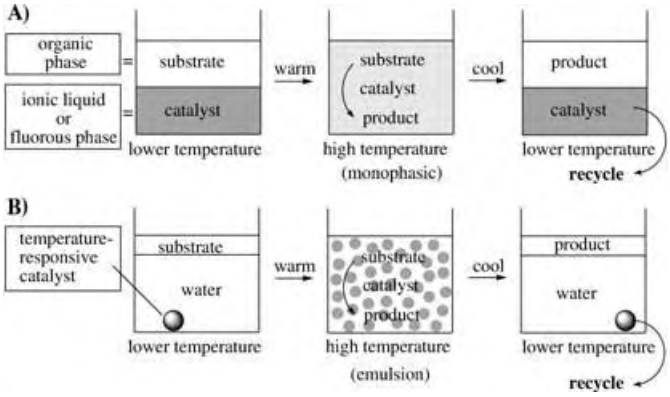
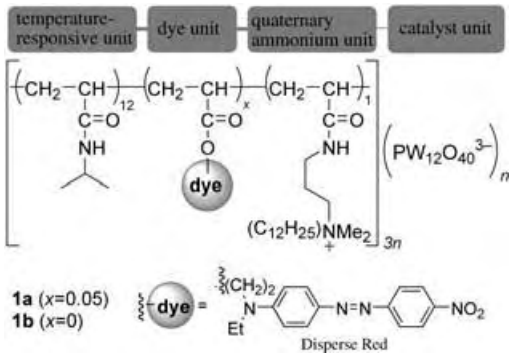


Figure 1. Simplified representation of thermomorphic catalysis. A) Use of a biphasic system comprising ionic liquids or fluorous solvents and an organic solvent. B) Use of a recyclable micellar-type reaction system.

Previously, we investigated the self-assembly of poly(*N*-isopropylacrylamide)-based (PNIPAAm-based) polymer ligands and an inorganic species.[5] This process afforded a networked supramolecular complex in which the polymers are cross-linked by the inorganic species. The complex thus obtained is insoluble in water and functions as an efficient triphase catalyst. In contrast, PNIPAAm polymers intrinsically have temperature-responsive behavior and have been applied to various fields such as drug-delivery systems, column-packing materials, and cell-culture substrates by changing the temperature.[6–8] PNIPAAm polymers undergo thermally reversible changes between water soluble and insoluble states across a lower critical solution temperature (LCST) from 30 to 40 °C. Thus, the polymer chains of NIPAAm are hydrated below the LCST and dehydrated with aggregation above the LCST.[7] The efficient application of soluble PNIPAAm-supported catalysts to biphasic systems has already been reported by Bergbreiter et al.[9]

Colloidal aggregation, such as emulsions formed by amphiphilic molecules in water, has been regarded as an attractive reaction media.[10] This work focuses much attention on the use of the specific hydrophobic species formed by PNIPAAm as a novel organic reaction media in water and provides a recyclable micellar-type reaction system based on PNIPAAm (Figure 1 B). In many cases, the use of a recyclable polymeric catalyst would be advantageous when isolating the product from solution and when removing surfactants that cause environmental pollution.

To design a new recyclable catalytic system from micellar-type aggregates, a dye-labeled catalyst comprising a phosphotungstic acid ($H_3PW_{12}O_{40}$), a PNIPAAm polymer, and a Disperse Red moiety was synthesized (Scheme 1).[5d] Using



Scheme 1. Design of thermomorphic polymer-supported $PW_{12}O_{40}^{3-}$ complex **1**.

this model catalyst **1a**, we investigated the effect of temperature on phase transformation in the presence of an organic substrate and solvent. Although **1a** was insoluble in most solvents at room temperature, the formation of a stable emulsion was observed in water at high temperature (Figure 2 A). Furthermore, an optical micrograph of the mixture at 80 °C showed the presence of hydrophobic beads in water, while such species could not be observed at room temperature (Figure 3). In contrast, **1a** was insoluble in nonpolar solvents such as toluene or octane and soluble in polar organic solvent such as MeCN or *tert*-butyl alcohol at high temperature (Figures 2 B and C).

The results mentioned above prompted us to develop a new reaction system based on the thermomorphic catalyst **1b** for the oxidation of primary and secondary alcohols with hydrogen peroxide.[11] In the oxidation of 1-phenyl-1-propanol in water, the thermoregulated formation of a stable

[*] Dr. H. Hamamoto, Y. Suzuki, Y. M. A. Yamada, H. Tabata, Dr. H. Takahashi, Prof. Dr. S. Ikegami
School of Pharmaceutical Sciences
Teikyo University
Sagamiko, Kanagawa, 199-0195 (Japan)
Fax: (+81) 426-85-1870
E-mail: shi-ike@pharm.teikyo-u.ac.jp

[**] This work was partially supported by a Grant-in-Aid of the Ministry of Education, Science, Sports, and Culture. We thank J. Shimode and A. Tonoki for spectroscopic measurements.

 © 2005 Wiley-VCH Verlag GmbH & Co. KGaA, Weinheim DOI: 10.1002/anie.200500574

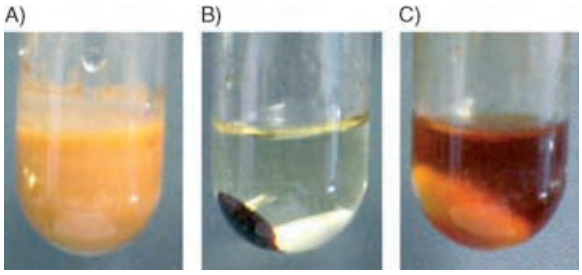


Figure 2. Photographs of a mixture of **1a** and 1-phenyl-1-propanol at 80°C: A) in water; B) in toluene; C) in *t*BuOH.

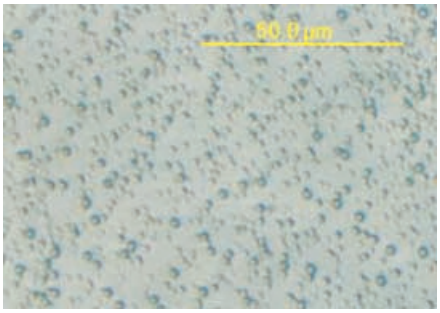


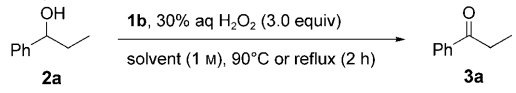
Figure 3. Optical micrograph of a mixture of **1a** and 1-phenyl-1-propanol in water at 80°C.

emulsion was detected at 90°C and higher activity was observed. In contrast, the oxidation hardly proceeded in the absence of catalyst (Table 1, entries 1 and 2). Furthermore, the oxidation proceeded smoothly even when only 0.1 mol% of **1b** was present (entry 3). Recovery of catalyst was very easy; **1b** precipitated on cooling and cleanly separated from the reaction mixture after the addition of diethyl ether (Figure 4). The ^{31}P NMR spectrum of recovered **1b** was unchanged relative to that of **1b** before the reaction and no other species was evident.[11,12] Moreover, recovered **1b** could also be used for consecutive reactions without any significant loss of catalytic efficacy (Scheme 2). The reaction was also carried out in various organic solvents (Table 1, entries 4–7). However, no significant activity was observed in each case. It is noteworthy that this catalytic system based on micellar-type aggregates in water is more effective than homogeneous systems.[13]

Having obtained these results, we extended our catalytic system to the oxidation of other alcohols. Oxidation of the secondary alcohols **2b–e** afforded the corresponding ketones **3b–e** in good yields (Table 2). However, the oxidation of the primary alcohols, **2f** and **2g**, with 3.0 equivalents of hydrogen peroxide afforded selectively the corresponding carboxylic acids **4a** and **4b**.

In summary, we have designed a unique and facile recyclable reaction system based

Table 1: Solvent effect on the oxidation of 1-phenyl-1-propanol (**2a**) catalyzed by **1b**.



Entry	Solvent	c(**1b**) [mol%]	Yield [%][a]	Reaction system
1	H_2O	0.0	<1	–
2	H_2O	0.5	92	emulsion
3	H_2O[b]	0.1	92	emulsion
4	toluene	0.5	10	heterogeneous
5	*n*-C_8H_{18}	0.5	18	heterogeneous
6	$C_2H_4Cl_2$	0.5	12	heterogeneous
7	*t*BuOH	0.5	35	homogeneous
8	CH_3CN	0.5	34	homogeneous

[a] Yield of isolated products. [b] 10% aq H_2O_2 (1.5 equiv).

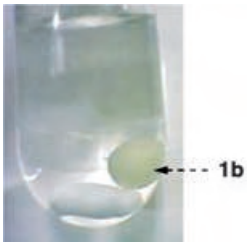
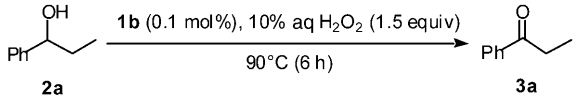


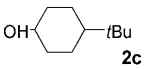
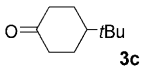
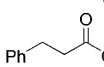
Figure 4. Photograph of recovered **1b**.



yield after 1st use: 92 %; 2nd use: 92 %; 3rd use: 90 %

Scheme 2. Oxidation of 1-phenyl-1-propanol by recycled **1b**.

Table 2: Oxidation of primary and secondary alcohols catalyzed by **1b**.

Entry	Substrate	Product	10% aq H_2O_2 [equiv]	Yield [%][a] (1st use)	(2nd use)	(3rd use)
1[b]	 **2b**	 **3b**	1.5	92	89	90
2[b]	 **2c**	 **3c**	1.5	88	87	87
3[c]	 **2d**	 **3d**	1.5	93	93	89
4[c]	 **2e**	 **3e**	1.5	92	88	90
5[c]	 **2f**	 **4a**	3.0	89	90	87
6[d]	 **2g**	 **4b**	3.0	84	80	81

[a] Yield of isolated products. [b] **1b** (0.1 mol%), 90°C (6 h). [c] **1b** (0.2 mol%), 90°C (6 h). [d] **1b** (0.4 mol%), 90°C (8 h).

 © 2005 Wiley-VCH Verlag GmbH & Co. KGaA, Weinheim

on a thermomorphic catalyst comprising PNIPAAm. Formation of a stable emulsion, derived from hydrophobic PNIPAAm at high temperature, raises the catalytic activity in the oxidation of alcohols with hydrogen peroxide. Moreover, the catalyst is easily recovered and reused. The results described herein highlight the potential use of PNIPAAm in the field of organic synthesis. Further investigation into the catalytic properties of temperature-responsive catalysts are currently in progress.

Experimental Section

General procedure for the catalytic reaction: A mixture of **1b** (80 mg, 0.01 mmol) and **2** (10 mmol) in 10% aq H_2O_2 (4.5 mL, 15 mmol) was heated to 90°C and stirred for 6 h. After the reaction mixture had been allowed to cool to room temperature, Et_2O (2.5–5 mL) was added and this mixture stirred for 5–10 min. The organic and aqueous phases were removed, and recovered **1b** was washed with ether and distilled water, which were then added to the aqueous phase. The aqueous phase was extracted three times with Et_2O and the combined organic extracts were washed with brine. The organic phase was then dried over $MgSO_4$ and concentrated under reduced pressure. The residual crude reaction mixture was purified by silica-gel column chromatography to give the pure products of **3**. Recovered **1b** was dried under vacuum for 12 h and reused for subsequent catalytic experiments.

Received: February 16, 2005
Revised: May 2, 2005
Published online: June 21, 2005

Keywords: green chemistry · micelles · oxidation · polymers · supported catalysts

[1] a) J. A. Gladysz, *Pure Appl. Chem.* **2001**, *73*, 1319–1324; b) U. Kragl, T. Dwars, *Biotechnology* **2001**, *19*, 442–449; c) J. A. Gladysz, *Chem. Rev.* **2002**, *102*, 3215–3216; d) D. J. Cole-Hamilton, *Science* **2003**, *299*, 1702–1706.

[2] a) D. P. Curran, *Angew. Chem.* **1998**, *110*, 1230–1255; *Angew. Chem. Int. Ed.* **1998**, *37*, 1174–1196; b) I. T. Hováth, *Acc. Chem. Res.* **1998**, *31*, 641–650; c) J. A. Gladysz, D. P. Curran, *Tetrahedron* **2002**, *58*, 3823–3825; d) C. C. Tzschucke, C. Market, W. Bannwarth, S. Roller, A. Hebel, R. Haag, *Angew. Chem.* **2002**, *114*, 4136–4173; *Angew. Chem. Int. Ed.* **2002**, *41*, 3964–4000.

[3] a) Y. Wang, J. Jiang, R. Zhang, X. Liu, Z. Jin, *J. Mol. Catal. A* **2000**, *157*, 111–115; b) K. Ishihara, K. Kondo, H. Yamamoto, *Synlett* **2001**, 1371–1374; c) M. Wende, R. Meier, J. A. Gladysz, *J. Am. Chem. Soc.* **2001**, *123*, 11490–11491; d) J. N. Xiang, A. Orita, J. Otera, *Adv. Synth. Catal.* **2002**, *344*, 84–90; e) K. Ishihara, A. Hasegawa, H. Yamamoto, *Synlett* **2002**, 1299–1301; f) M. Wende, J. A. Gladysz, *J. Am. Chem. Soc.* **2003**, *125*, 5861–5872.

[4] a) X. Zuwei, Z. Ning, S. Yu, K. Li, *Science* **2001**, *292*, 1139–1141; b) V. K. Dioumaev, R. M. Bullock, *Nature* **2003**, *424*, 530–533.

[5] a) Y. M. A. Yamada, M. Ichinohe, H. Takahashi, S. Ikegami, *Org. Lett.* **2001**, *3*, 1837–1840; b) Y. M. A. Yamada, K. Takeda, H. Takahashi, S. Ikegami, *Org. Lett.* **2002**, *4*, 3371–3374; c) Y. M. A. Yamada, K. Takeda, H. Takahashi, S. Ikegami, *J. Org. Chem.* **2003**, *68*, 7733–7741; d) Y. M. A. Yamada, H. Tabata, M. Ichinohe, H. Takahashi, S. Ikegami, *Tetrahedron* **2004**, *60*, 4087–4096.

[6] H. G. Schild, *Prog. Polym. Sci.* **1992**, *17*, 163–249.

[7] M. Heskins, J. E. Guillet, *J. Macromol. Sci. Chem.* **1968**, *2*, 1441–1455.

[8] a) Y. H. Bae, T. Okano, S. W. Kim, *J. Polym. Sci., Part B: Polym. Phys.* **1990**, *28*, 923–936; b) G. Chen, A. S. Hoffman, *Nature* **1995**, *373*, 49–52; c) H. Kanazawa, K. Yamamoto, Y. Matsushima, N. Takai, A. Kikuchi, Y. Sakurai, T. Okano, *Anal. Chem.* **1996**, *68*, 100–105; d) B. Jeong, Y. H. Bae, D. S. Lee, S. W. Kim, *Nature* **1997**, *388*, 860–862; e) Z. Hu, Y. Chen, C. Wang, Y. Zheng, Y. Li, *Nature* **1998**, *393*, 149–152; f) T. G. Park, *Biomaterials* **1999**, *20*, 517–521; g) D. Umeno, M. Maeda, *Chem. Lett.* **1999**, *28*, 381–382; h) S. Juodkazis, N. Mukai, R. Wakaki, A. Yamaguchi, S. Matsuo, H. Misawa, *Nature* **2000**, *408*, 178–181; i) H. Ichikawa, Y. Fukumori, *J. Controlled Release* **2000**, *63*, 107–119; j) T. Ito, T. Hioki, T. Yamaguchi, T. Shinbo, S. Nakao, S. Kimura, *J. Am. Chem. Soc.* **2002**, *124*, 7840–7846.

[9] Selected lead references: a) D. E. Bergbreiter, B. L. Case, Y.-S. Liu, J. W. Caraway, *Macromolecules* **1998**, *31*, 6053–6062; b) D. E. Bergbreiter, P. L. Osburn, A. Wilson, E. M. Sink, *J. Am. Chem. Soc.* **2000**, *122*, 9058–9064; c) D. E. Bergbreiter, R. Hughes, J. Besinaiz, C. Li, P. L. Osburn, *J. Am. Chem. Soc.* **2003**, *125*, 8244–8249.

[10] a) M.-J. Schwuger, K. Stickdorn, R. Schomäcker, *Chem. Rev.* **1995**, *95*, 849–864; b) S. Tascioglu, *Tetrahedron* **1996**, *52*, 11113–11152; c) C.-J. Li, T.-H. Chan, *Organic Reactions in Aqueous Media*, Wiley, New York, **1997**; d) *Organic Synthesis in Water* (Ed.: P. A. Grieco), Blackie Academic and Professional, London, **1998**; e) U. M. Lindström, *Chem. Rev.* **2002**, *102*, 2751–2772; f) S. Kobayashi, K. Manabe, *Acc. Chem. Res.* **2002**, *35*, 209–217.

[11] a) C. Venturello, R. D'Aloisio, J. C. T. Bart, M. Ricci, *J. Mol. Catal.* **1985**, *32*, 107–110; b) Y. Ishii, K. Yamawaki, T. Ura, H. Yamada, T. Yoshida, M. Ogawa, *J. Org. Chem.* **1988**, *53*, 3591–3593; c) C. Venturello, G. Mario, *J. Org. Chem.* **1991**, *56*, 5924–5931; d) C. Aubry, G. Chottard, N. Platzer, J. M. Bregeault, R. Thouvenot, F. Chauveau, C. Huet, H. Ledon, *Inorg. Chem.* **1991**, *30*, 4409–4415; e) R. Neumann, A. K. Khenkin, *J. Org. Chem.* **1994**, *59*, 7577–7579; f) L. Salles, C. Aubry, R. Thouvenot, F. Robert, C. D. Morin, G. Chottard, H. Ledon, Y. Jeannin, J.-M. Brégeault, *Inorg. Chem.* **1994**, *33*, 871–878; g) D. C. Duncan, R. C. Chambers, E. Hecht, C. L. Hill, *J. Am. Chem. Soc.* **1995**, *117*, 681–691; h) D. Sloboda-Rozner, P. Witte, P. L. Alsters, R. Neumann, *Adv. Synth. Catal.* **2004**, *346*, 339–345; i) L. Plault, A. Hauseler, S. Nlate, D. Astruc, J. Ruiz, S. Gatard, R. Neumann, *Angew. Chem.* **2004**, *116*, 2984–2988; *Angew. Chem. Int. Ed.* **2004**, *43*, 2924–2928.

[12] The absence of the dye-labeled polymer unit of **1a** in both organic and aqueous phases after oxidation catalyzed by **1a** indicates that tungsten leaching is negligible. Furthermore, the recovered aqueous phase did not show any catalytic activities for the oxidation of alcohols in the presence of surfactant and hydrogen peroxide.

[13] The oxidation of alcohol in water was not accelerated by the presence of $(Bu_4N)_3[PW_{12}O_{40}]$: Yields = 9% (in H_2O), < 5% (in toluene), 55% (in *t*BuOH); conditions: catalyst 0.5 mol%, solvent 1M, H_2O_2 1.5 equiv, 90°C, 2 h.

 © 2005 Wiley-VCH Verlag GmbH & Co. KGaA, Weinheim

Heterogeneous Catalysis

Pt–Cu Core–Shell and Alloy Nanoparticles for Heterogeneous NO_x Reduction: Anomalous Stability and Reactivity of a Core–Shell Nanostructure**

Shenghu Zhou, Bindhu Varughese, Bryan Eichhorn, Greg Jackson, and Kevin McIlwrath*

Metallic nanoparticles of the noble metals find wide applications in heterogeneous gas-phase and solution-phase catalytic processes.[1–4] Small particle sizes optimize the dispersion of precious metals, such as platinum and palladium, and can also show anomalous reactivities not observed for the bulk metals. Bimetallic nanoparticles have been studied because of modified (enhanced) activities of noble metals and their abilities to catalyze multistep processes in which each metal participates in a different elementary step.[5–7] Toshima and Wang[8] first reported the synthesis of colloidal PtCu particles and showed their utility in the catalytic hydrogenation in solution. Recent studies[9,10] have suggested that supported PtCu bimetallic catalysts may be effective in NO_x reduction, but coprecipitation/impregnation methods typically used in these studies make it difficult to identify and evaluate the actual catalytic species. While some catalysts have been reported to have high activity for NO_x reduction,[11,12] the best activity and selectivity for N_2 formation (a desirable feature) is typically found with monometallic platinum catalysts.[13–15] To fully understand the catalytic activity of PtCu bimetallic catalysts and compare the activities with the monometallic materials, a detailed understanding of the composition, phase behavior, activation processes, and stabilities of the catalytic components is essential. To this end, we have embarked on a systematic investigation of the synthesis and study of bimetallic PtCu nanoparticles to evaluate their heterogeneous catalytic activities for reduction of gas phase NO with H_2 as the reducing agent.

[*] S. Zhou, B. Varughese, Prof. B. Eichhorn
Department of Chemistry and Biochemistry
University of Maryland
College Park, MD 20742 (USA)
Fax: (+1) 301-314-9121
E-mail: eichhorn@umd.edu
Prof. G. Jackson
Department of Mechanical Engineering
University of Maryland
College Park, MD 20742 (USA)
K. McIlwrath
Hitachi Instruments
Hitachi High Technologies America
5100 Franklin Drive, Pleasanton, CA 94588 (USA)

[**] This work was supported by the U.S. Department of Energy's Oak Ridge National Lab under the Advanced Reciprocating Engine Systems Program (Tim Theiss, Program Manager) and the NSF (CHE/DMR).

Supporting information for this article is available on the WWW under http://www.angewandte.org or from the author.

In addition to monometallic and alloy particles, various core–shell architectures have recently been reported, such as the gold nucleated seeded growth structures.[16–20] These nanoparticles are of interest for catalytic, optical, and magnetic applications, but their synthesis and characterization are often difficult and less studied. In particular, the synthetic routes to many target structures are challenging and the exact composition and/or phase of the resulting core and shell components are often not well understood. Systematic, detailed investigations of core–shell structures are also needed to gain a full understanding of bimetallic systems.

We report herein the synthesis and characterization of the new reciprocal core–shell structures, Pt@Cu and Cu@Pt, as well as their compositional makeup and unusual thermal stabilities. In addition, we describe a modified synthesis of PtCu alloy nanoparticles from a polyol co-reduction process and compare the thermal stability and catalytic properties with those of the core–shell structures and pure metal particles. Preliminary evaluation of γ-Al_2O_3 supported nanoparticles for catalytic NO reduction shows that the Cu@Pt nanoparticles have high activity equal to that of pure platinum nanoparticles but with significantly greater selectivity for N_2 formation.

Platinum and copper monometallic nanoparticles, PtCu alloy nanoparticles, and the Pt@Cu and Cu@Pt core–shell structures were all prepared by polyol reductions with either PVP_{55000} polymer (polyvinylpyrrolidone $M_w = 55000$) or oleylamine/oleic acid stabilizers to control particle sizes. While the individual synthetic methods are quite reproducible in producing particles of a specific size, each type of particle has a different mean particle size. Monometallic platinum and copper nanoparticles were prepared by polyol reduction of $[Pt(acac)_2]$ and $[Cu(acac)_2]$ (acac = acetylacetonate), respectively, in glycol at reflux in the presence of PVP. The mean diameters of the platinum and copper monometallic nanoparticles thus formed are 15 nm and 4 nm, respectively. An alternative method using oleylamine/oleic acid stabilizers gave much smaller platinum particles (3–7-nm particles; mean diameter 4.5 nm). Transmission electron microscopy (TEM) and X-ray diffraction (XRD) data for these materials can be found in the Supporting Information. The PtCu alloy nanoparticles were prepared by a modified version of that of Toshima and Wang[8] in which $[Pt(acac)_2]$ and $Cu(SO_4)\cdot 5H_2O$ (1:1 mole ratio) were heated at reflux in glycol with PVP to give 2–5-nm spherical particles (mean diameter 3.3 nm). Monometallic nanoparticle impurities or sulfur contamination were not detected in the PtCu samples according to TEM, XRD, EDX (energy-dispersive X-ray spectroscopy) and UV/Vis analysis. The TEM image of a representative sample is shown in Figure 1 a. The Cu@Pt nanoparticles were prepared by sequential deposition involving the reduction of $[Cu(acac)_2]$ with glycol at reflux in the presence of PVP and subsequent addition and reduction of $[Pt(acac)_2]$. TEM images showed predominately 9–10-nm hexagonal particles (mean diameter 8.8 nm) with some smaller particles of 5 nm diameter. Field emission scanning TEM (FE-STEM) phase maps qualitatively show that all particles contain platinum and copper in approximately equal quantities (Figure 1 b–d). The Pt@Cu nanoparticles were prepared in a similar fashion

 DOI: 10.1002/anie.200500919 © 2005 Wiley-VCH Verlag GmbH & Co. KGaA, Weinheim

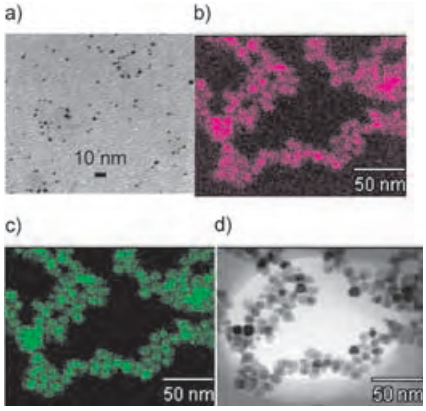


Figure 1. a) Bright-field TEM image (100 kV) of PtCu alloy nanoparticles. b–d) FE-STEM images (200 kV) of Cu@Pt nanoparticles showing b) Cu spectral map, c) Pt spectral map, and d) bright-field image.

with the initial glycol reduction of $[Pt(acac)_2]$ in the presence of PVP followed by a deposition of copper from $Cu(SO_4)\cdot 5H_2O$. FE-STEM analysis showed a broad distribution of particle sizes in the 8–20-nm size range with a mean diameter of 18.3 nm. However, all the particles again had approximately equal quantities of platinum and copper (FE-STEM phase map). A single particle EDX line scan for Cu@Pt is given in the Supporting Information. The presence of both platinum and copper in the core–shell structures is consistent with either PtCu alloys or the formation of the proposed core–shell particles. However, XRD and activity studies (see below) clearly show that the particles are not alloys. As expected, the mean diameters of each core–shell structure is larger than the diameters of the monometallic core particles.

No single analytical technique is sufficient to characterize the complex nanostructure of the core–shell particles. Comparison of several techniques is required to determine the general nature of the structure. The proposed structural models for the nanoparticle architectures described above are based on the evaluation of the combined TEM, EDX, XPS (X-ray photoelectron spectroscopy), XRD, and UV/Vis analyses. The XRD patterns of "as-prepared" PtCu alloy show the expected face-centered cubic (FCC) structure type with broad diffraction peak widths owing to the small particle sizes (mean diameter 3.3 nm, see above). After annealing the sample at 300 °C for 2 h, the peaks sharpen slightly and show 2θ peak positions[21] consistent with the target 1:1 (Pt/Cu) stoichiometry of the reaction mixture. This annealing process seems to have a dramatic effect on the catalytic activity of the particles as discussed below.

To evaluate the importance of the alloy structure in catalytic NO_x reductions, we prepared the core–shell nanoparticles Pt@Cu and Cu@Pt for comparison. The XRD data of the Pt@Cu and Cu@Pt particles are consistent with both the proposed core–shell structures and phase-separated monometallic particles. However, the FE-STEM studies described above and the activity studies (see below) are inconsistent with monometallic particles and allow us to exclude the phase-separated species from consideration. The XRD study (see Figure 2a) shows that the as-prepared Pt@Cu nanoparticles have a Pt FCC core with a $Pt_{1-x}Cu_x$ alloy shell ($x \approx 0.8$). Annealing the sample at 370 °C for 5 h converts the sample into PtCu (Figure 2b) as expected on the basis of the Pt–Cu phase diagram. In contrast, the as-prepared Cu@Pt nanoparticles have an FCC Cu core with an FCC Pt shell (Figure 2c). Surprisingly, annealing the samples at 370 °C for 5 h does not give the PtCu alloy but instead gives a Cu-rich $Pt_{1-x}Cu_x$ core and essentially a pure Pt shell (Figure 2d).

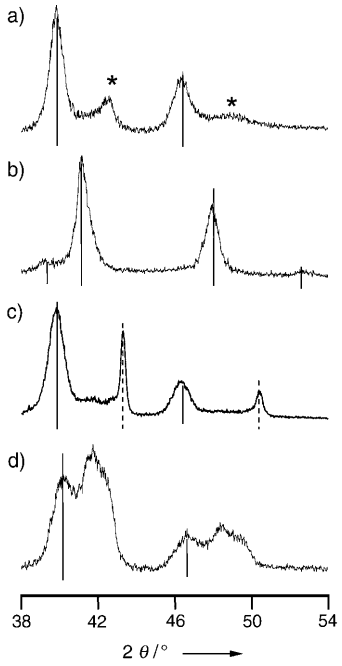


Figure 2. XRD profiles and JCPDS data (compound and file number)[21] for a) Pt@Cu (Pt, 04-0802; the asterisks indicate reflections from the $Pt_{0.2}Cu_{0.8}$ alloy), b) Pt@Cu after annealing (PtCu, 42-1326), c) Cu@Pt (Pt, 04-0802 solid vertical line; Cu, 04–0836 dashed vertical line) d) Cu@Pt after annealing (Pt, 01-1194).

We attribute this anomalous stability to Kirkendall mass-transport phenomena[22] in which the relative rates of migration of one metal into the other kinetically stabilize the Cu@Pt nanoparticles. Because the diffusion of Pt into Cu is fast (approximately $6\times10^{-7}\,cm^2h^{-1}$ at 960 °C) relative to Cu diffusion into Pt (approximately $8\times10^{-8}\,cm^2h^{-1}$ at 1041 °C),[23] the net migration at a Pt–Cu interface strongly favors Pt diffusion into the vacancies of the Cu bulk (i.e. the Kirkendall effect). In the Cu@Pt core–shell structure, the confined Cu core has a small, finite number of vacancies, which impedes net diffusion and thereby retards the alloying process. In contrast, the Cu-rich shell in the Pt@Cu nanoparticle system can maintain a high vacancy population and unhindered Pt-to-Cu diffusion. Therefore, alloying in the Pt@Cu is unimpeded but should result in a hollow PtCu alloy structure. While we know that the PtCu alloy is formed (Figure 2b), we do not yet know if the particles are hollow.

We are confident that the Pt@Cu and Cu@Pt nanoparticles are core–shell particles and not physical mixtures of monometallic components on the basis of the following experiments. 1) Annealing intimately mixed physical mixtures of Cu and Pt nanoparticles under the conditions described above does not result in alloy formation. The

 © 2005 Wiley-VCH Verlag GmbH & Co. KGaA, Weinheim

XRD profiles of the annealed physical mixture show clean peaks for FCC Cu and Pt after 5 h at 370 °C, which is in contrast to annealing behavior of both types of core–shell particles. 2) XPS spectra of the core–shell particles (Figure 3)

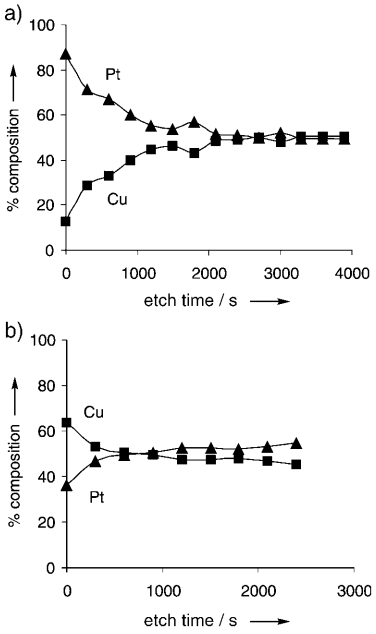


Figure 3. XPS data for a) Cu@Pt and b) Pt@Cu nanoparticles showing Pt (▲) and Cu (■) atomic percentages. Sequential Ar plasma etch sequences are shown as a function of etch time.

show atomic compositions that are highly enriched in the respective shell elements. For example, the Cu@Pt sample shows a Pt/Cu ratio of 88:12 that is indicative of a Pt-rich surface (Figure 3a). A series of 5-minute Ar plasma etches show that the composition becomes more Cu-rich as more of the particle core is exposed (or alloying takes place). After nine etches, the particles reach a 50:50 atomic ratio, which is the stoichiometric composition of the particles. The reciprocal particle, Pt@Cu, does not show the same initial large difference in surface elemental composition but achieves approximately 50:50 ratio after etching in a similar manner (Figure 3b). This behavior is consistent with the formation of the $Pt_{\approx 0.2}Cu_{\approx 0.8}$ alloy shell in contrast to a pure Cu shell and is consistent with the XRD experiments. 3) The STEM images show compositional maps that qualitatively indicate equal concentrations of each element and no monometallic particles (see Figure 1). 4) UV/Vis data show that Cu nanoparticles are not present in the colloid (no surface plasmon resonance band at around 590 nm).[1] 5) The catalytic activities of the core–shell particles are quite different to those of the monometallic particles, their alloys, and physical mixtures.

As an initial screening of the catalytic activity for NO reduction, we prepared samples of the different PtCu nanoparticles on γ-Al_2O_3 (1.06% total Pt loading) by direct deposition from colloidal suspensions. The NO conversions were evaluated by monitoring the formation of N_2, NH_3, NO_2, N_2O, and H_2O from an NO feed and H_2 reductant (0.75% NO, 3% H_2 diluted in Ar). The feed gas was passed across the catalyst (total loading, 105 mg of supported catalyst, pre-reduced in H_2) in a fixed bed reactor with a constant residence time. The reactants and products were measured (mass spectrometry) as a function of temperature. Figure 4 shows

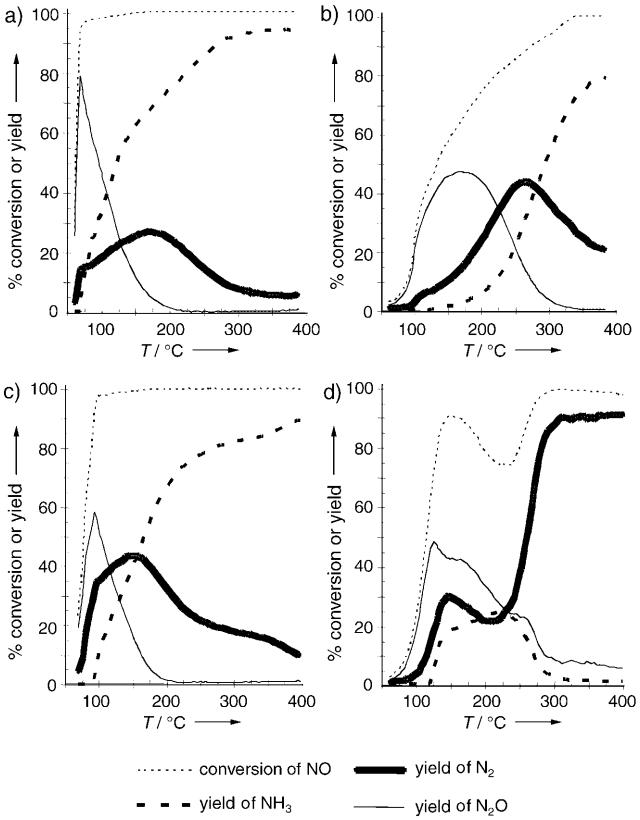


Figure 4. Temperature-programmed reactor studies of Pt–Cu bimetallic nanoparticle structures on NO reduction by H_2: a) pure Pt nanoparticles, b) PtCu alloy nanoparticles, c) Cu@Pt core–shell particles with a 4:1 ratio of H_2/NO, and d) Cu@Pt core–shell particles with a 1:1 ratio of H_2/NO. N_2 selectivity is calculated by dividing the yield of N_2 by the percentage conversion of NO.

the reactivities of a) 4.5-nm Pt, b) PtCu alloy, and c) Cu@Pt catalysts with a 4:1 ratio of H_2 to NO. The net Pt loading is the same in each. The Pt nanoparticles show a very high activity (low light off) with essentially complete NO conversion at 78 °C. However, the optimal selectivity for N_2 formation (vs. NH_3, N_2O, and NO_2) is quite low (26% at 160 °C, Figure 4a). In contrast, the PtCu alloy shows significantly better N_2 selectivity ($\approx$50% at 270 °C) but has significantly poorer activity (Figure 4b). Interestingly, the Cu@Pt core–shell nanoparticles show the high reactivity of the Pt nanoparticles and the high selectivity of the PtCu alloy (Figure 4c). For comparison, a physical mixture of Pt and PtCu alloy nanoparticles shows decreased activity and selectivity relative to the Cu@Pt core–shell system. Moreover, Pt@Cu nanoparticles show very little NO conversion under the same conditions, which is consistent with the Cu-rich shell structure (see Supporting Information).

Varying the H_2-to-NO ratio shows that the Cu@Pt core–shell catalyst can provide N_2 selectivities as high as 93% (at

 © 2005 Wiley-VCH Verlag GmbH & Co. KGaA, Weinheim

0.75% NO/0.75% H_2/98.5% Ar) over temperatures ranging from 275°C to 400°C as shown in Figure 4d. These remarkably high selectivities coincide with high NO conversion and are significantly better than the monometallic Pt systems. For example, we find 80% selectivity for the 15-nm Pt/Al_2O_3 catalyst at 400°C under identical conditions and Pt loading (see Supporting Information). These results are in good agreement with those of Burch and Coleman who reported approximately 80% selectivity for a Pt/SiO_2 catalyst (5% Pt loading) under similar conditions.[24] The 4.5-nm Pt particles show even better performance (88% selectivity at 400°C; data not shown) but are still not as selective as the Cu@Pt particles under 1:1 or 4:1 H_2/NO reaction conditions.

Further evidence of the kinetic stabilization of the Cu@Pt particles can be found in the stability tests shown in Figure 5.

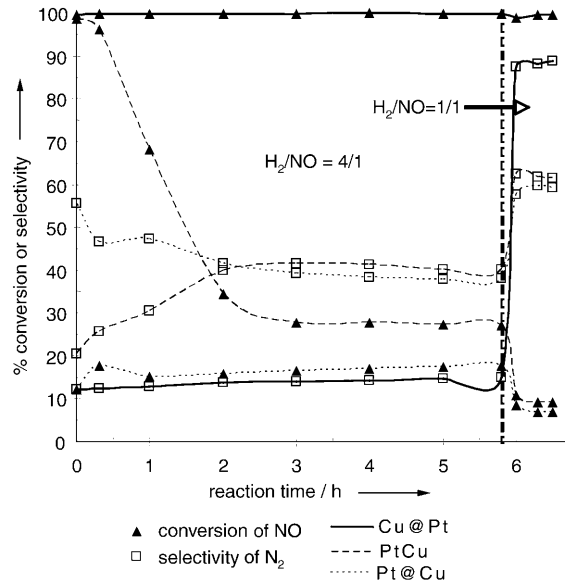


Figure 5. Stability tests for PtCu, Pt@Cu, and Cu@Pt nanocatalysts in the reduction of NO with H_2. The profiles for a 4:1 H_2/NO mixture (reaction time up to 5.8 h) are shown on the left. The subsequent reaction profiles for a 1:1 H_2/NO mixture are shown on the right.

In these experiments, NO conversion was monitored for 5.8 h at 360°C with the three different bimetallic catalysts (Cu@Pt, Pt@Cu, and PtCu) using a 4:1 H_2/NO feed. To highlight the differences in the three systems and test the thermal stability of the Cu@Pt particles under the most severe conditions, we conducted the experiments at 360°C even though the selectivity for N_2 is not optimal at these temperatures in the hydrogen-rich feed. After the 5.8-h runs, the catalysts were evaluated for NO conversion using 1:1 H_2/NO feeds for an additional 0.7 h at 360°C (Figure 5, right). For Cu@Pt, the conversion and selectivity in each feed are stable and the conversion is significantly higher than the other bimetallic systems. Post-reaction XRD analysis shows no sign of PtCu alloy formation (see Supporting Information) indicating that the particles are stable under these conditions. In contrast, the PtCu alloy catalyst rapidly loses activity (% NO conversion) but increases in N_2 selectivity during the first three hours of reaction. This change in performance is accompanied by an increase in crystallinity of the particles that may signify changes in surface structure. Interestingly, the selectivity of the Pt@Cu catalyst decreases during the first three hours and becomes equivalent to that of the PtCu alloy. This finding is consistent with the post-reaction XRD analysis that shows complete alloying of the Pt@Cu particles (see Supporting Information). The final % NO conversion of the alloyed Pt@Cu particle (17%) is lower than that of the PtCu alloy (27%), which is consistent with the significantly larger mean particle size of the Pt@Cu catalysts. Importantly, the stability and activity of the Cu@Pt nanocatalysts are markedly better than the other two bimetallic systems.

The origin of the enhanced performance of the Cu@Pt and related core–shell systems is not completely clear at present but may be related to near surface alloy (NSA) effects described by Greeley and Mavrikakis.[25] In their models, subsurface metal and alloy layers affect the binding of adsorbates (e.g. NO and H) to the particle surface. Changes in binding enthalpies can, in theory, enhance rates and selectivities in catalytic processes. Further studies designed to test these theories are in progress.

Experimental Section

The PtCu nanoparticles were prepared from $[Pt(acac)_2]$ (0.109 mmol), $Cu(SO_4)\cdot 5H_2O$ (0.109 mmol) in glycol (5 mL) with PVP_{55000} (3 mg). The solution was heated under reflux for 2 h to give a stable black colloidal suspension of PtCu nanoparticles. The Cu@Pt nanoparticles were prepared by sequential deposition involving the reduction of $[Cu(acac)_2]$ (0.156 mmol) with glycol (32 mL) and PVP_{55000} (116 mg) at reflux (20 min) to give a reddish colloidal solution. After cooling to 80°C, $[Pt(acac)_2]$ (0.156 mmol) was added and the mixture was slowly heated back to reflux (1 h) to give a black colloidal solution. The Pt@Cu nanoparticles were prepared in a similar fashion with the initial reduction of $[Pt(acac)_2]$ (0.315 mmol) in glycol (7.7 mL) at reflux for 2 h in the presence of PVP_{55000} (18.8 mg) followed by a deposition of Cu from $Cu(SO_4)\cdot 5H_2O$ (0.315 mmol) at reflux for 2 h. The 15-nm Pt particles and 4-nm Cu particles were prepared as described above but without the addition of the second metal. Smaller Pt particles (mean diameter 4.5 nm) were prepared as follows: A solution of $[Pt(acac)_2]$ (41 mg), oleic acid (133 μL; >99%), and oleylamine (133 μL; 70%, technical grade) in decahydronaphthalene (4.2 mL) was injected into decahydronaphthalene (8.3 mL) containing 1,2-hexadecanediol (83 mg; 90%, technical grade) at reflux. After 3 h under reflux, the solution was cooled to room temperature to give a black colloidal suspension of Pt nanoparticles.

Compositional phase maps were acquired using the Hitachi HD-2300 200 kV dedicated FE-STEM with an EDX detector with high sensitivity. Owing to the unique large solid angle, 2-nm spatial resolution is attainable in a relatively short time. NO reduction activity was measured by placing the supported catalyst in a packed bed arrangement in a 6.4-mm internal diameter (ID) quartz tube centered in a vertical programmable tube furnace. The catalyst charge was 5.5 mm in height. The packed bed consisted of 105 mg of catalyst (including support) intermixed with 135 mg of 1-μm quartz particles to provide adequate flow through the bed. The bed was held in place by quartz wool above and beneath, which assisted in preheating the gases to the prescribed furnace temperature. Computer-controlled electronic mass-flow controllers were used to vary flow rates and to fix reactor residence times and the reactor gas velocity (0.16 $m\,s^{-1}$). Product gases were measured continuously with a carefully calibrated magnetic sector mass spectrometer (VG Prima δB). Product compo-

 © 2005 Wiley-VCH Verlag GmbH & Co. KGaA, Weinheim

sitions were determined from the calibrated sensitivities and ion-cracking patterns for the analyzed gases.

Received: March 11, 2005

Keywords: copper · core–shell particles · heterogeneous catalysis · nanoparticles · nitrogen oxides · platinum

[1] R. M. Crooks, M. Q. Zhao, L. Sun, V. Chechik, L. K. Yeung, *Acc. Chem. Res.* **2001**, *34*, 181.
[2] Y. H. Niu, R. M. Crooks, *C. R. Chim.* **2003**, *6*, 1049.
[3] M. C. Daniel, D. Astruc, *Chem. Rev.* **2004**, *104*, 293.
[4] M. Moreno-Manas, R. Pleixats, *Acc. Chem. Res.* **2003**, *36*, 638.
[5] N. Toshima, T. Yonezawa, *New J. Chem.* **1998**, *22*, 1179.
[6] S. U. Son, Y. Jang, J. Park, H. B. Na, H. M. Park, H. J. Yun, J. Lee, T. Hyeon, *J. Am. Chem. Soc.* **2004**, *126*, 5026.
[7] R. W. J. Scott, A. K. Datye, R. M. Crooks, *J. Am. Chem. Soc.* **2003**, *125*, 3708.
[8] N. Toshima, Y. Wang, *Langmuir* **1994**, *10*, 4574.
[9] A. Obuchi, A. Ogata, K. Mizuno, A. Ohi, H. Ohuchi, *Colloids Surf. A* **1993**, *80*, 121.
[10] C. U. I. Odenbrand, J. Blanco, P. Avila, C. Knapp, *Appl. Catal. B* **1999**, *23*, 37.
[11] C. N. Costa, P. G. Savva, C. Andronikou, P. S. Lambrou, K. Polychronopoulou, V. C. Belessi, V. N. Stathopoulos, P. J. Pomonis, A. M. Efstathiou, *J. Catal.* **2002**, *209*, 456.
[12] C. N. Costa, A. M. Efstathiou, *J. Phys. Chem. B* **2004**, *108*, 2620.
[13] R. Burch, S. Scire, *Catal. Lett.* **1994**, *27*, 177.
[14] R. Burch, A. A. Shestov, J. A. Sullivan, *J. Catal.* **1999**, *186*, 353.
[15] R. Burch, A. A. Shestov, J. A. Sullivan, *J. Catal.* **1999**, *188*, 69.
[16] Y. Shiraishi, D. Ikenaga, N. Toshima, *Aust. J. Chem.* **2003**, *56*, 1025.
[17] M. S. Nashner, A. I. Frenkel, D. Somerville, C. W. Hills, J. R. Shapley, R. G. Nuzzo, *J. Am. Chem. Soc.* **1998**, *120*, 8093.
[18] N. S. Sobal, U. Ebels, H. Mohwald, M. Giersig, *J. Phys. Chem. B* **2003**, *107*, 7351.
[19] Y. Wang, N. Toshima, *J. Phys. Chem. B* **1997**, *101*, 5301.
[20] H. Yu, P. C. Gibbons, K. F. Kelton, W. E. Buhro, *J. Am. Chem. Soc.* **2001**, *123*, 9198.
[21] Powder diffraction files from the International Centre for Diffraction Data (ICDD), 12 Campus Blvd., Newtown Square, PA 19073. (http://www.icdd.com). File number 48-1549.
[22] Y. D. Yin, R. M. Rioux, C. K. Erdonmez, S. Hughes, G. A. Somorjai, A. P. Alivisatos, *Science* **2004**, *304*, 711.
[23] A. K. Sinha, *Physical Metallurgy Handbook*, McGraw-Hill, New York, **2003**.
[24] R. Burch, M. D. Coleman, *J. Catal.* **2002**, *208*, 435.
[25] J. Greeley, M. Mavrikakis, *Nat. Mater.* **2004**, *3*, 810.

 © 2005 Wiley-VCH Verlag GmbH & Co. KGaA, Weinheim

Host–Guest Chemistry

Host–Guest Interactions: Design Strategy and Structure of an Unusual Cobalt Cage That Encapsulates a Tetrafluoroborate Anion**

Hani Amouri, Lamia Mimassi, Marie Noelle Rager, Brian E. Mann, Carine Guyard-Duhayon, and Laurence Raehm*

The rational design of inorganic artificial receptors for host–guest chemistry is one of the most attractive areas in contemporary supramolecular chemistry.[1] Self-assembly is emerging as an elegant "bottom-up" method for fabricating elaborate architectures[2] such as helicates,[3] cages,[4] metallocryptands,[5] metallomacrocyles,[6] and coordination polymers.[7] This approach is particularly powerful when the ease of control offered by the self-assembly of organic components is combined with electronic, ion-sensing, catalytic, magnetic, or photonic properties of inorganic components.

Over the last decade there has been intensive research into the preparation of inorganic macrocycles, which have shown particular promise in host–guest chemistry.[8]Although the coordination chemistry of cations is well developed, the chemistry of anion encapsulation is still in its infancy despite the fact that anion-coordination chemistry is of interest from environmental, industrial, and health-related perspectives.[9]

We recently reported the self-assembly of iridocryptates that encapsulate BF_4^- anions through hydrogen bonding,[5a] but the present work differs completely to that reported previously in terms of coordination and binding. Herein, we report a rational high-yield strategy (> 90 %) for the preparation of unusual inorganic cages **1a**–**c** (Scheme 1) based on the coordination chemistry of cobalt and demonstrate their properties as hosts for anions. Prior to this work, only a few examples of supramolecular, inorganic-anion receptors had been reported: a metallohelicate that encapsulates a PF_6^- ion[10] and a supramolecular tetrahedral complex that encapsulates a BF_4^- ion[11] are two examples.

[*] Dr. H. Amouri, L. Mimassi, Dr. C. Guyard-Duhayon, Dr. L. Raehm
Laboratoire de Chimie Inorganique et Matériaux Moléculaires
UMR CNRS 7071
Université Pierre et Marie Curie
4 place Jussieu, case 42, 75252 Paris Cedex 05 (France)
Fax: (+33) 1-4427-3841
E-mail: amouri@ccr.jussieu.fr

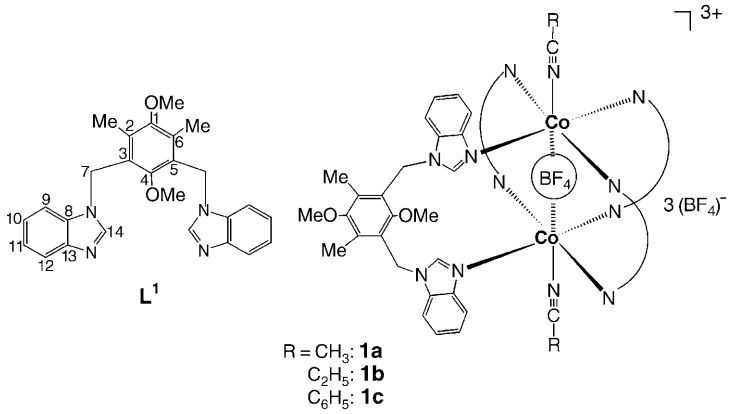
Dr. M. N. Rager
NMR Services of Ecole Nationale Supérieure de Chimie de Paris
11 rue Pierre et Marie Curie, 75231 Paris Cedex 05 (France)

Prof. Dr. B. E. Mann
Department of Chemistry
The University of Sheffield
Sheffield, S3 7HF (UK)

[**] We gratefully acknowledge the CNRS and the Université Pierre et Marie Curie for support of this work.

Supporting information for this article is available on the WWW under http://www.angewandte.org or from the author.

 DOI: 10.1002/anie.200500786 © 2005 Wiley-VCH Verlag GmbH & Co. KGaA, Weinheim



Scheme 1. Schematic drawings of ligand L^1 (with atom numbering scheme for ^{1}H NMR assignments) and the related $[Co_2(L^1)_4]$ cages **1a–c**.

The novelty of our work is the use of $Co^{II}(BF_4)_2{\cdot}6H_2O$ as a precursor and a coordinatively unsaturated connector to promote a dative interaction between the metal cation and the weakly coordinating anions in the final supramolecular structure. Rational design of these materials is complicated by uncertain factors such as the counteranion, the solvent, and the ligand geometry. Support for this complication is manifested in the only known Co^{II}-based cage anion $[Co_4L_6]$ (L = di(pyrazolylpyridine)-1,2-phenylene),[12] in which the geometry about each cobalt center is octahedral with the three bidentate ligands, and the encapsulated BF_4^- anion is bound by Coulombic attraction and a symmetry match between the host and the guest. Here, our system behaves completely different. To the best of our knowledge, we describe the first coordinatively unsaturated cobalt-based $[M_2(L^1)_4]$ cage (see Scheme 1) and demonstrate its encapsulation of BF_4^- anions through direct coordination of the unsaturated metal center and the guest anion.

Treatment of two equivalents of ligand L^1 with $Co(BF_4)_2{\cdot}6H_2O$ in a solution of methanol/chloroform for several hours yielded a blue precipitate, which was characterized as $[(CH_3OH)_2Co_2(L^1)_4](BF_4)_4$. The precipitate was recrystallized from CH_3CN/Et_2O to quantitatively afford bright pink crystals, which were characterized as $[(CH_3CN)_2Co_2(L^1)_4](BF_4)_4$ (**1a**). In a similar way, the two other supramolecular cages $[(C_2H_5CN)_2Co_2(L^1)_4](BF_4)_4$ (**1b**) and $[(C_6H_5CN)_2Co_2(L^1)_4](BF_4)_4$ (**1c**) were obtained as light pink and salmon-colored crystals, respectively, through recrystallization from a mixture of the related nitrile solvent RCN ($R = C_2H_5$-; C_6H_5-) in Et_2O. The NMR spectra (^{1}H,^{11}B) of **1a–c** recorded in CD_3CN were all very similar, however, **1b** and **1c** showed displacement of the nitrile solvent RCN ($R = C_2H_5$-; C_6H_5-) by the more strongly coordinating NMR solvent CD_3CN.

The ^{1}H NMR spectrum (400 MHz) of **1a** was recorded in CD_3CN at 292 K, and owing to the presence of Co^{II} atoms the spectrum spanned a broad range from $\delta = 45.70$ to -6.06 ppm, a range that is consistent with the presence of paramagnetic compounds. The spectrum of **1a** shows the presence of 10 signals, which were all assigned by means of peak integration ratios, COSY experiments performed at 352.5 K, and T_1 measurements at 292 K using the Solomon equation[13] (Figure 1). As T_1^{-1} is proportional to $\Sigma(r_{ij}^{-6})$, where r_{ij} is the distance between the hydrogen atoms and the cobalt

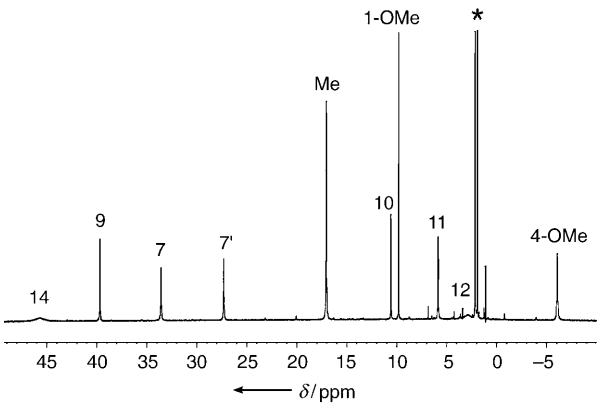


Figure 1. ^{1}H NMR spectrum of **1a** recorded in CD_3CN at 292 K. The symbol * denotes the residual solvent peak (CH_3CN/CD_2HCN).

ions, the relative values of T_1 were estimated and normalized to obtain the best fit with experimental measurements (see Supporting Information). The COSY spectrum showed connectivity between H^{10} and both H^9 and H^{11}, and between H^7 and $H^{7'}$ (see Supporting Information).

Significantly the methylene protons -CH_2^7- are inequivalent and show two signals at $\delta = 33.59$ and 27.30 ppm. The inequivalency results from the formation of a rigid cage, with the arene rings lying along the equator of the approximate sphere of the complexed ion. This result suggests that the presence of a guest anion inside the cavity of the cage increases the rigidity. Remarkably the ^{11}B NMR spectrum of **1a** recorded in CD_3CN showed not only the presence of a sharp singlet at $\delta = -0.82$ ppm that we attribute to the free BF_4^- anion but also another broad signal at $\delta = -105.1$ ppm that was assigned to an encapsulated BF_4^- ion (see Supporting Information). We attribute this large difference in chemical shift values to the paramagnetic nature of the Co ions.

The electrospray mass spectrum of **1a** clearly indicated the formation of the $[Co_2(L^1)_4]$ species in association with varying numbers of BF_4^- anions (see Supporting Information). To ascertain unambiguously the structure of **1a**, an analysis of the crystal structure was undertaken. Crystals of **1a** were grown by vapor diffusion of diethyl ether into a solution of the complex in CH_3CN/CH_3NO_2.[14] The compound crystallized in the monoclinic space group $P2_1/n$. The structure shows the formation of a $[Co_2(L^1)_4]$ tetragonal cage (Figure 2), in which each cobalt ion adopts a square-pyramidal geometry. The equatorial positions are filled by four benzimidazole arms of the bridging ligands L^1, and the axial position is coordinated by a solvent molecule, CH_3CN. The two methoxy groups are arranged in a *trans* fashion with one pointing towards the encapsulated BF_4^- anion while the other is directed in the opposite sense away from the cage cavity. The coordinatively unsaturated cobalt center binds to a BF_4^- anion located inside the cavity through a metal–anion coordination bond with a

 © 2005 Wiley-VCH Verlag GmbH & Co. KGaA, Weinheim

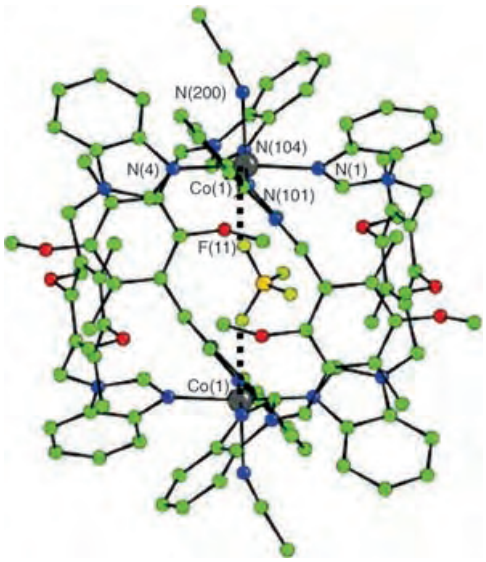


Figure 2. X-ray crystal structure of $[BF_4{\subset}(CH_3CN)_2Co_2(L^1)_4]^{3+}$ (C green, O red, N blue, B yellow, F pale green, Co gray; H atoms omitted for clarity). Selected bond lengths (Å) and angles (°): Co(1)–N(1) = 2.082(8), Co(1)–N(101) = 2.094(9), Co(1)–N(4) = 2.088(8) Co(1)–N(104) = 2.110(9), Co(1)–F(11) = 2.405(8); N(1)-Co(1)-N(4) = 175.5(3), N(101)-Co(1)-N(104) = 174.5(3), Co(1)-N(1)-C(1) = 123.6(7).

bond length of 2.405 Å (Co···F). The two nonbridging fluorine atoms (-FB*F*$_2$F-) occupy four sites (each fluorine atom was refined with half-occupancy). The other three BF_4^- anions are located outside the cavity. The Co···N bond lengths lie in the range of 2.08–2.11 Å, typical for complexes of high-spin Co^{II}.[12] The Co–Co distance is 7.1 Å, and the average distance between two facing phenyl rings is 11 Å.

The present example describes the first structure of a coordinatively unsaturated cobalt cage, which encapsulates a fluorinated anion through an unusual direct Co···F coordination bond. Anions such as BF_4^- are generally considered to be highly noncoordinating and only weakly interacting. The only previous example of a direct host metal/guest anion interaction was reported for a PF_6^- ion encapsulated through interaction with two Pd centers of a quadruply stranded helicate.[10]

We then examined the behavior of the cage **1a** in solution by recording the ^{1}H and ^{11}B NMR spectra at variable temperatures in the range of 292–352.5 K. The observation of separate signals for the -CH_2- protons shows that the structure is rigid. No exchange of the protons H[7] was detected by EXSY (exchange spectroscopy) at the higher temperature which gave a lower limit for the exchange process of $\Delta G^{\neq} = 80\ kJ\,mol^{-1}$. The ^{11}B NMR spectrum at room temperature showed two signals, as discussed earlier. Neither magnetization-transfer measurements nor EXSY showed any evidence of exchange at 60 °C. This result permits a lower limit of $\Delta G^{\neq} = 75\ kJ\,mol^{-1}$ to be set for the release of the encapsulated BF_4^- ion from the cavity. Therefore, the anion is trapped in the cavity with no or slow exchange with the free anions on the NMR timescale.

Ward and co-workers have prepared several cages of the general formula $\{BF_4{\subset}[Co_4(L^2)_6](BF_4)_7\}$, where L^2 is a tetradentate ligand that comprises two pyrazolylpyridine units attached to a 1,2-phenylene or to a 1,2-naphthylene spacer.[15] They found that the ease of exchange of the encapsulated anion depends on the size of the spacer, with facile exchange ($\Delta G^{\neq} = 50\ kJ\,mol^{-1}$) for the complex with a 1,2-naphthylene spacer, while for the rigid bridging 1,2-phenylene spacer the exchange was very slow on the NMR timescale.

In our system the encapsulated BF_4^- anion is an essential part of the structure. In **1a–c** the encapsulated BF_4^- anion plays a pivotal role as a template, around which the two Co^{II} metal ions and the four ligands self-assemble. Furthermore, the rigid nature of the bridging ligand L^1 in which a 1,4-phenylene spacer holds two benzimidazole arms to provide a rigid cage (Scheme 1) means that the encapsulated BF_4^- anion is locked in the cavity and is not released. Future objectives are directed towards the preparation of other bidentate ligands that comprise larger spacers so as to develop flexible cages, destined to encapsulate a variety of anions of different sizes and geometries.

Experimental Section

All experimental manipulations were carried out under argon using Schlenk techniques. ^{1}H and ^{11}B NMR spectra were recorded in CD_3CN using a Bruker AMX-2 400 NMR spectrometer at 400.13 and 128.38 MHz, respectively, and also a Bruker Avance 400 NMR instrument. The temperature of the sample was determined by means of a thermocouple and measured using a Comark N9009 thermometer.

1a: Ligand L^1 (403 mg, 1 mmol; see Scheme 1) in $CHCl_3$ (15 mL) was added to a pink solution of $Co(BF_4)_2{\cdot}6H_2O$ (120 mg, 0.352 mmol) in CH_3OH (15 mL). The solution was stirred at room temperature for 12 h, during which time a deep blue precipitate formed. The solids were collected by filtration, washed with $CHCl_3$, and dried under vacuum. This material was characterized as $[(CH_3OH)_2Co_2(L^1)_4](BF_4)_4$; elemental analysis (%): calcd for $C_{106}H_{112}N_{16}O_{10}Co_2B_4F_{16}$ (2235.24 g mol^{-1}): C 56.96, H 5.05, N 10.03; found: C 56.83, H 5.20, N, 10.13.

The precipitate was then dissolved in CH_3CN and recrystallized from CH_3CN/Et_2O to provide bright pink crystals of $\{[BF_4{\subset}(CH_3CN)_2Co_2(L^1)_4](BF_4)_3\}$ (**1a**); elemental analysis (%): calcd for $C_{108}H_{110}N_{18}O_8Co_2B_4F_{16}$ (2253.28 g mol^{-1}): C 57.57, H 4.92, N 11.19; found: C 55.49, H 5.05, N 10.09; ^{1}H NMR (see Supporting Information); ^{11}B NMR (128 MHz, CD_3CN): $\delta = -0.82$ (sh, free BF_4), -105.1 ppm (br, encapsulated BF_4); IR (KBr disk): $\tilde{\nu}$(B-F) = 1071 cm^{-1}; ES-MS (*m*/*z*): calcd for $C_{104}H_{104}O_8N_{16}Co_2B_4F_{16}$ $[M^{4+} + 3BF_4^-]^+$: 2083.5; found: 2084.54; calcd for $[M^{4+} + 2BF_4^-]^{2+}$: 998.35; found: 998.35; calcd for $[M^{4+} + BF_4^-]^{3+}$: 636.63; found: 636.82; calcd for $[M^{4+}]$: 455.77; found: 456.05.

1b: This supramolecular cage was prepared in a similar way as described for **1a**, but was recrystallized from C_2H_5CN/Et_2O to afford the title compound quantitatively as light pink crystals of $\{[BF_4{\subset}(C_2H_5CN)_2Co_2(L^1)_4](BF_4)_3\}$ (**1b**); elemental analysis (%): calcd for $C_{110}H_{114}N_{18}O_8Co_2B_4F_{16}$ (2281.31 g mol^{-1}): C 57.91, H 5.04, N 11.05; found: C 56.18, H 5.11, N 10.03; the NMR data recorded in CD_3CN were similar to those observed for **1a**, but we note the presence of free displaced C_2H_5CN in the ^{1}H NMR spectrum at δ = 2.38 (q, 4H, CH_2) and 1.23 ppm (t, 6H, CH_3); ^{11}B NMR (128 MHz, CD_3CN) $\delta = -0.74$ (sh, free BF_4), -105.2 ppm (br, encapsulated

 © 2005 Wiley-VCH Verlag GmbH & Co. KGaA, Weinheim

BF_4); IR (KBr disk): $\tilde{\nu}$(B-F) = 1083 cm^{-1}; ES-MS (*m*/*z*): calcd for $C_{104}H_{104}O_8N_{16}Co_2B_4F_{16}$ $[M^{4+} + 3\,BF_4^-]^+$: 2083.5; found: 2084.91; calcd for $[M^{4+} + 2\,BF_4^-]^{2+}$: 998.35; found: 998.35; calcd for $[M^{4+} + BF_4^-]^{3+}$: 636.63; found: 636.82; calcd for $[M^{4+}]$: 455.77; found: 456.05.

1c: This complex was prepared in a similar fashion to **1a**, but was recrystallized from C_6H_5CN/Et_2O to afford the title compound quantitatively as salmon-colored crystals of $\{[BF_4\subset(C_6H_5CN)_2Co_2(L^1)_4](BF_4)_3\}$ (**1c**); elemental analysis (%): calcd for $C_{110}H_{114}N_{18}O_8Co_2B_4F_{16}$ (2377.4 g mol^{-1}): C 59.62, H 4.83, N 10.60; found: C 57.41, H 4.82, N 10.48; the NMR data recorded in CD_3CN were analogous to those for **1a**, but we note the presence of free displaced C_6H_5CN in the ^{1}H NMR spectrum at δ = 7.76 (m, C_6H_5) and 7.57 ppm (m, C_6H_5); ^{11}B NMR (128 MHz, CD_3CN): δ = −0.98 (sh, free BF_4), −108.2 ppm (br, encapsulated BF_4); IR (KBr disk): $\tilde{\nu}$(B-F) = 1073 cm^{-1}.

Received: March 3, 2005
Revised: April 11, 2005
Published online: June 21, 2005

Keywords:
host–guest systems · boron · cage compounds · cobalt · supramolecular chemistry

[1] a) J.-M. Lehn, *Supramolecular Chemistry: Concepts and Perspectives*, VCH, Weinheim, **1995**; b) J. W. Steed, J. L. Atwood, *Supramolecular Chemistry*, Wiley, Chichester, **2000**.

[2] a) S. Leininger, B. Olenyuk, P. J. Stang, *Chem. Rev.* **2000**, *100*, 853 – 908, and references therein; b) B. J. Holiday, C. A. Mirkin, *Angew. Chem.* **2001**, *113*, 2076 – 2097; *Angew. Chem. Int. Ed.* **2001**, *40*, 2022 – 2043; c) M. Fujita, *Chem. Soc. Rev.* **1998**, *27*, 417 – 425; d) L. D. Caulder, K. N. Raymond, *Acc. Chem. Res.* **1999**, *32*, 975 – 982; e) F. A. Cotton, C. Lin, C. A. Murillo, *Acc. Chem. Res.* **2001**, *34*, 759 – 771.

[3] B. Hasenknopf, J.-M. Lehn, N. Boumediene, A. Dupont-Gervais, A. Van Dorsselaer, B. Kneisel, D. Fensker, *J. Am. Chem. Soc.* **1997**, *119*, 10956 – 10962.

[4] a) L. J. Barbour, G. W. Orr, J. L. Atwood, *Nature* **1998**, *393*, 671 – 673; b) L. Raehm, L. Mimassi, C. Guyard-Duhayon, H. Amouri, M. N. Rager, *Inorg. Chem.* **2003**, *42*, 5654 – 5659; c) C.-Y. Su, Y.-P. Cai, C.-L. Chen, H.-X. Zhang, B.-S. Kang, *J. Chem. Soc. Dalton Trans.* **2001**, 359 – 361.

[5] a) H. Amouri, M. N. Rager, F. Cagnol, J. Vaissermann, *Angew. Chem.* **2001**, *113*, 3748 – 3750; *Angew. Chem. Int. Ed.* **2001**, *40*, 3636 – 3638; b) R. W. Saalfrank, A. Dresel, V. Seitz, S. Trummer, F. Hampel, M. Teichert, D. Stalke, C. Stadler, J. Daub, V. Schunemann, A. X. Trautwein, *Chem. Eur. J.* **1997**, *3*, 2058 – 2062.

[6] C.-Y. Su, Y.-P. Cai, C.-L. Chen, M. D. Smith, W. Kaim, H.-C. zur Loye, *J. Am. Chem. Soc.* **2003**, *125*, 8595 – 8613.

[7] a) L. Mimassi, C. Guyard-Duhayon, L. Raehm, H. Amouri, *Eur. J. Inorg. Chem.* **2002**, 2453 – 2457; b) O. Mamula, A. von Zelewsky, T. Bark, G. Bernardinelli, *Angew. Chem.* **1999**, *111*, 3129 – 3133; *Angew. Chem. Int. Ed.* **1999**, *38*, 2945 – 2948; c) J. A. Ramsden, W. Weng, A. M. Arif, J. A. Gladysz, *J. Am. Chem. Soc.* **1992**, *114*, 5890 – 5891; d) W. Weng, J. A. Ramsden, A. M. Arif, *J. Am. Chem. Soc.* **1993**, *115*, 3824 – 3825; e) T. Bartik, W. Weng, J. A. Ramsden, S. Szafert, S. B. Falloon, A. M. Arif, J. A. Gladysz, *J. Am. Chem. Soc.* **1998**, *120*, 11071 – 11081; f) R. Dembinski, T. Bartik, B. Bartik, M. Jaeger, J. A. Gladysz, *J. Am. Chem. Soc.* **2000**, *122*, 810 – 822; g) W. Mohr, J. Stahl, F. Hampel, J. A. Gladysz, *Inorg. Chem.* **2001**, *40*, 3263 – 3264; h) N. Le Narvor, L. Toupet, C. Lapinte, *J. Am. Chem. Soc.* **1995**, *117*, 7129 – 7138.

[8] a) D. Fiedler, R. G. Bergman, K. N. Raymond, *Angew. Chem.* **2004**, *116*, 6916 – 6919; *Angew. Chem. Int. Ed.* **2004**, *43*, 6748 – 6751; b) D. Fiedler, D. H. Leung, R. G. Bergman, K. N. Raymond, *Acc. Chem. Res.* **2005**, *38*, 349 – 358, and references therein.

[9] M. Staffilani, K. S. B. Hancock, J. W. Steed, K. T. Holman, J. L. Atwood, R. K. Juneja, R. S. Burkhalter, *J. Am. Chem. Soc.* **1997**, *119*, 6324 – 6335, and references therein.

[10] D. A. McMorran, P. J. Steel, *Angew. Chem.* **1998**, *110*, 3495 – 3497; *Angew. Chem. Int. Ed.* **1998**, *37*, 3295 – 3297.

[11] S. Manne, G. Huttner, L. Zsolnai, K. Heinze, *Angew. Chem.* **1996**, *108*, 2983; *Angew. Chem. Int. Ed. Engl.* **1996**, *35*, 2808 – 2809.

[12] J. S. Fleming, K. L. V. Mann, C.-A. Carraz, E. Psillakis, J. C. Jeffery, J. A. McCleverty, M. D. Ward, *Angew. Chem.* **1998**, *110*, 1315 – 1318; *Angew. Chem. Int. Ed.* **1998**, *37*, 1279 – 1281.

[13] I. Solomon, *Phys. Rev.* **1955**, *99*, 559 – 565.

[14] Structural data for **1a**: $C_{112}H_{116}B_4Co_2F_{16}N_{20}O_8$, M_r = 2335.36, pink crystals, crystal dimensions: 0.10 × 0.10 × 0.10 mm^3; monoclinic $P2_1/n$, a = 14.418(3) Å, b = 22.387(5) Å, c = 18.844(4) Å, V = 5875.4(21) $Å^3$, Z = 4, D = 1.32 g cm^{-3}, T = 180 K, R (*Rw*) 0.0838 (0.0879) for 10923 observed independent reflections, GOF = 1.11; Nonius KAPPA CCD diffractometer, $Mo_{K\alpha}$ radiation (λ = 0.71069 Å) collection range 2θ = 2–51°. Empirical DIFABS absorption correction was applied. The structure was determined by direct methods and subsequent difference Fourier syntheses, and refined by full-matrix least-squares on F by using the PC version of the CRYSTALS package. All non-hydrogen atoms were refined anisotropically. Hydrogen atoms were located on a difference Fourier map, but they were introduced in the refinement in calculated positions and were affected by an overall isotropic thermal parameter. CCDC 265267 contains the supplementary crystallographic data for this paper. These data can be obtained free of charge from the Cambridge Crystallographic Data Centre via www.ccdc.cam.ac.uk/data_request/cif.

[15] R. L. Paul, S. P. Argent, J. C. Jeffery, L. P. Harding, J. M. Lynam, M. D. Ward, *Dalton Trans.* **2004**, 3453 – 3458.

 © 2005 Wiley-VCH Verlag GmbH & Co. KGaA, Weinheim

Combinatorial Chemistry

Molecular-Weight-Tagged Glycopeptide Library: Efficient Construction and Applications**

*Hiromi Ito, Akihiko Kameyama, Takashi Sato, Katsue Kiyohara, Yoshiaki Nakahara, and Hisashi Narimatsu**

Combinatorial chemistry has become indispensable for drug discovery and biotechnological research with high-throughput screening. Recently, glycoproteomics or glycomics has become a major academic and clinical research priority. Oligosaccharides on glycoconjugates, including glycoproteins and glycolipids, play vital roles in biological processes by influencing the stability of proteins, protein conformation, intra- and intercell signaling, and binding specificity for other biomolecules.[1] However, the functions of glycoconjugates are little understood at the molecular level, mostly because of a lack of sensitive and high-throughput methods for analyzing the structure and interaction of oligosaccharides. To overcome these problems, technologies such as an observational multistage tandem mass-spectral (MS^n) library[2] and arrays for carbohydrate and lectin[3] have been developed. However, a large variety of structurally defined oligosaccharides, that is, an oligosaccharide library,[4] is prerequisite for these technologies. A convenient and effective method for the construction of an oligosaccharide library is desired. Herein, we describe a method for the efficient construction of a glycopeptide library which can be easily converted to an oligosaccharide library by using human recombinant glycosyltransferases.[5] Furthermore, applications for the screening of ligand specificity for lectins by mass spectrometry are demonstrated.

We have developed a method for the construction of molecular-weight-tagged libraries, in which the structure and molecular weight of the components were designed to correspond one-to-one by using glycosyltransferases. Our general strategy for the construction of the libraries is shown in Figure 1. To achieve a diversity of oligosaccharides, the starting peptide or glycopeptide **X**, enzyme **I**, and the donor substrate **A** were added to a reaction mixture, and the reaction was stopped at around a 50% yield of the product

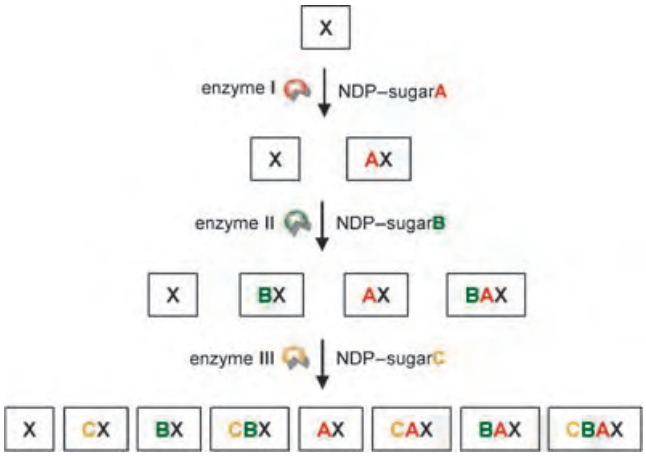


Figure 1. Basic strategy for the construction of oligosaccharide and glycopeptide libraries.

AX by monitoring the time course of the reaction using mass spectrometry. The reaction mixture was kept at 0°C during monitoring to stop the enzymatic reaction from proceeding. After enzyme **I** had been irreversibly denatured and inactivated by heat, enzyme **II** and the donor substrate **B** were added to the mixture of **X** and **AX**, and the mixture was again incubated. Then the transfer reaction of **B** was stopped at around a 50% yield, and enzyme **II** was inactivated. Sequentially, enzyme **III** and substrate **C** were added to the above solution containing **X**, **BX**, **AX**, and **BAX**, and the reaction was stopped at around a 50% yield. Finally, the glycopeptides were easily purified using a solid-phase extraction device, such as a reversed-phase microcolumn. After the three reactions, a mixed library, which theoretically contains eight different compounds (**X**, **CX**, **BX**, **CBX**, **AX**, **CAX**, **BAX**, and **CBAX**), should be generated.

The major advantages of our method are as follows: First, the formation of glycosidic linkages can be strictly controlled because of the excellent regio- and stereoselectivity of glycosyltransferases, which exhibit a clear specificity for substrates.[5] Second, by terminating each enzyme reaction halfway, it is possible to construct a library that has theoretically 2^n (n is the number of reaction steps) structures of oligosaccharides in a single tube. Third, the structure of each component in the library can be identified immediately by mass spectrometry alone, because these libraries are designed as molecular-weight-tagged libraries, that is, each product has a different molecular weight.

Our strategy has the limitation of not allowing the repetitive use of the same glycosyl donor or of diastereomeric donors (e.g., mannose and galactose donors) to achieve variation. Therefore, it is important for the systematic construction of the libraries to design reaction protocols that include the selection of enzymes, the reaction sequence, and the structure of the starting materials.

To demonstrate this strategy, we attempted to construct a library of O-linked glycopeptides, most of which are not commercially available. Extensions of the carbohydrate chain of glycopeptide **1** (β3Gal-Core 3-Muc1a) were achieved by sequential addition of each enzyme (ST6GalNAcI, fucosyl-

[*] Dr. H. Ito, Dr. A. Kameyama, Dr. T. Sato, K. Kiyohara, Prof. Dr. H. Narimatsu
Research Center for Glycoscience
National Institute of Advanced Industrial Science and Technology (AIST)
1-1-1 Umezono, Tsukuba, Ibaraki 305-8568 (Japan)
Fax: (+81) 29-861-3201
E-mail: h.narimatsu@aist.go.jp
Prof. Dr. Y. Nakahara
Department of Applied Biochemistry
Institute of Glycotechnology, Tokai University
Kitakaname 1117, Hiratsuka, Kanagawa 259-1292 (Japan)

[**] This work was performed as a part of the R&D Project of the Industrial Science and Technology Frontier Program supported by the New Energy and Industrial Technology Development Organization (NEDO).

 DOI: 10.1002/anie.200500802 © 2005 Wiley-VCH Verlag GmbH & Co. KGaA, Weinheim

transferase 2 (FUT2), and α3GalNAcT (A enzyme)) and its donor substrate (cytidine 5′-monophospho-*N*-acetylneuraminic acid (CMP-Neu5Ac), guanosine 5′-diphospho-β-L-fucose (GDP-Fuc), and uridine 5′-diphospho-*N*-acetylgalactosamine (UDP-GalNAc), respectively) in a single tube (Figure 2a). The time course of each reaction was monitored with a MALDI-TOF MS instrument (ReflexIV, Bruker-Daltonik) by directly applying the reaction solution to the target plate, and the reaction was stopped at around a 50% yield by inactivating the enzyme at 100°C for five minutes. Figure 2b shows the mass spectrum of the final reaction mixture. As α3GalNAcT transfers a GalNAc residue in the α1–3 linkage to the terminal Fucα1–2Gal structure, this library has six (over eight possible) compounds in this case. To each peak, the structure could be instantly assigned from the *m*/*z* value. In the same way, we synthesized a glycopeptide library having various *O*-linked oligosaccharides, that is, B antigen, Lewis^X and sialyl Lewis^X epitope, or Lewis^A and sialyl Lewis^A epitope elongated on the Core 2 and Core 3 structures, respectively (data not shown).

Reductive β elimination[6] by incubating the library at 50°C overnight in 20 μL of NaOH (50 mM) and $NaBH_4$ (500 mM) afforded the corresponding oligosaccharide library (Figure 3). Collision-induced dissociation (CID) spectra were acquired with a MALDI-QIT-TOF MS instrument (AXIMA-QIT, Shimadzu), and deposited in a CabosML database.[7]

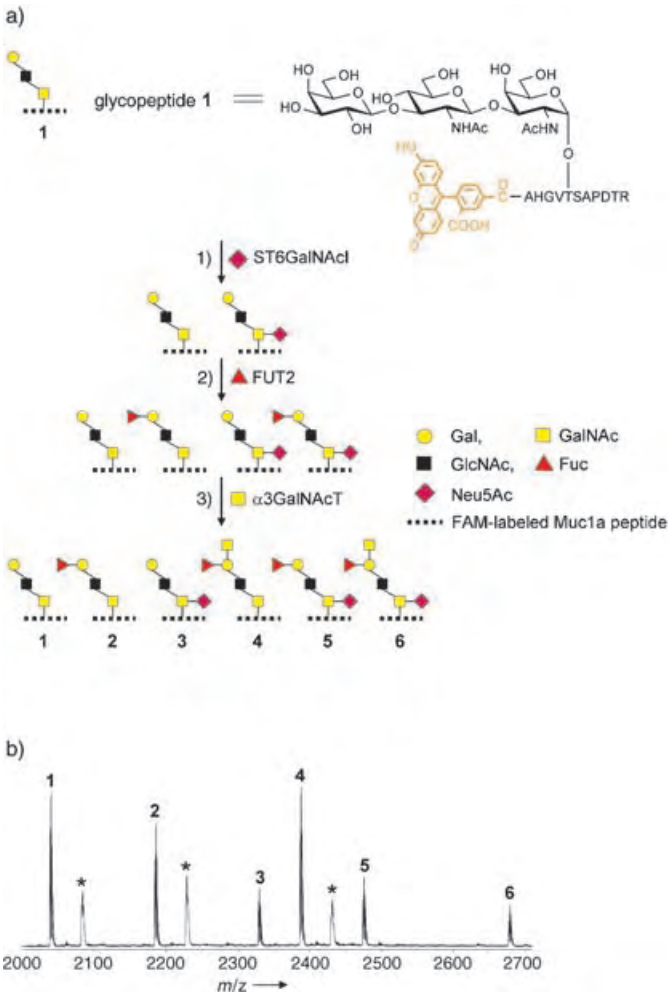


Figure 2. Demonstration of our construction strategy. a) Synthesis of an *O*-linked glycopeptide library including A antigen structures. b) MALDI-TOF mass spectrum of the prepared library. The asterisks indicate metastable ions from the sialylated compounds. Conditions for the enzymatic reactions: 1) ST6GalNAcI (5 μL), *N*-(2-hydroxylethyl)-piperazine-*N*′-2-ethanesulfonic acid (HEPES buffer) (25 mM, pH 7.0), $MnCl_2$ (10 mM), CMP-Neu5Ac (25 nmol), glycopeptide **1** (1 nmol), 37°C, 12 h; 2) FUT2 (2 μL), GDP-Fuc (5 nmol), 37°C, 2 h; 3) α3GalNAcT (2 μL), UDP-GalNAc (2 nmol), 37°C, 3 h. The recombinant glycosyltransferases are bound to anti-Flag M1 affinity gel (Sigma).

a)

Peak	Epitope	Structure of glycan moiety	*m*/*z* glycopeptide	*m*/*z* alditol
1	β4Gal-Core 3	Galβ1–4GlcNAcβ1–3GalNAc–	2037.66	611.32
2	blood group H	Fucα1–2Galβ1–4GlcNAcβ1–3GalNAc–	2183.72	757.40
3	blood group B	Galα1 (3) Fucα1–2Galβ1–4GlcNAcβ1–3GalNAc–	2345.77	919.50
4	blood group A	GalNAcα1 (3) Fucα1–2Galβ1–4GlcNAcβ1–3GalNAc–	2386.80	960.53

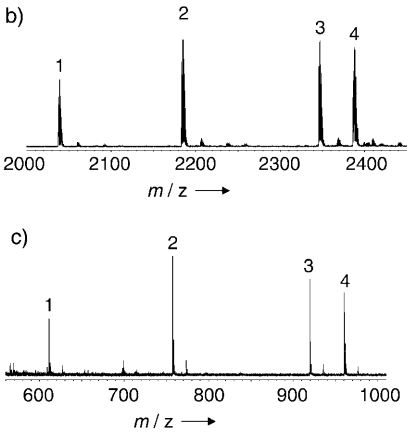


Figure 3. Conversion of a glycopeptide library to an oligosaccharide library. a) Structures and observed signals before and after β-elimination. b) MALDI-TOF mass spectrum of a glycopeptide library. c) MALDI-TOF mass spectrum of the released glycan from this glycopeptide library. The glycopeptides were observed as $[M+H]^+$ ions, the alditols as $[M+Na]^+$ ions.

The libraries described above have many uses. Herein, we demonstrate the screening of ligand specificity for lectins by using mass spectrometry. Ligand specificity for jacalin was determined quite easily by using the prepared library (Figure 4a). Jacalin covalently linked to agarose beads (0, 1, 2.5, and 5 μL) was added to library solutions. Bovine serum albumin (BSA)-conjugated agarose beads were used as the negative control. The solutions were incubated and centrifuged, and the glycopeptides remaining in the supernatants were identified by directly applying the supernatants with the matrix solution to the MS target plate. In this screening system, if the immobilized lectin has binding affinity for a

 © 2005 Wiley-VCH Verlag GmbH & Co. KGaA, Weinheim

a)

Epitope	Structure	*m/z* $[M+H]^+$
Tn	GalNAcα1-peptide	1672.64
Core 1	Galβ1-3GalNAcα1-peptide	1834.72
Core 2	GlcNAcβ1 (6) Galβ1-3GalNAcα1-peptide	2037.85
Core 3	GlcNAcβ1-3GalNAcα1-peptide	1875.77
Core 4	GlcNAcβ1 (6) GlcNAcβ1-3GalNAcα1-peptide	2078.88

b)

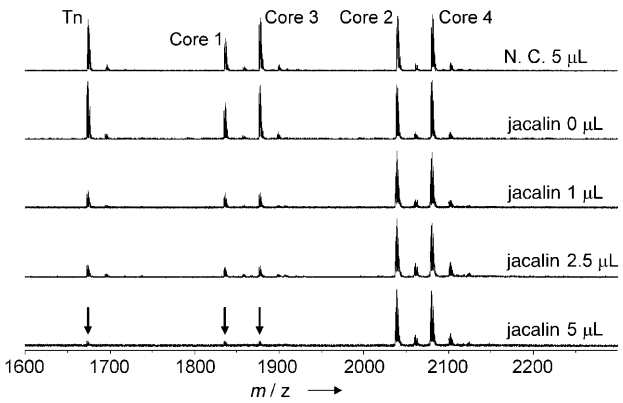


Figure 4. Screening of ligand specificity for jacalin by mass spectrometry. a) Components of the library used for screening. b) MALDI-TOF mass spectra of the library solution at various concentrations of jacalin. BSA covalently linked to agarose beads (5 μL) was used as the negative control (N.C.).

component of the library solution, the corresponding peak of this component becomes small or disappears on the mass spectrum. The intensities of three peaks corresponding to Tn, Core 1, and Core 3 structures in the mass spectra gradually decreased as the amount of added jacalin increased, whereas the intensity of two peaks, Core 2 and Core 4, did not decrease (Figure 4b). These results are consistent with the report that jacalin recognizes Tn and Core 1 residues,[8] and also include some additional findings: 1) jacalin binds to O-linked oligosaccharides, which are linearly elongated on the Gal residue of Core 1 and the GlcNAc residue of Core 3; 2) jacalin does not bind to *O*-glycans in which the O6 position of the GalNAc residue is occupied, that is, Core 2 and Core 4 structures.

In conclusion, we developed molecular-weight-tagged libraries thar were rapidly and readily prepared as mixtures, and the structure of each component in the libraries could be identified immediately by mass spectrometry alone. The libraries were useful for rapid and easy screening for ligand specificity of carbohydrate-binding proteins, such as lectins and antibodies. In the past few years, we have developed more than 160 human glycosyltransferases as recombinant enzymes.[5] It is possible to prepare libraries containing a large variety of natural oligosaccharide structures with these glycosyltransferases. We are increasing the variety of libraries as much as possible, based on different combinations of many enzymes and acceptor substrates, by carefully designing the reaction protocols, thus avoiding the complication attributable to components with the same molecular weight. In addition, this method will be applied to an automated system as a synthesizer for glycan and glycopeptide libraries. The libraries can also be used as carbohydrate microarrays in various fields of research, such as functional glycomics and drug discovery.

Received: March 4, 2005
Published online: June 27, 2005

Keywords: combinatorial chemistry · glycopeptides · high-throughput screening · mass spectrometry · transferases

[1] a) A. Varki, *Glycobiology* **1993**, *3*, 97–130; b) G. E. Ritchie, B. E. Moffatt, R. B. Sim, B. P. Morgan, R. A. Dwek, P. M. Rudd, *Chem. Rev.* **2002**, *102*, 305–320; c) A. Dove, *Nat. Biotechnol.* **2003**, *19*, 913–917.

[2] A. Kameyama, N. Kikuchi, S. Nakaya, H. Ito, T. Sato, T. Shikanai, Y. Takahashi, T. Takahashi, H. Narimatsu, *Anal. Chem.* **2005**, *77*, in press.

[3] a) T. Feizi, F. Fazio, W. Chai, C.-H. Wong, *Curr. Opin. Struct. Biol.* **2003**, *13*, 637–645; b) S. Park, I. Shin, *Angew. Chem.* **2002**, *114*, 3312–3314; *Angew. Chem. Int. Ed.* **2002**, *41*, 3180–3182; c) C. O. Mellet, J. M. Garcia Fernández, *ChemBioChem* **2002**, *3*, 819–822; d) D. Wang, *Proteomics* **2003**, *3*, 2167–2175; e) I. Shin, S. Park, M.-R. Lee, *Chem. Eur. J.* **2005**, *11*, 2894–2901; f) M. F. Templin, D. Stoll, M. Schrenk, P. C. Traub, C. F. Vöhringer, T. O. Joos, *Trends Biotechnol.* **2002**, *20*, 160–166.

[4] a) P. M. St. Hilaire, M. Meldal, *Angew. Chem.* **2000**, *112*, 1210–1228; *Angew. Chem. Int. Ed.* **2000**, *39*, 1162–1179; b) O. J. Plante, E. R. Palmacci, P. H. Seeberger, *Adv. Carbohydr. Chem. Biochem.* **2003**, *58*, 35–54; c) V. Wittmann, S. Seeberger, *Angew. Chem.* **2004**, *116*, 918–921; *Angew. Chem. Int. Ed.* **2004**, *43*, 900–903.

[5] a) *Handbook of Glycosyltransferases and Related Genes* (Eds.: N. Taniguchi, K. Honke, M. Fukuda), Springer, Tokyo, **2001**; b) H. Narimatsu, *Glycoconjugate J.* **2004**, *21*, 17–24.

[6] B. L. Schulz, N. H. Packer, N. G. Karlsson, *Anal. Chem.* **2002**, *74*, 6088–6097.

[7] N. Kikuchi, A. Kameyama, S. Nakaya, H. Ito, T. Sato, T. Shikanai, Y. Takahashi, H. Narimatsu, *Bioinformatics* **2005**, *21*, 1717–1718.

[8] a) M. V. Sastry, P. Banarjee, S. R. Patanjali, M. J. Swamy, G. V. Swarnalatha, A. Surolia, *J. Biol. Chem.* **1986**, *261*, 11726–11733; b) A. M. Wu, J. H. Wu, L.-H. Lin, S.-H. Lin, J.-H. Liu, *Life Sci.* **2003**, *72*, 2285–2302.

 © 2005 Wiley-VCH Verlag GmbH & Co. KGaA, Weinheim

Imaging Agents

Water-Soluble Photoluminescent Silicon Quantum Dots**

*Jamie H. Warner, Akiyoshi Hoshino, Kenji Yamamoto, and Richard. D. Tilley**

The quantum confinement of excitons in semiconductor quantum dots leads to interesting optical properties that can be exploited in a range of photonic applications including biological fluorescence imaging[1–6] and optoelectronic devices.[7–13] Quantum dots are becoming popular as replacements for fluorescent dyes in biological fluorescence imaging because of their superior stability against photobleaching. To date, considerable emphasis has been placed on using CdSe quantum dots with a ZnS shell as biological chromophores since they emit light that can be tuned throughout the visible spectrum.[14] However, concerns have been raised about the toxicological issue of using cadmium in biological systems.[15] In particular, Derfus et al. showed that CdSe quantum dots without a ZnS shell were toxic to liver cells after exposure to UV light.[15] The potential biocompatibility of silicon makes photoluminescent silicon quantum dots an ideal candidate for biological fluorescence imaging and should eliminate any potential toxicology problems that might arise from having a CdSe core.[16,17]

Strong quantum confinement in silicon increases the probability of radiative recombination through the direct band gap transitions and reduces phonon-assisted indirect band gap transitions.[18] In silicon, this requires the physical dimensions of the quantum dots to be on the order of or less than the bulk exciton Bohr radius of 4 nm.[19,20] Quantum dot sizes of less than 8 nm are easily achieved using wet chemistry techniques.[19–22] The remarkably successful advances in the synthesis of the semiconductor groups II/VI and III/V have not been applied to silicon as a consequence of the relatively high temperatures required to degrade the precursor and to produce highly crystalline quantum dots. The greatest success in producing silicon quantum dots with strong quantum confinement to date has been by the solution-phase reduction of silicon salts.[19,21,22]

[*] J. H. Warner, R. D. Tilley
School of Chemical and Physical Sciences
MacDiarmid Institute of Advanced Materials and Nanotechnology
Victoria University of Wellington
P.O. Box 600, Wellington (New Zealand)
Fax: (+64) 4-463-5237
E-mail: richard.tilley@vuw.ac.nz
A. Hoshino, K. Yamamoto
Department of Medical Ecology and Informatics
Research Institute
International Medical Center of Japan
Toyama 1-21-1, Shinjuku, Tokyo 162-8655 (Japan)

[**] J.W. and R.D.T. thank the MacDiarmid Institute of Advanced Materials and Nanotechnology for funding. J.W. and R.D.T. thank H. Rubinsztein-Dunlop for the use of the time-resolved PL spectroscopy system at The University of Queensland.

The solution-phase synthesis of silicon quantum dots has previously been reported by Kauzlarich and co-workers[21,22] through the use of a variety of reducing agents, by Korgel and co-workers[19,23] through the use of high temperatures and pressures, and by Wilcoxon et al. by using micelles.[20,24] The current problem associated with the simpler room-temperature syntheses [20–22] is the large size distribution produced. The large size distribution prevents a simple interpretation of the optical spectra. Post-synthesis treatments for narrowing the size distribution of the silicon quantum dots, such as high-pressure gas chromatography (HPGC), have revealed sharp features in the absorption spectra and narrow photoluminescence spectra attributed to direct band gap transitions.[20] We have recently reported the synthesis of 1–2-nm silicon quantum dots that were surface-passivated by 1-heptene. These dots had a narrower size distribution than previously reported and gave a strong blue photoluminescence.[25]

For silicon quantum dots to be used in biomedical applications it is essential that they have a substantial photoluminescence quantum yield in the visible region, have a fast radiative recombination rate, and are water soluble and hydrophilic to prevent aggregation and precipitation in a biological environment. The chemical process used to terminate the surfaces of the silicon quantum dots changes the internal electronic structure and thus plays an important role in the resultant emission wavelength and radiative lifetime, and ultimately determines the solubility.[18] Silicon quantum dots with an oxide surface passivation typically display a dipole-forbidden yellow-red emission with radiative lifetimes of 10^{-3}–10^{-6} s.[18,26] This slow rate of recombination limits the use of oxide-passivated silicon quantum dots in biological imaging. However, silicon quantum dots with a hydrogen or carbon surface passivation have electric-dipole-allowed direct band gap transitions that lead to blue photoluminescence with fast recombination rates of 10^{-8}–10^{-9} s.[18,20]

In this study we describe a simple room-temperature synthesis for producing water-soluble silicon quantum dots that exhibit strong blue photoluminescence with a rapid rate of recombination. The use of hydride reducing agents in these experiments produce hydrogen-terminated particle surfaces.[20,24,25] The Si–H surface bond can then be treated with both a compound containing a C=C bond and a platinum catalyst to produce a variety of surface types through formation of a Si–C surface bond. The surface of the silicon quantum dots are modified with allylamine to form hydrophilic silicon quantum dots (Figure 1). Previous reports of changing the surface-capping molecules of silicon particles have involved treating chloride-terminated particle surfaces with Grignard reagents to produce particles capped with organic molecules[27] or utilized a Si–OR bond.[22] Silicon quantum dots with a chlorine-terminated surface are restricted to a small range of available Grignard reagents, whilst Si–OR bonds have been shown to greatly affect the electronic charge distribution in the silicon quantum dots and consequently reduce the energy of indirect transitions.[18,26]

Figure 2 shows a high-resolution transmission electron microscope (HRTEM) image of a number of allylamine-capped silicon quantum dots on a carbon-coated copper grid.

 © 2005 Wiley-VCH Verlag GmbH & Co. KGaA, Weinheim DOI: 10.1002/anie.200501256

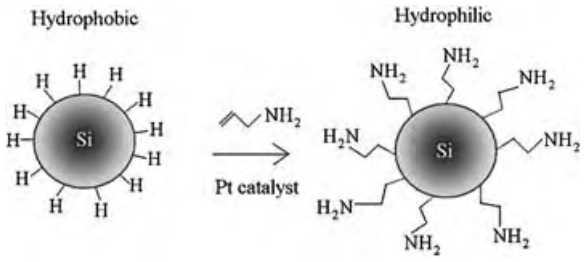


Figure 1. Schematic diagram of the procedure used to change the surface chemistry of the silicon quantum dots from hydrogen to allylamine.

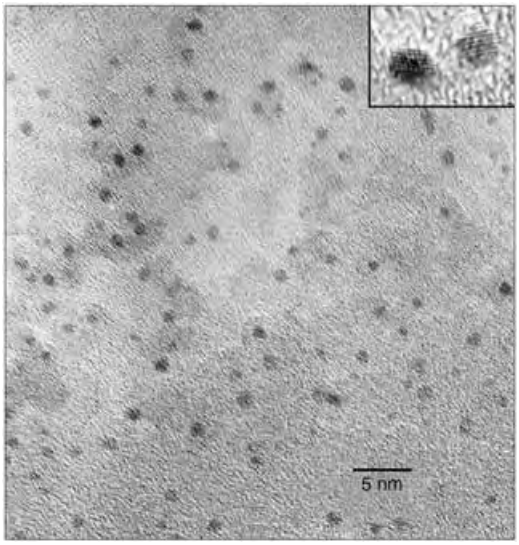


Figure 2. High-resolution transmission electron microscopy (HRTEM) image of a large number of allylamine-capped silicon quantum dots. Inset: HRTEM image of two silicon quantum dots showing the crystal lattice planes.

The water-soluble silicon quantum dots were highly crystalline and the atomic lattice planes of two separate silicon quantum dots can be clearly seen in the inset of Figure 2. Fast Fourier transform (FFT) analysis of the crystal structure shown in the inset of Figure 2 could be matched with the (2,1,−1) and (2,−1,1) planes of diamond silicon when viewed down the [011] direction. The low atomic weight of silicon relative to other metallic and semiconductor quantum dots combined with their extremely small dimensions resulted in low contrast in the HRTEM images. Only by removing almost all of the surfactant (TOAB) could such small (1–2 nm) silicon quantum dots be imaged by HRTEM. Figure 2 shows a relatively high contrast HRTEM image of the 1–2-nm silicon quantum dots along with minimal surfactant, thus indicating that a high level of purification had been achieved. The high purity of the silicon quantum dots enables the photoluminescence to be assigned to the quantum dots and not to other by-products of the reaction, such as silicon-based organosilane polymer/oligomers.

The small dimensions of the silicon quantum dots limits the selected-area electron-diffraction and X-ray diffraction measurements, and no conclusive results have as yet been obtained by using these techniques. The silicon quantum dots were also faceted, which reflects the controlled growth environment.[19] A mean size and size distribution of 1.4 ± 0.3 nm of the allylamine-capped silicon quantum dots was obtained by analyzing 648 quantum dots from different regions on the TEM grid. This small size distribution is a significant improvement on previous reports of 1–2-nm silicon quantum dots synthesized in inverse micelles.[20–22] Energy-dispersive X-ray spectroscopy (EDS) performed on the quantum dots showed a strong peak associated with silicon and no peaks for platinum. This observation confirmed that the platinum catalyst had successfully been removed during purification.

The bonding of allylamine to the surface of the silicon quantum dots was confirmed by FTIR spectroscopy (Figure 3). Peaks were observed at 1460 and 1260 cm^{-1} and

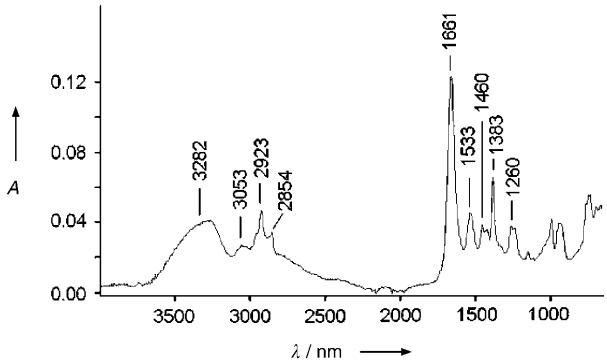


Figure 3. FTIR spectrum of allylamine-capped silicon quantum dots.

attributed to the vibrational scissoring and symmetric bending of Si−CH_2.[27] The absorbance between 2500 and 3500 cm^{-1} is attributed to symmetric and asymmetric vibrations of the C−CH_2 and C−NH_3 molecular components of the allylamine, while the dominant peak at 1661 cm^{-1} is attributed to the allylamine and clearly indicates its attachment to the silicon quantum dots. The peaks between 1000 and 1100 cm^{-1} are attributed to the vibrational stretching of Si−OR.[21] Despite the fact that the silicon quantum dots were heated in atmospheric conditions to remove the solvent for FTIR measurements, the magnitude of the Si−OR vibration is very small when compared to the FTIR reports of siloxane-coated silicon quantum dots, which have a total Si−OR surface coverage.[21] This difference highlights the strength and stability of the Si−C bond formed between the silicon quantum dots and the allylamine as well as the minimal number of Si−OR surface bonds present.

The absorption spectrum of the allylamine-capped silicon quantum dots in water (Figure 4a, curve I) displays a feature at 320 nm which is attributed to the Γ-Γ direct band gap transition.[19,20] This direct band gap transition has blue-shifted because of the effect of quantum confinement in the quantum dots—from the bulk value of 3.4 to 3.8 eV in these silicon quantum dots—and is in good agreement with other reports.[19,20]

The photoluminescence (PL) spectra recorded at 300 and 400 nm (Figures 4a, curves II and III) show a peak at 480 nm

 © 2005 Wiley-VCH Verlag GmbH & Co. KGaA, Weinheim

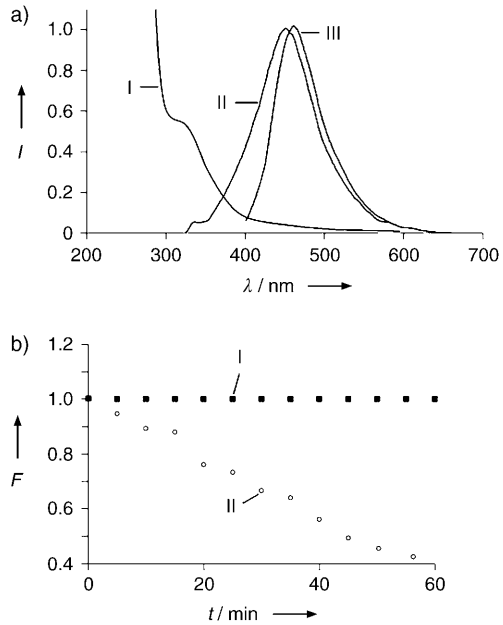


Figure 4. a) Curve I: Absorption spectrum of allylamine-capped silicon quantum dots in water; curve II: photoluminescence spectrum of allylamine-capped silicon quantum dots in water with excitation at 300 nm; curve III: photoluminescence spectrum of allylamine-capped silicon quantum dots in water with excitation at 400 nm. b) Integrated photoluminescence as a function of time of allylamine-capped silicon quantum dots in water (curve I) and rhodamine 6G in water (curve II). An excitation wavelength of 400 nm was used in both cases.

with a full-width at half maximum height (FWHM) of 70–80 nm. All the spectra in Figure 4 have been scaled for clarity of presentation.

Photoluminescence quantum yields of the allylamine-capped silicon quantum dots in water were obtained by using the comparative method of Williams et al.[28] PL quantum yields of up to 10% were obtained relative to the standard, 9,10-diphenylanthracene, in cyclohexane.[29] The optical properties of the colloidal solutions of the allylamine-capped silicon quantum dots were stable for several months. The silicon quantum dots showed better photobleaching stability than the fluorescent dye, rhodamine 6G in water, on excitation with UV light (Figure 4b). The silicon quantum dots showed no signs of any measurable photobleaching (Figure 4b, curve I) under the same illumination conditions during which the photoluminescence from rhodamine 6G dropped by 60% (Figure 4b, curve II).

The origin of the photoluminescence observed in Figure 4 is complicated by the combination of both indirect and direct band gap transitions present in silicon quantum dots and is actively debated.[19] However, there is strong theoretical evidence suggesting that 1–2-nm silicon quantum dots with a hydrogen or carbon surface termination have direct band gap optical transitions that lead to photoluminescence in the UV/blue region of the electronic spectrum.[18] The emission observed in Figure 4a is consistent with the theoretical predictions of direct band gap recombination in silicon quantum dots with carbon surface termination rather than from trap states or surface states, or of silicon quantum dots with oxygen surface termination. Emission from a Si–OR-terminated silicon quantum dot is typified by an emission centered at 600 nm.[20,30]

Further insights into the nature of the photoluminescence can be obtained by analyzing the time-resolved photoluminescence spectra from the allylamine-capped silicon quantum dots in water. Figure 5 shows the time-resolved photoluminescence decays from an aqueous solution of allylamine-capped silicon quantum dots at two different emission wavelengths. The PL decay measured at 420 nm (Figure 5, curve a) is noticeably shorter than the PL decay measured at 500 nm in curve b. Both PL decays required a three exponential fit with an overall average decay of 4 ns.

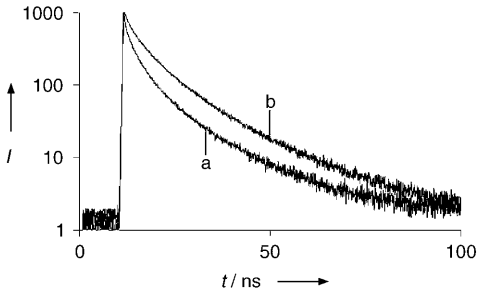


Figure 5. Time-resolved photoluminescence decays of allylamine-capped silicon quantum dots in water measured at emission wavelengths a) 420 nm and b) 500 nm. An excitation wavelength of 380 nm was used.

Indirect band gap materials, such as silicon, generally have slow recombination with PL lifetimes on the order of tens of microseconds to milliseconds, whereas direct band gap materials, such as GaAs and CdSe, have fast recombination with PL lifetimes on the order of 1–10 ns.[31] The PL lifetime measurements obtained here are in good agreement with the experimental findings of the research groups of Korgel [23] and Wilcoxon[20] as well as the theoretical predictions of Zhou et al.[18] The rapid rates of recombination measured here provide strong evidence that the observed emission results from dipole-allowed recombination across the direct band gap transition in silicon quantum dots with a carbon surface termination.

The suitability of allylamine-capped silicon quantum dots as a chromophore for biological imaging is demonstrated in Figure 6, for which an excitation wavelength of 365 nm was used and the emission at 480 nm was monitored. The control image (Figure 6a) shows minimal fluorescence from the HeLa cells relative to the HeLa cells with the incorporated silicon quantum dots (Figure 6b). Thus, the fluorescence observed in the HeLa cells in Figure 6b arises from the emission from silicon quantum dots and not autofluorescence from the cells. The inset in the top left corner of Figure 6b shows the bright blue fluorescence from a vial of allylamine-capped silicon quantum dots in water when excited with UV light. The bright blue fluorescence from the silicon quantum dots is distributed uniformly inside the cytosol of the HeLa cells and this shows the possibility of using these hydrophilic silicon quantum dots as chromophores in biological fluorescence imaging. This result has major implications towards

 © 2005 Wiley-VCH Verlag GmbH & Co. KGaA, Weinheim

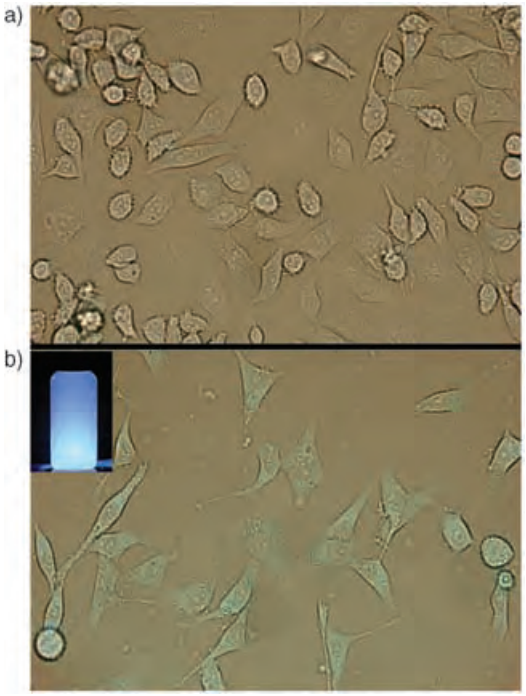


Figure 6. Overlay of the transmission and fluorescence microscope images of a) HeLa cells in the absence of any quantum dots and b) HeLa cells with silicon quantum dots incorporated inside the cytosol. Inset: fluorescence from a vial of allylamine-capped silicon quantum dots in water when excited with a UV lamp.

using colloidal silicon quantum dots effectively in biological fluorescence imaging.

In summary, silicon quantum dots with a narrow size distribution were synthesized using reverse micelles and powerful hydride reducing agents at room temperature and pressure. The surface of the silicon quantum dots was made hydrophilic by modification with allylamine. The silicon quantum dots dispersed in an aqueous environment displayed strong photoluminescence in the blue region of the visible spectrum, with a 10% quantum yield for the photoluminescence. The optical properties of the silicon quantum dots displayed features in both the absorption and emission spectra attributed to the direct band gap transitions in silicon quantum dots with a carbon surface termination. Time-resolved photoluminescence spectroscopy revealed a rapid recombination normally associated with direct band gap materials. The ease of synthesis and optical properties make the silicon quantum dots reported here excellent candidates for biomedical applications, as demonstrated by the imaging of allylamine-capped silicon quantum dots in HeLa cells.

Experimental Section

Synthesis of allylamine-capped silicon quantum dots: Silicon quantum dots were synthesized in reverse micelles by the solution-phase reduction of $SiCl_4$ with 1M $LiAlH_4$ in THF (Aldrich). The surfactant and solvent combination used to form the micelles were tetraoctylammonium bromide (TOAB, Merck) in toluene. Surface modification of the silicon quantum dots was achieved by treating the surface of the particles with allylamine (Aldrich). All experiments were carried out in an argon atmosphere in a glove box to prevent oxidation of the silicon. Oxygen levels were below 10 ppm at all times.

In a typical experiment, $SiCl_4$ (92 μL, 0.0008 mol) was dissolved in TOAB (1.5 g) and anhydrous toluene (100 mL) by using a homogenizer. Silicon quantum dots were then formed by adding a twofold excess of reducing agent. The mixture was left to react for 3 h and then anhydrous methanol (20 mL) was slowly added to quench any excess reducing agent. At this point it is expected that the surface of the particles were terminated with hydrogen.[20,25] Hydrophilic particles were formed by modifying the surface silicon–hydrogen bonds by reaction with 0.05M H_2PtCl_6 (40 μL) in isopropanol as the catalyst and allylamine (2 mL). After modification of the surface, the sample was removed from the glove box and purified by removing the surfactant.[32] The solvent was then removed using a rotary evaporator to produce a white powder consisting of mainly TOAB and silicon quantum dots. Distilled water (50 mL) was then added to the flask and resulted in the hydrophilic silicon quantum dots dissolving, but not the TOAB. The TOAB was then removed by successive filtration through a 0.22-μm membrane filter.

Incorporation of silicon quantum dots into HeLa cells: The HeLa cells were cultured in DMEM/F12 supplemented with 10% heat-inactivated fetal bovine serum at 37°C. The cells were plated at a volume of 1×10^6 cells/well on a 6-well culture plate (Iwaki technoglass, Japan) and were stimulated with a solution of 0.2 nM Si quantum dots. After incubation of the mixtures for 12 h, the cells were washed with a phosphate-buffered saline (PBS) twice to remove the nonspecific binding quantum dots. The cells were then fixed with 1% paraformaldehyde in PBS for 5 min.[33] Fluorescence images of the HeLa cells were acquired with a digital camera D1X (Nikon) on a fluorescent microscope IX-81 (Olympus) using a mirror unit to adjust the excitation wavelength to 365 nm and an oil immersion objective lens. The blue fluorescent light was detected in the cytosol of each cell.

Received: April 11, 2005
Published online: June 23, 2005

Keywords: imaging agents · luminescence · nanostructures · quantum dots · silicon

[1] W. C. Chan, S. Nie, *Science* **1998**, *281*, 2016.
[2] M. Bruchez, M. Moronne, P. Gin, S. Weiss, A. P. Alivisatos, *Science* **1998**, *281*, 2013.
[3] M. Green, *Angew. Chem.* **2004**, *116*, 4221; *Angew. Chem. Int. Ed.* **2004**, *43*, 4129.
[4] A. Wu, H. Liu, J. Liu, K. N. Haley, J. A. Tradway, J. P. Larson, N. Ge, F. Peale, M. P. Bruchez, *Nat. Biotechnol.* **2003**, *21*, 41.
[5] B. Dubertret, P. Skourides, D. J. Norris, V. Noireaux, A. H. Brivanlou, A. Libchaber, *Science* **2002**, *298*, 1759.
[6] D. R. Larson, W. R. Zipfel, R. M. Williams, S. W. Clark, M. P. Bruchez, F. W. Wise, W. W. Webb, *Science* **2003**, *300*, 1434.
[7] L. Bakueva, G. Konstantatos, L. Levina, S. Musikhin, E. H. Sargent, *Appl. Phys. Lett.* **2004**, *84*, 3459.
[8] S. A. McDonald, P. W. Cyr, L. Levina, E. H. Sargent, *Appl. Phys. Lett.* **2004**, *85*, 2089.
[9] S. Coe, W. Woo, M. Bawendi, V. Bulovic, *Nature* **2002**, *420*, 800.
[10] T. Tsutsui, *Nature* **2002**, *420*, 752.
[11] W. U. Huynh, J. J. Dittmer, A. P. Alivisatos, *Science* **2002**, *295*, 2425.
[12] R. A. M. Hikmet, D. V. Talapin, H. Weller, *J. Appl. Phys.* **2003**, *93*, 3509.
[13] B. Sun, E. Marx, N. C. Greenham, *Nano Lett.* **2003**, *3*, 961.
[14] C. B. Murray, D. J. Norris, M. G. Bawendi, *J. Am. Chem. Soc.* **1993**, *115*, 8706.
[15] A. M. Derfus, W. C. W. Chan, S. N. Bhatia, *Nano Lett.* **2004**, *4*, 11.

 © 2005 Wiley-VCH Verlag GmbH & Co. KGaA, Weinheim

[16] D. K. Nagesha, M. A. Whitehead, J. L. Coffer, *Adv. Mater.* **2005**, *17*, 921.
[17] L. T. Canham, C. L. Reeves, J. P. Newey, M. R. Houlton, T. I. Cox, J. M. Buriak, M. P. Stewart, *Adv. Mater.* **1999**, *11*, 1505.
[18] Z. Zhou, L. Brus, R. Friesner, *Nano Lett.* **2003**, *3*, 163.
[19] J. D. Holmes, K. J. Ziegler, C. Doty, L. E. Pell, K. P. Johnson, B. A. Korgel, *J. Am. Chem. Soc.* **2001**, *123*, 3748.
[20] J. P. Wilcoxon, P. P. Provencio, G. A. Samara, *Phys. Rev. B* **1999**, *60*, 2704.
[21] R. K. Baldwin, K. A. Pettigrew, E. Ratai, M. P. Augustine, S. M. Kauzlarich, *Chem. Commun.* **2002**, 1822.
[22] J. Zou, R. K. Baldwin, K. A. Pettigrew, S. M. Kauzlarich, *Nano Lett.* **2004**, *4*, 1181.
[23] D. S. English, L. E. Pell, Z. Yu, P. F. Barbara, B. A. Korgel, *Nano Lett.* **2002**, *2*, 681.
[24] J. P. Wilcoxon, G. A. Samara, *Appl. Phys. Lett.* **1999**, *74*, 3164.
[25] R. D. Tilley, J. H. Warner, K. Yamamoto, I. Matsui, H. Fujimori, *Chem. Commun.* **2005**, *14*, 1836.
[26] A. Puzder, A. J. Williamson, J. C. Grossman, G. Galli, *J. Am. Chem. Soc.* **2003**, *125*, 2786.
[27] C. Yang, R. A. Bley, S. M. Kauzlarich, H. W. H. Lee, G. R. Delgado, *J. Am. Chem. Soc.* **1999**, *121*, 5191.
[28] A. T. R. Williams, S. A. Winfield, J. N. Miller, *Analyst* **1983**, *108*, 1067.
[29] S. Hamai, F. Hirayama, *J. Phys. Chem.* **1983**, *87*, 83.
[30] Y. Kanemitsu, T. Futagi, T. Matsumoto, H. Mimura, *Phys. Rev. B* **1994**, *49*, 14732.
[31] J. H. Warner, E. Thomsen, A. R. Watt, N. R. Heckenberg, H. Rubinsztein-Dunlop, *Nanotechnology* **2005**, *16*, 175.
[32] R. D. Tilley, S. Saito, *Langmuir* **2003**, *19*, 5115.
[33] A. Hoshino, K. Fujioka, T. Oku, M. Suga, Y. F. Sasaki, T. Ohta, M. Yasuhara, K. Suzuki, K. Yamamoto, *Nano Lett.* **2004**, *4*, 2163.

 © 2005 Wiley-VCH Verlag GmbH & Co. KGaA, Weinheim

Electrochemistry

Electrochemical Control of the Photocurrent Direction in Intercalated DNA/CdS Nanoparticle Systems**

*Ron Gill, Fernando Patolsky, Eugenii Katz, and Itamar Willner**

In memory of Chava Lifshitz

The use of molecular[1–4] and biomolecular[5–7] assemblies that perform logic gate functions has attracted substantial interest directed toward information storage and processing. In these efforts, nanoparticles have been employed to switch the conductivity properties across interfaces.[8,9] The integration of biomaterials with nanoparticles as active hybrid components in bioelectronic systems is interesting, as the unique recognition properties of biomolecules are combined with the optoelectronic functions of nanoparticles.[10,11] Double-stranded DNA (dsDNA) could act as a matrix to assemble signal-triggered functional nanoparticle structures by binding molecular units to the dsDNA. The conductivity of DNA has been a subject of extensive controversy,[12] and it is accepted that DNA exhibits poor conductivity.[13] However, the conductivity of DNA could be controlled by appropriate ordering of the base sequence[14] or by the incorporation of redox-active intercalators into dsDNA.[15] Herein, we report the design of CdS nanoparticle/DNA conjugates on gold surfaces and describe the effects of intercalators and the applied potential on the photoelectrochemical features of the system. We demonstrate that the resulting photocurrent can be reversibly switched between cathodic and anodic directions by controlling the redox state of the intercalated species.

In a previous study,[16] CdS nanoparticles were linked to gold surfaces and low-value anodic photocurrents in the presence of a sacrificial electron donor were recorded. This photocurrent was explained to originate from CdS nanoparticles that were in intimate contact with the electrode, owing to a low surface coverage of the nanoparticles, and thus the DNA matrix acted only as a linker in this system. In the present study, a dithiol-tethered single-stranded DNA (ssDNA) molecule **1** was self-assembled on the surface of a gold electrode and then hybridized with a complementary dithiolated ssDNA **2** to yield a double-stranded DNA (Figure 1). The resulting surface was treated with CdS nanoparticles to yield a semiconductor nanoparticle interface linked to the surface of the electrode by the dsDNA (Figure 1a). The surface coverage of the different components on the electrode support was determined by quartz-crystal-microbalance (QCM) measurements on Au/quartz crystals and by complementary electrochemical experiments. The surface coverages of the ssDNA **1** and the dsDNA complex were determined by chronocoulometry using $[Ru(NH_3)_6]^{3+}$ as a redox label.[17] The surface coverage of **1** and the dsDNA were found to be 1.8×10^{12} molecules cm^{-2} and 1.46×10^{12} molecules cm^{-2}, respectively. From the frequency changes of the Au/quartz crystal upon the assembly of the CdS nanoparticles, their surface coverage was estimated to be 4.9×10^{11} particles cm^{-2}. Thus, approximately three units of dsDNA link a single CdS nanoparticle to the electrode surface.

Figure 2a, curve 1, shows the photocurrent action spectrum of the CdS nanoparticle/dsDNA system in the presence of triethanolamine, TEOA, as a sacrificial electron donor. A very low anodic photocurrent is observed. The intercalation of doxorubicin (**3**) into dsDNA is well-established.[18] The intercalation of **3** into the dsDNA here results in a fivefold higher photocurrent (Figure 2a, curve 2). The electrolyte solution in the photoelectrochemical experiment is free of **3**, and the enhancement in the resulting photocurrent originates only from intercalated **3**. The coverage of the dsDNA with the intercalator **3** could not be assessed quantitatively, but differential pulse voltammetry experiments clearly indicated

[*] R. Gill, Dr. F. Patolsky, Dr. E. Katz, Prof. I. Willner
Institute of Chemistry
The Hebrew University of Jerusalem
Jerusalem 91904 (Israel)
Fax : (+972) 2-652-7715
E-mail: willnea@vms.huji.ac.il

[**] This research was supported by the EC STREP Project MOLDYN-LOGIC. This work is dedicated to Professor Chava Lifshitz, who passed away on March 1, 2005.

 © 2005 Wiley-VCH Verlag GmbH & Co. KGaA, Weinheim DOI: 10.1002/anie.200500830

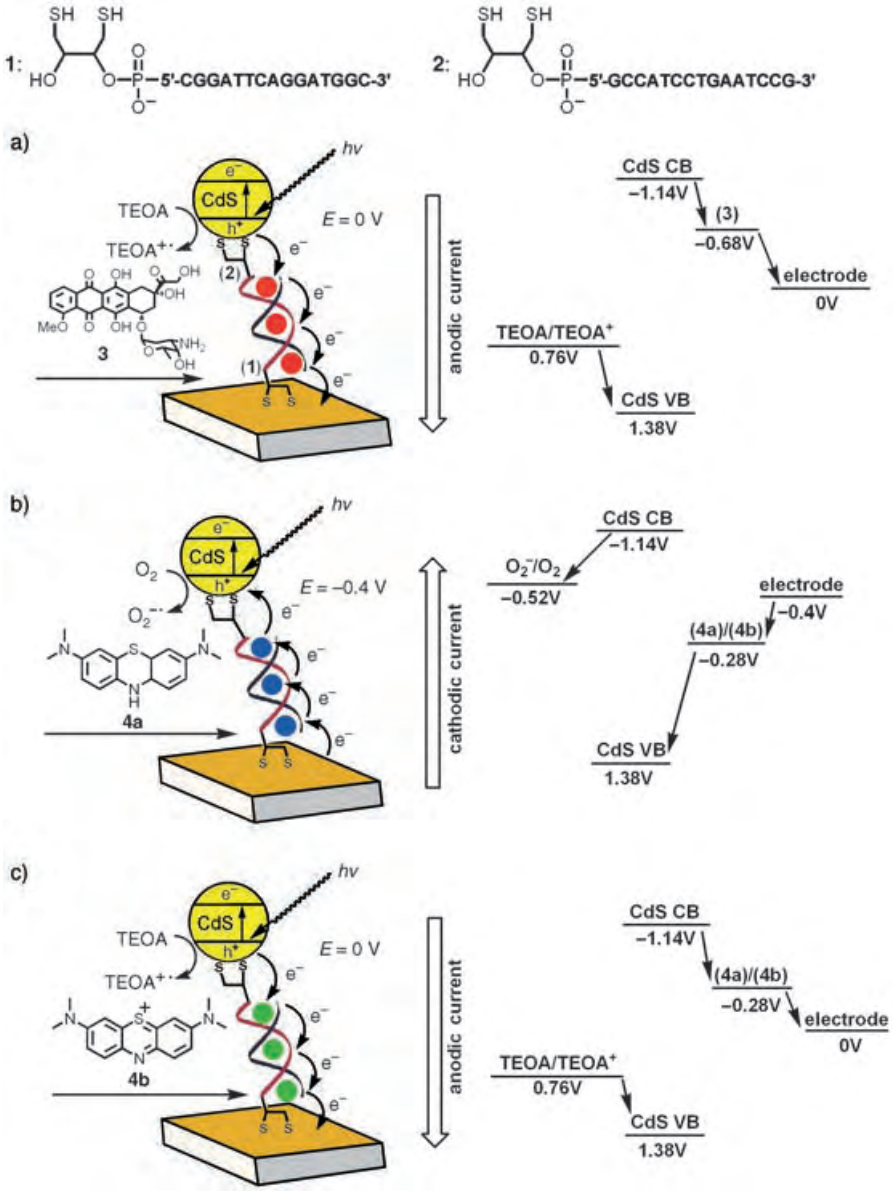


Figure 1. Directional electroswitchable photocurrents in the CdS nanoparticle/dsDNA/intercalator system. a) Enhanced generation of an anodic photocurrent in the presence of the doxorubicin intercalator (**3**; applied potential $E = 0$ V). b) Enhanced generation of a cathodic photocurrent in the presence of the reduced methylene blue intercalator (**4a**; applied potential $E = -0.4$ V). c) Enhanced generation of an anodic photocurrent in the presence of the oxidized methylene blue intercalator (**4b**; applied potential $E = 0$ V). The redox levels of the components that participate in the different photocurrent-generating systems are presented on the right side of the scheme. TEOA = triethanolamine; CB = conduction band; VB = valence band.

the binding of **3** to the dsDNA ($E° = -0.68$ V at pH 7.0). The photocurrent action spectra (Figure 2a) follow the absorbance features of the CdS nanoparticles (Figure 2b) which implies that the photocurrents originate from the photoexcitation of the semiconductor nanoparticles. Control experiments indicate that in the absence of TEOA, or without the association of the CdS nanoparticles, no photocurrents are generated in the systems. The fact that no photocurrent is generated in the presence of doxorubicin ($\lambda_{max} = 480$ nm) when the CdS nanoparticles are excluded from the dsDNA assembly prohibits the possibility that the **3**/TEOA pair contributes to the observed photocurrents. Thus, the enhanced photocurrent in the system that consists of the dsDNA with intercalated **3** is attributed to charge transport of conduction-band electrons to the bulk electrode by the intercalated quinone **3** (Figure 1a). Photoexcitation of the semiconductor nanoparticles yields an electron–hole pair. The transfer of the conduction-band electrons to intercalated **3** facilitates charge separation and the transport of electrons to the electrode to yield enhanced photocurrents. The redox levels of the components that participate in the generation of the photocurrent are presented in Figure 1.[19]

In a second configuration of the CdS nanoparticle/dsDNA system we employed methylene blue (**4**) as intercalator[15,18] (Figure 1b and c). A cyclic voltammogram of the system demonstrated a reversible redox process of intercalated **4** ($E° = -0.28$ V at pH 7.0) that can exist in the reduced state (**4a**; $\lambda_{max} = 400$ nm) or oxidized state (**4b**; $\lambda_{max} < 665$ nm), depending on the applied potential. Coulometric analysis of the reduction wave indicates that the surface coverage of **4** is 3.8×10^{12} molecules cm^{-2}. This value translates to the association of about two to three units of **4** with each dsDNA linked to the electrode. Figure 2c depicts the resulting photocurrents in the CdS nanoparticle/dsDNA system under an applied potential of $E = -0.4$ V and in the presence of O_2 as a sacrificial electron acceptor, in the absence of the intercalator (curve 1) and in the presence of the intercalator (curve 2). At this potential, the intercalator **4** exists in its reduced leuko form, **4a**. Whereas in the absence of **4a** a very low photocurrent is detected, in the presence of the reduced intercalator **4a**, the photocurrent is approximately fourfold higher. Control experiments reveal that upon the elimination of oxygen or the CdS nanoparticles from the assembly, no photocurrent is generated in the system. The photocurrent observed in the system is in the opposite direction to that observed in the presence of **3**. Thus, the enhanced cathodic photocurrent observed in the presence of **4a** originates from facilitated electron transport by the reduced intercalator **4a** (Figure 1b). Photoexcitation of the

 © 2005 Wiley-VCH Verlag GmbH & Co. KGaA, Weinheim

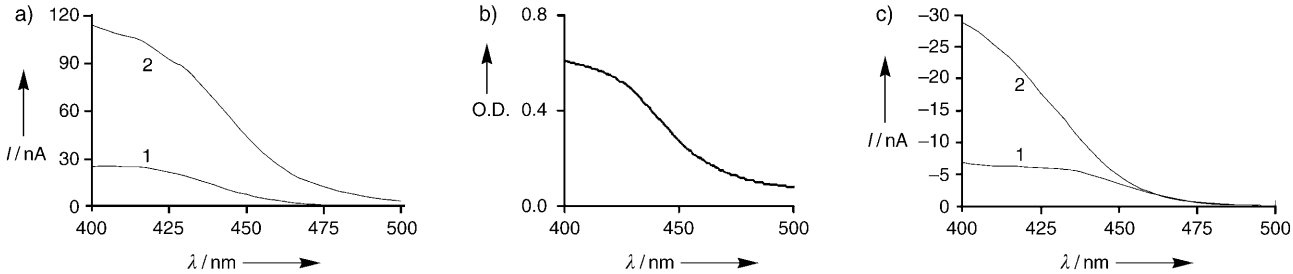


Figure 2. Photocurrent action spectra generated in the CdS nanoparticle/dsDNA systems: a) Anodic photocurrents generated in the absence (1) and in the presence (2) of the doxorubicin intercalator (**3**). The data were obtained at the applied potential $E = 0$ V and in the presence of TEOA (20 mM). b) Absorption spectrum of the CdS nanoparticles (OD = optical density). c) Cathodic photocurrents generated in the absence (1) and in the presence (2) of reduced methylene blue intercalator (**4a**). The data were obtained at the applied potential $E = -0.4$ V and in the presence of O_2 (under equilibrium with air).

semiconductor nanoparticles generates the electron–hole pair. Filling the valence-band holes with electrons that originate from the reduced intercalator **4a** facilitates charge separation and enables the enhanced reduction of O_2 by conduction-band electrons and the continuous generation of the photocurrent in the cathodic direction. The intercalation of the reduced methylene blue (**4a**) in the dsDNA allows charge transport from the electrode to the semiconductor nanoparticles, a process that leads to the effective generation of the cathodic photocurrent. Thus, the nature of the intercalator and its redox state control the direction of the photocurrent in the CdS nanoparticle/dsDNA/intercalator systems. The redox levels of the components that participate in the generation of the cathodic or anodic photocurrents are given in Figure 1.[19]

Inspection of the quasi-reversible cyclic voltammogram of the intercalated methylene blue (**4**) suggests, however, that one might use the same dsDNA intercalator for controlling the direction of the photocurrent by the application of an appropriate potential. That is, at an applied potential of 0 V, the intercalated **4** exists in its oxidized state **4b**, which behaves as electron acceptor. Thus, in the presence of the TEOA electron donor, an anodic photocurrent will be generated in the system (Figure 1c). Switching the potential on the electrode to −0.4 V yields the reduced state of the intercalator, **4a**, and in the presence of O_2 as electron acceptor the photocurrent will be switched to the cathodic direction (Figure 1b). Thus, in the presence of TEOA and O_2, one anticipates the possibility to switch the direction of the photocurrent by the applied potential. Switchable vectorial photocurrent generation was recently demonstrated by Yasutomi et al.[20] who employed helical peptides tethered to two different chromophores that acted as acceptor or donor units, respectively, upon photoexcitation. In contrast to their system, which requires the use of different wavelengths to switch the direction of the photocurrent, our system uses a dsDNA template and an intercalator to switch the direction of the photocurrent by alteration of the applied potential. Figure 3 shows the potential-induced switching of the direction of the photocurrent using the CdS nanoparticle/dsDNA system and either **4a** or **4b** as the intercalator. Photoexcitation of the system at $\lambda = 405$ nm results in an anodic current that is switched "on" and "off" by light at an applied potential

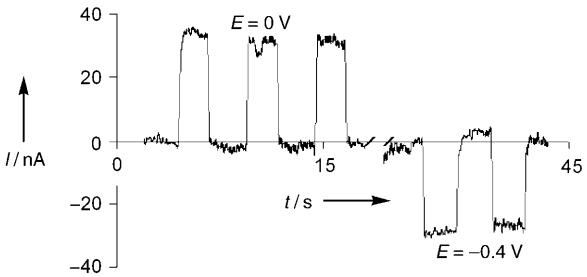


Figure 3. Electrochemically switched anodic and cathodic photocurrents generated in the CdS nanoparticle/dsDNA/**4b** (or **4a**) systems at 0 V and −0.4 V, respectively, in the presence of TEOA (20 mM) and O_2 (under equilibrium with air). Photocurrents were generated upon irradiation at $\lambda = 405$ nm.

of 0 V. Turning the applied potential to −0.4 V switches the photocurrent to the cathodic direction. The electroswitchable directional generation of the photocurrent is reversible and controlled by the applied potential.

The photocurrent generated by the CdS nanoparticle/dsDNA with the use of the intercalators corresponds to an AND logic gate, in which the photocurrent is generated only if the optical signal and the intercalator are introduced as activation stimuli to the system. The potential-controlled generation of the photocurrent in the **4a**/**4b**-intercalated CdS nanoparticle/dsDNA system not only allows the direction of the output current to be controlled but also allows regulation of the extent of opening of the gate and the resulting magnitude of the photocurrent.

To conclude, the present study has demonstrated the use of CdS nanoparticle/dsDNA assemblies on an electrode for the potential-induced switching of the directions of the photocurrents. The dsDNA acts as the template for the accommodation of the intercalators and its electrical contacting with the electrode.

Experimental Section

Dithiolated ssDNA (**1** and **2**) were prepared in situ during oligonucleotide synthesis using dithiophosphoamidite (Glen Research Inc.) by Sigma-Genosys Inc. DNA strands **1** and **2** were then reduced with dithiothreitol (DTT) and purified on a Sephadex G-25 column prior

 © 2005 Wiley-VCH Verlag GmbH & Co. KGaA, Weinheim

to the modification of the surfaces. CdS nanoparticles (5.5 nm) were prepared in water using polyphosphate as a capping agent.[21] Glass slides (AF-45) coated with a 250-nm thick layer of gold (Evaporated Coatings Inc) were used as working electrodes. The Au electrode was modified using reduced **1** (10 μM) for 2 h in phosphate buffer (50 mM, pH 7.4) containing NaCl (0.5 M). The electrode was then washed three times with phosphate buffer (0.1M, pH 7.4) and modified with mercaptohexanol (1 mM) in water for 10 min to prevent nonspecific absorption of DNA on the surface. For the hybridization step, the **1**-functionalized electrode was treated with reduced **2** (10 μM) for 2 h in phosphate buffer (50 mM, pH 7.4) containing NaCl (0.5 M). The dsDNA- (**1**·**2**)-functionalized gold electrode was washed three times with phosphate buffer (0.1M, pH 7.4) and incubated in a solution of CdS (50 nM) for 12 h. Doxorubicin (**3**) or methylene blue (**4**) intercalators were incorporated into the dsDNA/CdS nanoparticle assembly by the interaction of the modified electrodes with a 50 μM solution of **3** or **4**, respectively, for 30 min, followed by rinsing of the electrode with phosphate buffer (0.1M, pH 7.4). Electrochemical and photoelectrochemical measurements were performed as described previously.[22] The photocurrents were measured in phosphate buffer (0.1M, pH 7.0) in the presence of either TEOA (20 mM) or oxygen (under equilibrium with air) or both. The working electrode area was 2.1 cm^2. All reported photocurrents represent the difference between the currents observed under light and dark conditions. The electrical potentials are reported relative to the saturated calomel electrode (SCE).

Received: March 6, 2005
Revised: April 13, 2005
Published online: June 23, 2005

Keywords: DNA · electrochemistry · intercalations · nanostructures · semiconductors

[1] A. P. de Silva, *Nat. Mater.* **2005**, *4*, 15 – 16.
[2] A. P. de Silva, N. D. McClenaghan, *Chem. Eur. J.* **2004**, *10*, 574 – 586.
[3] V. Balzani, A. Credi, M. Venturi, *ChemPhysChem* **2003**, *4*, 49 – 59.
[4] F. M. Raymo, *Adv. Mater.* **2002**, *14*, 401 – 414.
[5] M. N. Stojanovic, D. Stefanovic, *Nat. Biotechnol.* **2003**, *21*, 1069 – 1074.
[6] I. Willner, S. Rubin, *Angew. Chem.* **1996**, *108*, 419 – 437; *Angew. Chem. Int. Ed. Engl.* **1996**, *35*, 367 – 385.
[7] I. Willner, *Acc. Chem. Res.* **1997**, *30*, 347 – 356.
[8] D. I. Gittins, D. Bethell, D. J. Schiffrin, R. J. Nichols, *Nature* **2000**, *408*, 67 – 69.
[9] G. K. Ramachandran, T. J. Hopson, A. M. Rawlett, L. A. Nagahara, A. Primak, S. M. Lindsay, *Science* **2003**, *300*, 1413 – 1416.
[10] E. Katz, I. Willner, *Angew. Chem.* **2004**, *116*, 6166 – 6235; *Angew. Chem. Int. Ed.* **2004**, *43*, 6042 – 6108.
[11] C. M. Niemeyer, *Angew. Chem.* **2001**, *113*, 4254 – 4287; *Angew. Chem. Int. Ed.* **2001**, *40*, 4128 – 4158.
[12] D. Porath, G. Cuniberti, R. Di Felice, *Top. Curr. Chem.* **2004**, *237*, 183 – 227.
[13] P. J. De Pablo, F. Moreno-Herrero, J. Colchero, *Phys. Rev. Lett.* **2000**, *85*, 4992 – 4995.
[14] M. A. O'Neill, J. K. Barton, *J. Am. Chem. Soc.* **2004**, *126*, 11 471 – 11 483.
[15] T. G. Drummond, M. G. Hill, J. K. Barton, *Nat. Biotechnol.* **2003**, *21*, 1192 – 1199.
[16] I. Willner, F. Patolsky, J. Wasserman, *Angew. Chem.* **2001**, *113*, 1913 – 1916; *Angew. Chem. Int. Ed.* **2001**, *40*, 1861 – 1864.
[17] A. B. Steel, T. M. Herne, M. K. Tarlov, *Anal. Chem.* **1998**, *70*, 4670 – 4677.
[18] *Small-Molecule DNA and RNA Binders* (Eds.: M. M. Demeunynck, C. Bailly), Wiley-VCH, Weinheim, **2003**.
[19] a) M. I. Bodnarchuk, M. V. Kovalenko, A. L. Stroyuk, S. Y. Kuchmii, *Theor. Exp. Chem.* **2004**, *40*, 287 – 292; b) T. Akiyama, S. Nitahara, S. Inoue, S. Yamada, *Photochem. Photobiol. Sci.* **2004**, *3*, 26 – 28.
[20] S. Yasutomi, T. Morita, Y. Imanishi, S. Kimura, *Science* **2004**, *304*, 1944 – 1947.
[21] Y. Tian, C. Wu, J. H. Fendler, *J. Phys. Chem.* **1994**, *98*, 4913 – 4918.
[22] E. Granot, F. Patolsky, I. Willner, *J. Phys. Chem. B* **2004**, *108*, 5875 – 5881.

 © 2005 Wiley-VCH Verlag GmbH & Co. KGaA, Weinheim

Supramolecular Chemistry

Rare and Diverse Binding Modes Introduced through Mechanical Bonding**

David A. Leigh, Paul J. Lusby, Alexandra M. Z. Slawin, and D. Barney Walker*

Interest in catenanes and rotaxanes has largely focused on the stimuli-induced change in the position of their components for possible exploitation in molecular devices,[1] but other properties and features of these architectures are becoming apparent.[2] Here, we report a previously unrecognized consequence of kinetic stabilization of an otherwise unfavorable association of molecular fragments through mechanical bonding (Figure 1). The raised energy of the interlocked components—brought about by the enforced high local concentration of convergent functional groups, the limitation in the number of conformations and co-conformations that each component can adopt, and the poor solvation of their inner surfaces—facilitates (kinetically and thermodynamically) the formation of internal and external binding motifs that are either not observed or much weaker when the same groups are not confined in this way. The effect is illustrated through a remarkable series of binding modes (including orthogonal bifurcated pyridine–pyridine hydrogen bonding,

[*] Prof. D. A. Leigh, Dr. P. J. Lusby, D. B. Walker
School of Chemistry
University of Edinburgh
The King's Buildings
West Mains Road, Edinburgh EH9 3JJ (UK)
Fax: (+44) 131-667-9085
E-mail: david.leigh@ed.ac.uk
Prof. A. M. Z. Slawin
School of Chemistry
University of St. Andrews
Purdie Building, St. Andrews, Fife KY16 9ST (UK)

[**] We thank Anne-Marie Fuller for the synthesis of H_2**4**. This work was supported by the European Union Future and Emerging Technology Program MechMol and by the EPSRC.

Supporting information for this article is available on the WWW under http://www.angewandte.org or from the author.

 DOI: 10.1002/anie.200500004 © 2005 Wiley-VCH Verlag GmbH & Co. KGaA, Weinheim

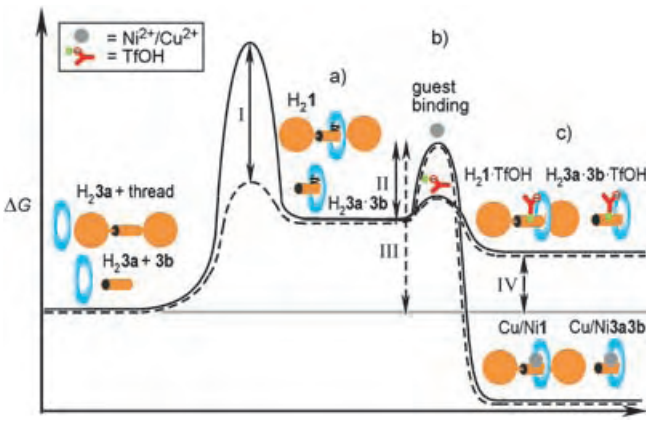


Figure 1. Effects of kinetic stabilization of an otherwise unfavorable association of molecular fragments through mechanical bonding. a) The kinetic stabilization (I) of a mechanically interlocked architecture that features only weakly attractive interactions between the macrocycle and thread permits noncovalent interactions to be observed (as in H_2**1**) which are too weak to stabilize the corresponding host–guest complex (H_2**3a**·**3b**). b) For a rotaxane that is not thermodynamically stable with respect to its free components, the activation energy for tertiary component complex formation is lower than for the analogous noninterlocked system (barrier II is less than III). This arises because the entropic cost of bringing the two components of the rotaxane together has already been paid, some degrees of freedom of the components are already restricted in the mechanically interlocked architecture, and the desolvation of the internal rotaxane surfaces is less energetically demanding than those of the free components. c) The higher energy of such a rotaxane means that a host–guest complex which involves the rotaxane can be favorable (e.g. H_2**1**·TfOH) even when the equivalent trimolecular complex (H_2**3a**·**3b**·TfOH) is not (IV). It also ensures that metal complexes derived from such rotaxanes, such as Cu**1** and Ni**1**, are inherently thermodynamically more stable than the analogous complexes derived from noninterlocked fragments and, in principle, kinetically easier to form. The association/dissociation pathways are shown by black solid (interlocked components) and dashed (noninterlocked components) lines; the horizontal gray line corresponds to the free energy of the nonassociated individual components.

cooperative binding to a sulfonic acid guest through deprotonation by one component and anion–amide hydrogen bonding by the other, enforced square-pyramidal coordination of Cu^{II} and Ni^{II}, and second-sphere coordination in a square-planar $Pd^{II}Cl$ complex) exhibited in solution and the solid state by a [2]rotaxane and an analogous [2]catenane, but not seen with either threadable (but nonmechanically interlocked) versions of the components or flexible covalently bonded systems (Figure 2).

Most catenanes and rotaxanes are synthesized by utilizing templates to thermodynamically favor interlocking,[1a] but subsequent removal of the template can leave a molecule that is energetically unstable with respect to the noninterlocked components and is only held intact by virtue of the mechanical bond. We recently described[3] the assembly of a mechanically interlocked architecture about a Pd^{II} template to give a square-planar [2]rotaxane–metal coordination complex, Pd**1**.[4] We were intrigued to find that upon protic demetalation of the complex to give H_2**1**, the ^{1}H NMR spectrum in $CDCl_3$ indicated significant intercomponent hydrogen bonding between the amide groups of the macrocycle and the pyridine nitrogen atom of the rotaxane thread (the protons of the amide groups in the macrocycle appear 1.7 ppm downfield relative to the corresponding protons in the free macrocycle). Such a binding motif, which requires essentially orthogonal pyridine rings with the nitrogen atoms bridged by bifurcated hydrogen bonds, is extremely rare (a search of the Cambridge Crystallographic Database reveals only one other example[5]) but is somewhat reminiscent of the hydrogen bonding that occurs at 90° to the plane of the lone pairs of amide groups in threads seen extensively in other hydrogen-bonded rotaxanes.[6] Slow cooling of a hot, saturated solution of H_2**1** in acetonitrile/chloroform (10:1) yielded single crystals that were of sufficient quality to confirm the interaction in the solid state by X-ray crystallography (Figure 3a, b) but were inadequate to confidently characterize the interaction in detail.[7] However, when we prepared a [2]catenane that incorporated the same functional groups, H_2**2**, a similar noncovalent interaction was observed in solution in $CDCl_3$ and, in this case, single crystals of excellent quality were obtained by slow cooling of a hot, saturated solution of H_2**2** in acetonitrile. The solid-state structure of H_2**2** (Figure 3c) closely mirrors the hydrogen-bonding motif seen in the crystal structure of H_2**1**, with unsymmetrical intercomponent hydrogen-bond distances (2.28 and 3.10 Å in H_2**2**; 2.3 and 2.8 Å in H_2**1**) and the angle between the planes of the

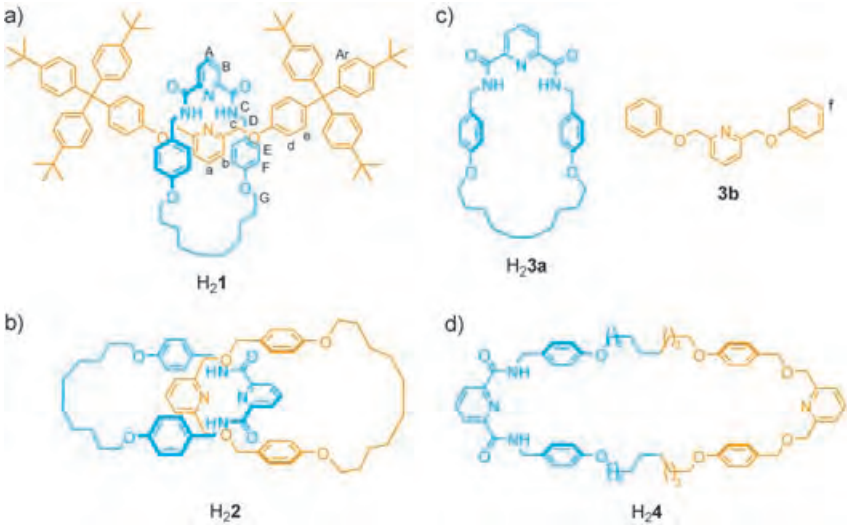


Figure 2. Different ways of linking a 2,6-dialkylpyridine unit with a 2,6-dicarboxamidepyridine unit which lead to significantly different noncovalent binding properties: a) on different components within a [2]rotaxane architecture, H_2**1**; b) on different components within a [2]catenane architecture, H_2**2**; c) on separate threadable, but not mechanically interlocked, molecular components H_2**3a** and **3b**; and d) on a flexible but wholly covalently bonded system, H_2**4**. For ^{1}H NMR spectroscopic assignments (see Figure 4), hydrogen atoms have been labeled A–G and a–f/Ar for the macrocycle and thread, respectively.

 © 2005 Wiley-VCH Verlag GmbH & Co. KGaA, Weinheim

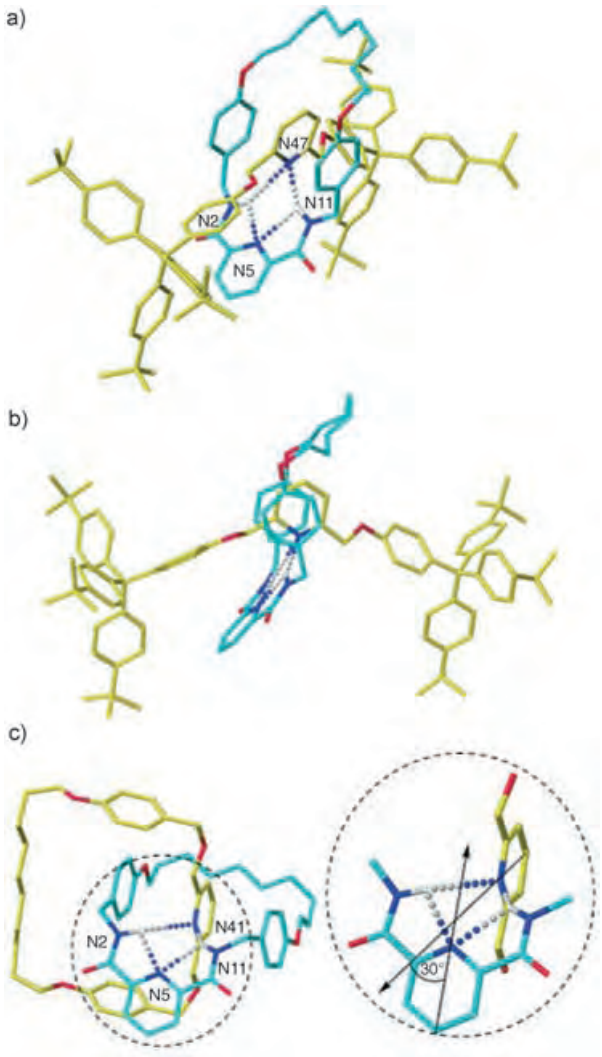


Figure 3. X-ray crystal structures[7] of [2]rotaxane H_2**1** and [2]catenane H_2**2**: a) H_2**1** (twisted view); b) H_2**1** (side view which shows the macrocycle circumscribing the pyridine residue of the thread; disorder in the alkyl chain region and solvent molecules, not the central hydrogen-bonding region, results in a high overall *R* factor of 33%); c) H_2**2** (*R* factor <5%; the intercomponent hydrogen-bond motif mirrors that shown in (a) and (b)). Inset: the lone pairs of the pyridine nitrogen atoms do not point directly at each other, but are tilted 30.0° apart. C (macrocycle) turquoise; C (thread) yellow; O red; N dark blue; H white. For clarity only nitrogen-bound hydrogen atoms are shown. Selected bond lengths [Å] for H_2**1**: N2H–N5 2.4; N11H–N5 2.6; N2H–N47 2.8; N11H–N47 2.3. Selected bond angles [°] for H_2**1**: N2H-N5 151; N11H-N5 153; N2H-N47 96; N11H-N47 108. Selected bond lengths [Å] for H_2**2**: N2H–N5 2.18; N11H–N5 2.33; N2H–N41 2.28; N11H–N41 3.10. Selected bond angles [°] for H_2**2**: N2H-N5 107.1; N11H-N5 102.2; N2H-N41 146.5; N11H-N41 129.0.

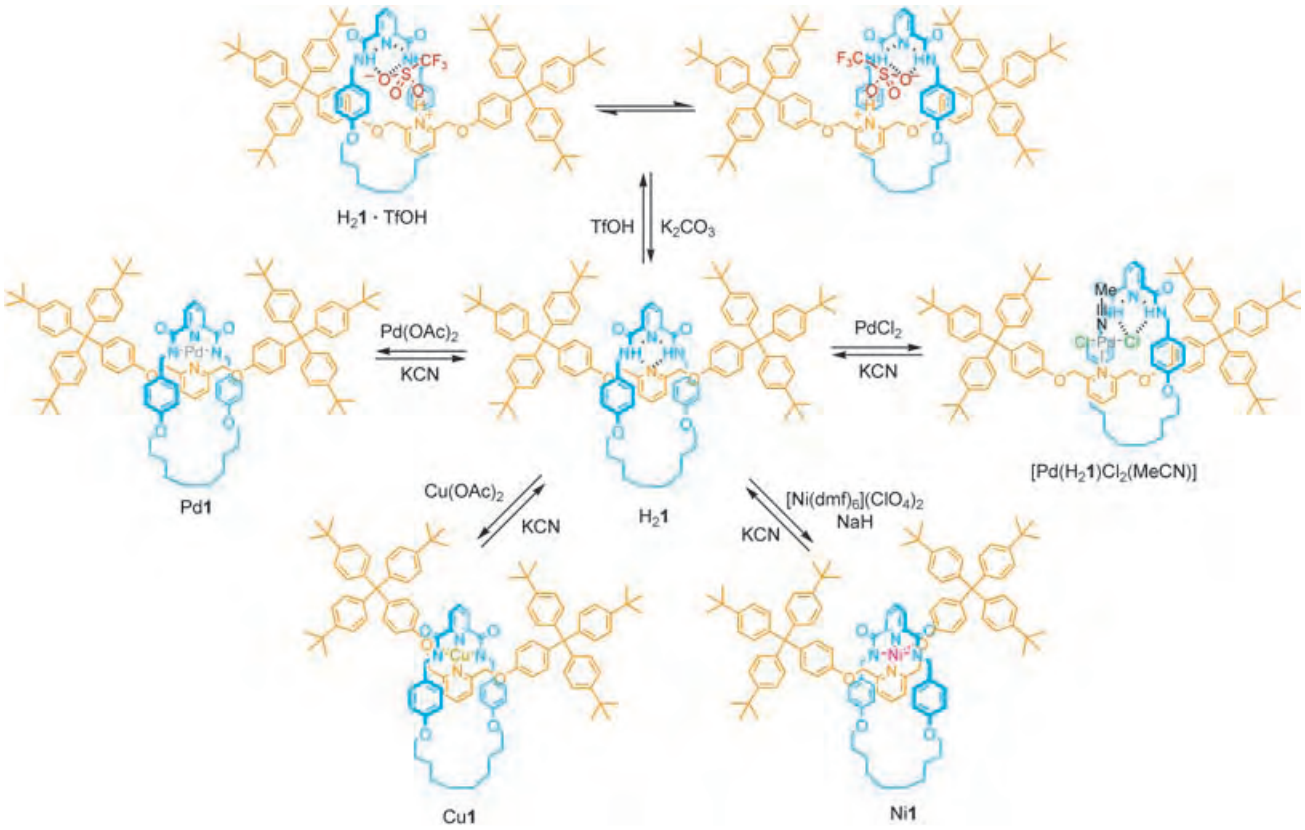
pyridine rings nearly orthogonal (90.7° in H_2**2**; 82° in H_2**1**) but tilted (30.0° in H_2**2** (Figure 3c, inset); 34° in H_2**1**) away from linearity to avoid too close an interaction between the lone pairs on the pyridine nitrogen atoms.

To investigate this atypical binding motif further, we titrated an unstoppered analogue of the thread, **3b**, with the free macrocycle, H_2**3a**, and monitored the titration by ^{1}H NMR spectroscopy ($CDCl_3$) to determine the energetics of the interaction in the absence of the kinetic barrier to dissociation provided by the mechanical bond. However, there was virtually no shift in the amide protons of H_2**3a** in the presence of up to 20 equivalents of **3b** (4–80 mM) which indicates that the bimolecular association constant must be less than $5\,M^{-1}$—the approximate limit of this detection method with the large shifts typically observed through hydrogen-bonding amide groups. Interestingly, the ^{1}H NMR spectrum of the wholly covalently linked analogue H_2**4** in $CDCl_3$ also gave no indication of hydrogen-bonding interactions between the pyridine-2,6-carboxamide protons and the second pyridine residue, even though this very large macrocycle is certainly flexible enough to adopt such a geometry without steric hindrance.

Rare hydrogen-bond motifs have previously been observed within rotaxane architectures (e.g. amide NH to ester acyl oxygen atoms,[8,9] and amide NH to ester alkyl oxygen atoms[9]). The propensity for such unusual interactions in mechanically bonded structures presumably arises for a number of reasons: 1) the enforced high local concentration of functional groups for which there is a low steric cost to relative movement within the vector of the thread; 2) the limited number of conformations and co-conformations that each component can adopt that do not put functional groups into convergent orientations; 3) the imposed orthogonalization of components which can preclude normally preferred noncovalent bonding geometries; 4) freezing out of a single co-conformation for an intercomponent binding event only costs a reduction of two degrees of freedom (translation and rotation of the macrocycle about the thread) in contrast to the multiple degrees of rotational freedom of the alkyl chains that would be lost by internal hydrogen bonding in H_2**4**; 5) the inefficient solvation of internal or congested surfaces of an interpenetrated architecture means that desolvation of binding sites is likely to occur at a lower energetic cost than for conventional structures. All of these factors effectively do the same thing, that is, raise the energy of the rotaxane with respect to the free components. However, the kinetic stabilization of the architecture provided by the stoppers prevents dethreading (the rotaxane is not in equilibrium with the free components). This increase in free energy is actually a form of host preorganization, which serves to enhance binding properties as outlined by Cram over 30 years ago.[10] The result is that interactions which are not strong enough to stabilize a host–guest complex can become thermodynamically favorable if the components are held together by a mechanical bond (Figure 1).

We reasoned that it should be possible to disrupt the intercomponent hydrogen-bonding interaction in H_2**1** by protonation of the more basic 2,6-dioxymethylenepyridine nitrogen atom (Scheme 1). Although treatment of H_2**1** with one equivalent of trifluoromethanesulfonic acid (TfOH) resulted in protonation of the desired site (Figure 4d), the downfield shift of the H_C amide protons indicated that strong hydrogen bonding was still present. The shielding and broadening of particular thread signals at 298 K (Figure 4d) suggests that instead of residing over the pyridine residue as in H_2**1**, the macrocycle is displaced to the side and shuttles between the two halves of the thread relatively slowly on the

 © 2005 Wiley-VCH Verlag GmbH & Co. KGaA, Weinheim



Scheme 1. Binding modes observed for [2]rotaxane H_2**1**. All of the complexation reactions are fully reversible. A similar range of complexes are exhibited by [2]catenane H_2**2** (for an X-ray crystal structure of Pd**2**, see ref. [12]). The hydrogen bonding in [Pd(H_2**1**)Cl_2(MeCN)] is observed only in the solid state. Tf = trifluoromethanesulfonyl, DMF = *N*,*N*-dimethylformamide.

NMR timescale. This was confirmed by the ^{1}H NMR spectrum recorded at 238 K (Figure 4e) in which many of the thread resonances were split into two inequivalent sets (H_b/$H_{b'}$, H_c/$H_{c'}$, H_d/$H_{d'}$, H_e/$H_{e'}$) that correspond to solvent-exposed and encapsulated (and thus magnetically shielded by the macrocycle) protons, respectively. The rationale for this behavior was provided by the crystal structure of single crystals grown from acetonitrile (Figure 5a). The [2]rotaxane acts as a host for an entire molecule of TfOH; one component (the thread) deprotonates the acid, and both components hydrogen bond to the resulting anion to generate a neutral complex, H_2**1**·HOTf. The X-ray crystal structure is consistent with the specific shielding effects seen in the ^{1}H NMR spectra, including the upfield shift of the signal for the pyridinium proton (see Figure 4c) as a consequence of other hydrogen-bond donors binding to the triflate anion, and with the noncovalent binding of the sulfonic acid acting as a transient steric barrier to shuttling of the macrocycle between the two halves of the thread.[12] In contrast (Scheme 2), a 1:1 mixture of H_2**3a** and **3b**H^+TfO^- in $CDCl_3$ shows neither upfield shift of resonances H_c, H_d, and H_e (compare Figure 4b with the spectrum of the protonated thread in Figure 4c) nor downfield shifts of the protons from the amide groups in H_2**3a**. Similarly, the absence of shifts in the amide resonances of the protonated covalently linked structure H_2**4**·H^+TfO^- suggests that it does not internally associate through hydrogen bonding.

The mechanically interlocked assemblies also differ from their noninterlocked counterparts in their ability to adopt a range of overall neutral binding modes with metals. Treatment of H_2**1** or H_2**2** with $Cu(OAc)_2$ in MeOH/CH_2Cl_2 with heating at reflux resulted in double deprotonation of the ligand and the generation of the corresponding 1:1 neutral metal-interlocked ligand complex. Recrystallization of the copper [2]rotaxane complex, Cu**1**, from acetonitrile gave single crystals that were suitable for X-ray crystallographic studies (Figure 5b). The solid-state structure shows a square-based pyramidal coordination motif that involves one of the thread oxygen atoms as well as the four nitrogen atoms of the rotaxane which form the near-planar base of the pyramid (N47 lies approximately 10° above the plane defined by N2-N11-N5-Cu). Treatment of H_2**3a**/**3b** or H_2**4** with $Cu(OAc)_2$ under the same conditions gave no indication of formation of a complex nor deprotonation of the amide groups of the macrocycle.

The synthesis of complexes of the mechanically interlocked ligands with nickel required more vigorous conditions ($[Ni(dmf)_6](ClO_4)_2$, NaH, DMF, 60 °C, 1 h) but nonetheless resulted in Ni**1** and Ni**2**, both isolated as orange crystalline compounds. In this case, a similarly colored complex could also be generated with H_2**3a**/**3b**, but unlike Ni**1** or Ni**2** the isolated compound rapidly decomposed and we were unable to isolate or characterize it. The X-ray crystal structure of single crystals of Ni**1** grown from slow cooling of a saturated

 © 2005 Wiley-VCH Verlag GmbH & Co. KGaA, Weinheim

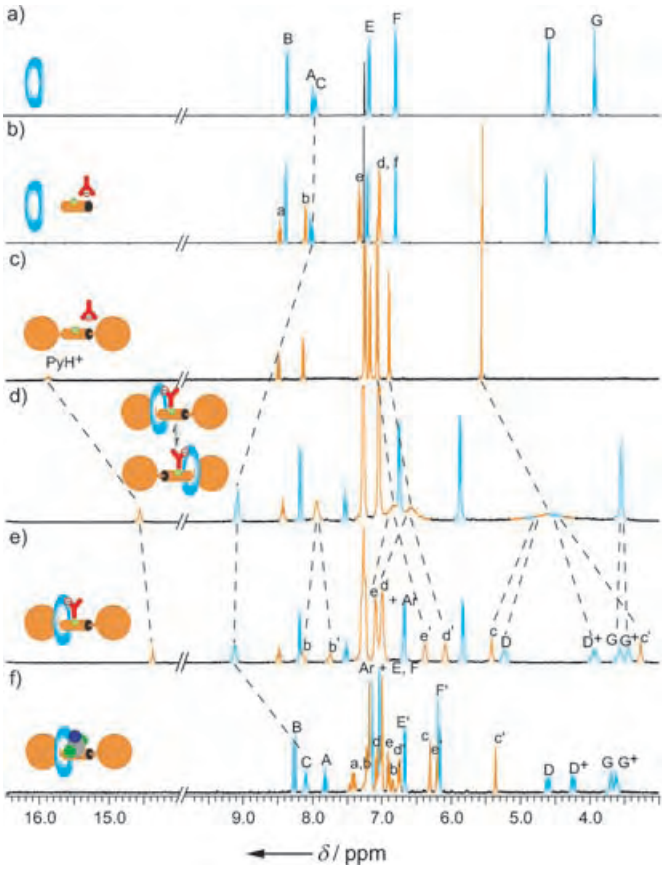


Figure 4. ^{1}H NMR spectra ($CDCl_3$, 400 MHz, 298 K unless otherwise stated): a) macrocycle H_2**3a**; b) H_2**3a** and unstoppered thread **3b** and HOTf; c) thread and HOTf (Py = pyridine); d) [2]rotaxane complex H_2**1**·HOTf showing fast exchange (shuttling) of the macrocycle between equivalent sites on both halves of the thread; e) [2]rotaxane complex H_2**1**·HOTf at 238 K showing slow exchange (reversible noncovalent bonding of the triflate anion provides a transient steric barrier to shuttling); f) [Pd(H_2**1**)Cl_2(MeCN)] showing slow exchange (coordination of [$PdCl_2$(MeCN)] provides a fixed steric barrier to shuttling up to at least 325 K). See Figure 2 for atom labeling scheme.

solution in acetonitrile is shown in Figure 5c and is closely related to the structure obtained for Cu**1**. Treatment of any of the rotaxane or catenane metal complexes with KCN in CH_2Cl_2/MeOH regenerated the original interlocked molecule, H_2**1** or H_2**2**. The differences in both the ease of formation and the stability of the metal complexes with the catenane and rotaxane relative to the noninterlocked ligands is, again,

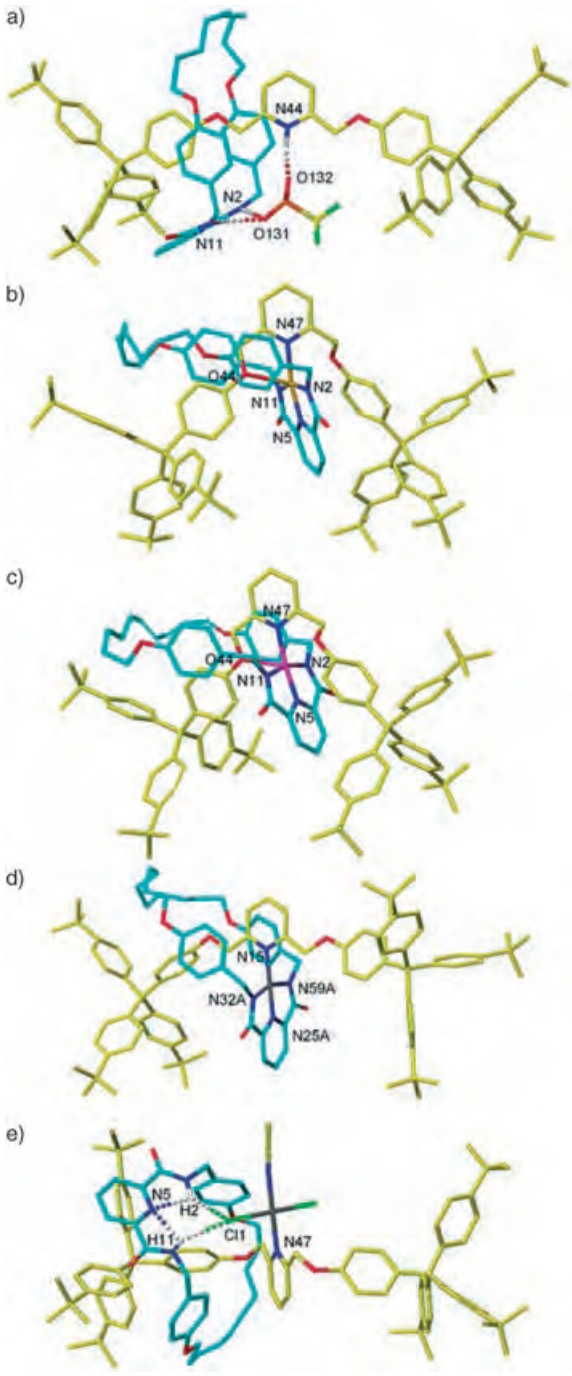
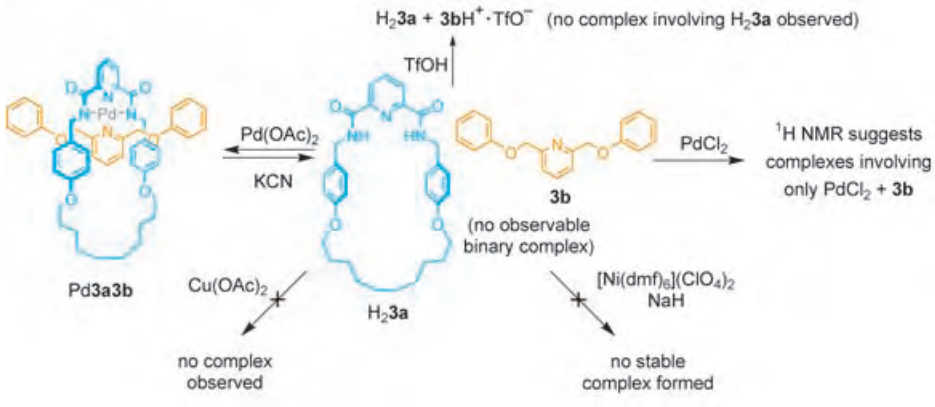


Figure 5. X-ray crystal structures[7] of various complexes of **1**: a) neutral [2]rotaxane–triflic acid complex, H_2**1**·HOTf. Note the macrocycle is displaced to one side of the central region of the thread relative to free H_2**1** (Figure 3b); b) square-pyramidal coordination complex Cu**1**; c) square-pyramidal coordination complex Ni**1**; d) square-planar coordination complex Pd**1**; e) square-planar coordination complex [Pd(H_2**1**)Cl_2(MeCN)]. C (macrocycle) turquoise; C (thread) yellow; O red; N dark blue; H white; S orange; F light green; Cl dark green; Cu tan; Ni pink; Pd dark gray. For clarity only amide hydrogen atoms are shown. Selected hydrogen-bond lengths [Å] for H_2**1**·HOTf: N2H–O131 2.14; N11H–O131 2.17; N44H–O132 1.72. Selected bond angles [°] for H_2**1**·HOTf:N2H-O131 159.0; N11H-O131 148.1; N44H-O132 159.7. Selected bond lengths [Å] for Cu**1**: N2–Cu 2.00; N11–Cu 1.98; N5–Cu 1.92; N47–Cu 2.02; O44–Cu 2.41. Selected bond angles [°] for Cu**1**: N2-Cu-N5 80.3; N5-Cu-N11 80.7; N11-Cu-N47 101.3; N5-Cu-O44 116.6; N5-Cu-N47 169.7. Selected bond lengths [Å] for Ni**1**: N2–Ni 1.94; N11–Ni 1.93; N5–Ni 1.81; N47–Ni 1.93; O44-Cu 2.52. Selected bond angles [°] for Ni**1**: N2-Ni-N5 82.6; N5-Ni-N11 82.4; N11-Ni-N47 98.5; N5-Ni-O44 113.8; N5-Ni-N47 172.1. Selected bond lengths [Å] for Pd**1**: Pd–N15 1.95, Pd–N25 1.86, Pd–N32 2.04, Pd–N59 2.02, N15–N25 3.81. Selected bond angles [°] for Pd**1** N59-Pd-N32 160.0. Selected bond lengths [Å] for [Pd(H_2**1**)Cl_2(MeCN)]: Pd–N47 1.98, Pd–Cl1 2.27, Cl1–H2 2.67, Cl1–H11 2.64, N5–H2 2.36, N5–H11 2.15. Selected bond angles [°] for [Pd(H_2**1**)Cl_2(MeCN)]: N2-H2-Cl1 139.8, N11-H11-N5 114.1, N11-H11-Cl1 125.0.

 © 2005 Wiley-VCH Verlag GmbH & Co. KGaA, Weinheim



Scheme 2. Attempted complexation experiments involving H_2**3a**/**3b**. Similar results were obtained with macrocycle H_2**4** (for an X-ray crystal structure of Pd**4**, see ref. [12]).

consistent with the intrinsic effect of kinetic stabilization of a mechanically interlocked architecture (Figure 1c).

Each of the four ligand sets reacts with $Pd(OAc)_2$ (H_2**1**, H_2**2**, and H_2**4** directly in $MeCN/CH_2Cl_2$; H_2**3a**/**3b** requires preliminary reaction of $Pd(OAc)_2$ with H_2**3a** in MeCN followed by treatment of the resulting complex with **3b** in CH_2Cl_2) to give the corresponding square-planar coordination complexes (Schemes 1 and 2 and Figure 5d). However, the rotaxane and catenane also formed a different type of neutral square-planar coordination complex when treated with $PdCl_2$, an initial palladium salt that features significantly stronger coordinating ligands (chloride is also less basic than acetate). Slow cooling of saturated solutions of either complex in acetonitrile afforded crystals that were suitable for X-ray crystallography, and the structure of the rotaxane complex, $[Pd(H_2$**1**$)Cl_2(MeCN)]$, is shown in Figure 5e (the solid-state structure of the [2]catenane complex is similar but features intermolecular rather than intramolecular NH···Cl–Pd hydrogen bonding). From the crystal structures it can be seen that although Pd coordinates to the thread as in Pd**1**, the original metal chloride ligands remain intact and the macrocycle amides are not deprotonated. In solution the coordination of the $[PdCl_2(MeCN)]$ unit to the pyridine ring of the thread acts as a steric barrier to shuttling (Figure 4f). This is similar to the effect seen with H_2**1**·TfOH, but unlike the complex held together by hydrogen bonds the coordination to the metal is not kinetically labile and persists as a barrier to shuttling up to at least 325 K (close to the boiling point of the solvent $CDCl_3$).[11]

The solid-state structure of $[Pd(H_2$**1**$)Cl_2(MeCN)]$ features hydrogen bonding between the amide groups of the macrocycle and the chloride ligands of the metal (Figure 5e). However, the ^{1}H NMR spectrum shows that this interaction is not present to any significant extent in $CDCl_3$ (the chemical shift of H_C is virtually unchanged compared to H_2**3a**; Figure 4f). Wisner and co-workers recently used a similar interaction to direct an elegant synthesis of a pseudorotaxane.[13] During the course of that work, a macrocycle binding constant that largely results from two sets of isophthalamide groups hydrogen bonding to the chloride ligands of a Pd^{II} complex was determined to be $5\times10^3\,M^{-1}$ in $CDCl_3$.[13] In contrast, Crabtree and co-workers determined the association constant for a single isophthalamide group with Cl^- to be $6\times10^4\,M^{-1}$ in CD_2Cl_2.[14] Accordingly, a C(O)NH···Cl–Pd interaction must be somewhat less than half the strength of a C(O)NH···Cl^- hydrogen bond. This is consistent with the observation that the interaction is too weak to significantly bind the macrocycle in $[Pd(H_2$**1**$)Cl_2(MeCN)]$ in $CDCl_3$, despite the high effective molarity introduced by the mechanical bond, and is in marked contrast to the effective bifurcated pyridine–pyridine hydrogen bonding in H_2**1**. This suggests that the intercomponent binding mode in H_2**1** is not particularly weak and its scarcity as an observed interaction may arise because the geometry of the interlocked architecture precludes otherwise preferred noncovalent bonding geometries.

In conclusion, the kinetically enforced association of molecular fragments within an interlocked architecture facilitates the formation of diverse, and sometimes rare and unusual, binding motifs both in solution and the solid state. These interactions can produce interesting effects in their own right; the cooperative hydrogen bonding of an organic guest by both components of a [2]rotaxane can present an effective barrier to shuttling at low temperatures, whereas a stronger metal–ligand coordination mode can be used to restrict the same motion even at higher temperatures. The fact that many of the observed modes of binding are weaker or not seen at all when the components are not mechanically interlocked makes this consequence of the mechanical bond particularly noteworthy.[15]

Received: January 1, 2005
Revised: February 18, 2005
Published online: June 23, 2005

Keywords: catenanes · coordination modes · hydrogen bonds · noncovalent interactions · rotaxanes

 © 2005 Wiley-VCH Verlag GmbH & Co. KGaA, Weinheim

[1] For reviews, see: a) *Molecular Catenanes, Rotaxanes, and Knots: A Journey Through the World of Molecular Topology* (Eds.: J.-P. Sauvage, C. Dietrich-Buchecker), Wiley-VCH, Weinheim, **1999**; b) V. Balzani, A Credi, F. M. Raymo, J. F. Stoddart, *Angew. Chem.* **2000**, *112*, 3484–3530; *Angew. Chem. Int. Ed.* **2000**, *39*, 3348–3391; c) V. Balzani, M. Venturi, A. Credi, *Molecular Devices and Machines—A Journey into the Nanoworld*, Wiley-VCH, Weinheim, **2003**; d) A. H. Flood, R. J. A. Ramirez, W.-Q. Deng, R. P. Muller, W. A. Goddard, J. F. Stoddart, *Aust. J. Chem.* **2004**, *57*, 301–322; e) "Synthetic Molecular Machines": E. R. Kay, D. A. Leigh in *Functional Artificial Receptors* (Eds.: T. Schrader, A. D. Hamilton), Wiley-VCH, Weinheim, **2005**, 333–406.

[2] For examples in which encapsulation and/or preorganization of the coordinating ligand geometry in a mechanically interlocked architecture can bring about significant property effects, see: (stabilization of oxidation state/complex geometry) a) C. O. Dietrich-Buchecker, J.-P. Sauvage, *J. Am. Chem. Soc.* **1984**, *106*, 3043–3045; b) N. Armaroli, L. De Cola, V. Balzani, J.-P. Sauvage, C. O. Dietrich-Buchecker, J.-M. Kern, A. Bailal, *J. Chem. Soc. Dalton Trans.* **1993**, 3241–3247; (protection of functional groups) c) D. Leigh, A. Murphy, J. P. Smart, A. M. Z. Slawin, *Angew. Chem.* **1997**, *109*, 752–756; *Angew. Chem. Int. Ed. Engl.* **1997**, *36*, 728–731; d) M. R. Craig, M. G. Hutchings, T. D. W. Claridge, H. L. Anderson, *Angew. Chem.* **2001**, *113*, 1105–1108; *Angew. Chem. Int. Ed.* **2001**, *40*, 1071–1074; e) J. E. H. Buston, F. Marken, H. L. Anderson, *Chem. Commun.* **2001**, 1046–1047; f) T. Oku, Y. Furusho, T. Takata, *Org. Lett.* **2003**, *5*, 4923–4925; g) D. A. Leigh, E. M. Pérez, *Chem. Commun.* **2004**, 2262–2263; (solubility) h) H. W. Gibson, S Liu, P. Lecavalier, C. Wu, Y. X. Shen, *J. Am. Chem. Soc.* **1995**, *117*, 852–874; i) A. G. Johnston, D. A. Leigh, A. Murphy, J. P. Smart, M. D. Deegan, *J. Am. Chem. Soc.* **1996**, *118*, 10662–10663; j) S. Anderson, H. L. Anderson, *Angew. Chem.* **1996**, *108*, 2075–2078; *Angew. Chem. Int. Ed. Engl.* **1996**, *35*, 1956–1959; (conformation of a component) k) W. Clegg, C. Gimenez-Saiz, D. A. Leigh, A. Murphy, A. M. Z. Slawin, S. J. Teat, *J. Am. Chem. Soc.* **1999**, *121*, 4124–4129; (electroluminescence) l) F. Cacialli, J. S. Wilson, J. J. Michels, C. Daniel, C. Silva, R. H. Friend, N. Severin, P. Samori, J. P. Rabe, M. J. O'Connell, P. N. Taylor, H. L. Anderson, *Nat. Mater.* **2002**, *1*, 160–164; (membrane transport) m) V. Dvornikovs, B. E. House, M. Kaetzel, J. R. Dedman, D. B. Smithrud, *J. Am. Chem. Soc.* **2003**, *125*, 8290–8301.

[3] A.-M. Fuller, D. A. Leigh, P. J. Lusby, I. D. H. Oswald, S. Parsons, D. B. Walker, *Angew. Chem.* **2004**, *116*, 4004–4008; *Angew. Chem. Int. Ed.* **2004**, *43*, 3914–3918.

[4] For a recent example of a [2]rotaxane that utilizes square-planar Pd^{II} coordination, see: I. Yoon, M. Narita, T. Shimizu, M. Asakawa, *J. Am. Chem. Soc.* **2004**, *126*, 16740–16741.

[5] S. L. Jain, P. Bhattacharyya, H. L. Milton, A. M. Z. Slawin, J. A. Crayston, J. D. Woollins, *Dalton Trans.* **2004**, 862–871.

[6] F. Biscarini, M. Cavallini, D. A. Leigh, S. León, S. J. Teat, J. K. Y. Wong, F. Zerbetto, *J. Am. Chem. Soc.* **2002**, *124*, 225–233.

[7] Structural data for H_2**1**, Cu**1**, and Ni**1** were collected at 93 K using a Rigaku Saturn diffractometer (MM007 high-flux RA/$Mo_{K\alpha}$ radiation, confocal optic); for H_2**2** and $[Pd(H_2\mathbf{1})Cl_2$-(MeCN)] at 93 K using a Rigaku Mercury diffractometer (MM007 high-flux RA/$Mo_{K\alpha}$ radiation, confocal optic); and for H_2**1**·TfOH at 125 K using a Bruker SMART diffractometer (sealed tube $Mo_{K\alpha}$ radiation, graphite monochromator, $\lambda = 0.71073$ Å). All data collections employed narrow frames (0.3–1.0°) to obtain at least a full hemisphere of data. Intensities were corrected for Lorentz polarization and absorption effects (multiple equivalent reflections). Structures were solved by direct methods, non-hydrogen atoms were refined anisotropically with CH protons being refined in riding geometries (SHELXTL) against F^2. In most cases, amide protons were refined isotropically subject to a distant constraint. Any other restraints or additional features of the refinement are detailed for each structure below. The structure determination for H_2**1** proved particularly problematic; we collected full datasets using a variety of collection routines on more than 15 different crystals from several different crystallization experiments. The data were always poor, principally because of disorder arising from the alkyl chain and solvated molecules. The structure was refined isotropically with no protons included in the refinement. H_2**1**: $C_{112}H_{130}N_4O_6$, $M_r = 1628$, crystal size $= 0.2 \times 0.1 \times 0.03$ mm^3, orthorhombic, *Pbca*, $a = 18.338(4)$, $b = 23.545(5)$, $c = 44.922(9)$ Å, $V = 19396(7)$ Å^3, $Z = 8$, $\rho_{calcd} = 1.115$ Mg m^{-3}; $\mu = 0.068$ mm^{-1}, 18573 data (17303 unique), $R = 0.3339$ for F values of reflections with $F_o > 4\sigma F_o$), $S = 4.90$ for 463 parameters. Residual electron density extremes were 1.665 and −4.557 eÅ^{-3}. H_2**2**: $C_{62}H_{76}N_4O_8$, $M_r = 1005.27$, colorless prism, crystal size $= 0.2 \times 0.2 \times 0.2$ mm^3, triclinic, *P*-1, $a = 11.3539(11)$, $b = 12.0635(11)$, $c = 20.445(2)$ Å, $\alpha = 82.323(6)$, $\beta = 88.351(7)$, $\gamma = 80.397(7)$°, $V = 2736.2(5)$ Å^3, $Z = 2$, $\rho_{calcd} = 1.220$ Mg m^{-3}; $\mu = 0.080$ mm^{-1}, 15494 data (8824 unique, $R_{int} = 0.0176$), $R = 0.0499$, $S = 0.987$ for 677 parameters. Residual electron density extremes were 0.759 and −0.336 eÅ^{-3}. H_2**1**·TfOH: $C_{113}H_{131}F_3N_4O_9S$, $M_r = 1778.28$, colorless prism, crystal size $= 0.15 \times 0.1 \times 0.1$ mm^3, monoclinic, $P2_1/c$, $a = 20.555(2)$, $b = 18.7503(19)$, $c = 27.853(3)$ Å, $\beta = 109.574(2)$°, $V = 10114.6(17)$ Å^3, $Z = 4$, $\rho_{calcd} = 1.168$ Mg m^{-3}; $\mu = 0.096$ mm^{-1}, 59606 data (18472 unique, $R_{int} = 0.0449$), $R = 0.1058$, $S = 1.028$ for 1149 parameters. Residual electron density extremes were 1.366 and −0.649 eÅ^{-3}. Cu**1**: $C_{117}H_{135.5}CuN_{6.5}O_6$, $M_r = 1792.36$, violet platelet, crystal size $= 0.2 \times 0.1 \times 0.01$ mm^3, triclinic, *P*-1, $a = 16.404(3)$, $b = 17.516(3)$, $c = 20.046(4)$ Å, $\alpha = 100.573(3)$, $\beta = 106.016(3)$, $\gamma = 96.178(3)$°, $V = 5365.3(17)$ Å^3, $Z = 2$, $\rho_{calcd} = 1.109$ Mg m^{-3}; $\mu = 0.258$ mm^{-1}, 41166 data (17787 unique, $R_{int} = 0.0318$), $R = 0.1507$, $S = 1.812$ for 1163 parameters. Residual electron density extremes were 2.325 and −1.107 eÅ^{-3}. The half-weight acetonitrile solvent molecules were refined isotropically. Ni**1**: $C_{117}H_{137.5}N_{6.5}NiO_7$, $M_r = 1805.54$, orange needle, crystal size $= 0.15 \times 0.015 \times 0.015$ mm^3, triclinic, *P*-1 $a = 16.423(3)$, $b = 17.582(3)$, $c = 20.056(3)$ Å, $\alpha = 100.0161(19)$, $\beta = 106.234(3)$, $\gamma = 96.2695(18)$°, $V = 5398.6(15)$ Å^3, $Z = 2$, $\rho_{calcd} = 1.111$ Mg m^{-3}; $\mu = 0.235$ mm^{-1}, 40853 data (17841 unique, $R_{int} = 0.0506$), $R = 0.1302$, $S = 1.465$ for 1184 parameters. Residual electron density extremes were 1.874 and −0.891. The half-weight acetonitrile and quarter-weight water solvent molecules were refined isotropically. The protons on all solvated molecules were discounted in the refinement. $[Pd(H_2\mathbf{1})Cl_2(MeCN)]$: $C_{122}H_{145}N_9O_6Cl_2Pd$, $M_r = 2010.77$, yellow platelet, crystal size $= 0.2 \times 0.1 \times 0.01$ mm^3, monoclinic, *C*2/*c*, $a = 29.6525(12)$, $b = 23.2314(10)$, $c = 32.6559(14)$ Å, $\beta = 99.071(3)$°, $V = 22214.3(16)$ Å^3, $Z = 8$, $\rho_{calcd} = 1.202$ Mg m^{-3}; $\mu = 0.273$ mm^{-1}, 58779 data (19158 unique, $R_{int} = 0.1733$), $R = 0.1416$, $S = 1.090$ for 1253 parameters. Residual electron density extremes were 0.946 and −0.925 eÅ^{-3}. The half-weight acetonitrile solvent molecules were refined isotropically. The protons on solvated molecules were discounted in the refinement. CCDC 259162–259166 contain the supplementary crystallographic data for this paper. These data can be obtained free of charge from the Cambridge Crystallographic Data Centre via www.ccdc.cam.ac.uk/data_request/cif.

[8] F. G. Gatti, D. A. Leigh, S. A. Nepogodiev, A. M. Z. Slawin, S. J. Teat, J. K. Y. Wong, *J. Am. Chem. Soc.* **2001**, *123*, 5983–5989.

[9] J. S. Hannam, S. M. Lacy, D. A. Leigh, C. G. Saiz, A. M. Z. Slawin, S. G. Stitchell, *Angew. Chem.* **2004**, *116*, 3322–3326; *Angew. Chem. Int. Ed.* **2004**, *43*, 3260–3264.

 © 2005 Wiley-VCH Verlag GmbH & Co. KGaA, Weinheim

[10] D. J. Cram, *Angew. Chem.* **1988**, *100*, 1041 – 1052; *Angew. Chem. Int. Ed. Engl.* **1988**, *27*, 1009 – 1020.
[11] For temporary steric barriers to shuttling, see: a) A. S. Lane, D. A. Leigh, A. Murphy, *J. Am. Chem. Soc.* **1997**, *119*, 11092 – 11093; b) L. Jiang, J. Okano, A. Orita, J. Otera, *Angew. Chem.* **2004**, *116*, 2173 – 2176; *Angew. Chem. Int. Ed.* **2004**, *43*, 2121 – 2124.
[12] A.-M. L. Fuller, D. A. Leigh, P. J. Lusby, A. M. Z. Slawin, D. B. Walker, unpublished results.
[13] B. A. Blight, K. A. Van Noortwyck, J. A. Wisner, M. C. Jennings, *Angew. Chem.* **2005**, *117*, 1523 – 1528; *Angew. Chem. Int. Ed.* **2005**, *44*, 1499 – 1504.
[14] K. Kavallieratos, S. R. de Gala, D. J. Austin, R. H. Crabtree, *J. Am. Chem. Soc.* **1997**, *119*, 2325 – 2326.
[15] *Note added in proof*: A paper recently appeared (Y. Furusho, T. Matsuyama, T. Takata, T. Moriuchi, T. Hirao, *Tetrahedron Lett.* **2004**, *45*, 9593 – 9597) that reproduces some of the previous work[3] on the square-planar template rotaxane system. Although the authors do not comment on it, the ^{1}H NMR chemical shifts show that the bifurcated pyridine–pyridine hydrogen-bonding motif also exists in their demetalated rotaxane.

 © 2005 Wiley-VCH Verlag GmbH & Co. KGaA, Weinheim

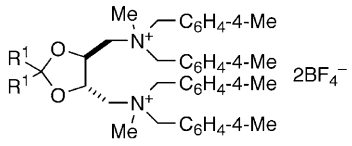
Phase-Transfer Catalysis

Enantio- and Diastereoselective Catalytic Mannich-Type Reaction of a Glycine Schiff Base Using a Chiral Two-Center Phase-Transfer Catalyst**

Akihiro Okada, Tomoyuki Shibuguchi, Takashi Ohshima, Hyuma Masu, Kentaro Yamaguchi, and Masakatsu Shibasaki**

α,β-Diamino acids are key structural components in molecules such as peptides and β-lactam antibiotics and in medicinally relevant compounds;[1,2] for example, 2,3-diamino-3-phenylpropanoic acid is used as an advanced alternative to the side chain of taxol to improve its water solubility.[3] Various methods for the preparation of optically active α,β-diamino acid derivatives have been reported. Almost all of them, however, require the use of stoichiometric amounts of chiral sources. One common method involves the displacement of the hydroxy group of serine derivatives with an azide moiety followed by reduction of the azide group,[1,4] and another is the addition of glycine ester derivatives to chiral *N*-sulfinyl imines.[5,6] Jørgensen and co-workers reported an efficient catalytic method that relies on the aza-Henry reaction of silyl nitronates with imines.[7] The catalytic asymmetric synthesis of chiral serine derivatives by the Sharpless asymmetric aminohydroxylation reaction is another useful method.[8] Recently, more direct and atom-economically favorable methods using a Mannich-type reaction of a glycine Schiff base with imines were reported by Jørgensen and co-workers[9] and Maruoka and co-workers.[10] Although these methods are highly enantioselective, there is still much room for improvement. For example, the removal of *para*-toluenesulfonate (tosyl) groups is difficult in the method of Jørgensen and co-workers, and low substrate generality is a problem in the method of Maruoka and co-workers. Both methods are also only moderately diastereoselective. Herein, we report a new direct method to access a variety of optically active *syn*-α,β-diamino acid derivatives by a Mannich-type reaction of a glycine Schiff base that uses a new chiral two-center phase-transfer catalyst. The selection of the imine-protecting group was pivotal to achieving high diastereoselectivity (up to 99:1). Moreover, the usefulness of the obtained products was successfully demonstrated by their transformation into a tripeptide and the key intermediate of CP-99,994 through chemoselective deprotection of the *N*-diphenylmethylene and *N*-*tert*-butoxycarbonyl (Boc) protecting groups.

To develop efficient methods for the synthesis of α,β-diamino acid derivatives, we used Mannich protocols under asymmetric phase-transfer reaction conditions because of the preparative advantages of the phase-transfer process, such as simple procedures and mild conditions.[11] Recently, we developed the tartrate-derived diammonium salt (TaDiAS) **1**, which efficiently catalyzes asymmetric phase-transfer alkylations and Michael reactions of a glycine Schiff base **2**.[12]



(*S*,*S*)-TaDiAS **1a**: R^1 = Pr
1b: R^1 = Bu

We initially examined a Mannich-type reaction of **2** using *N*-diphenylphosphinoyl (dpp) imine **3a** as an electrophile because the dpp group can be readily removed under mild conditions.[13] Under phase-transfer conditions using TaDiAS **1b**, which is a suitable catalyst for asymmetric phase-transfer Michael reactions,[12] and fluorobenzene and cesium carbonate were determined to be the best solvent and base, respectively; this reaction afforded the desired Mannich

[*] A. Okada, T. Shibuguchi, Dr. T. Ohshima, Prof. Dr. M. Shibasaki
Graduate School of Pharmaceutical Sciences
The University of Tokyo
Hongo, Bunkyo-ku, Tokyo 113-0033 (Japan)
Fax: (+81) 3-5684-5206
E-mail: ohshima@chem.es.osaka-u.ac.jp
mshibasa@mol.f.u-tokyo.ac.jp
Dr. H. Masu, Prof. Dr. K. Yamaguchi
Faculty of Pharmaceutical Sciences at Kagawa Campus
Tokushima Bunri University
Shido, Sanuki-city, Kagawa 769-2193 (Japan)

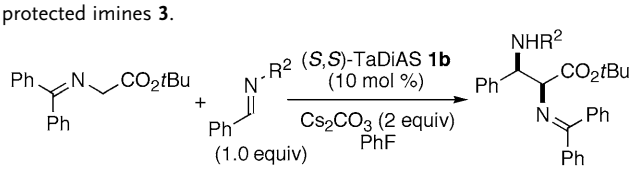
[**] This work was supported by RFTF, a Grant-in-Aid for the Encouragement of Young Scientists (A), and a Grant-in-Aid for Specially Promoted Research from the Japanese Society for the Promotion of Science (JSPS) and the Ministry of Education, Culture, Sports, Science, and Technology (MEXT).

Supporting information for this article is available on the WWW under http://www.angewandte.org or from the author.

 © 2005 Wiley-VCH Verlag GmbH & Co. KGaA, Weinheim DOI: 10.1002/anie.200500927

product **4a** in high yield (95%) and moderate selectivity (*syn*/*anti* = 77:23, 51% *ee*; Table 1, entry 1).[14] Various N-protected imines were screened under the optimized conditions (Table 1, entries 2–5). Although the reaction did not proceed

Table 1: Catalytic asymmetric Mannich-type reaction with various *N*-protected imines **3**.



2 **3a–e** **4a–e**

Entry	Imine **3**	R^2	*T* [°C]	*t* [h]	Yield [%]	d.r. [*syn*/*anti*][a]	*ee* [%][b]
1	**3a**	dpp	4	2	95	77:33	51
2	**3b**	$CHPh_2$	RT	72	n.r.[c]		
3	**3c**	CH_2Ph	RT	72	n.r.[c]		
4	**3d**	Boc	4	2	quant	>95:5	53
5	**3e**	tosyl	RT	2.5	97	70:30	0

[a] Determined by HPLC analysis. [b] The *ee* value of the *syn* product was determined by HPLC analysis. [c] n.r. = no reaction.

when diphenylmethyl imine **3b** (Table 1, entry 2) and benzyl imine **3c** (Table 1, entry 3) were used, *N*-Boc imine **3d** (Table 1, entry 4) gave the product **4d** in quantitative yield with high diastereoselectivity (*syn*/*anti* = >95:5) and moderate enantioselectivity (53% *ee*). These results suggested that the electron-withdrawing imine-protecting group plays an important role in the reactivity. On the other hand, the *N*-tosyl imine was less reactive and produced a low enantioselectivity (Table 1, entry 5). Thus, we chose the *N*-Boc imine **3d** as a substrate for further investigation because of these results and the fact that a Boc protecting group can be readily removed.

We next examined the structure of the catalyst to improve enantioselectivity. We had previously synthesized a variety of TaDiAS salts **1**, and they had been examined in catalytic asymmetric phase-transfer alkylations and Michael reactions. However, rational design of the catalyst was still difficult because of the lack of conformational information about **1**, except for preliminary computational analysis that suggested the formation of a tight ion complex between the two cation centers in **1** and the enolate of **2**. Thus, on the basis of the above analysis, we performed a conformational investigation of **1**. Although no useful information was obtained by NMR spectroscopy, the structure of **1a** was determined by X-ray crystallographic analysis. A tetrafluoroborate anion is situated very close to each of the ammonium units, thus creating an attractive C_2-symmetrical chiral environment (Figure 1). Another interesting fact is that the alkyl chains of the acetal moiety snake up in a direction perpendicular to the dioxolane ring. A previous examination of substituent effects in asymmetric phase-transfer catalysis revealed that both aromatic and acetal moieties strongly affected enantioselectivity. This unexpected substituent effect by the acetal moiety can be understood from the proximity of the counteranions to the

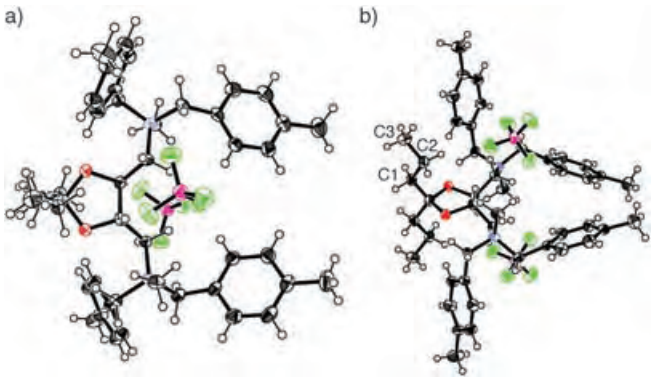
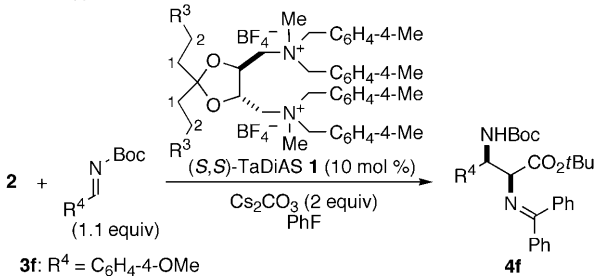


Figure 1. Crystal structure of (*S*,*S*)-TaDiAS (**1a**). a) Top view and b) side view.

acetal side chains, especially to the C2 and C3 positions (Figure 1b).

In the reaction, the enolate of **2** was expected to be replaced with the BF_4^- ion and form a tight complex with the cationic centers of **1**. Therefore, we assumed that longer or more sterically congested acetal substituents would prevent an unfavorable approach by the imines to the enolate of **2**. On the basis of this hypothesis, the substituent effects of the acetal moiety were examined (Table 2).[15] As expected, the

Table 2: Optimization of the catalyst structure for the asymmetric Mannich-type reaction.



3f: $R^4 = C_6H_4$-4-OMe **4f**

Entry	Cat. **1**	R^3	*T* [°C]	*t* [h]	Yield [%]	d.r. [*syn*/*anti*][a]	*ee* [%][b]
1	**1a**	H	4	1	96	>95:5	58
2	**1b**	Me	4	1	quant	>95:5	59
3	**1c**	Ph	4	0.5	quant	98:2	62
4	**1d**	CH_2Ph	4	0.5	quant	>95:5	57
5	**1e**	4-$tBuC_6H_4$	4	0.5	quant	98:2	60
6	**1f**	2,4,6-$Me_3C_6H_2$	4	0.5	97	98:2	48
7	**1g**	4-FC_6H_4	4	0.5	99	97:3	65
8[c]	**1g**	4-FC_6H_4	−45	48	95	95:5	82

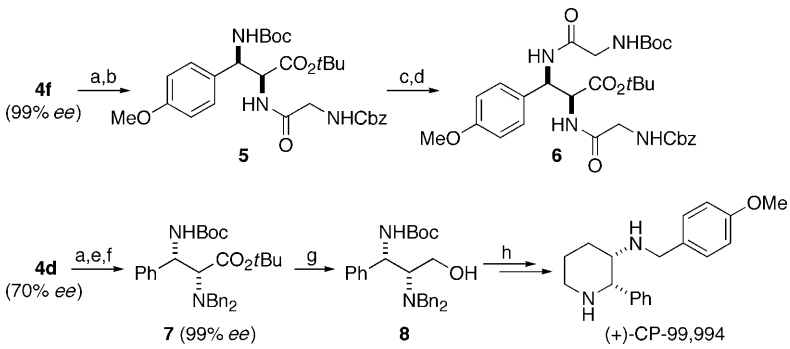
[a] Determined by HPLC analysis. [b] The *ee* value of the *syn* product was determined by HPLC analysis. [c] Solvent was PhF/pentane (4:1).

introduction of an aromatic ring at the C2 positions of the acetal side chains improved the enantioselectivity (Table 2, entry 3). On the other hand, the introduction of a benzyl group at C2, which results in an aromatic ring at the C3 position (Table 2, entry 4), and a bulky substituent at C2 (Table 2, entry 6) gave only moderate enantioselectivity. Finally, the best results were obtained from the use of the 4-fluorophenyl-substituted catalyst **1g** (Table 2, entry 7), which

 © 2005 Wiley-VCH Verlag GmbH & Co. KGaA, Weinheim

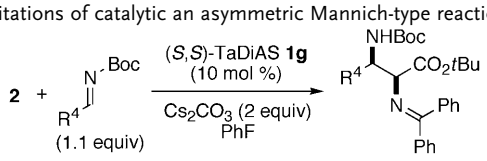
suggests the possibility of π–π interactions.[16] Performing the latter reaction at lower temperature (−45 °C) further improved the enantioselectivity to 82 % *ee* (Table 2, entry 8).

We examined the scope and limitations of the reaction under the optimized conditions using various *N*-Boc imines. As summarized in Table 3, all the asymmetric Mannich-type reactions proceeded in high yield with high diastereoselectivity (*syn*/*anti* = 95:5–99:1) when 10 mol % of TaDiAS **1g** was used with Cs_2CO_3 in fluorobenzene. In terms of enantioselectivity, *C*-phenyl imine derivatives with an electron-donating group at the 4-position were suitable substrates (Table 3, entries 2 and 3). On the other hand, 4-chlorophenyl and 2-naphthyl substituents (Table 3, entries 7 and 8) were only moderately enantioselective.



Scheme 1. Syntheses of tripeptide **6** and the key intermediate **8** of CP-99,994. Reagents and conditions: a) 0.5 M citric acid, THF, RT; b) *N*-Cbz-gly, WSC, HOBt, CH_2Cl_2, 4 °C (90 % over 2 steps); c) 2 N HCl, MeOH, RT; d) *N*-Boc-gly, WSC, HOBt, CH_2Cl_2, 4 °C (92 % over 2 steps); e) BnBr, K_2CO_3, THF, reflux; f) recrystallization from EtOAc/hexane (42 % over 3 steps, 99 % *ee*); g) $LiAlH_4$, 4 → 40 °C (91 %); h) see ref. [19] Cbz = carbobenzoxy, Bn = benzyl, gly = glycine, HOBt = 1-hydroxybenzotriazole, WSC = *N*-ethyl-*N*′-(3-dimethylaminopropyl)carbodiimide.

Table 3: Scope and limitations of catalytic an asymmetric Mannich-type reaction.



Entry	Imine **3**	R^4	*T* [°C]	*t* [h]	Yield [%]	d.r. [*syn*/*anti*][a]	*ee* [%][b]
1	**3d**	Ph	−30	19	98	99:1	70
2[c]	**3f**	4-OMe-C_6H_4	−45	48	95	95:5	82 (99)[d]
3	**3g**	4-Me-C_6H_4	−40	48	98	98:2	80
4[c]	**3h**	3-Me-C_6H_4	−45	72	96	95:5	70
5	**3i**	2-Me-C_6H_4	−20	66	99	97:3	68
6	**3j**	4-F-C_6H_4	−40	48	99	98:2	72
7	**3k**	4-Cl-C_6H_4	−20	20	87	98:2	58
8	**3l**	2-naphthyl	−20	72	87	> 95:5	60
9	**3m**	2-thiophenyl	−40	48	98	98:2	80
10	**3n**	(*E*)-PhCH=CH_2	−30	48	86	98:2	66

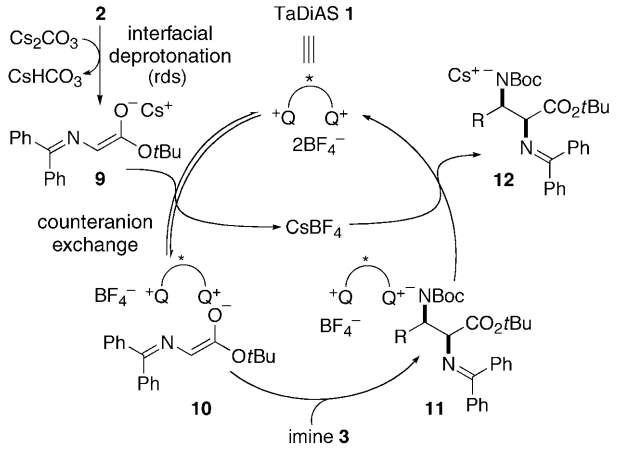
[a] Determined by HPLC analysis. [b] The *ee* value of the *syn* product was determined by HPLC analysis. [c] Solvent was PhF/pentane (4:1). [d] The *ee* value after a single recrystallization.

Although *N*-Boc C-aliphatic imines could not be applied because of the difficulties in synthesizing them, the use of α,β-unsaturated imines for the Mannich-type reaction followed by hydrogenation is an alternative method (Table 3, entry 10). Another beneficial feature of this process is that most of the products were obtained as crystalline solids, and in fact a single recrystallization of **4f** (82 % *ee*) provided an optically pure compound in 74 % yield. Although the enantioselectivity of the reaction was not very satisfactory, to the best of our knowledge, this diastereoselectivity is the highest reported for a catalytic Mannich-type reaction of a glycine Schiff base **2** with imines.

The synthetic utility of the resulting optically active α,β-diamino acid derivatives was demonstrated by straightforward transformations into tripeptide **6** and key intermediate **8** for the synthesis of the selective and potent neurokinin substance P antagonist (+)-CP-99,994[17–19] through deprotection of the *N*-diphenylmethylene and *N*-Boc groups (Scheme 1, top). Highly chemoselective deprotection of the *N*-diphenylmethylene group of **4f** by aqueous citric acid, followed by a subsequent peptide-coupling reaction gave dipeptide **5**. Next, the *N*-Boc group was readily deprotected with a 2 N solution of HCl in methanol to afford, after another peptide-coupling reaction, the optically pure tripeptide **6** in good yield. Moreover, the protected α,β-diamino ester **4d**, which was synthesized by using (*R*,*R*)-TaDiAS **1g**, was successfully converted into the key intermediate **8**[19] in an optically pure form (Scheme 1, bottom).

Information about the reaction mechanism is essential to improve the efficiency of the catalyst, TaDiAS **1**. Despite the value of mechanistic investigations in catalyst development, however, only limited mechanistic studies on asymmetric phase-transfer catalysis have been reported.[20] To gain insight into the mechanism of this asymmetric phase-transfer catalytic reaction, we performed initial rate kinetic studies.[21] First-order dependency was observed for the glycine Schiff base **2** and Cs_2CO_3, whereas the reaction rate had zero-order dependency for the imine **3** and the catalyst **1**. These results indicated that the rate-determining step of the Mannich-type reaction is deprotonation of **2** by Cs_2CO_3; unexpectedly, **1** was not involved in this step. On the basis of these results, we propose a catalytic cycle for the asymmetric Mannich-type reaction (Scheme 2). Deprotonation of **2** by Cs_2CO_3 at the interface between the liquid and solid phase followed by counteranion exchange with the catalyst **1** gives complex **10**.[22] An asymmetric C–C bond-forming reaction of **10** with the imine **3** gives the Mannich product **11**. Finally, counteranion exchange between **11** and the resulting $CsBF_4$ provides **12** and generates **1**. The very low reaction efficiency that results from the use of a catalytic amount of Cs_2CO_3 indicates that the formation of **10** through direct deprotonation of **2** in

 © 2005 Wiley-VCH Verlag GmbH & Co. KGaA, Weinheim



Scheme 2. Proposed catalytic cycle of the asymmetric Mannich-type reaction. rds = rate-determining step.

the liquid phase with **11** or a hydroxide complex of the chiral ammonium cation is slow, thus making the interfacial deprotonation (**2**→**9**) the rate-determining step.

In summary, we have developed a highly efficient (up to quantitative yield) and *syn*-selective (up to 99:1) enantio- and diastereoselective catalytic Mannich-type reaction of a glycine Schiff base **2** with *N*-Boc imines **3** using the newly designed phase-transfer catalyst **1g**. Moreover, we have demonstrated the synthetic utility of the α,β-diamino acid products. Further mechanistic studies and investigations to improve the enantioselectivity are in progress.

Received: March 14, 2005
Published online: June 14, 2005

Keywords: amino acids · asymmetric catalysis · Mannich reaction · phase-transfer catalysis · Schiff bases

[1] Y. Luo, M. A. Blaskovich, G. A. Lajoie, *J. Org. Chem.* **1999**, *64*, 6106, and references therein.
[2] a) N. Subasinghe, M. Shulte, R. J. Roon, J. F. Koerner, R. L. Johnson, *J. Med. Chem.* **1992**, *35*, 4602; b) M. Wang, S. J. Gould, *J. Org. Chem.* **1993**, *58*, 5176; c) E. S. Lee, J. Jurayj, M. Cushman, *Tetrahedron* **1994**, *50*, 9873.
[3] F. M. Rossi, E. T. Powers, R. Yoon, L. Rosenberg, J. Meinwald, *Tetrahedron* **1996**, *52*, 10279.
[4] a) O. Mitsunobu, *Synthesis* **1981**, 1; b) M. Otsuka, A. Kittaka, T. Iimori, H. Yamashita, S. Kobayashi, M. Ohno, *Chem. Pharm. Bull.* **1985**, *33*, 509.
[5] a) A. Viso, R. Fernández de la Pradilla, C. Guerrero-Strachan, M. Alonso, M. Martínez-Ripoll, I. André, *J. Org. Chem.* **1997**, *62*, 2316; b) A. Viso, R. Fernández de la Pradilla, A. García, C. Guerrero-Strachan, M. Alonso, M. Tortosa, A. Flores, M. Martínez-Ripoll, I. Fonseca, I. André, A. Rodríguez, *Chem. Eur. J.* **2003**, *9*, 2867; c) A. Viso, R. Fernández de la Pradilla, M. L. López-Rodríguez, A. García, A. Flores, M. Alonso, *J. Org. Chem.* **2004**, *69*, 1542.
[6] F. A. Davis, J. Deng, *Org. Lett.* **2004**, *6*, 2789.
[7] K. R. Knudsen, T. Risgaard, N. Nishiwaki, K. V. Gothelf, K. A. Jørgensen, *J. Am. Chem. Soc.* **2001**, *123*, 5843.
[8] a) H. Han, J. Yoon, K. D. Janda, *J. Org. Chem.* **1998**, *63*, 2045; b) S.-H. Lee, J. Yoon, S.-H. Chung, Y.-S. Lee, *Tetrahedron* **2001**, *57*, 2139.
[9] L. Bernardi, A. S. Gothelf, R. G. Hazell, K. A. Jørgensen, *J. Org. Chem.* **2003**, *68*, 2583.
[10] T. Ooi, M. Kameda, J. Fujii, K. Maruoka, *Org. Lett.* **2004**, *6*, 2397.
[11] For recent reviews of asymmetric phase-transfer catalysis, see: a) M. J. O'Donnell, *Aldrichimica Acta* **2001**, *34*, 3; b) K. Maruoka, T. Ooi, *Chem. Rev.* **2003**, *103*, 3013; c) M. J. O'Donnell, *Acc. Chem. Res.* **2004**, *37*, 506; d) B. Lygo, B. I. Andrews, *Acc. Chem. Res.* **2004**, *37*, 518.
[12] a) T. Shibuguchi, Y. Fukuta, Y. Akachi, A. Sekine, T. Ohshima, M. Shibasaki, *Tetrahedron Lett.* **2002**, *43*, 9539; b) T. Ohshima, T. Shibuguchi, Y. Fukuta, M. Shibasaki, *Tetrahedron* **2004**, *60*, 7743; for application of the TaDiAS-catalyzed phase-transfer reaction to the synthesis of aeruginosins, see: c) T. Ohshima, V. Gnanadesikan, T. Shibuguchi, Y. Fukuta, T. Nemoto, M. Shibasaki, *J. Am. Chem. Soc.* **2003**, *125*, 11206; d) Y. Fukuta, T. Ohshima, V. Gnanadesikan, T. Shibuguchi, T. Nemoto, T. Kisugi, T. Okino, M. Shibasaki, *Proc. Natl. Acad. Sci. USA* **2004**, *101*, 5433.
[13] a) R. Ramage, D. Hopton, M. J. Parrott, G. W. Kenner, G. A. Moore, *J. Chem. Soc. Perkin Trans. 1* **1984**, 1357; b) R. Ramage, B. Atrash, D. Hopton, M. J. Parrott, *J. Chem. Soc. Perkin Trans. 1* **1985**, 1217; c) H. M. I. Osborn, J. B. Sweeney, *Synlett* **1994**, 145.
[14] The absolute configuration of **4a** was determined to be the *S* enantiomer by optical rotation studies of the cyclic urea derived from **4a**; see ref. [5b] and the Supporting Information for details.
[15] Modification of the aromatic moiety gave only unsatisfactory results.
[16] a) U.-H. Dolling, P. Davis, E. J. J. Grabowski, *J. Am. Chem. Soc.* **1984**, *106*, 446; b) S.-S. Jew, Mi.-S. Yoon, B.-S. Jeong II, Y. Park, H.-G. Park, *Org. Lett.* **2002**, *4*, 4245; c) C. A. Hunter, K. R. Lawson, J. Perkins, C. J. Urch, *J. Chem. Soc. Perkin Trans. 2* **2001**, 651.
[17] M. C. Desai, S. L. Lefkowiz, P. F. Thadeio, K. P. Longo, R. M. Snider, *J. Med. Chem.* **1992**, *35*, 4911.
[18] For recent total syntheses of (+)-CP-99,994, see: a) N. Tsuritani, K. Yamada, N. Yoshikawa, M. Shibasaki, *Chem. Lett.* **2002**, 276; b) N. Yamazaki, M. Atobe, C. Kibayashi, *Tetrahedron Lett.* **2002**, *43*, 7979; c) P. -Q. Huang, L. -X. Liu, B.-G. Wei, Y.-P. Ruan, *Org. Lett.* **2003**, *5*, 1927; d) M.-R. Tsai, B.-F. Chen, C.-C. Cheng, N.-C. Chang, *J. Org. Chem.* **2005**, *70*, 1780.
[19] For the transformation of **8** into CP-99,994, see: S. Chandrasekhar, P. K. Mohanty, *Tetrahedron Lett.* **1999**, *40*, 5071.
[20] a) D. L. Hughes, U.-H. Dolling, K. M. Ryan, E. F. Schoenewaldt, E. J. J. Grabowski, *J. Org. Chem.* **1987**, *52*, 4745; b) K. B. Lipkowitz, M. W. Cavanaugh, B. Baker, M. J. O'Donnell, *J. Org. Chem.* **1991**, *56*, 5181; c) I. A. Esikova, M. J. O'Donnell in *ACS Symposium Series 659*, *Phase-Transfer Catalysis* (Ed.: M. E. Halpern), American Chemical Society, Washington, DC, **1997**, chap. 7.
[21] See the Supporting Information.
[22] The precise geometry of enolate **10** remains unclear despite extensive attempts, although we assume that the reaction proceeds through the *Z* enolate of **10**; see ref. [12b].

 © 2005 Wiley-VCH Verlag GmbH & Co. KGaA, Weinheim

Structure Elucidation

An Anomalous Endohedral Structure of Eu@C_{82} Metallofullerenes**

*Bao-Yun Sun, Toshiki Sugai, Eiji Nishibori, Kenichi Iwata, Makoto Sakata, Masaki Takata, and Hisanori Shinohara**

Trivalent metallofullerenes such as La@C_{82} and Ce@C_{82}, in which the metal ions prefer to take a trivalent charge state, have been extensively investigated.[1] However, studies on metallofullerenes encapsulating divalent Sm, Eu, Tm, and Yb metal ions have been limited because of the known low yields in the production of these metallofullerenes despite the development of some improved production and extraction methods during the past several years.[2] This situation has resulted in the structures of such metallofullerenes not having been studied in detail. The variety of encaged metal ions and charge transfer as well as the movement of entrapped metal ions are expected to provide different physical properties. Therefore, it is necessary to study the structure and electronic properties of metallofullerenes in this divalent group.

The Eu ion in Eu@C_{82} was shown by experiment to transfer two electrons to the fullerene cage.[2c] There are no unpaired electrons on the Eu@C_{82} cage and charge transfer results in the $4f^7 5d^0 6s^0$ electronic configuration, which gives rise to the fullerene having paramagnetic character. It is thus difficult to determine the structure of the cage and the symmetry of the complex by NMR spectroscopy. XRD measurements have become the only way to access the detailed structure of Eu@C_{82} fullerenes.

X-ray analysis performed using a combination of the maximum entropy method (MEM) and Rietveld refinement (the MEM/Rietveld method[3]) has proven to be a powerful method for the accurate determination of the structures of metallofullerenes. The endohedral nature of a series of metallofullerenes, such as La, Y, Sc, and Gd@C_{82},[4] Sc_3@C_{82}, La_2@C_{80}, Sc_2@C_{84}, Sc_2@C_{66}, and Sc_2C_2@C_{84}[5] has been determined successfully by this method.

In the present study the structures of the two isomers of Eu@C_{82}(I, III) were successfully determined by the MEM/Rietveld method using synchrotron X-ray powder diffraction data. The endohedral structure of Eu@C_{82}(III) is exceptional in view of the fact that the Eu ion is adjacent to the C–C double bond on the C_2 axis of the C_{2v} carbon cage, whereas the metal ions (such as La, Y, Sc, Er, Lu) in the normal monometallofullerenes are adjacent to a hexagon of the C_{82} cage, except for Gd@C_{82}.[4d,6]

Similar to previous studies of La-, Y-, Sc-, and Gd@C_{82},[4] Sc_3@C_{82},[5a] La_2@C_{80},[5b] as well as Sc_2@C_{84},[5c] the Eu@C_{82}(I, III) crystals are assigned to monoclinic $P2_1$ (no. 4) space groups from the peak positions of the Bragg reflections. The lattice parameters for both isomers are slightly different from each other, namely, $a = 18.2870(4)$, $b = 11.2381(2)$, $c = 11.2371(2)$ Å, $\beta = 107.769(3)°$ for isomer I of Eu@C_{82} and $a = 18.3143(5)$, $b = 11.2478(2)$, $c = 11.2308(3)$ Å, and $\beta = 107.706(3)°$ for isomer III.

The experimental data were analyzed by the MEM/Rietveld method.[3] The reliability factors of the final Rietveld refinement for Eu@C_{82}(I and III) are $R_I = 4.58\,\%$ and $R_{wp} = 2.64\,\%$ and $R_I = 4.57\,\%$ and $R_{wp} = 1.79\,\%$, respectively. The fitting results of the final Rietveld refinement for the two isomers are shown in Figure 1a,b. The number of observed structure factors derived in this analysis was 623 and 602 for isomers I and III, respectively. The MEM analysis was carried out by dividing the unit cell into $90 \times 60 \times 60$ pixels using a MEM program called ENIGMA.[7]

The obtained MEM charge-density distribution (from 0.0 to 2.0 e Å^{-3} with 0.2 e Å^{-3} intervals) and the equicontour density map of the MEM charge density of the half section of Eu@C_{82}(I) (drawn at 1.67 e Å^{-3}) are shown in Figure 2. Both the mirror plane and the double bond at the mirror plane are parallel to the Figure plane and vertical to the Figure plane in Figure 2a and b, respectively.

The MEM charge-density distribution in Figure 2a and b shows clearly that there is a charge-density maximum inside the C_{82} cage which can be assigned to the entrapped metal ion. The density maximum is not at the center but close to the carbon cage, as in other metallofullerenes such as La-, Y-, Sc-, and Gd@C_{82}.[4] The charge densities at the middle points between the Eu ion and the neighboring carbon atoms in positions A, B, and C of Eu@C_{82}(I) are 0.218, 0.207, and 0.224 e Å^{-3}, respectively, which are much less than the corresponding density for Gd@C_{82}.[4d]

The equicontour density map of the MEM charge density of the half section in Figure 2c visualizes the three-dimen-

[*] Dr. B.-Y. Sun, Dr. T. Sugai, Prof. Dr. H. Shinohara
Department of Chemistry
Nagoya University
Nagoya 464-8602 (Japan)
and
CREST, Japan Science Technology Corporation
c/o Department of Chemistry
Nagoya University
Nagoya 464-8602 (Japan)
Fax: (+81) 52-789-1169
E-mail: noris@cc.nagoya-u.ac.jp
Dr. E. Nishibori, K. Iwata, Prof. Dr. M. Sakata
Department of Applied Physics
Nagoya University
Nagoya 464-8603 (Japan)
Prof. Dr. M. Takata
Japan Synchrotron Radiation Research Institute
1-1-1 Kato, Mikazuki-cho, Sayo-gun, Hyogo 679-5198 (Japan)
and
CREST, Japan Science Technology Corporation

[**] H.S. thanks a CREST Program on Novel Carbon Nanotube Materials by the JST. The study was also supported by the Special Coordination Funds for Promoting Science and Technology of MEXT. B.-Y.S. thanks the Japan Society for the Promotion of Science (JSPS) for the postdoctoral fellowship for foreigner research. E.N. thanks the Iketani Foundation and the Toyota Riken Foundation. The synchrotron radiation experiments were performed at SPring-8 BL02B2 with the approval of the Japan Synchrotron Radiation Research Institute (JASRI).

Supporting information for this article (the relative yields of the three isomers and experimental section) is available on the WWW under http://www.angewandte.org or from the author.

 © 2005 Wiley-VCH Verlag GmbH & Co. KGaA, Weinheim DOI: 10.1002/anie.200500876

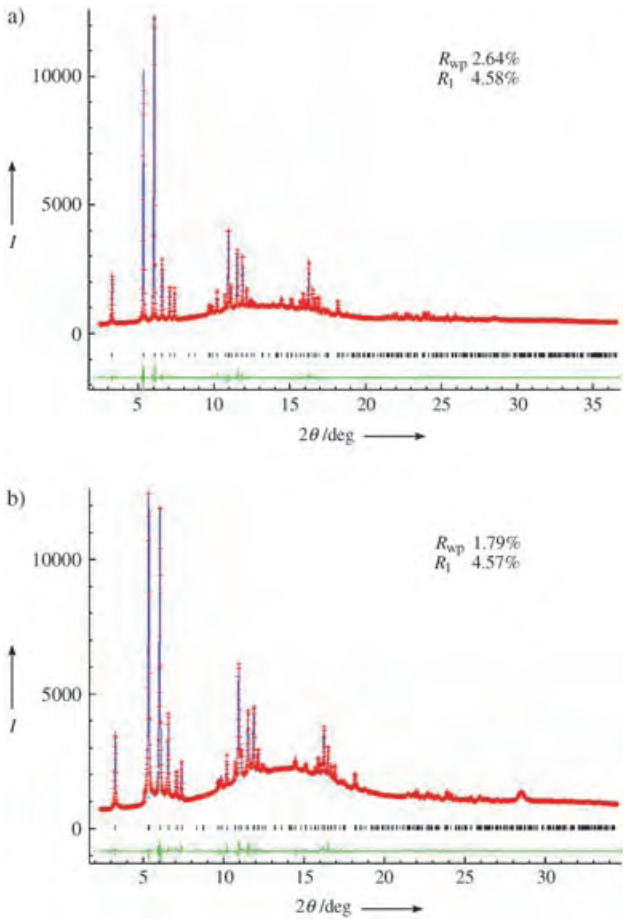


Figure 1. The Rietveld fitting results of Eu@C_{82}: a) isomer I with C_s (no. 6) symmetry and b) isomer III with C_{2v} symmetry.

sional structure of the cage and the entrapped metal ion. The obtained endohedral cage structure has a network of six- and five-membered rings corresponding to C_s (no. 6) symmetry.[8] The charge density of the Eu ion can clearly be seen inside the cage. The total number of electrons inside the region described by the red circle was estimated to be 61.0(8) e, which is very close to that of the divalent Eu ion (61 e). This result indicates that the Eu ion is encaged within C_{82} and the formal electronic structure should be expressed as $Eu^{2+}@C_{82}^{2-}$, which is consistent with the previous result based on EELS analysis.[2c] This finding confirms that the Eu ion prefers to take a +2 charge state in the C_{82} fullerene cage and to form the $4f^7 5d^0 6s^0$ half-filled configuration.

Figure 3 shows the side and top views of the corresponding schematic molecular structure of Eu@C_{82}(I) based on the

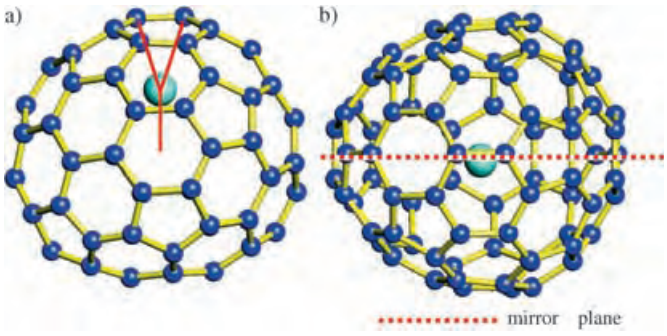


Figure 3. The side view (a) and the top view (b) of Eu@C_{82}(I) with C_s (no. 6) symmetry.

X-ray analysis. The obtained structural model indicates that the metallofullerene has C_s (no. 6) symmetry.[8] The mirror plane is on the Figure plane in the side view (Figure 3a) and is vertical to the Figure plane in the top view (Figure 3b). The Eu ion (colored turquoise) is located near the top of the carbon cage in Figure 3a, adjacent to the C–C double bond on the mirror plane but not to the six-membered ring at the other end of the cage. A similar endohedral structure was reported from a theoretical calculation for Ca@C_{82} with C_s(c), namely, C_s (no. 6) symmetry.[9] The distance between the Eu ion and the cage center is 1.59(4) Å and that between the Eu ion and the nearest (two) carbon atoms is 2.51(3) Å, which is much less than the calculated Ca···C distance in C_s-Ca@C_{82} (2.639(2) Å).[9]

There are nine distinct isomers for the C_{82} cage which satisfy the so-called isolated pentagon rule (IPR).[8] Three of them have C_s symmetry, which are designated as C_s (no. 2), C_s (no. 4), and C_s (no. 6) according to Fowler and Manolopoulos.[8] It is known that the minor isomer of La@C_{82} and one isomer of Tm@C_{82}, normally designated as La@C_{82}(I) and Tm@C_{82}(I), respectively, have been determined to have C_s symmetry by ^{13}NMR spectroscopic studies.[2a,10] However, one-dimensional ^{13}NMR measurements can not determine

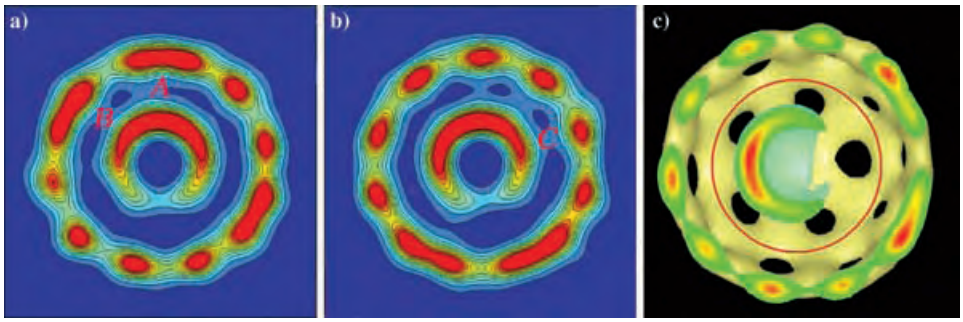


Figure 2. The MEM charge-density distribution (a, b; contour lines are drawn from 0.0 to 2.0 e Å^{-3} with 0.2 e Å^{-3} intervals) and the equicontour density map of the MEM charge density of the half section (c; drawn at 1.67 e Å^{-3}) of Eu@C_{82}(I) with C_s (no. 6) symmetry. Positions *A*–*C* are discussed in the text.

 © 2005 Wiley-VCH Verlag GmbH & Co. KGaA, Weinheim

definitively the final C_s symmetry, that is, whether it is no. 2, 4, or 6. The present XRD experiment enables us, for the first time, to identify that Eu@C_{82}(I) possesses C_s (no. 6) symmetry.

Only one of the nine IPR isomers of C_{82} has C_{2v} symmetry.[8] Most of the C_{82}-caged metallofullerenes, such as La-, Y-, Sc-, and Gd@C_{82}, have been determined to have C_{2v} symmetry by synchrotron X-ray diffraction studies.[4] The present X-ray measurement shows that Eu@C_{82}(III) also possesses C_{2v} symmetry.

The MEM charge-density distribution (from 0.0 to 2.0 e Å^{-3} with 0.2 e Å^{-3} steps, as for isomer I) and the contour line surface of Eu@C_{82}(III) (drawn at 1.67 e Å^{-3}, as for isomer I) are shown in Figure 4. The direction of the C_2 axis is vertical to the double bond at the C_2 axis and parallel to the Figure plane in both Figure 4a and b, but the direction of the double bond at the C_2 axis is parallel to the Figure plane in Figure 4a and vertical to the Figure plane in Figure 4b. The MEM charge density clearly shows that the cage structure of Eu@C_{82}(III) has C_{2v} symmetry (Figure 4a and b). Similar to isomer I, a charge-density maximum is located at an off-center position, which should be the encaged Eu ion. The overlapped charge densities between the Eu ion and the neighboring carbon atoms in Eu@C_{82}(III) are 0.186, 0.215, and 0.189 e Å^{-3} for positions A, B, and C, respectively, which are similar to those in isomer I. The number of electrons contained within the red circle is 61.2(7) e (see Figure 4c). This value is also close to that of an Eu^{2+} ion with 61 e, thus indicating that the Eu center also takes a divalent charge state in this isomer. The six- and five-membered rings can clearly be seen, and the structure has C_{2v} symmetry.

The corresponding schematic molecular structure based on the analysis of Eu@C_{82}(III) is shown in Figure 5. The side and the top views show that the Eu ion (colored turquoise) is located in the C_{2v}-symmetric cage and is adjacent to the C–C double bond along the C_2 axis in Eu@C_{82}(III). These endohedral structures of Eu@C_{82}(I and III) can be contrasted to those of the conventional C_{82}-based mono-metallofullerenes such as La-, Y-, and Sc@C_{82}.[4a–c] Only the mono-metallofullerene Gd@C_{82}[4d] is similar to the present Eu@C_{82} case, in which the Gd ion located close to the C–C double bond on the C_2 axis of C_{2v}-C_{82}. The distance between the Eu ion and the cage center is 1.70(5) Å, which is less than that between the La ion and the cage center in C_{2v}-La@C_{82} (1.96(9) Å).[4a]

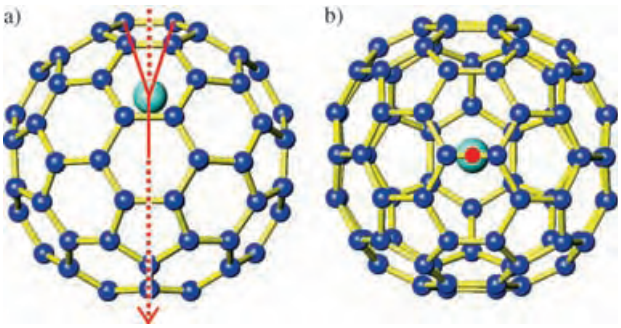


Figure 5. The side view (a) and the top view (b) of Eu@C_{82}(III) with C_{2v} symmetry.

The nearest Eu···C distance (between the Eu ion and two C atoms of the double bond) is 2.50(1) Å in the C_{2v} cage, which is close to those in La-, Y-, and Sc@C_{82} (ca. 2.5 Å).[4a–c]

A recent theoretical calculation[6] on Gd@C_{82} showed that the position of the metal near the C–C double bond is preferred to the position adjacent to a hexagon if relaxation of the cage is considered. The strong overlap in the charge density between the Gd ion and the cage and the back donation of electrons from the C–C double bond stabilize the Gd ion at the position adjacent to the double bond.[6] The calculated total energy is 2.83 eV lower than that at the position adjacent to the six-membered ring. It should be noted that both Gd^{3+} and Eu^{2+} ions have a half-filled configuration $[Xe]^{54}4f^7$.

The overlap in the charge density between the Eu ion and the cage is different from that in Gd@C_{82}. The charge density at the middle point between the Eu ion and the nearest carbon atoms in C_{2v}-Eu@C_{82}(III) (position A in Figure 4) is 0.186 e Å^{-3}, which is only about one-fifth of that found in C_{2v}-Gd@C_{82} (0.996 e Å^{-3}).[4d] Similarly, the charge density at the middle point between the Eu ion and the nearest carbon atoms in the C_s-Eu@C_{82}(I) case (position A in Figure 2) is only 0.218 e Å^{-3}, which is similar to that found in C_{2v}-Eu@C_{82}(III). The results strongly suggest that the interaction between the entrapped Eu ion and the carbon cage is much weaker than that exerted in Gd@C_{82}. This weaker interaction has also been suggested by a downfield shift of the Raman vibration frequency of the metal cage[2e,11] in Tm@C_{82} and Eu@C_{74}. Such low-energy modes in Tm@C_{82} and Eu@C_{74} are

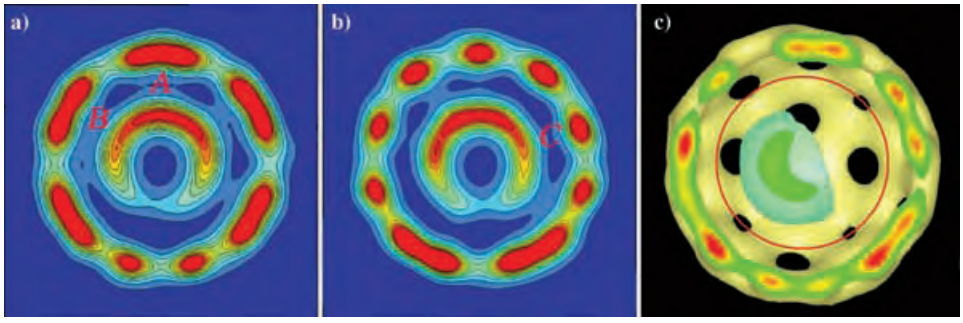


Figure 4. The MEM charge density distribution (a, b; contour lines are drawn from 0.0 to 2.0 e Å^{-3} with 0.2 e Å^{-3} intervals) and the equicontour density map of the MEM charge density of the half section (c; drawn at 1.67 e Å^{-3}) of Eu@C_{82}(III) with C_{2v} symmetry. Positions *A*–*C* are discussed in the text.

 © 2005 Wiley-VCH Verlag GmbH & Co. KGaA, Weinheim

lower in frequency than those in trivalent metallofullerenes. The present MEM charge density reveals that the nature of the chemical bonding between the Eu ion and the cage should be highly ionic.

The overlapped charge densities in positions B and C in Eu@C_{82}(III) in Figure 4 are 0.215 and 0.189 e Å^{-3}, respectively, which is similar to that between the Eu ion and the nearest carbon atoms (0.186 e Å^{-3}). The charge densities in Eu@C_{82}(I) in Figure 2 are 0.207 and 0.224 e Å^{-3} for positions B and C, respectively, which are similar to 0.218 e Å^{-3} at position A as in Eu@C_{82}(III). Figures 2 and 4 show that the Eu ion moves over a spatially confined domain both in the C_s (no. 6) and C_{2v} cages. The obtained charge density of the Eu ion exhibits a hemispherical shape at room temperature, which is much wider than those observed in Sc@C_{82} and Gd@C_{82}.[4c,d]

As previously mentioned, the endohedral structure of C_{2v}-Eu@C_{82} is significantly different from that of C_{2v}-Sc@C_{82}[4c] although both of them are divalent metallofullerenes. Firstly, the Eu metal ion is located at the opposite position of that of the Sc ion along the C_2 symmetry axis. Secondly, the Sc ion does not move inside the C_{82} cage even at room temperature and shows a spherical charge-density distribution, whereas the Eu ion floats inside the cage as is clearly seen in Figure 4. The different interaction in Eu@C_{82} and Sc@C_{82} evidently induces the different endohedral structure of the metal ions in the C_{82} cage.

In the present study, a weak intramolecular interaction between the Eu ion and the carbon cage should be one of the important reasons why the yield of Eu–metallofullerenes has been the lowest of the metallofullerenes so far studied. Undoubtedly, if the interaction between the cage and the metal is weak, such as in Eu–metallofullerenes, the probability of losing the metal ion before the closure (that is, completion) of the fullerene cage should increase. The fact that the relative yield of Eu@C_{82} is only about 3% of that of Er@C_{82} or La@C_{82} is consistent with this growth process.

The cage structures of Eu@C_{82} (isomers I and III) have been determined to have C_s (no. 6) and C_{2v} symmetry, respectively, by XRD measurements combined with the MEM/Rietveld analysis. Unlike other M@C_{82} (M = Sc, Y, La, and other lanthanide elements) mono-metallofullerenes (except Gd@C_{82}), the Eu ion is adjacent to the C–C double bond on the mirror plane of the C_s (no. 6) symmetric structure in Eu@C_{82}(I) and adjacent to the C–C double bond (not to a hexagon) on the C_2 axis of a C_{2v} structure of Eu@C_{82}(III). The obtained charge-density mappings for Eu@C_{82}(I, III) show that the charge densities of the Eu ions form a nearly hemispherical shape at room temperature, thus indicating that the Eu ion is floating in the C_{82} cage.[12]

Received: March 9, 2005
Published online: June 27, 2005

Keywords: electronic structure · inclusion complexes · metallofullerenes · structure elucidation · X-ray diffraction

[1] H. Shinohara, *Rep. Prog. Phys.* **2000**, *63*, 843 – 892.

[2] a) T. Kodama, N. Ozawa, Y. Miyake, K. Sakaguchi, H. Nishikawa, I. Ikemoto, K. Kikuchi, Y. Achiba, *J. Am. Chem. Soc.* **2002**, *124*, 1452 – 1455; b) T. Okazaki, K. Suenaga, K. Hirahara, S. Bandow, S. Iijima, H. Shinohara, *J. Am. Chem. Soc.* **2001**, *123*, 9673 – 9674; c) B. Y. Sun, T. Inoue, T. Shimada, T. Okazaki, T. Sugai, K. Suenaga, H. Shinohara, *J. Phys. Chem. B* **2004**, *108*, 9011 – 9015; d) Y. F. Lian, Z. J. Shi, X. H. Zhou, X. R. He, Z. N. Gu, *Chem. Mater.* **2001**, *13*, 39 – 42; e) P. Kuran, M. Krause, A. Bartl, L. Dunsch, *Chem. Phys. Lett.* **1998**, *292*, 586 – 586; f) K. Kikuchi, K. Akiyama, K. Sakaguchi, T. Kodama, H. Nishikawa, I. Ikemoto, T. Ishigaki, Y. Achiba, K. Sueki, H. Nakahara, *Chem. Phys. Lett.* **2000**, *319*, 472 – 476.

[3] M. Takata, E. Nishibori, M. Sakata, H. Shinohara, *Struct. Bonding (Berlin)* **2004**, *109*, 59 – 84.

[4] a) M. Takata, B. Umeda, E. Nishibori, M. Sakata, Y. Saito, M. Ohno, H. Shinohara, *Nature* **1995**, *377*, 46 – 49; b) E. Nishibori, M. Takata, M. Sakata, M. Tanaka, H. Hasegawa, H. Shinohara, *Chem. Phys. Lett.* **2000**, *330*, 497 – 502; c) E. Nishibori, M. Takata, M. Sakata, M. Inakuma, H. Shinohara, *Chem. Phys. Lett.* **1998**, *298*, 79 – 84; d) E. Nishibori, K. Iwata, M. Sakata, M. Takata, H. Tanaka, H. Kato, H. Shinohara, *Phys. Rev. B* **2004**, *69*, 113412.

[5] a) M. Takata, E. Nishibori, M. Sakata, M. Inakuma, E. Yamamoto, H. Shinohara, *Phys. Rev. Lett.* **1999**, *83*, 2214 – 2217; b) E. Nishibori, M. Takata, M. Sakata, A. Taninaka, H. Shinohara, *Angew. Chem.* **2001**, *113*, 3086 – 3087; *Angew. Chem. Int. Ed.* **2001**, *40*, 2998 – 2999; c) M. Takata, E. Nishibori, B. Umeda, M. Sakata, E. Yamamoto, H. Shinohara, *Phys. Rev. Lett.* **1997**, *78*, 3330 – 3333; d) C. R. Wang, T. Kai, T. Tomiyama, T. Yoshida, Y. Kobayashi, E. Nishibori, M. Takata, M. Sakata, H. Shinohara, *Nature* **2000**, *408*, 426 – 427; e) C. R. Wang, T. Kai, T. Tomiyama, T. Yoshida, Y. Kobayashi, E. Nishibori, M. Takata, M. Sakata, H. Shinohara, *Angew. Chem.* **2001**, *113*, 411 – 413; *Angew. Chem. Int. Ed.* **2001**, *40*, 397 – 399.

[6] L. Senapati, J. Schrier, K. B. Whaley, *Nano. Lett.* **2004**, *4*, 2073 – 2078.

[7] H. Tanaka, M. Takata, E. Nishibori, K. Kato, T. Iishi, M. Sakata, *J. Appl. Crystallogr.* **2002**, *35*, 282 – 286.

[8] P. W. Fowler, D. E. Manolopoulos, *An Atlas of Fullerenes*, Clarendon, Oxford, **1995**.

[9] K. Kobayashi, S. Nagase, *Chem. Phys. Lett.* **1997**, *274*, 226 – 230.

[10] T. Akasaka, T. Wakahara, S. Nagase, K. Kobayashi, M. Waelchli, K. Yamamoto, M. Kondo, S. Shirakura, Y. Maeda, T. Kato, M. Kako, Y. Nakadaira, X. Gao, E. V. Caemelbecke, K. M. Kadish, *J. Phys. Chem. B* **2001**, *105*, 2971 – 2974.

[11] M. Krause, M. Hulman, H. Kuzmany, P. Kuran, L. Dunsch, T. J. S. Dennis, M. Inakuma, H. Shinohara, *J. Mol. Struct.* **2000**, *521*, 325 – 340.

[12] CCDC-265613(Eu@C_{82}(I)) and CCDC-265614(Eu@C_{82}(III)) contains the supplementary crystallographic data for this paper. These data can be obtained free of charge from the Cambridge Crystallographic Data Centre via www.ccdc.cam.ac.uk/data_request/cif.

 © 2005 Wiley-VCH Verlag GmbH & Co. KGaA, Weinheim

Reaction Mechanisms

Elucidation of the Reaction Mechanism for the Palladium-Catalyzed Synthesis of Vinyl Acetate**

*Dario Stacchiola, Florencia Calaza, Luke Burkholder, Alan W. Schwabacher, Matthew Neurock, and Wilfred T. Tysoe**

Two basic mechanisms have been proposed for the palladium-catalyzed synthesis of the vinyl acetate monomer (VAM) from acetic acid, ethylene, and oxygen [Eq. (1)]:[1]

$$CH_3COOH + C_2H_4 + {}^1/_2O_2 \rightarrow CH_3COOC_2H_3 + H_2O \quad (1)$$

The first, suggested by Samanos et al., involves the coupling of ethylene directly with chemisorbed acetate.[2] The resulting acetoxyethyl–palladium intermediate then undergoes β-hydride elimination to form vinyl acetate. Alternatively, ethylene could first dehydrogenate to form a vinyl–palladium intermediate, which then couples with an acetate species adsorbed on the surface to form the VAM directly. This latter mechanism was proposed by Moiseev et al.[3,4] as well as by Nakamura and Yasui.[5] We have recently shown that ethylene in the gas phase reacts with a model-catalyst surface of η^2-acetate moieties adsorbed on a Pd(111) surface precovered with a (2×2) oxygen overlayer to form the VAM,[6] thus implying that the acetate species is the precursor to formation of the VAM.

The structures of the adsorbed η^2-acetate[7] and ethylene[8] species were determined separately on a Pd(111) surface by using low-energy electron diffraction (LEED) and reflection-absorption IR spectroscopy (RAIRS),[6–9] which showed that both species adsorb on the bridge site. Herein, we discuss the investigation into the nature of the reaction pathway by using isotopically labeled reactants, which allowed the mechanism for the formation of the VAM to be unequivocally identified. The RAIRS experiments were performed in an ultrahigh vacuum apparatus; the experimental procedure has been described in detail elsewhere.[10] Kinetic measurements were typically carried out by the collection of spectra over 100 scans, which is a relatively short procedure that took 25 seconds because of the large intensity of the asymmetric vibrational mode of the acetate moiety (O-C-O) at 1414 cm^{-1}.[6] Some experiments were carried out with a larger number of scans to yield spectra with better signal-to-noise ratios and, therefore, allow additional surface species to be identified. A flux of ethylene impinged onto the sample from a collimated dosing source to obtain an enhanced flux at the Pd(111) single-crystal surface while the background pressure was minimized.[6] C_2H_4 (Matheson, Research Grade), acetic acid (Aldrich, 99.99+%), C_2D_4 (CIL, 98% D), CD_2CH_2 (CDN, 99% D), CHDCHD (CDN, *cis*/*trans* mixture, 99% D), and $^{18}O_2$ (CIL, 95% $^{18}O_2$) were transferred into glass bottles, which were attached to the gas-handling line for introduction into the vacuum chamber.

It has been shown previously that acetate species adsorbed on a Pd(111)–O(2×2) surface undergoes reaction with ethylene in the gas phase to yield the VAM.[6] The experimental titration curves obtained with acetate species can be explained by using a procedure described previously,[6] in which it was assumed that adsorbed ethylene underwent reaction with the acetate species and that ethylene adsorption was blocked by the acetate species. Acetate species adsorbed on clean Pd(111) surfaces (namely, in the absence of the (2×2) oxygen overlayer) are also removed by reaction with ethylene and also can be analyzed by using the same procedure used to reproduce the kinetic data for the oxygen-covered Pd(111) surface; furthermore, these acetate species yield similar rate constants to those found for reactions on the oxygen-covered surface, and therefore the presence of coadsorbed oxygen does not substantially affect the reaction kinetics.

A series of IR spectra for the reaction of the acetate species on a clean Pd(111) surface was collected just after the acetate moieties had been completely removed using C_2H_4, C_2H_4 (on an ^{18}O-covered surface), and C_2D_4 (Figure 1). The spectrum of CO on the Pd(111) surface is shown for comparison (Figure 1a). The CO exposure was selected to

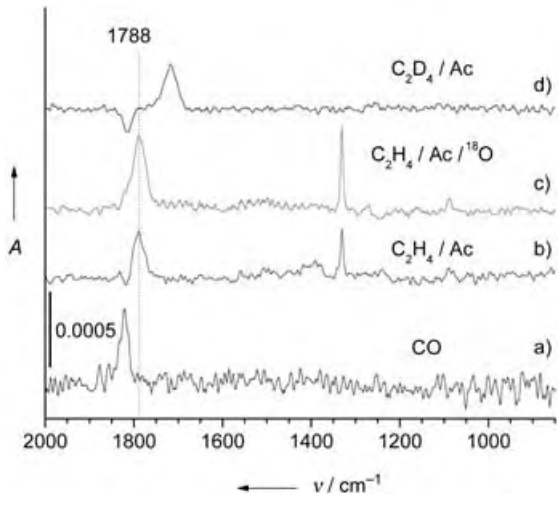


Figure 1. IR spectra of the reaction of acetate species with ethylene at 327 K after the acetate species had been removed. Spectra are given for the reactions of: b) C_2H_4 on an acetate-covered Pd(111) surface, c) C_2H_4 on an acetate-covered Pd(111)–^{18}O(2×2) surface, and d) C_2D_4 with a acetate-covered Pd(111) surface. a) IR spectrum of CO on a Pd(111) surface is shown for comparison. Ac = acetate.

[*] Dr. D. Stacchiola, F. Calaza, L. Burkholder, Prof. Dr. A. W. Schwabacher, Prof. Dr. W. T. Tysoe
Department of Chemistry and Biochemistry and Laboratory for Surface Studies
University of Wisconsin—Milwaukee
Milwaukee, WI 53211 (USA)
Fax: (+1) 414-229-5036
E-mail: wtt@uwm.edu
Prof. Dr. M. Neurock
Department of Chemical Engineering
University of Virginia
Charlottesville, VA 22904-4741 (USA)

[**] We gratefully acknowledge support of this work by the US Department of Energy, Division of Chemical Sciences, Office of Basic Energy Sciences (Grant No. DE-FG02-92ER14289).

 © 2005 Wiley-VCH Verlag GmbH & Co. KGaA, Weinheim DOI: 10.1002/anie.200500782

yield a similar intensity of signals to those produced by the reaction between ethylene and the adsorbed acetate species, thus indicating that none of the signals result from CO adsorbed from the background. The signals at 1330 and 1090 cm^{-1} in the spectra in Figure 1b and c arise from the ethylidyne species.[6] Deuterated ethylidyne has very weak IR features and is not detected in the spectrum in Figure 1d. The spectrum in Figure 1b demonstrates that surface oxygen does not participate in the formation of surface species. A signal is evident at 1788 cm^{-1} following the reaction with C_2H_4, whereas another is present at 1718 cm^{-1} following the reaction with C_2D_4. A deuterium isotope effect is measured which indicates that C_2D_4 undergoes reaction with the acetate species approximately six times more slowly than with C_2H_4 (see below). To establish whether the signal at 1718 cm^{-1} results from an isotopic shift of the absorption at 1788 cm^{-1} or a different species and to help establish the nature of the species that gives rise to the signal at 1788 cm^{-1}, both perdeuterated and undeuterated vinyl acetate were adsorbed on an ethylidyne-saturated Pd(111) surface at 300 K (data not shown). The RAIRS spectra revealed that the VAM exhibits a single signal at approximately 1780 cm^{-1} for both the perdeuterated and undeuterated vinyl acetate. The signal at 1718 cm^{-1} evidently does not result from either the vinyl acetate or the monodentate acetate species,[11,12] as the latter would have also been observed during reaction with C_2H_4. The presence of this signal does, however, provide a clue to the reaction pathway. The only species expected to be present on the surface in the pathway proposed by Moiseev et al.[3] are ethylene, the vinyl and acetate moieties, and vinyl acetate. Once the characteristic frequencies of these species are considered, however, it is clear that the signal at 1718 cm^{-1} does not arise from any of these.[6–9] The species present in the pathway proposed by Samanos et al. are ethylene, acetate, vinyl acetate, and the acetoxyethyl–palladium intermediate that results from insertion of ethylene into the acetate–Pd bond. Again bearing in mind their characteristic frequencies, the signal at 1718 cm^{-1} does not arise from ethylene,[9] acetate,[6,11,12] or vinyl acetate.

Density functional theory (DFT) calculations demonstrate that an acetoxyethyl–palladium intermediate has a C=O stretching frequency approximately 80 cm^{-1} lower than that of vinyl acetate. The calculations were carried out by using periodic plane-wave DFT calculations with the DMOL^3 code[13] and the Perdew–Wang91[14] form of the generalized gradient approximation. Pure ethyl acetate has a C=O stretching frequency substantially lower than that of vinyl acetate,[15] and a proposed acetoxyethyl–palladium species on a Pd–Al_2O_3 surface has a characteristic frequency of well below 1788 cm^{-1}.[16] The signal at 1718 cm^{-1} is, therefore, assigned to an acetoxyethyl–palladium intermediate, the presence of which can only be rationalized on the basis of the pathway proposed by Samanos et al.,[2] where this intermediate decomposes to form the VAM by β-hydride elimination. The decomposition rate of the acetoxyethyl–palladium intermediate will be slowed substantially by deuteration at the β position, thus accounting for the appearance of this intermediate when C_2D_4 reacts with the surface acetate species. Reaction with C_2H_4 results in a faster decomposition rate of the intermediate such that insufficient quantities accumulate to allow detection by IR spectroscopy.

In view of this isotope effect, the acetate species on the Pd(111) surface was treated with C_2D_4, CH_2CD_2, and CHDCHD, and the resulting plots of the acetate coverage versus time are displayed, along with the data for C_2H_4, in Figure 2. There are substantial differences in the reaction

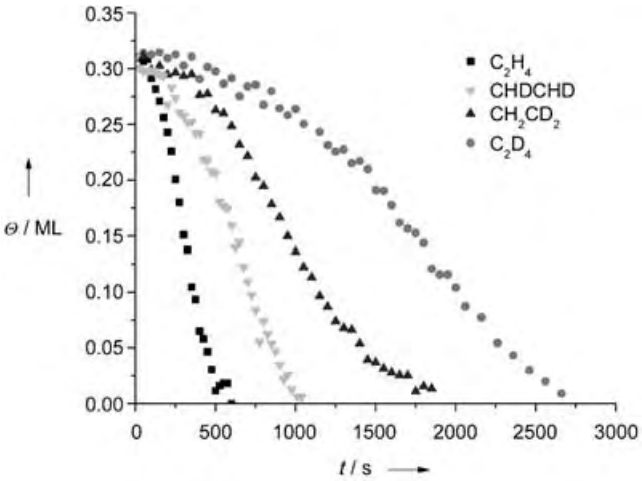


Figure 2. Plot of time versus coverage Θ, as measured from the intensity of the signal at 1414 cm^{-1} of the acetate species, for the reaction of C_2H_4 (■), CH_2CD_2 (▲), CHDCHD (▼), and C_2D_4 (●) carried out with the acetate species adsorbed on a Pd(111) surface, with an ethylene pressure of 2×10^{-7} Torr, and at a reaction temperature of 327 K.

rates between C_2H_4 and C_2D_4 which indicate, as noted above, that hydrogen is involved in the rate-limiting step. Interestingly, the reaction rates for [D_2]ethylene depend on the position of the deuterium isotope: the reaction is slower for the 1,1-dideuterated reactant than for 1,2-dideuteroethylene. This observation allows us to exclude the model proposed by Moiseev et al. immediately as, in this case, the rate-limiting step, which involves hydrogen, must be hydrogen abstraction from ethylene to form the vinyl species. An analysis of the experimental data[6] (Figure 2) yields $k_H/k_D \approx 6$, which is a reasonable value for a primary isotope effect. In the case of the reaction with [D_2]ethylene, and according to the pathway of Moiseev et al., the rate constant should be $(k_H + k_D)/2$ irrespective of the location of the deuterium atom, thus yielding an isotope effect of $2/(1+(k_D/k_H)) \approx 1.7$.

At first sight, a similar effect should occur with the model proposed by Samanos et al. In the case of the reaction with CH_2CD_2, there is an equal probability of CH_2 or CD_2 units being in the β position in the acetoxyethyl–palladium intermediate, thus yielding an isotope effect of approximately 1.7; whereas there will always be a CHD unit at the β position in CHDCHD, thus yielding a similar isotope effect of approximately 1.7. If it is assumed that the acetoxyethyl–palladium intermediate blocks the adsorption of ethylene, however, any intermediates formed from CH_2D_2, which has two deuterium atoms at the β position, will decompose more slowly than those with hydrogen atoms at the β position, thus blocking ethylene adsorption and lowering the reaction rate. For the reaction with CHDCHD, hydrogen atoms will always be

 © 2005 Wiley-VCH Verlag GmbH & Co. KGaA, Weinheim

present at the β position, so the intermediate decomposes more rapidly, which results in decreased blocking of ethylene adsorption by the intermediate. These observations suggest that reaction with CH_2CD_2 should be slower than with CHDCHD, as was found experimentally (Figure 2). This proposal is in accord with the identification of the acetoxyethyl–palladium intermediate in the reaction between the acetate species and C_2D_4 (Figure 1). In this case, there is always a deuterium atom at the β position which results in slower decomposition of the acetoxyethyl–palladium intermediate, thus allowing it to be detected by IR spectroscopic analysis. The detection of this species confirms that sufficient quantities can accumulate on the surface to affect the relative reaction rates of the 1,1- and 1,2-dideuteroethylenes, as found by the data shown in Figure 2.

Thus, the experimental results provide clear evidence that the reaction of ethylene with the acetate species proceeds through the pathway proposed by Samanos et al.,[2] that is, by insertion of ethylene into an adsorbed acetate species and subsequent β-hydride elimination to form vinyl acetate. First, when a reaction is carried out using C_2D_4, a vibrational mode at 1718 cm^{-1} is identified, which is assigned to the acetoxyethyl–palladium intermediate (Figure 1). Second, the differences in the reaction rates for CHDCHD and CH_2CD_2 can only be rationalized by the route of Samanos et al.; therefore, the reasonable assumption can be made that the acetoxyethyl–palladium intermediate blocks the adsorption of ethylene (Figure 2). Our mechanism is essentially the same as that observed for the stoichiometric oxidation of ethylene to the VAM by soluble palladium acetate.[17] Although it was a reasonable proposal that the surface-mediated reaction would be parallel to that of the related solution-phase process, the distinctly different reactivity of ethylene towards the two palladium species made disparate mechanisms plausible. Now that the intermediacy of an acetoxyethyl–palladium species in the surface-mediated process has been established, questions still remain that concern the geometry of each step. Whether the insertion of ethylene proceeds in an *anti* mode, as observed in the solution phase,[17] or by a *syn* process, which is apparently more appropriate for a surface, will be investigated in future studies.

Received: March 3, 2005
Published online: June 29, 2005

Keywords: IR spectroscopy · isotopes · palladium · reaction mechanisms · surface chemistry

[1] L. Horning, H. Fernholz, H.-J. Schmidt, F. Wunder, T. Quadflieg; Farbwerke Hoechst AG, US Patent 365888, **1972**.
[2] B. Samanos, P. Boutry, R. Montarnal, *J. Catal.* **1971**, *23*, 19–30.
[3] I. I. Moiseev, M. N. Vargaftic, Y. L. Syrkin, *Dokl. Akad. Nauk SSSR* **1960**, *133*, 377–380.
[4] I. I. Moiseev, *Catalytic Oxidation* (Ed.: R. A. Sheldon), World Scientific, **1995**, p. 203.
[5] S. Nakamura, T. Yasui, *J. Catal.* **1970**, *17*, 366–374.
[6] D. Stacchiola, F. Calaza, L. Burkholder, W. T. Tysoe, *J. Am. Chem. Soc.* **2004**, *126*, 15384–15385.
[7] J. James, D. K. Saldin, T. Zheng, W. T. Tysoe, D. S. Sholl, *Catal. Today*, in press.
[8] T. Zheng, D. Stacchiola, H. C. Poon, D. K. Saldin, W. T. Tysoe, *Surf. Sci.* **2004**, *564*, 71–78.
[9] D. Stacchiola, L. Burkholder, W. T. Tysoe, *Surf. Sci.* **2002**, *511*, 215–228.
[10] M. Kaltchev, A. W. Thompson, W. T. Tysoe, *Surf. Sci.* **1997**, *391*, 145–149.
[11] S. M. Augustine, J. P. Blitz, *J. Catal.* **1993**, *142*, 312–324.
[12] R. D. Haley, M. S. Tikov, R. M. Lambert, *Catal. Lett.* **2001**, *76*, 125–130.
[13] a) B. Delley, *J. Chem. Phys.* **2000**, *113*, 7756–7764; b) DMOL^3 V.2.1, Accelrys Inc., **2002**.
[14] J. P. Perdew, J. A. Chaevary, S. H. Vosko, K. A. Jackson, M. R. Pederson, D. J. Singh, C. Fiolhais, *Phys. Rev. B* **1992**, *46*, 6671–6687.
[15] L. J. Bellamy, *The Infrared Spectra of Complex Molecules*, Wiley, New York, **1959**.
[16] T. Bürgi, *J. Catal.* **2005**, *229*, 55–63.
[17] For example, see: J. E. Backvall, *Acc. Chem. Res.* **1983**, *16*, 335–342; T. Hosokawa, S.-I. Murahashi, *Acc. Chem. Res.* **1990**, *23*, 49–54.

 © 2005 Wiley-VCH Verlag GmbH & Co. KGaA, Weinheim

Host–Guest Chemistry

Tweezering the Core of a Dendrimer: A Photophysical and Electrochemical Study**

Vincenzo Balzani, Paola Ceroni, Carlo Giansante, Veronica Vicinelli, Frank-Gerrit Klärner,* Carla Verhaelen, Fritz Vögtle,* and Uwe Hahn*

Dendrimers[1] are complex, yet well-defined, branched compounds that exhibit a high degree of constitutional order, with the possibility of containing selected chemical units at predetermined sites of their structure (core, branches, periph-

[*] Prof. Dr. V. Balzani, Dr. P. Ceroni, C. Giansante, Dr. V. Vicinelli
Dipartimento di Chimica "G. Ciamician"
Università di Bologna
Via Selmi 2, 40126 Bologna (Italy)
Fax: (+39) 051-209-9456
E-mail: vincenzo.balzani@unibo.it

Prof. Dr. F.-G. Klärner, Dipl.-Chem. C. Verhaelen
Institut für Organische Chemie
Universität Essen-Duisburg, Campus Essen
Universitätsstrasse 5, 45117 Essen (Germany)
Fax: (+49) 201-183-4252
E-mail: frank.klaerner@uni-essen.de

Prof. Dr. F. Vögtle, Dr. U. Hahn
Kekulé-Institut für Organische Chemie und Biochemie
Universität Bonn
Gerhard-Domagk Strasse 1, 53121 Bonn (Germany)
Fax: (+49) 228-735-662
E-mail: voegtle@uni-bonn.de

[**] We thank Professors Mauro Maestri and Margherita Venturi for useful discussions, and Heinz Bandmann for NMR measurements. This work was supported by the MIUR (Supramolecular Devices Project) and the Deutsche Forschungsgemeinschaft (SFB 452).

Supporting information for this article is available on the WWW under http://www.angewandte.org or from the author.

 © 2005 Wiley-VCH Verlag GmbH & Co. KGaA, Weinheim DOI: 10.1002/anie.200501025

ery). As a result of their nanoscopic size and fractal structure, dendrimers resemble biocomponents such as viruses, enzymes, and proteins.[2] Dendrimers that contain redox-active units are currently attracting much attention.[3] When a large number of redox-active units are placed in the periphery and/or along the branches, dendrimers can undergo multiple electron-transfer processes and perform, for example, as molecular batteries, sensors, and catalysts.[4] Dendrimers with a single redox site as a core are the simplest examples of systems with an encapsulated redox center,[5] and their redox properties are usually modulated by the size and nature of the dendritic branches.[6]

Despite their large structures, which usually render dendrimers attractive as host molecules, suitably designed dendrimers can be equally involved as guests in molecular-recognition phenomena.[7] In such cases, the host species does not interact with the whole dendritric structure, but only with specific component units. Usually, the guest behavior of the dendrimer is connected with the threading of dendritic branches by ring-shaped molecules such as crown ethers,[8] cyclodextrins,[9] and cucurbiturils.[10]. More recently, Kaifer and co-workers[7,11] prepared several dendrimers that contain a single-site, potential guest unit and have investigated their adducts with cucurbit[7]uril, β-cyclodextrin, and bis-*para*-phenylene[34]crown-10.

When the potential guest unit constitutes the core of a dendrimer, the formation of a host–guest complex through threading of ring-shaped hosts cannot take place. It occurred to us that in such a case, tweezer-shaped molecules could be used to enclose the dendritic core into a host structure. Herein, we show that this strategy works in solution when suitably designed host and guest units are used.[12]

Several molecular tweezers and clips that exhibit electron-donating properties have been prepared recently in one of our laboratories.[13] Molecular tweezer **T**, which comprises one naphthalene and four benzene components bridged by four methylene units, was prepared and purified as previously reported (Figure 1).[14] NMR spectroscopy (see Supporting Information for details) showed that tweezer **T** forms a stable 1:1 complex with 4,4′-*N*,*N*-bis(3,5-di-*tert*-butylbenzyl)-bipyridinium $[\mathbf{D0}]^{2+}$. Solvent-dependent binding constants ($K_a = 730\,\text{M}^{-1}$ in [D$_6$]acetone/$CDCl_3$ (2:1) and $K_a = 8400\,\text{M}^{-1}$ in CD_2Cl_2), and complexation-induced upfield shifts of the chemical shifts for the protons of the guest ($\Delta\delta_{max} = 1.01$ or 0.91 ppm (H^o), and 4.12 or 3.22 ppm (H^m)) were determined by ^{1}H NMR titration experiments (500 MHz, Bruker DRX 500) at 25 °C, and the 1:1 stoichiometry of the complex was determined through Job plot analysis. The observed large $\Delta\delta_{max}$ values and the specific broadening of the ^{1}H NMR signals assigned to the bridgehead protons of the complexed tweezer at low temperature are evidence that one of the pyridinium rings of $[\mathbf{D0}]^{2+}$ is positioned inside the cavity of the tweezer and that tweezer **T** shuttles from one pyridinium ring of $[\mathbf{D0}]^{2+}$ to the other. At room temperature the shuttling process is fast and leads to an averaging of the ^{1}H NMR signals of the guest molecule lying inside/outside of the tweezer cavity, while at −75 °C the process is slow with respect to the NMR timescale ($\Delta G^{\ddagger}(\text{shuttle}) = 10\,\text{kcal mol}^{-1}$, estimated from the line broadening). As the 3,5-di-*tert*-butylben-

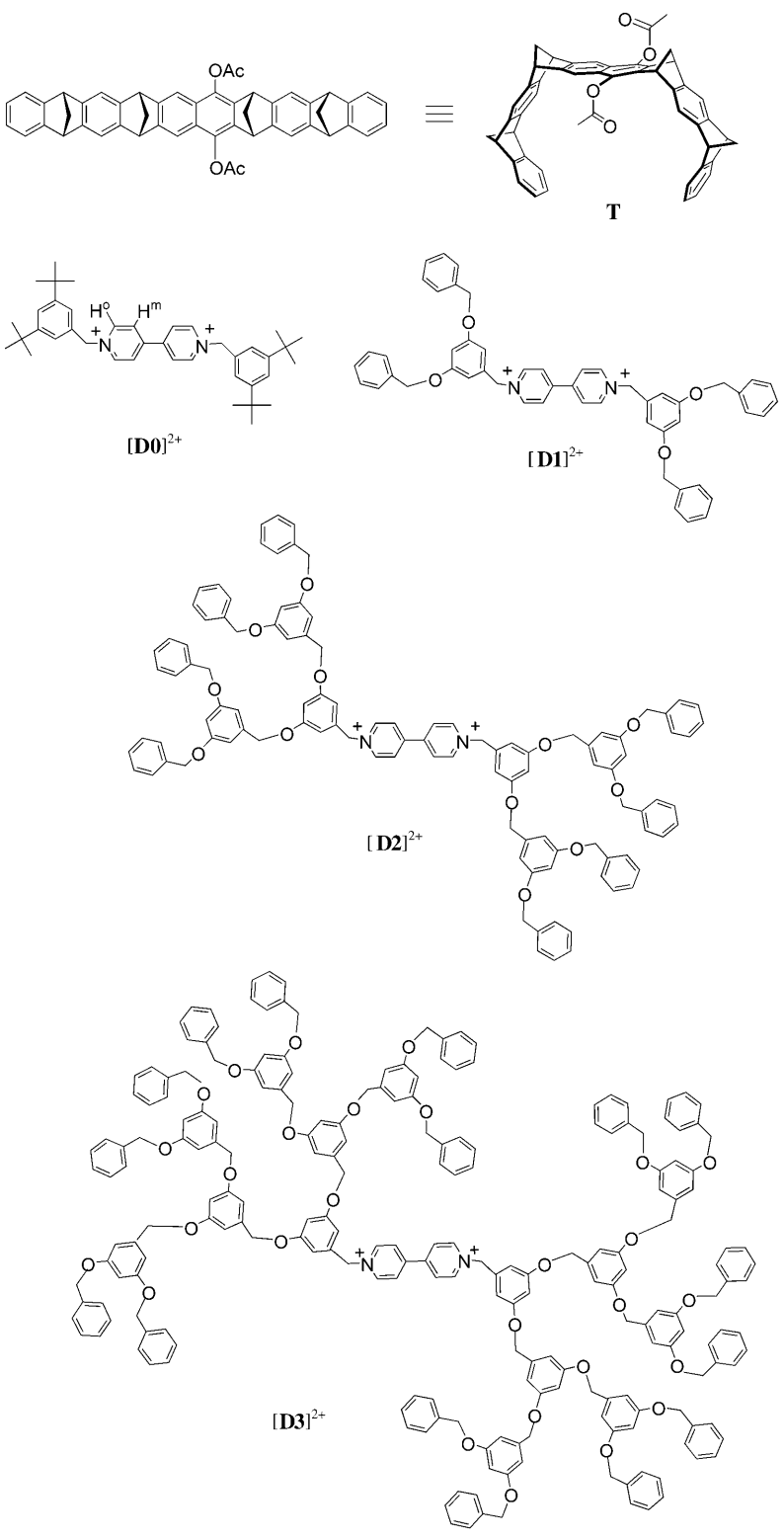


Figure 1. Formulae of the investigated tweezer (**T**) and dendrimeric compounds (**D*n*** where ***n*** indicates the dendron generation: ***n*** = 0,1,2,3).

 © 2005 Wiley-VCH Verlag GmbH & Co. KGaA, Weinheim

zyl stopper groups in $[\mathbf{D0}]^{2+}$ are already too bulky to form a complex with tweezer **T** by threading and as the complexation has to proceed by clipping of the guest molecule through the tips of the tweezer, we thought that **T** should also be able to interact with the bipyridinium core (bpy^{2+}) of the first-, second-, and third-generation dendrimers $[\mathbf{D}n]^{2+}$ ($n = 1, 2$ and 3; see Figure 1). NMR spectroscopy, however, could not provide information on the formation of a complex in the case of the dendrimers because of solubility problems and line broadening. Therefore we carried out a photophysical and electrochemical investigation of the interactions.

The hexafluorophosphate salts of the $[\mathbf{D}n]^{2+}$ dendrimers had been prepared during the course of previous work.[15] The equipment used for the photophysical and electrochemical measurements has been described elsewhere.[16] All the experiments were performed at room temperature (293 K) in air-equilibrated solution. Quantum yields of fluorescence were measured following the methods of Demas and Crosby[17], using terphenyl in cyclohexane ($\Phi = 0.82$) as the standard.[18] Dichloromethane was used as the solvent for the photophysical experiments, and mixtures of dichloromethane/acetonitrile (3:1 or 9:1 v/v) were used for the electrochemical experiments. The association constants were obtained from fluorescence titration experiments.

The absorption and emission spectra of tweezer **T** in dichloromethane are shown in Figure 2. The strong fluorescence emission band at $\lambda_{max} = 344$ nm ($\tau = 9.5$ ns, $\Phi = 0.53$)

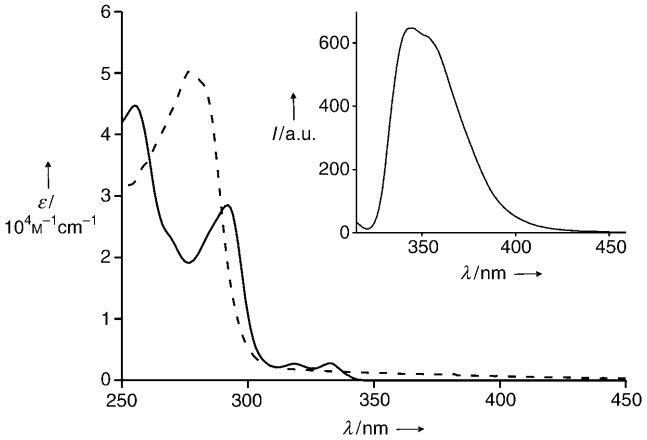


Figure 2. Absorption spectra of tweezer **T** (——) and dendrimer $[\mathbf{D3}]^{2+}$ (as PF_6^- salt; -----) in dichloromethane at room temperature. Inset: Emission spectrum of tweezer **T** in dichloromethane at 293 K ($\lambda_{ex} = 334$ nm).

can be assigned to the naphthalene unit. The absorption spectra of dendrimers $[\mathbf{D}n]^{2+}$ (see Figure 2 for an example) display a strong absorption band around $\lambda = 260$ nm from the bipyridinium unit, while the 1,3-dimethyleneoxybenzene units of the dendrons show an absorption around $\lambda =$ 280 nm. The fluorescence of the 1,3-dimethyleneoxybenzene units is completely quenched in the dendrimers.[15]

In a solution of 9:1 dichloromethane/acetonitrile, tweezer **T** shows an irreversible oxidative process at $+1.6$ V, whereas no reduction process could be observed in the potential window of the solvent used (up to -2.0 V vs. SCE). The $[\mathbf{D}n]^{2+}$ dendrimers[15,19] show two one-electron-transfer processes that correspond to the successive reductions of the 4,4′-bipyridinium core: $bpy^{2+} \rightarrow bpy^{+}$ and $bpy^{+} \rightarrow bpy$. The values of the potentials are gathered in Table 1, and the cyclic voltammetric curve for $[\mathbf{D2}]^{2+}$ is shown in Figure 3.

Table 1: Half-wave potentials versus SCE (saturated calomel electrode)[a] and association constants.[b]

	$bpy^{2+} \rightarrow bpy^{+}$ [V]	$bpy^{+} \rightarrow bpy$ [V]	$K_a \times 10^{-3}$ [M^{-1}]
$[\mathbf{D1}]^{2+}$[c]	−0.25	−0.73	
$[\mathbf{D1}]^{2+}\cdot\mathbf{T}$[c]	−0.30	−0.73	27
$[\mathbf{D2}]^{2+}$	−0.24	−0.72	
$[\mathbf{D2}]^{2+}\cdot\mathbf{T}$	−0.31	−0.72	18
$[\mathbf{D3}]^{2+}$	−0.24	−0.72	
$[\mathbf{D3}]^{2+}\cdot\mathbf{T}$	−0.30	−0.72	9

[a] Solvent: dichloromethane/acetonitrile (9:1), unless otherwise noted; $(NBu_4)PF_6$ (0.1 M); under these conditions more than 95% of the electroactive species are in the complexed form. [b] Solvent: dichloromethane; from fluorescence titration experiments. [c] Solvent: dichloromethane/acetonitrile (3:1).

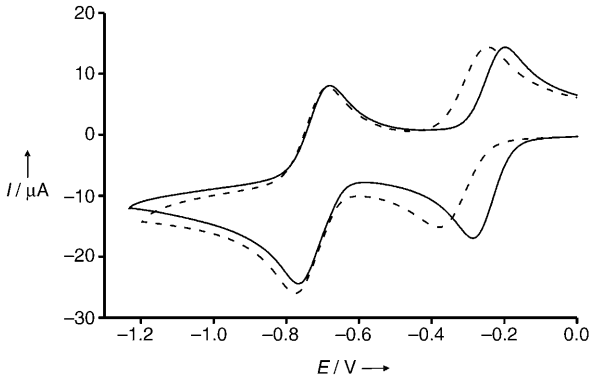


Figure 3. Cyclic voltammetry (CV) curves for a solution of $[\mathbf{D2}]^{2+}$ at 1.0×10^{-3} M in dichloromethane/acetonitrile (9:1) in the absence (——) and presence (-----) of tweezer **T** (3.2×10^{-3} M). Scan rate: 0.2 V s^{-1}; $(NBu_4)PF_6$ (0.1 M).Under such conditions, the association constant (Table 1) shows that about 98% of the species are associated.

Titrations of solutions of tweezer **T** at approximately 10^{-5} M in dichloromethane with the dendrimers did not cause any changes in the absorption spectra relative to the spectra expected from the absorptions of the two components. The fluorescence band of **T** ($\lambda_{max} = 344$ nm), however, was quenched, as shown in Figure 4 for the case of $[\mathbf{D3}]^{2+}$. As dynamic quenching can be ruled out because of the short excited-state lifetime of **T** ($\tau = 9.5$ ns), these results indicate that the tweezer and dendrimers give rise to adducts. We also verified that the fluorescence of **T** is not quenched upon addition to the solution of the dendrons used to construct the dendrimers. Therefore we conclude that adduct formation must involve an interaction between the tweezer and the bipyridinium dendritic cores.

To elucidate the stoichiometry and the strength of adduct formation, fluorescence titration experiments were performed by taking into account[20] the fraction of light absorbed

 © 2005 Wiley-VCH Verlag GmbH & Co. KGaA, Weinheim

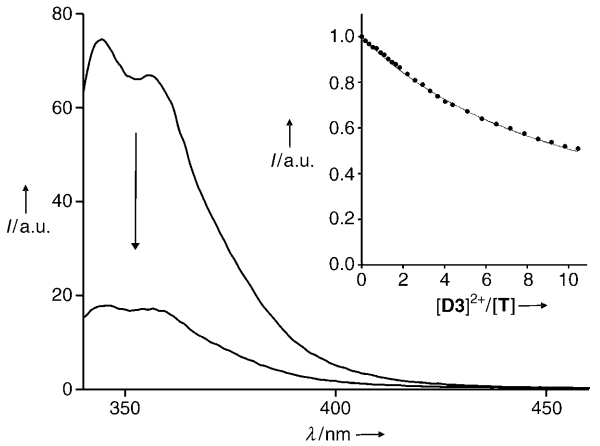


Figure 4. Changes in the fluorescence spectrum of a solution of **T** at 1.6×10^{-5} M in dichloromethane at room temperature upon addition of 10 equivalents of $[\mathbf{D3}]^{2+}$ ($\lambda_{ex}=334$ nm). Inset: The titration curve obtained by plotting the emission intensity at $\lambda=356$ nm as a function of the equivalents of $[\mathbf{D3}]^{2+}$ added, after correction for the fraction of light absorbed by **T**. The solid line shows the fit based on formation of a 1:1 complex. a.u. = arbitrary units.

by the dendrimer. The titration plot obtained for a solution of **T** at 1.6×10^{-5} M in dichloromethane upon addition of $[\mathbf{D3}]^{2+}$ is shown in the inset of Figure 4. As the fluorescence lifetime ($\tau=9.5$ ns) is not affected upon addition of the dendrimer and as there is no evidence of a double-exponential decay, we conclude that even after addition of an excess of dendrimer a significant fraction of tweezer remains uncomplexed in such a dilute solution and that the adducts do not show any appreciable fluorescence.

The results obtained from the titration plots show that 1:1 $[\mathbf{D}\boldsymbol{n}]^{2+}\cdot\mathbf{T}$ adducts are formed, with values for the association constants of the order of $10^4\,\text{M}^{-1}$ which decrease with increasing dendrimer generation (Table 1). A similar dependence of the stability of the complex on the size of the dendrimer was observed in the gas phase by mass spectroscopy.[12] Apparently, even in solution the bipyridinium core is stabilized by "intramolecular solvation", which results from the back-folding of the electron-donor branches, an effect that increases with increasing dendrimer generation.

The CV patterns for reduction of the dendritic cores are affected by the presence of tweezer **T** (Table 1 and Figure 3) which shows that the formation of the adduct involves an interaction between the tweezer and the bipyridinium dendritic cores. In particular, both the cathodic and anodic peaks which correspond to the first one-electron-reduction process of the dendritic core move to more negative values upon addition of the tweezer, whereas the peaks that correspond to the second reduction process are almost unaffected. Such a behavior shows that 1) formation of the adduct is caused by a charge-transfer interaction and 2) the adduct dissociates upon one-electron reduction of the dendritic core.

In conclusion, we have shown that the 4,4′-bipyridinium core of first-, second-, and third-generation $[\mathbf{D}\boldsymbol{n}]^{2+}$ dendrimers that bear Fréchet-type dendrons can be hosted by the molecular tweezer **T**, which comprises a naphthalene moiety and four benzene components bridged by four methylene units. The assembly/disassembly process can be monitored by fluorescence and electrochemical measurements. The tweezering process between **T** and $[\mathbf{D}\boldsymbol{n}]^{2+}$ is quite similar to the threading/dethreading processes observed with bipyridinium-based wire-type units and ring-shaped molecules,[21] with the advantage that tweezering can occur also when the wire-type unit terminates with bulky groups.

Received: March 21, 2005
Published online: June 27, 2005

Keywords: dendrimers · electrochemistry · fluorescence · molecular tweezers · supramolecular chemistry

[1] a) G. R. Newkome, C. Moorefield, F. Vögtle, *Dendrimers and Dendrons: Concepts, Syntheses, and Perspectives*, VCH, Weinheim, **2001**; b) Special issue on *Dendrimers and Nanoscience*, D. Astruc, *C. R. Chim.* **2003**, *6*, 709; c) V. Balzani, P. Ceroni, M. Maestri, C. Saudan, V. Vicinelli, *Top. Curr. Chem.* **2003**, *228*, 159; d) J-P. Majoral, A.-M. Caminade, V. Maraval, *Chem. Commun.* **2002**, 2929; e) S. Hecht, J. M. J. Fréchet, *Angew. Chem.* **2001**, *113*, 76; *Angew. Chem. Int. Ed.* **2001**, *40*, 74; f) M. W. P. L. Baars, E. W. Meijer, *Top. Curr. Chem.* **2001**, *210*, 131.

[2] a) B. Alonso, D. Astruc, J.-C. Blais, S. Nlate, S. Rigaut, J. Ruiz, V. Sartor, C. Valério, *C. R. Acad. Sci. Ser. IIc* **2001**, *173*; b) L. Liu, R. Breslow, *J. Am. Chem. Soc.* **2003**, *125*, 12110; c) M. F. Ottaviani, S. Jockusch, N. J. Turro, D. A. Tomalia, A. Barbon, *Langmuir* **2004**, *20*, 10238.

[3] a) P. A. Chase, R. J. M. K. Gebbink, G. van Koten, *J. Organomet. Chem.* **2004**, *689*, 4016; b) D. Astruc, *Pure Appl. Chem.* **2003**, *75*, 461; c) F. Diederich, B. Felber, *Proc. Natl. Acad. Sci. USA* **2002**, *99*, 4778; d) A. Juris, M. Venturi, P. Ceroni, V. Balzani, S. Campagna, S. Serroni, *Collect. Czech. Chem. Commun.* **2001**, *66*, 1; e) C. B. Gorman, J. C. Smith, *Acc. Chem. Res.* **2001**, *34*, 60; f) I. Cuadrado, M. Morán, C. M. Casado, B. Alonso, J. Losada, *Coord. Chem. Rev.* **1999**, *193–195*, 395.

[4] a) H. D. Abruña, *Anal. Chem.* **2004**, *76*, 310A; b) M.-C. Daniel, F. Ba, J. A. Ruiz, D. Astruc, *Inorg. Chem.* **2004**, *43*, 8649; c) B. Alonso, C. M. Casado, I. Cuadrado, M. Morán, A. E. Kaifer, *Chem. Commun.* **2002**, 1778.

[5] C. M. Cardona, S. Mendoza, A. E. Kaifer, *Chem. Soc. Rev.* **2000**, *29*, 37.

[6] a) T. L. Chasse, C. B. Gorman, *Langmuir* **2004**, *20*, 8792; b) F. Marchioni, M. Venturi, P. Ceroni, V. Balzani, M. Belohradsky, A. M. Elizarov, H.-R. Tseng, J. F. Stoddart, *Chem. Eur. J.* **2004**, *10*, 6361; c) N. D. McClenahan, R. Passalacqua, F. Loiseau, S. Campagna, B. Verheyde, A. Hameurlaine, W. Dehaen, *J. Am. Chem. Soc.* **2003**, *125*, 5356; d) Y. Rio, G. Accorsi, N. Armaroli, D. Felder, E. Levillain, J.-F. Nierengarten, *Chem. Commun.* **2002**, 2830; e) P. J. Dandliker, F. Diederich, M. Gross, C. B. Knobler, A. Louati, *Angew. Chem.* **1994**, *106*, 1821; *Angew. Chem. Int. Ed. Engl.* **1994**, *33*, 1739.

[7] W. Ong, M. Gomez-Kaifer, A. E. Kaifer, *Chem. Commun.* **2004**, 1677.

[8] H. W. Gibson, N. Yamaguchi, L. Hamilton, J. W. Jones, *J. Am. Chem. Soc.* **2002**, *124*, 4653.

[9] K. J. C. van Bommel, G. A. Metselaar, W. Verboom, D. N. Reinhoudt, *J. Org. Chem.* **2001**, *66*, 5405.

[10] J. W. Lee, Y. H. Ko, S.-H. Park, K. Yamaguchi, K. Kim, *Angew. Chem.* **2001**, *113*, 769; *Angew. Chem. Int. Ed.* **2001**, *40*, 746.

[11] a) W. Ong, J. Grindstaff, D. Sobransingh, R. Toba, J. M. Quintela, C. Peinador, A. E. Kaifer, *J. Am. Chem. Soc.* **2005**, *127*, 3353; b) M. Moon, J. Grindstaff, D. Sobransingh, A. E. Kaifer, *Angew. Chem.* **2004**, *116*, 5612; *Angew. Chem. Int. Ed.* **2004**, *43*, 5496; c) W. Ong, A. E. Kaifer, *Angew. Chem.* **2003**, *115*,

 © 2005 Wiley-VCH Verlag GmbH & Co. KGaA, Weinheim

2214; *Angew. Chem. Int. Ed.* **2003**, *42*, 2164; d) R. Toba, J. M. Quintela, C. Peinador, E. Román, A. E. Kaifer, *Chem. Commun.* **2002**, 1768; e) C. M. Cardona, T. D. McCarley, A. E. Kaifer, *J. Org. Chem.* **2000**, *65*, 1857.

[12] For a somewhat related gas-phase study of these systems, see: C. A. Schalley, C. Verhaelen, F.-G. Klärner, U. Hahn, F. Vögtle, *Angew. Chem.* **2005**, *117*, 481; *Angew. Chem. Int. Ed.* **2005**, *44*, 477.

[13] a) F.-G. Klärner, B. Kahlert, *Acc. Chem. Res.* **2003**, *36*, 919; b) F. Marchioni, A. Juris, M. Lobert, U. P. Seelbach, B. Kahlert, F.-G. Klärner, *New J. Chem.* in press.

[14] F.-G. Klärner, U. Burkert, M. Kamieth, R. Boese, *J. Phys. Org. Chem.* **2000**, *13*, 604.

[15] P. Ceroni, V. Vicinelli, M. Maestri, V. Balzani, W. M. Müller, U. Müller, U. Hahn, F. Osswald, F. Vögtle, *New J. Chem.* **2001**, *25*, 989.

[16] D. B. Amabilino, M. Asakawa, P. R. Ashton, R. Ballardini, V. Balzani, M. Belohradsky, A. Credi, M. Higuchi, F. M. Raymo, T. Shimizu, J. F. Stoddart, M. Venturi, K. Yase, *New J. Chem.* **1998**, *22*, 959.

[17] J. N. Demas, G. A. Crosby, *J. Phys. Chem.* **1971**, *75*, 991.

[18] I. B. Berlman, *Handbook of Fluorescence Spectra of Aromatic Molecules, 2nd ed.*, Academic Press, New York, **1971**.

[19] R. Toba, J. M. Quintela, C. Peinador, E. Roman, A. E. Kaifer, *Chem. Commun.* **2001**, 857.

[20] A. Credi, L. Prodi, *Spectrochim. Acta Part A* **1998**, *54*, 159.

[21] V. Balzani, A. Credi, M. Venturi, *Molecular Devices and Machines, A Journey into the Nano World*, Wiley-VCH, Weinheim, **2003**.

 © 2005 Wiley-VCH Verlag GmbH & Co. KGaA, Weinheim

Nanotechnology

Locking and Unlocking of Polyelectrolyte Brushes: Toward the Fabrication of Chemically Controlled Nanoactuators**

*Sergio Moya, Omar Azzaroni, Tamer Farhan, Vicky L. Osborne, and Wilhelm T. S. Huck**

Polymers are ideal building blocks for nanofabrication and the engineering of surfaces because of their response in shape and size to environmental changes in polymer concentration, ionic strength, pH, temperature, and solvent. Furthermore, since they are easy to synthesize, as well as chemically and mechanically robust, polymers are ideal materials to bridge the gap between biological nanomachines and silicon-based devices. Of particular interest herein is the exploration of the use of polymer brushes as nanoactuators.[1]

Polyelectrolytes, that is, polymers containing charged monomers, change from an extended conformation in a solution of low ionic strength to a coiled conformation in solutions of high ionic strength.[2] When polyelectrolytes are covalently attached to a surface to form a brush, the polymer chains show a strongly extended (stretched) conformation in pure water, as a result of both the repulsion between neighboring chains and the repulsion between the monomers.[3–6] In contrast, when polymer brushes are placed in electrolyte solutions, the charges of the pendant groups in the polymer chains are screened, and the minimization of the electrostatic repulsions leads to entropically more favorable collapsed conformations.[4–8] This collapse is comparable to transitions from extended to coil-like conformations commonly observed for polyelectrolytes in solution.[3,4] In the case of polymer brushes, there are constraints on the degrees of freedom related to conformational changes, and as a result the height and the amount of water on the inner brush environment are reduced.[5,8]

Our aim is to use the ionic-strength-sensitive behavior of polyelectrolyte brushes[9–11] in combination with specific binding interactions and ion-size-exclusion effects to design smart polymer surfaces that can be switched between a permanently collapsed and an extended state, where both states have different surface properties. In addition, we aim to find a route toward a "fast switch" that reversibly alternates between different polymer brush conformations, and as a consequence gain control over surface properties[12,13] such as wettability, hydration, and stiffness. Reversibly manipulating the polymer-brush conformation in a chemically selective way (not only by changing the ionic strength) will be a crucial step toward the use of surface-confined polyelectrolytes as nanoactuators.

Cationic brushes of [2-(methacryloyloxy)ethyl]trimethylammonium chloride (METAC)[14] were grown from gold surfaces, patterned into regions containing either initiator or methyl-terminated monolayers (Figure 1a,b), by atom-transfer radical polymerization (ATRP) in an oxygen-free methanol/water (4:1) mixture.[15,16] The responsive behavior of the METAC brushes in different electrolyte environments (NaCl and $MgSO_4$) was studied under liquids using atomic force microscopy (AFM) and a quartz crystal microbalance with dissipation (QCM-D).[17]

The conformational changes in the METAC brush in the presence of 1M NaCl electrolyte solution can be followed with QCM-D,[18,19] where additional information about the water content and the rigidity of the polymer brush can be obtained. Furthermore, QCM-D is well-suited to study the kinetics of the collapse process, which is not possible with AFM, since it takes approximately 15 min before stable images can be acquired after the addition of salt. QCM-D measurements on 50-nm-thick METAC brushes (thickness measured in the dry state with ellipsometry) clearly show an immediate increase in the frequency (Figure 2a) and a decrease in the dissipation (Figure 2b) of the METAC brush/quartz crystal system upon addition of 1M NaCl. The timescales involved in this collapse

[*] Dr. O. Azzaroni, T. Farhan, Dr. V. L. Osborne, Dr. W. T. S. Huck
Melville Laboratory for Polymer Synthesis
Department of Chemistry, University of Cambridge
Lensfield Road, Cambridge CB21EW (UK)
Fax: (+44) 1223-334-866
E-mail: wtsh2@cam.ac.uk
Dr. S. Moya, Dr. W. T. S. Huck
The Nanoscience Center, University of Cambridge
11 J. J. Thomson Avenue, Cambridge CB30FF (UK)

[**] This research was supported financially by the IRC in Nanotechnology, EPSRC (GR/T11555/01), a Marie Curie Research Fellowship (O.A.), DuPont Teijin Films (T.F.), and ICI-Vinamul (V.L.O.).

 © 2005 Wiley-VCH Verlag GmbH & Co. KGaA, Weinheim DOI: 10.1002/anie.200500228

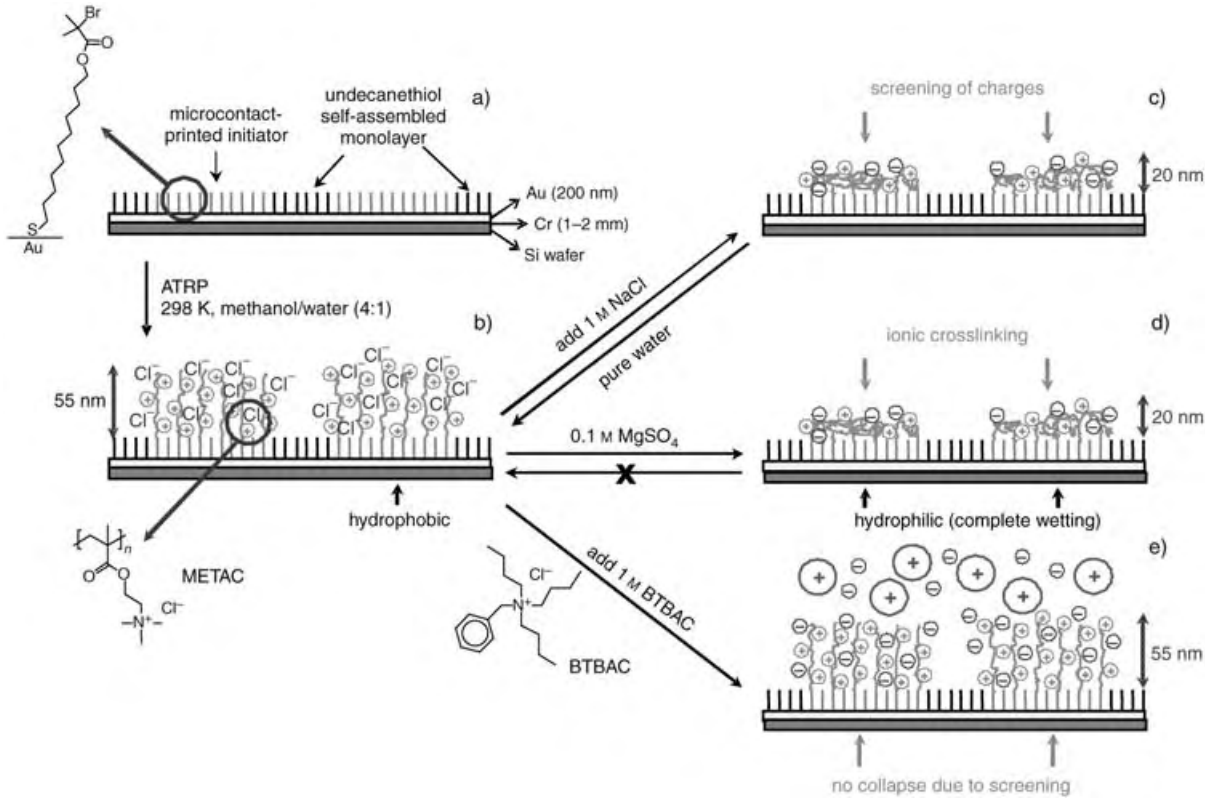


Figure 1. The synthesis (a, b) of polyelectrolyte brushes and their different possible behaviors in response to changes in ionic strength: c) reversible collapse by pure changes in ionic strength, d) irreversible collapse by increases in ionic strength combined with ion pairing, and e) no responsive behavior with the ionic strength because of steric effects.

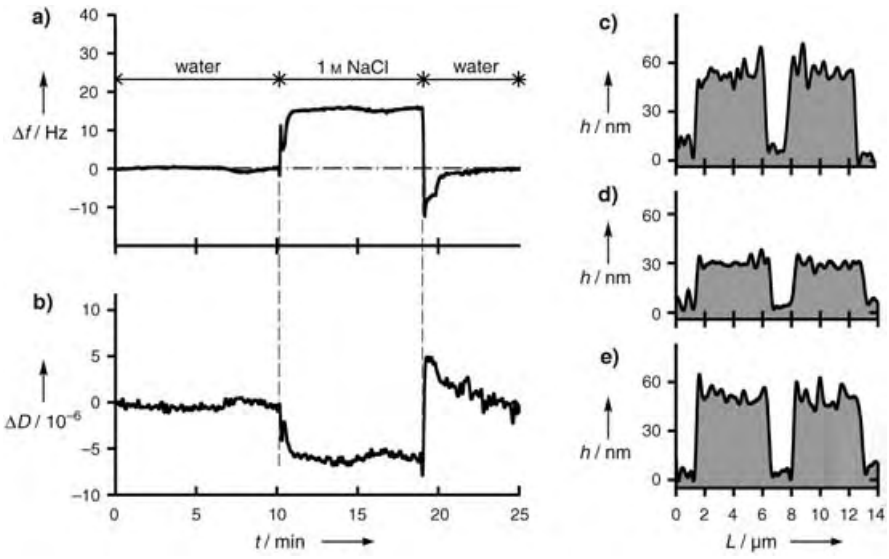


Figure 2. QCM response on a) frequency and b) dissipation when METAC brushes are in the presence of 1 M NaCl. c) Cross-sectional analysis derived from AFM imaging of METAC brushes in water. d) Cross-sectional analysis of patterned METAC brushes imaged in 1 M NaCl. e) Cross-sectional analysis of METAC brushes in water after treatment with 1 M NaCl.

process are less than 3 s. The increase in frequency is related to the loss of water molecules from the polyelectrolyte brush during the collapse process. The decrease in the dissipation (Figure 2b) can be understood as a change from a rather soft polymer film (viscoelastically coupled to the solution) to a more rigid collapsed structure. As shown in Figure 2, when the NaCl solution is replaced with pure water, the frequency and dissipation return to their original values, which indicates that the METAC brush resumes the "extended conformation". To estimate the magnitude of the collapse (brush height, h) under different liquid environments we performed in situ AFM measurements on patterned METAC brushes grown as depicted in Figure 1a and b. By combining AFM imaging (at low loads) under liquids with patterned responsive brushes (Figure 1b) it is possible to obtain reliable information about the actual h value of the polymer brush in the liquid environment. When imaged under pure water (Figure 2c), METAC brushes show $h \approx 55$ nm (extended conformation). In the presence of 1M NaCl electrolyte solutions the polyelectrolyte brushes are completely collapsed, which results in a change in h from ≈ 55 to ≈ 26 nm (Figure 2d). Notably, for NaCl solutions with concentrations lower than 0.1M the

 © 2005 Wiley-VCH Verlag GmbH & Co. KGaA, Weinheim

collapse takes place to a lesser degree. As previously indicated by QCM-D measurements, AFM shows that this collapsed state of the METAC brush in the presence of 1 M NaCl can be easily and completely reversed by simply washing the surface-confined polyelectrolyte with pure water (Figure 2e).

A different effect is observed when $MgSO_4$ is used as the electrolyte instead of NaCl. Addition of 0.5 M $MgSO_4$ electrolyte solution promotes a frequency decrease, while the dissipation is strongly increased (Figure 3a, b). These effects are predominantly a result of the strong changes in viscosity and ionic strength of the liquid environment. AFM imaging (not shown) confirmed, however, that METAC brushes are completely collapsed for $MgSO_4$ concentrations above 10 mM. Surprisingly, the replacement of the 0.5 M $MgSO_4$ electrolyte solution by pure water resulted in an increase of the frequency and simultaneous decrease of the dissipation over the values previously obtained in pure water before flushing with 0.5 M $MgSO_4$. This result can be interpreted as the METAC brushes remaining in a collapsed state while immersed in pure water. When the samples were stored in the QCM cell in pure water overnight, no changes in frequency or dissipation were detected. This finding implies an irreversible collapse of METAC brushes in the presence of SO_4^{2-} anions. However, these collapsed brushes can be "unlocked" by passing a concentrated NaCl solution (1 M) through the QCM chamber and then flushing with water. Figure 3 shows that after this unlocking procedure, both the frequency and dissipation signals return to the original values for fully stretched brushes in water. AFM cross-sectional analysis of METAC brushes ($h \approx 55$ nm in the extended conformation) clearly shows that the surface-confined polyelectrolytes remain collapsed ($h \approx 28$ nm) in pure water after treatment with 0.5 M $MgSO_4$ (Figure 3c).

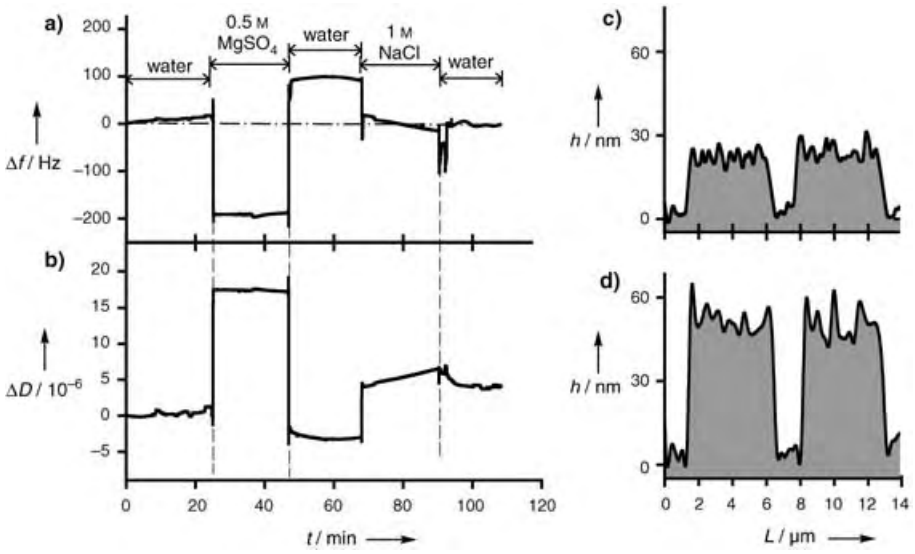


Figure 3. QCM response on a) frequency and b) dissipation when METAC brushes are placed in different electrolyte environments (0.5 M $MgSO_4$ and 1 M NaCl). Cross-sectional analysis, derived from AFM imaging performed under pure water, corresponding to c) patterned METAC brushes placed in 0.5 M $MgSO_4$ for 20 min and d) patterned METAC brushes placed in 0.5 M $MgSO_4$ for 20 min, rinsed with water, and then placed for 30 min in 1 M NaCl.

Figure 3d shows that after treatment of the SO_4^{2-}-collapsed METAC brushes with 1 M NaCl and subsequently storage in pure water, the extended conformation of the brushes is clearly restored ($h \approx 53$ nm). The excess of NaCl can be used to displace the equilibrium SO_4^{2-}/quaternary ammonium ion in such a way that the original chemical/ionic (Cl^--coordinated METAC) composition inside the brush is restored. In addition, washing with water depletes the NaCl excess and leads to the fully extended conformation.

The next step was to measure the contact angle to further characterize the surface properties of collapsed and extended brushes. Surfaces modified with METAC brushes ($h \approx 39$ nm) have a static contact angle of approximately 58° (Figure 4a). Treatment of brushes with 0.5 M $MgSO_4$ and washing with water results in a completely hydrophilic surface (Figure 4b), and the brush is in a collapsed state. The wettability of the surface is not affected by extensive rinsing with water, which demonstrates the robustness of the switch to the wetting behavior (Figure 4c).

The wetting properties are quite surprising, as we expected that the collapsed state (which involves a significant loss of water) would be more hydrophobic than the fully hydrated extended brushes. We hypothesize that during the collapse a considerable quantity of electrolyte (Mg^{2+} and SO_4^{2-} ions) is retained within the polyelectrolyte brush. This excess of strongly hydrated ions results in a highly hydrophilic behavior of the polymer film. QCM measurements confirmed that the collapsed brushes did not exchange salts with a pure water phase for at least 12 hours. "Unlocking" the brushes with NaCl and subsequent rinsing with water restores the original wetting properties (static contact angle: 58°).

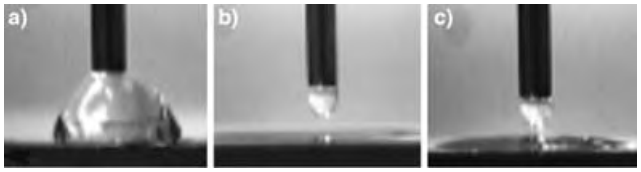


Figure 4. Contact-angle measurements of different METAC-modified gold substrates corresponding to a) Cl^--coordinated METAC brushes, b) SO_4^{2-}-treated METAC brushes, and c) SO_4^{2-}-treated METAC brushes after the substrate was stored for 8 min in pure water.

As a further extension of the combination of ionic strength effects and the chemical switching of the brush, we characterized the responsive behavior of METAC brushes with salts of different cation sizes. We treated METAC brushes with NaCl and benzyltributylammonium chloride

 © 2005 Wiley-VCH Verlag GmbH & Co. KGaA, Weinheim

(BTBAC, see Figure 1e). Both electrolytes have the same anion but a very different cation size. The AFM cross-sectional analysis in Figure 5 clearly shows that in the presence of 10 mM BTBAC the brushes remain fully extended, whereas the same brushes collapse to $h \approx 31$ nm in 10 mM NaCl. Chloride anion transport into the brush cannot be separated from the transport of their cationic counterions. When a bulky cation such as BTBA is chosen, whose permeability into the brush is hindered by steric effects, the ionic strength within the brush environment remains low, despite a high concentration of electrolyte outside the brush. As a result, the brushes do not collapse, thus opening up the possibility to decouple the conformational response of the brush from the external solution.

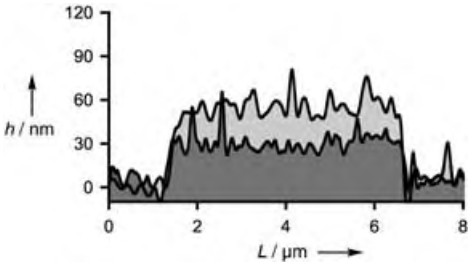


Figure 5. Cross-sectional analysis, derived from AFM imaging performed in 10 mM benzyltributylammonium chloride (light gray) and in 10 mM NaCl (dark gray).

In conclusion, the characterization of polyelectrolyte brushes by using the powerful combination of QCM-D and AFM techniques[20] has enabled us to demonstrate three different cases of brush behavior in the presence of salts: a) their response to the ionic strength, b) strong ion-pairing effects in the case of SO_4^{2-} ions, and c) the exclusion of the ions introducing steric effects. This rich responsiveness can be exploited to create surfaces where the brush is collapsed or extended in either low- or high-ionic-strength conditions (Figure 1). These states not only correspond to changes in thickness, but also to changes in hydration state and wettability. We think that this responsive behavior makes polymer brushes excellent candidates to be used as nano-actuators. By using strong binding interactions between the SO_4^{2-} anions and the quaternary ammonium pendant groups on the METAC brush, we have been able to "lock" the polyelectrolyte conformation in a completely hydrophilic collapsed state. To achieve the actuating character of the polyelectrolyte brush and to "unlock" it we exchanged the "locking" SO_4^{2-} counterions coordinated to the quaternary ammonium pendant groups for Cl^- anions, which restored the original extended state and surface properties.

The extended state could also be "locked" by introducing chloride salts with very bulky cations, decoupling the brush response from the ionic strength in solution, and introducing selectivity. The "lock" and "unlock" METAC brush conformation is also a simple and reversible way to change surface properties, thickness, and wettability, which could control the permeability of brushes if used as a barrier on a coating, and could stop or change the speed of a fluid in a liquid-cell device.

Received: January 20, 2005
Published online: June 21, 2005

Keywords: nanotechnology · polyelectrolytes · scanning probe microscopy · surface chemistry · surface properties

[1] R. A. L. Jones in *Soft Machines*, Oxford University Press, Oxford, **2004**, 134–143.
[2] P. G. De Gennes, *J. Chem. Phys.* **1974**, *60*, 5030–5042.
[3] S. Alexander, *J. Phys. (Paris)* **1977**, *28*, 977–981.
[4] P. G. DeGennes, *Macromolecules* **1980**, *13*, 1069–1075.
[5] E. B. Zhulina, O. V. Borisov, V. A. Pryamitsyn, T. M. Birshtein, *Macromolecules* **1991**, *24*, 140–149.
[6] E. B. Zhulina, O. V. Borisov, T. M. Birshtein, *Macromolecules* **1999**, *32*, 8189–8196.
[7] E. B. Zhulina, J. Klein Wolterink, O. V. Borisov, *Macromolecules* **2000**, *33*, 4945–4953.
[8] R. S. Ross, P. Pincus, *Macromolecules* **1992**, *25*, 2177–2183.
[9] E. P. K. Currie, A. B. Sieval, M. Avena, H. Zuilhof, E. J. R. Sudhoelter, M. A. Cohen-Stuart, *Langmuir* **1999**, *15*, 7116–7118.
[10] E. P. K. Currie, A. B. Sieval, G. J. Fleer, M. A. Cohen-Stuart, *Langmuir* **2000**, *16*, 8324–8333.
[11] R. Konradi, J. Ruehe, *Macromolecules* **2004**, *37*, 6954–6961.
[12] J. Klein, E. Kumacheva, D. Mahalu, D. Perahia, L. J. Fetters, *Nature* **1994**, *370*, 634–636.
[13] J. Rühe in *Polymer Brushes* (Eds.: R. C. Advincula, W. J. Brittain, K. C. Caster, J. Rühe), Wiley-VCH, Weinheim, **2004**, pp. 1–28.
[14] V. L. Osborne, D. M. Jones, W. T. S. Huck, *Chem. Commun.* **2002**, 1838–1839.
[15] D. M. Jones, A. A. Brown, W. T. S. Huck, *Langmuir* **2002**, *18*, 1265–1269.
[16] W. X. Huang, G. L. Baker, M. L. Bruening, *Angew. Chem.* **2001**, *113*, 1558–1560; *Angew. Chem. Int. Ed.* **2001**, *40*, 1510–1512.
[17] F. Höök, M Rodahl, B. Kasemo, P. Brzezinski, *Proc. Natl. Acad. Sci. USA* **1998**, 12271–12276.
[18] F. Höök, B. Kasemo, T. Nylander, C. Fant, K. Scott, H. Elwing, *Anal. Chem.* **2001**, *73*, 5796–5804.
[19] G. Zhang, *Macromolecules* **2004**, *37*, 6553–6557.
[20] S. M. Notley, S. Briggs, V. S. J. Craig, L. Wågberg, *Phys. Chem. Chem. Phys.* **2004**, *6*, 2379–2386.

 © 2005 Wiley-VCH Verlag GmbH & Co. KGaA, Weinheim

Protein Engineering

An *S*-Selective Lipase Was Created by Rational Redesign and the Enantioselectivity Increased with Temperature**

*Anders O. Magnusson, Mohamad Takwa, Anders Hamberg, and Karl Hult**

Lipases have characteristics that make them attractive tools for the synthesis of fine chemicals. They catalyze acyl-transfer reactions and are stable in organic solvents and at high temperatures. The possibility of modifying the performance of enzymes by biomolecular methods gives the opportunity to create tailor-made catalysts for each desired application. The high enantioselectivity of lipases toward secondary alcohols is a property often used in organic synthesis.[1] The enantioselectivity follows the Kazlauskas rule which normally predicts an *R* selectivity.[2] Structural explanations now exist for the strong chiral preference of many lipases.[3] Efforts to modify their properties have resulted in large improvements of the catalyst, such as increased stability and activity, but few articles report large effects on the enantioselectivity.[4,5] The largest changes in enantioselectivity of lipases concern substrates with a chiral center on the acyl chain of the substrate.[6] We redesigned the active site of *Candida antarctica* lipase B (CALB) to modify its specificity toward secondary alcohols. The enantioselectivity was greatly changed and an *S*-selective enzyme was created, mainly as a result of the increased activity toward the slow-reacting enantiomer. The mutant had very unusual behavior: the enantioselectivity increased strongly with temperature, and thermodynamic analysis showed that the altered enantioselectivity was dominated by entropy. In dynamic kinetic resolution, lipases can be used to produce close to 100% of the *R* enantiomer.[7] The creation of an *S*-selective lipase affords the possibility of achieving high yields of the *S* enantiomer.

CALB is a very robust and efficient catalyst that shows a high regio- and enantioselectivity.[8] The active site contains the catalytic triad Ser-His-Asp, an oxyanion hole that stabilizes the transition states, and a cavity called the stereospecificity pocket.[9] The strong *R* selectivity of CALB toward secondary alcohols is explained by the different binding modes of the enantiomers in the stereospecificity pocket.[10,11] The fast-reacting enantiomer positions its medium-sized substituent in the stereospecificity pocket and its large substituent toward the active-site entrance. For the slow-reacting enantiomer, the medium-sized substituent points toward the active-site entrance and the large substituent is placed in the stereospecificity pocket. Although the large substituent is not easily fitted in the stereospecificity pocket, this is the catalytically active binding mode for the slow-reacting enantiomer. The largest substituent that is well accommodated in the stereospecificity pocket is an ethyl group. This steric limitation makes CALB very selective toward secondary alcohols with a medium-sized substituent not larger than an ethyl group and a large substituent bigger than an ethyl group. When both substituents are larger than an ethyl group, the selectivity is low and the catalytic activity drops drastically.[11] To overcome this limitation in size and to increase the number of secondary alcohols that are good substrates for CALB, we earlier redesigned the volume of the stereospecificity pocket. Trp 104, which forms the bottom of the stereospecificity pocket, was replaced by smaller amino acids. The redesigned stereospecificity pockets were shown to readily accommodate much larger substituents than the stereospecificity pocket of the wild-type lipase. The mutant with the largest stereospecificity pocket, Trp 104 Ala, had a specificity constant (k_{cat}/K_M) of 830 $s^{-1}M^{-1}$ toward 5-nonanol, 5500 times greater than that of the wild-type enzyme.[12]

A larger stereospecificity pocket should affect the enantioselectivity of the lipase. Chiral secondary alcohols might easily position their large substituent in the redesigned stereospecificity pocket of the Trp 104 Ala mutant, which would lead to a low enantioselectivity. Computer modeling was used to compare the binding of secondary alcohols in the active site of the Trp 104 Ala mutant and wild-type CALB. Energy minimizations were performed on the tetrahedral intermediate of both lipase variants with the butanoate ester of (*R*)- and (*S*)-1-phenylethanol covalently bound to the catalytic serine (Figure 1). The *R* enantiomer was similarly positioned in both wild-type CALB and the Trp 104 Ala mutant; the large substituent (phenyl group) was oriented toward the active-site entrance and the medium-sized substituent (methyl group) was positioned in the stereospecificity pocket. The *S* enantiomer had different orientations in the two enzyme variants. In the wild-type lipase the slow-reacting enantiomer could not be accommodated in a catalytically active tetrahedral intermediate, as the phenyl group was too large to fit in the stereospecificity pocket. This finding is in accordance with a low reaction rate for the *S* enantiomer and a high enantioselectivity favoring the *R* enantiomer. However, the redesigned stereospecificity pocket of the Trp 104 Ala mutant comfortably accommodated the phenyl group.

We tested the low enantioselectivity expected for the Trp 104 Ala mutant by performing acyl-transfer reactions from vinyl butanoate to four secondary alcohols in cyclohexane. With 3-methyl-2-butanol, the selectivity for the *R* enantiomer dropped by a factor of 160 as a result of the mutation (Table 1, entries 6 and 7). With 2-hexanol, the *R* selectivity of several hundred for the wild-type enzyme changed into a low *S* selectivity for the mutant (Table 1, entry 5). Thus methyl, isopropyl, and butyl groups are almost equally well-accommodated in the stereospecificity pocket of the Trp 104 Ala

[*] A. O. Magnusson, M. Takwa, A. Hamberg, Prof. K. Hult
Royal Institute of Technology (KTH)
Department of Biochemistry, School of Biotechnology
AlbaNova University Center
10691 Stockholm (Sweden)
Fax: (+46) 8-5537-8468
E-mail: kalle@biotech.kth.se

[**] This work was supported by the Swedish Research Council and the Erasmus program. The graphical material presenting the active sites of the lipases was prepared by Linda Fransson.

Supporting information for this article is available on the WWW under http://www.angewandte.org or from the author.

 © 2005 Wiley-VCH Verlag GmbH & Co. KGaA, Weinheim DOI: 10.1002/anie.200500971

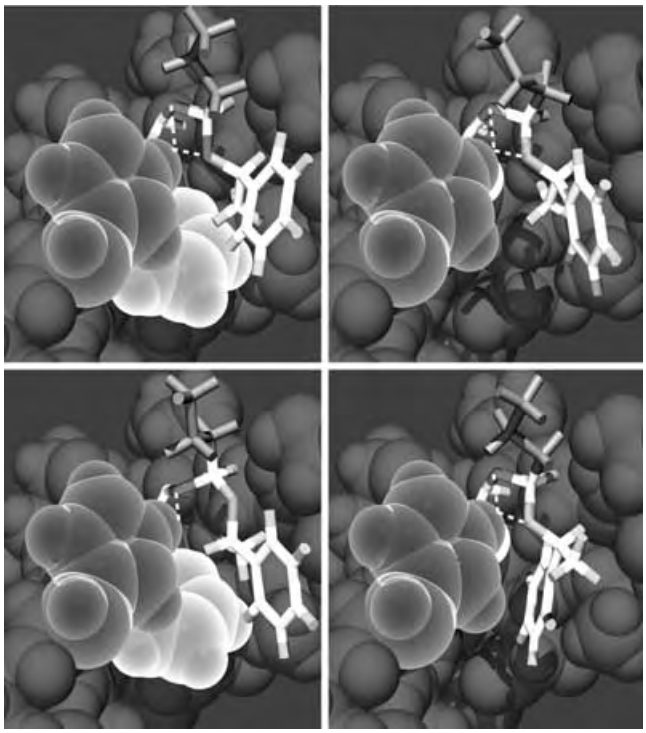


Figure 1. The active site of wild-type CALB (left) and Trp104Ala mutant (right) with the butanoate ester of (*R*)-1-phenylethanol (top) and (*S*)-1-phenylethanol (bottom) covalently bound to the catalytic serine in the tetrahedral reaction intermediate. The substrate is presented with a stick model and amino acid 104 with a space-filling model in white. The *R* enantiomer has a similar configuration in the wild-type CALB and Trp104Ala mutant: the large substituent (phenyl) points toward the active-site entrance and the medium-sized substituent (methyl) is positioned in the stereospecificity pocket. In the wild-type CALB, the *S* enantiomer cannot position its phenyl group in the stereospecificity pocket, and not all the hydrogen bonds required for catalysis can be formed. In the Trp104Ala mutant, the phenyl group is comfortably accommodated in the space liberated by the mutation in the stereospecificity pocket.

mutant. Interestingly, while wild-type CALB has a very high *R* selectivity, the mutant has a moderate *S* selectivity toward the two secondary alcohols with the bulky phenyl group as the large substituent (Table 1, entries 3 and 4). The phenyl group can probably fit well in the space liberated by the Trp104Ala mutation.

The enantioselectivity of wild-type CALB is very sensitive to the solvent used in the incubation.[13] The effects of the solvent and temperature on the enantioselectivity of the Trp104Ala mutant were investigated. We resolved 1-phenylethanol in three solvents and at temperatures between 10 and 70°C (Figure 2). Both the solvent and the temperature had

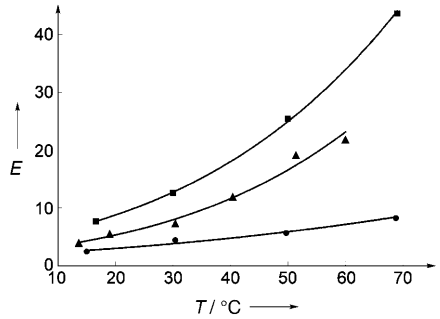
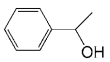
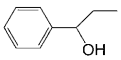
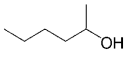


Figure 2. The *S* selectivity increased with temperature in the resolution of 1-phenylethanol catalyzed by the Trp104Ala mutant of CALB in acetonitrile (●), cyclohexane (▲), and *cis*-decalin (■). Trend lines are plotted according to Equation (1) using the values of the entropy and enthalpy terms in Table 1.

large effects on the enantioselectivity. The *S* selectivity increased to a large extent with the molecular size of the solvent. An increase in the temperature also favored the *S* enantiomer, which resulted in the unusual behavior of an increasing enantioselectivity with temperature. These effects gave an *S* selectivity of 44 for the Trp104Ala mutant toward 1-phenylethanol at 69°C in *cis*-decalin. Wild-type CALB is

Table 1: Thermodynamic components for acyl-transfer reactions from vinyl butanoate to secondary alcohols in various solvents catalyzed by wild-type CALB and the Trp104Ala mutant. Differential entropy ($\Delta_{S-R}\Delta S^{\neq}$) and enthalpy ($\Delta_{S-R}\Delta H^{\neq}$) and their standard errors were determined from the linear regression of $R\times\ln E$ versus T^{-1}. The entropic contribution ($T\Delta_{S-R}\Delta S^{\neq}$), Gibbs free energy ($\Delta_{S-R}\Delta G^{\neq}$), and the enantioselectivity (E) were calculated for 303 K. The preferred enantiomer (Pe) and the racemic temperature (T_R) are also presented.

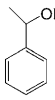
Entry	CALB variant	Sec. alcohol	Solv.	Pe	E[a]	$\Delta_{S-R}\Delta G^{\neq}$[a] [kJ mol^{-1}]	$T\Delta_{S-R}\Delta S^{\neq}$[a] [kJ mol^{-1}]	$\Delta_{S-R}\Delta H^{\neq}$ [kJ mol^{-1}]	$\Delta_{S-R}\Delta S^{\neq}$ [J K^{-1} mol^{-1}]	T_R [K]
1	Trp104Ala		CH_3CN	*S*	3.8	−3.3	21	18±2	70±8	250
2	Trp104Ala		Deca[b]	*S*	13	−6.4	34	27.5±0.3	112±1	250
3	Trp104Ala		cHex[c]	*S*	7.9	−5.2	35	30±2	116±5	260
4	Trp104Ala		cHex[c]	*S*	12	−6.3	26	20±1	87±4	230
5	Trp104Ala		cHex[c]	*S*	2.2	−1.9	23	21±2	77±5	280
6	Trp104Ala		cHex[c]	*R*	2.8	2.6	26	28±2	84±5	330
7	wild-type		cHex[c]	*R*	470	15	7.8	23±2	26±7	900

[a] Calculated for 303 K from the linear relation of Equation (1). [b] *cis*-Decalin. [c] Cyclohexane.

 © 2005 Wiley-VCH Verlag GmbH & Co. KGaA, Weinheim

used in dynamic kinetic resolution to achieve the *R* enantiomer,[14] and by using the Trp104Ala mutant in the same processes a high yield and enantiomeric excess could be achieved for the *S* enantiomer. The CALB mutant also has a higher activity (Table 2) and stability compared to those of subtilisin, which has been used in dynamic kinetic resolution to achieve the *S* enantiomer.[15]

Table 2: Apparent kinetic constants, specificity constants, preferred enantiomer (Pe), and *E* value of the wild-type CALB and Trp104Ala mutant for the acylation of the pure enantiomers of 1-phenylethanol in cyclohexane at 30°C with 500 mM vinyl butanoate.

CALB variant	Substrate enantiomer		k_{cat}^{app} [s^{-1}]	K_M^{app} [mM]	k_{cat}/K_M [$s^{-1}\,M^{-1}$][a]	Pe	E[a]
Wild-type		*R*	570	61	9300	*R*	1300000
		S	0.00053	71	0.0075		
Trp104Ala		*R*	4.4	29	150	*S*	6.6
		S	34	34	1000		

[a] Calculated from k_{cat}^{app} and K_M^{app}.

The Trp104Ala variant showed the very unusual behavior of increasing enantioselectivity with temperature for all the substrates tested, except for 3-methyl-2-butanol where the selectivity changed from the *R* to the *S* enantiomer. The selectivity between the two enantiomers depends on the difference in activation free energy ($\Delta_{S-R}\Delta G^{\ddagger}$), which can be divided into its enthalpic ($\Delta_{S-R}\Delta H^{\ddagger}$) and entropic components ($\Delta_{S-R}\Delta S^{\ddagger}$) according to Equation (1), where *R* is the gas constant and *T* is the temperature in Kelvin.

$$E = e^{-\Delta_{S-R}\Delta G^{\ddagger}/RT} = e^{(-\Delta_{S-R}\Delta H^{\ddagger} + T\Delta_{S-R}\Delta S^{\ddagger})/RT} \quad (1)$$

The value of the thermodynamic components can be calculated by determining the enantioselectivity (*E*) at several temperatures. This was done for the Trp104Ala mutant with 1-phenylethanol in three solvents (see Figure 2) and with three other secondary alcohols in cyclohexane. The enantioselectivity of the wild-type enzyme was determined for only one of the substrates at several temperatures; with the other substrates the *R* selectivity was too large to be accurately determined by resolution. Equation (1) was rearranged into Equation (2) and, if one assumes that the thermodynamic components are constant within the experimental temperature range, there is a linear correlation between $R\ln E$ and T^{-1}.[16] A good linearity was also seen, which justified this assumption. The differential entropy and enthalpy terms and their standard errors were calculated (Table 1) by linear regression to Equation (2).

$$R\ln E = -\frac{\Delta_{S-R}\Delta G^{\ddagger}}{T} = -\frac{\Delta_{S-R}\Delta H^{\ddagger}}{T} + \Delta_{S-R}\Delta S^{\ddagger} \quad (2)$$

In all the resolutions tested, the *R* enantiomer was favored by the enthalpy ($\Delta_{S-R}\Delta H^{\ddagger} > 0$) and the *S* enantiomer by the entropy ($\Delta_{S-R}\Delta S^{\ddagger} > 0$). The resolution of 3-methyl-2-butanol catalyzed by wild-type CALB afforded the *R* enantiomer, as the enthalpic contribution was larger than the entropic one (Table 1, entry 7). The magnitudes of the thermodynamic components agree well with the values obtained for the resolution of other secondary alcohols catalyzed by the same enzyme.[17] For the resolutions catalyzed by the Trp104Ala mutant, the enthalpic contribution was not significantly different from that of the wild-type enzyme. However, the entropic contribution increased so much that the enantioselectivity was eliminated or reversed. An enantioselectivity dominated by the entropy afforded a very unusual temperature dependence that has rarely been seen before.[18] The enantioselectivity of CALB Trp104Ala increased strongly with temperature: in the resolution of 1-phenylethanol in *cis*-decalin an *E*-value of 44 in favor of the *S* enantiomer was reached at 69°C (Figure 2). The racemic temperature ($T_R = \Delta_{S-R}\Delta H/\Delta_{S-R}\Delta S$),[19] at which the enantioselectivity is 1, was 330 K for this mutant toward 3-methyl-2-butanol; below this temperature the mutant was *R*-selective and above it, *S*-selective. A racemic temperature outside the experimental range should only be used to compare enthalphic and entropic contributions. Resolutions catalyzed by the Trp104Ala mutant have a much lower racemic temperature (Table 1) than those catalyzed by the wild-type lipase. This corresponds to the three to four times higher entropy contribution of the mutant.

The enantioselectivity toward 1-phenylethanol changed from a strong *R* selectivity with wild-type CALB to an *S* selectivity with the Trp104Ala mutant. The Trp104Ala mutation increases the size of the stereospecificity pocket, which should facilitate the binding of the *S* enantiomer in an orientation conducive to catalysis. This would lead to a higher ratio of productive binding of the *S* enantiomer in the Trp104Ala mutant compared to that in the wild-type CALB, and accordingly to a higher reaction rate. The apparent kinetic constants (k_{cat}^{app} and k_M^{app}) were determined for wild-type CALB and Trp104Ala mutant for the acylation of (*R*)- and (*S*)-1-phenylethanol with vinyl butanoate (500 mM) in cyclohexane at 30°C (Table 2). The specificity constant (k_{cat}/K_M) and the enantioselectivity (*E*) were calculated using the kinetic constants determined for both enzyme variants (Table 2).

The enantioselectivity was changed by a factor of 8300000 by the carefully selected point mutation in the stereospecificity pocket of CALB, which is more than any other example found in the literature. Rational design has been used to create variants of a phosphotriesterase with 6900000-fold difference in enantioselectivity, but the largest difference compared to the wild-type enzyme was 18000-fold.[5] The huge change in enantioselectivity by the Trp104Ala mutation of CALB was mainly achieved by increasing the apparent catalytic constant (k_{cat}^{app}) toward the slow-reacting enantiomer. The apparent catalytic constant toward (*S*)-1-phenylethanol was 64000 times larger for the mutant than for the wild-type CALB, while the same constant decreased by a factor of 130 toward the *R* enantiomer. However, the mutation did not affect the apparent Michaelis constant (k_M^{app}) to a large extent. The apparent Michaelis constants for the Trp104Ala mutant

 © 2005 Wiley-VCH Verlag GmbH & Co. KGaA, Weinheim

were almost equal toward the *R* and *S* enantiomers, and they both decreased by a factor of two compared to those of the wild-type enzyme.

In summary, the redesigned stereospecificity pocket of *Candida antarctica* lipase B (CALB) was able to accommodate much larger groups than that of the wild-type lipase. This change transformed the strongly *R*-selective wild-type CALB into an *S*-selective mutant. The *S* selectivity increased with temperature and it was dominated by entropy. For 1-phenylethanol the enantioselectivity changed by a factor of 8300000 as a result of the mutation. This was mainly achieved by an increased reaction rate toward the *S* enantiomer, which resulted in a very effective catalyst with a high specificity constant of $1000\ s^{-1}M^{-1}$. The *S* selectivity of the Trp104Ala mutant could be increased to a respectable value of $E = 44$ when the reaction was conducted in *cis*-decalin at 69 °C. The altered enantioselectivity of CALB is a demonstration of the possibilities offered by protein redesign and shows the importance of the entropy contribution in enzyme catalysis.

Received: March 16, 2005
Published online: June 23, 2005

Keywords: enantioselectivity · enzyme catalysis · hydrolases · protein engineering · thermodynamics

[1] T. Ema, *Curr. Org. Chem.* **2004**, *8*, 1009.
[2] R. J. Kazlauskas, A. N. E. Weissfloch, A. T. Rappaport, L. A. Cuccia, *J. Org. Chem.* **1991**, *56*, 2656.
[3] a) M. Cygler, P. Grochulski, R. J. Kazlauskas, J. D. Schrag, F. Bouthillier, B. Rubin, A. N. Serreqi, A. K. Gupta, *J. Am. Chem. Soc.* **1994**, *116*, 3180; b) A. Kovac, H. Scheib, J. Pleiss, R. D. Schmid, F. Paltauf, *Eur. J. Lipid Sci. Technol.* **2000**, *102*, 61; c) R. V. Muralidhar, R. R. Chirumamilla, R. Marchant, V. N. Ramachandran, O. P. Ward, P. Nigam, *World J. Microbiol. Biotechnol.* **2002**, *18*, 81.
[4] H. Scheib, J. Pleiss, P. Stadler, A. Kovac, A. P. Potthoff, L. Haalck, F. Spener, F. Paltauf, R. D. Schmid, *Protein Eng.* **1998**, *11*, 675.
[5] M. Chen-Goodspeed, M. A. Sogorb, F. Wu, F. M. Raushel, *Biochemistry* **2001**, *40*, 1332.
[6] a) Y. Koga, K. Kato, H. Nakano, T. Yamane, *J. Mol. Biol.* **2003**, *331*, 585; b) D. Zha, S. Wilensek, M. Hermes, K.-E. Jaeger, M. T. Reetz, *Chem. Commun.* **2001**, *24*, 2664.
[7] B. A. Persson, A. L. E. Larsson, M. Le Ray, J.-E. Baeckvall, *J. Am. Chem. Soc.* **1999**, *121*, 1645.
[8] a) E. M. Anderson, K. M. Larsson, O. Kirk, *Biocatal. Biotransform.* **1998**, *16*, 181; b) D. Rotticci, J. Ottosson, T. Norin, K. Hult, *Methods Biotechnol.* **2001**, *15*, 261.
[9] a) J. Uppenberg, N. Oehrner, M. Norin, K. Hult, G. J. Kleywegt, S. Patkar, V. Waagen, T. Anthonsen, T. A. Jones, *Biochemistry* **1995**, *34*, 16838; b) C. Orrenius, F. Haeffner, D. Rotticci, N. Ohrner, T. Norin, K. Hult, *Biocatal. Biotransform.* **1998**, *16*, 1.
[10] F. Haeffner, T. Norin, K. Hult, *Biophys. J.* **1998**, *74*, 1251.
[11] D. Rotticci, F. Haeffner, C. Orrenius, T. Norin, K. Hult, *J. Mol. Catal. B* **1998**, *5*, 267.
[12] A. O. Magnusson, J. C. Rotticci-Mulder, A. Santagostina, K. Hult, *ChemBioChem* **2005**, *6*, 1051.
[13] J. Ottosson, L. Fransson, J. W. King, K. Hult, *Biochim. Biophys. Acta* **2002**, *1594*, 325.
[14] B. Martin-Matute, M. Edin, K. Bogar, J.-E. Baeckvall, *Angew. Chem.* **2004**, *116*, 6697; *Angew. Chem. Int. Ed.* **2004**, *43*, 6535.
[15] M.-J. Kim, Y. I. Chung, Y. K. Choi, H. K. Lee, D. Kim, J. Park, *J. Am. Chem. Soc.* **2003**, *125*, 11494.
[16] P. L. A. Overbeeke, J. Ottosson, K. Hult, J. A. Jongejan, J. A. Duine, *Biocatal. Biotransform.* **1999**, *17*, 61.
[17] J. Ottosson, L. Fransson, K. Hult, *Protein Sci.* **2002**, *11*, 1462.
[18] a) R. S. Phillips, *Enzyme Microb. Technol.* **1992**, *14*, 417; b) K. Watanabe, T. Koshiba, Y. Yasufuku, T. Miyazawa, S.-I. Ueji, *Bioorg. Chem.* **2001**, *30*, 65; c) P. Lopez-Serrano, M. A. Wegman, F. van Rantwijk, R. A. Sheldon, *Tetrahedron Asymmetry* **2001**, *12*, 235; d) B. Galunsky, S. Ignatova, V. Kasche, *Biochim. Biophys. Acta* **1997**, *1343*, 130.
[19] R. S. Phillips, *Trends Biotechnol.* **1996**, *14*, 13.

 © 2005 Wiley-VCH Verlag GmbH & Co. KGaA, Weinheim

Photocatalyis with Visible Light

Photocatalytic Nanodiodes for Visible-Light Photocatalysis**

*Hyun G. Kim, Pramod H. Borse, Wonyong Choi, and Jae S. Lee**

Photocatalysts that respond to visible light ($\lambda < 400$ nm) are needed to utilize the main part of the solar spectrum for production of hydrogen energy by splitting water,[1,2] purification of water and air,[3] and other applications.[4] Traditional visible-light photocatalysts are either unstable upon illumination with light (e.g., CdS, CdSe)[5] or have low activity (e.g., WO_3, Fe_2O_3).[6] Recently, some UV-active oxides functioned as visible-light photocatalysts by substitutional doping of metals (as in $MTiO_2$ (M = Fe, V, Mn)[7] and $Ni_xIn_{1-x}TaO_4$[8]), reduction of TiO_2 (as in TiO_x ($x < 2$)),[9] and anion doping with N, C, and S (as in $TiO_{2-x}N_x$,[10] $TiO_{2-x}C_x$,[11] TaON,[12] and $Sm_2Ti_2O_5S_2$[13]). However, these doped materials, in general, show a small absorption in the visible-light region, leading to low activities.[14] New and more efficient visible-light photocatalysts are needed to meet the requirements of future environmental and energy technologies driven by solar energy.

Herein we describe a novel configuration of composite solids designated as photocatalytic nanodiodes (PCD). These contain nano-islands of p-type $CaFe_2O_4$ interfaced over a highly crystalline layered perovskite base lattice (n-type $PbBi_2Nb_{1.9}W_{0.1}O_9$), yielding nanodimensional p–n junctions.

[*] Dr. H. G. Kim, Dr. P. H. Borse, Prof. W. Choi, Prof. J. S. Lee
Department of Chemical Engineering and
School of Environmental Science & Engineering
Pohang University of Science and Technology
San-31 Hyoja-dong, Pohang 790-784 (Korea)
Fax: (+81) 54-279-5528
E-mail: jlee@postech.ac.kr

[**] This work was supported by the Hydrogen Energy R&D Center, the Research Center for Energy Conversion and Storage, the National R&D Center for Nano Science and Technology, the National Research Laboratory Program, and the General Motors R&D Center.

Supporting information for this article is available on the WWW under http://www.angewandte.org or from the author.

 DOI: 10.1002/anie.200500064 © 2005 Wiley-VCH Verlag GmbH & Co. KGaA, Weinheim

This nanodiode material shows greatly enhanced and stable photocatalytic activity for degradation of toxic organic pollutants (acetaldehyde, isopropyl alcohol), oxidation of water to gaseous oxygen, and photocurrent generation, all under visible light ($\lambda > 420$ nm).

In the rational design of this composite material, we employed a combination of concepts that optimize the photocatalytic activity. It has been demonstrated in photovoltaic cells and photoelectrochemical (PEC) cells that diode structures made of n- and p-type semiconductors show greatly enhanced activities compared to devices consisting of a single semiconductor. For example, the fundamental unit of current silicon solar cells consists of p–n junctions with p-type and n-type silicon. Multijunction solar cells and PEC cells with remarkable energy conversion efficiencies have been reported.[15] Nojik constructed an n-TiO_2/p-GaP diode electrode for a PEC cell that was much more active than either n-TiO_2 or p-GaP single-component electrodes for the decomposition of water.[16] He designated his monolithic device a p–n type photochemical diode. We attempted to create a particulate version of the p–n junction on a nanometer scale for photocatalytic applications; this junction should be stable under typical photocatalytic reaction conditions and highly active under visible light. Owing to the employment of the p–n junction concept, the nanoscale size, and the particulate form of our device material, we designated it a p–n type photocatalytic nanodiode (PCD).

The first step in fabricating the PCD was to select proper p- and n-type semiconductors that could absorb visible light. We identified $PbBi_2Nb_2O_9$ as a suitable n-type semiconductor. This material is an Aurivillius-phase layered perovskite, and is an efficient photocatalyst for the oxidation of water to O_2 and the degradation of isopropyl alcohol to CO_2 under visible light.[17] For $PbBi_2Nb_2O_9$ to show n-type semiconductivity, it was doped with tungsten(VI) to provide n-$PbBi_2Nb_{1.9}W_{0.1}O_9$. In addition to the valency, the similarity in size between W^{VI} (0.74 nm) and Nb^{V} (0.78 nm) was a further consideration in our choice. For the p-type semiconductor we chose $CaFe_2O_4$, a metal oxide with a bulk band gap of 1.9 eV.[18] The material by itself shows very low photocatalytic activity under visible light. Yet, we selected it because of its p-type semiconductivity and expected stability in water under illumination.

The next challenge was to combine these two semiconductor particles to form a p–n junction. For the efficient use of such a diode structure, the interfacing area should be maximized. However, in preliminary experiments, we learned that $PbBi_2Nb_{1.9}W_{0.1}O_9$ must be in a highly crystalline state to obtain high activity; this requires a high-temperature synthesis that inevitably produces large particles of 0.1–1 μm in diameter. We therefore devised the configuration of the diode particles as follows: 1) Nanocrystals of p-type $CaFe_2O_4$ and 2) a perovskite lattice of n-type $PbBi_2Nb_{1.9}W_{0.1}O_9$ as a submicron-sized base material. The $CaFe_2O_4$ nanoparticles and $PbBi_2Nb_{1.9}W_{0.1}O_9$ submicron particles were synthesized individually by sol–gel methods and a solid-state reaction, respectively. The individual components were then combined by placing them in a hydrothermal reactor (150 °C for 7 d) to form $CaFe_2O_4$ nano-islands over larger particles of $PbBi_2Nb_{1.9}W_{0.1}O_9$.

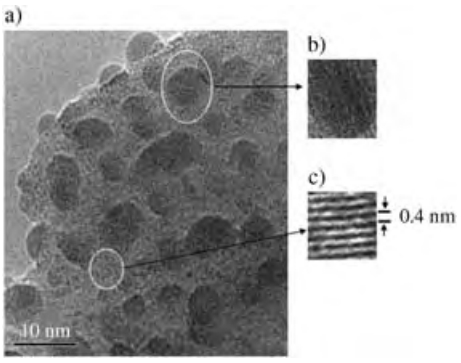


Figure 1. a) HRTEM image of the p–n type photocatalytic nanodiode (PCD). The magnified views show the nanocrystalline p-type $CaFe_2O_4$ (b) interfaced on layers of the n-type $PbBi_2Nb_{1.9}W_{0.1}O_9$ base (c).

Figure 1a shows a HRTEM image of a typical PCD particle. It clearly exhibits the existence of nano-islands dispersed over a single particle of perovskite base material. The micrograph shows many nanocrystalline islands of 5–10 nm, and the magnified view of a nano-island reveals the nanocrystallinity of $CaFe_2O_4$ (Figure 1b). The magnified view of the fringes also demonstrates the existence of a highly crystalline, layered base material corresponding to $PbBi_2Nb_{1.9}W_{0.1}O_9$ (layer thickness 0.4 nm, Figure 1c). The phase identification was also confirmed by elemental analysis with in situ energy-dispersive X-ray microanalysis carried out during the microscopic study.

Based on these experimental observations we propose a model for the PCD as illustrated in Figure 2a. Each island forms a nanoscale p–n junction at the interface, which plays a crucial role in the photocatalytic process. The working principle of PND is shown as an energy band model for one p–n junction (Figure 2b). At thermal equilibrium, the Fermi levels of two semiconductors align. When the device is immersed in an electrolyte, the band edges of the conduction and valence bands bend as indicated. The operation of the PCD is initiated by the absorption of the band-gap photons in both the n- and p-type semiconductors. Photogenerated holes and electrons separate under the influence of the electric field, corresponding to the energy diagram in Figure 2b. Thus,

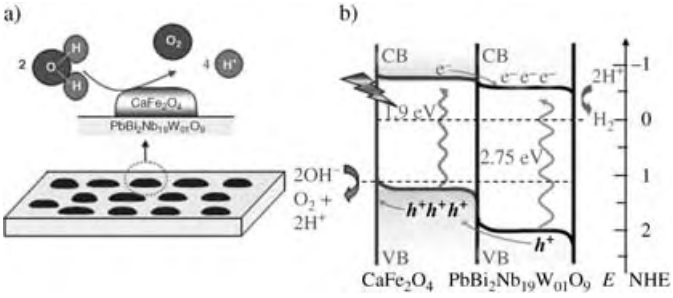


Figure 2. a) Schematic drawing of a PCD. B) Schematic drawing of the energy band model of a PCD showing the formation of the p–n junction and the process of water oxidation. The band positions were derived from flat band potential measurements as described in the Supporting Information. CB = conduction band, VB = valence band, NHE = normal hydrogen electrode.

 © 2005 Wiley-VCH Verlag GmbH & Co. KGaA, Weinheim

holes move to the p-$CaFe_2O_4$ side, and electrons to the n-$PbBi_2Nb_{1.9}W_{0.1}O_9$ side. The net effect of the p–n diode formation is the efficient separation of electron–hole pairs to minimize the energy-wasteful electron–hole recombination. This effect leads to the higher photocatalytic activity.

The optical properties of these compounds were probed by UV/Vis diffuse reflectance spectroscopy (Figure 3a). Then a comparison was made with the base material, $PbBi_2Nb_2O_9$, and nitrogen-doped TiO_2, that is, $TiO_{2-x}N_x$. The latter material is considered to be the standard example of a visible-light photocatalyst; the band structure of TiO_2 is modified by nitrogen doping to induce absorption of visible light.[10] From these spectra, we estimated the band gap energies of these materials (Table 1). The PCD powders showed a steep onset of absorption around $\lambda = 530$ nm, corresponding to green light; the band corresponding to this onset covers a major part of the visible region, compared to the other two standards considered here. The $TiO_{2-x}N_x$ sample showed two absorption edges typical of doped materials, the main edge due to the oxide at 390 nm and a shoulder due to the nitride at 451 nm. $PbBi_2Nb_2O_9$ and the PCD showed single sharp edges. Thus, the PCD would absorb more visible-light photons than $TiO_{2-x}N_x$, although their absorption edges were almost the same around 450 nm. Both $PbBi_2Nb_2O_9$ and $TiO_{2-x}N_x$ are yellow, and the PCD is orange, indicating that all these materials absorb visible light.

We then examined the photocatalytic properties of these materials. To investigate the generation of a photocurrent, aqueous suspensions of the materials containing acetate (donor) and Fe^{3+} (acceptor) were illuminated with visible light ($\lambda > 420$ nm).[19] Figure 3b indicates that the PCD generates a photocurrent approximately three and five times faster than $PbBi_2Nb_2O_9$ and $TiO_{2-x}N_x$, respectively. The higher activities of PCD and $PbBi_2Nb_2O_9$ for photocurrent generation result from the beneficial effect of forming photocatalytic p–n nanodiodes. Unmodified TiO_2, with a wide band gap, as well as all catalysts in the dark did not generate a photocurrent, as expected. The generation of photoelectrons is the critical initial step of photocatalytic reactions upon absorption of light, and the rate should directly correlate with the photocatalytic activity of the material.

The materials were then tested for the photooxidation of acetaldehyde, a hazardous air pollutant as well as a common model compound to test the photodegradation capability of photocatalysts. Figure 3c shows the time curves of CO_2 evolution from the reaction $CH_3CHO + 5/2\,O_2 \rightarrow 2\,CO_2 + 2\,H_2O$. The concentration of CO_2 increased steadily with irradiation time at a decomposition rate of about 0.02 μmol h^{-1} under irradiation with light. The CO_2 production stopped when the light was turned off and resumed at the same rate when the light was turned on again. No intermediate reaction products were detected. The superiority of the PCD over $PbBi_2Nb_2O_9$ and $TiO_{2-x}N_x$, as expected from the photocurrent generation behavior, was confirmed. Similar results were obtained for the photodecomposition of isopropyl alcohol, another common organic pollutant of air (not shown).

As the final test reaction, we studied the photodecomposition of water in the presence of sacrificial agents. These

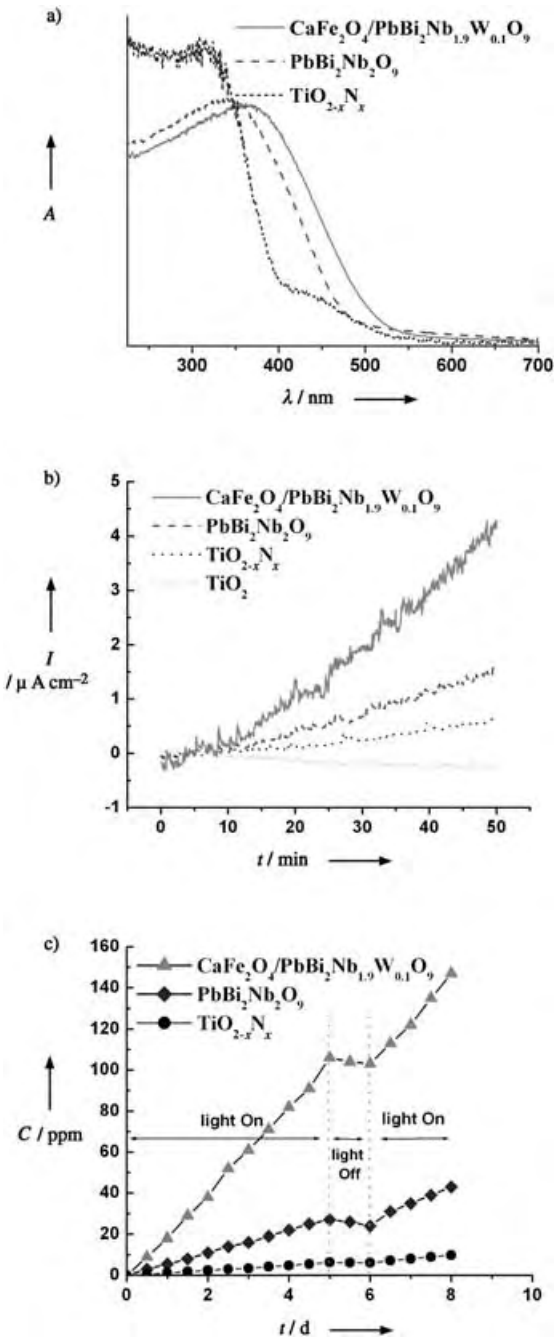


Figure 3. a) UV/Vis absorbance *A* of the various catalysts tested. b) Photocurrent *I* generated with time under visible light over various materials suspended with acetate and Fe^{3+}. c) Concentration *c* of evolved CO_2 as a function of time during photooxidation of acetaldehyde with various photocatalysts (0.3 g). The acetaldehyde (200 ppm) was mixed with air in a 500-mL Pyrex reaction cell.

experiments give individual hydrogen- and oxygen-producing activities from each half-reaction of water splitting. In these reactions, two reference catalysts were loaded with 0.1 wt% Pt as a co-catalyst to collect photoelectrons away from holes by forming a Schottky-type junction structure.[16] The rates of oxygen evolution from water in the presence of $AgNO_3$ as the electron scavenger ($2\,H_2O + 4\,Ag^+ \rightarrow O_2 + 4\,H^+$) are listed in Table 1. Again, the PCD demonstrated the best performance

 © 2005 Wiley-VCH Verlag GmbH & Co. KGaA, Weinheim

Table 1: Photocatalytic activities for oxygen evolution from an aqueous $AgNO_3$ solution as tested for the various catalysts.[a]

Catalyst	Band gap energy		Oxygen evolution	
	E_g [eV]	λ_{ab} [nm][b]	[μmol][c]	QY [%][d]
$CaFe_2O_4/PbBi_2Nb_{1.9}W_{0.1}O_9$	2.75	450	675	38
$PbBi_2Nb_2O_9$	2.88	431	520	29
$TiO_{2-x}N_x$	2.73[e]	451	221	14

[a] Catalyst 0.3 g; light source 450-W Xe-arc lamp (Oriel) with UV cut-off filter ($\lambda \geq 420$ nm). The reaction was performed in an aqueous $AgNO_3$ solution (0.05 mol L^{-1}, 200 mL). [b] The wavelength at the absorption edge was determined as the intercept on the wavelength axis for a tangent drawn on absorption spectra. [c] Per gram of catalyst and hour. [d] QY = quantum yield (see the Experimental Section). [e] The minimum energy of photoabsorption was estimated from the intercept of the shoulder peak onset.

even without a co-catalyst. The quantum yield of O_2 evolution over the PCD was estimated to be about 38%. To the best of our knowledge, this is the highest value ever reported for the reaction over semiconductor photocatalysts under visible light. The hydrogen evolution with methanol as a hole scavenger was also studied ($H_2O + CH_3OH \rightarrow 3H_2 + CO_2$). The relative activity trend among the three photocatalysts was the same, but the rates were lower than those for oxygen evolution by factors of at least 10, and thus are not reported herein.

It has been demonstrated that PCD is a highly active novel photocatalyst. Application of the p–n diode concept commonly employed in the synthesis of monolithic energy conversion devices and the employment of techniques for nanomaterial synthesis have allowed the production of a nanocomposite between the high-order oxides with a unique configuration. It appears that the p–n diode formation results in the efficient separation of electron–hole pairs to minimize the energy-wasteful electron–hole recombination, which leads to the high photocatalytic activity. The materials involved are all stable oxides, which means less stability problems under irradiation with light. Indeed, the crystal structure did not change during the reaction, and the post-reaction analysis showed no indication of dissolved catalyst components, even after more than 100 h of water decomposition.

The PCD catalyst appears to be particularly active for photooxidation reactions. The activity could be directly exploited for the degradation of toxic organic pollutants, as demonstrated for acetaldehyde and isopropyl alcohol. Cheap and abundant sunlight or weak indoor lighting could be employed as the light source. The high activity for the oxidation of water and the generation of a photocurrent could be of advantage for producing a photoelectrochemical cell that converts optical energy into chemical energy by decomposing water.[2] The overall performance of such a device is determined by the ability of the semiconductor anode[2] to oxidize water, and our PCD photocatalyst with the remarkable oxygen-producing capability could be used for this purpose. Furthermore, since the concept of PCD fabrication could be applied for other visible-light absorbing semiconductors, further improvement in performance may be possible by a materials screening of a wider scope.

Experimental Section

To synthesize the PCD, $PbBi_2Nb_{1.9}W_{0.1}O_9$ was first prepared by the conventional solid-state method. A stoichiometric mixture of PbO (Aldrich 99.999%), Bi_2O_3 (Aldrich 99.99%), Nb_2O_5 (Aldrich 99.999%), and WO_3 (Aldrich 99.999%) was ground in a mortar. The pelletized powders were calcined at 1123 K for 24 h in static air and sintered at 1323 K for 24 h. Next, the sol–gel route was adopted to synthesize the $CaFe_2O_4$ nanoparticles: A stoichiometric ratio of $Ca(NO_3)_2{\cdot}4H_2O$ (Aldrich 99.999%) and $Fe(NO_3)_3{\cdot}9H_2O$ (Aldrich 99.999%) was mixed in 30% aqueous NH_3 solution, and the mixture was stirred at room temperature for 24 h. The PCD composite of $CaFe_2O_4/PbBi_2Nb_{2-x}W_xO_9$ was made by hydrothermal treatment of preformed $PbBi_2Nb_{1.9}W_{0.1}O_9$ and $CaFe_2O_4$ sol at 150°C for 7 d to obtain 2 wt% $CaFe_2O_4$ loading on $PbBi_2Nb_{2-x}W_xO_9$. The $CaFe_2O_4/PbBi_2Nb_{1.9}W_{0.1}O_9$ thus obtained was characterized by high-resolution transmission electron microscopy (HRTEM, Phillips Model CM 200) and UV/Vis diffuse reflectance spectroscopy (Shimadzu, UV 2401).

Prior to the water-splitting reactions, all the catalysts (except the PCD) were loaded with 0.1 wt% Pt by impregnation with $PtCl_2$. The photocatalytic reactions in aqueous solution were carried out at room temperature in a closed system using a 450-W Xe-arc lamp (Oriel) with UV cut-off filter ($\lambda \geq 420$ nm) placed in an inner irradiation-type 200-mL Pyrex reaction cell. The H_2 evolution was examined in an aqueous solution (distilled H_2O (170 mL) + CH_3OH (30 mL)), and the O_2 evolution in an aqueous $AgNO_3$ solution (0.05 mol L^{-1}, 200 mL), both containing 0.3 g of the catalyst. The quantum yield (QY) was calculated as twice the number of generated H_2 molecules or four times the number of generated O_2 molecules divided by the number of photons absorbed by the photocatalyst. The number of absorbed photons was determined with a light flux meter (1815-C, Newport) with the light sensor attached to the photocatalytic reactor.

About 200 ppm of gaseous CH_3CHO or isopropyl alcohol was injected into a 500-mL Pyrex reaction cell filled with air and containing 0.3 g of a catalyst. The concentration of the reaction products (H_2, O_2, CO_2) was determined by a gas chromatograph equipped with a thermal conductivity detector and a molecular sieve 5-Å column. For photocurrent measurements, 25 mg of photocatalyst was suspended in distilled H_2O (75 mL) containing acetate (0.1 M) and Fe^{3+} (0.1 mM) as an electron donor and acceptor, respectively, and the pH value of the suspension was adjusted to 1.4 with $HClO_4$. A Pt plate (1×1 cm^2, 0.125 mm thick, both sides exposed to solution), a saturated calomel electrode (SCE), and a Pt gauze were immersed in the reactor as working (collector), reference, and counter electrodes, respectively. With continuous N_2 purging of the suspension, photocurrents were measured by applying a potential (+0.6 V vs. SCE) to the Pt electrode using a potentiostat (EG&G).

Received: January 7, 2005
Revised: April 13, 2005
Published online: June 27, 2005

Keywords: green chemistry · nanotechnology · photocatalysis · photooxidation · semiconductors

[1] A. Fujishima, K. Honda, *Nature* **1972**, *238*, 37.
[2] M. Gratzel, *Nature* **2001**, *414*, 338.
[3] M. R. Hoffman, S. T. Martin, W. Choi, D. W. Bahnemann, *Chem. Rev.* **1995**, *95*, 69.
[4] R. Wang, K. Hashimoto, A. Fujishima, M. Chikuni, E. Kojima, M. Shimohigoshi, T. Watanabe, *Nature* **1997**, *388*, 431.
[5] G. C. De, A. M. Roy, S. S. Bhattacharya, *Int. J. Hydrogen Energy* **1996**, *21*, 19.
[6] D. W. Hwang, J. Kim, T. J. Park, J. S. Lee, *Catal. Lett.* **2002**, *80*, 53.
[7] H. Yamashita, M. Harada, *J. Photochem. Photobiol. A* **2002**, *148*, 257.

 © 2005 Wiley-VCH Verlag GmbH & Co. KGaA, Weinheim

[8] Z. Zou, J. Ye, K. Sayama, H. Arakawa, *Nature* **2001**, *414*, 625.
[9] R. G. Breckenridge, W. R. Hosler, *Phys. Rev.* **1953**, *91*, 79.
[10] R. Asahi, T. Morikawa, T. Ohwaki, K. Aoki, Y. Taga, *Science* **2001**, *293*, 269; S. Sakthivel, H. Kisch, *ChemPhysChem* **2003**, *4*, 487.
[11] S. U. M. Khan, M. Al-Shahry, W. B. Ingler, Jr., *Science* **2002**, *297*, 2243; S. Sakthivel, H. Kisch, *Angew. Chem.* **2003**, *115*, 5057; *Angew. Chem. Int. Ed.* **2003**, *42*, 4908.
[12] G. Hitoki, T. Takata, J. N. Kondo, M. Hara, H. Kobayashi, K. Domen, *Chem. Commun.* **2002**, 1698.
[13] A. Ishikawa, T. Takata, J. N. Kondo, M. Hara, H. Kobayashi, K. Domen, *J. Am. Chem. Soc.* **2002**, *124*, 13547.
[14] D. W. Hwang, H. G. Kim, J. S. Lee, J. Kim, W. Li, S. H. Oh, *J. Phys. Chem. B* **2005**, *109*, 2093.
[15] O. Khaselev, J. Turner, *Science* **1998**, *280*, 425.
[16] A. J. Nojik, *Appl. Phys. Lett.* **1976**, *29*, 150; A. J. Nojik, *Appl. Phys. Lett.* **1977**, *30*, 567.
[17] H. G. Kim, D. W. Hwang, J. S. Lee, *J. Am. Chem. Soc.* **2004**, *126*, 8912.
[18] Y. Matsumoto, *J. Solid State Chem.* **1996**, *126*, 227.
[19] H. Park, W. Choi, *J. Phys. Chem. B* **2003**, *107*, 3885.

 © 2005 Wiley-VCH Verlag GmbH & Co. KGaA, Weinheim

Mesoporous Films

Thermally Stable Nanocrystalline γ-Alumina Layers with Highly Ordered 3D Mesoporosity**

*Monika Kuemmel, David Grosso, Cédric Boissière, Bernd Smarsly, Torsten Brezesinski, Pierre A. Albouy, Heinz Amenitsch, and Clement Sanchez**

Mesostructured materials can be obtained by combining ionic surfactants[1] or block copolymers[2] with the synthesis of metallic oxides through soft chemistry. Amongst the non-silicate mesoporous materials, alumina is very attractive since the Al_2O_3 has perfectly controlled mesoporosity associated with hardness, hydrolytic stability, amphoteric character, and thermal stability of the γ-transition-oxide phases. Indeed, alumina offers a range of possibilities for applications in ultrafiltration of salts,[3] as an adsorbent in environmental cleanup,[4] as an automobile exhaust catalyst,[5] as a heterogeneous catalyst support for hydrodechlorination,[6] and in petroleum refinement.[7] In state-of-the-art syntheses, ordered mesoporosity has been reported for boehmite,[8] gibbsite,[9] and alumina[2,5,10] through the template approach, and also by porogen bead inclusion,[11] by ordered mesoporous carbon (CMK) nanocasting,[12] and by anodization.[8a] However, none of these materials combines pure crystalline γ-Al_2O_3 of high thermal stability with a well-ordered porosity that has a narrow distribution and is adjusted on the mesoscopic scale.

Herein, we describe the preparation and characterization of nanocrystalline γ-Al_2O_3 layers with contracted face-centered cubic (fcc) mesoporosity that are stable up to 900 °C. These coatings were prepared by combining the block copolymer structuring approach[13] and the evaporation-induced self-assembly (EISA) method associated with layer deposition,[14] which has already led to mesoporous silica,[11] transition-metal oxide,[15] and even perovskite[16] layers. Here we show that such fcc-mesostructured alumina layers can be prepared reproducibly by a simple method by which one may

- adjust the mesopore dimension with a relatively narrow size distribution,
- tune the nature of the oxide framework between amorphous alumina to fully nanocrystalline γ-Al_2O_3,
- create up to 55 % volume of open porosity at 900 °C,
- adjust the layer thickness up to 1000 nm, and
- tune the refractive index from 1.19 to that of pure alumina (measured at 700 nm in a dry atmosphere).

These layers can thus find potential applications as low-refractive-index optical thin films or in the various domains mentioned above if used as coatings. In addition, we present the first fcc mesostructure ever reported for a non-silica system. The complete study of such a layer is assessed by 2D small-angle X-ray scattering (SAXS), transmission electron microscopy (TEM), electronic diffraction, atomic force microscopy (AFM), and ellipsometric porosimetry (EP). Finally, explanations for the high-temperature stability are given.

Layers (300-nm thick) of nanocrystalline γ- Al_2O_3 with optical quality were prepared as reported in the Experimental Section. Figure 1 shows the evolution of in situ 2D SAXS patterns obtained during thermal treatment. Indexation of the diffraction spots (Figure 1 b) reveals that the initial structure at 25 °C is a perfect fcc structure with lattice parameters of 36 and 60 nm when the KLE22 (Figure 1 a) and KLE23 block copolymer templates (Figure 1 d) are used, respectively (for KLE composition, see the Experimental Section). The diffraction rings (Figure 1 c, inset) are characteristic of the preferential monoorientation with the [111] direction normal to the surface (direction of shrinkage). Figure 1 c shows the diffraction pattern of a KLE22-templated alumina film calcined for 20 min at 900 °C. For clarity, diffraction points

[*] M. Kuemmel, Dr. D. Grosso, Dr. C. Boissière, Dr. C. Sanchez
Chimie de la Matière Condensée, UMR UPMC-CNRS 7574
4 place Jussieu, 75252 Paris 05 (France)
Fax: (+33) 1-4427-4769
E-mail: clems@ccr.jussieu.fr
Dr. B. Smarsly, T. Brezesinski
Max Planck Institute of Colloids and Interfaces
Research Campus Golm, 14424 Potsdam (Germany)
Dr. P. A. Albouy
Laboratoire de Physique des Solides
Université Paris-Sud, 91405 Orsay (France)
Dr. H. Amenitsch
Institute of Biophysics and X-ray Structure Research
Austrian Academy of Sciences
Steyrergasse 17/VI, 8010 Graz (Austria)

[**] We thank the European Network of Excellence FAME and the CNRS for funding, and Dr. Markus Antonietti from the Max Planck Institute of Colloids and Interfaces (Golm, Germany) for providing the KLE block copolymers. D. Jalabert from the Center of Electronic Microscopy of Orléans (France) is acknowledged for TEM and HRTEM analyses.

Supporting information for this article is available on the WWW under http://www.angewandte.org or from the author.

 DOI: 10.1002/anie.200500037 © 2005 Wiley-VCH Verlag GmbH & Co. KGaA, Weinheim

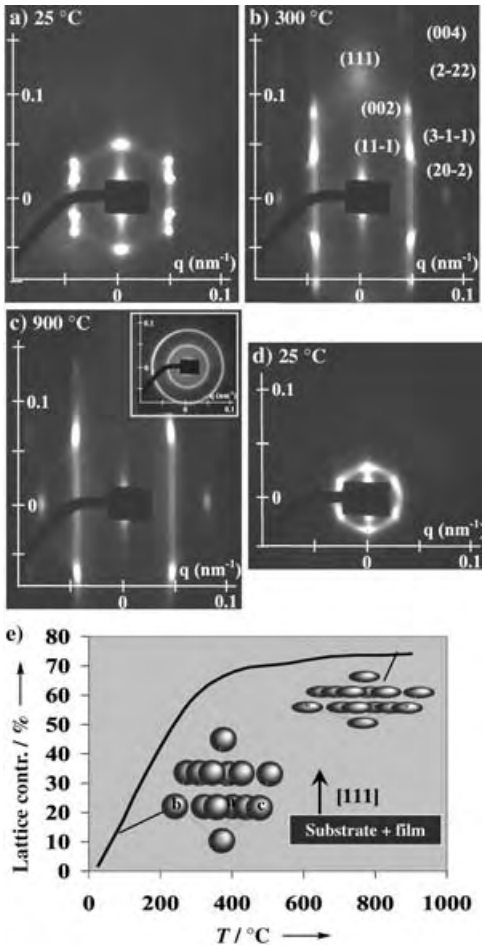


Figure 1. a)–c) 2D SAXS patterns of KLE22-templated alumina layers treated at various temperatures. c) Inset: diffraction rings. d) 2D SAXS patterns of KLE23-templated alumina layer at room temperature. e) Evolution of the fcc lattice contraction in the direction normal to the layer surface ([111] direction of the fcc domains) versus temperature.

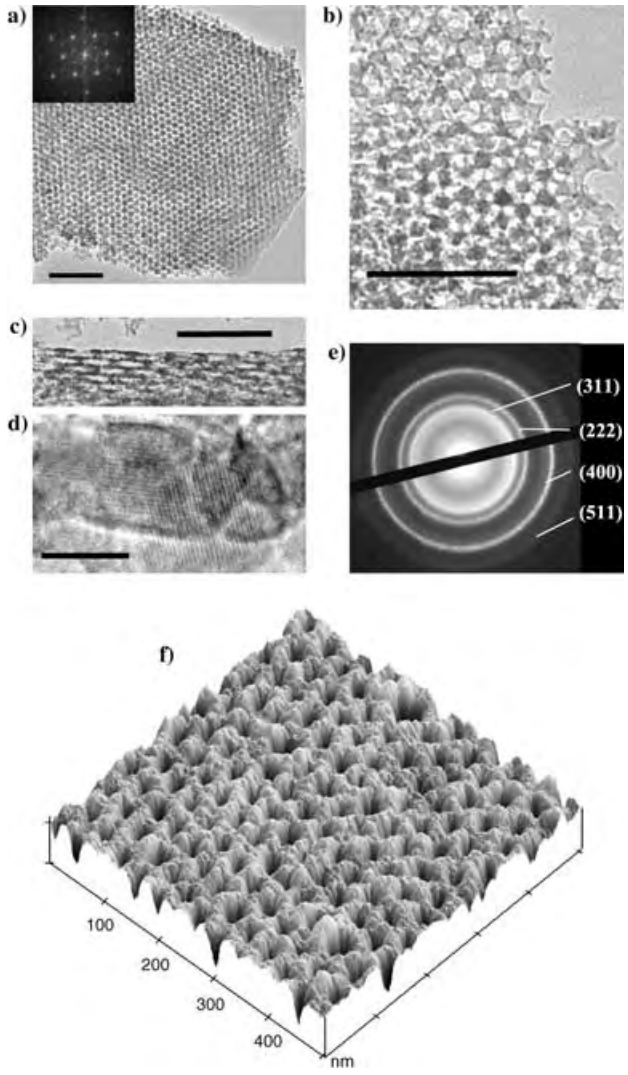


Figure 2. Electronic microscopy and diffraction investigations of KLE22-templated alumina layers treated at 400 °C (a) and at 900 °C (b–e). AFM topography of KLE23-templated layer treated at 900 °C (f). Images of the contracted fcc domains are given in the [111] zone axis for (b) and (c) and in the [1-10] zone axis for (c). Scale bars: 50 nm for (a) and (b), 25 nm for (c), and 5 nm for (d).

corresponding to these contracted systems are indexed with the original fcc structure.

Despite the significant lattice contraction found in Figure 1, the diffraction peaks are still very intense and well-resolved. The initial contraction of 68 % took place between room temperature and 400 °C, while the remaining 6 % occurred between 400 and 900 °C. The cubic structure is clearly confirmed by TEM analysis (see Figure 2), where the [111] view plane of the contracted fcc arrangement of pores exhibits the expected hexagonal arrays (Figure 2 a and b). The side view of the film in Figure 2 c confirms the fcc-based structure. It also reveals that pores are highly anisotropic as a result of the high degree of contraction induced by the thermal treatment. Energy-dispersive X-ray analysis confirmed that the whole mesostructure contains only Al and O elements. The surfaces of the thin films were probed by AFM, and the image obtained for the corresponding KLE23-templated film treated at 900 °C is shown in Figure 2 f.

AFM observations indicated that the porosity is open to the atmosphere through a hexagonal array of well-calibrated circular pores of average diameter 23 nm (see the Supporting Information). This topography is characteristic of the [111] plane from the contracted fcc arrangement of spherical pores with dimension similar to the size of templating micelles. The average pore depth was probed at 6 ± 1 nm. The HRTEM image (Figure 2 d) shows crystalline nanoparticles of around 5 nm in diameter with reticular distances corresponding to the (311) and (222) d spacing of the γ-Al_2O_3 phase. The corresponding diffraction pattern of the latter very stable alumina phase was also observed by electronic diffraction (Figure 2 e). Films treated for 20 min at 400 °C show no crystallinity, which suggests that the alumina framework is amorphous and crystallizes into γ-Al_2O_3 progressively from 400 to 900 °C. Electronic diffraction (see the Supporting Information) revealed that upon treatment above 900 °C, the d spacing slightly decreased, and diffraction spots clearly appeared on the diffraction rings. This finding is attributed to the γ-Al_2O_3 particles coalescing into larger crystalline particles of δ-Al_2O_3

 © 2005 Wiley-VCH Verlag GmbH & Co. KGaA, Weinheim

through the combined effect of γ-to-δ phase transformation and diffusive sintering of nanoparticles. This transformation is accompanied by a degradation of the mesostructure. δ-Al_2O_3 is the transition alumina phase lying between γ- and α-Al_2O_3 (corundum). Before thermal treatment the inorganic network is probably composed of Al^{3+}-based polymeric species from the initial slightly acidic aqueous solution (hydrated gibbsite or boehmite phases).[9a] Starting at 400 °C, progressive crystallization into transition alumina phases occurs. At 900 °C the structure is that of γ-Al_2O_3 (*Fd3m* lacunar spinel) with the lattice parameter $a = 7.9$ Å. Above 900 °C, the original lattice distorts into δ-Al_2O_3 as a result of the increase in Al atoms located in octahedral sites. Such a particular sequence of transformation is usually observed during thermal decomposition of the boehmite precursor.[17]

It is well known that pore morphology is difficult to assess in thin films as a result of the very low quantity of material. The actual KLE22 and KLE23 block copolymer templates form spherical organic domains that have a given diameter of around 10 and 20 nm, respectively.[18] It is evident from the lattice contraction (Figure 1) that, after thermal treatment, pores adopt an ellipsoidal disk morphology with a large axis (d_w) close to the initial dimension of the porogen template, while the small axis depends on the contraction. For instance, an aspect ratio of 4 can be roughly measured in Figure 2c. Such pore dimensions, their interconnection, and therefore the diffusion through the layer were investigated by EP (see the Supporting Information).[19] Isotherms of water adsorption–desorption of KLE22- and KLE23-templated layers thermally treated at 900 °C are given in Figure 3. A volume of water up to 55 % is adsorbed inside the matrix at high relative humidity, which corresponds to the volume of accessible porosity. The main capillary condensation takes place at narrow relative pressure domains above 0.6, which suggests that mesopores of both layers are relatively well-calibrated. Very little water is adsorbed at low relative pressure, therefore only a tiny fraction of the porosity is expected to consist of micropores. Capillary condensation takes place at higher relative pressures when KLE23 is used because of the wider pores obtained with such a template. The pore-size distributions presented in Figure 3 are evaluated using Kelvin's equation modified for ellipsoidal pores (see the Supporting Information). The characteristics of the porosity are given in Table 1.

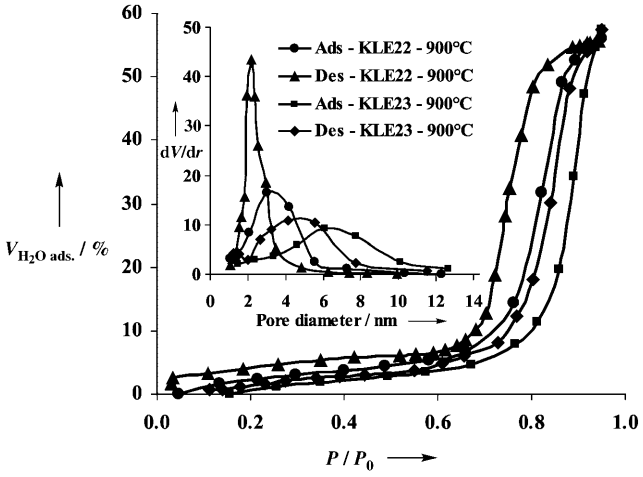


Figure 3. Water adsorption–desorption isotherms obtained from EP measurements performed on KLE22- and KLE23-templated alumina layers thermally treated at 900 °C. Inset: corresponding pore-size distributions deduced from the adsorption and desorption branches.

Table 1: Crystalline phase, pore volume *P*, pore small axis D_s deduced from adsorption, pore wide diameter D_w deduced from pore anisotropic factor, and interconnection diameter D_i deduced from desorption of KLE22- and KLE23-templated alumina layers depending on treatment temperature *T*.

Film	*T* [°C]	Phase	*P* [%]	D_s [nm]	D_w [nm]	D_i [nm]
AlKLE22	900	γ-Al_2O_3	55	3.3 ± 1	13 ± 4	2 ± 0.5
AlKLE22	940	δ-Al_2O_3	55	5 ± 2	–	–
AlKLE23	900	γ-Al_2O_3	55	6 ± 2	24 ± 5	5 ± 2

After crystallization into γ-Al_2O_3, the pore dimensions deduced from the isotherm adsorption branches are 3.3 and 6 nm for KLE22-and KLE23-templated structures, respectively. Both dimensions correspond to the smaller axes of the ellipsoidal pores, whereas their corresponding large axes (13 and 24 nm, respectively) are deduced from the pore aspect ratio. These results are in agreement with the TEM and AFM investigations and confirm the ellipsoidal-disk morphology of the pore, as expected when spherical shapes are unidirectionally contracted. The slightly greater value of the larger pore diameter is related to the matrix densification (crystallization and sintering) at high temperatures. The pore-size distributions become wider after transformation into δ-Al_2O_3 at 940 °C, as a result of the slight degradation of the mesoporous order already observed by TEM and electronic diffraction. No clear pore-size distribution could be deduced from the desorption branches. The dimensions deduced from the desorption branches are characteristic of the pore interconnection (bottleneck) that limits the diffusion of species within the porosity and delays the desorption. Both γ-Al_2O_3 mesostructures present pore-size distributions from desorption branches that are smaller than the dimension of their primary disk-shaped pores (that is, 2 and 5 nm for KLE22 and KLE23, respectively, deduced from the ellipsoidal geometry model). According to the fcc initial structure, every ellipsoidal-disk pore has six first neighbors since they are in an octahedral environment. The pores hold three interconnecting windows on each face of the disk as a result of contraction. A scheme of such an open, contracted-fcc mesostructure is represented in Figure 4.

In summary, the ability to stabilize γ-Al_2O_3 nanoparticles into a well-ordered three-dimensional mesostructured network is first attributed to the stability of the KLE22 template above the dehydration temperature of the inorganic phase. When the treatment reaches the KLE decomposition temperature at 350 °C, the amorphous inorganic dehydrated framework is rigid enough to prevent the mesostructure from collapsing. Above 400 °C, progressive crystallization by nucleation and growth slowly takes place, as expected for transition alumina phases, but the diffusive sintering usually responsible for the collapse of the transition-metal-oxide

 © 2005 Wiley-VCH Verlag GmbH & Co. KGaA, Weinheim

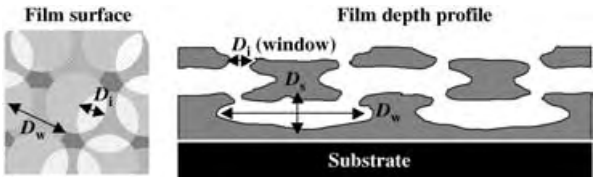


Figure 4. Scheme of the contracted-fcc nanocrystalline mesoporous film structure showing the corresponding surface ([111] zone axis) and depth-profile views ([1-10] zone axis). Pores of small and large diameter (D_s and D_w) with their interconnection dimension (D_i) are represented with respect to the arrangement of the disk-shaped pores.

mesostructure[20] is limited here by the spatial separation of the inorganic walls associated with the ordered mesostructure. The final nanocrystalline mesostructure is composed of ellipsoidal disk-shaped pores, which result from the unidirectional contraction associated with organic decomposition and the densification of the inorganic walls. The porosity (50% volume) is composed of well-calibrated mesopores and is accessible through interconnecting windows 2 or 5 nm in diameter, which is fixed by the template size.

Experimental Section

Isotropic solutions were prepared by dissolving $AlCl_3{\cdot}6\,H_2O$ precursor (0.3 g) and block copolymer KLE22 (BH_{79}-*b*-EO_{89}) or KLE23 (BH_{320}-*b*-EO_{568}) (BH = hydrogenated poly-*b*-butadiene-coethylene; EO = polyoxyethylene) template (0.06 g) in ethanol (5 mL) and H_2O (0.2 mL; 0.1 M NH_4OH). The solutions were aged for 7 days at room temperature before deposition. Films were prepared by dip-coating at a constant relative humidity of 30%. Amorphous ordered mesoporous layers were obtained at 400 °C (10 °C min^{-1} under air) whereas γ- and δ-Al_2O_3 nanocrystalline mesoporous networks were formed at 900 and 940 °C, respectively.

Received: January 5, 2005
Revised: March 22, 2005
Published online: June 24, 2005

Keywords: aluminum · mesoporous materials · nanostructures · template synthesis · thin films

[1] C. T. Kresge, M. E. Leonowicz, W. J. Roth, J. C. Vartuli, J. S. Beck, *Nature* **1992**, *359*, 710 – 712.
[2] P. Yang, D. Zhao, D. I. Margolese, B. Chmelka, G. Stucky, *Nature* **1998**, *396*, 152 – 155.
[3] J. Schaep, C. Vandecasteele, B. Peeters, J. Luyten, C. Dotremont, D. Roels, *J. Membr. Sci.* **1999**, *163*, 229 – 237.
[4] Y. Kim, C. Kim, I. Choi, S. Rengaraj, J. Yi, *Environ. Sci. Technol.* **2004**, *38*, 924 – 931.
[5] C. K. Narula, J. E. Allison, D. B. Bauer, H. S. Gandhi, *Chem. Mater.* **1996**, *8*, 984 – 1003
[6] P. Kim, Y. Kim, C. Kim, H. Kim, Y. Park, J. H. Lee, I. K. Song, J. Yi, *Catal. Lett.* **2003**, *89*, 185 – 192.
[7] Z. Zhang, R. W. Hicks, T. R. Pauly, T. J. Pinnavaia, *J. Am. Chem. Soc.* **2001**, *123*, 1592 – 1593.
[8] R. W. Hicks, T. J. Pinnavaia, *Chem. Mater.* **2003**, *15*, 78 – 82.
[9] a) L. Pidol, D. Grosso, G. J. de A. A. Soler-Illia, E. Crepaldi, P. A. Albouy, H. Amenitsche, P. Euzen, C. Sanchez, *J. Mater. Chem.* **2002**, *3*, 557 – 564; b) N. Idrissi-Kandri, A. Ayral, M. Klotz, P.-A. Albouy, A. El Mansouri, A. Van der Lee, C. Guizard, *Mater. Lett.* **2001**, *50*, 57 – 60.
[10] a) F. Schüth, *Chem. Mater.* **2001**, *13*, 3184 – 3195; b) J. Cejka, P. J. Kooyman, L. Vesela, J. Rathousky, A. Zukal, *Phys. Chem. Chem. Phys.* **2002**, *4*, 4823 – 4829; c) V. González-Peña, I. Díaz, C. Márquez-Alvarez, E. Sastre, J. Pérez-Pariente, *Microporous Mesoporous Mater.* **2001**, *44–45*, 203 – 210; d) S. Rana, S. Ram, *Phys. Status Solidi A* **2004**, *201*, 427 – 444; e) X. Zhang, F. Zhang, K.-Y. Chan, *Mater. Lett.* **2004**, *58*, 2872 – 2877.
[11] S. Vaudreuil, M. Bousmina, S. Kaliaguine, L. Bonneviot, *Microporous Mesoporous Mater.* **2001**, *44–45*, 249 – 258.
[12] J. M. Kim, M. Kang, S. H. Yi, J. E. Yie, S. H. Joo, R. Ryoo, *Stud. Surf. Sci. Catal.* **2003**, *146*, 53 – 56.
[13] G. J. de A. A. Soler-Illia, E. L. Crepaldi, D. Grosso, C. Sanchez, *Curr. Opin. Colloid Interface Sci.* **2003**, *8*, 109 – 126.
[14] D. Grosso, F. Cagnol, G. J. de A. A. Soler-Illia, E. L. Crepaldi, P. A. Albouy, H. Amenitch, A. Brunet-Bruneau, C. Sanchez. *Adv. Funct. Mater.* **2004**, *14*, 309 – 322.
[15] E. L. Crepaldi, G. J. de A. A. Soler-Illia, D. Grosso, F. Cagnol, F. Ribot, C. Sanchez, *J. Am. Chem. Soc.* **2003**, *125*, 9770 – 9786.
[16] D. Grosso, C. Boissière, B. Smarsly, T. Brezesinski, N. Pinna, P. A. Albouy, H. Amenitsch, M. Antonietti, C. Sanchez, *Nat. Mater.* **2004**, *3*, 787 – 792.
[17] C. Pecharroman, I. Sobrados, J. E. Iglesias, T. Gonzales-Carreno, J. Sanz, *J. Phys. Chem. B* **1999**, *103*, 6160 – 6170.
[18] A. Thomas, H. Schlaad, B. Smarsly, M. Antonietti, *Langmuir* **2003**, *19*, 4455 – 4459.
[19] A. Brunet-Brunneau, A. Bourgeois, F. Cagnol, D. Grosso, C. Sanchez, J. Rivory, *Thin Solid Films* **2004**, *455*, 656 – 660.
[20] D. Grosso, G. J. de A. A. Soler-Illia, E. L. Crepaldi, F. Cagnol, C. Sinturel, A. Bourgeois, A. Brunet-Bruneau, H. Amenitsch, P. A. Albouy, C. Sanchez, *Chem. Mater.* **2003**, *15*, 4562 – 4570.

 © 2005 Wiley-VCH Verlag GmbH & Co. KGaA, Weinheim

Bridging Ligands

Triatomic EP_2 Triangles (E = Ge, Sn, Pb) as μ_2:η^3,η^3-Bridging Ligands**

*Joshua S. Figueroa and Christopher C. Cummins**

Three-membered, 2π-electron rings comprised of main-group elements are of interest as compact manifestations of $4n+2$ Hückel aromaticity in which $n=0$.[1] The cyclopropenium ion $[cyclo\text{-}C_3H_3]^+$ serves as the prototypical organic representative of this class,[2] while the prospect of substituting one or more CH units of the cyclopropenium ring by an isolobal heteroatom has spurred investigations seeking to extend the concept of π delocalization throughout the p block of the

[*] J. S. Figueroa, Prof. Dr. C. C. Cummins
Department of Chemistry
Massachusetts Institute of Technology, Room 2-227
77 Massachusetts Avenue, Cambridge, MA 02139-4307 (USA)
Fax: (+1) 617-258-5700
E-mail: ccummins@mit.edu

[**] We gratefully acknowledge the US National Science Foundation (CHE-0316823) for financial support, Dr. Peter Müller for assistance with the X-ray crystallographic studies, and Prof. Daniel G. Nocera for a generous gift of computer time.

Supporting information for this article is available on the WWW under http://www.angewandte.org or from the author.

 © 2005 Wiley-VCH Verlag GmbH & Co. KGaA, Weinheim DOI: 10.1002/anie.200500707

periodic table.[3,4] Reactive unsaturated rings, such as cyclobutadiene, may be stabilized through complexation with a metal center. With this idea in mind, we present herein a study on the synthesis of triatomic {*cyclo*-EP_2} triangles (E = Ge, Sn, and Pb) stabilized within the coordination sphere of a sterically protected diniobium unit. This particular family of {*cyclo*-EP_2} triangles has not been considered previously in either its free or complexed form. Furthermore, divalent atoms from Group 14 have received relatively little attention as components in three-membered, 2π-electron rings. In fact, only the neutral cyclopropene carbene *cyclo*-:$C(C_2H_2)$, diazacyclopropene carbene *cyclo*-:CN_2, and silacyclopropenylidene *cyclo*-:$Si(C_2H_2)$ molecules have been considered theoretically,[5,6] with three-membered rings containing the heavier atoms from Group 14 having been completely neglected to date.

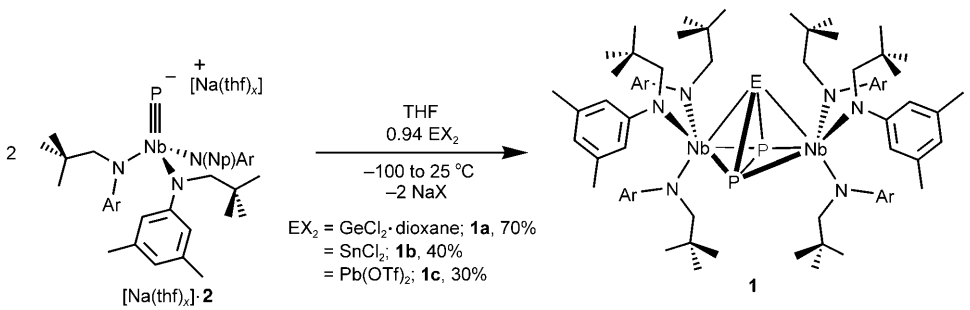
The title complexes [(μ_2:η^3,η^3-*cyclo*-EP_2){Nb[N(Np)Ar]$_3$}$_2$] (**1a–c**; E = Ge, Sn, and Pb, respectively; Np = neopentyl, Ar = 3,5-$Me_2C_6H_3$) were formed as a consequence of the propensity of the niobium phosphide anion [P≡Nb{N(Np)Ar}$_3$]$^-$ (**2**)[7] to undergo electronic rearrangement when functionalized at the phosphorus atom.[7,8] This tendency has already afforded both a new synthesis of phosphaalkynes[8] and of diorganophosphanylphosphinidene complexes.[7] The current manifestation of this phenomenon, which is characterized by the exchange of a niobium/phosphorus multiple-bond interaction for a main-group element/phosphorus bonding interaction, is simply derived from salt elimination reactions of divalent Group 14 halides with the [Na(thf)$_x$]$^+$ derivative of anion **2**.[7]

$^{31}P\{^1H\}$ NMR spectroscopic analysis on a room-temperature solution containing equimolar quantities of [Na(thf)$_x$]·**2** and $SnCl_2$ after mixing in cold THF revealed a single new resonance centered at $\delta = 47.8$ ppm, which is well upfield of the range expected for a niobium phosphinidene complex.[7,9] X-ray structural analysis of a crystal harvested from the reaction mixture established the identity of complex **1b** as containing a central {SnP_2} ring and as the product of a double addition of [Na(thf)$_x$]·**2** to $SnCl_2$ with elimination of NaCl. A purposeful synthesis was then devised and extended to the Ge- and Pb-containing derivatives. Accordingly, the slow addition of 0.47 equivalents of the respective divalent Group 14 source ($GeCl_2$·dioxane, $SnCl_2$, or $Pb(OTf)_2$[10]) to [Na(thf)$_x$]·**2** in cold THF provided dark-red **1a** and forest-green **1b** and **1c**, respectively, in moderate yields of isolated product (**1a**: 65%, **1b**: 40%, **1c**: 30%) after removal of the salt by-product and crystallization from Et_2O (Scheme 1).

Diamagnetic complexes **1a–c** are obtained as crystalline solids, which are soluble in ethereal and aromatic solvents. Complexes **1a** and **1b** retain their integrity in solution at elevated temperatures ([D_6]benzene, 80–100 °C, 2 days), whereas complex **1c** decomposed in solution at room temperature to Pb^0 and the known bridging diphosphide ligand complex [(μ_2:η^2,η^2-P_2){Nb[N(Np)Ar]$_3$}$_2$] (**3**),[11] over several hours; furthermore, the absence of light did not retard the decomposition of **1c**. Therefore, considering the fragile nature of **1c**, the mild conditions of the present synthesis,[12] condition which permitted it to be isolated in pure form, can be further appreciated.

The solid-state structures for complexes **1a–c** are depicted in Figure 1. The μ_2:η^3,η^3 disposition of the {*cyclo*-EP_2} ring between the two niobium centers is evident in each structure. The {*cyclo*-EP_2} units in **1b** and **1c** are near-perfect isosceles triangles, in which the ∢P-E-P angle in **1c** (48.85(5)°) is slightly more acute than that in **1b** (51.23(7)°) as a result of the larger covalent radius of the lead center. Indeed, the average E–P bond lengths in **1b** and **1c** (Sn–P: 2.571 Å, Pb–P: 2.677 Å) follow the trend of the covalent radii going from Sn to Pb and reflect values typical of Sn–P and Pb–P single bonds.[13] Additionally, the P–P distances of 2.223(2) and 2.213(3) Å for **1b** and **1c**, respectively, are in the range typical of P–P single bonds,[14] thus indicating a saturated electronic framework for these {*cyclo*-EP_2} rings when sandwiched between two reducing d^2 niobium centers.[11] Complex **1a**, however, was found to crystallize in the cubic space group $P2_13$ with its Nb–Nb vector coincident with a crystallographic C_3 axis. Unfortunately, this morphology resulted in a crystallographically imposed threefold compositional disorder of the ring atoms in the {*cyclo*-GeP_2} unit. Consequently, chemically suspect metrical parameters were obtained for the complexed {GeP_2} ring, in which the edge distance of 2.460 Å clearly exceeds the value for a P–P single bond and reflects structural dominance by the larger Ge component.[15]

To garner further insight into the geometrical structure of **1a**, the model construct [(μ_2:η^3,η^3-*cyclo*-GeP_2){Nb(NH_2)$_3$}$_2$] (**4a**) was subjected to full geometric optimization at the density functional level (ADF 2004.01, ZORA-TZ2P/BP86). Using the experimental metrical parameters of **1a** as the basis for the initial computational model structure, **4a** converged to a geometry with P–P (2.242 Å) and P–Ge (2.4465 Å av)



Scheme 1. Formation of complexes [(μ_2:η^3,η^3-*cyclo*-EP_2){Nb[N(Np)Ar]$_3$}$_2$] (**1a–c**). E = Ge, Sn, or Pb, respectively; Np = neopentyl, Ar = 3,5-$Me_2C_6H_3$, OTf = O_3SCF_3.

 © 2005 Wiley-VCH Verlag GmbH & Co. KGaA, Weinheim

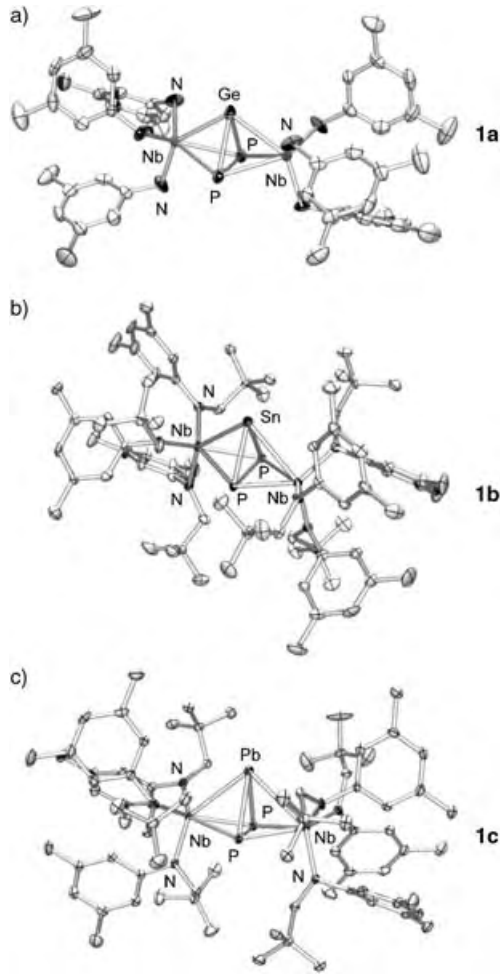


Figure 1. ORTEP diagrams of a) **1a**, b) **1b**, and c) **1c** at the 35% probability level. All the hydrogen atoms and the neopentyl residues of **1a** have been omitted for clarity.

separations consistent with both P–P and P–Ge single bonds.[13,14] All other overall structural features for **4a** were similarly consistent with those found experimentally for **1b** and **1c**. Furthermore, the calculated structural parameters for models **4b** and **4c** were in excellent agreement with their experimental counterparts (**1b** and **1c**, respectively). Therefore, we contend that **4a** represents the molecular geometry for complex **1a** in the absence of crystallographic disorder.

Of particular interest are the electronic-structure attributes attendant with {*cyclo*-EP_2} complexation in **1a–c**. The highest occupied molecular orbitals (HOMOs) calculated for **4b** are shown in Figure 2.[16] The HOMO-1 is part of the σ framework of the {*cyclo*-SnP_2} unit, whereas complexation of the Nb centers consists of a pair of mutually orthogonal two-electron π backbonds. The HOMO involves the out-of-plane valence p orbital of the Sn center as the acceptor component in one of these bonds, whereas the HOMO-2 utilizes a P–P π* orbital as the acceptor component in the other bond. Accordingly, a pair of d^2 niobium trisamide fragments is seen to be electronically complementary to a formally neutral {*cyclo*-EP_2} ring. However, summation of the

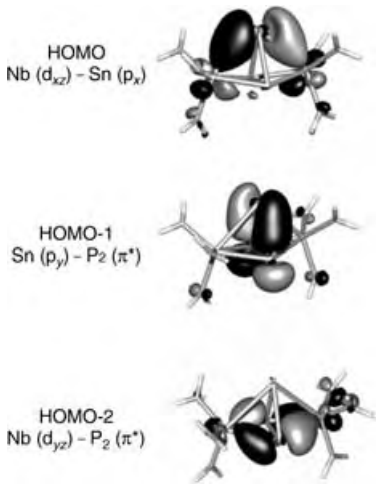


Figure 2. Selected frontier molecular orbitals calculated for **4b**.

calculated multipole-derived charges (MDC-q)[17] on the ring atoms in **4a–c** indicate that each complexed {*cyclo*-EP_2} unit bears a net charge of approximately −1.0 ($\Sigma_{MDC\text{-}q} = -1.186$, −0.917, and −0.837 a.u. for **4a–c**, respectively). Thus, although formally neutral as free entities, complexation by two electropositive d^2 Nb centers renders these {*cyclo*-EP_2} rings moderately anionic. The latter interpretation is consistent with the saturated nature of the {*cyclo*-EP_2} framework, as determined crystallographically for **1b** and **1c**.

It is noteworthy that the net negative charge calculated for the {*cyclo*-EP_2} rings in models **4a–c** decreases in the order Ge > Sn > Pb according to the decreasing electronegativity of the Group 14 atom.[18] Indeed, the negative charge at the phosphorus center is calculated to remain relatively constant between models **4a–c** (−0.384 ± 0.016 a.u.), and the variation in the net charge between each {*cyclo*-EP_2} ring is dictated by the charge at the E center (MDC-q = −0.390, −0.185, and −0.057 a.u. for **4a–c**, respectively). A similar dependence on the identity of the Group 14 atom is observed experimentally in the $^{31}P\{^1H\}$ NMR spectra of complexes **1a–c** in solution ($\delta^{31}P = -15.7$, 47.8, and 115.2 ppm for **1a–c**, respectively). The downfield progression in the resonances is attributed qualitatively to the increase in the paramagnetic component σ_{para} of the total ^{31}P nuclei shielding tensor σ_{total} as the Group 14 atom becomes less electronegative.[19] NMR calculations performed on models **4a–c** are consistent with this suggestion, thus revealing that variation in σ_{para} dominates σ_{total} and increases in the order Pb > Sn > Ge.[20] Mapping the principal components of σ_{para} onto the molecular frame of **4a–c** (Figure 3) reveals that $R(\sigma_{11})$ mediates an occupied–virtual coupling between the Nb_2–P_2 π* backbond (occupied) and the σ* framework (virtual) of the {EP_2} ring in the presence of an applied magnetic field. Thus, a molecular-orbital description of ^{31}P nuclei deshielding as influenced[21] by the identity of the Group 14 atom[22] within the {*cyclo*-EP_2} ring is afforded.

In conclusion, new triatomic molecules are of interest both as synthetic targets and theoretical constructs.[3,4] We have identified that complexed forms of {*cyclo*-EP_2} triangles

 © 2005 Wiley-VCH Verlag GmbH & Co. KGaA, Weinheim

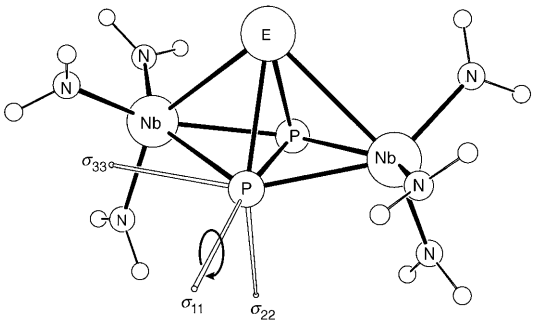


Figure 3. Principal components of σ_{para} for models **4a–c**.

containing germanium, tin, and lead can be synthesized as a direct consequence of the remarkable chemistry of the niobium–phosphorus triple bond in phosphide anion **2**.[7,8] Future prospects in this area include chemical liberation of the {*cyclo*-EP_2} triangles, with an aim of establishing their reactivity patterns.

Experimental Section

$[(\mu_2{:}\eta^3,\eta^3\text{-}cyclo\text{-}EP_2)\{Nb[N(Np)Ar]_3\}_2]$ (**1a–c**):[10] Solutions of $[Na(thf)_x]\cdot$**2** (0.300 g, 0.380 mmol) in THF (5 mL) and the corresponding divalent Group 14 salt (0.47 equiv; $GeCl_2$·dioxane, $SnCl_2$, or $Pb(OTf)_2$ for **1a–c**, respectively) in THF (2 mL) were frozen separately in a glove-box cold well. On removal of the solutions from the cold well, the thawing solution containing the salt was added dropwise (approximately 0.6 mL) over 1 min to the thawing solution of $[Na(thf)_x]\cdot$**2**. The reaction mixture was stirred for an additional 3 min, whereupon both solutions were placed back into the cold well. This procedure was repeated twice more until complete addition of the divalent Group 14 salt was achieved. The reaction mixture was then allowed to warm to room temperature and stirred for an additional 30 min before being evaporated to dryness in vacuo. The residue was extracted with *n*-pentane (3 mL), the extract filtered through celite, and the filtrate evaporated to dryness in vacuo. Crystallization of each complex was effected by storing a saturated solution of Et_2O at −35 °C for 1–3 days.

1a: Red crystals, 70% yield; ^{1}H NMR (500 MHz, [D_6]benzene, 20 °C): $\delta = 6.69$ (s, 6H, *o*-Ar), 6.60 (s, 3H, *p*-Ar), 4.42 (s, 6H, N-CH_2), 2.20 (s, 18H, Ar-CH_3), 1.02 ppm (s, 27H, *t*Bu); ^{13}C{^{1}H} NMR (125.7 MHz, [D_6]benzene, 20 °C): $\delta = 155.9$ (*ipso*-aryl), 137.7 (*m*-Ar), 126.4 (*p*-Ar), 125.2 (*o*-Ar), 80.3 (N-CH_2), 37.3 ($C(CH_3)_3$), 30.8 ($C(CH_3)_3$), 21.9 ppm (Ar-CH_3); ^{31}P{^{1}H} NMR (202.5 MHz, [D_6]benzene, 20 °C): $\delta = -15.7$ ppm (s); elemental analysis (%) calcd for $C_{78}H_{120}N_6P_2GeNb$: C 64.07, H 8.27, N 4.97; found: C 65.50, H 8.98, N 5.50.

1b: Green crystals, 40% yield; ^{1}H NMR (500 MHz, [D_6]benzene, 20 °C): $\delta = 6.76$ (s, 6H, *o*-Ar), 6.60 (s, 3H, *p*-Ar), 4.35 (s, 6H, N-CH_2), 2.22 (s, 18H, Ar-CH_3), 1.02 ppm (s, 27H, *t*Bu); ^{13}C{^{1}H} NMR (125.7 MHz, [D_6]benzene, 20 °C): $\delta = 156.2$ (*ipso*-aryl), 137.7 (*m*-Ar), 126.3 (*p*-Ar), 125.0 (*o*-Ar), 80.0 (N-CH_2), 37.4 ($C(CH_3)_3$), 30.8 ($C(CH_3)_3$), 21.9 ppm (Ar-CH_3); ^{31}P{^{1}H} NMR (202.5 MHz, [D_6]benzene, 20 °C): $\delta = 47.8$ ppm (t, ^1J(Sn-P) = 205.2 Hz); ^{119}Sn NMR (186.5 MHz, [D_6]benzene, 20 °C): $\delta = -696.4$ ppm (br s, $\nu_{1/2}$ = 1300.8 Hz); elemental analysis (%) calcd for $C_{78}H_{120}N_6P_2SnNb$: C 62.11, H 8.02, N 5.57; found: C 61.75, H 7.91, N 5.66.

1c: Green crystals, 30% yield; ^{1}H NMR (500 MHz, [D_6]benzene, 20 °C): $\delta = 6.78$ (s, 6H, *o*-Ar), 6.62 (s, 3H, *p*-Ar), 4.45 (s, 6H, N-CH_2), 2.23 (s, 18H, Ar-CH_3), 1.02 ppm (s, 27H, *t*Bu); ^{31}P{^{1}H} NMR (202.5 MHz, [D_6]benzene, 20 °C): $\delta = 115.2$ ppm (s with shoulders); satisfactory ^{13}C{^{1}H} NMR spectroscopic and elemental analyses could not be obtained because of the rapid decomposition of **1c**.[23]

Received: February 25, 2005
Published online: June 30, 2005

Keywords: aromaticity · bridging ligands · main-group elements · niobium · phosphorus

[1] P. J. Garratt, *Aromaticity*, Wiley, New York, **1986**, p. 137.
[2] a) R. Breslow, J. T. Groves, G. Ryan, *J. Am. Chem. Soc.* **1967**, *89*, 5048; b) G. Farnum, G. Mehta, R. S. Silberman, *J. Am. Chem. Soc.* **1967**, *89*, 5049; c) R. Breslow, J. T. Groves, *J. Am. Chem. Soc.* **1970**, *92*, 984.
[3] For example, see: a) M. W. Wong, L. Radom, *J. Am. Chem. Soc.* **1989**, *111*, 6976; b) Y.-G. Byun, S. Seabo, C. U. Pittman, Jr., *J. Am. Chem. Soc.* **1991**, *113*, 3689; c) J. R. Flores, A. Largo, *J. Phys. Chem.* **1992**, *96*, 3015; d) W. W. Schoeller, U. Tubbesing, *THEOCHEM* **1995**, *343*, 49; e) Y. Xie, P. R. Schreiner, H. F. Schaefer, X.-W. Li, G. H. Robinson, *J. Am. Chem. Soc.* **1996**, *118*, 10635; f) W. Eisfeld, M. Regitz, *J. Org. Chem.* **1998**, *63*, 2814; g) Y. Xie, P. R. Schreiner, H. F. Schaefer, X.-W. Li, Robinson, G. H. *Organometallics* **1998**, *17*, 114; h) R. Salcedo, C. Olvera, *THEOCHEM* **1999**, *460*, 221.
[4] Experimentally realized heteroatom-containing 2π-electron three-membered rings: a) {*cyclo*-BC_2}: J. J. Eisch, B. Shafii, A. L. Rheingold, *J. Am. Chem. Soc.* **1987**, *109*, 2526; J. J. Eisch, B. Shafii, J. D. Odom, A. L. Rheingold, *J. Am. Chem. Soc.* **1990**, *112*, 1847; b) [*cyclo*-PC_2]$^+$: K. K. Laali, B. Geissler, O. Wagner, J. Hoffmann, R. Armbrust, W. Eisfeld, M. Regitz, *J. Am. Chem. Soc.* **1994**, *116*, 9407; c) [*cyclo*-Ga_3]$^{2-}$: X.-W. Li, W. T. Pennington, G. H. Robinson, *J. Am. Chem. Soc.* **1995**, *117*, 7578; d) [*cyclo*-CP_2]$^+$: D. Bourissou, G. Bertrand, *Top. Curr. Chem.* **2002**, *220*, 1; D. Bourissou, Y. Canac, M. I. Collado, A. Barceirdo, G. Bertrand, *J. Am. Chem. Soc.* **1997**, *119*, 9923; D. Bourissou, Y. Canac, H. Gornitzka, A. Barceirdo, G. Bertrand, *Eur. J. Inorg. Chem.* **1999**, 1479.
[5] B. S. Jursic, *THEOCHEM* **1999**, *491*, 33.
[6] G. Frenking, R. B. Remington, H. F. Schaefer III, *J. Am. Chem. Soc.* **1986**, *108*, 2169.
[7] J. S. Figueroa, C. C. Cummins, *Angew. Chem.* **2004**, *116*, 1002; *Angew. Chem. Int. Ed.* **2004**, *43*, 984.
[8] J. S. Figueroa, C. C. Cummins, *J. Am. Chem. Soc.* **2004**, *126*, 13917.
[9] A. H. Cowley, *Acc. Chem. Res.* **1997**, *30*, 445.
[10] The corresponding dichloride, $PbCl_2$, did not react with $[Na(thf)_x]\cdot$**2** under the reaction conditions employed because of its low solubility in THF; a full description of general synthetic procedures can be found in the Supporting Information; see also the Supporting Information of reference [7].
[11] J. S. Figueroa, C. C. Cummins, *J. Am. Chem. Soc.* **2003**, *125*, 4020.
[12] An alternate synthesis of **1b** was attempted by treatment of **3** with an excess of Sn dust in THF; however, no reaction was observed when intermittently assayed for 24 h. We tentatively attribute this observation to the inability of elemental Sn to reduce the $\{P_2\}$ unit in **3**.
[13] L. Pauling, *The Nature of the Chemical Bond*, 3rd ed., Cornell University Press, Ithaca, NY, **1960**, chap. 11, p. 405.
[14] The experimentally determined P–P distance in P_4 is 2.21 Å: N. N. Greenwood,A. Earnshaw, *Chemistry of the Elements*, 2nd ed., Butterworth-Heinemann, Oxford, **1997**, chap. 12, p. 479.
[15] Separation of the Ge and P centers within the asymmetric unit is possible by allowing each atom to refine freely with the appropriate site occupancy factor (namely, $Ge_{0.33}P_{0.67}$); however, we suggest that the true molecular geometry in **1a** is marred by the crystallographically imposed symmetry, as the inherent

 © 2005 Wiley-VCH Verlag GmbH & Co. KGaA, Weinheim

translations of the {Nb[N(Np)Ar]$_3$} fragments, which are required to reveal a chemically sensible molecular geometry, are masked relative to the central ring (see the Supporting Information for full details).

[16] The molecular-orbital splitting patterns calculated for models **4a**–**c** are qualitatively identical.

[17] M. Swart, P. T. van Duijnen, J. G. Snijders, *J. Comput. Chem.* **2001**, *22*, 79.

[18] a) Y.-R. Luo, S. W. Benson, *J. Phys. Chem.* **1989**, *93*, 7333; b) J. Kapp, M. Remko, P. von R. Schleyer, *Inorg. Chem.* **1997**, *36*, 4241; c) C. H. Suresh, N. Koga, *J. Am. Chem. Soc.* **2002**, *124*, 1790.

[19] a) G. Schreckenbach, T. Ziegler, *J. Phys. Chem.* **1995**, *99*, 606; b) T. M. Gilbert, T. Ziegler, *J. Phys. Chem. A* **1999**, *103*, 7537.

[20] The calculated σ_{para} values are −558.6, −626.9, and −682.7 ppm for models **4a**–**c**, respectively; the total ^{31}P nuclei chemical shielding σ_{total} is the sum of the individual paramagnetic σ_{para}, diamagnetic σ_{dia}, and spin orbit σ_{so} tensor components; note that σ_{dia} was found to be essentially invariant between models **4a**–**c** (961.9 ± 0.5 ppm) and σ_{so} made a negligible contribution (13–21 ppm).

[21] a) Y. Ruiz-Morales, G. Schreckenbach, T. Ziegler, *Organometallics* **1996**, *15*, 3920; b) Y. Ruiz-Morales, G. Schreckenbach, T. Ziegler, *J. Phys. Chem.* **1996**, *100*, 3359; c) Y. Ruiz-Morales, G. Schreckenbach, T. Ziegler, *J. Chem. Phys.* **1996**, *104*, 8605.

[22] Complex **1b** gives rise to a broad, upfield ^{119}Sn NMR signal at $\delta = -696.4$ ppm ($\nu_{1/2} = 1300.8$ Hz, [D$_6$]benzene, 20 °C). Typical ^{119}Sn NMR chemical shifts for divalent Sn species are significantly deshielded relative to that of **1b**. We attribute this disparity to ground-state electronic population of the normally empty p orbital of the Sn^{II} center. For a discussion of ^{119}Sn NMR chemical shifts in divalent Sn complexes, see: a) B. E. Eichler, B. L. Phillips, P. P. Power, M. P. Augustine, *Inorg. Chem.* **2000**, *39*, 5450; b) B. E. Eichler, A. D. Phillips, S. T. Haubrich, B. V. Mork, P. P. Power, *Organometallics* **2002**, *21*, 5622. Attempts to locate the corresponding ^{203}Pb NMR shift for **1c** were unsuccessful.

[23] CCDC-262173–262175 contain the supplementary crystallographic data for [(μ_2:η^3,η^3-*cyclo*-SnP$_2$){Nb[N(Np)Ar]$_3$}$_2$] (**1b**), [(μ_2:η^3,η^3-*cyclo*-GeP$_2$){Nb[N(Np)Ar]$_3$}$_2$] (**1a**), and [(μ_2:η^3,η^3-*cyclo*-PbP$_2$){Nb[N(Np)Ar]$_3$}$_2$] (**1c**), respectively. These data can be obtained free of charge from the Cambridge Crystallographic Data Center via www.ccdc.cam.ac.uk/data request/cif.

 © 2005 Wiley-VCH Verlag GmbH & Co. KGaA, Weinheim

Glycopeptide Synthesis

A General Strategy toward S-Linked Glycopeptides**

*Desiree A. Thayer, Henry N. Yu, M. Carmen Galan, and Chi-Huey Wong**

Glycosylation, the most complex posttranslational modification of proteins, is involved in a number of biological processes. Such highly complex glycan structures have challenged present methods used in the functional study of glycoproteins.[1–4] Therefore, the development of new methods for the syntheses of natural and unnatural homogeneously glycosylated proteins[5–7] is needed for a systematic understanding of glycan function. In this context, the syntheses of natural and modified glycopeptides represent a means for additional glycoprotein studies and therapeutic developments.[8–11]

Naturally occurring glycopeptides most commonly incorporate an O- or N-glycosidic linkage between the saccharide moiety and the side chain of an appropriate amino acid residue. Replacement of the anomeric oxygen or nitrogen atom by sulfur results in the corresponding S-linked glycopeptide, which is known to be more stable chemically,[12] more resistant to the action of glycosidases, and tolerated by most biological systems. Furthermore, members of the closely related S-linked oligosaccharides have been used as enzyme inhibitors[13,14] and are suggested to be better immunogens than their natural O-linked analogues.[15–18] An alternate modification is the C-glycosyl linkage, for which several synthetic methods exist.[19]

The common synthetic approach for S-linked glycosyl amino acids uses an anomeric thiolate nucleophile in reaction with an alanine derivative equipped with a leaving group (Figure 1). The major side reaction is β-elimination, and the subsequent Michael addition results in a diastereomeric mixture at the α-carbon of the amino acid product. Several procedures have since emerged to overcome this problem.[20–24] The most advanced among these is a method reported by Schmidt and co-workers,[24–27] in which the reaction of the thiosugar **1** with β-bromoalanine was performed in an ethyl acetate/water two-phase system containing tetra-*n*-butylammonium hydrogen sulfate (TBAHS) and $NaHCO_3$ (Figure 2). We have used this protocol for the

[*] D. A. Thayer,[+] Dr. H. N. Yu,[+] Dr. M. C. Galan, Prof. C.-H. Wong
Department of Chemistry and
The Skaggs Institute for Chemical Biology
The Scripps Research Institute
10550 North Torrey Pines Road, La Jolla, CA 92037 (USA)
Fax: (+1) 858-784-2409
E-mail: wong@scripps.edu

[+] Contributed equally to this work.

[**] This work was supported by the National Institutes of Health (C.-H.W.) and National Science Foundation Predoctoral and Norton B. Gilula Graduate Student fellowships (D.A.T.).

Supporting information for this article is available on the WWW under http://www.angewandte.org or from the author.

 © 2005 Wiley-VCH Verlag GmbH & Co. KGaA, Weinheim DOI: 10.1002/anie.200500090

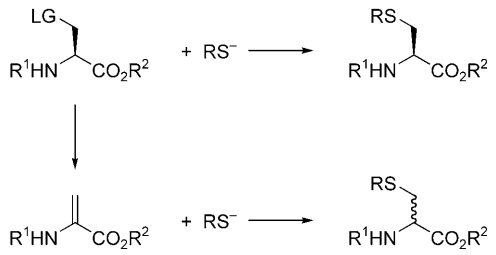


Figure 1. The common synthetic approach used for the synthesis of S-linked glycosyl amino acids.

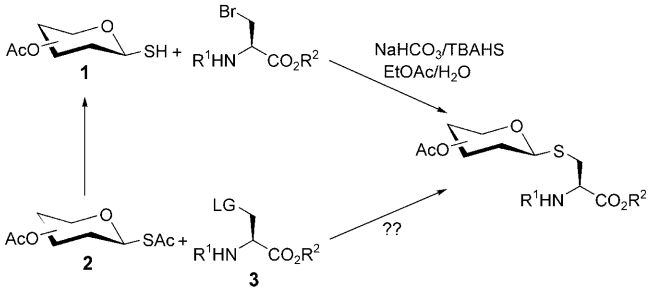


Figure 2. Reported procedure for the two-step synthesis of S-linked glycosyl amino acids and an alternative one-pot approach.

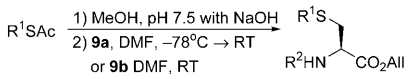
preparation of several different S-linked Boc- and Fmoc-modified glycosyl amino acids (Boc = *tert*-butoxycarbonyl, Fmoc = 9-fluorenylmethyloxycarbonyl). The Fmoc-protected compounds, however, can only be obtained indirectly from the S-linked Boc-modified glycosyl amino acids owing to the basicity of the reaction. The step for the generation of 1-thiosugars requires a special precaution, as it may give low yields due to the facile formation of disulfides during deacetylation of the sulfur atom and subsequent silica gel chromatography.

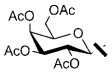
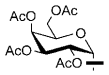
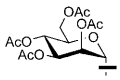
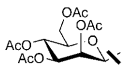
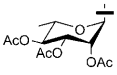
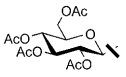
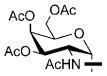
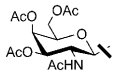
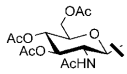
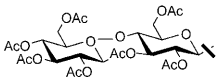
We therefore explored alternate reaction conditions in which thioacetate **2** and the alanine derivative **3** can be subjected to a one-pot reaction to generate the desired thio-linked glycosyl amino acid product (Figure 2). Such reaction conditions should meet several important criteria: first, deacetylation of the thioacetate group should be selective to generate the desired thiolate anion in situ, and to avoid β-elimination of the alanine derivative; second, dimethyl formamide (DMF) should be the solvent of choice, as solubility of large peptides in other solvents can be problematic;[24] furthermore, a set of optimal amino acid protecting groups should be employed to facilitate large-scale solid-phase peptide synthesis (SPPS).

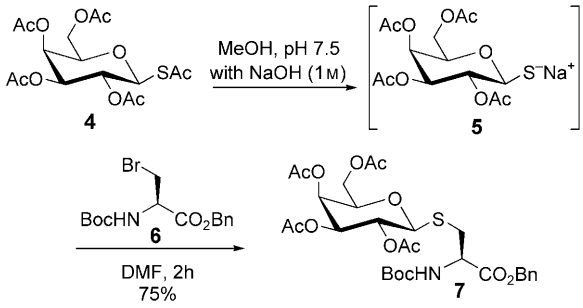
With these goals in mind, we first screened numerous one-pot reaction conditions (Table 1, Supporting Information). A simple "two-step one-pot" reaction emerged as the method of choice (Scheme 1). Therein, with 2,3,4,6-tetra-*O*-acetyl-1-*S*-acetyl-1-thio-β-D-galactopyranose (**4**)[28] as a starting material, the anomeric thioacetate was selectively deprotected in situ with NaOH in anhydrous methanol (pH ≈7.5). After removing the methanol solvent, the resulting thiolate sodium salt **5** was subjected to nucleophilic substitution with β-bromoalanine **6** in dry DMF to give the desired S-linked galactosyl amino acid **7**. This reaction is simple yet very effective. It selectively deacetylates the sulfur atom, preserves the anomeric configuration,[29] and carries out the S_N2 displacement reaction effectively without disrupting the integrity of the α-carbon center. It is necessary to remove the methanol before the nucleophilic substitution reaction, as electrophile **6** would otherwise undergo β-elimination with sodium methoxide generated in situ.

As the Fmoc protecting group is labile in basic conditions, most of the procedures reported in the literature use Boc as

Table 1: General applicability of the synthesis of S-linked glycosyl amino acids.



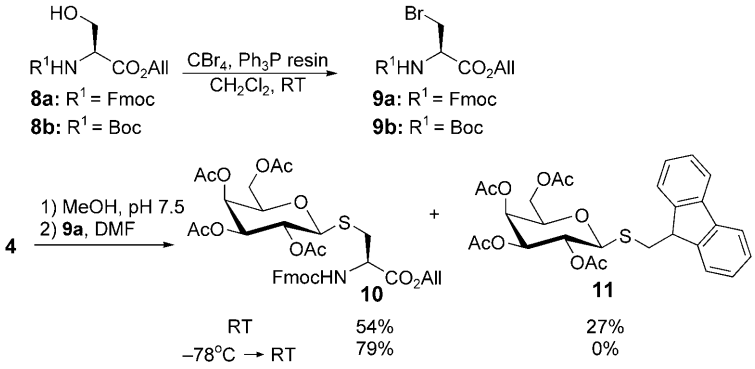
R^1SAc	R^1	R^2 = Fmoc (Yield [%])	R^2 = Boc (Yield [%])
4		**12** (79)	**19** (75)
20		**20a** (74)	
21		**21a** (77)	
22		**22a** (81)	
23		**23a** (75)	
24		**24a** (71)	
25		**25a** (66)	**25b** (75)
26		**26a** (68)	**26b** (70)
27		**27a** (71)	**27b** (78)
28		**28a** (78)	



Scheme 1. A two-step one-pot synthesis of a Boc-protected glycosyl amino acid (Bn = benzyl).

 © 2005 Wiley-VCH Verlag GmbH & Co. KGaA, Weinheim

the temporary protecting group to sustain the alkaline conditions in the nucleophilic substitution reaction.[20,24] However, the Boc group must then be replaced with the Fmoc protecting group for the preferred Fmoc SPPS of glycopeptides.[30,31] After the reaction shown in Scheme 1 was carried out following this traditional method, we hypothesized that the basicity of intermediate **5** in DMF would be sufficiently mild to permit the S_N2 reaction with the Fmoc-protected β-bromoalanine species without affecting the Fmoc group itself. Thus, compound **8a** was prepared as reported in the literature (Scheme 2).[32] The allyl ester protecting group

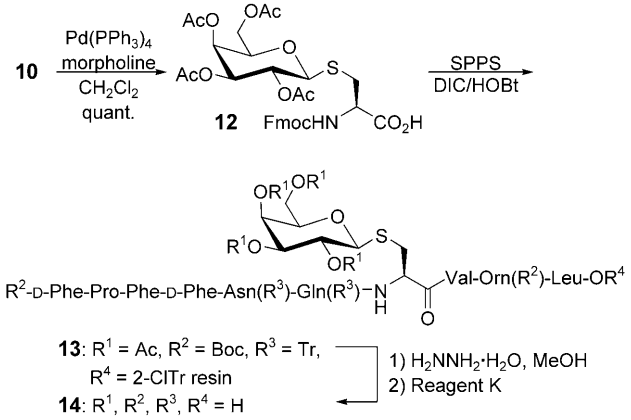


Scheme 2. A direct two-step one-pot synthesis of the S-linked Fmoc-modified glycosyl amino acid **10** with suppression of side product **11**.

was favored over the benzyl ester group, as it is easier to remove in high yield. Bromination of **8a** went smoothly with the solid-support Ph_3P resin and CBr_4 in dichloromethane to give **9a** (100%, TLC),[33] which was pure enough to carry out the next step without purification.[34] Upon performing the S_N2 reaction at ambient temperature, the desired amino acid **10** was obtained (54%), along with side-product **11** (27%). Thiolate **5** presumably attacks Fmoc-CH_2 to give **11**. To suppress the formation of this side-product, the reaction was performed at −78 °C to room temperature. We were gratified to observe that only compound **10** (79%) was formed without any trace of side product **11**.

S-linked glycosyl amino acid **10** was treated with tetrakis(triphenylphosphine)palladium(0) catalyst and morpholine in dichloromethane to give the Fmoc-modified building block **12** swiftly (100%, TLC), which was used without purification to afford the protected S-linked glycodecapeptide **13** (Scheme 3). Deacetylation of the sugar moiety was carried out on-resin by transesterification with hydrazine hydrate in methanol. Removal of the acid-labile amino acid protecting groups concomitant with cleavage from the 2-chlorotrityl resin by Reagent K afforded free S-linked glycopeptide **14** in pure form after HPLC. The whole process, starting from the readily available peracetylated 1-thio galactose to the final glycopeptide **14**, involved only two purifications (silica gel chromatography for **10** and HPLC for **14**). In fact, it is also possible to start with thiolate salt **5**, which can be stored under argon for up to a month without degradation.

Glycopeptide **14** is a linear analogue of tyrocidine A, which is a cyclic cationic decapeptide antibiotic produced in *Bacillus brevis* with an antiparallel amphipathic β-sheet



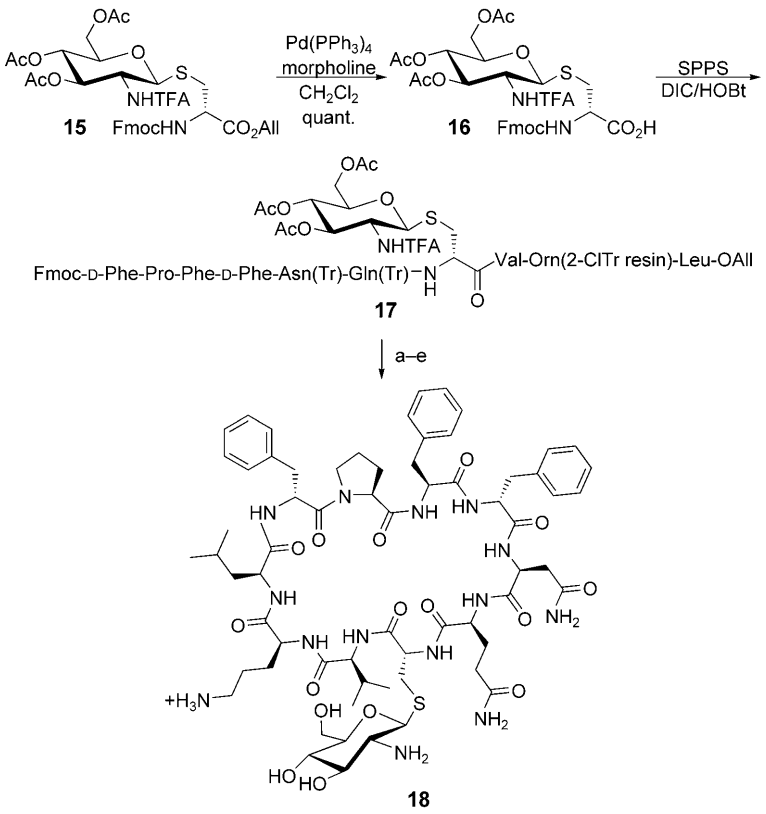
Scheme 3. Solid-phase peptide synthesis of glycopeptide **14** with Fmoc-modified glycosyl amino acid **12**. The yield from **12** to **14** is 60% (DIC = 1,3-diisopropylcarbodiimide, HOBt = 1-hydroxybenzotriazole, Tr = trityl).

conformation in solution.[35–38] A recent report has shown that several cyclic glycopeptide analogues of tyrocidine A retain biological activity as antibiotics.[39] To further test the method reported herein for the synthesis of S-linked glycopeptides, glycosyl amino acid **15** was synthesized and converted into **16**. After the removal of palladium by scavenger resin, the tyrocidine analogue precursor **17** was produced (Scheme 4). Conversion of **17** to cyclic glycopeptide **18** (an analogue of tyrocidine A in which the wild-type Tyr group at position 7 is replaced by a D-Ser(β-*S*-GlcNH$_2$) residue) was carried out in four steps on solid support followed by cleavage and amino acid side chain deprotection (29% overall yield from **16** to **18**). The biological activity of this glycosylated tyrocidine analogue was evaluated with the minimal inhibitory concentration (MIC) against *B. subtilis* as a measure of the antibiotic activity and the minimal hemolytic concentration (MHC) against human erythrocytes as an evaluation of eukaryotic membrane toxicity. The S-linked glycopeptide analogue **18** was shown to have a better antibiotic profile than tyrocidine A, with MIC values of 12.5 μM for both and MHC values of 100 and 50 μM, respectively.

Although Fmoc SPPS is preferred for glycopeptides, the synthetic approach reported herein should also be applicable for the synthesis of Boc-modified amino acid building blocks. Therefore, Boc-protected S-linked glycosyl amino acid building block **19** (Table 1) was synthesized from **4** and **9b** (Scheme 2) in a similar fashion.

To demonstrate that our approach is also applicable to other thiosugars, we synthesized several different peracetylated 1-thiosugars (Supporting Information). These represent all four possible classes of products: 1,2-*trans*-α (**21** and **23**[15]); 1,2-*trans*-β (**4**,[28] **24**,[40] **26**,[41] **27**,[42] and **28**[43]); 1,2-*cis*-α (**20** and **25**[23]); and 1,2-*cis*-β (**22**[29]). They are conveniently grouped based on the stereochemistry at C1 and its relationship to the functional group at C2 of the sugar ring. All compounds were subjected to the "two-step one-pot" conditions mentioned above to give the corresponding Fmoc- or Boc-protected S-linked glycosyl amino acid building blocks, in yields ranging from 66 to 81%.

 © 2005 Wiley-VCH Verlag GmbH & Co. KGaA, Weinheim



Scheme 4. Solid-phase glycopeptide synthesis of the tyrocidine analogue **18**. Reagents and conditions: a) $[Pd(PPh_3)_4]$/4-methylmorpholine, $CHCl_3$; b) piperidine/DMF (20%); c) PyBOP/HOBt, DMF; d) $H_2NNH_2{\cdot}H_2O$, MeOH; e) TFA/CH_2Cl_2/triisopropylsilane (80:15:5); 29% overall yield from **16**. PyBOP = 1-benzotriazolyloxy-tris-(pyrollidino)phosphonium; TFA = trifluoroacetate.

In summary, we have developed a general strategy for S-linked glycopeptide synthesis. With a simple "two-step one-pot" reaction, peracetylated thiosugars are quickly converted into masked S-linked amino acid building blocks. Under such reaction conditions, deacetylation at the sulfur atom is selective, anomeric integrity is retained, and S_N2 substitution is stereoselective. Unmasking the building blocks by deallylation affords Fmoc- or Boc-protected amino acids, which are ready for SPPS. This strategy is applicable for large-scale S-linked glycopeptide synthesis and could also be used for other S-linked glycoconjugates.

Received: January 11, 2005
Revised: April 21, 2005
Published online: June 30, 2005

Keywords: glycopeptides · S-linked glycopeptides · solid-phase synthesis · sulfur

[1] R. A. Dwek, *Chem. Rev.* **1996**, *96*, 683.
[2] H. Lis, N. Sharon, *Eur. J. Biochem.* **1993**, *218*, 1.
[3] A. Varki, *Glycobiology* **1993**, *3*, 97.
[4] R. S. Rush, P. L. Derby, D. M. Smith, C. Merry, G. Rogers, M. F. Rohde, *Anal. Chem.* **1995**, *67*, 1442.
[5] H. T. Liu, L. Wang, A. Brock, C. H. Wong, P. G. Schultz, *J. Am. Chem. Soc.* **2003**, *125*, 1702.
[6] Z. W. Zhang, J. Gildersleeve, Y. Y. Yang, R. Xu, J. A. Loo, S. Uryu, C. H. Wong, P. G. Schultz, *Science* **2004**, *303*, 371.
[7] J. D. Warren, J. S. Miller, S. J. Keding, S. J. Danishefsky, *J. Am. Chem. Soc.* **2004**, *126*, 6576.
[8] O. Sietz, *ChemBioChem* **2000**, *1*, 214.
[9] H. Herzner, T. Reipen, M. Schultz, H. Kunz, *Chem. Rev.* **2000**, *100*, 4495.
[10] P. M. St. Hilaire, M. Meldal, *Angew. Chem.* **2000**, *112*, 1210; *Angew. Chem. Int. Ed.* **2000**, *39*, 1162.
[11] B. G. Davis, *Chem. Rev.* **2002**, *102*, 579.
[12] B. Capon, *Chem. Rev.* **1969**, *69*, 407.
[13] H. Driguez, *Top. Curr. Chem.* **1997**, *187*, 85.
[14] Z. J. Witczak, *Curr. Med. Chem.* **1999**, *6*, 165.
[15] H. N. Yu, PhD Thesis, University of Alberta, **2002**.
[16] E. Bousquet, A. Spadaro, M. S. Pappalardo, R. Bernardini, R. Romeo, L. Panza, G. Ronsisvalle, *J. Carbohydr. Chem.* **2000**, *19*, 527.
[17] J. R. Rich, D. R. Bundle, *Org. Lett.* **2004**, *6*, 897.
[18] B. Kuberan, S. A. Sikkander, H. Tomiyama, R. J. Linhardt, *Angew. Chem.* **2003**, *115*, 2119; *Angew. Chem. Int. Ed.* **2003**, *42*, 2073.
[19] A. Dondoni, A. Marra, *Chem. Rev.* **2000**, *100*, 4395.
[20] Y. Ohnishi, M. Ichikawa, Y. Ichikawa, *Bioorg. Med. Chem. Lett.* **2000**, *10*, 1289.
[21] L. Jobron, G. Hummel, *Org. Lett.* **2000**, *2*, 2265.
[22] S. B. Cohen, R. L. Halcomb, *Org. Lett.* **2001**, *3*, 405.
[23] S. Knapp, D. S. Myers, *J. Org. Chem.* **2002**, *67*, 2995.
[24] X. M. Zhu, R. R. Schmidt, *Chem. Eur. J.* **2004**, *10*, 875.
[25] X. M. Zhu, R. R. Schmidt, *Tetrahedron Lett.* **2003**, *44*, 6063.
[26] X. M. Zhu, K. Pachamuthu, R. R. Schmidt, *J. Org. Chem.* **2003**, *68*, 5641.
[27] X. M. Zhu, K. Pachamuthu, R. R. Schmidt, *Org. Lett.* **2004**, *6*, 1083.
[28] K. P. R. Kartha, P. Cura, M. Aloui, S. K. Readman, T. J. Rutherford, R. A. Field, *Tetrahedron: Asymmetry* **2000**, *11*, 581.
[29] H. N. Yu, C. C. Ling, D. R. Bundle, *J. Chem. Soc. Perkin Trans. 1* **2001**, 832.
[30] E. Atherton, R. C. Sheppard, *Solid Phase Peptide Synthesis: A Practical Approach*, IRL Press at Oxford University Press, Oxford, **1989**.
[31] G. B. Fields, R. L. Noble, *Int. J. Pept. Protein Res.* **1990**, *35*, 161.
[32] S. Friedrich-Bochnitschek, H. Waldmann, H. Kunz, *J. Org. Chem.* **1989**, *54*, 751.
[33] D. H. Drewry, D. M. Coe, S. Poon, *Med. Res. Rev.* **1999**, *19*, 97.
[34] Compound **9a** is not stable in silica gel.
[35] R. D. Hotchkiss, R. J. Dubos, *J. Biol. Chem.* **1940**, *132*, 791.
[36] R. D. Hotchkiss, R. J. Dubos, *J. Biol. Chem.* **1940**, *132*, 793.
[37] R. D. Hotchkiss, R. J. Dubos, *J. Biol. Chem.* **1940**, *136*, 803.
[38] M.-C. Kuo, W. A. Gibbons, *Biophys. J.* **1980**, *32*, 807.
[39] H. Lin, D. A. Thayer, C. H. Wong, C. T. Walsh, *Chem. Biol.* **2004**, *11*, 1635.
[40] Obtained by the same procedure as used for compound **22**.
[41] Obtained by the same procedure as used for compound **4**, but with DMF as the solvent.
[42] Obtained by the same procedure as used for compound **4**, but with acetone as the solvent.
[43] V. Moreau, J.-L. Viladot, E. Samain, A. Planas, H. Driguez, *Bioorg. Med. Chem.* **1996**, *4*, 1849.

 © 2005 Wiley-VCH Verlag GmbH & Co. KGaA, Weinheim

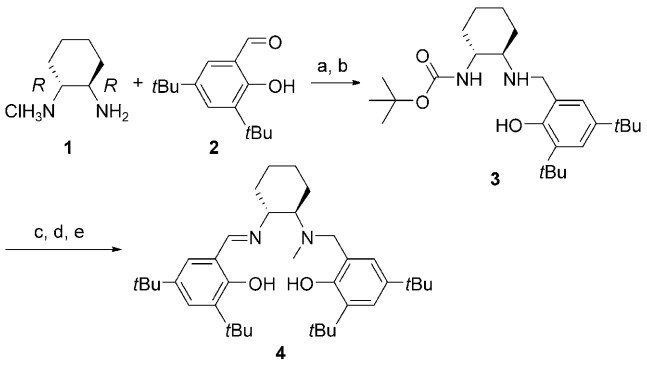
Asymmetric Catalysis

Synthesis of an Optically Active C_1-Symmetric Al(salalen) Complex and Its Application to the Catalytic Hydrophosphonylation of Aldehydes**

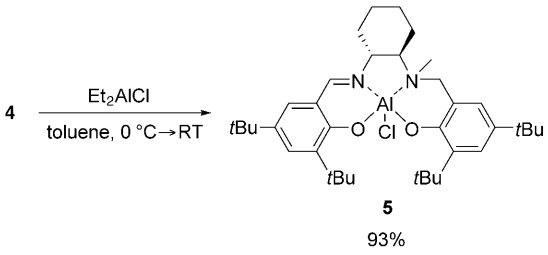
*Bunnai Saito and Tsutomu Katsuki**

For the last few decades asymmetric catalysis of optically active complexes has been a major topic in synthetic chemistry, and various types of chiral ligands have been introduced.[1] Among these, tetradentate ligands have been widely used because of their good ability to form complexes. In particular, chiral salen ligands have received a great deal of attention owing to their high asymmetry-inducing ability and ready availability. Chiral metallosalen complexes show potent and diverse asymmetric catalytic activities and have been used as catalysts for a wide range of enantioselective reactions, including epoxidation, aziridination, sulfoxidation, Michael reaction, epoxide opening, etc.[2] Salen complexes adopt mostly an octahedral configuration in which two ancillary ligands are *trans*-oriented. However, recent studies have disclosed that *cis*-β isomers show unique catalytic behavior.[2c] For example, a di-μ-oxo Ti(salen) complex that bears chiral *cis*-β-salen ligands catalyzes asymmetric cyanation with high enantioselectivity.[3] Furthermore, a di-μ-oxo Ti(salen) complex has been found to be an excellent pre-catalyst for asymmetric sulfoxidation, in which a monomeric *cis*-β-peroxo complex has been proven to be the active species.[4] Kol and co-workers reported quite recently that treatment of an achiral hybrid salan/salen tetradentate [ONN(Me)O]-type ligand (hereafter referred to as salalen) with titanium and zirconium tetraethoxides yielded the corresponding octahedral Ti- and Zr(salalen)$(OEt)_2$ complexes, in which the two diastereotopic ethoxy groups are *cis*-oriented and the coordinated amino nitrogen atom that is closer to the metal ion by one C–C bond than the ethylene carbon is chiral.[5] Thus, we expected that the chiral salalen ligand would establish a unique asymmetric reaction site that induces a high extent of asymmetry. Herein, we describe the synthesis of a chiral aluminum salalen complex and its application to the asymmetric hydrophosphonylation of aldehydes to give optically active α-hydroxy phosphonates.

We initially attempted the synthesis of an optically active salalen ligand according to Kol's procedure, but the attempt ended in failure because the key Mannich condensation of 2,4-di(*tert*-butyl)phenol and chiral secondary amines derived from cyclohexane-1,2-diamine and 1,2-diphenylethylenediamine did not proceed. Thus, the salalen ligand **4** was synthesized in a stepwise manner (Scheme 1). Reductive amination of aldehyde **2** with monoammonium salts of diamine **1**[6] in the presence of sodium borohydride, followed by *N*-protection with the *tert*-butoxycarbonyl (Boc) group, gave the corresponding amine **3** in 67% yield. The *N*-methylation of amine **3**, deprotection of the Boc group with aqueous HCl, and condensation of the resulting primary amine with aldehyde **2** afforded the desired ligand **4** in 76% yield. The salalen ligand **4** was then treated with Et_2AlCl to give the corresponding Al(salalen) complex **5** in high yield (Scheme 2). Recrystallization of **5** from heptane and dichloromethane gave single crystals, one of which was submitted for X-ray diffraction analysis (Figure 1).[7] This analysis demonstrated that complex **5** has a unique structure that is different from that of Al(salen) complexes:[8] it adopts a distorted trigonal-bipyramidal configuration, and the absolute configuration of the coordinated tertiary amine is *S*. As the chiral ligand adopts a unique *cis*-β-like structure and as the methyl group on the nitrogen atom is located in the middle of the chiral ligand and close to the chloro ligand that should be replaceable by a substrate such as an aldehyde, we expected that the orientation of the substrate ligated to the



Scheme 1. Synthesis of the optically active salalen ligand **4**: a) **1** and **2**, MeOH, room temperature, then $NaBH_4$ (2.5 equiv), 0°C → RT; b) $(Boc)_2O$, EtOH, room temperature (67%, 2 steps); c) aq. CH_2O, Pd/C, H_2, MeOH, room temperature; d) 3 M HCl, MeOH, room temperature; e) **2**, MeOH, room temperature (76%, 3 steps). Boc = *tert*-butoxycarbonyl.



Scheme 2. Synthesis of Al(salalen) complex **5**.

[*] B. Saito, Prof. T. Katsuki
Department of Chemistry, Faculty of Science
Graduate School, Kyushu University
33, Hakozaki, Higashi-ku, Fukuoka 812-8581 (Japan)
Fax: (+81) 92-642-2607
E-mail: katsuscc@mbox.nc.kyushu-u.ac.jp

[**] Financial support was provided by CREST of the Japan Science and Technology Agency. B.S. is grateful for research fellowships from the Japan Society for the Promotion of Science for Young Scientists. Salalen refers to an achiral hybrid salan/salen tetradentate ligand.

Supporting information for this article is available on the WWW under http://www.angewandte.org or from the author.

 © 2005 Wiley-VCH Verlag GmbH & Co. KGaA, Weinheim DOI: 10.1002/anie.200501008

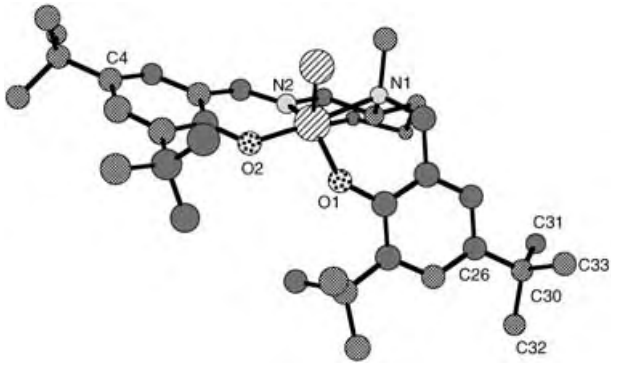


Figure 1. X-ray crystal structure of **5**. Hydrogen atoms have been omitted for clarity. The *tert*-butyl group (C30–C33) attached to C26 is disordered (disorder omitted for clarity).

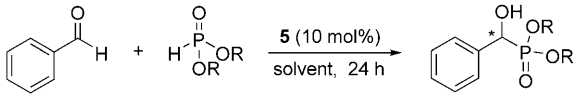
aluminum ion should be efficiently regulated by the ligand. Thus, we considered that **5** should be a highly efficient chiral Lewis acid catalyst. To explore the catalytic behavior of **5**, we first examined the asymmetric hydrophosphonylation of aldehydes.

Optically active α-hydroxy phosphonates and phosphonic acids are biologically active compounds that are widely used in pharmaceutical applications, and much effort has been directed toward the development of asymmetric hydrophosphonylation of carbonyl compounds (the Pudovik reaction).[9,10] To the best of our knowledge, LLB ($LaLi_3$tris(binaphthoxide)) and ALB (AlLibis(binaphthoxide)) reported by Shibasaki and co-workers are the most efficient catalysts for this reaction and have been complementarily used as catalysts for the reaction of various aldehydes.[10d,f] Recently, Kee and co-workers reported that chiral Al(salen) complexes serve as catalysts for asymmetric hydrophosphonylation; however, the enantioselectivities obtained were modest (up to 49% *ee*).[11] The introduction of a novel catalyst that can show wide applicability for various aldehydes, especially aliphatic ones, is therefore still required to achieve a highly efficient Pudovik reaction.

With the Al(salalen) complex **5** in hand, we first examined the asymmetric hydrophosphonylation of benzaldehyde with dimethyl phosphite at room temperature under various conditions (Table 1, entries 1–5). All the reactions proceeded smoothly to give the desired product in acceptable yields and the best enantioselectivity was observed in the reaction with diisopropyl ether as solvent. The reactions with dialkyl phosphites, especially dimethyl phosphite, showed better enantioselectivities than those with diphenyl phosphite (see entries 1–3). Lowering the temperature of the reaction in diisopropyl ether to 0°C improved the enantioselectivity to 89% *ee* (entry 7), whereas a further reduction of the temperature affected the reproducibility of the enantioselectivity (entry 9).[12] The enantioselectivity of the reaction in THF was inferior to that in diisopropyl ether at room temperature, but the reaction at −15°C showed the best and most reproducible enantioselectivity of 90% *ee*, albeit with some reduction of the chemical yield (entry 8).

Thus, we examined the asymmetric hydrophosphonylation of various aldehydes with complex **5** as catalyst at −15°C in THF (Table 2). The electronic effect on enantioselectivity was investigated with *para*-substituted benzaldehyde derivatives, and we found that an electron-withdrawing group increases the enantioselectivity (entries 1–3); the highest enantioselectivity of 94% *ee* was observed in the reaction with *p*-nitrobenzaldehyde (entry 1), although the reaction of *o*-chlorobenzaldehyde also proceeded with high enantioselectivity (entry 4). The reaction of an α,β-unsaturated aldehyde (cinnamaldehyde) was a little slow and showed a slightly reduced enantioselectivity of 83% *ee* (entry 5). To our delight, high enantioselectivity was also observed in the reactions of aliphatic aldehydes. Both nonbranched (entries 6 and 8) and branched (entry 7) aliphatic aldehydes gave the corresponding α-hydroxy phosphonates with high enantioselectivities and in good yields. To the best of our knowledge, this is the first example where a molecular catalyst can be

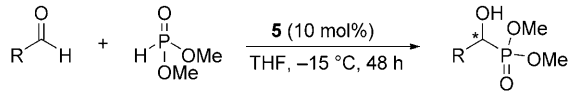
Table 1: Asymmetric hydrophosphonylation of benzaldehyde.



Entry	R	Solvent	*T* [°C]	Yield [%][a]	*ee* [%][b]	Config.[c]
1	Me	THF	RT	92	73	*S*
2	Et	THF	RT	96	70	
3	Ph	THF	RT	87	17	
4	Me	Et_2O	RT	97	68	*S*
5	Me	iPr_2O	RT	94	79	*S*
6	Me	THF	0	91	87	*S*
7	Me	iPr_2O	0	94	89	*S*
8[d]	Me	THF	−15	87	90	*S*
9[d]	Me	iPr_2O	−15	80	81–90	*S*

[a] Yield of isolated product. [b] Determined by HPLC analysis using a chiral stationary phase column (Daicel Chiralpak AS-H; hexane/*i*PrOH 4:1). [c] Determined by chiroptical comparison (ref. [10d]). [d] The reaction was carried out for 48 h.

Table 2: Asymmetric hydrophosphonylation of various aldehydes.



Entry	R	Yield [%][a]	*ee* [%]	Config.
1	*p*-$O_2NC_6H_4$	95	94[b]	*S*[c]
2	*p*-ClC_6H_4	88	88[b]	*S*[c]
3	*p*-$MeOC_6H_4$	87	81[b]	*S*[c]
4	*o*-ClC_6H_4	96	91[b]	
5	(*E*)-PhCH=CH	77	83[b]	*S*[c]
6	$PhCH_2CH_2$	94	91[b]	
7	$(CH_3)_2CH$	89	89[d]	
8	CH_3CH_2	61	89[d]	*S*[e]

[a] Yield of isolated product. [b] Determined by HPLC analysis using a chiral stationary phase column (Daicel Chiralpak AS-H; hexane/*i*PrOH 7:3). [c] Determined by chiroptical comparison (ref. [10d]). [d] Determined by HPLC analysis using a chiral stationary phase column (Daicel Chiralpak AS-H; hexane/*i*PrOH 9:1) after conversion of the product into the corresponding benzoate. [e] Determined by chiroptical comparison (ref. [13]).

 © 2005 Wiley-VCH Verlag GmbH & Co. KGaA, Weinheim

applied to the reactions of both aromatic and aliphatic aldehydes with enantioselectivities greater than 80% *ee*.

In conclusion, we have synthesized a chiral, trigonal-bipyramidal aluminum(salalen) complex **5** that provides a unique asymmetric reaction site in which an asymmetric nitrogen atom is bound to the metal ion and the *N*-methyl group is *cis* to the chloro ligand. Moreover, complex **5** is an efficient catalyst for the enantioselective hydrophosphonylation of various aldehydes with dimethyl phosphite. Further application of this novel aluminum complex to other asymmetric reactions is under investigation.

Experimental Section

Complex **5** (12.5 mg, 0.02 mol) and dimethyl phosphite (10.1 μL, 0.21 mmol) were dissolved in THF (1.0 mL) under nitrogen, and the solution was stirred for 10 min at room temperature. After cooling to −15 °C, aldehyde (0.20 mmol) was added to the solution and the solution was stirred for 48 h. The reaction was quenched with 1 M HCl and extracted with AcOEt (3 × ca. 1 mL), and the combined organic phase was passed through a pad of Celite and Na_2SO_4. After removal of the solvent under reduced pressure, the residue was chromatographed on silica gel (hexane/acetone, 7:3–3:7) to give the corresponding α-hydroxy phosphonate. The *ee* values were determined by HPLC on a chiral stationary phase under the conditions described in the footnotes to Table 1 and Table 2.

Received: March 19, 2005
Published online: June 27, 2005

Keywords: aldehydes · aluminum · asymmetric catalysis · hydrophosphonylation · N,O ligands

[1] a) *Comprehensive Asymmetric Catalysis* (Eds.: E. N. Jacobsen, A. Pfaltz, H. Yamamoto), Springer, Berlin, **1999**; b) *Catalytic Asymmetric Synthesis* (Ed.: I. Ojima), *2nd ed.*, Wiley-VCH, New York, **2000**.

[2] a) L. Canali, D. C. Sherrington, *Chem. Soc. Rev.* **1999**, *28*, 85–93; b) T. Katsuki, *Synlett* **2003**, 281–297; c) T. Katsuki, *Chem. Soc. Rev.* **2004**, *33*, 437–444; d) J. F. Larrow, E. N. Jacobsen, *Top. Organomet. Chem.* **2004**, *6*, 123–152.

[3] Yu. N. Belokon', S. Caveda-Cepas, B. Green, N. Ikonnikov, V. Khrustalev, V. Larichev, M. Moskalenko, M. North, C. Orizu, V. Tararov, M. Tasinazzo, G. Timofeeva, L. Yashkina, *J. Am. Chem. Soc.* **1999**, *121*, 3968–3973.

[4] a) B. Saito, T. Katsuki, *Tetrahedron Lett.* **2001**, *42*, 3873–3876; b) B. Saito, T. Katsuki, *Tetrahedron Lett.* **2001**, *42*, 8333–8336.

[5] A. Yeori, S. Gendler, S. Groysman, I. Goldberg, M. Kol, *Inorg. Chem. Commun.* **2004**, *7*, 280–282.

[6] E. J. Campbell, S. T. Nguyen, *Tetrahedron Lett.* **2001**, *42*, 1221–1225.

[7] CCDC-264917 contains the supplementary crystallographic data for this paper. These data can be obtained free of charge from the Cambridge Crystallographic Data Centre via www.ccdc.cam.ac.uk/data_request/cif.

[8] D. A. Atwood, M. S. Hill, J. A. Jegier, D. Rutherford, *Organometallics* **1997**, *16*, 2569–2664.

[9] a) D. F. Wiemer, *Tetrahedron* **1997**, *53*, 16609–16644; b) H. Gröger, B. Hammer, *Chem. Eur. J.* **2000**, *6*, 943–948, and references therein.

[10] a) T. Yokomatsu, T. Yamagichi, S. Shibuya, *Tetrahedron: Asymmetry* **1993**, *4*, 1779–1782; b) T. Yokomatsu, T. Yamagishi, S. Shibuya, *Tetrahedron: Asymmetry* **1993**, *4*, 1783–1784; c) N. P. Rath, C. D. Spilling, *Tetrahedron Lett.* **1994**, *35*, 227–230; d) T. Arai, M. Bougauchi, H. Sasai, M. Shibasaki, *J. Org. Chem.* **1996**, *61*, 2926–2927; e) T. Yokomatsu, T. Yamagichi, K. Matsumoto, S. Shibuya, *Tetrahedron* **1996**, *52*, 11725–11738; f) H. Sasai, M. Bougauchi, T. Arai, M. Shibasaki, *Tetrahedron Lett.* **1997**, *38*, 2717–2720; g) T. Yokomatsu, T. Yamagishi, S. Shibuya, *J. Chem. Soc. Perkin Trans. 1*, **1997**, 1527–1533; h) M. D. Groaning, B. J. Rowe, C. D. Spilling. *Tetrahedron Lett.* **1998**, *39*, 5485–5488; i) D. M. Cermak, Y. Du, D. F. Wiemer, *J. Org. Chem.* **1999**, *64*, 388–393; j) T. Yamagichi, T. Yokomatsu, K. Suemune, S. Shibuya, *Tetrahedron* **1999**, *55*, 12125–12136; k) D. Skropeta, R. R. Schmidt, *Tetrahedron: Asymmetry* **2003**, *14*, 265–273.

[11] a) J. P. Duxbury, A. Cawley, M. Thornton-Pett, L. Wantz, J. N. D. Warne, R. Greatrex, D. Brown, T. P. Kee, *Tetrahedron Lett.* **1999**, *40*, 4403–4406; b) C. V. Ward, M. Jiang, T. P. Kee, *Tetrahedron Lett.* **2000**, *41*, 6181–6184; c) J. P. Duxbury, J. N. D. Warne, R. Mushtaq, C. Ward, M. Thornton-Pett, M. Jiang, R. Greatrex, T. P. Kee, *Organometallics* **2000**, *19*, 4445–4457.

[12] Complex **5** and the product, dimethyl α-hydroxyphenylmethylphosphonate, are weakly soluble in diisopropyl ether. A suspension of **5** in diisopropyl ether became homogeneous upon addition of dimethyl phosphite, but the solution became heterogeneous again as the reaction proceeded. This turbidity might reduce the reproducibility of the enantioselectivity of the reaction at −15 °C.

[13] Y. Zhang, C. Yuan, Z. Li, *Tetrahedron* **2002**, *58*, 2973–2978.

 © 2005 Wiley-VCH Verlag GmbH & Co. KGaA, Weinheim

Natural Products Synthesis

Mining the Tetraene Manifold: Total Synthesis of Complex Pyrones from *Placobranchus ocellatus***

*Aubry K. Miller and Dirk Trauner**

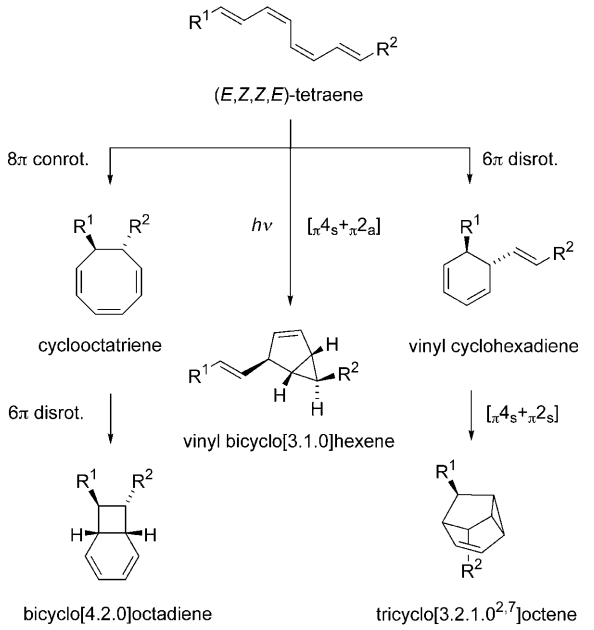
Conjugated tetraenes featuring *Z*-configured double bonds can undergo various cyclizations to rapidly generate molecular complexity. Different modes of thermal or photochemical electrocyclizations and cycloadditions afford structurally diverse scaffolds from a relatively simple (*E*,*Z*,*Z*,*E*)-tetraene precursor (Scheme 1).[1] If the tetraene is unsymmetrical ($R^1 \neq R^2$), additional pathways exist that lead to regioisomers and diastereomers. Isomerizations of the polyene geometry further increase the number of potential cyclization products, thus rendering this reaction manifold dauntingly complex.

[*] A. K. Miller, Prof. D. Trauner
Department of Chemistry
University of California
Berkeley, CA 94720-1460 (USA)
Fax: (+1) 510-643-9480
E-mail: trauner@cchem.berkeley.edu

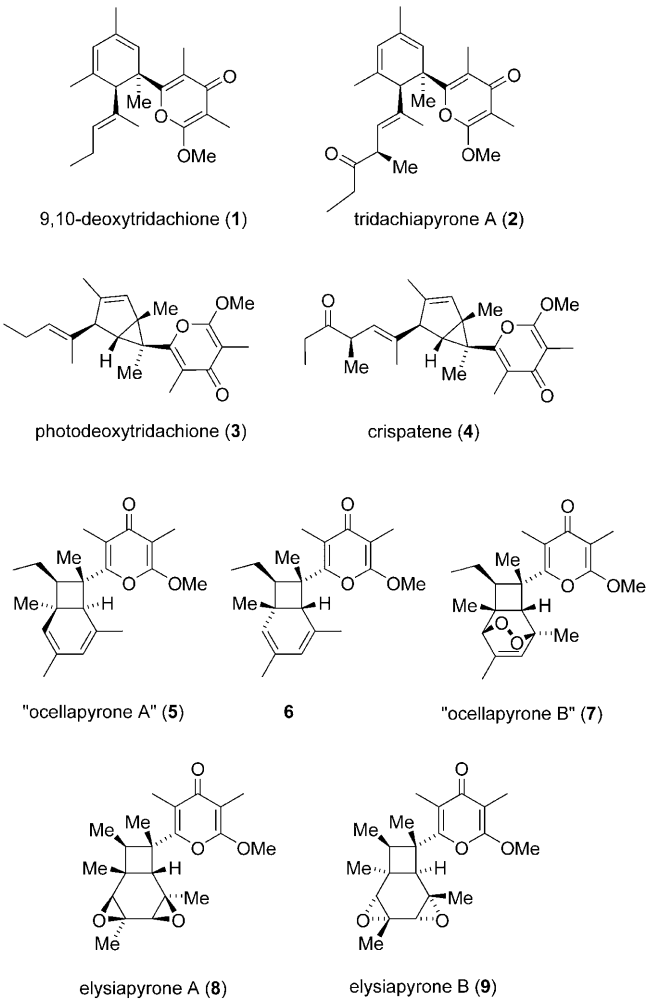
[**] This work was supported by the National Institutes of Health (Grant R01 GM067636). We thank Dr. Frederick J. Hollander and Dr. Alan G. Oliver (UC Berkeley) for X-ray crystal-structure determinations. A.K.M. thanks the NSF for a predoctoral fellowship.

Supporting information for this article is available on the WWW under http://www.angewandte.org or from the author.

 © 2005 Wiley-VCH Verlag GmbH & Co. KGaA, Weinheim DOI: 10.1002/anie.200500488



Scheme 1. The tetraene manifold. conrot. = conrotatory, disrot. = disrotatory.



Scheme 2. Polypropionate pyrones isolated from saccoglossan mollusks.

Many of the molecular scaffolds shown in Scheme 1 have been found among natural products isolated from saccoglossan mollusks (Scheme 2). The cyclohexadienes 9,10-deoxytridachione (**1**) and tridachiapyrone A (**2**) were isolated from sea slugs of the genus *Elysia*, which also yielded the bicyclo[3.1.0]hexenes photodeoxytridachione (**3**) and crispatene (**4**).[2]

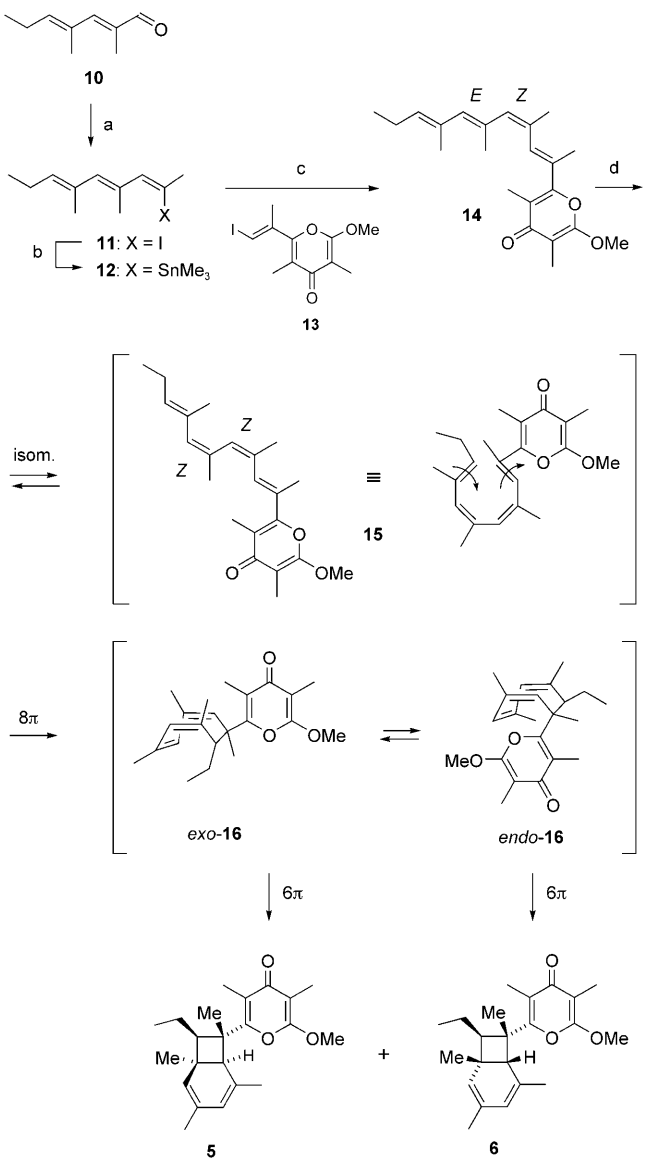
Recently, several new α-methoxy-γ-pyrones that feature a bicyclo[4.2.0]octane, -octene, or -octadiene skeleton were also found in saccoglossan mollusks. Two unnamed natural products, bicyclo[4.2.0]octadiene **5** and endoperoxide **7**, were found in *Placobranchus ocellatus* which we propose to call ocellapyrones A and B, respectively.[3] Although structure **6** was originally proposed for the bicylco[4.2.0]octadiene natural product (ocellapyrone A), our results (see below) and a recent report by Baldwin and co-workers[4] lead to the reassignment of its structure as **5**. Furthermore, two pyrones with a bicyclo[4.2.0]octane skeleton, elysiapyrones A (**8**) and B (**9**), were isolated from *Elysia diomedea*.[5] Their unusual bisepoxide moiety was proposed to arise biosynthetically from rearrangement of an *endo* peroxide analogous to **7**, which in turn would stem from the corresponding bicyclo[4.2.0]hexadiene through a Diels–Alder reaction that involved singlet oxygen. Note that the elysiapyrones contain one carbon atom less than the ocellapyrones, presumably because of the incorporation of an acetate moiety rather than a propionate unit into their biosynthetic precursor.

Biosynthetically, bicyclo[4.2.0]octadienes **5** and **6** and their oxidized analogues **7**–**9** probably stem from 8π–6π electrocyclization cascades.[6] Similar cascades have been proposed in the biosynthesis of the endiandric acids,[7] as well as the immunosuppressants SNF4435 C/D,[8] and verified by total synthesis.[9]

Herein, we report a synthesis of the racemic ocellapyrones A (**5**) and B (**7**), which originated from a serendipitous discovery. In our previous reports on the total synthesis of photodeoxytridachione (**3**) and crispatene (**4**), we speculated on the possibility of a unified synthetic approach toward both the bicyclo[3.1.0]hexene and cyclohexadiene natural products that would start from an α-methoxy-γ-pyronyl tetraene of type **14** (Scheme 3).[10] To test this hypothesis, vinyl stannane **12** was prepared from the known aldehyde **10** in two steps[11] and then subjected to the Stille coupling procedure[12] with the previously described pyrone building block **13**.[10c,13] The resultant pyronyl tetraene **14**, however, turned out to be quite unstable, as judged by TLC and NMR spectroscopic analysis.

When **14** was heated to 45 °C in $CHCl_3$, a very complex mixture of isomers was formed initially, which over five days gradually converged into bicylo[4.2.0]octadiene **6** accompanied by smaller amounts of ocellapyrone A (**5**). Presumably, *E/Z* isomerization of **14** took place under these conditions to yield (*E*,*Z*,*Z*,*E*)-tetraene **15**. This intermediate then underwent conrotatory 8π electrocyclization to afford cyclooctatriene **16**, which exists as a mixture of *exo* and *endo* conformers. Subsequent 6π electrocyclization of *exo*-**16** gave (±)-ocellapyrone A (**5**), whereas cyclization of *endo*-**16** afforded **6**. Since purified ocellapyrone A (**5**) could not be converted into **6** under the same reaction conditions, this product ratio presumably reflects kinetic control.[14]

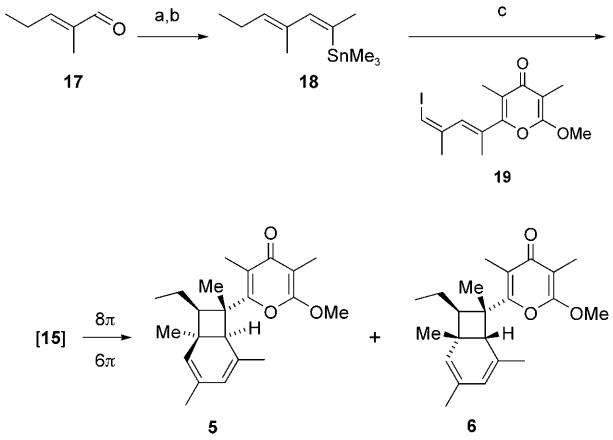
 © 2005 Wiley-VCH Verlag GmbH & Co. KGaA, Weinheim



Scheme 3. Synthesis of γ-pyronyl tetraene **14** and cyclization to **5** and **6**. Reagents and conditions: a) $Ph_3P{=}CHCH_3$, I_2, NaHMDS, −78 °C, THF (59%); b) *n*BuLi, $SnMe_3Cl$, −78 °C, THF (69%); c) **13**, 5 mol% $[Pd(PPh_3)_4]$, 350 mol% CsF, 10 mol% CuI, DMF, 1.5 h, 45 °C (89%); d) $CDCl_3$, 45 °C, 5 days (13% **5**; 66% **6**). HMDS = hexamethyldisilazide, DMF = *N*,*N*-dimethylformamide, isom. = isomerization.

The ^1H and ^{13}C NMR spectra of synthetic ocellapyrone A (**5**) match the reported spectra of the previously unnamed bicylo[4.2.0]octadiene natural product isolated from *Placobranchus ocellatus*, whereas the spectra of **6**, which represents the originally proposed structure, show marked differences.[15] The detailed structures of **5** and **6** were elucidated by extensive NOE interaction studies and the conversion of **6** into ocellapyrone B (**7**), whose relative configuration has been unequivocally assigned.[3,16]

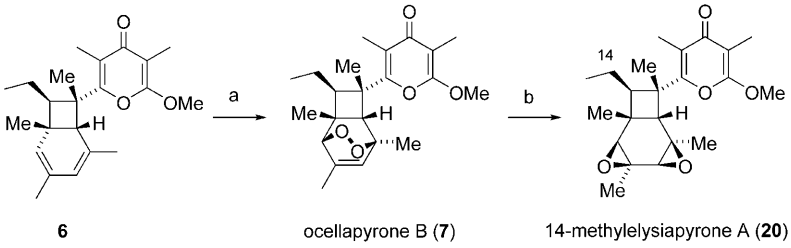
A more rational synthesis of **5** and **6** is shown in Scheme 4. Olefination of the known aldehyde **17**[17] followed by iodine–tin exchange, as before, gave vinyl stannane **18**. This material was then coupled to the known vinyl iodide **19**[4,18] under Stille conditions. The resultant tetraene **15** underwent 8π–6π electrocyclization in situ to give a 1:9 mixture of **5** and **6**. Note that the *endo* isomer **6** again prevailed. The much faster formation of the bicyclo[4.2.0]octadienes under these conditions presumably reflects the fact that **15** does not need to undergo *E*/*Z* isomerization to trigger the electrocyclization cascade, which is apparently the rate-determining step in the conversion of **14** into **5** and **6**.



Scheme 4. Rational synthesis of ocellapyrones A and B. Reagents and conditions: a) $Ph_3PCHICH_3$, NaHMDS, −78 °C, THF (12%); b) *n*BuLi, $SnMe_3Cl$, −78 °C, THF (86%); c) **13**, 6 mol% $[Pd(PPh_3)_4]$, 180 mol% CsF, 17 mol% CuI, DMF, 1 h, 45 °C (8% **5**; 78% **6**).

Racemic ocellapyrone B (**7**) was obtained in high yield from cyclohexadiene **6** by a [4+2] cycloaddition of singlet oxygen (Scheme 5). The synthetic material was identical in all respects (^1H and ^{13}C NMR, IR, MS) to the natural product.[3] Finally, ruthenium-catalyzed isomerization[19] of ocellapyrone B (**7**) gave bisepoxide **20**, which is a homologue of elysiapyrone A. Although this compound has not been isolated from natural sources so far, it seems entirely possible that it could be found, as endoperoxides can be readily converted into bisepoxides both under thermal and photochemical conditions.[20] The X-ray crystal structure of **20**, with its appealing "crouched" shape, is shown in Figure 1.[21]

In summary, we have demonstrated that complex pyrones isolated from saccoglossan molluscs can be synthesized by isomerization of stereochemically labile tetraenes followed by pericyclic reaction cascades. In combination with our previous



Scheme 5. Synthesis of ocellapyrone B and 14-methylelysiapyrone A. Reagents and conditions: a) O_2, methylene blue, $CHCl_3$, *hν*, reflux, 30 min (89%); b) 10 mol% $[RuCl_2(PPh_3)_3]$, CH_2Cl_2, 2 h (86%).

 © 2005 Wiley-VCH Verlag GmbH & Co. KGaA, Weinheim

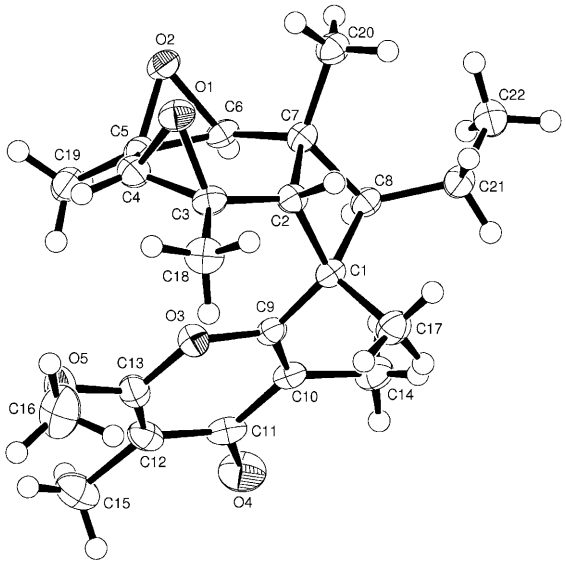


Figure 1. X-ray structure of 14-methylelysiapyrone A (20).

total syntheses of photodeoxytridachione[10a,b] and crispatene,[10c] these results demonstrate the remarkable versatility of conjugated polyenes as precursors for complex polycyclic molecular skeleta. On the basis of our experience with these compounds,[22] we predict that further bicylo[4.2.0]octadiene natural products and oxidized versions thereof, in particular isomers of crispatene and tridachiapyrone A, will be found. Studies toward asymmetric electrocyclization cascades and the total synthesis of the elysiapyrones are well underway and will be reported in due course.

Received: February 9, 2005
Published online: June 27, 2005

Keywords: biomimetic synthesis · electrocyclic reactions · isomerization · natural products synthesis · reaction cascades

[1] a) R. B. Woodward, R. Hoffmann, *The Conservation of Orbital Symmetry*, VCH, Weinheim, **1970**; b) E. N. Marvell, *Thermal Electrocyclic Reactions*, Academic Press, New York, **1980**; c) E. N. Marvell, J. Seubert, G. Vogt, G. Zimmer, G. Moy, J. R. Siegmann, *Tetrahedron* **1978**, *34*, 1323.

[2] M. T. Davies-Colman, M. J. Garson, *Nat. Prod. Rep.* **1998**, *15*, 477, and references therein.

[3] E. Manzo, M. L. Ciavatta, M. Gavagnin, E. Mollo, S. Wahidulla, G. Cimino, *Tetrahedron Lett.* **2005**, *46*, 465.

[4] J. E. Moses, R. M. Adlington, R. Rodriguez, S. J. Eade, J. E. Baldwin, *Chem. Commun.* **2005**, *13*, 1687.

[5] M. Cueto, L. D'Croz, J. L. Maté, A. San-Martín, J. Darias, *Org. Lett.* **2005**, *7*, 415.

[6] R. Huisgen, A. Dahmen, H. Huber, *J. Am. Chem. Soc.* **1967**, *89*, 7130.

[7] W. M. Bandaranayake, J. E. Banfiled, D. St. C. Black, G. D. Fallon, B. M. Gatehouse, *J. Chem. Soc. Chem. Commun.* **1980**, 162.

[8] a) C. M. Beaudry, D. Trauner, *Org. Lett.* **2002**, *4*, 2221; b) J. E. Moses, J. E. Baldwin, R. Marquez, R. M. Adlington, A. R. Cowley, *Org. Lett.* **2002**, *4*, 3731.

[9] a) K. C. Nicolaou, N. A. Petasis, J. Uenishi, R. E. Zipkin, *J. Am. Chem. Soc.* **1982**, *104*, 5555; b) K. A. Parker, Y. H. Lim, *J. Am. Chem. Soc.* **2004**, *126*, 15968; M. F. Jacobsen, J. E. Moses, R. M. Adlington, J. E. Baldwin, *Org. Lett.* **2005**, *7*, in press.

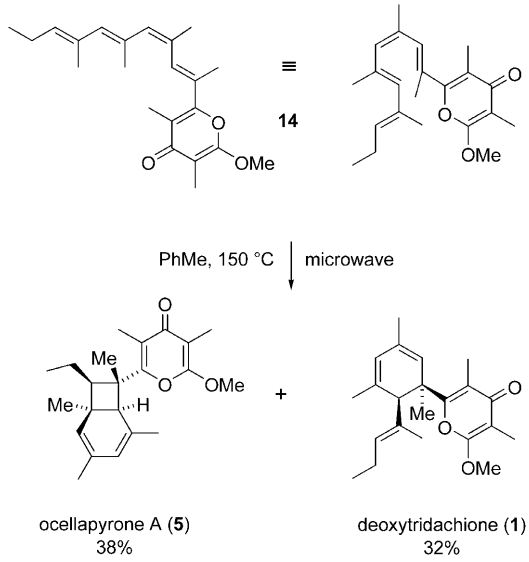
[10] a) A. K. Miller, D. Trauner, *Angew. Chem.* **2003**, *115*, 567; *Angew. Chem. Int. Ed.* **2003**, *42*, 549; b) A. K. Miller, M. R. Banghart, J. M. Suh, D. Trauner, *Tetrahedron* **2003**, *59*, 8919; c) A. K. Miller, D. H. Byun, C. M. Beaudry, D. Trauner, *Proc. Natl. Acad. Sci. USA* **2004**, *101*, 12019.

[11] G. Dahmann, R. W. Hoffman, *Liebigs Ann. Chem.* **1994**, 837.

[12] S. P. H. Mee, V. Lee, J. Baldwin, *Angew. Chem.* **2004**, *116*, 1152; *Angew. Chem. Int. Ed.* **2004**, *43*, 1132.

[13] G. Liang, A. K. Miller, D. Trauner, *Org. Lett.* **2005**, *7*, 819.

[14] The outcome of this isomerization was found to be strongly dependent on the conditions employed; for example, tetraene **14** underwent isomerization under microwave irradiation (PhMe, 150 °C, 20 min) to afford 9,10-deoxytridachione (**1**) and ocellapyrone A (**5**) in approximately equal amounts.



[15] In the reported isolation of bicyclo[4.2.0]octadiene **5** and endoperoxide **7** (Ref. [3]), the relative structure of ocellapyrone A was "… mainly determined on the basis of NOE difference and NOESY experiments recorded on the peroxide derivative [= ocellapyrone B]".

[16] Independent confirmation of the structure of **5** was obtained by conversion into the corresponding *endo* peroxide, whose structure was determined by X-ray crystallographic analysis. CCDC-269389 contains the supplementary crystallographic data for this paper. These data can be obtained free of charge from the Cambridge Crystallographic Data Centre via www.ccdc.cam.ac.uk/data_request/cif.

[17] A. Mordini, S. Pecchi, G. Capozzi, A. Capperucci, A. Degl'Innocenti, G. Reginato, A. Ricci, *J. Org. Chem.* **1994**, *59*, 4784.

[18] J. E. Barbarow, A. K. Miller, D. Trauner, submitted.

[19] M. Suzuki, H. Ohtake, Y. Kameya, N. Hamanaka, R. Noyori, *J. Org. Chem.* **1989**, *54*, 5292.

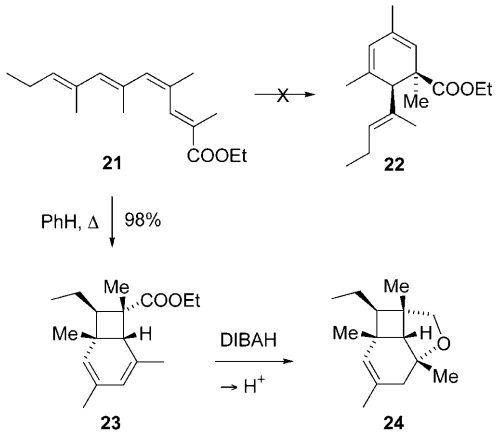
[20] S. Nitz, H. Kollmannsberger, M. H. Spraul, F. Drawert, *Phytochemistry* **1989**, *28*, 3051.

[21] CCDC-269388 contains the supplementary crystallographic data for this paper. These data can be obtained free of charge from the Cambridge Crystallographic Data Centre via www.ccdc.cam.ac.uk/data_request/cif.

[22] In our previous reports on photodeoxytridachione (Ref. [10a,b]), we erroneously reported the 6π electrocyclization

 © 2005 Wiley-VCH Verlag GmbH & Co. KGaA, Weinheim

of tetraenoic ester **21** to afford cyclohexadiene **22**. The "upfield shift" of a vinyl proton ($\delta = 2.93$ ppm) was rationalized with an anisotropic effect exerted by the nearby ester carbonyl group. In fact, double-bond isomerization followed by a stereoselective 8π–6π electrocyclization cascade had taken place. Therefore, the product of this very high-yielding and stereoselective reaction is reassigned as **23**. The structure of **23** was confirmed by reduction of the ester function to a primary alcohol followed by acid-catalyzed ring closure to the caged tricyclic compound **24**. (DIBAH = diisobutylaluminum hydride.)



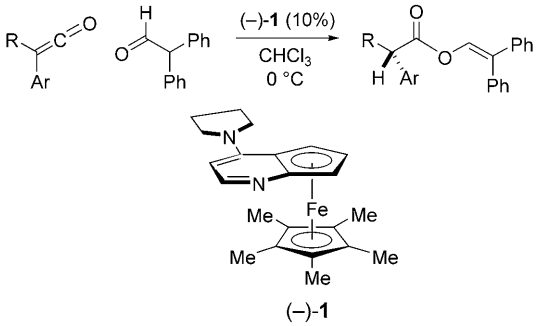
 © 2005 Wiley-VCH Verlag GmbH & Co. KGaA, Weinheim

Asymmetric Catalysis

Catalytic Asymmetric Couplings of Ketenes with Aldehydes To Generate Enol Esters**

*Carsten Schaefer and Gregory C. Fu**

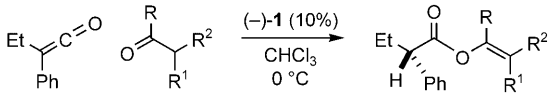
The synthesis of enantiopure α-arylalkanoic acids is an objective of significant interest, due in part to the bioactivity and commercial importance of this family of compounds.[1] One approach that has been pursued in industry is the asymmetric addition of alcohols to aryl alkyl ketenes to generate chiral esters (which can then be hydrolyzed to α-arylalkanoic acids).[2–5] Herein, we report a new method for the enantioselective synthesis of esters: the catalytic asymmetric coupling of a ketene with an aldehyde [Eq. (1)].

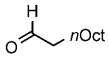
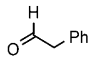
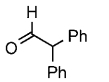
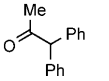


(1)

In the presence of planar-chiral dimethylaminopyridine (DMAP) derivative **1**,[6] we observed no reaction between phenyl ethyl ketene and *n*-decanal (Table 1, entry 1). In contrast, phenylacetaldehyde coupled with the ketene to furnish an enol ester in modest yield and with very good enantioselectivity (entry 2). Diphenylacetaldehyde was an excellent reaction partner (entry 3: 91% *ee*, 84% yield), whereas a related ketone was not (entry 4).[7,8]

Table 1: Survey of carbonyl compounds: Catalytic asymmetric couplings with ketenes.[a]



Entry	Carbonyl compound	*ee* [%]	Yield [%][b]
1		–	0
2		92	55
3		91	84
4		–	0

[a] All data are the average of two experiments. [b] Isolated product.

As illustrated in Table 2, we achieved the catalytic asymmetric synthesis of a wide array of enol esters of α-arylalkanoic acids through couplings of ketenes with diphenylacetaldehyde.[9–11] Thus, reactions of phenyl alkyl ketenes, in which the alkyl group ranges in size from methyl to *tert*-butyl, proceeded with moderate to excellent enantioselectivity (Table 2, entries 1–6). Furthermore, the addition occurred with very good stereoselectivity regardless of whether the aromatic group of the ketene was bulky (Table 2, entries 7 and 8), electron-rich (entries 8 and 9), or electron-poor (entry 10).

Enol esters are attractive targets in synthetic organic chemistry, in part as a result of the ease with which they can be

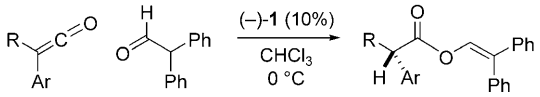
[*] Dr. C. Schaefer, Prof. Dr. G. C. Fu
Department of Chemistry
Massachusetts Institute of Technology
Cambridge, MA 02139 (USA)
Fax: (+1) 617-324-3611
E-mail: gcf@mit.edu

[**] Support was provided by the NIH (NIGMS, GM57034), the Deutsche Forschungsgemeinschaft (postdoctoral fellowship to C.S.), Merck Research Laboratories, and Novartis. Funding for the MIT Department of Chemistry Instrumentation Facility was furnished in part by the National Science Foundation (CHE-9808061 and DBI-9729592).

Supporting information for this article is available on the WWW under http://www.angewandte.org or from the author.

 © 2005 Wiley-VCH Verlag GmbH & Co. KGaA, Weinheim DOI: 10.1002/anie.200501434

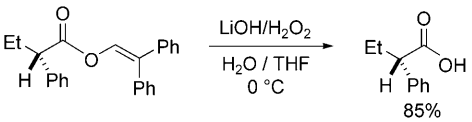
Table 2: Catalytic asymmetric couplings of aldehydes with ketenes to generate enol esters.[a]



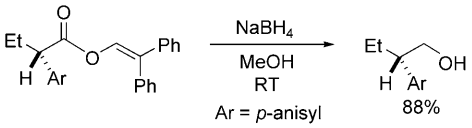
Entry	Ar	R	*ee* [%]	Yield [%][b]
1	Ph	Me	78	74
2	Ph	Et	91	84
3	Ph	*i*Bu	77	81
4	Ph	*i*Pr	98	95
5	Ph	cyclopentyl	97	99
6	Ph	*t*Bu	88	96
7	*o*-tolyl	Et	98	99
8	*o*-anisyl	Me	97	95
9	*p*-anisyl	Et	92	89
10	4-chlorophenyl	Et	88	96

[a] All data are the average of two experiments. [b] Isolated product.

converted into other useful families of compounds. We have established that our diphenyl-substituted enol esters can be hydrolyzed and reduced under mild conditions without racemization [Eqs. (2) and (3)].[12]



(2)



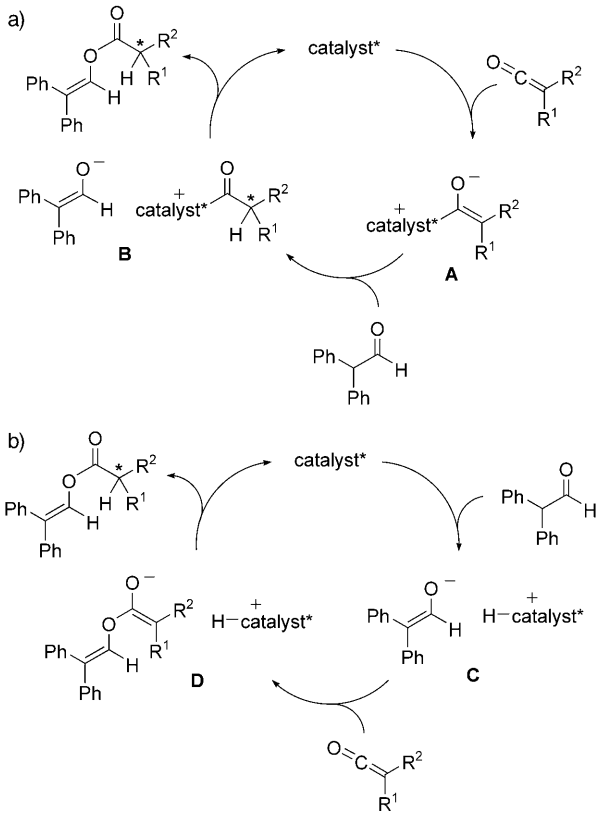
(3)

A number of mechanisms, two of which are illustrated in Scheme 1, can be envisioned for this new catalytic asymmetric coupling of ketenes with aldehydes to generate enol esters. In one possible pathway (Scheme 1a), catalyst **1** serves as a nucleophile and adds to the ketene to afford chiral enolate **A**,[13] which undergoes diastereoselective protonation by the aldehyde to furnish the ion pair **B**. Acylation of the enolate by the acylpyridinium ion then produces the enantioenriched enol ester and regenerates the catalyst.

Alternatively, the role of catalyst **1** may be to serve as a Brønsted base/acid (Scheme 1b). According to this hypothesis, the catalyst deprotonates the aldehyde to furnish an achiral enolate **C**. This nucleophilic enolate then adds to the electrophilic ketene to produce a new achiral enolate **D**,[14] which undergoes enantioselective protonation by its counterion (protonated **1**, a chiral Brønsted acid) to thereby generate the enol ester.[15]

To date, we have made the following observations with respect to the reaction pathway:

- The *ee* value of the product correlates linearly with that of the catalyst;[16]
- When catalyst **1** is mixed with one equivalent of diphenylacetaldehyde, there is no evidence for deprotonation of the aldehyde to form an ion pair;[17]



Scheme 1. Two of the possible mechanisms for the coupling of ketenes with aldehydes to form enol esters: a) nucleophilic catalysis and b) Brønsted acid/base catalysis.

- In the presence of catalyst **1**, the α proton of diphenylacetaldehyde exchanges rapidly with D_2O at 0 °C (in the absence of **1**, there is essentially no exchange after 3 days at room temperature);
- A small primary kinetic isotope effect is observed ($k_H/k_D \approx 2$ for the reaction of diphenylacetaldehyde relative to α-*d*-diphenylacetaldehyde).[18]

These data can be accommodated by either of the pathways illustrated in Scheme 1, as well as by others. A detailed mechanistic investigation will be required in order to gain improved insight into this interesting process.

In summary, we have developed a new method for the synthesis of enantioenriched esters: the catalytic asymmetric coupling of ketenes with aldehydes. We have established that this approach provides access to a wide array of α-arylalkanoic acid derivatives. Future studies will build upon our preliminary mechanistic observations to elucidate the reaction pathway for this intriguing transformation.

Received: April 26, 2005

Keywords: aldehydes · asymmetric catalysis · esters · ketenes

 © 2005 Wiley-VCH Verlag GmbH & Co. KGaA, Weinheim

[1] For leading references to bioactive α-arylalkanoic acid derivatives, see: a) "Fenvalerate": *The Merck Index*, *13th ed.*, Merck, Whitehouse Station, NJ, **2001**, pp. 710–711; b) J. Robichaud, R. Oballa, P. Prasit, J.-P. Falgueyret, M. D. Percival, G. Wesolowski, S. B. Rodan, D. Kimmel, C. Johnson, C. Bryant, S. Venkatraman, E. Setti, R. Mendonca, J. T. Palmer, *J. Med. Chem.* **2003**, *46*, 3709–3727; c) M. F. Landoni, A. Soraci, *Curr. Drug Metab.* **2001**, *2*, 37–51; d) C. D. W. Brooks, A. O. Stewart, T. Kolasa, A. Basha, P. Bhatia, J. D. Ratajczyk, R. A. Craig, D. Gunn, R. R. Harris, J. B. Bouska, P. E. Malo, R. L. Bell, G. W. Carter, *Pure Appl. Chem.* **1998**, *70*, 271–274; e) K. Brune, G. Geisslinger, S. Menzel-Soglowek, *J. Clin. Pharmacol.* **1992**, *32*, 944–952; f) H. R. Sonawane, N. S. Bellur, J. R. Ahuja, D. G. Kulkarni, *Tetrahedron: Asymmetry* **1992**, *3*, 163–192; g) J.-P. Rieu, A. Boucherle, H. Cousse, G. Mouzin, *Tetrahedron* **1986**, *42*, 4095–4131; h) N. Bodor, R. Woods, C. Raper, P. Kearney, J. J. Kaminski, *J. Med. Chem.* **1980**, *23*, 474–480.

[2] For examples of industrial interest in using asymmetric additions to ketenes to produce arylpropionic acid derivatives, see: a) R. D. Larsen, E. G. Corley, P. Davis, P. J. Reider, E. J. J. Grabowski, *J. Am. Chem. Soc.* **1989**, *111*, 7650–7651; b) C. G. M. Villa, S. P. Panossian in *Chirality in Industry* (Eds.: A. N. Collins, G. N. Sheldrake, J. Crosby), Wiley, New York, **1992**, chapt. 15; c) G. P. Stahly, R. M. Starrett in *Chirality in Industry II* (Eds.: A. N. Collins, G. N. Sheldrake, J. Crosby), Wiley, New York, **1997**, chapt. 3.

[3] For pioneering studies of asymmetric catalysis of this process, see: a) H. Pracejus, *Justus Liebigs Ann. Chem.* **1960**, *634*, 9–22; b) H. Pracejus, H. Mätje, *J. Prakt. Chem.* **1964**, *24*, 195–205, and references therein.

[4] For our studies of asymmetric catalysis of this process, see: a) B. L. Hodous, J. C. Ruble, G. C. Fu, *J. Am. Chem. Soc.* **1999**, *121*, 2637–2638; b) S. L. Wiskur, G. C. Fu, *J. Am. Chem. Soc.* **2005**, *127*, 6176–6177.

[5] For reviews of enantioselective protonations of enols/enolates, see: a) A. Yanagisawa in *Comprehensive Asymmetric Catalysis* (*Supplement 2*) (Eds.: E. N. Jacobsen, A. Pfaltz, H. Yamamoto), Springer, New York, **2004**, pp. 125–132; A. Yanagisawa, H. Yamamoto in *Comprehensive Asymmetric Catalysis* (Eds.: E. N. Jacobsen, A. Pfaltz, H. Yamamoto), Springer, New York, **1999**, chapt. 34.2; b) J. Eames, N. Weerasooriya, *Tetrahedron: Asymmetry* **2001**, *12*, 1–24; c) C. Fehr in *Chirality in Industry II* (Eds.: A. N. Collins, G. N. Sheldrake, J. Crosby), Wiley, New York, **1997**, chapt. 16; C. Fehr, *Angew. Chem.* **1996**, *108*, 2726–2748; *Angew. Chem. Int. Ed. Engl.* **1996**, *35*, 2567–2587.

[6] For leading references, see: G. C. Fu, *Acc. Chem. Res.* **2004**, *37*, 542–547.

[7] For a report of the O-acylation of β-ketoesters upon treatment with excess ketene ($O{=}C{=}CH_2$) and pyridine, see: K. W. Rosenmund, G. Kositzke, H. Bach, *Chem. Ber.* **1959**, *92*, 494–501.

[8] In contrast, treatment of a ketene with catalyst **1** and a non-enolizable aldehyde (e.g., PhCHO) leads to [2+2] cycloaddition to generate a β-lactone with good stereoselectivity: J. E. Wilson, G. C. Fu, *Angew. Chem.* **2004**, *116*, 6518–6520; *Angew. Chem. Int. Ed.* **2004**, *43*, 6358–6360.

[9] Interestingly, under these conditions, catalyst **1** does not rearrange the enol ester to a 1,3-dicarbonyl compound. For example, see: I. D. Hills, G. C. Fu, *Angew. Chem.* **2003**, *115*, 4051–4054; *Angew. Chem. Int. Ed.* **2003**, *42*, 3921–3924.

[10] General procedure: Under argon, a solution of the ketene (1.0 equiv) in $CHCl_3$ was added by syringe over 7 min to a solution of the catalyst (10%) and diphenylacetaldehyde (1.1 equiv) in $CHCl_3$ at 0 °C. The resulting solution was stirred at 0 °C, and then the reaction was quenched by the addition of MeOH (1 mL). The solvent was removed by rotary evaporation, and the residue was purified by column chromatography.

[11] Notes: a) The reaction of phenyl ethyl ketene with diphenylacetaldehyde proceeds in moderate to excellent enantioselectivity in a variety of solvents (e.g., toluene, Et_2O, EtOAc, 1,2-dimethoxyethane, THF, and CH_2Cl_2; however, not *N*-methylpyrrolidone); b) Slightly lower *ee* values were observed at room temperature; c) Typically, ca. 85% of catalyst **1** can be recovered at the end of the reaction.

[12] These enol esters are more reactive than the aryl esters produced by the addition of 2-*tert*-butylphenol to ketenes (see ref. [4b]).

[13] For other processes catalyzed by **1** that are believed to proceed through chiral enolate **A**, see: a) B. L. Hodous, G. C. Fu, *J. Am. Chem. Soc.* **2002**, *124*, 1578–1579; b) Ref. [8].

[14] For a pioneering study of the O-acylation of enolates by ketenes, see: K. Yoshida, Y. Yamashita, *Tetrahedron Lett.* **1966**, *7*, 693–696.

[15] For a process catalyzed by **1** that is believed to proceed through an analogous chiral Brønsted base/acid pathway, see ref. [4b].

[16] For a review of nonlinear effects in asymmetric catalysis, see: H. B. Kagan, T. O. Luukas in *Comprehensive Asymmetric Catalysis* (Eds.: E. N. Jacobsen, A. Pfaltz, H. Yamamoto), Springer, New York, **1999**, chapt. 4.1.

[17] This behavior contrasts with enantioselective additions of 2-*tert*-butylphenol to ketenes catalyzed by **1** in which the catalyst deprotonates the phenol; the mechanism is likely a chiral Brønsted acid catalyzed pathway (see ref. [4b]).

[18] Owing to the rapidness of the reaction at 0 °C, this experiment was conducted at −90 °C ($t_{1/2} \approx 1$ h).

 © 2005 Wiley-VCH Verlag GmbH & Co. KGaA, Weinheim

Organic Synthesis

Synthesis of Seven-Membered-Ring Ketones by Arylative Ring Expansion of Alkyne-Substituted Cyclobutanones**

*Takanori Matsuda, Masaomi Makino, and Masahiro Murakami**

Medium-sized carbocyclic ring systems are often present as the structural core in natural products of interesting biological activities. Thus, the development of new synthetic methods for medium-sized carbocyclic rings has been one of the prime targets in organic synthesis.[1] Fragmentation of an easily accessible bicyclic system circumvents unfavorable enthalpic and entropic factors associated with direct formation of the medium-sized ring by annulation or cyclization.[2] A number

[*] Dr. T. Matsuda, M. Makino, Prof. Dr. M. Murakami
Department of Synthetic Chemistry and Biological Chemistry
Kyoto University
Katsura, Kyoto 615–8510 (Japan)
Fax: (+81) 75-383-2748
E-mail: murakami@sbchem.kyoto-u.ac.jp

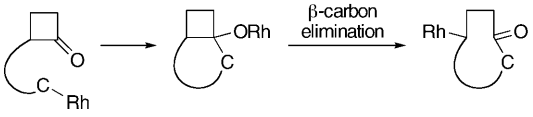
[**] This work was supported by a Grant-in-Aid for Young Scientists (B; No. 15750085) from the Ministry of Education, Culture, Sports, Science, and Technology, Japan.

Supporting information for this article is available on the WWW under http://www.angewandte.org or from the author.

 © 2005 Wiley-VCH Verlag GmbH & Co. KGaA, Weinheim DOI: 10.1002/anie.200500799

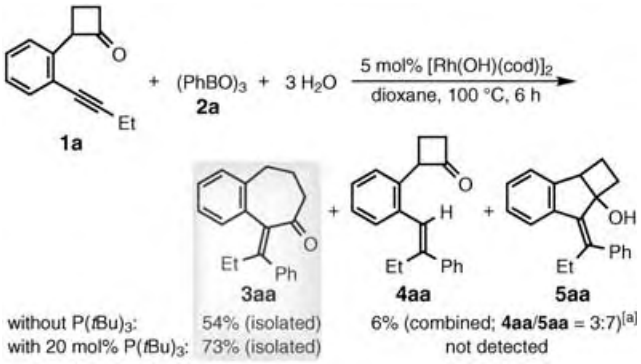
of ring-expansion reactions, which are promoted by acids, radicals, and transition metals, as well as heat, have been developed. Most of them are aided by the release of ring strain as the driving force.

Recently, we found that an arylrhodium adds to a cyclobutanone intermolecularly to afford a ring-opened ketone through β-carbon elimination from the resulting rhodium cyclobutanolate.[3] We then envisaged that intramolecular addition of an organorhodium group to cyclobutanone[4] followed by β-carbon elimination would provide a ring-expansion process [Eq. (1)]. Herein, we describe a new method for construction of seven-membered ring skeletons.



(1)

To establish a route to an organorhodium species necessary for such intramolecular additions, cyclobutanones **1** that bear an alkyne moiety were designed (Scheme 1). 2-(2-But-1-ynylphenyl)cyclobutanone (**1a**) was synthesized in three steps

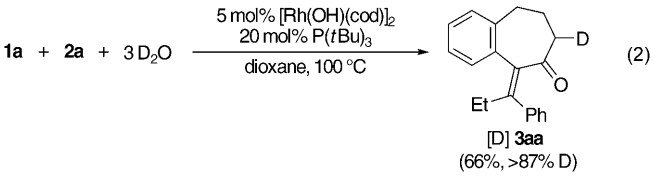


Scheme 1. Rhodium-catalyzed reaction of alkyne-substituted cyclobutanone **1a** with triphenylboroxin (**2a**). [a] Estimated from ^{1}H NMR spectroscopy of the crude reaction mixture.

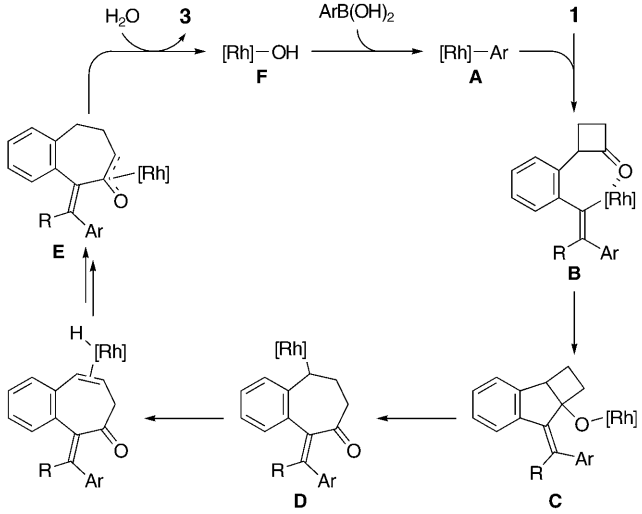
starting from commercially available 2-bromobenzaldehyde.[5] As a rhodium catalyst, we initially employed hydroxo(diolefin)rhodium(I) complexes, which have recently been used successfully in the rhodium-catalyzed reactions of arylboronic acids.[4b,d] Thus, a mixture of **1a**, triphenylboroxin (**2a**, 1.0 equiv), and water (3.0 equiv)[6] was heated in the presence of $[Rh(OH)(cod)]_2$ (10 mol% Rh; cod = cyclo-1,5-octadiene) in 1,4-dioxane at 100 °C. After heating for 6 h, seven-membered-ring ketone **3aa** was isolated in 54% yield along with small amounts of 1,2-adduct **4aa** and cyclobutanol **5aa**. The use of $P(tBu)_3$ as the additional ligand improved the yield of **3aa** to 73% without the formation of **4aa** and **5aa**.

The reaction in the presence of D_2O gave [D]**3aa** with deuterium incorporated exclusively at the α position of the carbonyl group, suggesting the formation of η^3-oxaallylrhodium prior to protonolysis, as previously reported [Eq. (2)].[3]

We propose the following mechanism for the transformation, which consists of a consecutive array of two C–C bond-forming and one C–C bond-cleaving steps (Scheme 2).



(2)



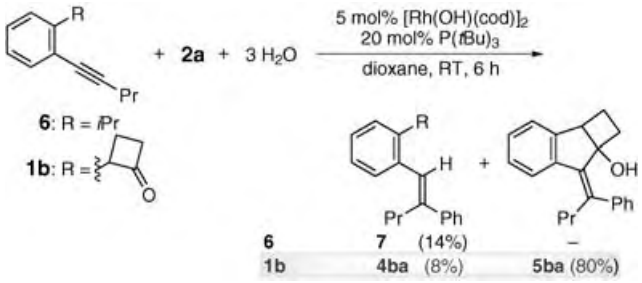
Scheme 2. Proposed mechanism for the formation of **3** from **1**.

Arylrhodium species **A**, generated from hydroxorhodium **F** and arylboronic acid, adds regioselectively across the carbon–carbon triple bond[4b–d,6b,7] of **1** in preference to the carbonyl group to afford vinylrhodium species **B**. Then, 1,2-addition to the adjacent carbonyl group of the cyclobutanone[4] forms rhodium cyclobutanolate **C**. β-Carbon elimination occurs regioselectively with the benzylic carbon atom,[8] and thus the bicyclic [3.2.0] skeleton of **C** is expanded with release of the ring strain to give alkylrhodium **D**. Successive β-hydride elimination/readdition processes take place, leading to the formation of η^3-oxaallylrhodium **E**.[9] Finally, protonolysis of **E** yields **3** and regenerates **F**.

Compound **4aa** is produced when the vinylrhodium species **B** is protonated through a 1,4-shift of rhodium. Protonolysis of the cyclobutanolate **C** affords **5aa**.

To examine the effect of coordination of the carbonyl group of **1**, a control experiment was carried out using 2-isopropyl-1-(pent-1-ynyl)benzene (**6**), whose alkyne structure is sterically similar to that of **1**, which comprises a cyclobutanone moiety (Scheme 3). The reaction of **6** with **2a** was sluggish at room temperature to give 1,2-adduct **7** in 14% yield after 6 h. In contrast, the analogous alkyne **1b** with a cyclobutanone substituent furnished 80% of cyclobutanol **5ba** as well as 8% of **4ba**. These contrasting results obtained with **6** and **1b** clearly indicate that the carbonyl group of **1b** facilitates the initial arylrhodation of the carbon–carbon triple bond by coordination. It also proved that the arylrhodation of **1b** and the following intramolecular carbonyl addition take place at room temperature and that the only ring-opening step by β-carbon elimination requires an

 © 2005 Wiley-VCH Verlag GmbH & Co. KGaA, Weinheim



Scheme 3. Effect of coordination of the carbonyl group of **1**.

elevated temperature. It is conceivable that the coordination of the carbonyl group retards the 1,4-shift of rhodium[4c,6b,10] which possibly occurs with the intermediate **B** to produce **4**.

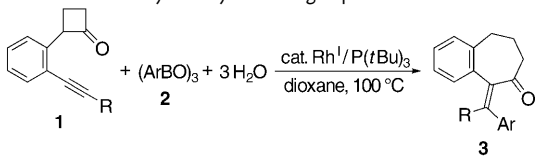
Arylboroxins **2b**–**2d** were subjected to the arylative ring-expansion reaction with cyclobutanone **1a** to give **3ab**–**3ad** in 63–71% yields (Table 1, entries 1–3).[11] Next, substituents at the alkyne termini of **1** were examined. Cyclobutanones **1b**–**1d**, which have other alkyl substituents (R), reacted with **2a** to afford the corresponding seven-membered-ring ketones **3ba**–**3da** (Table 1, entries 4–6).

In the reaction of **1e**, which contains a methyl ether linkage, 1,2-adduct **8ea** arising from arylrhodation with the opposite regiochemistry was formed as a byproduct (Scheme 4). Coordination of the ether oxygen center at the propargylic position might cause the regioisomeric 1,2-addition to produce **8ea**. With phenyl-substituted substrate **1f**, a mixture of **3** and **8** in a ratio of almost 1:1 was formed as a result of the barely biased alkyne structure.

Further studies on the scope and limitation of the arylative ring-expansion reaction (Table 2) were carried out. Both fluoro and methoxy substituents at the aryl ring of **1** were tolerated (Table 2, entries 1 and 2). Even a thiophene-derived substrate afforded the corresponding ketone **3ia** in 72% yield (Table 2, entry 3). We failed to obtain the seven-membered-ring ketones from cyclobutanone **1j**, which has an additional methyl substituent at the 2-position; instead, the corresponding cyclobutanol **5ja** was isolated (Table 2, entry 4). It is likely that migration of the rhodium from the oxygen atom to the tertiary carbon atom is difficult for steric reasons.[12] The reaction of **1k**, which contains a tether that is longer by one carbon atom, worked far less efficiently to result in the formation of the eight-membered-ring ketone **3ka** in only 17% yield (Table 2, entry 5).

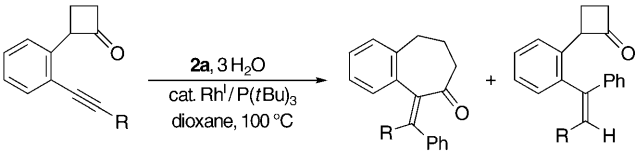
In summary, a new rhodium-catalyzed ring-expansion reaction was developed in which seven-membered-ring ketones **3** were produced from alkyne-substituted cyclobutanones **1** and arylboroxins **2** through ring opening by β-carbon elimination.

Table 1: Rhodium-catalyzed arylative ring expansion of **1** with **2**.[a]



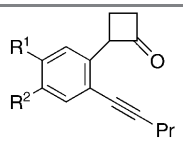
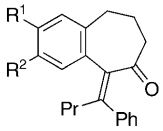
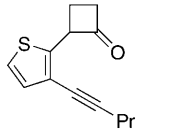
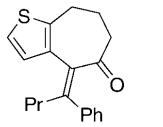
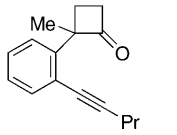
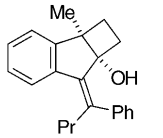
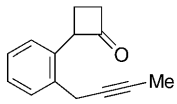
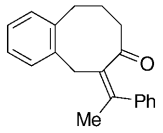
Entry	1	R	2	Ar	3	[%][b]
1	**1a**	Et	**2b**	4-MeC_6H_4	**3ab**	71
2	**1a**	Et	**2c**	4-$MeOC_6H_4$	**3ac**	70
3	**1a**	Et	**2d**	4-FC_6H_4	**3ad**	63
4	**1b**	Pr	**2a**	Ph	**3ba**	74
5	**1c**	*i*Bu	**2a**	Ph	**3ca**	76
6	**1d**	$(CH_2)_2OTBS$[c]	**2a**	Ph	**3da**	50

[a] All reactions were carried out using **1** (0.20 mmol), **2** (0.20 mmol), H_2O (0.60 mmol), $[Rh(OH)(cod)]_2$ (0.010 mmol, 10 mol% Rh), and $P(tBu)_3$ (0.04 mmol, 20 mol%) in 1,4-dioxane (1.0 mL) at 100 °C for 6 h. [b] Isolated yield. [c] TBS = *tert*-butyldimethylsilyl.



Scheme 4. Rhodium-catalyzed arylative ring expansion of **1e** and **1f**. [a] Estimated by ^1H NMR spectroscopy of the crude reaction mixture.

Table 2: Scope and limitation of the Rh-catalyzed arylative ring-expansion reaction.[a]

Entry	Cyclobutanone **1**		Product **3** or **5**		Yield [%][b]
1		$R^1 = R^2 = OMe$ **1g**		**3ga**	67
2		$R^1 = F$, $R^2 = H$ **1h**		**3ha**	58
3		**1i**		**3ia**	72
4		**1j**		**5ja**	63
5		**1k**		**3ka**	17

[a] All reactions were carried out using **1** (0.20 mmol), **2** (0.20 mmol), H_2O (0.60 mmol), $[Rh(OH)(cod)]_2$ (0.010 mmol, 10 mol% Rh), and $P(tBu)_3$ (0.06 mmol, 20 mol%) in 1,4-dioxane (1.0 mL) at 100 °C for 6 h. [b] Isolated yield.

Received: March 4, 2005
Published online: June 28, 2005

 © 2005 Wiley-VCH Verlag GmbH & Co. KGaA, Weinheim

Keywords:
rhodium · boron · elimination · ketones · ring expansion

[1] a) N. A. Petasis, M. A. Patane, *Tetrahedron* **1992**, *48*, 5757 – 5821; b) C. J. Roxburgh, *Tetrahedron* **1993**, *49*, 10749 – 10784; c) G. Mehta, V. Singh, *Chem. Rev.* **1999**, *99*, 881 – 930; d) L. Yet, *Chem. Rev.* **2000**, *100*, 2963 – 3007.

[2] a) G. Illuminati, L. Mandolini, *Acc. Chem. Res.* **1981**, *14*, 95 – 102; b) C. Galli, L. Mandolini, *Eur. J. Org. Chem.* **2000**, 3117 – 3125.

[3] a) T. Matsuda, M. Makino, M. Murakami, *Org. Lett.* **2004**, *6*, 1257 – 1259; b) T. Matsuda, M. Makino, M. Murakami, *Bull. Chem. Soc. Jpn.* **2005**, in press.

[4] For intramolecular additions of an organorhodium(I) to a carbonyl group, see: a) A. Takezawa, K. Yamaguchi, T. Ohmura, Y. Yamamoto, N. Miyaura, *Synlett* **2002**, 1733 – 1735; b) R. Shintani, K. Okamoto, Y. Otomaru, K. Ueyama, T. Hayashi, *J. Am. Chem. Soc.* **2005**, *127*, 54 – 55; c) T. Miura, T. Sasaki, H. Nakazawa, M. Murakami, *J. Am. Chem. Soc.* **2005**, *127*, 1390 – 1391; d) T. Miura, M. Shimada, M. Murakami, *Synlett* **2005**, 667 – 669; For intermolecular additions, see: e) M. Sakai, M. Ueda, M. Miyaura, *Angew. Chem.* **1998**, *110*, 3475 – 3477; *Angew. Chem. Int. Ed.* **1998**, *37*, 3279 – 3281; f) C. Krug, J. F. Hartwig, *J. Am. Chem. Soc.* **2002**, *124*, 1674 – 1679; g) M. Pucheault, S. Darses, J.-P. Genet, *J. Am. Chem. Soc.* **2004**, *126*, 15356 – 15357.

[5] Wittig olefination of the aldehyde with cyclopropylidenephosphorane afforded 2-bromobenzylidenecyclopropane (71%). Oxidation of the methylenecyclopropane with *m*-chloroperbenzoic acid followed by treatment with aqueous HBF_4 gave 2-(2-bromophenyl)cyclobutanone (58%). Introduction of a but-1-ynyl moiety by palladium-catalyzed coupling furnished **1a** (55%). See Supporting Information for details.

[6] Triphenylboroxin and water were used to generate phenylboronic acid in situ, see: a) T. Senda, M. Ogasawara, T. Hayashi, *J. Org. Chem.* **2001**, *66*, 6852 – 6856; b) T. Hayashi, K. Inoue, N. Taniguchi, M. Ogasawara, *J. Am. Chem. Soc.* **2001**, *123*, 9918 – 9919.

[7] a) M. Murakami, H. Igawa, *Helv. Chim. Acta* **2002**, *85*, 4182 – 4188; b) M. Lautens, M. Yoshida, *Org. Lett.* **2002**, *4*, 123 – 125; c) M. Lautens, T. Marquardt, *J. Org. Chem.* **2004**, *69*, 4607 – 4614; d) T. Miura, M. Shimada, M. Murakami, *J. Am. Chem. Soc.* **2005**, *127*, 1094 – 1095.

[8] For a review on β-carbon eliminations from palladium(II) cyclobutanolates, see: T. Nishimura, S. Uemura, *Synlett* **2004**, 201 – 216.

[9] For examples of related migrations of transition metals leading to enolates, see: a) H. Qian, R. A. Widenhoefer, *J. Am. Chem. Soc.* **2003**, *125*, 2056 – 2057; b) S. V. Gagnier, R. C. Larock, *J. Am. Chem. Soc.* **2003**, *125*, 4804 – 4807.

[10] a) K. Oguma, M. Miura, T. Satoh, M. Nomura, *J. Am. Chem. Soc.* **2000**, *122*, 10464 – 10465; b) R. Shintani, K. Okamoto, T. Hayashi, *J. Am. Chem. Soc.* **2005**, *127*, 2872 – 2873; c) H. Yamabe, A. Mizuno, H. Kusama, N. Iwasawa, *J. Am. Chem. Soc.* **2005**, *127*, 3248 – 3249.

[11] The reaction with *o*-tolylboroxin resulted in the formation of a complex mixture of products, in which 1,2-adduct **4** was the only identifiable product.

[12] Ring expansion by β-carbon elimination failed to occur even when the isolated **5ja** was heated at 160 °C in the presence of the rhodium catalyst.

 © 2005 Wiley-VCH Verlag GmbH & Co. KGaA, Weinheim

Addition Reactions

Chiral Phosphine–Olefin Bidentate Ligands in Asymmetric Catalysis: Rhodium-Catalyzed Asymmetric 1,4-Addition of Aryl Boronic Acids to Maleimides**

*Ryo Shintani, Wei-Liang Duan, Takashi Nagano, Atsushi Okada, and Tamio Hayashi**

Transition-metal-catalyzed asymmetric transformations in the presence of chiral ligands have proved to be one of the most efficient methods for the construction of enantioenriched chiral compounds from achiral precursors.[1] The design and synthesis of novel chiral ligands have therefore been a topic of great interest in organic and organometallic chemistry in the past few decades. In late-transition-metal catalysis, the development of phosphorus- and/or nitrogen-based chiral ligands has been most extensively investigated. As conceptually novel chiral ligands, a series of chiral dienes were recently introduced, which opened up a new dimension in the field of asymmetric catalysis.[2,3] Herein we describe the development of chiral phosphine–olefin ligands **1** and their use in the rhodium-catalyzed asymmetric 1,4-addition of aryl boronic acids to maleimides with the highest enantioselectivity reported to date in this class of substrates.

Chiral diene ligands that we developed have been shown to be highly effective in various rhodium-catalyzed asymmetric processes[2] and are superior to conventional chiral bisphosphine ligands in some cases. There are, however, some drawbacks in the use of these chiral dienes: for example, diene ligands are generally weaker than phosphorus-based ligands in their coordination ability to transition metals.[4] To overcome this problem while still maintaining the advantages of chiral dienes, we decided to develop chiral phosphine–olefin ligands as a hybrid of bisphosphines and dienes which would incorporate positive features of both frameworks, namely, the high coordination ability of phosphines and the good chiral environment created around the olefins (Figure 1).

To realize the desired features of these phosphine–olefins, we chose compound **1** as the target. During the course of our study directed toward this goal, Grützmacher described the preparation of chiral phosphine–olefin **2** and utilized it as a

[*] Dr. R. Shintani, W.-L. Duan, Dr. T. Nagano, A. Okada, Prof. Dr. T. Hayashi
Department of Chemistry
Graduate School of Science, Kyoto University
Sakyo, Kyoto 606-8502 (Japan)
Fax: (+81) 75-753-3988
E-mail: thayashi@kuchem.kyoto-u.ac.jp

[**] Support was provided in part by a Grant-in-Aid for Scientific Research, the Ministry of Education, Culture, Sports, Science, and Technology, Japan (21 COE on Kyoto University Alliance for Chemistry).

Supporting information for this article is available on the WWW under http://www.angewandte.org or from the author.

 DOI: 10.1002/anie.200501305 © 2005 Wiley-VCH Verlag GmbH & Co. KGaA, Weinheim

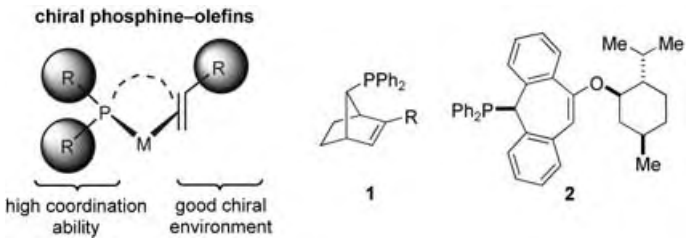
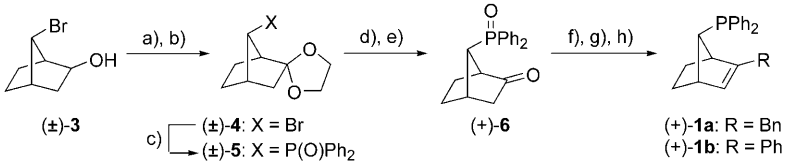


Figure 1. Chiral phosphine–olefin ligands designed to incorporate positive features of bisphosphine and diene ligands.

ligand for the iridium-catalyzed asymmetric hydrogenation of an imine with 86% *ee*.[5]

The synthesis of **1** began with known compound (±)-**3**[6] (Scheme 1). Swern oxidation of alcohol (±)-**3** followed by ketalization with ethylene glycol provided (±)-**4**, which was further converted into (±)-**5** by lithiation, phosphination, and then oxidation. Phosphine oxide (±)-**5** was resolved by chiral HPLC on a Chiralcel OD-H column to give each enantiomer



Scheme 1. a) oxalyl chloride, DMSO, Et_3N, CH_2Cl_2, 96%; b) cat. TsOH, ethylene glycol, C_6H_6, 94%; c) 1) *t*BuLi, THF; then $ClPPh_2$; 2) aqueous H_2O_2, acetone, 63% (over two steps); d) chiral HPLC resolution (OD-H column); e) aqueous HCl (1 N), THF, 99%; f) LDA, THF; then $PyNTf_2$, 89%; g) cat. [$NiCl_2$(dppp)], BnMgBr, Et_2O, 86% (for R = Bn); or cat. [$PdCl_2$(dppf)], PhMgBr, Et_2O, 86% (for R = Ph); h) $HSiCl_3$, Et_3N, C_6H_6, 90% for (+)-**1a** and 84% for (+)-**1b**. DMSO = dimethylsulfoxide; Ts = *p*-toluenesulfonyl; LDA = lithium diisopropylamide; Tf = trifluoromethanesulfonyl; dppp = propane-1,3-diylbis(diphenylphosphane); dppf = 1,1′-bis(diphenylphosphino)ferrocene.

of **5**, and then the ketal was cleaved to afford enantiopure ketone (+)-**6**. Conversion of (+)-**6** into its enol triflate, followed by Grignard cross-coupling and reduction with silane, completed the synthesis of (+)-**1a** (R = Bn, 39% overall yield) and (+)-**1b** (R = Ph, 36% overall yield).

We then carried out some complexation experiments with several transition metals to observe their mode of coordination. Thus, treatment of ligand (+)-**1b** (^{31}P NMR: $\delta = -17.1$ ppm; ^{1}H NMR: $\delta = 6.31$ ppm for the olefinic H atom) with 1 equivalent of [Rh(acac)$(C_2H_4)_2$] (acac = acetylacetonate) in dichloromethane at room temperature generated a new species, which showed a doublet at $\delta = 65.0$ ppm (J = 185 Hz) in the ^{31}P NMR spectrum and the signal for the olefinic H atom of (+)-**1b** was shifted upfield to $\delta = 3.82$ ppm in the ^{1}H NMR spectrum, thus indicating that both the phosphorus atom and the olefin were directly bound to rhodium. Similarly, a 1:1 mixture of (+)-**1b** and [$PdCl_2$-$(MeCN)_2$] in benzene led to the clean formation of [$PdCl_2$((+)-**1b**)]. Recrystallization of this complex from dichloromethane/benzene afforded single crystals suitable for X-ray crystallographic analysis.[7] As shown in Figure 2, (+)-**1b** does act as a phosphine–olefin bidentate ligand with

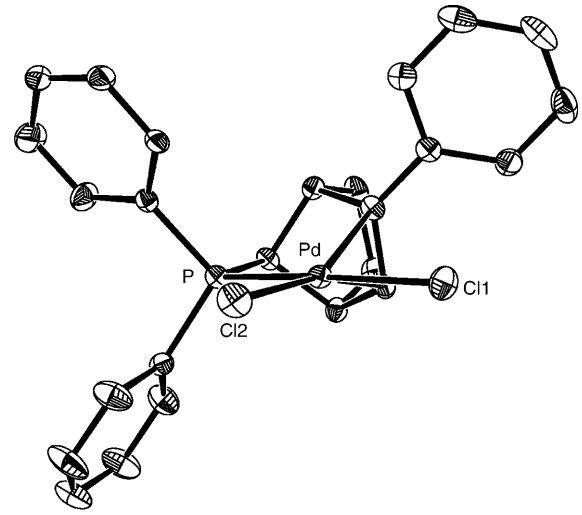
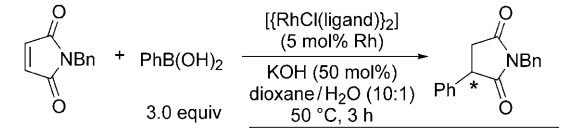


Figure 2. ORTEP illustration of [$PdCl_2$((+)-**1b**)] with thermal ellipsoids drawn at the 50% probability level (hydrogen atoms are omitted for clarity).

palladium, in accordance with the initial design of this novel hybrid ligand. The X-ray crystal structure also establishes the absolute configuration of (+)-**1b** as 1*R*,4*S*,7*R*.[8] Furthermore, it shows that the local structure around the phosphorus center is achiral and that the chirality mostly originates from the steric difference between the two substituents (Ph and H) on the olefin.

To investigate the potential of these ligands **1** in asymmetric catalysis, we chose to explore the rhodium-catalyzed 1,4-addition of aryl boronic acids to maleimides. As shown in Equation (1), the reaction of *N*-



(1)



(*R*,*R*)-**7**: Ar = 2,4,6-$Me_3C_6H_2$

ligand	result
(*R*)-binap	70% yield, 58% *ee* (*R*)
(*R*,*R*)-**7**	88% yield, 69% *ee* (*R*)
(+)-**1a**	96% yield, 91% *ee* (*S*)
(+)-**1b**	98% yield, 93% *ee* (*S*)

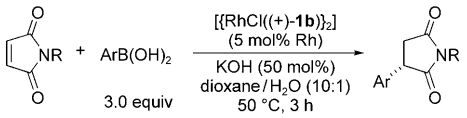
benzylmaleimide with $PhB(OH)_2$ in the presence of (*R*)-binap, a typical chiral bisphosphine ligand for rhodium-catalyzed asymmetric 1,4-additions,[9] gave the 1,4-adduct with only 58% *ee*. The use of chiral norbornadiene (*R*,*R*)-**7**, which was reported by us as the benchmark ligand in the 1,4-addition to maleimides,[2b] led to the desired product with 69% *ee*. The use of benzyl-substituted phosphine–olefin (+)-**1a** significantly improved the enantioselectivity to 91% *ee*. By changing the substituent on the olefin from benzyl to phenyl ((+)-**1b**), the selectivity was improved further (93% *ee*).

Under these conditions with (+)-**1b** as the ligand, various *N*-substituted maleimides can be employed in the reaction

 © 2005 Wiley-VCH Verlag GmbH & Co. KGaA, Weinheim

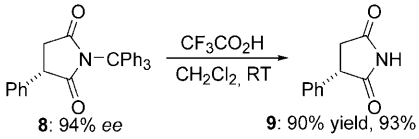
with $PhB(OH)_2$ to furnish the 1,4-adducts in uniformly high yield and enantioselectivity (Table 1, entries 1–5). With respect to the nucleophilic component, a variety of aryl boronic acids can be coupled with *N*-benzylmaleimide with high stereoselectivity as well (Table 1, entries 6–10).

Table 1: Rh–(+)-**1b**-catalyzed asymmetric 1,4-addition of aryl boronic acids to maleimides.



Entry	R	Ar	Yield [%]	*ee* [%]
1	Me	Ph	91	88
2	Cy	Ph	96	94
3	$CHPh_2$	Ph	95	94
4	CPh_3	Ph	95	94
5	Ph	Ph	88	90
6	Bn	Ph	98	93
7	Bn	4-$MeOC_6H_4$	98	93
8	Bn	4-FC_6H_4	90	89
9	Bn	3,5-$MeO_2C_6H_3$	90	92
10	Bn	2-MeC_6H_4	98	95

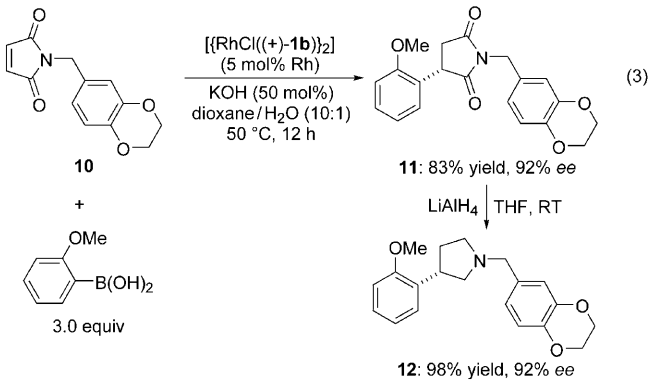
To show the utility of this highly enantioselective 1,4-addition to maleimides catalyzed by Rh–(+)-**1b**, we conducted a deprotection reaction of *N*-trityl 1,4-adduct **8** with 94% *ee* [Eq. (2)]. Thus, treatment of **8** with trifluoroacetic



(2)

acid in dichloromethane at room temperature furnished the desired product **9** in 90% yield with minimal erosion of the *ee* value.

The present asymmetric catalysis can also be applied to an enantioselective synthesis of biologically active compounds. Thus, addition of 2-$MeOC_6H_4B(OH)_2$ to maleimide **10** under Rh–(+)-**1b** catalysis led to 1,4-adduct **11** in 83% yield with 92% *ee* [Eq. (3)]. Reduction of the two carbonyl groups of **11**



(3)

with $LiAlH_4$ furnished pyrrolidine **12** in 98% yield, which is an enantiomer of the potent α-2-adrenoceptor antagonist developed by Novartis.[10]

The stereochemical outcome of these Rh–(+)-**1b**-catalyzed 1,4-additions can be rationalized as depicted in Figure 3,

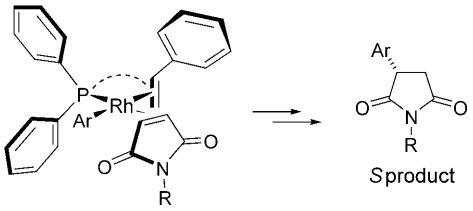
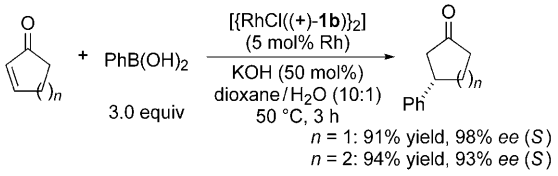


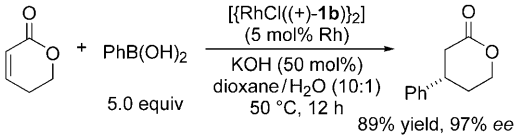
Figure 3. Proposed stereochemical pathway for the asymmetric 1,4-addition to a maleimide catalyzed by Rh–(+)-**1b**.

assuming that the maleimide approaches the aryl rhodium species bearing ligand (+)-**1b** *cis* to the olefin portion of the ligand. To avoid the steric repulsion between the imide moiety of maleimide and the phenyl group on the olefin, the product thus obtained should be an *S* isomer, which is consistent with the observed stereochemistry.

The Rh–(+)-**1b** catalyst is highly effective for asymmetric 1,4-addition to other α,β-unsaturated carbonyl compounds as well. For example, both cyclic enones and enoates[11] furnish the corresponding 1,4-adducts in high yield and enantioselectivity [Eq. (4) and Eq. (5)].



(4)



(5)

In summary, we have designed and synthesized novel chiral phosphine–olefin ligands. These ligands act as bidentate with some transition metals and have proved to be highly effective in the rhodium-catalyzed asymmetric 1,4-addition of aryl boronic acids to maleimides. Future studies will involve the exploration of further applications of these ligands to various transition-metal-catalyzed asymmetric processes.

Experimental Section

Procedure for Table 1: KOH (0.10 mL, 0.10 mmol; 1.0 M aqueous) was added to a solution of $[\{RhCl((+)\text{-}\mathbf{1b})\}_2]$ (4.9 mg, 10 μmol Rh) in 1,4-dioxane (0.50 mL), and the resulting solution was stirred for 5 min at room temperature. After addition of $ArB(OH)_2$ (0.60 mmol) and stirring for 5 min, this mixture was transferred to a vessel containing maleimide (0.20 mmol) with additional 1,4-dioxane (0.50 mL). The

 © 2005 Wiley-VCH Verlag GmbH & Co. KGaA, Weinheim

resulting mixture was stirred for 3 h at 50 °C and was then passed through a pad of silica gel with EtOAc. The solvent was removed under vacuum, and the residue was purified by chromatography on silica gel with EtOAc/hexane to afford the 1,4-adduct.

Received: April 14, 2005
Revised: May 12, 2005
Published online: June 23, 2005

Keywords: alkenes · asymmetric catalysis · boron · P ligands · rhodium

[1] a) *Catalytic Asymmetric Synthesis*, 2nd ed. (Ed.: I. Ojima), Wiley-VCH, New York, **2000**; b) *Comprehensive Asymmetric Catalysis*, *Vol. 1–3* (Eds.: E. N. Jacobsen, A. Pfaltz, H. Yamamoto), Springer, New York, **1999**.
[2] a) T. Hayashi, K. Ueyama, N. Tokunaga, K. Yoshida, *J. Am. Chem. Soc.* **2003**, *125*, 11508; b) R. Shintani, K. Ueyama, I. Yamada, T. Hayashi, *Org. Lett.* **2004**, *6*, 3425; c) N. Tokunaga, Y. Otomaru, K. Okamoto, K. Ueyama, R. Shintani, T. Hayashi, *J. Am. Chem. Soc.* **2004**, *126*, 13584; d) R. Shintani, K. Okamoto, Y. Otomaru, K. Ueyama, T. Hayashi, *J. Am. Chem. Soc.* **2005**, *127*, 54; e) Y. Otomaru, K. Okamoto, R. Shintani, T. Hayashi, *J. Org. Chem.* **2005**, *70*, 2503; f) Y. Otomaru, N. Tokunaga, R. Shintani, T. Hayashi, *Org. Lett.* **2005**, *7*, 307; g) Y. Otomaru, A. Kina, R. Shintani, T. Hayashi, *Tetrahedron: Asymmetry* **2005**, *16*, 1673.
[3] a) C. Fischer, C. Defieber, T. Suzuki, E. M. Carreira, *J. Am. Chem. Soc.* **2004**, *126*, 1628; b) C. Defieber, J.-F. Paquin, S. Serna, E. M. Carreira, *Org. Lett.* **2004**, *6*, 3873; for an overview, see: c) F. Glorius, *Angew. Chem.* **2004**, *116*, 3444; *Angew. Chem. Int. Ed.* **2004**, *43*, 3364.
[4] Diene ligands, such as 1,5-cyclooctadiene and norbornadiene, are often used as dummy ligands for various transition metals to be replaced by highly coordinating ligands such as bisphosphines.
[5] P. Maire, S. Deblon, F. Breher, J. Geier, C. Böhler, H. Rüegger, H. Schönberg, H. Grützmacher, *Chem. Eur. J.* **2004**, *10*, 4198.
[6] L. H. Zalkow, A. C. Oehlschlager, *J. Org. Chem.* **1964**, *29*, 1625.
[7] CCDC-266682 contains the supplementary crystallographic data for this paper. These data can be obtained free of charge from the Cambridge Crystallographic Data Centre via www.ccdc.cam.ac.uk/data_request/cif.
[8] The Flack parameter is 0.00(2) with this configuration (see Supporting Information for details): H. D. Flack, *Acta Crystallogr. Sect. A* **1983**, *39*, 876.
[9] For reviews, see: a) T. Hayashi, K. Yamasaki, *Chem. Rev.* **2003**, *103*, 2829; b) K. Fagnou, M. Lautens, *Chem. Rev.* **2003**, *103*, 169; c) C. Bolm, J. P. Hildebrand, K. Muñiz, N. Hermanns, *Angew. Chem.* **2001**, *113*, 3382; *Angew. Chem. Int. Ed.* **2001**, *40*, 3284.
[10] M. P. Seiler, J. Nozulak, WO EP861 20010126, **2001**.
[11] a) Y. Takaya, T. Senda, H. Kurushima, M. Ogasawara, T. Hayashi, *Tetrahedron: Asymmetry* **1999**, *10*, 4047; b) M. T. Reetz, D. Moulin, A. Gosberg, *Org. Lett.* **2001**, *3*, 4083.

 © 2005 Wiley-VCH Verlag GmbH & Co. KGaA, Weinheim

Host–Guest Systems

An Unstable Ligand-Unsupported Cu^{I} Dimer Stabilized in a Supramolecular Framework**

Shao-Liang Zheng, Marc Messerschmidt, and Philip Coppens**

The attractive interactions that exist between d^{10} "closed-shell" elements of Group 11 have received extensive attention.[1,2] The term "aurophilicity" has been coined to describe the Au^{I}–Au^{I} bonding interactions that are evident in many molecular and solid-state structures and have been attributed to correlation and relativistic effects.[3] However, relativistic effects cannot be invoked for $Cu^{I}\cdots Cu^{I}$ interactions, which are generally referred to as "cuprophilicity". These interactions are found in inorganic lattices, polynuclear compounds with bridging ligands[2] or stabilized by electrostatic interactions,[4] and polymeric systems, such as infinite ···Cu-ligand-Cu··· chains with short sideways $Cu^{I}\cdots Cu^{I}$ interactions.[5] The existence of ligand-bridged $Cu^{I}\cdots Cu^{I}$ interactions is supported by spectral evidence[6] and has been examined by a series of theoretical calculations, which have sometimes reached different conclusions.[7] However, a recent comprehensive analysis[8] has shown that only a small part of the intermolecular interaction energy is often gained in the ground state from the $Cu^{I}\cdots Cu^{I}$ interaction, whereas a large component results from $Cu^{I}\cdots$ligand interactions, even in the case of ligand-unsupported $Cu^{I}\cdots Cu^{I}$ species.

Only a few examples of ligand-unsupported Cu^{I} aggregates have been described, most of which have been reported quite recently. These examples include the dimer of trimers based on a substituted pyrazolate;[9] the dimer of dimers with a substituted phenanthroline/bipyridyl ligand;[10] the infinite arrays of $[Cu(t\mathrm{Bu})(CN)Li(OEt_2)_2]$, in which neighboring Cu^{I} dimers are connected through Li^{+} ions;[11] the one- and three-dimensional infinite arrays of Cu^{I} ions in $[Cu(NH_3)_2]Br$ and $[Cu(NH_3)Cl]$, respectively;[12] the one-dimensional chains of Cu^{I} atoms in $[Cu(C_6F_6)(py)]$ (py = pyridine);[13] and the $[(CuCl_2)_2]^{2-}$ dimer cocrystallized with the monomeric $[CuCl_3]^{-}$ ion and with amidinium cations.[14] Except for the $[(CuCl_2)_2]^{2-}$ dimer, all the ligand-unsupported Cu^{I} dimers ("dimer" refers to two Cu^{I} fragments with a short $Cu^{I}\cdots Cu^{I}$ distance) form one-dimensional infinite $Cu^{I}\cdots Cu^{I}$ or π–π-stacked chains.

[*] Dr. S.-L. Zheng, Dr. M. Messerschmidt, Prof. Dr. P. Coppens
Department of Chemistry
State University of New York at Buffalo
Buffalo, NY 14260–3000 (USA)
Fax: (+1) 716-645-6948
E-mail: coppens@buffalo.edu

[**] This work was supported by the Petroleum Research Fund of the American Chemical Society (PRF32638AC3) and the National Science Foundation (CHE0236317). The authors thank Dr. Irina Novozhilova and Dr. Anatoliy Volkov for help with the theoretical calculations.

Supporting information for this article is available on the WWW under http://www.angewandte.org or from the author.

 © 2005 Wiley-VCH Verlag GmbH & Co. KGaA, Weinheim DOI: 10.1002/anie.200501154

Much stronger d^{10} metal–metal bonding with a possible formal metal–metal single bond has been predicted to exist in the electronically excited state of $[\{Ag(CN)\}_2^-]_n$.[15] The recently developed method of time-resolved (TR) diffraction allows experimental confirmation of such predictions.[16] A recent TR diffraction experiment on trimeric [{Cu[3,5-$(CF_3)_2$pyrazolate]}$_3$] at 17 K indeed shows a strong contraction of one of the intermolecular $Cu^I\cdots Cu^I$ distances in the one-dimensional infinite chains, thus leading to the formation of an excimer with a lifetime of 52 μs.[17] The systematic luminescence investigations of a series of substituted Cu/pyrazolate trimers showed that the lifetime and wavelength of the luminescence emission were strongly dependent on the temperature and the wavelength of the excitation,[18] thus suggesting the possible population of different excited states at different temperatures.

Supramolecular host matrices provide a well-defined environment in which the encapsulated luminescent guest molecules may occur in different states of aggregation and orientation relative to their environment, thus offering an attractive possibility for isolating photoactive molecular species in a dilute yet crystalline environment.[19] For example, we have shown recently that the xanthone molecule occurs as a monomer and as a dimer in two crystalline resorcinarene-based inclusion complexes and results in significant variation of its spectral properties.[20] On excitation, the xanthone dimer forms a phosphorescing excimer.[21] Its geometry has been determined by TR diffraction methods.[22]

The ligand-unsupported $[\{Ag(NH_3)_2\}_2]^{2+}$ ion has been trapped in a polymeric silver(I) hexamethylenetetramine coordination framework,[23] thus suggesting that a favorable supramolecular system may give rise to a discrete ligand-unsupported Cu^I dimer with the monodentate ammonia ligand. As part of our investigations of well-defined excimers in supramolecular environments,[24] we isolated the analogous Cu^I species in a supramolecular framework composed of tris(hydroxyphenyl)ethane anions (H_2THPE; see the Supporting Information). This structure led to a solid with the composition $[\{Cu(NH_3)_2\}_2][H_2THPE]_2\cdot 3.25\,H_2O$ (**1**), in which no photoactive molecules other than the Cu^I dimer were present, thus simplifying a future TR diffraction analysis.

X-ray diffraction studies[25] show that crystals of **1** contain two crystallographically independent H_2THPE anions connected by hydrogen-bonding interactions (Figure 1; see also the Supporting Information). The dimeric unit is further linked by hydrogen bonds to its center-of-symmetry related equivalent (symmetry code: $-x+2,\ -y,\ -z+1$) which extends into a two-dimensional wavy hydrogen-bonded layer (O···O: 2.435(3)–2.593(4) Å; see the Supporting Information) parallel to the (011) plane. The wavy layer contains square-shaped channels (effective dimension: 2.1×2.1 Å), which constitute 4.8% of the crystal volume and run along the *a* axis.[26] Adjacent hydrogen-bonded layers are juxtaposed along the *b* axis, so as to leave larger channels with an effective cross-section of 5.90 Å (again parallel to the *a* axis), and account for 17.6% of the crystal volume.

Each of the larger channels contains two crystallographically independent Cu^I centers in proximity in each unit cell. Each Cu^I center is ligated by two nitrogen atoms from ammonia (Cu–N: 1.886(3)–1.892(3) Å, N-Cu-N: 176.3(1) and 177.3(2)°; see the Supporting Information). The Cu^I-centers are separated by only 3.0248 Å with N-Cu···Cu-N torsion angles of 73.2(2) and 77.6(2)° for the two cations, respectively (see the Supporting Information). As the $Cu^I\cdots Cu^I$ distance is within the range reported for ligand-

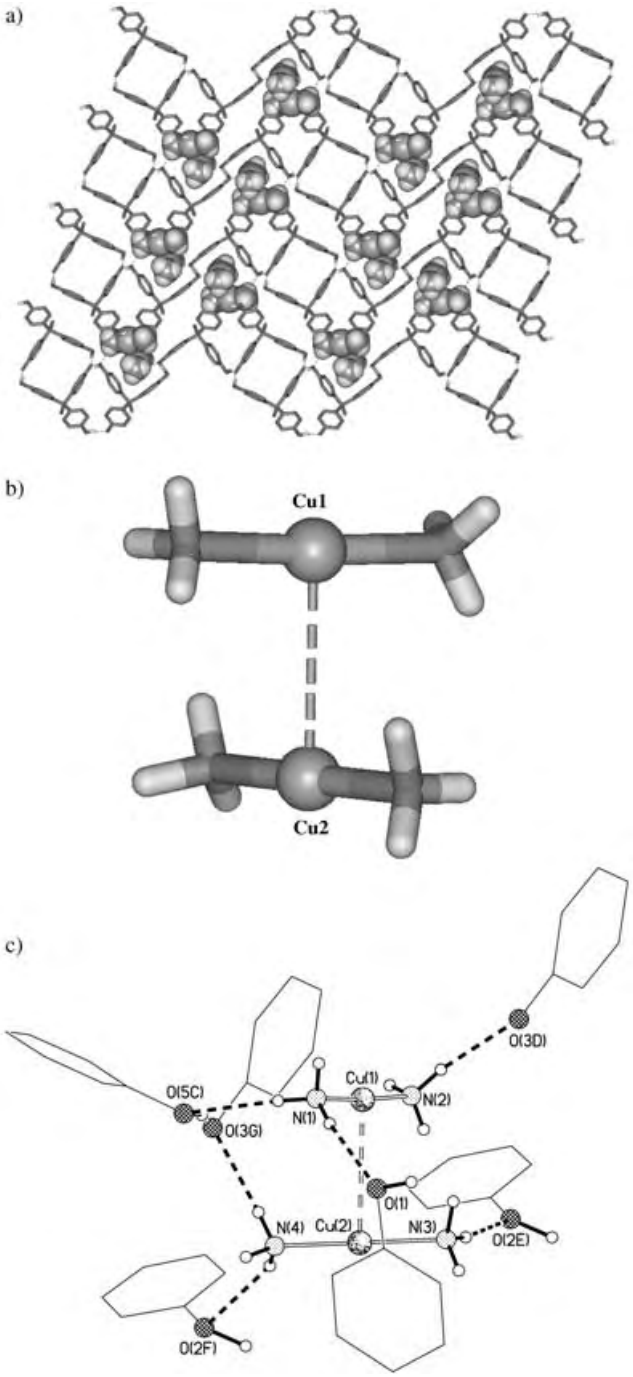


Figure 1. a) Three-dimensional supramolecular architecture of **1** viewed along the *a* axis, b) discrete dimeric $[\{Cu(NH_3)_2\}_2]^{2+}$ species in **1**, and c) the $[\{Cu(NH_3)_2\}_2]^{2+}$ species trapped in the supramolecular framework (selected distances [Å]: N(1)···O(5C) 2.968(4), N(1)···O(1) 3.185(4), N(2)···O(3D) 2.850(3), N(3)···O(2E) 2.996(4), N(4)···O(2F) 3.258(4), N(4)···O(3G) 2.889(4); see the Supporting Information. The water molecules included in the lattice are omitted for clarity.)

 © 2005 Wiley-VCH Verlag GmbH & Co. KGaA, Weinheim

unsupported $Cu^{I}\cdots Cu^{I}$ separations (2.71–3.60 Å),[9–14] the complex can be described as a novel dimeric $[\{Cu(NH_3)_2\}_2]^{2+}$ species. The ammonia ligands act as donors in hydrogen-bonding interactions with the oxygen atoms of the hydroxy groups in the adjacent H_2THPE anions (N···O: 2.850(3)–3.258(4) Å; Figure 1c), so that the supramolecular framework provides support and allows the dimeric $[\{Cu(NH_3)_2\}_2]^{2+}$ species to exist. One fully ordered water molecule is clathrated in each larger channel to fill the gap left between the Cu^{I} dimers. The water molecules form hydrogen-bonding interactions with the oxygen atom of the hydroxy group (O(1W)-H···O: 2.772(1) Å) of the host network. The smaller square-shaped channels are occupied by disordered water molecules.

The molecular dilution of the $[\{Cu(NH_3)_2\}_2]^{2+}$ species trapped in the supramolecular framework is pronounced: its concentration is 1.75 mol L^{-1} for **1**, relative to 7.35 mol L^{-1} for two $[Cu(NH_3)_2]^{+}$ ions in $[Cu(NH_3)_2]Br$ crystals.[12] The $Cu^{I}\cdots Cu^{I}$ distance is slightly longer than that found in the one-dimensional infinite $[Cu(NH_3)_2]^{+}$ chains (2.93 Å) in $[Cu(NH_3)_2]Br$.[12]

Molecular-orbital calculations were performed with the X-ray geometry of the $[\{Cu(NH_3)_2\}_2]^{2+}$ dimer to gain insight into the $Cu^{I}\cdots Cu^{I}$ interactions in the dimer. An intermolecular perturbation theory (IMPT)[27] calculation indicates that the Cu^{I} dimer with the geometry found in crystals of **1** is less stable by 309.1 kJ mol^{-1} than the isolated monomers.[28] Variation of the $Cu^{I}\cdots Cu^{I}$ distance shows no local minimum with the observed configuration (see the Supporting Information), thus suggesting that such a dimer is unlikely to occur in solution. Nevertheless, it can be stabilized in the supramolecular environment, as is evident from the crystal structure of **1**. Bimolecular $Cu^{I}\cdots Cu^{I}$ aggregates that have like charges have been calculated to be repulsive.[8] In the ground state, often only a small part of the intermolecular interaction energy gained results from the direct $Cu^{I}\cdots Cu^{I}$ interaction, whereas a large component of this energy results from $Cu^{I}\cdots$ligand interactions. In accordance with the calculations reported by Carvajal et al., the IMPT calculations show that the electrostatic repulsion, which is purely Coulombic in origin, is dominant in the current case (311.8 kJ mol^{-1}; see the Supporting Information). Nevertheless, the orbital interactions, including induction, charge transfer, and dispersion, are stabilized by -27.2 kJ mol^{-1} and so fall into the range of cuprophilic interactions estimated from spectroscopic or theoretical studies.[6–8] The results of the DFT calculations indicate that the HOMO-1 (HOMO = highest occupied molecular orbital) is a $Cu^{I}\cdots Cu^{I}$ σ bonding molecular orbital, the HOMO is a $Cu^{I}\cdots Cu^{I}$ σ antibonding molecular orbital, and the lowest unoccupied molecular orbital (LUMO) has $Cu^{I}\cdots Cu^{I}$ bonding character with 4d, 5s, and 5p contributions from the Cu^{I} center (Figure 2). The Mayer bond order[17,29] of the $Cu^{I}\cdots Cu^{I}$ interaction is calculated to be 0.187 (see the Supporting Information), which is in agreement with the IMPT analysis and shows the orbital interactions to be weakly attractive.

Optimization of the excited triplet state results in a shorter $Cu^{I}\cdots Cu^{I}$ distance of 2.6 Å (see the Supporting Information), which indicates a much stronger metal–metal bonding interaction on population of the $Cu^{I}\cdots Cu^{I}$ bonding LUMO (Figure 2). Emission measurements show an intense photoluminescence at 17 K with emission at 495 nm and a lifetime of approximately 4.2 μs, thus indicating that crystals of **1** may be suitable for TR diffraction studies.[19]

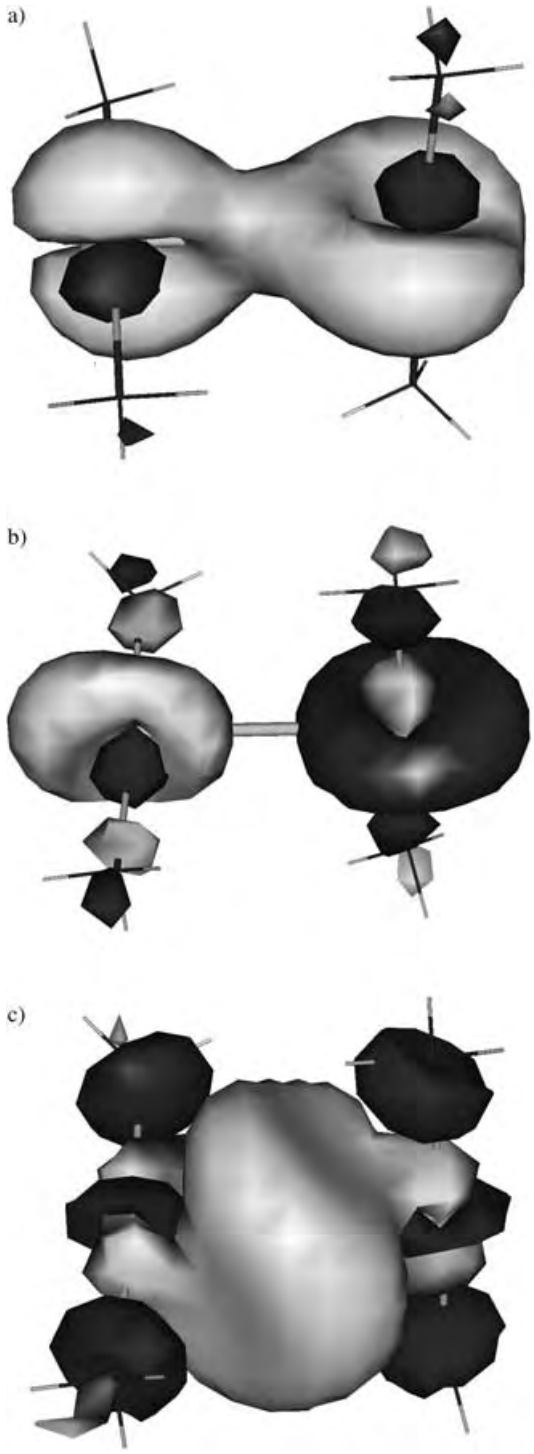


Figure 2. Contour plots (isosurfaces at ±0.04 au) of the frontier molecular orbitals of the $[\{Cu(NH_3)_2\}_2]^{2+}$ species: a) HOMO-1, b) HOMO, and c) LUMO.

In summary, a ligand-unsupported Cu^{I} dimer that is unstable by itself is stabilized in the cavities of a supramolec-

 © 2005 Wiley-VCH Verlag GmbH & Co. KGaA, Weinheim

ular framework to give **1**, thus offering the opportunity for systematic studies of the ground state of a Cu^{I} dimer with weak cuprophilicity and of its excited state by the use of TR diffraction methods. Analysis of the isolated dimeric species eliminates effects that occur in infinite chains of species linked through $Cu^{I}\cdots Cu^{I}$ interactions and provides the background needed for analysis of more complicated systems.

Experimental Section

1: Freshly prepared $Cu(OH)_2$ (0.5 mmol), H_3THPE (0.5 mmol), aqueous ammonia (25%, 2.0 mL), and toluene (2 mL) were sealed in a 6-mL pyrex glass tube. The tube was maintained at 160 °C for 40 h and then cooled to room temperature over 2 days. Pale-yellow needle-shaped crystals appeared during the cooling period.

CCDC-267412 contains the supplementary crystallographic data for this paper. These data can be obtained free of charge via www.ccdc.cam.ac.uk/conts/retrieving.html (or from the Cambridge Crystallographic Data Centre, 12 Union Road, Cambridge CB2 1EZ, UK; fax: (+44) 1223-336-033; or deposit@ccdc.cam.ac.uk).

Received: March 31, 2005

Keywords: copper · density functional calculations · host–guest systems · metal–metal interactions

[1] H. Schmidbaur, *Chem. Soc. Rev.* **1995**, *24*, 391 – 400.
[2] a) P. D. Harvey, *Coord. Chem. Rev.* **1996**, *153*, 175 – 198; b) P. Pyykkö, *Chem. Rev.* **1988**, *88*, 563 – 594; c) P. Pyykkö, *Chem. Rev.* **1997**, *97*, 597 – 636.
[3] P. Pyykkö, *Angew. Chem.* **2004**, *116*, 4512 – 4557; *Angew. Chem. Int. Ed.* **2004**, *43*, 4412 – 4456, and references therein.
[4] J. M. Poblet, M. Benard, *Chem. Commun.* **1998**, *11*, 1179 – 1180.
[5] For example, see: a) K. Jin, X. Huang, L. Pang, J. Li, A. Appel, S. Wherland, *Chem. Commun.* **2002**, 2872 – 2873; b) X.-C. Huang, J.-P. Zhang, X.-M. Chen, *J. Am. Chem. Soc.* **2004**, *126*, 13218 – 13219.
[6] a) C.-M. Che, Z. Mao, V. M. Miskowski, M.-C. Tse, C.-K. Chan, K.-K. Cheung, D. L. Phillips, K.-H. Leung, *Angew. Chem.* **2000**, *112*, 4250 – 4254; *Angew. Chem. Int. Ed.* **2000**, *39*, 4084 – 4088; b) D. L. Phillips, C.-M. Che, K.-H. Leung, Z. Mao, M.-C. Tse, *Coord. Chem. Rev.* DOI: 10.1016/j.ccr.2004.09.015, and references therein.
[7] For example, see: a) F. A. Cotton, X. Feng, M. Matusz, R. Poli, *J. Am. Chem. Soc.* **1988**, *110*, 7077 – 7083; b) H. L. Hermann, G. Boche, P. Schwerdtfeger, *Chem. Eur. J.* **2001**, *7*, 5333 – 5342; c) L. Magnko, M. Schweizer, G. Rauhut, M. Schütz, H. Stoll, H.-J. Werner, *Phys. Chem. Chem. Phys.* **2002**, *4*, 1006 – 1013; d) E. O'Grady, N. Kaltsoyannis, *Phys. Chem. Chem. Phys.* **2004**, *6*, 680 – 687.
[8] M. A. Carvajal, S. Alvarez, J. J. Novoa, *Chem. Eur. J.* **2004**, *10*, 2117 – 2132.
[9] a) K. Singh, J. R. Long, P. Stavropoulos, *J. Am. Chem. Soc.* **1997**, *119*, 2942 – 2943; b) M. K. Ehlert, S. J. Rettig, A. Storr, R. C. Thompson, J. Trotter, *Can. J. Chem.* **1990**, *68*, 1444 – 1449; c) H. V. R. Dias, S. A. Polach, Z. Wang, *J. Fluorine Chem.* **2000**, *103*, 163 – 169; d) H. V. R. Dias, H. V. K. Diyabalanage, M. A. Rawashdeh-Omary, M. A. Franzman, M. A. Omary, *J. Am. Chem. Soc.* **2003**, *125*, 12072 – 12073.
[10] a) X.-M. Zhang, M.-L. Tong, M.-L. Gong, H.-K. Lee, L. Luo, K.-F. Li, Y.-X. Tong, X.-M. Chen, *Chem. Eur. J.* **2002**, *8*, 3187 – 3194; b) J.-P. Zhang, Y.-B. Wang, X.-C. Huang, Y.-Y. Ling, X.-M. Chen, *Chem. Eur. J.* **2005**, *11*, 552 – 561.
[11] G. Boche, F. Bosold, M. Marsch, K. Harms, *Angew. Chem.* **1998**, *110*, 1779 – 1781; *Angew. Chem. Int. Ed.* **1998**, *37*, 1684 – 1686.
[12] G. Margraf, J. W. Bats, M. Bolte, H.-W. Lerner, M. Wagner, *Chem. Commun.* **2003**, 956 – 957.
[13] A. Sundararaman, L. N. Zakharov, A. L. Rheingold, F. Jäkle, *Chem. Commun.* **2005**, 1708 – 1710.
[14] R. D. Kön, G. Seifert, Z. Pan, M. F. Mahon, G. Kociok-Kön, *Angew. Chem.* **2003**, *115*, 818 – 821; *Angew. Chem. Int. Ed.* **2003**, *42*, 793 – 796.
[15] a) M. A. Omary, H. H. Patterson, *J. Am. Chem. Soc.* **1998**, *120*, 7696 – 7705; b) H. H. Patterson, S. M. Kanan, M. A. Omary, *Coord. Chem. Rev.* **2000**, *208*, 227 – 241, and references therein.
[16] P. Coppens, O. Gerlits, I. I. Vorontsov, A. Yu. Kovalevsky, Y.-S. Chen, T. Graber, I. V. Novozhilova, *Chem. Commun.* **2004**, 2144 – 2145; P. Coppens, I. I. Vorontsov, T. Graber, M. Gembicky, A. Yu. Kovalevsky, *Acta Crystallogr. A* **2005**, *61*, 162 – 172, and references therein.
[17] P. Coppens, I. I. Vorontsov, A. Yu. Kovalevsky, Y.-S. Chen, T. Graber, I. V. Novozhilova, *Phys. Rev. Lett.* **2005**, *94*, 193003.
[18] a) H. V. R. Dias, H. V. K. Diyabalanage, M. A. Rawashdeh-Omary, M. A. Franzman, M. A. Omary, *J. Am. Chem. Soc.* **2003**, *125*, 12072 – 12073; b) H. V. R. Dias, H. V. K. Diyabalanage, M. G. Eldabaja, O. Elbjeirami, M. A. Rawashdeh-Omary, M. A. Omary, *J. Am. Chem. Soc.* **2005**, *127*, 7489 – 7501.
[19] P. Coppens, B.-Q. Ma, O. Gerlits, Y. Zhang, P. Kulshrestha, *CrystEngComm* **2002**, *4*, 302 – 309.
[20] S.-L. Zheng, P. Coppens, *Chem. Eur. J.* **2005**, *11*, 3583 – 3590.
[21] N. N. Barashkov, T. V. Sakhno, R. N. Nurmukhanmetov, O. V. Khakel', *Uspekhi Khimii* **1993**, *62*, 579 – 593; *Russ. Chem. Rev.* **1993**, *62*, 539 – 552, and references therein.
[22] S.-L. Zheng, M. Gembecky, I. Vorontsov, T. Graber, M. Messerschmidt, P. Dominiak, P. Coppens, unpublished results.
[23] S.-L. Zheng, M.-L. Tong, X.-M. Chen, S. W. Ng, *J. Chem. Soc. Dalton Trans.* **2002**, 360 – 364.
[24] S.-L. Zheng, P. Coppens, *Cryst. Growth Des.*, submitted.
[25] Crystal data for **1**: triclinic, space group $P\bar{1}$, $a = 6.8426(3)$, $b = 12.0173(5)$, $c = 23.859(1)$ Å, $\alpha = 78.507(1)$, $\beta = 89.118(1)$, $\chi = 79.825(1)°$, $U = 1892.0(1)$ Å^3, $Z = 2$, $\rho_{calcd} = 1.517$ g cm^{-3}, $Mo_{K\alpha} = 0.71073$ Å, $R_1 = 0.0437$, $wR_2 = 0.1262$, GOF = 1.050 (see the Supporting Information).
[26] A. L. Spek, *PLATON, A Multipurpose Crystallographic Tool*, Untrecht University, Utrecht, The Netherlands, **2003**.
[27] a) I. C. Hayes, A. J. Stone, *Mol. Phys.* **1984**, *53*, 83 – 105; b) A. J. Stone, *The Theory of Intermolecular Forces*, Clarendon, Oxford, **1996**.
[28] Similar values of 305.7 and 242.1 kJ mol^{-1} are obtained with MP2 BSSE correlation calculations in GAUSSIAN03 and with DFT calculations in Amsterdam Density Functional Program (ADF), respectively.
[29] a) I. Mayer, *Chem. Phys. Lett.* **1983**, *97*, 270 – 274; b) I. Mayer, *Int. J. Quantum Chem.* **1984**, *26*, 151 – 154; c) A. J. Bridgeman, G. Cavigliasso, L. R. Ireland, J. Rothery, *J. Chem. Soc. Dalton Trans.* **2001**, 2095 – 2108.

 © 2005 Wiley-VCH Verlag GmbH & Co. KGaA, Weinheim

Bioinorganic Chemistry

Zn– and Cd–Metallothionein Recombinant Species from the Most Diverse Phyla May Contain Sulfide (S^{2-}) Ligands**

Mercè Capdevila, Jordi Domènech, Ayelén Pagani, Laura Tío, Laura Villarreal, and Sílvia Atrian*

After much multidisciplinary research into metallothioneins (MTs), the ubiquitous metal-binding proteins first described by Vallee and Margoshes[1] in 1957, there is still little information on the structures and functions[2,3] of the biological metal–MT complexes. There are two main obstacles to studying the physiological features of MTs. First, although MTs are present in all living organisms except Eubacteria, most of the existing data refers to mammalian MTs, which precludes any homology-driven structural, functional, or evolutionary inference because of the extreme sequence heterogeneity of this family of metalloproteins (see http://www.biochem.unizh.ch/mtpage/MT.html). Second, the difficulties encountered when trying to obtain homogeneous native preparations have led to the common utilization of in vitro reconstituted metal–MT complexes, based on the assumption that they represent genuine structural and functional native MT species. Thus, most of the data available to date, especially referring to MT structure, comes from nonbiological characterization of metal–MT complexes.[4] Following the MT discovery, another class of eukaryote metal-coordinating molecules was reported in plants and fungi: the enzymatically synthesized γ-glutamyl (γ-EC) peptides, also called phytochelatins and cadystins, which have always been considered as providing a very different mechanism of metal detoxification compared to the gene-encoded MTs, sharing few, if any, structural and functional features with them. From the chemical point of view, MTs bind a variety of metal ions giving rise to individual polynuclear clusters that are linked exclusively to cysteine residues through thiolate bonds. In contrast, γ-EC peptides create oligomeric clusters with a variable number of units that, most significantly, include acid-labile sulfide (S^{2-}) ions as additional ligands which induce the clusters to evolve to peptide-coated particles, so-called crystallites.[5]

Herein, we report the first definite evidence that sulfide ions are also present in nearly all the recovered Zn^{II}–MT and Cd^{II}–MT complexes, but never in the Cu^{I}–MT species of a wide range of recombinant metal–MT aggregates, thus sulfide ions are found in species formed in vivo, that is, in a physiological, although heterologous, environment. We have determined the presence of the acid-labile S^{2-} ligands both qualitatively and quantitatively by analytical, spectroscopic, and spectrometric techniques, and it is clear that the features of the recovered Zn^{II}–MT and Cd^{II}–MT complexes correlate well with those reported for plant and yeast Zn– or Cd–γ-glutamyl peptides,[5] therefore bridging the behavior gap between both types of metal-binding molecules.

Recombinant expression in *E. coli* has permitted the routine synthesis of a large number of proteins that are difficult or even impossible to obtain in their native forms. MTs stand out among them because of their extreme complexity and heterogeneity. Nearly ten years ago we developed an *E. coli* expression system that allows the biosynthesis of intact Zn^{II}–, Cd^{II}–, and Cu^{I}–MT complexes, isolated domains, and mutant variants, in sufficient quantity and purity for analytical, spectrometric, and spectroscopic characterization. As a first characterization on the mouse Zn–MT1 system[6,7] fully validated the correspondence between native and recombinant complexes, research was expanded to mammalian MT isoforms (MT1[8–10] and MT4[11]), the crustacean MTH,[12] *Drosophila* MTs (MTN[13] and MTO[14]), and the plant *Quercus suber* QsMT.[15]

We are now focused on studying MT species from the most diverse taxa (Table 1) and in the course of this work we found that many experimental results from analyzing Zn–MT, and particularly Cd–MT complexes, made little sense, as shown in Table 1. First, the stoichiometry of the Cd–MT complexes determined by inductively coupled plasma atomic emission spectroscopy (ICP-AES) was unusually low in comparison with the values expected from the corresponding Zn–MT complexes and the number of cysteine residues available for metal coordination. The metal-binding stoichiometries are assessed directly from the total sulfur and metal content of the sample provided by ICP-AES,[16] assuming that the total sulfur in the preparation arises from the summation of cysteine and methionine residues within the polypeptide. The unusually low stoichiometries calculated first suggested a partial oxidation of thiol groups and consequent loss of MT metal-binding capacity, but the Ellman reaction[17] quantification of the thiol groups in the samples did not support this prediction. Furthermore, ESI-MS analyses of most of the Cd–MT isolates revealed, besides the expected species, the presence of complexes whose mass did not match any

[*] Dr. M. Capdevila, L. Villarreal[+]
Departament de Química
Facultat de Ciències
Universitat Autònoma de Barcelona
08193 Bellaterra, Barcelona (Spain)
Fax: (+34) 93-581-3101
E-mail: merce.capdevila@uab.es
J. Domènech,[+] A. Pagani,[+] L. Tío,[+] Prof. S. Atrian
Departament de Genètica
Facultat de Biologia
Universitat de Barcelona
Av. Diagonal 645, 08028 Barcelona (Spain)
[+] These authors contributed equally to this work.

[**] This work was financially supported by the Spanish Ministerio de Educación y Ciencia (grants BIO2003-03892 to S.A. and CTQ2004-00359/BQU to M.C.). We thank the Serveis Científico-Tècnics de la Universitat de Barcelona and the Servei d'Anàlisi Química de la Universitat Autònoma de Barcelona for allocating instrument time. We thank Dr. I. Casals for his help in setting up the GC-FPD assay, and Dr. R. Bofill for manuscript comments. The cDNA clone of *S. purpuratus* MT (SpMTA), for which full characterization is in progress, was kindly provided by J. Kägi (Zürich, Switzerland). Finally, we are indebted to D. Winge (Utah, USA) for an invigorating exchange of ideas.

Supporting information for this article is available on the WWW under http://www.angewandte.org or from the author.

 © 2005 Wiley-VCH Verlag GmbH & Co. KGaA, Weinheim DOI: 10.1002/anie.200501183

Table 1: Analytical characterization of several purified metal–MT aggregates, corresponding to organisms of the most diverse taxa.[a]

Metal–MT	[MT][b] [$\times10^{-4}$ M]	[MT][c] [$\times10^{-4}$ M]	Metal/MT[d]	Metal/MT[e]	$AgNO_3$ test	S^{2-}/MT[f] (GC-FPD)	ESI-MS major species
Zn-QsMT	2.62	2.18	2.3	3.9	+	1.90	Zn_4-QsMT[15]
Cd-QsMT	1.49	0.58	2.5	6.5	+	3.44	Cd_6S_5-QsMT[15]
Cu-QsMT	0.29	0.26	5.8[g]	7.2[g]	–	n.d.	M_8-QsMT[15]
Zn-CRS5	1.72	1.67	5.7	5.8	–	0.44	Zn_6-CRS5[h]
Cd-CRS5	6.01	0.92	3.4	8.5	+	1.85	Cd_8-CRS5[h]
Cu-CRS5	3.22	3.16	11.3	11.4	–	n.d.	Cu_{11}-CRS5[h]
Zn-MTN	0.40		3.5				Zn_4-MTN[13]
Cd-MTN	1.80	0.80	1.7	3.8	+	2.34	Cd_4-MTN[h]
Cu-MTN	0.42		7.0		–		Cu_8-MTN[13]
Zn-MTO	0.78	0.63	3.2	3.7		0.90	Zn_4-MTO[14]
Cd-MTO	0.50	0.30	3.2	4.1	+	2.63	Cd_4-MTO[h]
Cu-MTO	0.37		8.9		–		Cu_9-MTO[14]
Zn-SpMTA	1.40	1.22	5.2	5.6	+	2.33	Zn_8/Zn_7S_2-SpMTA[h]
Cd-SpMTA	0.81	0.62	6.3	7.2	+	3.62	Cd_7-SpMTA[h]
Cu-SpMTA	0.41	0.39	7.1[g]	7.1[g]	–	n.d.	M_8-SpMTA[h]
Zn-ckMT	1.51	1.09	5.5	7.5		3.75	Zn_7-ckMT[h]
Cd-ckMT	2.29	0.63	3.7	8.8	+	4.70	Cd_7-ckMT[h]
Cu-ckMT	0.39		9.9[g]		–	n.d.	M_{10}-ckMT[h]
Zn-MT1	1.38	1.13	6.0	7.3		1.50	Zn_7-MT1[7]
Cd-MT1	1.90	1.13	3.7	6.4	+	3.17	Cd_7-MT1[11]
Cu-MT1	0.13		9.6[g]		–	n.d.	M_{10}-MT1[10]
Zn-MT4	2.18	1.18	6.7	7.0		3.5	Zn_7-MT4[11]
Cd-MT4	0.19	0.11	5.5[g]	6.9[g]	+	14	M_7-MT4[11]
Cu-MT4	0.36		9.4		–	n.d.	Cu_{10}-MT4[11]

[a] QsMT = *Quercus suber* MT; CRS5 = a *S. cerevisiae* MT; MTN and MTO are *Drosophila* MT forms; SpMTA = *S. purpuratus* type A MT; ckMT = chicken MT; MT1 = mammalian isoform 1 MT; MT4 = mammalian isoform 4 MT. Equivalent analyses with *T. pyriformis* MT1, *C. elegans* MT2, and *M. edulis* MT10IV yielded comparable results with regard to the presence of sulfide in their metal–MT complexes (data not shown). [b] Protein concentration calculated from conventional ICP-AES results. [c] Protein concentration calculated from acid ICP-AES results. Amino acid analysis led to identical values ±0.01. [d] Metal/MT ratio deduced from the metal content measured by conventional ICP-AES and results in (b). [e] Metal/MT ratio deduced from the metal content measured by ICP-AES and the acid ICP-AES and the results in (c). [f] n.d. = not detectable. [g] In this case, the metal/MT ratio represents the mean metal content per MT of preparations which had heterometallic composition (Zn and Cu or Zn and Cd). [h] This work. The corresponding manuscripts including the full MT characterization are in preparation.

possible Cd^{II} metallated complexes. These unknown mass peaks did not arise from the presence of other metal ions in putative heterometallic MT species, as Cd was the only metal detected by ICP-AES. Finally, circular dichroism (CD) spectroscopy of the Cd–MT samples showed features in the 260–280 nm range that clearly were not attributable to the known tetrahedral $Cd(SCys)_4$ chromophores that absorb at approximately 250 nm, which were also present in the spectra (Figure 1).

At this stage, the most likely explanation for our observations was the presence of an additional ligand in the purified Zn–MT and Cd–MT species, but none of the reported possibilities (chloride participation,[18] phosphate-driven dimerization[19]) were consistent with the analytical and spectral features of the samples. However, transitions between 260 and 300 nm have been reported in the CD spectra of Cd-phytochelatins containing sulfide anions[5,20] and we have already suggested that these ligands could be present in *Drosophila* Cd–MTN species.[13] The presence of extra sulfur in our samples as sulfide ligands would provide a sound explanation for all the bizarre results mentioned above as well as the negative oxidation degrees measured by reactions with the 3,3′-dithiobis(6-nitrobenzoic acid) (DTNB).[21] Therefore, we performed a quick test[22] to assess the presence of S^{2-} ions in our panel of recombinant metal–MTs by determining hydrogen sulfide gas generation after acidification of the samples with HCl. Blackening of a filter paper moistened with a solution of $AgNO_3$ which was capping the sample tube, as a consequence of silver sulfide precipitation, unequivocally identified the presence of sulfide in all the Cd–MT and some Zn–MT samples, but not from the control (sample without MT) or any Cu–MT preparations.

Zn–, Cd–, and Cu–MT species from different taxa were analyzed more thoroughly to determine whether sulfide ion binding was common in the diverse metal–MT complexes. If sulfide ions were present, then the ICP-AES approach for global metal–MT ratio calculation was not valid, as the sulfur quantization would not report exclusively on Cys and Met

 © 2005 Wiley-VCH Verlag GmbH & Co. KGaA, Weinheim

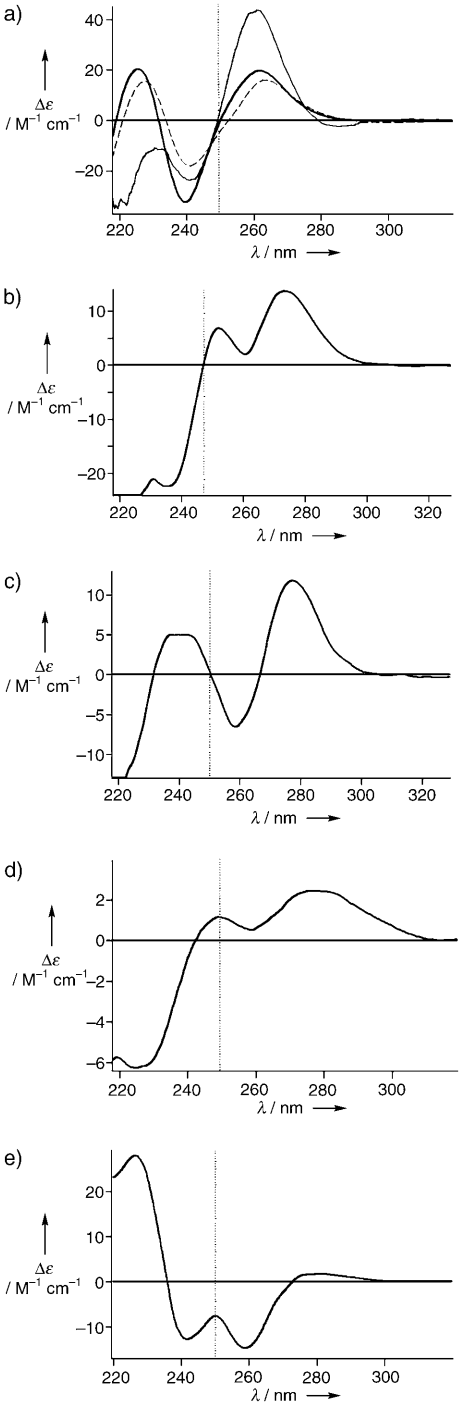


Figure 1. Representative CD spectra of several Cd–MT species from the most diverse taxa. Spectra have been grouped as a) type A (conventional spectra expected for Cd–MT species): Cd–MT1 (solid black line), Cd–SpMTA (solid gray line), and Cd–ckMT (dashed black line); b) type B: Cd–QsMT; c) type C: Cd–MTN; d) type D: Cd-CRS5; e) type E: Cd–MTO. All spectra show the characteristic absorption features of the $Cd(SCys)_4$ chromophores at approximately 250 nm (vertical dotted line) either as derivative shaped signals of different signs (A and B versus C), Gaussian bands (D) or more complex absorptions mixed with chloride participation[18] in Cd binding (E). The most (B, C, D and E) and least (A) intense absorptions at approximately 280 nm could be attributed to the presence of $Cd–S^{2-}$ bonds.

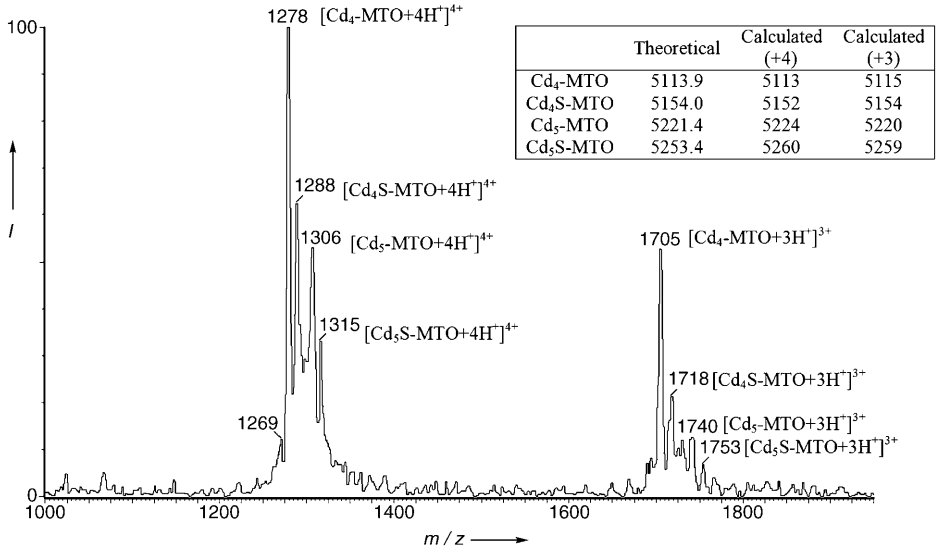
concentrations. Protein concentrations were then redetermined simultaneously by two methods: acid ICP-AES and amino acid analysis. Acid ICP-AES involves acidification of the sample with 1M HCl prior to the conventional method[16] to favor the loss of the acid-labile ligands such as H_2S and thus ensure that all the sulfur remaining in the sample corresponded to Cys and Met. Acid ICP-AES results gave new metal–MT ratios that were now highly consistent with the expected stoichiometries (Table 1). The amino acid analysis was used to quantify protein levels, and these data nicely matched those obtained by acid ICP-AES. Finally, considering single or multiple 32 Dalton (sulfur atomic weight) additions to the value of the mass of the canonical metal–MT species yielded values that were coincident with the unassigned ESI-MS peaks of the sample.

We attempted quantification of the sulfide content in all the samples, initially using a methylene blue method[23] similar to that applied for Cd–phytochelatin analyses.[20] However, this method has serious drawbacks, as some degree of interference with cadmium ions has been reported[24] and it is not suitable for samples containing copper owing to the insolubility of copper sulfide. As a consequence, we adapted a GC-FPD (flame photometric detector) approach initially reported for solid samples.[25] Both methods gave consistent results and permitted the mean S^{2-} ion content per MT to be determined (Table 1). These data demonstrated that acid-labile sulfide was present in all the recombinant Cd–MT samples and in many Zn–MT isolates, although always at lower ratios than in the corresponding Cd–MT samples. Furthermore, ESI-MS analyses of the Zn– and Cd–MT preparations not only accounted for the presence of S^{2-} ions as additional ligands but also showed coexistence of S^{2-}-containing and S^{2-}-devoid metal–MT species (Figure 2), indicating an equilibrium between the two forms in the original preparations. None of the MT proteins synthesized in Cu-supplemented media gave any evidence of sulfide ligands in their complexes. All of these findings are consistent with the features reported for the presence/absence of sulfide in Zn– or Cd–, and Cu–phytochelatins, respectively.[5,26] As for the spectroscopic analyses, evidence that sulfide in the Cd–MT complexes is associated with absorptions in the 260–280 nm range came from acidification/reneutralization experiments(see Supporting Information).

The data presented herein support the hypothesis that recombinant synthesis in *E. coli* of diverse MTs results in the recovery of sulfide-containing complexes in addition to the expected non-sulfide-containing canonical species. This is the first demonstration that Zn–MT and Cd–MT species have the capacity to form Zn- and Cd-thiolate complexes in which labile sulfide ligands contribute to the Zn^{II} and Cd^{II} binding.

This situation has major practical and theoretical implications. From a practical point of view, it is important that the ever-growing community of MT researchers using recombinant strategies to produce metal–MT complexes evaluates the presence of S^{2-} in their preparations to attain a true interpretation of their analytical, spectroscopic, and spectrometric data. From a theoretical angle, the presence of S^{2-} ions in metal–MT aggregates raises significant questions. Because of the observed metal and protein dependency and the

 © 2005 Wiley-VCH Verlag GmbH & Co. KGaA, Weinheim



	Theoretical	Calculated (+4)	Calculated (+3)
Cd_4-MTO	5113.9	5113	5115
Cd_4S-MTO	5154.0	5152	5154
Cd_5-MTO	5221.4	5224	5220
Cd_5S-MTO	5253.4	5260	5259

Figure 2. ESI-MS spectrum of the recombinant Cd–MTO preparation. The two sets of peaks corresponding to two charge states (+4 and +3) are shown, to illustrate the coexistence of sulfide-loaded and sulfide-devoid Cd–MTO forms. The table gives the corresponding molecular weights of the species as calculated from the MS data and predicted.

equilibrium between S^{2-}-containing and S^{2-}-devoid forms, it is unlikely that S^{2-} binding is a mere artifact, thus it is pertinent to ask if sulfide incorporation also occurs in endogenous metal–MT complexes, that is, in native forms. Should this be the case, it is intriguing why it has not been previously detected. A likely explanation is that for nearly half a century most of the MT research has been carried out using in vitro reconstituted metal–MT species, which are prepared by adding the corresponding metal ions to apo-MT (metal-devoid MT) polypeptides. These species are obtained after heavy acidification of the purified metal–MT forms and thus, any sulfide ions involved in the initial Zn^{II} or Cd^{II} complexation would be lost. Furthermore, the native isolates of MT complexes from many species contain significant heterogeneity of isoforms and metal compositions.[27,28] Therefore a lot of effort has been devoted to obtaining pure chromatographic fractions, which may involve discarding other minor metal–MT species originally present in the sample and that are assumed to be impurities, mixed-metal species, or simply, non-MT metal-containing aggregates.

The S^{2-} ion is a species not restricted to *E. coli*, but rather a universal cell component. At present, evidence is being gathered that relates the presence of S^{2-} ions with physiological events, which have also been proposed for MT function candidates (redox equilibrium,[29] neurotransmission, and neuromodulation[30]). Consequently, evaluation of the sulfide-binding MT capability in endogenous MT forms is worth considering in further studies of native MT forms, especially Zn–MT, as new data could shed light into the physiological significance of this poorly understood protein in view of the recently revised relationship between the biological and inorganic zinc clusters in nature.[31] But, in any case, knowledge of the capability of divalent metal–MTs to include S^{2-} ions in their aggregates, or in other words, to build metal-MT aggregates that include S^{2-} ions would be highly significant for structural, nanobiological, biotechnological, and biomedical applications in which MTs are involved. In conclusion, a new attribute must be added to the already long list of peculiar features of these versatile proteins.

Experimental Section

Zn–, Cd–, and Cu–MT complexes were synthesized according to a recombinant fusion-protein strategy (GST-MT) fully reported in references [6,7]. This method is based on cultures of *E. coli* cells transformed with the corresponding expression constructs in LB (Luria Bertini) medium supplemented with Zn^{II}, Cd^{II}, or Cu^{II} (300 μM, 300 μM, and 500 μM, respective final concentrations). After cell sonication, all the steps were performed under argon atmosphere. The total protein extract was only submitted to Glutathione-Sepharose affinity chromatography, thrombin digestion, and FPLC (fast performance liquid chromatography) in 50 mM Tris-HCl (Tris = 2-amino-2-(hydroxymethyl)-1,3-propanediol), pH 7.5 buffer. All MT complexes were synthesized and purified under identical conditions.

The molecular mass of the metal–MT species was determined by electrospray ionization mass spectrometry (ESI-MS) on a Fisons Platform II Instrument, equipped with MassLynx software and calibrated with horse-heart myoglobin (0.1 mg mL^{-1}). The assay conditions for the Zn- and Cd-containing species were as follows: 20 μL of protein solution injected at 40 μL min^{-1}; the use of an HPLC Uptisphere C_4 33 mm × 2 mm × 5 μm column to separate analytes; capillary counterelectrode voltage, 4.5 kV; lens counterelectrode voltage, 1.0 kV; cone potential, 60 V; source temperature, 120 °C; *m*/*z* range, 850–1950; scanning rate, 3 s scan^{-1}; interscan delay, 0.3 s. The assay conditions for the Cu-containing species were: 20 μL of protein solution injected at 30 μL min^{-1}; capillary counterelectrode voltage, 3.5 kV; lens counterelectrode voltage, 1.0 kV; cone potential, 35 V; source temperature, 160 °C; *m*/*z* range, 850–1950; scanning rate, 3 s scan^{-1}; interscan delay, 0.3 s. In all cases, the running buffer was an appropriate mixture of acetonitrile and 5 mM ammonium acetate/ammonia, pH 7.5.

Electronic absorption measurements were performed on an HP-8453 Diode array UV/Vis spectrophotometer. A Jasco spectropolarimeter (J-715) interfaced to a computer (GRAMS 32 Software)

 © 2005 Wiley-VCH Verlag GmbH & Co. KGaA, Weinheim

was used for CD determinations. The temperature for all measurements was kept at 25 °C by means of a Peltier PTC-351S apparatus.

ICP-AES, using a Polyscan 61E (Thermo Jarrell Ash) spectropolarimeter, allowed determination of S (182.040 nm), Zn (213.856 nm), Cd (228.802 nm), and Cu (324.803 nm) sample contents. Two alternative methods were used: conventional ICP implied no previous sample treatment,[16] while acid ICP included acid incubation of the sample (1 M HCl, 65 °C, 5 min) prior to ICP measurements. In both cases, protein concentration was calculated from the S content, assuming it was only contributed to by the Cys and Met residues of the peptides. In addition, protein concentration was assessed by amino acid analysis (hydrolysis in 6 M HCl at 110 °C for 22 h) on an Alpha Plus Amino Acid Autoanalyzer (Pharmacia LKB). Ser, Lys, and Gly contents were used to extrapolate MT concentrations.

GC-FPD[32] was used as the most suitable methodology for direct (i.e. without sample derivatization) S^{2-} detection at low concentrations, since it presents a quadratic response to compounds including one unique S atom.[25] H_2S was generated by strong acidification (H_2SO_4, pH 0.0) of the sample to ensure disruption of the metal–MT complex and to avoid precipitation of insoluble ZnS and CdS. The calibration curve was determined with dilute standards of S^{2-} at 0, 0.25, 0.5, 1, 1.5, 2.5, and 3 ppm prepared from a stock solution of S^{2-} at 1000 ppm which was obtained by dissolving a single crystal of $Na_2S{\cdot}9H_2O$ in oxygen-free water and standardized by iodine titration using $NaIO_3$.[22] Sample aliquots, as well as the standard solutions, were transferred to airtight 2-mL vials, acidified to a final volume of 0.5 mL, and immediately sealed. Vials were then incubated at 40 °C for 2 h with agitation (250 rpm) to accelerate the evolution of H_2S from the aqueous phase and equilibration of gas phase in the head-space. 500 μL of the head-space gas were subjected to gas chromatography (HP 5890 Serie II coupled to a FPD80 CE Instruments (Thermo Finnigan) detector). The gaseous mixture was carried by a 6.6 mL min^{-1} flux of He through the GC glass column (SPB 608 30 m × 0.25 mm i.d. with 0.5 μm particle size). Both the injection and the detection port were kept at 110 °C while the column was operated at a constant temperature of 35 °C. The H_2S peak generated from MT samples was readily identified by a retention time coincident with that of the standard solutions. All determinations were performed in duplicate with independent samples.

Received: April 4, 2005

Keywords: bioinorganic chemistry · cadmium · metallothioneins · S ligands · zinc

[1] M. Margoshes, B. Vallee, *J. Am. Chem. Soc.* **1957**, *79*, 4813 – 4814.
[2] R. Palmiter, *Proc. Natl. Acad. Sci. USA* **1998**, *95*, 8428 – 8430.
[3] P. Coyle, J. C. Philcox, L. C. Carey, A. M. Rofe, *Cell. Mol. Life Sci.* **2002**, *59*, 62 – 647.
[4] P. Gonzalez-Duarte in *Comprehensive Coordination Chemistry II*, *Vol. 8* (Eds.: J. A. McCleverty, T. J. Meyer), Elsevier-Pergamon, Amsterdam, **2003**, pp. 213 – 228.
[5] D. Winge, C. T. Dameron, R. K. Mehra in *Metallothioneins* (Eds.: M. J. Stillman, F. C. Shaw III, K. T. Suzuki), VCH, New York, **1992**, pp. 257 – 270.
[6] M. Capdevila, N. Cols, N. Romero-Isart, R. González-Duarte, S. Atrian, P. González-Duarte, *Cell. Mol. Life Sci.* **1997**, *53*, 681 – 688.
[7] N. Cols, N. Romero-Isart, M. Capdevila, B. Oliva, P. González-Duarte, R. González-Duarte, S. Atrian, *J. Inorg. Biochem.* **1997**, *68*, 157 – 166.
[8] N. Cols, N. Romero-Isart, R. Bofill, M. Capdevila, P. González-Duarte, R. González-Duarte, S. Atrian, *Protein Eng.* **1999**, *12*, 265 – 269.
[9] R. Bofill, O. Palacios, M. Capdevila, N. Cols, R. Gonzàlez-Duarte, S. Atrian, P. Gonzàlez-Duarte, *J. Inorg. Biochem.* **1999**, *73*, 57 – 64.
[10] R. Bofill, M. Capdevila, N. Cols, S. Atrian, P. González-Duarte, *J. Biol. Inorg. Chem.* **2001**, *6*, 405 – 417.
[11] L. Tío, L. Villarreal, S. Atrian, M. Capdevila, *J. Biol. Chem.* **2004**, *279*, 24404 – 24413.
[12] M. Valls, R. Bofill, R. González-Duarte, P. González-Duarte, M. Capdevila, S. Atrian, *J. Biol. Chem.* **2001**, *276*, 32835 – 32843.
[13] M. Valls, R. Bofill, N. Romero-Isart, R. Gonzàlez-Duarte, J. Abián, M. Carrascal, P. Gonzàlez-Duarte, M. Capdevila, S. Atrian, *FEBS Lett.* **2000**, *467*, 189 – 194.
[14] J. Domenech, O. Palacios, L. Villarreal, P. González-Duarte, M. Capdevila, S. Atrian, *FEBS Lett.* **2003**, *533*, 72 – 78.
[15] G. Mir, J. Domènech, G. Huguet, W. Guo, P. Goldsbrough, S. Atrian, M. Molinas, *J. Exp. Bot.* **2004**, *55*, 2483 – 2493.
[16] J. Bongers, C. D. Walton, D. E. Richardson, J. U. Bell, *Anal. Chem.* **1988**, *60*, 2683 – 2686.
[17] W. Birchmeier, P. Christen, *FEBS Lett.* **1971**, *18*, 209 – 213.
[18] L. Villarreal, L. Tío, S. Atrian, M. Capdevila, *Arch. Biochem. Biophys.* **2005**, *435*, 331 – 335.
[19] P. Palumaa, M. Vasak, *Eur. J. Biochem.* **1992**, *205*, 1131 – 1135.
[20] R. N. Reese, D. R. Winge, *J. Biol. Chem.* **1988**, *263*, 12832 – 12835.
[21] D. N. Weber, F. Shaw III, D. H. Petering, *J. Biol. Chem.* **1987**, *262*, 6962 – 6964.
[22] A. I. Vogel in *A Text-Book of Macro and Semimicro Qualitative Inorganic Analysis*, Longmans, **1954**, p. 335.
[23] In *Standard Methods for the Examination of Water and Wastewater* (Eds. L. S. Clesceri, A. E. Greenberg, A. D. Eaton), American Public Health Association, Washington D. C., **1998**.
[24] T. E. King, R. O. Morris, *Methods Enzymol.* **1967**, *10*, 634 – 637.
[25] A. Marcó, R. Compañó, R. Rubio, I. Casals, L. Krotz, L. Ragaglia, G. Giazzi, *Analyst* **2001**, *126*, 1820 – 1825.
[26] R. N. Reese, R. K. Mehra, E. B. Tarbet, D. R. Winge, *J. Biol. Chem.* **1988**, *263*, 4186 – 4192.
[27] J. H. R. Kägi, S. R. Himmelhoch, P. D. Whanger, J. L. Bethune, B. L. Vallee, *J. Biol. Chem.* **1974**, *249*, 3537 – 3542.
[28] D. R. Winge, R. Premakumar, K. V. Rajagopalan, *Arch. Biochem. Biophys.* **1975**, *170*, 242 – 252.
[29] W. Maret, *Biochemistry* **2004**, *43*, 3301 – 3309.
[30] D. E. Barañano, C. D. Ferris, S. H. Snyder, *Trends Neurosc.* **2001**, *24*, 99 – 106.
[31] C. Blindauer, P. Sadler, *Acc. Chem. Res.* **2005**, *38*, 62 – 69.
[32] T. Ubuka, *J. Chromatogr. B* **2002**, *781*, 227 – 249.

 © 2005 Wiley-VCH Verlag GmbH & Co. KGaA, Weinheim

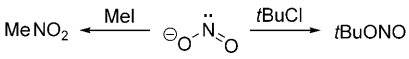
Ambident Anions

Ambident Reactivity of the Nitrite Ion Revisited**

*Alexander A. Tishkov, Uli Schmidhammer, Stefan Roth, Eberhard Riedle, and Herbert Mayr**

Dedicated to Professor Horst Kessler on the occasion of his 65th birthday

Extensive investigations on the reactions of the nitrite ion with alkylating agents[1] led Kornblum to the conclusion "*The greater the carbonium contribution to the transition state the greater is the yield of nitrite ester and the smaller is the yield of nitroparaffin.*"[1a] However, Pearson's specification of this rule, "*tC_4H_9Cl reacts with the hard oxygen atom of NO_2^-, while the softer CH_3I reacts with the softer nitrogen atom,*"[2a] which was expressed by Equation (1) in later theoretical treatments of ambident reactivity,[2b–d] is not in line with experimental findings, because CH_3I and other primary haloalkanes yield mixtures of alkyl nitrites and nitroalkanes with either $NaNO_2$ or $AgNO_2$.[1,2e]



(1)

Fleming's statement "*Although silver nitrite does react with alkyl halides to give nitrites, sodium nitrite gives more nitroalkane than alkyl nitrite*" [Eqs. (2) and (3)][3a] is contradicted by Streitwieser, Heathcock, and Kosower, who compare the reactions of iodoalkanes with $NaNO_2$ and $AgNO_2$ and conclude "*Yields of nitroalkane are higher when silver nitrite is used, but this added economy is tempered by the cost of silver salt*" [Eq. (4)].[3b]

$$AgNO_2 + RBr \rightarrow RONO \quad (2)$$

$$NaNO_2 + RBr \rightarrow RNO_2 \quad (3)$$

$$CH_3(CH_2)_6CH_2I + AgNO_2 \rightarrow CH_3(CH_2)_6CH_2NO_2\ (83\,\%) + CH_3(CH_2)_6CH_2ONO\ (11\,\%) \quad (4)$$

[*] Dr. A. A. Tishkov, Prof. Dr. H. Mayr
Department Chemie und Biochemie
Ludwig-Maximilians-Universität München
Butenandtstrasse 5–13 (Haus F), 81377 München (Germany)
Fax: (+49) 89-2180-77717
E-mail: herbert.mayr@cup.uni-muenchen.de
Dipl.-Phys. U. Schmidhammer, Dipl.-Phys. S. Roth, Prof. Dr. E. Riedle
Lehrstuhl für BioMolekulare Optik
Ludwig-Maximilians-Universität München
Oettingenstrasse 67, 80538 München (Germany)

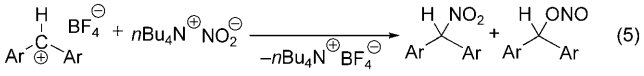
[**] This research was supported by the Alexander von Humboldt Foundation (stipend to A.A.T.) and the Deutsche Forschungsgemeinschaft.

Supporting information for this article is available on the WWW under http://www.angewandte.org or from the author.

This confusion prompted us to reinvestigate the ambident reactivity of the nitrite ion with emphasis on absolute rate constants.

We have recently reported that the knowledge of absolute rate constants and of the diffusion control limit is a key to understanding the ambident reactivity of the thiocyanate[4a] and cyanide ions[4b] in alkylation reactions. These ambident anions are preferentially attacked at the soft S or C termini by hard and soft alkylating agents. Only when diffusion control is reached, can the attack of carbocations at the hard nitrogen compete with attack at sulfur (SCN^-) or carbon (CN^-), respectively. We now report on the kinetics and selectivities of alkylations of the nitrite ion.

Reactions of the blue benzhydrylium salts (**1a–d**)-BF_4 (see Table 1) with $n Bu_4N^+NO_2^-$ in anhydrous acetonitrile [Eq. (5)], which gave colorless adducts, were followed photo-

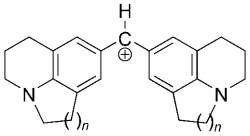
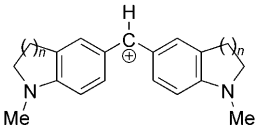
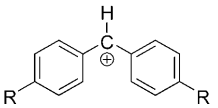


(5)

metrically using the stopped-flow technique described previously.[5] For $[\mathbf{1a–d}]_0 = (1–10) \times 10^{-6}$ M and $[NO_2^-]_0 = (1–100) \times 10^{-5}$ M, pseudo-first-order conditions were employed resulting in exponential decays of the benzhydrylium absorptions, from which the pseudo-first-order rate constants $k_{1\psi}$ (s^{-1}) were derived. The second-order rate constants k_2 ($M^{-1}s^{-1}$) listed in Table 1 were obtained as the slopes of the plots of $k_{1\psi}$ vs. $[NO_2^-]$.[6] From the linearity of these correlations one can infer that ion pairing does not play a role under these conditions.

The reactions with the highly electrophilic benzhydrylium ions **1e–k** (see Table 1) were too fast to be followed by stopped-flow techniques. Therefore, these carbocations were generated photolytically in the presence of the nitrite ion. For this purpose, solutions of (**1e–h**)-NO_2 (obtained according to

Table 1: Rate constants of the reactions of nitrite ions with the benzhydrylium cations **1a–k** (20 °C, MeCN).

Benzhydrylium ion			E[a]	k_2 [$M^{-1}s^{-1}$]
	$n=1$	**1a**	−10.04	1.58×10^5
	$n=2$	**1b**	−9.45	3.30×10^5
	$n=1$	**1c**	−8.76	9.85×10^5
	$n=2$	**1d**	−8.22	2.76×10^6
	R = NMe_2	**1e**	−7.02	1.56×10^7
	R = NMePh	**1f**	−5.89	1.49×10^8
	R = $NMe(CH_2CF_3)$	**1g**	−3.85	1.09×10^9
	R = $NPh(CH_2CF_3)$	**1h**	−3.14	3.41×10^9
	R = OMe	**1i**	0.00	–[b]
	R = Me	**1j**	3.63	2.50×10^{10}
	R = H	**1k**	5.90	2.2×10^{10}[c]

[a] Electrophilicity parameter as defined by Equation (6), see ref. [5a]. [b] Not determined. [c] From ref. [6].

 DOI: 10.1002/anie.200501274 © 2005 Wiley-VCH Verlag GmbH & Co. KGaA, Weinheim

Eq. (5)) or **1j**-Cl and nBu$_4$N$^+$NO$_2^-$ in acetonitrile were irradiated by laser pulses (< 1 ps, ca. 1.5 μJ, center wavelengths between 250 and 300 nm) to yield the benzhydrylium ions **1e–j** in less than 2 ps. The behavior of these transients (λ_{max} = 460–612 nm) was monitored on different timescales, and we detected reactions with 10 ms > $\tau_{1/2}$ > 10 ns.[7] As in the stopped-flow experiments, these reactions were also performed under pseudo-first-order conditions [Ar$_2$CH$^+$] ≪ [NO$_2^-$], and the second-order rate constants listed in Table 1 were again derived from plots of $k_{1\psi}$ vs. [NO$_2^-$].

In previous work we have shown that the reactions of carbocations with nucleophiles can be described by Equation (6), where k is the second-order rate constant, E is a

$$\log k_{20^\circ C} = s(E + N) \quad (6)$$

nucleophile-independent electrophilicity parameter, and N and s are electrophile-independent nucleophilicity parameters.[5,8] Figure 1 correlates the second-order rate constants listed in Table 1 with the previously determined electrophilicity parameters of benzhydrylium ions[5] and shows that the reactions of carbocations **1a–f** with NO$_2^-$ follow Equation (6).

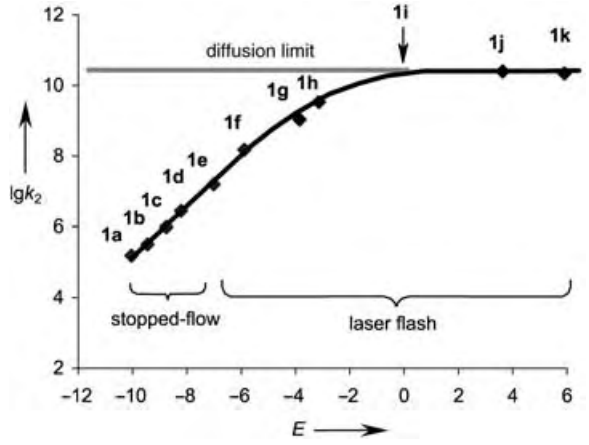
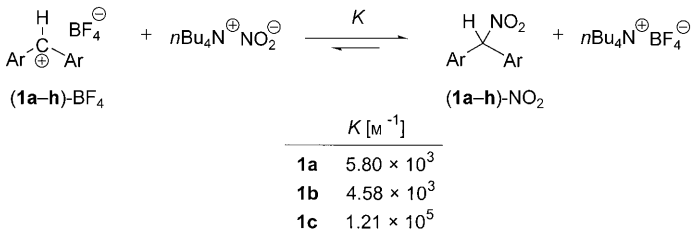


Figure 1. Plot of lg k_2 for the reactions of the nitrite ion with the benzhydrylium ions **1a–k** versus their electrophilicity parameters E (20 °C, MeCN).[5a]

From the linear part of this correlation (**1a–f**) one can derive N = 17.2 and s = 0.72 for the nitrite ion in acetonitrile. For the more electrophilic benzhydrylium ions **1g–k**, a flattening of the curve can be seen, and the observed diffusion limit is in accord with the previously reported value of (2.2–2.7) × 10^{10} M^{-1} s^{-1} for reactions of carbocations with anions in acetonitrile.[6]

Which reactions are responsible for the decay of the benzhydrylium absorbances? Addition of an excess of nBu$_4$N$^+$NO$_2^-$ to solutions of benzhydrylium tetrafluoroborates (**1a–h**)-BF$_4$ in CD$_3$CN gives rise to the exclusive formation of the nitromethanes (**1a–h**)-NO$_2$[9] (Scheme 1), as revealed by the characteristic ^{1}H NMR chemical shifts of the benzhydryl protons (δ = 6.5–6.8 ppm) and the ^{15}N NMR



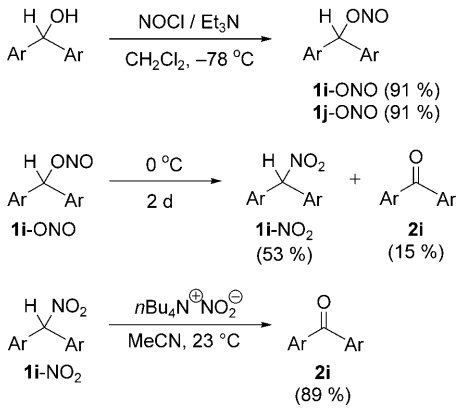
Scheme 1. Reactions of benzhydrylium tetrafluoroborates with nBu$_4$N$^+$NO$_2^-$ (equilibrium constants K in CH$_3$CN at 20 °C).

chemical shift of the nitro group (δ = 3.8 ppm) in **1e**-NO$_2$.[10] For the least reactive carbocations **1a–c** an excess of nBu$_4$N$^+$NO$_2^-$ is needed to drive the reactions toward completion. The equilibrium constants, which were determined by UV/Vis spectroscopy (see the Supporting Information), are listed in Scheme 1.[11]

These observations clearly indicate that the photometrically monitored process for the reactions of **1a–c** with NO$_2^-$ is N attack: Since alkyl nitrites are thermodynamically less stable than the corresponding nitro compounds,[12] the equilibrium constants for the formation of (**1a–c**)-ONO must be much smaller, and one can exclude that the observed rates of carbocation decay are due to the formation of (**1a–c**)-ONO, which rearrange to the observed nitro compounds (**1a–c**)-NO$_2$ in consecutive reactions.[13]

For the more electrophilic benzhydrylium ions **1d–h** one cannot a priori exclude the possibility that the UV/Vis spectroscopically monitored process is the formation of (**1d–h**)-ONO, which successively rearrange to the observed nitro compounds (**1d–h**)-NO$_2$. However, since the obtained rate constants for the reactions of **1d–h** with NO$_2^-$ are on the same correlation line as the rate constants for N attack at **1a–c** (Figure 1), the observed rate constants are compatible only with exclusive N attack or with simultaneous N and O attacks that occur with similar rates. In none of these cases could a biexponential decay be observed as in the reactions of some benzhydrylium ions with SCN$^-$, where the faster reversible S attack was followed by the slower irreversible N attack.[4a]

Pure benzhydrylium nitrites **1i**-ONO and **1j**-ONO were obtained by treatment of the corresponding benzhydrols with NOCl/Et$_3$N (Scheme 2), while analogous attempts to synthe-

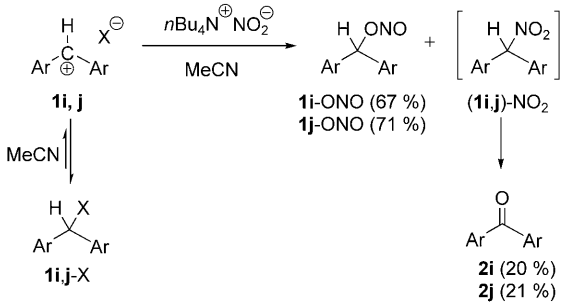


Scheme 2. **i**: Ar = 4-MeOC$_6$H$_4$; **j**: Ar = 4-MeC$_6$H$_4$.

 © 2005 Wiley-VCH Verlag GmbH & Co. KGaA, Weinheim

size (**1a**–**h**)-ONO failed.[14] Whereas pure **1j**-ONO remained unchanged when stored at room temperature for several days, **1i**-ONO rearranged within two days at 0 °C into **1i**-NO_2, which decomposed to **2i** either spontaneously or upon treatment with nBu$_4$N$^+$NO$_2^-$ in MeCN (Scheme 2).[15]

Both benzhydrylium nitrites **1i**-ONO and **1j**-ONO were recovered unchanged when kept in a solution of nBu$_4$N$^+$NO$_2^-$ in acetonitrile for 3 h. These experiments show that benzhydryl nitrites **1i**-ONO and **1j**-ONO are kinetically stable under the conditions of the experiment described in Scheme 3. Treatment of the benzhydrylium halides **1i**-Cl and **1j**-Br with



Scheme 3. X = Cl, Br.

nBu$_4$N$^+$NO$_2^-$ in MeCN gave 7:2 mixtures of **1i**-ONO and benzophenone **2i**, and **1j**-ONO and benzophenone **2j**, respectively, which were analyzed by comparison of the NMR spectra of the product mixtures with those of authentic compounds. Since **1i**-ONO and **1j**-ONO are stable under the conditions of the experiment, and the benzophenones **2i** and **2j** are consecutive products of the corresponding diarylnitromethanes **1i**-NO_2 and **1j**-NO_2, the product ratios described in Scheme 3 imply a k_O/k_N ratio of 3.4 for the diffusion-controlled reactions of NO_2^- with the benzhydrylium ions **1i** and **1j**.

We thus conclude that diffusion-controlled reactions of benzhydrylium ions with NO_2^- occur preferentially at the O terminus.[16] Since Figure 1 shows that carbocations with $E > 0$ (i.e., carbocations less stabilized than **1i**) generally undergo diffusion-controlled reactions with NO_2^-, it is evident that the reactions of NO_2^- with most carbocations typically generated in S_N1 processes (e.g., *tert*-alkyl, allyl, and benzyl cations) proceed without an activation barrier. Explanations of the ambident reactivity of NO_2^- based on transition-state models, therefore, cannot apply. On the other hand, those benzhydryl nitrites, which are formed by activation-controlled reactions of benzhydrylium ions with NO_2^-, are thermodynamically unstable and rapidly isomerize to the corresponding nitro compounds.

Let us now turn to S_N2 reactions with the nitrite ion. Silver ion was proven to assist the cleavage of the C–Hal bond during the reactions of $AgNO_2$ with alkyl halides.[1a] However, in contrast to statements in the secondary literature (e.g., see ref. [3a]) silver ions were reported not to exert a significant influence on the O/N selectivity (Table 2, entries 1–4).[2e] On the other hand, the methyl nitrite/nitromethane ratio is changed significantly by variation of the solvent (Table 2, entries 5–8).[17]

We have now studied the reactions of nBu$_4$N$^+$NO$_2^-$ with soft (MeI) and hard ($MeOSO_2Me$, $MeOSO_2CF_3$, and $Me_3O^+BF_4^-$) methylating agents in $CDCl_3$. The yields were determined by integration of the ^{1}H NMR spectra with MeOAc as the internal standard. Overall yields were close to quantitative in all cases, and the methyl nitrite/nitromethane ratios (Table 2, entries 9–12) clearly indicate that the effect of the leaving groups on the O/N selectivities is small. Changing from the soft methylating agent MeI to the hard Me_3O^+ changes the O/N selectivities by only a factor of 2.4, while a larger difference is found among the hard methylating agents $MeOSO_2Me$ and $MeOSO_2CF_3$.

In conclusion, neither S_N1 nor S_N2 alkylations of the nitrite ion are satisfactorily described in the framework of perturbation molecular orbital theory (PMO). The reactions of carbocations with NO_2^- only yield kinetically controlled product mixtures when $k > 1 \times 10^9\,M^{-1}s^{-1}$, that is, when they proceed without an activation barrier. Therefore PMO approaches, such as the Klopman–Salem model, which aim at comparing relative activation energies cannot be applied. Furthermore, O/N selectivities of the methylations of the nitrite ion (Table 2) also do not correlate well with the hardness of the methylating agents. Thus, NO_2^- is the third prototype of the ambident anions (after SCN^- and CN^-)[4] for which the previously accepted rationalization by frontier orbital theory has to be withdrawn.

Table 2: O/N selectivities for methylations of nitrite ions.[a]

Entry	Nitrite	Methylation agent	Solvent	Me-ONO/Me-NO_2
1	$AgNO_2$	MeI	DMSO	46:54[b]
2	$NaNO_2$	MeI	DMSO	54:46[b]
3	$AgNO_2$	MeI	DMF	54:46[b]
4	$NaNO_2$	MeI	DMF	54:46[b]
5	KNO_2/[18]crown-6	$MeOSO_2Me$	EtOH	30:70[c]
6	KNO_2/[18]crown-6	$MeOSO_2Me$	MeCN	50:50[c]
7	KNO_2/[18]crown-6	$MeOSO_2Me$	THF	92:8[c]
8	KNO_2/[18]crown-6	$MeOSO_2Me$	C_6H_6	85:15[c]
9	nBu$_4$N$^+$NO$_2^-$	MeI	$CDCl_3$	30:70[d]
10	nBu$_4$N$^+$NO$_2^-$	$MeOSO_2Me$	$CDCl_3$	32:67[d]
11	nBu$_4$N$^+$NO$_2^-$	$MeOMe_2^+BF_4^-$	$CDCl_3$	50:50[d]
12	nBu$_4$N$^+$NO$_2^-$	$MeOSO_2CF_3$	$CDCl_3$	59:41[d]

[a] At room temperature. [b] Determined by LC with radioactivity detection for reactions of $^{11}CH_3I$ (see ref. [2e]). [c] Determined by GC (see ref. [17]). [d] Determined by integration of ^{1}H NMR spectra (this work, see the Supporting Information).

Received: April 12, 2005

Keywords: HSAB principle · kinetics · Klopman–Salem equation · Kornblum's rule · nitro compounds

 © 2005 Wiley-VCH Verlag GmbH & Co. KGaA, Weinheim

[1] a) N. Kornblum, R. A. Smiley, R. K. Blackwood, D. C. Iffland, *J. Am. Chem. Soc.* **1955**, *77*, 6269 – 6280; b) N. Kornblum, H. O. Larson, R. K. Blackwood, D. D. Mooberry, E. P. Oliveto, G. E. Graham, *J. Am. Chem. Soc.* **1956**, *78*, 1497 – 1501; c) N. Kornblum, R. A. Smiley, H. E. Ungnade, A. M. White, B. Taub, S. A. Herbert, Jr., *J. Am. Chem. Soc.* **1955**, *77*, 5528 – 5533; d) N. Kornblum, H. O. Larson, D. D. Mooberry, R. K. Blackwood, E. P. Oliveto, G. E. Graham, *Chem. Ind.* **1955**, *78*, 443; e) N. Kornblum, *Organic Reactions*, *Vol. 12* **1962**, 101 – 156; f) N. Kornblum, L. Fishbein, R. A. Smiley, *J. Am. Chem. Soc.* **1955**, *77*, 6261 – 6266.

[2] a) R. G. Pearson, J. Songstad, *J. Am. Chem. Soc.* **1967**, *89*, 1827 – 1836; b) G. Klopman, *J. Am. Chem. Soc.* **1968**, *90*, 223 – 234; c) R. F. Hudson, *Angew. Chem.* **1973**, *85*, 63 – 84; *Angew. Chem. Int. Ed. Engl.* **1973**, *12*, 36 – 57; d) S. J. Formosinho, L. G. Arnaut, *J. Chem. Soc. Perkin Trans. 2* **1989**, 1947 – 1952; e) K.-O. Schoeps, C. Halldin, S. Stone-Elander, B. Långström, T. Greitz, *J. Labelled Compd. Radiopharm.* **1988**, *25*, 749 – 758.

[3] a) I. Fleming, *Frontier Orbitals and Organic Chemical Reactions*, Wiley, Chichester, **1976**, p. 41 – 42; b) A. Streitwieser, C. H. Heathcock, E. M. Kosower, *Introduction to Organic Chemistry*, Macmillan, New York, **1992**, p. 779; This statement is in line with Kornblum's report (p. 114 in ref. [1e]): "*In the synthesis of saturated primary nitro compounds, silver nitrite gives nitroparaffins in about 80% yield as against about 60% yields obtained with sodium nitrite. While silver nitrite is, therefore, the reagent of choice here, the lower cost and ready availability of sodium nitrite, the not very large disparity in yield, and the shorter reaction time all combine to make sodium nitrite an excellent second choice.*"

[4] a) R. Loos, S. Kobayashi, H. Mayr, *J. Am. Chem. Soc.* **2003**, *125*, 14126 – 14132; b) A. A. Tishkov, H. Mayr, *Angew. Chem.* **2005**, *117*, 145 – 148; *Angew. Chem. Int. Ed.* **2005**, *44*, 142 – 145.

[5] a) H. Mayr, T. Bug, M. F. Gotta, N. Hering, B. Irrgang, B. Janker, B. Kempf, R. Loos, A. R. Ofial, G. Remennikov, H. Schimmel, *J. Am. Chem. Soc.* **2001**, *123*, 9500 – 9512; b) H. Mayr, B. Kempf, A. R. Ofial, *Acc. Chem. Res.* **2003**, *36*, 66 – 77.

[6] J. Bartl, S. Steenken, H. Mayr, *J. Am. Chem. Soc.* **1991**, *113*, 7710 – 7716.

[7] The laser flash photolysis was performed using state-of-the-art femtosecond pulses as excitation and light-emitting diodes (LEDs) as sources of monitoring beams. New instrumentation was developed that is compatible with standard pump probe setups. Details of this method will be published separately: U. Schmidhammer, S. Roth, E. Riedle, A. A. Tishkov, H. Mayr, *Rev. Sci. Instrum.* **2005**, submitted.

[8] a) S. Minegishi, R. Loos, S. Kobayashi, H. Mayr, *J. Am. Chem. Soc.* **2005**, *127*, 2641 – 2649; b) S. Minegishi, H. Mayr, *J. Am. Chem. Soc.* **2003**, *125*, 286 – 295; c) R. Lucius, R. Loos, H. Mayr, *Angew. Chem.* **2002**, *114*, 97 – 102; *Angew. Chem. Int. Ed.* **2002**, *41*, 91 – 95; d) T. Bug, H. Mayr, *J. Am. Chem. Soc.* **2003**, *125*, 12980 – 12986; e) T. Bug, T. Lemek, H. Mayr, *J. Org. Chem.* **2004**, *69*, 7565 – 7576.

[9] Because of the ease of the transformation of diarylnitromethanes into the corresponding benzophenones (see Scheme 2) these reactions were performed in NMR tubes and analyzed immediately after the reagents had been mixed.

[10] D. M. Grant, R. K. Harris, *Encyclopedia of Nuclear Magnetic Resonance*, *Vol. 5*, Wiley, Chichester, **1996**, p. 3232.

[11] The nonobservance of tetraarylethanes indicates that electron-transfer processes do not occur under these conditions; see: a) N. Kornblum, L. Cheng, T. M. Davies, G. W. Earl, N. L. Holy, R. C. Kerber, M. M. Kestner, J. W. Manthey, M. T. Musser, H. W. Pinnick, D. H. Snow, F. W. Stuchal, R. T. Swiger, *J. Org. Chem.* **1987**, *52*, 196 – 204; b) N. Kornblum, T. M. Davies, G. W. Earl, N. L. Holy, R. C. Kerber, M. T. Musser, D. H. Snow, *J. Am. Chem. Soc.* **1967**, *89*, 725 – 727.

[12] a) J. F. Liebman, M. S. Campbell, S. W. Slayden in *The Chemistry of Amino, Nitroso, Nitro and Related Groups, Supplement F2* (Ed.: S. Patai), Wiley, Chichester, **1996**, chap. 8, p. 340; b) B. M. Rice, S. V. Pai, J. Hare, *Combust. Flame* **1999**, *118*, 445 – 458; c) "Neutral Thermochemical Data": H. Y. Afeefy, J. F. Liebman, S. E. Stein in *NIST Chemistry WebBook* (Eds.: P. J. Linstrom, W. G. Mallard), NIST Standard Reference Database Number 69, National Institute of Standards and Technology, Gaithersburg MD, 20899, **2003** (http://webbook.nist.gov).

[13] These results disagree with the claim that malachite green ((4-$Me_2NC_6H_4)_2PhC^+$) reacts with NO_2^- in acetone and ethyl acetate yielding (4-$Me_2NC_6H_4)_2PhC$-ONO as the kinetic product followed by slow (for a UV/Vis spectrometer with a regular mixing mode) irreversible formation of the more stable (4-$Me_2NC_6H_4)_2PhC$-NO_2: O. H. Abed, N. S. Isaacs, *J. Chem. Soc. Perkin Trans. 2* **1983**, 839 – 842. Since the electrophilicity parameter of (4-$Me_2NC_6H_4)_2PhC^+$ ($E = -10.29$, ref. [8b]) is comparable to that of **1a** ($E = -10.04$), the rate constant reported by Isaacs for the reaction of (4-$Me_2NC_6H_4)_2PhC^+$ with NO_2^- in acetonitrile is more than six orders of magnitude smaller than expected for the formation of either (4-$Me_2NC_6H_4)_2PhC$-NO_2 or (4-$Me_2NC_6H_4)_2PhC$-ONO.

[14] Addition of NOCl to solutions of benzhydrols (**1a**–**h**)-OH in the presence of Et_3N led to the immediate development of blue color characteristic for the corresponding benzhydryl cations.

[15] a) Ph_2CH-NO_2 was reported to convert into benzophenone spontaneously: H. Feuer, H. Friedman, *J. Org. Chem.* **1975**, *40*, 187 – 190; b) For the conversion of secondary nitro compounds into ketones in the presence of NO_2^-, see: N. Kornblum, R. K. Blackwood, D. D. Mooberry, *J. Am. Chem. Soc.* **1956**, *78*, 1501 – 1504; c) A. Gissot, S. N'Gouela, C. Matt, A. Wagner, C. Mioskowski, *J. Org. Chem.* **2004**, *69*, 8997 – 9001.

[16] Preferential or exclusive formation of nitrites was reported for reactions of *tert*-alkyl halides as well as 4-methoxybenzyl bromide and 1-phenylethyl chloride with $AgNO_2$ in Et_2O (see refs. [1a,c,f]).

[17] H. Lemmetyinen, L. Lehtinen, J. Koskikallio, *Finn. Chem. Lett.* **1979**, *6*, 72 – 75.

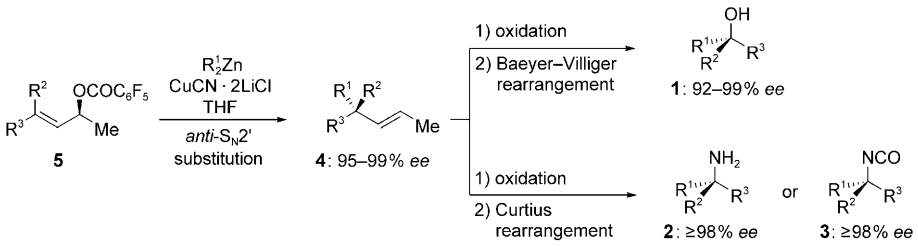
 © 2005 Wiley-VCH Verlag GmbH & Co. KGaA, Weinheim

Asymmetric Synthesis

Highly Enantioselective Preparation of Tertiary Alcohols and Amines by Copper-Mediated Diastereoselective Allylic S_N2' Substitutions**

*Helena Leuser, Sylvie Perrone, Frédéric Liron, Florian F. Kneisel, and Paul Knochel**

The asymmetric preparation of tertiary alcohols and amines is an important synthetic problem that has been the subject of numerous studies.[1,2] Copper-catalyzed S_N2' substitutions are an excellent method for setting up chiral centers in cyclic and acyclic systems.[3–5] Only a few of these reactions can be applied to the construction of quaternary carbon centers.[6] We have recently reported an efficient *anti*-S_N2' allylic substitution reaction with pentafluorobenzoates of trisubstituted allylic alcohols that produces quaternary centers with almost complete transfer of the chiral information.[7] Herein, we report applications of this method for preparing chiral tertiary alcohols **1** and amines and isocyanates such as **2** and **3**, which bear a tertiary chiral center, with high enantioselectivity starting from the chiral allylic substitution products **4**, which were obtained from the allylic pentafluorobenzoates **5** (Scheme 1).



Scheme 1. Enantioselective preparation of tertiary alcohols **1**, amines **2**, and isocyanates **3** bearing a tertiary chiral carbon center.

In a typical procedure the *E* pentafluorobenzoate **5a** (97% *ee*, entry 1 of Table 1) was treated with $Pent_2Zn$ (2 equiv) and CuCN·2 LiCl (1 equiv) in THF at −30 to −10 °C for 14 h to afford the expected *anti*-S_N2' substitution product **4a** (70%, 96% *ee*) with an almost perfect transfer of chiral information. Functionalized diorganozinc reagents such as $(EtO_2C(CH_2)_3)_2Zn$[8] reacted in a similar way providing the corresponding chiral esters **4b** (68%, 96% *ee*) and **4c** (58%, 96% *ee*) with the same level of enantioselectivity. In all these substitutions, allylic pentafluorobenzoates were used as substrates. Other allylic alcohol derivatives such as 2,6-difluorobenzoate **5c** (99% *ee*) underwent the allylic substitution with optimum enantioselectivity leading to the *E* alkene **4d** in 85% yield and 98% *ee* (entry 4). These substrates also gave excellent results with purely alkyl-substituted allylic reagents such as **5d** (99% *ee*, entry 5). In this case, the substitution with Et_2Zn provided the *E* alkene **4e** (80%, 96% *ee*) bearing a quaternary center with three different alkyl substituents. Although allylic acetates react only sluggishly with diorganozinc reagents, in the case of the allylic acetate **5e** (97% *ee*), which bears small substituents (Me and Et) at the double bond, an efficient substitution with $Pent_2Zn$ took place providing the *E* alkene **4f** in 60% yield and 95% *ee*.

This substitution reaction proceeded with a reliable transfer of chirality (entries 7 and 8) and was also performed with secondary diorganozinc reagents like iPr_2Zn to furnish the sterically hindered alkene **4i** (73%, 95% *ee*; entry 9). Interestingly, functionalized allylic pentafluorobenzoates such as **5i** (99% *ee*) and **5j** (99% *ee*) provided useful chiral building blocks like **4j** (69%), **4k** (90%), and **4l** (80%) in enantiomerically pure form (99% *ee*; entries 10–12).

With the chiral alkenes of type **4** in hand, we then developed a straightforward oxidation sequence for the conversion of chiral alkenes **4** to either the corresponding aldehydes **12** or carboxylic acids **13** (Scheme 2). The former intermediate undergoes stereoselective Baeyer–Villiger rearrangement[9] to afford the chiral tertiary alcohol **1**, and the latter undergoes stereoselective Curtius rearrangement[10] leading to the isocyanates **3**, which can be converted to the corresponding amines **2**. In this way the ozonolysis of the alkene **4d** followed by a reductive workup (PPh_3, −78 to 25 °C, 2 h) provided the aldehyde **12a** in 85% overall yield and 98% *ee*. Treatment of **12a** with MCPBA (3 equiv, Na_2HPO_4, CH_2Cl_2, RT, 2 h) furnished, after saponification of the intermediate formyl ester, the tertiary alcohol **1a** (70%, 97% *ee*) with perfect retention of configuration (entry 1 of Table 2). Alternatively, the conversion of **4d** to the corresponding carboxylic acid **13a** (entry 2) was achieved when the ozonolysis was followed by a Jones oxidation. Heating **13a** with $(PhO)_2P(O)N_3$ in toluene for 1 h in the presence of Et_3N afforded an intermediate isocyanate, which was converted to the corresponding chiral amine **2a** (20% HCl, reflux, 18 h, 65%, 98% *ee*) with very high retention of the configuration for the chiral tertiary center.

These reaction sequences proved to be general, and the alkenes **4e** (96% *ee*) and **4g** (98% *ee*) afforded the alcohols **1b** (76%, 92% *ee*; entry 3) and **1c** (68%, 93% *ee*; entry 4), respectively, and the isocyanate **3a** (68%, 98% *ee*). Polyfunc-

[*] Dr. H. Leuser, Dipl.-Chem. S. Perrone, Dr. F. Liron, Dr. F. F. Kneisel, Prof. Dr. P. Knochel
Department Chemie
Ludwig-Maximilians-Universität München
Butenandtstrasse 5–13, Haus F, 81377 München (Germany)
Fax: (+49) 89-2180-77680
E-mail: paul.knochel@cup.uni-muenchen.de

[**] We thank the Fonds der Chemischen Industrie, the Deutsche Forschungsgemeinschaft (DFG), and Merck Research Laboratories (MSD) for financial support. We also thank Chemetall GmbH (Frankfurt) and BASF AG (Ludwigshafen) for generous gifts of chemicals.

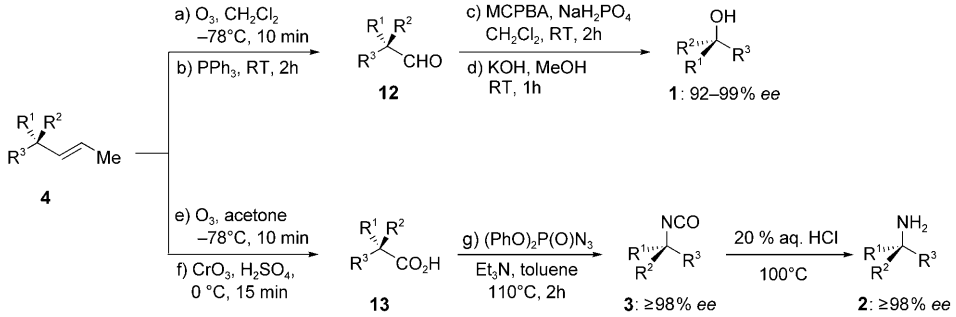
Supporting information for this article is available on the WWW under http://www.angewandte.org or from the author.

 DOI: 10.1002/anie.200500672 © 2005 Wiley-VCH Verlag GmbH & Co. KGaA, Weinheim

Table 1: Products **4** resulting from the copper-mediated *anti*-S_N2' substitution of pentafluorobenzoates **5** with diorganozinc reagents.

Entry	Allyl substrate (*ee* [%][a])	Product	Yield [%][b]	*ee* [%][a]	Entry	Allyl substrate (*ee* [%][a])	Product	Yield [%][b]	*ee* [%][a]
1	**5a** (97)	**4a**: R = Pent	70	96	7	**5f** (99)	**4g**	88	98
2	**5a** (97)	**4b**: R = $(CH_2)_3CO_2Et$	68	96					
3	**5b** (98)	**4c**	58	96	8[c]	**5g** (97)	**4h**	90	95
4	**5c** (99)	**4d**	85	98	9	**5h** (99)	**4i**	73	95
5	**5d** (99)	**4e**	80	96	10	**5i** (99)	**4j**: R = Et	69	99
					11	**5i** (99)	**4k**: R = Pent	90	99
6	**5e** (97)	**4f**	60	95	12	**5j** (99)	**4l**	80	99

[a] The enantiomeric excess was determined by HPLC or GC analysis. In each case the racemic product was also prepared for HPLC or GC calibration. [b] Yield of analytically pure product. [c] In this case the reaction was performed in a 2:1 THF/*N*-methylpyrrolidinone.



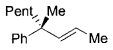
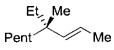
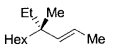
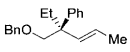
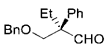
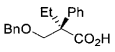
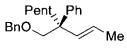
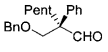
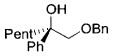
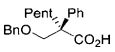
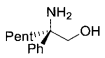
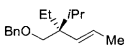
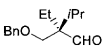
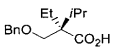
Scheme 2. Oxidation–rearrangement sequence for the preparation of chiral tertiary alcohols.

tional products such as selectively protected 1,2-diols bearing a tertiary hydroxyl group can be readily prepared starting from the chiral homoallylic benzyl ethers **4j** (99% *ee*), **4k** (99% *ee*) and **4l** (99% *ee*). After ozonolysis, the intermediate aldehydes **12d** (62%, 99% *ee*; entry 6), **12e** (66%, 99% *ee*; entry 8), and **12f** (71%, 99% *ee*; entry 10) were submitted to the Baeyer–Villiger reaction to provide the mono-protected diols **1d** (70%, 99% *ee*), **1e** (77%, 98% *ee*), and **1f** (93%, 96% *ee*), respectively. By performing the Curtius rearrangement on the corresponding carboxylic acids **13c** (65%, 99% *ee*; entry 7), **13d** (60%, 99% *ee*; entry 9), and **13e** (85%, 99% *ee*; entry 11), we obtained the amino alcohols **2b** (60%, 99% *ee*), and **2c** (88%, 99% *ee*), respectively, as well as the isocyanate **3b** (79%, 99% *ee*).

As an application of this methodology, we prepared the chiral 1,2-diol **14**, which is a key intermediate in the synthesis of the combined NK_1 and NK_2 tachykinin receptor antagonist (Scheme 3).[11] Thus, the S_N2' substitution of **5i** with $(PivO(CH_2)_3)_2Zn$ in the presence of CuCN·2 LiCl provided the chiral alkene **15** in 60% yield and 98% *ee*. The ozonolysis of **15** followed by reductive workup afforded the chiral aldehyde in 76% yield and 98% *ee*. Baeyer–Villiger oxidation of **16** in the presence of NaH_2PO_4 in CH_2Cl_2 followed by the saponification of the two ester functions gave the diol **17** in 70% yield. Quantitative protection of the remote primary hydroxy function as a TBDMS-silyl ether provided an intermediate alcohol, which underwent hydrogenolysis over Pd/C in 2-propanol (H_2 (1 atm), 25°C, 1 h) to furnish the

 © 2005 Wiley-VCH Verlag GmbH & Co. KGaA, Weinheim

Table 2: Tertiary alcohols **1** obtained by oxidation followed by Baeyer–Villiger rearrangement and chiral isocyanates **3** and amines **2** obtained by oxidation followed by Curtius rearrangement.

Entry	Alkene	Intermediate	Yield [%][b]	*ee* [%][a]	Product	Yield [%][b]	*ee* [%][a]
1	 **4d**	 **12a**	85	98	 **1a**	70	97
2	**4d**	 **13a**	79	98	 **2a**	65	98
3	 **4e**	 **12b**	63	96	 **1b**	76	92
4	 **4g**	 **12c**	65	98	 **1c**	68	93
5	**4g**	 **13b**	68	98	 **3a**	68	98
6	 **4j**	 **12d**	62	99	 **1d**	70	99
7	**4j**	 **13c**	65	99	 **2b**	60	99
8	 **4k**	 **12e**	66	99	 **1e**	77	98
9	**4k**	 **13d**	60	99	 **2c**	88	99
10	 **4l**	 **12f**	71	99	 **1f**	93	96
11	**4l**	 **13e**	85	99	 **3b**	79	99

[a] The enantiomeric excess was determined by HPLC or GC analysis. In each case the racemic product was also prepared for HPLC or GC calibration. [b] Yield of isolated analytically pure product.

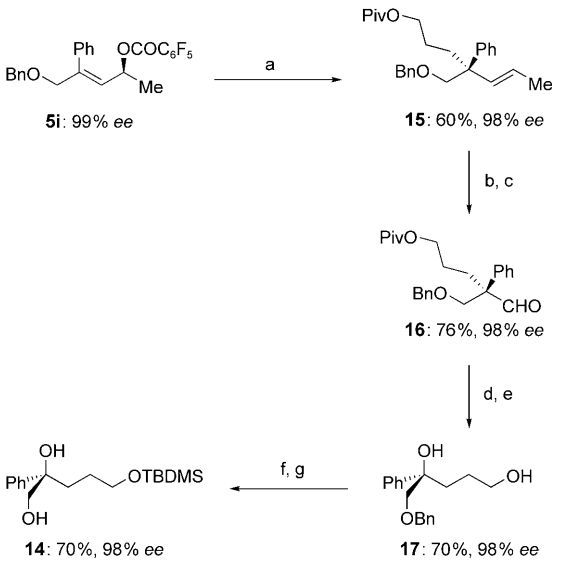
expected product **14**, an intermediate in the synthesis of a tachykinin receptor antagonist.

In summary, we have developed a straightforward sequence for the synthesis of tertiary alcohols with high enantioselectivity. We have shown that a Curtius rearrangement on the corresponding chiral carboxylic acids provides a stereoselective approach to amines bearing a tertiary center and to amino alcohol derivatives. Further applications of this method to the preparation of polyfunctional chiral building blocks are currently underway in our laboratories.

Experimental Section

Typical procedure for the copper(I)-mediated allylic substitution of fluorobenzoates with dialkylzinc reagents: **4d**:[7a]: $Pent_2Zn$ (2.35 mL, 11.3 mmol, 2.4 equiv) was added at −30 °C to a solution of CuCN·2-LiCl (5.6 mL, 5.6 mmol, 1.2 equiv, 1 M in THF) stirred under argon. The resulting mixture was stirred for 0.5 h at −30 °C, then **5c** (4.7 mmol in THF (2 mL), 1.0 equiv) was added dropwise. The reaction mixture was allowed to warm to −10 °C within 1.5 h and was stirred at −10 °C for 14 h. The reaction mixture was quenched by addition of aq. sat. NH_4Cl (5 mL) and was then poured into 25% aq. ammonia (2 mL), aq. sat. NH_4Cl (100 mL), and Et_2O (100 mL). After extraction with Et_2O (3 × 100 mL), the combined extracts were washed with brine (100 mL) and dried ($MgSO_4$). The solvents were

 © 2005 Wiley-VCH Verlag GmbH & Co. KGaA, Weinheim



Scheme 3. Preparation of the diol **14**, an intermediate in the synthesis of the tachykinin receptor antagonist. a) $(PivO(CH_2)_3)_2Zn$, CuCN·2 LiCl, THF, −30→−10 °C, 16 h; b) O_3, CH_2Cl_2, −78 °C; c) PPh_3, RT, 2 h; d) MCPBA, NaH_2PO_4, CH_2Cl_2, RT, 2 h; e) LiOH, MeOH, RT, 5 h; f) TBDMSCl, imidazole, DMF, RT, 5 h; g) 1 atm H_2, Pd/C, *i*PrOH, RT, 1 h. MCPBA = *meta*-chloroperbenzoic acid, TBDMS = *tert*-butyldimethylsilyl.

removed by evaporation and the residue purified by column chromatography to yield alkene **4d** (855 mg, 3.96 mmol, 85 %) as a colorless liquid.

Typical procedure for the oxidation[12] and Baeyer–Villiger rearrangement[9] sequence: **1a**: Ozone was passed through a solution of alkene **4d** (260 mg, 1.20 mmol, 1.0 equiv) in CH_2Cl_2 (30 mL) at −78 °C under N_2 until the solution turned blue (3–10 min); excess O_3 was removed with a stream of N_2. PPh_3 (408 mg, 1.5 mmol, 1.3 equiv) was added in one portion, and the mixture was warmed to 20 °C within 2 h. The reaction mixture was then diluted with Et_2O (10 mL) and washed with water and brine, and then dried ($MgSO_4$). The solvents were removed by evaporation in vacuo, and the residue was purified by column chromatography to give **12a** (194 mg, 0.95 mmol, 85 %, 98 % *ee*) as a colorless liquid. The enantiomeric excess was determined by GC analysis (column: Chiraldex B-PH; 100 °C (30 min), 0.5° min^{-1} until 120 °C: t_R = 78.3 (*R*), 79.7 min^{-1} (*S*)). To a solution of aldehyde **12a** (163 mg, 0.80 mmol, 1.0 equiv) in CH_2Cl_2 (2 mL) was added anhydrous MCPBA (260 mg, 1.2 mmol, 1.5 equiv). The reaction was stirred at room temperature for 24 h before it was quenched with water and extracted with Et_2O (3 × 50 mL). The combined organic layers were dried ($MgSO_4$), concentrated in vacuo, and purified by flash chromatography (pentane/Et_2O = 98:2). (2*S*)-2-phenylheptan-2-yl formate (123 mg, 70 %) was obtained as a colorless liquid. To a solution of (2*S*)-2-phenylheptan-2-yl formate (123 mg, 0.56 mmol, 1.0 equiv) in MeOH (2 mL) was added KOH (62 mg, 1.12 mmol, 2.0 equiv). The reaction mixture was stirred at 20 °C for 1 h, then diluted with Et_2O (10 mL), washed with brine, dried ($MgSO_4$), and concentrated in vacuo. Purification by flash chromatography (pentane/Et_2O = 9:1) yielded **1a** (75 mg, 0.39 mmol, 70 %, 97 % *ee*) as a colorless oil. The enantiomeric excess was determined by GC analysis (column: chiraldex B-PH; 100 °C (30 min), 0.5° min^{-1}, 120 °C (60 min)): t_R = 78.3 (*S*), 79.7 min^{-1} (*R*)). Na_2HPO_4 (1 equiv) can be used as a buffer in order to enhance the rate of the reaction (reaction time reduced to 2 h at 20 °C) and to improve the *ee* value. See the Supporting Information for the preparation of compounds **1b** and **1c**.

Typical procedure for the oxidation[12] and Curtius rearrangement:[10] **2a**: Ozone was passed through a solution of alkene **4d** (432 mg, 2.00 mmol, 1.0 equiv) in acetone (10 mL) at −78 °C under N_2 until the solution turned blue (3–10 min); excess O_3 was removed by a stream of nitrogen. The reaction mixture was cooled to 0 °C, and Jones reagent (2.0 mL, 2.67 M, 5.4 mmol, 2.7 equiv) was added dropwise until the orange color persisted. The mixture was stirred for 1 h at 20 °C, then *i*PrOH (8 mL) was added until the mixture turned green. The solvents were removed by evaporation, and the residue was dissolved in water/ (100 mL, 1:4). After acid–base workup[12c] the desired carboxylic acid **13a** (348 mg, 1.58 mmol, 79 %) was obtained as a colorless liquid. A mixture of **13a** (124 mg, 0.56 mmol, 1.0 equiv), $(PhO)_2P(O)N_3$ (231 mg, 0.84 mmol, 1.5 equiv) and NEt_3 (85 mg, 0.84 mmol, 1.5 equiv) in toluene (5 mL) was heated at reflux for 2 h. After removal of the solvent by evaporation in vacuo, the residue was taken up in ether (50 mL) and washed with water (3 × 50 mL). The organic layer was dried ($MgSO_4$), concentrated in vacuo, and purified by flash chromatography (pentane/Et_2O = 98:2). 1-((2*S*)-2-Isocyanatoheptan-2-yl)benzene (120 mg, quant., 98 % *ee*) was obtained as a colorless liquid. The enantiomeric excess was determined by GC analysis (column: Chiraldex B-PH; 100 °C const.: t_R = 57.8 (*S*), 61.9 min^{-1} (*R*)). 1-((2*S*)-2-isocyanatoheptan-2-yl)benzene (50 mg, 0.23 mmol) was heated at reflux in 20 % aq. HCl (5 mL) for 24 h. The reaction mixture was partitioned in Et_2O and water (4:1), and the layers were separated. The aqueous layer was treated with NaOH (20 %) and extracted with Et_2O (3 × 80 mL). The organic layer was dried ($MgSO_4$) and the solvent evaporated in vacuo to give **2a** (30 mg, 0.16 mmol, 65 %, 98 % *ee*) as a colorless oil.

Received: February 22, 2005

Keywords: allylic substitution · asymmetric synthesis · copper · rearrangements · zinc

[1] a) D. J. Ramon, M. Yus, *Angew. Chem.* **2004**, *116*, 286; *Angew. Chem. Int. Ed.* **2004**, *43*, 284; b) B. Weber, D. Seebach, *Angew. Chem.* **1992**, *104*, 96; *Angew. Chem. Int. Ed. Engl.* **1992**, *31*, 84; c) B. Weber, D. Seebach, *Tetrahedron* **1994**, *50*, 6117; d) P. I. Dosa, G. C. Fu, *J. Am. Chem. Soc.* **1998**, *120*, 445; e) C. Bolm, J. P. Hildebrand, K. Muniz, N. Hermanns, *Angew. Chem.* **2001**, *113*, 3382; *Angew. Chem. Int. Ed.* **2001**, *40*, 3284; f) P. G. Cozzi, *Angew. Chem.* **2003**, *115*, 3001; *Angew. Chem. Int. Ed.* **2003**, *42*, 2895; g) B. Jiang, Z. Chen, X. Tang, *Org. Lett.* **2002**, *4*, 3451; h) D. J. Ramon, M. Yus, *Tetrahedron Lett.* **1998**, *39*, 1239; i) D. J. Ramon, M. Yus, *Tetrahedron* **1998**, *54*, 5651; j) M. Yus, D. J. Ramon, O. Prieto, *Tetrahedron: Asymmetry* **2003**, *14*, 1103; k) C. Garcia, L. K. Larochelle, P. J. Walsh, *J. Am. Chem. Soc.* **2002**, *124*, 10970; l) S.-J. Jeon, P. J. Walsh, *J. Am. Chem. Soc.* **2003**, *125*, 9544; m) M. Yus, D. J. Ramon, O. Prieto, *Tetrahedron: Asymmetry* **2002**, *13*, 2291; n) M. Yus, D. J. Ramon, O. Prieto, *Eur. J. Org. Chem.* **2003**, 2745; o) O. Prieto, D. J. Ramon, M. Yus, *Tetrahedron: Asymmetry* **2003**, *14*, 1955; p) C. Garcia, P. J. Walsh, *Org. Lett.* **2003**, *5*, 3641; q) E. F. DiMauro, M. C. Kozlowski, *J. Am. Chem. Soc.* **2002**, *124*, 12668; r) E. F. DiMauro, M. C. Kozlowski, *Org. Lett.* **2002**, *4*, 3781.

[2] a) J. L. Wood, G. A. Moniz, D. A. Pflum, B. M. Stoltz, A. A. Holubec, H.-J. Dietrich, *J. Am. Chem. Soc.* **1999**, *121*, 1784; b) D. A. Cogan, J. A. Ellman, *J. Am. Chem. Soc.* **1999**, *121*, 268; c) H. Li, P. J. Walsh, *J. Am. Chem. Soc.* **2004**, *126*, 6538; d) E. Cleator, C. F. McCusker, F. Steltzer, S. V. Ley, *Tetrahedron Lett.* **2004**, *45*, 3077; e) B. M. Trost, N. G. Andersen, *J. Am. Chem. Soc.* **2002**, *124*, 14320; f) S. Casolari, D. D'Addario, E. Tagliavini, *Org. Lett.* **1999**, *1*, 1061.

[3] a) B. H. Lipshutz, S. Sengupta, *Org. React.* **1992**, *41*, 135; b) P. Rona, L. Tökes, J. Tremble, P. Crabbé, *J. Chem. Soc. Chem. Comun.* **1969**, 43; c) R. J. Anderson, C. A. Henrick, J. B. Siddall,

 © 2005 Wiley-VCH Verlag GmbH & Co. KGaA, Weinheim

R. Zurflüh, *J. Am. Chem. Soc.* **1972**, *94*, 5379; d) C. C. Tseng, S. D. Paisley, H. L. Goering, *J. Org. Chem.* **1986**, *51*, 2884; e) T. L. Underiner, H. L. Goering, *J. Org. Chem.* **1991**, *56*, 2563; f) N. Krause, A. Gerold, *Angew. Chem.* **1997**, *109*, 194; *Angew. Chem. Int. Ed. Engl.* **1997**, *36*, 186.

[4] a) Y. Yamamoto, S. Yamamoto, H. Yatagai, K. Maruyama, *J. Am. Chem. Soc.* **1980**, *102*, 2318; b) E. Nakamura, K. Sekiya, M. Arai, S. Aoki, *J. Am. Chem. Soc.* **1989**, *111*, 3091; c) M. Arai, B. H. Lipshutz, E. Nakamura, *Tetrahedron* **1992**, *48*, 5709; d) M. Arai, E. Nakamura, B. H. Lipshutz, *J. Org. Chem.* **1991**, *56*, 5489; e) M. Arai, T. Kawasuji, E. Nakamura, *J. Org. Chem.* **1993**, *58*, 5121; f) M. Arai, T. Kawasuji, E. Nakamura, *Chem. Lett.* **1993**, 357; g) A. Yanagisawa, Y. Noritake, N. Nomura, H. Yamamoto, *Synlett* **1991**, 251; h) A. S. E. Karlström, J.-E. Bäckvall in *Modern Organocopper Chemistry* (Ed.: N. Krause), Wiley-VCH, Weinheim, Germany, **2001**, p. 259.

[5] a) B. Breit, P. Demel, *Adv. Synth. Catal.* **2001**, *343*, 429; b) B. Breit, P. Demel, *Tetrahedron* **2000**, *56*, 2833; c) B. Breit, S. K. Zahn, *Polyhedron* **2000**, *19*, 513; d) J. L. Belelie, J. M. Chong, *J. Org. Chem.* **2001**, *66*, 5552; e) T. Ibuka, H. Habashita, A. Otaka, N. Fujii, Y. Oguchi, T. Uyehara, Y. Yamamoto, *J. Org. Chem.* **1991**, *56*, 4370; f) Y. Yamamoto, M. Tanaka, T. Ibuka, Y. Chounan, *J. Org. Chem.* **1992**, *57*, 1024; g) J. P. Marino, A. Viso, J.-D. Lee, R. Fernandez de la Pradilla, P. Fernandez, M. B. Rubio, *J. Org. Chem.* **1997**, *62*, 645; h) J. H. Smitrovich, K. A. Woerpel, *J. Org. Chem.* **2000**, *65*, 1601; i) C. Spino, C. Beaulieu, J. Lafreniere, *J. Org. Chem.* **2002**, *67*, 7091; For copper-catalyzed reactions using a chiral ligand, see: j) M. van Klaveren, E. S. M. Persson„ A. del Villar, D. M. Grove, J.-E. Bäckvall, G. van Koten, *Tetrahedron Lett.* **1995**, *36*, 3059; k) A. S. E. Karlström, F. F. Huerta, G. J. Meuzelaar, J.-E. Bäckvall, *Synlett* **2001**, 923; l) G. J. Meuzelaar, A. S. E. Karlström, M. van Klaveren, E. S. M. Persson, A. del Villar, G. van Koten, J.-E. Bäckvall, *Tetrahedron* **2000**, *56*, 2895; m) F. Dübner, P. Knochel, *Angew. Chem.* **1999**, *111*, 391; *Angew. Chem. Int. Ed.* **1999**, *38*, 379; n) F. Dübner, P. Knochel, *Tetrahedron Lett.* **2000**, *41*, 9233; o) A. Alexakis, C. Malan, L. Lea, C. Benhaim, X. Fourniou, *Synlett* **2001**, 927; p) A. Alexakis, K. Croset, *Org. Lett.* **2002**, *4*, 4147; q) H. Malda, A. W. Van Zijl, L. A. Arnold, B. L. Feringa, *Org. Lett.* **2001**, *3*, 1169; r) C. A. Luchaco-Cullis, H. Mizutani, K. E. Murphy, A. H. Hoveyda, *Angew. Chem.* **2001**, *113*, 1504; *Angew. Chem. Int. Ed.* **2001**, *40*, 1456.

[6] For recent examples, see: a) B. Breit, P. Demel, C. Studte, *Angew. Chem.* **2004**, *116*, 3874; *Angew. Chem. Int. Ed.* **2004**, *43*, 3785; see also: b) B. Breit, C. Herber, *Angew. Chem.* **2004**, *116*, 3878; *Angew. Chem. Int. Ed.* **2004**, *43*, 3790.

[7] a) N. Harrington-Frost, H. Leuser, M. I. Calaza, F. F. Kneisel, P. Knochel, *Org. Lett.* **2003**, *5*, 2111; see also: b) D. Soorukram, P. Knochel, *Org. Lett.* **2004**, *6*, 2409; c) M. I. Calaza, E. Hupe, P. Knochel, *Org. Lett.* **2003**, *5*, 1059.

[8] P. Knochel, N. Millot, A. L. Rodriguez, C. E. Tucker, *Org. React.* **2001**, *58*, 417.

[9] a) I. M. Godfrey, M. V. Sargent, J. A. Elix, *J. Chem. Soc. Perkin Trans. 1*, **1974**, 1353; b) P. F. Hudelik, G. Nagendrappa, T. Yimenu, E. T. Zeller, E. Chin, *J. Am. Chem. Soc.* **1980**, *102*, 6894.

[10] a) T. Shiori, K. Ninomiya, S. Yamada, *J. Am. Chem. Soc.* **1972**, *94*, 6203; b) J. M. Elliott, M. Jason, J. L. Castro, G. G. Chicchi, L. C. Cooper, K. Dinnell, G. J. Hollingworth, M. P. Ridgill, W. Rycroft, M. M. Kurtz, D. E. Shaw, C. J. Swain, K.-L. Tsao, L. Yang, *Bioorg. Med. Chem. Lett.* **2002**, *12*, 1755.

[11] T. Nishi, T. Fukazawa, K. Ishibashi, K. Nakajima, Y. Sugioka, Y. Iio, H. Kurata, K. Ithoh, O. Mukaiyama, Y. Satoh, T. Yamaguchi, *Bioorg. Med. Chem. Lett.* **1999**, *9*, 875.

[12] a) O. Lorenz, C. R. Parks, *J. Org. Chem.* **1965**, *30*, 1976; b) D. P. Higley, R. W. Murray, *J. Am. Chem. Soc.* **1976**, *98*, 4526; c) J. L. Belelie, J. M. Chong, *J. Org. Chem.* **2001**, *66*, 5552.

 © 2005 Wiley-VCH Verlag GmbH & Co. KGaA, Weinheim

Protein Folding

^{13}C-Labeled Tyrosine Residues as Local IR Probes for Monitoring Conformational Changes in Peptides and Proteins**

Sandra Tremmel, Michael Beyermann, Hartmut Oschkinat, Michael Bienert, Dieter Naumann, and Heinz Fabian**

Fourier transform infrared (FTIR) spectroscopy has become a valuable tool for studying the secondary structure of proteins and for monitoring conformational changes associated with protein unfolding, folding, and misfolding.[1–3] Most studies in the past have focused on components of the intense amide I band (primarily the C=O stretch of the secondary amide group) in the IR spectra between 1610 and 1700 cm^{-1} as established indicators of protein secondary structure. Besides the amide I band of the peptide backbone, several amino acid side-chain absorption bands may serve as intrinsic local monitors of conformational changes. Very useful is the relatively strong absorption band of the tyrosine side chain (C–C stretching vibration of the aromatic ring) at $\approx$1515 cm^{-1}, which can be distinguished particularly well in the infrared spectra of proteins.[4] The frequency of this band may change in a characteristic manner upon unfolding, folding, and aggregation of proteins. For proteins whose unfolding is reversible, a discontinuous high-frequency shift of the tyrosine vibration around the corresponding denaturation temperatures was observed.[5–7] In a structureless peptide, the tyrosine band displayed only a minor gradual shift to lower wavenumbers upon increasing temperature, reflecting a general effect of temperature.[5] A relatively large downshift of the tyrosine vibration was observed for proteins upon aggregation, which has been suggested as indicative of stronger hydrogen bonds of the tyrosine OH group with acceptors in the protein aggregates.[6,8] However, if the corresponding peptide or protein contains more than one tyrosine residue, the site-specific information is limited. Removal of all but one of the tyrosine residues by site-directed mutagenesis is one possible solution to this problem. However, if the corresponding residues are, for example, part

[*] S. Tremmel, Dr. M. Beyermann, Prof. H. Oschkinat, Prof. M. Bienert
Forschungsinstitut für Molekulare Pharmakologie
Robert-Rössle-Strasse 10, 13125 Berlin (Germany)
Fax: (+49) 30-9479-3159
E-mail: tremmel@fmp-berlin.de

Prof. D. Naumann, Dr. H. Fabian
Robert-Koch-Institut
Nordufer 20, 13353 Berlin (Germany)
Fax: (+49) 30-4547-2606
E-mail: fabianh@rki.de

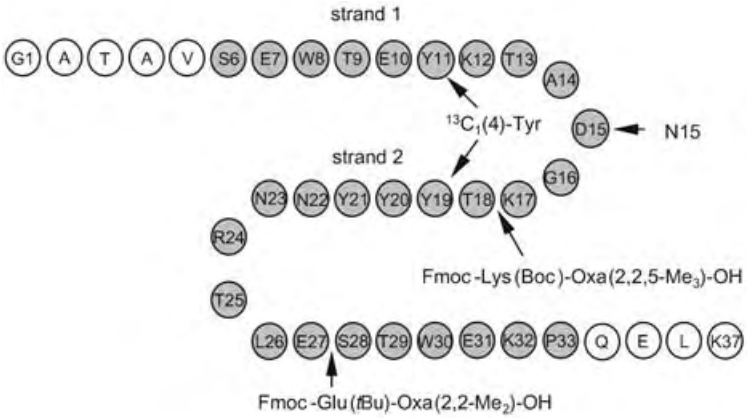
[**] The work at the Forschungsinstitut für Molekulare Pharmakologie was supported by the Deutsche Forschungsgemeinschaft (DFG-FOR 299). We thank Annerose Klose and Bernhard Schmikale for their assistance with the peptide synthesis.

Supporting information for this article is available on the WWW under http://www.angewandte.org or from the author.

 DOI: 10.1002/anie.200500547 © 2005 Wiley-VCH Verlag GmbH & Co. KGaA, Weinheim

of the hydrophobic core of the protein, mutating them may destabilize the protein and/or affect its function. Herein we demonstrate that an ideal alternative to site-directed mutagenesis is site-directed isotope labeling, such as the introduction of individual tyrosine residues labeled with ^{13}C at the C4 position of the phenol ring. Consequently site-specific structural specificity is added to the spectrum since the vibration of the labeled residue is shifted by $\approx 10\ cm^{-1}$,[9] thus providing a well separated unique spectroscopic signature. While isotopic labeling of tyrosines to probe proteins by IR spectroscopy is not new, the current application to obtain information on the microenvironment of distinct tyrosine side chains and to monitor simultaneously local conformational changes in different regions of proteins is novel.

To explore the potential of site-directed isotope labeling, we studied changes in the infrared-spectroscopic behavior of distinct tyrosine residues caused by the thermal unfolding of the formin-binding protein 28 (FBP28) WW domain. This protein contains four tyrosine residues, one located in strand 1 (position 11), whereas the remaining three (at positions 19, 20, and 21) are located in strand 2 (Scheme 1, peptide **1** in Table 1). WW domains are the smallest naturally occurring three-stranded β sheets identified so far. They are named after the two conserved tryptophan residues and function as noncatalytic domains of signaling proteins by recognizing proline-containing ligands.[10] Recently, several WW domains served as model systems for studies of β-sheet stability and folding.[11–19] Among them, the FBP28WW domain was reported to be monomeric and stable, although under certain conditions aggregation and even fibril formation have been observed.[18]



Scheme 1. Structural features of the FBP28WW domain. The sequence 6–33 (gray) forms a defined three-dimensional structure, including three strands and two loops.[11] The locations for the application of pseudo-proline building blocks to enable the successful synthesis and the positions for $^{13}C_1$(4)-tyrosine labeling are indicated (Oxa = Ser/Thr-derived oxazolidine-4-carboxylic acid).

Table 1: Sequences of FBP28WW peptides (*Y = $^{13}C_1$(4)-Tyr).

Peptide		Sequence
FBP28WW	**1**	GATAVSEWTEYKTADGKTYYYNNRTLESTWEKPQELK
[N^{15}]-FBP28WW[a]	**2**	GATAVSEWTEYKTANGKTYYYNNRTLESTWEKPQELK
[Q^{9,21,23,26,28},N^{15}]-FBP28WW[a]	**3**	GATAVSEWQEYKTANGKTYYQNQRTQEQTWEKPQELK
[Q^{9,21,23,26,28},F^{11,20},N^{15}]-FBP28WW	**4**	GATAVSEWQEFKTANGKTYFQNQRTQEQTWEKPQELK
[*Y^{11},Q^{9,21,23,26,28},N^{15}]-FBP28WW[a]	**5**	GATAVSEWQE*YKTANGKTYYQNQRTQEQTWEKPQELK
[*Y^{19},Q^{9,21,23,26,28},N^{15}]-FBP28WW[a]	**6**	GATAVSEWQEYKTANGKT*YYQNQRTQEQTWEKPQELK

[a] Amidated at the C terminus.

The preparation of WW analogues, including the incorporation of labeled amino acids, should be feasible by solid-phase peptide synthesis (SPPS).[20] However, initial attempts to synthesize wild-type FBP28WW (peptide **1**) by SPPS failed, which is not unexpected for the assembly of β-sheet-forming sequences.[21] Fortunately, the synthesis could be improved considerably by insertion of two X-Ser and X-Thr dipeptides (X = pseudo-proline) in the form of the corresponding pseudo-proline derivatives.[22] In addition, aspartate in position 15 was replaced by asparagine (peptide **2**) in order to minimize the high propensity for aspartimide formation[23] of the Asp15-Gly16 unit (Scheme 1; see the Supporting Information).

The low-temperature IR spectra (Figure 1a, blue traces) of the [Asn^{15}]-FBP28WW variant (peptide **2**) recorded between 10 and 90 °C during the course of a thermal denaturation experiment (see the Supporting Information) are characterized by a major amide I band centered at $1636\ cm^{-1}$ and a weaker band component at $1679\ cm^{-1}$, indicating the presence of antiparallel β-sheet structures.[1–3] The infrared bands between 1500 and $1612\ cm^{-1}$ are due to absorptions of amino acid side chains: tyrosine (1515 and $1612\ cm^{-1}$), glutamate ($1565\ cm^{-1}$), and arginine ($1587\ cm^{-1}$).[4] The amide I region of the spectrum recorded at 90 °C is dominated by bands at 1616 and $1685\ cm^{-1}$ (Figure 1a, black trace). These bands are characteristic of intermolecular β-sheet structures,[1–3] indicating that thermal denaturation of the [Asn^{15}]-FBP28WW variant involves aggregation.

During our search for FBP28WW analogues with a reduced tendency toward aggregation, we surprisingly found that insertion of Gln residues in certain positions was very successful (peptide **3**, Table 1). Peptide **3** displayed the typical fold of the FBP28WW domains when it was characterized by NMR spectroscopy[27] and did not form intermolecular β-sheet structures at high temperatures, which is indicated by the lack of the characteristic IR "aggregate" bands at 1616 and $1685\ cm^{-1}$. Instead, the high-temperature spectra of peptide **3** are dominated by a broad and featureless amide I band centered at $1648\ cm^{-1}$ (Figure 1b), indicative of structureless proteins.[1–3] This is also valid for peptide **4** (spectra not shown), in which additionally two Tyr residues have been replaced by Phe in order to permit the assignment of tyrosine-mediated spectroscopic changes to a single Tyr residue. The temperature-induced decrease in intensity of the low-frequency component of the amide band at $1636\ cm^{-1}$ (Figure 2a) and the frequency shift of the stretching vibration of tyrosine's aromatic ring at $\approx 1515\ cm^{-1}$ (Figure 2b) revealed sigmoidal unfolding transitions between 10 and 90 °C for the two peptides.

The Tyr→Phe substitution, however, decreased the denaturation temperature

 © 2005 Wiley-VCH Verlag GmbH & Co. KGaA, Weinheim

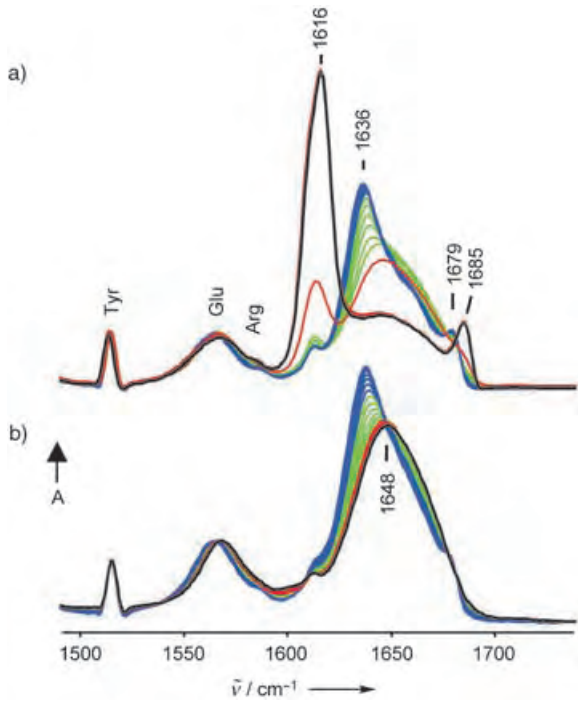


Figure 1. Deconvolved infrared spectra of a) peptide **2** and b) peptide **3** in D_2O buffer (50 mM phosphate, 50 mM sodium chloride, pD 7.6) as a function of temperature. Blue traces, 10–40 °C; green traces, 45–70 °C; red traces, 75–85 °C; black traces, 90 °C.

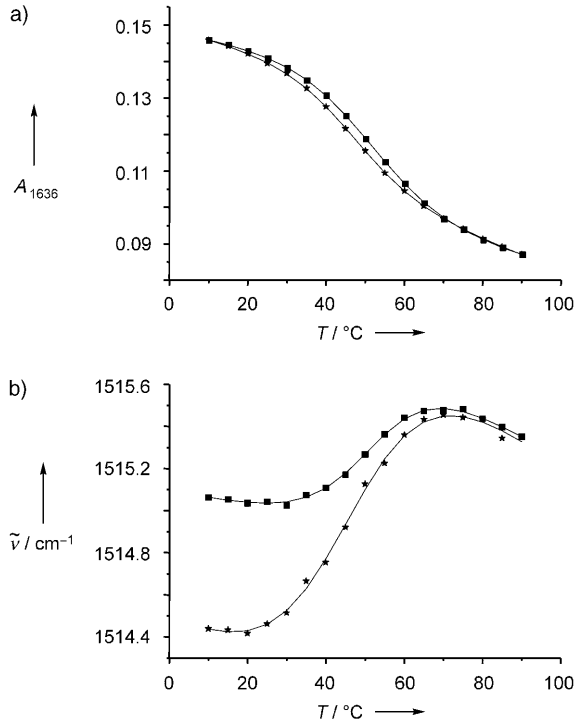


Figure 2. a) Temperature dependence of the peak intensity of the amide I band at 1636 cm^{-1} and b) temperature dependence of the position of the tyrosine band for peptide **3** (■) and peptide **4** (⋆). The peak intensities at 1636 cm^{-1} were normalized relative to the signal obtained at 90 °C. The solid lines represent the best fit used to estimate the denaturation temperatures (T_m).

by ≈5 K,[24] which demonstrates a drawback of the mutation approach. Therefore, we labeled peptide **3** with $^{13}C_1$(4)-Tyr residues site-specifically. In order to probe simultaneously temperature-induced changes in the local environment of Tyr11 located in strand 1 of the WW domain (see Scheme 1), and of Tyr19, a highly conserved residue of the second strand of WW proteins,[11] we synthesized the labeled peptides **5** and **6**. As expected, selective $^{13}C_1$(4)-labeling of Tyr11 (Figure 3, middle trace) or of Tyr19 (Figure 3, upper trace) led to a drop of intensity at 1515 cm^{-1} and the appearance of a new band at 1505 cm^{-1}.

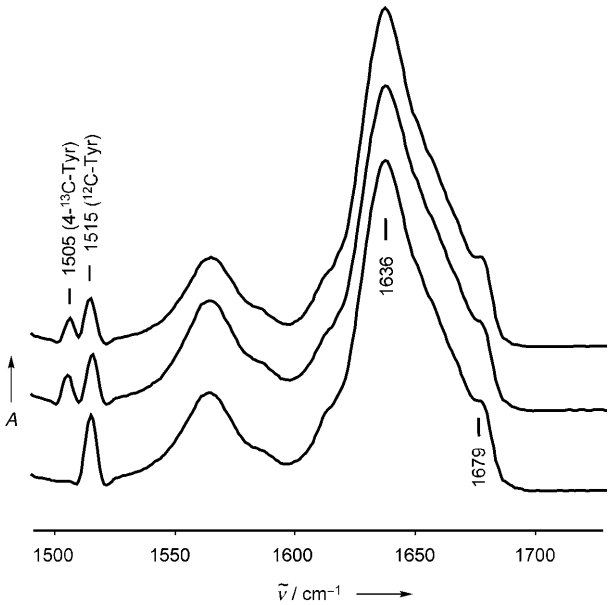


Figure 3. Deconvolved infrared absorbance spectra of unlabeled (peptide **3**, lower trace), site-specifically $^{13}C_1$(4)-Tyr11-labeled (peptide **5**, middle trace), and site-specifically $^{13}C_1$(4)-Tyr19-labeled (peptide **6**, upper trace) FBP28WW peptides in D_2O buffer (50 mM phosphate, 50 mM sodium chloride, pD 7.6) at 10 °C.

The temperatures of thermal denaturation, derived from the IR bands of Tyr11 in strand 1 and of Tyr19 in strand 2, were found to be practically identical,[25] suggesting no major differences in the thermal response of the conformational changes in both strands of the FBP28WW peptide **3**. An inspection of the transition profiles, however, revealed striking differences between the bands of the labeled Tyr11 and Tyr19 residues (Figure 4b). While the band due to Tyr11 displayed only minor frequency changes, a relatively large shift to higher frequencies by ≈0.6 cm^{-1} was observed for Tyr19. At high temperatures, the peak positions were practically identical, as expected for an unfolded peptide. Moreover, the frequency changes of less than 0.2 cm^{-1} due to labeled Tyr11 observed around the thermal denaturation temperature of peptide **5** (Figure 4b) were comparable to the minor mean spectroscopic changes due to unlabeled Tyr11 and Tyr20 in peptide **6** (Figure 4a), suggesting a very similar temperature response of Tyr11 and Tyr20. Altogether, this indicates that in the folded state of the peptides the local

 © 2005 Wiley-VCH Verlag GmbH & Co. KGaA, Weinheim

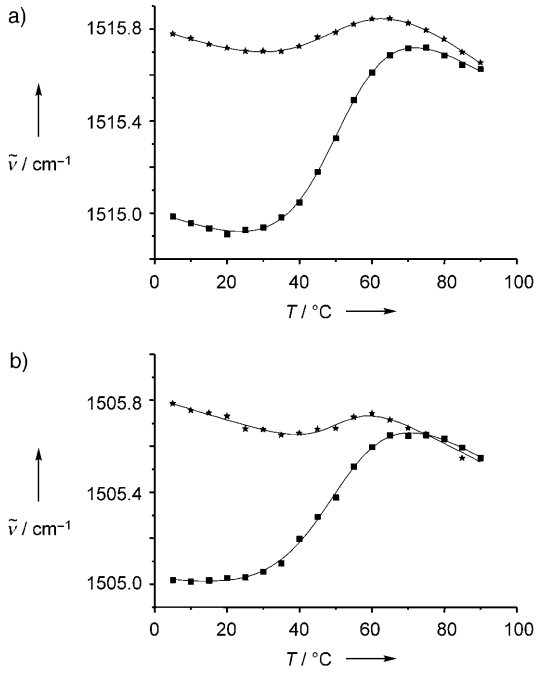


Figure 4. Temperature dependence of the position of the tyrosine bands of site-specifically $^{13}C_1(4)$-Tyr11- and $^{13}C_1(4)$-Tyr19-labeled [Gln^{9,21,23,26,28},Asn^{15}]-FBP28WW. a) Positions of the unlabeled tyrosines of peptide **5** (■) and of peptide **6** (⋆). b) Positions of the labeled tyrosine of peptide **5** (⋆) and of peptide **6** (■).

environments of Tyr19, on one side, and of Tyr11/Tyr20, on the other side, must differ considerably.

A plausible explanation for a strong shift of the tyrosine band to higher frequencies upon protein unfolding would be a strengthening of tyrosine O–H bonds, caused by loosening of hydrogen bonds between the tyrosine OH group and neighboring acceptors.[5,6] The available information on the FBP28WW structure, however, provides no hints for tyrosine OH groups being involved in hydrogen bonding. This suggests that effects other than hydrogen bonding may also affect the spectroscopic features of the corresponding ring vibration. A possible explanation may be altered π–π interactions between tyrosine rings and conjugated systems of other residues.[6,26] In the FBP28WW domain Trp30 is close to Tyr19.[11] Thus, the temperature-dependent shift of the Tyr19 side-chain band observed herein might reflect a disruption of π–π interactions between Tyr19 and the indole ring of Trp30. If so, than the infrared band of Tyr19 provides a local probe of specific interactions between residues located in strands 2 and 3 of the WW domain.

In summary, we have demonstrated that FTIR spectroscopy along with site-directed $^{13}C_1(4)$-labeling of tyrosine residues is a promising new approach to obtain information on the microenvironment of distinct tyrosine side chains and to monitor simultaneously temperature-induced local conformational changes in different regions of a given protein. In combination with time-resolved IR-spectroscopic techniques, this strategy offers novel possibilities for studying protein unfolding and folding events at the level of individual groups in a peptide or protein. We are currently conducting both peptide synthesis and spectroscopic studies in order to improve our insights into the role of the tyrosine residues in the stabilization and unfolding of the β-sheet structure of FBP28WW and other WW domains.

Received: February 14, 2005
Published online: June 24, 2005

Keywords: IR spectroscopy · isotope effects · peptide synthesis · protein folding · WW domains

[1] M. Jackson, H. H. Mantsch, *Crit. Rev. Biochem. Mol. Biol.* **1995**, *30*, 95–120.
[2] H. Fabian, W. Mäntele in *Handbook of Vibrational Spectroscopy. Infrared Spectroscopy of Proteins* (Eds.: J. M. Chalmers, P. R. Griffiths), Wiley, Chichester, **2002**, pp. 3399–3425.
[3] A. Barth, C. Zscherp, *Q. Rev. Biophys.* **2002**, *35*, 369–430.
[4] Y. N. Chirgadze, O. V. Fedorov, N. P. Trushina, *Biopolymers* **1975**, *14*, 679–694.
[5] H. Fabian, C. Schultz, J. Backmann, U. Hahn, W. Saenger, H. H. Mantsch, D. Naumann, *Biochemistry* **1994**, *33*, 10725–10730.
[6] C. Zscherp, H. Aygün, J. W. Engels, W. Mäntele, *Biochim. Biophys. Acta* **2003**, *1651*,139–145.
[7] J. Torrent, P. Rubens, M. Ribo, K. Heremans, M. Vilanova, *Protein Sci.* **2001**, *10*, 725–734.
[8] J. L. R. Arrondo, N. M. Young, H. H. Mantsch, *Biochim. Biophys. Acta* **1988**, *952*, 261–268.
[9] R. Hienerwadel, A. Boussac, J. Breton, B. A. Diner, C. Berthomieu, *Biochemistry* **1997** *36*, 14712–14723.
[10] a) M. Sudol, T. Hunter, *Cell* **2000**, *103*, 1001–1004; b) L. J. Ball, R. Kühne, J. Schneider-Mergener, H. Oschkinat, *Angew. Chem.* **2005**, *117*, 2912-–2930; *Angew. Chem. Int. Ed.* **2005**, *44*, 2852–2869.
[11] M. J. Macias, V. Gervais, C. Civera, H. Oschkinat, *Nat. Struct. Biol.* **2000**, *7*, 375–379.
[12] R. Kaul, A. R. Angeles, M. Jäger, E. T. Powers, J. W. Kelly, *J. Am. Chem. Soc.* **2001**, *123*, 5206–5212.
[13] M. Jäger, H. Nguyen, J. C. Crane, J. W. Kelly, M. Gruebele, *J. Mol. Biol.* **2001**, *311*, 373–393.
[14] a) G. T. Ibragimova, R. C. Wade, *Biophys. J.* **1999**, *77*, 2191–2198; b) N. Ferguson, J. R. Pires, F. Toepert, C. M. Johnson, Y. P. Pan, R. Volkmer-Engert, J. Schneider-Mergener, V. Daggett, H. Oschkinat, *Proc. Natl. Acad. Sci. USA* **2001**, *98*, 13008–13013.
[15] N. Ferguson, C. M. Johnson, M. Macias, H. Oschkinat, A. Fersht, *Proc. Natl. Acad. Sci. USA* **2001**, *98*, 13002–13007.
[16] J. Karanicolas, C. L. Brooks III, *Proc. Natl. Acad. Sci. USA* **2003**, *100*, 3954–3959.
[17] H. Nguyen, M. Jäger, A. Moretto, M. Gruebele, J. W. Kelly, *Proc. Natl. Acad. Sci. USA* **2003**, *100*, 3948–3953.
[18] N. Ferguson, J. Berriman, M. Petrovich, T. D. Sharpe, J. T. Finch, A. R. Fersht, *Proc. Natl. Acad. Sci. USA* **2003**, *100*, 9814–9819.
[19] S. Deechongkit, H. Nguyen, E. T*. Powers, P. E. Dawson, M. Gruebele, J. W. Kelly, *Nature* **2004**, *430*, 101–105.
[20] G. B. Fields, R. L. Noble, *Int. J. Pept. Protein Res.* **1990**, *35*, 161–214.
[21] a) M. Beyermann, M. Bienert, *Tetrahedron Lett.* **1992**, *33*, 3745–3748; b) M. Dettin, S. Pegoraro, P. Rovero, S. Bicciato, A. Bango, C. Di Bello, *J. Pept. Res.* **1997**, *49*, 103–111; c) C. Hyde, T. Johnson, D. Owen, M. Quibell, R. C. Sheppard, *Int. J. Pept. Protein Res.* **1994**, *43*, 431–440.
[22] a) T. Haack, M. Mutter, *Tetrahedron Lett.* **1992**, *33*, 1589–1592; b) T. Wöhr, F. Wahl, A. Nefzi, B. Rohwedder, T. Sato, X. Sun, M. Mutter, *J. Am. Chem. Soc.* **1996**, *118*, 9218–9227; c) W. R. Sampson, H. Patsiouras, H. J. Ede, *J. Pept. Sci.* **1999**, *5*, 403–409.
[23] a) E. Nicolas, E. Pedroso, E. Giralt, *Tetrahedron Lett.* **1989**, *30*, 497–500; b) R. Dölling, M. Beyermann, J. Haenel, F. Kernchen,

 © 2005 Wiley-VCH Verlag GmbH & Co. KGaA, Weinheim

E. Krause, P. Franke, M. Brudel, M. Bienert, *J. Chem. Soc. Chem. Commun.* **1994**, 853 – 854; c) Y. Yang, W. V. Sweeney, K. Schneider, S. Thornqvist, B. T. Chait, J. P. Tam, *Tetrahedron Lett.* **1994**, *35*, 9689 – 9692.

[24] The denaturation temperatures (T_m) of the FBP28WW variants were estimated either from the intensity/temperature plot of the β band at 1636 cm^{-1} and from the frequency/temperature changes of the tyrosine-ring vibration at 1515 cm^{-1} (in brackets); peptide **3**: 50.9 (52.8) °C, peptide **4**: 46.2 (46.4) °C.

[25] The denaturation temperatures of strand 1 and strand 2 of the [$Gln^{9,21,23,26,28}$,Asn^{15}] FBP28WW variant were estimated from the frequency/temperature changes of the corresponding bands of ^{13}C-labeled tyrosine at 1505 cm^{-1}. For comparison, the T_m (°C) values calculated from the frequency/temperature changes of the unlabeled tyrosine bands at 1515 cm^{-1} are also shown: Tyr11 (strand 1): 51.5; Tyr19 (strand 2): 51.1; Tyr11/20: 52.3; Tyr19/20: 51.1.

[26] IR studies of the histone-like protein of *Bacillus subtilis*, HBsu, revealed that also the absorption band of the phenylalanine side chain at 1498 cm^{-1} may show a pronounced discontinuous high-frequency shift around the denaturation temperature: H. Fabian, unpublished results.

[27] J. H. Holtmann, H. Oschkinat, unpublished results.

 © 2005 Wiley-VCH Verlag GmbH & Co. KGaA, Weinheim

Molecular Devices

Geometrically Precisely Defined Multinanometer Expansion/Contraction Motions in a Resorcin[4]arene Cavitand Based Molecular Switch**

*Vladimir A. Azov, Anna Schlegel, and François Diederich**

The invention of molecular devices that undergo reversible controlled mechanical movements on the nanometer scale and thereby mimic natural phenomena such as muscle expansion/contraction is a hot target in contemporary chemistry.[1] Elegant examples of molecular and supramolecular switches with bistable conformations of profoundly different geometry have been described in recent years.[2–7] On the other hand, the conformational space available in the contracted and expanded states of the reported systems often is rather large and the geometric differences not always well defined. We became interested in developing a rigid molecular system in which both states adopt a precisely defined geometry and report here a first example based on a bridged resorcin[4]arene scaffold. These cavitands, first introduced by Cram and co-workers,[8] can be reversibly switched between a contracted (vase) and an expanded (kite) conformation upon variation of temperature[8–10] or pH,[11] or upon metal-ion addition.[12]

Recent advances in the synthesis of partially or differently bridged resorcin[4]arene cavitands[13,14] enabled the preparation of **1**, in which two opposite cavity walls are greatly extended by attachment of rigid oligo(phenylene ethynylene) arms. A donor–acceptor BODIPY (dipyrromethene boron difluoride) dye pair[15] is attached to the oligomeric termini to allow observation of the switching process by fluorescence resonance energy transfer (FRET).[16] BODIPY dyes were chosen for the targeted pH-induced switching, since their emission behavior features low sensitivity to pH and environmental polarity, as we could confirm in model studies. Computer model building,[17] based on X-ray crystal structures of bridged resorcin[4]arene cavitands in both vase and kite conformations,[12,13b] suggested a ≈1000% difference in the distance between the dye pair in the contracted (≈7 Å) and expanded (≈7 nm) states (Figure 1), which should allow convenient detection of different FRET behavior in the two states.[16a]

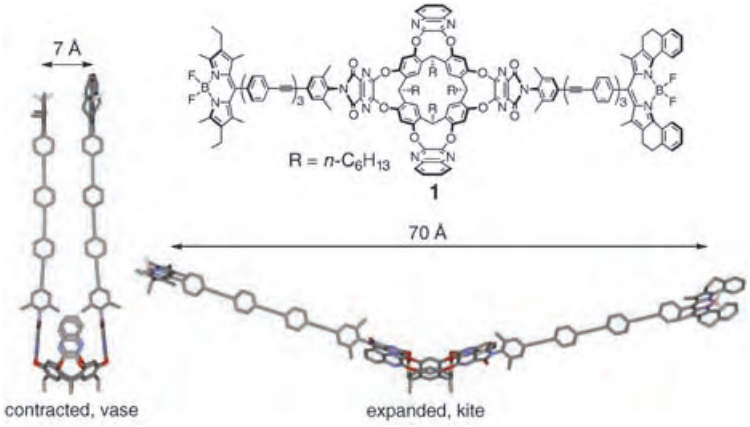


Figure 1. Donor–acceptor dye-labeled cavitand **1** and its extensions in the contracted (vase) and expanded (kite) states. In the models, the alkyl chains ("legs") of the cavitand are omitted.

The synthesis of **1** proceeded in a highly convergent manner. Sonogashira cross-coupling[18] of **2**[15b] with Me_3Si-C≡CH afforded **3**, which was deprotected to give **4**. A second cross-coupling with aryl iodide **5**[19] provided **6**, which was deprotected to yield the donor dye-appended **7**. A similar route led from **8**[15a] (via **9**→**10**→**11**) to the acceptor building block **12** (Scheme 1).

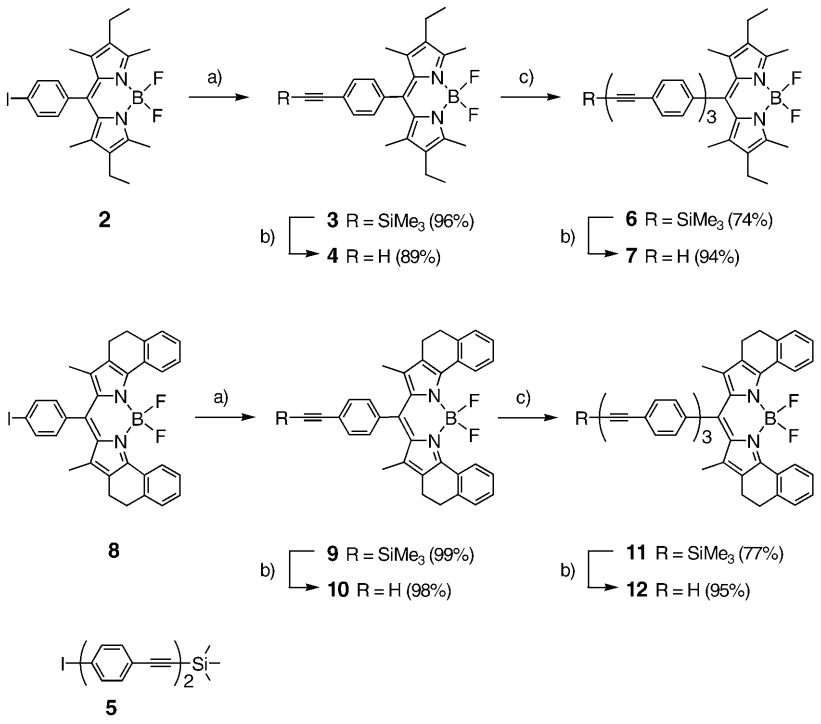
The cavitand core **13** was prepared by bridging **14**[13,14] with imide **15** (Scheme 2). ^{1}H NMR investigations revealed reversible vase–kite switching of **13** induced either by changes in temperature or pH. Upon addition of trifluoroacetic acid (TFA) to a solution of **13** in CH_2Cl_2 or when the temperature was lowered from 60 °C to −60 °C, the signals of the methine

[*] Dr. V. A. Azov, A. Schlegel, Prof. Dr. F. Diederich
Laboratorium für Organische Chemie
ETH-Hönggerberg, HCI
8093 Zürich (Switzerland)
Fax: (+41) 1-632-1109
E-mail: diederich@org.chem.ethz.ch

[**] This research was supported by the Swiss National Science Foundation (NFP-47 "Supramolecular Functional Materials" and NCCR "Nanoscience"). We thank Rolf Häfliger for providing high-resolution mass spectra.

Supporting information for this article is available on the WWW under http://www.angewandte.org or from the author.

 DOI: 10.1002/anie.200500970 © 2005 Wiley-VCH Verlag GmbH & Co. KGaA, Weinheim



Scheme 1. Synthesis of the donor dye (**7**) and acceptor dye (**12**) building blocks. a) Me_3Si-C≡CH, $[Pd(PPh_3)_4]$, CuI, $Et(iPr)_2N$, tetrahydrofuran (THF), 20 °C, 1–3 d; b) Bu_4NF, THF, −78 °C, 30 min; c) **5**, $[Pd(PPh_3)_4]$, CuI, $Et(iPr)_2N$, THF, 20 °C, 1–3 d.

protons in the resorcin[4]arene core shifted upfield from ≈5.6 ppm to ≈3.6 ppm, which is characteristic for the expansion process (see the Supporting Information). Sonogashira cross-coupling of **13** with **7** afforded a mixture of the three cavitands **13**, **16**, and **17**, which was separated by gel permeation chromatography (GPC, Biorad-BioBeads SX-1, CH_2Cl_2; see the Supporting Information). A second cross-coupling of **16** with **12** provided the target structure **1** as a stable, high-melting dark-violet solid after GPC purification. The reversed sequence of dye addition to **13** (first **12** followed by **7**) was much less fruitful due to the poor solubility of the singly labeled intermediate. The spectroscopic data fully support the structural assignment for **1**. The base peak in the high-resolution matrix-assisted laser-desorption-ionization mass spectrum (HR-MALDI-MS, matrix: 3-hydroxypicolinic acid (3-HPA)) corresponds to the molecular ion after loss of one F atom at *m/z* 2880.2161 ($[M-F]^+$, $C_{188}H_{156}B_2F_3N_{14}O_{12}^+$; calcd 2880.2160).

To test distance-dependent FRET between the chosen donor and acceptor BODIPY dye pair, we also prepared the three oligo(phenylene ethynylene)s **18a–c** of different lengths (Figure 2). Fluorescence spectroscopy in very dilute $CHCl_3$ solution ($c = 0.5 \times 10^{-7}$ M) showed that the FRET efficiency strongly decreases with increasing length of the rigid spacer from about 98% for **18a** (distance $r = 19$ Å between the B atoms of the dyes), to ≈85% for **18b** ($r = 32$ Å), and to ≈35% for **18c** ($r = 53$ Å). Importantly, addition of TFA (up to $c = 0.3$ M) does not affect the emission behavior.

The two bis(BODIPY dye)-appended cavitands **1** and **17** were shown by ^{1}H NMR spectroscopy to adopt the contracted (vase) conformation in CD_2Cl_2 or $CHCl_3$ above 25 °C (see the Supporting Information). Upon lowering the temperature to −60 °C or upon addition of TFA (up to 0.27 M), they both undergo expansion to the kite forms as clearly evidenced by the characteristic large upfield shift (≈5.6 → ≈3.6 ppm) of the resorcinarene methine protons.[20]

Whereas the fluorescence spectrum of bis(donor dye)-appended **17** is nearly identical in the contracted and expanded forms (see the Supporting Information), the emission behavior of target compound **1** differs dramatically in the two states. The UV/Vis spectrum of **1** (Figure 3a) in $CHCl_3$ ($c = 1.0 \times 10^{-5}$ M) displays three strong absorption bands assigned to the oligo(phenylene ethynylene) spacers (λ_{max} 332 nm), the donor dye (529 nm), and the acceptor dye (619 nm); these bands are not affected by the addition of TFA. The emission spectrum in $CHCl_3$ ($c = 0.5 \times 10^{-7}$ M, $\lambda_{exc} = 490$ nm, 20 °C) features two strong peaks at 542 nm (donor dye) and 630 nm (acceptor dye) with an integral ratio of the donor/acceptor fluorescence intensity of 45:55. In view of the prevalence of the contracted vase conformation under these conditions, as demonstrated by ^{1}H NMR spectroscopy, this relatively low FRET efficiency is rather surprising. We tentatively explain it by either a) the dynamic behavior of the cavitand,[20] with constant wagging vibrations separating the two dyes one from another for a statistically important amount of time, or b) unfavorable orientations of the transition dipole moments of the dyes.

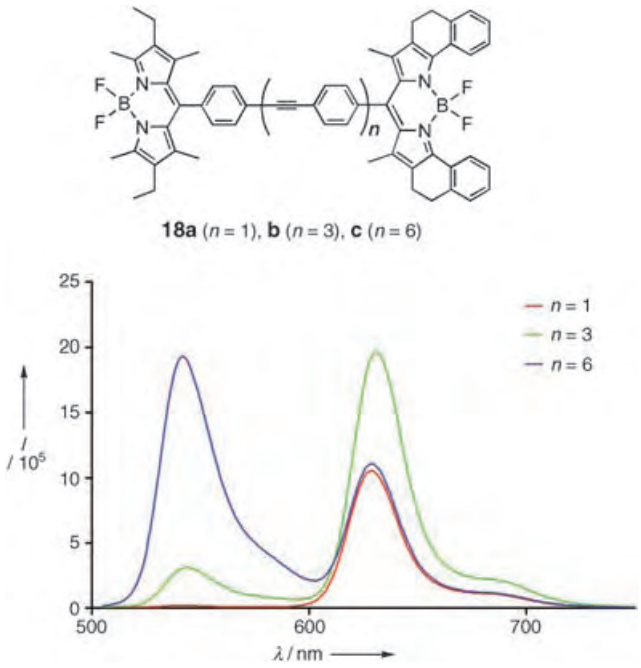
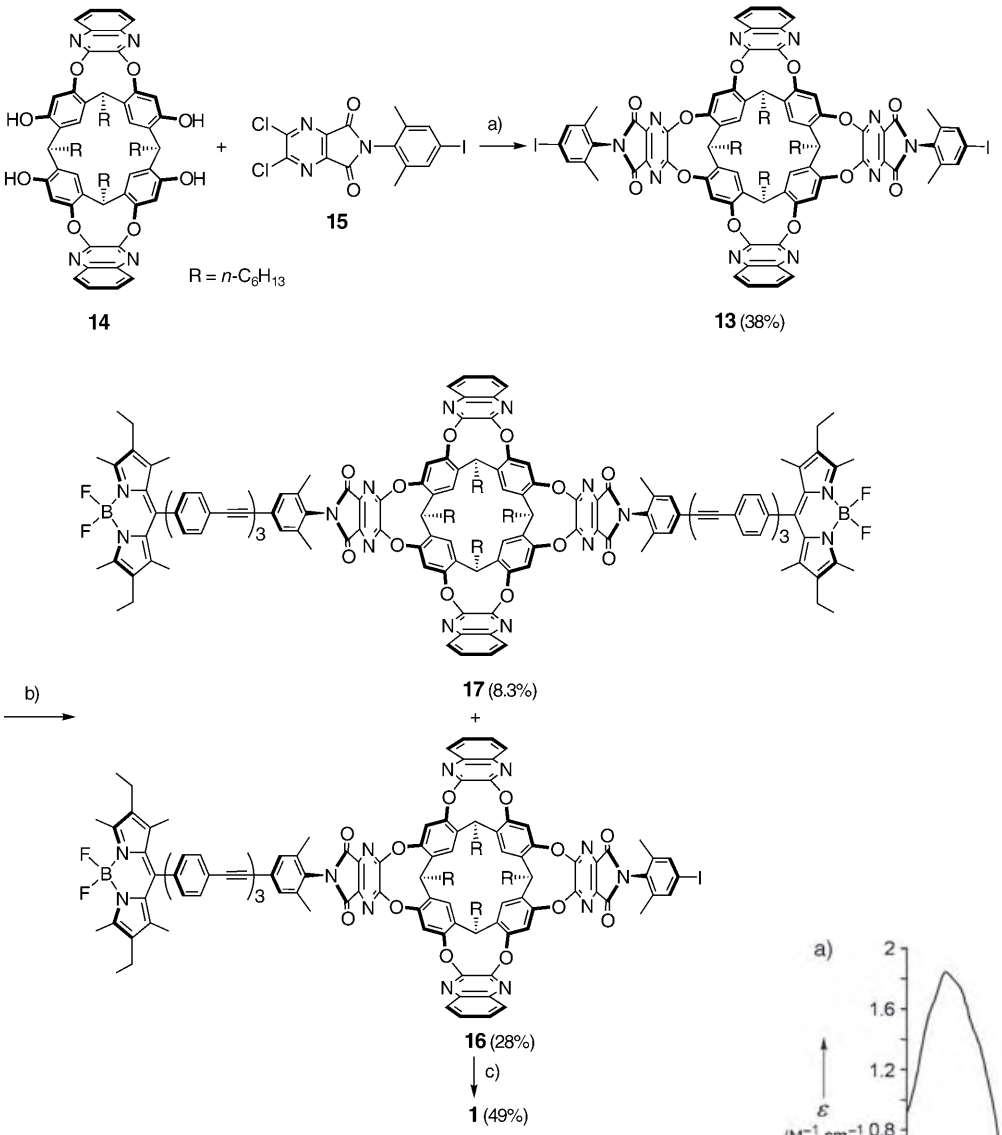


Figure 2. FRET intensities of **18a–c** in $CHCl_3$ ($c = 0.5 \times 10^{-7}$ M). The higher energy band is the donor emission and the lower energy band the acceptor emission.

 © 2005 Wiley-VCH Verlag GmbH & Co. KGaA, Weinheim



Scheme 2. Synthesis of target compound **1**. a) K_2CO_3, Me_2SO, 35 °C, 2 d; b) **7** (0.75 equiv), [Pd(PPh_3)$_4$], CuI, Et(*i*Pr)$_2$N, THF, 35 °C, 2 d; c) **12** (2.25 equiv), [Pd(PPh_3)$_4$], CuI, Et(*i*Pr)$_2$N, THF, 35 °C, 2 d.

Upon addition of TFA, (Figure 3b) the acceptor fluorescence vanishes nearly completely, whereas the donor fluorescence doubles in intensity. In the expanded state, with a separation of donor and acceptor of ≈ 7 nm, the FRET efficiency is dramatically reduced. This result could only be obtained since the expanded conformation of **1** is very rigid, strongly limiting the available conformational space. Intermolecular FRET is clearly not effective at the low concentration range of the experiment ($c = 0.5 \times 10^{-7}$ M). The spectral changes are reversed upon reneutralization with base (Et(*i*Pr)$_2$N).

Thus, the large-scale expansion/contraction movement of **1** (Figure 1) is clearly proven by both ^{1}H NMR spectroscopy and FRET measurements. We are now further investigating the dynamics of the switching motion in single-molecule studies using confocal fluorescence microscopy.[21]

Experimental Section

Compound **1**: Cavitand **16** (13.2 mg, 5.73 μmol), **12** (9.3 mg, 13 μmol, 2.25 equiv), [Pd(PPh_3)$_4$] (1.3 mg, 0.11 μmol), and CuI (0.22 mg, 0.11 μmol) were mixed together in a Schlenk apparatus filled with Ar. $CHCl_3$ (0.3 mL) and THF (0.3 mL) were added, and the mixture was degassed by freeze-pump-thaw cycles. Et(*i*Pr)$_2$N (0.02 mL, 120 mmol) was added and the mixture degassed again, then stirred at 35 °C for 2 d. The mixture was concentrated to dryness, and flash chromatography (SiO_2; CH_2Cl_2/EtOAc gradient 0→0.5 %) yielded crude **1**. Further purification by repeated GPC (Biorad BioBeads SX-1, CH_2Cl_2), afforded **1** (8.2 mg, 49 %) as a dark-violet solid. M.p. > 300 °C (decomp.); $R_f = 0.32$ (SiO_2; CH_2Cl_2/EtOAc 99.4:0.6); ^{1}H NMR (300 MHz, $CDCl_3$): $\delta =$ 0.91–1.02 (m, 18H), 1.26–1.54 (m, 50H), 2.23 (s, 6H), 2.22–2.36 (m, 12H), 2.49–2.54 (m, 10H), 2.86 (br t, $J = 7$, 4H), 5.62 (t, $J = 8.1$, 2H), 5.71 (t, $J = 8.1$, 2H), 7.24–7.62 (m, 38H), 7.66–7.74 (m, 4H), 7.86–7.91 (m, 4H), 8.25 (s, 4H), 8.80 ppm (br d, $J = 7.8$, 2H); ^{13}C NMR (125 MHz, $CDCl_3$): $\delta = 12.10$, 12.55, 12.75,

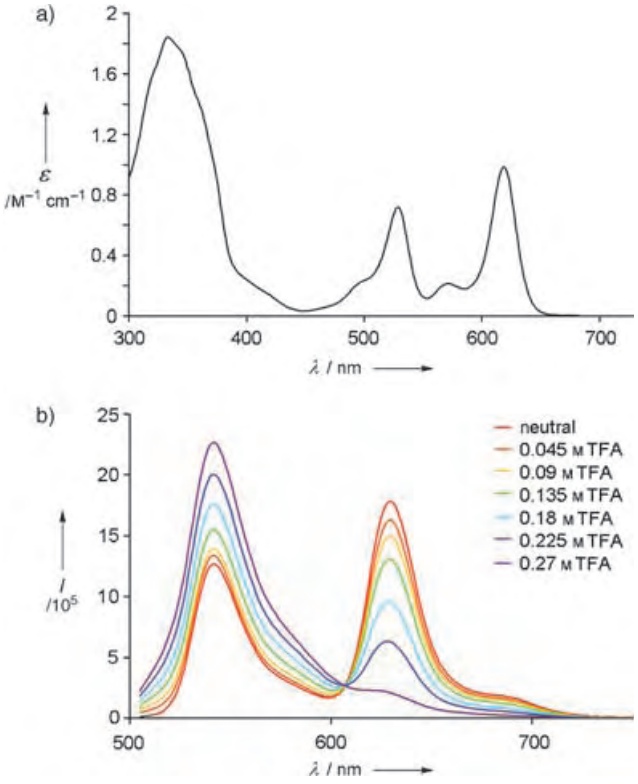


Figure 3. a) UV/Vis spectrum of **1** in $CHCl_3$ at 20 °C ($c = 1.0 \times 10^{-5}$ M). b) Fluorescence spectra of **1** in $CHCl_3$ at 20 °C ($c = 0.5 \times 10^{-7}$ M) recorded at different concentrations of TFA.

 © 2005 Wiley-VCH Verlag GmbH & Co. KGaA, Weinheim

14.29, 14.81, 17.26, 18.33, 18.36, 20.66, 22.89, 28.16, 28.20, 29.58, 29.59, 30.70, 32.09, 32.10, 32.39, 32.89, 34.42, 34.51, 90.57, 90.61, 90.76, 91.00, 91.35, 91.40, 119.02, 123.13, 123.19, 123.50, 123.83, 123.97, 124.00, 125.37, 127.57, 128.32, 128.55, 128.60, 128.86, 129.21, 129.33, 129.66, 129.72, 130.73, 131.59, 131.87, 131.89, 131.93, 131.98, 132.41, 132.47, 132.55, 133.24, 133.92, 134.92, 135.93, 135.98, 136.29, 136.37, 136.72, 137.08, 137.68, 138.31, 139.28, 140.03, 140.92, 141.72, 151.18, 152.28, 152.46, 153.31, 154.36, 159.08, 161.68 ppm; ^{19}F NMR ($CDCl_3$, 282.5 MHz): $\delta = -134.5$ (q, $J = 33.5$), -145.1 ppm (q, $J = 32.5$); IR (neat): $\tilde{\nu} = 2957$ (w), 2924 (m), 2855 (w), 1739 (s), 1524 (m), 1479 (m), 1444 (m), 1411 (s), 1362 (s), 1326 (s), 1275 (m), 1231 (m), 1190 (s), 1158 (s), 1116 (m), 1103 (m), 1083 (m), 1018 (m), 979 (m), 898 (m), 837 (m), 760 (m), 708 (m), 669 (w), 604 cm^{-1} (w); UV/Vis ($CHCl_3$): λ_{max} (ε) = 332 (184000), 529 (72000), 571 (21000), 619 nm (98000); Fluorescence ($CHCl_3$, $\lambda_{exc} = 490$ nm): $\lambda_{max} = 542$ nm, 630 nm; HR-MALDI-MS (matrix: 3-HPA): 2880.2161 ([$M-$F]$^+$, $C_{188}H_{156}B_2F_3N_{14}O_{12}^+$, calcd 2880.21599).

Received: March 16, 2005

Keywords: cavitands · conformation analysis · FRET (fluorescence resonance energy transfer) · molecular devices

[1] a) Special issue on molecular machines: *Acc. Chem. Res.* **2001**, *34*, 410 – 522; b) *Molecular Switches* (Ed.: B. L. Feringa), Wiley-VCH, Weinheim, **2001**.

[2] a) S. Kang, S. A. Vignon, H.-R. Tseng, J. F. Stoddart, *Chem. Eur. J.* **2004**, *10*, 2555 – 2564; b) H.-R. Tseng, S. A. Vignon, J. F. Stoddart, *Angew. Chem.* **2003**, *115*, 1529 – 1533; *Angew. Chem. Int. Ed.* **2003**, *42*, 1491 – 1495.

[3] G. Bottari, D. A. Leigh, E. M. Pérez, *J. Am. Chem. Soc.* **2003**, *125*, 13360 – 13361.

[4] a) M. C. Jimenez-Molero, C. Dietrich-Buchecker, J.-P. Sauvage, *Chem. Commun.* **2003**, 1613 – 1616; b) M. C. Jimenez, C. Dietrich-Buchecker, J.-P. Sauvage, *Angew. Chem.* **2000**, *112*, 3422 – 3425; *Angew. Chem. Int. Ed.* **2000**, *39*, 3284 – 3287.

[5] a) M. Barboiu, L. Prodi, M. Montalti, N. Zaccheroni, N. Kyritsakas, J.-M. Lehn, *Chem. Eur. J.* **2004**, *10*, 2953 – 2959; b) M. Barboiu, G. Vaughan, N. Kyritsakas, J.-M. Lehn, *Chem. Eur. J.* **2003**, *9*, 763 – 769; c) M. Barboiu, J.-M. Lehn, *Proc. Natl. Acad. Sci. USA* **2002**, *99*, 5201 – 5206.

[6] a) T. Lougheed, V. Borisenko, T. Hennig, K. Rück-Braun, G. A. Woolley, *Org. Biomol. Chem.* **2004**, *2*, 2798 – 2801; b) D. C. Burns, D. G. Flint, J. R. Kumita, H. J. Feldman, L. Serrano, Z. Zhang, O. S. Smart, G. A. Woolley, *Biochemistry* **2004**, *43*, 15329 – 15338.

[7] M. J. Pandya, E. Cerasoli, A. Joseph, R. G. Stoneman, E. Waite, D. N. Woolfson, *J. Am. Chem. Soc.* **2004**, *126*, 17016 – 17024.

[8] a) J. R. Moran, S. Karbach, D. J. Cram, *J. Am. Chem. Soc.* **1982**, *104*, 5826 – 5828; b) D. J. Cram, H.-J. Choi, J. A. Bryant, C. B. Knobler, *J. Am. Chem. Soc.* **1992**, *114*, 7748 – 7765.

[9] P. Soncini, S. Bonsignore, E. Dalcanale, F. Ugozzoli, *J. Org. Chem.* **1992**, *57*, 4608 – 4612.

[10] T. Haino, D. M. Rudkevich, A. Shivanyuk, K. Rissanen, J. Rebek, Jr., *Chem. Eur. J.* **2000**, *6*, 3797 – 3805.

[11] P. J. Skinner, A. G. Cheetham, A. Beeby, V. Gramlich, F. Diederich, *Helv. Chim. Acta* **2001**, *84*, 2146 – 2153.

[12] M. Frei, F. Marotti, F. Diederich, *Chem. Commun.* **2004**, 1362 – 1363.

[13] a) V. A. Azov, F. Diederich, Y. Lill, B. Hecht, *Helv. Chim. Acta* **2003**, *86*, 2149 – 2155; b) V. A. Azov, P. J. Skinner, Y. Yamakoshi, P. Seiler, V. Gramlich, F. Diederich, *Helv. Chim. Acta* **2003**, *86*, 3648 – 3670.

[14] P. P. Castro, G. Zhao, G. A. Masangkay, C. Hernandez, L. M. Gutierrez-Tunstad, *Org. Lett.* **2004**, *6*, 333 – 336.

[15] a) J. Chen, A. Burghart, A. Derecskei-Kovacs, K. Burgess, *J. Org. Chem.* **2000**, *65*, 2900 – 2906; b) A. Burghart, H. Kim, M. B. Welch, L. H. Thoresen, J. Reibenspies, K. Burgess, F. Bergström, L. B.-Å. Johansson, *J. Org. Chem.* **1999**, *64*, 7813 – 7819; c) J. Karolin, L. B.-A. Johansson, L. Strandberg, T. Ny, *J. Am. Chem. Soc.* **1994**, *116*, 7801 – 7806.

[16] a) T. Förster, *Ann. Phys.* **1948**, *2*, 55 – 75; b) P. R. Selvin, *Methods Enzymol.* **1995**, *246*, 300 – 334.

[17] AM1 calculations: Spartan 04 for Windows, Wavefunction Inc., 18401 Von Karman Ave., Irvine, CA 92612 USA, **2003**.

[18] J. A. Marsden, M. M. Haley in *Metal-Catalyzed Cross-Coupling Reactions*, *2nd ed.*, *Vol. 1* (Eds.: A. de Meijere, F. Diederich), Wiley-VCH, Weinheim, **2004**, pp. 317 – 394.

[19] O. Lavastre, L. Ollivier, P. H. Dixneuf, S. Sibandhit, *Tetrahedron* **1996**, *52*, 5495 – 5504.

[20] For further details of the analysis of the contracted/expanded conformations by NMR spectroscopy as well as for the kinetics and thermodynamics of vase/kite switching, see: V. A. Azov, B. Jaun, F. Diederich, *Helv. Chim. Acta* **2004**, *87*, 449 – 462.

[21] Ongoing studies in collaboration with Prof. B. Hecht (University of Basel), see: a) S. Weiss, *Science* **1999**, *283*, 1676 – 1683; b) B. Hecht, B. Sick, U. P. Wild, V. Deckert, R. Zenobi, O. J. F. Martin, D. W. Pohl, *J. Chem. Phys.* **2000**, *112*, 7761 – 7774.

 © 2005 Wiley-VCH Verlag GmbH & Co. KGaA, Weinheim

Cover Picture

Jesse L. C. Rowsell and Omar M. Yaghi*



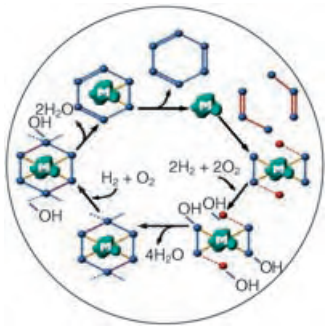
Hydrogen storage strategies for metal–organic frameworks have been developed recently to enhance their applicability in this role, as shown in the cover picture. In their Minireview on page 4670 ff., O. M. Yaghi and J. L. C. Rowsell discuss the various approaches used to reach the required compromise between high porosity and smaller pore size for stronger binding of H_2 under ambient conditions. In their Communication on page 4745, B. Chen, O. M. Yaghi, and co-workers report a promising hydrogen-storage material with open metal sites.



Aldol Reactions
In their Review on page 4682 ff., S. E. Denmark et al. explore the scope and limitations of the catalytic, enantioselective, vinylogous aldol reaction, in which dienolates derived from γ-enolizable α,β-unsaturated carbonyl compounds are added to aldehydes.



Pharmaceutically Active "Prils"
Chiral building blocks for the synthesis of these angiotensin-converting-enzyme inhibitors can be produced on a large scale. Their application in the structure-guided redesign of the active site of almond (*R*)-*Pa*HNL5 is discussed by K. Gruber, A. Glieder, and co-workers in their Communication on page 4700 ff.



No Pressure
The coupling of propylene to generate benzene at 70 °C and atmospheric pressure is discussed by E. W. McFarland and co-workers in the Communication on page 4735 ff. The selectivity of the benzene formation depends on the size of the Pd^0 cluster and on the presence of hydrogen and oxygen.

Contents

The following Communications have been judged by at least two referees to be "very important papers" and will be published online at www.angewandte.org soon:

*V. Lavallo, Y. Canac, C. Präsang, B. Donnadieu, G. Bertrand**
Stable Cyclic (Alkyl)(amino)carbenes as Rigid or Flexible, Bulky, Electron-Rich Ligands for Transition-Metal Catalysts

S. Aime, D. Delli Castelli, E. Terreno*
Highly Sensitive MRI-CEST Agents using Liposomes (LIPOCEST)

H. Braunschweig, K. Radacki, D. Rais, D. Scheschkewitz*
A T-Shaped Platinum(II) Boryl Complex as the Precursor to a Base-Stabilized Borylene of Platinum

X. Liang, D. Fu, R. Liu,* Q. Zhang, T. Y. Zhang, X. Hu**
Highly Efficient $NaNO_2$-Catalyzed Destruction of Trichlorophenol using Molecular Oxygen

*P. Maire, T. Büttner, F. Breher, P. Le Floch, H. Grützmacher**
Heterolytic Hydrogen Splitting with Novel Rhodium(I) Amides

D. Banser, M. Schnell, J.-U. Grabow, E. J. Cocinero, A. Lesarri, J. L. Alonso*
The Internuclear Potential, Electronic Structure, and Chemical Bond of Tellurium Selenide

News

M. Quack to give Jost Lectures — **4662**

M. Chisholm Elected to US Academy — **4662**

DuPont Awards for P. Baran, T. Odom, and D. Zhao — **4662**

Books

The 1702 Chair of Chemistry at Cambridge — Mary Archer, Christopher Haley — *reviewed by D. H. Rouvray* — **4663**

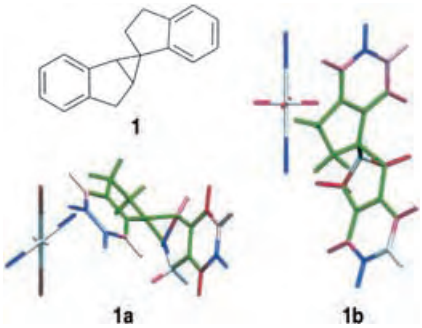
Molecular Reaction Dynamics — Raphael D. Levine — *reviewed by O. S. Vasyutinskii* — **4664**

Highlights

NMR Spectroscopy

R. M. Gschwind* — **4666 – 4668**

Residual Dipolar Couplings—A Valuable NMR Parameter for Small Organic Molecules



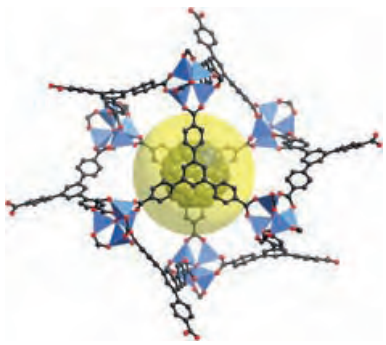
The partial alignment of small organic molecules is now also possible in organic solvents by mechanically constrained polymer gels or modified liquid-crystalline phases. This paves the way to apply residual dipolar couplings to small molecules and thus to use an additional NMR parameter to determine the structure and configuration of small organic molecules (e.g. spiroindene (**1**), see picture).

Minireviews

Microporous Materials

J. L. C. Rowsell, O. M. Yaghi* — **4670 – 4679**

Strategies for Hydrogen Storage in Metal–Organic Frameworks



Reaching a compromise: Metal–organic frameworks such as MOF-177 (see picture) are potential hydrogen-storage materials, but the pores (yellow sphere) are much larger than the molecular diameter of H_2, thus limiting their effectiveness. Their hydrogen uptake may be improved by impregnation with other moieties (such as C_{60}, gray) to provide additional adsorptive sites and stronger H_2 binding at the expense of high porosity.

© 2005 Wiley-VCH Verlag GmbH & Co. KGaA, Weinheim

Reviews



The power of the aldol reaction is extended through the use of γ-enolizable α,β-unsaturated carbonyl substrates as "extended dienolates" in the addition to aldehydes. This process gives δ-hydroxy carbonyl compounds **1** or **2** with up to two new stereocenters (see scheme). New methods for the catalytic, enantioselective, vinylogous aldol reaction are summarized, and the scope and limitations of these systems are discussed.

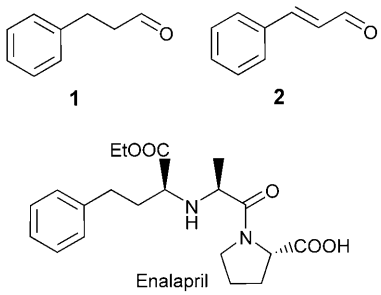
Asymmetric Catalysis

S. E. Denmark,* J. R. Heemstra, Jr., G. L. Beutner ——— **4682 – 4698**

Catalytic, Enantioselective, Vinylogous Aldol Reactions

Communications

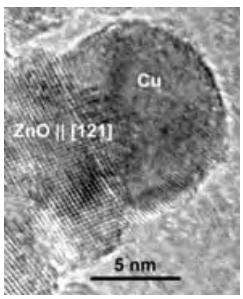
Structure-guided redesign of the active site of almond (*R*)-*Pa*HNL5 for increased enantioselectivity resulted in four improved muteins. In particular, mutation V360I gave enhanced conversion rates and enantioselectivities higher than 96% *ee* for two structurally related substrates **1** and **2**. Chiral building blocks for the synthesis of pharmaceutically active "prils" (example shown) can thus be produced on a large scale.



Protein Engineering

R. Weis, R. Gaisberger, W. Skranc, K. Gruber,* A. Glieder* ——— **4700 – 4704**

Carving the Active Site of Almond *R*-HNL for Increased Enantioselectivity



Approaching reality: Copper zinc oxide catalysts that were prepared similarly to industrial catalysts were studied by high-resolution electron microscopy. The microstructure of the Cu/ZnO catalysts (see picture) deviates considerably from that of idealized copper model systems. Future model systems for copper catalysts in methanol chemistry must take into account the "real" structure of active copper catalysts.

Heterogeneous Catalysis

T. Ressler,* B. L. Kniep, I. Kasatkin, R. Schlögl ——— **4704 – 4707**

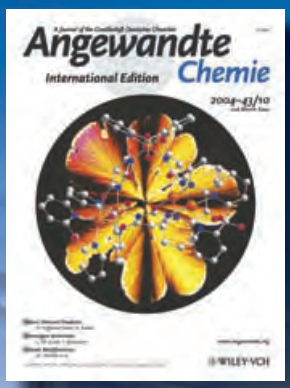
The Microstructure of Copper Zinc Oxide Catalysts: Bridging the Materials Gap

For the USA and Canada:
ANGEWANDTE CHEMIE International Edition (ISSN 1433-7851) is published weekly by Wiley-VCH PO Box 191161, D 69451 Weinheim, Germany. Air freight and mailing in the USA by Publications Expediting Inc. 200 Meacham Ave., Elmont, NY 11003. Periodicals postage paid at Jamaica NY 11431. US POSTMASTER: send address changes to *Angewandte Chemie*, Wiley-VCH, 111 River Street, Hoboken, NJ 07030. Annual subscription price for institutions: US$ 4948.00/4498.00 (valid for print and electronic / print or electronic delivery); for individuals who are personal members of a national chemical society, or whose institution already subscribes, or who are retired or self-employed consultants, print only: US$ 394.00. Postage and handling charges included. All Wiley-VCH prices are exclusive VAT.

 © 2005 Wiley-VCH Verlag GmbH & Co. KGaA, Weinheim

The best in chemistry –

for more than a hundred years



A Journal of the Gesellschaft Deutscher Chemiker

Angewandte International Edition **Chemie**

www.angewandte.org

1888: ***The beginning of a success story***

Constant Innovations

1962: *First issue of the International Edition*
1976: *Graphical abstracts*
1979: *Cover pictures*
1988: *Centenary of Angewandte*
1989: *Routine use of color*
1991: *New section: Highlights*
1992: *Computerized editorial tracking system*
1995: *Internet service for readers*
1998: *Regular press service; full-text online*
2000: *New section: Essays; EarlyView: Communications available online ahead of the printed version*
2001: *New section: Minireviews*
2002: *Online submission of manuscripts*
2003: *Weekly publication; new section: News; new layout*
2004: *Backfiles (1962-1997); ManuscriptXpress: Online system for authors and referees*



Angewandte's advisors...

J. Fraser Stoddart
University of California, Los Angeles

» When it comes to informing myself, I have two weekly fixations. The Economist and ***Angewandte Chemie****. Both are compulsive browsing and there are many articles in each that are essential reading. I simply cannot afford not to know what's in every issue of* ***Angewandte****. Being on the board of* ***Angewandte Chemie*** *has been a real pleasure. Whether or not it's true, I have the feeling that I have really been able to influence how some of the most creative chemistry in my time has been presented to the scientific community at large. «*

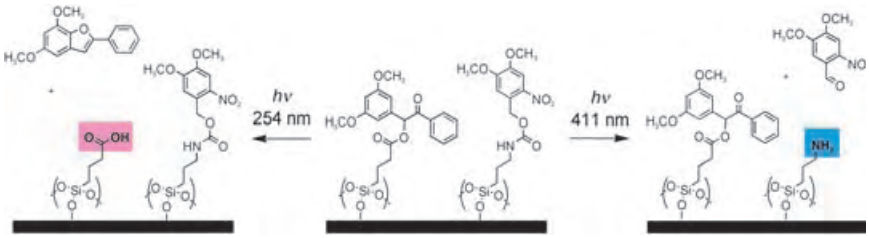
Angewandte Chemie International Edition *is a journal of the German Chemical Society (GDCh)*

GDCh

WILEY InterScience® DISCOVER SOMETHING GREAT

WILEY-VCH

11931404_gu



Monolayer lithography: The concept of orthogonal cleavage of photolabile protecting groups was demonstrated with self-assembled silane layers on solid surfaces. Nitroveratryloxycarbonyl and benzoin derivatives can be addressed independently by light of different wavelengths to selectively liberate amino and carboxylic acid groups, respectively, in mixed silane layers. Specific colloid adsorption on such photopatterned surfaces was investigated.

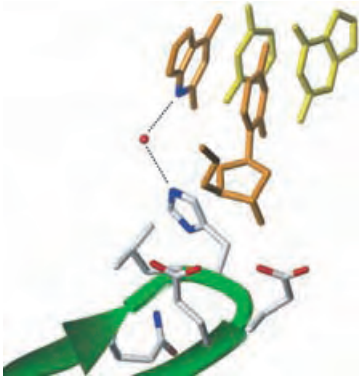
Chemical Photolithography

A. del Campo, D. Boos, H. W. Spiess, U. Jonas* ——— **4707 – 4712**

Surface Modification with Orthogonal Photosensitive Silanes for Sequential Chemical Lithography and Site-Selective Particle Deposition

---

How is a selective enzyme made even more selective? With a combinatorial approach to redesign an enzyme motif (see figure; red = O, blue = N), the mismatch extension selectivity of DNA polymerases was increased. The results impart new and deeper insight into the mechanisms of DNA polymerases and provide new tools for applications such as efficient genotyping.

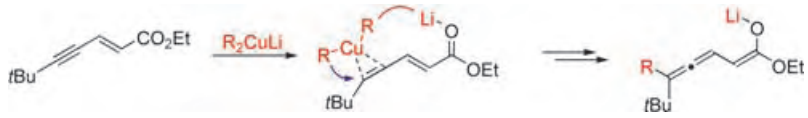


DNA Polymerase

D. Summerer, N. Z. Rudinger, I. Detmer, A. Marx* ——— **4712 – 4715**

Enhanced Fidelity in Mismatch Extension by DNA Polymerase through Directed Combinatorial Enzyme Design

---



A combination of experimental and theoretical studies of ^{13}C kinetic isotope effects have led to a comprehensive mechanistic picture of the 1,6-cuprate addition to acceptor-substituted enynes. In the rate-determining step, the new bond is formed from the triple bond of the substrate to the incoming alkyl group (see scheme).

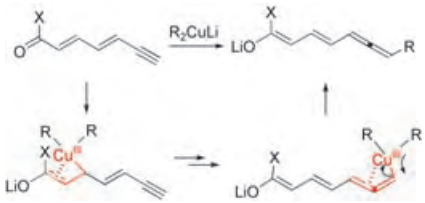
Reaction Mechanisms

S. Mori,* M. Uerdingen, N. Krause,* K. Morokuma* ——— **4715 – 4719**

Elucidation of the Mechanism of the 1,6-Cuprate Addition to Acceptor-Substituted Enynes through ^{13}C Kinetic Isotope Effects: Experimental and Theoretical Studies

---

Passing the buck: Rapid copper migration along the conjugated system results in regioselective remote conjugate addition of a lithium organocuprate to a polyenynyl carbonyl compound, as revealed by density-functional calculations (see scheme). The unique structural/electronic properties of the σ/π-allenyl–copper(III) intermediates are responsible for the selective C–C bond formation at the terminal acetylenic position.



Reaction Mechanisms

N. Yoshikai, T. Yamashita, E. Nakamura* ——— **4721 – 4723**

Mechanism of Remote Conjugate Addition of a Lithium Organocuprate to a Polyconjugated Carbonyl Compound

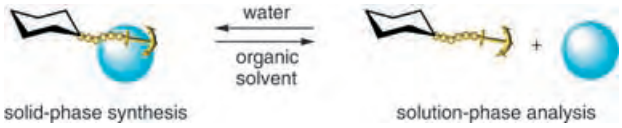
 © 2005 Wiley-VCH Verlag GmbH & Co. KGaA, Weinheim

Contents

Solid-Phase Synthesis

A. Porzelle, W.-D. Fessner* **4724 – 4728**

Reversible Substrate Anchoring: NC-SPOS as a Sustainable Approach to Solid-Supported Organic Synthesis

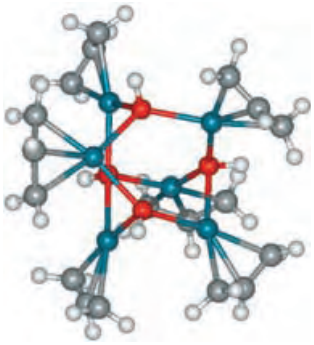


An on–off relationship: The main problems of conventional solid-phase organic synthesis (SPOS) are overcome by a freely reversible attachment strategy. Hydrophobic labeling of organic substrates allows noncovalent (NC) binding to hydrophobic carriers in water for solid-phase-assisted reactions ("NC-SPOS"; see scheme). NC-SPOS reactions are free of the diffusion limitations typical for polymer supports and highly environmentally benign.

Cluster Compounds

A. Gogoll,* L. Toom, H. Grennberg **4729 – 4731**

Ligand-Induced Formation of an Adamantanoid Hexanuclear (π-Allyl)Pd^{II}(μ_3-Hydroxo) Cluster Stacked as Hydrogen-Bonded Double Strands



Stranded clusters: The treatment of (η^3-propenyl)palladium chloride with a bulky, basic dinitrogen ligand in the presence of traces of water results in the formation of an unusual adamantanoid [{(η^3-propenyl)Pd}$_6$(μ_3-OH)$_4$] cluster (see picture). The clusters are linked into double strands through hydrogen bonds and bridging counterions.

Self-Assembly

B. Song, Z. Wang, S. Chen, X. Zhang,* Y. Fu, M. Smet, W. Dehaen **4731 – 4735**

The Introduction of π–π Stacking Moieties for Fabricating Stable Micellar Structure: Formation and Dynamics of Disklike Micelles

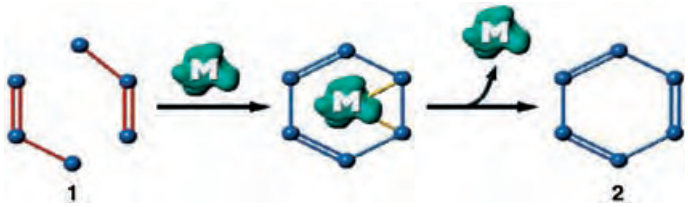


Enhancing the intermolecular interactions between micelles by introducing a strong π–π stacking moiety and flexible spacers of appropriate length results in the formation of disklike micelles that can maintain their monomolecule-layered structures even when being transferred to hydrophilic substrates (see AFM image, 3 μm × 3 μm).

Nanocluster Catalysts

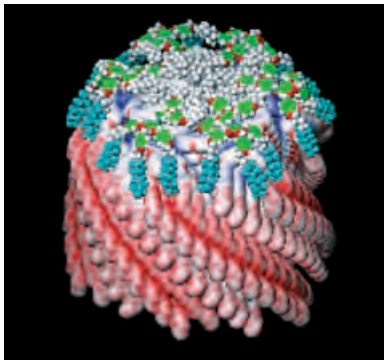
J. Chou, S. Zhang, S. Sun, E. W. McFarland* **4735 – 4739**

Benzene Formation at 70 °C by Coupling of Propylene on Supported Pd Nanoclusters



The pressure's off: The coupling of propylene (**1**) to generate benzene (**2**) at 70 °C and atmospheric pressure was observed together with propylene hydrogenation and oxygenation on titania-supported Pd nanoclusters (in green). The catalysts consist predominately of metallic Pd^0. The selectivity of benzene formation is dependent on cluster size ($\varnothing$ = 3–12 nm) and the presence of both hydrogen and oxygen.

 © 2005 Wiley-VCH Verlag GmbH & Co. KGaA, Weinheim



Two faces: Semifluorinated Janus-dendritic benzamides self-assemble into supramolecular bilayered pyramidal columns with diameters over twofold greater than those of columns generated from twin-dendritic benzamides (see model). The Janus-dendritic benzamides are synthesized by selectively replacing the aliphatic chains from the periphery of one of the two dendrons of a twin-dendritic benzamide with semifluorinated chains.

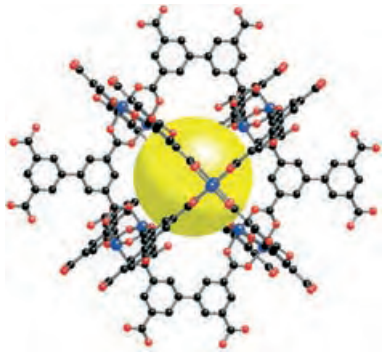
Liquid Crystal Dendrimers

V. Percec,* M. R. Imam, T. K. Bera, V. S. K. Balagurusamy, M. Peterca, P. A. Heiney ——— **4739 – 4745**

Self-Assembly of Semifluorinated Janus-Dendritic Benzamides into Bilayered Pyramidal Columns

---

A copper-based metal–organic framework (MOF) has been synthesized, and its structure has been solved by X-ray crystallography (see picture; Cu blue, C black, O red, framework pore yellow). The remarkably high hydrogen adsorption properties (2.47 wt%) of this compound have been studied.

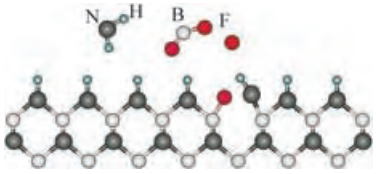


Microporous Materials

B. Chen,* N. W. Ockwig, A. R. Millward, D. S. Contreras, O. M. Yaghi* ——— **4745 – 4749**

High H_2 Adsorption in a Microporous Metal–Organic Framework with Open Metal Sites

---



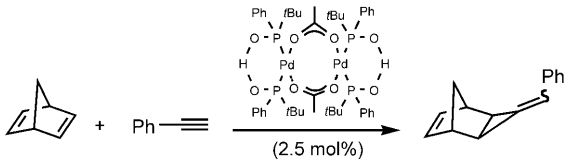
Growing pains: A new surface reaction mechanism for the growth of films of cubic BN (cBN) in an electron cyclotron resonance plasma fed with a reactive gas mixture ($BF_3/H_2/N_2$) is revealed. The excited plasma contains reactive H, F, BF_x, and NH_x species which are responsible for the etching of hexagonal BN (mainly through F atoms) and for the growth of the cBN crystals (through BF_x and NH_x species; see picture).

Chemical Vapor Deposition

W. J. Zhang,* C. Y. Chan, X. M. Meng, M. K. Fung, I. Bello, Y. Lifshitz, S. T. Lee, X. Jiang ——— **4749 – 4753**

The Mechanism of Chemical Vapor Deposition of Cubic Boron Nitride Films from Fluorine-Containing Species

---



Two plus one makes three-membered rings in an unusual [2+1] cycloaddition of phenylethyne with norbornadiene as catalyzed by a new palladium(II) complex with phosphinous acid ligands (see scheme). A related complex (cyclohexyl replaces *t*Bu) efficiently catalyzes the [2+1] cycloaddition of norbornene derivatives with various terminal alkynes to provide functionalized *exo*-alkylidenecyclopropanes.

Palladium-Catalyzed Chemistry

J. Bigeault, L. Giordano, G. Buono* ——— **4753 – 4757**

[2+1] Cycloadditions of Terminal Alkynes to Norbornene Derivatives Catalyzed by Palladium Complexes with Phosphinous Acid Ligands

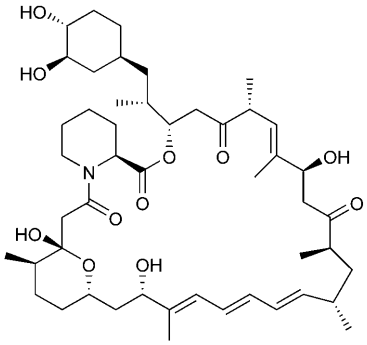
 © 2005 Wiley-VCH Verlag GmbH & Co. KGaA, Weinheim

Contents

Biosynthesis

M. A. Gregory, H. Petkovic, R. E. Lill, S. J. Moss, B. Wilkinson, S. Gaisser, P. F. Leadlay, R. M. Sheridan* ——— **4757 – 4760**

Mutasynthesis of Rapamycin Analogues through the Manipulation of a Gene Governing Starter Unit Biosynthesis



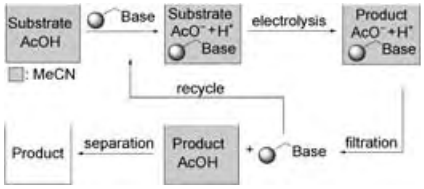
The surprising discovery has been made that the gene product RapK is required for production of the starter unit in the rapamycin polyketide cluster. It is shown that a deletion mutant (*Streptomyces hygroscopicus* MG2–10) provides a clean background for the mutasynthesis of prerapamycin (the precursor to rapamycin, see structure) when fed with novel starter units.

Electrochemistry

T. Tajima, T. Fuchigami* ——— **4760 – 4763**

An Electrolytic System That Uses Solid-Supported Bases for In Situ Generation of a Supporting Electrolyte from Acetic Acid Solvent

Re-usability is trumps: The electrolytic system presented here (see graphic) has been used for the anodic acetoxylation of various compounds to provide the corresponding acetoxylated products in good to excellent yields. The acetoxylated products and the solid-supported bases can easily be separated by filtration, and the separated solid-supported bases can be re-used many times.

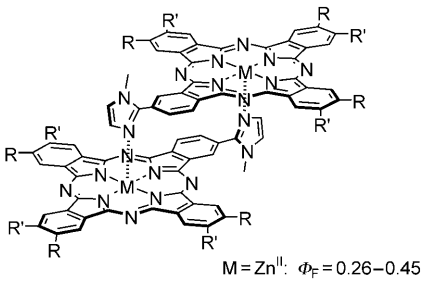


Metallophthalocyanines

K. Kameyama, M. Morisue, A. Satake, Y. Kobuke* ——— **4763 – 4766**

Highly Fluorescent Self-Coordinated Phthalocyanine Dimers

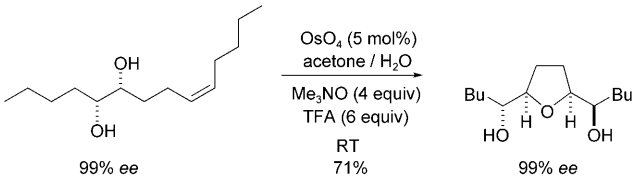
Head-to-tail self-assembly of two imidazolylphthalocyaninatozinc(II) or -magnesium(II) units through mutual imidazole–metal interactions leads to strongly fluorescent dimers (see picture, Φ_F = fluorescence quantum yield) that exhibit high association constants estimated at over $10^{11}\ M^{-1}$ in toluene.



Asymmetric Catalysis

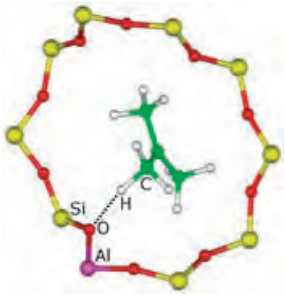
T. J. Donohoe,* S. Butterworth ——— **4766 – 4768**

Oxidative Cyclization of Diols Derived from 1,5-Dienes: Formation of Enantiopure *cis*-Tetrahydrofurans by Using Catalytic Osmium Tetroxide; Formal Synthesis of (+)-*cis*-Solamin



High yields and high levels of stereocontrol are observed in the oxidative cyclization of vicinal diols using catalytic amounts of a transition metal (see scheme; TFA = trifluoroacetic acid). The product stereochemistry is controlled completely by the starting material, and, importantly, single enantiomers can be accessed readily. The reaction sequence is demonstrated in a very short formal synthesis of the natural product (+)-*cis*-solamin.

 © 2005 Wiley-VCH Verlag GmbH & Co. KGaA, Weinheim



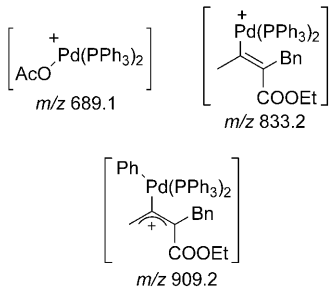
Substantially red-shifted as a result of hydrogen-bond formation with the zeolite framework: This characteristic of a C–H infrared band can be used to identify the *tert*-butyl carbenium ion in zeolite ferrierite (see picture). Above 120 K, this complex becomes more stable than the *tert*-butoxide or the isobutoxide of ferrierite.

Isobutene in Zeolites

C. Tuma, J. Sauer* ——— **4769 – 4771**

Protonated Isobutene in Zeolites: *tert*-Butyl Cation or Alkoxide?

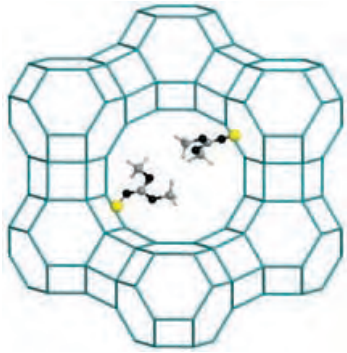
Three key intermediates in the palladium-catalyzed reaction of allenes with organoboronic acids in the presence of AcOH have been characterized by high resolution ESI-FT mass spectrometry (see picture). Their observation allows a better understanding of the reaction mechanism.



Mass spectrometry

R. Qian, H. Guo, Y. Liao, Y. Guo,* S. Ma* ——— **4771 – 4774**

Probing the Mechanism of the Palladium-Catalyzed Addition of Organoboronic Acids to Allenes in the Presence of AcOH by ESI-FTMS



Insight into the catalytic activity of NaY zeolite in dimethyl carbonate based methylation and carboxymethylation reactions is provided by a combination of vibrational spectroscopy and DFT-based computational methods. The enhanced activity and selectivity is due to the electric fields present in the confined spaces of the supercages (see picture).

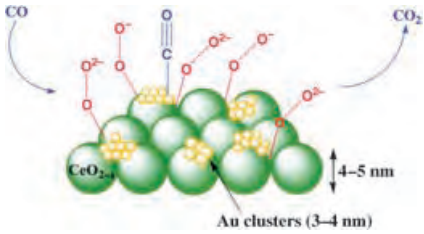
Zeolites

F. Bonino, A. Damin, S. Bordiga, M. Selva, P. Tundo, A. Zecchina* ——— **4774 – 4777**

Dimethyl Carbonate in the Supercages of NaY Zeolite: The Role of Local Fields in Promoting Methylation and Carboxymethylation Activity

---

Beneficial defects: Reactive η^1-superoxide and peroxide species at one-electron defect sites are formed at the metal–support interface in gold nanoclusters on nanocrystalline CeO_{2-x}. These intermediates oxidize CO adsorbed on gold to form CO_2. The reactive oxygen species are formed on nanocrystalline CeO_{2-x} (see picture) but not on conventional CeO_2, and their formation is enhanced by the gold.



Heterogeneous Catalysis

J. Guzman, S. Carrettin, J. C. Fierro-Gonzalez, Y. Hao, B. C. Gates, A. Corma* ——— **4778 – 4781**

CO Oxidation Catalyzed by Supported Gold: Cooperation between Gold and Nanocrystalline Rare-Earth Supports Forms Reactive Surface Superoxide and Peroxide Species

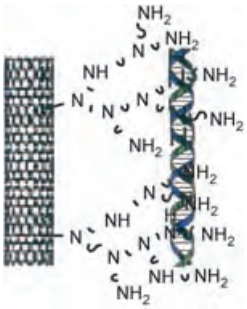
 © 2005 Wiley-VCH Verlag GmbH & Co. KGaA, Weinheim

Contents

Gene Technology

Y. Liu,* D.-C. Wu, W.-D. Zhang, X. Jiang, C.-B. He, T. S. Chung, S. H. Goh, K. W. Leong _____ **4782 – 4785**

Polyethylenimine-Grafted Multiwalled Carbon Nanotubes for Secure Noncovalent Immobilization and Efficient Delivery of DNA



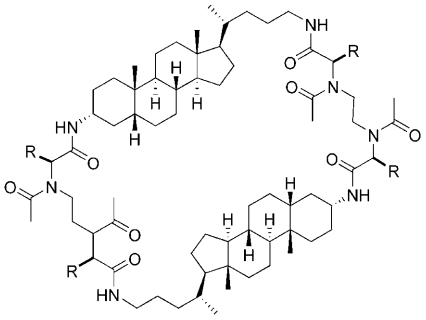
DNA hits the wall: DNA is immobilized securely onto the surface of multiwalled carbon nanotubes through electrostatic interactions with grafted polyethylenimine (PEI; see picture). The polyethylenimine-graft multiwalled carbon nanotubes carrying DNA show transfection efficiency for DNA delivery similar to or even several times higher than PEI.

Macrocycle Synthesis

L. A. Wessjohann,* B. Voigt, D. G. Rivera _____ **4785 – 4790**

Diversity Oriented One-Pot Synthesis of Complex Macrocycles: Very Large Steroid–Peptoid Hybrids from Multiple Multicomponent Reactions Including Bifunctional Building Blocks

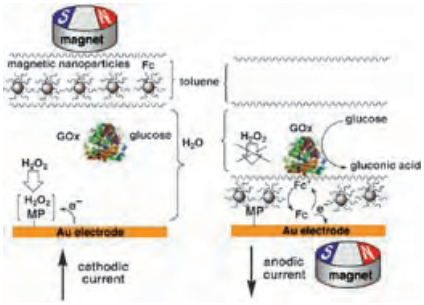
Sixteen in one go: Up to 16 new bonds connect 12 building blocks to form 54-membered macrocycles (46-membered example shown) in a one-pot procedure combining bifunctional components with multicomponent reactions. The large rings are not made of repetitive subunits and form an ideal basis for the fast construction of libraries of chiral host molecules.



Electrochemistry

E. Katz, I. Willner* _____ **4791 – 4794**

Switching of Directions of Bioelectrocatalytic Currents and Photocurrents at Electrode Surfaces by Using Hydrophobic Magnetic Nanoparticles



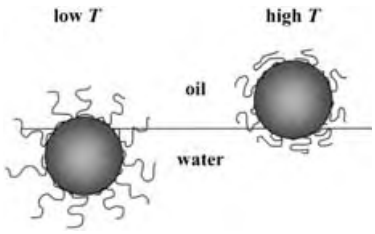
Magnetic switch: The direction of bioelectrocatalytic currents and photocurrents is demonstrated to be reversibly switched by the attraction and retraction of hydrophobic magnetic nanoparticles to and from the electrode surface in a water/toluene biphasic system (see picture; Fc = decamethylferrocene; MP = microperoxidase-11; GOx = glucose oxidase).

Nanoparticles

B. P. Binks,* R. Murakami, S. P. Armes, S. Fujii _____ **4795 – 4798**

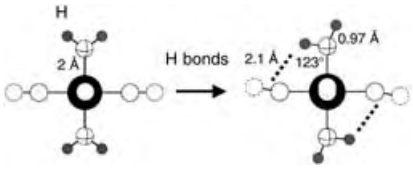
Temperature-Induced Inversion of Nanoparticle-Stabilized Emulsions

A change for the wetter: The effect of temperature *T* on the position of a sterically stabilized polystyrene latex particle adsorbed at an oil–water interface is described. Emulsions stabilized by such particle monolayers are oil-in-water at low *T* and water-in-oil at high *T* (see scheme). The results are also in line with the predicted change in the wettability of the particles in emulsions.



 © 2005 Wiley-VCH Verlag GmbH & Co. KGaA, Weinheim

Unexpectedly small: The Co^{II} crystal-field parameter in CoFe Prussian blue analogues is smaller than for any other octahedral Co^{II}(high-spin) molecular entity and it seems to be determined by the geometry of the Co coordination polyhedron, which is imposed by weak and strong cooperative interactions within the 3D structure rather than by the chemical nature of the ligands (see picture).

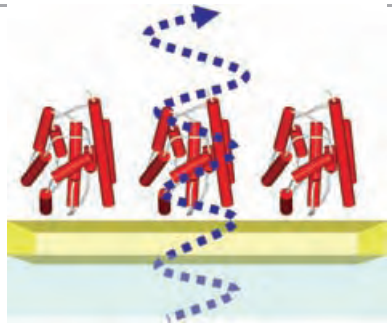


Prussian blue derivatives

V. Escax, G. Champion, M.-A. Arrio, M. Zacchigna, C. Cartier dit Moulin, A. Bleuzen* ——— **4798 – 4801**

The Co Ligand Field: A Key Parameter in Photomagnetic CoFe Prussian Blue Derivatives

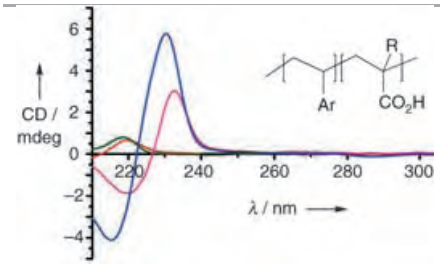
Thin but not invisible: The single layers of proteins needed for screening arrays and nanostructures can be studied by standard UV circular dichroism methods (see picture: colicin N P-domain on Au surface). In this way the conformational integrity of immobilized proteins can be measured under aqueous conditions, as is currently possible with their soluble counterparts.



Protein Folding

N. Keegan, N. G. Wright, J. H. Lakey* ——— **4801 – 4804**

Circular Dichroism Spectroscopy of Folding in a Protein Monolayer



Chirality chain: Copolymerization of (−)-sparteine zinc(II) dimethacrylate or diacrylate with styrene or 2-vinylnaphthalene monomers followed by removal of the zinc (−)-sparteine template yields the corresponding methacrylic or acrylic acid copolymers, with specific optical rotations that arise from the configurations of the main-chain stereogenic carbon atoms (see picture; R = H, Me; Ar = styryl, 2-vinylnaphthyl).

Chiral Polymerization

S. Jana, D. C. Sherrington* **4804 – 4808**

Transfer of Chirality from (−)-Sparteine Zinc(II) (Meth)acrylate Complexes to the Main Chains of Their (Meth)acrylate Polymer Derivatives

Sources

Product and Company Directory

You can start the entry for your company in "Sources" in any issue of ***Angewandte Chemie***.

If you would like more information, please do not hesitate to contact us.

Wiley-VCH Verlag – Advertising Department
Tel.: 0 62 01 - 60 65 65
Fax: 0 62 01 - 60 65 50
E-Mail: MSchulz@wiley-vch.de

Service

Keywords ——— ***4810***

Authors ——— ***4811***

Preview ——— ***4813***

 © 2005 Wiley-VCH Verlag GmbH & Co. KGaA, Weinheim

Corrigendum

Metallophosphite-Induced Nucleophilic Acylation of α,β-Unsaturated Amides: Facilitated Catalysis by a Diastereoselective Retro [1,4] Brook Rearrangement

M. R. Nahm, X. Linghu, J. R. Potnick, C. M. Yates, P. S. White, J. S. Johnson* _____ **2377–2379**

Angew. Chem. Int. Ed. **2005**, *44*

DOI 10.1002/anie.200462795

An important reference was omitted from this paper. Reich and co-workers reported the metallophosphite-induced Brook rearrangement nine years before the work cited in reference [10]. The authors apologize for this error. Reference [10] should read:

[10] a) H. J. Reich, R. C. Holtan, C. Bolm, *J. Am. Chem. Soc.* **1990**, *112*, 5609 – 5617; b) K. Takeda, T. Tanaka, *Synlett* **1999**, 705 – 708.

Technology for industrial applications and products in our modern life

14,000 pages at a special price. Save 85 % with the softcover edition



Cahn, R.W., Haasen, P., Kramer, E.J. (Eds.)

Materials Science and Technology – A Comprehensive Treatment

The Classic Softcover Edition
ISBN 3-527-31395-8
May 2005
Approx. 14,000 pages
11 Volumes. English.
€ 599.-/ SFr 886.- / US$ 780.-

The right choice of materials is essential for satisfying the consumers and customers needs.

"Materials Science and Technology" is forming the basis for modern research in the interdisciplinary field of materials science. It encompasses all different classes of materials - metals, alloys, ceramics, composites, semiconductors and polymers – and is essential for anyone involved in production and development of new products in modern industry.

This softcover edition offers the wealth of information of the renowned series "Materials Science and Technology" in one complete set of eleven volumes.

For ordering information, please contact our customer service:

Wiley-VCH · Tel.: +49 (0) 6201 606-400
E-Mail: service@wiley-vch.de · www.wiley-vch.de

John Wiley & Sons, Inc. · Tel.: +1 877-762-2974
E-Mail: custserv@wiley.com · www.wiley.com

John Wiley & Sons, Ltd. · Tel.: +44 (0) 1243-843-294
E-Mail: cs-books@wiley.co.uk · www.wiley.com

WILEY InterScience

WILEY-VCH WILEY

1908150_4_gu

 © 2005 Wiley-VCH Verlag GmbH & Co. KGaA, Weinheim



M. Quack to give Jost Lectures

Martin Quack (ETH Zürich, Switzerland) is to deliver the Wilhelm Jost Memorial Lecture Series of the Academy of Sciences in Göttingen (Germany) and the German Bunsen Society of Physical Chemistry. Quack studied chemistry in Darmstadt (Germany), Grenoble (France), and Göttingen. He obtained a doctorate from the Ecole Polytechnique Fédérale de Lausanne (Switzerland) for work on unimolecular reactions in the group of J. Troe. In 1976/77, he worked as a postdoc in the group of W. H. Miller (UC Berkeley). In 1978, he obtained a habilitation in physical chemistry from the University of Göttingen, where he subsequently worked as a professor until 1982. He then moved to the University of Bonn (Germany) and on to Zurich a year later. Quack has been a member of the editorial board of *Angewandte Chemie* since 2001.



M. Quack

Quack's research is focused on molecular kinetics and spectroscopy and the understanding of the fundamental physical and chemical processes. He successfully combines theoretical and experimental techniques, in particular high-resolution and time-resolved IR spectroscopy. Theoretical aspects of his work include approximations in quantum dynamics and time-resolved quantum dynamics of intramolecular energy flow and vibrational redistribution. His group also studies fundamental symmetry principles in molecular processes as well as molecular chirality and parity violation. He discussed progress in this area in a review in 2002 and in a recent communication in *Angewandte Chemie*.[1]

M. Chisholm Elected to US Academy

Last year, Malcolm H. Chisholm (Ohio State University, Columbus, USA) was recognized with the Fred Basolo Medal for Inorganic Chemistry of the American Chemical Society. He was also elected to the Akademie der Naturforscher Leopoldina in Halle (Germany). This year the trend continues: He was recently elected to the US National Academy of Sciences. The Chisholm group has developed a new generation of polymers by using alkoxide catalysts. They also investigate complexes with metal–metal multiple bonds, π-donor ligands in organometallic chemistry, and the synthesis of polyesters from cyclic esters which are obtained from biomass. A communication on polythiophenes with metal–metal bonds will appear in *Angewandte Chemie* soon.



M. Chisholm

Chisholm earned a PhD under the guidance of D. C. Bradley from London University (UK) in 1969, and subsequently moved to the University of Western Ontario (Canada) as a postdoc and lecturer in H. C. Clark's group. He moved to Princeton University in 1972 and to Indiana University in 1978. In 2000, he accepted his current professorship at the Ohio State University. From 1995 to 2001, he was a member of the editorial board of *Chemistry—A European Journal*.

DuPont Awards for P. Baran, T. Odom, and D. Zhao

The following researchers are among the recipients of the DuPont Young Professor Award 2005:

- Phil S. Baran, Scripps Research Institute in La Jolla, CA (USA), for his work on the total syntheses of complex natural products, such as Avrainvillamide and Stephacidin B;[2]
- Teri W. Odom, Northwestern University in Evanston, IL (USA), for her work on the synthesis and characterization of nanoscale materials, for example the directed growth of small-diameter ZnO nanowires in ordered arrays,[3] the development of new methods for this purpose, and the design of functional assemblies from nano- and mesostructures;
- Dongyuan Zhao, Fudan University in Shanghai (China), for his research on nanophase materials for embedded passive applications. His communication on mesoporous bioactive glasses was published in *Angewandte Chemie* recently.[4]

[1] a) M. Quack, *Angew. Chem.* **2002**, *114*, 4812; *Angew. Chem. Int. Ed.* **2002**, *41*, 4618, b) R. Berger, G. Laubender, M. Quack, A. Sieben, J. Stohner, M. Willeke, *Angew. Chem.* **2005**, *117*, 3689, *Angew. Chem. Int. Ed.* **2005**, *44*, 3623.

[2] P. S. Baran, C. A. Guerrero, B. D. Hafensteiner, N. B. Ambhaikar, *Angew. Chem.* **2005**, *117*, 3960, *Angew. Chem. Int. Ed.* **2005**, *44*, 3892.

[3] E. C. Greyson, Y. Babayan, T. W. Odom, *Adv. Mater.* **2004**, *16*, 1341.

[4] X. Yan, C. Yu, Xufeng Zhou, J. Tang, D. Zhao, *Angew. Chem.* **2004**, *114*, 6106, *Angew. Chem. Int. Ed.* **2004**, *43*, 5980.

 © 2005 Wiley-VCH Verlag GmbH & Co. KGaA, Weinheim DOI: 10.1002/anie.200502265

NMR Spectroscopy

Residual Dipolar Couplings—A Valuable NMR Parameter for Small Organic Molecules

*Ruth M. Gschwind**

Keywords:
gels · liquid crystals · NMR spectroscopy · polymers · structure elucidation

In the last ten years the structure determination of biomacromolecules by NMR spectroscopy has made vast progress owing to the development of new and valuable structural parameters. In addition to classical structural parameters (NOE/ROE data and scalar coupling constants), distance and/or angular information can now be gained from cross-correlated relaxation interferences, chemical shift anisotropies, or residual dipolar couplings (RDCs).[1] Especially RDCs, which require partially aligned molecules in the sample, have come to occupy a very important place in the structure determination of biomacromolecules, since they are quite easy to detect experimentally and the structural information gained from them is very valuable.[2a,b]

To recognize the tremendous potential of RDCs, it is essential to understand their physical basis. In principle, dipolar couplings are quite large interactions and well known from solid-state NMR spectroscopy. Through space the magnetic flux lines of one NMR-active nucleus affect the magnetic field at the site of another nucleus and vice versa, changing the effective fields at both nuclei. The size of the resultant coupling depends on the distance between the two nuclei as well as the direction of their internuclear vector relative to the external magnetic field (B_0). In isotropic solutions the angle-dependent dipolar interactions typically average to zero, owing to the uniform distribution of all orientations (rotational Brownian diffusion). As a result of this isotropic tumbling, the high-resolution NMR spectra show narrow linewidths in solution, which enable the assignment of large or complicated molecules. However, the valuable structural information on the orientations of the internuclear vectors is lost.

The challenge is now to preserve the small linewidths and to additionally gain the vectorial information about the structure from dipolar couplings. This is possible in partially anisotropic media, in which the dissolved molecules are still mobile but show some slightly preferred orientations. The slightly anisotropic tumbling of the molecules, that is, the alignment, is described by an alignment tensor, which is used to analyze the RDCs. At best, the dipolar couplings are reduced by about three orders of magnitude from many kHz in the static case to a few Hz in the partially aligned sample. In the resulting NMR spectra, the RDCs add to the corresponding scalar couplings and cause a splitting $J + D$ (Figure 1).

Although RDCs were originally discovered and theoretically explained for small molecules by A. Saupe in 1968,[2c] RDCs have only rarely been used for the structure determination of small organic molecules up to now. This lack of applications compared to their widespread use in biomacromolecular NMR spectroscopy is attributed to the design of the known alignment media for aqueous solutions. Now recent research results considerably extended the applications of RDCs to small molecules by developing and applying two kinds of alignment media for organic solvents: liquid-crystalline phases[3,4] and mechanically constrained polymer gels.[5] A disadvantage of liquid-crystalline phases is basically that a minimum concentration and thus a minimum alignment exists, which sometimes leads to problems in the analysis of standard spectra.[4b] This problem was solved

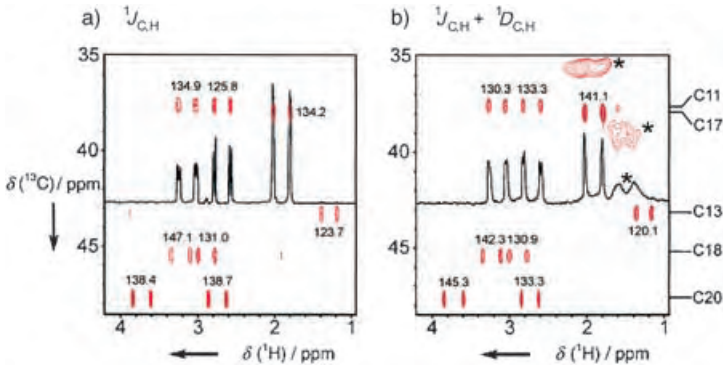


Figure 1. Sections of ^{1}H,^{13}C-HSQC spectra and traces through the HSQC spectra recorded on a strychnine sample without decoupling during acquisition in $CDCl_3$ without (a) and with anisotropic polystyrene gel (b).[5a]

[*] Prof. Dr. R. M. Gschwind
Institut für Organische Chemie
Universität Regensburg
Universitätsstrasse 31
93053 Regensburg (Germany)
Fax: (+49) 941-943-4617
E-mail:
ruth.gschwind@chemie.uni-regensburg.de

 © 2005 Wiley-VCH Verlag GmbH & Co. KGaA, Weinheim DOI: 10.1002/anie.200500634

elegantly by scaling the RDCs by variable angle spinning in a solid-state NMR spectrometer.[7] At present the most flexible approach that can be applied to several organic solvents and can include scalable alignment, without the employment of a solid-state NMR spectrometer, is the use of polymeric gels. This method is called "strain-induced alignment in a gel" (SAG) and was already applied successfully to biomacromolecules in aqueous solution. Initially, cross-linked polymers (e.g. polystyrene,[5a] poly(dimethylsiloxane),[5b] poly(vinyl acetate)[5c] or poly(acryl amide)[5d]) are synthesized. A cylindrical stick of the polymer is put into a standard NMR tube and after addition of an organic solvent the polymer swells to a gel. Owing to the shape of the NMR tube the gel does not swell isotropically but anisotropically along the glass wall of the tube (Figure 2). The resulting alignment of the dissolved molecules inside these gels can be easily adjusted by different amounts of cross-linking in the polymer as well as by varying the diameters of the unswollen polymer stick.

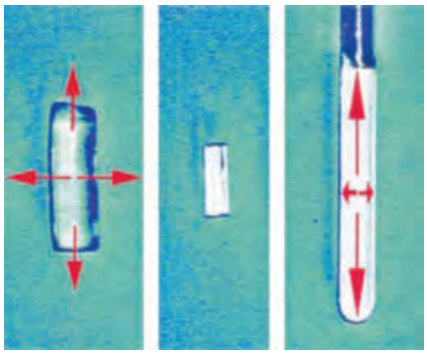


Figure 2. Isotropic (left) and anisotropic (right) swelling of a polystyrene stick (center: unswollen polymer stick).[5a]

The availability of anisotropic gels raises the question about the potential, the limitation, and the application of RDCs as structural parameters for small organic molecules. In principle the potential is tremendous: The distance dependence of RDCs is r^{-3} (versus r^{-6} for NOEs), which therefore allows longer-range internuclear interactions to be monitored. Provided that the distance is known (e.g. in CH moieties), valuable angular information about internuclear vectors relative to the static magnetic field can be obtained. This means that an absolute reference system can be used for the structure determination in solution. This fact is particularly important for molecules with a dearth of protons for which the elucidation of the configuration is not possible as long as only NOEs and scalar couplings are used.

The actual requirements and limitations of the method become apparent when describing the conventional way in which the calculations are performed. Initially, the alignment tensor, that is, the level and direction of order introduced by the partial alignment in the gel or liquid crystal, is calculated on the basis of the experimentally determined RDCs. For this purpose, a reliable structural model is necessary as well as at least five RDCs per fixed moiety that are independent of each other, as nonparallel C–H vectors. Taking into account the structural model used and the determined alignment tensor, the theoretical RDCs are calculated and compared with the experimental data. This cycle is repeated for all proposed structures and the actual structure is identified through significant differences in the correlation between theoretical and experimental RDCs (Figure 3). It is nontrivial to fulfil the described requirements especially for small molecules. First, reliable structural models have to be available from crystal structures or calculations. Second, molecular flexibilities lead to an averaging of the orientation-dependent RDCs, and third, single RDC values are not one-to-one but can originate from several vectorial orientations. This means that only in molecules with a fixed conformation or by a combination of different types of RDCs (e.g., $^{1}D_{C,H}$, $^{2}D_{C,H}$, $^{1}D_{C,C}$) from several spectra is it possible to reach the required high amount of RDCs per fixed molecular moiety. However, once systems meet these conditions, previously undreamt-of possibilities open up for determining the configuration of small organic molecules, which, on the basis of classical structural parameters, have not been possible up to now.

Present applications of RDCs in achiral alignment media are: assigning diastereotopic protons, determining the relative orientation of protons far away from each other, and elucidating the absolute configuration of diastereomers. In chiral gels or liquid crystals it is additionally possible to discriminate enantiomers.[6] Owing to the described requirements, up to now only molecules with rigid units have been used such as sugars,[8,9b] polycyclic molecules,[3,4b,5a–5c,9a] or molecules with fixed conformations in their cyclic moieties.[4a,c,5d]

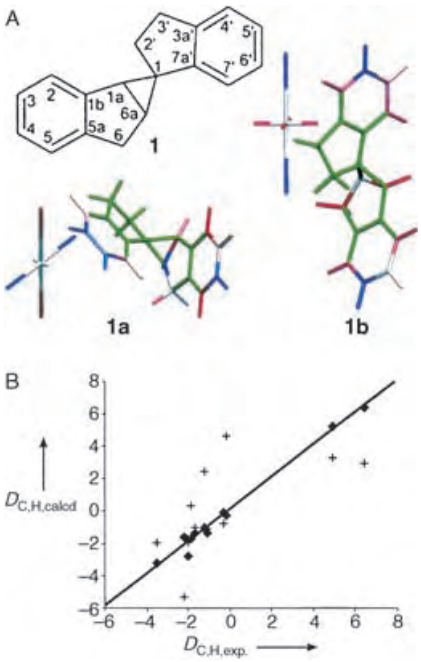


Figure 3. A) Differentiation of the diastereomers (**1a** and **1b**) of spiroindene (**1**) by RDCs (red: negative RDCs, blue: positive RDCs, green: no RDCs or RDCs not used in the analysis). B) A comparison of the experimental and the calculated RDCs, which shows a clear preference for **1b** in a poly(dimethylsiloxane) gel (PDMS gel); + **1a**, ◆ **1b**.[5b]

At first glance, the applicability of RDCs to small molecules seems to be limited by the calculation of the alignment tensor, the required rigidity of the investigated molecules, and the possibly stronger intermolecular interactions of small molecules with the alignment medium. However, the methodical development of RDCs for small organic molecules is still in its infancy.[10] Thus, first approaches exist to analyze RDCs without alignment tensors,[9b] the ambiguity of RDCs can be reduced by using several independent alignment media and the averaging of the RDCs due to internal motion is already used in bio-

 © 2005 Wiley-VCH Verlag GmbH & Co. KGaA, Weinheim

macromolecules to study dynamic processes on a time scale range between femtoseconds and milliseconds.[11] If the methodology of RDCs for organic molecules increases only half as much as it did for biomacromolecules, the structure determination of small organic molecules will be revolutionized during the next few years.

Published online: June 27, 2005

[1] O. Zerbe, *BioNMR in Drug Research*, *Vol. 16*, Wiley-VCH, Weinheim, **2003**.

[2] a) B. Simon, M. Sattler, *Angew. Chem.* **2002**, *114*, 453; *Angew. Chem. Int. Ed.* **2002**, *41*, 437; b) J. H. Prestegard, C. M. Bougault, A. I. Kishore, *Chem. Rev.* **2004**, *104*, 3519; c) A. Saupe, *Angew. Chem.* **1968**, *80*, 99; *Angew. Chem. Int. Ed. Engl.* **1968**, *7*, 97, and references therein.

[3] C. M. Thiele, *J. Org. Chem.* **2004**, *69*, 7403.

[4] a) C. Aroulanda, V. Boucard, F. Guibé, J. Courtieu, D. Merlet, *Chem. Eur. J.* **2003**, *9*, 4536, and references therein; b) C. M. Thiele, S. Berger, *Org. Lett.* **2003**, *5*, 705; c) L. Verdier, P. Sakhaii, M. Zweckstetter, C. Griesinger, *J. Magn. Reson.* **2003**, *163*, 353.

[5] a) B. Luy, K. Kobzar, H. Kessler, *Angew. Chem.* **2004**, *116*, 1112; *Angew. Chem. Int. Ed.* **2004**, *43*, 1092; b) J. C. Freudenberger, P. Spiteller, R. Bauer, H. Kessler, B. Luy, *J. Am. Chem. Soc.* **2004**, *126*, 14690; c) J. C. Freudenberger, S. Knör, K. Kobzar, D. Heckmann, T. Paululat, H. Kessler, B. Luy, *Angew. Chem.* **2005**, *117*, 427; *Angew. Chem. Int. Ed.* **2005**, *44*, 433; d) P. Haberz, J. Farjon, C. Griesinger, *Angew. Chem.* **2005**, *117*, 431; *Angew. Chem. Int. Ed.* **2005**, *44*, 427.

[6] a) M. Sarfati, P. Lesot, D. Merlet, J. Courtieu, *Chem. Commun.* **2000**, 2069; b) K. Kobzar, H. Kessler, B. Luy, *Angew. Chem.* **2005**, *117,* 3205; *Angew. Chem. Int. Ed.* **2005**, *44,* 3145, and references therein.

[7] C. M. Thiele, *Angew. Chem.* **2005**, *117*, 2847; *Angew. Chem. Int. Ed.* **2005**, *44*, 2787.

[8] D. I. Freedberg, *J. Am. Chem. Soc.* **2002**, *124*, 2358.

[9] a) J. L. Yan, F. Delaglio, A. Kaerner, A. D. Kline, H. P. Mo, M. J. Shapiro, T. A. Smitka, G. A. Stephenson, E. R. Zartler, *J. Am. Chem. Soc.* **2004**, *126*, 5008; b) J. L. Yan, A. D. Kline, H. P. Mo, M. J. Shapiro, E. R. Zartler, *J. Org. Chem.* **2003**, *68*, 1786.

[10] J. L. Yan, E. R. Zartler, *Magn. Reson. Chem.* **2005**, *43*, 53.

[11] a) W. Peti, J. Meiler, R. Brüschweiler, C. Griesinger, *J. Am. Chem. Soc.* **2002**, *124*, 5822; b) J. R. Tolman, *J. Am. Chem. Soc.* **2002**, *124*, 12020.

 © 2005 Wiley-VCH Verlag GmbH & Co. KGaA, Weinheim

Microporous Materials

Strategies for Hydrogen Storage in Metal–Organic Frameworks

*Jesse L. C. Rowsell and Omar M. Yaghi**

Keywords:
adsorption · hydrogen · metal–organic frameworks · microporous materials · organic–inorganic hybrid composites

Increased attention is being focused on metal–organic frameworks as candidates for hydrogen storage materials. This is a result of their many favorable attributes, such as high porosity, reproducible and facile syntheses, amenability to scale-up, and chemical modification for targeting desired properties. A discussion of several strategies aimed at improving hydrogen uptake in these materials is presented. These strategies include the optimization of pore size and adsorption energy by linker modification, impregnation, catenation, and the inclusion of open metal sites and lighter metals.

1. Introduction

The scope of the United States Hydrogen Initiative[1] has captured the attention of industrial and academic researchers around the world.[2] A measure of success has already been achieved by the initiative; specifically, the uncovering of the extent by which current technology must advance to bring about the use of hydrogen as an energy carrier.[3] Among the challenges facing hydrogen production, distribution, storage, and usage, the improvements required for the safe and efficient storage of the volatile fuel have been cited as the most formidable. As a corollary, it has been claimed that if a breakthrough in hydrogen storage were realized, a favorable impetus would be applied to resolving the other issues. Several reviews have appeared on the use of hydrogen as a fuel and its storage in various media, many of which are cited below. Herein, a brief discussion is presented on hydrogen storage requirements and the current state-of-the-art of established systems. This Review is focused on the use of metal–organic frameworks (MOFs) as new hydrogen storage materials.

[*] J. L. C. Rowsell, Prof. Dr. O. M. Yaghi
Materials Design and Discovery Group
Department of Chemistry
Ann Arbor, MI 48109-1055 (USA)
Fax: (+1) 734-615-9751
E-mail: oyaghi@umich.edu

2. Hydrogen Storage Requirements

The most compelling goals for hydrogen storage involve transportation (on-board) applications. There are two reasons for this: first, the transportation sector represents the largest consumer of oil, thus making it one of the largest sources of airborne pollutants such as carbon and nitrogen oxides. Secondly, the efficiency and economic demands to make hydrogen competitive with fossil-fuel technology are more challenging than for stationary storage. The current targets set by the U.S. Department of Energy (DOE) have been made with the concept that today's vehicles will be powered by tomorrow's higher efficiency fuel-cell power sources. The vehicles should have a similar range (480 km or 300 miles), operate at close to ambient conditions, and be quickly and safely refueled. As hydrogen has approximately three times the gravimetric energy density of petrol, and fuel cells are expected to perform at least twice as efficiently as internal combustion engines, only 5–10 kg of hydrogen must be stored (although 4 kg or less would be required by smaller, more practical passenger cars[4]). The 2010 energy density targets for the hydrogen storage system (including container and necessary components) are 7.2 MJ kg^{-1} and 5.4 MJ L^{-1}, which translates as 6.0 wt % and 45 kg H_2 per m^3.[3] The goals for 2015 are even more demanding: 9.0 wt % and 81 kg H_2 per m^3, which approach the expectations of the automotive industry.[5] This daunting task is easily put into perspective by noting that the mass density of elemental hydrogen is only 70.8 kg m^{-3} in its liquid state at 20 K (1 atm), and that 5 kg of hydrogen gas

 © 2005 Wiley-VCH Verlag GmbH & Co. KGaA, Weinheim DOI: 10.1002/anie.200462786

fills a volume of 56 m^3 under ambient conditions. Furthermore, both of these insights ignore the contribution of the mass of the necessary container.

3. Current Storage Technologies

Compressed hydrogen gas and cryogenically stored liquid hydrogen are the most developed technologies, and are currently utilized in the demonstration vehicles of several automotive manufacturers. While a systems analysis shows that they meet the technical aspects of the DOE 2010 targets, they are unlikely to comply with future ones.[6] In all cases, the containment vessel contributes at least 90% of the system mass, but there is still room for improvement with respect to the maximum pressure that can be maintained (operation at 825 bar is now being demonstrated[7]) or the minimization of liquid boil-off in cryogenic systems.[8] A significant drawback of cryogenic storage is the large amount of energy input necessary for condensation, approximately 40–50% of the fuel's lower heating value.

Understandably, the possibility of breakthroughs in storage efficiency has been sought by chemical means.[9] Solid metal hydrides[10] have been studied for many years, particularly for understanding the process of metal embrittlement upon absorption of hydrogen at interstitial sites. After surface adsorption, molecular hydrogen may dissociate into atoms that form a solid solution of a hydride phase in the metal or alloy or generate an intermetallic region. The uptake of hydrogen continues at nearly constant pressure until the pure hydride phase is formed, which may have volumetric densities of 150 kg H_2 per m^3 (Mg_2NiH_4).[4] In favorable cases this process is reversible and cycling can occur at desirable pressures (1–10 bar). For materials with a significant capacity for hydrogen, however, desorption usually occurs at a higher temperature than the targeted conditions. Improving the uptake/release kinetics and retention of cycling capacity are currently the major areas of materials research. The disadvantages of these compounds include high cost, susceptibility to impurities, and low reversible gravimetric capacity (typically less than 3 wt%).

To circumvent some of these issues chemical hydrides (also called complex or covalent hydrides) such as $NaAlH_4$ have been studied and shown to reversibly cycle hydrogen on doping with a catalyst.[11] Indeed, the DOE has deemed this material worthy of extensive study, as a result of its reversible release of 4.5 wt% hydrogen.[3] Other alanates and borohydrides of Groups 1, 2, and 13 elements have large gravimetric capacities (> 7 wt%), but the extent to which their hydrogen sorption is reversible requires continued investigation. Hydrolysis of alkali metals and their hydrides is also a convenient route for hydrogen release, but requires off-board recycling of the decomposition products.[3,12] Most of these chemical methods still require demonstration of both physical and economic viability.

The fastest way to charge and discharge a storage vessel with hydrogen is to maintain its molecular identity. To reduce the mechanical requirements of pressurized vessels highly porous materials have been investigated for their ability to physisorb molecular hydrogen. This arrangement could potentially allow the confinement of greater masses of fuel within a smaller volume. Carbon materials have received the most attention in this area, because of their low density, high surface area, good chemical stability, and amenability to a wide range of processing conditions. It is precisely this last aspect that has led to controversy with respect to the maximum volume they can adsorb. Since the first account of hydrogen adsorption by carbon nanotubes,[13] a wide range of uptake values have been reported, from negligible to fantastically large. Recently, more consistent results have been achieved by research groups examining many varieties of sample preparations, morphologies, and activations in a single study. Unfortunately, these have revealed adsorption of approximately 5% at 77 K and < 1% at room temperature under high pressure.[14] Theoretical modeling studies of the interaction of hydrogen with carbon in systems of many geometries and scales has been performed to provide a rationale for the larger uptake values. The general conclusion reached is that uptake of only a few wt% is achievable with this class of materials.[15] However, reports of improved uptake on changing the morphology have appeared recently.[16]

Research surrounding hydrogen uptake in carbon materials has highlighted several key points, including the importance of sample and measurement reproducibility by independent investigators, the necessity of establishing standard samples for instrumental calibration (especially for gravimetric methods where adsorbate contamination is a significant



Omar M. Yaghi was born in Amman, Jordan (1965). He received his BS in chemistry from the State University of New York--Albany (1985) and his PhD from the University of Illinois-Urbana (1990) with Prof. Walter Klemperer. After postdoctoral research at Harvard University with Prof. Richard Holm (1990 to 1992) he joined the faculty at Arizona State University. In 1999, he moved to the University of Michigan as a Professor of Chemistry and was later awarded the Robert W. Parry Collegiate Chair. His research concerns the reticular synthesis of discrete polyhedra and extended frameworks from organic–inorganic building blocks.



Jesse Rowsell was born in Black River-Matheson, Ontario, and began his studies of chemistry at the University of Waterloo in Canada. While obtaining his BSc, he performed research on diverse projects including reversible lithium-ion batteries, aluminum hydrolysis, and atmospheric aerosols. With fellowships from the NSERC and the Link Foundation, he is continuing to explore his research interests of the structure and physical properties of solids at the University of Michigan. His efforts there have earned graduate awards for both teaching and research.

 © 2005 Wiley-VCH Verlag GmbH & Co. KGaA, Weinheim

issue), and the utility of theoretical studies to gain insight into the details of the uptake mechanism. These lessons can (and should) be applied to the future studies of novel adsorbents. The other point that has been gleaned from this period of research is that hydrogen storage is still awaiting its breakthrough material.

4. Crystalline MOFs as New Materials for Hydrogen Storage

Metal–organic frameworks (MOFs) are crystalline solids that are assembled by the connection of metal ions or clusters through molecular bridges.[17] As such, they have the potential to exhibit properties inherent to the building blocks, such as geometric rigidity, chemical functionality, or chirality. Their simple preparations are generally high yielding and scalable, and by careful use of the building blocks a certain degree of design can be wielded to produce targeted products from the vast number of MOFs that are potentially accessible. One simple outcome of the use of molecular, rather than monatomic, bridges is the extension of the length between the metal centers, which can lead to the definition of large void regions (Figure 1). Considerations of the geometric requirements for a target framework and implementation of the design and synthesis of such a framework have been termed reticular synthesis. This process requires both an understanding of the local coordination patterns of the metal and organic units and foreknowledge of what net topologies they will adopt.[18] The accumulation of knowledge that has given rise to such precepts has primarily resulted from their crystalline nature, which allows a high degree of structural characterization to be achieved through X-ray diffraction methods.

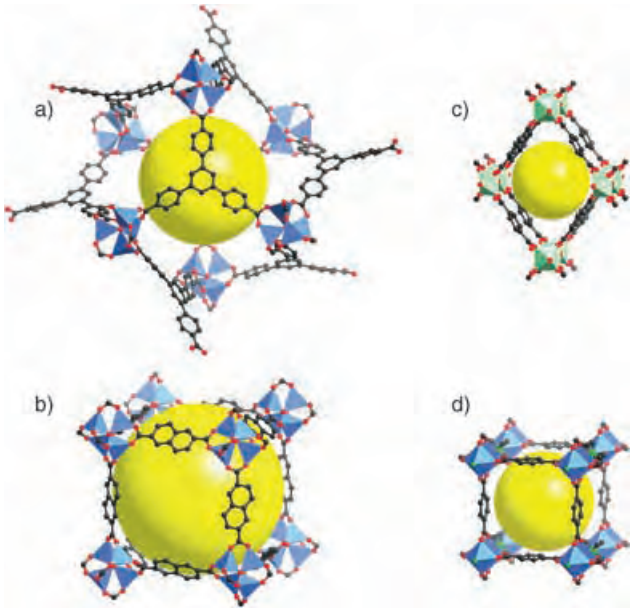


Figure 1. Examples of metal–organic frameworks (MOFs) studied for hydrogen adsorption include a) MOF-177, $Zn_4O(btb)_2$ (btb = benzene-1,3,5-tribenzoate), b) IRMOF-8, $Zn_4O(ndc)_3$ (ndc = naphthalene-2,6-dicarboxylate), c) MIL-53, M(OH)(bdc) (M = Al^{3+} or Cr^{3+}), and d) $Zn_2(bdc)_2(dabco)$ (dabco = 1,4-diazabicyclo[2.2.2]octane). The properties of these compounds are listed in Table 1. Pores in the evacuated crystalline frameworks are illustrated by yellow spheres that contact the van der Waals radii of the framework atoms (C: black, N: green, O: red, Zn: blue polyhedra, M: green octahedra).

Highly crystalline MOFs are also inherently pure in form. The materials are generally prepared in "one-pot" solvothermal syntheses under mild conditions. Powder X-ray diffraction is a simple and effective technique to establish the purity of the crystalline fraction, which often approaches 100% of the sample. Synthetic reproducibility with high purity is essential for the establishment of structure–property relationships, and this issue has been reiterated many times in the studies of hydrogen storage materials.

The cavities within MOFs are filled with solvent molecules in their as-synthesized forms. Successful establishment of permanent porosity has been accomplished in many cases, with the material stable upon removal of the guest species. This is most conveniently demonstrated by the measurement of gas adsorption isotherms, typically using dinitrogen at its normal boiling point. All porous MOFs to date are microporous by IUPAC definition, having cavities less than 2 nm in size and displaying type I isotherms.[19] Two values are typically calculated from these measurements to allow the porosity to be compared: surface area and pore volume. Type I isotherms can often be described by the Langmuir model, which assumes that a homogenous monolayer of the adsorbate is formed on the walls of the adsorbent. An extension to this model to describe multilayer adsorption has given rise to the commonly used Brunauer, Emmett, and Teller (BET) equation, which is primarily used to determine the point at which monolayer coverage is obtained. In either case, the apparent surface area is calculated as the product of the estimated value of monolayer uptake and an accepted value for the area occupied by an adsorbate molecule. While these models do allow simple comparisons of microporous materials, their assumptions are not always appropriate, especially since pore-filling is the predominant mode of uptake. When multilayer adsorption is possible (such as when the width of the pore is greater than three times the adsorbate diameter) or the assumed molecular area is too large (as can occur if the N_2 molecules are oriented as a consequence of strong quadrupolar interactions with surface sites), then an overestimation of the "true" surface area is possible. Sensibly, all equations and parameters used to calculate surface areas should be reported to facilitate adequate comparisons. The micropore volume, usually calculated by the Dubinin–Radushkevich method, is a complementary and perhaps better descriptor of the porosity of a material.[20]

An outstanding property of MOFs that has prompted their study as hydrogen storage candidates is their large apparent surface areas. Many MOFs are now reported in the literature with surface areas greater than 1000 $m^2 g^{-1}$, which is higher than that demonstrated for zeolites. In particular, the dinitrogen isotherm measured for MOF-177 (Figure 1a) at 77 K exhibits the highest uptake of N_2 for any material to date, and gives rise to a monolayer-equivalent surface area of 4500 $m^2 g^{-1}$.[21] The micropore volume is calculated to be 0.69 $cm^3 cm^{-3}$, and single-crystal X-ray diffraction studies

 © 2005 Wiley-VCH Verlag GmbH & Co. KGaA, Weinheim

reveal the framework has cavities of 10.9–11.8 Å diameter connected in all directions by channels. The initial study of the hydrogen uptake by this material at 77 K revealed that while it did not reach saturation at 1 atm, it adsorbed comparatively less than other related materials displaying smaller surface areas.[22] Supercritical hydrogen, as expected, adsorbs more weakly than dinitrogen at 77 K, and pore-filling is not possible at reasonable pressures. Thus, both pore geometry and surface structure must be optimized to increase the uptake in these materials. This study was particularly instructive in demonstrating the diversity in MOFs over nanostructured carbon materials, which show a positive trend in hydrogen uptake with surface area.[14c,15a] As MOFs are composed of a great assortment of chemical moieties that are characterized to a higher degree (by crystallography), they hold more promise for establishing which structural factors are most effective in adsorbing hydrogen.

5. Strategies for Hydrogen Adsorption in MOFs

In the initial report of hydrogen uptake by MOFs alteration of the linking moiety in isoreticular frameworks was shown to improve the uptake to a level of 2.0 wt% in IRMOF-8 (Figure 1b) at 293 K and 10 bar.[23] Saturation uptake is not reached under these conditions and increased pressure results in greater adsorption. For experimental convenience, most reports since then have studied the uptake at 77 K up to 1 atm. The gravimetric uptakes measured under these conditions on a larger subset of Zn_4O-based MOFs also did not exhibit saturation.[22] Calculation of the fraction of the void volume occupied by hydrogen in each material revealed it to be quite low, that is, only a small amount of the surface—let alone the pore volume—is occupied by the guests. This study and others[15a,24] have highlighted the need to optimize pore size to reduce the fraction of under-utilized void space, thereby increasing the volumetric capacity and attractive adsorbate–adsorbent interactions.

5.1. High Porosity with Appropriate Pore Size

The ideal pore size for maximal attraction of an adsorbate is the same as its diameter. This situation results in optimal interaction with all the surrounding adsorbent walls, regardless of geometry, thus maximizing the total van der Waals force on the adsorbate. For adsorbents with thick or dense walls, however, this situation leads to impractically low hydrogen uptake values, as demonstrated for slit and cylindrical pores in nanostructured carbon materials.[15a] Instead, a simple geometric structure resembling a scaffold is preferable. In terms of general considerations, the walls of an adsorbent should be composed of light elements, be as thin as possible (that is, one atomic layer thick, as in graphite), and be highly segmented. A simple calculation demonstrating the advantage of segmenting graphene sheets has recently been reported.[21] The incision process that isolates groups of aromatic rings from each other results in an increased surface area as more edges become exposed. The challenge is to separate these isolated units, and this has already been addressed in MOFs by reticular synthesis. Organic units that represent isolated graphene segments include phenylene, terphenylene, and benzene-1,3,5-triphenylene. These moieties can be reticulated into frameworks where they are isolated from each other by functionalizing their termini with coordinating groups and linking them with metal ions or clusters, as illustrated in Figure 1. This is an alternative perspective of the approach first used to engender porosity in these solids, as described above.

Many MOFs reported, however, have spacings between their walls (or links) that are too large for the effective adsorption of hydrogen. For example, the distance between phenylene faces in MOF-5 describe an approximately spherical pore that is 15 Å in diameter, which is much larger than the 2.89 Å kinetic diameter of H_2 (Figure 2).[25] There would be an unused void volume at the center of these pores that would detract from the volumetric packing density, even at monolayer coverage. To approach the targeted guidelines for H_2 storage it is ultimately required that the density of the adsorbed hydrogen surpasses that of its liquid state. To improve this situation in MOFs, smaller pores are necessary. This arrangement can be afforded by the use of shorter links and the investigation of new topologies. A rigid linear dicarboxylate such as acetylenedicarboxylate is required to stabilize a smaller pore analogue of MOF-5. This is an attractive target for future syntheses, but it is not necessary to only consider simple cubic topologies of this type. By simply distorting the primitive cubic net—for example, by shearing along the face or body diagonals—the pores become elliptical and their shortest dimension is reduced. There are a vast number of smaller pore structures with various topologies that have been published, and their H_2 adsorption requires investigation. While MOFs with constricted pores may exhibit smaller gravimetric capacities, gains may be made in volu-

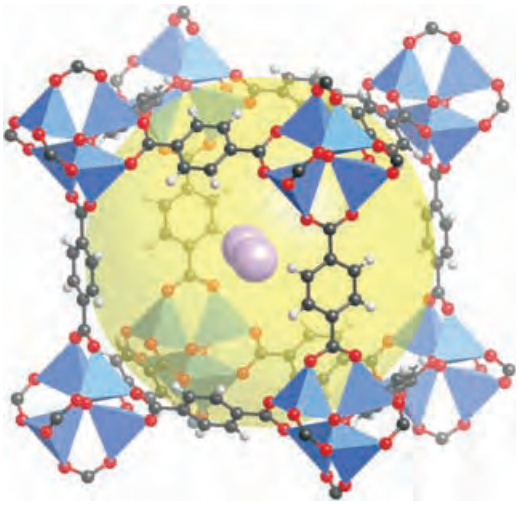


Figure 2. The large pore (yellow sphere) in MOF-5 is 15.2 Å in diameter, much larger than the size of a hydrogen molecule (lilac, shown with atomic van der Waals radii of 1.2 Å) which has a kinetic diameter of 2.89 Å. Framework atoms C: black, H: white, O: red, Zn: blue tetrahedra.

 © 2005 Wiley-VCH Verlag GmbH & Co. KGaA, Weinheim

metric capacity.[24] In addition, MOFs with very short linkers that may at first not appear to be porous from dinitrogen adsorption studies, may be composed of apertures that are too small to admit N_2, but are large enough to allow the passage of H_2.[26] From a design perspective, however, it must always be borne in mind that as the framework density increases, the gravimetric H_2 capacity decreases and therefore a compromise must be found.

5.2. Impregnation

Another approach for pore-size and hydrogen volumetric density optimization is to insert another adsorbate surface within large-pore MOFs. This can be achieved by either impregnation with a nonvolatile guest or catenation by another identical framework. It has been shown that large molecules such as C_{60} and Reichardt's dye can be included into MOF-177 from the solution phase.[21] In addition to reducing the free diameter of the pores, such guests may provide additional adsorptive sites (Figure 3). Impregnation with reactive species could provide the more attractive sites that are ultimately necessary to improve hydrogen uptake at room temperature. As expected, there is a doping level that is reached where the additional mass added by the guest is not compensated by additional hydrogen uptake. The guest should also not block the existing adsorptive sites on the framework, instead straddling the pore with minimal framework contacts. Conversely, the guest must be well-anchored or have very low vapor pressure to prevent its desorption along with the hydrogen. These considerations imply that lightweight and reactive, but large and spindly molecules or complexes are required. Structure–property relationships of impregnated MOFs are essentially unexamined to date.

5.3. Catenation

Framework catenation has long been a topic of interest in MOF research. The intergrowth of two or more frameworks is allowed for many high-symmetry, default topologies and is often observed when long linkers are used. Catenation can take the form of interpenetration, where the frameworks are maximally displaced from each other, or interweaving, where they are minimally displaced and exhibit many close contacts.[27] The most immediate consequence of catenation is a reduction of the free diameter of the pores (shown schematically in Figure 4a–c), therefore, it is a viable strategy for improving hydrogen uptake. There is already some evidence supporting this: in a series of Zn_4O carboxylates studied, the interwoven IRMOF-11 material showed the greatest hydrogen uptake at 77 K.[22] Fourfold catenated IRMOFs have been reported recently to adsorb approximately 1 wt% hydrogen at room temperature and 48 bar.[28]

Interpenetration rather than interweaving is desirable to maximize the exposed surfaces of catenated frameworks. Although interweaving can lead to reinforcement of the individual frameworks, by improving the rigidity and favoring stability in the absence of guests, this is a result of an effective

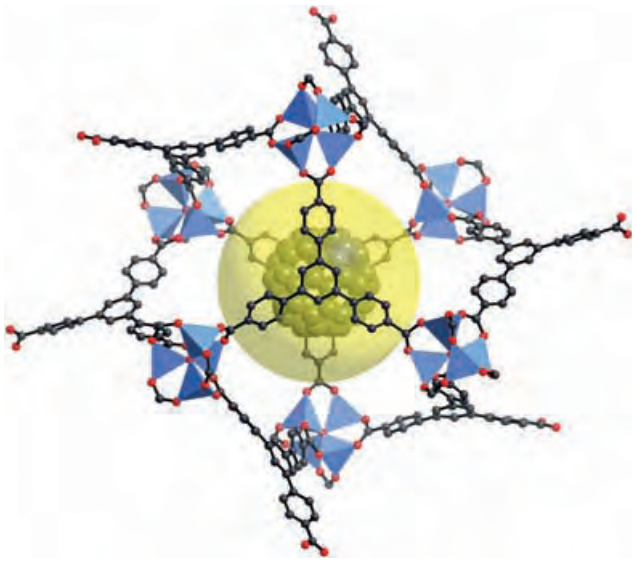


Figure 3. The large pore (yellow sphere) in MOF-177 is 11.8 Å in diameter, large enough to include C_{60} molecules that may provide additional surface sites for the physisorption of H_2.

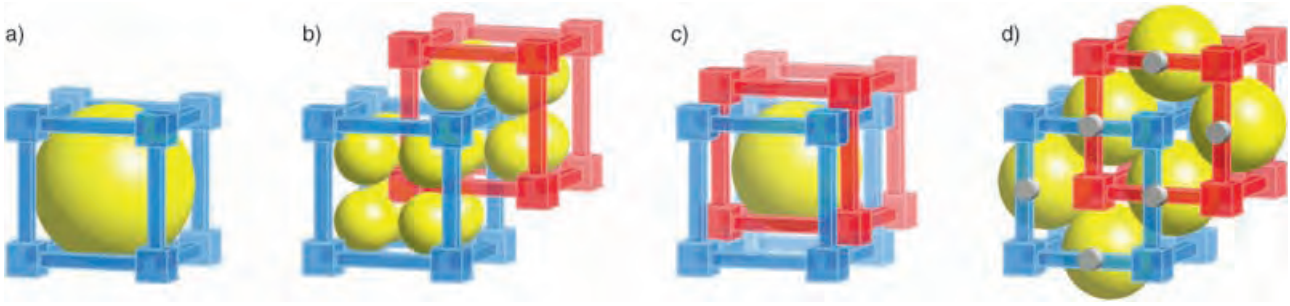


Figure 4. a) Schematic representation of the repeat unit of a crystalline, single-framework MOF with secondary building units (SBUs) shown as cubes and linkers depicted as rods. The yellow sphere represents the large pore defined within the framework. Catenation of two identical frameworks can be used to restrict the dimensions of the pore considerably by interpenetration (b) or to a lesser extent by interweaving (c). Interweaving can improve the material's rigidity by mutual reinforcement; however, this is a result of thicker walls and results in the blockage of potential adsorptive sites. An alternative catenation mode (d) can be achieved by reducing the close contacts between the frameworks to only the midpoints of a proportion of the linkers, as represented by gray discs. The pore dimensions are considerably reduced while a large proportion of the framework atoms, including the SBUs, are still exposed.

 © 2005 Wiley-VCH Verlag GmbH & Co. KGaA, Weinheim

thickening of the walls. Thus, the number of framework atoms and their associated adsorptive sites that are exposed to the pore volume is reduced. Conversely, interpenetration decreases the pore size without blocking any adsorptive sites and in most cases also leads to a more convoluted void region. This is not expected to have an appreciable impact on the diffusion rate of supercritical hydrogen through the solid unless the apertures constrict to the size of the H_2 kinetic diameter.

Although conceptually it seems that interpenetrated frameworks should be targeted over interwoven ones, this mode of catenation is unlikely to be sustained in the evacuated state. Most catenated frameworks to date in fact exhibit interweaving, while those that are truly interpenetrated have free solvent molecules separating the individual frameworks where void regions do exist. Examples of the latter include MOF-9[29] and IRMOF-15.[30] It is inevitable that during the evacuation process attractive interactions between catenated frameworks will result in their interweaving. The extent to which this occurs, that is, the proportion of framework atoms that are involved in close contacts, could be minimized by incorporating specified chemical features that would locally attract each other. For example, the inclusion of a hydrogen bond donor–acceptor group at the midpoint of a linker could lead to localized interframework contacts only at the linker midpoints, thus leaving ample distance between the secondary building units (SBUs, Figure 4d). This arrangement would be optimal in the situation where the primary adsorptive sites are on the SBUs and blocking of them results from full interweaving.

5.4. Open Metal Sites

Perhaps the most attractive structural element of secondary building units in some MOFs is coordinative unsaturation, which can be achieved for metal clusters that have additional terminal ligands bound to them. Quite often these are solvent molecules coordinated to the metal by a Lewis acid/base interaction, and may be liberated with heating as neutral guest species. In the most favorable cases, the terminal ligand is removed without detriment to the framework and an open metal site is exposed to the void region. This has typically been achieved for axial ligands bound to metals displaying a Jahn–Teller distortion, most prominently Cu^{2+} ions.[31] Ligand field effects result in the binding of the axial ligand being sufficiently weak to allow its release. In addition, the resulting geometry (square planar for the example of the dimeric Cu^{2+} "paddlewheel", Figure 5a) is stable and consistent with the symmetry requirements of topologies such as those adopted by MOF-11 and HKUST-1 (Figure 5b and c, respectively). MOFs composed of metal clusters with lesser rigidity or constructed of metal ions that lack the electronic requirements to sustain an open metal site commonly collapse after loss of the terminal ligands, but may rearrange to a new form displaying permanent porosity.[32] Another strategy for constructing MOFs with open metal sites is to embed these within the linker. This has been achieved using the equatorially chelating ligand *N*,*N*′-phenylenebis(salicylideneimine)dicarboxylate, that can be used to construct a framework isoreticular with MOF-69[33] after binding a metal ion at its center.[34] The solvent molecules axially coordinated to the linker-bound metal should be removable after framework construction, since the metal is not a key component of the framework. The prospects of exposing open metal sites in a porous material are exciting indeed. To date, these have been divalent cations that are too electron deficient to be expected to form metal hydrides or hydrogen σ complexes. Their coordinative unsaturation, however, may lead to stronger physisorption and is concurrent with a decrease in the density of the framework as a result of the loss of the terminal ligands. Evidence for stronger binding of H_2 to open Ni^{2+} sites has been presented recently for an open-framework phosphate.[35] The possibility of incorporating other metals with coordinative unsaturation that will reversibly chemisorb hydrogen is plausible and this is an admirable target for future syntheses.

5.5. MOFs of Light Metals

One consideration that should not be overlooked while exploring MOFs composed of other metals is the need to reduce the framework density to enhance gravimetric hydro-

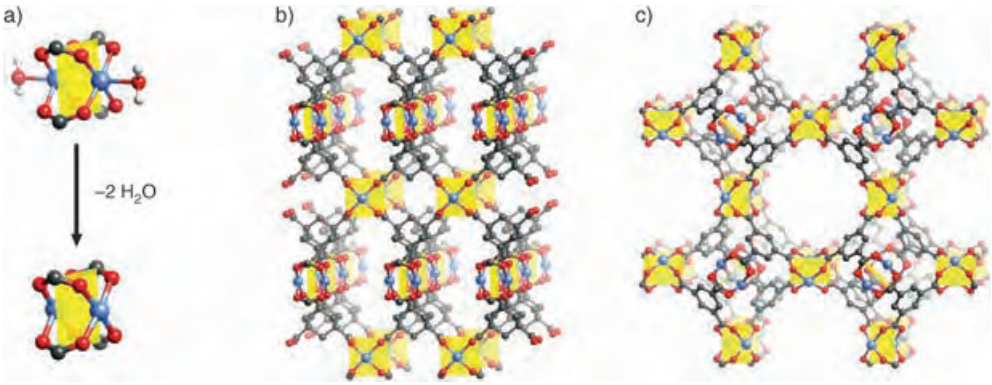


Figure 5. a) The Cu^{II} carboxylate "paddlewheel" cluster is an important square SBU used in some reticulated MOFs. Axial ligands, such as water (shown), may be removed without rearrangement of the cluster and consequent collapse of frameworks such as in MOF-11 (b) and HKUST-1 (c) to yield materials with permanent porosity and a periodic array of open metal sites. Atoms shown as spheres, C: black, H: white, O: red, Cu: blue.

 © 2005 Wiley-VCH Verlag GmbH & Co. KGaA, Weinheim

gen capacity. This approach requires investigating the MOFs formed by light main group metal cations such as Li^+, Na^+, Mg^{2+}, and Al^{3+}. While the monovalent cations will most likely produce frameworks that are susceptible to hydrolysis, the large polarizing power of Mg^{2+} and Al^{3+} should give rise to relatively strong coordination bonds. Oxophilicity and predominantly octahedral coordination are well-known characteristics of the two cations, and novel solvent systems will probably need to be employed to avoid formation of dense oxide/hydroxide phases. The only aluminum MOF to date was prepared hydrothermally by using fluoride ions as a mineralizer. The aluminum hydroxide terephthalate MIL-53 (Figure 1c) displays an uptake of 3.8 wt% at 77 K and 16 bar, but an unusual amount of hysteresis upon desorption.[36] Magnesium MOFs are also very rare, in fact few systematic studies of Group 2 MOFs have been reported, as has been recently discussed.[37] None have displayed permanent porosity.

5.6. Functionalized Linkers, SBU Adsorptive Sites, and the Energetics of Physisorption

The impetus for constructing MOFs with constricted pores stems from the need to increase the heat of adsorption of hydrogen in host materials. Ideally, the adsorbent should have both large gravimetric and volumetric capacities at ambient temperature, with the additional criterion of facilitating quick uptake and release of the gas. Since the van der Waals forces that underlie physisorption are weak, the hydrogen capacity of even materials with a very high surface area becomes small at room temperature. An energy of interaction of about 20 kJ mol^{-1} has been suggested for porous materials to maintain high capacity at ambient temperatures. A great deal of work, both theoretical and experimental, has gone into estimating the interaction energy of hydrogen with nanostructured carbon materials. There is now reasonable agreement that this value is approximately 5 kJ mol^{-1}, both from high-level calculations of the gas-phase interaction of H_2 with substituted and expanded aromatic compounds[38] as well as variable-temperature adsorption studies on various carbon materials.[14a,d] Most experimental evidence regarding desorption of hydrogen from activated carbon materials at elevated temperatures have attributed this to chemisorbed hydrogen at dangling bonds.[39] Importantly, it appears that the influence of chemical substitution or nanostructuring of carbon materials on the physisorptive interaction energy is rather small.

Organic linkers with aromatic backbones such as phenylene, naphthalene, bipyridine, and biphenylene have been employed in MOF structures to increase the rigidity of the frameworks. These molecular units mimic the nanostructure of activated carbon materials and nanotubes which are primarily composed of sp^2-hybridized carbon atoms, and hence it is believed that adsorption energetics should be similar for both classes of materials. This situation would be especially true for MOFs where only a small proportion of the framework is composed of metal, such as those with small nuclearity secondary building units. Ab initio calculations indicate that the energy of interaction of hydrogen with substituted benzene is marginally enhanced by the addition of electron-donating groups.[38] The effects of these modifications remain untested in MOFs. Chemical modification with the retention of topology has been demonstrated for a large series of Zn_4O-based MOFs,[30] and initial studies reveal that the linker length and width appear to have an influence on the hydrogen uptake at 77 K[22] and room temperature.[23] As the metrics of the linker have a profound impact on the framework pore size, it is not clear at present whether gains in uptake are more easily achieved by the surface energetics of the linker or the resulting geometric changes in the pore. Further alteration of the linker energetics, such as inclusion of heteroatoms in the aromatic backbone also requires investigation.

With respect to adsorption energetics, MOFs have the additional advantage of a heterogeneous surface structure with local dipoles that may enhance the attraction of hydrogen. These are mainly associated with the SBUs where ionic and dative bonding occur. MOFs composed of $Zn_4O(CO_2)_6$ SBUs such as MOF-5 and MOF-177 can be considered as an assembly of six-membered rings (Figure 6). Here one notes that each benzene ring is attached to two six-membered Zn-O-Zn-O-C-O rings which we believe alter the polarizability of

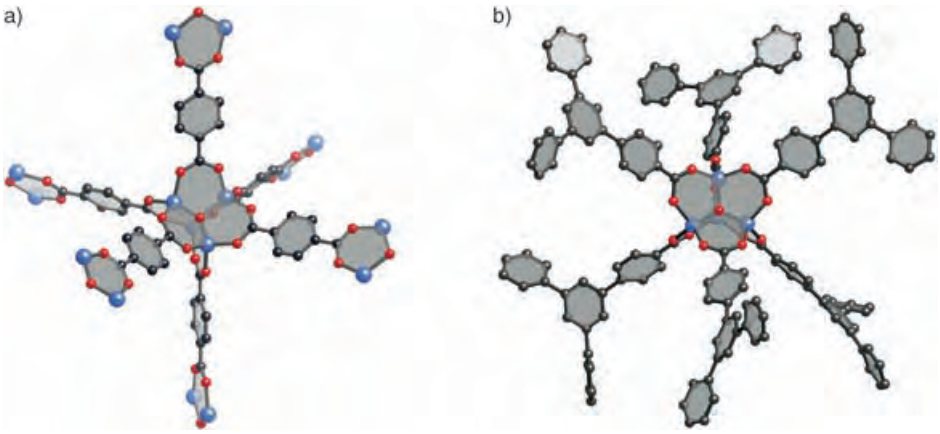


Figure 6. Six-membered rings exist throughout the organic and inorganic backbones of Zn_4O MOFs such as MOF-5 (a) and MOF-177 (b). Atoms shown as spheres, C: black, O: red, Zn: blue.

 © 2005 Wiley-VCH Verlag GmbH & Co. KGaA, Weinheim

the π electrons of the link and lead to a higher binding energy for H_2 relative to that of the six-membered rings in graphite and carbon nanotubes. Evidence for stronger binding of H_2 in MOFs was obtained by inelastic neutron scattering experiments.[23] Thus, the composition of such metal-containing ring systems which are incorporated in the SBUs is critical to hydrogen binding. Understanding the details of the hydrogen interaction at the SBUs is particularly important for larger clusters as they begin to resemble an array of metal oxide nanoparticles in a porous organic matrix. As it is clear that the use of alternative metals generates new SBUs and possibly new framework topologies, the search for new MOFs with enhanced uptake is limitless.

6. Characterization of Hydrogen Uptake in MOFs

Metal–organic frameworks have only recently been proposed as candidates for hydrogen storage, but already several reports of uptake in these materials have entered the literature. The uptake is typically characterized by adsorption isotherms measured at 77 K up to 1 atm (the operating range of a typical commercial adsorption apparatus), but data collected at room temperature and high pressure have also been reported. These data have been summarized in Table 1. The high-pressure conditions are more relevant for practical applications, especially as the pressure limits in commercial hydrogen tanks increase. As the low-temperature hydrogen isotherms can be measured using essentially the same apparatus as that used to determine the MOF surface area, these data are also very useful at this early stage of exploration. As always, care must be taken to ensure the accuracy of the results, especially when gravimetric methods are used. As H_2 gas has the lowest molecular weight and physisorbs weakly, ultrahigh-purity gas must be used and the adsorption apparatus adequately tested for leaks. Ideally, the results should be confirmed by a complementary method, such as volumetric adsorption.[22] More extensive measurements are required to quantify the heat of adsorption in the most promising compounds.

Spectroscopic investigation of the hydrogen–framework interaction has been performed using inelastic neutron scattering studies. This technique provides a sensitive probe of the adsorptive sites for molecular hydrogen as it monitors the hindered rotational transitions of bound molecules. Promising observations were made for MOF-5 loaded with varying amounts of hydrogen.[23] These spectra revealed that at least two distinct adsorptive sites exist on the framework,

Table 1: Summary of hydrogen adsorption in MOFs.

Material[a]	Free/fixed diameters[b,c] [Å]	Accessible volume fraction[b,d]	Apparent surface area[e] [$m^2 g^{-1}$]	Pore volume[i] [$cm^3 g^{-1}$]	H_2 uptake [wt%]	Conditions	Reference
$Zn_4O(bdc)_3$, IRMOF-1	7.8/15.2	0.59	3362	1.19	1.32	77 K, 1 atm	[22]
					1.0	RT, 20 bar	[23]
					1.65	RT, 48 atm	[24]
$Zn_4O(R^6\text{-}bdc)_3$, IRMOF-6	5.9/15.2	0.50	2630	0.93	1.0	RT, 10 bar	[23, 30]
$Zn_4O(ndc)_3$, IRMOF-8	8.4/18.0	0.66	1466	0.52	1.50	77 K, 1 atm	[22]
					2.0	RT, 10 atm	[23]
$Zn_4O(hpdc)_3$, IRMOF-11	6/12.4	0.40	1911	0.68	1.62	77 K, 1 atm	[22]
$Zn_4O(tmbdc)_3$, IRMOF-18	5.4/13.8	0.42	1501	0.53	0.89	77 K, 1 atm	[22]
$Zn_4O(btb)_2$, MOF-177	9.6/11.8	0.63	4526	1.61	1.25	77 K, 1 atm	[22]
Al(OH)(bdc), MIL-53(Al)	6.4/6.4	0.29	1590, 1020[f]	–	3.8	77 K, 16 bar	[36, 45]
Cr(OH)(bdc), MIL-53(Cr)	6.6/6.6	0.29	1500, 1026[f]	–	3.1	77 K, 16 bar	[36, 46]
$Mn(HCO_2)_2$	3/4.7	0.10	297[g]	–	0.9	77 K, 1 atm	[26]
$Cu_2(hfipbb)_2(H_2hfipbb)$	3/4.7	0.03	–	–	1.0	RT, 48 atm	[24]
Ni(cyclam)(bpydc)	6.1/7.6	0.18	817	0.37	1.1	77 K, 1 atm	[47]
$Zn_2(bdc)_2(dabco)$	7.8/9.5	0.45	1450[f]	–	2.0	77 K, 1 atm	[48]
$Ni_2(bpy)_3(NO_3)_4$ (M)	2.4/4.0	0.05	–	0.181[j]	0.8	77 K, 1 atm	[49]
$Ni_2(bpy)_3(NO_3)_4$ (E)	2.1/4.2	0.05	–	0.149[j]	0.7	77 K, 1 atm	[49]
$Ni_3(btc)_2(3\text{-}pic)_6(pd)_3$	8.5/10.7	0.30	–	0.63	2.1	77 K, 14 bar	[49]
$Zn_4O(L^1)_3$	3.8/7.8	0.21	502[h]	0.20	1.12	RT, 48 atm	[28]
$Zn_4O(L^2)_3$	3.8/5.4	0.17	396[h]	0.13	0.98	RT, 48 bar	[28]
$Cu_2(pzdc)_2(pyz)$, CPL-1	3.4/5.0	0.04	–	–	0.2	89 K, 1 atm	[40]
$Cu_2(bptc)$, MOF-505	6.7/10.1	0.37	1646	0.63	2.48	77 K, 1 atm	[50]

[a] Acronyms: bdc = benzene-1,4-dicarboxylate, R^6-bdc = 1,2-dihydrocyclobutylbenzene-3,6-dicarboxylate, ndc = naphthalene-2,6-dicarboxylate, hpdc = 4,5,9,10-tetrahydropyrene-2,7-dicarboxylate, tmbdc = 2,3,5,6-tetramethylbenzene-1,4-dicarboxylate, btb = benzene-1,3,5-tribenzoate, hfipbb = 4,4′-(hexafluoroisopropylidene)bisbenzoate, cyclam = 1,4,8,11-tetraazacyclotetradecane, bpydc = 2,2′-bipyridyl-5,5′-dicarboxylate, dabco = 1,4-diazabicyclo[2.2.2]octane, bpy = 4,4′-bipyridine, btc = benzene-1,3,5-tricarboxylate, 3-pic = 3-picoline, pd = 1,2-propanediol, L^1 = 6,6′-dichloro-2,2′-diethoxy-1,1′-binaphthyl-4-4′-dibenzoate, L^2 = 6,6′-dichloro-2,2′-dibenzyloxy-1,1′-binaphthyl-4,4′-dibenzoate, bptc = biphenyl-3,3′,5,5′-tetracarboxylate. [b] Calculations were performed using the Cerius² software package. Crystallographic data for the evacuated frameworks was used where available. [c] Free and fixed diameters correspond to the largest spheres that can pass through the apertures and fit in the largest pores of the frameworks, respectively. [d] Calculated using a probe radius of 1.45 Å, which corresponds to the kinetic diameter of H_2. [e] Calculated from N_2 adsorption data collected at 77 K using the Langmuir model except where indicated. [f] BET surface area from N_2 at 77 K. [g] BET surface area from CO_2 at 195 K. [h] BET surface area from CO_2 at 273 K. [i] Calculated from N_2 adsorption data collected at 77 K using the Dubinin–Radushkevich method except where indicated. [j] Methanol used as adsorbate.

 © 2005 Wiley-VCH Verlag GmbH & Co. KGaA, Weinheim

which were assigned to the inorganic and organic components. MOFs have a further advantage over nanostructured carbon materials and amorphous adsorbents in that they have a high degree of long-range order. If such adsorptive sites are indeed localized, they are additionally periodically arranged. It therefore may be possible to detect the adsorbed hydrogen molecules at very low temperatures by a diffraction experiment. A report has recently appeared describing the modeling of electron density, measured by synchrotron powder X-ray diffraction, of adsorbed H_2 in the small channels of CPL-1.[40] Neutrons are again the ideal scattering probes for such experiments as X-rays are insensitive to the low electron density of hydrogen atoms.

Computational modeling studies of the hydrogen interaction with metal–organic frameworks and their chemical components will also be important for our understanding of physisorption in these materials. The simplicity and high symmetry of some of the structures should make them ideal candidates for study, to the level that has been achieved for zeolites such as Na-A.[41] Grand Canonical Monte Carlo simulations of argon and methane in MOFs have been reported, and these display good agreement with measured isotherms.[42] The physisorption of hydrogen in MOF-5 has also been examined recently, in addition to more detailed calculations for H_2 with models of its inorganic and organic moieties, by using second-order Møller–Plesset perturbation theory.[38,43,44] The Monte Carlo study indicates that binding at the $Zn_4O(CO_2)_6$ clusters is perhaps 1.5 kJ mol^{-1} higher in energy than at the phenylene groups, but a broad range of interaction energies was determined for their system at 300 K corresponding to occupation of a broad distribution of sites.[44] Further computations of the hydrogen dynamics in MOFs will be indispensable in providing future directions for materials optimization.

7. Concluding Remarks

The series of considerations proposed above are multifaceted and we expect that significant exploration will be required to satisfy many of them simultaneously. A material with high gravimetric and volumetric hydrogen capacity at practical conditions should have a high surface area with pores of appropriate dimension for hydrogen and a large heat of adsorption. The strategies of impregnation, catenation, and the inclusion of open metal sites are just a few possibilities to be tested. To date, nearly 5000 2D and 3D MOF structures have been reported in the literature, but only a fraction of these have been examined for their porosity and far fewer of them have been tested for their hydrogen storage capacity. This fact, combined with the advantages of MOFs such as ease of synthesis and functionalization of their organic linkers and inorganic SBUs are favorable circumstances for achieving the DOE target for on-board hydrogen storage.

Received: December 2, 2004
Revised: May 1, 2005

[1] a) "National Hydrogen Energy Roadmap", United States Department of Energy, results from the National Hydrogen Energy Roadmap Workshop, Washington DC, April 2–3, **2002**. http://www.eere.energy.gov/hydrogenandfuelcells/pdfs/national_h2_roadmap.pdf; b) "Hydrogen Posture Plan", United States Department of Energy, February **2004**. http://www.eere.energy.gov/hydrogenandfuelcells/pdfs/hydrogen_posture_plan.pdf.

[2] a) "The Hydrogen Initiative", American Physical Society Panel on Public Affairs, March **2004**; b) P. M. Grant, *Nature* **2003**, *424*, 129; c) R. Coontz, B. Hanson, *Science* **2004**, *305*, 957, and other articles in this issue.

[3] a) "Hydrogen Storage Materials Workshop Proceedings", United States Department of Energy, August 14–15, **2002**. http://www.eere.energy.gov/hydrogenandfuelcells/pdfs/h2_stor_mat_work_proceedings.pdf; b) "Basic Research Needs for the Hydrogen Economy", United States Department of Energy, report of the Basic Energy Sciences Workshop on Hydrogen Production, Storage, and Use, May 13–15, **2003**. http://www.sc.doe.gov/bes/hydrogen.pdf; c) E. Tzimas, C. Filiou, S. D. Peteves, J.-B. Veyret, "Hydrogen Storage: State-of-the-Art and Future Perspective", European Commission DG JRC Institute for Energy, Petten **2003**. http://www.jrc.nl/publ/2003_publ.html.

[4] L. Schlapbach, *MRS Bull.* **2002**, *27*, 675.

[5] B. Wicke, presentation for the *Hydrogen Storage Materials Workshop*, United States Department of Energy, Argonne, IL, August 14–15, **2002**.

[6] W. P. Teagan, M. Rona, presentation for the *Hydrogen Storage Materials Workshop*, United States Department of Energy, Argonne, IL, August 14–15, **2002**.

[7] a) R. S. Irani, *MRS Bull.* **2002**, *27*, 680; b) S. Franzky, *Fuel Cells Bull.* **2002**, *9*, 9.

[8] J. Wolf, *MRS Bull.* **2002**, *27*, 685.

[9] W. Grochala, P. P. Edwards, *Chem. Rev.* **2004**, *104*, 1283.

[10] a) G. Sandrock, *J. Alloys Compd.* **1999**, *293–295*, 877; b) R. C. Bowman, Jr., B. Fultz, *MRS Bull.* **2002**, *27*, 688.

[11] a) B. Bogdanović, M. Schwickardi, *J. Alloys Compd.* **1997**, *253–254*, 1; b) F. Schüth, B. Bogdanović, M. Felderhoff, *Chem. Commun.* **2004**, 2249.

[12] Hydrogen release by hydrolysis has been commercialized in the past by Millenium Cell and Powerball; see Ref. [3] for further details.

[13] A. C. Dillon, K. M. Jones, T. A. Bekkedahl, C. H. Kiang, D. S. Bethune, M. J. Heben, *Nature* **1997**, *386*, 377.

[14] a) P. Bénard, R. Chahine, *Langmuir* **2001**, *17*, 1950; b) G. G. Tibbetts, G. P. Meisner, C. H. Olk, *Carbon* **2001**, *39*, 2291; c) M. G. Nijkamp, J. E. M. J. Raaymakers, A. J. van Dillen, K. P. de Jong, *Appl. Phys. A* **2001**, *72*, 619; d) H. G. Schimmel, G. J. Kearley, M. G. Nijkamp, C. T. Visser, K. P. de Jong, F. M. Mulder, *Chem. Eur. J.* **2003**, *9*, 4764; e) M. Becher, M. Haluska, M. Hirscher, A. Quintel, V. Skakalova, U. Dettlaff-Weglikovska, X. Chen, M. Hulman, Y. Choi, S. Roth, V. Meregalli, M. Parrinello, R. Ströbel, L. Jörissen, M. M. Kappes, J. Fink, A. Züttel, I. Stepanek, P. Bernier, *C. R. Phys.* **2003**, *4*, 1055.

[15] a) M. Rzepka, P. Lamp, M. A. de la Casa-Lillo, *J. Phys. Chem. B* **1998**, *102*, 10894; b) M. S. Dresselhaus, K. A. Williams, P. C. Eklund, *MRS Bull.* **1999**, *24*, 45; c) A. Züttel, P. Sudan, P. Mauron, T. Kiyobayashi, C. Emmenegger, L. Schlapbach, *Int. J. Hydrogen Energy* **2002**, *27*, 203.

[16] G. Gundiah, A. Govindaraj, N. Rajalakshmi, K. S. Dhathathreyan, C. N. R. Rao, *J. Mater. Chem.* **2003**, *13*, 209.

[17] For reviews, see: a) J. L. C. Rowsell, O. M. Yaghi, *Microporous Mesoporous Mater.* **2004**, *73*, 3; b) S. Kitagawa, R. Kitaura, S.-I. Noro, *Angew. Chem.* **2004**, *116*, 2388; *Angew. Chem. Int. Ed.* **2004**, *43*, 2334; c) C. Janiak, *Dalton Trans.* **2003**, 2781.

[18] O. M. Yaghi, M. O'Keeffe, N. W. Ockwig, H. K. Chae, M. Eddaoudi, J. Kim, *Nature* **2003**, *423*, 705.

 © 2005 Wiley-VCH Verlag GmbH & Co. KGaA, Weinheim

[19] K. S. W. Sing, D. H. Everett, R. A. W. Haul, L. Moscou, R. A. Pierotti, J. Rouquerol, T. Siemieniewska, *Pure Appl. Chem.* **1985**, *57*, 603.
[20] For further reading on the topic of surface-area and porosity determination of microporous materials, see: F. Rouquerol, J. Rouquerol, K. Sing, *Adsorption by Powders and Porous Solids*, Academic Press, London, **1999**.
[21] H. K. Chae, D. Y. Siberio-Pérez, J. Kim, Y. Go, M. Eddaoudi, A. J. Matzger, M. O'Keeffe, O. M. Yaghi, *Nature* **2004**, *427*, 523.
[22] J. L. C. Rowsell, A. R. Millward, K. S. Park, O. M. Yaghi, *J. Am. Chem. Soc.* **2004**, *126*, 5666.
[23] N. L. Rosi, J. Eckert, M. Eddaoudi, D. T. Vodak, J. Kim, M. O'Keeffe, O. M. Yaghi, *Science* **2003**, *300*, 1127.
[24] L. Pan, M. B. Sander, X. Huang, J. Li, M. Smith, E. Bittner, B. Bockrath, J. K. Johnson, *J. Am. Chem. Soc.* **2004**, *126*, 1308.
[25] D. W. Breck, *Zeolite Molecular Sieves*, Wiley, New York, **1974**.
[26] D. N. Dybtsev, H. Chun, S. H. Yoon, D. Kim, K. Kim, *J. Am. Chem. Soc.* **2004**, *126*, 32.
[27] a) S. R. Batten, R. Robson, *Angew. Chem.* **1998**, *110*, 1558; *Angew. Chem. Int. Ed.* **1998**, *37*, 1460; b) B. Chen, M. Eddaoudi, S. T. Hyde, M. O'Keeffe, O. M. Yaghi, *Science* **2001**, *291*, 1021.
[28] B. Kesanli, Y. Cui, M. R. Smith, E. W. Bittner, B. C. Bockrath, W. Lin, *Angew. Chem.* **2005**, *117*, 74; *Angew. Chem. Int. Ed.* **2005**, *44*, 72.
[29] T. M. Reineke, M. Eddaoudi, D. Moler, M. O'Keeffe, O. M. Yaghi, *J. Am. Chem. Soc.* **2000**, *122*, 4843.
[30] M. Eddaoudi, J. Kim, N. Rosi, D. Vodak, J. Wachter, M. O'Keeffe, O. M. Yaghi, *Science* **2002**, *295*, 469.
[31] a) B. Chen, M. Eddaoudi, T. M. Reineke, J. W. Kampf, M. O'Keeffe, O. M. Yaghi, *J. Am. Chem. Soc.* **2000**, *122*, 11559; b) K. Schlichte, T. Kratzke, S. Kaskel, *Microporous Mesoporous Mater.* **2004**, *73*, 81.
[32] H. Li, M. Eddaoudi, T. L. Groy, O. M. Yaghi, *J. Am. Chem. Soc.* **1998**, *120*, 8571.
[33] N. L. Rosi, M. Eddaoudi, J. Kim, M. O'Keeffe, O. M. Yaghi, *Angew. Chem.* **2002**, *114*, 294; *Angew. Chem. Int. Ed.* **2002**, *41*, 284.
[34] R. Kitaura, G. Onoyama, H. Sakamoto, R. Matsuda, S.-I. Noro, S. Kitagawa, *Angew. Chem.* **2004**, *116*, 2738; *Angew. Chem. Int. Ed.* **2004**, *43*, 2684.
[35] P. M. Forster, J. Eckert, J.-S. Chang, S.-E. Park, G. Férey, A. K. Cheetham, *J. Am. Chem. Soc.* **2003**, *125*, 1309.
[36] G. Férey, M. Latroche, C. Serre, F. Millange, T. Loiseau, A. Percheron-Guégan, *Chem. Commun.* **2003**, 2976.
[37] A. P. Côté, G. K. H. Shimizu, *Chem. Eur. J.* **2003**, *9*, 5361.
[38] O. Hübner, A. Glöss, M. Fichtner, W. Klopper, *J. Phys. Chem. A* **2004**, *108*, 3019.
[39] X. Sha, B. Jackson, *J. Am. Chem. Soc.* **2004**, *126*, 13095.
[40] Y. Kubota, M. Takata, R. Matsuda, R. Kitaura, S. Kitagawa, K. Kato, M. Sakata, T. C. Kobayashi, *Angew. Chem.* **2005**, *117*, 942; *Angew. Chem. Int. Ed.* **2005**, *44*, 920.
[41] a) C.-R. Anderson, D. F. Coker, J. Eckert, A. L. R. Bug, *J. Chem. Phys.* **1999**, *111*, 7599; b) J. A. McKinnon, D. F. Coker, J. Eckert, A. L. R. Bug, *J. Chem. Phys.* **2001**, *114*, 10137.
[42] a) A. Vishnyakov, P. I. Ravikovitch, A. V. Neimark, M. Bülow, Q. M. Wang, *Nano Lett.* **2003**, *3*, 713; b) A. I. Skoulidas, *J. Am. Chem. Soc.* **2004**, *126*, 1356; c) T. Düren, L. Sarkisov, O. M. Yaghi, R. Q. Snurr, *Langmuir* **2004**, *20*, 2683.
[43] a) T. Heine, L. Zhechkov, G. Seifert, *Phys. Chem. Chem. Phys.* **2004**, *6*, 980; b) S. Hamel, M. Côté, *J. Chem. Phys.* **2004**, *121*, 12618.
[44] T. Sagara, J. Klassen, E. Ganz, *J. Chem. Phys.* **2004**, *121*, 12543.
[45] T. Loiseau, C. Serre, C. Huguenard, G. Fink, G. Taulelle, M. Henry, T. Bataille, G. Férey, *Chem. Eur. J.* **2004**, *10*, 1373.
[46] F. Millange, C. Serre, G. Férey, *Chem. Commun.* **2002**, 822.
[47] E. Y. Lee, M. P. Suh, *Angew. Chem.* **2004**, *116*, 2858; *Angew. Chem. Int. Ed.* **2004**, *43*, 2798.
[48] D. N. Dybtsev, H. Chun, K. Kim, *Angew. Chem.* **2004**, *116*, 5143; *Angew. Chem. Int. Ed.* **2004**, *43*, 5033.
[49] X. Zhao, B. Xiao, A. J. Fletcher, K. M. Thomas, D. Bradshaw, M. J. Rosseinsky, *Science* **2004**, *306*, 1012.
[50] B. Chen, N. W. Ockwig, A. R. Millward, D. S. Contreras, O. M. Yaghi, *Angew. Chem.* **2005**, *117*, 4823; *Angew. Chem. Int. Ed.* **2005**, *44*, 4745.

 © 2005 Wiley-VCH Verlag GmbH & Co. KGaA, Weinheim

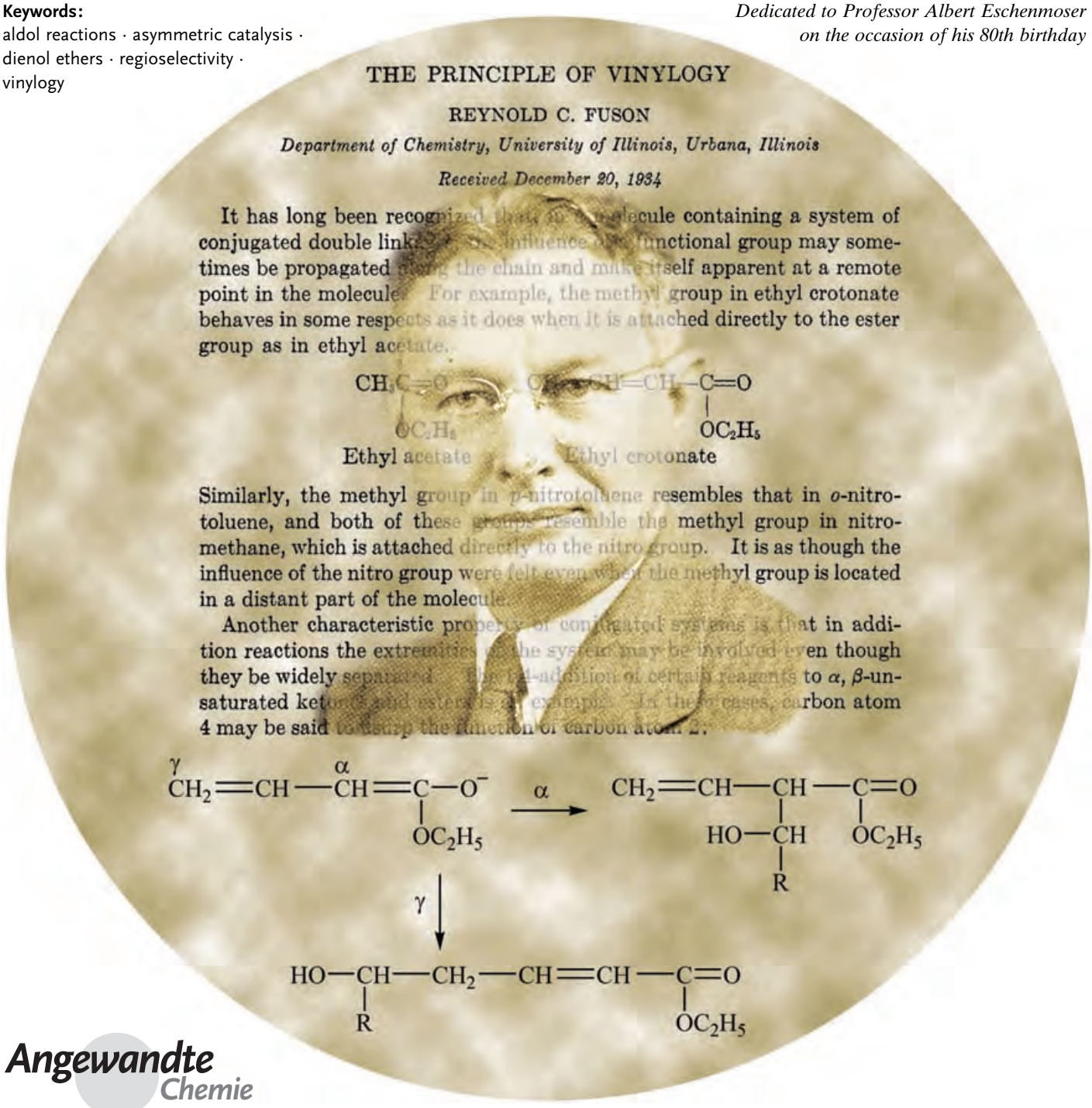
Asymmetric Catalysis

Catalytic, Enantioselective, Vinylogous Aldol Reactions**

Scott E. Denmark, John R. Heemstra, Jr., and Gregory L. Beutner*

Keywords:
aldol reactions · asymmetric catalysis · dienol ethers · regioselectivity · vinylogy

Dedicated to Professor Albert Eschenmoser on the occasion of his 80th birthday



Angewandte Chemie

 © 2005 Wiley-VCH Verlag GmbH & Co. KGaA, Weinheim DOI: 10.1002/anie.200462338

In 1935, R. C. Fuson formulated the principle of vinylogy to explain how the influence of a functional group may be felt at a distant point in the molecule when this position is connected by conjugated double-bond linkages to the group. In polar reactions, this concept allows the extension of the electrophilic or nucleophilic character of a functional group through the π system of a carbon–carbon double bond. This vinylogous extension has been applied to the aldol reaction by employing "extended" dienol ethers derived from γ-enolizable α,β-unsaturated carbonyl compounds. Since 1994, several methods for the catalytic, enantioselective, vinylogous aldol reaction have appeared, with which varying degrees of regio- (site), enantio-, and diastereoselectivity can be attained. In this Review, the current scope and limitations of this transformation, as well as its application in natural product synthesis, are discussed.

From the Contents

1. Introduction 4683
2. Early Developments in the Vinylogous Aldol Reaction 4684
3. Synthetic Equivalents of Acetoacetate Ester Dianions 4686
4. Simple Ester-Derived Silyl Dienol Ethers 4691
5. Lactone-Derived Dienol Ethers 4695
6. Ketone-Derived Dienol Ethers 4696
7. Conclusions and Outlook 4696

1. Introduction

The potent biological activity and structural diversity of the polyketide class of natural products has provided inspiration and impetus for research in many subfields of the chemical sciences. A main characteristic of these natural products is presence of complex polyol subunits with repeating 1,3-diol relationships within their core structure. Through elegant biosynthetic studies it is now well established that these polyol chains are synthesized in nature by multifunctional enzymes termed polyketide synthetases.[1] By using small carboxylic acid building blocks (primarily acetate, propionate, and butyrate), which are activated as thioesters bound to a ketosynthase protein and through carboxylation (e.g. with malonyl-CoA and 2-methylmalonyl-CoA), the carbon backbone of the polyketide is assembled two carbon atoms at a time as the result of enzymatic, decarboxylative Claisen condensations (Scheme 1). Reduction of the β-keto thioester intermediate by NADPH generates a β-hydroxy thioester, which can undergo acyl-group transfer to a subsequent ketosynthase protein. This sequence is repeated until the appropriate polyol chain length is reached. Each stereogenic center is created with high selectivity owing to the ability of the enzyme to rigidly fix the orientation of the reactive components relative to each other and relative to the enzyme.

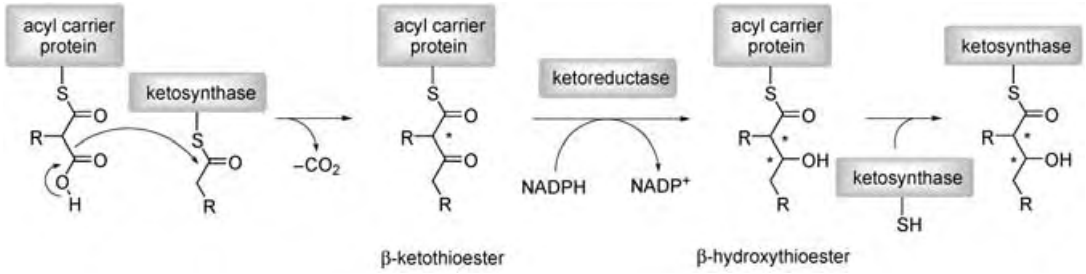
A challenge for the modern synthetic chemist is the development of non-enzymatic asymmetric reactions for the construction of polyol subunits with equally high selectivity and efficiency as achieved in nature. With regard to many criteria, the asymmetric aldol addition reaction, which provides β-hydroxy carbonyl compounds with up to two new stereocenters from readily available starting materials, has met this challenge.[2] Indeed, the selectivity, scope, and predictability associated with current aldol-addition methods have allowed this reaction to emerge as a strategy-level reaction in natural product synthesis. Although the aldol addition reaction has found widespread application in the synthesis of linear acyclic polyol structures, it is certainly not the only method available. Other transformations, such as allylations,[3] alkylations of 4-cyano-1,3-dioxanes,[4] and nucleophilic epoxide-opening reactions of epoxyalkynols,[5] have also been developed as viable alternatives to the aldol reaction.

Nevertheless, despite some limitations, the aldol addition is ideally suited for efficient access to the targeted polyol structures. Moreover, the polar nature of the enolate precursor in the addition makes a vinylogous extension of this reaction possible. Defined as the transmission of electronic effects through a conjugated π system, the principle of vinylogy allows the extension of the nucleophilic or electrophilic character of a functional group through the π system of a carbon–carbon double bond.[6] Accordingly, a γ-enolizable α,β-unsaturated carbonyl substrate can be employed as an "extended dienolate" in a vinylogous aldol addition to an aldehyde to give δ-hydroxy-β-ketoesters **2** (Scheme 2) or α,β-unsaturated δ-hydroxy carbonyl compounds **4** (Scheme 3) in which up to two stereocenters and one double bond can be created. These functional arrays are common structural motifs that have found application in synthesis. The newly created hydroxy-substituted stereocenter is adjacent to a double bond or carbonyl group, and these versatile intermediates can therefore be further elaborated by using various highly selective substrate-directable reactions (see Schemes 2 and 3).[7] Among the most useful of these reactions are

[*] Prof. Dr. S. E. Denmark, J. R. Heemstra, Jr., Dr. G. L. Beutner
Roger Adams Laboratory
University of Illinois at Urbana-Champaign
600 South Mathews Avenue
Urbana, IL 61801 (USA)
Fax: (+1) 217-333-3984
E-mail: denmark@scs.uiuc.edu

[**] Seventy years ago, Reynold C. Fuson formulated the concept of vinylogy that constitutes the conceptual underpinning of the vinylogous aldol reactions described in this Review. (Reprinted with permission from *Chem. Rev.* **1935**, *16*, 1–27. Copyright 1935, American Chemical Society. Photograph courtesy of the University of Illinois at Urbana-Champaign Archives (Record Series 39/2/26)).

 DOI: 10.1002/anie.200462338 © 2005 Wiley-VCH Verlag GmbH & Co. KGaA, Weinheim



Scheme 1. The biosynthesis of polyol compounds by polyketide synthetases.[1]

conjugate additions to the double bond, oxidations or reductions of the double bond, or in the case of the β-keto carbonyl compounds, directed reductions or cyclizations.

For all its advantages, the vinylogous aldol reaction is still a challenging transformation because the additional problem of site selectivity overlays the issues of diastereo- and enantioselectivity already present in simple aldol reactions. Reactions of dienol ethers or ketene acetals can occur at either the α or the γ carbon atom of the extended conjugated system (Scheme 4). In comparison to the progress of the classic aldol addition reaction, the development of methods that combine high levels of regio- (site), diastereo-, and enantioselectivity in vinylogous aldol reactions has lagged significantly behind. Since 1994, a number of creative and practical solutions have been developed for highly selective catalytic, enantioselective, vinylogous aldol reactions. Their direct application in the total synthesis of natural products, as well as their use in the rapid assembly of complex synthetic intermediates, attests to the utility of these methods. This Review summarizes the scope and limitations of the catalytic, enantioselective, vinylogous aldol reaction and highlights its potential as a powerful and perhaps underutilized method for the synthesis of a number of useful structural motifs when used in conjunction with substrate-directable reactions.



Scott E. Denmark completed his SB degree with Richard H. Holm and Daniel S. Kemp (MIT, 1975), and his DScTech with Albert Eschenmoser (ETH Zürich, 1980). He then moved to the University of Illinois and became full professor in 1987. Since 1991 he has been Reynold C. Fuson Professor of Chemistry. His research interests include new synthetic reactions, exploratory organoelement chemistry, and stereocontrol in C–C bond-forming processes. He is on the Board of Editors of Organic Reactions and Organic Syntheses, was a founding Associate Editor of Organic Letters, and is Co-Editor of Topics in Stereochemistry.



John R. Heemstra, Jr. was born in Oak Lawn, IL in 1978. He graduated from North Central College (Naperville, IL) in 2000 with a BA degree in chemistry. He is currently a graduate student at the University of Illinois in the research group of Scott E. Denmark. His PhD thesis work concerns the development of catalytic, enantioselective vinylogous aldol additions of ketone- and amide-derived silyl dienol ethers.



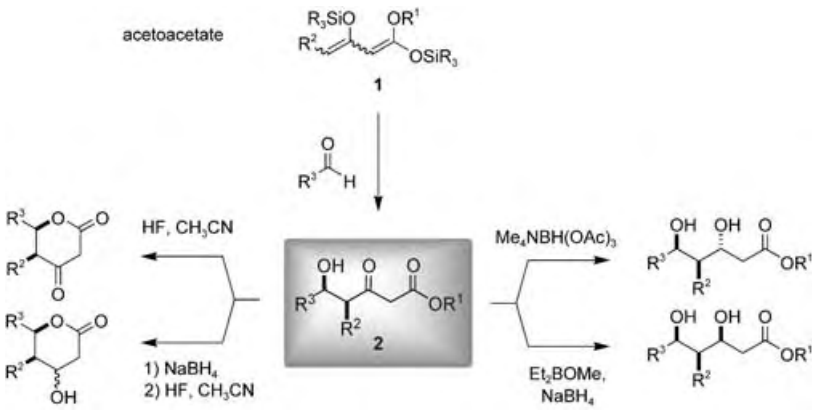
Gregory L. Beutner was born in Malden, MA in 1976. He graduated in 1998 with a BS in chemistry from Tufts University, where he carried out research with Arthur Utz and Marc d'Alarcao. He completed his PhD in 2004 at the University of Illinois, Urbana-Champaign under the guidance of Scott E. Denmark. He is currently an NIH postdoctoral research associate at the California Institute of Technology in the research group of Robert Grubbs.

2. Early Developments in the Vinylogous Aldol Reaction

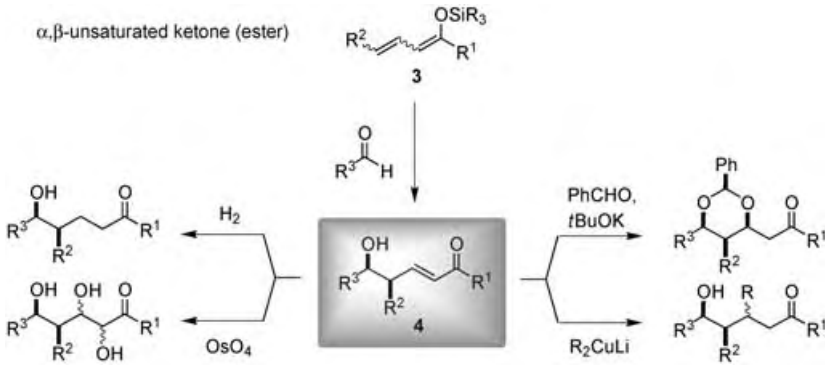
Historically, the development of a successful catalytic asymmetric vinylogous aldol reaction had to provide solutions to two major problems: 1) viable access to the requisite dienolates and dienol ethers, and 2) methods to control the site selectivity of the addition. As the formation of the acetoacetate-derived dienol ether **1** has recently been reviewed,[8] this discussion will focus on the formation of dienolates and dienol ethers derived from α,β-unsaturated carbonyl compounds. Early studies on the use of metallodienolates showed that direct deprotonation of unsaturated ester **5** with strong amide bases such as lithium diisopropylamide (LDA) was not possible owing to competitive conjugate addition of the base [Scheme 5, Eq. (1)].[9] In 1972, Rathke and Sullivan reported the first successful enolization of an α,β-unsaturated ester, **5**, by the combination of a bulky amide base (lithium *N*-isopropylcyclohexylamide (LiICA)) and HMPA [Scheme 5, Eq. (2)].[10] Trapping of the enolate intermediate with MeI led to the deconjugated α-alkylation product **7** in good yield and selectivity. Subsequently, Schlessinger and co-workers discovered that a 1:1 mixture of LDA and HMPA generated a non-nucleophilic base that could readily enolize a variety of unsaturated esters. These reactions gave the products of α alkylation in high yields [Scheme 5, Eq. (3)].[9]

The high α-site selectivity observed in these alkylations illustrates an important feature of dienolate chemistry: The vinylogous transmission of electronic effects does not guarantee that reaction at the remote position will be favored or

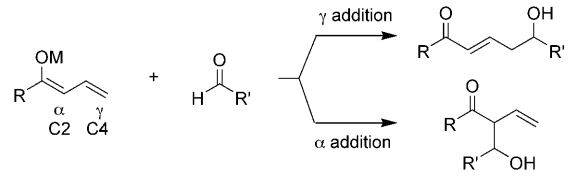
 © 2005 Wiley-VCH Verlag GmbH & Co. KGaA, Weinheim



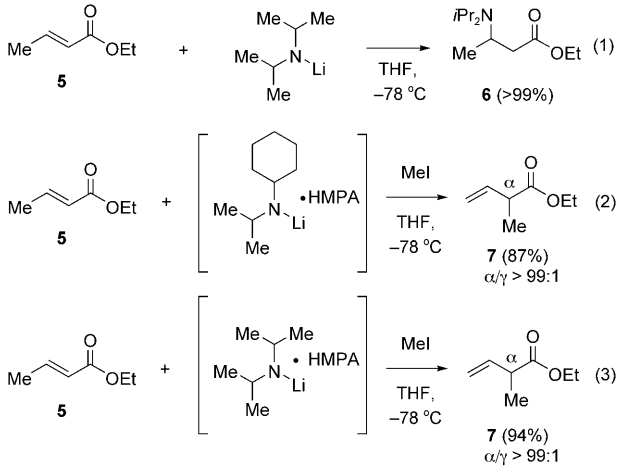
Scheme 2. Substrate-controlled methods for elaboration of adduct **2**.



Scheme 3. Substrate-controlled methods for elaboration of adduct **4**.



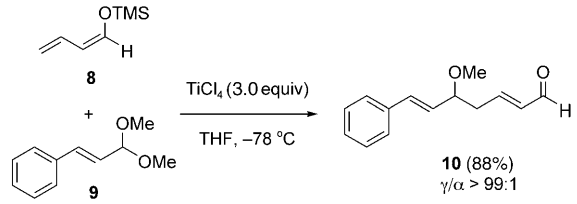
Scheme 4. Site selectivity in the vinylogous aldol reaction.



Scheme 5. Successful methods for the preparation of metallodienolates derived from α,β-unsaturated esters.[9,10] HMPA = hexamethyl phosphoramide.

even observed. However, high γ selectivity is possible through the use of latent dienolate equivalents in Mukaiyama-type aldol reactions[2] promoted by Lewis acids. First reported by Mukaiyama and Ishida, a vinylogous alkylation of the crotonaldehyde-derived silyl dienol ether **8** with dimethyl acetal **9** takes place under activation by $TiCl_4$ (Scheme 6).[11] Since this initial report, the vinylogous aldol addition of silyl dienol ethers to aldehydes has also been demonstrated and high regioselectivities for γ addition have been observed for a variety of dienolate structures.[12]

The reason for the different regioselectivities of the metallodienolate and the silyl dienol ether can be understood by considering the electronic structure of the two reagents. Metallodienolates and their silyl congeners are highly electron rich species, and their reactions are therefore governed by electrostatic interactions, that is, by the total electron density at each carbon atom.[13] Whereas HOMO coefficients and partial charges on the constituent atoms have historically been cited to predict site selectivity,[13] a more meaningful and computationally more accurate measure is the frontier-orbital density recommended by Fukui et al.[14] The frontier-orbital density



Scheme 6. The first reported vinylogous alkylation of a silyl dienol ether.[11]

can be calculated for attack both by electrophiles (electrophilic susceptibility) and nucleophiles (nucleophilic susceptibility). The diagrams in Figure 1 show the HOMO orbital coefficients (O.C.) and electrophilic susceptibility (E.S.) of the lithium enolate (*E*)-**11** of methyl crotonate, the corresponding trimethylsilyl ketene acetal (*E*)-**12**, and the trimethylsilyl enol ether (*E*)-**13** of methyl 2-propenyl ketone.[15] In the lithium enolate (*E*)-**11**, both the HOMO coefficient and the electrophilic susceptibility are greater at C2 than at C4; a preference for the α-addition product is therefore predicted. On the other hand, both silyl ketene acetal (*E*)-**12** and silyl enol ether (*E*)-**13** display larger HOMO coefficients and electrophilic susceptibilities at C4 than at C2, so that selectivity for the formation of the γ-addition products is predicted. The smaller difference between the values at C2 and C4 in (*E*)-**13** relative to that in (*E*)-**12** suggests that the

 © 2005 Wiley-VCH Verlag GmbH & Co. KGaA, Weinheim

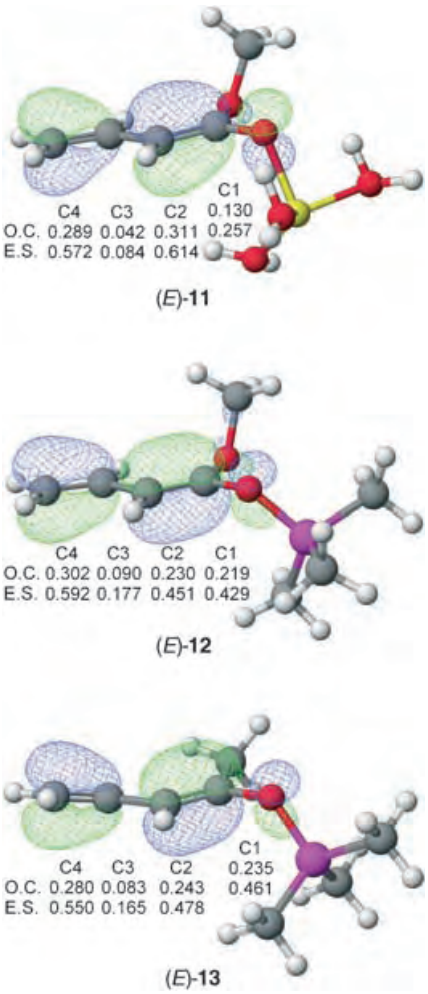


Figure 1. The electronic structures of the lithium dienolate (*E*)-**11**, silyl ketene acetal (*E*)-**12**, and silyl enol ether (*E*)-**13**.

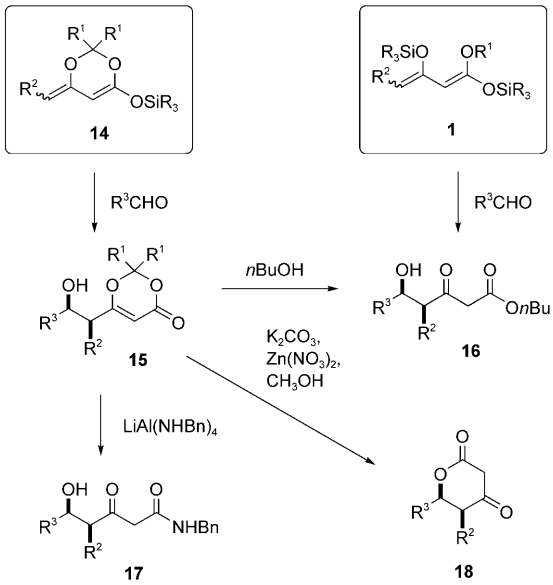
selectivity in ketone dienol ethers may be attenuated compared to silyl ketene acetals.

In rationalizing site selectivity, steric effects cannot be underestimated. In (*E*)-**12** and (*E*)-**13**, C2 is the more sterically hindered site owing to its proximity to the silyl group and the alkyl group of the ester; therefore, the approach of the electrophile to the less sterically encumbered C4 position is favored when C4 is not similarly substituted. For this reason, consideration of both the electrophilic susceptibilities and the steric environment around C2 and C4 is necessary to rationalize the high selectivity for the γ-addition products.

The inherent γ selectivity of silyl dienol ethers in Lewis acid promoted vinylogous Mukaiyama aldol additions has provided an ideal platform for the development of several catalytic enantioselective variants. Furthermore, various dienol ether structures derived from acetoacetates, lactones, esters, and ketones have been used successfully in additions to aldehydes. The following discussion is organized around the individual dienol ether structural types in catalytic, enantioselective, vinylogous aldol additions.

3. Synthetic Equivalents of Acetoacetate Ester Dianions

The frequent occurrence of δ-hydroxy-β-ketoesters **2** and their *syn*- and *anti*-β,δ-diol ester derivatives as structural subunits in biologically active natural products has suggested the use of acetoacetate-derived dienolates **14** and **1** in catalytic, asymmetric, vinylogous aldol reactions (Scheme 7).[8] Whereas the addition of dienolate **1** to aldehydes affords δ-hydroxy-β-ketoesters **16** directly, the addition of the 1,3-dioxin-4-one-derived dienolate **14** affords the protected acetoacetate aldol adduct **15**. To demonstrate the synthetic versatility of this adduct **15**, Singer and Carreira showed that compounds with the dioxinone functionality can be converted not only into a δ-hydroxy-β-ketoesters, but also into amides **17** or lactones **18**.[16] Furthermore, highly diastereoselective reductions of **16** afford both *anti*- and *syn*-dihydroxy esters, which are synthetically useful polyacetate building blocks (Scheme 2). The lactones formed through the cyclization of these adducts are also valuable synthetic subunits, and have been used for the synthesis of several pyran derivatives found in natural products.[8,12a]



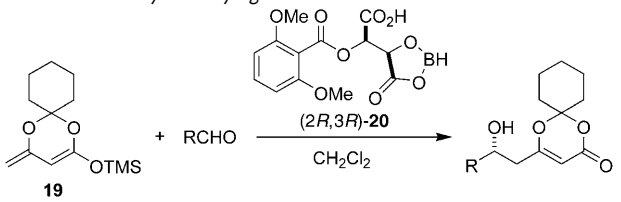
Scheme 7. The vinylogous aldol addition of acetoacetate-derived dienol ethers **14** and **1**;[8,16] Bn = benzyl.

The first asymmetric vinylogous aldol reactions of the dioxinone-derived dienol ether **19** were reported by Sato et al. They employed a boron catalyst that had already proven highly selective for Mukaiyama aldol reactions of simple silyl ketene acetals.[17] Under the catalysis of the chiral acyloxyborane (CAB) complex (2*R*,3*R*)-**20**, the vinylogous aldol reaction of dienol ether **19** with a number of aldehydes proceeds in moderate yields and enantioselectivities (Table 1).[18]

Similar problems are encountered in this reaction to those observed in the reactions of silyl ketene acetals catalyzed by **20**, such as a competitive achiral-silyl-cation-catalyzed path-

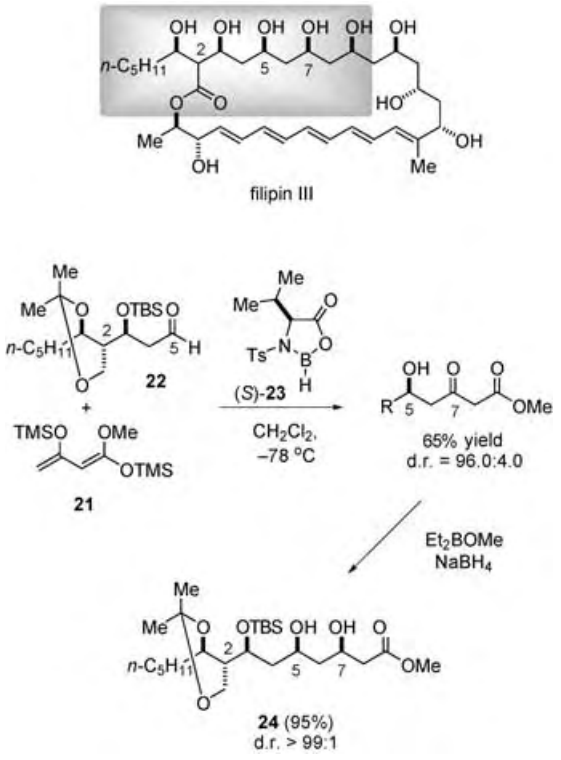
 © 2005 Wiley-VCH Verlag GmbH & Co. KGaA, Weinheim

Table 1: CAB-catalyzed vinylogous aldol reactions.[18]



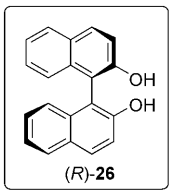
Entry	R	Catalyst [%]	*T* [°C]	Yield [%]	*R*/*S*
1	Ph	50	−78	69	83.5:16.5
2	Ph	100	−98	91	86.5:13.5
3	PhCH=CH	50	−78	56	86.5:13.5
4	PhCH=CH	100	−98	93	88:12
5	*n*Bu	50	−78	52	15:85
6	*n*Bu	100	−98	39	18:82

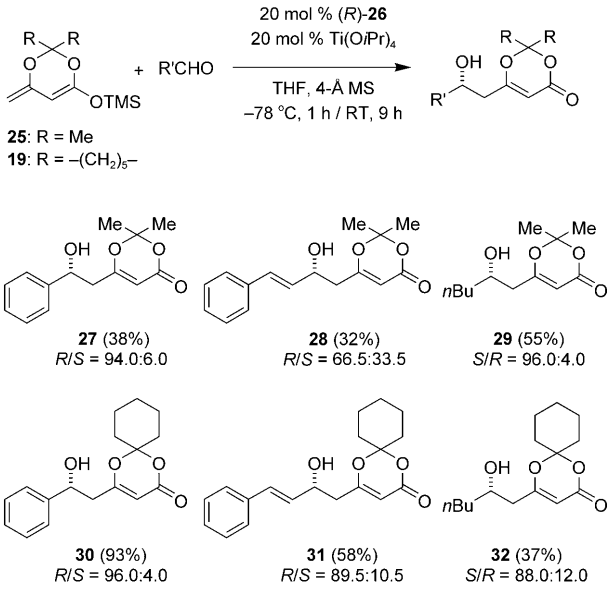
way.[17]. Therefore, slow addition of the silyl dienol ether, low temperatures, and high catalyst loadings (50–100 mol%) are required to attain high selectivities. 1,3,2-Oxazaborolidine catalysts, although not commonly used because of their low selectivity, were employed by Kiyooka and co-workers in the synthesis of a key fragment of the polyol portion of filipin III[19] and in a partial synthesis of the macrolide acutiphycin.[20] In the synthesis of filipin III, the direct product of the vinylogous aldol addition of dienolate **21** to aldehyde **22** catalyzed by oxazaborolidine complex **23** was further elaborated through a substrate-controlled *syn* reduction with Et_2BOMe and $NaBH_4$ to afford polyol **24** (Scheme 8).



Scheme 8. Oxazaborolidinone-promoted vinylogous aldol addition in the total synthesis of filipin III;[19] TBS = *tert*-butyldimethylsilyl; TMS = trimethylsilyl; Ts = toluenesulfonyl.

As part of their ongoing program on the synthesis of dioxanone-containing compounds, Sato et al. sought an improved protocol for these vinylogous aldol reactions. By adopting another well-known Lewis acid catalyst for aldol additions,[21] they found that a titanium(IV)–1,1′-binaphthol (binol) complex generated in situ could be employed (Scheme 9).[22] This complex is also a highly efficient and



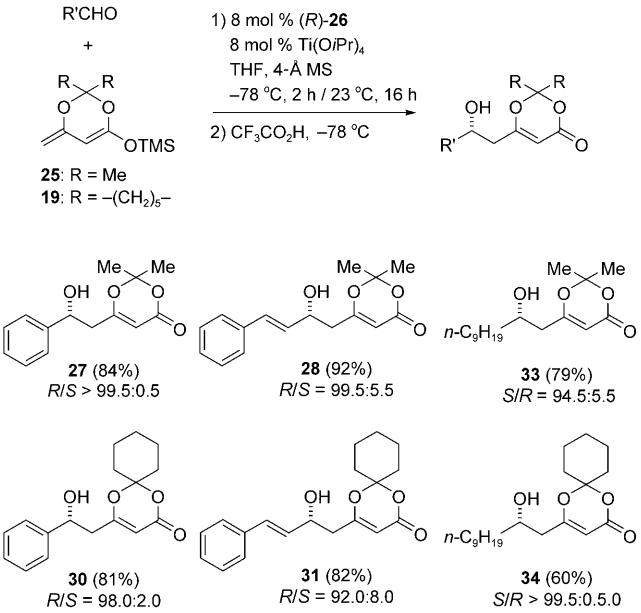


Scheme 9. The $Ti(OiPr)_4$/(*R*)-binol-catalyzed vinylogous aldol reaction of dienolates **25** and **19** developed by Sato et al.[22]

selective catalyst for aldol additions of simple silyl ketene acetals. However, in this case, the high selectivities observed with acetate- and propanoate-derived silyl ketene acetals translate well to the reactions of dioxinone-derived silyl dienol ethers. High, although not exceptional, selectivities are observed for a variety of aldehyde substrates. Interestingly, the structure of the dioxinone-derived silyl dienol ether has a dramatic effect on both the yield and the selectivity. Whereas dienolate **25** is superior for reactions with aliphatic aldehydes, the use of the spirodioxinone-derived silyl dienol ether **19** leads to higher yields and selectivities with aromatic and olefinic aldehydes.

The titanium(IV)–binol catalyst has become popular for the vinylogous aldol reaction, and several recent reports from Scettri and co-workers expand the scope of this catalytic method as well as improve upon its selectivity (Scheme 10).[23] During their investigation of the catalyst structure, Scettri and co-workers observed that these reactions exhibit a strong, positive nonlinear effect. The magnitude of the effect is not

 © 2005 Wiley-VCH Verlag GmbH & Co. KGaA, Weinheim

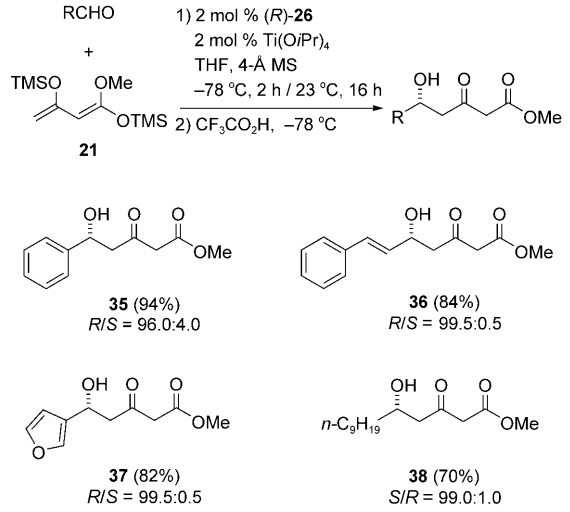


Scheme 10. The Ti(O*i*Pr)$_4$/(*R*)-binol-catalyzed vinylogous aldol reaction of dienolates **25** and **19** developed by Scettri and coworkers.[23]

concentration dependent. This behavior is indicative of an ML_2 catalyst system and suggests that two binol units are incorporated in the active catalytic species.[24] Furthermore, the addition of dienolate **25** to benzaldehyde proceeds through an autoinductive process with an amplification of the enantioselectivity when the reaction is performed in the presence of the enantiomerically enriched aldol product as an additive. These observations led to further refinements in the protocol for the in situ generation of the catalyst, so that reproducibly high enantioselectivities could be attained in the addition of dioxinone-derived dienolates **19** and **25** to a wide range of aldehydes. In a reversal of the trend observed when Sato et al. employed the titanium(IV)–binol catalyst system, dienolate **19** is now more effective in reactions with aliphatic aldehydes, whereas dienolate **25** is superior for aromatic and olefinic aldehydes.

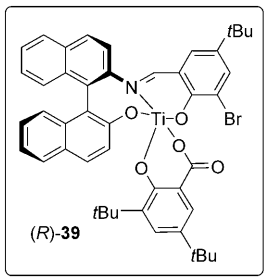
Scettri and co-workers reported that the protocol developed in their laboratories for the in situ generation of the titanium(IV)–binol catalyst system is also suitable for the addition of the Chan diene (**21**) to a wide variety of aldehydes (Scheme 11).[25] Dienolates of this type are extremely reactive and require catalyst loadings of only 2 mol% to afford aldol products in high yields and excellent selectivities. To isolate the aldol product in high selectivity, the use of the procedure developed by Carreira and co-workers for cleaving the silyl protecting group in the aldolate intermediate is essential, as racemization of the newly created stereocenter occurs when other methods are employed.

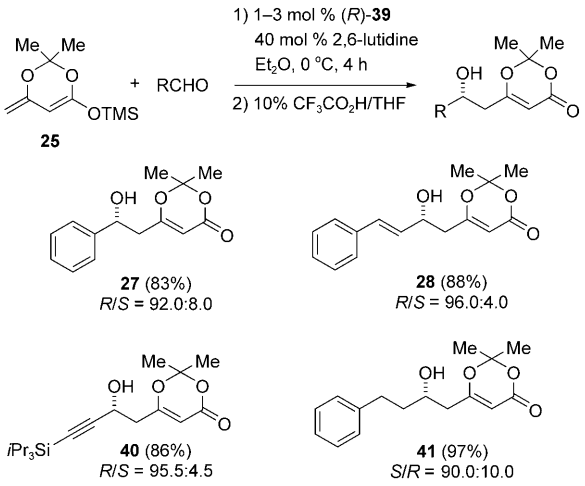
Although this titanium-based system provides high levels of enantioselectivity for a wide variety of substrates, it is less than ideal for synthetic planning because of its poorly defined catalyst structure and the fact that the autoamplification observed in the case of some substrates may not be general. In 1995, Singer and Carreira reported a well-defined catalyst system with which consistently high enantioselectivities and



Scheme 11. The vinylogous aldol reaction of dienolate **21** catalyzed by the Ti(O*i*Pr)$_4$/(*R*)-binol complex;[25] MS = molecular sieves.

yields can be attained (Scheme 12).[16] The titanium(IV)–Schiff base complex (*R*)-**39**, which had also proven successful for aldol reactions of simple silyl ketene acetals, presents several practical and advantages for synthesis over the catalysts described above. This catalyst system, unlike most catalysts for aldol reactions, provides high yields and enantioselectivities with alkynyl aldehydes as well as aromatic, olefinic, and aliphatic aldehydes.

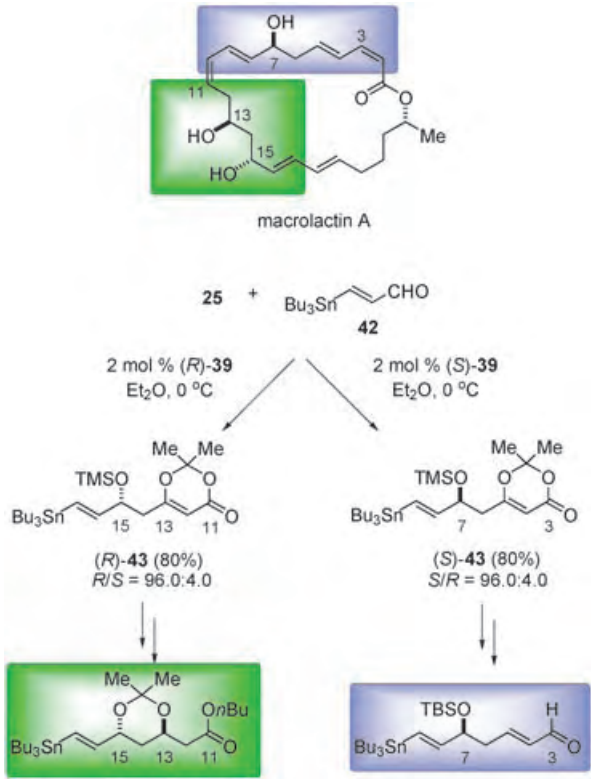




Scheme 12. The Ti^{IV}/Schiff base catalyzed vinylogous aldol reaction of dienolate **25**.[16]

 © 2005 Wiley-VCH Verlag GmbH & Co. KGaA, Weinheim

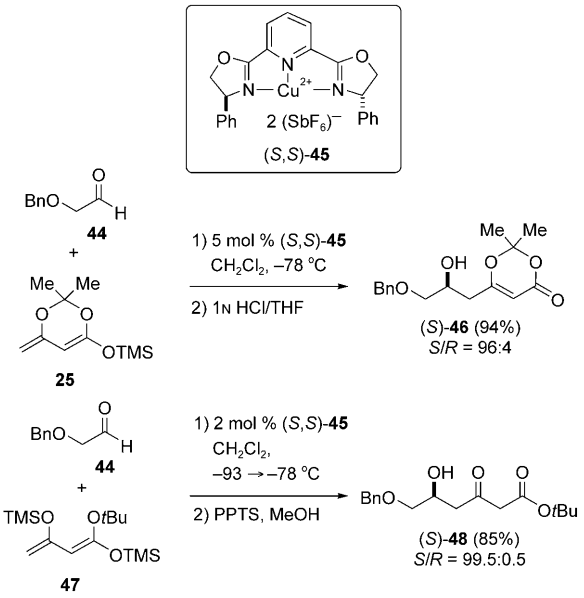
The high selectivity and wide substrate scope of this method makes it useful in complex-molecule total synthesis, as illustrated by the synthesis of macrolactin A[26] and dihydroxy vitamin D_3.[27] In the synthesis of macrolactin A, both enantiomeric forms of the titanium(IV)–Schiff base complex are employed to construct hydroxy-bearing stereocenters present in two key subunits of the molecule (Scheme 13). The protected acetoacetate adducts (*R*)-**43**



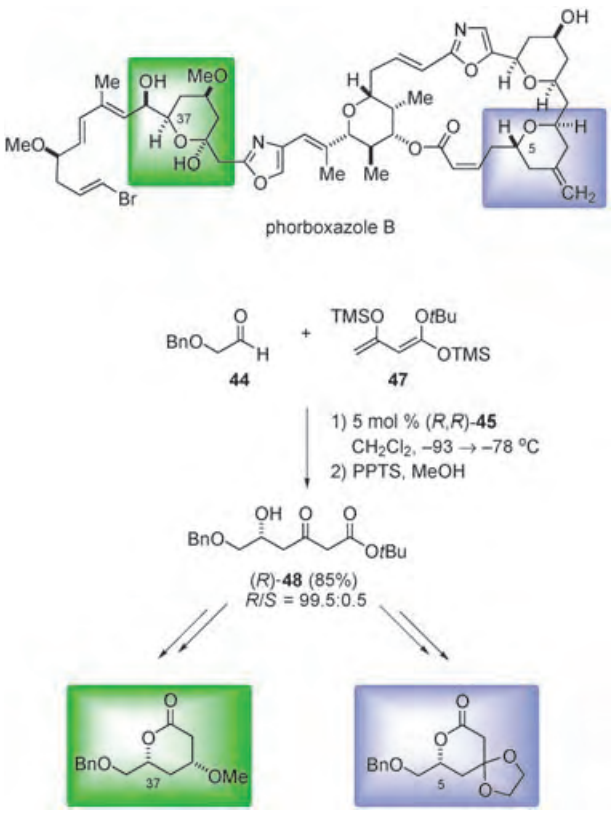
Scheme 13. Application of the Ti(IV)/Schiff base catalyzed vinylogous aldol reaction in the total synthesis of macrolactin A.[26]

and (*S*)-**43** were then further elaborated into the C11–C17 and C3–C9 fragments, respectively. The 1,3-*anti*-diol relationship between the C13 and C15 stereocenters is created through a highly selective, substrate-controlled reduction.

Evans and co-workers have applied the well-defined and versatile copper–bisoxazoline catalyst (*S*,*S*)-**45** for vinylogous aldol reactions of the dioxinone- and acetoacetate-derived silyl dienol ethers **25** and **47** with the α-heteroatom-substituted aldehyde **44** (Scheme 14).[28] Because this catalyst requires a potentially chelating substrate for high selectivity, the reaction remains somewhat limited in terms of aldehyde scope. Nevertheless, this method affords the products in high yields and selectivities and has been applied in successful syntheses of phorboxazole B[29] and bryostatin 2.[30] To demonstrate the versatility of the acetoacetate aldol adduct **48**, Evans and co-workers constructed two different pyran rings in phorboxazole B from this product of a vinylogous aldol addition (Scheme 15).



Scheme 14. The Cu^{II}/pybox-catalyzed vinylogous aldol addition of dienolates **25** and **47** to aldehyde **44**;[28] PPTS = pyridinium *p*-toluenesulfonate.

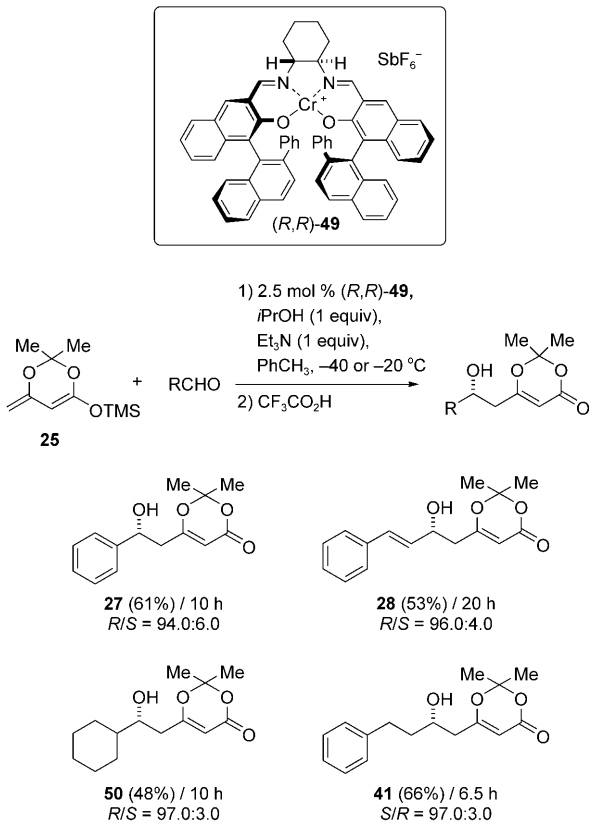


Scheme 15. Application of the vinylogous aldol reaction catalyzed by the Cu^{II}/pybox complex (*R*,*R*)-**45** in the total synthesis of phorboxazole B.[29]

Katsuki and co-workers showed that the chiral, cationic chromium–salen complex (*R*,*R*)-**49** is an effective catalyst for vinylogous aldol reactions of the dioxinone-derived silyl

 © 2005 Wiley-VCH Verlag GmbH & Co. KGaA, Weinheim

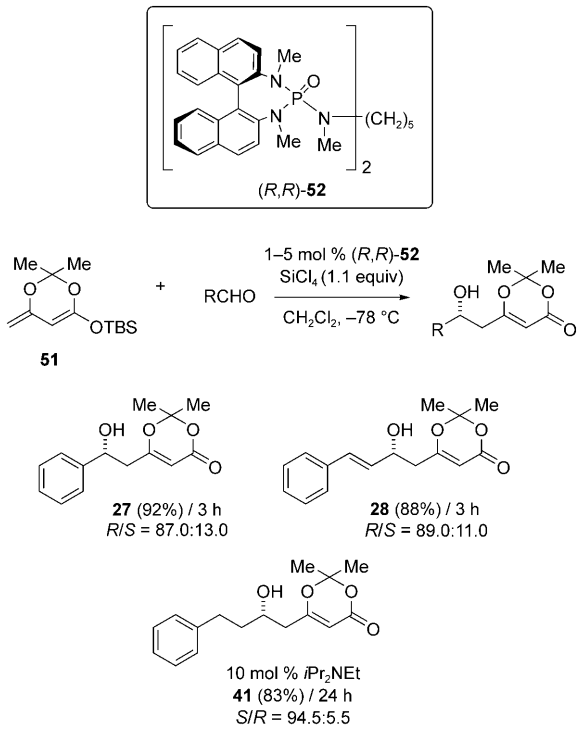
dienol ether **25** (Scheme 16).[31] The enantioselectivity of these reactions is highly sensitive to both the rate of addition of the silyl dienol ether and the solvent used. The low enantioselectivities can be attributed to a competitive silyl-



Scheme 16. The vinylogous aldol reaction of dienolate **25** catalyzed by the cationic chromium–salen complex (*R*,*R*)-**49**.[31]

cation-catalyzed pathway. Slow addition of dienolate **25** with a syringe pump and the presence of protic cosolvents greatly increase the rate of catalyst turnover from the chromium aldolate relative to the release of the silyl cation and lead to an increase in enantioselectivity. Although a protic cosolvent, such as an alcohol, is essential for excellent enantioselectivities to be attained, it also has the detrimental effect of decreasing the yield of the aldol adduct. However, reactions performed in the presence of both an alcohol and an amine base provide the products in improved yields while high enantioselectivities are maintained. The authors propose that coordination of the alcohol to the chromium ion generates a Brønsted acid, which, if not neutralized by the amine base, can effect protodesilylation of dienolate **25**. Under optimized conditions that include 2-propanol as a cosolvent and the addition of Et_3N, a catalyst loading of only 2.5 mol% is adequate to attain moderate to good yields and excellent enantioselectivities with a variety of aldehydes.

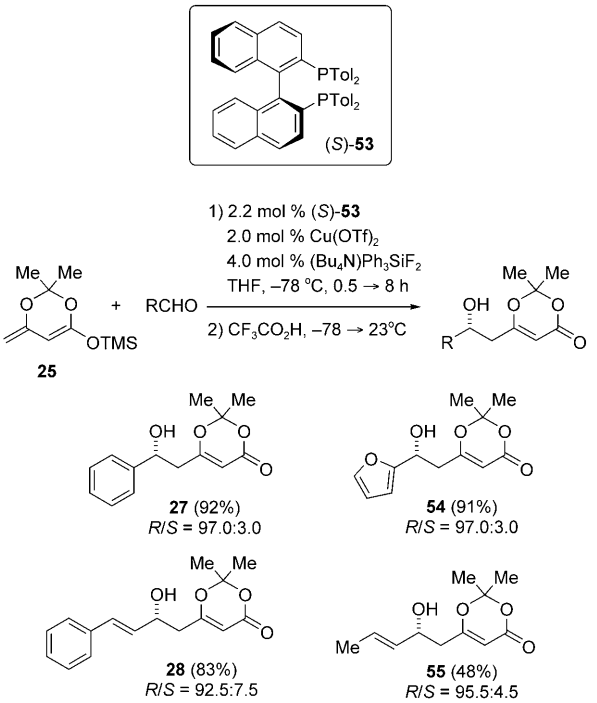
As is clear from the preceding examples of enantioselective Lewis acid catalysis, developments in the aldol reactions of simple silyl enol ethers are typically echoed in the vinylogous aldol reaction. The application of "Lewis base activation of Lewis acid" catalysis to the aldol reaction of silyl ketene acetals has also been extended to the vinylogous aldol reaction.[32] In this case, the use of the chiral bisphosphoramide catalyst (*R*,*R*)-**52** in conjunction with $SiCl_4$ leads to the in situ formation of a putative chiral siliconium ion that promotes the addition of the dioxinone-derived dienol ether **51** to a variety of aldehydes in high yields (Scheme 17). Although the aromatic and olefinic aldehydes studied reacted with only moderate enantioselectivity, the addition to the aliphatic aldehyde leads to the aldol adduct with high enantioselectivity.



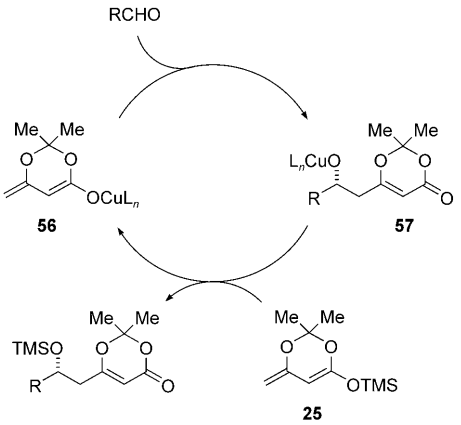
Scheme 17. The vinylogous aldol reaction of dienolate **51** catalyzed by $SiCl_4$ and bisphosphoramide (*R*,*R*)-**52**.[32]

The catalyst systems discussed thus far represent extensions of asymmetric methods for simple aldol reactions to vinylogous aldol reactions. The active catalyst is a chiral Lewis acid, which binds to the aldehyde and participates in the catalytic cycle by providing electrophilic activation. The first catalyst system that was specifically designed for use in the vinylogous aldol reaction is a copper(II) fluoride/Tol-binap catalyst reported by Carreira and co-workers in 1998 (Scheme 18).[33] Reactions with this catalyst proceed by a different mechanism to that of the reactions discussed previously (Scheme 19). Initial studies suggested that the copper(II) fluoride catalyst reacts with the silyl dienol ether to generate a chiral copper dienolate **56**, which is the active species in the subsequent carbon–carbon bond-forming step. This hypothesis was confirmed by ReactIR studies, in which both the copper dienolate **56** and the copper aldolate **57** were observed. This reaction system leads to high yields and

 © 2005 Wiley-VCH Verlag GmbH & Co. KGaA, Weinheim



Scheme 18. The vinylogous aldol reaction of dienolate **25** catalyzed by the (*S*)-Tol-binap·CuF_2 complex.[33]



Scheme 19. Catalytic cycle for the vinylogous aldol reaction catalyzed by the Tol-binap·CuF_2 complex.

enantioselectivities for aromatic, heteroaromatic, and olefinic aldehydes in the addition to the dioxinone-derived dienol ether **25**; diminished yields are observed with aliphatic aldehydes, while high selectivity is maintained. This reaction is featured as a key step in the syntheses of leucascandrolide A,[34] salicylihalamide A,[35] a subunit of the group-A streptogramin antibiotics,[36] and the amphotericin B polyol subunit.[37]

In a total synthesis of salicylihalamide A, the ability to override the inherent Cram selectivity of chiral aldehyde (*S*)-**58** in a catalytic, asymmetric vinylogous aldol addition is illustrated.[35] Although Felkin–Heathcock analysis predicts that attack at the *Si* face of the carbonyl group in (*S*)-**58** is preferred, coupling of aldehyde (*S*)-**58** to dienolate **25** in the presence of $Cu(OTf)_2$, (*S*)-Tol-binap, and $(Bu_4N)Ph_3SiF_2$ affords an 81:19 mixture of diastereomers in favor of the aldol adduct *anti*-**59** formed from *Re*-face addition (Scheme 20). In contrast, use of the (*R*)-Tol-binap ligand in an overall matched case of double diastereoselection, produces an 86:14 mixture of diastereomers in favor of the adduct *syn*-**59**. Although the catalyst with the (*S*)-Tol-binap ligand can override the intrinsic facial selectivity of the aldehyde in the mismatched case to afford moderate *anti* selectivity, the inherent Cram selectivity, which favors the *syn* aldol adduct, is low for aldehyde (*S*)-**58**.

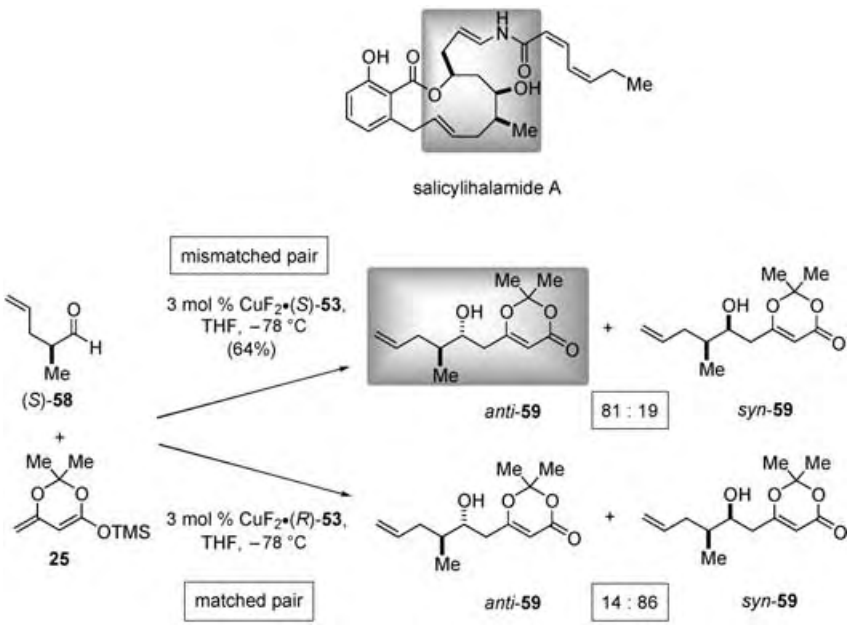
Although several highly selective catalyst systems have been developed for enantioselective, vinylogous aldol additions of the 6-methyldioxinone-derived dienolate **25**, a general, highly selective catalyst for the 6-ethyldioxinone-derived analogue **60** has not been reported.[38] In 1995, Sato et al. disclosed the only examples of catalytic, enantioselective, vinylogous aldol additions with dienolate **60** (Scheme 21).[22] Under catalysis with the titanium(IV)–binol complex, the addition of dienolate **60** to benzaldehyde proceeds in modest yield and with *syn* diastereoselectivity. Remarkably, the *syn* diastereomer is produced in enantiomerically pure form. When the CAB complex **20** is employed for the addition of the same substrates, poor *anti* diastereoselectivity is observed along with moderate to good enantioselectivity for both diastereomers.

4. Simple Ester-Derived Silyl Dienol Ethers

Dienol ethers **1** and **14** are synthetic equivalents of ketoester dianions that react with exclusive γ-site selectivity owing to the high nucleophilicity at C4. However, as exemplified in Figure 1, silyl dienol ethers (*E*)-**12** derived from α,β-unsaturated esters are not as electronically biased, and steric effects also need to be considered. Indeed, both α- and γ-addition products have been observed in vinylogous aldol reactions with ester-derived dienol ethers. Although achieving high site selectivity with these dienol ethers is more challenging than with the acetoacetate-derived dienol ethers, it is well worth the effort, as the α,β-unsaturated δ-hydroxy carbonyl adducts **4** are chiral homoallylic alcohols, which can be further functionalized through conjugate addition to, or oxidation or reduction of, the double bond (Scheme 3).

In 1999, Bluet and Campagne expanded the scope of the catalytic, enantioselective, vinylogous aldol reaction to simple ester-derived silyl dienol ethers **3** by employing the titanium(IV)–binol catalyst system (Scheme 22).[39] In this initial study, only the ethyl tiglate derived silyl dienol ether **62** was investigated. Although γ-aldol adducts were obtained exclusively, these less nucleophilic species were found to lead to lower yields and enantioselectivities than more highly oxygenated silyl dienol ethers, such as **25**. Nevertheless, the vinylogous aldol addition of simple ester-derived silyl dienol ethers has found application in the synthesis of complex natural products, such as callipeltoside A (Scheme 23).[40] The C13 stereocenter and the *E*-configured trisubstituted C10–

 © 2005 Wiley-VCH Verlag GmbH & Co. KGaA, Weinheim



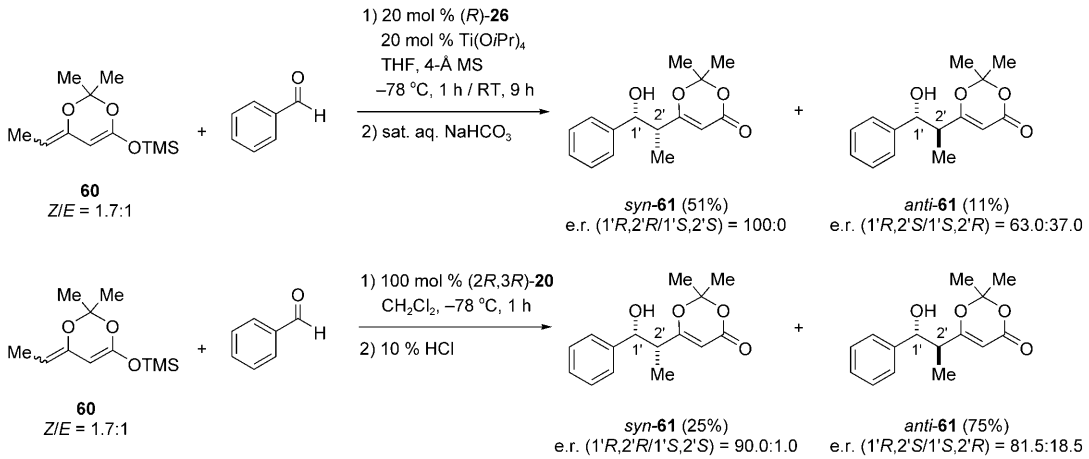
Scheme 20. Addition of dienolate **25** to chiral aldehyde (*S*)-**58** catalyzed by the Tol-binap·CuF_2 complex.[35]

C11 double bond were installed with excellent selectivity by an asymmetric, vinylogous aldol reaction of the methyl senecioate derived silyl dienol ether **67** with dienal **68**. However, high catalyst loadings and long reaction times are required to obtain a high yield because of the low reactivity of the dienolate.

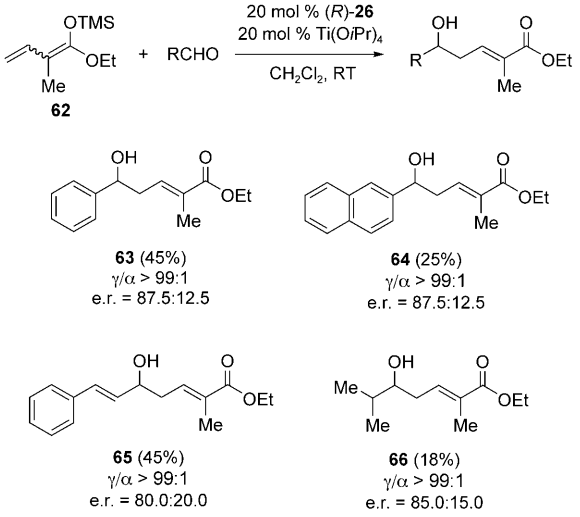
In an earlier approach to callipeltoside A, Evans et al. developed a catalytic, asymmetric, vinylogous aldol reaction with ethyl senecioate derived silyl dienol ether **70** to construct the same hydroxy-substituted stereocenter and trisubstituted *E* double bond (Scheme 24).[41] The addition of dienolate **70** to 2-(4-methoxybenzyloxy)acetaldehyde (**71**) afforded the vinylogous aldol adduct **73** in high yield with complete *E* selectivity and excellent enantioselectivity under catalysis with the air-stable complex (*R*,*R*)-**72**.

Whereas in the preceding system a Lewis acidic copper catalyst was employed to activate the aldehyde prior to the addition, Bluet and Campagne have explored the use of copper as an activator of ester-derived silyl dienol ethers through generation of chiral copper metallodienolates. The use of the Carreira catalyst (*S*)-Tol-binap·CuF_2 produces a metallodienolate that provides exclusive γ-site selectivity along with high yields and moderate enantioselectivities for the vinylogous aldol addition of dienol ether **62** to aromatic and aliphatic aldehydes (Scheme 25).[42] However, in the addition to cinnamaldehyde a 1:1 mixture of the vinylogous aldol adduct and the 1,4-addition product was obtained. Chemical degradation of **63** to a previously described enantiomerically pure compound and comparison of the optical rotation showed that the major enantiomer is the aldol adduct derived from *Si*-face attack on the aldehyde. Remarkably, the sense of asymmetric induction observed in this reaction with the (*S*)-Tol-binap ligand is opposite to that observed by Carreira and co-workers in the addition of the dioxinone-derived silyl dienol ether **25** to aldehydes under catalysis by (*S*)-Tol-binap·CuF_2.[33]

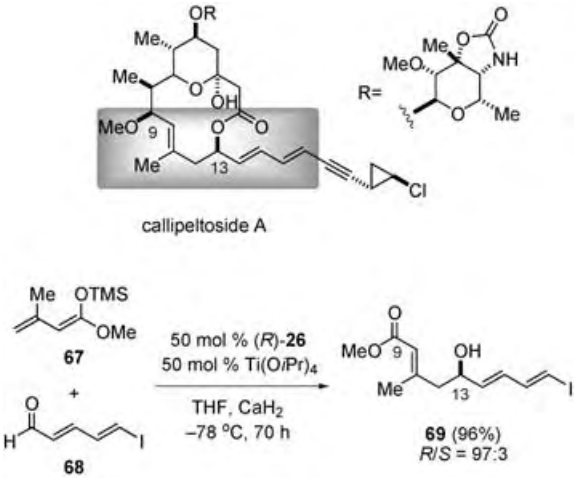
Campagne and co-workers also studied the effect of γ substitution on the dienolate in the addition to aldehydes in the presence of the (*S*)-Tol-binap·CuF_2 catalyst (Scheme 26).[43] The addition of the methyl pentenoate derived silyl dienol ether **74** to various aldehydes yielded mixtures of lactones **75** and vinylogous aldol products **76**. Whereas lactones **75** were formed with excellent *anti* selectivity (>98:2) along with high enantioselectivity in all cases, the linear products **76** were isolated as a 1:1 mixture of racemic *syn* and *anti* diastereomers. The lactones are obtained with high diastereo- and enantioselectivity from the reaction with aromatic, heteroaromatic, olefinic, and aliphatic aldehydes. However, the ratio of the lactone to the linear product, a measure of the *E*/*Z* selectivity in the formation of the double bond, is highly substrate dependent. Whereas aro-



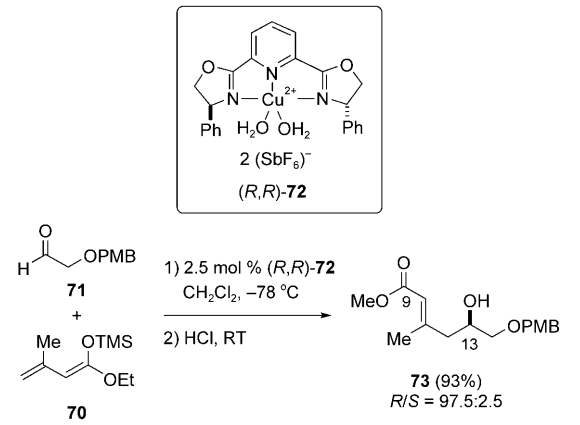
Scheme 21. Vinylogous aldol additions of dienolate **60** to benzaldehyde catalyzed by CAB and Ti(O*i*Pr)$_4$/(*R*)-binol.[22]



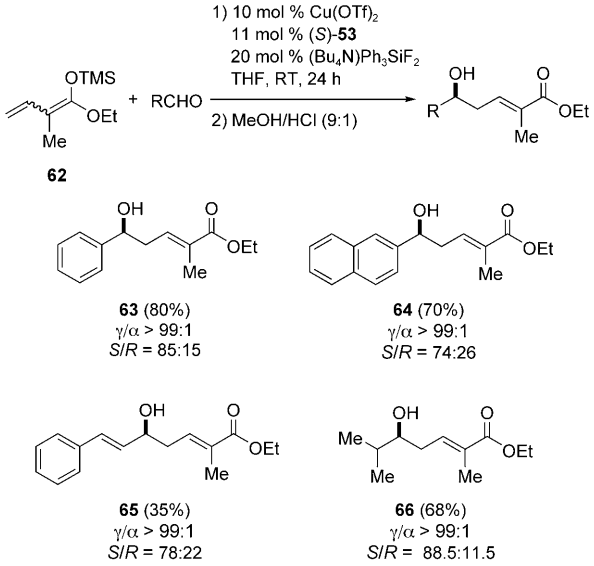
Scheme 22. The Ti(O*i*Pr)$_4$/(*R*)-binol-catalyzed vinylogous aldol reaction of the ester-derived dienolate **62** (absolute configurations were not established by the authors).[39]



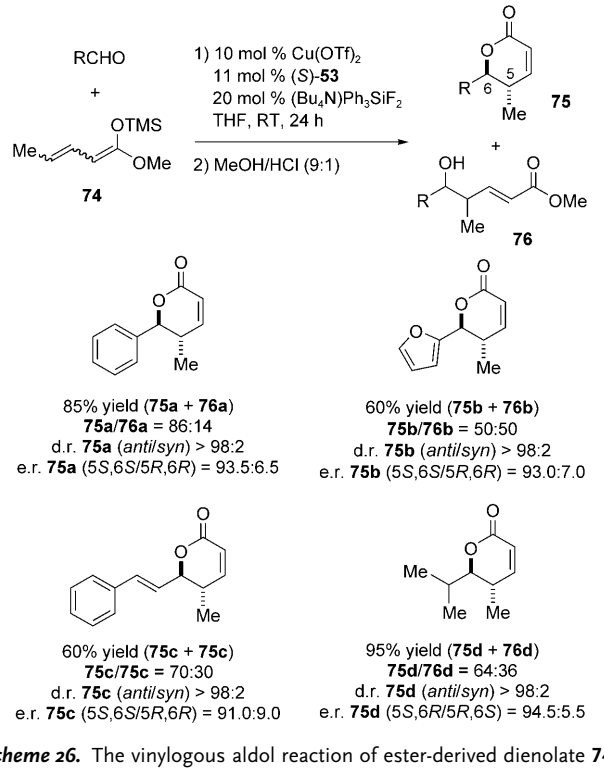
Scheme 23. Application of the Ti(O*i*Pr)$_4$/(*R*)-binol-catalyzed vinylogous aldol reaction in the total synthesis of callipeltoside A.[40]



Scheme 24. Application of the vinylogous aldol reaction catalyzed by the Cu^{II}/pybox complex (*R*,*R*)-**72** in the total synthesis of callipeltoside A;[41] PMB = *p*-methoxybenzyl.



Scheme 25. The vinylogous aldol reaction of ester-derived dienolate **62** catalyzed by the (*S*)-Tol-binap·CuF$_2$ complex.[42]

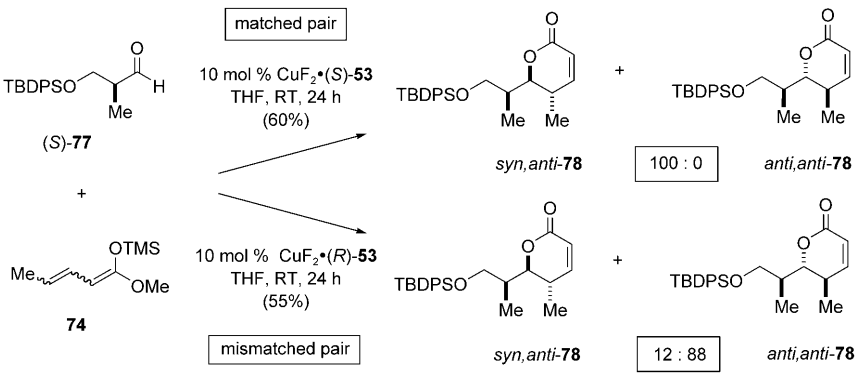


Scheme 26. The vinylogous aldol reaction of ester-derived dienolate **74** catalyzed by the Tol-binap·CuF$_2$ complex (**a**: R = Ph, **b**: R = 2-furyl, **c**: R = cinnamyl, **d**: R = isopropyl).[43]

matic aldehydes afford the highest proportion of the lactone product, aliphatic and olefinic aldehydes are less selective, and 2-furaldehyde affords both the linear product and the lactone in a 1:1 ratio.

In an extension of this method, the addition of dienol ether **74** to the chiral aldehyde (*S*)-**77** was investigated (Scheme 27).[43] Felkin–Heathcock analysis of the *S*-config-

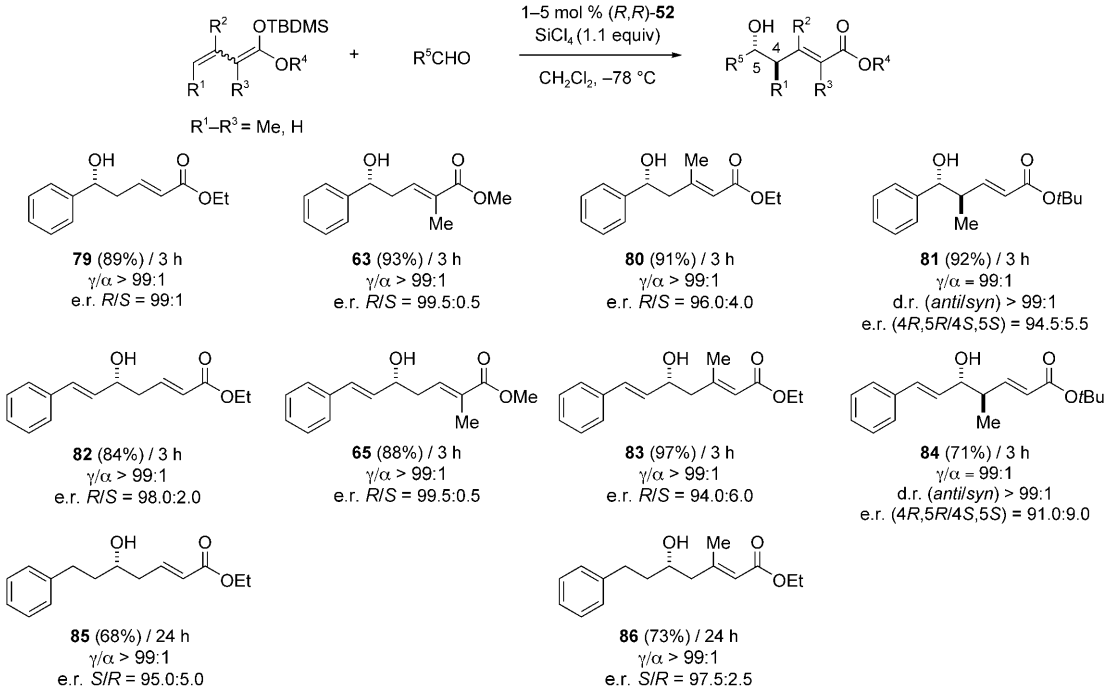
 © 2005 Wiley-VCH Verlag GmbH & Co. KGaA, Weinheim



Scheme 27. The vinylogous aldol addition of ester-derived dienolate **74** to chiral aldehyde (*S*)-**77** catalyzed by the Tol-binap·CuF_2 complex;[43] TBDPS = *tert*-butyldiphenylsilyl.

ured aldehyde (*S*)-**77** predicts that approach to the *Si* face of the carbonyl group should be preferred, thus leading to the *syn* diastereomer. Additionally, the (*S*)-Tol-binap ligand has the same facial bias for attack at the *Si* face of the aldehyde, as shown above. When the (*S*)-Tol-binap·CuF_2 catalyst system is used, *syn*/*anti*-**78** is formed as the only lactone diastereomer, with the linear product reported to account for less than 10% of the crude reaction mixture. However, when the (*R*)-Tol-binap ligand is employed, an 88:12 mixture of lactones is formed, with a switch in diastereoselectivity now favoring the *anti*/*anti* lactone **78**. Again, the amount of linear product formed is reported to be less than 10% of the crude reaction mixture. Although the selectivity in both the matched and the mismatched case is high, the yields of the isolated product are low for both addition reactions (60 and 55%, respectively).

A systematic study of the effect on the addition to aldehydes of various substitution patterns on the dienol ether further expanded the scope of the vinylogous aldol reaction of ester-derived dienol ethers (Scheme 28).[32] The $SiCl_4$–phosphoramide catalyst system used for the addition of the acetoacetate-derived dienol ether **51** also effectively promotes the addition of the unsubstituted ethyl crotonate derived dienol ether as well as α-, β-, and γ-substituted dienol ethers. Remarkably, excellent γ-site selectivity and *E*-double-bond selectivity are maintained for all substitution patterns on the dienolate in the addition to aromatic, olefinic, and aliphatic aldehydes. Furthermore, this catalyst system maintains the high level of *anti* diastereoselectivity (> 99:1) that is observed in the additions of propanoate-derived silyl ketene acetals.[44] With aromatic and olefinic aldehydes, catalyst loadings of 1 mol% are sufficient to provide vinylogous aldol adducts in high yields and selectivities with all four dienolates surveyed. However, aliphatic aldehydes require higher catalyst loadings and longer reaction times for acceptable yields to be attained in the additions of the unsubstituted crotonate-derived and β-substituted senecioate-derived dienol ethers. Dienol ethers with methyl groups in the γ and α positions were found to be unreactive with aliphatic aldehydes. The aldol adducts are produced with excellent *E* selectivity regardless of the substitution on the dienol ether, including γ substitution. This result stands in contrast to catalysis with Tol-binap·CuF_2. Whereas the addition of the α-substituted methyl tiglate derived dienol ether occurs with exclusive *E* selectivity in the presence of this catalyst, the γ-substituted methyl pentenoate derived dienol ether affords the aldol adduct with modest *Z* selectivity.

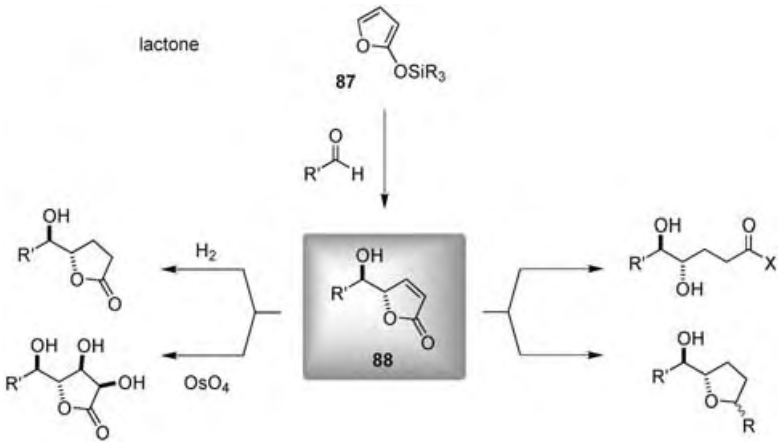


Scheme 28. The vinylogous aldol reaction of various ester-derived dienolates catalyzed by $SiCl_4$ and bisphosphoramide (*R*,*R*)-**52**.[32]

 © 2005 Wiley-VCH Verlag GmbH & Co. KGaA, Weinheim

5. Lactone-Derived Dienol Ethers

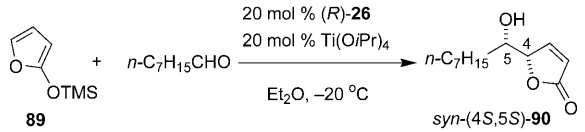
The Lewis acid catalyzed vinylogous aldol addition of lactone-derived dienol ether **87** to aldehydes leads to the formation of a γ-substituted butenolide **88**, a structural motif that is found in several biologically active natural products (Scheme 29). Furthermore, these adducts are useful chiral building blocks for the preparation of functionalized γ-lactones through manipulation of the double bond. Butenolide **88** has also been used for the preparation of compounds containing 1,2-diol functionality, and for the construction of optically active pyrans.[12a]



Scheme 29. The vinylogous aldol addition of lactone-derived dienol ether **87** and elaboration of the butenolide product.

Figadère and co-workers disclosed the first catalytic, enantioselective addition involving a lactone-derived dienolate in 1998.[45] The titanium-based chiral catalyst system developed by Sato et al. and improved upon by Scettri and co-workers for acetoacetate-derived dienol ethers can also promote highly site-selective additions of the lactone-derived silyl dienol ether **89** to aldehydes. Interestingly, reactions performed in the presence of a 1:1:1 mixture of $Ti(OiPr)_4$, binol, and a second chiral alcohol afforded the aldol addition product in higher yields and enantioselectivities than those carried out in the presence of only $Ti(OiPr)_4$ and binol. The authors suspected that the aldol product becomes incorporated into the catalytic species to generate a new catalyst structure and therefore explored the possibility of an autoinductive aldol reaction (Table 2). The first experiment established that the aldol addition product was produced with higher enantioselectivity in the presence of 5 mol% of the enantiomerically enriched aldolate *syn*-(4*S*,5*S*)-**90** than in the reaction performed in the absence of additives (Table 2, entries 1 and 2). Furthermore, the inclusion of the minor enantiomer *syn*-(4*R*,5*R*)-**90** under the same reaction conditions causes a decrease in enantioselectivity (Table 2, entry 3). To allow amplification of the enantioselectivity through the incorporation of the major *syn* butenolide formed during the reaction into the catalyst structure, a general procedure

Table 2: Modification of the $Ti(OiPr)_4$/binol-catalyzed vinylogous aldol reaction.[45]

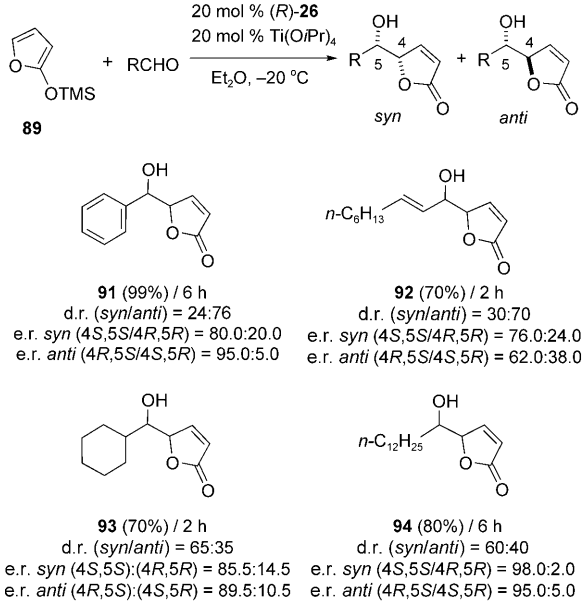


Entry	Additive	Yield [%]	*syn*:*anti*	e.r. (*syn*)
1[a]	none	99	70:30	85:15
2	5% (4*S*,5*S*)-**90**	99	70:30	>98:2
3	5% (4*R*,5*R*)-**90**	99	70:30	70:30
4[b]	none	90	60:40	>98:2

[a] Dienolate **89** was added in one portion. [b] Dienolate **89** was added stepwise in four portions. e.r. = enantiomeric ratio.

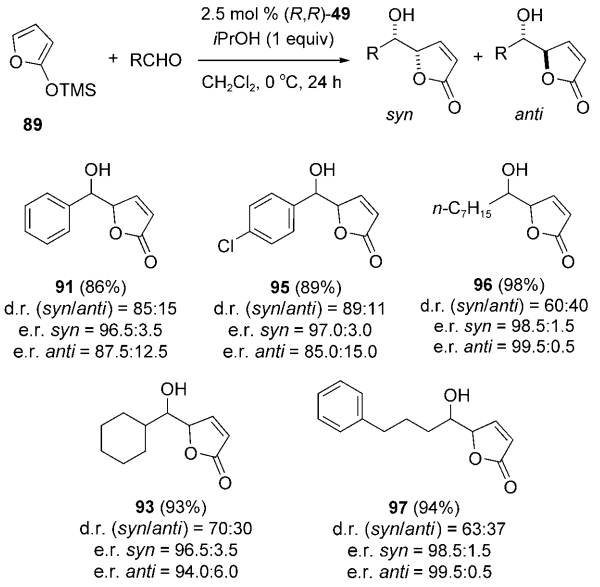
involving stepwise addition of dienolate **89** was developed (Table 2, entry 4). This method has been applied to vinylogous aldol reactions of silyl dienol ether **89** and affords adducts with modest to excellent enantioselectivities and modest diastereoselectivities (Scheme 30). Interestingly, the substrate determines which product is formed as the major diastereomer in the addition reaction; whereas aliphatic aldehydes lead to the formation of the *syn* isomer, olefinic and aromatic aldehydes produce the *anti* isomer.

The chromium–salen catalyst (*R*,*R*)-**49** used by Katsuki and co-workers for the addition of dioxinone-derived dienol ether **25** to aldehydes also catalyzes the addition of **89** to aldehydes with high enantioselectivity (Scheme 31).[46] As is the case for the reaction with dienol ether **25**, the addition of a protic cosolvent to the reaction mixture is essential for high and reproducible selectivities to



Scheme 30. The $Ti(OiPr)_4$/(*R*)-binol-catalyzed vinylogous aldol reaction of lactone-derived dienolate **89**.[45]

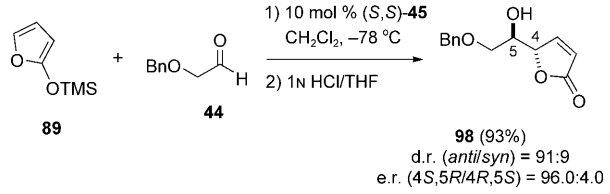
 © 2005 Wiley-VCH Verlag GmbH & Co. KGaA, Weinheim



Scheme 31. The vinylogous aldol reaction of lactone-derived dienolate **89** catalyzed by the cationic chromium–salen complex (*R*,*R*)-**49** (absolute configurations were not established by the authors).[46]

be attained. The authors propose that the protic cosolvent is needed to suppress the undesired retroaddition reaction by rapidly converting the aldolate into the hydroxyl lactone product, thereby enabling the isolation of the adduct formed under conditions of kinetic control. Although only modest to good *syn* diastereoselectivities are observed with aromatic and aliphatic aldehydes, both the *syn* and *anti* isomers are formed with good to excellent enantioselectivities.

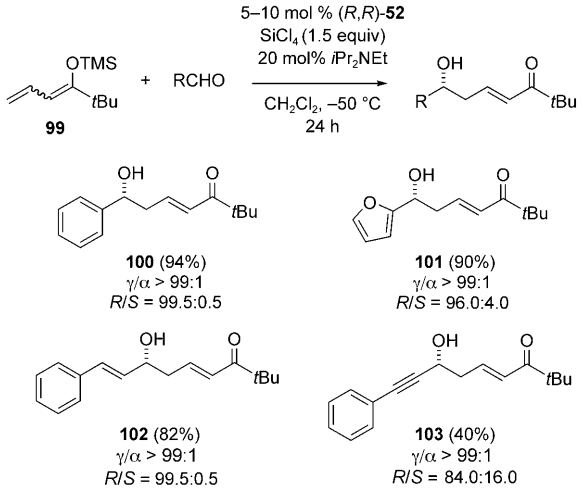
Whereas the two previously described catalyst systems afford only modest diastereoselectivities, the copper–bisoxazoline catalyst (*S*,*S*)-**45** developed by Evans and co-workers affords the *anti* product with high diastereo- and enantioselectivity from the vinylogous aldol reaction of **89** with (benzyloxy)acetaldehyde (**44**; Scheme 32).[28] However, the addition only to aldehyde **44** was demonstrated.



Scheme 32. The vinylogous aldol reaction of lactone-derived dienolate **89** to aldehyde **44** in the presence of the Cu(II)/pybox complex (*S*,*S*)-**45**.[28]

6. Ketone-Derived Dienol Ethers

Although the catalytic, enantioselective, vinylogous aldol addition of dienol ethers derived from α,β-unsaturated esters has been successfully demonstrated, extension of the nucleophile scope to other acyclic α,β-unsaturated carbonyl compounds has remained virtually unexplored. The first use of ketone-derived dienol ethers in catalytic, asymmetric, vinylogous aldol reactions was recently reported from these laboratories.[47] The combination of catalytic amounts of the chiral bisphosphoramide (*R*,*R*)-**52** and $SiCl_4$ promotes the addition of silyl dienol ethers derived from simple acyclic α,β-unsaturated ketones to aldehydes. In this initial report, dienol ether **99** reacts with aromatic, heteroaromatic, olefinic, and propargylic aldehydes with exclusive γ-site selectivity and high enantioselectivity (Scheme 33). However, the failure of aliphatic aldehydes to undergo this reaction remains a limitation of this method.



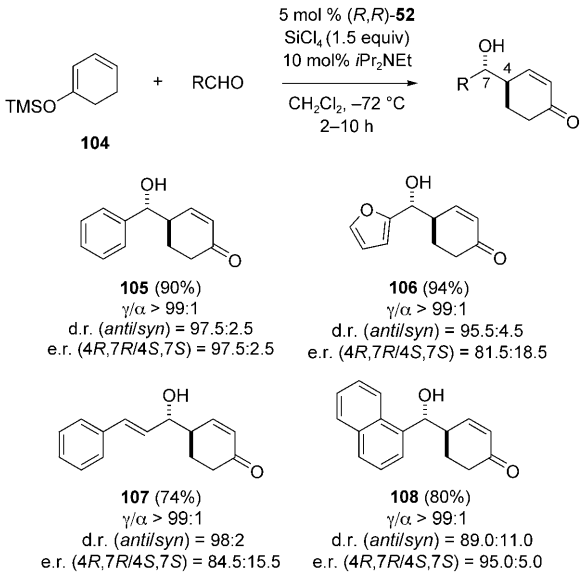
Scheme 33. The vinylogous aldol reaction of acyclic-ketone-derived dienolate **99** catalyzed by $SiCl_4$ and bisphosphoramide (*R*,*R*)-**52**.[47]

The reactivity of the cyclic-ketone-derived dienol ether **104** was examined to evaluate the diastereoselectivity in the addition to form γ-substituted ketones (Scheme 34).[47] Aldol adducts formed from aromatic, olefinic, and heteroaromatic aldehydes could be obtained with exclusive γ-site selectivity and good to excellent *anti* diastereoselectivity. However, as in the case of acyclic-ketone-derived dienol ethers, **104** did not react with aliphatic aldehydes.

7. Conclusions and Outlook

Excellent progress has been made in the development of the catalytic, enantioselective, vinylogous aldol reaction since the initial report in 1994. Through the extension of existing catalyst systems and the invention of novel ones, several general and highly selective methods now exist for the addition of acetoacetate-derived silyl dienol ethers **1** and **14** to a wide variety of aldehydes (see **111**, Figure 2). Moreover, recent studies with dienolates derived from esters have shown that crotonate-derived silyl dienol ethers, as well as dienolates with α and β substituents, react with a wide range of aldehydes with high selectivity (**120**). This method also allows for high selectivity in the addition of dienolates derived from γ-substituted esters to aromatic and olefinic aldehydes to give compounds **123**. Furthermore, high enan-

 © 2005 Wiley-VCH Verlag GmbH & Co. KGaA, Weinheim



Scheme 34. The vinylogous aldol reaction of cyclic-ketone-derived dienolate **104** catalyzed by $SiCl_4$ and bisphosphoramide (*R*,*R*)-**52**.[47]

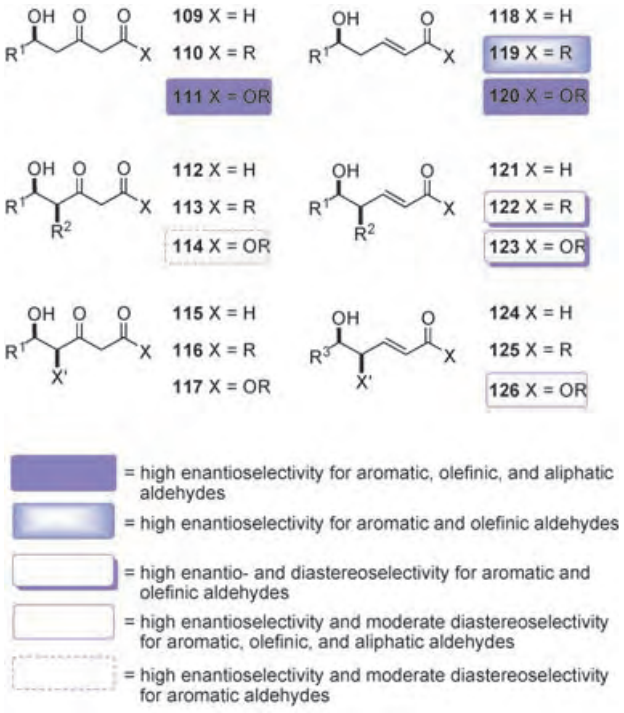


Figure 2. Vinylogous aldol adducts created from simple aldehydes and dienol derivatives derived from β-dicarbonyl compounds or α,β-unsaturated carbonyl compounds.

tioselectivity can be attained in the vinylogous aldol addition of lactone-derived dienol ethers to different aldehyde structures, although a general method that affords high diastereoselectivity is still lacking (**126**).

When one considers the wide range of structural motifs that can be created by employing the vinylogous aldol reaction, the limited number of dienol ethers thus far examined becomes apparent. Figure 2 provides an overview of the aldol adducts that can be created by using catalytic, asymmetric methods through the combination of dienol derivatives derived either from β-dicarbonyl compounds or α,β-unsaturated carbonyl compounds with simple aldehydes. A number of important conclusions are readily apparent. First, the range of nucleophiles is limited primarily to ester-derived reagents. With only a single report of dienol ethers derived from α,β-unsaturated ketones (see **119** and **122**) and no examples of dienol ethers derived from α,β-keto aldehydes (**109**, **112**, and **115**), β-diketones (**110**, **113**, and **116**), or α,β-unsaturated aldehydes (**118**, **121**, and **124**), this is clearly an area for future development. Another serious omission is the lack of methods for the addition of any nucleophile to a wide range of aldehydes with excellent diastereoselectivity. Although progress has been made in the addition of dienol ethers derived from γ-substituted esters, ketones, and lactones, the analogous reactions of dienolates derived from γ-substituted acetoacetates or 1,3-diketones represent opportunities for future investigation.

The presence of the vinylogous aldol motif in many natural products, and the easily manipulated functionalities contained in the resulting α,β-unsaturated δ-hydroxy carbonyl or δ-hydroxy-β-ketoester vinylogous aldol adducts, render this reaction an interesting alternative for the synthesis of many natural products. Although the use of complex enzymes for the synthesis of polyketides is highly successful, the unique strengths and weaknesses of small-molecule asymmetric catalysis inspire the synthetic chemist to find different and innovative solutions to this challenge. The combination of well-established, substrate-controlled asymmetric transformations with these highly selective, catalytic, enantioselective vinylogous aldol reactions is destined to generate new strategies for synthesis in the years to come.

We are grateful to the National Science Foundation (NSF CHE-0105205 and NSF CHE-0414440) for generous financial support. We also thank Dr. Martin Eastgate for performing the DFT calculations.

Received: October 18, 2004
Published online: June 7, 2005

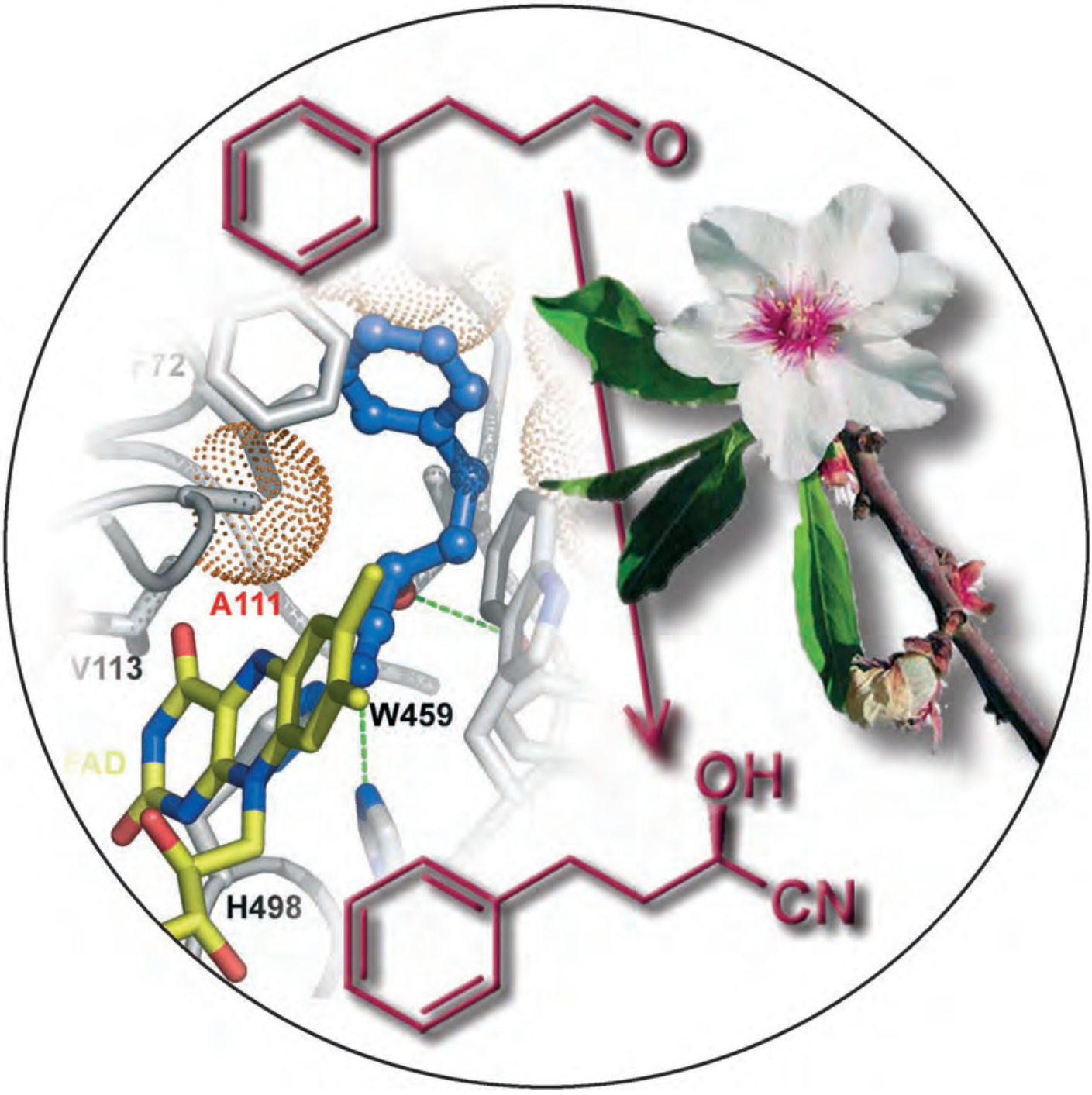
[1] For a recent review, see: J. Staunton, K. J. Weissman, *Nat. Prod. Rep.* **2001**, *18*, 380.
[2] a) E. M. Carreira in *Modern Carbonyl Chemistry*, (Ed.: J. Otera), Wiley-VCH, Weinheim, **2000**, chap. 8; b) E. M. Carreira in *Comprehensive Asymmetric Catalysis*, *Vol. III* (Eds.: E. N. Jacobsen, A. Pfaltz, H. Yamamoto), Springer, Heidelberg, **1999**, chap. 29; c) I. Paterson, C. J. Cowden, D. J. Wallace in *Modern Carbonyl Chemistry* (Ed.: I. Otera), Wiley-VCH, Weinheim, **2000**, chap. 9; d) E. M. Carreira in *Catalytic Asymmetric Synthesis*, 2nd Ed. (Ed.: I. Ojima), Wiley-VCH, Weinheim, **2000**, chap. 8B2; e) M. Braun in *Stereoselective Synthesis, Methods of Organic Chemistry (Houben-Weyl)*, *Vol. 3*, *Edition E21* (Eds.: G. Helmchen, R. Hoffman, J. Mulzer, E. Schaumann), Thieme, Stuttgart, **1996**, p. 1603; f) S. G. Nelson, *Tetrahedron: Asymmetry* **1998**, *9*, 357; g) R. D. Norcross, I. Paterson, *Chem. Rev.* **1995**, *95*, 2041; h) T. Mukaiyama, S. Kobayashi, *Org. React.* **1994**, *46*, 1.
[3] W. R. Roush, A. D. Palkowitz, K. Ando, *J. Am. Chem. Soc.* **1990**, *112*, 6348.

 © 2005 Wiley-VCH Verlag GmbH & Co. KGaA, Weinheim

[4] S. D. Rychnovsky, B. N. Rogers, T. I. Richardson, *Acc. Chem. Res.* **1998**, *31*, 9.
[5] S. A. Burova, F. E. McDonald, *J. Am. Chem. Soc.* **2004**, *126*, 2495.
[6] a) R. C. Fuson, *Chem. Rev.* **1935**, *16*, 1; b) S. Krishnamurthy, *J. Chem. Educ.* **1982**, *59*, 543; c) P. Bruneau, P. J. Taylor, A. J. Wilkinson, *J. Chem. Soc. Perkin Trans. 2* **1996**, 2263.
[7] A. M. Hoveyda, D. A. Evans, G. C. Fu, *Chem. Rev.* **1993**, *93*, 1307.
[8] A. Soriente, M. De Rosa, R. Villano, A. Scettri, *Current Org. Chem.* **2004**, *8*, 993.
[9] J. L. Herrmann, G. R. Kieczykowski, R. H. Schlessinger, *Tetrahedron Lett.* **1973**, *14*, 2433.
[10] M. W. Rathke, D. Sullivan, *Tetrahedron Lett.* **1972**, *13*, 4249.
[11] T. Mukaiyama, A. Ishida, *Chem. Lett.* **1975**, 319.
[12] a) G. Casiraghi, F. Zanardi, G. Appendino, G. Rassu, *Chem. Rev.* **2000**, *100*, 1929; b) J. Hassfeld, M. Kalesse, *Synlett* **2002**, 2007; c) M. Christmann, M. Kalesse, *Tetrahedron Lett.* **2001**, *42*, 1269; d) X. Moreau, J.-M. Campagne, *Tetrahedron Lett.* **2001**, *42*, 4467; e) G. Rassu, P. Carta, L. Pinna, L. Battistini, F. Zanardi, D. Acquotti, G. Casiraghi, *Eur. J. Org. Chem.* **1999**, 1395; f) B. Dudot, L. Micouin, I. Baussanne, J. Royer, *Synthesis* **1999**, 688; g) P. Spanu, G. Rassu, L. Pinna, L. Battistini, G. Casiraghi, *Tetrahedron: Asymmetry* **1997**, *8*, 3237; h) C. W. Jefford, D. Jaggi, J. Boukouvalas, *Tetrahedron Lett.* **1987**, *28*, 4037; i) H.-F. Chow, I. Fleming, *Tetrahedron Lett.* **1985**, *26*, 397.
[13] I. Fleming, *Frontier Orbitals and Organic Chemical Reactions*, Wiley-Interscience, New York, **1996**, p. 45.
[14] K. Fukui, T. Yonezawa, C. Nagata, H. Shingu, *J. Chem. Phys.* **1954**, *22*, 1433.
[15] The ground-state conformations of the dienolates and dienol ethers were found by using the PC GAMESS version of GAMESS (US) QC package at the STO-3G(p,d)** level. The orbital analysis, HOMO-coefficient data (C.O.), and electrophilic susceptibility (E.S.) were then calculated from these structures by using density functional theory at the B88-LYP level with the CAChe program. a) A. A. Granovsky, http://classic.chem.msu.su/gran/gamess/index.html; b) M. W. Schmidt, K. K. Baldridge, J. A. Boatz, S. T. Elbert, M. S. Gordon, J. J. Jensen, S. Koseki, N. Matsunaga, K. A. Nguyen, S. Su, T. L. Windus, M. Dupuis, J. A. Montgomery, *J. Comput. Chem.* **1993**, *14*, 1347; c) CAChe WorkSystem Pro, Version 6.1.10, **2004**, CAChe Group, Fujitsu America, Inc., Beaverton, OR.
[16] R. A. Singer, E. M. Carreira, *J. Am. Chem. Soc.* **1995**, *117*, 12360.
[17] a) K. Furuta, T. Maruyama, H. Yamamoto, *J. Am. Chem. Soc.* **1991**, *113*, 1041; b) K. Furuta, S. Shimizu, Y. Miwa, H. Yamamoto, *J. Org. Chem.* **1989**, *54*, 1481.
[18] M. Sato, S. Sunami, Y. Sugita, C. Kaneko, *Chem. Pharm. Bull.* **1994**, *42*, 839.
[19] S.-I. Kiyooka, M. A. Hena, T. Yabukami, K. Murai, F. Goto, *Tetrahedron Lett.* **2000**, *41*, 7511.
[20] S.-I. Kiyooka, M. A. Hena, *J. Org. Chem.* **1999**, *64*, 5511.
[21] K. Mikami, S. Matsukawa, *J. Am. Chem. Soc.* **1993**, *115*, 7039.
[22] M. Sato, S. Sunami, Y. Sugita, C. Kaneko, *Heterocycles* **1995**, *41*, 1435.
[23] a) M. De Rosa, M. R. Acocella, R. Villano, A. Soriente, A. Scettri, *Tetrahedron: Asymmetry* **2003**, *14*, 2499; b) M. De Rosa, M. R. Acocella, R. Villano, A. Soriente, A. Scettri, *Tetrahedron Lett.* **2003**, *44*, 6087; c) R. Villano, M. De Rosa, C. Salerno, A. Soriente, A. Scettri, *Tetrahedron: Asymmetry* **2002**, *13*, 1949; d) M. De Rosa, M. R. Acocella, A. Soriente, A. Scettri, *Tetrahedron: Asymmetry* **2001**, *12*, 1529; e) M. De Rosa, A. Soriente, A. Scettri, *Tetrahedron: Asymmetry* **2000**, *11*, 3187; f) A. Soriente, M. De Rosa, A. Apicella, A. Scettri, G. Sodano, *Tetrahedron: Asymmetry* **1999**, *10*, 4481; g) M. De Rosa, R. Dell'Aglio, A. Soriente, A. Scettri, *Tetrahedron: Asymmetry* **1999**, *10*, 3659; h) A. Soriente, M. De Rosa, P. Dovinola, G. Sodano, A. Scettri, *Tetrahedron: Asymmetry* **1998**, *9*, 2197.
[24] C. Girard, H. B. Kagan, *Angew. Chem.* **1998**, *110*, 3088; *Angew. Chem. Int. Ed.* **1998**, *37*, 2923.
[25] a) R. Villano, M. R. Acocella, M. De Rosa, M. A. Soriente, A. Scettri, *Tetrahedron: Asymmetry* **2004**, *15*, 2421; b) A. Soriente, M. De Rosa, M. Stanzione, R. Villano, A. Scettri, *Tetrahedron: Asymmetry* **2001**, *12*, 959; c) A. Soriente, M. De Rosa, R. Villano, A. Scettri, *Tetrahedron: Asymmetry* **2000**, *11*, 2255.
[26] Y. Kim, R. A. Singer, E. M. Carreira, *Angew. Chem.* **1998**, *110*, 1321; *Angew. Chem. Int. Ed.* **1998**, *37*, 1261.
[27] S. Anne, W. Yong, M. Vandewalle, *Synlett*, **1999**, 1435.
[28] a) D. A. Evans, M. C. Kozlowski, J. A. Murry, C. S. Burgey, K. R. Campos, B. T. Connell, R. J. Staples, *J. Am. Chem. Soc.* **1999**, *121*, 669; b) D. A. Evans, J. A. Murry, M. C. Kozlowski, *J. Am. Chem. Soc.* **1996**, *118*, 5814.
[29] D. A. Evans, D. M. Fitch, T. E. Smith, V. J. Cee, *J. Am. Chem. Soc.* **2000**, *122*, 10033.
[30] D. A. Evans, P. H. Carter, E. M. Carreira, A. B. Charette, J. A. Prunet, M. Lautens, *J. Am. Chem. Soc.* **1999**, *121*, 7540.
[31] Y. Shimada, Y. Matsuoka, R. Irie, T. Katsuki, *Synlett* **2004**, 57.
[32] S. E. Denmark, G. L. Beutner, *J. Am. Chem. Soc.* **2003**, *125*, 7800.
[33] a) B. L. Pagenkopf, J. Krüger, A. Stojanovic, E. M. Carreira, *Angew. Chem.* **1998**, *110*, 3312; *Angew. Chem. Int. Ed.* **1998**, *37*, 3124; b) J. Krüger, E. M. Carreira, *J. Am. Chem. Soc.* **1998**, *120*, 837.
[34] A. Fettes, E. M. Carreira, *Angew. Chem.* **2002**, *114*, 4272; *Angew. Chem. Int. Ed.* **2002**, *41*, 4098.
[35] B. B. Snider, F. Song, *Org. Lett.* **2001**, *3*, 1817.
[36] C. J. Brennan, J.-M. Campagne, *Tetrahedron Lett.* **2001**, *42*, 5195.
[37] J. Krüger, E. M. Carreira, *Tetrahedron Lett.* **1998**, *39*, 7013.
[38] During the completion of this Review, the diastereo- and enantioselective addition of dienolate **60** to aromatic, heteroaromatic, olefinic, and aliphatic aldehydes in the presence of 8 mol% of the $Ti(OiPr)_4$/(*R*)-binol complex was reported; the adducts were afforded in yields of 26–98% with d.r.(*syn*/*anti*) = 79:21–87:13 and e.r.(1′*R*,2′*R*/1′*S*,2′*S*) = 93.0:7.0–99.5:0.5; M. De Rosa, M. R. Acocella, M. F. Rega, A. Scettri, *Tetrahedron: Asymmetry* **2004**, *15*, 3029.
[39] G. Bluet, J.-M. Campagne, *Tetrahedron Lett.* **1999**, *40*, 5507.
[40] I. Paterson, R. D. M. Davies, A. C. Heinmann, R. Marquez, A. Meyer, *Org. Lett.* **2003**, *5*, 4477.
[41] D. A. Evans, E. Hu, J. D. Burch, G. Jaeschke, *J. Am. Chem. Soc.* **2002**, *124*, 5654.
[42] G. Bluet, J.-M. Campagne, *J. Org. Chem.* **2001**, *66*, 4293.
[43] G. Bluet, B. Bazan-Tejeda, J.-M. Campagne, *Org. Lett.* **2001**, *3*, 3807.
[44] S. E. Denmark, T. Wynn, G. L. Beutner, *J. Am. Chem. Soc.* **2002**, *124*, 13405.
[45] a) M. Szlosek, B. Figadère, *Angew. Chem.* **2000**, *112*, 1869; *Angew. Chem. Int. Ed.* **2000**, *39*, 1799; b) M. Szlosek, X. Franck, B. Figadère, A. Cavé, *J. Org. Chem.* **1998**, *63*, 5169.
[46] a) S. Onitsuka, Y. Matsuoka, R. Irie, T. Katsuki, *Chem. Lett.* **2003**, *32*, 974; b) Y. Matsuoka, R. Irie, T. Katsuki, *Chem. Lett.* **2003**, *32*, 584.
[47] S. E. Denmark, J. R. Heemstra, Jr., *Synlett* **2004**, 2411.

 © 2005 Wiley-VCH Verlag GmbH & Co. KGaA, Weinheim

Communications



The active site of almond hydroxynitrile lyase was redesigned to give highly enantioselective enzyme variants for the synthesis of (*R*)-2-hydroxy-4-phenylbutyronitrile. K. Gruber, A. Glieder et al. describe their rationalization and realization of these biocatalysts in their communication on the following pages.

 © 2005 Wiley-VCH Verlag GmbH & Co. KGaA, Weinheim DOI: 10.1002/anie.200500435

Protein Engineering

Carving the Active Site of Almond *R*-HNL for Increased Enantioselectivity**

Roland Weis, Richard Gaisberger, Wolfgang Skranc, Karl Gruber, and Anton Glieder**

Hydroxynitrile lyases (HNLs) catalyze quantitative, stereoselective carbon–carbon bond formation in the addition of HCN to aldehydes or ketones yielding enantiopure cyanohydrins, which are key intermediates for numerous synthetic routes.[1] Both *R*- and *S*-selective HNLs are widely present in nature, and several genes have been cloned and expressed.[1] Recombinant almond (*Prunus amygdalus*) (*R*)-HNL isoenzyme 5 (*Pa*HNL5) is secreted to the culture supernatant of *Pichia pastoris*, which can be directly used for biocatalytic conversions in water or biphasic systems without prior enzyme purification or immobilization. Further prerequisites for an industrial application of this enzyme are its stability at acidic pH (suppression of the unselective non-enzymatic background reaction) and its enantioselectivity. Although the high stability of recombinant *Pa*HNL5 already enabled stereoselective enzymatic syntheses in water or biphasic systems even with slow-reacting substrates,[1,2] the enantioselectivity of *Pa*HNL5 is in some cases still too low for biocatalysis on a large scale.

Among the broad substrate range accepted by *Pa*HNL5[3] those with the aldehyde functionality separated from an aromatic moiety by an aliphatic linker represent an especially interesting group. The aromatic ring, which plays an important role in the correct recognition and binding of the natural substrate mandelonitrile (benzaldehyde cyanohydrin),[4] still has to fit into the closer region around the active site. On the other hand its distance from the functional group and the conformational flexibility of the alkyl linker reduce its influence on the stereoselectivity of the reaction. Among such aromatic substrates, 3-phenylpropionaldehyde (**1a**) and 3-phenylpropenal (**2a**, *trans*-cinnamaldehyde), and their corresponding cyanohydrins (*R*)-2-hydroxy-4-phenylbutyronitrile (**1b**) and (*R*)-2-hydroxy-4-phenyl-3-butene nitrile (**2b**) emerged as the most interesting representatives in terms of commercial use. Enantiopure α-hydroxycarboxylic acids, which are important intermediates for the synthesis of a class of angiotensin-converting enzyme inhibitors (ACEi) known as "prils",[5] can be derived from these cyanohydrins by acid hydrolysis. Compound **2a** was described as a notoriously recalcitrant substrate, but palladium-catalyzed hydrogenation of **2b** also yields (*R*)-2-hydroxy-4-phenylbutyric acid.[6] In addition **2b** can be used as a versatile intermediate for asymmetric epoxidation, dihydroxylation, and halogen addition.[7] Only *R* enantiomer **2b** is a building block of pharmacologically active "prils", and commercial production calls for high enantiomeric excesses (> 95 % *ee*), high yields (> 95 %), an environmentally benign process, and economic reaction times with a low enzyme/substrate ratio. Enantiomer separation is feasible by preferential crystallization of diastereomers, although with limited yields (68 %).[8] Other synthetic routes, for example, enantioselective reduction of keto or diketo esters, suffer from complicated procedures or require expensive starting compounds.[5,9]

Considering implementation of these chiral building blocks on a large scale, we investigated a biocatalytic route using very low amounts (i.e. 17 μg enzyme per mmol **1a**) of recombinant *Pa*HNL5 (Scheme 1). This route starts with cheap substrates, minimizes the number of unit operations, and offers optional crystallization after cyanohydrin hydrolysis to recover pure product. Conversion of **1a** to **1b** using recombinant *Pa*HNL5 was almost complete (93 %) after 4 h with 89.4 % *ee* (Table 1, entry 1). However, to avoid enantioselective crystallization as an additional step in the synthetic route, we needed a more selective mutein.

Directed evolution of enzymes has proved to be an efficient tool to influence the enantioselectivity of many (mostly bacterial) enzymes.[10] However, although expression of *Pa*HNL isoenzymes by *E. coli* is feasible, highly active *Pa*HNL5 could only be expressed in *Pichia pastoris*,[1,11] which is not a reliable host system for laboratory evolution. Furthermore a codon dilemma[12] impedes access to all possible amino acid exchanges by point mutations, especially when only a few thousand mutants can be screened. Because of our recent success in designing a more active mutein for sterically demanding mandelonitrile derivatives,[1a] we started a structure-guided approach to increase the enantioselectivity of this lyase. To our knowledge this is the first report on a successful structure-guided design of lyases to improve enantioselectivity, although rational approaches to *Manihot esculenta* HNL variants with reduced substrate transport limitations resulted in improved enantioselectivity for a variety of substrates as well.[13]

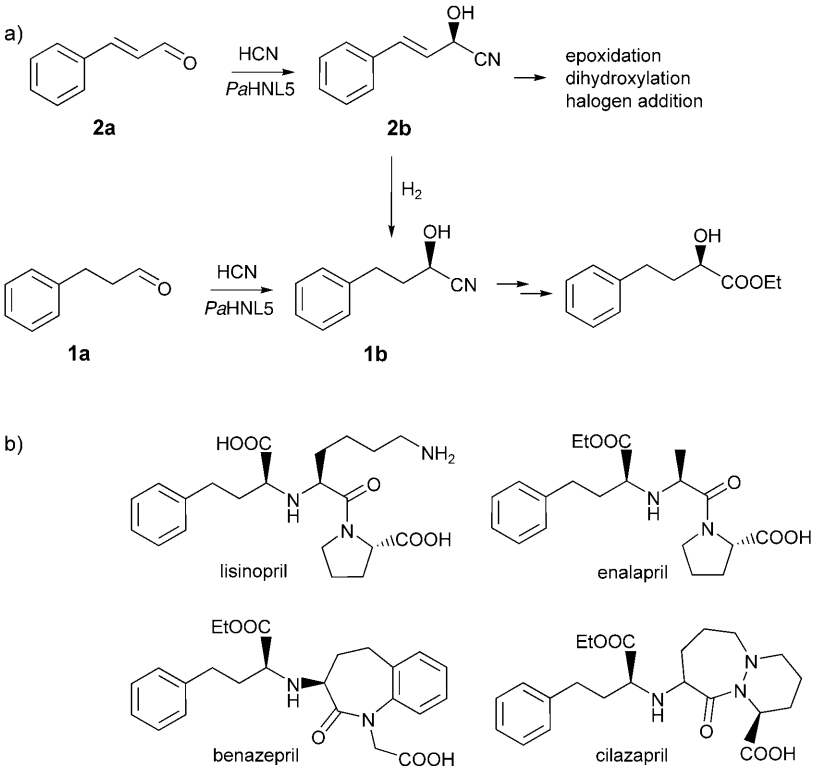
We modeled the complexes of *Pa*HNL5 with (*R*)-**1b** and (*S*)-**1b.** For both substrates equivalent binding modes were observed with respect to the position of the phenyl group as well as the mechanistically important polar interactions of the hydroxy and cyano groups with His 498 and His 460 (Figure 1).[4] Differences were observed only for the interactions of *Pa*HNL5 with the alkyl linker chain of **1b**, which was oriented towards Ala 111 in the *S* enantiomer and towards Val 360 in the *R* enantiomer (Figure 1, see also

[*] R. Weis, R. Gaisberger, Prof. Dr. K. Gruber, Prof. Dr. A. Glieder
Research Centre Applied Biocatalysis GmbH
Petersgasse 14, 8010 Graz (Austria)
Fax: (+43) 316-873-4072
E-mail: karl.gruber@a-b.at
glieder@glieder.com
Dr. W. Skranc
DSM Fine Chemicals Austria Nfg. GmbH & Co KG
R & D Center Linz
St.-Peter-Strasse 25, 4021 Linz (Austria)

[**] This research was supported by DSM, the FFG, the province of Styria, the SFG, and the city of Graz. We thank H. Mandl from the Research Centre Applied Biocatalysis, I. Wirth and O. Maurer from DSM for excellent technical support, and K. Faber, C. Kratky, and W. Kroutil for valuable comments on the manuscript, and P. Naggl for the color artwork.

Supporting information for this article is available on the WWW under http://www.angewandte.org or from the author.

 © 2005 Wiley-VCH Verlag GmbH & Co. KGaA, Weinheim



Scheme 1. a) Enantioselective synthesis of (*R*)-2-hydroxy-4-phenylbutyronitrile (**1b**) and (*R*)-2-hydroxy-4-phenylbutene nitrile (**2b**) from 3-phenylpropionaldehyde (**1a**) and 3-phenylpropenal (**2a**), respectively, for the production of (*R*)-2-hydroxy-4-phenylbutyric acid, an intermediate for "prils". b) Examples of "prils".

Table 1: Comparison of the constructed muteins to the unmodified *Pa*HNL5 for the enantioselective hydrocyanation of **1a**.[a]

Entry	Enzyme	Conv. [%]	*ee* [%]
1	*Pa*HNL5	93	89.4
2	A111VL331A	30	≈0
3	A111G	40	15.2
4	A111VL343A	40	27.6
5	A111V	16	60.2
6	L331F	80	63.1
7	A111GV360M	75	64.7
8	L343A	83	68.8
9	L343F	95	74.4
10	V360M	93	86.7
11	A111GV360I	92	87.6
12	L331A	94	88
13	V360I	98	95.3

[a] Reaction conditions: 30 mmol of **1a** and 0.5 mg of enzyme (17 μg mmol^{-1} substrate), 4 h, 10 °C, pH 3.4.

video material in the Supporting Information). We took advantage of this pseudo mirror symmetry and redesigned the substrate binding site of *Pa*HNL5 to tailor the accessible volume for one or the other enantiomer, similarly to other successful examples of laboratory-evolved enzymes.[14] Amino acids in the binding site were exchanged with residues of different sizes while preserving hydrophobicity. Ala111 and Val360 interact with the alkyl chain of the substrate from opposite sides and therefore are promising sites for mutations. The same is true for Leu331 and Leu343, which mainly interact with the phenyl group and form part of the access tunnel leading to the active site. In total, we studied 24 mutants in silico, and 12 of those—with the largest predicted changes in enantioselectivity—were prepared and analyzed experimentally. In a first test of the hydrocyanation of **1a** with only low amounts of each mutein, V360I yielded the most selective enzyme (Table 1, entry 13). As expected, A111G was less stereoselective. In a more detailed examination, 1 mg each of the best four muteins (entries 10–13) were analyzed for conversion of 2 g (15 mmol) of **1a** (i.e. 67 μg enzyme per mmol substrate). L331A, V360M, and V360I (Table 2, entries 3–5) resulted in almost complete substrate conversion within 4 h with significantly improved enantioselectivity. At the end of the conversion **1b** produced with mutein A111GV360I also showed slightly higher enantiopurity (91.8% *ee*), although the conversion was a little slower.

To explore turnover rates, the amount of the enzyme was adjusted such that with each individual mutein the conversion of 2 g (15 mM) of **1a** was in a roughly linear range during the first 20 min. Specific activities under these conditions (Table 2) served for comparison of the individual muteins for cyanohydrin synthesis, although due to the nonlinear kinetics of *Pa*HNL5-catalyzed reactions in biphasic systems, such numbers cannot be translated to k_{cat} values for higher enzyme concentrations. The introduction of isoleucine at position 360 raised the *ee* to more than 96% and accelerated the transformation of **1a** almost sixfold. Thus the conversion

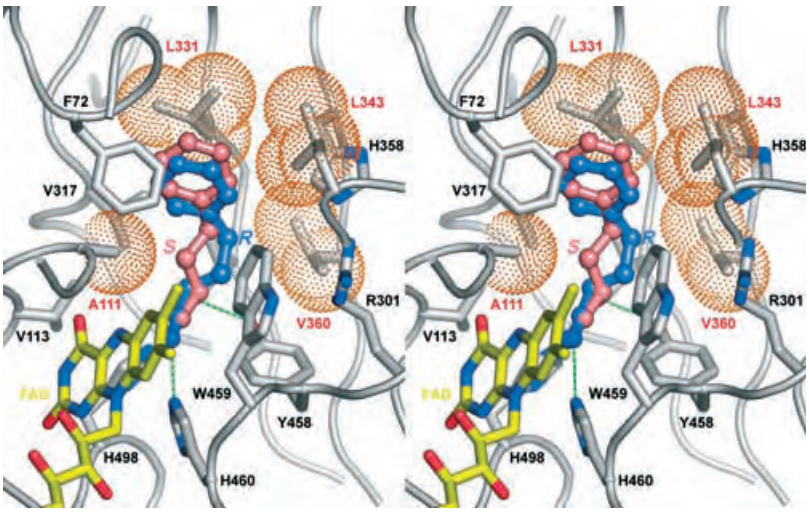


Figure 1. Stereoimage of the superposition of modeled complexes of (*R*)-**1b** (blue) and (*S*)-**1b** (pink) bound to the active site of *Pa*HNL5. Amino acid side chains are shown in light gray, the FAD cofactor in yellow. N and O atoms are shown in blue and red, respectively. Residues selected for mutagenesis are labeled in red, and their van der Waals volumes are represented by small spheres. The image was prepared with the software PyMol (http://www.pymol.org).

 © 2005 Wiley-VCH Verlag GmbH & Co. KGaA, Weinheim

was complete within a couple of hours despite a low enzyme/substrate ratio. In contrast, in a recent report at least 30 times more enzyme[6] was employed. Mutations L331A and, surprisingly, A111GV360I also resulted in a moderately increased catalytic rate. Compared to other muteins, however, the turnover rate of A111GV360I decreased during the course of the reaction.

All muteins with increased enantioselectivity for the synthesis of **1b** were also tested in the conversion of 15 mmol of the more rigid **2a** to **2b** (Table 3). Two muteins were also more selective with **2a**, reaching ≈98% *ee* with mutation V360I. In addition all mutations except V360M caused a faster conversion of **2a** than with the original enzyme *Pa*HNL5. The higher rigidity of **2a** compared to **1a** and the larger volume of the methionine residue are likely reasons for the weaker activity of the V360M variant. With only 27 μg of *Pa*HNL5-V360I per mmol **2a**, conversion to **2b** was almost complete after 3 h with an excellent enantiomeric excess of ≈98%. In contrast, Gerrits and co-workers reported a reaction time of 168 h for 97% yield and 98% *ee*.[15] Recently also the Sheldon lab reported highly enantioselective and fast reactions by employing cross-linked enzyme aggregates of native almond HNL.[16]

Structure-guided design was employed to generate recombinant *Pa*HNL5 variants suitable for large-scale stereoselective synthesis of aromatic cyanohydrins in water-based systems. From 24 desigend enzyme variants, 12 of which were prepared, four well-expressed, sit-specific mutants of the *Pa*hnl5 gene with significantly increased stereoselectivity were obtained. All muteins were stable at low pH. As a highlight, the variant *Pa*HNL5-V360I exhibited extraordinary catalytic properties. The enantiomeric excess for the conversion of **1a** was improved to >96% despite a very low enzyme/substrate ratio. This particular mutein reduced the required amount of biocatalyst 10- to 30-fold to produce enantiopure (*R*)-2-hydroxy-4-phenylbutyric acid and derivatives thereof. From *trans*-cinnamaldehyde (**2a**) very low amounts of catalyst with mutation V360I were needed to produce cyanohydrin **2b** with an optical purity of ≈98% *ee* within 3 h. The conversion time for this recalcitrant substrate was reduced from 168 h to 3 h. Interestingly our designed and more selective muteins were also more active. This is in contrast to reports on the design of more selective hydrolases, where just the reactivity with the wrong enantiomer was reduced.[17] *Pa*HNL5-V360I is currently the most efficient catalyst for syntheses of enantiomerically pure building blocks for pharmaceutically active "prils", therefore suggesting itself for industrial application on a large scale.

Received: February 4, 2005
Published online: July 6, 2005

Keywords: ACE inhibitors · asymmetric synthesis · biocatalysis · hydroxynitrile lyase · protein engineering

[1] a) A. Glieder, R. Weis, W. Skranc, P. Poechlauer, I. Dreveny, S. Majer, M. Wubbolts, H. Schwab, K. Gruber, *Angew. Chem.* **2003**, *115*, 4963–4966; *Angew. Chem. Int. Ed.* **2003**, *42*, 4815–4818; b) M. H. Fechter, H. Griengl, *Food Technol. Biotechnol.* **2004**, *42*, 287–294.

[2] a) M. Bauer, R. Geyer, M. Boy, H. Griengl, W. Steiner, *J. Mol. Catal. B* **1998**, *5*, 343–347; b) U. Kragl, U. Niedermeyer, M. R. Kula, C. Wandrey, *Ann. N. Y. Acad. Sci.* **1990**, *613*, 167–175.

[3] a) F. Effenberger, B. Horsch, F. Weingart, T. Ziegler, S. Kuhner, *Tetrahedron Lett.* **1991**, *32*, 2605–2608; b) F. Effenberger, *Angew. Chem.* **1994**, *106*, 1609–1619; *Angew. Chem. Int. Ed. Engl.* **1994**, *33*, 1555–1564.

Table 2: Conversion and enantioselectivity of selected muteins and the original *Pa*HNL5 for the hydrocyanation of **1a**.[a]

		Reaction time						
		1 h		2 h		4 h		
Entry	Enzyme	Conv.[b] [%]	*ee* [%]	Conv.[b] [%]	*ee* [%]	Conv.[b] [%]	*ee* [%]	TOF[c] [s^{-1}]
1	*Pa*HNL5	72	89.0	87	90.1	96	90.2	2497 ± 208
2	A111GV360I	70	90	83	90.6	94	91.8	3379 ± 208
3	L331A	78	90.7	90	93.3	95	92.9	2865 ± 312
4	V360M	78	93.6	93	94.0	97	94.6	6812 ± 837
5	V360I	86	96.0	96	96.6	98	96.7	14397 ± 416

[a] Reaction conditions: 15 mmol of **1a** and 1 mg of enzyme (67 μg enzyme mmol^{-1} substrate), 10°C, pH 3.4. [b] Conversions. [c] TOF: turnover frequency.

Table 3: Conversion and enantioselectivity of selected muteins and the parent *Pa*HNL5 for the hydrocyanation of **2a**.[a]

		Reaction time						
		1 h		2 h		3 h		
Entry	Enzyme	Conv.[b]	*ee*	Conv.[b]	*ee*	Conv.[b]	*ee*	TOF[c] [s^{-1}]
1	*Pa*HNL5	13	95.2	22	96.2	30	96.4	110 ± 19
2	V360M	9	90.3	14	92.7	18	92.6	n.d.[d]
3	L331A	19	94.5	29	95.4	39	95.7	n.d.[d]
4	A111GV360I	21	95.8	36	96.8	47	96.8	149 ± 16
5	V360I	70	98.0	90	97.9	97	97.6	458 ± 32

[a] Reaction conditions: 15 mmol of **2a** and 0.4 mg of enzyme (27 μg enzyme mmol^{-1} substrate), 10°C, pH 3.4). [b] Conversion and *ee* are shown in percent. [c] TOF: turnover frequency. [d] n.d.: not determined since the *ee* was not improved.

 © 2005 Wiley-VCH Verlag GmbH & Co. KGaA, Weinheim

[4] a) I. Dreveny, K. Gruber, A. Glieder, A. Thompson, C. Kratky, *Structure* **2001**, *9*, 803 – 815; b) I. Dreveny, C. Kratky, K. Gruber, *Protein Sci.* **2002**, *11*, 292 – 300.
[5] R. K. Tikare, WO 0242244A, **2004** [*Chem. Abstr.* **2002**, *136*, 401540].
[6] A. Matsuyama, I. Takase, Y. Ueda, Y. Kobayashi, US 5429935, **1995** [*Chem. Abstr.* **1995**, *123*, 141884].
[7] a) A. Schummer, H. Yu, H. Simon, *Tetrahedron* **1991**, *47*, 9019 – 9034; b) H. Yu, H. Simon, *Tetrahedron* **1991**, *47*, 9035 – 9052.
[8] M. Kottenhahn, K. Drauz (Degussa AG), US 5616727, **1997** [*Chem. Abstr.* **1997**, *126*, 305791].
[9] a) H. U. Blaser, E. Schmidt, *Asymmetric Catalysis on Industrial Scale: Challenges, Approaches and Solutions*, VCH, Weinheim, **2004**, pp. 91 – 103; b) M. Studer, S. Burkhardt, A. F. Indolese, H.-U. Blaser, *Chem. Commun.* **2000**, 1327 – 1328.
[10] a) O. May, P. T. Nguyen, F. H. Arnold, *Nat. Biotechnol.* **2000**, *18*, 317 – 320; b) K. E. Jaeger, T. Eggert, *Curr. Opin. Biotechnol.* **2004**, *15*, 305 – 313; c) B. Lingen, J. Groetzinger, D. Kolter, M.-R. Kula, M. Pohl, *Protein Eng.* **2002**, *15*, 585 – 593.
[11] a) H. Ayguen, S. Wojczewski, S. Rosmus (Biospring GmbH), DE 10251547, **2004** [*Chem. Abstr.* **2002**, *140*, 401356]; b) R. Weis, P. Poechlauer, R. Bona, R. Luiten, M. Wubbolts, H. Schwab, A. Glieder, *J. Mol. Catal. B* **2004**, *29*, 211 – 218.
[12] B. Steipe, *Curr. Top. Microbiol. Immunol.* **1999**, *243*, 55 – 86.
[13] H. Buhler, F. Effenberger, S. Forster, J. Roos, H. Wajant, *ChemBioChem* **2003**, *4*, 211 – 216.
[14] M. Chen-Goodspeed, M. A. Sogorb, F. Wu, F. M. Raushel, *Biochemistry* **2001**, *40*, 1332 – 1339; M. T. Reetz, F. Daligault, B. Brunner, H. Hinrichs, A. Deege, *Angew. Chem.* **2004**, *116*, 4170 – 4173; *Angew. Chem. Int. Ed.* **2004**, *43*, 4078 – 4081.
[15] J. P. Gerrits, W. F. Willeman, A. J. J. Straathof, J. J. Heijnen, J. Brussee, A. van der Gen, *J. Mol. Catal. B* **2001**, *15*, 111 – 121.
[16] L. M. van Langen, R. P. Selassa, F. van Rantwijk, R. A. Sheldon, *Org. Lett.* **2005**, *7*, 327 – 329.
[17] a) U. T. Bornscheuer, *Curr. Opin. Biotechnol.* **2002**, *13*, 543 – 547; b) M. T. Reetz, *Proc. Natl. Acad. Sci. USA* **2004**, *101*, 5716 – 5722; c) D. Rotticci, J. C. Rotticci-Mulder, S. Denman, T. Norin, K. Hult, *ChemBioChem* **2001**, *2*, 766 – 770.

 © 2005 Wiley-VCH Verlag GmbH & Co. KGaA, Weinheim

Heterogeneous Catalysis

The Microstructure of Copper Zinc Oxide Catalysts: Bridging the Materials Gap**

Thorsten Ressler, Benjamin L. Kniep, Igor Kasatkin, and Robert Schlögl*

The progressing shift in resources used in the petrochemical industry from crude oil to natural gas increases the importance of methanol as a basic chemical for the production of synthetic fuels and polymers. In modern MegaMethanol plants that produce more than 5000 tons of methanol per day, supported copper nanoparticles are employed as highly active heterogeneous catalysts. For the efficient use of natural resources the design of more active and selective catalysts is required. However, structure–activity relationships are often deduced from model systems exhibiting structural characteristics very different from those of industrial catalysts. Here we describe the microstructure[1] of copper nanoparticles on zinc oxide prepared similar to industrially used copper catalysts and exhibiting comparable catalytic activities.

Supported copper nanoparticles are active catalysts for methanol synthesis, methanol oxidation, and methanol steam reforming. Structure–activity relationships for copper catalysts have been studied extensively with a variety of materials ranging from single-crystal model systems to multiple-component industrial catalysts with copper concentrations of more than 50%.[2] Several suggestions were made as to the nature of the "real" structure[3] of the copper phase under reaction conditions, including the simplifying assumption that the activity increases linearly with the copper surface area.[4] Conversely, copper nanoparticles were prepared recently with surfaces displaying different catalytic activities. In addition to the surface area, bulk structural parameters like microstrain in the copper particles were identified to correlate with the catalytic activity of these catalysts.[5–7]

Only few microscopic studies of the "real" structure of active copper catalysts have been reported.[8–10] High-resolution transmission electron microscopy (TEM) and in situ TEM studies have been performed on copper particles supported on ZnO with a copper concentration of less than 10%.[11,12] These studies showed faceted well-ordered Cu particles on a large and well-defined ZnO support. Changes in the morphology of the Cu particles, the ratio of the copper facets, and the surface area upon varying the reduction potential of the gas phase were impressively illustrated by in situ TEM. However, these copper model systems were prepared by impregnation of ZnO crystals with a solution of copper acetate. This preparation procedure deviates considerably from the preparation of industrial copper catalysts,[13] and hence, the well-defined model systems studied probably exhibit a microstructure different from that of a catalyst prepared for industrial application. Industrial $Cu/ZnO/Al_2O_3$ catalysts are commonly prepared by precipitating copper zinc hydroxycarbonates from metal nitrate solutions. In addition to the precipitation method, each step in the subsequent treatment of the precipitate and the resulting oxide precursor (i.e. ageing, washing, drying, calcination, and reduction) affects the microstructure of the active copper phase (chemical memory).

Precipitate ageing strongly influences the activity of the resulting Cu/ZnO catalysts.[14–17] The superior activity of Cu/ZnO catalysts obtained from precipitates aged for more than 30 min was shown to correlate with the increasing microstrain in the copper nanoparticles.[18] Apparently, structure–activity relationships revealed for idealized copper model systems should not be extrapolated to the microstructure and catalytic properties of industrial catalysts.

Here we report HRTEM investigations of the microstructure of reduced Cu/ZnO catalysts obtained from differ-

[*] Priv.-Doz. Dr. T. Ressler, Dipl.-Chem. B. L. Kniep, Dr. I. Kasatkin, Prof. Dr. R. Schlögl
Abteilung Anorganische Chemie
Fritz-Haber-Institut der Max-Planck-Gesellschaft
Faradayweg 4–6, 14195 Berlin (Germany)
Fax: (+49) 30-8413-4405
E-mail: ressler@fhi-berlin.mpg.de

[**] Financial support from the German Research Foundation (DFG SPP 1091) is acknowledged. We thank K. Weiss for his assistance with the TEM measurements.

 © 2005 Wiley-VCH Verlag GmbH & Co. KGaA, Weinheim DOI: 10.1002/anie.200462942

ently aged hydroxycarbonate precipitates. Electron micrographs of Cu/ZnO catalysts obtained from a nonaged (0 min) and an aged (120 min) precipitate are depicted in Figure 1 together with a plot of the the corresponding catalytic

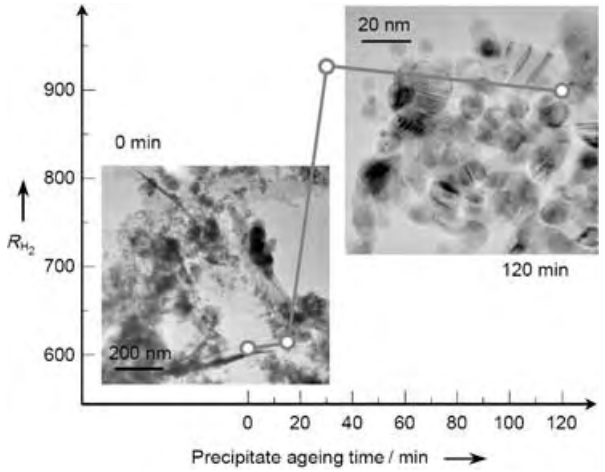


Figure 1. TEM images of Cu/ZnO catalysts obtained from hydroxycarbonate precipitates aged for 0 min and 120 min together with the H_2 production rate R_{H_2} [μmol g^{-1} s^{-1}] of four catalysts as a function of precipitate ageing time (methanol-synthesis activity and ageing time exhibited a similar correlation).

activities in the steam reforming of methanol. Electron diffraction and electron energy-loss spectroscopy identified only Cu metal and ZnO in the samples studied. Various morphologies of Cu and ZnO particles were detected in the Cu/ZnO catalyst obtained from nonaged precipitates, such as large isolated Cu particles, large ZnO plates and needles, and to a lesser degree nanostructured Cu and ZnO particles (Figure 1).

When the precipitate was aged for more than 30 min, a transition to a homogeneous microstructure was observed. In these Cu/ZnO catalysts mostly nanostructured Cu/ZnO particles were found with only minute amounts of isolated Cu particles and ZnO particles detectable (Figure 1). The increase in catalytic activity observed for Cu/ZnO catalysts obtained from precursors aged for more than 30 min (Figure 1) clearly correlates with the distinct change in the microstructure of the catalysts. While the less active Cu/ZnO catalysts comprise a heterogeneous mixture of large and isolated Cu and ZnO particles, the more active catalysts show small and intimately mixed Cu and ZnO particles. The homogeneous microstructure of the more active Cu/ZnO catalysts may constitute a potential lead for future preparations of improved catalysts for methanol chemistry.

The HRTEM images of the Cu/ZnO catalysts show a marked interface between the Cu and ZnO particles (Figure 2a,b). Well-defined copper clusters on large ZnO particles, like the ones observed in the model systems described above,[11] are clearly absent in Cu/ZnO catalysts prepared similarly to industrial copper catalysts. The Cu and ZnO particles in the Cu/ZnO catalysts obtained from more aged precipitates are round-shaped (Figure 2) or oval-shaped independent of their size. The HRTEM images reveal a

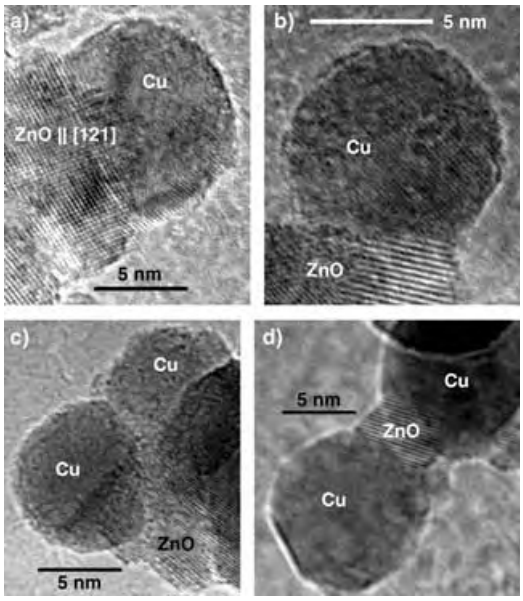


Figure 2. HRTEM images of a Cu/ZnO catalyst obtained from a copper zinc hydroxycarbonate precipitate aged for 120 min.

variety of epitaxial relations between Cu and ZnO (e.g. Cu[110]||ZnO[100], Cu[111]||ZnO[100], Figures 2 and 3) with an average contact angle between the Cu and ZnO

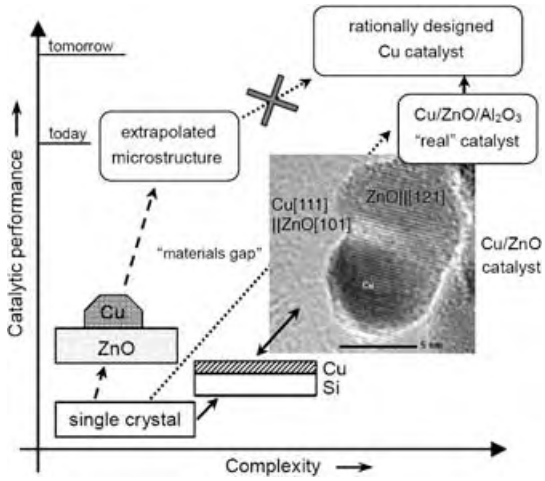


Figure 3. Representation of the relationship between structural complexity and catalytic performance and the requirement of suitable model systems to bridge the materials gap between the structure–activity correlations for industrial copper catalysts and the understanding of elemental processes on catalyst surfaces on a microscopic level.

particles of about 61°. Zinc oxide exhibits a higher degree of structural order than the copper nanoparticles in the reduced Cu/ZnO catalyst (Figure 2), and the distinct defects in the ZnO structure may be indicative of the oxygen-deficient nature of the ZnO particles in the catalysts. Moreover, ZnO particles are often located between Cu particles, thus efficiently preventing the Cu particles from sintering (Figure 2c,d).

 © 2005 Wiley-VCH Verlag GmbH & Co. KGaA, Weinheim

The nonlinearity frequently observed in correlations of copper surface area and catalytic activity in methanol chemistry is strong evidence for the existence of additional bulk or surface structural parameters that govern the activity of copper nanoparticles.[5–7] The distinct interface between the Cu particles and the ZnO support in the homogeneous microstructure of the more active Cu/ZnO catalysts can be correlated to the previously reported increased degree of strain in the Cu particles in the highly active Cu/ZnO catalysts as determined by averaging bulk structural techniques (XRD, NMR).[18] Thus, the higher degree of disorder in the Cu nanoparticles, which corresponds to an increased deviation from the "ideal" structure of bulk copper metal, results from the increased interface area between Cu and ZnO and is indicative of a more active copper catalyst.

The Cu/ZnO catalysts described are less complex than the most active industrial $Cu/ZnO/Al_2O_3$ catalysts and are thus suitable model systems for investigating the microstructure of copper nanoparticles in methanol-synthesis catalysts (Figure 3). In studies of industrial catalysts the microscopic processes on the surface of heterogeneous catalysts are difficult to unravel because of their huge complexity and the multiple-parameter dependence of catalytic properties. Hence, a detailed understanding of heterogeneous catalysis on an atomistic level will most likely arise from investigations of simplified model systems from which one can elucidate the influence of individual structural parameters on catalytic properties.

The results described here indicate that new and more suitable model systems should be designed according to established structure–activity relationships of copper catalysts that are prepared similarly to industrial catalysts (Figure 3). These second-generation model systems must take into account the deviation from the ideal copper structure to provide a meaningful representation of microscopic processes in catalysis. On the one hand, model systems that closely resemble ideal bulk copper metal may be of limited value in advancing our understanding of the "real" structure of methanol catalysts under reaction conditions and designing suitable preparation routes to improved copper catalysts (Figure 3). On the other hand, copper catalysts obtained by a wet-chemical preparation appear to be less suited mostly because of the inherent difficulty to vary the "real" structure of the resulting materials without changing other relevant structural and chemical parameters (e.g. chemical composition and copper crystallite size). Thin copper films on substrates such as silicon and polyimide, for instance, are currently considered as suitable model systems (Figure 3). With these systems the microstrain in the copper can be adjusted dynamically by thermal treatment or mechanical forceto elucidate the corresponding effect on the electronic structure and the catalytic properties of the copper surface.[19–21]

The "real" structure of the copper catalysts described here deviates considerably from that of ideal bulk copper metal and emphasizes that structural complexity is a prerequisite for an active heterogeneous catalyst. Hence, for an atomistic understanding of catalytic reactions, second-generation model systems are required that reduce complexity yet take the characteristic "real" structure of active copper catalysts into account. Eventually, this will bridge the materials gap and provide the basis for the knowledge-driven improvement of heterogeneous catalysts.

Experimental Section

Preparation of Cu/ZnO catalysts: Copper zinc hydroxycarbonate precursors of Cu/ZnO catalysts with a Co/Zn molar ratio of 70:30 were prepared according to a conventional coprecipitation route.[16] The coprecipitation was performed in a flask filled with 400 mL of doubly distilled water (353 K) by simultaneously addition of 600 mL of an aqueous solution of metal nitrates ($Cu(NO_3)_2{\cdot}3H_2O$ (0.7 M) and $Zn(NO_3)_2{\cdot}6H_2O$ (0.3 M)) and an aqueous solution of sodium carbonate (1.2 M) at constant pH 7. The resulting precipitates were aged under continuous stirring in the mother liquor at 353 K for 0 min, 15 min, 30 min, and 120 min. After filtering, the precipitates were washed six times with deionized water (80 mL) under continuous stirring at 333 K. Finally, the samples were dried at 393 K for 10 h in static air followed by calcination at 603 K in static air for 3 h (heating rate 6 K min^{-1}). The resulting CuO/ZnO materials were reduced in 2.0 vol % H_2 at 523 K for 30 min (heating rate 6 K min^{-1}) to obtain the Cu/ZnO catalysts.

TEM studies were performed on a Phillips CM 200 FEG TEM. The reduced Cu/ZnO catalysts were deposited on holey-carbon films supported on gold grids. The samples were prepated in a glove box to prevent exposure of the reduced Cu/ZnO catalysts to air.

Received: December 15, 2004
Revised: January 26, 2005
Published online: July 1, 2005

Keywords: copper · heterogeneous catalysis · methanol · structure–activity relationships · transmission electron microscopy

[1] In addition to the crystallography, the "microstructure" of the material also includes those morphological features that are revealed by a microscopic examination of a suitably prepared specimen sample (from D. Brandon, W. D. Kaplan, *Microstructural Characterization of Materials*, Wiley, New York, **1999**).
[2] J. B. Hansen, *Handbook of Heterogeneous Catalysis*, *Vol. 4* (Eds.: G. Ertl, H. Knoezinger, J. Weitkamp), VCH, Weinheim, **1997**.
[3] In addition to the "ideal (crystallographic) structure" of copper metal, the "real structure" comprises all defects such as strain, impurities, etc. present in the bulk structure of the copper catalysts.
[4] G. C. Chinchen, K. C. Waugh, D. A. Whan, *Appl. Catal.* **1986**, *25*, 101.
[5] K. C. Waugh, *Catal. Lett.* **1999**, *58*, 163.
[6] M. M. Günter, T. Ressler, B. Bems, C. Büscher, T. Genger, O. Hinrichsen. M. Muhler R. Schlögl, *Catal. Lett.* **2001**, *71*, 37.
[7] M. Kurtz, H. Wilmer, T. Genger, O. Hinrichsen, M. Muhler, *Catal. Lett.* **2003**, *86*, 77.
[8] S. Metha, G. W. Simmons, K. Klier, R. G. Herman, *J. Catal.* **1979**, *57*, 339.
[9] J. M. Dominquez, G. W. Simmons, K. Klier, *J. Mol. Catal.* **1983**, *20*, 369.
[10] G. J. Millar, I. H. Holm, P. J. R. Uwins, J. Drennan, *J. Chem. Soc. Faraday Trans.* **1998**, *94*, 593.
[11] P. L. Hansen, J. B. Wagner, S. Helveg, J. R. Rostrup-Nielsen, B. S. Clausen, H. Topsoe, *Science* **2002**, *295*, 2053.

 © 2005 Wiley-VCH Verlag GmbH & Co. KGaA, Weinheim

[12] J. B. Wagner, P. L. Hansen, A. M. Molenbroek, H. Topsoe, B. S. Clausen, S. Helveg, *J. Phys. Chem. B* **2003**, *107*, 7753.
[13] Industrial $Cu/ZnO/Al_2O_3$ catalysts for methanol synthesis may contain more than 50% copper and are commonly prepared by coprecipitating mixed metal hydroxycarbonates from metal nitrate solutions.
[14] D. Waller, D. Stirling, F. S. Stone, M. S. Spencer, *Faraday Discuss.* **1989**, *87*, 107.
[15] S. H. Taylor, G. J. Hutchings, A. A. Mirzaei, *Chem. Commun.* **1999**, 1373.
[16] D. M. Whittle, A. A. Mirzaei, J. S. J. Hargreaves, R. W. Joyner, C. J. Kiely, S. H. Taylor, G. J. Hutchings, *Phys. Chem. Chem. Phys.* **2002**, *4*, 5915.
[17] B. Bems, M. Schur, A. Dassenoy, H. Junkes, D. Herein, R. Schlögl, *Chem. Eur. J.* **2003**, *9*, 2039.
[18] B. L. Kniep, T. Ressler, A. Rabis, F. Girgsdies, M. Baenitz, F. Steglich, R. Schlögl, *Angew. Chem.* **2004**, *116*, 114; *Angew. Chem. Int. Ed.* **2004**, *43*, 112.
[19] M. Hommel, O. Kraft, E. Arzt, *J. Mater. Res.* **1999**, *14*, 2373.
[20] R. M. Keller, S. P. Baker, E. Arzt, *J. Mater. Res.* **1998**, *13*, 1307.
[21] F. Girgsdies, T. Ressler, U. Wild, T. Wübben, T. J. Balk, G. Dehm, L. Zhou, S. Günther, E. Arzt, R. Imbihl, R. Schlögl, *Catal. Lett.* **2005**, *102*, 91.

 © 2005 Wiley-VCH Verlag GmbH & Co. KGaA, Weinheim

Chemical Photolithography

Surface Modification with Orthogonal Photosensitive Silanes for Sequential Chemical Lithography and Site-Selective Particle Deposition**

*Aránzazu del Campo, Diana Boos, Hans Wolfgang Spiess, and Ulrich Jonas**

The site-selective adsorption of molecules and mesoscopic objects at predefined positions on solid surfaces is a key fabrication step and a major challenge in many applications, such as multifunctional biosensors and novel electronic, mechanical, and photonic devices. The adsorption process is strongly influenced by the functional groups on the surfaces, which can be introduced by different strategies for depositing molecular layers (e.g. self-assembled monolayers, SAMs). In order to direct the adsorption process to predefined regions of the substrate, chemical patterning of these surface layers with discrete micro- to nanometer features is required; this is a critical stage in device fabrication and usually involves iterative combinations of several patterning and surface activation steps.

For this purpose various patterning techniques have been developed, like photolithography and electron beam lithography,[1] microcontact printing,[2] micromachining, and several techniques based on scanning probe microscopy.[3] Light is a particularly convenient medium to introduce lateral patterns, as multiple methods for its generation, handling, and control are available that exploit different mechanisms of how light interacts with molecular surface layers.

In the following, a very brief overview of the fundamental photopatterning strategies is provided with some representative references:

1) Irradiation at very short wavelengths (< 250 nm, high-energy UV) in the presence of oxygen can lead to the chemical degradation of a whole molecular layer; this was shown for aryl- and alkylsilanes at 193 nm.[4]
2) For certain materials under similar irradiation conditions, but often longer wavelengths, specific photoconversion of only the anchor group might take place (rather than degradation of the whole layer). This method has been employed for the photooxidation of thiol monolayers on gold to sulfonates, which bind more weakly to the substrate and can displaced by a second thiol.[5]
3) Instead of photocleavage from the surface, the opposite process of light-induced attachment of a molecular layer onto the substrate was demonstrated with aldehydes and 1-alkenes onto hydrogenated silicon surfaces,[6a] and the photografting polymer layers onto benzophenone-modified silane layers.[6b]
4) Photopolymerization and cross-linking of physisorbed monomers can lead to permanent layer immobilization in the exposed areas due to substantially increased mechanical stability and reduced solubility of the polymerized species. This patterning technique was applied to polydiacetylene lipid layers with subsequent dissolution of the monomeric lipids in the nonirradiated regions.[7]
5) Finally, photoactivation of a surface layer can be achieved if the monolayer-forming molecules are functionalized with a photosensitive group. This is a particularly interesting approach, since a large variety of photosensitive and -reactive species are known that can be combined with many different functional groups.[8] The typical procedure for preparing monolayers with such photosensitive moieties usually involves two steps. First, the surface-active molecules with unprotected functional groups are deposited onto the substrate. These functional groups determine the properties of the newly formed surface, like reactivity, polarity, and charge. In the second step, the photosensitive moieties are introduced into the monolayer by reaction with the functional surface groups.[9] Restrictions of this method are the limited control over the protection step (the coexistence of free and protected functional groups depends on the surface

[*] Dr. A. del Campo,[+] Dr. D. Boos, Prof. Dr. H. W. Spiess, Dr. U. Jonas
Max-Planck-Institut für Polymerforschung
Ackermannweg 10, 55128 Mainz (Germany)
Fax: (+49) 6131-379-100
E-mail: jonas@mpip-mainz.mpg.de

[+] Present address: Max-Planck-Institut für Metallforschung
Heisenbergstrasse 3, 70569 Stuttgart (Germany)

[**] Financial support from the European Union (Marie Curie Fellowship for A.d.C, grant HPMF-CT-2000-01063) and the Bundesministerium für Bildung und Forschung (grant 01RC0175–01RC0178) is gratefully acknowledged. We thank H. J. Menges and K. Wendt for their help with the irradiation experiments, as well as C. G. Bochet for helpful advice.

Supporting information for this article is available on the WWW under http://www.angewandte.org or from the author.

 DOI: 10.1002/anie.200500092 © 2005 Wiley-VCH Verlag GmbH & Co. KGaA, Weinheim

reaction yield) and the limited choice over the layer composition, since mixing of incompatible functional groups in their free form is nontrivial.

A consequential improvement is based on the synthesis of surface-active molecules (like thiols and silanes) with the photosensitive moieties directly attached to the functional groups prior to monolayer preparation.[10] The surface layers are thus intrinsically protected, as we demonstrate here with novel triethoxysilanes bearing light-sensitive nitroveratryl and benzoin protecting groups on terminal amino, hydroxy, and carboxylic acid functionalities.

This advanced silane chemistry opens attractive possibilities for simplying the preparation of chemically patterned surfaces. A major advantage of this method lies in the highly defined, quantitative reactions of the protected surface functionalities (achieved during synthesis and purification prior to layer fabrication) and full control over the layer preparation process. Lateral patterning can be achieved easily by direct irradiation and deprotection of the silane layer through a mask, as performed in standard photolithography. Thus, no additional investment is required for its implementation in current industrial processes, and further processing steps (like developing and removing photoresists) can be minimized. In addition, mixed surface layers can be prepared in one step with different types of functional groups (which may be incompatible in their free form and cause reactions, segregation, or salt formation) and different protecting groups that can be independently addressed by their specific deprotection wavelengths (in line with the orthogonality concept, see Figure 1).[11] The surface density of the free functional groups can be tuned conveniently by irradiation time and intensity during the photolysis reaction, which cleaves the protecting group and restores the initial activity of the functional groups.[9b] Further chemical modification or specific adsorption of targets is possible at the deprotected functionalities in the irradiated regions. A schematic representation of the process is provided in Figure 1.

The principle of orthogonality is defined as the possibility to selectively remove one type of protecting group in the presence of others in any chronological sequence. It represents a mayor challenge but is also the primary virtue of protecting group chemistry. In the case of photosensitive protecting groups, individual addressing requires specific differences in sensitivity to selected wavelengths and intensities, as has been recently demonstrated by C. G. Bochet et al. for nitroveratryl and benzoin derivatives in solution.[11] Amongst the reported photoprotecting groups, 3,5-dimethoxybenzoin esters are known to be effectively cleaved by low-intensity irradiation at wavelengths below 300 nm,[12] while nitroveratryl (Nvoc) derivatives, being less reactive, are cleaved at much longer wavelengths (up to 420 nm).[13]

Based on our previous experience with the Nvoc-protected aminosilane **1**, and to transfer and extend the orthogonality concept from solution to solid surfaces (Scheme 1) we synthesized photoprotected triethoxysilanes with terminal amino- (**1**), hydroxy- (**2**), and carboxylic acid groups (**3**, **4**) with nitroveratryloxycarbonyl (NH-Nvoc for **1**/-NH_2; O-Nvoc **2**/-OH; and CO-Nvoc **3**/-COOH[14]) and 3,5-dimethoxybenzoin substituents (CO-Bzn for **4**/-COOH). The synthesis was achieved by first linking the protecting groups to the corresponding functional 1-alkenes by reported coupling procedures, followed by hydrosilylation to introduce the triethoxysilyl anchor group.[15] The triethoxysilyl anchor group was chosen since it favors the formation of a dense monolayer through the three alkoxy valences and at the same time it is less reactive than chlorosilanes), which facilitates handling of the compounds under laboratory conditions (no inert-gas atmosphere required). Furthermore, the silane anchor group is particularly attractive for the modification of a large variety of technologically relevant materials like silica (SiOH groups on glass, quartz, and oxidized Si wafers) and other oxide surfaces (e.g. ITO, TiO_2, Fe_3O_4, ZrO_2, and oxidized polymer surfaces).

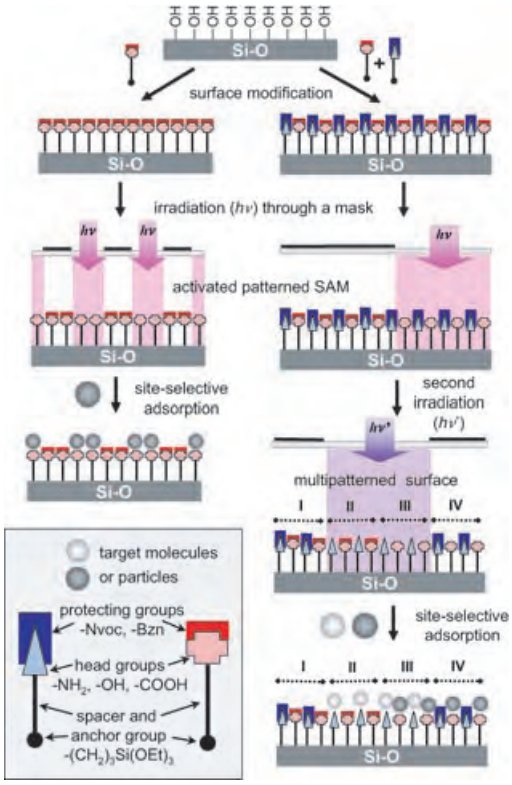
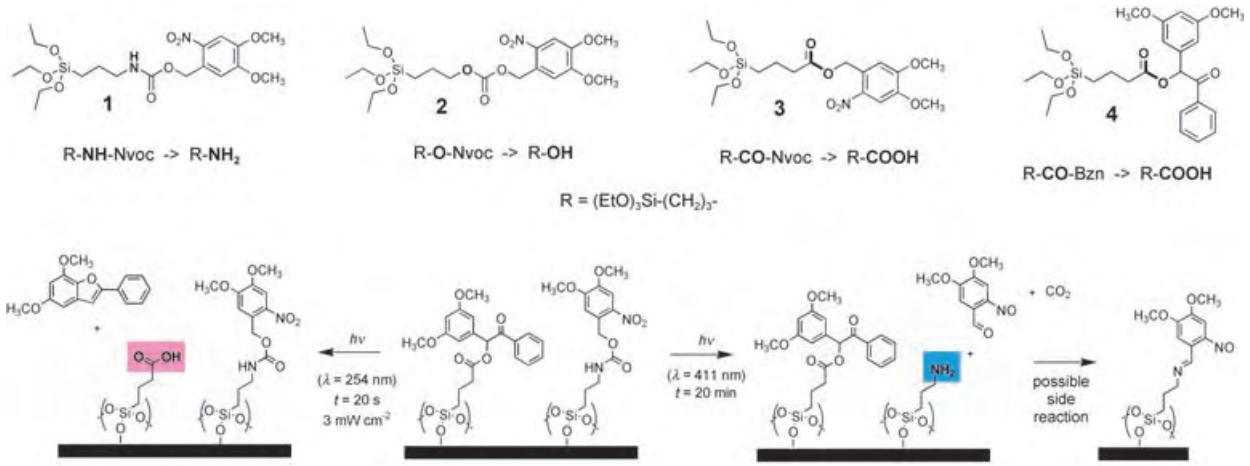


Figure 1. Surface modification and direct monolayer patterning with photosensitive silanes. Left: Formation of a homogenous monolayer by chemisorption of a photosensitive silane. Selected regions of the monolayer are activated by irradiation through a photomask to liberate functional groups. Right: Simultaneous coadsorption of two different silanes (with different functionalities and orthogonal protecting groups) leads to mixed monolayers. Each type of protecting group can be addressed individually in two deprotection steps by irradiation with their corresponding wavelength ($h\nu$ and $h\nu'$), leading to four chemically distinct surface types: I) nonirradiated, fully protected region, II) one in which only one functional group (A) is activated, III) one in which both functional groups are deprotected, and IV) one in which only the second group (B) is liberated. In the deprotected regions adsorption and chemical modification may be achieved for each individual functionality. Nvoc = nitroveratryl, Bzn = benzoin.

During the surface modification process two types of reactions take place simultaneously. First, the trialkoxysilyl groups hydrolyze to give the highly reactive silanol species,

 © 2005 Wiley-VCH Verlag GmbH & Co. KGaA, Weinheim



Scheme 1. Chemical structures of the photoprotected triethoxysilanes synthesized and used in this study. Selective deprotection of the amino (blue, from NH-Nvoc **1**) and the carboxylic acid function (red, from CO-Bzn **4**) is shown for a mixed monolayer. A possible side reaction between the liberated amino group and the benzaldehyde fragment might lead to an imine.

which condense in a second step with each other and with free OH groups of the surface to form stable Si-O-Si bonds. In this reaction sequence oligomerization to 1D, 2D, and 3D structures competes with covalent binding to the surface and requires particular consideration. Extensive oligomerization may lead to larger 3D aggregates that would ultimately result in substantial surface roughness.[18b] The progression of these reactions and consequently the characteristics of the final surface layer critically depend on experimental variables such as type of solvent, temperature, and reaction time, as well as on the catalyst and the concentration of the organosilane. Post-silanization curing of the modified substrates at elevated temperature has been shown to improve the stability of the silane films by covalent cross-linking of free silanol groups.

The synthesized silanes were chemisorbed from solution onto quartz substrates and Si wafers at individually optimized prehydrolysis and surface reaction conditions in order to obtain homogeneous and smooth surface layers.[10a,15] The flat layer topography was confirmed by AFM measurements (average roughness of the silane layers was similar to that of the bare substrate, rms ca. 0.4 nm over several 10^4 nm^2). The layer thickness from ellipsometric measurements was in the range of 1–2 nm (±0.5 nm), and advancing water contact angles were around 65–70° (±2)° for the Nvoc surfaces (**1**, **2**, and **3**) and 56 (±2)° for the CO-Bzn **4** layer (bare silica surface ≈0°). After irradiation and deprotection the water contact angles dropped by 10–20° (±5)°, indicating the liberation of the more polar functional groups. The ellipsometric thickness was slightly reduced after irradiation by about 0.2–0.5 nm (within the error range).

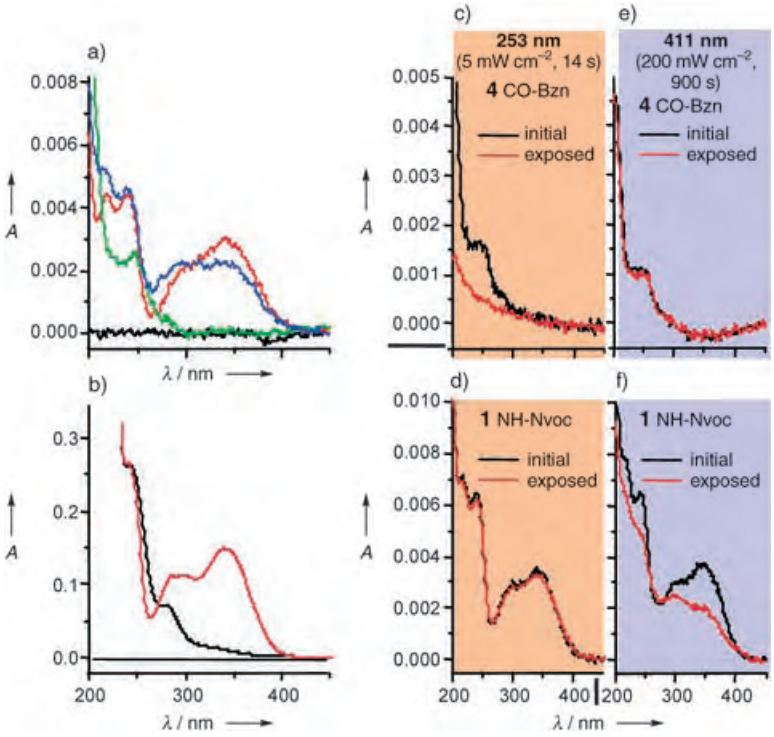


Figure 2. a) UV/Vis spectra of quartz substrates modified with the individual silanes **1** (Nvoc-protected; red), **4** (Bzn-protected; green), a binary mixture of both silanes (blue), and the bare substrate (black). b) UV/Vis spectra of the silanes **1** and **4** in THF; for **4** the absorption band tails far into the visible range. c, d) The absorption for the layer of CO-Bzn **4** decays upon irradiation at 253 nm (c), while that for the layer of NH-Nvoc **1** remains stable at this wavelength (d). During irradiation at 411 nm the layer of CO-Bzn **4** (e) remains stable, while NH-Nvoc **1** (f) is cleaved.

The presence of the photoprotecting groups in the surface layers was also confirmed by their characteristic chromophore absorption in the UV/Vis spectroscopic analysis of silanized quartz substrates. This is demonstrated in Figure 2a for substrates modified with silane **1** (characteristic absorption of the NH-Nvoc group, red curve), with **4** (CO-Bzn group, green curve), and with an equimolar mixture of both (blue curve). These spectroscopic profiles are identical for the corresponding silanes in solution (Figure 2b). The coexistence of both chromophores (Nvoc and Bzn) in the mixed layer corroborates that combinations of different functionalities and protecting groups can be obtained in a single chemisorption

 © 2005 Wiley-VCH Verlag GmbH & Co. KGaA, Weinheim

step, as also shown for the NH-Nvoc silane and a quaternary ammonium silane.[10a]

A possible problem with the coadsorption of different silanes from a mixture in solution might result from a deviation of the relative ratio of silanes in the adsorbed state and the ratio in solution. Based on the relative UV absorption intensities of the individual components **1**, **4**, and the mixed layer (Figure 2a) and the assumption of random chromophore orientation in the disordered silane layers, one can infer an equimolar coadsorption. The different absorbance maxima of the Nvoc (λ_{max} above 300 nm, tailing beyond 400 nm) and Bzn (λ_{max} below 300 nm, tailing up to 380 nm) protecting groups explain the specific wavelength sensitivity of the deprotection process. In fact, irradiation at 254 nm (5 mW cm^{-2}) for 14 s results in almost quantitative cleavage of the Bzn group of **4** (see Figure 2c), while the NH-Nvoc layer **1** remains fully stable under identical conditions (Figure 2d).[16] The Nvoc group can be effectively photolyzed at its absorbance maximum around 365 nm, but also the Bzn derivative **4** fragments at this wavelength (for a more detailed kinetic analysis see Figure S1 in the Supporting Information). This instability of the Bzn group at 365 nm may be a consequence of the weak absorbance band up to 380 nm evident in the solution spectrum (Figure 2b). In contrast, irradiation at 411 nm leads to a strong decrease of the Nvoc chromophore in layer **1** (Figure 2f), while the CO-Bzn layer **4** remains stable (Figure 2e, see also Figure S1 in the Supporting Information). These results clearly illustrate the possibility of orthogonal deprotection at the substrate surface.

Closer analysis of the photolysis reactions reveals that the relative chromophore intensity in the Nvoc-protected amine **1** never drops below 40–50% even in the presence of a carbonyl scavenger.[17] In contrast, the Nvoc-protected alcohol **2** and carboxylic acid **3** can be cleaved almost quantitatively under identical conditions. This particular behavior might be explained by imine formation between the benzaldehyde fragment and the primary amino group at the surface as a side reaction after photolysis (Scheme 1); this is not possible for **2** and **3**. This result is indicative of a diffusion-controlled process at the substrate surface, in which the separation of the photofragments is slow (compared to the imine formation) due to the 2D confinement imposed by the solid surface.

When the substrates are irradiated through a mask, a pattern of activated and nonactivated areas with the shape of the mask is generated. The resulting chemical contrast between exposed and nonirradiated regions can be used to direct the assembly process of specific targets onto the activated areas (like colloidal particles[10a,18] and fluorescence dyes, see Figure S2 in the Supporting Information). Figure 3 shows the site-selective assembly structures from carboxylated poly(butylmethacrylate) (PBMA) colloids[18a] after photolytic patterning of the surface groups for substrates modified with **1** (a: NH-Nvoc/NH_2), **2** (b: O-Nvoc/-OH), **3** (c: CO-Nvoc/-COOH), and **4** (d: CO-Bzn/-COOH).[15] The contrast in the optical-microscope images (dark-field mode) results from differences in the density of adsorbed particles, which is higher in the brighter areas. On the free amino surface of the irradiated layer **1** a relatively high particle density of 3.5(±0.5) particles per μm^2 is found, while essentially no particles adsorbed onto the nonirradiated regions. This is similar to results obtained by direct functionalization with an aminopropylsilane.[10a] Strong electrostatic attraction between the partially protonated and positively charged amino groups at the substrate and the partially deprotonated and negatively charged carboxyl functions on the latex particles may drive the assembly process. The individual particles at the NH_2 surface are isolated due to a strong repulsion between the like-charged colloids, as seen at higher magnification in the SEM image (inset Figure 3a). On the hydroxy-modified surface of the irradiated layer **2** the

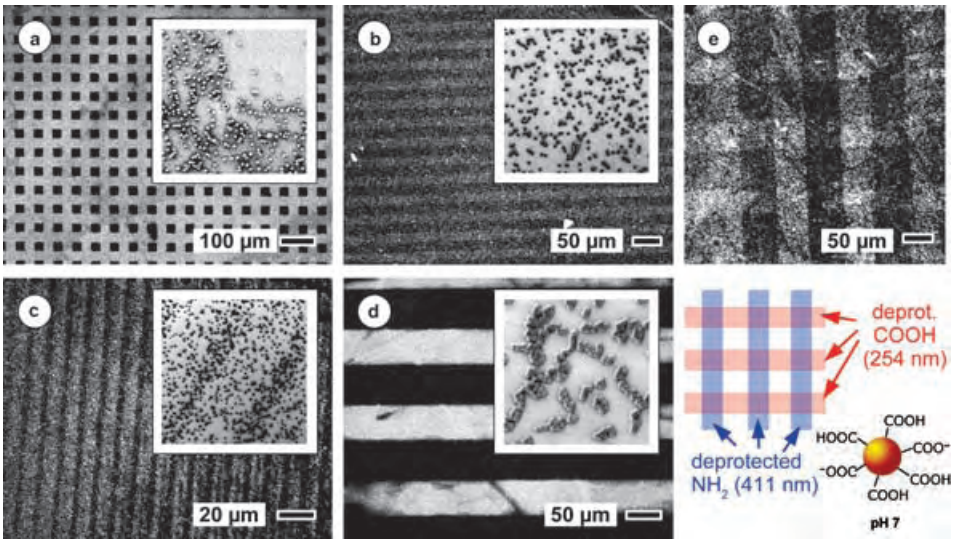


Figure 3. Optical-micrographic images (dark field) of assembly patterns from carboxylated PBMA particles (diameter 183 nm) adsorbed from aqueous suspension at pH 7 onto silane layers of a) **1** (NH-Nvoc/NH_2), b) **2** (O-Nvoc/-OH), c) **3** (CO-Nvoc/-COOH), and d) **4** (CO-Bzn/-COOH) irradiated through a mask. The insets show SEM images of individual particles at higher magnification (width ≈5 μm). Image (e) shows the colloid assembly pattern on a mixed layer of **1** and **4**, which has been irradiated at two different wavelengths (254 and 411 nm) a 90°-rotated line masks (according to the color scheme).

 © 2005 Wiley-VCH Verlag GmbH & Co. KGaA, Weinheim

particle affinity is apparently weaker and a low density of individually dispersed colloids is observed (1.7 particles per μm^2) with unspecific adsorption in the nonirradiated areas (1.3 particles per μm^2). In this case the adsorption process might be driven primarily by polar and hydrogen-bonding interactions between the OH and COOH groups.

Surprisingly, on COO surfaces from exposed layers **3** and **4** a relatively strong colloid adsorption (4.1/1.4 particles per μm^2 for irradiated/nonirradiated **3**; 8.5/1.2 particles per μm^2 for **4**) and substantial particle clustering is found (seen at higher magnification in the SEM image, Figure 3d). This is in contrast to initial expectations, since the carboxy functions on the particles and at the substrate surface should show electrostatic repulsion. Indeed, no particle adsorption is achieved when pure water is used instead of buffer solution as the suspending medium; this indicates the important role of charge screening by the salt. Colloidal adsorption onto a mixed layer of **1** and **4** after successive irradiation through a striped mask, first at 254 nm (CO-Bzn deprotection) and secondly with the mask rotated by 90° at 411 nm (NH-Nvoc deprotection), leads to the checkered pattern shown in Figure 3e, in which the particle density depends on the activated functional groups and the irradiation dose (highest particle density in cross regions).

Other methods for particle assembly have been reported,[19] and one prominent example of orthogonal particle deposition is based on DNA-assisted specific recognition between DNA-modified spots on a substrate and DNA-labeled particles.[20] This method was demonstrated successfully for two different kinds of particles,[20b] but it requires specific DNA labeling of both the substrate and the particles. The advantage of the method presented here is the the fact that a simple silanization process introduces the mixed protected functionalities and patterning is achieved by means of standard photolithographic irradiation; the particles need not be specifically modified with complementary recognition elements (besides the functional surface groups introduced during particle synthesis).

In conclusion, the new photosensitive silanes presented here can be used for direct monolayer lithography and the introduction of functional surface groups, which is not possible directly by silanization (OH and COOH functions are incompatible with the triethoxysilane anchor group). Complex combinations of different functional and protecting groups can thus be achieved by simultaneous coadsorption of the corresponding silane mixtures and orthogonal activation, as demonstrated here for NH-Nvoc **1** and CO-Bzn **4**. Specific colloid assembly onto the photoactivated regions is possible and mediated by the free surface functionalities. Further experiments are currently directed to the selective immobilization of DNA fragments onto the photopatterned mixed layers (relevant for biochip applications) and the extension of the Bzn group to other functionalities.

Received: January 11, 2005
Revised: April 11, 2005
Published online: July 1, 2005

Keywords: monolayers · photolithography · silanes · surface chemistry

[1] a) G. M. Wallraff, W. D. Hinsberg, *Chem. Rev.* **1999**, *99*, 1801 – 1821; b) P. M. Mendes, J. A. Preece, *Curr. Opin. Colloid Interface Sci.* **2004**, *9*, 236- 248.
[2] Y. Xia, G. M. Whitesides, *Angew. Chem.* **1998**, *110*, 568 – 594; *Angew. Chem. Int. Ed.* **1998**, *37*, 550 – 575.
[3] a) R. M. Nyffenegger, R. M. Penner, *Chem. Rev.* **1997** *97*, 1195 – 1230; b) S. Krämer, R. R. Fuierer, C. B. Gorman, *Chem. Rev.* **2003**, *103*, 4367 – 4418.
[4] C. S. Dulcey, J. H. Georger, Jr., V. Krauthamer, D. A. Stenger, T. L. Fare, J. M. Calvert, *Science* **1991**, *252*, 551 – 554.
[5] M. J. Tarlov, D. R. F. Burgess, Jr., G. Gillen, *J. Am. Chem. Soc.* **1993**, *115*, 5305 – 5306.
[6] a) F. Effenberger, G. Götz, B. Bidlingmaier, M. Weztein, *Angew. Chem.* **1998**, *110*, 2651 – 2654; *Angew. Chem. Int. Ed.* **1998**, *37*, 2462 – 2464; b) O. Prucker, C. A. Naumann, J. Ruehe, W. Knoll, C. W. Frank, *J. Am. Chem. Soc.* **1999**, *121*, 8766 – 8770.
[7] K. Morigaki, T. Baumgart, U. Jonas, A. Offenhäusser, W. Knoll, *Langmuir* **2002**, *18*, 4082 – 4089.
[8] a) V. N. R. Pillai, *Synthesis* **1980**, *1*, 1 – 26; b) A. S. Blawas, W. M. Reichert, *Biomaterials* **1998**, *19*, 595 – 609; c) C. G. Bochet, *J. Chem. Soc. Perkin Trans. 1* **2002**, 125 – 142.
[9] a) S. P. A. Fodor, J. L. Read, M. C. Pirrung, L. Stryer, A. T. Lu, D. Solas, *Science* **1991**, *251*, 767 – 771; b) G. H. McGall, A. D. Barone, M. Diggelmann, S. P. A. Fodor, E. Gentalen, N. Hgo, *J. Am. Chem. Soc.* **1997**, *119*, 5081 – 5090; c) T. Vossmeyer, S. Jia, E. Delonno, M. R. Diehl, S.-H. Kim, X. Peng, A. P. Alivisatos, J. R. Heath, *J. Appl. Phys.* **1998**, *84*, 3664 – 3670; d) G. Elender, M. Kühner, E. Sackmann, *Biosens. Bioelectron.* **1996**, *11*, 565 – 577.
[10] a) U. Jonas, A. del Campo, C. Krüger, G. Glasser, D. Boos, *Proc. Natl. Acad. Sci. USA* **2002**, *99*, 5034 – 5039; b) B. Zhao, J. S. Moore, D. J. Beebe, *Langmuir* **2003**, *19*, 1873 – 1879; c) K. Lee, F. Pan, G. T. Carroll, N. J. Turro, J. T. Koberstein, *Langmuir* **2004**, *20*, 1812 – 1818; d) D. Ryan, B. A. Parviz, V. Linder, V. Semetey, S. K. Sia, J. Su, M. Mrksich, G. M. Whitesides, *Langmuir* **2004**, *20*, 9080 – 9088.
[11] a) C. G. Bochet, *Angew. Chem.* **2001**, *113*, 2140 – 2142; *Angew. Chem. Int. Ed.* **2001**, *40*, 2071 – 2073; b) A. Blanc, C. G. Bochet, *J. Org. Chem.* **2002**, *67*, 5567 – 5577.
[12] a) G. Papageorgiou, J. E. T. Corrie, *Tetrahedron* **1997**, *53*, 3917 – 3932; b) R. S. Rock, S. I. Chan, *J. Org. Chem.* **1996**, *61*, 1526 – 1529.
[13] M. Kessler, R. Glatthar, B. Giese, C. G. Bochet, *Org. Lett.* **2003**, *5*, 1179 – 1181.
[14] For molecule **3** the nitroveratryl group is directly linked to the carboxylic acid function through an ester linkage (without a oxycarbonyl moiety), but for simplicity it is referred to as CO-Nvoc.
[15] See the Supporting Information for details.
[16] In analogy to the irradiated silane layers, nonirradiated reference substrates were also washed to identify and account for any intensity loss due to simple removal of the silane layer by washing. All absorbances remained constant after this procedure, corroborating the high stability of these silane layers.
[17] During irradiation a thin film of methanol was sandwiched between the substrate and a covering quartz plate to allow dissolution of the generated protecting-group fragments. In the case of the Nvoc-protected amine **1**, semicarbazide hydrochloride (55 mM solution in methanol) was added as a carbonyl scavenger to capture the photogenerated benzaldehyde and prevent potential imine formation with the free amino surface (Scheme 1).

 © 2005 Wiley-VCH Verlag GmbH & Co. KGaA, Weinheim

[18] a) C. Krüger, U. Jonas, *J. Colloid Interface Sci.* **2002**, *252*, 331 – 338; b) U. Jonas, C. Krüger, *J. Supramol. Chem.* **2002**, *2*, 255 – 270.

[19] a) "Self-Organization of Colloidal Nanoparticles": J. Dutta, H. Hofmann in *Encyclopedia of Nanoscience and Nanotechnology* (Ed.: H. S. Nalwa), American Scientific, Stevenson Ranch, **2004**, *9*, pp. 617 – 639; b) "Colloidal Micro- and Nanostructures Assembled at Patterned Surfaces": A. del Campo, A. S. Duwez, C. A. Fustin, U. Jonas in *Dekker Encyclopedia of Nanoscience and Nanotechnology* (Eds.: J. A. Schwarz, C. Contescu, K. Putyera), Marcel Dekker, New York, **2004**, pp. 725 – 738.

[20] a) S. Esener, D. Hartmann, S. Güncer, C. Fan, M. Heller, J. Cable, *Proc. Spatial Light Modulators. Topical Meeting. OSA Trends in Optics and Photonics Series* **1997**, *14*, 65 – 68; b) L. M. Demers, S.-J. Park, T. A. Taton, Z. Li, C. A. Mirkin, *Angew. Chem.* **2001**, *113*, 3161 – 3163; *Angew. Chem. Int. Ed.* **2001**, *40*, 3071 – 3073; c) R. Bashir, *Superlattices Microstruct.* **2001**, *29*, 1 – 16.

 © 2005 Wiley-VCH Verlag GmbH & Co. KGaA, Weinheim

DNA Polymerase

Enhanced Fidelity in Mismatch Extension by DNA Polymerase through Directed Combinatorial Enzyme Design**

*Daniel Summerer, Nicolas Z. Rudinger, Ilka Detmer, and Andreas Marx**

Dedicated to Professor Bernd Giese on the occasion of his 65th birthday

The fidelity of DNA polymerase activity is of central importance for numerous biotechnological applications.[1,2] The imperfect fidelity of DNA polymerases under the unnatural conditions of several techniques such as those of the polymerase chain reaction (PCR) either restricts the application of these enzymes or demands their tedious optimization. Thus, a prime target for the design of DNA polymerases with altered functions is high fidelity in the formation of Watson–Crick base pairs during DNA synthesis. Progress in this area generates valuable tools for many biological applications like PCR, sequencing protocols, mutagenesis techniques, and genotyping. Through the engineering of DNA and RNA polymerases, it has been possible to design enzymes that accept dideoxynucleoside triphosphates,[3] exhibit an altered substrate spectrum and lower fidelity, higher thermostability, decreased activity at low temperatures, and enhanced resistance to inhibitors.[4]

Herein, we describe an efficient automated high-throughput setup for the rapid parallel screening of DNA polymerase mutant libraries. The readout is based exclusively on enzyme activity through detection of the reaction product by fluorescence. By the randomization of a gene cassette of the Klenow fragment of *E. coli* DNA polymerase I (3′→5′-exonuclease deficient, KF$^-$) and subsequent comparative automated screening, several active variants with significantly higher extension fidelity than the wild-type enzyme were identified. The new properties of mutated KF$^-$ forms were transferred to the thermostable *Thermus aquaticus* (*Taq*) DNA polymerase to provide tools that supersede the wild-type enzyme in highly accurate PCR-based genotyping techniques.

Motif C was recently suggested to be involved in a reaction mechanism shared by members of the A and B families of DNA polymerases, in which mismatches in the primer–template substrate are recognized through indirect H-bonding between the minor groove and a histidine side chain (Figure 1).[5] This β-strand–turn–β-strand structure harbors acidic side chains that bind catalytically essential magnesium ions, reflected in the high conservation among family A DNA polymerases like KF$^-$, and also among sequence families B, RT, X, single subunit RNA polymerases, and the lesion bypass DNA polymerases of family Y.[6] Therefore, motif C seemed a promising target for directed polymerase engineering through focused randomization and subsequent screening.

To modify motif C, we constructed a library of 1316 KF$^-$ mutants randomized at the consensus residues 879–881 (Q879, V880, and H881).[7] This QVH consensus sequence is directly adjacent to the essential catalytic carboxylate group of D882 and forms the main part of a loop that connects the two β strands of motif C. It closely interacts with the deoxyribose moiety of the 3′-terminal primer nucleotide (Figure 1b).

Protein expression was conducted in 96-well plates. Enzymes were screened directly after lysis and dilution, and further purification steps were not required. DNA polymerase activity was monitored after reaction termination by quantitation of synthesized double stranded DNA through staining with Sybr green I (Figure 1c). This setup links enzyme activity to a signal without the need for artificial substrates, which could interfere with the enzymatic reaction. To determine if DNA binding and modifying agents or bacterial DNA in the crude lysate perturbs signal generation, we assayed lysates of *E. coli* expression cultures containing the KF$^-$ wild-type coding vector against those without the KF$^-$ coding vector. Fluorescence measurements revealed low background activity of the negative control with a considerable signal-to-noise ratio of ≈5:1. This enabled the assessment of a large dynamic range in enzyme activity.

We assayed single clones in 384-well plates for the ability to extend primer–template complexes with either a T_{primer}/$A_{template}$ match or a T/G mismatch at the 3′ end of the primer (Figure 1). An automated pipetting device and the fluorescent readout allowed the screening and evaluation of 384

[*] Dr. D. Summerer, Dipl.-Biol. N. Z. Rudinger, Dipl.-Chem. I. Detmer, Prof. Dr. A. Marx
Fachbereich Chemie, Universität Konstanz
Universitätsstrasse 10, M 726, 78457 Konstanz (Germany)
Fax: (+49) 7531-88-5140
E-mail: andreas.marx@uni-konstanz.de

[**] We thank the Volkswagen Foundation for financial support and M. Strerath for his support in the preparation of the manuscript.

Supporting information for this article is available on the WWW under http://www.angewandte.org or from the author.

 © 2005 Wiley-VCH Verlag GmbH & Co. KGaA, Weinheim DOI: 10.1002/anie.200500047

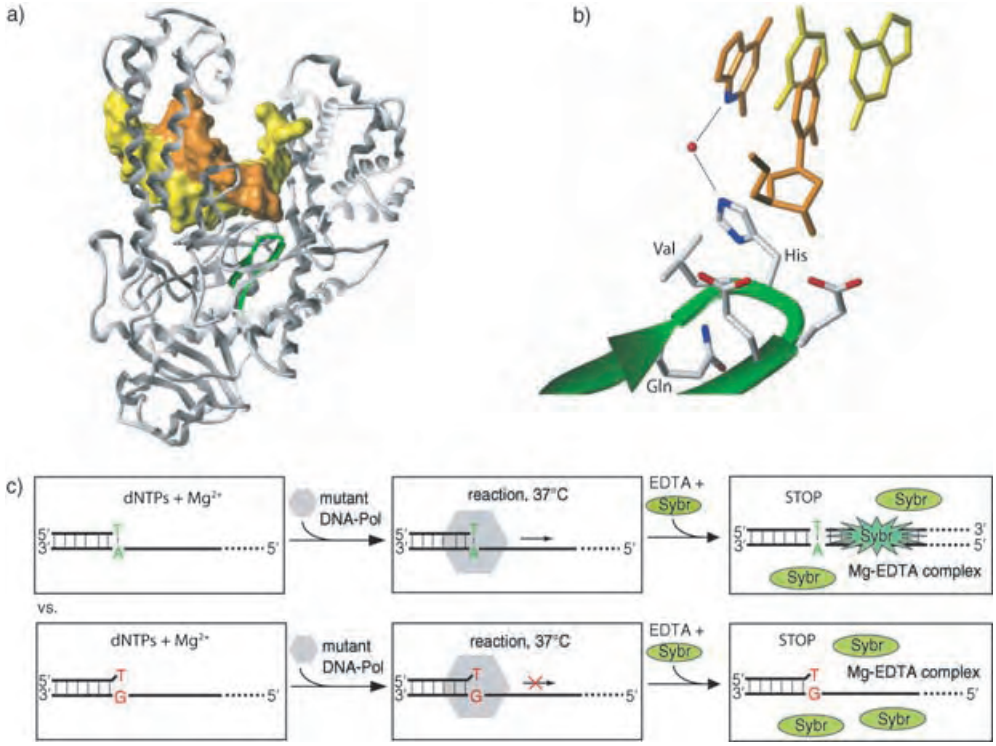


Figure 1. Structural properties of motif C and screening for DNA polymerase variants with increased selectivity. a) Overall view of *Bst* DNA polymerase I (PDB entry 2BDP), which shares high homology with KF^-.[16] The enzyme is shown in gray, motif C in green. The substrate DNA is depicted as a Connolly surface with primer in orange, and template strand in yellow. b) Detailed view of the turn of motif C and the two nucleotide pairs at the 3′ terminus of the primer. For clarity, the sugar–phosphate groups are not depicted for each nucleotide. Primer nucleotides are in orange, template nucleotides in yellow. The indirect hydrogen bond between N3 of histidine (blue) and the 3′-penultimate primer nucleotide is shown in black and is mediated by a water molecule (red sphere). c) General scheme of the screening approach for DNA polymerases with increased extension fidelity. Enzyme variants that extend the canonical primer–template duplex but fail to extend the noncanonical duplex are identified with the DNA duplex-specific dye Sybr green I in a subsequent fluorescence read-out.

reactions in approximately 40 minutes. Extension fidelity was measured by determining the ratios of fluorescence of primer extensions from matched versus mismatched substrates. The template sequences were derived from the human single nucleotide polymorphism (SNP) G1691A of the Factor V Leiden (FVL) gene.[8] The screen revealed considerable mutability of the targeted QVH sequence. Despite the fact that this motif is highly conserved among several DNA and RNA polymerase families,[6] 47% of the mutants exhibited measurable primer extension activity.

The three most selective mutants, PLQ, LVG, and LVL, were chosen for further characterization. First, we assayed the purified enzymes in radiometric primer extensions (Figure 2). All possible base-pair combinations at the primer 3′ terminus were tested under conditions that promote mismatch extension: excess enzyme over primer–template complex and high dNTP concentrations.[7] Measurements revealed that wild-type KF^- is capable of extending almost all mismatches under the chosen conditions, albeit to varying extents consistent with previous studies (Figure 2b).[9] In contrast, all three selected mutants show a marked decrease in the efficiency of mismatch extension. Particularly, mutant LVL fails to fully extend mismatched primer termini in most cases. Steady-state kinetics measurements of single-nucleotide extensions show that in all cases of processing a properly matched primer–template complex, mutants display similar steady-state k_{cat} values as the wild-type enzyme.[7] K_M values of the mutants were generally higher than those for wild-type KF^-, reflected by a slight decrease in DNA synthesis efficiency by the mutant forms. Remarkably, no significant elongation of mismatched primer termini by the mutants was detected under steady-state and single-turnover conditions, whereas the results obtained for wild-type KF^- are consistent with previous reports.[9] This indicates that the k_{cat} values for all base-pair combinations assayed were drastically lower for the KF^- variants than for the wild-type polymerase. Binding studies were performed to determine whether the effects on mismatch extension fidelity are caused by a decrease in substrate-binding affinity in the mutants.[7] Interestingly, only mutant PLQ exhibits a significant decrease in binding affinity to a mismatched primer terminus. For this reason, altered binding affinity does not generally appear to be mandatory for an increase in mismatch extension fidelity.

We next investigated whether the observed effects could be transferred to wild-type *Taq* DNA polymerase (*Taq* wt). Though *Taq* wt and KF^- are both members of the DNA polymerase family A, they differ in several properties such as thermostability and fidelity.[10] The *Taq* QVH consensus sequence was mutated into LVL and the extension fidelity of the resulting mutant polymerase was investigated. We

 © 2005 Wiley-VCH Verlag GmbH & Co. KGaA, Weinheim

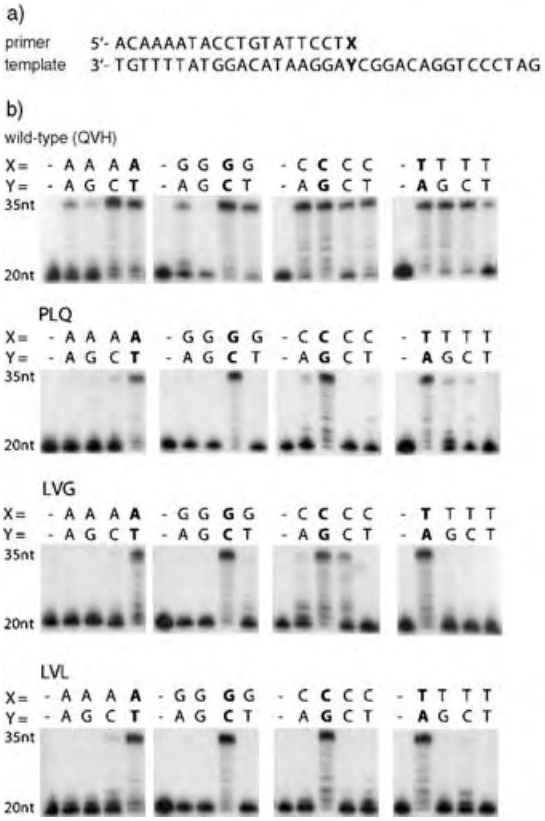


Figure 2. Increased primer extension fidelity of the KF$^-$ mutants PLQ, LVL, and LVG (positions 879–881) in comparison with the wild-type enzyme in different sequence contexts. The conditions were chosen to promote mismatch extension. All reactions contained equal amounts of primer–template complex, enzyme, and dNTPs.[7] a) The sequence of the primer–template duplex employed is derived from the human FVL SNP G1691A.[7] b) Primer extensions catalyzed by the depicted enzyme variants. The first lane of each gel represents a control reaction without enzyme. Nucleotide sequences at the 3′ end of the primer are shown on top of each gel image. Unextended primer (20 nt) and full-length product (35 nt) are indicated at the left side of each image. X = 3′-terminal primer nucleotide, Y = template nucleotide pairing with X leading to matched (bold) or mismatched primer termini.[7]

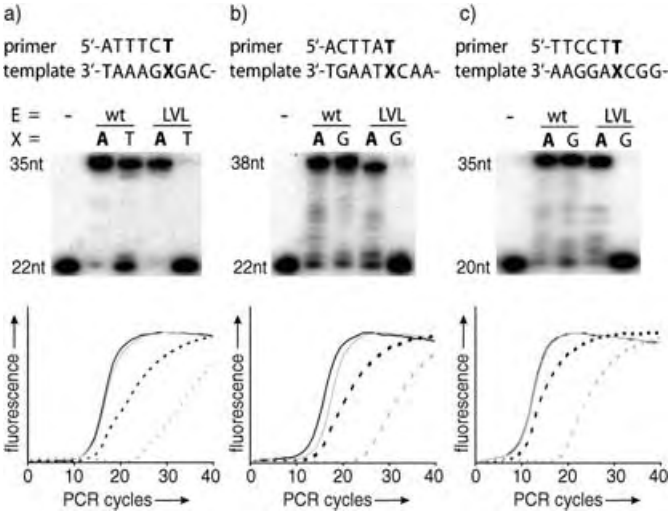


Figure 3. The impact of LVL mutations on the fidelity of *Taq* DNA polymerase within three sequence contexts. Top panel: partial nucleotide sequences of primer–template complexes used for primer extensions. The first lane of each gel represents a control reaction without enzyme. The lengths (nt) of primer and full-length product are shown on the left side of each gel; E = enzyme, X = template nucleotide. Lower panel: real-time allele-specific PCR experiments with either wild-type or mutant LVL *Taq* DNA polymerase in three sequence contexts.[7] Solid lines: wild-type *Taq* DNA polymerase; dashed lines: LVL *Taq* DNA polymerase; black: matched primer–template substrates; gray: mismatched primer–template substrates. Experiments conducted in a) the human BRAF somatic SNP T1796A, b) in the human DPYD SNP G735A, and c) in the FVL SNP G1691A sequence context.[7]

conducted primer extension reactions in three sequence contexts that contain prominent SNPs.[11,12] These experiments show that there are only subtle differences between the extension of matches and mismatches with *Taq* wt under the chosen conditions (Figure 3).

In contrast, the mutant *Taq* DNA polymerase (*Taq* LVL) is clearly capable of discriminating transversion and transition SNPs (Figure 3). *Taq* LVL might greatly expand the technical scope and allow an improvement of PCR-based techniques like allele-specific PCR (asPCR).[13] To test the applicability of *Taq* LVL for asPCR, we performed real-time PCR reactions with the substrate sequence contexts described above. We measured the difference in the threshold-crossing cycle number (ΔC_t) between a matched and a mismatched primer–template complex (Figure 3). *Taq* wt displays weak or no discrimination, whereas *Taq* LVL leads to ΔC_t values of 10 for all sequence contexts. Therefore, the mutant *Taq* LVL shows greater discrimination than *Taq* wt in asPCR, regardless of the sequence context applied or enzyme and template concentrations tested, as shown in additional experiments (Supporting Information).[7]

In summary, the identification of several active DNA polymerase variants that display increased primer extension fidelity shows that none of the chosen amino acid positions is essential for catalysis, and that all positions tolerated substitutions. However, the nature of the side chain of V880 seems to be most conserved, as all identified active and more selective mutants bear a nonpolar amino acid side chain at this position. Furthermore, the absence of any charged residues within the selected active mutants indicates that the introduction of ionic residues in this region might inactivate the enzyme by interference with D882, the magnesium ions, or the incoming dNTP substrate.

The fact that the apparent increased fidelity is not limited to the sequence context employed during screening, is suggestive of a common mechanism for error sensing. It was recently proposed that the histidine group of QVH might be involved in DNA polymerase extension fidelity mechanisms by editing H-bonding patterns in the minor groove of the primer–template duplex (Figure 1b).[5] One of the mutants that exhibits increased extension fidelity has three amino acid substitutions at the targeted site (QVH to PLQ), in which a glutamine side chain replaces histidine at position 881. As mentioned above, glutamine can often replace the H-bond donating ability of the imidazole ring of histidine.[14] Thus, improved editing of H-bond patterns by Q881 in the context of the PLQ sequence might be the cause for the increased fidelity in this variant. However, we identified mutants LVG

 © 2005 Wiley-VCH Verlag GmbH & Co. KGaA, Weinheim

and LVL, both of which lack hydrogen bonding capability within the wild-type QVH region, yet have significantly higher extension fidelity. Thus, abolishing hydrogen bonding to the minor groove results in enhanced polymerase fidelity. Similar results for another KF^- variant (H881A) were recently reported.[15] The origins of the observed selectivity currently remain elusive. It could be that a loss of hydrogen bonding in a complex that is already destabilized (upon mismatch extension catalysis) actually facilitates the editing capacity over that of the wild-type polymerase, in which hydrogen bonding is present.

The approach of rapid DNA polymerase screening discussed herein, which has led to highly valuable enzyme variants, can be used to further tailor DNA polymerase activities for obtaining insight into biological processes and new tools for biotechnological applications.

Received: January 16, 2005
Revised: April 18, 2005
Published online: July 1, 2005

Keywords: DNA polymerase · DNA recognition · molecular evolution · polymerase chain reaction

[1] a) T. A. Kunkel, K. Bebenek, *Annu. Rev. Biochem.* **2000**, *69*, 497 – 529; b) E. T. Kool, *Annu. Rev. Biochem.* **2002**, *71*, 191 – 219.
[2] J. Sambrook, D. W. Russell, *Molecular cloning: A Laboratory Manual*, Cold Spring Harbor Laboratory Press, Cold Spring Harbor, NY, USA **2001**.
[3] Y. Li, V. Mitaxov, G. Waksman, *Proc. Natl. Acad. Sci. USA* **1999**, *96*, 9491 – 9496.
[4] a) F. J. Ghadessy, J. L. Ong, P. Holliger, *Proc. Natl. Acad. Sci. USA* **2001**, *98*, 4552 – 4557; b) S. Brakmann, S. Grzeszik, *ChemBioChem* **2001**, *2*, 212 – 219; c) G. Xia, L. Chen, T. Sera, M. Fa, P. G. Schultz, F. E. Romesberg, *Proc. Natl. Acad. Sci. USA* **2002**, *99*, 6597 – 6602; d) P. H. Patel, L. A. Loeb, *J. Biol. Chem.* **2000**, *275*, 40266 – 40272; e) M. B. Kermekchiev, A. Tzekov, W. M. Barnes, *Nucleic Acids Res.* **2003**, *31*, 6139 – 6147; f) M. Fa, A. Radeghieri, A. A. Henry, F. E. Romesberg, *J. Am. Chem. Soc.* **2004**, *126*, 1748 – 1754; g) F. J. Ghadessy, N. Ramsay, F. Boudsocq, D. Loakes, A. Brown, S. Iwai, A. Vaisman, R. Woodgate, P. Holliger, *Nat. Biotechnol.* **2004**, *22*, 755 – 759.
[5] M. C. Franklin, J. Wang, T. A. Steitz, *Cell* **2001**, *105*, 657 – 667.
[6] M. Delarue, O. Poch, N. Tordo, D. Moras, P. Argos, *Protein Eng.* **1990**, *3*, 461 – 467.
[7] Detailed experimental procedures are provided in the Supporting Information.
[8] H. Engel, L. Zwang, H. van Vliet, J. J. Michiels, J. Stibbe, J. Lindemans, *Thromb. Haemostasis* **1996**,*75*, 267 – 269.
[9] a) C. M. Joyce, X. C. Sun, N. D. Grindley, *J. Biol. Chem.* **1992**, *267*, 24485 – 24500; b) D. T. Minnick, K. Bebenek, W. P. Osheroff, R. M. Turner, Jr., M. Astatke, L. Liu, T. A. Kunkel, C. M. Joyce, *J. Biol. Chem.* **1999**, *274*, 3067 – 3075.
[10] M. Suzuki, A. K. Avicola, L. Hood, L. A. Loeb, *J. Biol. Chem.* **1997**, *272*, 11228 – 11235.
[11] H. Davies, G. R. Bignell, C. Cox, P. Stephens, S. Edkins, S. Clegg, J. Teague, H. Woffendin, M. J. Garnett, W. Bottomley, N. Davis, N. Dicks, R. Ewing, Y. Floyd, K. Gray, S. Hall, R. Hawes, J. Hughes, V. Kosmidou, A. Menzies, C. Mould, A. Parker, C. Stevens, S. Watt, S. Hooper, R. Wilson, H. Jayatilake, B. A. Gusterson, C. Cooper, J. Shipley, D. Hargrave, K. Pritchard-Jones, N. Maitland, G. Chenevix-Trench, G. J. Riggins, D. D. Bigner, G. Palmieri, A. Cossu, A. Flanagan, A. Nicholson, J. W. C. Ho, S. Y. Leung, S. T. Yuen, B. L. Weber, H. F. Siegler, T. L. Darrow, H. Paterson, R. Marais, C. J. Marshall, R. Wooster, M. R. Stratton, P. A. Futreal, *Nature* **2002**, *417*, 949 – 954.
[12] X. X. Wei, H. L. McLeod, J. McMurrough, F. J. Gonzalez, P. Fernandez Salguero, *J. Clin. Invest.* **1996**, *98*, 610 – 615.
[13] a) A. C. Syvänen, *Nat. Rev. Genet.* **2001**, *2*, 930 – 942; b) M. M. Shi, *Clin. Chem.* **2001**, *47*, 164 – 172; c) M. V. Myakishev, Y. Khripin, S. Hu, D. H. Hamer, *Genome Res.* **2001**, *11*, 163 – 169.
[14] A. Fersht in *Structure and Mechanism in Protein Science*, Freeman, New York, **1999**, p. 425.
[15] D. T. Minnick, K. Bebenek, W. P. Osheroff, R. M. Turner, M. Astatke, L. Liu, T. A. Kunkel, C. M. Joyce, *J. Biol. Chem.* **1999**, *274*, 3067 – 3075.
[16] J. R. Kiefer, C. Mao, J. C. Braman, L. S. Beese, *Nature* **1998**, *391*, 304 – 307.

 © 2005 Wiley-VCH Verlag GmbH & Co. KGaA, Weinheim

Reaction Mechanisms

Elucidation of the Mechanism of the 1,6-Cuprate Addition to Acceptor-Substituted Enynes through ^{13}C Kinetic Isotope Effects: Experimental and Theoretical Studies**

Seiji Mori, Marc Uerdingen, Norbert Krause,* and Keiji Morokuma**

The use of organocopper compounds (in particular organocuprates) has opened new avenues in organic and organometallic chemistry.[1] Among many different reaction principles, Michael additions to extended acceptors that bear a triple bond are particularly interesting as they provide efficient access to functionalized allenes.[2] The prototype of these

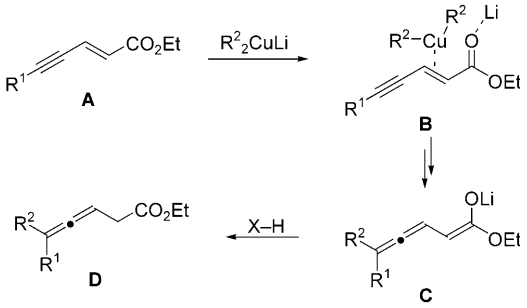
[*] Prof. Dr. S. Mori
Faculty of Science, Ibaraki University
Bunkyo, Mito 310-8512 (Japan)
Fax: (+81) 29-228-8403
E-mail: smori@mx.ibaraki.ac.jp
Dr. M. Uerdingen, Prof. Dr. N. Krause
Organic Chemistry II, Dortmund University
44221 Dortmund (Germany)
Fax: (+49) 231-755-3884
E-mail: norbert.krause@uni-dortmund.de
Prof. Dr. K. Morokuma
Cherry L. Emerson Center for Scientific Computation and
Department of Chemistry, Emory University
Atlanta, GA 30322 (USA)
Fax: (+1) 404-727-7412
E-mail: morokuma@emory.edu

[**] Financial support by the Deutsche Forschungsgemeinschaft, and generous allotment of computational time from the Research Center for Computational Science, National Institutes of Natural Sciences (Japan), the National Center for Supercomputing Applications (University of Illinois at Urbana-Champaign, USA), and the Cherry L. Emerson Center for Scientific Computation (Emory University, Atlanta, U.S.A.) are gratefully acknowledged.

Supporting information for this article is available on the WWW under http://www.angewandte.org or from the author.

 DOI: 10.1002/anie.200462976 © 2005 Wiley-VCH Verlag GmbH & Co. KGaA, Weinheim

transformations is the 1,6-cuprate addition to 2-en-4-ynoates **A** and similar acceptor-substituted enynes which has found numerous applications in allene chemistry (Scheme 1).[2,3] Moreover, 1,6-addition has provided deep insight into the



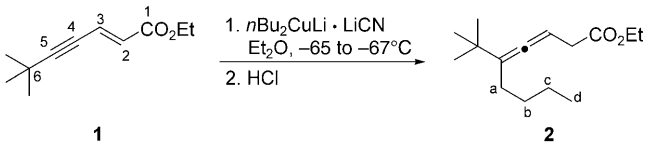
Scheme 1. 1,6-Cuprate addition to 2-en-4-ynoates **A** via π complexes **B** provides allenyl enolates **C**, which are protonated to give β-allenic esters **D**.

mechanistic details of copper-promoted reactions.[4] Early NMR spectroscopic investigations have proven the presence of π complexes **B**, which were characterized by their unique chemical shifts and $^{13}C,^{13}C$ coupling constants.[5] In contrast, less is known about further intermediates on the way to the allenyl enolates **C**, whose protonation furnishes β-allenic esters **D** and derivatives thereof.

Kinetic measurements have provided an activation energy value of 70 kJ mol^{-1} for the 1,6-addition of $Me_2CuLi{\cdot}LiI$ to ethyl 6,6-dimethylhept-2-en-4-ynoate;[6] however, the rate-determining step along the reaction pathway has not yet been identified unambiguously. The aim of the study described herein is to close this gap and to provide, with experimental and theoretical tools, a comprehensive mechanistic picture of the 1,6-cuprate addition to acceptor-substituted enynes.

The most powerful and straightforward experimental tool for identifying the rate-limiting step of a transformation is the determination of primary kinetic isotope effects (KIEs), that is, the rate change due to isotopic substitution at the site of bond breaking or bond making in the rate-determining step of a reaction. Instead of actually measuring the reaction rates of different isotopomers of a given substrate, small KIEs are normally determined by competition experiments of isotopically labeled and unlabeled compounds. Singleton and co-workers introduced a powerful NMR spectroscopic technique for measuring ^{2}H and ^{13}C KIEs at natural isotopic abundance which has found widespread application in diverse transformations such as pericyclic reactions,[7] palladium-catalyzed couplings,[8] and copper-promoted reactions.[9–11] The method involves the NMR spectroscopic determination of the relative proportion of the isotope in question for the product (from a reaction with very low conversion) and the substrate (for a reaction with very high conversion) under carefully controlled conditions.

The application of the Singleton technique to the 1,6-cuprate addition to acceptor-substituted enynes required a choice of reactants that allowed the starting material to be isolated readily from a mixture that contained large amounts of the product, and vice versa. We selected the reaction of ethyl 6,6-dimethylhept-2-en-4-ynoate (**1**) with lithium di-*n*-butylcyanocuprate ($nBu_2CuLi{\cdot}LiCN$) in diethyl ether at temperatures between −65 and −67 °C (Scheme 2). A set of three reactions on the 20-mmol scale went to 85, 94, or 92 %



Scheme 2. Reaction used for the determination of experimental ^{13}C KIEs.

completion after a reaction time of 15–16 min, and the unconverted enynoate **1** (200–320 mg) was recovered by repeated vacuum distillation. Conversely, allene **2** (280–550 mg) was isolated by distillation from three reactions that went to 13, 11, or 7 % completion.

The relative amounts of ^{13}C at different positions of the starting enyne **1** and of the product **2** were determined by ^{13}C NMR spectroscopy[25] in relation to the original starting material from the same lot and to an authentic sample of the allene **2** prepared by S_N2' substitution of a propargylic mesylate.[12] The quaternary carbon atom C6 was selected as the internal standard for both the substrate **1** and the product **2** under the assumption that the isotopic ratio remains unchanged in this position during the reaction. The ^{13}C KIEs were calculated by using the standard equations from the work of Singleton and Thomas,[7] and the error analysis was carried out accordingly. The results are summarized in Table 1.

Table 1: Experimental ^{13}C KIEs for the 1,6-addition of $nBu_2CuLi{\cdot}LiCN$ to enynoate **1**.

	KIE from substrate **1**		
	Experiment 1	Experiment 2	Experiment 3
C1	1.001(1)	1.003(2)	1.002(1)
C2	1.001(2)	1.003(2)	1.003(3)
C3	1.002(1)	1.001(3)	1.003(3)
C4	1.005(1)	1.009(3)	1.006(2)
C5	1.011(1)	1.013(3)	1.011(3)
C6		1.000 (internal standard)	
	KIE from product **2**		
	Experiment 1	Experiment 2	Experiment 3
C_a	1.005(1)	1.002(2)	1.009(3)
C_b	1.002(2)	1.001(2)	1.004(1)
C_c	1.001(3)	1.000(3)	1.002(4)
C_d	1.000(3)	1.000(4)	1.000(3)
C6		1.000 (internal standard)	

The ^{13}C kinetic isotope effects for the starting enyne **1** are appreciable at C4 and even more so at C5, thus indicating that bond formation takes place from the triple bond of the substrate in the rate-limiting step of the reaction. This is in accordance with the KIEs determined for the butyl group in product **2**, as the small but distinct isotope effect for C_a suggests a bonding change at this position. To corroborate

 © 2005 Wiley-VCH Verlag GmbH & Co. KGaA, Weinheim

these experimental results, the B3LYP density-functional theory was employed with an Ahlrichs SVP basis set for the Cu atom and 6-31G(d) basis sets for others (denoted as 631A)[13,14] for geometry optimization of stationary points of the 1,6-addition of a model system, that is, the reaction of the methyl cuprate $Me_2CuLi{\cdot}LiCl$ with methyl 6,6-dimethylhept-2-en-4-ynoate (Figure 1).[15] To describe the energy profile more accurately, the Stuttgart–Dresden quasirelativistic effective core potential with a (311111/22111/411) contracted basis set[16] and an additional *f* polarization function (exponent $\alpha = 3.72$ optimized according to the procedure by Ehlers et al.[17]) with 6-311G(d) basis sets for the other atoms (denoted as 6311S) were employed. Thermal corrections for enthalpy and Gibbs energy were performed for all stationary points by normal coordinate analyses at the B3LYP/631A level. The reactants (**RT**), a complex with a closed cuprate aggregate (**CPcl**), an open complex (**CPop1**) in which Cu is coordinated to π system of the C=C double bond, another open complex (**CPop2**) in which Cu is coordinated to the π system of the C–C triple bond, the transition state for the C–C bond formation in the 1,6-addition (**TScc**), and the 1,6-adduct (**PD**) were found (Figure 1). The transition state (**TSiso1**) between **CPcl** and **CPop1** is not very high in energy, according to previous theoretical studies for addition reactions of acrolein[18] and cyclohex-2-enone.[19] The transition state **TSiso2** of the isomerization between **CPop1** and **CPop2** was also found. The energy profile is shown in Figure 2:

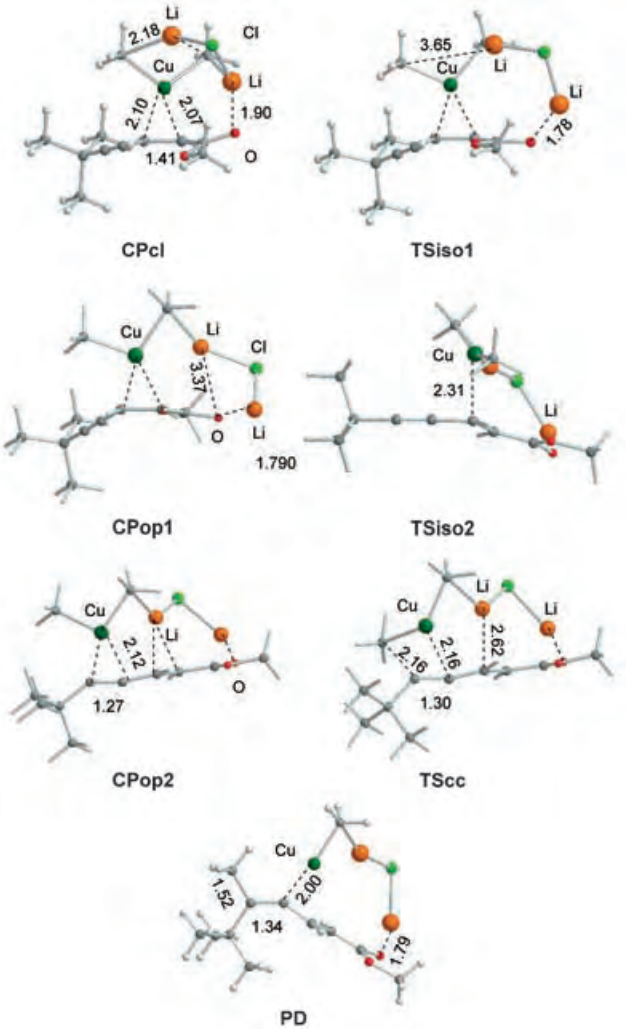


Figure 1. Intermediates, transition states, and the product in the 1,6-addition of $Me_2CuLi{\cdot}LiCl$ to (*E*)-*t*BuC≡CCH=$CHCO_2Me$ calculated at the B3LYP/631A level (bond lengths in Å).

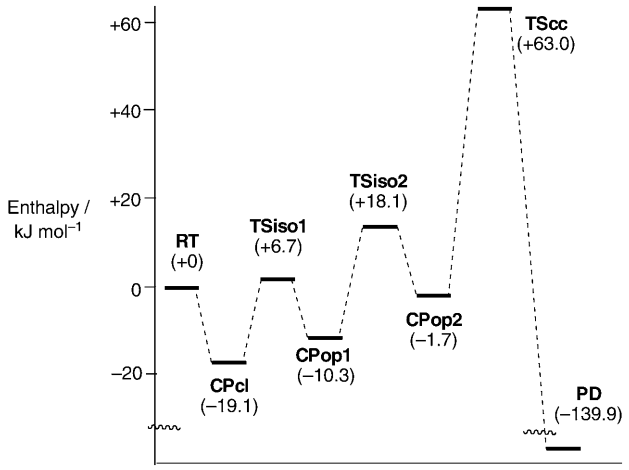


Figure 2. Enthalpy changes in the 1,6-addition of $Me_2CuLi{\cdot}LiCl$ to (*E*)-*t*BuC≡CCH=$CHCO_2Me$ at 208.15 K (B3LYP/6311S//B3LYP/631A). Values below the name of the stationary structures are enthalpies relative to the reactants (**RT**) in kJ mol^{-1}.

CPop2 is higher in enthalpy than **CPop1**, and **CPcl** is lower than **CPop1. TScc** is higher in enthalpy (208.15 K) than **TSiso2** by 44.9 kJ mol^{-1} which suggests that the rate-determining step of the 1,6-addition is the C–C bond formation (in line with the experimental ^{13}C KIEs). The theoretical activation energy ($RT + \Delta H^{\neq}$) was calculated as 66.4 kJ mol^{-1} (gas phase) and 67.5 kJ mol^{-1} (PCM method in solution in Et_2O ($\varepsilon_0 = 4.335$) with the UAKS cavities)[20] at 208.15 K and is also in good agreement with the experimental value of 70 kJ mol^{-1} determined for the reaction of Me_2Cu-Li·LiI with enynoate **1**,[6] in particular if one considers that explicit solvent effects are not included in the present calculation.[21]

The ^{13}C kinetic isotope effects (KIEs)[22] for the formation of the 1,6-addition product in a similar model system, that is, for the reaction of EtMeCuLi·LiCl with (*E*)-*t*BuC≡CCH=$CHCO_2Me$ were calculated at the B3LYP/631A level on the basis of the Bigeleisen equation with Wigner tunnel correction.[23] The theoretical KIE values of **TScce** (the most stable transition state for the rotation about the C_aH_2–C_bH_3 bond; "**e**" denotes the ethyl residue of the EtMeCuLi·LiCl moiety) based on the precursor open Cu π complex **CPop2e** with a C4≡C5 bond (Figure 3) are in good agreement with experimental values (Table 2).[24] The KIE values (1.024 for C_a at the incoming ethyl group and 1.016 for C5) are much larger than those for the other positions of the substrate and the product (0.996–1.002). On the other hand, the theoretical KIE values of **TScce** based on **CPop1e** (the open Cu π complex at the C2=C3 bond) deviate from the experimental values, in

 © 2005 Wiley-VCH Verlag GmbH & Co. KGaA, Weinheim

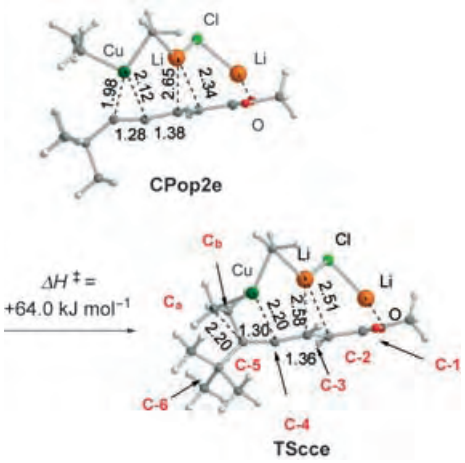


Figure 3. π Complex **CPop2e** and transition state **TScce** for the C–C bond formation in the reaction of EtMeCuLi·LiCl with (*E*)-*t*BuC≡CCH=CHCO$_2$Me (B3LYP/6311S//B3LYP/631A).

Table 2: Theoretical KIE values at −65 °C (C1 to C5) and −67 °C (C_a and C_b) at the B3LYP/631 A level for the reaction of EtMeCuLi·LiCl with (*E*)-*t*BuC≡CCH=CHCO$_2$Me (based on **CPop2e**, **CPop1e, CPcle**).

	CPop2e	CPop1e	CPcle
C1	1.002	1.000	1.002
C2	1.000	0.992	1.000
C3	0.998	0.993	0.995
C4	1.002	1.007	1.007
C5	1.016	1.021	1.022
C6		1.000 (internal standard)	
C_a	1.024	1.023	1.015
C_b	0.996	0.995	0.995

particular for C2 (Table 2). These results show that **CPcle** or **CPop2e** is the "starting material" for the rate-limiting step of the 1,6-addition.

In conclusion, our combined experimental and theoretical studies with ^{13}C kinetic isotope effects have revealed that the C–C bond formation is the rate-determining step of the 1,6-cuprate additions to 2-en-4-ynoates. The reaction proceeds via intermediates **CPop1** and **CPop2**, and the calculated activation barrier for transition state **TScc** is in good agreement with the experimental value. Thus, the mechanism of the 1,6-cuprate additions can be considered as solved, which to date can only be said for very few transition-metal catalyzed transformations.[26]

Received: December 17, 2004
Revised: April 5, 2005
Published online: July 1, 2005

Keywords: allenes · cuprates · density functional calculations · isotope effects · Michael addition

[1] *Modern Organocopper Chemistry* (Ed.: N. Krause), Wiley-VCH, Weinheim, **2002**.
[2] N. Krause, A. Gerold, *Angew. Chem.* **1997**, *109*, 194–213; *Angew. Chem. Int. Ed. Engl.* **1997**, *36*, 186–204.
[3] a) N. Krause, A. Hoffmann-Röder in *Modern Organocopper Chemistry* (Ed.: N. Krause), Wiley-VCH, Weinheim, **2002**, pp. 145–166; b) A. Hoffmann-Röder, N. Krause in *Modern Allene Chemistry* (Ed.: N. Krause, A. S. K. Hashmi), Wiley-VCH, Weinheim, **2004**, pp. 51–92.
[4] For reviews on structures and reaction mechanisms of organocuprates in organic chemistry, see: a) E. Nakamura, S. Mori, *Angew. Chem.* **2000**, *112*, 3902–3924; *Angew. Chem. Int. Ed.* **2000**, *39*, 3750–3771; b) S. Mori, E. Nakamura in *Modern Organocopper Chemistry* (Ed.: N. Krause), Wiley-VCH, Weinheim, **2002**, pp. 315–346; c) S. Woodward, *Chem. Soc. Rev.* **2000**, *29*, 393–401.
[5] a) N. Krause, *J. Org. Chem.* **1992**, *57*, 3509–3512; b) N. Krause, R. Wagner, A. Gerold, *J. Am. Chem. Soc.* **1994**, *116*, 381–382; c) J. Canisius, T. A. Mobley, S. Berger, N. Krause, *Chem. Eur. J.* **2001**, *7*, 2671–2675.
[6] J. Canisius, A. Gerold, N. Krause, *Angew. Chem.* **1999**, *111*, 1727–1730; *Angew. Chem. Int. Ed.* **1999**, *38*, 1644–1646.
[7] D. A. Singleton, A. A. Thomas, *J. Am. Chem. Soc.* **1995**, *117*, 9357–9358.
[8] L. K. Vo, D. A. Singleton, *Org. Lett.* **2004**, *6*, 2469–2472.
[9] a) D. E. Frantz, D. A. Singleton, J. P. Snyder, *J. Am. Chem. Soc.* **1997**, *119*, 3383–3384; b) D. E. Frantz, D. A. Singleton, *J. Am. Chem. Soc.* **2000**, *122*, 3288–3295.
[10] K. Nakano, Y. Bessho, M. Kitamura, *Chem. Lett.* **2003**, 224–225.
[11] N. Yoshikai, E. Nakamura, *J. Am. Chem. Soc.* **2004**, *126*, 12264–12265.
[12] M. Laux, N. Krause, U. Koop, *Synlett* **1996**, 87–88.
[13] E. Nakamura, S. Mori, M. Nakamura, K. Morokuma, *J. Am. Chem. Soc.* **1997**, *119*, 4887–4899.
[14] a) A. Schäfer, H. Horn, R. Ahlrichs, *J. Chem. Phys.* **1992**, *97*, 2571–2577; b) W. J. Hehre, L. Radom, P. v. R. Schleyer, J. A. Pople, *Ab Initio Molecular Orbital Theory*, Wiley, New York, **1986**, and references therein.
[15] Gaussian 03 (Revision B.03), M. J. Frisch, G. W. Trucks, H. B. Schlegel, G. E. Scuseria, M. A. Robb, J. R. Cheeseman, J. A. Montgomery, Jr., T. Vreven, K. N. Kudin, J. C. Burant, J. M. Millam, S. S. Iyengar, J. Tomasi, V. Barone, B. Mennucci, M. Cossi, G. Scalmani, N. Rega, G. A. Petersson, H. Nakatsuji, M. Hada, M. Ehara, K. Toyota, R. Fukuda, J. Hasegawa, M. Ishida, T. Nakajima, Y. Honda, O. Kitao, H. Nakai, M. Klene, X. Li, J. E. Knox, H. P. Hratchian, J. B. Cross, V. Bakken, C. Adamo, J. Jaramillo, R. Gomperts, R. E. Stratmann, O. Yazyev, A. J. Austin, R. Cammi, C. Pomelli, J. W. Ochterski, P. Y. Ayala, K. Morokuma, G. A. Voth, P. Salvador, J. J. Dannenberg, V. G. Zakrzewski, S. Dapprich, A. D. Daniels, M. C. Strain, O. Farkas, D. K. Malick, A. D. Rabuck, K. Raghavachari, J. B. Foresman, J. V. Ortiz, Q. Cui, A. G. Baboul, S. Clifford, J. Cioslowski, B. B. Stefanov, G. Liu, A. Liashenko, P. Piskorz, I. Komaromi, R. L. Martin, D. J. Fox, T. Keith, M. A. Al-Laham, C. Y. Peng, A. Nanayakkara, M. Challacombe, P. M. W. Gill, B. Johnson, W. Chen, M. W. Wong, C. Gonzalez, J. A. Pople, Gaussian, Inc., Wallingford, CT, **2004**.
[16] M. Dolg, U. Wedig, H. Stoll, H. Preuss, *J. Chem. Phys.* **1987**, *86*, 866–872.
[17] A. W. Ehlers, M. Böhme, S. Dapprich, A. Gobbi, A. Hollwarth, V. Jonas, K. F. Köhler, R. Stegmann, A. Veldkamp, G. Frenking, *Chem. Phys. Lett.* **1993**, *208*, 111–114.
[18] E. Nakamura, S. Mori, K. Morokuma, *J. Am. Chem. Soc.* **1997**, *119*, 4900–4910.
[19] S. Mori, E. Nakamura, *Chem. Eur. J.* **1999**, *5*, 1534–1543.
[20] a) M. Cossi, G. Scalmani, N. Rega, V. Barone, *J. Chem. Phys.* **2002**, *117*, 43–54; b) Y. Takano, K. N. Houk, *J. Chem. Theory. Comput.* **2005**, *1*, 70–77.
[21] Differences in solvation are observed, for example, in the 1,6-addition of Me_2CuLi·LiCl to (*E*)-HC≡CCH=CHCOOMe with 2 Me_2O molecules as model solvent: One Me_2O molecule is

 © 2005 Wiley-VCH Verlag GmbH & Co. KGaA, Weinheim

coordinated to the Cu center in the TS, but none in the open complex (see Supporting Information). Due to this solvent effect, the theoretical activation energy at 208.15 K is raised from 41.5 to 57.1 kJ mol^{-1}.

[22] L. Melander, W. H. Saunders, Jr., *Reaction Rates of Isotopic Molecules*, Wiley, Chichester, USA, **1980**.

[23] a) J. Bigeleisen, M. G. Mayer, *J. Chem. Phys.* **1947**, *15*, 261 – 267; b) J. Bigeleisen, M. Wolfsberg, *Adv. Chem. Phys.* **1958**, *1*, 15 – 76.

[24] The slight difference between experimental and theoretical KIE values can be attributed to the difference between the experimental and model systems and the absence of solvent effects in theoretical calculations; see: P. Czyryca, P. Paneth, *J. Org. Chem.* **1997**, *62*, 7305 – 7309; see also: M. Yamanaka, E. Nakamura, *Organometallics* **2001**, *20*, 5675 – 5681.

[25] For each sample, five spectra were recorded on a Bruker DRX 400 spectrometer with a receiver delay of 120 s (> 5 T1; the longest T1 relaxation time for the compounds examined in this study was determined to be 17.0 s). The spectra were collected with 256 scans and 200032 points, zero-filled to 524288 points (spectral resolution 0.042 Hz/point), and the integrals were taken in the ± 3.0 Hz region around the center of each peak.

[26] For a related article, see the following Communication in this issue: N. Yoshikai, T. Yamashita, E. Nakamura, *Angew. Chem.* **2005**, *117*, 4799 – 4801; *Angew. Chem. Int. Ed.* **2005**, *44*, 4721 – 4723.

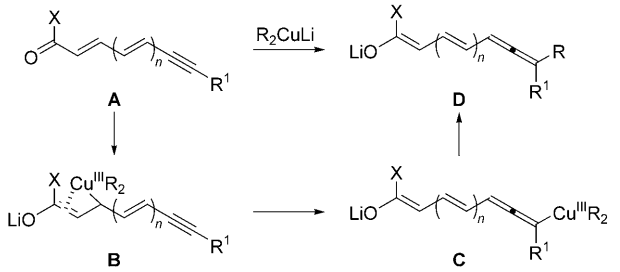
 © 2005 Wiley-VCH Verlag GmbH & Co. KGaA, Weinheim

Reaction Mechanisms

Mechanism of Remote Conjugate Addition of a Lithium Organocuprate to a Polyconjugated Carbonyl Compound**

*Naohiko Yoshikai, Tatsuya Yamashita, and Eiichi Nakamura**

Conjugate addition[1] of a nucleophile to a polyconjugated carbonyl compound is an intriguing reaction as it can potentially result in C–C bond formation at one of the remote carbon atoms. In many cases, however, the regioselectivity may be poor, unpredictable, or condition-dependent, and the origin of the regioselectivity often difficult to determine with certainty.[2,3] The particular combination of a polyenynyl carbonyl compound **A** and a lithium organocuprate is unique in all respects in that the C–C bond formation takes place always at the remote acetylenic carbon atom to give an adduct **D** (Scheme 1).[4,5] Although important



Scheme 1. Regioselective conjugate addition of a lithium organocuprate to a polyenynyl carbonyl compound.

pieces of information—NMR spectroscopic identification of the reaction intermediate and the activation energy of the reaction—have been reported,[4b,c] they do not give an answer to the fundamental question as to why the cuprate addition takes place at the acetylene terminal. We report herein a density-functional study on the reaction pathway and the origin of the regioselectivity of this reaction.[6]

[*] Dr. N. Yoshikai, T. Yamashita, Prof. Dr. E. Nakamura[+]
Department of Chemistry
The University of Tokyo
Bukyo-ku, Tokyo 113-0033 (Japan)
Fax: (+81) 3-5800-6889
E-mail: nakamura@chem.s.u-tokyo.ac.jp

[+] Additional affiliation:
Nakamura Functional Carbon Cluster Project
ERATO, Japan Science and Technology Agency
Bunkyo-ku, Tokyo 113-0033 (Japan)

[**] We thank the Ministry of Education, Culture, Sports, Science, and Technology of Japan for financial support, a Grant-in-Aid for Specially Promoted Research, and for the 21st Century COE Program for Frontiers in Fundamental Chemistry.

Supporting information for this article is available on the WWW under http://www.angewandte.org or from the author.

What is intriguing is that the low-temperature NMR spectroscopic analysis of the reaction showed the formation of only one species that can be ascribed to a copper/olefin complex structurally best represented by a σ/π-allyl structure such as **B**, but none of what might be more relevant to the formation of the remote addition product (i.e., **C**).[4b,7] This underscores the importance of the copper/lithium aggregate structure of the organocuprate reagent: Thus, initial formation of the complex **B** can be understood as the result of a sequence of coordination of the Lewis acidic lithium atom to the carbonyl group and the copper atom to the nearest C–C unsaturated bond.[7] On the basis of this background information, we examined the reaction of Me_2CuLi and hepta-2,4-dien-6-ynal (and its shorter homologues; see Supporting Information) as a model reaction, starting from a complex **1**. The pathways for the formation of 1,4-, 1,6-, and 1,8-adducts, and the energy diagram are summarized in Scheme 2 and Figure 1, respectively.[8]

The energy diagram immediately suggests that the kinetically and thermodynamically most favorable pathway is the 1,8-addition pathway that involves three organocopper(III) intermediates **1**, **3**, and **5**. Double migration of the copper atom (**1**→**3**→**5**) and reductive elimination of the final intermediate **5** via **TS5** gives the 1,8-adduct; the first copper migration is the rate-determining step. Reductive elimination of **1** and **3** (via **TS1** and **TS3**) can produce the 1,4- and 1,6-adducts **2** and **4**, respectively, but these routes are kinetically unfavorable relative to the copper migration pathways.[9] Remarkably, the reductive elimination of **5** requires a much lower activation energy than that of **1** and **3**. The reaction pathway is discussed in detail below.

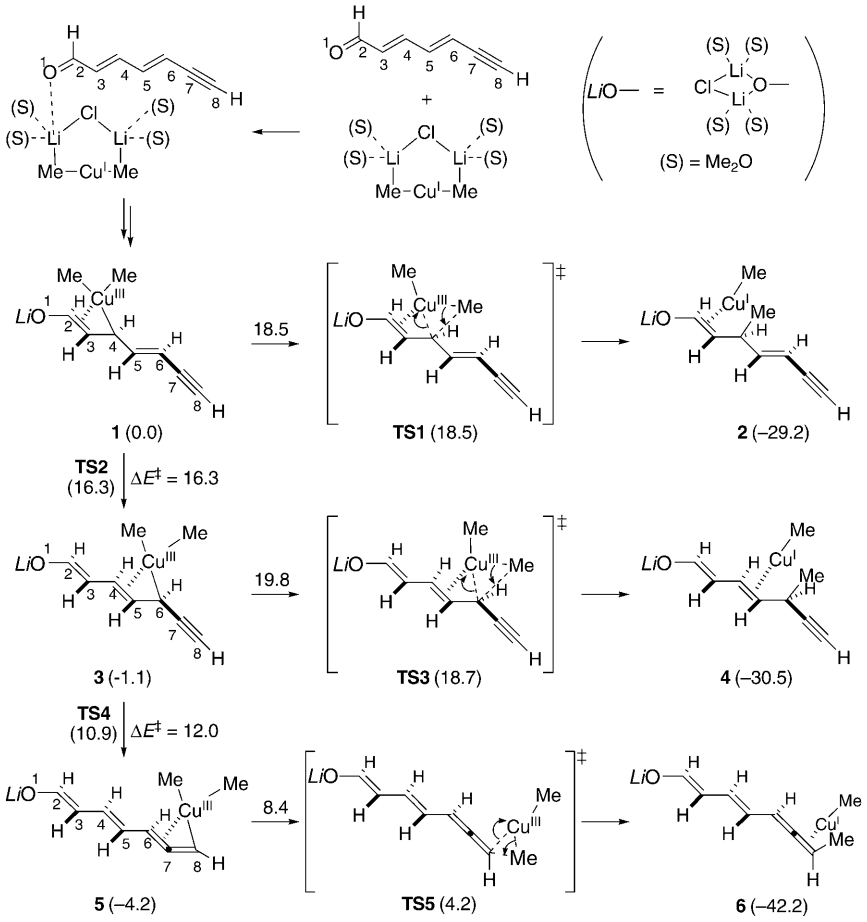
The first intermediate **1** has a structure essentially the same as that of the intermediate generally found in a 1,4-conjugate addition of Me_2CuLi to an α,β-unsaturated carbonyl compound,[7] and can undergo reductive elimination via **TS1** to give the 1,4-addition product **2**. The activation energy (18.5 kcal mol^{-1}) is higher than that of simple 1,4-addition to an acrolein or a cyclohexenone ($\approx$12–15 kcal mol^{-1}),[7] since the C–C bond formation disturbs the polyenyne conjugation system present in **1**.[10]

Alternatively, the Me_2Cu moiety in **1** can migrate to the C5–C6 double bond (via **TS2**) to form a new σ/π-allyl–copper(III) intermediate **3**. The migration ($\Delta E^{\ddagger} = 16.3$ kcal mol^{-1}) is kinetically preferred by 2.2 kcal mol^{-1} over C–C bond formation. **TS2** contains an intrinsically unstable T-shaped triorganocopper(III) geometry (see Supporting Information),[11] but is partially stabilized by the neighboring C5–C6 double bond.

The second intermediate **3** is a σ/π-allyl–copper(III) complex that can either form a C–C bond via **TS3** or undergo further Cu migration to the C7–C8 triple bond via **TS4** to give another copper(III) intermediate **5**. The former process again disturbs the conjugation system, and the latter pathway is overwhelmingly favored by 7.8 kcal mol^{-1}.

The low activation energy of the Cu migration is due to coordination of the terminal acetylene moiety in **TS4** (Figure 2). Intermediate **5** has a distorted square-planar geometry in which the copper atom is much more strongly bonded to the terminal C8 atom (Cu–C8: 2.02 Å) than to the

 DOI: 10.1002/anie.200501107 © 2005 Wiley-VCH Verlag GmbH & Co. KGaA, Weinheim



Scheme 2. Reaction pathways and potential energy changes for 1,4-, 1,6-, and 1,8-addition of Me_2CuLi to hepta-2,4-dien-6-ynal. Potential energies (kcal mol^{-1}, calculated at the B3LYP/631SDD//B3LYP/321SDD level) relative to **1** are shown in parentheses. Energy changes are shown together with arrows.

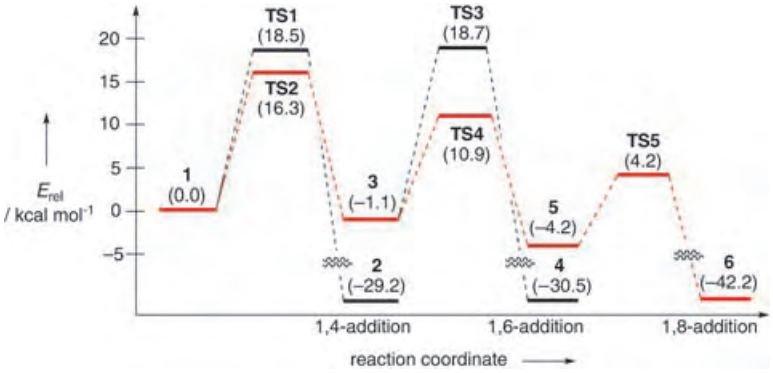


Figure 1. Potential energy profiles for 1,4-, 1,6-, and 1,8-addition pathways (B3LYP/631SDD//B3LYP/321SDD). The energetically most favored 1,8-pathway is shown in red.

C6 atom (Cu–C6: 2.47 Å). This structural feature indicates that the copper atom is σ-bonded to C8 and π-coordinated by the C6–C7 bond, and hence in this case **5** may be called a σ/π-allenyl–copper(III) complex.[10,12] The dissymmetric bonding would be the result of the intrinsic stability of a C(sp^2)–metal bond (relative to a C(sp^3)–metal bond) and the electron-rich dienolate substituent at C6.[10]

The complex **5** undergoes reductive elimination at C8 (via **TS5**) with very low activation energy (8.4 kcal mol^{-1}) owing to the intrinsic linear geometry of the allene: The C6-C7-C8 bond strain (153.9°) is released, and the C6–C7 double bond of **5** is easily detached from the copper(III) center to give a kinetically unstable triorganocopper(III) species,[11] which undergoes rapid reductive elimination (see inset of Figure 2). Furthermore, participation of the allenyl C7–C8 π orbital orthogonal to the Cu–C8 σ bond in C–C bond formation may also contribute to the low activation barrier.[13]

We also studied in some detail the 1,6-addition reaction to the less conjugated analogues pent-2-en-4-ynal and penta-2,4-dienal (see Supporting Information). The former reaction proceeds in essentially the same manner as the 1,8-reaction described above: The 1,6-adduct is formed through a rate-determining Cu migration ($\Delta E^{\ddagger} = 12.2$ kcal mol^{-1}) and quick reductive elimination of the σ/π-allenyl copper(III) intermediate ($\Delta E^{\ddagger} = 8.4$ kcal mol^{-1}). In the latter case, Cu migration takes place with an activation energy of 15.8 kcal mol^{-1} to give a σ/π-allyl–copper(III) intermediate, the reductive elimination of which requires a much higher activation energy (13.3 kcal mol^{-1}) than that of σ/π-allenyl–copper(III) intermediates. Furthermore, theoretical ^{13}C NMR spectroscopic data calculated for the initially formed olefin complex, employing ethyl 6,6-dimethyl-hept-2-en-4-ynoate as a substrate, showed reasonable agreement with experimental findings (see Supporting Information).[4b]

In summary, we proposed a general mechanistic framework for remote conjugate addition of an organocuprate to a polyconjugated Michael acceptor. Interaction between the two reactants initially generates a β-cuprioenolate intermediate, which undergoes sequential copper migration via σ/π-allyl–copper(III) intermediates. The final migration to the acetylene terminal gives a key σ/π-allenyl–copper(III) intermediate, the kinetic instability of which results in rapid C–C bond formation at the terminal carbon atom. C–C bond formation at the internal carbon atoms is disfavored as it disturbs the conjugation system. This mechanism for polyenyne substrates also explains why conjugate addition to polyenyl carbonyl compounds tends to be unpredictable: The copper intermediates formed from a polyene substrate lack such a decisive structural feature as that in **5** and may undergo C–C bond formation at any possible carbon atom, depending on structure and reaction conditions.[2] The present mechanistic framework should apply to remote substitution reactions,[14] and we consider also that rapid 1,3 copper migration similar to that reported herein is responsible for the remarkably high regioselectivity of the multi-

 © 2005 Wiley-VCH Verlag GmbH & Co. KGaA, Weinheim

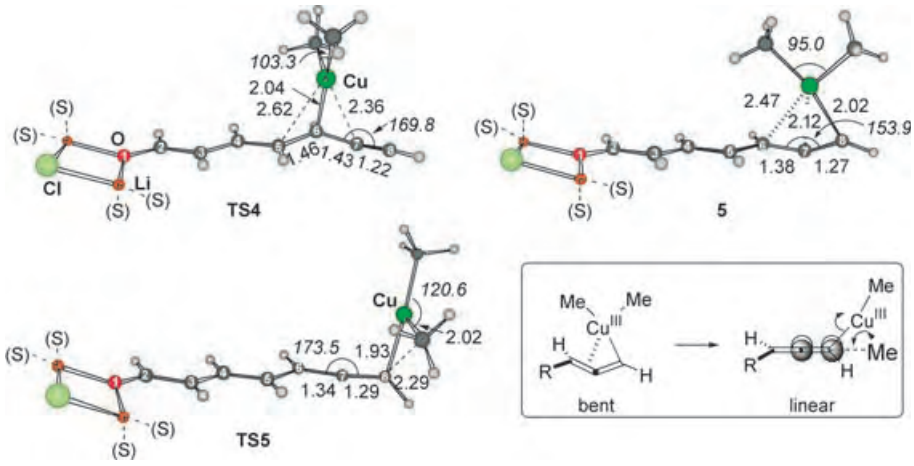


Figure 2. Structures of the copper migration transition state **TS4**, the π-propargyl/allenyl–copper(III) intermediate **5**, and the 1,8-reductive elimination transition state **TS5** (B3LYP/321SDD), and a schematic representation for reductive elimination of a σ/π-allenyl–copper(III). (S) represents a Me_2O molecule coordinated to a Li atom. The values refer to bond lengths (Å) and bond angles (°, italics).

addition of organocopper reagents to [60]- and [70]fullerenes.[15] The relevance of the present mechanism to the dynamic behavior of transition-metal complexes of polyconjugated molecules[16] is worthy of further consideration.[17]

Received: March 29, 2005
Published online: June 29, 2005

Keywords: conjugate addition · density functional calculations · organocuprates · reaction mechanisms · regioselectivity

[1] *Comprehensive Organic Synthesis, Vol. 3* (Eds.: B. M. Trost, I. Fleming), Pergamon, New York, **1991**, pp. 1–268; P. Perlmutter, *Conjugate Addition Reactions in Organic Synthesis*, Pergamon, New York, **1992**.

[2] a) J. A. Marshall, R. A. Ruden, L. K. Hirsch, M. Phillippe, *Tetrahedron Lett.* **1971**, 3795; b) E. J. Corey, N. W. Boaz, *Tetrahedron Lett.* **1985**, *26*, 6019; c) H. Wild, L. Born, *Angew. Chem.* **1991**, *103*, 1729; *Angew. Chem. Int. Ed. Engl.* **1991**, *30*, 1685.

[3] Examples other than organocuprate addition: a) M. P. Cooke, R. J. Goswami, *J. Am. Chem. Soc.* **1977**, *99*, 642–644; b) P. Magunus, T. Gallagher, J. Schultz, Y-S. Or, T. P. Ananthanarayan, *J. Am. Chem. Soc.* **1987**, *109*, 2706–2711.

[4] a) N. Krause, A. Hoffmann-Röder in *Modern Organocopper Chemistry* (Ed.: N. Krause), Willey-VCH, Weinheim, **2001**, pp. 145–166; b) J. Canisius, T. A. Mobley, S. Berger, N. Krause, *Chem. Eur. J.* **2001**, *7*, 2671–2675; c) J. Canisius, A. Gerold, N. Krause, *Angew. Chem.* **1999**, *111*, 1727–1730; *Angew. Chem. Int. Ed.* **1999**, *38*, 1644–1646, and references therein.

[5] L. Ernst, H. Hopf, N. Krause, *J. Org. Chem.* **1987**, *52*, 398–405.

[6] All calculations were performed at the B3LYP/631SDD//B3LYP/321SDD level using a Gaussian 03 package: Gaussian 03 (Revision C.02), M. J. Frisch et al., see Supporting Information. For computational methods, see: M. Yamanaka, S. Inagaki, E. Nakamura, *J. Comput. Chem.* **2003**, *24*, 1401–1409.

[7] a) M. Yamanaka, E. Nakamura, *Organometallics* **2001**, *20*, 5675–5681; b) E. Nakamura, S. Mori, *Angew. Chem.* **2000**, *112*, 3902–3924; *Angew. Chem. Int. Ed.* **2000**, *39*, 3750–3771; c) S. Mori, E. Nakamura in *Modern Organocopper Chemistry* (Ed.: N. Krause), Wiley-VCH, Weinheim, **2001**, pp. 315–346, and references therein.

[8] Potential energies at the B3LYP/631SDD//B3LYP/321SDD level are reported throughout the paper. Potential energies and Gibbs free energies (at 298 K) at the B3LYP/321SDD are essentially the same (see Supporting Information).

[9] The 1,4- and 1,6-addition products can also form through reductive elimination of **3** at C4 and of **5** at C6, respectively. However, these processes require much high activation energies (>20 kcal mol^{-1}) and were therefore omitted from the main text. See Supporting Information for the complete reaction pathways.

[10] M. Yamanaka, S. Kato, E. Nakamura, *J. Am. Chem. Soc.* **2004**, *126*, 6287–6293.

[11] A. E. Dorigo, J. Wanner, P. v. R. Schleyer, *Angew. Chem.* **1995**, *107*, 492; *Angew. Chem. Int. Ed. Engl.* **1995**, *34*, 476–478; J. P. Snyder, *J. Am. Chem. Soc.* **1995**, *117*, 11025–11026; E. Nakamura, M. Yamanaka, S. Mori, *J. Am. Chem. Soc.* **2000**, *122*, 1826–1827.

[12] For examples of related η^3-metal complexes, see: a) K. Tsutsumi, S. Ogoshi, S. Nishiguchi, H. Kurosawa, *J. Am. Chem. Soc.* **1998**, *120*, 1938–1939; b) S. Ogoshi, Y. Fukunishi, K. Tsutsumi, H. Kurosawa, *J. Chem. Soc. Chem. Commun.* **1995**, 2485–2486.

[13] E. Nakamura, M. Yamanaka, *J. Am. Chem. Soc.* **1999**, *121*, 8941–8942; M. Yamanaka, E. Nakamura, *J. Am. Chem. Soc.*, **2005**, *127*, 4697–4706.

[14] M. Purpura, N. Krause, *Eur. J. Org. Chem.* **1999**, 267–275.

[15] a) M. Sawamura, H. Iikura, E. Nakamura, *J. Am. Chem. Soc.* **1996**, *118*, 12850–12851; b) M. Sawamura, H. Iikura, A. Hirai, E. Nakamura, *J. Am. Chem. Soc.* **1998**, *120*, 8285–8286.

[16] For example, see: B. E. Mann, *Chem. Soc. Rev.* **1986**, *15*, 167–187.

[17] For a related article, see the previous Communication in this issue: S. Mori, M. Uerdingen, N. Krause, K. Morokuma, *Angew. Chem.* **2005**, *117*, 4795–4798; *Angew. Chem. Int. Ed.* **2005**, *44*, 4715–4719.

 © 2005 Wiley-VCH Verlag GmbH & Co. KGaA, Weinheim

Solid-Phase Synthesis

Reversible Substrate Anchoring: NC-SPOS as a Sustainable Approach to Solid-Supported Organic Synthesis**

*Achim Porzelle and Wolf-Dieter Fessner**

Dedicated to Professor George M. Whitesides

The goal of solid-phase organic synthesis (SPOS) is to accelerate and standardize synthetic operations to be compatible with parallel and automated approaches. In conventional SPOS, substrates are covalently attached to an insoluble matrix and time-consuming workup procedures are simplified to physical separation steps. Products are released after multiple reaction cycles by the chemoselective cleavage of a linker moiety.[1] A major problem with this technology is the difficulty in analytical characterization of synthetic intermediates and impossibility of purification from covalently bound side-products. Moderate loading capacities, limited mechanical stability, and unsatisfactory reagent penetration are further disadvantages of the polymeric supports common to this approach. Matrix material is usually discarded after use because regeneration of the matrix–linker construct is inconvenient and uneconomical. In the search for superior options, alternative concepts[2] have recently been investigated that attempt to amalgamate the advantages of a high-molecular-weight carrier with solution-phase chemistry, such as in soluble-polymer-supported[3] and dendrimer-supported organic synthesis.[4] In other studies distinct techniques for product isolation have been introduced, for example, special product-precipitation methods[5] and liquid/liquid phase separation, including the use of ionic liquids and fluorous phases.[2,6] Inverse approaches consist of the application of immobilized reagents, catalysts, and scavengers.[7] In contrast to reactions with solid-phase resins, reactions with soluble supports can be performed (and analyzed) under homogeneous conditions. Method validation is thus facilitated, but often the practical simplicity and efficiency gained by the use of insoluble supports are lost.[2]

Our interest in the efficacious generation of molecular diversity within biocatalytic synthesis[8] has led us to develop a novel approach to SPOS by using the *noncovalent attachment of substrates* to a solid matrix through hydrophobic interactions (noncovalent SPOS, NC-SPOS).[9] When tagged with a hydrophobic anchor unit, substrates in a highly polar, hydrophilic solvent, such as water, become immobilized on a hydrophobic matrix (Figure 1). Thus, standard SPOS operations, including washing and filtration steps, may be performed on immobilized substrates. As the anchoring affinity depends on the partition coefficient ($\lg P$) of the anchor unit between the matrix and the solution phase,[10] anchored products are released into the solution phase when switched to a nonpolar organic solvent. A typical NC-SPOS reaction procedure would thus consist of three steps: 1) adsorption of the anchor–substrate unit onto the matrix, 2) single or multiple reactions under aqueous conditions, each followed by washing, and 3) final desorption and/or cleavage of the anchor–product unit.

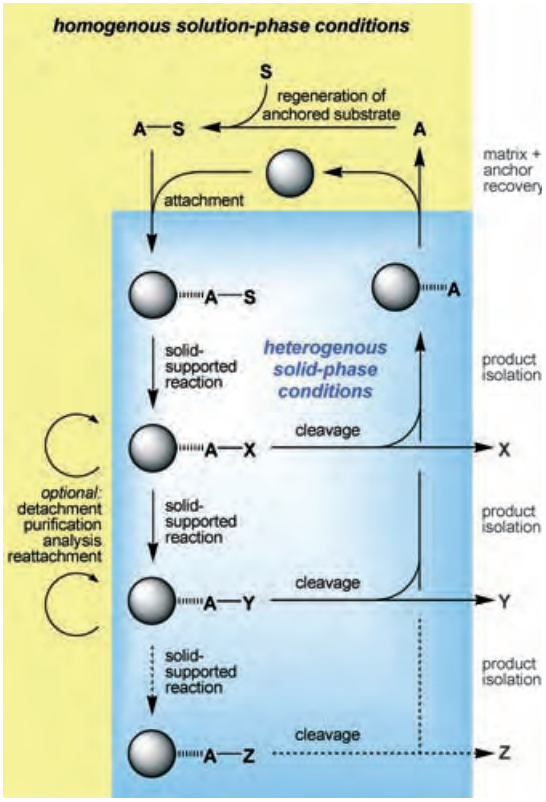


Figure 1. Basic concept of NC-SPOS. A = hydrophobic anchor unit; S = substrate; X, Y, and Z = products. Bead symbols indicate a hydrophobic solid-phase support. Dashed bonds represent noncovalent attachment. The yellow area denotes the nonpolar organic phase, while the blue box indicates the polar hydrophilic phase.

As the attachment is reversible, phase switching may be performed, in principle, at any stage of a given reaction sequence; in this way the NC-SPOS technique displays the same advantages as common solution-phase chemistry. Thus, the reaction can be monitored conveniently by conventional TLC, and reaction intermediates are amenable to spectroscopic analysis (or even optional chromatographic purification) by application of an organic solvent under homogenous conditions. As phase switching is freely reversible, compounds released into solution for analysis may be readsorbed onto the solid matrix by subsequent change to the polar

[*] Dr. A. Porzelle, Prof. Dr. W.-D. Fessner
Institut für Organische Chemie und Biochemie
Technischen Universität Darmstadt
Petersenstrasse 22, 64287 Darmstadt (Germany)
Fax: (+49) 6151-166-636
E-mail: fessner@tu-darmstadt.de

[**] NC-SPOS = Noncovalent solid-phase organic synthesis. This work was supported by the Fonds der Chemischen Industrie. Professor Whitesides received the 2005 Emanuel Merck Award.

Supporting information for this article is available on the WWW under http://www.angewandte.org or from the author.

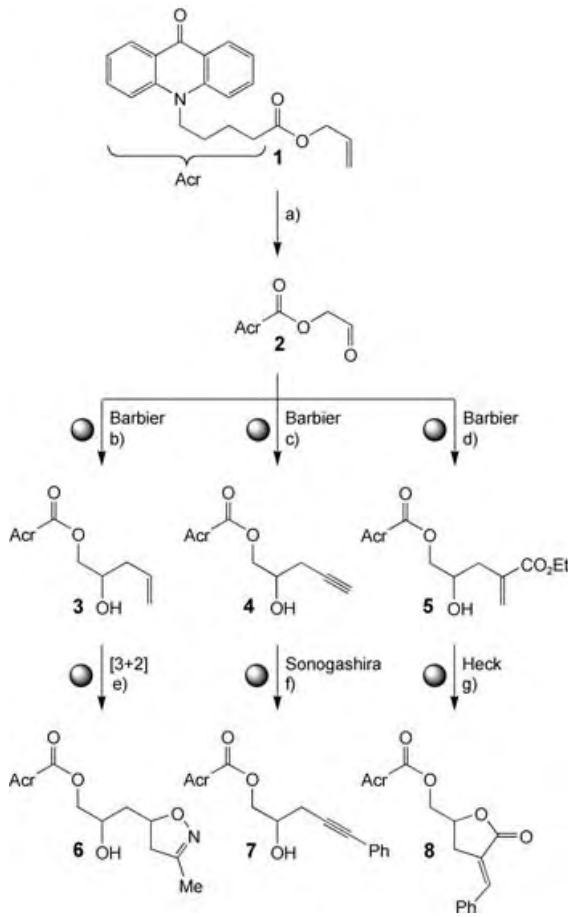
 © 2005 Wiley-VCH Verlag GmbH & Co. KGaA, Weinheim DOI: 10.1002/anie.200462278

solvent. Likewise, it is immediately obvious that in a multistep synthetic sequence, for example, individual steps may also be performed under nonaqueous conditions if the type of reaction or the choice of reagent is incompatible with SPOS operations or requires a moisture-free organic solvent; thereafter, the NC-SPOS process can be continued after reattachment of the intermediates to the matrix under aqueous conditions.

The final product is released from the hydrophobic anchor unit by conventional linker cleavage and isolated from the solid matrix by washing (Figure 1). Both the collected solid phase and the hydrophobic anchor unit can be recycled. Loading capacity is broadly adjustable and limited only by the accessible hydrophobic surface area of the solid matrix. A broad variety of suitable solid-phase supports with designed properties is commercially available, because the NC-SPOS concept relies on the same phenomenon as conventional solid-phase extraction (SPE) and reversed-phase (RP) chromatography.[11] Although it is very simplistic in design, this approach of reversible substrate binding as a fully integrated strategy of SPOS has, to the best of our knowledge, not been pursued previously.[12] However, polycyclic-arene-based protecting groups with high adsorptive affinity to charcoal or graphite have been reported to facilitate the recovery of tagged products from organic solvent media[13] or for chromatographic purification.[14]

For a first realization of the NC-SPOS concept, we chose standard C_{18}-modified RP silica gel as the hydrophobic matrix and *N*-alkylated acridone derivatives as the hydrophobic anchor moieties (usually 0.5 g of RP matrix per mmol of substrate). The choice of an acridone tag, aside from its low polarity and high (photo)chemical stability, was based on its extremely efficient, bright blue fluorescence, which facilitates the effective establishment of ultrasensitive reaction screening by TLC or HPLC analysis.[15] Indeed, initial experiments with an anchored allyl ether moiety demonstrated that basic alkene functionalization (epoxidation by peracids, dihydroxylation by $KMnO_4$ or by acid epoxide hydrolysis, cleavage by O_3) and carbonyl reactions (aldehyde reduction/oxidation by $NaBH_4/H_2O_2$, hydrazone condensation) could be achieved selectively by typical SPOS procedures.[9]

To test the suitability of the NC-SPOS concept as a rapid reactivity-screening system (Scheme 1), the allyl ester **1** was initially chosen as a generic example of an anchor–substrate unit from which products could be released by simple adjustment of the pH value without further addition of contaminating reagents. The ester functionality has been applied successfully in many SPOS operations because it is easy to generate and can be cleaved selectively under mild conditions that are tolerated by a very broad variety of further functional groups. At an experimental lg *P* value of ≈ 2.5, no remaining **1** could be detected in the solution phase of a RP-matrix/water mixture by UV measurement at $\lambda = 399$ nm, and less than 2% of **1** became desorbed in the presence of 10% methanol as an organic cosolvent. However, when small aliquots of the NC-SPOS slurry were transferred to a TLC plate that was then dried and developed with an organic solvent, a sharp homogenous spot of **1**, indistinguishable from an unbound reference sample, was observed.



Scheme 1. Screening for NC-SPOS reactions. Reagents and conditions: a) O_3, MeOH, −78 °C, then DMS, RT, 24 h, quantitative; b) $SnCl_2$/KI, allyl bromide (6 equiv), H_2O, RT, 90%; c) $SnCl_2$/KI, ethyl 2-bromomethylacrylate (6 equiv), H_2O, RT, 85%; d) $SnCl_2$/KI, propargyl bromide (6 equiv), H_2O, RT, 70%; e) $CH_3CH{=}NOH$ (3 equiv), NaOCl, 0 °C→RT, 8 h, 79%; f) 5 mol% $Pd(OAc)_2$/TPPTS, PhI (1.1 equiv), NEt_3 (2.5 equiv), RT, 20 h, 90%; g) 5 mol% $Pd(OAc)_2$/TPPTS, PhI (1.1 equiv), NEt_3 (2.5 equiv), RT, 20 h, 40%. Bead symbols indicate reactions performed by hydrophobic attachment of the substrates to a reversed-phase silica support. DMS = dimethyl sulfide; TPPTS = tris-(*m*-sulfonatophenyl)phosphane, trisodium salt.

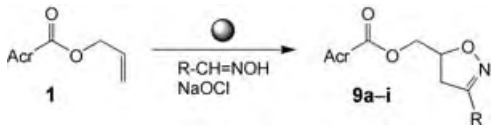
Subsequent to early findings of Breslow, Grieco, and their respective co-workers[16] that water can increase the rate and selectivity of Diels–Alder reactions, a large variety of reactions have been adapted to aqueous conditions.[17] As an entry to the multistep construction of larger entities, we tested metal-mediated Barbier-type allyl additions[18] as one of the best developed reactions in aqueous media by using aldehyde **2** under NC-SPOS conditions. As to be expected, in situ formation of the organometallic allyl reagents from elemental Zn or Sn was largely unsuccessful since the metal surface must be activated by acid treatment or sonication, which also led to partial cleavage of the linker cleavage and unsatisfactory yields. In contrast, in the case of In-mediated reactions good yields were obtained, but inorganic precipitates hampered filtration and matrix purification for reuse. However, the homogenous reagents generated from $SnCl_2$/KI[19] with allyl

 © 2005 Wiley-VCH Verlag GmbH & Co. KGaA, Weinheim

bromide, ethyl 2-bromomethylacrylate,[20] and even propargyl bromide consistently gave high yields of isolated adducts **3**–**5**.

Further reactivity screening included 1,3-dipolar cycloaddition of nitrile oxides[21] and Pd-catalyzed C–C cross-coupling reactions[22] to carrier-adsorbed alkenes as consecutive synthesis steps. Generation of the nitrile oxide reagent could be performed advantageously in situ from the corresponding oxime by using 11% aqueous NaOCl at 0°C to furnish Δ^2-isoxazoline **6** in good yield. Also, Pd-catalyzed C–C cross-coupling reactions such as Heck and Sonogashira reactions, which have emerged as valuable tools in organic synthesis to build new C–C bonds, were performed successfully in water by using water-soluble phosphine ligands. In the latter case, air sensitivity of the catalytic Pd complex proved challenging because of the difficulty of degassing the RP-silica solid phase in a practical manner. The Heck reaction, performed without added organic cosolvent, was compromised by competing partial cleavage of the ester linker under the slightly alkaline conditions, because an equivalent of base is needed to scavenge the acid by-product. The reported yield for isolated product thus accounts only for the anchor-conjugated adduct (40%, nonoptimized; *E*/*Z* ratio 16:1) that remained adsorbed to the solid phase, an adduct that, interestingly, proved to be lactone **8** formed by an intramolecular transesterification (>95% purity). In addition, a considerable quantity of further unlabeled Heck product was detected in the aqueous phase. Therefore, the unsatisfactory yield is due to the insufficient stability of the anchoring ester under the reaction conditions, but it should be pointed out that this is not a limitation inherent to the NC-SPOS approach. The ester conjugate was chosen as a simple, uniform linker moiety in this demonstration of reaction screening, but it could be readily replaced by more appropriate functionalities for more focused studies on Heck-type conversions.[1]

In a first attempt to address the potential of the NC-SPOS technique for diversity generation in parallel syntheses, we focused on isoxazoline formation by [3+2] cycloaddition because these reactions are highly atom economical and usually give high yields, and, for comparison, they are well documented under various reaction conditions.[21] Also, isoxazolines are medicinally important pharmacophores and provide versatile building blocks for the synthesis of complex natural products.[23] A series of oximes (Scheme 2, Table 1) was subjected to NaOCl oxidation as before in the presence of RP-silica-bound allyl ester **1**, and product formation was conveniently determined by TLC monitoring. After the usual aqueous washing, all the resulting isoxazolines **9a**–**h** were obtained as single regioisomers by methanol desorption from the solid phase. The crude products from aromatic oximes



Scheme 2. Examples of 1,3-dipolar additions of nitrile oxides to alkene **1** by NC-SPOS. Reagents and conditions: R–CH=NOH (1.5 equiv), NaOCl, 0°C→RT, 16 h.

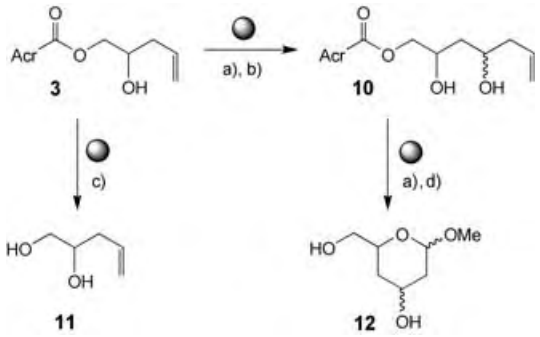
Table 1: Solid-supported 1,3-dipolar cycloaddition of different dipoles to alkene **1**.

R^1	Product	Yield [%][a]
Ph	**9a**	84
p-F-C_6H_4	**9b**	70
p-NO_2-C_6H_4	**9c**	45
p-Me_2N-C_6H_4	**9d**	65
o,*p*-$(MeO)_2$-C_6H_3	**9e**	70
o-Py[b]	**9f**	40
Me	**9g**	46[c]
Et-$(CHCH_3)_2$	**9h**	67[c]
Ph-$(CH_2)_2$	**9i**	80[c]

[a] Yield of chromatographically purified products after isolation. [b] Py = pyridyl. [c] Reaction performed with 3 equivalents of oxime.

were pure by NMR spectroscopic analysis, with only minor impurities from excess reagent and some anchor carboxylic acid arising from undesired cleavage of the anchoring ester linkage. Owing to the lower stability of alkyl oximes (**6** and **9g**–**i**) more reagent was required (up to 3 equiv), and extended exposition to strongly alkaline medium (pH ≈ 11) resulted in diminished yields. For full characterization, products were purified by conventional column chromatography. Yields were within the usual range observed for conventional solution-phase and solid-phase synthesis protocols.[21]

The effectiveness of the protocols for cleavage and matrix/anchor regeneration is illustrated in an exemplary manner by the NC-SPOS synthesis of a small stereocombinatorial[24] library of dideoxyglycosides (Scheme 3). By diverging from



Scheme 3. Examples of cleavage reactions for NC-SPOS products. Reagents and conditions: a) O_3, MeOH, −78°C, then DMS, RT, quantitative; b) $SnCl_2$/KI, allyl bromide (6 equiv), H_2O, RT, 90%; c) aqueous HCl/EtOH, reflux, 2 h, 85%; d) HCl/MeOH, reflux, 30 min, 89%.

the racemic alkene intermediate **3**, ozonolytic generation of the corresponding aldehyde electrophile followed by a second Barbier-type allyl addition gave a mixture of diastereomeric *syn*/*anti* adducts **10** in a 1:1 ratio. Ozonolysis and reductive workup furnished an anchored mixture of 2,4-dideoxysugars, consisting of four distinct α,β anomers (all pairs of enantiomers, eight different stereoisomers altogether) as evident by NMR analysis of a desorbed aliquot (later readsorbed by slurrying with fresh RP silica in water). For cleavage, the solid-phase material was treated with HCl in methanol at room temperature. Solvent exchange to water followed by

 © 2005 Wiley-VCH Verlag GmbH & Co. KGaA, Weinheim

filtration provided a fraction of solid matrix containing the free anchor moiety and an aqueous solution of free methyl dideoxyglycosides **12.** The latter were isolated in 89% yield by evaporation of the water and characterized by NMR spectroscopic analysis; the expected diastereomers were obtained in a 3:3:1:1 ratio. Finally, the solids were leached with methanol to furnish the regenerated RP matrix (98% total recovery) and the detached hydrophobic anchor unit as the methyl ester ready for reuse (86% total recovery; >95% purity). Similarly, diol **11** was isolated by acidic cleavage (HCl/EtOH) in 96% total yield together with the ethyl ester of the anchor unit. Cleavage from the anchor could also be performed under aqueous alkaline conditions; this, however, required an additional ion-exchange treatment for neutralization.

In conclusion, we have proposed NC-SPOS as a novel concept for facilitated organic processes and have demonstrated that many modern synthetic reactions can be carried out under such conditions. For all the reactions screened, aided by highly sensitive fluorescent labeling, we have been able to replace an organic-substrate-solubilizing phase with a hydrophobic surface-modified solid matrix and use reagents in water as an environmentally friendly solvent. A general NC-SPOS reaction procedure often takes less time than the equivalent common SPOS process, because there are none of the diffusion limitations that are typical for polymer supports and tedious washing cycles are thus unnecessary. We have generally been able to avoid the use of a vast excess of reagent, which is otherwise typical for SPOS conditions, and thereby minimize potential product contamination from hydrophobic reagents. Clearly, limitations can arise for aqueous NC-SPOS reactions with building blocks or reagents that are poorly soluble in water because these components may stick to the support and lower the reaction rates. However, for those individual reactions investigated, but not optimized, yields so far are comparable to conventional solution-phase conversions and may be improved with further experimentation.

The main problems of conventional SPOS, that is, analysis and purification of intermediates, particularly during multistep syntheses, are overcome by our new freely reversible attachment strategy. The recovery of the RP-silica solid phase and anchor units is facile and efficient, so the technique is highly environmentally benign, in keeping with the philosophy of green chemistry.[25] The NC-SPOS strategy offers practical simplicity that is readily applicable to both automation and scaleup. The study of more sophisticated aspects, such as multiparallel and combinatorial synthesis, asymmetric catalysis, use of anchored scavengers and/or other anchor–linker combinations, further reaction types, and application to multistep syntheses, is currently underway.

Experimental Section

Example synthesis of **3**: A solution of **1** (335 mg, 1 mmol) in MeOH (10 mL) at −78 °C was treated with ozone until a blue color persisted. After the mixture had been purged with O_2 for a further 5 min, dimethyl sulfide (0.5 mL) was added, and the mixture was then allowed to warm to room temperature for 2 h. RP silica 100 (C_{18}, endcapped, 230–400 mesh; 500 mg) was added, and the solvent was removed in vacuo. Further portions of MeOH (3 × 10 mL) were added and evaporated to remove all volatile compounds. In a separate flask, an aqueous solution (10 mL) containing KI (510 mg, 3.0 mmol) and $SnCl_2$ (342 mg, 1.8 mmol) was stirred with allyl bromide (0.14 mL, 6.4 mmol) to give an orange-red reagent solution. This mixture was added to the adsorbed RP silica, and the resulting slurry was stirred at room temperature overnight, during which time the color faded away. After filtration through a thin RP-silica layer (prewashed with MeOH), the solid residue was washed with water (50 mL) and dried. For product release, the solid was washed with methanol, and the filtrates were evaporated to give **3** as a yellow oil (350 mg, 90%); $R_f = 0.4$ (40% EtOAc/cyclohexane); ^{1}H NMR (300 MHz, $CDCl_3$): $\delta = 8.52$ (dd, 2H, $J = 8.0$, 1.7 Hz, H_{ar}), 7.68 (ddd, 2H, $J = 8.0$, 7.0, 1.7 Hz, H_{ar}), 7.41 (br d, 2H, $J = 8.7$ Hz, H_{ar}), 7.22 (ddd, 2H, $J = 8.0$, 7.0, 0.7 Hz, H_{ar}), 5.72 (m, 1H, H-4′), 5.08 (m, 2H, H-5′), 4.30 (t, 2H, $J = 7.5$ Hz, H-5), 4.11 (dd, 1H, $J = 11.4$, 3.2 Hz, H-1′a), 3.97 (dd, 1H, $J = 11.4$, 7.0 Hz, H-1′b), 3.85 (m, 1H, H-2′), 2.44 (t, 2H, $J = 6.9$ Hz, H-2), 2.23 (m, 2H, H-3′), 1.95–1.80 ppm (m, 4H, H-3, H-4); ^{13}C NMR (75 MHz, $CDCl_3$): $\delta = 177.94$ (C=O), 173.09 (C-1), 141.76 (C_{ar}), 134.01 (C_{ar}), 133.41 (C-4′), 128.11 (C_{ar}), 122.54 (C_{ar}), 121.35 (C_{ar}), 118.65 (C-5′), 114.46 (C_{ar}), 69.41 (C-2′), 68.42 (C-1′), 45.77 (C-5), 38.18 (C-3′), 33.93 (C-2), 26.68 (C-4), 22.20 ppm (C-3); MS (70 eV): *m*/*z* (%): 379 (49) [M^+], 208 (100).

Cleavage of **3**: A sample of **3** (100 mg, 0.26 mmol) adsorbed to RP silica (500 mg) was heated at reflux in a mixture of EtOH (30 mL) and concentrated HCl (1 mL) for 2 h. After complete conversion (according to TLC), the solvent was removed by evaporation, and then water (15 mL) and further RP silica (1 g) were added. The resulting slurry was filtered, the solids washed with water (15 mL), and the combined filtrates were evaporated to yield **11** (26 mg, 96%) as a colorless liquid; ^{1}H NMR (300 MHz, $CDCl_3$): $\delta = 5.82$ (m, 1H, H-4), 5.14 (m, 2H, H-5), 3.80 (m, 1H, H-2), 3.67 (dd, 1H, $J = 11.2$, 3.1 Hz, H-1a), 3.48 (dd, 1H, $J = 11.2$, 7.2 Hz, H-1b), 2.25 ppm (m, 2H, H-3); ^{13}C NMR (75 MHz, $CDCl_3$): $\delta = 132.77$ (C-4), 119.84 (C-5), 71.75 (C-2), 66.54 (C-1), 37.81 ppm (C-3); MS (70 eV): 124.1 [M+Na]$^+$. The filtered solids were washed with acetone, and the filtrates were evaporated to give the ethyl ester of the anchor unit as a yellow solid (80 mg, 94%).

Synthesis of **12**: A sample of **1** (335 mg, 1 mmol) was processed as above to give adduct **3**, still anchored to the RP silica. The dried solid was taken up in MeOH (10 mL), and the mixture was treated with ozone. This was then followed by reductive workup and solvent removal as above. The resulting RP silica containing the anchored aldehyde was treated again with the aqueous allylation reagent to give the corresponding 1,3-diol adduct **10** (1:1 diastereomeric ratio verified by NMR spectroscopic analysis on a small aliquot); ^{1}H NMR ($CDCl_3$, 300 MHz): $\delta = 8.50$ (dd, 2H, $J = 8.0$, 1.7 Hz, H_{ar}), 7.65 (ddd, 2H, $J =$ 8.0, 7.0, 1.7 Hz, H_{ar}), 7.41 (br d, 2H, $J = 8.7$ Hz, H_{ar}), 7.23 (ddd, 2H, $J = 8.0$, 7.0, 0.7 Hz, H_{ar}), 5.85–5.70 (m, 1H, H-6′), 5.15–5.05 (m, 2H, H-7′), 4.27 (t, 2H, $J = 7.5$ Hz, H-5), 4.16–4.04 (m, 4H, H-1′, H-2′, H-4′), 2.44 (t, 2H, $J = 6.9$ Hz, H-2), 2.27 (m, 2H, H-3′), 1.94–1.87 (m, 4H, H-3, H-4), 1.64–1.60 ppm (m, 2H, H-5′); ^{13}C NMR ($CDCl_3$, 75 MHz): $\delta = 178.03$ (C=O), 173.26 (C-1), 141.61 (C_{ar}), 134.62 (C-6′), 134.21 (C_{ar}), 127.91 (C_{ar}), 122.19 (C_{ar}), 121.46 (C_{ar}), 118.45 (C-7′), 114.62 (C_{ar}), 71.31, 70.41 (C-2′), 68.80, 68.62 (C-1′), 67.74, 67.07 (C-4′), 45.87 (C-5), 42.58, 42.13 (C-3′), 38.85, 38.57 (C-5′), 33.66 (C-2), 26.61 (C-4), 22.15 ppm (C-3); MS (70 eV) *m*/*z* (%): 423 (9) [M^+], 296 (100).

Ozonolysis of **10** under standard conditions resulted in the anchored 2,4-dideoxysugars (NMR spectroscopic analysis). For cleavage, the RP silica containing the adsorbed product was heated under reflux in HCl-saturated MeOH (30 mL) for 2 h. After complete conversion (according to TLC), the solvent was removed, and then water (15 mL) and further RP silica (500 mg) were added. After filtration, the remaining solids were washed with water (15 mL), and the solution was evaporated to yield the stereoisomeric mixture of **12** (116 mg, 79% overall) as a colorless syrup; ^{1}H NMR ($CDCl_3$,

 © 2005 Wiley-VCH Verlag GmbH & Co. KGaA, Weinheim

500 MHz): $\delta = 4.81$ (d, 0.3H, $J = 3.2$ Hz), 4.74 (dd, 0.1H, $J = 9.5$, 2.2 Hz), 4.28 ppm (d, 0.3H); ^{13}C NMR ($CDCl_3$, 125 MHz): $\delta = 101.77$, 99.83, 99.52 ppm.

Received: October 12, 2004
Published online: June 21, 2005

Keywords:
solid-phase synthesis · green chemistry · noncovalent interactions · synthetic methods · water chemistry

[1] a) D. Hudson, *J. Comb. Chem.* **1999**, *1*, 333 – 360; b) F. Guillier, D. Orain, M. Bradley, *Chem. Rev.* **2000**, *100*, 2091 – 2157; c) F. Zaragoza Dörwald, *Organic Synthesis on Solid Support*, Wiley-VCH, Weinheim, **2000**.

[2] a) D. P. Curran, *Angew. Chem.* **1998**, *110*, 1230 – 1255; *Angew. Chem. Int. Ed.* **1998**, *37*, 1174 – 1196; b) C. C. Tzschucke, C. Markert, W. Bannwarth, S. Roller, A. Hebel, R. Haag, *Angew. Chem.* **2002**, *114*, 4136 – 4173; *Angew. Chem. Int. Ed.* **2002**, *41*, 3964 – 4000.

[3] a) D. J. Gravert, K. D. Janda, *Chem. Rev.* **1997**, *97*, 489 – 509; b) P. H. Toy, K. D. Janda, *Acc. Chem. Res.* **2000**, *33*, 546 – 554.

[4] R. Haag, *Chem. Eur. J.* **2001**, *7*, 327 – 335.

[5] For examples, see: a) H. Perrier, M. Labelle, *J. Org. Chem.* **1999**, *64*, 2110 – 2113; b) S. V. Ley, A. Massi, F. Rodriguez, D. C. Horwell, R. A. Lewthwaite, M. C. Pritchard, A. M. Reid, *Angew. Chem.* **2001**, *113*, 1088 – 1090; *Angew. Chem. Int. Ed.* **2001**, *40*, 1053 – 1055; c) T. Bosanac, J. Yang, C. S. Wilcox, *Angew. Chem.* **2001**, *113*, 1927 – 1931; *Angew. Chem. Int. Ed.* **2001**, *40*, 1875 – 1879.

[6] a) D. P. Curran, *Synlett* **2001**, 1488 – 1496; b) W. Zhang, *Tetrahedron* **2003**, *59*, 4475 – 4489.

[7] a) S. V. Ley, I. R. Baxendale, R. N. Bream, P. S. Jackson, A. G. Leach, D. A. Longbottom, M. Nesi, J. S. Scott, R. I. Storer, S. J. Taylor, *J. Chem. Soc. Perkin Trans. 1* **2000**, 3815 – 4195; b) A. Kirschning, H. Monenschein, R. Wittenberg, *Angew. Chem.* **2001**, *113*, 670 – 701; *Angew. Chem. Int. Ed.* **2001**, *40*, 650 – 679.

[8] a) W.-D. Fessner, C. Walter, *Top. Curr. Chem.* **1996**, *184*, 97 – 194; b) A. N. Phung, M. T. Zannetti, G. Whited, W.-D. Fessner, *Angew. Chem.* **2003**, *115*, 4970 – 4972; *Angew. Chem. Int. Ed.* **2003**, *42*, 4821 – 4824.

[9] a) M. Knorst, PhD Dissertation, RWTH Aachen, **1999**; b) A. Porzelle, PhD Dissertation, TU Darmstadt, **2003**; c) W.-D. Fessner, M. Knorst, A. Porzelle, DE 10021883 [*Chem. Abstr.* **2002**, *136*, 5544].

[10] a) W. Blokzijl, J. B. F. N. Engberts, *Angew. Chem.* **1993**, *105*, 1610 – 1648; *Angew. Chem. Int. Ed. Engl.* **1993**, *32*, 1545 – 1579; b) F. Schmidt, B. Schilling, R. Jäger, J. Brickmann, *J. Comput.-Aided Mol. Des.* **2000**, *14*, 1 – 16.

[11] a) D. Flynn, *Med. Res. Rev.* **1999**, *19*, 408 – 430; b) *Solid-Phase Extraction: Principles, Techniques, and Applications* (Ed.: N. J. K. Simpson), Marcel Dekker, New York, **2000**.

[12] The adsorptive nature of unmodified silica gel or that of an alkylated SiO_2 sol–gel emulsion system has also been observed to facilitate heterogeneous reactions in water; see: a) R. Abu-Reziq, D. Avnir, J. Blum, *Angew. Chem.* **2002**, *114*, 4306 – 4308; *Angew. Chem. Int. Ed.* **2002**, *41*, 4132 – 4134; b) S. Minakata, D. Kano, Y. Oderaotoshi, M. Komatsu, *Angew. Chem.* **2004**, *116*, 81 – 83; *Angew. Chem. Int. Ed.* **2004**, *43*, 79 – 81.

[13] a) A. M. Hay, S. Hobbs-Dewitt, A. A. MacDonald, R. Ramage, *Synthesis* **1999**, 1979 – 1985; b) X. Wang, J. J. Parlow, J. A. Porco, *Org. Lett.* **2000**, *2*, 3509 – 3512; c) X. Li, C. Abell, M. S. Congreve, B. H. Warrington, M. Ladlow, *Org. Biomol. Chem.* **2004**, *2*, 989 – 998.

[14] a) R. Ramage, G. Raphy, *Tetrahedron Lett.* **1992**, *33*, 385 – 388; b) R. Ramage, F. O. Wahl, *Tetrahedron Lett.* **1993**, *34*, 7133 – 7136.

[15] a) J.-L. Reymond, T. Koch, J. Schröder, E. Tierney, *Proc. Natl. Acad. Sci. USA* **1996**, *93*, 4251 – 4256; b) E. González-García, V. Helaine, G. Klein, M. Schuermann, G. A. Sprenger, W.-D. Fessner, J.-L. Reymond, *Chem. Eur. J.* **2003**, *9*, 893 – 899.

[16] a) D. C. Rideout, R. Breslow, *J. Am. Chem. Soc.* **1980**, *102*, 7816 – 7817; b) R. Breslow, U. Maltra, D. C. Rideout, *Tetrahedron Lett.* **1983**, *24*, 1901 – 1904; c) P. A. Grieco, P. Garner, Z. He, *Tetrahedron Lett.* **1983**, *24*, 1897 – 1900.

[17] a) C.-J. Li, *Chem. Rev.* **1993**, *93*, 2023 – 2035; b) C.-J. Li, T.-H. Chan, *Organic Reactions in Aqueous Media*, Wiley-Interscience, New York, **1997**; c) *Aqueous-Phase Organometallic Catalysis* (Eds.: B. Cornils, W. A. Hermann), Wiley-VCH, Weinheim, **1998**; d) C.-J. Li, *Green Chem.* **2002**, *4*, 1 – 4; e) U. M. Lindström, *Chem. Rev.* **2002**, *102*, 2751 – 2772; f) S. Kobayashi, K. Manabe, *Chem. Eur. J.* **2002**, *8*, 4094 – 4101; g) D. Sinou, *Adv. Synth. Catal.* **2002**, *344*, 221 – 237.

[18] a) C.-J. Li, *Chem. Rev.* **1993**, *93*, 2023 – 2035; b) A. Lubineau, J. Auge, Y. Queneau, *Synthesis* **1994**, 741 – 760; c) C.-J. Li, *Tetrahedron* **1996**, *52*, 5643 – 5668; d) C.-J. Li, T.-H. Chan, *Tetrahedron* **1999**, *55*, 11149 – 11176.

[19] a) D. Houllemare, F. Outurquin, C. Paulmier, *J. Chem. Soc. Perkin Trans. 1* **1997**, 1629 – 1632; b) D. E. Gremyachinskiy, L. L. Smith, P. H. Gross, V. V. Samoshin, *Green Chem.* **2002**, *4*, 317 – 318.

[20] S. Steurer, J. Podlech, *Eur. J. Org. Chem.* **1999**, 1551 – 1560.

[21] a) "Nitrile Oxides": V. Jaeger, P. A. Colinas in *Synthetic Applications of 1,3-Dipolar Cycloaddition Chemistry Toward Heterocycles and Natural Products* (Eds.: A. Padwa, W. H. Pearson), Wiley, Chichester, **2002**, pp. 361 – 472; b) K. V. Gothelf, Jørgensen, *Chem. Rev.* **1998**, *98*, 863 – 909. c) For solid-phase approaches, see: G. Faita, M. Mella, A. Mortoni, A. Paio, P. Quadrelli, P. Seneci, *Eur. J. Org. Chem.* **2002**, 1175 – 1183, and references therein.

[22] J. P. Genêt, M. Savignac, *J. Organomet. Chem.* **1999**, *576*, 305 – 317.

[23] A. P. Kozikowski, *Acc. Chem. Res.* **1984**, *17*, 410 – 416.

[24] U. Müllenmeister, W.-D. Fessner in *Innovation and Perspectives in Solid Phase Synthesis & Combinatorial Libraries 2000* (Ed.: R. Epton), Mayflower Worldwide, Birmingham, **2001**, pp. 149 – 152.

[25] P. T. Anastas, J. C. Warner, *Green Chemistry: Theory and Practice*, Oxford University Press, Oxford, **1998**.

 © 2005 Wiley-VCH Verlag GmbH & Co. KGaA, Weinheim

Cluster Compounds

Ligand-Induced Formation of an Adamantanoid Hexanuclear (π-Allyl)Pd^{II}(μ_3-Hydroxo) Cluster Stacked as Hydrogen-Bonded Double Strands

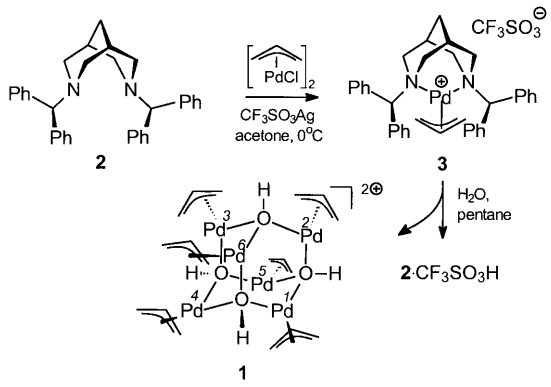
Adolf Gogoll, Lauri Toom, and Helena Grennberg*

Hydroxo complexes of transition metals are of interest in materials science as precursors for intricate metal oxides,[1] and as intermediates in metal-mediated or -catalyzed processes. Hydroxopalladium intermediates have been postulated in some palladium-catalyzed reactions,[2] and they may explain the unexpected stability of some palladium catalysts in the presence of water.[3] In most of its hydroxo complexes, palladium is coordinated to further heteroatom ligands containing P and/or N atoms. Notable exceptions are (μ_2-hydroxo)bis(η^2,η^2-cyclooctadiene)dimethyldipalladium(II) hexafluoroantimonate[4a] and bis(tetrabutylammonium)-bis[(μ_2-hydroxo)bis(pentafluorophenyl)palladium],[4b] which contain palladium coordinated to η^2-alkene or σ-C ligands, respectively.

Isolated hydroxopalladium complexes usually display polynuclearity.[5] The formation of a trinuclear palladium complex was attributed to the presence of traces of water during purification.[6] Trinuclear, mixed-metal complexes were obtained by reaction between hydroxopalladium and metal hydride complexes.[7] Larger clusters of Pd atoms with predominantly carbon monoxide ligands are known, and non-hydroxopalladium clusters of catalytic interest have been studied.[8] A mixed-metal cluster (Pd/Cu) with an adamantanoid Pd–oxygen substructure (hexanuclear in Pd) but without organic ligands on the Pd atoms has been described.[9]

Herein, we report an organometallic, homonuclear hydroxo(π-allyl)Pd cluster **1**, [{(1,3-η^3-propenyl)Pd}$_6$(μ_3-OH)$_4$](CF$_3$SO$_3$)$_2$, without further heteroatom (P or N) ligands. The cluster has a distorted adamantanoid geometry, and the crystal lattice consists of clusters linked into double strands by hydrogen bonds via bridging counterions.

Cluster **1** was obtained during the attempted complexation of the sterically hindered bispidine ligand *N*,*N*′-bis(diphenylmethyl)-3,7-diazabicyclo[3.3.1]nonane (**2**) with a (π-allyl)palladium species, from which we expected to obtain complex **3** (Scheme 1). The formation of **3** was proven by ^{1}H NMR spectroscopy.[10] However, when trying to isolate solid **3** from the acetone solution, we observed the initial formation of colorless, needle-shaped crystals of the protonated ligand salt, **2**·CF$_3$SO$_3$H. Upon further undisturbed standing, the precipitation of yellow, rhomboid crystals was observed in experiments using technical-grade solvent. Under dry conditions, Pd black precipitated. The yellow crystals



Scheme 1. Ligand-induced formation of cluster **1** via complex **3**. The Pd$_6$(OH)$_4$ subunit is emphasized. The trifluorosulfonate ions are omitted for clarity.

were stable for several days at refrigerator temperature (below 4 °C) while covered by the crystallization solvent. Isolated crystals were reasonably stable in air at ambient temperature for several hours. To our surprise, the yellow crystals were not of the expected complex **3**, but of the adamantanoid (π-allyl)Pd^{II} cluster **1** with bridging hydroxo ligands. To the best of our knowledge, this is the first example of an organometallic cluster of palladium of this type.[11,14]

The Pd···C distances in cluster **1** (Figure 1) vary between 2.048 and 2.082 Å (propenyl C-2) and between 2.093 and 2.115 Å (propenyl C-1 and C-3). These distances are shorter

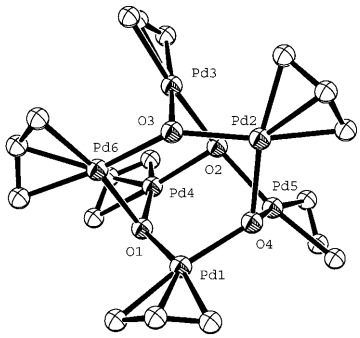


Figure 1. Molecular structure of cluster **1** (counterions omitted for clarity).

than those in the chloro dimer bis[(1,3-η^3-propenyl)palladium chloride] (2.121 Å for C-2, 2.108–2.123 Å for C-1 and C-3),[12] and in (*N*,*N*′-diphenyl-1,5-dimethyl-3,7-diazabicyclo[3.3.1]-nonane-9-one)(1,3-η^3-propenyl)palladium trifluoromethanesulfonate (2.128 Å for C-2 and 2.125–2.126 Å for C-1 and C-3),[15] most likely because of the small *trans* influence of μ_3-hydroxo ligands on the Pd–C bond compared to that of Cl or N ligands.

The Pd···O distances in cluster **1**, which range from 2.133 to 2.179 Å, are shorter than those in the only other reported Pd–(μ_3-OH) cluster, [{Pd(8-methylquinoline)}$_3$(μ_3-Ph$_2$PCH-COOC$_2$H$_5$)(μ_3-OH)]PF$_6$, which are between 2.144 and 2.281 Å.[4] In comparison with a series of μ_2-OH complexes, the Pd···(μ_3-OH) distances in **1** are similar to[16a] or signifi-

[*] Dr. A. Gogoll, L. Toom, Prof. Dr. H. Grennberg
Department of Chemistry, Organic Chemistry
Uppsala University
Box 599, 751 24 Uppsala (Sweden)
Fax: (+46) 18-471-3818
E-mail: adolf.gogoll@kemi.uu.se

 DOI: 10.1002/anie.200500750 © 2005 Wiley-VCH Verlag GmbH & Co. KGaA, Weinheim

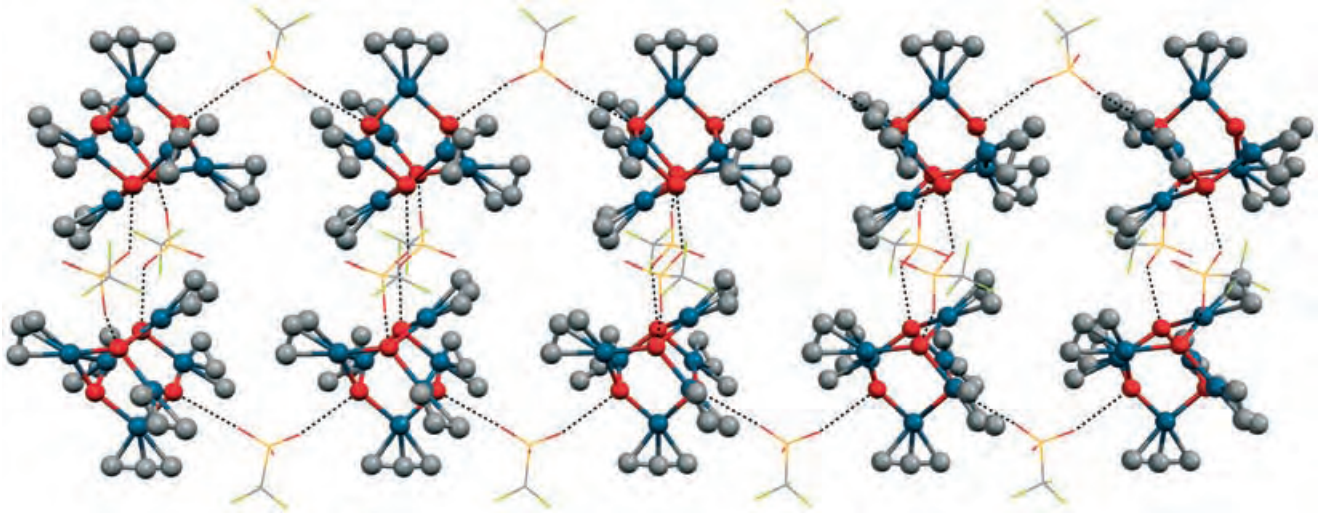


Figure 2. Double strands of clusters of **1**. Cluster pairs bonded via two $CF_3SO_3^-$ ions are linked into strands via two other $CF_3SO_3^-$ ions. Hydrogen bonds are indicated (••••, hydrogen atoms omitted for clarity). The lattice contains one acetone molecule per cluster (not shown).

cantly longer than[4,16b–e] those in the μ_2-OH complexes, where a common feature is that the Pd–(μ_2-O) bond experiences significantly less *trans* influence from other ligands than that exerted by the η^3-propenyl ligands in **1**.

The dicationic clusters of complex **1** are grouped into pairs, linked by two $CF_3SO_3^-$ ions hydrogen-bonded to the hydroxy ligands (connecting O3···O4′ and O4···O3′). These pairs are then linked into double strands of clusters by two more $CF_3SO_3^-$ ions connecting O1···O2′ and O2···O1′, respectively (Figure 2). Hydrogen-bond lengths are shorter between pairs than in the chains of clusters, with CF_3SO_3···(μ_3-H*O*) distances at 2.839 and 2.872–2.921 Å, respectively. Thus, each cluster is surrounded by four shared anions, which leads to a regular crystal lattice composed of double strands.

Hydroxo complexes of transition metals are usually formed by ligand exchange with water.[5b,17] We propose that this is also the case in the formation of cluster **1**. The sequence of steps leading to **1** is coupled to the dynamic process of apparent π-allyl rotation observed in (π-allyl)Pd complexes with chelating dinitrogen ligands.[18] Most likely, steric interactions between the organic ligands in complex **3** favor dissociation of one of its nitrogen atoms. Next, protonation of the basic nitrogen prevents reattachment to the palladium. Instead, the resulting coordinatively unsaturated complex is stabilized by coordination of hydroxy ions, generated by deprotonation of water by the strongly basic ligand **2**.[19] Involvement of η^3–η^1 isomerism of the π-allyl ligand is unlikely, since no exchange between *syn* and *anti* protons of complex **3** was detected by ^{1}H NMR spectroscopy.[10] Furthermore, the cluster **1** is not formed when bispidine ligands other than **2** are used.[15,18b,c]

In conclusion, ligand **2**, although itself not part of the cluster **1**, appears to be responsible for the formation of this new type of palladium complex.

Received: February 28, 2005
Revised: May 6, 2005
Published online: June 29, 2005

Keywords: allyl ligands · cluster compounds · hydrogen bonds · ligand effects · palladium

[1] a) R. G. Bergman, *Polyhedron* **1995**, *14*, 3227; b) J. W. Gilje, H. W. Roesky, *Chem. Rev.* **1994**, *94*, 895.
[2] V. V. Grushin, H. Alper, *Organometallics* **1993**, *12*, 1890.
[3] C. W. Kohlpaintner, M. Beller, *J. Mol. Catal. A* **1997**, *116*, 259.
[4] a) A. Klein, A. Dogan, M. Feth, H. Bertagnolli, *Inorg. Chim. Acta* **2003**, *343*, 189; b) G. López, J. Ruiz, G. García, C. Vicente, J. Casabó, E. Molins, C. Miravitlles, *Inorg. Chem.* **1991**, *30*, 2605.
[5] a) V. V. Grushin, H. Alper, *Organometallics* **1996**, *15*, 5242; b) M. C. Pilon, V. V. Grushin, *Organometallics* **1998**, *17*, 1774.
[6] P. Braunstein, J. Fischer, D. Matt, M. Pfeffer, *J. Am. Chem. Soc.* **1984**, *106*, 410.
[7] V. F. Kuznetsov, C. Bensimon, G. A. Facey, V. V. Grushin, H. Alper, *Organometallics* **1997**, *16*, 97.
[8] P. D. Harvey, Y. Mugnier, D. Lucas, D. Evrard, D. F. Lemaître, A. Vallat, *J. Cluster Sci.* **2004**, *15*, 63.
[9] T. Hosokawa, M. Takano, S.-I. Murahashi, *J. Am. Chem. Soc.* **1996**, *118*, 3990.
[10] Full characterization of **3** will be presented in a separate paper.
[11] Formation of **1** and **2**·CF_3SO_3H: Ligand **2**[12] (7.6 mg, 16.6 μmol) was dissolved in a mixture of acetone (0.3 mL) and $CHCl_3$ (0.2 mL) in a small test tube. After cooling to 0 °C a solution of bis[(1,3-η^3-propenyl)palladium chloride][13] (3.1 mg, 8.5 μmol) in acetone (0.2 mL) was added, followed by a solution of CF_3SO_3Ag (4.3 mg, 16.7 μmol) in acetone (0.2 mL). After stirring (30 s), the precipitated AgCl was separated by centrifugation. The clear, slightly yellow solution was transferred with a Pasteur pipette into a screw-cap vial, and carefully layered with the same volume of cold hexane, which became slightly cloudy. The closed vial was stored at 4 °C. After one day, colorless needles of **2**·CF_3SO_3H had formed. After two days, yellow rhomboid crystals of **1** appeared (yield ca. 0.1 mg, 4 %).
[12] F. Binnig, L. Friedrich, H. P. Hofmann, H. Kreiskott, M. Raschack, C. Müller, Ger. Offen. DE2726571, **1978**.
[13] A. E. Smith, *Acta Crystallogr.* **1965**, *18*, 331.
[14] Crystal data for **1**: $C_{23}H_{40}F_6O_{11}Pd_6S_2$, $M_r = 1309.07$, yellow rhombohedra, crystal size $0.20 \times 0.18 \times 0.16$ mm^3, triclinic, space group $P\bar{1}$, $a = 10.321$, $b = 13.86770(10)$, $c = 14.531$ Å, $\alpha = 99.0800(10)$, $\beta = 107.3650(10)$, $\gamma = 94.5410(10)$°, $V = 1942.494(14)$ Å^3, $Z = 2$, $\rho_{calcd} = 2.238$ g cm^{-3}, $\mu = 2.901$ mm^{-1},

 © 2005 Wiley-VCH Verlag GmbH & Co. KGaA, Weinheim

$\theta = 2.09$–$32.89°$, $F(000) = 1256$, $T = 173(2)$ K, $R_1 = 0.0334$, $wR_2 = 0.0780$. Independent reflections = 13422 [R(int) = 0.0274], restraints = 240, parameters = 435. Crystal data for **2**·CF_3SO_3H: $C_{34}H_{35}F_3N_2O_3S$, $M_r = 608.70$, colorless needles, $1.00 \times 0.04 \times 0.04$ mm^3, monoclinic, space group $P2_1/n$, $a = 9.1585(2)$, $b = 14.3750(3)$, $c = 23.3428(5)$ Å, $\alpha = \gamma = 90$, $\beta = 90.073(1)°$, $V = 3073.16(11)$ Å^3, $Z = 4$, $\rho_{calcd} = 1.316$ g cm^{-3}, absorption coefficient = 0.161 mm^{-1}, $\theta = 0.87$–$25.12°$, $F(000) = 1256$, $T = 173(2)$ K, $R_1 = 0.0519$, $wR_2 = 0.1078$. Independent reflections = 5418 [R(int) = 0.0823], restraints = 0, parameters = 424. Siemens SMART CCD area-detector diffractometer, $Mo_{K\alpha}$ radiation, wavelength = 0.71073 Å, multiscan, SADABS (Sheldrick, 2002). The structures were solved by direct methods, and refined with the SHELX software package and with full-matrix least-squares on F^2. All non-hydrogen atoms were refined anisotropically. Hydrogen atoms were assigned idealized positions and were included in structure-factor calculations. The authors acknowledge Dr. V. Langer, Chalmers University of Technology, Goteborg (Sweden), for the data collection. CCDC-264283 (for **1**) and CCDC-264284 (for **2**·CF_3SO_3H) contain the supplementary crystallographic data for this paper. These data can be obtained free of charge from the Cambridge Crystallographic Data Centre via www.ccdc.cam.ac.uk/data_request/cif.

[15] A. Gogoll, H. Grennberg, A. Axén, *Organometallics* **1997**, *16*, 1167.

[16] a) V. V. Grushin, H. Alper, *Organometallics* **1993**, *12*, 1890; b) C. Pisano, G. Consiglio, A. Sironi, M. Moret, *Chem. Commun.* **1991**, 421; c) G. Pieri, M. Paasquali, P. Leoni, U. Englert, *J. Organomet. Chem.* **1995**, *491*, 27; d) R.-D. Schnebeck, E. Freisinger, B. Lippert, *Eur. J. Inorg. Chem.* **2000**, 1193; e) U. Thewalt, S. Müller, *Z. Naturforsch. B* **1989**, *44*, 1206.

[17] T. G. Appleton, J. A. Bailey, D. R. Bedgood, J. R. Hall, *Inorg. Chem.* **1994**, *33*, 217.

[18] a) A. Gogoll, J. Örnebro, H. Grennberg, J. E. Bäckvall, *J. Am. Chem. Soc.* **1994**, *116*, 3631; b) A. Gogoll, C. Johansson, A. Axén, H. Grennberg, *Chem. Eur. J.* **2001**, *7*, 396; c) A. Gogoll, H. Grennberg, A. Axén, *Organometallics* **1998**, *17*, 5248.

[19] The pK_a of (**2**·H)$^+$ in acetonitrile is 17.81: L. Toom, A. Kütt, I. Kaljurand, I. Leito, H. Grennberg, A. Gogoll, unpublished results.

 © 2005 Wiley-VCH Verlag GmbH & Co. KGaA, Weinheim

Self-Assembly

The Introduction of π–π Stacking Moieties for Fabricating Stable Micellar Structure: Formation and Dynamics of Disklike Micelles**

Bo Song, Zhiqiang Wang, Senlin Chen, Xi Zhang, Yu Fu, Mario Smet, and Wim Dehaen*

Amphiphiles can self-organize into micellar structures with defined sizes and shapes[1,2] that may be used in applications such as templates for making nanostructured materials and mimicking biomineralization processes. Engineering robustness is required to make these applications practical, as the micellar structures are inherently dynamic and fluid. Enhancing the intermolecular interactions among the aggregates is one possible method for stabilizing the micellar structures. This approach may rely on generating a strong association among its assembling units through a combination of different interactions, including van der Waals interactions and hydrogen bonding.[3–5] Herein, we report the introduction of a strong π–π stacking moiety into bolaamphiphiles[6] so as to increase the robustness of the self-organized entities, thus providing a new approach to fabricating organic nanostructured materials.

The diaryldiketopyrrolopyrrole (DPP) dye is a recently developed technical pigment with remarkable properties such as a high fade-proof nature, extraordinary thermal stability, and very low solubility as a consequence of strong intermolecular interactions.[7] We attempted to introduce a DPP dye as a strong π–π stacking moiety into bolaamphiphiles, and hoped that such a bolaamphiphile might give rise to a stable micellar nanostructure with light-emitting properties. For this

[*] Dr. Z. Wang, S. Chen, Prof. X. Zhang
Key Lab of Optoelectronics and Molecular Engineering
Department of Chemistry
Tsinghua University
Beijing 100084 (China)
Fax: (+86) 010-6277-1149
E-mail: xi@mail.tsinghua.edu.cn

B. Song
Key Lab of Supramolecular Structure and Materials
Jilin University
Changchun, 130023 (China)

Dr. Y. Fu, Dr. M. Smet, Prof. W. Dehaen
Department of Chemistry
Katholieke Universiteit Leuven
Celestijnenlaan 200F, 3001 Leuven (Belgium)

[**] We thank the major state basic research development program (G2000078102) and the National Natural Science Foundation of China (20334010, 20473045) for financial support. The Flemish and Belgian governments, as well as the University of Leuven, supported this work with a bilateral grant (BIL02/03), the grant IAP-V-4, and a postdoctoral fellowship to Y.F., respectively. M.S. thanks F. W. O. Vlaanderen for a postdoctoral fellowship. Professor Lei Jiang and Huan Liu of the Institute of Chemistry, Chinese Academy of Sciences are thanked for their help with FE-SEM measurements.

Supporting information for this article is available on the WWW under http://www.angewandte.org or from the author.

 DOI: 10.1002/anie.20050980 © 2005 Wiley-VCH Verlag GmbH & Co. KGaA, Weinheim

purpose, a series of bolaamphiphiles bearing diaryldiketopyrrolopyrrole units with different spacer lengths were synthesized, namely, 2,5-bis(*n*-(1-pyridinium)alkyl)-3,6-bis-(2-thienyl)-1,4-dioxopyrrolo[3,4-*c*]pyrrole ditosylate salts, abbreviated as DPP-*n*, where *n* ($n = 7$, 11, 15) corresponds to the number of methylene units in the alkyl chain spacer.

For DPP-11, for example, there exists a critical micelle concentration (cmc) at 5.5×10^{-5} M, as indicated by the plot of the conductivity as a function of the concentration (Figure 1).

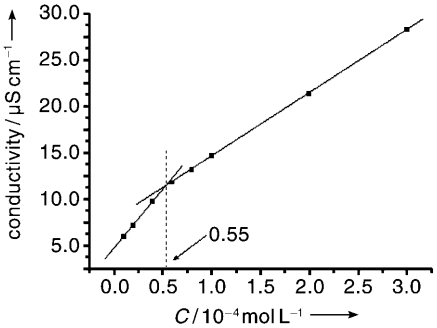


Figure 1. Dependence of the solution conductivity of DPP-11 on concentration; the cmc is around 5.5×10^{-5} M.

When the concentration is above this critical value the bolaamphiphiles self-organize into micelles in aqueous solution. The formation of a micellar structure is also supported by ^{1}H NMR spectroscopic analysis. As seen in Figure 2, the

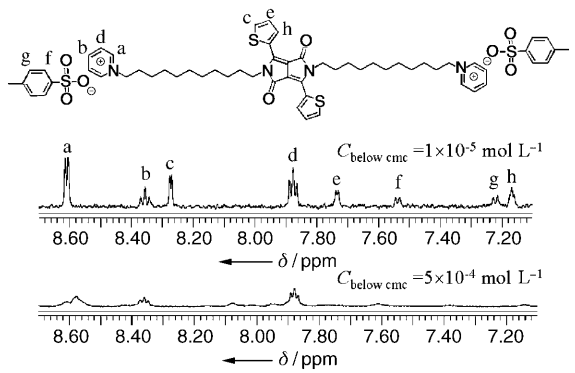


Figure 2. ^{1}H NMR spectra of DPP-11 in D_2O with concentrations lower and higher than its cmc.

^{1}H NMR signals of the aromatic rings from the two terminal pyridinium groups as well as from the rigid unit are well resolved below its cmc. However, all the ^{1}H NMR signals become broad and weak when the concentration is above its cmc. The change in the ^{1}H NMR signals of the thienyl residues in the rigid moiety is even greater than that of the two terminal pyridinium groups. This change can be rationalized by the restricted motion of the amphiphilic molecule in the associated state.[3,8] The segregation of the hydrophobic and hydrophilic parts of the molecule during the self-assembly in water results in the thienyl groups residing in the inner part of the micelles and the terminal pyridinium groups at the outer part of the micelles. Therefore, interaction between the water and the pyridinium groups is stronger than that with the thienyl residues, thus leading to increased local mobility and less line broadening of the NMR signals.

We found that if the concentration of the DPP-11 solution was above the cmc the solution turned from bright red to dark purple. We anticipated that the color change was indicative of the formation of micelles, which was further supported by spectroscopic studies: We first identified the UV/Vis spectral absorption bands of the DPP-11 monomer and aggregate. As shown in Figure 3, there are two absorption bands around 514

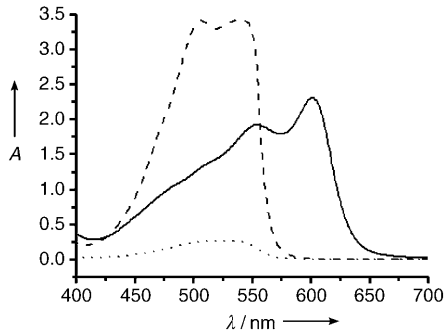


Figure 3. Concentration-dependent UV/Vis spectra of DPP-11: in methanol at 1.0×10^{-4} M (dashed line); in aqueous solution at 1.0×10^{-4} M, above the cmc (solid line); in aqueous solution at 1.0×10^{-5} M, below the cmc (dotted line).

and 540 nm in dilute aqueous solution (below the cmc, dotted curve) or in the good solvent, methanol (dashed curve). These bands are assigned to the monomer of DPP-11. In concentrated solution (above the cmc), a new absorption band appears around 601 nm (solid curve), which is attributed to the aggregate state of DPP-11. The bathochromic shift of the absorption bands is caused by the strong π–π stacking of the diketopyrrolopyrrole units in the amphiphiles upon self-assembly into micellar structures. Interestingly, in contrast with the normal formation of micelles that reaches equilibrium in a very short time, we found that DPP-11 requires a relatively long period to self-assemble, thus allowing the dynamic process to be monitored (Figure 4). Only absorption bands at around 514 and 540 nm corresponding to the monomer absorption exist at the beginning. The monomer absorption becomes weaker and weaker over time and concomitantly the absorption band of the aggregate around 601 nm appears and then becomes greater and greater, thus indicating the formation of micelles and the increase in their numbers. There is an isosbestic point around 560 nm. Figure 4b shows that the absorption change of DPP-11 almost reaches a plateau after about 10 minutes, thus suggesting an equilibrium situation.

To determine whether the aggregation is temperature-dependent in solution we carried out systematic experiments of the variation of the UV/Vis spectrum with temperature. As shown in Figure 5, the UV/Vis absorption experiment indeed shows that the aggregate can disassemble as the temperature increases and reassemble as the temperature decreases. The increase and decrease of the characteristic absorption bands of the aggregates (601 nm) and monomers of the DPP-11

 © 2005 Wiley-VCH Verlag GmbH & Co. KGaA, Weinheim

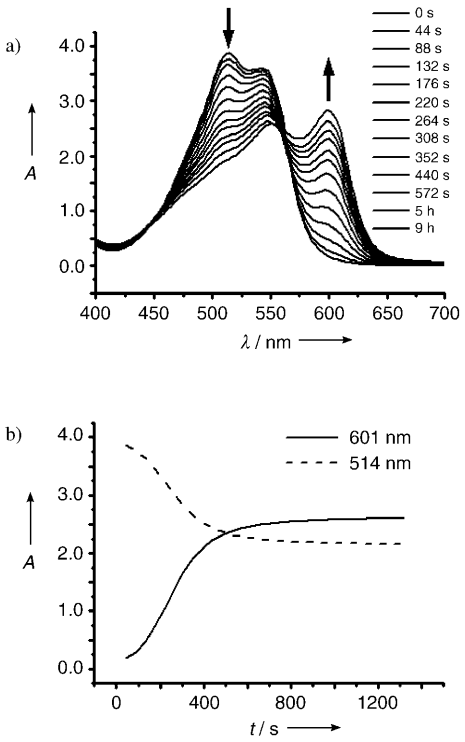


Figure 4. a) Time-resolved absorbance of DPP-11 in aqueous solution at a concentration of 1.0×10^{-4} M. b) The change in the absorbance with time at 601 nm (solid line) and 514 nm (dashed line).

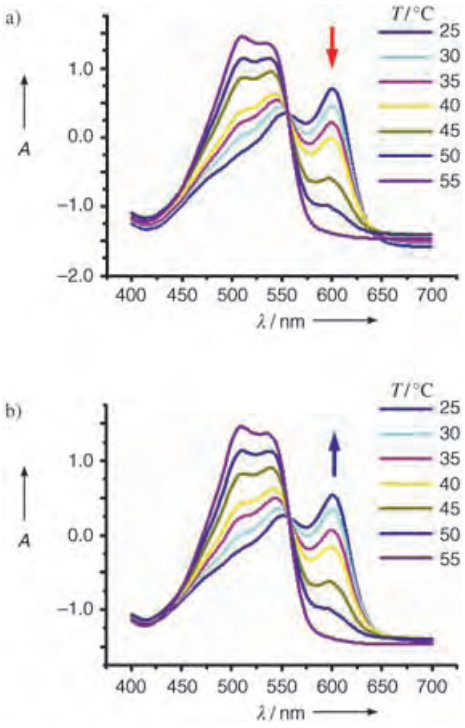


Figure 5. Temperature-dependent UV/Vis spectra of DPP-11 in aqueous solution at 1.0×10^{-4} M. The temperature increase (a) and decrease (b) are in intervals of 5 °C.

molecules (514 nm) show aggregation is a reversible process. At the same time, the reversible phenomena also indicate the DPP-11 molecules experience self-assembly through supramolecular interactions.

The micelles formed in aqueous solution could be adsorbed on freshly cleaved mica sheets and visualized by ex situ atomic force microscopy (AFM). As exhibited in Figure 6, DPP-11 forms disklike micelles with diameters

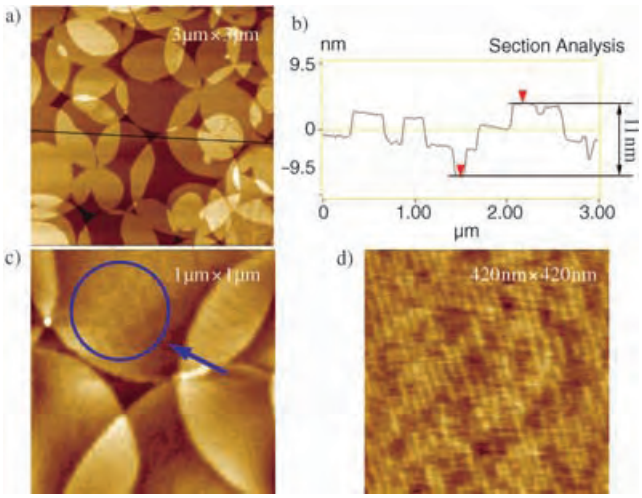


Figure 6. Ex situ AFM images of DPP-11 micellar structures adsorbed on a mica sheet: a) large area image; b) section analysis of (a); c) and d) magnified images.

ranging from several hundreds of nanometers to one micrometer. Adjacent disklike micelles partially overlap, and the overlapping parts stack together to form double layers, triple layers, or even multilayers. The section analysis (Figure 6b) shows that the disk has an average thickness of about 3.7 nm. This value agrees well with the length of a single DPP-11 molecule, thus suggesting that the disks form a monolayer structure with the thickness of a single molecule. Although the self-assembly of the amphiphiles is mainly driven by the hydrophobic effect, once the disklike micelle forms, the π–π stacking interaction becomes another dominating factor that enhances the stability of the disks. This is the reason why we can readily observe the micellar structure by ex situ AFM: the micellar structure formed in this way is stable enough toward the drying process. When looking more closely at the disks we found that there were uniform stripes with a width of about 10 nm (Figure 6c, d). These stripes have a preferred orientation within one disk, although the orientation can be different in different disks. Thus, the surface disklike micelle is a combination of micro- and nanostructures, which can be explained in terms of a compromise between the different intermolecular interactions. The intermolecular π–π stacking in the middle part of the aggregate forces the molecules to pack closely, while the repulsive interaction of the positively charged head groups has the reverse effect. We believe that the repulsion between the charged head groups may be enhanced as a consequence of water evaporation during the drying process. A compromise between these two types of

 © 2005 Wiley-VCH Verlag GmbH & Co. KGaA, Weinheim

interaction could lead to crystallization of the amphiphiles, which is responsible for the formation of the observed stripelike structure.

The disklike micellar structure in the dry state as revealed by ex situ AFM should also reflect its associated structure in solution. This speculation is supported by the following experimental facts. First, in situ AFM studies demonstrate the presence of similar disks as those observed by ex situ AFM, thus excluding the possibility that the disks are formed during the air-drying process. Second, the disks can also be observed when adsorbed onto hydrophilic quartz slides. This fact indicates that formation of the disks is not induced by the mica substrate, and that the disklike micelles formed in the aqueous solution are robust enough to resist the effect of the substrate. Third, the UV/Vis absorption bands for the adsorbates on both a mica sheet and quartz slide are almost the same as that for the micellar suspension, which indicates the micelles are resistant to the transferring and drying processes. Fourth, the enhanced stability is also supported by AFM studies at elevated temperature. The disks undergo no apparent changes until the substrate is heated to 80 °C, after which they gradually melt as the temperature is further increased.

In addition, an appropriate length of the flexible spacers is also necessary for such bolaamphiphile to self-organize into the disklike micellar structure. We performed similar studies on DPP-7 and DPP-15, but failed to obtain self-assembled structures for these two bolaamphiphiles where the spacers are shorter and longer than DPP-11, respectively. Neither the concentration/conductivity plot nor the UV/Vis spectra for DPP-7 show any distinct phase transition, thus indicating that this compound can not form micellar structures in aqueous solution. Analysis of the adsorbate on a hydrophilic substrate by AFM showed no regular structures were formed. The self-assembly of DPP-15 is inhibited by its poor solubility, since the increase in the spacer length decreases its solubility in water significantly.

In summary, interesting disklike micelles have been obtained by self-assembly of a novel bolaamphiphile, and the dynamics of disk formation have been investigated. The disklike micelles can maintain their monomolecule-layered structures even when being transferred to hydrophilic substrates, thus showing their high stability as a result of the introduction of a strong π–π stacking moiety into the amphiphile. Although micelles are inherently dynamic and fluid, they can be stabilized by enhancing the intermolecular interactions, thus providing a new approach for the fabrication of organic nanostructured materials.

Experimental Section

A commercial multimode Nanoscope IV AFM was used to characterize the surface structure. In situ AFM: The substrate was mounted under a liquid cell and the solution injected into the cell. After leaving the solution to stand for at least 30 minutes to reach equilibrium, it was scanned in the tapping mode. Ex situ AFM: The substrate was incubated in the solution for at least 30 minutes, before a sample was removed from the solution and air-dried. The sample was then scanned in the tapping mode. UV/Vis spectra were measured with a HITACHI U-3010 spectrophotometer. A weighed amount of DPP-11 was dissolved in a minimum quantity of methanol (a good solvent for DPP-11) and then the solution injected into a certain volume of water. The UV/Vis spectrum was then recorded immediately by capturing one spectrum every 44 s. ^{1}H NMR spectroscopic analysis (600 MHz) was performed in deuterium oxide. The substrates used in the AFM studies were commercial mica and quartz slides. Before each use, the mica was freshly cleaved, and the quartz slides treated with piranha solution (concentrated sulfuric acid and 30% H_2O_2 (7:3)) to obtain a hydrophilic surface.

The three bolaamphiphiles DPP-7, DPP-11, and DPP-15 were synthesized in an analogous way. The synthesis of DPP-11 is presented as an example. 3,6-Bis-(2-thienyl)-1,4-dioxopyrrolo[3,4-*c*]pyrrole (DPP) was synthesized as reported before.[9] 7-Bromo-1-heptanol was obtained by monobromination of 1,7-heptanediol with HBr, and 15-bromo-1-pentadecanol was prepared by cleaving ω-pentadecalactone with H_2SO_4/HBr, followed by reduction with borane·methyl sulfide complex (2 M solution in THF).

2,5-Bis-(11-hydroxyundecyl)-3,6-bis-(2-thienyl)-1,4-dioxopyrrolo-[3,4-*c*]pyrrole (**1**): 11-Bromo-1-undecanol (1.7 g, 6.8 mmol), K_2CO_3 (1 g, 7.2 mmol), and NaI (1 g, 6.7 mmol) were added to a solution of DPP (1 g, 3.3 mmol) in dry DMF (40 mL). The mixture was stirred at 60 °C for 18 h. After cooling the mixture to room temperature, it was poured into water and extracted with ethyl acetate. The organic phase was dried over $MgSO_4$ and the solvent was evaporated in vacuo. The product (0.6 g, 28%) was obtained by column chromatography (SiO_2, CH_2Cl_2). ^{1}H NMR (300 MHz, $CDCl_3$, 25 °C, tetramethylsilane (TMS)): $\delta = 8.92$ (d, ^3J(H,H) = 4.2 Hz, 2H,), 7.64 (d, ^3J(H,H) = 4.2 Hz, 2H), 7.28 (t, ^3J(H,H) = 4.2 Hz, 2H), 4.07 (t, ^3J(H,H) = 7.2 Hz, 4H), 3.64 (t, ^3J(H,H) = 3.6 Hz, 4H), 1.29–1.74 ppm (m, 36H).

2,5-Bis-(11-tosyloxyundecyl)-3,6-bis-(2-thienyl)-1,4-dioxopyrrolo-[3,4-*c*]pyrrole (**2**): Tosyl chloride (TosCl; 0.6 g, 3 mmol) and 4-dimethylaminopyridine (0.6 g, 4.9 mmol) were added to a solution of **1** (0.6 g, 0.9 mmol) in dichloromethane (140 mL). The mixture was stirred at room temperature for 24 h, and then the solvent evaporated in vacuo. The product (0.16 g, 19%) was obtained by column chromatography (SiO_2, CH_2Cl_2). ^{1}H NMR (300 MHz, $CDCl_3$, 25 °C, TMS): $\delta = 8.92$ (d, ^3J(H,H) = 4.2 Hz, 2H), 7.80 (d, ^3J(H,H) = 8.7 Hz, 4H), 7.64 (d, ^3J(H,H) = 4.2 Hz, 2H), 7.34 (d, ^3J(H,H) = 8.7 Hz, 4H), 7.28 (t, ^3J(H,H) = 4.2 Hz, 2H), 3.99–4.09 (m, ^3J(H,H) = 7.2 Hz, 8H), 2.44 (s, 6H), 1.29–1.74 ppm (m, 36H).

DPP-11: Dry pyridine (4 mL) was added to a solution of **2** (0.165 g, 0.17 mmol) in dry chloroform (10 mL). The solution was refluxed under nitrogen for 20 h. After cooling the mixture to room temperature, it was added dropwise to toluene (150 mL). The resulting red precipitate (0.18 g, 93%) was purified by two precipitations by adding a solution of the product in methanol to diethyl ether. ^{1}H NMR (300 MHz, DMSO, 25 °C, TMS): $\delta = 9.07$ (d, ^3J(H,H) = 6.0 Hz, 4H; 2-H, 6-H Py), 8.80 (d, ^3J(H,H) = 4.2 Hz, 2H; 3-H Th), 8.58 (t, ^3J(H,H) = 7.2 Hz, 2H; 4-H Py), 8.14 (t, ^3J(H,H) = 7.2 Hz, 4H; 3-H 5-H Py), 8.10 (d, ^3J(H,H) = 4.2 Hz, 2H; 5-H Th), 7.47 (d, ^3J(H,H) = 8.1 Hz, 4H; 2-H, 6-H Tos), 7.40 (t, ^3J(H,H) = 4.2 Hz, 2H; 4-H Th), 7.10 (d, ^3J(H,H) = 8.1 Hz, 4H; 3-H, 5-H Tos), 4.57 (t, ^3J(H,H) = 7.2 Hz, 4H; CH_2Py), 3.99 (t, ^3J(H,H) = 7.2 Hz, 4H; CH_2DPP), 2.50 (t, ^3J(H,H) = 1.7 Hz, 6H; CH_3 Tos), 1.88 (m, 4H; CH_2CH$_2$Py), 1.62 (m, 4H; CH_2CH$_2$DPP), 1.20 ppm (m, 28H; CH$_2$CH$_2$(CH_2)$_7$CH$_2$CH$_2$).

DPP-7: ^{1}H NMR (300 MHz, DMSO, 25 °C, TMS): $\delta = 9.07$ (d, ^3J(H,H) = 6.0 Hz, 4H; 2-H 6-H Py), 8.80 (d, ^3J(H,H) = 4.2 Hz, 2H; 3-H Th), 8.58 (t, ^3J(H,H) = 7.2 Hz, 2H; 4-H Py), 8.14 (t, ^3J(H,H) = 7.2 Hz, 4H; 3-H 5-H Py), 8.10 (d, ^3J(H,H) = 4.2 Hz, 2H; 5-H Th), 7.47 (d, ^3J(H,H) = 8.1 Hz, 4H; 2-H, 6-H Tos), 7.40 (t, ^3J(H,H) = 4.2 Hz, 2H; 4-H Th), 7.10 (d, ^3J(H,H) = 8.1 Hz, 4H; 3-H; 5-H Tos), 4.57 (t, ^3J(H,H) = 7.2 Hz, 4H; CH_2Py), 3.99 (t, ^3J(H,H) = 7.2 Hz, 4H; CH_2DPP), 2.50 (t, ^3J(H,H) = 1.7 Hz, 6H; CH_3 Tos), 1.90 (m, 4H; CH_2CH$_2$Py), 1.62 (m, 4H; CH_2CH$_2$DPP), 1.37 ppm (m, 12H; CH$_2$CH$_2$(CH_2)$_7$CH$_2$CH$_2$).

 © 2005 Wiley-VCH Verlag GmbH & Co. KGaA, Weinheim

DPP-15: ^{1}H NMR (300 MHz, DMSO, 25 °C, TMS): $\delta = 9.07$ (d, ^3J(H,H) = 6.0 Hz, 4H; 2-H, 6-H Py), 8.80 (d, ^3J(H,H) = 4.2 Hz, 2H; 3-H Th), 8.58 (t, ^3J(H,H) = 7.2 Hz, 2H; 4-H Py), 8.14 (t, ^3J(H,H) = 7.2 Hz, 4H; 3-H 5-H Py), 8.10 (d, ^3J(H,H) = 4.2 Hz, 2H; 5-H Th), 7.47 (d, ^3J(H,H) = 8.1 Hz, 4H; 2-H, 6-H Tos), 7.40 (t, ^3J(H,H) = 4.2 Hz, 2H; 4-H Th), 7.10 (d, ^3J(H,H) = 8.1 Hz, 4H; 3-H; 5-H Tos), 4.57 (t, ^3J(H,H) = 7.2 Hz, 4H; CH_2Py), 3.99 (t, ^3J(H,H) = 7.2 Hz, 4H; CH_2DPP), 2.50 (t, ^3J(H,H) = 1.7 Hz, 6H; CH_3 Tos), 1.90 (m, 4H; CH_2CH_2Py), 1.62 (m, 4H; CH_2CH_2DPP), 1.20 ppm (m, 44H; CH_2CH_2(CH_2)$_7$CH_2CH_2).

Received: March 17, 2005
Revised: May 20, 2005
Published online: July 1, 2005

Keywords: bolaamphiphiles · micelles · nanostructures · noncovalent interactions · self-assembly

[1] a) H. Ringsdorf, B. Schlarb, J. Venzmer, *Angew. Chem.* **1988**, *100*, 117; *Angew. Chem. Int. Ed. Engl.* **1988**, *27*, 113; b) M. Ahlers, W. Mueller, A. Reichert, H. Ringsdorf, J. Venzmer, *Angew. Chem.* **1990**, *102*, 1310; *Angew. Chem. Int. Ed. Engl.* **1990**, *29*, 1269; c) T. Kunitake, *Angew. Chem.* **1992**, *104*, 692; *Angew. Chem. Int. Ed. Engl.* **1992**, *31*, 709; d) J.-M. Lehn, *Supramolecular Chemistry, Concepts and Perspectives*, VCH, Weinheim, **1995**.

[2] S. J. Candau, E. Hirsch, R. Zana, M. Adam, *J. Colloid Interface Sci.* **1988**, *122*, 430.

[3] Y. Okahata, T. Kunitake, *J. Am. Chem. Soc.* **1979**, *101*, 5231.

[4] Y. Yan, W. Xiong, J. B. Huang, Z. C Li, X. S. Li, N. N. Li, H. L. Fu, *J. Phys. Chem. B* **2005**, *109*, 357.

[5] a) B. Zou, M. F. Wang, D. L. Qiu, X. Zhang, L. F. Chi, H. Fuchs, *Chem. Commun.* **2002**, 1008; b) M. F. Wang, D. L. Qiu, B. Zou, T. Wu, X. Zhang, *Chem. Eur. J.* **2003**, *9*, 1876; c) B. Zou, L. Y. Wang, T. Wu, X. Y. Zhao, L. X. Wu, X. Zhang, S. Gao, M. Gleiche, L. F. Chi, H. Fuchs, *Langmuir* **2001**, *17*, 3682; d) S. Gao, B. Zou, L. F. Chi, H. Fuchs, J. Q. Sun, X. Zhang, J. C. Shen, *Chem. Commun.* **2000**, 1273.

[6] a) J. H. Fuhrhop, H. H. David, J. Mathieu, U. Liman, H. J. Winter, E. Boekemat, *J. Am. Chem. Soc.* **1986**, *108*, 1785; b) J. H. Fuhrhop, T. Y. Wang, *Chem. Rev.* **2004**, *104*, 2901.

[7] O. Wallquist, R. Lenz, *Macromol. Symp.* **2002**, *187*, 617.

[8] X. F. Wang, Y. Z. Shen, Y. Pan, Y. Q. Liang, *Langmuir* **2001**, *17*, 3162.

[9] a) A. Iqbal, M. Jost, R. Kirchmayr, J. Pfenninger, A. Rochat, O. Wallquist, *Bull. Soc. Chim. Belg.* **1988**, *97*, 615; b) A. C. Rochat, L. Cassar, A. Iqbal, *Eur. Patent* 0094911, **1983**; c) N. Avcibasi, M. Smet, B. Metten, W. Dehaen, F. C. De Schryver, G. Bultynck, G. Callewaert, H. De Smedt, L. Missiaen, N. Boens, *Int. J. Photoenergy* **2004**, *6*, 159.

 © 2005 Wiley-VCH Verlag GmbH & Co. KGaA, Weinheim

Nanocluster Catalysts

Benzene Formation at 70 °C by Coupling of Propylene on Supported Pd Nanoclusters**

*Ju Chou, Siyan Zhang, Shouli Sun, and Eric W. McFarland**

Reactions on supported transition metal clusters have important applications and often display unexpected reactivity when the cluster size is on the nanometer scale.[1] As reliable methods of preparing size-selected supported clusters have been developed, relationships between the preparation method, size, and/or support have become apparent, albeit poorly understood. Metal clusters can be synthesized by using micelle encapsulation, and this method has been further developed to make nanocluster powders supported on metal oxides.[2–4] The metal ions are initially dissolved homogeneously within the hydrophilic block copolymer cores of the micelle solutions, and the length and structure of the copolymers can be used to control the sizes of the clusters.[3,5] A uniform distribution of metal nanoclusters is created throughout the polymer matrix[5] and in the resulting powder catalyst.

Supported Pd clusters on metal oxides are widely used as industrial heterogeneous catalysts.[6] They are known catalysts for the hydrogenation of olefins,[7] propylene epoxidation,[8–9] and the production of hydrogen peroxide.[10] Coupling or cyclization of the alkynes acetylene[11–14] and propyne[15–16] has also been observed. The cyclotrimerization of acetylene on Pd deposited on MgO thin films or W surfaces was observed to occur at 330 K and higher, and was found to be dependent on the size and coverage of Pd nanoclusters. This coupling reaction leads to the formation of benzene through C activation on the Pd surface and end-to-end C–C coupling. Propyne has also been observed to couple to benzene on a Cu surface at 260 K in an ultra high vacuum (UHV) system.

[*] Dr. J. Chou
Department of Chemistry and Physics
Southeastern Louisiana University
Hammond, LA, 70402 (USA)
Dr. S. Sun, Prof. E. W. McFarland
Gas Research Technology, Inc.
861 Ward Drive, Santa Barbara, CA 93111 (USA)
Fax: (+1) 805-893-4731
E-mail: mcfar@engineering.ucsb.edu
S. Zhang, Prof. E. W. McFarland
Department of Chemical Engineering
University of California
Santa Barbara, CA, 93106-5080 (USA)

[**] The authors are grateful for financial support from the U.S. Department of Energy (DE-FG03-89ER14048), the U.S. Air Force Office of Scientific Research (DURINT grant F49620-01-1-0459), and the National Science Foundation (CHE-9626338). The authors thank Professor Galen Stucky and Professor Horia Metiu for helpful discussions, and Dr. Tom Mates and Dr. Jinping Zhang for technical assistance with XPS and TEM. The authors made use of the MRL Central Facilities, supported by the MRSEC Program of the NSF under Award DMR-00-80034.

 DOI: 10.1002/anie.200500022 © 2005 Wiley-VCH Verlag GmbH & Co. KGaA, Weinheim

Head-to-tail interaction of two propyne molecules takes place to produce benzene with the elimination of hydrogen.[16] Though observations of propylene coupling to form aromatic compounds on acid or bifunctional catalysts has been previously observed, these have all been attributed to radical processes that require high temperatures (> 300 °C).[17] To our knowledge, there are as yet no reports of propylene coupling to benzene on supported metal catalysts at low temperature.

In our previous investigations of propylene partial oxidation (epoxidation) on supported Au in the presence of hydrogen and oxygen, we observed traces of benzene while using Au–Pd alloys. With an increased Pd/Au ratio we observed an increase in the rate of benzene production. Herein, we describe our subsequent follow-up to the preliminary observations in which we addressed the following questions: what are the conditions under which Pd clusters supported on TiO_2 can catalyze propylene coupling to produce benzene? Is the propylene coupling reaction size-dependent? What is the mechanism involved in the formation of benzene from propylene coupling?

Three Pd nanocluster sizes were prepared in micelles of three different block copolymers respectively and supported on TiO_2 by impregnation. The powders were dried and calcined at 300 °C. The calcination procedure removed the polymer surrounding the metal cluster (observed by MS, $M_r = 44$) and partially reduced Pd^{II} to metallic Pd^0. The calcination was followed by treatment with hydrogen at 250 °C to complete the reduction of Pd^{II} to Pd^0. The final powder catalysts, Pd/TiO_2, were characterized by HRTEM (Figure 1).

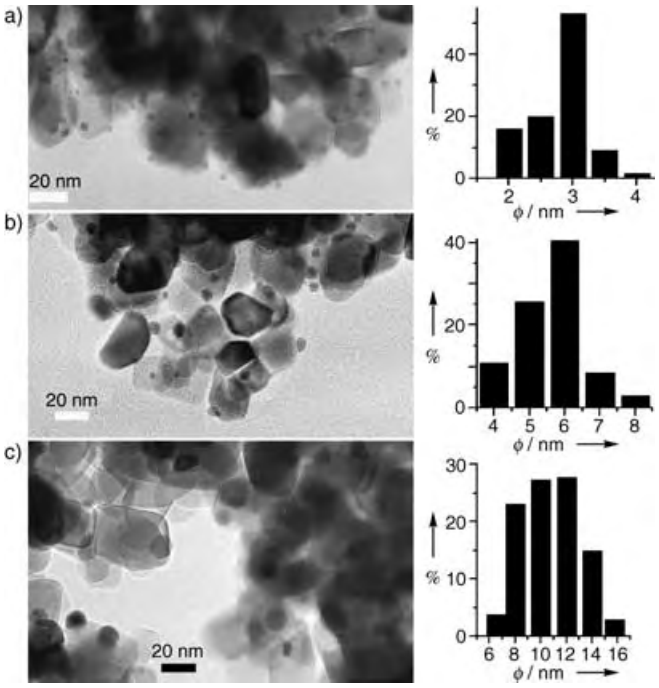


Figure 1. TEM images (left) of Pd nanoparticles prepared on titania supports from polymers with three different head sizes after calcination and reduction. Histograms (right) show the corresponding Pd size distributions obtained for: a) PS(54300)-P2VP(8800), $\varnothing = 3 \pm 1$ nm; b) PS(81000)-P2VP(14200), $\varnothing = 6 \pm 2$ nm; c) PS(53000)-P2VP(43800), $\varnothing = 12 \pm 3$ nm.

The micrographs and corresponding histograms show Pd nanoclusters uniformly dispersed on TiO_2 with a narrow size distribution. The diameters of the nanoclusters from the three different polymers were determined by HRTEM to be 3 ± 1, 6 ± 2, and 12 ± 3 nm.

X-ray photoelectron spectra (XPS) were collected with the Pd/TiO_2 catalyst to determine the Pd oxidation states before and after calcination, after reduction in hydrogen, and after the reaction. Figure 2 shows the measured Pd 3d core-level spectra of the Pd/TiO_2 ($\varnothing = 6$ nm). While still surrounded by the polymer micelle before calcination, the binding energy (E_b) of the Pd catalyst is observed as two broad peaks which are thought to be the superposition of two pairs of peaks at $E_b = 336.3$ and 341.6 eV, and at $E_b = 338.1$ and 343.3 eV. The former pair is assigned to PdO[10] and the latter ($E_b = 338.1$ and 343.3 eV) we believe corresponds to Pd^{II} bound to the CH_3COO^- groups of the micelle. Both peaks are consistent with Pd^{II}.

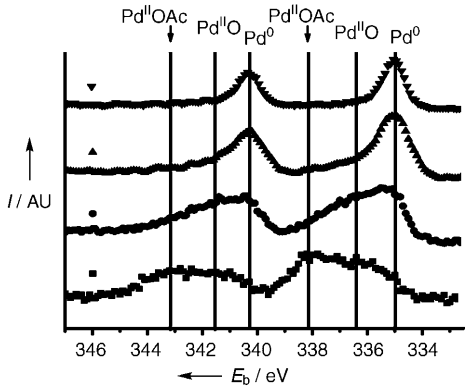


Figure 2. XPS of the Pd 3d region of the Pd/TiO_2 catalyst before calcinations (■), after calcinations (●), after reduction in hydrogen (▲), and after propylene reaction (▼).

After calcination the binding energy decreases, and two chemical states of Pd are observed. Peaks at 336.3 and 341.6 eV are still assigned to $Pd^{II}O$; however, the peaks at 335.0 and 340.3 eV are attributed to Pd^0.[18] Therefore, calcination partially reduces palladium(II) and removes the measurable polymer surrounding Pd. After reduction in hydrogen, the major peaks are at 335.0 and 340.3 eV which arise from Pd^0; a small tail of $Pd^{II}O$ remains, however.

The activity of Pd/TiO_2 in a mixture of propylene, hydrogen, and oxygen was measured in a packed bed reactor with argon as a carrier and calibration standard. The mixture was controlled by a mass flow controller at 2 mL min^{-1} for each gas with a total flow rate of 8 mL min^{-1}. The reaction products were analyzed by MS, GC, and ^{1}H NMR spectroscopy.[4,19]

Figure 3 shows the products of the reaction of propylene, hydrogen, and oxygen on Pd/TiO_2 as measured by on-line MS during a temperature increase at a rate of 2.5 °C min^{-1}. At approximately 70 °C, a rapid increase in benzene production ($M_r = 78$) was observed as well as increases in the production of species with $M_r = 44$ (CO_2 and C_3H_8), $M_r = 43$ (C_3H_8), and $M_r = 58$ (C_3H_6O). The masses of both CO_2 and C_3H_8 are 44;

 © 2005 Wiley-VCH Verlag GmbH & Co. KGaA, Weinheim

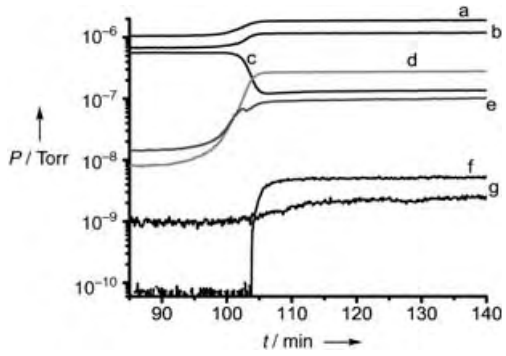


Figure 3. On-line MS data from the reaction of propylene, hydrogen, and oxygen on Pd/TiO_2 ($\varnothing = 3$ nm) as the catalyst temperature is increased from room temperature to 70 °C. Species shown and their corresponding M_r values are: a) Ar, 40; b) C_3H_6, 42; c) O_2, 32; d) ($CO_2 + C_3H_8$), 44; e) C_3H_8, 43; f) C_6H_6, 78; g) C_3H_6O, 58.

however, C_3H_8 has a unique fragment at $M_r = 43$. Therefore, the change in $M_r = 44$ results from the presence of both CO_2 and C_3H_8, whereas the signal at $M_r = 43$ is solely that of C_3H_8. The signal at $M_r = 58$ is also ambiguous and could be from the isomers acetone, propanal, or propylene oxide.

Further identification of each product was confirmed by both GC and NMR spectroscopy. On-line GC analysis shows that the products include CO_2, acetone, propane, and benzene. Finally, the reaction products were collected by a cold trap of $CDCl_3$. Figure 4 shows the ^1H NMR spectrum of

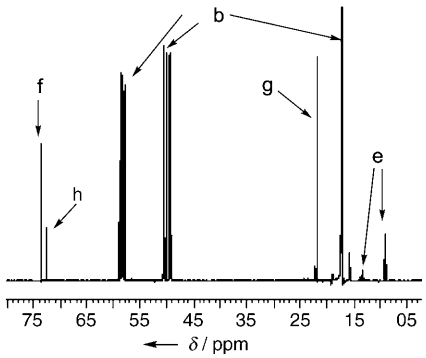


Figure 4. ^1H NMR spectrum of the products of the catalytic reaction at 25 °C on Pd/TiO_2 ($\varnothing = 3$ nm). The peaks are assigned to b) C_3H_6; e) C_3H_8; f) C_6H_6; g) C_3H_6O (acetone); h) $CDCl_3$.

collected products. The chemical shift at $\delta = 7.4$ ppm is that of benzene. Propane and acetone were also observed in the NMR spectrum (Figure 4), which is in good agreement with our analysis of the GC and MS results. For all cases in which benzene was formed, we observed that it is preceded by oxidation and hydrogenation, and is accompanied by the condensation of water at the reactor outlet.

The activities of the different Pd nanocluster sizes on TiO_2 were determined, and Table 1 shows product conversion and selectivity as a function of nanocluster size at 70 °C. Under the same experimental conditions, the 3-nm diameter Pd clusters were the most active. The selectivity for deep oxidation to carbon dioxide is inhibited on the smallest clusters, which

Table 1: Performance of TiO_2-supported Pd nanoclusters (≈1% by weight) of different sizes for the reaction of a mixture of propylene, hydrogen and oxygen.

Pd Size [nm]	T [°C]	Selectivity [%]				Conversion C_3H_6 [%]
		Benzene	Acetone	Propane	CO_2	
3	70[a]	4.9	1.7	69.5	23.9	20.3
6	70[a]	4.2	0.7	36.5	58.6	12.0
6	70[b]	4.3	0.9	19.8	75.0	33.5
12	70[a]	2.5	0.4	31.1	66.0	11.4

Reactant gas molar ratios: [a] $Ar/O_2/H_2/C_3H_6 = 2:2:2:2$. [b] $Ar/O_2/H_2/C_3H_6 = 1:3:2:2$.

favor hydrogenation, coupling, and partial oxidation. As a control, large (bulk) Pd clusters were prepared by sintering the powder catalyst to 1000 °C. The large cluster sizes were confirmed by SEM and were inactive for propylene coupling to form benzene at 70 °C; the only observed products in this case were propane and acetone.

After reaction, XPS analysis of the catalyst shows the presence of only Pd^0. To test the hypothesis that Pd^0 is required for the formation of benzene, the reaction was carried out with a Pd catalyst lacking prior reduction, leaving $Pd^{II}O$ on the surface. Under the same reaction conditions as above, benzene formation was not observed, which suggests that metallic Pd^0 is necessary for the formation of benzene.

The production of benzene requires the co-reactants oxygen and hydrogen; on Pd/TiO_2 ($\varnothing = 3$ nm) in the presence of both oxygen and hydrogen ($O_2/H_2/C_3H_6 = 2:2:2$ mL min^{-1}), benzene formation was observed. Upon replacement of hydrogen with Ar to maintain the total flow rate at 6 mL min^{-1} ($Ar/O_2/C_3H_6 = 2:2:2$ mL min^{-1}), the production of benzene and all other products (CO_2, propane, and acetone) stopped. No activity was observed at 70 °C without hydrogen.

When oxygen was absent, not surprisingly, oxidation of propylene to CO_2 and acetone stopped; however, hydrogenation to propane was observed by both MS and NMR spectroscopy. Upon returning to the original flow rates of propylene, oxygen, and hydrogen (2:2:2 mL min^{-1}) on the same catalyst, the formation of benzene was again observed.

These observations indicate that both oxygen and hydrogen are required for the production of benzene at low temperatures on the Pd clusters. The product reactions are summarized in Equations (1)–(4):

$$H_3C{-}CH{=}CH_2 + H_2 \rightarrow H_3C{-}CH_2{-}CH_3 \quad (1)$$

$$H_3C{-}CH{=}CH_2 + O_2 + H_2 \rightarrow (H_3C)_2{-}C{=}O + H_2O \quad (2)$$

$$H_3C{-}CH{=}CH_2 + 5\,O_2 + H_2 \rightarrow 3\,CO_2 + 4\,H_2O \quad (3)$$

$$H_3C{-}CH{=}CH_2 + O_2 + \frac{1}{2}\,H_2 \rightarrow \frac{1}{2}\,C_6H_6 + 2\,H_2O \quad (4)$$

For the reaction of propylene to produce benzene we tentatively propose a mechanism on the Pd cluster surface that involves H-atom abstraction that initially couples two propylene molecules. This is energetically driven by the

 © 2005 Wiley-VCH Verlag GmbH & Co. KGaA, Weinheim

formation of water with C–H bond activation through an activated intermediate of the hydrogen/oxygen reaction. Figure 5 illustrates the proposed reaction cycle. The observation that benzene formation from propylene is preceded by

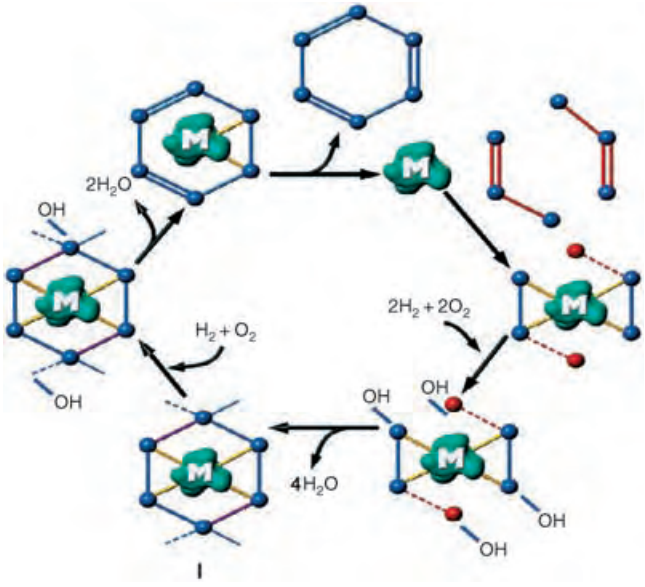


Figure 5. Mechanism of propylene coupling, leading to the formation of benzene. M represents one or more metal sites.

hydrogenation and oxidation suggests that the Pd surface is populated by hydroxy and/or peroxide species that result from the dissociative chemisorption of hydrogen and oxygen.[10,20] These species abstract a hydrogen atom from the terminal methyl group of a π-bound propylene molecule on the surface. This initial hydrogen abstraction produces a symmetric allyl intermediate[21] which then cyclizes with an adjacent allyl group to form the cyclic intermediate **I** and water. Although it is known that on a bifunctional catalyst, two allyl groups can couple to form 1,5-hexadiene as a by-product and benzene by dehydrogenation, 1,5-hexadiene products were not observed by MS. Thus, in the low-temperature Pd-catalyzed propylene coupling reaction, the cyclization apparently does not follow the conventional mechanism via 1,5-hexadiene; instead, it may proceed to form intermediate **I** (Figure 5). The mechanism of propyne coupling to form benzene via cyclohexadiene intermediates has been proposed.[16] The formation of water provides the energetic drive necessary for the removal of hydrogen. The fact that Pd nanoclusters are required for efficient low-temperature coupling suggests that either the very low coordination (giving rise to the suggested structures analogous to bis-(allyl)palladium complexes) and/or surface intermediates that are sufficiently different from the pure metal (or metal–ligand complexes previously studied) are responsible for this unusual reactivity.

Experimental Section

Block copolymers of poly(styrene)–block–poly(2-vinylpyridine) (PS-b-P2VP) of three molecular weights were used to make Pd micelle solutions.[3,17] Pd/TiO_2 catalysts were prepared by using Pd acetate with the following procedure: 50 mg block copolymer PS(x)-b-P2VP(y) (54300/8800, 81000/14200, 54000/43800, Polymer Source, Inc., Canada) was dissolved in toluene (10 mL) and stirred for 5 h. This was followed by the addition of 20 mg Pd acetate (or 16 mg for 3-nm diameter Pd) into the solution and continuous stirring for 48 h. The different Pd nanocluster sizes were obtained by changing the length of the polymer head (PS). The Pd micelle precursors were then deposited onto anatase TiO_2 (1 g, donated by Siant-Gobain) which was ground into powder and filtered by a sieve (mesh size 60). The surface area of the support was 34.8 $m^2 g^{-1}$. The solvent was slowly evaporated in air until the sample was completely dry. The dry sample (200 mg) was calcined in the mixture of oxygen and argon (20:80 *v*/*v*) at 300 °C after increasing the temperature 5 °C min^{-1} for 1 hour, after which the temperature was decreased to 50 °C. The sample was reduced at 250 °C for 30 min in the hydrogen/argon mixture (10:80 *v*/*v*). The sample was cooled to room temperature before starting the reaction studies. Bulk Pd catalyst was prepared by mixing Pd (2 mg) with TiO_2 (198 mg). The sample was calcined at 1000 °C for 4 h to form large Pd and was also reduced with hydrogen at 250 °C before the catalytic reaction.

A continuous-flow packed-bed reactor (0.6 × 30 cm) was used for the activity studies. In a typical run, the volumetric flow ratios of argon, propylene, hydrogen, and oxygen were 1:1:1:1, controlled by mass flow controllers. The total flow rate was 480 mL h^{-1}. The products were analyzed by GC (SRI 8010 A), MS (SRI), and NMR spectroscopy (Varian UNITY INOVA 400 MHz). A Porapack column was used for the separation of products. Both a thermal conductivity detector and flame ionization detector were used. For NMR spectroscopic analysis, the products were collected in a $CDCl_3$ solvent cold trap.

The Pd/TiO_2 catalysts were imaged by HRTEM (JEOL 2010FX) to determine the morphology and size of the Pd nanoclusters. The binding energies of Pd in the Pd/TiO_2 catalyst were monitored by XPS (Kratos, Axis Ultra) with a monochromated $Al_{K\alpha}$ source.

Received: January 4, 2005
Revised: April 15, 2005
Published online: June 28, 2005

Keywords: benzene · heterogeneous catalysis · nanostructures · palladium · propylene coupling

[1] A. K. Sinha, S. Seelan, S. Tsubota, M. Haruta, *Angew. Chem.* **2004**, *116*, 1572–1574; *Angew. Chem. Int. Ed.* **2004**, *43*, 1546–1548.
[2] H.-G. Boyen, G. Kästle, F. Weigl, B. Koslowski, C. Dietrich, P. Ziemann, J. P. Spatz, S. Riethmüller, C. Hartmann, M. Möller, *Science* **2002**, *297*, 1533–1536.
[3] B. R. Cuenya, S.-H. Baeck, T. F. Jaramillo, E. W. McFarland, *J. Am. Chem. Soc.* **2003**, *125*, 12928–12934.
[4] J. Chou, N. Franklin, S.-H Baeck, T. F. Jaramillo, E. W. McFarland, *Catal. Lett.* **2004**, *95*, 107–111.
[5] G. Kästle, H.-G. Boyen, F. Weigl, G. Lengl, T. Herzog, P. Ziemann, S. Riethmüller, O. Mayer, C. Hartmann, J. P. Spatz, M. Möller, M. Ozawa, F. Banhart, M. G. Garnier, P. Oelhafen, *Adv. Funct. Mater.* **2003**, *13*, 853–861.
[6] a) C. N. Satterfield in *Heterogeneous Catalysis in Industrial Practice*, 2nd ed., McGraw-Hill, New York, **1991**, pp. 6–18; b) Y. Takasu, T. Sakuma, Y. Matsuda, *Chem. Lett.* **1985**, *8*, 1179.
[7] T. Ueno, M. Suzuki, T. Goto, T. Matsumoto, T. Nagayama, Y. Watanabe, *Angew. Chem.* **2004**, *116*, 2581–2584; *Angew. Chem. Int. Ed.* **2004**, *43*, 2527–2530.
[8] K. Murata, Y. Liu, N. Mimura, M. Inaba, *J. Catal.* **2003**, *220*, 513–518.

 © 2005 Wiley-VCH Verlag GmbH & Co. KGaA, Weinheim

[9] W. Laufer, R. Meiers, W. Hölderich, *J. Mol. Catal. A* **1999**, *141*, 215 – 221.
[10] G. Blanco-Brieva, E. Cano-Serrano, J. M. Campos-Martin, J. L. G. Fierro, *Chem. Commun.* **2004**, 1184 – 1185.
[11] R. Barnes, I. M. Abdelrehim, T. E. Madey, *Top. Catal.* **2001**, *14*, 53 – 61.
[12] S. Abbet, U. Heiz, A. M. Ferrari, L. Giordano, C. D. Valentin, G. Pacchioni, *Thin Solid Films* **2001**, *400*, 37 – 42.
[13] S. Abbet, A. Sanchez, U. Heiz, W.-D. Schneider, *J. Catal.* **2001**, *198*, 122 – 127.
[14] K. G. Pierce, M. A. Barteau, *J. Phys. Chem.* **1994**, *98*, 3882 – 3892.
[15] R. L. Middleton, R. M. Lambert, *Catal. Lett.* **1999**, *59*, 15 – 20.
[16] A. Clotet, J. M. Ricart, F. Illas, G. Pacchioni, R. M. Lambert, *J. Am. Chem. Soc.* **2000**, *122*, 7573 – 7578.
[17] B. Grzybowska, J. Haber, J. Janas, *J. Catal.* **1977**, *49*, 150 – 163.
[18] J. F. Moulder, W. F. Stickle, P. E. Sobol, K. Bomben in *Handbook of X-Ray Photoelectron Spectroscopy* (Eds.: J. Chastain, R. C. King, Jr.), Physical Electronics, Inc. USA **1995**, pp. 118 – 119.
[19] J. Chou, E. W. McFarland, *Chem. Commun.* **2004**, *16*, 1648 – 1649.
[20] H. Fornander, L.-G. Ekedahl, H. Dannetun, *Catal. Lett.* **1999**, *59*, 107 – 113.
[21] A. Bielanski, J. Habe, *Oxygen in Catalysis*, Marcel Dekker, New York, **1991**, pp. 294 – 298.

 © 2005 Wiley-VCH Verlag GmbH & Co. KGaA, Weinheim

Liquid Crystal Dendrimers

Self-Assembly of Semifluorinated Janus-Dendritic Benzamides into Bilayered Pyramidal Columns**

Virgil Percec, Mohammad R. Imam, Tushar K. Bera, Venkatachalapathy S. K. Balagurusamy, Mihai Peterca, and Paul A. Heiney*

Amphiphilic dendrons that adopt the shape of a disk or disk fragment can self-assemble into supramolecular columns which self-organize into *p6mm* hexagonal or *p2mm* and *c2mm* rectangular 2D periodic assemblies.[1,2] The apex of such dendrons generates the hollow[1l] or occupied[1a–k] functional core of the supramolecular column (Figure 1 a). Twin-tapered dendritic benzamides self-assemble into supramolecular columns generated by an orthogonal hydrogen-bonded stack of dendritic benzamide units (Figure 1 b).[3] These supramolecular columns self-organize into periodically ordered *p6mm* hexagonal assemblies or co-assemble into more complex hexagonal superlattices.[3] Amphiphilic dendrons that adopt the shape of a sphere fragment can self-assemble into spherical supramolecular dendrimers, which self-organize into periodic $Pm\bar{3}n$,[1d,h,4a–4c] $Im\bar{3}m$[4d–f] 3D cubic and $P4_2/mnm$ 3D tetragonal,[4g] and quasiperiodic 3D 12-fold symmetry-forbidden liquid quasicrystals.[4h] It was recently reported that semifluorination of the conical dendron $(3,4,5)^2$12G2-CO_2CH_3 yields the crownlike dendron $(3,4,5)^2$12F8G2-CO_2CH_3 as one of the two products.[5] This

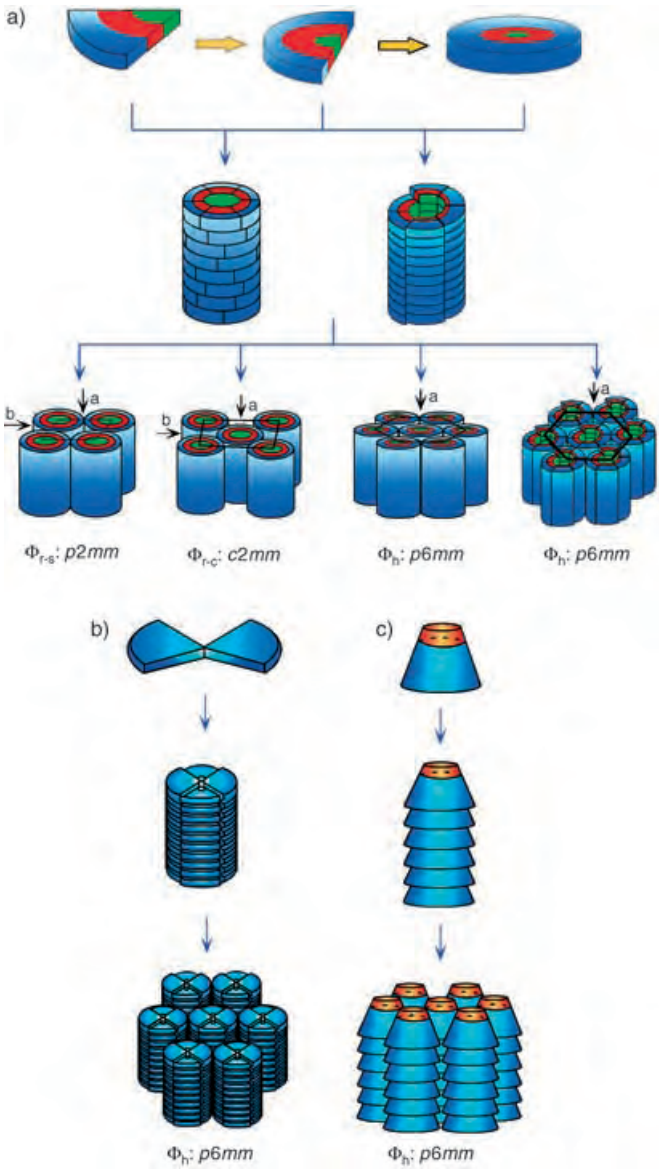


Figure 1. Self-assembly of building blocks based on a) flat, tapered dendrons into hollow and occupied supramolecular columns; b) twin dendrons into cylindrical columns; and c) crownlike dendrons into pyramidal columns and their subsequent self-organization into *p6mm* hexagonal columnar (Φ_h), *p2mm* simple rectangular columnar ($\Phi_{r\text{-}s}$), or *c2mm* centered rectangular columnar ($\Phi_{r\text{-}c}$) lattices.

[*] Prof. V. Percec, M. R. Imam, Dr. T. K. Bera, Dr. V. S. K. Balagurusamy
Roy & Diana Vagelos Laboratories, Department of Chemistry
Laboratory for Research on the Structure of Matter
University of Pennsylvania
Philadelphia, PA 19104-6323 (USA)
Fax: (+1) 215-573-7888
E-mail: percec@sas.upenn.edu
Dr. V. S. K. Balagurusamy, M. Peterca, Prof. P. A. Heiney
Department of Physics and Astronomy
Laboratory for Research on the Structure of Matter
University of Pennsylvania
Philadelphia, PA 19104-6396 (USA)

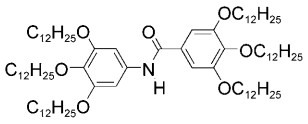
[**] Financial support by the National Science Foundation (DMR-9996288 and DMR-0102459) is gratefully acknowledged.

Supporting information for this article is available on the WWW under http://www.angewandte.org or from the author.

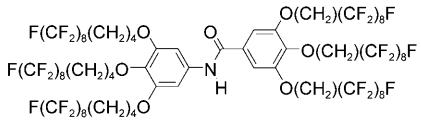
 DOI: 10.1002/anie.200501254 © 2005 Wiley-VCH Verlag GmbH & Co. KGaA, Weinheim

process changes the mode of self-assembly from a supramolecular sphere (for $(3,4,5)^2$12G2-CO_2CH_3) to a supramolecular pyramidal column for $(3,4,5)^2$12F8G2-CO_2CH_3 (Figure 1c). Herein, we report that semifluorination of one of the two dendrons of the twin-dendritic benzamides (that is, a benzamide containing two identical dendrons)[3b,c] changes the mode of self-assembly from a single-layer supramolecular column to an unprecedented bilayered pyramidal supramolecular column. The supramolecular pyramidal columns generated from these semifluorinated Janus-dendritic benzamides (that is, a benzamide containing two different dendrons) exhibit diameters more than twice as large as their nonfluorinated or semifluorinated twin-dendritic benzamide counterparts. Nonfluorinated Janus-dendritic benzamides continue to self-assemble like twin-dendritic benzamides.

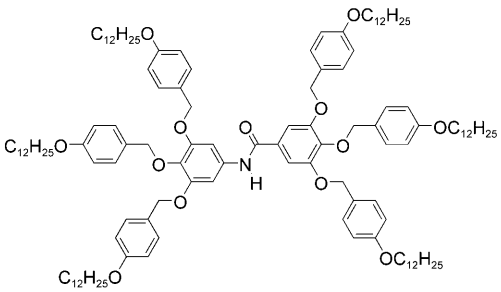
Our study involved two nonfluorinated benzamides (3,4,5)12G1-(3,4,5)12G1-BzA **1** and (4-3,4,5)12G1-(4-3,4,5)12G1-BzA **3**, one fluorinated twin-dendritic benzamide (3,4,5)12F8G1-(3,4,5)12F8G1-BzA **2**, and a nonfluorinated Janus-dendritic benzamide (3,4,5)12G1-(4-3,4,5)12G1-BzA **4**. The synthesis, structural analysis, and mechanism of self-assembly of the two nonfluorinated twin-dendritic benzamides **1** and **3** were reported previously.[3b,c] Both **1** and **3** self-assemble into supramolecular columns by the orthogonal hydrogen-bonded stack mechanism outlined in Figure 1b. The fluorinated twin-dendritic benzamide **2** was synthesized with the procedure used for the corresponding nonfluorinated twin-dendritic benzamides[3b] (see Supporting Information). The semifluorinated twin-dendritic benzamides self-assemble into supramolecular columns by a mechanism similar to that of the nonfluorinated twin-dendritic benzamides (Figure 1b). The phase transitions for these three twin-dendritic benzamides, identified by a combination of



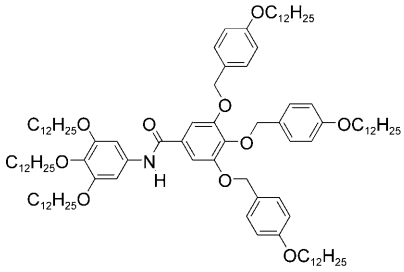
1



2



3



4

Table 1: Thermal analysis of the supramolecular dendrimers self-assembled from twin-dendritic and Janus-dendritic benzamides.[a]

Compound		Heating			Cooling	
	Phase Transition	T [°C]	ΔH [kcal mol^{-1}]	Phase Transition	T [°C]	ΔH [kcal mol^{-1}]
1	k→Φ_h	76.9	35.04	i→Φ_h	112.7	−0.77
	Φ_h→i	121.3	0.63	Φ_h→k($\Phi_{r\text{-}c}$)	47.1	−13.94
s.h.[b]	k→Φ_h	73.5	14.60			
	Φ_h→i	120.6	0.42			
2	k→Φ_h	134.9	16.28	i→Φ_h	146.5	−2.26
	Φ_h→i	150.1	2.38	Φ_h→k	49.9	−10.06
s.h.	k_1→k_2	104.6	−0.64			
	k_2→Φ_h	134.8	16.65			
	Φ_h→i	149.8	2.29			
3	k_1→k_2	66.3	20.34	i→Φ_h	179.5	−2.54
	k_2→Φ_h	101.0	11.16	Φ_h→k	78.3	−10.72
	Φ_h→i	182.8	2.43			
s.h.	k_1→k_2	−5.9	2.37			
	k_2→Φ_h	101.5	12.41			
	Φ_h→i	181.9	2.76			
4	k→N_c	45.7	8.63	i→Φ_h	138.3	−1.41
	N_c→Φ_h	56.3	2.81	Φ_h→k	34.9	−0.74
	Φ_h→i	141.6	1.62			
s.h.	k→Φ_h	48.5	0.91			
	Φ_h→i	141.6	1.61			
5	k→Φ_h	106.1	9.40	i→Φ_h	153.1	−1.88
	Φ_h→i	156.9	1.82	Φ_h→k($\Phi_{r\text{-}c}$)	69.8	−9.16
s.h.	k→Φ_h	105.8	9.95			
	Φ_h→i	156.5	2.03			
6	k_1→k_2	62.6	0.57	i→N_c	72.2	−15.33
	k_1→i	105.6	23.11			
s.h.	k→N_c	94.7	8.92			
	N_c→i	101.7	0.89			
7	k_1→k_2	39.1	1.44	Φ_h dec →k	131.2	−3.15
	k_2→$\Phi_{r\text{-}s}$	88.4	3.14			
	$\Phi_{r\text{-}s}$→Φ_h dec[c]	137.3	3.16			
s.h.	k→Φ_h dec	137.3	3.70			

[a] k: Crystalline; Φ_h: *p6mm* hexagonal columnar LC phase; i: isotropic; k($\Phi_{r\text{-}c}$): *c2mm* centered rectangular columnar crystalline; N_c: columnar nematic LC phase; $\Phi_{r\text{-}s}$: *p2mm* simple rectangular columnar LC phase. [b] s.h.: Data from the second heating. [c] The compound exhibits a decomposition temperature at 240.9 °C.

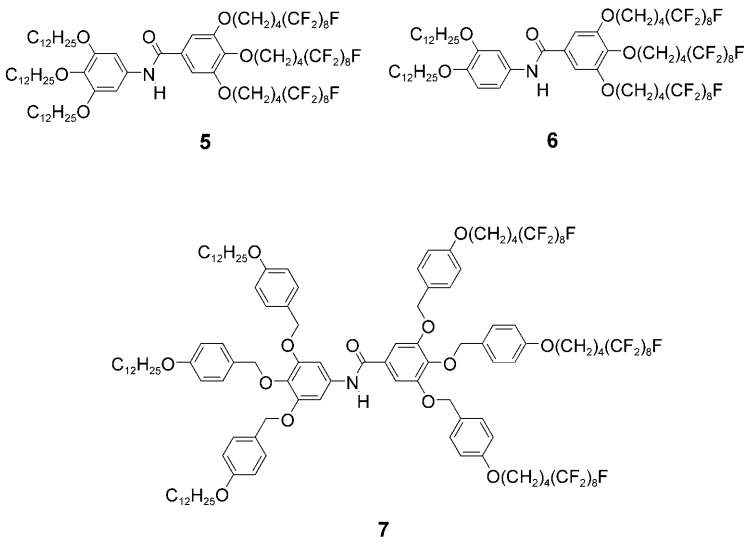
 © 2005 Wiley-VCH Verlag GmbH & Co. KGaA, Weinheim

differential scanning calorimetry (DSC) and X-ray diffraction (XRD) experiments, are reported in Table 1. Their structural and retrostructural analysis by a combination of XRD, thermal optical polarized microscopy (TOPM), and molecular modeling experiments is reported in Table 2. Surprisingly, the nonfluorinated Janus-dendritic benzamide **4** also self-assembles into a supramolecular column by a mechanism similar to that of the twin-dendritic benzamides (Figure 1b).

The semifluorinated Janus-dendritic benzamides (3,4,5)12G1-(3,4,5)12F8G1-BzA **5** and (4-3,4,5)12G1-(4-3,4,5)12F8G1-BzA **7** were synthesized from dendrons with identical structures, except one is semifluorinated and the other has hydrogenated alkyl groups on the periphery. Both dendritic benzamides self-assemble into supramolecular columns that self-organize in a *p6mm* columnar hexagonal (Φ_h) liquid crystal (LC) lattice (Table 1 and Table 2). However, the diameter of the supramolecular column self-assembled from **5** is twice that of the column self-assembled from the twin-dendritic benzamides **1** and **2**. A similar result was observed for the diameter of the supramolecular column self-assembled from **7**. The benzamide (3,4)12G1-(3,4,5)12F8G1-BzA **6** self-assembles into a less perfect supramolecular column with a diameter approximately twice as large as that of the column generated from **2** (Table 1 and Table 2). The less perfect supramolecular column produced by **6** self-organizes in a columnar nematic mesophase.

The XRD and TOPM textures of the columnar hexagonal lattices generated from nonfluorinated twin-dendritic benzamides are compared with those of semifluorinated Janus-dendritic benzamides in Figure 2 and Figure 3. Electron density calculations were performed to elucidate the origin of the difference between the diameters of the supramolecular columns self-organized from twin- and Janus-dendritic benzamides.

The Janus-dendritic benzamide **4**, which contains hydrogenated aliphatic chains, shows a strong and a very weak reflection in the XRD pattern recorded at 70 °C. The *d* spacings of these reflections are 27.4 Å and 15.9 Å, respectively (Table 2). The ratio of these *d* spacings is 1.72:1, which is very close to $\sqrt{3}$. This ratio demonstrates a Φ_h phase that exhibits only (10) and (11) reflections. Furthermore, these reflections give a column diameter of 31.7 Å. This is



5 **6**

7

Table 2: Structural and retrostructural analysis of 2D lattices self-organized from twin- and Janus-dendritic benzamides.

Compound	*T* [°C]	LC Phase	*d* Spacings [Å] and Indices					Lattice Dimension or Column Diameter [Å][h]	ρ [g cm^{-3}] [i]	μ[j]
			d_{20}[a]	d_{11}	d_{31}	d_{40}	d_{22}			
			d_{51}[b]	d_{42}	d_{13}	d_{33}	d_{53}			
			d_{10}[c]	d_{11}	d_{20}	d_{21}				
			d_{30}[d]	d_{22}	d_{40}					
			d_{10}[e]	d_{11}						
			d_{10}[f]	d_{11}	d_{12}	d_{21}				
			d_{04}[g]	d_{30}	d_{31}	d_{15}				
1	21	$\Phi_{r\text{-}c}$	22.8[a]	18.6	–	11.3	–	a = 45.5	–	–
		$\Phi_{r\text{-}c}$	8.3[b]	7.6	6.8	–	–	b = 20.5	–	–
	90	Φ_h	21.7[c]	12.8	–	–	–	25.3 ± 0.4	0.98	1.8
2	78	Φ_h	28.8[c]	16.7	14.3	10.9	–	33.2 ± 0.2	–	–
3	94	Φ_h	29.2[c]	17.2	–	–	–	34.1 ± 0.5	0.93	2.1
4	50	N_c	42.5[e]	23.9	–	–	–	48.4	–	–
	70	Φ_h	27.4[c]	15.9	–	–	–	31.7	0.99	2.3
5	19	$\Phi_{r\text{-}c}$	45.3[a]	–	24.8	–	20.4	a = 90.3	–	–
		$\Phi_{r\text{-}c}$	16.6[b]	15.6	–	13.1	11.7	b = 44.7	–	–
	120	Φ_h	51.9[c]	–	25.4	19.2	–	59.0 ± 1.0	1.57	9.2
		Φ_h	16.9[d]	–	–	–	–	–	–	–
6	50	N_c	45.9[e]	–	–	–	–	53.0	–	–
7	100	$\Phi_{r\text{-}s}$	66.1[f]	56.1	41.3	32.4	–	a = 66.9	–	–
		$\Phi_{r\text{-}s}$	22.6[g]	21	21.7	20.1	–	b = 106.1	–	–
	150	Φ_h	64.8[c]	–	32.6	24.5	–	75.0	1.30	9.6
		Φ_h	21.6[d]	18.8	16.3	–	–	–	–	–

[a] *d* Spacings with indices for a *c2mm* simple rectangular columnar lattice ($\Phi_{r\text{-}c}$): (20), (11), (31), (40), and (22); [b] for indices (51), (42), (13), (33), and (53). [c] *d*-Spacings with indices for a *p6mm* hexagonal columnar lattice (Φ_h): (10), (11), (20), and (21); [d] for indices (30), (22), and (40); the *d*-spacing ratios are as expected for the 2D hexagonal columnar lattice: $d_{10}/d_{11}/d_{20}/d_{21}/d_{30}/d_{22}/d_{40} = 1:(1/\sqrt{3}):(1/\sqrt{4}):(1/\sqrt{7}):(1/\sqrt{9}):(1/\sqrt{12}):(1/\sqrt{16})$. [e] *d* Spacings with indices for a nematic columnar lattice (N_c). [f] *d*Spacings with indices for a *p2mm* simple rectangular columnar lattice ($\Phi_{r\text{-}s}$): (10), (11), (12), and (21); [g] For indices (04), (30), (31), and (15). [h] For the Φ_h LC phase, lattice dimension *a* is the same as the column diameter; for $\Phi_{r\text{-}c}$ and $\Phi_{r\text{-}s}$ phases, lattice dimensions *a* and *b* are given. [i] Experimental density of the molecule in the LC phase. [j] Number of monodendrons per cylindrical stratum of the supramolecular column: $\mu = (\sqrt{3} N_A a^2 t \rho)/2M$; ($N_A = 6.022045 \times 10^{23}$ mol^{-1}, t = 7.2 Å = average column stratum height, ρ = average density of the molecule in the LC phase, a = lattice dimension, M = molar mass of the monodendron).

 © 2005 Wiley-VCH Verlag GmbH & Co. KGaA, Weinheim

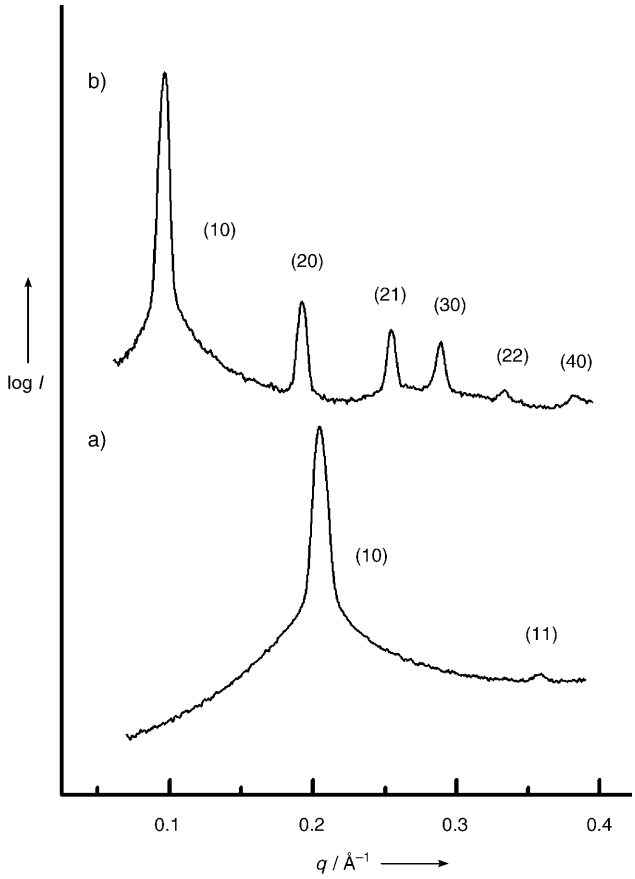


Figure 2. XRD pattern in the Φ_h phase of a) **3** and b) **7**. In b), the observed peaks shift to larger *d* spacings, which leads to a greater than twofold increase in column diameter.

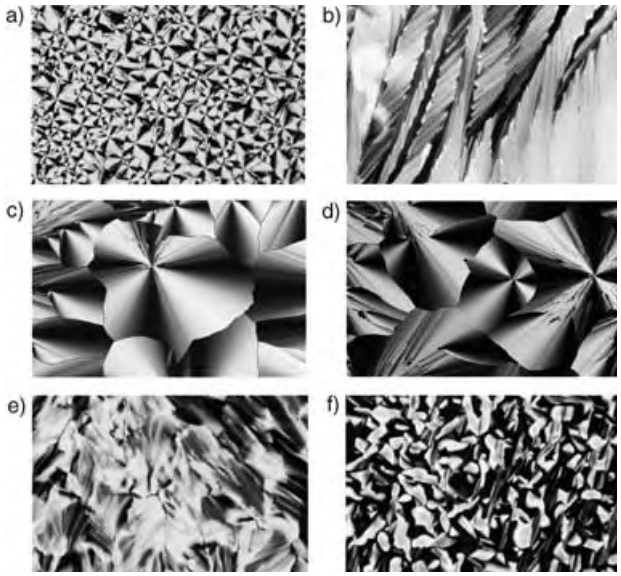


Figure 3. Representative TOPM textures of the hexagonal columnar (Φ_h) mesophase, obtained by cooling at a rate of 1 °C min^{-1} from isotropic phase of a) **1**; b) **2**; c) **3**; d) **4**; e) **5**; and f) **7**.

smaller than that of the twin-dendritic benzamide **3** (a = 34.1 Å, Figure 2a and Table 2), which forms an orthogonal stack of dendrons in its supramolecular column.[3c] However, the column diameter of the Janus benzamide **4** (a = 31.7 Å) is larger than that of the supramolecular column generated from the twin benzamide **1** (a = 25.3 Å).[3b] This indicates that the nonfluorinated Janus-dendritic benzamide **4** forms an orthogonal stack of dendrons in the column of its Φ_h phase that is similar to those of the columns self-assembled from nonfluorinated twin-dendritic benzamides **3** and **1**.

The twin-dendritic benzamide **2**, which contains only semifluorinated aliphatic chains, shows four reflections in the XRD pattern at 78 °C. They are indexed to the (10), (11), (20), and (21) peaks of a 2D Φ_h phase generated from columns with a diameter of 33.2 Å (Table 2). This diameter is substantially larger than that of the nonfluorinated twin-dendritic benzamide **1**. However, the column diameter is close to that of the supramolecular column of the nonfluorinated Janus-dendritic benzamide **4**, evidence that its corresponding supramolecular column is constructed from an orthogonal stack of building blocks.

The semifluorinated Janus-dendritic benzamide **7**, which contains hydrogenated aliphatic chains in one dendron and semifluorinated aliphatic chains in the other, forms a Φ_h phase above 137.3 °C. The X-ray diffraction pattern at 150 °C shows the reflections (10), (20), (21), (30), (22), and (40) that index to a 2D Φ_h lattice with a column diameter of 75.0 Å (Figure 2b). This column diameter is about 2.2-fold larger than that of the twin-based column of **3** (a = 34.1 Å), suggesting that in the semifluorinated Janus column, the fluorinated aliphatic regions do not mix with the hydrogenated aliphatic regions as a result of a fluorophobic effect.[6] If they mixed, they would generate only an orthogonal stack with a column diameter expected to be very close to that of the nonfluorinated Janus-dendritic benzamide **4**. Similarly, the semifluorinated Janus-dendritic benzamide **5** self-assembles into a supramolecular column with a column diameter of 59 Å (Table 2), which is 2.3-fold larger than that of the corresponding nonfluorinated twin-dendritic benzamide, **1** (a = 25.3 Å). These results suggest that the semifluorinated Janus-dendritic benzamides **5** and **7** self-assemble into a bilayered disc or crown in which the semifluorinated regions are segregated from hydrogenated aliphatic regions, with the aromatic part of the molecules occupying the intermediate region between the core and the periphery. The disc or crownlike aggregate generates the supramolecular column. This arrangement contrasts with the orthogonal stack formed by nonfluorinated or semifluorinated twin-dendritic benzamides and by nonfluorinated Janus-dendritic benzamides.

Electron density profiles were computed with the aid of the integrated intensity data calculated from the X-ray diffraction peaks obtained in the Φ_h phase to visualize the molecular organization of the dendrons in various supramolecular columns (Figure 4).[4a] The XRD of the nonfluorinated Janus benzamide **4** in the Φ_h phase shows a very strong (10) peak and a very weak (11) peak that are expected from the orthogonal stacks formed by these molecules.[3c] The electron density profile computed with the phase choice "+ −" for these two reflections exhibits a maximum in the core. The maximum electron density of the core decreases towards the periphery of the column, becoming almost constant on the periphery (Figure 4a). This variation of the electron density

 © 2005 Wiley-VCH Verlag GmbH & Co. KGaA, Weinheim

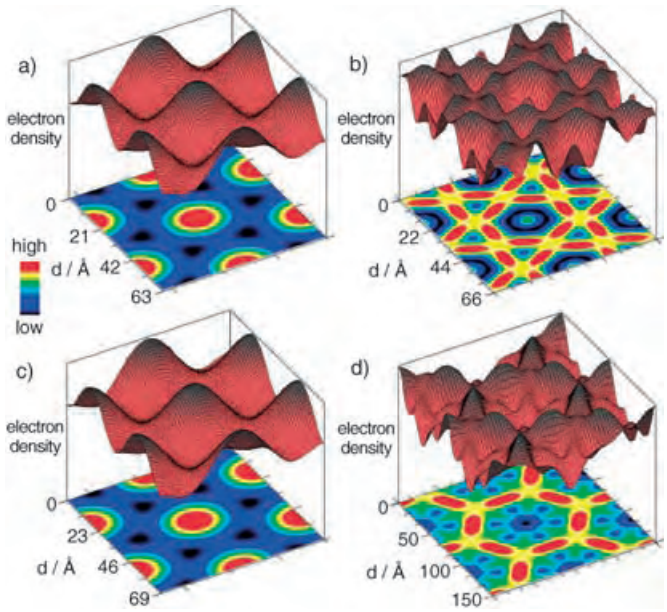


Figure 4. Electron density profiles and contour plots of the twin- and Janus-dendritic benzamides a) **4** showing the center of the supramolecular columns with high electron density (red) due to the aromatic parts; b) **2** with high electron density (red) in the periphery of the columns which corresponds to the semifluorinated aliphatic chains, and the low electron density (black), which corresponds to the hydrogenated aliphatic chains; c) **3** showing the center of the supramolecular columns with high electron density (red), which corresponds to the aromatic parts; and d) **7** with high electron density (red) in the periphery of the columns which corresponds to the semifluorinated aliphatic chains.

profiles is consistent with the nanophase segregation expected in these systems.[1c,d,4a] The maximum and the surrounding high electron density regions correspond to the aromatic portion of the molecules, and the near-constant peripheral regions represent the aliphatic part of the molecules from the orthogonal stack of the twin-dendritic benzamides. Similar electron density profiles were observed for the supramolecular columns self-assembled from the twin-dendritic benzamide **1**.

The semifluorinated twin-dendritic benzamide **2** shows additional reflections in the Φ_h phase that correspond to a strong (10) peak, a moderately strong (21) peak, a very weak (20) peak, and a weak (11) peak. The observation of a moderately strong (21) peak rather than a sequence of higher order peaks with decreasing intensity suggests that the semifluorinated aliphatic chains of the molecules occupy the peripheral regions of the columns. The electron density profiles computed with the phases "$- - + +$" for the peaks (10), (11), (20), and (21), respectively, show high and nearly constant electron density regions on the periphery of the columns (Figure 4b). They also show an intermediate electron density region near the core of the columns that corresponds to the aromatic portions. As one moves toward the periphery from the aromatic regions of the column, the electron density reaches a minimum and then rises toward the semifluorinated regions on the periphery. The regions surrounding the minima in the electron density correspond to the hydrogenated aliphatic part of the molecule. Notably, the electron density profile is similar to that observed in the Φ_h phase of a pyramidal columnar supramolecular dendrimer with semifluorinated aliphatic chains that was reported previously.[5a]

The electron density profiles of the twin-dendritic benzamide **3** is shown in Figure 4c. These profiles show maximum electron density in the center of the columns corresponding to the aromatic regions and low electron density corresponding to the aliphatic region in the periphery. The semifluorinated Janus-dendritic benzamide **7** shows the reflections (10), (20), (21), (30), (22), and (40). Whereas the peak with the strongest intensity is (10), the intensities of (20) and (30) peaks are higher than that of the (21) peak (Figure 2b). This is consistent with the semifluorinated aliphatic chains occupying the peripheral region of the column. Accordingly, the electron density profiles for the phases "$- + - - + -$" has high electron density in the peripheral region of the column and low electron density in the central region of the column (Figure 4d). Starting from the center of the column, the electron density increases from the lowest value to a small local maximum that corresponds to the aromatic part of the molecules. As one moves closer to the periphery from the aromatic region, the electron density decreases slightly owing to the hydrogenated part of the semifluorinated aliphatic chains. Therefore, the electron density profiles are consistent with the bilayered columnar structure containing the hydrogenated aliphatic chains in the core and the semifluorinated aliphatic chains in the periphery with the aromatic part occupying the intermediate region. Molecular models of the bilayered supramolecular columns obtained from small- and wide-angle XRD of oriented fibers are shown in Figure 5,

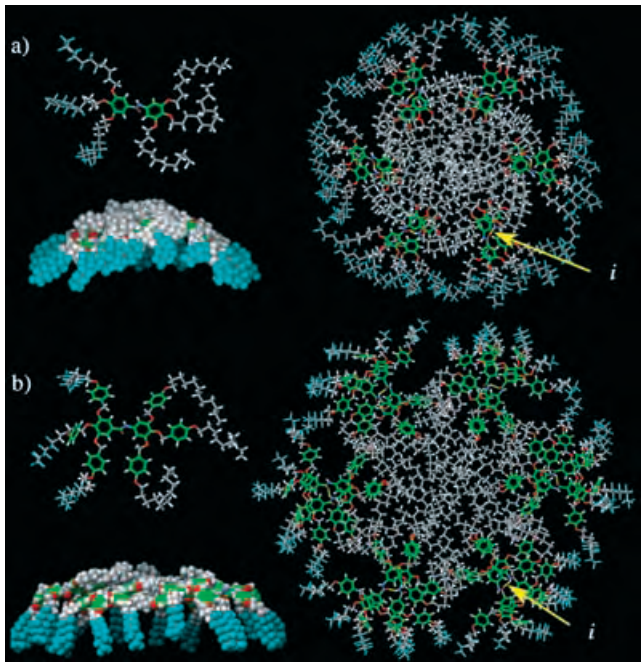


Figure 5. Structures of a) **5** and b) **7**. Top left: single dendron with the semifluorinated tails in blue; bottom left: space-filling side view of one crownlike layer; right: top view of two consecutive crownlike layers (*i* indicates the hydrogen bonding between layers).

 © 2005 Wiley-VCH Verlag GmbH & Co. KGaA, Weinheim

Figure 6, and Figure 7. These models illustrate the location of the nonfluorinated alkyl chains in the central region of the column and the perfluorinated regions in the periphery of the column. Nonorthogonal hydrogen bonding is available in the crownlike stratum of the pyramidal column (Figure 5 and Figure 6). *N*-methylation of the –NH– groups of the Janus-dendritic benzamides almost destroys the pyramidal columnar assembly. The *N*-methylated Janus-benzamide derivative **5** displays a monotropic crystalline *p2mm* simple rectangular phase before melting at 67 °C (see Supporting Information). The crystals of its precursor benzamide **5** melt into a Φ_h phase at 106 °C, followed by isotropization at 157 °C (Table 1). The behavior of the latter demonstrates that hydrogen bonding is responsible for the formation of the LC phases of the Janus-dendritic benzamides.

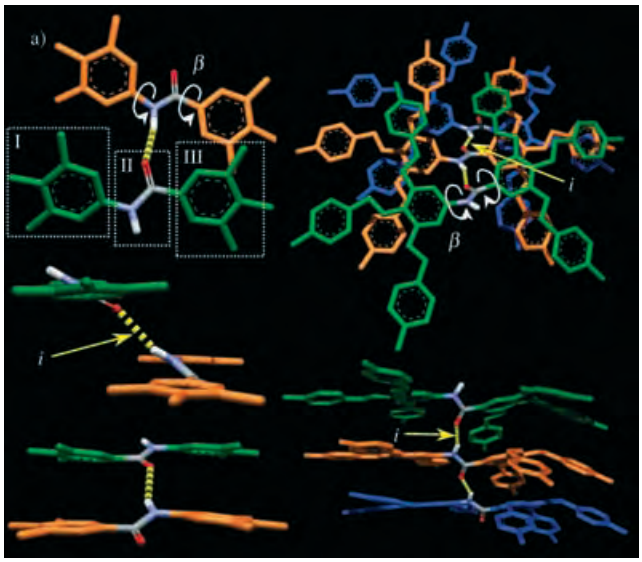


Figure 6. Hydrogen-bonding details for Janus benzamides a) **5** and b) **7**; only the aromatic regions are shown, with each dendron molecule colored differently. The formation of hydrogen bonds (*i*) requires a benzamide torsion angle (β) of about 30°, as the layer spacing is approximately 4.5–5.0 Å. Top left: dihedral angles between planes I and II, approximately 30°; between planes II and III, approximately 30° (Ref. [7]); and between planes I and III, 0°. The dihedral angle between planes I and III was chosen to be 0° instead of 62.6°, as reported in Ref. [7], to decrease the steric constrains and to facilitate better packing.

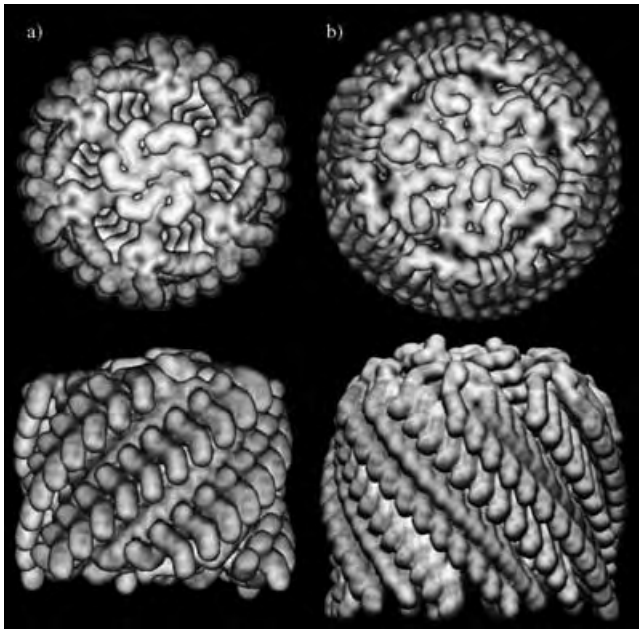


Figure 7. Supramolecular assembly models of a) **5** and b) **7**, indicating the higher electron density on the semifluorinated periphery and the short-range helical order of the supramolecular assembly.

In conclusion, the selective attachment of nonfluorinated aliphatic chains on one dendron and semifluorinated aliphatic chains on the other dendron of the twin-tapered dendritic benzamides generates semifluorinated Janus-dendritic benzamides. These, in turn, self-assemble into supramolecular pyramidal columns that exhibit diameters more than double those of the columns generated from nonfluorinated or semifluorinated twin-dendritic benzamides. This new mode of self-assembly of the semifluorinated Janus-dendritic benzamides results from the tendency of the semifluorinated aliphatic chains to segregate from the hydrogenated aliphatic chains. Aside from providing an unusual example of the fluorophobic effect in self-assembly[8,9] and the second example of supramolecular pyramidal dendrimers[5a,b] self-assembled from supramolecular crowns, this novel bilayered supramolecular pyramidal columnar structure opens numerous new strategies for the construction of complex supramolecular nanosystems.[2m,n,10] This initiates a new direction in the area of Janus-derived supramolecular liquid crystals,[2h,i] complements pyramidal mesophases generated from covalent crownlike molecules,[11] and raises the question about the generality of this concept.

Received: April 10, 2005
Published online: July 1, 2005

Keywords: amides · dendrimers · liquid crystals · self-assembly · supramolecular chemistry

[1] a) V. Percec, G. Johansson, J. Heck, G. Ungar, S. V. Batty, *J. Chem. Soc. Perkin Trans. 1* **1993**, 1411–1420; b) G. Johansson, V. Percec, G. Ungar, D. Abramic, *J. Chem. Soc. Perkin Trans. 1* **1994**, 447–459; c) V. Percec, G. Johansson, G. Ungar, J. Zhou, *J. Am. Chem. Soc.* **1996**, *118*, 9855–9866; d) S. D. Hudson, H.-T. Jung, V. Percec, W.-D. Cho, G. Johansson, G. Ungar, V. S. K. Balagurusamy, *Science* **1997**, *278*, 449–452; e) V. Percec, W.-D. Cho, P. E. Mosier, G. Ungar, D. J. P. Yeardley, *J. Am. Chem. Soc.* **1998**, *120*, 11061–11070; f) V. Percec, W.-D. Cho, G. Ungar, D. J. P. Yeardley, *Angew. Chem.* **2000**, *112*, 1661–1666; *Angew. Chem. Int. Ed.* **2000**, *39*, 1597–1602; g) V. Percec, W.-D. Cho, G. Ungar, *J. Am. Chem. Soc.* **2000**, *122*, 10273–10281; h) V. Percec, W.-D. Cho, G. Ungar, D. J. P. Yeardley, *J. Am. Chem. Soc.* **2001**, *123*, 1302–1315; i) V. Percec, W.-D. Cho, G. Ungar, D. J. P. Yeardley, *Chem. Eur. J.* **2002**, *8*, 2011–2025; j) V. Percec, M Glodde, T. K. Bera, Y. Miura, I. Shiyanovskaya, K. D. Singer, V. S. K. Balagurusamy, P. A. Heiney, I. Schnell, A. Rapp, H.-W. Spiess, S. D. Hudson, H. Duan, *Nature* **2002**, *419*, 384–387; k) V. Percec, C. M. Mitchell, W.-D. Cho, S. Uchida, M. Glodde, G. Ungar, X. Zeng, Y. Liu, V. S. K. Balagurusamy, P. A. Heiney, *J. Am. Chem. Soc.* **2004**, *126*, 6078–6094; l) V. Percec, A. E.

 © 2005 Wiley-VCH Verlag GmbH & Co. KGaA, Weinheim

Dulcey, V. S. K. Balagurusamy, Y. Miura, J. Smidrkal, M. Peterca, S. Nummelin, U. Edlund, S. D. Hudson, P. A. Heiney, H. Duan, S. N. Magonov, S. A. Vinogradov, *Nature* **2004**, *430*, 764 – 768.

[2] a) D. J. Pesak, J. S. Moore, *Angew. Chem.* **1997**, *109*, 1709 – 1712; *Angew. Chem. Int. Ed. Engl.* **1997**, *36*, 1636 – 1639; b) H. Meier, M. Lehmann, *Angew. Chem.* **1998**, *110*, 666 – 669; *Angew. Chem. Int. Ed.* **1998**, *37*, 643 – 645; c) M. Marcos, A. Omenat, J. L. Serrano, *C. R. Chim.* **2003**, *6*, 947 – 957; d) M. Marcos, R. Gimenez, J. L. Serrano, B. Donnio, B. Heinrich, D. Guillon, *Chem. Eur. J.* **2001**, *7*, 1006 – 1013; e) M. Suarez, J.-M. Lehn, S. C. Zimmerman, A. Skoulios, B. Heinrich, *J. Am. Chem. Soc.* **1998**, *120*, 9526 – 9532; f) T. Chuard, M.-T. Beguin, R. Deschenaux, *C. R. Chim.* **2003**, *6*, 959 – 962; g) M. W. P. L. Baars, S. H. M. Söntjens, H. M. Fischer, H. W. I. Peerlings, E. W. Meijer, *Chem. Eur. J.* **1998**, *4*, 2456 – 2466; h) I. M. Saez, J. W. Goodby, *Chem. Eur. J.* **2003**, *9*, 4869 – 4877; i) I. M. Saez, J. W. Goodby, *Chem. Commun.* **2003**, 1726 – 1727; j) M. Kimura, Y. Saito, K. Ohta, K. Hanabusa, H. Shirai, N. Kobayashi, *J. Am. Chem. Soc.* **2002**, *124*, 5274 – 5275; k) C. Kim, K. T. Kim, Y. Chang, H. H. Song, T.-Y. Cho, H.-J. Jeon, *J. Am. Chem. Soc.* **2001**, *123*, 5586 – 5587; l) B.-K. Cho, A. Jain, S. M. Gruner, U. Wiesner, *Science* **2004**, *305*, 1598 – 1601; m) C. Tschierske, *Curr. Opin. Colloid Interface Sci.* **2002**, *7*, 69 – 80; n) S. A. Ponomarenko, N. I. Boiko, V. P. Shibaev, *J. Polym. Sci. Part C* **2001**, *43*, 1 – 45.

[3] a) G. Ungar, D. Abramic, V. Percec, J. A. Heck, *Liq. Cryst.* **1996**, *21*, 73 – 86; b) V. Percec, C.-H. Ahn, T. K. Bera, G. Ungar, D. J. P. Yeardley, *Chem. Eur. J.* **1999**, *5*, 1070 – 1083; c) V. Percec, T. K. Bera, M. Glodde, Q. Fu, V. S. K. Balagurusamy, P. A. Heiney, *Chem. Eur. J.* **2003**, *9*, 921 – 935.

[4] a) V. S. K. Balagurusamy, G. Ungar, V. Percec, G. Johansson, *J. Am. Chem. Soc.* **1997**, *119*, 1539 – 1555; b) V. Percec, C.-H. Ahn, G. Ungar, D. J. P. Yeardley, M. Möller, S. S. Sheiko, *Nature* **1998**, *391*, 161 – 164; c) G. Ungar, V. Percec, M. N. Holerca, G. Johansson, J. A. Heck, *Chem. Eur. J.* **2000**, *6*, 1258 – 1266; d) D. J. P. Yeardley, G. Ungar, V. Percec, M. N. Holerca, G. Johansson, *J. Am. Chem. Soc.* **2000**, *122*, 1684 – 1689; e) H. Duan, S. D. Hudson, G. Ungar, M. N. Holerca, V. Percec, *Chem. Eur. J.* **2001**, *7*, 4134 – 4141; f) V. Percec, M. N. Holerca, S. Uchida, W. -D. Cho, G. Ungar, Y. Lee, D. J. P. Yeardley, *Chem. Eur. J.* **2002**, *8*, 1106 – 1117; g) G. Ungar, Y. Liu, X. Zeng, V. Percec, W.-D. Cho, *Science* **2003**, *299*, 1208 – 1211; h) X. Zeng, G. Ungar, Y. Liu, V. Percec, A. E. Dulcey, J. K. Hobbs, *Nature* **2004**, *428*, 157 – 160; i) G. H. Mehl, *Angew. Chem.* **2005**, *117*, 678 – 679; *Angew. Chem. Int. Ed.* **2005**, *44*, 672 – 673.

[5] a) V. Percec, M. Glodde, G. Johansson, V. S. K. Balagurusamy, P. A. Heiney, *Angew. Chem.* **2003**, *115*, 4474 – 4478; *Angew. Chem. Int. Ed.* **2003**, *42*, 4338 – 4342; b) D. A. Tomalia, *Nat. Mater.* **2003**, *2*, 711 – 712.

[6] For fundamental reports on fluorinated materials, see: a) B. E. Smart in *Organofluorine Chemistry. Principles and Commercial Applications* (Eds.: R. E. Banks, B. E. Smart, J. C. Tatlow), Plenum, New York, **1994**; b) *Modern Fluoropolymers* (Ed.: J. Scheirs), Wiley, New York, **1997**; c) D. F. Eaton, B. E. Smart, *J. Am. Chem. Soc.* **1990**, *112*, 2821 – 2823.

[7] S. Kashino, K. Ito, M. Haisa, *Bull. Chem. Soc. Jpn.* **1979**, *52*, 365 – 369.

[8] For examples of fluorinated molecules in self-assembly, see: a) G. W. Coates, A. R. Dunn, L. M. Henling, D. A. Dougherty, R. H. Grubbs, *Angew. Chem.* **1997**, *109*, 290; *Angew. Chem. Int. Ed. Engl.* **1997**, *36*, 248 – 251; b) W. J. Feast, P. W. Lövenich, H. Puschmann, C. Taliani, *Chem. Commun.* **2001**, *5*, 505 – 506; c) D. R. Dukeson, G. Ungar, V. S. K. Balagurusamy, V. Percec, G. Johansson, M. Glodde, *J. Am. Chem. Soc.* **2003**, *125*, 15974 – 15980.

[9] For examples of fluorinated compounds in self-organization, see: a) U. Dahn, C. Erdelen, H. Ringsdorf, R. Festag, J. H. Wendorff, P. A. Heiney, N. C. Maliszewskyj, *Liq. Cryst.* **1995**, *19*, 759; b) G. Johansson, V. Percec, G. Ungar, K. Smith, *Chem. Mater.* **1997**, *9*, 164 – 175; c) V. Percec, D. Schlueter, G. Ungar, *Macromolecules* **1997**, *30*, 645 – 648; d) F. Guittard, E. T. de Givenchy, S. Geribaldi, A. Cambon, J. *Fluorine Chem.* **1999**, *100*, 85 – 96; e) X. H. Cheng, S. Diele, C. Tschierske, *Angew. Chem.* **2000**, *112*, 605; *Angew. Chem. Int. Ed.* **2000**, *39*, 592 – 595; f) C. Rocaboy, F. Hampel, J. A. Gladysz, *J. Org. Chem.* **2002**, *67*, 6863 – 6870; g) A.-M. Caminade, C.-O. Turrin, P. Sutra, J.-P. Majoral, *Curr. Opin. Colloid Interface Sci.* **2003**, *8*, 282 – 295.

[10] a) J.-M. Lehn, *Proc. Natl. Acad. Sci. USA* **2002**, *99*, 4763 – 4768; b) J. W. Goodby, *Curr. Opin. Colloid Interface Sci.* **1999**, *4*, 361 – 368; c) D. Guillon, R. Deschenaux, *Curr. Opin. Colloid Interface Sci.* **2002**, *6*, 515 – 525; d) T. Emrick, J. M. J. Fréchet, *Curr. Opin. Colloid Interface Sci.* **1999**, *4*, 15 – 23.

[11] a) H. Zimmermann, R. Poupko, Z. Luz, J. Billard, *Z. Naturforsch. A* **1985**, *40*, 149 – 160; b) J. Malthête, A. Collet, *Nouv. J. Chim* **1985**, *9*, 151 – 153; c) A.-M. Levelut, J. Malthête, A. Collet, *J. Phys.* **1986**, *47*, 351 – 357; d) J. Malthête, A. Collet, *J. Am. Chem. Soc.* **1987**, *109*, 7544 – 7545; e) R. Poupko, Z. Luz, N. Spielberg, H. Zimmermann, *J. Am. Chem. Soc.* **1989**, *111*, 6094 – 6105; f) H. Zimmermann, V. Bader, R. Poupko, E. J. Wachtel, Z. Luz, *J. Am. Chem. Soc.* **2002**, *124*, 15286 – 15301.

 © 2005 Wiley-VCH Verlag GmbH & Co. KGaA, Weinheim

Microporous Materials

High H_2 Adsorption in a Microporous Metal–Organic Framework with Open Metal Sites**

Banglin Chen, Nathan W. Ockwig, Andrew R. Millward, Damacio S. Contreras, and Omar M. Yaghi**

Metal–organic frameworks (MOFs) are a rapidly growing class of porous materials that are studied for their amenability to design[1] and extraordinary permanent porosity.[2] The recent discovery that MOFs take up significant amounts of

[*] Prof. B. Chen, D. S. Contreras
Department of Chemistry
University of Texas-Pan American
Edinburg, TX 78541-2999 (USA)
Fax: (+1) 956-384-5006
E-mail: banglin@utpa.edu
N. W. Ockwig, A. R. Millward, Prof. O. M. Yaghi
Materials Design and Discovery Group
Department of Chemistry
University of Michigan
Ann Arbor, MI 48109-1055 (USA)
Fax: (+1) 734-615-9751
E-mail: oyaghi@umich.edu

[**] This work was supported by the University of Texas-Pan American through a start-up fund and a Faculty Research Council award to B. Chen, and, in part, by a Welch Foundation grant (BG-0017) to the Department of Chemistry at UTPA, a grant from the National Science Foundation to O.M.Y. (DMR-0242630), and the Department of Energy (O.M.Y.).

Supporting information for this article is available on the WWW under http://www.angewandte.org or from the author.

 DOI: 10.1002/anie.200462787 © 2005 Wiley-VCH Verlag GmbH & Co. KGaA, Weinheim

hydrogen has further intensified research in this area.[3] In particular, the focus remains on identifying strategies for designing MOFs with high hydrogen-storage capacities. We have already found that both the metal-oxide units and the organic links are important features for hydrogen binding,[3a,d] and that interpenetrating MOFs take up more hydrogen than their noninterpenetrating counterparts.[3d] In this report, we highlight the synthesis and structure of a MOF (named MOF-505) based on the NbO topology which has two kinds of pores, open metal sites, permanent porosity, and a high capacity for hydrogen adsorption.

We have previously synthesized MOFs with $Cu_2(CO_2)_4$ "paddle-wheel" units, and illustrated their use in the design of 0-periodic discrete[4] and 3-periodic extended structures.[5,10] MOF-505 was synthesized under analogous conditions: the solvothermal reaction of 3,3′,5,5′-biphenyltetracarboxylic acid (H_4bptc; 25 mg, 0.076 mmol)[6] and $Cu(NO_3)_2{\cdot}(H_2O)_{2.5}$ (52 mg, 0.22 mmol) in *N*,*N*-dimethylformamide (DMF)/ethanol/H_2O (3:3:2 *v*/*v*/*v*) at 65 °C for 24 h gave green, block-shaped crystals (47 mg, 86 % yield based on H_4bptc). The compound was formulated as $[Cu_2(bptc)(H_2O)_2(dmf)_3(H_2O)]$ by elemental microanalysis[7] and single-crystal X-ray diffraction studies.[8]

The $Cu_2(CO_2)_4$ unit is a square secondary building unit (SBU; Figure 1 A) that is defined by the carboxylate carbon atoms, and the $bptc^{4-}$ unit is a rectangular SBU that is defined by the 3, 3′, 5, and 5′ carbon atoms (Figure 1 B). The carboxylate functionalities of the $bptc^{4-}$ ligand are nearly coplanar with the biphenyl rings (the dihedral angle between the carboxylate group and the phenyl ring is 7.4°).[2] Thus, when the square SBUs are linked to the biphenyl rings, they must be mutually orthogonal (Figure 1 C), an aspect that is the hallmark of the NbO topology.[9,10] The crystal structure of MOF-505 (Figures 1 D and E) clearly shows that the link has predisposed the inorganic square SBUs at nearly 90° angles (94.4°) to the organic rectangular SBUs. This arrangement yields an overall 3-periodic network which has two kinds of pores. The first of these pores is defined by six inorganic SBUs (representing the faces of a cubic NbO subunit) with a spherical volume of 290 Å^3 and a pore diameter of 8.30 Å (Figures 1 D and F), while the second, and larger, pore is defined by six organic SBUs (again representing the faces of a cubic NbO subunit) and has a solvent-accessible void of 540 Å^3 with a pore diameter of 10.10 Å (Figures 1 E and G).[11] These roughly spherical pores are arranged in a rhombohedrally distorted CsCl-type fashion with the small pores surrounded by eight large pores, each of which is also surrounded by eight small pores. There are a total of six pores (three large and three small) per unit cell, which are coupled through an interconnected porous network of 6.70 Å diameter apertures. This provides a total accessible free volume of 2713 Å^3 (37.1 %).[11,12]

Thermal gravimetric analysis (TGA) and powder X-ray diffraction (PXRD) patterns were used to evaluate the framework stability under solvent-exchange conditions. PXRD reveals the same pattern of intense diffraction lines in each of the simulated, as-synthesized, and acetone-exchanged materials (see Supporting Information). However, upon desolvation of the exchanged material, decreased

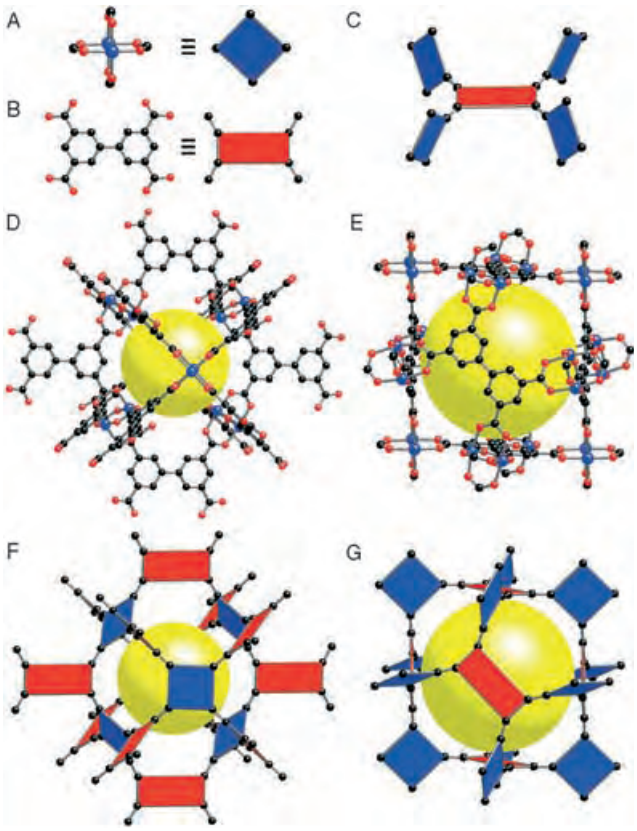


Figure 1. The single-crystal X-ray structure of MOF-505 showing A) $Cu_2(CO_2)_4$ units (blue, square SBUs) and B) $bptc^{4-}$ units (red, rectangular SBUs) that are C) orthogonally joined. The overall 3-periodic crystal structure (D, E; Cu blue, C black, O red, and the yellow sphere represents the largest sphere that would occupy the cavity without contacting the interior van der Waals surface) has two different types of pores and an underlying NbO-type net (F, G). Hydrogen atoms, guest molecules, and terminal solvent molecules have been omitted for clarity.

diffraction intensities and broadened reflections were observed in the PXRD pattern. This indicates some loss of long-range order but not necessarily loss of porosity, as detailed below. To examine the thermal stability of MOF-505 and estimate the temperature of desolvation we conducted a TGA study: the weight loss of 30.83 % below 250 °C corresponds to the liberation of 2.5 acetone molecules and three water molecules per Cu_2bptc formula unit (calcd: 30.53 %).

To evaluate whether the framework structure is maintained upon evacuation of the pores, we obtained the gas sorption isotherms using a Cahn C-1000 microgravimetric balance to measure the change in mass of samples suspended within a glass enclosure under a chosen gas atmosphere. The as-synthesized MOF-505 crystalline sample was activated by immersion in acetone for 72 h (3 × 50 mL for 24 h each) to exchange the dmf guests. The resulting damp, blue-green solid (617 mg) was loaded into the apparatus and evacuated ($<10^{-3}$ Torr) in three stages (I–III), with both weight loss and color changes being recorded (stage I: 15 h at room temperature (weight decreased to 358 mg, 42.0 % weight loss, light blue); stage II: heating at 70 °C for 15 h (weight

 © 2005 Wiley-VCH Verlag GmbH & Co. KGaA, Weinheim

decreased to 325 mg, 5.3% weight loss, dark blue); and stage III: a final dehydration at 120°C for 12 h (weight decreased to 296 mg, 4.7% weight loss, purple)), to leave the evacuated sample. Nitrogen and hydrogen isotherms were obtained at each of these activation stages (I–III) as elaborated below. To ensure complete removal of all volatile contaminants from the system, the gas manifold was evacuated overnight and heated to 100°C prior to the introduction of gas. The system was purged three times at room temperature with the gas to be studied (ultra-high-purity grade, 99.999%) before cooling to 77 K with liquid nitrogen. The sample temperature was monitored by a thermocouple suspended in close proximity to the sample. Pressures were measured with two MKS Baratron 622 A pressure transducers (10 and 1000 Torr, accuracy $\pm 0.25\%$ of range). The gas was introduced incrementally and data points were recorded when no further change in mass was observed (< 0.02 mg per 10 min). An empirical buoyancy correction was applied to all data points based on the buoyancy experienced by standard aluminum foil weights within the pressure range of the gas at 77 K.

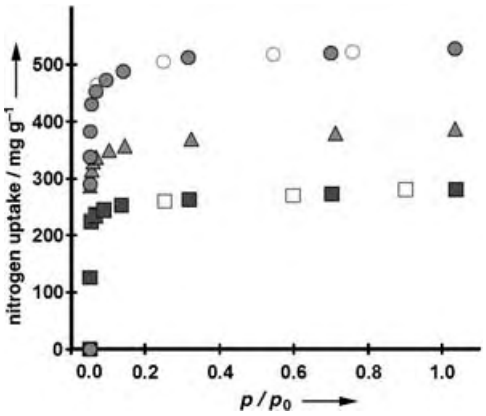


Figure 2. N_2 isotherms for MOF-505 (77 K) after three different activation stages: stage I (25°C, squares), stage II (70°C, triangles), and stage III (120°C, circles); filled shapes indicate adsorption and open shapes indicate desorption data points.

Nitrogen sorption by this material clearly shows reversible type-I isotherms at each of the activation stages (Figure 2), indicative of permanent porosity. At stage I (25°C), an uptake of 278 mg g^{-1} is achieved, with an equivalent Langmuir surface area (A_s) of 967 m^2 g^{-1}, and $K_{N_2} = 0.193$ for a 16.2 Å^2 molecular cross-section. Assuming liquid-nitrogen density (0.808 g cm^{-3}) in the pores, extrapolation of the Dubinin–Radushkevich equation[13] from the low-pressure data points yields an available micropore volume (V_p) of 0.33 cm^3 g^{-1}. Further evacuation of the pores (stage II) removes an additional 5.3% of guests, providing a 36% greater uptake (386 mg g^{-1}, $A_s = 1343$ m^2 g^{-1}, $K_{N_2} = 0.327$, and $V_p = 0.45$ cm^3 g^{-1}) than that observed in the first stage. The fully activated material obtained after stage III shows a substantial increase in the sorption to give a final N_2 uptake of 526 mg g^{-1} ($A_s = 1830$ m^2 g^{-1}, $K_{N_2} = 0.362$, and $V_p = 0.63$ cm^3 g^{-1}). These data are summarized in Table 1.

Table 1: Sorption data for MOF-505.

Activation Stage	T [°C]	Uptake [mg g^{-1}] N_2	H_2	A_s [m^2 g^{-1}][a]	K_{N_2} [Torr^{-1}][a,c]	K_{H_2} [Torr^{-1}][a,d]	V_p [cm^3 g^{-1}][b]
I	25	278	14.1	967	0.193	0.0071	0.33
II	70	386	19.7	1343	0.327	0.0070	0.45
III	120	526	24.7	1830	0.362	0.0086	0.63

[a] Calculated from a Langmuir fit of the data. [b] Calculated by extrapolation of the Dubinin–Radushkevich equation. [c] Calculated from N_2 data. [d] Calculated from H_2 data.

The hydrogen isotherms of MOF-505 measured at 77 K at the same stages of activation are shown in Figure 3. This temperature is well above the critical temperature (33 K) for hydrogen,[14] which suggests that condensation in the pores would be unlikely and complete saturation would not be achieved without much higher pressures. The isotherms measured (0 to 750 Torr) did not show saturation; however, the maximum uptake at 750 Torr for each of the three hydrogen isotherms demonstrates similar increases in capacity to those observed in the nitrogen isotherms, with the fully activated MOF-505 adsorbing an exceptional 2.47 wt% hydrogen at 750 Torr and 77 K. This extraordinary hydrogen sorption capacity is unprecedented in previously reported MOF materials under these conditions.[3h]

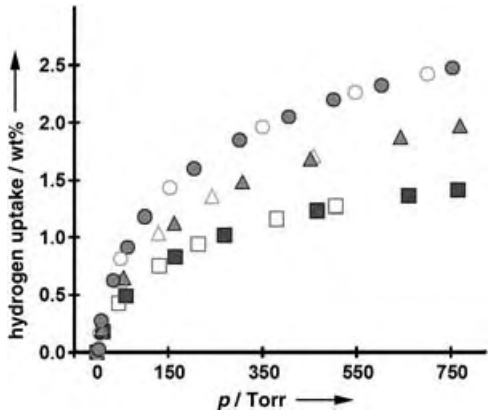


Figure 3. H_2 isotherms for MOF-505 (77 K) after three different activation stages: stage I (25°C, squares), stage II (70°C, triangles), and stage III (120°C, circles); filled shapes indicate adsorption and open shapes indicate desorption data points.

Removal of noncoordinated guests during activation has at least two positive effects on the adsorption capacity: a decrease of sample mass and an increase of available micropore volume and specific surface area. However, removal of the water ligands (bound axially to the copper centers) has the same benefits and also introduces open metal sites that we think enhance the hydrogen–framework interaction. The existence of such open metal sites in MOFs has been confirmed previously by single-crystal X-ray diffraction of

 © 2005 Wiley-VCH Verlag GmbH & Co. KGaA, Weinheim

MOF-11.[5b] Room temperature evacuation overnight (stage I) yields an initial hydrogen uptake of 14.1 mg g^{-1} (1.41 wt% H_2; Table 1). The second activation step (stage II) removes an additional 5.3 wt% (partial dehydration) and increases the hydrogen uptake by 5.6 mg g^{-1} (19.7 mg g^{-1}, 1.97 wt% H_2). Further removal of 4.7 wt% (stage III, complete dehydration) increases the hydrogen uptake capacity by an additional 5.0 mg g^{-1} to 24.7 mg g^{-1} or 2.47 wt% H_2. Upon comparison, the initial activation step (stage I, evacuation of bulk guests) shows an increase in hydrogen sorption of 0.34 mg g^{-1} per percent mass loss whereas the last two activation steps (stages II and III, dehydration with loss of six water molecules per Cu_2bptc formula unit) show a corresponding increase of 1.06 mg g^{-1} per percent mass loss during activation. Indeed, at stage I the H_2 uptake (77 K) is 14.1 mg g^{-1}, while the fully activated material (stage III) containing open metal sites displays an uptake nearly twice as high (24.7 mg g^{-1}) despite only a 10% mass loss. The lack of any hysteresis in the isotherm illustrates that this physisorption process is completely reversible, and that the presence of these open metal sites does not hamper the desorption process, nor do the pore apertures of 6.70 Å significantly hinder small-molecule diffusion through the host framework. Although there are slight curvatures in the Langmuir plots (leading to some degree of uncertainty) some insight pertinent to this specific system can still be gleaned. Increasing K_{H_2} values reveal a trend toward increasing hydrogen affinity of the fully dehydrated framework relative to the partially evacuated material (Table 1).

Although we speculate that the open metal sites have a favorable impact on the hydrogen sorption capacity of MOF-505, further experimentation is required to verify this. Another plausible explanation for the high hydrogen uptake capacity of MOF-505 is a simple correlation between specific surface area (A_s) and uptake. Similar correlations have been made for activated carbons and zeolites[15] but have yet to be established for MOF materials. In fact, we would like to specifically point out that, so far, MOF materials with very high surface areas (1000–4500 m^2 g^{-1}) do not cleanly follow this correlation.[3d] Nevertheless, we do observe that each stage of activation is accompanied by distinct changes in sample color, which is consistent with a change in the coordination environment of the metal sites as a result of the removal of terminal ligands. As-synthesized MOF-505 is blue-green and the first-stage activation changes this to light blue; further activation deepens the blue color, while the final activation step yields a deep-purple material. An activated sample exposed to ambient air for 36 h shows a dramatic color change from purple back to blue-green, with the subsequent TGA showing a loss of 18.7 wt% below 250 °C, corresponding to the loss of six water molecules per Cu_2bptc formula unit (calcd: 19.3%). Undoubtedly, two of these water molecules are axially coordinated to the paddle wheels, while the remaining four may be located in the equatorial quadrants defined by adjacent carboxylate groups of every paddle wheel.

At present, we are targeting the application of MOFs to gas sorption and selective separations in order to establish their optimal performance and to establish principles for improved inert-gas storage capacities. The unprecedented 2.47 wt% H_2 uptake of MOF-505 is an important milestone toward achieving these objectives.

Received: December 2, 2004
Revised: March 24, 2005
Published online: May 27, 2005

Keywords: adsorption · copper · hydrogen · metal–organic frameworks · microporous materials

[1] a) O. M. Yaghi, M. O'Keeffe, N. W. Ockwig, H. K. Chae, M. Eddaoudi, J. Kim, *Nature* **2003**, *423*, 705–714; b) N. W. Ockwig, O. Delgado-Friedrichs, M. O'Keeffe, O. M. Yaghi, *Acc. Chem. Res.* **2005**, *38*, 176–182; c) C. Mellot-Draznieks, J. Dutour, G. Férey, *Angew. Chem.* **2004**, *116*, 6450–6456; *Angew. Chem. Int. Ed.* **2004**, *43*, 6290–6296.

[2] a) H. Li, M. Eddaoudi, M. O'Keeffe, O. M. Yaghi, *Nature* **1999**, *402*, 276–279; b) H. K. Chae, D. Y. Siberio-Pérez, J. Kim, Y. Go, M. Eddaoudi, A. J. Matzger, M. O'Keeffe, O. M. Yaghi, *Nature* **2004**, *427*, 523–527; c) H. Li, M. Eddaoudi, T. L. Groy, O. M. Yaghi, *J. Am. Chem. Soc.* **1998**, *120*, 8571–8572; d) G. Férey, C. Serre, C. Mellot-Draznieks, F. Millange, S. Surble, J. Dutour, I. Margiolaki, *Angew. Chem.* **2004**, *116*, 6456–6461; *Angew. Chem. Int. Ed.* **2004**, *43*, 6296–6301; e) R. Kitaura, K. Seki, G. Akiyama, S. Kitagawa, *Angew. Chem.* **2003**, *115*, 444–447; *Angew. Chem. Int. Ed.* **2003**, *42*, 428–431; f) X. Zhao, B. Xiao, A. J. Fletcher, K. M. Thomas, D. Bradshaw, M. J. Rosseinsky, *Science* **2004**, *306*, 1012–1015.

[3] a) N. L. Rosi, J. Eckert, M. Eddaoudi, D. T. Vodak, J. Kim, M. O'Keeffe, O. M. Yaghi, *Science* **2003**, *300*, 1127–1129; b) D. N. Dybstev, H. Chun, S. H. Yoon, D. Kim, K. Kim, *J. Am. Chem. Soc.* **2003**, *125*, 32–33; c) G. Férey, M. Latroche, C. Serre, F. Millange, T. Loiseau, A. Percheron-Guegan, *Chem. Commun.* **2003**, 2976–2977; d) J. L. C. Rowsell, A. R. Millward, K. S. Park, O. M. Yaghi, *J. Am. Chem. Soc.* **2004**, *126*, 5666–5667; e) D. N. Dybstev, H. Chun, K. Kim, *Angew. Chem.* **2004**, *116*, 5143–5146; *Angew. Chem. Int. Ed.* **2004**, *43*, 5033–5036; f) E. Y. Lee, M. P. Suh, *Angew. Chem.* **2004**, *116*, 2858–2861; *Angew. Chem. Int. Ed.* **2004**, *43*, 2798–2801; g) L. Pan, M. B. Sander, X. Huang, J. Li, M. Smith, E. Bittner, B. Bockrath, J. K. Johnson, *J. Am. Chem. Soc.* **2004**, *126*, 1308–1309; h) J. L. C. Rowsell, O. M. Yaghi, *Angew. Chem.* **2005**, *117*, accepted; *Angew. Chem. Int. Ed.* **2005**, *44*, accepted.

[4] M. Eddaoudi, J. Kim, J. B. Wachter, H. K. Chae, M. O'Keeffe, O. M. Yaghi, *J. Am. Chem. Soc.* **2001**, *123*, 4368–4369.

[5] a) M. Eddaoudi, D. B. Moler, H. Li, B. Chen, T. M. Reineke, M. O'Keeffe, O. M. Yaghi, *Acc. Chem. Res.* **2001**, *34*, 319–330; b) B. Chen, M. Eddaoudi, T. M. Reineke, J. W. Kampf, M. O'Keeffe, O. M. Yaghi, *J. Am. Chem. Soc.* **2000**, *122*, 11559–11560; c) B. Chen, M. Eddaoudi, S. T. Hyde, M. O'Keeffe, O. M. Yaghi, *Science* **2001**, *291*, 1021–1023.

[6] H_4bptc was prepared according to published methods: S. J. Coles, R. Holmes, M. B. Hursthouse, D. J. Price, *Acta Crystallogr. Sect. E* **2002**, *58*, o626.

[7] Elemental analysis (%) for MOF-505 ($C_{25}H_{33}Cu_2N_3O_{14}$): calcd: C 41.32, H 4.54, Cu 17.49, N 5.78; found: C 41.09, H 4.35, Cu 17.20, N 5.61.

[8] X-ray crystallographic data: φ and ω scans were performed on a Bruker SMART APEX CCD area detector with graphite-monochromated $Mo_{K\alpha}$ radiation ($\lambda = 0.71073$ Å). SAINT was used for data integration, SADABS for absorption correction, and XPREP for correction of Lorentz and polarization effects. Structure solution was performed by direct methods and subsequent difference Fourier techniques using the SHELX-

 © 2005 Wiley-VCH Verlag GmbH & Co. KGaA, Weinheim

TL software suite. Data collection for a green, block-shaped crystal of MOF-505 ($0.06 \times 0.06 \times 0.04\ mm^3$) was performed at $-120\,^{\circ}C$; rhombohedral space group $R\bar{3}m$ (no. 166) with $a = 18.4826(8)$, $c = 24.713(2)$ Å, $V = 7311.2(7)$ Å^3, $Z = 18$, $\rho_{calcd} = 0.992\ g\,cm^{-3}$, $\mu(Mo_{K\alpha}) = 1.338\ mm^{-1}$, $F(000) = 2160$; a total of 10057 reflections (2072 unique, $R_{int} = 0.0488$) within $2\theta_{max} = 55.16^{\circ}$, $T_{max} = 0.9484$, $T_{min} = 0.9240$. All non-hydrogen atoms of the extended structure, except for solvent molecules, were refined anisotropically. Electron-density contributions from diffuse scattering and disordered guest molecules were handled using the SQUEEZE procedure from the PLATON software suite. Hydrogen atoms were generated with idealized geometries. The final full-matrix least-squares refinement (based on 2072 observed reflections) on F^2 converged to $R1$ ($I > 2\sigma(I)$) = 0.0361 and $wR2$ (all data) = 0.0896 with GOF = 0.945. The maximum and minimum peaks on the final difference Fourier map corresponded to 0.549 and $-0.269\ e^-\,Å^{-3}$, respectively. CCDC 257470 contains the supplementary crystallographic data for this paper. These data can be obtained free of charge from the Cambridge Crystallographic Data Centre via www.ccdc.cam.ac.uk/data_request/cif.

[9] M. Eddaoudi, J. Kim, D. Vodak, A. Sudik, J. Watcher, M. O'Keeffe, O. M. Yaghi, *Proc. Natl. Acad. Sci. USA* **2002**, *99*, 4900 – 4904.

[10] M. Eddaoudi, J. Kim, M. O'Keeffe, O. M. Yaghi, *J. Am. Chem. Soc.* **2001**, *124*, 376 – 377.

[11] The van der Waals radii of C (1.70 Å) and Cu (1.43 Å) were employed in the determination of distance parameters: A. Bondi, *J. Phys. Chem.* **1964**, *68*, 441 – 451.

[12] As calculated using the accessible free volume method in Cerius^2 4.2 from Accelrys with a probe radius of 1.45 Å.

[13] F. Rouquerol, J. Rouqerol, K. Sing, *Absorption by Porous Solids*, Academic Press, London, **1999**.

[14] R. C. Reid, J. M. Prausnitz, B. E. Poling, *The Properties of Gases and Liquids*, *4th ed.*, McGraw-Hill, New York, **1987**.

[15] M. G. Nijkamp, J. E. M. J. Raaymakers, A. J. van Dillen, K. P. de Jong, *Appl. Phys. A* **2001**, *72*, 619 – 623.

 © 2005 Wiley-VCH Verlag GmbH & Co. KGaA, Weinheim

Chemical Vapor Deposition

The Mechanism of Chemical Vapor Deposition of Cubic Boron Nitride Films from Fluorine-Containing Species**

W. J. Zhang, C. Y. Chan, X. M. Meng, M. K. Fung, I. Bello, Y. Lifshitz, S. T. Lee, and X. Jiang*

The unique properties of cubic boron nitride (cBN) make it an excellent material for mechanical and electronic applications. Powders of cBN were synthesized by using a high-pressure, high-temperature method[1] and films of cBN were deposited by energetic ion-assisted physical vapor deposition (PVD).[2–5] The latter technique involves two distinct stages: nucleation and growth. The nucleation of cBN is preceded by a soft incubation interlayer of, first, amorphous BN (aBN) and, second, turbostratic BN (tBN). cBN nucleates on the edges of the basal planes of tBN. Energetic particle bombardment is crucial to cBN nucleation but results in highly stressed, nanocrystalline cBN films with poor adhesion and a limited thickness, thus hindering both mechanical and electronic applications. Deposition through energetic particle bombardment is a shallow implantation ("subplantation") process,[6] that is, nucleation and growth occur at several atomic layers below the surface.[7] This process is the origin of the sp^2-bonded aBN/tBN top surface layer that covers the cBN crystallites in PVD cBN films.

[*] Dr. W. J. Zhang,[+] C. Y. Chan, X. M. Meng,[+] Dr. M. K. Fung, Dr. I. Bello, Prof. S. T. Lee[+]
Center Of Super-Diamond and Advanced Films (COSDAF) and Department of Physics and Materials Science
City University of Hong Kong
Kowloon, Hong Kong SAR (China)
Fax: (+852) 2788-7830
E-mail: apwjzh@cityu.edu.hk

Prof. Y. Lifshitz
Center Of Super-Diamond and Advanced Films (COSDAF) and Department of Physics and Materials Science
City University of Hong Kong
Kowloon, Hong Kong SAR (China)
and
Department of Materials Engineering, Technion
Israel Institute of Technology
Haifa 32000 (Israel)

Prof. X. Jiang
Institute of Materials Engineering
University of Siegen
Paul-Bonatz-Strasse 9–11, 57076 Siegen (Germany)

[+] Additional address:
Nano-Organic Photoelectronic Laboratory
Technical Institute of Physics and Chemistry
The Chinese Academy of Science
Beijing 100101 (China)

[**] This work was supported by the Research Grants Council of the Hong Kong Special Administrative Region, China (Project Nos. CityU 1131/04E and CityU 1130/04E). W.J.Z. acknowledges the Alexander von Humboldt Foundation for supporting the collaboration between the City University of Hong Kong and the University of Siegen.

 DOI: 10.1002/anie.200500320 © 2005 Wiley-VCH Verlag GmbH & Co. KGaA, Weinheim

Chemical vapor deposition (CVD) of diamond employs hydrogen chemistry to selectively etch sp^2-bonded carbon atoms to grow high-quality, thick films. Hydrogen does not selectively etch sp^2-bonded BN, thus attempts to grow cBN by hydrogen-based CVD methods failed.[8] However, the deposition of films of up to around 20-μm thick of cBN by fluorine-based bias-assisted CVD methods was recently reported.[9–11] Similar to the CVD of diamond, the nucleation stage of cBN requires an ion-assisted physical mechanism that involves a tBN incubation interlayer as described previously.[10] The application of fluorine-containing species for the growth stage that follows this nucleation enables a drastic decrease in the required bombarding ion energy (< 20 eV),[11] especially for the direct deposition of cBN on diamond, upon which no interlayer (no nucleation stage) forms.[12]

Herein, we show the successful development of a surface CVD growth process of cBN and outline a new mechanism initiated by the introduction of fluorine-containing species. Our study involves a combination of high-resolution transmission electron microscopy (HR-TEM) characterization of the topmost layers of cBN films, X-ray photoelectron spectroscopy (XPS) analysis of the composition of the surface of the film, and optical emission spectroscopy (OES) of the composition of the plasma. The possibility of growing cBN by a true surface CVD process and the understanding of the growth mechanism paves the way to the growth of single-crystal, electronic-grade wafers of cBN for electronic applications.

Deposition of the cBN film was performed in an electron cyclotron resonance (ECR)-enhanced microwave (MW) plasma of a $He(Ar)/N_2/BF_3/H_2$ gas mixture generated by an ASTeX 1.5 kW MW source with a magnetic field of approximately 875 G.[13] The deposition conditions were as follows: MW power, 1.4 kW; pressure, 2×10^{-3} Torr; Ar and He (plasma-processing gases) flow, 10 and 140 std $cm^3 min^{-1}$, respectively; N_2, BF_3, and H_2 (reactant gases) flow, 50, 1.5, and 3 std $cm^3 min^{-1}$, respectively. During deposition, a bias voltage of -20 to -40 V was applied to the substrate, which was maintained at about 950 °C as measured by an optical pyrometer.

We first discuss a comparative HR-TEM study of the structure of the topmost layers of two samples, A (deposited by CVD) and B (deposited by bias-enhanced radio-frequency magnetron sputtering PVD[14]). Both samples were coated with a protecting layer of gold (10-nm thick) directly after deposition of cBN. Specimens for cross-sectional TEM were prepared by the standard procedure, that is, grinding, dimpling, and final ion milling. A 200 kV field-emission TEM apparatus (Philips CM200) was used.

Figure 1 displays cross-sectional overviews of samples A (Figure 1a) and B (Figure 1b). Figure 1a (CVD sample) shows a clear interface between the cBN film and the gold layer and that the cBN and gold lattices are in direct contact; there is no amorphous interlayer. Figure 1b (PVD sample) shows a much more defective, nanocrystalline cBN structure with aBN and tBN impurities and a thin aBN top layer (indicated) that clearly covers the surface of the cBN film with a thickness of about three atomic layers.

A layer of aBN is absent from the top of the CVD cBN film, yet it is present on the film obtained by PVD. This

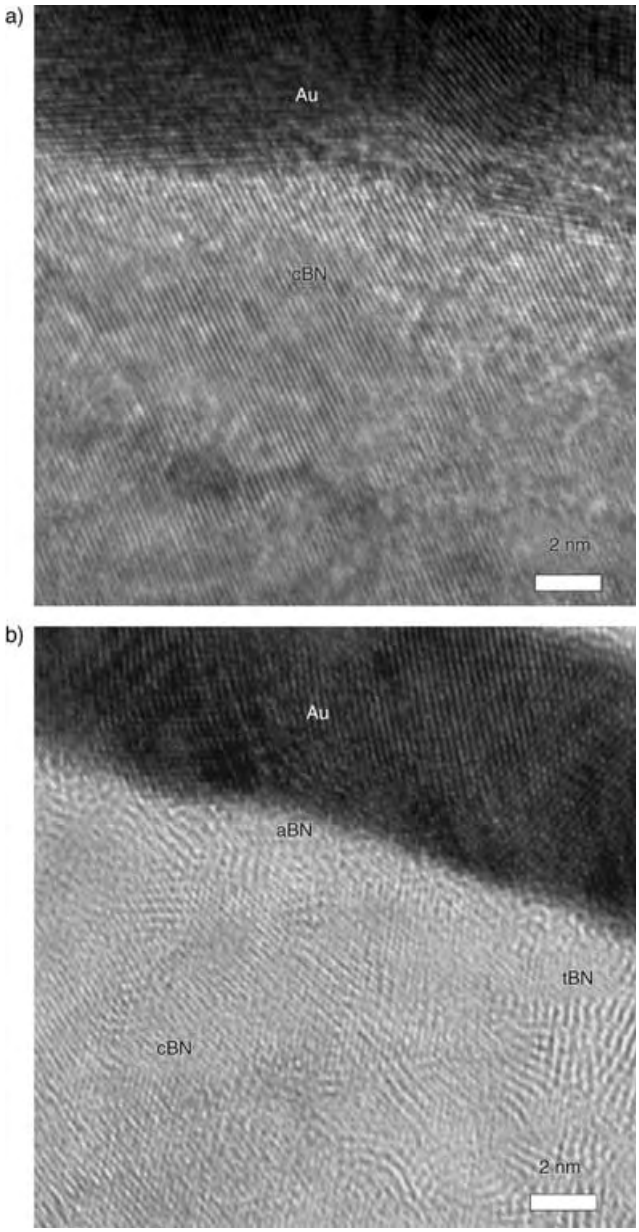


Figure 1. Cross-sectional HR-TEM image of the surface region of the film deposited by a) ECR MW CVD and b) magnetron sputtering. A gold coating on the cBN surface protects and marks the surface region.

indicates the difference between the growth mechanisms in the two deposition schemes: CVD involves a surface-growth process associated with surface etching, whereas PVD involves a subsurface growth that leads to a typical aBN skin. In accord with the TEM data, SEM images (not shown) indeed show the faceted nature of the CVD films[15] which is not observed for the PVD films. The HR-TEM data thus substantiate the conclusion that cBN growth by chemical pathways was obtained by the introduction of fluorine-containing species.

Optical emission spectroscopy of the plasma used for cBN growth reveals the reactive gas species and provides insight into the growth mechanism. The small quantity of BF_3 and H_2

 © 2005 Wiley-VCH Verlag GmbH & Co. KGaA, Weinheim

used relative to the much larger amounts of Ar, He, and N_2 present inhibit the observation of most reactant species in the actual plasma used for cBN growth. Hence, we chose to study the composition of the $BF_3 + H_2$ plasma with different H_2/BF_3 ratios (0:1 to 5:1) instead. The study was performed by using a substrate holder made of hBN to enable the observation of hBN etching by $BF_3 + H_2$ plasma. OES of pure BF_3 plasma (Figure 2a) indicates the formation of atomic F, BF, H, and N_2

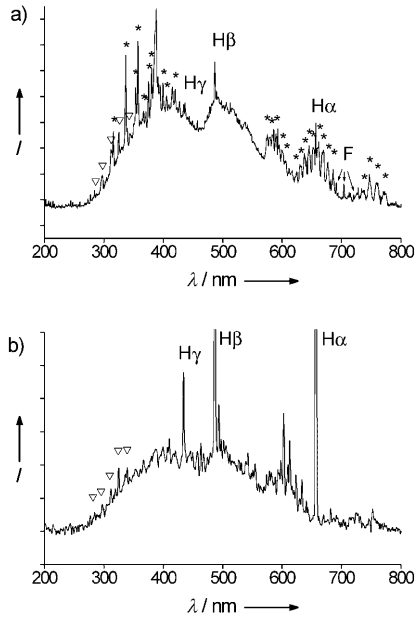


Figure 2. OES data of the plasma (impinging an hBN holder) with a gas flow of a) 5 std $cm^3 min^{-1}$ BF_3 and b) 5 std $cm^3 min^{-1}$ BF_3 and 10 std $cm^3 min^{-1}$ H_2. Emissions from N_2 (*) and BF (▽) are indicated.

clusters; F and BF clusters are expected in the BF_3 plasma. The small quantity of atomic hydrogen evident, which decreased with time, is likely to have arisen from residual H_2 released from the surfaces of the chamber. The signal corresponding to N_2 was constant with time and no N_2 was introduced into the system. The emission intensity of both N_2 and F decreased with the introduction of H_2 and finally disappeared (Figure 2b) for a gas flow rate of 5 std $cm^3 min^{-1}$ for BF_3 and 10 std $cm^3 min^{-1}$ for H_2. The signal corresponding to N_2 that followed a periodic decrease and increase of the H_2 flow rate was studied and observed only for low flow rates of H_2. This observation rules out residual N_2 in the system as the N_2 source. Therefore, the etching of the hBN substrate holder by F atoms, which are formed in pure BF_3 plasma or BF_3 plasma with low H_2 concentrations, is the only plausible source of N_2. The concentration of F atoms decreases with the introduction of H_2 as a result of the formation of HF, which seems not to react with hBN. Hence, the hBN etching (revealed by the N_2 signal) stops at a sufficiently high concentration of H_2. The etching of hBN at only low H_2/BF_3 ratios is in accord with the optimal window of the H_2/BF_3 ratio for successful cBN deposition, whereas at higher H_2/BF_3 ratios only hBN films evolve.[16] The flow rate of H_2 controls the production rate of solid BN from the gas phase, and the ratio of H to F atoms controls the equilibrium between film formation and etching.

The last observation from this OES study is the nearly constant emission intensity of the BF_x cluster with increasing hydrogen flow rates, whereas no signal pertaining to BH_x clusters could be detected. This result suggests that the growth species are clusters of BF_x rather than of BH_x. This finding from OES is consistent with the higher bond energy of the B–F bond (757 kJ mol^{-1}) relative to that of the B–H bond (340 kJ mol^{-1}). Quantum mechanical calculations indicate that B–F termination stabilizes the boron surface of cBN.[17,18] The F-terminated boron surface, however, was found by quantum mechanical calculations to be resistant to abstraction and adsorption of N-containing growth species for further cBN growth.[17,18] B–F bond breaking followed by surface abstraction and adsorption of N-containing species may be facilitated by low-energy ion bombardment, which is still needed for cBN growth from F-containing species.[9,11]

Angle-resolved XPS (VG, EscaLab 220i-XL, $Al_{K\alpha}$ radiation) of cBN films grown by the ECR system was used to gain further insight into the cBN growth process. Spectra were collected at emission angles of 10° and 90° to evaluate the elemental depth distributions, as the probing depth at 90° ($\approx$5 nm) is much larger than that at 10° ($\approx$1 nm).[19] Table 1

Table 1: Elemental concentration calculated from XPS data.

	Elemental Concentration [%]	
Emission angle	90°	10°
B	43.7	39.4
N	47.6	47.7
C	5.7	8.7
O	2.3	3.2
F	0.7	1.0

summarizes the elemental concentration of the film, which includes mainly boron and nitrogen and small amounts of fluorine, carbon, and oxygen. The B/N ratio is less than 1 and decreases from 0.92 to 0.83 with decreasing emission angle (90°→10°) thus indicating boron-deficient surfaces. The low concentration of fluorine (0.7% and 1.0% for 90° and 10°, respectively) indicates that only a small portion of the surface is terminated by F atoms. These results are in accord with the feeding gas composition of the plasma ($BF_3/N_2 = 1.5{:}50$). The high concentration of N_2 in the gas phase leads to a high probability of termination with N atoms. This point was further verified by exposing the film to a $BF_3 + Ar + He$ plasma, which lead to a significant increase of both the B/N ratio (to greater than 1:1) and the concentration of F atoms (to approximately 6%). Further exposure to $N_2 + H_2$ plasma decreased the B/N ratio and the concentration of fluorine to their initial values. Finally, the O and C atoms are mostly surface contaminants from the atmosphere as revealed by the angle-dependent XPS analysis.

We note that N_2 molecules fed to the plasma decompose to N atoms and then combine with H or F atoms. The bonding energies of N–H ($\approx$340 kJ mol^{-1}) and N–F (343 kJ mol^{-1}) are similar,[17,18] so both NH_x and NF_x clusters may exist.

 © 2005 Wiley-VCH Verlag GmbH & Co. KGaA, Weinheim

However, the low concentration of F atoms in our present XPS data ($\approx 1\,\%$) rules out the possibility of N–F termination of the cBN surface, and the results of secondary ion mass spectrometry (SIMS) of a cBN film suggest that N atoms are partly bonded to H atoms.[20] It is therefore most likely that only NH_x clusters contribute to the surface processes that lead to cBN growth. Furthermore, we note that the adsorption energy of NH_x clusters ($416\,kJ\,mol^{-1}$) is larger than that of NF_x clusters ($17\,kJ\,mol^{-1}$) on F-terminated boron surfaces.[17,18] N–H bonds are also found to be much more effective than N–F bonds in incorporating B-containing species after H abstraction, and in stabilizing and maintaining sp^3-hybridized surface atoms.[17,18]

Our experimental findings lead to the following conclusions regarding the growth of cBN through the introduction of fluorine-containing species: 1) the growth of cBN is a surface process (HR-TEM data); 2) hBN constituents are etched by F atoms in the plasma (OES data); 3) BF_x and NH_x species are responsible for the growth of cBN (OES and XPS data); 4) the cBN film surface is boron-deficient and the termination of dangling bonds by F atoms is minor (XPS data). On the basis of these conclusions, we now offer the following sequence of cBN growth from fluorine-containing species, as shown in Figure 3:

1) The excited plasma contains reactive species, namely, H, F, BF_x, NH_x, which are responsible for the etching of hBN (mainly F atoms) and cBN crystal growth (BF_x and NH_x) (Figure 3a). The cBN surface at any stage contains a large number of N atoms terminated by H atoms but a very small number of B atoms terminated by F atoms.

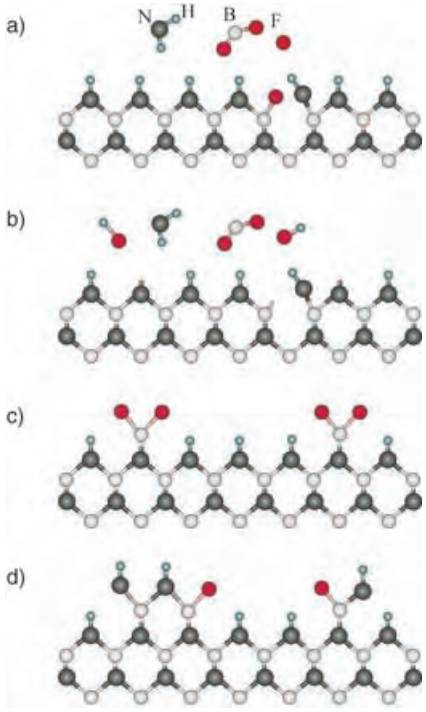


Figure 3. A proposed cBN growth sequence in fluorine-based ECR-assisted MW CVD. The growth is illustrated on a (001) surface (see text for details).

2) The cBN crystal surface is activated by surface abstraction by the impingement of plasma species, thus providing free unsaturated sites for further growth (Figure 3b). B–F bond breaking is most likely assisted by energetic particle bombardment (bias of about 20 V) while N–H bond breaking is easier.
3) B atoms are added to N-activated sites by incorporation of BF_x species, whereas N atoms are added to B-activated sites by incorporation of NH_x species (Figure 3c).
4) Each B surface site is subject to deposition by an NH_x molecule at a much higher rate than the deposition of BF_x on N surface sites (the BF_3/N_2 flow rate feeding the plasma is 1.5:50), thus leading to a B-deficient surface at any stage (Figure 3d).

Layer-by-layer growth of a cBN crystal requires the alternate deposition of B atoms on the nitrogen surface and the deposition of N atoms on the boron surface, which means (on a macroscopic scale) equal surface concentrations of B and N atoms. The surface of our ECR films is B-deficient owing to the plasma composition needed for cBN growth (BF_3/N_2 flow rate = 1.5:50). As stated above, our experimental findings support that N surface atoms are terminated by H atoms, whereas B surface atoms are terminated by F atoms. The N–H bonds of N–H terminated surface sites were found to be energetically effective in abstraction and adsorption of incoming B-containing species.[17,18] The H atom that terminates an N surface atom is abstracted by plasma F atoms to form HF and leave room for BF_x adsorption. The chemical bond strength of B–F is large, which makes it resistant to abstraction and adsorption of NH_x molecules. In our work, the breaking of B–F bonds and formation of a dangling bond needed for NH_x adsorption and further cBN growth are most likely to be facilitated by the low-energy ion bombardment of the growing surface (Figure 3b).

The high abundance of N-containing clusters in the plasma (relative to B-containing clusters) dictates that the coverage rate of each B surface atom (F terminated) by N atoms will be much larger than the coverage rate of N surface atoms (H terminated) by B atoms. This rules out the possibility of a layer-by-layer growth and leaves island formation of cBN with a major surface coverage of H-terminated N atoms as the dominant growth mechanism (Figure 3d). The hydrogen concentration in the plasma determines 1) the concentration of NH_x species (needed for growth) which increases with the concentration of H atoms; 2) the concentration of F atoms (needed for activation of H-terminated N surface atoms and for etching of noncubic BN constituents) which decreases with H concentration. This is how the hydrogen/fluorine ratio controls the deposition rate and phase purity resulting in an optimal window of the H_2/BF_3 ratio for cBN growth.[16]

In conclusion, a combination of HR-TEM, OES, and XPS studies has revealed that ECR fed by a gas mixture of $He(Ar)/N_2/BF_3/H_2$ leads to the surface CVD growth of cBN, which is fundamentally different from PVD growth by ion-assisted methods. The new data collectively support a cBN surface-growth sequence, which includes 1) formation of H, F, BF_x, and NH_x species in the plasma in which the amount of F

 © 2005 Wiley-VCH Verlag GmbH & Co. KGaA, Weinheim

and NH_x species is balanced by the concentration of hydrogen atoms, 2) abstraction of H atoms and activation of N sites by F atoms, 3) abstraction of F atoms and activation of B sites by energetic particle bombardment, 4) growth by adsorption of BF_x (boron source) on N surfaces and NH_x (N source) on B surfaces, and 5) etching of noncubic BN phases by F atoms. The possibility to grow cBN through surface reactions with little damage from ion bombardment suggests that the growth of electronic grade, single-crystal cBN wafers is feasible (similar to electronic grade, single-crystal diamond wafers grown by CVD).

Received: January 27, 2005
Revised: April 15, 2005
Published online: July 1, 2005

Keywords: chemical vapor deposition · crystal growth · nitrides · plasma chemistry · reaction mechanisms

[1] R. H. Wentorf, *J. Chem. Phys.* **1962**, *36*, 1990 – 1991.
[2] P. B. Mirkarimi, K. F. McCarty, D. L. Medlin, W. G. Wolfer, T. A. Friedmann, E. J. Klaus, G. F. Cardinale, D. G. Howitt, *J. Mater. Res.* **1994**, *9*, 2925 – 2938.
[3] T. Yoshida, *Diamond Relat. Mater.* **1996**, *5*, 501 – 507, and references therein.
[4] W. J. Zhang, I. Bello, Y. Lifshitz, S. T. Lee, *MRS Bull.* **2003**, *28*, 184 – 188, and references therein.
[5] X. W. Zhang, H. G. Boyen, N. Deyneka, P. Ziemann, F. Banhart, M. Schreck, *Nat. Mater.* **2003**, *2*, 312 – 315.
[6] Y. Lifshitz, S. R. Kasi, J. W. Rabalais, W. Eckstein, *Phys. Rev. B* **1990**, *41*, 10468 – 10480.
[7] Y. Lifshitz, T. Kohler, T. Frauenheim, I. Guzmann, A. Hoffman, R. Q. Zhang, X. T. Zhou, S. T. Lee, *Science* **2002**, *297*, 1531 – 1533.
[8] P. B. Mirkarimi, K. F. McCarty, D. L. Medlin, *Mater. Sci. Eng. R* **1997**, *21*, 47 – 100, and references therein.
[9] W. J. Zhang, S. Matsumoto, *Appl. Phys. A* **2000**, *71*, 469 – 472.
[10] W. J. Zhang, S. Matsumoto, K. Kurashima, Y. Bando, *Diamond Relat. Mater.* **2001**, *10*, 1881 – 1885.
[11] C. Y. Chan, W. J. Zhang, X. M. Meng, K. M. Chan, I. Bello, Y. Lifshitz, S. T. Lee, *Diamond Relat. Mater.* **2003**, *12*, 1162 – 1168.
[12] W. J. Zhang, I. Bello, Y. Lifshitz, K. M. Chan, X. M. Meng, Y. Wu, C. Y. Chan, S. T. Lee, *Adv. Mater.* **2004**, *16*, 1405 – 1408.
[13] W. J. Zhang, C. Y. Chan, K. M. Chan, I. Bello, Y. Lifshitz, S. T. Lee, *Appl. Phys. A* **2003**, *76*, 953 – 955.
[14] Z. F. Zhou, I. Bello, M. K. Lei, K. Y. Li, C. S. Lee, S. T. Lee, *Surf. Coat. Technol.* **2000**, *128*, 334 – 340.
[15] W. J. Zhang, X. Jiang, S. Matsumoto, *Appl. Phys. Lett.* **2001**, *79*, 4530 – 4532.
[16] W. J. Zhang, S. Matsumoto, *Chem. Phys. Lett.* **2000**, *330*, 243 – 248.
[17] K. Larsson, J. O. Carlsson, *J. Phys. Chem. B* **1999**, *103*, 6533 – 6538.
[18] B. Mårlid, K. Larsson, J. O. Carlsson, *Phys. Rev. B* **1999**, *60*, 16065 – 16072.
[19] M. P. Seah, W. A. Dench, *Surf. Interface Anal.* **1979**, *1*, 2 – 11.
[20] X. Jiang, K. Helming, W. J. Zhang, S. Matsumoto, *Chem. Vap. Deposition* **2002**, *8*, 262 – 265.

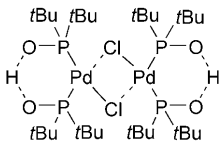
 © 2005 Wiley-VCH Verlag GmbH & Co. KGaA, Weinheim

Palladium-Catalyzed Chemistry

[2+1] Cycloadditions of Terminal Alkynes to Norbornene Derivatives Catalyzed by Palladium Complexes with Phosphinous Acid Ligands**

*Julie Bigeault, Laurent Giordano, and Gérard Buono**

Secondary phosphine oxides (SPOs) have been widely used for the synthesis of tertiary phosphine oxides and have found applications as Wittig–Horner reagents[1–2] and, later, as effective ligands for transition-metal complexes.[3] Recently, Li et al. showed that SPOs form air-stable palladium complexes, such as POPd1, when they are mixed with $PdCl_2(MeCN)_2$ and then treated with Et_3N.[4] These complexes proved efficient as catalysts in several cross-coupling reactions[4–5] as well as in asymmetric allylic alkylations.[6] Recent reports showed also that these new ligands are suitable for other types of catalyzed reactions such as the hydrolysis of nitriles[7] and the asymmetric hydrogenation of imines[8] and alkenes.[9] Our continued interest in the metal-catalyzed cycloaddition reactions between alkynes and norbornadiene[10] prompted us to investigate the catalytic behavior of palladium(II) complexes coordinated by SPOs.



POPd1

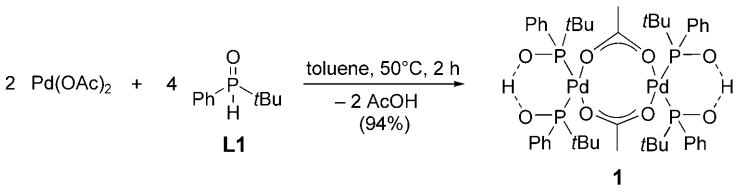
First, we developed an easier way to synthesize the palladium catalyst **1**. Upon treatment of $Pd(OAc)_2$ with *tert*-butyl(phenyl)phosphane oxide (**L1**), dihydrogen di-μ-acetatotetrakis(*tert*-butylphenylphosphinito-κ-*P*)dipalladate (**1**) was quantitatively obtained without further treatment (Scheme 1).[11] Second, as a model we examined the reaction of phenylethyne (**3a**) with norbornadiene (**2**) in the presence of 2.5 mol% of **1** in toluene at 50°C for 24 h. Unexpectedly, the palladium(II) complex **1** coordinated by **L1** favored the formation of benzylidenecyclopropane (**4a**) as a single diastereomer in 17% yield (Scheme 2) and contaminated by an unidentified byproduct (5%). Surprisingly, a similar reaction using the known chloro-bridged analogue **5**[6a–12] as catalyst did not work. Furthermore, in the reaction catalyzed by **5**, the addition of 10 mol% of AgOAc (4 equiv relative to

[*] J. Bigeault, Dr. L. Giordano, Prof. Dr. G. Buono
Laboratoire de Synthèse Asymétrique
UMR 6180 CNRS "Chirotechnologies: Catalyse et Biocatalyse"
Case A62, Université d'Aix-Marseille P. Cézanne
Faculté des Sciences et Techniques de St Jérôme, EGIM
Avenue Escadrille Normandie Niemen
13397 Marseille Cedex 20 (France)
Fax: (+33) 4-9128-2742
E-mail: gerard.buono@univ.u-3mrs.fr

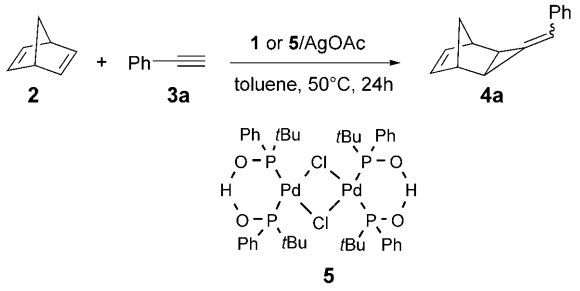
[**] The authors thank the CNRS for financial support. J.B. thanks MENRT for a doctoral fellowship. We also thank Dr. N. Vanthuine for kind assistance with chiral HPLC separation of **L1** and **L2**, Dr. M. Giorgi for X-ray analyses, and Dr. L. Charles for ESI-MS measurements.

Supporting information for this article is available on the WWW under http://www.angewandte.org or from the author.

 DOI: 10.1002/anie.200500879 © 2005 Wiley-VCH Verlag GmbH & Co. KGaA, Weinheim

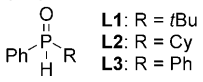


Scheme 1. Synthesis of the new air-stable palladium(II) complex **1** with phosphinous acid ligands.



Scheme 2. Palladium(II) complexes **1** or **5** catalyze an unusual [2+1] cycloaddition of **2** with **3a**. Conditions: **2**/**3a**/**1** = 2:1:0.025; **2**/**3a**/**5**/AgOAc = 2:1:0.025:0.1.

Table 1: Benzylidenecyclopropanation of **2** with **3a**.



Entry[a]	L	*T* [°C]	Yield [%][b]
1	**L1**	25	trace
2	**L1**	50	42
3	**L2**	50	76
4	**L2**	25	80
5	**L3**	25	21
6	**L3**	50	58

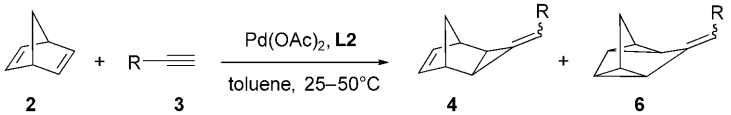
[a] All reactions were carried out with **2**/**3a**/$Pd(OAc)_2$/**L** in a ratio of 2:1:0.05:0.1 for 24 h. [b] Yield of isolated product. Cy = cyclohexyl.

Having established the feasibility of the cycloaddition reaction, we tested various terminal alkynes **3a**–**k** to extend its applicability. Under optimized conditions, all reactions proceeded cleanly and various functional groups such as ethers, esters, alcohols, sulfones, or tertiary amines present in the alkyne were tolerated (Table 2). Propargylic alcohols **3f** and **3g**, sulfone **3i**, and tertiary amine **3j** also reacted with **2** to afford **4f**, **4g**, **4i**, and **4j**, respectively, in 57–75% yields

catalyst **5**) led to the formation of **4a** in 15% yield.[13] Even if few examples of ruthenium-[14] or palladium-catalyzed[15] cyclopropanations of norbornene derivatives with alkynes are known, a catalytic process that is able to favor the direct formation of alkylidenecyclopropanes as illustrated in Scheme 2 has, to our knowledge, not been reported. Herein, we show that palladium(II) complexes stabilized by secondary phosphine oxides are active catalysts for an unusual [2+1] cycloaddition of norbornene derivatives with terminal alkynes to produce various alkylidenecyclopropanes.

In a preliminary study, we found that the addition of 5 mol% of acetic acid was beneficial to the reaction and led to the formation of **4a** as the exclusive product in 26% yield. This finding revealed that acetate plays an important role in the reaction. Indeed, AcOH was released in the reaction medium during the formation of catalyst **1**. This observation prompted us to test the formation of catalysts in situ. Two other SPOs, **L2** and **L3**, were tested under similar conditions by generating the catalyst in situ (Table 1). The best result was observed when $Pd(OAc)_2$ was associated with **L2** (1:2 molar ratio), affording **4a** in satisfactory yield at room temperature (entry 4).[16–17] Similarly, palladium catalyst systems generated with **L1**[18] or **L3** proved active but less efficient (entries 2 and 6).

Table 2: Palladium-catalyzed alkylidenecyclopropanation of **2** with terminal alkynes **3**.

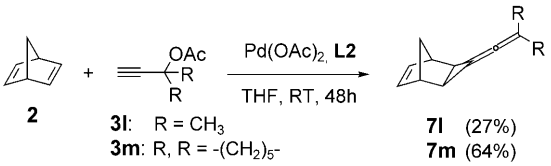


Entry[a]	Alkyne	R	*T* [°C]	*t* [h]	Cycloadduct	Yield [%][b]
1	**3a**	Ph	25	20	**4a**	80
2	**3b**	*n*Bu	50	20	**4b**	9
3	**3c**	CH_2TMS	50	48	**4c**	–
4	**3d**	CH_2OBn	25	50	**4d**	70
5	**3e**	CH_2OAc	25	50	**4e**	73
6	**3f**	CH_2OH	25	50	**4f**	34
7	**3f**	CH_2OH	50	48	**4f**	57
8	**3g**	$C(Me)_2OH$	50	36	**4g**	75
9	**3h**	$CH_2CH(CO_2Me)_2$	50	50	**4h**	52
10	**3i**	CH_2SO_2Ph	25	48	**4i**	66
11	**3j**	CH_2Mp	25	48	**4j**	34
12	**3j**	CH_2Mp	50	36	**4j**	60
13	**3k**	CO_2Me	25	60	**6k**	56

[a] Experiments were performed on a 1-mmol scale using 5 mol% of $Pd(OAc)_2$ and 10 mol% of **L2** (**2**/**3**/Pd/**L2** = 2:1:0.05:0.1). [b] Yield of isolated product. TMS = trimethylsilyl; Bn = benzyl; Mp = morpholinyl (C_4H_8NO).

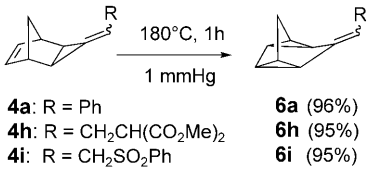
(Table 2, entries 7, 8, 10, and 12). For an unknown reason, no product was obtained with propargylsilane **3c** (entry 3).[19] Likewise, with an unfunctionalized alkyne such as **3b**, the reaction was slow and conversion was very low (Table 2, entry 2). Surprisingly, an acetate group in a propargylic position such as in **3e** afforded the desired cyloadduct **4e** without formation of byproducts (entry 5).[20] A notable difference in reactivity was observed for tertiary acetates such as **3l** and **3m**. In this case, known allenylidenecyclopropanes[21] **7l** and **7m** were obtained in 27% and 64% yield, respectively (Scheme 3).

 © 2005 Wiley-VCH Verlag GmbH & Co. KGaA, Weinheim



Scheme 3. Synthesis of allenylidenecyclopropanes **7l** and **7m** from tertiary acetates. Conditions: **2**/**3**/Pd/**L2** = 2:1:0.05:0.1.

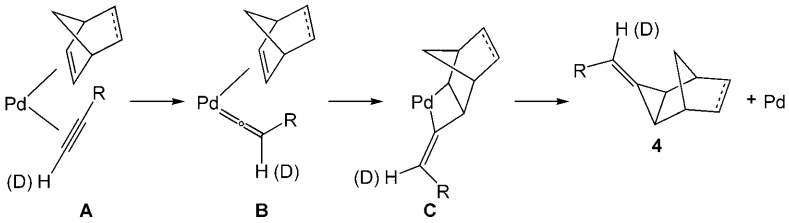
With the electron-deficient alkyne **3k** (Table 2, entry 13), the expected cycloadduct **4k** and the rearranged (valence isomerization) product **6k** were observed in 1:1 ratio in the crude reaction mixture. After purification by chromatography on silica gel, only **6k** was isolated in 56% yield. Valence isomerization proved to be effective on cycloadducts **4a**, **4h**, and **4i** under thermal conditions in the absence of solvent: heating these cycloadducts to 180 °C at 1 mm Hg resulted in clean and complete conversion after 1 h (Scheme 4).[22–23]



Scheme 4. Thermal rearrangements (valence isomerization) of **4**.

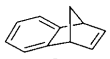
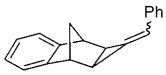
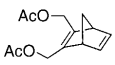
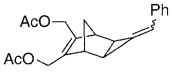
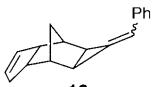
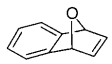
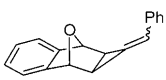
The cycloaddition reaction was extended to other norbornene derivatives by using phenylethyne (**3a**) as a partner (Table 3).[24] The cyclopropanation of alkenes **8**–**12** afforded expected benzylidenecyclopropanes **13**–**17** in moderate to good yields. The best yields were observed for norbornene (**8**) or benzonorbornene (**9**; entries 2 and 3). The cycloaddition with functionalized norbornenes gave the products in fair yields (entries 4 and 6). For cyclopentadiene dimer **11**, the cyclopropanation occurred exclusively at the most strained double bond to yield the cycloadduct **16** in 51% as a 1:1 mixture of diastereomers (Table 3, entry 5). Note the exclusive formation of cyclopropane **15** from **10** (entry 4). Indeed, diacetate **10** has been previously used in palladium(0)-catalyzed elimination[25] and alkylation[26] reactions and proceeds via an intermediate π-allyl complex.

Although the mechanism of this unusual cyclopropanation remains unclear at the moment, we assume that the reaction may involve palladium vinylidene species as key intermediates in a catalytic process that favors the formation of [2+1] cycloadducts over dimerization[27] products of alkynes (Scheme 5). Palladium vinylidene complex **B** may be generated from 1-alkyne **3**,[28,29] and **B** could allow a [2+2] cycloaddition with the double bond of the norbornene. The resulting 2-alkylidene palladacyclobutane (**C**) would release cycloadduct **4** after reductive elimination. The formation of this unprecedented Pd vinylidene complex is supported by results from deuterium-labeling experiments. Starting from monodeuterophenylacetylene [D$_1$]**3a** and **2**,



Scheme 5. A possible pathway for the palladium-catalyzed [2+1] cycloaddition of norbornadienes and alkynes. (D) denotes the proton exchanged for deuterium in labeling experiments.

Table 3: Cyclopropanation of various norbornenes **8**–**12** with phenylethyne (**3a**).

Entry[a]	Alkene	*T* [°C]	*t* [h]	Cycloadduct	Yield [%][b]
1	 **8**	25	60	 **13**	51
2		50	48		94
3	 **9**	25	60	 **14**	84
4	 **10**	50	36	 **15**	58
5	 **11**	50	72	 **16**	51
6	 **12**	50	48	 **17**	56

[a] Experiments were performed on a 1-mmol scale using 5 mol% of Pd(OAc)$_2$ and 10 mol% of **L2**. [b] Yield of isolated product.

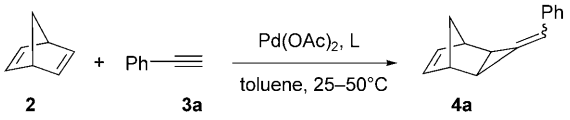
under similar conditions the reaction led to compound [D$_1$]**4a** in 88% yield with 80% incorporation of deuterium on the external double bond (Scheme 5).[30] For the formation of allenylidenecyclopropanes **7l** and **7m**, the reaction is thought to proceed through a similar mechanism via a palladium allenylidene intermediate (Pd=C=C=CR$_2$).[31]

Finally, we briefly examined the interesting asymmetric version of this cycloaddition by using chiral secondary phosphine oxides (−)-**L1** and (−)-**L2** obtained by separation with chiral HPLC.[32] Indeed, alkylidenecyclopropanes synthesized from symetrical **2** showed geometrical enantiomorphic isomerism.[33–34] Preliminary results obtained are encouraging: an asymmetric induction of 59% *ee* was achieved with (−)-**L1** without optimization of the reaction conditions (Table 4, entry 1).

In conclusion, we have shown that palladium(II) complexes stabilized by secondary phosphine oxide ligands catalyze a very unique [2+1] cycloaddition of norbornene derivatives with various terminal alkynes to afford functionalized alkylidenecyclopropanes.[35–36] Moreover, our results suggest a Pd vinylidene complex as a key intermediate. A detailed investigation of the mechanism and the development

 © 2005 Wiley-VCH Verlag GmbH & Co. KGaA, Weinheim

Table 4: Enantioselective benzylidenecyclopropanation of **2** with **3a** using a chiral secondary phosphine oxide ligand.



2 **3a** **4a**

Entry[a]	L	*T* [°C]	*t* [h]	Yield [%][b]	*ee* [%][c]
1	(−)-**L1**	50	60	53	59
2	(−)-**L2**	25	20	80	22

[a] Experiments were performed using 5 mol% of $Pd(OAc)_2$ and 10 mol% of ligand L. [b] Yield of isolated product. [c] *ee* values determined on a Daicel Chiralcel OJ-H column at $\lambda = 254$ nm using hexane/*i*PrOH 99:1 as eluent with a flow rate of 1 mL min^{-1}; $t_1 = 6.4$ min, $t_2 = 7.1$ min.

of asymmetric cycloaddition reactions are underway in our laboratory.

Received: March 9, 2005
Revised: April 28, 2005
Published online: June 27, 2005

Keywords: alkynes · cycloaddition · cyclopropanes · palladium · phosphane ligands

[1] "Methods of Preparation of Phosphine Chalcogenides": A. K. Bhattacharya, N. K. Roy in *The Chemistry of Organophosphorous Compounds*, *Vol. 2* (Ed.: F. R. Hartley), Wiley, Chichester, **1992**, pp. 195–285.

[2] "Chemical Properties and Reactions of Phosphine Chalcogenides": R. S. Edmundson in *The Chemistry of Organophosphorous Compounds*, *Vol. 2* (Ed.: F. R. Hartley), Wiley, Chichester, **1992**, pp. 287–407.

[3] a) D. M. Roudhill, R. P. Sperline, W. B. Beaulieu, *Coord. Chem. Rev.* **1978**, *26*, 263–279; b) B. Walther, *Coord. Chem. Rev.* **1984**, *60*, 67–105; c) T. Appleby, J. D. Woollins, *Coord. Chem. Rev.* **2002**, *235*, 121–140.

[4] a) G. Y. Li, G. Zheng, A. F. Noonan, *J. Org. Chem.* **2001**, *66*, 8677–8681; b) G. Y. Li, *Angew. Chem.* **2001**, *113*, 1561–1564; *Angew. Chem. Int. Ed.* **2001**, *40*, 1513–1516; c) G. Y. Li, P. J. Fagan, P. L. Watson, *Angew. Chem.* **2001**, *113*, 1140–1143; *Angew. Chem. Int. Ed.* **2001**, *40*, 1106–1109; d) G. Y. Li, *J. Org. Chem.* **2002**, *67*, 3643–3650.

[5] a) W. Yang, Y. Wang, J. R. Corte, *Org. Lett.* **2003**, *5*, 3131–3134; b) C. Wolf, R. Lerebours, *J. Org. Chem.* **2003**, *68*, 7077–7084; c) C. Wolf, R. Lerebours, E. H. Tanzani, *Synthesis* **2003**, *68*, 2069–2073; d) C. Wolf, R. Lerebours, *Org. Lett.* **2004**, *6*, 1147–1150.

[6] a) W. Dai, K. K. Y. Yeung, W. H. Leung, K. K. Haynes, *Tetrahedron: Asymmetry* **2003**, *14*, 2821–2826; b) T. Nemoto, T. Matsumoto, T. Masuda, T. Hitomi, K. Hatano, Y. Hamada, *J. Am. Chem. Soc.* **2004**, *126*, 3690–3691.

[7] a) T. Ghaffar, A. W. Parkins, *Tetrahedron Lett.* **1995**, *36*, 8657–8660; b) C. J. Cobley, M. van den Heuvel, A. Abbadi, J. G. de Vries, *Tetrahedron Lett.* **2000**, *41*, 2467–2470; c) T. Ghaffar, A. W. Parkins, *J. Mol. Catal. A* **2000**, *160*, 249–261; d) X. Jiang, A. J. Minaard, B. L. Feringa, J. G. de Vries, *J. Org. Chem.* **2004**, *69*, 2327–2331.

[8] X. Jiang, A. J. Minnaard, B. Hessen, B. L. Feringa, A. L. L. Duchateau, J. G. O. Andrien, J. A. F Boogers, J. G. de Vries, *Org. Lett.* **2003**, *5*, 1503–1506.

[9] X. Jiang, M. Van den Berg, A. J. Minnaard, B. L. Feringa, J. G. de Vries, *Tetrahedron: Asymmetry* **2004**, *15*, 2223–2229.

[10] a) O. Pardigon, G. Buono, *Tetrahedron: Asymmetry* **1993**, *4*, 1977–1980; b) O. Pardigon, A. Tenaglia, G. Buono, *J. Org. Chem.* **1995**, *60*, 1868–1871; c) A. Tenaglia, O. Pardigon, G. Buono, *J. Org. Chem.* **1996**, *61*, 1129–1132; d) O. Pardigon, A. Tenaglia, G. Buono, *J. Mol. Catal. A* **2003**, *196*, 157–164.

[11] With enantiopure **L1**, the complex **1** was clearly identified by NMR spectroscopy. The acetato-bridged structure was supported by the ESI mass spectrum of the palladium complex **1** (see Supporting Information).

[12] Complex **5** was prepared according to Li's procedure[4] from **L1**. As shown by ^{31}P NMR spectra and X-ray crystallography, only one diastereomeric complex was obtained which exhibits C_2 symmetry and retention of configuration at phosphorus (see Supporting Information). During the course of our work, Leung and co-workers reported chiral bisphosphinite metalloligands derived from a P-chiral secondary phosphine oxide: E. Y. Y. Chan, Q. F. Zhang, Y.-K. Sau, S. M. F. Lo, H. H. Y. Sung, I. D. Williams, R. K. Haynes, W.-H. Leung, *Inorg. Chem.* **2004**, *43*, 4921–4926.

[13] Cycloadduct **3a** was also contaminated with 5% of an unidentified byproduct.

[14] a) H. Kikuchi, M. Uno, S. Takahashi, *Chem. Lett.* **1997**, 1273–1274; b) Y. Matsushima, H. Kikuchi, M. Uno, S. Takahashi, *Bull. Chem. Soc. Jpn.* **1999**, *72*, 2475–2482; c) Y. Yamamoto, H. Kitahara, R. Ogawa, H. Kawaguchi, K. Tatsumi, K. Itoh, *J. Am. Chem. Soc.* **2000**, *122*, 4310–4319; For pertinent reviews on ruthenium-catalyzed C–C bond formations, see: d) B. M. Trost, F. D. Toste, A. B. Pinkerton, *Chem. Rev.* **2001**, *101*, 2067–2096; e) *Ruthenium Catalysts and Fine Chemistry* (Eds.: C. Bruneau, P. H. Dixneuf), Springer, Berlin, **2004**; f) Y. Yamamoto, K. Itoh in *Ruthenium in Organic Synthesis* (Ed.: S-I. Murahashi), Wiley-VCH, Weinheim, **2004**, chap. 4, pp. 95–127.

[15] a) C. H. Liu, C. H. Cheng, M. C. Cheng, S. M. Peng, *Organometallics* **1994**, *13*, 1832–1839; b) D. Brown, R. Grigg, V. Sridharan, V. Tambyrajah, M. Thornton-Pett, *Tetrahedron* **1998**, *54*, 2595–2606.

[16] Other catalysts associated with two PPh_3 ligands such as $[PdCl\{\eta^3\text{-}(C_3H_5)\}_2]$, $Pd(OAc)_2$, and $[Pd_2(dba)_3]\cdot CHCl_3$ (dba = dibenzylideneacetone) did not promote the reaction at all.

[17] Toluene gave the best results. The [2+1] cycloaddition proceeded well in heterogeneous media in solvents such as Et_2O (74% yield), THF (59% yield), or CH_2Cl_2 (49% yield). The lowest yields were obtained with more polar solvents such as *N*,*N*-dimethylformamide (10% yield) or CH_3CN (6% yield).

[18] The catalytic system was stable under the experimental conditions described and could be recovered after the reaction by column chromatography.

[19] A difference in reactivity was observed by using trimethylsilylacetylene in place of propargylsilane **3c**: Only an adduct of hydroalkynylation was obtained as a single diastereomer in 68% yield.

[20] The reaction is probably catalyzed by a Pd^{II} catalyst. Indeed, Pd^0-catalyzed reactions of various propargylic compounds proceed by the formation of either σ-allenyl or σ-prop-2-ynylpalladium species; see: J. Tsuji, *Palladium Reagents and Catalysts: New Perspectives for the 21st Century*, Wiley, Chichester, **2004**, chap. 6, pp. 543–563; for the Pd^0- and Pd^{II}-catalyzed reactions of alkynes, see: J. Tsuji, *Palladium Reagents and Catalysts: New Perspectives for the 21st Century*, Wiley, Chichester, **2004**, chap. 7, pp. 565–599.

[21] a) D. H. Aue, M. J. Meshishnek, *J. Am. Chem. Soc.* **1977**, *99*, 223–231; b) T. Sasaki, S. Eguchi, M. Ohno, F. Nakata, *J. Org. Chem.* **1976**, *41*, 2408–2410.

[22] These rearrangments are geometrically constrained to occur by a $\sigma^2s + \sigma^2\pi$ mechanism, which is a symmetry-forbidden reaction.

 © 2005 Wiley-VCH Verlag GmbH & Co. KGaA, Weinheim

They have therefore been generally interpreted to occur by cleavage to a diradical followed by rapid intramolecular trapping of the diradical by the π bond (see reference [21a]).
[23] The structure and stereochemistry of compounds **4i** and **6i** were confirmed by X-ray analysis (see reference [36]).
[24] The same reaction carried out with cyclopentene in place of norbornene derivatives did not work. No oligomers or self-coupling adducts of the phenylethyne **3a** have been observed.
[25] G. Muchow, J. M. Brunel, M. Maffei, G. Buono, *J. Org. Chem.* **1995**, *60*, 852 – 855.
[26] a) J. M. Brunel, M. Maffei, G. Muchow, G. Buono, *Eur. J. Org. Chem.* **2000**, 1799 – 1803; b) J. M. Brunel, M. Maffei, G. Muchow, G. Buono, *Eur. J. Org. Chem.* **2001**, 1009 – 1012.
[27] For examples of terminal alkyne–alkyne couplings catalyzed by palladium, see: B. M. Trost, M. T. Sorum, C. Chan, A. E. Harms, G. Rühter, *J. Am. Chem. Soc.* **1997**, *119*, 698 – 708.
[28] a) C. Bruneau, P. H. Dixneuf, *Acc. Chem. Res.* **1999**, *32*, 311 – 323; b) M. I. Bruce, *Chem. Rev.* **1991**, *91*, 197 – 257; c) B. Weyerhausen, K. H. Dötz, *Eur. J. Inorg. Chem.* **1999**, 1057 – 1066; d) C. Menéndez, D. Morales, J. Pérez, V. Riera, D. Miguel, *Organometallics* **2001**, *20*, 2775 – 2781.
[29] There are two possible mechanisms for the formation of Pd vinylidene complexes **B** from η^2-coordinated alkyne intermediate **A**. The first involves a direct 1,2-hydrogen migration over the carbon triple bond. In contrast, the second mechanism occurs through a 1,3-shift of the hydride to the alkynyl ligand after oxidative addition of the C–H bond to Pd.
[30] The position of the deuterium was based on the disappearance of the signal of C_{sp^2}-H at $\delta = 6.55$ ppm (see Supporting Information).
[31] For recent reviews, see: a) H, Werner, *Chem. Commun.* **1997**, 903 – 910; b) D. Touchard, P. H. Dixneuf, *Coord. Chem. Rev.* **1998**, 178 – 180, 409 – 429; c) V. Cadierno, M. P. Gamasa, J. Gimeno, *Eur. J. Inorg. Chem.* **2001**, 571 – 591.
[32] Pure enantiomers were obtained by semipreparative chiral HPLC on chiralpak AD or AS (250×10 mm^2) columns using hexane/ethanol (90:10) or ethanol as eluents. For **L2**, the absolute configuration at phosphorus is currently unknown.
[33] a) R. E. Lyle, G. G. Lyle, *J. Org. Chem.* **1957**, *22*, 856 – 856; b) G. G. Lyle, E. T. Pelosi, *J. Am. Chem. Soc.* **1966**, *88*, 5276 – 5279; c) For a pertinent review, see: V. Prelog, G. Helmchen, *Angew. Chem.* **1982**, *94*, 614 – 631; *Angew. Chem. Int. Ed. Engl.* **1982**, *21*, 567 – 583.
[34] This type of chirality known under the name of "geometric enantiomerism" is also called *cis–trans* enantiomerism. *Stereochemistry of Organic Compounds* (Eds.: E. L. Eliel, S. H. Wilen), Wiley, New York, **1994**, chap. 14-3, pp. 1155 – 1156.
[35] Alkylidenecyclopropanes have served as useful building blocks in organic synthesis. For recent reviews, see: a) I. Nakamura, Y. Yamamoto. *Adv. Synth. Catal.* **2002**, *344*, 111 – 217; b) A. Brandi, S. Cicchi, F. M. Cordero, A. Goti, *Chem. Rev.* **2003**, *103*, 1213 – 1270.
[36] See Supporting Information for full synthetic details and characterization of new compounds. CCDC 265344–265346 (**4i**, **6i**, and **5**) contain the supplementary crystallographic data for this paper. These data can be obtained free of charge from the Cambridge Crystallographic Data Centre via www.ccdc.cam.ac.uk/data_request/cif.

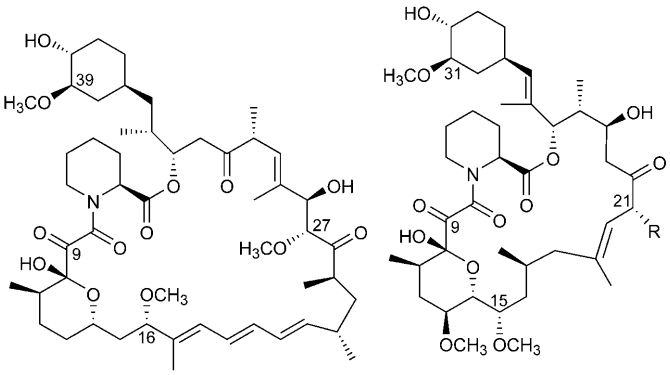
 © 2005 Wiley-VCH Verlag GmbH & Co. KGaA, Weinheim

Biosynthesis

Mutasynthesis of Rapamycin Analogues through the Manipulation of a Gene Governing Starter Unit Biosynthesis**

*Matthew A. Gregory, Hrvoje Petkovic, Rachel E. Lill, Steven J. Moss, Barrie Wilkinson, Sabine Gaisser, Peter F. Leadlay, and Rose M. Sheridan**

Rapamycin **1**, FK506 **2**, and FK520 **3** are biogenetically related natural products which are synthesized by mixed polyketide synthase (PKS)/nonribosomal peptide synthetase (NRPS) systems and which possess potent antifungal and immunosuppressive activities. Compounds **1**–**3** possess a



1: Rapamycin

2: FK506, R =

3: FK520, R = Et

common structural motif which is responsible for their specific binding to FK506-binding proteins (FKBPs). This binding triggers the subsequent binding of the binary complex to a downstream protein target, either mTOR (mammalian target of rapamycin) or calcineurin (FK506, FK520) which mediate their biological effects.[1] Inhibition of mTOR by

[*] Dr. M. A. Gregory,[+] Dr. H. Petkovic,[+] Dr. R. E. Lill, Dr. S. J. Moss, Dr. B. Wilkinson, Dr. S. Gaisser, Dr. R. M. Sheridan
Biotica Technology Ltd
Chesterford Research Park
Little Chesterford
Near Saffron Walden CB10 1XL (UK)
Fax: (+44) 179-953-2921
E-mail: rose.sheridan@biotica.co.uk
Prof. P. F. Leadlay
Department of Biochemistry
80 Tennis Court Road, Cambridge CB2 1GA (UK)

[+] These authors contributed equally to the work.

[**] We thank Dr. Jens Fuchser and Dr. Matthias Witt (Bruker Daltonik GmbH, Bremen (Germany)) and Dr. Paul Gates (University of Cambridge) for help with FT-ICR-MS experiments, and Dr. Apoorva Bhatt for helpful discussions. Work carried out in Cambridge was supported by a project grant from the BBSRC (UK).

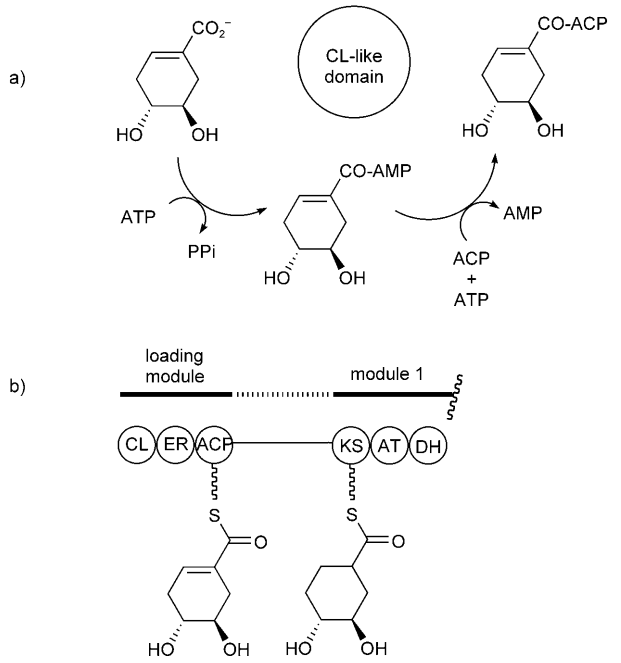
Supporting information for this article is available on the WWW under http://www.angewandte.org or from the author.

 DOI: 10.1002/anie.200462784 © 2005 Wiley-VCH Verlag GmbH & Co. KGaA, Weinheim

rapamycin is also the basis for current interest in such compounds as anticancer drugs.

The dihydroxycyclohexane moiety of rapamycin arises through the incorporation of a 4,5-dihydroxycyclohex-1-enecarboxylic acid (DHCHC) starter unit derived from shikimic acid in an analogous manner to that of FK520.[2] Cyclohexanecarboxylic acid (CHC), the starter unit for asukamycin[3] and phoslactomycin,[4] also arises from shikimic acid. These biosynthetic pathways share a common first step, the 1,4-conjugate elimination of water from shikimic acid.

Selection and activation of the carboxylic acid group of the rapamycin PKS starter unit is carried out by a carboxylic acid ligase (CL) like domain, in a manner analogous to that of adenylation domains of NRPS systems (Scheme 1a). Following covalent tethering to the ACP domain, the double bond of



Scheme 1. a) Proposed pathway for CL-catalyzed activation and subsequent attachment of the natural starter unit to the rapamycin PKS. b) Translocation of ACP-bound starter unit involves reduction of the Δ^1 bond by the ER domain of the loading module of RAPS1, the N-terminus of which is shown with a linear arrangement of the predicted catalytically active domains. AMP = adenosine monophosphate, PPi = inorganic phosphate, CL = carboxylic acid ligase like domain, KS = β-ketoacyl synthase, ACP = acylcarrier protein, AT = acyltransferase, DH = dehydratase.

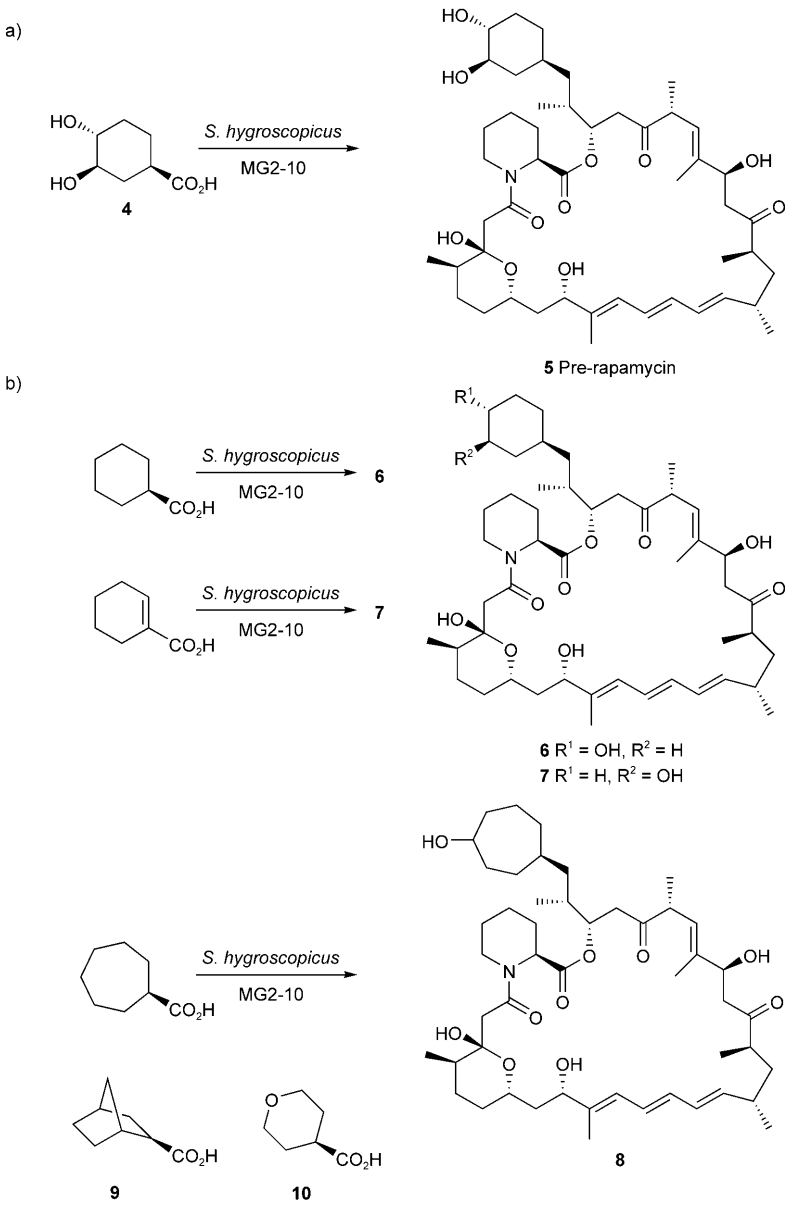
DHCHC is reduced by the action of the enoyl reductase (ER) domain of the rapamycin PKS loading module (Scheme 1b). Efficient incorporation of the pseudostarter acid 1,2-dihydro-DHCHC was also observed during feeding experiments with stable isotopes, thus leading to speculation that the domains of the PKS involved in selection of the starter unit might have broad substrate tolerance.[2,5] Indeed, a recent report has shown that novel analogues of rapamycin are biosynthesized in addition to rapamycin when simple analogues of the natural starter unit are fed to the rapamycin-producing organism.[6]

The immediate product of the rapamycin PKS is pre-rapamycin **5**, which is then modified by a series of two cytochrome P450 monooxygenases (RapJ and RapN) and three O-methyltransferases (RapI, RapM, and RapQ). When a region of DNA including the genes thought to encode these enzymes was excised (*rapKIJMNOQL*) from the rapamycin biosynthetic gene cluster, no production of rapamycins was observed from the resulting strain, *Streptomyces hygroscopicus* MG2–10. The mutant strain MG2–10 was then independently complemented with full-length copies of each of the genes which had been removed. Surprisingly, the production of **5** was only observed when *rapK* was reintroduced and expressed in the strain.[7] The gene *rapK* has previously been proposed as a candidate gene to encode a pteridine-dependent dioxygenase,[8] which (like its homologue in the FK506 cluster, *fkbO*) might catalyze the oxidation of the C9 hydroxy group after initial hydroxylation at C9 catalyzed by the cytochrome P450 RapJ.[9] However, we now have clear evidence that RapJ alone is capable of both oxygen insertion and further oxidation to give a C9 keto group.[10]

Furthermore, comparison of the sequences between RapK[11] and its homologues from the FK520 (FkbO),[12] FK506 (FkbO),[13] and hyg (ORF5)[14] biosynthetic gene clusters have revealed that the proposed binding motif for a pteridine derivative present in RapK[8] is not present in any of the other three proteins. These findings. together with the surprising effect of *rapK* on pre-rapamycin production in strain MG2–10,[7] have led us to reexamine the role of this gene, and of its product, in rapamycin biosynthesis.

We first carried out a series of experiments in an attempt to explain the lack of production of the rapamycin macrocycle by *S. hygroscopicus* MG2-10. These included feeding experiments in which exogenous pseudostarter carboxylic acid **4** was added to the fermentation medium to verify that the supply of this component was not a limiting factor. To our surprise, the addition of **4** to the fermentation led to the efficient production of **5** (Scheme 2a), which was fully characterized by mass spectrometry and NMR spectroscopy and shown to be identical to authentic pre-rapamycin.[7] Furthermore, the addition of other carboxylic acids in place of **4**, as reported for the wild-type organism,[6,15] was found to lead to the specific production of pre-rapamycin analogues in which these non-natural starter acids had been incorporated, in most cases after prior hydroxylation (Scheme 2b). CHC, cyclohex-1-enecarboxylic acid, and cycloheptanecarboxylic acid were all fed separately to *S. hygroscopicus* MG2–10, which led to the production of analogues **6**–**8**, respectively. Compounds **7** (22 mg) and **8** (77 mg) were isolated from the fermentation broth[16] by preparative chromatography[7] and their structures were confirmed by using high-resolution FT-ICR-MS^n.[17] Compound **6** (100 mg) was isolated and its structure confirmed by a combination of high-resolution FT-ICR-MS^n and multidimensional NMR spectroscopy experiments.[18] The MS and NMR data were in complete harmony with the results of previous work on the fully processed variants of these compounds.[6] Other compounds were fed, including norbornane carboxylic acid **9**, which had previously been unsuccessfully fed to the wild-type strain.[15] LC-MS analysis showed the production of low levels of a pre-rapamycin analogue arising

 © 2005 Wiley-VCH Verlag GmbH & Co. KGaA, Weinheim



Scheme 2. a) Reestablishment of pre-rapamycin **5** production in *S. hygroscopicus* MG2–10 by feeding the pseudostarter unit **4**. b) Exclusive production of the analogues **6**–**8** of pre-rapamycin by feeding, respectively, cyclohexanecarboxylic acid, cyclohex-1-enecarboxylic acid, and cycloheptanecarboxylic acid to *S. hygroscopicus* MG2–10.

from incorporation (after hydroxylation) of **9**, thus demonstrating that removal of competition from the natural starter acid allows a more efficient mutasynthesis of pre-rapamycin analogues.

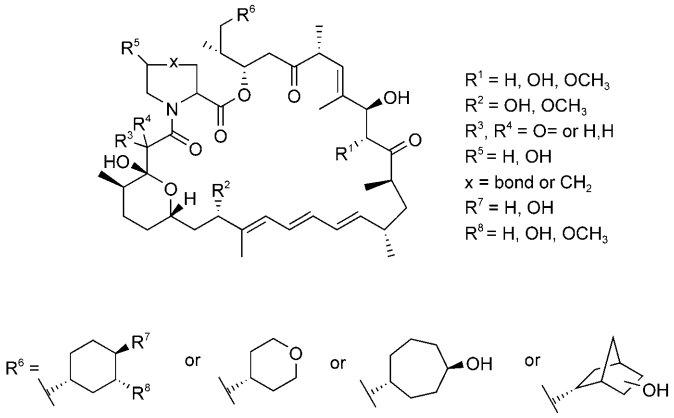
The hydroxylation of the incorporated starter acids appears to occur before synthesis of the polyketide chain.[6] Consistent with this idea, the hydroxylation seen in strain MG2–10 shows that none of the *rapKIJMNOQL* genes are involved. The enzyme or enzymes responsible remain to be identified. Interestingly, when the heterocycle tetrahydro-2*H*-pyran-4-carboxylic acid (**10**)[19] was fed to MG2-10, LC-MS studies revealed low levels of incorporation without hydroxylation. This observation reveals that hydroxylation is not essential for incorporation.

To test whether *fkbO*, the *rapK* homologue found in the FK520 cluster, has a similar function to *rapK*, *fkbO* was amplified by the polymerase chain reaction (PCR) from *S. hygroscopicus* var. *ascomyceticus* genomic DNA and ligated into the expression plasmid pSGSet1, which contains the P_{act} promoter.[10] This unit was introduced into *S. hygroscopicus* MG2–10 and the strain was analyzed for production of **5**. Levels of **5** were observed similar to those produced by *S. hygroscopicus* MG2–10 when complemented by *rapK*. This result indicates that FkbO has a similar function to RapK and opens the way to analogous mutasynthesis of FK506 and FK520 analogues.

The surprising observation that feeding exogenous starter unit carboxylic acids to *S. hygroscopicus* MG2-10 complements the absence of *rapK* provides strong evidence that the product of this gene is involved directly in the biosynthesis of DHCHC or in its regulation. Further sequence comparisons (data not shown) have revealed that *rapK* and its three homologues so far identified share a C-terminal domain which is present in a broadly distributed family of over 200 proteins—members of the YjgF/YER057c/UK114 family.[20] These proteins have been tentatively implicated in a range of regulatory functions. We propose that RapK is involved in the regulation of DHCHC production from shikimate.

Rapamycin and its analogues are the only established inhibitors of mTOR and the most selective inhibitors of kinase activity known to date, and therefore represent exciting candidates for the development of anticancer therapeutics.[21] All of the rapamycin analogues presently in clinical trials (for example, CCI-779, SDZ-RAD, and ABT-578) contain semisynthetic alterations at positions derived from the starter unit.[22] We have shown here that novel starter units can be efficiently and exclusively incorporated into the rapamycin molecule by feeding them to a *rapK*-deleted mutant of *S. hygroscopicus* MG2–10. The advantages of such mutasynthesis in a strain background not capable of producing natural rapamycins are clear (compare with the production of the modified avermectin analogue doramectin).[23] By combining alternative starter units, with controlled late-stage processing, by the selective expression of the methyltransferases RapI, RapM, and RapQ as well as monooxygenases RapJ and RapN (along with the ferridoxin RapO),[10] and with potential incorporation of alternative amino acid analogues in place of the natural pipecolic acid,[24] combinatorial biosynthesis of a wide range of rapamycin analogues is now possible (Scheme 3) even before engineered alterations of the macrocycle by PKS/NRPS engineering are considered. Such analogues offer great potential as chemical genetic probes of the molecular path-

 © 2005 Wiley-VCH Verlag GmbH & Co. KGaA, Weinheim



Scheme 3. Illustration of selected rapamycin analogues possible by feeding complemented strains of *S. hygroscopicus* MG2–10 with natural starter and/or pipecolic acid analogues.

ways involved in rapamycin action, and as new agents with enhanced therapeutic properties.

Received: December 2, 2004
Revised: April 1, 2005
Published online: June 24, 2005

Keywords: biosynthesis · macrocycles · mutasynthesis · natural products · polyketides

[1] A. G. DiLella, R. J. Craig, *Biochemistry* **1991**, *30*, 8512–8517; E. J. Brown, M. W. Albers, T. B. Shin, K. Ichikawa, C. T. Keith, W. S. Lane, S. L. Schreiber, *Nature* **1994**, *369*, 756–758.
[2] P. A. S. Lowden, B. Wilkinson, G. A. Böhm, S. Handa, H. G. Floss, P. F. Leadlay, J. Staunton, *Angew. Chem.* **2001**, *113*, 799–801; *Angew. Chem. Int. Ed.* **2001**, *40*, 777–779; A. Fang, A. L. Demain, *Folia Microbiol.* **1995**, *40*, 607–610.
[3] K. Kakinuma, N. Ikekama, A. Nakagawa, S. Omura, *J. Am. Chem. Soc.* **1979**, *101*, 3402–3403.
[4] N. Palaniappan, B. S. Kim, Y. Seikiyama, H. Osada, K. A. Reynolds, *J. Biol. Chem.* **2003**, *278*, 35552–35557.
[5] P. A. S. Lowden, G. A. Böhm, J. Staunton, P. F. Leadlay, *Angew. Chem.* **1996**, *108*, 2395–2397; *Angew. Chem. Int. Ed. Engl.* **1996**, *35*, 2249–2251.
[6] P. A. S. Lowden, G. A. Böhm, S. Metcalfe, J. Staunton, P. F. Leadlay, *ChemBioChem* **2004**, *5*, 535–538.
[7] M. A. Gregory, S. Gaisser, R. E. Lill, H. Hong, R. M. Sheridan, B. Wilkinson, H. Petkovic, A. J. Weston, I. Carletti, H.-L. Lee, J. S. Staunton, P. F. Leadlay, *Angew. Chem.* **2004**, *116*, 2605–2607; *Angew. Chem. Int. Ed.* **2004**, *43*, 2551–2553.
[8] I. Molnár, J. F. Aparicio, S. F. Haydock, L. E. Khaw, T. Schwecke, A. König, J. Staunton, P. F. Leadlay, *Gene* **1996**, *169*, 1–7.
[9] H. Motamedi, A. Shafiee, S.-J. Cai, S. L. Streicher, B. H. Arison, R. R. Miller, *J. Bacteriol.* **1996**, *178*, 5243–5248.
[10] S. J. Moss, S. Gaisser, M. A. Gregory, H. Petkovic (Biotica Technology Ltd), WO 04/007709, **2004**.
[11] T. Schwecke, J. F. Aparicio, I. Molnár, A. König, L.-E. Khaw, S. F. Haydock, M. Oliynyk, P. Caffrey, J. Cortés, J. B. Lester, G. A. Böhm, J. Staunton, P. F. Leadlay, *Proc. Natl. Acad. Sci. USA* **1995**, *92*, 7839–7843.
[12] K. Wu, L. Chung, W. P. Revill, L. Katz, C. D. Reeves, *Gene* **2000**, *251*, 81–90.
[13] H. Motamedi, A. Shafiee, *Eur. J. Biochem.* **1998**, *256*, 528–534.
[14] X. Ruan, D. Stassi, S. A. Lax, L. Katz, *Gene* **1997**, *203*, 1–9.
[15] P. A. S. Lowden, PhD Thesis, University of Cambridge (UK), **1999**.
[16] See Supporting Information for fermentation methods.
[17] See Supporting Information for FT-ICR-MS-MS data.
[18] The NMR spectra of rapamycins are complicated by the existence of rotamers.[7] See Supporting Information for NMR data.
[19] Tetrahydro-2H-pyran-4-carboxylic acid was synthesized by the method of: C. Strässler, A. Linden, H. Heimgartner, *Helv. Chim. Acta* **1997**, *80*, 1528–1554.
[20] S. Sinha, P. Rappu, S. C. Lange, P. Mantsala, H. Zalkin, J. L. Smith, *Proc. Natl. Acad. Sci. USA* **1999**, *96*, 13074–13079; L. Parsons, N. Bonander, E. Eisenstein, M Gilson, V. Kairys, J. Orban, *Biochemistry* **2003**, *42*, 80–89; A. Farkas, G. Nardai, P. Csermely, P. Tompa, P. Friedrich, *Biochem. J.* **2004**, *383*, 165–170.
[21] S. Huang, P. J. Houghton, *Curr. Opin. Pharmacol.* **2003**, *3*, 371–377.
[22] K. Yu, L. Toral-Barza, C. Discafani, W. G. Zhang, J. Skotnicki, P. Frost, J. J. Gibbons, *Endocr.-Relat. Cancer* **2001**, *8*, 249–258; R. Sedrani, S. Cottens, J. Kallen, W. Schuler, *Transplant. Proc.* **1998**, *30*, 2192–2194; D. K. Campbell, M. D. Rogers, *Rev. Cardiovascular Med.* **2004**, *5*(S2), S9–S15.
[23] H. A. I. McArthur, *Developments in Industrial Microbiology—BMP'97.* Society for Industrial Microbiology, Fairfax, VA, USA, **1998**, pp. 43–48; B. S. Moore, C. Hertweck, *Nat. Prod. Rep.* **2002**, *19*, 70–99.
[24] L. E. Khaw, G. A. Böhm, S. Metcalfe, J. Staunton, P. F. Leadlay, *J. Bacteriol.* **1998**, *180*, 809–814.

 © 2005 Wiley-VCH Verlag GmbH & Co. KGaA, Weinheim

Electrochemistry

An Electrolytic System That Uses Solid-Supported Bases for In Situ Generation of a Supporting Electrolyte from Acetic Acid Solvent**

*Toshiki Tajima and Toshio Fuchigami**

Electroorganic synthesis is one of the most useful methods in organic synthesis and is even applied in large-scale industrial processes.[1] It has recently attracted much interest as an environmentally friendly method because electrodes are inherently environmentally friendlier reagents than conventional oxidizing and reducing reagents. However, large

[*] T. Tajima, Prof. Dr. T. Fuchigami
Department of Electronic Chemistry
Tokyo Institute of Technology
Nagatsuta, Midori-ku, Yokohama 226-8502 (Japan)
Fax: (+81) 45-924-5489
E-mail: fuchi@echem.titech.ac.jp

[**] This work was supported by the Nissan Motor Co., the Mizuho Foundation for the Promotion of Sciences, the foundation "Hattori–Hokokai", and the Venture Business Laboratory of the Tokyo Institute of Technology.

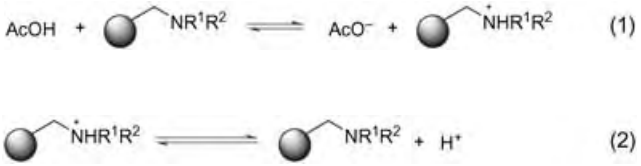
Supporting information for this article is available on the WWW under http://www.angewandte.org or from the author.

 © 2005 Wiley-VCH Verlag GmbH & Co. KGaA, Weinheim DOI: 10.1002/anie.200500977

amounts of supporting electrolytes are necessary to provide sufficient electrical conductivity to the solvents for electrolyses. Therefore, after the electrolyses, separation of the supporting electrolytes is required, and these separated supporting electrolytes generally become industrial waste because they are mostly unrecyclable, except for some industrialized cases.[2] Furthermore, the inefficient separation of supporting electrolytes from solvents requires a huge consumption of energy and produces large amounts of additional industrial waste.

To solve such separation and industrial-waste problems, a capillary-gap cell,[3] distillation of supporting electrolytes,[2] solid polymer electrolytes,[4] electrochemical microreactors,[5] and a thin-layer flow cell[6] have been developed. To the best of our knowledge, an ideal electroorganic synthetic system from the viewpoint of green sustainable chemistry should be one that does not require the addition of any supporting electrolytes. Although solid polymer electrolytes, electrochemical microreactors, and the thin-layer flow cell provide such an ideal electroorganic synthetic system, they require special equipment.

It is well known that electron transfer between one solid and another is very difficult.[7] Therefore, it can be expected that solid-supported bases should act as bases in bulk solutions and at the same time be electrochemically inactive reagents at an electrode surface. In the presence of solid-supported bases such as amines, protic organic solvents such as acetic acid should dissociate into anions and protons to some extent [Eqs. (1) and (2)]. This system would be suitable



for electroorganic synthesis because the protons derived from the protic organic solvent would play the role of the main carrier of an electronic charge via ammonium ions [Eq. (2)].[8] In this system, protic organic solvents would therefore serve both as a solvent and a supporting electrolyte generated in situ. We report herein a novel electrolytic system using solid-supported bases for the generation of a supporting electrolyte in situ from acetic acid as the solvent.

The cyclic voltammograms of *N*-methylmorpholine (**1**) and polystyrene-supported morpholine (**2**) were first measured in nBu$_4$NBF$_4$/anhydrous acetonitrile. As shown in Figure 1a, **1** is easily oxidized at around 1.2 V vs. SCE, while **2** is not oxidized at all, even when stirring. This means that solid-supported bases are not oxidized at the electrode surface. Next, the cyclic voltammogram of **2**/AcOH (0.1 M based on the concentration of morpholine) was measured; however, and rather unexpectedly, neither an oxidation current nor a reduction current was observed. Acetonitrile was then added as a co-solvent and the cyclic voltammogram of 0.1 M **2**/AcOH/MeCN was measured. As shown in Figure 1b, both an oxidation wave for AcO^- at about 2.1 V vs. SCE and a reduction current for H^+ were observed.[9] Therefore, it is clear that solid-supported bases cause acetic acid to dissociate into acetate anions and protons, and the resulting protons seem to act as the main carrier of the electronic charge.

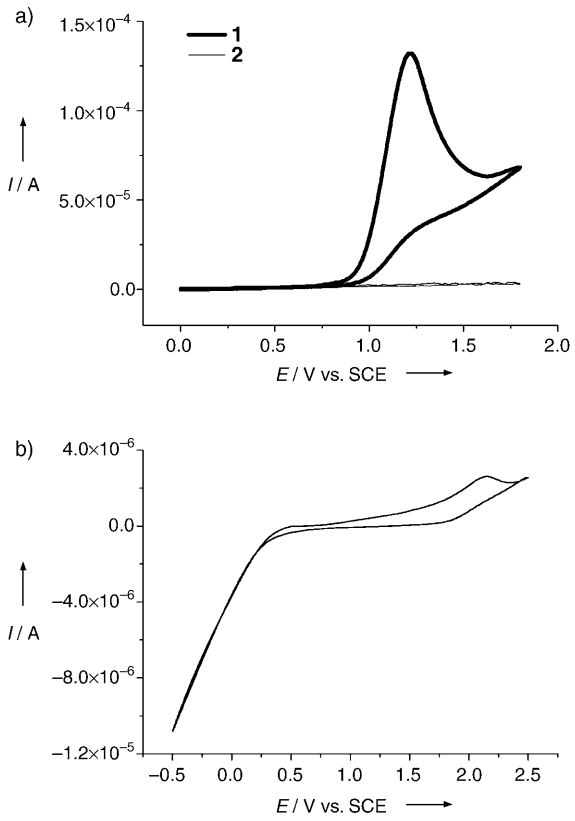


Figure 1. Cyclic voltammograms of a) *N*-methylmorpholine (**1**, 0.1 M) and polystyrene-supported morpholine (**2**, 0.1 M) in 0.1 M nBu$_4$NBF$_4$/MeCN, and b) AcOH/MeCN (50/50 v/v) in the presence of **2** (0.1 M) recorded at a Pt disk anode (ϕ = 0.8 mm). The scan rate was 100 mV s^{-1}.

We then investigated anodic α-acetoxylation using solid-supported bases with phenyl 2,2,2-trifluoroethylsulfide (**3**)[10] as the model compound as anodic acetoxylation is one of the most useful reactions in electroorganic synthesis.[11] The overall experimental procedure is illustrated in Figure 2.

The results with various solid-supported bases are shown in Table 1; polystyrene-supported morpholine gave the α-acetoxylated product **4** in low yield (entry 1), while similar

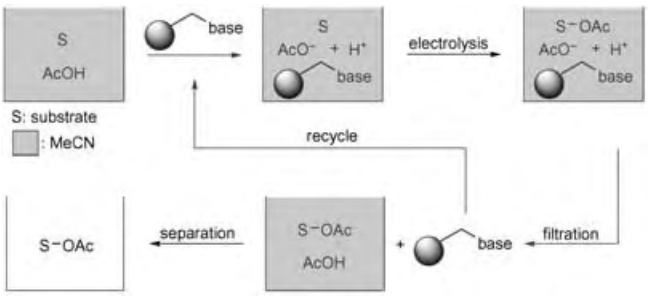
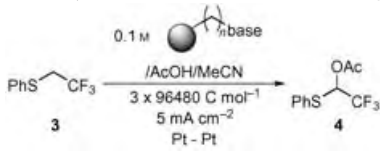


Figure 2. Schematic presentation of the experimental procedure.

 © 2005 Wiley-VCH Verlag GmbH & Co. KGaA, Weinheim

Table 1: Anodic acetoxylation of **3** with various solid-supported bases.



Entry	Solid	*n*	Base	Yield[a] [%]
1	PS[b]	1	 $pK_a = 8.33$	39
2	PS[c]	2		81 (77)[d]
3	SiO_2[e]	3		72 (68)
4	SiO_2	3	 $pK_a = 5.22$	24
5	SiO_2	3	 $pK_a = 6.95$	56 (54)
6	SiO_2	3	 **5** $pK_a = 24.3$	25

[a] ^{19}F NMR spectroscopically determined yield based on the CF_3 group and using monofluorobenzene as an internal standard. [b] Polystyrene. [c] Porous polystyrene. [d] Yield of isolated product in parentheses. [e] Silica gel.

reactions with porous polystyrene-supported and silica gel supported morpholine proceeded efficiently to provide **4** in good to high yields (entries 2 and 3). These results indicate that the solvent compatibility of the solids is highly significant. The acetoxylated product **4** was obtained in only 24% yield with silica gel supported pyridine, whose basicity is lower than that of morpholine (Table 1, entry 4), which means it does not dissociate acetic acid into acetate anions and protons efficiently. On the other hand, the acetoxylated product **4** was formed in 56% yield with silica gel supported imidazole (Table 1, entry 5). Unexpectedly, anodic acetoxylation of **3** resulted in a low yield (25%; Table 1, entry 6) when silica gel supported **5** was used, even though its basicity is much higher than that of morpholine. This can be explained as follows. Silica gel supported **5** can dissociate acetic acid into acetate anions and protons efficiently; however, **5** is protonated by the resulting protons because it is strongly basic. Therefore, the equilibrium of Equation (2) shifts to the left, and the resulting proton mobility is much lower than those of the other bases.[12]

Anodic acetoxylation of **3** was successfully carried out 10 times after recycling of the silica gel supported morpholine. In this recycling process, silica gel supported morpholine is easily separated and recovered by simple filtration (Figure 2). As shown in Figure 3, the yield of **4** was always more than 65%

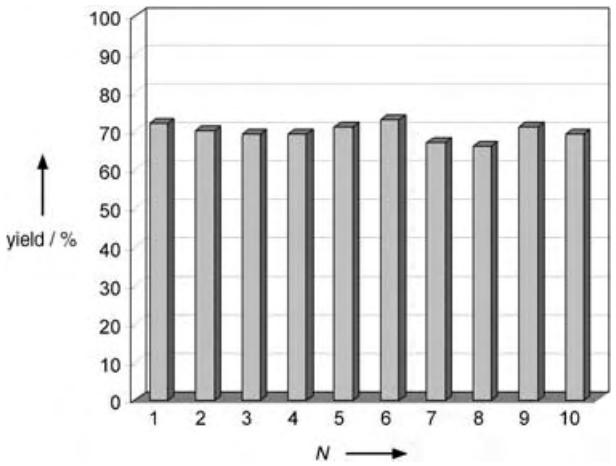
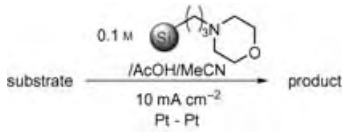


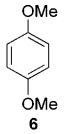
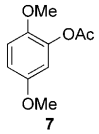
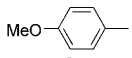
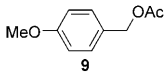
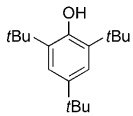
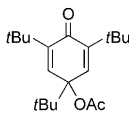
Figure 3. Yield of acetoxylated product **4** depending on the number *N* of reuses of the silica gel supported morpholine.

and did not decrease at all upon reuse of the silica gel supported morpholine. This clearly shows that solid-supported bases are not subject to oxidative decomposition at the electrode surface and therefore recyclable many times.

The generality of the new electrolytic system is shown in Table 2. Anodic acetoxylation of **6** was carried out to provide

Table 2: Anodic acetoxylation of various compounds with silica gel supported morpholine.



Entry	Substrate	Electricity [×96480 C mol^{-1}]	Product	Yield[a] [%]
1	 **6**	6	 **7**	91
2	 **8**	6	 **9**	72[b]
3	 **10**	5	 **11**	95

[a] Yield of isolated product. [b] The benzylic diacetoxylated product was also formed.

the corresponding acetoxylated product **7** in excellent yield. Anodic benzylic acetoxylation of **8** also proceeded to provide the acetoxylated product **9** in good yield. Furthermore, anodic acetoxylation of **10**, a phenol derivative, took place to provide the acetoxylated product **11** in excellent yield.

In conclusion, we have developed a novel electrolytic system for anodic acetoxylation that uses solid-supported bases. This system has many practical advantages and characteristics. For instance, it does not require addition of

 © 2005 Wiley-VCH Verlag GmbH & Co. KGaA, Weinheim

supporting electrolytes as the supporting electrolyte is generated in situ from acetic acid as the solvent. Furthermore, it allows a simple separation of the acetoxylated products and solid-supported bases by filtration, and the solid-supported bases are electrochemically stable and recyclable. The limitations of this new methodology and its further application for electroorganic synthesis are now under investigation. In addition, we plan to apply this system to a capillary-gap cell to reduce the high internal resistance compared with conventional methods.

Received: March 17, 2005
Revised: April 19, 2005
Published online: June 29, 2005

Keywords: acetoxylation · electrochemistry · electroorganic synthesis · green chemistry · solid-supported base

[1] *Organic Electrochemistry*, *4th ed.* (Eds.: H. Lund, O. Hammerich), Marcel Dekker, New York, **2001**.
[2] D. Degner, DE 2601541, **1977**.[*Chem. Abstr.* **1977**, *87*, 92655q].
[3] a) F. Beck, H. Guthke, *Chem. Ing. Tech.* **1969**, *41*, 943–950; b) L. Eberson, K. Nyberg, H. Sternerup, *Chem. Scr.* **1973**, *3*, 12–14.
[4] a) Z. Ogumi, T. Mizoe, C. Zhen, Z. Takehara, *Bull. Chem. Soc. Jpn.* **1990**, *63*, 3365–3368; b) D. Hoormann, C. Kubon, J. Jörissen, L. Kröner, H. Pütter, *J. Electroanal. Chem.* **2001**, *507*, 215–225.
[5] a) A. Ziogas, H. Löwe, M. Küpper, W. Ehrfeld in *Microreaction Technology* (Ed.: W. Ehrfeld), Springer, Berlin, **1998**, pp. 136–150; b) V. M. Schmidt, *Elektrochemische Verfahrenstechnik*, Wiley-VCH, Weinheim, **2003**, pp. 328–329.
[6] a) C. A. Paddon, G. J. Pritchard, T. Thiemann, F. Marken, *Electrochem. Commun.* **2002**, *4*, 825–831; b) D. Horii, M. Atobe, T. Fuchigami, F. Marken, *Electrochem. Commun.* **2005**, *7*, 35–39; c) R. Horcajada, M. Okajima, S. Suga, J. Yoshida, *Chem. Commun.* **2005**, 1303–1305.
[7] S. Nad, R. Breinbauer, *Angew. Chem.* **2004**, *116*, 2347–2349; *Angew. Chem. Int. Ed.* **2004**, *43*, 2297–2299.
[8] K. D. Kreuer, A. Fuchs, M. Ise, M. Spaeth, J. Maier, *Electrochim. Acta* **1998**, *43*, 1281–1288.
[9] N. Sato, T. Sekine, K. Sugino, *J. Electrochem. Soc.* **1968**, *115*, 242–246.
[10] T. Fuchigami, K. Yamamoto, Y. Nakagawa, *J. Org. Chem.* **1991**, *56*, 137–142.
[11] a) A. J. Baggaley, R. Brettle, *Chem. Commun.* **1966**, 108; b) L. Eberson, K. Nyberg, *J. Am. Chem. Soc.* **1966**, *88*, 1686–1691; c) T. Shono, A. Ikeda, J. Hayashi, S. Hakozaki, *J. Am. Chem. Soc.* **1975**, *97*, 4261–4264; d) T. Fuchigami, K. Yamamoto, H. Yano, *J. Org. Chem.* **1992**, *57*, 2946–2950; e) K. Surowiec, T. Fuchigami, *J. Org. Chem.* **1992**, *57*, 5781–5783.
[12] E. Grunwald, E. Price, *J. Am. Chem. Soc.* **1964**, *86*, 2970–2977.

 © 2005 Wiley-VCH Verlag GmbH & Co. KGaA, Weinheim

Metallophthalocyanines

Highly Fluorescent Self-Coordinated Phthalocyanine Dimers**

*Kazuya Kameyama, Mitsuhiko Morisue, Akiharu Satake, and Yoshiaki Kobuke**

Phthalocyanines have been studied for many possible applications because of their excellent optical and electronic properties as well as their chemical, thermal, and light stability.[1] Their expanded π orbitals create the large oscillator strength in the Q band (S_1) region and result in high quantum yields of fluorescence. Pigments, dyes, nonlinear optics,[2] and optical data storage devices are important applications for phthalocyanines. Phthalocyanines are also ideal for applications in electronic conduction[3] as a result of the extra stabilization of electrons/holes in their large π-electronic frameworks.

In the related field of porphyrin chemistry, Kobuke et al. previously reported a methodology for supramolecular organization. For imidazolyl-substituted porphyrins, complementary coordination of the imidazolyl group from one porphyrin molecule to the central Zn^{II} ion in a second porphyrin molecule causes a "slipped cofacial dimer", with an extremely large stability constant of $10^{11}\,M^{-1}$. This organization has served as a basic building block of linear and macrocyclic porphyrin arrays, which have increased the utilities of porphyrins for photosynthesis and functional dyes.[4]

The organization of phthalocyanines into controlled structures has been the target of extensive investigations. Besides π–π interactions in solution,[5] in thin films,[6] and in the solid state,[7] metal–ligand,[8] hydrogen-bonding,[9] and donor–acceptor interactions[10] have been reported for the phthalocyanines. It is well-known that J-aggregates of organic dyes are fluorescent[11] whereas H-aggregates are not.[12] Therefore, head-to-tail dimers and J-aggregates are highly desirable to maximize their optical properties. However, except for a few fluorescent phthalocyanines[13,14] only face-to-face dimers and H-aggregates have been observed. Herein, we report highly fluorescent phthalocyanine dimers that result from complementary coordination of imidazolyl groups to zinc and magnesium ions.

[*] K. Kameyama, M. Morisue, A. Satake, Prof. Y. Kobuke
Graduate School of Materials Science
Nara Institute of Science and Technology
Ikoma 630-0192 (Japan)
Fax: (+81) 743-72-6119
E-mail: kobuke@ms.naist.jp

[**] This work was supported by a Grant-in-Aid for Scientific Research (A) and Scientific Research on Priority Areas (No. 15036248): Reaction Control of Dynamic Complexes, from the Ministry of Education, Culture, Sports, Science, and Technology, Japan, and the JSPS (Japan Society for the Promotion of Science).

Supporting information for this article is available on the WWW under http://www.angewandte.org or from the author.

 DOI: 10.1002/anie.200501199 © 2005 Wiley-VCH Verlag GmbH & Co. KGaA, Weinheim

Zinc(II) hexa-*n*-butoxyimidazolylphthalocyanine (**1**) was prepared from the condensation of 6-cyanodiiminoisoindoline with 5 equivalents of 6,7-dibutoxydiiminoisoindoline in the presence of $Zn(OAc)_2$, followed by treatment with *N*-methylethylenediamine to convert the cyano groups into imidazolinyl substituents (29% yield based on 6-cyanodiiminoisoindoline). Oxidation of the imidazolinyl derivative with 5% Pt/C in boiling diphenyl ether afforded **1** in 95% yield (see Supporting Information). The MALDI-TOF mass spectrum of purified **1** revealed a peak for the molecular ion at $m/z = 1091.6$ $[M+H]^+$ as well as a peak for the dimer $[\mathbf{1}]_2$ at $m/z = 2182.0$ $[M+H]^+$ in a ratio of 6:5. Similarly, zinc(II) and magnesium(II) tri-*tert*-butylimidazolylphthalocyanines **2** and **3** were synthesized from zinc(II) and magnesium(II) tri-*tert*-butylcyanophthalocyanines, respectively.

The self-association behavior of **1**–**3** was first examined with UV/Vis spectroscopy by performing titrations in toluene. Phthalocyanine **1** (1.07×10^{-6} M) showed split Q bands at 670 and 700 nm (Figure 1a, solid line). If we assume that dimer $[\mathbf{1}]_2$ forms (Scheme 1),[15] the split Q bands are best interpreted in terms of exciton interactions of Q_x and Q_y transition dipoles to give red-shifted Q_x and blue-shifted Q_y bands (Figure 1c).[16] These Q bands converged into a single peak through isosbestic points at 624, 650, and 693 nm upon addition of *N*-methylimidazole (Im; Figure 1b), and the spectra reached a stationary state after adding 1.44×10^{-2} M Im. The final converged spectrum (Figure 1a, dashed line) resembles that of zinc(II) octa-*n*-butoxyphthalocyanine (**4**) in toluene with axial coordination of Im.

On the basis of the association constants determined for **4** with Im ($K_{\mathbf{4}\text{-Im}} = 2.8 \times 10^5\ M^{-1}$) from another titration experiment (data not shown), the constant for self-association of **1** in toluene was evaluated as $K_{\mathbf{1}\text{-}\mathbf{1}} = 1.1 \times 10^{12}\ M^{-1}$. The extremely large association constant is thought to originate from the

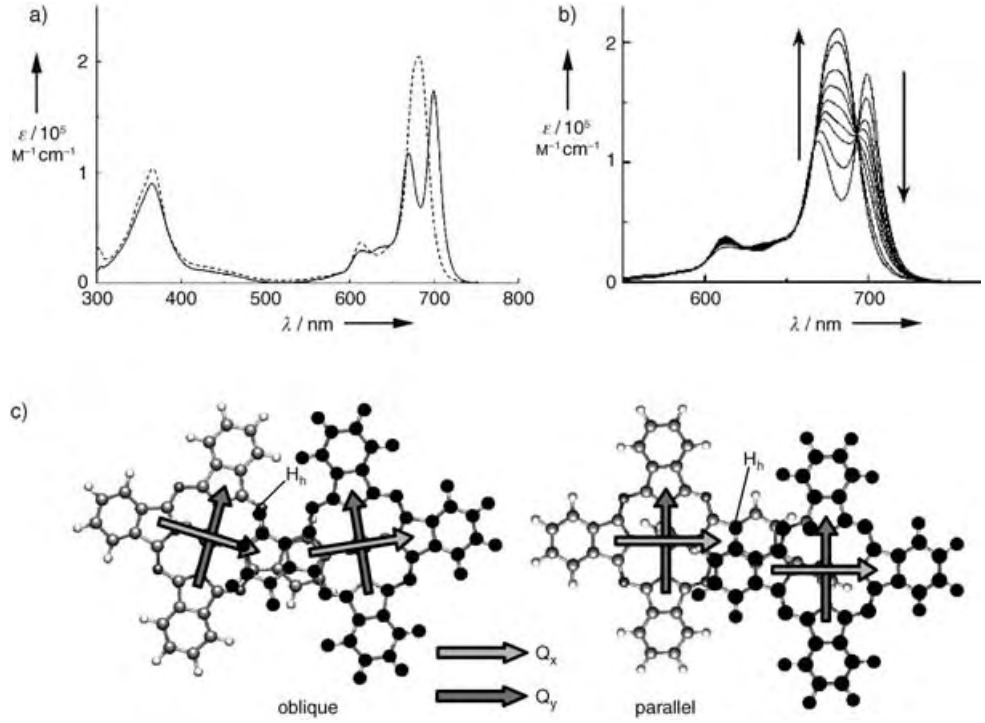
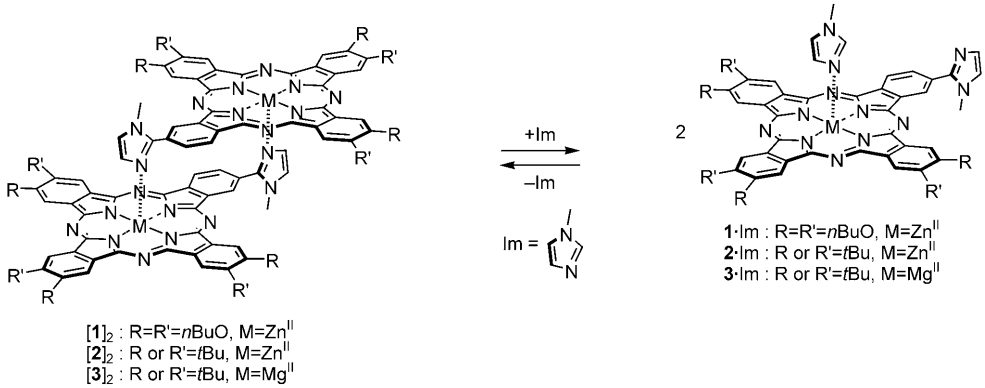


Figure 1. a) UV/Vis spectra of dimer $[\mathbf{1}]_2$ (——) and dissociated monomer **1**·Im (-----) in toluene. b) Changes in the spectra of $[\mathbf{1}]_2$ upon addition of Im (0.00, 0.32×10^{-3}, 0.73×10^{-3}, 1.04×10^{-3}, 1.44×10^{-3}, 2.01×10^{-3}, 2.93×10^{-3}, 4.45×10^{-3}, and 1.44×10^{-2} M). c) Oblique and parallel geometric isomers of $[\mathbf{1}]_2$, and the directions of the transition dipoles. Hydrogen atom H_h is highlighted (see Figure 2).



Scheme 1. Dimer⇌monomer equilibrium of metalloimidazolylphthalocyanines **1**–**3**.

 © 2005 Wiley-VCH Verlag GmbH & Co. KGaA, Weinheim

complementary nature of the coordination. Dilution of $[\mathbf{1}]_2$ down to 1.03×10^{-9} M did not lead to any spectral changes, which is in accord with the high association constant. As the UV/Vis spectra followed Beer's law, at least, up to 2×10^{-4} M,[17] further aggregation of $[\mathbf{1}]_2$ caused by commonly observable π–π stacking is considerably suppressed relative to zinc tetra-*tert*-butylphthalocyanine (dimerization constant in toluene, $K=2.5\times10^{4}\,\mathrm{M}^{-1}$).[18]

The formation of stable dimers was also observed in other noncoordinating solvents such as $CHCl_3$ and CH_2Cl_2. Furthermore, **2** and **3** also showed similar split Q bands at 671 and 700 nm for **2** and at 672 and 701 nm for **3**, and their self-association constants in toluene were $K_{\mathbf{2}\text{-}\mathbf{2}}=1.7\times10^{11}$ and $K_{\mathbf{3}\text{-}\mathbf{3}}=1.4\times10^{11}\,\mathrm{M}^{-1}$. These results indicate that the Zn and Mg imidazolylphthalocyanine motifs lead to stable dimeric complexes of defined structure, regardless of the nature of the peripheral substituents.

A detailed structural analysis was carried out by NMR spectroscopy using various techniques. As the imidazolyl substituent does not lie along the symmetry axis defined by the pyrrolic N···N atoms, two isomeric dimers should emerge upon coordination: one parallel, with the two metallophthalocyanine units aligned but slip-stacked; and the other oblique, with the imidazolyl group of one unit aligned with the pyrrolic symmetry axis of the other (see Figure 1c). The presence of two dimeric structures was clearly displayed in the ^{1}H NMR (Figure 2) and heteronuclear multiple quantum coherence (HMQC) spectra. The hydrogen atom H_k, which lies closest to the plane of the second phthalocyanine unit upon coordination, appeared characteristically as two highly shielded peaks at $\delta=2.91$ and 2.83 ppm. The second closest hydrogen atom H_j and imidazolyl-*N*-methyl H_i atoms were observed as moderately shielded pairs of peaks at $\delta=5.57$ and 5.47 ppm and at $\delta=2.55$ and 2.39 ppm, respectively. When trifluoroacetic acid (TFA) was gradually added to the dimer, the two peaks for H_k at $\delta=2.91$ and 2.83 ppm shifted downfield and converged at $\delta=7.71$ ppm. Similarly, the peaks for the other imidazolyl protons, H_i and H_j, also shifted downfield and converged as indicated by arrows in Figure 2b. These results reveal that the coordinated dimers dissociates into the corresponding monomer upon addition of TFA and that the twin peaks originate from two isomeric dimers upon coordination.

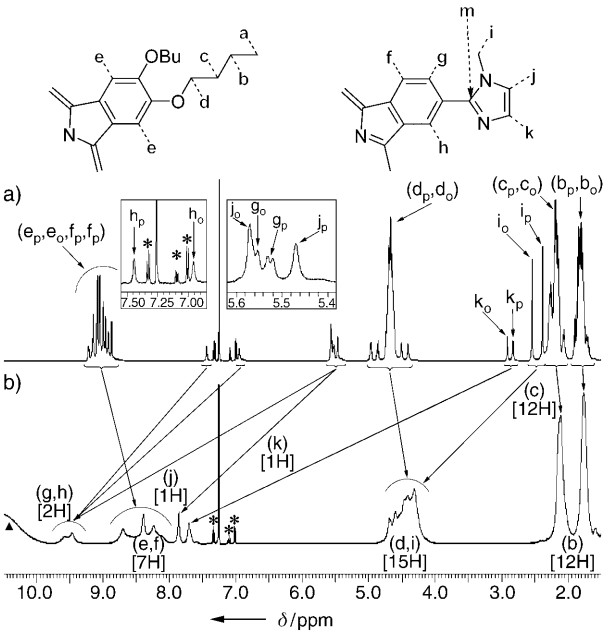


Figure 2. ^{1}H NMR spectra of a) dimer $[\mathbf{1}]_2$ (20 mM) in $CDCl_3$ at room temperature and b) monomer **1**·TFA, from the dissociation of the dimer by the addition of 10% TFA. The subscripts o and p denote oblique and parallel, respectively, and refer to the isomers shown in Figure 1. Symbols ⋆ and ▲ indicate the residual peaks of the solvent (diphenyl ether) and TFA, respectively. Relative integration intensities are provided in square parentheses in (b).

Two sets of signals for all the protons were assigned by total correlation and heteronuclear multiple bond coherence NMR spectroscopy (TOCSY and HMBC). Proton H_h was the most sensitive to the isomeric structures and appeared at $\delta=$ 6.96 and 7.44 ppm. The proton H_h in the oblique configuration is located closer to the center of the molecule, and the signal for H_h at $\delta=6.96$ ppm was assigned to the oblique isomer whereas that at $\delta=7.44$ ppm was assigned to the parallel isomer. The ratio of parallel to oblique dimers for $[\mathbf{1}]_2$ was approximately 1:1 from the integration of the areas for various well-separated peaks. All the NMR signals were consistent with the expected J-type phthalocyanine dimers. ^{1}H NMR spectra of dimers **2** and **3** were assigned to similar isomeric dimers.

All of the J-type dimers emit strong fluorescence in toluene. The quantum yield of $[\mathbf{1}]_2$ ($\Phi_F=0.45$) is identical to that of the dissociated monomer **1**·Im ($\Phi_F=0.45$), and the same pattern is observed for the other dimers, with $\Phi_F=0.26$ for $[\mathbf{2}]_2$ ($\Phi_F=0.27$ for **2**·Im) and $\Phi_F=0.76$ for $[\mathbf{3}]_2$ ($\Phi_F=0.76$ for **3**·Im). These results indicate that both the oblique and parallel conformational isomers emit in the same way as the monomeric metallophthalocyanines. In the case of a previously reported noncomplementary coordination dimer,[13b] the fluorescence quantum yield was decreased by a half as a result of its flexible structure. Other supramolecular motifs reported so far have weaker interactions, such that J-type dimerization only occurred under specific conditions of concentration, composition of solvent mixture, and temperature.[13] The orientation and spatial position of the two phthalocyanines units were not reported in those cases, but the imidazolylphthalocyanine motif developed here constitutes a unique basis set for supramolecular expression.

Analysis by differential pulse voltammetry of $[\mathbf{1}]_2$ showed split oxidation waves at 510 and 619 mV (versus Ag/AgCl)[19] for oxidation of the phthalocyanine ring that correspond to one- and two-electron oxidations from the dimer, respectively. The first oxidation potential was almost identical to that of the dissociated monomer **1**·Im, and the second wave appeared at a higher potential. This pattern suggests delocalization of the cation radical over the two π–π interacting phthalocyanine units. Such so-called charge–resonance interaction[20] is effective in lowering the charge density of the cation generated on the phthalocyanine rings and decreases the solvent reorganization energy and is therefore beneficial for efficient charge separation.[4b]

 © 2005 Wiley-VCH Verlag GmbH & Co. KGaA, Weinheim

In conclusion, we have demonstrated a complementary phthalocyanine dimer. This report is the first example of a noncovalent J-type dimer of fluorescent phthalocyanines with well-defined structural analysis. This supramolecular dimer unit will be useful in applications that require efficient excitation-energy transfer, charge separation, and hole-transfer reactions, as was shown previously with a porphyrin dimer.[4] The present methodology which employs a slipped-cofacial dimer of imidazolyl-appended phthalocyanine is expected to produce advanced materials with excellent fluorescence properties combined with stabilities toward various external sources.

Received: April 5, 2005
Published online: June 29, 2005

Keywords: aggregation · fluorescence · phthalocyanines · self-assembly · supramolecular chemistry

[1] N. B. McKeown, *Phthalocyanine Materials*: *Synthesis, Structure and Function*, Cambridge University Press, Cambridge, **1998**.
[2] G. Torre, P. Vázquez, F. Agullü-Lüpez, T. Torres, *Chem. Rev.* **2004**, *104*, 3723 – 3750.
[3] T. J. Marks, *Science* **1985**, *227*, 881 – 889.
[4] a) Y. Kobuke, H. Miyaji, *J. Am. Chem. Soc.* **1994**, *116*, 4111 – 4112; b) H. Ozeki, A. Nomoto, K. Ogawa, Y. Kobuke, M. Murakami, K. Hosoda, M. Ohtani, S. Nakashima, H. Miyasaka, T. Okada, *Chem. Eur. J.* **2004**, *10*, 6393 – 6401; c) K. Ogawa, Y. Kobuke, *Angew. Chem.* **2000**, *112*, 4236 – 4239; *Angew. Chem. Int. Ed.* **2000**, *39*, 4070 – 4073; d) R. Takahashi, Y. Kobuke, *J. Am. Chem. Soc.* **2003**, *125*, 2372 – 2373.
[5] A. W. Snow in *The Porphyrin Handbook*, *Vol. 17* (Eds.: K. M. Kadish, K. M. Smith, R. Guilard), Elsevier Science, USA, **2003**, pp. 129 – 176.
[6] M. J. Cook, I. Chambrier in *The Porphyrin Handbook*, *Vol. 17*, Elsevier Science, USA, **2003**, pp. 37 – 127.
[7] a) D. Dini, M. Hanack in *The Porphyrin Handbook*, *Vol. 17*, Elsevier Science, USA, **2003**, pp. 1 – 36; b) M. K. Engel in *The Porphyrin Handbook*, *Vol. 20*, Elsevier Science, USA, **2003**, pp. 1 – 242; c) P. Thordarson, R. J. M. Nolte, A. E. Rowan in *The Porphyrin Handbook*, *Vol. 18*, Elsevier Science, USA, **2003**, pp. 281 – 301.
[8] a) M. Hanack, D. Dini in *The Porphyrin Handbook*, *Vol. 18*, Elsevier Science, USA, **2003**, pp. 251 – 280; b) M. J. Cook, A. Jafari-Fini, *J. Mater. Chem.* **1997**, *7*, 2327 – 2329; c) X. Li, D. K. P. Ng, *Eur. J. Inorg. Chem.* **2000**, 1845 – 1848; d) N. Kobayashi, A. Muranaka, V. N. Nemykin, *Tetrahedron Lett.* **2001**, *42*, 913 – 915; e) K. Ishii, Y. Watanabe, S. Abiko, N. Kobayashi, *Chem. Lett.* **2002**, 450 – 451.
[9] M. V. Martinez-Diaz, M. S. Rodriguez-Morgade, M. C. Feiters, P. J. M. van Kan, R. J. M. Nolte, J. F. Stoddart, T. Torres, *Org. Lett.* **2000**, *2*, 1057 – 1060.
[10] A. Escosura, M. V. Martínez-Díaz, P. Thordarson, A. E. Rowan, R. J. M. Nolte, T. Torres, *J. Am. Chem. Soc.* **2003**, *125*, 12300 – 12308.
[11] a) E. E. Jelley, *Nature* **1936**, *138*, 1009 – 1010; b) E. E. Jelley, *Nature* **1937**, *139*, 631 – 632.
[12] N. Kobayashi, A. B. P. Lever, *J. Am. Chem. Soc.* **1987**, *109*, 7433 – 7441.
[13] For fluorescent phthalocyanines, see: a) Y. Kaneko, T. Arai, K. Tokumaru, D. Matsunaga, H. Sakuragi, *Chem. Lett.* **1996**, 345 – 346; b) K. Ishii, S. Abiko, M. Fujitsuka, O. Ito, N. Kobayashi, *J. Chem. Soc. Dalton Trans.* **2002**, 1735 – 1739; c) X.-Y. Li, D. K. P. Ng, *Tetrahedron Lett.* **2001**, *42*, 305 – 309; d) M. Kimura, T. Kuroda, K. Ohta, K. Hanabusa, H. Shirai, N. Kobayashi, *Langmuir* **2003**, *19*, 4825 – 4830.
[14] For reports on noncovalent head-to-tail dimers and J-aggregates of porphyrin derivatives, see: a) R. F. Pasternack, P. R. Huber, P. Boyd, G. Engasser, L. Francesconi, E. Gibbs, P. Fasella, G. C. Venturo, L. deC. Hinds, *J. Am. Chem. Soc.* **1972**, *94*, 4511 – 4517; b) J. Chiefari, K. Griebenow, N. Griebenow, T. S. Balaban, A. R. Holzwarth, K. Schaffner, *J. Phys. Chem.* **1995**, *99*, 1357 – 1365; c) J. Vasudevan, R. T. Stibrany, J. Bumby, S. Knapp, J. A. Potenza, T. J. Emge, H. J. Schugar, *J. Am. Chem. Soc.* **1996**, *118*, 11676 – 11677; d) J.-C. Chambron, V. Heitz, J.-P. Sauvage in *The Porphyrin Handbook*, *Vol. 6*, Academic Press, USA, **2000**, pp. 1 – 42.
[15] Two kinds of configurational isomers, oblique and parallel, are possible. The energy-minimized structures and their excited states were calculated using MOPAC (AM1) and INDO/S (see Supporting Information).
[16] M. Kasha, M. *Radiat. Res.* **1963**, *20*, 55 – 70.
[17] 2×10^{-4} M is the upper concentration limit to analyze $[\mathbf{1}]_2$ by UV/Vis absorption spectroscopy in a cell of 1-mm path length.
[18] D. A. Fernandez, J. Awruch, L. E. Dicelio, *Photochem. Photobiol.* **1996**, *63*, 784 – 792.
[19] DPV conditions: $[\mathbf{1}]_2$ (0.1 mM with respect to the monomer), nBu$_4$NPF$_6$ (0.1M), CH_2Cl_2, at 298 K (see Supporting Information).
[20] D. E. Richardson, H. Taube, *Inorg. Chem.* **1981**, *20*, 1278 – 1285.

 © 2005 Wiley-VCH Verlag GmbH & Co. KGaA, Weinheim

Asymmetric Catalysis

Oxidative Cyclization of Diols Derived from 1,5-Dienes: Formation of Enantiopure *cis*-Tetrahydrofurans by Using Catalytic Osmium Tetroxide; Formal Synthesis of (+)-*cis*-Solamin**

Timothy J. Donohoe and Sam Butterworth*

In 1965, Klein and Rojahn discovered that treatment of 1,5-hexadiene with $KMnO_4$ afforded *cis*-2,5-bis(hydroxymethyl)-tetrahydrofuran.[1] The mechanism of the reaction was a matter of some debate but eventually was considered to be a concerted cyclization of a metal–glycolate complex across a distal alkene.[2] This mechanism is consistent with the fact that the addition across both alkenes is stereospecific (*syn*) and also that stereoselective formation of *cis*-tetrahydrofurans is observed. Since the original reports using $KMnO_4$, several

[*] Prof. T. J. Donohoe, Dr. S. Butterworth
Department of Chemistry
University of Oxford, Chemistry Research Laboratory
Mansfield Road, Oxford, OX1 3TA (UK)
Fax: (+44) 186-527-5708
E-mail: timothy.donohoe@chem.ox.ac.uk

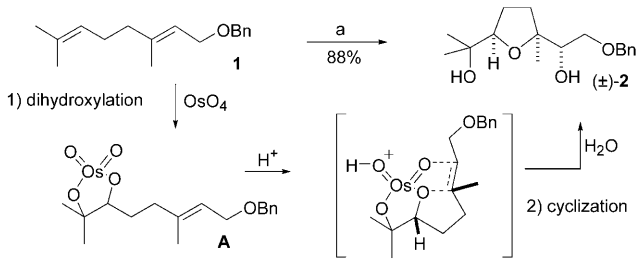
[**] We thank the EPSRC and Merck for supporting this project. AstraZeneca, Pfizer, Novartis, and Merck are thanked for unrestricted funding. R. C. D. Brown is thanked for providing the NMR spectra of compound **19**.

Supporting information for this article is available on the WWW under http://www.angewandte.org or from the author.

 © 2005 Wiley-VCH Verlag GmbH & Co. KGaA, Weinheim DOI: 10.1002/anie.200500513

other metals have been shown to mediate this type of cyclization, including ruthenium[3] and, more recently, osmium.[4]

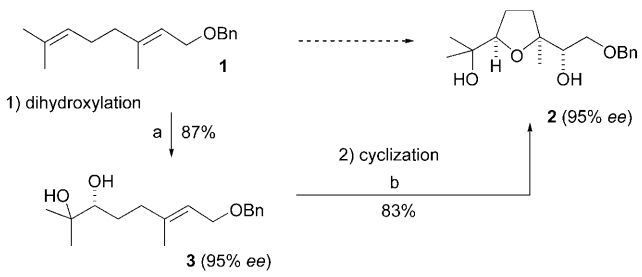
We recently described the development of the oxidative cyclization of 1,5-dienes using catalytic amounts of OsO_4 (5 mol%) under acidic conditions (see **1**→**2**, Scheme 1).[5] This sequence is remarkable for its high yields, especially during the oxidation of mono- and disubstituted alkenes, which tend to give overoxidation products with manganese and ruthenium oxidants.



Scheme 1. Oxidative cyclization of 1,5-dienes. Reagents and conditions: a) OsO_4 (5 mol%), Me_3NO (4 equiv), camphor sulfonic acid (6 equiv), CH_2Cl_2. Bn = benzyl.

A major obstacle to the application of this sequence in synthesis is the fact that racemic mixtures are produced. Attempts to introduce asymmetric induction into this reaction by the addition of chiral amine ligands failed, presumably because the pH values of the solutions were too low to enable efficient coordination of the amines to the osmium center. However, we now report a reaction sequence that overcomes this hurdle, allows the formation of tetrahydrofuran (THF) systems with complete control over both the relative and absolute stereochemistries, and uses catalytic amounts of a transition metal. We have discovered that vicinal diols derived from 1,5-dienes will cyclize to form the THF ring system when they are subjected to oxidative cyclization conditions (see **3**→**2**, Scheme 2). This cyclization reaction becomes a powerful methodology because the starting diols can be obtained from 1,5-dienes in a regio- and stereoselective manner by using, for example, the Sharpless asymmetric dihydroxylation (AD) reaction.[6] We have proven unambiguously by HPLC analysis that there is no loss of stereochemical integrity during the cyclization process.

The cyclization of diol **3** gave **2**, which was identical to the product obtained from the corresponding diene. This result



Scheme 2. Two-step procedure for the formation of enantiopure *cis*-THF rings. Reagents and conditions: a) AD-mix-β; b) OsO_4 (5 mol%), Me_3NO (4 equiv), trifluoroacetic acid (TFA; 6 equiv), acetone/H_2O, RT.

suggests that the 1,2-diol forms a chelated osmate ester in situ (see intermediate **A**, Scheme 1) that then cyclizes as before.

Naturally, we were intrigued by the oxidation state of the osmium center in **A**, because the diene cyclization protocol provides Os^{VI} directly and the diol cyclization route commences with Os^{VIII}.[7] Therefore, we examined the role of additives in the cyclization of **3** (Table 1) and found that a range of

Table 1: Oxidation of (+)-**3**→(−)-**2**.

Entry	Sacrificial alkene[a]	*t* [h]	Conversion [%][b]
1	none	6	30
2	none	30	85 (55)
3	cyclohexene (5)	6	40
4	cyclohexene (5)	30	100 (83)
5	isoprene (5)	6	45

[a] Equivalents given in brackets. [b] Yield of isolated product given in brackets.

sacrificial alkenes improved the yield (5 equiv were best). It is possible that this second alkene is able to generate Os^{VI} in situ (from Os^{VIII}) by a dihydroxylation reaction and thus acts to increase the amount of active Os^{VI} catalyst in the reaction mixture.

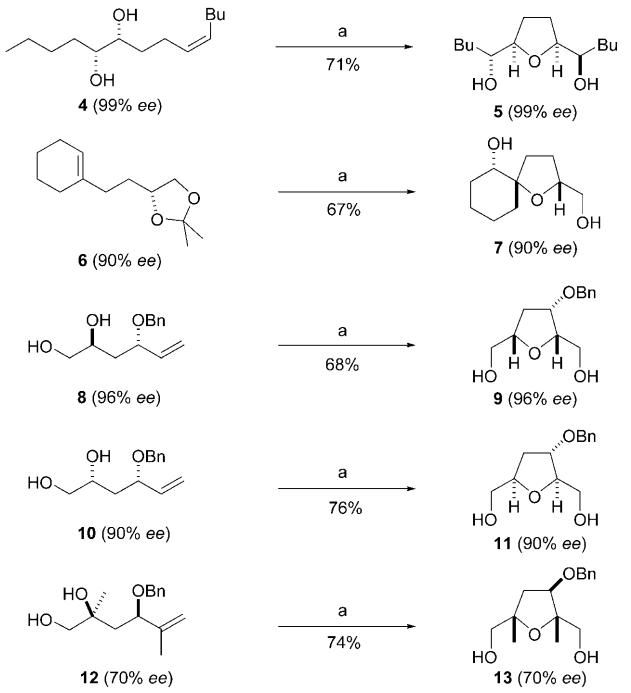
Although we could find no advantage to using cyclohexene rather than isoprene, the choice of sacrificial alkene becomes important in the purification as the product occasionally coelutes with the diol derived from this second alkene.

This investigation is related to the oxidative cyclization of bishomoallylic alcohols using Re^{VII} reagents (to give *trans*-tetrahydrofurans)[8] and diols using Cr^{VI} reagents[9] (the yields for this process are low), which have both been used successfully in synthesis.[10] However, both sets of conditions use stoichiometric amounts of the metal reagent to accomplish these transformations, and the advantages of catalytic metal oxidants are clear.

Next, we examined the oxidative cyclization of a range of diols derived from 1,5-dienes (Scheme 3). The diol starting materials were made by a regio- and stereoselective dihydroxylation of a diene by using the Sharpless AD reaction—although there are other viable routes to the diol precursors. The cyclization was shown to be tolerant of a variety of different substitution patterns on the alkene, diol unit, and even the backbone (Scheme 3). The yields were good and the products from the diol cyclizations were identical, as shown by NMR spectroscopic analysis, to a (racemic) compound formed by the cyclization of the corresponding 1,5-diene under the conditions shown in Scheme 1. As expected, the sequence is highly selective in each case for the formation of *cis*-tetrahydrofurans. Moreover, the enantiomeric purity of the diol was transferred completely to the THF product.

We then sought to exemplify this new cyclization reaction in synthesis. Our target was *cis*-solamin, which is an annonaceous acetogenin with potent biological activity (e.g., *cis*-solamin displays cytotoxicity and hemolytic activity).[11,12] Brown and co-workers[12] recently reported a clever synthesis of this molecule, whereby $KMnO_4$ was used to oxidatively cyclize a 1,5-diene precursor that was loaded with a chiral

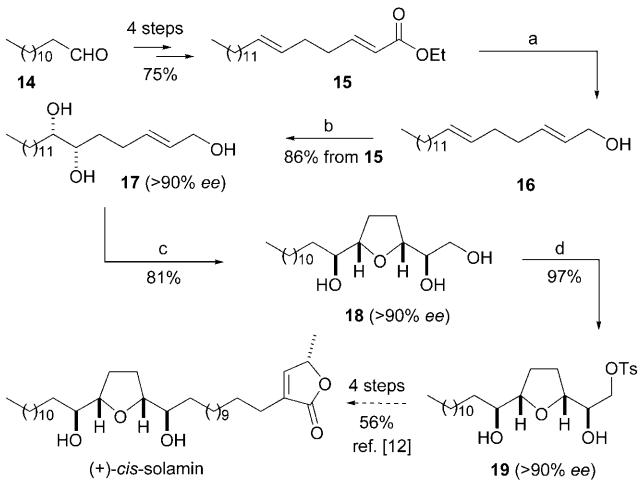
 © 2005 Wiley-VCH Verlag GmbH & Co. KGaA, Weinheim



Scheme 3. Oxidative cyclization of various diols. Reagents and conditions: a) OsO_4 (5 mol%), Me_3NO (4 equiv), TFA (6 equiv), acetone/H_2O, RT. Isoprene (5 equiv) was used as an additive in each entry, except for **4** in which cyclohexene was used.

auxiliary to control the absolute stereochemistry of the product.

This literature route was used to prepare compound **15** in four steps (Scheme 4). The ester group was then reduced and a regioselective AD reaction was performed on hydroxy-substituted diene **16** to yield **17** in 86% yield from **15** and with >90% *ee*. The key oxidative cyclization reaction of **17** worked well and gave THF product **18** in 81% yield. This product was subsequently transformed into tosylate **19** (>90% *ee* as determined by HPLC), which was spectroscopically identical to the product reported by Brown and co-workers. This investigation constitutes a formal synthesis of the target as **19** can be converted into (+)-*cis*-solamin in four steps and 56% yield by using a literature precedent.[12] This osmium-catalyzed oxidation methodology compares well with the permanganate-based alternative (e.g., **15**→**18**: obtained in five steps and 46% overall yield from the method of Brown and co-workers[12] compared with three steps and 70% overall yield from our new approach).



Scheme 4. The synthesis of *cis*-solamin. Reagents and conditions: a) diisobutylaluminum hydride; b) AD-mix-α,$(DHQ)_2PHAL$; c) OsO_4 (5 mol%), Me_3NO (4 equiv), TFA (6 equiv), isoprene (5 equiv), acetone/H_2O, RT; d) Bu_2SnO, *p*-toluenesulfonyl chloride (TsCl), benzene. $(DHQ)_2PHAL$ = hydroquinine 1,4-phthalazinediyl diether.

To conclude, we present herein a new catalytic oxidation reaction that promotes the cyclization of vicinal diols onto a proximal alkene with a high level of stereocontrol. The diol precursors are readily prepared as single enantiomers, which means that the oxidation products (tetrahydrofurans) can also be accessed in enantiopure form. This method is simple to perform, high yielding, and tolerant of substitution on the THF backbone. The usefulness of this method has been proved in a short and extremely efficient (formal) synthesis of (+)-*cis*-solamin.

Received: February 10, 2005
Revised: April 14, 2005
Published online: June 29, 2005

Keywords: asymmetric catalysis · natural products · osmium · oxidation · stereoselectivity

[1] E. Klein, W. Rojahn, *Tetrahedron* **1965**, *21*, 2353.
[2] J. E. Baldwin, M. J. Crossley, E.-M. M. Lehtonen, *J. Chem. Soc. Chem. Commun.* **1979**, 918; D. M. Walba, M. D. Wand, M. C. Wilkes, *J. Am. Chem. Soc.* **1979**, *101*, 4396.
[3] P. H. J. Carlsen, T. Katsuki, V. S. Martin, K. B. Sharpless, *J. Org. Chem.* **1981**, *46*, 3936; V. Piccialli, N. Cavallo, *Tetrahedron Lett.* **2001**, *42*, 4695; V. Piccialli, T. Caserta, *Tetrahedron Lett.* **2004**, *45*, 303.
[4] M. de Champdore, M. Lasalvia, V. Piccialli, *Tetrahedron Lett.* **1998**, *39*, 9781; T. J. Donohoe, J. J. G. Winter, M. Helliwell, G. Stemp, *Tetrahedron Lett.* **2001**, *42*, 971.
[5] T. J. Donohoe, S. Butterworth, *Angew. Chem.* **2003**, *115*, 978; *Angew. Chem. Int. Ed.* **2003**, *42*, 948.
[6] For a review, see: H. C. Kolb, M. S. VanNieuwenhze, K. B. Sharpless, *Chem. Rev.* **1994**, *94*, 2483.
[7] Preliminary studies have shown that the vicinal diol must be intact for cyclization to occur: monoprotected derivatives of **4** and bishomoallylic alcohols gave no THF products under these cyclization conditions.
[8] S. H. Tang, R. M. Kennedy, *Tetrahedron Lett.* **1992**, *33*, 5299; F. E. McDonald, T. B. Towne, *J. Am. Chem. Soc.* **1994**, *116*, 7921; F. E. McDonald, T. B. Towne, C. C. Schultz, *Pure Appl. Chem.* **1998**, *70*, 355.
[9] D. M. Walba, G. S. Stoudt, *Tetrahedron Lett.* **1982**, *23*, 727.
[10] E. J. Corey, D.-C. Ha, *Tetrahedron Lett.* **1988**, *29*, 3171; Y. Morimoto, K. Muragaki, T. Iwai, Y. Morishita, T. Kinoshita, *Angew. Chem.* **2000**, *112*, 4248; *Angew. Chem. Int. Ed.* **2000**, *39*, 4082; for a review of Re reagents used in oxidative cyclization reactions, see: E. Keinan, S. C. Sinha, *Pure Appl. Chem.* **2002**, *74*, 93.
[11] C. Gleye, P. Duret, A. Laurens, R. Hocquemiller, A. Cavé, *J. Nat. Prod.* **1998**, *61*, 576; H. Makabe, Y. Hattori, A. Tanaka, T. Orltani, *Org. Lett.* **2002**, *4*, 1083; J. Defretin, C. Gleye, D. Cortes, X. Franck, R. Hocquemiller, B. Figadere, *Lett. Org. Chem.* **2004**, *1*, 316.
[12] A. R. L. Cecil, Y. Hu, M. J. Vincent, R. Duncan, R. C. D. Brown, *J. Org. Chem.* **2004**, *69*, 3368.

 © 2005 Wiley-VCH Verlag GmbH & Co. KGaA, Weinheim

Isobutene in Zeolites

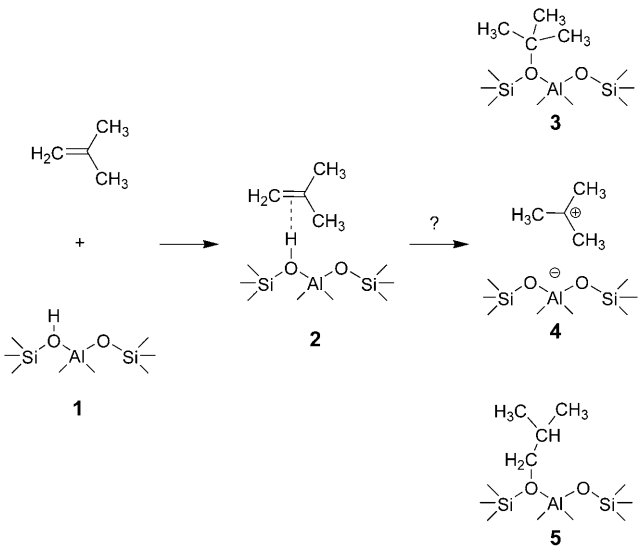
Protonated Isobutene in Zeolites: *tert*-Butyl Cation or Alkoxide?**

*Christian Tuma and Joachim Sauer**

Acid zeolite catalysts are industrially used for a variety of hydrocarbon transformation processes. Initially it was assumed that these reactions follow mechanisms known from chemistry in superacidic media, and involve carbocations as intermediates formed upon protonation of hydrocarbons by Brønsted acid sites.[1] However, NMR spectroscopic studies failed to find simple carbenium ions as intermediates, and instead produced evidence for surface alkoxides.[2,3] Around the same time, quantum chemical calculations employing small cluster models showed that alkoxides are minima on the potential energy surface (PES) and, hence, intermediates, while carbenium ions represent saddle points on the PES and are only present as extremely short-lived transition states.[4] So far, evidence for persistent carbenium ions has only been produced for cyclic alkenyl or aromatic carbenium ions by NMR,[5] UV/Vis,[6] and IR spectroscopy[7] or computational techniques.[8]

Among the carbenium ions derived from small alkenes, the *tert*-butyl cation has attracted much interest because it is more stable than primary or secondary carbenium ions; the competing formation of *tert*-butoxide may be sterically hindered. Previous computational studies have shown that, depending on the framework and the position at the zeolite wall to which they are bound, *tert*-butoxides may be as unstable as the *tert*-butyl cation.[9–12] Only the embedded cluster study by Boronat et al.[12] reports a local minimum on the PES for the *tert*-butyl cation in mordenite. It is, however, about 26 kJ mol^{-1} less stable than the adsorption π complex of isobutene with the Brønsted site. Nevertheless, all experimental attempts[13,14] to produce evidence for either the *tert*-butyl cation or an alkoxide have been unsuccessful so far, and the existence of *tert*-butyl cations in zeolites remains controversial.

Herein we report density functional theory (DFT) calculations for the reaction of isobutene with H-ferrierite (H-FER, **1**) with formation of the π complex **2** (Scheme 1). We applied periodic boundary conditions to a large simulation cell of dimensions $1870 \times 1417 \times 1496$ pm^3.[15] We show that the complex with the *tert*-butyl cation (**4**)—one possible structure formed upon proton transfer to isobutene in **2**—is a local minimum on the potential energy surface. For the first time we have evaluated entropy contributions to assess the stability of **4** relative to the adsorption π complex **2** and other possible proton transfer products, that is, surface alkoxides (**3**, **5**), at finite temperatures.



Scheme 1. Reactions considered for the protonation of isobutene in H-FER (**1**).

Our simulation cell of H-FER (**1**) has the composition $HAlSi_{71}O_{144}$. After aluminum substitution at the crystallographic position T2,[16] the proton is most stable at O7.[15] We used the Perdew–Burke–Ernzerhof (PBE) density functional[17] with a plane wave basis set.[18] Stationary points obtained by relaxation of the positions of all atoms in the cell are characterized by harmonic frequencies, from which zero-point vibrational energies, finite temperature energy, and entropy contributions are obtained.[19] All calculations employed the CPMD code.[20]

The calculated structures and the corresponding reaction energies are shown in Figure 1 and Table 1. Formation of the π complex of isobutene with the Brønsted acidic site is exothermic (**2**, $\Delta E_0 = -6.6$ kJ mol^{-1}). In contrast, chemisorption of isobutene is an endothermic process. Of the two different alkoxides, the isobutoxide (**5**) is more stable than the *tert*-butoxide (**3**). The longer C–O bond in *tert*-butoxide (161 pm) compared to isobutoxide (151 pm) indicates increased steric constraints due to the three methyl groups at the C–O carbon atom. Both the adsorbed isobutene and the *tert*-butyl cation are connected by hydrogen bonds to the zeolite framework. The corresponding bond lengths are 190.2 and 242.5 pm for r(AlOH···C^1) and r(AlOH···C^2) in the π complex and 174.0 pm for r(AlO···HC) in the carbenium ion structure. The carbenium ion complex **4** is electronically least favored. It is 46 kJ mol^{-1} less stable than the adsorption π complex, while isobutoxide is 14 kJ mol^{-1} and *tert*-butoxide is 27 kJ mol^{-1} less stable.

Similar relative energies have been found in a previous DFT (PW91) study for chabasite, ZSM-22, and mordenite[11]

[*] Dipl.-Chem. C. Tuma, Prof. Dr. J. Sauer
Humboldt-Universität zu Berlin
Institut für Chemie
Unter den Linden 6, 10099 Berlin (Germany)
Fax: (+49) 30-2093-7136
E-mail: sek.qc@chemie.hu-berlin.de

[**] This work was supported by the Deutsche Forschungsgemeinschaft (priority programme 1155). We also thank the Norddeutscher Verbund für Hoch- und Höchstleistungsrechnen (HLRN) for computing time. Parameters for the generation of Vanderbilt-type pseudopotentials were provided by Bernd Meyer, University of Bochum.

Supporting information for this article is available on the WWW under http://www.angewandte.org or from the author.

 DOI: 10.1002/anie.200501002 © 2005 Wiley-VCH Verlag GmbH & Co. KGaA, Weinheim

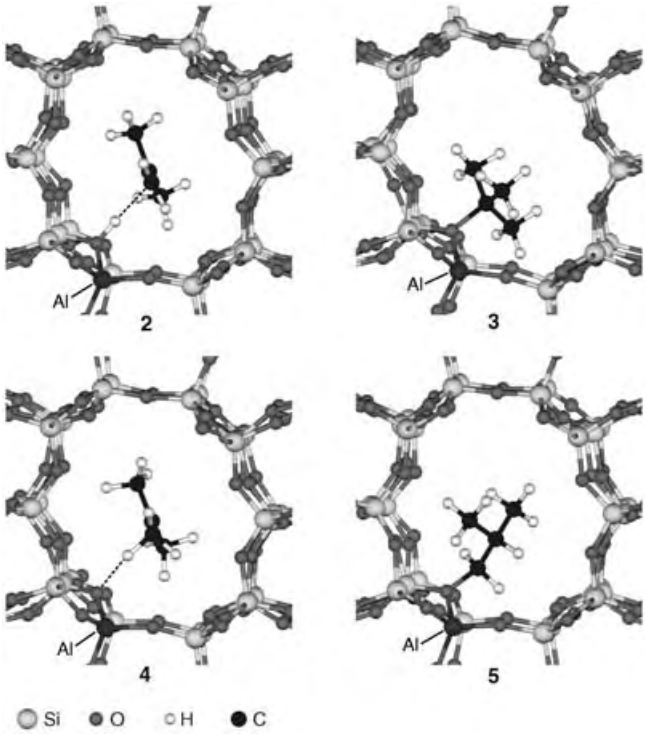


Figure 1. Portions of the structures calculated for the π complex of isobutene in ferrierite (**2**), for the *tert*-butyl cation in ferrierite (**4**), and for the *tert*-butoxide (**3**) and isobutoxide (**5**) of ferrierite.

Table 1: Electronic (ΔE) and ZPVE-corrected (ΔE_0) reaction energies, enthalpies (ΔH_{298}), and Gibbs energies (ΔG_{298}; pressure 1 atm) in kJ mol^{-1} for the formation of structures **2**–**5** from isobutene and H-FER (**1**).

Compound	ΔE	ΔE_0	ΔH_{298}	ΔG_{298}
2	−9.4	−6.6[a]	−4.9	40.4
3	17.2	35.0	27.5	119.0
4	36.2	32.2	34.9	76.0
5	4.8	24.4	18.8	96.8

[a] For comparison, ΔE_0 for isobutene in mordenite is −6.4 kJ mol^{-1} (B3PW91).[12]

as well as in a B3PW91 study on mordenite.[12] The density functionals that are currently used do not properly account for dispersion interactions (see, e.g., references [21,22]). This results in too low energies of adsorption, but may also change the relative energies of chemisorbed species compared to adsorption π complexes and carbenium ions.[15] Future refinements of the present results by explicit inclusion of dispersion interactions may be obtained by an MP2/DFT hybrid technique[23] or by adding a damped dispersion term.[22] The results obtained with the PBE/PW91 family of functionals require less correction than those with functionals including Becke exchange.[21,22,24]

Inclusion of zero-point vibrations and finite temperature effects stabilizes the *tert*-butyl carbenium ion relative to the chemisorbed species (see ΔE_0 and ΔH_{298} in Table 1). An important new finding of the present study is the effect of entropy on the Gibbs energy: At temperatures higher than about 120 K, the *tert*-butyl cation complex **4** becomes favored over the alkoxides (**3**, **5**, Figure 2). The different slopes for the change in Gibbs energy for the alkoxides compared to the π complex and the carbenium ion reflect different entropy contributions. The existence of an additional covalent bond in the alkoxides (C–O) limits the mobility of the hydrocarbon species, and suggests a lower entropy compared to the other two structures.

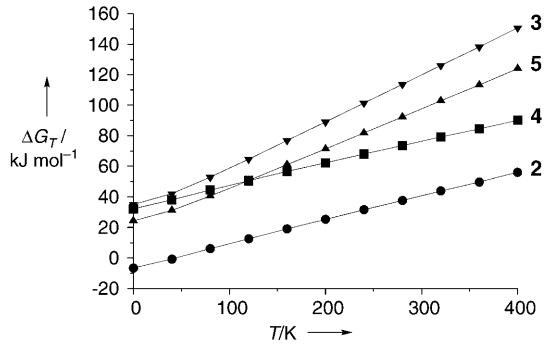


Figure 2. Plot of the Gibbs energy ΔG_T as a function of temperature T (at 1 atm) for the formation of **2**–**5** from isobutene and H-FER (**1**).

The vibrational states obtained from our frequency calculations are shown in Figure 3 (the vibrational frequencies can be found in the Supporting Information). A nearly continuous vibrational region from 1250 cm^{-1} down to far infrared with a window between about 1000 and 800 cm^{-1} is seen for unloaded H-FER (**1**) as well as for the hydrocarbon-containing structures. This is characteristic of zeolite lattice vibrations. The calculated frequencies for the zeolitic O–H and O–D stretching modes in unloaded H-FER (3643 and 2652 cm^{-1}, respectively) compare well with experimental data (3609 and 2663 cm^{-1}, respectively).[25] Quantitative agreement is not expected because of the limited accuracy of DFT and neglected anharmonicities. The vibrational spectra of structures **2**–**5** approximately resemble superpositions of those of the unloaded zeolite and the gas-phase species. In the isobutene π complex **2**, hydrogen bond formation shifts the zeolitic O–H and O–D stretching mode by −819 and

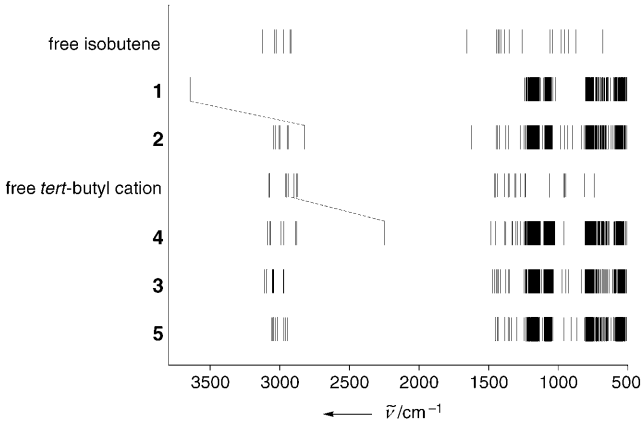


Figure 3. Vibrational spectra calculated for isobutene and the *tert*-butyl cation (both in the gas phase) as well as for structures **1**–**5**.

 © 2005 Wiley-VCH Verlag GmbH & Co. KGaA, Weinheim

−585 cm^{-1}, respectively. Corresponding measurements on deuterated forms of different zeolites yield somewhat smaller O−D shifts: −416 cm^{-1} (mordenite)[14] and −388 cm^{-1} (faujasite).[26] It is known[27] that the PBE functional overestimates O−H frequency shifts upon hydrogen bond formation.

A significant change is predicted for the IR spectrum of the carbenium ion complex **4**: Only 8 instead of 9 vibrational modes are seen in the C−H stretching region around 3000 cm^{-1}; the remaining mode corresponding to the O···HC hydrogen bond is found at 2245 cm^{-1}, that is, well separated from the others. This is a new prediction which may help to identify the *tert*-butyl cation as a transient species in future laser-spectroscopic experiments.[28]

Received: March 18, 2005
Published online: June 29, 2005

Keywords: carbenium ions · density functional calculations · heterogeneous catalysis · hydrocarbons · zeolites

[1] a) G. A. Olah, G. K. S. Prakash, J. Sommer, *Superacids*, Wiley, New York, **1985**; b) P. A. Jacobs, *Carboniogenic Activity of Zeolites*, Elsevier, New York, **1977**.
[2] M. T. Aronson, R. J. Gorte, W. E. Farneth, D. White, *J. Am. Chem. Soc.* **1989**, *111*, 840.
[3] a) T. Xu, J. Zhang, E. J. Munson, J. F. Haw, *J. Chem. Soc. Chem. Commun.* **1994**, 2733; b) J. F. Haw, J. B. Nicholas, T. Xu, L. W. Beck, D. B. Ferguson, *Acc. Chem. Res.* **1996**, *29*, 259.
[4] a) I. N. Senchenya, V. B. Kazansky, *Catal. Lett.* **1991**, *8*, 317; b) V. B. Kazansky, M. V. Frash, R. A. van Santen, *Appl. Catal. A* **1996**, *146*, 225.
[5] J. F. Haw, *Phys. Chem. Chem. Phys.* **2002**, *4*, 5431.
[6] M. Bjørgen, F. Bonino, S. Kolboe, K.-P. Lillerud, A. Zecchina, S. Bordiga, *J. Am. Chem. Soc.* **2003**, *125*, 15863.
[7] a) S. Yang, J. N. Kondo, K. Domen, *J. Phys. Chem. B* **2001**, *105*, 7878; b) S. Yang, J. N. Kondo, K. Domen, *Catal. Today* **2002**, *73*, 113.
[8] a) L. A. Clark, M. Sierka, J. Sauer, *J. Am. Chem. Soc.* **2003**, *125*, 2136; b) L. A. Clark, M. Sierka, J. Sauer, *J. Am. Chem. Soc.* **2004**, *126*, 936.
[9] P. E. Sinclair, A. de Vries, P. Sherwood, R. A. Catlow, R. A. van Santen, *J. Chem. Soc. Faraday Trans.* **1998**, *94*, 3401.
[10] a) M. Boronat, P. Viruela, A. Corma, *Phys. Chem. Chem. Phys.* **2001**, *3*, 3235; b) M. Boronat, C. M. Zicovich-Wilson, P. Viruela, A. Corma, *J. Phys. Chem. B* **2001**, *105*, 11169.
[11] X. Rozanska, R. A. van Santen, T. Demuth, F. Hutschka, J. Hafner, *J. Phys. Chem. B* **2003**, *107*, 1309.
[12] M. Boronat, P. M. Viruela, A. Corma, *J. Am. Chem. Soc.* **2004**, *126*, 3300.
[13] N. D. Lazo, B. R. Richardson, P. D. Schettler, J. L. White, E. J. Munson, J. F. Haw, *J. Phys. Chem.* **1991**, *95*, 9420.
[14] H. Ishikawa, E. Yoda, J. N. Kondo, F. Wakabayashi, K. Domen, *J. Phys. Chem. B* **1999**, *103*, 5681.
[15] V. Nieminen, M. Sierka, D. Yu. Murzin, J. Sauer, *J. Catal.* **2005**, *231*, 393.
[16] P. A. Vaughan, *Acta Crystallogr.* **1966**, *21*, 983.
[17] J. P. Perdew, K. Burke, M. Ernzerhof, *Phys. Rev. Lett.* **1996**, *77*, 3865.
[18] The cutoff for the kinetic energy of the plane wave basis set is 30 Rydberg. Core electrons are described using atomic pseudopotentials constructed either by a normconserving procedure (G. B. Bachelet, D. R. Hamann, M. Schlüter, *Phys. Rev. B* **1982**, *26*, 4199, core cutoff radii of 1.4 and 1.6 a_0 for aluminum and silicon, respectively) or according to an ultrasoftness scheme (D. Vanderbilt, *Phys. Rev. B* **1990**, *41*, 7892, core cutoff radii of 0.8, 1.1, and 1.1 a_0 for hydrogen, carbon, and oxygen, respectively).
[19] All atom positions were fully relaxed until the maximum component of cartesian atomic forces was smaller than 1.0×10^{-5} E_h/a_0. Force constants were calculated by numerical differentiation of forces, stepsize 0.01 a_0. Vibrational modes were projected.
[20] CPMD 3.7.2: Copyright MPI für Festkörperforschung, Stuttgart, **1997–2001**, and IBM Research Division, Zürich, **1990–2003**.
[21] T. A. Wesolowski, O. Parisel, Y. Ellinger, J. Weber, *J. Phys. Chem. A* **1997**, *101*, 7818.
[22] S. Grimme, *J. Comput. Chem.* **2004**, *25*, 1463.
[23] C. Tuma, J. Sauer, *Chem. Phys. Lett.* **2004**, *387*, 388.
[24] X. Xu, W. A. Goddard III, *Proc. Natl. Acad. Sci. USA* **2004**, *101*, 2673.
[25] J. N. Kondo, E. Yoda, H. Ishikawa, F. Wakabayashi, K. Domen, *J. Catal.* **2000**, *191*, 275.
[26] a) J. N. Kondo, H. Ishikawa, E. Yoda, F. Wakabayashi, K. Domen, *J. Phys. Chem. B* **1999**, *103*, 8538; b) J. N. Kondo, L. Shao, F. Wakabayashi, K. Domen, *J. Phys. Chem. B* **1997**, *101*, 9314.
[27] C. Tuma, A. D. Boese, N. C. Handy, *Phys. Chem. Chem. Phys.* **1999**, *1*, 3939.
[28] K. Onda, K. Tanabe, H. Noguchi, K. Domen, A. Wada, *J. Phys. Chem. B* **2003**, *107*, 11391.

 © 2005 Wiley-VCH Verlag GmbH & Co. KGaA, Weinheim

Mass spectrometry

Probing the Mechanism of the Palladium-Catalyzed Addition of Organoboronic Acids to Allenes in the Presence of AcOH by ESI-FTMS**

Rong Qian, Hao Guo, Yuanxi Liao, Yinlong Guo, and Shengming Ma**

The products of transition-metal-catalyzed reactions are usually explained and predicted in terms of four elementary reactions.[1] However, deduction of the real mechanism

[*] R. Qian, Y. Liao, Prof. Y. Guo
Shanghai Mass Spectrometry Center
Shanghai Institute of Organic Chemistry
Chinese Academy of Sciences
354 Fenglin Road, Shanghai 200032 (P. R. China)
Fax: (+86) 21-6416-6128
E-mail: ylguo@mail.sioc.ac.cn

H. Guo, Prof. S. Ma
State Key Laboratory of Organometallic Chemistry
Shanghai Institute of Organic Chemistry
Chinese Academy of Sciences
354 Fenglin Road, Shanghai 200032 (P. R. China)
Fax: (+86) 21-6416-7510
E-mail: masm@mail.sioc.ac.cn

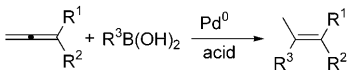
[**] We gratefully acknowledge financial support from the Major State Basic Research Development Program (grant no. G2000077500), the National Nature Science Foundation of China (no. 20175034, no. 20475059), and the Chinese Academy of Sciences.

Supporting information for this article is available on the WWW under http://www.angewandte.org or from the author.

 DOI: 10.1002/anie.200463101 © 2005 Wiley-VCH Verlag GmbH & Co. KGaA, Weinheim

usually requires the isolation and characterization of organometallic species, which is usually not easy and is often time-consuming.[2] Thus, the interception and detection of reaction intermediates by instrumental analysis is a facile and reliable alternative method.[3–5] Molecular analysis by mass spectrometry (MS) has greatly benefited from the development of electrospray ionization (ESI) techniques,[6,7] since molecules and supramolecules of high polarity and molecular complexity can be easily ionized by ESI for investigation by MS.[4,5] ESI-MS is a technique that allows the ions present in solution to be transferred into the gas phase, where they can be analyzed and eventually characterized, with minimal fragmentation. Thus, straightforward analytical applications of ESI-MS to the characterization of organometallic intermediates have started to catch the attention of chemists.[8] Here we report our recent observation of the high resolution and high-mass-accuracy MS characterization of several organometallic species, which leads to a better understanding of the reaction mechanism of the palladium-catalyzed highly regio- and stereoselective addition of organoboronic acids to allenes in the presence of AcOH.

Although allenes have been considered as highly unstable,[9] recent studies show that they demonstrate useful reactivities and selectivities.[9–11] During our systematic study on the chemistry of allenes,[12] we have developed a palladium-catalyzed highly regio- and stereoselective hydroarylation or hydroalkenylation of allenes with organic boronic acids that gives tri- or tetrasubstituted alkenes (Scheme 1).[13] Despite the importance of its synthetic utility this reaction still has a number of unaccountable features, including the mechanistic details.



Scheme 1. The Pd-catalyzed addition reaction of allenes with organoboronic acids in the presence of an acid.

After some preliminary studies, we successfully found that the ESI-FTMS monitoring of the $[Pd(PPh_3)_4]$-catalyzed reaction of 2,3-allenoate with two organoboronic acids (**2a** and **2b**, Scheme 2) in the presence of AcOH in THF yielded some interesting information about the reaction intermediates. A solution of allenoate **1**[14] (0.05 mmol), organoboronic acid (0.1 mmol), $[Pd(PPh_3)_4]$ (0.005 mmol), and AcOH (0.05 mmol) in THF (6 mL) was stirred at room temperature under N_2 atmosphere for the time indicated in Figure 1.[13] Then, 20 μL of this solution was diluted with 80 μL of methanol and transferred into the ESI source at a flow rate of 10 μL min^{-1} for the MS detection.

The palladium intermediates involved in the catalytic cycle were intercepted, detected, and characterized by high resolution accurate mass measurements of their corresponding ions with the ESI-FTMS instrument in the positive-ion mode. After three minutes of the reaction with organoboronic acid **2a**, ions assigned to intermediate **5** (principal ion of *m*/*z* 689.1004; calcd. for $C_{38}H_{33}O_2P_2{}^{106}Pd^+$: *m*/*z* 689.1003; Figure 1a) and the by-product **6** (principal ion of *m*/*z* 465.2276; calcd. for $C_{28}H_{33}O_6^+$: *m*/*z* 465.2277; Figure 1a) were detected.

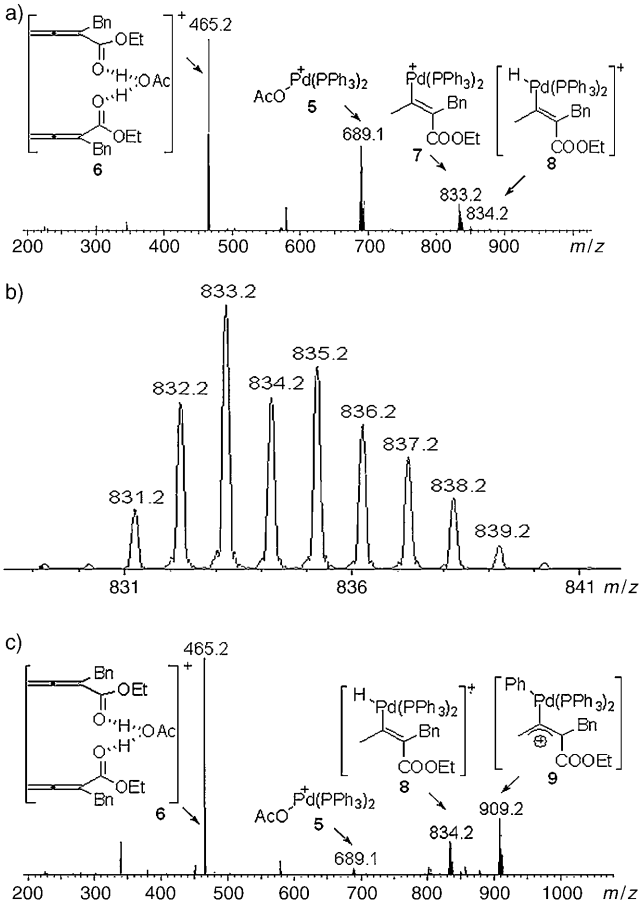
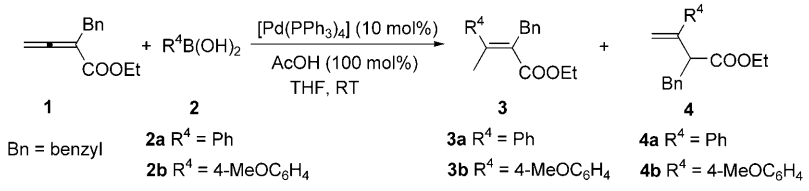


Figure 1. ESI-(+)-MS of the sample taken at a) 3 min and c) 2 h after mixing allenoate **1** and organoboronic acid **2a**. b) Experimental isotopic distribution of the mixture of **7** and **8**.

The composition of the major cationic intermediates changes dramatically with time. Continuous monitoring of these intermediates by ESI-FTMS also allowed us to detect three other ions: the palladium cation **7** (principal ion of *m*/*z* 833.1993; calcd. for $C_{49}H_{45}O_2P_2{}^{106}Pd^+$: *m*/*z* 833.1945; Figure 1a), which usually disappeared five minutes after initiation of the reaction, the palladium cation **8** (principal ion of *m*/*z* 834.2025; calcd. for $C_{49}H_{46}O_2P_2{}^{106}Pd^{\bullet+}$: *m*/*z* 834.2023; Figure 1a and Figure 1c), which might result from the oxidation of the neutral intermediate $HPd(PPh_3)_2$–vinyl species during the ESI process,[15,16] and the

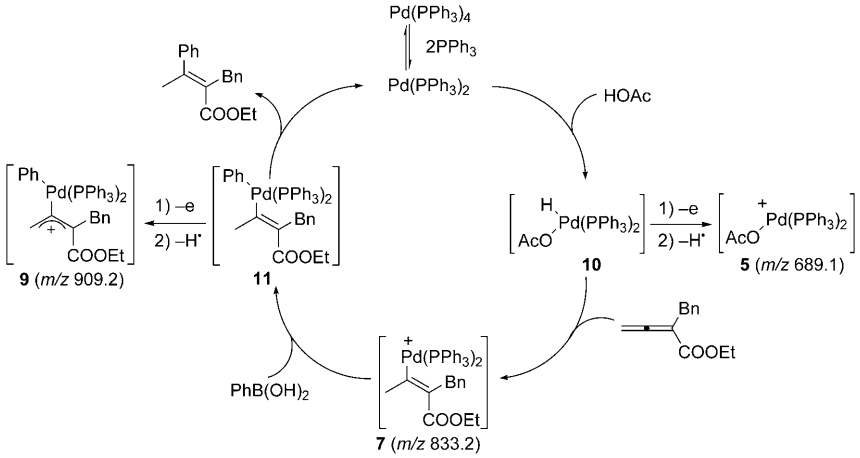


Scheme 2. The reaction of a 2,3-allenoate with two organoboronic acids, as monitored by ESI-FTMS.

 © 2005 Wiley-VCH Verlag GmbH & Co. KGaA, Weinheim

cationic π-allyl intermediate **9** (principal ion of *m/z* 909.2265; calcd. for $C_{55}H_{49}O_2P_2{}^{106}Pd^+$: *m/z* 909.2259; Figure 1c), which may be formed by sequential oxidation during the ESI process and elimination of H· from the (η^3-allyl)palladium complex in the gas phase.[8,17,18] Similar results were observed for organoboronic acid **2b** (see the Supporting Information). All the experimental isotopic distributions of the palladium-containing species matched the theoretical isotopic distributions, as simulated with the Bruker Xmass 6.1.2 program.

For further structural characterization of the intermediates of this reaction, all isotopolog ions forming the isotopic clusters of **7**, **8**, and **9** were isolated for a SORI-CAD (sustained off-resonance irradiation collision-activated dissociation) experiment with argon in a tandem mass spectrometric analysis.[19] Figure 2a–c show that intermediates **7** (principal ion of *m/z* 833.1993), **8** (principal ion of *m/z* 834.2025), and **9** (principal ion of *m/z* 909.2265) yield palladium cations **7A** (principal ion of *m/z* 571.1046; calcd. for $C_{31}H_{30}O_2P^{106}Pd^+$: *m/z* 571.1029; Figure 2a), **8A** (principal ion of *m/z* 572.1105; calcd. for $C_{31}H_{31}O_2P^{106}Pd^{\cdot+}$: *m/z* 572.1107; Figure 2b), and **9A** (principal ion of *m/z* 647.1342; calcd. for $C_{37}H_{34}O_2P^{106}Pd^+$: *m/z* 647.1344; Figure 2c) by loss of one PPh_3 ligand. The above results allow us to propose a mechanism for the reaction, which is shown in Scheme 3 with organoboronic acid **2a** as an example. Firstly, the oxidative addition reaction between AcOH and Pd^0 affords the palladium hydride species **10**, which may undergo hydropalladation with the less-sterically hindered terminal C=C bond in the allene moiety, with elimination of OAc^-, to afford alkenylpalladium intermediate **7**.[20] Transfer of the aryl group from the arylboronic acid to **7** gives **11**, which affords the final product by reductive elimination.[21]



Scheme 3. Proposed catalytic cycle for the palladium-catalyzed addition of an organoboronic acid to an allene in the presence of AcOH based on the MS study.

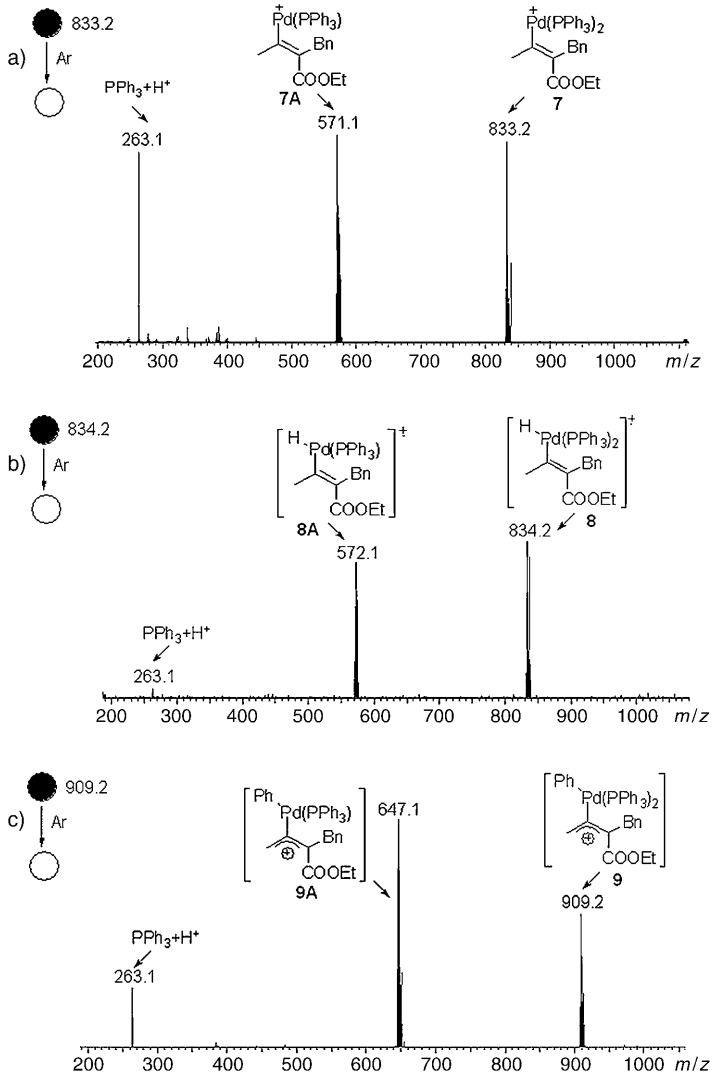


Figure 2. ESI-(+)-MS/MS of a) intermediate **7** (principal ion of *m/z* 833.1993), b) intermediate **8** (principal ion of *m/z* 834.2025), and c) intermediate **9** (principal ion of *m/z* 909.2265).

In conclusion, we have successfully characterized some key intermediates in the Pd^0-catalyzed addition reaction of allenes with boronic acids in the presence of AcOH by ESI-FTMS, and this has led to the mechanism shown in Scheme 3. Further studies in this area are being carried out in our laboratory.

Received: December 30, 2004
Revised: March 25, 2005
Published online: June 29, 2005

Keywords: allenes · mass spectrometry · organoboronic acid · palladium · reaction mechanisms

[1] a) J. P. Collman, L. Hegedus, *Principles and Applications of Organotransition Metal Chemistry*, University Science Books, Mill Valley, **1980**; b) A. Yamamoto, *Organotransition Metal Chemistry: Fundamental Concepts and Applications*, Wiley, New York, **1986**; c) R. H. Crabtree, *The Organometallic Chemistry of the Transition Metals*, 3rd ed., Wiley-Interscience, New York, **2001**; d) S. Ma,

 © 2005 Wiley-VCH Verlag GmbH & Co. KGaA, Weinheim

Transition Metal Involved Modern Synthetic Organic Reactions, 2nd ed., Guangdong Science Press, Guangzhou, **2003**.

[2] For some recent reports, see: a) U. Nettekoven, J. F. Hartwig, *J. Am. Chem. Soc.* **2002**, *124*, 1166–1167; b) K. H. Wu, H. M. Gau, *Organometallics* **2004**, *23*, 580–588.

[3] a) J. Zhou, M. C. Ye, Z. Z. Huang, Y. Tang, *J. Org. Chem.* **2004**, *69*, 1309–1320; b) B. M. Choudary, S. Madhi, M. L. Kantam, B. Sreedhar, Y. Iwasawa, *J. Am. Chem. Soc.* **2004**, *126*, 2292–2293.

[4] A. A. Sabino, A. H. L. Machado, C. R. D. Correia, M. N. Eberlin, *Angew. Chem.* **2004**, *116*, 2568–2572; *Angew. Chem. Int. Ed.* **2004**, *43*, 2514–2518.

[5] L. S. Santos, C. H. Pavam, W. P. Almeida, F. Coelho, M. N. Eberlin, *Angew. Chem.* **2004**, *116*, 4430–4433; *Angew. Chem. Int. Ed.* **2004**, *43*, 4330–4333.

[6] a) C. M. Whitehouse, R. N. Dreyer, M. Yamashita, J. B. Fenn, *Anal. Chem.* **1985**, *57*, 675–679; b) J. B. Fenn, M. Mann, C. K. Meng, S. F. Wong, C. M. Whitehouse, *Science* **1989**, *246*, 64–71; c) R. B. Cole, *Electrospray Ionization Mass Spectrometry*, Wiley, New York, **1997**.

[7] a) T. Kotiaho, M. N. Eberlin, P. Vainiotalo, R. Kostiainen, *J. Am. Soc. Mass Spectrom.* **2000**, *11*, 526–535; b) K. J. Koch, F. C. Gozzo, S. C. Nanita, Z. Takats, M. N. Eberlin, R. G. Cooks, *Angew. Chem.* **2002**, *114*, 1797–1800; *Angew. Chem. Int. Ed.* **2002**, *41*, 1721–1724; c) V. Rioli, F. C. Gozzo, A. S. Heimann, A. Linardi, J. E. Krieger, C. S. Shida, P. C. Almeida, S. Hyslop, M. N. Eberlin, E. S. Ferro, *J. Biol. Chem.* **2003**, *278*, 8547–8555; d) E. C. Meurer, A. A. Sabino, M. N. Eberlin, *Anal. Chem.* **2003**, *75*, 4701–4709.

[8] D. A. Plattner in *Modern Mass Spectrometry* (Ed.: C. A. Schalley), Springer, Heidelberg, **2003**, pp. 154–155 and 176–178.

[9] A. Hoffmann-Röder, N. Krause, *Angew. Chem.* **2004**, *116*, 1216–1236; *Angew. Chem. Int. Ed.* **2004**, *43*, 1196–1216.

[10] a) *The Chemistry of Ketenes, Allenes, and Related Compounds*, Part 1 (Ed.: S. Patai), Wiley, New York, **1980**; b) H. F. Schuster, G. M. Coppola, *Allenes in Organic Synthesis*, Wiley, New York, **1984**.

[11] For reviews, see: a) R. Zimmer, C. U. Dinesh, E. Nandanan, F. A. Khan, *Chem. Rev.* **2000**, *100*, 3067–3126; b) J. A. Marshall, *Chem. Rev.* **2000**, *100*, 3163–3186; c) A. S. K. Hashmi, *Angew. Chem.* **2000**, *112*, 3737–3740; *Angew. Chem. Int. Ed.* **2000**, *39*, 3590–3593; d) R. W. Bates, V. Satcharoen, *Chem. Soc. Rev.* **2002**, *31*, 12–21; e) S. Ma in *Handbook of Organopalladium Chemistry for Organic Synthesis* (Ed.: E. Negishi), Wiley, New York, **2002**, p. 1491; f) L. K. Sydnes, *Chem. Rev.* **2003**, *103*, 1133–1150. For some of the most representative recent reports, see: g) A. S. K. Hashmi, L. Schwarz, J. H. Choi, T. M. Frost, *Angew. Chem.* **2000**, *112*, 2382–2385; *Angew. Chem. Int. Ed.* **2000**, *39*, 2285–2288; h) S. Kang, Y. Ha, B. S. Ko, Y. Lim, J. Jung, *Angew. Chem.* **2002**, *114*, 353–355; *Angew. Chem. Int. Ed.* **2002**, *41*, 343–345; i) K. Lee, D. Seomoon, P. H. Lee, *Angew. Chem.* **2002**, *114*, 4057–4059; *Angew. Chem. Int. Ed.* **2002**, *41*, 3901–3903; j) K. M. Brummond, H. Chen, P. Sill, L. You, *J. Am. Chem. Soc.* **2002**, *124*, 15186–15187; k) S. Ma, Z. Yu, *Angew. Chem.* **2003**, *115*, 1999–2001; *Angew. Chem. Int. Ed.* **2003**, *42*, 1955–1957; l) J. Franzén, J. Bäckvall, *J. Am. Chem. Soc.* **2003**, *125*, 6056–6057; m) B. M. Trost, C. Jakel, B. Plietker, *J. Am. Chem. Soc.* **2003**, *125*, 4438–4439; n) H. Ohno, K. Miyamura, Y. Takeoka, T. Tanaka, *Angew. Chem.* **2003**, *115*, 2751–2754; *Angew. Chem. Int. Ed.* **2003**, *42*, 2647–2650; o) F.-Y. Yang, M. Shanmugasundaram, S.-Y. Chuang, P.-J. Ku, M.-Y. Wu, C.-H. Cheng, *J. Am. Chem. Soc.* **2003**, *125*, 12576–12583.

[12] For accounts of our own work, see: a) S. Ma, L. Li, *Synlett* **2001**, *8*, 1206–1213; b) S. Ma, *Acc. Chem. Res.* **2003**, *36*, 701–712.

[13] a) S. Ma, N. Jiao, L. W. Ye, *Chem. Eur. J.* **2003**, *9*, 6049–6056; b) C. H. Oh, T. W. Ahn, R. Ready, *Chem. Commun.* **2003**, 2622–2623.

[14] The starting allenoate **1** was prepared according to a literature procedure: S. Ma, N. Jiao, S. Zhao, H. Hou, *J. Org. Chem.* **2002**, *67*, 2837–2847.

[15] C. S. Christ, J. R. Eyler, D. E. Richardson, *J. Am. Chem. Soc.* **1990**, *112*, 596–607.

[16] We thank the referee who suggested this possibility.

[17] D. E. Richardson, N. G. Alameddin, M. F. Ryan, T. Hayes, J. R. Eyler, A. R. Siedle, *J. Am. Chem. Soc.* **1996**, *118*, 11244–11253.

[18] a) T. Zhang, S. P. Palii, J. R. Eyler, A. Brajter-Toth, *Anal. Chem.* **2002**, *74*, 1097–1103; b) S. Meyer, R. Koch, J. O. Metzger, *Angew. Chem.* **2003**, *115*, 4848–4851; *Angew. Chem. Int. Ed.* **2003**, *42*, 4700–4703; c) C. S. Christ, J. R. Eyler, D. E. Richardson, *J. Am. Chem. Soc.* **1988**, *110*, 4038–4039.

[19] C. T. Yu, Y. L. Guo, G. Q. Chen, Y. W. Zhong, *J. Am. Soc. Mass Spectrom.* **2004**, *15*, 795–802.

[20] a) B. M. Trost, V. J. Gerusz, *J. Am. Chem. Soc.* **1995**, *117*, 5156–5157; b) L. Besson, J. Goré, B. Cazes, *Tetrahedron Lett.* **1995**, *36*, 3853–3856; c) T. Doi, K. Yamamoto, *Curr. Org. Chem.* **1997**, *1*, 219–234; d) W. Oppolzer, A. Pimm, B. Stammen, W. E. Hume, *Helv. Chim. Acta* **1997**, *80*, 623–639.

[21] a) A. Suzuki, *Pure Appl. Chem.* **1985**, *57*, 1749–1758; b) A. Suzuki, *Pure Appl. Chem.* **1991**, *63*, 419–422; c) A. Suzuki, *Pure Appl. Chem.* **1994**, *66*, 213–222.

 © 2005 Wiley-VCH Verlag GmbH & Co. KGaA, Weinheim

Zeolites

Dimethyl Carbonate in the Supercages of NaY Zeolite: The Role of Local Fields in Promoting Methylation and Carboxymethylation Activity**

*Francesca Bonino, Alessandro Damin, Silvia Bordiga, Maurizio Selva, Pietro Tundo, and Adriano Zecchina**

In the last two decades the need for safer processes has focused a great deal of attention on the use of small organic carbonates, especially dimethyl carbonate ($MeOCO_2Me$: DMC). DMC is a nontoxic compound that can profitably

[*] Dr. F. Bonino, Dr. A. Damin, Prof. Dr. S. Bordiga, Prof. Dr. A. Zecchina
Department of IFM Chemistry and
NIS Centre of Excellence
Università di Torino
Via P. Giuria 7, 10125 Torino (Italy)
Fax: (+39) 011-670-7855
E-mail: adriano.zecchina@unito.it
and
INSTM
UdR di Torino (Italy)
Prof. Dr. M. Selva, Prof. Dr. P. Tundo
Department of Environmental Science
Università Ca'Foscari
Dorsoduro 2137, 30123 Venezia (Italy)
and
Interuniversity Consortium "Chemistry for the Environment"
UdR di Venezia (Italy)

[**] This project was supported by COST Action D29.

Supporting information for this article is available on the WWW under http://www.angewandte.org or from the author.

 © 2005 Wiley-VCH Verlag GmbH & Co. KGaA, Weinheim DOI: 10.1002/anie.200500110

replace very harmful methyl halides (or dimethyl sulfate) and phosgene in both methylation and carboxymethylation processes.[1] In recent times it has been observed that methylation of primary aromatic amines with DMC is efficiently catalyzed by alkali-metal-exchanged faujasites (e.g. NaY). The peculiarity of the process is that DMC-mediated methylation of amines proceeds with unprecedented monomethyl selectivity (up to 99%) and complete chemoselectivity at the amino group in the case of ambident nucleophiles. Another peculiarity of NaY is that it also catalyzes carboxymethylation reactions. These findings suggest that under the appropriate conditions the DMC/NaY interaction leads to weakening (activation) of both $O-CH_3$ and $C-OCH_3$ bonds. The discovery of highly selective catalysts for reactions involving DMC is of special interest from both environmental and synthetic standpoints because it offers important and innovative protocols for the synthesis of high-value-added pharmaceutical intermediates and dyestuffs.[2]

It has been reasonably hypothesized that activation of DMC in the restricted spaces of the internal cavities (supercages) of NaY occurs by an electric-field-induced polarization of the molecule, which is accompanied by elongation and weakening of the $O-CH_3$ and/or $C-OCH_3$ bonds. To clarify this fundamental point, the aim of this investigation is to shed light on the structural perturbation induced in DMC upon interaction with the positively charged counterions present in the supercages. For this purpose a study of the modification of the IR properties of DMC, induced by the interaction with NaY, has been performed; the experimental results obtained are compared with ab initio simulations. It will be shown that the interaction of DMC with Na^+ ions fully explains why NaY is so effective in promoting the methylation and carboxymethylation activity of DMC.

This spectroscopic investigation takes advantage of the fact that, as DMC is a liquid, it can be easily dosed from the gas phase onto activated NaY and that, upon diffusion inside the pores, the IR spectrum of DMC can easily be recorded in situ.[3]

The available frequency range for the IR study on NaY ($\tilde{\nu} > 1300\ cm^{-1}$) only allows the observation of the $\nu(CO)$ mode of the $C-O_1$ bond (see Figure 1a), the $\nu_{asymm.}(CO_2)$ mode of the O_2-C-O_3 moiety (see Figure 1b), and the $\delta(CH_3)$ modes of the methyl groups. The bands associated with $\nu_{symm.}(CO_2)$, $\nu_{symm.}(O-CH_3)$, and $\nu_{asymm.}(O-CH_3)$, which would be of high diagnostic utility, cannot be observed because they fall within the zeolite framework region.

The dashed line in Figure 2a represents the background-subtracted spectrum of DMC completely filling the supercages (DMC/$Na^+ > 1$) (obtained by equilibration at the vapor pressure of DMC). Under these conditions the spectrum is characterized by broad and complex absorptions in both the $\nu(CO)$ (1805–1710 cm^{-1}) and $\nu_{asymm.}(CO_2)$ (1340–1235 cm^{-1}) ranges due to the superposition of the contributions from DMC interacting directly with the cations of the walls and liquid-like DMC filling the residual spaces of the supercages. Because of this multiple contribution, this spectrum is of little utility.

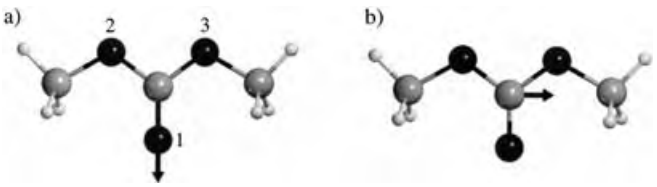


Figure 1. Pictorial representation of the normal modes of DMC1: a) $\nu(CO)$; b) $\nu_{asymm.}(CO_2)$. White spheres: H atoms; gray spheres C atoms; black spheres: O atoms.

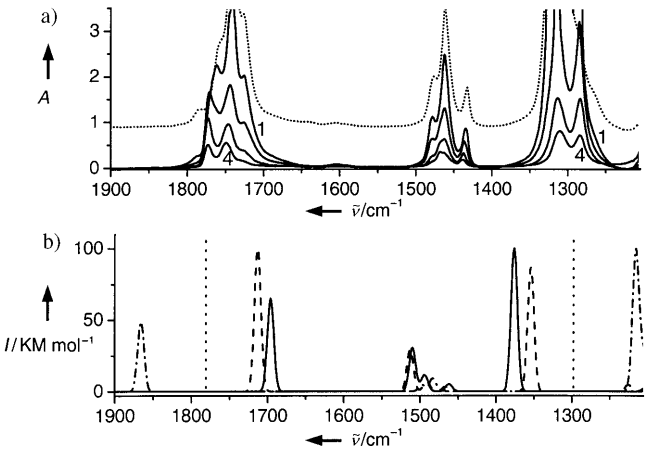


Figure 2. a) Dashed line: background-subtracted spectrum of vapor pressure of DMC on NaY zeolite outgassed at 673 K. Curves 1–4: effect of progressive outgassing at 353, 393, 423, and 453 K respectively. b) Computed IR spectra of structures **b**, **c**, and **d** reported in Figure 4. Dotted lines correspond to the computed spectrum of the DMC1 isomer.

To reveal the contribution of DMC in direct contact with the Na^+ ions present on the walls, we removed the liquid-like fraction by controlled desorption and collected a series of spectra corresponding to decreasing DMC/Na^+ ratios (curves 1–4, solid lines in Figure 2a). It can be seen that, after removal of liquid-like DMC, the $\nu(CO)$ and $\nu_{asymm.}(CO_2)$ modes clearly split into two major components at 1772–1747 and 1311–1284 cm^{-1}, respectively, while the bending frequencies of the methyl groups are essentially unaffected. The half-width of the components of the 1747–1311 cm^{-1} pair is larger than that of the 1772–1284 cm^{-1} pair, which suggests that they are caused by a family of similar species, instead of a single one. A shoulder is also observable at 1728 cm^{-1}. The relative intensity of the doublets' components changes with coverage, which allows us to conclude that the 1772–1284 and the 1747–1311 doublets belong to two different species (I and II, respectively). For the reasons described above, species II has a composite structure. A relevant observation concerning the species I and species II pairs is that the frequency difference $\Delta\nu$ between the $\nu(CO)$ and $\nu_{asymm.}(CO_2)$ modes is such that $\Delta\nu_I > \Delta\nu_{gas} > \Delta\nu_{II}$. This observation will be of great utility for comparison with the theoretical results (see below). In conclusion, from the IR spectroscopic data we can infer that the interaction of DMC with the Na^+ ions present in the supercages induces a relevant perturbation of the molecule, which influences the vibrational properties, and hence the force constants, of bonds with C–O character. On the basis of these results, it was not possible to advance an unambiguous

 © 2005 Wiley-VCH Verlag GmbH & Co. KGaA, Weinheim

structural interpretation of the observed vibrational perturbations. Consequently, B3-LYP calculations of the structural, energetic, and vibrational features of model Na^+/DMC adducts were performed. To this end both *cis–cis* and *cis–trans* DMC structures (hereafter DMC1 and DMC2, respectively; see stick-and-ball representations in Figure 3) were

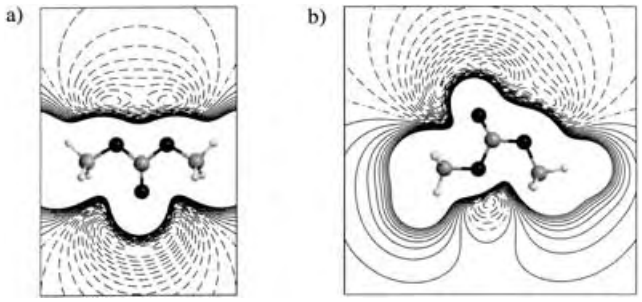


Figure 3. Pictorial representation of the computed electrostatic potential (ESP) of a) DMC1 and b) DMC2. Solid line: ESP > 0. Dashed line: ESP < 0. White spheres: H atoms; gray spheres: C atoms; black spheres: O atoms.

considered because they are very similar from the stability point of view (DMC2 being less stable by only about 12.9 kJ mol^{-1}), and hence they could be both present in the supercages as the result of an isomerization process. The computational scheme adopted (see Experimental Section for further details) is fully appropriate for this type of computation because the geometry and vibrational frequencies obtained for the DMC1 conformer are in agreement with the experimental observations.[4,5] The analysis of the molecular electrostatic potential (ESP) of DMC1 and DMC2 is shown in Figure 3, and reveals that: 1) DMC1 possesses two distinct nucleophilic sites (ESP < 0) on the oxygen of the C–O_1 bond and on the oxygen atoms of the O_2–C–O_3 moiety, and 2) DMC2 has only one nucleophilic site on the C–O_1 bond. On this basis three different DMC adducts with the complete series of naked alkali-metal cations were considered (Figure 4, structures **b**, **c**, and **d**). Such an approach has been demonstrated to be able to describe the electrostatic origin of

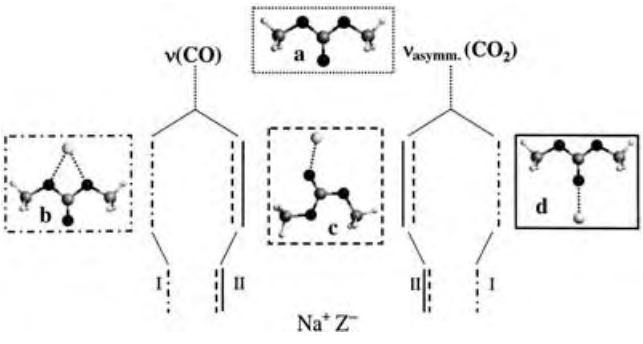


Figure 4. Vertical lines represent schematically ν(CO) and $\nu_{asymm.}(CO_2)$ of DMC under different conditions. Gas phase: isomer **a** top part; adducts **b**, **c**, and **d** middle part; experimental values obtained for NaY bottom part. The models are represented as sticks and balls with the same color code used in Figure 3. Na^+ ions in clusters **b**–**d** are represented as white spheres.

the interaction between the CO molecule and counterions in exchanged zeolites.[6] A subsequent article[7] has shown that the presence of the $AlH(OH)_3^-$ counteranion does not substantially change the conclusions reached in reference [6]. The stabilities of the adducts, as evaluated by binding energy calculations (DMC1 taken as reference reactant, BSSE accounted for),[8] are in the order **c** > **d** > **b**. As shown in Figure 5a, there is a linear correlation (positive slope)

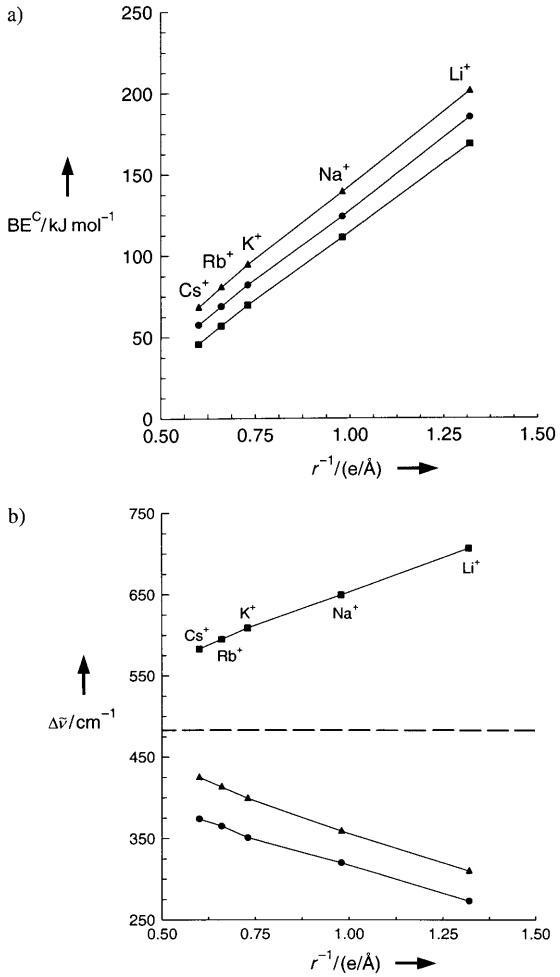


Figure 5. a) Computed BE^c (binding energy corrected for the BSSE) versus the charge density of the interacting alkali-metal cations. (■), (▲), and (●) refer to adducts **b**, **c**, and **d**, respectively. b) Computed $\Delta\nu$ ($\nu(CO) - \nu_{asymm.}(CO_2)$) versus the charge density of the interacting alkali-metal cations. (■), (▲), and (●) refer to adducts **b**, **c**, and **d**, respectively.

between the computed binding energy for the three adducts and the charge density (i.e. the reciprocal of the ionic radius for monovalent cations), thus confirming the pure electrostatic origin of the interaction. When the interaction occurs through the oxygen of the C–O_1 moiety (structures c and d in Figure 4), the calculations predict an elongation (weakening) of the C–O_1 and the $O_{2/3}$–CH_3 bonds, the remaining two C–$O_{2/3}$ bonds being shortened (strengthened). When the interaction occurs through the latter two oxygen atoms (structure **b** in Figure 4), the C–O_1 moiety undergoes a shortening

 © 2005 Wiley-VCH Verlag GmbH & Co. KGaA, Weinheim

(strengthening), while the $C{-}O_{2/3}$ and the $O_{2/3}{-}CH_3$ bonds undergo a lengthening (weakening). Further interesting results come from the computed frequencies of the adducts: in structures **c** and **d** of Figure 4 the ν(CO) and $\nu_{asymm.}(CO_2)$ are red- and blue-shifted, respectively, with respect to isolated DMC1, whereas in structure **b** of Figure 4 the opposite behavior is observed. The computed spectra obtained in the case of Na^+ are shown in Figure 2b and in Figure 4 as dotted (**a**), dot-dashed (**b**), dashed (**c**), and full (**d**) lines, and show that $\Delta\nu_{\mathbf{b}} > \Delta\nu_{gas} > \Delta\nu_{\mathbf{c}} \approx \Delta\nu_{\mathbf{d}}$. A similar trend is observed for the other alkali-metal cations, as shown in Figure 5b, from which it is clear that this observation also correlates with the charge density of the interacting cations.

These values are clearly in qualitative agreement with the experimental observations (reported in Figure 2a and schematized in Figure 4). Another interesting result is that structures **c** and **d** have very similar spectroscopic features and hence they behave as a family of similar species, in agreement with the observed half-width of the components of species II. Of course, the computed Δν values are higher than the experimental ones, because the model adducts involve bare Na^+ ions; in fact their polarizing power is higher than that of the Na^+ counterions in the supercage, whose positive charge is partially counterbalanced by the negative charge of the framework.

In conclusion, on the basis of a comparison of the experimental and computed data we have been able to conclude that both *cis–cis* and *cis–trans* species are present in the NaY supercages and to identify the properties of the adducts formed by these species with the Na^+ ions. In particular, the electrostatic perturbation in adducts **c** and **d** induces an elongation (weakening) of the $O{-}CH_3$ bonds, a fact which can explain the catalytic activity of NaY in methylation reactions. In adduct **b** an elongation of the $C{-}OCH_3$ occurs, which justifies the catalytic activity of NaY in carboxymethylation reactions. Finally, the observation that the IR components associated with structure **b** are the preferred ones at lowest coverage (higher evacuation temperature) could explain a different selectivity of the DMC/NaY system towards carboxymethylation reactions.

Taken together, these results afford, in a simple and direct manner, a reasonable explanation why NaY is a useful catalyst for methylation and carboxymethylation reactions with DMC. The role of polarization forces associated with the Na^+ counterions that are present in the restricted spaces of the supercages in DMC activation is also clearly demonstrated.[2c]

Experimental Section

An NaY sample (Aldrich, Si/Al ≈ 3), in the form of a thin, self-supported wafer, was activated at 673 K in vacuo (up to 10^{-5} mbar) before contact with DMC. Liquid DMC (ACROS Organics, 99% in purity) was dosed in the gas phase in a vacuum manifold directly connected to the measurement cell. IR spectra were recorded with a Bruker IFS 66 FTIR spectrometer equipped with an HgCdTe cryodetector (4000–700 cm^{-1} range) with a resolution of 2 cm^{-1}.

All calculations were performed by density functional theory procedures[9] with the B3-LYP[10] Hamiltonian, as implemented in Gaussian 98.[11] Li, Na, K, Rb, and Cs atoms were described with basis-set adopted by Ferrari et al.[6]. For C and O atoms, the fully optimized triple-ζ valence basis-set (TZV) of Ahlrichs et al.[12] was emplyed. A double set of diffuse p functions on the cations was added ($\zeta_p(Na) = 0.131$ and 0.0196 $Bohr^{-2}$). Moreover, the TZV basis sets for C and O atoms (hereafter TZV2d) were also supplemented by a double set of polarization d functions: ζ_d values were derived from the standard ones[13] following an even-tempered recipe ($\zeta_d(C) = 1.6$ and 0.4 $Bohr^{-2}$; $\zeta_d(O) = 2.4$ and 0.6 $Bohr^{-2}$). Hydrogen atoms in the DMC molecule were described by means of a standard Pople 6-311 + G(d,p) basis set.

Received: January 12, 2005
Revised: March 25, 2005
Published online: June 29, 2005

Keywords: density functional calculations · green chemistry · IR spectroscopy · methylation · zeolites

[1] a) P. Tundo, M. Selva, *Acc. Chem. Res.* **2002**, *35*, 706–716; b) Z. H. Fu, Y. Ono, *Catal. Lett.* **1993**, *22*, 277–281; c) P. R. H. P. Rao, P. Massiani, D. Barthomeuf, *Catal. Lett.* **1995**, *31*, 115–120.
[2] a) M. Selva, P. Tundo, A. Perosa, *J. Org. Chem.* **2002**, *67*, 9238–9247; b) M. Selva, P. Tundo, A. Perosa, *J. Org. Chem.* **2003**, *68*, 7374–7378; c) M. Selva, P. Tundo, *Tetrahedron Lett.* **2003**, *44*, 8139–8142.
[3] T. Beutel, *J. Chem. Soc. Faraday Trans.* **1998**, *94*, 985–993.
[4] F. C. Mijlhoff, *J. Mol. Struct.* **1977**, *36*, 334–335.
[5] H. Bohets, B. J. van der Veken, *Phys. Chem. Chem. Phys.* **1999**, *1*, 1817–1826, and references cited therein.
[6] A. M. Ferrari, P. Ugliengo, E. Garrone, *J. Chem. Phys.* **1996**, *105*, 4129–4139.
[7] A. M. Ferrari, K. M. Neyman, N. Rösch, *J. Phys. Chem. B* **1997**, *101*, 9292–9298.
[8] G. Lendvay, I. Mayer, *Chem. Phys. Lett.* **1998**, *297*, 365–373.
[9] a) P. Hohenberg, W. Kohn, *Phys. Rev.* **1964**, *136*, B864–B871; b) W. Kohn, L. J. Sham, *Phys. Rev.* **1965**, *140*, A1133–A1138.
[10] a) C. Lee, W. Yang, R. G. Parr, *Phys. Rev. B: Condens. Matter* **1988**, *37*, 785–789; b) A. D. Becke, *J. Chem. Phys.* **1993**, *98*, 1372–1377; c) A. D. Becke, *J. Chem. Phys.* **1993**, *98*, 5648–5652.
[11] Gaussian 98, Revision A.11, M. J. Frisch et al., see Supporting Information.
[12] A. Schafer, C. Huber, R. Ahlrichs, *J. Chem. Phys.* **1994**, *100*, 5829–5835.
[13] A. Schafer, H. Horn, R. Ahlrichs, *J. Chem. Phys.* **1992**, *97*, 2571–2577.

 © 2005 Wiley-VCH Verlag GmbH & Co. KGaA, Weinheim

Heterogeneous Catalysis

CO Oxidation Catalyzed by Supported Gold: Cooperation between Gold and Nanocrystalline Rare-Earth Supports Forms Reactive Surface Superoxide and Peroxide Species**

*Javier Guzman, Silvio Carrettin, Juan C. Fierro-Gonzalez, Yalin Hao, Bruce C. Gates, and Avelino Corma**

Novel catalysts for environmental and energy-related conversions are increasingly emerging from rational design based on the understanding of relationships between structure at the molecular level and catalyst performance. Gold that is highly dispersed on metal oxides has surprisingly been found to be an active and selective catalyst for numerous reactions,[1,2] including CO oxidation.[3] Contradictory hypotheses have been advanced to account for the CO oxidation activity,[4–13] and the nature of the active sites and reactive oxygen intermediates remains elusive.[14,15] Herein we show by time-resolved spectroscopy of working catalysts consisting of gold nanoclusters on nanocrystalline CeO_{2-x} that η^1-superoxide and peroxide intermediates are formed at one-electron defect sites at the metal–support interface and oxidize adsorbed CO to CO_2. The reactive oxygen species are not formed on conventionally prepared CeO_2, and their formation on nanocrystalline CeO_{2-x} is enhanced by the presence of the gold. This report is the first that unambiguously identifies and quantifies reactive oxygen species in low-temperature CO oxidation catalysis. The new concept advanced here is the representation of the catalytically active species as a composite that uniquely facilitates the formation of reactive oxygen species at the metal–support interface. The generality of the concept is exemplified by results showing that the nanocrystalline oxide can be either CeO_{2-x} or Y_2O_3.[16] This concept opens new avenues to the design of novel materials with improved activities and selectivities for catalytic oxidation.

We prepared high-surface-area ($S_{BET} = 180\ m^2 g^{-1}$; BET refers to Brunauer, Emmett, and Teller) and thermally stable nanocrystalline CeO_{2-x} with the fluorite structure by self-assembly in a liquid-crystal phase of individual CeO_2 nanoparticles with an average diameter of 5 nm.[17] Calcination of the nanocrystalline CeO_{2-x} at 873 K either in the absence or in the presence of 20 wt% H_2O produced minor changes in the BET surface area ($S_{BET} = 160\ m^2 g^{-1}$). CeO_2 was also prepared by a conventional precipitation–calcination method to facilitate a comparison with the nanocrystalline material and to allow investigation of the influence of the surface structure.[12] Deposition–precipitation of gold on the two supports yielded samples with gold loadings in the range of 0.9–4.6 wt%. These samples were characterized by the following spectroscopic methods as they functioned as catalysts for CO oxidation at steady state in flow reactors: X-ray absorption near edge structure (XANES); extended X-ray absorption fine structure (EXAFS); Raman; IR. Each of the samples catalyzed CO oxidation but gold supported on conventional CeO_2 was much less active than that on the nanocrystalline support. The spectra provide information that characterizes the oxidation state(s) and structure of the gold atoms as well as reactive oxygen species derived from the support and reactants.

Highly active gold supported on nanocrystalline CeO_{2-x} was characterized during treatment in He and during catalytic CO oxidation at room temperature; in each case, the EXAFS first-shell Au–Au coordination number $N_{Au\text{-}Au}$ was close to 4 (Table 1), thus indicating the presence of small gold nanoclusters. The absence of higher-shell Au–Au contributions confirms that the nanoclusters did not aggregate during catalysis. Time-resolved XANES spectra (see Supporting Information) indicate cationic gold clusters in the catalyst, which were stable during CO oxidation and this result is consistent with those that show cationic gold clusters in other supported catalysts.[4,5,12]) EXAFS contributions from Au–O at a distance of approximately 2.1 Å demonstrate covalent bonding between gold atoms in the supported clusters and oxygen atoms of the support,[18] and Au–O contributions for longer distances (3.5 Å) indicate nonbonding interactions of gold clusters with oxygen of the support surface (Table 1).

The data that represent the family of samples show a striking correlation: the catalytic activity of nanocrystalline CeO_{2-x}-supported gold clusters increases approximately in proportion to the EXAFS coordination number that represents the Au–O contribution for longer distances (Figure 1). This result indicates the participation of oxygen species at the support surface in CO oxidation. Bolstering this inference, IR spectra recorded for the sample treated with CO in the absence of O_2 indicate formation of CO_2 (see Supporting Information). Thus, the results indicate that nanocrystalline CeO_{2-x} supplies reactive oxygen to the active gold species in CO oxidation, which is consistent with the idea of CeO_2 acting as an oxygen reservoir by releasing and taking up oxygen through redox processes that involve the Ce^{4+}/Ce^{3+} couple.[6] The correlation between catalytic activity and the number of oxygen atoms surrounding—but not bonded to—the gold

[*] Dr. J. Guzman, Dr. S. Carrettin, Prof. Dr. A. Corma
Instituto de Tecnología Química
UPV-CSIC
Universidad Politécnica de Valencia
Avda. de los Naranjos s/n, Valencia 46022 (Spain)
Fax: (+34) 96-387-7809
E-mail: acorma@itq.upv.es
J. C. Fierro-Gonzalez, Y. Hao, Prof. Dr. B. C. Gates
Department of Chemical Engineering and Materials Science
University of California Davis
One Shields Ave.
Davis, CA 95616 (USA)

[**] We thank CICYT (MAT 2003-07945-C02-01), the Auricat European Union network (HPRN-CT-2002-00174), the US National Science Foundation (CTS-0121619; JCF-G), and the US Department of Energy (FG02-04ER15513; YH) for financial support. We also thank the NSLS (supported by the US Department of Energy, DE-AC02-98CH10886) for beam time and the staff of the electron microscopy group at UPV.

Supporting information for this article is available on the WWW under http://www.angewandte.org or from the author.

 © 2005 Wiley-VCH Verlag GmbH & Co. KGaA, Weinheim DOI: 10.1002/anie.200500659

Table 1: Structural parameters characterizing 2.8 wt% gold on CeO_2 before and during CO oxidation catalysis.[a]

Support	Conditions	$N_{Au\text{-}Au}$	$R_{Au\text{-}Au}$ [Å]	$N_{Au\text{-}O_s}$[b]	$R_{Au\text{-}O_s}$ [Å]	$N_{Au\text{-}O_i}$[c]	$R_{Au\text{-}O_i}$ [Å]	$N_{Au\text{-}C}$	$R_{Au\text{-}C}$ [Å]
conventional CeO_2	He[d]	6.2	2.82						
	catalysis[e]	6.2	2.82						
nanostructured CeO_2	He[d]	4.1	2.84	1.0	2.02	1.3	3.66		
	catalysis[e]	4.1	2.83	1.5	2.06	1.0	3.51	0.2	1.93

[a] N: EXAFS coordination number (error approximately ±10% for metal–metal contributions and ±20% for metal–oxygen contributions); R: EXAFS interatomic distance (error approximately ±1%). [b] $N_{Au\text{-}O_s}$: for shorter Au–$O_{support}$ distance. [c] $N_{Au\text{-}O_i}$: for longer Au–$O_{support}$ distance. [d] He flow of 30 mL min^{-1} at 760 Torr and 298 K. [e] Reaction conditions: 298 K (molar ratio CO/air/He = 0.2:19.8:80.0) and an inverse space velocity of 94 $g_{cat}\,h\,mol_{CO}^{-1}$.

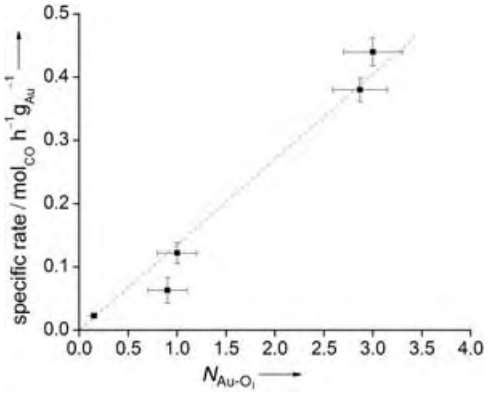


Figure 1. Catalytic activity as a function of the EXAFS coordination number of Au–O_i during CO oxidation catalyzed by gold supported on nanoparticulated CeO_2.

clusters implies that these species are involved in the catalysis, possibly as reactive intermediates that are continuously regenerated by reaction of the surface with O_2.

In contrast, the EXAFS data that characterize gold clusters supported on conventional CeO_2 (which was barely active as a catalyst under the same conditions) do not indicate any Au–O contributions distinguishable above the noise.[19,20] We attribute the near absence of catalytic activity of gold species on the conventional support to the lack of oxygen atoms at the cluster–support interface that can interact fruitfully with the gold atoms. Consistent with this interpretation, we did not detect CO_2 during IR experiments when CO alone was brought in contact with the sample. Furthermore, the differences in catalytic activity between the gold catalysts prepared with conventional and nanocrystalline supports cannot be associated with effects from the different size of the gold particles because the two catalysts have similar distributions of particle size (with an average diameter of about 3–4 nm; see TEM images in the Supporting Information).

To elucidate the nature of the reactive oxygen species on the nanocrystalline support that interact with the gold clusters, we recorded Raman spectra during the room-temperature adsorption of O_2 on CeO_{2-x} alone and on the sample consisting of gold on nanocrystalline CeO_{2-x}; the samples were subsequently exposed to 10% CO in He (Figure 2).

The precise identity of the reactive oxygen species on supported metal catalysts remains to be clarified, although various types of oxygen species have been characterized on cerium oxide.[21] Our results contribute to the understanding of these species and give evidence of a correlation that connects the concentration of reactive oxygen species, their rate of consumption, and the catalytic rate of formation of CO_2 on our catalyst. The spectrum that characterizes the products of O_2 adsorption on nanocrystalline CeO_{2-x} presents bands at 1123, 964, 871, and 831 cm^{-1}, which, on the basis of published data,[22–24] are assigned to η^1-superoxide, peroxide at one-electron defect sites, nonplanar bridging peroxide, and η^2-peroxide species, respectively (see Supporting Information). When CO came into contact with this sample, the intensities of the bands of the oxygen species remained constant and no CO oxidation was detected. In contrast, when O_2 was adsorbed on the gold supported on nanocrystalline CeO_{2-x}

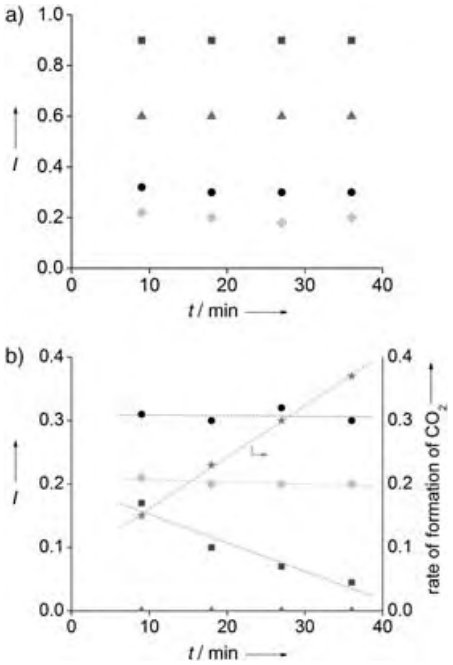


Figure 2. Raman spectra characterizing the formation and reactivity of oxygen species on Au supported on nanostructured CeO_2. Operating conditions were 298 K and 760 Torr: a) adsorption of O_2; b) subsequent exposure to 10% CO in He. The Raman intensities I corresponding to various oxygen species were obtained from the following bands: η^1 superoxide: 1123 cm^{-1} (squares); peroxide at one-electron defect site: 966 cm^{-1} (triangles); nonplanar bridging peroxide: 871 cm^{-1} (circles); and η^2 peroxide: 831 cm^{-1} (diamonds). The rate of formation of CO_2 (stars in (b)) was determined from analysis of the evolved gas phase.

 © 2005 Wiley-VCH Verlag GmbH & Co. KGaA, Weinheim

(Figure 2a), the intensities of the bands representing η^1-superoxide and peroxide species at one-electron defect sites were greater than those characterizing the support alone, whereas the intensities of the bands representing nonplanar bridging peroxide and η^2-peroxide species were almost the same. These results indicate a promoting effect of the gold species on the formation of η^1-superoxide and peroxide at one-electron defect sites on the support.

It has been suggested that the presence of gold clusters weakens the bonding of the oxygen species on CeO_2 and facilitates the formation of more reactive species.[6,25] Consistent with this suggestion, we observed that the peroxide species at one-electron defect sites were completely depleted when CO interacted with the sample to form CO_2 (observed in the gas phase); η^1-superoxide species were consumed simultaneously (Figure 2b). There is a correlation between the concentration of each of these species and its rate of consumption and also with the catalytic rate of formation of CO_2 (Figure 2b). In contrast, the concentrations of nonplanar bridging peroxide and η^2-peroxide species remained unchanged (Figure 2b), which indicates that these species do not participate directly in the CO oxidation. Thus, η^1-superoxide and peroxide at one-electron defect sites are identified as reaction intermediates under our conditions, whereas nonplanar bridging peroxide, η^2-peroxide, and molecular oxygen species are either spectators or involved in virtually equilibrated elementary steps in the catalytic cycle.

Consistent with this interpretation, when we performed the same experiments but with a barely active catalyst consisting of gold supported on conventional CeO_2, the only oxygen species observed were nonplanar bridging peroxide adspecies, η^2-peroxide, $O_2^{\delta-}$ $(0<\delta<1)$, and molecular oxygen; no CO_2 formation was detected with this sample under our conditions.

Results of temperature-programmed reduction (TPR) with CO characterizing the catalytically active gold on nanocrystalline CeO_{2-x} confirm the participation of the separate surface oxygen species, which are reactive under various conditions (see Supporting Information). The species reduced at high temperature (820 K) are associated with lattice oxygen, which does not participate in CO oxidation at low temperatures. The oxygen species with maximum CO uptakes at 385 and at 473 K may be attributed to superoxide and peroxide adspecies, respectively. Cyclic TPR experiments (see Supporting Information) demonstrate the regeneration of the active gold sites during reduction and oxidation of the catalyst.

Our results imply a cooperation between gold and the nanocrystalline CeO_{2-x} which promotes the formation of reactive oxygen species (Figure 3). An explanation for the enhanced activity of the catalysts prepared with nanocrystalline CeO_{2-x} is based on the stabilization of cationic gold (indicated by previous reports and supported by our own XANES data)[5,12] and reactive intermediate oxygen species, all at the cluster–support interface; the stabilization is inferred to be caused in part by oxygen vacancies on the nanocrystalline support and facilitated by a synergistic effect associated with the smallness (nanoscale) of both the gold and the support. Consistent with this interpretation, the high surface/grain–boundary area that is characteristic of the CeO_{2-x} nanocrystals is associated with the presence of defects that enhance the electron-transport properties of sintered nanostructured CeO_{2-x} relative to that of bulk CeO_2.[17]

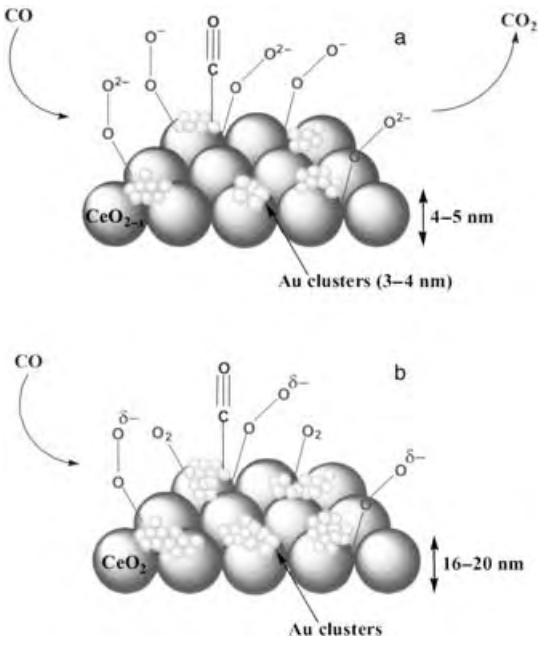


Figure 3. Schematic representation of CO oxidation catalyzed by gold on nanocrystalline (a) and regular (b) CeO_2. a) CO is adsorbed on the gold, whereas the oxygen is supplied through the nanocrystalline CeO_2 support as η^1-superoxide and peroxide adspecies at one-electron defect sites to give CO_2. b) CO is adsorbed on the gold atoms and the oxygen is adsorbed as molecular O_2 and $O_2^{\delta-}$. The size of the atoms is not scaled.

As described in reference [16], a catalyst consisting of gold on Y_2O_3, both nanocrystalline and conventionally prepared, showed similar differences in the catalytic activity as the one studied here; the activity of the catalyst prepared from nanocrystalline Y_2O_3 was shown to be comparable to the activities of the most active supported gold catalysts under similar conditions,[3,13] and the reactive intermediate oxygen species identified by Raman spectroscopy during catalysis were peroxide and superoxide species (see Supporting Information). These results bolster those observed for the CeO_{2-x}-supported samples and demonstrate a general synergistic effect associated with the interfaces between gold and nanocrystalline redox-active supports in promoting the formation of reactive oxygen species that participate in catalytic CO oxidation.

In summary, we have shown a correlation between the catalytic activity of gold supported on nanocrystalline CeO_{2-x} and reactive η^1-superoxide and peroxide species at one-electron defect sites on the support. The formation of reactive oxygen species on the nanocrystalline support is enhanced by the gold. The pattern extends to Y_2O_3 supports, and we infer that the existence of reactive peroxides at gold nanocluster–support interfaces is general and will be useful in the design of novel materials with enhanced catalytic activity and selectivity for oxidation reactions.

 © 2005 Wiley-VCH Verlag GmbH & Co. KGaA, Weinheim

Experimental Section

Nanocrystalline CeO_2 and Y_2O_3 were prepared from colloidal dispersions of CeO_2 and Y_2O_3 nanoparticles with average diameters of 5 nm. The conventional CeO_2 support was prepared by precipitation of $Ce(NO_3)_4$; conventional Y_2O_3 was supplied by Nyacol, Inc. Gold was deposited on each support by deposition–precipitation of $HAuCl_4$ with NaOH, as described elsewhere.[12,16] The catalysts were not calcined. The total Au content of each final catalyst was determined by chemical analysis.

Raman spectra, with a resolution of 2 cm^{-1}, were collected with a Renishaw inVia Raman spectrometer equipped with a Leica DMLM microscope and a 514-nm Ar^+ ion laser as an excitation source and with a laser power at the sample of 2.0 mW. Each reported spectrum is the average of 20 scans with an exposure time each of 10 s. O_2 adsorption and CO oxidation experiments were conducted with an in situ cell (Linkam Scientific, THMS 600). The catalysts were pretreated at 323 K under vacuum (10^{-2} Pa) for 1 h before adsorption experiments.

The X-ray absorption spectroscopy experiments were performed at beamline X-18B at the National Synchrotron Light Source, Brookhaven National Laboratory, Upton, NY, USA. The storage ring electron energy was 2.8 GeV and the ring current varied within the range of 110 to 250 mA. Spectra were collected in the fluorescence mode. Higher harmonics in the X-ray beam were minimized by detuning the Si(111) double-crystal monochromator by 20 to 25 % at the Au L_{III} edge (11919 eV). A PIPS detector was used, and each reported spectrum is the average of six scans. Data were recorded during CO oxidation catalysis at 298 K and also with the catalysts in flowing He at atmospheric pressure and 298 K. Catalyst powder (0.3 g) was loaded into a cell/reactor and installed in the flow system at the beamline.

CO oxidation catalysis was carried out at atmospheric pressure in a standard once-through, nearly isothermal tubular packed-bed flow reactor (9 mm in diameter). Total feed flow rate to the reactor was 100 mL (normal temperature and pressure) per minute with a molar ratio of CO/air/He of 0.2:19.8:80.0, with an inverse space velocity of 18.6–94.0 $g_{cat}\,h\,mol_{CO}^{-1}$. The conversions were determined by gas chromatographic analysis of the product stream with an accuracy of about $\pm 5\,\%$. An on-line gas chromatograph (Varian, Star 3400 CX) equipped for column switching (Porapak and molecular sieves) in combination with two-channel detection (with a thermal conductivity detector and a flame-ionization detector) was used to analyze the gas stream.

Received: February 22, 2005
Revised: April 20, 2005
Published online: June 29, 2005

Keywords:
heterogeneous catalysis · cerium · EXAFS spectroscopy · gold · nanostructures

[1] B. Nkosi, M. D. Adams, N. J. Coville, G. J. Hutchings, *J. Catal.* **1991**, *128*, 378 – 386.
[2] a) T. Hayashi, K. Tanaka, M. Haruta, *J. Catal.* **1998**, *178*, 566 – 575; b) E. E. Stangland, K. B. Stavens, R. P. Andres, W. N. Delgass, *J. Catal.* **2000**, *191*, 332 – 386.
[3] M. Haruta, N. Yamada, T. Kobayashi, S. Iilima, *J. Catal.* **1989**, *115*, 301 – 309.
[4] J. Guzman, B. C. Gates, *J. Phys. Chem. B* **2002**, *106*, 7659 – 7665.
[5] J. Guzman, B. C. Gates, *J. Am. Chem. Soc.* **2004**, *126*, 2672 – 2673.
[6] Q. Fu, H. Saltsburg, M. Flytzani-Stephanopoulos, *Science* **2003**, *301*, 935 – 938.
[7] M. Valden, X. Lai, D. W. Goodman, *Science* **1998**, *281*, 1647 – 1650.
[8] N. Lopez, J. K. Nørskov, *J. Am. Chem. Soc.* **2002**, *124*, 11262 – 11263.
[9] M. S. Chen, D. W. Goodman, *Science* **2004**, *306*, 252 – 255.
[10] C. Lemire, R. Meyer, S. Shaikhutdinov, H. J. Freund, *Angew. Chem.* **2004**, *116*, 121 – 124; *Angew. Chem. Int. Ed.* **2004**, *43*, 118 – 121.
[11] V. A. Bondzie, S. C. Parker, C. T. Campbell, *Catal. Lett.* **1999**, *63*, 143 – 151.
[12] S. Carrettin, P. Concepción, A. Corma, J. M. López Nieto, V. F. Puntes, *Angew. Chem.* **2004**, *116*, 2592 – 2594; *Angew. Chem. Int. Ed.* **2004**, *43*, 2538 – 2540.
[13] G. C. Bond, D. T. Thompson, *Catal. Rev. Sci. Eng.* **1999**, *41*, 319 – 388.
[14] R. J. Davis, *Science* **2003**, *301*, 926 – 927.
[15] C. T. Campbell, *Science* **2004**, *306*, 234 – 235.
[16] J. Guzman, A. Corma, *Chem. Commun.* **2005**, *6*, 743 – 745.
[17] A. Corma, P. Atienzar, H. Garcia, J.-Y. Chane-Ching, *Nat. Mater.* **2004**, *3*, 394 – 397.
[18] A. M. Argo, J. F. Odzak, F. S. Lai, B. C. Gates, *Nature* **2002**, *415*, 623 – 626.
[19] These samples contained slightly larger gold clusters than those supported on the nanocrystalline support, with an average diameter of about 15 Å as indicated by the Au–Au first- and second-shell coordination numbers of 6 and 1 at interatomic distances of (2.8 ± 0.1) Å and (4.0 ± 0.1) Å, respectively. There are other supported metal samples with clusters almost as small as these for which the EXAFS metal–oxygen contributions are also negligible.[4,20]
[20] J. Guzman, B. C. Gates, *Nano Lett.* **2001**, *1*, 689 – 692.
[21] a) E. S. Putna, J. M. Vohs, R. J. Gorte, *J. Phys. Chem.* **1996**, *100*, 17862 – 17865; b) Q. Fu, A. Weber, M. Flytzani-Stephanopoulos, *Catal. Lett.* **2001**, *77*, 87 – 95; c) A. Boulahouache, G. Kons, H.-G. Lintz, P. Schulz, *Appl. Catal. A* **1992**, *91*, 115 – 123.
[22] V. V. Pushkarev, V. I. Kovalchuk, J. L. d'Itri, *J. Phys. Chem. B* **2004**, *108*, 5341 – 5348.
[23] R. Q. Long, Y. P. Huang, H. L. Wan, *J. Raman Spectrosc.* **1997**, *28*, 29 – 32.
[24] J. Guzman, S. Carrettin, A. Corma, *J. Am. Chem. Soc.* **2005**, *127*, 3286 – 3287.
[25] D. Andreeva, V. Idakiev, T. Tabakova, L. Ilieva, P. Falaras, A. Bourlinos, A. Travlos, *Catal. Today* **2002**, *72*, 51 – 57.

 © 2005 Wiley-VCH Verlag GmbH & Co. KGaA, Weinheim

Gene Technology

Polyethylenimine-Grafted Multiwalled Carbon Nanotubes for Secure Noncovalent Immobilization and Efficient Delivery of DNA

Ye Liu, De-Cheng Wu, Wei-De Zhang, Xuan Jiang, Chao-Bin He, Tai Shung Chung, Suat Hong Goh, and Kam W. Leong*

The functionalization of carbon nanotubes (CNTs) has been carried out in various ways for numerous applications in biotechnology,[1–15] including for the preparation of sensors,[2,3] as scaffolds for cell growth,[4] imaging reagents,[5] and transporters for drug delivery.[6–8,13,15] One way is to immobilize DNA onto the surface of CNTs through noncovalent interactions[8–13] or covalent bonds.[3,12–15] Covalent-bond approaches might compromise and even spoil the functions of DNA owing to chemical reactions and the difficulty in releasing DNA.[13,14b,15] Nevertheless, noncovalent approaches developed to date may only provide metastable immobilization of DNA onto the surface of CNTs. It was reported that the migration of DNA linked covalently to CNTs was retarded in gel electrophoresis but noncovalent interactions between DNA and CNTs did not completely prevent migration.[14b] Polyethylenimine (PEI) is a type of polymer with a high density of amines, thus DNA may be immobilized securely onto the surface of multiwalled carbon nanotubes (MWNTs) that have been functionalized with PEI through strong electrostatic interactions arising from these amines. Hence, we have adopted a grafting-from approach to prepare polyethylenimine-graft multiwalled carbon nanotubes (PEI-g-MWNTs). DNA has been immobilized securely onto the surface of PEI-g-MWNTs as demonstrated by the total inhibition of the migration of DNA in gel electrophoresis, and PEI-g-MWNTs showed transfection efficiency for delivery of DNA that was similar to or even several times higher than that of PEI (25 K) and several orders of magnitude higher than that of naked DNA.

PEI was grafted onto the surface of MWNTs by performing a cationic polymerization of aziridine in the presence of amine-functionalized MWNTs (NH_2–MWNTs). NH_2–MWNTs were obtained by introducing carboxylic acid groups onto the surface of MWNTs by heating at reflux in 3.0 M nitric acid. The carboxylic acid groups were transformed into acyl chloride groups by treatment with thionyl chloride[16] followed by treatment with ethylenediamine.[14] The grafting of PEI was realized through two mechanisms, the activated monomer mechanism (AMM) or the activated chain mechanism (ACM), by which protonated aziridine monomers or the terminal iminium ion groups of propagation chains, respectively, are transferred to amines on the surface of MWNTs.[17] (see Supporting Information.)

The relative amount of PEI grafted onto the surface of MWNTs was investigated by thermogravimetric analysis (TGA) performed under nitrogen. MWNTs were thermally stable up to 600 °C (Figure 1 A, curve a) whereas pure PEI degraded completely at about 500 °C (Figure 1 A, curve d). At 500 °C, pristine MWNTs, NH_2–MWNTs, and PEI-g-MWNTs showed negligible, about 2.3 %, and 10.5 % weight losses, respectively, thus PEI-g-MWNTs contained about 8.2 % PEI. Grafting with PEI made PEI-g-MWNTs easy to disperse in water, and the resulting suspension was still stable after six months. However, NH_2–MWNTs dispersed poorly in water and precipitation occurred within several hours (see Supporting Information). Transmission electron microscopy (TEM) provides direct evidence of grafting of PEI onto the surface of MWNTs. Figure 1 B shows TEM images of PEI-g-MWNTs on a holey carbon film: individually dispersed MWNTs are separated from others. High-resolution TEM (Figure 1 B, inset) indicates that PEI was grafted onto the surface of MWNTs as lumps with different sizes instead of as a uniform coating. This clumping results from the carboxylic acid groups, the ethylenediamine, and the PEI adhering preferably to the defects, which are the most active locations for chemical or physical functionalization;[18] these defects tend to cluster at the bends along the surface of MWNTs grown by chemical vapor deposition (CVD).[19] In Figure 1 C, the ^{1}H NMR spectrum of PEI-g-MWNTs in D_2O is compared with that of PEI in D_2O (pH 7.0). The signal at about $\delta =$ 3.1 ppm for PEI-g-MWNTs is attributed to grafted PEI, but the significantly decreased mobility of the PEI chains in PEI-g-MWNTs leads to broadening of the resonances. Some of the amine groups of PEI were protonated (pK_a of PEI is greater than 8.0); we found that protonation or partial protonation of PEI was necessary for the formation of a stable aqueous suspension of PEI-g-MWNTs and neutralizing PEI by adjusting the pH value to 9 or higher led to precipitation of dispersed PEI-graft-MWNTs within several hours.

PEI obtained by cationic polymerization of aziridine has a dendritic structure that contains primary, secondary, and tertiary amines with a molar ratio of about 1:2:1.[20] Grafting PEI onto the surface of MWNTs should have a negligible effect on the chemistry. The migration of DNA was totally inhibited in gel electrophoresis when the weight ratio of PEI-

[*] Dr. Y. Liu, D.-C. Wu, Dr. W.-D. Zhang, Dr. C.-B. He
Institute of Materials Research and Engineering
3 Research Link, Singapore 117602 (Singapore)
Fax: (+65) 6872-7528
E-mail: ye-liu@imre.a-star.edu.sg
D.-C. Wu, Prof. S. H. Goh
Department of Chemistry
National University of Singapore
3 Science Drive 3, Singapore 117543 (Singapore)
X. Jiang
Division of Johns Hopkins in Singapore
Singapore 138669 (Singapore)
Prof. T. S. Chung
Department of Chemical and Biomolecular Engineering
National University of Singapore
Singapore 119260 (Singapore)
Prof. K. W. Leong
Department of Biomedical Engineering
Johns Hopkins University School of Medicine
Baltimore, MD 21205 (USA)

Supporting information for this article is available on the WWW under http://www.angewandte.org or from the author.

 © 2005 Wiley-VCH Verlag GmbH & Co. KGaA, Weinheim DOI: 10.1002/anie.200500042

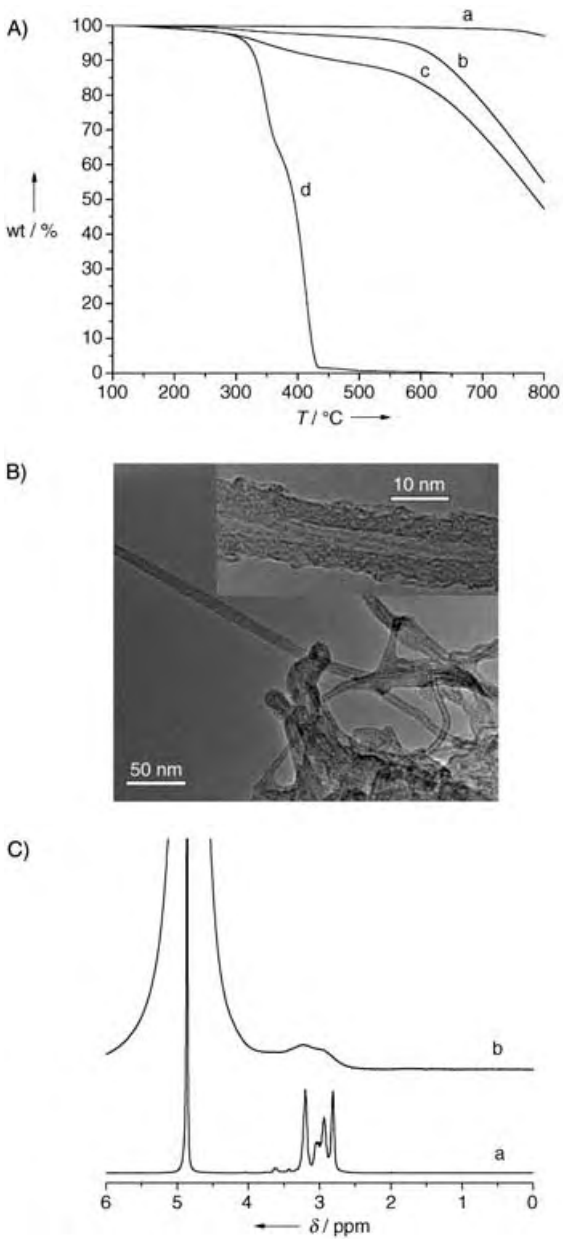


Figure 1. A) TGA curves of a) pristine MWNTs, b) NH_2–MWNTs, c) PEI-g-MWNTs, and d) PEI. B) TEM images of PEI-g-MWNTs; inset, high-resolution TEM image of PEI-g-MWNTs . C) ^1H NMR spectra of a) PEI in D_2O (pH 7) and b) PEI-g-MWNTs in D_2O.

g-MWNTs to DNA was about 4:1 (see Supporting Information). This result indicated that the dendritic grafted PEI with a high content of primary, secondary, and tertiary amines could function as anchor points for the secure immobilization of DNA onto the surface of MWNTs. In contrast, the presence of pristine MWNTs and NH_2–MWNTs showed little effect on the migration of DNA, even at a high weight ratio of 100:1 (see Supporting Information). Furthermore, a monolayer of PEI (25 K) was adsorbed onto the surface of CNTs directly after thorough rinsing,[21] but this monolayer of PEI did not prevent the migration of DNA (see Supporting Information). Thus, DNA could not be securely immobilized onto the surface of pristine MWNTs, NH_2–MWNTs, and MWNTs that were covered by a physically absorbed monolayer of PEI (25 K) because the interaction was too weak.

Recently it was demonstrated that amine-terminal oligoethylene glycol functionalized MWNTs (*f*-MWNTs) are promising for the delivery of DNA into cells, but the in vitro transfection efficiency of *f*-MWNTs was much less effective than that of lipids and only ten times higher than that of naked DNA.[8] In comparison, PEI-g-MWNTs that we have developed showed good transfection efficiency for DNA delivery. Figure 2 compares the transfection efficiency of PEI-g-MWNTs for DNA delivery in 293 cells with that of naked DNA and PEI (25 K), one of the most efficient polymers for the delivery of DNA.[22] The optimal weight ratio for PEI-g-MWNTs to DNA was about 45:1, with a N/P ratio of about 28.5:1 (10:1 for PEI at 25 K).[22] Under these conditions, the transfection efficiency of PEI-g-MWNTs was more than three times higher than that of PEI (25 K), and four orders of magnitude higher than that of naked DNA. PEI-g-MWNTs showed good transfection efficiency of DNA in other cells as well. The transfection efficiencies of PEI-g-MWNTs in COS7 and HepG2 cells were around twice and half, respectively, of those of PEI (25 K) and much higher than those of naked DNA under an optimal N/P ratio of between 10 to 16:1 (see Supporting Information).

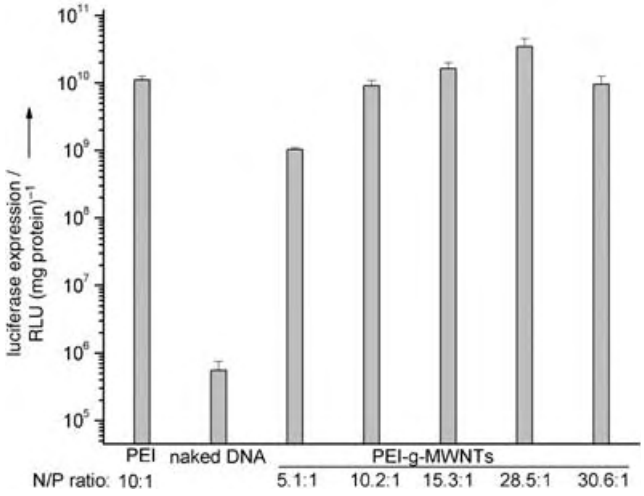


Figure 2. Transfection efficiency of PEI-g-MWNTs for DNA delivery relative to that of PEI (25 K) and naked DNA in 293 cells. The level of gene (pCMV-Luc) expression is given in relative light units (RLU) per mg of protein for quadruplicate runs (mean ± standard deviation ($n = 4$)).

The uptake of CNTs or their conjugates by the cells was suggested to occur by phagocytosis[5] or endocytosis,[6] which is in contrast to an insertion and diffusion mechanism in which MWNTs function as nanoneedles that inject DNA through the cell membranes.[7,8] We labeled PEI-g-MWNTs with fluorescein isothiocyanate (FITC); confocal microscope imaging demonstrated that the complexes of DNA with fluorescently labeled PEI-g-MWNTs entered cells after incubation for 1 h at 37 °C, but only very weak green fluorescence could be detected after incubation for 1 h at 4 °C (see Supporting Information). Therefore, the uptake of

 © 2005 Wiley-VCH Verlag GmbH & Co. KGaA, Weinheim

the complexes of PEI-g-MWNTs and DNA should occur by endocytosis as reported.[5,6] The high transfection efficiency of PEI-g-MWNTs is attributed to several factors. The first factor is the secure immobilization of DNA onto the surface of MWNTs which leads to the formation of stable complexes that protect DNA well from degradation. The second factor is that the proton-sponge effect of the grafted PEI would allow the PEI-g-MWNTs/DNA complexes to escape easily from endosomes or other vesicles in cells, as has been well documented.[22] Furthermore, the larger complexes of PEI-g-MWNTs and DNA would improve the proton-sponge effects of PEI and facilitate a more effective sedimentation onto the cells.[23]

Pristine and some functionalized carbon nanotubes have been demonstrated to be of low cytotoxicity.[5–8] In 293 cells, the complexes of PEI-g-MWNTs/DNA with a weight ratio of 10:1 showed no significant effects on cellular metabolism but higher ratios led to a decreased cell number. Pure PEI-g-MWNTs showed a higher cytotoxicity. Figure 3A shows that

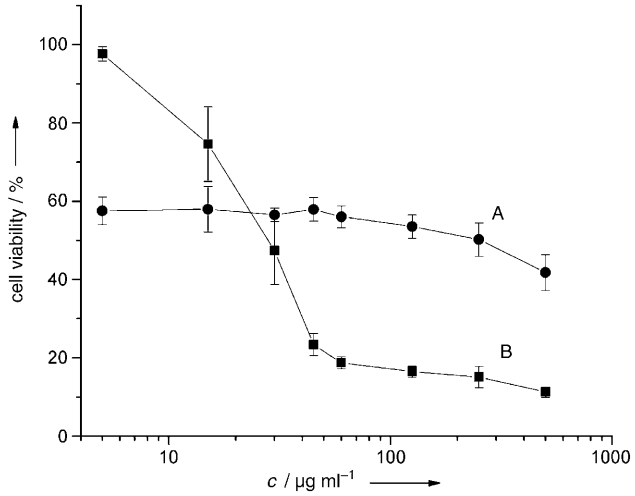


Figure 3. Cytotoxicity of A) PEI-g-MWNTs and B) PEI (25 K) in 293 cells.

about 60% of the cells were viable when the concentration of PEI-g-MWNTs was about 5 $\mu g\,mL^{-1}$, but the increased concentration of PEI-g-MWNTs showed less effect on the cell viability as compared with PEI (25 K; Figure 3B). Similar results were observed in COS7 and HepG2 cells (see Supporting Information). The cytotoxicity of PEI is related to the molecular weight: a higher molecular weight results in a higher cytotoxicity.[23] One PEI-g-MWNT may behave as high-molecular-weight PEI and thus it would have a certain degree of cytotoxicity.

In conclusion, we have prepared PEI-g-MWNTs. The grafted PEI chains function as efficient anchors to securely immobilize DNA onto the surface of MWNTs. This approach might be exploited to prepare highly sensitive CNT-based DNA sensors or probes and novel safe and efficient gene-delivery systems by fine-tailoring the PEI or by adopting other low toxic and biocompatible substitutes.

Experimental Section

PEI-graft-MWNTs: MWNTs were prepared by catalytic CVD of methane on Co–Mo/MgO catalysts. NH_2–MWNTs[14] and aziridine[25] were prepared by procedures similar to those reported. In a typical process for preparing PEI-g-MWNTs, NH_2–MWNTs (0.1 g) were dispersed in 1,2-dichloroethylene (20 mL) by ultrasonication over 20 min; aziridine (0.45 mL) was then added into the mixture under stirring followed by HCl (10 M; 10 μL). The reaction mixture was left at 80 °C for 24 h, after which time PEI-g-MWNTs were collected by filtration through a 0.2-μm pore polycarbonate membrane then washed with dichloromethylene ten times. PEI-g-MWNTs were purified by dispersing in deionized water, filtering through a 0.2-μm pore PVDF membrane, and washing with deionized water followed by drying under vacuum at 60 °C.

TGA was performed by scanning from 100 to 820 °C under nitrogen at a heating rate of 20 °C min^{-1} by using a Perkin Elmer TGA7. TEM was performed on a Philips CM300 FEGTEM instrument at 300 kV, and the samples were prepared by dropping one droplet of an aqueous suspension of PEI-g-MWNTs onto a holey copper mesh covered with carbon. NMR spectra were obtained on a Bruker DRX-400 spectrometer. The procedures for gel electrophoresis, evaluation of transfection efficiency for delivery of DNA, and cytotoxicity, were similar to those reported previously,[26] and these procedures are described in the Supporting Information together with the preparation of FTIC-labeled PEI-g-MWNTs, their incubation with cells, and confocal microscopy experiments.

Received: January 6, 2005
Revised: April 4, 2005
Published online: July 1, 2005

Keywords: amines · carbon nanotubes · DNA · gene technology · polymerization

[1] a) Y. Lin, S. Taylor, H. P. Li, K. A. S. Fernando, L. W. Qu, W. Wang, L. R. Gu, B. Zhou, Y. P. Sun, *J. Mater. Chem.* **2004**, *14*, 527; b) E. Katz, I. Willner, *ChemPhysChem* **2004**, *5*, 1084; c) J. J. Davis, K. S. Coleman, B. R. Azamian, C. B. Bagshaw, M. L. H. Green, *Chem. Eur. J.* **2003**, *9*, 3732; d) X. Chen, G. S. Lee, A. Zettl, C. R. Bertozzi, *Angew. Chem.* **2004**, *116*, 6237; *Angew. Chem. Int. Ed.* **2004**, *43*, 6112.

[2] a) R. J. Chen, S. Bangsaruntip, K. A. Drouvalakis, N. W. S. Kim, M. Shim, Y. Li, W. Kim, P. J. Utz, H. Dai, *Proc. Natl. Acad. Sci. USA* **2003**, *100*, 4984; b) K. A. Williams, P. T. M. Veenhuizen, B. G. de la Torre, R. Eritja, C. Dekker, *Nature* **2002**, *420*, 761.

[3] a) C. V. Nguyen, L. Delzeit, A. M. Cassell, J. Li, J. Han, M. Meyyappan, *Nano Lett.* **2002**, *2*, 1079; b) J. Li, H. T. Ng, A. Cassell, W. Fan, H. Chen, Q. Ye, J. Koehne, J. Han, M. Meyyappan, *Nano Lett.* **2003**, *3*, 597.

[4] H. Hu, Y. Ni, V. Montana, R. C. Haddon, V. Parpura, *Nano Lett.* **2004**, *4*, 507.

[5] P. Cherukuri, S. M. Bachilo, S. H. Litovsky, R. B. Weisman, *J. Am. Chem. Soc.* **2004**, *126*, 15638.

[6] a) N. W. S. Kam, T. C. Jessop, P. A. Wender, H. Dai, *J. Am. Chem. Soc.* **2004**, *126*, 6850; b) N. W. S. Kam, H. Dai, *J. Am. Chem. Soc.* **2005**, *127*, 6021.

[7] Q. Lu, J. M. Moore, G. Huang, A. S. Mount, A. M. Rao, L. L. Larcom, P. C. Ke, *Nano Lett.* **2004**, *4*, 2473.

[8] a) D. Pantarotto, R. Singh, D. McCarthy, M. Erhardt, J.-P. Briand, M. Prato, K. Kostarelos, A. Bianco, *Angew. Chem.* **2004**, *116*, 5354; *Angew. Chem. Int. Ed.* **2004**, *43*, 5242; b) R. Singh, D. Pantarotto, D. McCarthy, O. Chaloin, J. Hoebeke, C. D. Partidos, J.-P. Briand, M. Prato, A. Bianco, K. Kostarelos, *J. Am. Chem. Soc.* **2005**, *127*, 4388.

 © 2005 Wiley-VCH Verlag GmbH & Co. KGaA, Weinheim

[9] S. C. Tsang, Z. Guo, Y. K. Chen, M. L. H. Green, H. A. O. Hill, T. W. Hambley, P. J. Sadler, *Angew. Chem.* **1997**, *109*, 2291; *Angew. Chem. Int. Ed. Engl.* **1997**, *36*, 2198.
[10] Z. Guo, P. J. Sadler, S. C. Tsang, *Adv. Mater.* **1998**, *10*, 701.
[11] M. Zheng, A. Jagota, M. S. Strano, A. P. Santos, P. Barone, S. G. Chou, B. A. Diner, M. S. Dresselhaus, R. S. Mclean, G. B. Onoa, G. G. Samsonidze, E. D. Semke, M. Usrey, D. J. Walls, *Science* **2003**, *302*, 1545.
[12] B. J. Taft, A. D. Lazareck, G. D. Withey, A. Yin, J. M. Xu, S. O. Kelley, *J. Am. Chem. Soc.* **2004**, *126*, 12750.
[13] T. E. McKnight, A. V. Melechko, G. D. Griffin, M. A. Guillorn, V. I. Merkulov, F. Serna, D. K. Hensley, M. J. Doktycz, D. H. Lowndes, D. H. Lowndes, M. L. Simpson, *Nanotechnology* **2003**, *14*, 551.
[14] a) S. E. Baker, W. Cai, T. L. Lasseter, K. P. Weidkamp, R. J. Hamers, *Nano Lett.* **2002**, *2*, 1413; b) C. Dwyer, M. Guthold, M. Falvo, S. Washburn, R. Superfine, D. Erie, *Nanotechnology* **2002**, *13*, 601.
[15] T. E. McKnight, A. V. Melechko, D. K. Hensley, D. G. J. Mann, G. D. Griffin, M. L. Simpson, *Nano Lett.* **2004**, *4*, 1213.
[16] J. Chen, M. A. Hamon, H. Hu, Y. Chen, A. M. Rao, P. C. Eklund, R. C. Haddon, *Science* **1998**, *282*, 95.
[17] a) Y. Liu, H. B. Wang, C. Y. Pan, *Macromol. Chem. Phys.* **1997**, *198*, 2613; b) S. J. Oh, S. J. Cho, C. O. Kim, J. W. Park, *Langmuir* **2002**, *18*, 1764; c) H. Petersen, A. L. Martin, S. Stolnik, C. J. Roberts, M. C. Davies, T. Kissel, *Macromolecules* **2002**, *35*, 9854.
[18] A. Hirsch, *Angew. Chem.* **2002**, *114*, 1933; *Angew. Chem. Int. Ed.* **2002**, *41*, 1853.
[19] M. Endo, K. Takeuchi, S. Igarashi, K. Kobori, M. Shiraishi, H. W. Kroto, *J. Phys. Chem. Solids* **1993**, *54*, 1841.
[20] A. V. Harpe, H. Petersen, Y. X. Li, T. Kissel, *J. Controlled Release* **2000**, *69*, 309.
[21] M. Shim, A. Javey, N. W. S. Kam, H. Dai, *J. Am. Chem. Soc.* **2001**, *123*, 11512.
[22] O. Boussif, F. Lezoualc'h, M. A. Zanta, M. D. Mergny, D. Scherman, B. Demeneix, J. P. Behr, *Proc. Natl. Acad. Sci. USA* **1995**, *92*, 7297.
[23] M. Ogris, P. Steinlein, M. Kursa, K. Mechtler, R. Kircheis, E. Wagner, *Gene Ther.* **1998**, *5*, 1425.
[24] D. Fischer, T. Bieber, Y. X. Li, H. P. Elsasser, T. Kissel, *Pharm. Res.* **1999**, *16*, 1273.
[25] H. Wenker, *J. Am. Chem. Soc.* **1935**, *57*, 2328.
[26] Y. Liu, D. C. Wu, Y. X. Ma, G. P. Tang, S. Wang, C. B. He, T. S. Chung, S. H. Goh, *Chem. Commun.* **2003**, 2630.

 © 2005 Wiley-VCH Verlag GmbH & Co. KGaA, Weinheim

Macrocycle Synthesis

Diversity Oriented One-Pot Synthesis of Complex Macrocycles: Very Large Steroid–Peptoid Hybrids from Multiple Multicomponent Reactions Including Bifunctional Building Blocks**

Ludger A. Wessjohann, Brunhilde Voigt, and Daniel G. Rivera*

Dedicated to Professor Armin de Meijere on the occasion of his 65th birthday

One of the most fascinating challenges in modern organic chemistry is the design of strategies capable of providing structurally diverse and complex molecules, which are useful either for the study of important biological processes[1] or for the development of supra- and nanomolecular systems.[2] The chemical genomics approach especially has focused efforts towards the rapid generation of molecules able to modulate protein functions, with the hope of thereby achieving a better understanding of the role of these molecules in many cellular pathways as well as providing new targets for drug development.[3] Frank in his recent review on chemical genomics concludes:[1e] "A general concept for the construction of protease-resistant (protein-like) synthetics for the interference of such (protein–protein) interactions is not yet available." Also, in contrast to small classic enzyme inhibitors, molecules to study protein–protein interactions are believed to require much larger interaction surfaces with an interplay of lipophilic and polar interaction areas. A promising solution could be the one-pot construction of extended, highly complex structures in which spatially separated recognition motifs combine to achieve overall binding. For this purpose, macrocyclic skeletons are considered to be an especially remarkable class of target scaffolds, as they can combine conformational preorganization with flexibility and biological stability.[4]

A useful prospect has been the development of diverse routes towards synthetic and natural-product-like macrocycles.[5,6] However, most (large) macrocycles utilized by the chemical community so far are either of the repetitive type (for example, the homooligomeric cyclodextrins and calixarenes) or have to be made by multistep, complex synthetic routes, which allow the generation of a single specimen but do not easily provide the diverse libraries required for holistic or evolutionary approaches and activity/property screenings.

[*] Prof. Dr. L. A. Wessjohann, Dr. B. Voigt, D. G. Rivera
Department of Bioorganic Chemistry
Leibniz Institute of Plant Biochemistry
Weinberg 3, 06120 Halle/Saale (Germany)
Fax: (+49) 345-5582-1309
E-mail: wessjohann@ipb-halle.de

[**] We are grateful to Dr. Jürgen Schmidt for the HRMS spectra and Angela Schaks for experimental assistance. We also gratefully acknowledge the Deutsche Forschungsgemeinschaft for financial support (Grant GRK/894).

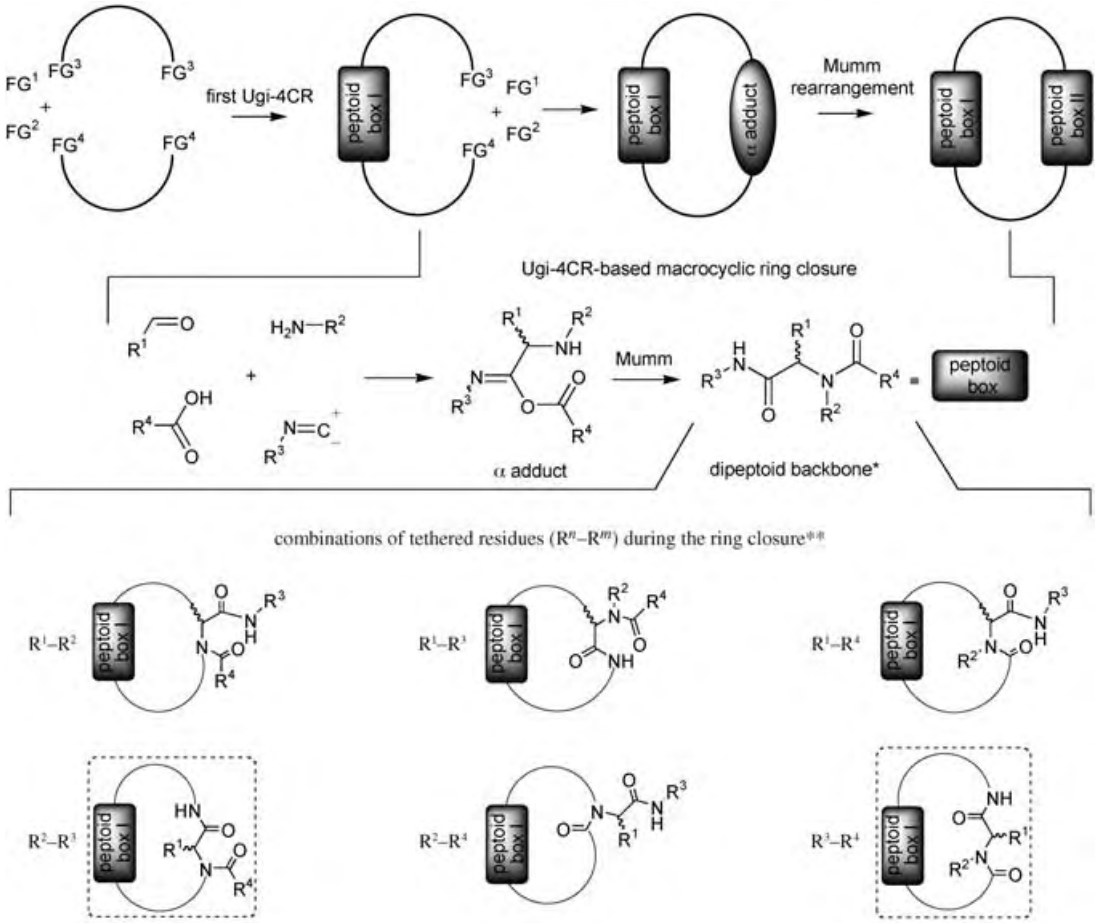
 DOI: 10.1002/anie.200500019 © 2005 Wiley-VCH Verlag GmbH & Co. KGaA, Weinheim

Naturally occurring macrocycles are usually endowed with unique structural complexity[4] which, for example, enables the disruption of protein–protein interactions or binding to specific protein domains. Whilst diversity-oriented approaches have been devised to create the crucial complexity and diversity,[7] improvements are still required for macrocyclization strategies to rapidly and readily access diversity and to simultaneously introduce, for example, protein binding motifs in a unified task in the macrocyclization step itself.

We have recently addressed this quest and devised a new strategy for developing macrocycle diversity, in which the proper application of multiple multicomponent macrocyclizations including bifunctional building blocks (MiBs) allows rapid access to libraries of constitutionally defined peptoid-containing macrocycles.[6] Herein we describe the first applications of this concept for the straightforward synthesis of very large macrocycles (up to 60-membered rings), in which up to 4 multicomponent reactions (including the macrocyclization step) incorporate 12 components in 1 pot.

The Ugi four-component reaction (Ugi-4CR) has evolved as one of the most useful reactions in diversity-oriented approaches toward drug discovery.[8] The only by-product of this (atom) economic process is water. Moreover, bifunctional building blocks have been appropriately utilized to access a variety of structurally diverse cyclic scaffolds.[9] However, the multicomponent reaction itself has previously not been exploited for recognition-motif generation or, with some exceptions,[6,10] as a ring-closing reaction in macrocyclization strategies.

A simple survey of the skeletal (peptoid-core) diversity achieved by employing different symmetrically bifunctionalized (Ugi) components in a bidirectional macrocyclization is presented in Scheme 1. The ring size of the final macrocycle depends on the chosen combination of bifunctional building blocks. As either endo- or exocyclic amide bonds can be formed, higher or lower flexibility can be generated for both the ring and the differently tethered residues. However, it is important to note that even in the simplest double Ugi-4CR based approach, the two Ugi-4CRs do not occur simultaneously because a linear macrocycle precursor is formed initially. To understand the proper design of macrocycles, the final cyclization step is crucial to assess the ring size (multiplicity) and efficiency (yield), and thereby the result of the overall process.[5a,g] In the case of Ugi-type reactions, the analysis should not only be directed to the strain of the final macrocycle but also to the cyclic precursor α-adduct, as well as the possibly strained 1,3-*ansa*-like intermediate of the Mumm rearrangement, both resulting from the various



Scheme 1. Skeletal diversity of the peptoid backbones that can be obtained in a *m*ultiple *m*ulticomponent *m*acrocyclization *i*ncluding *b*ifunctional *b*uilding *b*locks (MiBs) of the bidirectional Ugi type. *: The C→N terminus of box I runs parallel to that of box II (bidirectional peptoids), that is, even if the same FG^1 and FG^2 residues are included, the boxes are not identical owing to the asymmetry of the steroid tether.[6] **: The different *endo*/*exo* peptoid cores available by the MiBs. Dashed boxes indicate examples used herein.

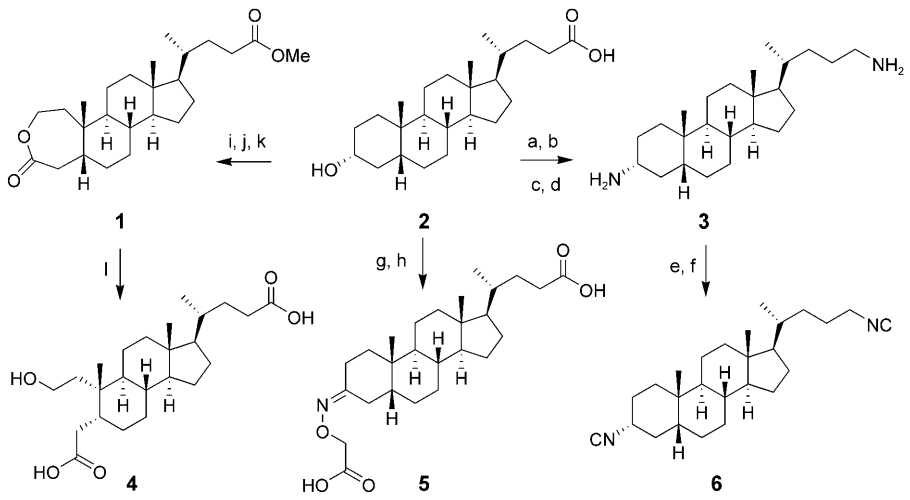
 © 2005 Wiley-VCH Verlag GmbH & Co. KGaA, Weinheim

bifunctional building block combinations (Scheme 1; for example, aldehyde/acid building blocks bridging R^1 and R^4).[6]

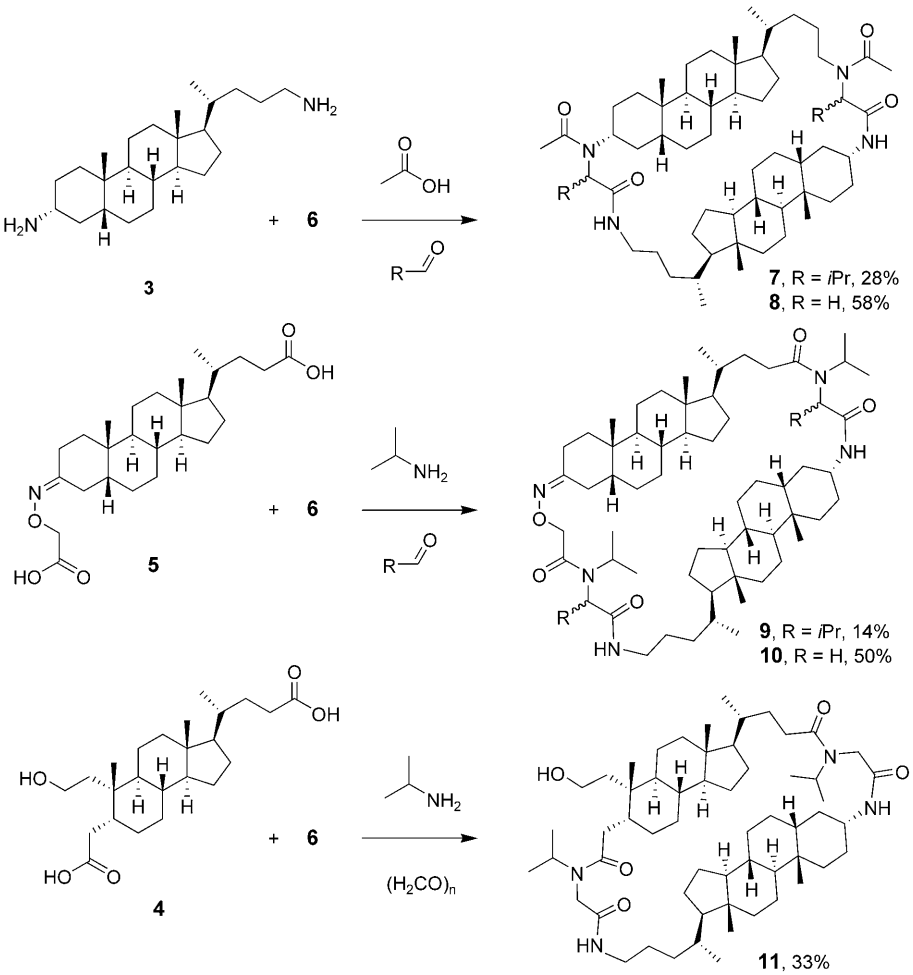
With a view to applying this concept in the work described herein, we concentrated on a straightforward strategy towards steroid–peptoid hybrid macrocycles through a one-pot multiple Ugi-4CR of steroidal bifunctional building blocks. Steroids combine several structural features that render them suitable architectural components in macrocycle synthesis. They present one of the few extended, readily available, chiral units that can be additionally functionalized by a large set of established procedures. The natural stereochemical diversity and rigid array of concave-directed differentiable functionalities in the steroidal nucleus have been previously used in the (target-oriented) design of macrocyclic frameworks for biomimetic and molecular recognition applications.[11]

Scheme 2 summarizes the synthesis of the steroidal bifunctional building blocks from lithocholic acid (**2**). Synthesis of diamine **3** and diisonitrile **6** proceeded by a double Mitsunobu reaction to the corresponding reduced acid, followed by azide displacement,[12a] reduction, and subsequent isonitrile formation.[12b] Steroidal dicarboxylic acids are a source of additional skeletal diversity. They are most rapidly obtained from the 3-oxo derivative through lactone formation by a Baeyer–Villiger reaction[13] and consecutive ring-opening saponification or alternatively by condensation with *O*-(carboxymethyl)hydroxylamine; these reactions afforded the dicarboxylic acids **4** and **5**, respectively.

All multiple macrocyclizations by the Ugi-4CR presented here were carried out under pseudodilution conditions by adding the diisonitrile building block at a rate of $0.1\ mL\,h^{-1}$ ($c = 0.05\ mmol\,mL^{-1}$) to a mixture of the other components. Competing oligomerization was successfully minimized and an almost equal mixture of head-to-head (H-H) and head-to-tail (H-T) isomers resulted in all cases with at least two bifunctional asymmetric building blocks.[6,14] Three examples, highlighted in Scheme 3, illustrate the initial attempt to explore our strategy. By using the diamine **3** and the diacids **4** and **5** as counterparts of the common diisonitrile **6** in the Ugi-4CR, two different types of peptoid backbones are produced, according to the considerations summarized in Scheme 1. The diamine/diisonitrile combination is characterized by an



Scheme 2. Synthesis of the steroidal bifunctional building blocks. a) $LiAlH_4$, THF; b) DIAD, Ph_3P, $MeSO_3H$; c) NaN_3, DMPU; d) H_2, PtO_2; e) HCO_2Et, Δ; f) $POCl_3$, iPr_2NEt; g) PCC, CH_2Cl_2; h) $NH_2OCH_2CO_2H$, Py; i) TMSCl, MeOH; j) PCC, CH_2Cl_2; k) urea/H_2O_2, $(CF_3CO)_2O$; l) KOH, MeOH. DIAD = diisopropylazodicarboxylate, DMPU = 1,3-dimethyl-3,4,5,6-tetrahydro-2(1*H*)-pyrimidone, PCC = pyridinium chlorochromate, Py = pyridine, THF = tetrahydrofuran, TMS = trimethylsilyl.



Scheme 3. Double Ugi-4CR based macrocyclization of steroidal bifunctional building blocks (bidirectional MiBs of diamine/diisonitrile and diacid/diisonitrile type). Head-to-head (H-H) and head-to-tail (H-T) regiomers are formed in almost equal amounts. Yields refer to the mixture; however, for clarity, only the H-T isomer is shown.[14]

 © 2005 Wiley-VCH Verlag GmbH & Co. KGaA, Weinheim

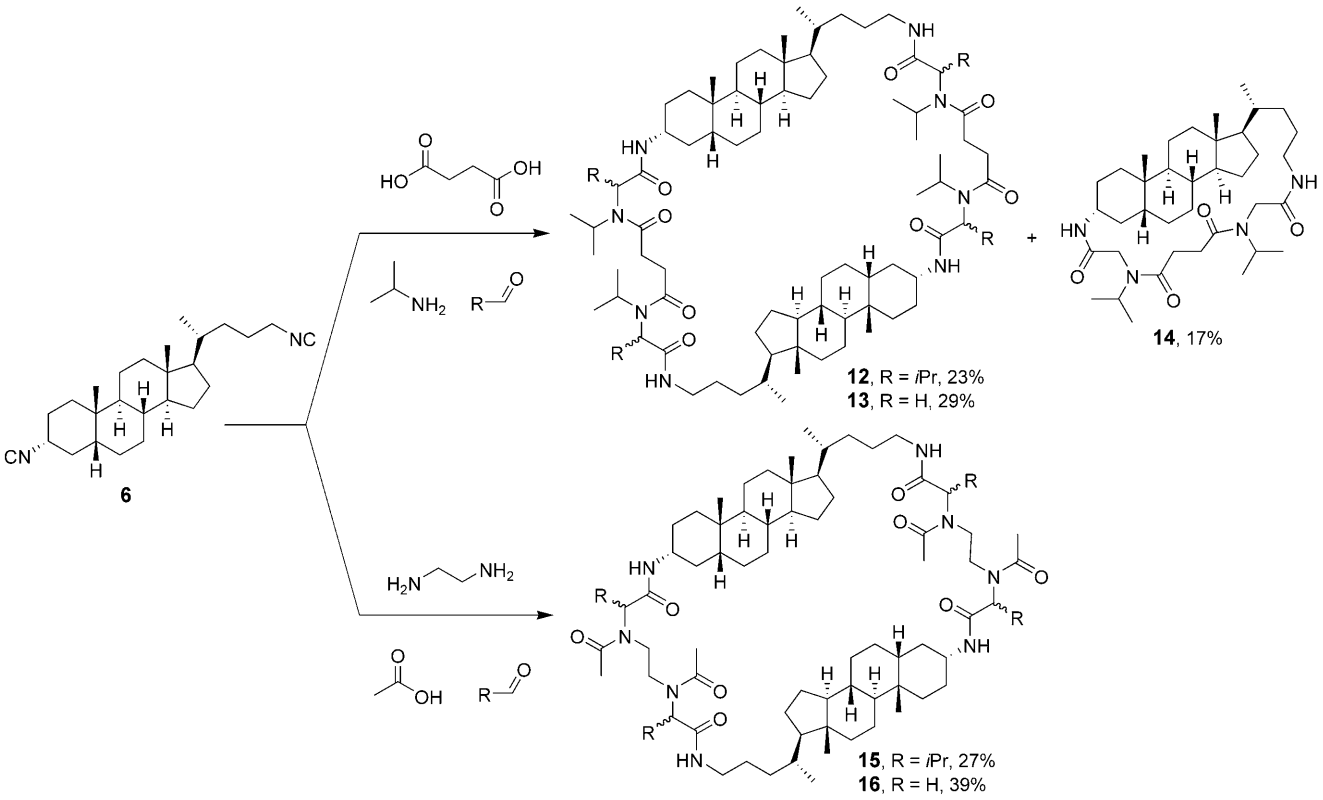
exocyclic amide bond which shortens the tether chain but increases the flexibility of the peptoid portion.

Of the various components that can be varied, the oxo component exhibits special influence on ring formation and stereochemical complexity. Thus, macrocycles **7**–**10** were isolated as almost equally distributed mixtures of diastereomers.[15] The Ugi approach facilitates the rapid generation of stereochemical diversity that is much more difficult to access in a multistep synthetic strategy, although it could also be considered a drawback owing to the required (but often easy) separation and difficult characterization work. Furthermore, when isobutyraldehyde was replaced by paraformaldehyde there was a marked increase in the macrocyclization yields, which is probably the result of lower steric hindrance or a significantly modified prefolding bias.

To improve the size as well as recognition-motif diversity of the peptoid core of the macrocyclic skeleton, we set out to design a fourfold Ugi-4CR macrocyclization by using two equivalents of the steroidal diisonitrile **6** and another (at this stage simpler) bifunctional building block. This complementary and direct approach, which allows manipulation of the nature and length of the steroid bridging tethers, succeeded for the synthesis of the fourfold macrocycles **12**–**16** (Scheme 4) with ethylenediamine or succinic acid as the simpler bifunctional building blocks. Interestingly, in the case with succinic acid and with paraformaldehyde as the oxo component the smaller macrocycle **14** was also formed, although in lower yield, a result confirming that the succinate-bridged double dipeptoid chain is just long enough to span the distance between the two functional groups of the steroidal skeleton. An alternative third pathway, isonitrile (imidate) induced condensation to succinic anhydride leading to the Ugi three-component product, was not observed, but it was also not specifically looked for, as the desired macrocycles were formed in typical combined yield.

The different outcomes in these macrocyclizations by using different aldehydes pinpoint the importance of understanding the effect of a bulky aldehyde side chain on the success and result of the overall process. In addition to pure steric effects, the favoring (or disfavoring) of double[16] or fourfold Ugi-4CR based macrocyclizations is dependent on the length, flexibility, and prefolding characteristics of the acyclic precursor. The strain and strain change of the cyclic α-adduct are also crucial aspects which determine the formation and further ability to rearrange to the final macrocycle. Thus, the sterically demanding isopropyl groups might cause significant steric strain or incorrect prefolding in the formation of the cyclic α-adduct, thereby prohibiting the formation of the smaller macrocycle. Larger (for example, sixfold Ugi-4CR based) macrocycles, in contrast, could not be identified to any significant amount by ESI-FT-ICR mass spectrometry.

After reliable fourfold Ugi-4CR macrocyclizations were established and because of the intriguing result obtained with a diacid as the bridging building block, we extended our plan to cover other types of peptoid tethers for the steroids. This could be achieved with diacids that have a significant influence either on the molecular recognition behavior or on the internal folding of the obtained macrocycle. Terephthalic and cyclopropane-1,1-dicarboxylic acids were chosen as the counterparts, and consequently macrocycles **17**–**20** were



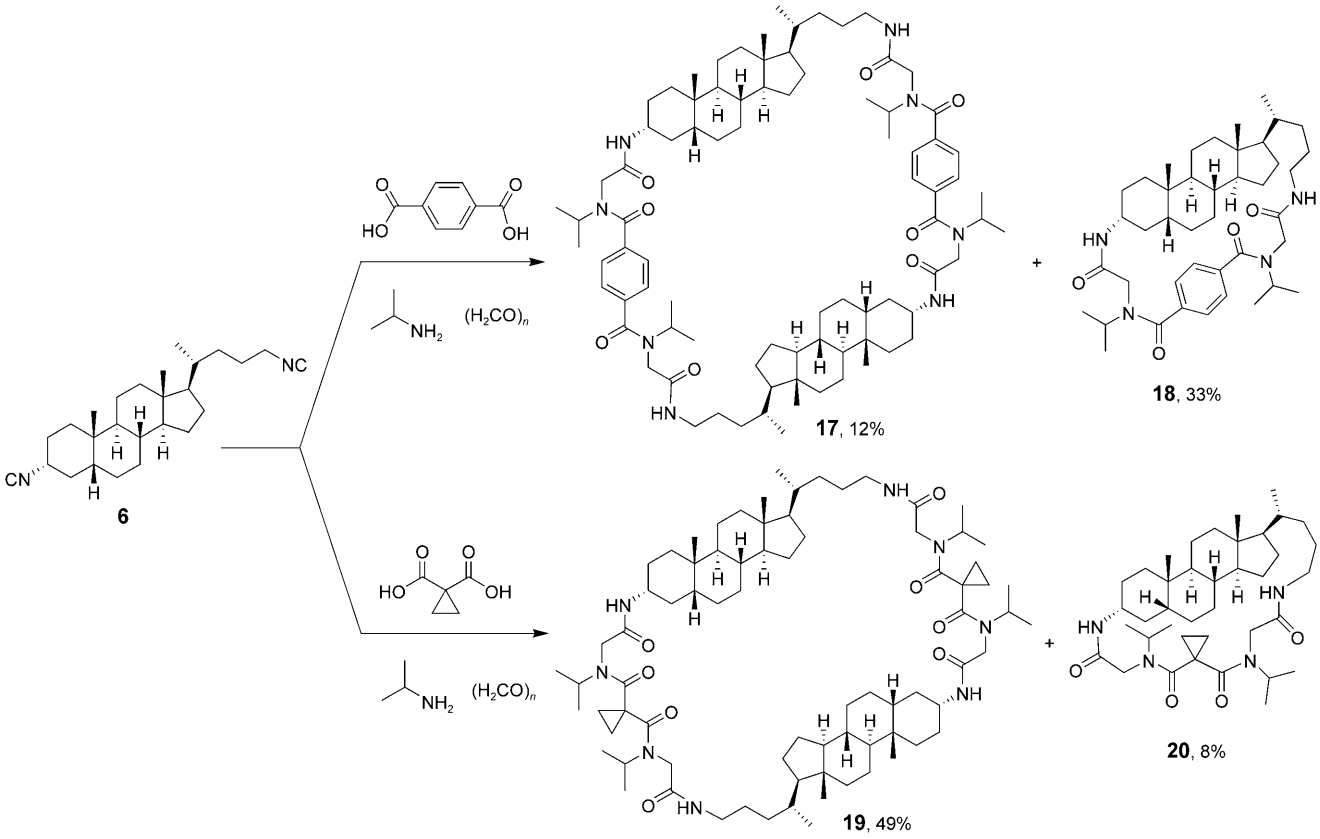
Scheme 4. Fourfold Ugi-4CR based macrocyclization of bifunctional building blocks (MiBs of diacid/diisonitrile and diamine/diisonitrile type). A mixture of H-H and H-T isomers is observed for fourfold reactions, (i.e., not for **14**).[14,16]

 © 2005 Wiley-VCH Verlag GmbH & Co. KGaA, Weinheim

synthesized in a similar fashion, with paraformaldehyde as the best oxo component for analytical purposes. Scheme 5 highlights the convincing results of our design. It also shows the effect of a more strained chain on the success of the fourfold Ugi-4CR macrocyclization versus the double reaction. With the long and straight terephthalic acid, the double Ugi-4CR based small macrocycle **18** was the main product, whereas the short, kinked 1,1-cyclopropane diacid led to the formation of the fourfold Ugi-4CR based large macrocycle **19** as the major product; this result shows that the formation of the cyclopropane-bridged double dipeptoid chain is disfavored owing to its significantly lower flexibility and shorter length to span the steroidal moiety. At this point it should be mentioned that, for example, a yield of 49% for isolated **19** corresponds to an approximately 96% calculated yield for each individual reaction/bond formed, *including* the macrocyclization.

Apart from the vast array of functionalities that could be placed inside the macrocyclic cavity by altering one of the differentiable faces of the steroidal moiety, the proven degree of complexity and diversity accessible through this one-pot synthetic process can be highlighted by considering four distinct issues: 1) additional binding elements or biologically or catalytically interesting motifs can be appended as side chains to some of the Ugi components, 2) the macrocyclization can be performed in a template-based manner to control the size of the cavity, 3) further skeletal diversity can be achieved by varying the nature of the building blocks, and 4) conformational diversity of the cavity can be designed either a) from geometrically varied building blocks (for example, straight or kinked, as shown above) or b) by generating new stereogenic centers. While the first issues are being developed in connection with ongoing projects, an efficient access to diastereoselective Ugi reactions (4b) is the last problem that remains unsolved—with a few exceptions.[17] Supported by the possible automation of the Ugi-4CR,[5,6,8] the current strategy may be extended to independently modify the different access points of diversity generation in a parallel (or mixed) combinatorial fashion. Moreover, the whole system is suitable for evolutionary-based or holistic approaches, for the generation of sets of biologically relevant molecules or biomimetic supramolecular systems, or for any application that requires large, constitutionally defined complex molecules of a nonrepetitive or only partly repetitive nature.

In conclusion, we have presented a very straightforward strategy to generate a collection of chimeric peptoid macrocycles—here specifically with steroid moieties—of a size and structural complexity that bears no resemblance to any known natural product but that is potentially useful in chemical genomics approaches, as well as for artificial receptors for molecular recognition studies or as bottom-up building units for nanotechnology. To our knowledge, multicomponent reactions have not so far been used to directly form macrocycles of this size and complexity that can easily incorporate and display chemical motifs previously identified as suitable, for example, for anion and carbohydrate recognition.[18] We believe that no other macrocycle synthesis is known that better combines ease, versatility, functionality,



Scheme 5. Fourfold versus double Ugi-4CR based macrocyclizations of geometrically different bifunctional building blocks. A mixture of H-H and H-T isomers is observed for **17** and **19**.[14]

 © 2005 Wiley-VCH Verlag GmbH & Co. KGaA, Weinheim

size control, and speed in one pot than the process presented here. Finally, the principal concept of MiBs[6] should not be limited to Ugi type multicomponent reactions only.

Experimental Section

General procedure for the Ugi-4CR based macrocyclizations: A solution of the oxo component (2 mmol) and the amino component (2 mmol) in MeOH (250 mL) was stirred for 1 h at room temperature. The diacid building block (0.5 mmol) was then added and the stirring was continued for another 30 min. A solution of diisocyanide **6** (0.5 mmol) in MeOH (10 mL) was added slowly to the reaction mixture by using a syringe pump (flow rate of 0.1 $mL\,h^{-1}$). After addition was complete, the reaction mixture was concentrated under decreased pressure and the crude material was purified by flash column chromatography or preparative HPLC to afford the corresponding macrocycles, usually as amorphous solids.

Received: January 4, 2005
Revised: April 4, 2005
Published online: June 29, 2005

Keywords: combinatorial chemistry · macrocycles · molecular recognition · multicomponent reactions · steroids

[1] For reviews, see: a) G. Mitsopoulos, D. P. Walsh, Y.-T. Chang, *Curr. Opin. Chem. Biol.* **2004**, *8*, 26; b) R. S. Lokey, *Curr. Opin. Chem. Biol.* **2003**, *7*, 91; c) D. L. Boger, J. Desharnais, K. Capps, *Angew. Chem.* **2003**, *115*, 4270; *Angew. Chem. Int. Ed.* **2003**, *42*, 4138; d) T. Berg, *Angew. Chem.* **2003**, *115*, 2562; *Angew. Chem. Int. Ed.* **2003**, *42*, 2462; e) R. Frank, *BIOspektrum* **2002**, *8*, 474; f) P. Arya, R. Joseph, D. T. H. Chou, M.-G. Baek, *Angew. Chem.* **2001**, *113*, 351; *Angew. Chem. Int. Ed.* **2001**, *40*, 339; g) S. L. Schreiber, *Bioorg. Med. Chem.* **1998**, *6*, 1127.

[2] a) H.-J. Schneider, A. Yatsimirsky, *Principles and Methods in Supramolecular Chemistry*, Wiley, Chichester, **2000**; b) C. A. Schalley, J. Rebek in *Stimulating Concepts in Chemistry* (Eds.: F. Vögtle, S. Stooddart, M. Shibasaki), Wiley-VCH, Weinheim, **2000**.

[3] For selected reports, see: a) D. Barnes-Seeman, S. B. Park, A. N. Koehler, S. L. Schreiber, *Angew. Chem.* **2003**, *115*, 2478; *Angew. Chem. Int. Ed.* **2003**, *42*, 2376; b) S. M. Khersonsky, D. W. Jung, T. W. Kang, D. P. Walsh, H. S. Moon, H. Jo, E. M. Jacobson, V. Shetty, T. A. Neubert, Y. T. Chang, *J. Am. Chem. Soc.* **2003**, *125*, 11804; c) F. G. Kuruvilla, A. F. Shamji, S. M. Sternson, P. J. Hergenrother, S. L. Schreiber, *Nature* **2002**, *416*, 653; d) H. E. Pelish, N. J. Westwood, Y. Feng, T. Kirchhausen, M. D. Shair, *J. Am. Chem. Soc.* **2001**, *123*, 6740; e) T. U. Mayer, T. M. Kapoor, S. J. Haggarty, R. W. King, S. L. Schreiber, T. J. Mitchison, *Science* **1999**, *286*, 971.

[4] a) L. A. Wessjohann, E. Ruijter, D. G. Rivera, W. Brandt, *Mol. Diversity* **2005**, *9*, 171; b) M. Feher, J. M. Schmidt, *J. Chem. Inf. Comput. Sci.* **2003**, *43*, 218.

[5] a) L. A. Wessjohann, E. Ruijter, *Top. Curr. Chem.* **2005**, *243*, 137; b) P. Cristau, J.-P. Vors, J. Zhu, *Tetrahedron* **2003**, *59*, 7859; c) B. Beck, G. Larbig, B. Bejat, M. Magnin-Lachaux, A. Picard, E. Herdtweck, A. Dömling, *Org. Lett.* **2003**, *5*, 1047; d) J. K. Sello, P. R. Andreana, D. Lee, S. L. Schreiber, *Org. Lett.* **2003**, *5*, 4125; e) L. A. Wessjohann, *Curr. Opin. Chem. Biol.* **2000**, *4*, 303; f) D. Lee, J. K. Sello, S. L. Schreiber, *J. Am. Chem. Soc.* **1999**, *121*, 10648; g) J. Blankenstein, J. Zhu, *Eur. J. Org. Chem.* **2005**, 1949.

[6] L. A. Wessjohann, E. Ruijter, *Mol. Diversity* **2005**, *9*, 159.

[7] a) M. A. Burke, S. L. Schreiber, *Angew. Chem.* **2004**, *116*, 48; *Angew. Chem. Int. Ed.* **2004**, *43*, 46; b) D. Lee, J. K. Sello, S. L. Schreiber, *Org. Lett.* **2000**, *2*, 709; c) S. L. Schreiber, *Science* **2000**, *287*, 1964.

[8] For reviews, see: a) A. Dömling, I. Ugi, *Angew. Chem.* **2000**, *112*, 3300; *Angew. Chem. Int. Ed.* **2000**, *39*, 3168; b) C. Hulme, T. Nixey, *Curr. Opin. Drug Discovery Dev.* **2003**, *6*, 921; c) R. V. A. Orru, M. de Greef, *Synthesis* **2003**, 1471; d) L. Weber, *Curr. Med. Chem.* **2002**, *9*, 1241; e) L. Weber, *Drug Discovery Today* **2002**, *2*, 143; f) H. Bienaymé, C. Hulme, G. Oddon, P. Schmitt, *Chem. Eur. J.* **2000**, *6*, 3321; g) C. Hulme, V. Gore, *Curr. Med. Chem.* **2003**, *10*, 51.

[9] B. Beck, A. Picard, E. Herdtweck, A. Dömling, *Org. Lett.* **2004**, *6*, 39, and references therein.

[10] a) P. Janvier, M. Bois-Choussy, H. Bienaymé, J. Zhu, *Angew. Chem.* **2003**, *115*, 835; *Angew. Chem. Int. Ed.* **2003**, *42*, 811; b) A. Failli, H. Immer, M. D. Götz, *Can. J. Chem.* **1979**, *57*, 3257.

[11] For reviews, see: a) A. P. Davis, R. P. Bonar-Law, J. K. M. Sanders in *Comprehensive Supramolecular Chemistry*, *Vol. 4* (Eds.: J. L. Atwood, J. E. D. Davies, D. D. MacNicol, F. Vögtle), Elsevier, Oxford, **1996**, pp. 257–286; b) P. Wallimann, T. Marti, A. Fürer, F. Diederich, *Chem. Rev.* **1997**, *97*, 1567; c) Y. Li, J. R. Dias, *Chem. Rev.* **1997**, *97*, 283; d) J. Tamminen, E. Kolehmainen, *Molecules* **2001**, *6*, 21; e) E. Virtanen, E. Kolehmainen, *Eur. J. Org. Chem.* **2004**, 3385.

[12] a) A. P. Davis, S. Dresen, L. J. Lawless, *Tetrahedron Lett.* **1997**, *38*, 4305; b) R. Obrecht, R. Herrmann, I. Ugi, *Synthesis* **1985**, 400.

[13] M. S. Cooper, H. Heaney, A. J. Newbold, W. R. Sanderson, *Synlett* **1990**, 533.

[14] For bidirectional MiBs with at least two bifunctional asymmetric building blocks, see ref. [6]. For simplicity reasons only the head-to-tail (H-T) isomers are shown in all schemes. The yields refer to the mixture of both isomers, which often cannot be distinguished by the available structural determination techniques (HRMS, NMR) prior to chromatographic separation. This separation, however, is usually not problematic.

[15] HPLC and LC-MS spectra showed the presence of all diastereomers in the mixture in close to equal amounts.

[16] The double MiBs of Schemes 4 and 5 are different from those in Scheme 3 in that only one bifunctional building block is steroidal. This results in a different multiplicity bias (disfavoring the double MiBs) and the absence of regioisomers (H-H/H-T isomers).

[17] For lead references for stereoselective Ugi and Passerini reactions, see: a) D. J. Ramón, M. Yus, *Angew. Chem.* **2005**, *117*, 1628; *Angew. Chem. Int. Ed.* **2005**, *44*, 1602; b) K. Oertel, G. Zech, H. Kunz, *Angew. Chem.* **2000**, *112*, 1489; *Angew. Chem. Int. Ed.* **2000**, *39*, 1431; c) H. Kunz, W. Pfrengle, *J. Am. Chem. Soc.* **1988**, *110*, 651; d) I. Ugi, K. Offermann, *Angew. Chem.* **1963**, *75*, 917; *Angew. Chem. Int. Ed. Engl.* **1963**, *2*, 624; e) P. R. Andreana, C. C. Liu, S. L. Schreiber, *Org. Lett.* **2004**, *6*, 4231; f) U. Kusebauch, B. Beck, K. Messer, E. Herdtweck, A. Dömling, *Org. Lett.* **2003**, *5*, 4021; g) G. Cuny, R. Gamez-Montano, J. Zhu, *Tetrahedron* **2004**, *60*, 4879; h) R. Frey, S. F. Galbraith, S. Guelfi, C. Lamberth, M. Zeller, *Synlett* **2003**, 1536; i) T. Ziegler, H.-J. Kaisers, R. Schlomer, C. Koch, *Tetrahedron* **1999**, *55*, 8397; j) S. E. Denmark, Y. Fan, *J. Am. Chem. Soc.* **2003**, *125*, 7825.

[18] a) A. P. Davis, J. F. Gilmer, J. J. Perry, *Angew. Chem.* **1996**, *108*, 1410; *Angew. Chem. Int. Ed. Engl.* **1996**, *35*, 1312; b) R. P. Bonar-Law, A. P. Davis, B. A. Murray, *Angew. Chem.* **1990**, *102*, 1497; *Angew. Chem. Int. Ed. Engl.* **1990**, *29*, 1407; c) K. M. Bhattarai, R. P. Bonar-Law, A. P. Davis, B. A. Murray, *J. Chem. Soc. Chem. Commun.* **1992**, 752; d) A. P. Davis, R. S. Wareham, *Angew. Chem.* **1999**, *111*, 3160; *Angew. Chem. Int. Ed.* **1999**, *38*, 2979.

Electrochemistry

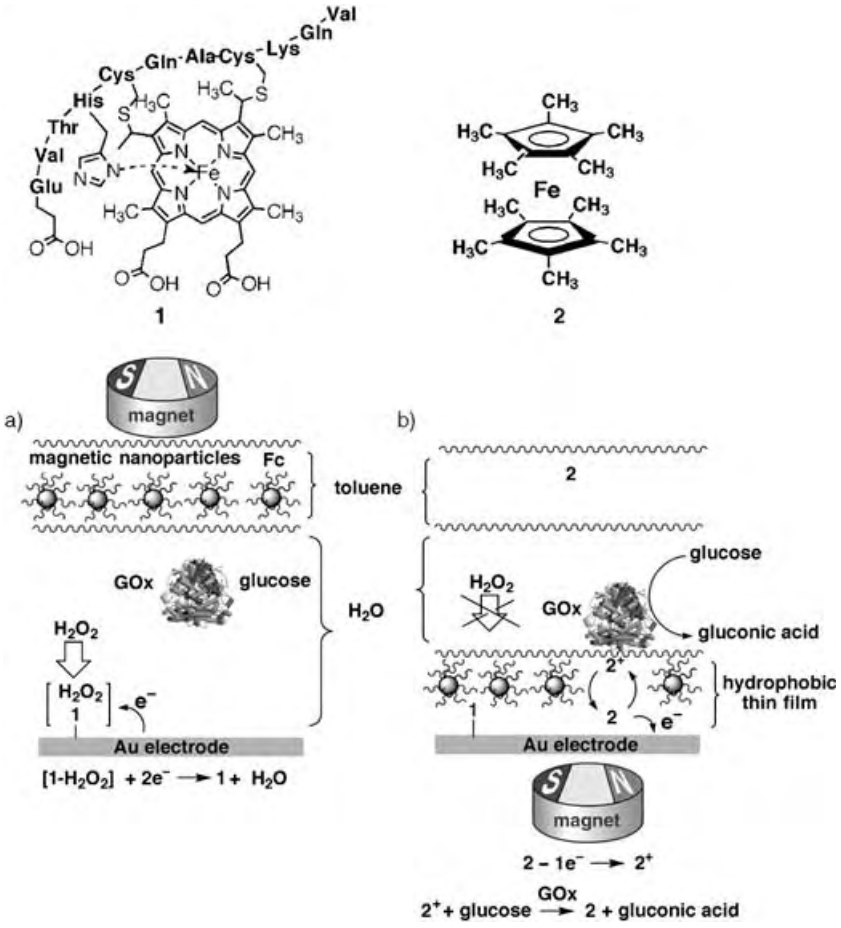
Switching of Directions of Bioelectrocatalytic Currents and Photocurrents at Electrode Surfaces by Using Hydrophobic Magnetic Nanoparticles**

*Eugenii Katz and Itamar Willner**

Magnetic particles—microspheres, nanospheres, and ferrofluids—are widely studied and applied in various fields of biology and medicine, such as magnetic targeting (drugs, genes, radiopharmaceuticals), magnetic resonance imaging, diagnostics, immunoassays, RNA and DNA purification, gene cloning, and cell separation and purification.[1] Extensive research efforts were recently directed towards the application of functionalized magnetic particles for controlling electrochemical transformations at electrode interfaces or chemical reactivity at solid supports.[2] The magnetic attraction or retraction of magnetic particles that are functionalized with redox units to and from electrode surfaces was used to switch "on" and "off" redox processes and subsequently activate/deactivate bioelectrocatalytic transformations.[3] Similarly, catalytic magnetic particles such as nickel nanoparticles were used to switch on and off electrocatalytic processes at electrode supports by using an external magnet.[4] The rotation of magnetic particles on electrode supports was reported to enhance electrocatalytic and bioelectrocatalytic processes by the hydrodynamic transport of the reacting substrates to the electrode.[5] Enhanced electrochemically generated chemiluminescence was reported in the presence of rotating magnetic particles,[6] and the system was employed for the amplified detection of DNA,[6,7] antigen–antibody complexes,[6] and cancer cells.[8] Recently, magnetic nanoparticles with a hydrophobic capping layer were employed to reversibly separate surface-confined and diffusional redox processes at electrodes.[9,10] By dissolving the hydrophobic magnetic nanoparticles in an organic phase, the magnetic nanoparticles were transported to the electrode surface with a colayer of hydrophobic solvent. This layer enabled a change of electrochemical processes of the electrode-confined species from aqueous type to organic-phase type, and the co-transport of hydrophobic substrates to the electrode surfaces allowed switchable electrocatalysis.[10]

Herein, we demonstrate the use of hydrophobic magnetic nanoparticles in a water/toluene biphasic system to switch reversibly at a fixed potential the bioelectrocatalytically and photoelectrochemically generated currents from cathodic to anodic directions.

Magnetite nanoparticles (diameter ca. 5 nm, saturation magnetization ca. 36.4 emu g^{-1}) functionalized with a monolayer of undecanoic acid[9] were dissolved in toluene (1 mg mL^{-1}), and the solution was added to the electrochemical cell to yield a system in which the upper organic layer was immiscible with the aqueous electrolyte solution. In the first system (Scheme 1), a gold surface placed at the bottom of the electrochemical cell was modified with the hemo-undecapeptide microperoxidase-11 (MP-11; **1**) by covalent linkage of MP-11 to a monolayer of cystamine.[11] Glucose oxidase (GOx, 1 mg mL^{-1}), glucose (50 mM), and H_2O_2 (50 mM) were added to the aqueous electrolyte solution. The upper toluene phase contained the hydrophobic magnetic nanoparticles and decamethylferrocene (**2**; 2 mM). When the external magnet was positioned above the electochemical cell, the magnetic nanoparticles were confined to the organic phase and the system adopted the configuration shown in



Scheme 1. Magnetoswitchable anodic/cathodic currents generated at the electrode functionalized with microperoxidase-11 (**1**) by using hydrophobic magnetic nanoparticles to gate the bioelectrocatalytic processes.

[*] Dr. E. Katz, Prof. I. Willner
Institute of Chemistry
The Hebrew University of Jerusalem
Jerusalem 91904 (Israel)
Fax: (+972) 2-652-7715
E-mail: willnea@vms.huji.ac.il

[**] This research is supported by the Israel–China Binational Program, The Israel Ministry of Science.

 DOI: 10.1002/anie.200501126 © 2005 Wiley-VCH Verlag GmbH & Co. KGaA, Weinheim

Scheme 1a. The cyclic voltammogram of the system is depicted in Figure 1a, curve 2. The electrocatalytic cathodic wave that starts at approximately 0.35 V is attributed to the electrocatalyzed reduction of H_2O_2 by **1**, as previously shown.[11a] In the absence of H_2O_2 in the aqueous phase, the cyclic voltammogram recorded at positive potentials shows a background current (Figure 1a, curve 1) while the quasi-reversible redox wave of the surface-confined MP-11 (**1**) is observed at negative potentials ($E^\circ = -0.4$ V; $\approx 1.4 \times 10^{-10}$ mole cm^{-2} surface coverage of **1**; Figure 1b). The shift in the reduction potential of H_2O_2 relative to the quasi-reversible wave of **1** observed in the absence of H_2O_2 was attributed to the formation of a complex between H_2O_2 and the heme center of MP-11 (**1**) that stimulated the reduction of H_2O_2 at the positive potentials.[11a]

Positioning of an external magnet below the electrode attracted the hydrophobic magnetic nanoparticles to the electrode. The magnetic attraction of the hydrophobic magnetic nanoparticles, which were associated with a layer of toluene that also includes **2**, to the electrode surface resulted in the cyclic voltammogram shown in Figure 1c, curve 3. In the absence of glucose in the aqueous phase, the quasi-reversible cyclic voltammogram of **2** associated with the hydrophobic magnetic nanoparticles was detected (Figure 1c, curve 2; the low voltammetric response is due to the slow scan rate). The electrocatalytic anodic current shown in Figure 1c, curve 3, is attributed to the bioelectrocatalytic oxidation of glucose by GOx mediated by **2**; that is, the oxidation of **2** in the toluene film yields the respective ferrocenyl cation that mediates the oxidation of glucose by GOx (Scheme 1b). Note, however, that upon attraction of the magnetic nanoparticles to the electrode surface, the electrocatalyzed reduction of H_2O_2 by **1** is totally blocked as a result of the formation of the hydrophobic thin film on the electrode which impedes contact between H_2O_2 dissolved in the aqueous phase and the **1**-functionalized electrode. Indeed, in the absence of **2** in the toluene phase and upon magnetic attraction of the nanoparticles from the organic phase to the electrode surface, the system shows complete blocking of the currents as a result of the isolation of the electrode surface by the hydrophobic thin film (Figure 1c, curve 1).

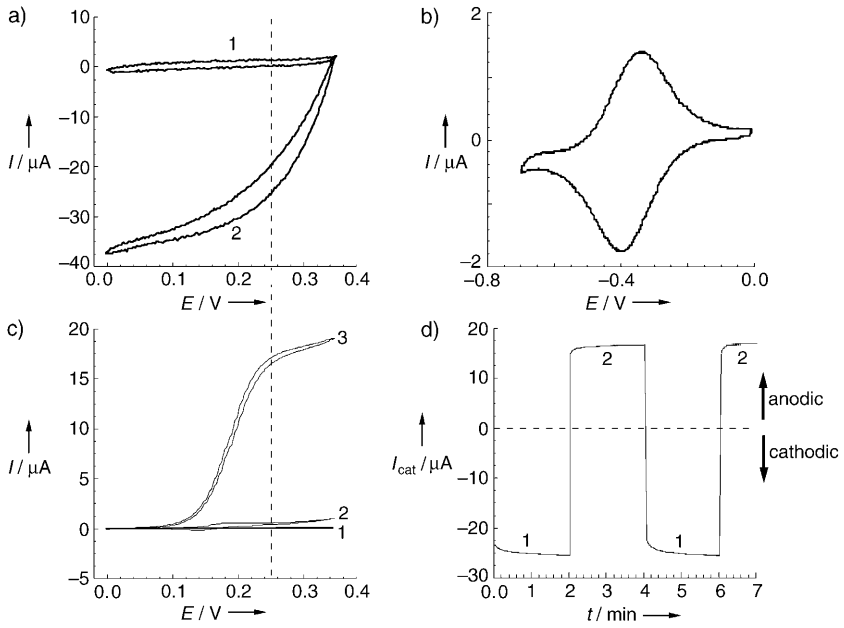
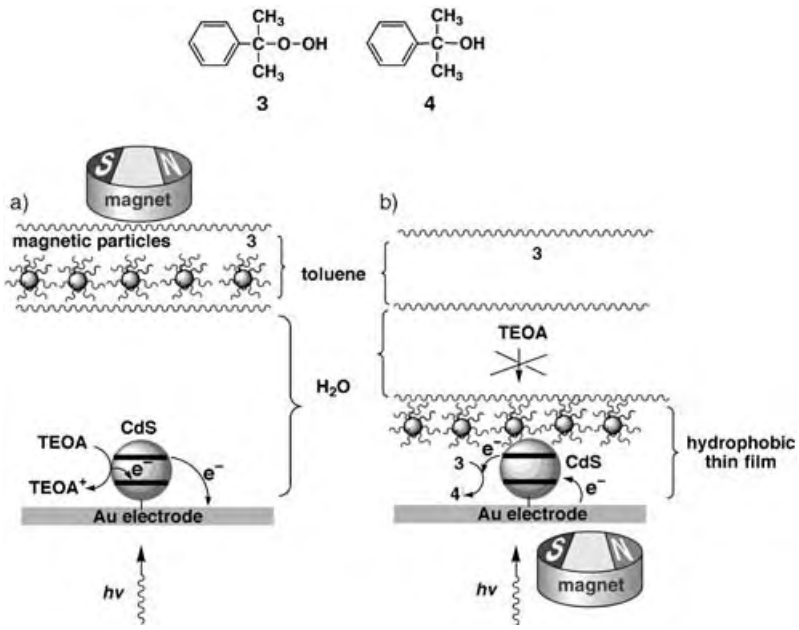


Figure 1. a) Cyclic voltammograms (potential scan rate: 5 mV s^{-1}) recorded in the presence of the **1**-functionalized electrode when the magnetic nanoparticles are retracted from the surface: 1) in the absence of H_2O_2 and 2) in the presence of H_2O_2 (50 mM). b) Cyclic voltammogram of the **1**-functionalized electrode recorded in the absence of H_2O_2 at a potential scan rate of 100 mV s^{-1}. c) Cyclic voltammograms (potential scan rate: 5 mV s^{-1}) recorded in the presence of the **1**-functionalized electrode when the magnetic nanoparticles are attracted to the surface: 1) in the absence of decamethylferrocene (**2**) in the toluene phase, 2) in the presence of **2** (2 mM) in the toluene phase and the absence of glucose in the aqueous phase, and 3) in the presence of **2** (2 mM) in the toluene phase and of glucose (50 mM) in the aqueous phase. d) Switchable bioelectrocatalytic currents generated in the system upon application of a fixed potential at 0.25 V, in the presence of H_2O_2 (50 mM) and glucose (50 mM) in the aqueous phase and **2** (2 mM) in the toluene phase, when the magnetic nanoparticles are retracted from the surface (1) or attracted to the surface (2). The data were recorded in a solution of phosphate buffer (0.1 M, pH 7.0) containing GOx (1 mg mL^{-1}).

The selective activation of the bioelectrocatalyzed reduction of H_2O_2 (by **1**) or the bioelectrocatalyzed oxidation of glucose (by **2** and GOx) enables the selection of a fixed potential value (e.g. 0.25 V vs. SCE) at which the direction of the current at the electrode surface can be reversibly switched by the hydrophobic magnetic nanoparticles (Figure 1d). When the nanoparticles are retracted from the electrode surface (Figure 1d, domains 1), the bioelectrocatalyzed reduction of H_2O_2 by **1** proceeds and a cathodic current of approximately -25 μA is observed at the applied potential of 0.25 V. Attraction of the magnetic nanoparticles to the electrode surface blocks the electrocatalytic reduction of H_2O_2, but the ferrocene-mediated bioelectrocatalyzed oxidation of glucose by GOx proceeds (Figure 1d, domains 2). A bioelectrocatalytic anodic current of about 15 μA is observed in the system at the applied potential of 0.25 V. By the cyclic retraction and attraction of the magnetic nanoparticles from or to the electrode surface, the current is switched between cathodic and anodic values, respectively.

By using a similar concept, the photoelectrochemical currents generated upon the illumination of a layer of CdS nanoparticles associated with an electrode could be switched between cathodic and anodic photocurrents by means of the hydrophobic magnetic particles (Scheme 2). A monolayer of CdS nanoparticles (diameter 5 nm) functionalized with a layer of 3-mercaptopropionic acid/3-mercaptoethanesulfonic acid was covalently linked to a cystamine-functionalized gold electrode.[12] Parallel microgravimetric quartz-crystal microbalance measurements indicated a surface coverage of approximately 3×10^{12} particles cm^{-2}. The system comprised the electrode functionalized with CdS nanoparticles and a biphasic system composed of an aqueous solution of triethanolamine (TEOA; 20 mM) as electron donor in phosphate

 © 2005 Wiley-VCH Verlag GmbH & Co. KGaA, Weinheim



Scheme 2. Magnetoswitchable anodic/cathodic photocurrents generated at the electrode functionalized with CdS nanoparticles by using hydrophobic magnetic nanoparticles to gate the photoelectrochemical processes.

buffer (0.1 M, pH 7.0) and a solution in toluene of cumene hydroperoxide (**3**; 2 mM) and the hydrophobic magnetic nanoparticles (Scheme 2a).

Irradiation of the CdS nanoparticles through a semitransparent gold-coated glass electrode, while confining the magnetic nanoparticles to the toluene phase, resulted in an anodic photocurrent (Figure 2a, curve 1). This photocurrent is generated only if TEOA is dissolved in the aqueous medium. The photocurrent action spectrum follows the absorbance spectrum of the CdS nanoparticles, which implies that it originates from the photoexcitation of the nanoparticles; that is, upon irradiation of the CdS nanoparticles an electron–hole pair is generated. The oxidation of TEOA by the holes and the transport of the conduction-band electrons to the electrode result in the formation of the anodic photocurrent (Scheme 2a).

The magnetic attraction of the hydrophobic magnetic nanoparticles from the toluene phase containing **3** to the electrode resulted in a cathodic photocurrent (Scheme 2b and Figure 2a, curve 3). In the absence of **3** in the toluene phase, no photocurrent was generated (Figure 2a, curve 2). Thus, the cathodic photocurrent originates from the transfer of the photoexcited conduction-band electrons in CdS nanoparticles to cumene hydroperoxide (**3**) to yield the respective reduction product cumene alcohol **4** and the concomitant transfer of electrons from the electrode to the semiconductor valence-band holes (Scheme 2b). Thus, the magnetic attraction of the hydrophobic magnetic nanoparticles to the surface functionalized with CdS nanoparticles results in the blocking of the electrode surface towards the aqueous solution of TEOA, while allowing the contact of the electrode surface with the electron acceptor **3** associated with the generated hydrophobic thin film. By the cyclic attraction and retraction of the magnetic nanoparticles to and from the electrode surface, the photocurrents generated by the semiconductor nanoparticles are switched between cathodic and anodic directions, respectively (Figure 2b). The quantum yields for the generation of photocurrents (taking into account the light flux, its reduction by the semitransparent electrode, and the absorbance of the CdS monolayer) were estimated to be approximately 5% and 3% for the anodic and cathodic photocurrents, respectively.

Note that in a previous study,[13] the direction of photocurrents at an electrode was switched between cathodic and anodic values by tethering two different chromophores (an electron acceptor or electron donor) to helical peptides associated with the electrode, and the photocurrents in this system were generated by irradiation of the system at two different wavelengths. In the present study, the switchable photocurrents originate from irradiation of the system in the same spectral region and through the control of the composition of the system at the electrode surface.

In conclusion, we have demonstrated switchable systems that can be gated between anodic and cathodic currents or photocurrents at a defined potential region or upon irradiation. To the best of our knowledge, these systems represent the first examples of inherent switchable amperometric responses that originate from the tailored local composition at the electrode interface. We believe that the results present a new concept for electron transfer at electrode surfaces and for the future design of bioelectronic and optobioelectronic systems.

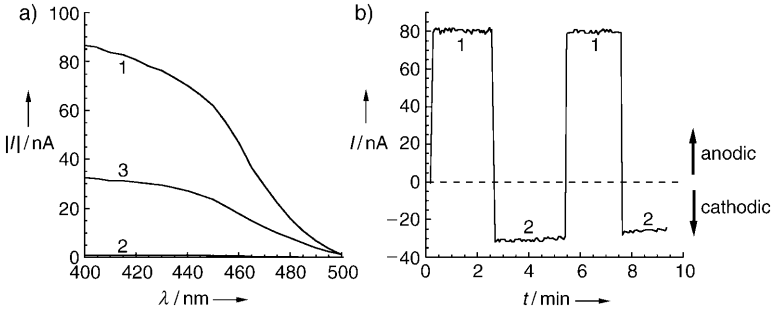


Figure 2. a) Photocurrent action spectra recorded on the electrode functionalized with CdS nanoparticles: 1) Anodic photocurrents generated when the magnetic nanoparticles are retracted from the surface; 2) cathodic photocurrents generated when the magnetic nanoparticles are attracted to the surface from the toluene phase containing cumene hydroperoxide (**3**; 2 mM); 3) no photocurrent is observed when the magnetic nanoparticles are attracted to the surface in the absence of associated **3**. b) Switchable photocurrents generated in the system upon 1) retraction from the electrode and 2) attraction to the electrode of the magnetic nanoparticles associated with **3**. The data were recorded in solutions of phosphate buffer (0.1 M, pH 7.0) containing TEOA (20 mM) and upon application of a potential of 0 V (vs. SCE).

 © 2005 Wiley-VCH Verlag GmbH & Co. KGaA, Weinheim

Experimental Section

Microperoxidase-11 (**1**), glucose oxidase (GOx, EC 1.1.3.4; type X-S from *Aspergillus niger*), β-D-glucose, decamethylferrocene (**2**), cumene hydroperoxide (**3**), cystamine (2,2′-diaminodiethyldisulfide), undecanoic acid, triethanolamine (TEOA), 4-(2-hydroxyethyl)piperazine-1-ethanesulfonic acid sodium salt (HEPES), 1-ethyl-3-(3-dimethylaminopropyl)-carbodiimide (EDC), and all other chemicals were purchased from Sigma or Aldrich and used without further purification. CdS nanoparticles coated with a shell composed of 3-mercaptopropionic acid and 3-mercaptoethanesulfonic acid were prepared according to a published procedure.[12] Magnetic nanoparticles of Fe_3O_4 coated with a shell of undecanoic acid were prepared according to a published procedure except that only a single capping layer was generated on the surface of the nanoparticles.[14] Ultrapure water from NANOpure Diamond (Barnstead) was used throughout all the experiments.

A gold-coated (50-nm thick layer) glass plate (Analytical μ-Systems, Germany) was used as a working electrode. Cystamine was self-assembled on the electrode, and the resulting amine-functionalized gold electrode was treated with microperoxidase-11 (**1**; 10 mM) in HEPES buffer (0.1M, pH 7.2) in the presence of EDC (1 mM) for 2 h to yield the **1**-functionalized gold electrode.[11] Alternatively, the amine-functionalized gold electrode was treated with carboxylated CdS nanoparticles (1 mg mL^{-1}) in HEPES buffer (0.1M, pH 7.2) in the presence of EDC (1 mM) for 2 h to yield the nanoparticle-functionalized electrode.[12]

Cyclic voltammetry measurements were performed using an electrochemical analyzer (model 6310, EG&G) connected to a personal computer with EG&G 270/250 software). The photoelectrochemical measurements were performed using a homemade system that allows recording of action spectra of photocurrents.[12] The measurements were carried out at ambient temperature (25 ± 2 °C) in a conventional electrochemical cell consisting of a modified Au working electrode (0.3 cm^2 area exposed to the solution) assembled at the bottom of the electrochemical cell, a glassy carbon auxiliary electrode, and a saturated calomel electrode (SCE) connected to the working volume with a Luggin capillary. All potentials are reported with respect to this SCE reference electrode. Phosphate buffer (0.1M, pH 7.0) was used as an aqueous background electrolyte. The magnetic nanoparticles functionalized with undecanoic acid were added to the cell as a solution in toluene (0.5 mL, 1 mg mL^{-1}) to yield an immiscible system of an organic layer (upper) and the aqueous electrolyte solution (lower). Cumene hydroperoxide (**3**; 2×10^{-3} M) or decamethylferrocene (**2**; 2×10^{-3} M) was added to the toluene phase. The functionalized magnetic nanoparticles were attracted to the surface of the Au electrode from the upper organic layer by positioning a 12-mm-diameter magnet (NdFeB/Zn-coated magnet with a remnant magnetization of 10.8 kG) below the bottom electrode. The magnetic nanoparticles were removed from the electrode surface and retransported to the organic phase by positioning the external magnet above the electrochemical cell. A flow of argon through the solution was used to remove oxygen from the electrochemical cell. The cell was placed in a grounded Faraday cage.

Received: March 30, 2005
Published online: July 1, 2005

Keywords: biocatalysis · biphasic systems · magnetic properties · nanostructures · photocurrents

[1] a) *Scientific and Clinical Applications of Magnetic Carriers* (Eds.: U. Häfeli, W. Schütt, J. Teller, M. Zborowski), Plenum, New York, **1997**; b) *Advances in Biomagnetic Separation* (Eds.: M. Uhlén, E. Hornes, O. Olsvik), Eaton, Natick, **1994**; c) Y. H. Zhu, X. L. Yang, P. L. Li, H. Ying, *Prog. Chem.* **2003**, *15*, 512–517; d) A. M. Koch, F. Reynolds, M. F. Kircher, H. P. Merkle, R. Weissleder, L. Josephson, *Bioconjugate Chem.* **2003**, *14*, 1115–1121; e) A. K. Gupta, A. S. G. Curtis, *Biomaterials* **2004**, *25*, 3029–3040; f) D. Wang, J. He, N. Rosenzweig, Z. Rosenzweig, *Nano Lett.* **2004**, *4*, 409–413; g) A. K. Gupta, C. Berry, M. Gupta, A. Curtis, *IEEE Trans. Nanobiosci.* **2003**, *2*, 255–261.

[2] I. Willner, E. Katz, *Angew. Chem.* **2003**, *115*, 4724–4737; *Angew. Chem. Int. Ed.* **2003**, *42*, 4576–4588.

[3] a) R. Hirsch, E. Katz, I. Willner, *J. Am. Chem. Soc.* **2000**, *122*, 12053–1254; b) E. Katz, L. Sheeney-Haj-Ichia, A. F. Bückmann, I. Willner, *Angew. Chem.* **2002**, *114*, 1399–1402; *Angew. Chem. Int. Ed.* **2002**, *41*, 1343–1346; c) E. Katz, L. Sheeney-Haj-Ichia, I. Willner, *Chem. Eur. J.* **2002**, *8*, 4138–4148; d) J. Wang, A. N. Kawde, *Electrochem. Commun.* **2002**, *4*, 349–352.

[4] J. Wang, M. Musamesh, R. Laocharoensuk, *Electrochem. Commun.* **2005**, *7*, 652–656.

[5] E. Katz, I. Willner, *J. Am. Chem. Soc.* **2002**, *124*, 10290–10291.

[6] Y. Weizmann, F. Patolsky, E. Katz, I. Willner, *J. Am. Chem. Soc.* **2003**, *125*, 3452–3454.

[7] F. Patolsky, Y. Weizmann, E. Katz, I. Willner, *Angew. Chem.* **2003**, *115*, 2474–2478; *Angew. Chem. Int. Ed.* **2003**, *42*, 2372–2376.

[8] F. Patolsky, Y. Weizmann, E. Katz, I. Willner, *ChemBioChem* **2004**, *5*, 943–948.

[9] E. Katz, L. Sheeney-Haj-Ichia, B. Basnar, I. Felner, I. Willner, *Langmuir* **2004**, *20*, 9714–9719.

[10] E. Katz, R. Baron, I. Willner, *J. Am. Chem. Soc.* **2005**, *127*, 4060–4070.

[11] a) T. Lötzbeyer, W. Schuhmann, E. Katz, H.-L. Schmidt, *J. Electroanal. Chem.* **1994**, *377*, 291–0294; b) A. N. J. Moore, E. Katz, I. Willner, *J. Electroanal. Chem.* **1996**, *417*, 189–192.

[12] L. Sheeney-Haj-Ichia, S. Pogorelova, Y. Gofer, I. Willner, *Adv. Funct. Mater.* **2004**, *14*, 416–424.

[13] S. Yasutomi, T. Morita, Y. Imanishi, S. Kimura, *Science* **2004**, *304*, 1944–1947.

[14] L. Shen, P. E. Laibinis, T. A. Hatton, *Langmuir* **1999**, *15*, 447–453.

 © 2005 Wiley-VCH Verlag GmbH & Co. KGaA, Weinheim

Nanoparticles

Temperature-Induced Inversion of Nanoparticle-Stabilized Emulsions**

Bernard P. Binks, Ryo Murakami, Steven P. Armes, and Syuji Fujii*

Emulsions are mixtures of immiscible liquids where one liquid is dispersed as micrometer-sized drops in the continuous phase of the other. They occur as end products in a wide range of areas including the food, cosmetic, and pharmaceutical industries. To prevent phase separation, surfactants or proteins are usually added to cover the liquid–liquid interfaces.[1] It has been shown recently that certain solid nanoparticles act as excellent emulsifiers alone[2–5] and novel materials can be made from them.[6,7] Inversion of such emulsions from oil-in-water (o/w) to water-in-oil (w/o) or vice versa can be effected by changes in the oil:water ratio,[8] pH value,[9] or oil type.[10] Herein we describe for the first time temperature-modulated emulsion inversion using sterically stabilized polystyrene latex particles as the sole emulsifier. The steric stabilizer is a diblock copolymer in which one block is thermo-responsive, exhibiting inverse temperature solubility behavior. Thus the particle surface becomes less hydrophilic at higher temperature, causing inversion from o/w to w/o to occur in batch emulsions.

Emulsions stabilized by ionic surfactant invert from w/o to o/w with increasing temperature as a result of the increased dissociation of counterions bound to surfactant head groups, making the surfactant more hydrophilic.[11] In contrast, nonionic surfactant-stabilized emulsions invert the other way around; increasing temperature causes dehydration of head groups, making them more hydrophobic.[11] Inversion with respect to temperature is important industrially and is exploited to prepare fine emulsions of increased stability.[12] Small solid particles act in many ways like surfactant molecules in that they adsorb at fluid–fluid interfaces, allowing stabilization of droplets in emulsions and bubbles in foams.[3] However, it is only recently that their precise role has begun to be elucidated in surfactant-free systems. The wettability of the particles at the oil–water interface is crucial in determining which type of emulsion is formed, with hydrophilic particles preferentially forming o/w emulsions and hydrophobic particles forming w/o emulsions. Although the influence of temperature on the stability of either w/o[13] or o/w[14] emulsions stabilized solely by nanoparticles has been reported, the ability to phase invert such emulsions with temperature has not been demonstrated.

The particulate emulsifier employed in this study was a sterically stabilized polystyrene (PS) latex of 152 nm diameter. The steric stabilizer was a near-monodisperse diblock copolymer, poly[2-(dimethylamino)ethyl methacrylate-*block*-methyl methacrylate], PDMA-*b*-PMMA.[15] The hydrophobic PMMA block is designed to adsorb onto the latex surface and the solvated PDMA block acts as the hydrophilic steric stabilizer. As reported earlier,[16] the cationic charge density of the PDMA block can be adjusted by controlling the solution pH value and this dictates the emulsification performance of these PS latex particles. At 25 °C, batch emulsions containing equal volumes of *n*-hexadecane and 2 wt % aqueous PS latex are o/w at all pH values above 3, and the stability of these emulsions towards coalescence increases progressively on increasing the pH from 3 to 8. It was argued that this effect was due to progressive deprotonation of the PDMA-based stabilizer chains with increasing pH, causing the sterically stabilized PS latex particles to become less hydrophilic and hence better emulsifiers.[16]

In this work, we investigate the effect of temperature on emulsions stabilized by the same particles as above, prepared at pH 8.1, which are completely stable to coalescence at 25 °C. In one series of experiments, an *n*-hexadecane/water (1:1) emulsion stabilized by 2 wt % particles was prepared at room temperature and heated progressively up to 70 °C with gentle shaking. Although the emulsion remained o/w at all temperatures, substantial coalescence occurred at and above 60 °C. In a second series, an emulsion was prepared at each temperature after pre-equilibration of the two phases at that temperature. The difference between the two is that particles are already adsorbed at oil–water interfaces in the first series, whereas they are free to become adsorbed at different temperatures in the second series. Importantly in the second series, phase inversion of the emulsions occurs from o/w at low temperatures to w/o at higher temperatures. This result is shown in Figure 1, which summarizes the emulsion conductivities (κ) and the drop test findings obtained at various temperatures. At temperatures below 52 °C, the conductivities are relatively high ($\kappa_{aq} = 25$, $\kappa_{oil} = 0.1\ \mu S\,cm^{-1}$), the emulsions disperse in water and not in oil and are therefore water continuous. At and above 65 °C, the emulsions exhibit low conductivities, disperse in oil rather than in water, and are therefore oil continuous. At intermediate temperatures indicated by the dotted lines (53–64 °C), emulsions can be either of the two types, which may co-exist.

Optical micrographs of the emulsions of the second series are shown in Figure 2. At 25 °C (Figure 2a) oil drops in an o/w emulsion are discrete and some appear non-spherical. At 55 °C (Figure 2b) in addition to simple emulsions, there is some evidence for multiple emulsions, in this case of water-in-oil-in-water (w/o/w), in which water drops are present within oil globules themselves dispersed in water. The appearance of

[*] Prof. B. P. Binks, Dr. R. Murakami
Surfactant & Colloid Group
Department of Chemistry
University of Hull
Hull HU6 7RX (UK)
Fax: (+44) 1482-466-410
E-mail: b.p.binks@hull.ac.uk
Prof. S. P. Armes, Dr. S. Fujii
Department of Chemistry
Dainton Building, University of Sheffield
Sheffield S3 7HF (UK)

[**] This work was funded by the EPSRC (UK) (GR/S69283 and GR/S69276). S.P.A. is the recipient of a Royal Society/Wolfson Research Merit award. We thank Dr. J. I. Amalvy for the synthesis of the sterically-stabilized polystyrene latex used in this study.

 DOI: 10.1002/anie.200501073 © 2005 Wiley-VCH Verlag GmbH & Co. KGaA, Weinheim

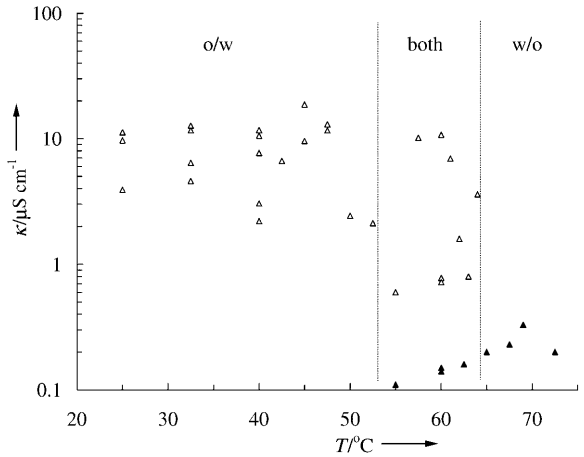


Figure 1. Conductivity κ of batch emulsions (second series, see text for details) comprising equal volumes of *n*-hexadecane and 2 wt% aqueous PDMA-*b*-PMMA-stabilized PS latex (152 nm diameter, pH 8.1) as a function of temperature. Emulsions are only o/w (△) to the left of the first dotted line and only w/o (▲) to the right of the second dotted line, but can be either type or multiple at intermediate temperatures. The labels for emulsion type are based on drop test results.

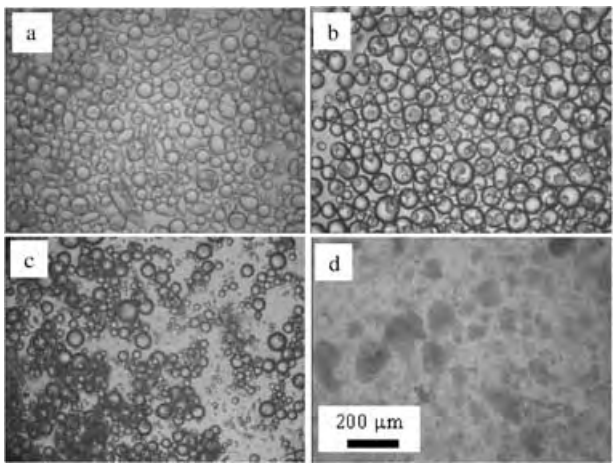


Figure 2. Optical micrographs of emulsions prepared as in Figure 1 at a) 25 (o/w), b) 55 (w/o/w), and c) 65 °C (w/o). Also shown is micrograph of the 2 wt% aqueous PS latex (pH 8.1) held at 70 °C for 30 min on a glass slide (d). The scale bar refers to all images.

multiple emulsions around conditions of phase inversion in surfactant-stabilized systems is common; the balanced surfactant satisfies the preference for both types of emulsion simultaneously.[12] Such emulsions are notoriously unstable to coalescence (of both drops and globules), whereas these solid-particle-stabilized emulsions are stable. The stabilization of multiple emulsions by only one type of particle has been reported for silica.[17] At 65 °C, water drops in a w/o emulsion are characteristically flocculated (Figure 2c), since any repulsion between particle surfaces on neighboring drops is mediated through the oil phase, which has a low dielectric constant, and little steric stabilization is provided by the PDMA chains in this oil.

A measure of the average diameter of drops in both types of emulsion is plotted against temperature in Figure 3. For

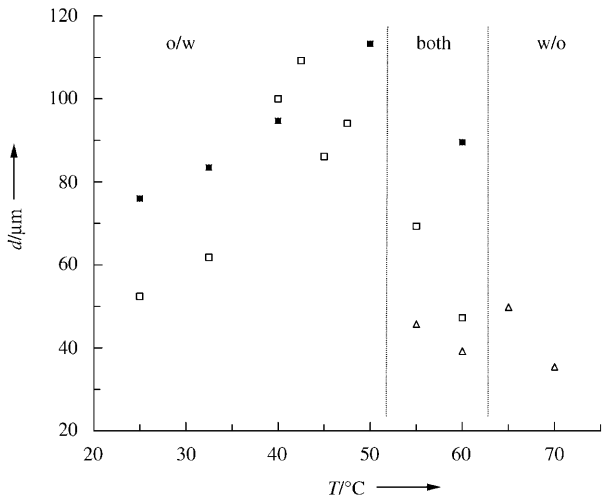


Figure 3. Average drop diameter *d* versus temperature for batch emulsions prepared as in Figure 1 immediately after preparation. Sizes determined by optical microscopy (□ o/w, △ w/o) and using light diffraction (■ o/w) are shown.

o/w emulsions, the number-average mean determined by optical microscopy (40 drops) is shown, as is the median diameter measured using light diffraction. For w/o emulsions, only the mean by microscopy has been determined. The average oil-drop size increases with temperature on approaching inversion and the size of water drops is less than that of oil drops. Assuming that particles form a hexagonally close-packed monolayer around oil drops, we calculate that at 25 °C approximately 35 % of the particles originally in water become adsorbed around drops of average diameter 76 μm. This number falls to 24 % for the larger drops of 113 μm at 50 °C. On this basis, there is thus a distribution of particles between interface and bulk, although no exchange is likely because of the high energies of particle attachment to interfaces.[3]

The stabilities of these latex-stabilized emulsions six months after preparation are summarized in Figure 4. The parameters *f*(oil) (and *f*(water)) are defined as the volumes of oil (or water) resolved relative to the initial volumes of oil (or water). At temperatures prior to inversion, the oil drops in o/w emulsions cream within 1–2 h at all temperatures with no further change subsequently. The oil volume fraction in the cream is now increased beyond 0.5 and, apart from the stable emulsion at 25 °C, a low degree of coalescence occurs in emulsions approaching 50 °C. At intermediate temperatures (between the dotted lines), the creaming of o/w emulsions is reduced and w/o emulsions sediment but are stable to coalescence. At temperatures above inversion, sedimentation of water drops occurs gradually in the first 24 h followed by their coalescence. Eventually, virtually complete phase separation ensues as indicated by near unity values of both *f*(oil) and *f*(water).

We seek to understand the origin of emulsion phase inversion with temperature, which occurs in the same sense as that for non-ionic surfactants. Some clues to this can be found in the behavior of the aqueous PS latex particle dispersions in the absence of oil. Dynamic light-scattering studies indicate

 © 2005 Wiley-VCH Verlag GmbH & Co. KGaA, Weinheim

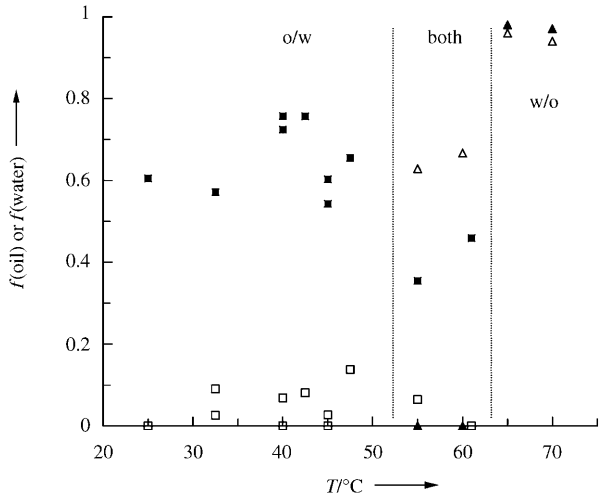


Figure 4. Stability of batch emulsions after six months at different temperatures. For o/w, f(water) (■) relates to creaming and f(oil) (□) relates to coalescence. For w/o, f(oil) (△) relates to sedimentation and f(water) (▲) relates to coalescence.

that the mean hydrodynamic diameter remains constant at 152 nm between 20 and 50 °C and increases to 173 nm at 53 °C, above which significant flocculation is apparent. Optical microscopy investigations of a drop of dispersion on a glass slide shows no features above 1 μm up to 50 °C but particle aggregates of increasing size above this critical temperature (Figure 2d). Since PDMA homopolymer in water at pH 8.1 exhibits a lower consolute solution temperature between 32 and 46 °C (depending on its mean degree of polymerization),[18] it is likely that the temperature-induced flocculation of the latex particles reflects the thermo-responsive character of the PDMA block in the stabilizer chains. This hypothesis was verified by performing contact-angle measurements of water drops under *n*-hexadecane on spin-coated films of PDMA homopolymer at different temperatures. As shown in Table 1, the contact-angle measured through water increases with temperature from near-wetting (hydrophilic) at 25 °C to values that are characteristic of hydrophobic surfaces above 60 °C. They are also in line with the predicted change in the wettability of the particles in emulsions, from predominantly hydrophilic at low temperatures (o/w) to more hydrophobic at high temperatures (w/o).

Table 1: Effect of temperature on the contact angle θ of a water drop.[a]

T [°C]	θ (w/o) [°]	θ (o/w) [°]
25	4	3
35	6	6
45	11	12
55	28	28
60	34	32
65	33	30
75	58 ± 10	65 ± 10

[a] At pH 8.1 under *n*-hexadecane, measured through water, on a glass slide coated with a film of PDMA homopolymer. Data given for water (w/o) or oil (o/w) contacting the substrate first.

Two competing effects caused by increasing temperature may cause this change. The first is the disruption of hydrogen bonds surrounding the PDMA chains, leading to an increase in their hydrophobicity. The second is an increase in the degree of protonation of tertiary amine groups resulting in increased particle hydrophilicity. For trimethylamine in water, this has been measured as an increase in K_b (equilibrium constant) with temperature, taking into account the increase in the dissociation constant of pure water.[19] It is therefore clear that for these sterically stabilized PS latex particles, the dominant influence of temperature is in reducing the degree of hydration of the PDMA chains to such an extent that these particles become preferentially wetted by oil.

Nanoparticles are effective emulsifiers of oil and water. Appropriate design of the latex surface allows the particle wettability to be controlled by adjusting the temperature, which in turn allows the preparation of either o/w or w/o emulsions. The emulsions described herein are temperature-dependent but not temperature-responsive. Manipulating the behavior of particles adsorbed at fluid interfaces in this way augurs well for the development of a novel range of simple and multiple emulsions for use in cosmetic, food, and drug and formulations.

Experimental Section

The synthesis and characterization of the PDMA-*b*-PMMA-stabilized PS particles (diameter = 152 nm, M_n = 38400 g mol^{-1}, M_w/M_n = 1.14) was described earlier.[15,16b] Dynamic light scattering of 2 wt% aqueous PS latex at pH 8.1 was measured using a Malvern Nano ZS ZEN3600 instrument under a N_2 atmosphere at a scattering angle of 173°. Three measurements were made at each temperature, with 30 min being allowed for equilibration. Batch emulsions of equal volumes (2 mL) of *n*-hexadecane and aqueous PS latex (pH 8.1), equilibrated at the appropriate temperature, were prepared at that temperature using an Ultra Turrax T25 homogenizer (1 cm head) operating at 11000 rpm for 2 min. Emulsion type was determined by conductivity measurements and the drop test. Their stabilities at different temperatures were measured by monitoring the movement of the oil–emulsion and water–emulsion interfaces. Drop size distributions of o/w emulsions were measured using a Malvern MasterSizer 2000 instrument using either cold or hot water as diluting phase. For microscopy, a dilute sample of emulsion/dispersion was placed in a haemocytometer cell (Weber Scientific) and viewed with a Nikon Labophot microscope fitted with a DIC-U camera (World Precision Instruments). Images were processed using Adobe Photoshop 5.0 software. The contact angles of water drops (10 μL, pH 8.1) under *n*-hexadecane on films of PDMA homopolymer (M_n = 21300 g mol^{-1}) spin-coated onto glass slides from a 5 wt% solution in methanol (Speciality Coating Systems model P6700, 2000 rpm for 1 min) were determined using a Krüss DSA10 apparatus with a thermostatted cell. At least five separate drops were used at each temperature.

Received: March 24, 2005
Published online: June 29, 2005

Keywords: emulsions · inversion · latex · nanoparticles · wettability

 © 2005 Wiley-VCH Verlag GmbH & Co. KGaA, Weinheim

[1] *Modern Aspects of Emulsion Science* (Ed.: B. P. Binks, The Royal Society of Chemistry, Cambridge, **1998**.
[2] N. X. Yan, M. R. Gray, J. H. Masliyah, *Colloids Surf. A* **2001**, *193*, 97 – 107.
[3] B. P. Binks, *Curr. Opin. Colloid Interface Sci.* **2002**, *7*, 21 – 41.
[4] E. Vignati, R. Piazza, T. P. Lockhart, *Langmuir* **2003**, *19*, 6650 – 6656.
[5] S. Stiller, H. Gers-Barlag, M. Lergenmueller, F. Pflücker, J. Schulz, K. P. Wittern, R. Daniels, *Colloids Surf. A* **2004**, *232*, 261 – 267.
[6] A. D. Dinsmore, M. F. Hsu, M. G. Nikolaides, M. Marquez, A. R. Bausch, D. A. Weitz, *Science* **2002**, *298*, 1006 – 1009.
[7] P. F. Noble, O. J. Cayre, R. G. Alargova, O. D. Velev, V. N. Paunov, *J. Am. Chem. Soc.* **2004**, *126*, 8092 – 8093.
[8] B. P. Binks, S. O. Lumsdon, *Langmuir* **2000**, *16*, 2539 – 2547.
[9] B. P. Binks, J. A. Rodrigues, *Angew. Chem.* **2005**, *117*, 445 – 448; *Angew. Chem. Int. Ed.* **2005**, *44*, 441 – 444.
[10] B. P. Binks, S. O. Lumsdon, *Phys. Chem. Chem. Phys.* **2000**, *2*, 2959 – 2967.
[11] See Chapter 7 by A. S. Kabalnov in ref. [1].
[12] K. Shinoda, H. Saito, *J. Colloid Interface Sci.* **1969**, *30*, 258 – 266.
[13] B. P. Binks, C. P. Whitby, *Colloids Surf. A* **2003**, *224*, 241 – 249.
[14] T. Ngai, S. H. Behrens, H. Auweter, *Chem. Commun.* **2005**, 331 – 333.
[15] F. L. Baines, S. Dionisio, N. C. Billingham, S. P. Armes, *Macromolecules* **1996**, *29*, 3096 – 3102.
[16] a) J. I. Amalvy, S. P. Armes, B. P. Binks, J. A. Rodrigues, G.-F. Unali, *Chem. Commun.* **2003**, 1826 – 1827; b) J. I. Amalvy, G.-F. Unali, Y. T. Li, S. Granger-Bevan, S. P. Armes, B. P. Binks, J. A. Rodrigues, C. P. Whitby, *Langmuir* **2004**, *20*, 4345 – 4354.
[17] B. P. Binks, J. A. Rodrigues, *Langmuir* **2003**, *19*, 4905 – 4912.
[18] V. Bütün, S. P. Armes, N. C. Billingham, *Polymer* **2001**, *42*, 5993 – 6008.
[19] D. H. Everett, W. F. K. Wynne-Jones, *Proc. R. Soc. London Ser. A* **1941**, *177*, 499 – 516.

 © 2005 Wiley-VCH Verlag GmbH & Co. KGaA, Weinheim

Prussian blue derivatives

The Co Ligand Field: A Key Parameter in Photomagnetic CoFe Prussian Blue Derivatives**

*Virginie Escax, Guillaume Champion, Marie-Anne Arrio, Michele Zacchigna, Christophe Cartier dit Moulin, and Anne Bleuzen**

Various interesting electrochemical,[1] magnetic,[2] or photomagnetic[3] properties have been revealed in Prussian blue and its analogues. In the face-centered-cubic structure of the CoFe Prussian blue analogues of chemical formula $C_xCo_4[Fe(CN)_6]_{(8+x)/3}\square_{(4-x)/3}\cdot n H_2O$, where C^+ is an alkali-metal cation and $\square$ represents the intrinsic $[Fe(CN)_6]$ vacancies, both of which are randomly distributed throughout the solid,[4] the Wyckoff positions 4a (0,0,0) are occupied by Fe ions or $\square$ and the 4b positions (1/2,1/2,1/2) are occupied by Co ions.[5] The alkali-metal cations are distributed over the tetrahedral sites.[5] Such compounds may display unusual photomagnetic effects due to a light-induced Co^{III}(low spin, $S=0$)–Fe^{II}(S=0)→(Co^{II}(high spin, $S=3/2$)–Fe^{III}(S=1/2))* electron transfer accompanied by a spin change of Co and a lengthening of the Co–ligand bonds from 1.91 Å for Co^{III}(LS) to 2.08 Å for Co^{II}(HS).[3,6,7]

It has been proposed that the stabilization of the Co^{III}(LS)–Fe^{II} switchable pairs is correlated with the average number of cyanide ligands in the Co coordination sphere. The average chemical composition of the Co coordination polyhedron is given by $Co(NC)_{(8+x)/2}(OH_2)_{(4-x)/2}$. When x increases,

[*] Dr. V. Escax, Dr. G. Champion, Dr. M.-A. Arrio, Prof. Dr. A. Bleuzen[+]
Laboratoire de Chimie Inorganique et Matériaux Moléculaires
UMR CNRS 7071, Université Pierre et Marie Curie
Bât. F, 4, place Jussieu, 75252 Paris Cedex 05 (France)
E-mail: annebleuzen@icmo.u-psud.fr

Dr. G. Champion, Dr. C. Cartier dit Moulin
Laboratoire pour l'Utilisation du Rayonnement Electromagnétique,
UMR CNRS 130-CEA-MENRS
Bât. 209d, Université Paris Sud
BP34, 91898 Orsay Cedex (France)

Dr. M.-A. Arrio
Laboratoire de Minéralogie Cristallographie
UMR CNRS 7590-IPGP, Universités Paris 6 et 7
4, place Jussieu, 75252 Paris Cedex 05 (France)

Dr. M. Zacchigna
Laboratorio TASC, INFM
Universita catholica
via Trieste 17, 25121 Brescia (Italy)

[+] Present address:
Laboratoire de Chimie Inorganique
UMR CNRS 8613, Université Paris Sud
91405 Orsay Cedex (France)
Fax: (+33) 169-154-754

[**] This research was supported by the European Community (grant no. ERBFMRXCT980181), the contract TMR/TOSS (FMRX-CT98-0199), and the CNRS (Programme Materiaux). We acknowledge Michel Verdaguer for fruitful discussions.

Supporting information for this article is available on the WWW under http://www.angewandte.org or from the author.

 © 2005 Wiley-VCH Verlag GmbH & Co. KGaA, Weinheim DOI: 10.1002/anie.200500647

weak-field H_2O ligands are replaced by stronger ones (CN^-) in the Co coordination sphere. An increase of the number of cyanide ligands in the Co coordination sphere should then lead to an increase of the Co ligand field and of the reducing power of Co, and therefore stabilize the Co^{III}(LS)–Fe^{II} photoactive diamagnetic pairs.[4,8,9] As the $[Fe(CN)_6]$ entity is stable and rigid,[10–12] the Co ligand field appears to be a key parameter for understanding the switchable properties of CoFe Prussian blue analogues.

Since a quantitative UV-vis spectroscopic investigation is impossible due to the existence of large charge-transfer bands in the visible range (the compounds are all dark violet or dark brown),[9] we used X-ray absorption spectroscopy (XAS) to determine the Co crystal-field parameter ($10\,Dq$) in two well-crystallized compounds for which the Co coordination sphere is expected to be different. For $Co^{II}_4[Fe^{III}(CN)_6]_{2.7}\square_{1.3}\cdot 18\,H_2O$[6] (**1**) and for $Rb_{1.8}Co^{III}_{3.3}Co^{II}_{0.7}[Fe^{II}(CN)_6]_{3.3}\square_{0.7}\cdot 13\,H_2O$[6] (**2**), which has photomagnetic properties, the average Co coordination spheres and cell parameters are $Co(NC)_4(OH_2)_2$ ((10.32 ± 0.05) Å) and $Co(NC)_5(OH_2)$ ((9.96 ± 0.05) Å), respectively.[12] This study allowed us to measure unexpected $10\,Dq$ values and to propose a structural model that explains the Co crystal-field parameter and the oxidation- and spin-states of Co in these compounds.

The L_3 edge can be used to directly probe the 3d levels of the metallic ion ($2p^63d^n \rightarrow 2p^53d^{n+1}$ transitions) as it is sensitive to the crystal-field parameter. X-ray absorption spectra of **1** and **2** were therefore recorded at the Co L_3 edge and compared to the spectrum of $[Co^{II}(OH_2)_6](NO_3)_2$ (Figure 1).

Peaks A to D are the signature of Co^{II}(HS) in an octahedrally symmetric environment,[7,13] and peaks E to G, at higher energy, the signature of Co^{III}(LS) also for octahedral symmetry.[7] Given the spectral shapes of compounds **1** and **2**, any Co coordination number other than six can be excluded.[14]

Simulation of the spectra using the ligand-field multiplet model[13,15] reproduces very well the experimental data

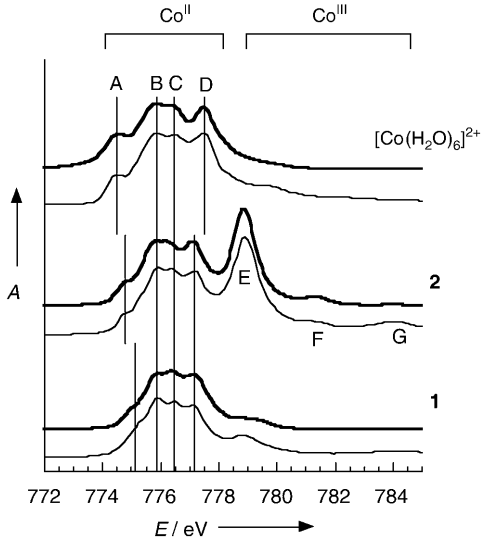


Figure 1. Experimental Co L_3-edge spectra (——) and best simulations (——) obtained from the ligand-field multiplet model for $[Co^{II}(OH_2)_6](NO_3)_2$, **1**, and **2**.

(Figure 1). The Co^{II} signature is different from one spectrum to the other. These differences in the energy positions of the multiplet features are significant. Multiplet calculations show that an increase of the energy gap between the peaks A and D of Co^{II} species corresponds to an increase of $10\,Dq(Co^{II})$.[14] Attempts to reproduce any of the Co^{II} experimental contributions with more than one $10\,Dq(Co^{II})$ value, that is, different Co environments, failed. This surprisingly shows that $10\,Dq$(Co) is the same (within the experimental error) for all Co^{II} atoms in a single compound. In the same way, $10\,Dq(Co^{III})$ is, within the experimental error, the same for all Co^{III} atoms in **2**.

To characterize the influence of the ligands on $10\,Dq$, the model developed by Jorgensen[16] to formulate the spectrochemical series for octahedral complexes was used. In this model, the crystal-field parameter is treated as the product of two independent factors f and g ($10\,Dq = fg$), where f describes the strength of a ligand relative to water, which is assigned a value of 1, and g is characteristic of the metal ion. The $10\,Dq$ values given by multiplet calculations, and the corresponding f values, are gathered in Table 1.

Table 1: $10\,Dq$ parameters, obtained by multiplet calculations, and the corresponding f values.

	$10\,Dq$ [eV]	f
Co^{II} in $[Co(OH_2)_6]^{2+}$	1	1
Co^{II} in **1**	0.55	0.55
Co^{II} in **2**	0.7	0.7
Co^{III} in **2**	2.4	1.2[a]

[a] This value was calculated from the ratio $g(Co^{III})/g(Co^{II}) = (18\,600/9300) = 2$.[17]

The $10\,Dq$ values of Co^{II} in $[Co(OH_2)_6](NO_3)_2$ and of Co^{III} in **2** are in the expected spectral range for Co^{II}(HS) and Co^{III}(LS) molecular species, respectively.[18] The f factor corresponding to the environment of Co^{III} in **2** is the expected one for a metal ion surrounded by an average of five CN^- and one H_2O ligands, in the range of the f factors of most N-ligating ligands (NH_3 ($f = 1.25$), $NH_2CH_2CH_2NH_2$ (1.28), CH_3CN (1.22)).[17]

Surprisingly, the f factors corresponding to the environment of Co^{II} in **1** and **2** are, to the best of our knowledge, much weaker than any f value reported for octahedral Co^{II}(HS) molecular coordination compounds ($f = 0.7$ for the weak-field bromide ion and almost always > 1 for N-ligating ligands[17]). Such weak crystal fields, which have never been found in molecular compounds, are probably associated with three-dimensional network strains. The replacement of H_2O in the Co^{II} coordination sphere by CN^- does not strengthen the Co crystal field and does not explain the stabilization of the Co^{III}–Fe^{II} photoactive pairs in CoFe Prussian blue analogues. The stabilization of the Co^{II}(HS)–Fe^{III} or of the Co^{III}(LS)–Fe^{II} state is not simply due to a local chemical effect but to a cooperative structural one associated with the three-dimensional character of the compounds.

To explain these values, we have proposed a hypothesis based on structural considerations. In a molecular compound without steric hindrance, linear most-stable Co^{II}–NC bonds

 © 2005 Wiley-VCH Verlag GmbH & Co. KGaA, Weinheim

are expected with an f value close to 1.2.[17] In **1**, we propose that the geometry of the Co^{II}–NC–Fe entities deviates from the linear one: as a consequence of 3D network strains they are bent,[10] as shown for the (100) plane of one unit cell of **1** in Figure 2a. This bending leads to a weaker orbital interaction

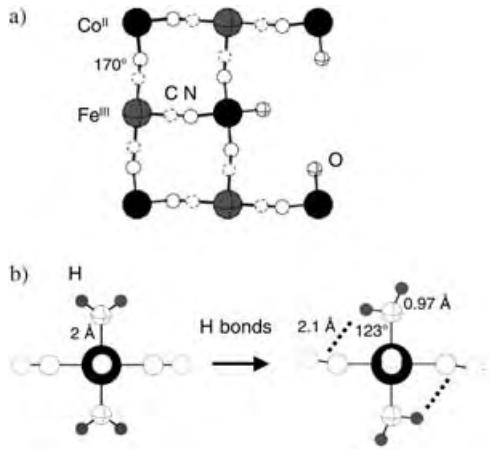


Figure 2. Proposed scheme for the (100) plane of one unit cell (a) and the Co^{II} coordination polyhedron with sensible structural parameters (b) for compound **1**.

between Co and CN^- and a weaker ligand field than for a linear geometry. The geometry of the Co–OH_2 entities also deviates from the most stable one,[19] leading again to a decrease of the ligand field exerted by H_2O. These deviations can be explained by the formation of hydrogen bonds between H_2O bonded to Co and the electronic density on the CN^- ligand, as shown, with sensible structural parameters,[20] in Figure 2b. As a consequence of these interactions, the H_2O ligands rotate around the O position so that the orbital interaction between Co and H_2O is also weakened. Such interactions may also explain the bending of the Co–NC–Fe entities in **1**. A bent Co-N-C geometry, probably stabilized by an H bond, stabilizes the Co^{II}(HS) state in **1**.

Complex **2** contains a majority of Co^{III}(LS), with an $f(Co^{III})$ value corresponding to linear Co^{III}–NC–Fe entities.[10] These globally impose the short cell parameters and the structure of the compound. The relatively high X-ray crystallinity of a sample containing a mixture of Co^{III}(LS) and Co^{II}(HS), which have very different Co-to-ligand bond lengths,[6] implies that the remaining 20% of the Co^{II}(HS) ions are situated in particular positions and fit into the structure as proposed in Figure 3. They are close to the $[Fe(CN)_6]$ vacancies (□), and are displaced slightly from the crystallographic site toward the vacancy. Along the Co^{II}–□ fourfold axis, the Co–NC entity prefers the most stable geometry due to the presence of the vacancy on the opposite site of this Co–NC bond. In the equatorial plane, the four Co–NC entities are bent (due to network strains), with an angle fixed by the Co^{II}–N bond lengths along the fourfold axis. The $f(Co^{II})$ value in **2** (0.73), which is close to the experimental value (0.7), can be estimated by assuming an average f value for bent Co–NC entities deduced from **1** (0.55), an approximate f value for linear Co–NC entities deduced from **2** (1.2),

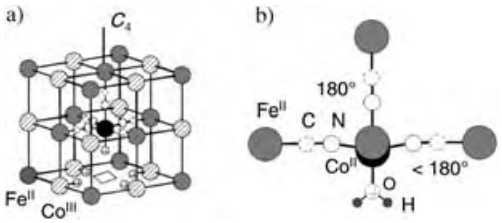


Figure 3. Co^{II} coordination polyhedron in a) a conventional unit cell, in which the alkali-metal cations have been omitted for clarity, and b) extracted from the unit cell of compound **2**.

and the f value for the Co–OH_2 entity in the most stable geometry (1).[21]

In **2**, 80% of the Co ions are low-spin with an oxidation state of +3. These oxidation- and spin-states of Co are probably due to the linearity of the Co–NC–Fe entities associated with a stronger orbital interaction between Co and CN^- and a stronger Co ligand field. We can propose three ways to explain this linear geometry: 1) the stoichiometry (x) implies a reduced amount of H_2O in the Co coordination sphere, which means that it is no longer able to form enough hydrogen bonds to impose the bent Co–NC geometry; 2) Rb in the tetrahedral sites interacts with the CN bridges,[10] and this interaction imposes the linear geometry; 3) the interactions between Rb and the CN bridges reduce the number of CN bridges available to form hydrogen bonds with Co-linked water molecules.

This is the first experimental determination of Co crystal-field parameters in photomagnetic CoFe Prussian blue analogues by XAS. We have shown that, contrary to expectation, the Co^{II} crystal-field parameter is, to the best of our knowledge, smaller than for any other octahedral Co^{II}(HS) molecular entities.[18] The $10Dq$ value is essentially determined by the geometry of the Co coordination polyhedron, which is imposed by weak and strong cooperative interactions within the three-dimensional structure rather than by the chemical nature of the ligands.

It is noticeable that the Co crystal-field parameter values are all far from HS–LS frontier values. In the switch from one state to the other, the Co spin-state change is therefore probably not the driving effect. Work is in progress to determine $10Dq$(Co) in the photo-induced metastable state of **2**.

Experimental Section

The syntheses of compounds **1** and **2** have been described elsewhere.[6]

The Co L_3-edge spectra were collected at the Beamline for Advanced diCHroism (BACH)[22] at the ELETTRA Synchrotron Radiation Source in Trieste, Italy.

XAS data parameters of the calculated spectra, a brief description of the simulation method, and determination of the f parameters are available as Supporting Information.

Received: February 21, 2005
Revised: April 22, 2005
Published online: June 29, 2005

Keywords: crystal-field parameters · electron transfer · prussian blue analogues · spin crossover · X-ray absorption spectroscopy

 © 2005 Wiley-VCH Verlag GmbH & Co. KGaA, Weinheim

[1] a) K. Honda, J. Ochiachi, H. Hayashi, *J. Chem. Soc. Chem. Commun.* **1986**, 168; b) D. R. Rosseinsky, H. Lim, X. Zhang, H. Jiang, J. W. Chai, *Chem. Commun.* **2002**, 2988 – 2989.

[2] a) T. Mallah, S. Thiébault, M. Verdaguer, P. Veillet, *Science* **1993**, *262*, 1554 – 1557; b) S. Ferlay, T. Mallah, R. Ouhaès, P. Veillet, M. Verdaguer, *Nature* **1995**, *378*, 701; c) S. M. Holmes, G. S. Girolami, *J. Am. Chem. Soc.* **1999**, *121*, 5593 – 5594; d) N. Shimamoto, O. Ohkoshi, O. Sato, K. Hashimoto, *Inorg. Chem.* **2002**, *41*, 678 – 684.

[3] O. Sato, T. Iyoda, A. Fujishima, K. Hashimoto, *Science* **1996**, *272*, 704 – 705.

[4] V. Escax, A. Bleuzen, C. Cartier dit Moulin, F. Villain, A. Goujon, F. Varret, M. Verdaguer, *J. Am. Chem. Soc.* **2001**, *123*, 12536 – 12543.

[5] A. Lüdi, H. U. Güdel, *Structure and Bonding*, Springer, Berlin, **1973**, pp. 1 – 21.

[6] A. Bleuzen, C. Lomenech, V. Escax, F. Villain, F. Varret, C. Cartier dit Moulin, M. Verdaguer, *J. Am. Chem. Soc.* **2000**, *122*, 6648 – 6652.

[7] C. Cartier dit Moulin, F. Villain, A. Bleuzen, M.-A. Arrio, P. Sainctavit, C. Lomenech, V. Escax, F. Baudelet, E. Dartyge, J. J. Gallet, M. Verdaguer, *J. Am. Chem. Soc.* **2000**, *122*, 6653 – 6658.

[8] M. Verdaguer, *Science* **1996**, *272*, 698 – 699.

[9] O. Sato, Y. Einaga, A. Fujishima, K. Hashimoto, *Inorg. Chem.* **1999**, *38*, 4405 – 4412.

[10] A. Bleuzen, V. Escax, A. Ferrier, F. Villain, M. Verdaguer, P. Münsch, J.-P. Itié, *Angew. Chem.* **2004**, *116*, 3814 – 3817; *Angew. Chem. Int. Ed.* **2004**, *43*, 3728 – 3731.

[11] T. Yokoyama, T. Ohta, O. Sato, K. Hashimoto, *Phys. Rev. B: Condens. Matter* **1998**, *58*, 8257 – 8266.

[12] V. Escax, A. Bleuzen, J. P. Itié, P. Münsch, F. Varret, M. Verdaguer, *J. Phys. Chem. B* **2003**, *107*, 4763 – 4767.

[13] M. A. Arrio, P. Sainctavit, C. Cartier dit Moulin, T. Mallah, M. Verdaguer, E. Pellegrin, C. T. Chen, *J. Am. Chem. Soc.* **1996**, *118*, 6422 – 6427.

[14] G. van der Laan, I. W. Kirkman, *J. Phys.: Condens. Matter* **1992**, *4*, 4189 – 4204.

[15] a) R. Cowan, *The Theory of Atomic Structure and Spectra*, University of California Press, Berkeley, **1981**; b) P. Butler, *Point Group Symmetry—Methods and Tables*, Plenum Press, New York, **1981**.

[16] C. K. Jorgensen, *Modern Aspects of Ligand Field Theory*, North-Holland, Amsterdam, **1971**.

[17] I. B. Bersuker, *Electronic Structure and Properties of Transition Metal Compounds*, Wiley, New York, **1996**, p. 354.

[18] A. Lever, *Inorganic Electronic Spectroscopy*, 2nd ed., Elsevier, Amsterdam, **1984**.

[19] If only the geometry of the Co–NC entities were responsible for the small $10Dq(Co^{II})$ values in **1** and **2**, with the Co–OH_2 bonds being similar to those in $[Co^{II}(OH_2)_6]^{2+}$, one would expect a smaller $10Dq(Co^{II})$ for **2** than for **1**, firstly because the number of CN^- ligands involved in bent Co–NC entities in the Co coordination sphere would be higher in **2** than in **1** (due to the stoichiometry), and secondly because the cell parameters, which are smaller in **2** than in **1**, imply a shorter Co^{II}–Fe distance (fixed by the Co^{III}–Fe distance) in **2** and therefore a narrower Co-N-C angle and weaker orbital interaction between Co and NC. However, the reverse is observed experimentally. The geometry of the Co–NC entities is therefore probably not the only effect responsible for the small $10Dq(Co^{II})$ values.

[20] I. D. Brown, *Acta Crystallogr. Sect. A* **1976**, *32*, 24.

[21] $f = 1/6 + 4 \times 0.55/6 + 1.2/6 = 0.73$.

[22] M. Zangrando, M. Finazzi, G. Paolucci, G. Comelli, B. Diviacco, R. P. Walker, D. Cocco, F. Parmigiani, *Rev. Sci. Instrum.* **2001**, *72*, 1313 – 1316.

 © 2005 Wiley-VCH Verlag GmbH & Co. KGaA, Weinheim

Protein Folding

Circular Dichroism Spectroscopy of Folding in a Protein Monolayer**

*Neil Keegan, Nicholas G. Wright, and Jeremy H. Lakey**

DNA arrays on surfaces have caused a revolution in nucleic acid analysis, and a similar revolution is required for proteins if high-throughput screening of their functions is to be realized.[1,2] In addition, proteins can also form the basis of self-assembling nanostructures.[3,4] One important obstacle is the assembly of functional protein monolayers on useful surfaces. Unlike DNA, proteins must retain an intricate three-dimensional structure to function, and measurement of these conformations under changing solution conditions is difficult in monomolecular films. However, our increasing awareness of natively unfolded proteins, which adopt defined conformations only upon interaction with ligands or receptors, means that structural change is also an important readout for protein–protein and protein–DNA interactions.[5] Finally, measurement of changes in protein secondary structure that lead to insoluble protein aggregates is crucial to the study and identification of conditions such as Alzheimer's disease and Creutzfeldt–Jacob disease (CJD).[6]

Fourier-transform infrared spectroscopy in either attenuated total internal reflection or grazing incidence modes is very useful for measuring protein structure in monolayers,[3,7] but its use is limited by its sensitivity to bulk water. Fluorescence spectroscopy is a sensitive but not a generic assay for protein folding, as it relies upon the presence of aromatic amino acids in suitable positions. Circular dichroism (CD) spectroscopy in the ultraviolet range ($\lambda = 180$–250 nm) measures the conformation of the core peptide backbone and is insensitive to the presence of bulk water.[8] The characteristic spectra for helix, sheet, or random structures, which arise from the π–π^* and n–π transitions, make this the spectroscopic method of choice for protein scientists who wish to monitor folding, stability, and conformational change.[9] Small sample size, accessible concentrations, and relatively inexpensive instrumentation mean that CD spectroscopy is the

[*] N. Keegan, Prof. J. H. Lakey
Institute of Cell and Molecular Biosciences and
Institute for Nanoscale Science and Technology
University of Newcastle upon Tyne
Newcastle NE2 4HH (UK)
Fax: (+44) 191-222-7424
E-mail: j.h.lakey@ncl.ac.uk
Prof. N. G. Wright
School of Electrical, Electronic, & Computer Engineering and
Institute for Nanoscale Science and Technology
University of Newcastle upon Tyne
Newcastle NE1 7RU (UK)

[**] This work was supported by the Medical Research Council, the Biological and Biotechnological Research Council, and the Wellcome Trust.

Supporting information for this article is available on the WWW under http://www.angewandte.org or from the author.

 DOI: 10.1002/anie.200462977 © 2005 Wiley-VCH Verlag GmbH & Co. KGaA, Weinheim

most commonly used noncrystallographic method for protein structure characterization. It is also the only method that can measure the changing structure of proteins exposed to different aqueous bulk solutions. In the past, sensitivity has been a problem, but modern spectrometers easily resolve signals as small as $10^{-5}\,\Delta A$ (0.3 mdeg), and synchrotron sources now allow us to access data at wavelengths shorter than 180 nm.[10] Recently, CD spectra have been collected for proteins on gold films using extended acquisition times (10^3 scans).[11] With this in mind we investigated the practical limits for CD spectroscopy on a single protein monolayer, and we found that high-quality data can be collected with reasonable acquisition times on an unmodified commercial spectrometer.

The C-terminal, pore-forming (P) domains of colicins have been extensively studied by CD spectroscopy,[12,13] and we chose the 22.4-kDa colicin N P-domain (ColN-P) to test the sensitivity of CD to a protein monolayer. It is helix rich with a globin fold found in many protein families.[14] The exposed alanine residue at position 351 was replaced by a single cysteine (A351C) moiety by site-directed mutagenesis (Figure 1). The mutant protein ColN-P-Cys and the cysteine-free wild-type ColN-P were purified as described[15] and gave the expected helix-rich CD spectrum.



Figure 1. Structure of the pore-forming domain of colicin N (PDB:1A84) showing the position of alanine replacement by cysteine. The shape of the observed CD spectrum (Figure 3A) results from the 60% α-helix content.

If one treates ColN-P as a sphere of 3-nm diameter, a 1-mm^2 area of a *perfectly packed* protein monolayer should contain 1.1×10^{11} protein molecules (2.7 $ng\,mm^{-2}$). In a normal solution experiment using a 0.2-mm-pathlength CD cuvette and a protein concentration of 0.5 $mg\,mL^{-1}$ (2.2×10^{-5} M), an equivalent 1-mm^2 light beam will traverse a volume of 0.2 mm^3 or 0.2 μL containing 4.4×10^{-12} mol of protein or 2.6×10^{12} protein molecules. Thus the densest monolayer will provide a signal about 20-fold smaller than normal.

We created a reproducible protein monolayer by sulfur–gold chemisorption. All experiments were performed in buffer A, which comprised sodium phosphate (50 mM, pH 7.0) and NaCl (300 mM), with additions as specified. The ColN-P-Cys mutant was reduced with β-mercaptoethanol (2-sulfanylethanol, 10 mM), which was subsequently removed by gel filtration (Pharmacia PD-10 column or equivalent). Surface plasmon resonance (SPR; Biacore model X, Biacore Ltd., St. Albans, UK) was used to measure monolayer formation. Bare gold surfaces (Biacore AU-Chip) bound > 2200 resonance units (RU; 2.2 $ng\,mm^{-2}$ [16]) of both ColN-P and ColN-P-Cys proteins (Figure 2A). A wash step with sodium dodecyl sulfate (Buffer A + 0.5% w/v SDS) removed only some of the nonspecifically bound ColN-P from the surface, thus leaving 1200 RU. Under the same conditions 1900 RU of ColN-P-Cys protein remained, of which much is likely to be nonspecifically bound. Pretreatment of the gold

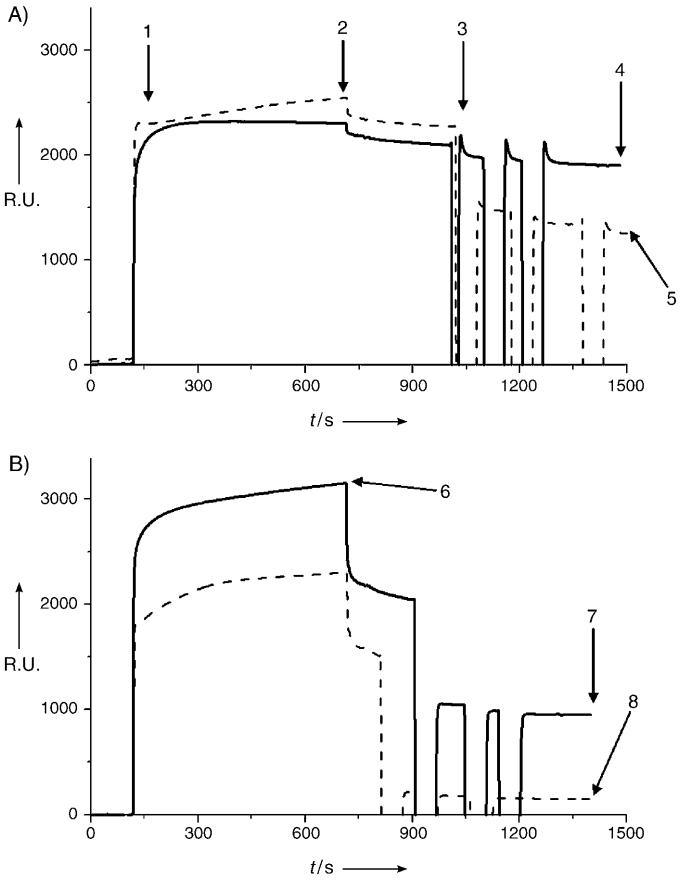


Figure 2. Surface plasmon resonance. A) Injection of ColN-P (2.5 $mg\,mL^{-1}$; -----) and ColN-P-Cys (——) in buffer A over a bare gold surface starting at point 1 (5 μL min^{-1}). Both proteins bind strongly to the surface and do not desorb upon washing with buffer (point 2). After washes with 0.5% SDS, indicated by regions with a negative baseline (point 3), the cysteine-free wild-type protein shows significant nonspecific binding (1200 RU (point 5)). ColN-P-Cys shows additional binding (1900 RU (point 4)). B) Pretreatment of the gold surface with β-mercaptoethanol (5 mM) increases the specificity of binding during identical injections both before, and especially after, the SDS washes. The upward slope on the ColN-P-Cys trace during injection indicates that the protein monolayer has not saturated during this short assembly period (point 6). ColN-P-Cys shows 1000 RU (point 7) final binding whereas ColN-P only binds 150 RU (point 8). All solutions contain phosphate (50 mM)/NaCl (300 mM) as buffer (pH 7.0).

with short-chain thiols inhibits nonspecific protein interactions with gold,[3] and therefore the surface was pretreated with β-mercaptoethanol (5 mM) in buffer A. When ColN-P was applied to this thiol-functionalized surface, which was then washed with 0.5% SDS, only 150 RU remained bound compared to 1000 RU (equivalent to 1 $ng\,mm^{-2}$) of ColN-P-Cys[16] (Figure 2B). Thus, 85% is likely to be bound through the cysteine residue, and the continuing upward slope of the SPR signal during the injection phase (Figure 2B) indicates that higher densities would result from longer incubation times.[3]

CD spectroscopy was performed in a standard demountable 0.2-mm-pathlength quartz-glass cuvette (106-QS, Hellma) and, as calculated above, a far-UV spectrum of a 20-fold diluted ColN-P solution (0.025 $mg\,mL^{-1}$ or $1.1\times$

 © 2005 Wiley-VCH Verlag GmbH & Co. KGaA, Weinheim

10^{-6} M) provided a clearly resolvable signal (Figure 3A). For monolayer measurements the flat cover was coated by evaporation on one side with 2 nm of chromium followed by 10 nm of gold. This layer gave a characteristic absorption spectrum (not shown[11]), a CD spectrum (accumulated mean of 50 scans) which deviated by less than ± 1 mdeg from air baseline values (Figure 3A), and a photomultiplier voltage that only exceeded the empirical limit of >600 V at wavelengths below 196 nm (Figure 3B). The gold-layer baselines differed slightly between samples, possibly as a result of small variations in gold thickness, so the corresponding baseline for the cuvette containing the relevant buffer was subtracted from each set of data. Correct repositioning of the cuvette each time was also important. After baseline acquisition the gold was incubated with ColN-P-Cys (0.7 mg mL^{-1}, buffer A) for 3 h. Without pretreatment with β-mercaptoethanol, the protein bound strongly to the surface, and after a buffer wash it gave a signal larger (2 mdeg at 208 nm; Figure 3A) than the theoretical maximum, which indicated that, as in the SPR experiment, large amounts of nonspecific binding had occurred. A subsequent wash with 0.5% SDS reduced the value to the theoretical maximum seen in the diluted standard (1.5 mdeg at 208 nm). However, the SPR data indicate that this is still likely to contain nonspecifically bound protein.

To overcome this problem and ensure that data from a single monolayer of thiol-immobilized protein was collected, the gold surface was pretreated with β-mercaptoethanol (5 mM) in ethanol for 1 h. Incubation of this surface with ColN-P-Cys followed by washing steps with 0.5% SDS resulted in a lower intensity of 0.6 mdeg at 208 nm (Figure 3C). This value, which resulted from a longer assembly period than in the SPR experiment, equates to a protein density of 1.6 ng mm^{-2} (60% higher than that recorded by SPR). The signal corresponds to 62% of the maximum calculated packing and compares well with the 50% of maximum packing observed for OmpF (*Escherichia coli* outer membrane protein F) on gold surfaces.[3] Thus, the CD arises from a less than fully packed monolayer and could be further improved.

The utility of immobilized proteins was demonstrated by an unfolding–refolding cycle commonly used in protein stability measurements. This cycle would normally require a series of protein samples pre-equilibrated at a range of increasing denaturant concentrations.[17] A spectrum of the ColN-P-Cys monolayer was measured in phosphate buffer. This buffer was replaced by 2 M urea, which partially unfolded the secondary structure. Then the same sample was equilibrated in 8 M urea causing a complete loss of secondary

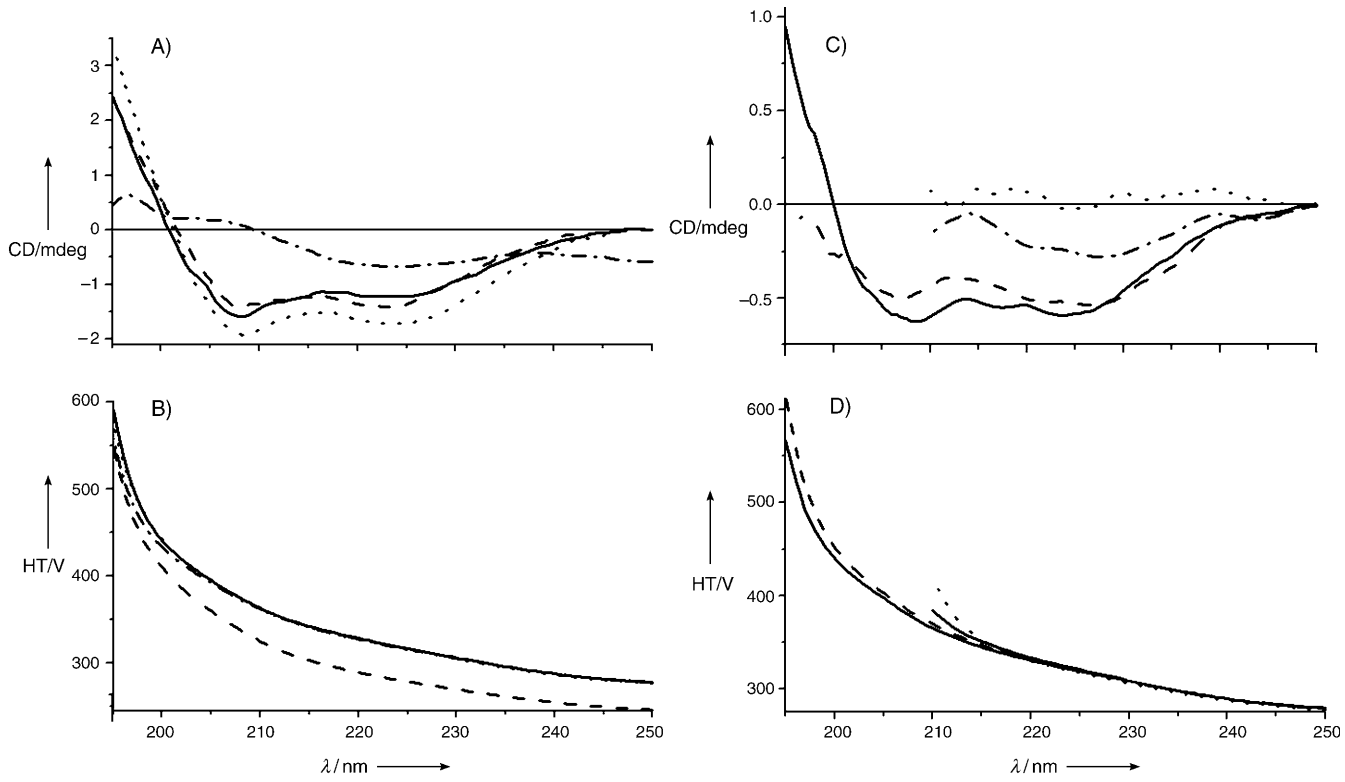


Figure 3. Circular dichroism. A) Solution measurement of ColN-P (0.025 mg mL^{-1}) in a 0.2-mm-pathlength cuvette (10 scans; ——). The gold baseline spectrum (–•–•) in the appropriate buffer was subtracted from all the following spectra. ColN-P-Cys bound to untreated gold (••••) and after SDS wash (-----; see Figure 2A). B) Photomultiplier voltage for the spectra in (A). C) Specific binding of ColN-P-Cys on β-mercaptoethanol-functionalized gold (see Figure 2B). Immobilized ColN-P-Cys in phosphate buffer (——) was then treated with 2 M urea (–•–•; absorption of urea limits data to >210 nm), 8 M urea (••••), and again in urea-free phosphate buffer (-----). D) Photomultiplier voltage for the spectra in (C); data from voltages >600 V were removed. Conditions: displayed data are means of 50 spectra collected at 20 nm min^{-1}, 4 s response time, 0.5 nm data pitch, bandwidth 2 nm, 25 °C, smoothed with a seven-point Savitzky–Golay[20] method (Jasco Spectra Analysis Software 1.53) on a Jasco J-810 spectrometer. All solutions contain phosphate (50 mM)/NaCl (300 mM) as buffer (pH 7.0). Further data showing untreated spectra, examples of data treatment, and Figure 3A, C with error bars added are to be found in the Supporting Information. HT is the photomultiplier voltage and is inversely related to light intensity passing through the sample.

 © 2005 Wiley-VCH Verlag GmbH & Co. KGaA, Weinheim

structure. This finding repeats published solution data,[13] and refolding was achieved by simply incubating the sample again in buffer A.

The results demonstrate that even a crude system in which the protein is directly coupled to gold can be used to study the unfolding and refolding of the same protein sample rather than a series of different samples. The method could be improved by binding the proteins through a linker group to further reduce interaction with the gold surface.[2] Solutions can now flow over the immobilized proteins, so it is possible to add or remove ligands and denaturants easily, and the longer data collection times could be compensated for by designing overnight unfolding–refolding experiments where buffers are exchanged automatically on one fixed protein sample. Combined with the ability to assemble membrane proteins on gold and perform parallel SPR on these surfaces,[3,18] the use of immobilized protein monolayers in CD spectroscopy offers a way to extend the applications of this technique. Methods that increase the surface roughness of the gold[19] could further increase the sensitivity of the procedure.

Received: December 17, 2004

Keywords: circular dichroism · monolayers · nanostructures · protein folding · surface plasmon resonance

[1] a) C. M. Niemeyer, *Angew. Chem.* **2001**, *113*, 4254; *Angew. Chem. Int. Ed.* **2001**, *40*, 4128; b) G. MacBeath, S. L. Schreiber, *Science* **2000**, *289*, 1760; c) G. MacBeath, A. N. Koehler, S. L. Schreiber, *J. Am. Chem. Soc.* **1999**, *121*, 7967.
[2] B. H. Lee, T. Nagamune, *Biotechnol. Bioprocess Eng.* **2004**, *9*, 69.
[3] S. Terrettaz, W.-P. Ulrich, H. Vogel, Q. Hong, L. G. Dover, J. H. Lakey, *Protein Sci.* **2002**, *11*, 1917.
[4] U. B. Sleytr, P. Messner, D. Pum, M. Sara, *Angew. Chem.* **1999**, *111*, 1098; *Angew. Chem. Int. Ed.* **1999**, *38*, 1034.
[5] a) A. K. Dunker, C. J. Brown, J. D. Lawson, L. M. Iakoucheva, Z. Obradovic, *Biochemistry* **2002**, *41*, 6573; b) H. J. Dyson, P. E. Wright, *Curr. Opin. Struct. Biol.* **2002**, *12*, 54; c) G. Anderluh, I. Gokce, J. H. Lakey, *J. Biol. Chem.* **2004**, *279*, 22002.
[6] C. M. Dobson, *Nature* **2003**, *426*, 884.
[7] P. Rigler, W. P. Ulrich, H. Vogel, *Langmuir* **2004**, *20*, 7901.
[8] G. D. Fasman, *Circular Dichroism and the Conformational Analysis of Macromolecules*, Plenum, New York, **1996**, p. 738.
[9] R. W. Woody, *Energ. Biol. Macromol. E* **2004**, *380*, 242.
[10] a) B. A. Wallace, R. W. Janes, *Curr. Opin. Chem. Biol.* **2001**, *5*, 567; b) W. A. Stanley, A. Sokolova, A. Brown, M. Wilmanns, D. T. Clarke, D. I. Svergun, *J. Synchrotron Radiat.* **2004**, *11*, 490.
[11] M. Shimizu, K. Kazutoshi, H. Morii, K. Mitsui, W. Knoll, T. Nagamune, *Biochem. Biophys. Res. Commun.* **2003**, *310*, 606.
[12] a) F. G. van der Goot, J. M. González-Mañas, J. H. Lakey, F. Pattus, *Nature* **1991**, *354*, 408; b) S. L. Fridd, J. H. Lakey, *Biochemistry* **2002**, *41*, 1579.
[13] L. J. A. Evans, M. L. Goble, K. Hales, J. H. Lakey, *Biochemistry* **1996**, *35*, 13180.
[14] a) I. R. Vetter, M. W. Parker, A. D. Tucker, J. H. Lakey, F. Pattus, D. Tsernoglou, *Structure* **1998**, *6*, 863; b) L. Holm, C. Sander, *Febs Lett.* **1993**, *315*, 301.
[15] S. L. Fridd, I. Gokce, J. H. Lakey, *Biochimie* **2002**, *84*, 477.
[16] E. Stenberg, B. Persson, H. Roos, C. Urbaniczky, *J. Colloid Interface Sci.* **1991**, *143*, 513.
[17] C. N. Pace, B. A. Shirley, J. A. Thompson in *Protein Structure: A Practical Approach* (Ed.: T. E. Creighton), IRL, Oxford, **1989**, p. 311.
[18] a) B. Hu, D. Finsinger, K. Peter, Z. Guttenberg, M. Barmann, I. Kessler, A. Escherich, L. Moroder, J. Bohm, W. Baumeister, S. F. Sui, E. Sackmann, *Biochemistry* **2000**, *39*, 12284; b) R. Naumann, T. Baumgart, P. Graber, A. Jonczyk, A. Offenhausser, W. Knoll, *Biosens. Bioelectron.* **2002**, *17*, 25; c) S. Terrettaz, W. P. Ulrich, R. Guerrini, A. Verdini, H. Vogel, *Angew. Chem.* **2001**, *113*, 1790; *Angew. Chem. Int. Ed.* **2001**, *40*, 1740.
[19] H. Raether, *Springer Tracts Mod. Phys.* **1988**, *111*, 1.
[20] A. Savitzky, M. J. E. Golay, *Anal. Chem.* **1964**, *36*, 1627.

 © 2005 Wiley-VCH Verlag GmbH & Co. KGaA, Weinheim

Chiral Polymerization

Transfer of Chirality from (−)-Sparteine Zinc(II) (Meth)acrylate Complexes to the Main Chains of Their (Meth)acrylate Polymer Derivatives**

*Satyasankar Jana and David C. Sherrington**

Optically active polymers represent a class of materials of importance because of their unique properties and potential application as chiral chromatographic stationary phases, as supports for or ligands in asymmetric catalysts, and as components in nonlinear optical and liquid-crystalline materials. However, vinyl and related polymers that are optically active as a result of the configuration of their main chains, rather than chiral side-chain substituents, are very rare as this requires very special stereoregular symmetries of consecutive repeat units.

In general, symmetry operations are more difficult to recognize in a long polymer chain made up of uniformly repeating units than in low-molecular-weight compounds. Wulff, however, recognized that only one specific sequence of eight possible hexad sequences of a homopolymer of a monosubstituted vinyl monomer is chiral.[1] Not surprisingly it is extremely difficult to control a vinyl polymerization to introduce such a chiral hexad sequence in a polymer backbone. One of the methods proposed by Wulff to reduce this difficulty was to introduce a second repeat unit in the polymer backbone to help break down the overall symmetry. For such copolymers, triad sequences (Figure 1) in which a syndiotactic

[*] S. Jana, Prof. Dr. D. C. Sherrington
Department of Pure and Applied Chemistry
University of Strathclyde
Glasgow G1 1XL, Scotland (UK)
Fax: (+44) 141-548-4246
E-mail: d.sherrington@strath.ac.uk

[**] S.J. acknowledges the receipt of an Overseas Research Studentship from the UK Committee of Vice-Chancellors and a maintenance grant from the University of Strathclyde. We thank Dr. A. R. Kennedy for single-crystal X-ray diffraction analysis.

Supporting information for this article is available on the WWW under http://www.angewandte.org or from the author.

 © 2005 Wiley-VCH Verlag GmbH & Co. KGaA, Weinheim DOI: 10.1002/anie.200501308

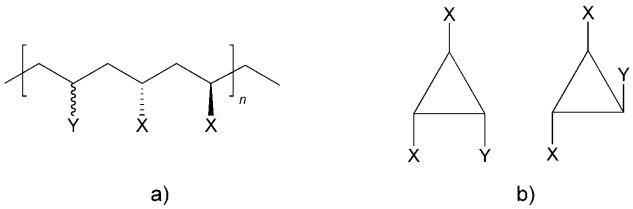


Figure 1. Chiral triad in a linear chain (a) and in a ring structure (b) (see Reference [1]).

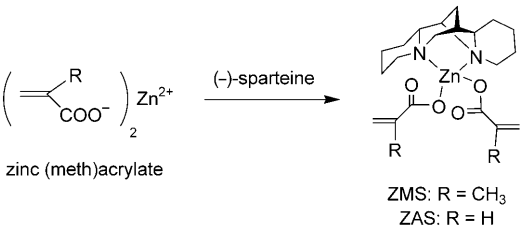
(or racemic) diad sequence of one comonomer is spaced apart by a repeat unit of another comonomer would be chiral.[1] Indeed Wulff et al. went on to complete some extremely elegant syntheses that involved the use of covalently bound chiral templates to confirm that his rationalizations were correct.[1,2]

Kakuchi and Obata,[3] Sivaram and co-workers,[4] and Sherrington and co-workers[5] have subsequently used essentially the same synthetic strategy with different templates to confirm the generality of Wulff's approach. In all of these cases, multifunctional vinyl monomers have been covalently bonded to a chiral moiety and then polymerized, followed by cleavage and washing away of the template, to produce main-chain chiral polymers.

Although this strategy has been valuable, the use of covalently bound chiral templates is not particularly convenient nor is it versatile, as, in effect, specifically functionalized monomers need to be synthesized. A more attractive methodology in this context would be one that exploited a noncovalently or more weakly bound chiral template that could be readily synthesized and later easily removed from the polymer product once asymmetry is induced. If in addition such a template could be employed with a routinely available monomer, then the potential for application would be far greater. Preliminary work on this alternative noncovalent approach was carried out by Sherrington and co-workers,[6] who showed that hydrogen bonding and metal coordination also can be exploited in synthesizing carbon–carbon main-chain optically active polymers. However, to date, these approaches have been useful only for a very limited number of monomers and the levels of specific optical rotation that have been reported is limited. Herein, we report the use of metal coordination as the source of weaker interaction between the chiral template and the monomer, with the latter being simply a methacrylate or acrylate anion.

In our search for a new noncovalent or more weakly bound template–monomer system, two chiral (−)-sparteine zinc (meth)acrylate complexes ZMS and ZAS (Scheme 1) were prepared by mixing a solution of (−)-sparteine in methanol with commercially available zinc(II) methacrylate or zinc(II) acrylate (Aldrich), respectively, in chloroform. Addition of cold diethyl ether to the mixtures led to crystallization of the products. The structures of the white crystalline products (yields: 82% ZMS and 92% ZAS) were deduced by elemental microanalysis, FTIR and ^{1}H and ^{13}C NMR spectroscopy, single-crystal X-ray crystallography (Figure 2), and polarimetry (Table 1). The specific rotations of ZAS proved to be 6–8-times higher than those of ZMS (Table 1).

The solution copolymerization of each complex with styrene (St; Scheme 2) using AIBN as initiator (2 wt% relative to total C=C content) in methanol at 70 °C (oil-bath temperature) under a nitrogen atmosphere for 20 h resulted in the spontaneous precipitation of the polymer products **1a**, **3a**, **5a**, and **7a** (Table 2), which were collected by simple filtration and washed repeatedly with methanol. These copolymers were insoluble in all organic solvents tested, which is perhaps not surprising as both ZMS and ZAS are in effect difunctional monomers and so are likely to yield cross-linked products on (co)polymerization. Surprisingly, however, when dichloroethane (DCE) was used as the polymerization solvent (Table 2), even after 20 h of reaction the reaction mixtures remained homogeneous and the products **2a**, **4a**, **6a**, and **8a** had to be recovered by precipitation in excess methanol. These copolymers were readily resoluble in DCE and chloroform which, together with the absence of any signals from pendent vinyl groups in the ^{1}H NMR and FTIR spectra, is most easily explained in terms of the ZMS and ZAS comonomers undergoing selective cyclopolymerization of



Scheme 1. Synthesis of (−)-sparteine Zn (meth)acrylate complexes, ZMS and ZAS.

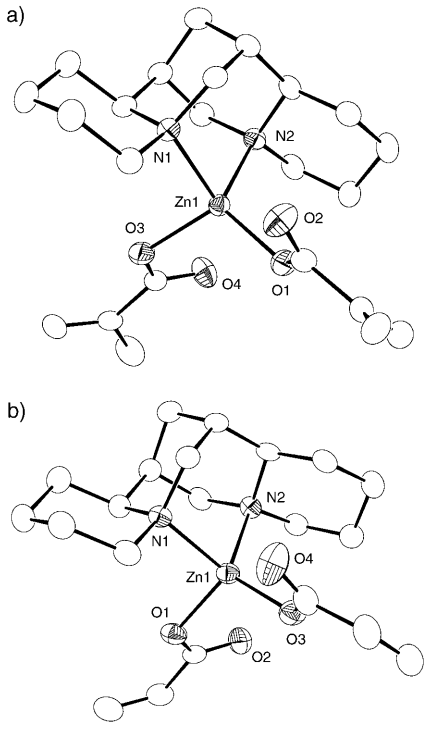


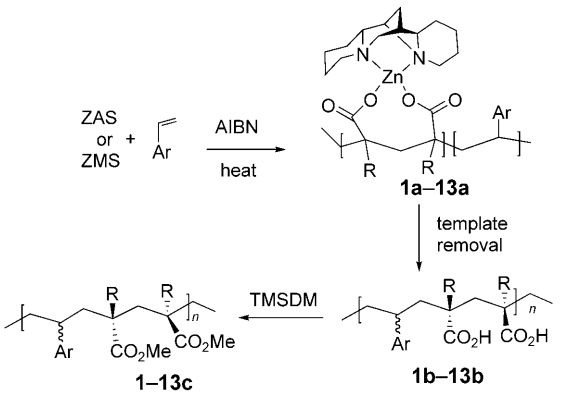
Figure 2. Molecular structures of (−)-sparteine Zn (meth)acrylate complexes a) ZMS and b) ZAS, from single-crystal X-ray diffraction studies.

 © 2005 Wiley-VCH Verlag GmbH & Co. KGaA, Weinheim

Table 1: Optical activities of ZMS and ZAS, and their respective copolymers with styrene and 2-vinylnaphthalene.

Sample[a]	Solvent[b]	Specific optical rotation, $[\alpha]^{23}$ [deg dm^{-1} g^{-1} cm^3]		
		$\lambda = 365$ nm	$\lambda = 436$ nm	$\lambda = 589$ nm
ZMS	CH_3OH[c]	−12.0	−9.5	−5.5
ZAS	$CHCl_3$[c]	−98.0	−61.5	−30.5
1b (St-co-MAA)	THF	+0.95	+0.65	+0.20
1c (St-co-MMA)	$CHCl_3$	+1.65	+1.05	+0.40
2a (St-co-ZMS)	$CHCl_3$	−2.95	−2.15	−1.00
2b (St-co-MAA)	THF	+1.25	+0.60	+0.25
2c (St-co-MMA)	$CHCl_3$	+2.70	+0.80	+0.40
3b (St-co-AA)	THF	+1.45	+0.50	+0.00
3c (St-co-MA)	$CHCl_3$	+0.40	+0.20	+0.00
4b (St-co-AA)	THF	+3.10	+1.20	+0.50
4c (St-co-MA)	$CHCl_3$	+1.75	+0.75	+0.00
5b (St-co-AA)	THF	+1.60	+0.75	+0.20
5c (St-co-MA)	$CHCl_3$	+1.65	+0.80	+0.50
6a (St-co-ZAS)	$CHCl_3$	−14.90	−9.80	−5.40
6b (St-co-AA)	THF	+2.40	+1.10	+0.45
6c (St-co-MA)	$CHCl_3$	+1.25	+0.30	+0.10
7b (St-co-AA)	THF	+1.10	+0.50	+0.00
7c (St-co-MA)	$CHCl_3$	+1.40	+0.70	+0.50
8b (St-co-AA)	THF	+2.00	+0.90	+0.30
8c (St-co-MA)	$CHCl_3$	+0.90	+0.25	+0.15
9b (2VN-co-MAA)	THF[d]	+10.80	+4.50	+2.10
10b (2VN-co-MAA)	THF[d]	+8.15	+3.50	+1.40
10c (2VN-co-MMA)	THF[d]	+11.40	+5.80	+2.50
11b (2VN-co-AA)	THF[d]	+24.40	+12.40	+4.60
12b (2VN-co-AA)	THF[d]	+23.00	+11.30	+4.60
12c (2VN-co-MA)	THF[d]	+19.20	+10.00	+3.80
13b (2VN-co-AA)	THF[d]	+12.80	+6.20	+1.70

[a] Copolymer compositions: ZMS = sparteine zinc methacrylate; ZAS = sparteine zinc acrylate; St = styrene; MAA = methacrylic acid; MMA = methyl methacrylate; AA = acrylic acid; MA = methyl acrylate; 2VN = 2-vinylnaphthalene. [b] 0.5–1.5 g/100 mL. [c] 2.0 g/100 mL. [d] 0.25 g/100 mL.



Scheme 2. Ideal cyclopolymerization of chiral zinc (meth)acrylates ZMS (R = Me) and ZAS (R = H) with vinyl arene monomers (Ar) to yield main-chain chiral Ar-MAA and Ar-AA copolymers, followed by methylation of the latter to yield main-chain chiral Ar-MMA and Ar-MA copolymers. AIBN = azobis(isobutyronitrile); TMSDM = (trimethylsilyl)-diazomethane.

their two vinyl groups, as elegantly demonstrated by Wulff with his covalently templated bis-styrylboronate comonomer.[1] Whether or not some ZMS- or ZAS-derived segments are incorporated with insertion of one or more styrene segments between the (meth)acrylate segments is impossible for us to say. However homopolymerization of ZMS in DCE and copolymerization of ZMS with methyl methacrylate in DCE both result in gelation, which suggests that in these two polymerization processes the reaction of the various methacrylate functions is statistical and results in cross-linked products. In contrast, in copolymerizations of ZMS or ZAS with the electron-rich monomer styrene in DCE, the latter plays an important role in generating linear soluble copolymers.

We believe therefore that copolymerization of styrene with ZMS or ZAS in DCE results in the formation of at least some Wulff-type chiral triads (Figure 1; Y = St, X,X = ZMS or ZAS) in the backbone of the resultant copolymers and most likely with some of these triads also present in the copolymers prepared in methanol as well. The workup of **1a**–**8a** (see Table 2 and Supporting Information) destroys the template Zn complex and removes the Zn and (−)-sparteine components to yield the corresponding styrene–(meth)acrylic acid copolymers St-MAA and St-AA (**1b**–**8b**; Scheme 2 and Table 2). This was confirmed by the appearance of the signal for CO_2H and disappearance of the resonances for (−)-sparteine in the ^{1}H NMR spectrum, by the appearance of a peak for the C=O group of the carboxylic acid in the FTIR spectrum, and by the absence of nitrogen upon elemental analysis of the products. Copolymers **1b**–**8b** were readily soluble in THF, consistent with the loss of any cross-links arising from removal of bridging Zn centers in ZMS- or ZAS-derived segments. Polarimetric measurements of solutions of copolymers **1b**–**8b** showed small but definite dextrorotatory specific optical rotation (Table 1), in contrast to the levorotatory rotations of (−)-sparteine, ZMS, ZAS, and the unpurified template-containing copolymers **2a** and **6a** (Table 1). Furthermore compounds **2b**, **4b**, **6b**, and **8b**, which were derived respectively from **2a**, **4a**, **6a**, and **8a**, with the latter group prepared as a soluble species in DCE, consistently show a greater specific rotation than **1b**, **3b**, **5b**, and **7b**, which were each derived respectively from **1a**, **3a**, **5a**, and **7a**, with the latter group formed as precipitates in MeOH (Table 2).

Methylation of copolymers **1b**–**8b** using (trimethylsilyl)-diazomethane (TMSDM) in a 1:3 mixture of methanol/THF under nitrogen at room temperature yielded quantitatively the corresponding styrene–methyl (meth)acrylate copolymers St-MMA and St-MA (**1c**–**8c**; Scheme 2). These were isolated by precipitation into hexane and were characterized by microanalyses and also FTIR and ^{1}H NMR spectroscopy. The specific rotation values of **1c**–**8c** are also dextrorotatory (Table 1). As a control, copolymers were synthesized with styrene using achiral zinc methacrylate or zinc acrylate in methanol. The polymers precipitated from solution as they formed and were decomplexed by stirring with dilute HCl to

 © 2005 Wiley-VCH Verlag GmbH & Co. KGaA, Weinheim

Table 2: Copolymerization of ZMS and ZAS with styrene and 2-vinylnaphthalene to yield main-chain chiral (meth)acrylate copolymers.

Monomers (mole ratio)	Copolymerization[a] Solvent	Copolymer	Isolated yield [%]	Solubility	Template-removal method[b]	After template removal Copolymer	Recovery [%]	Solubility	Composition[c]	Copolymer after methylation
ZMS/St 1:2	MeOH[d]	**1a**, precipitate	53	insoluble	A	**1b**	47	THF, DMSO	St/MAA 1.6:1.0	**1c**
	DCE[d]	**2a**, solution	37	DCE, $CHCl_3$	A	**2b**	26	THF, DMSO	St/MAA 1.6:1.0	**2c**
ZAS/St 1:1	MeOH	**3a**, precipitate	32	insoluble	B	**3b**	32	THF, DMSO	St/AA 1.0:1.0	**3c**
	DCE	**4a**, solution	30	DCE,[e] $CHCl_3$[e]	B	**4b**	28	THF, DMSO	St/AA 0.9:1.0	**4c**
ZAS/St 1:2	MeOH	**5a**, precipitate	43	insoluble	B	**5b**	46	THF, DMSO	St/AA 1.4:1.0	**5c**
	DCE	**6a**, solution	33	DCE, $CHCl_3$	B	**6b**	34	THF, DMSO	St/AA 1.3:1.0	**6c**
ZAS/St 1:3	MeOH	**7a**, precipitate	50	insoluble	B	**7b**	49	THF, acetone	St/AA 1.7:1.0	**7c**
	DCE	**8a**, solution	32	DCE, $CHCl_3$	B	**8b**	31	THF, acetone	St/AA 1.8:1.0	**8c**
ZMS/2VN 1:1	DCE	**9a**, solution	45	DCE, $CHCl_3$	B	**9b**	39	THF, acetone	2VN/MAA 1.1:1.0	–
ZMS/2VN 1:2	DCE	**10a**, solution	43	DCE, $CHCl_3$	B	**10b**	45	THF, $CHCl_3$	2VN/MAA 1.5:1.0	**10c**
ZAS/2VN 1:1	DCE	**11a**, solution	40	DCE, $CHCl_3$	B	**11b**	42	THF, DMSO	2VN/AA 1.3:1.0	–
ZAS/2VN 1:2	DCE	**12a**, solution	46	DCE, $CHCl_3$	B	**12b**	47	THF, acetone	2VN/AA 3.0:1.0	**12c**
ZAS/2VN 1:4	DCE	**13a**, solution	46	DCE	B	**13b**	45	THF, $CHCl_3$	2VN/AA 6.0:1.0	–

[a] Conditions: AIBN = 2 wt% of total C=C content, 24 h, 70°C (oil-bath temp), concentration of C=C in solution = 1 M. [b] See Supporting Information. [c] From elemental analysis. [d] 20 h, concentration of C=C in solution = 0.75 M. [e] Partially soluble.

yield St-MAA and St-AA copolymers, both of which exhibited no optical rotation.

The effect of varying the polymerization feed ratio of ZAS/St is also shown in Tables 1 and 2. As the proportion of ZAS in the monomer feed decreases, the optical activity of the resulting St-AA copolymers also decreases. The effect is most obvious in the copolymers prepared in DCE, that is, **4b**, **6b**, and **8b**. Reassuringly, this observation tends to confirm that the degree of induction of chirality into the carbon–carbon main chain of the copolymer is indeed controlled by the chiral ZAS or ZMS complex. Furthermore, analysis of the St-MMA and St-MA copolymers by double-detection (refractive index/light scattering) size-exclusion chromatography (SEC) confirms that the copolymers are indeed macromolecular species with number-average molecular weights, M_n, in the range 15000–50000.

Copolymerization of ZMS and ZAS, respectively, with other monomers were also evaluated, and some remarkable results were attained. Most interestingly, 2-vinylnaphthalene (2VN) was used to prepare copolymers **9a**–**13a**. Removal of the template afforded the corresponding 2VN–(meth)acrylic acid copolymers **9b**–**13b**, and methylation of selected examples of these produced the 2VN–methyl (meth)acrylate copolymers 2VN-MMA and 2VN-MA (**10c** and **12c**; Table 2). These show significantly enhanced values of specific optical rotation (Table 1) which we believe is associated, at least in part, with the increased bulk of the naphthyl group relative to the phenyl group in the analogous styrene copolymers. Also, the rotations of the methacrylate copolymers are lower than those of the corresponding acrylate species, as found with the styrene copolymers. SEC data confirmed the molecular weights of the 2VN-MMA and 2VN-MA copolymers **10c** and **12c** to be indeed in the polymeric range ($M_n \approx 15000$).

Finally, the circular dichroism spectra of some selected chiral carboxylic acid copolymers, namely **2b, 4b, 9b**, and **11b**, all showed the Cotton effect around their maximum absorption in their UV spectra (Figure 3). The styrene-based

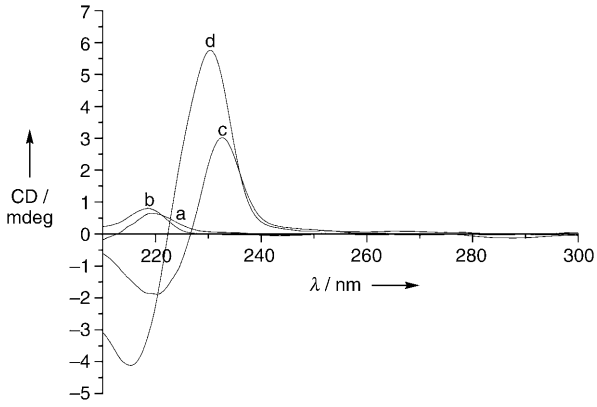


Figure 3. Circular dichroism data of chiral polymers measured in THF solution (1 mg mL^{-1}) using 0.1 mm path-length cuvette cell at room temperature. a) **2b**, b) **4b**, c) **9b**, and d) **11b**.

 © 2005 Wiley-VCH Verlag GmbH & Co. KGaA, Weinheim

species **2b** and **4b** showed small but positive Cotton effects around 218 nm, whereas the 2-vinylnaphthalene-based species **9b** and **11b** showed larger, both positive and negative Cotton effects around 230 and 218 nm, respectively. A similar type of behavior was observed earlier by Wulff and Dhal[7] and Kakuchi et al.[8] for their carbon–carbon main-chain copolymers synthesized using covalently linked chiral templates.

In conclusion, a novel methodology has been developed for the synthesis of chiral vinyl polymers in which the chirality is associated only with the configuration of the backbone stereogenic centers. The methodology is somewhat more convenient than those previously reported, as a chiral (−)-sparteine Zn complex is used as an easily cleavable template and the source of asymmetry control, with chirality being transferred to the polymer main chain. If required, the complex can be prepared in situ just prior to polymerization. The method also allows the direct use of methacrylic acid and acrylic acid monomers as their respective anions, with no covalent chemical modification of these required. The liberation of the chiral copolymers from the template therefore involves only decomplexation, and the resulting macromolecules are readily available for further chemical derivatization if required as they are simple methacrylic and acrylic acid copolymers. Overall we believe the facile and core nature of the methodology will provide a convenient and cost-effective source of main-chain optically active vinyl polymers perhaps even in large quantities. The new methodology does, of course, still require a stoichiometric relationship between the chiral ligand and the (meth)acrylate monomers, and the major challenge that remains is to develop a similar templating methodology that is substoichiometric or catalytic in this respect—we are currently considering how this might be achieved.

Received: April 14, 2005
Published online: July 1, 2005

Keywords: chirality · polymerization · template synthesis · zinc

[1] G. Wulff, *Angew. Chem.* **1989**, *101*, 22; *Angew. Chem. Int. Ed. Engl.* **1989**, *28*, 21; G. Wulff, *CHEMTECH* **1991**, 384; Y. Okamoto, T. Nakano, *Chem. Rev.* **1994**, *94*, 349.
[2] G. Wulff, A. Matussek, C. Hanf, S. Gladow, C. Lehmann, R. Croddard, *Angew. Chem.* **2000**, *112*, 2364; *Angew. Chem. Int. Ed.* **2000**, *39*, 2275; G. Wulff, S. Gladow, S. Krieger, *Macromolecules* **1995**, *28*, 7434.
[3] T. Kakuchi, M. Obata, *Macromol. Rapid Commun.* **2002**, *23*, 395.
[4] B. B. De, S. Sivaram, P. K. Dhal, *Macromolecules* **1995**, *28*, 3733.
[5] I. H. Donnelly, P. Kambouris, D. C. Nohebel, T. Rohr, D. C. Sherrington, *J. Chem. Soc. Perkin Trans. 2* **1996**, 1821.
[6] J. H. G. Steinke, I. R. Dunkin, D. C. Sherrington, *TrAC Trends Anal. Chem.* **1999**, *18*, 159; B. J. L. Royals, D. C. Sherrington, *J. Mater. Chem.* **2000**, *10*, 2035.
[7] G. Wulff, P. K. Dhal, *Macromolecules* **1990**, *23*, 100.
[8] T. Kakuchi, O. Haba, N. Fukui, K. Yokota, *Macromolecules* **1995**, *28*, 5941.

 © 2005 Wiley-VCH Verlag GmbH & Co. KGaA, Weinheim